CONCREEP 10

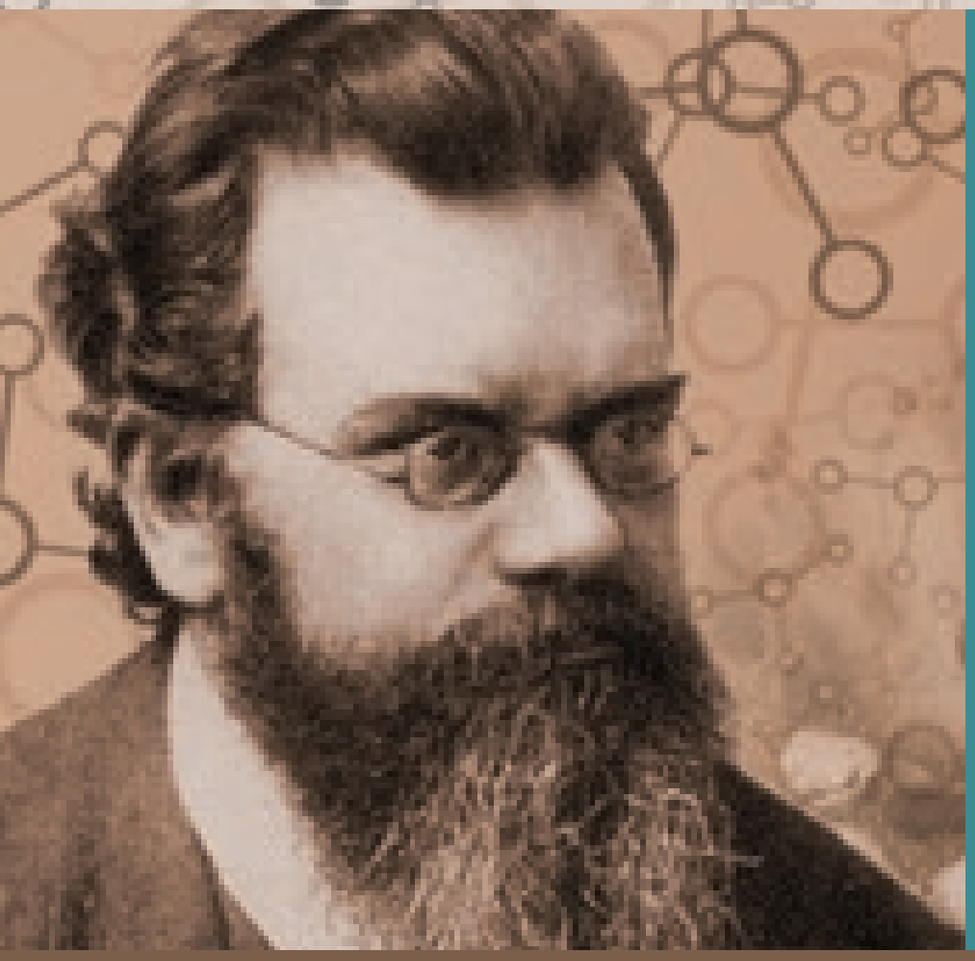

Mechanics and Physics of Creep, Shrinkage, and Durability of Concrete and Concrete Structures

Commemorating Ludwig Boltzmann

EDITED BY Christian Hellmich, Bernhard Pichler, and Johann Kollegger

ASCE

EMI 1687 ASCE ENGINEERING MECHANICS INSTITUTE

TU WIEN TECHNISCHE UNIVERSITÄT WIEN Vienna University of Technology

CONCREEP 10

Mechanics and Physics of Creep, Shrinkage, and Durability of Concrete and Concrete Structures

PROCEEDINGS OF THE 10TH INTERNATIONAL CONFERENCE ON MECHANICS AND PHYSICS OF CREEP, SHRINKAGE, AND DURABILITY OF CONCRETE AND CONCRETE STRUCTURES

September 21-23, 2015
Vienna, Austria

SPONSORED BY
RILEM
Engineering Mechanics Institute of ASCE

EDITED BY
Christian Hellmich
Bernhard Pichler
Johann Kollegger

Published by the American Society of Civil Engineers

Published by American Society of Civil Engineers
1801 Alexander Bell Drive
Reston, Virginia, 20191-4382
www.asce.org/publications | ascelibrary.org

Errata: Errata, if any, can be found at http://dx.doi.org/10.1061/9780784479346

ISBN 978-0-7844-7934-6 (PDF)
Manufactured in the United States of America.

Introduction

Christian Hellmich[1], Bernhard Pichler[1], and Johann Kollegger[2]

[1]Vienna University of Technology (TU Wien), Institute for Mechanics of Materials and Structures, Karlsplatz 13/202, A-1040 Vienna, Austria; E-mail: Christian.Hellmich@tuwien.ac.at, Bernhard.Pichler@tuwien.ac.at
[2]Vienna University of Technology (TU Wien), Institute of Structural Engineering, Karlsplatz 13/212, A-1040 Vienna, Austria; E-mail: Johann.Kollegger@tuwien.ac.at

Dear Participants of CONCREEP-10,

It is our great pleasure to cordially welcome you at the Vienna University of Technology (TU Wien), the oldest of its type in Central Europe, situated in the heart of one of the culturally richest and most liveable cities in the world; on the occasion of the Tenth International Conference on Mechanics and Physics of Creep, Shrinkage, and Durability of Concrete and Concrete Structures – CONCREEP-10@TUWien.

With a history going back to 1958, the CONCREEP conference series has remained the key driving force whenever it came to gathering prominent scientists and engineers from around the world to discuss the peculiar time-dependent behavior of one of the oldest and most used, yet at the same time least fundamentally understood construction materials: concrete. Distinct from the traditional, standards-driven approaches, CONCREEP has always fostered an interdisciplinary approach, exemplified already at the first conferences held in Munich, organized by the civil engineer Hubert Rüsch and the physicist Folker Wittmann. This approach has ever since been intensified, in particular through the ceaseless efforts of Zdeněk Bažant from Northwestern University, hosting the 1986 conference, and thereby triggering a strong transatlantic cooperation on the topic, which culminated in the 2013 CONCREEP9@MIT-conference, co-sponsored by the French National Research Center - CNRS.

During these developments, the intricacies of concrete have led experimental and computational investigators to enter ever smaller scales. Presently, we face the great chance and, at the same time, the equally great challenge, to effectively link atomistic physics to real-life civil engineering design, by incorporating the sheer boundless wealth of insights provided by modern materials sciences, further progressing at a fast pace.

It has also become a tradition to dedicate each CONCREEP conference to a scientist or engineer who particularly shaped the field: e.g., the 1986 conference in Evanston honored Robert L'Hermite (1910-1982), whose report from 1948 entitled

"The Science of Concrete" (Fickelson, 1988) exemplifies his broad and unifying vision on the topic, and whose quest for realistic mathematical descriptions for creep and shrinkage phenomena marked a turning point in concrete mechanics and physics. The corresponding idea that realistic material modeling may drive concrete building design (at least) as much as structural creep analysis, has defined, to a large part, the unparalleled career of the person honored at the previous CONCREEP9@MIT-conference, Zdeněk Bažant. Among various other pioneering contributions in the mechanics and physics of solids, Zdeněk Bažant has been ceaselessly working on the continuous improvement of creep functions, and their relation to underlying microscopic and nanoscopic physical phenomena taking place in aging concrete – with large impact on structural design and safety (Bažant et al, 2011). In this context, it is natural to ask who actually brought up the very concept of creep functions in the first place; and this brings us right back to Vienna and Austria: It was Ludwig Boltzmann (1844-1906), who presented, in the 1874 Proceedings of the Imperial Academy of Sciences in Vienna, a paper on the "delayed elastic action" under general loading histories (Boltzmann, 1874), and since then he has been widely regarded as one of the fathers of creep analysis and viscoelasticity. More specifically, three aspects in his 1874 paper are particularly noteworthy in the present context: (i) he mentions the importance of "considerations on the molecular constitution"; (ii) he discusses forces and deformations evolving with the logarithm of time; and (iii) he presents an experimental campaign on glass threads. And perhaps surprisingly, these issues have been dominating, possibly more than ever, the discussion on concrete creep in the most recent past, as well as here and now – namely, (i) tackling molecular approaches to realistic properties of calcium silicate hydrates (Pellenq et al., 2009), the logarithmic (or power-law) deformation characteristics of the latter upon nanoindentation (Vandamme et al, 2009), and the use of glass physics to reveal the origins of the mechanical behavior of concrete (Youssef et al, 2011). This is why CONCREEP-10@TUWien is dedicated to Ludwig Boltzmann, the man who is most famous for his contributions to gas kinetics, thermodynamics, statistical mechanics, and atomistic physics – but who also "invented" continuum creep mechanics.

We are very grateful for the support of CONCREEP-10 from two organizations intrinsically tied to the CONCREEP conference series: RILEM – The International Union of Laboratories and Experts in Construction Materials, Systems, and Structures, having played a particularly important role in the early editions of the International Conferences on Creep and Shrinkage; and the Engineering Mechanics Institute (EMI) of the American Society of Civil Engineers (ASCE), extending, through its involvement in CONCREEP-10, the fruitful interaction developed through CONCREEP9@MIT. This testifies the international perspective of the EMI, and at the same time the long-lasting tradition of scientific exchange and technological cooperation between Austria and the United States of America: In the case of concrete, this actually goes back to the days of Boltzmann, when the Austrian bridge pioneer Joseph Melan (an alumnus of TU Wien) invented a system for arch bridges built of reinforced concrete, with one of the first such bridges having been realized in the US, triggering a worldwide success. The aforementioned support was complemented on the international level by promotion activities of the members of the Advisory Committee, the Scientific Committee, the

Mini-symposium Organizers, and of our Gold Sponsor Lafarge, to all of which we extend our deep thankfulness. While this international support proves invaluable when it comes to outreach and dissemination of CONCREEP-10 activities, the very existence of CONCREEP-10 exclusively results from the smooth local organizational support, and in particular so from the deep dedication, administrative talent, and logistical diligence of Martina Pöll – to whom we express our most sincere gratitude.

Finally, we take honor in cordially thanking you, the participants of CONCREEP-10! Through your extraordinary efforts for this conference, having resulting in a proceedings volume with 187 contributions published by ASCE, the 2015 state of the art in the mechanics and physics of creep, shrinkage, and durability of concrete and concrete structures, has now been defined and documented. This alone makes us very optimistic concerning the short- und long-term impact of CONCREEP-10. The latter is probable to result from intensive discourses and interactions during the conference, as these are key ingredients to any true progress in science and engineering. In this sense, we wish you inspiring, lively, and constructive discussions in the unique setting provided by the City of Vienna!

Christian Hellmich, Bernhard Pichler, Johann Kollegger
Chairmen CONCREEP-10

REFERENCES

Z.P. Bažant, M.H. Hubler, and Q. Yu (2011), Pervasiveness of excessive segmental bridge deflections: wake-up call for creep, *ACI Structural Journal*, 108 (6), 766-774.

L. Boltzmann (1874), Zur Theorie der elastischen Nachwirkung (Theory of delayed elasticity), *Proceedings of the Imperial Academy of Sciences in Vienna,* 70, 275-306.

Maurice Fickelson (1988), *Robert L'Hermite and his legacy*, in Z. Bažant, editor, Mathematical Modeling of Creep and Shrinkage of Concrete, Wiley.

R.J.-M. Pellenq, A. Kushima, R. Shahsavari, K.J. Van Vliet, M.J. Buehler, S. Yip, and F.-J. Ulm (2009), A realistic molecular model of cement hydrates, *Proceedings of the National Academy of Sciences of the United States of America*, 106 (38) 16102-16107.

M. Vandamme and F.-J. Ulm (2009), Nanogranular origin of concrete creep, *Proceedings of the National Academy of Sciences of the United States of America,* 106 (26) 10552-10557.

M. Youssef, R.J.-M. Pellenq, B. Yildiz (2011), Glassy nature of water in an ultraconfining disordered material: the case of calcium-silicate-hydrate, *Journal of the American Chemical Society*, 133 (8), 2499-2510.

Contents

Plenary Keynote Lecture

Evaluating the Performance of Recycled Aggregate Concrete

Nanotechnology Applied to Concrete

Constitutive and Numerical Modeling

Simulation and Design of Concrete Structures

New Insights from Macroscopic Material Testing

Creep and Shrinkage Properties of New Cementitious Materials

Creep and Shrinkage of Concrete under Extreme Conditions

Interaction of Concrete Creep, Shrinkage and Swelling with Water, Hydration and Damage: Nano-Macro-Chemo

Z.P. Bažant[1], A. Donmez[1], E. Masoero[2], and S. Rahimi Aghdam[1]

[1]Department of Civil and Environmental Engineering, Northwestern University, 60208, Evanston IL, USA; PH (+1) 847 491 4025; emails: z-bazant@northwestern.edu, abdullah.donmez@northwestern.edu, saeedrahimiaghdam2013@u.northwestern.edu
[2]School of Civil Engineering and Geosciences, Newcastle University, NE1 7RU, Newcastle upon Tyne, United Kingdom; PH (+44) 191 208 7686; email: enrico.masoero@newcastle.ac.uk

ABSTRACT

It has generally been accepted that the volume of cement hydration products is slightly smaller than the original volume of cement and water. However, this does not mean that the hydration reaction causes the hardened cement paste and concrete to contract. In fact, C-S-H shells that grow around anhydrous cement grains push the neighbors apart by crystallization pressure and thus cause the solid framework of cement paste to expand. Proposed here is a new idea—this expansion *always* dominates over the contraction, i.e., the hydration is, in the bulk, *always expansive*, while the source of all of the observed shrinkage, whether autogenous or due to external drying, is a compressive elastic strain in the solid caused by a decrease of chemical potential of pore water, with the corresponding changes in pore humidity, surface tension and disjoining pressure. From recent observations of autogenous shrinkage growing logarithmically in time over many years it follows that the growing C-S-H shells surrounding cement grains must act as diffusion barriers for water and ions, which slow down the hydration process and can extend it over many years and even decades. The new idea implies that all of the autogenous shrinkage must be caused by elastic compression (probably with no, or almost no, creep) of crystalline nano-sheets in the solid framework subjected to stresses that arise as a reaction to pore water stresses. Swelling under water immersion is explained by insufficient elastic compression when water is permanently supplied to the pores. The lecture first presents the aforementioned theory and then summarizes some recent advances in related phenomena, particularly a model for oriented damage due to alkali-silica reaction and a method for shrinkage extrapolation.

INTRODUCTION AND OBSERVATIONS REQUIRING A NEW COMPREHENSIVE MATHEMATICAL MODEL

The interaction of creep, shrinkage, pore humidity changes, water transport and cement hydration is a complex problem that has been debated for a decades. Although

various useful models have been developed, a sufficiently comprehensive model is not yet available. This is made particularly clear by the following recent experimental observations on multi-year behavior of modern concretes with pronounced autogenous shrinkage (Fig. 1 a,b).

1) The drying and autogenous shrinkages have traditionally been considered as separate phenomena. However, after a specimen is exposed to drying, the autogenous shrinkage continues in the core until the arrival of the drying front. After that, the drying and autogenous shrinkages occur simultaneously. Is it their sum or maximum which takes place? It would be the sum if the autogenous shrinkage were of direct chemical origin, unrelated to selfdesiccation; but the maximum if not only the drying shrinkage but also the autogenous one were caused by a decrease of pore humidity, h, i.e., if the autogenous shrinkage were driven by selfdesiccation. If the former were true, then in normal concretes with negligible selfdesiccation the autogenous shrinkage would have to be at least as large as it is in modern concretes with strong selfdesiccation. But far from that. Therefore both drying and autogenous shrinkages must be driven by a decrease of pore humidity.

2) In water immersion, most concretes are swelling. But since $h = 1$, the expansion cannot be driven by pore humidity. So it must be driven by chemical expansion during hydration. Since the hydration cannot be expansive in water immersion and contractive without immersion, it must be assumed that the hydration always causes the hardened cement paste to expand, even in specimens exposed to drying. It follows that, in drying specimens, the magnitude of contraction due to a decrease of pore humidity is greater, even much greater, than the magnitude of expansion due to hydration.

3) As established at the dawn of cement research by Le Chatelier and confirmed by Powers and others, the cement hydration reaction is always contractive, i.e., the volume of the cement gel produced by hydration is always smaller than the sum of the original volumes of anhydrous cement and water. So how can the hardened cement paste expand? The reason is porosity. The growth of adjacent C-S-H shells around the cement grains pushes the adjacent shells apart, producing crystallization pressure. This is what causes the porous solid to expand (see Fig. 2 a).

4) Misled by an illusion of approach to an asymptotic bound caused by plots in linear time scale, vast majority of experimenters have terminated the selfdesiccation, autogenous shrinkage and swelling tests within a few months. But some recent data show autogenous shrinkage as well as swelling in water to continue logarithmically for almost ten years. This conflicts with the calorimetric studies of normal pastes which show the hydration to terminate within a year.

5) Aside from the delay caused by the diffusion barriers of C-S-H shells, another phenomenon that might be thought to explain the decade-long logarithmic evolution of autogenous shrinkage is the creep. Maintaining thermodynamic equilibrium requires equality of the chemical potential μ in all the phases of pore water. So a decrease of pore humidity h must produce tensile stress changes in all the phases, which must be balanced by compressive stress changes, which in turn might be thought to

cause compressive creep in the solid skeleton of cement paste. However, this kind of creep might be smaller, even far smaller, than the creep due to loads applied externally on the macroscale because the stresses introduced by a drop in h fluctuate between tensile and compressive on the micro- and nano-scales. A drop in disjoining pressure p_d in the nanopore will be balanced by compressive forces in the solid bridges across the nanopores and in the adjacent crystalline C-S-H sheets. These bridges and sheets surely deform elastically but not by creep because macroscopic creep must, for other reasons, occur by sliding in the connections between the sheets, not within the sheets. Thus the role of creep might be very weak or nonexistent.

6) If humidity-induced creep existed, it would have to be compressive. Hence, the observed logarithmic multi-year swelling under water immersion cannot be explained by creep. But it can be explained by diffusion of water and ions through the barrier shell of C-S-H. The diffusion halftimes increase as the square of shell thickness. So a thick enough shell can slow down hydration to take years or decades (Fig. 2 b).

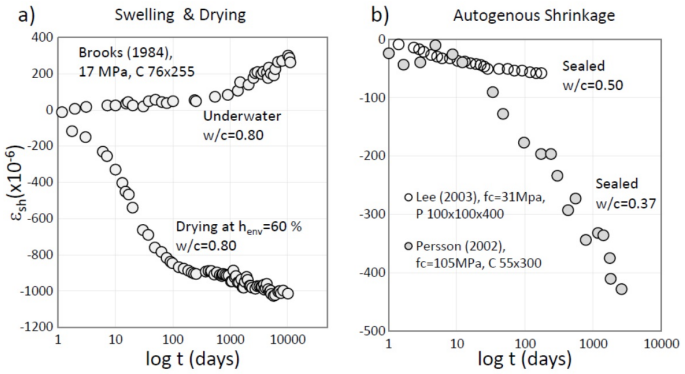

Figure 1: a) Logarithmic log-term evolution of swelling and drying, and b) of autogenous shrinkage for high and low w/c ratio.

EQUATIONS GOVERNING CONTRACTION AND EXPANSION DURING HYDRATION AND HUMIDITY CHANGES

The main governing equations may be formulated as follows (Bažant, 2015). The hydration occurs at the surface of anhydrous cement (chiefly C_3S) grain when in contact with water. At contact, the hydration reaction is virtually immediate and leads to cement set, i.e., the formation of a solid framework, in just a few hours. What slows down the hydration to proceed for months, or even years and decades, is the diffusion barrier of a growing C-S-H shell, which controls the hydration rate (except the during the first 50 hours). The inward water volume discharge, Q_w, of the flow of water per unit cell of material from capillary pores through the mid-surfaces of the solid cement gel shells toward all the anhydrous cement grains in the cell, may be expressed by

Darcy law as

$$Q_w = -Ab\,\frac{h-h^*}{z-r} \qquad \text{where } h = \frac{p_v}{p_{sat}},\ \ h^* = e^{(\mu_0-\mu_1)M/RT} \tag{1}$$

which is written here, as a simplification, in terms of the average gradient; r = decreasing radius of anhydrous cement grain; z = increasing outer radius of the C-S-H shell around the grain, with the initial value $z_0 = r_0$; A = mid-surface area of the barrier shell; b = permeability of C-S-H, which xhas the dimension of m; h = relative humidity at the outer surface of the shells, i.e., in the capillary pores (Fig. 1a); T = absolute temperature, R = gas constant and M = molecular weight of water; h^* is, in absence of vapor, defined as the h-value corresponding to the chemical potential μ_0 of water in C-S-H nanopores (or hindered adsorbed layers) at the interface of C-S-H and anhydrous cement grain (μ_1 = chemical potential in nanopores at saturation, i.e., at $p_v = p_{sat}$); h^* must be equal to the h-value at which hydration of alite stops, which also equals the limiting value of selfdesiccation; $h^* \approx 0.80$ (Flatt et al., 2011). The outward diffusion of ions (mainly silicate ions, of silicic acid) has a different discharge Q_i, governed by the gradient of chemical potential (or Fick's law). But here Q_i need not be formulated because it is in one-to-one stoichiometric relation to Q_w. For this reason, whether the water or ion diffusion controls is mathematically irrelevant.

The loss of water by diffusion through the C-S-H shells causes the humidity in the capillary pores of cement paste to decrease. This may be described by the secant desorption relation:

$$1-h = K(h)\left(1-\frac{w}{w_1}\right) = K(h)\left(1-\frac{\phi\xi}{\phi_0}\right),\quad 1-h^* = K_0\left(1-\frac{w_0}{w_1}\right) = K_0(1-\xi_0) \tag{2}$$

in which $w = \rho_w\phi\xi$, $w_0 = \rho_w\phi_0\xi_0$, $w_1 = \rho_w\phi_0$; $K(h)$ = inverse secant slope of the desorption isotherm (Fig. 2c), i.e. of w/w_1 as a function of h (it must also depend on the age, which is here neglected); w, w_0 = current and initial mass of water in the capillary pores (per m^3 of concrete), and w_1 = mass of water when the capillary pores are fully saturated; ρ_w = mass density of liquid water; ϕ = current capillary porosity decreasing in time; ϕ_0 = initial ϕ = initial water volume fraction; ξ = capillary saturation degree = current volume fraction of water within capillary pore space ϕ; ξ_0 = initial value of ξ (equal to 1 if w/c is high but < 1 for modern concretes with low w/c).

The cement volume $\mathrm{d}V_c$ that combines chemically with water volume $\mathrm{d}V_w$ is defined by the stoichiometric ratio

$$\zeta_{cw} = \frac{\mathrm{d}V_c}{\mathrm{d}V_w} = \frac{A_c}{Q_w}\,\frac{\mathrm{d}r}{\mathrm{d}t} \tag{3}$$

where A_c = surface area of anhydrous cement and $1/\zeta_{cw} \approx 0.74$ by volume (which corresponds to 0.22 by weight). For simplicity, assume now that all cement grains have about the same size and let n_g be the number of anhydrous cement grains within a unit

cell of hardened cement paste or concrete (dimension 1/m^3). The inward flux of water at the surface of cement grains within a unit cell may then be written as

$$q_w = \frac{Q_w}{A} = \frac{1}{\zeta_{cw}} \left(\frac{2r}{r+z} \right)^2 \frac{\mathrm{d}r}{\mathrm{d}t} \tag{4}$$

where the shells are assumed to be spherical. The change of pore volume ϕ due to radius increment dz may be approximately expressed as $\mathrm{d}\phi = -4\pi\hat{z}^2 n_g \mathrm{d}z$, where $\hat{z}$ should equal z only initially, when $x = z - r_0$ is negligible. Later, as the adjacent shells distort in contact, one may use $\hat{z}^2 = (\phi_0/4\pi n_g a)e^{-x/a}$, with $a = \phi_0/(4\pi r_0^2 n_g)$. This gives $\mathrm{d}\phi = (\phi_0/a)e^{-x/a}\mathrm{d}z$ and $\phi = \phi_0 e^{-x/a}$, which is an asymptotic matching approximation satisfying also the condition that $\phi \to 0$ for $z \to \infty$. Finally, the pore volume loss due to hydration must be equal to the gain of C-S-H volume, i.e.,

$$4\pi\hat{z}^2 n_g \, \mathrm{d}z = -Q_w \zeta_{cw}(\zeta_{gc} - 1)\mathrm{d}t \tag{5}$$

Note that, for the sake of simplicity, we do not distinguish between the inner and outer C-S-H, the inner one being denser (generalization is, of course, possible).

At this point, equations for all the basic processes are formulated. To reduce their number, the total discharge Q_w may be eliminated by combining Eqs. (1) and (3):

$$\frac{\mathrm{d}r}{\mathrm{d}t} = -b\zeta_{cw} \frac{h - h^*}{z - r} \left(\frac{r+z}{2r} \right)^2 \tag{6}$$

Elimination of Q_w from Eqs. (4) and (5) further yields:

$$\frac{\mathrm{d}z}{\mathrm{d}r} = -(\zeta_{gc} - 1)\frac{r^2}{\hat{z}^2} \tag{7}$$

Finally, using Eqs. (1) and (2) with the volume balance of water, one obtains:

$$\frac{\mathrm{d}h}{\mathrm{d}t} = -4\pi r^2 n_g \, \frac{K(h)b}{\phi_0} \, \frac{h - h^*}{z - r} \tag{8}$$

Eqs. (6). (7) and (8) represent a system of three nonlinear differential equations for $r(t), z(t)$ and $h(t)$, governing the hydration reaction for cement grains of one size. Generalization to distributed particle sizes will be needed. Another important generalization is needed for a combination of selfdesiccation with external drying. In that case, Eq. (8) is extended as

$$\frac{\partial h}{\partial t} = -4\pi r^2 n_g \, \frac{K(h)b}{\phi_0} \, \frac{h - h^*}{z - r} + \nabla[C(h)\nabla h] \tag{9}$$

where $C(h)$ = diffusivity of cement paste or concrete, which decreases with decreasing h by more than an order of magnitude (Bažant and Najjar 1972). At saturation, $C(1) \approx$ 0.1 m^2/day in mature concrete.

Permeability b of C-S-H, a hydration product that includes nanopores but not capillary pores, has apparently not been directly measured. However, the diffusivity of C-S-H can be estimated from the fact that, in normal concretes, the hydration terminates in about 1 year. This means that the halftime, τ_{sh}, of water diffusion is about 1 month. According to the common parabolic approximation of the pressure profile, $\tau_{sh} = (z-r)^2/12C_s$ where, for grains of 50 μm diameter, the shell thickness $z-r$ attains about 15 μm. So $C_S = (z-r)^2/12\tau_{sh} \approx (15\mu\text{m})^2/(1\text{ month}) = 2\cdot 10^{-16}$ m^2/s. This is 7 orders of magnitude less than the diffusivity of cement paste or concrete, which is at saturation about 0.1 cm^2/day or 10^{-9} m^2/s, according to transient drying tests (Bažant and Najjar 1972) as well as Scherer's viscoelastic bending tests (Vickit-Vadakan and Scherer, 2002).

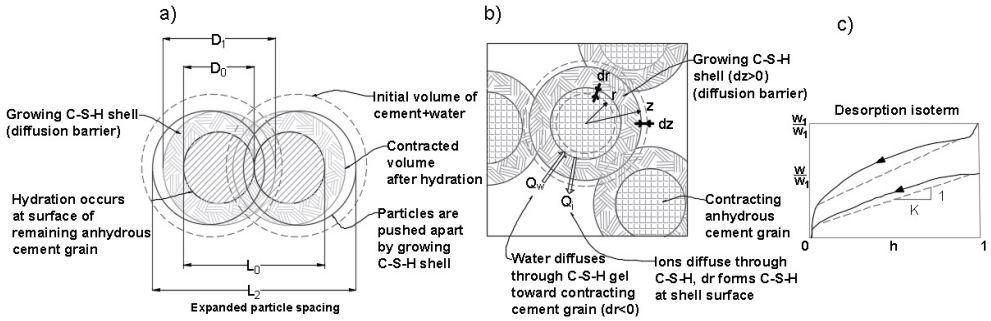

Figure 2: a) C-S-H shells pushing adjacent cement grains apart; b) C-S-H shells growing around anhydrous cement grains and partially filling the capillary pore space; c) Desorption isotherm.

HUMIDITY-INDUCED COMPRESSIVE STRESSES IN SOLID MICROSTRUCTURE

Three sources of compressive changes of stress in the solid framework of hardened cement paste may be distinguished (Fig. 3 a-c):

a) increase in capillary tension ($p_c < 0$) based on to the Kelvin-Laplace (KL) theory;

b) decrease Δp_d of disjoining pressure p_d in nanopores (Bažant 1972; Bažant and Bazant 2012); and

c) decrease δp_s of pressure p_s caused by increase $\Delta\gamma$ of solid-fluid surface tension caused by decrease of spreading pressure in adsorbed water layer on the surface on nano-scale globules of C-S-H.

Similar to Pinson et al. (2015), we neglect p_c in pores smaller than 2 nm (in which p_d is so large that the KL theory fails), and p_d in pores larger than 2 nm (according to Bažant and Bazant, 2012) in which $p_d = 0$, because such pores are wider than ~ 2.6. Since vapor pressure p_v is negligible, and the p_d-dominated pores may be assumed to be always saturated (see Fig. 3), the volumetric equilibrium condition for a

three-phase extension of Biot two-phase medium (Coussy 2004) may be written as:

$$S_V \;=\; (1-\phi-\psi)\sigma_V - \xi\phi\, p_c - \psi\Delta p_d - p_s\Delta\gamma, \qquad S_{ij} = S_{Dij} + \delta_{ij} S_V \tag{10}$$

Here $p_c = \Delta p_c$; S_V, S_{Dij} = volumetric (or hydrostatic) and deviatoric total stresses (per unit surface of the representative unit cell of material), σ_V = volumetric stress in the solid only, ϕ = volume fraction of KL-dominated pores with saturation degree ξ, ψ = volume fraction of p_d-dominated pores in the unit cell, and δ_{ij} = Kronecker's delta ($\sigma_V > 0 \rightarrow$ tension; $p > 0 \rightarrow$ compression).

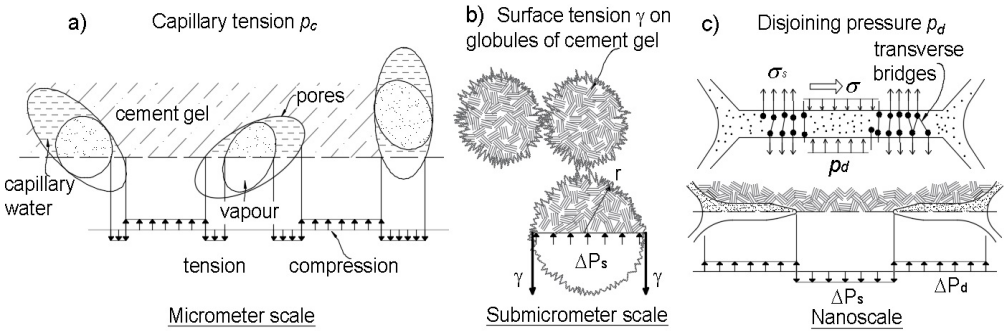

Figure 3: Schematic free diagram of pore pressures.

Pore pressures p_c and p_s are usually evaluated with reference to $h = 1$ (complete saturation), but p_d in reference to the humidity $h = h_f$ at which a pore gets filled by multi-layer BET adsorption ($h_f = 0.6$ for all the p_d-dominated pores, which corresponds to a half-width of ~ 1.3 nm). This leads to:

$$\xi\phi\, p_c + \psi\, p_d + p_s(\Delta\gamma) = RT(\omega_c + \omega_s + \omega_d)\ln h + \psi C_d \tag{11}$$

where $C_d = (RT/M)\,\ln\left({h_f}^{-1}\right)\rho_a/(1+2\kappa)$ = constant depending on the liquid density in the adsorbed layer ρ_a (probably $\sim$ 1100 kg/m^3 for water in C-S-H; Qomi et al., 2014); coefficient κ is the transverse-to-longitudinal pressure ratio in the adsorbed water confined within nanopores ($\neq 1$ since adsorbed water is not a liquid, Bažant and Bazant 2012); R = universal gas constant, T absolute temperature, and M molar mass of bulk liquid water. The ω coefficients in Eq. (11) are related to the pressures:

$$p_c \;=\; \frac{\rho_w RT}{M}\ln(h), \quad p_s = \frac{A}{V}\frac{k_B T\beta}{a_w^2}\ln\left(\frac{1+\beta h}{1+\beta}\right) \tag{12}$$

$$p_d \;=\; 0 \text{ for } h < h_f \;\text{ and }\; \frac{\rho_a}{1+2\kappa}\frac{RT}{M}\ln\left(\frac{h}{h_f}\right) \;\text{ for }\; h \geq h_f \tag{13}$$

Here ρ_w = density of bulk liquid water, A/V = pore surface area per unit volume (varying during hydration), k_B = Boltzmann's constant, $a_w \sim 0.26$ nm is the effective

diameter of a water molecule, β = fluid dependent material quantity related to the heat of adsorption (a monolayer from BET adsorption at $h = 0.11$ implies $\beta = 65$, (Pinson et al., 2015), and so the parenthesis in p_s is $\sim h$); p_s in Eq. (13) comes from Langmuir adsorption (Langmuir, 1917) and Gibbs free energy equilibrium in the unit cell between the gas phase and adsorbed water.

Choosing $h = 1$ and h_f as the reference pressures provides upper bound absolute values for all three pore pressures. In a hydrating paste, one could instead assume that every newly formed gel is self-equilibrated at the humidity h_i at which it forms. If h_f is the average of h_i across the whole gel volume (or, more accurately, the value corresponding to the average pressure), Eq. (11) becomes:

$$\xi\phi\, p_c + \psi\Delta p_d + p_s\Delta\gamma = RT(\omega_c + \omega_s + \omega_d)\ln(h/h_f) + (\phi - \phi_g)C_c \tag{14}$$

where $C_c = \rho_w(RT/M)\ln h_f$ assumes saturated gel pores; ϕ_g is the volume fraction of KL-dominated gel pores. Eq. (14) provides a lower bound for the pore pressures and reduces the swelling induced by Δp_d.

MODELING OF ALKALI-SILICA REACTION IN CONCRETE

Another chemical process which usually interacts with humidity changes as well long-term hydration is alkali-silica reaction, or ASR (aka the alkali-aggregate reaction, AAR). After a few decades, it causes serious deterioration of concrete in numerous structures, such as dams and bridges. Recently it became a problem for very old nuclear reactor containments and dry-cask containers for storage of radioactive waste.

ASR is a chemical reaction between alkalis in Portland cement paste and amorphous or imperfectly crystalline silica in a variety of natural aggregate. The ASR produces a soft viscous substance called the ASR gel. When the ASR gel imbibes water from the pores in cement paste, it can expand to many times its original volume and thus exert high pressures on the surrounding matrix, causing extensive cracking in concrete. Thus, the strength and stiffness of concrete can be degraded substantially.

Once ASR gel migrates from the reacted aggregate and reaches the cement paste, it takes up calcium and loses alkali. So its composition approaches that of C-S-H gel and thus the potential for expansion is lost (Katayama, 2008). Therefore, the ASR gel produced can be divided into two parts: 1) the part of gel that reaches cement paste will cause little or no expansion; 2) the part of gel that accumulates in gel regions, comprising the aggregate or interfacial transition zone (ITZ) and becomes expansive if water is supplied. To simulate the ASR damage, first the specimen is randomly discretized into small parts. Some parts are considered as the gel regions and others as normal concrete. The volume of gel regions can expand, and damage concrete, due either to production of new gel or to expansion of old gel when water can be imbibed.

The gel production is simulated in time according to Bažant and Steffens' model (2000) and its modification by Alnaggar and Cusatis (2013). The produced gel can migrate from the reacted aggregate or remain in or near the aggregate. The part that

migrates appears to be unimportant for swelling. The ASR gel can also be extruded into damaged regions and this extrusion will alleviate the pressure in gel regions. The total volume increment of gel and the induced pressure can be calculated as

$$\Delta V_{eff} = \Delta V_{gel} - \Delta V_{in}; \quad \Delta p = \Delta V_{eff}/\kappa_g \tag{15}$$

Here ΔV_{gel} = total volume of produced gel, and ΔV_{in} = gel extruded into the damaged regions, which is the only unknown; κ_g = bulk modulus of the gel and p = its pressure. Since the expanded gel consists mostly of water, its properties are considered as those of liquid water. To model concrete and its damage, microplane damage constitutive model M7 (Caner and Bažant, 2013) is adopted. The damage is characterized by inelastic strain increments defined as

$$\Delta\epsilon''_{ij} = \Delta\epsilon_{ij} - \frac{(1+\nu)}{E}\,\Delta\sigma_{ij} - \frac{\nu}{E}\,\Delta\sigma_{kk}\delta_{ij} \tag{16}$$

where E, ν = Young's modulus and Poisson's ratio of concrete, and $d\epsilon''$represent inelastic strain. In calculating these strains, the unloading in each increment is assumed to be linear. The principal inelastic strains are then calculated from using the inelastic strain tensor. Finally, using the principal inelastic strains and element volume, the inelastic volume increment can be calculated. The volumetric inelastic strain is regarded as the volume (per unit cell) that is available to the ASR gel, and its increment represents the currently empty volume;

$$\Delta V'' = V_{element}(\Delta\epsilon''_1 + \Delta\epsilon''_2 + \Delta\epsilon''_3); \quad V''_{new} = V''_{old} + \Delta V'' \tag{17}$$

Here $\Delta\epsilon''_1$, $\Delta\epsilon''_2$ and $\Delta\epsilon''_3$ are the principal inelastic strain increments, and V'' represents the currently empty inelastic volume. The empty volume must be distinguished from the part of inelastic volume (per unit cell) that has already been filled by the gel in previous time increments. The accumulated gel will move into the inelastic volume regions and will fill them. The gel volume ΔV_{in} that will get extruded during time increment Δt depends on the gel pressure p in the gel regions and the partition of inelastic volume into empty and full; $\Delta V_{in} = V''_{new}\, e^{-p/p_A}\, \Delta t/\tau_A$, where p_A, τ_A are empirical constants of metric dimensions Pa and s.

The duration of ASR experiments is usually long enough for creep and shrinkage to be significant sources of deformation. The creep and shrinkage were calculated according to model B3 (Bažant and Baweja, 2000) because model B4 (2015) was not yet available. Model B3 was combined with the microplane damage constitutive model M4 (M4 is necessary to capture oriented cracking, which is caused by ASR in presence of external loads and cannot be captured by the classical tensorial constitutive models). To model creep properly and efficiently, the rate-type creep model combined with the exponential algorithm (Bažant and Yu 2012) is used. The rate-type, rather than hereditary integral-type, approach is inevitable since the ASR extent, humidity and cracking damage vary in time. The exponential algorithm is unconditionally stable and allows arbitrarily increasing the time step as the creep rate decays.

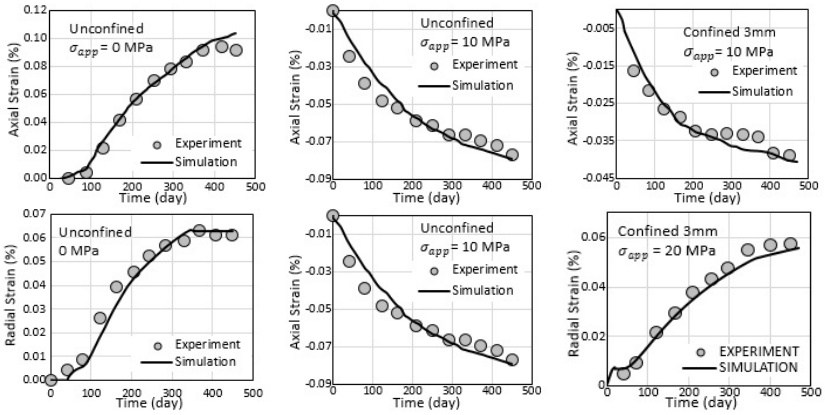

Figure 4: Comparison between simulated and experimental results on ASR damage

To verify and calibrate the model, the ASR damage tests reported by Multon and Toutlemonde (2005) were simulated (Fig. 4). They were performed on sealed cylindrical specimens (of 240 mm length and 130 mm diameter). xxFig. 4 documents good agreement.

EXTRAPOLATION OF SHORT-TIME DRYING SHRINKAGE TESTS BASED ON MEASURED DIFFUSION SIZE EFFECT

Analysis of humidity effects is also important for the prediction of shrinkage. Because of the tremendous variety of concrete compositions, prior to designing or building a structure it is often necessary to perform short-time creep and shrinkage tests of the concrete to be used. Typically, the acceptable test duration, t_e, is 1 to 3 months. Extrapolation of the basic creep test (i.e., the test of a sealed specimen) is relatively easy (Bažant and Baweja, 2000) since the compliance curve of concrete is, in the logarithmic time scale, rising at nearly constant slope and no final asymptotic final value exists. However, extrapolation of the drying shrinkage test is far more difficult.

Figs. 5 a and b show the extrapolations from the short times (3 months) in which the circle data points are used for calculation and the cross data points are predicted. In Fig. 5, the shrinkage data are shifted according to diffusion theory to improve the extrapolation (Bažant et.al., 1987; Burg and Ost, 1992; Bažant and Donmez, 2015). Comparison with various data showed some good extrapolations, some not too good. But the same is true of the previously proposed weight loss method. The fact that neither the present method nor the water loss method are completely satisfactory must be viewed in the context of the current practice, which is intuitive graphical extrapolation, with much bigger errors.

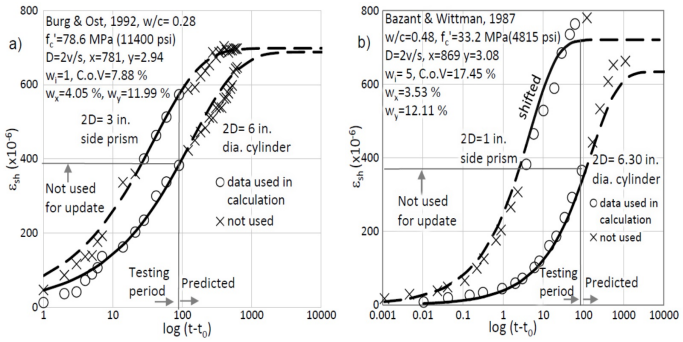

Figure 5: a) Shrinkage data of (Burg and Ost, 1992) and b)(Bažant et.al., 1987) and their extrapolations

REFERENCES

Alnaggar, M., Cusatis, G., and Di Luzio, G. (2013 "Lattice discrete particle modeling (LDPM) of alkali silica reaction (ASR) deterioration of concrete structures." *Cement and Concrete Composites*, 41, 45-59.

Bažant, ZP (1972). "Thermodynamics of hindered adsorption and its implications for hardened cement paste and concrete." *Cem. Concr. Res.* 2(1), 1-16.

Bažant, Z.P. (2015). "Note privately communicated to A. Donmez, S. Rahimi and E. Masoero." March 21.

Bažant, Z.P., and Baweja, S. (2000). "Creep and shrinkage prediction model for analysis and design of concrete structures: Model B3." *Adam Neville Symposium: Creep and Shrinkage—Structural Design Effects*, ACI SP–194, A. Al-Manaseer, ed., Am. Concrete Institute, Farmington Hills, Michigan, 1-83.

Bažant, Z.P., and Bazant, M.A. (2012). "Theory of sorption hysteresis in nanoporous solids: Part I: Snap-through instabilities." *J. Mech. Phys. Solids* 60(9), 1644-1659.

Bažant, Z.P., and Donmez, A. (2015). "Extrapolation of short-time drying shrinkage tests based on measured diffusion size effect: concept and reality." DOI:10.1617/s11527-014-0507-0.

Bažant ZP, Najjar LJ (1972) "Nonlinear water diffusion in nonsaturated concrete." *Materials and Structures* (RILEM, Paris), 5, 3-20.

Bažant, Z.P., and Steffens, A. (2000). "Mathematicalmodel for kinetics of alkali–silica reaction in concrete." *Cem. Concr. Res.*, 30(3), 419-428.

Bažant, Z.P., Wittmann, F. H., Kim, Jenn-Keun, and Alou, F. (1987)."Statistical extrapolation of shrinkage data—Part I: Regression." *ACI Materials Journal*, 84, 20-34.

Bažant, Z.P., Yu, Qiang, and Li, Guang-Hua (2012). Excessive long-time deflections of prestressed box girders: I. Record-span bridge in Palau and other paradigms. ASCE J. of Structural Engrg. 138 (6), 676686.

Brooks, J.J. (1984). "Accuracy of Estimating Long-Term Strains in Concrete." *Magazine of Concrete Research*, 36 (128), 131-145.

Burg, R.G., and Ost, B.W. (1992). "Engineering Properties of Commercially Available High-Strength Concretes." Research and Development Bulletin RD 104T, *Portland Cement Association*, Skokie, Illinois.

Caner, F.C., and Bažant, Z.P. (2013). "Microplane model M7 for plain concrete: I. formulation." *ASCE J. of Engrg. Mechanics* 139(12), 1714-1723.

Coussy, O. (2004). "Momentum Balance. Stress Tensor" *Poromechanics.* John Wiley & Sons, 19.

Flatt, R.J., Scherer, G.W., and Bullard, J.W. (2011). "Why alite stops hydrating below 80% relative humidity." *Cem. Concr. Res.*, 41(9), 987-992.

Katayama, T. (2008). "ASR gel in concrete subject to freezethaw cyclescomparison between laboratory and field concretes from Newfoundland, Canada." Proceedings of the 13th International Conference on AlkaliAggregate Reaction (ICAAR), 174183, (Trondheim, Norway).

Langmuir, I. (1917). "The evaporation, condensation and reflection of molecules and the mechanism of adsorption." *J. Franklin Inst.* 183(1), 101-102.

Lee, H.K., Lee, K.M., and Kim, B.G. (2003). "Autogeneous shrinkage of high-performance concrete containing fly ash." *Magazine of Concrete Research*, 55 (6), 507-515.

Multon, S., and Toutlemonde, F. (2006). "Effect of applied stresses on alkali–silica reaction-induced expansions." *Cem. Concr. Res.*, 36(5), 912-920.

Persson, B. (2002) "Eight-years exploration of shrinkage in high-performance concrete." *Cem. Concr. Res.*, 32, 12291237.

Pinson, M.B., Masoero, E., Bonnaud, P.A., Manzano, H., Ji, Q., Yip, S., Thomas, J.J., Bazant, M., Van Vliet, K.J., and Jennings, H.M. (2015). "Hysteresis from multiscale porosity: water sorption and shrinkage in cement paste." Under review.

Powers, T.C. (1900). "Physical properties of cement paste." *Chemistry of Cement: Proceedings of the Fourth International Symposium*, Washington D.C., 43(2), 577-609.

Qomi, M.J.A., Bauchy, M., Ulm, F.J., and Pellenq, R.J.M. (2014). "Anomalous composition-dependent dynamics of nanoconfined water in the interlayer of disordered calcium-silicates." *J. Chem. Phys.* 140(5), 054515.

Vichit-Vadakan, W. and Scherer, G.W. (2002). "Measuring permeability of rigid materials by a beam-bending method: III, cement paste." *J. Am. Ceram. Soc.* 85(6), 1537-1544.

Shrinkage Due to Colloidal Force Interactions

Franz-Josef Ulm[1] and Roland J. M. Pellenq[2]

[1]Department of Civil and Environmental Engineering, Massachusetts Institute of Technology; and CNRS-MIT Lab <MSE>[2]: MultiScale Materials Science for Energy and Environment, Cambridge, MA 02139. E-mail: ulm@mit.edu
[2]Department of Civil and Environmental Engineering, Massachusetts Institute of Technology; and CNRS-MIT Lab <MSE>[2]: MultiScale Materials Science for Energy and Environment, Cambridge, MA 02139. E-mail: pellenq@mit.edu

Abstract

It has long been argued that shrinkage in cementitious materials can occur even in the absence of drying phenomena. Herein we argue that such shrinkage is attributable to colloidal forces that develop between C-S-H particles during the hydration in an out-of-equilibrium process. We base our argument on meso-scale simulation results, and show via microporomechanics theory that such colloidal forces can lead to the build-up of solid eigenstresses causing macroscopic shrinkage deformation.

INTRODUCTION

There is a renewed interest in shrinkage deformation of cementitious materials at early ages when such materials are subject to almost saturated conditions. The account of such deformation turns out to be critical for estimating the risk of fracture of e.g. oil- and gas well cement liners that hydrate under high pressure and temperature applications (Ardakani and Ulm, 2013). Such conditions appear –on first sight– quite distinct from the classical autogeneous shrinkage conditions and their occurrence in normal concrete applications, which have been attributed to self-desiccation mechanisms, and the generation of capillary pressure under sealed conditions (Hua et al., 1995) which possibly entail –by analogy with external drying phenomena– a shrinkage of the solid.

To fully appreciate the difference between pressures generated in the pore space and eigenstresses generated in the solid phase, we evoke the framework of microporomechanics (Dormieux et al., 2006), employed for early age cementitious materials in an incremental form – as the response of the system at a given hydration degree to deformation, pressure and eigenstresses (Ulm et al., 2014). Specifically, consider an incremental (mean) stress distribution in the heterogeneous microstructure (solid volume V_s, pore volume V_p) of the form:

$$d\sigma(z) = k(z)d\epsilon + d\sigma^p(z) \qquad d\sigma^p(z) = \begin{cases} d\sigma^* \; in \; V_s \\ -dp \; in \; V_p \end{cases} \tag{1}$$

with $k(z) = k^s$ in V_s and $k(z) = 0$ in V_p the stiffness distribution; whereas $d\sigma^*$ is an (incremental) prestress prevailing in the solid phase, while $-dp$ is the pressure at the surface of the solid phase in contact with the pore space (which eventually could be negative when accounting for the surface tensions at the liquid-gas interface). Such a stress-distribution in the microstructure entails (under regular boundary conditions, and provided scale separability) the macroscopic incremental state equation of the form:

$$d\Sigma = KdE + d\Sigma^p \qquad d\Sigma^p = (1-b)d\sigma^* - b\,dp \qquad (2)$$

where $K = (1-b)k^s$ is the drained bulk modulus, while $b = 1 - K/k^s$ is the Biot coefficient, which captures the influence of the evolving compressibility of the solid system. Specifically, at early ages, the fresh material is a suspension which is incompressible, $b = 1$. Yet, as the system sets, and the solid phase percolates with hydration products precipitating into the pore volume, the system gains in compressibility, mainly related to the nanoporosity in the C-S-H gel (Constantinides and Ulm, 2007). From Eq. (2), it is then understood, that a macroscopic deformation ($dE = -d\Sigma^p/K$) due to a solid pre-stress is intimately related to the increase in compressibility of the hydrating matter; while it is the opposite for a pressure loading at the solid-liquid interface. The question then arises what is the origin of such a solid prestress. An experimental approach to the determination of this eigenstress was recently presented. Here, we shall make use of meso-scale simulation results.

COLLOIDAL PRESTRESS DEVELOPMENT

Recent advances in meso-scale simulations of cement hydrates consider nanometer-sized polydisperse particles to simulate the packing of hydration products (Masoero et al., 2012; 2014; Del Gado et al. 2014). The key in these simulations is a scaling of the interaction energy ε (well depth) between particles with particle size σ, of the form $\varepsilon \propto M\sigma^3$, where M is the contact modulus between particles (akin to Hertz' contact problem). As particles are filling the pore space, colloidal forces develop in between them, which can be repulsive (typically at short distances) or attractive (. If the precipitation was followed by a complete relaxation, these forces would relax bringing the system close to the hard-sphere relaxed situation. However, due to a finite hydration-precipitation rate, there is never enough time for these forces to relax, before another particle precipitates (or is inserted in the confined space (constant volume). Furthermore, since the repulsion forces at short distances are so much greater than the attraction forces at further distance, the overall pressure that is measured (as a reaction) at the boundary of system is always negative (i.e. tension!). This is illustrated in Figure 1 showing this pre-stress development determined by meso-scale simulations. The figure also displays indirect measurements of this prestress from oedometric measurements on cement paste carried out under saturated conditions that have been reported by Ulm et al. (2014).

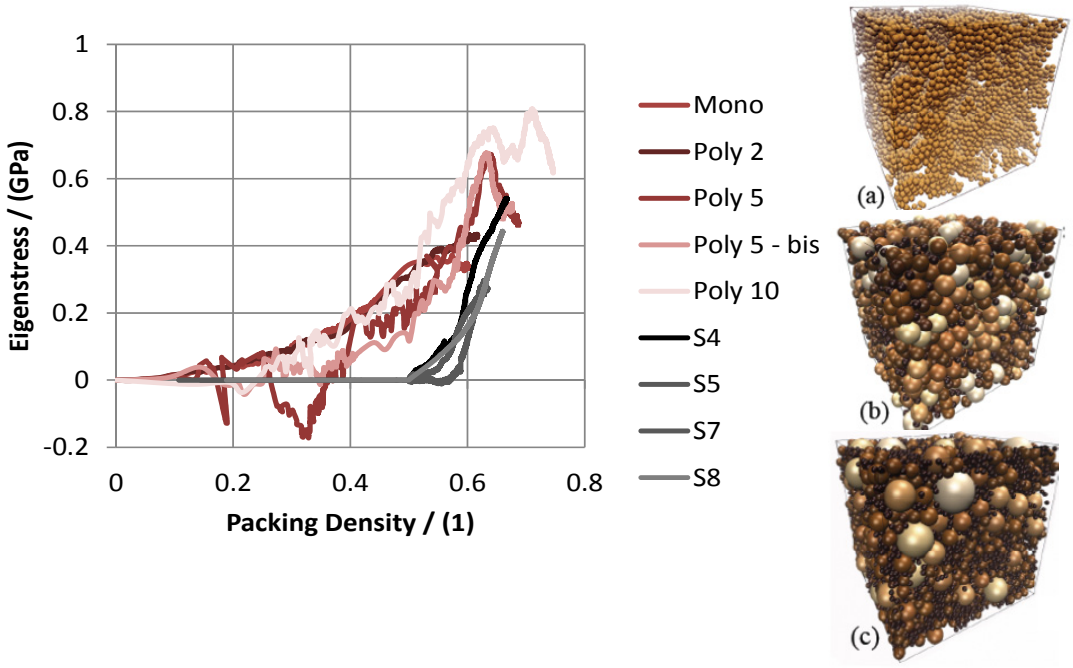

Figure 1. Eigenstress development in function of C-S-H packing density during hydration for different polydisperse meso-scale systems (Mono, Poly 2, 5 5 – bis, 10), and from oedometric mesaurements of hydrating cement paste carried out under saturated conditions. [Simulation results provided by Enrico Masoero at MIT, Experimental Data provided by Muhannad Abuhaikal, MIT]

CONCLUSIONS

The eigenstresses that develop in the solid phase during hydration are a consequence of an out-of-equilibrium situation. Precipitating nano-scale particles are stuck in the attractive well, causing on-average a tension stress under constant volume. We view this tension as a good candidate to explain the hydration shrinkage which occurs at early ages even under saturated conditions. While there is no doubt that other phenomena related to pore pressure developments (incl. negative pressure) may also induce some deformation, the order of magnitude of this solid eigenstress may well explain (at least a part) of the deformation attributable to autogeneous shrinkage. In fact, the macroscopic deformation is scaled by the materials compressibility, see Eq. (2) (in contrast to pore pressure driven deformation that scales with the matter's incompressibility). Thus far, if such deformation occurs with setting and the simultaneous solid's percolation, there is a good chance that it is such solid eigenstresses –and not pore pressure developments– that cause said shrinkage deformation.

The account of this prestress in advanced engineering applications appears to us critical, specifically when fracture processes risk jeopardizing the structural integrity and sealing functions of cement-based material-structural solutions; such as cement liners in oil- and gas well applications.

REFERENCES

Ardakani, S.M., and Ulm, F.-J. (2013). "Chemoelastic fracture mechanics model for cement sheath integrity". *J. Eng. Mech.*, 140(4), 04013009.

Constantinides, G. and Ulm, F.-J. (2007). "The nanogranular nature of C-S-H", *Journal of the Mechanics and Physics of Solids* 55 (1), 64-90.

Del Gado, E., Ioannidou, K., Masoero, E., Baronnet, A., Pellenq, RJM, Ulm, RJM , and Yip, S. (2014). "A soft matter in construction–Statistical physics approach to formation and mechanics of C–S–H gels in cement", The European Physical Journal Special Topics 223 (11), 2285-2295.

Dormieux, L., Kondo, D., and Ulm, F.-J. (2006). *Microporomechanics*, J. Wiley & Sons, Chichester UK.

Hua, C., Acker, P., and Ehrlacher, A. (1995). "Analysis and models of autogeneous shrinkage of hardening cement paste." *Cem. Concr. Res.*, 25(7), 1457-1468.

Masoero, E., Del Gado, E., Pellenq, R.J-M., Ulm, F.-J., and Yip, S. (2012). "Nanostructure and nanomechanics of cement: polydisperse colloidal packing", *Physical review letters* 109 (15), 155503.

Masoero, E., Del Gado, E., Pellenq, R.J-M., Ulm, F.-J., and Yip, S. (2012). "Nano-scale mechanics of colloidal C–S–H gels", *Soft matter* 10 (3), 491-499.

Ulm, F.-J., Abuhaikal, M., Petersen, T., and Pellenq, R.J-M., (2014). "Poro-chemo-fracture-mechanics…bottom-up: Application to risk of fracture design of oil and gas cement sheath at early ages", In: *Computational Modelling of Concrete Structures*, N. Bicanic, H. Mang, G. Meschke, de Borst R., eds. CRC Press/Balkema, London, Vol. I, 61-70.

Influence of Aggregate Restraint on Volume Changes: Experiments and Modelling

P. Lura[1,2] and M. Wyrzykowski[1,3]

[1]Empa, Swiss Federal Laboratories for Materials Science and Technology, Concrete/Construction Chemistry Laboratory, Switzerland. E-mail: pietro.lura@empa.ch
[2]ETH Zürich, Institute for Building Materials (IfB), Zürich, Switzerland.
[3]Department of Building Physics and Building Materials, Lodz University of Technology, Poland.

Abstract

Aggregates in cementitious composites restrain the volume changes of the matrix, which reduces the overall shrinkage of the composite and may lead to internal microcracking. In this paper, autogenous shrinkage of cement pastes and mortars with different amounts of aggregates was measured. While in the case of thermal deformations it is possible to estimate the volume changes of the composites with reasonable accuracy using effective medium approaches, predictions of early-age shrinkage tend to be less accurate, possibly because it is difficult to fully take into account the viscoelastic behavior of the cement paste, which is particularly pronounced at early ages.

INTRODUCTION

Concrete subject to drying, autogenous or thermal shrinkage develops stresses when the shrinkage strains are internally or externally restrained. Stresses resulting from restraint of deformations need to be considered not only at the macroscopic scale, where they may lead to macrocracking of concrete structures due to the restraining action of foundations, adjacent elements, etc., but also at the microscopic level, where microcracking may originate from the heterogeneity of the mesostructure. Internal stresses in concrete due to drying and autogenous shrinkage develop due to the restraining effect of stiff aggregates on the shrinkage of the matrix. In concrete subjected to temperature changes, internal stresses and cracking occur due to the much higher coefficient of thermal expansion of the cement paste compared to the aggregates. Aggregate restraint has positive aspects, since it results in smaller deformation of the concrete compared to cement paste (Pickett 1956, Hobbs 1974). However, tangential tensile stresses arising in the matrix restrained by the aggregates induce microcracks (Goltermann 1995). The ensuing micro-cracking depends on the relative stiffness of aggregates and matrix, the viscoelastic properties of the cement paste, its tensile strength and its bond strength with the aggregates.

In the models for drying shrinkage by Pickett (1956) and Hobbs (1974) (also applicable to thermal expansion and contraction), concrete is considered as a composite of two elastic phases, in which the cement paste shrinks while the aggregates do not. The aggregates act as rigid, non-shrinking inclusions that restrain the deformation of the paste the more rigid they are and the less rigid the cement paste is. The final expressions of the composite shrinkage based on the shrinkage of the matrix and the elastic properties of matrix and inclusions are different in Pickett (1956) and Hobbs (1974), because of the different assumptions employed in the derivation of the formulas. However, both these models and equivalent ones, e.g. (Rosen and Hashin 1970) tend to overestimate the shrinkage of the composite. Better estimations of drying or autogenous shrinkage are obtained when the viscoelastic properties of the cement paste are taken into account either explicitly (Grasley et al. 2005) or indirectly, by decreasing the elastic properties of the matrix used in the calculations.

In this study, autogenous shrinkage of high-performance of a cement paste and of mortars with the same cement paste but different amounts of aggregates were measured. Compared to drying shrinkage experiments, no shrinkage gradients are present in samples tested for autogenous shrinkage, which avoids the need for slow drying of thin samples (Weiss et al. 2008). Another advantage is that autogenous shrinkage usually takes days to weeks to develop, much faster than drying shrinkage, which is controlled by the comparatively slower kinetics of drying. Gaining a deeper understanding of the effect of aggregates on autogenous shrinkage or mortars and concrete would allow to predict the autogenous shrinkage of a concrete from that of the corresponding cement paste or mortar. This would be of practical importance for limiting the costs of laboratory measurements, especially considering that the only international standard for autogenous strain measurements, ASTM C1698-09 (ASTM 2009) based on the corrugated tubes method (Jensen and Hansen 1995), can only be applied to mixtures with small aggregates.

MATERIALS AND METHODS

Materials and sample preparation. The cement pastes and mortars had all water-to-cement ratio 0.30 and 20% silica fume addition (water-to-binder ratio 0.25). The cement was a CEM I 52.5 R with Blaine fineness 420 m^2/kg. The silica fume (BET specific surface 17.5 m^2/g) was added as a dry powder. Quartz aggregate of different sizes (0.5-1 mm and 2-3 mm) and low water absorption (<0.36%) were added to the mortars in amounts corresponding to 15, 30 and 50% aggregate by volume. One additional mixture with 60% by volume of aggregate was obtained by combining the 0.5-1 mm and 2-3 mm fractions in equal volumes. The cement pastes were mixed in a 5-l epicyclic mixer.

Autogenous deformation measurements. Linear autogenous shrinkage of mortars was measured using the corrugated tube method (Jensen and Hansen 1995, ASTM 2009). The measuring bench was placed in a temperature-controlled oil bath (20 ± 0.1 °C), which allowed reducing moisture loss from the tubes and at the same time maintaining stable temperature of the samples. Automatic measurements by means of LVDTs allowed recording the deformation starting 30 min after mixing. All the

results were referenced to the length at final set (measured by Vicat needle on the cement paste) in order to comply with the well-established standard ASTM protocol (ASTM 2009). Duplicate samples were measured for each mixture.

EXPERIMENTAL RESULTS AND DISCUSSION

In this paper, only a small part of the obtained results is presented and discussed. The autogenous deformation of cement paste and mortars with different amounts of quartz aggregates is shown in Figure 1. The initial rapid shrinkage of the cement paste (up to about 1 day after mixing) does not induce a corresponding high and rapid shrinkage in the mortars. The restraining effect of the aggregates on the deformation of the mortars is highly non-linear. For examples, 15% aggregate by volume result in about 40% shrinkage reduction.

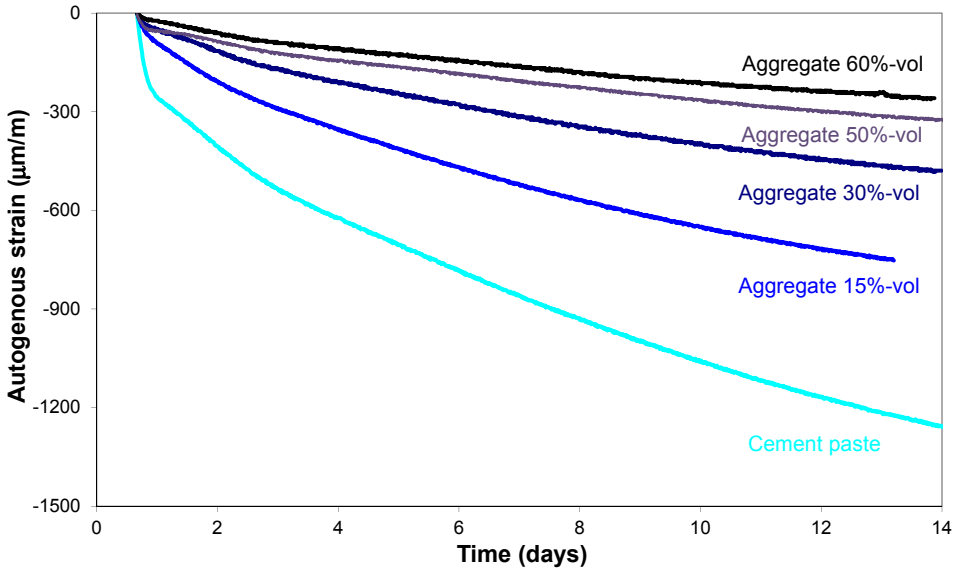

Figure 1. Autogenous deformation of cement paste and mortars with different amounts of quartz aggregates. The curves were zeroed at 16 hours from mixing.

MODELLING AND DISCUSSION

In the following calculations, concrete is assumed to consist of two phases, namely aggregate particles dispersed in a cement paste matrix. If the shrinkage of the paste is greater than the one of the aggregates, the aggregates restrain the shrinkage of the paste. According to this approach, concrete shrinkage is a function of the paste shrinkage, the aggregate shrinkage, the stiffness of the paste and of the aggregate, and the aggregate volume concentration.

Different approaches for the calculation of concrete shrinkage upon the aggregate volume concentration and the properties of the constituents were followed in the past, e.g. (Pickett 1956, Hobbs 1974). However, exact solutions for concrete shrinkage cannot be obtained because of the geometric complexity of concrete and

the many interacting particles. In order to obtain a solution, simplifying assumptions have to be made and as a consequence the solutions are only approximate.

Basic assumptions common to the solutions are (Hobbs 1974):

1) Concrete consists of two homogenous phases, aggregates and cement paste;
2) Aggregate and paste behave elastically;
3) Elastic properties are not influenced by shrinkage, i.e. microcraking of the paste, if it occurs, does not reduce the stiffness.
4) The total volume occupied by shrinkage cracks is independent of aggregate grading.

In the following, only Hobbs' model (Hobbs 1974) will be discussed and applied to quantify the reduction of autogenous shrinkage in the mortars compared to the cement paste (Figure 1).

Hobbs' model

Hobbs' model (1974) was developed for drying shrinkage, where the elastic modulus of the paste is constant. According to the model, the shrinkage of the concrete, ε_C [m/m], is equal to:

$$\varepsilon_C = \frac{\varepsilon_P \cdot (1-\phi_A) \cdot (K_P + K_A) + 2 \cdot \varepsilon_A \cdot \phi_A \cdot K_A}{K_P + K_A + \phi_A \cdot (K_A - K_P)} \quad (1)$$

where ε_P [m/m] is the shrinkage of the cement paste, ε_A [m/m] the shrinkage of the aggregates, K_A [MPa] the bulk modulus of the aggregates, and K_P [MPa] the bulk modulus of the paste.

This model is more general than Pickett's, taking into account also the possible shrinkage of the aggregates upon drying. A further difference is that the elastic modulus of the paste, rather than that of the concrete, is used in the computations.

In the common case the shrinkage of the aggregates is negligible, Hobbs' model reduces to:

$$\frac{\varepsilon_C}{\varepsilon_P} = \frac{(1-\phi_A) \cdot (K_P + K_A)}{K_P + K_A + \phi_A \cdot (K_A - K_P)} \quad (2)$$

Tazawa et al. [1997] applied equation (2) to compare autogenous shrinkage of paste and concrete at 28 days, finding a good agreement with the measurements.

In previous research of the authors (Wyrzykowski and Lura 2014), it was found that the Rosen-Hashin (1970) upper bounds (a model developed for calculating the coefficient of thermal expansion, CTE, of two-phase composites) overlap with Hobbs' model.

Comparison of model and measurements

Figure 2 shows a plot of the ratio of the shrinkage of the mortars to the shrinkage of the aggregates. For the experimental values (single markers), two sets are shown, corresponding to the period between 16 hours and 4 days and the period between 4 days and 13 days (see Figure 1). It is noticed that at earlier ages, a lower proportion of the shrinkage of the paste results into shrinkage of the mortar compared to later ages.

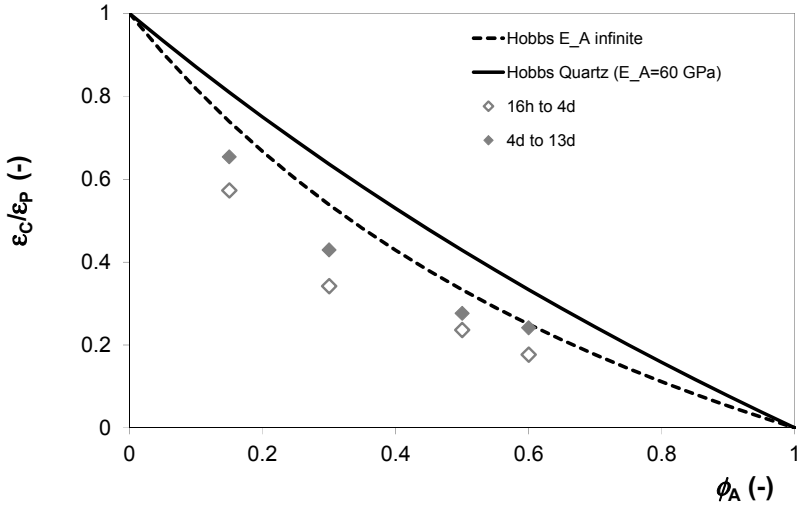

Figure 2. Ratio of the autogenous deformation of the mortars compared to the autogenous deformation of the corresponding cement paste as a function of the volume fraction of quartz aggregates in the mortar. In addition to the experimental results (single points), calculations according to Hobbs' model are also shown (continuous and dotted lines).

The curves corresponding to Hobbs' model (continuous line) were calculated assuming an elastic modulus of the aggregates of E_A = 60 GPa (a common value for quartz), an elastic modulus of the cement paste of E_P = 30 GPa and Poisson's ratios of both aggregates and pastes equal to 0.2. In addition, the dotted line shows the results of Hobbs' model when $E_A \Rightarrow \infty$ ($K_A \Rightarrow \infty$). In the limit of $E_A >> E_P$, which also covers the case in which the modulus of the paste is very low, equation (2) reduces to:

$$\frac{\varepsilon_C}{\varepsilon_P} = \frac{1-\phi_A}{1+\phi_A} \tag{3}$$

It is noticed that equation (3) is a better approximation of the experimental results compared to the original model by Hobbs, equation (2). On the contrary, in previous work on the CTE (Wyrzykowski and Lura 2014) it was possible to obtain good predictions of the CTE of mortars based on that of the corresponding cement paste using equation (2). This difference between the thermal expansion/contraction behavior (which is quasi-instantaneous) and the autogenous shrinkage behavior (a process that takes hours to days or even weeks to develop) is an indication that the viscoelastic properties of the cement paste might act to reduce the amount of shrinkage of the paste that results into shrinkage of the mortar. This effect can be taken into account by artificially reducing the elastic modulus of the cement paste (for example using an effective modulus about 1/3 of the measured one (Lura et al. 2004)) in equation (2) or by applying equation (3). It must be pointed out that even equation (3) appears to overestimate the deformation of the mortars. However, the predictions appear to improve at higher aggregate content (50 and 60% by volume), which is encouraging for practical applications in which the aggregate content of the content is higher than 60% and typically around 70% or higher.

Following these considerations, the lower $\varepsilon_C/\varepsilon_P$ measured at early ages compared to later ages (empty diamonds compared to full diamonds in Figure 2) may be due both to the lower elastic modulus of the cement paste at early ages and to its more pronounced viscoelastic behavior.

Effect of microcracking

The presence of aggregates restrains the deformation of the cement paste. According to the linear elastic solution (Goltermann 1995), the aggregates will be under hydrostatic compression and the paste in radial compression and in tangential tension at the interface. As a consequence of the low tensile strength of the cement paste, radial cracks in the paste around the aggregates may form (Goltermann 1995). Opening microcracks may result in a reduction of the global shrinkage of the concrete, and also of its stiffness.

Detection and quantification of microcracks caused by restrained autogenous shrinkage in high-performance concrete is a difficult task. Available techniques either lack the required resolution or may produce additional cracks that are indistinguishable from the original ones. A recently developed technique allows identification of microcracks while avoiding artefacts induced by unwanted restraint, drying, or temperature variations during sample preparation (Lura et al. 2009). Small cylindrical samples of cement paste were cast with steel rods of different diameters in their centre, to restrain the autogenous shrinkage of the paste and cause crack formation. The crack pattern was identified by impregnation with gallium and analyzed by optical and scanning electron microscopy. Both experimental results and the numerical analysis showed that samples with larger steel rods had the highest probability of developing microcracks. In addition, the pattern and the width of the observed microcracks showed good agreement with the simulation results.

While these results on 2D composites show an approach to quantify microcracking due to autogenous shrinkage, the real case is much more complicate. On the one hand, the stress fields generated by the aggregates will interact, resulting in localization of cracks [Moon et al. 2005, Idiart et al. 2012]. Most important, one would need to measure and simulate crack nucleation and propagation in a realistic 3D concrete mesostructure.

CONCLUSIONS

Preliminary results on autogenous shrinkage of cement pastes and mortars show that 2-phase models like Hobbs' model tend to overestimate the autogenous shrinkage of the mortars, while previous work showed that they give reliable predictions of the coefficient of thermal expansion. The fraction of the paste shrinkage that results in shrinkage of the composite is lower at early ages. Based on this evidence, models taking into account the viscoelastic properties of the cement paste should be developed (a first example is [Grasley et al. 2005]). A more practical approach is to apply Hobbs model with a reduced bulk modulus of the paste (or an increased bulk modulus of the aggregates) that takes into account its viscoelastic properties in an indirect manner.

REFERENCES

ASTM, ASTM C1698-09 Standard Test Method for Autogenous Strain of Cement Paste and Mortar, ASTM International, West Conshohocken, PA, 2009.

Goltermann, P. (1995). Mechanical predictions on concrete deterioration. Part 1: Eigenstresses in concrete. ACI Materials Journal, 91(6).

Grasley, Z.C., Lange, D.A., Brinks, A.J., D'Ambrosia, M.D (2005). Modeling autogenous shrinkage of concrete accounting for creep caused by aggregate restraint. 4th Int Conf on Self-Desiccation, NIST, Gathersburg, 78-94.

Hobbs, D. W. (1974). Influence of aggregate restraint on the shrinkage of concrete. In ACI Journal Proceedings (Vol. 71, No. 9). ACI.

Idiart, A., Bisschop, J., Caballero, A., & Lura, P. (2012). A numerical and experimental study of aggregate-induced shrinkage cracking in cementitious composites. Cement and Concrete Research, 42(2), 272-281.

Jensen, O. M., & Hansen, P. F. (1995). A dilatometer for measuring autogenous deformation in hardening Portland cement paste. Materials and Structures, 28(7), 406-409.

Lura, P., Ye, G., & van Breugel, K. (2004). Effect of cement type on autogenous deformation of cement-based materials. ACI Special Publication, 220.

Lura, P., Jensen, O. M., & Weiss, J. (2009). Cracking in cement paste induced by autogenous shrinkage. Materials and structures, 42(8), 1089-1099.

Moon, J. H., Rajabipour, F., Pease, B. J., & Weiss, J. (2005). Autogenous shrinkage, residual stress, and cracking in cementitious composites: The influence of internal and external restraint. 4th Int Conf on Self-Desiccation, NIST, Gathersburg.

Pickett, G. (1956). Effect of aggregate on shrinkage of concrete and a hypothesis concerning shrinkage. In ACI Journal Proceedings (Vol. 52, No. 1). ACI.

Rosen, B. W., & Hashin, Z. (1970). Effective thermal expansion coefficients and specific heats of composite materials. International Journal of Engineering Science, 8(2), 157-173.

Tazawa, E., & Miyazawa, S. (1997). Influence of constituents and composition on autogenous shrinkage of cementitious materials. Magazine of Concrete Research, 49(178), 15-22.

Weiss, J., Lura, P., Rajabipour, F., & Sant, G. (2008). Performance of shrinkage-reducing admixtures at different humidities and at early ages. ACI Materials Journal, 105(5).

Wyrzykowski, M., & Lura, P. (2013). Controlling the coefficient of thermal expansion of cementitious materials–a new application for superabsorbent polymers. Cement and Concrete Composites, 35(1), 49-58.

Aging and deterioration of concrete structures. Learning from the past, assessing the present, and predicting the future: science or magic?

G. Cusatis[1], M. Alnaggar[2], P. Gardoni[3], M. D'Ambrosia[4], and J. Qu[1]

[1] Department of Civil and Environmental Engineering, Northwestern University, Evanston, IL 60208-3109; PH (847) 491-4027; email: g-cusatis@northwestern.edu & j-qu@northwestern.edu
[2] Department of Civil and Environmental Engineering, Renselear Polytechnic Institute, Troy, NY 12180; PH (518) 276-3956; email: alnagm2@rpi.edu
[3] Department of Civil and Environmental Engineering, University of Illinois at Urbana Champaign, Urbana, IL 61801; PH (217) 333-5103; email: gardoni@illinois.edu
[4] CTLGroup, Skokie, IL 60077; PH (847) 972-3264; email: mdambrosia@ctlgroup.com

Abstract

This paper deals with important issue of the aging and deterioration of concrete structures: a problem at the forefront of civil engrineering research that has profound impact on our society and our way of living. Despite the recognized importance of such issue, entrenched practice and remediation approaches are, for the most part, empirical and fundamentally related only to the lifetime experience of few capable professionals. We all need to thank the work of these people but this paper argues that such "modus operandi" is only slightly better than predicting the future of infrastructure by looking into a crystal ball – it is more magic than science. On the contrary, this paper presents a different vision in which "predictions" are based on a rigourous structural reliability framework equipped with physically-sound computational models that are rigorously validated and continually updated on the basis of reliable experimental data obtained from both destructuve and non-destructuve techniques.

Introduction

Sustainability – the ability of being durable, reliable, and economically affordable during the entire lifetime – is one of the most important properties of modern infrastructures. Unfortunately, many of our critical infrastructures, such as bridges, dams, and roads, fall short of fitting within this definition. In the US and around the world, concrete structures suffer from serious deterioration and damage due to aging after only a relatively small portion of their expected lifetime, which often exceeds a hundred years. Inspection, maintenance, and repair costs are on the rise and our society does not seem on track to meet the required commitment to maintain a state of good repair of our national infrastructures (www.infrastructurereportcard.org). The American Society of Civil Engineers (ASCE), for example, estimates that a 3.6 trillion

dollars investment will be needed by 2020 in order to improve the condition of infrastructures to an acceptable level. This is 2 trillion dollars over the anticipated funding level. In addition to the problems of aging infrastructure, there is also a compelling need to develop new infrastructure technologies, especially in regard to transportation and communication systems, to stimulate and sustain continuing economic growth in both developed and developing countries. These technologies will likely be required to be built and used in harsh environments and/or service conditions to fit societal needs, which places high demand on the structural performance, resulting in increased construction costs. Worldwide increasing consciousness for sustainable use of natural resources has made "overcoming the apparent contradictory requirements of low cost and high performance a challenging task" (Mihashi and Nishiwaki, 2010) as well as a major concern for the civil engineering community. For concrete structures, deterioration is due to the effect of several chemical and physical phenomena including shrinkage, alkali-silica reaction (ASR), freeze-thaw damage, sulphate and salt attack, delayed ettringite formation (DEF), and fatigue. These types of phenomena lead to cracking which, while may not affect significantly the load carrying capacity in the short-term, does dramatically influence moisture diffusion through concrete. This, in turn, leads corrosive agents to reach the reinforcing steel whose strength, as a consequence, declines overtime, posing significant safety risks. In addition, cracking may induce degradation of other non-mechanical properties for which concrete is widely used. One critical example is the loss of radiation shielding in elements used in nuclear power plants.

Predicting the lifetime of infrastructures

The prediction of the service lifetime of infrastructures requires the accurate prediction of the evolution of the probability of failure with time. Recent studies (e.g., Kumar and Gardoni 2014a,b) have shown that the probability of failure of infrastructure systems increases with time with either continuous or discrete increments (Figure 1, top). Continuous increments often result from a gradual deterioration of the system properties due to various deterioration phenomena. Discrete increments can be due to shocks that cause sudden changes in the system properties and these include loads and deterioration mechanisms that are active for a short duration of time such as impact loads, seismic events, and other man-made and natural hazards.

Figure 1 (top) depicts the evolution of the probability of failure for a concrete structure in two different scenarios. The first scenario (red lines) is relevant to a situation in which an increase of the probability of failure beyond a level requiring retrofitting and/or repair is not followed but any action, leading to the end of the service life of the structure at a certain point in time shortly after – especially if unexpected events occur. The second scenario (blue lines), on the contrary, shows a situation in which the probability of failure is reduced through appropriate structural retrofitting and/or repair. As a consequence the service lifetime of the structure is increased, but

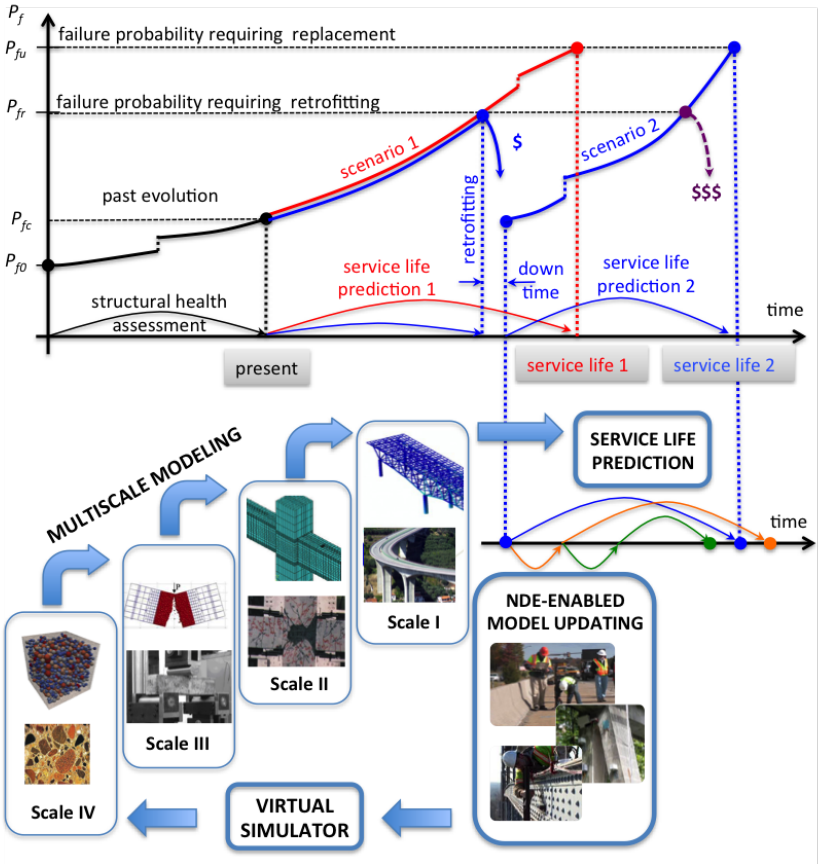

Figure 1. Evolution of the probability of failure for infrastructure systems (top) and its prediction through virtual experiments (bottom).

the magnitude of such increase is directly related to reduction of probability of failure, which, in turn, depends on the extent, and consequently the cost, of the performed retrofitting/repair. Multiple retrofitting/repair scenarios can be of course envisioned during the service lifetime of the structure with the understanding, however, that subsequent repairs do require increasing resources for achieving the same reduction in the probability of failure. x The current societal demand for "sustainability" calls for the optimal management of infrastructures, which can be achieved only by accounting for numerous conflicting requirements associated with, for examples, economic costs, environmental impact, safety, aesthetics, transportation need of the public, etc. For this reason, infrastructure owners necessitate of a quantitative characterization of all these requirements so that they can find an optimal solution to their management and maintenance goals. At any given time in the life of a structure ("present" in Figure 1) there are two aspects that contribute to the estimation of the remaining service life of a structure: (1) the assessment of the current probability of failure ("the status quo"), P_{fc}, and (2) the prediction of the evolution of the probability of failure in the

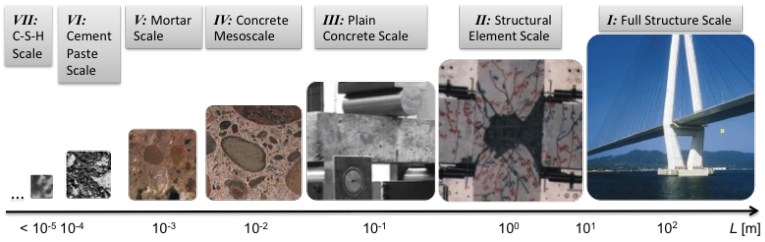

Figure 2. Concrete multiple length scales

future and, in particular, the prediction of the time needed for the structure to reach some predetermined values of the probability of failure associated with the need of retrofitting/repair or replacement (P_{fr} and P_{fu}, respectively). The latter corresponds to the service life of the structure. While, in the current practice, the combination of current destructive and nondestrutive evaluation technologies provide a robust procedure for the assessment of the status quo from a qualitatively point of view, a quantitative accurate assessment of the current probability of failure is still hampered by the lack of a comprehensive framework able to link destructive and nondestructive measurements to the fundamental deterioration and failure mechanisms of the material. This is even more an issue when the evaluation is solely based on nondestructive evaluation as required by the fact that destructive evaluations tend to be too invasive as far as the infrastructure operations are concerned and too expensive to be performed on a regular basis. Furthermore, for infrastructure with no specific evidence of deterioration nobody would ever consider performing destructive evaluations but it is common practice to perform preventive nondestructive evaluations as part of continuous structural health monitoring and periodic maintenance activities.

Once evaluation of the current degradation level is performed, even more complicated is to predict the future. For this aspect, current practice only rely on the lifetime experience of few capable professionals. While we all need to thank the work of these experienced people, this paper argues that such “modus operandi” is only slightly better than predicting the future of infrastructure by looking into a crystal ball – it is more magic than science. On the contrary, this paper presents a different vision in which “predictions” are based on physically-sound computational models that are rigorously validated and continually updated on the basis of reliable experimental data obtained from non-destructuve evaluation (NDE) techniques. More specifically, the overarching vision consist in using of computational technologies enabling the calculation of the probability of failure (and the remaining service life) on the basis of NDE measurements; and performing (real-time) NDE-enabled model updating to continuously improve the prediction of the service life of concrete structures.

Multiscale and multiphysics modeling of concrete

A recently discussed in Cusatis et Al. (2014), reinforced concrete structures are multiscale systems in which a large variety of length scales can be identified as shown in Figure 2. Scale *I* is the largest scale, the scale of the full structure or, as typically

referred to in the literature, the macroscopic engineering scale. Characteristic lengths of Scale I go from meters to tens of meters, for small to medium size structures such as buildings, urban overpasses, foundations, etc.; and up to hundreds of meters for large structures such as, long-span bridges, skyscrapers, and dams. The analysis of Scale I is typically done through well-established structural theories implemented in robust and computationally efficient software. These theories require knowledge of the behavior of each structural element beams, columns, connections, etc. composing the structure. The structural element scale is Scale *II* in Figure 2 and it is characterized by lengths in the order of tens to hundreds of centimeters. Reinforced concrete elements consist of concrete and steel reinforcement in the form of rebars, prestressed strands and cables, stirrups, and other type of steel detailing. At this scale the mechanical behavior can be described by simulating concrete as a statistically homogeneous and isotropic quasi-brittle continuum; steel as an elasto-plastic continuum; and the concrete-steel interface as a third material characterized by its own peculiar properties. Formulation of appropriate constitutive equations at Scale *II* depends on the appropriate mathematical description of deformation and failure mechanisms that are often identified through laboratory experiments on samples whose size is in the order of few to several centimeters – see the plain concrete scale (Scale *III*) in Figure 2. For many decades, researchers have tried to formulate continuum constitutive equations for plain concrete but these attempts, although successful in many ways, failed to capture to the full extent the most important aspect of concrete behavior characterized by cracking and fracture. Fracturing behavior is strongly influenced by its heterogeneous internal structures. At the mesoscale (Scale *IV* in Figure 2) concrete is considered as a two-phase composite in which hard and stiff inclusions, the coarse aggregate particles (several millimeters to few centimeters large in standard concrete), are embedded in a softer and weaker mortar matrix. Modeling the effect of the major material heterogeneities is instrumental in order to capture the intrinsic material characteristic length associated with fracture and the consequent reduction of the structural strength as a function of the structural size the so-called Size Effect. At the mortar scale, also called concrete mini-scale and indicated as Scale *V* in Figure 2, concrete can be regarded as a three-phase composite composed of (1) a porous matrix, the cement paste; (2) aggregate particles of all size (from several microns to few centimeters in standard concrete); and (3) a thin layer (size of several microns) of material at the interface between cement paste and aggregate pieces, the so called Interfacial Transition Zone (ITZ), which has distinctly different properties compared to the cement paste bulk. Scale *VI* is the scale of cement paste and ITZ whose internal structure features a very complex system of pores with size spanning various orders of magnitude (from nanometers to millimeters). The six concrete scales described above are not the only ones: multiple other fine scales can be defined all the way down to the atomic structure (Figure 2). The formulation of a multiscale computational framework requires three fundamental ingredients: (1) A mathematical model describing the behavior of interest at a certain given scale; (2) Experimental data, from destructive and nondestructive testing conducted not neces-

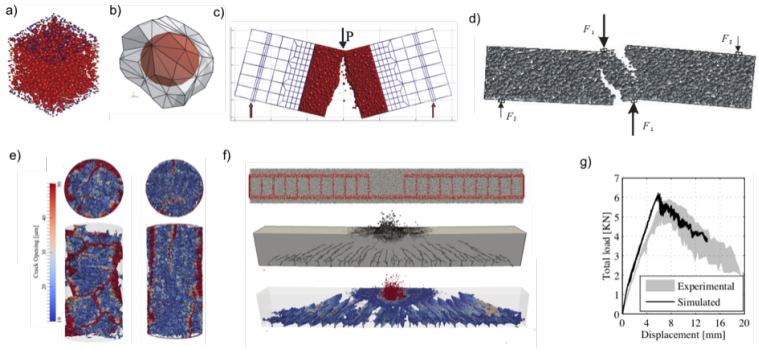

Figure 3. The Lattice Discrete Particle Model (LDPM)

sarily at the same scale of the selected model, for calibration identification of model parameters and validation proof of predictive capability; and (3) multiscale theories and technologies allowing the upscaling of the selected model to Scale *I*.

One effective model to simulate concrete at Scale *IV* is the so-called Lattice Discrete Particle Model (LDPM) formulated and extensively calibrated/validated by Cusatis and coworkers (Smith et Al., 2014; Alnaggar et Al., 2013; Schauffert et Al., 2012a; Schauffert et Al., 2012b; Cusatis et Al., 2011a; Cusatis et Al., 2011b; Cusatis 2011) in the last several years. LDPM simulates the mesostructure of concrete by a three-dimensional assemblage of particles (Figure 3a) that are generated randomly according to the given grain size distribution. An algorithm, based on Delaunay tetrahedralization and three-dimensional domain tessellation, allows the generation of a system of cells interacting through triangular facets (Figure 3b). Discrete compatibility equations are formulated by means of displacements and rotations of adjacent particles and adopting rigid body kinematics. A mesoscale constitutive law that simulates cohesive fracture, compaction due to pose collapse, frictional slip, and rate effect, is formulated at each cell facet. The formulation is completed by the equilibrium equations of each single particle. LDPM has been extensively calibrated and validated and it has shown superior capabilities in reproducing and predicting (qualitatively and quantitatively) concrete behavior under a wide range of loading conditions ranging from uniaxial and multiaxial compression to fragmentation. Figure 3 shows a collection of typical LDPM results.

Recently, LDPM was also further extended to simulate the deterioration associated with Alkali-Silica reaction (ASR) and, as shown in Figure 3e, it can reproduce very well the resulting crack patterns and effect of applied load. Figure 3f and 3g show the numerical simulation of an over-reinforced beam in which the rebars are simulated as elastic beams and the LDPM-rebar coupling is obtained through a simple penalty algorithm. The LDPM formulation also account for early age behavior, drying and autogenous shrinkage, and creep. LDPM is also coupled with a multiphisics solver (Di Luzio and Cusatis, 2009a and Di Luzio and Cusatis, 2009b) allowing the simulation of heat transfer as well as as transport of moisture and other chemical species. Furthermore, LDPM can be up-scaled from Scale IV to Scale III by using a multiscale

procedure. The classical homogenization approach has been applied successfully in a wide variety of situations and can be used to obtain the macroscopic stress versus strain curves that can be used for Scale *III* and higher analyses especially for cases featuring distributed damage as for deteriorating concrete.

Non destructive evaluation and its numerical interpretation

To operate safely, structures and components need to be inspected or monitored either periodically or in real time for potential failure. For this purpose, ultrasonic non-destructive evaluation (NDE) techniques have been used extensively. The vast majority of these ultrasonic NDE techniques utilize only the linear behavior of the ultrasound, which however cannot characterize fully diffuse damage as the one occurring from aging and deterioration of concrete structures. Nonlinear ultrasounds represent a valid and more appealing alternative. Qu and his coworkers (Kim et Al., 2006; Liu et Al., 2012) have recently adopted nonlinear wave mixing tecniques to characterize ASR deterioration. As an ultrasonic wave of monolithic frequency propagates in a concrete sample, a second harmonic wave of frequency will be generated by the damage in the material. The amplitude of the second harmonic wave is proportional to the acoustic nonlinearity parameter (ANLP) β. It has been shown that β is an intrinsic material property and is well correlated with the degree of ASR damage in concrete. For example, when a concrete bar is immersed in an alkaline solution at elevated temperature to accelerate the ASR damage, the bar will elongate, and the magnitude of the elongation indicates the degree of ASR damage. Figure 4a shows the elongation of a concrete bar (Samples L1) versus the number of days of alkaline solution immersion. As a comparison, Sample L2 was left in an ambient environment (about 50 % RH and 250°C). The corresponding ANLP β for Samples L1 and L2 is plotted in Figure 4b. The error bars are the ranges of values measured at different locations of the same sample. In order for NDE measurements to be used for model updating, a direct relationship between the increase of nonlinearity parameter and degradation of material properties need to be established. This is not a trivial task due to the fact that all NDE techniques measure the occurrence and evolution of nonlinear phenomena but cannot distinguish between various nonlinear phenomena that might occur in the material internal structure. Recent work of the Authors (Alnaggar et Al. 2014) has shown that a precise interpretation of NDE measurements in concrete can be obtained by performing accurate LDPM simulations of the wave propagation phenomena through the affected concrete. Figure 4c show how metrics of LDPM-calculated ASR-induced cracking (for example max or mean crack opening) correlates very well with the nonlinearity parameter β (both experimental and numerical) for the case of a classical accelerated ASR mortar bar test.

Predictive structural reliability framework

Following the conventional notation in structural reliability theory, the probability of failure can be expressed as $P_f(t) = P((g(C(t), D(t)) \leq 0)$ where $C(t)$ = capac-

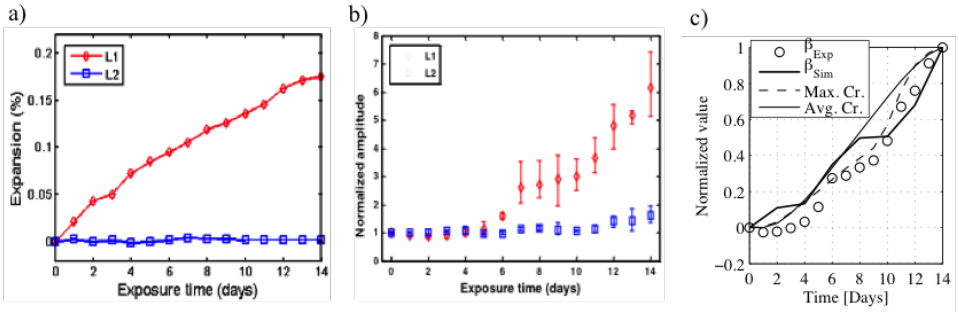

Figure 4. (a) Expansion versus exposure time, and (b) ANLP versus exposure time. (c) Correlation between nonlinearity parameter and LDPM-simulated cracking metrics.

ity model, $D(t)$ = demand model, $g(\cdot)$ = limit state function, such that $g(C(t), D(t)) \leq 0$ refers to the failure at time t. In order to be predictive, the probabilistic capacity and demand models must be well calibrated and rigorously validated. The probabilistic model should account for all the prevailing uncertainties, including model error arising from potential inaccuracies in the model form and potentially missing variables, as well as measurement errors and statistical uncertainties (Gardoni et al. 2002). NDE data can be used to calibrate the probabilistic models (Huang et al. 2012 and Gardoni et al 2012).

Both probabilistic capacity and demand models are function of a number of measurable variables $\mathbf{x}(t)$, that in general might change with time and can be partitioned in a vector of random variables, $\mathbf{x}_r(t)$, like, for example, the elastic modulus of concrete, and in a vector of parameters, $\mathbf{x}_s(t)$, such as the height of a column, or the mean and standard deviation of a random variable. Thus, $\mathbf{x}(t)$ can be written as $\mathbf{x}(t) = [\mathbf{x}_r(t), \mathbf{x}_s(t)]$. Sensitivity analysis can be used to study which parameters the reliability of the structure being analyzed is most sensitive to and importance analysis can determine which random variables have more effect on the reliability analysis. Therefore, by conducting a sensitivity analysis and an importance analysis, one can identify which terms are most crucial and need to be detected. In the adopted formulation, the most sensitive parameters and the most important random variables are indicated as $\mathbf{x}^*(t) = [\mathbf{x}_r^*(t), \mathbf{x}_s^*(t)]$. By updating $\mathbf{x}^*(t)$ based on the monitored NDE data, the probability density function (PDF) of the capacity and demand will change: the mean of PDF may be increased or decreased. Also the updated PDFs will become less flat because the incorporated monitored information reduces the uncertainties of the probabilistic models. The essence of the adaptive reliability framework discussed here is to use the monitored data to update $\mathbf{x}^*(t)$ in the capacity model and the demand model through a Bayesian approach (Huang et A., 2011). Since the monitoring is (possibly) continuous, the same updating process can be repeated any number of times. If there are m groups of independent monitored data corresponding to m times monitoring, the posterior model can be updated after each group of monitored data becomes available. The likelihood associated with the m^{th} group of monitored data updates the

posterior model that accounts for the information content of the previous $m-1$ groups of monitored data.

Conclusion

This paper introduced an overall vision for the rational prediction of the deterioration evolution of concrete structures. The fundamental idea is that meaningful predictions must be based on an accurate and predictive structural reliability framework in which the demand model depends on deterioration and aging. Furthermore, such dependence must be formulated by using a reliable physically sound stochastic computational framework that, in turn, should be calibrated and validated through past available experimental data as well as destructive and non-destructive evaluation assessing the current structural deterioration level. Furthermore, the model should be continually updated with rigorous model updating techniques and by using experimental data mostly obtained through continuous structural monitoring.

Acknowledgements

Financial support of National Regulatory Commission (NRC) through Award No NRC-HQ-60-14-G-0003 is gratefully acknowledged.

REFERENCES

Alnaggar, M.,G. Cusatis, and G. Di Luzio. (2013) "Lattice Discrete Particle Modeling of Alkali-Silica-Reaction (ASR) Deterioration of Concrete Structures". *Cement and Concrete Composites Journal*. Volume 41, August 2013, Pages 45-59.

Alnaggar, M., G. Cusatis, J. Qu, M. Liu (2014). "Simulating acoustic nonlinearity change in accelerated mortar bar tests: a discrete mesoscale approach". *IALCEE Conference 2014*, 16-19 November, 2014. Tokyo, Japan.

Cusatis, G., Rezakhani, R., Alnaggar, M. , Zhou, X. and Pelessone, D. (2014). "Multiscale computational models for the simulation of concrete materials and structures". *Proceedings of EURO-C 2014, Computational Modelling of Concrete and Concrete Structures*, 24-27 March, 2014. St. Anton, Austria.

Cusatis, G., A. Mencarelli, D. Pelessone, and J.T. Baylot. (2011a) "Lattice Discrete Particle Model (LDPM) for Failure Behavior of Concrete. II: Calibration and Validation". *Cement and Concrete Composites*. 2011, 33(9), pp. 891-905.

Cusatis, G., D. Pelessone, and A. Mencarelli. (2011b) "Lattice Discrete Particle Model (LDPM) for Concrete failure Behavior of Concrete. I: Theory". *Cement and Concrete Composites*. 2011, 33(9), pp. 881-890.

Cusatis, G. (2011). "Strain Rate Effects on Concrete Behavior". *International Journal of Impact Engineering*. 2011, 38(4), pp. 162-170.

Di Luzio, G. and G. Cusatis. (2009a) "Hygro-Thermo-Chemical Modeling of High Performance Concrete. II: Calibration and Validation". *Cement and Concrete Composites*. 2009, 31(5), pp. 309-324.

Di Luzio, G. and G. Cusatis. (2009b) "Hygro-Thermo-Chemical Modeling of High Performance Concrete. I: Theory". *Cement and Concrete Composites*. 2009, 31(5), pp. 301-308.

Gardoni, P., Der Kiureghian A., Mosalam K.M., (2002). "Probabilistic capacity models and fragility estimates for RC columns based on experimental observations," *ASCE Journal of Engineering Mechanics*, 128 (10), 1024-1038.

Gardoni P., Pagnotta, A., Huang, Q., and Trejo, D., (2012), "Evaluation of concrete structures affected by alkali-silica reaction and delayed ettringite formation", TxDOT Report No. 0-6491-1, Texas Transportation Institute, Texas Department of Transportation, Austin, Texas, USA.

Huang, Q., Gardoni, P., and Hurlebaus, S., (2011). "Adaptive reliability analysis of reinforced concrete bridges using nondestructive testing," Proceedings of the ASCE's International Conference on Vulnerability and Risk Analysis and Management (ICVRAM) and Fifth International Symposium on Uncertainty Modeling and Analysis (ISUMA), Hyattsville, Maryland.

Huang, Q., Gardoni P., and Hurlebaus, S., (2012). A probabilistic damage detection approach using vibration-based nondestructive testing, Structural Safety, 38 (2012), 11-21.

Kim,J.-Y. , L. J. Jacobs, J. Qu, and J. W. Littles, (2006) "Experimental characterization of fatigue damage in a nickel-base superalloy using nonlinear ultrasonic waves", *The Journal of the Acoustical Society of America*, 120(3):1266–1273, 2006.

Kumar, R., and Gardoni, P., (2014a). "Effect of seismic degradation on the fragility of reinforced concrete bridges". *Engineering Structures*, 79, 267-275.

Kumar, R., and Gardoni, P., (2014b). "Renewal theory-based life-cycle analysis of deteriorating engineering systems". *Structural Safety,* 50, 94-102.

Liu, M., G. Tang, L. J. Jacobs, and J. Qu (2012), "A nonlinear wave mixing method for detecting Alkali-Silica reactivity of aggregates", *AIP Conference Proceedings 1430, 1524 (2012); doi: 10.1063/1.4716396*, 1430, 2012.

Mihashi, H. and Nishiwaki, T. (2010). "Development of engineered self-healing and self-repairing concrete. State-of-art report." *J. Adv. Concr. Techn.*; 10; 170-184.

Schauffert, E. A. , G. Cusatis, Pelessone, D., O'Daniel, J., and Baylot, J. (2012a) "Lattice Discrete Particle Model for Fiber Reinforced Concrete (LDPM-F): II Tensile Fracturing and Multiaxial Loading Behavior". *ASCE Journal of Engineering Mechanics*. 2012, 138(7), 834-841.

Schauffert, E. A. and G. Cusatis. (2012b) "Lattice Discrete Particle Model for Fiber Reinforced Concrete (LDPM-F): I Theory". *ASCE Journal of Engineering Mechanics*. 2012, 138(7), 826-833.

Smith, J., G. Cusatis, D. Pelessone, Eric Landis, J. O'Daniels, and J. Baylot. (2014) "Lattice Discrete Particle Modeling of Ultra High-Performance Fiber-Reinforced Concrete for Projectile Penetration Simulations". *International Journal of Impact Engineering*. Volume 65, March 2014, Pages 13-32.

The Meso-Scale Texture of Cement Hydrate Gels: Out-of-Equilibrium Evolution and Thermodynamic Driving

Emanuela Del Gado[1,2]; Katerina Ioannidou[3]; Enrico Masoero[4]; Roland J.-M. Pellenq[3,5]; Franz-Josef Ulm[3]; and Sidney Yip[6]

[1]Department of Physics, Institute for Soft Matter Synthesis and Metrology, Georgetown University, Washington, DC.
E-mail: emanuela.del.gado@georgetown.edu
[2]Department of Civil, Environmental and Geomatic Engineering, ETH Zurich, Switzerland.
[3]Department of Civil and Environmental Engineering, Massachusetts Institute of Technology, Cambridge.
[4]School of Civil Engineering and Geosciences, Newcastle University, Newcastle upon Tyne, U.K.
[5]CINaM, CNRS and Aix-Marseille University, Marseille, France.
[6]Department of Nuclear Science and Engineering, Massachusetts Institute of Technology, Cambridge.

Abstract

By the end of cement hydration calcium-silicate-hydrate (C-S-H) gels extends over tens and hundreds of nanometers. Their complex texture affects directly, and to a large extent, the macroscopic hygrothermal and mechanical behavior of cement. Here we review a statistical physics approach recently developed, which allows us to investigate the gel formation under the out-of-equilibrium conditions typical of cement hydration and the role of the nano-scale structure in C–S–H mechanics upon hardening. Our investigations have unveiled the role, in the C-S-H gels, of nano-scale structural and mechanical heterogeneities that develop due to the the far-from-equilibrium physico-chemical environment in which the material forms. A subtle interplay between the out-of-equilibrium evolution and the effective interactions emerging between the nano-scale units of the gels at different stages of the hydration process ultimately determines the mesoscale texture of cement hydrates and their material properties.

INTRODUCTION

Upon dissolution of cement powder in water, calcium-silicate-hydrates C-S-H precipitate and assemble into a cohesive meso-porous gel that fills the pore space in the cement paste over hundreds of nanometers, eventually binding the different components of concrete [1]. C-S-H mechanics and microstructure are key to concrete performance and durability [2-6], but the understanding needed to design more durable cements with a reduced carbon footprint (up to 5-8% of global man-made

CO2 comes from cement production for concrete) is far from being reached. Most of the experimental characterization and models used to predict and design cement performance have been developed at a macroscopic level and hardly include the material heterogeneity over lengths scales smaller than microns [3-8]. However, internal stresses emerging over length scales between a few and hundreds of nanometers are a major obstacle to design the material properties and control its durability, being responsible for early age or delayed non-linear deformations, such as shrinkage or creep.

We have developed a statistical physics approach to investigate the mesoscale texture of cement hydrates. Our model accounts for cohesive interactions between nanoscale units, structural and mechanical heterogeneities as well as far-from-equilibrium conditions in the development of the C-S-H structure over a hundred nanometers. With these ingredients, the hydration kinetics and the material properties naturally emerge and provide a first consistent characterization of the complex and elusive meso-scale structure of cement hydrates.

GEL GROWTH AND DENSIFICATION

In our model for the early stages of the hydration the gel is formed via the anisotropic growth of branches that eventually interconnect and progressively thicken and densify. The assembly of C-S-H gels during cement hydration is quite different from most gelation processes investigated typically for soft materials because of the underlying hydration kinetics that continuously produces the material as gelation proceeds. We consider a small volume contained in a capillary pore of the wet paste and approximate it to an open system of interacting nano-scale units. The nano-scale units in the model can be thought of as colloidal hydrates or simply as coarse graining elements in our description of the material. In a simple first approximation, we consider such units to be spherical and monodisperse in size. Size polydispersity and shape anisotropy are certainly important in a material like C-S-H and are included in the model in the work currently in progress. Because of the gelation and of the strong cohesion that C-S-H develops by the end of the hydration, it is clear that the net effective interactions must be attractive. Strong non-contact attractive forces, more than one order of magnitude stronger than Van der Waals interactions, are expected indeed in presence of high surface charges and of divalent counter-ions Ca^{2+} in the pore solution [9-11]. Experiments, simulations and theory also indicate that a narrow and deep attractive short range interaction can be accompanied by a medium range repulsion, whose strength is mainly determined by the lime concentration, which in general changes with time during cement hydration, hence changing the effective nano-scale interactions overtime [1]. These features have been included in the interaction potential between the nano-scale units in our model. The other important component is in the specific out-of-equilibrium conditions for gelation due to the hydrate precipitation, which in our modeling and numerical simulations are realized by coupling MD simulations with a Grand-canonical Monte Carlo scheme (GCMC) that mimics the precipitation of C-S-H. The chemical potential in the GCMC here represents the free energy gain corresponding to the formation of the C-S-H hydrates (i.e., its value would set the equilibrium density of C-S-H ideally reached in the pore).

In Figure 1 we show three snapshots from the simulations, illustrating the gel growth and densification, due to the precipitation of the hydrates, the aggregation and the change in the effective interactions governing the phenomenon. A detailed report of the model and of the simulations can be found in Refs.[12-15].

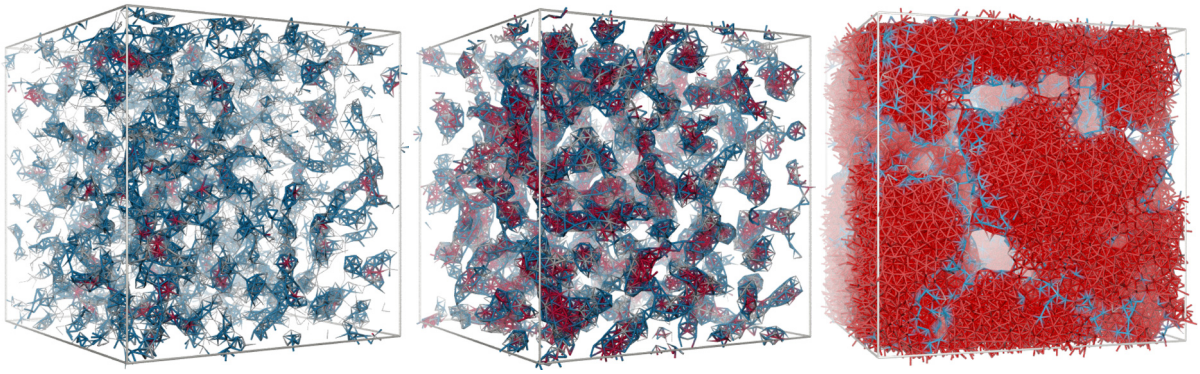

Figure 1. Snapshots from the simulations of C-S-H gelation with evolving effective interactions during cement hydration.

HARDENED GELS: MECHANICS AND NANOSCALE PORES.

As hydration proceed the gel branches progressively densify. We have characterized the elastic properties and the pore size distribution of the dense gel branches that should be mainly responsible for the mechanical properties of the gel. In particular, we have investigated the role of structural and mechanical heterogeneities that can be present even in these dense domains, due to the complex and out-of-equilibrium aggregation and densification process. We find that such heterogeneities, mimicked in the model in terms of strong size polydispersity and size dependent interaction strengths of the nano-scale units, are crucial to attain the high packing fractions needed to develop the mechanical strength typical of hardened cement pastes. The mechanical properties are computed in the simulations in presence of nano-scale structure and dynamical heterogeneities by means of Non-Equilibrium-Molecular-Dynamics and using the stress fluctuation method [16]. This approach allows us to obtain the full microscopic tensor of elasticity, from which we can compute bulk, shear and indentation moduli, and can be extended to investigate also the non-linear response of the material [14,16].

Figure 2 displays a comparison of the results obtained in the simulations for the indentation modulus M with the results of nanoindentation experiments [13,14,17,18]. The agreement between experiments and simulations indicates that the structural and mechanical heterogeneities included in the model are at the core of the material properties up to the micrometer scale. Hence they should be included in models aimed at elucidating the mechanical response detected at the micrometer scale [19]. Interestingly enough, the simulations also unveiled that significantly softer domains, typically associated to the mechanical heterogeneities, are significantly more liable to local rearrangements, while the stiffer domains constitute the high

stiffness backbone of the microstructure [14]. These findings suggest that the nano-scale mechanical and structural heterogeneities may also be at the origin of the physical mechanisms responsible for the aging and the stress relaxation in the C-S-H gels.

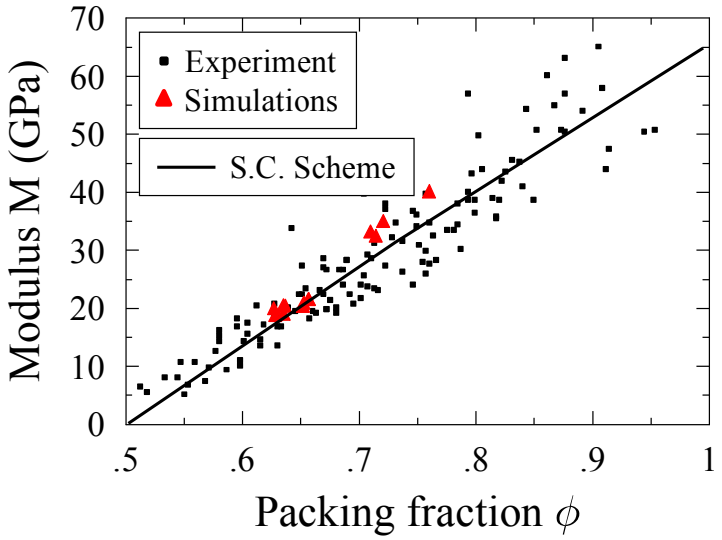

Figure 2. Comparison of the simulations results for the indentation modulus of the structurally heterogeneous dense gel branches and nanoindentation experimens (from Ref. [15]).

CONCLUSION

We have given an overview of recent developments obtained in investigating aggregation, gelation and development of mechanical properties in cement hydrates thanks to a statistical physics approach that addresses specifically their mesoscale texture. The results highlight the role of structural and mechanical heterogeneities emerging from the complex interplay between the out-of-equilibrium physico-chemical environment and the effective interactions between the nano-scale units of the material. This first attempt to rationalize the structural and mechanical complexity of cement hydrates over sub-micron lengthscales opens the way to new scientific developments in cement and concrete science.

AKNOWLEDGMENTS

The authors acknowledge support from the Swiss National Science Foundation (SNSF) (Grants No. PP00P2_150738), Schlumberger (SDR Cambridge, U.S./SRPC Clamart, France) and the CSHub at MIT.

REFERENCES

[1]R.J.M. Pellenq, H. Van Damme, MRS Bull. **29** (5), 319 (2004)

[2]R.J. Flatt, N.Roussel, C.R. Cheeseman, J. Eur. Ceram. Soc. **32** (11), 2787 (2012)

[3] A. Nonat, Cem. Con. Res. **34** (9), 1521 (2004)

[4] A.J. Allen, J.J. Thomas, H.M. Jennings, Nature Mater. 6, 311 (2007)

[5]L.B. Skinner, S.R. Chae, C.J. Benmore, H.R. Wenk, P.J.M. Monteiro, Phys. Rev. Lett. **104**, 195502 (2010)

[6] J.J. Thomas, H.M. Jennings, Cem. Con. Res. **36**, 30 (2006)

[7] J.W. Bullard, H.M. Jennings, R.A. Livingston, A. Nonat, G.W. Scherer, J.S. Schweitzer, K.L. Scrivener, J.J. Thomas, Cem. Con. Res. **41**, 1208 (2011)

[8] S.Bishnoi, K.L. Scrivener, Cement and Concrete Research **39**, 266 (2009)

[9] R.J.M. Pellenq, J.M. Caillol, A.~Delville, The Journal of Physical Chemistry B **101**, 8584 (1997)

[10]B. Jonsson, A.Nonat, C.Labbez, B.Cabane, H.Wennerstrom, Langmuir **21,** 9211 (2005)

[11]R.M. Pellenq, N.Lequeux, H.Vandamme, Cem. Con. Res. **38,** 159 (2008)

[12] K.Ioannidou, R.J.M. Pellenq, E. Del Gado, Soft Matter **10,**1121 (2014)

[13] E. Masoero, E. Del Gado, R.J.M. Pellenq, F.J. Ulm, S. Yip, Phys. Rev. Lett. **109**, 155503 (2012) □

[14] E. Masoero, E. Del Gado, R.J.M. Pellenq, S. Yip, F.J. Ulm, Soft Matter **10**, 491 (2014)

[15] E. Del Gado, K. Ioannidou, E. Masoero, A. Baronnet, R.J. Pellenq, F.-J. Ulm and S. Yip, Eur. Phys. J. Special Topics **223**, 2285 (2014).

[16] J.F. Lutsko, J. Appl. Phys. **65**, (1989)

[17] G. Constantinides, F.J. Ulm, J. Mech. Phys. Solids **55**, 64 (2007)

[18] M. Vandamme, F.J. Ulm, Proc. Nat. Acad. Sci. **106**, 10552 (2009)

[19] E. Masoero, J.J. Thomas, H.M. Jennings, J. Am. Ceram. Soc (2013)

C-S-H across Length Scales: From Nano to Micron

M. J. Abdolhosseini Qomi[1]; E. Masoero[2]; M. Bauchy[3]; F.-J. Ulm[1,4]; E. Del Gado[5]; and R. J.-M. Pellenq[1,4,6]

[1]Concrete Sustainability Hub, Department of Civil and Environmental Engineering, Massachusetts Institute of Technology, 77 Massachusetts Ave., Cambridge, MA 02139. E-mail: javad@mit.edu; ulm@mit.edu
[2]School of Civil Engineering and Geosciences, Newcastle University, Newcastle upon Tyne, NE1 7RU, U.K. E-mail: Enrico.Masoero@newcastle.ac.uk
[3]Department of Civil and Environmental Engineering, University of California, Los Angeles, CA 90095. E-mail: bauchy@ucla.edu
[4]<*MSE*>[2], the MIT-CNRS Joint Laboratory at Massachusetts Institute of Technology, 77 Massachusetts Ave., Cambridge, MA 02139. E-mail: pellenq@mit.edu
[5]Department of Physics, Georgetown University, Washington, DC 20057. E-mail: ed610@georgetown.edu
[6]Centre Interdisciplinaire des Nanosciences de Marseille, CNRS and Aix-Marseille University, Campus de Luminy, Marseille, 13288 Cedex 09, France.

Abstract

Despite their impact on longevity, serviceability, and environmental footprint of our built infrastructure, the chemo-physical origins of nanoscale properties of cementitious materials, and their link to macroscale properties still remain rather obscure. Here, we discuss a multi-scale approach that describes different aspects of physical properties of C-S-H at the nano- and meso-scales. These include dynamics of water, thermal properties and mechanical behavior of C-S-H and its effect on properties of cement paste at different scales.

INTRODUCTION

With an average annual consumption rate of one cubic meter per capita, concrete is the most used man-made material on Earth. This unrestrained consumption of concrete contributes to 5–10% of annual worldwide anthropogenic emissions. This environmental footprint necessitates the enhancement of concrete's physical properties by either optimizing the clinker phases(Manzano et al. 2011) or the molecular-level properties of calcium-silicate-hydrates (C-S-H), the binding phase of concrete. The complexity of physical properties of C-S-H is in parts associated with its hierarchical multiscale structure (see Figure 1.a-c). One can recognize at least three separate length scales in C-S-H, when conceptualized in a 3-level hierarchical thought-model, Figure 1. At the nanoscale, molecular properties of individual phases become available via tools of statistical physics. Both neutron scattering(Allen et al. 2007; Chiang et al. 2012) and statistical nano-indentation

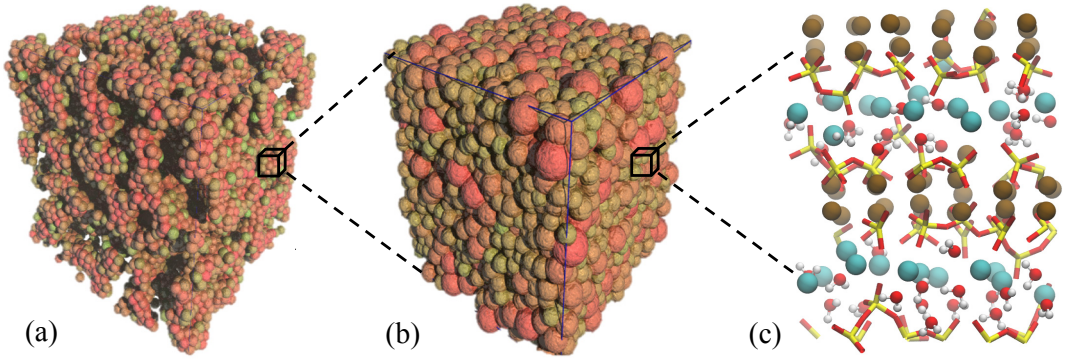

Figure 1: a) A snapshot of C-S-H's meso-scale structure at the early stages. b) A snapshot of a dense region of CSH at the meso-scale. c) The molecular structure of CSH at the nano-scale.

experiments(Constantinides and Ulm 2007) provide growing evidences that C-S-H has a nanogranular meso-texture (see Figure 1.b). In this light, the C-S-H gel at mesoscale is considered to be comprised of poly-disperse nanoscale C-S-H particles(Masoero et al. 2012). At micro-scale, the C-S-H gel is regarded as an isotropic and homogeneous material with gel porosity that holds anhydrous cement clinkers and the other hydration products together, which is consistent with a composite view of cement paste. In this sense, we regard laboratory measurements as the homogenized response of this multiscale porous composite at engineering macroscale. In this paper, we focus on understanding the physical origins of macroscopic physical properties of cement paste starting from the atomic scale. The paper is organized into five sections. First, we describe the molecular structures of C-S-H phases in cement paste and provide details of atomistic simulations and force fields. Next, We explore the water dynamics across length scales in terms of diffusion coefficients. Afterwards, we discuss the thermal properties at different length scales. This is followed by a discussion on the effect of C-S-H density on the mechanical properties of C-S-H at the nano- and meso-scale. Finally, conculsive remarks close the paper.

THE MOLECULAR STRUCTURE OF C-S-H

The nano-texture of C-S-H strongly depends on its chemical composition. In addition to 11Å tobermorite, we utilize a set of 150 molecular models constructed to cover a wide range of calcium-to-silicon ratio (Ca/Si) spanning from 1.1 to 2.1(Abdolhosseini Qomi et al. 2012, 2014; Qomi et al. 2014). Following a combinatorial scheme, these models are constructed by structural and chemical modification of 11Å tobermorite(Hamid 1981). The Ca/Si ratio of 11Å tobermorite is systematically increased by randomly removing charge-neutralized SiO_2 groups from its infinitely long silica chains. We create 5 models for each Ca/Si ratio to ensure proper statistical sampling by altering the arrangement of vacancies. As shown in Figure 1.c, C-S-H is consisted of negatively-charged defective calcium-silicate layers separated by an inter-layer spacing, which is filled with water molecules and charge-

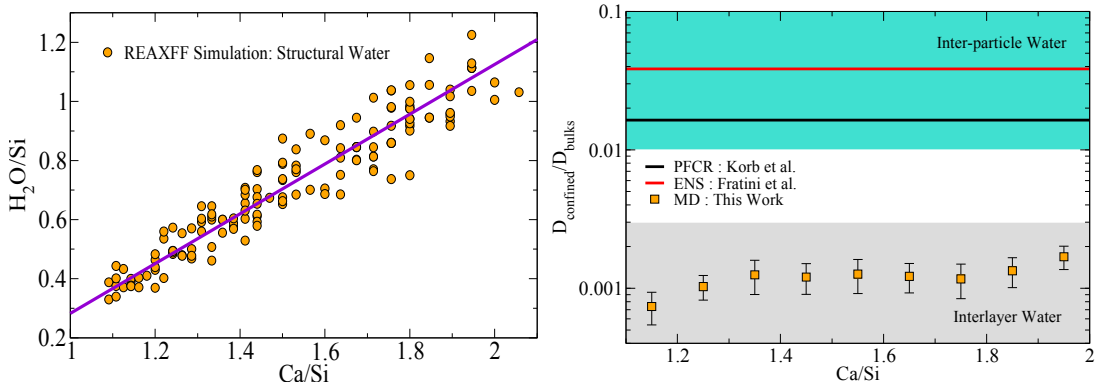

Figure 2: Water dynamics across length scales. a) Water content in C-S-H nano-structure as a function of Ca/Si ratio. b) Diffusion coefficient of water in C-S-H's nano and meso confinements.

balancing calcium cations. Vacancies in the silicate chains provide possible adsorption sites for water molecules. The adsorption of water molecules in defect sites was performed via Grand Canonical Monte Carlo (GCMC) simulation ensuring equilibrium with bulk water at constant volume and room temperature. Some of the above-mentioned adsorbed water molecules are chemically unstable and dissociate into hydroxyl groups and protons upon first principle or reactive force field modeling(Abdolhosseini Qomi et al. 2014). REAXFF potential is subsequently utilized to enforce reaction between the inter-layer water molecules and defective calcium-silicate layers. Figure 2.a presents the number of unreacted water molecules in terms of Ca/Si ratio. These molecular structures are extensively validated against Nuclear Magnetic Resonanace, Elastic and Inelastic Neutron Scattering, X-ray Diffraction and drying experiments (for further details on model constructions and validations see abdolhosseini et. al(Abdolhosseini Qomi et al. 2014; Bauchy et al. 2014d; a; Qomi et al. 2014). These realistic molecular structures are consistent with the averaged stoichiometry of $Ca_xSiO_{2.75}$ $(OH)^{Ca}_{0.85(x-1)}$ $(OH)^{Si}_{1.15(x-1)+0.5}$ $[0.8(x-1)+0.3]H_2O$, where x is the Ca/Si ratio and $(OH)^{Ca}$ and $(OH)^{Si}$ represent hydroxyl groups coordinated to inter-layer calcium atoms and silica groups, respectively. The collective topological observation of these 150 models indicates that, while at low Ca/Si ratios (Ca/Si<1.2) C-S-H exhibits a lamellar crystalline structures with strong transversely isotropic mechanical response , the structure of C-S-H at high Ca/Si ratios (Ca/Si>1.7) is fairly amorphous exhibiting isotropic mechanical properties.

ATOMISTIC SIMULATION AND FORCE FIELDS

In this work, we use molecular dynamics (MD), energy minimization and phonon analysis techniques to study thermal properties CSH using LAMMPS(Plimpton 1995), Gulp(Gale 1997; Gale and Rohl 2003) and a series of in-house codes. In MD, the equations of motion were integrated via the Velocity-Verlet algorithm with periodic boundary conditions applied in all directions. After performing extensive convergence studies, the suitable time steps were found to be as small as 0.1 fs for C-S-H. The size of C-S-H simulation boxes are 5 to 6 times larger

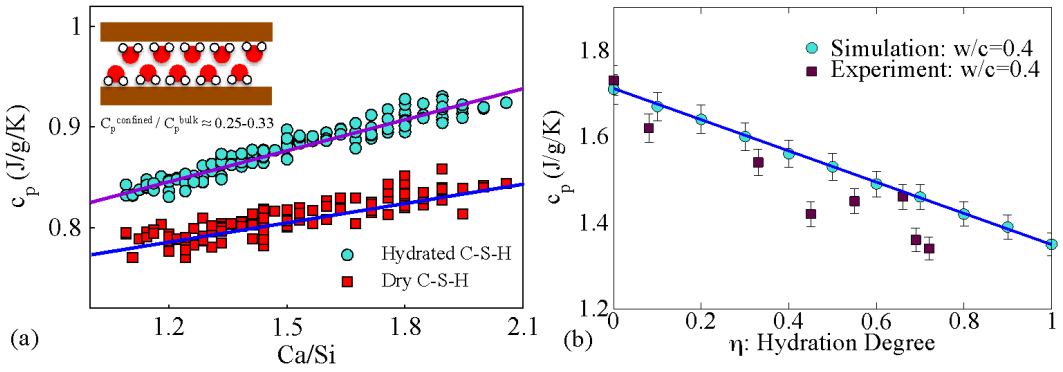

Figure 3: Thermal properties across length scales. a) The effect of Ca/Si ratio on the specific heat capacity of C-S-H at the nano-scale. b) The evolution of heat capacity of cement paste during the hydration process.

than the characteristic medium range length scale of calcium oxide layers and silica chains (Abdolhosseini Qomi et al. 2014). Therefore, we expect no size effect in our simulations. Initially, all C-S-H models were relaxed in isobaric isothermal ensemble (NPT) at room temperature and pressure of 0 atm. To exclude the impact of fictitious forces on the trajectories of atoms affecting velocities and heat fluxes along the MD trajectory, further simulations were carried out in the microcanonical ensemble (NVE). In order to properly calculate the statistical errors for each model, 10 independent simulations are performed, each 10^6 time steps long. Core-only CSH-FF (Shahsavari et al. 2011) potential was used in. To avoid the computational expenses incurred by the calculation of coulombic interactions in real and reciprocal spaces, such interactions are calculated via the Wolf method (Wolf et al. 1999).

WATER DYNAMICS

The self-diffusivity of water in the interlayer of C-S-H, DC–S–H, is normalized by that of bulk SPC water at 300 K, DH2O , 4.17 × 10−9 m2 s−2 . As show in Figure 2.b, DC–S–H increases linearly in the crystalline domain and maintains a constant value at the glassy regimes. Due to the high H2O/Si ratio at very high Ca/Si ratios, the self-diffusivity increases further because of the screening effect. DC–S–H in high Ca/Si ratio, 0.0018 × DH2 O , is almost three times higher than that of low Ca/Si ratio, 0.0006 × DH2 O . This highlights the effect of substrate composition on the diffusion of water molecules in the ultraconfined hydrophilic environments. On average, the self-diffusivity of water in the interlayer spacing inside C–S–H particles is thousand times slower than that of bulk water. This emphasizes that part of the mobile interlayer water diffuses with significantly slow dynamics, however distinguishable from the dynamics of immobile water and hydroxyl groups. It is noteworthy that water in tobermorite minerals (Ca/Si < 1) is immobile as it does not have translational motion at the scale of 10 ns (water molecules experience liberating motion). This means that tobermorite minerals cannot provide insightful information for studying water in C–S–H with common composition of Ca/Si = 1.7. In C–S–H, the diffusion of mobile interlayer water is different from inter-particle water molecules and those on the surface of larger pores.

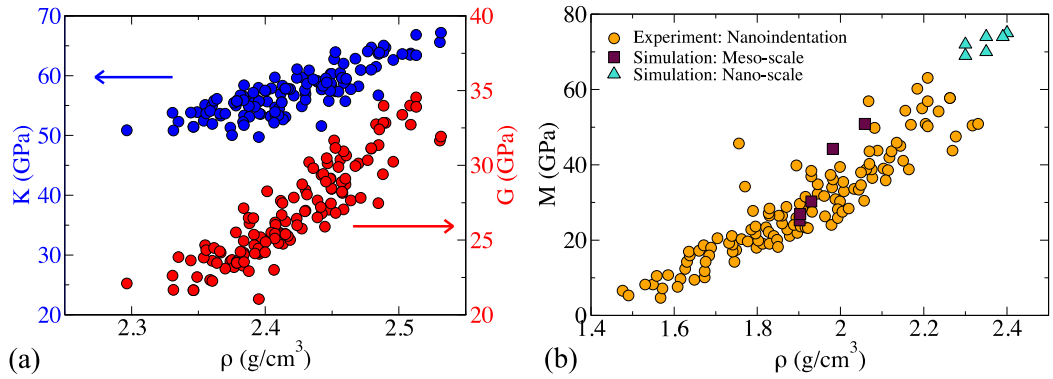

Figure 4: Mechanical properties across length scales. a) The effect of density on the bulk and shear moduli of C-S-H at the nano-scale. b) The effect density on the mechanical properties of CSH gel at the meso-scale.

The values of self-diffusivities presented in this study are at least one order of magnitude less than that measured by PFCR by Korb et al.(Korb et al. 2007a) ($D_{H2O}/80$) and Incoherent Elastic Neutron Scattering measurements of Fratini et al.(Fratini et al. 2013) ($D_{H2O}/60$). Recent ENS experiments suggest that slow self-diffusion in the paste is associated with inter-particle water(Kalinichev et al. 2007). PFCR experiments are interpreted to capture the dynamical behavior of water adsorbed on the pore surfaces(Korb et al. 2007a). In particular, Kalinichev et al.(Kalinichev et al. 2007) reported MD simulation of adsorbed water on [100] surfaces of anomalous tobermorite with self- diffusions comparable to that of Korb et al.(Korb et al. 2007b) Since the inter- particle pore-size distribution is shown to be significantly larger than interlayer spacing, the significant difference in characteristic length of confinement explains the difference between the self-diffusion inside and in between C–S–H grains.

THERMAL PROPERTIES

Figure 3.a displays the specific heat capacity of both dry (all molecular inter-layer water removed), c_p^{dry}, and hydrated, c_p^{hyd}, C-S-H in function of Ca/Si ratio. The specific heat capacities in both dry and hydrated samples increase almost linearly with Ca/Si with a minor scatter attributable to the polymorphic structure of C-S-H(Abdolhosseini Qomi et al. 2014). Similar to the experimentally observed increase in heat capacity of rocks(Clauser and Huenges 1995) and Vycor glass(Tombari et al. 2005), the heat capacity of hydrated C-S-H is higher than that of dry samples. The constant pressure specific heat capacities can be written in the form of c_p^{dry}=0.66x+0.75$ and c_p^{hyd}=1.00x+0.75, where x is the Ca/Si ratio. The difference between dry and hydrated samples indicates the effect of inter-layer water on the heat capacity of C-S-H. In fact, the apparent heat capacity of nano-confined water can be considered as the difference between the specific heat capacities of wet and dry C-S-H. The inset of Figure 3.a shows the relation between the normalized apparent heat capacity of the nanoconfined water. The heat capacity of water in the ultra-confining interlayer spacing of C-S-H (d<1.0 nm) is noticeably smaller than that of bulk water

at room temperature, roughly 4.2 J/g/K. This is in full agreement with Bentz's postulate stating that the heat capacity of chemically and physically bound water within the hydration gel should be significantly lower than that of bulk water(Bentz 2007). Similar to dynamical properties presented in Figure 2.b, the heat capacity of nanoconfined water in C-S-H and its trend with density behaves like supercooled water. In fact, although being at room temperature, the heat capacity of nano-confined water is on the order of those observed at 150 K(Angell 2008). This is mainly due to the strong interactions between the water molecules and the substrate(Qomi et al. 2014). By considering the hydration reaction and using the specific heat capacity values of the individual phases in the cement paste, the constant pressure specific heat capacity of hydrating cement paste can be estimated in terms of hydration degree(Abdolhosseine Qomi et al. 2015). Figure 3.b presents the constant pressure specific heat capacities of three hydrating cement pastes with water-to-cement ratios (w/c) of 0.4 and its comparison with macroscopic experimental measurements of Bentz(Bentz 2007). According to the mixture rule, simulation results are necessarily linear in terms of hydration degree and are in good agreement with the experimental measurements. The slight difference between the experiment and simulation are attributed to the presence of other phases in OPC systems and the difference between the properties of bulk and interfacial water. Nevertheless, both simulation and experiments indicate that the heat capacity of the paste decreases with increasing hydration degree. This can be understood by proper consideration of the role of water during the course of hydration. The specific heat capacity of bulk water is considerably high (4.18 J/g/K), which makes the heat capacity of the mixture of water and clinker relatively high. Throughout the hydration process, the water is consumed to precipitate C-S-H, which has significantly lower specific heat capacity (see Figure 3.a). Also, part of this water is trapped within the C-S-H's molecular structure, which exhibits features of super-cooled water with considerably lower specific heat capacity compared to that of room temperature bulk water (see the inset of Figure 3.a).

MECHANICAL PROPERTIES

Based on our atomistic simulation, the density of C-S-H at the atomic scale decreases linearly with increasing Ca/Si ratio(Abdolhosseini Qomi et al. 2013; Bauchy et al. 2014d; a; b; c, 2015). This is merely because by removing a chage-neutralized SiO_2 group, two water molecules are adsorbed in the interlayer of C-S-H. However, two water molecules are lighter than a SiO_2 group, which results in lowering the density. Here, we have calculated the Voight-Reuss-hill bounds of both shear and bulk moduli for all of the C-S-H models (see Figure 4.a). As we expect, the elastic properties of C-S-H at the nano-scale decrease linearly with decreasing density. In fact, this signals that tuning the density of C-S-H is the key to achieve high mechanical properties. This conclusion is also valid at the meso-scale (see Figure 4.b). The indentation modulus of C-SH at the meso-scale also decreases with decreasing density of C-S-H. In fact, the results of our meso-scale models are in good agreement with that of experimental nano-indentation analysis without the use of micro-mechanical back-analysis. It is noteworthy to mention that the both the

simulation and experiment point to the results of the atomistic simulation with density of 2.4 g/cm^3.

CONCLUSION

In this work, we discussed the structure of C-S-H across length scales, from nano to meso-scale. We described how does the nano- and meso-texture of C-S-H affect the physical properties of C-S-H. We showed that the water mobility in the nano-pores of C-S-H are at least one order of magnitude slower than that of meso-pores. The heat capacity of both dry and saturated C-S-Hs are found to scale linearly with Ca/Si ratio. The heat capacity of nano-confined water is found to be three to four times smaller that of bulk water. The mechanical properties of C-S-H are found to scale linearly with density both at the nano- and meso-scales.

ACKNOWLEDGEMENTS

This work was supported the MIT-Schlumberger XCEM research program and by the CSHub@MIT. This work has been partially carried out within the framework of the ICoME2 Labex (ANR-11-LABX-0053) and the A*MIDEX projects (ANR-11-IDEX-0001-02) co-funded by the French program ”Investissements d’Avenir” which managed by the ANR, the French National Research Agency.

REFERENCES

Abdolhosseine Qomi, M. J., Ulm, F.-J., and Pellenq, R. J.-M. (2015). “The Physical Origins of Thermal Properties of Cement Paste.” *Physical Review Applied*, at press.

Abdolhosseini Qomi, M. J., Bauchy, M., Pellenq, R. J.-M., and Ulm, F.-J. (2013). “Applying Tools from Glass Science to Study Calcium-Silicate-Hydrates.” *Mechanics and Physics of Creep, Shrinkage, and Durability of Concrete: A Tribute to Zdenk P. Bazant*, American Society of Civil Engineers, 78–85.

Abdolhosseini Qomi, M. J., Krakowiak, K. J., Bauchy, M., Stewart, K. L., Shahsavari, R., Jagannathan, D., Brommer, D. B., Baronnet, A., Buehler, M. J., Yip, S., Ulm, F.-J., Van Vliet, K. J., and Pellenq, R. J.-M. (2014). “Combinatorial molecular optimization of cement hydrates.” *Nature Communications*, 5:4960 doi: 10.1038/ncomms5960.

Abdolhosseini Qomi, M. J., Ulm, F.-J., and Pellenq, R. J.-M. (2012). “Evidence on the dual nature of aluminum in the calcium-silicate-hydrates based on atomistic simulations.” *Journal of the American Ceramic Society*, 95(3), evidence on the dual nature of aluminum in the calcium–silicate–hydrates based on atomistic simulations.

Allen, A. J., Thomas, J. J., and Jennings, H. M. (2007). "Composition and density of nanoscale calcium–silicate–hydrate in cement." *Nature Materials*, 6(4), 311.

Angell, C. A. (2008). "Insights into Phases of Liquid Water from Study of Its Unusual Glass-Forming Properties." *Science*, 319(5863), 582–587.

Bauchy, M., Abdolhosseini Qomi, M. J., Bichara, C., Ulm, F.-J., and Pellenq, R. J.-M. (2014a). "Nanoscale Structure of Cement: Viewpoint of Rigidity Theory." *The Journal of Physical Chemistry C*, 118(23), 12485–12493.

Bauchy, M., Laubie, H., Qomi, M. J. A., Hoover, C. G., Ulm, F.-J., and Pellenq, R. J.-M. (2014b). "Fracture toughness of calcium-silicate-hydrate grains from molecular dynamics simulations." *arXiv:1410.2915 [cond-mat]*.

Bauchy, M., Qomi, M. J. A., Bichara, C., Ulm, F.-J., and Pellenq, R. J.-M. (2014c). "Topological Origin of Fracture Toughening in Complex Solids: the Viewpoint of Rigidity Theory." *arXiv:1410.2916 [cond-mat]*.

Bauchy, M., Qomi, M. J. A., Bichara, C., Ulm, F.-J., and Pellenq, R. J.-M. (2015). "Rigidity Transition in Materials: Hardness is Driven by Weak Atomic Constraints." *Physical Review Letters*, 114(12), 125502.

Bauchy, M., Qomi, M. J. A., Ulm, F.-J., and Pellenq, R. J.-M. (2014d). "Order and disorder in calcium–silicate–hydrate." *The Journal of Chemical Physics*, 140(21), 214503.

Bentz, D. P. (2007). "Transient plane source measurements of the thermal properties of hydrating cement pastes." *Materials and Structures*, 40(10), 1073–1080.

Chiang, W.-S., Fratini, E., Baglioni, P., Liu, D., and Chen, S.-H. (2012). "Microstructure Determination of Calcium-Silicate-Hydrate Globules by Small-Angle Neutron Scattering." *The Journal of Physical Chemistry C*, 116(8), 5055–5061.

Clauser, C., and Huenges, E. (1995). "Thermal Conductivity of Rocks and Minerals." *Rock Physics & Phase Relations*, T. J. Ahrens, ed., American Geophysical Union, New York, NY, 105–126.

Constantinides, G., and Ulm, F.-J. (2007). "The nanogranular nature of C–S–H." *Journal of the Mechanics and Physics of Solids*, 55(1), 64–90.

Fratini, E., Faraone, A., Ridi, F., Chen, S.-H., and Baglioni, P. (2013). "Hydration Water Dynamics in Tricalcium Silicate Pastes by Time-Resolved Incoherent Elastic Neutron Scattering." *The Journal of Physical Chemistry C*, 117(14), 7358–7364.

Gale, J. D. (1997). “GULP: A computer program for the symmetry-adapted simulation of solids.” *Journal of the Chemical Society-Faraday Transactions*, 93(4), 629–637.

Gale, J. D., and Rohl, A. L. (2003). “The General Utility Lattice Program (GULP).” *Molecular Simulation*, 29(5), 291–341.

Hamid, S. (1981). “The crystal-structure of the 11A natural tobermorite Ca2.25[Si3O7.5(OH)1.5].1H2O.” *Zeitschrift Fur Kristallographie*, 154(3-4), 189–198.

Kalinichev, A. G., Wang, J., and Kirkpatrick, R. J. (2007). “Molecular dynamics modeling of the structure, dynamics and energetics of mineral–water interfaces: Application to cement materials.” *Cement and Concrete Research*, 37(3), 337–347.

Korb, J.-P., McDonald, P. J., Monteilhet, L., Kalinichev, A. G., and Kirkpatrick, R. J. (2007a). “Comparison of proton field-cycling relaxometry and molecular dynamics simulations for proton–water surface dynamics in cement-based materials.” *Cement and Concrete Research*, 37(3), 348–350.

Korb, J.-P., Monteilhet, L., McDonald, P. J., and Mitchell, J. (2007b).“Microstructure and texture of hydrated cement-based materials: A proton field cycling relaxometry approach.” *Cement and Concrete Research*, 37(3), 295–302.

Manzano, H., Durgun, E., Abdolhosseine Qomi, M. J., Ulm, F.-J., Pellenq, R. J. M., and Grossman, J. C. (2011). “Impact of chemical impurities on the crystalline cement clinker phases determined by atomistic simulations.” *Crystal Growth & Design*, 11(7), 2964–2972.

Masoero, E., Del Gado, E., Pellenq, R. J.-M., Ulm, F.-J., and Yip, S. (2012). “Nanostructure and nanomechanics of cement: polydisperse colloidal packing.” *Physical Review Letters*, 109(15), 155503.

Plimpton, S. (1995). “Fast parallel algorithm for short range Molecular Dynamics.” *Journal of computational physics*, 117(1), 1–19

Qomi, M. J. A., Bauchy, M., Ulm, F.-J., and Pellenq, R. J.-M. (2014). “Anomalous composition-dependent dynamics of nanoconfined water in the interlayer of disordered calcium-silicates.” *The Journal of Chemical Physics*, 140(5), 054515.

Shahsavari, R., Pellenq, R. J.-M., and Ulm, F.-J. (2011). “Empirical force fields for complex hydrated calcio-silicate layered materials.” *Physical chemistry chemical physics: PCCP*, 13(3), 1002–1011.

Tombari, E., Salvetti, G., Ferrari, C., and Johari, G. P. (2005). “Heat capacity of water in nanopores.” *The Journal of Chemical Physics*, 123(21), 214706.

Wolf, D., Keblinski, P., Phillpot, S. R., and Eggebrecht, J. (1999). “Exact method for the simulation of Coulombic systems by spherically truncated, pairwise r−1 summation.” *The Journal of Chemical Physics*, 110(17), 8254–8282.

Coupled Effects between Damage and Permeability with a View to Discrete Modelling

G. Pijaudier-Cabot; F. Khaddour; D. Grégoire; and L. Ecay

Laboratoire de Fluides Complexes et leurs Réservoirs, UMR 5150 UPPA – CNRS – Total, Allée du Parc Montaury, F-64600 Anglet, France. E-mail: Gilles.Pijaudier-Cabot@univ-Pau.fr

Abstract

The purpose of this work is to achieve a better understanding of the relationship between mechanical damage and the transport properties of cementitious materials. In the literature, analyses are usually restricted to intrinsic permeability of the material and the evolution of the apparent permeability with respect to the pressure gradient and to the nature of the fluid considered are left aside. A new model capable to provide the apparent permeability of a porous material to gas, directly from the pore size distribution and from the properties of the gas is discussed. Comparisons with experimental data on mortar specimens show that the model can reproduce the intrinsic permeability and its evolution when the material is subjected to mechanical damage, provided the pore size distributions are available. For a given pore size distribution, the evolution of the apparent permeability is also provided and test data with several types of gases compare quite well with the model.

INTRODUCTION

In this work, we aim at a better understanding of the relationship between damage, and the transport properties in cementitious materials, namely permeation of gas. This is typically of utmost importance in the long-term assessment of tightness of vessels and containment facilities.

Many authors have looked for predictive models of porous media permeability based on the pore size distribution of the material. Pioneering work by Kozeny [1] related the permeability to the porosity, to the tortuosity and to an average pore size and later on Katz & Thompson [2] predicted the permeability from the electrical conductivity of the porous material through a critical pores radius. There are also several studies in which the pore size distribution was modeled, e.g. with a bimodal [3] or multimodal distribution [4], and then entered into some capillary bundle model. Recently, models for the calculation of the intrinsic permeability derived directly from the experimental PSD, without any idealization have been also discussed [5]. Here, we shall follow this approach which requires (i) to transform the pore size distribution into a hydraulic network, and (ii) to solve the equations governing fluid flow once the hydraulic network has been set.

As far as the porous network in the material is concerned, we shall use here a description that is consistent with the Pore Size Distribution (PSD) characterization technique used for this study, mercury intrusion. The pore network is not defined in the material space, e.g. with a distribution of pores connected to each other following a topological distribution characterised e.g. by microtomography, but rather following a stochastic hierarchical bundle model. The technique yields a pore network, which mimics the porous space measured experimentally.

Usually, analyses are restricted to the intrinsic permeability of the material and to the evolution of the apparent permeability, with respect to the pressure gradient. Here, the model is capable to provide estimates of the apparent permeability directly from the pore size distribution and from the properties of the fluid. The intrinsic permeability and the evolution of the apparent permeability with mean pressure are provided by combining Darcy's law [6], which represents the flow in the porous media at the macroscale and a combination of Poiseuille [7] and Knudsen laws [8], which represent respectively viscous flow and diffusion flow at the microscale. For typical gases, the contributions of laminar flow and of Knudsen diffusion are of the same order for pores of diameter in the range of a few hundred of nanometers [9].

Comparisons with experimental data on mortar specimens show that the model can reproduce the intrinsic permeability and its evolution when the material is subjected to mechanical damage, provided the pore size distributions are available at each level of damage. For a given pore size distribution, the evolution of the apparent permeability is also obtained, for several gases, and compares quite well with experiments. The model provides also the condition of permeation of mixture of two gases. Knudsen effect being different for each species, selective permeation is obtained and preliminary comparisons with experiments are provided.

STOCHASTIC HIERARCHICAL BUNDLE MODEL

We consider here that the microstructure of the porous material consists in cylindrical pores of different lengths and diameters. Assuming that the porous space has been characterized in term of PSD by mercury intrusion technique, we may link, for each pore size, the pore length to the pore volume fraction.

A simple assembling technique consists in distributing all the pores of a given size (or interval of size) in parallel and in a regular manner, assuming that all pores have an identical length corresponding to the cubic root of the total porous volume times the tortuosity. Predictions of permeability based on such parallel assembly of pores have been discussed in [5], and it was observed that tuning parameters were required in order to obtain relevant results in term of apparent and intrinsic permeability. Large pores drive the permeability and since the model assumes that they cannot be connected to smaller ones, their effect on permeability has to be moderated.

We thus developed a different approach where the different pores sizes are organized randomly within the material and are randomly connected to each other, while

satisfying the PSD description under the condition that a given pore may only be connected to a smaller one.

Let V_t be the total porous volume, characterized by mercury intrusion, which may be organized according to the PSD into a series of volumes V_{pi} of mean diameter d_i. Hence, we discretize the PSD into a finite set of pore diameters, $i = 1,2, \ldots n$. We may now relate, for each pore size, the total pore length L_i to the pore diameter d_i and to the pore volume fraction V_{pi} assuming that pores are cylindrical:

$$L_i = \frac{4.V_{pi}}{\pi.{d_i}^2} \qquad (1)$$

This pore length is then cut into small segments of random length ΔL_i (see Figure 1.a). Their assembly is performed from larger pores to smaller pores. Each pore segment either creates a new assembling site (on which subsequent segment will be connected) or is connected to an existing one of larger or equal size on an existing assembling site (Figure 1.b). We then define the average pore length L_e and a critical length L_c as

$$L_e = \sqrt[3]{V_t}\,,\ L_c = T.L_e \quad T = \text{tortuosity} \qquad (2)$$

As soon as the sum of all pore segment lengths reaches the critical length on one assembling site, further segments cannot be added anymore and the permeability of the resulting capillary is estimated and added to the global permeability.

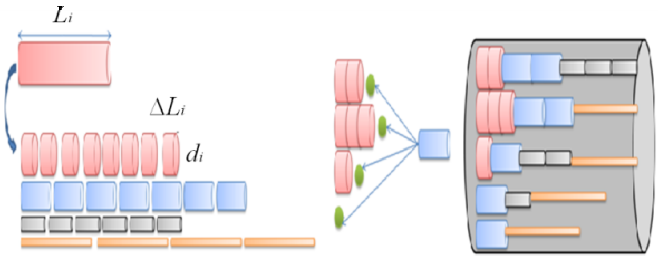

(a). Discretization of pores (b). Random assembly

Fig.1. Random network assembly of pores.

This random process is performed until the overall permeability does not change by adding a new assembled capillary (with some specified tolerance). This criterion is used to speed up the process: there is a huge amount of pore segments of very small diameter but they do not contribute so much to the global permeability, which is mostly driven by larger pores. As soon as this criterion is reached, the remaining porosity is organized according to a parallel capillary bundle, each capillary being of the same diameter. Their contribution is also taken into account in the global permeability.

Some adjustments need to be discussed with respect to the mercury intrusion technique from which the PSD is obtained. During mercury intrusion, two different phases are performed. Firstly, mercury is introduced at low pressure (from 0 MPa to 0.2 MPa) and large diameter pores are characterized. Secondly, mercury is introduced at high pressure (from 0.2 MPa to 200 MPa) in order to drive mercury into smaller pores. Unfortunately, the data obtained at low pressure are quite noisy and the distribution of sizes for very large pores is not characterized accurately. Since large pores drive the permeability, this may be very problematic in order to predict the permeability accurately. Usually, the solution to circumvent this artifact consists in removing the low-pressure information. Here we adopt another, less arbitrary technique, motivated by the fact that upon damage, pores (or cracks) of large aperture might contribute significantly to the permeability.

Figure 2.a presents a typical PSD response of a cementitious material (mortar). We observe both the low-pressure signal and the high-pressure one (in the range of 100 micrometers). In order to keep the relevant low-pressure information and at the same time to remove the noisy artifacts, we implement a specific filtering of the low-pressure information: let us consider the pores of size corresponding to the low-pressure measurements only. These pores are discretized randomly into segments of equal size. We now count the number of segments corresponding to these pore sizes. Figure 2.b shows this number for several random realizations. We observe that the number of segments lies below 10000 for the material that is typically considered in this study. Instead of removing these pores, we assume that each segment below this threshold of 10000 is forced to create a new assembling site. Consequently pores of such sizes cannot percolate throughout the material, unless the total number of segments is over the threshold.

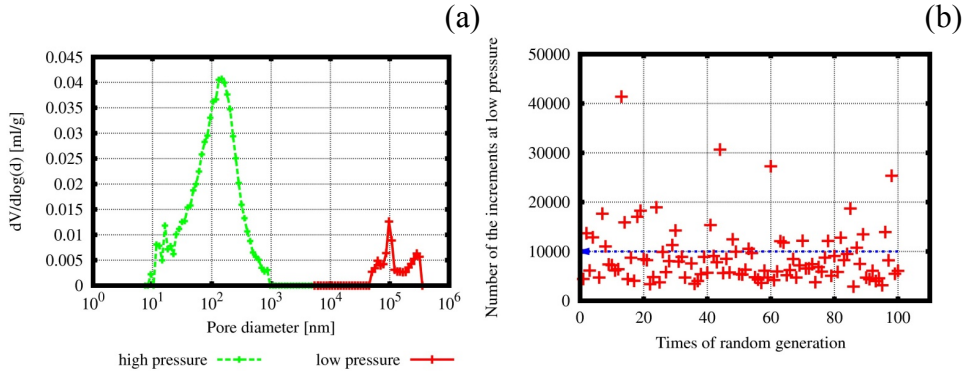

Fig. 2. Method of eliminating of the noise at low pressure for an undamaged sample: (a) pore size distribution corresponding to the low and high pressures; (b) statistical study of the low frequency for 100 random realizations.

In the hierarchical assembly forming the porous network, the random function that decides if the current pore segment should be connected to an existing site or will create a new site is weighted by the following exponential function:

$$f(x) = \exp\left(-\frac{x-B}{A}\right) \qquad (3)$$

where x is the index of the current pore segment dealt with, A and B are parameters. B controls the pore diameter from which new pore segments may be connected to existing assembling sites. If the index x is lower than B, the current pore segment is forced to create a new site. From the PSD in (Figure 2.a), the parameter B is chosen in such a way it assures that the first 10000 low-pressure pore segments are forced to create a new assembling site. Upon damage, if meaningful information appear in the low-pressure part of the PSD, the number of pore segments characterized under low pressure will increase and then they will be taken into account when $x>B$.

Parameter A controls the pore diameter from which new pore increments have almost no chance to create a new assembling site. Therefore, it controls indirectly the time at which the stochastic assembling of pore segments will start to be in parallel deterministically. Since the transition between a random assembly and a deterministic assembly is also driven by a criterion on the global permeability, the influence of parameter A is not determinant if this last criterion is met first (which is the case in our calculations).

FLUID FLOW IN THE PORE NETWORK

From a given hierarchical assembly of capillary pores, the objective is now to estimate not only the intrinsic but also the apparent permeability. The apparent permeability is obtained by combining Darcy's law, which represents the flow at the macro-scale, and Poiseuille and Knudsen laws, which represent the flow at the micro-scale.

Poiseuille's flow at the micro-scale

Let us consider a cylindrical pore of diameter d_i. The flow (i.e. volume of fluid per unit time) passing through the pore of length L_c is given by:

$$Q_P^v = \left(\frac{1}{2}\right)\frac{\pi}{128}\frac{d_i^4}{\mu}\frac{(P_1^2 - P_2^2)}{L_c\, P_2} \qquad (4)$$

where (P_1, P_2) are the upstream and downstream pressures respectively, Q_P^v is the volume of fluid estimated at the outlet pressure and μ is the fluid dynamic viscosity. This classical expression relies on the assumption of laminar flow [7].

Knudsen flow at the micro-scale

In the Knudsen region, the mass transfer of a gas occurs due to free-molecule flow [8]. This region is defined for each pore diameter from the Knudsen number N_i^{Kn}:

$$N_i^{Kn} > 1$$

$$N_i^{Kn} = \frac{\lambda}{d_i} = \left(\frac{1}{d_i}\right) \frac{R\ T}{\pi\ \sqrt{2}\ d_j^2\ N_{Av}\ P_m} \qquad (5)$$

where $(\lambda,\ d_j, P_m)$ are the average free path, the molecule diameter and the average pressure of the considered gas respectively, and (N_{Av}) is the Avogadro's number. When the Knudsen number is greater than one, the interaction between the walls of the pore and the gas, at the molecular level, are dominant and the fluid flow is quite different from Poiseuille's flow. The volume of fluid per unit time passing in the pore is:

$$Q_{Kn}^v = \frac{\pi}{12} \frac{d_i^3}{L_c} \sqrt{\left(\frac{8\ R\ T}{\pi\ \ M}\right)} \frac{\Delta P}{P_2} \qquad (6)$$

where $\Delta P = P_1 - P_2$ is the difference between the upstream and downstream pressures.
In the transition regime defined as $(0.01 < N_i^{Kn} < 1)$ the flow rate through a pore (i) due to a pressure gradient is given as the sum of Poiseuille flow (Eq. 4) and Knudsen flow (Eq. 6):

Macroscopic transport properties
At the macro-scale, the flow rate is described by Darcy's law [6]:

$$Q_D^v = \frac{K_a}{\mu} S \frac{\Delta P\ P_m}{L_e\ P_2} \qquad (7)$$

For hierarchical assembly of capillaries, the transport properties are obtained by adding the contribution of each capillary pore. Comparison between Eq. (7) and the equations at the micro-scale provides the expression of the apparent permeability K_a.

EXPERIMENTAL DATA AND COMPARISONS WITH THE MODEL

Experiments have been performed on mortars specimens with water/cement ratio of 0.7 and a maximum aggregate diameter of 3mm. Mortar hollow cylinders were cast in aluminum molds (outer diameter: 24.5mm; inner diameter: 6.5mm; height: 40 mm). Top and bottom surfaces were rectified and the samples were cured in a ventilated oven at 80°C at constant humidity during 48 hours.

The testing apparatus consists in a conventional electro-mechanical compressive machine coupled with a nitrogen permeameter in order to measure in-situ the permeability under loading [5]. The initial permeability is measured before applying a given compressive load corresponding to a given level of damage (measured by the variation of the Young's modulus of the material upon unloading [9,11]). Permeability is measured under load and after load. Several load levels are

considered, corresponding to several levels of damage ranging from 0% to 12% (in the pre-peak regime).

The apparent permeability has been measured by applying a pressure gradient and measuring the radial gas flow through the sample (see e.g.[11]):

$$K_a = \frac{Q_i\ \mu\ P_i \ln(\frac{R_2}{R_1})}{\pi\ h\ (P_i^2 - P_2^2)} \qquad (8)$$

where Q_i is the gas volumetric flow, (h, R_2, R_1) are the sample height, outer and inner diameters respectively and (P_i, P_2) are the gas upstream and downstream pressure respectively. Typically P_2 is the atmospheric pressure. In order to derive the intrinsic permeability from experimental data, the approach of Klinkenberg [10] is applied:

$$K_a = K_{in}\ (1 + \frac{\beta}{P_m}) \qquad (9)$$

where β is the coefficient of Klinkenberg, K_{in} is the intrinsic permeability and P_m is the mean pressure.

After complete unloading, the middle part of the sample (15mm over 40mm) is cut out in order to characterize the PSD. The PSD measurements has been performed by mercury intrusion (Micromeritics–AutoPore IV). Figure 3 shows the evolution of pore size distribution of different samples subjected to different mechanical damage (from 0 to 12%). Initially, a peak at 150nm is observed with no porosity higher than 1000nm. As damage increases, a slight shift of the PSD is observed between 1000nm and 3000nm. Moreover new porosity is created around 10000nm. This new porosity leads to the increase of the intrinsic permeability of two orders of magnitude.

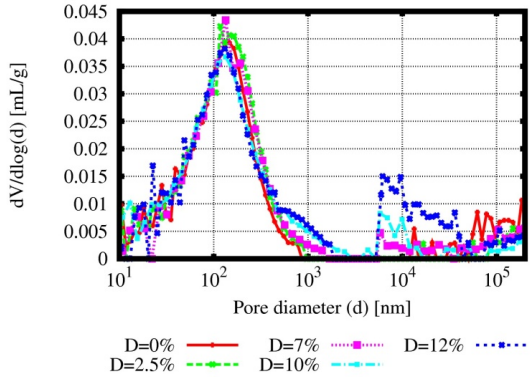

Fig. 3. Evolution of pore size distribution upon damage.

Figure 4 present a comparison between the measured and predicted intrinsic permeabilities and Klinkerberg coefficient evolutions upon damage from 0% to 12%. It is shown that the predicted values are in good agreement with the experimental

ones whatever the state of damage. Note that no tortuosity parameter has been introduced in the model (tortuosity equals 1).

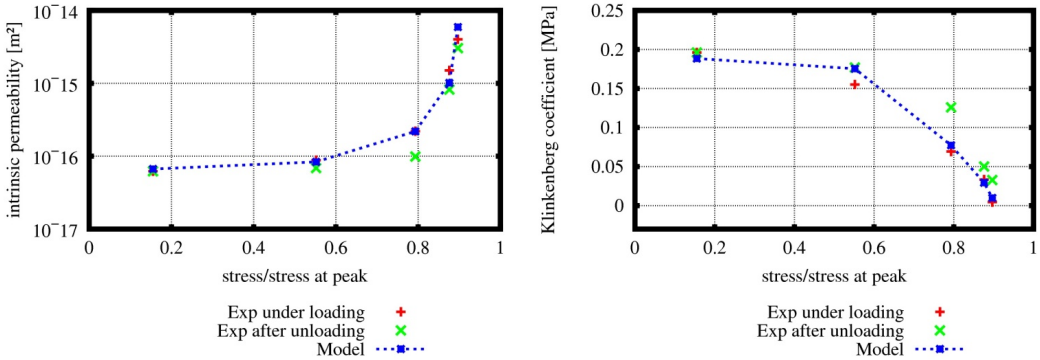

Fig. 4. Comparison between the measured and predicted intrinsic permeability (left) and Klinkenberg coefficients (right).

Figure 5 shows a comparison between the apparent permeability to nitrogen and to helium for an undamaged sample measured experimentally and computed according to the same PSD measured experimentally. We observe again a good agreement. It is important to notice that when performing the comparisons, no specific model parameter is set to predict the apparent permeability with the proposed model upon a change of the nature of the gas. Since the helium mean free path is greater than the nitrogen one, the slip flow effect is higher for helium and then the slope of the apparent permeability vs. mean pressure curve is also higher compared to the other gases.

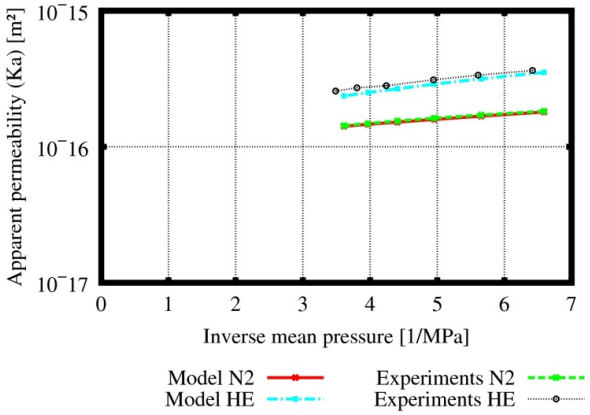

Fig. 5. Comparison between the model and the experimental results of apparent permeabilities for N2 and He.

CONCLUSIONS AND EXTENSIONS

A theoretical model aimed at computing the apparent permeability of a porous material to gas has been presented. The model uses the pore size distribution of the material as an input. The porous network is generated according to a hierarchical

scheme in which bundles of capillaries are assembled randomly. Within each capillary pore, fluid flow is described by a combination of Poiseuille Flow and Knudsen (diffusion) flow. The outcome at the macroscopic scale results into a Klinkerberg-type of apparent permeability.

The model has been compared with experiments on mortar subjected to compression. The theoretical model captures experimental trends very consistently. In addition, the same model is also capable of predicting the permeability of the material to a different gas, without any adjustment of the parameters.

This theoretical model can be extended to several cases, among which the permeability to a mixture of gases is a first step. According to Poiseuille flow, the separation of gases upon permeation through a porous material cannot occur. By separation, we mean that the composition of the mixture measured upstream, before entering the porous material, and downstream is not the same. Because Knudsen effect depends on the molecular sizes of each species, separation will occur and will depend on the relative amount of species. Hence, a deviation from the linear variation of the downstream molar fractions with the change of composition of the mixture upstream, obtained according to Poiseuille flow, is to be expected.

The experimental set-up has been modified in order to accommodate the case of a mixture of two gases and the analysis of the composition of the mixture upstream and downstream has been added. Figure 6 shows the case of He/CH_4 mixture considered as a test case. On the horizontal axis is plotted the molar fraction of He on the upstream face of the specimen. On the vertical axis are plotted the molar fraction of each gas downstream. Deviation from straight lines is due to Knudsen effect and show that the porous material separates the gas components.

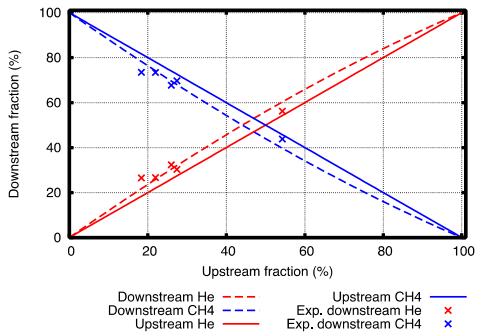

Fig. 6: Separation of He/CH_4 mixture (predicted and measure experimentally)

Further developments are currently being considered, investigating the case of a mixture of phases of the same fluid, for instance water and vapour where as opposed to He/CH_4, phase change may occur depending on the diameter of the pores and on the temperature and pressure conditions.

ACKNOWLEDGEMENTS

Financial supports from the *European Research Council* through the ERC advanced grant Failflow (27769), and from the French *Région Aquitaine* through the grant CEPAGE (20121105002) are gratefully acknowledged. F. Khaddour is grateful to the Syrian Ministry of Higher Education for its support (13153/4/W).

REFERENCES

1. Kozeny, J. 1927. Über Kapillare Leitung Des Wassers Im Boden [About capillary pipe of water in soil]. *Wien, Akad. Wiss*, 136: 271–306.
2. Katz, A. J. and A. H. Thompson. 1986. Quantitative prediction of permeability in porous rock. *Physical review B*, 34: 8179–8181.
3. Aït-Mokhtar, A., O. Amiri, P. Dumargue and S. Sammartino. 2002. A new model to calculate water permeability of cement materials from MIP results. *Magazine of Concrete Research*, 14: 43–49.
4. Amiri, O., A. Aït-Mokhtar and M. Sarhani. 2005. Tri-dimensional modelling of cementitious materials permeability from polymodal pore size distribution obtained by mercury intrusion porosimetry tests. *Magazine of Concrete Research*, 17: 39–45.
5. Khaddour, F., D. Grégoire and G. Pijaudier-cabot. 2012. Upscaling Permeation Properties in Porous Materials from Pore Size Distributions. In *Geomechanical Issues in CO2 Storage Facilities*, eds G. Pijaudier-Cabot and J.-M. Pereira, 44–56.
6. Darcy, H. 1856. *Les fontaines publiques de la ville de Dijon* [The public fountains of the city of Dijon]. Paris: Dalmont.
7. Poiseuille, J. 1840. Recherches expérimentales sur le mouvement des liquides dans les tubes de très petits diamètres [Experimental research on the movement of liquids in capillary of very small diameters]. *Comptes rendus hebdomadaires des séances de l'Académie des sciences*, T11: 1041–1048.
8. Steckelmacher, W. 1986. Knudsen flow 75 years on: the current state of the art for flow of rarefied gases in tubes and systems. *Rep. Prog. Phys*, 49: 1083–1107.
9. F. Khaddour, D. Grégoire and G. Pijaudier-Cabot. 2015. Capillary bundle model for the computation of the apparent permeability from pore size distributions. *European journal of environmental and civil engeneering,* 9: 168–183.
10. Klinkenberg, L. J. 1941. The permeability of porous media to liquids and to gases. In *Drilling and Production Practice*, ed. American Petroleum Institute, 200–213.
11. Choinska, M., A. Khelidj, G. Chatzigeorgiou and G. Pijaudier-Cabot. 2007. Effects and interactions of temperature and stress-level related damage on permeability of concrete. *Cement and Concrete Research*, 37: 79–88.

Recent Experimental Results about the Basic Creep of Concretes and a New Approach to Model It

Pierre Rossi

Institut Français des Sciences et Technologies des Transports, de l'Aménagement et des Réseaux (IFSTTAR), Department of Materials and Structures, Cité Descartes, 14-20 bd Newton, 77447 Champs-sur-Marne cedex 2, France. E-mail: pierre.rossi@ifsttar.fr

Abstract

This paper presents a summary of recent experimental researches about basic creep of concretes. From the analysis of these researches, a proposal is made concerning the dominant physical mechanism at the origin of this basic creep. Based on this physical mechanism, a new way to model, by using finite elements method, basic creep of concrete structures is proposed.

INTRODUCTION

The international literature on basic creep of concrete is considerable. Despite this, there is no, today, an international consensus about the physical mechanisms related to this mechanical behaviour.

It should be noted that several experimental studies have been conducted over the last five years [1 to 6] which converge to the high probability of existence of a dominant physical mechanism that is responsible for this basic creep.

This dominant physical mechanism leads to the questioning of the way usually chosen to model the creep behaviour of concrete structures.

The first part of this paper summarizes the experimental evidences obtained in the frame of the studies evocated above and the physical mechanism proposed in relation with these evidences.

The second part of the paper presents the basis of a new numerical model which takes into account the physical mechanism proposed.

The third and last part presents the way to determine experimentally the values of the mechanical parameters of the model.

EXPERIMENTAL EVIDENCES RELATED TO THE BASIC CREEP OF CONCRETE

The experimental studies, above referenced, led to the following evidences:

- The basic creep strain is directly leaked to the creation of microcracks during the creep loading.
- The basic creep in uniaxial tension is about three times less than the basic creep in compression when tests are performed on specimens of similar volume (usually used in the laboratories).
- The basic creep in uniaxial tension depends on the stressed volume of material. The higher the volume, the greater the basic creep is. This volume effect has to be related to the one existing when the static tensile behaviour of concrete is concerned.
- The compressive basic creep is not volume effect dependent.
- The compressive basic creep can be considered as linear until a stress level of about 50% of the compressive strength of the material.
- The tensile basic creep can be considered as linear until a stress level of about 70% of the uniaxial tensile strength of the material.
- The residual strains observed after unloading are related to the initial stresses existing in the material which are released during the creep loading when micro-cracks are created.

All these experimental evidences leaded to a proposal concerning a predominant physical mechanism at the origin of the basic creep of concrete. This physical mechanism can be summarized as following:

Under the effect of creep loading, concrete undergoes a micro-cracking process. This process results in an increase in the density of micro-cracks over time. This evolution leads to the creation of an additional self-drying shrinkage. In other words, the basic creep of concretes can be considered as self-drying shrinkage under stresses.

These experimental evidences lead to these logical consequences: ***the basic creep has no more to be modelled like in the past***. It is thus necessary:

- To stop considering that the total strain under creep loading can be considered as the sum of the strain related to self-drying shrinkage and the strain related to basic creep. This decomposition has no physical meaning.
- To stop considering that the basic creep in tension is identical to the basic creep in compression.
- To take into account the volume effects related to the basic creep in tension.

A new way to model basic creep of concrete is then proposed in the frame of finite elements method. This approach which is more physically relevant than those existing today is presented below.

A NEW NUMERICAL MODEL TO DESCRIBE THE BASIC CREEP OF CONCRETE

Taking into account what is proposed concerning the physical origin of the basic creep of concrete, it is possible to identify the main assumptions of a numerical model physically based. Thus, such a model should (not exhaustive list):

- Be able to describe explicitly the cracking process during the creep loading.
- Take into account the existence of initial stresses within the material.
- Take into account the volume effects related to the static tensile behaviour of concrete.
- Explicitly connect the cracking process during the creep loading to the self-drying shrinkage induced by this cracking process,

A numerical model consistent with the respect to the explicit modelling of cracking process was developed since several years [8 to 10] at IFSTTAR. This fully validated model is a probabilistic one. It serves as the basis of the model proposed to describe creep of concrete.
Some recalls related to the probabilistic explicit cracking model are presented below.

The probabilistic explicit cracking model. The numerical model is based on three physical evidences:

- Concrete is a heterogeneous material in which the heterogeneities can be modeled through a random spatial distribution of mechanical properties considered as dominant in the cracking process, namely the Young's modulus and the tensile strength;
- Scale effects of concrete cracking (experimentally proved) are taken into account by the fact that the mechanical properties of the material depend on the size of the mesh elements chosen for the finite element analysis.
- Cracking is explicitly treated through the creation of random kinematic discontinuities, which provides access to quantitative information on the cracking state (number of cracks, opening and spacing). Numerically speaking, these cracks are represented by interface elements.

The criterion for the crack creation is very simple: the interface element opens when the normal tensile stress at the centre of the interface element reaches a critical value (probabilized through a Weibull distribution function [10]). This means that the rigidity of the interface element becomes equal to zero (perfect brittle behaviour). As mentioned above, the value of this critical value depends on the total volume of the two volumetric elements interfaced by the considered interface element. The criterion of crack creation is schematically presented in the Figure 1.

Remark. It is very important to introduce a random distribution of the Young modulus to generate local tensile stresses (and so cracks) when the compressive behaviour of a specimen is concerned. The random distribution of the Young modulus depending of the size of the element mesh is a log-normal one [11].

From the above model, it is necessary to introduce strains versus time evolution in relation with the cracking process to describe basic creep of concrete in the frame of the physical mechanism proposed in chapter II. So, an extension of the probabilistic explicit cracking model is presented in the following.

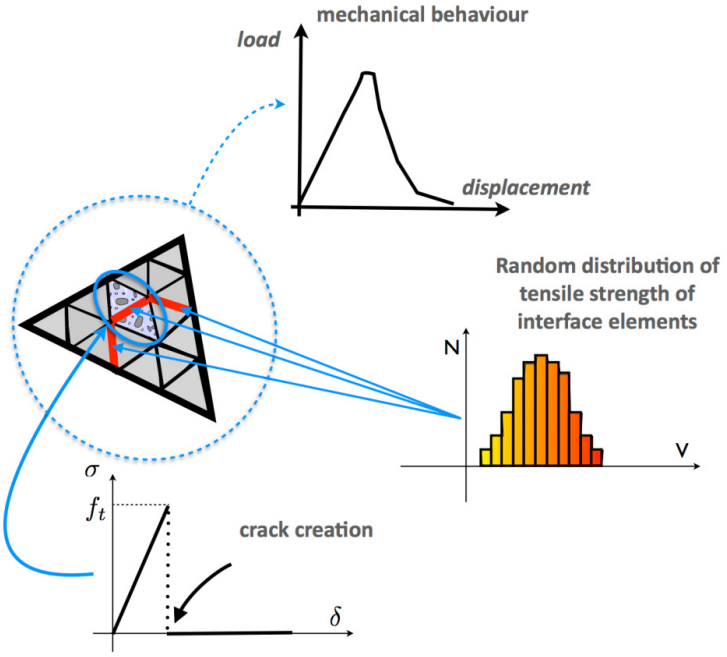

Figure1. Criterion of crack creation (explicit probabilistic cracking model)

Strains versus time evolution generated by the cracking process. From the cracking model presented above, it is important to take into account the self-drying shrinkage generated by this cracking and so to model the strain versus time induced by this mechanism. Two types of approaches are considered and actually in development to model the effect of this self-drying shrinkage:

- a direct one which consists in introducing, in the volume elements surrounding the interface elements considered as opened, an additional negative strain which evolutes during time.
- a second one, indirect, which consists in decreasing during time the value of the Young modulus of the volume elements surrounding the interface elements considered as opened.

These two strategies have for consequence, in complement to the fact that a global strain versus time is generated during the creep loading, to induce a stress redistribution around the (static) cracks. This redistribution allows the creation of new cracks during the creep loading and, by this way, allows the evolution of this global strain.

The cracking process obtained by the use of the probabilistic explicit cracking model described above is mesh independent. To conserve this same type of mesh independency with the model extensions presented above, the additional strain versus time law or the Young modulus versus time law are considered as dependent of the mesh size.

Remarks. The residual strain observed when a creep specimen is unloaded is generated, in the proposed numerical model, by the fact that initial stresses are introduced before any mechanical loading and released during the cracking process.

The experimental evidence related to the fact that the basic creep in tension is different of the basic creep in compression is taken into account by the cracking model itself.

The strategy to quantify the additional strain versus time law or the Young modulus versus time law in function of the mesh size is presented in chapter IV.

EXPERIMENTAL STRATEGY TO QUANTIFY THE MODEL PARAMETERS OF THE BASIC CREEP OF CONCRETES

It is needed to define an experimental strategy for determining the input data of the proposed model.

Considering what is said in paragraph II and the works it refers [1 to 6], the inevitable material parameters to be considered in the experimental strategy are:

- The ability of the concrete to micro-cracking (creating of greater or lesser density of micro-cracks) under a given stress ratio.
- The *water/binder* ratio of the concrete. This ratio will determine on the one hand the amount of movable water and vapour and, on the other hand, will determine the potentiality of the material to create self-drying shrinkage.
- The temperature within the material. This temperature can increase the density of micro-cracks (the coefficients of thermal expansion between the cement paste and the aggregates being different, they can generate tensile stresses and therefore local micro-cracks), an increase of the water viscosity, as well as changes in the *water/vapour* equilibrium. These last two points can induce changes in the amplitude and the kinetics of the additional self-drying shrinkage.

Taking into account these material parameters the mechanical test to be performed to quantify the mechanical parameters of the proposed model are:

- Compressive basic creep tests on specimens of any dimension (the basic compressive creep being no sensitive to the volume effects). These tests can be performed in a range of loading ratios comprised between 10% and 85% (it has been shown in the past that this last loading ratio is convenient to performed and control a creep test for studying all the steps of the creep behaviour until the rupture of the specimen).
- Bending basic creep tests on specimens of different dimensions (to perform uniaxial tensile creep tests on specimens of different dimension being very difficult). The range of loading ratio will be identical to the one of the compressive creep tests. From these bending basic creep tests, the basic creep in uniaxial tension, integrating volume effects, can be determined by using an inverse approach. As matter of fact, knowing the basic creep in compression, it is easy to determine, by using a numerical model (finite elements method), the basic creep in uniaxial tension that correctly reproduces the basic creep in bending. To do this, it is necessary to use the same numerical model as the one chosen to analyse the basic creep of concrete structures.

Remarks.

- If, as mentioned above, the basic creep of a given concrete is mainly linked to that of *its matrix through the water/binder ratio, it is necessary, for each type of test (compressive and bending creep tests), to test various concrete with different water/binder* ratios and different volumes of binder.
- In a fairly comprehensive experimental study related to the compressive basic creep of normal concrete [7], it was clearly shown that this basic creep is a mechanical characteristic for which the dispersion is relatively large. It therefore seems necessary to develop a probabilistic approach to model the basic creep behaviour rather than a deterministic one as usually done. To do this, it is imperative, for each type of basic creep test above mentioned and for each type of concrete, to perform enough tests to get enough experimental data for this probabilistic approach.

From these experimental tests, the mechanical parameters of the model are obtain through the use of an inverse approach. It means that the tests have to be simulate with the model. The parameters values of the cracking model being known [8 to 11], the additional strain versus time law or the Young modulus versus time law are obtained by fitting the tests results.

The dispersion related to the creep tests are considered as the consequence of the dispersion related to the cracking process. So, for each type of test and for a given meshing of the specimen, several simulations are performed. To get the additional strain versus time law or the Young modulus versus time law in function of the mesh size, different meshing of the specimens has to be considered.

CONCLUSIONS

This paper proposes a new numerical model for analysing basic creep behaviour of concrete structures. This model is based on experimental evidences which led to the proposal concerning the predominant physical mechanism at the origin of the basic creep of concretes. This paper proposes also an experimental strategy to quantify the mechanical parameters of the numerical model proposed.

The originality of the paper is based on the overall consistency of the approach (which integrates a proposal of the main physical mechanism of basic creep of concrete, a numerical model taking into account this physical mechanism and an experimental strategy to quantify the mechanical parameters of the model).

The next paper will present quantitative comparisons between the proposed model and experimental results (this work is in progress).

REFERENCES

Clément, J.L., Le Maou, F. (2001). "Experimental repeatability of creep and shrinkage concrete tests - data statistical analysis and modelling." *Concreep 6, 6th international conference on creep, shrinkage and durability mechanics of concrete and other quasi-brittle materials*, MIT Cambridge USA.

Rossi, P., Richer, S. (1987). "Numerical modelling of concrete cracking based on a stochastic approach." *Materials and Structures,* vol. 20, pp. 334-337.

Rossi, P., Wu, X. (1992). "A probabilistic model for material behaviour analysis and appraisement of the concrete structures." *Magazine of Concrete Research*, vol. 44, n°161, pp. 271-280.

Rossi, P., Ulm, F.J., Hachi, F. (1996) "Compressive behaviour of concrete: physical mechanisms and modelling." *ASCE Engineering Mechanics*, vol. 122 (11), pp-1038-1043.

Rossi, P., Tailhan, J.L., Le Maou, F., Gaillet, L., Martin, E. (2012). "Basic Creep Behaviour of Concretes. Investigation of the physical mechanisms by using acoustic emission." *Cement and Concrete Research*, Vol. 42, pp.61-73.

Rossi, P., Tailhan, J.L., Le Maou, F. (2013). "Comparison between concrete creeps in tension and in compression: influence of the concrete age at the loading and of the drying conditions." *Cement and Concrete Research*, 51, 78-84.

Rossi, P., Tailhan, J.L., Le Maou, F., Martin, E (2013). "Creep strain versus residual strain of a concrete loaded under various levels of compressive stress." *Cement and Concrete Research*, 51, 32-37.

Rossi, P., Charron, J.P., Bastien-Masse, M..Tailhan, J.L, Le Maou, F., Ramanich, S. (2014). "Tensile basic creep versus compressive basic creep at early ages: comparison between normal strength concrete and a very high strength fibre reinforced concrete."*Materials and Structures*, vol. 47, pp. 1773-1785

Rossi, P., Boulay, C., Tailhan, J.L., Martin, E (2014). "Macrocrack propagation in a concrete specimen under sustained loading: study of the physical mechanisms." *Cement and Concrete Research*, vol. 63, pp. 98-104.

Tailhan, J.L., Dal Pont, S., Rossi, P. (2010). "From local to global probabilistic modelling of concrete cracking." *Ann. Solid. Struct. Mech.*, vol. 1, pp. 103-115.

Tailhan, J.L., Boulay, C., Rossi, P., Le Maou, F., Martin E. (2012). "Compressive,tensile and bending basic creep behaviours related to the same concrete."*Structural Concrete*, 14, n°2, pp. 124-130.

The Three-Fluids Model for Concrete and Beyond

B. A. Schrefler

Department of Civil, Environmental and Architectural Engineering, University of Padua, Via Marzolo 9, 35131 Padova, Italy; and Department of Translational Imaging and Department of Nanomedicine, Houston Methodist Research Institute, 6670 Bertner Ave., Houston, TX 77030.
E-mail: Bernhard.schrefler@dicea.unipd.it

Abstract

Recent advances in the application of the three fluids model for concrete will be discussed where creep matters such as in repair problems. As known, this model considers concrete as composed of a deformable solid matrix with pores filled by dry air, capillary water and water vapor. The interaction of the constituents as well as phase change is taken into account. It will also be shown that the same material free balance equations can successfully be adopted for the simulation of tumor growth and drug delivery. In this case the solid phase is the extracellular matrix and the three fluids are formed by the healthy cells, the tumor cells and the interstitial fluid which transports the chemical species (therapeutic agents). The extracellular matrix is an elasto-visco-plastic porous solid of the Perzyna type. Applications for both forms of the general model will be shown.

INTRODUCTION

In the last couple of decades we have developed two major three fluid flow models in deforming porous solids. The first is our three fluids model for concrete which has been developed from the late nineties on and extended to many applications in concrete technology, such as concrete under high temperatures (Gawin et al. 1999, 2006 c), leaching in isothermal and non-isothermal conditions (Gawin et al. 2008 a,b, 2009), Alkali-Aggregate Reactions (Pesavento et al. 2012), young concrete and repair problems (Gawin et al, 2006 a,b, Sciumè et al. 2013 a), and recently also freezing/thawing (Koniorczyk et al. 2015). It considers concrete as formed by a deformable solid matrix the pores of which are filled with dry air, water vapour and liquid water. The interactions between all the constituents are duly taken into account. The second one is our recently developed tumor growth model which considers tumors as comprised of different compartments: the extracellular matrix as deformable porous solid, the pores of which are filled with healthy cells, tumor cells, both living and necrotic, and the interstitial fluid which carries nutrients, therapeutic agents, and waste products (Sciumè et al. 2012 a, 2013c, 2014 a-c, Bao et al. 2014). The vasculature/neovasculature is a separate compartment with only mass exchange with the other compartments. The cells are treated as adhesive fluids. Both models are hence de facto three fluid flow models in a deforming porous medium. The same set of material free balance equations apply to these apparently completely different problems, governing the structure of the code for numerical solution.

This insight allowed us to build the second model in very short time starting from the concrete model even if the constitutive behavior and evolution laws differ substantially. Both models are implemented in the code CAST3M (2003) of the French Atomic Energy Commission (CEA) and are easily accessible. In the following we show the balance equations for both cases to convince the reader of the analogy, and a recent application for each of the two cases.

THREE-FLUIDS MODEL FOR CONCRETE AND APPLICATION

The balance equations are written by considering concrete as a multi-phase porous material assumed to be in thermal-, hygral- and mechanical equilibrium state locally, even if chemical reactions (hydration process) are progressing with a certain rate. The local chemical equilibrium is reached only at the end of the spontaneous hydration process and from that time local thermodynamic equilibrium state is reached at a given point. Characteristic times of the local thermal, hygral and mechanical processes are much smaller than that of hydration reaction; hence, for these processes we use the equilibrium relations (with the actual value of hydration degree being 'frozen') (Gawin et al. 2006 a). The solid skeleton voids are filled partly by liquid water and partly by a gas phase. The liquid phase consists of bound water, which is present in the whole range of moisture content, and capillary water, which appears when the degree of water saturation exceeds the upper limit of the hygroscopic region. The gas phase is a mixture of dry air and water vapor (condensable gas constituent) and is assumed to behave as an ideal gas. The model equations are obtained by means of the Thermodynamically Constrained Averaging Theory TCAT (Gray and Miller, 2014, Gray et al., 2013) which is used to transform known micro scale relations to mathematically and physically consistent macro scale relations. The balance equations are here written already at macroscopic level for sake of brevity.

The mass balance equation for the solid phase *s* is

$$\frac{\partial\left(\varepsilon^s\rho^s\right)}{\partial t}+\nabla\cdot\left(\varepsilon^s\rho^s\mathbf{v}^{\bar{s}}\right)=\overset{l\to Hs}{M}$$

The mass balance equation of liquid water *l* is

$$\frac{\partial\left(\varepsilon^l\rho^l\right)}{\partial t}+\nabla\cdot\left(\varepsilon^l\rho^l\mathbf{v}^{\bar{l}}\right)=-\overset{l\to Hs}{M}-\overset{l\to Wg}{M}$$

The mass balance of water vapor *Wg* reads

$$\frac{\partial\left(\varepsilon^g\rho^g\omega^{\overline{Wg}}\right)}{\partial t}+\nabla\cdot\left(\varepsilon^g\rho^g\omega^{\overline{Wg}}\mathbf{v}^{\bar{g}}\right)+\nabla\cdot\left(\varepsilon^g\rho^g\omega^{\overline{Wg}}\mathbf{u}^{\overline{\overline{Wg}}}\right)=\overset{l\to Wg}{M}$$

and that of dry air *Ag* is

$$\frac{\partial\left(\varepsilon^g \rho^g \omega^{\overline{Ag}}\right)}{\partial t} + \nabla\cdot\left(\varepsilon^g \rho^g \omega^{\overline{Ag}} \mathbf{v}^{\overline{g}}\right) + \nabla\cdot\left(\varepsilon^g \rho^g \omega^{\overline{Ag}} \mathbf{u}^{\overline{\overline{Ag}}}\right) = 0$$

where $\overset{l\to Hs}{M}$ is the chemically combined water, $\overset{l\to Wg}{M}$ the vaporized water, g indicates the gaseous phase, mixture of dry air and water, ε the volume fraction, ω the mass fraction, $\mathbf{v}$ the phase velocity, $\mathbf{u}$ the relative velocity and ρ the density.
Finally the linear momentum balance equation is

$$\nabla\cdot\left(\frac{\partial \mathbf{t}^s_{eff}}{\partial t} - \frac{\partial p^s}{\partial t}\mathbf{1}\right) = 0$$

where $\mathbf{t}^s_{eff}$ is the effective stress and p^s the solid pressure (Gawin et al. 2007).
These balance equations have to be supplemented with appropriate constitutive equations and evolution laws for which the reader is referred to the relevant papers in the References.
As typical application of the model we show the results of the numerical simulation of cracking of a massive concrete beam. The analyzed test is a large beam specimen built for ConCrack (2011): the international Benchmark for Control of Cracking in Reinforced Concrete Structures (Figure 1). This benchmark has been organized within the French national project CEOS (Comportement et Evaluation des Ouvrages Speciaux vis-à-vis de la fissuration et du retrait) dedicated to the analysis of the behavior of special large specimens concerning cracking and shrinkage.

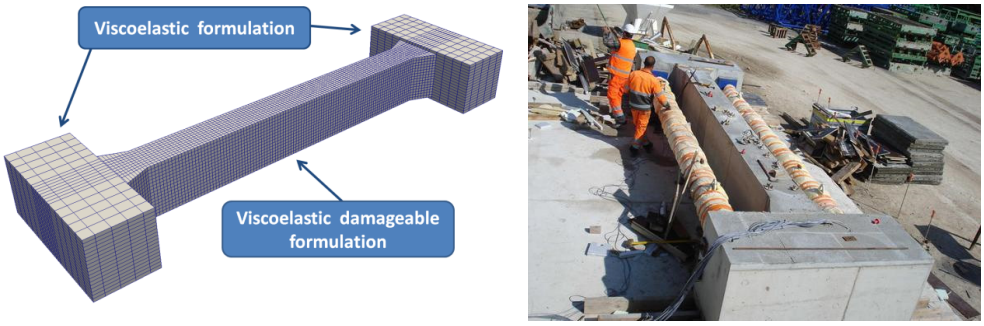

Figure 1. Experimental specimen (right) and finite elements mesh (left), Reprinted from Simoni and Schrefler (2014), Copyright (2014), with permission from Elsevier.

Here one of the experiments of the benchmark program and its numerical simulation are presented. The test is divided in two phases. During the first 48 hours after casting, the structure is thermally isolated and protected from drying. Then after two days the isolation and the formwork are removed and the structure is conserved during two months in the open environment. During the two phases of the test the longitudinal strains of the structure are globally restrained by two metallic struts. After two months the structure is loaded by a static bending test.

For more details on the analyzed test see the reference web page of the benchmark (www.concrack.org). The mesh of concrete is made of 3D elements (Figure 1, left). Truss elements rigidly linked with the concrete 3D mesh are used to model the struts. The local damage model of Mazars (1986) has been used. This approach allows predicting cracking in mode I (De Sa et al. 2008, and De Sa and Benboudjema 2012) which is the case here, since cracking is induced by shrinkage restraint. The model is regularized in tension with the introduction of a characteristic length, *lc*, related to the size of each finite element (Rots, 1988, and Cervera and Chiumenti, 2006) to overcome the possible mesh dependency. The model for concrete at early age is that of Sciumè et al. (2013 a).

The boundary conditions are assumed to be of convective type for both heat and mass exchange, see (Simoni and Schrefler, 2014) for details. For the material parameters see Sciumè et al. (2012 b).

During the first and second phase the longitudinal displacements of the specimen have been globally restrained by the two metallic struts. Therefore during hydration the thermal extension of the concrete has been restrained and so in this phase the concrete cross-section was compressed. After the hydration it is the shrinkage of the beam that has been contrasted. The position of the displacement measurement points are depicted in Figure 2 and the deformed configuration and the damage at day 60 in Figure 3. The solution is not symmetric due to the non-symmetric solar irradiation: this has been experimentally measured by the benchmark organizers and taken into account in the modeling process.

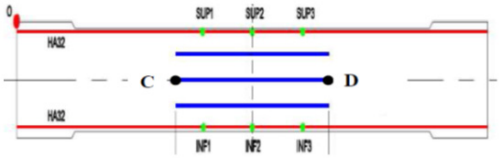

	x (m)	y (m)	z (m)
C	1.26	2.6	0.49
D	1.26	5.1	0.49

Figure 2. Position of the displacement measurement points (and coordinates). Reprinted from Simoni and Schrefler (2014), Copyright (2014), with permission from Elsevier.

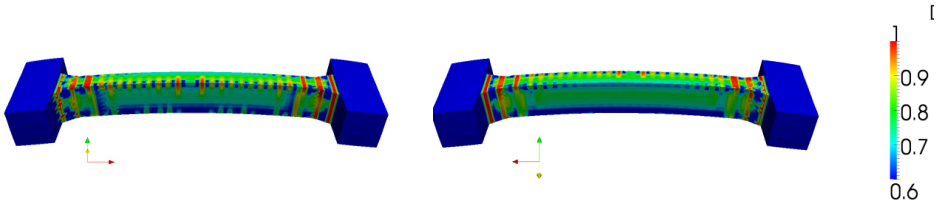

Figure 3. Deformed configuration (x 500) and damage after 60 days. Face exposed to the sun (left) and face not exposed to the sun (right). Reprinted from Simoni and Schrefler (2014), Copyright (2014), with permission from Elsevier.

The comparison between the experimentally and numerically obtained relative displacements and axial force is shown in Figure 4. Note the complex displacement evolution.

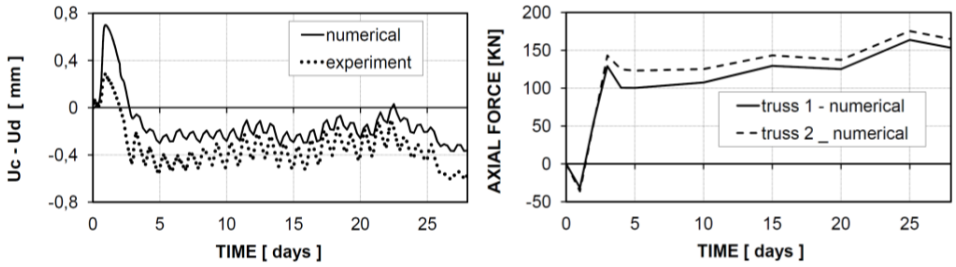

Figure 4. Relative displacement between the point C and D (left). Axial force in the two metallic struts that restrain shrinkage (right). Reprinted from Simoni and Schrefler (2014), Copyright (2014), with permission from Elsevier.

After two months a static four point bending test has been carried out until rupture. Compression has been applied by eight jacks and live controlled by a pressure sensor with an independent data registration system. The load is applied with increments of 50 kN and each loading step is kept during 20 min. The comparison between the experimental and numerical crack pattern and the force versus displacement diagram are shown in Figure 5. The comparison in Figures 4 and 5 with experimental results shows that the adopted approach is able to simulate such complicated multi-field fracture phenomena in realistic engineering structures. For more results concerning hydration and thermal field the reader is referred to the website of ConCrack (2011) and the final report.

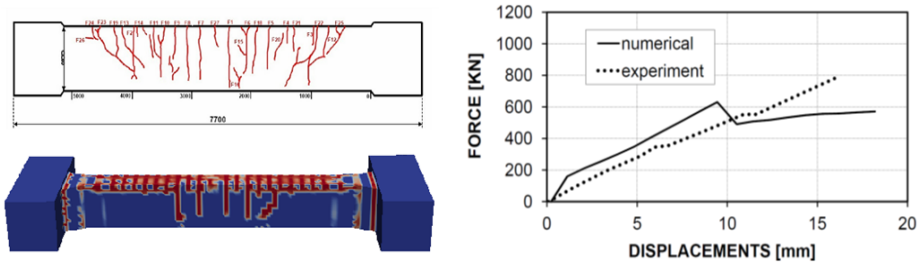

Figure 5. Comparison between the numerical and experimental crack pattern (left). Force vs displacements during the bending test (right). Reprinted from Simoni and Schrefler (2014), Copyright (2014), with permission from Elsevier.

TUMOR GROWTH MODEL AND APPLICATION

From review papers of numerical models for tumor growth such as Roose et al. (2007), Deisboeck et al. (2011) and Sciumè et al. (2013 c), it appears clearly that in the realm of a continuum approach a vast majority of models describe the malignant mass (TC), the host cells (HC) and the interstitial fluid (IF) as homogeneous, viscous fluids and employ reaction-diffusion-advection equations

for predicting the distribution and transport of nutrients. The Extracellular matrix (ECM) is absent in almost all the models.

In our model the tumor is comprised of the following phases: i) tumor cells (TC), which partition into living cells (LTC) and necrotic cells (NTC); ii) healthy cells (HC); iii) extracellular matrix (ECM); and iv) interstitial fluid (IF); see Sciumè et al. (2012 a, 2013c, 2014 a-c). The ECM is a porous solid, while all other phases are fluids. The tumor cells may become necrotic upon exposure to low nutrient concentrations or excessive mechanical pressure. The IF is a mixture of water and biomolecules, such as nutrients, oxygen, therapeutic agents and waste products. In the following mass and momentum balance equations, α denotes a generic phase, t the tumor cells (TC), h the healthy cells (HC), s the solid phase (ECM), and l the interstitial fluid (IF).

The balance equations are listed below to show the analogy with the concrete model. For the full development the reader is referred to Sciumè et al. (2013 b, and 2014 a-c).

The mass balance equations of the solid s is

$$\frac{\partial\left(1-\varepsilon\right)}{\partial t}+\nabla\cdot\left[\left(1-\varepsilon\right)\mathbf{v}^{s}\right]=0$$

where $\mathbf{v}^s$ is the solid phase velocity.

The mass balance equations of the tumor cell phase t, the host cell phase h and interstitial fluid l are respectively

$$\frac{\partial\left(\varepsilon S^{t}\right)}{\partial t}+\nabla\cdot\left(\varepsilon S^{t}\mathbf{v}^{s}\right)-\nabla\cdot\left(\frac{k_{rel}^{t}\bar{\mathbf{k}}^{ts}}{\mu^{t}}\left\langle 1-\frac{a_{t}}{\left|\nabla p^{t}\right|}\right\rangle_{+}\nabla p^{t}\right)=\frac{1}{\rho}\overset{l\to t}{\underset{growth}{M}}$$

$$\frac{\partial\left(\varepsilon S^{h}\right)}{\partial t}+\nabla\cdot\left(\varepsilon S^{h}\mathbf{v}^{s}\right)-\nabla\cdot\left(\frac{k_{rel}^{h}\bar{\mathbf{k}}^{hs}}{\mu^{h}}\left\langle 1-\frac{a_{h}}{\left|\nabla p^{h}\right|}\right\rangle_{+}\nabla p^{h}\right)=0$$

$$\frac{\partial\left(\varepsilon S^{l}\right)}{\partial t}+\nabla\cdot\left(\varepsilon S^{l}\mathbf{v}^{s}\right)-\nabla\cdot\left(\frac{k_{rel}^{l}\bar{\mathbf{k}}^{ls}}{\mu^{l}}\nabla p^{l}\right)=-\frac{1}{\rho}\overset{l\to t}{\underset{growth}{M}}$$

where a_α is the adhesion (a_l =0), μ^α is the dynamic viscosity, k_{rel}^{α} is the relative permeability which takes care of the presence of the other two fluid phases (Sciumè et al. 2014 a), $\bar{\mathbf{k}}^{\alpha s}$ is the absolute permeability, p^α is the pressure and ρ is the common density; $\overset{l\to t}{\underset{growth}{M}}$ is the rate of growth term. The linear momentum balance equations of the fluid phases have here already been introduced to show the difference between cells and IF.

Assuming that: i) there is no diffusion of either necrotic or living cells; ii) there is no exchange of necrotic cells with other phases; the mass conservation equation for the necrotic portion of the tumor cells phase reads

$$\frac{\partial\left(\varepsilon^{t}\rho\omega^{N\bar{t}}\right)}{\partial t}+\nabla\cdot\left(\varepsilon^{t}\rho\omega^{N\bar{t}}\mathbf{v}^{\bar{t}}\right)-\varepsilon^{t}r^{Nt}=0$$

where $\omega^{N\bar{t}} = \dfrac{\varepsilon^{N\bar{t}}\rho^{N\bar{t}}}{\varepsilon^{t}\rho^{t}}$ is the mass fraction of necrotic cells in the tumor cells phase t, $\varepsilon^{t} r^{Nt}$ the rate of generation of necrotic cells and $\mathbf{v}^{\bar{t}}$ the velocity of the tumor cells phase.

The mass balance equation of the nutrient species in the interstitial fluid is

$$\frac{\partial\left(\varepsilon S^{l} c^{g}\right)}{\partial t} - \nabla\cdot\left(\varepsilon S^{l} D_{eff}^{\bar{gl}} \nabla c^{g}\right) = -\overset{gl\to t}{M}$$

where $D_{eff}^{\bar{gl}}$ is the effective diffusion coefficient depending on the available pore space, (Sciumè et al., 2014 a) and $\overset{gl\to t}{M}$ is the nutrient consumption rate which depends on the local nutrient availability. Finally the linear momentum balance equation of the solid phase in rate form reads as

$$\nabla\cdot\left(\frac{\partial \mathbf{t}_{eff}^{s}}{\partial t} - \frac{\partial p^{s}}{\partial t}\mathbf{1}\right) = 0$$

where $\mathbf{t}_{eff}^{s}$ is the effective stress tensor in the solid and $\mathbf{1}$ is the unit tensor. The interaction between solid and the fluids, inclusive of the cell populations, has been accounted for through the effective stress principle (Gray and Schrefler, 2007). Clearly these balance equations have to be completed with the appropriate constitutive equations which can be found in Sciumè et al. (2013 b, 2014 a-c).

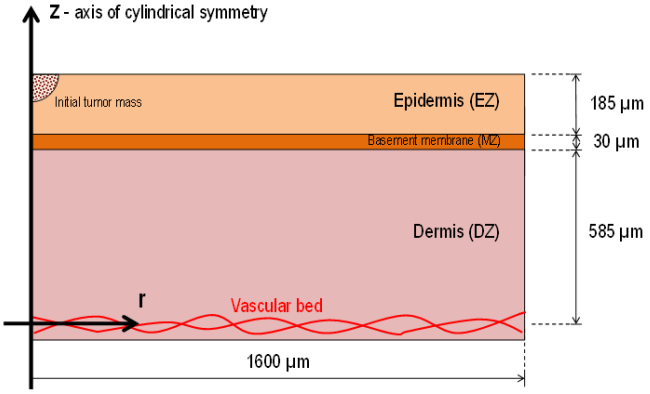

Figure 6. Skin structure and geometry of the modeled case. Reprinted from Sciumè et al. (2014 c), Copyright (2014), with permission from IOP publishing.

We show here as application the evolution of a melanoma during the avascular stage. Cutaneous melanoma is the most dangerous form of skin cancer. It arises in the melanocytes, the specialized melanin producing cells, which are scattered along the epidermis-dermis border, Figure 6 . It is recalled that the outer structure of the skin has a layered structure where three compartments can be evidenced: the epidermis, an outer epithelium of stratified cells; the dermis, an intermediate cushion of vascularized connective tissue; and the hypodermis, the lowermost

layer made of loose tissue and adipose cells. The dermis is separated from the epidermis by the basement membrane or basal laminae, a tough sheet of ECM, see Figure 6. The following example deals with the evolution of a melanoma during the avascular stage (Sciumè et al. 2014 c). Figure 7 shows the melanoma after two weeks of growth and a qualitative comparison with a clinical observed case of Chung et al. (2010).

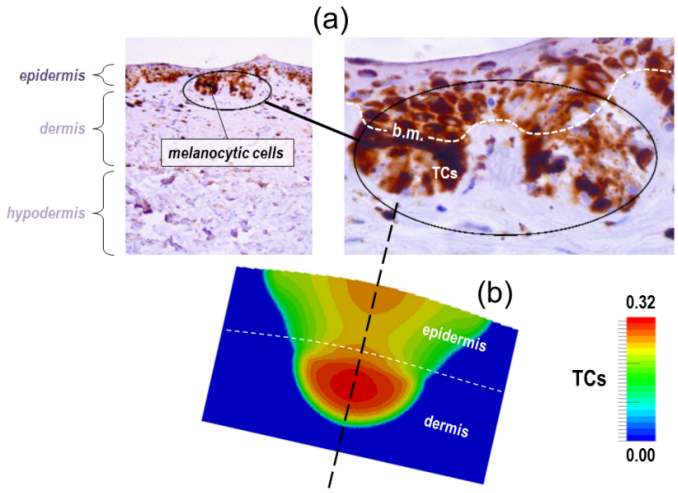

Figure 7. Paraffin-embedded tissue sections of a melanocytic lesion, Chung et al. (2010); b.m. stands for basement membrane (a); numerical results (volume fraction of TCs) after two weeks of growth (b). Reprinted from Sciumè et al. (2014 c), Copyright (2014), with permission from IOP publishing.

CONCLUSION

Three fluid flow models in deforming porous media have several applications ranging from geo-material mechanics such as concrete, to reservoir engineering such as water, gas and oil flowing in a deforming formation, and to mechanics in medicine such as tumor growth models. Two of such applications have been shown. With a general framework in place it is relatively easy to pass from one application to another in a different field. However a good aptitude to out of the box thinking is needed as well as collaboration with experts of the fields concerned.

Acknowledgment: the author wishes to thank Paolo Decuzzi, Mauro Ferrari, Dariusz Gawin, William G. Gray, Francesco Pesavento, Raffaella Santagiuliana, Giuseppe Sciumè, and Luciano Simoni for their precious collaboration.

REFERENCES

Bao, G., Bazilevs, Y., Chung, J-H., Decuzzi, P., Espinosa, H. D., Ferrari, M., Gao, H., Hossain, S. S., T. J. R. Hughes, T. J. R., R. D. Kamm, R. D., Liu, W. K., Marsden, A., and Schrefler, B. (2014). "USNCTAM perspectives on mechanics in medicine." *J Royal Soc Interface*, 11, 20140301.

Cast3M (2003) FE code developed by the French Atomic Agency (CEA), France. www.cast3m.cea.fr.

Cervera, M., Chiumenti, M. (2006). "Mesh objective tensile cracking via a local continuum damage model and a crack tracking technique." *Comp. Methods Appl. Mech. Engng.*, 196, 304–320.

Chung, L. S., Man, Y-G. and Lupton, G. P. (2010). "WT-1 expression in a spectrum of melanocytic lesions: Implication for differential diagnosis." *Journal of Cancer*, 1, 120.

ConCrack. (2011)." International benchmark for control of cracking in R.C. Structures." <www.concrack.org>.

De Sa, C., Benboudjema, F., Thiery, M., and Sicard, J. (2008). "Analysis of microcracking induced by differential drying shrinkage." *Cement and Concrete Composites*, 30, 947–956.

De Sa, C., and Benboudjema, F. (2012). "Modeling of concrete nonlinear mechanical behavior at high temperatures with different damage-based approaches." *Materials and Structures*, 44, 1411–1429.

Deisboeck, T. S., Wang. Z., Macklin, P., and Cristini, V. (2011) "Multiscale cancer modeling" *Annual Rev. Biomed. Eng.* 13.

De Schutter, G., and Taerwe, L. (1997). "Fracture energy of concrete at early ages." *Materials andStructures*, 30, 67–71.

Gawin, D., Majorana, C.E., and Schrefler, B.A. (1999). "Numerical analysis of hygro-thermic behaviour and damage of concrete at high temperature." *Mech. Cohesive-Frictional Materials*, 4, 37-76.

Gawin, D., Pesavento, F., and Schrefler, B.A. (2006 a). "Hygro-thermo-chemo-mechanical modelling of concrete at early ages and beyond. Part I: Hydration and hygro-thermal phenomena." *Int. J. Num. Methods Eng.*, 67, 299-331.

Gawin, D., Pesavento, F., and Schrefler, B.A. (2006 b). "Hygro-thermo-chemo-mechanical modelling of concrete at early ages and beyond. Part II: Shrinkage and creep of concrete." *Int. J. Num. Methods Eng.*,67, 332-363.

Gawin, D., Pesavento, F., and Schrefler, B. A. (2006 c). "Towards prediction of the thermal spalling risk through a multi-phase porous media model of concrete." *Comput. Methods Appl. Mech. Engrg.*, 195, 5707-5729.

Gawin, D., Pesavento, F., and Schrefler, B. A. (2007). "Modelling creep and shrinkage of concrete by means of effective stress." *Materials and Structures*, 40, 579-591.

Gawin, D., Pesavento, F., and Schrefler, B. A. (2008 a). "Modeling of cementitious materials exposed to isothermal calcium leaching, with considering process kinetics and advective water flow. Part 1: Theoretical model." *Solids and Structures*, 45, 6221-6240.

Gawin, D., Pesavento, F., and Schrefler, B. A. (2008 b). "Modeling of cementitious materials exposed to isothermal calcium leaching, with considering process kinetics and advective water flow. Part 2: Numerical solution." *Solids and Structures*, 45, 6241-6286.

Gawin, D., Pesavento, F., and Schrefler, B. A. (2009). "Modeling deterioration of cementitious materials exposed to calcium leaching in non-isothermal conditions." *Comput. Methods Appl. Mech. Engrg.*, 198 3051-3083.

Gray, W. G., Miller, C. T., and Schrefler, B. A. (2013). " Averaging theory for description of environmental problems: What have we learned?" *Adv. Water Res.,* 51, 123-38.

Gray, W. G., and Miller, C. T. (2014). Introduction to the Thermodynamically Constrained Averaging Theory for Porous Medium Systems. Springer.

Koniorczyk, M., Gawin, D., and Schrefler B. A. (2015). Modelling evolution of frost damage in fully saturated porous materials, submitted.

Mazars, J. (1986). "A description of micro and macroscale damage of concrete structures." *Engineering Fracture Mechanics*, 25, 729–737.

Pesavento, F., Gawin, D., Wyrzykowski, M., Schrefler, B. A., and Simoni, L. (2012). "Modeling alkali-silica reaction in non-isothermal, partially saturated cement based materials." *Comp-Meth. Appl. Mech. Engrg.,* 225-228, 95-115.

Roose, T., Chapman, S. J. and Maini, P. K. (2007) "Mathematical models of avascular tumor growth." *Siam Review*, 49(2), 179-208.

Rots, J. G. (1988). "Computational modeling of concrete fracture." PhD Thesis, Delft University of Technology.

Sciumè, G., Shelton, S. E., Gray, W. G., Miller, C. T., Hussain, F., Ferrari, M., Decuzzi, P., and Schrefler, B.A. (2012 a). "Tumor growth modeling from the perspective of multiphase porous media mechanics." *Molecular and Cellular Biomechanics*, 9(3), 193-212.

Sciume`, G., Schrefler, B. A., and Pesavento, F. (2012 b). "Thermo-hygro-chemo-mechanical modelling of the behaviour of a massive beam with restrained shrinkage." CONCRACK 3, International workshop on crack control of mass concrete and related issues concerning early-age concrete structures, RILEM, JCI, Paris, France.

Sciume`, G., Benboudjema, F., De Sa, C., Pesavento, F., Berthaud, Y., and Schrefler, B. (2013 a). "A multiphysics model for concrete at early age applied to repairs problems." *Engineering Structures*, 57, 374–387.

Sciumè, G, Shelton, S. E., Gray, W. G., Miller, C. T., Hussain, F., Ferrari. M., Decuzzi, P. and Schrefler, B. A. (2013 b). "A multiphase model for three-dimensional tumor growth." *New Journal of Physics,* 15(1), 015005.

Sciumè, G., Gray, W. G., Ferrari, M., Decuzzi, P., and Schrefler, B.A. (2013 c). "On computational modeling in tumor growth." *Archives Comp. Methods Eng.,* 20, 327-52.

Sciumè, G., Gray, W. G., Hussain, F., Ferrari, M., Decuzzi, P., and Schrefler B. A. (2014 a). "Three phase flow dynamics in tumor growth." *Comp. Mech*., 53, 465-484.

Sciumè, G., Ferrari, M., and Schrefler, B. A. (2014 b). "Saturation–pressure relationships for two-and three-phase flow analogies for soft matter." *Mech. Res. Com*., 62, 132-137.

Sciumè, G., Santagiuliana, R., Ferrari, M., Decuzzi, P., and Schrefler, B. A. (2014 c). "A tumor growth model with deformable ECM." *Phys. Biol.,* 11, 065004.

Simoni, L., and Schrefler, B. A. (2014). "Multi Field Simulation of Fracture." Chapter 4 in *Advances in Applied Mechanics*, Bordas, S., P., A., ed. Vol 47, AAMS, Academic Press, UK, 367-519.

A Few Analogies Between the Creep of Cement and of Other Materials

M. Vandamme

Université Paris-Est, Laboratoire Navier (École des Ponts ParisTech, IFSTTAR, CNRS), 6-8 Av. B. Pascal, 77420 Champs-sur-Marne, France; PH (+33) 1 64 15 37 04; FAX (+33) 1 64 15 37 41; email: matthieu.vandamme@enpc.fr

ABSTRACT

Creep is not observed for cementitious materials only: most materials creep, in particular materials very relevant for civil engineering applications, namely clay or wood. Although each of those materials possesses its own specific features, some analogies between their respective creep behaviors can be drawn. From these analogies, we can try to obtain meaningful pieces of information on the physical processes at stake during creep. After having introduced the topic, I present a few of those analogies and discuss briefly what can be learned from them.

INTRODUCTION

Cementitious materials creep, i.e., slowly deform under the application of a sustained load. Most materials also do, some of which are relevant for civil engineering applications, e.g., clay, wood, or rock.

In terms of microstructure, cement, clay, and wood, exhibit several common features (for a description of the multiscale structure of each material, see Constantinides and Ulm (2004), Bobko and Ulm (2008), and Rafsanjani et al. (2012), respectively): 1) they are heterogeneous, 2) they are multiscale, 3) they are porous, 4) their porosity spans several orders of magnitude down to micropores (i.e., to pores with a diameter smaller than 2 nm). However, a feature that significantly distinguishes cement from clay or wood is that, in cement, the microstructure continuously evolves over time because of hydration, while, in absence of any external solicitation, the microstructure of clay or wood does not evolve with time.

At the scale of the nanometric building blocks of which they are made, cementitious materials and clay-based materials exhibit strikingly similar features. Indeed, C-S-H (i.e., calcium silicate hydrate) is made of Ca-O sheets covalently bonded with silicate chains, which form stacks of parallel solid layers separated by a few layers of water molecules. Clays are phyllosilicates made of stacks of layers combining silicate tetahedra with aluminum octahedra: Again, those parallel solid layers are separated by a few layers of water. Therefore, both C-S-H and clay are microporous layered systems at the nanometric scale. In contrast, at this same scale, wood is very different, as the main layer (namely S2) of the cell wall is composed of stiff cellulose microfibrils

surrounded by a soft amorphous polymeric matrix made of hemicelluloses reinforced with lignin.

Cement, clay, and wood all creep, and their creep properties have been studied in depth. In the next sections, we underline some analogies in their creep behavior.

QUALITATIVE FEATURES OF CREEP

Cementitious materials are known to creep in a logarithmic manner with respect to time in the long term. Such are clay-based materials, for which this logarithmic feature is so intrinsic that it actually defines how creep experiments on those materials are analyzed: A creep test on clay makes it possible to identify its so-called coefficient of secondary compression (noted C_α), defined as $C_\alpha = de/d(\log(t)$, where de is a small increment of the void ratio and is proportional to the volume strain classically used in solid mechanics. In fact, this logarithmic feature of long-term creep is not limited to clays only, but is observed for all soils, including sands. In soils, the non-logarithmic short-term creep is known to be due to movements of water and dissipation of pore pressure. In contrast, as is the case in cement science, what causes long-term logarithmic creep is still under debate, even for sands. For those latter, whether such feature is due to the behavior of individual contacts between grains or, in contrast, whether it is the result of a collective behavior (e.g., some propose that creep of sand is due to the progressive breakage of grains (Leung et al., 1996)) is unclear. In any case, if the reason for a logarithmic creep is the same in cement and in clay, then this observation teaches us that the origin of logarithmic creep is not due to a chemical specificity of C-S-H (as the chemical structures of clay and C-S-H are different), and is not due to hydration *per se* (as clays are usually not subjected to chemical processes).

An interesting observation is that, for clays, creep in tension is also a logarithmic function of time after a transient period. To reach this conclusion, we performed creep experiments on self-standing clay films manufactured by deposition and evaporation of montmorillonite (Carrier, 2013). The manufactured films (which were a few dozens of microns in thickness) were solicited in tension and we measured the resulting strains by Digital Image Correlation: For the various films tested, creep became a logarithmic function of time after a few seconds. This observation makes it possible to discard the idea that logarithmic creep in clays could be explained by free-volume dynamics as, under tension, the free volume (and thus the creep rate) should increase with time.

Another qualitative feature of both scientific and practical interests is the effect of the age of loading on the creep of cementitious materials. Even in absence of any chemical process, i.e., in the hypothetical case where the material would be fully hydrated, one can wonder whether the age of loading should still have an impact. According to the microprestress theory (Bažant et al., 1997), which can successfully explain why long-term creep is a logarithmic function of time, even if the hydration degree has reached an asymptotic value, the age at loading still plays a role, as the microprestress

decreases over time. Therefore, according to the microprestress theory, a concrete that would be fully hydrated should creep differently if creep testing is performed 1 year after pouring or 10 years after pouring. To the best of my knowledge, for clays, the age of the tested sample is never taken into account, even though soil scientists not only work with geologically old intact samples, but also with recompacted samples obtained by consolidating a clay slurry directly in the lab.

SENSITIVITY OF MECHANICAL PROPERTIES TO WATER

The creep properties of cement, clay, and wood, depend on the hydric state: As could be thought intuitively, the more humid the material, the more it creeps. Such trend is observed for wood (Hunt, 1999), we observed it for C-S-H by microindentation (Zhang, 2014) and also for our self-standing clay films solicited in tension (Carrier, 2013).

Actually, on those materials, the hydric state is known to affect not only the creep, but also the short-term mechanical properties, namely swelling and elastic properties, in an amount that varies according to the material. Regarding the impact on those properties, one can wonder what the most relevant parameter is to quantify the hydric state. For wood, in the range of hydric states for which an effect is observed, dimensional variations depend somewhat linearly on the moisture content (i.e., on the water content), and the effect on the stiffness is also expressed as a function of the moisture content (Glass & Zelinka, 2010). For the clay films we manufactured, we observed that both their swelling and stiffness depended on the hydric state: however, although we observed an hysteresis when plotting swelling and stiffness versus relative humidity, the hysteresis fully disappeared when plotting those data versus water content (Carrier, 2013; Carrier et al., 2013). As is the case for wood, swelling depended roughly linearly on water content. Those observations suggest that the main physical parameter to consider when focusing on the effect of the hydric state should be the water content rather than the relative humidity (although expressing constitutive laws in terms of relative humidity also has its advantages). It is likely that such suggestion can be extended to creep properties and cementitious materials.

THE PICKETT EFFECT

The Pickett effect, also called drying creep, is the fact that the creep of a sample submitted to a varying relative humidity is more important than what one would expect from a mere addition of the effects of creep at constant relative humidity and of drying shrinkage (Pickett, G., 1942). Interestingly, this effect is also observed in wood (Armstrong and Kingston, 1960), under the name of mechano-sorptive creep. Actually, creep enhancement due to moisture variations is quite general, as it is also observed in keratin and synthetic or semi-synthetic polymers (Vlahinić et al., 2012). The fact that Pickett-type effects are observed on so different materials shows that the Pickett effect in cement is not due to a chemical specificity of C-S-H or to the fact that C-S-H is lay-

ered. A likely candidate to creep enhancement would be the presence of micropores, which are present in all materials mentioned by Vlahinić et al. (2012).

Although models of drying creep can describe the hydric state through the internal relative humidity (Bažant & Yunping, 1994), based on the discussion in the previous section, one can wonder what the hydric driving force for the Pickett effect is. As an alternative to variations of relative humidity, this driving force could be variations of local water content, or flow of water. Note that those latter two alternatives are not equivalent: local variations of water content always require a flow of water, but flow can occur without variations of relative humidity and/or water content. Such is the case for a system with different faces exposed to different relative humidities: in a steady state, one observes a flow of water but no variations of relative humidity or water content. Actually, such experiment was performed on wood (Armstrong, 1972): different relative humidities were imposed inside and outside the wood core and, in the steady state, no creep enhancement was observed. For the variety of materials on which Pickett-type effects are observed, Vlahinić et al. (2012) propose the driving force to be the local flow of water from and to the microporosity.

CREEP MODELING

For the modeling of the creep behavior of clays, one approach which has been particularly successful is the isotache approach (Šuklje, 1957; Leroueil, 2006), which postulates that the strain rate $\dot{\varepsilon}$ at a given time is only a function of the state of the material (characterized by its actual strain ε) and of the stress σ to which the material is submitted, i.e.:

$$\dot{\varepsilon} = R(\varepsilon, \sigma) \tag{1}$$

where R is a function. For clays, such approach has been verified experimentally and proves to be very useful: Indeed, the creep of clays is known to be nonlinear with respect to the applied stress, so that, in contrast to cementitious materials, linear viscoelasticity (and thus the principle of superposition) is not relevant.

Interestingly, an equivalent approach has been proposed for cementitious materials, which is called the incremental model or “equivalent time method” (Acker et al., 1989) and starts by postulating the exact same relation as Eq. (1). An appealing feature of those 2 approaches for clay or cement-based materials is that the strain rate does not depend *per se* on the full loading history, but only depends on the actual state of the material (i.e., actual stress and strains), which, at least from a physical point of view, makes sense. Note that linear viscoelasticity and isotache approach are not antagonistic models: the isotache approach can also be used for linear viscoelastic materials.

Given the success of the isotache approach in the modeling of creep for clay materials, revisiting the “equivalent time method” to the light of the isotache approach could be of interest for the cement science community. In the same spirit, one could imagine modeling the creep of concrete by starting from an isotache-type model of the

creep of C-S-H and upscaling it to the scale of concrete through micromechanics by intermixing C-S-H with pores and several classes of elastic inclusions.

CONCLUSIONS

Although each type of materials possesses its own unique features, here we have shown that some phenomenology observed on cementitious materials is not specific to them but can be observed for clay or for wood, e.g., a logarithmic long-term creep, a sensitivity of the mechanical properties to water, or the Pickett effect. Assuming that, when the same phenomenology is observed for various types of materials, the underlying physical mechanisms are the same, we infer that: 1) The logarithmic feature of long-term creep of cement is not due to the hydration process *per se* or to any chemical specificity of C-S-H, since such feature is also observed with clay and 2) the Pickett effect is not due to the layered structure of the C-S-H or to its specific chemistry, since it is observed over a wide variety of materials.

When aiming at modeling the effect of water on mechanical properties, making use of the water content as the parameter to describe the hydric state of the material may have some advantages. Also, we observe that the "equivalent time method" for cementitious materials is equivalent to the isotache approach for clays, which has been proposed more than 50 years ago and is still of great value today for the soil science community.

ACKNOWLEDGMENTS

I thank P. Acker for his constructive feedback on the manuscript.

REFERENCES

Acker, P., Lau, M. Y., & Collet, F. (1989). "Comportement différé du béton: validation expérimentale de la méthode du temps équivalent." *Bulletin de Liaison Des Laboratoires Des Ponts et Chaussées*, 163, 31-39.

Armstrong, L. D. (1972). "Deformation of wood in compression during moisture movement." *Wood Science*.

Armstrong, L. D., & Kingston, R. S. T. (1960). "Effect of moisture changes on creep in wood." *Nature*, 185, 862-863.

Bažant, Z. P., Hauggaard, A. B., Baweja, S., & Ulm, F.-J. (1997). "Microprestress-solidification theory for concrete creep. I: Aging and drying effects." *Journal of Engineering Mechanics*, 123(11), 1188-1194.

Bažant, Z. P., & Yunping, X. I. (1994). "Drying creep of concrete: constitutive model and new experiments separating its mechanisms." *Materials and Structures*, 27(1), 3-14.

Bobko, C., & Ulm, F.-J. (2008). "The nano-mechanical morphology of shale." *Mechanics of Materials*, 40(4-5), 318-337.

Constantinides, G., & Ulm, F.-J. (2004). “The effect of two types of C-S-H on the elasticity of cement-based materials: Results from nanoindentation and micromechanical modeling.” *Cement and Concrete Research*, 34(1), 67-80.

Carrier, B. (2013). *Effect of water on the short- and long-term mechanical properties of swelling clays: experiments on self-standing films and molecular simulations*, Ph.D. thesis, Université Paris-Est.

Carrier, B., Wang, L., Vandamme, M., Pellenq, R. J.-M., Bornert, M., Tanguy, A., & Van Damme, H. (2013). “ESEM study of the humidity-induced swelling of clay film.” *Langmuir: The ACS Journal of Surfaces and Colloids*, 29(41), 12823-33.

Glass, S. V., & Zelinka, S. L. (2010). “Chapter 4: Moisture Relations and Physical Properties of Wood.” In *Wood Handbook - Wood as an Engineering Material. General technical report FPL: GTR-190*.

Hunt, D. G. (1999). “A unified approach to creep of wood.” *Proceedings of the Royal Society A: Mathematical, Physical and Engineering Sciences*, 455(1991), 4077-4095.

Leroueil, S. (2006). “The isotache approach. Where are we 50 years after its development by Professor Šuklje? (2006 Prof . Šukljes Memorial Lecture).” In *Proceedings of the XIII Danube-European Conference on Geotechnical Engineering*. Ljubljana, Slovenia.

Leung, C. F., Lee, F. H., & Yet, N. S. (1996). “The role of particle breakage in pile creep in sand.” *Canadian Geotechnical Journal*, 33(6), 888-898.

Šuklje, L. (1957). “The analysis of the consolidation process by the isotache method.” In *Proceedings of the 4th International Conference on Soil Mechanics and Foundation Engineering. Vol. 1*. London, England.

Vlahinić, I., Thomas, J. J., Jennings, H. M., & Andrade, J. E. (2012). “Transient creep effects and the lubricating power of water in materials ranging from paper to concrete and Kevlar.” *Journal of the Mechanics and Physics of Solids*, 60(7), 1350-1362.

Zhang, Q. (2014). *Creep properties of cementitious materials: effect of water and microstructure. An approach by microindentation*, Ph.D. thesis, Université Paris-Est.

Useful Fundamentals of Shrinkage and Creep of Concrete

Folker H. Wittmann[1]

[1]Aedificat Institute Freiburg, D-79100 Freiburg, Schlierbergstr. 80; and Swiss Federal Institute of Technology Zurich (ETHZ). E-mail: wittmann@aedificat.de

Abstract

In this contribution selected fundamental properties of concrete are presented and discussed. Basic mechanisms of shrinkage are first described in some detail. With increasing age of concrete different mechanisms of shrinkage become activated. During the first hours after mixing dissolution of cement is the main shrinkage mechanism. Depending on the humidity of the surrounding air capillary pressure in the pore water may cause serious damage in the first hours. After this initial loss of water, the remaining aqueous solution is retreated in the free spaces between fine aggregates and first hydration products. The role of disjoining pressure is pointed out in detail. In this context it becomes clear that the influence of capillary pressure on shrinkage of hardened concrete can be neglected. In equilibrium with RH lower than 50 % the dominating mechanism is the increasing surface energy of the drying gel particles. Shrinkage of high strength concrete has a totally different time evolution as the time-dependent moisture distribution in aging high strength concrete is completely different. If high strength concrete is exposed to an environment with RH higher than 80% there will be no shrinkage at all but swelling. Creep of concrete can be described in a realistic way by means of rate theory. Elements of rate theory are briefly described in the last section. Prediction of creep can be significantly improved if these useful fundamentals are taken into consideration.

INTRODUCTION

There are few properties of concrete, which have been presented and discussed in such a contradictory way as creep and shrinkage. For quite some time creep was characterized by a simple creep number that means the elastic deformation was multiplied by a factor of 2 to 3 to obtain a so-called total deformation. Shrinkage was given as a basic value, which depends on the environmental humidity and a factor, which takes the dimensions of the structural element into consideration. In the meantime the complex nature of creep and shrinkage was widely realized and more sophisticated models for prediction of creep and shrinkage in real structures were developed. In this way material properties can be described more precisely and hopefully some disasters which happened in the past due to underestimation of shrinkage and creep can be avoided in the future. There are fundamentals, which are of interest for scientists exclusively and there are fundamentals, which may be helpful for practitioners.

In the meantime several codes for prediction of creep and shrinkage were published and they are permanently further checked and refined. Model B3, based on several precursors, was first published as a RILEM Draft Recommendation in 1995 (RILEM Draft Recommendation, 1995). Statistical aspects and the sensitivity as well as the theoretical basis were further outlined in two follow-up papers (Bazant, Z. P., and Baweja, S., 1995(1)) and (Bazant, Z. P., and Baweja, S., 1995(2)). Another code was prepared by ACI committee 209 (ACI committee 209, 1992). And a third alternative is the CEB-FIP Model Code (CEB-FIP Model Code, 1990). In fact there exist still more models all with different advantages and shortcomings. All codes are critically checked, compared, and improved on the basis of ever growing databases (see for example: Akthem Al-Manaseer, and Armando Prado, 2015). At the moment the most comprehensive database is probably the NU-ITI database (Bazant, Z.P., and G.-H. Li, 2007).

Scatter plots of measured versus predicted values of shrinkage of concrete are shown for instance in Bazant Z. P., and Baveja S., 1995(1). Prediction models predict the average value reasonably well. The average value as measured on many different types of concrete is not necessarily of primary interest. The type and amount of cement, the water-cement ratio, and the type of aggregates is not taken into consideration adequately. If we consider for instance in the scatter plots of the models a predicted shrinkage value of $0.4 \cdot 10^{-3}$ the measured values may vary between 0.2 and $0.6 \cdot 10^{-3}$. Because of this enormous scatter the value for long term prediction is limited in practice. If, however, some characteristic properties of the material, which can be deduced from fundamental mechanisms of creep and shrinkage of concrete, are taken into consideration in addition, this will be helpful to obtain more realistic results by applying predictive models. It has already been suggested by several authors that short-time tests followed by extrapolation will be necessary to reduce the enormous scatter of data obtained from the different prediction models (see for example: Bazant, Z. P., and Li, G.-H., 2008). Results of short-time tests, however, should be evaluated carefully and understood on the basis of real mechanisms of creep and shrinkage. Then and then only the prediction will be based on a more solid basis and predictions will become more reliable.

In this contribution dominant mechanisms of shrinkage and creep shall be briefly presented. On the basis of real mechanisms it will be possible to predict the influence of a number of parameters on creep and shrinkage. This may help to make predictions of model codes even more reliable. Because of obvious limitations of time and space a selected number of examples can be presented only.

SHRINKAGE

Dissolution and capillary shrinkage

Fresh concrete behaves in the first few hours like a mixture of fine and coarse particles mixed with water. During this early phase the volume of the mix is reduced by evaporation and in particular by dissolution of cement in water. Both evaporation and the dissolution shrinkage lead to an early volume reduction of the fresh mix, which in most cases leads to a vertical movement of the top surface (Beltzung F., and

Wittmann, F. H., 2001). Dissolution shrinkage may be of particular interest for the technology of steel pipes filled with concrete for instance. But it can also create problems when the fresh concrete is placed in complex formwork.

If evaporation of water continues the water film on the surface will be replaced by menisci between the particles near the surface. A capillary pressure p_c will be created in the water under these menisci:

$$p_c = \frac{2\,\sigma\,cos\theta}{r} \tag{1}$$

σ in equ.(1) stands for the surface energy, θ for the wetting angle and r represents the average radius of the menisci. The capillary shrinkage of fresh concrete under the drying surface is shown in Fig. 1. It can be seen that initially the capillary shrinkage follows the evolution of the capillary pressure but after few hours capillary pressure collapses and capillary shrinkage approaches a final value. At this moment the aqueous system in the mix becomes unstable and the remaining water moves into the spaces between the particles (Wittmann, F. H., 1976). By the way this sudden transition can be visually observed easily on the surface of concrete.

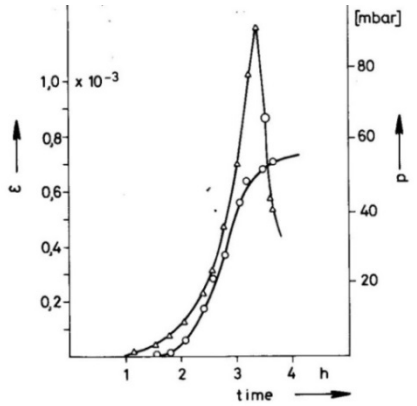

Figure 1. Evolution of capillary pressure p in fresh concrete and resulting capillary shrinkage ε as function of age of concrete (Wittmann F. H., 1976).

It is a wide spread heresy that capillary pressure is a major mechanism of shrinkage of hardened concrete (Wittmann, F. H., 2009). Wide cracks can be formed by capillary pressure in the first hours after compacting fresh concrete, but these cracks can be easily avoided by keeping the surface of fresh concrete wet (Slowik et al. 2009). But after few hours capillary shrinkage becomes negligible.

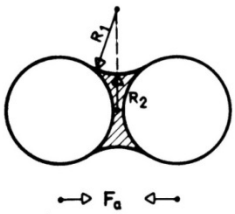

Figure 2. Water layer between two spherical particles

In Figure 2 two spherical particles are shown which are connected by a thin water layer. We may consider fresh concrete to be built up by many of these elements forming a three-dimensional network. The free water layer between the solid particles

can be characterized by two Radii R_1 and R_2 as shown in Fig. 2. From this geometry follows a capillary pressure P_c in the water:

$$P_c = \sigma \cos\theta \left(\frac{1}{R_1} + \frac{1}{R_2}\right) \quad (2)$$

If water evaporates from this system both radii R_1 and R_2 decrease and as a consequence the capillary pressure P_c increases. As capillary pressure increases, the surface of contact between the liquid and the solid particles decreases. It can be shown that under these conditions the attractive force F_a between the two particles remains practically constant (Schubert H., 1972). The green strength of the young concrete also remains constant. That clearly shows that other mechanisms than capillary pressure must be at the origin of drying shrinkage. We will discuss most important mechanisms in the following section.

Drying Shrinkage, influence of disjoining pressure

Let us first have a look at results of an experiment to observe the action of disjoining pressure. In thin water layers between two particles disjoining pressure is created. The theoretical background of disjoining pressure has been studied in great detail (see for instance Churaev, N. V., and Derjaguin, B. V., 1985). Splittgerber has visualized the action of disjoining pressure (Splittgerber, H., 1974, and Splittgerber, H., 1976). The experimental set-up of Splittgerber is shown schematically in Fig. 3 (left). A thin quartz plate is kept at constant distance from a polished quartz block at the right end, while the left end is free. In the dry state the left end is in direct contact with the quartz block and from the bending of the plate van der Waals attractive force can be determined. When the relative humidity of the surrounding air is increased above 55 % the thin glass plate is separated from the support by a thin water layer which squeezes in between y capillary condensation. The increasing distance with increasing RH is shown in Fig. 3 (right).

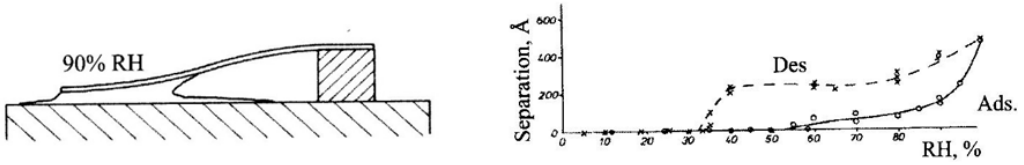

Figure 3. (left) Thin glass plate separated from the quartz support by disjoining pressure of water; (right) Distance from the free end of the thin glass plate from the support as function of RH. The adsorption and desorption branches are shown.

In Fig. 3 (right) a pronounced hysteresis between the adsorption and desorption branches can be observed. This explains essentially the origin of the hysteresis of sorption isotherms as measured on hardened cement paste or concrete. Based on this information we have to subdivide the influence of RH on properties of cement-based materials into two regions: (I) Below 40 % RH adsorbed water reduces the surface energy of gel particles. This leads to expansion of all particles. (II) At higher RH the disjoining pressure modifies the nano-structure of the material by separating existing gaps. This change of the system is also reflected in the change of strength and elastic modulus of the material. Strength of dry concrete decreases with

increasing RH until a value of about 50 % is reached, because surface energy decreases. At higher RH strength decreases even more due to the action of disjoining pressure.

In Fig. 4 hygral length change is plotted as function of RH. The observed length change can be subdivided into two parts. (I) At low RH adsorbed water reduces surface energy of the gel particles. All particles expand until RH reaches a value around 50%. (II) At higher RH additional length change is due to the action of disjoining pressure (dashed zone in Fig. 4). In systems where capillary pressure is at the origin of shrinkage and swelling, shrinkage and not swelling is observed when capillary condensation takes place.

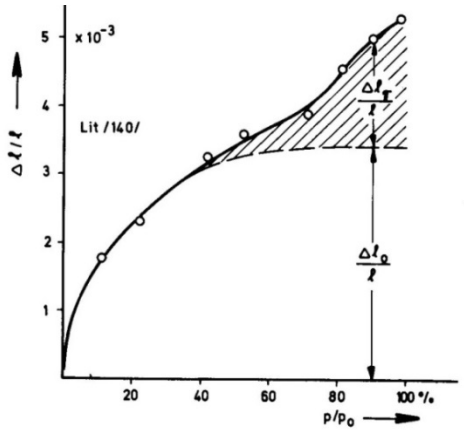

Figure 4. Hygral length change of hardened cement paste as function of RH.

It is well-known that disjoining pressure can be modified by the type and concentration of ions dissolved in the pore water. If disjoining pressure increases shrinkage will increase. In Fig. 5 the total shrinkage of a given type of concrete is plotted as function of the alkali content in the pore water. The final shrinkage increases approximately linearly with increasing alkali content. This observation cannot be explained by the action of capillary pressure. Taking the influence of disjoining pressure into consideration shrinkage can be modified and reduced within limits by choosing cement, which contains a small amount of alkali only. This will also help to use shrinkage prediction in a more realistic way of course.

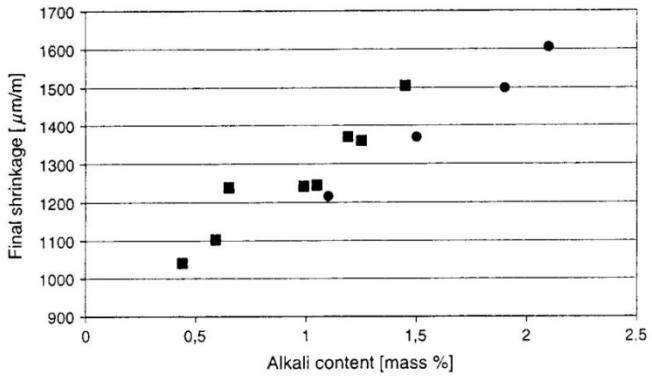

Figure 5. Final shrinkage of concrete as function of the alkali content (■ Na_2O and ● K_2O), (F. Beltzung et al., 2001).

A striking example of the role of disjoining pressure in the complex process of shrinkage can be observed in the so-called Chichibu GRC Cement. This cement is composed in such a way that the portlandite, which is formed during hydration of C_3S and C_2S is progressively consumed by secondary pozzolanic reactions and formation of ettringite. Concrete and mortar fabricated with this special cement has extremely low shrinkage. If, however, $Ca(OH)_2$ is added to the mix, the usual shrinkage deformation is observed. Surface tension of pore water is not changed by Chichibu GRC Cement, nor is it changed by the addition of $Ca(OH)_2$. Shrinkage can be changed within wide borders by the influence of Ca ions on disjoining pressure.

Shrinkage of high performance concrete

So far we have considered dissolution shrinkage, capillary shrinkage and drying shrinkage. In looking into the different mechanisms we could find ways to modify under given circumstances the prediction of model codes and come to more realistic predictions. With the advent of high strength concrete another important aspect became apparent. In high strength concrete a considerable amount of the mixing water is consumed by hydration of cement. In normal concrete the relative humidity in the pore space may be reduced to 95 % at most. Under these conditions an influence on shrinkage exists but it remains modest. With high strength concrete, however, RH in the pore space may be reduced to values below 80 % at an early age. Under these conditions self-desiccation and autogenous shrinkage can be observed. In Fig. 6 results of Miyazawa S. and Tazawa E. ,2001, are shown. It can be seen that shrinkage of high strength concrete differs fundamentally from shrinkage of normal concrete. Due to hydration of cement a considerable amount of mixing water is consumed after seven days already. This rapid self-desiccation leads to considerable shrinkage at very early age. After seven days high strength concrete has reached shrinkage deformation, which can be observed on normal concrete after several years only.

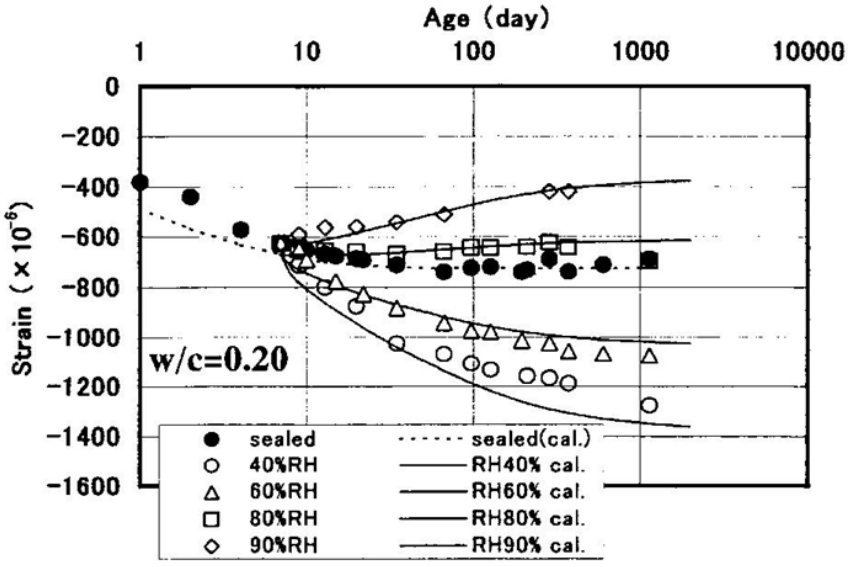

Figure 6. Self-desiccation and autogenous shrinkage of high strength concrete, (S. Miyazawa and E. Tazawa, 2001)

If this type of concrete is exposed to an environment with RH = 80 % no shrinkage can be observed at all, but in contrast the material absorbs humidity from the environment and swells. It will swell even more if placed in an environment with RH of 90 %. Obviously in this case predictions of most model codes are far from the observed deformations. To understand the fundamental differences of shrinkage of normal and high strength concrete we have to look into the moisture distributions as function of time. In Fig. 7 the distributions of relative humidity of normal strength and high strength concrete are shown for the first five years after casting (Alvaredo, A. M., and Wittmann, F. H., 1995). In this case the concrete is supposed to be exposed to an environment with an average relative humidity of 50 %. The concrete sample is supposed to have a thickness of 500 mm. The quick self-desiccation of high strength concrete leads to a decrease of RH to approximately 80 % over the entire cross section after two weeks and finally a value of slightly more than 70 % is reached after six months. The RH will not decrease further in the center because the hydration of cement is practically stopped at this low relative humidity. The remaining pore water is not available for further hydration of cement. The slow loss of water by drying continues of course for many years and finally equilibrium with 50 % RH will be reached. Based on the time-dependent moisture distributions shown in Fig. 7 shrinkage of specimens made with the two types of concrete can be numerically determined. Results are shown for the first 5 years in Fig.8 (left). It is obvious that the time-dependence of shrinkage is totally different. From these results follows that it is not realistic to assume a common shrinkage law for concrete with significantly different water-cement ratio.

If the drying specimens of normal and high strength concrete are fixed at both ends a time-dependent restraint reaction can be observed. Results of numerical predictions are shown in Fig.8 (right). The normal strength concrete will fail under tension after 500 days of drying. The high strength concrete, however, will fail after 13 days already because of the quick endogenous drying process.

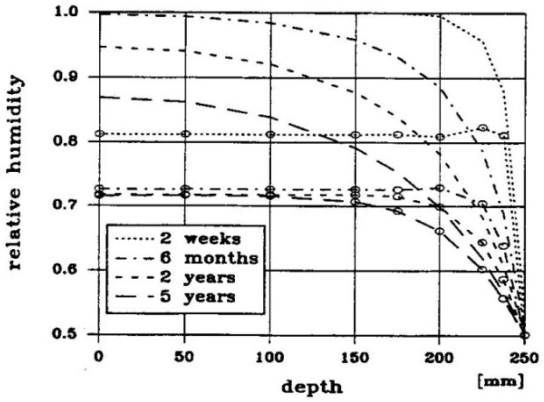

Figure 7. Moisture distribution in normal and high strength concrete (curves plotted with circles) in the first five years

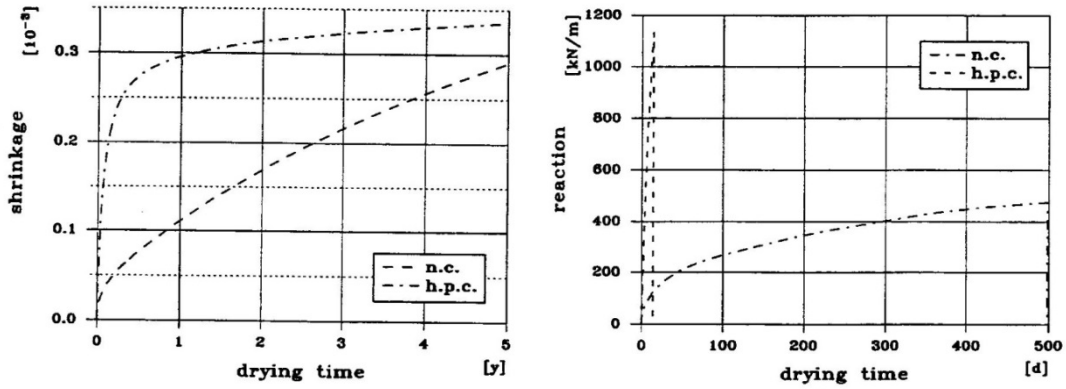

Figure 8. (left) Evolution of shrinkage of normal (n.c.) and high performance concrete (h.p.c.) as determined along the centre of the specimens; (right) Evolution of restraint reaction of fully restraint members of normal (n.c.) and of high performance concrete (h.p.c.)

CREEP

Creep of different materials such as metals, ceramics, and polymers can be described in a realistic way by rate theory. This very general approach can also be applied to cement-based materials (Wittmann, F. H., 1977, Klug, P. and Wittmann, F. H., 1974, Wittmann, F. H. and Lukas J., 1974). On this basis creep strain ε as function of time t can be expressed by the following equation:

$$\varepsilon = at^n \exp\left(-\frac{Q}{RT}\right) \sinh\left(\frac{V}{RT}\,\sigma\right) \tag{3}$$

In Eq.(3) Q stands for the activation energy and V for the activation volume of the material. The activation energy of concrete is in most cases approximately 4.5 kcal/Mol. The activation volume varies with water-cement ratio and with humidity content. An average value of 10^{-17} mm^3 has been determined (Klug, P. and Wittmann, F. H., 1974)

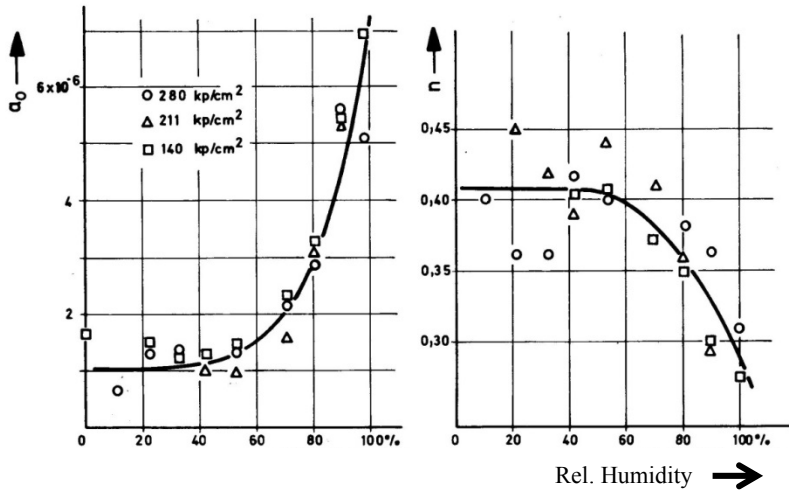

Figure 9. a_0 and n of Eq. (4) as function of relative humidity

If creep at constant temperature and at moderate applied stress is to be described, Eq.(3) can be simplified:

$$\varepsilon = a_0\, t^n\, \sigma \tag{4}$$

Under constant moisture content creep follows a simple power law. But the moisture content has a significant influence on the activation volume. The lower the moisture content, the lower will be the creep strain. Values for a_0 and n of Eq. (4) are plotted in Fig. 9. As expected, creep of saturated specimens is at maximum. In high strength concrete the equilibrium humidity in the mass may be reduced after one week already to values around 75 %. According to Fig. 9 creep of high strength concrete will then be reduced to one third of the value at saturation.

CONCLUSIONS

Shrinkage of porous materials such as concrete is a complex process based on a number of different mechanisms. The most important mechanisms at an early stage are dissolution shrinkage and capillary shrinkage. In the hardened state of concrete shrinkage is essentially due to loss of water in the pore space. Water can get lost by drying to the environment and by internal drying by continuing hydration (self-desiccation). Disjoining pressure in concrete depends strongly on the amount and type of ions dissolved in the pore water. When all these mechanisms are taken into consideration prediction of shrinkage by model codes can be significantly improved. For high strength concrete and for concrete produced with blended cements existing model codes are applicable with certain limits only. When obvious fundamental properties are taken into consideration, model codes can be modified for given applications and for special types of concrete they can be made more realistic.

REFERENCES

ACI committee 209, “Prediction of creep, shrinkage and temperature effects in concrete structures”, ACI 209 R-92, American Concrete Institute, Detroit.

Al-Manaseer A., and Prado A., (2015) “Statistical comparison of creep and shrinkage prediction models using RILEM and NU-ITI Databases, ACI Material Journal 112(1) 125-135

Alvaredo, A. M., and Wittmann, F. H.,(1995) “Shrinkage and cracking of normal and high performance concrete”, in High Performance Concrete: Material Properties and Design, Wittmann F. H. and Schwesinger P., editors, Aedificaatio Publishers, Freiburg, 91-110

Bazant, Z. P., and Baweja, S., (1995(1)) “Justification and Refinements of Model B3 for concrete creep and shrinkage, 1. Statistics and sensitivity” Materials and Structures 28, 415-430.

Bazant, Z. P. and Baweja, S., (1995(2) “Justification and refinements of model B3 for concrete creep and shrinkage, 2. Updating and theoretical basis” Materials and Structures 28, 488-495.

Bazant, Z. P., and Li, G.-H., (2007) “NU Database of Laboratory Creep and Shrinkage Data” available for download from www.civil.northwestern.edu/people/Bazant.html.

Bazant, Z. P., and Li, G.-H., (2008) “Unbiased statistical comparison of creep and shrinkage prediction models” ACI Materials Journal 105(6) 610-621.
Beltzung, F., and Wittmann, F. H., (2001) “Early chemical shrinkage due to dissolution and hydration of cement” Materials and Structures 34, 279-283
Beltzung, F., Wittmann, F. H., and Holzer, L.,(2001) „Influence of composition of pore solution on drying shrinkage“ in Creep, Shrinkage and Durability Mechanics of Concrete and other Quasi-brittle Materials, edited by Ulm F.-J., Bazant Z. P. and Wittmann F. H., Elsevier Science Ltd., 39-48
Beltzung, F., and Wittmann, F. H., (2005) “Role of disjoining pressure in cement based materials” Cement and Concrete Research 35, 2364-2370.
CEB-FIP Model Code, Design Code, (1990), Thomas Telford, London,
Churaev, N. V., and Derjaguin, B. V., (1985) “Inclusion of structural forces in the theory of stability of colloids and films” J. Coll. Interf. Sci. 103(2), 542-553
Klug, P. and Wittmann, F.H., (1974) “Activation energy and activation volume of creep of hardened cement paste”, Mat. Sci. and Eng. 15, 63-66
Miyazawa, S., and Tazawa, E., (2001) “Prediction model for shrinkage of concrete including autogenous shrinkage”, in Creep, Shrinkage and Durability Mechanics of Concrete and other Quasi-brittle Materials, edited by Ulm F.-J., Bazant Z. P. and Wittmann F. H., Elsevier Science Ltd., 735-740
RILEM Draft Recommendation, Projets de Recommendation de la RILEM, (1995) 107-GCS Guidelines for the Formulation of Creep and Shrinkage Prediction Models, Creep and Shrinkage Prediction Model for Analysis and Design of Concrete Structures – Model B3, Materials and Structures 28, 357-365.
Schubert, H.,(1972) “Untersuchungen zur Ermittlung von Kapillardruck und Zugfestigkeit von feuchten Haufwerken aus körnigen Stoffen“, Dissertation, Karlsruhe University of Technology.
Schubert, H., (1992) “Kapillarität in porösen Feststoffsystemen“, Springer Verlag.
Slowik, V., Neumann, A., Dorow, J., and Schmidt, M., (2009) “ Early age cracking and its influence on durability of concrete structures” in Creep, Shrinkage and Durabiity Mechanics of Concrete and Concrete Strucutres, Tanabe T., Sakata, K., Mihashi, H., Sato, R., Maekawa, K., and Nakamura, H., editors, CRC Press, 471-477.
Splittgerber, H., (1974) “Einfluss adsorbierter Wasserfilme auf die van der Waals Kraft zwischen Quarzglasoberflächen“, Surface Science 41, 504-514
Splittgerber, H., (1976) “Spaltdruck zwischen Festköpern und Auswirkung auf Probleme in der Technik“, Cement and Concrete Research 6, 29-36.
Wittmann, F. H., and Lukas, J., (1074) “The application of rate theory to time-dependent deformation of concrete “, Mag. of Concr. Res. 26, 191-197.
Wittmann, F. H., (1976) “On the action of capillary pressure in fresh concrete” Cement and Concrete Research 6, 49-56
Wittmann, F. H., (1977) “Grundlagen eines Modells zur Beschreibung charakteristischer Eigenschaften des Betons“ , Deutscher Ausschuss für Stahlbeton, Schriftenreihe Heft 290, 43-101
Wittmann, F. H., (2009) “Heresies on shrinkage and creep mechanisms” in Creep, Shrinkage and Durability Mechanics of Concrete and Concrete Structures, Tanaba et al., editors, Taylor and Francis Group, London, 3-9.

Fracture and damage spreading in amorphous materials

Elisabeth Bouchaud

PSL Research University, ESPCIParisTech, UMR Gulliver, 10 rue Vauquelin, 75231 Paris Cedex 05, FRANCE; email: elisabeth.bouchaud@cea.fr

ABSTRACT

Although amorphous materials are usually brittle, and break without deforming irreversibly at observable sclaes, their fracture involves some dissipation. By examining the *post-mortem* fracture surfaces, by following *in situ* the progession of a stress corrosion crack in silicate glasses and by measuring the depth of penetration of water in the material during slow fracture, we show that glass behaves in fact in a quasi-brittle manner, with a damage zone of $\approx$10 nm developping ahead of the crack tip. In order to make these damage scales observable optically, we have started to work on colloidal systems, where "atoms" have the size of a few micrometers. Direct observation of crack propagation through these materials show that damage is not of plastic origin as in ductile metals, for example, but of a quasi-brittle nature.

Amorphous materials are often brittle macroscopically: they break without deforming irreversibly prior to fracture. One noticeable counterexample, however, concerns metallic glasses, which may be either brittle or ductile [1, 2, 3]. On the contrary, silicate glasses are considered as the archetype of brittle materials. As a consequence, no energy dissipation is expected to take place during fracture, and Griffith's energy balance criterion should be perfectly fulfilled: the stored elastic energy should exactly compensate for the creation of two free surfaces. Let us remark that if this is the physical definition of "brittleness", then the cleavage of perfect crystals is indeed brittle. As a matter of fact, in a perfect crystal, all the atomic bonds having identical energies, the first one to break is the one located exactly at the crack tip, where the stress is the largest. Cleavage thus proceeds by successive openings of atomic bonds at the crack tip, and the fracture energy is exactly equal to the product of the number of cut bonds by their energy. Cleavage surfaces are also perfectly flat, and used for that quality in surface science experiments.

If one considers now an amorphous material, the balance is not as simple. Some bonds may require less energy to be broken, and, in consequence, they may break first even if they are located somewhat away from the crack tip. Furthermore, the orientation of the bond at the crack tip may not be adequate: if the bond is perpendicular to the direction of the applied tension, it undergoes a much smaller tension than if it is

parallel to it. In the case of silica, knowing that the only bonds which can be broken are the Si-O bonds linking together silica tetrahedra, and knowing their energy, 110 kcal/mole [4], one can estimate the energy needed to break all the Si-O bonds per unit area to be 2J.m^{-2}. It can be compared to the fracture energy, $\simeq K_{Ic}^2/E \simeq 9$J.m^{-2}, where $K_{Ic} \simeq 0.8$ MPa.m$^{-1/2}$ and $E \simeq 70$ GPa are respectively the fracture toughness and the Young's modulus of silica. In a humid environment, as recalled in the following, a crack propagates at a lower stress intensity factor, depending on the humidity rate. Typically, propagation was observed to take place at a velocity $v \simeq 10^{-11}$ m.s^{-1} for a stress intensity factor $\simeq 0.4$ MPa.m$^{-1/2}$ at 40% humidity. Even in this case, the fracture energy is $\simeq$ 4.5 J.m^{-2}, a value more than twice higher than the expected one. Since glass is deprived of plasticity when loaded in tension – the plastic zone size can be estimated to be of the order of $R_c = \pi/8(K_{Ic}/\sigma_Y)^2 \simeq 1.7$ nm [5] (σ_Y being the yield stress)– the central question is the nature of the dissipated energy.

The only possibility seems to be a quasi-brittle damage spreading similar to the one which can be observed at a macroscopic scale in materials which are highly disordered, such as wood, concrete, or paper, for example [6]. This is indeed what is suggested by Molecular Dynamics (MD) simulations for other amorphous materials [7] and for silica [8], independently of the interaction potential used [9]. Such processes were actually observed in metallic glasses. In these materials, where the matrix is not compeltely deprived of plasticity, damage cracks extend into cavities under tension, and their traces could be observed on fracture surfaces [2].

We have performed several experiments on silica, in order to track quasi-brittle damage. We have first examined, with an Atomic Force Microscope (AFM), the morphology of glass fracture surfaces, and compared it to observations performed on other materials [10]. We have shown that glass fracture surfaces are *self-affine*, i.e. that the distribution of heights h has a second moment which involves a roughness index ζ in the direction perpendicular to the direction of crack propagation, and an exponent $\beta \neq \zeta$ in the direction of crack propagation [11].
where $\Delta h(\Delta x, \Delta z)$ is the mean heigth difference between points of the fracture surface separated by a distance Δx along the direction of crack propagation and by a distance Δz in the perpendicular direction.
The so-called "dynamic exponent" κ is simply the ratio of the roughness indices ζ and β: $\kappa = \zeta/\beta$.

For different humidity rates, i.e. for different crack velocities ranging from $\sim 10^{-12}$m.s^{-1} to $\sim 10^{-4}$m.s^{-1}, it was observed that: $\zeta \simeq 0.8$ and $\beta \simeq 0.6$.

Because it has been shown that there are indeed two classes of universality corresponding to [12] (i) purely brittle fracture of disordered materials for which $\zeta \simeq 0.4$ and $\beta \simeq 0.5$, (ii) quasi-brittle or ductile fracture, for which $\zeta \simeq 0.75$ and $\beta \simeq 0.6$, our observations showed that quasi-brittleness exists in silica at the scale of a few tens of nanometers.

Another set of observations consists in direct observation of damage spreading around a propagating crack tip, using AFM [14, 15]. Because scanning with an AFM

takes time, we were constrained to follow very slow propagating cracks. This cannot be achieved in UHV conditions, this is why we have decided to follow stress corrosion cracks [5]. Under very moderate external tensile stresses, corresponding to stress intensity factors K_I lower than K_{Ic}, cracks may indeed grow in silicate glasses, thanks to hydrolysis of the Si-O bonds, a chemical reaction which involves the water molecules of the surrounding environment. This is a complex phenomenon, which started to be studied in the sixties [16, 17] and is not yet fully understood (see [18] for a review). In the classical picture, proposed first by Michalske and Bunker [19], water molecules break the Si-O bonds located exactly at the crack tip. For small enough external loads, the crack velocity is controlled by the rate of the chemical reaction, which depends both on the degree of ambient humidity and on the applied stress. It is in this regime, traditionally refered to as "Stage I" [5], that our AFM experiments have been performed.

We have observed the formation of depressions ahead of the main crack tip, and we have concluded that, indeed, secondary cracks form and contribute to energy dissipation.

However, in this case also, several artifacts could alter the results [20, 21, 22]. Other authors, by using digital image correlation techniques applied to AFM frames, concluded that there is no departure from elasticity at distances larger or equal than $\sim$ 10nm (resolution of their experiments) from the crack tip [23]. Hence a more accurate technique had to be used in order to understand whether failure in glass is indeed preceded by damage at very small scales. Neutron reflexion indeed provides the required sensitivity. It also allows to probe the bulk of the specimen, which is unaccessible to AFM. As a matter of fact, stresses at the surface of the specimen – where plane stress conditions apply – are different from the ones in volume - plane strain conditions -. But, much more importantly, the surface is in contact with an infinite reservoir of water molecules. On the contrary, water has to diffuse within the bulk in order to provoke damage.

Nevertheless, if one considers the diffusion coefficient of water in silica, in order to estimate the plausibility of our scenario, it seems unlikely. Although experiments have been performed at high temperature only [24, 25], a rough extrapolation of Tomozawa et al's results [26] suggests a water diffusion coefficient in silica of the order of $\sim 10^{-21}$ cm^2.s^{-1} at room temperature. This means that the penetration length of water molecules into unstrained glass should be approximately 3 pm (respectively 0.3 Å) during the time it takes for a crack moving at 10^{-6} m.s^{-1} (respectively at 10^{-8} m.s^{-1}) to cover 100 μm.

However, because of the huge stresses concentrated at the crack tip, diffusion is enhanced by orders of magnitude in the vicinity of the tip during fracture, as observed in several other materials. Therefore, water is expected to penetrate into the glass and, because of the heterogeneity of the material mentioned above, starts breaking bonds and create microcracks ahead of the crack tip. This in turn increases further the diffusion of water, thereby creating more corrosion and potentially leading to a substantial damaged zone. If this scenario is correct, a rather thick layer of water should remain

trapped underneath the nominal fracture surface after the crack has propagated and stresses have relaxed. Since the diffusion constant is so small in unloaded silica glass (more than 100 days for travelling 1 nm), one should observe post-mortem a "fossil" water profile, essentially frozen-in at the time of its creation, with a thickness of the order of the size of the damaged zone.

Specular Neutron Reflectivity (SNR) measurements have been carried out on the horizontal time-of-flight EROS reflectometer (CEA-Saclay, France) to test this scenario, with a neutron white beam covering wavelengths λ from 4 Å to 25 Å, corresponding to an accessible range of diffusion vectors ranging from from 0.005 $Å^{-1}$ to 0.032 $Å^{-1}$.

Our results have shown a huge change in the reflectivity of broken samples when compared to the reflectivity of an unbroken control specimen. By fitting the refectivity curves (reflectivity as a function of the wave vector), we have shown that a damage zone of extension $\sim 10 - 15$nm had to form during fracture to explain the presence of water stored under the fracture surface.

In order to analyze damage spreading using standard and confocal optical microscopy, we have recently started to study fracture of colloidal gels, in collaboration with Peter Schall's group at the University of Amsterdam. Close to the critical point of a binary liquid, P. Schall and collaborators have shown that concentration fluctuations become long range, and the confinement of these long-range fluctuations gives rise to critical Casimir interactions [27, 28] which amount to an attraction between the colloids. Critical Casimir interactions are induced by approaching the phase-separation temperature of the binary solvent. In order to trigger gelification of the colloidal system of 2 micrometer size microgels, temperature has to be controlled with a 0.1K precision.

We have constructed a microfluidic cell [29] in stainless steel, the temperature of which can be controlled precisely enough in order to trigger the sol-gel transition *in situ*. Displacement is applied to the formed gel by pumping out the solvent at a prescribed flow rate. Observations were made within a plane in the bulk of the material in confocal microscopy. Damage formation ahead of the main crack tip could be observed directly. A Digital Image Correlation method due to Hild and Roux [30] allowed us to locate precisely bond breakings ahead of the main tip, and to evaluate the size of the damage zone (several tens of micrometers).

These colloidal systems, which exhibit an amorphous structure at a scale much larger than silicate or polymeric glasses, are good candidates to study damage and crack propagation mechanisms. More concentrated solutions leading to glassy systems will be considered in a near future.

REFERENCES

X. K. Xi, D. Q. Zhao, M. X. Pan, W. H. Wang, Y. Wu, and J. J. Lewandowski. Fracture of brittle metallic glasses: Brittleness or plasticity. *Phys. Rev. Lett.*, 94:125510, 2005.

E. Bouchaud, D. Boivin, J.-L. Pouchou, D. Bonamy, B. Poon, and G. Ravichandran. Fracture through cavitation in a metallic glass. *Europhys. Lett.*, 83:66006, 2008.

P. Guan, S. Lu, M. J. B. Spector, P. K. Valavala, and M. Falk. Cavitation in amorphous solids. *Phys. Rev. Lett*, 110:185502, 2013.

R. T. Sanderson. *Chemical bonds and bond energy*. Academic Press, 1971.

B. Lawn. *Fracture of Brittle Solids- Second Edition*. Cambridge University Press, 1993.

D. Bonamy and E. Bouchaud. Failure of heterogeneous materials: A dynamic phase transition? *Physics Reports*, 498:1–44, 2011.

A. Nakano, R. K. Kalia, and P. Vashishta. Dynamics and morphology of brittle cracks: A molecular-dynamics study of silicon-nitride. *Phys. Rev. Lett.*, 75:3138–3141, 1995.

C. L. Rountree, R.K. Kalia, E. Lidorikis, A. Nakano, L. Van Brutzel, and P. Vashishta. Atomistic aspects of crack propagation in brittle materials: multimillion atom molecular dynamics simulations. *Annual Review of Materials Research*, 32:377–400, 2002.

M. L. Falk. Molecular-dynamics study of ductile and brittle fracture in model noncrystalline solids. *Phys. Rev. B*, 60:7062–7070, 1999.

P. Daguier, S. Hénaux, E. Bouchaud, and F. Creuzet. Quantitative analysis of a fracture surface by atomic force microscopy. *Phys. Rev. E*, 53:5637, 1996.

L. Ponson, D. Bonamy, and E. Bouchaud. Two dimensional scaling properties of experimental fracture surfaces. *Phys. Rev. Lett.*, 96:035506, 2006.

L. Ponson. Crack propagation in disordered materials: how to decipher fracture surfaces. *Annales de Phys.*, 32:1, 2007.

F. Lechenault, G. Pallares, M. George, C. Rountree, E. Bouchaud, and M. Ciccotti. Effects of finite probe size on self-affine roughness measurements. *Phys. Rev. Lett.*, 104:025502, 2010.

F. Célarié, S. Prades, D. Bonamy, L. Ferrero, E. Bouchaud, C. Guillot, and C. Marlière. Glass breaks like metals, but at the nanometer scale. *Phys. Rev. Lett.*, 90:075504, 2003.

S. Prades, D. Bonamy, D. Dalmas, E. Bouchaud, and C. Guillot. Nano-ductile propagation in glasses under stress corrosion: spatio-temporal evolution of damage in the vicinity of the crack tip. *Int. J. of Sol. and Struct.*, 42:637–645, 2004.

S. M. Wiederhorn. Moisture assisted crack growth in ceramics. *Int. J. of Fract. Mech.*, 4:171–177, 1968.

S. M. Wiederhorn. Fracture surface energy of glass. *J. Am. Ceram. Soc.*, 52, 1969.

M. Ciccotti. Stress-corrosion mechanisms in silicate glasses. *J. Phys. D: Appl. Phys.*, 42, Special Issue "Fracture: from the atomic to the geophysical scale", Guest Editors E. Bouchaud and P. Soukiassian:214006, 2009.

T.A. Michalske and B.C. Bunker. Slow fracture model based on strained silicate structures. *J. Appl. Phys.*, 56:2686–2693, 1984.

J.-P. Guin and S. M. Wiederhorn. Fracture of silicate glasses: Ductile or brittle? *Phys. Rev. Lett.*, 92:215502, 2004.

J.M. Lòpez-Cepero, S.M. Wiederhorn, T. Fett, and J.-P. Guin. Do plastic zones form at crack tips in silicate glasses? *Int. J. Mater. Res.*, 98:1170–1176, 2007.

T. Fett, G. Rizz, D. Creek, S. Wagner, J. P. Guin, J. M. López-Cepero, and S. M. Wiederhorn. Finite element analysis of a crack tip in silicate glass: No evidence for a plastic zone. *Phys. Rev. B*, 77:174110, 2008.

K. Han, M. Ciccotti, and S. Roux. Measuring nanoscale stress intensity factors with an atomic force microscope. *Europhys. Lett.*, 89:66003–p1/p5, 2010.

K.M. Davis and M. Tomozawa. An infrared spectroscopic study of water-related species in silica glasses. *J. of Non-Cryst. Sol.*, 201:177–198, 1996.

S. Berger and M. Tomozawa. Water diffusion into a silica glass optical fiber. *J. of Non-Cryst. Sol.*, 324:256–263, 2003.

M. Tomozawa and K. M. Davis. Time dependent diffusion coefficient of water into silica glass at low temperatures. *Mat. Sci. and Eng. A*, 272:114119, 1999.

D. Bonn, J. Otwinowski, S. Sacanna, H. Guo, G. Wegdam, and P. Schall. Direct observation of colloidal aggregation by critical casimir forces. *Phys. Rev. Lett.*, 103:156101, 2009.

V. D. Nguyen, S. Faber, Z. Hu, G. H. Wegdam, and P. Schall. Controlling colloidal phase transitions with critical casimir forces. *Nature Comm.*, 4:1584:1–6, 2013.

M. Lefranc and E. Bouchaud. Mode i fracture of a biopolymer gel: rate-dependent dissipation and large deformations disentangled. *Extreme Mech. Lett.*, 2014.

F. Hild and S. Roux. Comparison of local and global approaches to digital image correlation. *Exp. Mech.*, 52:1503–1519, 2012.

Shape Correction Factor for Drying Shrinkage in a Concrete Cross-Section

N. Reybrouck[1]; P. Criel[1]; R. Caspeele[1]; and L. Taerwe[1]

[1]Magnel Laboratory for Concrete Research, Department of Structural Engineering, Ghent University, Technologiepark-Zwijnaarde 904, Ghent. E-mail: Nicky.Reybrouck@UGent.be

Abstract

A concrete member is subjected to loads for a long period of time, during which creep and shrinkage of concrete develop gradually. The prediction of this time-dependent behaviour is important as it may cause serious serviceability problems in concrete structures. A time-dependent analysis is commonly based on empirical equations according to design codes where the function describing the time dependent increment of shrinkage and creep is commonly, among others, defined based on the notional size of the element. In case of imbedded steel or insulated boundaries the moisture transport can be partially affected or prevented. Also, the geometry and size of the cross-section have an important effect on the shrinkage behaviour of a concrete member. Hence, the performance of commonly used empirical formulas may be improved by applying a correction factor on the notional size. In order to investigate the impact of these various factors on the net macroscopic shrinkage used in analysis and design, a discretized 2D physical model was developed. The model was used to simulate drying of a concrete cross-section by determining the moisture distribution in the cross-section as function of time.

INTRODUCTION

Creep and shrinkage of concrete result in long-term deformations that may cause serviceability problems and it is therefore important to predict this effect properly. The mechanisms causing creep and shrinkage of concrete show significant correlation with the moisture distribution of the concrete cross–section. This study is focussing on the determination of the influence of the geometry of a concrete member on the drying shrinkage response.

The effect of moisture transportation has shown considerable effect on shortening of concrete members in case of imbedded steel profiles (Seol 2008). The differential moisture distribution should therefore be taken into account in order to enhance the accuracy of the prediction of strain development. The deformation of concrete members depends highly on the possible moisture transport routes affected by for example a different shape geometry (T-beams), hollow areas (hollow core elements), obstructions (imbedded steel) and boundary conditions (isolations and exposed surfaces).

The moisture diffusion and differential drying shrinkage was determined using finite element analysis. This behaviour is determined by analysing the progress of moisture at each point of the concrete section in time.

NUMERICAL ANALYSIS OF DRYING CREEP AND SHRINKAGE

The creep and shrinkage behaviour is modelled using a finite element method combined with Fick's second law of diffusion, which describes the transient phenomena within the concrete section during each time–step of the analysis. The drying of a concrete cross-section with time is given by (Sue-Tae 2011):

$$\frac{\partial H}{\partial T} = \nabla \cdot (D_s(H,T)\nabla \mathrm{H})$$

where H is the relative pore humidity and t is time. The progress of moisture diffusion through these specimens was calculated using the non-linear moisture diffusion equation (Bazant 1972). For isothermal conditions the non–linear diffusion coefficient D can be expressed as a function of the relative pore humidity H as defined in Model Code 2010 (Fib 2010) as:

$$D(H) = D_1\left(\alpha + \frac{1-\alpha}{1+\left(\frac{1-H}{1-H_c}\right)^n}\right)$$

where D_1 is the maximum of $D(H)$; D_0 is the minimum of $D(H)$; $\alpha = D_0/D_1$ (assumed 0.05); H_c = the relative pore humidity at $D(H) = 0.5D_1$ (assumed 0.80) and n is an exponent (assumed 15). The free shrinkage at each point of the section is determined based on local drying and calculated as suggested by (Kim 2012; Bazant 1994):

$$\Delta\varepsilon_{sh}(t_i, t_{i-1}) = \varepsilon_s^0 g_s(t_i)(1 - h(t_i,x,y)^3) - \varepsilon_s^0 g_s(t_{i-1})(1 - h(t_{i-1},x,y)^3)$$

where $\Delta\varepsilon_{sh}(t_i, t_{i-1})$ is the shrinkage strain during time period (t_i, t_{i-1}); ε_s^0 is the magnitude of the final shrinkage; $g_s(t_i) = E_c(t_0)/E_c(t_i)$; $E_c(t)$ is the Young modulus at time t and $h(t,x,y)$ is the local moisture content at time t.

The moisture distribution at each time step and each material point within the concrete section is determined using the initial strains and induce non-uniform restraining stresses. An example of the moisture distribution of a T-shaped cross-section is shown in Figure 1. This analysis of shrinkage and creep strains was performed by using a numerical step-by-step procedure in time in combination with transformed section properties adjusted in time.

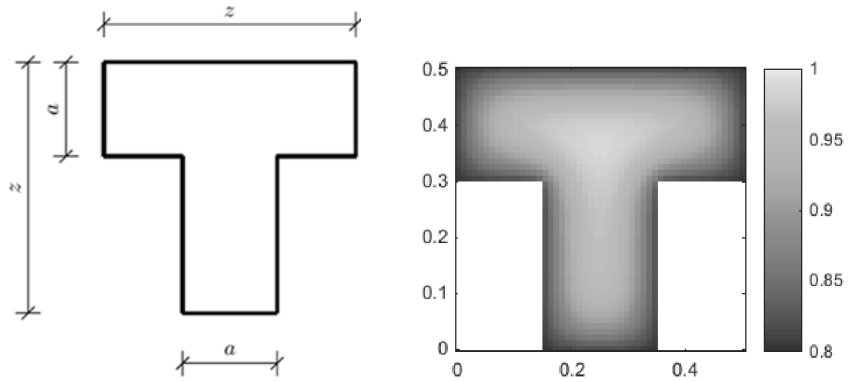

Figure 1. Geometry of the studied T cross-section and moisture content example.

The local shrinkage behaviour in a specific point of the cross-section is determined based on the local moisture content history. This local strain response throughout the structural element in space/time is then transformed to a section-wide temporal shrinkage response by applying the principle of Navier-Bernoulli. The fictitious force ΔN and bending moment ΔM_x corresponding to restrain the local free shrinkage increment $\Delta\varepsilon_{sh}(x, y, t_i, t_{i-1})$ at time interval (t_i, t_{i-1}) is determined by (Ghali 2011):

$$\Delta N = \int_A E_c(t)\Delta\varepsilon_{sh}(x, y, t_i, t_{i-1})\, dA$$

$$\Delta M_x = \int_A E_c(t)\Delta\varepsilon_{sh}(x, y, t_i, t_{i-1})\ y\, dA$$

in which y is the y-coordinate of the observed material point and A is the area of the cross-section. The strain increment $\Delta\varepsilon_{\mathrm{sh}}(t_i, t_{i-1})$ and curvature increment $\Delta\kappa_{\mathrm{sh}}(t_i, t_{i-1})$ are then calculated by:

$$\begin{Bmatrix}\Delta\varepsilon_{\mathrm{sh}}(t_i, t_{i-1})\\ \Delta\kappa_{\mathrm{sh}}(t_i, t_{i-1})\end{Bmatrix} = \frac{1}{E_c(t)}\begin{bmatrix}EA & ES\\ ES & EI\end{bmatrix}^{-1}\begin{Bmatrix}-\Delta N\\ -\Delta M_x\end{Bmatrix}$$

in which EA, ES and EI are respectively the area, the first moment of area and the second moment of area of the transformed cross-section multiplied with the modulus of elasticity $E_c(t)$. The final shrinkage $\varepsilon_{sh}(t)$ is given by:

$$\varepsilon_{sh}(t) = \sum_{i=1}^{n} \Delta\varepsilon_{sh}(t_i, t_{i-1})$$

RESULTS OF THE NUMERICAL SIMULATION

The size of each element used in the numerical analysis was chosen equal to 5 mm and the simulation was performed for a period of 10 years using time step increments of 5 hours. An example of the drying shrinkage development obtained by the numerical analysis for different geometries such as rectangular, circular and T-shaped cross-sections are given in Figure 2.

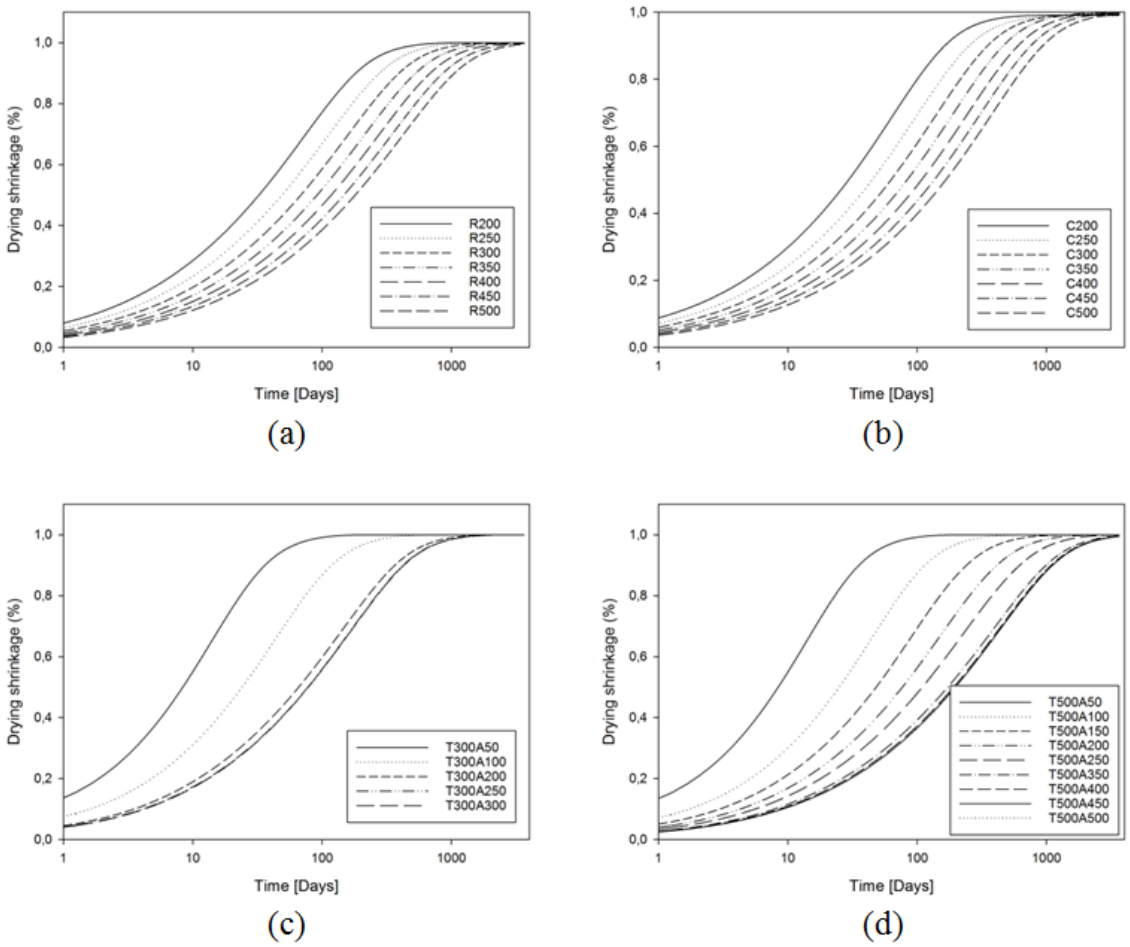

Figure 2. Drying shrinkage development for different cross-sections (a) Rectangular (b) Circular (c) T-beam with z = 300 mm, variable flange thickness a (d) T-beam with z = 500 mm, variable flange thickness a.

REMARK

Drying shrinkage results in a shortening of the concrete element. Cross-sections who do not have two axis of symmetry will also produce a curvature (inclined plane) due to the non-uniform shrinkage (see Figure 3). The curvatures as function of time obtained from the numerical analysis of a T-beam with a width of 500 mm are shown in Figure 4.

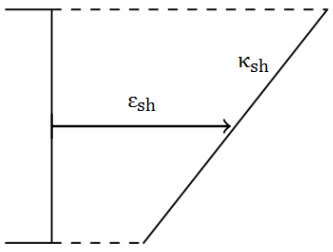

Figure 3. Curvature due to the non-uniform development of shrinkage.

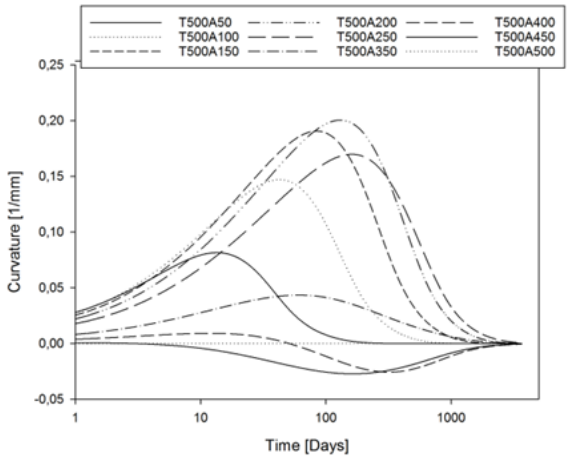

Figure 4. Curvature due to the development of shrinkage in case of T-beams. (example z = 500 mm)

SHAPE CORRECTION FACTOR

An averaged cross-sectional approach in which the behaviour of the structural member is equal for the whole cross-section is a simple, fast and efficient method for the analysis of creep and shrinkage in concrete structures and is widely used in engineering practice. The formulations given in Model Codes and guidelines such as CEB-FIP (fib 2010), ACI (ACI 1998), B3 (Bazant 1995), B4 (RILEM 2015) are generally used to calculate the shortening of concrete members. These methods provide fairly good results as an average for plain concrete cross–sections. It considers mix properties, size and exposed ambient conditions. The progress of drying shrinkage in Eurocode 2 is expressed as a function of the notional size of the element. Non–uniform behaviour of the cross-section cannot be captured correctly using these methods but can be accounted for using correcting parameters. The shrinkage and creep equations found in Eurocode have been modified to predict the shortening of the concrete element more accurately for different shapes. In this paper a modified shrinkage model is suggested to a determine shape correction factor α_T to improve the accuracy of the formulations for drying creep of concrete by modifying the notional size h_0 in Eurocode 2. It is assumed that the differences between the different shapes are caused only by the moisture diffusion process. Consequently, the proposed method was used to perform a numerical analysis on a wide range of different shapes and dimensions for T-shaped beams to improve the local drying shrinkage prediction. The function $\beta_{ds}(t, t_s)$ (EN 1992-1-1) describes the time-development of the drying shrinkage $\varepsilon_{cds}(t, t_s)$ and is given as (with an additional proposed correction parameter α_T) :

$$\beta_{ds}(t, t_s) = \frac{t - t_s}{(t - t_s) + 0.04\sqrt{(\alpha_T h_0)^3}}$$

where $h_0 = 2\,A_c/u$; A_c is the cross-section and u is the perimeter of the member in contact with the atmosphere.; α_T is a proposed shape correction factor for T-beams. Some examples for h_0 are shown in Table 1.

Table 1. Expected value for notional size h_0 according to Eurocode 2 applied to a square, circle and T-beam.

Shape geometry of cross-section	*Shape description*	$h_0 = \frac{2A_c}{u}$ *(EN1992-1-1)*
	Square	$\frac{z}{2}$
	Circle	$\frac{D}{2}$
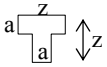	T-beam (see figure 1)	$\frac{2az - a^2}{2z}$

The parameter $\alpha_T h_0$ was determined based on the equation for $\beta_{ds}(t, t_s)$ using a least squares approximation of the drying shrinkage behaviour obtained by the numerical simulations. A comparison of the estimated notional size with correction factor $\alpha_T h_0$ obtained from simulations and the notional size parameter h_0 as defined by Eurocode 2 ($h_0 = 2\,A_c/u$) is shown in Table 2 and Figure 5.

Table 2. Comparison of estimated values for notional size h_0 with the expected value according to Eurocode 2.

	$\alpha_T h_0$	h_0	α_T		$\alpha_T h_0$	h_0	α_T
R200	76.8	100	0.77	T400A200	120.9	150.0	0.81
R250	100.0	125	0.80	T400A250	152.2	171.9	0.89
R300	125.1	150	0.83	T400A300	165.2	187.5	0.88
R350	152.1	175	0.87	T400A350	181.1	196.9	0.92
R400	181.0	200	0.90	T500A50	25.1	47.5	0.53
R450	211.7	225	0.94	T500A100	53.7	90.0	0.60
R500	244.3	250	0.98	T500A150	86.5	127.5	0.68
C200	82.5	100	0.82	T500A200	122.7	160.0	0.77
C250	97.8	125	0.78	T500A250	160.5	187.5	0.86
C300	121.4	150	0.81	T500A300	184.4	210.0	0.88
C350	144.9	175	0.83	T500A350	223.9	227.5	0.98
C400	170.8	200	0.85	T500A400	240.1	240.0	1.00
C450	199.3	225	0.89	T500A450	245.0	247.5	0.99
C500	231.2	250	0.92	T800A800	478.6	400.0	1.20
T300A50	25.3	45.8	0.55	T800A600	455.9	375.0	1.22
T300A100	53.8	83.3	0.65	T800A400	303.5	300.0	1.01
T300A150	76.2	112.5	0.68	T800A200	123.7	175.0	0.71
T300A200	111.8	133.3	0.84	T1000A1000	661.7	500.0	1.32
T300A250	124.4	145.8	0.85	T1000A800	649.8	480.0	1.35
T400A50	25.2	46.9	0.54	T1000A600	521.5	420.0	1.24
T400A100	53.7	87.5	0.61	T1000A400	309.6	320.0	0.97
T400A150	86.3	121.9	0.71	T1000A200	124.3	180.0	0.69

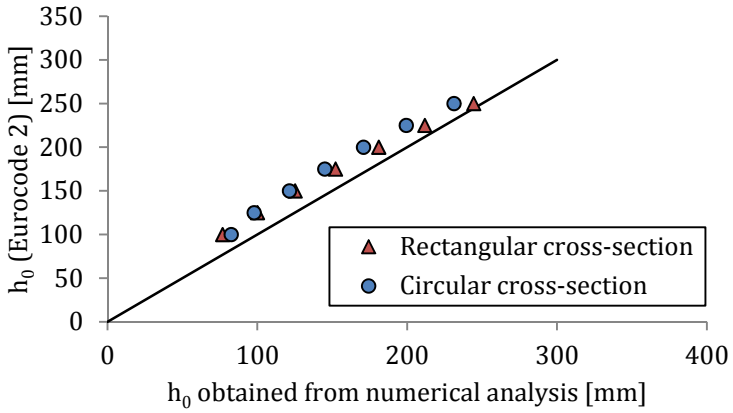

Figure 5. Comparison $\alpha_T h_0$ obtained by simulations and h_0 according to Eurocode 2 for rectangular and circular cross-sections.

The goal of this paper is to define a general parameter α_T to denote the influence of the shape and size of T-beams on the drying shrinkage development. The following equation is proposed (with R^2 equal to 0.93):

$$\alpha_T = 1.3 \cdot a^{0.33}$$

in which α_T is the shape correction factor for T-beams and a is the thickness of the flange in meters (see Figure 1). A comparison of the proposed correction factor α_T given by the proposed equation and the value of α_T obtained by numerical results is shown in Figure 6.

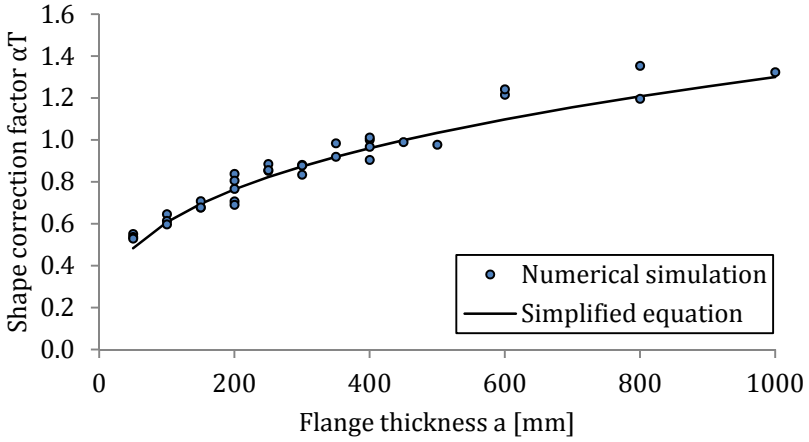

Figure 6. Comparison proposed equation for $\alpha_T h_0$ and numerical results.

CONCLUSION

- The time-development of the drying shrinkage behaviour obtained by the numerical analysis for prisms and cylinders is comparable with the function $\beta_{ds}(t, t_s)$ given by EN 1992-1-1 based on the notional size h_0.

- The presented results are based on simplifications and give agreeable results even in the case in which the effect of creep is neglected. Further refinements can be included to enhance the modelling of drying shrinkage.
- There is a large influence of the geometry of T-shaped beams on the drying shrinkage behaviour caused by the different flow paths for moisture transport and a simple modification parameter α_T was proposed in order to account for this effect.

REFERENCES

ACI 209R. (1998). Prediction of creep, shrinkage, and temperature effects in concrete structures. *Amer concr inst Detroit*.

Bazant, Z. P., & Baweja, S. (1995). Justification and refinement of Model B3 for concrete creep and shrinkage. 1. Statistics and sensitivity. *Materials and structures, Vol.28*.

Bazant, Z. P., & Najjar, L. J. (1972). Nonlinear water diffusion In nonsaturated concrete. *Materiaux et Constructions, Vol.5*(No.25).

Bazant, Z. P., & Xi, Y. (1994). Drying creep of concrete: constitutive model and new experiments separating its mechanisms. *Materials and structures, Vol.27*, pp.3-14.

Fib. (2010). CEB-FIP Model Code 2010 In Comite Euro-Int Du Beton (Ed.), *Design code*.

Ghali, A., Favre, R., & Elbadry, M. (2011). *Concrete Structures: Stresses and Deformations: Analysis and Design for Sustainability (4th edition)*: CRC Press.

Jefferson, A. D., & Lyons, P. (2010). *Comparison of approaches for simulating moisture content changes in concrete*. Paper presented at the EURO-C 2010.

Kim, J. K., & An, G. H. (2012). *An Analytical Study of Long-term Deformation in SRC Columns Considering Differential Moisture Distribution*. Paper presented at the Proceedings of the 3rd JCI-KCI-TCI Symposium on Recent Advancement of Technologies in Concrete Engineering Japan Concrete Institute.

Reybrouck, N., Maes, M., Caspeele, R., Criel, P., & Taerwe, L. (2014). *Modeling the effect of random environmental influences on stochastic creep in concrete members.* Paper presented at the 12th international probabilistic workshop.

RILEM. (2015). Model B4 for creep, drying shrinkage and autogenous shrinkage of normal and high-strength concretes with multi-decade applicability. In TC-242-MDC (Ed.), (Vol. Vol.48). Materials and Structures.

Seol, H. C., Kwon, S.-H., Yang, J.-K., Kim, H.-S., & Kim, J.-K. (2008). *Effect of differential moisture distribution on the shortening of steel-reinforced concrete columns*. Paper presented at the Magazine of Concrete Research.

Su-Tae, K., Jeong-Su, K., Yun, L., Yon-Dong, P., & Jin-Keun, K. (2011). Moisture Diffusivity of Early Age Concrete Considering Temperature and Porosity. *KSCE Journal of Civil Engineering*.

Accelerated Corrosion of Steel Reinforcement in Concrete: Experimental Tests and Numerical 3D FE Analysis

J. Ožbolt[1,2]; E. Sola[1]; and G. Balabanić[2]

[1]Institute of Construction Materials, University of Stuttgart, Pfaffenwaldring 4, 70560 Stuttgart, Germany. E-mail: ozbolt@iwb.uni-stuttgart.de; emiliano.sola@iwb.uni-stuttgart.de
[2]Faculty of Civil Engineering, University of Rijeka, Radmile Matejčić 3, 51000 Rijeka, Croatia. E-mail: gojko.balabanic@gradri.hr

Abstract

Chloride-induced corrosion of steel reinforcement in concrete is one of the major causes for deterioration of reinforced concrete (RC) structures. RC structures exposed to aggressive environmental conditions, such as structures close to the sea or highway bridges and garages exposed to de-icing salts, very often exhibit damage due to corrosion. Therefore, to predict durability of RC structure it is important to have a numerical tool, which is able to predict corrosion processes and their consequences for the structural safety. In order to speed up corrosion of reinforcement in concrete the experimental tests are almost always accelerated by imposing external electric potential and by adding chlorides to concrete mix. Therefore, the corrosion rate becomes much faster than the fastest corrosion rate in the nature, which can have significant consequences on the non-mechanical and mechanical processes related to the corrosion of reinforcement, i.e. the experimental results can lead to unrealistic conclusions. In the present paper recently performed experiments under accelerated conditions are simulated and compared with corrosion process that approximately corresponds to natural conditions. For the investigated geometry and environmental conditions it is shown that accelerated corrosion rate, which is approximately 20 times faster than corrosion rate under natural conditions, leads to corrosion induced damage of concrete, which is similar to the damage predicted assuming natural conditions.

INTRODUCTION

Degradation of reinforced concrete (RC) structures caused by chloride-induced corrosion is one of the major concerns for durability of RC structures (Tuutti, 1993). Especially vulnerable are structures located in coastal marine environment or highways and garages treated with de-icing salts during winter seasons (Tuutti, 1993; Cairns, 1998). Consequences of chloride-induced corrosion of steel reinforcement have negative effects on structural behavior and involve several aspects related to the life cycle of the structure, such as serviceability, safety and structural performance. The main effect of the corrosive attack is manifested as cracking and spalling, due to the expansion of the

corrosion products, which have greater volume than the steel. Direct and indirect costs of maintenance and repair are very high. Therefore, is very important to develop and improve numerical tools, which can realistically predict the corrosion processes and the related mechanism of deterioration in RC structures.

Before depassivation of reinforcement a surface layer of ferric oxide covers and protects the steel in concrete. Upon this layer being damaged or depassivated, the corrosion of reinforcement in concrete can be activated. Depassivation of the protective layer can occur by reaching a critical threshold concentration of free chloride ions near the reinforcement bar surface or as a consequence of carbonation of concrete (Tuutti, 1993). Here is discussed only the chloride-induced type of corrosion, which is generally the most severe one. Corrosion of steel in concrete is an electrochemical process dependent on the electrical conductivity of the concrete and steel surfaces, presence and conductivity of electrolyte in the concrete and the concentration of dissolved oxygen in the pore water near the reinforcement (Bažant, 1979; Glasstone, 1964; Page and Treadway, 1982). Recently developed 3D chemo-hygro-thermo-mechanical model, which is employed in the present numerical simulations, couples the above mentioned physical and electrochemical processes with mechanical behaviour of concrete (damage). The model can simulate processes before and after depassivation of steel reinforcement in concrete under natural or accelerated corrosion conditions (Ožbolt et al. 2010, 2011, 2012, 2014; Oršanić, 2015).

In order to calibrate and verify numerical models, experimental tests are required. However, corrosion tests under natural conditions are time consuming. Therefore, experimental tests are frequently carried out under accelerated conditions with corrosion rates that can be 100 or even more times faster than corrosion rates under natural conditions. This can significantly influence the test results and possibly lead to incorrect conclusions. To bring more light into the effect of accelerated corrosion on the related effects, such as corrosion induced damage of concrete, experimental tests under accelerated conditions are carried out. The first part of the paper gives a short overview of the experimental work and in the second part the numerical simulations of accelerated tests are carried out. The results are compared with simulations obtained assuming natural corrosion conditions and conclusions are drawn out.

CHEMO-HYGRO-THERMO-MECHANICAL MODEL FOR CONCRETE

In order to predict the rate of rust production and related effects, it is necessary to simulate the following physical, electrochemical and mechanical processes: (1) Transport of capillary water, oxygen and chloride through the concrete cover; (2) Immobilization of chloride in the concrete; (3) Crystallization and dissolution of free chloride as a consequence of drying and wetting of concrete as well as related hysteretic property of concrete; (4) Transport of OH^- ions through electrolyte in concrete pores; (5) Cathodic and anodic polarization; (6) Transport of corrosion products in concrete and cracks; (7) Creep and shrinkage of concrete and (8) Damage of concrete due to mechanical and non-mechanical actions (8). Presently, there are only a limited number of coupled 3D chemo-

hygro-thermo-mechanical models capable to realistically predict corrosion process in cracked concrete (Ožbolt et al., 2010, 2011; Marsavina et al., 2009). Recently coupled chemo-hygro-thermo-mechanical model for simulation of processes before and after depassivation of steel reinforcement in concrete is developed and implemented into a 3D FE code. For more detail see Ožbolt et al. (2010, 2011, 2012, 2014) and Oršanić (2015). In the present paper the code is used to study the effect of accelerated and natural corrosion of steel reinforcement on damage of concrete specimens.

ACCELERATED CORROSION – EXPERIMENT AND 3D FE ANALYSIS

Recently an extensive experimental test program was initiated, which is still in progress, to calibrate the parameters needed for the above mentioned 3D chemo-hygro-thermo-mechanical model. Samples used in the experimental tests are cylinders with cast-in reinforcement bars of different sizes. They are exposed to accelerated corrosion under different laboratory controlled conditions by imposing an external electric potential. In addition, chlorides are added to concrete mix to accelerate depassivation of reinforcement. Moreover, experiments under natural corrosion conditions are also underway. The casting of the samples and the experiments are carried out at the University of Stuttgart, Institute of Construction Materials.

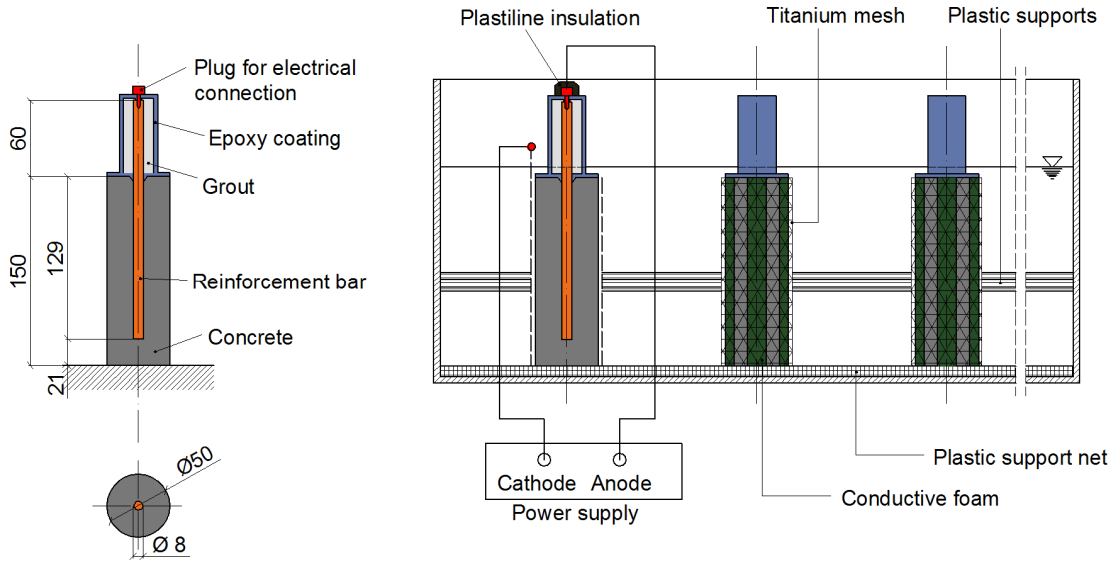

Figure 1. Geometry of the specimen and details of the accelerated corrosion tests (measures in mm)

Geometry and material properties

The samples discussed in the present paper are concrete cylinders with a diameter of 50 mm and height of 150 mm, with a cast-in steel bar of 8 mm in diameter and cover of 21 mm, as shown in Fig. 1. Concrete is manufactured using Portland cement CEM I

42.5 N and water/cement ratio of 0.7. Siliceous sand and aggregates were used with a maximum aggregate size of 8 mm. Approximately 2.5 % of NaCl by weight of cement was added to the mixture to accelerate depassivation of steel. The specimens were cast in PVC cylindrical molds held from a wooden assembly with an appropriate hole to fix position of the steel bar and assuring the designed embedment length of the reinforcement.

The specimens were cured 7 days under constant temperature of 20°C and relative humidity (RH) of 100%. Subsequently they were stored in a temperature controlled chamber at 20°C with RH of 60%. The uni-axial compressive strength of concrete was measured before testing on standard cubes of 150x150x150 mm. The average strength (three specimens) is f_c = 40 MPa. Based on f_c the concrete properties were estimated as: Young's modulus E_c = 31.6 GPa, Poisson's ratio ν = 0.18, tensile strength f_t = 3.10 MPa and fracture energy G_F = 55 J/m². Mass density of concrete is assumed to be ρ_c = 2400 kg/m³. The reinforcement bar is normal steel with the following properties: Young's modulus E_c = 210.0 GPa, Poisson's ratio ν = 0.33 and mass density ρ_s = 7800 kg/m³.

Accelerated corrosion test set-up and testing environment

After curing, the samples were dried and coating of grout and epoxy resin was applied onto external part of the reinforcement. In order to accelerate the corrosion process, an imposed constant potential was applied between the rebar (anode) and a cylindrical shell of platinized titanium mesh (cathode), located around the lateral surface of the specimen. Four stripes of conductive foam, at 90° to each other, were used to electrically connect the external titanium mesh with the concrete surface (see Fig. 1). To investigate the influence of corrosion rate, two different voltages were used. During the experiment readings of current were continuously recorded measuring the drop of voltage, over a resistance unit of 10 Ω, and were performed by a digital multimeter data acquisition and data logging system, KEITHLEY 2701. Specimens were exposed to cyclic wetting/drying regime, 1 day of wetting by 2.5 % NaCl solution, followed by 6 days of drying at relative humidity of approximately 60%. As mentioned above, because of the extensive experimental program and numerous specimens, here are discussed only the results obtained for the smallest specimens, with reinforcement bar of 8 mm and concrete cover of 21 mm, exposed to wetting/drying cycles with two imposed potentials, 100 mV (specimen A, B, C) and 500 mV (specimen D, E, F).

Numerical analysis of experimental tests

The main aim of the numerical study is to verify and calibrate the above mentioned 3D chemo-hygro-thermo-mechanical model for the case of accelerated corrosion. Furthermore it should be investigated the influence of water content and concrete conductivity on current density and crack pattern. Moreover, the influence of the imposed electric potential and related current density on the transport of rust and related crack pattern should be studied. Finally, based on the calibrated model parameters for accelerated corrosion, the comparison between natural and accelerated corrosion

should be possible to highlight the differences, which could be important for objective evaluation of test results obtained from accelerated corrosion.

The geometry of the specimen is the same as in the experiment except that the length of only 50 mm is simulated assuming axisymmetric conditions (geometrical, mechanical and environmental). The finite element discretization is performed using solid 8-node finite elements and as localization limiter crack band method is used (Bažant and Oh, 1983). The mechanical model for concrete is based on the microplane model (Ožbolt et al., 2001). In contrast to mechanical part, in the non-mechanical part of the model transient finite element analysis based on the direct integration of implicit type is carried out. It is assumed that entire length of the steel bar is activated as anode (depassivated) at the start of the analysis. Consequently, only water content, electric potential, current density at the surface of reinforcement, transport of rust through pores and cracking of concrete are computed. Note that corrosion rate at the surface of reinforcement is calculated from computed electrical current density. The coefficient of proportionality between the anodic current density and rate of rust production is calculated using the stoichiometry of chemical reactions and Faraday's law (Ožbolt et al., 2011, 2012; Martín-Pérez, 1999).

The parameters of hysteretic moisture model were calibrated from experimental results obtained for two different levels of imposed electric potential: 100 and 500 mV HSE. The used sorption isotherms (concrete w/c = 0.65) are plotted in Fig. 2 and the corresponding parameters are listed in Table 1 (isothermal conditions, temperature = 20°C). Furthermore, electrical conductivity of concrete (see Table 2) was calibrated based on the experimentally measured average current density and from the experimentally measured conductivity on fully saturated concrete cube specimens using the "Two Electrodes Method" (TEM). The conductivity is relevant for the computation of current density especially in chloride contaminated concrete (Osterminski and Schießl, 2012).

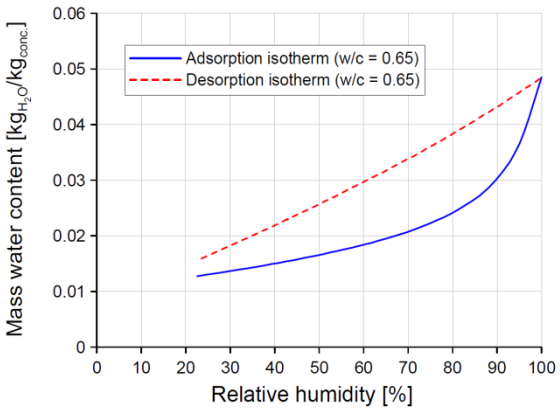

Figure 2. Input main adsorption and desorption curves from the experiments by Hansen (1986) for concrete with w/c=0.65

As discussed in Ožbolt et al. (2012, 2014) for the corrosion induced damage the expansion factor of rust and the transport of rust through concrete plays important role. In the used model transport of rust through pores of concrete and cracks is modeled as diffusion-convection governed process (mathematical interpretation). Note that from the physical point of view the rust is not transported, instead ions are transported and corrosion products are generated in the pores around the reinforcement bar and in cracks. The relation between diffusivity of rust and crack width is obtain based on the calibration of the experimental data. The initial diffusion coefficient for un-cracked concrete is set to $D_r = 2.2x10^{-13}$ m²/s. The volume expansion factor of rust is assumed to be congruent with $\alpha_r = \rho_s/\rho_r = 4.0$ for natural conditions (red rust) and $\alpha_r = \rho_s/\rho_r = 1.9$ in accelerated conditions (black-green rust, Goethite, Lepidocrocite) (Fischer, 2012; Fischer and Ožbolt, 2012). Note that especially in case of imposed potential (relatively high corrosion current density and admixed chlorides) the type, the rate and the distribution of corrosion products are highly influenced. These products are in comparison with products generated under natural conditions (red rust) significantly different.

Table 1. Model parameters relevant for computation of relative humidity.

Hysteretic moisture model for concrete	
Sorption isotherms	w/c=0.65
Water vapour permeability [s]	$5.0x10^{-10}$
Surface humidity trans. Coeff [m/s]	$4.5x10^{-6}$

Table 2. Electrical conductivity of concrete (w/c=0.7) [$10^{-3}\Omega^{-1}m^{-1}$]

Saturation[%]	*50*	*55*	*60*	*65*	*70*	*75*	*80*	*85*	*90*
$\sigma_{natural}$	2.75	3.00	4.28	8.70	9.52	10.50	11.50	12.50	13.50
$\sigma_{accelerated}$	8.75	9.54	13.61	27.67	30.27	33.39	36.57	39.75	42.93

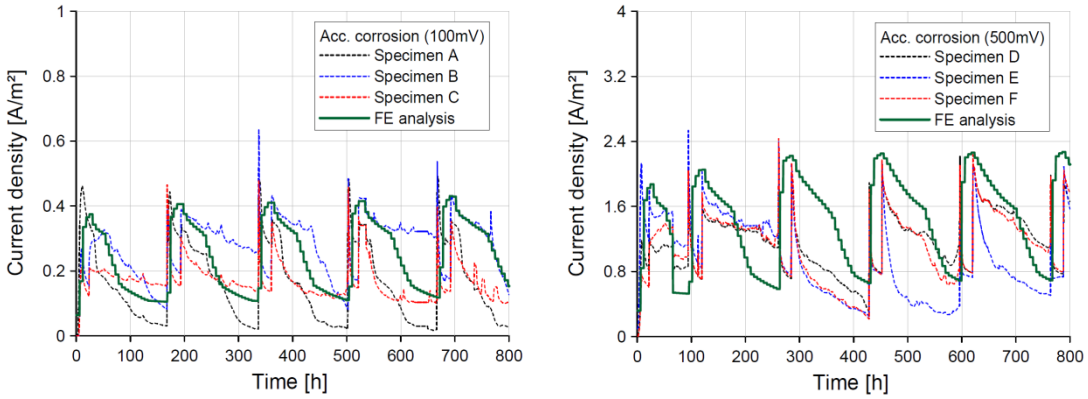

Figure 3. Time dependent distribution of the average anodic current density for an imposed electric potential of 100 mV and 500mV.

Comparison between numerical and test results

The average experimental and numerical values of anodic current density-time curves for three different specimens with imposed potential of 100 mV (specimen A, B, C) and 500 mV (specimen D, E, F) are plotted in Fig. 3. The experimental data are average values on the anodic surface area calculated on the base of measured current intensity. As can be seen, the numerical model is able to realistically simulate anodic current density time history curve. The analysis and the experiment exhibit sudden increase of current density that is related with sudden wetting of concrete cylinder (1 day wetting). Subsequently the water is removed and current density gradually decreases (6 days drying). As expected, with increase of imposed electric potential from 100 mV to 500 mV, average current density increases approximately proportionally with imposed electric potential, i.e. with the factor of five.

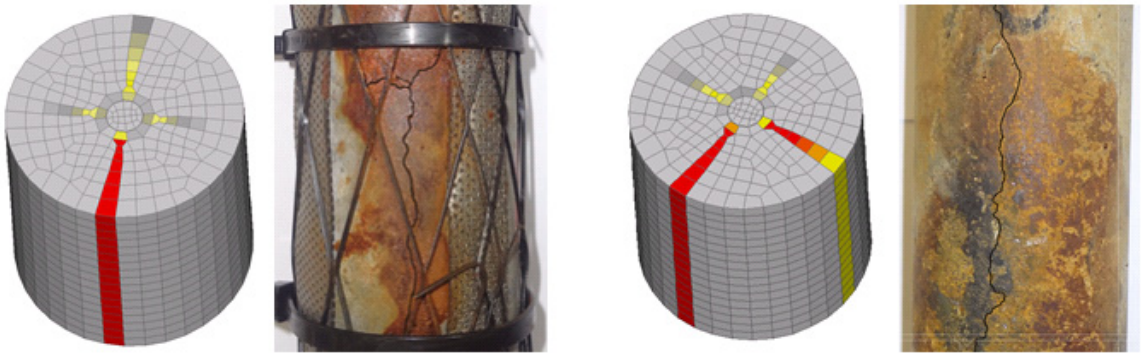

Figure 4. Predicted (crack initiation at surface) and experimentally observed crack patterns for potential of 100 mV (left) and 500 mV (right), (red = crack opening ≥ 0.05 mm

It can be noted that the moisture content and anodic current density are strongly influenced by the corrosion induced cracks, which leads to ingress of water into specimen and increase of saturation in un-cracked concrete. Consequently with increasing wetting-drying cycles current density tends to increase, especially in case of higher imposed potential (500 mV). Moreover, once the crack is generated the water content gradually increases in time. This accelerates the transport of rust from the reinforcement surface through the cracks into direction of concrete specimen surface. It has to be noticed that during wetting periods, in which the specimens are completely under water, the analysis does not indicate significant change in current density, as in experimental tests. This is probably a consequence of the assumption that the accelerated corrosion process is independent from the oxygen content.

Fig. 4 shows the observed and calculated crack patterns (crack initiation). For lower and higher imposed potential in the experiment the first crack at the surface of the cylinder (crack width = 0.05 mm) appeared after 20 and 6 days, respectively, and in the analysis after 17 and 4 days, respectively. Having on mind the complexity of the problem

this is relatively good agreement and the crack patterns are also similar. There is one dominant vertical crack in the experiment and in the analysis. Furthermore, it can be seen that there is a large amount of rust at the concrete surface. This indicates that a lot of corrosion products are transported from the reinforcement through cracks onto the surface of concrete cylinder.

NATURAL CORROSION – EXPERIMENT AND 3D FE ANALYSIS

In order to be able to investigate the difference between corrosion induced damage between natural and accelerated corrosion the above specimen is numerically analyzed assuming natural corrosion conditions. Only active phase of corrosion is computed, i.e. the phase after depassivation of steel. It is assumed that the concrete cylinder is exposed to the constant air temperature of 20ºC with humidity conditions which correspond to Stuttgart, i.e. variation of air relative humidity in the range from 63% (May) up to maximum 80% (December). To calculate corrosion rate it is necessary to compute distribution of relative humidity, oxygen and electric potential. Electric potential is computed based on the Butler-Volmer kinetics (Ožbolt et al. 2014) assuming anodic and cathodic surfaces as shown in Fig. 5 (left). The volume expansion factor is assumed to be congruent with $\alpha_r = \rho_s/\rho_r = 4.0$ (red rust) and diffusivity for rust transport is set to $D_r = 2.2 \times 10^{-16}$ m^2/s (Ožbolt et al. 2014). The electrical conductivity of concrete used in the analysis is specified in Table 2. More details related to other relevant model parameters can be found in Ožbolt et al. (2012, 2014). Note that in contrast to accelerated case for the natural corrosion also creep of concrete is accounted for (Ožbolt and Reinhardt, 2001).

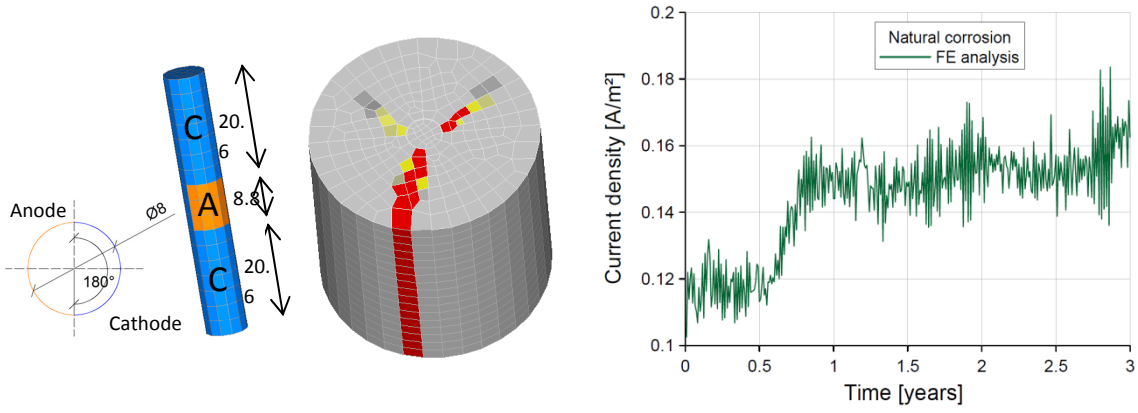

Figure 5. Assumed position of anode and cathode [mm], first visible crack at concrete surface (180 days, red=0.05 mm crack width) and time history of current density at the anode-cathode transition zone

Fig. 5 shows typical crack pattern at crack initiation, 180 days after depassivation. The time history of average current density at the anodic-cathodic transition zone is

plotted in Fig. 5 (right). As can be seen, maximum current density reaches approximately the value of 0.16 A/m^2, which is, for the assumed concrete quality (w/c=0.70) and given environmental conditions, a realistic value. Compared to accelerated corrosion, the computed corrosion rate is approximately 3 (100 mV) and 15 (500 mV) times higher. In spite of this, the computed crack pattern is very similar to that obtained for the accelerated corrosion. There are two reasons for this: (i) In case of accelerated corrosion Goethite and Lepidocrocite are produced, which have expansion factor ($\rho_s/\rho_r = 1.9$) lower than the red rust ($\rho_s/\rho_r = 4.0$) produced in case of natural conditions; (ii) In accelerated corrosion there is relative large amount of water present, which accelerate transport of rust and consequently reduce the pressure of rust around the reinforcement bar.

CONCLUSIONS

In the present paper are performed experimental tests and numerical analysis of accelerated corrosion of steel reinforcement embedded in concrete cylinders. The results are compared with numerical results assuming natural corrosion conditions. Based on the results, the following conclusions can be drawn out. (1) The recently proposed coupled 3D chemo-hygro-thermo-mechanical model is able to realistically simulate experimental tests on accelerated corrosion of reinforcement in concrete. (2) Computed current density and related time of cracking and crack patterns are similar to the experimentally observed ones. (3) The transport of rust through cracks in concrete plays important role in corrosion induced damage of concrete. This is especially true if there is relatively high saturation of concrete. (4) In case of accelerated corrosion different types of rust are produced with expansion factor lower of that observed in case of natural corrosion (red rust). (5) Although for natural corrosion, current density is up to 20 times lower than in accelerated corrosion (500 mV) and crack patterns are very similar. Therefore it can be concluded that for the present geometry and environmental conditions accelerated conditions with imposed electric potential up to 500 mV yields to results that are comparable with the results obtained assuming natural corrosion. (6) Further experimental and numerical work is needed in order to investigate the influence of accelerated corrosion for different geometries and environmental conditions.

REFERENCES

Bažant ZP. (1979). “Physical Model for Steel Corrosion in Concrete Sea Structures – Theory.” J Struct Div-ASCE, 105(6),1137–1153.

Bažant ZP, Oh BH. (1983). “Crack band theory for fracture of concrete.” *Mater Struct*, 16(93), 155–177.

Bažant ZP, Kaplan MF. (1996). Concrete at high temperature. Longman. Essex, UK.

Cairns JW. (1998). “State of the art report on bond of corroded reinforcement.” Technical report No. CEB-TG-2/5.

Fischer C. (2012). “Beitrag zu den Auswirkungen der Bewehrungsstahlkorrosion auf den Verbund zwischen Stahl und Beton.” Dissertation. Stuttgart.

Fischer C, Ožbolt J. (2012). “Influence of bar diameter and concrete cover on bond degradation due to corrosion”. Bond in Concrete 2012. Proceedings of the International Conference, p. 445-451.

Glasstone S. (1964). “ An introduction to electrochemical behaviour of steel in concrete.” ACI J, 61,177–188.

Hansen KK. (1986). Sorption Isotherms. A-catalogue. Technical University of Denmark.

Marsavina L, Audenaert K, Schutter G de, Faur N, Marsavina D. (2009). “Experimental and numerical determination of the chloride penetration in cracked concrete”. *Constr Build Mater*, 23(1), 264–274.

Martín – Pérez B. (1999). “Service life modelling of RC highway structures exposed to chlorides.” Dissertation. University of Toronto.

Oršanić F (2015). “Chemo-hygro-thermo-mechanical model for simulation of corrosion induced damage in reinforced concrete.” Dissertation. Stuttgart.

Osterminski K, Schießl P. (2012). “Voll-probabilistische Modellierung von Bewehrungskorrosion. Ein Beitrag zur Dauerhaftigkeitsbemessung. Projekt D.” Deutscher Ausschuss für Stahlbeton. Berlin.

Ožbolt J, Li Y, Kožar I. (2001). “Microplane model for concrete with relaxed kinematic constraint.” Int J Solids Struct, 38(16), 2683–2711.

Ožbolt, J. and Reinhardt, H.W. (2001). Three-dimensional finite element model for creep-cracking interaction of concrete. Proceedings of the sixth international conference CONCREEP-6, Ed. By Ulm, Bažant & Wittmann, 221-228.

Ožbolt J., Reinhardt HW. (2002). “Numerical study of mixed mode fracture in concrete.” *Int J Fract*, 118, 145-161.

Ožbolt J, Balabanić G, Periškić G, Kušter M. (2010). “Modelling the effect of damage on transport processes in concrete.” *Constr Build Mater*, 24(9), 1638–1648.

Ožbolt J, Balabanić G, Kušter M. (2011). “3D Numerical modelling of steel corrosion in concrete structures.” *Corros Sci*, 53(12), 4166–4177.

Ožbolt J, Oršanić F, Balabanić G, Kušter M. (2012). “Modeling damage in concrete caused by corrosion of reinforcement: coupled 3D FE model”. *Int J Fract*, 178(1-2), 233–244.

Ožbolt J, Oršanić F, Kušter M, Balabanić G. (2012). “Modelling bond resistance of corroded reinforcement.” Bond in Concrete 2012. Proceedings of the International Conference, p. 437-444.

Ožbolt J, Oršanić F, Balabanić G. (2014). “Modeling pull-out resistance of corroded reinforcement in concrete: Coupled three-dimensional finite element model”. *Cement and Concrete Composites*, 46, 41–55.

Page CL, Treadway KWJ. (1982). “Aspects of the electrochemistry of steel in concrete”. *Nature*, 297, 109–15.

Tuutti K. (1982). Corrosion of steel in concrete. Report No. 4. Stockholm.

Tuutti K. (1993). Corrosion of steel in concrete. Technical report. Stockholm.

Simulating the Deteriorating Effect of the Alkali-Silica Reaction in Concrete via a Micro-Poro-Fracture-Mechanical Model

Rita Esposito[1] and Max A.N. Hendriks[2,3]

[1]Delft University of Technology, Stevinweg 1, 2628 CN, Delft, The Netherlands; email: r.esposito@tudelft.nl
[2]Delft University of Technology, Stevinweg 1, 2628 CN, Delft, The Netherlands; email: m.a.n.hendriks@tudelft.nl
[3]Norwegian University of Science and Technology, Rich. Birkelandsvei 1A, 7491 Trondheim, Norway

ABSTRACT

The deteriorating effect of alkali-silica reaction in concrete has a relevant impact both on the material and on the structural performance. This effect is mainly considered in terms of concrete expansion and microscopic damage within the aggregates. Limited attention is reserved to the degradation of mechanical properties, which are often used in the structural assessment. In this paper the attention is focussed on the relationship between ASR-induced concrete expansion and mechanical degradation (e.g. elastic modulus, tensile strength, compressive strength). The results of a statistical analysis are presented. The elastic modulus results the best indicator to identify the reaction, by showing the earliest degradation and the lowest residual values. The non-linear stress-strain behaviour of ASR-affected concrete appears substantially different from the one of unaffected concrete. Experimental observations are simulated via a multiscale micro-poro-fracture-mechanical model. The linear elastic pressure-based single porosity model overestimates the stiffness-expansion relationship. It reasonably approximates the degradation ratio between strengths and stiffness.

INTRODUCTION

The alkali-silica reaction (ASR) deteriorates concrete and concrete structures on different levels. The chemical process involves silica ions, available in the aggregates, and alkali ions mainly present in pore solution together with water (reaction products level). The formed alkali-silica gel, when exposed to moisture, tends to swell. Its expansion, while confined in the pores structure of concrete, builds up an internal pressure with the consequent formation of cracks in the aggregates and in the cement

paste (aggregate level). As a result, the concrete is expanding and its mechanical properties are degrading (concrete level). The reduction in material resistance compromises the performance of the structure in terms of both capacity and durability (structural level).

The interaction of the various phenomena at the different scales is a particular characteristic of ASR in concrete structures. The applied external load substantiated by affected structures can be redistributed due to the differential resistance of the material (structural to concrete level interaction). The stress state of the material influences the redistribution of the gel, thus the expansion and the cracking formation (concrete to aggregate level interaction). Eventually, the redistribution of cracks modifies the equilibrium of the system at the reaction products level (e.g. water ingress), thus the chemical process can be (re)activated or stopped (aggregate to reaction products level interaction).

To evaluate the deteriorating impact of ASR on concrete material a multi-scale material model, based on micro-poro-fracture-mechanics concepts, is adopted. The concrete is micromechanically modeled, at aggregate level, as a saturated porous medium subjected to internal pressure, generated by the expansive reaction products of ASR, and external loading. The macroscopic properties at concrete level are evaluated with the Mori-Tanaka analytical homogenization approach. The state equations of the problem are derived in the framework of poromechanics theory. The damage propagation is associated to the cracks, which represent the pore space at aggregate level, adopting linear fracture mechanics theory. This approach allows studying the combined effect of mechanical loading and an ASR-induced pressure load, which is controlled by a unique micro-mechanical damage parameter.

In this paper the model is applied to describe the deteriorating impact of ASR in terms of concrete expansion and degradation of its mechanical properties (e.g. elastic modulus, tensile and compressive strengths). First, experimental observations are presented and statistically analysed. Second, the presented micro-poro-fracture-mechanical model is adopted to simulate the effect of ASR on the mechanical properties of concrete.

ASR-INDUCED CONCRETE DEGRADATION

The alkali-silica reaction in concrete is a long-term deterioration process, which consequences are strongly related to the environmental and mechanical state of the material. The interaction between the chemical load, provoked by the ASR gel swelling, and the mechanical load is the key point which make standard laboratory tests different from the real behaviour of ASR-affected structures. An understanding of first the mechanical effect of ASR and second the interaction, opens the way to explain the behaviour of ASR-affected concrete structures.

To quantify the mechanical degradation of concrete provoked by ASR, an extensive research was made [1]. Available experimental data [1, 2, 3, 4, 5, 6, 7, 8, 9, 10]

were collected and statistically analysed to determine trends in degradation behaviour. The majority of the authors studied the degradation of the compressive strength (10 authors out of 12) and of the static elastic modulus (9 authors out of 12). The tensile behaviour was studied by 7 authors out of 12, who preferred the splitting tensile strength, above the modulus of rupture and the direct tensile strength. Non-destructive tests for the determination of the dynamic elastic modulus were chosen by 4 authors out of 12. A normalization procedure was applied to statistically analyse the data: each property was normalized with respect to its reference value, taken at an expansion equal to 0.05%. Subsequently the trend between the normalized properties versus the concrete expansion was analysed by means of curve fitting. The fitting included two degradation laws: the S-shaped curve, which is inspired by [11], and the piecewise linear curve.

In Figure 1a the best curve fitting results are presented together with the error band equal to 2σ. The piecewise linear curve is chosen for the description of the compressive strength behaviour, while the S-shaped curve for the other properties. Only splitting test results are accounted for the description of the tensile properties. Both static and dynamic elastic modulus data are adopted to describe the stiffness degradation. The curve fitting defines the elastic modulus as the best indicator of ASR signs in concrete. It presents a relevant degradation already at early expansion; moreover, its degradation rate is the fastest one. For high expansion values ($\epsilon > 2.00\%$) the maximum degradation reaches 80%. Conversely, the compressive strength behaviour is characterized by an initial increase of 15% and a maximum reduction of 46%. However, the estimation error is high, around 13%. The tensile property starts to degrade at higher expansion values with respect to the elastic modulus and it reaches a residual value of 64%.

In Figure 1b the differences in degradation behaviour are shown in an alternative way. When the elastic modulus reaches 85% of its original value, both strengths reduce with a similar rate, but still slower than the degradation rate of the elastic modulus. At a normalized value of 0.50 for the elastic modulus, the normalized splitting strength reaches an asymptotic value of 0.60. The compressive strength is subjected to a drastic deterioration for a normalized value of the elastic modulus of 0.20. In engineering it is common practice to express the stiffness and the tensile strength of unaffected concrete as a function of its compressive strength. Using the strength-stiffness relationships proposed by Model Code 2010 [12], it resulted that for unaffected concrete the degradation rate of compressive and tensile strength is lower than the one for elastic modulus (Figure 1b). This demonstrated that, in the case of ASR-affected concrete, the engineering strength-stiffness relationships cannot be applied to determine the elastic modulus and the tensile strength from the measured compressive strength.

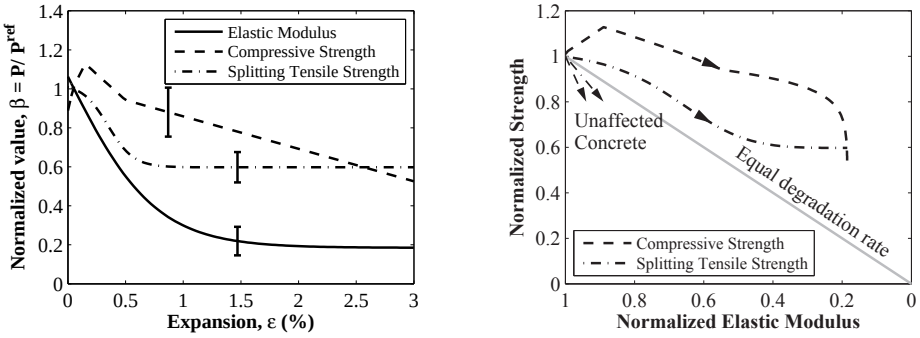

(a) (b)

Figure 1: (a) Relation between normalised properties and concrete expansion; (b) Relation between normalised elastic modulus and normalised strengths.

MICRO-PORO-FRACTURE-MECHANICAL MODEL

The deterioration process induced by the ASR in concrete has a multiscale nature. The phenomenon starts within the constituent phases of concrete and create damage at aggregate level. The induced degradation can impact on the mechanical characteristics of concrete, with consequent modification of the structural performance.

In the wider framework of structural analyses for ASR-affected concrete structures, a multiscale material model is adopted to understand the deteriorating impact of ASR on concrete. The model takes advantage of the micro-pore-mechanics theory, developed by Dormieux et al. [14], which blends the concepts of poro-mechanics and micro-mechanics approaches. This theory has been adopted also by Lemarchand et al. [15] and Charpin and Ehrlacher [16], who studied the evolution of ASR-induced concrete expansion under free-expansion and confined conditions, respectively.

At aggregate level, the concrete is considered as a heterogeneous material formed by the solid matrix and the porosity space, modelled as cracks. To simulate the ASR effects, it is assumed that the expansive alkali-silica gel saturates the entire porosity space and exerts a pressure on the solid matrix phase.

The porosity space is composed by three orthogonal families of cracks ($m = 3$). Within each family the cracks are aligned in one plane with normal $\boldsymbol{n}_i$. Algorithmically, there is no limit to the number of planes (e.g. Bazant et al. [13] considered 21 families in a refined version of their microplane models). The cracks of the *i*-th family are represented by penny-shaped inclusions, with radius a_i in the inclusion's plane and radius c_i in thickness direction. Their aspect ratio, X_i, and volume fraction, ϕ_{ci}, are defined as:

$$X_i = \frac{c_i}{a_i}; \quad \phi_{ci} = \frac{4}{3}\pi c_i n_i a_i^2 \tag{1}$$

where n_i is the number of cracks per unit of volume. The porosity of concrete Φ is defined as the sum of the volume fraction of each crack family. The solid matrix is considered a uniform material, which properties (Y_{m} and ν_{m}) are related to mechanical characteristics of the aggregates and the cement paste (Y_{agg}, Y_{cem} and $\nu_{\mathrm{agg}} = \nu_{\mathrm{cem}}$). Consequently, no explicit distinction is made between cracks in the aggregates or in the cement paste. The aggregates are modelled as spherical inclusions, having a volume fraction ϕ_{agg}, embedded in the cement paste matrix.

The state equations are based on the linear poro-elasticity theory for saturated media. The concrete is subjected to a uniform strain tensor $\boldsymbol{E}$ induced by the external mechanical loading and an pressure P, simulating the swelling of the ASR gel. The macroscopic stress tensor $\boldsymbol{\Sigma}$ and the change in porosity $\Phi - \Phi^*$ can be defined as:

$$\boldsymbol{\Sigma} = \mathbb{C} : \boldsymbol{E} - \boldsymbol{B}P; \quad \Phi - \Phi^* = \boldsymbol{B} : \boldsymbol{E} + \frac{P}{N} \tag{2}$$

where $\mathbb{C}$ is the drained stiffness tensor, $\boldsymbol{B}$ is the Biot tensor and $1/N$ is the Biot modulus. They are calculated by the Mori-Tanaka homogenization method, which defines the macroscopic mechanical characteristics of concrete on the basis of it constituent phases. The method is analytically solved.

The damage criterion is formulated in the framework of linear fracture mechanics theory, on the basis of thermodynamic concepts [14].
For the *i*-th crack family, the crack density parameter ϵ_i [17] is defined as:

$$\epsilon_i = n_i a_i^3 \tag{3}$$

where n_i is the number of crack per unit of volume and a_i is the crack radius of the *i*-th family. The *i*-th crack family is propagating, by increasing its crack radius a_i, if the energy release rate G_i is greater than its critical value $G_{\mathrm{c},i}$.
The energy release rate G_i is calculated on the basis of the potential energy Ψ_i of the system, which represents the macroscopic dissipation:

$$G_i\left(\boldsymbol{E}, P, \epsilon_i\right) = \frac{\partial \Psi_i}{\partial \epsilon_i} = -\frac{1}{2}\left\langle \boldsymbol{E} + P\mathbb{C}_0^{-1} : \boldsymbol{I} \right\rangle : \frac{\partial \mathbb{C}\left(\epsilon_i\right)}{\partial \epsilon_i} : \left\langle \boldsymbol{E} + P\mathbb{C}_0^{-1} : \boldsymbol{I} \right\rangle$$

where $\boldsymbol{E} + P\mathbb{C}_0^{-1} : \boldsymbol{I} = \boldsymbol{E}'$ is the effective strain controlling the damage. To distinguish between the damage provoked by tension and compression loading, only the positive part $\langle \boldsymbol{E}' \rangle$ of the effective strain is accounted in the damage criterion. This concept is inspired by the work of Mazars [18].
The critical energy release rate $G_{\mathrm{c},i}$ can be expressed as function of the current damage parameter ϵ_i [14]:

$$G_{\mathrm{c},i} = \frac{2\pi}{3} g_{\mathrm{f}} \left(\frac{n_i}{\epsilon_i}\right)^{1/3} = \frac{2\pi}{3} \frac{g_{\mathrm{f}}}{a_i} \tag{4}$$

with g_{f} the microscopic fracture energy, which is a material parameter.

Table 1: Initial parameters of the model.

Input parameters			Calibrated and dependent parameters		
Y_{in}	36.3	GPa	$X_{i,\mathrm{in}}$ $(i = 1, 2, 3)$	0.057	
$f_{\mathrm{t,in}}$	2.970	MPa	g_{f}	$3.48\ 10^{-4}$	N/mm
Y_{cem}	43.3	GPa	Y_{m}	68.6	GPa
Y_{agg}	86.5	GPa	ν_{m}	0.200	
$\nu_{\mathrm{cem}} = \nu_{\mathrm{agg}}$	0.200		n_i $(i = 1, 2, 3)$	0.025	mm^{-3}
ϕ_{agg}	0.680		$a_{i,\mathrm{in}}$ $(i = 1, 2, 3)$	1.762	mm
$\Phi_{\mathrm{in}} = 3\phi_{\mathrm{c}i,\mathrm{in}}$	0.098		$\epsilon_{i,\mathrm{in}}$ $(i = 1, 2, 3)$	0.138	
c_i $(i = 1, 2, 3)$	0.100	mm			

MODEL SIMULATION

The micro-poro-fracture-mechanical model is employed to simulate the mechanical degradation induced by the ASR in concrete. First, a free-expansion test is simulated imposing that the concrete is only subjected to an internal pressure P. Second, subsequent uniaxial tension and compression tests are performed at various level of expansion to determine the mechanical properties. The simulation uses one set of date from the statistical analysis [1].

The model is based on a limited number of initial parameters that can be divided in input and calibrated parameters. The former are retrieved by experimental observations, such as mix design proportion, nano-indentation test and porosity measurements. The latter are the initial shape of the cracks and the microscopic fracture energy, which are calibrated against the elastic modulus and the tensile strength of unaffected concrete (e.g. 28-day properties). The initial variables are listed in Table 1.

Figure 2a reports the comparison between experimental and model results in terms of normalized mechanical properties versus concrete expansion. The model results are normalized with respect to the initial properties, while the experimental results are presented similarly as in Section "ASR-induced concrete degradation". The model overestimates the degradation of concrete properties, in correlation with the expansion.

Figure 2b shows that the model is able to capture the relation between strength and stiffness degradation. As already presented in Figure 1b, this relationship is substantially different from the one observed for unaffected concrete under mechanical loading. As a consequence, the refinement of the model should focus on the relation between the stiffness and the expansion.

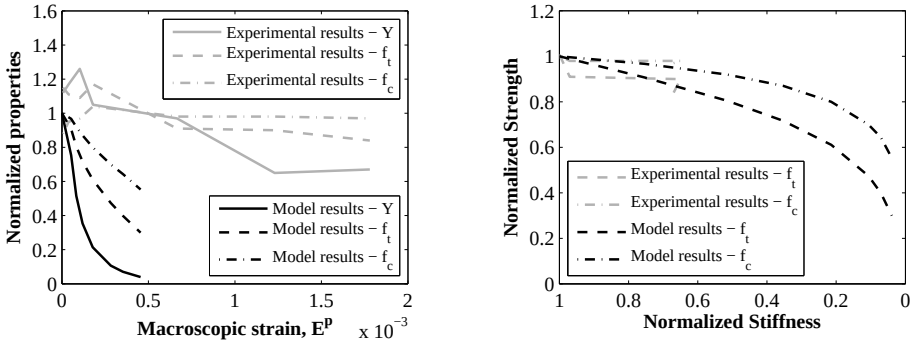

(a) (b)

Figure 2: Simulation of ASR-induced concrete degradation: (a) Degradation of Young's modulus, tensile strength and compressive strength as a function of expansion; (b) Ratio between stiffness and strengths degradation.

DISCUSSION AND CONCLUSIONS

The alkali-silica reaction (ASR) in concrete is a deterioration process which acts on different scales and creates damage from the aggregate up to the structural level. The chemical reaction starts among the concrete constituents and produces an expansive gel. The gel saturates the concrete porosity and creates microscopic and macroscopic damage.

Due to the multiscale characteristic of the phenomenon, various influencing factors can modify the damage evolution. The most known one is the stress-induced anisotropic expansion: the concrete expansion is re-distibuted on the basis of the macroscopic external loading. This process is mainly governed by the re-distribution of cracks at aggregate level. By explaining the damage process at the various level, it is possible to understand the complex phenomenon of ASR in concrete structure.

In the structural engineering framework, the damage process is usually identified with the evolution of mechanical properties of concrete. As a consequence, the deteriorating impact of ASR in concrete is considered here, not only in terms of concrete expansion, but also with respect to the mechanical degradation. First, as statistical analysis of available literature data is performed to identify the correlation between concrete expansion and mechanical properties degradation. Second, a multiscale material model is adopted to simulated the experimental observations.

Experimental observations reveals that the ASR process has a relevant impact on the elastic modulus, a moderate effect on the tensile strength and a limited impact on the compressive strength. The degradation of the elastic modulus starts already at small expansion values and it can reach a maximum residual value of 20%. The tensile strength shows an initial delay with respect to the degradation of the elastic modulus but

a similar deterioration rate for high expansion value. The compressive strength exhibits an initial gain of approximately 15% and a subsequent decrease to 46% of its original value.

Comparing the degradation trend in terms of strength versus stiffness, it appears that the known strength-stiffness relationships, frequently adopted within the structural assessments, cannot be applied for ASR-affected concrete. The observed non-linear relationship betweens strengths and stiffness of affected concrete shows a lower degradation rate with respect to the one proposed by Model Code 2010 for unaffected concrete.

A multiscale micro-poro-fracture-mechanical model is adopted to simulate the deteriorating impact of ASR in concrete. The model describes the phenomenon between aggregate and concrete level. The concrete is modelled as a porous medium composed by penny-shaped cracks embedded into a linear elastic solid matrix. The matrix is formed by aggregates and cement paste phases. The swelling of ASR gel is simulated by an internal pressure, which together with the macroscopic strain, represents the loading parameter of the system. The damage criterion is defined within the linear fracture mechanics framework, on the basis of thermodynamic concepts.

The model is adopted to simulate the degradation of mechanical properties observed in ASR-affected concrete in free-expansion conditions. The model overestimates the degradation of mechanical properties as a function of the concrete expansion. On the contrary, the degradation rate between strength and stiffness is well captured.

Model modifications should thus focus on the evaluation of elastic modulus degradation as a function of the concrete expansion. Various model modifications can be considered.

The model is defined as a one-scale single porosity approach, which simplified the complex hierarchical microstructure of the concrete. Accurate micro-mechanical models define concrete as an heterogeneous material composed by various phases and multiple porosity systems. The presence of pores of different sizes can influence the distribution of the internal pressure, thus of the macroscopic expansion.

The ASR reaction products are here considered as a fluid saturating the porosity space. However, microscopic observation reveals that the ASR gel can be present in various forms with different density. The presence of calcium can interfere with the chemical reaction. As a results a more dense and less expansive reaction product is formed, which can contribute to the global stiffness of concrete.

The damage propagation is here evaluated in the framework of linear fracture mechanics; however, non-linear phenomena can be present. The development of plastic strains, within the solid matrix, during cracking can delay the degradation mechanism.

In conclusion, the deteriorating effect of ASR in concrete should be considered, not only in terms of concrete expansion, but also with respect to the degradation of mechanical properties. A multiscale material model base on micro-poro-fracture mechanics can be adopted to simulate the phenomenon. The current model results in an overestimation of the expansion-stiffness relationship for ASR-affected concrete. However, it appears as a flexible tool, due to its analytical solution, and it is based on

a limited number of input parameters. The model can be easily implemented in finite element software for structural assessment or adopted as a complementary tool. The chemo-mechanical coupling can be accounted by formulating a reaction kinetics law to evaluate the pressure.

ACKNOWLEDGEMENTS

This work is part of the project "Performance Assessment Tool for Alkali-Silica Reaction" (PAT-ASR, http://pat-asr.blogspot.nl/), which is developed in the context of the IS2C program (http://is2c.nl/). The authors wish to express their thanks to the Dutch National Foundation (STW), the Dutch Ministry of Infrastructures and the Environment (Rijkswaterstraat), SGS and TNO DIANA BV for their financial support.

REFERENCES

[1] Esposito, R., Anaç, C., Hendriks, M.A.N. and Çopuroğlu, O. "The Influence of Alkali-Silica Reaction on the Mechanical Degradation of Concrete." *Submitted for publication in ASCE Journal of Materials in Civil Engineering*.

[2] Larive, C. (1998). *Apports combinès de l expèrimentation et de la modèlesllisation á la comprehènsion de l'alcali-rèaction et de ses effets mècaniques.* Ph.D. Dissertation, Laboratoire Central des Ponts et Chaussèes (LCPC).

[3] Monette, L.J., Gardner, N.J. and Grattan-Bellew, P.E. (2002). "Residual Strength of Reinforced Concrete Beams Damaged by Alkali-Silica Reaction- Examination of Damage Rating Index Method." *ACI Journal of Materials*, 99(1).

[4] Ahmed, T. and Burley, E. and Rigden, S. and Abu-Tair, A.I. (2003). "The effect of alkali reactivity on the mechanical properties of concrete." *Construction and Building Materials*,17(2), 123-144.

[5] Multon, S. (2004). *Èvaluation expèrimental et thèorique des effets mècaniques de l'alcali-rèaction sur des structures modéles.* Ph.D. Dissertation, Universitè de Marne-la-Vallèe (in collaboration with LCPC-EDF).

[6] Ben Haha, M. (2006). *Mechanical Effects of ASR in Concrete Studied by SEM-Image Analysis.* Ècole Polytechnique Fédérale de Lausanne (EPFL).

[7] Giaccio, G. and Zerbino, R. and Ponce, J.M. and Batic, O.R. (2008). "Mechanical behavior of concretes damaged by alkali-silica reaction". *Cement and Concrete Research*, 38(3), 993-1004.

[8] Sargolzahi, M., et al. (2010). "Effectiveness of nondestructive testing for the evaluation of alkalisilica reaction in concrete." *Construction and Building Materials*, 24(8),1398-1403.

[9] Lindgård, J. (2013). *Alkali-silica reaction (ASR) - Performance testing.* Ph.D. Dissertation, Norwegian University of Science and Technology.

[10] Sanchez, L.F.M. and Fournier, B. and Jolin, M. and Bastien, J. (2014). "Evaluation of the stiffness damage test (SDT) as a tool for assessing damage in concrete due to ASR: Test loading and output responses for concretes incorporating fine or coarse reactive aggregates." *Cement and Concrete Research*, 56, 213-229.

[11] Saouma, V. and L. Perotti (2006). "Constitutive model for alkali-aggregate reactions." *ACI Journal of Materials*, 103(3), 194-202.

[12] CEB-FIP (2011). *Model Code for Concrete Structures (MC2010).* International Federation for Structural Concrete (fib), Lausanne, Switzerland.

[13] Bažant, Z.P. and Oh, B.-H. (1996). "Microplane model for fracture analysis of concrete structures." *Symposium on Interaction of NonNuclear Munitions with Structures*, U.S. Air Force Academy, Colorado, Springs, 49-53.

[14] Dormieux, L. and Kondo, D. and Ulm, F.-J. (2006). *Microporomechanics.* John Wiley & Sons.

[15] Lemarchand, E. and Dormieux, L. and Ulm, F.-J. (2005). "Micromechanics investigation of expansive reactions in chemoelastic concrete." *Philosophical Transactions of the Royal Society a-Mathematical Physical and Engineering Sciences*, 363(1836), 2581-2602.

[16] Charpin, L. and Ehrlacher, A. (2014). "Microporomechanics study of anisotropy of ASR under loading." *Cement and Concrete Research*, 63, 143-157.

[17] Budiansky, B. and O'Connell, R.J. (1976). "Elastic moduli of a cracked solid" *International Journal of Solids and Structures*, 12(2), 81-97.

[18] Mazars, J. (1986). "A description of micro-and macroscale damage of concrete structures" *Engineering Fracture Mechanics*, 25(5), 729-737

Numerical and experimental study of creep and shrinkage in a high-performance concrete

G. Di Luzio[1], R. Felicetti[1], and L. Cedolin[1]

[1]Politecnico di Milano, Department of Civil and Environmental Engineering, Politecnico di Milano University, Milan, Piazza Leonardo da Vinci, 32; PH (+39) 02-2399-4278; FAX (+39) 02-2399-4300; email: giovanni.diluzio@polimi.it

ABSTRACT

In this study, an experimental investigation on a high-performance concrete used for the construction of a pre-stressed bridge is presented, together with the numerical assessments of the material properties, such as strength, modulus of elasticity, creep, and shrinkage. In this experimental investigation cylindrical specimens were used to measure shrinkage strains under both sealed and drying conditions, with environmental relative humidity of 50% and temperature of 20°C. In addition, basic and drying creep tests were also conducted under the same aforementioned environmental conditions starting at the age of 2 and 28 days. The rate-type creep model, entitled solidification-microprestress-microplane (SMM) model (Di Luzio and Cusatis, 2013), which amalgamates a microplane model and the solidification-microprestress theory is adopted to simulate the age-dependent response of sealed and unsealed specimens observed in the experimental investigation previously mentioned. Comparison with experimental data shows that the SMM model can explain well the interplay of shrinkage (autogenous and drying), creep, and cracking phenomena.

INTRODUCTION

The short- and long-term behavior of long-span prestressed concrete continuous box girder bridges is significantly sensitive to creep and shrinkage properties of the adopted concrete. The short-term rheological behavior governs all the construction operations, while the long-term behavior governs the serviceability limit state of deflection control. In this study, an experimental investigation on the concrete used for the construction of a pre-stressed ”balanced cantilever girder” type bridge is presented. Cylindrical specimens were used to measure shrinkage strains under both sealed and drying conditions, with environmental relative humidity of 50% and temperature of 20°C. In addition, basic and drying creep tests were conducted by applying a 14 MPa compressive stress under the same aforementioned environmental conditions applying the load at two different age, 2 and 28 days.

Numerical analyses were performed to assess the evolution of the material properties, such as strength, modulus of elasticity, creep, and shrinkage. The adopted

rate-type creep model, entitled solidification-microprestress-microplane (SMM) model (Di Luzio and Cusatis, 2013), amalgamates a microplane model and the solidification-microprestress theory and it is able to take into account all the most significant aspects of concrete behavior, such as creep, shrinkage, thermal deformation, and cracking, starting from the initial stages of curing up to several years of age. The calibration of the model parameters is performed through the numerical simulations of the age-dependent response of sealed and unsealed specimens, subjected to loading and unloading conditions, obtained in experimental investigation previously described. Comparison with experimental data shows that the SMM model can reproduce well the interplay of shrinkage (autogenous and drying), creep, and cracking phenomena during the curing and drying phases. The proposed model requires the hydration degree, humidity and temperature fields which are obtained through the Hygro-Thermo-Chemical (HTC) model for high-performance concrete formulated and proposed by Di Luzio and Cusatis (2009a, 2009b).

Complete details of the presented work will be soon published in a journal paper.

EXPERIMENTS

The concrete used in the experiments has the following mix composition: cement CEM III A 42.5 N-LH; polycarboxylic superplasticiser; natural calcareous aggregates with maximum aggregate size of 25 mm with a water/cement ratio of 0.37 and superplasticizer/cement ratio of 1% (by weight).

Cylindrical and cubic specimens were casted using paperboard and plastic molds and consolidated with a high frequency vibrating table, removed from the mold after 24 h, and cured in climatic room at a temperature of 20°C and relative humidity of 95% until the time of test. The compressive strength and the modulus of elasticity were measured on cylindrical specimens (diameter of 150 mm and height of 300 mm) at different ages.

The main purpose of the experiment is to determine the time-dependent properties of high-strength concrete used in the Bridge construction. The cylindrical (diameter of 150 mm and height of 360 mm) creep specimens were loaded using two creep frames (Fig. 1a) at constant-temperature (20 °C) and relative humidity (approximately 50%) room. Each frame accepted four specimens (two for basic creep and and two for drying creep) and was loaded at different concrete ages (2 and 28 days).

The strains of all creep specimens were measured by using electric 200-mm-long gauges and a mechanical manual extensometer (Huggenberger's extensometer) with a measuring base of 250 mm, delimited at the extremities by steel bases with conical cavities. Both the electrical and mechanical readings were taken longitudinally on two diametrically opposite sides of the specimen, and the average of the two strain readings was regarded as the axial strain.

Eight shrinkage specimens were tested: three specimens for autogenous shrink-

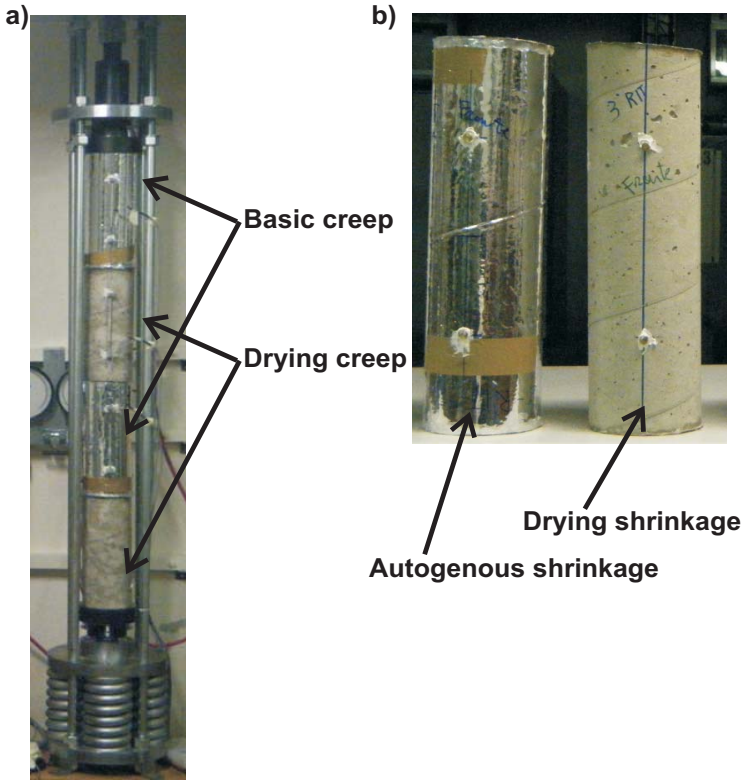

Figure 1. Experimental set-up: a) creep loading frame; b) specimens used for shrinkage measurement.

age were sealed using adhesive aluminium sheet at the age of 2 days; three specimens for total shrinkage at the age of 2 days; two specimens for total shrinkage at the age of 28 days. Fig. 1b shows a couple of concrete specimens, one for sealed and one for drying conditions. The shrinkage specimens were exposed to the same ambient conditions as creep specimens.

SMM MODEL

The SMM formulation (Di Luzio and Cusatis 2013) consists of a multi-physics framework that is capable of simulating the mechanical behavior of concrete, including visco-elasticity (creep/relaxation), cracking and damage, hygro-thermal deformations (shrinkage or swelling due to relative humidity variations and thermal expansion/contraction), heat transfer, moisture variation and/or diffusion, and aging. The SSM model is based on the assumption that the strain additivity holds, so the total strain rate, $\dot{\boldsymbol{\epsilon}}$, is given by

$$\dot{\boldsymbol{\epsilon}} = \dot{\boldsymbol{\epsilon}}^i + \dot{\boldsymbol{\epsilon}}^v + \dot{\boldsymbol{\epsilon}}^f + \dot{\boldsymbol{\epsilon}}^d + \dot{\boldsymbol{\epsilon}}^s + \dot{\boldsymbol{\epsilon}}^t \tag{1}$$

where $\dot{\boldsymbol{\epsilon}}^i$ is the instantaneous strain rate; $\dot{\boldsymbol{\epsilon}}^v$ is the viscoelastic strain rate; $\dot{\boldsymbol{\epsilon}}^f$ is the purely viscous strain rate; $\dot{\boldsymbol{\epsilon}}^d$ is the inelastic strain rate due to cracking and damage; and $\dot{\boldsymbol{\epsilon}}^s$, $\dot{\boldsymbol{\epsilon}}^t$ are hygral and thermal strains caused by variations of relative humidity and temperature, respectively. The strain additivity assumption, from the constitutive point of view, is equivalent to a rheological model in which the different elements of the chain are coupled in series under constant stress state.

Instantaneous, viscoelastic, and purely viscous strain rate. The instantaneous strain rate, $\dot{\boldsymbol{\epsilon}}^i$, is the strain increment appearing immediately after the application of a stress increment, $\dot{\boldsymbol{\sigma}}$, and can be expressed as $\dot{\boldsymbol{\epsilon}}^i = q_1 \mathbf{G} \dot{\boldsymbol{\sigma}}$ in which the parameter q_1 (in MPa^{-1}) can be assumed age independent and the matrix $\mathbf{G}$ is the elastic compliance matrix with a unit Young modulus with constant Poisson's ratio ($\nu = 0.18$).

The viscoelastic strain rate, $\dot{\boldsymbol{\epsilon}}^v$, is obtained according to the solidification theory (Bažant and Prasannan, 1989a,1989b), and it can be formulated as

$$\dot{\boldsymbol{\epsilon}}^v(t) = \frac{1}{v(\alpha)} \dot{\boldsymbol{\gamma}} \quad \text{and} \quad \boldsymbol{\gamma} = \int_0^t \Phi(t-\tau) \mathbf{G} \dot{\boldsymbol{\sigma}} \mathrm{d}\tau \tag{2}$$

where $\dot{\boldsymbol{\gamma}}$ is the visco-elastic micro-strain rate of cement gel. The aging function, $v(\alpha)$, represents the volume fraction of cement gel produced by early-age chemical reactions and it depends on the total reaction degree, $\alpha(t)$, as $1/v(t) = [\alpha_\infty/\alpha(t)]^n$ where α_∞ is the degree of reaction at infinite time and n is an empirical parameter. The degree of reaction, $\alpha(t)$, is an average measure of the total binder reaction which in the case of portland cement coincides with the degree of hydration provided by the HTC model (Di Luzio and Cusatis 2013, Di Luzio and Cusatis 2009a). The non-aging micro-compliance function of cement gel is defined as $\Phi(t-t_0) = q_2 \ln\left[1 + (t-t_0)^{0.1}\right]$, in which $t - t_0$ is the loading time duration, q_2 (in MPa^{-1}), is a model parameter.

The purely viscous strain rate, $\dot{\boldsymbol{\epsilon}}^f$, represents the completely irrecoverable part of the creep strain, which it has been explained in the literature by slippage between adsorbed water layers hindered in cement nanopores. Bažant and coworkers (Bažant et al. 1997a,1997b, Bažant et al. 2004) modeled purely viscous creep by introducing the concept of micro-prestress, S, which was assumed to represent an average measure of the stresses acting on the transverse nanopore bonds. Accordingly, under general temperature and relative humidity variations, viscous creep flow and evolution of micro-prestress can be formulated as

$$\dot{\boldsymbol{\epsilon}}^f = q_4 \kappa_0 S \psi \mathbf{G} \boldsymbol{\sigma} \qquad \text{and} \qquad \dot{S} + \omega \kappa_0 S^2 = \kappa_1 \left| \dot{T} \ln h + T \, \dot{h}/h \right| \tag{3}$$

where ψ is the reduced time coefficient, $\omega = [0.1 + 0.9h^2] \exp\left[Q_s/(RT_0 - RT)\right]$, $Q_s/R \approx 3000$ °K. Finally, κ_0 (in MPa^{-1} day^{-1}), κ_1 (in MPa K^{-1}), and q_4 (in MPa^{-1}) are material parameters that need to be calibrated from experimental data. Note that while the general formulation depends separately on κ_0, κ_1, and q_4, only parameter q_4 governs long-term basic creep behavior (Bažant et al. 2004).

Humidity changes cause free hygrometric strain expressed as $\dot{\boldsymbol{\epsilon}}^s = k_{sh}\dot{h}\mathbf{I}$ where the coefficient k_{sh} is assumed to be constant. Similarly, temperature changes cause thermal strain rates, which can be expressed as $\dot{\boldsymbol{\epsilon}}^t = k_t\dot{T}\mathbf{I}$ where, again, the coefficient k_t is assumed to be a constant.

Cracking strain rate. Cracking and damage strain, $\boldsymbol{\epsilon}^d$, is described through a modified version of the Microplane Model M4 (Di Luzio 2007). In order to amalgamate the microplane theory with the formulation presented earlier it is convenient to rewrite Eq. 1 as

$$\dot{\boldsymbol{\epsilon}} = \dot{\boldsymbol{\epsilon}}^i + \dot{\boldsymbol{\epsilon}}^v + \dot{\boldsymbol{\epsilon}}^f + \dot{\boldsymbol{\epsilon}}^m - \dot{\boldsymbol{\epsilon}}^e + \dot{\boldsymbol{\epsilon}}^s + \dot{\boldsymbol{\epsilon}}^t \tag{4}$$

where $\dot{\boldsymbol{\epsilon}}^e = \bar{E}^{-1}\mathbf{G}\dot{\boldsymbol{\sigma}}$ is an average elastic strain rate that needs to be subtracted from the strain rate calculated according to the microplane model in order to obtain the cracking/damage strain: $\dot{\boldsymbol{\epsilon}}^d = \dot{\boldsymbol{\epsilon}}^m - \dot{\boldsymbol{\epsilon}}^e$. Parameter $\bar{E}$, according to the original microplane formulation, has the meaning of average elastic modulus and serves as dimensional parameter for the microplane boundaries (see Bažant et al. 2000). On the contrary, in the current formulation $\bar{E}$ does not have physical meaning, since it is introduced only for numerical convenience, and it can be assigned prior to the model calibration and without loss of generality. An interested reader can find additional details of the adopted microplane constitutive equations in Bažant et al. (2000), Di Luzio (2007), Di Luzio (2009). The macroscopic stress tensor can be expressed formally as $\boldsymbol{\sigma} = \mathbf{F}^{mpl}(\boldsymbol{\epsilon}^m)$ and, consequently, one can write the inverse formula as $\dot{\boldsymbol{\epsilon}}^m = \left(\partial\mathbf{F}^{mpl}/\partial\boldsymbol{\epsilon}^m\right)^{-1}\dot{\boldsymbol{\sigma}}$. Unfortunately, in general, the gradient of $\mathbf{F}^{mpl}$ cannot be computed analytically and $\dot{\boldsymbol{\epsilon}}^m$ must be computed numerically according the procedure proposed by Di Luzio (2009). The concept of aging degree is used to account for early age phenomena within the modified microplane model M4 formulation. This is achieved by assuming that some material parameters governing the microplane constitutive equations (stress-strain boundaries) are functions of the aging degree (see for further details Di Luzio and Cusatis 2013).

Heat Transfer and Moisture Diffusion. The behavior of concrete, especially at early age, depends heavily on internal relative humidity, h, and temperature, T, whose distributions can be computed by imposing moisture mass balance and enthalpy balance equations in the volume of interest. For concrete mixes in which the binder is only Portland cement and for temperature not exceeding $90°$C, one can write (Di Luzio and Cusatis 2009a)

$$\nabla\cdot(D_h\nabla h) - \frac{\partial w_e}{\partial h}\frac{\partial h}{\partial t} - \frac{\partial w_e}{\partial \alpha_c}\dot{\alpha}_c - \dot{w}_n = 0 \tag{5}$$

and

$$\nabla\cdot(\lambda_t\nabla T) - \rho c_t\frac{\partial T}{\partial t} + \dot{\alpha}_c\, c\, \tilde{Q}_c^{\infty} = 0 \tag{6}$$

where D_h is moisture permeability, w_e is evaporable water – adsorption/desorption isotherm (see Di Luzio and Cusatis 2009a); α_c = hydration degree; $\dot{w}_n = 0.253\dot{\alpha}_c c$ is

rate of non-evaporable water; $\rho =$ mass density of concrete; $c_t =$ isobaric heat capacity (specific heat); $\lambda_t =$ heat conductivity; $c =$ cement content; $\tilde{Q}_c^\infty =$ hydration enthalpy. In Di Luzio and Cusatis 2009b one can find additional details of the formulation and Di Luzio and Cusatis 2009c reports detailed calibration and validation of the theory.

Cement hydration and aging degree. Cement hydration can be characterized by the hydration degree (Ulm and Coussy 1995, Cervera et al 1999, Gawin et al 2006, Di Luzio and Cusatis 2009b) α_c, that represents the fraction of Portland clinker fully reacted with water. Its evolution law can be formulated as

$$\dot{\alpha}_c = \frac{A_{c1} e^{-\eta_c \alpha_c/\alpha_c^\infty} e^{-E_{ac}/RT}}{1+(5.5-5.5h)^4} \left(\frac{A_{c2}}{\alpha_c^\infty} + \alpha_c \right) \cdot (\alpha_c^\infty - \alpha_c) \tag{7}$$

where E_{ac} is the hydration activation energy; R is the universal gas constant; η_c, A_{c1}, A_{c2} are material parameters; and α_c^∞ is the asymptotic value of the hydration reaction degree.

The strength evolution is assumed to depend on the aging degree, λ, defined as (Cervera et al 1999) $\dot{\lambda} = [(T_{max}-T)/(T_{max}-T_{ref})]^{n_\lambda} (B_\lambda - 2A_\lambda \alpha)\dot{\alpha}$ for $\alpha > \alpha_0$ and $\dot{\lambda} = 0$ otherwise. The parameter $\alpha_0 = 0.1 \div 0.4$ defines the value of the reaction degree at the end of the setting phase, that is when concrete may begin to be considered a solid; T_{max} represents the maximum temperature at which hardening of concrete is possible under standard conditions (≈ 100°C); T_{ref} is the reference temperature for the experimental calibration of the aging model. By imposing these conditions one obtains $B_\lambda = [1 + A_\lambda(\alpha_\infty^2 - \alpha_0^2)]/(\alpha_\infty - \alpha_0)$, in which n_λ, A_λ are model parameters that need to be identified from experimental data.

Numerical Simulation of Experimental Data

The experimental investigation presented in the previous section is numerically simulated using the above model.

Moisture distribution and degree of hydration were calculated by solving the hygro-thermo-chemical (HTC) model with the standard parameters reported in Di Luzio and Cusatis (2009b).

The SSM model parameters were identified on the basis of the available experimental data: evolution of compressive strength (Fig. 2a), autogenous shrinkage test (Fig. 2b), basic creep curves (Fig. 2c), and drying creep curves (Fig. 2d). All the other experimental results were used to validate the reliability of the SSM model (see Fig. 3). Note that the broken line reports the strain which is total strain, i.e. it includes creep strain due to loading; shrinkage strain due to drying and self desiccation; and cracking strain. On the other hand the dashed line reports the numerical strain obtained using a liner elastic constitutive law, i.e. cracking strain set to zero.

Fig. 3c and 3d present the numerical analyses of the basic and drying creep tests at 28 days using the model with the parameters previously calibrated. Fig. 3c and

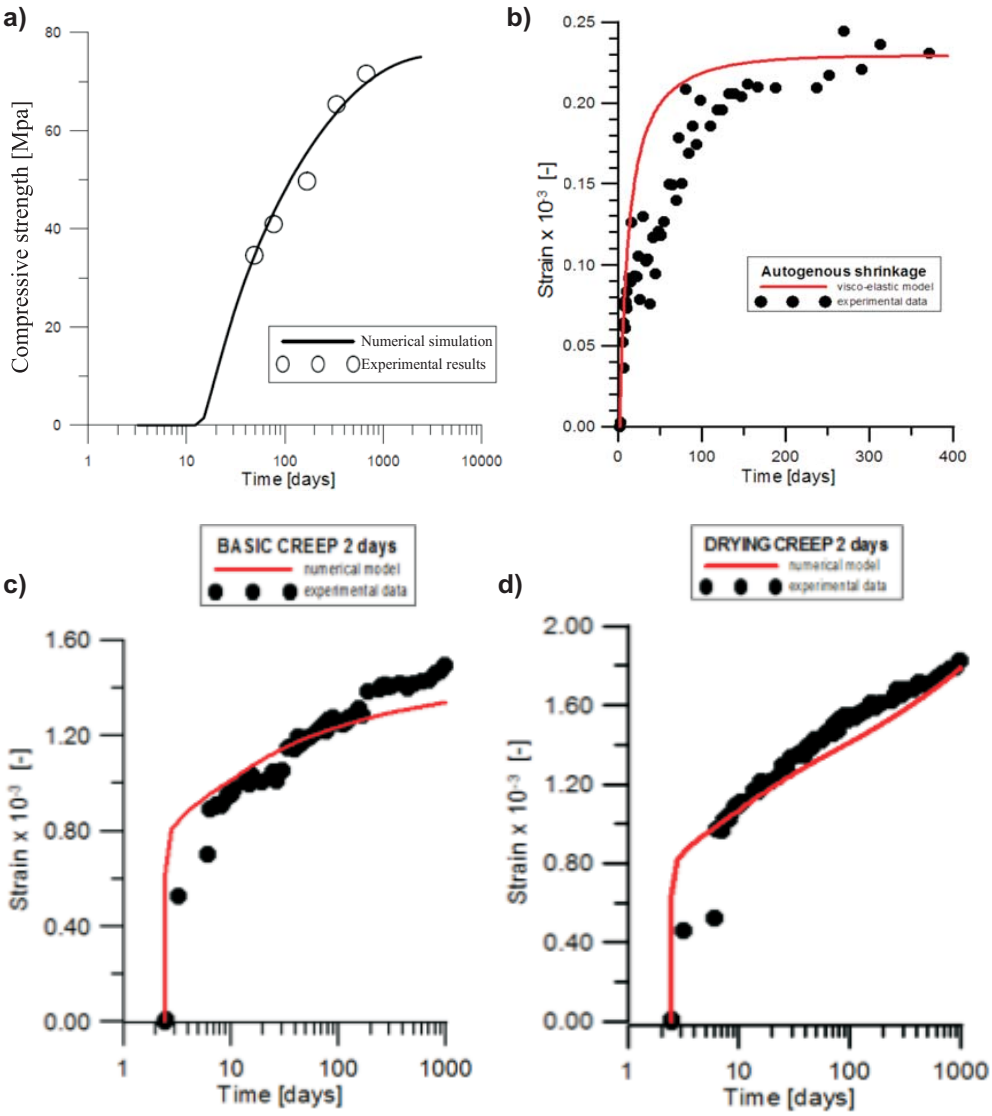

Figure 2. Numerical analyses used for the model calibration.

3d show the simulations of the drying shrinkage tests. As one can see, the numerical results are in very good agreement with the experiments. Moreover, in the studied concrete the additional creep observed in drying condition is due only to the effect of microprestress which is able to reproduce the effect of the so-called shrinkage-induced stresses (Bažant and Chern 1985).

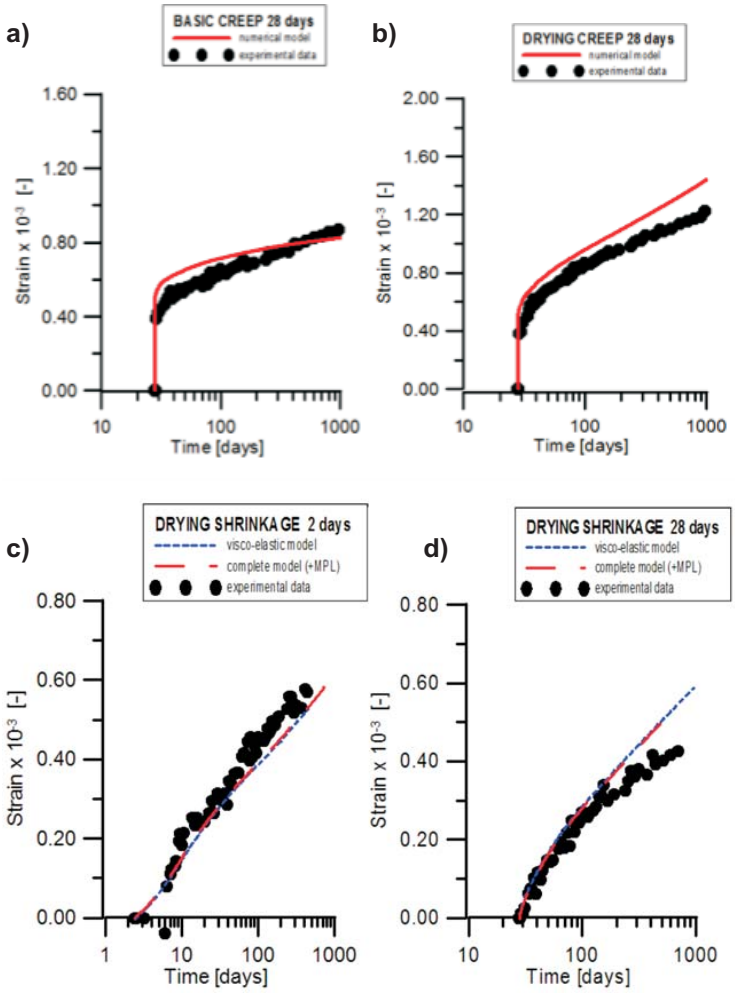

Figure 3. Numerical analyses for model validation.

CONCLUSION

The paper presents a numerical and experimental investigation on the evolution of strains in a high-strength concrete. Based on the experimental evidence, the following conclusions can be drawn. The strength increases quite rapidly in the studied concrete with a strength of about 37 MPa at the age of two days. The autogenous shrinkage is quite high compared to the total (drying) shrinkage. This fact can explain why the contribution of cracking is negligible in the drying shrinkage tests.

The results of the numerical analyses show that the SSM model together with the HTC model is capable of simulating the observed experimental data. The numerical simulations revealed the different contributions in the deformation observed in the specimens.

Acknowledgments The authors acknowledge the financial contribution of Italrom Inginerie Internationala S.r.l. Besides, the authors wish to thank the graduate student Sergio Borlini for his contribution to experimental and numerical work. Special thanks are due to the technicians Tonino Cocco and Paolo Broglia who have contributed to the experimental work.

REFERENCES

Bažant, Z.P., F.C. Caner, I. Carol, M.D. Adley, and S.A. Akers (2000). "Microplane model M4 for concrete. I: Formulation with work-conjugate deviatoric stress." *Journal of Engineering Mechanics,* ASCE, 126(9), 944-953.

Bažant, Z.P., J.C. Chern (1985). "Concrete creep at variable humidity: constitutive law and mechanisms." *Materials and Structures,* 103(18), 1-20.

Bažant, Z.P., G. Cusatis, and L. Cedolin (2004). "Temperature effect on concrete creep modeled by microprestress-solidification theory." *Journal of Engineering Mechanics,* ASCE, 130(6), 691-699.

Bažant, Z.P., A.B. Hauggaard, S. Baweja, and F.J. Ulm (1997a). "Microprestress-Solidification Theory for Concrete Creep. I: Aging and Drying Effects." *Journal of Engineering Mechanics,* ASCE, 123, 1188-1194.

Bažant, Z.P., A. B. Hauggaard, and S. Baweja (1997b). "Microprestress-Solidification Theory for Concrete Creep. II: Algorithm and Verification." *Journal of Engineering Mechanics,* ASCE, 123, 1195-1201.

Bažant, Z.P., and S. Prasannan (1989a). "Solidification theory for concrete creep. I: Formulation." *Journal of Engineering Mechanics,* ASCE, 115, 1691-1703.

Bažant, Z.P., and S. Prasannan (1989b). "Solifification theory for concrete creep. II: Verification and application." *Journal of Engineering Mechanics,* ASCE, 115, 1704-1725.

Cervera, M., J. Oliver, and T. Prato (1999a). "Thermo-chemo-mechanical model for concrete. I: Hydration and aging." *Journal of Engineering Mechanics,* ASCE, 125(9), 1018-1027.

Di Luzio, G. (2007). "A symmetric over-nonlocal microplane model m4 for fracture in concrete." *International Journal of Solids and Structures,* 44(13), 4418-4441.

Di Luzio, G. (2009). "Numerical model for time-dependent fracturing of concrete." *Journal of Engineering Mechanics,* ASCE, 135(7), 632-640.

Di Luzio, G. and G. Cusatis (2009a). "Hygro-thermo-chemical modeling of high performance concrete. I: Theory." *Cement and Concrete Composites,* 31(5), 301-308.

Di Luzio, G. and G. Cusatis (2009b). "Hygro-thermo-chemical modeling of high performance concrete. II: Numerical implementation, calibration, and validation." *Cement and Concrete Composites,* 31(5), 309-324.

Di Luzio, G. and G. Cusatis (2013). "Solidification-microprestress-microplane (SMM) theory for concrete at early age: Theory, validation and application." *International Journal of Solids and Structures,* 50(6), 957-975.

Gawin, D. and Pesavento, F. and Schrefler, B. A. (2006). "Hygro-thermo-chemo-mechanical modelling of concrete at early ages and beyond. Part I: hydration and hygro-thermal phenomena." *International Journal for Numerical Methods in Engineering,* (3), 299-331.

Ulm, F.J. and O. Coussy (1995). "Modeling of thermo-chemo-mechanical couplings of concrete at early ages." *Journal of Engineering Mechanics,* ASCE, 121(7), 785-794.

Stress Redistribution of Concrete Prisms Due to Creep and Shrinkage: Long-Term Observations and Analysis

P. Criel[1]; R. Caspeele[1]; N. Reybrouck[1]; S. Matthys[1]; and L. Taerwe[1]

[1]Magnel Laboratory for Concrete Research, Department of Structural Engineering, Ghent University, Ghent, Belgium. E-mail: Pieterjan.Criel@UGent.be

Abstract

In 1979, 16 concrete prisms with dimensions 140x150x4000 mm were casted in the Magnel Laboratory for Concrete Research. These prisms differ by the amount of passive reinforcement and by the applied loading level. Four reinforcement ratios were considered, i.e. 0%, 1.5%, 3% and 6%. For each reinforcement ratio a prism was subjected to an axial load corresponding to a concrete stress of 0, 5, 10 or 15 MPa. The combination of both parameters results in a total of 16 specimens. The compressive stress was applied to the prisms by means of post-tensioned unbonded strands at an age of 28 days. The stress level was kept constant during the first 12 years of the experiment by re-adjusting the force in the strands when the deviation exceeded 2% of the initial value. Afterwards, no re-adjusting of the strands took place. Significant redistribution of the stresses between the concrete and the steel can be expected due to the creep and shrinkage of concrete. This redistribution is larger for the prisms with a higher reinforcement ratio, resulting in lower creep and shrinkage strains. The time-dependent response of these prisms was modelled taking into account the prestress losses and stress redistribution between the concrete and the steel. For reasons of numerical efficiency, the compliance function was approximated by a Dirichtlet series using continuous retardation spectra. A comparison between the predicted results and the measurements is given for two prisms.

INTRODUCTION

Creep and shrinkage are important time-dependent phenomena in reinforced concrete structures. Although consensus on the details of the different mechanisms responsible for the time-dependent behaviour is not yet reached (Koenders et al., 2009; Yue, 1992), the effects of creep and shrinkage are well known and many reliable material models are available in literature. A large part of this research is the result of experiments on plain concrete without any reinforcing steel present and under constant loading conditions. However, in reality the load on concrete elements is rarely constant in function of time and reinforcement steel is mostly present. In order to determine the influence of reinforcing steel on the time-dependent deformations of concrete a series of 16 prisms with dimensions 140x150x4000 mm³ were manufactured at the Magnel Laboratory for Concrete Research (Lambotte et al., 1986, 1988). These prisms differ by the amount of passive reinforcement - respectively 0, 1.5, 3 and 6% of the concrete section - and by the applied level of

axial stress - respectively 0, 5, 10 and 15 MPa. One prism for each combination was tested. An overview of the experimental programme is given in Figure 1.

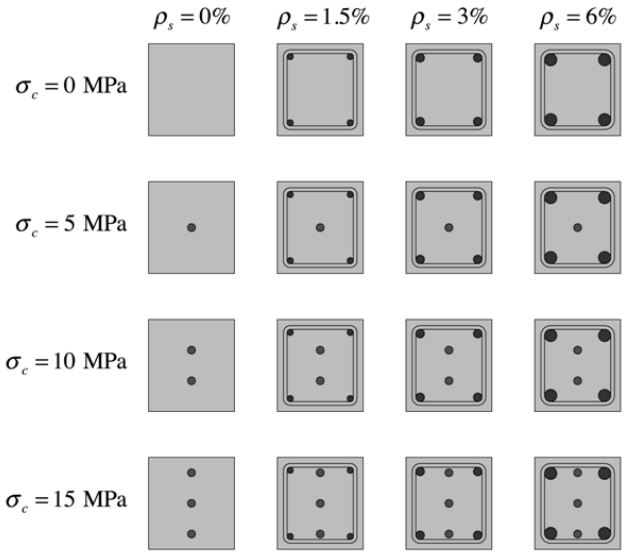

Figure 1 Reinforcing bars and unbounded strands arrangements for the 16 combinations of passive reinforcement ratios and applied stress levels.

Each prism is designated with a prefix "W" followed by the percentage of passive reinforcing steel, a dash and the level of applied stress; e.g. prism W0-0 is the prism in the top-left position in Figure 1, containing 0% reinforcing steel and zero applied stress.

The compatibility of the longitudinal deformations has as a consequence that the creep and shrinkage of the prisms are partly restrained by the reinforcement steel. This results in a redistribution between the stress in the concrete, which will decrease, and the stress in the reinforcement steel, which will increase in order for the cross-section to remain in longitudinal equilibrium. In the scope of this paper it is assumed that the bond between the concrete and the reinforcement steel is perfect.

TEST PROCEDURE

One day after casting, each prism was placed in a frame on two supports, of which one support allows for horizontal movements. The distance between the two supports was determined in such a way that the bending moments above the supports and in the mid-section due to the self-weight would have the same (minimal) value.

The prisms are axially prestressed with unbonded strands at 28 days. The strands were placed in a prestressing bed 96 hours before anchorage to reduce long-term relaxation losses. The prestressing force of each strand was measured using a load cell placed between the bearing plate attached to the endpoints of the prisms and the strand anchorage. An illustration of the test setup for each of the prims is given in Figure 2.

Figure 2 Test setup of the prisms

The axial force in the strands P_0 is determined in such a way that the resulting stress in the concrete is equal to respectively 0, 5, 10 or 15 MPa for the specified cases according to

$$P_0 = \sigma_c(A_c + \alpha A_S)$$

where A_c is the area of the concrete section, A_s is the area of the passive reinforcement, σ_c is the required concrete stress and α is the ratio between the moduli of elasticity of concrete and steel respectively. For α a theoretical value of 6 was assumed.

Each time the prestress losses reached 2% of the initial prestressing force, the force in the tendons was adjusted to 1.02 times the initial value. In this manner the external compressive force was kept approximately constant during the experiment.

MATERIALS

A traditional concrete with a water-cement ratio equal to 0.46 was used. The composition of the mixture in given in Table 1.

Table 1. Concrete mixture.

Component	*kg/m^3*
Cement CEM I 52.5 N	360
Gravel 8/16	1060
Gravel 4/8	190
Sand 2/5	100
Sand 0/2	535
Water	165

The mean compressive strength (cubes with side lengths158mm) at 28 days was equal to 47.4 MPa.

The unbonded tendons have a nominal diameter of 12.7 mm and have a very low relaxation. There are respectively 0, 1, 2 and 3 tendons used for the considered stress levels in the prisms

High-bond reinforcement bars with diameters 10, 14 and 20 mm were used for the passive reinforcement.

MEASUREMENT RESULTS

Nearly all reinforced prisms developed small cracks with a maximum crack width of 0.02 mm during the first 28 days of the experiment (when no axial loading was applied). These cracks can be attributed to the restrained shrinkage of the concrete.

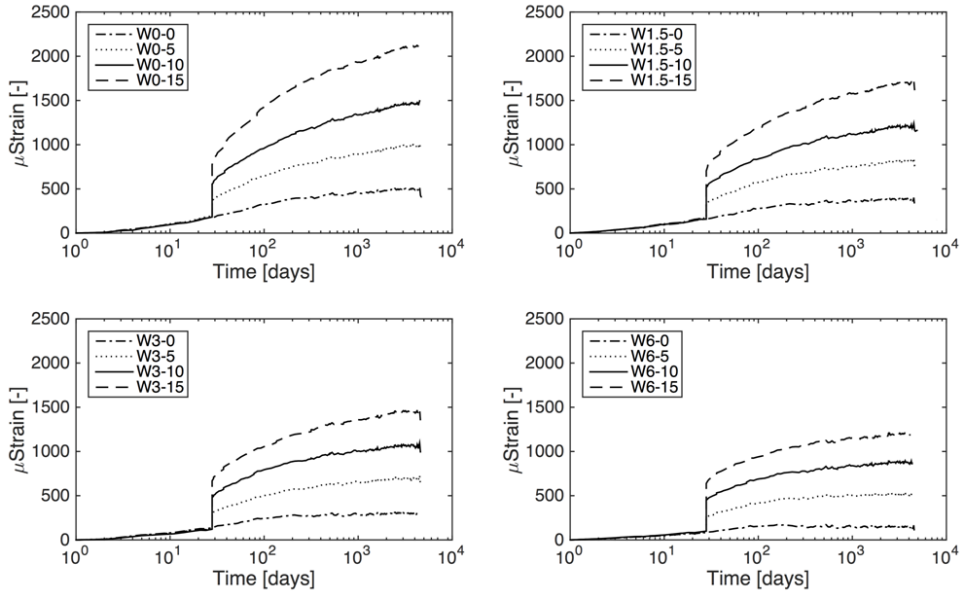

Figure 3 Measurement results of the axial deformation of the prisms.

The strain measurements of the prisms are given in Figure 3 up to 4500 days (12 years). It is observed that the measured concrete strain is proportional to the applied stress for the different reinforcement ratios.
Comparing W0-0 till W6-0, it is noted that the strain for the prisms with passive reinforcement steel is significantly less than the strain measured in the prism where no steel is present. This difference is attributed to the passive reinforcing steel, which limits the free shrinkage of the concrete.

It is noted that the strain of prism W6-0 shows a constant value starting from approximately 200 days. The concrete shrinkage continues but the total deformation does not increase any further. Due to the high percentage of passive reinforcement, tensile stresses are introduced in the concrete and the concrete cracked. This is visually confirmed by the many cracks in this particular prism.

NUMERICAL PROCEDURE

Creep strain
The uniaxial constitutive relation defining concrete as an ageing viscoelastic material is given by (Bažant, 1988):

$$\varepsilon(t) = \int_0^t J(t,t')\, d\sigma(t') + \varepsilon_{sh}(t)$$

in which t is the time of interest, t' is the time of application of the concrete stress, σ is the concrete stress , $\varepsilon(t)$ is the total concrete strain, $\varepsilon_{sh}(t)$ is the concrete shrinkage strain.

$J(t,t')$ is the creep compliance function. This integral is known as a *Stieltjes* integral. There is no compliance function $J(t,t')$ which is sufficiently accurate for this integral to be solvable in an analytically closed form. A numerical solution of this integral is possible, but this requires that the complete stress history is kept in memory for each new time-step (Gilbert & Ranzi, 2010). This is only feasible for simple problems.

In order to make the calculation of the *Stieltjes* integral more feasible, the creep compliance function can be approximated by a series of exponential functions with real exponents, so called Dirichlet series (Bažant, 1975, 1988). Hence, the compliance function $J(t,t')$ can be rewritten as:

$$J(t,t') = \frac{1}{E(t')} + \sum_{\mu=1}^{m} \frac{1}{\hat{E}_\mu}\left(1 - e^{-(t-t')/\tau_\mu}\right)$$

in which τ_μ are the chosen retardation times, $E(t')$ is the modulus of elasticity of the concrete at time t' and $\hat{E}_\mu$ are coefficients which depend on the age of load application t'. The coefficients $\hat{E}_\mu$ have the same dimension as the modulus of elasticity and must be determined in such a way that the error between the theoretical creep compliance function and the series approximation is minimal. Notice that the Dirichtlet series is written in function of the time lag $t - t'$ for a given application time t'. To determine the coefficients $\hat{E}_\mu$ it is most convenient to first select a number of t' values and fit $J(t,t')$ as a function of the lag time $t - t'$ for each fixed t'. Since the concrete stress gradually decreases, a Dirichtlet series was defined for each time step in the analysis. A uniform distribution of the time-step in log-time recommended choice (Jendele & Phillips, 1992).

Fitting a Dirichlet series on a function is not as straightforward as a Fourier series (Bažant, 1973). The coefficients $\hat{E}_\mu$ should be regarded as a discrete spectrum of the Dirichtlet series for given retardation times τ_μ. If the Dirichlet series is composed out of an infinite number of terms, each with a coefficient $\hat{E}_\mu$ and a retardation time τ_μ, a continuous function $L(\tau)$ is created. This function $L(\tau)$ can be regarded as the continuous spectrum of a Dirichtlet series with an infinite number of terms (Jirásek & Havlásek, 2014).

Jirásek & Havlásek (2014) showed that an approximation of $L(\tau)$ can be obtained analytically be using the *Post-Widdler* formula

$$L(\tau)_{(k)} = -\frac{(-k\tau)^k}{(k-1)!}\varphi^{(k)}(k\tau)$$

It was shown that a sequence of approximations converges to the continuous spectrum $L(\tau)$, in which $\varphi(\cdot)$ is the creep function, $\varphi^{(k)}(\cdot)$ is the k^{th} derivative of the creep function and k is the order of approximation.

Values for the coefficients $\hat{E}_\mu$ can be determined by integration of $L(\tau)$. With these coefficient an approximated compliance function $J(t,t')$ is constructed which allows for an analytical solution of the *Stieltjes* integral.

Stress redistribution
the strain of the steel and the strain of the concrete should be equal at each time t:

$$\varepsilon_c(t) = \varepsilon_s(t) = \varepsilon(t)$$

The steel stress can be written as:

$$\sigma_s(t) = E_s\varepsilon(t)$$

where E_s is the modulus of elasticity of the reinforcement steel. The longitudinal equilibrium of the prisms can be written as:

$$P(t) = A_s\sigma_s(t) + A_c\sigma_c(t)$$

The concrete stress which would induce by a strain $\Delta\varepsilon$ is given by:

$$\sigma_c = \Delta\varepsilon E_c$$

The corresponding force on the concrete area A_c is given by:

$$F = \sigma_c A_c = \Delta\varepsilon E_c A_c$$

If the same force is exerted on a concrete section that contains passive reinforcement the following equality can be written:

$$\Delta\varepsilon E_c A_c = \Delta\varepsilon_{corr}(E_c A_c + E_s A_s)$$

with A_s the area of the steel section and $\Delta\varepsilon_{corr}$ the strain of the section containing both concrete and reinforcement steel.

The ratio between the corrected strain $\Delta\varepsilon_{corr}$ and the assumed free strain of $\Delta\varepsilon$ is given by:

$$\frac{\Delta\varepsilon_{corr}}{\Delta\varepsilon} = \frac{E_c A_c}{E_c A_c + E_s A_s}$$

The same reasoning can be applied to shrinkage strains as well as creep strains, with the difference that the creep strain will depend on the concrete stress in the considered time-step, while the shrinkage strain is independent of the stresses in the concrete.

Prestress losses

Due to the concrete creep and shrinkage the unbonded tendons will lose part of their prestressing force. The equivalent lost prestress force for a given strain $\Delta\varepsilon_{corr}$ is given by:

$$\Delta P = \Delta\varepsilon_{corr} A_p E_p$$

where A_p is the area of the prestressing tendons and E_p is the modulus of elasticity of the prestressing steel.

General procedure

As in (Taerwe, 1990), also in this paper the creep and shrinkage models suggested by Model Code 90 are applied (fib, 1993).

A series of times $t_1, t_2, \dots, t_r, \dots, t_{200}$ is chosen, distributed uniformly on a log-scale. A total of 200 calculation steps were considered in the analysis. Since the nature of this problem results in a continuous decreasing concrete stress, the Dirichlet series to approximate the compliance function needs to be determined for each time t_r in the time series.

During the first 28 days no prestressing is applied on the prisms. The prisms will shrink during this period, introducing tensile stresses in the concrete due to the restraining effect. After 28 days the prestressing force is applied. Starting from this point the prisms will start to creep. To avoid erroneous predictions of the instantaneous response of the prisms, the instantaneous response is calculated by considering a very short time step after 28 days. In each time step the creep and shrinkage strains of the concrete are corrected as mentioned above taking into account the restraining effect of the reinforcement steel. With this correction, the stresses in the reinforcing steel and in the concrete are adjusted so that an equilibrium is reached with the prestressing force $P(t)$.

RESULTS

The procedure described above is applied for prism W1.5-10 of the experimental test programme. The results of the calculation is given in Figure 4.

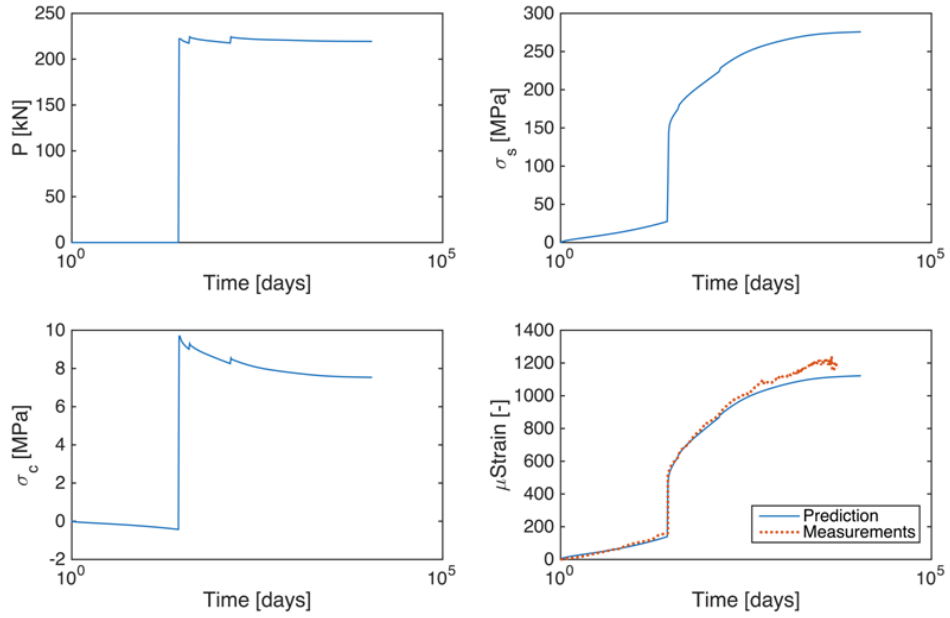

Figure 4 Results of the calculation for prism W1.5-10. (a) The prestressing force (b) The stress in the reinforcement (c) The stress in the concrete (d) The predicted and measured deformation of the prism

In the period before the application of the load the model shows a build-up of tensile stress in the concrete, as shown in Figure 4 (c). This is due to the restrained shrinkage. The load is applied at 28 days. The predicted deformation shows good agreement with the measurements. The concrete stress decreases over time starting from a pre-defined stress equal to 10 MPa and drops to 7.5 MPa. The stress in the reinforcement steel is almost doubled compared to the stress immediately after the application of the load.

CONCLUSIONS

From the available experiments and the numerical analysis the following conclusions can be drawn.

- Measurements of axial deformations of concrete prisms subjected to a quasi-sustained load during 12 years are presented. The experiments show that the time-dependent deformations of reinforced prisms are strongly affected by the presence of passive reinforcement steel. This is due to the significant redistribution of the stresses in the concrete section.
- An approximation of the creep compliance function by a Dirichtlet series allows for the *Stieltjes* integral to be solvable in an analytically closed form. Additionally, the load history does not need to be stored in order to calculate the deformation in a next time-step.
- The predicted axial deformations taking into account the stress redistribution and the prestress losses show good agreement with the measurements.

ACKNOWLEDGEMENTS

The authors would like to thank the Agency for Innovation by Science and Technology in Flanders (IWT) and the Buildsoft company for supporting this research.

REFERENCES

Bažant, Z. P. (1973). Dirichlet Series Creep Function for Aging Concrete *Journal of the Engineering Mechanics Division, 99*(2), 367-387.

Bažant, Z. P. (1975). I. - Theory of Creep and Shrinkage in Concrete Structures: A Précis of Recent Developments. In S. Nemat-Nasser (Ed.), *Mechanics Today* (pp. 1-93): Pergamon.

Bažant, Z. P. (1988). *Mathematical Modeling of Creep and Shrinkage of Concrete*. New York: John Wiley & Sons.

fib. (1993). *CEB-FIP Model Code 90*. London: Thomas Telford

Gilbert, R. I., & Ranzi, G. (2010). *Time-Dependent Behaviour of Concrete Structures*: Taylor & Francis.

Jendele, L., & Phillips, D. V. (1992). Finite element software for creep and shrinkage in concrete. *Computers & Structures, 45*(1), 113-126. doi: 10.1016/0045-7949(92)90349-5

Jirásek, M., & Havlásek, P. (2014). Accurate approximations of concrete creep compliance functions based on continuous retardation spectra. *Computers & Structures, 135*(0), 155-168. doi: http://dx.doi.org/10.1016/j.compstruc.2014.01.024

Koenders, E. A. B., van der Ham, H. W. M., van Breugel, K., & Lokhorst, S. J. (2009). *Modelling creep by microstructural changes.* Paper presented at the Concreep 8, Ise-Shima, Japan.

Lambotte, H., Van Nieuwenburg, D., & Cocquyt, F. (1986). Influence of Non-Prestressed Steel on Shrinkage and Creep deformations and on Steel-Concrete Stress Redistribution. In M. Z. Cohn (Ed.), Partial Prestressing, From Theory to Practice (NATO ASI Series E: Applied Sciences, V. 2) (pp. 45-56). Doordrecht: Martinus Nijhoff Publishers.

Lambotte, H., Van Nieuwenburg, D., & Taerwe, L. (1988). *Cracking and Crack Widths of Partially Prestressed Concrete Members*. Paper presented at the European Conference on Cracking of Concrete and Durability of Constructions, AFREM-CCE, Saint-Remy-Les-Cheveuse.

Taerwe, L. (1990). Simplified Analysis of Stress Redistribution in Partially Prestressed Concrete Sections. *Aci Structural Journal, 87*(11), 93-98.

Yue, L. L. (1992). *Creep Recovery of Plain Concrete under Uniaxial Compression.* PhD thesis, Ghent University, Ghent.

Advanced Evaluation of the Fracture Response of Steel Fibre-Reinforced Concrete Specimens

D. Lehký[1]; I. Havlíková[1]; Z. Keršner[1]; D. Novák[1]; H. Šimonová[1]; L. Řoutil[1]; A. Abdulrahman[1]; P. Schmid[1]; and B. Krug[2]

[1]Brno University of Technology, Veveří 331/95, 602 00 Brno, Czech Republic. E-mail: lehky.d@fce.vutbr.cz
[2]Franz Oberndorfer GmbH & Co KG, Lambacher Straße 14, 4623 Gunskirchen, Austria. E-mail: b.krug@oberndorfer.at

Abstract

Selected results of extensive fracture testing of steel fibre reinforced concrete (developed in industry for the production of prefabricated concrete elements) after different period of hardening are presented in the paper. Experiments were performed on notched specimens in a three-point bending test configuration. The fracture parameters were evaluated using three models/approaches: double-*K* fracture model, effective crack length method, and work-of-fracture method. The obtained parameters can be used to quantify the structural resistance against crack initiation and propagation – or the brittleness and toughness/ductility of the structural members – as well as for the comparison of the studied or developed cement based composites or the structural members of buildings. They can be also employed for the definition of the material models for deterministic or stochastic simulation of the quasi-brittle/ductile response of cement based composites/members using Stochastic Finite Element Method model with nonlinear fracture mechanics principles implemented – this approach can help to the optimal design of developed prefabricated concrete elements.

INTRODUCTION

The natural heterogeneity of composites containing steel fibres leads to the natural variability of fracture parameters. The correct representation for stochastic nonlinear modelling is essential in order to capture the behaviour of prefabricated concrete elements made of these composites. Numerical modelling of failure and fracture phenomena in concrete as well as other cementitious materials became a field of an intensive research in the recent years. With respect to the accuracy and the efficiency of corresponding numerical models one open question exits: How the heterogeneity of cementitious materials can be taken into consideration in the most realistic way using commercially available finite element programs? The classical approach is to introduce a stochastic probability distribution of the properties of concrete into the finite elements. With respect to the strength and deformation behaviour of quasi-brittle materials a better knowledge of its fracture properties is required to enable a realistic prediction of its failure using virtual nonlinear finite

element simulation. Therefore, it is necessary to take into account the random character of mechanical fracture parameters while employing a suitable method when conducting statistical and reliability analyses of concrete structures (Bergmeister et al. 2009, Novák et al. 2007, 2014, Pukl et al. 2003, Strauss et al. 2009, 2014, Zimmermann et al. 2014).

The contribution focuses on the characterization of the mechanical fracture properties (including statistical characteristics) of specific steel fibre reinforced concrete. One of the primary aims was monitoring the values of selected parameters and their variability in time. Note that presented work follows a previous study of the same concrete type but without addition of steel fibres (Řoutil et al. 2014). The testing program was carried out in cooperation of the Faculty of Civil Engineering, Brno University of Technology in Czech Republic with the University of Natural Resources and Life Sciences in Vienna and concrete plant company Franz Oberndorfer GmbH & Co KG.

EXPERIMENTS

The part of testing program focused on C50/60 strength class concrete reinforced with steel fibres is presented. For details of concrete mixture see Table 1. This mixture is being developed for the production of prefabricated pre-stressed concrete elements. Steel fibres were Dramix 5D fibers (Figure 1c). According to the manufacture certification the fibres have a tensile strength of $R_{m,nom}$ = 2300 MPa, a modulus of elasticity of E_s = 210000 MPa and a wire ductility of 6 %. The length of the fibres is 60 mm and the diameter is 0.9 mm. The experiments were carried out after 7, 28 and 126 days of hardening in order to obtain time dependent changes of the material parameters.

The testing program involves tests on freshly mixed concrete as well as on hardened concrete. On freshly mixed concrete, slump value and air void contents were determined. On hardened concrete three-point bending tests on notched beams of nominal sizes 150 × 150 × 550 mm were carried out first. The loading span was 500 mm. The notch depth was about 1/3 of the depth of the specimen. See Figure 1 for test configuration and example of typical crack initiation and propagation. Two fractured parts of each specimen were cut to nominal size of 150 × 150 × 150 mm used for consequent compression tests.

Note that within mentioned extensive testing also other influences like e.g. amount of fibres, different storing conditions and specimen sizes on values of the fracture parameters were studied – the review can be found in (Lehký et al. 2015).

Figure 2 shows load–crack mouth opening displacement (*CMOD*) diagrams obtained from testing specimens of nominal size 150 × 150 × 550 mm tested at 7, 28 and 126 days of concrete hardening. Shapes of diagrams are typical for steel fibre reinforced concrete with two peaks – the first corresponds to concrete cracking when fibres are still not fully activated; the second correspond to ultimate capacity of the composite. From time of curing point of view diagrams show slight increase of mean values of strength corresponding to the first peak and more significant increase of mean value of strength corresponding to the second peak – for comparison see Figure 2.

Table 1. Concrete mixture composition and selected parameters.

Component/property	*Unit*	*Amount*
Aggregate 0/4 edge	kg	99.54
Aggregate 0/4 round	kg	845.76
Aggregate 4/8 round	kg	373.71
Aggregate 8/16 edge	kg	535.61
Water content	kg	159
Cement CEM I 52.5 R	kg	459.36
Sky 657	kg	6.45
Sky 911	kg	0.92
Steel fibers	kg/m^3	25
Water to cement ratio *w*/*c*	–	0.35
Air void contents	vol.%	0.8
Slump value	cm	58 (F5)
Density	kg/m^3	2488

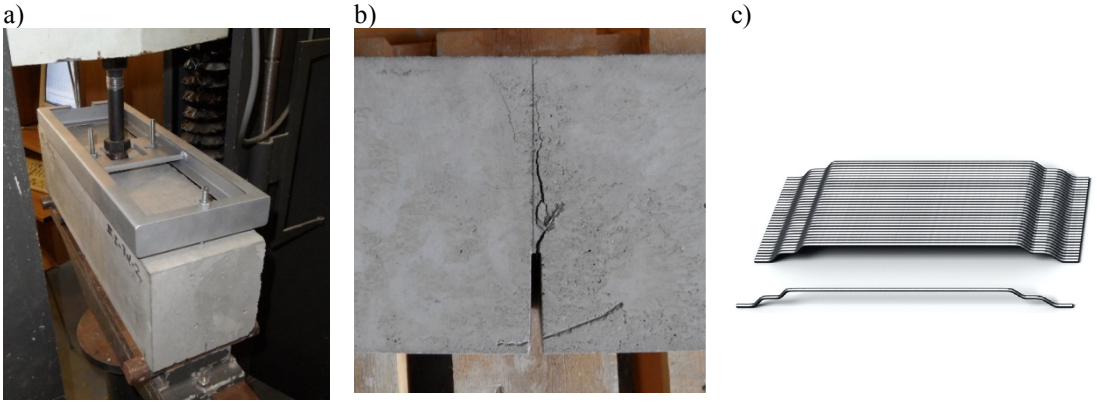

Figure 1. a) Three-point bending test configuration, b) example of crack initiation and propagation, c) Dramix 5D fibres.

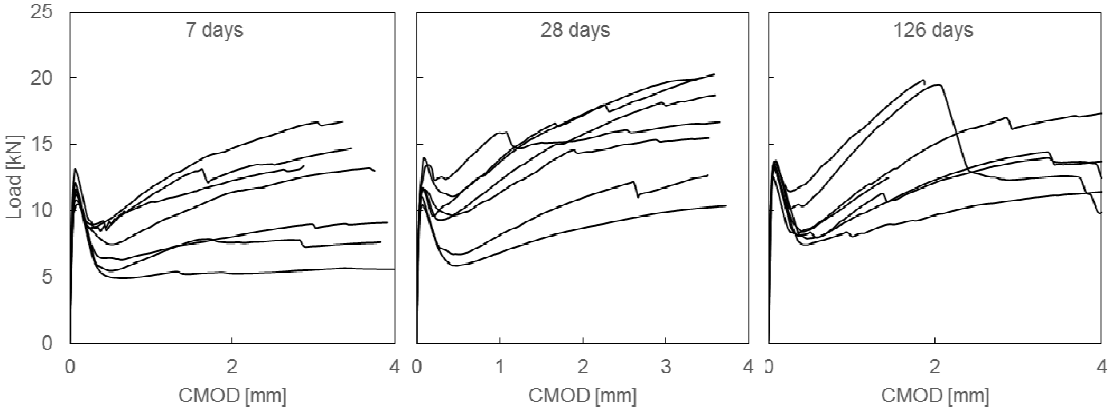

Figure 2. Load vs. crack mouth opening displacement (*CMOD*) diagrams obtained for specimens tested at 7, 28 and 126 days of concrete hardening.

EVALUATION OF MECHANICAL FRACTURE PARAMETERS

Three models/approaches were utilized to evaluate mechanical fracture parameters from diagrams load vs. crack mouth opening displacement (*CMOD*) and load vs. deflection: double-*K* fracture model, effective crack length method, and work-of-fracture method.

Double-K fracture model

In principle, the double-*K* fracture model combines the concept of cohesive forces acting on the faces of the fictitious (effective) crack increment with a criterion based on the stress intensity factor. The advantage of this model is that it describes different levels of crack propagation: an initiation part which corresponds to the beginning of stable crack growth (at the level where the stress intensity factor, K_{Ic}^{ini}, is reached), and a part featuring unstable crack propagation (after the unstable fracture toughness, K_{Ic}^{un}, has been reached).

In this paper, the unstable fracture toughness K_{Ic}^{un} was numerically determined first, followed by the cohesive fracture toughness K_{Ic}^{c}. When both of these values were known, the following formula was used to calculate the initiation fracture toughness K_{Ic}^{ini}:

$$K_{Ic}^{ini} = K_{Ic}^{un} - K_{Ic}^{c}. \tag{1}$$

Details regarding the calculation of both unstable and cohesive fracture toughness can be found in book (Kumar and Barai 2011). Calculation of parameter K_{Ic}^{un} is dependent on geometry function $F_1(\alpha)$ which for the case of three-point bending fracture test is defined as:

$$F_1(\alpha) = \frac{1.99 - \alpha(1-\alpha)\left(2.15 - 3.93\cdot\alpha + 2.7\cdot\alpha^2\right)}{(1+2\cdot\alpha)(1-\alpha)^{3/2}}, \quad \text{and} \quad \alpha = \frac{a_c}{D}, \tag{2}$$

where a_c is the critical effective crack length and D is the specimen depth.

To determine the cohesive part of fracture toughness, K_{Ic}^{c}, it is necessary to accept the assumption of the distribution of the cohesive stress σ along the fictitious crack. Generally, in the cohesive crack model, the relation between the cohesive stress σ and the effective crack opening displacement, w, is referred to as the cohesive stress function $\sigma(w)$. The cohesive stress $\sigma(CTOD_c)$ at the tip of the initial notch of length a_0 at the critical state can be obtained from the softening curve. In this paper, the bilinear softening curve was used when two cases may occur:

In case I ($CTOD_c \le w_s$), $\sigma(CTOD_c)$ value can be obtained according to:

$$\sigma(CTOD_c) = f_t - (f_t - \sigma_s)\frac{CTOD_c}{w_s}, \tag{3}$$

where f_t is the tensile strength, $CTOD_c$ is critical crack tip opening displacement (see e.g. Kumar and Barai 2011), σ_s and w_s are the ordinate and abscissa at the point of slope change of the bilinear softening curve, respectively. According to Petersson (Petersson 1981), the σ_s and w_s values can be considered using the following equations:

$$\sigma_s = \frac{1}{3} f_t, \quad \text{and} \quad w_s = \frac{2}{9} w_c, \tag{4}$$

where w_c is the critical crack tip opening displacement. In this paper, w_c is constant value (w_c = 0.16 mm) for all specimens.

The value of tensile strength is estimated using the measured value of compressive strength f_{cu} using the following relation (Červenka et al. 2012):

$$f_t = 0.24 f_{cu}^{\frac{2}{3}}. \tag{5}$$

In case II ($w_s \leq CTOD_c \leq w_c$), $\sigma(CTOD_c)$ value can be calculated using the following formula:

$$\sigma\left(CTOD_c\right) = \frac{\sigma_s}{w_c - w_s}\left(w_c - CTOD_c\right). \tag{6}$$

Finally, the value of the load P_{ini} was determined according to equation (7). This value can be defined as the load level at the beginning of stable crack propagation from the initial crack/notch:

$$P_{ini} = \frac{4WK_{\mathrm{Ic}}^{ini}}{SF_1\left(\alpha_0\right)\sqrt{a_0}}, \tag{7}$$

where W is section modulus determined as $W = 1/6BD^2$, B is the specimen width, S is the load span, $F_1(\alpha_0)$ is geometry function according to formula (2), which is dependent on α_0, i.e. ratio a_0/D, a_0 is the initial notch length.

Effective crack length method, work-of-fracture method

To determine the mechanical fracture parameters of the tested concretes, experimental load vs. deflection diagrams were treated also by the standard technique – the two-parameter effective crack model and work-of fracture method (RILEM 1985, Karihaloo 1995). The effective fracture toughness and specific fracture energy values were obtained. Effective fracture toughness was calculated as:

$$K_{\mathrm{Ice}} = \frac{3P_{max}S}{BW^2} Y\left(\alpha_e\right)\sqrt{a_e}. \tag{8}$$

Symbols in equation (8) are as follows: W (B) – width (breadth) of the specimen, P_{max} – maximum load (first peak corresponds to concrete cracking), S – loading span of the specimen, a_e – effective crack length and $Y(\alpha_e)$ – function of geometry. Note that introduction of effective crack length is essential to capture the quasi-brittle behavior of cement based composites.

Fracture energy G_F is defined as the energy needed to create a crack surface of unit area. According to the "work-of-fracture method", the fracture energy is calculated as the area under the load vs. *CMOD* curve recorded during the fracture test and divided by the area of the initial specimen ligament. To approach the value of the part of "true fracture energy" two limit values were determined for selected stages of cracking process. Lower (upper) limit value for each step was set up according to Eq. 9 (Eq. 10). In each case the different reduction of the area under the *load–CMOD* curve was employed for the calculation of the part of value of work of fracture. Mentioned reductions are shown at Figure 3 for both the upper as well as the lower limit value. To obtain the value of corresponding part of specific fracture energy the (reduced) work of fracture is divided by the area of ligament which corresponds to current effective crack length (Figure 3). This approach can be applied with respect to actual value of $CMOD_i$. Spread of described values for *CMODi* between 0 and 4 mm can be found at Figure 5. Note that this estimation of the part of specific fracture energy is more general and suitable than values presented in (Řoutil et al. 2014) or (Lehký et al. 2015).

$$G^*_{F,\min} = \frac{W^*_{F,\min}}{B(a_e - a_0)} \tag{9}$$

$$G^*_{F,\max} = \frac{W^*_{F,\max}}{B(a_e - a_0)} \tag{10}$$

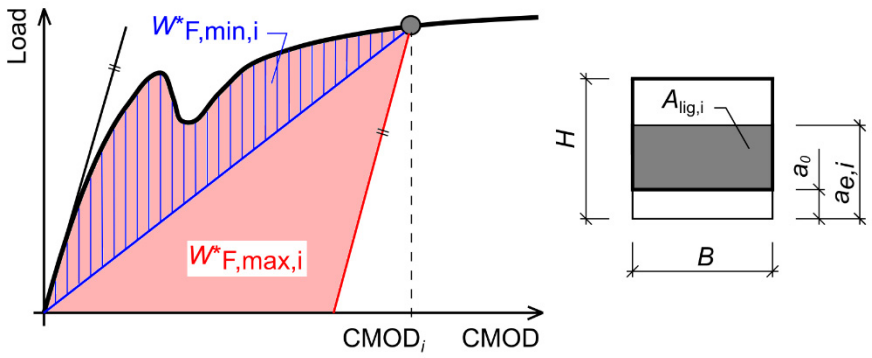

Figure 3. To evaluation of minimal and maximal part of specific fracture energies corresponding to $CMOD_i$.

RESULTS

The resulting mechanical fracture parameters are presented in Table 2 and Figures 4 and 5; namely compressive strength f_{cu}, modulus of elasticity E, effective fracture toughness K_{Ice}, unstable fracture toughness K_{Ic}^{un}, initiation to unstable fracture toughness ratio K_{Ic}^{ini}/K_{Ic}^{un}, and ratio P_{ini}/P_{max}, i.e. the ratio between the force at the beginning of stable crack propagation from the initial stress concentrator and the maximal force, as well as the parts of minimal and maximal specific fracture energies corresponded to actual *CMOD* were determined. For parameters with potential utilization in numerical modelling, i.e. compressive strength and modulus of elasticity, the most suitable probability distribution function was determined by goodness of fit test (Kolmogorov–Smirnov test) implemented in FReET probabilistic software (Novák et al., 2014).

Table 2. Statistical characteristics of selected mechanical fracture parameters.

Parameter		Days of hardening 7d	28d	126d
Compressive strength f_{cu} [MPa]	mean	78.0	86.3	91.8
	std	1.8	2.9	5.6
	PDF	WBMn	WBMx	LN3
Modulus of elasticity E [GPa]	mean	25.9	25.5	28.3
	std	4.1	3.3	4.4
	PDF	Ray	GBMx	GBMx
Effective fracture toughness K_{Ice} [MPa.m$^{1/2}$]	mean	1.907	2.018	2.112
	std	0.117	0.199	0.172
Unstable fracture toughness K_{Ic}^{un} [MPa.m$^{1/2}$]	mean	1.573	1.715	1.779
	std	0.134	0.343	0.223
Ratio K_{Ic}^{ini}/K_{Ic}^{un} [–]	mean	0.369	0.340	0.418
	std	0.101	0.094	0.042
Ratio P_{ini}/P_{max} [–]	mean	0.527	0.515	0.582
	std	0.079	0.143	0.065

Notes: std – standard deviation; PDF – probability density function; WBMx – Weibull Maximum (3 par.), WBMn – Weibull Minimum (3 par.), LN3 – Lognormal (3 par.), Ray – Rayleigh, GBMx – Gumbel Maximum.

Results show that there is a gradual increase of compressive strength in time. Similar values were obtained also for plain concrete (see Řoutil et al. 2014 for more details). As expected, variability of compressive strength is quite small compared to other parameters with slight increase over time.

In case of modulus of elasticity, not large differences occur among values obtained for different age of concrete. Variability of modulus of elasticity is more or less constant over time. The higher age of specimens show increase of values of both effective fracture toughness and unstable fracture toughness respectively.

The K_{Ic}^{ini}/K_{Ic}^{un} ratio means the relative resistance to stable crack propagation – it was shown that there is no significant trend on the resistance to stable crack

propagation (with respect to variability of this parameter) over time. Similar trend can be found for the ratio between the force at the beginning of stable crack propagation from the initial stress concentrator and the maximal force (P_{ini}/P_{max}). In this case we can see higher variability of values for the age of testing equal to 28 days.

Values of parts of specific fracture energies corresponded to actual *CMOD* show significant variability. Spread of values of parts of minimal as well as maximal specific fracture energies for increasing *CMOD* are presented graphically for 7, 28 and 126 days of concrete hardening.

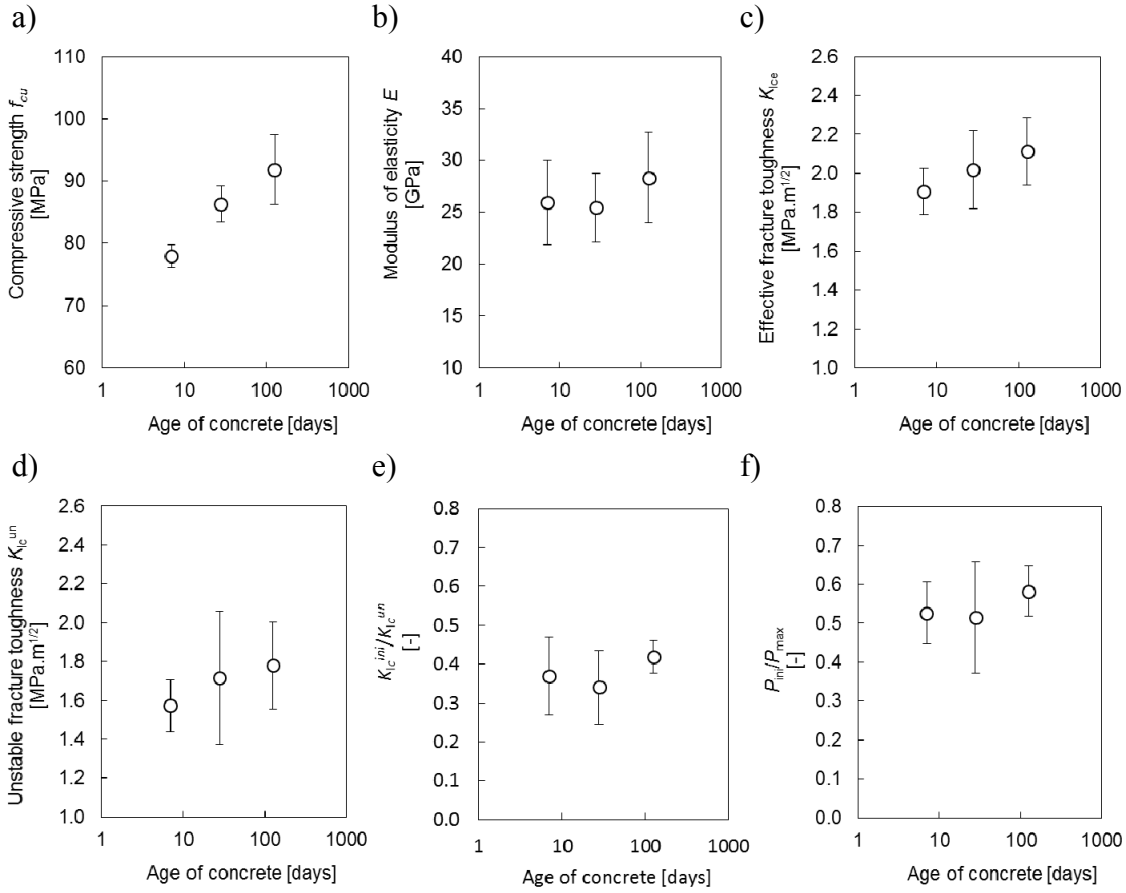

Figure 4. Mean values and standard deviations of selected parameters: a) compressive strength, b) modulus of elasticity, c) effective fracture toughness, d) unstable fracture toughness, e) initiation to unstable fracture toughness ratio, and f) crack initiation load to maximum load ratio.

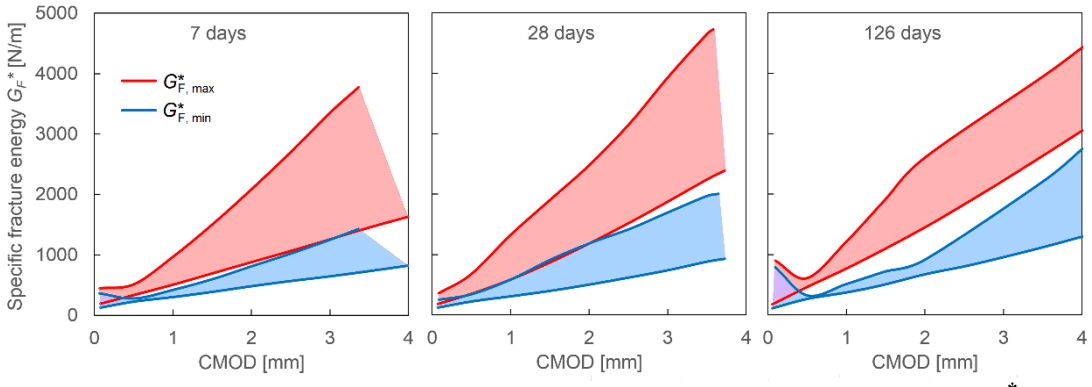

Figure 5. Spread of values of parts of minimal specific fracture energy $G^*_{F,\,min}$ and maximal specific fracture energy $G^*_{F,\,max}$ with respect to actual crack mouth opening displacement obtained for specimens tested in 7, 28 and 126 days of concrete hardening.

CONCLUSION

Within the paper selected results of the extensive testing program carried out to obtain mechanical fracture parameters of concrete with steel fibres tested at different ages are presented. The investigated material parameters were basic mechanical ones as well as fracture–relevant. Obtained set of material parameters was statistically evaluated and suitable models of probabilistic distribution functions were assessed using goodness of fit tests. Finally, these research results can serve as a basis for the further numerical assessment and optimization of real structural elements fabricated from tested concrete types, including probabilistic aspects.

ACKNOWLEDGEMENTS

The authors give thanks for the support of the project FRAPA No. P104-13-03662S provided by the Grant Agency of the Czech Republic and the project No. LO1408 "AdMaS UP – Advanced Materials, Structures and Technologies", supported by Ministry of Education, Youth and Sports under the „National Sustainability Programme I".

REFERENCES

Bergmeister, K., Novák, D., Pukl, R., and Červenka, V. (2009). "Structural assessment and reliability analysis for existing engineering structures, theoretical background." *Structure and Infrastructure Engineering*, 5(4), 267–275.

Červenka, V., Jendele, L., and Červenka, J. (2012). *ATENA Program documentation – Part 1: theory*. Cervenka Consulting, Praha.

Karihaloo, B. L. (1995). *Fracture mechanics of concrete*. Longman Scientific & Technical, New York.

Kumar, S., and Barai, S. V. (2011). *Concrete Fracture Models and Applications*. Springer, Berlin.

Lehký, D., Řoutil, L., Keršner, Z., Novák, D., Šimonová, H., Havlíková, I., and Schmid, P. (2015). "Experimental determination of mechanical fracture parameters of steel fiber reinforced concrete for probabilistic life-cycle assessment." In *FIB Symposium 2015*, Copenhagen (in print).

Novák, D., Vořechovský, M., Lehký, D., Bergmeister, K., Pukl, R., and Červenka, V. (2007). "Stochastic nonlinear analysis of concrete structures - Part I: From simulation of experiment and parameters identification to reliability assessment." In *10th Int. Conf. on Applications of Statistics and Probability in Civil Engineering – ICASP10*, Tokyo, Japan.

Novák, D., Vořechovský, M., and Teplý, B. (2014). "FReET: Software for the statistical and reliability analysis of engineering problems and FReET-D: Degradation module." *Advances in Engineering Software*, 72, 179–192.

Petersson, P. E. (1981). "Crack growth and development of fracture zone in plain concrete and similar materials." *Report No. TVBM-1006*, Lund Institute of Technology.

Pukl, R., Červenka, V., Strauss, A., Bergmeister, K., and Novák, D. (2003). "An advanced engineering software for probabilistic-based assessment of concrete structures using nonlinear fracture mechanics." In *Proc. of 9th Int. Conf. on Applications of Statistics and Probability in Civil Engineering – ICASP 9*, San Francisco, USA, Rotterdam Millpress, 1165–1171.

RILEM TC – 50 FMC (Recommendation). (1985). "Determination of the fracture energy of mortar and concrete by means of three-point bend test on notched beams." *Materials and Structures*, 18(107), 285–290.

Řoutil, L., Lehký, D., Šimonová, H., Kucharczyková, B., Keršner, Z., Novák, D., Zimmermann, T., Strauss, A., and Krug, B. (2014). "Experimental-computational determination of mechanical fracture parameters of concrete for probabilistic life-cycle assessment." In: *Proceedings of the Fourth International Symposium on Life-Cycle Civil Engineering (IALCCE 2014) – Life-Cycle of Structural Systems: Design, Assessment, Maintenance and Management*, Tokyo, Japan, Furuta, Frangopol & Akiyama (Eds.), © 2015 Taylor & Francis Group, London, UK, 801–807.

Strauss, A., Hoffmann, S., Wendner, R., and Bergmeister, K. (2009). "Structural assessment and reliability analysis for existing engineering structures, applications for real structures." *Structure and Infrastructure Engineering*, 5(4), 277–286.

Strauss, A., Zimmermann, T., Lehký, D., Novák, D., and Keršner, Z. (2014). "Stochastic fracture-mechanical parameters for the performance-based design of concrete structures." *Structural Concrete*, 15(3), 380–394.

Zimmermann, T., Strauss, A., Lehký, D., Novák, D., and Keršner, Z. (2014). "Stochastic fracture-mechanical characteristics of concrete based on experiments and inverse analysis." *Construction and Building Materials*, 73, 535–543.

Simulating the Effect of ASR on the Performance of Concrete Structures

J. J. Kim[1]; T. Fan[2]; and M. M. Reda Taha[2]

[1]Department of Civil Engineering, Kyungnam University, Changwon-si, South Korea. E-mail: jungkim@kyungnam.ac.kr
[2]Department of Civil Engineering, University of New Mexico, MSC 01 1070, Albuquerque, NM 87131-0001. E-mail: mrtaha@unm.edu

Abstract

Concrete is a time-dependent and multi-scale composite. Alkalis in cement react with reactive silica in aggregate in the presence of water and forms a gel in what is known as alkali-silica reaction (ASR). When ASR gel absorbs water, it swells. Swelling of ASR gels can damage concrete and cause cracking which reflects on long-term structural performance. In this paper, the mechanical consequences of ASR on concrete are simulated using a discrete homogenization model. Representative volume element (RVE) of concrete is established as a cluster of cement paste and aggregate particles connected using an interfacial transition zone (ITZ), which includes contact and cracking mechanisms to consider particle interaction. The mechanical evolution of concrete subjected to ASR is achieved from microstructural behaviors: volume expansion of reactive elements induces internal stresses and cause debonding and cracking. The mechanical evolution of concrete characteristics due to continuous cement hydration is also considered. The constitutive model of concrete is attained via the homogenization approach. The proposed method allows considering the effect of ASR on performance of concrete structures. A case study, in the literature, is used to demonstrate the efficiency of the proposed meso-scale homogenization approach. The proposed model shows good agreement with experimental observations of concrete behavior with ASR.

INTRODUCTION

Since its discovery of ASR by Stanton (1940), Alkali-silica reaction (ASR) became a well-known problem in concrete materials that can affect the integrity and performance of concrete structures (Mehta and Monteiro 2014; Sharp 2006). ASR takes place when alkalis in cement react with reactive silica in aggregate in the presence of water, When ASR takes place, it produces a gel which swells (Bažant et al. 2000). ASR swelling would not necessary produce immediate problem as the swelling gels would first occupy concrete voids and then exert internal pressure on concrete (Multon et al. 2006). Many researchers examined ASR mechanism and showed that the growing ASR pressure can result in inducing microcracks inside the concrete and thus deterioration that can affect the concrete structures. Examples of reinforced concrete structures deteriorated because of ASR have been reported

worldwide including bridges, viaducts, dams and nuclear power plants (den Ujil et al. 2002, Takakura et al. 2005, Sellier et al. 2009).

Several methods to prevent ASR were reported in the literature (Mehta and Monteiro 2014). Such methods include adding high silica content admixtures such as fly ash and/or silica fume, reducing concrete permeability and keeping concrete dry, and using nonreactive aggregate. Although these methods proved efficient for mitigating ASR in new concrete structures, they cannot be used for protecting existing concrete structures with ASR potential. This becomes a critical issue dealing with sensitive structures such as nuclear power plants or storage casks. ASR, therefore, represents a hazard to existing concrete structures that can affect its performance integrity. Computational models to predict service life of existing concrete structures under ASR hazard are warranted.

The details of the chemical reaction responsible for ASR lie beyond the scope of this study but can be understood from other work in the literature (e.g. Bažant et al. 2000). Generally, it is believed that ASR happens when alkalis in the cement paste chemically react with silica from reactive aggregate in the existence of water. Water is then used to transport reactants and so is indispensable to complete the reaction. If the amount of ASR gels is relatively small, voids in concrete will be filled and no internal pressure is then induced. On the contrary, concrete mechanical performance might be improved due to the reduced porosity and the increased integrity of concrete microstructure as shown by Ulm et al. (2000) and Multon et al. (2006). If ASR reaction continues, then internal pressure will be induced inside the concrete, these stresses will result in inducing microcracks that can grow to be macrocrack (Ulm et al. 2000) or at least reduce the concrete integrity and shortens its service life.

A simplification to examine the effect of ASR on the mechanical response of concrete was suggested by Multon et al. (2005) where ASR effect is simulated as superposition of two mechanisms; first: damage in concrete material due to ASR expansion and second: confinement effect on cement paste by the aggregate particles. Experimental investigations showed that ASR expansion is far more complex than the above approach and that other factors controlling void distribution in concrete might significantly affect the final behavior. For instance, it was shown that ASR expansion is affected by concrete casting direction (Grimal et al. 2010). ASR expansion in concrete casting direction was shown to be about 1.5 times of that in lateral direction. This was attributed to the fact that microbleeding tend to increase the voids in the casting direction than the lateral direction (Grimal et al. 2010). Furthermore, researchers also reported that ASR expansion can be reduced by externally applied compressive stresses and was shown to decrease gradually from surface to center in a concrete member (Ulm et al. 2000, Multon et al. 2005). This directional dependency of ASR (casting direction and radial direction towards element center) makes it difficult to believe that a standard cylinder or prism test can reflect the strength of concrete in an element exposed to ASR with such varying ASR level and boundary conditions. The above challenges make multi-scale simulation of ASR very challenging but yet very necessary for accurate prediction of RC service life.

In this article, we present a framework on simulation of ASR in concrete structures. We suggest using microstructural homogenization approach to extract the constitutive model of concrete subject to ASR reaction. ASR expansion ratio in

concrete is selected as the controlling parameter to indicate the progress of ASR. The simulated constitutive model is then used to predict the structural behavior of reinforced concrete element subjected to external loads and ASR expansion is then simulated using the finite element method. The results are compared to experimental observations reported in the literature (Fan et al. 1999).

MICROSTRUCTURAL HOMOGENIZATION OF CONCRETE

First, we start by modeling concrete microstructure using a mesoscale model descriping a representative volume element (RVE) of concrete. The concrete RVE is established using a cluster incorporating cement paste and aggregate particles connected by interfacial transition zone (ITZ). Cement paste and aggregate particles are assumed to follow linear elasticity. We developed a computational framework integrating methods of image processing for the generation of the RVE model aided with geometrical descriptors using two point correlation functions after (Torquato, 2001). This framework enables generating a representative volume element of concrete using its microstructure. This process is described schematically in **Figure 1** and is further discussed elsewhere for space limitation (Kim et al. 2011).

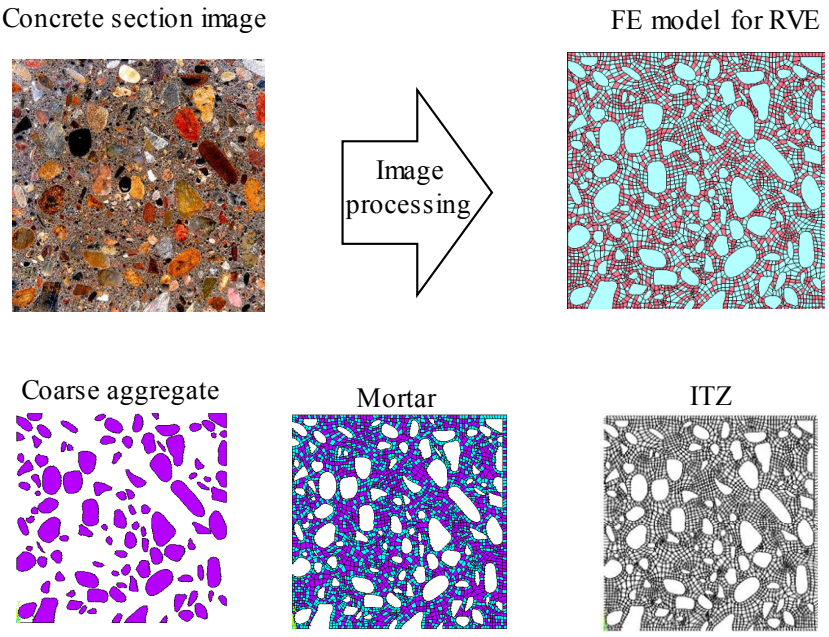

Figure 1. Computation framework used to generate RVE of concrete.

Properties of cement paste are derived from cement hydration simulation package HYMOSTRUC® (van Burgel 1995). Aggregate's properties are determined by experiments. As the mechanical characteristics (constitutive model) of ITZ are unknown, an optimization algorithm is developed and employed to identify the characteristics of ITZ such that the final constitutive model of concrete extracted the simulation framework meets the experimentally observed stress-strain curve of concrete described by the model presented in Equation (1) after Loov (1991).

$$\frac{f_c}{f_c^{'}} = \frac{\varepsilon_c}{\varepsilon_{c0}} \left(\frac{1 + k + \frac{1}{\eta - 1}}{1 + k(\varepsilon_c / \varepsilon_{c0}) + \frac{(\varepsilon_c / \varepsilon_{c0})^{\eta}}{\eta - 1}} \right) \quad (1)$$

where f_c fc and ε_c are stress and strain respectively. ε_{c0} is the strain when the stress is $f_c^{'}$ and 0.0022 is used for normal concrete. k and η are numerical coefficients for curve fitting shown to be equal to 0 and 4 respectively for normal concrete ($f_c^{'}$ < 40 MPa). The use of the above constitutive model for describing the stress-strain of concrete is attributed for its ability to describe a considerably wide range of concrete ranging from 20 to 200 MPa (Loov 1991).

The suggested concrete RVE and the boundary conditions used to extract concrete constitutive models are shown in Figure 2. In addition to the cement paste, the aggregate and ITZ phases described above, the model RVE includes special contact and cracking mechanisms to consider particle interaction. These mechanisms are proven essential to accurately consider the mixed contribution of Mode I and Mode II fractures such that realistic simulation of initiation and propagation of ITZ debonding can be simulated. Details of these models are not listed here for space limitations and can be found elsewhere (Reda Taha et al. 2015).

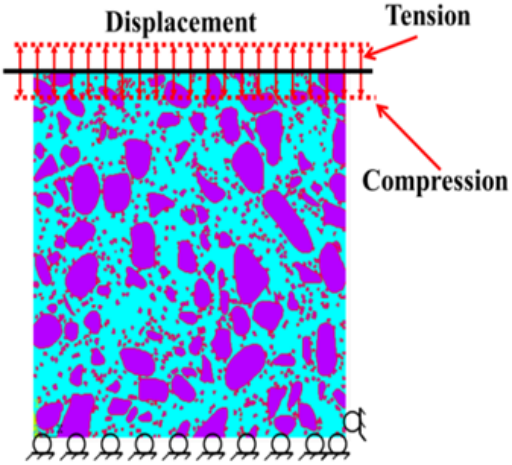

Figure 2. Concrete RVE model and its and boundary conditions.

To extract the stress-strain relationship of concrete, the average strain and average stress of the RVE model shall be extracted at each displacement step. The average strain is attained using Equation (2).

$$\varepsilon_A = \frac{d}{L_{RVE}} \quad (2)$$

ε_A is the average strain; d is the displacement applied; L_{RVE} is the length of RVE edge. The average stress of the RVE is based on elastic strain energy calculations. This approach is presented in Equation (3).

$$U_d = \frac{1}{2} \cdot \varepsilon_A \cdot \sigma_A \cdot \varepsilon_A \quad (3)$$

U_d is the elastic strain energy for the imposed displacement, σ_A is the average stress. An important challenge is the absence of experimental observations that correlate the level of cement hydration and ITZ properties. With that in mind, two methods were considered: first; the properties of ITZ are allowed to change to reflect continuous cement hydration and second; the properties of the ITZ are assumed to reach a maximum constant value. The second approach is considered here. A characteristic stress-strain relationships in compression and tension for concrete extracted using the above RVE model is shown in Figure 3.

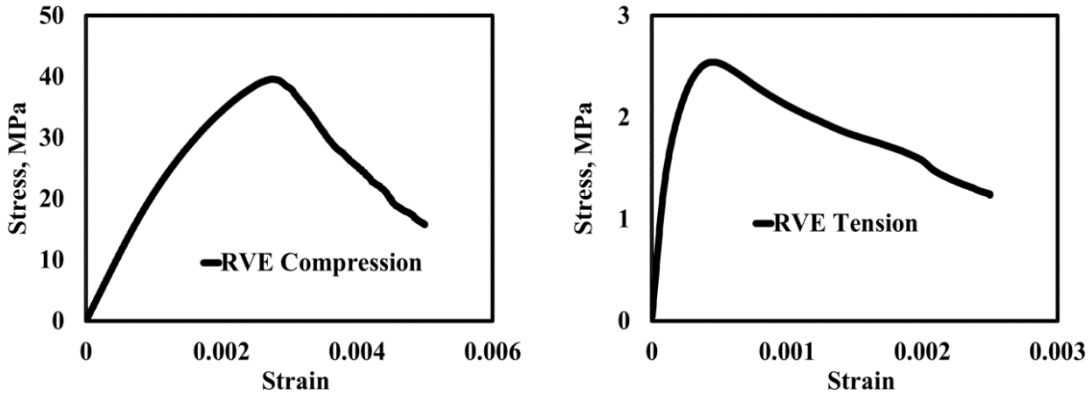

Figure 3. Stress-strain relationship of concrete extracted using RVE model (left) compression (right) tension.

MODELING ASR IN CONCRETE HOMOGENIZATION

ASR expansion is modelled as part of the concrete homogenization model by expanding the aggregate elements, as shown in Figure 4. This assumption meets the observation by many researchers that ASR gel generation and swelling are concentrated at the aggregate surface. The expansion of aggregate elements will produce stresses in the cement paste and the ITZ phases and can therefore damage the ITZ and deteriorate concrete mechanical properties.

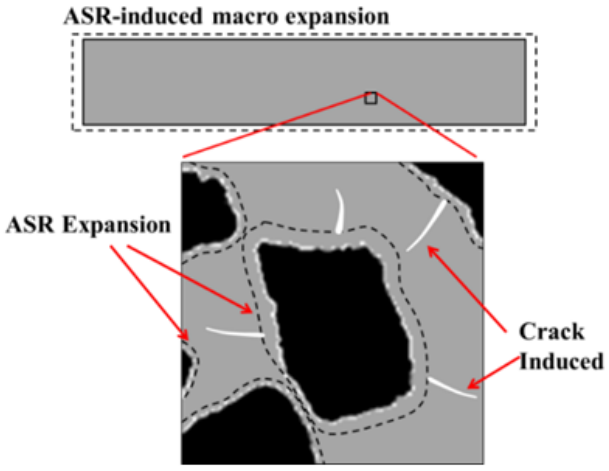

Figure 4. ASR-induced expansion achieved by expanding aggregate particles

The proposed expansion of aggregate is implemented by applying temperature rise with coefficient of thermal expansion meeting the aggregate type. When the target expansion ratio is achieved the temperature is held constant. ASR expansion then results in exerting stresses in the RVE model. After ASR expansion is implemented, a tensile or compressive displacement is then applied to the RVE and the new stress-strain relationship for the RVE is extracted. The elastic strain energy equation, Equation (3), is thus modified to Equation (4) to account for the new energy component representing ASR as

$$U_{Total} = U_{ASR} + U_d \tag{4}$$

U_{ASR} is the strain energy generated by ASR expansion; U_d is the elastic strain energy caused by the applied displacement; U_{Total} is the total strain energy. In doing so, ASR action is similar to an internal prestressing condition. By applying ASR expansion of aggregates in the RVE, the RVE is subject to the initial strain of U_{ASR}. Applying additional compressive displacement to the RVE model with the initial strain energy of U_{ASR}, the additional strain energy U_d is added to the existing energy. For this case, the total strain stored in the RVE increases regardless of the ASR expansion ratio. However, when tensile displacement is applied to the RVE model, the total strain energy is not additive. On the contrary, with a relatively high ASR expansion ratio (above 0.2%), the total strain energy U_{Total} decreases until all the initial strain energy U_{ASR} is released. The above energy approach would significantly reduce concrete capacity when ASR is combined with tensile stresses. To overcome this challenge by the energy approach, a stress averaging approach can be implemented. In this approach, all elements' stresses are averaged, as described by Equation (5), to extract the stress-strain of concrete subjected to ASR

$$\sigma_A = \frac{\sum_{i=1}^{N} \sigma_{ei} A_{ei}}{A_{Total}} \tag{5}$$

σ_A is the average stress of RVE; N is the total element number; σ_{ei} is the average stress of element i; A_{ei} is the area of element i; A_{Total} is the total area of RVE. The difference between the two approaches is demonstrated for concrete with ASR in Figure 5. It is evident that the strain energy approach underestimates the strength of concrete specifically for concrete under tensile stresses. The average stress approach derived using Equation (5) was used further for simulating ASR effect on structural concrete performance.

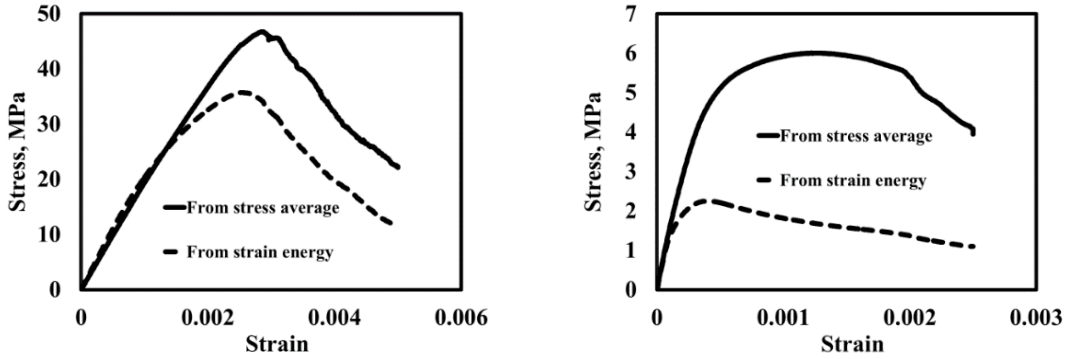

Figure 5. Stress-strain curve extracted using RVE model of concrete subjected to ASR; (left) compression; (right) tension.

CASE STUDY

Experimental results presented by Fan et al. (1999) were used to validate the ASR homogenization model described here. Fan et al. (1999) cast 40 reactive and 40 nonreactive concrete Φ100mm×200mm cylinders and measured their mechanical properties. The homogenization approach was used to simulate ASR for the concrete mix reported by Fan et al. (1999). A comparison between the homogenization model and the experimental observations of ASR significance on compressive and tensile strengths of concrete are shown in Figure 6. Furthermore, the cracking patterns of the homogenization model incorporating ASR reaction under both compressive and tensile stresses are shown in Figure 7. It is evident from Figure 6 that the proposed mesoscale homogenization approach can simulate the significance of ASR on the mechanical response of concrete with acceptable accuracy. It is also evident that considering a time-independent ITZ characteristics might yield acceptable results. Finally, Figure 7 confirms that ASR would result in much higher number of multiple cracks under compressive stresses compared to those observed under tensile stresses. Such observations match basic principles of fracture mechanics of concrete (Wang et al. 1995).

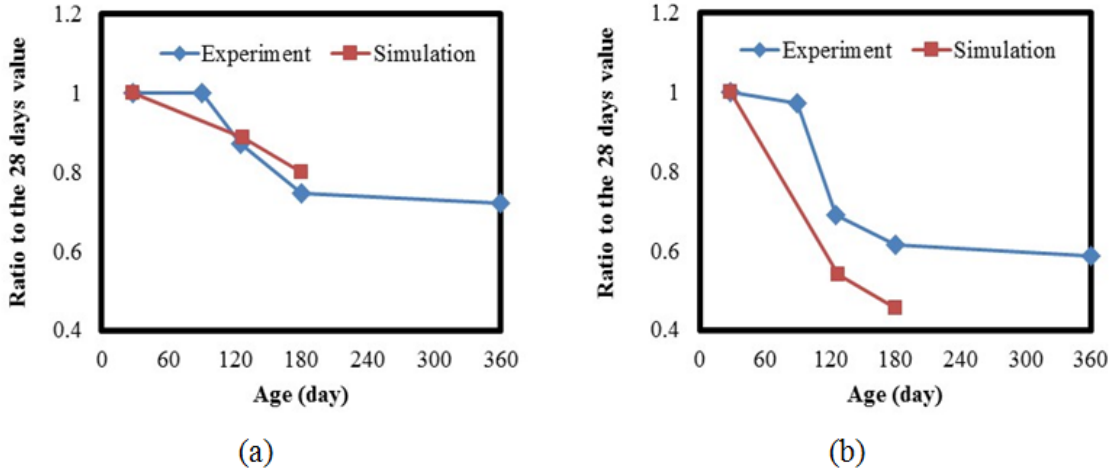

Figure 6. Simulated vs. experimental strength by Fan et al. (1999) (a) compression (b) tension.

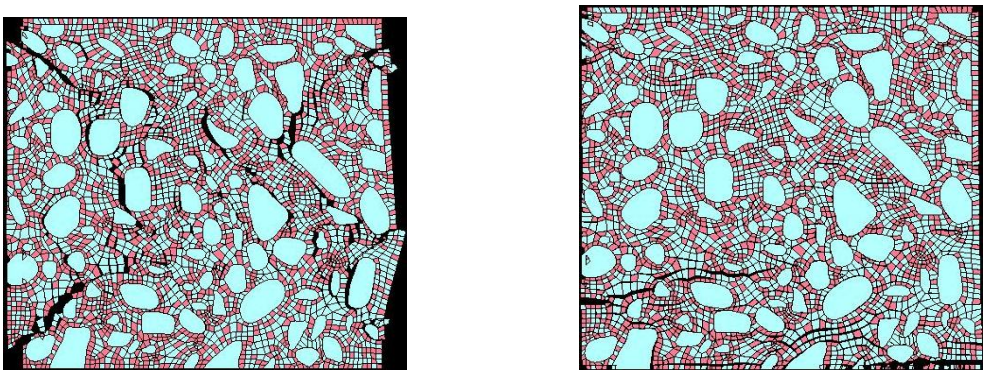

Figure 7. Cracking pattern in concrete mix with ASR (left) compression (right) tension showing the significantly higher number of cracks in concrete with ASR under compressive stresses compared with that under tensile stresses.

CONCLUSION

A microstructural homogenization model framework for modeling of concrete subjected to ASR is presented. Cement paste, aggregate and ITZ are modelled separately and cohesive model approach is used to describe bond at the ITZ. ASR reaction is simulated as uniform increase in temperature in aggregate resulting in cement paste cracking and debonding of the ITZ. Elastic strain energy and a stress averaging methods are examined to extract the constitutive model of concrete under ASR. Model results show that the stress averaging method can predict the constitutive model of concrete subjected to ASR accurately. The proposed framework is validated using ASR data in the literature. The model is capable of predicting the strength loss of concrete cylinders subjected to ASR. The model shows that acceptable accuracy can be achieved in ASR simulations if the ITZ phase mechanical characteristics are kept constant. It is apparent that continuous cement hydration might compensate some of the negative effects of ASR. Cracking patterns of the proposed model meets expectations of concrete failure under tension and compression stresses. The proposed microstructural homogenization framework can be used to predict the service life of reinforced concrete structures subjected to ASR. Further research results are underway to present this approach.

REFERENCES

Bažant, Z.P. and Steffens, A., Mathematical model for kinetics of alkali-silica reaction in concrete. *Cement and Concrete Research*, Vol. 30, 2000, pp. 419-428.

den Uijl, J.A. and Kaptijn, N., Structural consequences of ASR: An example on shear capacity. *Heron*, Vol. 47, Issue 2, 2002, pp. 125-139.

Fan, S., Hanson, J. M. Effect of Alkali Silica Reaction Expansion and Cracking on Structural Behavior of Reinforced Concrete Beams. *ACI Structural Journal*, Vol. 95, 1999, pp: 498-505.

Grimal, E., Sellier, A., Multon, S., Le Pape, Y. and Bourdarot, E., Concrete modelling for expertise of structures affected by alkali aggregate reaction. *Cement and Concrete Research*, Vol. 40, 2010, pp. 502-507.

Kim, J. J. Fan, T., & Reda Taha M. M. A homogenization approach for uncertainty quantification of deflection in RC beams considering microstructural variability. *Structural Engineering and Mechanics-An International Journal*, Vol. 38, No. 4, 2011. pp. 503-516.

Loov, R. E. A General Stress-Strain Curve for Concrete: Implications for High Strength Concrete Columns. *Annual Conference of the Canadian Society for Civil Engineering*, 1991, pp. 302-311.

Mehta, P. K., Monteiro, P., *Concrete: Microstructure, Properties, and Materials*, 4th Edition, 2014, McGraw Hill.

Multon, S. and Toutlemonde, F., Effect of applied stresses on alkali-silica reaction-induced expansions. *Cement and Concrete Research*, Vol. 36, 2006, pp. 912-920.

Multon, S., Seignol, J.-F. and Toutlemonde, F., Structural behavior of concrete beams affected by alkali-silica reaction. *ACI Materials Journal*, Vol. 102, No. 2, 2005, pp. 67-76.

Reda Taha, M. M., Douba, A., Kim, J. J., Fan, T. A computational framework using microstructure homogenization approach to simulate alkali-silica reaction in concrete structures, *ACI Materials Journal*, In Review (2015).

Sellier, A., Bourdarot, E., Multon, S., Cyr, M. and Grimal, E., Combination of structural monitoring and laboratory tests for assessment of alkali-Aggregate reaction swelling: Application to gate structure dam. *ACI Materials Journal*, Vol. 106, No. 3, 2009, pp. 281-290.

Sharp, J.H., Surely we know all about cement – don't we?. 48th Mellor Memorial Lecture, *Advanced in Applied Ceramics*, Vol. 105, No. 4, 2006, pp. 162-174.

Stanton, T. H., Expansion of concrete through reaction between cement and aggregate. *Proceedings of American Society of Civil Engineering,* Vol. 66, 1940, pp. 1781-1811.

Takakura, M., Watanabe, Y., Hosokawa, T., Ishii, T., Takiguchi, K. and Masuda, Y., Vibration measurement and simulation analysis on a reinforced concrete structure with alkali-silica reaction. *Proceedings of 18th International Conference on Structural Mechanics in Reactor Technology* (SMiRT 18), Beijing, China, 2005, pp. 2026-2035.

Torquato, S., Random Heterogeneous Materials, Microstructure and Macroscopic Properties, Springer, 2001.

Ulm, F.-J., Coussy, O., Li, K.F., and Larive, C., .Thermo-chemo-mechanics of ASR expansion of concrete structures. *Journal of Engineering Mechanics*, Vol. 126, No. 3, 2000, pp. 233-242.

van Breugel, K., Numerical simulation of hydration and microstructural development in hardening cement-based materials (I): Theory. *Cement and Concrete Research,* Vol. 25, No. 2, 1995, pp. 319-331.

Wang, E. Z. and Shrive, N.G. Brittle fracture in compression: mechanisms, models and criteria, *Engineering Fracture Mechanics*, Vol. 52, No. 6, 1995, pp. 1107-1126.

A Hygro-Thermo-Chemo-Mechanical Model for the Simulation of Early Age Behavior of Ultra High Performance Concrete

Lin Wan[1], Roman Wendner[2] and Gianluca Cusatis[3]

[1] Graduate Research Assistant, Department of Civil and Environmental Engineering, Northwestern University, 2145 Sheridan Rd. A120, Evanston IL, 60208 USA. E-mail: lin.wan@u.northwestern.edu
[2]Director Christian Doppler Laboratory LiCRoFast, Department of Civil Engineering and Natural Hazards, University of Natural Resources and Life Sciences (BOKU) Vienna, Austria. E-mail: roman.wendner@boku.ac.at
[3]Associate Professor, Department of Civil and Environmental Engineering, Northwestern University, 2145 Sheridan Rd. A123, Evanston IL, 60208 USA. E-mail: g-cusatis@northwestern.edu

Abstract

Ultra-high performance concretes (UHPCs) are cementitious composite materials with high level of performance including but not limited to high compressive strength, tensile strength and durability, reached by a low water-to-binder ratio, an optimized aggregate size distribution, thermal activation, and fiber reinforcement. In the past couple of decades, more and more UHPCs have been developed and found their way into practice. Thus, also the demand for computational models capable of describing and predicting relevant aging phenomenon to assist design and planning is increasing. This paper presents the early age experimental characterization as well as the results of subsequent simulations of a typical UHPC. Performed and simulated tests include unconfined compression, splitting, and 3-point-bending tests. The computational framework is formulated by coupling a hygro-thermal-chemical (HTC) theory with a comprehensive mesoscale discrete model: the HTC component allows taking into account various types of curing conditions with varying temperature and relative humidity and predicting the level of concrete aging, while the mechanical component, based on a recently formulated discrete model, the Lattice Discrete Particle Model (LDPM), permits the simulation of the failure behavior of concrete at the coarse aggregate level. The obtained results provide both insight in UHPC early age mechanisms and a computational model for the analysis of aging UHPC structures.

Introduction

Ultra high performance concretes (UHPCs) are cementitious composites characterized by high compressive strength, typically greater than 150 MPa (21.7 ksi), by a low water-to-binder ratio, an optimized gradation curve, thermal activation, and fiber

reinforcement. Moreover, UHPC has a discontinuous pore structure that reduces liquid ingress and permeability, significantly enhancing durability as compared to conventional and high-performance concretes. Consequently the service life can be expanded and the costs for maintenance and repair of UHPC structures can be lowered.

With the increased adoption of UHPC materials in practice, also the demand for computational models that can be utilized in design is increasing. Di Luzio and Cusatis [2009] formulated, calibrated, and validated the Hygro-Thermo-Chemical (HTC) model suitable for the analysis of moisture transport and heat transfer for regular as well as high performance concrete. Classical macroscopic mass and energy conservation laws are written in terms of humidity and temperature as primary variables and by taking into account explicitly various chemical reactions, such as cement hydration, silica fume reaction, and silicate polymerization [DiLuzio&Cusatis 2009]. Furthermore, Di Luzio and Cusatis [2013], coupled the HTC model with the microplane model and the solidification-microprestress theory account for the most significant aspects of concrete behavior, such as creep, shrinkage, thermal deformation, and cracking from the initial stages of curing up to several years of age.

While finite element solvers are broadly utilized for analyzing the mechanical behavior of concrete structures, the Lattice Discrete Particle Model (LDPM) [Cusatis 2011] is very suitable for the simulation of the failure behavior of concrete. LDPM simulates concrete at the length scale of coarse aggregate pieces (mesoscale) and is formulated within the framework of discrete models, which enable capturing the salient aspects of material heterogeneity while keeping the computational cost manageable [Cusatis 2011].

The HTC and LDPM models are selected as basis for the presented early age model for concrete. On the one hand, the HTC model can comprehensively capture the hygral and thermal evolutions and chemical reactions during aging. The LDPM model, on the other hand, can not only provide great insights into the concrete behavior on the mesoscale level but also simulate well the mechanical behavior of concrete structures under various loads at the macroscopic level. The two models are linked by introducing proper aging functions for the LDPM parameters.

Experimental Characterization of Early Age Behavior of UHPC

The material composition of the adopted UHPC consists of LaFarge Type H cement, F-50 sand, Sil-co-sil 75 silica flour, Elkem ES-900W silica fume, ADVA-190 Superplasticizer and tap water. The maximum particle size, 0.6 mm, is limited to that of silica sand, which is a foundry grade Ottawa sand [Roth et al. 2009]. Two curing protocols with and without hot water bath curing were explored. A first group of specimens was kept in a humidity room (HR) for 14 days. A second group, instead, was kept in a humidity room for 7 days after which the specimens were placed in a hot water bath (WB) at 85°C for another 7 days. Both groups were let to dry at constant laboratory conditions (about 22 °C and 50% RH). Unconfined compression tests using 2×2”

(50.8×50.8 mm) cylinders, 3-point-bending tests with half-depth notched 1×1×5" (25.4×25.4×127 mm) beams, and tensile splitting tests using 3×1" (76.2×25.4 mm) disks were carried out on nominal ages of 3, 7, 14, and 28 days. Circumferential expansion control for compression tests and CMOD opening control for three-point bending and splitting tests were utilized to avoid brittle failure and to obtain full post-peak behavior. Furthermore, boundary effects in compression tests were reduced through the application of a friction reducing material (dry-moly lubricant).

In order to calibrate the HTC model RH measurements inside specimens as well as at the specimen boundaries (ambient environment) were conducted with three curing routines: 14 days HR, 7 days HR + 7 days WB, and fully sealed (self desiccation) at room temperature, each using five 2x2" (50.8×50.8 mm) cylinders, with compact coupled RH sensors. At the time of casting, a straw with one side bent, closed, and pinned with holes, was vertically inserted into each specimen with the perforated end centered in the specimen. After humidity room curing, where 100% RH was ensured, the other end of the straw was opened up and sealed again housing a RH sensor in the perforated area, which remains sealed during data recording. Self desiccation specimens were sealed with plastic molds.

Computational Framework for the Simulation of UHPC at Early Age

The proposed hygro-thermo-chemo-mechanical coupled early age model for concrete consists of two major components: HTC model and LDPM model, with aging functions bringing the two together. The behavior of concrete at early age heavily depends on moisture transport and heat transfer. The internal relative humidity and temperature distributions can be calculated by imposing moisture mass balance and enthalpy balance equations in the volume of interest [DiLuzio&Cusatis 2013]. Arrhenius type of equations are found to govern cement hydration, pozzolanic reactions, and silicate polymerization [DiLuzio&Cusatis 2009], which are adopted in HTC to calculate an overall aging degree of concrete. The LDPM, on the other hand, simulates the concrete meso-structure on the scale of coarse aggregates. The lattice system which represents the meso-structure topology is defined by a Delaunay tetrahedralization of the particle centers together with the nodes utilized to describe the external surface of the volume. Mesostructure deformation is described in LDPM through the adoption of rigid-body kinematics [Cusatis 2011]. While the mechanical behavior is dominated by mesoscale material parameters in LDPM, their magnitude evolutions at early age are constructed as functions of aging degree, which, as aforementioned, is an output of the HTC model.

Hygro-thermo-chemical (HTC) model

Moisture Transport and Heat Transfer

The overall moisture transport, including water in various phases [Powers 1946] is described through the Fick's law that expresses the flux of water mass per unit time **J** as a function of the spatial gradient of the relative humidity h. The moisture mass balance requires the change in water content dw to be equal to the divergence of moisture flux **J**. The water content w is the sum of evaporable water w_e (capillary water, water vapor, and absorbed water) and non-evaporable (chemically bound) water w_n [Mills 1966, Panta 1995]. Assuming that w_e is a function of relative humidity h, degree of hydration α_c, and degree of silica fume reaction α_s, one can write $w_e = w_e(h, \alpha_c, \alpha_s)$ as age-dependent sorption/desorption isotherm. By mathematical substitution, the moisture balance equation relating hydration/reaction degrees [DiLuzio&Cusatis 2009] is achieved:

$$\nabla \cdot (D_h \nabla h) - \frac{\partial w_e}{\partial h}\frac{\partial h}{\partial t} - (\frac{\partial w_e}{\partial \alpha_c}\dot{\alpha_c} + \frac{\partial w_e}{\partial \alpha_s}\dot{\alpha_s} + \dot{w_n}) = 0 \tag{1}$$

Similarly, heat conduction in concrete can be expressed, at least for a temperature not exceeding 100 ° C [Bazant 1996], based on Fourier's Law:

$$\nabla \cdot (\lambda \nabla T) - \rho c_t \frac{\partial T}{\partial t} + \dot{\alpha}_s s \tilde{Q}_s^{\infty} + \dot{\alpha}_c c \tilde{Q}_c^{\infty} = 0 \tag{2}$$

where $\tilde{Q}_c^{\infty}$ = hydration enthalpy, and $\tilde{Q}_s^{\infty}$ = latent heat of silica-fume reaction per unit mass of reacted silica-fume.

Cement Hydration and Silica Fume Reaction

With the assumption that the thermodynamic force conjugate to the hydration extent, named the *chemical affinity*, is governed by an Arrhenius-type equation and that the viscosity governing the diffusion of water though the layer of cement hydrates is an exponential function of the hydration extent [Ulm 1995], Cervera et al. [1999] proposed the evolution equation for the hydration degree: $\dot{\alpha}_c = A_c(\alpha_c)e^{-E_{ac}/RT}$, and $A_c(\alpha_c) = A_{c1}(\frac{a_{c2}}{\alpha_c^{\infty}} + \alpha_c)(\alpha_c^{\infty} - \alpha_c)e^{-\eta_c \alpha_c/\alpha_c^{\infty}}$, where α_c^{∞} is the asymptotic degree of hydration, $A_c(\alpha_c)$ is the *normalized chemical affinity*, E_{ac} is the hydration activation energy, R is the universal gas constant, and η_c,A_{c1}, and A_{c2} are material parameters. To account for the situation that the hydration process slows down and may even stop if the relative humidity decreases below a certain value ($h \approx 75\%$), the equation can be rewritten as: $\dot{\alpha}_c = A_c(\alpha_c)\beta_h(h)e^{-E_{ac}/RT}$, where $\beta_h(h) = [1+(a-ah)^b]^{-1}$. The function $\beta_h(h)$ is an empirical function that was first proposed for the definition of the equivalent hydration period by Bazant and Prasannan [1989]. The parameters a and b can be calibrated by comparison with experimental data but values a = 5.5 and b = 4 can be generally adopted [Bazant 1989, Gawin 2006]. The theory adopted for cement hydration can

be as well utilized for silica fume (SF) reaction since pozzolanic reactions can also be assumed to be diffusion controlled. Accordingly, the degree of SF reaction α_s is introduced [DuLuzio&Cusatis 2009].

Aging Degree

Experimental studies show that the strength evolution at early age depends not only on the degree of chemical reactions, but also on the kinetics of the reactions, e.g. relative humidity and curing temperature [Cervera 2000]. The aging degree λ is formulated such that it approaches the normalized asymptotic value of 1 at time of infinity [Cervera1999], correspondingly the material properties, which can be assumed to depend on the aging degree, also go to asymptotic values when concrete fully cures:

$$\dot{\lambda} = \left(\frac{T_{max} - T}{T_{max} - T_{ref}} \right)^{n_\lambda} (B_\lambda - 2A_\lambda \alpha)\dot{\alpha} \tag{3}$$

where $B_\lambda = [1 + A_\lambda(\alpha_\infty^2 - \alpha_0^2)]/(\alpha_\infty - \alpha_0)$, n_λ and A_λ are model parameters obtained from experiments, and α is the overall degree of reaction [DiLuzio&Cusatis 2013].

Age-dependent Lattice Discrete Particle Model

In 2011, Cusatis et. al. developed the Lattice Discrete Particle Model (LDPM), a mesoscale discrete model that simulates the mechanical interaction of coarse aggregate pieces embedded in a cementitious matrix (mortar). The geometrical representation of the concrete meso-structure is constructed through the following steps. First, the coarse aggregate pieces, assumed to have spherical shapes, are introduced into the concrete volume by a try-and-reject random procedure. Secondly, nodes as zero-radius aggregate pieces are randomly distributed over the external surfaces to facilitate the application of boundary conditions. Thirdly, a three-dimensional domain tessellation, based on the Delaunay tetrahedralization of the generated particle centers, creates a system of polyhedral cells interacting through triangular facets and a lattice system composed by the line segments connecting the aggregate centers.

LDPM has been utilized successfully to simulate concrete behavior under various loading conditions [Cusatis 2011]. Furthermore it has been properly formulated to account for fiber reinforcement [Schauffert 2012] and has the ability to simulate the ballistic behavior of ultra-high performance concrete (UHPC) [Smith 2014]. In addition, LDPM showed success in structural scale analysis using multiscale methods [Cusatis 2014].

The concept of aging degree is used in the proposed aging model to account for early age phenomena. The individual material properties, which govern the mesoscale constitutive equations, can be introduced as functions of the aging degree, λ, each capable of modifying part of the mechanical behavior. The proposed aging functions relating the local mesoscale material parameters with the aging degree are listed in Eq.

$4 \sim 6$. As seen, normal modulus, which is related to the elastic modulus, or Young's modulus, has a linear relation with aging degree, by multiplying the asymptotic normal modulus E_0^∞. Tensile strength, compressive strength, and transitional stress, on the other hand, have "power law" type relations with aging degree, by multiplying the corresponding asymptotes (σ_t^∞, σ_c^∞, σ_{N0}^∞). Last, the tensile characteristic length has a linear relation with aging degree, however rewritten to show the asymptotic tensile characteristic length, L_{ct}^∞. L_{ct} decreases as concrete ages. Note, all the functions are structured such that when λ approaches the asymptotic value of 1 the corresponding parameters also approach their asymptotes.

The proposed aging functions for UHPC at early age with constants C_1 and C_2 are a linear relationship for the normal modulus,

$$E_0 = E_0^\infty * \lambda \tag{4}$$

power laws in the form

$$\sigma = \sigma^\infty * \lambda^{C_1} \tag{5}$$

for the evolution of tensile strength, compressive strength, and transitional stress, and a linear function for the tensile characteristic length:

$$L_{ct} = L_{ct}^\infty (C_2(1-\lambda) + 1) \tag{6}$$

LDPM modeling of UHPC: Calibration and Validation

The HTC model is calibrated by self desiccation RH measurements of 40 days starting from casting and validated by HR, HR+WB curing RH measurements of 50 and 62 days of data respectively. Also included in the output results are the simulated time history of cement hydration degree, silica fume reaction degree, total reaction degree, and overall aging degree, calculated by Eq. 3.

The HTC input data include boundary conditions and material properties. The environmental boundary conditions are as follows: for HR curing: 22°S and 100% RH for 14 days then 50% RH afterwards; for HR+WB curing: 22°S and 100% RH for 7 days, then 85°C and 100% RH for the next 7 days and afterwards 50% RH at room temperature; and for self desiccation curing: sealed and room temperature.

The calibrated and validated HTC model provides the spatial distribution of the aging degree which serves as input for the aging functions defining the local mesoscale mechanical properties of LDPM. The aging functions , Eq. $4 \sim 6$, are formulated in such a way as to capture the aging mechanical properties with the simplest possible functional relationship and hence the lowest number of parameters that have to be calibrated. The aging mechanical properties are captured by the mesoscale model parameters: normal modulus, tensile strength, stress at pore collapse, transitional stress, and tensile characteristic length.

For the UHPC in this study a good agreement between experiments and simulations can be obtained by using C_1 = 2.33, and C_2 = 22.2, for the aging functions. All the LDPM simulations utilize a coarse aggregate size $2 \sim 4$ mm.

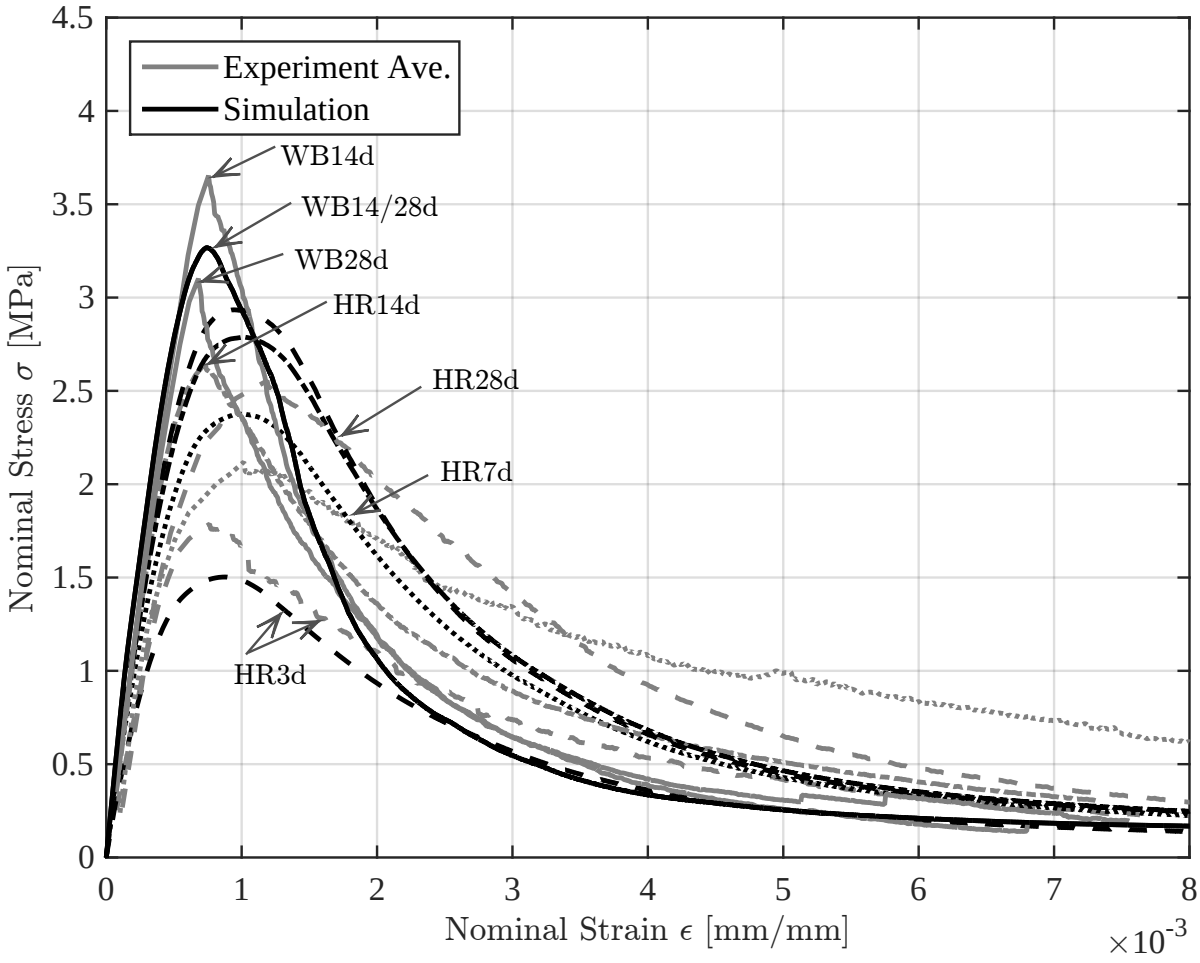

Figure 1. LDPM Simulations for 3-point-bend Test

Generally speaking, the model is calibrated first by 3-point-bending (notched) test results and later validated by the other types of tests including unconfined cylinder compression, circular disk Brazilian, cube compression, and unnotched beam bending tests, as well as size effect tests (see related work of the authors). Averaged experimental data as well as simulation results of beam 3-point-bending (50% notched) for different ages can be found in Fig. 1, where the nominal flexural stress is obtained by equation $\sigma = 3Pl/2DH^2$ ([3×load×test span]/[2×specimen depth×specimen height^2]) and nominal strain by ϵ = extensometer/specimen height. The strength gain and stress-strain curve shapes from simulations match those from experiments quite well. As the UHPC ages, its strength increases while ductility decreases.

Conclusion

This paper describes a LDPM-based hygro-thermo-chemo-mechanical early age model, for UHPC, calibrated and validated by relative humidity measurements and experimental mechanical test data. By coupling the HTC model and the LDPM, the development of the internal structure of the cement phase and its effects on mechanical properties can be accurately and comprehensively captured by the proposed computational framework. The aging functions developed as a bridge between HTC and LDPM have great simplicity and easy applicability.

REFERENCES

Bazant Z. P. and Prasannan S. (1989). Solidification theory for concrete creep. I: formulation. Journal of Engineering Mechanics, ASCE 115, 1691-1703.

Bazant Z. P. and Kaplan M. F. (1996). Concrete at high temperatures: material properties and mathematical models. London: Longman Addison-Wesley.

Bentz D. P. , Waller V. , and De Larand F. (1998). Prediction of adiabatic temperature rise in conventional and high-performance concretes using a 3-D microstructure model. Cement Concrete Research; 28(2):285-97.

Cervera M., Oliver J., and Prato T. (1999). Thermo-chemo-mechanical model for concrete. I: hydration and aging. Journal of Engineering Mechanics.

Cervera M., Oliver J., and Prato T. (1999). Thermo-chemo-mechanical model for concrete. II: damage and creep. Journal of Engineering Mechanics.

Cervera M., Oliver J., and Prato T. (2000). Simulation of construction of RCC dams. I: temperature and aging. Journal of Structural Engineering. Vol. 126, No. 9.

Cusatis G., Pelessone D., and Mencarelli A. (2011). Lattice discrete particle model (LDPM) for failure behavior of concrete. I: Theory. Cement Concrete Composites, 33(9), 881-890.

Cusatis G., Pelessone D., and Mencarelli A. (2011). Lattice discrete particle model (LDPM) for failure behavior of concrete. II: Calibration and validation. Cement Concrete Composites, 33(9), 891-905.

Cusatis G., Rezakhani R., Alnaggar M., Zhou X., and Pelessone D. (2014). Multiscale computational models for the simulation of concrete materials and structures, pages 23-38, CRC Press, 2015/02/26, ISBN 978-1-138-00145-9.

Di Luzio G. and Cusatis G. (2009). Hygro-thermo-chemical modeling of high performance concrete. I: Theory. Cement and Concrete composites 31 (5), 301-308.

Di Luzio G. and Cusatis G. (2009). Hygro-thermo-chemical modeling of high performance concrete. II: Numerical implementation, calibration, and validation. Cement and Concrete composites 31 (5), 309-324.

Di Luzio G. and Cusatis G. (2013). Solidification-microprestress-microplane (SMM) theory for concrete at early age: Theory, validation and application. International Journal of Solids and Structures 50, 957-975.

Gawin D., Pesavento F., and Schrefler B.A. (2006). Hygro-thermo-chemo-mechanical modelling of concrete at early ages and beyond, Part I: hydration and hygrothermal phenomena. Int J Numer Methods Eng;67:299-331.

Gawin D., Pesavento F., and Schrefler B.A. (2006). Hygro-thermo-chemo-mechanical modelling of concrete at early ages and beyond, Part II: shrinkage and creep of concrete. Int J Numer Methods Eng;67:332-363.

Mills. R. H. (1966). Factors influencing cessation of hydration in water-cured cement pastes. In: Proceeding of the symposium on the structure of Portland cement paste and concrete. Washington (DC): Highway research board; p. 406-24 [Special report no. 90].

Pantazopoulo S. J. and Mills R.H. (1995). Microstructural aspects of the mechanical response of plain concrete. ACI Mater J;92(6):605-16.

Powers TC. and Brownyard TL. (1946). Physical properties of hardened cement paste. American Concrete Institute Journal Proc, 18(3), 250-336.

Roth M. J., Rushing T. S., Flores O. G., Sham D. K., and Stevens J. W. (2009). Laboratory Characterization of Cor-Tuf Flexural and Splitting Tensile Properties U.S. Army Engineer Research and Development Center, Vicksburg, MS.

Schauffert E. A. and Cusatis G. (2012). Lattice discrete particle model for fiber-reinforced concrete. I: theory. Journal of Engineering Mechanics, ASCE. 826-833.

Schauffert E. A. and Cusatis G., Pelessone D., O'Daniel J. L., and Baylot J. T. (2012). Lattice discrete particle model for fiber-reinforced concrete. II: tensile fracture and multiaxial loading behavior. Journal of Engineering Mechanics, ASCE. 834-841.

Smith J., Cusatis G., Pelessone D., Landis E., O'Daniel J., Baylot J. (2014). Discrete modelling of ultra-high-performance concrete with application to projectile penetration International Journal of Impact Engineering 65, 13-32.

Ulm F-J. , and Coussy O. (1995). Modeling of thermo-chemicalmechanical couplings of concrete at early age. Journal of Engineering Mechanics, ASCE; 121(7): 785-794.

Gamma Processes for the Long-Term Prediction of Creep Deflections

Alfred Strauss[1]; Roman Wendner[1,2]; Anja Vidovic[1]; and Ivan Zambon[1]

[1]Institute of Structural Engineering, Dept. of Civil Engineering and Natural Hazards, University of Natural Resources and Life Sciences Vienna, 1190 Vienna, Austria.
[2]Christian Doppler Laboratory LiCRoFast, Dept. of Civil Engineering and Natural Hazards, University of Natural Resources and Life Sciences Vienna, 1190 Vienna, Austria.

Abstract

The design and long-term performance of long-span bridges is to a large part determined by serviceability related considerations. For prestressed concrete bridges the relevant phenomena are concrete creep and shrinkage, coupled with steel relaxation. It has been shown that stochastic processes and in particular continuous Gamma processes are suitable to describe the deterioration of infrastructure systems within the frameworks of performance assessment and life-time prediction. This paper investigates the applicability of gamma processes for the prediction of creep related deformations in prestressed concrete bridges and attempts to provide guidance regarding the parameter selection. Deflection and shortening histories obtained by a probabilistic nonlinear rate-type analysis of the Colle Isarco Viaduct utilizing different creep models serves as data basis for this case study.

INTRODUCTION

Well-defined specifications for the design and assessment of structures and their behavior are being used around the world. The main purpose of those specifications is to ensure a sufficiently high degree of reliability. Periodic assessments based on inspection and sometimes on monitoring data are required due to the wide range of processes affecting any infrastructure system in the course of its lifetime. When necessary, the performance of these infrastructure systems and their components is restored through carefully optimized maintenance and rehabilitation measures. Recently, new concepts and theories were developed for the accurate description of physical processes affecting concrete. Furthermore, this development is accompanied by a rapid increase in the availability of data for calibration and validation, which can be gained through monitoring (Strauss et al. 2011; Strauss et al. 2012; Wendner and Strauss, A. 2014). All this creates a solid ground for reevaluating the effectiveness of long established inspection procedures for infrastructure systems, which are paramount for the predicted performance and safety of structural systems. An essential element for the engineers, in field of the verification and improvement of current models and design concepts, is the systematic collection of a wide range of site-specific data. This contribution focuses on the long-term serviceability of long-span prestressed concrete bridges related to concrete creep and shrinkage. In particular, it focuses on the possibility of using stochastic processes for the performance prediction of those systems as an efficient alternative to computationally expensive mechanical models.

LONG-TERM PREDICTION OF CREEP EFFECTS

Currently established creep and shrinkage prediction models are deterministic and provide no quantification of uncertainty. Degradation in its nature can be described by nonnegative continuous functions characterized by nonnegative increments with independent path and variable uncertainty. Furthermore, the residual period of time of an observed undesirable event is typically associated with considerable uncertainty and dependent on the structural behavior. Therefore, stochastic processes can be used as an approximate approach for capturing the creep and shrinkage behavior of structural components and systems. During the 1970s stochastic processes for the prediction of creep started to be investigated (Cinlar, Bazant, and Osman 1977; Bazant and Chern 1984). Frangopol et al. (2004) and van Noortwijk (2009) acknowledged stochastic process predictions and probabilistic modeling as key elements within the framework of life cycle. A major problem for the application of reliability methods is the lack of failure data for buildings and bridges since no calibration or validation is possible. Time dependent uncertain structural properties, for example the deterioration rates of structures or structural components, are frequently computed using random variables. Stochastic processes are commonly described as either discrete Markov processes, e.g. Markov chains, or continuous Markov processes, such as Brownian movement, Levy and gamma processes. Non-correlated incremental stochastic processes on the other hand cannot realistically capture the physical processes behind structural deterioration, as the current condition of a structure is clearly not independent of previous time steps. This fact was acknowledged by Pandey et al. (2009) and van Noortwijk (2009) who suggested using continuous gamma processes for the description of a gradually developing deterioration processes. These are, among others, corrosion of reinforcement bars, creep and shrinkage, fatigue of concrete and reinforcement, and crack propagation.

CASE STUDY

Recently, the multi-decade creep behavior of the Colle Isarco Viaduct (Figure 1), a 167.5 m long fully post-tensioned box girder bridge located in Northern Italy was investigated (Wendner et al. 2014). The data created in course of a sensitivity study serves as basis for the here investigated gamma prediction process. Each of the four identical main structural elements of the bridge consists of a main span of 91.0 m, a long cantilever of 59.0 m, and a short cantilever of 17.5 m (Strauss et al. 2009). The cross-section height varies between 10.8 m at the main pier and 2.85 m at the tip of the cantilever. The box girder itself has a width of 6.0 m whereas the top slab is 10.6 m wide. The bridge is erected sequentially out of 44 segments, 497 pre-stressing tendons in total and 149 tendons above the main support.

Figure 1: A view on the Colle Isarco Viaduct, Italy (Colle Isarco Viaduct, n.d.)

In the recent investigation by Wendner et al. (2014) the following creep and shrinkage models were examined: ACI92 (ACI Committee 209 2008), B3 (Bažant and Baweja 1995), B4 (Bažant, Hubler, and Wendner 2014), CEB-FIP90 (CEB-FIP 1993), fib2010 (fib 2013). The full discussion of the different models' characteristics and the respective consequences for long term predictions is based on most realistic deterministic and probabilistic structural analyses. Moreover, it provides important insights into the creep behavior that could not be derived based on laboratory data and theoretical considerations as presented in Hubler et al. (2015). The bridge was modeled in ABAQUS using symmetry, with solid elements for the concrete members and truss elements for the discretely modeled pre-stressing tendons.

With the exception of the concrete properties, all input variables are considered to be statistically independent and were used in terms of mean value and coefficient of variation. The correlation matrix for the concrete properties, described by pairwise linear correlation coefficients according to Pearson (1895) and Stigler (1989), is given in Table 1. A statistically representative number of samples was generated utilizing the Latin hypercube sampling scheme (Iman and Conover 1982) combined with simulated annealing (Kirkpatrick, Gelatt, and Vecchi 1983; Vořechovský and Novák 2009) with a population size of 45 samples. The resulting scattering response serves both for the derivation of sensitivity factors between model inputs and structural response quantities (Bergmeister et al. 2007; Strauss et al. 2013) and as an input for the performance prediction using the concept of gamma processes as introduced in the subsequent section.

Table 1: Correlation matrix of concrete properties (Strauss, 2003)

	E_{28}	f_c	c	w/c	a/c
E_{28}	1	0.19	0.06	-0.07	0.05
f_c	0.19	1	0.5	-0.52	0.36
c	0.06	0.5	1	-0.86	-0.86
w/c	-0.07	-0.52	-0.86	1	0.8
a/c	0.05	0.36	-0.86	0.8	1

Figure 2 presents the scattering predictions of the horizontal shortening of the main girder *w* of the Colle Isarco Viaduct, on which the subsequent investigations are based. Deformations are simulated in 100-day increments, from the end of the construction up to the age of approximately 12,000 days, i.e. 32 years.

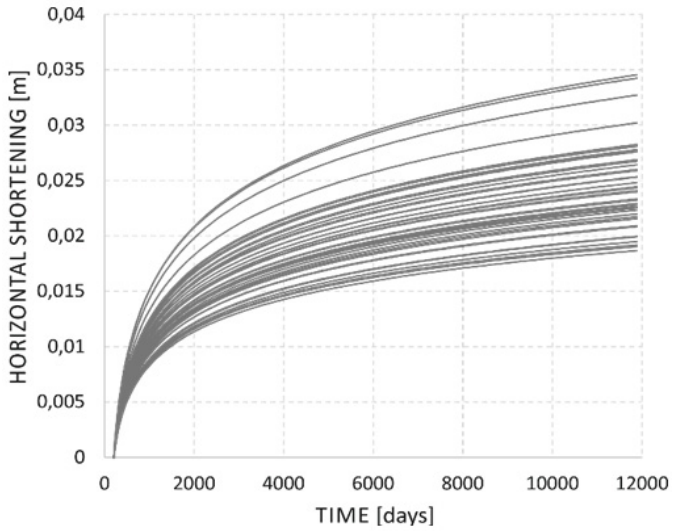

Figure 2: Numerically computed creep responses of the Colle Isarco Viaduct Bridge

A gamma process formulation and calculation models were provided by van Noortwijk (2009) and Ohadi and Micic (2011) (for a comprehensive description see also Strauss et. al, 2014). The gamma prediction process was carried out with a time dependent shape parameter following the power law equation $\alpha(t)=c\cdot t^b$ and a constant scale parameter ß. Two parameters *c* and ß have been determined through the statistical analysis Method of Moments, following a recommendation by Ellingwood and Mori (1993), fixing the exponent $b = 1.0$. Additionally, a parameter study varying the exponent *b* for creep phenomena is presented.

The assumption is that n=10 observations at times $t_{1\ldots n} = 212, 473, 773, 1533, 3033, 4533, 6033, 7533, 9033, 10533$ days are available. The gamma distributions Ga_k^i were estimated for prediction time horizons $i = 1,\ldots,10$ based on information up to assessment time periods k=3,…,10. The constant scale parameter β was determined based on information up to $k = 10$. Figure 3 portrays the predicted expected values of the horizontal shortening of the main girder *w*, and Figure 4 the associated relative deviations Δw_k^i in percentage. With increasing assessment time period *k* and/or reduction of the distance to the prediction horizon *i* the bias in the prediction decreases. In order to evaluate the required observation time for a given prediction quality or to assess the prediction quality for a given set of observations the data contained within Figure 4 is crucial.

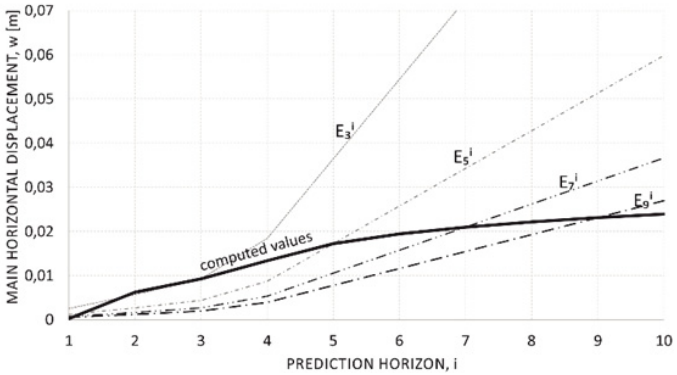

Figure 3: Expected values of the gamma process prediction, of the time periods for prediction time horizons *i*

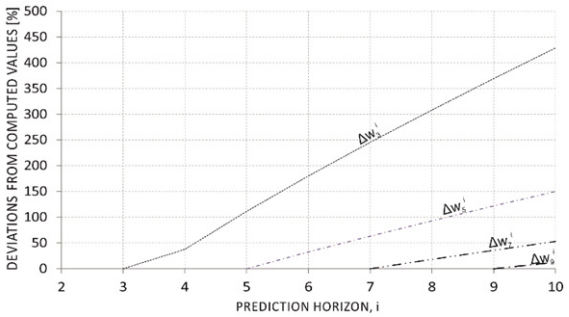

Figure 4: Deviations of the gamma process predictions from the real values of displacement

Van Noortwijk et al. (2007) recommended using a constant exponent b which should be adapted according to the considered deterioration process. Ellingwood and Mori (1993) suggested a value of $b = 1$ for the corrosion of reinforcement, $b = 2$ for sulphate attacks and $b = 0.5$ for diffusion controlled ageing. Through their investigation of gamma process for a concrete creep prediction, Bažant and his coworkers recommended $b = 0.125$ (Cinlar, Bazant, and Osman 1977). Figure 5 is showing deviations of prediction in the time horizon i=10, for various values of b. In general, for the considered time period k and time horizon i=1…10, values of b between $b = 0.30$ and $b = 0.39$ are resulting in the smallest deviations Δw_k^i. If the prediction is made with the information of at least 5 observations, the most suitable values of b would be between $b = 0.22$ and $b = 0.30$.

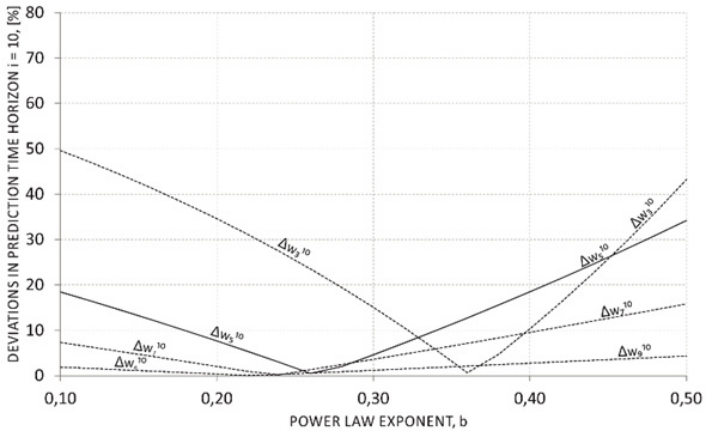

Figure 5: Deviations of prediction from computed values Δw_k^{10} of the assessment horizon k in the prediction horizon $i = 10$, for different values of an exponent b

CONCLUSION

In this paper the suitability of the gamma process for the prediction of creep processes was analyzed. It is demonstrated that the horizontal displacement can be predicted with the information of 7 observations, i.e. within the first 6033 days, with an error less than 30 %. The exponent b of the power law is not only dependent on the considered deterioration phenomenon, but also on the assessment horizon k and the prediction horizon i. Furthermore, a stationary gamma process (where the power law exponent is b=1.0) has higher deviations of predictions. Therefore, the optimum value of the exponent b would be b≈0.35.

ACKNOWLEDGEMENT

The authors would like to acknowledge the invaluable contributions to the research made by their many multidisciplinary colleagues at the Institute of Structural Engineering, Department of Natural Hazards and Life Sciences and the ATLASS Center of Lehigh University. The support of the ZIT Center for Innovation and Technology within the project “Lifetime assessment of fatigue endangered concrete structures, MSLeB, Call From Science to Products 2011; ID 699219 is appreciated. The financial support by the Austrian Federal Ministry of Economy, Family and Youth and the National Foundation for Research, Technology and Development is gratefully acknowledged.

REFERENCES

ACI Committee 209. 2008. *Guide for Modeling and Calculating Shrinkage and Creep in Hardened Concrete*. 209.2R-08. Farmington Hills.

Bazant, Zdenek P., and Jenn-Chuan Chern. 1984. “Bayesian Statistical Prediction of Concrete Creep and Shrinkage.” *Journal of the American Concrete Institute* 81 (4): 319–30.

Bažant, Z. P., and S. Baweja. 1995. “Creep and Shrinkage Prediction Model for Analysis and Design of Concrete Structures - Model B3.” *Matériaux et Constructions* 28 (180): 357–65.

Bažant, Z. P., M. H. Hubler, and R. Wendner. 2014. “RILEM Draft Recommendation: Model B4 for Creep, Drying Shrinkage and Autogenous Shrinkage of Normal and High-Strength Concretes with Multi-Decade Applicability.” *Materials and Structures (RILEM)*, (accepted).

Bergmeister, K., A. Strauss, Novák D., and R. Pukl. 2007. “Structural Analysis and Reliability Assessment: SARA Part I.” In , edited by B. Bakht and A.A. Mufti.

CEB-FIP. 1993. *CEB-FIP MODEL CODE 1990*. Bulletin d’information No. 195. Committee Euro-International du Béton.

Cinlar, Erhan, Zdenek P. Bazant, and ElMamoun Osman. 1977. “Stochastic Process for Extrapolating Concrete Creep.” *ASCE J Eng Mech Div* 103 (6): 1069–88.

Ellingwood, B. R., and Y. Mori. 1993. “Probabilistic Methods for Condition Assessment and Life Prediction of Concrete Structures in Nuclear Power Plants.” *Nuclear Engineering and Design* 142 (2–3): 155–66.

fib. 2013. *Model Code for Concrete Structures 2010*. Berlin: Wilhelm Ernst & Sohn.

Frangopol, D. M., M. J. Kallen, and J. M. van Noortwijk. 2004. “Probabilistic Models for Life–cycle Performance of Deteriorating Structures: Review and Future Directions.” *Progress in Structural Engineering and Materials* 6 (4): 197–212.

Hubler, Mija H., Roman Wendner, and Zdeněk P. Bažant. 2015. “Statistical Justification of Model B4 for Drying and Autogenous Shrinkage of Concrete and Comparisons to Other Models.” *Materials and Structures* 48 (4): 797–814. doi:10.1617/s11527-014-0516-z.

Iman, R. L., and W. J. Conover. 1982. “A Distribution–free Approach to Inducing Rank Correlation among Input Variables.” *Communications in Statistics–Simulation and Computation* 11 (3): 311–34.

Kirkpatrick, S., C. Gelatt, and M. Vecchi. 1983. “Optimization by Simulated Annealing.” *Science* 220: 671–80.

Ohadi, A., and T. Micic. 2011. “Stochastic Process Deterioration Modelling for Adaptive Inspections.” In *Applications of Statistics and Probability in Civil Engineering*, 1085–91. London: Taylor & Francis Group.

Pandey, M. D., X. X. Yuan, and J. M. van Noortwijk. 2009. “The Influence of Temporal Uncertainty of Deterioration on Life–cycle Management of Structures.” *Structure and Infrastructure Engineering* 5 (2): 145–56.

Pearson, K. 1895. “Notes on Regression and Inheritance in the Case of Two Parents.” *Proceedings of the Royal Society of London* 58: 240–42.

Stigler, S. M. 1989. “Francis Galton’s Account of the Invention of Correlation.” *Statistical Science* 4 (2): 73–79.

Strauss, A., S. Hoffmann, R. Wendner, and K. Bergmeister. 2009. “Structural Assessment and Reliability Analysis for Existing Engineering Structures, Applications for Real Structures.” *Structure and Infrastructure Engineering* 5 (4): 277–86. doi:10.1080/15732470601185638.

Strauss, A., R. Wendner, K. Bergmeister, M. Adley, and J. Horvatits. 2011. "Monitoring and influence lines based performance indicators." *Beton- und Stahlbetonbau* 106 (4): 231–40. doi:10.1002/best.201100003.

Strauss, A., R. Wendner, K. Bergmeister, and C. Costa. 2013. "Numerically and Experimentally Based Reliability Assessment of a Concrete Bridge Subjected to Chloride-Induced Deterioration." *Journal of Infrastructure Systems* 19 (2): 166–75. doi:10.1061/(ASCE)IS.1943-555X.0000125.

Strauss, A., R. Wendner, D. M. Frangopol, and K. Bergmeister. 2012. "Influence Line-Model Correction Approach for the Assessment of Engineering Structures Using Novel Monitoring Techniques." *Smart Structures and Systems* 9 (1): 1–20. doi:10.12989/sss.2012.9.1.001.

Van Noortwijk, J. M. 2009. "A Survey of the Application of Gamma Processes in Maintenance." *Reliability Engineering & System Safety* 94 (1): 2–21.

Van Noortwijk, J. M., J. A. M. van der Weide, M. D. Kallen, and M. D. Pandey. 2007. "Gamma Processes and Peaks-over-Threshold Distributions for Time-Dependent Reliability." *Reliability Engineering & System Safety* 92 (12): 1651–58.

Vořechovský, M., and D. Novák. 2009. "Correlation Control in Small–sample Monte Carlo Type Simulations I: A Simulated Annealing Approach." *Probabilistic Engineering Mechanics* 24 (3): 452–62.

Wendner, R., and Strauss, A. 2014. "Inclined Approach Slab Solution for Jointless Bridges: Performance Assessment of the Soil–Structure Interaction." *J. Perform. Constr. Facil.*, (in press). doi:10.1061/(ASCE)CF.1943-5509.0000522.

Wendner, R., T. Tong, A. Strauss, and Q. Yu. 2014. "A Case Study on Correlations of Axial Shortening and Deflection with Concrete Creep Asymptote in Segmentally-Erected Prestressed Box Girders." *Structure and Infrastructure Engineering*, (in press). doi:10.1080/15732479.2014.992442.

Lattice Discrete Particle Modeling for coupled concrete creep and shrinkage using Solidification Microprestress Theory

M. Abdellatef[1],M. Alnaggar[2],G. Boumakis[3],G. Cusatis[4],G. Di-Luzio[5],R. Wendner[6]

[1]PhD Graduate Student, Department of Civil and Environmental Engineering, Rensselaer Polytechnic Institute, Troy, NY 12180, USA; abdelm4@rpi.com
[2]Assistant Professor, Department of Civil and Environmental Engineering, Rensselaer Polytechnic Institute, Troy, NY 12180, USA; alnagm2@rpi.edu
[3]PhD Graduate Student, University of Natural Resources and Life Sciences, Vienna, Austria, giannis.boumakis@boku.ac.at
[4]Associate Professor, Department of Civil and Environmental Engineering, Northwestern University, Evanston, IL 60208-3109, USA; g-cusatis@northwestern.edu
[5]Assistant Professor, Department of Structural Engineering, Politecnico di Milano, Milan, Italy: giovanni.diluzio@polimi.it
[6]Director Christian Doppler Laboratory, University of Natural Resources and Life Sciences, Vienna, Austria, roman.wendner@boku.ac.at

ABSTRACT

The macroscopic continuum creep simulation always neglect internal creep/relaxation at lower scales due to the internal self-equilibrated stresses. So far, a comprehensive model for concrete creep at the meso-scale level has been lacking. In this paper, such a shortcoming is over come by the explicit implementation of the solidification-microprestress (SM) theory within the Lattice Discrete Particle Model (LDPM). Aging effect is obtained using a global reaction degree of concrete obtained by a multi physics model evolving temperature, humidity and cement degree of reaction in full coupling over time and space leading to an elegant and simple implementation within the LDPM framework through an imposed eigenstrain. This leaves the features of the LDPM constitutive equation simulating material strength and toughness completely unaltered. To show the superiority of the proposed model, extensive calibration and validation of the model is pursued by numerical simulations of experimental data from literature.

INTRODUCTION

Creep and shrinkage deformations are known to be two major factors affecting serviceability and integrity of concrete structures on the long term. For more than a century, different experimental programs for creep and shrinkage have been performed, in order to provide adequate data sets for extensive understanding. In parallel, several models have been proposed and developed, giving explanation and prediction tools for

such behavior. Extensive modes were proposed to predict concrete behavior. From concrete early ages, concrete exhibits shrinkage behavior due to change in moisture content (Khan et al., 1997). This leads to cracking or strain-softening damage for internally and or externally constrained volumes (Cusson and Hoogeveen, 2007). In this paper, Lattice Discrete Particle Model (LDPM) is used (Cusatis et al., 2011b,a), along with Microprestress Solidification Theory (SM) (Di-Luzio and Cusatis, 2013), to model creep and shrinkage behavior. The Microprestress is a visco-elastic behavior modeling through two the merge of two theories: Microprestress (Bazant et al., 1997) and Solidification (Bazant and Prasannan, 1989) theories. Also, the model implements the idea of reaction degree to account for the aging behavior of concrete(Di-Luzio and Cusatis, 2009a). The formulation and numerical implementations are presented in this paper, followed by experimental calibration and validation.

MECHANICAL BEHAVIOR

The mechanical behavior of concrete undergoing creep and shrinkage deformations is simulated by expressing each deformation as an eigenstrain to be imposed on the concrete meso-structure. The constitutive behavior of concrete is modeled using the Lattice Discrete Particle Model (LDPM). In the same discrete setting for the LDPM framework, assuming strain additivity to be valid throughout the whole procedure, one can rewrite in rate form, the total vectorial strain rate $\dot{\boldsymbol{\epsilon}}$ as a sum of the individual vectorial strains rates from different phenomena involved as follows:

$$\dot{\boldsymbol{\epsilon}} = \dot{\boldsymbol{\epsilon}}^{*} + \dot{\boldsymbol{\epsilon}}^{s} + \dot{\boldsymbol{\epsilon}}^{t} + \dot{\boldsymbol{\epsilon}}^{v} + \dot{\boldsymbol{\epsilon}}^{f} \tag{1}$$

where $\dot{\boldsymbol{\epsilon}}^{*}$ represents the elastic, damage and cracking strain rates computed LDPM, $\dot{\boldsymbol{\epsilon}}^{s}$ and $\dot{\boldsymbol{\epsilon}}^{t}$ are shrinkage and thermal strain rates (respectively) formulated following the same assumptions in Ref. (Di-Luzio and Cusatis, 2013); $\dot{\boldsymbol{\epsilon}}^{v}$ is the viscoelastic strain rate and $\dot{\boldsymbol{\epsilon}}^{f}$ is the purely viscous strain rate representing in sum, the creep strain rate and formulated based on the Micro-Prestress Solidification theory recently presented in Ref. (Di-Luzio and Cusatis, 2013). Eq. 1 can be interpreted as the rheological model depicted in fig. 1a.

The Lattice Discrete Particle Model (LDPM)

The Lattice Discrete Particle Model (LDPM) (Cusatis et al., 2011a,b) is a mesoscale discrete model that simulates the mechanical interaction of coarse aggregate pieces embedded in a cementitious matrix (mortar). The concrete mesostructure is geometrically represented through a system of polyhedral cells (see Figure 1b) interacting through triangular facets and a lattice system composed by the line segments connecting the particle centers. In LDPM, rigid body kinematics is used to describe the deformation of the lattice/particle system and the displacement jump, $[\![\mathbf{u}_C]\!]$, at the centroid of each facet is used to define measures of strain as $e_N = \mathbf{n}^{\mathrm{T}}[\![\mathbf{u}_C]\!]/\ell$, $e_L = \mathbf{l}^{\mathrm{T}}[\![\mathbf{u}_C]\!]/\ell$ and

$e_M = \mathbf{m}^{\mathrm{T}}[\![\mathbf{u}_C]\!]/\ell$. Where ℓ = interparticle distance; and $\mathbf{n}$, $\mathbf{l}$, and $\mathbf{m}$, are unit vectors defining a local system of reference attached to each facet. Next, a vectorial constitutive law governing the behavior of the material is imposed at the centroid of each facet. In the elastic regime, the normal and shear stresses are proportional to the corresponding strains: $t_N = E_N e_N^* = E_N(e_N - e_N^0)$; $t_M = E_T e_M^* = E_T(e_M - e_M^0)$; $t_L = E_T e_L^* = E_T(e_L - e_L^0)$, where $E_N = E_0$, $E_T = \alpha E_0$, E_0 = effective normal modulus, and α = shear-normal coupling parameter; and e_N^0, e_M^0, e_L^0 are mesoscale eigenstrains that might arise from a variety of phenomena such as, but not limited to, thermal expansion, shrinkage, corrosion, sulphate attack and ASR expansion. For constitutive relations of stresses and strains beyond the elastic limit, one can refer to (Cusatis et al., 2011a). LDPM has been used successfully to simulate concrete behavior under a large variety of loading conditions. Furthermore it was successfully used to: account for fiber reinforcement (Schauffert and Cusatis, 2012); simulate the ballistic behavior of ultra-high performance concrete (UHPC) (Smith et al., 2014); simulate Alkali-Silica Reaction (ASR) deterioration (Alnaggar et al., 2013) and nondestructive evaluation (Alnaggar et al., 2014); and Reinforced concrete flexural and shear behavior (Alnaggar, 2014). In addition, LDPM was successfully used in structural element scale analysis using multiscale methods (Alnaggar and Cusatis, 2012, Cusatis et al., 2014).

Thermal and hygral deformations

Thermal and hygral variation effects on concrete skeleton are treated as eigenstrains inducing only volumetric deformations (no shear deformations) assuming that they only change the material physical state. For the range of application of the current model which is only below boiling temperature and above freezing temperature for water, the thermal strain rate is $\dot{\boldsymbol{\epsilon}}^t = [\alpha_{th}\dot{T}, 0, 0]^{\mathrm{T}}$ with a constant coefficient of thermal expansion α_{th}. Similarly, using only a constant shrinkage coefficient κ_{sh} the shrinkage strain rate is $\dot{\boldsymbol{\epsilon}}^s = [\kappa_{th}\dot{h}, 0, 0]^{\mathrm{T}}$.

Microprestress Solidification Theory for viscous and visco-elastic deformations

According to the Microprestress Solidification (MS) Theory (Di-Luzio and Cusatis, 2013), the visco-elastic behavior of concrete is modeled through the sum of three components. Following the original formulation of the MS theory, all the macroscopic components were reformulated at the meso-scale and equivalent parameters were used. The first is the instantaneous strain rate $\dot{\boldsymbol{\epsilon}}^i$ corresponding to the elastic deformations induced by instantaneous change of stress $\dot{\boldsymbol{\sigma}}$. It is modeled by defining an instantaneous elastic modulus of concrete as $E = 1/q_1$, where q_1 is an age independent model parameter. LDPM elastic behavior is used to simulate this behavior by redefining the mesoscale elastic modulus as $E_0 = 1/\xi_1$ where ξ_1 (in MPa^{-1}) is a mesoscale model parameter that corresponds to q_1 in the original formulation. When all stresses are within their elastic limits, this formulation gives $\dot{\boldsymbol{\epsilon}}^* = \xi_1 \mathbf{G}\dot{\boldsymbol{\sigma}}$. The sec-

ond component is the viscoelastic strain rate which is formulated as $\dot{\boldsymbol{\epsilon}}^v(t) = \dot{\boldsymbol{\gamma}}/v(\alpha_c)$ where$\boldsymbol{\gamma} = \int_0^t \Phi(t_r(t) - t_r(\tau))\mathbf{G}\dot{\boldsymbol{\sigma}}d\tau$, where $\dot{\boldsymbol{\gamma}}$ represents the cement gel visco-elastic micro-strain rate, $v(\alpha_c) = (\alpha_c/\alpha_c^\infty)^{n_\alpha}$ is a function that represents the volume fraction of cement gel produced by early-age chemical reactions and it depends on the total reaction degree α_c and material parameters n_α and α_c^∞ , $\Phi(t-t_0) = \xi_2 \ln\left[1 + (t-t_0)^{0.1}\right]$ is the non-aging micro-compliance function of cement gel, with $t - t_0$ as the loading time interval and ξ_2 is another mesoscale model parameter that corresponds to the macroscale parameter q_2 in the original formulation, and the reduced time concept is introduced to account for the effect of change in relative humidity and temperature, where $t_r(t) = \int_0^t \psi(\tau)d\tau$ and $\psi(t) = [0.1 + 0.9h(t)^2]\exp[Q_v/R(1/T_0 - 1/T(t))]$, where $h(t)$, $T(t)$ are the relative humidity and temperature (in Kelvin) at time t, R is the universal gas constant and Q_v is the activation energy for the creep processes. The third component is the purely viscous strain rate which represents the unrecoverable part of the creep deformation and is given by $\dot{\boldsymbol{\epsilon}}^f = \xi_4\kappa_0\psi(t)S\mathbf{G}\boldsymbol{\sigma}$, where S is the microprestress computed by solving the differential equation $\dot{S} + \psi_s(t)\kappa_0 S^2 = \kappa_1 \left|\dot{T}\ln(h) + T\dot{h}/h\right|$, where κ_0 and κ_1 are model parameters, ξ_4 is a mesoscale model parameter that corresponds to the macroscale parameter q_4 in the original formulation, and $\psi_s(t) = [0.1 + 0.9h(t)^2]\exp[Q_s/R(1/T_0 - 1/T(t))]$. In this differential equation, the initial value S_0 at time $t = t_0$ is assumed to be a model parameter.

HYGRO-THERMO-CHEMICAL (HTC) MODEL

To accurately simulate shrinkage and creep behavior of concrete, the values of temperature, T, relative humidity, h, and cement hydration degree, α_c must be defined both spatially and temporally over the simulated geometry. Without such presentation, key mesoscale mechanisms will not be correctly captured including cracks induced by inhomogenous shrinkage strains. In this regard, a comprehensive three dimensional Hygro-thermo-Chemical (HTC) model for the evolution of temperature, humidity and cement hydration degree is utilized here (Di-Luzio and Cusatis, 2009a). Based on this model, h and T distributions can be computed by imposing moisture mass balance and enthalpy balance equations in the volume of interest. For temperature not exceeding 90°C, moisture mass balance can be given by $\boldsymbol{\nabla}\cdot(D_h\boldsymbol{\nabla}h) - \frac{\partial w_e}{\partial h}\frac{\partial h}{\partial t} - \frac{\partial w_e}{\partial \alpha_c}\dot{\alpha}_c - \dot{w}_n = 0$ and enthalpy balance is given by $\boldsymbol{\nabla}\cdot(\lambda_t\boldsymbol{\nabla}T) - \rho c_t\frac{\partial T}{\partial t} + \dot{\alpha}_c\, c\, \tilde{Q}_c^\infty = 0$. Cement hydration can be characterized by the hydration degree α_c, that represents the fraction of Portland clinker fully reacted with water. Its evolution law can be formulated as $\dot{\alpha}_c = (A_{c1}e^{-\eta_c\alpha_c/\alpha_c^\infty}e^{-E_{ac}/RT})/(1+(a-ah)^4)\,(A_{c2}/\alpha_c^\infty + \alpha_c)\,(\alpha_c^\infty - \alpha_c)$. The detailed description of the model is presented in (Di-Luzio and Cusatis, 2009a).

NUMERICAL IMPLEMENTATION OF VARIOUS STRAIN COMPONENTS

All strain rates described and formulated in the previous section are integrated in the LDPM framework. For each one, its three vectorial components at a generic facet

connecting two aggregate pieces are integrated explicitly to compute its corresponding strain increments during the time step Δt. For the procedure to be fully explicit, all state variables (h, T, α_c, S and $\boldsymbol{\sigma}$) are assumed to remain constant during the time step. Their values at the beginning of the time step are used to advance the solution in time. This is a fairly acceptable assumption provided that the time step used is small enough to guarantee stability and minimal integration errors.

In this study, for the first time in literature, all environmentally induced strains are treated as completely imposed strains, so, it is only required to evaluate the LDPM strain rate at the beginning of each time step by rearranging of Eq. 1 in an incremental form as $\Delta\boldsymbol{\epsilon}^* = \Delta\boldsymbol{\epsilon} - \left(\Delta\boldsymbol{\epsilon}^s + \Delta\boldsymbol{\epsilon}^t + \Delta\boldsymbol{\epsilon}^v + \Delta\boldsymbol{\epsilon}^f\right)$.

Given the total facet strain rate $\dot{\boldsymbol{\epsilon}}$ at the beginning of each time step, the total strain increment is computed by $\Delta\boldsymbol{\epsilon} = \Delta t\dot{\boldsymbol{\epsilon}}$. Then, all imposed strain increments are subtracted from $\Delta\boldsymbol{\epsilon}$ to compute the concrete skeleton strain increment $\Delta\boldsymbol{\epsilon}$ which is used by the LDPM constitutive law to compute the corresponding facet stress vector increment $\Delta\boldsymbol{\sigma}$ and update the stress vector at the end of the time step.

Shrinkage $\Delta\boldsymbol{\epsilon}^s$ and thermal $\Delta\boldsymbol{\epsilon}^t$ strain increments are computed at the beginning of the time step as $\Delta\boldsymbol{\epsilon}^s = \kappa_{sh}\Delta t\dot{h}[1\ 0\ 0]^T$ and $\Delta\boldsymbol{\epsilon}^t = \alpha_{th}\Delta t\dot{T}[1\ 0\ 0]^T$.

Creep strain is formulated at the facet level using the assumption of constant stress in the time step increment as stated earlier. The viscoelastic creep strain is modeled as an aging multi Kelvin chain model. For a one dimensional single Kelvin model with spring constant E_j and damper coefficient η_j the stress σ is given by $\sigma = E_j\gamma_j + \eta_j\dot{\gamma}_j$, where γ_j is the strain. Let $\tau_j = E_j/\eta_j$ be the system time constant. For the time step from t_i to t_{i+1} with $\Delta t = t_{i+1} - t_i$, the stress is constant: $\sigma(t) = \sigma(t_i) = \sigma^i$. The strain increment for a chain of N Kelvin elements at time t_{i+1} is given by $\Delta\gamma^i = \sum_{j=0}^{N}\left(\sigma^i/E_j - \gamma_j^i\right)\left(1 - e^{-\Delta t/\tau_j}\right)$ and following (Bazant and Xi, 1995), the non-aging compliance $1/E_j = A_j$ is computed for each chain to satisfy $A_0 + \sum_{j=1}^{N} A_j\left(1 - e^{-\Delta t/\tau_j}\right) \approx \xi_2\ln\left[1 + (\Delta t)^{0.1}\right]$. Ten chains are used ranging from 10^{-4} to 10^5 days. This gives $A_0 = 0.279\xi_2\ln(10)$ for $\tau_0 = 0$ (Bažant et al., 2004). With these values for τ_j, $A_j = L_j\ln(10)$ where L_j is computed based on an approximate retardation spectrum of order 3 (Bazant and Xi, 1995). Also by considering a constant $\psi(t^i) = \psi(t^{i+1}) = \psi^i$ over the time step, one can write, $\Delta t_r = \psi^i\Delta t$. So, including all effects, the viscoelastic strain increment becomes $\Delta\boldsymbol{\epsilon}^v = \sum_{j=0}^{N}\left(\mathbf{G}A_j\boldsymbol{\sigma}^i - \boldsymbol{\gamma}_j^i\right)\left(1 - e^{-\psi^i\Delta t/\tau_j}\right)/v(\alpha_c)$. Also, assuming constant stress $\boldsymbol{\sigma}^i$, constant ψ^i and similarly constant $\psi_s^i = \psi_s(t^i)$. The purely viscous strain increment at the facet level is $\Delta\varepsilon^f = \Delta t\xi_4\kappa_0\psi^i S^i\mathbf{G}\boldsymbol{\sigma}^i$ and the microprestress S update is $\Delta S^i = -\psi_s^i\kappa_0 S^{i^2}\Delta t + \kappa_1\left|\Delta T^i\ln(h^i) + T^i\Delta h^i/h^i\right|$.

IDENTIFICATION OF MODELS PARAMETERS

The proposed models contain three sets of material parameters that need to be identified from experimental data. The first set consists of the LDPM parameters, reported in Ref (Cusatis et al., 2011a). Ideally, a full set of mechanical tests are needed

in order to calibrate all parameters. For creep and shrinkage experiments, only compressive strength f'_c and elastic modulus E are usually reported. The LDPM model is calibrated to match these values. Some LDPM parameters were assumed based on (Cusatis et al., 2011a) as they have minimal effects on f'_c and E. These parameters are $\alpha = 0.25$, $\sigma_{c0} = 150$ MPa, $n_t = 0.2$, $H_{c0}/E_0 = 0.6$, $\kappa_{c0} = 4$, $\mu_0 = 0.2$, $\mu_\infty = 0$, $\sigma_{N0} = 600$ MPa, $\kappa_{c1} = 1$ and $\kappa_{c2} = 5$. The remaining parameters are calibrated and listed in Table 1.

The second set of material parameters is relevant to the HTC model which was extensively calibrated and validated in (Di-Luzio and Cusatis, 2009b). In the current study, only the relevant parameters that correspond to the experiments used are calibrated and listed in Table 1. All other parameters were reasonably assumed based on (Di-Luzio and Cusatis, 2009b) as follows, $A_{c2} = 2e - 4$, $E_{ac}/R = 5000°K$, $a = 5.5$, $b = 4$, $E_{ad}/R = 2700°K$, $c_t = 1100$ J/kg$°C$, and $\tilde{Q}_c^\infty = 450$ kJ/kg. Parameters controlling evaporable water (which directly affects the level of self desiccation), g_1 and k_{vg}^c are calibrated first, to match autogenous shrinkage profile, then diffusion parameters, D_0, D_1 and n_h, are calibrated to match drying shrinkage.

The third set of material parameters is relevant to creep and shrinkage models. The shrinkage parameter κ_{th} is calibrated through sealed and/or drying shrinkage tests. For Creep, parameters ξ_2 and ξ_4 are calibrated through sealed and/or drying creep tests, to match initial compliance value and the slope of the compliance function at the end, respectively. First, ξ_2 combined with E_n are calibrated to match initial elasticity. Second, ξ_4 is calibrated to fit basic creep strain evolution. Finally, κ_1 is calibrated to match drying creep evolution. Similar to others, typical values of previously calibrated parameters were used which were $k_t = 1e-5°C^{-1}$, $n = 0.1$ and $n_\alpha = 1.9$ as presented in (Di-Luzio and Cusatis, 2009b).

NUMERICAL SIMULATIONS OF EXPERIMENTAL DATA

This section presents numerical simulations of experimental data relevant to concrete specimens creep and shrinkage. The simulations demonstrate the capability of the formulated framework to capture hygral and thermal deformations along with creep deformations and their dependence on temperature, humidity and concrete aging under varying environmental conditions. A total of 6 different experimental campaigns were used in the calibration/validation of the model. Set1: Sealed and drying prisms (150mmX150mmX600mm) by (Bryant and Vadhanavikkit, 1987), Set2: Cycles of wetting and drying of prisms (70mmX70mmX280mm) by (L'hermite et al., 1965), Set3: Sealed and drying Cylinders (38mmX255mm) by (Brooks, 2005), Set4: Sealed and drying cylinders (40mmX270mm) (Mazloom et al., 2004), Set5: Sealed cylinders (76mmX235mm) by (Nasser and Neville, 1965) and Set6: Sealed cylinders (150mmX406mm) by (York et al., 1970).

Simulation of shrinkage deformations

Figure 1c shows the simulation of autogenous shrinkage of Set4 sealed specimens and Figures 1d,e and f show the simulation of drying shrinkage of Set4, Set3 and Set1 respectively. The model was able to capture both sealed and drying shrinkage behavior. The simulation of cyclic drying and rewetting by For (L'hermite et al., 1965) is shown in Figure 1h with the cycles shown in Figure 1g, both swelling and shrinkage behavior were approximated using the same coefficient K_{sh}. This should explain the difference between the experimental and numerical results, but with an overall acceptable simulation.

Simulations of basic creep deformations

Figures 1i and j show the effect of temperature on basic creep behavior and represent the simulation of Set5 and Set6 respectively. In addition, Figure 1k shows the effect of initial time of loading (7 and 14 days) by Set1. In all Figures 1i,j and k, one curve is used for calibration and the other is for validation. Additional simulations are presented in Figures 1l and m. It is clearly shown that the model is able to capture basic creep behavior, under different loading times and environmental conditions.

Simulations of drying creep deformations

Finally, Figure 1n shows the simulations for drying creep at 7, 14, 28, 84 and 182 days of initial time of loading comparing to the experiments from Set1. It has to be said that creep parameters were only calibrated based on the 28 days case and all others are validations. Also, Figure 1o shows another drying creep simulation for Set4. Considering the large scatter usually encountered in experimental data, the model shows excellent capturing of long term drying creep as shown in the figures.

CONCLUSIONS

In this work, coupling of LDPM with Microprestress-Solidification theory was performed including the effect of moisture transport and heat transfer. The aging viscoelastic strain was numerically implemented explicitly as an imposed eigenstrain to the LDPM framework. The model was calibrated and validated by the simulation of drying creep, basic creep and cycles of wetting and drying. This extension will allow the introduction of long term aging and deterioration mechanisms and multi-physical phenomena within LDPM framework.

References

Alnaggar, M. (2014). "Multiscale modeling of aging and deterioration of reinforced concrete structures." Ph.D. thesis, Northwestern University, Northwestern University.

Alnaggar, M. and Cusatis, G. (2012). "Automatic parameter identification of discrete mesoscale models with application to the coarse-grained simulation of reinforced concrete structures." *ASCE 2012 Structures Congress*, 36, 406–417.

Alnaggar, M., Cusatis, G., and Di-Luzio, G. (2013). "Lattice discrete particle modeling (ldpm) of alkali silica reaction (asr) deterioration of concrete structures." *Cement and Concrete Composites*, 41, 45–59.

Alnaggar, M., Cusatis, G., Qu, J., and Liu, M. (2014). *Simulating acoustic nonlinearity change in accelerated mortar bar tests: A discrete meso-scale approach*. CRC Press, 451–458.

Bažant, Z. P., Cusatis, G., and Cedolin, L. (2004). "Temperature effect on concrete creep modeled by microprestress-solidification theory." *Journal of Engineering Mechanics*, 130(Special Issue: Constitutive Modeling of Geomaterials), 691–699.

Bazant, Z. P., Hauggaard, A. B., Baweja, S., and Ulm, F.-J. (1997). "Microprestress-solidification theory for concrete creep. i: Aging and drying effects." *Journal of Engineering Mechanics*, 123(11), 1188–1194.

Bazant, Z. P. and Prasannan, S. (1989). "Solidification theory for concrete creep. i: Formulation." *Journal of engineering mechanics*, 115(8), 1691–1703.

Bazant, Z. P. and Xi, Y. (1995). "Continuous retardation spectrum for solidification theory of concrete creep." *Journal of Engineering Mechanics*, 121, 281–288.

Brooks, J. (2005). "30-year creep and shrinkage of concrete." *Magazine of concrete research*, 57(9), 545–556.

Bryant, A. H. and Vadhanavikkit, C. (1987). "Creep, shrinkage-size, and age at loading effects." *ACI Materials Journal*, 84(2).

Cusatis, G., Mencarelli, A., Pelessone, D., and Baylot, J. (2011a). "Lattice discrete particle model (ldpm) for failure behavior of concrete. ii: Calibration and validation." *Cement and Concrete Composites*, 33(9), 891–905.

Cusatis, G., Pelessone, D., and Mencarelli, A. (2011b). "Lattice discrete particle model (ldpm) for concrete failure behavior of concrete. i: Theory." *Cement and Concrete Composites*, 33(9), 881–890.

Cusatis, G., Rezakhani, R., Alnaggar, M., Zhou, X., and Pelessone, D. (2014). *Multi-scale computational models for the simulation of concrete materials and structures*. CRC Press, 23–38.

Cusson, D. and Hoogeveen, T. (2007). "An experimental approach for the analysis of early-age behaviour of high-performance concrete structures under restrained shrinkage." *Cement and Concrete Research*, 37(2), 200–209.

Di-Luzio, G. and Cusatis, G. (2009a). "Hygro-thermo-chemical modeling of high performance concrete. I: Theory.." *Cement and Concrete Composites*, 31(5), 301–308.

Di-Luzio, G. and Cusatis, G. (2009b). "Hygro-thermo-chemical modeling of high performance concrete. II: Numerical implementation, calibration, and validation.." *Cement and Concrete Composites*, 31(5), 309–324.

Di-Luzio, G. and Cusatis, G. (2013). "Solidification–microprestress–microplane (smm) theory for concrete at early age: Theory, validation and application." *International Journal of Solids and Structures*, 50, 957–975.

Khan, A. A., Cook, W. D., and Mitchell, D. (1997). "Creep, shrinkage, and thermal

strains in normal, medium, and high-strength concretes during hydration." *ACI Materials Journal*, 94(2).

L'hermite, R., Mamillan, M., and Lefèvre, C. (1965). "Nouveaux résultats de recherches sur la déformation et la rupture du béton." *Annales de l'Institut technique du bâtiment et des travaux publics*, Vol. 18, 323–360.

Mazloom, M., Ramezanianpour, A., and Brooks, J. (2004). "Effect of silica fume on mechanical properties of high-strength concrete." *Cement and Concrete Composites*, 26(4), 347–357.

Nasser, K. W. and Neville, A. M. (1965). "Creep of concrete at elevated temperatures." *ACI Journal Proceedings*, Vol. 62, ACI.

Schauffert, E. A. and Cusatis, G. (2012). "Lattice discrete particle model for fiber reinforced concrete (ldpm-f): I. theory." *Journal of Engineering Mechanics*, 138(7), 826–833.

Smith, J., Cusatis, G., Pelessone, D., Landis, E., O'Daniel, J., and Baylot, J. (2014). "Discrete modeling of ultra-high-performance concrete with application to projectile penetration." *International Journal of Impact Engineering*, 65, 13–32.

York, G. P., Kennedy, T. W., and Perry, E. S. (1970). *Experimental investigation of creep in concrete subjected to multiaxial compressive stresses and elevated temperatures*. Department of Civil Engineering, University of Texas at Austin.

Table 1: Calibrated LDPM, HTC, creep and shrinkage models parameters

Parameter	Set 1	Set 2	Set 3	Set 4	Set 5	Set 6
E_0 [MPa]	93700	30000	32081	60273	92000	90000
σ_t [MPa]	4.5	4.5	3.7	3.44	4.55	5.3
σ_s/σ_t	2.35	2.35	1.9	2.6	4.3	3.5
l_t [mm]	200	200	50	500	95	95
A_{c1} [h^{-1}]	1.5e7	1.5e7	3e7	1e8	1.5e7	1.5e7
η_c	5	5	2	5.5	5	5
D_0	2e-5	3e-4	2.4e-3	1e-4	9e-3	9e-3
D_1	2.5	0.06	3.22	2	1.25	1.25
n_h	6.5	6	3.25	4	3	3
λ_t [W/m°C]	5.4	5.4	2.3	2.3	5.4	5.4
g_1	1.75	1.75	1.5	1.8	1.25	1.25
k_{vg}^c	0.11	0.11	0.2	0.2	0.2	0.2
k_{sh} [h^{-1}]	2e-3	5e-4	2.3e-3	1.14e-3	5e-4	3.5e-4
ξ_2 [1/MPa]	1e-5	5e-6	1.55e-5	1.03e-5	7.5e-7	5e-6
ξ_4 [1/MPa]	5.5e-6	5e-6	1.6e-5	9.3e-6	6.5e-6	4.5e-6
κ_0 [1/MPa/day]	1.0e-8	1.0e-8	1.0e-3	1.0e-3	1.0e-8	1.0e-8
κ_1 [1/MPa/K]	1.25e18	1.25e18	5e6	5e6	1.25e18	1.25e18

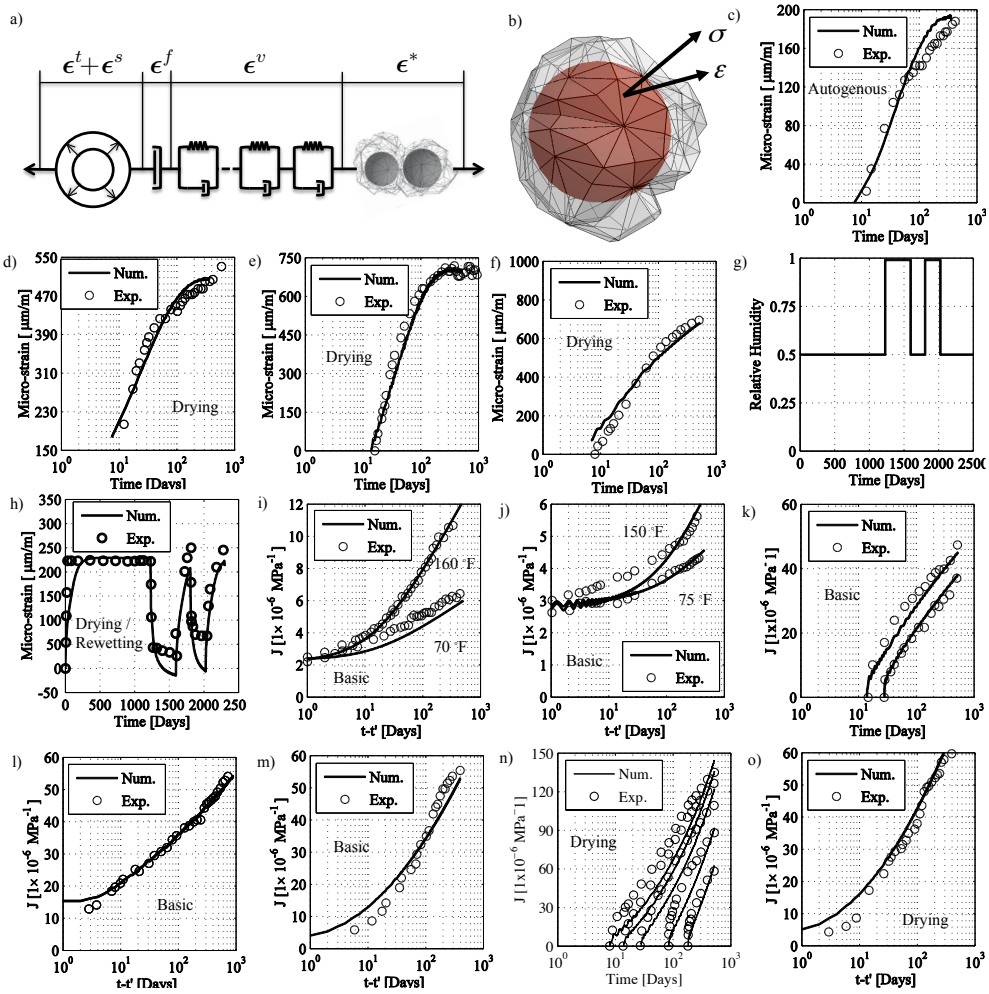

Figure 1: a) Equivalent rheological model based on strain additivity, b) One LDPM Cell around an aggregate piece with facet stress and strain vector, c) Autogenous shrinkage strain for (Mazloom et al., 2004), Drying shrinkage strain for d) (Mazloom et al., 2004), e) (Brooks, 2005), and f) (Bryant and Vadhanavikkit, 1987), (L'hermite et al., 1965) g) Humidity profile, h) Drying and rewitting strain, Compliance function of basic creep for i) (Nasser and Neville, 1965) , j) (York et al., 1970) , k) (Bryant and Vadhanavikkit, 1987) , l) (Brooks, 2005) , m) (Mazloom et al., 2004) , Compliance function of drying creep for n) (Bryant and Vadhanavikkit, 1987) , and o) (Mazloom et al., 2004)

Computational Modeling of Concrete Degradation due to Alkali Silica Reaction

Jithender J. Timothy [1], Minh N. Nguyen[2] and Günther Meschke [3]

Institute for Structural Mechanics, Ruhr University Bochum, 44801, Germany;
[1] PH (49) 234 32 29070; FAX (49) 234 32 - 14149; email: timothy.jithenderjaswant@rub.de,
[2] PH (49) 234 32 29056; FAX (49) 234 32 - 14149; email: nguyenmy@rub.de
[3] PH (49) 234 32 29051; FAX (49) 234 32 - 14149; email: guenther.meschke@rub.de

ABSTRACT

This paper presents a computational multi-level model for the description of alkali and moisture transport in concrete structures coupled to a macroscopic ASR induced phase-field damage model. Concrete is modeled as a heterogeneous material consisting of a partially saturated pore space with diffusively distributed microcracks and the solid skeleton (cement paste and potentially reactive and inert aggregates). The influence of the topology of the pore space and the presence of oriented micro-cracks on ion diffusion and moisture transport is taken into account through a novel continuum micromechanics homogenization model. The transport model is connected to a phenomenological reaction kinetics model to account for the ASR induced volume expansion of the affected aggregates. At the macroscopic scale, crack propagation and effects of induced topological changes on the fluid and ion transport are taken into account using a phase-field model.

Introduction

Alkali-silica reaction (ASR) is a major cause for premature loss of durability of concrete structures. In recent years, ASR damage resulting to a major extent from the external ingress of alkalis has been extensively detected in concrete pavements in Germany. ASR occurs in concrete pavements when diffusing alkali in the pore fluid and hydroxyl ions break the silanol and siloxane bonds in reactive aggregates, forming an alkali-silica gel. Once the volume of the gel exceeds the available volume of the pore space, the induced pressure generates stresses and swelling occurs, which results in the nucleation and propagation of micro-cracks in and around the aggregates. The ASR induced volume expansion eventually causes macro cracks at the surface of concrete road pavements, which in turn accelerate the alkali transport into the pavement and leads to the structural degradation of concrete pavements.

At the scale of the pore-fluid the nano-physics of diffusion and interaction of the alkalis is modelled by the Nernst-Planck-Poisson equation (Samson et al., 2005; Krabbenhøft and Krabbenhøft, 2008). The Nernst-Planck equation extends the Fick's law for a diffusing substance in a fluid subject to electrostatic forces. These electrostatic

forces result from the interaction of charged ions such as alkalis. The Poisson equation is used to close the system of equations for estimating the electric potential. To take into consideration of the complex pore-space induced tortuousity of the diffusing alkali, the intrinsic diffusivity in the pore-fluid is upscaled to the macroscopic scale using the cascade micromechanics model (Timothy and Meschke, 2011, 2014) that provides a homogenized diffusivity as a function of the porosity and of the complexity of the pore-space given that the pore structure of concrete spans multiple scales ranging from the gel pores at the nm scale, the capillary pores around the μm scale and the air pores at the mm scale.

In addition to pre-existing micro-cracks, e.g. resulting from shrinkage in concrete, cyclic traffic loading on road pavements due to traffic cause diffusely distributed micro-cracks, which in general, have an anisotropic orientation and strongly affect the alkali and moisture transport by enhancing the transport pathways in preferred directions. This influence of diffusely distributed micro-cracks is taken into account by a micro-mechanics homogenization model with embedded penny-shaped inclusions representing micro-cracks surrounded by an intact porous concrete matrix (Timothy and Meschke, 2011). To simulate the fracture pattern induced by ASR at the macroscopic scale, the alkali-silica reaction induced strain is modelled by an empirical ASR reaction model (Poyet et al., 2007; Nguyen et al., 2014b). The ASR induced damage at the macroscopic scale is simulated using the phase-field method (Miehe et al., 2010; Borden et al., 2012) based on energy minimization (Francfort and Marigo, 1998).

Modelling alkali diffusion and water transport in intact and micro-cracked concrete pavements

During winter, deicing salts such as $NaCl$, $CaCl_2$ and KCl are used for clearing snow and ice from the road pavement surfaces. These salts dissolve in water producing ions. The relevant ions for the alkali silica reaction are the alkalis. Ion diffusion in concrete pavements can be described by the Nernst-Planck equation for the concentration c_i and the POISSON equation for the variation of the electric potential ψ at the macroscopic level:

$$\frac{\partial(\phi c_i)}{\partial t} - \text{div}\left(\mathbf{D}_i^c \cdot \left(\nabla c_i + z_i c_i \frac{F}{RT}\nabla\psi\right)\right) = 0, \tag{1}$$

$$\text{div}(\boldsymbol{\varepsilon}^c \cdot \nabla\psi) + F\sum(z_i c_i) = 0. \tag{2}$$

c_i is the concentration of the i^{th} ion species, R is the ideal gas constant, F is the Faraday constant, T is the temperature measured in KELVIN and z_i is the valence number. $\mathbf{D}_i^c$ and $\boldsymbol{\varepsilon}^c$ are the upscaled diffusivity of the i^{th} ion species and the upscaled permittivity of pore fluid of micro-cracked concrete that can be estimated using a multi-level continuum micro-mechanics model (Timothy and Meschke, 2011) whose expressions are given below.

$$\mathbf{D}_i^c = D_i^{int}\mathbf{I} + \varphi_c \boldsymbol{\Upsilon} D_i\,, \tag{3}$$

$$\boldsymbol{\varepsilon}^c = \varepsilon^{int}\mathbf{I} + \varphi_c \boldsymbol{\Upsilon} \varepsilon. \tag{4}$$

φ_c is the micro-crack volume fraction and $\boldsymbol{\Upsilon}$ takes into account the effects of the micro-crack orientation, shape and its interaction with the porous microstructure. For intact concrete $\varphi_c = 0$.

Given the intrinsic quantities D_i and ε at the level of the pore fluid, the respective macroscopic quantities D_i^{int} and ε^{int} are obtained by upscaling to the macroscopic level using the cascade micromechanics scheme recently proposed by Timothy and Meschke (2014).

$$D_i^{int} = \phi A_f\left(n, \phi\right) D_i,$$
$$\varepsilon^{int} = \phi A_f\left(n, \phi\right) \varepsilon.$$

This cascade homogenization model takes into account the complexity of the pore-space using a cascade parameter n respectively. For cementitious materials (Timothy and Meschke, 2013, 2014) the complexity parameter was found to be in the range $4 < n < 8$.

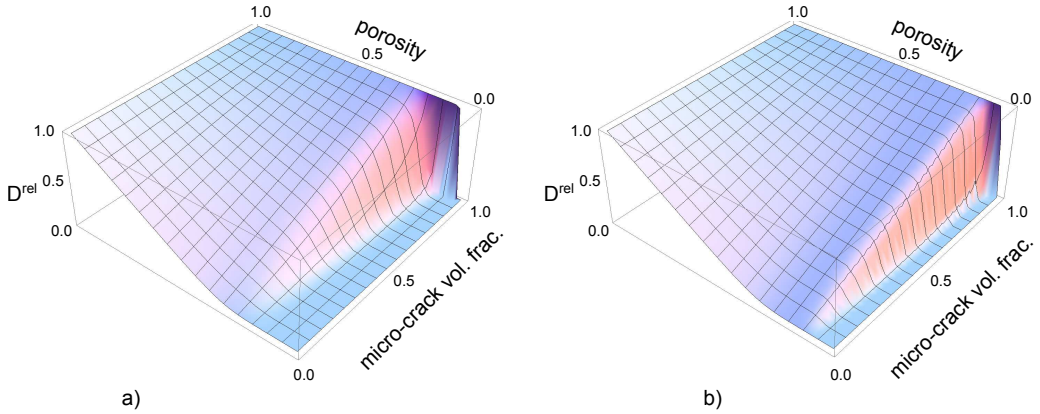

Figure 1. Homogenized relative diffusivity D^{rel} as a function of the porosity and the micro-crack volume fraction a) micro-crack aspect ratio 0.01, b) micro-crack aspect ratio 0.00001.

Defining the relative diffusivity as $\mathbf{D}^{rel} = \frac{\mathbf{D}_i^c}{\mathbf{D}_i}$, Figure 1 shows the relative diffusivity as a function of the aspect ratio of the micro-cracks assuming an anisotropic distribution of micro-cracks tangential to the alkali flux. It should be noted, that the model is able to predict a percolation threshold for diffusion below which transport is not possible. This percolation threshold is strongly influenced by the micro-crack topology. Longer and slender cracks reduce the percolation threshold by increasing the connectivity in contrast to shorter and thicker cracks.

Water flow into the concrete pavements due to rain and snow in addition to advecting the diffusing ions also act as a catalyst for the alkali-silica reaction. Water

transport can be either described by Darcy's law for the fully saturated case and the Richards equation for the partially saturated case (Celia et al., 1990; Samson et al., 2005). Similar in philosophy of modelling the influence of micro-cracks on diffusion, the enhanced permeability of micro-cracked concrete can be written as (Timothy and Meschke, 2011; Nguyen et al., 2014a):

$$\mathbf{k}^c = k^{int}\mathbf{I} + \varphi_c \boldsymbol{\Upsilon} k^{cr}. \tag{5}$$

$\boldsymbol{\Upsilon}$ is the interaction tensor, k^{int} is the permeability of the intact porous concrete matrix and k^{cr} is the equivalent intrinsic permeability in the micro-cracks. For this intrinsic permeability of the micro cracks, Poiseulle flow is assumed in the current model (Dormieux et al., 2006). Further details about the interaction tensor, $\boldsymbol{\Upsilon}$ can be found in Timothy and Meschke (2011).

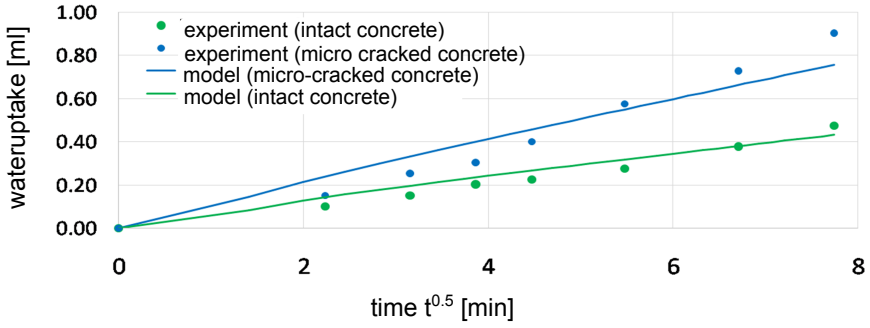

Figure 2. Water uptake in intact and micro-cracked concrete: Comparison of model predictions and experimental data (Przondziono et al., 2015)

Figure 2 compares model predictions and experimental data for water uptake in micro-cracked and intact partially saturated concrete specimens. In partially saturated concrete, the alkalis can diffuse only in the saturated zone of the pore space which is a fraction of the total porosity. Water transport due to capillary suction and/or external pressure provides an additional fluid velocity induced advective flux for alkali diffusion which is also considered in the model. In the validation analysis shown in Figure 2, water transport is modelled using the Richards equation (Celia et al., 1990; Samson et al., 2005) and the relative hydraulic conductivity is computed using the model proposed by van Genuchten (1980). Adsorption is also accounted for in the developed model. However, since it was shown to have negligible effect on the results, it was not considered in the presented analysis.

From the comparison of the experimental and model results, we can infer that the presence of oriented micro-cracks ($\varphi_c = 0.1$) significantly increase water transport. It should be noted, that ignoring the influence of the micro-cracks would not only affect

the anisotropic ion diffusivity as described by Eqs. 3 and 4, but also the advective flux, which is highly controlled by the enhanced fluid velocity due to micro-cracks according to the second term in Eq. 5.

Macroscopic fracture patterns due to ASR

The alkalis penetrating through the connected pore space and the micro cracks eventually reach reactive aggregates and partially diffuse into the porous aggregates. Depending on the type of aggregate, the alkalis present on the surface and inside the aggregate react in the presence of water with silicious components to produce an alkali-silica gel that is hydrophilic. Existing micro-cracks and pores act as reservoirs for gel accumulation. However, large pressures are generated once the gel volume is larger than the volume of the reservoir that results in an expansion of the aggregates, micro-cracking and eventually, at the scale of the concrete pavement, to a network of cracks visible at the surface. Macroscopic cracks, i.e. fractures at the scale of the concrete pavement are represented numerically by a zone of damage $d(\mathbf{x}, t) \in [0, 1]$ using the phase field method. $d = 0$ indicates the point inside the crack and $d = 1$ a point at the edge of the crack zone. The Griffith's fracture energy G_c required to create a fully open crack is then approximated by

$$\int_\Gamma G_c \mathrm{d}\Gamma \approx \int_\Omega G_c \left[\frac{(d-1)^2}{4l_0} + l_0 \nabla \cdot \nabla d \right] \mathrm{d}\Omega. \tag{6}$$

l_0 is a model parameter controlling the width of the smooth approximation of the crack and also numerically approximates the damage zone. In the limit of $l_0 = 0$, the phase field approximation converges to a sharp discrete fracture surface. The elastic energy density that takes into account the loss of material stiffness in the failure zone is a function of the phase field and the elastic strain tensor $\boldsymbol{\varepsilon}_e$ (Miehe et al., 2010)

$$\psi_e(\boldsymbol{\varepsilon}_e, d) = ((1-k)d^2 + k)\psi_{e0}^+ + \psi_{e0}^-, \tag{7}$$

where ψ_{e0}^+ and ψ_{e0}^- are the tensile and compressive parts of the elastic energy density $\psi_{e0} = \frac{1}{2}\boldsymbol{\varepsilon}_e : \mathbf{C} : \boldsymbol{\varepsilon}_e$ in the intact material. Assuming that crack propagation is a purely Mode-I driven process the phase-field influences only the tensile term in the decomposed elastic energy expression (see Eq. 7 and (Miehe et al., 2010)). The elastic strain tensor $\boldsymbol{\varepsilon}_e = \boldsymbol{\varepsilon} - \boldsymbol{\varepsilon}^{asr}$ depends on the total strain tensor $\boldsymbol{\varepsilon}$ and the ASR-induced strain $\boldsymbol{\varepsilon}^{asr}$ obtained by coupling the transport equation to a phenomenological ASR reaction model proposed by Poyet et al. (2007). The ASR induced strain $\boldsymbol{\varepsilon}^{asr}$ is a function of the asymptotic strain in free swelling β, the reaction extant ξ as a function of the alkali concentration c_{Na}, the fraction of ions involved in the reaction k, the maximum concentration of the gel produced c_{gel}^{max} and the initial volume fraction available for strain free filling of the pores and the ITZ region around the aggregate ξ_0. Denoting $\overline{\xi} = \xi(c_{Na}, c_{gel}^{max}, k) - \xi_0$ as the effective reaction extant and H the Heaviside function, the ASR induced strain has the following expression:

$$\varepsilon^{asr} = \beta H[\bar{\xi}]\bar{\xi}\mathbf{I} \tag{8}$$

By substituting the elastic energy density and the phase field approximation of the fracture energy into the Lagrangian energy functional (Borden et al., 2012), one obtains the following equation for evolution of the phase field

$$(\frac{4l_0(1-k)\psi_{e0}^{+}}{G_c} + 1)d - 4l_0^2\nabla\cdot\nabla d = 1. \tag{9}$$

The coupling between the transport model, the ASR reaction kinetics model and the phase field fracture model is illustrated in Figure 3. It shows, that the alkali concentration provokes ASR induced strains, which in case of restrained deformations, lead to the opening of cracks. The presence of cracks, on the other hand, modify the permeability and the diffusivity according to Eqs. 3 and 5 and thus further accelerate the transport process.

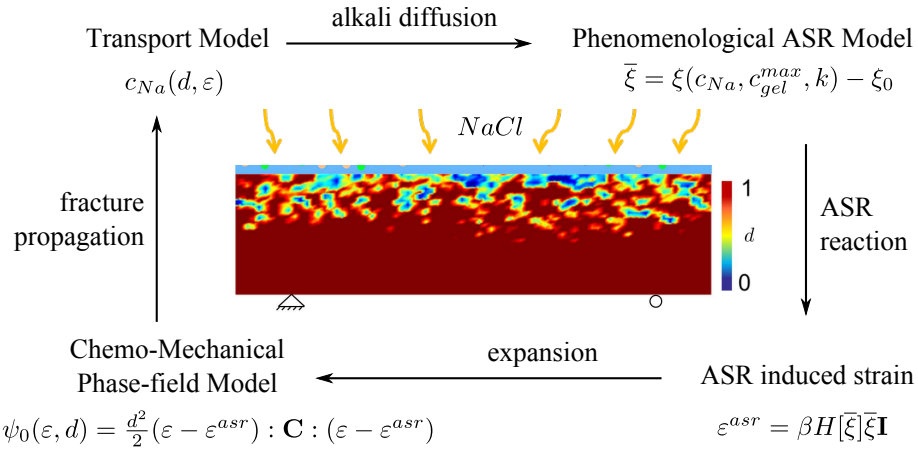

Figure 3. Coupling between the transport model, ASR reaction kinetics model and the phase field model for ASR induced crack propagation. Inset: Simulated ASR induced fracture pattern in a concrete beam subject to $NaCl$ after 360 days

The inset in Figure 3 shows the simulation of the fracture pattern induced by ASR in a fully saturated concrete beam (200 $\times$ 50 cm) with an initial porosity ϕ= 0.2 after 360 days. The top surface is subjected to a $NaCl$ concentration of $500 mol/m^3$.

CONCLUSIONS

A multi-level modeling strategy is presented for simulating alkali diffusion, water transport and ASR damage in concrete structures. A major novel component of this paper is the synthesis of a multi-level continuum micromechanics model to characterize the topology of the pore-structure and the presence of micro-cracks in the framework

of a numerical model for alkali diffusion and water transport and a phase-field model for the representation of ASR induced macroscopic cracks. The effective diffusivity, permittivity and permeability of micro-cracked concrete is anisotropic and depends on the micro-crack distribution, the aspect ratio and the diffusivity, permittivity and permeability of the intact concrete. The coupling between the transport and the fracture model is two-fold: The alkali concentration provokes ASR gel expansion, which may result in cracking of the material. On the other hand, ASR induced fractures influence and accelerate diffusion by enhancing the diffusivity in specific fracture orientations dependent on the fracture network which in turn further accelerates ASR. The modular nature of the proposed multi-level model allows to incorporate more refined ASR reaction kinetics models replacing the phenomenological model used here. This will be the subject of further research.

ACKNOWLEDGEMENT

Financial support was provided by the German Research Foundation (DFG) within the scope of subproject TP 3 of the Research Unit FOR 1498 ”Alkali-Silica Reaction in concrete structures considering external alkali supply”. This support is gratefully acknowledged.

References

Borden, M. J., Verhoosel, C. V., Scott, M. A., Hughes, T. J., and Landis, C. M. (2012). A phase-field description of dynamic brittle fracture. *Computer Methods in Applied Mechanics and Engineering*, 217-20:77 – 95.

Celia, M. A., Bouloutas, E. T., and Zarba, R. L. (1990). A general mass-conservative numerical solution for the unsaturated flow equation. *Water Resources Research*, 26(7):1483–1496.

Dormieux, L., Kondo, D., and Ulm, F. (2006). *Microporomechanics*. Wiley & Sons.

Francfort, G. and Marigo, J. (1998). Revisiting brittle fracture as an energy minimization problem. *Journal of Mechanics and Physics of Solids*, 46(8):1319–1342.

Krabbenhøft, K. and Krabbenhøft, J. (2008). Application of the Poisson-Nernst-Planck equations to the migration test. *Cement and Concrete Research*, 38:77–88.

Miehe, C., Welschinger, F., and Hofacker, M. (2010). Thermodynamically consistent phase-field models of fracture: Variational principles and multi-field fe implementations. *International Journal for Numerical Methods in Engineering*, 83(10):1273–1311.

Nguyen, M. N., Timothy, J. J., Beckhuis, S., and Meschke, G. (2014a). Hydraulic effects of fracture in brittle porous materials. *PAMM*, 14(1):135–136.

Nguyen, M. N., Timothy, J. J., and Meschke, G. (2014b). Numerical analysis of multiple ion species diffusion and alkali-silica reaction in concrete,. In Minh N. Nguyen*, Jithender J. Timothy, G. M., editor, *Computational Modelling of Concrete and Concrete Structures (EURO-C 2014)*, pages 789–796. CRC Press/Balkema, NL.

Poyet, S., Sellier, A., Capra, B., Foray, G., Torrenti, J.-M., Cognon, H., and E., B. (2007). Chemical modelling of alkali silica reaction: influence of the reactive aggregate size distribution. *Materials and Structures*, 40:229–239.

Przondziono, R., Timothy, J., Nguyen, M., Weise, F., Breitenbücher, R., Meschke, G., and Meng, B. (2015). Vorschädigung in Beton infolge zyklische Beanspruchungen und deren Auswirkungen auf Transportprozesse im hinblick auf eine schädigende AKR. *Beton und Stahlbetonabu*, 110(1):3–12.

Samson, E., Marchand, J., Snyder, K., Beaudoin, J., and j. Schroder (2005). Modeling ion and fluid transport in unsaturated cement systems in isothermal conditions. *Cement and Concrete Research*, 35:141–153.

Timothy, J. J. and Meschke, G. (2011). Micromechanics model for tortuosity and homogenized diffusion properties of porous materials with distributed micro-cracks. *Proceedings in Applied Mathematics and Mechanics (PAMM)*, 11(1):555–556. Article first published online : 9 DEC 2011, DOI: 10.1002/pamm.201110267.

Timothy, J. J. and Meschke, G. (2013). Diffusion in fracturing porous materials: Characterizing topological effects using cascade micromechanics and phase-field models. In *Poromechanics V*, pages 2250–2259.

Timothy, J. J. and Meschke, G. (2014). A micromechanics model for molecular diffusion in materials with complex pore structure. *Int. Journal for Numerical and Analytical Methods in Geomechanics*. submitted for publication.

van Genuchten, M. (1980). A closed-form equation for predicting the hydraulic conductivity of unsaturated soils. *Soil Science Society of America*, 44:892–898.

Measurements of Shrinkage Strain and Stress of an Existing Reinforced Concrete Structure in Japan

Keiko Arai[1]; Kei-ichi Imamoto[2]; and Chizuru Kiyohara[3]

[1]Imamoto Laboratory, Tokyo University of Science Laboratory, 125-0051 6-3-1, Niijuku, Katsushika-ku, Tokyo. E-mail: 25.secret.base.25@gmail.com

Abstract

In this study, authors measured strain and temperature of existing reinforced concrete structure using embedded strain gauge for the purpose to predict the shrinkage crack risk of the concrete structure. Authors also measured shrinkage and restrained of stresses relationship of concrete at laboratory. As a result, the shrinkage of the concrete under actual environmental condition was approximately $300*10^{-6}$ at 1.5 years after casting of the concrete. The shrinkage stress of wall was approximately $1.0N/mm^2$.In addition, shrinkage strain of underground beam was 70 $\times 10^{-6}$ and it's temperature changes ranged from -5 ℃ to +5 ℃ throughout a year.

1 INTRODUCTION

It is well known that cracks of concrete affect durability of structure. However shrinkage behavior of existing concrete structure isn't sufficiently understood. This research inquired about shrinkage behavior of exposed reinforced concrete structure with 2stories. Photo1 shows appearance of the structure and table1 tabulates outline of the building. This paper is reports results on restrained stresses and shrinkage of the existing concrete structure.

Picture-1 Appearance of the structure

Table-1 Outline of the building

Floor area	About 260m^2
Total floor area	About 270m^2
The number of stories	The 2nd floor of ground
Height	The ground 10m
Structure	Reinforced concrete structure

2 MEASUREMENT OF THE LINEAR EXPANSION COEFFICIENT

Mixture proportions and mechanical properties of concretes are shown in table2 and table3, respectively.

Table-2 Mixture proportions

	W/c	s/a	Unit quantity						Concrete admixture	Slump	Air
	(%)	(%)	C	W	S①	S②	G①	G②	(C×%)	(cm)	volume
Underground beam	54.5	50.1	323	176	275	643	912	—	2.91	15.0	4.5
1st･2nd floor wall･beam	60	48	292	175	429	434	675	289	2.92	18.0	4.5

Table-3 Mechanical properties of concretes (28days)

	Compressive strength (N/mm^2)	Young's modulus (×10^{3}N/mm^2)	Splitting tensile strength (N/mm^2)
Underground beam	36.4	-	-
1st･2nd floor wall･beam	32.0	29.9	3.0

Shrinkage strain was measured with embedded gage. Prior to analysis of shrinkage data, linear expansion coefficient of concrete was investigated using the same concrete with the structure. The measurement was performed at laboratory condition. The surface of the specimen were sealed aluminum foil tape. Contact-type strain gauge was used for the measurement. Length changes of the specimens were shown in figure-1. This inclination indicates the linear expansion coefficient of concrete.

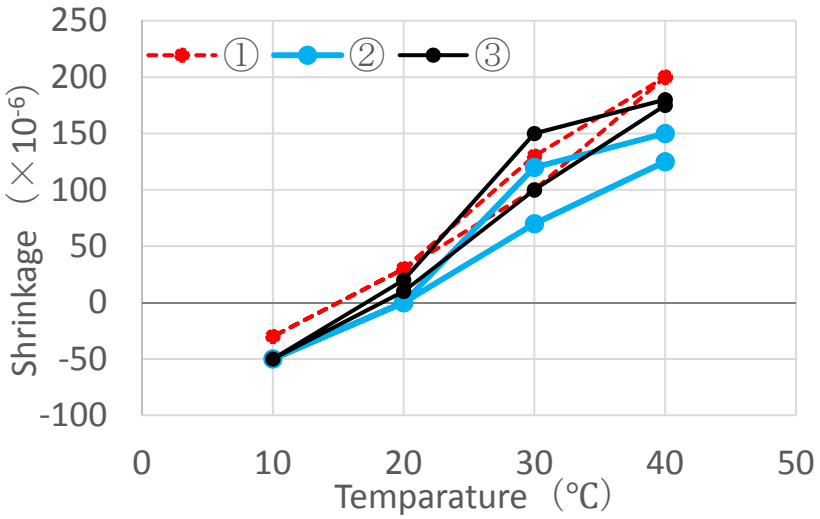

Figure 1 Length changes of concrete

Table 4 Linear expansion coefficient(Unit×10^{-6}/℃)

Temperature (℃)	Ascending line	Descending line
10～20	7	6.75
20～30	12.2	8.67
30～40	6	6.5
Average	8.4	7.31
Average	7.855	

Obtained values were smaller than well-known magnitude of 10 x 10^{-6}/℃. The linear expansion coefficient of concrete in this study was supposed to be 7.86 10^{-6}/℃ in table-4. Using this value, temperature compensation was performed.

3 STRAIN MEASUREMENT OF EXISING

3.1 Measurement outline

Shrinkage strains of 2 stories reinforced concrete structure were measured. Embedded type strain gauges with a thermocouple was installed in 5 points of a wall, a beam and an underground beam like picture-2. Plan and section of the building is shown in figure -2. To grasp behavior of concrete shrinkage under unrestrained, dummy specimens of the wall and the beam were constructed under the same environment to the existing structure like picture-3. Outline of dummy specimens is shown in figure -3 and table-5.

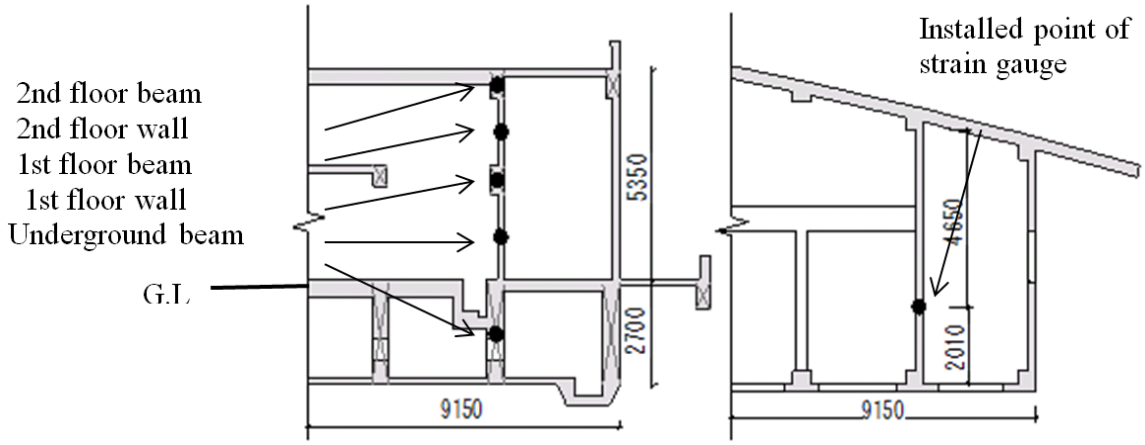

Figure-2 Left: Section, Right: Plan

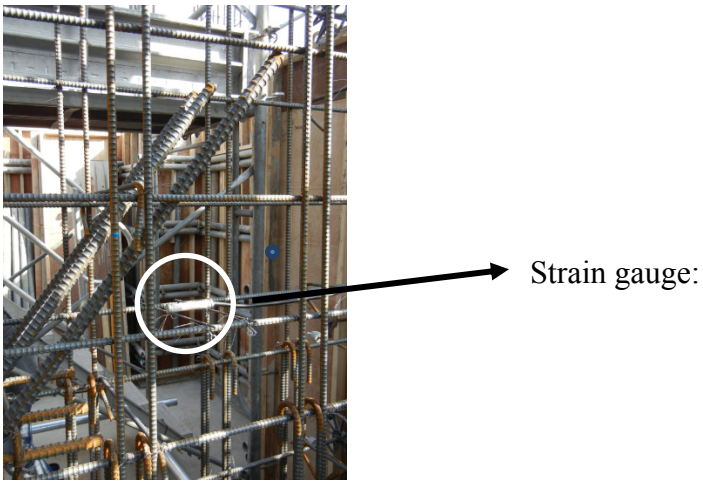

Picture-2 Strain gauge installation situation

Picture-3 Dummy specimens installation situation

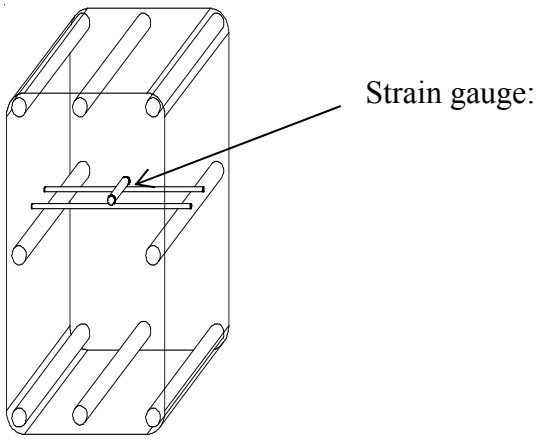

Figure-3 Outline of dummy specimens

Table-5 Specimens size

	The thickness(mm)	The height(mm)
The 1, 2nd floor wall	220	600
The 1, 2nd floor beam	370	710

3.2 Shrinkage of the measurement and temperature change.

Shrinkage behaviors of concrete members are shown in figure-4. The Shrinkage behaviors considering the linear expansion coefficient of concrete in this study are shown in figure-5.

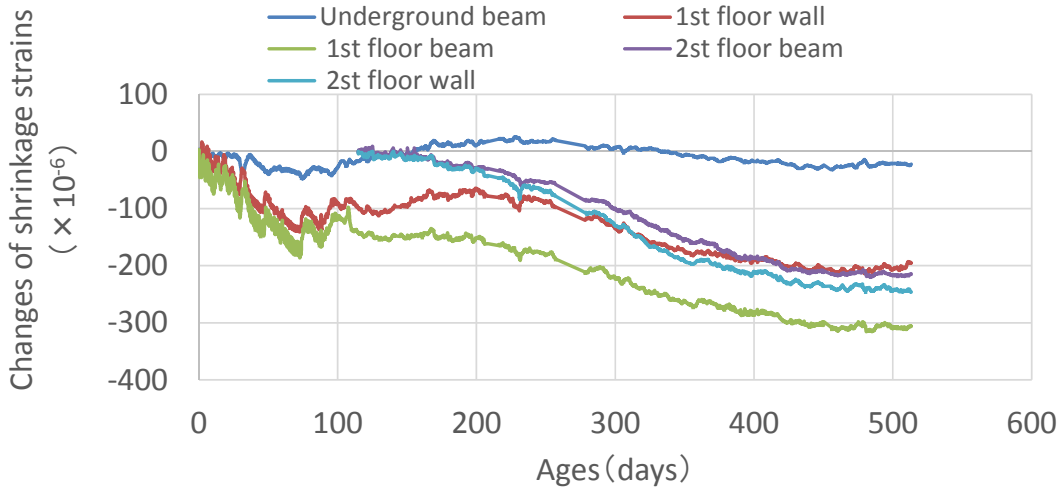

Figure-4 Shrinkage behaviors of concrete members

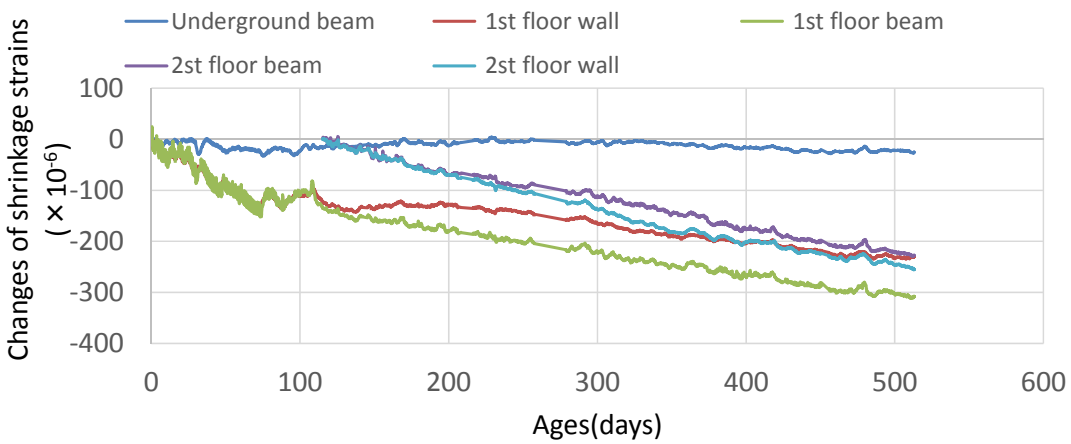

Figure-5 Shrinkage behaviors considering the linear expansion coefficient of concrete in this study

The shrinkage strains become slightly smooth by considering the linear expansion coefficient obtained from the same concrete. Strains of underground beam were stable and varied from +25 ($\times 10^{-6}$) to -50 ($\times 10^{-6}$) .

3.3 Restriction stress of existing structure.

Restrained stresses of wall and beam of existing structure at 1F and 2F are shown in figure-6. Restrained stresses were calculated with constant effective Young's modulus obtained from controlled-restraining test with restrained ratio of 50% at air conditioned(20℃and 60%R.H.)laboratory by Equation(1).

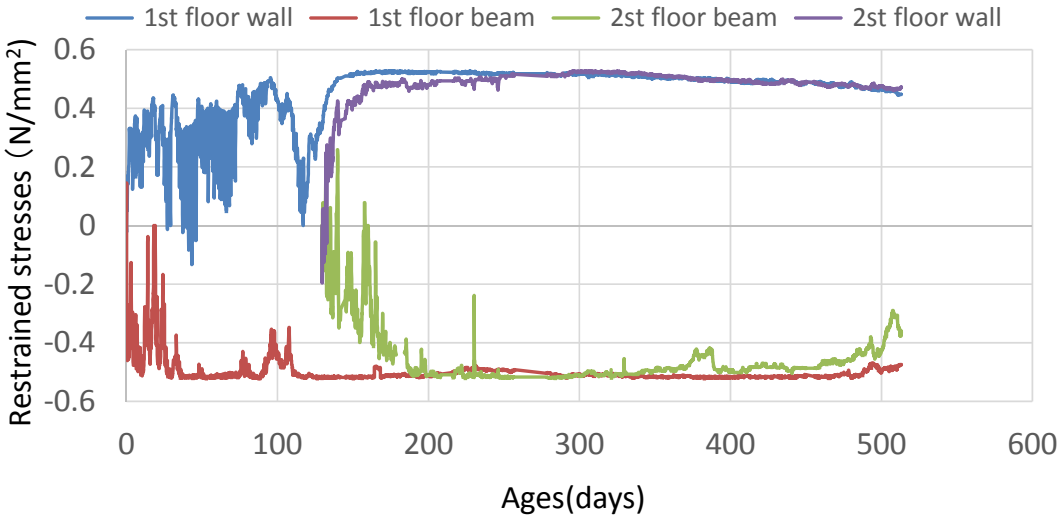

Figure-6 Restrained stresses

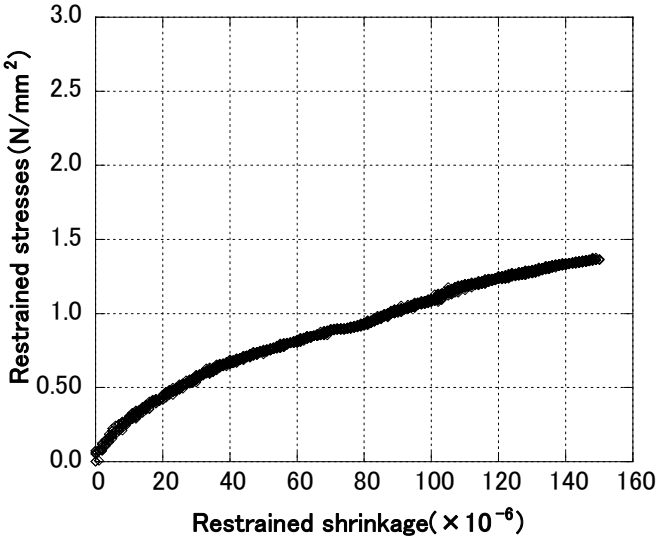

Figure-7 Stress-strain relationship 【Controlled-restraining test with restrained ratio of 50% at air conditioned(20℃and 60%R.H.)laboratory 】

$\sigma_s=(\varepsilon_f-\varepsilon_m)\cdot Ee$ Equation(1)
σ_s : Restrained stresses(N/mm^2)
ε_f : Shrinkage of dummy specimen
ε_m : Shrinkage of RC building
Ee : Effective Young's modulus

Shrinkage stress stabilized with the stabilization of drying shrinkage strain as shown in figure-6. Figure-7 shows stress-strain relationship of concrete at restrained test. The tangent angle is evaluated as "effective Young's modulus" of concrete used in this study. The effective Young's modulus method was used to calculate the restrained stresses. As shown in figure-7, magnitude of the effective Young's modulus change with restrained shrinkage strain. Hence, the shrinkage stress of concrete was evaluated according to the magnitude of restrained strain. The result is shown in figure-8.

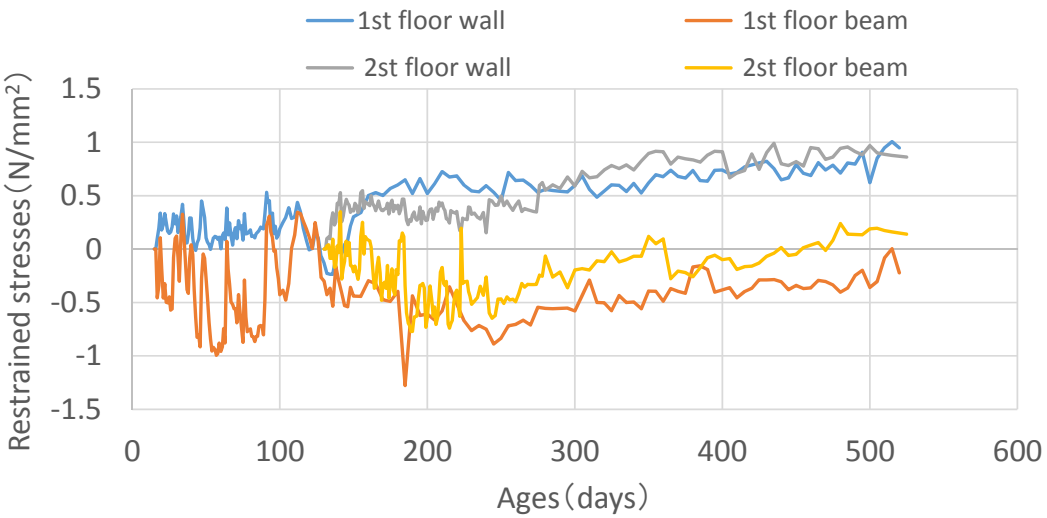

Figure-8 Restrained stresses(an effective Young's modulus way)

Restrained stresses of 1F and 2F wall increased gradually until 250 days after form removal. The stress reached 1.0 N/mm^2 at 400 days. On the other hand, the restrained stresses of the beam shifted to tensile region gradually after 250 days. Using the restrained stresses, the stress strength ratio was calculated as shown in figure-9.

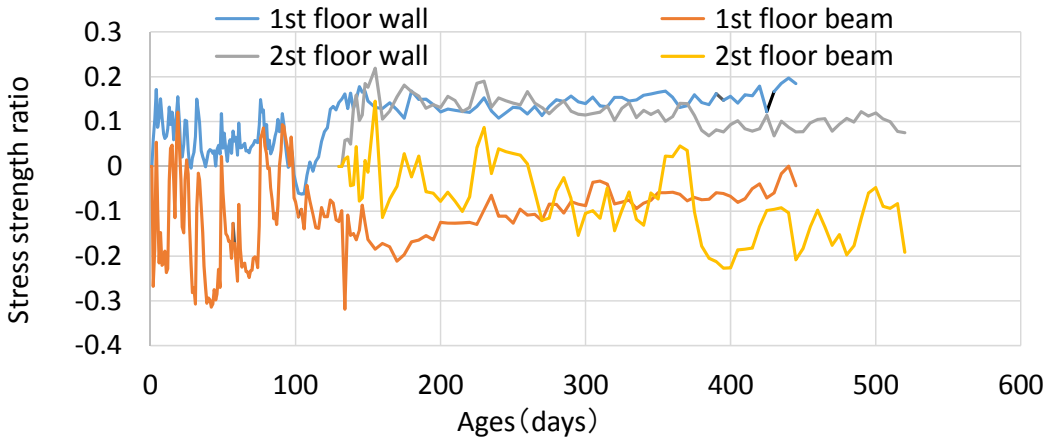

Figure-9 Stress strength ratio

Tensile strengths were obtained with equation proposed by Noguchi and CFB-FIP1990 model code based on the measured value at 28days. [2)] Shrinkage stresses of walls in 1F and 2F ranged within 0~1 N/mm^2. On the other hand, behaviors of beam was different between 1F and 2F. Shrinkage stress of beam at 1F was higher than other parts until the concrete placement of 2F. The stress-strength ratio of 2F beam reached to 0.1 at 500 days. The stress-strength ratio at failure of concrete in a laboratory test was 0.48. Hence crack would not be occurred and, at present, cracks have not been observed.

CONCLUSION

As a result, the following know ledges were obtained.

(1) Strains of underground beam were stable and varied from +25 ($\times 10^{-6}$) to -50 ($\times 10^{-6}$) .
(2) Restrained stresses of 1F and 2F wall increased gradually until 250 days after form removal. The stress reached 1.0 N/mm^2 at 400 days. On the other hand, restrained stresses of the beam shifted to tensile stress gradually after 250 days.
(3) Shrinkage stresses of walls in 1F and 2F ranged within 0~1 N/mm^2. On the other hand, behaviors of beam was different between 1F and 2F.

REFERENCES

(1) Keiko Arai, Keiichi Imamoto and Chizuru Kiyohara: Study about shrinkage behavior of 2 story strike release reinforced concrete structure, Kanto branch collected papers,2013
(2) Takafumi Noguchi, Fuminori Tomozawa: Relation between the compression strength of the high-strength concrete and all kinds' mechanical characteristic, Architectural Institute of Japan structural collected papers, No.472, pp.11-16, 1995

Concrete Pavement Joint Durability: A Sorption-Based Model for Saturation, the Role of Distributed Cracking, and Calcium Oxychloride Formation

W. Jason Weiss[1]

[1]Jack and Kay Hockema Professor, School of Civil Engineering, School of Materials Engineering, Purdue University, 550 Stadium Mall Dr., West Lafayette, IN 47906. E-mail: wjweiss@purdue.edu

Abstract

Concrete pavement joints have shown the potential to deteriorate, thereby compromising the service life of an otherwise healthy pavement. It is proposed that this damage is due to fluid collecting at the joint. The collection of fluid makes concrete 1) susceptible to freeze and thaw damage when it reaches a critical degree of saturation and 2) susceptible to damage due to a chemical reaction between the salt and matrix. Currently, models that describe the rate of water absorption in concrete consider the concrete as uncracked. In service however, concrete can develop cracks that increase the rate of transport. The first part of this paper will begin by discussing water absorption in undamaged concrete. The second part of this paper discusses the influence of distributed cracking. The third part of this paper discusses a potential chemical reaction between cement and deicing salt that forms calcium oxychloride.

BACKGROUND ON THE PROBLEM OF CONCRETE JOINT DAMAGE

While many concrete pavements in North America provide excellent long-term performance, a portion of the concrete pavements have exhibited premature deterioration primarily at the saw-cut joints (Jones et al. 2014). Joint deterioration is problematic because it compromises the performance and service life of an otherwise healthy pavement. Repairing joint damage can be expensive and these repairs are disruptive to the travelling public. It is commonly observed that the joints that frequently exhibit this damage contain standing fluid. Two primary types of deterioration can be observed: 1) cracking parallel to the joint resulting in 2 mm to 12 mm flakes of concrete being removed from the joint or 2) spalling that begins with a hollowed out region at the bottom of the saw cut resulting in a crack to the surface of pavement that is typically 75 to 150 mm from the edge of the joint. This paper provides a short update of recent research investigating the role of 1) saturation and freezing, 2) the influence of distributed cracking on the rate of saturation and freezing, and 3) the reaction between deicing salts (in this case calcium chloride) and the cementitious matrix.

A WATER ABSORPTION BASED MODEL FOR FREEZE THAW DAMAGE

Fagerlund (1977) pioneered the use of an approach for modeling freeze-thaw damage that considered that concrete would not be able to withstand saturation levels above a certain value. This value has been measured to be 86% for some concrete (Li et al. 2012) and will be assumed to be 85% for this paper. A two stage absorption approach was used to describe the rate at which concrete reached a critical level of saturation. Bentz et al. (2011) simplified the approach assuming a single sorption rate by assuming a weather event (e.g., rain) of longer than a particular time (6 hrs) was required to reach the second level of saturation. Bentz et al. (2001) used this approach with weather data to predict freeze-thaw damage in concrete pavements. Lucero et al. (in press) used neutron radiography to illustrate that the initial sorption was related to the filling of gel and capillary pores while the secondary rate of sorption was related to the filling of larger pores like air voids (Todak et al. 2015).

This paper examines the role of the mixture proportions on saturation response. It is assumed that the transition between the initial absorption and secondary absorption (commonly referred to as the nick point) can be described by a value of saturation that fills in all the pores in a concrete with the exception of the air voids. Powers model (Powers and Brownyard 1942) can be used to determine the degree of saturation at the nick point (Figure 1a) where the degree of saturation is shown as a function of the entrained air volume. Concrete with more air has a lower degree of saturation (i.e., is further away from reaching critical saturation). It has been shown that when water is in contact with a small sample of concrete (50 mm thick sample) the nick point will generally occur during the first 24 hours for typical paving concrete (Lucero et al. in press). This value can be used with the secondary rate of sorption to predict the time required to reach the critical degree of saturation as shown in equation 1:

$$S_{CR} = S_{NICK} + \Delta S\sqrt{t} \qquad \text{Equation 1}$$

where S_{CR} is the critical degree of saturation, S_{NICK} is the degree of saturation between the initial and secondary absorption which occurs when all the pores are filled except the air entrainment, ΔS is the secondary rate of absorption and t is time.

While S_{NICK} is dependent on the entrained air volume, the secondary rate of absorption is strongly related to the quality of the matrix. Figure 1b illustrates the impact of the sorption rate on the time to achieve critical saturation for a concrete made with an air content of 5.5% and a water to cement ratios (w/c) of 0.39 to 0.45 (with S_{NICK} varying from 66% to 70% respectively. The range of secondary sorption was measured by Castro et al. (2011) with 0.033 being representative of a mixture with a w/c of 0.39 and 0.053 being representative of a mixture with a w/c of 0.45.

Figure 2a provides an illustration of the influence of air content on the time it takes to saturate the concrete. It can be seen that the volume of air has a substantial influence

on the time to reach critical saturation. Figure 2b illustrates the influence of w/c where the impact is due to the change in the rate of water absorption.

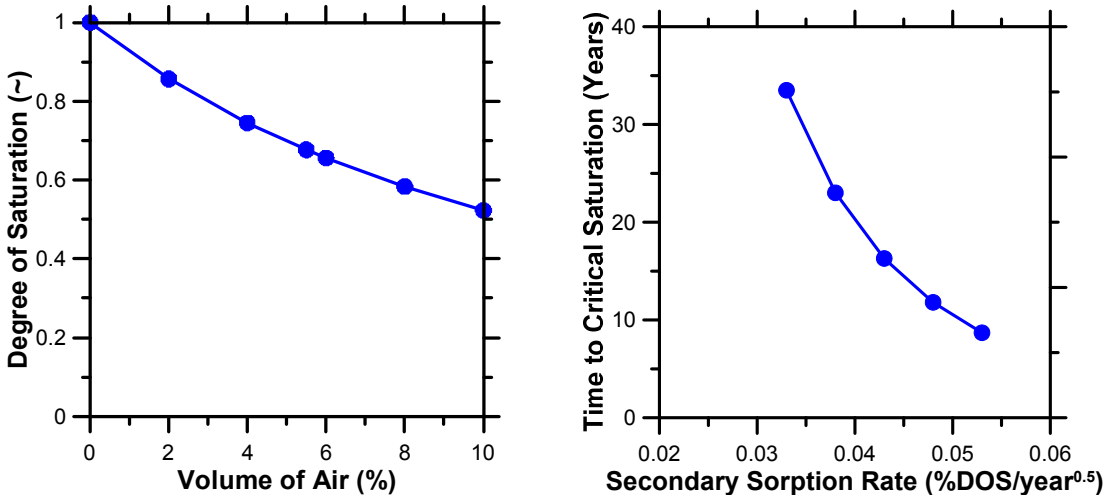

(a) (b)

Figure 1. a) Influence of Air Content on Degree of Saturation and b) Influence of the Secondary Rate of Sorption on the Time to Reach Critical Saturation

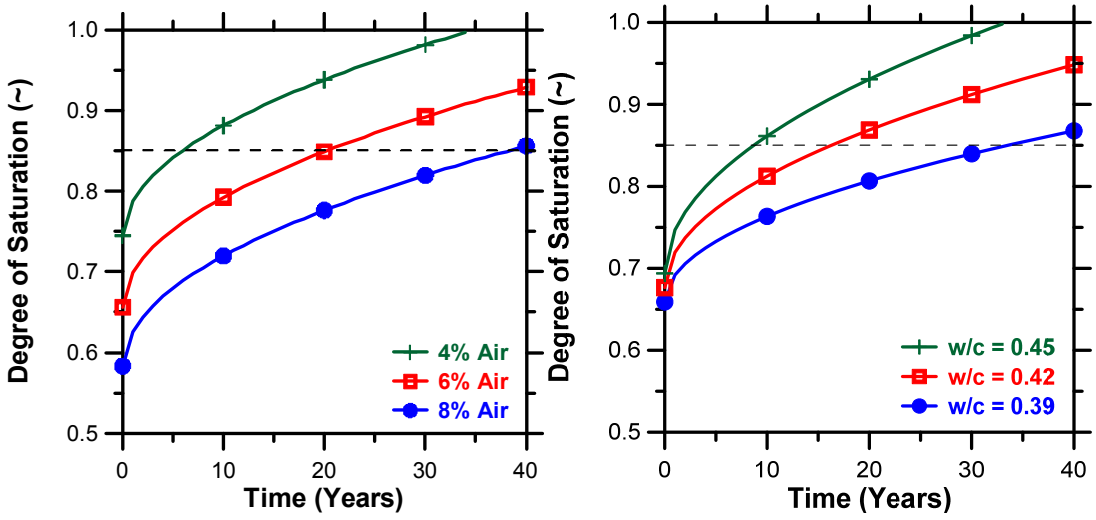

(a) (b)

Figure 2. a) The Illustration of the Air Content on the Degree of Saturation and b) the Influence of Water to Cement Ratio on the Degree of Saturation

A WATER ABSORPTION BASED MODEL THAT CONSIDERS CRACKING

While the previous section of the paper discussed the time to reach the critical degree of saturation for a concrete that was undamaged, this portion of the paper will begin

to discuss the role that cracking or damage may have in accelerating the rate of water absorption. Previous research by Yang et al. (2006, 2007) has indicated that there are two very distinctive types of crack morphology that can occur in a concrete pavement. Crack morphology can be divided into two main types of cracking: 1) localized discrete cracks which are consistent with mechanical loading and 2) distributed crack networks which are consistent of those occurring due to freeze thaw damage or alkali silica reactivity. The localized cracking can result in localized water ingress creating regions with higher degrees of saturation. The distributed crack networks are influenced by the crack distribution, orientation, and morphology. The cracked networks influence the overall rate of fluid absorption. Yang et al. (2006) showed that a cracked network that was consistent with connected cracking and a decrease in sample stiffness of 30% resulted in a sorption that was 1.9 times higher than that of the undamaged concrete. This is more complicated when the crack network is not completely connected. Figure 3a illustrates the influence of damage on the projected time to saturation. Figure 3b illustrates the projected time for the concrete to reach critical saturation.

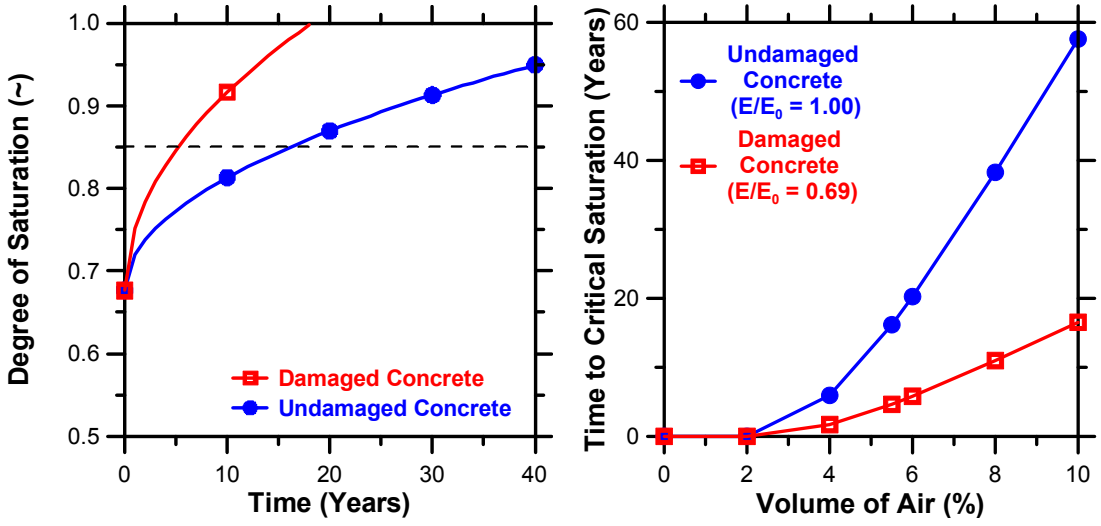

(a) (b)

Figure 3. a) The Influence of Damage on the Degree of Saturation and b) The Influence of Damage on the Time to Reach Critical Saturation

CHEMICAL REACTIONS BETWEEN DEICING SALT AND CONCRETE

The fluid that collects in the pavement joints is not pure water but contains deicing salts. While the use of deicing salts is an effective method for melting the ice and increasing the safety to the travelling public, it may also be partially responsible for joint deterioration issues that develop at the joints in the pavement. The reactions that occur depend on the salt that is used. It appears that NaCl results in an expansive and damaging sulfo-aluminate phase (Farnam et al. 2014a) while $CaCl_2$ and $MgCl_2$ result in the formation of a calcium oxychloride (Farnam et al. 2014b, Farnam et al. 2015, Farnam et al. submitted, Sutter et al. 2008, Villani et al. 2015).

A procedure was developed to measure the heat flow of a salt-hydrated cement powder sample using low-temperature differential scanning calorimetry (LT-DSC) (Monical et al. in preparation). The LT-DSC test is performed by cooling the sample to -80C, performing a small cooling loop, then reheating the material at a rate of 0.3 C/min while measuring the heat release. Three main events occur resulting in heat release. At approximately -50C heat is released as the eutectic solid changes phase becoming a highly concentrated salt liquid (the concentration is the eutectic composition). In the range between the eutectic temperature to the liquidus temperature a second feature in the heat flow curve occurs that is related to the melting of ice. The third feature in the heat flow curve occurs at temperatures between those associated with the melting of ice and approximately 50C are associated with the formation of calcium oxychloride. By integrating the heat flow peak associated with the calcium oxychloride the total heat released can be obtained. Oxychloride requires the presence of calcium chloride from the salt and calcium hydroxide from the cementitious matrix. Figure 4 compares the amount of calcium oxychloride that forms for cement matrixes made using a variety of cementitous binders. It can be observed that when supplementary cementitious materials are used (slag, fly ash or silica fume) the amount of calcium oxychloride that is produced decreases and the pavement joint would be expected to be more durable.

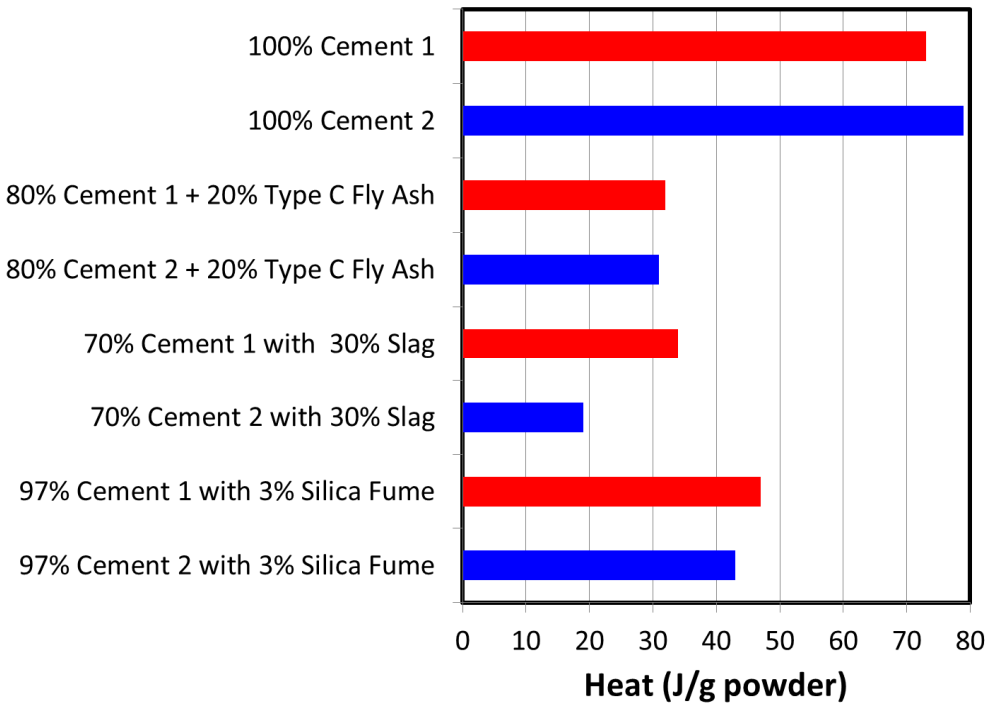

Figure 4. An Illustration of the Composition of the Matrix and the Potential Formation of Calcium Oxychloride

DISCUSSION ON IMPROVING JOINT DURABILITY IN CONCRETE

The durability of concrete pavement joints in North America have shown signs of deterioration. This deterioration has been previously proposed by the author (2005) to be related to fluid collecting in the joint that can lead to hydraulic pressure during freezing and/or a chemical reaction between the deicing salt and matrix. The fluid collects when the joint sealant fails and the joint does not crack or the crack does not open to a sufficient width to allow it to drain. Many agencies are searching for ways to mitigate this damage. The increase of the air content has been proposed which may help to reduce the initial degree of saturation and increase the time for the concrete to reach a critical saturation. This has been shown to be an effective way to reduce the degree of saturation when the pores in the matrix saturate and this is beneficial. It should be noted however that the volume of the air void system (and saturation) may be compromised when the deicing salt enters the pavement reacting with the calcium aluminate phase resulting in Friedels salt or Kuzel's salt. It has also been proposed that decreasing the water – to cement ratio of the pavement can increase life by reducing the rate of fluid absorption. While both of these approaches are valid their benefits can not completely solve the problem. It has been shown that damage can be caused by saw-cutting (Raoufi et al. 2008) in a heart shaped region at the base of the saw-cut. It is proposed that this damaged region could lead to an increase in the rate of saturation and damage. By improving the timing of saw-cutting using maturity to minimize damage at the base of the saw cut has great potential. Coates et al. (2008) and Golias et al (2012) have suggested that the use of a concrete sealant can reduce the rate of fluid ingress and thereby reducing the rate of fluid ingress and potential for the concrete to reach critical saturation or the potential chemical reaction between the salt and concrete resulting in an increase in the durability of the concrete pavement joint. The use of supplementary cementitious materials (SCM, fly ash, silica fume, slag) is beneficial. While use of SCM reduces the transport properties (similar to reducing the water to cement ratio) they can also reduce the potential for reaction between calcium chloride and calcium hydroxide.

CONCLUSION

Concrete is susceptible to freeze and thaw damage when it reaches a critical degree of saturation. Currently, most models that describe the rate of water absorption in concrete consider the concrete as uncracked. In service however, concrete can develop cracks. These cracks can dramatically influence the transport of liquids and ions. However not all cracks are created equal. This paper will discuss the rate at which water is absorbed in concrete and the rate at which concrete reaches this critical degree of saturation. Specifically the first portion of this paper will begin by discussing water absorption in undamaged concrete. In the second part of the paper the influence of cracking was discussed on the rate of water absorption. Specifically, crack morphology will be divided into two main sources of cracking: 1) localized discrete cracks and 2) distributed crack networks. This paper used data that shows how distributed microcracking, similar to the cracking that is expected during freeze thaw or alkali silica reaction, can alter the rate of absorption. Finally the potential

damage that occurs due to a reaction between the deicing salt (calcium chloride) and the calcium hydroxide in the cementitious matrix.

ACKNOWLEDGEMENTS

This work was supported in part by the Joint Transportation Research Program administered by the Indiana Department of Transportation (SPR 3864) and the Portland Cement Association/National Ready Mix Concrete Association through the CSH HUB initiative. The contents of this paper reflect the views of the authors, who are responsible for the facts and the accuracy of the data presented herein, and do not necessarily reflect the official views or policies of the Federal Highway Administration, the Indiana Department of Transportation, Portland Cement Association or National Ready Mix Concrete Association, nor do the contents constitute a standard, specification, or regulation.

REFERENCES

Bentz, D. P., Ehlen, M., Ferraris, C., Garboczi, E., (2001) "Sorptivity-Based Service Life Predictions for Concrete Pavements," International Conference on Concrete Pavements, September 2001

Castro, J., Bentz, D., & Weiss, J. (2011). Effect of sample conditioning on the water absorption of concrete. Cement and Concrete Composites, 33(8), 805–813. doi:10.1016/j.cemconcomp.2011.05.007

Coates, K., Mohtar, S., Tao, B., and Weiss, W. J., (2009) "Can Soy Methyl Esters Reduce Fluid Transport and Improve the Durability of Concrete?" Transportation Research Board, Volume 2113, pp. 22-30

Fagerlund, G. (1977). The international cooperative test of the critical degree of saturation method of assessing the freeze / thaw. Materials and Structures, 10(4), 231–253.

Farnam, Y., Bentz, D. P., Hampton, A., & Weiss, W. J. (2014). Acoustic Emission and Low Temperature Calorimetry Study of Freeze and Thaw Behavior in Cementitious Materials Exposed to Sodium Chloride Salt. Journal of the Transportation Research Record, 2441, 81–90.

Farnam. Y., Bentz, D. P., Sakulich, A., Flynn, D., and Weiss, W. J., (2014) "Using A Low Temperature Guarded Comparative Longitudinal Calorimeter and Acoustic Emission to Measure Freeze and Thaw Damage in Mortars Containing Deicing Salt" Journal of Advances in Civil Engineering Materials, ASTM, Vol. 3, No. 1, 2014, pp. 316–337, doi:10.1520/ACEM20130095

Farnam, Y., Wiese, A., Bentz, D., Davis, J. and Weiss, W. J., (2015), Damage Development in Cementitious Materials Exposed to Magnesium Chloride Deicing Salt, Accepted for Publication in the Journal of Construction and Building Materials, Elsevier (In Press).

Farnam, Y., Dick, S., Wiese, A., Davis, J., Bentz, D. P. and Weiss, W. J., (Submitted) "Influence of Calcium Chloride Deicing Salt on Phase Changes and Damage Development in Cementitous Materials," Cement & Concrete Composites

Farnam, Y. Esmaeeli, H.S. Bentz, D. Zavattieri, P. and Weiss J. (2015) "Experimental and Numerical Investigation on the Effect of Cooling/Heating Rate on the Freeze-Thaw Behavior of Mortar Containing Deicing Salt Solution," International Conference on the Regeneration and Conservation of Concrete Structures (RCCS), Nagasaki, Japan, June 2015, pp. 1-12

Golias, M., Castro, J., Peled, A., Nantung, T., Tao, B., and Weiss, J., (2012) "Can Soy Methyl Ester (SME) Improve Concrete Pavement Joint Durability," Transportation Research Record, Vol. 10 p. 60-68

Jones, W., Y. Farnam, P. Imbrock, J. Spiro, C. Villani, M. Golias, J. Olek, and W. J. Weiss. An Overview of Joint Deterioration in Concrete Pavement: Mechanisms, Solution Properties, and Sealers. Purdue University, West Lafayette, Indiana, 2013. doi: 10.5703/1288284315339

Li, W., Pour-Ghaz, M., Castro, J., & Weiss, J. (2012). Water Absorption and Critical Degree of Saturation Relating to Freeze-Thaw Damage in Concrete Pavement Joints. Journal of Materials in Civil Engineering, (March), 299–307. doi:10.1061/(ASCE)MT.1943-5533.0000383.

Lucero, C., Bentz, D. P., Hussey. D., Jacobsen, D. and Weiss, W. J. (in press) "Using Neutron Radiography to Quantify Water Transport and the Degree of Saturation in Entrained Air Cement Based Mortar," Physics procedia

Monical, J., Villani, C., Farnam, Y., Unal, E., and Weiss, W. J., (in preparation) "Using Low Temperature Differential Scanning Calorimetery to Quantify Calcium Oxychloride Formation for Different Cementitious Materials in the Presence of $CaCl_2$," ASTM Advances in Civil Engineering Materials

Raoufi, K., Radlinska, A., Nantung, T., and Weiss, W. J., (2008) "Practical Considerations To Determine The Time And Depth Of Saw-Cuts In Concrete Pavements," Transportation Research Record

Spragg, R., Castro, J., Li, W., Pour-Ghaz, M., Huang, P., and Weiss, W. J., (2011) "Wetting and Drying of Concrete in the Presence of Deicing Salt Solutions", Cement and Concrete Composites, Volume 33, Issue 5, May, Pages 535-542

Sutter, L., Peterson, K., Julio-Betancourt, G., Hooton, D., Van Dam, T., & Smith, K. (2008). The deleterious chemical effects of concentrated deicing solutions on Portland cement concrete. Pierre, South Dakota

Todak, H., Lucero, C., and Weiss, W. J., (2015) "Why is the Air There? Thinking about Freeze-Thaw in Terms of Saturation," Concrete In Focus

Villani, C., Farnam, Y., Washington, T., Jain, J., & Weiss, W. J. (2015). Performance of Conventional Portland Cement and Calcium Silicate Based Carbonated Cementitious Systems During Freezing and Thawing in the presence of Calcium Chloride Deicing Salts. Transportation Research Record

Yang, Z., Weiss, J., Olek, J., & Lafayette, W. (2007). Water absorption in partially saturated fractured concrete. In RILEM workshop: transport mechanism in cracked concrete (pp. 1–8). Ghent

Yang, Z., Weiss, W. J., and Olek, J., (2006) "Water Transport in Concrete Damaged by Tensile Loading and Freeze-Thaw Cycling," ASCE Journal of Civil Engineering Materials, Vol. 18, No. 3, pp. 424-434

Prediction of the Time-Variant Behaviour of Concrete Sewer Collection Pipes Undergoing Deterioration Due to Biogenic Sulfuric Acid

L. Řoutil[1]; M. Chromá[1]; B.Teplý[1]; and D. Novák[1]

[1]Faculty of Civil Engineering, Brno University of Technology, Veveří 95, 60200 Brno, Czech Republic. E-mail: routil.l@fce.vutbr.cz; chroma.m@fce.vutbr.cz; teply.b@fce.vutbr.cz; novak.d@fce.vutbr.cz

Abstract

The influence of microbiologically induced corrosion on the bearing capacity of concrete sewer pipes is modeled as a time dependant and stochastic problem. The potential of the model and software is shown in this presentation of a parametric study of a corroding pipe, the comparison of crushing strength to test results and an approach for the complex analysis of a buried pipe.

INTRODUCTION

In sewage collection systems a corrosion problem exists involving the destruction of concrete pipes or structures by sulfuric acid produced by sulfur-oxidizing bacteria from hydrogen sulfide. This type of corrosion is termed *microbiologically induced corrosion* (MIC), or more precisely biogenic sulfuric acid corrosion (Neville 2004), (Yuan et al. 2013), and its effect may be intensified in combination with mechanical loading actions (RILEM 2013). The influence of this corrosion on the service life, bearing and deformation capacity of such concrete structures is obvious. Tremendous resources are being spent worldwide on the maintenance and repair of sewer networks. The degradation problems affecting concrete sewer pipes and the modelling of such problems were previously dealt with e.g. in (Tee et al. 2011), (Yamamoto et al. 2013), (Wells & Melchers 2014) and (De Belie et al. 2004).

In the context of concrete degradation processes, time is the decisive variable and the durability issues affecting concrete structures are significant. With respect to the tremendous number of possible variants and combinations as regards materials, exposure, loading and structure type, it is not feasible to perform a comprehensive investigation using experimental techniques. Analytical modelling is a reasonable alternative which also enables the consideration of the existing scatter of different quantities involved. This is also clearly reflected in recent standardization activities where design for durability is dealt with: (ISO 13823 2008), (*fib* 2012) and (ISO 16204 2012). These documents deal with probabilistic approaches and introduce the design of structures for durability – i.e. a time-dependent limit state approach which takes service life into account. It appears that predictive models are needed to estimate how resistance (and/or loads) will change over time, and the involved uncertainties (both epistemic and eleatoric) need to be given proper consideration.

In (Tee et al., 2011) a relatively detailed stochastic analysis of corrosion-affected concrete sewer pipes is presented and the expected service life of pipes subjected to hydrogen sulfide-induced corrosion is predicted. However, structural failures are determined in a rather simplified way only. In (Yamamoto et al. 2013) the method of estimating bending strength based on endoscopic camera diagnostics and Japanese design recommendations is discussed; simplified formulae for structural analysis are employed and only a deterministic formulation is provided.

The present paper aims at presenting a complex stochastic method for the assessment of bearing capacity (in the sense of the serviceability, ultimate effects and durability) of concrete sewer pipes. The modeling approach considers the effects of the combination of biogenic sulfuric acid corrosion with mechanical loading actions and its influence on the structural performance of concrete sewer pipes. Structural changes over time due to the MIC corrosion of a circular structure are studied.

BIOGENIC SULFURIC ACID CORROSION

Large amounts of concrete and cementitious materials are used in wastewater systems and sulfate attack is one of the major threats to the durability of such infrastructure. Concrete pipes, walls and other structures can be affected by sulfate directly from wastewater (in the bottom part of pipelines) or produced by microbiological activity (on the sewer crown). Although there are various microorganisms in sewage pipes which can generate many kinds of aggressive species which may damage concrete and reduce the material's service life, the most prominent biodeterioration is caused by biogenic sulfuric acid corrosion (Neville 2004), (Yuan et al. 2013), (Belie et al. 2004). Chemical sulfate attack on concrete results in the neutralisation of the concrete surface, the cracking and scaling of concrete material accelerated by the sewage flow, and the disruption of the concrete and the significant loss of its mechanical strength (Sun et al. 2013), (Sarkar et al. 2010), (Stein 1999). From this aspect, sulfate attack in a sewage system is very dangerous, especially in areas where waste water is rich in sulfates or H_2S.

LIMIT STATES, MODELLING AND A SOFTWARE TOOL

Limit states

The *Ultimate Limit State* (ULS) and the *Serviceability Limit State* (SLS) are generally evaluated while designing/assessing a concrete structure. The general condition for the probability of failure P_f reads:

$$P_f = P(S \geq R) < P_d \tag{1}$$

where S is the action effect, R is the resistance (barrier) and P_d is the design (acceptable, target) probability value. The index of reliability is alternatively utilized instead of P_f in practice.

Generally, both S and R (and hence P_f) are time dependent and random. Durability is related to the design working life t_D (or service life) (Teplý & Vořechovská 2012). Two types of P_f assessment can be distinguished that consider the randomness of concrete degradation due to biogenic sulfuric acid corrosion:

(i) Focusing on the pipe wall only, in which case the following holds for the action effect (for a degraded concrete layer)

$$S = c\,t \tag{2}$$

where c stands for the rate of corrosion; R in condition (1) represents in this case for a value limiting the thickness of the concrete pipe wall in the sense of ULS (bearing capacity) or SLS (deflection limit or crack opening). See Section "Parametric study" for an example.

(ii) In a more complex case the action effect S is the bearing capacity of the (buried) pipe (ULS or SLS) with a degraded wall, under given conditions and load; the barrier R is a relevant limiting value.

Modeling of concrete degradation

The rate of concrete deterioration depends, among other things, upon local conditions and material characteristics. The degradation of concrete sewer pipes due to sulfuric acid attack can be assessed by the frequently cited model (Pomeroy & Parkhurst 1977) for the average deterioration rate c of concrete (mm/year):

$$c = 11.5\,k\,\Phi\,A^{-1}\psi \tag{3}$$

where ψ is the coefficient of model uncertainty (optional), k is the factor representing the proportion of acid reacting (only an estimated value and ranging from 1.0 when acid formation is slow to 0.3 when it forms rapidly), Φ is the flux of H_2S (or sulfide release [g $H_2S/(m^2$ hr)]), and A is acid-consumption capability, i.e. the alkalinity of the concrete, expressed as the proportion of equivalent calcium carbonate (g $CaCO_3$/g concrete). For granitic aggregate concretes A ranges from 0.17 to 0.24, while for calcareous aggregates it ranges from 0.9 to 1.1, the equivalent A value for mortar-lined pipes being 0.4.

The average rate of corrosion represents the total loss of pipe wall over the total surface area considered. Moreover, the crown of the pipe tends to exhibit a greater rate of corrosion then the intermediate perimeter. Also, areas of greater turbulence have higher corrosion. Eq. (3) is thus modified with flux Φ analyzed according to (Tee et al. 2011) and included in the equation used for the determination of the maximum rate of corrosion $c_{\max}$ (ASCE 2007). The resulting equation reads:

$$c_{\max} = k_{ccf}\;k_{tcf}\;4{,}025\cdot 10^{-3}\;k\;j\;A^{-1}\left[BOD\right](1{,}07)^{T-20}\left(P\big/(\pi D - P)\right)\psi \tag{4}$$

where k_{ccf} is the crown corrosion factor (typically 1.5 to 2), k_{tcf} is the turbulence corrosion factor (typically 1 to 2 for well-designed drop structures and 5 to 10 for sharp drops or other turbulent junctions), j is the pH-dependent factor for the proportion of H_2S (e.g. for pH = 7.4 it follows that j = 0.28), P is the wetted perimeter of the pipe wall (m), D is the diameter of the pipe, [BOD] is the biochemical oxygen demand concentration (mg/l) and T is the sewage temperature (°C).

Software tool

The FReET-D software package, a feasible and user-friendly combination of analytical models and simulation techniques, has been used for the purposes of the present paper. Models for carbonation, chloride ingress, reinforcement corrosion, acid attack and frost attack are available, as well as the model for sulfate attack on concrete in sewage collection systems shown in previous section. Altogether, 32 models are implemented as pre-defined dynamic-link library functions selected from the literature. Fully probabilistic safety formats are employed, serving also for the provision of quantitative information concerning a structure's safety level. The uncertainties associated with parameters involved in deterioration processes are modelled by random variables. Statistical, sensitivity and reliability analyses are provided. Several features are offered, including parametric studies and Bayesian updating. Some of the models selected from the literature and originally developed as deterministic models have been converted into a probabilistic form for the purposes of this software. For more details see www.freet.cz (Novák et al 2014).

Parametric study

An ad-hoc example of the degradation of concrete sewer pipes induced by sulfuric acid attack is described here in order to show the potential of the used model and software. The focus is placed on the influence of two kinds of parameters – the wetted perimeter of the pipe wall and the type of aggregate in the concrete. Utilizing model (4), the stochastic analysis of biogenic sulfate corrosion rate c (mm/year) is accomplished using the input data set listed in Table 1. The wetted perimeter of the pipe wall is varied (reflecting the filling of the pipe by 10 % – 80 %) for two types of concrete, which is made either from granitic aggregates (according to (ASCE 2007) the acid-consumption capability value ranges from 0.17 up to 0.24; A = 0.20 is chosen in present example) or calcareous aggregates (A = 0.9 up to 1.1; A = 1.0 is used).

The resulting corrosion rates are depicted in Figure 1 (mean ± standard deviation; the best fitted being the Gumbel max and Lognormal PDFs) demonstrating the use of the stochastic approach.

The aggregate type appeared to influence concrete degradation to the largest extent (Belie et al. 2004) – this effect is also clearly evident from the presented example. Note that in reality the pipe is usually 20 % – 40 % full, which leads in our example to a corrosion rate at the crown of about 2 mm/year (granitic aggregate) or 0.4 mm/year (calcareous aggregate). This appears rather realistic with regard to results mentioned in other sources; e.g. in (ASCE 2007) examples with a rate of 0.7 up to 4 mm/year for calcareous aggregates are given.

An example of reliability and assessment of type (i), Section 3.1 can be presented together with the service life prediction as follows. Considering a limiting value for the degraded pipe thickness of 40 mm (i.e. the barrier in Eq. (1), regarding an SLS case with the design reliability index value β = 1.5), if the reliability analysis is carried out for granitic aggregate, the corresponding service life is about 18 years. In the case of calcareous aggregate it would be more than 50 years.

Table 1. Input variables.

Variable	Unit	Mean value	COV (%)	PDF	Reference
Uncertainty factor of model	–	1	15	Lognormal (2par)	(JCSS 2014)
Crown corrosion factor – k_{ccf}	–	1.75	–	Rectangular (a = 1.5; b = 2.0)	(ASCE 2007)
Turbulence corrosion factor – k_{tcf}	–	1.5	–	Deterministic	(ASCE 2007)
Proportion of acid reacting – k	–	0.80	5	Beta (a = 0.3; b = 1.0)	(Bellie et al. 2004)
Acid-consumption capability – A	–	i) 0.20 ii) 1.00	10	TwoBounded Normal i) a = 0.17; b = 0.24 ii) a = 0.9; b = 1.1	(ASCE 2007)
Factor for the proportion of H_2S – j	–	0.28	15	Beta (a = 0; b = 1)	(Pomeroy 1976)
Biochemical oxygen demand - [BOD]	mg/l	350	15	Normal	Typical value
Sewage temperature – T	°C	22	10	Normal	Typical value
Diameter of the pipe wall – D	m	1.8	0.5	Normal	
Wetted perimeter of the pipe wall – P	m	1.158 – 3.986	–	Deterministic	(Pomeroy 1976)

MODELING OF STRUCTURAL BEARING CAPACITY

Ring failure

The stochastic structural analysis of buried concrete sewer pipes with the consideration of biogenic sulfuric acid corrosion is an involved, time dependant task. Therefore, as a first step, a stochastic study for the strength analysis of the impact of corrosion on concrete pipes has been performed, based on experimental results presented in (Karihaloo 1995 – Chapter 9, with reference to Gustafsson 1985).

The ring failure (or crushing strength f_{cr}) of a non-degraded thin-walled pipe corresponding to a single force on the top of the pipe (specifically: a linear load, Fig. 2) is studied utilizing concrete fracture theory, namely the FCM (Fictitious Crack Model), which exhibits a good match to the test summary (2366 samples altogether!). Note that tests on pipes with a wall thickness (t)/inner diameter (D_i) ratio of 1/7 were considered. Simple linear elasticity proved not to be relevant in this case. In this paper the crack band model implemented in FEM was used (Atena software ─

Červenka et al. 2007) to simulate the variation in the crushing strength f_{cr} (Eq. 5, Karihaloo 1995) of concrete pipes with different wall thickness. The ultimate experimental top load P_u in Eq. 5 is replaced in this case by the ultimate value from the nonlinear model.

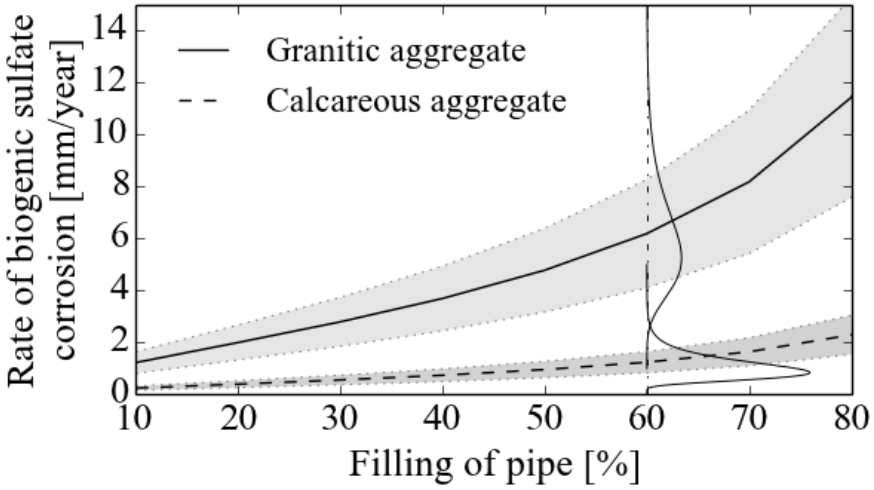

Figure 1. Rate of corrosion vs. filling of pipe for two types of aggregate.

The obtained numerical results are compared to experiments in Fig. 2. Note that the 3D Nonlinear Cementitious material model (plain strain idealization; Červenka et al. 2007) was employed – tensile strength f_t was equal to 4.52 MPa and characteristic length l_{ch} was equal to 380 mm (the same parameters were determined for experimentally investigated specimens). As l_{ch} is defined by Eq. 6, a combination of fracture energy G_f = 210 N/m and modulus of elasticity E = 37 GPa was used. These parameters are in close agreement with those of concrete recently developed and investigated for other applications (Řoutil et al. 2014). For crushing strength the following holds

$$f_{cr} = \frac{6}{\pi}\frac{\left(P_u / S\right)}{D_0}\frac{\left(1 + D_i / D_0\right)}{\left(1 - D_i / D_0\right)^2}, \tag{5}$$

where D_i (D_0) is the inner (outer) diameter of the pipe and P_u/S is the intensity of the ultimate linear load. Note that t/D_i = 1/7. The characteristic length is defined as

$$l_{ch} = \frac{EG_f}{f_t^2}, \tag{6}$$

The final model was consequently used to study the influence of the rate of concrete deterioration on the variation in the crushing strength f_{cr} of concrete pipes with wall thickness – the results of the study can be seen in Fig. 2. The considered reference rate of concrete deterioration was 0.5 mm/year at the crown of the pipe (see scheme in Fig. 2). The study was carried out for 30, 60 and 90 years.

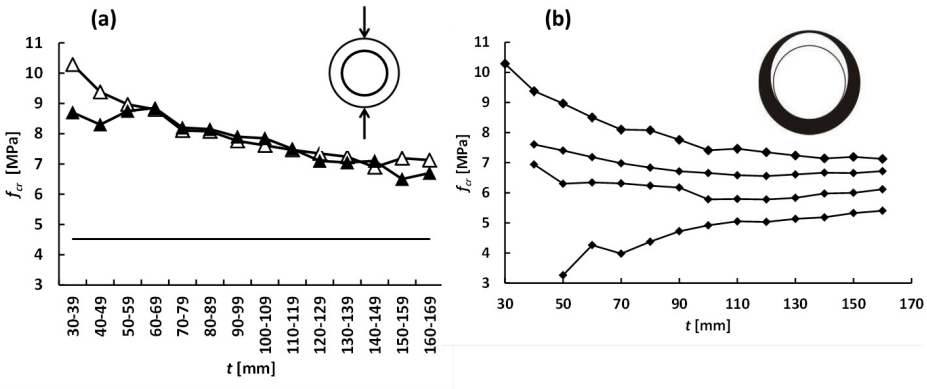

Figure 2. (a) Variation in the crushing strength f_{cr} of concrete pipes with wall thickness – experiments (Karihaloo 1995; black symbols), simulations (white symbols) and the value of $f_{cr} = f_t$ (linear elasticity prediction; horizontal line), (b) Simulated influence of the rate of concrete deterioration on the variation in the crushing strength of concrete pipes with wall thickness (from above ― 0, 30, 60 and 90 years of degradation).

Moreover, the study was also realised at the stochastic level using the approach published in (e.g. Novák et al. 2007, Strauss et al. 2008). The rate of concrete deterioration as well as the following dominant concrete parameters of the material model were considered to be random variables: Modulus of elasticity, compressive and tensile strength, and fracture energy. All of the input basic random variables involved, and the particular set of their statistical parameters (mean value, coefficient of variation (*COV*), and probability distribution function (*PDF*)) are summarized in Tab. 2. Statistical correlation among the input basic random variables was also considered (employing simulated annealing – Novák et al. 2007); see Tab. 3. Correlation coefficients were set up based on previous experiments (e.g. Novák et al. 2007, Řoutil et al. 2014). The Latin Hypercube Sampling method (Novák et al. 2014) was used and 16 simulations of crushing strength f_{cr} were performed for selected concrete pipe profiles and degradation times (0, 30, 60 and 90 years). The obtained results – values of crushing strength f_{cr} and their statistical parameters – are shown in Fig. 3 and Tab. 3, and can be used as inputs in the subsequent reliability and durability analysis of concrete pipes.

The results summarized in Tab. 3 show an interesting trend – the value of f_{cr} for the pipe with DN 400 (wall thickness 60 mm) after 30 years of degradation is nearly the same as for the non-degraded pipe DN 600, etc. – see the bold numbers in the diagonals.

Table 2. Basic random variables of concrete deterioration and dominant material parameters.

Variable [Unit]	Mean value	*COV*	*PDF*
Modulus of elasticity E [GPa]	37	0.1	Log-normal
Compressive strength f_c [MPa]	69.5	0.1	Log-normal
Tensile strength f_t [MPa]	4.52	0.12	Log-normal
Fracture energy G_f [J/m^2]	210	0.2	Normal
Deterioration rate of concrete [mm/years]	0.5	0.33	Log-normal

Table 3. Correlation coefficients between dominant material parameters.

Variable	E	f_c	f_t	G_f
E	1	0.9	0.7	0.37
f_c		1	0.9	0.6
f_t			1	0.9
G_f	Sym.			1

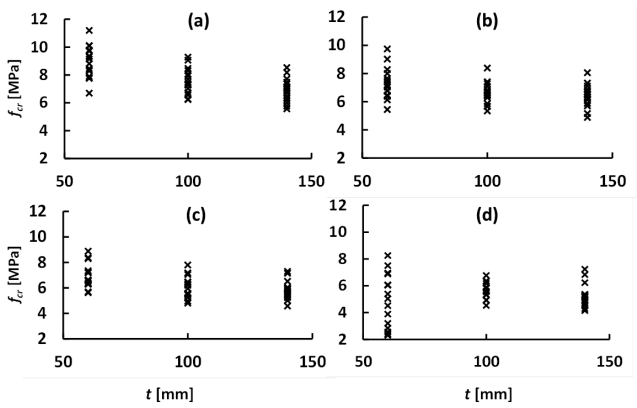

Figure 3. Crushing strengths f_{cr} for selected wall thicknesses (60, 100 and 140 mm) and deterioration times – 0 (a), 30 (b), 60 (c) and 90 (d) years - obtained using a stochastic model.

Table 4. Basic statistical parameters of crushing strengths for selected wall thickness and times of deterioration.

		t = 0 years	t = 30 years	t = 60 years	t = 90 years
DN400	mean [*MPa*]	**8.91**	**7.26**	**6.89**	4.99
	COV	12.8	15.2	13.6	39.0
	PDF	Weibull max (3 par)	Gumbel Max. EV I	Gumbel Max. EV I	Weibull min (3 par)
DN700	Mean [*MPa*]	**7.55**	**6.56**	**6.06**	**5.71**
	COV	12.2	11.5	13.8	10.7
	PDF	Weibull max (3 par)	Normal	Rayleigh	Weibull max (3 par)
DN1000	Mean [*MPa*]	**6.90**	**6.42**	**5.78**	**5.25**
	COV	12.1	12.2	12.4	16.3
	PDF	Normal	Weibull min (3 par)	Gumbel Max. EV I	Gumbel Max. EV I

Buried pipe analysis

The strength analysis of buried concrete sewer pipe behaviour with consideration given to material nonlinearity, contact with different soil layers, the MIC degradation of the concrete, and the involved uncertainties, as well as the assessment of reliability and the prediction of service life, are all complex tasks. They can be solved employing materially nonlinear FE analysis combined with a suitable numerical simulation technique in a similar manner to that described in the previous section. Note that different limit states and relevant reliability index values can be assessed in this way.

Creep effect

The behaviour of the buried sewer pipe is time-dependant due to the MIC degradation effect. Evidently the creep of concrete is an additional time-variant effect which can play a considerable role. It can be incorporated into the above described approach in a simplified way: at each time step a creep strain value (associated with actual compressive stress) is added to the strain value due to mechanical loading in

each element. The statistical parameters of the creep strain can be gained using a special FreET module which employs e.g. the B3 model.

Note that the approach described briefly in the last two sub-sections is part of work which is currently ongoing; some results will be reported at the conference.

CONCLUSION

The microbiologically induced corrosion of reinforced concrete sewers and manholes is a problem with significant global repair costs. When corrosion is sufficiently advanced it can lead to diminished service life or to structural failures. Therefore, for the life cycle management of sewage facilities proper and effective tools are needed; they may serve in this respect in several ways, e.g.:

(i) Utilizing suitable models, the assessment of concrete deterioration rate affected by different material or operational parameters can be studied, e.g. in the form of parametric studies, service life prognosis, etc.

(ii) Using a model and considering a given time period, material and operational parameters, the thickness of a buried concrete pipe weakened due to corrosion is specified. Based on such a degraded structural configuration, the reliability of the bearing capacity of the pipe can be assessed (durability, SLS or ULS).

(iii) In a reciprocal manner with regard to variant (ii), first the bearing capacity of the buried pipe is determined, i.e. the necessary (minimal) cross sectional and material characteristics. Then, utilizing a relevant degradation model, a service life prognosis can be performed.

This can help managers make more realistic decisions concerning the safe and cost-effective operation of pipes during their service life.

Acknowledgement

This work has been supported by projects No. 14-10930S and 13-22899P awarded by the Czech Science Foundation and by project CZ.1.07/2.3.00/30.0005 – "Support for the creation of excellent interdisciplinary research teams at Brno University of Technology".

REFERENCES

ASCE (American Society of Civil Engineers). (2007) *Manuals and Reports of Engineering Practice*, No. 60, 2007, Gravity Sewers, NY, USA.

Červenka, V., Jendele, L. and Červenka, J. (2007). "ATENA program documentation – Part 1: theory." Prague, Czech Republic: Cervenka Consulting.

De Belie De, N. et al. (2004). "Experimental research and prediction of the effect of chemical and biogenic sulphuric acid on different types of commercially produced concrete sewer pipes." *Cem. Concr. Res*., 34, 2223–2236.

Fernardes, I. et al. (2012). "Identification of acid attack on concrete of a sewage system." *Mat. Struct*., 45(3), 337–350.

fib Model Code 2010 (2012). fib Bulletins No. 65 and 66. International Federation for Structural Concrete, Lausanne, Switzerland.

ISO 13823 (2008). *General Principles on the Design of Structures for Durability*.

ISO 16204 (2012). *Durability – Service life design of concrete structures*.
JCCS (Joint Committee on Structural Safety) (2014). Accessible from <http://www.jcss.byg.dtu.dk/Publications/Probabilistic_Model_Code.aspx >.
Karihaloo, B. L. (1995). *Fracture Mechanics and Structural Concrete*. Longman.
Neville, A. (2004). "The confused world of sulfate attack on concrete." *Cem. Concr. Res.*, 24, 1275–1296.
Novák, D., Vořechovský, M., Lehký, D., Bergmeister, K., Pukl, R., and Červenka V. (2007). "Stochastic nonlinear analysis of concrete structures – Part I." Proc. of *ICASP10*, Tokyo, ISBN 978-0-415-45211-3.
Novák, D., Vořechovský, M. and Teplý, B. (2014). "FReET – Software for the statistical and reliability analysis of engineering problems and FReET-D: Degradation Module." *Advances in Engineering Software,* 72, 179–192.
Pomeroy, R. D. and Boon, A. G. (1976). *The problem of hydrogen sulphide in sewers*. Clay Pipe Development Association, Ltd.
Pomeroy, R. D. and Parkhurst, J. D. (1977). "The forecasting of sulfide build-up rates in sewers." *Progr. Water Technol*., 9(3), 621–628.
RILEM Report rep043 (2013). *Publications on Durability of Reinforced Concrete Structures under Combined Mechanical Loads and Environmental Actions: An Annotated Bibliography.* Edited by Yao Yan, Wang Ling, Wittmann Folker H.
Řoutil, L., Lehký, D., Šimonová, H., Kucharczyková, B., Keršner, Z., Novák, T., Zimmermann, T., Strauss, A. and Krug B. (2014). "Experimental-computational determination of mechanical fracture parameters of concrete for probabilistic life-cycle assessment." Proc. of *IALCCE 2014*, Tokyo, 801−807.
Sakar, S., Mahadevan, S., Meeussen, J.C.L., Sloot, H. van der and Kosson, D.S. (2010). "Numerical simulation of cementitious materials degradation under external sulfate attack." *Cem. Concr. Com.,* 32, 241–252.
Stein, D. (1999). *Instandhaltung von Kanalisationen*. 3rd edition, Berlin: Ernst, p. 141. ISBN 3-433-01315-2. (in German)
Strauss A, Bergmeister K, Hoffmann S, Pukl R and Novak D. (2008). "Advanced life-cycle analysis of existing concrete bridges." *J. Mater. Civil Eng.* (ASCE) 20(1), 9–19.
Sun, Ch., Chen, J., Zhu, J., Zhang, M. and Ye, J.(2013). "A new diffusion model of sulfate ions in concrete." *Constr. Build. Mater.*, 39, 39–45.
Tee, K. F., Li, CH. Q. and Mahmoodian, M. (2011). "Prediction of time-variant probability of failure for concrete sewer pipes." *Proc. of XII DBMC*, Porto, Vol. I, 447–454.
Teplý, B. and Vořechovská, D. (2012). "Reinforcement corrosion: Limit states, reliability and modelling." *J. of Advanced Concrete Technology,* 10, 353–362.
Wells, T. and Melchers, R. E. (2014). "An observation-based model for corrosion of concrete sewers under aggressive conditions." *Cem. Concr. Res.*, 61-62. 1–10.
Yamamoto, D., Hamada, H., Sagawa, Y and Md Noor, N. (2013). "Diagnostic of load bearing capacity of sewage pipes deteriorated by sulphate attack." *Proc. of CONSEC13*, 1280–1288.
Yuan, H., Dangla, P., Chatellieur, P. and Chaussadent, T. (2013). "Degradation modelling of concrete submitted to sulphuric acid attack." *Cem. Concr. Res.*, 53, 267–277.

Coupled Effects of Static Creep, Cyclic Creep, and Damage on the Long-Term Performance of Prestressed Concrete Bridges: A Case Study Based on Rate-Type Formulation

Qiang Yu[1] and Teng Tong[2]

[1]Department of Civil and Environmental Engineering, University of Pittsburgh, PA 15261. E-mail: qiy15@pitt.edu

[2]Department of Civil and Environmental Engineering, University of Pittsburgh, PA 15261. E-mail: tet16@pitt.edu

Abstract

One of the challenges in bridge engineering is to predict the long-term deflection and damage accumulation in large-span prestressed concrete girders during their lifespan. For prestressed concrete bridges, a salient by-product of time-dependent deformation resulting primarily from concrete creep is unexpected stress redistribution, which triggers damage and cracking in the critical structural components. To deepen the understanding of the coupled effects of deflection and damage on bridge performance, a case study is carried out in this investigation, in which a large-span prestressed concrete bridge is modeled in ABAQUS based on its blueprints available. To capture the concrete behavior during service, a constitutive law formulated based on a damage model is employed to approximate the nonlinear softening after concrete cracking. This formulation is further integrated with a rheological model resting on Kelvin units for concrete creep. Using a rate-type algorithm, the long-term behavior of the bridge is probed.

INTRODUCTION

With the increasing demands in construction sustainability, a longer lifespan, i.e., over 100 years, is now generally expected for critical prestressed concrete girders. A serious challenge to this goal is the low predictive capacity of the current design models for bridge long-term performance, a complex outcome of time-dependent interactions between concrete creep, shrinkage, steel relaxation, and deterioration processes (Strauss *et al*. 2013, Wendner *et al*. 2010), coupled with other physical and mechanical influences.

In a recent survey (Bažant *et al.* 2012), deflections exceeding design expectation are found prevalent in large-span prestressed concrete girders. The excessive deflection triggers unexpected cracking in concrete members, and thus significantly compromises the safety and serviceability of prestressed concrete bridges. A primary source of the inaccuracy is identified to be the inadequacy existing in the current concrete creep models used in bridge design (Bažant *et al.* 2013, Wendner *et al.* 2015). In addition, lack of coupling between deflection and other important physical and chemical processes further exacerbates the prediction accuracy. It is found the popular, yet primitive formulation based on integral form used in the current creep structural analyses, which is incapable of taking into account time-independent phenomena (e.g., concrete cracking), leads to substantial underestimate of long-term deflection (Yu *et al.* 2012).

To overcome these obstacles in creep structural analysis and bridge design, rate-type formulation residing on improved creep models was recently developed and implemented in long-term deflection analysis (Bažant *et al.* 2013, Wendner *et al.* 2015, Yu *et al.* 2012). In the rate-type formulation, concrete creep is approximated by a rheological model and continuous spectrum method is employed to uniquely identify the viscoelastic parameters based on the given creep compliance function.

A prominent advantage of rate-type formulation is that it allows the creep structural analysis to be coupled with other time-independent phenomena, especially concrete cracking trigged by stress redistribution. Unfortunately, the research effort to explore the coupled effects of time-dependent deformation and concrete damage is limited in bridge structural analysis, especially for long-term performance prediction. The objective of this study is to build a unified rate-type formulation to capture the coupled effects of concrete creep and cracking on bridge long-term performance. A case study based on a large-span bridge will be carried out and the results obtained from FEM simulation will be compared with the in-situ measurements.

GENERAL FRAMEWORK

Under service load, concrete creep can be deemed as an ageing linear viscoelastic phenomenon, which can be accurately approximated by a rheological model (Bažant and Prasannan 1989 a, b, Yu *et al.* 2012). Although Maxwell units are equivalently effective, Kelvin units are popularly used in creep structural analysis due to their direct correlation with the parameters observed in creep tests. As shown in Fig. 1, Kelvin units characterized by moduli D_i and retardation time τ_i are coupled in a series connection.

Unexpected deformation causes stress redistribution, which triggers damage and cracking in concrete. To capture the nonlinear softening of concrete after cracking, the rheological model is further enriched by constitutive laws hinging on isotropic damage. When stress exceeds the threshold (e.g., concrete tensile strength), damage happens and it influences the behaviour of Kelvin units. Correspondingly, a damage factor will be assigned to D_i in an isotropic manner.

In addition to static creep which is characterized by strain growth under sustained stress, cyclic creep due to cyclic loading contributes to the time-dependent deformation. For bridges under moderate traffic loads or bridges of a short lifespan (e.g., less than 30 years), cyclic creep does not play an important role (Bažant and Hubler, 2014). However, for large-span critical bridges of an extended lifespan (over 100 years), the contribution of cyclic creep cannot be ignored.

As shown in Fig. 1, the total strain of concrete ε_{ij} can be conceptually expressed as

$$\varepsilon_{ij} = \underbrace{(\varepsilon_{ij}^{e})}_{\varepsilon_{ij}^{i}} + \underbrace{(\varepsilon_{ij}'' + \varepsilon_{ij}^{cc} + \varepsilon_{ij}^{sh})}_{\varepsilon_{ij}^{t}}$$

where ε_{ij}^{i} is the instantaneous strain after loading, and ε_{ij}^{t} is its time-dependent counterpart consisting of inelastic strain induced by concrete static creep $\varepsilon_{ij}^{''}$, cyclic creep ε_{ij}^{cc} and shrinkage ε_{ij}^{sh}. In this study, autogeneous shrinkage is neglected and only the drying shrinkage resulting from moisture loss is taken into account.

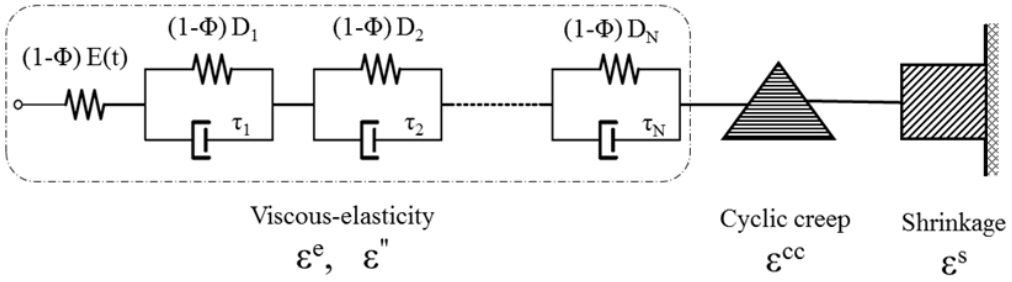

Figure 1. One dimensional illustration of the proposed unified concrete model

RATE-TYPE FORMULATION

Within the service stress level, concrete static creep is assumed to follow the constitutive law of ageing linear viscoelasticity (Jirásek and Bažant 2002, Bažant *et al*. 2012 a, b). Due to concrete ageing, the compliance function $J(t, t')$, serving as kernel in Volterra integral form, is not of a convolution type. Therefore, it may be approximated by a rheological model in the rate-type formulation so as to capture the strain growth under a general stress history $\sigma(t)$.

If Kelvin units are employed, the compliance function can be approximated as (Hardy and Riesz 2013, Schapery 1962, Jirásek and Bažant 2002):

$$J(t,t') \approx \frac{1}{E(t)} + \sum_{i=1}^{M} \frac{1}{D_i(t')}[1-\exp(-\frac{t-t'}{\tau_i})]$$

where t is current time and t' is the loading age. To avoid thermodynamically inadmissible D_i obtained through data fitting, continuous spectrum method is adopted

to uniquely and efficiently identify the compliance spectrum A_i. Utilizing Laplace transformation inversion supplemented by Widder's approximate inversion formula (Widder 1971), the analytical solution of A_i for a given compliance function can be attained; see Yu *et al.* 2012.

Damage in concrete can be approximated by a number of forms based on different formulation. Here a damage model resting on an isotropic damage variable Φ will be employed (Kachonov, 1958). Using the strain equivalence hypothesis and generalized Hook's law, the effective (undamaged) stress tensor $\bar{\sigma}_{ij}$ can be expressed as:

$$\bar{\sigma}_{ij} = \bar{E}_{ijkl}(t)\bar{\varepsilon}^{e}_{kl} = \bar{E}_{ijkl}(t)\varepsilon^{e}_{kl}$$

where $\bar{E}_{ijkl}(t)$ is the fourth-order effective (undamaged) isotropic elasticity tensor, expressed as a function of concrete age t. After concrete cracking, concrete stress-strain relation can be described by a simplified softening law as:

$$\sigma_{ij} = (1-\Phi)\bar{\sigma}_{ij} = (1-\Phi)\bar{E}_{ijkl}(t)\varepsilon^{e}_{ij}$$

here the evolution of damage variable Φ follows an isotropic damage rule hinging on the critical principle strain of concrete. In the formulation, this damage variable will be assigned to all Kelvin units based on the assumption that same degree of damage happens in each Kelvin unit.

For the cyclic creep, a power law-type equation similar to Paris law will be used. The development of cyclic creep after N cycles is approximated as (Bažant and Hubler, 2014):

$$\varepsilon^{cc} = C_1\bar{\sigma}(\frac{\Delta\sigma}{f'_c})^m N$$

Here f'_c is the compressive strength of concrete, $\Delta\sigma$ is the amplitude of stress variation and $\bar{\sigma}$ is the average stress in concrete. Note that ε^{cc} depends on both $\bar{\sigma}$ and N linearly, which agrees with the test measurements available in literature and is convenient for structural analysis. In this study, the exponent value m is set as 4, and C_1 is about 46×10^{-6}.

For a rate-type formulation, the 3D quasi-elastic stress-strain incremental relation at any time step can be written as:

$$\Delta\bar{\sigma} = \bar{E}''\Delta\varepsilon^{e}$$

where $\bar{E}''$ is the effective incremental modulus considering viscoelasticity and concrete cracking. The increment of the effective elastic strain $\Delta\varepsilon^{e}$ is:

$$\Delta\varepsilon^{e}_{ij} = \Delta\varepsilon_{ij} - \Delta\varepsilon^{cc}_{ij} - \Delta\varepsilon^{sh}_{ij} - \Delta\varepsilon''_{ij}$$

It can be seen that in the rate-type formulation, the creep calculation is coupled with other time-dependent processes in the structural analysis. The general algorithm to be implemented in FEM can be illustrated in Fig.2.

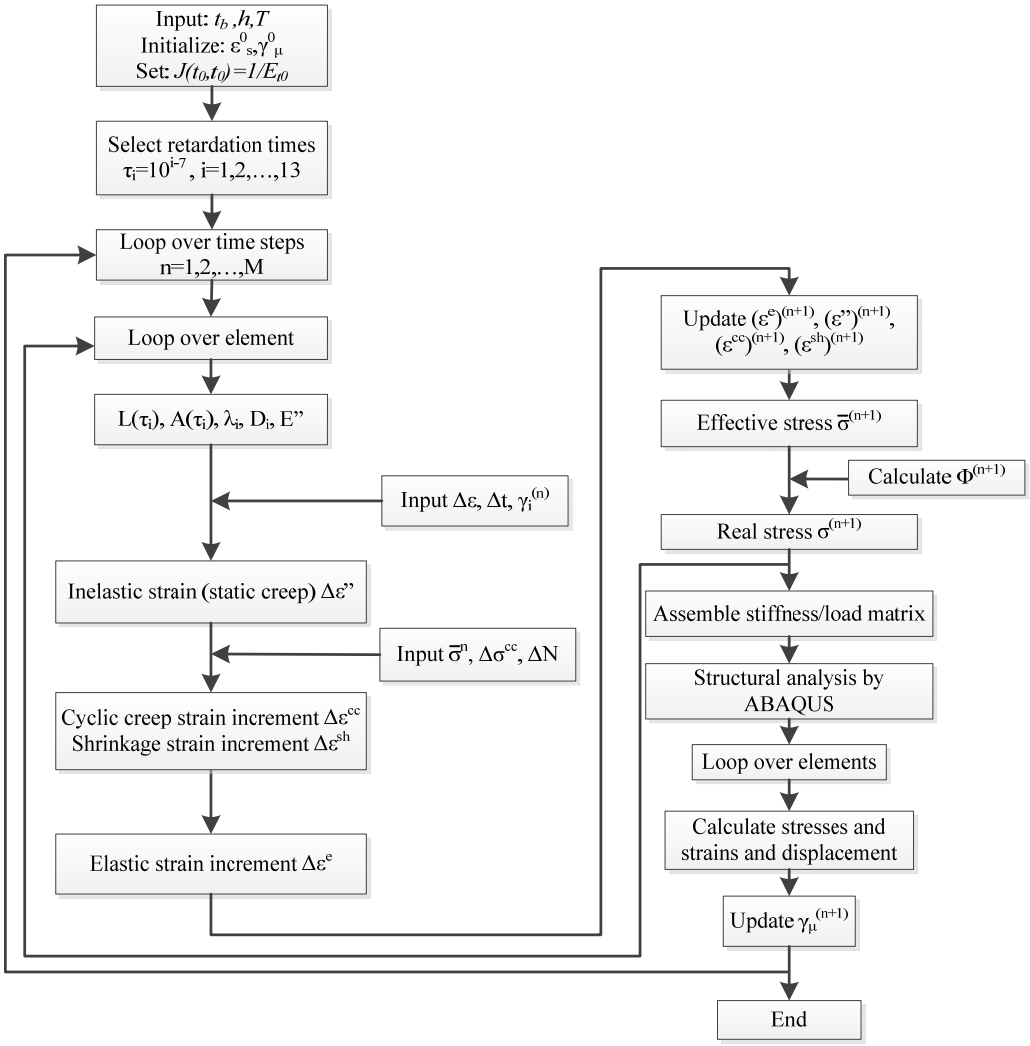

Figure 2. Overall algorithm for rate-type formulation.

CASE STUDY BASED ON A LARGE-SPAN BRIDGE

To explore the coupled effects of time-dependent deformation and concrete cracking, a case study based on a large-span prestressed concrete bridge is carried out. Utilizing the information available in the blueprints, a 3D model of the bridge is built in ABAQUS; see Fig. 3. As a segmentally erected bridge, the bridge consists of 138 cast-in-situ segments and its main span is over 270 m. In order to focus on the post-construction behavior, the camber generated in segmental construction, which is varied for different creep models, will not be considered in the deflection comparison.

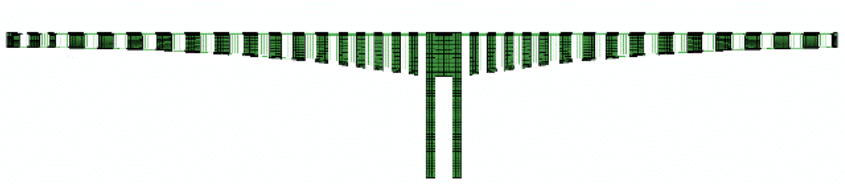

Figure 3. 3D finite element model of a large-span bridge (half-model)

In the modelling, ACI (ACI, 2008), *fib* MC2010 (fib, 2012) and B4 (Wendner *et al.* 2015) models are employed for concrete creep and shrinkage. Among these models, ACI model is purely empirical and the only intrinsic parameter employed to represent concrete characteristics in its compliance function is concrete strength $f_c^{'}$. The fib MC2010 is similar to its old version, namely CEB-FIP MC90 model, except for introducing a split into basic and drying creep with a logarithmic time function to capture the long-term behaviour of creep observed in long-term creep tests (Brooks 1984, Brooks 2004). B4 model, based on the solidification theory (Bažant and Prasannan 1989 a, b, Bažant and Baweja 2000), split concrete creep into basic creep and drying creep, the former being unbounded and consisting of short-term strain, viscous strain and a flow term, while the latter being bounded and related to moisture loss. Besides $f_c^{'}$, multiple intrinsic parameters are employed in B4 model to represent concrete composition characterized by water-cement ratio (w/c), aggregate-cement ratio (a/c), and cement content (c).

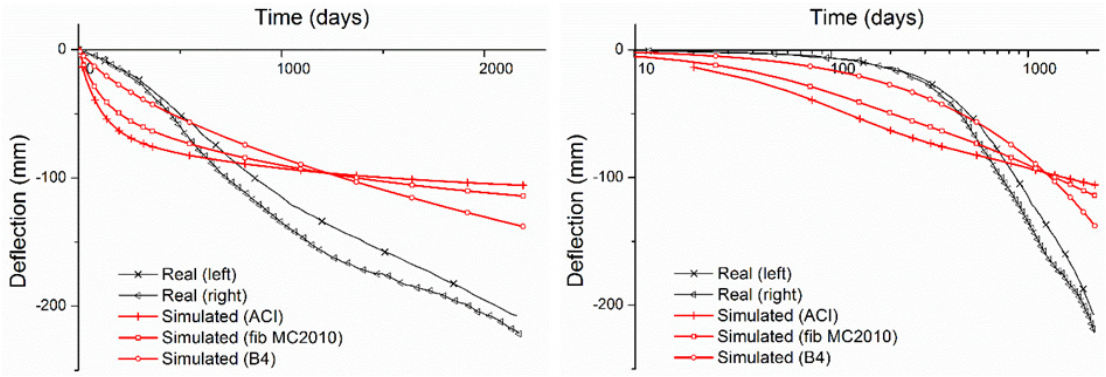

(a) Linear time scale (b) Logarithmic time scale

Figure 4. Comparison of deflection at midspan 7 years after construction.

As for prestressing steel, a bilinear law featured with Young's modulus E and yield strength f_y is used in the simulations. Its relaxation is modelled based on the CEB relaxation formulas (CEB 1990). To simplify the calculation of cyclic creep, a normalized cyclic traffic load based on annual traffic report is used in the modelling.

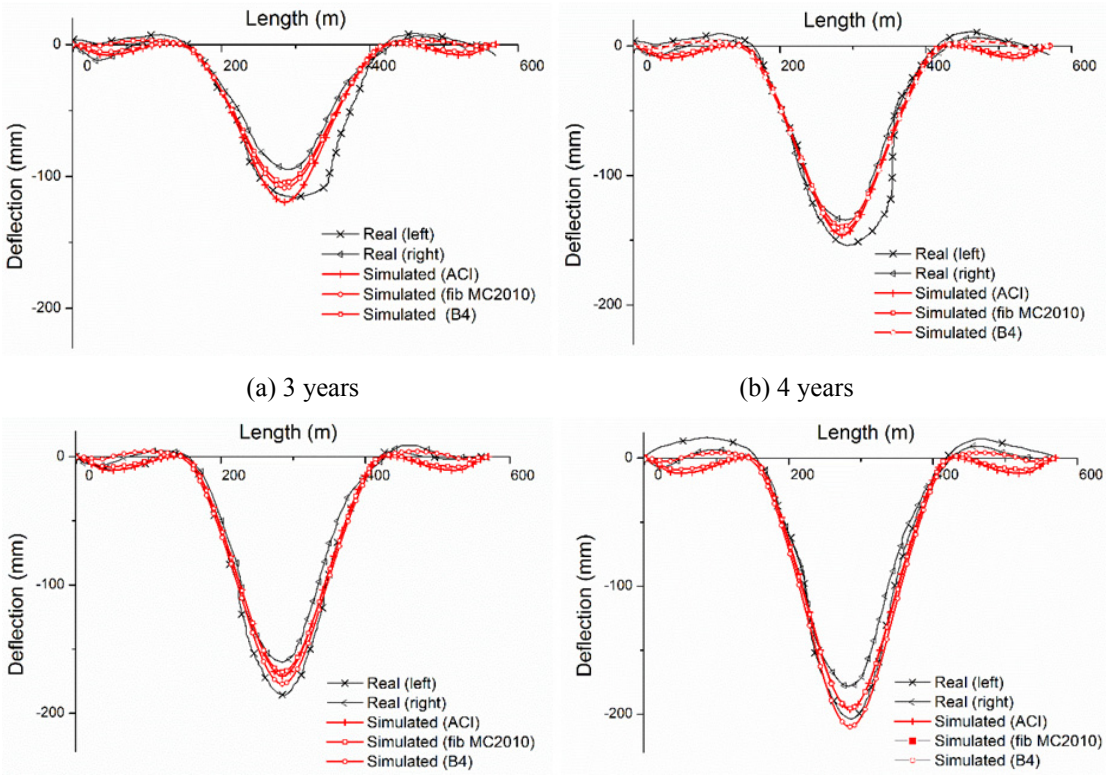

(a) 3 years (b) 4 years

(c) 5 years (d) 6 years

Figure 5. Comparison of the deflection profile.

Fig 4 shows the comparison between the in-situ measurements and predictions from ACI, fib MC 2010 and B4 models without considering damage and cyclic creep. After 7 years, the predicted deflection at midspan is about 100, 110 and 140 mm for the ACI, fib MC 2010 and B4 models, respectively. While, the measured deflection is about 210 mm. The substantial deviation indicates that the neglect of damage and cyclic creep of the concrete will lead to significant underestimate of long-term deflection, especially for bridges carrying heavy traffic load.

If concrete damage and cyclic creep are considered, remarkable improvement can be achieved in deflection prediction. In Fig. 5, the simulated deflection profiles of the bridge are plotted. From Figs 5(a) to (d), comparison is made with the in-situ measurements obtained after 3-, 4-, 5- and 6-year service respectively. Clearly, the prediction based on all models agrees well with the measured deflection history.

CONCLUSIONS

In this study, a unified concrete model coupling the time-dependent behaviour of concrete (e.g. quasi-static and cyclic creep, shrinkage, etc.) with concrete damage is developed and its effectiveness is demonstrated in a case study. Based on the FEM simulation, the following conclusions can be drawn:

(1) For the prestressed concrete bridges carrying heavy traffic flow cyclic creep of concrete must be taken into account in bridge design. The neglect of cyclic creep may lead to unrealistic long-term deflection prediction.
(2) Due to the time-dependent deformation, cracking will happen in concrete as a consequence of stress redistribution. The interaction between concrete damage and creep will augment the time-dependent deflection of prestressed bridges.
(3) To capture the coupled effect of damage and time-dependent deformation, rate-type formulation is needed. In addition to cyclic creep and concrete cracking, it can be further extended to incorporate other physical and chemical processes, e.g., corrosion.

REFERENCES

ACI Committee (2008). *Building Code Requirements for Structural Concrete (ACI 318-08) and Commentary*. Farmington Hills: American Concrete Institute.

Bažant, Z. P., and Prasannan, S. (1989 a). "Solidification theory for concrete creep II: verification and application." *Journal of Engineering mechanics*, 115(8), 1704-1725.

Bažant, Z. P., and Prasannan, S. (1989 b). "Solidification theory for concrete creep I: formulation." *Journal of engineering mechanics*, 115(8), 1691-1703.

Bažant, Z. P., and Baweja, S. (2000). "Creep and shrinkage prediction model for analysis and design of concrete structures: Model B3." *ACI SPECIAL PUBLICATIONS*, 194, 1-84.

Bažant, Z. P., Hubler, M. H., and Jirásek, M. (2012). "Improved estimation of long-term relaxation function from compliance function of aging concrete." *ASCE J. of Engrg. Mech*, 139 (2), 146–152.

Bažant, Z. P., Yu, Q., & Li, G. H. (2012 a). "Excessive long-time deflections of prestressed box girders. I: Record-span Bridge in Palau and other paradigms." *Journal of Structural Engineering*, 138(6), 676-686.

Bažant, Z. K. P., Yu, Q., & Li, G. H. (2012 b). "Excessive long-time deflections of prestressed box girders. II: Numerical analysis and lessons learned." *Journal of Structural Engineering*, 138(6), 687-696.

Bažant, Z. P., Hubler, M. H., and Jirásek, M. (2013). "Improved Estimation of Long-Term Relaxation Function from Compliance Function of Aging Concrete." *Journal of Engineering Mechanics*, 139(2), 146-152.

Bažant, Z. P., & Hubler, M. H. (2014). "Theory of cyclic creep of concrete based on Paris law for fatigue growth of subcritical microcracks." *Journal of the Mechanics and Physics of Solids*, 63, 187-200.

Brooks, J. J. (1984). "Accuracy of estimating long-term strains in concrete." *Magazine of Concrete Research*, 36(128), 131-145.

Brooks, J. J. (2005). "30-year creep and shrinkage of concrete." *Magazine of concrete research*, 57(9), 545-556.

Fédération Internationale du Béton (2012). *International Federation for Structural Concrete Special Activity Group New Model Code*. Lausanne: International Federation for Structural Concrete.

Hardy, G. H., and Riesz, M. (2013). *The general theory of Dirichlet's series.* Courier Corporation.

Jirásek, M., and Bažant, Z. P. (2002). *Inelastic analysis of structures*. NewYork: John Wiley & Sons.

Kachonov, L.M. (1958). "On the creep fracture time." *Izvestiya Akademii Nauk USSR Otd. Tech*. 8, 26–31 (in Russian).

Schapery, R. A. (1962). "Approximate methods of transform inversion for viscoelastic stress analysis." *In Proceedings Fourth US National Congress of Applied Mechanics*, 2, 1075-1085.

Strauss, A., Wendner, R., Bergmeister, K., and Costa, C. (2013). "Numerically and Experimentally Based Reliability Assessment of a Concrete Bridge Subjected to Chloride Induced Deterioration." *Journal of Infrastructure Systems*, 19(2), 166-175.

Wendner, R., Strauss, A., Guggenberger, T., Bergmeister, K., and Teply, B. (2010). "Approach for the Assessment of Concrete Structures Subjected to Chloride Induced Deterioration." *BETON- STAHLBETONBAU*, 105(12), 778-786.

Wendner, R., Hubler, M.H., and Bažant, Z.P. (2015). "Statistical justification of model B4 for multi-decade concrete creep using laboratory and bridge databases and comparisons to other models." *Materials and Structures*, 1-19.

Widder, D. V. (1971). *An introduction to transform theory (Vol. 42)*. Academic Press.

Yu, Q., Bažant, Z. P., and Wendner, R. (2012). "Improved Algorithm for Efficient and Realistic Creep Analysis of Large Creep-Sensitive Concrete Structures." *ACI Structural Journal*, 109(5), 665-675.

Creep of Concrete and Its Instant Nonlinear Deformation in the Calculation of Structures

Rudolf Sanjarovskiy[1]; Tatyana Ter-Emmanuilyan[2]; and Maksim Manchenko[3]

[1]Department of Theoretical Mechanics, Saint-Petersburg State University of Architecture and Civil Engineering (SPSUACE), 2-nd Krasnoarmeiskaya St., 4, St. Peterburg 190005, Russia. E-mail: milasanj@gmail.com
[2]Department of Petroleum Engineering, Kazakh-British Technical University (KBTU), Tolebi St., 59, Almaty 050000, Republic of Kazakhstan. E-mail: tanya_ter@mail.ru
[3]FSUE "Krylov State Research Center", Moscow Highway, 44, St. Petersburg 196158, Russia. E-mail: salsa87@bk.ru

Abstract

This article is a continuation of the series of publications of authors to produce instant nonlinear properties of the concrete. The theory, which is a substantial development of the methods for calculating the long resistance of reinforced concrete structures, allows almost exactly the instant nonlinear properties of the concrete.

1. INTRODUCTION

Concrete is essentially nonlinear structural material. The diagram instantaneous compression $\sigma - \varepsilon_M$ (Figure 1) has a decreasing portion bounded by the limiting deformation ε_{B2}. The parameters of this nonlinear diagram normalized to Eurocode 2 in the section on the calculation of reinforced concrete structures.

In the theory of creep of concrete (linear, nonlinear), instead of a real nonlinear diagrams used fictitious linear diagram that satisfies Hooke's law (Figure 1). This diagram makes calculations in the two types of errors, corresponding to the four points of the fictitious 1-4, accompanied by a realistic point of M. For example, at a given instant deformation ε_M fictitious stress $\sigma_f = \varepsilon_M E_B$ is significantly greater than the actual stress σ for a given real stress σ fictitious elastic deformation $\varepsilon_e = \sigma / E_B$ is much less real deformation ε_M. Replacing the actual nonlinear diagram $\sigma - \varepsilon_M$ makes large errors in the calculation of total deformations during prolonged uploading designs.

This approach is justified misleading statement that "experiments instantaneous deformation of concrete, even at high levels of loading are linearly dependent on the stress".

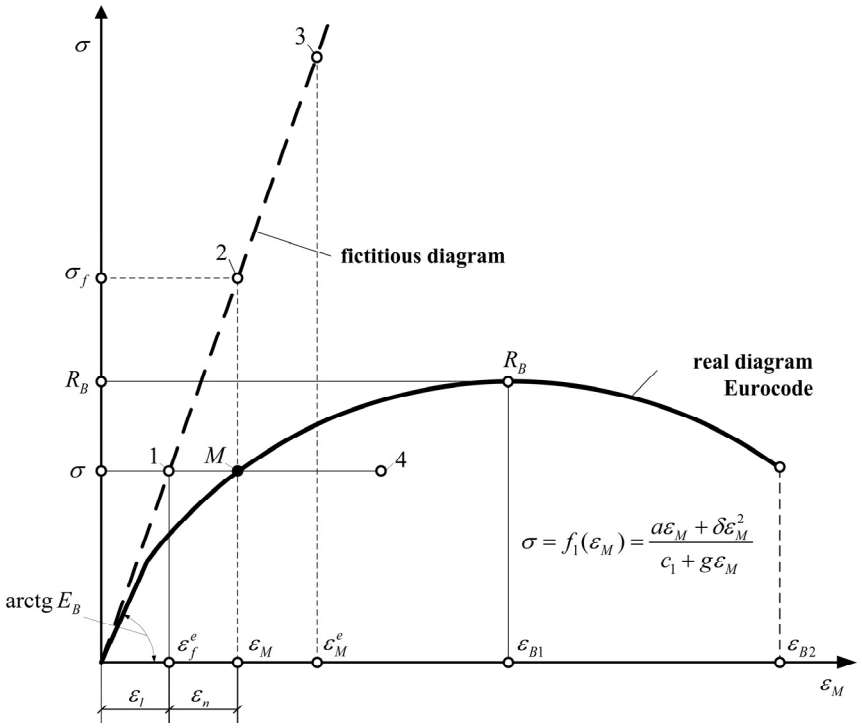

Figure 1 - The diagram $\sigma - \varepsilon_M$ instantaneous deformation of concrete

In the theory of creep of concrete (linear, nonlinear), instead of a real nonlinear diagrams used fictitious linear diagram that satisfies Hooke's law (Figure 1). This diagram makes calculations in the two types of errors, corresponding to the four points of the fictitious 1-4, accompanied by a realistic point of M. For example, at a given instant deformation ε_M fictitious stress $\sigma_f = \varepsilon_M E_B$ is significantly greater than the actual stress σ; for a given real stress σ fictitious elastic deformation $\varepsilon_e = \sigma / E_\text{B}$ is much less real deformation ε_M. Replacing the actual nonlinear diagram $\sigma - \varepsilon_M$ makes large errors in the calculation of total deformations during prolonged uploading designs.

This approach is justified misleading statement that "experiments instantaneous deformation of concrete, even at high levels of loading are linearly dependent on the stress".

As is known, the curved diagrams concrete have obtained experimentally for a long time ago. For example, Tal K. in 1955 revealed the real diagram $\sigma - \varepsilon_M$ in concrete by testing prisms reinforced with high-strength steel wire. As can be seen from Fig. 1, the total instantaneous deformation in the experiments is the sum of the linear and nonlinear component: $\varepsilon_\text{M} = \varepsilon_l + \varepsilon_\text{n}$. With prolonged uploading total deformation consists of two components: the total instantaneous and creep: $\varepsilon = \varepsilon_\text{м} + \varepsilon_\text{c}$. The total instantaneous deformation ε_M is determined for the time measured in minutes (at the Alexandrovsky S. listed 4 min.). Creep deformation is

manifested in the time measured for days and years, which creates problems for their joint consideration.

2. BASES OF THE METHOD

In the traditional theory of hereditary creep deformation nonlinear component $\varepsilon_{н}$ is not considered, so the total deformation is composed of elastic deformation $\varepsilon_{л}$ and creep deformation: $\varepsilon = \varepsilon_l + \varepsilon_c$ .These theories include the creep equation: Kelvin, Boltzmann (1887), Volterra (1913), Maslow-Harutyunyan (1952). In this regard, Gvozdev in 1955, on the basis of experiments Borishansky M. pointed out that the traditional theory of creep is not suitable for the theory of reinforced concrete. This theory does not reflect the experimentally observed rapid leakage of creep deformation at the time of observation, close to the time of loading of the samples. The initial portions of the creep curves constructed from these theories creep, do not have the characteristic outlines of curves at time τ, close to the time *t*.

The error lies in the fact that the nonlinear part of the instantaneous deformation is transferred to her inappropriate discharge creep deformation and formally joins them. This approach requires compliance with the relevant mathematical transformations that have not been fulfilled. The above translation is required to the traditional form of the equation of linear viscoelasticity

$$\varepsilon(t) = \frac{\sigma(t)}{E(t)} - \int_{\tau_1}^{t} \sigma(\tau) \frac{\partial}{\partial \tau} \frac{1}{E(\tau)} d\tau - \int_{\tau_1}^{t} \sigma(\tau) \frac{\partial}{\partial \tau} C(t,\tau) d\tau , \qquad (1)$$

with instantaneous elastic deformation.

Retaining the first two terms describing the elastic deformation, the model recommends transfer to account for deformation ε_n (Figure 1) to clarify the kind of measures the creep *C(t, τ)*. Since deformation ε_n increases nonlinearly with increasing stress σ, and then measure the nonlinear creep should depend on the stress $C_n(\sigma, t, \tau)$. Unfortunately, this requirement was not taken into account by researchers.

Accounting instantaneous deformation creep of concrete was performed for the first time Yashin A. and Katin N. in 1959, then Alexandrovsky S. and many foreign scientists. We found that in the entry (1) contains a number of inaccuracies, introducing an error in the calculation results.

Consider first elastic deformation in equation (1). Generally linear (potential) forces allows us to find the speed of the elastic deformation

$$\dot{\varepsilon}_e(\tau) = \dot{\sigma}(\tau) \frac{1}{E(\tau)} + \sigma(\tau) \frac{d}{d\tau} \frac{1}{E(\tau)}$$

and its significance

$$\varepsilon_e(\tau)=\frac{\sigma(\tau_1)}{E(\tau_1)}+\int_{\tau_1}^{t}\dot{\sigma}(\tau)\frac{1}{E(\tau)}d\tau+\int_{\tau_1}^{t}\sigma(\tau)\frac{d}{d\tau}\frac{1}{E(\tau)}d\tau.$$

After transformations we have $\varepsilon_e(t)=\sigma(t)/E(t)$. It follows that the second term in (1) is superfluous, and used form of the principle of superposition is incorrect:

$$\varepsilon_e(\tau)=\frac{\sigma(\tau_1)}{E(\tau_1)}+\int_{\tau_1}^{t}\frac{1}{E(\tau)}d\sigma.$$

The error is a loss of the deformation portion, which corresponds to the rate of change of stiffness. The same error exists in the last integral term. Under the conditions of nonlinear creep further this loss leads to the formulation of the principle of superposition strange that violates not only the principles of Newtonian mechanics, but also the conditions of the affine scaling experimental creep curves. Consider the third term in (1), and write with the help of that part of the linear creep, which is called instantaneous.

$$\varepsilon_n(t)=\int_{\tau_1}^{t}\sigma(\tau)\frac{\partial}{\partial\tau}C_n(\sigma,t,\tau)d\tau=\int_{\tau_1}^{t}\dot{\sigma}(\tau)\sigma(\tau)\frac{\partial C_n(\sigma,t,\tau)}{\partial\sigma}d\tau+\int_{\tau_1}^{t}\sigma(\tau)\frac{\partial C_n(\sigma,t,\tau)}{\partial\tau}d\tau.$$

However, the calculation of the instantaneous creep does not operate, and the integral is usually written in the form

$$\varepsilon_n(t)=\int_{\tau_1}^{t}\sigma(\tau)\frac{\partial}{\partial\tau}C_n(t,\tau)d\tau. \qquad (2)$$

Here are the values $\varepsilon_n(t)$, linearly depends on the stresses, that corresponds neither to experiment to find $\varepsilon_n(t)$, or the data in Fig. 1 of the nonlinear coupling ε_n and σ.

To describe $C_n(t,\tau)$ used a variety of complex formulas that do not meet the obvious experimental data. For example, in the approximation of the diagram $\sigma-\varepsilon_M$ square parabola, we have the exact value of the deformation $\varepsilon_n=\beta_2\sigma^2$:

$$\varepsilon_n(t)=\beta_2\sigma^2(t)=\int_{\tau_1}^{t}\sigma(\tau)\frac{\partial}{\partial\tau}C_n(t,\tau)d\tau,$$

which should correspond to the right side, including its function $C(t, \tau)$, that it is impossible to perform traditional records, for example, at Alexandrovsky S.

$$C(t,\tau)=\psi(\tau)-\psi(t)\frac{1-A_2e^{-\gamma\tau}}{1-A_2e^{-\gamma t}}e^{-\gamma(t-\tau)}+\Delta(\tau)\left[1-e^{-\gamma(t-\tau)}\right].$$

Complex formulas in the description of *C(t, τ)*, designed to take into account the instantaneous creep significantly increase the order of the corresponding differential equation of creep of concrete. This complicates the solution of practical problems of ordinary calculation of reinforced concrete structures.

Update the last term in (1), using the properties of potential forces under creep conditions (Sanzharovsky R., 2014). Find the velocity of creep deformation-

$$\dot{\varepsilon}_c(t,\tau)=\dot{\sigma}(\tau)C(t,\tau)+\sigma(\tau)\frac{\partial C(t,\tau)}{\partial\tau}+\sigma(\tau)\frac{\partial C(t,\tau)}{\partial t},$$

its magnitude and

$$\varepsilon_c(t)=\sigma(\tau_1)C(t,\tau_1)+\int_{\tau_1}^{t}\dot{\sigma}(\tau)C(t,\tau)\,d\tau+\int_{\tau_1}^{t}\sigma(\tau)\frac{\partial C(t,\tau)}{\partial\tau}d\tau+\int_{\tau_1}^{t}\sigma(\tau)\frac{\partial C(t,\tau)}{\partial t}d\tau.$$

Finally, we have after transformation

$$\varepsilon_c(t)=\int_{\tau_1}^{t}\sigma(\tau)\frac{\partial C(t,\tau)}{\partial t}d\tau. \qquad (3)$$

The last term in (1) and the value of (3) in linear creep may not differ from each other only by using the difference of the nuclei. This fact characterizes the corresponding superposition principle, as well as the correctness of its further application in the nonlinear creep.

These unauthorized principles and errors have a significant impact on the results of the calculations of reinforced concrete structures creep. They also show that in the conventional form of (1) the equation for creep regulation and mass use in reinforced concrete structures is unacceptable.

Previously, the authors of this paper (Sanzharovsky R., 2013) proposed a method of accounting instantaneous nonlinearity of concrete creep. According to the hypothesis of linear concrete creep basic equation by creep can be written as

$$\varepsilon(t)=f_2\left[\sigma(t)\right]+\int_{\tau_1}^{t}f_1\left[\varepsilon_M(\tau)\right]\frac{\partial}{\partial t}C(t,\tau)\,d\tau, \qquad (4)$$

which $f_1\left[\varepsilon_M(\tau)\right]$, $f_2\left[\sigma(t)\right]$ represent the direct and inverse function of nonlinear diagrams instantly $\sigma-\varepsilon_M$ concrete parameters which change over time.

For example, the use of concrete for nonlinear diagram with the descending parts in the form proposed by Eurocode 2

$$\sigma = f_1(\varepsilon_M) = \frac{a\varepsilon_M + \delta\varepsilon_M^2}{c_1 + g\varepsilon_M};\ \varepsilon_M = f_2(\sigma) = \frac{a_0\sigma + \delta_0\sigma^2}{c_0 + g_0\sigma};\ a = E_B(t);\ a_0 = \frac{1}{E_B(t)};$$

$$\delta = -\frac{R_\delta(t)}{\varepsilon_{B1}^2};\ g = \frac{E_B(t)\varepsilon_{B1} - 2R_B(t)}{R_B(t)\varepsilon_{B1}};\ c_1 = c_0 = 1 \text{ and so on.}$$

In its simplest form using square parabola

$$\sigma = f_1\left[\varepsilon_M(t)\right] = E_B(t)\varepsilon_M - A_2(t)\varepsilon_M^2, \tag{5}$$
$$\varepsilon_M = \frac{1}{E_B(t)}\sigma + B_2(t)\sigma^2 = f_2\left[\sigma(t)\right],$$

where $E_в(t)$, $A_2(t)$, $B_2(t)$ - known functions.

To measure the creep of concrete $C(t, \tau)$ can use any sentence of the famous scientists.

For the calculation of the valuation of the most common structures (reinforced concrete beams and columns), the average consumer friendly (Sanzharovsky R., 1978), the function $C(t, \tau)$ should be presented in a degenerate form. In this case, equation (4) reduces to a differential form, and final recommendations for designers are represented in a simple tabular form. When a degenerate form of the type $C(t,\tau) = \theta(\tau)\left[1 - e^{-\gamma(t-\tau)}\right]$ proposed by Prokopovich I. and Karapetyan K. the differential equation of creep of concrete will be first order. Here we use a measure of creep in the form proposed McHenry

$$C(t,\tau) = C_0\left[1 - e^{-\gamma(t-\tau)}\right] + C_1 e^{-\gamma_2\tau}\left[1 - e^{-\gamma_3(t-\tau)}\right], \tag{6}$$

where the differential equation will have a second order. Measure the creep of the Alexander S. lead to differential equations of the fifth order. Pay attention to the important requirement to the function $C(t,\tau)$. The equations of second and higher orders appear drag force proportional to the total acceleration $\ddot{\varepsilon}(t)$. This is incompatible with Newtonian mechanics and violates its fundamental principle of the independence of the forces.

Saving the form action creep Harutyunyan N., Prokopovich I., Karapetyan K., we obtain the differential equation of the first order that is convenient for practical tasks

$$\dot{\varepsilon}(t) + \gamma\varepsilon(t) = \dot{\varepsilon}_M(t) + \gamma\theta(t)\frac{a(t)\varepsilon_M(t) + \delta(t)\varepsilon_M^2(t)}{1 + g(t)\varepsilon_M(t)} + \gamma\varepsilon_M(t), \tag{7}$$

or

$$E_{\sec}\left[\sigma(t)\right]\left[\dot{\varepsilon}(t)+\gamma\varepsilon(t)\right]=\frac{E_{\sec}\left[\sigma(t)\right]}{E_{\tan}\left[\sigma(t)\right]}\dot{\sigma}(t)+\gamma\left\{1+\theta(t)E_{\sec}\left[\sigma(t)\right]\right\}\sigma(t). \qquad (8)$$

Let's pay attention to the important results. The presence in the creep law (7) instantaneous deformation $\varepsilon_м$ concrete and its relation to the total strain ε opens opportunities for almost an exact solution of a number of fundamental design problems, such as long-term resistance to compression of concrete columns and beams (Sanzharovsky R., 1978). It is possible, under the conditions of nonlinear creep and instantaneous nonlinearity of concrete, to take into account the exact stress distribution over the cross section within the deformation model of Eurocode 2, and thereby bridge the gap that exists between the theories of short-term and prolonged resistance reinforced concrete structures. It is possible in the evaluation of long-term ultimate bearing capacity of structures to apply the criterion to achieve the normalized value of the limiting compressive deformation $\varepsilon_{в2}$ Eurocode 2. Parallel accounted for the change over time of concrete strength R_B.

3. EXAMPLE

For example, consider the definition of the carrying capacity of eccentrically compressed main regulatory elements in the design scheme. After integration over the cross section on the basis of deformation model section of Eurocode 2 and diagrams (5) we can write the equilibrium condition:

$$\begin{cases} N=\dfrac{ba}{g^2}\dfrac{c}{\varepsilon_{2M}}\left[g\varepsilon_{2м}-\ln\left(1+g\varepsilon_{2M}\right)\right]+ \\ +\dfrac{b\delta}{g^3}\dfrac{c}{\varepsilon_{2M}}\left[\dfrac{1}{2}g^2\varepsilon_{2M}^2-g\varepsilon_{2M}+\ln\left(1+g\varepsilon_{2M}\right)\right]+ \\ +A_s'E_s'\dfrac{\varepsilon_2}{c}\left(c-a'\right)-A_sE_s\dfrac{\varepsilon_2}{c}\left(h_0-c\right), \\ M=N\left(e+f\right)=\dfrac{b\delta}{g^4}\dfrac{c^2}{\varepsilon_{2M}^2}\left[\dfrac{1}{3}g^3\varepsilon_{2M}^3-\dfrac{1}{2}g^2\varepsilon_{2M}^2+g\varepsilon_{2M}-\ln\left(1+g\varepsilon_{2M}\right)\right]+ \\ +\dfrac{b\delta}{g^3}\dfrac{c^2}{\varepsilon_{2M}^2}\left[\dfrac{1}{2}g^2\varepsilon_{2M}^2-g\varepsilon_{2M}+\ln\left(1+g\varepsilon_{2M}\right)\right]-A_s'E_s'\dfrac{\varepsilon_2}{c}\left(c-a'\right)^2+ \\ +A_s'E_s'\dfrac{\varepsilon_2}{c}\left(h_0-c\right)^2, \end{cases} \qquad (9)$$

where b, h_0 - cross-sectional dimensions of the column; c - the height of the compression zone of the section; h_0-c - depth of cracks in the concrete; ε_2, $\varepsilon_{2м}$ - complete and instantaneous deformation extreme fiber compressed zone; a, δ, g - regulatory options diagram by Sarzhin; e - eccentricity; f - the deflection of the middle column.

Equilibrium equation is differentiable with respect to *t*

$$\begin{cases} \dfrac{\partial N}{\partial \varepsilon_2}\dot{\varepsilon}_2(t)+\dfrac{\partial N}{\partial c}\dot{c}(t)+\dfrac{\partial N}{\partial \varepsilon_{2M}}\dot{\varepsilon}_{2M}(t)=0, \\ N\dfrac{\partial f}{\partial \varepsilon_2}\dot{\varepsilon}_2(t)+N\dfrac{\partial f}{\partial c}\dot{c}(t)=\dfrac{\partial M}{\partial \varepsilon_2}\dot{\varepsilon}_2(t)+\dfrac{\partial M}{\partial c}\dot{c}(t)+\dfrac{\partial M}{\partial \varepsilon_{2M}}\dot{\varepsilon}_{2M}(t)=0. \end{cases} \tag{10}$$

If using a second-order equation of creep, the equation (10) is differentiated once again and so on.

From equations (10), read in conjunction with (7), we have a complete system of governing equations for calculating the deformation of reinforced concrete columns under creep conditions, which can easily transform (mean linearity) to the normal form of Cauchy

$$\begin{aligned} \dot{\varepsilon}_2(t)&=\Phi_2\left[\varepsilon_2(t),\varepsilon_{2M}(t),c(t)\right], \\ \dot{\varepsilon}_{2M}(t)&=\Phi_{2M}\left[\varepsilon_2(t),\varepsilon_{2M}(t),c(t)\right], \\ \dot{c}(t)&=\Phi_c\left[\varepsilon_2(t),\varepsilon_{2M}(t),c(t)\right]. \end{aligned} \tag{11}$$

Integration of (11) is carried out according to standard programs; it repeatedly performed as the authors themselves and their numerous students. Settlement of (11) is accompanied by three independent test conditions characterizing achievement column limit state, and indicates a loss of bearing capacity:

a) $\varepsilon_{2M}(t)\le\varepsilon_{B2}=350\cdot10^{-5}$ in the compressed zone of concrete

b) $\varepsilon_{1s}=\varepsilon_2(t)\dfrac{h_0-c(t)}{c(t)}\le\dfrac{R_s}{E_s}$ in the tension reinforcement

c) the condition of the critical state, based on the calculation of the second-order nonlinear.

Condition critical condition characterized by the loss of stability of the column moment during creep, according to the data, is found by varying the isochronous quasistatic equilibrium equations:

$$\begin{cases} \dfrac{\partial N}{\partial \varepsilon_2}\delta\varepsilon_2+\dfrac{\partial N}{\partial c}\delta c+\dfrac{\partial N}{\partial \varepsilon_{2M}}\delta\varepsilon_{2M}=0, \\ N\dfrac{\partial f}{\partial \varepsilon_2}\delta\varepsilon_2+N\dfrac{\partial f}{\partial c}\delta c=\dfrac{\partial M}{\partial \varepsilon_2}\delta\varepsilon_2+\dfrac{\partial M}{\partial c}\delta c+\dfrac{\partial M}{\partial \varepsilon_{2м}}\delta\varepsilon_{2M}=0, \\ \delta\varepsilon_2=\delta\varepsilon_{2M}. \end{cases} \tag{12}$$

Determinant of the system (12) is equal to zero, is the condition of the critical state. This determinant is calculated together with the system of equations (11). It captures the moment of the ultimate state, the time loss of bearing capacity of the structure, including the duration of the existence of the structure.

4. CONCLUSIONS

Developed theory of partitions and covers short-term bearing capacity of the structure by identifying the values of ε_2, ε_{2M}. This theory covers cases of alternating periods of short-term and long-term existence of reinforced concrete structures. In this theory, a unified manner is taken into account together six types of nonlinear behavior of reinforced concrete structures:

1. Instantaneous deformation elastoplastic concrete;
2. The elastic-plastic deformation of the valve;
3. The presence of cracks in the tension zone of the concrete;
4. The linear and nonlinear creep of concrete;
5. Creep special types of reinforcement (reinforced plastics, polymers, etc.), which leads to higher order differential equations;
6. The two types of geometric nonlinearity in the approximate and exact expression for the curvature of the curved axis of the column.

According to the results of the theory developed practical methods of calculation of reinforced concrete structures, which are more reliable and cost-effective for the following reasons. The theory is based on estimated Principles and Rules of Eurocode 2 corresponds to the current state of the theory of elastic-plastic analysis of structures and foundations of classical Newtonian mechanics. In theory not used questionable or controversial assumptions. Computational procedures are based on the classical method of numerical solution of the Cauchy problem for normal systems of differential equations. Numerical results are consistent with the theory of multiple reliable experiments Tal K. and Chistyakov E. conducted in the Research Institute of Concrete. They also coincide with the limit values obtained during the transition to the linear theory. Used functions and their parameters describing the phenomenological creep curves of concrete substantiated by numerous experiments of famous scientists.

We can show the results for practical design in the table, which lists the expansion coefficient of resistance reinforced concrete structure. They demonstrate, in accordance with the standard method, to increase economic efficiency for ordinary consumers, as well as economy of materials and energy costs at the State level.

Table 1. is an example and contains a set of coefficients prolonged resistance compressed concrete structures corresponding φ_∞=0,8. It is compared with a standard value 0,555 and demonstrates the great convention of the existing standard for concrete in terms of accounting creep of concrete.

Table 1. Prolonged resistance coefficients

Value reinforcement	Eccentricity					
	0,1	0,2	0,3	0,4	0,5	0,8
0,2	0,838	0,845	0,855	0,860	0,875	0,890
0,15	0,830	0,835	0,843	0,850	0,862	0,875
0,125	0,821	0,825	0,828	0,835	0,845	0,855
0,10	0,817	0,820	0,821	0,822	0,828	0,828
0,075	0,815	0,815	0,815	0,815	0,815	0,815
0,05	0,795	0,795	0,791	0,790	0,787	0,785
0,025	0,785	0,780	0,772	0,767	0,755	0,740
0,01	0,765	0,757	0,750	0,737	0,715	0,695
	1,0	1,2	1,4	1,6	1,8	2,0
0,2	0,910	0,928	0,945	0,968	0,980	0,990
0,15	0,885	0,900	0,915	0,925	0,937	0,950
0,125	0,865	0,880	0,890	0,900	0,910	0,922
0,10	0,847	0,855	0,865	0,875	0,882	0,895
0,075	0,815	0,815	0,820	0,822	0,825	0,830
0,05	0,782	0,780	0,777	0,775	0,770	0,765
0,025	0,730	0,712	0,690	0,670	0,650	0,625
0,01	0,670	0,645	0,625	0,600	0,575	0,550

REFERENCES

Sanzharovsky, RS 1978, *Stability of construction elements during creep*, LSU. (in Russian)

Sanzharovsky, RS 2013, 'Problems of the theory of creep', *Structural Mechanics engineering structures and buildings,* no. 3, pp. 28-34. (in Russian)

Sanzharovsky, RS 2014, 'Nonlinear hereditary creep theory', *Building mechanics engineering structures and buildings*, no. 1, pp. 63-68. (in Russian)

.

Massive Structure Monitoring: Relevance of Surface Strain Measurement

Maxime Boucher[1]; Matthieu Briffaut[1]; and Frédéric Dufour[1,2]

[1]Univ. Grenoble Alpes, 3SR, F-38000 Grenoble, France; and CNRS, 3SR, F-38000 Grenoble, France.
[2]Chair Professor PERENITI.
E-mail: maxime.boucher@3sr-grenoble.fr

Abstract

Most of large civil engineering concrete structures have been instrumented for decades with embedded sensors. To prevent the eventual loss of data, complementary instrumentation of external surface has recently been deployed. This new instrumentation can take different forms but in all cases, to avoid damaging the structure, it will be only superficially anchored. Near the outer surfaces, thermo-hydro-mechanical concrete behaviour is more sensitive to varying environmental conditions than in the centre of the structures. Therefore, the strain measured near the outer surfaces is not identical to the strain measured by embedded sensors. Consequently the methods of classical physical-statistical analysis must be reviewed. Using a thermo-hydro-mechanical finite element modeling calibrated on a representative concrete and applied on a current part of a thick structure, this work confirms a dependence of strain on the depth. First results show that the depth impact affects both kinetic and amplitude strain.

Keywords:
Thermo-hydro-mechanical behavior; Concrete; Massive structure; Variable environnemental conditions; Surface monitoring.

INTRODUCTION

For nearly 80 years, most of large civil engineering concrete structures are instrumented with vibratory strain gauge. On some structures such as confinement vessels of nuclear power plants (highly prestressed), operators have to cope with the

loss of signal from some sensors. This can be explained by several reasons including a default in the electrical system that excite the wire or by the excess of frequency limit measurement due for instance to important creep strains (*Simon and Courtois, 2011; Simon et al. 2013*). Most of these sensors have been embedded in the concrete during construction and are thus irreplaceable. To overcome this loss of information, one of the solutions is to replace these defective embedded sensors by surface sensors (Figure 1).

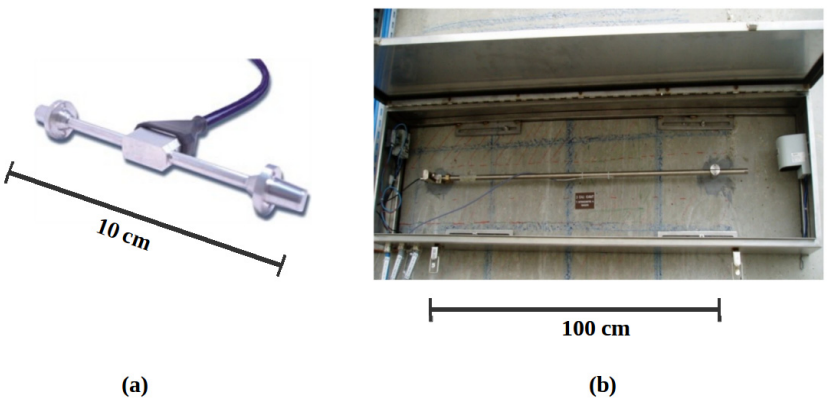

Figure 1: Embedded strain sensor (a) and surface strain sensor (b).

Nevertheless, unlike central strain (far from outer surface), skin strain (near outer surfaces) is strongly affected by the environmental condition variations. Temperature and humidity cycles (daily and seasonal) generate thermo-hydric variations of volume. Other phenomena such as sunshine, rain or wind, also disrupt these two main fields. Finally, characteristic times and so influence depths of these phenomena are very different. For these reasons, the analysis of this new data is more complex than embedded measures for which usual statistical analysis methods exist.
The aim of the present contribution is to compare the strain evolution through the depth in thick structure. This can be considered as a first step toward the complete definition of a space and time transfer functions between both strain vs time signals.

For this purpose, a visco-elastic finite element model able to represent thermo-hydro-mechanical behaviour of concrete submitted to variable thermo-hydric boundary conditions is presented in the first part. Then, the calibration of the material constitutive parameters on laboratory tests is detailed. Finally, the strains at different depths from a simulation over thirty years on a current part of containment enclosure submitted to thermo-hygrometric variations are analysed.

NUMERICAL MODEL

Numerical strategy.
To be applicable to major civil engineering thick structures, the numerical model must account for thermal and hydric variation effects on strains. Thermo-mechanical (*Arthanari and Yu, 1967 ; Seki and Kawasumi, 1972 ; Kommendant et al, 1976*), hydro-mechanical (*Wittmann, 1970 ; Wittmann, 1973*) and thermo-hydric (*Caré, 2008*) chaining are retained. In contrast, the effects of mechanical strains on thermal and hydric properties (*Lassabatere et al, 1997*) and the modification of heat and water diffusivity due to cracked skin are neglected. Finally, for ageing structures, hydration reaction is supposed finished.

Complete simulations are carried out using *Code_Aster* by chaining three calculations: thermal field, hydric field and mechanical strains. Constitutive models adopted are for the most part empirical although based on physical approaches.

Thermal field.
Thermal field is assumed to be governed by a conventional linear heat equation with convective boundary conditions (Neumann type):

$$\begin{cases} \rho C_{th} \dot{T} = k_{th} \Delta T \\ \phi_{th} = h_{th}(T - T_\infty) \end{cases} \quad (1)$$

Specific heat capacity ρC_{th}, thermal conductivity k_{th} and heat transfer coefficient h_{th} (taking into account convection and radiation) are taken constant during all the calculation.

Hydric field.
Drying process is modeled by a nonlinear diffusion equation involving a diffusion coefficient (non-linear function of water content) usually written as:

$$\dot{C} = \nabla [D(C,T) \nabla T] \quad (2)$$

Several authors have proposed various relationships between drying coefficient and water content. The expression used, proposed by Granger (*1995*), is composed of the drying coefficient proposed by Mensi (*1988*) and the temperature dependence given by Bazant (*1972*):

$$D(C,T) = a e^{bC} \frac{T}{T_0} e^{\frac{-Q}{R}(\frac{1}{T} - \frac{1}{T_0})} \quad (3)$$

The coefficients a,b and the activation energy Q of Arrhenius' law are supposed to be constant. T_0 represents the reference temperature.
The calculation of drying is done by means of water content, although boundary conditions are prescribed in relative humidity. The isotherm between relative humidity of concrete and water content must be entered. In this study, the hysteresis existing between sorption and desorption cycles is neglected and the isotherm is supposed linear in the humidity range between 40% and 100%. Therefore, the used isotherm function is:

$$C(h) = \frac{C_{eq}[h_0 - h] - C_0[h - h_{eq}]}{h_0 - h_{eq}} \tag{4}$$

where h_0, C_0 are the relative humidity and initial moisture content and h_{eq}, C_{eq} are the relative humidity and water content at equilibrium.
The convective boundary condition used involves a water exchange coefficient h_{dr} which is assumed constant:

$$\phi_{dr} = h_{dr}[C - C(h_{air})] \tag{5}$$

By analogy with nonlinear thermal calculation, water field is obtained using the non-linear thermal module of *Code_Aster*.

Mechanical field.
This study focuses on operating structures during service life. Consequently damage rate is assumed to be low and a simple elastic model is used.
Under the assumption of small strains, the total strain tensor is assumed to be the sum of five tensors: elastic strain (ε_{El}), thermal strain (ε_{Th}), drying shrinkage strains (ε_{DS}), basic creep strains (ε_{BC}) and drying creep strains (ε_{DC}):

$$\underline{\varepsilon_{tot}} = \underline{\varepsilon_{El}} + \underline{\varepsilon_{Th}} + \underline{\varepsilon_{DS}} + \underline{\varepsilon_{BC}} + \underline{\varepsilon_{DC}} \tag{6}$$

- The thermal strain is assumed to be proportionnal to the temperature change: $\underline{\varepsilon_{El}} = \alpha_{Th}.\dot{T}.\underline{1}$.
- For the calculation of drying shrinkage, a phenomenological model assuming proportionality with water variation content is used: $\underline{\varepsilon_{DS}} = \alpha_{DS}.\dot{C}.\underline{1}$.
- The basic creep model is based on simple rheological models: an elastic body, a linear Kelvin-Voigt for modeling reversible creep and a Maxwell unit with a nonlinear viscosity to model the long time creep. The model also assumes complete decoupling between the spherical and deviatoric components. Both of these chains are however equivalent in their construction. A linear dependance with internal relative humidity is included.

- The model, proposed by Bazant (*1985*), is assumed to be a linear relation with strain and internal relative humidity variations: $\underline{\varepsilon_{DC}} = \alpha_{DC} . \underline{\dot{h}}$.

CALIBRATION

The numerical model presents 20 material parameters to be determined. For this, laboratory tests on specimens formed by a representative concrete of nuclear power plant are used. These tests are of two types:

- A first test campaign on 4 specimens of dimensions 25x50cm subjected to axial compression cycles from 0 to 12 MPa.
- A second test campaign on 14 specimens of dimensions 16x100cm subjected to various conditions:
  - Non-drying weight loss (1 specimen)
  - Drying weight loss (1 specimen)
  - Non drying shrinkage (3 specimens)
  - Drying shrinkage (3 specimens)
  - Non drying creep (3 specimens)
  - Drying creep (3 specimens)

Non-drying conditions were ensured by strips of self-adhesive aluminium. The temperature was maintained near to 20°C. The relative humidity has oscillated between 50% and 70%. All strain measurements were carried out with inductive sensors located outside the specimens.
Since the variability between specimen responses from the second campaign was low, only one out of the three (for shrinkage and creep tests) was carried out up to the end of the campaign. The model was calibrated with these last specimens.
For confidentiality reasons, the experimental results will be normalized and the parameter values will not be provided.

Thermal field.
The thermal diffusion and the specific capacity cannot be measured out of these tests. Thus, their retained values were obtained from the literature. It is the same for the heat exchange coefficient.

Hydric field.
Before calibrating the drying model, the sorption-desoprtion isotherm of the concrete must be determined in order to translate the boundary conditions (known in relative

humidity of the surrounding air) in concrete water content.
Initial relative humidity of concrete (h_0) is taken equal to 100% (saturated) and equal to the average of the relative humidity in the air during all the test at equilibrium (h_{eq}).
The initial water content (C_0) is defined as the amount of water used to make concrete minus the water used in hydration reaction (*Granger 1995*). The final water content (C_{eq}) is obtained by extrapolating the weight loss curve to infinity.
Finally, the drying model was calibrated on the drying mass loss test. The water exchange coefficient and the coefficient *b* (Equation 3) from diffusion coefficient have been fixed to reference values from the literature. Only the coefficient *a* from diffusion coefficient has been calibrated. The comparison between the experimental points and the numerical curve is presented in Figure 2a.

Elastic strain.
Measurements from the first campaign were used to determine the Young's modulus of concrete studied. A linear regression of the stress-strain curves (Figure 3a) allows to determine an average Young's modulus for these four specimens.
Since only axial strains were measured, the Poisson's ratio could not been determined. Therefore a standard value for concrete is used.

Thermal strain.
No thermal expansion test was made. But peaks of temperature up to 25°C were measured during the campaign. These variations have been felt on shrinkage and creep tests. These thermal anomalies have been used to calibrate the thermal expansion coefficient.
The analysis of the experimental results yields an increase of strain with temperature amplitude (Figure 3b). A linear regression of these points gives direct access to the thermal expansion coefficient α_{Th}.

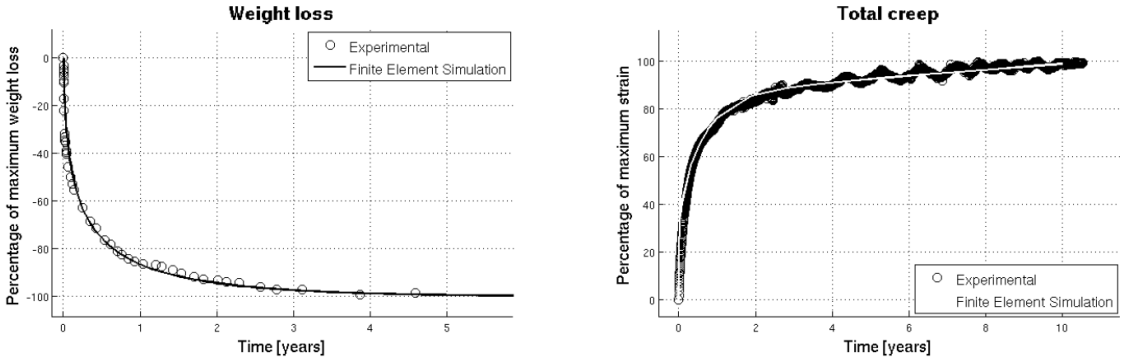

(a) (b)

Figure 2: Calibration of the thermo-hydro-mechanical model. Numerical simulations: weight loss (a) and total creep (b).

Drying shrinkage.

The drying shrinkage strain is assumed to be proportional to the variation of water content. Therefore, only one parameter must be identified (α_{DS}). Autogenous shrinkage was estimated at short-term from non-drying weight loss. Then, it was substracted to drying shrinkage test in order to obtain the drying shrinkage. The obtained curve is not exactly linear at the beginning (Figure 3c). Indeed, at the start of drying, the high tensile stress located near the exchange surfaces creates skin cracking, which relaxes the stress.

A linear regression of the central portion of the curve allows the calibration of the drying shrinkage parameter. Numerically, the strain obtained will be greater than the experimental measurement. However both kinetic and amplitude related to relative humidity cycles will be respected.

Drying creep.

It was decided arbitrarily to calibrate drying creep before basic creep (since it has only one parameter). Experimental curve of drying creep was obtained by subtracting non-drying creep and drying shrinkage to the drying creep test. Since drying creep was assumed proportional to the stress and the relative humidity variation, drying creep values were divided by the applied stress. Meanwhile, the mass loss was translated into relative humidity thanks to the sorption-desorption isotherm.

A quasi-linear increase of drying creep with relative humidity variation is highlighted by the analysis of experimental results in Figure 3d. Again, as for drying shrinkage, the resulting curve is not perfectly linear in its ends. For the beginning, explanations may be the same than in the case of drying shrinkage. For the long term, the

permeability of dessiccation protection is probably involved. It was found that after a few years, the mass loss from non-drying test increased significantly. Consequently, in our approach, by subtracting non-drying creep and drying shrinkage to drying creep, drying shrinkage is removed twice which explains the decrease at the end of the curve.
That is why, drying creep parameter is identified by linear regression of the central portion of the experimental curve only (Figure 3d).

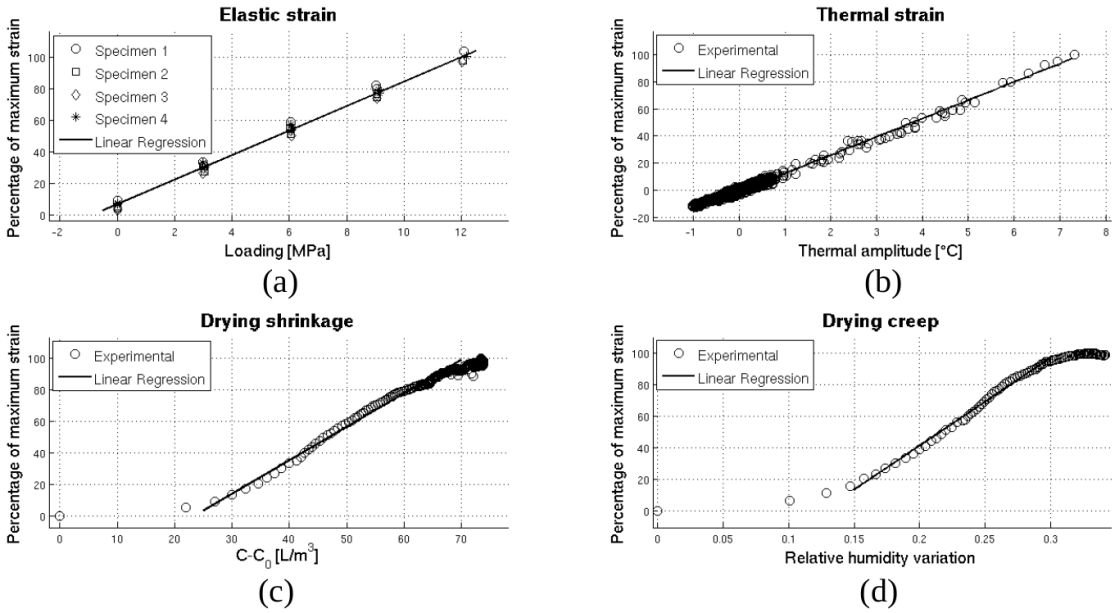

Figure 3: Calibration of the thermo-hydro-mechanical model. Linear regressions: elastic strain (a), thermal strain (b), drying shrinkage (c) and drying creep (e).

Basic creep.
Finally, basic creep is calibrated on the total creep test, taking into account the previously calibrated drying creep. Experimental and numerical results are presented in Figure 2b.

SIMULATION METHOD

After a thorough calibration of material parameters for each modeled phenomena, an application to a representative volume of a confinement vessel of a nuclear power plant was achieved. For this simulation, an inner containment wall of a

double containment vessel is studied which allows the suppression of the direct effects of rain, wind and sunshine; only thermal and humidity variations, load and prestressing were selected as thermo-hydro-mechanical boundary conditions.
The mesh of a current portion of containment in three dimensions (width of 2 meters, height of 1.8 meters, thickness of 1.2 meters and internal radius of 21.9 meters), taking into account reinforcements was used (Figure 4).

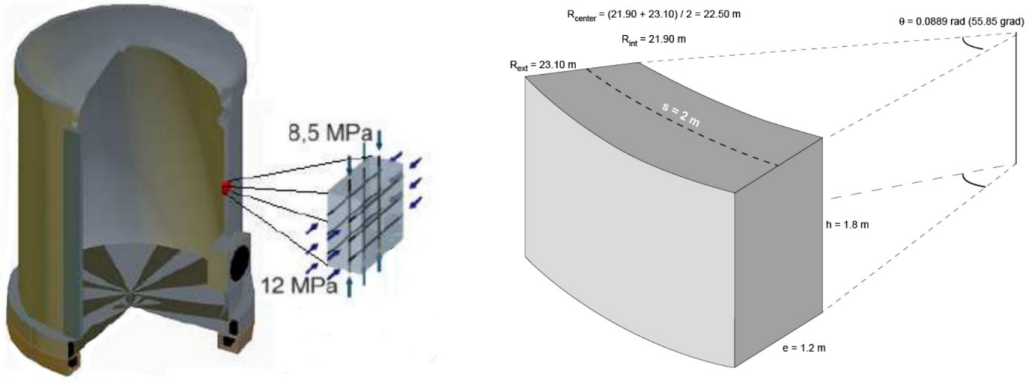

Figure 4: Geometry and dimensions of the studied structure.

The calculation simulates 30 years of service life of the structure. The thermo-hygrometric boundary conditions were created by duplicating periodic temperature and humidity measurements from the studied structure.

In-situ mechanical boundary conditions are represented by the following hypothesis: on the bottom and lateral faces, normal displacements are prohibited and the upper side is forced to remain parallel to the bottom side.

During the first three years, only the structural loading, the thermal and the moisture variations (identical on the inner and outer faces) are taken into account.
At 3.5 years, the vertical and horizontal preloading is added.
At 6 years, the reactor is operating. This yields a change in thermo-hygrometric boundary conditions (different on the inner and outer sides).
At 16 and 26 years, two containment pressure tests are simulated (pressurizing the reactor vessel for 3 days). For that, an overpressure is added on the inner side and an depression is added on the upper face (to represent the vertical stretch of the structure).

RESULTS :

The orthoradial strains obtained numerically on the outer surface and near the center of the structure are presented in Figure 5. Also for confidentiality reasons, the

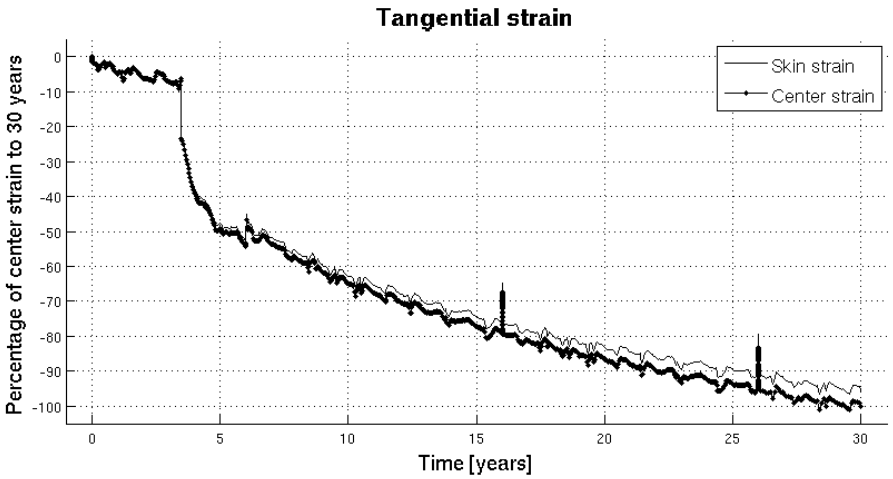

strains are normalized by the absolute value of the center strain at 30 years.

Figure 5: Tangential strain on outer surface and close to center of structure.

On this graph, one can remark that:

- Strain cycles related to thermal variations between the center and the skin are closed to each others.
- Given the thickness of the structure and a very low water diffusivity, in comparison to thermal strain and creep, the drying shrinkage of the concrete is only slightly perturbed by the changes in humidity of the air.
- Before prestressing, both strains observed in skin and in the center are similar. After prestressing the cables, the creep kinetics begin to dissociate: faster in the center (high water content) than at the surface (low water content). After 30 years, this difference is about 5%.

CONCLUSION

The results of this study show that, unlike thermal variations which affect the entire thickness of the structure, creep kinetics are not the same between the center and the surface of the structure. Creep is smaller near the exchange surfaces, where

concrete has a lower water content.
Under the hypothesis used in the numerical part, this contribution shows that the strain evolution between the core and the surface of the structure are not exactly the same. This confirms that the identification of a transfer function is necessary between strain measurement at various depth. Given the above results, a simple reduction of the strain depending on the distance to the outer sides could be accurate enough.
Benefiting from a representative structure, built in the same concrete used for the calibration procedure and instrumented with surface strain sensors for several years, this present work will continue with a comparison between simulated strain and measured strain.

Acknowledgments.

Work performed thanks to the support of EDF in context of Chair PERENITI run by the Fondation Partenariale Grenoble INP and using the monitoring data provided by EDF-DTG. Partners responsibility of the Chair cannot in any circumstances be blamed on the grounds of the content of the publication, which is only binding its author.

REFERENCES

Arthanari S., Yu C.W. (1967). "Creep of conrete under uniaxial and biaxial stresses at elevated temperatures". Mag. Concrete Res. 13(60), 149-156.

Bazant Z.P., Najjar L.J. (1972). "Nonlinear water diffusion in nonsaturated concrete". Materials and Constructions, 1972, Vol. 5, 3-20.

Bazant Z.P., Chern J.C. (1985). "Concrete creep at variable humidity: constitutive law and mechanism". Matériaux et Constructions, Vol. 18, n°103, pp 1-20.

Caré S. (2008). "Effect of temperature on porosity and on chloride diffusion in cement pastes". Construction and Building Materials 22, 1560-1573.

Code_Aster, Électricité De France (EDF), Code_Aster finite element code version 11.5, available at http://www.code-aster.org.

Granger L. (1995). "Comportement différé du béton dans les enceintes de centrales nucléaires: analyse et modélisation". Laboratoire Central des Ponts et Chaussées.

Kommendant G., Polivka M., Pirtz D. (1976). "Study of concrete properties for prestressed concrete reactor vessels". Rapport technique, Department of Civil Engineering.

Lassabatere T., Torrenti J.-M., Granger L. (1997). "Sur le couplage entre séchage du

béton et contrainte appliquée". Pages 331-338.
Mensi R., Acker P., Attolou A. (1988). "Séchage du béton : analyse et modélisation". Materials and Structures/Matériaux et Construction, 1988, 21, 3-12.
Seki S., Kawasumi M. (1972). "Creep of concrete at elevated temperatures". Concrete of Nuclear Reactors, 1:591-638.
Simon A., Courtois A. (2011). « Structural Monitoring of Prestressed Concrete Containments of Nuclear Power Plants for ageing management ». Transactions, SmiRT 21, 6-11 November, 2011, New Delhi, India.
Simon A., Oukhemanou E., Courtois A. (2013). « Structural Monitoring of Prestressed Concrete Containments of Nuclear Power Plants for ageing management ». Technical Innovation in Nuclear Civil Engineering – TINCE 2013, Paris (France), October 23-31, 2013.
Wittmann F. (1970). « Einfluss des feuchtigkeitsgehaltes auf das kriechen des zementsteines ». rheologica Acta, 9(2):282-287.
Wittmann F. (1973). « Interaction of hardened cement paste and water ». Journal of the American ceramic society, 56(8):409-415.

Interfacial Micromechanics Assessment of Rheological Chain Models and Their Application to Early-age Creep of Concrete

M. Shahidi[1,2] B. Pichler[2] R. Wendner[1] S. Scheiner[2] Ch. Hellmich[2]

[1]Christian Doppler Laboratory for Life-Cycle Robustness in Fastening Technology, University of Natural Resources and Life Sciences Vienna, Peter-Jordan-Strasse 82, A-1190 Vienna, Austria; email: Mehran.Shahidi@boku.ac.at; Roman.Wendner@boku.ac.at
[2]Institute for Mechanics of Materials and Structures, Vienna University of Technology, Karlsplatz 13/202, A-1040 Vienna, Austria; email: Bernhard.Pichler@tuwien.ac.at; Stefan.Scheiner@tuwien.ac.at; Christian.Hellmich@tuwien.ac.at

ABSTRACT

Nanoindentation testing suggests that creep of hydration products is the microscopic reason for macroscopic creep of cementitious materials. This is supported by a multiscale creep model which explains *aging* creep of young concretes as the consequence of *universal* creep of hydration products (Scheiner and Hellmich, 2009), whereby the latter is described with a rheological model consisting of linear springs and dashpots. We here extend the investigation of the origin of creep of cementitious materials further down to the nanoscale of hydration products, where we envision solid matter sliding (upon loading) along interfaces which are filled with lubricating thin layers of adsorbed water, i.e. water in a "glassy", "liquid crystal" state. As for the viscous behavior of the interfaces, we follow (Shahidi et al., 2014) and consider that the shear traction acting on an adsorbed water layer is proportional to the shear dislocation rate of the interface, with an interface viscosity as the proportionality constant. Our analysis starts from corresponding anisotropic creep and relaxation tensors of matrix-interface composites containing *parallel* interfaces (Shahidi et al., 2014). Considering that hydration products contain interfaces oriented isotropically in *all space directions*, we here compute complete spatial averages of parallel interface-related anisotropic creep and relaxation tensors, in order to derive isotropic creep and relaxation tensor bounds. Comparing them with creep and relaxation functions of the aforementioned rheological model for universal creep of hydration products allows for identification (i) of the interface density and (ii) of the product of interface size and viscosity. Based on the Reuss-type creep tensor bound, we obtain, interesting quantitative insight into microstructural features of hydration products.

INTRODUCTION

Creep is the slow and progressive deformation of materials under constant loading. In 1874, Boltzmann introduced the concept of linear creep functions, as well as the

associated superposition principle, and he confirmed these groundbreaking ideas by an initial experimental campaign (Boltzmann, 1874). Ever since, these ideas have remained the foundation of the theory of viscoelasticity, which has been developed up to high mathematical maturity, see (Gurtin and Sternberg, 1962; Salençon, 1983; Leitman and Fisher, 1973).

Creep and relaxation functions of *mature* concrete are typically modeled based on rheological chain models, either in form of Kelvin-Voigt chains or in form of Maxwell chains, see (Thomson, 1875; Voigt, 1890) and (Maxwell, 1868). The involved regression parameters are identified by means of fitting the chain model to experimental data from macroscopic material testing. When it comes to the more challenging problem of *aging* creep and relaxation of *hydrating* concrete, spring stiffnesses and damper viscosities are typically a function of material age (Bažant and Wu, 1974; Bažant, 2015; Wendner et al., 2015a,b; Hubler et al., 2015). Both in the non-aging case and in the aging case, modeling and identification activities remain macroscopic, such that the actual microscopic origin of creep or relaxation remains unattended.

Nanoindentation testing suggests that creep of hydration products is the microscopic reason for macroscopic creep of cementitious materials (Acker, 2004; Vandamme and Ulm, 2013; Zhang et al., 2014). This is supported by a multiscale creep model, see (Scheiner and Hellmich, 2009), which explains *aging* creep of young concretes as the consequence (i) of *universal* isochoric creep of hydration products, and (ii) of changes of volume fractions of basic constituents of cement paste, induced by the consumption of cement clinker and water, as well as by the corresponding production of hydrates. Notably, *universal* creep of hydration products is described with a rheological model consisting of linear springs and dashpots with *constant*, i.e. *non-aging* stiffnesses and viscosities. This knowledge serves as input for the developments communicated in this contribution, as described next.

We here extend the investigation for the origin of creep of cementitious materials further down to the nanoscale of cement hydrates, where we envision that solid matter slides (upon loading) along interfaces which are filled with lubricating thin layers of adsorbed water, i.e. water in a "glassy", "liquid crystal" state, (Shahidi et al., 2014). As for the viscous behavior of the interfaces, we follow (Shahidi et al., 2014) and consider that the shear traction T acting on an adsorbed water layer is proportional to the shear dislocation rate $[\![\dot{\xi}]\!]$ of the interface, with an interface viscosity η_i as the proportionality constant

$$T = \eta_i \, [\![\dot{\xi}]\!] \tag{1}$$

Our analysis starts from corresponding anisotropic creep and relaxation tensors of matrix-interface composites containing *parallel* circular interfaces of identical radius a, see (Shahidi et al., 2014), where creep and relaxation tensors were derived in the framework of eigenstrain homogenization schemes of continuum micromechanics (Pichler and Hellmich, 2011).

Considering that hydration products contain interfaces oriented isotropically in *all space directions*, we here use the mixture rule and compute complete spatial av-

erages of parallel interface-related anisotropic creep and relaxation tensors, in order to derive *isotropic* creep and relaxation tensor bounds. These Voigt and Reuss bounds are compared with creep and relaxation functions of the aforementioned rheological model for universal creep of hydration products. This allows for quantitative identification (i) of the interface density d and (ii) of the product of interface size a and viscosity η_i. Considering that the characteristic interface size a is equal to the characteristic size of solid C-S-H crystals (Pellenq et al., 2009; Garrault et al., 2005), allows for quantifying the order of magnitude of the interface viscosity η_i of adsorbed water in cementitious material systems.

POINTS OF DEPARTURE FOR THE PRESENT STUDY

We here revisit prerequisites for the present study, i.e. we recall essential results from previous multiscale analyses, including (i) creep and relaxation tensors of matrix-interface composites with parallel interfaces, and (ii) universal rheological properties of hydrates.

Creep and relaxation tensors of matrix-interface composites with parallel interfaces

In our previous work, see (Shahidi et al., 2014), we have derived the following anisotropic creep and relaxation tensors for matrix-interface composites containing parallel interfaces of identical size (Fig. 1)

$$\underline{\underline{\underline{\underline{J}}}}_{hyd,aniso} = \underline{\underline{\underline{\underline{C}}}}_s^{-1} + \frac{4\,d\,(1-\nu_s)}{3\,\mu_s(2-\nu_s)}\left[1-\exp\left(-\frac{t}{\tau_{c,IM}}\right)\right]\underline{\underline{\underline{\underline{I}}}}_{aniso} \tag{2}$$

$$\underline{\underline{\underline{\underline{R}}}}_{hyd,aniso} = \underline{\underline{\underline{\underline{C}}}}_s - \frac{16\,\mu_s\,d\,(1-\nu_s)}{3\,(2-\nu_s)+16\,d\,(1-\nu_s)}\left[1-\exp\left(-\frac{t}{\tau_{r,IM}}\right)\right]\underline{\underline{\underline{\underline{I}}}}_{aniso} \tag{3}$$

where $\underline{\underline{\underline{\underline{C}}}}_s^{-1}$ and $\underline{\underline{\underline{\underline{C}}}}_s$ denote the elastic compliance tensor and the elastic stiffness tensor of the solid matrix

$$\underline{\underline{\underline{\underline{C}}}}_s^{-1} = \frac{1}{3\,k_s}\,\underline{\underline{\underline{\underline{I}}}}_{vol} + \frac{1}{2\,\mu_s}\,\underline{\underline{\underline{\underline{I}}}}_{dev}\,, \qquad \underline{\underline{\underline{\underline{C}}}}_s = 3\,k_s\,\underline{\underline{\underline{\underline{I}}}}_{vol} + 2\,\mu_s\,\underline{\underline{\underline{\underline{I}}}}_{dev} \tag{4}$$

In (2), (3), and (4), μ_s, k_s, and ν_s, respectively, stand for bulk modulus, shear modulus and Poisson's ratio of the isotropic solid matrix. Tensors $\underline{\underline{\underline{\underline{I}}}}_{vol}$ and $\underline{\underline{\underline{\underline{I}}}}_{dev}$, respectively, denote the volumetric and the deviatoric part of the symmetric fourth-order identity tensor, and $\underline{\underline{\underline{\underline{I}}}}_{aniso}$ stands for an anisotropic identity tensor which reads for interfaces

with normals pointing in $\underline{e}_z$ direction (Fig. 1) as

$$\begin{aligned}\underline{\underline{\underline{\underline{I}}}}_{aniso} = \quad & \underline{e}_x \otimes \underline{e}_z \otimes \underline{e}_x \otimes \underline{e}_z + \underline{e}_x \otimes \underline{e}_z \otimes \underline{e}_z \otimes \underline{e}_x \\ & + \underline{e}_z \otimes \underline{e}_x \otimes \underline{e}_x \otimes \underline{e}_z + \underline{e}_z \otimes \underline{e}_x \otimes \underline{e}_z \otimes \underline{e}_x \\ & + \underline{e}_y \otimes \underline{e}_z \otimes \underline{e}_y \otimes \underline{e}_z + \underline{e}_y \otimes \underline{e}_z \otimes \underline{e}_z \otimes \underline{e}_y \\ & + \underline{e}_z \otimes \underline{e}_y \otimes \underline{e}_y \otimes \underline{e}_z + \underline{e}_z \otimes \underline{e}_y \otimes \underline{e}_z \otimes \underline{e}_y \end{aligned} \tag{5}$$

Finally, $\tau_{c,IM}$ and $\tau_{r,IM}$ in Eqs. (2) and (3), respectively, denote characteristic creep and relaxation times of the interfacial micromechanics model, and they read as (Shahidi et al., 2014)

$$\tau_{c,IM} = \frac{8\,a\,\eta_i\,(1-\nu_s)}{\mu_s\,\pi\,3\,(2-\nu_s)} \tag{6}$$

$$\tau_{r,IM} = \frac{8\,a\,\eta_i\,(1-\nu_s)}{\mu_s\,\pi\,[3\,(2-\nu_s)+16\,d\,(1-\nu_s)]} \tag{7}$$

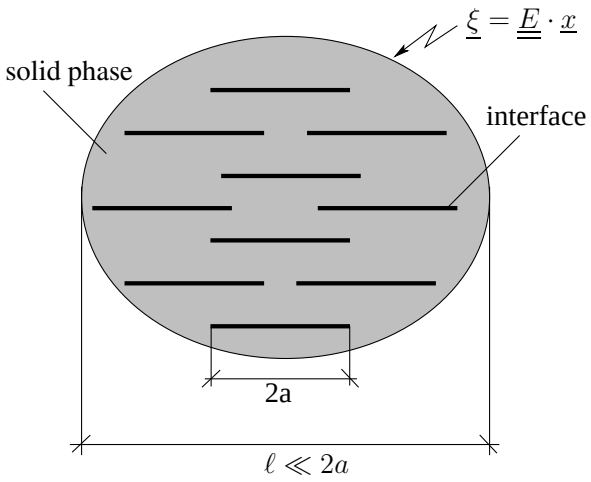

Figure 1: Matrix-interface composite containing parallel interfaces of identical size, after (Shahidi et al., 2014)

Multiscale model of concrete based on universal creep of hydrates

Scheiner and Hellmich (2009) have developed a multiscale model for aging creep of concrete (Fig 2). Hydrates were considered to behave purely elastic under isotropic loading, and viscoelastic under deviatoric loading, whereby short-term creep

behavior was essentially described by a Zener model, see (Zener, 1948) and Fig 2, with the following spring stiffnesses and damper viscosity[1]:

$$k_{hyd} = 14.1\,\text{GPa}\,, \quad \mu_{hyd} = 8.9\,\text{GPa}\,, \quad \mu_Z = 6.9303\,\text{GPa}\,, \quad \eta_Z = 1.9880 \cdot 10^6\,\text{GPa s} \tag{8}$$

Creep and relaxation functions of the Zener model, read as

$$\underset{\equiv\equiv}{J}_{hyd,Z} = \frac{1}{3\,k_{hyd}}\,\underset{\equiv\equiv}{I}_{vol} + \frac{1}{2}\left[\frac{1}{\mu_{hyd}} + \frac{1}{\mu_Z}\left\{1 - \exp\left(-\frac{t}{\tau_{c,Z}}\right)\right\}\right]\underset{\equiv\equiv}{I}_{dev} \tag{9}$$

$$\underset{\equiv\equiv}{R}_{hyd,Z} = 3\,k_{hyd}\,\underset{\equiv\equiv}{I}_{vol} + 2\left[\mu_{hyd} - \frac{\mu_{hyd}^2}{\mu_{hyd} + \mu_Z}\left\{1 - \exp\left(-\frac{t}{\tau_{r,Z}}\right)\right\}\right]\underset{\equiv\equiv}{I}_{dev} \tag{10}$$

where $\tau_{c,Z}$ and $\tau_{r,Z}$, respectively denote characteristic creep and relaxation times, defined as

$$\tau_{c,Z} = \frac{\eta_Z}{\mu_Z} \qquad \tau_{r,Z} = \frac{\eta_Z}{(\mu_{hyd} + \mu_Z)} \tag{11}$$

Notably, spring stiffnesses and damper viscosity (8) allow for a reliable prediction of short-term aging creep of young concretes, see Scheiner and Hellmich (2009).

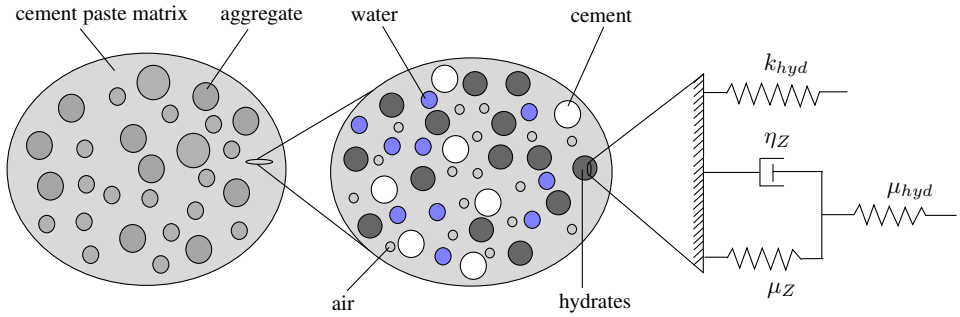

Figure 2: Multiscale organogram of concrete after (Scheiner and Hellmich, 2009)

CREEP OF HYDRATES REPRESENTED AS RANDOMLY ARRANGED MATRIX-INTERFACE BUILDING BLOCKS

We here resolve the microstructure of cement hydrates as a disordered arrangement of isotropically oriented building blocks of matrix-interface composites (Fig. 3).

[1] Notably, in (Scheiner and Hellmich, 2009), the full viscoelastic behavior of the hydrates was actually described by a Burgers model; the latter includes, in comparison to the Zener model, a further, serially added damper element, in order to account also for mid-term viscoelastic effects. When considering only short-term creep and relaxation, this additional damper element can be omitted, yielding the here employed Zener model.

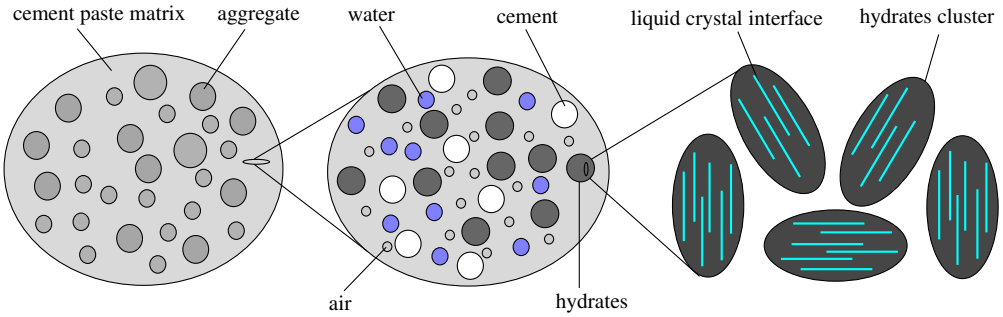

Figure 3: Multiscale organogram of concrete resolving the microstructure of cement hydrates as randomly oriented building blocks of matrix-interface composites

Isotropic creep and relaxation tensor bounds

In order to quantify the isotropic creep behavior of hydrates according to Fig. 3, we here use the mixture rule, i.e. we average the anisotropic creep and relaxation functions (2) and (3), respectively, over all possible space orientations, whereby the latter are described by the polar angle (= "zenith angle" or "colatitude") θ and the azimuthal angle ϕ of a spherical coordinate system:

$$\underline{\underline{\underline{\underline{J}}}}_{hyd,IM} = \int_{\phi=0}^{\phi=2\pi}\int_{\theta=0}^{\theta=\pi} \underline{\underline{\underline{\underline{J}}}}_{hyd,aniso} \frac{\sin\theta \,\mathrm{d}\theta \,\mathrm{d}\phi}{4\,\pi} \tag{12}$$

$$\underline{\underline{\underline{\underline{R}}}}_{hyd,IM} = \int_{\phi=0}^{\phi=2\pi}\int_{\theta=0}^{\theta=\pi} \underline{\underline{\underline{\underline{R}}}}_{hyd,aniso} \frac{\sin\theta \,\mathrm{d}\theta \,\mathrm{d}\phi}{4\,\pi} \tag{13}$$

Notably, $\underline{\underline{\underline{\underline{I}}}}_{aniso}$ is the only orientation-dependent element in Eqs. (2) and (3). Its complete spatial average follows as

$$\int_{\phi=0}^{\phi=2\pi}\int_{\theta=0}^{\theta=\pi} \underline{\underline{\underline{\underline{I}}}}_{aniso} \frac{\sin\theta \,\mathrm{d}\theta \,\mathrm{d}\phi}{4\,\pi} = \frac{4}{5}\underline{\underline{\underline{\underline{I}}}}_{dev} \tag{14}$$

The sought Reuss bound of the isotropic creep tensor is obtained by specifying (12) for (2) and by considering Eqs. (4) and (14) as

$$\underline{\underline{\underline{\underline{J}}}}_{hyd,IM} = \frac{1}{3\,k_s}\underline{\underline{\underline{\underline{I}}}}_{vol} + \frac{1}{2}\left[\frac{1}{\mu_s} + \frac{32\,d\,(1-\nu_s)}{15\,\mu_s\,(2-\nu_s)}\left\{1-\exp\left(-\frac{t}{\tau_{c,IM}}\right)\right\}\right]\underline{\underline{\underline{\underline{I}}}}_{dev} \tag{15}$$

The sought Voigt bound of the isotropic relaxation tensor is obtained by specifying (13) for (3) and by considering Eqs. (4) and (14) as

$$\underline{\underline{\underline{\underline{R}}}}_{hyd,IM} = 3\,k_s\,\underline{\underline{\underline{\underline{I}}}}_{vol} + 2\left[\mu_s - \frac{2}{5}\,\frac{16\,d\,(1-\nu_s)\,\mu_s}{3\,(2-\nu_s)+16\,d\,(1-\nu_s)}\left\{1-\exp\left(-\frac{t}{\tau_{r,IM}}\right)\right\}\right]\underline{\underline{\underline{\underline{I}}}}_{dev} \tag{16}$$

Creep and relaxation tensor bounds (15) and (16) suggest so-called "isochoric" creep and relaxation, i.e. time dependent behavior does not change the volume of hydrates, and, therefore, it is expected under deviatoric loading only. This is in perfect qualitative agreement with the validated modeling approach of (Scheiner and Hellmich, 2009).

Identification of interface density, size, and viscosity

In the sequel, we quantify interface density, size, and viscosity of cement hydrates, see Fig. 3. To this end, we compare the creep and relaxation tensor bounds (15) and (16), respectively, with creep and relaxation tensors (9) and (10) which are related to the Zener model of Scheiner and Hellmich (2009), see Fig. 2. Focusing on spontaneous elastic behavior, this comparison delivers

$$\mu_s = \mu_{hyd} = 8.9\,\text{GPa}\,, \qquad k_s = k_{hyd} = 14.1\,\text{GPa} \qquad \Rightarrow \qquad \nu_s = \nu_{hyd} = 0.24 \tag{17}$$

Next, we compare the time-dependent parts of the creep tensor bound (15) and of the Zener model-related creep tensor, see Eq. (9). In order to quantify interface density d, we extract from (15) and (9), respectively, the terms which are multiplied with the curled brackets containing the exponential function, we set the two terms equal, and we solve the resulting equation for the interface density d. This delivers, under consideration of the Zener model constants (8) and Eqs. (17),

$$d = \frac{\mu_s}{\mu_Z}\,\frac{15\,(2-\nu_s)}{32\,(1-\nu_s)} = 1.394 \tag{18}$$

In order to quantify the product of interface size a and interface density η_i, we set characteristic creep time $\tau_{c,Z}$, see (11), equal to the characteristic creep time $\tau_{c,IM}$, see (6). This delivers, under consideration of the Zener model viscosity (8) and of the interface density (18),

$$a\,\eta_i = \frac{4\,\pi\,d\,\eta_Z}{5} = 6.965\cdot 10^6\,\text{GPa s} \tag{19}$$

In order to get access to the interface viscosity η_i, we now consider characteristic interface sizes to range between $2a = 5\,\text{nm}$ and $2a = 60\,\text{nm}$ (Garrault et al., 2005; Pellenq et al., 2009) such that (19) yields

$$\eta_i \in [\,0.2322\,,\,2.7861\,]\cdot 10^{15}\,\text{GPa s m}^{-1} \tag{20}$$

The viscosity of adsorbed water follows from multiplying the interface viscosity η_i by the width of the interface which is envisioned to range between 1 and 2 nm:

$$\eta_{adsorbed-water} \in [\,0.2322\,,\,5.5722\,]\,10^{15}\,\text{Pa s} \tag{21}$$

Next, we compare the time-dependent parts of the relaxation tensor bound (16) and of the Zener model-related relaxation tensor, see Eq. (10). In order to quantify interface density d, we extract from (16) and (10), respectively, the terms which are multiplied with the curled brackets containing the exponential function, we set the two terms equal, and we solve the resulting equation for the interface density d. This delivers, under consideration of the Zener model constants and Eqs. (17),

$$d = \frac{15\,\mu_s\,(2-\nu_s)}{16\,(2\,\mu_Z - 3\,\mu_s)\,(1-\nu_s)} = -1.5 \tag{22}$$

Since a reasonable value of the interface density must be positive, Eq. (22) implies that the Voigt bound fails to exhibit mechanical relevance, rendering quantification of interface size and viscosity useless.

DISCUSSION AND CONCLUSIONS

We here used the mixture rule to compute *isotropic* creep and relaxation tensor bounds of cement hydrates, by averaging – over *all spatial orientations* – the *anisotropic* creep and relaxation tensors of composites containing an isotropic solid matrix and *parallel* interfaces. Comparing creep and relaxation tensor bounds with universal isochoric creep properties of cement hydrates allowed for identification not only of the interface density of cement hydrates, but – based on characteristic sizes of solid C-S-H crystals communicated in the open literature – also of the viscosity of water which is adsorbed in these interfaces. The creep tensor comparison delivers values of interface density and of adsorbed water viscosity on expected orders of magnitude when considering corresponding interface properties of hydroxyapatite (Qu et al., 2015). The relaxation tensor bound, in turn, fails to deliver a mechanically reasonable estimate of interface density, and this is reminiscent of a situation which is quite frequently encountered in homogenization, as described next. The Mori-Tanaka scheme is well-known to deliver reliable estimates of homogenized properties of matrix-inclusion composites and – for many two-phase composites – it can be shown to be equal to one of the Hashin-Shtrikman bounds. In other words, a bound may well exhibit the quality of a reliable estimate, as encountered herein in case of the creep tensor bound. In addition, upper and lower bounds may well quantify the limits of quite large domains, such that if one bound is close to reality, the second bound is naturally unrealistic, as encountered herein in case of the relaxation tensor bound. In the future, it will be interesting (i) to study this issue in more detail and (ii) to upscale – from the interface density and viscosity identified herein – aging short-term creep properties of hydrating concretes.

References

Acker, P. (2004). Swelling, shrinkage and creep: A mechanical approach to cement hydration. *Materials and Structures/Materiaux et Constructions*, 37(268):237–243.

Bažant, Z. (2015). RILEM draft recommendation: TC-242-MDC multi-decade creep and shrinkage of concrete: material model and structural analysis*: Model B4 for creep, drying shrinkage and autogenous shrinkage of normal and high-strength concretes with multi-decade applicability. *Materials and Structures/Materiaux et Constructions*, 48(4):753–770.

Bažant, Z. and Wu, S. (1974). Creep and shrinkage law for concrete at variable humidity. *Journal of Engineering Mechanics (ASCE)*, 100(6):1183–1209.

Boltzmann, L. (1874). Zur Theorie der elastischen Nachwirkung [Concerning the theory of the elastic aftereffect]. *Sitzungsberichte der Mathematisch-Naturwissenschaftlichen Classe der Kaiserlichen Akademie der Wissenschaften*, 70(2):275–306. In German.

Garrault, S., Finot, E., Lesniewska, E., and Nonat, A. (2005). Study of CSH growth on C3S surface during its early hydration. *Materials and Structures*, 38(4):435–442.

Gurtin, M. and Sternberg, E. (1962). On the linear theory of viscoelasticity. *Archives of Rational Mechanics and Analysis*, 11:291–356.

Hubler, M. H., Wendner, R., and Bažant, Z. (2015). Statistical justification of model B4 for drying and autogenous shrinkage of concrete and comparisons to other models. *Materials and Structures/Materiaux et Constructions*, 48(4):797–814.

Leitman, M. J. and Fisher, M. C. (1973). *The linear theory of viscoelasticity*. Springer-Verlag, Berlin-Heidelberg-New York.

Maxwell, J. C. (1868). On the dynamic theory of gases. *Phil. Mag*, 35:129 – 145.

Pellenq, R. J.-M., Kushima, A., Shahsavari, R., Van Vliet, K. J., Buehler, M. J., Yip, S., and Ulm, F.-J. (2009). A realistic molecular model of cement hydrates. *Proceedings of the National Academy of Sciences of the United States of America*, 106(38):16102–16107.

Pichler, B. and Hellmich, C. (2011). Upscaling quasi-brittle strength of cement paste and mortar: A multi-scale engineering mechanics model. *Cement and Concrete Research*, 41(5):467–476.

Qu, T., Verma, D., Shahidi, M., Pichler, B., Hellmich, C., and Tomar, V. (2015). Mechanics of organic-inorganic biointerfaces-implications for strength and creep properties. *MRS Bulletin*, 40(4):349–358.

Salençon, J. (1983). *Viscoélasticité [Viscoelasticity]*. Presses de l'Ecole Nationale des Ponts et Chaussées. In French.

Scheiner, S. and Hellmich, C. (2009). Continuum microviscoelasticity of model for aging basic creep of early-age concrete. *Journal of Engineering Mechanics (ASCE)*, 135(4):307–323.

Shahidi, M., Pichler, B., and Hellmich, C. (2014). Viscous interfaces as source for material creep: A continuum micromechanics approach. *European Journal of Mechanics, A/Solids*, 45:41–58.

Thomson, W. L. K. (1875). On the dynamic theory of gases. *Math. Phys.*, 4:27.

Vandamme, M. and Ulm, F.-J. (2013). Nanoindentation investigation of creep properties of calcium silicate hydrates. *Cement and Concrete Research*, 52:38–52.

Voigt, W. (1890). Ueber die innere reibung der festen Körper, insbesondere der Krystalle. *Abhandlungen der Königlichen Gesellschaft der Wissenschaften in Göttingen*, 36:3–48.

Wendner, R., Hubler, M. H., and Bažant, Z. (2015a). Optimization method, choice of form and uncertainty quantification of model B4 using laboratory and multi-decade bridge databases. *Materials and Structures/Materiaux et Constructions*, 48(4):771–796.

Wendner, R., Hubler, M. H., and Bažant, Z. (2015b). Statistical justification of model B4 for multi-decade concrete creep using laboratory and bridge databases and comparisons to other models. *Materials and Structures/Materiaux et Constructions*, 48(4):815–833.

Zener, C. (1948). *Elasticity and Anelasticity of Metal*. University of Chicago Press, IL, USA.

Zhang, Q., Le Roy, R., Vandamme, M., and Zuber, B. (2014). Long-term creep properties of cementitious materials: Comparing microindentation testing with macroscopic uniaxial compressive testing. *Cement and Concrete Research*, 58:89–98.

Modelling of Alkali-Silica Reaction (ASR)—Concrete Structures

S. Seręga[1]; A. Winnicki[2]; and F. Norys[3]

[1,2]Faculty of Civil Engineering, Cracow University of Technology, ul. Warszawska 24, 31-155 Kraków, Poland. E-mail: sserega@pk.edu.pl[1]; andrzej@hypatia.L5.pk.edu.pl[2]
[3]Ph.D. Candidate, Cracow University of Technology, ul. Warszawska 24, 31-155 Kraków, Poland. E-mail: filipnorys@interia.pl

Abstract

Paper deals with creep effects being combined with alkali-silica reaction (ASR) in concrete. At first description of reaction kinetics is discussed, then the creep model is presented based on Model Code 2010 (MC2010) approach. An approximation of MC2010 analytical formulation in the form of Kelvin chain is proposed. Presented numerical examples show that it renders analytical formulation really well. Next a numerical algorithm developed previously by authors in order to solve chemomechanical problems is recalled. Performed exemplary numerical computations for a gravity dam show clearly that the influence of creep on the overall behavior of the structure is relatively small in comparison with effects caused by ASR itself.

INTRODUCTION

Alkali-silica reaction (ASR) in concrete is nowadays a recognized cause of the progressive deterioration and damage in many plain and reinforced concrete structures (Hobbs 1988). The reaction was for the first time noted in 1940 by Stanton who studied causes of cracking of RC structures in California (Hobbs 1988). He suggested chemical reaction taking place between alkalis in cement Na_2O, K_2O and silica SiO_2 in aggregate in presence of water as a cause of concrete deterioration.

The commonly accepted fact is that the amorphous gel located in material pores is the final product of the reaction. The gel is highly hydrophilic, imbibes large amounts of water and swells considerably. In general gel is composed of alkali silica hydrate N(K)-S-H ($Na_2(K_2)O$-SiO_2-H_2O) and/or calcium alkali silica hydrate C-N(K)-S-H (CaO-$Na_2(K_2)O$-SiO_2-H_2O).

In the last two decades much effort was put into chemomechanical aspects of ASR and their influence on the behavior of existing structures. This effort resulted in development of many phenomenological chemomechanical models describing the behavior of concrete subjected to action of ASR dependent on both temperature and humidity – see for example Pietruszczak (1996), Poyet (2003), Ulm et al. (2000), Winnicki and Pietruszczak (2008). The presented paper is a continuation of the work on the numerical modelling of ASR which results were shown by Winnicki et al. (2014) and Winnicki et al. (2015), this time focusing on creep effects being combined with ASR action.

REACTION KINETICS

Following the approach proposed by Pietruszczak (1996) and Ulm et al. (2000) kinetics of the reaction is described with a nondimensional variable called reaction extent ξ which describes progress of the reaction and changes in the course of ASR from 0.0 to 1.0. In the case of the alkali-silica reaction which is characterized by the increase of the volume of the material (swelling) reaction extent can be linked to volumetric chemical strain caused by reaction using the equation:

$$\xi(t) = \frac{\varepsilon_{ASR}(t)}{\varepsilon_{ASR}^{\infty}} \quad , \quad \varepsilon_{ASR}^{\infty} = \varepsilon_{ASR}(t \to \infty), \quad 0.0 \le \xi(t) < 1.0$$

where $\varepsilon_{ASR}(t)$ is concrete expansion at time t, $\varepsilon_{ASR}^{\infty}$ is maximal linear concrete expansion.

In such a way internal variable ξ is associated with concrete expansion which is observable and measurable quantity. Kinetics of the reaction is governed by the equation:

$$A_m(\xi) = k_d \frac{d\xi}{dt}$$

where $A_m(\xi)$ is a change in the molar concentration of reactants, k_d is a reaction parameter. In the course of the reaction variable $A_m(\xi)$ decreases from the initial value $A_m(\xi = 0.0) = A_{m0}$ at which reaction starts to end value $A_m(\xi = 1.0) = 0.0$ when reaction stops. Order of the reaction kinetics is determined by relation of the function $A_m(\xi)$ to variable ξ. Following the work of Larive (1998) the modified form of the first order equation is assumed:

$$1 - \xi = t_c(\xi) \frac{d\xi}{dt} \tag{1}$$

This relation is not a pure first order equation because t_c is not a constant internal parameter but a variable changing in the reaction course according to the formula:

$$t_c(\xi) = \tau_{ch} \frac{1 + \exp(-\tau_{lat} / \tau_{ch})}{\xi + \exp(-\tau_{lat} / \tau_{ch})}$$

where τ_{lat} is latency time (describing the first stage of the reaction where gel is produced and fills pores of the material exerting only minimal pressure on material skeleton), τ_{ch} is characteristic time which governs the reaction rate. It is possible to get closed form solution of Eq. (1):

$$\xi(t,T) = \frac{1 - \exp\left(-t/\tau_{ch}(T)\right)}{1 + \exp\left(-\left(t - \tau_{lat}(T)\right)/\tau_{ch}(T)\right)}$$

for the case of constant temperature and humidity (when τ_{lat} and τ_{ch} remain constant). In the original work of Larive (1998) only dependence of τ_{lat} and τ_{ch} on temperature was taken into account following Arrhenius law:

$$\tau_{lat}(T) = \tau_{lat}(T_0) \exp\left(U_{lat}\left(\frac{1}{T} - \frac{1}{T_0}\right)\right) \qquad \tau_{ch}(T) = \tau_{ch}(T_0) \exp\left(U_{ch}\left(\frac{1}{T} - \frac{1}{T_0}\right)\right)$$

where U_{lat} and U_{ch} are the thermal activation constants for τ_{lat} and τ_{ch}, respectively.

Authors have modified Larive's (1998) formulae for the latency and characteristic times in order to include dependency on the relative humidity:

$$\tau_{lat}(T,RH)=\tau_{lat}(T_0)\exp\left(U_{lat}\left(\frac{1}{T}-\frac{1}{T_0}\right)\right)f_5(RH)$$

$$\tau_{ch}(T,RH)=\tau_{ch}(T_0)\exp\left(U_{ch}\left(\frac{1}{T}-\frac{1}{T_0}\right)\right)f_6(RH)$$

where $f_{5,6}(RH)=\left(\frac{RH}{100}\right)^{k,l}$.

In the above equations additional new parameters k, l are introduced. Authors have developed procedure for calibrating values of all (original and newly introduced) parameters for given experimental data using the least square method. The detailed analysis and comparison of assumed reaction kinetics model with available experimental data (Larive 1998, Poyet 2003) have been presented by Winnicki et al. (2014) and Winnicki et al. (2015). In authors' opinion the model renders experimental data reasonably well.

CREEP MODEL

As a novel element in the proposed approach creep model is introduced. ASR reaction takes place over the long period of time, therefore the mechanical analysis of ASR should also take into account the creep effects. In this paper MC2010 approach to creep is followed. MC2010 makes a distinction between basic and drying creep. For the time being as the only example the large concrete dam is analyzed. In such a case the large humidity exists almost in the whole structure during the analyzed time period therefore drying creep can be neglected. Additionally, in the creep model it is necessary to include ASR influence assuming that the concrete Young modulus is a function of current value of reaction extent ξ. In such a way coupling between ASR (causing deterioration of stiffness) and creep is introduced as:

$$J(t,\tau,\xi)=\frac{1}{E_0(\xi)}+\frac{\varphi_{bc}(t,\tau)}{E_0(\xi=0.0)} \tag{2}$$

where E_0 is concrete elastic modulus, φ_{bc} is basic creep coefficient.
In MC2010 analytical formulae are given for creep coefficient φ_{bc}. In Figure 1a the exemplary creep functions for different times of loading and reaction extent $\xi = 0.0$ are presented.

In the paper the creep function J is approximated in the form of truncated Dirichlet series. This degenerated form of creep function can be interpreted as Kelvin chain model:

$$\bar{J}(t,\tau,\xi)=\frac{1}{E_0(\xi)}+\sum_{i=1}^{n}\frac{1}{E_i(\tau)}\left(1-e^{-\frac{t-\tau}{\lambda_i}}\right) \tag{3}$$

where E_i are the stiffness of the individual springs in Kelvin chain and λ_i are retardation times. Kelvin chain model is, among others, implemented as a standard material model in DIANA code. Using the procedure for fitting material parameters

offered by DIANA the proper values of material parameters have been established. It appeared that in order to approximate MC2010 analytical formulae reasonably well, it is enough to take only three terms of the series. The fitting procedure has been performed for no ASR influence (i.e. $\xi = 0.0$). The values of the spring stiffness and retardation times adopted in the analysis are shown in Figure 1b.

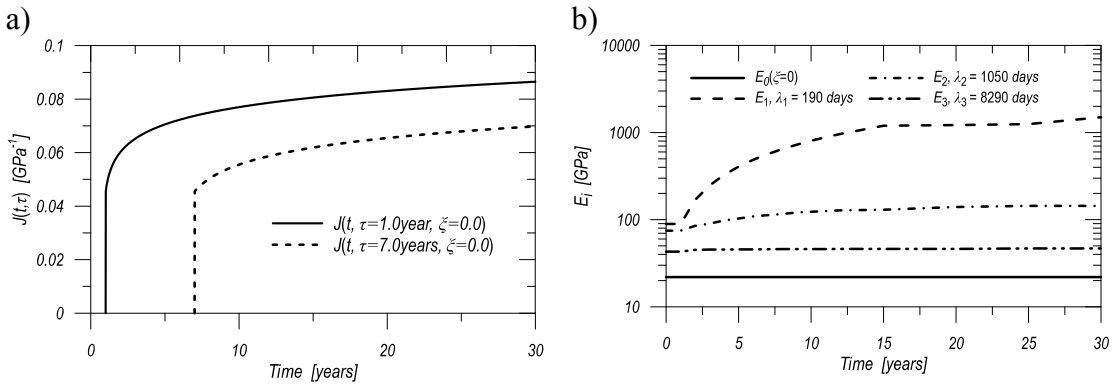

Figure 1. a) example of creep functions for concrete in analyzed dam, b) materials parameters for Kelvin chain model.

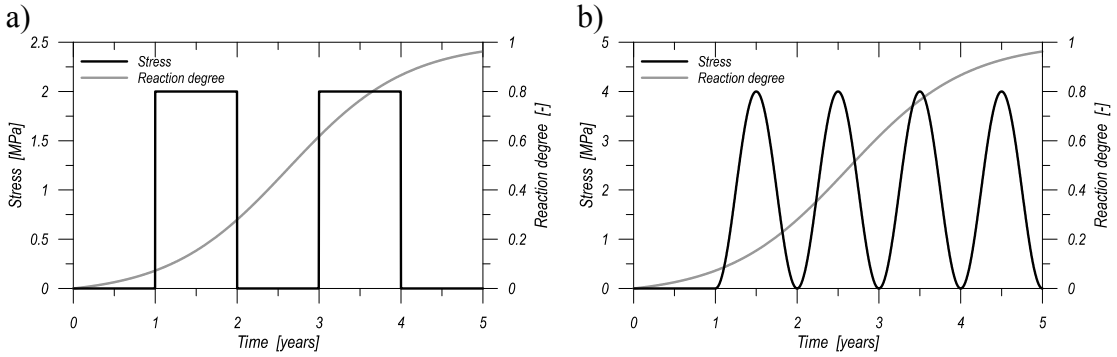

Figure 2. Loading scenarios and reaction course in time.

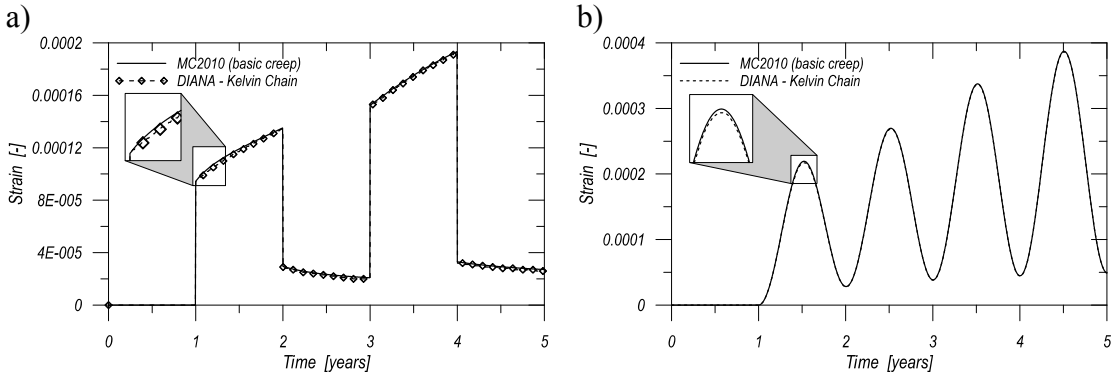

Figure 3. Calculated strains for creep functions according to Eq. (2) and (3).

Numerical examples at the material point level have been done using both the exact analytical formulation of MC2010 (coded in Mathcad) and Kelvin chain model (available in DIANA code) with the extent parameter ξ being defined in time domain as the input value. Figure 2 shows two analyzed loading scenarios and the reaction course in time. The first loading scenario is periodically constant load in time whereas the second one is described by the sine function. In both cases the extent parameter ξ increases continually in time domain form 0.0 to 1.0. The given examples show clearly that numerical approximation in form of finite Kelvin chain renders MC2010 approach in a very good way – see Figure 3.

NUMERICAL ALGORITHM

Authors elaborated a numerical algorithm enabling of the presented reaction kinetic model to be included in the FEM nonlinear analysis using standard commercial codes, as for example DIANA (Winnicki et al. 2014 and Winnicki at al. 2015). Below for sake of completeness the algorithm is briefly repeated.

The reaction extent is treated as input variable. Therefore for a given boundary and initial conditions in time domain the reaction extent ξ has to be computed as a scalar variable over the given area for every time instant. In turn the reaction extent ξ depends strongly on temperature and relative humidity fields. Therefore, at first temperature and relative humidity fields for the whole structure are computed in time domain solving Fourier-Kirchhoff equation for temperature and moisture transport equation given by Xi et al. (1994a) – Figure 4. For the Fourier-Kirchhoff equation the constant thermal capacity and conductivity coefficients are assumed. For the moisture transport equation both moisture capacity and diffusion coefficient are taken as functions of relative humidity according to approach by Xi et al. (1994b). These computations have been performed using standard transport models of DIANA code.

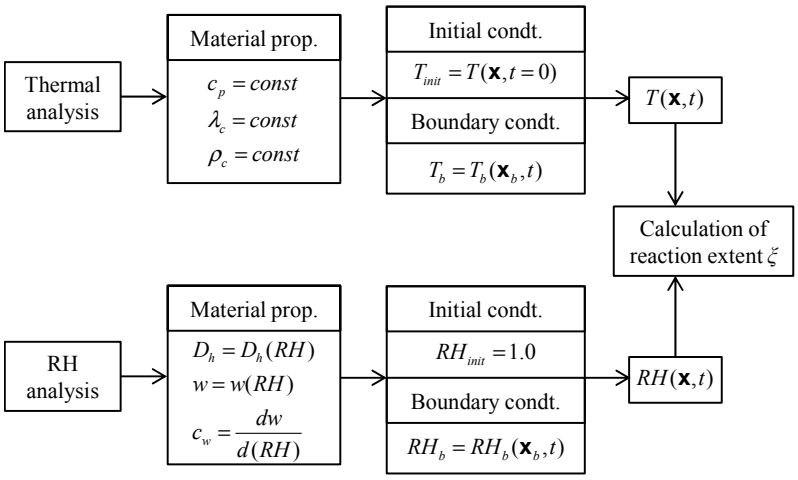

Figure 4. Computational algorithm (part 1).

Having temperature and relative humidity values computed for the whole structure in time domain the reaction extent ξ has been calculated according to the formulae presented above – Figure 5a. As the last stage of the algorithm the

mechanical analysis is performed for the given time instant using the reaction extent ξ as an input value – Figure 5b.

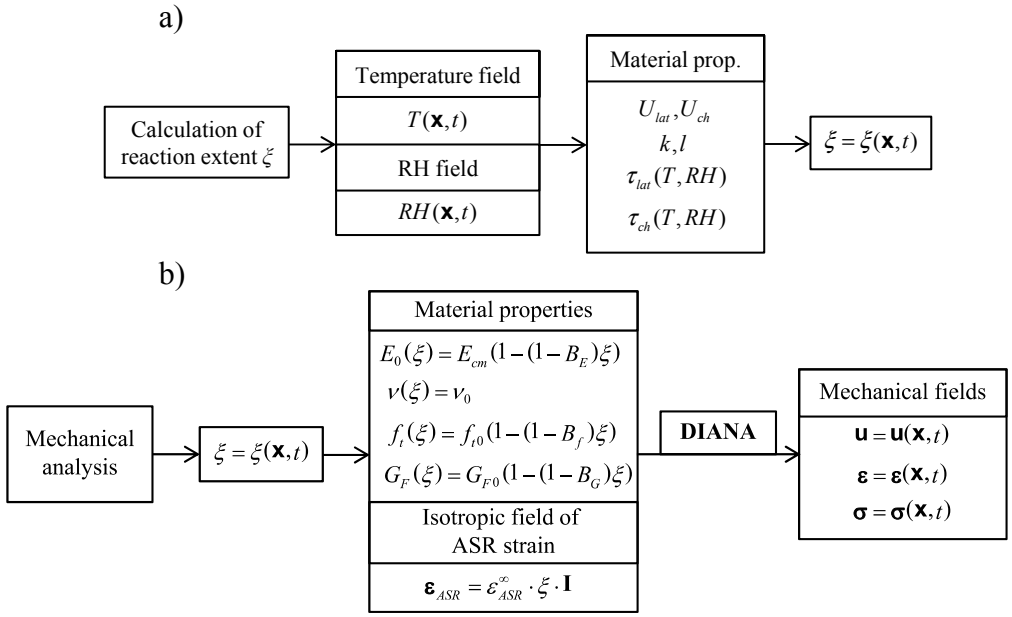

Figure 5. Computational algorithm (part 2).

In the mechanical analysis it is assumed that both elastic (Young modulus) and strength properties (tensile strength, fracture energy) are functions of the reaction extent ξ deteriorating with its increase. The swelling is accounted for by introducing imposed strain $\boldsymbol{\varepsilon}_{ASR}$ as an isotropic, linear function of the reaction extent ξ. As the mechanical model the smeared crack approach in the form of multidirectional fixed crack model (Borst 1987) together with Kelvin chain model for creep as implemented in DIANA code is used. Details of coupling between smeared cracking and creep are provided by Borst and Boogaard (1994). The regularization of obtained numerical results after cracking is provided by keeping the constant fracture energy value for a given area of a cracked element ("fracture energy trick" (Borst 1987)).

CASE STUDY – FONTANA DAM

As a numerical example Fontana gravity dam was chosen following the numerical analysis made by Comi et al. (2009). Fontana dam is located in Graham Country, North Carolina USA and its construction was finished in 1946. Three years after the end of completing (1949) for first time a pattern of cracking was observed together with an upstream movement of the structure. Later inspections (1972) found large cracks inside the dam. According to the information provided by Comi et al. (2009) petrographic examination made in 1999 revealed the presence of ASR. The detailed pattern of cracks in one of the damaged dam monoliths can be found in http://simscience.org/cracks. Analysed cross-section together with the subsoil is presented in Figure 6 showing assumed FE mesh and applied initial and boundary conditions. In the previous papers by Winnicki et al. (2014) and Winnicki et al. (2015) the detailed results of numerical analysis of ASR action together with dead

load and water pressure without creep effects were shown. In the presented paper new results connected with taking into account creep are described. Assumed mechanical and ASR parameters as well as initial and boundary conditions are given by Winnicki et al. (2014) and Winnicki et al. (2015).

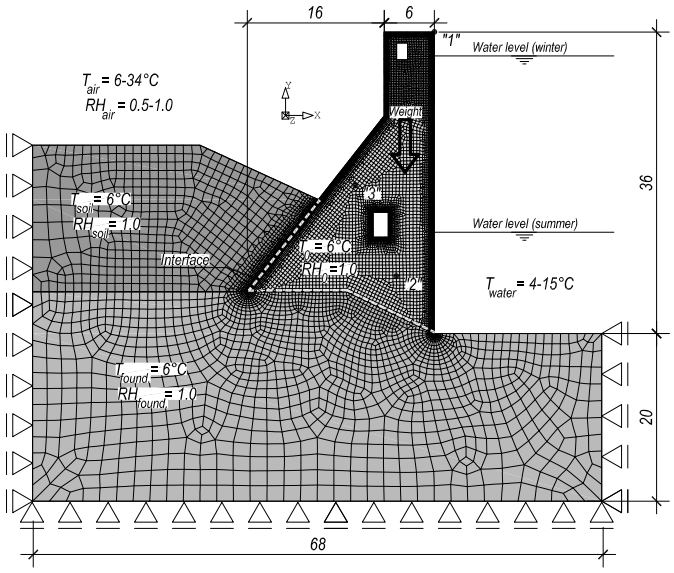

Figure 6. Cross section of Fontana dam together with foundation on subsoil.

Presented analysis of the Fontana dam comprises two parts. The first one is pertinent to the normal exploitation state of the dam within time period 30 years, the second one concerns the catastrophic situation in which the overtopping load till the failure of the dam is analyzed.

Following the numerical algorithm outlined above the relative humidity and temperature fields have been computed. On the basis of known humidity and temperature fields the reaction extent in time domain for the whole structure has been computed – Figure 7.

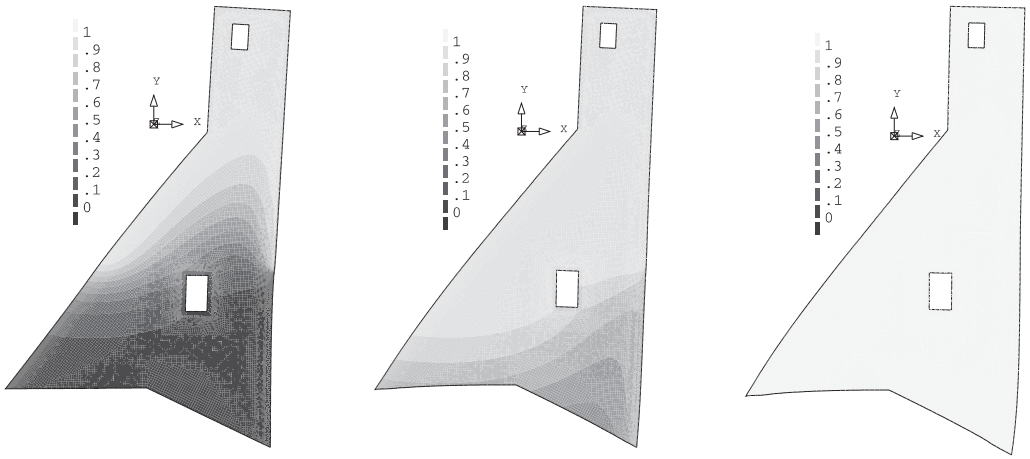

Figure 7. Reaction extent fields in dam: after 7, 14 and 30 years, respectively.

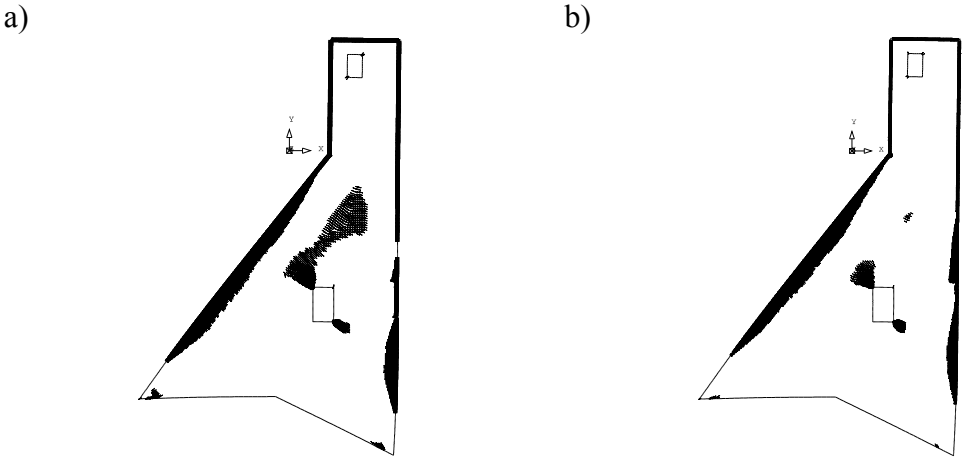

Figure 8. Crack pattern after 30 years, $\varepsilon_{ASR}^{\infty} = 0.075\%$: a) without creep, b) with creep (note that closed cracks are also shown).

In Figure 8 the crack patterns after 30 years of ASR action are shown for the cases with and without creep effects, respectively. It can be concluded from this figure that creep effects result in reducing the cracked area mainly in the middle part of the dam.

For a selected point at the crown of the dam the histories of the displacements are shown in Figure 9. It follows from this figure that after 30 years of ASR influence displacements are eventually stabilized. It can be also observed that the influence of creep on displacements is negligibly small.

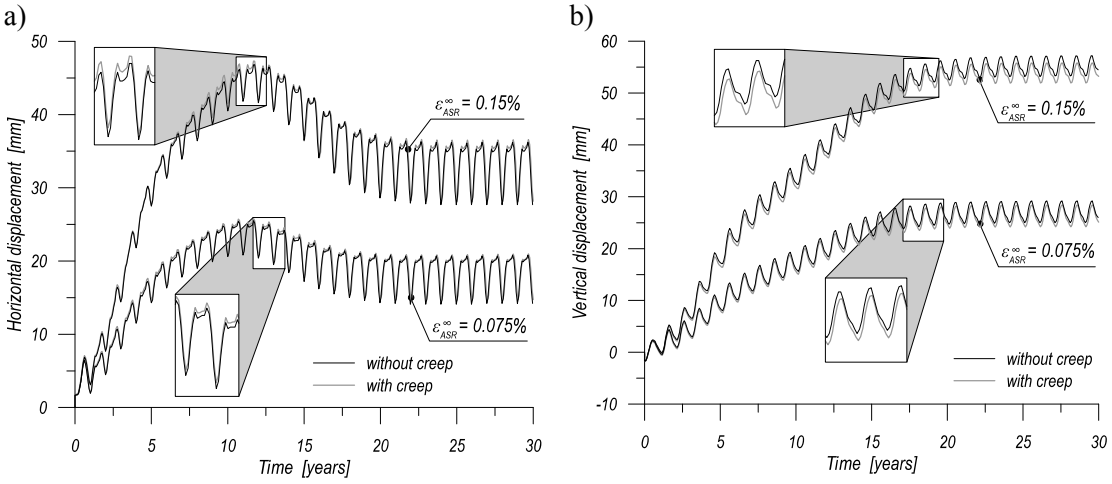

Figure 9. Displacements of the crown of dam: a) horizontal, b) vertical.

As a next case the overtopping load till the failure of the dam applied to the structure after 30 years of ASR action together with creep is analyzed. Figure 10 shows the overtopping ratio versus horizontal displacement of the crown (overtopping ratio is defined as H_{wave}/H_{dam}, where H_{wave} is the height of water level during flood, H_{dam} means the height of a dam). This overtopping ratio can be

considered as the global safety factor for the dam structure. The ratio H_{wave}/H_{dam} calculated after 30 years of ASR action is approximately equal to 2.1. In Figure 10 H_{wave}/H_{dam} values are also plotted for dam not affected by ASR. It turns out that in this case the overtopping ratio is less than for dam affected by ASR. This controversial observation can be explained by the fact that the chemical strains introduce compressive stresses at the upstream side of the dam, at the critical section located above the inspection gallery. From Figure 10 it follows that ASR affected dam behaves in the softer way (in the sense of the maximum load displacement curve) than ASR-free dam. This behavior is caused by the amount of accumulated cracks due to ASR.

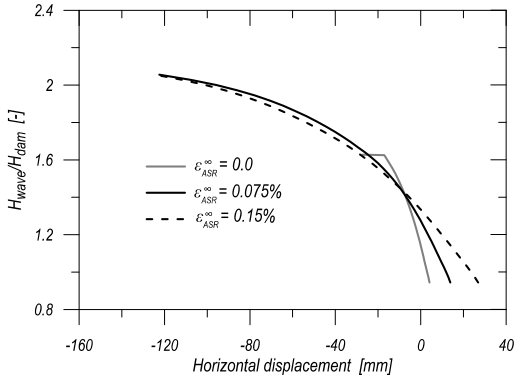

Figure 10. Overtopping ratio versus horizontal displacement.

Comparing the above presented results with previously published results concerning a case without creep effects (Winnicki et al. 2014 and Winnicki et al. 2015) it can be stated that influence of creep on the overtopping ratio is negligibly small.

CLOSING REMARKS

The presented paper is a continuation of the work on the numerical modelling of ASR which results were shown by Winnicki et al. (2014) and Winnicki et al. (2015), this time focusing on creep effects being combined with ASR action. For creep the model of MC2010 is adopted using numerical approximation in the form of Kelvin chain. The numerical examples show that this numerical approximation with only three terms of series being included renders the original analytical formulation very well.

Mechanical effects of ASR action together with creep at the structural level has been computed using DIANA code with numerical algorithm for solving chemomechanical problems developed by authors (Winnicki et al. 2014 and Winnicki et al. 2015). As the mechanical model the smeared crack approach in the form of multidirectional fixed crack model (Borst 1987) as implemented in DIANA code has been used. Coupling between smeared cracking and creep is made in the way described by Borst and Boogaard (1994).

As a numerical example the Fontana dam has been chosen analyzed by authors previously without creep effects (Winnicki et al. 2014 and Winnicki et al.

2015). Comparison between previously obtained numerical results and these presented now with creep being taken into account shows clearly that the creep influence on the overall behavior of structure is negligibly small. Therefore, a conclusion can be stated that in the case of massive plain concrete structures the ASR modelling without creep effects being taken into account is an acceptably good approximation usually on safe side.

REFERENCES

Comi, C., Fedele, R. and Perego, U. (2009). "A chemo-thermo-damage model for the analysis of concrete dams affected by alkali-silica reaction." *Mech. Mat.*, 41:210-230.

de Borst, R. (1987) "Smeared cracking, plasticity, creep and thermal loading - a unified approach." *Com. Meth. Appl. Mech. Eng.*, 62:89-110.

de Borst, R., and van den Boogaard, A. H. (1994). "Finite-element modeling of deformation and cracking in early-age concrete." *J. Eng. Mech. Div.*, ASCE 120, pp. 2519-2534.

Hobbs, D.W. (1988). *Alkali-silica reaction in concrete*. Thomas Telford, London.

Larive, C. (1998). *Apports combinés de l'expérimentation et de la modélisation a la comprehension de l'alcali reaction et de ses effets mécaniques*. Technical Report LPC, OA 28, Laboratoires des Ponts et Chaussées, Paris, France.

Pietruszczak, S. (1996). On the mechanical behaviour of concrete subjected to alkali-aggregate reaction. *Computers & Structures*, 58:1093-1097, 1996.

Poyet, S. (2003). *Etude de la dégradation des ouvrages en béton atteints par la réaction alcali-silice: Approche expérimentale et modélisation numérique multi-échelles des dégradations dans un environnement hydro-chemo-mécanique variable*. PhD thesis, Universite de Marne-La-Valleé.

Ulm, F.-J., Coussy O., Li, K., and Larive, C. (2000). "Thermo-chemomechanics of ASR expansion in concrete structures." *J. of Eng. Mech*., 126:233-242.

Winnicki, A. and Pietruszczak, S. (2008). "On mechanical degradation of reinforced concrete affected by alkali-aggregate reaction." *J. Eng. Mech.*, 134:611-628.

Winnicki, A., Seręga, S. and Norys, F. (2014). "Chemoplastic modelling of Alkali-Silica Reaction (ASR)." *Computational Modelling of Concrete Structures Euro-C 2014 Int. Conf*., 765-774, St. Anton am Arlberg, Austria.

Winnicki, A., Seręga, S. and Norys, F. (2015). „Alkali-silica reaction in concrete – chemomechanical description." *Cracow University of Technology Jubilee Monograph*, Kraków, Poland, accepted for publication.

Xi, Y., Bažant, Z. P., and Hamlin, M. J. (1994a). "Moisture diffusion in cementitious materials. Adsorption isotherms." *Adv. Cem. Bas. Mater.*, 1:248-257.

Xi, Y., Bažant, Z. P., and Hamlin, M. J. (1994b). "Moisture diffusion in cementitious materials. Moisture capacity and diffusivity." *Adv. Cem. Bas. Mater.*, 1:258-266.

DIANA (2014) *Finite Element Analysis. User's Manual.*

International Federation for Structural Concrete. (2012), *fib Model Code 2010. Final Draft – Volume 1*, Lausanne, Switzerland.

Modelling of the Drying Process in Pores and the Shrinkage of Cement Paste at High Relative Humidity

Lin Liu[1] and Huisu Chen[2]

[1]College of Civil and Transportation Engineering, Hohai University, Nanjing 210098, China (corresponding author). E-mail: LinLiuLinLiu@gmail.com
[2]Jiangsu Key Laboratory of Construction Materials, School of Materials Science and Engineering, Southeast University, Nanjing 211189, China. E-mail: chenhs@seu.edu.cn

Abstract

To fundamentally understanding the drying behavior of cementitious materials, this paper presents a microstructure-based approach to model the drying process in pores and the shrinkage of cement specimens. At high relative humidity (>84% RH), on the basis of Kelvin-Laplace equation and a microstructure model HYMOSTRUC3D, the drying process in capillary pores is simulated by several algorithms. Considering the drying deformation of C-S-H and assuming the capillary pressure in capillary pores as the main responsible stress for the drying deformation, the shrinkage of cement paste at different RH is calculated by three-dimensional lattice analyses.

INTRODUCTION

Drying shrinkage can be a major cause of the deterioration of concrete structures, especially in dry environment. When the environmental relative humidity decreases, the cement-based materials undergo a drying process and shrinkage occurs. Shrinkage generally leads to cracking at a restrained condition, and further it will affect the structural integrity and durability.

Capillary pressure mechanism can be predominant in the range of internal relative humidity (RH) that a typical concrete will experience, especially at high relative humidity. According to Kelvin equation, the capillary pressure p_{cap} is given by (Grasley Z.C. *et al.*, 2005, Coussy O. *et al.*, 2004),

$$p_{cap} = p_{atm} - p_L = -\frac{RT}{\overline{V}_L}\ln h_R \tag{1}$$

where p_L is pressure in pore fluid, MPa; p_{atm} is the atmospheric pressure, MPa; $\overline{V}_L$ is the molar volume of water, cm^3/mol; R is the universal gas constant, J/(mol•K); T is temperature, K; h_R represents the value of relative humidity. Based on a spherical meniscus, combing equation (1) and a Laplace equation, the pore radius threshold for drying at a specific h_R and T can be described as (Coussy O. *et al.*, 2004),

$$r_{\Delta u} = -\frac{2\gamma_{LV}}{(RT/\overline{V}_L)\ln h_R} \tag{2}$$

where $r_{\Delta u}$ represents the smallest pore access radius of the pore volume currently invaded by air; γ_{LV} is the surface tension of the liquid/vapor interface, J/m^2. At 293.15 *K*, *R*=8.314 J/(mol•K), $\overline{V}_L$=18.032 cm^3/mol and γ_{LV}=0.0728 J/m^2 are adopted in this paper (Lide D.R., 2001). At relative humidity larger than 85% RH, capillary pores larger than 12 nm get empty, while gel pores are remaining full of water (Jennings H.M., 2008).

In order to obtain a better understanding of the drying process and to evaluate the shrinkage behavior of cementitious materials, this paper presents a microstructure-based approach to model the drying process in pores and the shrinkage of cement specimens. In this paper, the drying and shrinkage behavior of cement paste with water-to-cement ratio of 0.4 after hydrating 28 days is studied.

SIMULATION OF DRYING PROCESS IN PORES

The microstructure of cement paste at a certain hydration degree is first generated by a numerical model HYMOSTRUC3D (van Breugel K. 1993, Ye G. 2003). Using CEM I 42.5N with a potential Bogue phase composition of 64% C_3S, 13% C_2S, 8% C_3A, and 9% C_4AF by mass, cubic cement paste samples with a length of 75 μm are generated. Cement particles with a Blaine surface area value of 420 m^2/kg and a discretized particle size distribution between 1 μm and 37 μm with an interval of 1 μm, are randomly distributed in the 3D cubes and then hydrate. Periodic boundary conditions are utilized during the particle placement. The microstructure of cement paste is represented by vectors which give the *x*, *y*, *z* values of each spherical hydrated cement particle in the 3D coordinate. For cement paste of water-to-cement (*w/c*) ratio 0.4, the hydration degree is 0.71 after hydrating 28 days. In figure 1, mixed phase represents the voxel partially occupied by outer C-S-H and partially occupied by pores, which will be further digitalized.

In order to characterize the pore structure of cement paste and to capture the pores we concerned, a multi-step digitalization algorithm is employed. Similar applications of the multi-step digitalization algorithm can be found in calculations of pore size distribution (Liu L. *et al.*, 2011 & 2012) and in water freezing in pores (Liu L. *et al.*, 2014a&b). Pores are represented by voxels of various sizes and are obtained by step-by-step digitalization. According to Kelvin-Laplace equation (equation (2)) and from the multi-step digitalized pore structure, the drying process in pores can be simulated, see figure 2. Pores are categorized as empty pores and water-filled pores in this stage. At a certain relative humidity, large pores connected to the surfaces of specimen are first emptied. As the environmental relative humidity decreases, the smaller pores connected to the emptied large pores then get emptied. Since the simulation in this study is performed at microscopic scale, the relative humidity gradients are not considered.

The pore structure filled with air and water at different relative humidity are illustrated in figure 3. As the environmental relative humidity decreases, changes of the water saturation degree S_w are given in figure 4. S_w is defined as ratio of the pore volume occupied by the fluid to the total pore volume.

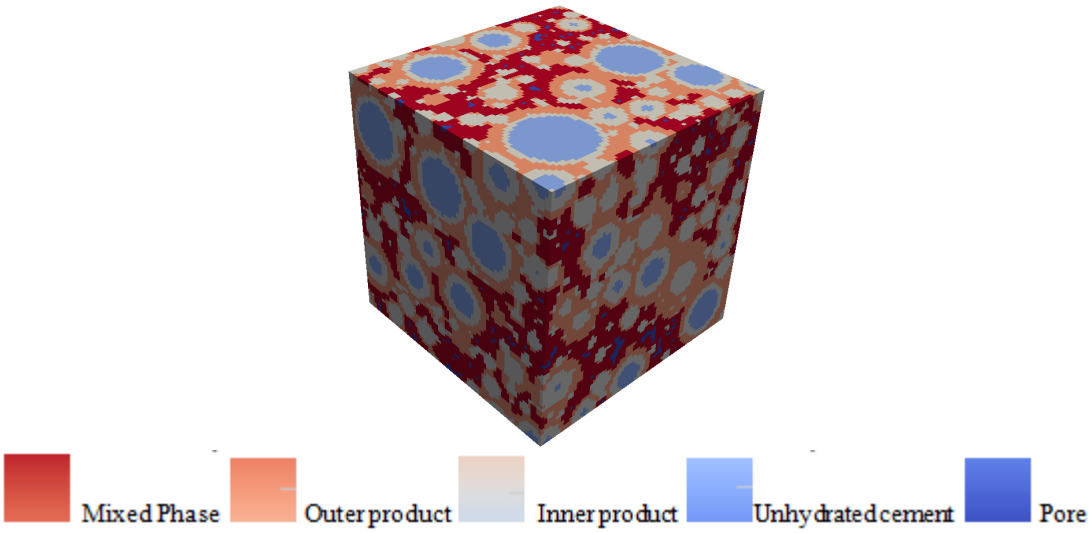

Figure 1. Microstructure of cement paste (w/c=0.4, hydration degree=0.69).

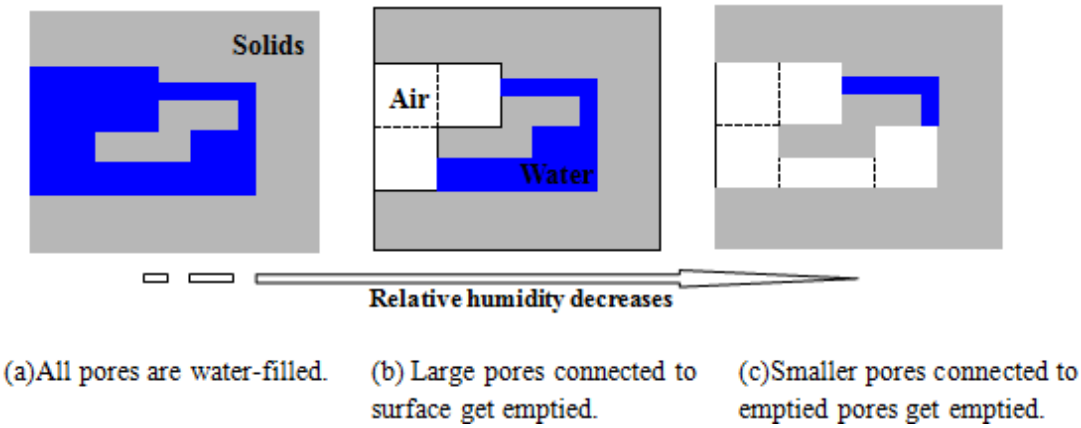

Figure 2. Two dimensional illustration diagram of drying in pores (reproduced after Liu L. *et al.*, 2014b).

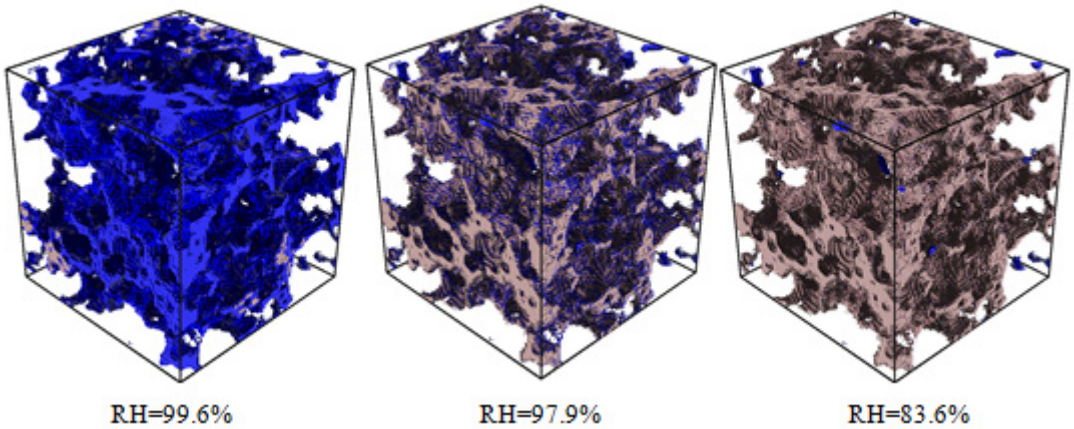

Figure 3. Pore structure under different relative humidity (yellow: air pores, blue: water pores).

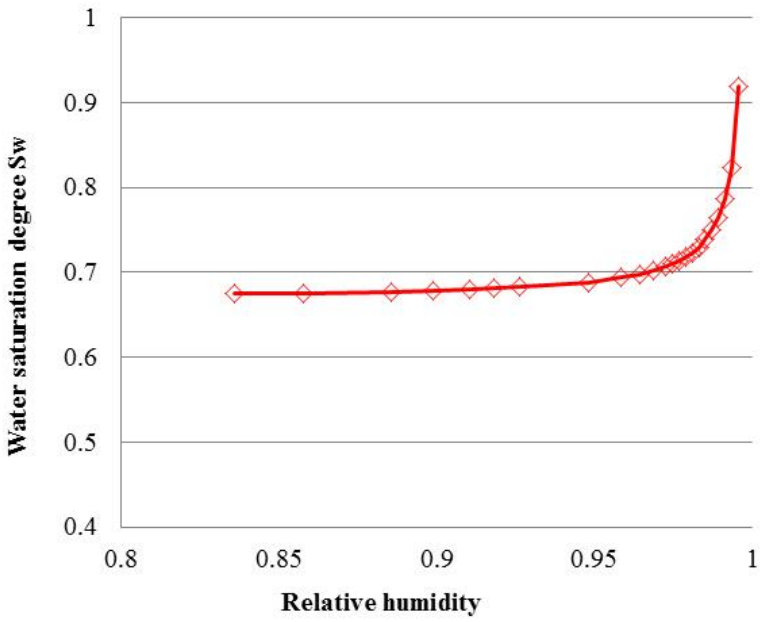

Figure 4. Water saturation degree versus RH.

SIMULATION OF SHRINKAGE DEFORMATION OF CEMENT PASTE

The liquid water remaining in small pores has a negative pressure which can be calculated according to equation (1). It is assumed that the water remaining in small pores is attributed to the shrinkage of cement paste. Therefore, the pressure in liquid water is the main responsible stress for the volume deformation during drying. By applying the internal loads resulting from liquid water in small pores, the drying shrinkage of cement paste at different relative humidity can be calculated by use of 3D lattice model.

Construction of lattice structure. The 3D lattice analyses are performed on a 3D lattice structure of cement paste (see figure 5) which is transformed from their corresponding voxel-presented microstructure (shown in figure 1). Lattice elements shown in figure 5 are colored according to its Young's modulus. The mechanical properties of lattice elements are determined by those of its component voxels. More detailed information about lattice construction and its property determination can be found in literature (Schlangen E. 1993, Qian Z. 2012, Liu L. *et al.*, 2014a&b).

Application of internal loads. Figure 6 shows how to apply internal loads resulting from liquid water in small capillary pores to the lattice structure of cement paste. The force is an integration of liquid water pressure on the associated surfaces.

Deformation of C-S-H. The shrinkage of C-S-H due to drying is a key factor determining the drying shrinkage of cementitious materials, and can not be ignored. On the basis of experimental evidence and concept models in literature, Liu L. et al. have introduced a granular particle packing model to construct the nanostructures of C-S-H, and then to predict the drying deformation of C-S-H by a three-dimensional

lattice model (Liu L. *et al.*, 2015). Simulation results about the drying deformation of C-S-H are employed to represent the action of water in small gel pores.

Results. Free boundary condition is applied to simulate the free shrinkage deformation without constrains. After 3D lattice analyses, the simulated linear shrinkage of cement paste versus relative humidity is given in figure 7. It is found that the shrinkage of cement paste is approximately inversely proportional to relative humidity in the range of 84% ~100% RH. This is in agreement with experimental test in literature (Bissonnette B. et al., 1999).

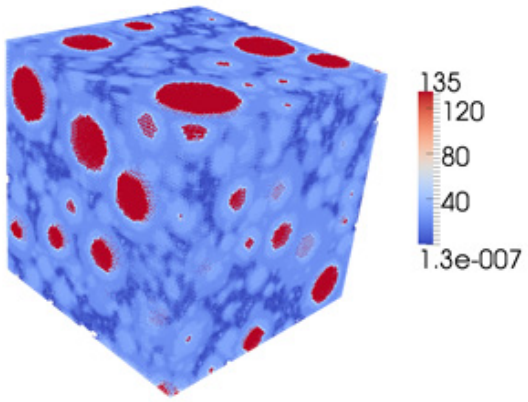

Figure 5. Lattice structure of cement paste.

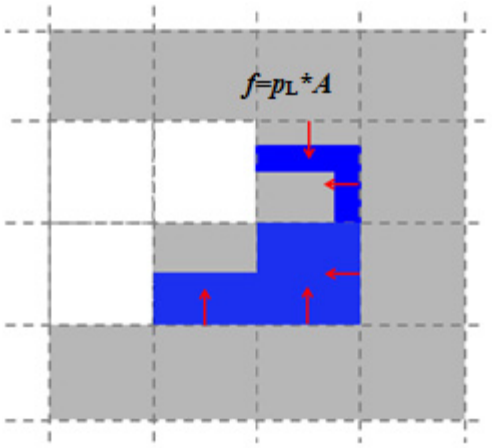

Figure 6. Illustration of applying internal loads resulting from liquid water in small pores.

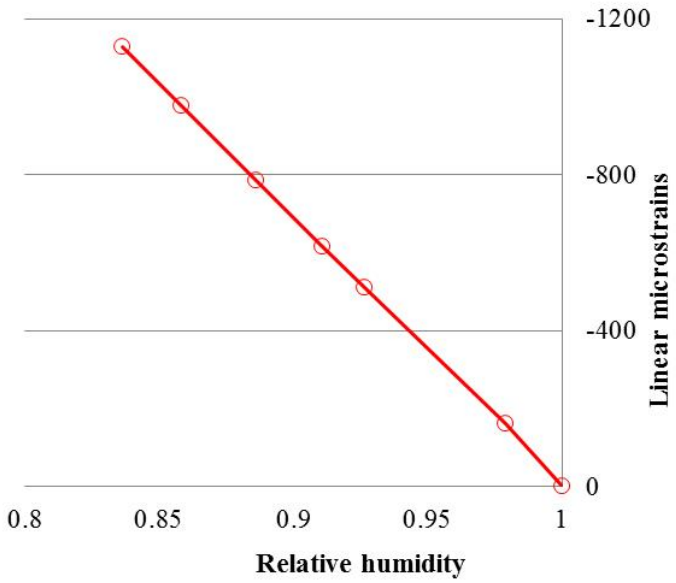

Figure 7. Simulated shrinkage of cement paste with relative humidity decreasing.

CONCLUSION

This paper presents a microstructure-based approach to model the drying process in pores and the shrinkage of cement specimens. By coupling a microstructure model HYMOSTRUC3D with a number of algorithms, the drying process in capillary pores is simulated in the range of 84% RH and100% RH. Considering the deformation of C-S-H and the capillary pressure effect in capillary pores, the drying shrinkage of cement paste is simulated by 3D lattice analyses.

ACKNOWLEDGEMENT

The financial support of National Natural Science Foundation of China (Grant No.51308187 and No. 51461135001), and Natural Science Foundation of Jiangsu Province via Grant No. BK20130837, are gratefully acknowledged.

REFERENCES

Bissonnette, B., Pierre, P. & Pigeon, M. (1999) "Influence of key parameters on drying shrinkage of cementitious materials." *Cement and Concrete Research*, 29 (10), 1655-1662.

Coussy, O., Dangla, P., Lassabatere, T. & Baroghel-Bouny, V. (2004) "The equivalent pore pressure and the swelling and shrinkage of cement-based materials." *Materials and Structures*, 37, 15-20.

Grasley, Z.C., Lange, D.A. & D'Ambrosia, M.D. (2005) "Drying stresses and internal relative humidity in concrete." in *Materials Science of Concrete*, vii, J. Skalny ed., American Ceramic Society, 265–305.

Jennings, H.M. (2008) "Refinements to colloid model of C-S-H in cement: CM-II." *Cement and Concrete Research*, 38, 275-289.

Lide, D.R. (2001) CRC Handbook of Chemistry and Physics, CRC Press.

Liu, L., Ye, G., Schlangen, E., Chen, H.S., Qian, Z.W., Sun, W. & van Breugel, K. (2011) "Modeling of the internal damage of saturated cement paste due to ice crystallization pressure during freezing." *Cement and Concrete Composites*, 33(5), 562-571.

Liu, L., Sun, W., Ye, G., Chen, H.S. & Qian, Z.W. (2012) "Estimation of the ionic diffusivity of virtual cement paste by random walk algorithm." *Construction and Building Materials*, 28(1), 405-413.

Liu, L., Shen, D.J., Chen, H.S., Sun, W., Qian, Z.W., Zhao, H.T. & Jiang, J.H. (2014a) "Analysis of damage development in cement paste due to ice nucleation at different temperatures." *Cement and Concrete Composites*, 53, 1-9.

Liu, L, Wu, S.X., Chen, H.S. & Zhao, H.T. (2014b) "Numerical investigation of the effects of freezing on micro-internal damage and macro-mechanical properties of cement pastes." *Cold Regions Science and Technology*, 106~107, 141-152.

Liu, L., Wang, X.C. & Chen H.S. (2015) "A drying shrinkage model of calcium silicate hydrate." *The 14th International Congress on the Chemistry of Cement* (ICCC2015). (Submitted).

Qian, Z. (2012) Multiscale modeling of fracture process in cementitious materials, PhD thesis, Delft University of Technology, Delft.

Schlangen, E. (1993) Experimental and numerical analysis of fracture processes in concrete, PhD thesis, Delft University of Technology, Delft.

van Breugel, K.(1991) Simulation of hydration and formation of structure in hardening cement-based materials. PhD thesis, Delft University of Technology, Delft.

Ye, G. (2003) Experimental study and numerical simulation of the development of the microstructure and permeability of cementitious materials. PhD thesis, Delft University of Technology, Delf.

Modeling Drying Shrinkage and Creep of Concrete at the Meso-level

Petr Havlásek[1] and Milan Jirásek[2]

[1]Department of Mechanics, Faculty of Civil Engineering, Czech Technical University in Prague, Thákurova 7, Prague 6, 166 29; PH (+420) 224 355 417; email: petr.havlasek@fsv.cvut.cz
[2]Department of Mechanics, Faculty of Civil Engineering, Czech Technical University in Prague, Thákurova 7, Prague 6, 166 29; PH (+420) 224 354 481; email: milan.jirasek@fsv.cvut.cz

ABSTRACT

Creep and shrinkage are complicated time-dependent processes taking place in cementitious materials. Creep refers to a stress-induced increasing deformation at constant stress while shrinkage is stress-independent. In typical concretes, the most significant part of shrinkage is represented by drying shrinkage; it is caused by a decrease in relative humidity of pores which leads to an increase in capillary tension of pore water and in the solid surface tension at pore walls.

Experimental data indicate that the ultimate value of drying shrinkage measured on concrete and mortar specimens is a nonlinear function of the ambient relative humidity. The nonlinear behavior is partially caused by microcracking, and partially by creep of the cement matrix. On the other hand, drying shrinkage of hardened cement paste, measured on very thin specimens at gradually decreasing relative humidity, is found to be a linear function of relative humidity.

The aim of this paper is to assess the nature of the macroscopic shrinkage computed employing finite element simulations at the meso-scale level in which the drying cement paste is described by a viscoelastic model based on the Microprestress-Solidification Theory (MPS) with tensile cracking and with a constant shrinkage coefficient.

INTRODUCTION AND MOTIVATION

In civil engineering practice, time-dependent behavior of concrete, such as creep and shrinkage, is experimentally assessed on both loaded and unloaded prismatic or cylindrical specimens. The height of the specimen is usually $4\times$–$5\times$ its diameter (or base), which is approximately 100 mm. Even though the specimens for experimental measurement of drying shrinkage are kept unloaded, internally they are not stress-free. Self-equilibrated stresses develop due to combination of structural restraint and self (or aggregate) restraint. The generated stresses are relieved by creep of the matrix and, if the tensile strength is exceeded, also by microcracking. The structural restraint appears

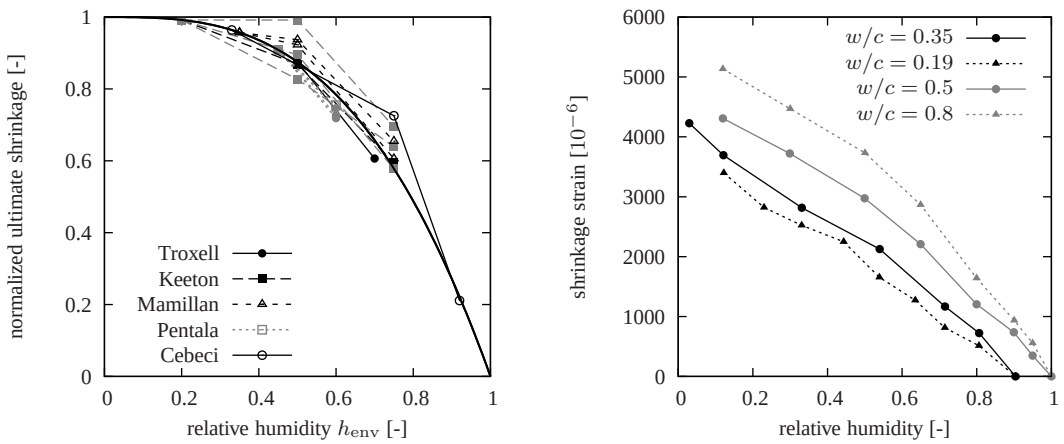

Figure 1. Influence of the ambient relative humidity on drying shrinkage: (a) comparison of experimental data measured on standard concrete specimens (Hubler et al., 2014; Cebeci et al., 1989) with the B3 model (data of concretes with $w/c > 0.45$ are shown in black), (b) experimental data measured on discs $D = 90$ mm, $h = 3$ mm (Baroghel-Bouny et al., 1999) (black) and prisms $20 \times 20 \times 160$ mm (Rougelot et al., 2009) (gray) showing drying shrinkage of hardened cement paste drying at gradually decreasing relative humidity.

whenever the cross section of the specimen cannot shrink freely, i.e., when the distribution of relative humidity is not uniform. This effect becomes more pronounced with increasing specimen size and with increasing drying rate. A typical consequence of the structural restraint is the surface (micro)cracking. Self-restraint is caused by differential shrinkage of the cement matrix and aggregates which do not shrink, or shrink considerably less. The latest experimental and numerical studies (Bisschop, 2002; Idiart et al., 2012; Grassl et al., 2010) conclude that the increasing aggregate size and decreasing volume fraction lead to smaller crack density but larger crack opening. However, these studies were focused merely on microcracking and did not consider the impact on volume changes.

The experimental data obtained from standard shrinkage experiments suggest that the resulting ultimate shrinkage strain measured on identical specimens is a strongly nonlinear function of ambient relative humidity at which these specimens are drying. This influence is anchored not only in academic models (Bažant and Baweja, 2000; Gardner, 2004; Sakata, 2004), but also in currently valid codes of practice for civil engineering (Fédération Internationale du Béton, 2012; ACI 209, 2008; Japan Society of Civil Engineers (JSCE), 2010). The comparison of normalized 12 relevant data sets (out of 1050 shrinkage tests, Hubler et al. (2014)) with the analytical formula given by the B3 model $1 - h_{\mathrm{env}}^3$ is shown in Figure 1a. Although the other models recommend different functions to describe this relationship, the result is very similar because the

models were calibrated on (almost) the same set of data.

On the other hand, drying shrinkage of hardened cement paste measured on very thin specimens at a gradually decreasing relative humidity is found to be an almost linear function of the relative humidity, at least in the typical range of relative humidity, as shown in Figure 1b.

The aim of this paper is to show whether or not the nonlinear dependence of concrete shrinkage on ambient relative humidity can be obtained if one uses a meso-scale model with a linear shrinkage-humidity relationship for the hardened cement paste. The material model that was chosen to capture the behavior of the matrix covers all essential phenomena: basic creep, drying creep, shrinkage and tensile cracking.

NUMERICAL SIMULATIONS

All presented results have been obtained by simulations employing the OOFEM finite element package (Patzák, 2012, 2000), the inputs and the FE meshes have been generated in the environment of Matlab and T3D (Rypl, 2004). The solution is based on the staggered approach; in each time step the moisture transport is solved first and the computed results are consequently utilized in the humidity-dependent structural analysis. The influence of the structural response on transport properties (i.e. increased diffusivity due to cracking) is neglected. Due to the high computational demands, the problem is solved only in 2D.

The finite element meshes for the structural and the moisture transport problems are different. The actual geometry of the aggregates is respected only by the mesh for the structural problem. The size distribution of the grains is defined by the Fuller curve and their position in the surrounding matrix is random. The aggregates are separated from the matrix by interface elements of infinitely small thickness.

In order to make the analysis computationally feasible, only the large grains are considered. In the presented example the aggregates represent 75% of the total area; the largest grain (sieve) size is 16 mm but only aggregates above 4 mm are modeled (i.e., the aggregates actually represent only 37.5% of the total area) while the remaining part is assumed to be lumped with the cement matrix. In order to compare and assess the influence of the structural and agregate restraint, the same finite element mesh is used in two different setups. The first one represents a section 50×50 mm cut out of an infinite 100 mm thick wall subjected to drying from both sides in the environment of constant relative humidity. In this configuration, both structural and self-restraints are activated while in the second setup the same segment is subjected to uniform drying resulting only into the self-restraint. In the first configuration, one vertical edge is the drying surface, the second one is the axis of symmetry (horizontal restraint), one horizontal edge is vertically supported and the master-slave condition in the vertical direction is imposed on the other horizontal edge. The notional element size is 0.4 mm.

Material Models

The nonlinear **moisture transport** problem uses the well-known material model proposed by Bažant and Najjar (1972). This model has been chosen in this study for two main reasons: one of them is its simple form (only four parameters) while the accuracy still remains fully sufficient for the present purpose, and the second is the choice of pore relative humidity as the primary unknown—the same variable is incorporated in the MPS model for creep and shrinkage and so there is no need for additional parameters describing the desorption isotherm (providing the link between relative humidity and moisture content or moisture ratio).

Viscoelastic behavior of the **matrix** is captured by a material model based on the Microprestress-Solidification Theory (Bažant et al., 1997a,b) in its reformulated version (Jirásek and Havlásek, 2014). In this alternative formulation the governing differential equation for the microprestress is replaced by a fully equivalent equation for viscosity of the corresponding unit of the rheological chain. Additionally, as shown in Bažant et al. (2014) and Havlásek (2014), the exponent p in that equation influences the size effect on drying creep. In the experiments, the average (cross-sectional) drying creep is decreasing with specimen size while for the standard value, $p = 2$, the MPS model exhibits the opposite trend. For $p = \infty$ the size effect disappears, and for $p < 0$ it corresponds to the experiments. Unfortunately, with negative or infinite value of p the underlying theory loses its original physical background. Shrinkage strains ε_{sh} are linked to the pore relative humidity h by a simple linear rate equation $\dot{\varepsilon}_{sh} = k_{sh}\dot{h}$, with constant coefficient k_{sh}.

Tensile cracking is taken into account using the concept of damage mechanics. If the tensile strength of the material is exhausted, the material stiffness is reduced, but only in the directions of positive principal stresses. The present implementation computes from the equivalent strain, which is defined by a Rankine-type criterion, based on the maximum principal effective stress. The parameters of the exponential damage law are adjusted with respect to the element size in spirit of the crack-band approach in order to guarantee proper energy dissipation, independent of the size of finite elements.

To make the analysis simpler, it is assumed that the **aggregates** are stronger than the surrounding matrix and can be accurately represented by linear elasticity. The material of the **interface** elements is described by a damage model with exponential softening. Here, damage is computed only from the normal (opening) displacement. For the virgin material, the normal and shear stiffnesses are the same, but once the material strength is reached, the shear stiffness is substantially reduced.

Calibration and Results

First of all, the meso-scale model was calibrated to match the basic creep compliance function given by the B3 model (Bažant and Baweja, 2000) for typical concrete cured for 28 days and loaded just afterwards. Consequently, the shrinkage and drying

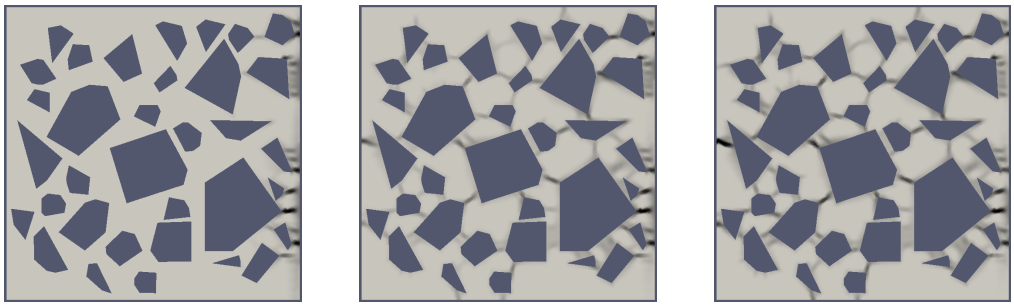

(a) (b) (c)

Figure 2. Computed crack pattern in 100 mm thick concrete wall (left edge = axis of symmetry, right edge = drying surface) after (a) 1 month, (b) 1 year, and (c) 3 years of drying.

compliance functions given by the same model for drying at $h_{\text{env}} = 50\%$ were used to determine the parameters of the transport model and the remaining parameters of the MPS model. Tensile strength and fracture energy of the matrix were set to 4 MPa and 15 N/m (3 MPa and 10 N/m for the interfaces); this choice leads to a brittle behavior and should maximize the influence of cracking.

The calibration has been done for three different versions of the creep model: A) MPS model with $p = \infty$, giving no size effect on drying creep; B) MPS model with $p = -1.5$, leading to the correct size effect; and C) no drying creep to emphasize even more the role of cracking. In the last case, the computed drying compliance is lower than for the B3 model, because its only source is the cracking strain.

The influence of nonuniform drying on crack formation in the unloaded specimen is shown in Figure 2; the darker the color the wider is the crack width. Fast changes in relative humidity near the drying surface lead not only to fast shrinkage but also to high compliance, which causes considerable relaxation of the stresses generated by shrinkage. The result is a crack pattern which does not start directly at the surface. In later stages of drying the cracks connect neighboring aggregates. If a crack forms, its width increases with the distance between the aggregates.

The dependence of the ultimate shrinkage strain on the ambient relative humidity is for the **non-uniform drying** presented in Figure 3a. The simulation has been run for nine levels of outer relative humidity (0.1–0.9) and several alternatives of the material model.

As expected, a linear response (and also the biggest shrinkage strain) is obtained with a linear elastic model, which is shown as the dashed black line. The elastic stiffness has been computed from the compliance function corresponding to the age of 28 days and duration of loading 0.01 day. For the current choice of the tensile strength and fracture energy, the lowest strain and the most nonlinear behavior is found for the damage model without creep (dashed grey curve); obviously, the higher the tensile strength

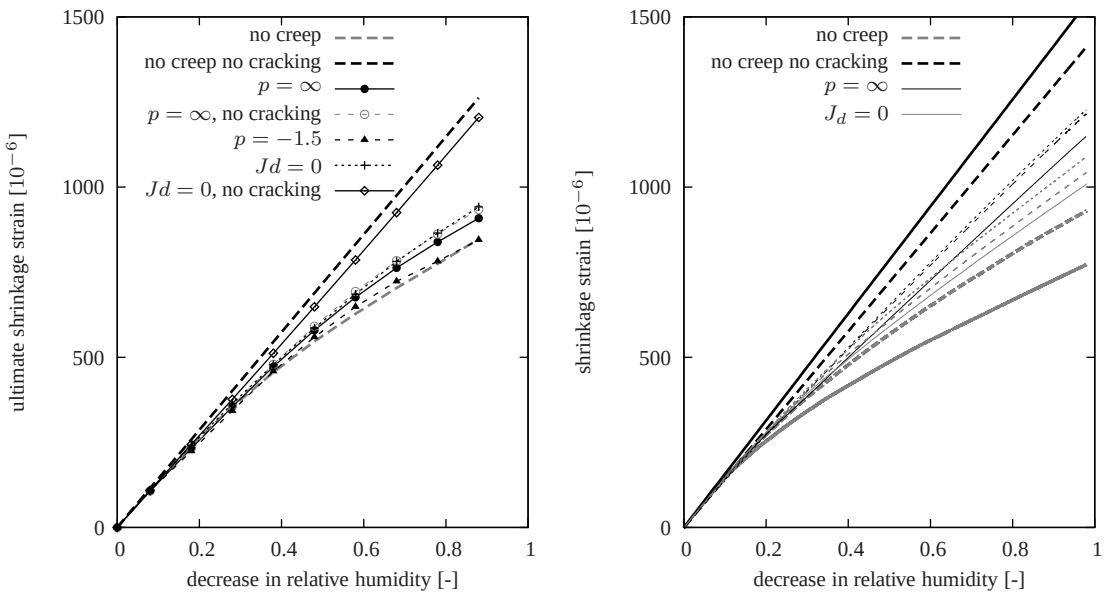

Figure 3. Comparison of computed shrinkage strain using different approaches for (a) nonuniform drying, (b) uniform drying.

the later the model starts deviating from the linear response, and the lower the fracture energy the earlier it converges to a straight line with a reduced slope. A transition between these two models is represented by the dashed line with crosses, which corresponds to the viscoelastic model without drying creep. Owing to the stress relaxation caused by basic creep which relieves the tensile stresses and also due to partial creep deformation of the material neighboring damaged elements (due to creep less prone to unloading), this model does not get much damaged and therefore its response is more linear. A very small reduction of the shrinkage strain is observed for the combination of basic creep without cracking, as shown by the thin solid line with diamonds. The models with considered (and calibrated) drying creep exhibit almost the same response when the cracking is considered or neglected—for $p = \infty$ see the full and empty circles. Very high reduction of the ultimate shrinkage strain is obtained for the model with $p = -1.5$ (shown by triangles); at variable humidity this model leads to extremely fast relaxation of stresses induced by shrinkage strains. The influence of the structural and aggregate restraints can be easily compared using the homogeneous model (calibrated with different values of parameters). If the drying creeep is considered, the structural effect plays a far more significant role than the aggregate restraint; the response of the homogeneous and meso-scale models turns out to be almost identical.

The computed results for the models subjected to **gradual uniform drying** are shown in Figure 3b. Thick black curves represent the solution without creep and cracking, the solid steeper curve is obtained with the asymptotic modulus E_0 while

the dashed one with the conventional modulus. The same two moduli have been used to compute the response of the model with cracking, which is shown by thick grey lines. Finally, two sets of three lines represent the response of the models with $p = \infty$ (black) and without drying creep (grey). The solid lines correspond to the fastest rate of drying, $\dot{h} = 10$ day^{-1}, the dashed lines to the moderate rate of 0.1 day^{-1}, and the dotted one to the slowest rate, $\dot{h} = 0.001$ day^{-1}. In the model without drying creep (grey), the difference between the curves is linked to the stress relaxation due to basic creep; the faster the drying the more is the curve approaching the thick dashed line for no creep. With the exception of very fast drying, the response of the model with $p = \infty$ is almost insensitive to the drying rate. If the exponent $p = -1.5$, the gradual continuous change in relative humidity leads to an enormous compliance; almost zero stresses are generated due to shrinkage.

CONCLUSIONS

Experimental data indicate that the ultimate value of drying shrinkage measured on concrete specimens is a nonlinear function of the ambient relative humidity; on the other hand, drying shrinkage of hardened cement paste measured on very thin specimens at gradually decreasing relative humidity was found to be a linear function of relative humidity. A simplified meso-scale model, which uses the modified material model based on the reformulated Microprestress-Solidification Theory to describe the properties of the matrix, has been calibrated against the basic creep, shrinkage and drying creep function of the B3 model and used in simulations of nonuniform and uniform drying. The results indicate that the most significant part of the nonlinear behavior stems from the presence of the drying creep and/or cracking, while the basic creep has a minor influence.

ACKNOWLEDGMENTS

The authors gratefully acknowledge the financial support received from the European Social Fund through the project on Support of Inter-Sectoral Mobility and Quality Enhancement of Research Teams at the Czech Technical University in Prague (CZ.1.07/2.3.00/30.0034).

References

ACI 209 (2008). *Guide for Modeling and Calculating Shrinkage and Creep in Hardened Concrete*. American Concrete Institute.

Baroghel-Bouny, V., M. Mainguy, T. Lassabatere, and O. Coussy (1999). Characterization and identification of equilibrium and transfer moisture properties for ordinary and high-performance cementitious materials. *Cement and Concrete Research 29*, 1225–1238.

Bažant, Z. and S. Baweja (2000). Creep and shrinkage prediction model for analysis and design of concrete structures: Model B3. *Adam Neville Symposium: Creep and Shrinkage - Structural Design Effects*.

Bažant, Z., P. Havlásek, and M. Jirásek (2014). Microprestress-solidification theory: Modeling of size effect on drying creep. In N. Bicanic, H. Mang, G. Meschke, and R. de Borst (Eds.), *Computational Modelling of Concrete Structures*, EH Leiden, The Netherlands, pp. 749–758. CRC Press/Balkema.

Bažant, Z. P., A. P. Hauggaard, and S. Baweja (1997b). Microprestress solidification theory for concrete creep. II: Algorithm and verification. *Journal of Engineering Mechanics 123*, 1195–1201.

Bažant, Z. P., A. P. Hauggaard, S. Baweja, and F. J. Ulm (1997a). Microprestress solidification theory for concrete creep. I: Aging and drying effects. *Journal of Engineering Mechanics 123*, 1188–1194.

Bažant, Z. P. and L. J. Najjar (1972). Nonlinear water diffusion in nonsaturated concrete. *Materials and Structures 5*, 3–20.

Bisschop, J. (2002). *Drying Shrinkage Microcracking in Cement-based Materials*. DUP Science.

Cebeci, O., S. Al-Noury, and W. Mirza (1989). Strength and drying shrinkage of masonry mortars in various temperature-humidity environments. *Cement and Concrete Research 19*, 53 – 62.

Fédération Internationale du Béton (2012). *Model Code 2010*. Number vol. 65 in fib Bulletin. International Federation for Structural Concrete (fib).

Gardner, N. (2004). Comparison and prediction provisions for drying shrinkage and creep of normal-strength concretes. *Canadian Journal for Civil Engineering 31*(5), 767–775.

Grassl, P., H. Wong, and N. Buenfeld (2010). Influence of aggregate size and volume fraction on shrinkage induced micro-cracking of concrete and mortar. *Cement and Concrete Research 40*, 85 – 93.

Havlásek, P. (2014). *Creep and Shrinkage of Concrete Subjected to Variable Environmental Conditions, PhD. Thesis*. Czech Technical University in Prague.

Hubler, M., R. Wendner, and Z. Bažant (2014). Comprehensive database for concrete creep and shrinkage: analysis and recommendations for testing and recording. *ACI (in press)*.

Idiart, A., J. Bisschop, A. Caballero, and P. Lura (2012). A numerical and experimental study of aggregate-induced shrinkage cracking in cementitious composites. *Cement and Concrete Research 42*(2), 272 – 281.

Japan Society of Civil Engineers (JSCE) (2010). *JSCE Guidelines for Concrete, Standard Specifications for Concrete Structures - 2007 "Design"*. Number 15 in JSCE Guidelines for Concrete. Subcommittee on English Version of Standard Specifications for Concrete Structures - 2007, Japan Society of Civil Engineers (JSCE).

Jirásek, M. and P. Havlásek (2014). Microprestress-solidification theory of concrete creep: Reformulation and improvement. *Cement and Concrete Research 60*, 51–62.

Patzák, B. (2000). OOFEM home page. http://www.oofem.org.

Patzák, B. (2012). OOFEM - an object-oriented simulation tool for advanced modeling of materials and structures. *Acta Polytechnica 52*(6), 59–66.

Rougelot, T., F. Skoczylas, and N. Burlion (2009). Water desorption and shrinkage in mortars and cement pastes: Experimental study and poromechanical model. *Cement and Concrete Research 39*(1), 36 – 44.

Rypl, D. (2004). T3d mesh generator. http://ksm.fsv.cvut.cz/ dr/t3d.html.

Sakata, K. (2004). Prediction of concrete creep and shrinkage. *Creep and Shrinkage of Concrete 31*(5), 767–775.

Creep Behavior of Cement Paste, Mortar, and Concrete: The Role of Relative Humidity and Interface Porosity

L. Sorelli[1]; J. Frech-Baronet[2]; and J.-P. Charron[3]

[1]Civil Engineering, Université Laval, 1065 avenue de la Médicine, PLT2928-A. E-mail: luca.sorelli@gci.ulaval.ca
[2]Civil Engineering, Université Laval, 1065 avenue de la Médicine, PLT2928-A. E-mail: jessy.frech-baronet.1@ulaval.ca
[3]Civil, Geological, and Mining Engineering, Polytechnique Montreal. E-mail: jean-philippe.charron@polymtl.ca

Abstract

Delayed deformations in concrete under sustained loading may depend on complex chemo-hydro-mechanical phenomena. Generally, the creep deformation of a cement paste is distinguished in the short-term and long-term. Simply speaking, the former can be associated to the diffusion of gel water in pores and cracks and it is mainly volumetric (i.e., volumetric deformation), reversible, and bounded. The latter can be associated to the sliding of the sheets of Calcium-Silicate-Hydrate (C-S-H), which is mainly deviatoric (i.e., shape deformation), irreversible and with an unbounded asymptotic deformation. From an experimental point of view, recent studies have shown that microindentation is a powerful technique to quickly characterize basic creep thanks to the reduced characteristic time of a sample size of few micrometers.
The objective of this project is twofold: (1) investigating the effect of relative humidity on the creep behavior by microindentation; (2) characterize the viscous behavior of the interface transition zones (ITZ) around a rigid inclusion. In particular, the project investigated two different relative humidity, 33% and 85%, by considering both creep and relaxation microindentation tests. The presented results show the effect of the moisture content on the creep behavior of cement paste both at short and long terms. In addition, the results showed that the ITZ zone around an aggregate showed higher creep than the bulk cement paste. Those results provide new insights to understand the role of water and interface porosity on the creep mechanisms of concrete.

INTRODUCTION

Creep can have beneficial as well as negative effects on concrete structure. For stress-to- strength ratio lower than 40%, compressive creep is considered linear and it is usually additively split into the basic creep (i.e. no moisture transfer) and the drying creep components. Creep in concrete is influenced by many factors, such as the microstructure constituents, the porous network, the type of curing, the temperature and relative humidity, and the loading time. Bernardi et al. employed a triaxial load cell test to show that the short term creep is mostly volumetric, while the long term creep is mostly deviatoric hinting on the coexistence of different mechanisms (Bernard et al. 2003). The mechanisms which are mostly recognized for

explaining concrete creep can be broadly classified as follows: (i) gel water diffusion theory (Powers 1965); (ii) sliding of C-S-H sheets (Vandamme et al. 2009; Sanahuja et al. 2010); (iii) gel compaction like a secondary consolidation process. More recently, Sahidi et al. (Shahidi et al. 2014) have recently described the kinetics of the creep by considering a viscous interface model which accounts for the lubricant role of water. As for non linear creep is considered, Rossi et al. have lately proposed that the interaction between the hygral gradients and the micro-cracks at the tip of propagating cracks may play an important role in the creep deformation under sustained loading (Rossi et al. 2012).

The role of relative humidity on concrete creep is recognized to be of paramount importance. However, the experimental results available in literature are sometimes contradictory as the initial hygral conditions within the sample is often not uniform since the hygral equilibrium within a sample of few centimeters can take several months (Neville 1971). The compressive creep test of Troxell et al. over 30 years on concrete cylinders of 100 mm diameter and 150 mm height showed that, after the hygral equilibrium has been reached at about 1 year, the rate of creep seems quite independent of the relative humidity (Troxell et al. 1958). Contrarily, Bazant proposed a parabolic relationship between the basic creep and the relative humidity (Bazant et al. 1985) based on the experimental results of Wittman on millimeter size samples (Wittmann 1968). Such apparent contradiction may be explained by the difficulty, if not impossibility, of decoupling basic and drying creep within the microstructure. The overall coupling was quantified by L'Hermite (L'Hermite 1959) which assumed that the drying creep is covariant (i.e., multiplicative) with respect to the shrinkage and the basic creep. Nowadays, microindentation technique have been emerging for measuring the creep properties of cement-based materials as it allows significant reduction of the time scale for observing creep phenomena (Nguyen et al. 2013; Pourbeik et al. 2013; Nguyen et al. 2014). Zhang et al. have proven that, for several mix designs, the long term creep rate measured by microindentation and the ones measured by compressive tests over 30 years are linearly correlated (Zhang et al. 2013). Furthermore, Zhang (Zhang 2014) recently showed that the relative humidity can increases the long term creep rate by a factor of 5 when the relative humidity level increases from 11% to 95%.

The scope of this work is to better understand the effect of humidity on the short term and long term creep mechanisms. *Does the relative humidity modify the creep response of a cement paste? Does creep and relaxation behave as dual mechanisms? Does the aggregate interface contribute to the overall creep?*

MATERIALS AND METHODS

Materials

This study employed a cement paste and a concrete made with ordinary Portland (type I) with water-to-cement ratio (w/c) of 0.4. The concrete mix design was adapted to have the same matrix characteristics of the cement paste. The samples were cast in cylinder molds of 100 mm and 150 mm diameters. They were then cured at 100% R.H for 28 days and then stored at 50% RH for 2 months. The samples were tested 90 days after casting to reduce the effect of aging. Before testing, a cubic sample of 30 mm side was cut out from the center of cement paste and concrete cylinders. Secondly, a coarse grinding was performed with the used of abrasive paper and water in order to smooth the edge of the samples. Thirdly, the surfaces were polished by 1 μm fineness diamond suspension oil-based solution. Finally, a 0.250 μm fineness diamond paste serve to finalize the polishing. Special attention was paid to keep the samples leveled since the angle of indentation could influence the results of measurement. After polishing, the samples were put in an ultrasonic bath to remove any trace of diamond particles left on the surface. The sample were cured for 2 weeks at the testing relative humidity before microindentation testing which is enough to guarantee the hygral equilibrium of the micrometer zone under testing.

Humidity Chamber

In order to control the relative humidity (RH) and CO_2 concentration, an hermetic enclosure was built specifically for this research project. The system consists of a closed circuit where the hermetic enclosure is connected in series to an Erlenmeyer flask containing a saturated salts solution and a pump. The use of saturated solution of salt is required to reach specific humidity equilibrium (Table 3. for details). The system being a hermetic closes loop allows the air to pass multiple times through the saturated salts solution. The relative humidity and CO_2 concentration are continuously monitored by two sensors within the chamber. In this work different relative humidity, such as 33% and 85% were considered.

Table 1. Salts used to control the relative humidity

Salts	RH at 20°C	Solubility in water (g/100mL)
Lithium Chloride (LiCl)	11.3 ± 0.3	84.25
Magnesium Chloride ($MgCl_2$)	33.1 ± 0.1	54.3
Magnesium Nitrate ($Mg(NO_3)_2$)	54.4 ± 0.2	125.0
Potassium Chloride (KCl)	85.9 ± 0.3	34.4
Lithium Chloride (LiCl)	11.3 ± 0.3	84.25

Surface roughness

The sample surface were carefully prepared for cement paste and concrete specimens according to a well established protocol (Miller et al. 2008). The Roughness Mean Square (RMS), which is a statistical parameter defined as follows $R_q^{\,2} = 1/n^2 \sum_{j=1}^{n} \sum_{i=1}^{n} z_{ij}^2$ where i and j are the position of each pixel in a plane, was checked by Atomistic Force Microscope (AFM). Topographic images were carried out on three different zones: the inclusion (granulates/sands) zone, the ITZ and the paste zone. A Gaussian filter was applied to filter out the wave larger than 8.0 μm (Miller, Bobko et al. 2008). The R_q value was obtained by averaging three selected topographic area of 50 µm by 50 µm per zone of interest. The Rq for the cement paste was about 65 ±36 nm, while the Rq for the ITZ was about 56 nm±31 nm (Figure 1).

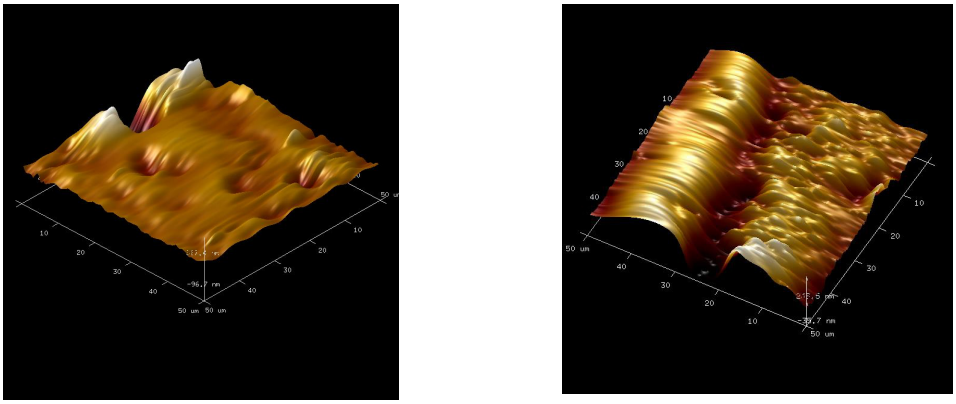

(a) *(b)*

Figure 1. AFM imag: (a) cement paste wit average R_q=65 nm; (b) ITZ with average R_q=56 nm.

Basics of microindentation

Microindentation has become a powerful technique to quantitatively measure the elasticity and hardness of cement paste and other hydrates products (Nguyen, Alizadeh et al. 2013; Pourbeik, Alizadeh et al. 2013; Nguyen, Alizadeh et al. 2014). During an indentation test, the force (*P*) and the penetration depth (*h*) are measured simultaneously, while the indenter tip penetrates into the film (Figure 2a). A typical P-h curve (Figure 2b) is constituted by a loading curve up to the maximum load P_{max}, followed by an unloading curve. Note that the loading curve profile parabolic in the ideal case of conical indenters with no friction on the tip-material interface. For this study we employed a Berkovich-type indenter which is three-sided pyramid with an equivalent cone semi-angle θ of 70.3º as shown in Figure 2a. The analysis of the P-h curve consists in extracting the indentation properties, such as: the indentation Modulus $M = \left(S\sqrt{\pi}\right)\Big/\left(2\beta A_C\right)$ and the indentation Hardness H = P_{max} /A_C. The coefficient β accounts for the non symmetrical shape of the indenter. The projected area A_C of the indenter-sample contact depends on the contact depth h_c (Figure 2.a). The contact stiffness S=dP/dh is the slope measured during the initial stages of the unloading curve (Figure 2.b). The Young modulus E of an isotropic material is estimated from the indentation modulus M as follows : $M^{-1} = (1-\upsilon^2)/E + (1-\upsilon^2)/E_i$, where E_i and ν_i are the elastic modulus and the Poisson's ratio of the diamond tip, which are equal to 1141 GPa and 0.07, respectively; while E and ν are the Young modulus and the Poisson's ratio of the material, respectively. Furthermore, to account for the tip imperfection, the contact area function, $A_C = \pi^2 a$, is calibrated according to a standard procedure on a reference fused silica sample. It is usually estimated by the Oliver and Pharr method with the next equation $A_C = 3\sqrt{3}h_C^2 \tan^2\theta$, where $h_c = h_m - \varepsilon P_{\max}/S$. The geometry correction factor β and the intercept factor ε are 1.034 and 0.75, respectively, for Berkovich-type indenter (Fischer-Cripps 2011).

Figure 2c shows an experiment where the load is linearly applied over a time τ_L, then held constant over a time τ_H, and finally reduced to zero over a time τ_U. While plastic deformation often occurs during loading, it is generally assumed that the unloading curve is elastic. Different coefficients have been defined to describe the creep mechanism from an indentation tests. As for a creep microindentation test, the asymptotic creep behavior ($t \to \infty$) can be characterized by the Long Term (LT) contact creep modulus C_{LT} proposed by (Vandamme and Ulm 2009), which essentially describes the logarithmic asymptote of the creep rate, as follows

$$C_{LT} \overset{def}{=} \lim_{t\to\infty} \frac{1}{\dot{t}\,\dot{L}(t)} = \lim_{t\to\infty} \frac{P_m}{\dot{t}\; 2a_U \dot{h}} = \frac{P_m}{2a_u x_1} \quad \text{[GPa]} \tag{1}$$

where the indentation compliance $L(t) = M(t)^{-1}$, x_1 is the term of the logarithmic penetration depth function. $h(t) = x_1 log\left(t/\tau_{ch} + 1\right)$ which is employed to fit the creep curve. We remind that a_U is the radius of the contact area at unloading, which is

supposed to be rather constant during the holding time. Vallée et al. (Vallée 2013) proposed to normalize C_{LT} by the initial indentation modulus as follows

$$c_{LT} \overset{def}{=} \frac{C_{LT}}{M_0} = \beta \frac{P_m}{S\, x_1} \quad [-] \tag{2}$$

Notably, c_{LT} is independent of the elastic stiffness of the material and the radius of the contact area.

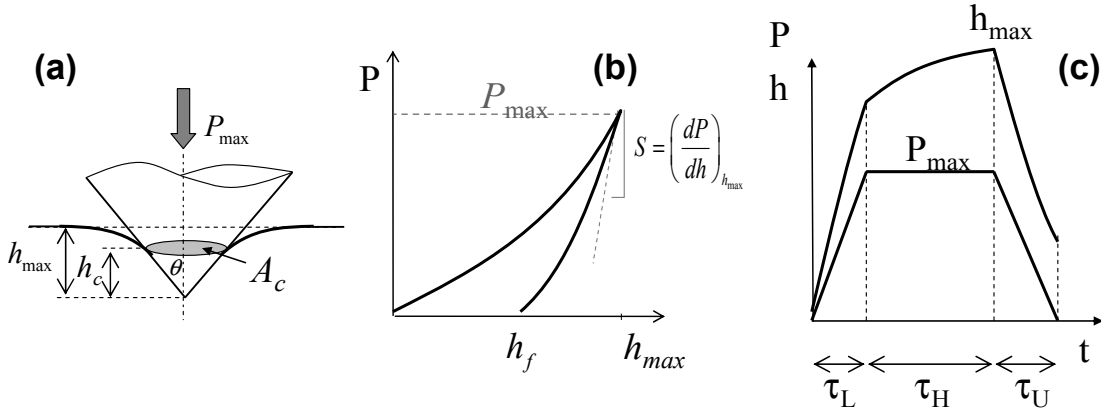

(a) (b) (c)

Figure 2. Indentation test (a); Curve P-h (b); Curves P-t and h-t for a creep microindentation test.

Herein, we define a contact Short Term (ST) creep modulus which describes the very short term creep as the asymptotic behavior right after the load is applied ($t \to 0^+$) as follows

$$c_{ST} \overset{def}{=} \lim_{t\to 0} \frac{\dot{M}(\mathrm{t})}{M_0} = \lim_{t\to 0} \frac{\dot{P}(\mathrm{t})}{P_m} = \beta \frac{P_{\mathrm{m}}\, \tau_{ch}}{S\, x_1} = \tau_{ch}\, c_{LT} \quad [-] \tag{3}$$

As for the relaxation indentation test, Vallée et al. (Vallée 2013) defined a dimensionless Long Term (LT) contact relaxation modulus r_∞ for describing the logarithmic asymptote as follows

$$r_{LT} \overset{def}{=} \lim_{t\to\infty} -\frac{M_0}{t\,\dot{M}(\mathrm{t})} = \lim_{t\to\infty} -\frac{P_m}{t\,\dot{P}(\mathrm{t})} = \frac{P_m}{x'_1} \quad [-] \tag{4}$$

where x_1 is the term of the logarithmic penetration depth function, $\Delta P(t) = -x'_1\, log\left(t/\tau'_{ch} + 1\right)$ which is employed to fit the creep curve. As for the short term relaxation behavior, we define here a contact Short Term (ST) relaxation modulus as follows:

$$r_{ST} \overset{def}{=} \lim_{t\to 0} -\frac{M_0}{\dot{M}(\mathrm{t})} = \lim_{t\to\infty} -\frac{P_m}{\dot{P}(\mathrm{t})} = \frac{P_m\, \tau'_{ch}}{x'_1} = \tau'_{ch}\, r_{LT} \quad [-] \tag{5}$$

The experimental tests are carried out as following. First a 5 x 5 grid of micro-indentation tests was performed on the cement paste for each relative humidity for both test condition, i.e., creep and relaxation. To check the repeatability the creep test series were repeated. Then, the ITZ zone was characterize by creep microindentation

tests over a grid of 5 lines of 20 indentation points in the proximity of the inclusion/cement paste interface at a relative humidity of 35%. The distance of each point from the interface was calculated by digital microscope. The results were averaged for indentations separated in groups according to the distance from the interface, such as: <20 μm, 20-40 μm, 40-60 μm, 60-80 μm and >80 μm.

RESULTS

The average results for the test series of creep and relaxation for different relative humidity are summarized in Table 2 in terms of indentation modulus M and hardness H. Figure 3 shows an example of indentation grid for the cement paste tested at 35% with the mapping of the indentation Modulus M and Hardness. As average, at lower humidity the material is slightly stiffer (+10%) and harder (+25%). Notably, those results confirm the previously one obtained by Zhang (Zhang 2014). Table 3. shows the results of the creep and relaxation tests on the cement paste at different relative humidity. Figure 4a shows the average creep curve penetration depth vs. time (h-t) for the different relative humidity. Figure 4b shows the average relaxation curve load vs. time (P-t) for the different relative humidity. A variation of humidty from 35% to 85% causes a reduction of the creep modulus C_{LT} of a factor between 2 and 3 (i.e., the creep increase). This result is again coherent with the results of Zhang (Zhang 2014). The effect of varying the humidity from 35% to 85% strongly increases the short term creep modulus c_{ST}, which means the short term creep reduces when the humidity is higher. Notably, those observations are confirmed by the relaxation tests for which the contact relaxation modulus (r_{LT}) reduces of about 100% when the humidity is increased from 35% to 85%, i.e., creep doubles. Analogously to the creep tests, the short term contact relaxation modulus (r_{CT}) increases when relative humidity increases, i.e., the short term creep reduces. Table 3 shows the depth rates calculated over a period of 3 seconds.

Table 2. Mean results of microindentation for all the test series.

	Indentation Modulus [GPa]	Indentation Hardness [MPa]
Creep test at 35% r.h.	14.3	214.6
Creep test at 35% r.h.	12.0	191.0
Creep test at 85% r.h.	13.3	187.6
Creep test at 85% r.h.	11.5	153.0
Relaxation test at 35% r.h.	15.5	202.6
Relaxation test at 35% r.h.	13.3	212.8
Relaxation test at 85% r.h.	13.1	135.8
Relaxation test at 85% r.h.	11.6	115.8

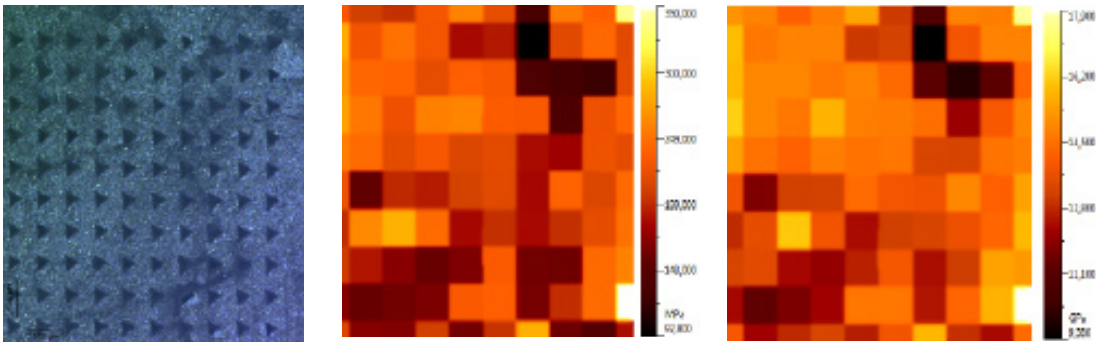

(a) (b) (c)

Figure 3. Example of indentation grid on the cement paste for r.h.=33% (a); mappingof the M-modulus (b); mappring of the Hardness (c).

Table 3. Mean results of creep and relaxation test on cement paste for different test series.

	Creep tests at P_m=8N						Relaxation test at h_m=40 µm				
R.H. ¶	C_{LT} [GPa]	τ_{ch} [sec] 10^{-3}	c_{LT} [-]	c_{ST} [-]10^{-3}	$\frac{dh}{dt}$ [µm/sec]		r_{LT} [-]	τ'_{ch} [sec] 10^{-3}	r_{ST} [-] 10^{-3}	$\frac{dh}{dt}$ [µm/sec]	
					t=0	t=300				t=0	t=300
35%	141	5.2	10	52	385	0.6	41	0.02	1	-710	-0.58
35%	98	13.5	8	110	434	1.0	35	0.20	7	-645	-0.66
85%	57	114.9	4	495	488	1.8	18	0.71	13	-832	-0.73
85%	45	84.7	4	334	560	1.8	19	0.45	9	-694	-0.64

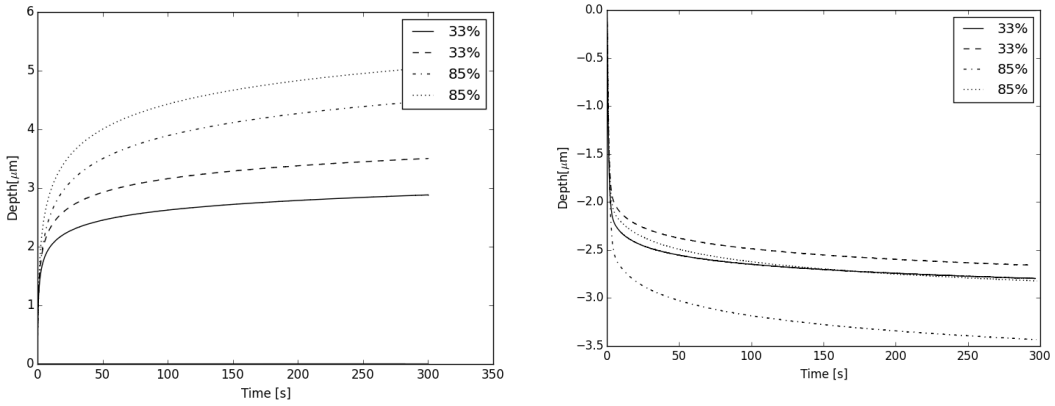

(a) (b)

Figure 4. Effect of the relative humidity on the mean response of a cement paste by microindentation: creep response (a); relaxation response (b)

The characterization of the ITZ in concrete samples is summarized Table 4. Figure 5 shows the indention grid on the interface aggregate-cement paste as well as the average creep curves for points within different distance ranges. It is evident that there exists a weakened zone of about 60 µm with reduced M and H likely, which is likely due to a greater porosity. As for creep, the ITZ zone showed a reduced C_{LT} with

respect to the point far away (>80 μm) which means that the creep rate of the ITZ zone can be up to twice that of the bulk cement paste.

Table 4. Average microindentation properties of the ITZ zone for creep tests at Pm=50 mN.

Distance from inclusion	h_m [μm]	M [GPa]	H [MPa]	C_{LT} [GPa]	τ_{ch} [sec] 10^{-3}	c_{LT} [-]	c_{ST} [-]10^3	$\frac{dh}{dt}$ [μm/sec]	
								t=0	t=300
<20 μm	2.4	16.2	250	157	16.2	10	34	290	32
20-40 μm	2.4	19.8	409	242	19.8	12	22	558	26
40-60 μm	2.1	26.3	556	259	26.3	10	53	188	24
60-80 μm	2.3	24.1	425	266	24.1	11	6	1928	26
>80 μm	2.2	24.9	476	333	24.9	13	31	434	21

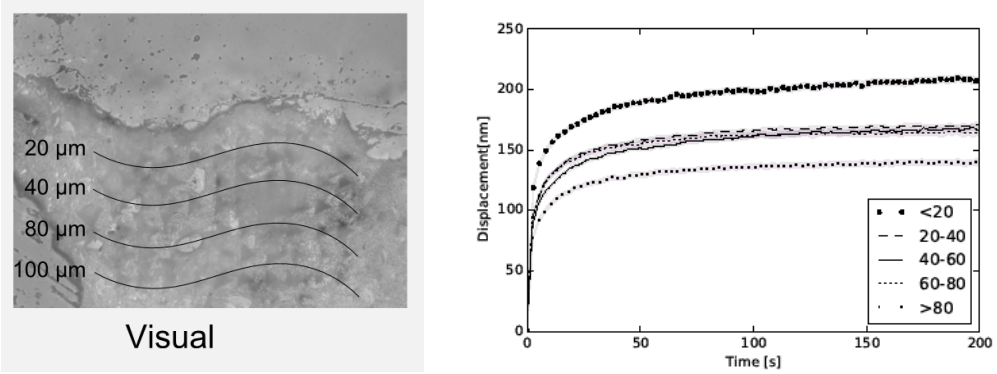

(a) (b)

Figure 5. Grid microindentation on ITZ of an aggregate (a) Average creep curves at different distance zone from the interface (b).

CONCLUDING REMARKS

This works present an original characterization of the creep of cement paste and ITZ of concrete by microindentation at various relative humidity (35% and 85%). The preliminary conclusions are drawn:

(1) The indentation modulus of cement paste is slightly greater for low humidity. The hardness is significantly greater for low humidity;

(2) The cement paste shows greater creep rate at higher humidity 85% as confirmed by both creep and relaxation results;

(3) The ITZ of 60-80 μm around an aggregate presents a lower stiffness and hardness and is more viscous that the bulk matrix.

The research is being extended to other relative humidity levels to statically confirm the present results.

REFERENCES

Bazant, Z. and J. Chern (1985). "Concrete creep at variable humidity: constitutive law and mechanism." Materials and structures **18**(1): 1-20.
Bernard, O., F.-J. Ulm, et al. (2003). "Volume and deviator creep of calcium-leached cement-based materials." Cement and concrete research **33**(8): 1127-1136.
Fischer-Cripps, A. C. (2011). Nanoindentation, Springer Science & Business Media.
L'Hermite, R. (1959). What do we know about the plastic deformation and creep of concrete? . R. Bulletin. **1:** 21-51.
Miller, M., C. Bobko, et al. (2008). "Surface roughness criteria for cement paste nanoindentation." Cement and concrete research **38**(4): 467-476.
Neville, A. M. (1971). "Creep of concrete: plain, reinforced, and prestressed."
Nguyen, D.-T., R. Alizadeh, et al. (2013). "Microindentation creep of secondary hydrated cement phases and C–S–H." Materials and structures **46**(9): 1519-1525.
Nguyen, D.-T., R. Alizadeh, et al. (2014). "Microindentation creep of monophasic calcium–silicate–hydrates." Cement and Concrete Composites **48**: 118-126.
Pourbeik, P., R. Alizadeh, et al. (2013). "Microindentation creep of 45 year old hydrated Portland cement paste." Advances in Cement Research **25**(5): 301-306.
Powers, T. C. (1965). "Mechanisms of shrinkage and reversible creep of hardened cement paste." The structure of concrete and its behaviour under load: 319-344.
Rossi, P., J.-L. Tailhan, et al. (2012). "Basic creep behavior of concretes investigation of the physical mechanisms by using acoustic emission." Cement and concrete research **42**(1): 61-73.
Sanahuja, J. and L. Dormieux (2010). "Creep of a CSH gel: a micromechanical approach." Anais da Academia Brasileira de Ciências **82**(1): 25-41.
Shahidi, M., B. Pichler, et al. (2014). "Viscous interfaces as source for material creep: A continuum micromechanics approach." European Journal of Mechanics-A/Solids **45**: 41-58.
Troxell, G. E., J. M. Raphael, et al. (1958). Long-term creep and shrinkage of plain and reinforced concrete, ASTM. **58:** 1101-1120.
Vallée, D. (2013). Mechanical and chemical characterization of the heterogeneous microstructure of green concrete with mineral additions. Civil Engineering. Quebec, Université Laval. **M.Sc.:** 167.
Vandamme, M. and F.-J. Ulm (2009). "Nanogranular origin of concrete creep." Proceedings of the National Academy of Sciences **106**(26): 10552-10557.
Wittmann, F. (1968). "Surface tension skrinkage and strength of hardened cement paste." Matériaux et Construction **1**(6): 547-552.
Zhang, Q. (2014). Creep properties of cementitious materials: effect of water and microstructure: An approach by microindentation, Université Paris-Est.
Zhang, Q., R. Le Roy, et al. (2013). Long-term creep properties of cementitious materials–comparing compression tests on concrete with microindentation tests on cement. American Society of Civil Engineers.

Modelling hysteresis in the water sorption and drying shrinkage of cement paste

E. Masoero[1], M.B. Pinson[2,3], P.A. Bonnaud[4], H. Manzano[5], Q. Ji[6], S. Yip[7], J.J. Thomas[8], M.Z. Bazant[9], K. Van Vliet[10], H.M. Jennings[11]

[1]School of Civil Engineering and Geosciences, Newcastle University, NE1 7RU, Newcastle upon Tyne, United Kingdom; PH (+44) 191 208 7686; email: enrico.masoero@newcastle.ac.uk
[2]Department of Physics, University of Chicago, 60637, Chicago, USA.; PH (+1) 773 702 3102; email: mpinson@uchicago.edu
[3]Department of Physics, Massachusetts Institute of Technology, Cambridge, MA 02139, USA.
[4]New Industry Creation Hatchery Center (NICHe), Tohoku University, 980-8579, Sendai, Japan; email: patrick@aki.niche.tohoku.ac.jp
[5]Molecular Spectroscopy Laboratory, Universidad del Pas Vasco/EHU, 48080 Bilbao, Spain; email: hegoi.manzano@ehu.es
[6]Inspur Group, State Key Laboratory of High-End Server & Storage Technology, Jinan, Shangdong, P.R. China
[7]Department of Nuclear Science and Engineering, Massachusetts Institute of Technology, Cambridge, MA 02139, USA; PH (+1) 617 253 3809; email: syip@mit.edu
[8]Schlumberger-Doll Research, Cambridge, MA 02139, USA; email; JThomas39@slb.com
[9]Department of Chemical Engineering and Department of Mathematics, Massachusetts Institute of Technology, Cambridge, MA 02139, USA; PH (+1) 617 324 2036; email: bazant@mit.edu
[10]Department of Materials Science and Engineering and Department of Mechanical Engineering, Massachusetts Institute of Technology, Cambridge, MA 02139, USA; PH (+1) 617 253 3315; email: krystyn@mit.edu
[11]Department of Civil and Environmental Engineering, Massachusetts Institute of Technology, Cambridge, MA 02139, USA; PH (+1) 617 253 7127; hmj@mit.edu

ABSTRACT

Shrinkage can be critical for the strength and durability of drying cement pastes. Shrinkage becomes particularly severe at very low relative humidity, $< 20\%$, which can be met in some activities involving extreme temperatures. Experiments and simulations suggest that small pores in the cement paste, with approximate thickness ≤ 1 nm, stay saturated unless the humidity drops below 20%. Here we suggest that this pore size can define two different categories of pores in the paste: pores thicker than 1 nm, where the Kelvin's equation and the corresponding capillary (Laplace) pressure apply, and pores thinner than 1 nm, which can be considered as part of the solid skeleton if the humidity stays above 20%. We show that a continuum model, incorporating

a pore-blocking mechanism for desorption and equilibrium thermodynamics for adsorption, explains well the sorption hysteresis for a paste that remains above $\sim 20\%$. At lower humidities, we assume that (1) during adsorpion water re-enters the smallest pores throughout the entire RH range (supported by experiments and simulations) and (2) there exists a simple linear relationship between water and strain in the smallest pores. These minimal assumptions are sufficient to explain the low-humidity hysteresis of water content and strain, but the underlying mechanistic explanation is still an open question. Combining the low-humidity and high-humidity models allows capturing the entire drying and rewetting hysteresis, and provides parameters to predict the corresponding dimensional changes.

INTRODUCTION

The isothermal water desorption and adsorption of unrestrained cement paste are accompanied by volume changes, respectively shrinkage and swelling (see Figure 1). Furthermore, the water content and strain are not unique functions of the relative humidity (RH); they depend also on the history of drying and wetting. This results in hysteresis, which complicates the long-term predictions of deformations and stresses in concrete structures that undergo cyclic humidity or temperature changes during their lifetime, for example nuclear reactor pressure vessels and nuclear waste dry casks.

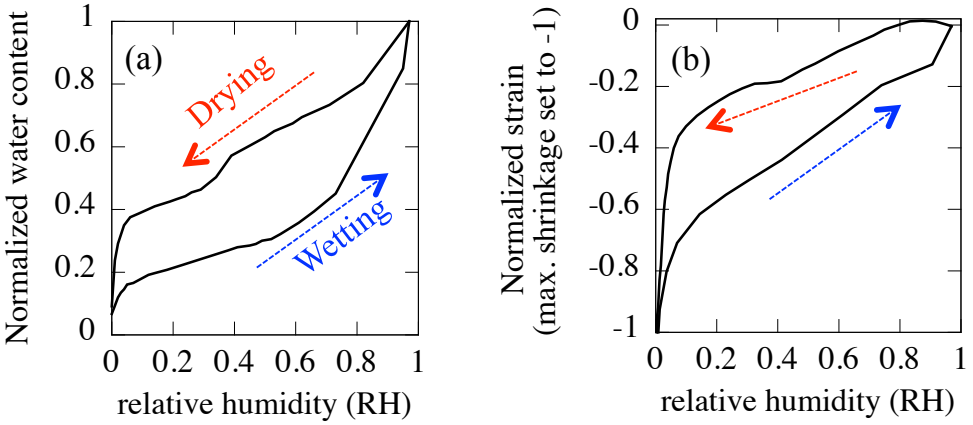

Figure 1. Typical (a) water sorption isotherm and (b) shrinkage isotherm for a cement paste (data from (Feldman and Sereda, 1968) normalized(Pinson et al., in press)).

The coupling between water content and volume changes as well as the hysteresis are common features in mesoporous materials like cement paste (according to IUPAC, a mesoporous material has pores with width between 2 and 50 nm). However, the strain hysteresis of cement paste has a peculiar shape, with the volume of the

sample being larger during desorption than during adsorption. This is analogous to the behaviour of clays, but is opposite to that of mesoporous glasses whose deformations are dominated by capillary menisci, e.g. Vycor. In analogy with clay, we expect the deformations of cement paste to be largely controlled by the behaviour of water in small interlayer spaces within the calcium-silicate-hydrate (C–S–H) phase, which is the main binding phase in ordinary cement pastes.

WATER ISOTHERMS: SEPARATING THE EFFECTS OF "SMALL" AND "LARGE" PORES

We argue that the experimentally measured water content can be split into two additive contributions based on the different physical behaviour of water in pores thinner and thicker than $\sim$1 nm. The value of 1 nm comes from the combination of experimental observations and molecular simulations. Namely, nuclear magnetic resonance (NMR) experiments (Muller et al., 2013) indicate that there exists a "class" of water in cement paste that does not evaporate until very low relative humidities are reached (RH $\sim$20%, see Figure 2). Molecular simulations indicate that this type of behaviour (remaining full of water between RH=100% and 20% in desorption) is to be expected from pores of $\sim$1 nm width (Bonnaud et al., 2012; Bonnaud et al., 2013). The NMR results agree also with older measurements from water isotherms which were also extended to the adsorption path and indicated a large hysteresis coming from the smallest pores (Feldman and Sereda,1968; Pinson et al., in press)

In Figure 2.b we subtract the estimated sorption isotherm for the smallest pores (Figure 2.a) from the overall water sorption hysteresis. This leads to a reduced water sorption isotherm that looks like nitrogen sorption isotherms and can be captured using a simple network model that combines the Kelvin equation with two mechanisms for hysteresis (Pinson et al., preprint): (1) different kinematics of water condensation and evaporation in cylindrical pores (multi-layer adsorption plus instability vs. retracting capillary meniscus), and (2) "ink-bottle effect", where only pores in contact with a vapour phase that is connected to the exterior of the sample can desaturate (or, possibly, at least to a very large pore). It turns out that the ink-bottle effect is responsible for most of the hysteresis in water content at RH$>$20%. The model is based on a fit pore size distribution and a scalar parameter quantifying the connectivity of the pore network. These parameters can be obtained via calibration on a full cycle of adsorption and desorption, and then can be used to predict the paste's response to an history of drying and wetting. Figure 3 shows a model-fitted sorption isotherm and a predicted scanning loop. Those were obtained combining both the interlayer and larger pore contributions, the former being taken directly from Figure 2.a and the latter being obtained by fitting the reduced isotherm in Figure 2.b using the model of (Pinson et al., preprint) just outlined.

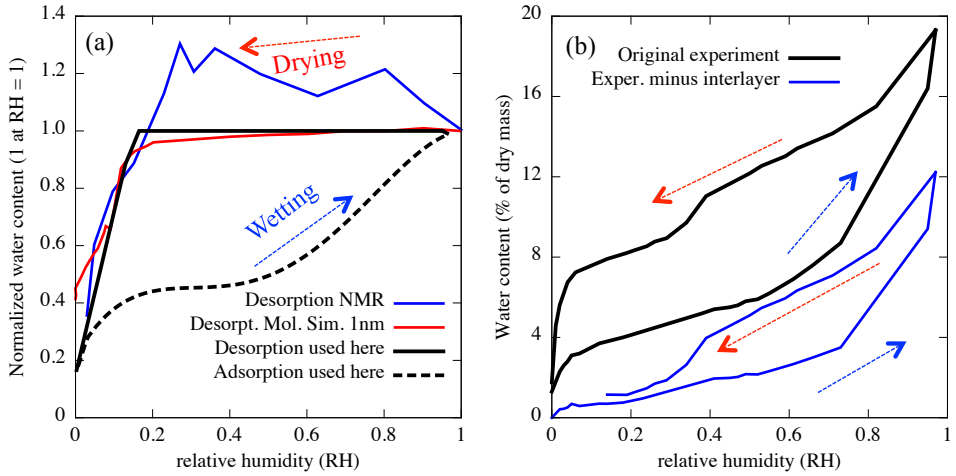

Figure 2. (a) Reconstructed sorption isotherm for pores smaller tha ∼1 nm. The curves are obtained using data from NMR (Muller et al., 2013), molecular simulations (Bonnaud et al., 2012; Bonnaud et al., 2013) and interpretation of cyclic isothermal water soprtion (Feldman and Sereda,1968; Pinson et al., in press). (b) Total sorption isotherm compared to reduced sorption isotherm for pores larger than 1 nm.

PREDICTING DRYING SHRINKAGE

With our model for hysteretic sorption isotherms we can quantify the saturation of interlayer spaces (here, spaces smaller than 1 nm), of gel and capillary pores which are sufficiently large for capillary pressure to develop, and also the amount of water adsorbed on the surface of unsaturated capillary pores. For the latter, we use the Langmuir isotherm, but we have also shown in (Pinson et al., in press) that the BET isotherm would yield very similar results. The information on these different categories of adsorbed water allows us to predict the drying shrinkage of the paste.

For pores larger then 1 nm we consider only the Laplace pressure associated with the capillary meniscus. For the water adsorbed on the surface of unsaturated capillary pores, we quantify the pressure generated by the increase of interfacial tension between the solid skeleton of the paste and the surface-adsorbed water. To this end, we combine the Bangham equation, the Gibbs equation, and the Langmuir sorption isotherm (see (Pinson et al., in press) for details; the reader might also find (Feldman and Sereda, 1968) a useful reference).

The strain contribution from the interlayer spaces (smaller than 1 nm) is poorly understood. Similar to the approach used in other mesoporous materials to estimate the strain contribution from micropores (Brochard et al., 2012), here we assume a linear relationship between water content in the interlayer spaces (see Figure 2.a) and strain.

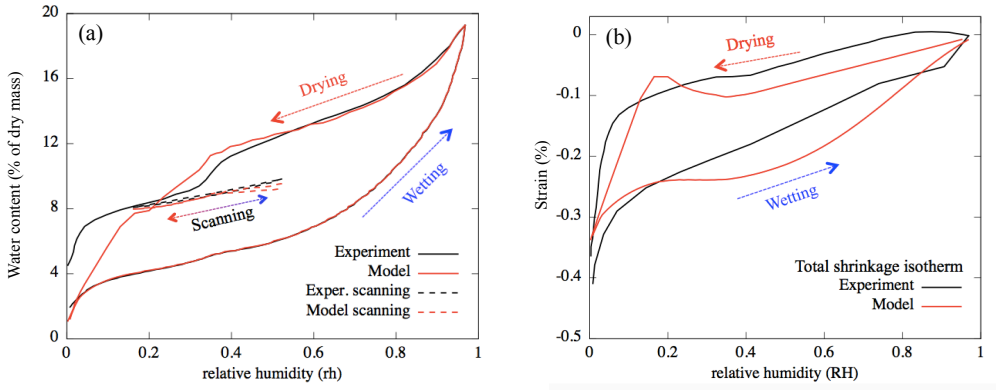

Figure 3. (a) Sorption and (b) strain isotherms: experiments vs. model fitting and predictions. The experiments are taken from (Feldman, and Sereda, 1968).

This hints to a mechanism of interlayer collapse upon water removal, but it turn out that the proportionality constant λ between water content and volume change needs be much smaller than unity in order to capture the low-RH strain isotherm Figure 3.b reasonably well. Nevertheless, the contribution from the interlayer spaces must be considered, otherwise the Laplace pressure and the change of interfacial tension would be insufficient to capture quantitatively the strong drying shrinkage at low RH $<$20%).

The small λ raises doubts about the mechanism of interlayer collapse upon drying below 20% RH. Namely, it is not clear why only a small portion of the local strain would be translated into macroscopic strain. At the present state, other mechanisms for strain development in interlayer spaces must be considered as well, for example the effect of disjoining pressure (Bažant, 1972). This is a field that can benefit significantly from developments in physical models and experiments(Pellenq and Van Damme, 2004; Plassard et al., 2005), molecular simulations (Bonnaud et al., 2012, Manzano et al., 2013), and mesoscale simulations of the mesoporous gel in cement (Masoero et al., 2012; Masoero et al., 2014; Ioannidou et al., 2014; Del Gado et al., 2014).

CONCLUSION

NMR experiments indicate that a considerable amount of pores in cement stay saturated unless the RH is decreased below 20%. Molecular simulations indicate that these pores should have width of $\sim$1 nm or less. We therefore made the assumption that water sorption and the associated dimensional changes can be spilt in two regimes: RH$>$20%, which is dominated by pore network effects and Kelvin-Laplace theory, and RH$<$20% which is dominated by molecular scale processes in very small pores, which we call interlayer spaces. For this paper, we consider the mechanism of pore blocking and the formation of capillary menisci as mechanisms for the hysteretic water sorp-

tion and strain contributions coming from pores larger than 1 nm. The contribution from interlayer spaces is instead taken phenomenologically from experimental results and considering a simple linear relationship between water content and strain for the shrinkage isotherm. Our results results capture satisfactorily the experiments in the whole range of adsorption and desorption, and predict the behaviour during scanning loops too. The mechanistic explanation of sorption isotherm and volumetric changes in the interlayer spaces requires further investigations which should reconcile the existing theories of pore collapse and disjoining pressure with the growing body of information generated by physical models and simulations, and new experiments.

REFERENCES

Bažant, ZP (1972). "Thermodynamics of hindered adsorption and its implications for hardened cement paste and concrete." *Cem. Concr. Res.* 2(1), 1-16.

Bonnaud, P.A., Ji, Q., Coasne, B., Pellenq, R.J.-M., and Van Vliet, K.J. (2012). "Thermodynamics of water confined in porous calcium-silicate-hydrates." *Langmuir* 28, 11422.

Bonnaud, P.A., Ji, Q., and Van Vliet, K.J. (2013). "Effects of elevated temperature on the structure and properties of calcium–silicate–hydrate gels: the role of confined water" *Soft Matter* 9, 6418.

Brochard, L., Vandamme, M, and Pellenq, R.J.-M. (2012). "Poromechanics of microporous media." *J. Mech. Phys. Solids* 60(4), 606-622.

Del Gado, E., Ioannidou, K., Masoero, E., Baronnet, A., Pellenq, R.J.-M., Ulm, F.-J., ans Yip, S. (2014) "A soft matter in constructionStatistical physics approach to formation and mechanics of CSH gels in cement" *Europ. Phys. J. Special Topics* 223(11), 2285-2295.

Feldman, R.F., and Sereda, P.J. (1968). "A model for hydrated Portland cement paste as deduced from sorption-length change and mechanical properties." *Mater. Constr.* 1(6), 509-520.

Ioannidou, K., Pellenq, R.J.-M., and Del Gado, E. (2014). "Controlling local packing and growth in calcium–silicate–hydrate gels" *Soft Matter* 10, 1121-1133.

Manzano, H., Masoero, E., Lopez-Arbeloa, I, and Jennings, H.M. (2013). "Shear deformations in calcium silicate hydrates" *Soft Matter* 9(30), 7333-7341.

Masoero, E., Del Gado, E., Pellenq, R.J.-M., Yip, S. and Ulm, F.-J. (2014) "Nano-scale mechanics of colloidal C–S–H gels" *Soft Matter* 109(15), 155503.

Masoero, E., Del Gado, E., Pellenq, R.J.-M., Yip, S. and Ulm, F.-J. (2014) "Nanostructure and nanomechanics of cement: polydisperse colloidal packing" *Phys. Rev. Lett.* 10(3), 491-499.

Muller, A.C.A., Scrivener, K.L., Gajewicz, A.M., and McDonald, P.J. (2013). "Use of bench-top NMR to measure the density, composition and desorption isotherm of C–S–H in cement paste." *Microporous Mesoporous Mater.* 178, 99.

Pellenq, R.J.-M. and Van Damme, H. (2004). "Why does concrete set?: The nature of cohesion forces in hardened cement-based materials" *MRS Bulletin* 29(5), 319-323.

Pinson, M.B., Jennings, H.M., and Bazant, M.Z. (preprint) "Inferring Pore Size and Network Structure from Sorption Hysteresis", *arXiv* 2014, 3377.

Pinson, M.B., Masoero, E., Bonnaud, P.A., Manzano, H., Ji, Q., Yip, S., Thomas, J.J., Bazant, M.Z., Van Vliet, K., and Jennings, H.M. (in press). "Hysteresis from multiscale porosity: water sorption and shrinkage in cement paste." *Phys. Rev. Appl.*.

Plassard, C., Lesniewska, E., Pochard, I., and Nonat, A. (2005). "Nanoscale Experimental Investigation of ParticleInteractions at the Origin of the Cohesion of Cement" *Langmuir* 21, 7263-7270.

Numerical Study of the Creep of Slit Nanopores: Role of Water

M. Vandamme[1], Z. P. Bažant[2], S. Keten[3]

[1]Université Paris-Est, Laboratoire Navier (École des Ponts ParisTech, IFSTTAR, CNRS), 6-8 Av. B. Pascal, 77420 Champs-sur-Marne, France; e-mail: matthieu.vandamme@enpc.fr
[2]Department of Civil and Environmental Engineering & Department of Mechanical Engineering & Department of Materials Science and Engineering, Northwestern University, 2145 Sheridan Road, Evanston, IL 60208; e-mail: z-bazant@northwestern.edu
[3]Department of Civil and Environmental Engineering & Department of Mechanical Engineering, Northwestern University, 2145 Sheridan Road, Evanston, IL 60208; e-mail: s-keten@northwestern.edu

ABSTRACT

Creep of cementitious materials is known to originate mostly from the creep of calcium silicate hydrates (i.e., C-S-H). Here, we study numerically a model for the C-S-H structure, and explicitly calculate the energy barriers that impact the rate at which two C-S-H layers slide over each other. In particular, we calculate how the viscosity scales with the microprestress. The obtained scaling is consistent with the microprestress theory which can explain why long-term creep of cementitious materials is a logarithmic function of time. Calculations are performed at various basal spacings (i.e., at various water contents), and model predictions are compared with experimental data obtained by micro-indentation of how the long-term logarithmic creep rate of C-S-H depends on the relative humidity. Considering properties of the interlayer water identical to those of bulk water, we obtain a good agreement with the experimental observations.

INTRODUCTION

Calcium silicate hydrates (i.e., C-S-H) are known to be responsible for the viscous behavior of cementitious materials. At the nanometer scale, C-S-H is formed of stacks of solid C-S-H layers separated by a few layers of interlayer water. The creep of concrete is generally thought to be due to the sliding of the C-S-H layers over each other.

In cementitious materials, hydration processes lead to a field of high self-equilibrated stress (called microprestress) in the C-S-H matrix. The microprestress originates from compressive stress normal to a C-S-H layer. But, because of the variety of orientations of randomly interconnected C-S-H layers in the C-S-H phases, the microprestress, along with the applied loads, inevitably induces shear stresses in the C-S-H layers (see Fig. 1), thus making this latter creep: Such a process leads to a

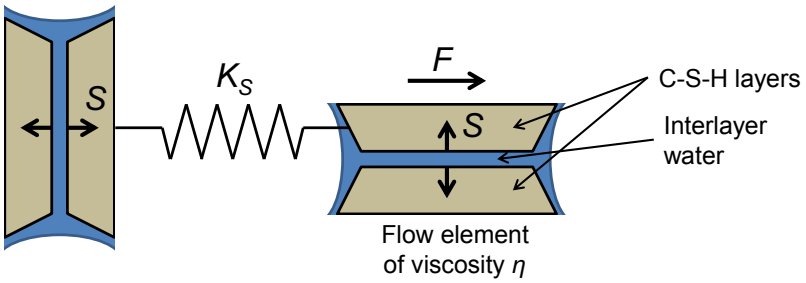

Figure 1. Principle of the microprestress theory, adapted from Bažant et al. (1997).

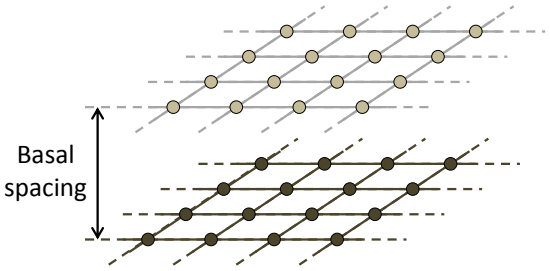

Figure 2. System considered.

relaxation of the microprestress over time, even when there is no external mechanical loading. The microprestress theory (Bažant et al., 1997) stipulates that the relaxation of the microprestress over time is such that the viscosity of the C-S-H layers increases linearly with time. Hence, under a constant mechanical load, one expects a creep rate that decreases with the inverse of time, and therefore a creep strain that increases linearly with the logarithm of time, as is observed experimentally in the long term. However, the microprestress theory relies on the assumption that the shear viscosity of the C-S-H layers scales as a power law of the microprestress.

In this study, we consider a simplified nanoscale model system for the C-S-H layers and aim at evaluating its viscosity from the energy barriers which the system needs to overcome for two adjacent C-S-H layers to slide over each other.

NUMERICAL STUDY OF SLIT NANOPORE

The model system we study (see Fig. 2) is a slit nanopore made of two rigid layers (thought to be representative of the C-S-H layers) parallel to each other and separated by water, seen as a continuum. Each atom of a solid layer interacts with each atom of the other layer through a Lennard-Jones potential. We apply both an in-plane force (i.e., acting in the plane of the layers) force F and a normal force S (i.e., the microprestress) to each atom of a layer. Since the self-equilibrated shear stresses are induced by the microprestress, we consider the in-plane force F to be proportional to the microprestress S.

For various microprestress S, various ratios F/S, and various equilibrium dis-

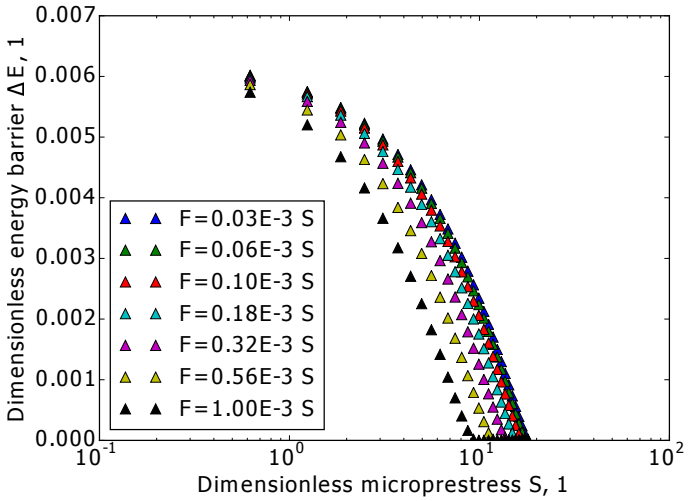

Figure 3. Effect of the dimensionless microprestress S on the dimensionless energy barrier ΔE that limits sliding of the C-S-H layers.

tances of the Lennard-Jones potential, we calculate numerically the energy barrier ΔE that the system needs to overcome for one solid layer to slide over the other one. We plot in Fig. 3 the energy barriers for the specific case of an equilibrium distance of the Lennard-Jones potential that is twice the lattice spacing. For large microprestress, we observe that the energy barrier decreases linearly with the logarithm of the microprestress. Moreover, how fast this energy barrier decreases with the microprestress (as indicated by $-d(\Delta E)/d(\ln S)$, which we denote α) is, in fact, independent of the (unknown) ratio F/S. By making use of an Arrhenius-type dependence of the viscosity on the energy barrier (i.e., $\eta \propto \exp(\Delta E/k_B T)$, where k_B is the Boltzmann constant and T the temperature (Debenedetti & Stillinger, 2001)), we find that the viscosity η of the C-S-H layers scales as $\eta \propto (1/S)^{\alpha/k_B T}$, i.e., the viscosity η scales as a power-law function of the microprestress S. Making use of the microprestress theory (Bažant et al., 1997), this scaling translates into a macroscopic creep rate $\dot{J}$ which evolves as:

$$\dot{J} \propto \frac{k_B T}{K_s \alpha} \frac{1}{t} \tag{1}$$

where K_s is imagined as the stiffness of a spring that resists the microprestress (see Fig. 1) and t is the time. Thus, after integration, we observe that the logarithmic feature of long-term creep is retrieved. Therefore, the calculations performed here provide some physical basis to the microprestress theory. We also observe that the rate of logarithmic creep depends on the parameter $\alpha = -d(\Delta E)/d(\ln S)$, which characterizes how the energy barriers decrease with the microprestress.

Note that the model provides reasonable orders of magnitude. We find typical energy barriers on the order of $k_B T$, so that the proposed mechanism of a viscosity impacted by the energy barriers due to the effective wall-wall interactions is plausible. Also, what we considered as large microprestress corresponds to a microprestress on

the order of 100 MPa, which is realistic as it corresponds to a typical order of magnitude of disjoining pressures.

INFLUENCE OF WATER CONTENT ON CREEP

The proposed slit nanopore model makes it possible to predict how variations of water content in the interlayer space modify the energy barriers which the system needs to overcome for the C-S-H layers to slide over each other and, consequently, how those variations modify the apparent viscosity of the layers. Then, through the microprestress theory, one can thus predict how the long-term creep rate of cementitious materials should evolve with water content (or relative humidity).

To estimate the effect of variations of water content, we repeat the numerical evaluations of the energy barriers presented in the previous section, but do so by varying the equilibrium distances of the Lennard-Jones potential. In all calculations, the well of the Lennard-Jones potential is identical. Such calculations indicate how parameter $\alpha = -d(\Delta E)/d(\ln S)$ evolves with the basal spacing. To estimate how the macroscopic viscosity evolves with the water content, one must recognize that Eq. (1) captures only the effect of the energy barriers on the viscosity of the C-S-H layers, but does not explicitly take into account the viscosity of the interlayer water itself. Taking into account this latter effect makes it possible to formulate the proportionality factor that intervenes in Eq. (1), and thus one finds that $\dot{J} \propto (d_w/\eta_w)(k_B T/K_S \alpha)(1/t)$, where η_w is the viscosity of the interlayer water and d_w is the interlayer spacing.

The predictions of the model are compared with long-term creep properties of C-S-H obtained by microindentation at various relative humidities (Zhang, 2014). To convert the relative humidities into the water content and the interlayer spacing, we use the adsorption isotherms gathered by Jennings (2008) and consider the density of the interlayer water to be equal to that of bulk water. We also consider that the viscosity of the interlayer water is equal to that of bulk water, which is a crude assumption since those two viscosities could in fact differ by a factor of about 3 (Raviv et al., 2001). Nevertheless, in spite of the assumptions, the proposed model system provides satisfactory predictions of how the relative humidity impacts the long-term logarithmic creep rate, as can be observed in Fig. 4 which displays the results of Zhang (2014) together with our model predictions.

CONCLUSIONS

The conclusions of this work are several:

- How the energy barriers that limit the sliding of C-S-H layers over each other evolve with the microprestress is consistent with the microprestress theory. This can explain why the long-term creep of cementitious materials is a logarithmic function of time.

- The proposed system model yields results consistent with the microprestress the-

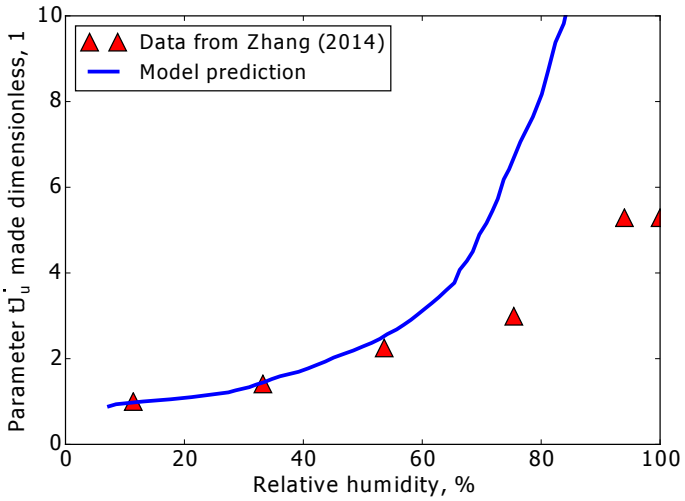

Figure 4. Effect of relative humidity on the long-term creep rate.

ory in spite of fully neglecting the chemical complexity of C-S-H. Such an observation shows that the logarithmic feature of long-term creep of C-S-H does not originate from a chemical specificity of C-S-H, but could originate from the nano-porosity and layered nano-scale structure of the C-S-H.

- For what concerns the dependence of creep on relative humidity, the proposed system model provides a reasonable agreement with the experimental data when, on top of the energy barriers due to the effective wall-wall interactions, the viscosity of the interlayer water is explicitly taken into account. Here, as a rough approximation, we consider the properties of the interlayer water and of the bulk water to be the same.

REFERENCES

Bažant, Z. P., Hauggaard, A. B., Baweja, S., and Ulm, F.-J. (1997). "Microprestress-solidification theory for concrete creep. I: Aging and drying effects." *Journal of Engineering Mechanics*, 123(11), 1188-1194.

Zhang, Q. (2014). *Creep properties of cementitious materials: effect of water and microstructure. An approach by microindentation*, Ph.D. thesis, Université Paris-Est.

Debenedetti, P. G., and Stillinger, F. H. (2001). "Supercooled liquids and the glass transition." *Nature*, 410(6825), 259-267.

Jennings, H. M. (2008). "Refinements to colloid model of C-S-H in cement: CM-II." *Cement and Concrete Research*, 38(3), 275-289.

Raviv, U., Laurat, P., and Klein, J. (2001). "Fluidity of water confined to subnanometre films." *Nature*, 413(6851), 51-54.

Shrinkage and Creep Caused by Dissolution

X. Li[1] and Z. C. Grasley[1]

[1]Zachry Department of Civil Engineering, Texas A&M University, College Station, TX. E-mail: xiaodanl@tamu.edu; zgrasley@civil.tamu.edu

Abstract

It has long been understood that creep and desiccation-driven shrinkage of concrete are coupled phenomena. Many mechanisms have been proposed over the past six decades by which creep and shrinkage are intertwined. Here, we propose that dissolution of solid, microscale constituents while under a state of stress leads to time-dependent deformation. As the state of stress may be incurred via external tractions on the microstructure, such time-dependent deformation may yield creep. As the state of stress may also be incurred through internal pore pressures, such time-dependent deformation may likewise generate shrinkage. By integrating the THAMES microstructural evolution model with a time-stepping finite element routine, simulations were performed to assess the magnitude of shrinkage deformations that may result from time-dependent dissolution. The simulation results indicate that the dissolution mechanism is significant, and may help explain the source of the irreversible component of desiccation shrinkage.

1. INTRODUCTION

Desiccation shrinkage, defined as the time-dependent deformation due to loss of water, is a characteristic property of cementitious materials. It can be induced by external drying (through diffusion and evaporation), or internal drying (when hydration consumes the capillary pore water) (see e.g., (Grasley & Leung, 2011; Hansen, 1987; Mindess, Young, & Darwin, 2002)). The origin of shrinkage has been primarily attributed to three most prominent mechanisms: surface free energy (R. F. Feldman, 1970; Treval C Powers, 1965; T. C Powers, 1968; Wittmann, 1973), capillary tension (R. Feldman & Sereda, 1970; R. F. Feldman & Sereda, 1968; Treval C Powers, 1965; T. C Powers, 1968; Young, Berger, & Bentur, 1978), and disjoining pressure (Bažant, 1972; Treval C Powers, 1965; T. C Powers, 1968; Wittmann, 1973, 1976). The activeness of these mechanisms depends on the internal relative humidity (RH), and at an intermediate to high internal RH (greater than ~50% RH) capillary tension and disjoining pressure are the primary mechanisms that induce drying shrinkage. The basis for both the disjoining pressure mechanism and capillary tension shrinkage mechanism is a reduction in the pore pressure, resulting in a negative pressure exerted by the pore fluid. One thing to note is that, even under constant RH and thus constant pore fluid pressure, shrinkage continues, resulting in a creep-like behavior of the cementitious composites (Lura, Jensen, & van Breugel, 2003). Despite extensive investigation into the shrinkage mechanisms, there is no unified

theory explaining the creep components related to desiccation shrinkage, as well as the irreversible components of shrinkage. Recently, a computational scheme coupling the THAMES microstructure evolution model and a time-stepping finite analysis routine has been developed to predict the long-term mechanical behavior of cementitious materials (Li, Grasley, Garboczi, & Bullard, 2015a, 2015b), and the simulation results from the scheme suggest that dissolution of solid load bearing constituents leads to significant time-dependent deformation while the microstructure is under external loading. As the state of stress inside cementitious composites may also be incurred through internal pore fluid pressure changes, it is hypothesized that a portion of early-age shrinkage (especially the irreversible component) is associated with dissolution of cement grains during the hydration process.

The objective of the research is to simulate the desiccation shrinkage behavior of cement paste due to combined elastic deformation of the composite microstructure and the concurrent dissolution of cement grains. The simulation results are analyzed and discussed to provide a more insightful view of the mechanisms leading to the creep and irreversible components of early-age desiccation shrinkage.

2. COMPUTATIONALLY IMPLEMENTED MODEL

2.1 Microstructure Model

The hydration model THAMES (Thermodynamic Hydration And Microstructure Evolution) (Bullard, Lothenbach, Stutzman, & Snyder, 2011; Lothenbach & Winnefeld, 2006) was used to simulate the microstructure evolution at the micrometer level during the hydration process. With the input of the original measured clinker constituent mass fractions, the particle size distribution of the cement and the water to cement mass ratio (*w/c*) at the sub-particle level, THAMES simulates the dissolution process of cement grains at different time steps (which represent different ages). According to empirically derived equations for clinker reaction rates (Parrot & Killoh, 1984), and based in part on phenomenological dissolution kinetics (Bullard et al., 2011), THAMES calculates the pore fluid elemental composition at each time step. A thermodynamic engine GEMS (Gibbs Energy Minimization)(Dmitrii A. Kulik, 2002; D.A. Kulik, 2006) was implemented in THAMES to calculate the equilibrium solution speciation and the mass of each solid constituent in equilibrium with the solution at each time step. More detailed description of the microstructure model THAMES can be found in (Bullard et al., 2011; Li et al., 2015a, 2015b).

2.2 Finite Analysis Conceptualization

To predict the time-dependent, apparent viscoelastic/viscoplastic (VE/VP) behavior of cementitious composites, the computational scheme was discretized in time to account for the time and (stress or strain) history dependent mechanical properties. Here, the term “apparent VE/VP” is reserved for modeling the constitutive behavior at the macroscale induced by smaller length scale mechanisms that are not due to

inherent VE or VP behavior of phases (e.g., C-S-H) within the composite material, but purely due to dissolution of load bearing phases. At each time step in the finite element calculations, THAMES provides 3D snapshots for cement paste as time evolves, where the 3D snapshots of microstructures are meshed into voxels using a spatially aligned numerical discretization (Ruetz, 1968) such that each voxel becomes an eight node tri-linear cubic finite element consisting of a unique phase with assigned elastic mechanical properties (e.g., Young's modulus and Poisson's ratio) from the literature. These 3D time-evolving microstructures generated by THAMES are subjected to strain-controlled periodic displacement boundary conditions in the finite element analyses, and through minimizing the total mechanical energy stored in the microstructure at each time step (Li et al., 2015a, 2015b), the volume averaged stress of the composite can be predicted. The composite moduli are calculated by solving the elastic equations on a regular finite element mesh (Zohdi, 2004), based on the volume averaged stress of the composite.

A key assumption in the model for dissolution of load bearing phases is that once phase changes occur inside one microstructure, the stress originally transmitted by the dissolved solid phases are transmitted into surrounding phases in order to satisfy conservation of linear momentum. Furthermore, the newly formed phases must form in a stress-free state within the deformed configuration that conforms to the preexisting phases. This condition implies that that stress redistribution takes place much faster than chemical phase changes, and the newly formed phases carry no memory of historical responses, resulting in the production of apparent strain inside the microstructure. The term "apparent strain" in this paper is defined, from a continuum mechanics perspective, as strain that exists independent of the state of stress. Unlike other 'free' strains (e.g., strain induced by changes in temperature or moisture state of the material), the apparent strain here does not involve a change in the atomic or molecular spacing from the reference configuration. However, from a book-keeping perspective, apparent strain is treated in the same fashion as free strains. This process of microstructure evolution (or load bearing solids dissolution) would lead to apparent VE/VP effects of cement paste even when each microscopic phase is strictly elastic. More detailed procedures, theoretical derivations, and the finite element formulation of the computational model may be found in (Li et al., 2015a, 2015b).

2.3 Shrinkage Prediction

Due to the limitation of the computational scheme that the microstructures in the model can only be subjected to strain-controlled periodic boundary conditions, to predict the time-evolving shrinkage strain of the macroscopic cement paste composite under zero external stress and negative internal pore fluid pressure, Boltzmann's superposition principle (Christensen, 2012; Wineman & Rajagopal, 2000) was applied. In the computational program, starting with one microstructure at a certain loading age, prescribed, periodic volumetric strain was applied on the boundaries of a series of isotropic, evolving microstructures to determine the evolution of the apparent VE/VP bulk modulus of the whole composite under a specific loading age.

In this way, the apparent VE/VP bulk modulus of the cement paste composite under a series of different loading ages can be predicted by the computational scheme. Meanwhile, for the same series of microstructures, through constraining the applied periodic boundary volumetric strain to be zero for all time steps while assigning a negative pore pressure to the fluid phases, the evolution of volumetric stress of the whole composite can be calculated in the computational implemented model. With the known apparent VE/VP bulk modulus at different ages and the time-evolving apparent volumetric stress, the strain that must necessarily be applied at each time step to maintain an overall spatially averaged zero stress state (corresponding to "free shrinkage") can be calculated according to the superposition principle. Thus, the predicted time-evolution of the shrinkage strain is due to concomitant elastic deformation of the solid microstructure with changes in pore fluid pressure and dissolution of cement grains and subsequent stress redistributions in the microstructure.

3. SIMULATION RESULTS AND DISCUSSIONS

3.1 Different Loading Age

Microstructures of hydrating cement composites with pure elastic phases (using elastic properties taken from (Haecker et al., 2005)) at different ages (from 1 d to 56 d) were examined in this project. In these simulations, the irreversible, time-dependent shrinkage of the cement pastes occurs strictly due to the time-dependent dissolution of cement grains. **Figure 1** shows the predicted irreversible shrinkage strain normalized by the applied pore fluid pressure for a 0.40 *w/c* cement paste at ages of 1 d and 4 d. The pore fluid pressure was applied here as a step function at the given ages.

From **Figure 1**, one can see that the cement paste irreversible shrinkage due to dissolution of cement grains is substantial. Once the desiccation process starts, negative pore water pressure is induced into the cement composite. Under the constant (step function applied) negative pore fluid pressure, younger specimens exhibit greater irreversible shrinkage because of the higher hydration rate (and thus dissolution rate of cement grains) at earlier ages. Another reason leading to the faster shrinkage for the younger specimen is that more water is present in younger specimens, and thus the negative pressure results in greater contraction of the solid skeleton. Meanwhile, the younger cement paste composite is less stiff than the older cement paste, and thus is more compliant to external and internal forces, resulting in a much larger deformation. Both specimens show decreasing shrinkage rate with age because hydration rate decreases as cement paste ages. Thus, in conclusion, from the simulation results, younger cement pastes are likely to exhibit greater irreversible shrinkage from cement grain dissolution than older cement pastes.

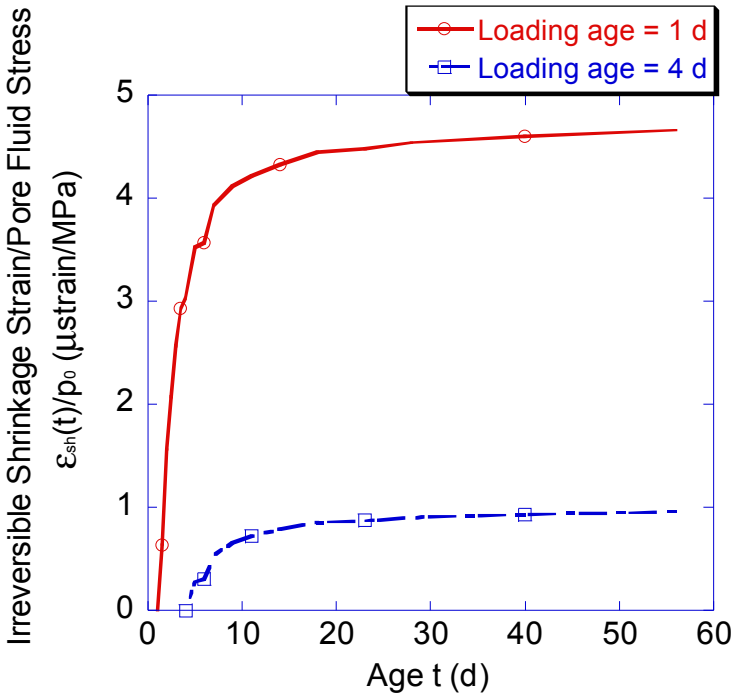

Figure 1 Irreversible shrinkage strain normalized by the applied pore fluid pressure in a 0.40 *w/c* cement paste when loaded at different ages (1 d and 4 d). In this graph, irreversible shrinkage strain was considered to increase strictly due to dissolution of load bearing cement grains.

3.2 Different w/c

To investigate the influence of different values of *w/c* on the irreversible shrinkage behavior of cement paste, microstructures of cement paste with purely elastic phases (with elastic properties taken from (Haecker et al., 2005)) and *w/c* from 0.35 to 0.50 were utilized. In this set of simulations, the irreversible shrinkage of cement paste occurred strictly due to dissolution of load bearing cement grains. **Figure 2** shows the predicted results of irreversible shrinkage strain divided by the step-applied pore fluid pressure for different values of *w/c* at loading ages of 1 d. As shown in **Figure 2**, higher *w/c* results in faster and larger shrinkage (normalized by pore fluid pressure) than lower *w/c* because of its higher water content and lower stiffness. All *w/c* cement pastes show decreasing shrinkage rate with age.

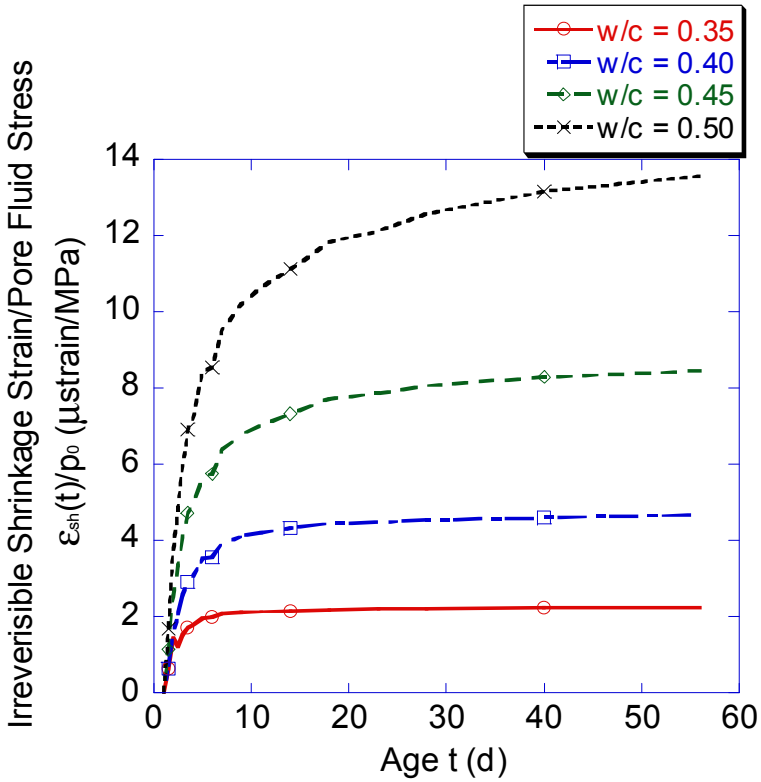

Figure 2 Irreversible shrinkage strain divided by the applied pore fluid pressure for different *w/c* at loading age of 1 d. The irreversible shrinkage strain was considered to increase strictly due to dissolution of load bearing cement grains.

3.3 Time-evolving RH

In the previous simulations, the pore fluid pressure were assigned as a step-function in the computational scheme, while in real life, the pore fluid pressure changes with age as a function of the time-evolving internal RH through the combined Kelvin-Laplace equation

$$p \approx -\ln(\frac{RH}{RH_0})\frac{RT}{v_w},$$

where p is the pore fluid pore pressure, RH is the current internal relative humidity, RH_0 is the initial internal relative humidity, R is the universal gas constant, v_w is the molar volume of water, and T is the temperature in Kelvins (Defay, Bellemans, & Prigogine, 1966). Here, we neglect the time-evolution of the effect of the dissolved species on the chemical potential of the pore fluid. With the experimental data of the time-evolving RH, the pore fluid pressure inside the cement paste composite can be calculated and implemented into the computational scheme to simulate the real life shrinkage behavior of cement paste.

Figure 3 shows the simulated results of the time-dependent shrinkage strain of 0.40 *w/c* cement paste utilizing experimental data of time-evolving RH at the loading age of 1 d under the temperature of 273 K. The experiments involved the measured

internal RH (starting at an age of 1 d) in a self-desiccating (sealed from external drying) mortar bar. In **Figure 3**, the solid line was obtained through utilizing the microstructure-evolving properties of cement paste at all different ages; it shows the increase of the shrinkage strain as a combination of both the elastic response to increasing internal pore fluid pressure as well as the dissolution effect of the load bearing cement grains. Meanwhile, the dashed shrinkage strain line in **Figure 3** was obtained by treating the cement paste composite at each time step as a purely elastic material with constant mechanic moduli independent of microstructures from other ages. In this way, the phase dissolution effect was neglected, and the dashed shrinkage strain line simply shows the increase of the cement paste shrinkage strain due to the elastic response to pore fluid pressure increase [i]. The shrinkage demonstrated by this dashed line can also be referred to as the recoverable shrinkage (as it occurs only due to the elastic deformation of cement paste), while the differences between the solid line and the dashed line are the irreversible components

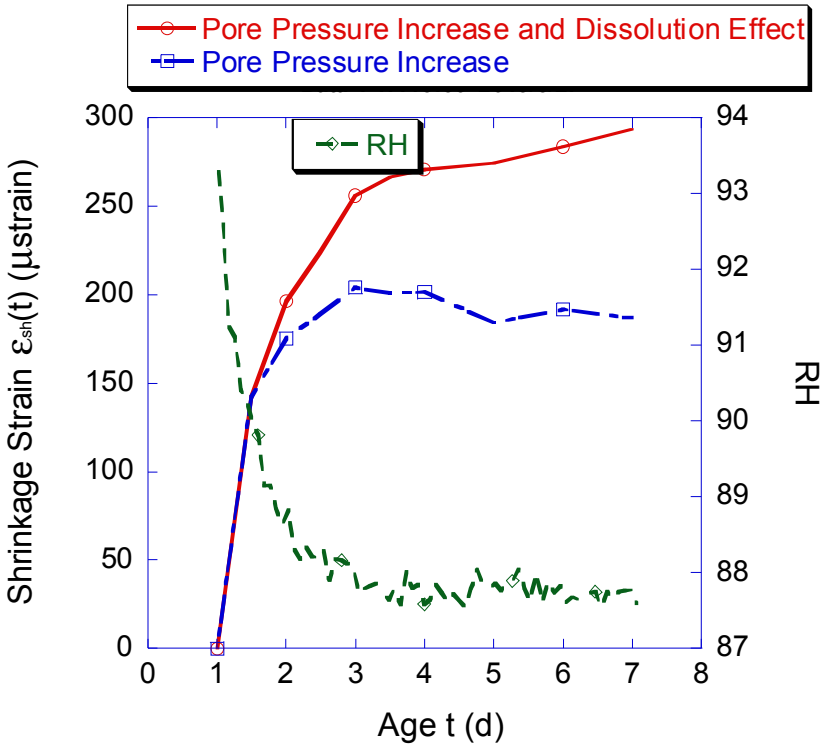

Figure 3 Predicted shrinkage strain of 0.40 *w/c* cement paste when loaded at an age of 1 d. In this graph, the dashed shrinkage strain line was obtained by treating cement paste as purely elastic while neglecting phase dissolution effects, while the solid line was obtained by treating cement paste at all ages as a microstructure-dependent time-evolving material. The dashed shrinkage line shows the shrinkage of cement paste occurring purely due to pore pressure increase, while the solid line shows both the reversible and irreversible shrinkage due to both pore pressure increase and cement grain dissolution effects. Measured RH history was also included in this graph on the right hand Y axis.

of shrinkage induced by cement grain dissolution. Thus, from the simulation results, the dissolution of load bearing cement grains during the shrinkage process appears to be a significant mechanism leading to irreversible shrinkage.

4. CONCLUSIONS

A computational scheme that couples a microstructure evolution model and a time-stepping finite element method capable of tracking phase formation/dissolution was utilized to predict the shrinkage strain evolution of cement paste with time. From the model simulations, dissolution of cement grains of hydrating cement paste is a significant factor leading to the irreversible component of cement paste shrinkage.

REFERENCES

Bažant, Z. (1972). Thermodynamics of hindered adsorption and its implications for hardened cement paste and concrete. *Cement and Concrete Research, 2*(1), 1-16.

Bullard, J. W., Lothenbach, B., Stutzman, P. E., & Snyder, K. A. (2011). Coupling thermodynamics and digital image models to simulate hydration and microstructure development of portland cement pastes. *Journal of Materials Research, 26*(4), 609-622.

Christensen, R. (2012). *Theory of viscoelasticity: an introduction*: Elsevier.

Defay, R., Bellemans, A., & Prigogine, I. (1966). Surface tension and adsorption.

Feldman, R., & Sereda, P. (1970). A new model for hydrated Portland cement and its practical implications. *Engineering Journal, 53*(8/9), 53-59.

Feldman, R. F. (1970). Sorption and length-change scanning isotherms of methanol and water on hydrated Portland cement.

Feldman, R. F., & Sereda, P. J. (1968). A model for hydrated Portland cement paste as deduced from sorption-length change and mechanical properties. *Materiaux et construction, 1*(6), 509-520.

Grasley, Z. C., & Leung, C. K. (2011). Desiccation shrinkage of cementitious materials as an aging, poroviscoelastic response. *Cement and Concrete Research, 41*(1), 77-89.

Haecker, C. J., Garboczi, E. J., Bullard, J. W., Bohn, R. B., Sun, Z., Shah, S. P., & Voigt, T. (2005). Modeling the linear elastic properties of Portland cement paste. *Cement and Concrete Research, 35*(10), 1948-1960. doi: 10.1016/j.cemconres.2005.05.001

Hansen, W. (1987). Drying shrinkage mechanisms in Portland cement paste. *Journal of the American Ceramic society, 70*(5), 323-328.

Kulik, D. A. (2002). Gibbs energy minimization approach to modeling sorption equilibria at the mineral-water interface: Thermodynamic relations for multi-site-surface complexation. *American Journal of Science, 302*(3), 227-279. doi: 10.2475/ajs.302.3.227

Kulik, D. A. (2006). Dual-thermodynamic estimation of stoichiometry and stability of solid solution end members in aqueous–solid solution systems. *Chemical Geology, 225*(3–4), 189-212. doi: 10.1016/j.chemgeo.2005.08.014

Li, X., Grasley, Z. C., Garboczi, E. J., & Bullard, J. W. (2015a). Computing the time evolution of the apparent viscoelastic/viscoplastic poisson's ratio of hydrating cement paste. *Cement and Concrete Composite, 56*, 121-133.

Li, X., Grasley, Z. C., Garboczi, E. J., & Bullard, J. W. (2015b). Modeling the apparent and intrinsic viscoelastic relaxation of hydrating cement paste. *Cement and Concrete Composite, 55*(0), 322-330. doi: http://dx.doi.org/10.1016/j.cemconcomp.2014.09.012

Lothenbach, B., & Winnefeld, F. (2006). Thermodynamic modelling of the hydration of portland cement. *Cement and Concrete Research, 36*(2), 209-226.

Lura, P., Jensen, O. M., & van Breugel, K. (2003). Autogenous shrinkage in high-performance cement paste: An evaluation of basic mechanisms. *Cement and Concrete Research, 33*(2), 223-232. doi: http://dx.doi.org/10.1016/S0008-8846(02)00890-6

Mindess, S., Young, J. F., & Darwin, D. (2002). *Concrete* (2nd ed.). Upper Saddle River, NJ: Prentice Hall.

Parrot, L., & Killoh, D. (1984). *Prediction of cement hydration.* Paper presented at the Proc. Br. Ceram. Soc.

Powers, T. C. (1965). Mechanisms of shrinkage and reversible creep of hardened cement paste. *The structure of concrete and its behaviour under load*, 319-344.

Powers, T. C. (1968). The thermodynamics of volume change and creep. *Matériaux et Construction, 1*(6), 487-507.

Ruetz, W. (1968). *A hypothesis for the creep of hardened cement paste and the influence of simultaneous shrinkage Proceedings of International Conference On the Structure of Concrete*. London, England: Cement and Concrete Association.

Wineman, A. S., & Rajagopal, K. R. (2000). *Mechanical response of polymers: an introduction*: Cambridge University Press.

Wittmann, F. (1973). Interaction of hardened cement paste and water. *Journal of the American ceramic society, 56*(8), 409-415.

Wittmann, F. (1976). The structure of hardened cement paste-a basis for a better understanding of the materials properties. *Hydraulic Cement Pastes: Their Structure and Properties. Cement and Concrete Association, Slough, United Kingdom*, 96-117.

Young, J., Berger, R., & Bentur, A. (1978). Shrinkage of Tricalcium silicate pastes: Superposition of several mechanisms. *Il Cemento, 75*(3), 391-398.

Zohdi, T. I. (2004). Homogenization Methods and Multiscale Modeling *Encyclopedia of Computational Mechanics*: John Wiley & Sons, Ltd

[i] The slight decay of the shrinkage illustrated by the dashed line is due to the fact that the shrinkage at a given time is a function of the pore pressure and material microstructure (and thus elastic stiffness) at that time. In reality, increases in stiffness that occur after a change in pore pressure would not reduce the shrinkage.

Thoughts on Curling in Plain and SRA Concrete Slabs: Moisture Gradients, Surface Tension, and Viscosity

W. Jason Weiss[1]

[1]Jack and Kay Hockema Professor, School of Civil Engineering, School of Materials Engineering, Purdue University, 550 Stadium Mall Dr., West Lafayette, IN 47906. E-mail: wjweiss@purdue.edu

Abstract

This paper is part of the mini-symposium on the interplay between water and shrinkage. The paper provides a short discussion of observations from a recent neutron radiography experiment where radiography was performed on plain concrete and concrete containing a shrinkage reducing admixture (SRA) when each sample was exposed to drying. While the results of the radiography test provided information on the moisture content and degree of saturation, the goal of this paper is to relate the moisture (degree of saturation) gradients, the relative humidity gradients, the shrinkage gradient and a corresponding stress gradient. The work provides evidence for the reduced curling that is often seen in concrete containing SRA. The reduced curling with SRA appears to be a combination of the reduced surface tension that limits shrinkage and the increased viscosity that reduces fluid flux.

MOISTURE (DEGREE OF SATURATION) GRADIENTS

While shrinkage is discussed in many applications, understanding moisture gradients is important to understanding the rate of drying, curling and cracking. Figure 1 plots the degree of saturation as obtained from neutron radiography (Villani et al. 2015) of a sample exposed to 4 days of drying in an environment with a temperature of 26-28C and a relative humidity of 20-40% RH. Both samples were made from a plain mortar that had a water to cement ratio of 0.42. The mortar was dried after it had hydrated for one year. After drying the mortar was resaturated (vacuum saturated) with either lime saturated water or with a solution consisting of SRA and lime saturated water where 5% of the water was replaced with SRA. It can be observed that both the plain sample and sample containing SRA have a very sharp moisture front with the drying surface having a substantially different degree of saturation than the core of the concrete. The plain concrete had an average degree of saturation of 82% between 10 and 50 mm while the sample containing SRA had an average degree of saturation of 86% between 10 and 50 mm. If the average degree of saturation between 10 and 50 mm is used to determine the depth of the drying front (i.e., the location where the degree of saturation first exceeds the average degree of saturation) the depth of the drying front is 8.93 mm for the plain sample and only 0.7 mm for the SRA sample. Figure 1c and 1d include the same data used in Figure 1a and 1b however the axis is changed to better resolve the surface effects.

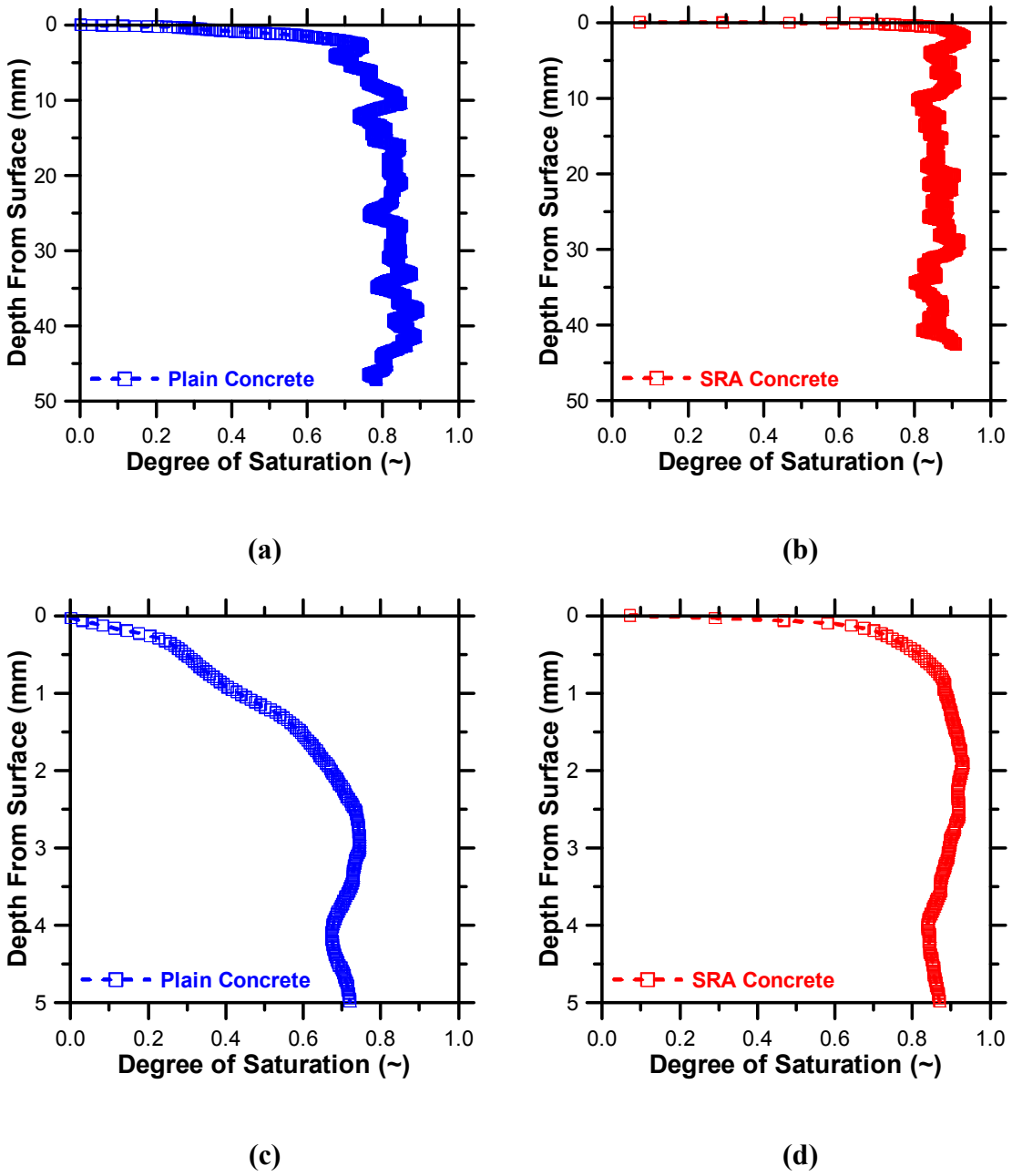

Figure 1. Degree of Saturation as a Function of Distance from the Drying Surface for Plain Concrete (a and c) and Concrete Containing SRA (b and d)

RELATIVE HUMIDITY GRADIENTS

While the degree of saturation shown in Figure 1 is useful, this can be related to the relative humidity using a desorption isotherm. The desorption isotherm was

measured using dynamic vapor sorption for these materials (Villani et al. 2015) abnd the result is shown in Figure 2.

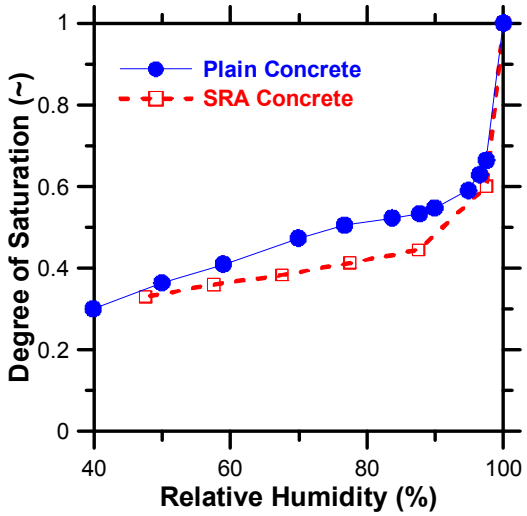

Figure 2. Desorption Isotherm

This desorption isotherm was fitted in a piece-wise manner and used to obtain the relative humidity gradients shown in Figure 3 using the data from neutron radiography shown in Figure 1. The plain concrete shows a sharp relative humidity gradient in the outer 2 mm of the sample near the drying surface. It can be noticed that the relative humidity is greater than 99% RH for all but the top 0.2 mm in the SRA concrete. In both samples the relative humidity in the outermost surface appears to result in values that would be less than that expected from the environment.

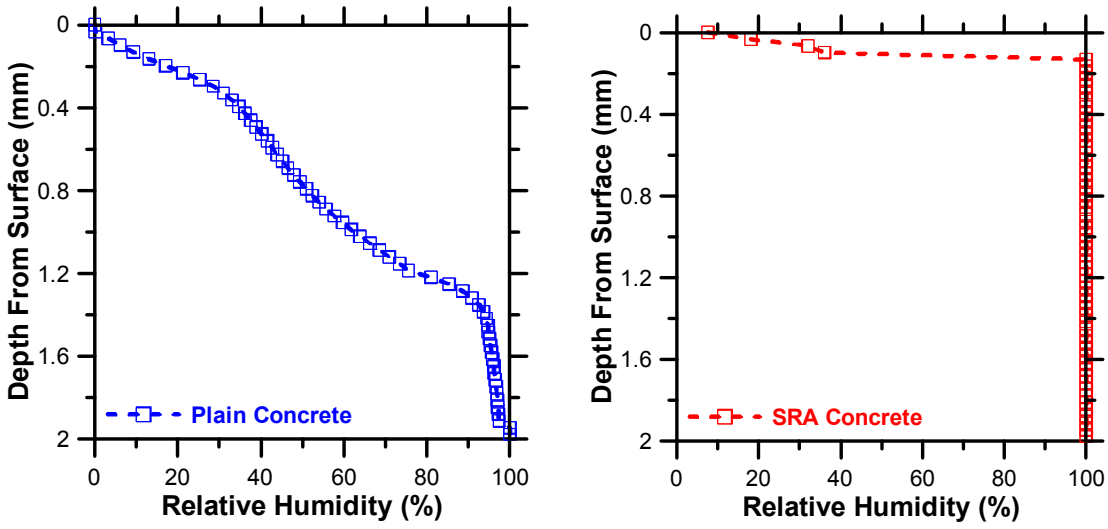

Figure 3. Relative Humidity Gradients as a Function of the Depth from the Drying Surface (a) Plain Concrete and (b) SRA Concrete

SHRINKAGE AND STRESS GRADIENTS

A model was developed by Vlahinic et al. (2009) where the shrinkage of porous body could be related to properties of the porous material shown in the following equation:

$$\varepsilon_{SH} = -\frac{1}{3}\frac{RT}{M} ln(RH)\left(\frac{1}{K_b} - \frac{1}{K_s - \frac{(K_s - K_b)(1 - S_w)}{(1 - S_w \emptyset_0)}}\right)$$

where R is the gas constant, T is the temperature, M is the molar volume of the water, RH is the relative humidity, K_s is the bulk modulus of the solid, K_b is the bulk modulus of the porous body, S_w is the degree of saturation and ϕ_o is the capillary porosity (assumed to be 0.35 which would correspond to complete hydration following Powers model for a sealed system). It can be assumed that the shrinkage strain is related to the stress (assuming that the system is elastic and Hooke's law applies, in reality aging viscoelastic effects should be considered; however for this analysis the assumption of elastic behavior is used). Figure 4 shows the stress gradients that can be expected. The resulting force in the plain system would be 5.5 times greater at an age of 4 days than the system with SRA and the resulting moment would be 2.7 times greater. This is consistent with trends observed by Weiss (1999).

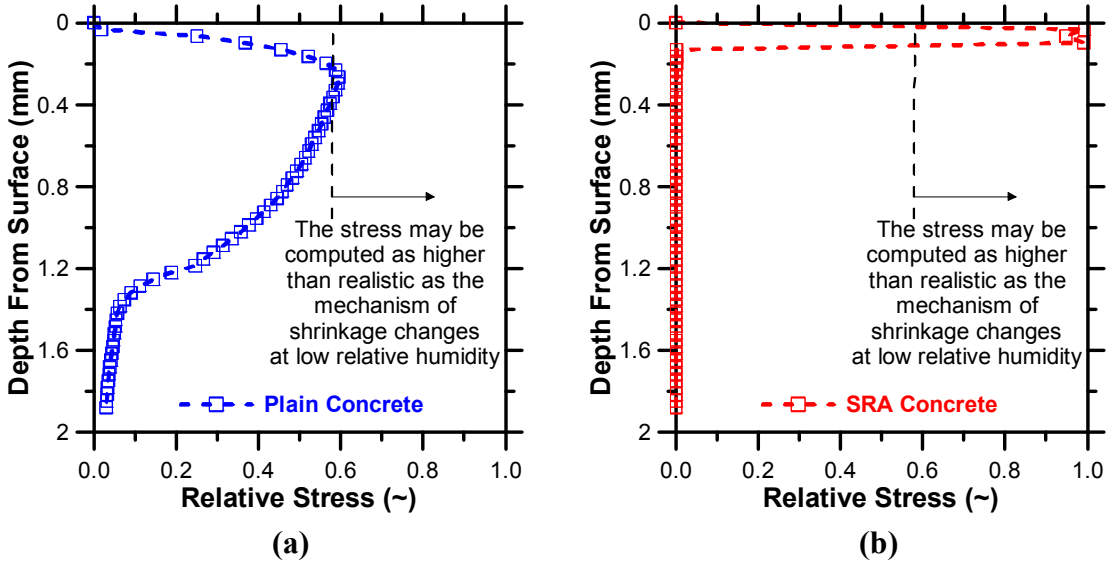

Figure 4. Relative Stress Profiles from the Depth from the Drying Surface (a) Plain Concrete and (b) SRA Concrete

Figure 4 however assumes that the shrinkage is entirely described by the Vhahinic previously discussed and this equation shows good correspondence for plain mixtures at humidities where capillary stress is the predominant stress in the system. It has been reported by Weiss et al. (2008) that if one assumes capillary stress effects only correspond with pores of a Kelvin radius of above 1.5 nm then the Vlahanic equation would only correspond to shrinkage values above approximately 50% RH for a plain system and 70% for the system with 5% SRA. As a result it may be expected that the

values of stress to the right of the dashed lines in Figure 4 are over estimates of the actual shrinkage that may be expected. This change in relative humidity due to the Kelvin radius accounts for the changes in surface tension that occur with the use of a shrinkage reducing admixture. This implies that for systems at the same relative humidity a smaller pore empties in the SRA system (Radlinska et al. 2008).

It should however be noted that in addition to changes in the surface tension the use of SRA alters the viscosity of the solution (Villani et al. 2014). This increase in viscosity can be used to describe the reduction in the vapor diffusion coefficient (Villani et al. 2015). The change in viscosity can also describe the change in fluid flux using an approach shown by Brinker and Scherer (1989) (chapter 8, section 2.1) where the fluid flux is inversely related to viscosity.

CONCLUSION

The paper begins with results from a recent neutron radiography experiment where a plain concrete and concrete containing a shrinkage reducing admixture (SRA) were exposed to drying. While the results of the radiography test provided information on the degree of saturation, this paper used this information to compute the relative humidity gradients, relative shrinkage gradient and a corresponding stress gradient. The work provides evidence for the reduced curling that is often seen in concrete containing SRA. The reduced curling with SRA appears to be a combination of the reduced surface tension that limits shrinkage and the increased viscosity that reduces fluid flux maintaining a higher degree of saturation in the concrete.

REFERENCES

Brinker, C.J., and Scherer, G. W., “Sol Gel Science”, Academic Press 1989

Radlinska, A., Rajabipour, F., Bucher, B., Henkensiefken, R., Sant, G., and Weiss, W. J., (2008), “Shrinkage Mitigation Strategies in Cementitious Systems: a Closer Look at Sealed and Unsealed Behavior,” Transportation Research Record, Volume 2070, pp. 59-67

Villani, C., Lucero, C., Bentz, D. P., Hussey, D., Jacobson, D. L., and Weiss, W. J., (2015) “Neutron Radiography Evaluation of Drying in Mortars with and without Shrinkage Reducing Admixtures,” ACI Special Publication, submitted

Villani, C., Spragg, R., Pour-Ghaz, M., and Weiss, W. J., (2014) “The Influence of Pore Solution Properties on Drying In Cementitious Materials,” Journal of the American Ceramic Society

Vlahinic, I., Jennings, H.M., and Thomas, J.J. (2009) “A Constitutive Model for Drying of a Partially Saturated Porous Material, Mechanics of Materials, Vol 41. pp 319-328

Weiss, W. J., (1999) “Prediction of Early-Age Shrinkage Cracking in Concrete Elements,” PhD Thesis, Northwestern University, Evanston Illinois

Weiss, W. J., Lura, P., Rajabipour, F., and Sant, G., (2008) “Performance Of Shrinkage Reducing Admixtures At Different Humidities And At Early Ages,” American Concrete Institute Materials Journal, Vol. 105, no. 5, pp. 478-486

Effects of humidity on the time dependent behaviour of geomaterials

J. M. Pereira[1] and V. De Gennaro[2]

[1]Université Paris-Est, Laboratoire Navier (UMR 8205), CNRS, ENPC, IFSTTAR, 77455 Marne-la-Vallée, France; PH +33 (0)164153548; FAX +33 (0)164153562; email: jeanmichel.pereira@enpc.fr
[2]Schlumberger, Pau, France; email: vdegennaro@slb.com

ABSTRACT

Geomaterials present a mechanical behaviour with a more or less pronounced time dependency. This sensitivity to time effects encompasses creep and effects of strain rate and its changes. This time dependent behaviour of geomaterials is affected by humidity, and also by humidity changes. In this paper, these effects are first reviewed, with an emphasis put on a series of experiments on chalk saturated by different fluids or pairs of fluids. The main observation is that less humidity implies less creep and a smaller sensitivity of the mechanical behaviour to strain rates effects. A constitutive model accounting for saturation level and time effects is then developed in the framework of elastoplasticity, at the macroscopic scale. The constitutive laws for the description of the time-dependent mechanical behaviour generalise the isotach concept to partially saturated states. It is shown that the model can predict creep or relaxation of geomaterials, when the applied load is close to the elastic limit. Finally, numerical predictions by the proposed model are compared with available experimental results on saturated and partially saturated chalk. It is shown that the model can capture satisfactorily creep and strain rate effects on the mechanical response of this soft rock at various water saturation states.

INTRODUCTION

All geomaterials present a mechanical behaviour with a more or less pronounced time dependency. This sensitivity to time effects encompasses creep and effects of strain rate and its changes. Time effects generally arise from various physico-chemical origins, such as water diffusion across different porosity scales, pressure-solution phenomenon, sub-critical crack propagation... These effects have been characterised experimentally in many studies. What has been less studied is the role that humidity plays on this susceptibility of the mechanical behaviour of geomaterials to time effects. In this paper, the effects of humidity on the time dependent behaviour of some geomaterials are first reviewed, with an emphasis put on a series of experiments on chalk saturated by several fluids or pair of fluids (air, water, oil, water-oil at different saturation levels). The main

observation is that less humidity implies less creep and a smaller sensitivity of the mechanical behaviour to strain rates effects.

In this paper, by convention, stresses and strain are accounted positively under compression and contraction. Stresses with a $'$ refer to effective stresses, in the sense of Terzaghi (total stress minus pore fluid pressure).

EXPERIMENTAL OBSERVATIONS

Time effects on the mechanical behaviour of soils and rocks have been investigated for a long time (e.g. Vaid and Campanella, 1977; Leroueil *et al.*, 1985; Di Benedetto *at al.*, 2002; Oldecop and Alonso, 2003; De Gennaro *et al.*, 2004). Creep constitutes the emblematic phenomenon of these effects. Strain rate effects have also been studied, the main reason being that strain rates applied in the laboratory are quite different from the observed ones in the field. It has been observed that the response of soils generally follow the so-called isotach behaviour, also known as reference time approach. Interestingly, experimental observations tend to show that the tendency of geomaterials to creep is consistent with their sensitivity to strain rate (isotach behaviour). Another significant observation is the link between materials' apparent stiffness and their creep modulus.

In the plastic regime, the following log-linear relation is generally used to predict volumetric strain change during an oedometric compression:

$$\mathrm{d}e = C_c \frac{\mathrm{d}\sigma'_v}{\sigma'_v} \tag{1}$$

where σ'_v is the vertical effective stress and $e = \phi/(1-\phi)$ is the void ratio (ϕ being the porosity of the material).

Under constant vertical effective stress, secondary consolidation (stage during which primary creep occurs during oedometric compression tests) may be described by the following equation:

$$\mathrm{d}e = C_{\alpha e} \frac{\mathrm{d}t}{t} \tag{2}$$

The ratio $C_{\alpha e}/C_c$ is observed to be approximately constant, with a value depending on the type of soil (Mesri and Godlewski, 1977). Alternatively, other studies investigated the evolution of the yield stress as a function of the strain rate. It has been concluded that the yield stress evolves as a power law of the applied strain rate:

$$\frac{\sigma'_y}{\sigma'^{ref}_y} = \left(\frac{\dot{\epsilon}_z}{\dot{\epsilon}^{ref}_z} \right)^{\alpha} \tag{3}$$

where ϵ_z denotes the vertical strain and α is a material constant. This relation has been first proposed for oedometric compression but similar relations hold for isotropic and drained triaxial compression tests, provided that an appropriate measure of the control strain variable is defined. This relation can even be extended to undrained triaxial tests

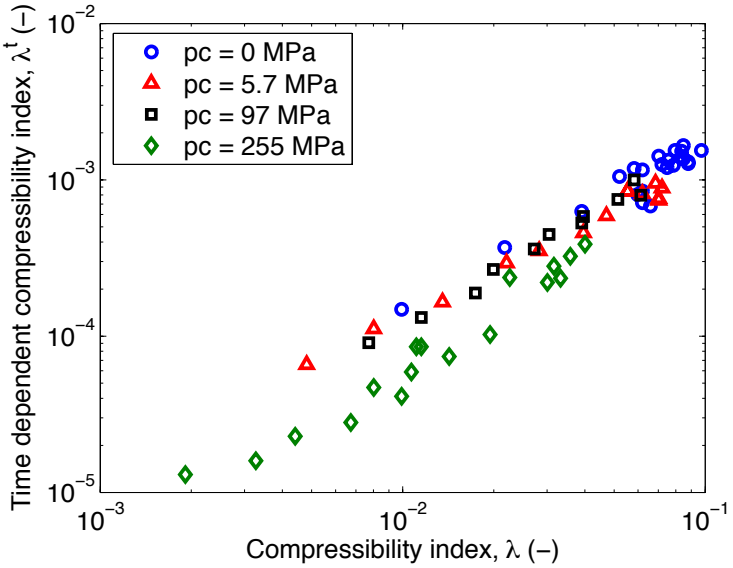

Figure 1. Time dependent compressibility and compressibility indices of rockfill material (Oldecop and Alonso, 2003).

(Sendir-Torisu *et al.*, 2012). It can be shown that $\alpha = C_{\alpha e}/C_c$, which leads to the conclusion that strain rate sensitivity and primary creep proceed from similar mechanisms. This relation

A few studies have investigated the effects that humidity or capillary pressure has on these empirical relations. The main conclusion from the available experiments is that reducing the water saturation reduces both strain rate sensitivity and tendency to creep of geomaterials (see Figures 1 and 2). These results show that as material's apparent compressibility decreases with increasing capillary pressures, its tendency to creep (or alternatively it sensitivity to strain rate) also decreases. However, Figure 2 shows that the ratio α depends on the value of the capillary pressure, or the saturation. Actually, this ratio even depends on the saturating fluid.

CONSTITUTIVE MODEL

Several approaches to the modelling of time dependent behaviour of soils have been used (Perzyna, 1964; Kim and Leroueil, 2001; De Gennaro *et al.*, 2003). In the present study, the Barcelona Basic Model –BBM– (Alonso *et al.*, 1990) developed for partially saturated soils is extended to account for strain rate sensitivity. BBM is based on the well-known Modified CamClay model –MCC– for saturated soils. These elastoplastic models account for strain hardening, the isotropic yield stress being the hardening variable associated to the volumetric plastic strain. The specificity of BBM is that this hardening is generalised to account for partial saturation effects. The main idea of the model presented here is to extend this apparent hardening to account for strain rate changes.

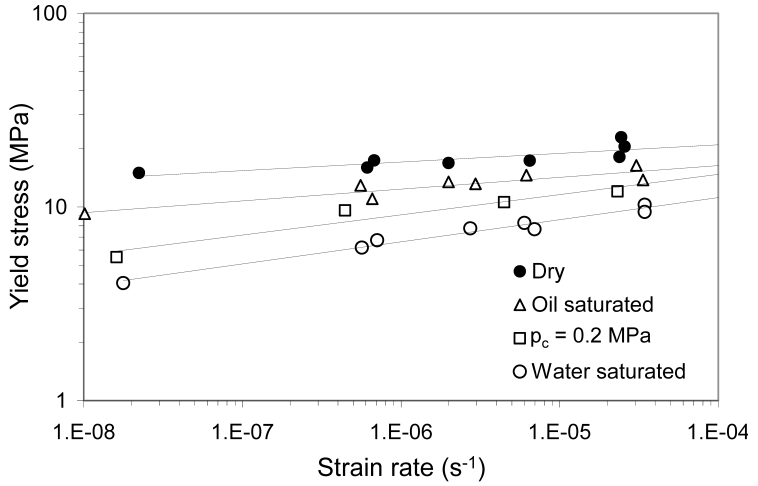

Figure 2. Yield stress as a function of applied strain rate in oedometric conditions (after De Gennaro *et al.*, 2004).

To do so, taking inspiration from the Equation (3), the yield stress of BBM (or MCC) is redefined as follows:

$$p_0 = p_0^{ref} \left(\frac{\dot{\epsilon}_v}{\dot{\epsilon}_v^{ref}} \right)^{\alpha(p_c)} \mathcal{H}(\epsilon_v^p) \tag{4}$$

where $\mathcal{H}(\epsilon_v^p)$ is a hardening function. In the present case, the hardening function of MCC is chosen. The evolution of parameter α with capillary pressure remains to be defined. Because of the lack of experimental data, a linear relationship is assumed.

$$\alpha(p_c) = \alpha(0) - \beta p_c \tag{5}$$

where p_c is the capillary pressure. It should also be pointed out that the evolution of the elastic limit prediction by Equation (4) has a range of validity that is limited to strain rates applied in the laboratory (typically, the range shown in Figure 2). Beyond this range, the yield stress is likely to evolve much less than predicted, for both low strain rates and high strain rates. In this later case, dynamic effects should also be accounted for if strain rate become significant.

The remaining equations to complete the definition of the model are practically identical to those of BBM and will not be presented in this work. Interested readers are referred to a detailed presentation of RASTRA model (De Gennaro and Pereira, 2013). The methodology presented here to extend BBM could easily be extended to other elastoplastic models, provided that they account for strain hardening. One of the main limitations of this model is that it cannot reproduce any viscoelastic behaviour. This assumption is reasonable for soils but should be reconsidered for stiffer materials, such as concrete.

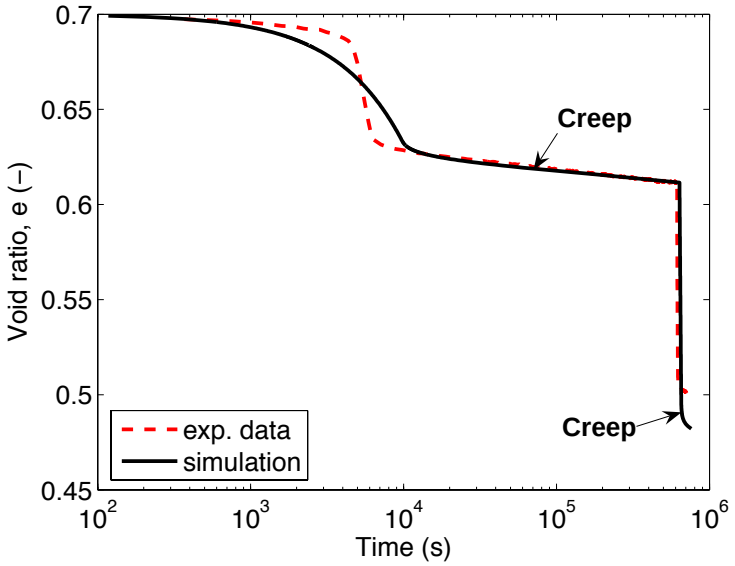

Figure 3. Simulation of isotropic compression followed by two creep stages (capillary pressure is constant, equal to 1 MPa).

VALIDATION

The isotropic compression under constant capillary pressure of a chalk specimen has been simulated. The model prediction is compared to experimental data in Figure 3. A good agreement is observed.

In order to verify the model prediction of creep for various saturation, creep stages at three imposed capillary pressures are simulated and shown in Figure 4. It can be seen that the model predicts smaller creep strains when the capillary pressure is higher.

CONCLUSION

Time dependent of a large class of geomaterials is affected by humidity. Either sensitivity to strain rate or creep are indeed saturation dependent, and saturated geomaterials are generally more viscous than dry ones.

An elastoplastic model has been presented. It is based on the extension of an existing model for partially saturated soils. The approach used to derive this model could be applied to other elastoplastic hardening models easily. The model reproduces satisfactorily the viscous behaviour of geomaterials in the plastic regime.

Practical applications of this model include modelling of (i) underground carries submitted to humidity changes including the assessment of flooding impacts on the mechanical stability of pillars, (ii) long term behaviour of oil reservoir formations during oil enhanced recovery by water injection or (iii) geological storage of CO2.

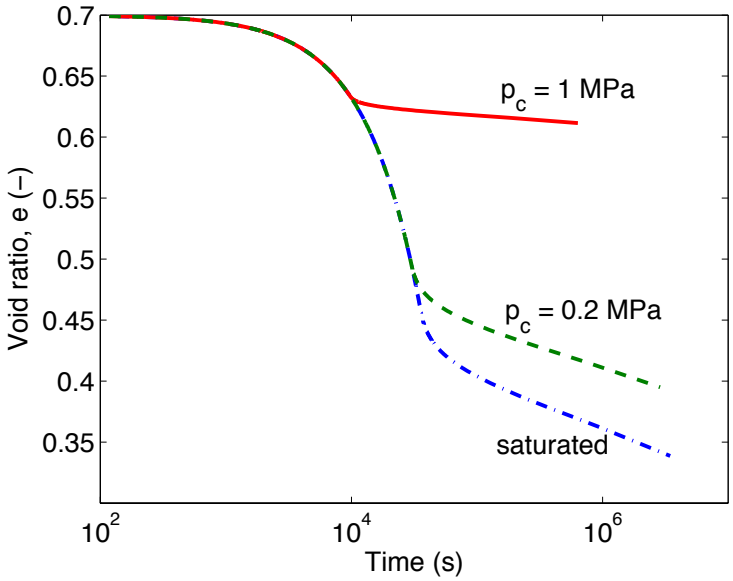

Figure 4. Prediction of the influence of capillary pressure on creep.

REFERENCES

Alonso, E. E., Gens, A., and Josa, A. (1990). "A constitutive model for partially saturated soils." *Géotechnique,* 40(3), 405430.

De Gennaro, V., Delage, P., Cui, Y. J., Schroeder, C., and Collin, F. (2003). "Time-dependent behaviour of oil reservoir chalk: a multiphase approach." *Soils and Foundations,* 43(4), 131-148.

De Gennaro, V., Delage, P., Priol, G., Collin, F., and Cui, Y. J. (2004). "On the collapse behaviour of oil reservoir chalk'." *Geotechnique,* 54(6), 415-420.

De Gennaro, V., and Pereira, J. M. (2013). "A viscoplastic constitutive model for unsaturated geomaterials." *Computers and Geotechnics,* 54(October), 143151.

Di Benedetto, H., Tatsuoka, F., and Ishihara, M. (2002). "Time-dependent shear deformation characteristics of sand and their constitutive modelling". *Soils and Foundations,* 42(2), 122.

Kim, Y. T., and Leroueil, S. (2001) "Modelling the viscoplastic behaviour of clays during consolidation: application to Berthierville clay in both laboratory and field conditions." *Canadian Geotechnical Journal,* 38(3), 484-497.

Leroueil, S., Kabbaj, M., Tavenas, F., and Bouchard, R. (1985). "Stress-strain-strain rate relation for compressibility of sensitive natural clays." *Géotechnique,* 35(2), 159180.

Mesri, G., Godlewski, P. M. (1977). "Time and stress compressibility interrelationships." *J. Geotech. Eng. Div.,* ASCE, 103(GT5), 417430.

Oldecop, L. A., and Alonso, E. E. (2003). "Suction effects on rockfill compressibility." *Gotechnique,* 53(2), 289292.

Perzyna, P. (1964) "The constitutive equations for rate sensitive plastic materials." *Quart Appl Mech,* 20, 32132.

Sendir-Torisu, S., Pereira, J. M., De Gennaro, V., Delage, P., and Puech, A. (2012) "Strain-rate effects in deep marine clays from the Gulf of Guinea." *Gotechnique,* 62(9), 767775.

Vaid, Y. P., and Campanella, R. G. (1977). "Time-dependent behaviour of undisturbed clay." *J. Geotech. Eng. Div.,* ASCE, 103(GT7), 693709.

RH Dependence upon Applied Load: Experimental Study on Water Redistribution in the Microstructure at Loading

M. Wyrzykowski[1,2] and P. Lura[1,3]

[1]Empa, Swiss Federal Laboratories for Materials Science and Technology, Concrete/Construction Chemistry Laboratory, Switzerland. E-mail: mateusz.wyrzykowski@empa.ch
[2]Department of Building Physics and Building Materials, Lodz University of Technology, Poland.
[3]ETH Zürich, Institute for Building Materials (IfB), Zürich, Switzerland.

Abstract

The influence of applied stresses on adsorbed water in cement paste has been proposed long ago (independently by Powers and by Ruetz) as a possible mechanism able to explain delayed deformations (creep) of concrete. Following this approach, the application of compressive stresses should lead to an increase in internal relative humidity (RH). This hypothesis has never been confirmed experimentally. Even though water redistribution due to loading was applied in some modeling approaches for description of short-term creep, the RH dependence upon the stress state has generally been neglected over the past decades. This study shows that instantaneous RH changes do accompany applied load and can be accurately measured. Moreover, the measured RH changes may in fact explain a large part of the short-term creep deformation and also the commonly-observed difference between static and dynamic elastic moduli. In this study, mortars made with water-to-cement ratio of 0.3 were loaded in uniaxial compression or tension, while internal RH was measured by means of embedded water activity sensors. At the same time, elastic moduli were measured in compression using both the standard static method and ultrasound resonance spectroscopy.

INTRODUCTION

The coupling between an applied mechanical stress and the hygral state in concrete is usually neglected in description of concrete behavior, e.g. (Ulm and Coussy 1995). This is based on the assumption that changes in pore volume due to loading have a negligible effect on changes of pores saturation. However, Powers (Powers 1965, 1968) suggested that upon loading, water may redistribute from hindered adsorption regions to larger pore spaces. A similar water redistribution mechanism was also proposed by Ruetz (Ruetz 1966). The microdiffusion mechanism would cause additional, delayed shrinkage deformation on compression. Powers postulated that this mechanism may be responsible for volumetric basic

creep, and proposed that the latter would better be named “stress-induced shrinkage” (Powers 1968). At the same time, an increase of internal relative humidity (RH) should take place as water is redistributed from gel to capillary pores (Powers 1968). Upon unloading, the opposite should take place.

Loading-induced microdiffusion of water was employed describe short-term creep in shotcrete by Sercombe et al. (Sercombe et al. 2000) and Hellmich et al. (Hellmich et al. 2001). Water redistribution due to loading was either responsible for, or accompanied, creep in other theoretical approaches, even when based on different mechanisms (Bažant 1972, Feldman 1972, Bažant and Chern 1985).

An alternative creep theory, referred to as the microprestress-solidification theory, proposes shear slip of the hydrate sheets as the microstructural origin of creep (Bažant et al. 1997). A number of experimental studies are in line with the shear slip theory, e.g. (Tamtsia and Beaudoin 2000, Beaudoin and Tamtsia 2004, Vandamme and Ulm 2009).

Studies of concrete creep by Bernard et al. (Bernard et al. 2003) and Grasley and Lange (Grasley and Lange 2007) at the macrostructural level revealed two to three stages of creep deformation. First, short-term volumetric creep occurring during the first few minutes after loading was proposed to be due to consolidation of the matrix and water redistribution. Later, short-term volumetric creep continues for another few days to few weeks at decreasing rate (decaying creep or viscous creep). Some researchers attribute it still to microdiffusion of water, e.g. (Acker and Ulm 2001, Hellmich et al. 2001). Other researchers attribute it to the C-S-H sliding deviatoric mechanism at the microscale, which is supposed to manifest macroscopically as volumetric creep since sliding of solid C-S-H sheets after being accommodated in free pore spaces would lead to volume reduction (Bernard et al. 2003, Grasley and Lange 2007). It should be noted that the macroscopic observations of concrete creep do not allow for excluding either of the proposed mechanisms, namely water redistribution due to microdiffusion and C-S-H sliding. Despite the mechanism responsible or accompanying creep is not agreed upon, the key role of water on creep deformations has been commonly accepted.

The basic hypothesis of our study presented here is that, no matter the mechanism responsible for creep, the reorganization of microstructure is expected to lead to a certain change in the state of water contained in the microstructure. Given that the water redistribution effects exist and are measurable, they could enable an explanation of concrete (delayed) deformations. As aforementioned, the theory by Powers (Powers 1968) states explicitly that the applied compressive load should lead to an increase of internal RH. Such effect has been however explicitly neglected later both in elaboration of microdiffusion mechanism (Bažant and Chern 1985) and the microprestress-solidification (shear slip) mechanism (Bažant et al. 1997).

In order to test the hypothesis of water redistribution upon mechanical loading, we performed measurements of internal RH changes at loading/unloading both in compression and in tension. We tested mortars with water-to-cement ratio (w/c) of 0.30. The samples were loaded with hydraulic presses and the RH was measured by means of water activity sensors nested in holes made in the specimens at casting. Further, in order to study the influence of water redistribution on short-term deformations, the elastic modulus was studied by static tests in compression and by

dynamic tests with resonance ultrasound spectroscopy according to the ASTM C215-08 standard.

Part of the results presented here has been recently published in (Wyrzykowski and Lura 2014), regarding RH changes accompanying compressive load; here the extension of the experimental framework to different stress levels and loading in tension is presented.

MATERIALS AND METHODS

Materials and sample preparation. Mortar with water-to-cement ratio (w/c) of 0.3 was prepared with ordinary Portland cement CEM I 42.5 N. Alluvial sand with particle sizes of 0-4 mm was used as aggregate in an amount corresponding to approximately 40% of the mortar's volume. A polycarboxylate-based superplasticizer was used in an amount of 0.3-0.4% by mass of cement. Mechanical properties were tested on 40×40×160 mm^3 prisms. Two types of measurements during loading were performed on two sample geometries. *Long-term (weeks-long) loads* in uniaxial compression were applied on massive prismatic samples of dimensions 120×120×360 mm^3. This test followed a standard procedure for basic creep measurements, with the main modification being performing simultaneous RH measurements. *Short-term (minutes-long) loads* (both in uniaxial compression and tension) were applied on 35×100×450 mm^3 prisms.

Directly after casting, steel cylinders of 12 mm diameter were cast in the central part of the samples used for RH measurements during loading. At demolding at the age of 24 h, the steel cylinders were removed in order to create openings able to accommodate later the RH sensors. The samples were next sealed with adhesive aluminum tape ad stored at 20±0.3°C until the age of loading.

Methods. Prisms of dimensions 120×120×360 mm^3 (see Figure 1a) used for long-term measurements were positioned at the age of 21 days in hydraulic load cells used for standard creep tests. Thermal insulation was provided with 30 mm plates of Styrofoam glued to the vertical faces of the samples. RH sensors were next inserted into the wholes prepared in the central parts of the samples at casting (Figure 1a) and the openings were carefully sealed with paraffin film. 4 samples were tested for deformations under compressive load, two of them with one embedded RH sensor each. At the age of 35 days, a compressive load corresponding to a stress of 18.2 MPa was applied and kept constant until the age of 56 days, when the samples were unloaded. At the age of 64 days, a compressive load corresponding to a stress of 26.3 MPa was applied and kept constant until the age of 108 days, when the samples were unloaded (see Figure 2). Axial deformations were measured by following distance changes between the steel plugs glued on the two apposite faces of each sample at given time intervals (Figure 1a). The base length (distance between the metal plugs) was equal to about 250 mm and the displacements were measured with a manual comparator with 0.001 mm resolution. The presented strains are the average results from 4 samples, with two faces measured for each sample. The standard deviation did not exceed 40 μm/m.

A prism of dimensions of 35×100×450 mm^3 (see Figure 1b) was loaded in compression at the age of 7 days. The applied compressive stress was equal to 2.5, 5.0, 7.5 and 10 MPa. Load in tension was later applied on the same sample at the age of 15 days. Tensile stress was equal to 2.5 MPa and 5 MPa. During tensile loading, the ends of the sample were clamped with metal grips with roughened faces and fastened by adjusting the screws. The stress was applied in cycles as follows: each stress level was reached within 1 min and kept constant during 15 min. Next, the sample was unloaded within 1 min and the break before the next loading step lasted 15 minutes.

A RH sensor was placed in the central part of the 35×100×450 mm^3 sample. Since the sample thickness was only 35 mm, thus not allowing for accommodating the whole RH sensor (the sensor length is about 50 mm), a plastic cylinder was glued to the sample to create additional space able to accommodate the sensor, Figure 1b.

RH sensors were miniature (5 mm diameter, 50 mm long) water activity sensors HC2-C05 by Rotronic. The nominal trueness of the sensors was ± 1.0 %RH / ± 0.3 °C, and the reproducibility was nominally <0.02 %RH / 0.01 °C. The nominal response time of the sensors was < 15 s. The sensors were calibrated with saturated salt solutions in the range 85-98 %RH before being placed in the sample and for long-term measurements additionally after the first and the second unloading. The absolute difference between the two sensors used in different 120×120×360 mm^3 samples each was approximately constant over time, 1.3 %RH on average. Differences regarding quasi-instantaneous RH changes at loading/unloading were much lower, up to about 0.1 %RH. For the smaller sample, 35×100×450 mm^3, only one sample with one embedded sensor was tested.

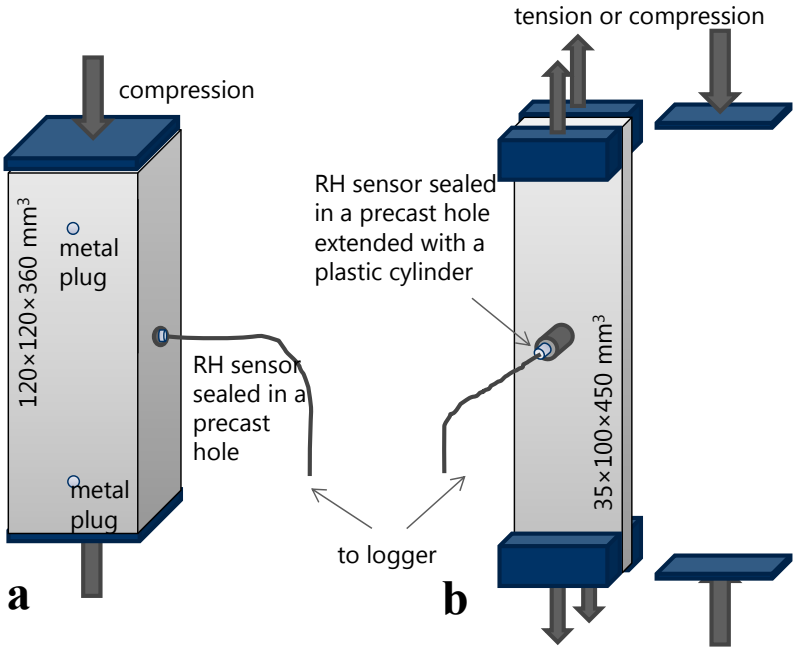

Figure 1. Scheme of samples during loading: a) long-term load experiments (see results in Figure 2); b) short-term load experiments (see results in Figure 3).

Mechanical properties were measured on 40×40×160 mm^3 prismatic samples. Three samples were used for strength and two samples for static elastic Young's modulus measurements at 28 and 90 days. In addition, the elastic Young's modulus was determined on four samples at the age of 140 days using the static method with stress of 26 MPa and loading duration of about 1 min and the dynamic method with resonance ultrasound spectroscopy according to the ASTM C215-08 standard. This standard was also used to determine the Poisson's ratio on the same samples.

RESULTS

The mechanical properties of the tested mortar are presented in Table 1. It can be seen that the compressive stress used in long-term loading experiments (Figure 2) never exceeded 1/3 of compressive strength. For the samples loaded with short term-load, the maximum compressive stress level used (10 MPa) was likely not exceeding 15% of compressive strength, while the tensile stress (2.5 MPa) was approximately equal to 1/2 of tensile strength (the sample failed when loaded to 5 MPa in direct tension).

Table 1. Mechanical properties (average ± standard deviation)

Property/Age	*28 days*	*90 days*	*140 days*
Compressive strength	83.0±0.8 MPa	92.5±2.0 MPa	-
Static elastic Young modulus	31.4±0.1 GPa	32.3±0.2 GPa	32.7±0.5 GPa
Dynamic elastic Young modulus	-	-	38.3±0.3 GPa
Dynamic Poisson's ratio	-	-	0.25±0.01

In Figure 2, deformations and corresponding RH evolution accompanying the applied long-term load are presented. The two figures correspond to two different levels of load applied on the same samples, corresponding to compressive stresses of 18.2 and 26.3 MPa, respectively.

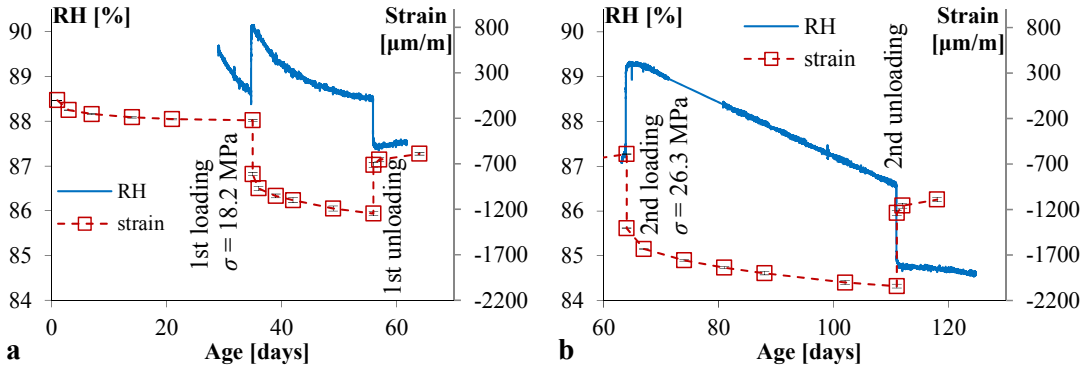

Figure 2. Axial strain and RH changes measured on the 120×120×360mm^3 prisms in long-term load experiments (see Figure 1a). Strain curves are average from 4 samples; RH curves are average from 2 samples.

The deformations follow a common trend observed during basic creep experiments, with quasi-instantaneous changes followed by delayed creep

deformations under constant load. At unloading, almost full recovery of instantaneous deformation takes place (90% and 99% recovery at first and second unloading, respectively), while delayed deformations are only partially recovered with time.

It can be seen in Figure 2 that an applied compressive load is accompanied by an almost instantaneous increase in RH. The increase takes place within some seconds/minutes, which corresponds to the response time of the RH sensors and the maximum difference is reached a few hours from loading. The quasi-instantaneous RH increase was equal to 1.45±0.03 %RH and 1.87±0.11 %RH for stresses equal to 18.2 MPa and 26.3 MPa, respectively. At unloading, the phenomenon seemed to be partially recovered at first unloading (decrease of 0.98±0.02 %RH), and almost fully recovered at second unloading (decrease of 1.81±0.06 %RH). The trend in the recovery of the RH levels is similar to that observed for deformations.

After the instantaneous RH increase following applied compressive stress, the RH decreases gradually while under constant load, Figure 2. The origins of such gradual decrease are not clear. The two following mechanisms are proposed here. First, the additional water provided due to redistribution at loading may be consumed by ongoing hydration, with the resulting self-desiccation being responsible for the gradual RH decrease. Another possible mechanism is further redistribution of water on a macroscopic scale. In this case, the water initially migrated from the hindered adsorption areas to larger gel or capillary pore spaces would further migrate into larger capillary voids, cracks, or eventually to the sample boundaries, in case the sealing was not perfect).

In order to study the dependence of the RH changes on the applied stress level, an additional series of experiments was performed with several short-term loading steps of low magnitude on a single sample (Figure 1b). As long as the RH measurements were prone to a considerable noise, the RH changes clearly take place even at low stress levels (Figure 3). Moreover, the phenomenon is apparently symmetrical considering applied force direction. Even though higher levels of stress could not be tested in tension due to sample failure, the RH decrease due to tensile loading was similar to that due to compressive loading with the same absolute stress value.

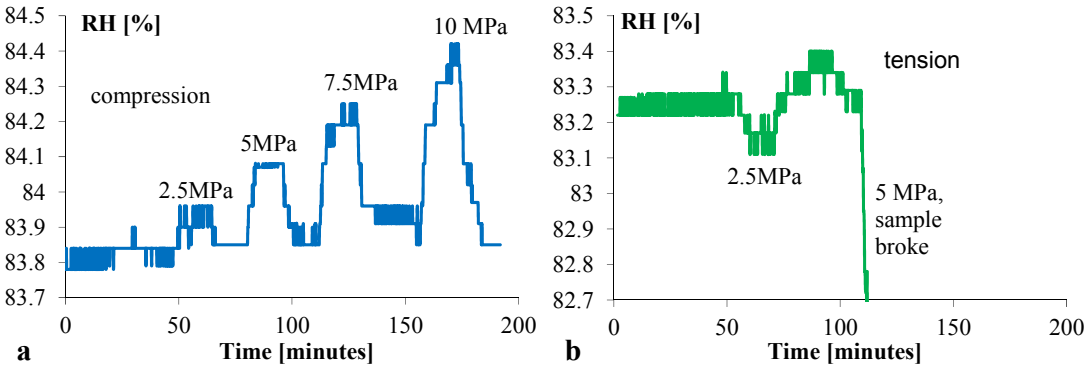

Figure 3. RH changes measured in the 35×100×450mm^3 prisms in short-term load experiments (see Figure 1b): a) load in compression, b) load in tension.

MODELLING AND DISCUSSION

As shown in the previous section, the influence of external load on internal RH is measurable and is not negligible. In this section it is studied whether such changes of RH are of relevance for understanding concrete deformations. In the following analysis it will be shown that the observed RH change accompanying loading is able to quantitatively explain the quasi-instantaneous deformations that are manifested by the commonly observed lower value of the static elastic modulus compared to the dynamic one, e.g. (Zech and Setzer 1988, Panesar and Shindman 2011).

Adopting the approach by Powers (Powers 1968), when external compressive load is applied, water is removed from the hindered adsorption to the larger capillary spaces and RH increases in the pores. The assumption that we follow is that the swelling that would normally follow an increase of RH in the absence of applied load is equal and opposite to the contraction that occurred upon removing water from the hindered adsorption areas and increasing the disjoining pressure. The RH change is linked to a change in capillary pressure by the Kelvin-Laplace equation, and it can be further related to a volumetric deformation $\Delta\varepsilon_V$ using a classic poroelastic approach:

$$\Delta\varepsilon_V = (\Delta p_c S + p_c \Delta S)(1/K - 1/K_s) \quad (1)$$

where K_s is the bulk modulus of the solid skeleton assumed as 44 GPa, K is the bulk modulus of porous body (calculated based on elastic Young modulus and Poisson's ratio), p_c is the capillary pressure (obtained based on the measured RH from the Kelvin-Laplace equation) and S is the saturation degree with water (obtained based on sorption isotherms measured in (Wyrzykowski et al. 2011)). The calculations were performed for the RH change observed at 2nd loading (Figure 2b). RH before and after loading at 64 days were equal to RH_1 = 87.4% and RH_2 = 89.3%, respectively, Figure 2b. The corresponding values of saturation degree were S_1=0.803 and S_2=0.812, respectively. Assuming no considerable development of elastic properties after the age of 28 days (see Table 1), mechanical properties determined at 140 days were used in the calculations.

The bulk modulus of the porous body K was calculated using the Poisson's ratio obtained from dynamic tests, ν=0.25 (Table 1) and elastic modulus assumed as the average between the static, E_{stat}, and dynamic, E_{dyn} elastic moduli, yielding K=23.7 GPa. Finally, the volumetric deformation calculated as an effect of the RH change (supposedly due to water removal from hindered adsorption areas) with a poroelastic approach (1) was equal to $\Delta\varepsilon_V$ = 48 μm/m.

In the next step, the additional delayed deformation occurring during static test compared to the assumed purely elastic deformation that would correspond to the value of dynamic elastic modulus is quantified using the following equation:

$$\Delta\varepsilon_V = \sigma\frac{(1-2\nu)}{E_{stat}} - \sigma\frac{(1-2\nu)}{E_{dyn}} \quad (2)$$

where σ = 26 MPa is the axial stress used both the static tests and during the second loading (Figure 2b), therefore leading to RH changes as used for calculations with equation (1). Equation (2) yields a value $\Delta\varepsilon_V$ = 58 μm/m. Equation (2) is a quantification of an apparent volumetric deformation leading to lower values of static

elastic modulus compared to the dynamic one, while equation (1) allows estimating the effects of the discussed water redistribution phenomenon. Since the values calculated with the two equations are reasonably close, one can conclude that the observed changes in RH are able to quantitatively explain the origin of quasi-instantaneous deformations occurring during applied loading. The origin of these quasi-instantaneous deformations seems to be due to water redistribution (microdiffusion) in the microstructure (supposedly from hindered adsorption areas to the larger pore spaces). Since the accompanying RH changes are in major part reversible (in particular during the second loading step), it is supposed that the redistribution mechanism is due to microdiffusion occurring in a form similar to that proposed originally by Powers (Powers 1965, 1968). However, our results show a contribution of water redistribution to only short-term deformations (occurring within the few minutes following loading), while the origin of long-term deformations is apparently different.

CONCLUSIONS

The experimental study presented here clearly shows that an increase of RH at loading in compression is not negligible and reaches approximately 2% RH at a compressive stress level of 26 MPa. An increase of RH was also clearly visible even at compressive stress levels as low as 2.5 MPa. On the long-term, after an initial increase of RH accompanying compressive loading, the internal RH decreases gradually. At the same time, a decrease of RH was observed when the sample was loaded in tension. The initial changes of RH on loading were in major part reversible on unloading.

The presented results are in line with the mechanism of water redistribution from hindered adsorption areas to larger pores occurring when compressive load is applied. According to the original description by Powers, this mechanism was supposed to be responsible for volumetric basic creep. According to our study, the redistribution of water at loading and the corresponding RH changes can explain only short-term (seconds-to-minutes) deformations of concrete. In particular, our analysis shows that the commonly observed difference between static and dynamic elastic moduli can be quantitatively explained based on the observed hygral state changes at loading.

REFERENCES

Acker, P. and F.-J. Ulm (2001). "Creep and shrinkage of concrete: physical origins and practical measurements." Nuclear Engineering and Design 203(2–3): 143-158.

Bažant, Z., A. Hauggaard, S. Baweja and F. Ulm (1997). "Microprestress-Solidification Theory for Concrete Creep. I: Aging and Drying Effects." Journal of Engineering Mechanics 123(11): 1188-1194.

Bažant, Z. P. (1972). "Thermodynamics of interacting continua with surfaces and creep analysis of concrete structures." Nuclear Engineering and Design 20(2): 477-505.

Bažant, Z. P. and J. C. Chern (1985). "Concrete creep at variable humidity: constitutive law and mechanism." Materials and Structures 18(1): 1-20.
Beaudoin, J. and B. Tamtsia (2004). "Creep of Hardened Cement Paste—The Role of Interfacial Phenomena." Interface Science 12(4): 353-360.
Bernard, O., F.-J. Ulm and J. T. Germaine (2003). "Volume and deviator creep of calcium-leached cement-based materials." Cement and Concrete Research 33(8): 1127-1136.
Feldman, R. F. (1972). "Mechanism of creep of hydrated portland cement paste." Cement and Concrete Research 2(5): 521-540.
Grasley, Z. and D. Lange (2007). "The viscoelastic response of cement paste to three-dimensional loading." Mechanics of Time-Dependent Materials 11(1): 27-46.
Hellmich, C., M. Lechner, R. Lackner, J. Macht and H. A. Mang (2001). Creep in Shotcrete Tunnel Shells. IUTAM Symposium on Creep in Structures. S. Murakami and N. Ohno, Springer Netherlands. 86**:** 217-229.
Panesar, D. K. and B. Shindman (2011). "Elastic properties of self consolidating concrete." Construction and Building Materials 25(8): 3334-3344.
Powers, T. C. (1965). Mechanisms of shrinkage and reversible creep of hardened cement paste. Proc. Int. Symp. Struct. Concr. London. London**:** 319-344.
Powers, T. C. (1968). "The thermodynamics of volume change and creep." Materials and Structures 1(6): 487-507.
Ruetz, W. (1966). Das Kriechen des Zementsteins im Beton und seine Beeinflussung durch gleichzeitiges Schwinden: experimentelle Studien zur Klärung des Mechanismus durchgeführt an der Materialprüfungsanstalt der Technischen Hochschule München, Ernst.
Sercombe, J., C. Hellmich, F. Ulm and H. Mang (2000). "Modeling of Early-Age Creep of Shotcrete. I: Model and Model Parameters." Journal of Engineering Mechanics 126(3): 284-291.
Tamtsia, B. T. and J. J. Beaudoin (2000). "Basic creep of hardened cement paste A re-examination of the role of water." Cement and Concrete Research 30(9): 1465-1475.
Ulm, F. and O. Coussy (1995). "Modeling of Thermochemomechanical Couplings of Concrete at Early Ages." Journal of Engineering Mechanics 121(7): 785-794.
Vandamme, M. and F.-J. Ulm (2009). "Nanogranular origin of concrete creep." Proceedings of the National Academy of Sciences 106(26): 10552-10557.
Wyrzykowski, M. and P. Lura (2014). "The effect of external load on internal relative humidity in concrete." Cement and Concrete Research 65(0): 58-63.
Wyrzykowski, M., P. Lura, F. Pesavento and D. Gawin (2011). "Modeling of internal curing in maturing mortar." Cement and Concrete Research 41(12): 1349-1356.
Zech, B. and M. Setzer (1988). "The dynamic elastic modulus of hardened cement paste. Part I: A new statistical model—water and ice filled pores." Materials and Structures 21(5): 323-328.

Minutes-long creep tests on young cement pastes provide access to creep properties relevant for ageing creep with a duration of 2 days

M. Irfan-ul-Hassan*, B. Pichler*, R. Reihsner*, and Ch. Hellmich*

*Institute for Mechanics of Materials and Structures, Vienna University of Technology (TU Wien), Karlsplatz 13/202, A-1040 Vienna, Austria;
E.mail: Muhammad.Irfan-ul-hassan@tuwien.ac.at, Bernhard.Pichler@tuwien.ac.at, Roland.Reihsner@tuwien.ac.at, Christian.Hellmich@tuwien.ac.at

ABSTRACT

Cementitious materials are particularly creep active at early ages. We here perform an ageing creep test on a cement paste sample exhibiting an initial water-to-cement mass ratio amounting to $w/c = 0.50$. The sample is conditioned to 20 °C. The creep test is started 24 hours after production and runs for 48 hours. The loading amounts to 15 % of the uniaxial compressive strength of the material at the time instant of loading. Inspired by a recently developed new testing protocol consisting of hourly-repeated three-minutes long creep tests [6], we exploit force and deformation readings recorded during the *first three minutes* of our 2-days creep test, i.e. we identify Young's modulus and power-law creep properties. Given that the chemical hydration process does not progress significantly during the analyzed three minutes, the identified creep properties refer to *non-ageing* creep. The identified properties are combined with measurements of autogenous shrinkage, in order to predict the strain evolution over the entire 2-days runtime of our ageing creep test. When fitting of the creep function targets, through an appropriately chosen weight functions, the end of three minutes creep interval, in terms of both absolute creep strain and creep strain rate, then the resulting creep function remarkably well predicts creep up to a time period of 2 days.

INTRODUCTION

Cementitious materials are known to be creep active [2, 3, 5, 7, 11, 15, 17], in particular at early ages [1, 16]. In order to study early-age basic creep of cement pastes, mortars, and concretes, we have developed a new testing protocol involving nondestructive, hourly repeated, three minutes long creep tests [6]. Three minutes are so short that the ongoing hydration process does not make a significant progress, i.e. our individual creep tests provide quantitative insight into the creep properties of specific (non-ageing) microstructures of cementitious materials. This raises the question, whether or not it is possible to extrapolate, based on observations carried out during three-minutes creep tests, the strain evolution of the material in much longer creep tests, say with a duration of two days. Herein, this question is exemplary answered based on

creep test data obtained from cement paste testing. At first, we describe the tested material and the used test method. Then, characteristic results are presented, followed by identification of Young's modulus and creep properties, based on the measurements obtained during the first three minutes, and the assessment of the extrapolation capabilities. The paper closes with a discussion and conclusions.

MATERIALS AND METHODS

Materials

Raw materials used for production of cement paste are a commercial cement of type CEM I 42.5 N and distilled water. The investigated cement paste exhibits an initial water-to-cement mass ratio amounting to $w/c = 0.50$. We cast cylindrical specimens with a diameter of 70 mm and a height of 300 mm. Right after production, the specimens are sealed against the ambient environment, in order to prevent them from drying. The specimens are stored in a climate chamber conditioned to 20 °C.

Methods

The compression tests are carried out using an electromechanical universal testing machine of type Walter and Bai LFM 150. The used test setup is strongly inspired by the one recently developed for early-age stiffness characterization of cement pastes, see [8]. In more detail, the tested specimen is covered with several layers of a food preservation foil, in order to avoid significant drying. The entire test setup is placed inside an insulated temperature chamber conditioned to 20 °C, see Fig. 1 a. The specimen is the central part of a serial arrangement described next. Bottlenecked steel cylin-

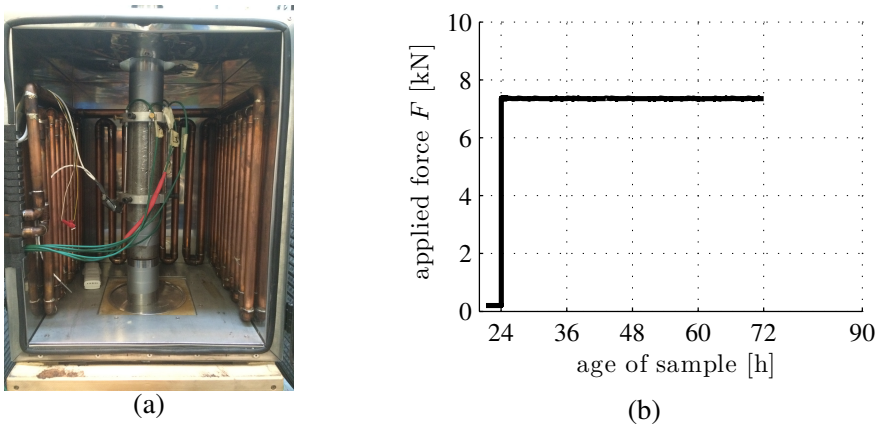

Figure 1. (a) Test setup consisting of the cement paste specimen, metal cylinders with bottlenecks, two aluminum rings holding five Linear Variable Differential Transducers (LVDTs): view into a climate chamber conditioned to 20 degrees Centigrade, and (b) force history prescribed during the 2-days creep test

ders are attached to the top and to the bottom of the specimens, respectively, in order to facilitate a central load application. The force acting on the serial arrangement is measured by means of a force sensor integrated into the testing machine. Deformations of the specimen are measured with five Linear Variable Differential Transducers (LVDTs). To this end, two aluminum rings are attached to the central part of the specimen, by means of three screws per ring. The distance between the two rings amounts to 164 mm. The LVDTs are equally distributed around the specimen, i.e. the spacing amounts to 72°. This setting allows for realization of virtually purely uniaxial stress states in the monitored central part of the specimen - as undesired shear stresses which result from unavoidable friction in the interfaces between steel cylinders and specimen, have decayed to a negligible amount towards this central part [8].

The 2-days creep tests was started 24 hours after the production of the specimen. Using a loading speed of 7.697 kN/s, corresponding to a specimen-related stress-rate amounting to 2 MPa/s, the loading of the specimen was increased up to 7.15 kN, corresponding to a compressive stress of 1.81 MPa. This amounts to 15 % of the uniaxial compressive strength of the material, predicted by a validated multiscale model for uniaxial compressive strength of cement pastes [9, 10] combined with the hydration degree evolution determined by quasi-isothermal calorimetry. The force was held constant for 48 hours, such that the test ended once the specimen had reached at an age of three days, see Fig. 1 b.

RESULTS

The five individual LVDT readings are averaged in order to compute the mean change of length between the two aluminum rings. Specimen strains are computed by dividing the mean change of length between the two aluminum rings by the distance of the two aluminum rings, amounting to 164 mm, see Fig. 2 a.

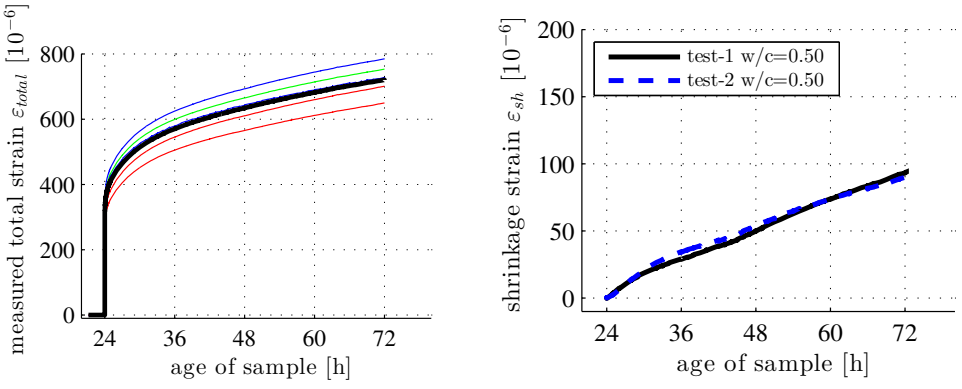

(a) (b)

Figure 2. (a) Strains measured during the 2-days creep test on cement paste with w/c = 0.50, subjected at an age of 24 h to a force amounting to 7.15 kN, and (b) shrinkage strain evolution, measured on independent specimens

During the second and third day after production, the chemical hydration reaction progresses significantly, such that significant autogenous shrinkage strains are expected to develop. They were measured in parallel to the 3-minutes creep testing activities described in [6], see Fig. 2 b.

IDENTIFICATION OF YOUNG'S MODULUS AND CREEP PROPERTIES DURING THE FIRST 3-MINUTES

Following the procedure for Young's modulus identification given in [6], the Young's modulus is determined from the 3 minutes creep test as

$$E = 6.3\,\text{GPa} \tag{1}$$

Based on the identified Young's modulus, and considering that no significant shrinkage happens within three minutes, it is straightforward to extract from the total strain evolution, see Fig. 2 a, the creep strain evolution:

$$\varepsilon_{creep}(t) = \varepsilon_{total}(t) - \varepsilon_{elastic}(t) = \varepsilon_{total}(t) - \frac{F(t)}{EA} \tag{2}$$

where $F(t)$ is the measured force history, see Fig. 1 b and $A = 3848.50$ mm^2 stands for the cross-sectional area of the tested specimen, see also Fig. 3.

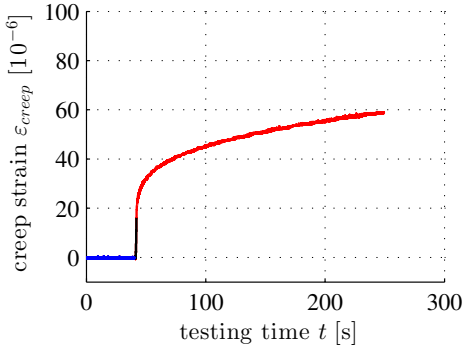

Figure 3. Creep strains developing during the first three minutes of the 2-days creep test

Power-law creep model

As for identification of creep properties, we follow Tamtsia and Beaudoin [16] who introduced a power-law model for the creep compliance rate:

$$\frac{dJ(t)}{dt} = C\left(\frac{t - t_0}{t_{ref}}\right)^{\gamma} \tag{3}$$

Considering a theoretical creep test, where the loading is (i) suddenly increased, at time t_0, to the the stress level σ_0, and (ii) held constant thereafter, the creep strain evolution reads as [6]

$$\varepsilon_{creep}^{mod}(t) = \frac{\sigma_0}{E_c}\left(\frac{t-t_0}{t_{ref}}\right)^{\beta} \qquad t \geq t_0 \tag{4}$$

where $E_c = (\gamma+1)/(C\,t_{ref})$ denotes the creep modulus at time $t = t_0 + t_{ref}$ and $\beta = \gamma + 1$ stands, by analogy to γ in Eq. (3), for a dimensionless power-law exponent.

The creep strain evolution derived from our experiments indicates a significant development of creep strains already during the loading phase. This is the motivation to model the force history as a superposition of many small load increments, and to consider Eq. (4) in the framework of Boltzmann's superposition principle [4].

$$\varepsilon_{creep}^{mod}(t) = \sum_{i=1}^{n} \frac{F(t_i)-F(t_{i-1})}{A}\left[\frac{1}{E_c}\left(\frac{t-t_i}{t_{ref}}\right)^{\beta}\right] \qquad t_n \leq t \leq t_{n+1} \tag{5}$$

FITTING OF CREEP EVOLUTION OVER 3-MINUTES - AND EXTRAPOLATION CAPABILITIES TO 2-DAYS

Creep modulus E_c and power-law exponent β are identified such that the square root of sum of squares error, $\mathcal{E}_{SRSS}$, attains a minimum. It quantifies the difference between creep strains evolution $\varepsilon_{creep}(t)$ derived from the experiments, see Fig. 3, and modeled creep strains evolution $\varepsilon_{creep}^{mod}(t)$, see Eq. (5),

$$\mathcal{E}_{SRSS}(E_c,\beta) = \sqrt{\frac{1}{N}\sum_{i=1}^{N}\left[\varepsilon_{creep}(t_i) - \varepsilon_{creep}^{mod}(t_i)\right]^2} \quad \rightarrow \quad \min \tag{6}$$

where $N = 5400$ is the total number of experimental readings collected during the first three minutes of the creep test. Optimization problem (6) is solved numerically. At first, intervals are defined for the creep modulus E_c and power-law exponent β. These intervals are subdivided into 7 equidistant values. For all $7\times7 = 49$ combinations, error function (6) is evaluated. The parameter combination associated with the smallest error value is treated as a close-to-optimum solution and serves as the basis for the definition of refined search intervals for the next iteration step [6]. This procedure converges towards the following solution,

$$E_c = 9.72\,\text{GPa} \quad \text{and} \quad \beta = 0.23 \tag{7}$$

see also Fig. 6 for the comparison of measured and model-predicted creep strain evolutions as well as for a contour plot of error function (6).

Young's modulus, see (1), and creep properties (7), which were identified from measurements captured during the first three minutes of the 2-days creep test, together

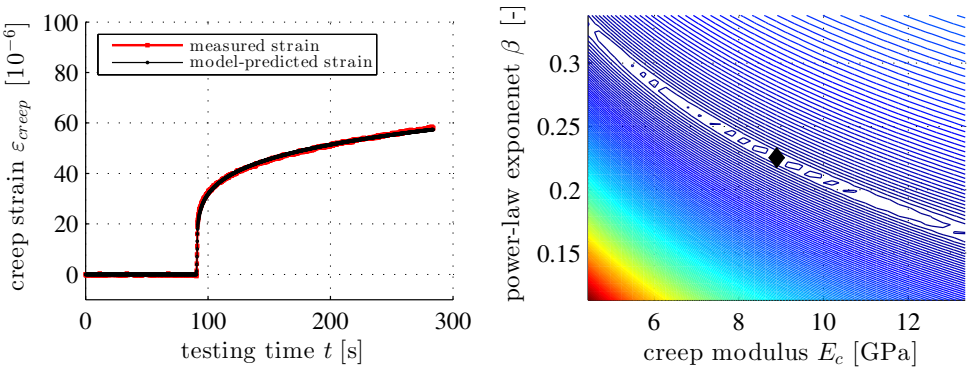

Figure 4. Illustration of creep property identification: (a) comparison of measured and modeled creep strain evolution, and (b) contour plot of error function (6) as a function of creep modulus and power-law exponent; the marked point refers to the optimal solution (7)

with the measured shrinkage strain evolution ε_{sh}, see Fig. 2 b, are now used to predict the total strain evolution for a 2-days creep test

$$\varepsilon_{total}^{mod}(t) = \frac{F(t)}{EA} + \sum_{i=1}^{n} \frac{F(t_i) - F(t_{i-1})}{A} \left[\frac{1}{E_c} \left(\frac{t - t_i}{t_{ref}} \right)^{\beta} \right] + \varepsilon_{sh}(t)$$
$$t_n \leq t \leq t_{n+1} \tag{8}$$

The predicted strain evolution is of the same order of magnitude as the actually measured strain evolution. Typical prediction errors amount to 14 %, see Fig. 7. The reason

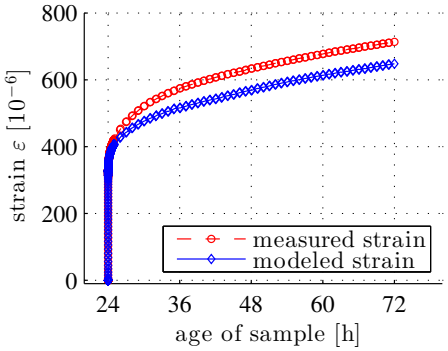

Figure 5. Comparison of extrapolated strain evolution, see (8) as well as (1) and (7), with measured strain evolution, see Fig. 3 b

for this difference is twofold

1. *Non-ageing* creep properties, valid for the microstructure formed 24 hours after

production, are used for predicting the *ageing* creep strain evolution measured during the second and third day after production.

2. Error function (6) is designed to identify a creep modulus and a power-law exponent which explain the measured creep strain evolution in an *overall* optimal fashion, i.e. emphasis is neither layed on the absolute strain values nor on the creep strain rate at the end of the 3-minutes interval.

FITTING OF CREEP EVOLUTION TARGETING THE END OF THE 3-MINUTES PERIOD - AND EXTRAPOLATION CAPABILITIES TO 2-DAYS

In order to improve the quality of extrapolation, we now re-formulate the error function (6) such that the optimization process puts emphasis on the absolute strain values and on the creep strain rate at the end of the 3-minutes interval. To this end, we introduce a weight function $w(t)$ which monotonously increases from the beginning to the end of the three minutes time interval

$$\mathcal{E}_{SRSS}(E_c, \beta, w) = \sqrt{\frac{\sum_{i=1}^{N} \left[\varepsilon_{creep}(t_i) - \varepsilon_{creep}^{mod}(t_i)\right]^2 w(t_i)}{\sum_{i=1}^{N} w(t_i)}} \quad \rightarrow \quad \min \tag{9}$$

Herein, we use an exponential for the weight function $w(t_i)$

$$w(t_i) = \exp\left[\ln(\max w)\frac{t_i - t_1}{t_N - t_1}\right] \quad \in \; [\,1\,;\,\max w\,] \tag{10}$$

The optimization problem (9) is solved for increasing values of $\max w$, starting with $\max w = 1$. With increasing value of $\max w$, the optimal value of the creep modulus is decreasing, and the optimal value of the power-law exponent is increasing, until $\max w$ amount to one million:

$$\max w = 10^6 \tag{11}$$

Further increase of $\max w$ has no influence on the optimal values of creep modulus and power-law exponent, i.e. a stationary solution is reached:

$$\max w \geq 10^6 : \qquad E_c = 7.36\,\text{GPa} \quad \text{and} \quad \beta = 0.25 \tag{12}$$

see also Fig. 6 for the comparison of measured and model-predicted creep strain evolutions as well as for a contour plot of error function (9) with weight function $w(t_i)$ according to (10) and (11).

Young's modulus, see (1), and creep properties (12), which were identified from measurements captured during the first three minutes of the 2-days creep test, together with the measured shrinkage strain evolution, see Fig. 2 b, are now used to predict the

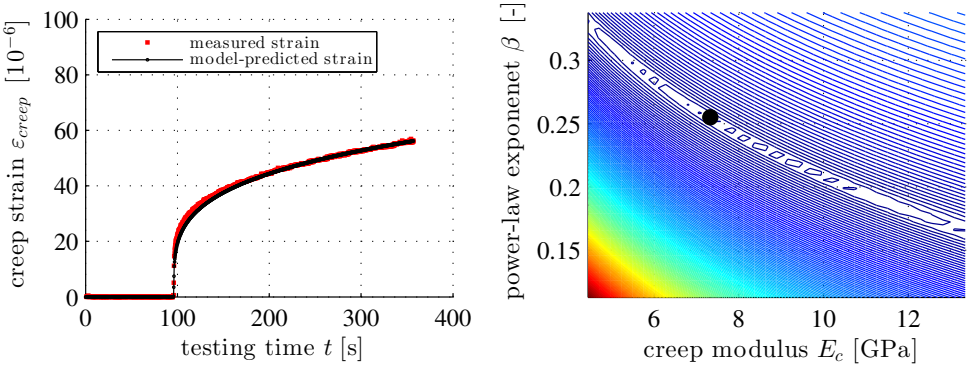

Figure 6. Illustration of creep property identification (a) comparison of measured and modeled creep strain evolution, and (b) contour plot of error function (9), see also (10) and (11), as a function of creep modulus and power-law exponent; the marked point refers to the optimal solution (12)

total strain evolution for a 2-days creep test according to Eq. (8). The predicted strain evolution is closer to the measured strain evolution than before, as quantified by the typical prediction errors which is reduced to 4.5 %, see Fig. 7.

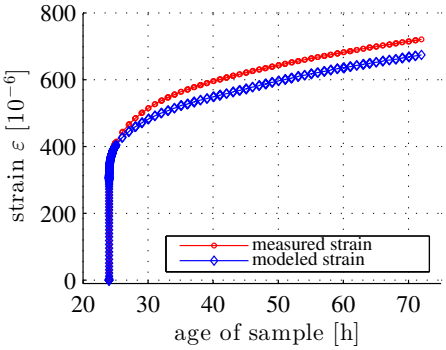

Figure 7. Comparison of extrapolated strain evolution, see (8) as well as (1) and (12), with measured strain evolution, see Fig. 2 a

DISCUSSION AND CONCLUSIONS

Herein, we have identified non-ageing creep properties of cement paste with w/c = 0.50 which cured at 20 °C for 24 hours. To this end, we have exploited measurements taken in the first three minutes of a 2-days creep test. Together with independent shrinkage measurements, we have used the *non-ageing* creep properties for predicting the strain that evolves during the entire duration of the 2-days *ageing* creep test. Extrapolation quality is satisfactory, and this is very remarkable, because three minutes are by a factor of 960 shorter than two days, i.e. the extrapolation distance is very large.

Contour plots of the here-studied error functions (6) and (9), exhibit a valley-shaped structure, see Fig. 4 b and and Fig. 6 b, respectively. Pairs of values of the creep modulus and the power-law exponent referring to the bottom of the valleys allow for an overall reliable explanation of the creep strain evolution measured in the first three minutes. In order to achieve an optimal extrapolation quality, it is of great importance to identify – among all the parameter combinations referring to the aforementioned valleys – the one parameter combination which explains the absolute strain values and the creep strain rate *at the end* of the three-minutes interval as good as possible.

The satisfactory extrapolation quality underlines that the microstructure formed at the time instant of loading plays an important role for ageing creep tests. In the future, it will be interesting to confront available multiscale models for ageing creep of cement paste [12, 13, 14] with the experimental data reported herein, and with similar data stemming from tests on cement pastes with different compositions.

REFERENCES

[1] Z.P. Bažant, A.A. Asghari, and J. Schmidt. Experimental study of creep of hardened Portland cement paste at variable water content. *Matériaux et Constructions*, 9(4):279 – 290, 1976.

[2] Z.P. Bažant, M.H. Hubler, and Q. Yu. Pervasiveness of excessive segmental bridge deflections: Wake-up call for creep. *ACI Structural Journal*, 108(6):766 – 774, 2011.

[3] Z.P. Bažant, Q. Yu, and G.-H. Li. Excessive long-time deflections of prestressed box girders. I: Record-span bridge in Palau and other paradigms. *Journal of Structural Engineering*, 138(6):676 – 686, 2012.

[4] L. Boltzmann. Zur Theorie der elastischen Nachwirkung. *Annalen Der Physik - Ann Phys-Berlin*, 241(11):430 – 432, 1878.

[5] M. Briffaut, F. Benboudjema, J.-M. Torrenti, and G. Nahas. Concrete early age basic creep: Experiments and test of rheological modelling approaches. *Construction and Building Materials*, 36:373 – 380, 2012.

[6] M. Irfan-ul-Hassan, B. Pichler, R. Reihsner, and Ch. Hellmich. Hourly-repeated minutes-long creep tests on young cement pastes provide access to power-law creep properties at early ages. 2015. In preparation.

[7] Ch. A. Jones and Z.C. Grasley. Short-term creep of cement paste during nanoindentation. *Cement and Concrete Composites*, 33(1):12 – 18, 2011.

[8] Ph. Karte, M. Hlobil, R. Reihsner, W. Dörner, O. Lahayne, J. Eberhardsteiner, and B. Pichler. Unloading-based stiffness characterization of cement pastes during the second, third, and fourth day after production. *Strain*, 51(2):156 – 169, 2015.

[9] B. Pichler and Ch. Hellmich. Upscaling quasi-brittle strength of cement paste and mortar: A multi-scale engineering mechanics model. *Cement and Concrete Research*, 41(5):467 – 476, 2011.

[10] B. Pichler, Ch. Hellmich, J. Eberhardsteiner, J. Wasserbauer, P. Termkhajornkit,

R. Barbarulo, and G. Chanvillard. Effect of gel-space ratio and microstructure on strength of hydrating cementitious materials: An engineering micromechanics approach. *Cement and Concrete Research*, 45(0):55 – 68, 2013.

[11] P. Rossi, N. Godart, J.L. Robert, J.P. Gervais, and D. Bruhat. Investigation of the basic creep of concrete by acoustic emission. *Materials and Structures*, 27(113):510 – 514, 1994.

[12] J. Sanahuja. Effective ageing viscoelastic behaviour of solidifying materials: estimations from homogenization of random media. In *Proceedings of the Fifth Biot Conference on Poromechanics*, pages 1715 – 1724, TU Vienna, 2013. BIOT-V.

[13] J. Sanahuja. Efficient homogenization of ageing creep of random media: Application to solidifying cementitious materials. In *Proceedings of the 9th International Conference on Creep, Shrinkage, and Durability Mechanics*, pages 201 – 210, MIT, 2013. CONCREEP IX.

[14] S. Scheiner and Ch. Hellmich. Continuum microviscoelasticity model for ageing basic creep of early-age concrete. *Journal of Engineering Mechanics*, 135(4):307 – 323, 2009.

[15] B.T. Tamtsia and J.J. Beaudoin. Basic creep of hardened cement paste. A reexamination of the role of water. *Cement and Concrete Research*, 30(9):1465 – 1475, 2000.

[16] B.T. Tamtsia, J.J. Beaudoin, and J. Marchand. The early age short-term creep of hardening cement paste: Load-induced hydration effects. *Cement and Concrete Composites*, 26(5):481 – 489, 2004.

[17] Q. Zhang, R.L. Roy, M. Vandamme, and B. Zuber. Long-term creep properties of cementitious materials: Comparing microindentation testing with macroscopic uniaxial compressive testing. *Cement and Concrete Research*, 58(0):89 – 98, 2014.

Modelling the Electric Corrosion of Rebar in Concrete Considering Electro-Mechanical Coupling

Di. Qiao[1]; Hikaru. Nakamura[2]; Yoshihito. Yamamoto[3]; and Taito. Miura[4]

[1]Department of Civil Engineering, Nagoya University, Furo-cho, Chikusa-ku, Nagoya, Japan. E-mail: rudyqiao@gmail.com
[2]Department of Civil Engineering, Nagoya University, Furo-cho, Chikusa-ku, Nagoya, Japan. E-mail: hikaru@nagoya-u.jp
[3]Department of Civil Engineering, Nagoya University, Furo-cho, Chikusa-ku, Nagoya, Japan. E-mail: y.yamamoto@civil.nagoya-u.ac.jp
[4]Department of Civil Engineering, Nagoya University, Furo-cho, Chikusa-ku, Nagoya, Japan. E-mail: t.miura@civil.nagoya-u.ac.jp

Abstract

The mutual effect between electric corrosion of reinforcing bars and concrete cracks development caused by corrosion is investigated experimentally and analytically. In the experiment, a salt-water pool was set on the concrete cover of each specimen containing single round rebar for the implementation of electric corrosion. Then the radius losses around the corroded rebars were measured for the corrosion patterns. It was shown that the corrosion rates at various positions around the rebar were related to the crack width nearby. In the analysis, a numerical model based on the rigid body spring method combined with a truss network is proposed to simulate the coupled process by assuming the relation of current efficiency to the crack width. Satisfied agreement with the test results of non-uniform corrosion process and associated crack propagation is obtained using this model, offering a good tool to assist in the employment of the electric corrosion method.

INTRODUCTION

Corrosion of reinforcing bars (rebars) embedded in concrete is the most common cause of deterioration of reinforced concrete (RC) structures. Since natural rebar corrosion is a slow process, for the evaluation of structural behavior of corroded RC members, researchers adopt several accelerating corrosion techniques to obtain the desired corrosion damage in a reasonably short time. The impressed current method, i.e. applying an external direct electric current to the rebar, is widely used as an accelerating method (Poursaee and Hansson, 2009). However, there is a mutual effect existing between corrosion and cracking, i.e. cracks enable quicker transport of chloride and water, thereby accelerating corrosion and causing more cracks, which makes the control of the electric corrosion process difficult. Both surface crack width and mass loss predicted by Faraday's law may be inappropriate as parameters to indicate corrosion damage (Malumbela et al., 2012). Hence a numerical model that can analyze the electric corrosion process and the caused damage is required.

Regarding the numerical models for the simulation of corrosion-induced cracking process, although a large amount of models verified with the electric corrosion test results are proposed (for example, Michel et al., 2014), the corrosion process described in these models is mostly simplified to be increments of corrosion amounts, which is not influenced by the cracking situation.

Aiming at this problem, this paper presents a time-dependent model to evaluate the crack effect on the electric corrosion process. Initially, an experimental study is carried out to measure the corrosion patterns around the corroded rebars, which are represented by radius losses along the rebar surfaces. The electric corrosion process was implemented using a salt-water pool on the concrete cover of each specimen. Then a numerical model based on the Rigid Body Spring Method (RBSM) and a truss network is developed to simulate the coupled process between local corrosion and cracks development. RBSM has a merit of obtaining crack width directly, with which local corrosion near cracks can be considered. The applicability of this model is verified by comparisons to the test results.

EXPERIMETNAL STUDY

Electric corrosion test. The specimens tested had a dimension of 200mm×500mm×200mm as shown in Figure 1. In each specimen, one 600mm long round rebar with a diameter of 16mm was partly embedded at 30mm cover depth and the rebar extended 200mm beyond the concrete specimen at each end. The length of the rebar part exposed to corrosion was confined to 180mm by coating the other parts with anti-corrosion paint, waterproof tape and insulating tape in sequence to prevent from corrosion. The mill scale of the area studied was left intact. Before casting, these rebar samples with anti-corrosion covers were weighted for the initial weight. Twelve specimens were made using early strength cement and coarse aggregates with a maximum diameter of 20mm. After casting the concrete, the specimens were cured in a room at 20℃ for 14days and then the electric corrosion test was conducted. Prior to the test, the concrete elastic modulus, compressive strength and splitting tensile strength were determined to be 30.75GPa, 38.45MPa and 2.94MPa respectively.

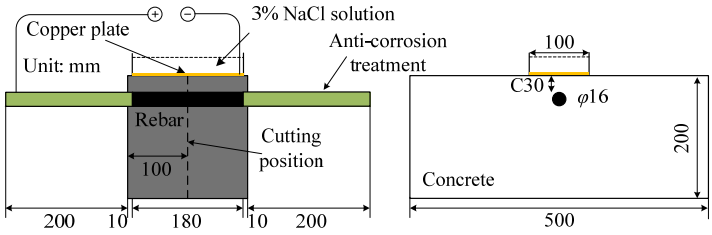

Figure 1. Electric corrosion test.

A 100mm wide water pool filled with 3% NaCl solution was set on the top surface of each specimen, right above the rebar. In the water pool, a copper plate was placed as the cathode. A schematic of the electric corrosion test is shown in Figure 1. The authors presumed that the corrosion current for the rebar upper part facing the concrete cover would be greater than that for the lower part, attributable to the smaller distance from the upper part to the cathode. Moreover, the cracks generated in

the concrete cover can cause faster chloride ingress (Djerbi et al., 2008), increasing the corrosion rate of the upper part. Therefore, the corrosion pattern around rebar can be expected to be non-uniform, i.e. the half circumference facing the concrete cover is more corroded. The nominal current density applied in the test was about 900μA/cm^2 to allow quick cracks generation, as referred to in other reported electric corrosion tests (Mangat & Elgarf, 1999; Yuan et al., 2007).

The testing time was varied as shown in Table 1 to obtain different concrete cracking situations. For each test series four specimens were used. Among them, one specimen was cut at the position shown in Figure 1 after the corrosion test for the investigation of internal cracks. For the other three specimens, the rebars were collected and cleaned by immersing them in 10% ammonium citrate solution for 24h and then using a steel brush to remove corrosion products. The mass loss Δm (g) of each rebar sample measured as the difference between the initial weight and the remaining weight was used to determine the corrosion degree η over 180mm long corroded area and the current efficiency N:

$$\eta = \frac{\Delta m}{180 m_u} \qquad (1) \qquad\qquad N = \Delta m \Big/ \left(\frac{ItM}{nF} \right) \qquad (2)$$

Where m_u is the unit mass (1.58g/mm), I is the current intensity (0.08A), t is the testing time (s), M is the molar mass of iron (55.85g/mol), n is the valency (2), and F is Faraday's constant (9.65×10^4 C/mol).

Table 1. Test series.

Series	*Testing time(hr)*	*Current flow(A*hr)*
T86, T205, T341	86.18, 204.53, 340.89	6.89, 16.36, 27.27

Figure 2 shows the development of corrosion degree against accumulated current flow, in which the corresponding current efficiencies are also indicated. The practical corrosion degrees η by the electric corrosion applied are 0.65%, 1.8% and 3.2% for the testing time ranged from 86 to 341 hours respectively. They are much smaller than those estimated based on Faraday's law (see N=1 in Figure 2) due to the occurrence of a competitive reaction, probably the splitting water to oxygen and hydrogen. During the corrosion test, it was noticed that some gases bubbled out of the water pool, which were considered to be oxygen and hydrogen. As the testing time increases, the current efficiency slightly increases, implying a rise of corrosion rate. Nossoni and Harichandran (2012) suggested that the current efficiency of the electric corrosion test increases when the chloride concentration in the concrete is increased. Therefore, the rise of corrosion rate is due to the chloride ions transport through the concrete cover.

Radius losses along rebar. The radius losses along the corroded rebars were measured using a laser meter with a precision of 0.1μm. Twelve measurement lines located at various circumferential positions around each rebar were tested, which had an interval of 30° (see Figure 3). The measurement interval along the line was 50μm. Each rebar sample studied was measured before casting the concrete specimens to obtain the initial level. The difference between the initial level and the measurement level after the corrosion test was calculated as the radius loss. Meanwhile, a Fast

Fourier Transform was performed to remove the influences of imperceptible vibrations during the measurements and then an Inverse Fourier Transform was conducted to obtain radius loss. Microwaves with frequencies of more than five wave periods in each 10mm of length were removed (Mada, 2000).

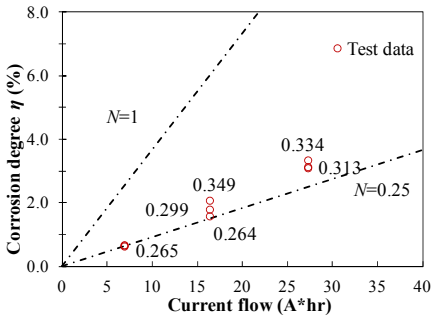

Figure 2. Measured corrosion degrees.

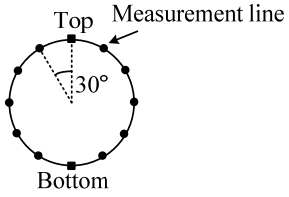

Figure 3. Measuring radius loss by laser meter.

Figure 4 shows the measured radius losses along the corroded part at the top and bottom of the rebar. With corrosion degree increasing, the radius losses along the top that is the nearest side to the cathode have a significant development, while the radius losses along the bottom hardly increase. It indicates that the applied electric method results in a non-uniform corrosion in the circumferential direction. Since the radius losses are similar along the rebar length direction, the average value for each measurement line was obtained to demonstrate the typical corrosion pattern around the rebar, which is shown in Figure 5. It is clear that the difference of the radius loss between the upper and the lower circumferences enlarges as the corrosion develops. This tendency may be attributed to the cracks appearing in the concrete, which accelerates the chloride transport and thereby increases the corrosion rate for the part near cracks.

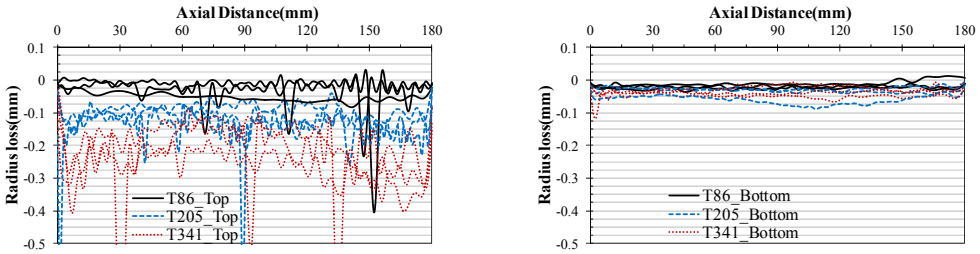

(a) top side **(b) bottom side**

Figure 4. Measured radius losses along rebar.

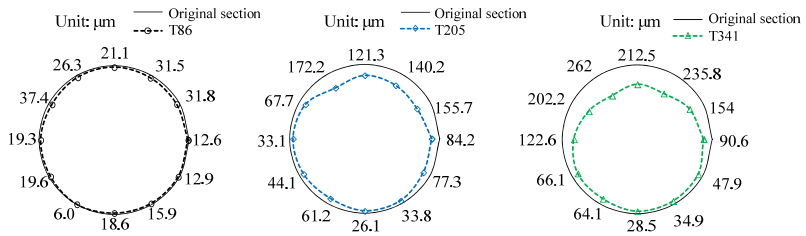

Figure 5. Rebar cross section after corrosion.

This corrosion pattern is distinct from the normal uniform corrosion reported in other electric corrosion tests (for example, Yuan et al., 2007), while it is similar to that observed from the specimens corroded under an artificial climate environment (Yuan and Ji, 2009). It is caused by the difference in test setup. Unlike the classic method in which the specimen is immersed in salt solutions or chloride is added to the concrete mix, in this method the salt-water pool is put on the concrete cover instead, which makes the chloride transport unidirectional. Thereby, it provides a better way for the reproduction of the corrosion occurring under practical chloride-contaminated conditions within a relatively short time.

Crack pattern. Figure 6 shows internal crack patterns of the specimens under different corrosion amounts. A visible crack (vertical crack) initiates from the concrete surface. As corrosion amount increases, the surface crack becomes wider and the vertical crack propagates to the rebar along with the appearance of lateral cracks. The developed vertical crack provides a flow channel for chloride ions and further increases the corrosion rate of the rebar upper part (see Figure 5), suggesting that the corrosion rates (the current efficiencies) at various positions around the rebar may be in a relation with the crack width nearby.

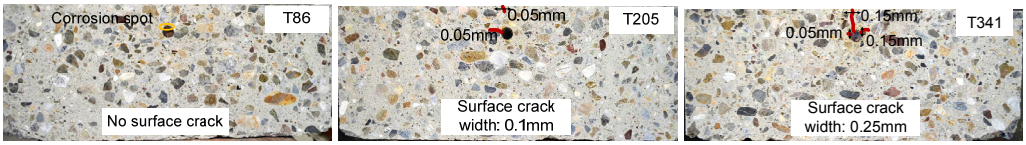

Figure 6. Internal crack patterns under various corrosion amounts.

ANALYTICAL MODEL

The experimental results demonstrate that cracks caused by corrosion expansion can in turn affect the electric corrosion process, especially the corrosion pattern around the rebar. In the analysis, a numerical model based on RBSM combined with a truss network is developed to investigate the mutual effect between local corrosion and cracks development, in which the relation between crack width and local current efficiency is assumed and verified with the test results. Such a model can be beneficial for the application of the electric corrosion method on the study of corrosion caused damage.

Three-dimensional RBSM. RBSM represents a continuum material as an assemblage of rigid particle elements interconnected by zero-length springs along their boundaries, as shown in Figure 7. The elements are randomly generated with Voronoi Diagram. Each of the elements has six degrees of freedoms at its nucleus. At the center points of every triangle formed by the center of gravity and the vertices of the boundary between two elements, three springs, one normal and two shears, are defined. Crack width can be automatically calculated as the relative displacement between the centers of each two elements. (Yamamoto et al., 2008)

Material models. Figure 8 shows the material models of concrete used in the analysis. Tensile and compressive models are introduced into normal springs. Shear

model is introduced into shear springs, where the shear strength is assumed to follow the Mohr-Coulomb type criterion with the tension and compression caps. The shear transferring capacity at the cracked interface changes according to the crack opening. Considering this effect, the shear stiffness is reduced using a function of the strain normal to the crack as shown in the shear reduction model of Figure 8b. Rebar is modeled as linear elastic with an elastic modulus of 200GPa.

Truss network. Field type problems and mass transfer situations that are governed by partial differential equations are usually dealt with a continuum model, whereas RBSM does not require continuality. Thus, a truss network (Nakamura et al., 2006) is incorporated with RBSM to cope with the analysis of electric potential distribution. The rigid particle elements are linked by truss elements with a node at each nucleus and at intermediate points on each particle boundary, as shown in Figure 9. A simplified one-dimensional partial differential equation is applied to the truss elements to carry the potential flow.

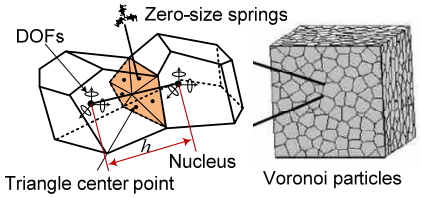

Figure 7. Rigid body spring method.

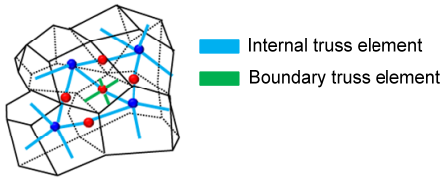

Figure 9. Truss network.

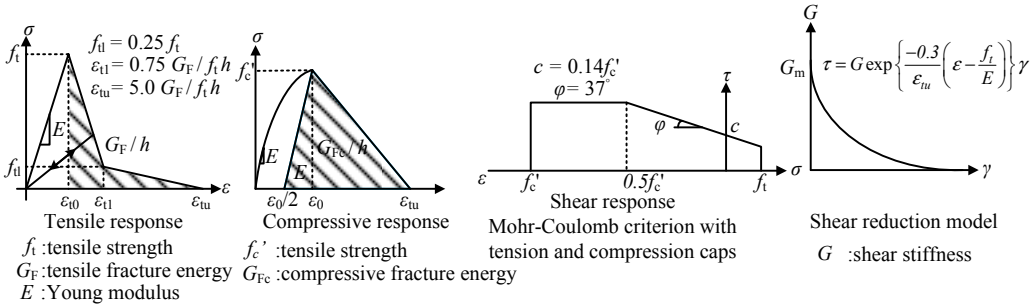

a. For normal springs b. For shear springs

Figure 8. Concrete material models.

Coupled electro-mechanical model. An electro-mechanical model is established to address the interaction of corrosion and cracking, which consists of corrosion current analysis using a truss network and corrosion expansion analysis by RBSM (see Figure 10). A three-phase material model including concrete, corrosion products and rebar is set up as shown in Figure 11. This model has the same dimensions as the tested specimen, although without the extended rebar part. The mesh sizes of the Voronoi particles in the cover area near rebar are 5mm, while the mesh size in the outer area is 20mm. In the corrosion current analysis, the potential distribution under the external applied electric field is calculated based on Laplace equation (Moliton, 2007). For the boundary conditions, the potential of the anode is simply assumed to be 10V, while the boundaries representing the cathode are fixed as zero (see Figure 11). The

potential difference between the anode and cathode has the same order of magnitude as that observed in the corrosion test. A zero influx condition is applied on the other boundaries. The analysis is controlled by ensuring the calculated current flows consistent with the test conditions listed in Table 1. Assuming only micro-cell corrosion circuit is involved in the electric corrosion process, the corrosion current I_i flowing through each truss element connecting the rebar layer and corrosion products layer can be easily determined with Ohm's law. Accordingly, the increment of mass loss Δm_i for each corroded rebar element i is calculated using Faraday's law, in which the current efficiency N_i related with the crack opening W nearby is introduced.

Djerbi et al. (2008) indicate that the diffusion coefficient of chloride ions through the crack increases as the crack width increases and almost becomes constant when the crack width is greater than 80μm. Considering that the current efficiency rises with an increase of chloride concentration (Nossoni and Harichandran, 2012), it can be considered that the current efficiency for a rebar element may be increased if a crack with sufficient crack width occurs at the neighboring concrete element. Thus, their relations are assumed in Figure 12. The current efficiency N is initially kept as 0.25 until a small crack width of 10μm and then increased linearly to 1 corresponding to a large crack width of 20μm.

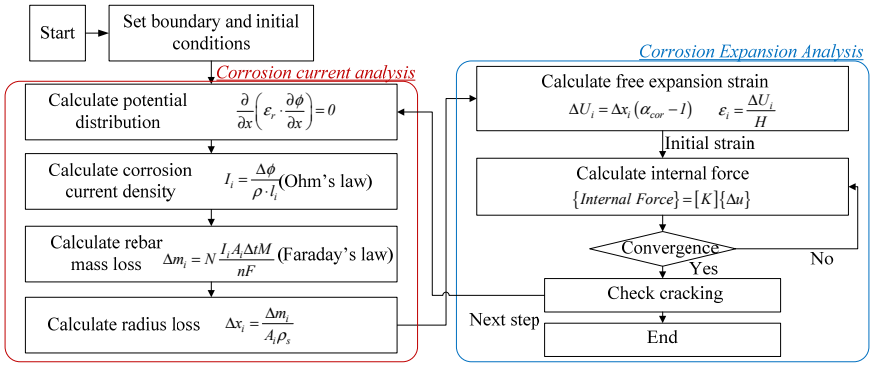

Figure 10. Coupled electro-mechanical model.

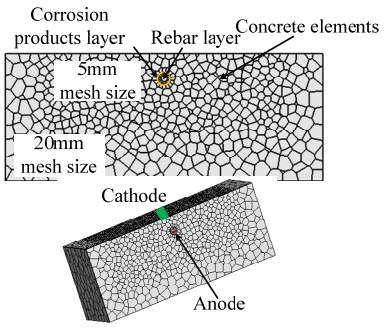

Figure 11. Three-phase material model.

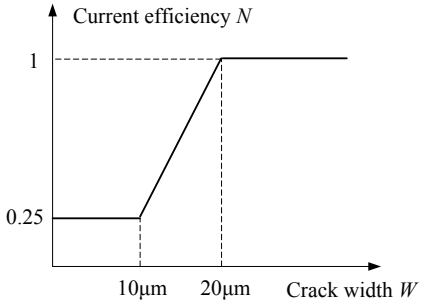

Figure 12. Relations of current efficiency to crack width

In the corrosion expansion analysis (see Figure 10), the internal expansion pressure is exerted on the elastic corrosion products layer, which has a constant thickness H. This pressure is simulated based on the initial strain problem with

increment of free increase of rebar radius ΔU_i in each analysis step. ΔU_i is calculated based on the increment of radius loss Δx_i and the volume-expansion ratio α_{cor} of corrosion products that is assumed as 2.5. Thereby, the expansion pressure distributed non-uniformly over the rebar surface can be automatically obtained from the corrosion current analysis. In consideration of the nature of corrosion expansion, the initial strain is only applied to the normal springs located on the boundary between the corrosion products layer and the rebar layer. The shear stiffness for shear springs of the corrosion products layer is set nearly zero to model free sliding of corrosion products layer in the shear direction. The previous work (Tran et al., 2011) shows that a thickness H of 1mm and an elastic modulus E_r of 500MPa for the corrosion products layer enable a correct prediction of cracks initiation comparing to the test results. They are also employed in this study. The cracking conditions obtained in the present step are used to determine the new series of current efficiencies N and to calculate the increment of initial strains around the rebar for the next step. The feature of this model is that the corrosion and cracking process is controlled only by the time increment Δt, which can contribute to the evaluation of time dependent behavior of concrete structures.

ANALYTICAL RESULTS

Without crack effect. To clarify the effect of cracks on the electric corrosion process, a case without considering the variation of current efficiency with crack width is carried out firstly. In this way, the two analyses in the coupled electro-mechanical model are independent with each other. The radius losses around the rebar can be calculated only using the corrosion current analysis. Figure 13 shows the simulated rebar sections under varied corrosion amounts, where the current efficiency is kept as a constant of 0.25. It appears that the modeled corrosion also concentrates at the upper circumference, which is similar to the characteristic of the corrosion induced in the test. However, the predicted radius losses at upper part are clearly smaller than those in tests, especially after crack initiating at the surface. Comparing the ratio of the radius loss at the top side to that at the bottom side (see Figure 14), it yields a constant of value of 2.47 in the analysis, whereas the ratio measured in the test gradually rises with the development of corrosion. It proves that cracks have a strong effect on the corrosion pattern around the rebar.

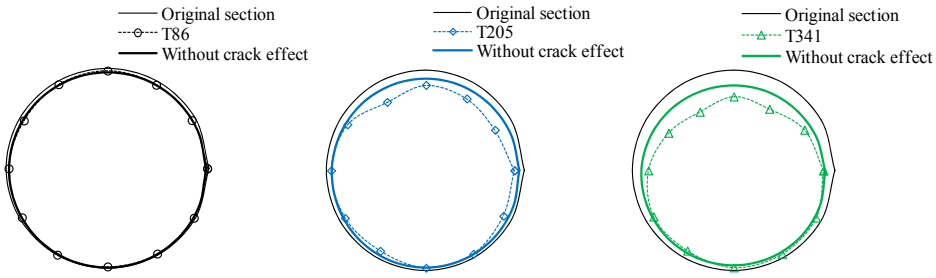

Figure 13. Simulated rebar section without crack effect.

With crack effect. The assumed relationship between local current efficiency and crack width is applied in the coupled model. The corrosion process simulated under

this assumption shows a good agreement with the test data in terms of the mass loss caused by the current flow studied (see in Figure 15) and the corrosion pattern (see Figure 14 and 16). The simulated internal crack patterns also correspond to the test result (see Figure 17). It suggests that generated cracks with a width of 20μm and more in the concrete cover may greatly increase the current efficiency.

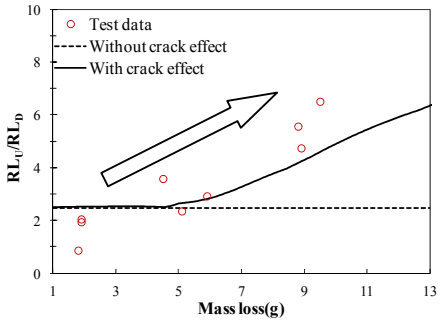

Figure 14. Ratio of radius losses between top and bottom sides.

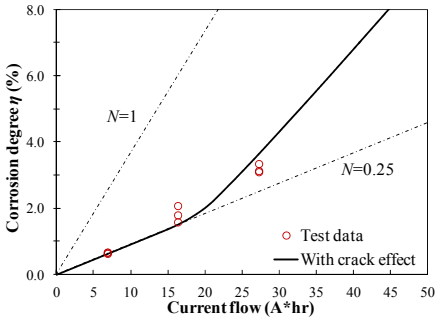

Figure 15. Development of corrosion degree with crack effect.

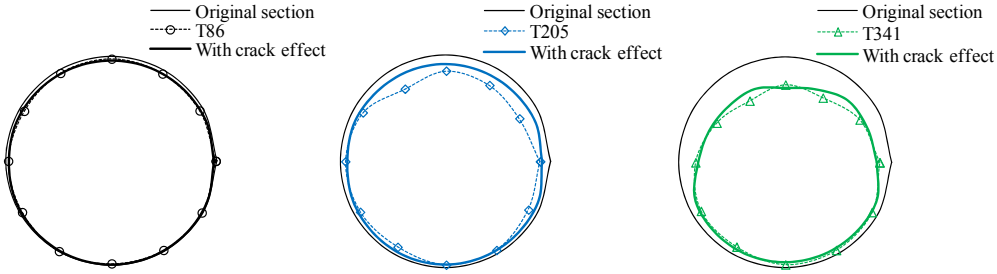

Figure 16. Simulated rebar section with crack effect.

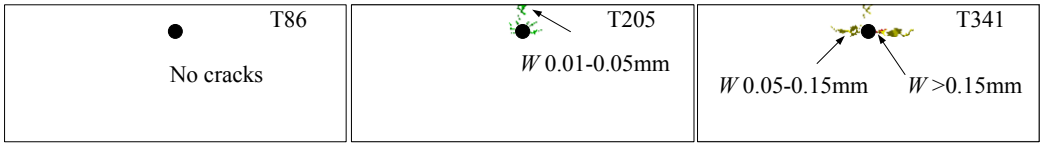

Figure 17. Simulated internal crack patterns.

CONCLUSION

The purpose of this study is to propose an analytical model that can assist in the employment of electric corrosion method on laboratory studies of corrosion-induced damage of RC structures. An experiment using the salt-water pool on the concrete cover was carried out to study the effect of generated cracks on the corrosion process, and to verify the applicability of the proposed model. The following conclusions can be derived from current study:

(1) The corrosion pattern around the rebar that is experimentally obtained using the salt-water pool is similar to that of natural corrosion. The circumference facing the concrete cover is more corroded and the cracks generated may enlarge the difference of corrosion rates between various positions.

(2) The electric corrosion process and the associated cracks evolution can be well predicted by the proposed electro-mechanical model, in which a relation between the current efficiency for Faraday's law and nearby crack width is assumed.

(3) The analysis shows that, under the electric corrosion process, when a crack with a width greater than 20μm is generated, the adjacent rebar part may be highly corroded.

The experimental study only obtained somewhat small corrosion degrees. There is a lack of test data for the calibration of the analytical model. Therefore, further experiments with higher objective corrosion degrees are in progress.

REFERENCES

Djerbi, A., Bonnet, S., Khelidj, A. and Baroghel-bouny, V., (2008)."Influence of traversing crack on chloride diffusion into concrete." *Cement &Concrete Research*, 38, 877-883.

Mada, T., (2011). "Automatic Fourier analysis by EXCEL." *Technical Report of Technical Service Division, Research Institute for Applied Mechanics, Kyushu University*, 12, 1-8. (in Japaneses)

Malumbela, G., Moyo, P. and Alexander, M., (2012). "A step towards standardizing accelerated corrosion tests on laboratory reinforced concrete specimen." *Journal of the South African Institution of Civil Engineering*, 54(2), 78-85.

Mangat, P. S. and Elgarf, M. S., (1999). "Flexural strength of concrete beams with corroding reinforcement." *ACI Structural Journal*, 96(1), 149-158.

Michel, A., Pease, B. J., Peterova, A., Geiker, M. R., Stang, H. and Thybo, A. E. A., (2014). " Penetration of corrosion products and corrosion-induced cracking in cementitious materials: Experimental investigations and numerical simulations." *Cement & Concrete Composites*, 47, 75-86.

Moliton, A., (2007). "*Basic electromagnetism and materials*." New York: Springer. 51-56.

Nakamura, H., Srisoros, W., Yashiro, R. and Kunieda, M., (2006). "Time-dependent structural analysis considering mass transfer to evaluate deterioration process of RC structures." *Journal of Advanced Concrete Technology*, 4(1), 147-158.

Nossoni, G. and Harichandran, R., (2012). " Current efficiency in accelerated corrosion testing of concrete." *Corrosion*, 68(9), 801-809.

Poursaee, A. and Hansson, C. M., (2009). "Potential pitfalls in assessing chloride-induced corrosion of steel in concrete." *Cement & Concrete Research*, 39, 391-400.

Tran, K. K., Nakamura, H., Kawamura, K. and Kunieda, M., (2011). "Analysis of crack propagation due to rebar corrosion using RBSM." *Cement & Concrete Composites*, 33, 906-917.

Yamamoto, Y., Nakamura, H., Kuroda, I. and Furuya, N., (2008). "Analysis of compression failure of concrete by three-dimensional rigid body spring model." *Doboku Gakkai Ronbunshuu*, 64(4), 612-630. (in Japaneses)

Yuan, Y., Ji, Y. and Shah, S. P., (2007). "Comparison of two accelerated corrosion techniques for concrete structures." *ACI Material Journa*l, 104(3), 344-347.

Yuan, Y. and Ji, Y., (2009). "Modeling corroded section configuration of steel bar in concrete structure." *Construction & Building Materials,* 23(6), 2461-2466.

Modelling the time dependence of transport properties of porous materials

Ignatios Athanasiadis, Simon Wheeler and Peter Grassl

School of Engineering, University of Glasgow, G12 8LT Glasgow UK; e-mails: i.athanasiadis.1@research, simon.wheeler@glasgow.ac.uk, peter.grassl@glasgow.ac.uk

ABSTRACT

A network model for the time dependence of transport properties of porous materials is proposed. A statistical volume element (SVE) of a capillary pore network of porous materials is idealised by a discrete lattice model consisting of spheres and pipes representing pores and throats, respectively, which can be filled with either liquid water or gas. The time dependence of the transport properties is modelled by incrementally decreasing the radius of the water filled pipes and spheres accounting for the evolution of the microstructure. The microstructural model is applied to investigate the change of macroscopic transport properties due to microstructural changes.

INTRODUCTION

The presence of moisture within porous materials is one of the key factors for their deterioration. Water movement is governed by the transport properties that depend on the material's microstructure. For water absorption in an inert porous material, the cumulative volume uptake scales linearly with the square root of time. However, for many materials, the response deviates from the square root of time law, which has been attributed to a number of different processes depending of the type of material, such as swelling in clays and rehydration in cement based materials (Hall et al., 1995,Martys and Ferraris, 1997, Kolstad et al., 2004). These processes result in a reduction of the size of pores through which water is transported. Therefore, the permeability of the network gradually reduces as the processes proceed. The aim of the present work is to investigate the influence of the microstructural evolution on the material's transport properties during wetting. The time evolution of the permeability and water retention curve of an SVE are presented.

MODEL

The analysis of the movement of liquid water and gas in the capillary pores of a porous material is based on a network of one dimensional pipes that connect spheres, representing throats and pores, respectively. The spatial arrangement of the network is determined from a Voronoi tessellation based on a irregular set of vertices representing the centres of particles. The locations of the pipes and spheres are determined by the edges

and vertices of the Voronoi polyhedra, respectively. The microstructure heterogeneity is imposed by considering random distributions for the radii of pipes and spheres.

Each sphere can be filled with either gas or liquid water based on the Young-Laplace equation. The procedure to determine the phase change of a sphere during a wetting process is illustrated in Figure 1a. The hatched and unhatched areas represent water and gas, respectively. Water is allowed to inflow from pipe 1. At each step of the analysis only one gas filled sphere that is connected to a water filled one is allowed to change phase. Therefore, spheres B and C are candidates to change phase. At the next step of the analysis, as suction (P_{c}) decreases, the candidate sphere with the highest P_{c} water entry value will change phase. During wetting, the P_{c} entry value increases with decreasing sphere radius. Therefore, sphere C is going to change phase since it has a smaller radius than sphere B. An analogue procedure has been implemented for a drying process, but in this case it is the pipe radius (rather than the sphere radius) that determines which sphere empties of water. The combination of these procedures for wetting and drying, is capable of describing complex macroscopic responses, such as hydraulic hysteresis (Athanasiadis et al., 2014). In the present work, the approach in Athanasiadis et al., (2014) is extended by a new approach for the evaluation of the degree of saturation (S_{r}) of the SVE.

The volume of spheres is generally much larger than the volume of pipes. Therefore, only sphere volumes are considered to contribute to the void space of the SVE. In porous materials, the pores (here spheres) with the smallest and the largest radii have almost an equal contribution to the void volume. The radii can vary by more than three orders of magnitude. Therefore, the number of smallest pores has to be more than nine orders of magnitude larger than that of the largest ones. In order to capture this feature, the number of spheres in the SVE has to be larger than a million, which is computationally inefficient. To overcome this problem, the initial volume of each sphere s is evaluated as $V_{\mathrm{s}} = 4/3\pi r_{\mathrm{s},0}^3 r_{\mathrm{m,s}}^3 / r_{\mathrm{s},0}^3$, where V_{s} is the volume of the sphere, $r_{\mathrm{m,s}}$ is the mean of the sphere radii distribution and $r_{\mathrm{s},0}$ is the initial radius of the sphere. Hence, each sphere has an equal contribution to the void volume of the SVE and represents a non integer number of spheres of the same size equal to $r_{\mathrm{m,s}}^3 / r_{\mathrm{s},0}^3$. When $r_{\mathrm{s},0}$ is less than $r_{\mathrm{m,s}}$, the number of spheres represented is greater than 1, otherwise it is less than 1. The rules for the filling of the spheres are evaluated based on the radius of the sphere $r_{\mathrm{s},0}$. When a pipe connects two water filled spheres, it is considered to be water filled and exhibits a conductivity based on the Hagen-Poiseuille equation. Otherwise, it is considered to be gas filled, with a much lower conductivity.

The influence of the time-dependent volume change of the macro pores is considered by incrementally reducing the radii of the water filled pipes and spheres. The change of the sphere and pipe radii is described by a simple linear expression

$$r(t) = \begin{cases} r_0 - \alpha\,(t - t_0) & \forall \;\; (t - t_0) < (r_0 - r_{\min})/\alpha \\ r_{\min} & \forall \;\; (t - t_0) \geq (r_0 - r_{\min})/\alpha \end{cases} \tag{1}$$

where $r(t)$ is the sphere or pipe radius at time t, r_0 is the initial radius of either the pipe

or the sphere, α is the constant radius change rate and t_0 is the time at which a pipe or sphere is filled, before that time $r(t) = r_0$. Furthermore, $r_{\min} = 1.35$ nm, which is the minimum radius at which a water meniscus can be formed (Bažant and Bazant 2012).

ANALYSIS AND RESULTS

The model was applied to the wetting of an SVE, which was generated with a target mean particle diameter in the range of $15-30$ μm. This was achieved by setting $d_{\min} = 15$ μm as a minimum distance of the Voronoi nuclei. The SVE edge length was chosen to be 7 times $d_{\min}$ (Figure 1b). The sphere and pipe distributions were chosen to obtain a porosity of 0.1 and an intrinsic permeability of $\kappa_{\mathrm{i}} = 2 \times 10^{-19}$ m^2, respectively. Also, the water retention curve for an inert SVE is presented in Figure 2a.

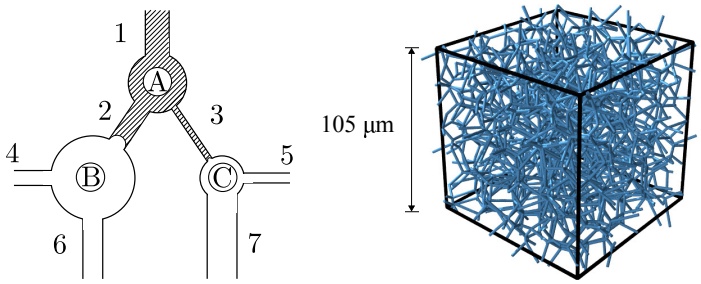

Figure 1. (a) Schematic representation of a simple network during wetting. The hatched areas represent the liquid water filled pipes and spheres. (b) Pipe network of an SVE.

The permeability for four evolution stages and varying P_{c} were investigated in Figure 2b. Here, the evolution is expressed by a dimensionless parameter $\bar{t} = \alpha t / r_{\mathrm{m}}$, where r_{m} is the mean of the pipe radii distribution. For each $\bar{t}$, which considers both time and microstructural change, the permeability κ of the SVE is evaluated for decreasing P_{c} starting with an almost dry condition. The results were normalised as $\bar{\kappa} = \kappa / \kappa_{\mathrm{i}}$. For high P_{c}, $\bar{\kappa}$ is almost the same for all $\bar{t}$, since only a small number of pipes are water filled. As P_{c} decreases, more pipes are water filled, so that, the decrease of $\bar{\kappa}$ is more pronounced for increasing $\bar{t}$.

CONCLUSION

A three dimensional transport model based on a network approach for the analysis of the time dependent evolution of the microstructure of porous materials and its influence on permeability during wetting was presented. Based on the present approach, the permeability of the SVE decreases for increasing time. This decrease is particularly

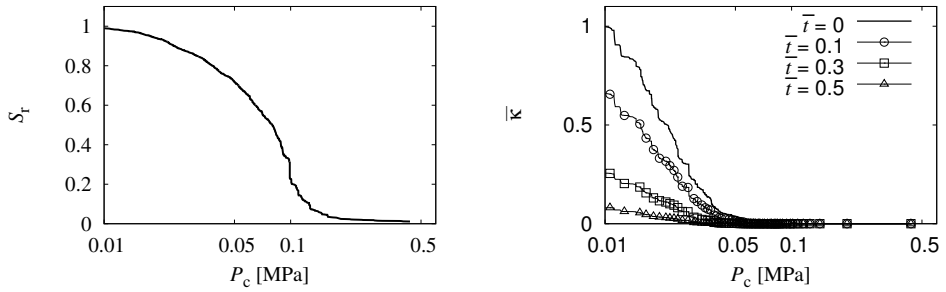

(a) (b)

Figure 2. (a) Water retention curve of an inert SVE. (b) Normalised permeability versus suction for four different $\bar{t}$ values.

pronounced for high levels of saturation.

ACKNOWLEDGEMENTS

The authors acknowledge funding received from the UKs Engineering and Physical Sciences Research Council (EPSRC) under Grant EP/I036427/1 and the funding from Radioactive Waste Management Limited (RWM) (http://www.nda.gov.uk/rwm), a wholly-owned subsidiary of the Nuclear Decommissioning Authority. RWM is committed to the open publication of such work in peer reviewed literature, and welcomes e-feedback to rwmdfeedback@nda.gov.uk. The simulations were performed with the object-oriented finite element package OOFEM (www.oofem.org) extended by the present authors.

REFERENCES

Athanasiadis, I., Wheeler, S., and Grassl, P. (2014). "Three-dimensional network modelling of the influence of microstructure on mass transport in unsaturated soils". In *International Symposium on Geomechanics from Micro to Macro*, IS Cambridge, 84-91.

Bažant, Z.P., and Bazant, M.Z. (2012). "Theory of sorption hysteresis in nanoporous solids: Part I Snap-through instabilities". *Journal of the Mechanics and Physics of Solids*, 60, 1644-1659.

Hall, C., Hoff, W., Taylor, S., Wilson, M., Yoon, B., Reinhardt, H., Sosoro, M., Meredith, P., and Donald, A. (1995). "Water anomaly in capillary liquid absorption by cement-based materials". *Journal of Materials Science Letters*, 17, 1178-1181.

Kolstad, D.C., Benson, C.H., and Edil, T.B. (2004). "Hydraulic conductivity and swell

of nonprehydrated geosynthetic clay liners permeated with multispecies inorganic solutions". *Journal of Geotechnical and Geoenvironmental Engineering*, 130, 1236-1249.

Martys, N. and Ferraris, C. (1997). "Capillary transport in mortars and concrete". *Cement and Concrete Research*, 27, 747-760.

3D modelling of the influence of microcracking on mass transport in concrete

P. Grassl and I. Athanasiadis

School of Engineering, University of Glasgow, G128LT Glasgow; emails: peter.grassl@glasgow.ac.uk, i.athanasiadis.1@research.gla.ac.uk

ABSTRACT

A three-dimensional lattice approach for modelling the coupling of fracture and transport was applied to micro-cracking induced by aggregate restrained shrinkage in concrete, which was idealised as a three phase material consisting of matrix, aggregates and interfacial transition zones. Shrinkage of the matrix and interfacial transition zones was modelled by applying incrementally a uniform eigenstrain. The influence of aggregate diameter and specimen thickness on cracking and transport properties was investigated. The results show that increasing aggregate diameter at constant volume fraction increases the crack widths and, therefore, permeability, which confirms previously obtained 2D modelling results.

INTRODUCTION

Microcracking due to aggregate restrained shrinkage significantly increases the permeability of materials, which, in turn, decreases their durability. The results of previous numerical studies indicate that the width of cracks produced by aggregate restrained shrinkage depends strongly on the size of aggregates (Grassl et al., 2010). It was found that increasing size of aggregates resulted in increasing crack widths and, as a result, increasing permeability, which is qualitatively in agreement with experimental observations. In the 2D numerical modelling, aggregates were idealised as cylindrical inclusions and all cracks were assumed to penetrate completely the specimen thickness. In experiments, it could be expected that the influence of cracking on permeability is dependent on the specimen thickness. In thicker specimens, more complicated 3D fracture networks could be generated, in which not all microcracks are fully connected and therefore do not equally contribute to the increase of permeability. The aim of the present study is to investigate numerically the separate influences of specimen thickness and aggregate size on the increase of permeability due to aggregate restrained

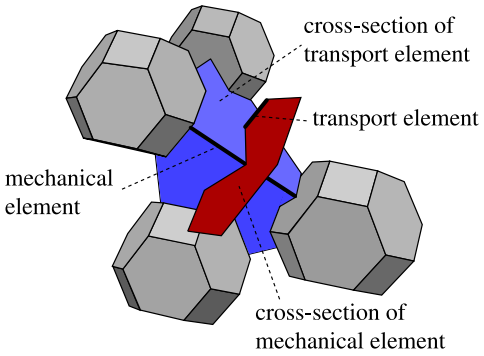

Figure 1: Spatial arrangement of mechanical and transport elements of the 3D hydro-mechanical lattice approach showing one tetrahedron and four polyhedra of the dual Delaunay and Voronoi tessellation. The four polyhedra and the mid-cross-section are shown smaller to improve the clarity of the illustration.

shrinkage induced microcracking. These influences are investigated by means of coupled 3D fracture and transport analyses using a lattice approach originally proposed in Grassl and Bolander (2009).

MODEL

The 3D numerical approach for modelling the interaction of fracture and transport is based on dual Delaunay and Voronoi tessellations of the domain based on a set of irregular vertices. The mechanical response is modelled by special lattice elements developed for efficiently modelling the evolution of displacement discontinuities, such as cracks. The nodes of these elements, which coincide with the random set of vertices used for the tessellations, possess 3 translational and 3 rotational degrees of freedom. The constitutive response of the mechanical elements is described by a damage-plasticity approach. The arrangement of the irregular lattice is chosen so that the mechanical elements are located on the edges of the Delaunay tetrahedra and their mid cross-sections are placed on the facets of the Voronoi polyhedra. Transport is modelled by a 3D network of one-dimensional conduit elements, which are placed at the edges of the Voronoi polyhedra. This dual spatial arrangement of mechanical and transport elements has been shown to be suitable for modelling the increase of flow due to fracture in 2D studies (Grassl, 2009). For the present 3D approach, the geometrical arrangement of mechanical and transport elements in relation to the spatial tessellation of the domain is shown in Figure 1.

The coupling of fracture and mass transport is modelled by setting the permeability of the transport elements to be dependent on the crack opening of adjacent mechanical elements, which form the boundary of cross-sections of the transport elements. This dependence of permeability on cracking is considered by a cubic function of the norm of the crack opening at the mid cross-section.

RESULTS

The coupled mechanical transport lattice model is applied to the analysis of aggregate restrained shrinkage of concrete prisms of varying thickness. Concrete is idealised as a three phase material consisting of matrix, interfacial transition zones and aggregates. The properties of the different phases are mapped onto the background lattice. Periodic aggregate arrangements and boundary conditions are applied for both the mechanical and transport model. The mechanical material properties are chosen according to the ones in Grassl et al. (2010), where aggregates are modelled to be elastic and stiffer than the matrix, and the interfacial transition zone has a smaller strength and fracture energy than the matrix. Loading is applied by subjecting the matrix and interfacial transition zones incrementally to a uniform eigenstrain, which results in nonzero internal forces due to the restraint of the aggregates. The resulting forces for the entire specimen are kept at zero. For the transport part, aggregates are assigned a much lower permeability than the matrix, whereby transport elements crossing the interface between aggregates and matrix are given a much higher permeability than the matrix. The permeability of the specimens is evaluated by stationary transport analysis with a pressure gradient applied in the vertical direction of the specimen.

In Figure 2, one of the thick specimens of the study with dimensions $5 \times 5 \times 7.5$ cm, with the largest considered aggregates of diameter $d = 16$ mm and a volume fraction of 0.125, is shown for three stages of shrinkage strain applied to the matrix. The blue spheres indicate the position of the aggregates. The orange polygons specify cross-sections at which the crack opening increases at this stage of analysis and is greater than 10 μm. The description of colours refers to the colour version of the figure. The aggregate restraint results in distributed crack networks, which result in a strong increase of the permeability of the material. Varying the diameter of the aggregates from 16 to 4 mm and the specimen thickness (in the vertical direction) from 7.5 to 2.5 cm indicates that the permeability is strongly influenced by the size of aggregates, but less by the specimen thickness. However, these preliminary results are obtained for a small sample of random aggregate arrangements (only 3 for each configuration). More analyses are required to obtain a more accurate description of the mean response.

CONCLUSIONS

A three-dimensional coupled mechanical transport lattice model is used for the analysis of the influence of microcracking on transport in concrete, and its relation to aggregate and specimen size. Preliminary results indicate that the microcracking results in a strong increase of the permeability of the material. Furthermore, the greater the aggregate size is at constant volume fraction, the greater is the increase of the permeability due to microcracking. The influence of the specimen thickness on the change of permeability is less pronounced. More analyses are needed to obtain an accurate eval-

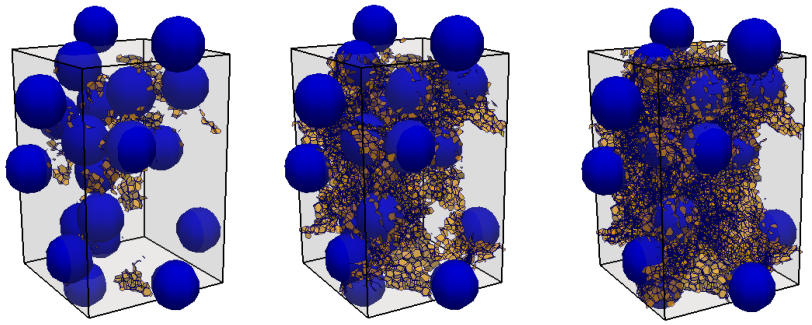

Figure 2: Crack patterns for three stages of shrinkage strain applied to the matrix. In the colour version, aggregates are shown in blue and the cracks are represented by yellow cross-sections of mechanical element in which crack openings increase at this stage of the analysis and are greater than 10 μm.

uation of the mean of the permeability for different spatial aggregate arrangements to draw clear conclusions about the influence of specimen thickness on the crack patterns and transport properties.

ACKNOWLEDGEMENTS

The numerical analyses were performed with the nonlinear analyses program OOFEM extended by the present authors. The authors acknowledge funding received from the UK Engineering and Physical Sciences Research Council (EPSRC) under grant EP/I036427/1 and from Radioactive Waste Management Limited (RWM) (http://www.nda.gov.uk/rwm), a wholly-owned subsidiary of the Nuclear Decommissioning Authority. RWM is committed to the open publication of such work in peer reviewed literature, and welcomes e-feedback to rwmdfeedback@nda.gov.uk.

References

[1] Grassl, P. (2009). “A lattice approach to model flow in cracked concrete”. *Cement and Concrete Composites*, 31, 454-460.

[2] Grassl, P. and Bolander, J. E. (2009) “Three-dimensional lattice model for coupling of fracture and flow”, *International Conference on Particle-Based Methods*, Barcelona, Spain, 154-157.

[3] Grassl, P., Wong H. S., and Buenfeld, N. R. (2010). “Influence of aggregate size and volume fraction on shrinkage induced micro-cracking of concrete and mortar”. *Cement and Concrete Research*, 40(1), 85-93.

Modelling the Effect of Microcracks on the Transport Properties of Concrete in Three Dimensions

S. D. Abyaneh[1]; H. S. Wong[2]; and N. R. Buenfeld[3]

Concrete Durability Group, Department of Civil and Environmental Engineering, Imperial College London, SW7 2AZ London, U.K. E-mail: s.dehghanpoor-abyaneh@imperial.ac.uk[1]; hong.wong@imperial.ac.uk[2]; n.buenfeld@imperial.ac.uk[3]

Abstract

This paper investigates the effect of microcracks on transport properties of concrete using a three-dimensional model. Concrete is idealised as consisting of aggregate particles (1-10 mm, 60% vol.), cement paste matrix and microcracks with widths of 1-50 μm. Using aligned meshing, aggregate particles are discretised with tetrahedral elements and the microcracks are incorporated as interface elements. The microcracks are either bond cracks at the aggregate-paste interface or matrix cracks that span nearest neighbouring aggregate particles. A finite-element model is applied to simulate diffusion and permeation. The model is used to perform a sensitivity analysis to examine the effect of microcrack width, density and percolation. It is found that the effect of microcracks is more pronounced for concretes with denser matrix. Furthermore, the effect of microcracks in non-percolated networks increases up to a finite limit, the value of which is independent of crack width but depends on other crack characteristics and transport property of the matrix. In all cases, microcracking has a greater effect on permeation than diffusion and this is more pronounced for percolated crack networks.

INTRODUCTION

Concrete structures in service are subjected to tensile stresses arising from mechanical loads, restrained shrinkage and thermal gradients. These often exceed the tensile strength of the concrete and generate microcracking. It has long been suspected that microcracks act as preferential paths for the ingress of aggressive species, but the significance of their influence on the bulk transport properties and durability of concrete is not well understood. The ability to model this influence is appealing, as it would assist the development of more accurate prediction of degradation and service life.

A number of studies have examined the transport properties of concrete containing traversing cracks such as the work of Wang et al. (1997), Gerald et al. (1997, 2000), Aldea et al. (1999), Kamali-Bernard and Bernard (2009), Picandet et al. (2009), Jang et al. (2011), Akhawan et al. (2012) and Djerbi Tegguer et al. (2013). Traversing cracks are cracks that go through the entire thickness of the sample. The transport properties of a medium containing such cracks can be modelled in a

relatively straightforward manner because the effective property can be related to crack characteristics such as width, area and transport property (e.g. free diffusivity) by using a parallel model. However, such cracks are not representative of microcracks observed in concrete, such as those induced by drying shrinkage or thermal effects (Wong et al., 2009; Grassl et al., 2010; Wu et al., 2015). Nevertheless, concrete with traversing cracks can be regarded as a worst-case scenario and the modelled results should provide upper-bound values of the transport property.

In contrast to the numerous modelling studies available on the effect of traversing cracks on transport properties of concrete, the influence of random and discontinuous microcrack networks has received much less attention. Furthermore, the effect of microcracks on permeability of cement-based materials has rarely been studied using numerical approaches. A major challenge in modelling the effect of microcracks is the huge computational resource needed to simulate a representative volume of concrete in three-dimensions at sufficient resolution to capture the microcracks. This is because the ratio of the size of the numerical sample to the discretisation is constrained by the available computational resource and this imposes a limit on the smallest feature that can be realistically modelled. For example, it would be too computationally demanding to have voxels small enough to represent the whole range of microcracks in a representative volume of concrete.

In this study, we attempt to overcome this limitation by using aligned meshing. With this approach aggregate particles are discretised using tetrahedral elements and triangulation to explicitly capture the particle surfaces more accurately and efficiently. This is in contrast to the regular meshing approach of using cubic elements that consequently replaces curved surfaces with perpendicular planar surfaces. With aligned meshing, microcracks are then incorporated as interface elements and can be explicitly considered as either bond or matrix cracks. Hence, the smallest microcracks can be represented independent of the size of the discretisation. The microcracks can be assigned with different widths, lengths, orientation and connectivity. The model is then used to perform a sensitivity analysis to examine the effect of the microcracks on diffusivity and permeability.

METHODOLOGY

Input structure

A mesostructure of concrete is generated by randomly placing spherical aggregate particles in a $25\times25\times25$ mm^3 computational cube, as shown in Figure 1a. The aggregate particles have a size distribution ranging from 1 mm to 10 mm, following the Fuller-Thompson gradation. Therefore, the numerical sample size is 2.5 times the largest aggregate particle and this provides representative results if sufficient number of realisations is simulated and averaged (Abyaneh et al., 2013). Around 1000 particles are required and they are placed in order of descending size with no overlaps. The total aggregate volume fraction is 60%. The smallest aggregate particle considered is 1 mm due to limitations of the mesh generator. It should be

noted however, that small aggregate particles have less contribution to microcracking as observed in several studies such as Bisschop and van Mier (2002), Grassl et al. (2010), Idiat et al. (2012) and Wu et al. (2015). These studies showed that the degree of microcracking (measured in terms of width, length, depth or density) decreases with decrease in aggregate size. Fracture mechanics predict that aggregate particles below a critical size do not cause microcracking (Goltermann, 1994). Here, we assume the critical size is 1 mm.

The mesostructure is meshed using the aligned meshing approach implemented in the finite-element package ABAQUS. Surfaces of the aggregate particles are first triangulated, and then the aggregate particles and cement paste matrix are filled with tetrahedral elements as shown in Figure 1b and 1c respectively. For the sake of demonstration, a rather coarse mesh is used in Figure 1b and 1c, where the global element size i.e. spacing between nodes is 1 mm. In the actual transport simulations, the global element size is reduced to 0.25 mm and the mesostructure contains about 6.5×10^6 tetrahedral elements. Microcracks are incorporated as interface elements and triangulated during the meshing process. Each crack is approximately a two-dimensional plane since its width is much smaller than the projections along the two other axes. Each crack can be assigned with its own characteristics such as width, length and orientation, and so the cracks are represented independent of the size of the discretisation of the aggregate particles and cement paste matrix. Each phase in the input structure is assigned a transport property and then a finite element technique described in the next section is applied to simulate diffusion or permeation through the cracked media.

Governing equations

Diffusion of the cracked concrete is modelled by considering the diffusivities of the porous cement paste matrix and cracks. Aggregate particles are assumed to be dense inclusions that do not contribute to transport. Assuming that the porous matrix has a diffusivity D_m that can vary with position, the local flux $\bar{j}_m$ in the matrix is provided by Fick's first law: $\bar{j}_m = -D_m \nabla c$, where c is concentration of the diffusing species. The conservation equation for local flux in the porous matrix at steady-state can be written as $\nabla . \bar{j}_m = 0$. Assuming that the crack has a width w_{cr} and diffusivity D_{cr} (= free diffusivity D_o), the flux in the crack is obtained by the following equation:

$$\boldsymbol{J_{cr}} = -w_{cr} D_{cr} \nabla_s c \tag{1}$$

The differential equations are solved using finite element method, and solutions are averaged on a larger scale. The total flux $\bar{\bar{j}}$ is obtained by integrating local fluxes over the porous matrix and cracks divided by the total sample volume:

$$\bar{\bar{\boldsymbol{j}}} = \frac{1}{\tau_0}\left(\int_{\tau_m} \bar{j}_m d\tau + \int_{S_{cr}} \boldsymbol{J_{cr}} ds\right) \tag{2}$$

Where τ_0, τ_m and S_{cr} are the sample volume, matrix volume and crack surface area respectively. The overall flux is related to the concentration gradient: $\bar{\bar{\boldsymbol{j}}} = -D_{eff}\overline{\nabla c}$. For an anisotropic medium, D_{eff} is a tensor. However, if the concentration gradient is imposed in one direction, the equation is simplified to $\bar{\bar{j}}_x = -D_{eff}\,\overline{\overline{\partial c}}/\partial x$.

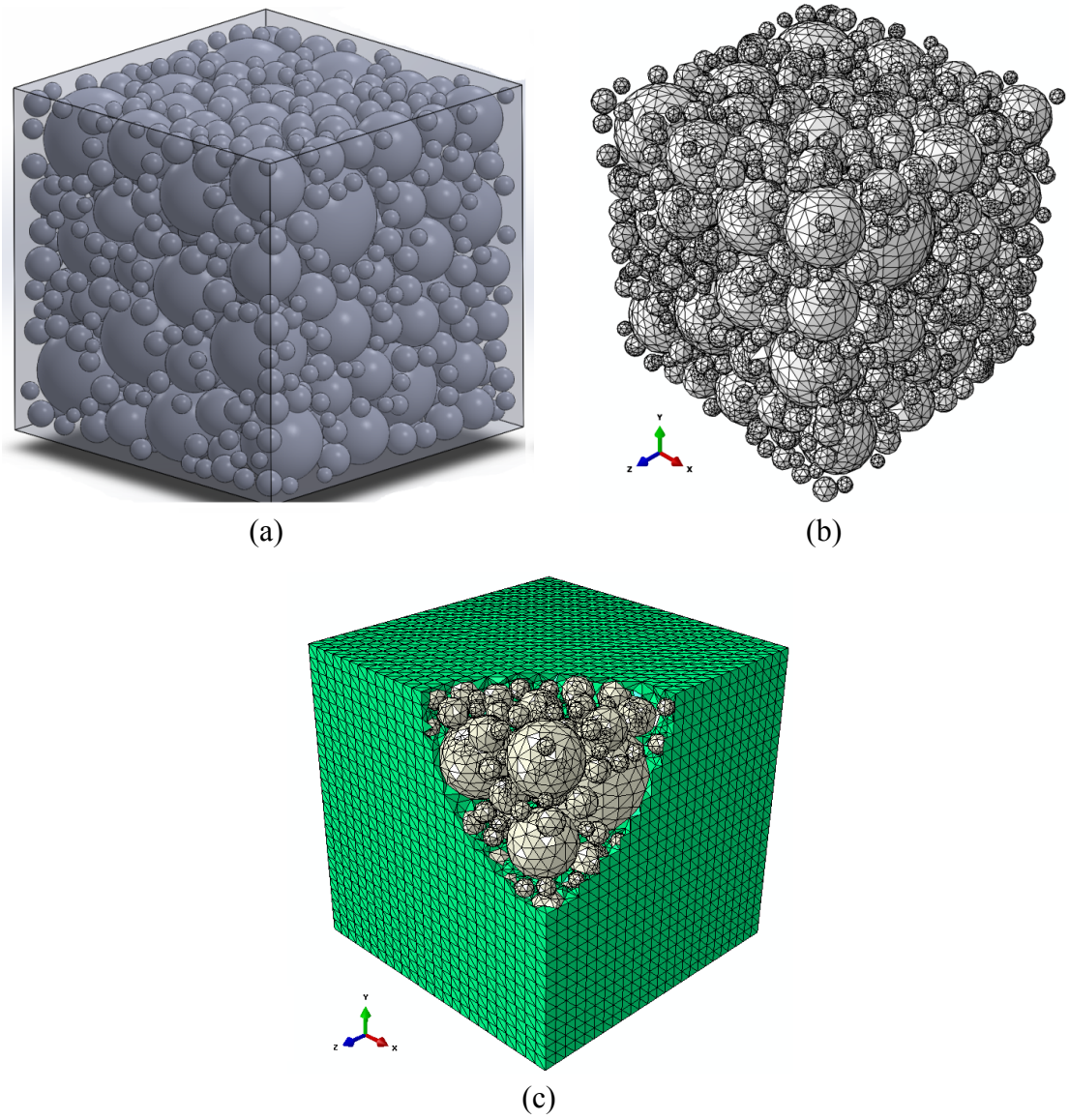

Figure 1. a) Mesostructure of concrete containing 60% volume of aggregate particles ranging from 1 to 10 mm (Fuller-Thompson gradation) in a 25×25×25 mm^3 computational cube, (b) triangulation on the surface of aggregate particles and (c) tetrahedral elements in the cement paste matrix.

This approach can also be applied to model pressure-induced flow by replacing Fick's law with Darcy's law at the mesoscale and Navier-Stokes equations at the microscale. The cement paste matrix is assigned a bulk permeability K_m that can vary with position, so the local fluid velocity $\bar{v}$ in the matrix is $\bar{v} = -K_m \nabla p/\mu$, where μ is the fluid viscosity and p is pressure. The conservation for local fluid velocity can be written as $\nabla . \bar{v} = 0$. Assuming that the crack has permeability K_{cr}, the flow rate in the crack is given by a two-dimensional Darcy's law:

$$J = -\frac{w_{cr} K_{cr}}{\mu} \nabla_s p \tag{3}$$

Where permeability of the crack is obtained from the equation $K_{cr} = w_{cr}^2/12$. This assumes the crack is of constant width and has no surface roughness. The differential equations are then solved using finite element method, noting that the pressure gradient is imposed in one direction and other surfaces are assumed to be impermeable. Subsequently, the solutions are averaged on a larger scale by integrating the flow rates over the porous matrix and crack surfaces divided by the total volume of the media to obtain the overall fluid velocity $\bar{\bar{v}}$

$$\bar{\bar{\boldsymbol{v}}} = \frac{1}{\tau_0}\left(\int_{\tau_m} \bar{\boldsymbol{v}}\, d\tau + \int_{S_{cr}} \boldsymbol{J}\, ds\right) \tag{4}$$

Where τ_0 is the total volume, τ_m is the matrix volume and S_{cr} is the crack surface area as before. The overall fluid velocity is related to the pressure gradient by Darcy's law $\bar{\bar{\boldsymbol{v}}} = -K_{eff}\overline{\nabla p}/\mu$. In the general case of anisotropic medium, K_{eff} is a tensor. But because pressure gradient is imposed in one direction and other surfaces are assumed to be impermeable, the above equation can be simplified as:

$$\bar{\bar{v}}_x = \frac{1}{\tau_0}\left(\int_{\tau_m} \bar{v}_x\, d\tau + \int_{S_{cr}} J_x\, ds\right) = -\frac{K_{eff}}{\mu}\frac{\overline{\overline{\partial p}}}{\partial x} \tag{5}$$

Sensitivity analysis

Six concrete mesostructures containing microcracks were generated and tested. An important issue is the placement of the microcracks, which should mimic actual cracks in concrete. It is known that microcracks initiate at the weak aggregate-paste interface and then propagate along the interface or across the cement paste matrix to span aggregate particles. These are referred to as bond cracks and matrix cracks respectively. As such, the first mesostructure was created by placing bond cracks around randomly selected aggregate particles and placing matrix cracks to span the nearest neighbouring aggregate particles (smallest distances first). The number of bond cracks and matrix cracks were gradually increased until the first crack network achieved a crack density (specific surface area) of 0.15 mm^2/mm^3. This process (illustrated in two dimensions in Figure 2) was repeated to produce six crack networks with increasing degree of microcracking, up to a crack density of 0.90 mm^2/mm^3. Table 1 shows the number of bond cracks, matrix cracks and specific surface area of the six crack networks. The ratio of matrix to bond cracks ranged between 1.24 and 1.28.

Percolation was determined using a burning algorithm (Stauffer, 1985). The transport property of the cracks was increased to infinity and if the bulk transport property of the media tended to infinity, then the crack network was deduced to be percolated. It was observed that the first four crack networks (a, b, c, d) are not percolated, while the last two crack networks (d and e) are percolated. For the sake of simplicity, the cracks were assumed to have equal widths of 1, 5, 10, 25 or 50 μm. Therefore, the crack volume fraction, calculated by multiplying the specific surface area with the crack width, of all the simulated mesostructures ranged from 0.015% to 4.5%. It should be noted that the simulated microcrack width, volume fraction and specific surface area are within the measured range for drying-induced microcracks in concrete (Wong et al., 2009; Wu et al., 2015).

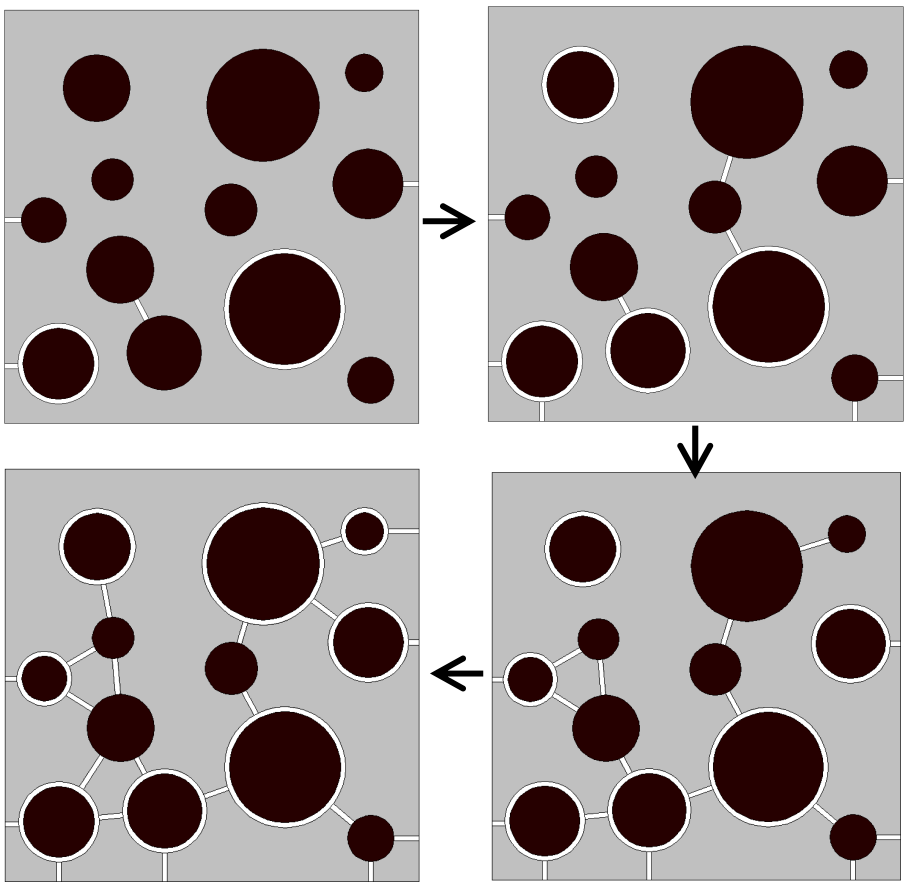

Figure 2. Schematic of generating crack networks with increasing degree of microcracking by placing bond cracks around randomly selected aggregate particles, and matrix cracks to span the nearest neighbouring aggregates.

Table 1 Characteristics of the generated crack pattern

Property	Crack network					
	a	*b*	*c*	*d*	*e*	*F*
Number of bond cracks	154	298	452	606	750	904
Number of matrix cracks	191	382	573	765	956	1147
Specific surface area (mm^2/mm^3)	0.15	0.29	0.43	0.58	0.74	0.90

RESULTS

The simulated diffusivity and permeability are shown in Figure 3 and 4 respectively. Simulations for diffusivity were carried out at three contrast ratios, i.e. ratio of diffusivity of microcrack to the diffusivity of uncracked concrete, of 100, 1000 and 10000. Simulations for permeability were carried out by assigning the permeability of uncracked concrete as 1E-19, 1E-18 or 1E-17 m^2. The reason for this is because the diffusivity of a crack is equal to the free diffusivity (independent of crack width), while the permeability of a crack is a function of its width.

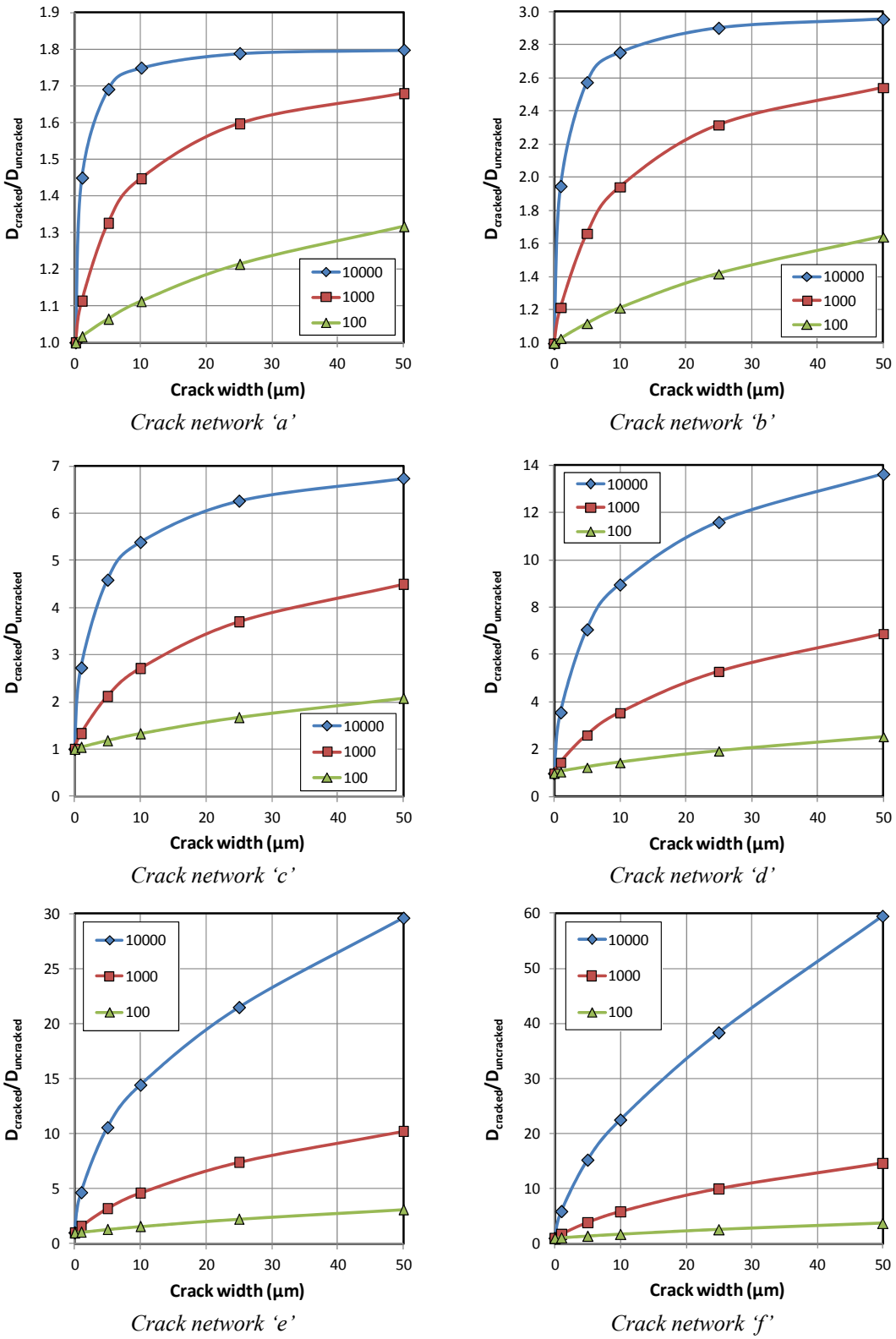

Figure 3 Effect of crack width on diffusivity of concrete with different crack patterns. Simulations were carried out at contrast ratios (i.e. ratio of diffusivity of crack to the diffusivity of uncracked media) of 100, 1000 and 10000.

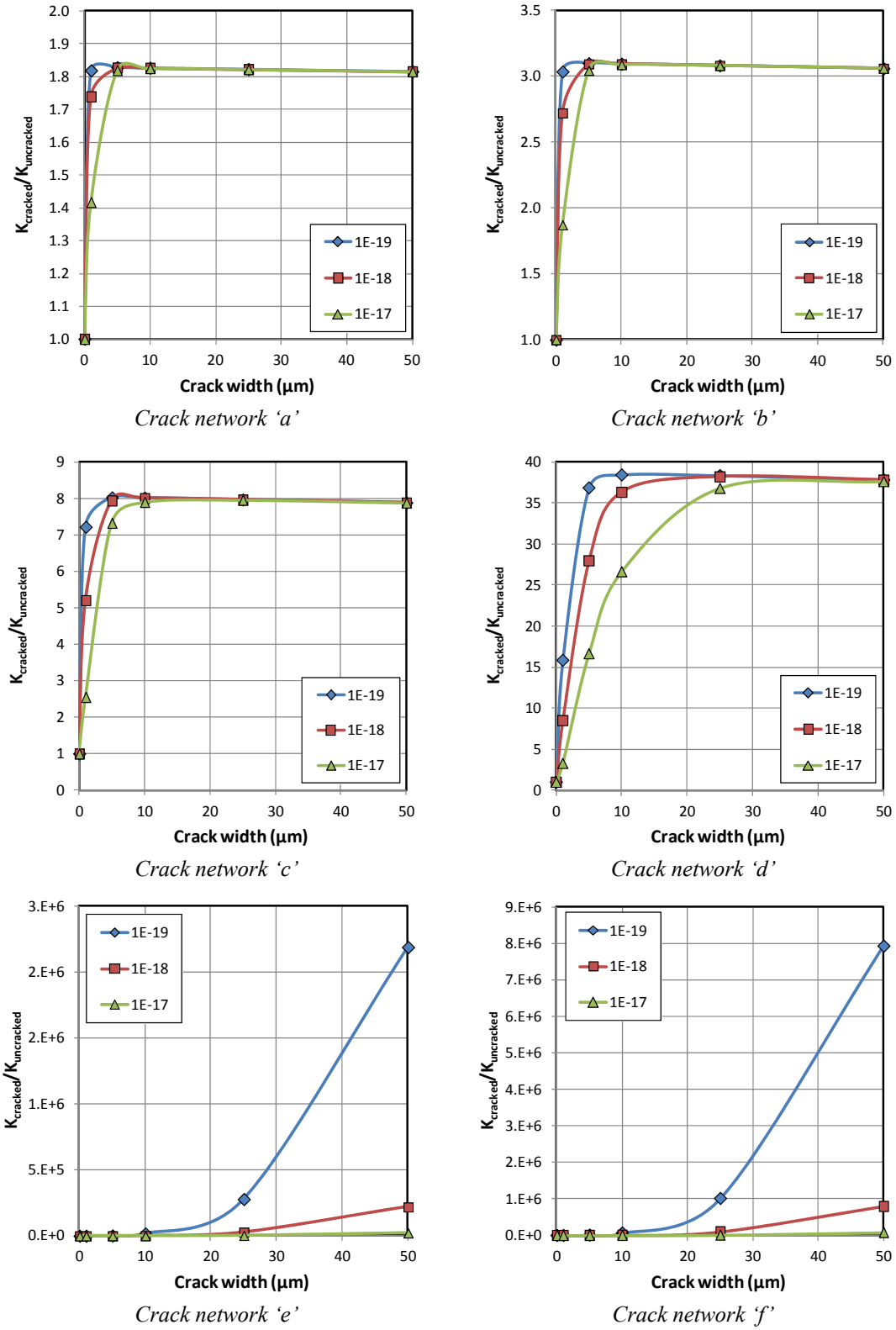

Figure 4 Effect of crack width on permeability of concrete with different crack patterns. Simulations were carried out assuming that the permeability of the uncracked concrete is either 1E-19, 1E-18 or 1E-17 m^2.

Results show that the effect of microcracking is more pronounced for materials with a denser matrix such as concretes with low water to cement ratio or high degree of hydration. These materials would have higher diffusivity contrast ratios and lower permeability in the uncracked state. Moreover, it can be seen that the effect of microcracks for non-percolated crack networks (a, b, c and d) always increases up to a finite limit with the increase in crack width. The value of the finite limit depends on the characteristics of the crack network and material properties. This finite limit exists for non-percolated crack networks because flux has to cross the uncracked cement paste matrix. The effective transport property does not increase beyond a certain crack width as it is governed by the transport property of the uncracked paste matrix. However, a slight decrease in permeability is observed for crack widths > 5 μm in Figure 4 (a to d). This is an artefact of the model that arises from the use of two-dimensional Darcy's law (Eq. 3) to calculate flux through the crack, causing an underestimation of transport property. The actual flux is three-dimensional, and the neglected component is in the direction of the crack width (i.e. perpendicular to crack surface). Although this component is small for microcracks, it increases with crack width and therefore the error of the underestimation increases.

For percolated crack networks (e and f), the transport property increases continuously with increase in crack width as expected. Increasing crack specific surface area increases the equivalent diffusivity and permeability for both non-percolated and percolated crack networks. This is because at higher specific surface area, there are more cracks present and the distance that the diffusing species has to travel across the matrix is decreased. However, it is interesting to note that the increase in diffusivity due to percolation (from crack network d to e) is very modest compared to that for permeability. The effect of percolation can be observed from the sudden increase in permeability for crack network 'd' and 'e'. This is more significant for denser matrix and for higher crack widths.

CONCLUSIONS

The effect of microcracks on diffusivity and permeability is more pronounced for concretes with denser matrix. In non-percolated crack network, microcracks increases bulk transport property up to a finite limit, the value of which is independent of crack width but depends on other crack characteristics and the transport property of the uncracked matrix. Transport property then remains relatively constant with increase in microcracks until percolation occurs. In all cases, the presence of microcracks has a greater effect on permeation compared to diffusion and this is more pronounced for percolated crack networks.

ACKNOWLEDGEMENTS

The research leading to these results has received funding from the European Union Seventh Framework Programme (FP7 / 2007-2013) under grant agreement 264448.

REFERENCES

Aldea, C. M., Shah, S. P., Karr, A. (1999). "Permeability of cracked concrete." *Mater. Struct.,* 32**,** 370-376.

Akhavan, A., Shafaatian, S.-M.-H., Rajabipour, F. (2012). "Quantifying the effects of crack width, tortuosity, and roughness on water permeability of cracked mortars." *Cem. Concr. Res.,* 42**,** 313-320.

Bisschop, J., van Mier, J.G.M. (2002). "Effect of aggregates on drying shrinkage microcracking in cement-based composites", *Mater. Struct.* 35, 453–461.

Djerbi Tegguer, A., Bonnet, S., Khelidj, A. & Baroghel-Bouny, V. (2013). "Effect of uniaxial compressive loading on gas permeability and chloride diffusion coefficient of concrete and their relationship." *Cem. Concr. Res.,* 52**,** 131-139.

Abyaneh, S.D., Wong, H.S., Buenfeld, N.R. (2013). "Modelling the diffusivity of mortar and concrete using a three-dimensional mesostructure with several aggregate shapes", *Computational Materials Science*, 78, 63-73.

Gérard, B. & Marchand, J. (2000). "Influence of cracking on the diffusion properties of cement-based materials: Part I: Influence of continuous cracks on the steady-state regime." *Cem Concr Res,* 30**,** 37-43.

Gérard, B., Reinhardt, H. W. & Breysse, D. (1997). "Measured transport in cracked concrete." *In:* Reinhardt, H. W. (ed.) *RILEM Report 16: Penetration and Permeability of Concrete: Barriers to Organic and Contaminating Liquids.* London.

Goltermann, P. (1994). "Mechanical predictions on concrete deterioration. Part 1: eigenstresses in concrete." *ACI Materials Journal,* 91**,** 543-550.

P. Grassl, H.S. Wong, N.R. Buenfeld (2010), "Influence of aggregate size and volume fraction on shrinkage induced micro-cracking of concrete and mortar." *Cem. Concr. Res.* 40, 85–93.

A. Idiart, J. Bisschop, A. Caballero, P. Lura (2012). "A numerical and experimental study of aggregate-induced shrinkage cracking in cementitious composites." *Cem. Concr. Res.* 42, 272–281.

Jang, S. Y., Kim, B. S. & Oh, B. H. (2011). "Effect of crack width on chloride diffusion coefficients of concrete by steady-state migration tests." *Cem. Concr. Res.* 41**,** 9-19.

Kamali-Bernard, S. & Bernard, F. (2009). "Effect of tensile cracking on diffusivity of mortar: 3D numerical modelling." *Computational Materials Science,* 47**,** 178-185.

Picandet, V., Khelidj, A. & Bellegou, H. (2009). "Crack effects on gas and water permeability of concretes". *Cem. Concr. Res.,* 39**,** 537-547.

Stauffer, D. (1985), *Introduction to Percolation Theory*, Taylor & Francis, London.

Wang, K. J., Jansen, D. C., Shah, S. P. & Karr, A. F. (1997). "Permeability study of cracked concrete." *Cem. Concr. Res.* 27**,** 381-393.

Wong, H. S., Zobel, M., Buenfeld, N. R. & Zimmerman, R. W. (2009). "Influence of the interfacial transition zone and microcracking on the diffusivity, permeability and sorptivity of cement-based materials after drying". *Magazine of Concrete Research,* 61**,** 571-589.

Grassl, P., Wong, H. S. & Buenfeld, N. R. (2010). "Influence of aggregate size and volume fraction on shrinkage induced micro-cracking of concrete and mortar." *Cem. Concr. Res.,* 40**,** 85-93.

Wu, Z., Wong, H. S. & Buenfeld, N. R. (2015). "Influence of drying-induced microcracking and related size effects on mass transport properties of concrete." *Cem. Concr. Res.,* 68**,** 35-48.

Prediction of the Cracking Effect on Mass Penetration into Unsaturated Concrete

L. C. Wang[1] and J. W. Bao[1]

[1]State Key Laboratory of Coastal and Offshore Engineering, Dalian University of Technology, Dalian, China. E-mail: wanglich@dlut.edu.cn

Abstract

Cracking of concrete, which may induced by environmental action or mechanical loading, has been identified as one of the major factors controlling the long-term performance of concrete structures because it can provide preferential pathways for the ingress agents (e.g. water or chloride ions). In the current work, the transport coefficients of water and chloride through a single crack are developed by treating it as a parallel-plate configuration. The physical migration models coupled with capillary absorption and convection-diffusion are utilized to predict water penetration and chloride ingress into cracked concrete. By means of the mesoscale computational method that concrete is modeled as a composite of impermeable coarse aggregate embedded in the porous matrix separated by vulnerable interfacial transition zone, the lattice network model is presented to investigate water and chloride transport properties in cracked concrete. The influence of cracking and the actual saturation level on the transport process of water and chlorides are investigated numerically. The numerical results indicated that the computational method is able to well represent the mass movement within cracked concrete. The effect of saturation level and cracks on water and chloride transport process is of great importance.

INTRODUCTION

Mass transport process in unsaturated concrete implies a complex interaction between the nonlinear dynamic phenomena and physical-chemical process, which is to a large extent dependent on the internal pore-structure of concrete, environmental condition, temperature, water saturation level, etc (Ababneh *et al*. 2003; Bastidas-Arteaga *et al*. 2011; Climent *et al*. 2002; Saetta *et al*. 1993). For concrete structures during the service life, cracks or microcracks always occur in concrete due to external loading and environmental action, which turn concrete materials from continuous media to discrete ones so as to change the mass transport processes (Aldea *et al.* 1999; Bentz *et al.* 2013; Boulfiza *et al*. 2003; Djerbi 2008; Ishida *et al.* 2009; Kato *et al.* 2005; Yang *et al.* 2006). Therefore, the degradation of mechanical properties and durability is related intimately to the initiation and propagation of cracks. To clarify the deterioration mechanism and predict the life-cycle performance of concrete structures, it is essential to conduct prediction of cracking effect on mass penetration into unsaturated concrete.

In terms of the characteristic of internal structure of concrete, numerical analysis of mass transport in concrete by mesoscale method, in which concrete is

described as a three-phase composite consisting of the coarse aggregate, hardened cement mortar and the interfacial transition zone between aggregate and mortar, not only may enhance understanding of the non-homogeneous characteristic of concrete but also can represent influence of material composition and cracking on transport properties. Principally, there are two groups of approaches within the finite element framework to account for the cracking effect on mass transport in concrete: (i) smeared approaches, which describe the increase of diffusivity of concrete by a damage variable in the cracked area (Ozbolt *et al.* 2010), and (ii) discrete approaches, in which the crack is explicitly represented by two surfaces with flow occurring between the surfaces, and an exchange of water and chloride ions is allowed between the crack and surrounding bulk concrete (Boulfiza 2003; Grassl 2009; Šavija *et al.* 2014; Wang and Ueda 2011a). On the basis of Voronoi tessellation, the lattice network model, which can be categorized to the second group, is presented to investigate the influence of cracking on transport properties of concrete.

This paper focuses on developing the 2D numerical mesoscale method that could systematically investigate the mass transport of concrete by coupling with capillary absorption of water and diffusion-convection of chloride, including the influence of crack obtained by Rigid Body Spring Model (RBSM) and the saturation degree of concrete. The objective lies on determination of the distribution of water content and chloride profiles within concrete samples.

MASS PENETRATION MODELS IN CRACKED CONCRETE

Water Penetration by Capillary Absorption Action

Unsaturated flow theory, which is commonly adopted to describe water uptake in soil, can also be utilized to explain water transport of porous concrete (Hall 1989, 2007; Leech *et al.* 2003; Lockington 1993). Capillary absorption has been the main transport mechanism in unsaturated or partially saturated concrete. For a 1D semi-infinite system, the governing equation can be presented as follows (Carpenter *et al.* 1993; Goual *et al.* 2000; Hall 1989; Wang and Ueda 2011b):

$$\frac{\partial \theta}{\partial t} = \frac{\partial}{\partial x}\left(D_w(\theta) \frac{\partial \theta}{\partial x} \right) \tag{1}$$

where x is the distance from the exposed surface; t is the absorption time; dimensionless variable θ is the normalized water content, scaled to be zero and one for the initial and saturated volumetric water content (i.e. volume of water/bulk volume of concrete), Θ_i and Θ_s, respectively. Thus θ can be written as $\theta=(\Theta-\Theta_i)/(\Theta_s-\Theta_i)$, in which Θ is the volumetric water content under any state, ranging between Θ_i and Θ_s; $D_w(\theta)$ is a material property, generally called the hydraulic diffusivity with dimensions $\mathbf{L^2T^{-1}}$. Because the functional relationship between D_w and θ is strongly non-linear and is not always feasible to be determined, for uncracked concrete, it is often approximated by the exponential-law, $D_w(\theta)=D_0 e^{n\theta}$.

In terms of the coupling of the unsaturated flow theory and the cubic law of water through a single crack, the diffusivities of mass transport in crack are developed by treating crack as a parallel-plate configuration. If the crack is treated as

a straight, smooth and parallel surface and the extended Darcy law is still applied, the Navier-Stokes equation can be used to describe the water transport process through a single crack (see Figure 1) (Zhou 2007).

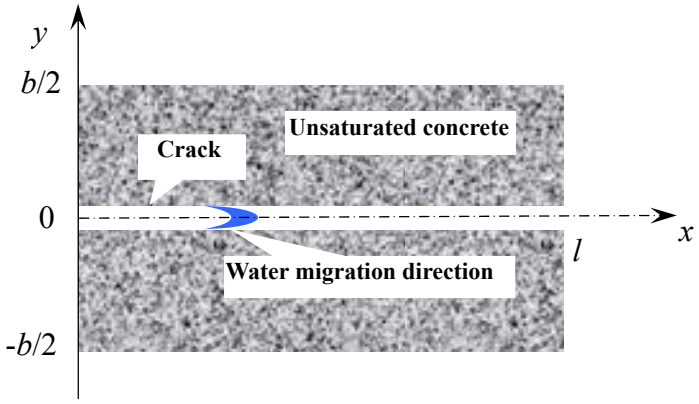

Figure 1. Diagram of water flow in crack of concrete

According to the definition formula of hydraulic diffusivity, $D_w(\theta)=-K(\theta)(\partial p_c/\partial\theta)$, the water diffusivity in a single crack with respect of the width can be written as

$$D_w^{cr}(\theta) = -K_{cr}(\theta)\cdot\frac{dp_c}{d\theta} = -\frac{k_r(\theta)}{\mu}\cdot k_s^{cr}\cdot\frac{dp_c}{d\theta}$$
$$= \frac{w_h^3}{12\mu l}\frac{p_r(1-m)}{m}\sqrt{\theta}\left[1-\left(1-\theta^{1/m}\right)^m\right]^2\theta^{-1/m-1}(\theta^{-1/m}-1)^{-m} \quad (2)$$

where $K(\theta)$ is the hydraulic conductivity function; p_c is capillary pressure; k_s^{cr} is the crack permeability under saturated condition with dimension $\mathbf{L}^2$; w_h is the equivalent width of a single crack; l is the crack length; μ is the viscous coefficient of water; p_r is the reference pressure, experimentally determined as 18.6237 N/mm^2 and the Van-Genuchten parameter m=0.4396 (Meschke and Grasberger 2003).

Chloride Penetration by Convection-Diffusion Action

For the unsaturated-cracked concrete, chloride transport process is very complex and mainly consists of diffusion, convection and electro-migration (usually neglected) (Ababneh *et al.* 2003; Saetta *et al.* 1993). In terms of convection suction, the driving force is mainly capillary absorption due to capillary pressure gradient. Therefore, the chloride transport process in unsaturated concrete can be described as

$$\frac{\partial C_t}{\partial t} = \underbrace{\frac{\partial}{\partial x}\left(D_{cl}(\theta)\frac{\partial C_f}{\partial x}\right)}_{\text{diffusion}} + \underbrace{C_f\frac{\partial}{\partial x}\left(D_w(\theta)\frac{\partial\theta}{\partial x}\right)}_{\text{convection}} \quad (3)$$

in which C_t=C_f+C_b, is the total chloride concentration, representing the sum of free concentration C_f and bound chloride concentration C_b (De Vera *et al.* 2007; Ishida *et al.* 2009). $D_{cl}(\theta)$ is chloride diffusivity in unsaturated state as follows:

$$D_{cl}(\theta) = D_{cl}\left(1+\frac{(1-\theta)^4}{(1-\theta_c)^4}\right)^{-1} \tag{4}$$

where θ_c is the critical relative water content and set as 0.83 (Nielsen and Geiker 2003); When cracks exit, the chloride diffusivity in saturated state (D_{cl}), which can be obtained by the rapid migration test (Nagesh and Bhattacharjee 1998; Care and Herve 2004; Otsuki *et al.* 2004), will be replaced by chloride diffusivity of a crack in saturated state (D_{cl}^{cr}). Djerbi (2008) suggested that the chloride diffusion coefficient as a function of crack width w_{cr}, D_{cl}^{cr}(m^2/s), can be expressed as

$$D_{cl}^{cr} = \begin{cases} 2\times10^{-11}w_{cr} - 4\times10^{-10} & (30\mu\text{m} \le w_{cr} \le 80\mu\text{m}) \\ 14\times10^{-10} & (w_{cr} \ge 80\mu\text{m}) \end{cases} \tag{5}$$

By using two sets of experiments performed by Ismail *et al.* (2004, 2008), in which the materials used are respectively brick and mortar, Šavija *et al.* (2013) obtained the value of D_{cl}^{cr} by the trial and error method. After validating the accuracy of values in the same method by comparing with cracked mortar, the value of D_{cl}^{cr} in brick was overestimated compared with that of the mortar. It was attributed to the crack nature of brittle and homogeneous brick material which has less crack branching and more pore structure. However, their results obtained by using Equation 5 were in well agreement with the test data of mortar sample. Therefore, in the current paper, Equation 5 is used to represent the chloride diffusivity within cracks under the saturated state.

ANALYTICAL METHOD AND APPLICATION

Mesoscale Lattice Network Model of Cracked Concrete

The mechanical analysis on the Voronoi diagram has been widely carried out in some previous works (Bolander *et al.* 1998). Grassl *et al.* (2009) and Šavija *et al.* (2013) used the Voronoi tessellation as lattices to describe mass transport and the dual Delaunay triangles to reflect mechanical response. A more detailed description of their models can be found in their publications. As has been stated, there are two groups of numerical strategies above-mentioned for representing the effect of cracks: smeared and discrete cracking. From the viewpoint of examining the influence such crack parameters as width and length, the discrete cracking approach is more appropriate. By connecting the centres of Voronoi cells and the intermediate nodes on their boundaries (see Figure 2), a network consisting of lines (or lattices) is generated. This lattice network can alter a 2D transport problem to a 1D process because the mass transporting through an area is idealized as a process moving through a conductive pipe.

Cracks are supposed to be present on the boundary of Voronoi cells, especially ITZ elements. These boundary lattices are formed to simulate the influence of potential occurrence of cracks because as stated above, cracks only appear on the boundaries of Voronoi cells. For a crack with width of w_{cr}, the sectional area of its corresponding lattice is determined as wcrt0 and its diffusivity has been discussed in the above sections. Here, t_0 is the out-of-plane thickness of the element assuming a rectangular cross-section. Obviously, for the sound or uncracked specimen, the sectional area and diffusivity of the boundary lattices are all set as zero except those on the ITZ (double dotted lines in Figure 2), which have their specific area and diffusivity even before cracking.

The outstanding advantage of this model is that it can realistically account for the physical process of flow through a single crack. For example, assuming a crack to occur on *mn*, the flow (water or chloride ions) will transport along it at very fast speed and can also penetrate into the bulk mortar by the lattices of *ji* and *jk*. Therefore the 2D transport process of a crack is well represented.

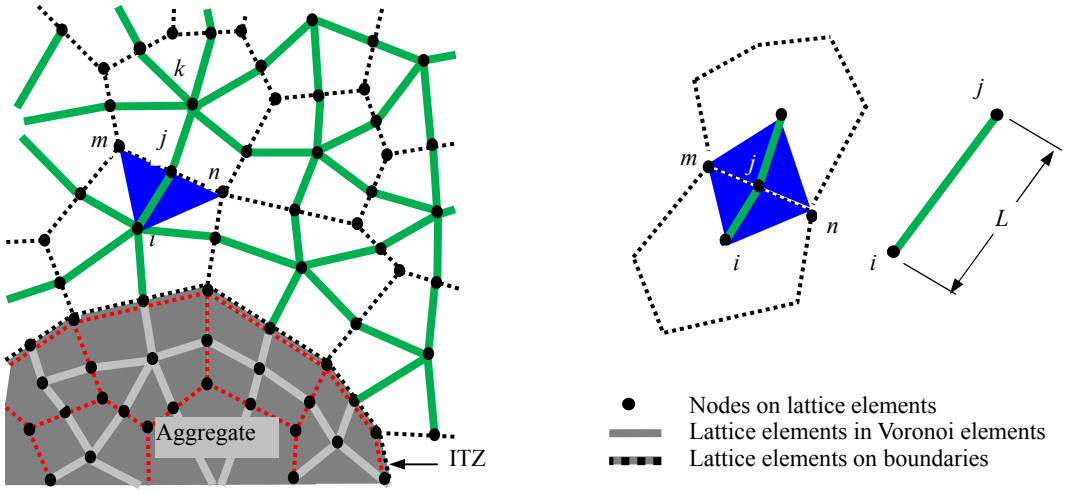

Figure 2. Schematic diagram of the lattice network model

Validation of Models

In the experiment carried out by neutron radiography technology (Zhang *et al.* 2010) on the cracked samples, *w/c* of the mortar specimens was 0.6 and the mix proportion of 1:3.3:0.6 cement/sand/water by volume was used. The specimens were used to generate a single crack with width of 0.35 mm and depth of 75 mm by three-point bending load. The comparisons of the penetration distributions of water along both vertical and horizontal directions of the crack between the calculation results and test data after the elapsed time of 60min and 120min are depicted in Figure 3. It can be observed that at the same 50mm-height position of the specimen, the relative water content from the test along the horizontal direction is slightly greater than that obtained from the numerical calculation. This deviation is attributed to the microcracks generated on the interface between steel bars and concrete when the lateral crack is induced in the experimental specimens. On the position of steel bars,

the water distribution perpendicular to the crack direction is obviously observed and indicated by the two "rings" along the crack (see Figure 3b).

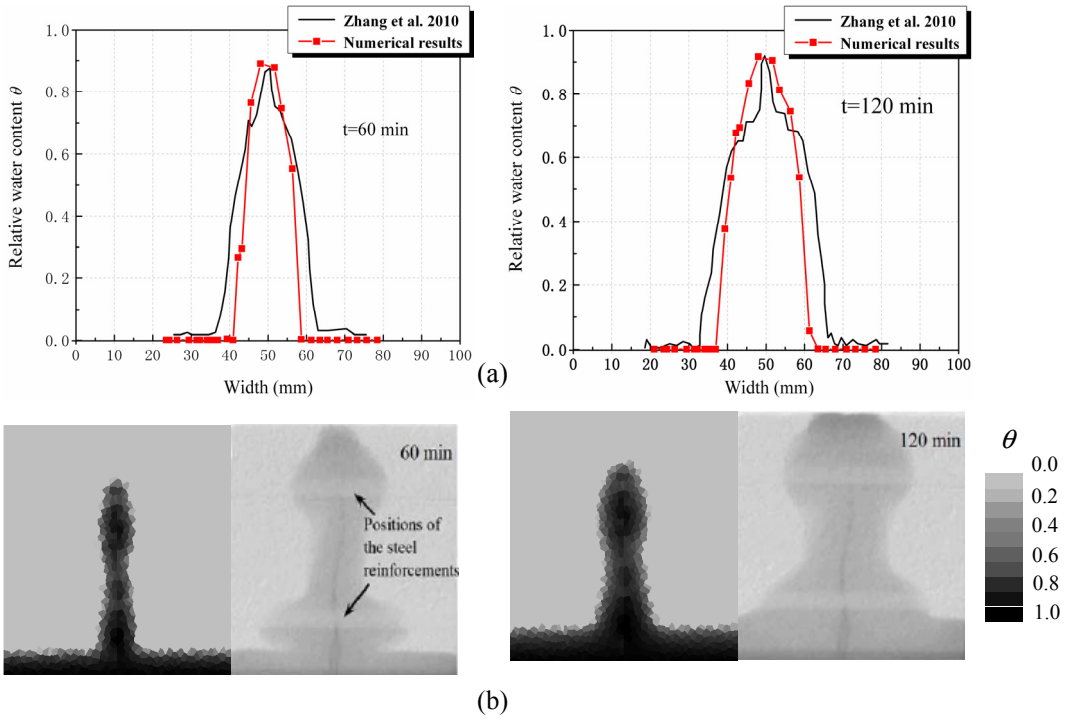

Figure 3. Comparison of water content between the numerical results and test data

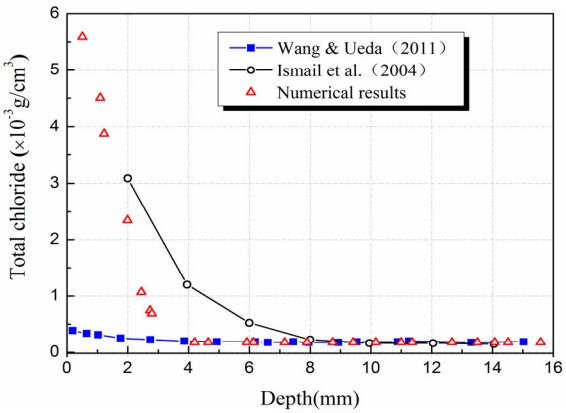

Figure 4. Chloride profiles perpendicular to the crack surface

The same model is used here to examine the effect of cracking on chloride ingress. The surface chloride concentration C_s is determined as 7.68×10^{-3}g/cm^3 based on test result (Ismail *et al.* 2004). When only diffusion process was considered and the diffusion coefficient through crack was set as a constant (equaling to the diffusivity in free water), Wang & Ueda (2011a) have found that the chloride profiles perpendicular-to-crack obtained by numerical analysis deviate much from those in test. According to the findings of Šavija *et al.* (2013), the brick specimens might have

not been fully saturated when the experiment begun. Thereafter, the capillary suction would play a significant role. From Figure 4, although the numerical results are still slightly less than brick's test data, compared with the case of only diffusion process (results of Wang & Ueda (2011a)), it exhibits better prediction. Similarly, Ishida *et al.* (2009) stated that mass transport in the crack spaces may be driven not only by concentration gradient of ions, but also by convection current due to the small temperature gradient and/or hydraulic pressure gradient. It reasonably demonstrates that the model of water diffusivity in a single crack, $D_w^{cr}(\theta)$, is feasible.

Analysis of model parameters

Initial relative water content θ_0 As stated above, the hydraulic diffusivity D for the sound or cracked concrete is expressed as a function of relative water content θ. Thus, the initial relative water content in concrete may influence the mass transport and distribution. The sound unsaturated concrete has been discussed above, in this part a single crack with the width of 0.2 mm and depth of 25 mm in the middle of model specimen, which is meshed by Voronoi tessellation and developed into lattice conduit elements, is adopted to predict water content distribution in the crack (see Figure 5). To further illustrate this phenomenon, three relative initial water contents for the specimen are selected, i.e., θ_0=0.1, 0.3 and 0.5 respectively. The results show the effect of different initial water content on water penetration through a single crack in Figure 6. The water content in crack itself is obviously higher than that in uncracked zone. Moreover, after the elapsed 24 hours, the relative water content drops rather sharply around 22 mm depth for all of three cases, which suggests the difference of flow rate and transport mechanism between the crack and uncracked zone.

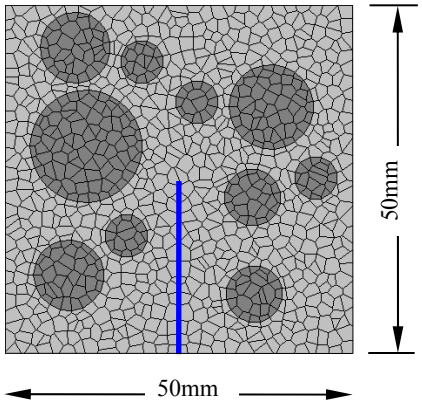

Figure 5. Calculation model for the effect of initial water content

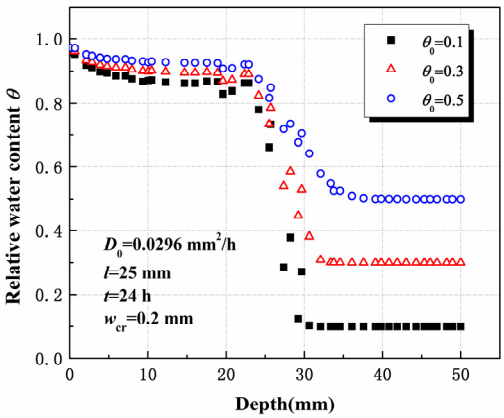

Figure 6. Profiles of water content with different initial water contents

Crack width w_{cr} In the previous experimental programs, the cracks with widths ranging from 0.02 to 0.68 mm were created by saw-cutting or mechanically loading the concrete specimens (splitting tensile test or expanding test) (Ismail *et al.* 2004; Aldea *et al.* 1999; Rodriguez & Hooton 2003). In present study, the concrete model of a single transverse crack with different crack widths and the diffusivity in crack

(Equation 2) are utilized to numerically investigate the effect of crack width on the water movement (see Figure 7). As shown in Figure 8, the relative water content and penetration depth do not increase with an increase of crack width up to about 50 μm. Over 50 μm in crack width, however, water movement in crack obviously speeds up so that the water content and depth start to increase. This value may be called as the threshold crack width for water passing through the transverse crack, which was same as the permeation found by Wang *et al* (1997).

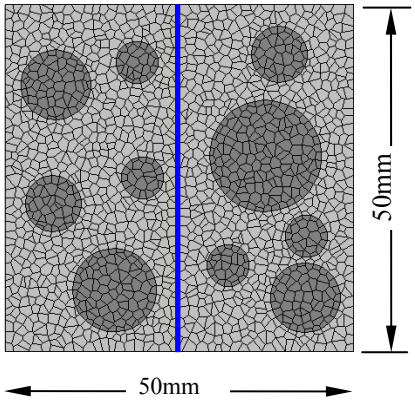

Figure 7. Model for the effect of crack width

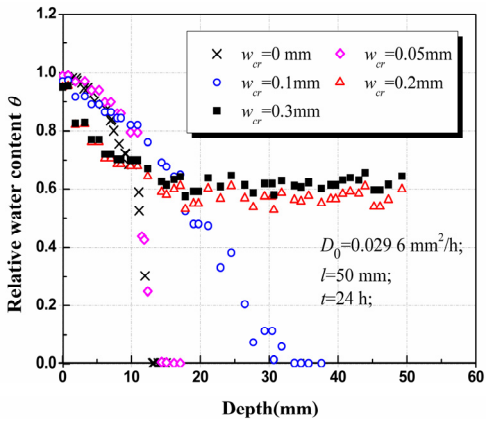

Figure 8. Water content distribution within different crack widths

CONCLUSIONS

In the present paper, an attempt has been made to address the effect of cracking and saturation degree on water and chloride transport process by coupling the mesoscale lattice network and mass transport models. The following conclusions can be drawn:

A 2D model for water and chlorides transport in cracked-unsaturated concrete is presented on the basis of the mesoscale structure of concrete and the corresponding lattice network. The unsaturated flow theory for capillary water absorption and chloride transport is coupled with the cubic law of mass transport through a single crack. The diffusivities of mass transport in the single crack are reasonably developed by treating it as a parallel-plate configuration. The comparison with existing experiment results of cracked specimens validates the feasibility of the models.

The effects of initial relative water content and crack width are illustrated in terms of the proposed mesoscale lattice network model, which show significant influence on the water distribution. The relative water content and penetration depth do not increase with an increase of crack width up to about 50 μm, but obviously speeds up over 50 μm crack width.

ACKNOWLEDGEMENT

This study was supported by the National Natural Science Foundation of China (Grant No. 51378090) and the National Key Basic Research Program of China (973 Program) (No. 2015CB057703; 2015CB057701).

REFERENCES

Ababneh, A., Benboudjema, F., and Xi, Y. P. (2003). "Chloride penetration in nonsaturated concrete." *J. Mater. Civil Eng.*, 15(2), 183-191.

Aldea, C. M., Shah, S. P. and Karr, A. (1999). "Effect of cracking on water and chloride permeability of concrete." *J. Mater. Civil Eng.*, 11(3), 181-187.

Bastidas-Arteaga, E., Chateauneuf, A., and Sanchez-Silva, M., et al. (2011). "A comprehensive probabilistic model of chloride ingress in unsaturated concrete." *Eng. Struct*., 33(3), 720-730.

Bentz, D. P., Garboczi, E. J. and Lu, Y. et al. (2013). "Modeling of the influence of transverse cracking on chloride penetration into concrete." *Cem. Concr. Comp.*, 38, 65-74.

Bolander, J. E. and Saito, S. (1998). "Fracture analyses using spring networks with random geometry." *Eng. Fract. Mech.* 61(5), 569-591.

Boulfiza, M., Sakai, K., and Banthia, N., *et al*. (2003). "Prediction of chloride ions ingress in uncracked and cracked concrete." *ACI Mater. J.*, 100(1), 38-48.

Care, S. and Herve, E. (2004). "Application of a n-phase model of the diffusion coefficient of chloride in mortar." *Trans. in Porous Media*, 56(2), 119-135.

Carpenter, T. A., Davies, E. S. and Hall C. et al. (1993). "Capillary water migration in rock: process and material properties examined by NMR imaging." *Mater. Struct.* 26(5), 286-292.

Climent, M. A., De Vera, G. and Lopez, J. F. et al. (2002). "A test method for measuring chloride diffusion coefficients through nonsaturated concrete Part I. The instantaneous plane source diffusion case." *Cem. Concr. Res.*, 32(7), 1113-1123.

De Vera, G., Climent, M. A. and Viqueira, E. et al. (2007). "A test method for measuring chloride diffusion coefficients through partially saturated concrete. Part II: The instantaneous plane source diffusion case with chloride binding consideration." *Cem. Concr. Res.* 37(5), 714-724.

Djerbi, A. (2008). "Influence of traversing crack on chloride diffusion into concrete." *Cem. Concr. Res.*, 38(6), 877-883.

Goual, M.S., De Barquin, F. & Benmalek, M.L. *et al.* (2000). "Estimation of the capillary transport coefficient of clayey aerated concrete using a gravimetric technique." *Cem. Concr. Res.*, 30(10), 1559-1563.

Grassl, P. (2009). "A lattice approach to model flow in cracked concrete." *Cem. Concr. Comp.*, 31(7), 454-460.

Hall, C. (1989). "Water sorptivity of mortars and concretes: a review." *Mag. Concr. Res.*, 41(147), 51-61.

Hall, C. (2007). "Anomalous diffusion in unsaturated flow: Fact or fiction?" *Cem. Concr. Res.*, 37(3): 378-385.

Ishida, T., Iqbal, P. O. N. and Anh, H. T. L. (2009). "Modeling of chloride diffusivity coupled with non-linear binding capacity in sound and cracked concrete." *Cem. Concr. Res.*, 39(10): 913-923.

Ismail, M., Toumia, A. and Francois, R. *et al.* (2004). "Effect of crack opening on the local diffusion of chloride in inert materials." *Cem. Concr. Res.* 34(4), 711-716.

Ismail, M., Toumia, A., & Francois, R. *et al.* (2008). "Effect of crack opening on the local diffusion of chloride in cracked mortar materials." *Cem. Concr. Res.*, 38(8/9), 1106-1111.

Kato, E., Kato, Y. & Uomoto, T. (2005). "Development of simulation model of chloride ion transportation in cracked concrete." *J. of Adv. Concr. Tech.*, 3(1): 85-94.

Leech, C., Lockington, D. & Dux, P. (2003). "Unsaturated diffusivity functions for concrete derived from NMR images." *Mater. Struct.*, 36(6), 413-418.

Lockington, D. (1993). “Estimating the sorptivity for a wide range of diffusivity dependence on water content.” *Transport in Porous Media*, 10(1), 95-101.

Meschke, G. and Grasberger, S. (2003). “Numerical modeling of coupled hygromechanical degradation of cementitious materials.” *J. Eng. Mech.*, 129(4), 383-392.

Nagesh, M. and Bhattacharjee, B. (1998). “Modelling of chloride diffusion in concrete and determination of diffusion coefficients.” *ACI Mater. J.*, 95(2), 113-120.

Nielsen, E. and Geiker, M. R. (2003). “Chloride diffusion in partially saturated cementitious material.” *Cem. Concr. Res.*, 33(1), 133-138.

Otsuki, N., Yodsudjai, W. and Nishida, H. *et al.* (2004). “New test the methods for measuring strength and chloride ion diffusion coefficient of minute regions in concrete.” *ACI Mater. J.*, 101(2), 146-153.

Ozbolt, J., Balabanic, G. and Periskic, G. *et al.* (2010). “Modeling the effect of damage on transport processes in concrete.” *Constr. Build. Mater.*, 24(9), 1638-1648.

Rodriguez, O. G. and Hooton, R. D. (2003). “Influence of cracks on chloride ingress into concrete.” *ACI Mater. J.*, 100(2), 120-126.

Saetta, A. V. Scotta, R. V. and Vitaliani, R. V. (1993). “Analysis of chloride diffusion into partially saturated concrete.” *ACI Mater. J.*, 90(5), 441-451.

Šavija, B., Pacheco, J. and Schlangen, E. (2013). “Lattice modeling of chloride diffusion in sound and cracked concrete.” *Cem. Concr. Comp.*, 42, 30-40.

Šavija, B., Luković, M. and Schlangen, E. (2014). “Lattice modeling of rapid chloride migration in concrete.” *Cem. Concr. Res.*, 61, 49-63.

Wang, K., Jansen, D. C. and Shah, S. P. (1997). “Permeability study of cracked concrete.” *Cem. Concr. Res.*, 27(3), 181-393.

Wang, L. C. and Ueda, T. (2011a). “Mesoscale modeling of the chloride diffusion in cracks and cracked concrete.” *J. Adv. Concr. Tech.*, 9(3), 241-249.

Wang, L.C. and Ueda, T. (2011b). “Mesoscale modeling of water penetration into concrete by capillary absorption.” *Ocean Eng.*, 38(4), 519-528.

Wang, Z. M., Kwan, A. K. H. and Chan, H. C. (1999). “Mesoscopic study of concrete I: generation of random aggregate structure and finite element mesh.” *Comp. Struct.*, 70(5), 533-544.

Yang, Z., Weiss, W. J. and Olek, J. (2006). “Water transport in concrete damaged by tensile loading and freeze-thaw cycling.” *J. Mater. Civil Eng.*, 18(3), 424-434.

Zhang, P., Wittmann, F. H. and Zhao, T. *et al.* (2010). “Neutron imaging of water penetration into cracked steel reinforced concrete.” *Physica B: Condensed Matter*, 405(7), 1866-1871.

Zhou, Z. F. (2007). *Theroy on dynamics of fluid in fractured medium*. Beijing: Higher Education Press. (in Chinese)

A Continuum Coupled Thermo-Hygro Mechanical Time-Dependent Model for Concrete

A. D. Jefferson[1] and Adriana Chitez[1]

[1]Cardiff University School of Engineering, The Parade, Cardiff CF24 3AA, U.K. E-mail: JeffersonAD@Cardiff.ac.uk; ChitezAS1@Cardiff.ac.uk

Abstract

An overview of a recently developed thermo-hygro-mechanical-hydration model (THMH) model for concrete is presented. The coupled flow aspect of the model solves a mass balance equation for moisture and an enthalpy balance equation for heat transport. A key assumption used to simplify the moisture flow component of the model is that the gas pressure is assumed to remain constant at atmospheric pressure. The model simulates early age concrete behaviour and therefore a hydration component is included in the formulation. This uses the approach of Schindler & Folliard, which was based on a comprehensive range of data and gives good predictions for a range of cement types. The mechanical component of the model simulates the dependence of the strength and stiffness properties of the model on the degree of hydration. Furthermore, the plastic-damage-contact model of Jefferson and Mihai; which simulates cracking, crushing and crack closure; has been extended to include hydration dependent behaviour. The hydration sub-model is also linked to a new creep model. The paper includes an example of the analysis of beam RL1 from the Concrack benchmark programme. The focus of the work from this benchmark is the accurate prediction of crack widths in reinforced concrete elements and reference is made to a recent study that explored the accuracy of the present model in this context. A critique of the model is presented which concludes that the moisture flow component of the model would be greatly improved by including coupling between the flow parameters and mechanical damage.

1. INTRODUCTION

This subject of the paper is a finite element model for the thermo-hygro-mechanical behaviour of concrete that was applied to the international benchmarking exercise Concrack (Jefferson et al, 2014). The particular focus of the work was on the computation of crack patterns for a beam in which the full casting, curing and loading history was available. This contribution will provide an overview of the model and then give a critique which highlights certain short-comings and areas for future development.

The model allows for concrete hydration, hygro and heat transport as well as time dependent mechanical behaviour. The hygro-thermal component of the model was inspired by the work of Gawin et al. (2006) but in the present model only one fluid phase is considered rather than two. Cement hydration is simulated using Schindler & Folliard's (2005) approach. Their model provides an accurate means of

simulating the heat and degree of hydration for a range of cement types, and includes expressions for a number of commonly used cement replacement materials (e.g. GGBS, FA). Expressions for the dependence of the elastic constants and uniaxial strengths on the degree of hydration are similar to those given by de Schutter (2002). Within the overall model is embedded a new approach for computing creep, which accounts for the gradual hardening of the cementitious material. This uses the ideas from Bazant et al.'s (1997) solidification creep model but introduces the idea of two age related material states, relating to short and long term creep behaviour. The basic mechanical constitutive model is based on a new smoothed plastic-damage-contact model (Jefferson & Mihai, 2015).

2. MODEL THEORY

2.1. Basic mechanics constitutive model component

The constitutive is based on a recently developed smoothed plastic-damage-contact model for concrete developed by Jefferson and Mihai (2015). The basic stress-strain relationship employed in the model is as follows;

$$\boldsymbol{\sigma} = \mathbf{D}_e\left((\boldsymbol{\varepsilon}-\boldsymbol{\varepsilon}_p-\boldsymbol{\varepsilon}_{tm})-\sum_{j=1}^{n_p}\mathbf{N}_j{}^T\breve{\boldsymbol{\varepsilon}}_j\right) \quad (1)$$

where $\boldsymbol{\sigma}$ is the stress tensor (in vector form), $\boldsymbol{\varepsilon}$ is the strain vector, $\breve{\boldsymbol{\varepsilon}}$ denotes the fracture strains for crack j and n_p is the number of crack planes at an element integration point, $\mathbf{N}_j$ is the stress transformation matrix, $\boldsymbol{\varepsilon}_p$ is a plastic strain vector and $\boldsymbol{\varepsilon}_{tm}$ denotes all time dependent strains (i.e. from shrinkage, creep and thermal effects).

The fracture strains are derived from a local crack-plane constitutive model which splits the local stress tensor ($\tilde{\boldsymbol{\sigma}}$) into damaged (d) and an undamaged (u) components as shown below;

$$\tilde{\boldsymbol{\sigma}} = (1-\omega)\tilde{\boldsymbol{\sigma}}_u + \omega\tilde{\boldsymbol{\sigma}}_d \quad (2)$$

where ω ($\in[0,1]$) is a local damage parameter, which is different on each crack plane.

This damage parameter is a function of an effective local strain parameter ζ, which in turn is a function of the local strains ($\breve{\boldsymbol{\varepsilon}}$) (Jefferson and Mihai, 2015). Bazant and Oh's (1983) crack-band approach is used to regularise the model with respect to mesh grading.

2.1. Hydration dependent properties

The mechanical properties are assumed to vary with the degree of hydration. The basis of the expressions adopted is the work of de Schutter (2002), although it is noted that the definition used here for the relative degree of hydration (Γ_r) differs from that used by de Schutter for reasons explained in Jefferson et al. (2014);

The expressions adopted for Young's modulus (E), and for the uniaxial compressive (f_c) and tensile (f_t) strengths are given below;

$$E(\Gamma_r) = E_f\Gamma_r^{c_E} \quad (3)$$

$$f_c(\Gamma_r) = f_{c_f}\Gamma_r^{c_{fc}} \quad (4)$$

$$f_t(\Gamma_r) = f_{t_f}\Gamma_r^{c_{ft}} \quad (5)$$

where C_E=0.7, C_{fc}=1.5 and C_{ft}=1.

2.3. Creep and shrinkage

The creep model is based on the following three assumptions (Jefferson et al 2014):

(i) concrete exhibits both short term and long term creep behaviour; over time, the gradual packing of the CSH blocks (Jennings 2008) increases the proportion of the material associated with the latter;

(ii) material always hardens in a stress free (or fluid pressure) state, as per Bazant *et al.*'s (1997) solidification theory; and

(iii) material elemental volumes mature from the short term to the long term state without changing stress.

As in the original solidification theory, it is assumed that hardened material forms with the elastic properties of the fully cured concrete. The following equation is used for the creep stress-strain relationship;

$$\boldsymbol{\sigma} = (1-\mathrm{v})\sigma_{\mathrm{f}}\mathbf{I}_{\mathrm{m}} + \mathrm{v}\mathbf{D}_{\mathrm{e}}\left(\boldsymbol{\varepsilon} - \boldsymbol{\varepsilon}_{\mathrm{vsT}}\right) \tag{6}$$

$$\text{in which } \boldsymbol{\varepsilon}_{\mathrm{vsT}} = (1-\alpha)\left(\beta_{\mathrm{S}}\boldsymbol{\varepsilon}_{\mathrm{vS}} + \boldsymbol{\varepsilon}_{\mathrm{sS}}\right) + \alpha\sum_{\mathrm{j=1}}^{3}\beta_{\mathrm{L_j}}\left(\boldsymbol{\varepsilon}_{\mathrm{vL_j}} + \boldsymbol{\varepsilon}_{\mathrm{sL_j}}\right)$$

in which σ_f = wet concrete fluid pressure (always assumed to be 0 in the present work), $\mathbf{I}_{\mathrm{m}}$ is the vector denoting hydrostatic components, $v=\Gamma_r^{0.7}$ is the proportion of solidified material, α=proportion of long term material component, β_S=elastic proportion of short-term component, β_{Li}=the relative proportions of the long-term material components, $\boldsymbol{\varepsilon}_{\mathrm{v}\pi}$ are the viscous strains , $\boldsymbol{\varepsilon}_{\mathrm{s}\pi}$ are the solidification-aging strains and subscript π represents S (short-term) or L (long-term). It is noted that $\alpha \in [0,1]$, $\sum_{\mathrm{j=1}}^{3}\beta_{\mathrm{L_j}} = 1$ and that $\boldsymbol{\varepsilon}_{\mathrm{vL_3}} = \mathbf{0}$, since the third component of the long term component is elastic.

The β proportion factors are set to the following fixed values

$$\beta_{\mathrm{S}} = 0.85, \boldsymbol{\beta}_{\mathrm{L}} = \begin{bmatrix}0.2 & 0.2 & 0.6\end{bmatrix}^{\mathrm{T}} \tag{7}$$

The model does not aim to provide a fundamental set of expressions for creep but rather to use an established basic creep model, or experimental data, to predict the basic creep factor for a specimen loaded at 28 days(φ_{28}). The creep factor (φ) at time (t) is given by;

$$\varphi = \varphi_{28}\beta_{\mathrm{age}}(\mathrm{t})\frac{\mathrm{v}_{28}}{\mathrm{v}(\Gamma_{\mathrm{r}})}\mathrm{S}_{\mathrm{w}} \tag{8}$$

The proportion factor (α), used in equation (6), is given by

$$\alpha = \frac{1}{\beta_{\mathrm{L_3}} - (1-\beta_{\mathrm{S}})}\left[\frac{1}{1+\varphi} - (1-\beta_{\mathrm{S}})\right] \tag{9}$$

where S_w is the degree of saturation, $\beta_{age}(t)$ is based on the EC2 aging factor, but normalised to the 28 day value.

The shrinkage strain rate is computed using the following expression;

$$\dot{\varepsilon}_{\mathrm{sh}} = \left(\beta_{\mathrm{ds}}\dot{\mathrm{S}}_{\mathrm{w}} - \beta_{\mathrm{cs}}\dot{\Gamma}_{\mathrm{r}}\right)\Gamma_{\mathrm{r}} \tag{10}$$

It is noted that a 'degree of hydration' term has been added to the shrinkage rate equation for reasons explained in Jefferson et al (2014).

2.3. Hygro-Thermal (HT) model component

The mass balance equations for liquid water and water vapour are as follows;

$$\dot{\bar{\rho}}_w + \nabla\bullet\mathbf{J}_w = -\dot{m}_v - \dot{m}_h \tag{11}$$

$$\dot{\bar{\rho}}v + \nabla\bullet\mathbf{J}_v = \dot{m}_v \tag{12}$$

where $\dot{m}_v$ is the rate of mass transfer during evaporation of liquid water, $\dot{m}_h$ is the rate of change of liquid water mass due to hydration, $\overline{\rho_\pi} = nS_\pi\rho^\pi$ is the averaged density of the phase π (π = w or v), n is the capillary porosity of the medium, S_π is the degree of saturation of phase π, ρ^π is the bulk density of phase. The superior dot denotes the time derivative with respect to the solid skeleton and $\mathbf{J}_\pi$ denotes the mass flux of phase π.

The heat energy balance equation is as follows:

$$\overline{\rho C}\dot{T} + \nabla\bullet\mathbf{J}_T = -\dot{m}_v H_v + \dot{Q}_h \tag{13}$$

where, $\mathbf{J}_\mathrm{w}$ is the heat flux, T is the temperature of the medium, $\overline{\rho C_p} = \sum_\pi(\overline{\rho_\pi}C_p^\pi)$ is the thermal capacity, H_v is the specific enthalpy of evaporation and $\dot{Q}_h$ is the rate of heat generation of hydration. It is noted that m_v is eliminated by combining equations (11) and (12) into a single moisture mass-balance equation.

Use of a single moisture mass balance equation is made possible by assuming that the gas pressure is constant at atmospheric pressure. This results in a formulation in which capillary pressure (P_c) and temperature (T) are the primary variables. The HT model requires a set of standard constitutive equations (Gawin *et al*. 2006, Lewis and Schrefler 1998) which are given in full in Jefferson et al. (2014).

2.4. Hydration model component

The variation of the degree of hydration (Γ) is computed using the following expression due to Schindler & Folliard's (2005)

$$\Gamma(t_e) = \Gamma_\infty exp\left[-\left(\frac{\tau_{sf}}{t_e}\right)^{\beta_{sf}}\right] \tag{14}$$

in which w/c is the water cement ratio, the ultimate degree of hydration is given by $\Gamma_\infty = (1.031\cdot w/c)/(0.194 + w/c) + 0.5\cdot p_{FA} + 0.3\cdot p_{slag} \le 1.0$; τ_{sf} and β_{sf} are parameters which depend on the cement type and t_e is the effective time given by

$$t_e(T_r) = \sum_0^t \exp\left(\frac{A_E}{R}\left(\frac{1}{T_r} - \frac{1}{T}\right)\right)\cdot\Delta t\,,$$

T_r and T are reference (294K) and current temperatures in Kelvin respectively, A_E is the activation energy and R is the universal gas constant.

The rate of heat generation by the hydration process is predicted by the following equation;

$$Q_h(t) = H_u \cdot C_c \cdot \left(\frac{\tau}{t_e}\right)^{\beta_{sf}} \cdot \beta_{sf} \cdot \Gamma(t_e) \cdot \exp\left[\frac{E}{R}\left(\frac{1}{T_r} - \frac{1}{T}\right)\right] \quad (15)$$

The relative degree of hydration is defined as;

$$\Gamma_r = \Gamma / \Gamma_\infty \quad (16)$$

3. CONCRACK BENCHMARK

The Concrack benchmark RL1 is described in the CEOS (2015) web site. The benchmark considered here was named RL1 and is illustrated in Figure 1. Full details of this benchmark test are available on the project website (CEOS, 2015).

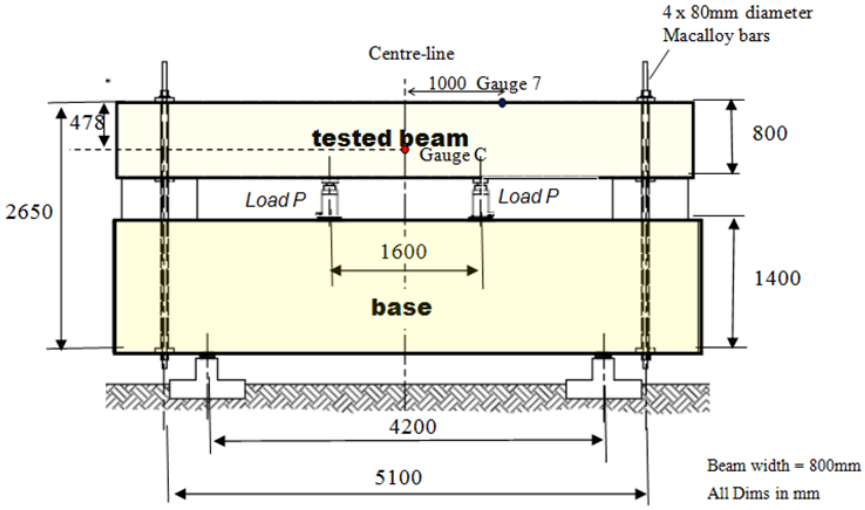

Figure 1. Details of the Concrack Benchmark RL1 (CEOS, 2015)

The benchmark beam has been analysed using the new model implemented in the finite element program LUSAS (www.LUSAS.com). Particular attention is focussed on predicting crack widths, and to this end, a comparison is provided between the numerical results and those obtained from the experiment in Figure 2 . The FE mesh showing crack widths is given in Figure 3. More details of the analysis and results may be found in Jefferson et al. (2014).

4. CRITIQUE

Many of the model components could be enhanced for improved accuracy but one particular short-coming is that the model currently assumes that the permeability and diffusion parameters remain constant. This ignores the fact that when damage occurs the permeability can greatly increase. This issue was investigated by Chatzigeorgiou et al. (2005), who proposed an approach for coupling between the damage and permeability of concrete by using lattice model.

Furthermore, a recent lattice model was developed by Grassl et al. (2015) to describe hydraulic fracturing. In their model fluid pressure and the mechanical response were coupled by using Biot's theory. The present authors believe that the combination of Grassl's recent approach and the model of Chatzigeorgiou et al. could be used to greatly improve the moisture modelling component of the present model.

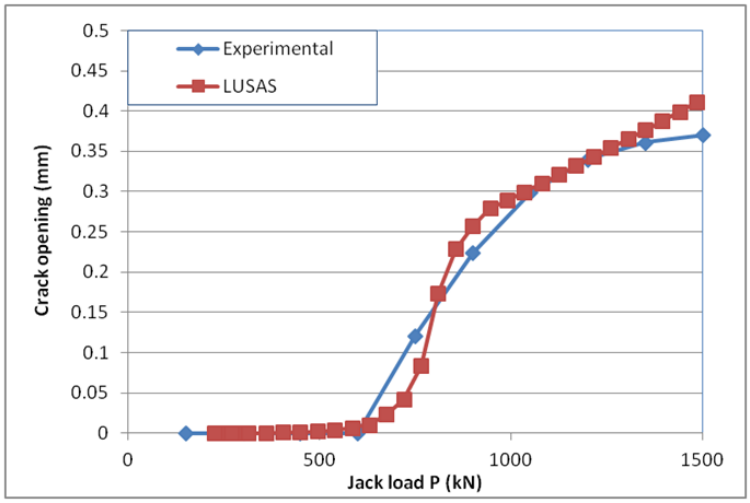

Figure 2. Crack width values versus load P

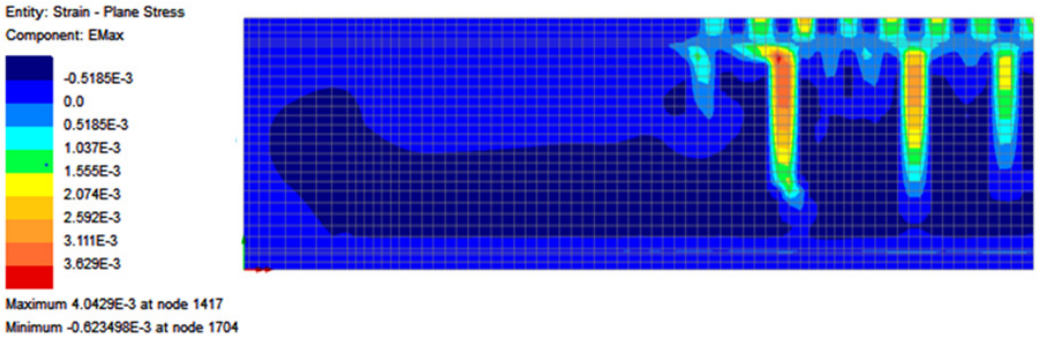

Figure 3. Localised strains at P=1000kN

5. CONCLUSIONS

The proposed model is able to simulate most of the important aspects of the thermo-hygro-mechnical and hydration behaviour of concrete, and is able to predict crack patterns with reasonable accuracy. One component of the model that is particularly lacking is a coupling between damage and the permeability parameters. A critique of the model leads to the conclusion that this aspect of the model could be improved by coupling the approaches of Chatzigeorgiou et al. (2005) and Grassl et al. (2015) and applying the resulting formulation to the present model.

REFERENCES

Bazant Z.P., Hauggaard A.B., Baweja S. and Ulm F-J. (1997). Microprestres-solidification theory for concrete. Creep. I: Ageing and Drying Effects. *ASCE Journal of Engineering Mechanics*, 1188-1194.

CEOS (2015). http://www.ceosfr.irex.asso.fr/en/. accessed 04/04/2015

Chatzigeorgiou G., PicandetV., Abdelhafid K. and Pijaudier-Cabot G. (2005). "Coupling between progressive damage and permeability of concrete: analysis with a discrete model". International Journal for Numerical and Analytical Methods in Geomechanics 29(10):1005 - 1018

De Schutter, G. (2002). Finite element simulation of thermal cracking in massive hardening concrete elements using degree of hydration based material laws. *Computers and Structures*, **80**, 2035-2042.

Gawin D., Pesavento F., Schrefler B.A. (2006). Hygro-thermo-chemo-mechanical Modelling of Concrete at Early Ages and Beyond. Part I: Hydration and Hygro-thermal Phenomena. *International Journal for Numerical Methods in Engineering*, **67**, 299-331.

Grassl P., Fahy C., Gallipoli D. and Wheeler S. J. (2015). "On a 2D hydro-mechanical lattice approach for modelling hydraulic fracture". Journal of the Mechanics and Physics of Solids. Vol. 75, pp. 104-118.

Jefferson A.D., Tenchev R., Chitez A., Mihai I, Coles G., Lyons P., Ou J. (2014). Finite element crack width computations with a thermo-hygro-mechanical-hydration model for concrete. European Journal of Environmental and Civil Engineering. 18(7) 793-813.

Jefferson A.D. and Mihai I.C. (2015). "The simulation of crack opening–closing and aggregate interlock behaviour in finite element concrete models" Int. J. Numer. Meth. Engng. DOI: 10.1002/nme.4934

Jennings H.M., (2008). Refinements to colloid model of C-S-H in cement: CM-II, *Cement and Concrete Research*, **38**, 275-289.

Schindler A.K. and Folliard K.J., (2005). Heat of hydration models for cementitious materials, *ACI Journal*, Feb 2005, 24-33.

Experimental and Numerical Study of Water Uptake in Strained SHCC

B. Šavija[1]; M. Luković[1]; and E. Schlangen[1]

[1]Microlab, Faculty of Civil Engineering and Geosciences, Delft University of Technology, The Netherlands.
E-mail: b.savija@tudelft.nl; m.lukovic@tudelft.nl; erik.schlangen@tudelft.nl

Abstract

Strain hardening cementitious composites are a class of cement based materials which show strain hardening behaviour in tension. This is achieved by multiple microcracking, which results in a tightly spaced crack pattern with relatively small crack widths (50-80μm, in general) and high strain capacity (up to 4-5%). Due to their ductile behaviour and tight crack widths, SHCCs are commonly used for concrete repair applications. However, due to the tight crack width and crack spacing, moisture uptake by capillary suction can take place very fast. This could result in rapid access of deleterious substances, such as chloride ions, resulting in corrosion initiation. In this study, X-ray tomography is used for monitoring and quantification of water uptake in SHCC. Specimens were first loaded to different strain levels in uniaxial tension. They are subsequently subjected to a capillary suction test. The performed test was subsequently modelled using a lattice model.

INTRODUCTION

Reinforced concrete structures are prone to cracking. Although most cracks do not present risks for structural safety and reliability of a structure, they can be fast routes for ingress of deleterious species such as chloride ions and CO_2 (Šavija, 2014). Therefore, it is necessary to limit the extent of cracking in reinforced concrete structures. It is believed that SHCCs should have higher durability compared to concrete (Šavija, 2014). In this study, moisture uptake in cracked SHCC is monitored non-destructively using X-ray absorption technique. First, SHCC specimens are loaded in uniaxial tension. After unloading, they are subjected to water penetration in a moisture uptake test. This was monitored by X-ray absorption. Finally, moisture uptake in cracked SHCC is simulated using an experimentally-informed modelling procedure within the lattice modelling framework.

EXPERIMENTS

Materials used in the SHCC mixture were Ordinary Portland Cement (CEM I 42.5N), limestone powder, blast furnace slag (BFS), water, superplasticizer, and polyvinyl alcohol (PVA) fibers. Mix proportions are given in Table 1. Coupon specimens were then cast for uniaxial tension tests (Figure 1). The specimens were sealed, demolded after one day, and cured in a fog room at 20°C and 95% RH for 28 days. Afterwards, the specimens were kept in laboratory conditions until testing (around 20°C and 50% RH). At the age of 40 days, they were subjected to uniaxial

tension. Afterwards, a slice was cut from the middle portion of the specimen to be subjected to the moisture-uptake test. Prior to testing, it was dried overnight in an oven at 35°C. The dry sample was subjected to moisture uptake by capillary suction, while X-ray absorption measurements were performed. More details on the measurement technique can be found elsewhere (Luković et al., 2015). In this work, results are shown only for one cracked specimen. Note that the selected specimen didn't exhibit real strain-hardening behavior (see Figure 1 right), even though multiple cracking was observed. It was selected for this study, however, because of its relatively large cracks (up to about 800μm), in order to facilitate the image processing procedure as described below.

Table 1. SHCC mix proportions (weight %) (Luković et al, 2014)

CEM I 42.5 N	Limestone powder	Blast furnace slag	Water/powder ratio	Super-plasticizer	PVA fiber (volume %)
0.6	2	1.4	0.26	0.02	2

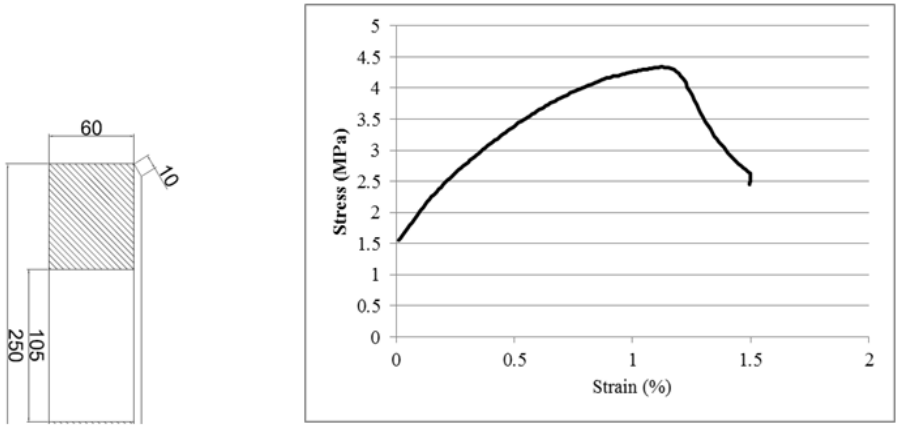

Figure 1. Left: Geometry of an SHCC coupon specimen (Hatched areas were glued and clamped, leaving the middle free to deform); Right: the stress/strain diagram of the analyzed SHCC specimen.

MODELING

Transport of water in cement based materials can be successfully simulated using discrete (lattice) models (Bolander and Berton, 2004). In this work, the following diffusion-type equation is used:

$$\frac{\partial \theta}{\partial t} = D(\theta)\frac{\partial^2 \theta}{\partial t^2}$$

where θ is the increase in moisture content due to capillary uptake, and D the moisture diffusivity which depends on the increase in the moisture content. The increase in moisture content was selected as a variable because it can be measured directly in the experiment. The moisture diffusivity can also be derived directly from the experimental data (Luković et al, 2015).

Cracking of the SHCC material can also be simulated by a lattice-type model (Luković et al, 2014). Then, the output of the mechanical analysis can be used as input for the transport simulation. However, in this work, a different approach is taken. Due to the level of microstructural detail obtained by the X-ray method (spatial resolution was 30μm) , it was decided to use the X-ray image as input for the transport simulation. The X-ray image was thresholded to reveal major pores and cracks. The thresholded image was skeletonized and processed, and then this image was used to generate a two-dimensional lattice mesh (Figure 2). Such a mesh had two distinct phases: the matrix phase, and the crack phase. The moisture diffusivity was calculated as $D(\theta) = 0.197e^{50.067\theta}$(based on the measurements of an uncracked specimen), while the diffusivity of the crack phase was taken as 5000 times higher, irrespective of the crack width. This was done because, due to the limitations in the spatial resolution, only cracks wider than 30μm could be detected.

RESULTS AND DISCUSSION

In figure 2, experimental and simulation results for different exposure times are compared. It can be seen that the moisture ingress in cracks is quite rapid in the first 20 minutes. Afterwards, moisture penetration inside the matrix material takes place, thereby widening the initially sharp moisture front. This general trend is observed in both the measured and simulated profiles. Similar observations were made by (Wang et al., 2014). However, there are some marked differences between the measurements and the simulations. Clearly, the simulation results underestimate the measured moisture uptake in terms of both maximum penetration depth and the total amount of moisture uptake. This is due to the limited spatial resolution of the X-ray attenuation measurement (around 30μm). Therefore, these cracks are not represented in the lattice mesh. It can be seen that, in the simulation, two main cracks are observed, while in reality there is also a multitude of small cracks between them, which also contribute to moisture uptake. Also, it is possible that damage has occurred at crack faces due to (partial) fiber pullout, thereby enhancing their diffusivity locally. Furthermore, these two large cracks are not of the same “depth” in the lattice mesh as in the specimen, due to the same effect: even though they are visible, some of their parts are disconnected, thereby slowing down the moisture ingress. This is also, a consequence of the averaging procedure: even though the specimen is thin in the direction of the X-rays (10mm), the result is the “average” over this thickness. It should be noted that, although the diffusivity of cracks was assumed to be independent of the crack width, it is unlikely that this has led to a large error. It seems that the limiting factor is not the rate of moisture ingress in cracks, but rather the diffusivity of the (damaged) matrix.

CONCLUSIONS

In this paper, a study of moisture uptake in cracked SHCC is presented. From this study, it can be concluded that cracked SHCC is prone to rapid capillary moisture uptake. Therefore, if it is to be used for corrosion protection, the maximum strain (and, indirectly, crack width and density) should be limited.

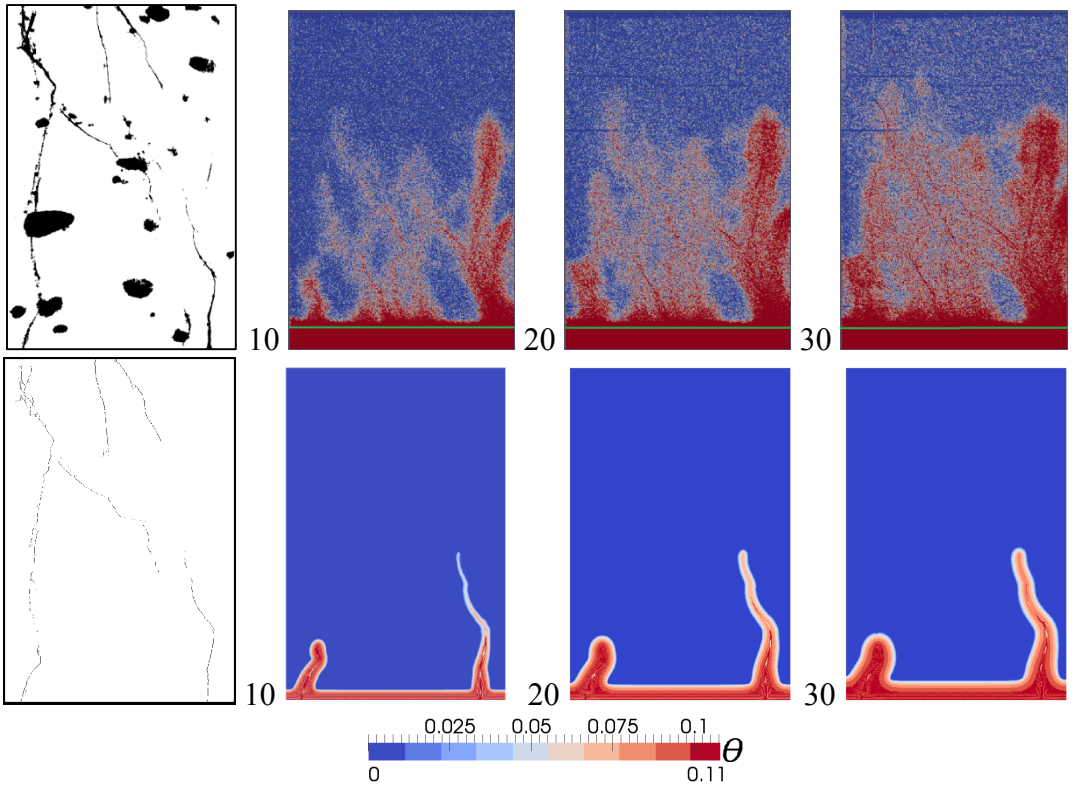

Figure 2. (Top). Experimental cracks and moisture uptake (green lines denote the water level at the start of the experiment); (bottom) 2D lattice mesh and simulated moisture uptake (exposure time is denoted in min)

ACKNOWLEDGEMENTS

The authors acknowledge the financial support of European Union Seventh Framework Programme (FP7/2007-2013) under grant agreement no 309451 (HEALCON).

REFERENCES

Bolander, J. E., & Berton, S. (2004). "Simulation of shrinkage induced cracking in cement composite overlays". *Cement Concrete Comp. 26*(7), 861-871.

Luković, M., Dong, H., Šavija, B., Schlangen, E., Ye, G., & van Breugel, K. (2014). "Tailoring strain-hardening cementitious composite repair systems through numerical experimentation". *Cement and Concrete Comp. 53*, 200-213.

Luković, M., Schlangen, E., Ye, G., and van Breugel, K. (2015)." Monitoring of moisture exchange in concrete repair systems", *14th International Congress on the Chemistry of Cement (ICCC 2015)*

Šavija, B. (2014). *Experimental and numerical investigation of chloride ingress in cracked concrete* (PhD thesis, Delft University of Technology).

Wang, P., Wittmann, F.H., Zhang, P., Lehmann, E., and Zhao, T. (2014). "Durability and service life of elements made with SHCC under imposed strain". *SHCC3: Proceedings of the 3rd International RILEM Conference on Strain Hardening Cementitious Composites, Dordrecht, The Netherlands*

A 3D Investigation of ITZ Porosity and Pore Connectivity Relevant to Damage and Transport Properties

Chula Gangsa, Lauren S. Flanders, and Eric N. Landis[1]

[1]Department of Civil and Environmental Engineering, University of Maine, Orono, ME 04469-5711 USA; PH +1 207 581-2173; FAX +1 581-3888; email: landis@maine.edu

ABSTRACT

In this work, we analyzed x-ray microtomographic images to quantify the porosity of small mortar specimens, with a particular focus on the porosity of the interfacial transition zone (ITZ). Specimens were nominally 5 mm diameter, 4 mm long cylinders with 0.5 mm diameter glass bead aggregates. Specimens were scanned via synchrotron-based x-ray microtomography while they were positioned in an *in situ* loading frame in a split cylinder configuration. Scans of undamaged specimens were evaluated for porosity both in the bulk paste and in the ITZ. Specifically, voids in the paste and porosity in the ITZ were superimposed onto a map of the tensile stress in the specimen in an attempt to identify critical flaws, and to measure their role in split cylinder strength. Preliminary results indicate that the ITZ porosity has a lower effect on split cylinder strength than the large flaws that occur either in the ITZ or the bulk cement past.

INTRODUCTION

Properties of the interfacial transition zone (ITZ) in concrete have long been recognized as critical to both transport properties and mechanical properties (e.g. Buyukozturk and Wecharatana 1995). The high porosity characteristic of the ITZ can provide a critical flaw that can dictate fracture toughness, as well as provide a path of least resistance for fluid transport. Despite its importance, high quality 3D quantitative measurements of ITZ porosity have been limited.

In this work, we have employed x-ray microtomography to make 3D measurements of porosity around artificial aggregates in a cement matrix. Within the resolution of the imaging technique, we are able to quantify porosity with respect to distance from the aggregate and spatial variation relative to casting direction and load axis. We are also able to look at the spatial variation of interface porosity in the zone of maximum split cylinder tension to partially examine variability of split cylinder strength. Finally, we are able to identify preferential pathways for mass transport via interfaces and shortest matrix distances.

The focus of the work described here is an analysis of voids in both the bulk cement past and the ITZ, and to assess the relative importance of the voids with respect

to average tensile stress at the location of the void. This analysis gives us the potential to identify critical flaws that dictate fracture behavior, and as such, the question we wish to answer is: is the ITZ porosity a better predictor of strength than the size of bulk voids in the matrix? Previous experiments and simulations (Asahina et al 2011) showed that an increasing fraction of coarse aggregates lowered the split cylinder strength. Presumably the strength is dictated by critical flaws, so these begs the question of whether a higher fraction of aggregates increases the probability of a critical flaw by having a greater overall ITZ region, or does a greater overall ITZ region by itself reduce the strength without necessarily introducing a larger flaw.

MATERIALS AND METHODS

Test Specimens

The specimens used for this work were prepared using a high early strength (ASTM Type III) portland cement, very fine silica (passing #80 sieve), small glass bead aggregates (nominally 0.5 mm), and water. The glass beads were used for their well-defined geometry, and because the surface can be easily modified to change interface properties. In this work, two different surfaces were considered: smooth (untreated) and etched using an ammonium bifluoride solution. The mix proportion of the mortar matrix was 1:2:0.5, by weight cement:fine sand:water. Glass beads were added as "coarse" aggregates at a dosages of roughly 10% and 50% by volume. Additionally, a set of specimens without glass beads was prepared to investigate properties of the cement matrix. The material was mixed with a benchtop rotary mixer and cured in wet conditions for seven days. The nominally 5 mm cylindrical test specimens were extracted from the bulk material using a 5.5 mm inside diameter diamond coring bit and then cut to size.

X-ray Microtomography

Three dimensional imaging of the specimens were made using x-ray microtomography (XMT), a radiographic technique by which hundreds of projection radiographs are made of a specimen at different angles, and the radiographs are reconstructed to form a 3D image of the specimen and its interior (Landis and Keane 2012). For these experiments, the x-ray source was a 30 keV monochromatic, collimated beam from a synchrotron at the Advanced Photon Source (APS). The high flux source led to high contrast images with a voxel size of 6 μm.

In the experiments, specimens were scanned in the x-ray beamline while positioned in an *in situ* loading frame that could monitor load and platen-to-platen displacement. Scans were made at nominally zero load and again after fracture.

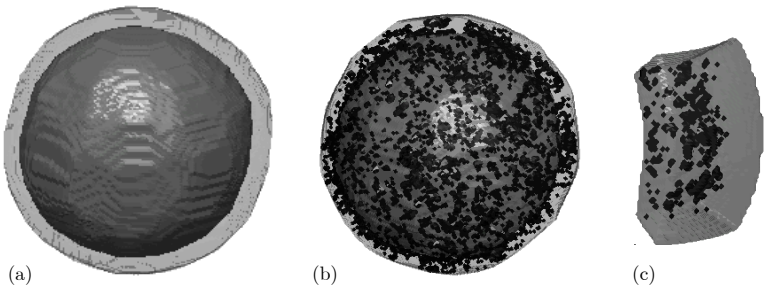

Figure 1. Illustration of (a) isolated bead and ITZ, (b) ITZ porosity, and (c) a section of the ITZ in a tension zone.

Image Processing

Digital image processing techniques were applied to the acquired 3D images. First, the images were segmented such that both individual aggregate particles could be isolated, as well as the porosity surrounding the aggregates. In order to isolate pores, beads, and other constituents, the specimen had to be isolated from the background. To achieve this, a shrinkwrapping function was employed. Then, the isolated volume could be used in conjunction with informed selection of a threshold and binary operators to isolate constituents such as pores, aggregates, and unhydrated cement particles. A similar but slightly more complicated process, which used a standard deviation filter to identify edges, was used to isolate the beads.

For the ITZ analysis, varying interfacial zone widths were applied as shells around the beads, and pores within those shells were isolated, resulting in information about ITZ width and porosity. A rough illustration of this process is presented in Fig. 1. In this work, we only considered ITZ zones in which the aggregate surface was nominally normal to the plane of maximum principal tensile stress. As detailed below, this was determined by superimposing the ITZ zone onto a map of the tensile stress in the specimen, and defining a shell defined by a 45° arc centered on the normal vector. Of interest here is the porosity of the ITZ, which could simply be calculated by dividing the number of void voxels by the total number of voxels in the defined ITZ zone.

Regarding the analysis of void space in the cement matrix, we simply conduct a connected component analysis of the void space (obtained through image segmentation) inside the specimen. The individual pore spaces are then analyzed for size and location. An example of the analysis is illustrated in Fig. 2.

ANALYSIS

The isolated ITZ regions and the bulk void spaces, while useful in predicting fracture strength, is incomplete information. de Wolski et al (2014) showed a correlation between bulk porosity and split cylinder strength, however, it was not a strong

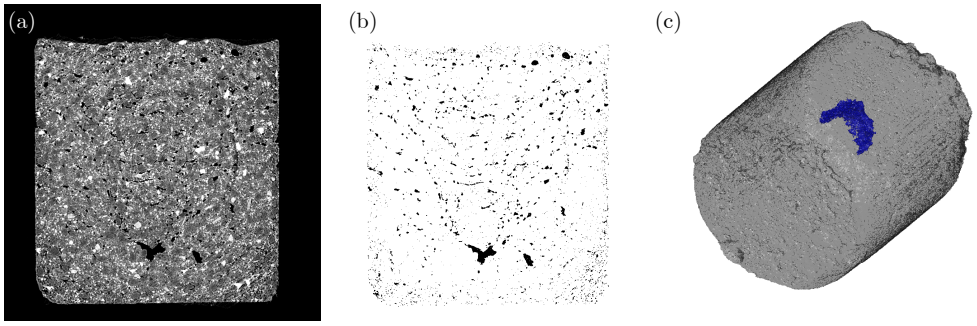

Figure 2. (a) Cross sectional slice, (b) slice segmented for pores, and (c) 3D rendering of largest pore in specimen.

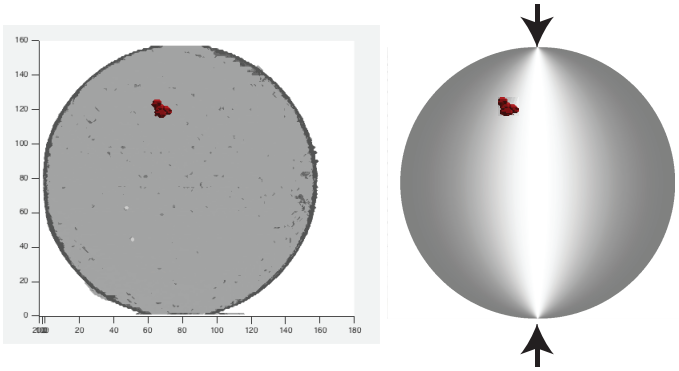

Figure 3. Void object isolated in specimen (left) superimposed on tension stress field (right).

correlation. The split cylinder configuration is a popular measure for tensile strength because the test is easy to run, and the tensile stress is fairly uniform along the axis of the load. Thus, for a void to truly have an impact on the tensile strength it must be located on or near that central axis. The effect of a large void decreases if it is away from that axis.

Using the well documented stress field for a split cylinder configuration (e.g. Petroski and Ojdrovic 1987), a 3D image could be constructed such that the voxel intensity is proportional to the principal tensile stress. The relative influence of the void space is assumed to be a function of its size and the tensile field where it lies. This can be visualized in Fig. 3, where a void object isolated in the specimen is superimposed on the tension field. The tension field is set based on a unit compressive force.

This superposition was applied two different ways in order to address the question of whether bulk pores have a greater affect on split cylinder strength than the ITZ porosity. First, the porosity of all tensile zone ITZ regions was evaluated as described

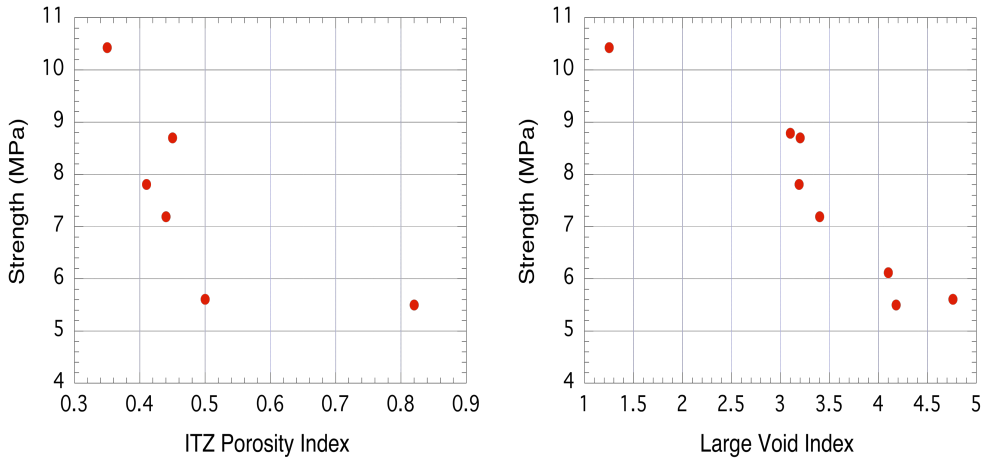

Figure 4. Plots illustrating the effect of ITZ porosity index and large void index on split cylinder strength.

above. Each tensile zone porosity value was then multiplied by the principal tensile stress acting at the centroid of the the ITZ region. We refer to this product as the ITZ porosity index, and of particular interest is the largest ITZ porosity index in each specimen.

A similar procedure was then applied to the isolated void objects. The volume of each object is multiplied by the maximum principal stress at the centroid of the object. We refer to this product as the Largest Void Index. The presumption, again, is that the combination will have the greatest impact on specimen strength.

The results of both of these analysis are plotted in Fig. 4, which show split cylinder strength plotted against ITZ porosity index and largest void index. Qualitatively, the results show that both indices correlate inversely with strength, as expected. While sample sizes are admittedly small, it would seem that the large void index shows less scatter, indicating perhaps a stronger relationship. It should be noted that the sample size is slightly larger for the large void index data due to the inclusion of specimens that did not include any bead aggregates (and thus no ITZ can be defined).

CONCLUSIONS

While not conclusive, the preliminary answer to the original question of the role of the ITZ in fracture strength, the results suggest that the largest void, relative to principal tensile stress, produces a stronger correlation, and is therefore a more important factor in dictating split cylinder strength than the high porosity regions in the ITZ. However, as previous results have shown that higher aggregate fractions reduce the split cylinder strength, this would imply that either the ITZ produces large voids, or the addition of more aggregates somehow promotes larger void spaces, perhaps due to

mixing or entrapped air issues.

Among the implications of the work are that the results can be incorporated into discrete models such that the models can properly incorporate spatial variability. Specifically, it shows the interacting role of ITZ variability and void distribution relative to stress fields as the likely source of fracture initiation.

ACKNOWLEDGMENTS

Portions of this work were per- formed at the DuPont-Northwestern-Dow Collaborative Access Team (DND-CAT) located at Sector 5 of the Advanced Photon Source (APS). DND-CAT is supported by E.I. DuPont de Nemours & Co., The Dow Chemical Company and the State of Illinois. Use of the APS was supported by the U. S. Department of Energy, Office of Science, Office of Basic Energy Sciences, under Contract No. DE- AC02-06CH11357. An additional acknowledgement goes to Dr. Denis Keane, DND-CAT director, for his assistance at the beamline.

REFERENCES

Asahina, D., Landis, E. N., and Bolander, J. E. (2011) "Modeling of Phase Interfaces During Pre-Critical Crack Growth in Concrete." *Cement and Concrete Composites,* 33(9), 966-977.

Buyukozturk, O., and Wecharatana, M. (1995) *Interface Fracture and Bond SP-156,* American Concrete Institute, Detroit.

de Wolski, S. C., Bolander, J. E., and Landis, E. N. (2014) "An *In-Situ* X-ray Microtomographic Study of Split Cylinder Fracture in Cement-Based Materials." *Experimental Mechanics*, 54(7), 1227-1235.

Landis, E. N., and Keane, D. T. (2010) "Tutorial Review: X-Ray Microtomography." *Materials Characterization*, 61(12), 1305-1316.

Petroski, H. J., and Ojdrovic, R. P. (1987) "The Concrete Cylinder: Stress Analysis and Failure Modes." *International Journal of Fracture*, 34, 263-279.

Dual-lattice Modeling of Transport in Heterogeneous Materials

J.E. Bolander[1], T. Saka[2], M.M. Rashid[3]

[1]University of California, Davis, California, USA; email: jebolander@ucdavis.edu
[2]Kajima Technical Research Institute, Tokyo, Japan; email: sakat@kajima.com
[3]University of California, Davis, California, USA; email: mmrashid@ucdavis.edu

ABSTRACT

Coupled elasticity and potential flow problems, such as drying shrinkage, can be solved using lattice models. Typically, both the displacement and relative humidity fields are represented by the same set of nodes. When considering crack development and its influences on transport, however, it may be advantageous to use a different lattice for each field. In this research, the structural problem is to be solved using a lattice defined by the edges of the Delaunay tessellation of a set of nodal points. The edges of the dual Voronoi diagram are used to solve the flow problem. In this way, flow elements are better positioned to simulate transport along cracks, the effects of crack opening on such flow, and transport from the crack faces into the bulk material. A complicating factor is the inevitable occurrence of arbitrarily small and/or poorly-shaped geometric objects associated with the Voronoi diagram. These features can both degrade the physical fidelity of the simulation results, and negatively impact the reliability of the overall simulation process. This research introduces the concept of automated tolerance-driven domain discretization, by which undesirable features of the Voronoi diagram are avoided at the mesh-generation stage. Corresponding improvements in the ability to reliably model flow in homogeneous and heterogeneous solids are demonstrated. Potential improvements in the modeling of fracture and flow through fractured media are discussed.

INTRODUCTION

Lattice models have been used to study the fracture of heterogeneous materials, including cement-based composites (Schlangen and van Mier 1992; Cusatis et al. 2011). The lattice nodes are typically positioned, either regularly or irregularly, in relation to an image of the material structure. For the case of irregularly positioned nodes, the topology of the lattice has been defined by a Delaunay tessellation of the nodes; the dual Voronoi tessellation serves to define properties of the lattice elements (Bolander and Saito 1998). This discretization scheme provides: (1) a polyhedral tiling of the material volume; (2) a versatile means for the grading of nodal point density; (3) explicit representations of material interfaces; and (4) an elastically homogenous description of the material under uniform straining. The last of these features results from the A_{ij}/h_{ij}

scaling of the element stiffness coefficients, where A_{ij} is the area of the Voronoi facet associated with nodes i and j, and h_{ij} is the distance between the same two nodes. One further attribute of lattice models is their simplicity. Since the model formulations rely only on low-order geometrical features, the solutions are typically well-behaved as long as those features are topologically correct (i.e., their measures are positive). In particular, the minimum size of h_{ij} is easily controlled by the constrained placement of nodes in the domain.

Lattice models are also being used to simulate transport processes within concrete materials (Bolander and Berton, 2004). There is interest in modeling the coupling between damage and mass transport, as it relates to the durability mechanics of materials and structures. Whereas most such couplings have been based on a single lattice topology, there are potential advantages to the use of distinctly different lattices for the structural and flow problems. One recent strategy involves the conventional use of Delaunay tessellation to define the structural lattice, but the flow lattice is defined by the edges of the dual Voronoi tessellation (Nakamura et al. 2006; Grassl 2009; Saka 2012; Grassl et al. 2015). In this way, the flow elements are aligned with potential crack directions and thus can directly account for the dependency of transport on crack opening.

This paper reports on qualities of such dual-lattice formulations for these coupled problems. As a complicating factor, edges of the Voronoi diagram may be of zero-length, which ill-conditions the system of equations representing the flow lattice. Of the various means for addressing this problem, this paper introduces the concept of tolerance-driven domain discretization, in which measures of the geometric features (in this case, the minimal allowable length of the Voronoi edges) are controlled. Potential uses of the dual-lattice formulation are discussed through the example of heat-affected concrete containing polypropylene fibers.

DUAL-LATTICE MODELING OF COUPLED PROBLEMS

Basic Concept

Element sharing of coincident sets of nodes simplifies coupled-field analyses prior to cracking. After crack formation, however, the flow elements are directed perpendicular to the crack path, which (in an approximate sense) follows the boundaries of the Voronoi cells (Fig. 1). This misalignment of the flow elements with the crack path complicates the simulation of crack-assisted flow and its dependence on crack opening. An alternative, more physically-based approach is being adopted herein: the structural and flow lattices are constructed on different (i.e., non-coincident) sets of nodal points. By defining the flow network on the edges of the Voronoi tessellation, both pre-cracking and postcracking flow can be simulated. As seen in Fig. 1b, flow elements are now aligned with potential cracks. The structural analysis provides values of crack opening, which govern the properties of the flow elements (Grassl 2009).

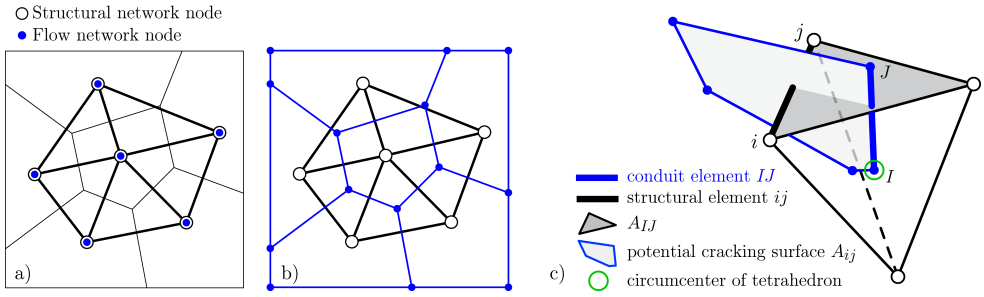

Figure 1. Lattice networks for coupled problems: a) conventional approach based on coincident nodes; b) dual-lattice approach based on non-coincident nodes; and c) 3D geometrical relationships.

Application Issues

Whereas improvements in the post-cracking representation of flow are anticipated, use of the dual-lattice approach entails several complicating factors.

- The lattice defined by the edges of the Voroni tessellation is computationally more expensive than its Delaunay counterpart. The number of Voronoi vertices is dramatically greater than the number of Delaunay vertices. The number of flow lattice elements is also much greater than the number of structural lattice elements.

- Coupling of the displacement and flow fields is complicated by the use of different nodal sets for each respective field (Figs. 1b and c).

- The occurrence of zero-length (or tiny) Voronoi edges can ill-condition the system of equations associated with the flow field analyses. Such zero-length edges rarely occur from the random placement of structural nodes, but precautionary measures are still necessary. Some regular arrangements of structural nodes lead to degenerate Delaunay tessellations, which produce zero-length Voronoi edges. For both cases, the problem can be circumvented by assigning a sufficiently large length to the elements in question. Alternatively, the minimum allowable edge length can be controlled using a tolerance-driven domain discretization scheme, as described next.

Tolerance-driven domain discretization

The computational lattice in the present modeling approach derives from partitioning of the physical problem domain via both Delaunay and Voronoi tessellations, relative to a given set of nodes. The nodes fully determine the computational lattice, and several essential features of the discrete model derive from it. For example, the stiffnesses of the structural elements scale with the areas of the Voronoi facets associated with the elements. Likewise, the fluid resistance of the elements in the flow network

– which are the edges of the Voronoi tessellation – is proportional to the lengths of these edges. These geometric-physical relationships suggest that near-degeneracies in the geometric tessellations may lead to undesirable singularities in the physical models. This is so even if the tessellations are properly generated and topologically correct. Of particular concern in this regard are arbitrarily short Voronoi edges, which cause ill-conditioning in the flow-field governing equations. We also note that tiny Voronoi facets produce structural elements with vanishingly small stiffness. While not a concern in relation to numerical conditioning, the presence of such elements causes at least two problems during event-by-event simulations of fracture:

- Element breakage extends the solution time without any appreciable effect on either the local stress conditions or the global load-displacement behavior.
- For displacement or energy-based convergence criteria, breakage of a small element could cause false convergence. Whereas the fracture criteria may be met for additional elements, the breakage of the small element does not produce sufficient imbalance in internal forces, nor large enough energy increment, to continue the iteration sequence.

It is evident that Voronoi tessellations with excessively small features (edges, facets) are unsuitable for the present purposes. Unfortunately, however, there is no simple way to constrain the placement of the generating nodes so that such features are excluded. Indeed, even well-separated nodal distributions can produce arbitrarily small features: a regular Cartesian array of nodes, for example, produces a highly degenerate Voronoi partition, while a small perturbation from such a distribution produces exactly the kind of small features that we wish to avoid. This difficulty is distinct from the problem of correctly generating a tessellation for near-degenerate nodal arrangements in the first place. This too is a challenging problem, and is a main focus of current research on *approximate Voronoi diagrams* e.g. (Vleugels 1998).

The present application would benefit from a Voronoi partitioning scheme whose output departs slightly from the exact Voronoi tessellation, in exchange for a guarantee that the tessellation will be free of Voronoi edges smaller than a specified threshold. This threshold is controlled by a tolerance parameter, such that the exact Voronoi tessellation is recovered in the limit as the tolerance decreases to zero. Such a *tolerance-driven algorithm* has been developed, and is being used to explore the dividends of guaranteed-freedom from small geometric features. An additional benefit of this algorithmic approach is that it is inherently robust numerically for tolerance values greater than a very small minimum value, even for arbitrarily degenerate nodal distributions.

Application Examples

Flow through a homogeneous material. A homogeneous material is discretized as shown in Fig. 2a. The Delaunay/Voronoi discretization of the domain is based on a set

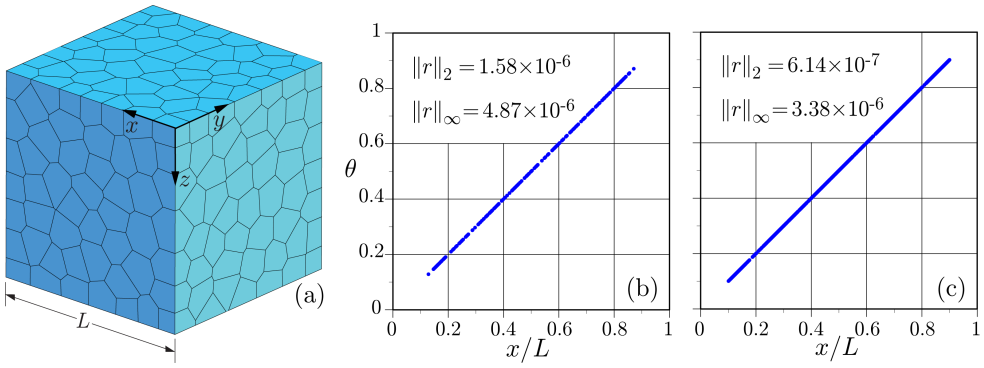

Figure 2. Steady-state simulation of potential flow: a) Voronoi tessellation of domain; b) conventional lattice solution; and c) dual-lattice solution.

of randomly inserted nodes. Table 1 compares the numbers of nodes/elements forming each type of lattice. It is clear that the dual-lattice is computationally more expensive.

Table 1. Lattice feature counts.

Lattice type	Node definition	Element definition	Nodal count*	Element count*
Conventional	Delaunay vertex	Delaunay edge	330	1800
Dual	Voronoi vertex	Voronoi edge	2880	5440

*rounded to nearest ten.

The material is subjected to a potential difference between the x-faces of the domain: $\theta(x=0)=0$ and $\theta(x=L)=1$. Both lattices accurately represent the steady-state solution, as shown by the nodal potentials plotted in Fig. 2. Potential values are not plotted for the nodes associated with prescribed boundary conditions. The discrete error norms presented in the figures are:

$$||r||_\infty = \max_{m=1,\ldots,M} |r_m| \tag{1}$$

$$||r||_2 = \left(\frac{1}{M} \sum_{m=1}^{M} |r_m|^2 \right)^{1/2} \tag{2}$$

where $r_m = \theta(\mathbf{x}_m) - \theta_h(\mathbf{x}_m)$ is the difference between the theoretical and numerical solutions, respectively, at the position of node m; and M is the number of unconstrained nodal points.

Flow through heat-affected concrete containing polypropylene fibers. The central portion a cubic domain is refined to simulate the effects cylindrical channels on

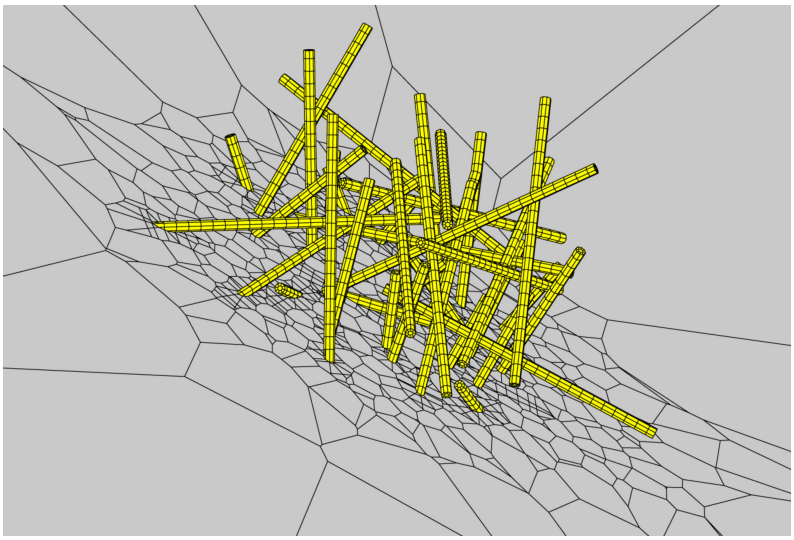

Figure 3. Discretization of multiple fiber inclusions (section of central region within a cubic domain).

the flow field (Fig. 3). These channels represent the volumes occupied by polypropylene fibers, which are assumed to have melted and decomposed under high temperature loading. Each fiber channel is discretized by a set of regularly positioned nodes, prior to random placement of nodes elsewhere in the domain.

Figure 4 shows streamlines of steady-state flow past these fiber channels, as obtained from a conventional lattice simulation. As expected, the empty channels provide preferential pathways for flow, increasing the effective permeability of the composite material. In some instances, the flow paths traverse intact matrix material between the channels. It is thought that microcracking in the vicinity of the fibers, possibly induced by fiber dilitancy during early heating, accentuates the effective permeability of the material. The dual-lattice is being developed for this type of investigation.

CONCLUSIONS

Several observations can be made regarding this dual-lattice approach:

- Whereas conventional approaches, based on coincident nodal sets, are effective prior to cracking, they lack physical bases for modeling the effects of cracking on the flow network. With the dual-lattice approach, flow lattice elements are defined by the Voronoi edges and therefore aligned with potential cracking directions.

- Use of the dual tessellation, in which the lattice topology is defined by the Voronoi vertices and edges, greatly increases computational demands.

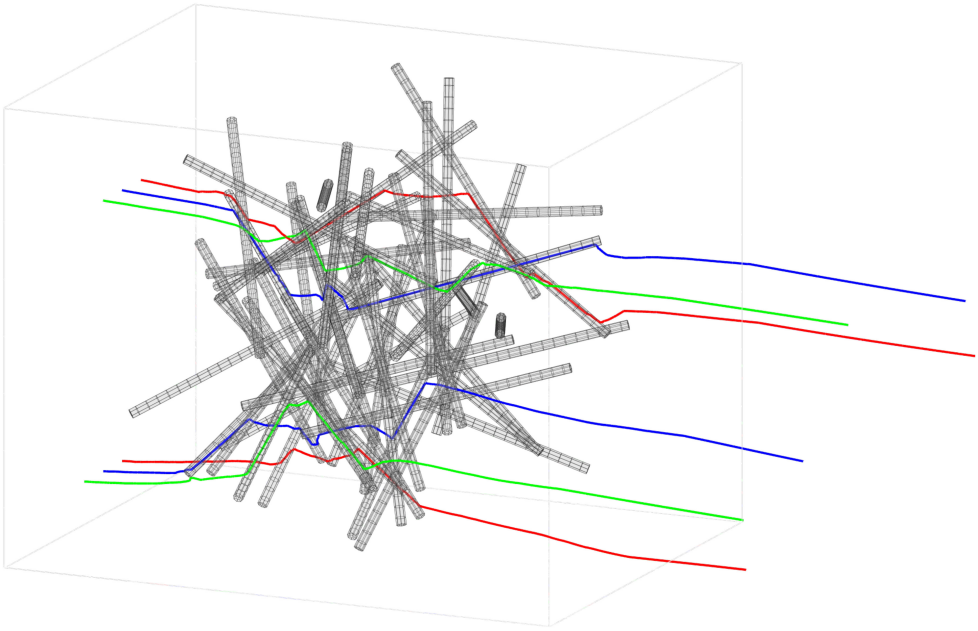

Figure 4. Flow past multiple fiber channels.

- Both the conventional and dual lattice accurately represent steady-state flow through homogeneous materials.
- The appearance of zero-length Voronoi edges is problematic for the dual-lattice, particularly for the case of regularly positioned nodes. This can be handled through tolerance-aware domain discretization. The applications of such novel approaches are under study.

REFERENCES

Bolander, J.E. and Saito, S. (1998) "Fracture analyses using spring networks with random geometry." *Engng. Fracture Mech.,* 61, 569-591.

Bolander, J.E. and Berton, S. (2004) "Simulation of shrinkage induced cracking in cement composite overlays." *Cem. Conc. Compos.,* 26(7), 861-871.

Cusatis, G., Pelessone, D., and Mencarelli, A. (2011) "Lattice discrete particle model (LDPM) for failure behavior of concrete. I: Theory." *Cem. Conc. Compos.,* 33(9), 881-890.

Grassl, P. (2009). "A lattice approach to model flow in cracked concrete." *Cem. Conc. Compos.,* 31(7), 454-460.

Grassl, P., Fahy, C., Gallipoli, D. and Wheeler, S.J. (2015) "A 2D hydro-mechanical lattice approach for modeling hydraulic fracture." *J. Mech. Phys. Solids,* 75, 104-118.

Nakamura, H., Worapong, S., Yashiro, R., and Kunieda, M. (2006) "Time-dependent structural analysis considering mass transfer to evaluate deterioration processes of RC structures." *J. Adv. Concrete Technology* 4(1), 147-158.

Saka, T. (2012) "Simulation of reinforced concrete durability: Dual-lattice models of crack-assisted mass transport." Ph.D. Dissertation, University of California, Davis, 179 pp.

Saka, T., Bolander, J.E., and Grassl, P. (2009) "Spalling potential of fire-exposed structural concrete: Numerical simulation of the effects of polypropylene fibres." In: 1st International RILEM Workshop on Concrete Spalling Due to Fire Exposure, 3-5 September, Leipzig, Germany, 510-518.

Schlangen, E. and van Mier, J.G.M. (1992) "Simple lattice model for numerical simulation of fracture of concrete materials and structures." *Materials and Structures,* 25, 534-542.

Vleugels, J. and Overmars, M. (1998) "Approximating Voronoi diagrams of convex sites in any dimension." *Int. J. Computational Geometry and Applications,* 8, 201-221.

Drying Shrinkage Damage in Concrete Repair Systems: A 3D Modelling Study

M. Lukovic[1]; B. Šavija[1]; E. Schlangen[1]; and G. Ye[1]

[1]Delft University of Technology, Faculty of Civil Engineering and Geosciences, Stevinweg 1, 2628 CN Delft, The Netherlands. E-mail: m.lukovic@tudelft.nl

Abstract

Differential shrinkage between repair material and concrete substrate is considered to be the main cause of premature failure of repair systems. Magnitude of induced stresses depends on many factors, for example the degree of restraint, moisture gradients caused by curing and drying conditions, type of repair material, etc. Numerical simulations combined with experimental observations can be of great use when determining the influence of these parameters on the performance of a repair system. In this work, a lattice type model is used first to simulate moisture transport inside a repair system and then to model time dependent damage. 3D simulations are performed, and damage patterns and crack widths are qualitatively verified with some experimental observations.

INTRODUCTION

Differential shrinkage (primarily drying shrinkage) is the major cause of damage in concrete repair systems. The aim of this paper is to understand parameters which influence drying shrinkage induced cracking in concrete repair systems. 3D mesoscale lattice models are used to simulate moisture distribution due to drying and substrate absorption and resulting damage in the repair system. Benefits of using lattice models for fracture simulations are that they can mimic physical structure and processes, so that realistic crack patterns can be achieved (Schlangen 1993, Landis and Bolander 2009). Such models have been used for modelling fracture of quasi-brittle materials (i.e. concrete, mortar or cement paste). Material structure is explicitly represented- in the lattice fracture model it is captured through assigning different fracture properties, and in the lattice transport model through assigning different diffusivity (conductivity) properties to lattice elements that represent a certain material phase (Šavija, Pacheco et al. 2013). In this work, the influence of substrate surface preparation (i.e. roughness) and thickness of the repair material on damage caused by drying shrinkage is investigated.

MODELLING APPROACH

In the transport lattice approach, concrete is treated as an assembly of one-dimensional “pipes”, through which the flow takes place. In the mechanical lattice approach, concrete is discretized as a set of beam elements which transfer forces. The output from the moisture transport model is used as an input for simulating fracture.

This is a one-way coupling – moisture transport does effect mechanical fracture, but there is no influence of the (micro) cracking on moisture transport.

The approach proposed here uses the same lattice network for both fracture and moisture simulations. For the spatial discretization of the specimen in three dimensions, the basis is the prismatic domain. The domain is divided into a number of cubic cells with linear dimension 1 mm. In each cell, a random location for a lattice node is selected. Voronoi tessellation of the prismatic domain is performed. Nodes with adjacent Voronoi cells are connected by lattice elements. In order to take material heterogeneity into account, different material properties (diffusivity and mechanical) are ascribed to elements representing coarse aggregate, substrate mortar, repair mortar and interface (Figure 1a-purple is substrate mortar, black are coarse aggregates).

Lattice moisture transport model. For the analysis of the time dependent drying shrinkage, a repair system is simulated. The model treats concrete as an assembly of one-dimensional linear ("pipe") elements, through which moisture transport takes place. A governing partial differential equation for moisture transport is:

$$\frac{\partial H}{\partial t} = \frac{\partial}{\partial x}\left(D(H)\frac{\partial H}{\partial x}\right) \quad (1)$$

where H is the relative humidity and $D(H)$ is a humidity dependent diffusion coefficient given as:

$$D(H) = \beta e^{\gamma H} \quad (2)$$

Transport properties and parameters for different material phases, used in all moisture transport simulations, are given in table 1 (top two rows). Film coefficient of the surface is 0.7mm/day and the system is exposed to environment with 50% relative humidity.

Lattice fracture model. In fracture simulations, different mechanical properties are ascribed to elements of a certain phase (table 1-bottom two rows). All individual elements have linear elastic behaviour. In each loading step, an element that exceeds limit stress is removed from the mesh.

Table 1. Diffusivity [mm^2/day] and mechanical [MPa] properties of lattice elements in the lattice moisture and fracture model (Lukovic, Šavija et al. 2014)

	Repair mortar	*Interface*	*Mortar substrate*	*ITZ*	*Aggregates*
β	0.022	0.022	0.022	0.066	0.00022
γ	7.5	7	4	4	0
E modulus	20000	15000	25000	15000	70000
Tensile strength	3.5	1	4	2.5	8

Coupling lattice moisture model with lattice fracture model. For coupling moisture and fracture analysis, it is assumed that shrinkage strain is proportional to the relative humidity change within the element. Therefore, due to hygral gradients, every element tends to change its length. As its deformation is restrained by its connectivity with other elements in the mesh, tensile stresses are generated. Once this stress exceeds the element strength, element is broken and removed from the mesh.

NUMERICAL RESULTS AND DISCUSSION

In order to verify the proposed modelling approach, crack development and distribution due to restrained shrinkage in the repair system are examined. Periodic boundary conditions are applied in horizontal directions. Dimensions of the repair system are 40x40mm^2 with the total height of 30mm. Simulated repair material thicknesses are 10mm and 6 mm. The substrate contains 30% of coarse aggregate particles (by volume), generated and packed using the Anm material model (Qian, Garboczi et al. 2014). Smooth and sandblasted surface roughness of the concrete substrate are imitated. Sandblasted surface is mimicked by exposing 3mm of aggregates at the surface (Figure 1a).

Due to drying and substrate absorption, moisture transport in repair system takes place (Figure 1c). Moisture loss triggers material shrinkage which, if unrestrained, does not cause stresses. In repair systems, however, the repair material is restrained by its bond with the substrate and the friction provided by the roughness profile. This results in stress concentrations inside the repair material, possibly leading to cracking and delamination. Boundary conditions and degree of restraint (bond with the substrate and thickness of the repair material), type of repair material (SHCC or repair mortar) and moisture gradient (environmental conditions and diffusivity properties of the repair system) are critical for damage pattern and maximum crack widths.

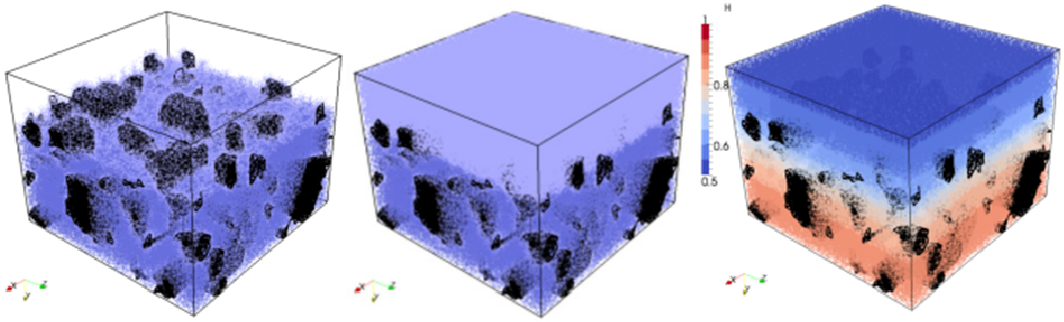

Figure 1: a) Imitating sandblasted surface b) "Casting" repair mortar with 10 mm thickness c) Moisture distribution in the repair system due to drying from the top and substrate absorption at 110 days

Influence of the substrate roughness and repair material thickness on the simulated crack pattern at 110 days is shown in figure 2. Deformation in the figure 2 is scaled 100x. Maximum crack width and debonding (0.12 mm and 0.056 mm, respectively) are observed when the substrate surface is smooth (Figure 2a). Cracks in the repair mortar form at close to 90° angle. Rough surface with the same interface strength enables a similar polygonal pattern with almost straight cracks (Figure 2b). However, due to more restraint and higher friction at the interface, provided by the higher roughness profile, more cracks with smaller crack spacing and smaller crack widths (maximum 0.090 mm) form. In figure 2c, repair mortar thickness is reduced to 6 mm. Maximum crack width is 0.049mm. In addition, crack patterns from Figure 2b and Figure 2c confirms that crack spacing is simply proportional to the thickness of the drying layer as previously experimentally concluded (Groisman and Kaplan 1994)

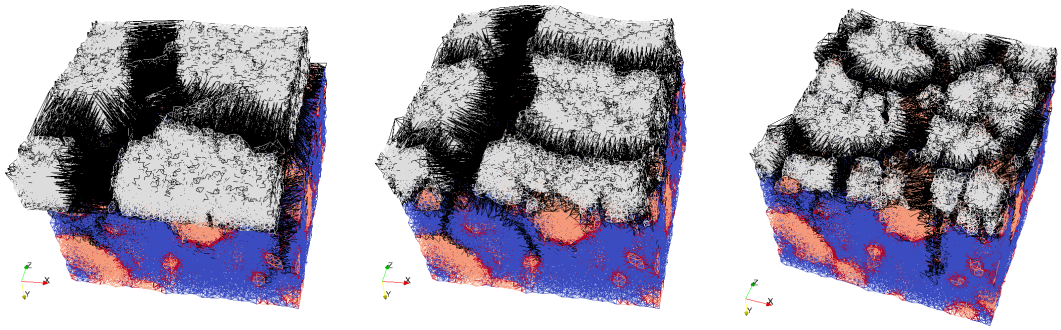

Figure 2: Influence of substrate surface roughness and repair material thickness on cracking and debonding after 110 days of drying: a) smooth surface, 10 mm thick b) rough surface, 10 mm thick and c) rough surface, 6mm thick

CONCLUSIONS

Simulation results show that, in general, performance of the repair system due to drying shrinkage can be well imitated by the model. It is found that the rough surface enables more restrain and more controlled cracking and delamination. It was also observed that more cracks with smaller spacing will form in thinner overlays, under the same exposure conditions. Furthermore, the influence of other parameters, such as bond strength and implementation of fibres in the repair material are investigated by the proposed modelling approach and will be published in (Lukovic 2015).

ACKNOLEDGMENTS

Financial support by the Dutch Technology Foundation (STW) for the project 10981- "Durable Repair and Radical Protection of Concrete Structures in View of Sustainable Construction" is gratefully acknowledged.

REFERENCES

Groisman, A. and E. Kaplan (1994). "An experimental study of cracking induced by desiccation." *Europhys. Lett.* 25(6): 415.

Landis, E. and J. Bolander (2009). "Explicit representation of physical processes in concrete fracture." *J. Phys. D Appl. Phys*. 42(21): 214002.

Lukovic, M. (2015*). Influence of interface and SHCC material properties on the performance of the repair system* (in preparation, PhD thesis, TU Delft).

Lukovic, M., B. Šavija, E. Schlangen and G. Ye (2014). A modelling study of drying shrinkage damage in concrete repair systems. *Proc. Int. Conf. Structural Faults & Repair,* London, UK.

Qian, Z., E. Garboczi, G. Ye and E. Schlangen (2014). "Anm: a geometrical model for the composite structure of mortar and concrete using real-shape particles." *Mater. Struct*: 1-10.

Šavija, B., J. Pacheco and E. Schlangen (2013). "Lattice modeling of chloride diffusion in sound and cracked concrete". *Cement Concrete Comp. 42*: 30-40.

Schlangen, E. (1993). *Experimental and numerical analysis of fracture processes in concrete* (PhD thesis, TU Delft).

Modelling of Non-Uniform Corrosion-Induced Cover Cracking in Reinforced Concrete

Santiago Guzmán[1]; Jaime C. Gálvez[2]; and José M. Sancho[3]

[1]Técnicas Reunidas, Natural Gas & Upstream Division, Initec PI, Department of LNG Tanks, C/ María de Portugal 9, Madrid 28050, Spain. E-mail: guzman.s@tecnicasreunidas.es
[2]Department of Civil Engineering Construction, ETSI Caminos, Canales y Puertos, Universidad Politécnica Madrid, C/ Profesor Aranguren s/n, Madrid 28040, Spain. E-mail: jaime.galvez@upm.es
[3]Group of Advanced Structural Materials, Universidad Politécnica Madrid, C/ Profesor Aranguren s/n, Madrid 28040, Spain. E-mail: jose.sancho@upm.es

Abstract

Cover cracking and spalling in concrete due to corrosion of reinforcement bars is one of the major concerns for durability of reinforced concrete structures and has been widely researched during recent years. Most approaches to the problem are based on a uniform corrosion and expansion pressure around the rebar. However, corrosion rust tends to accumulate around the steel circumference that faces the concrete cover. From this outer part of the rebar, the corrosion front gradually advances to the inner, which entails a non-uniform expansive pressure around the rebar. The purpose of the study is to simulate the effect of non-uniform rust distribution around the corroded rebar, taking advantage of an embedded cohesive crack finite element. The objective is to develop more realistic models for the estimation of the service life of reinforced concrete structures.

INTRODUCTION

Corrosion of reinforcement bars is one of the major reasons for deterioration of reinforced concrete (RC) structures. Oxidation of the reinforcement bars leads to the formation of rust which occupies a much greater volume than the original steel consumed by corrosion. Thus, tensile forces are generated in the surrounding concrete, with surface cracking eventually appearing.

Most approaches to the problem are based on a uniform corrosion and expansion pressure around the rebar. Such assumptions provide satisfactory results when modelling some laboratory accelerated corrosion tests (Andrade et al, 1993; Liu and Weyers, 1998; Bhargava et al, 2005; Chernin et al, 2010; Guzmán et al, 2011) and are generally accepted for the sake of simplicity.

However, a pitting or localised pattern represents the most common situation in concrete structures exposed to natural environments, especially regarding chloride-induced corrosion. The corrosion rust tends to accumulate around the steel circumference that faces the concrete cover. From this outer part of the rebar, the

corrosion front gradually advances to the inner, as chloride ions diffuse, which entails a non-uniform expansive pressure around the rebar. Although some recent studies have proposed elliptical or Gaussian distribution patterns (Liu and Li, 2004; Jang and Oh, 2010; Cao and Cheung, 2014; Du et al, 2014; Chen and Leung, 2015) for modelling, there is generally a lack of numerical simulation offered.

Therefore, the purpose of this study is to simulate the effect of non-uniform rust distribution around the corroded rebar. An embedded cohesive crack 2D finite element, as presented in previous work (Guzmán et al, 2012), is chosen here again in order to analyse the concrete fracture process. The objective is to develop more realistic models for the estimation of the service life of RC structures.

FINITE ELEMENT MODEL

Based on the so-called strong discontinuity approach (SDA), an embedded cohesive crack finite element (Sancho et al, 2007) is employed to model the non-linear fracture behaviour of concrete. In particular, a simple generalisation of the cohesive crack to mixed mode is used which assumes that the traction vector $\boldsymbol{t}$ transmitted across the crack faces is parallel to the crack displacement vector $\boldsymbol{w}$ (central forces model), i.e.:

$$\boldsymbol{t} = \frac{f(w)}{w}\boldsymbol{w}$$

where $f(w)$ is the classical softening function for pure opening mode (Figure 1). In order to avoid locking after a certain crack growth, the opportunity of crack adaptability within each element is provided, allowing the crack to adapt itself to the later variations in principal stress direction while its opening is small. Having exceeded a threshold value, the crack is considered consolidated and the crack direction becomes fixed. The finite element code FEAP (Taylor, 2013) is employed for numerical simulations. Plane strain formulation and the exponential softening curve are considered, assuming 100 N/m as the value of the specific fracture energy G_F.

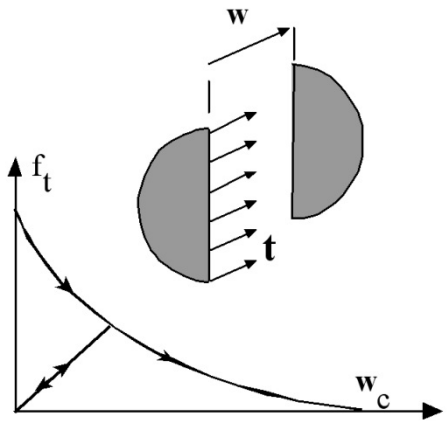

Figure 1. Softening curve for the cohesive crack model.

Regarding geometry, samples with a width of 150mm and with a middle side bar are considered, as indicated by Williamson and Clark (2000) who carried out experimental tests that will be compared with the present analysis results. Basic assumptions are the following:

1. Diameter of the bar, 16mm.
2. Cover depth-to-rebar diameter ratio (c/d) equals one.
3. Compressive strength of concrete f_c= 27.5/44.1 MPa. The corresponding Young's modulus is E_c= 24.8/31.4 GPa and tensile strength f_t= 1.83/2.55 MPa. In all cases, Poisson's ratio is v_c= 0.2.
4. For the sake of simplicity, the mechanical properties of oxide products are taken to be the same as those corresponding to steel. In addition, a perfect sliding contact is chosen to reproduce the oxide-concrete interface.
5. Free boundary conditions are considered in order to reproduce the single rebar case found in the laboratory tests.

CRACKING PRESSURE OF CONCRETE COVER

From real RC structures exposed to an aggressive environment, oxide products around the rebar usually take a pseudo-elliptical shape, in such a way that the closer to the concrete surface, the more corrosion takes place. Figure 2 shows the most used analytical models for reproducing non-uniform corrosion, through patterns of theoretical free expansion of the rebar. The parameter α is defined as the ratio of maximum rust expansion of that corresponding to the uniform case when the total corrosion product is kept constant.

Following Jang and Oh (2010), a first approach to the problem would be based on the concept of cracking pressure, i.e. the internal pressure required to cause cracking of concrete cover due to reinforcement corrosion. That involves the aim of obtaining the value of the cracking pressure depending upon the different values of α.

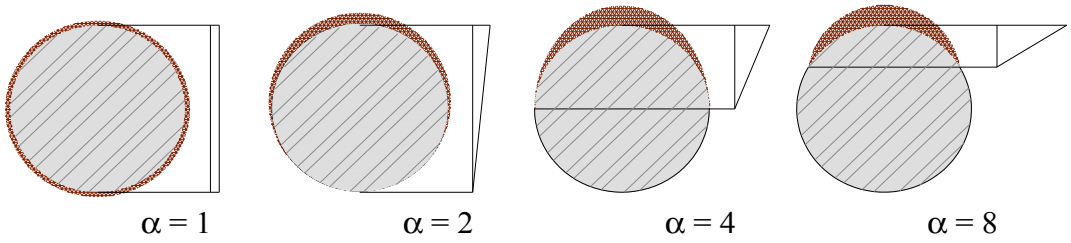

Figure 2. Different shapes of corrosion distribution in the reinforcement bar.

Contrary to the arguments offered by Jang and Oh (2010), in this case the reinforcement bar is considered explicitly in the finite element model. Conventional elastic parameters for steel are assumed (E_s= 210 GPa and v_s= 0.3). Figure 3 depicts the pressure distribution acting on both steel and concrete boundary surfaces as a function of α value. Figure 4 and Table 1 summarise the resulting cracking pressures in terms of α value.

For comparison purposes, cracking pressure is equal to p_{max}, $p_{max}/2$ and $p_{max}/4$ when α= 2, 4 and 8, respectively, in order to obtain an equivalent average uniform pressure on concrete and take into account both the action and reaction forces.

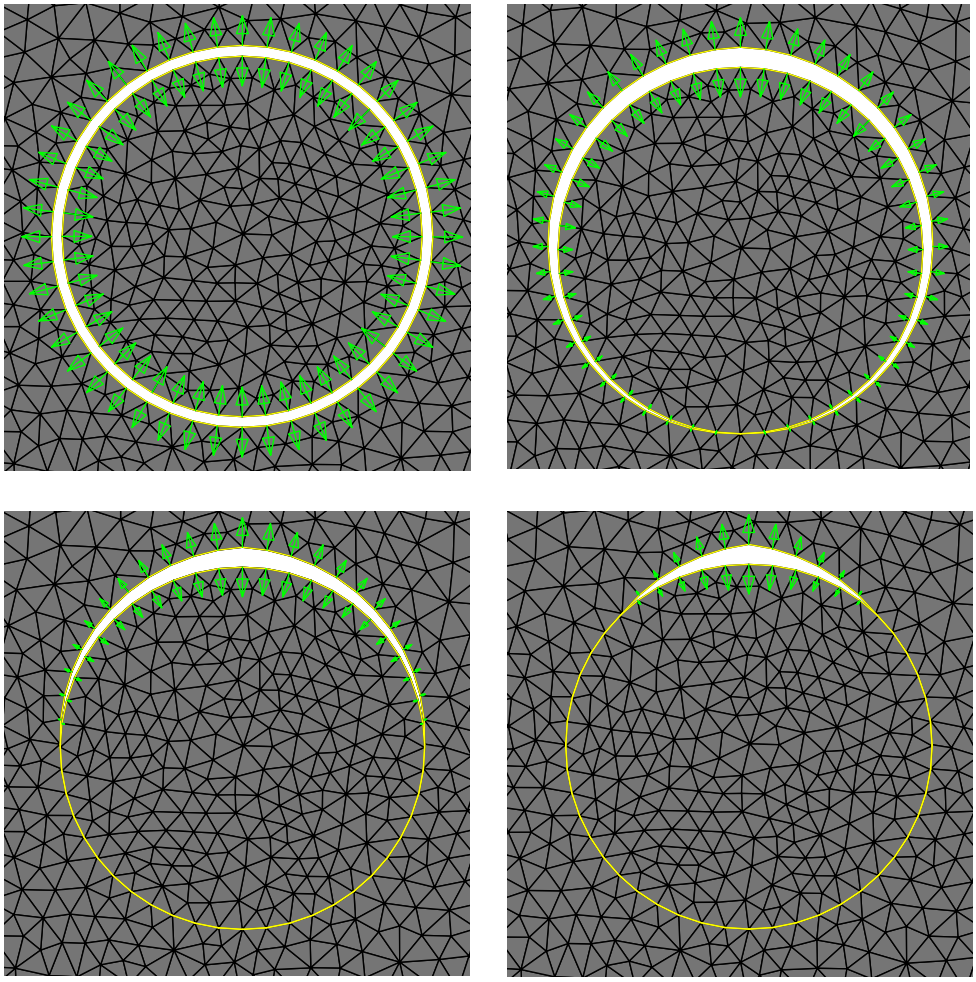

Figure 3. Pressure distribution around reinforcement bar (α= 1, 2, 4 and 8, respectively)

Two conclusions are derived: that cracking pressures clearly decrease as α value increases and that these strongly depend on tensile strength of concrete. The cracking pressure values obtained are similar to those found by Jang and Oh (2010), though some higher and experimental results provided by Williamson and Clark (2000) lead to greater cracking pressure for the uniform case (α= 1). This could be explained mainly because experimental tests are based on concretes with higher tensile strength ($f_t \approx$ 3.5 MPa). In addition, they are based on visual inspection of surface cracking and not when just the exact theoretical f_t value is reached at the concrete surface.

The effect of non-uniform corrosion over the first principal stress in concrete, when the first surface crack appears, is shown in Figure 5. In the bottom left corner of each diagram, nodal reactions on concrete inner boundary surface are also depicted.

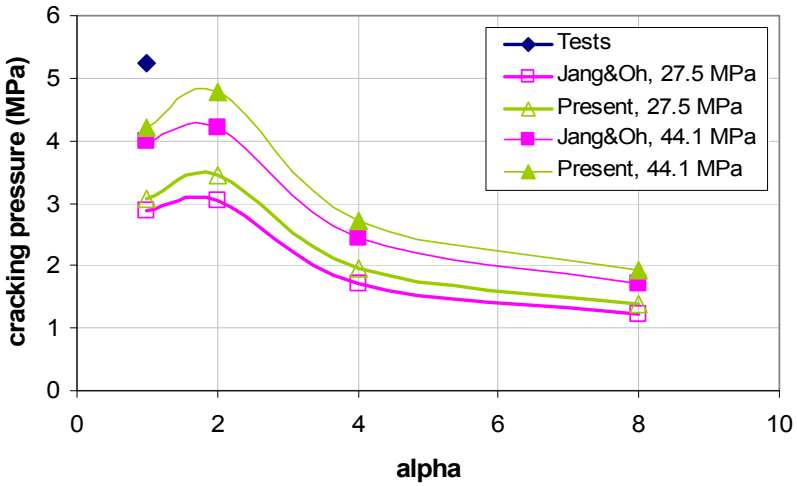

Figure 4. Cracking pressures as function of α. Please, see the text for references.

Table 1. Cracking pressures according to Figure 4 (MPa).

f_{ct} (MPa)	cover (mm)	A= 1	α= 2	α= 4	α= 8
27.5	16	3.1	3.4	2.0	1.4
44.1	16	4.2	4.8	2.7	1.9

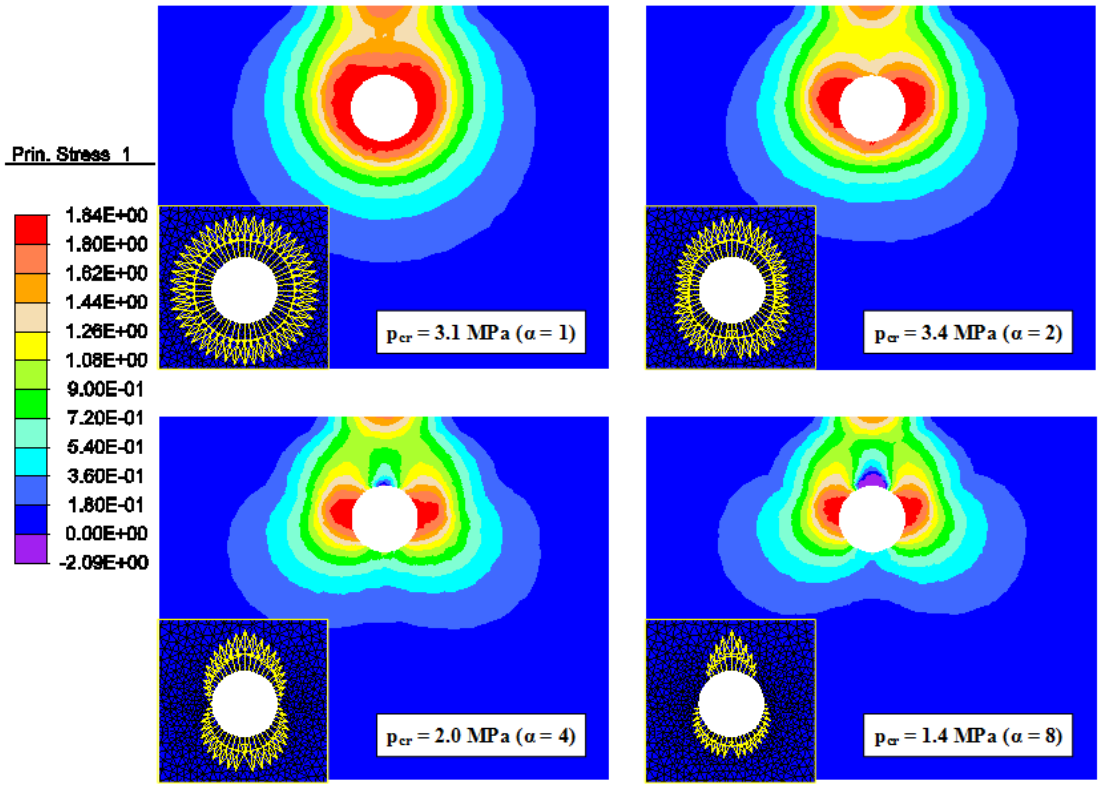

Figure 5. First principal stress and reactions in concrete under cracking pressure (MPa)

RUST EXPANSION

The next step is to introduce the effect of the rust expansion around the rebar, imposing displacement boundary conditions. Here, a fictitious increment of temperature in the rebar section will be used with a linear variation from 0 to ΔT_{max}, as shown in Figure 3. Then, the average ΔT_{avg} will be $\Delta T_{max}/2$, $\Delta T_{max}/4$ and $\Delta T_{max}/8$ when α= 2, 4 and 8, respectively. A conventional $\varepsilon = 10^{-5}$ is taken as the steel thermal expansion coefficient.

If Δ represents the rebar radius increment due to free expansion of corrosion products for the uniform case and R_i is the initial radius (nominal) of the rebar, Δ comes from the following:

$$\Delta = \varepsilon R_i \Delta T_{avg}$$

Figure 6 shows the corresponding free expansion of the 16 mm reinforcement bar (the vertical displacements are shown in a different colour) that obtains the same corrosion product volume (corresponding to Δ= 1.6 µm for the uniform case) but under different non-uniform cases. For the case α= 2, taking ΔT_{max}= 2 ΔT_{avg}, the same expansion unit volume is obtained directly. For the case α= 4, a factor equal to $3\pi/8 \approx$ 1.18 shall apply and, finally, for the case α = 8, this factor is 1.56.

For comparative purposes, the same figures as those shown in the previous section are obtained (Figure 7 and Figure 8).

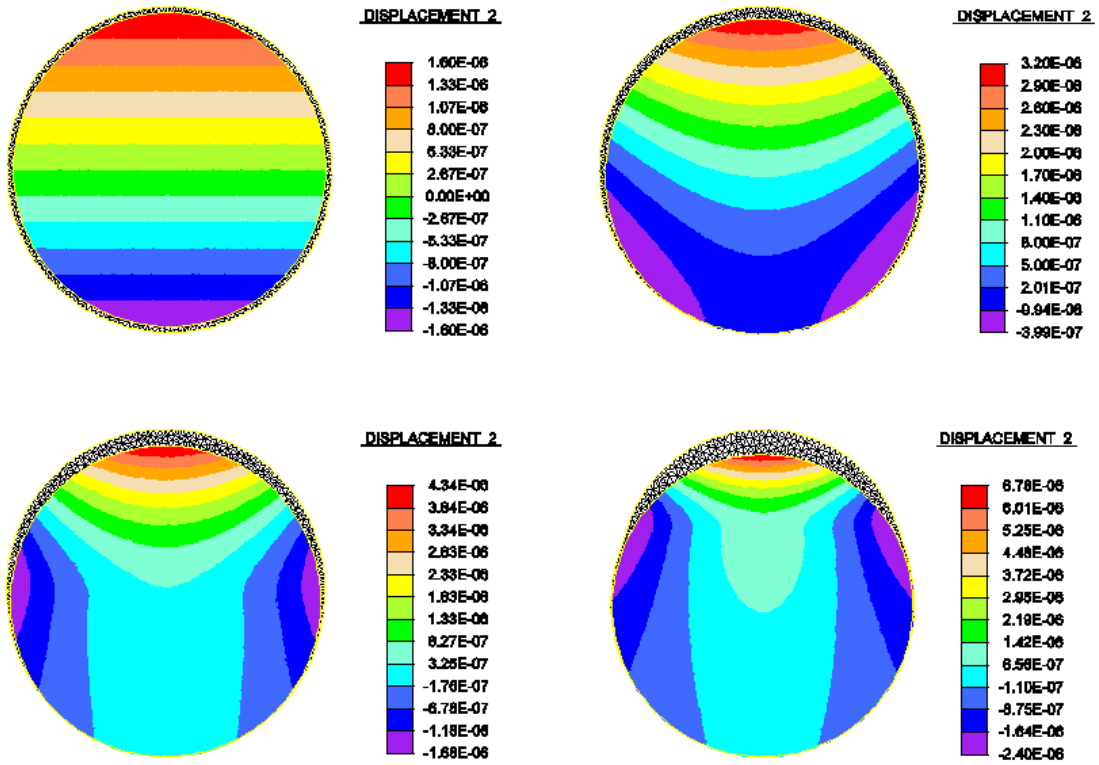

Figure 6. Free expansion of the reinforcement bar, ΔT_{avg}= 20ºC i.e. Δ_{avg}= 1.6 µm (α = 1, 2, 4 and 8, respectively).

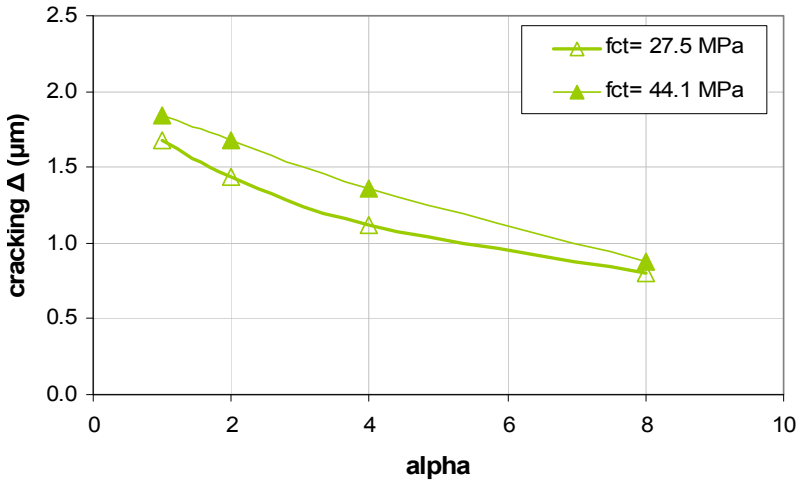

Figure 7. Cracking rebar radius increment as a function of α.

Table 2 Cracking rebar radius increment according to Figure 7 (μm)

f_{ct} (MPa)	cover (mm)	α= 1	α= 2	α= 4	α= 8
27.5	16	1.7	1.5	1.1	0.8
44.1	16	1.8	1.7	1.4	0.9

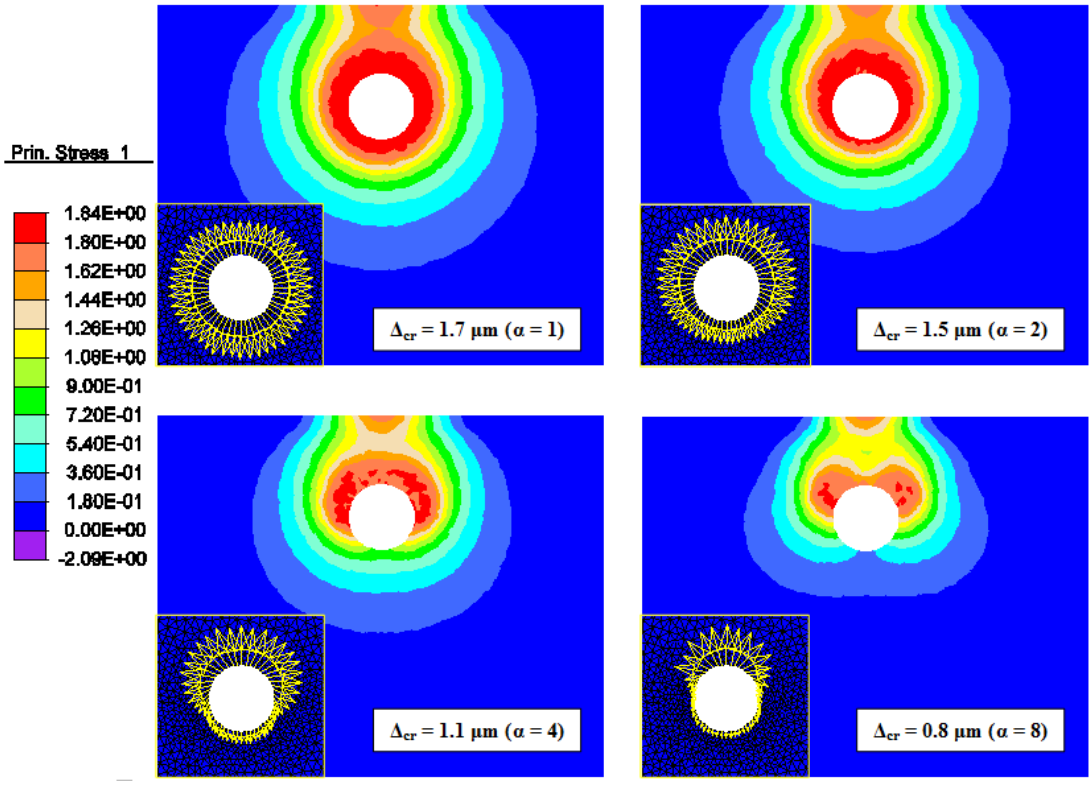

Figure 8. First principal stress and reactions in concrete under cracking rebar radius increment (MPa)

CONCLUSION

Taking advantage of an embedded cohesive crack finite element, the effects of non-uniform corrosion around a rebar on the surface cracking of concrete is explored under two approaches: imposed loads (cracking pressure) and displacements (rust expansion). Although the latter approach appears as a more realistic one, both do lead to a significant decrease of the corrosion amount needed to cause the concrete surface to crack when non-uniform corrosion is considered. As expected, the critical values depend on the compressive strength of concrete.

Further analysis would be required that considered certain other significant aspects, such as the influence of the ratio *c/d*, the determination of the rust mechanical properties and the penetration of these corrosion products in the microcracks of concrete.

ACKNOWLEDGEMENTS

The authors gratefully acknowledge the financial support provided by Ministry of Economy and Competitiveness of Spain by means of the Research Fund Project DPI 2011-24876.

REFERENCES

Andrade, C., Alonso, C., and Molina, F.J. (1993). “Cover cracking as a function of bar corrosion: part 1- Experimental test”. *Mater. Struct.*, 26: 453-464.

Bhargava, K., Ghosh, A.K., Mori, Y., and Ramanujam, S. (2005). “Modeling of time to corrosion-induced cover cracking in reinforced concrete structures”. *Cement Concrete Res.*, 35: 2203-2218.

Cao, C. and Cheung, M.M.S. (2014). “Non-uniform rust expansion for chloride-induced pitting corrosion in RC structures”. *Constr. Build. Mater.*, 51: 75-81.

Chen, E., and Leung, C. (2015). "Finite element modeling of concrete cover cracking due to non-uniform steel corrosion." *Eng. Fract. Mech.*, 134: 61-78.

Chernin, L., Val, D.V., and Volkh, K.Y. (2010). “Analytical modelling of concrete cover cracking caused by corrosion of reinforcement”. *Mater. Struct.*, 43(4): 543-556.

Du, X., Jin, L., and Zhang, R. (2014). "Modeling the cracking of cover concrete due to non-uniform corrosion of reinforcement." *Corros. Sci.*, 89: 189-202.

Guzmán, S., Gálvez, J.C., and Sancho, J.M. (2011). “Cover cracking of reinforced concrete due to rebar corrosion induced by chloride penetration”. *Cement Concrete Res.*, 41: 893-902.

Guzmán, S., Gálvez, J.C., and Sancho, J.M. (2012). “Modelling of corrosion-induced cover cracking in reinforced concrete by an embedded cohesive crack finite element”. *Eng. Fract. Mech.*, 93: 92-107.

Jang, B.S., and Oh, B.H. (2010). “Effects of non-uniform corrosion on the cracking and service life of reinforced concrete structures”. *Cement Concrete Res.*, 40: 1441-1450.

Liu, Y., and Li, Y. (2004). “Mechanistic model and numerical analysis for corrosion damage in reinforced concrete”. *Int. J. Fracture*, 126: 71-78.

Liu, Y., and Weyers, R. (1998). "Modeling the time-to-corrosion cracking in chloride contaminated reinforced concrete structures". *ACI Mater. J.*, 95(6): 675-681.

Sancho, J.M., Planas, J., Cendón, D.A., Reyes, E., and Gálvez, J.C. (2007). "An embedded crack model for finite element analysis of concrete fracture". *Eng. Fract. Mech.*, 74: 75-86.

Taylor, R.L. (2013). FEAP - A Finite Element Analysis Program, http://www.ce.berkeley.edu/projects/feap/.

Williamson S.J., and Clark, L.A. (2000). "Pressure required to cause cover cracking of concrete due to reinforcement corrosion". *Mag. Concrete Res.*, 52(6): 455-467.

Structural Performance Caused by Corrosion for RC Beams and Columns

Y. Shinohara[1]

[1]Structural Engineering Research Center, Tokyo Institute of Technology, Dr. Eng., G5-5 4259 Nagatsuta, Midori, Yokohama 226-8503, Japan. E-mail: shinohara.y.ab@m.titech.ac.jp

Abstract

Corrosion has known as a major problem on deterioration of RC structures because it may induce cracking of concrete cover as well as degradation of structural performance. Most of studies on the corrosion cracking have used a single bar in a concrete prism or a cylinder and absence of stirrup bars, which may not represent the real boundary condition of reinforced concrete members. The main objective of this paper is to investigate the influence of stirrup confinement, longitudinal bar diameter, concrete strength and corrosion rate on the cover crack propagation. Six beams were designed to experience a specified corrosion by performing an accelerated corrosion. The current flowed on each bar and the strains on the stirrups were recorded using data logger. The corrosion-crack behaviors were frequently observed using digital microscope. Furthermore, finite element analysis was performed to study the internal cracking behavior of RC beams and the structural behavior of corroded RC columns.

INTRODUCTION

Cracking of concrete cover due to corrosion product expansion of a steel bar is one of the main factors in determining durability performance and service life of RC structures. Although number of experimental studies evaluating the cracking behavior of concrete under corrosion of reinforcement for past years, most of studies used a single bar in concrete prism or cylinder and absence of transverse bars. The corrosion of steel induces not only cracking of concrete cover, but also stressing on the transverse bar. This may reduce the residual shear capacity of RC structures and it has not been widely explored in the previous studies.

The present study is intended to explore the influence of actual confinement provided by surrounding concrete and transverse bar on the cover cracking behaviors induced by corrosion of a longitudinal bar of RC beams, and to understand a general tendency on the structural performance or shear behaviors of corroded RC columns.

CORROSION TEST OF RC BEAMS

The proportion of concrete mixture used in an accelerated corrosion test is shown in Table 1. The beam specimens were cured for 28 days before accelerated corrosion test. The specified compressive concrete strength of 28 days was 22 N/mm^2 and 49 N/mm^2 for Fc24 and Fc48 respectively. The test variables include the ratio and

configuration of transverse bars, diameter of longitudinal bar and concrete strength (Table 2 and Figure 1). To measure the strain development on transverse bar due to corrosion cracking, three gages were installed at each transverse bar, as shown in Figure 1. The non-corroded transverse bars were used by covering with vinyl tape to protect gages during accelerated corrosion of longitudinal bars. The tank containing 3% of NaCl solution was put below the specimens and NaCl solution penetrated to the concrete through water sponge, as shown in Figure 2. The current and strain were monitored and recorded by data logger in 60 minutes increments.

The cracks on the surface of cover were visually observed and the crack width at certain locations was frequently measured using a digital microscope having a resolution of 0.01mm to measure the crack width increment, as shown in Figure 3.

Table 1. Mixture proportions.

Mix ID	w/c (%)	Cement (kg/m^3)	Water (kg/m^3)	Sand (kg/m^3)	Gravel (kg/m^3)
Fc24	74	257	190	830	979
Fc48	46	392	180	807	979

Table 2. List of specimen designations and test variables.

Designation	Concrete strength σ_B (N/mm^2)	Longitudinal bar	transverse bars ratio p_w
Fc24-LB4-Pw0	22	4D19	0%
Fc24-LB4-Pw015		4D19	0.15%
Fc24-LB4-Pw03		4D19	0.3%
Fc24-LB4-Pw03M		4D19	0.3%
Fc24-LB3-Pw03		3D22	0.3%
Fc48-LB4-Pw03	49	4D19	0.3%

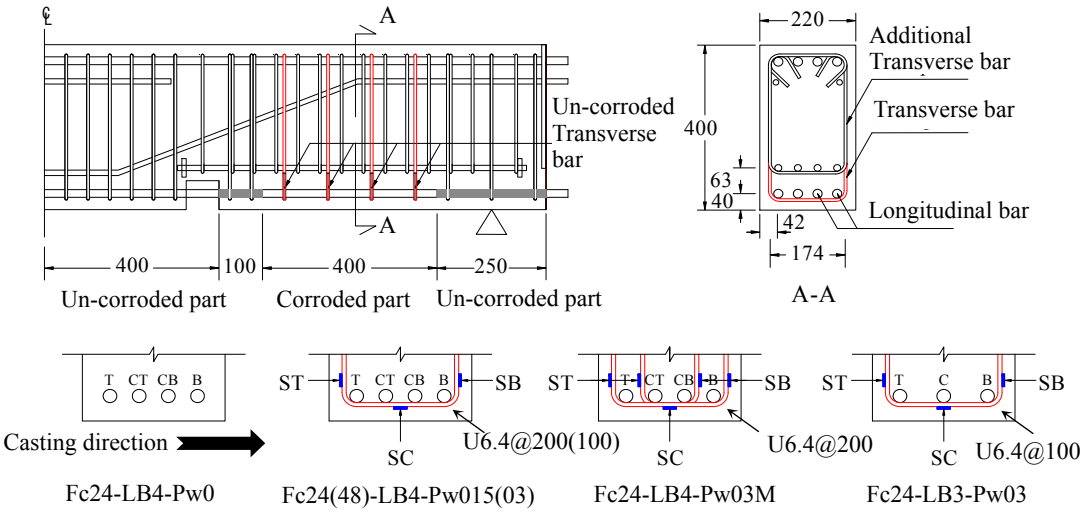

T, CT, CB, B: index of longitudinal bar location; ST, SC, SB: index of gages location at transverse bar

Figure 1. Typical specimen configuration and gage attachment.

The longitudinal bars were corroded up to approximately 6% of weight loss. To accurately determine the corrosion rate of bars, the steel bars were removed from the concrete, chemically and mechanically cleaned, and measured the weight loss.

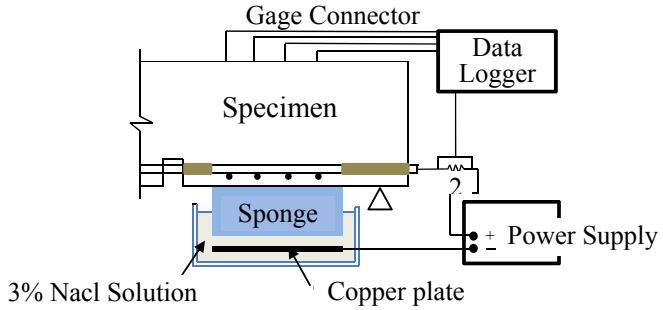

Figure 2. Overview of accelerated corrosion test.

Figure 3. Measurement of corrosion crack width using digital microscope.

CORROSION TEST RESULTS

Corrosion loss in weight. Table 3 shows a measured corrosion loss of each bar. A different corrosion loss of each bar (i.e. T, CT, CB and B) on each specimen was obtained although the measured current of them was relatively similar. The higher corrosion loss was obtained from the corner bar (T and B) having two directional surfaces and the largest one was located at top in casting. This can be because the bar located at top of concrete casting tends to have higher porosity than at bottom casting due to a settlement of fresh concrete. Furthermore, the corrosion process is given as a function of the time. If the average measured corrosion loss in one specimen is compared with estimated corrosion loss by Faraday's law, the difference between the two methods is approximately 10%.

Table 3. Corrosion in weight loss (%).

Designation	Bar Location (see Figure 1)					Predicted i
	T	CT	CB	B	Average	mA·hr/cm^2
Fc24-LB4-Pw0	10.6	4.7	3.8	5.6	6.2 (222)	210
Fc24-LB4-Pw015	8.9	4.9	4.4	4.9	5.8 (207)	210
Fc24-LB4-Pw03	8.2	4.4	5.4	6.3	6.1 (218)	210
Fc24-LB4-Pw03M	7.4	4.5	4.6	5.2	5.4 (195)	210
Fc24-LB3-Pw03	7.4	3.9		6.3	5.8 (243)	262
Fc48-LB4-Pw03	6.6	4.0	6.0	6.1	5.7 (205)	210

Note: number in the parenthesis shows the equivalent of accumulative current density estimated by Faraday's Law in mA·hr/cm^2

The appearance of localized corrosion (pitting) can be seen after removing the bar from the concrete and cleaning (see Figure 4). The sign of localized corrosion and more severe corrosion mostly occurred at the side of steel bar which faces to chloride solution penetration, i.e. the cover side. This could be attributed to current flow and diffusion chloride solution only came from one direction (the bottom side of a beam).

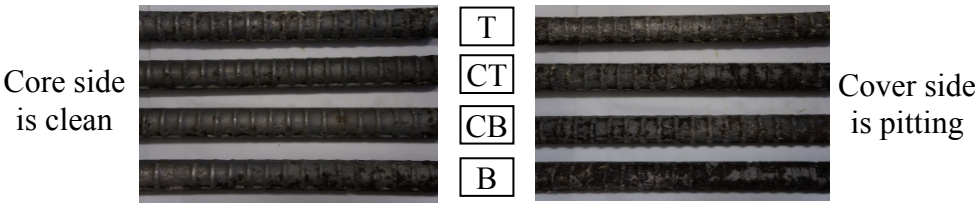

Figure 4. Appearance of corrosion from Fc24-LB4-Pw0 specimen.

Corrosion crack pattern. The first crack on the concrete surface was visually observed within a few days after accelerating for all specimens. The crack was initiated at bottom side of beams and mostly located near corner bar. The crack then propagated and formed a continuous crack approximately parallel to the longitudinal bar. The final crack patterns and the crack width up to corrosion loss of 6% are shown in Figure 5. A relatively close spacing of longitudinal bar seems to promote the corrosion crack among bars to propagate horizontally connecting each longitudinal bar. This can be confirmed from the stain in Figure 5 after removing the bottom cover.

The relations between observed maximum crack width and average corrosion penetration are shown in Figure 6. The average corrosion penetration was determined from means value for all longitudinal bars in one specimen. The corrosion penetration at first concrete cracking is around 30-60 micrometers for all specimens.

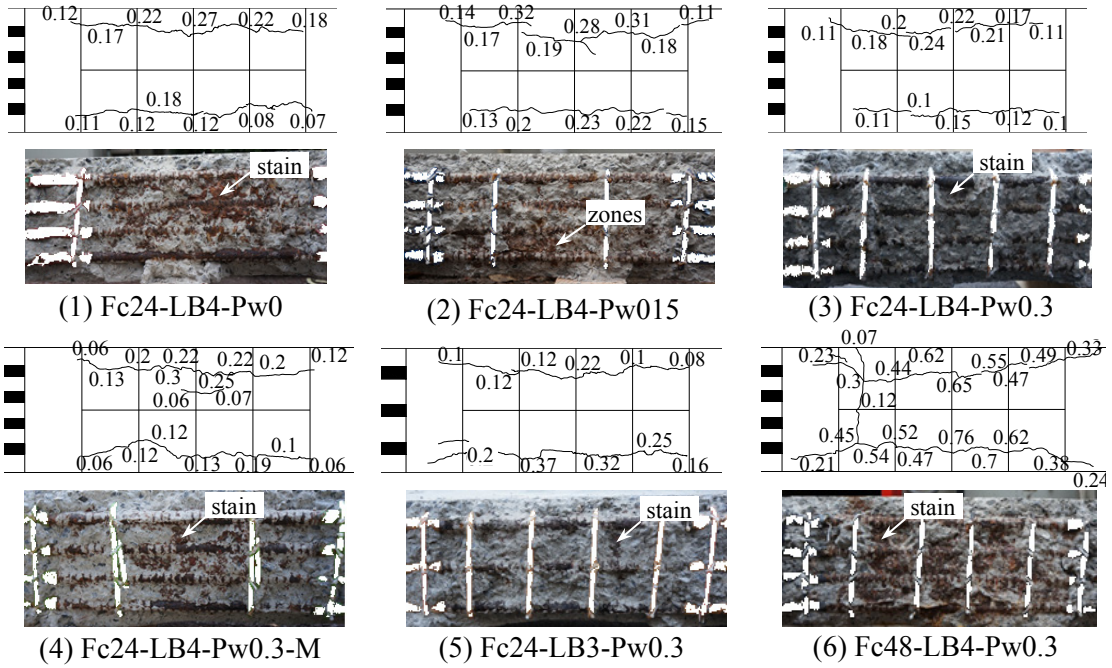

Figure 5. Crack patterns at final corrosion and stains after removing the cover.

For the higher strength Fc48-LB4-Pw03 specimen, it clearly shows that the crack width is larger than specimens having normal concrete strength at similar corrosion levels. This trend can be often attributed to the concentration of corrosion products in a crack because of lower porosity of high strength concrete, as shown in Figure 7 reported by Tanaka (2001). The effect of transverse bar seems insignificant on the cover crack width growth. This can be attributed to the use of vinyl taping.

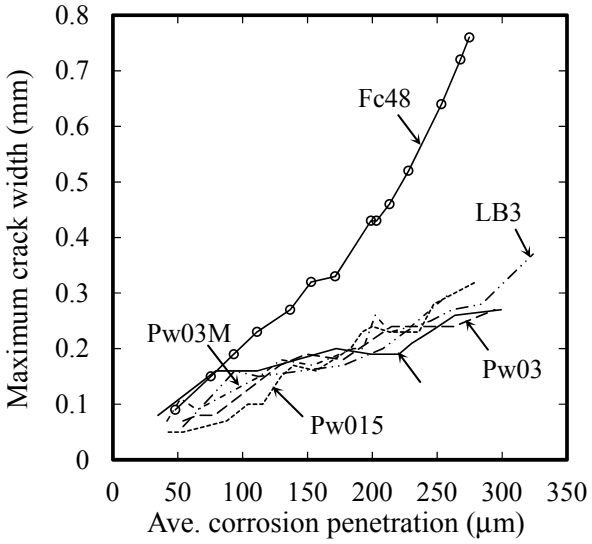

Figure 6. Relationship between maximum crack width and corrosion penetration.

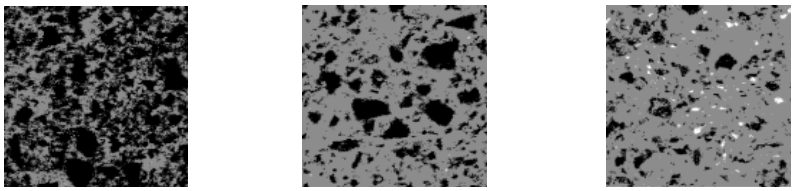

Figure 7. Effect w/c ratio on pore structure of hardened cement paste.

Transverse bar strain induced by corrosion. The strain of transverse bars will be also generated by the concrete cracking around corroded longitudinal bar and greatly depends on cracking behavior and the bond interaction. Figure 8 shows the relation between corrosion of longitudinal bar and measured strain of transverse bar. For specimen with normal concrete strength and transverse bar ratio of 0.15-0.3%, the observed strain on the transverse bar is relatively small lower than 200μm or 40 N/mm^2. However, a higher strain at transverse bar was observed for specimen with high strength concrete. Maximum strain generated at the bottom leg (SC) for Fc48-LB4-Pw03 is 700 μm or 140 N/mm^2 which will reduce almost 50% of its capacity for normal strength of transverse bars. Therefore, it may significantly reduce the residual shear capacity of RC structures under service loading or seismic loading.

The strain at the bottom leg (SC) tends to have larger tensile strain than at the side leg (ST and SB) because the majority of cracks are propagated at bottom side of

beams crossing the bottom leg of stirrups. Only one side crack is appeared in the high strength specimen, so that a strain of side leg increases, as shown in Figure 5 (6).

Assuming a complete bond between concrete and transverse bar, the strain on the transverse bar can be roughly estimated from the total crack width. For example, the strain of bottom leg of Fc24-LB4-Pw03 is approximately 0.39 mm/174 mm = 2300 μm. The observed stirrup strain from the test is not so large compared with the above estimation. It can be due to the bond is not perfect due to vinyl taping.

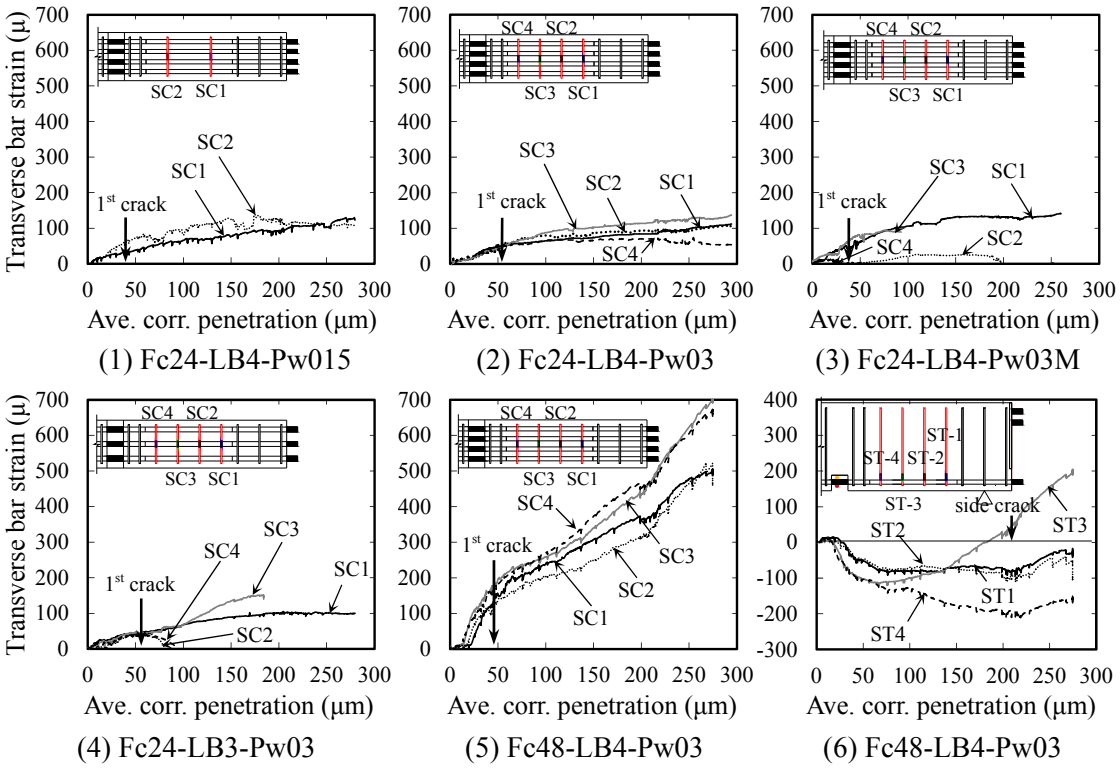

Figure 8 Measured strain of transverse bar at bottom leg (SC) and side leg (ST).

NONLINEAR ANALYSIS FOR CORROSION CRACK BEHAVIOR

Modeling approach. For the sake of simplicity, two-dimensional (2D) analysis with plane stress elements having a thickness of exposed length (400 mm) were used to model the concrete for a half of beam sections. The longitudinal bars were modeled as holes and the transverse bars were modeled using truss elements (Figure 9). To simulate corrosion-product expansion, the expansion pressure around corroded bar was applied by the internal pressure. The internal pressure of corner bars, which were greatly corroded in tests, was assumed to be two times of middle bars.

The mechanical properties of concrete, transverse steel and bond-slip relation are shown in Figure 10. The concrete behavior under compression was assumed to be linear because of low levels of compressive stresses. After cracking, bi-linear tension softening model was adopted. The transverse steel used a bi-linear model without strain hardening. The bond-slip relationship for a transverse bar covered by taping was determined according to CEB-FIP Model code as plain bars.

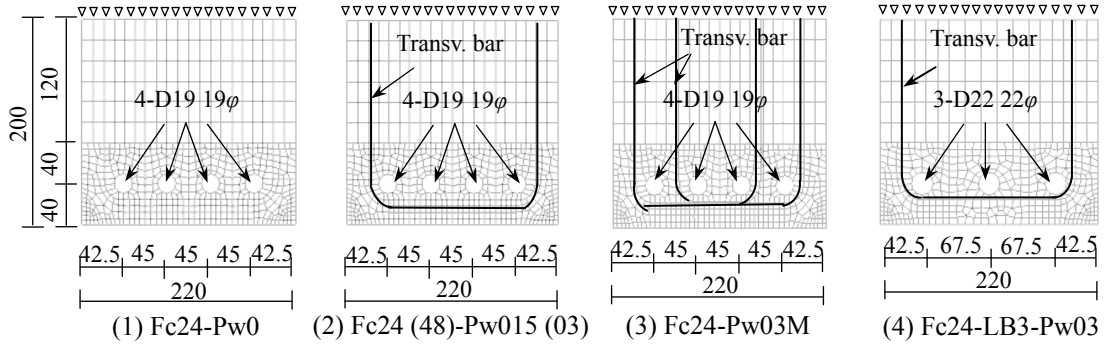

Figure 9. Typical finite element modeling.

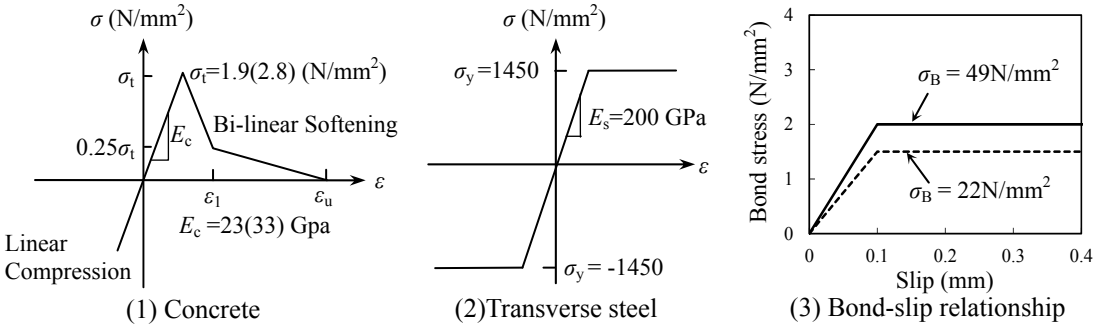

Figure 10. Mechanical properties for concrete, transverse steel and bond-slip.

Cover crack propagation. Figure 11 shows crack strain behaviors obtained from FE analysis at the first cracking of the surface. The expansive pressure p and the depth of corrosion penetration x, which was calculated using Lundgren (2002) models with the relative volume of the rust to corroded steel, v = 2, are also provided in the figure. From Figure 11, the crack initially tends to form a horizontal crack pattern connecting each longitudinal bar, and then mostly propagates to concrete surface near the corner beam indicated by higher crack strain. This crack pattern and corrosion penetration, x, show a good agreement with the experimental results (see Figures 5 and 6).

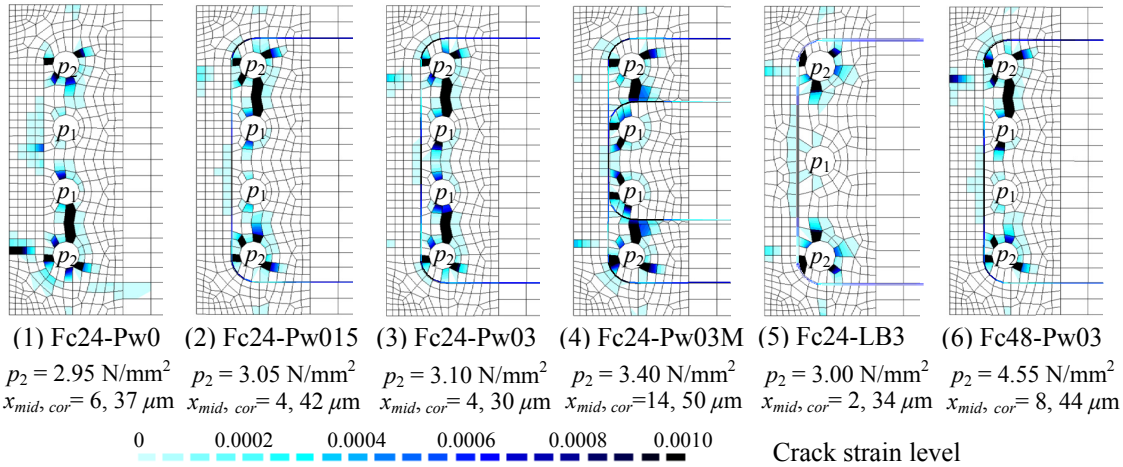

Figure 11. Crack strain behaviors and corrosion penetration at first cracking.

Cover crack width. A comparison of the total crack width on the concrete surface in the experimental and the analytical results are shown in Figure 12. The total crack width from the experiment was determined as the summation of crack width at one section of the exposed length. Meanwhile the total crack width from FE analysis was determined by the relative nodal displacement of two corner beam section because concrete tensile strain is generally negligible. For specimens with normal concrete strength, the analytical result shows a good agreement with the test by assuming $\nu = 2$. However, for specimens with high strength concrete, it generates an underestimate prediction compared with experimental results. This indicates that a large expansion ratio is required for high strength concrete because only a small amount of corrosion products can penetrate to the lower porosity. The ratio of volume increase of $\nu = 2.5$ to 3 gives a good agreement with test results.

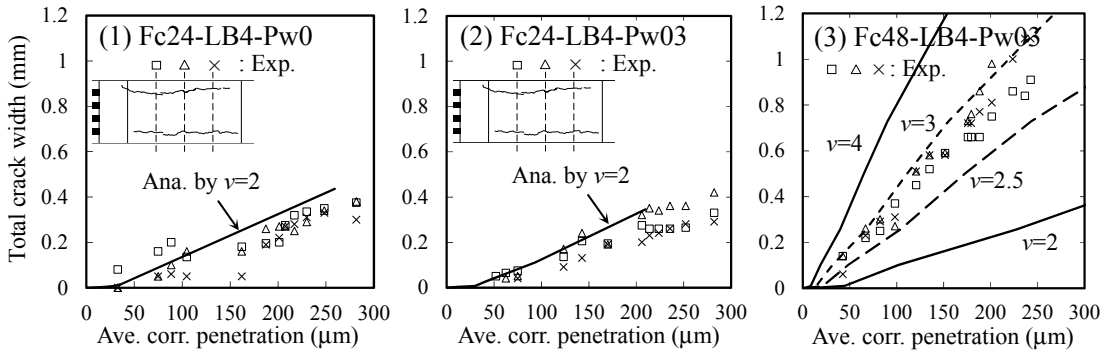

Figure 12. Corrosion penetration and total crack width relationship.

STRUCTURAL PERFOMANCE OF DETERIORATED RC COLUMNS

In order to evaluate the effect of corrosion on the serviceability and the safety performance of RC structural members, a finite element analysis was conducted on corroded RC columns with a special attention in transformation of material properties of reinforcements, concrete and bond properties due to corrosion. The configuration of column is based on the experimental specimen performed by Shinohara (2010). However, some modification was made by changing the longitudinal bars and the transverse bars to make the column failed in flexure for the uncorroded columns. FE model and boundary conditions are summarized in Figure 13. To assess the effect of corrosion, three different corrosion levels (3%, 6% and 10% in weight loss) are considered including the uncorroded columns as reference.

The mechanical properties of materials corresponding to corrosion level are summarized in Figure 14. The steel bars used a bi-linear model. The stress generated on transverse bars due to corrosion crack is also considered to be taken into account in the analysis using the apparent yield strength. The bond stress slip relationships of longitudinal bar proposed by Aris (2014) were adopted, as shown in Figure 15.

Figure16 shows the shear force and rotation angle of columns under (1) no axial force and (2) axial force ratio of 0.1. The stiffness decay can be explained from the chain of events corresponding to the formation of bending cracks, bending shear cracks, crushing of concrete cover, the yielding of transvers bars and longitudinal bars.

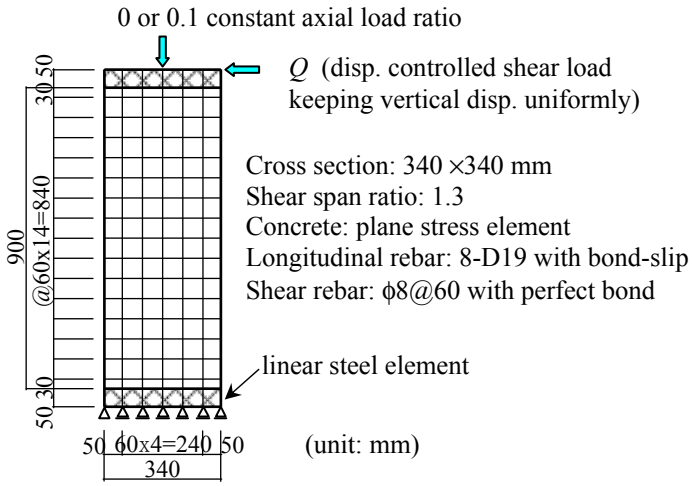

Figure 13. Finite element model and boundary conditions of RC column.

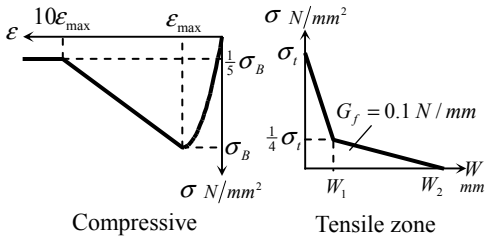

	Concrete			Longitudinal		Transverse	
Corr. level	σ_B N/mm^2	E_c N/mm^2	σ_t N/mm^2	σ_y N/mm^2	E_s N/mm^2	σ_{wy} N/mm^2	E_{ws} N/mm^2
0 %	48	34300	2.8	345	200000	295	205000
3 %	32	26700	1.9	325	193000	208	198000
6 %	26	24100	1.5	304	186000	130	191000
10 %	26	24100	1.5	277	171000	39	182000

Figure 14. Mechanical properties corresponding to corrosion level.

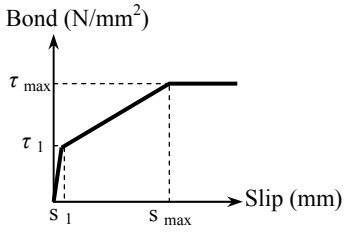

Corr. level	τ_1 N/mm^2	τ_{max} N/mm^2	s_1 mm	s_{max} mm
0 %	2.0	5.60	0.02	1.00
3 %	2.0	5.26	0.02	0.91
6 %	2.0	4.93	0.02	0.82
10 %	2.0	4.48	0.02	0.70

Figure 15. Analytical model for bond-slip corresponding to corrosion level.

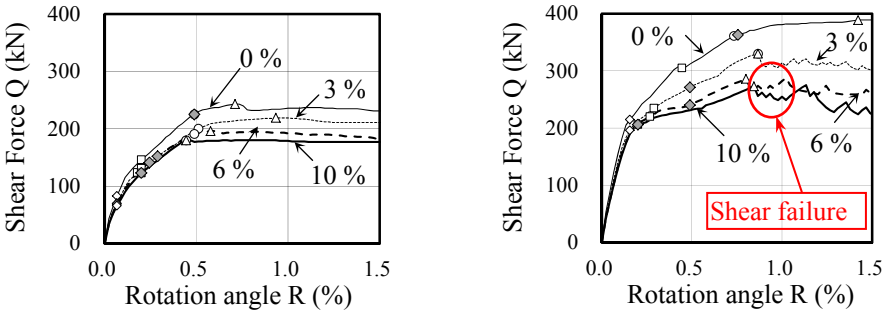

Figure 16. Numerical results of shear force-rotation responses of RC column.

Without an axial load, the cracking events and the yielding of bars for the corroded columns are almost similar to the uncorroded columns. However, the specimens having an axial force and corrosion levels of 6% and 10% behave quite differently, as shown in Figure 16 (2). They show that larger corrosion level increases the possibility to have the cracking and the yielding of transverse bars at lower shear force level. Moreover, the axial force promotes a shear failure before yielding of longitudinal bars. This can be attributed to the lower apparent yield strength of transverse bar and bond degradation induced by corrosion cracking. Thus, this analysis indicates that the failure mode of RC columns can be changed with increasing corrosion levels from flexural failure preceded by yielding of longitudinal bars to shear failure before bar yielding which displays a more brittle behavior.

CONCLUSION

1) Corrosion rate is not uniformly distributed among longitudinal bars in a beam and over perimeter of bar caused by the different of bar location in casting direction, the direction of chloride diffusion, and the supply of water and oxygen.
2) Both experimental and analytical results indicate that crack initiated in concrete surface occurs in small corrosion penetration around 30 to 60 micrometers.
3) The difference of porosity in hardened cement paste has a significant influence on the crack width growth and the stress increase of the transverse bars.
4) The relative volume of the rust to corroded steel, v=2 for normal strength concrete, and v =2.5 to 3 for high strength concrete give a good agreement with test results.
5) The failure mode of RC columns can be changed with increasing corrosion levels from flexural failure preceded by yielding of longitudinal bars to shear failure before bar yielding which indicate a brittle behavior.

ACKNOWLEDGEMENTS

The authors acknowledge the supports of the Nuclear Regulation Agency as a part of the project on Enhancement of Ageing Management and Maintenance of Nuclear Power Stations.

REFERENCES

Tanaka, K. and Kurumisawa, K. (2001). “Development of technique for observing pores in hardened cement paste.” Cement and Concrete Research, Vol.32, 1435-1441.

Lundgren, K. (2002). “Modelling the effect of corrosion on bond in reinforced concrete.” *Magazine of Concrete Research*, 54(3), 165-173.

Shinohara, Y. (2010). “Effect of Axial Load on the Shear-Transfer Mechanism during Shear Damage Progress in R/C Columns.” *The Third International Congress and Exhibition fib,* Paper ID 48.

Aryanto, A., and Shinohara, Y. (2014). “Bond Splitting Capacity of Corroded Reinforced Concrete Members.” *Proceedings of the Japan Concrete Institute,* Vol.36, No.2, 415-420.

Numerical Modelling of ASR Expansions in Concrete

J. Liaudat; A. Martínez; C. M. López; and I. Carol

Department of Geotechnical Engineering and Geo-Sciences, ETSECCPB (School of Civil Engineering)-UPC (Technical Univ. of Catalonia), c/Jordi Girona, 1-3 (D2), 08034 Barcelona, Spain. E--mail: joaquin.liaudat@upc.edu; ariadna.martinez.e@upc.edu; carlos.maria.lopez@upc.edu; ignacio.carol@upc.edu

Abstract

In the context of a project to characterize and model the Alkali-Silica Reaction in concrete, the results of a series of tests on specimens with a single interface between aggregate and cement paste, and the comparison to the numerical results of a simplified diffusion-reaction Finite Element model are presented. The tests are conceived as the simplest test to characterize the basic constituent reactions of the process. The model implemented is a first operational version of a more general three-species diffusion-reaction model already formulated and in the process of implementation. In spite of its relative simplicity, the model described seems capable of reproducing the experimental observations with specimens tested under different diffusion boundary conditions, and provides a satisfactory basis for further development.

INTRODUCTION

Expansion due to Alkali Silica Reaction (ASR) is the second most common cause of concrete deterioration, after reinforcement corrosion. First reported in 1940, its reaction-expansion mechanism is not yet fully understood. It is accepted that certain types of metastable silica present in aggregates are attacked by hydroxyl ions in concrete pore solution producing its dissolution into silicate ions. These ions recombine with alkalis and calcium ions in an expansive reaction forming Calcium-Alkali-Silicate-Hydrates of variable stoichiometry, molar volume and mechanical properties. The expansive gel is formed mainly around aggregates and in cracks within them or near them, leading to expansions and more cracking. This mutual influence of the cracking and expansions confers to the process the C-M coupled character that should be reflected in the formulation. Another characteristic feature of ASR expansions (that make them different from other expansive processes such as external sulfate attack for instance) is the interaction with mechanical actions, such as for instance in the case of lateral confinement a specimen tends to expand considerably more on the “free” direction so that the total volume expansion is preserved (Multon & Toutlemonde 2006).

This paper presents part of the ongoing research project which aiming to the formulation and experimental validation of a coupled chemo-transport-mechanic (C-T-M) reaction-expansion mechanism of ASR expansions in concrete as it has been done before by our research group for external sulfate attack (Idiart et al. 2011).

First, a new experimental set-up to study the expansion mechanisms at the level of a single matrix-aggregate interface using sandwich-like cylindrical specimens of cement paste/mortar and glass is described, and some results concerning with the effect of alkali diffusion in the development of ASR are presented.

Finally, as an intermediate step in the development of the complex C-T-M model, a simplified reaction mechanism is formulated and implemented in Finite Element Method (FEM) to interpret the experimental results presented.

AAR-INTER TESTS

The aim of this test is to measure the expansions at the level of a single interface aggregate-matrix due to the precipitation of ASR products. For this purpose, two kinds of cylindrical specimens of 33 mm diameter and 66 mm height are elaborated. The first type, named "Active specimens", involves sandwich–like specimens, with cement paste or mortar on top and bottom of a disc of reactive aggregate in the middle (Figure 1). The second one, called "Control specimens", involves purely mortar or cement paste specimens without reactive aggregate. Control specimens are used to assess the deformations of the matrix of cement paste or mortar, solely caused by phenomena such us drying shrinkage or thermal expansions. All the specimens count with stainless steel terminals on their symmetry axes to properly measure their length changes.

So far, soda-lime glass and borosilicate glass have been used as reactive aggregates because of their advantageous of homogeneity as industrial materials. Once the methodology has been demonstrated, natural reactive aggregates will be used.

After casting, the specimens are kept in the molds for 24hs in a humid chamber. Once unmolded, they are cured in airtight containers with a solution of sodium hydroxide of 1 mole/litre at 23ºC during 27 days (Curing Stage). Finally, the containers are introduced in an oven at 60ºC until the end of the test (Exposure Stage). The sodium hydroxide solution keeps the specimens saturated of water and prevents the leakage of alkali ions from the cement paste. During both stages, specimen length changes are measured regularly with a machinist's dial indicator until the end of the test.

It must be mentioned that a similar test has been previously proposed by Schlangen and Çopuroglu (Schlangen & Çopuroğlu 2007). However, they have not presented, to the best of the author's knowledge, any results since then.

Influence of alkali diffusion. One controversial issue of the AAR-INTER tests is that the matrix-aggregate interfaces are in direct communication with the alkaline solution. In conventional accelerated ASR test, namely ASTM 1260, where concrete or mortar specimens are used, most of the aggregates are completely surrounded by the cementitious matrix, so that alkaline ions from the exposure bath have to go through the Hardened Cement Paste (HCP) before reaching the Interfacial Transition Zone (ITZ) where the reaction takes place, i.e. the external alkali income to the ITZ will be determined by the HCP diffusivity. In the case of AAR-INTER specimens the external ionic flux of alkaline ions is expected to be highly influenced by the diffusivity of the ITZ, which is usually higher than HCP one (Ollivier et al. 1995) due

to its higher porosity or the presence interfacial cracks, preexistent or originated by the ASR.

In order to assess the influence of the alkali diffusion through the ITZ, three sets AAR-INTER specimens with different lateral sealing have been tested (Figure 1):

Set #1: Specimens without lateral sealing
Set #2: Specimens with complete lateral sealing
Set #3: Specimens with lateral sealing of 10mm width covering aggregate (glass), the ITZ and the immediate HCP.

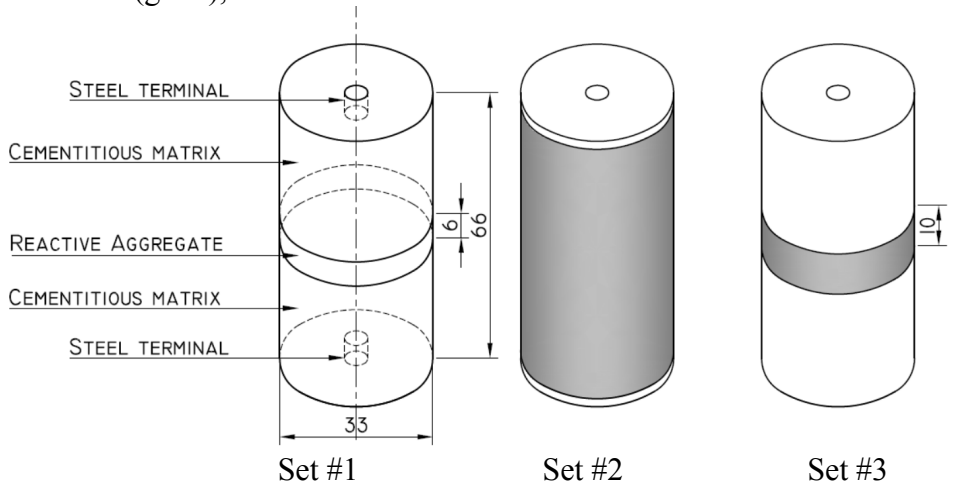

Figure 1. Configuration of AAR-INTER active specimens and schematic representation of the three sets of specimens tested with different lateral sealing.

The specimens where elaborated with cement paste as cementitious matrix and 6mm width soda-lime glass as reactive aggregate. Each set consisted in 4 active specimens and 4 control (without glass) specimens. The cement used was Type I 42.5R (UNE-EN 197:1) and the water/cement ratio was 0.47. Sodium Hydroxide was added to the mixing water in order to raise the equivalent sodium dioxide content to 1.1% of the cement weight. The lateral sealing was materialized with self-curing rubber tape once the curing period was end, just before putting the recipients into the oven.

From the length change measurements of active and control specimens during the exposition stage, the expansions d_I corresponding to the ASR reaction products precipitated in a single interface matrix-aggregate were obtained using

$$d_I = \frac{1}{2}\left[\Delta L - \bar{\varepsilon}^c(L - e) - e \propto_{glass} \Delta T\right]$$

where L and ΔL are the length and the length change of the active specimen respectively, e is the width of the glass disc, $\bar{\varepsilon}^c$ is the average deformation of the control specimens, α_{glass} is the linear thermal expansion coefficient of the glass and ΔT is temperature variation from curing (23ºC) to exposure (60ºC). In Figures 2 to 4 d_I is plotted against time for each tested specimen. Where indicated with a letter D over the last measurement, the test finished because one of the glass faces detached from the HCP.

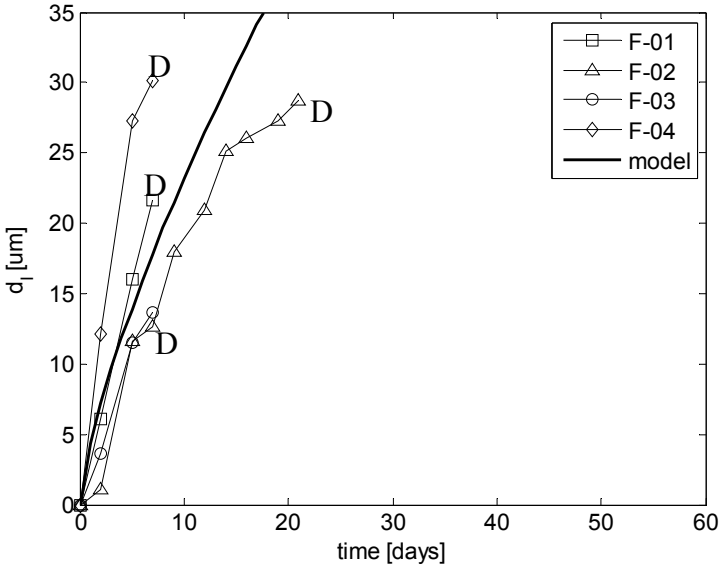

Figure 2. Specimens without lateral sealing (Set #1).

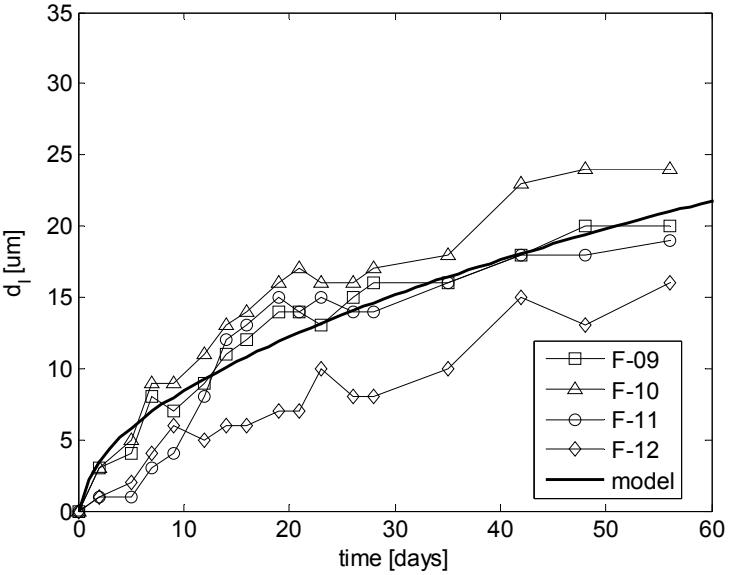

Figure 3. Specimens with complete lateral sealing (Set #2).

The dispersion of the results shall be attributed to the testing methodology. Measuring such a small elongation manually with a machinist's dial indicator taking the specimens out of the hot bath introduces both random and systematic errors due to thermal deformations and to the positioning of the specimen within the measuring frame. However, the overall expansive behavior and the influence of the sealing in the kinetics can be appreciated.

Specimens from set #1 (without any sealing) expand clearly faster than the remaining ones until one of the glass faces detached from the HCP. Comparing the curves of set #2 and #3, seems clear that sealing the ends of the specimens, (and therefore preventing the ingress of external alkalis from the bath through continuum

HCP) has a minor effect on the kinetics of the expansions. Therefore, the results seem to confirm our assumption that the kinetics of the expansion is mainly determined by the flux of external alkalis into the specimens, and that this flux is mainly localized along the ITZ.

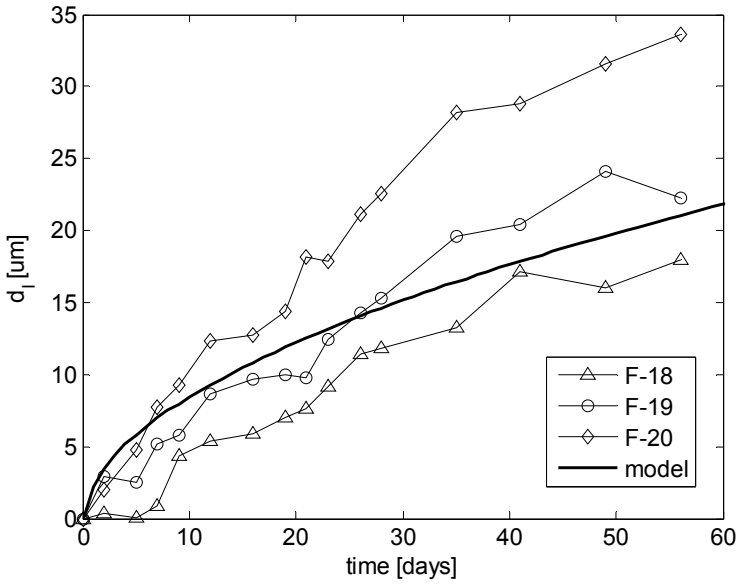

Figure 4. Specimens with lateral sealing only on the HCP-glass interface zone (Set #3).

NUMERICAL MODEL FOR ASR IN GLASS-HCP INTERFACES

As an intermediate step in the development of a chemo-transport-mechanic numerical model for ASR expansions in concrete, here is presented a simplified chemical formulation which is however considered valid for the simulation of the particular case of ASR expansions in a HCP-glass interface. This chemical formulation was implemented in the context of a preexistent FE code (DRAC-FLOW) for the analysis of diffusion problem. As a result of ASR, local expansions over time are calculated and written in an external file that is later read by a second FE code (DRAC) for the mechanical analysis which interpret them as local pseudo-thermal expansions, returning the stress-strain state of the material.

A more general and complex formulation for ASR in concrete has been proposed by the authors elsewhere (Liaudat et al. 2014), and it is the final goal of the research program to implement it in a coupled scheme in which the changes of the transport properties of the material due to cracking and the related effects in the development of the expansions could be assessed.

Simplified reaction mechanism. The reaction mechanism considered is based in two subsequent reactions occurring at pore solution in contact with the glass. First, the soda-lime glass in contact with the alkaline pore solution is attacked by hydroxyl ions, dissolving it in silicate, calcium and alkali ions

$$\underbrace{(SiO_2)(CaO)_x(Na_2O)_y}_{soda-lime\ glass} + (1-2x-2y)OH^- + (1+x+y)H_2O \rightarrow SiO_4H_3^- + xCa^{2+} + 2yNa^+$$

For the soda-lime glass used in AAR-INTER tests the correspondent stoichiometric coefficients are $x = 0.13$ and $y = 0.075$. Second, the resulting ions plus others already present in the pore solution react forming a Calcium-Alkali-Silicate Hydrate, called RPA,

$$SiO_4H_3^- + a_1Ca^{2+} + a_2R^+ + a_3OH^- + a_5H_2O \rightarrow \underbrace{(SiO_2)(CaO)_{a_1}(R_2O)_{a_2/2}(H_2O)_{2-a_1-a_2/2+a_3+a_5}}_{RPA}$$

with $a_3 = 2a_1 + a_2 - 1 \geq 0$, $a_1 > 1.0 > x$ and $1.0 > a_2 > 2y$. The calcium and alkali content of RPA have been measured by EDS analysis on SEM images of reacted glass/PCH in former AAR-INTER tests (not published here), giving stoichiometric coefficients $a_1 = 1.3$ and $a_2 = 0.25$, which are in good agreement with those published in the literature,(e.g. Rajabipour et al., 2010). Additionally, the following simplifications are assumed:

a) Pores are completely saturated with water and remain in this condition. Water consumed in the reactions is immediately replenished.

b) The concentration of hydroxyl ions is given by water self-ionization and it is approximated as equal to the alkali concentration.

c) Alkali ions (Na^+ and K^+) are treated indistinctly and named as R^+.

d) All the ionic species produced in the first reaction are immediately consumed in the second one, not given place to any diffusion out of the reaction site and generating a local consumption of calcium and alkali ions coming from elsewhere in the HCP proportional to $a_1 - x$ and $a_2 - 2y$.

e) The difference between the calcium ions produced by the first reaction and the ones consumed in the second ($a_1 - x$) is considered to be immediately provided by the portlandite and CSH surrounding the reaction site. On the other hand, the supply of the necessary alkaline is ions ($a_2 - 2y$) is given by a diffusion process from the HCP to the reaction site in the glass.

f) The second reaction will not occur, and consequently the ASR will stop, unless the alkali concentration surpasses a threshold value of 500 mmol/l, which approximately corresponds to the alkali concentration in pore solution for a cement with 0.6 wt $\%Na_2O_e$ and w/c ratio of 0.50 (Diamond 1989).

g) The volume occupied by a Mole of RPA is greater than the volume occupied by a mole of unreacted glass, giving place to a net local expansion as result of both reactions.

Formulation. Assuming that the alkali diffusion in the pore solution obeys Fick's diffusion law, averaging it in the saturated porous medium and posing the correspondent mass balance equation, the following diffusion-reaction equation for the continuum porous medium is obtained

$$\frac{\partial(\phi c^r)}{\partial t} = \boldsymbol{\nabla}^T(\boldsymbol{T}^r\boldsymbol{\nabla}c^r) + q^r; \quad \boldsymbol{\nabla} = \left[\frac{\partial}{\partial x} \quad \frac{\partial}{\partial y}\right]^T \tag{1}$$

where ϕ is the total porosity, c^r [mol/m^3] is the concentration of alkali ions in the pore solution expressed in moles per unit volume of pore solution, $\boldsymbol{T}^r$ [m^2/h] is the second order effective diffusivity tensor of alkali ions in the porous medium and q^r [mol/(m^3·h)] is the rate of production /consumption of alkali ions per unit volume of

porous medium. An analogous expression is obtained for the localized transport of alkali ions through a discontinuity, such as a crack or an ITZ,

$$\frac{\partial c_{mp}^r}{\partial t} = \frac{\partial}{\partial l}\left(T_l^r \frac{\partial c_{mp}^r}{\partial l}\right) + J^+ + J^-$$

where c_{mp}^r [mol/m^3] alkali concentration at the middle-plane (mp) of the discontinuity, T_l^r[m^2/h] is the longitudinal effective diffusivity, $J^+$and J^- [mol/(m^3·h)] are the leak-off terms, incoming from the surrounding porous medium and l [m] is the coordinate along the discontinuity axis. For a detailed discussion of diffusion process through discontinuities see Segura & Carol (2004). Note that non chemical have been considered to occur in the discontinuity. For the sake of simplicity, ϕ, T^r and T_l^r were assumed to remain constant along the simulations.

The rate q^r is given by

$$q^r = -2y\Gamma^S - a_2\Gamma^{RPA} \cong -(a_2 - 2y)\Gamma^{RPA}$$

where Γ^S and Γ^{RPA} [mol/(m^3·h)] are the rate of production/consumption of solid glass and RPA per unit volume of porous medium, respectively. Since the progress of each reaction depends on the progress of the other one, it can be assumed that $\Gamma^S \cong -\Gamma^{RPA}$. For the sake of simplicity, the kinetics of the two-step reaction is assumed to follow a unique law given by

$$\Gamma^{RPA} = \frac{dN^{RPA}}{dt} = -\Gamma^S = -\frac{dN^S}{dt} = k \cdot N^S \cdot [\langle c^r - c_{th}^r\rangle^+]^\alpha$$

where k and the exponent α are parameters of the kinetic law to be fitted, N^S [mol/m^3] is the molar concentration of glass per unit volume of porous medium, $c_{th}^r = 500$ mmol/m^3 is the threshold value of alkali concentration in pore solution. The operator $\langle X\rangle^+$ stands for "the positive part of X", i.e. if $X < 0, \langle X\rangle^+ = 0$ otherwise $\langle X\rangle^+ = X$.

The volume occupied by capillary pores ($\mathcal{U}^{cp}$), glass ($\mathcal{U}^S$) and RPA ($\mathcal{U}^{RPA}$) at the reaction site is given by

$$\mathcal{U}^S = \eta^S N^S;\ \mathcal{U}^{RPA} = \eta^{RPA} N^{RPA};\ \mathcal{U}^{cp} = \langle 1 - \mathcal{U}^S - \mathcal{U}^{RPA}\rangle^+$$

where $\eta^S$and η^{RPA}[m^3/mol] are the molar volume of glass and RPA, respectively. The total volume occupied by the porous material is $\mathcal{U} = \mathcal{U}^{cp} + \mathcal{U}^S + \mathcal{U}^{RPA}$. Being the initial volume equal to 1, the mechanic expansion induced by the production of RPA is $\mathcal{E}_v^{ASR} = \mathcal{U} - 1$. Note that the glass dissolution increases the capillary porosity, while RPA formation decreases it. No mechanical expansion will be induced until the capillary pores are completely filled with RPA. Finally, the porosity of the material is given by

$$\phi = (\mathcal{U}^{cp} + \phi^{RPA}\mathcal{U}^{RPA})/\mathcal{U}$$

where ϕ^{RPA}[-] is the intrinsic porosity of RPA. The intrinsic porosity is defined as the volumetric fraction of the phase occupied with physically bonded water through which the diffusion-reaction process can happen. The effective diffusivity of the glass has been assumed to depend on the evolution of the porosity according to

$$T^r = T_0^r[1 + \beta(\phi - \phi_0)\ ]$$

where T_0^r and ϕ_0 are the initial effective diffusivity and porosity, respectively, and β is a fitting parameter. However, the corresponding increment in the "capacity" of the system has not been considered, i.e. ϕ have been assumed constant in equation (1).

The molar volume η^S have been obtained from the glass density (neglecting minor components), being $\eta^S = 31.7E^{-06}$ m^3/mol. The molar volume η^{RPA} has been estimated to be in the range of 2.1 to 2.5 times greater than the glass one by the comparison of measured expansions of specimens with the correspondent width of RPA at the ITZ measured on SEM images of reacted glass/PCH interfase in former AAR-INTER tests. For this paper $\eta^{RPA} = 70.2E^{-06}$m^3/mol and $\phi^{RPA} = 0.37$ have been adopted.

Numerical implementation. The model has been implemented by means of Finite Elements Method in a way similar to other chemical attacks previously developed in the group (Idiart et al. 2011).

SIMULATION OF AAR-INTER TESTS

Model description. AAR-INTER specimens have been modeled as a plane stress/flux problem. The use of joint elements to simulate the ITZ excluded the possibility to model them as an axisymmetric problem. It shall be noted that assuming plane flux underestimates the radial flux of alkalis as well as assuming plane stresses overestimates the stiffness of the specimens in case of a non-uniform pattern of expansion at the ITZ. To compensate the underestimation of the radial flow, the horizontal effective diffusivity coefficient T_x^r was affected by a correction coefficient $\lambda > 1$, such that, in the case of pure radial flux, the average concentration of alkalis in the cross-section of the specimen in the plane flux model and in an axisymmetric model after a time interval Δt_c would be the same. The time interval Δt_c is defined qualitatively as the period of time in which most of the expansion has been developed in the experiment. These criteria lead, for Set #1, to Δt_c=7 days and $\lambda = 5.7$, and for sets #2 and #3, to Δt_c=14 days and $\lambda = 4.5$. No correction has been applied to the mechanical parameters.

The geometry and discretization of the FE model is schematically represented in Figure 5. The FE mesh consisted in 3715 linear continuum elements and 1500 linear joint elements, giving a total of 5281 nodes. Joint elements where inserted in between five horizontal layers of continuum elements: along the HCP-glass contact line, and in between the four first horizontal rows of glass elements. In the diffusion analysis, the first layer simulated the localized diffusivity of the ITZ. The remaining layers, on the other hand, played no role in the diffusion problem but they are kept in order to use the same FEM mesh in both analysis.

The mechanical boundary conditions consisted of zero horizontal displacements along the left vertical boundary, and zero vertical displacements along the bottom horizontal boundary. The diffusive boundary conditions consisted of fixed 1000 mmol/l concentration along the upper boundary, and on the right boundary the type of b.c. varied according with the test under simulation. Initial concentration of alkalis in pore solution was assumed to be 700 mmol/l for the HCP, and zero for glass.

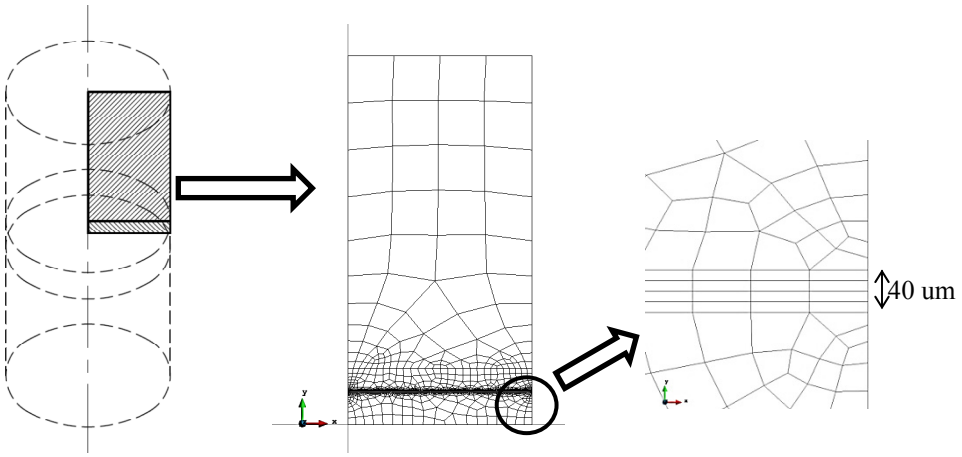

Figure 5. Model geometry and FE mesh.

The parameters of the kinetics law (*k=1.0E-05*, $\alpha = 2$), the parameters of the glass diffusivity law ($\beta = 1800, \phi_0 = 0.001$, $T_0^r = 3.3E^{-14}$ m^2/h), the effective diffusivity of the PCH ($\phi = 0.30, T^r = 2.0E^{-10}$ m^2/h) and the effective diffusivity of the interfase ($T_l^r = 6.6E^{-12}$ m^3/h, $T_t^r = 1.0$ m^3/h) have been estimated by fitting the expansion curves obtained with the model with the correspondent experimental curves. It shall be noted that the resulting effective diffusivity of the HCP has been about an order lower than the one expected for the mixture used. This difference can be attributed to the pore filling effect of the ASR gel precipitating in the HCP, which has not been considered in the model.

With regard to the mechanical analysis, Glass, HCP and the ITZ were modelled with linear elastic constitutive laws, with the following parameters: glass continuum elements, Young's modulus $E = 74$GPa and Poisson's coefficient $\nu = 0.20$; PCH continuum elements, $E = 25$GPa and $\nu = 0.15$; interface elements, Normal Stiffness $K_N = 1000\ GN/m$ and Tangential Stiffness $K_L = 0.001\ GN/m$.

Simulations Results. In figure 6, the alkali concentration pattern after 14 days of exposure obtained with the model is shown. It can be observed that the alkali concentration at the ITZ does not change significantly for sets #2 and #3, while set #1 shows a marked increment at the right hand side near the specimen surface.

The expansion curves obtained with the model are plotted together with the correspondent experimental ones in Figures 2 to 4. The model seems capable of capturing the effect of external alkali diffusion in the development of the expansions.

The longitudinal profiles along the interfacial zone showed the degradation of the glass and the formation of RPA in an affected zone of less than 30 micras width.

CONCLUDING REMARKS

A new experimental set-up to study the expansion mechanisms at the level of a single matrix-aggregate interface and some results concerning with the effect of alkali diffusion in the development of ASR have been presented.

As an intermediate step in the development of a C-T-M model, a simplified diffusion-reaction mechanism have been formulated and implemented in a FEM code, in order to interpret the experimental results presented. The simulation results

obtained have been in good agreement with the experimental ones. However, to fit the experimental results, it has been necessary to use an effective diffusivity of the HCP lower than expected. It seems that the pore filling effect of ASR gel precipitating at the HCP which has not been considered in the model could be the reason.

Next steps in this research project include implementing a C-T-M coupled model with the three diffusion-reaction mechanisms proposed in (Liaudat et al. 2014) and validating it with experimental results from AAR-INTER tests and from the literature.

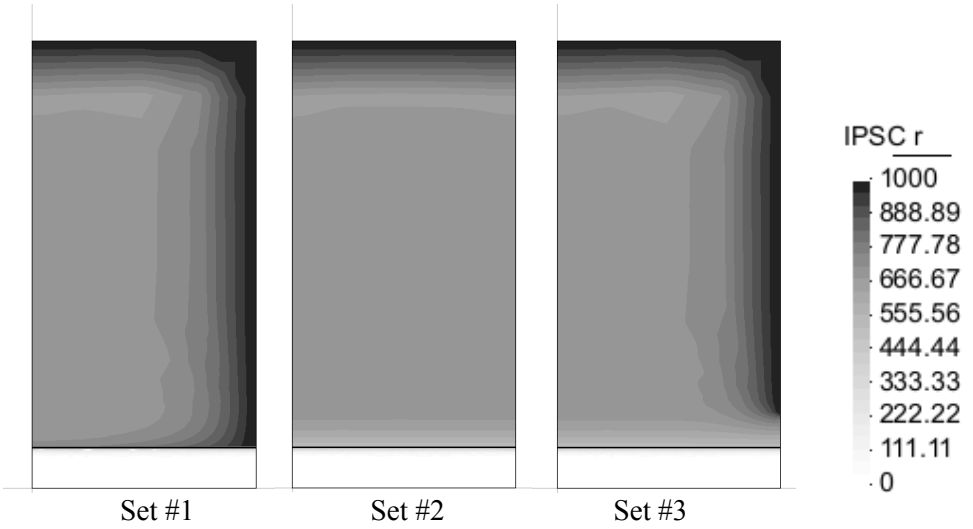

Figure 6. Alkali concentration in pore solution (mmol/l) at time 14 days.

ACKNOWLEDGMENTS

This research is supported by grants BIA-2012-36898 funded by MEC (Madrid), which includes FEDER funds, and 2014SGR-1523 from AGAUR-Generalitat de Catalunya (Barcelona). The first author also wishes to acknowledge MICINN (Madrid), for his FPI doctoral fellowship.

REFERENCES

Diamond, S., (1989). In *Proceedings of the 8th International Conference on Alkali-Aggregate Reaction.* Kyoto, pp. 83–94.

Idiart, A.E., López, C.M. & Carol, I., (2011). *Cement and Concrete Composites*, 33(3), pp.411–423.

Liaudat, J., López, C.M. & Carol, I., (2014). In *Proceedings of EURO-C 2014 Computational Modelling of Concrete and Concrete Structures*. St. Anton am Arlberg, Austria.

Multon, S. & Toutlemonde, F., (2006). *Cement and Concrete Research*, 36(5), pp.912–920.

Ollivier, J., Maso, J. & Bourdette, B., (1995). *Advanced Cement Based Materials*, 7355(94).

Rajabipour, F., Maraghechi, H. & Fischer, G., (2010). *Journal of Materials in Civil Engineering*, 22(12), pp.1201–1208.

Schlangen, E. & Çopuroğlu, O., (2007). In *Fracture Mechanics of Concrete and Concrete Structures - High-Performance Concrete and Environmental Aspects,* Carpinteri et al. editors, Catania, Italy, 17-22 June 2007.

Segura, J.M. & Carol, I., 2004. *International Journal for Numerical and Analytical Methods in Geomechanics*, 28(9), pp.947–962.

Experimental Study of the Influence of the Temperature and Duration of Heat Treatments at an Early Age on the Risk of Concrete Expansion Associated with Delayed Ettringite Formation

B. Kchakech[1]; R.-P. Martin[1]; O. Omikrine Metalssi[1]; and F. Toutlemonde[1]

[1]University Paris Est – IFSTTAR- Materials and Structures Department, Boulevard Newton, Champs sur Marne, 77447 Marne la Vallée Cedex 2, France.

Abstract

Delayed Ettringite formation (DEF) is an autogenous expansive reaction that can affect concrete. A long enough exposure to high enough temperature are the necessary conditions to develop DEF. The results of experimental laboratory investigations that aim to quantify the effect of thermal history on DEF characteristics (namely magnitude and kinetics of expansion) are presented. A threshold of temperature for the concrete at early age, a pessimum effect with the heating duration and a relation between thermal energy and swelling parameters (kinetics and magnitude) are highlighted.

INTRODUCTION

Delayed Ettringite Formation (DEF) is an internal swelling reaction that can affect concretes heated at a temperature higher than about 65°C [Scrivener et al. 1999]. This phenomenon is related to a late formation of a normal hydrate (ettringite) of cement in presence of many conditions related with temperature increase at early age, which is the necessary parameter to develop DEF. Thus, temperature limitation is recommended as one of the most efficient ways to avoid DEF expansions [Kretz et al. 2007]. This late formation of ettringite may affect concretes exposed to high temperatures at early age; it is the case of precast elements, and massive concrete parts heated due to cement hydration (combination of the exothermic hydration and the low heat transfer conditions). The development of this pathology leads to concrete swelling, cracking of the structure, decrease of the mechanical properties of the affected materials and thus potential problems in terms of serviceability of the affected structures [Godart & Divet 2013]. The objectives of this study are to quantify and predict the relation between thermal history and swelling characteristics (magnitude and kinetics) in order to propose recommendations for prevention of DEF, assessment and repair of structures affected by this pathology.

The experimental laboratory investigations about the effects of temperature and heating duration at early age have been carried out on concrete specimens, using highly DEF-reactive cement, aiming to quantify the expansion magnitudes and kinetics due to different thermal histories and to identify the possible existence of an eventual pessimum effect regarding the heating duration e.g. in [Brunetaud 2005]. A number of heat treatments at different temperatures (61, 71 and 81 °C) were applied after casting for durations ranging from 1 to 28 days. The monitoring of swelling was ensured by digital sensors and was coupled with a mass monitoring. This article, presents the results of expansion for the different thermal histories at early age. The swelling characteristics (magnitude and kinetics) are quantified using a mathematical

relation (Brunetaud's law), and compared to thermal histories at early age to determine the coupling between thermal history, swelling and kinetic parameters the studied concrete mix, and confronted to the predictions of the models available in the literature[Baghdadi 2008] [Martin et al. 2012]. Finally, the swelling magnitude and kinetic parameters in function of the thermal energy are discussed.

EFFECT OF TEMPERATURE ON DEF

The cement hydration is an exothermic reaction which can occur a high temperature in the case of massive concrete parts where the heat generation, associated with the reaction of hydration combined with the low heat transfer conditions leads to an extended heating of the material. Thus, the temperature may reach values significantly above 70°C [Divet & Pavoine 2002], exeeding the threshold temperature reported in the literature [Scrivener et al. 1999].

Namely, according to [Damidot & Glasser 1992], temperature influences the stability of ettringite. In addition, the high temperature leads to faster kinetics and higher magnitudes of expansion [Martin et al. 2012].

As temperature, heating duration is an important parameter for the development of DEF. The work of [Brunetaud 2005] and [Baghdadi 2008] show that the expansion increases with the heating duration for the same heating temperature. However, [Brunetaud 2005] showed the existence of a pessimum effect: for a given heat treatment temperature and above a certain threshold duration, the magnitude of expansion decreases with the heating duration. This requires that the coupling between temperature and heating duration should be considered during the DEF's study.

The studies of [Baghdadi et al. 2008, Martin et al. 2012] were based on the study of swelling due to DEF by coupling the effect of temperature and heating duration. These authors suggest a relationship based on experimental results using temperatures of 71°C to 86°C and heating durations of 1 to 5 days. They established relationships leading to predict the swelling in the massive parts [Seignol et al. 2009] by knowing their thermal history. The predictions of these coupling laws will be compared with experimental results of this study to define their domain of validity.

EXPERIMENTAL STUDY

The concrete mix used in this study (W/C=0.46) is given in Table 1. The binder used is a CEM I 52.5 R CE CP2 NF which is a high early strength cement. It was chosen because of its high aluminate, sulphate and alkali contents (respectively 3.46, 4.30 and 0.83%) highly DEF-prone. However, to ensure optimum conditions for expansion to occur, K_2O was added to mixing water up to a Na_2Oeq content of 1% of the cement content. The aggregates used are unreactive regarding AAR (Alkali-Aggregate Reaction)

Table 1 : Concrete mix (kg/m^3)

Cement	*Water*	*Sand NR 0/2*	*Coarse aggregate 4/8*	*Coarse aggregate 8/12*	*KOH*
410	188	854	100	829	1.745

Prismatic specimens (11x11x22 cm^3) were heat treated after casting. The heat treatments were performed in water in a specific device described in [Martin & Toutlemonde 2013]. A number of heat treatments at different temperatures at 71°C and 81 °C were applied after casting with durations ranging from 1 to 28 days to explore the domain of validity of the coupling laws, defined by [Baghdadi et al. 2008, Martin et al. 2012]. A heat treatment at 61 °C during 14 days has also been applied in order to understand this coupling for mass concrete structure (like in dams) subjected to smaller but longer heat treatment, and to determine the temperature threshold of DEF. Table 2 presents the heat treatments applied. The heating durations were adjusted to experimental requirements. The heat treatments were divided into four phases: a pre-treatment phase during 2 hours at 20°C, a heating phase at a rate of 5°C/h, a constant temperature plateau and a cooling phase at a rate of -5°C/h.

Table 2 : Heat treatments applied (plateau characteristics)

Mean temperature (°C)	*Standard deviation of temperature (°C)*	*Treatment 1*	*Treatment 2*	*Treatment 3*	*Treatment 4*	*Treatment 5*
81.3°C	0.1	1 day	3 days	5 days	7 days	14 days
71.1°C	0.1	2 days	7 days	14 days	12 days	28 days
61.0°C	0.1	14 days	-	-	-	-

A realistic heat treatment (called V_BIS) corresponding to the case of thermal history, of massive elements at early age was also applied to compare the expansion with those obtained after simplified trapezoid shaped heat treatments (61, 71 and 81 °C). It is intended to constitute a validation case. The result of Martin's study [Martin, 2010] is a second validation case. Indeed, the present study is based on the same material as [Martin, 2010], however the heat treatment (Figure 1-b) is different from the cases studied in this article, particularly in terms of heating and cooling rates.

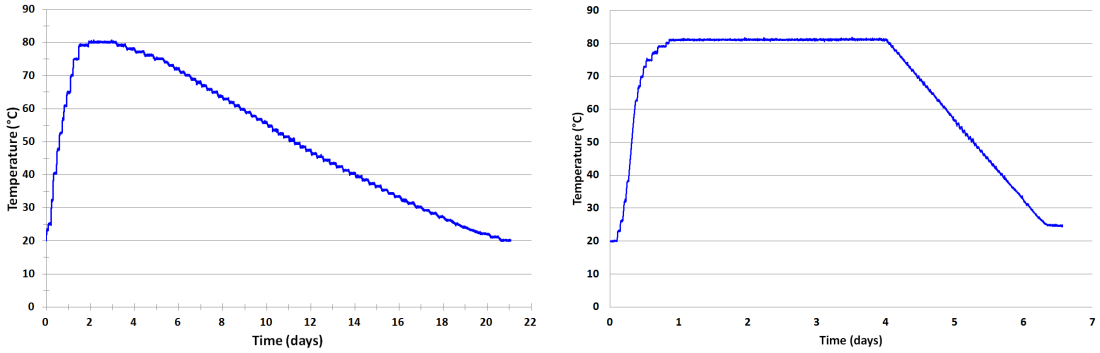

(a) (b)

Figure 1 : Heat treatments for the validation test: (a): realistic thermal history used for the validation test; (b): temperature profile applied in [Martin 2010]

After heat treatment, the specimens were stored in a climatic chamber at 38°C and 40% RH for 12 hours in order to start monitoring of swelling in a stable thermal

state. Figure 2 shows the thermal and hydric history of specimens. All specimens were stored in water at constant temperature of 38°C to speed up the kinetics of DEF. Three identical samples were prepared to gather statistically representative data (average value of expansion and its standard deviation). The swelling was monitored by digital device described in Figure 3. In this paper, each sample (11x11x22 cm^3) is referred as TT_DT, where TT and DT are respectively the temperature (°C) and heating duration (days) of the plateau of the applied heat treatment applied.

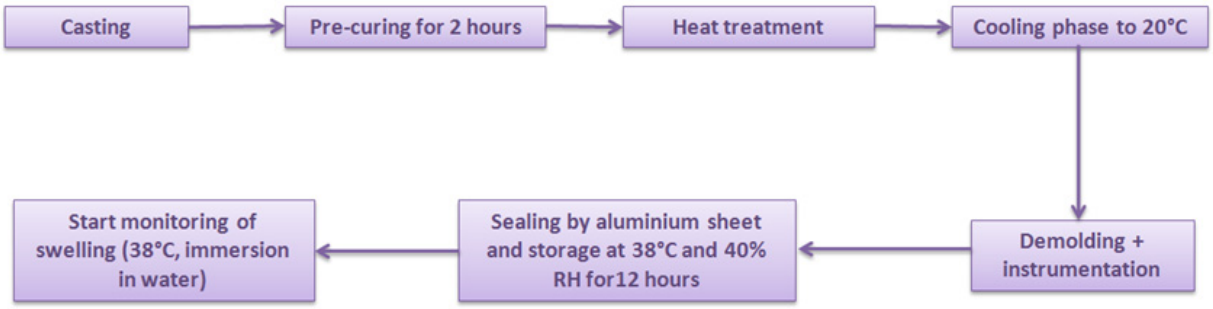

Figure 2 : Thermal and hydric history of specimens

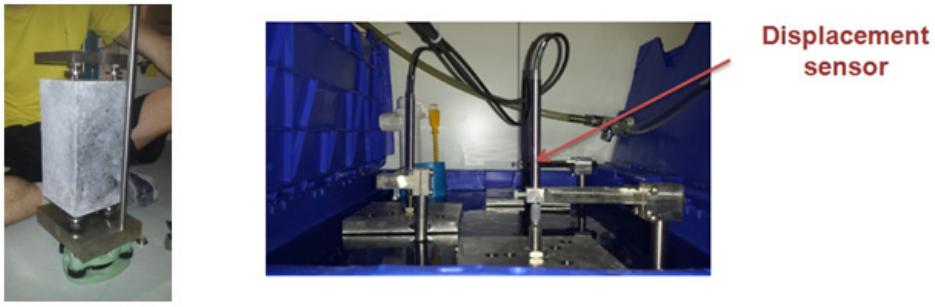

Figure 3 : Measurement instrument (a): leveling of instrument and specimens; (b): monitoring of specimens 11x11x22cm^3

RESULTS

The swelling characteristics (magnitude and kinetics) can be quantified using a mathematical relation (Brunetaud's law) [Equation (1)] [Brunetaud 2005], where ε_∞ is the final magnitude of expansion, τ_L and τ_c are respectively the latency and the characteristic times, and Φ and δ are two parameters to take into account a linear evolution of the last phase of swelling. A parameter (ε_{hyd}) was added to take into account an instantaneous hydric expansion during the first days of monitoring.

$$\varepsilon(t) = \varepsilon_\infty . \frac{1 - e^{\left(\frac{-t}{\tau_C}\right)}}{1 + e^{\left(-\frac{t-\tau_L}{\tau_C}\right)}} . \left(1 - \frac{\Phi}{\delta + t}\right) + \varepsilon_{hyd} \qquad (1)$$

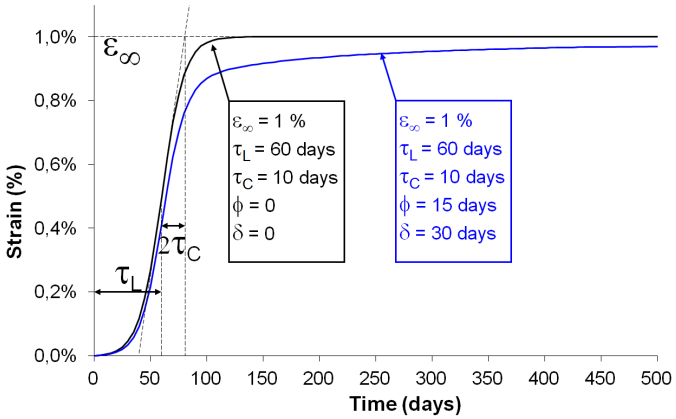

Figure 4 : Calibration of parameters describing the expansion curves [Brunetaud 2005]

Figures 5 and 6 present the results of swelling monitoring for the different studied cases. Each curve corresponds to the average expansion of 3 prismatic specimens, and the error bars correpond to plus or minus the standard deviation.

Figure 5 presents the expansion of the specimens heated at 61°C during 14 days. The maximal magnitude after 400 days is about 0.015%. It is almost unchanged from the first days of storage. In the absence of a significant tendency of expansions, it seems that, for this concrete, the threshold temperature of DEF is above 61°C. This has been recently confirmed with an additional case of thermal treatment with temperature plateau equal to 66°C and duration of 14 days Figure 5.

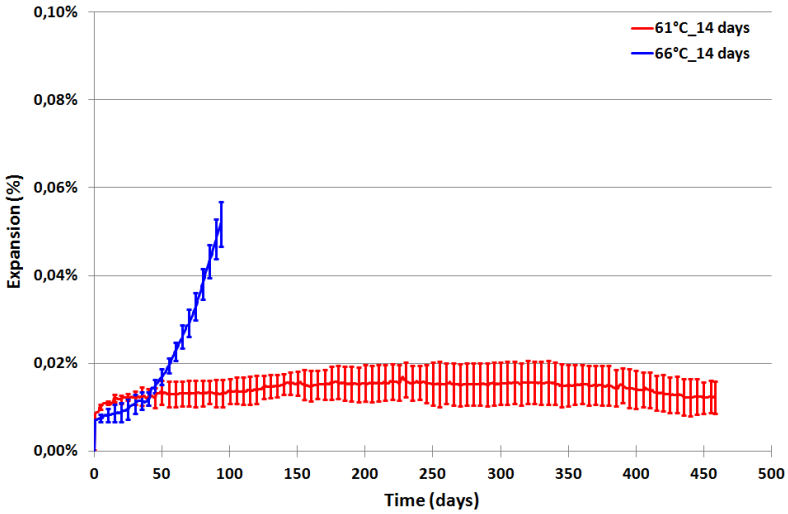

Figure 5 : Expansion of specimens heated at 61°C during 14 days

Figure 6 presents the recapitulative expansions of specimens heated at 71 ° C during 2, 7, 12, 14 and 28 days (Figure 6-a) and at 81 ° C during 1, 3, 5, 7 and 14 days (Figure 6-b). The kinetics of expansions are conform to the results expressed in [Baghdadi 2008]: for the same temperature plateau of heat treatment, the expansions have a latency time much shorter when the duration of the heating is longer. The parameters fitted on the experimental results are given in Table 3.

(a)

(b)

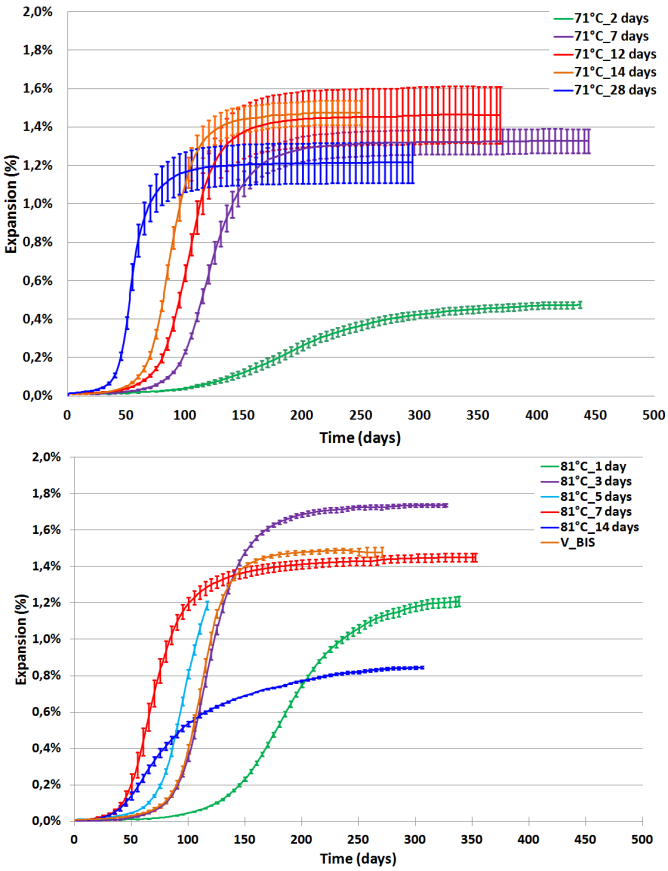

Figure 6 : Expansion of specimens heated at: (a) 71°C during 2, 7, 12, 14 and 28 days; (b) 81°C during 1, 3, 5, 7 and 14 days

Table 3 : Parameters of Brunetaud's model

	ε_∞ (%)	τ_L (days)	τ_C (days)	Φ (days)	δ (days)	eHyd (%)
71°C_2 days	0,49	187	39	41	122	0,0071
71°C_7 days	1,39	119	14	24	100	0,0061
71°C_12 days	1,53	101	12	29	200	0,0100
71°C_14 days	1,55	87	10	18	100	0,0100
71°C_28 days	1,28	55	7	20	100	0,0120
81°C_1 day	1,26	178	26	10	10	0,0054
81°C_3 days	1,81	118	14	50	240	0,0011
81°C_5 days	Not stabilized					
81°C_7 days	1,54	66	12	30	100	0,0071
81°C_14 days	0,92	54	15	91	150	0,0050

V_BIS	1,52	111	11	10	45	0,0020

A pessimum effect was confirmed in relation with heating duration (Figure 7). This effect corresponds to the lower final magnitude expansions in the case of heat treatment at 71 ° C for 28 days and heat treatment at 81 ° C for 7 days and 14 days (Figure 7), compared to the maximum obtained for each treatment temperature.

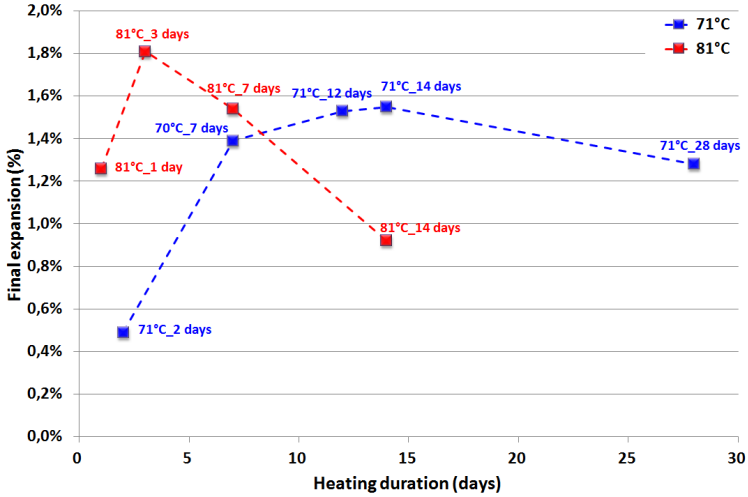

Figure 7 : Effect of temperature and duration of heat treatment on magnitude of expansion

DISCUSSION

To study the influence of thermal history at different temperatures, expansion parameters (ε_∞, τ_L and τ_c) were compared to the supplied thermal energy during the various thermal treatments. At first, it was considered the total thermal energy (ET), the integral of the temperature curve in fuction of time, with T> 20°C, which corresponds to the assumption that all thermal energy applied is responsible for the development of DEF. Then, an effective thermal energy (EU) was considered, taking 65 ° C as a threshold temperature [Equation (2)]. In this case it is assumed that only the thermal energy supplied beyond the threshold temperature 65 °C is responsible for DEF expansions. This hypothesis was chosen due to the absence of expansion for the heat treatment at 61 °C during 14 days and based on the information available in the literature [Scrivener et al. 1999].

$$Effective\ thermal\ energy = \begin{cases} \int\int (T(t) - 65)\, dt & if\ T(t) > 65°C \\ 0 & else \end{cases} \quad (2)$$

The representation of the final expansion magnitude in function of the total thermal energy ET shows that there is no satisfactory correlation between ET and final expansions due to DEF. Figure 8, however, presents the final expansions in function of the effective thermal energy EU (temperature threshold of 65 °C) assumed to be responsible for the destabilization of ettringite at early age, there seems

to be a master curve linking the effective thermal energy to the final expansion. Indeed, this final expansion increases with the EU provided up to a certain value of about 2000 °C.h beyond which expansions decrease. This may be related to the definitive aluminum substitution of silica in C-S-H eventually leading to the decrease of the quantity in ettringite precipitated, thus reducing the final expansion [Salgues 2013]. This relation well describes the pessimum effect.

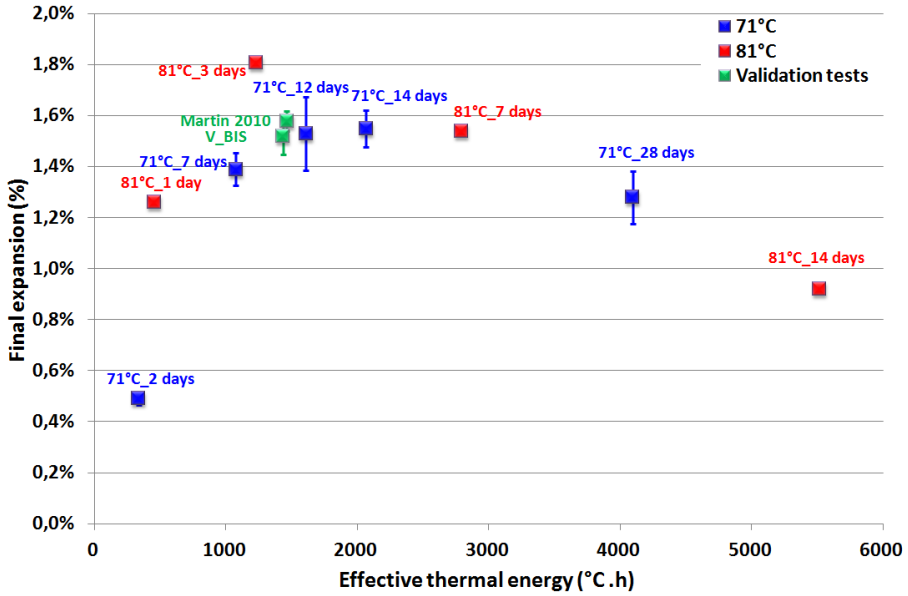

Figure 8 : Effect of effective thermal energy on magnitude of expansion

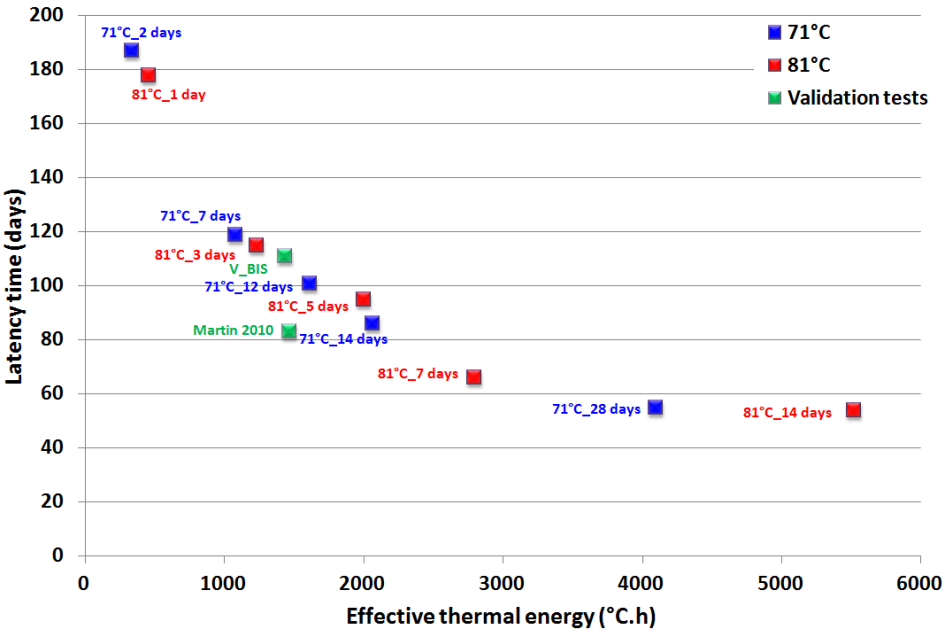

Figure 9 : Effect of effective thermal energy on latency time

The latency and characteristic time of expansions were expressed in function of the thermal energy EU. Figure 9 and 10 show that there exist a master curves

which link these two times (latency and characteristic) to this effective thermal energy. The development of DEF is faster when the effective energy supplied to destabilize ettringite increases, even though τ_c hardly.

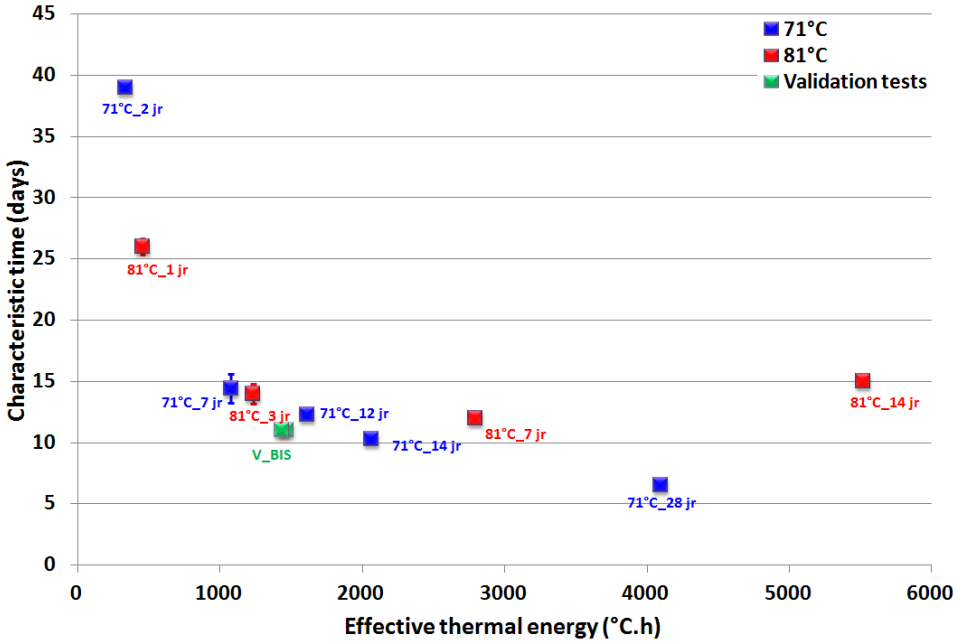

Figure 10 : Effect of effective thermal energy on characteristic time

CONCLUSIONS

The experimental study presented strove to improve the description of expansions due to DEF, based on the thermal history at early age, for a concrete subject to staggered protocols in the critical field of temperatures and heating duration which may trigger reaction

Magnitude and kinetics depends on the temperature and the heating duration. A pessimum effect with the heating duration was: for the same treatment temperature there is a heating duration beyond which the magnitude of expansion decreases significantly.

The absence of expansion after about 400 days for the case 61°C_14 days suggests that the threshold temperature of DEF is above 61°C, probably close to 65°C for the concrete mix under investigation.

The swelling parameters of the different expansions curves, determined with Brunetaud's law, have been linked to effective thermal energy (with a temperature threshold of 65 °C).

Master curves were identified linking the swelling parameters to the EU. Indeed, the final expansion increases with EU until to about 2000 °C.h, above which expansions decrease. This may be related to the definitive aluminum substitution of silica in C-S-H eventually leading to the decrease of the quantity of ettringite that can precipitate. The latency and characteristic times decrease when EU increases.

Chemical analyses and SEM observations are planned to explain the mechanisms of pessimum effect identified. Comparisons with the results obtained on

other concrete mixes subjected to other thermal histories are also scheduled to confirm the identification of master curves.

Références

Baghdadi N, 2008, Modélisation du couplage chimico-mécanique d'un béton atteint d'une réaction sulfatique interne, Thèse de l'Université Paris Est, Paris.

Baghdadi N, Seignol J.F, Martin R.P, Renaud J.C, Toutlemonde F, 2008, Effect of early age thermal history on the expansion due to delayed ettringite formation: experimental study and model calibration, Advances in Geomaterials and Structures, Vol 4, 661-666.

Brunetaud X, 2005, Etude de l'influence de différents paramètres et de leurs interactions sur la cinétique et l'amplitude de la réaction sulfatique interne. Thèse de l'Ecole Centrale de Paris.

Damidot D, Glasser F.P, 1992, Thermodynamic investigation of the CaOAl2O3-CaSO4-H2O system at 50°C and 85°C. Cement and Concrete Research, 22, 1179-1191

Divet L, Pavoine A, 2002, Delayed ettringite formation in massive concrete structures: an account of some studies of degraded bridges, International RILEM TC 186-ISA Workshop on Internal Sulfate Attack and Delayed Ettringite Formation, Villars, Switzerland.

Godart B, Divet L, 16-17 April 2013, Lessons learned from structures damaged by delayed ettringite formation and the French prevention strategy, Fifth international conference on Forensic Engineering, Institution of Civil Engineers, London.

Kretz, T., Godart, B. & Divet, L., 2007, Recommandations pour la prévention des désordres dus à la réaction sulfatique interne, Guide technique des Laboratoires des Ponts et Chaussées, Laboratoire Central des Ponts et Chaussées.

Martin R.P, 2010, Analyse sur structures modèles des effets mécaniques de la réaction sulfatique interne du béton. Mémoire de thèse de doctorat, Université Paris Est - LCPC Paris.

Martin R.P, Bazin C, Billo J, Estivin M, Renaud J.C, Toutlemonde F, 2012, Experimental evidence for understanding DEF sensitivity to early-age thermal history. RILEM PRO-85, 45-54.

Martin R.P, Toutlemonde F, 2013, Theoretical and experimental validation of a simple method to reproduce representative DEF-prone conditions in laboratory. Materials and Structures, Vol 46(8), 1245-1255.

Salgues M, 2013, Modélisation des effets structuraux des réactions sulfatiques internes et alcaligranulats : Application aux barrages en béton, Mémoire de thèse de doctorat, Université de Toulouse.

Scrivener K.L, Damidot D, Famy C, 1999, Possible mechanisms of expansion of concrete exposed to elevated temperatures during curing (also known as DEF) and implications for avoidance of field problems, Cement, Concrete and Aggregates, 21(1), 93-101.

Seignol J.-F, Baghdadi N and Toutlemonde F, 2009, A macroscopic chemo-mechanical model aimed at re-assessment of DEF affected concrete

structures, in '1st International conference on computational technologies in concrete structures CTCS’09', Jeju, Korea, 442-440.

Coupled Effects of Creep and Alkali-Silica Reaction in Concrete at the Meso-Scale

G. Xotta[1]; K. J. Willam[2]; E. Bombasaro[1,2]; V. A. Salomoni[1]; and C. E. Majorana[1]

[1]Department of Civil, Architectural and Environmental Engineering (DICEA), University of Padova, via F. Marzolo 9 35131, Padova, Italy.
E-mail: giovanna.xotta@dicea.unipd.it; elenabombasaro@gmail.com; valentina.salomoni@dicea.unipd.it; carmelo.maiorana@dicea.unipd.it
[2]Department of Civil and Environmental Engineering, Cullen College of Engineering, University of Houston, TX. E-mail: kwillam@uh.edu

Abstract

Concrete degradation is analyzed due to alkali silica reaction (ASR) in combination with creep and shrinkage. Environmental factors such as temperature and relative humidity are included in this study since they accelerate hydration and aging of cement-based materials due to the underlying transport of multiple chemical reaction processes. This study examines the performance of concrete at the meso-scale level of observation where aggregate particles and the embedding hydrated cement paste form interacting continua. Macro-scale numerical analyses are compared with corresponding meso-scale ones, in order to capture the chemo-physical damage and understand the role of the different concrete constituents. For this purpose a 3D fully coupled thermo-hygro-mechanical finite element code developed at Padua University, which treats concrete as a multi-phase material, has been adopted and updated to take into account the effects of ASR expansion in the interface transition zone, the aggregate particles and the hydrated cement based mortar.

INTRODUCTION

ASR is a chemical reaction, firstly observed by Stanton (1940) while analyzing cracking of structures, which occurs between reactive forms of silica in the aggregates and alkali and hydroxyl ions in the pore solution.

To reach a better comprehension of this complex, not fully understood, chemical process, many different models have been developed during last decades. ASR process can be simplified considering two macro stages: a first stage, when silica is dissolved from the aggregates an amorphous gel and precipitates are formed, and a second stage, when the gel, strongly hydrophilic, expands by imbibition of water, generating internal pressure in the concrete meso-structure. This pressure causes non-uniform deformations leading to pervasive cracking and a progressive reduction of the mechanical properties.

The role of water is of central importance for any dissolution, reaction, formation of amorphous gel and precipitates. Moreover, temperature plays a fundamental part in the ASR rate of reaction; that is, the higher the temperature, the faster is the chemical reactions process.

In this work concrete is treated as a heterogeneous medium, considering a meso-scale level of observation below the macroscopic scale of homogenized continua. The meso-level of observation provides a more realistic description of the global behaviour which is a direct consequence of the phenomena that take place at the heterogeneous level of composite materials. Concrete at the meso-level is a mixture of cement paste, aggregates of different sizes and a thin layer of matrix material between these two components called interfacial transition zone (ITZ).

In the specific case of ASR, the meso-level approach is essential to characterize and understand the mechanical interactions of the constituents and the composite action of concrete, resolving the internal material hyperstaticity that generate residual stress and triggers damage evolution. The paper takes into consideration time dependent creep and shrinkage effects; in fact neglecting visco-elastic behavior of the material could lead to an overestimation of the damage, as ASR affects concrete on time scales similar to those of the creep deformations.

For these purposes, a 3D coupled thermo-hydro-mechanical finite element code is adopted, to characterize concrete behaviour at the macro- and meso-scale levels and to consider ASR effects as well as creep and shrinkage. Particularly, it is here assumed that concrete creep is associated with the cement paste only, and that creep obeys the B3 model proposed by Bažant and Baweja, whereas damage obeys the Mazars'damage law with a non-local correction.

MODELLING ALKALI SILICA REACTION

ASR is modelled in this work as a two-stage process:

1. Gel formation process

The multiple complex processes during the first stage of ASR are described in this model as one overall chemical reaction driven by one overall kinetics. The experiments of Dron and Brivot (1992) confirmed that this stage of ASR may be described by a first-oder kinetic law. Larive's experiments (Larive, 1998) demonstrated that the process rate depends on both, the moisture content and the temperature of concrete.

The advancement of the first stage of ASR is described by means of one overall normalized chemical reaction $\xi_{ASR} \in [0,1]$ (ξ_{ASR}=0 at the beginning of ASR reactions and ξ_{ASR}=1 at the end) which includes all the multiple chemical reactions but has the same meaning as in thermodynamics of chemical reactions.

The extent of ASR reaction ξ_{ASR} is modelled by the first-order kinetic law in the form of:

$$\dot{\xi}_{ASR} = \frac{1-\xi_{ASR}}{t_r} \tag{1}$$

where t_r is the characteristic time of the ASR reaction.

Considering the combined effect of the material temperature T and relative humidity RH (in this work the effects of asborption and desorption are not taken into account; saturation degree are hence replaced by relative humidity (Wu et al., 2014) on the characteristic time of the ASR reaction (Ulm et al., 2000; Steffens et al., 2003; Pesavento et al., 2012).

$$t_r\left(RH,T,\xi_{ASR}\right)=\tau_r\left(RH,T\right)\frac{1+\exp\left[\dfrac{-\tau_L\left(RH,T\right)}{\tau_r\left(RH,T\right)}\right]}{\xi_{ASR}+\exp\left[\dfrac{-\tau_L\left(RH,T\right)}{\tau_r\left(RH,T\right)}\right]} \tag{2}$$

where τ_L and τ_r represent the reaction time and latency time for ASR. The dependence of these characteristic times on the temperature and relative humidity are given by:

$$\tau_L\left(RH,T,\xi_{ASR}\right)=\tau_{L0}\cdot U_L\left[\frac{1}{T}-\frac{1}{T_0}\right]\left(A_L\cdot RH+B_L\right) \tag{3}$$

$$\tau_r\left(RH,T,\xi_{ASR}\right)=\tau_{r0}\cdot U_r\left[\frac{1}{T}-\frac{1}{T_0}\right]\left(A_r\cdot RH+B_r\right) \tag{4}$$

with τ_{L0} and τ_{r0} being the reaction and latency times at the reference time T_0 and RH=100%, U_r and U_L are the Arrhenius activation energies, while A_L, A_r, B_L and B_r are material parameters.

2. Swelling process

The second stage of ASR, during water absorption and gel expansion is modelled similarly to Steffens et al. (2003), assuming that the ASR induced strains are volumetric and their rate, $\dot{\varepsilon}_{ASR}$, is proportional to the rate of water mass combination with the products of the first stage of ASR, $\dot{m}_{ASR}$

$$\dot{\varepsilon}_{ASR}=\frac{\alpha}{\rho_{ASR}}\cdot\dot{m}_{ASR}\left(t\right)\cdot\mathbf{I} \tag{5}$$

This expression, after assumptions and considerations (Steffens et al., 2003; Pesavento et al., 2012), can be rewritten as:

$$\dot{\varepsilon}_{ASR}=\frac{\alpha}{\rho_{ASR}}\cdot M_{ASR}\left(RH\right)\cdot\left(1-\xi_{ASR}\right)^{\beta}\dot{\xi}_{ASR}\cdot\mathbf{I} \tag{6}$$

where $\beta=\dfrac{\tau_{r0}}{t_{AGE}}$ and where t_{AGE} is the characteristic time of aging, α is the chemo-elastic dilation coefficient, ρ_{ASR} is the density of the formed gel and $M(RH)$ is the water absorption coefficient at the moisture content RH. This dependence can be approximated by the following relation:

$$M_{ASR}\left(RH\right)=M_{ASR,0}\cdot\exp\left(A_{ASR}\cdot RH+B_{ASR}\right) \tag{7}$$

where A_{ASR} and B_{ASR} are material parameters.

Finally, eq. (5) assumes the form:

$$\dot{\varepsilon}_{ASR}=\delta\cdot\exp\left(A_{ASR}\cdot RH+B_{ASR}\right)\cdot\left(1-\xi_{ASR}\right)^{\beta}\dot{\xi}_{ASR}\cdot\boldsymbol{I} \tag{8}$$

where $\delta=\dfrac{\alpha\cdot M_{ASR,0}}{\rho_{ASR}}$ denotes the swelling coefficient.

THE MATHEMATICAL MODEL

The basic features and equations of the FE hydro-thermal damage code (Baggio et al., 1995; Xotta et al., 2013) are briefly recalled in the following.

Concrete is treated as a multiphase system where the micropores of the skeleton are partially filled with liquid water, both in the form of bound or absorbed water and free or capillary water, and partially filled with a gas mixture composed of dry air (non-condensable constituent) and water vapor (condensable), supposed to behave like an ideal gas.

The coupled system of differential equations for dealing with humidity diffusion and heat transport can be written in the form:

$$k\frac{\partial h}{\partial t} - \nabla^T \mathbf{C}\nabla h - \frac{\partial h_s}{\partial t} - K\frac{\partial T}{\partial t} + \bar{\alpha}\mathbf{m}^T\frac{\partial \boldsymbol{\varepsilon}}{\partial t} = 0 \tag{9}$$

$$\rho C_q \frac{\partial T}{\partial t} - \nabla^T \boldsymbol{\Lambda}\nabla T - \frac{\partial Q_h}{\partial t} = 0 \tag{10}$$

where k is the cotangent of the isotherm slope, **C** is the (relative humidity) diffusivity diagonal matrix, dh_s the self-desiccation, K the hygrothermal coefficient, $\mathbf{m} = \{1 \quad 1 \quad 1 \quad 0 \quad 0 \quad 0\}^T$, $\bar{\alpha} = \left(\frac{\partial h}{\partial \boldsymbol{\varepsilon}_v}\right)\Big|_{T,w}$ equals the change in h due to unit change of volumetric strain ε_v at constant moisture content w and temperature T, ρC_q is the thermal capacity, $\boldsymbol{\Lambda}$ the thermal conductivity diagonal matrix and Q_h the outflow of heat per unit volume of solid. The last term in eq. (9) represents the coupling term for connecting hygro-thermal and mechanical response to capture the Dufour and Soret interaction effects.

As regards to the mechanical field, when considering creep and damage respectively, Model B3 (Bazănt and Baweja, 2000) and Mazars' damage law (Mazars, 1986) with non-local correction have been chosen and implemented.

The constitutive relationship can be written as:

$$\boldsymbol{\sigma}(t) = \left(1 - d\left(\tilde{\varepsilon}^*(t)\right)\right)\int_0^t \mathbf{D}' \sum_{\mu=1}^{n} E_\mu(t_e') e^{\left[y_\mu(t_v') - y_\mu(t_v)\right]}\left[d\boldsymbol{\varepsilon}(t) - d\boldsymbol{\varepsilon}^0(t)\right] \tag{11}$$

where d is the scalar damage factor, depending on the current equivalent strain $\tilde{\varepsilon}^*$ and where $\boldsymbol{\varepsilon}^0$ refers to imposed initial strains, not related to stresses.

In eq. (11), **D'** corresponds to the time-independent part of the compliance matrix; E^μ is the μ-th elastic modulus of the Maxwell unit; y_μ are the reduced times; t' is the time of first application of load and subscripts e and v refer to equivalent hydration and to humidity and temperature effects on creep velocity, respectively.

3D NUMERICAL MODELS

1. Model calibration

3D numerical models at the macro scale have been calibrated taking as reference the experimental tests performed by Larive (1998). In specific, cylindrical concrete specimens with dimension of 13cm of diameter and 24cm in height have been considered, subjected to different isothermal temperatures and relative humidities. We can identify two main different thermo-hygral conditions for these samples:

- kept at constant temperature of 38°C and different relative humidities, equal to 73%, 87.5% and 92.5%;
- kept at constant relative humidity and three different temperatures: 23°C, 38°C and 60°C.

The parameters assumed for the simulations are summarized in Table 1, while in Figure 1 the sample geometry and the mesh is reported. As can be observed the sample has been reduced due to symmetry.

Table 1. Parameters adopted for the simulations.

Parameter	*Value*	
Young Modulus	34,536	[MPa]
Poisson's Ratio	0.2	[--]
τ_{r0}	19	[days]
τ_{L0}	40	[days]
U_r	2,500	[J]
U_L	6,000	[J]
A_r	-7	[--]
A_L	-9	[--]
B_r	8	[--]
B_L	10	[--]
δ	0.0028	[--]
t_{AGE}	150	[days]
A_{ASR}	3.7	[--]
B_{ASR}	-3.4	[--]

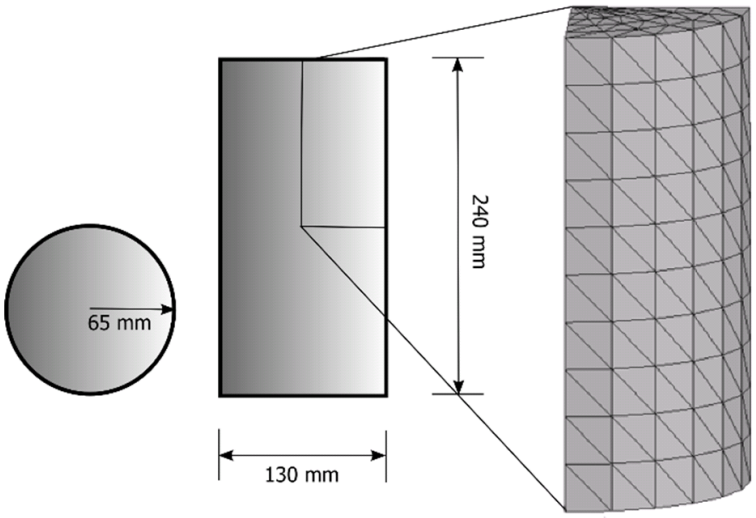

Figure 1. Sample geometry and FE mesh considered.

Calibration results obtained in terms of ASR expansion strains vs. time at different temperatures and with different moisture content are reported in Figure 2 and in Figure 3. As can be noticed by these figures there is a good agreement between numerical predictions and experimental observations. For completeness the time transient evolution of the ASR reaction extent for the considered constant relative humidities and temperatures is presented in Figure 4.

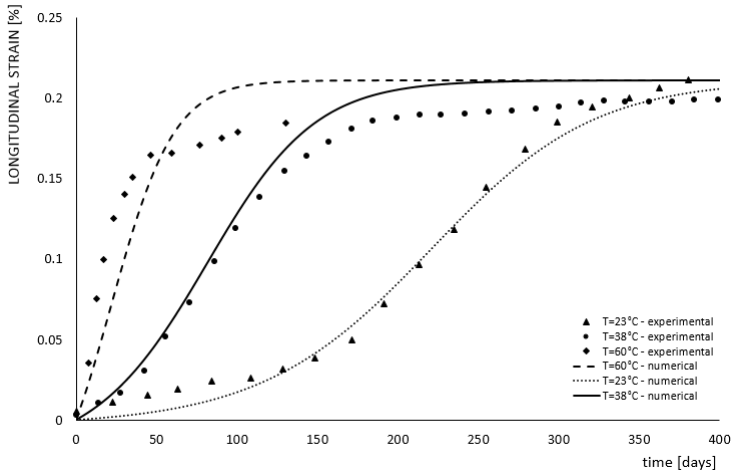

Figure 2. Comparison between the experimental ASR strains curves obtained by Larive (1998) and the numerical ones at three different temperatures.

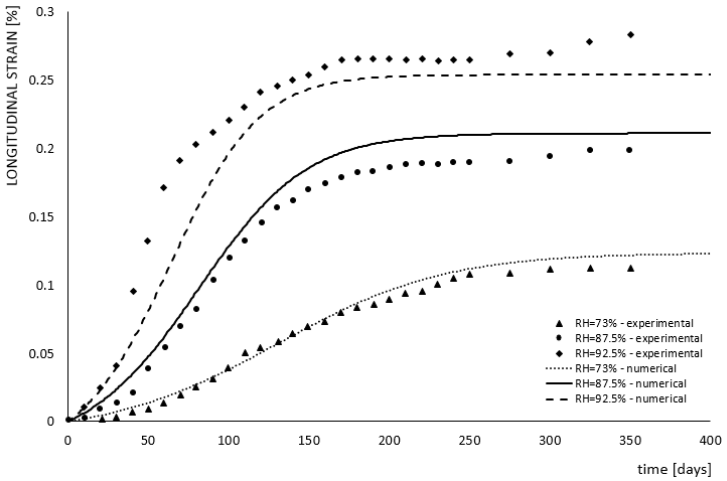

Figure 3. Comparison between the experimental ASR strains curves obtained by Larive (1998) and the numerical ones at three different relative humidities.

2. Macro-meso results

The experimental tests here considered for the calibration are tests in so-called "free expansion"; therefore at the macro-scale level our samples will be subjected to an isotropic expansion due to the formation and the expansion of the alkali-silica gel.

Considering in the numerical model only a mechanical damage, such as the non local Mazars' damage model, we will not see any degradation, even if in reality, as observed by Larive, the material will be subject by pervasive micro-cracking and a drastic reduction of the mechanical properties. This is due to the amorphous gel, strongly hydrophilic, that swells by imbibition of water and, after filling up the available pore space, that creates increasing internal pressure.

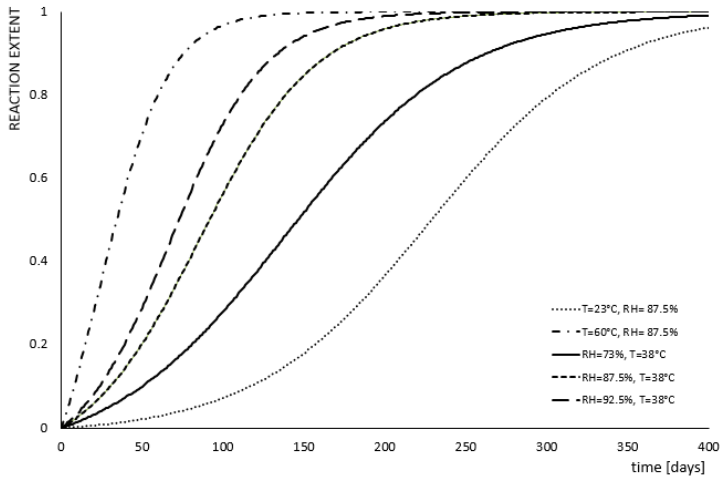

Figure 4. Evolution of ASR reaction extent in time for the different relative humidities and temperatures considered by Larive (1998).

In order to come up with a representative degradation behaviour due to ASR, the idea in this work is to move down to the meso-scale level, and characterize concrete as a multiphase material made of cement paste, aggregates and ITZ. Here we assume that the ASR will affect the aggregates, which behave elastically and will expand isotropically, whereas the ITZ and the cement paste are subjected to creep and

damage. This time, due to the different material characterization and the different behaviour and properties of the constituent components, the ASR will induce damage in the specimens.

For the meso-scale studies, starting from the mesh considered in the macro-scale simulations and reported in Figure 1, we consider as cell base a cylinder of 2cm of diameter and 2cm in height and for this cell base we consider different coarse aggregates distributions, as can be seen in Figure 5.

For all the different meso-scale models we consider the same aggregate/concrete ratio equal approximately to 0.45, as reported in Larive work, and we assume appropriate properties for the three constituent components.

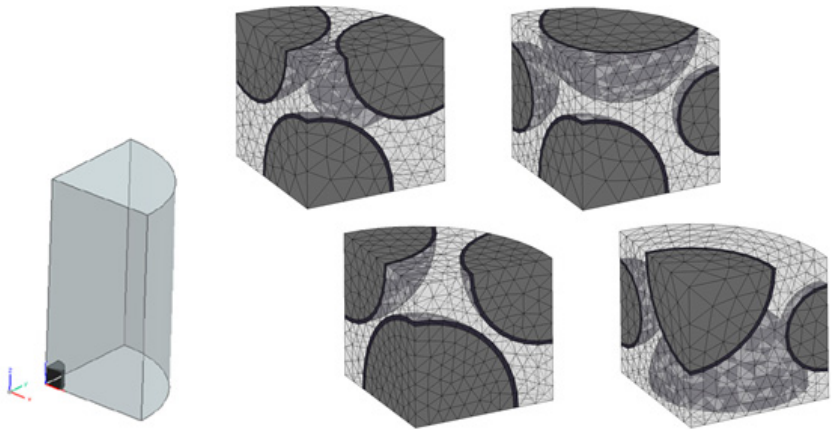

Figure 5. Meso-scale cell base, taken from the macro-scale sample, and four different coarse aggregates distributions for the cell base.

Damage evolution for two different temperatures (38°C and 60°C) at the meso-level is reported in Figure 6. It can be noticed that the advancement of damage is accelerated by the increase of temperature form 38°C TO 60°C; indeed, for the higher temperature case, at 10 days the ITZ exhibits significant deterioration.

In contrast, damage due to material mismatch between aggregates and cement paste and ITZ remains invisible at the macro-scale for uniform hygro-thermal conditions under unrestrained free expansion.

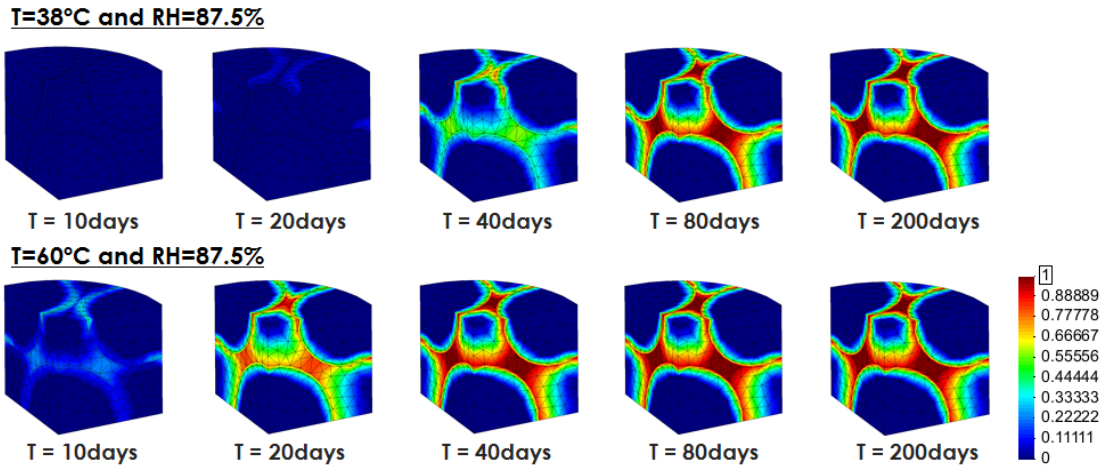

Figure 6. Damage evolution at the meso level for two different temperatures, 38°C and 60°C.

The damage values for each Gauss point at each time step, are weighted, based on the element size, to come up with a homogenized damage measure able to describe the time history of macroscopic degradation (Comi et al., 2012) shown in Figure 7.

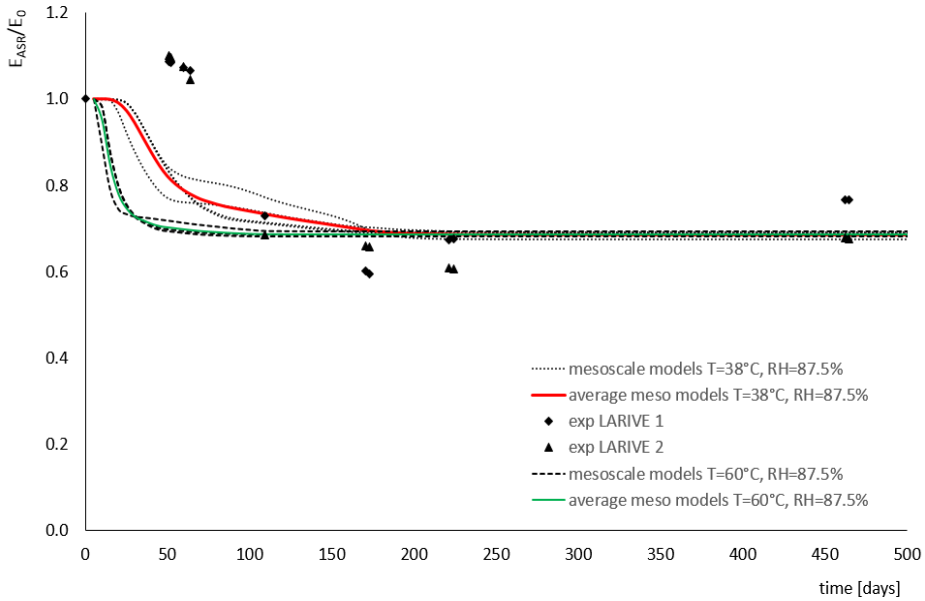

Figure 7. Experimental vs. numerical elastic modulus reduction obtained from meso-scale models using damage homogenization.

A comparison between the experimental and numerical longitudinal strain curves at the macro- and meso-scale levels for the two different temperatures already considered is depicted in Figure 8.

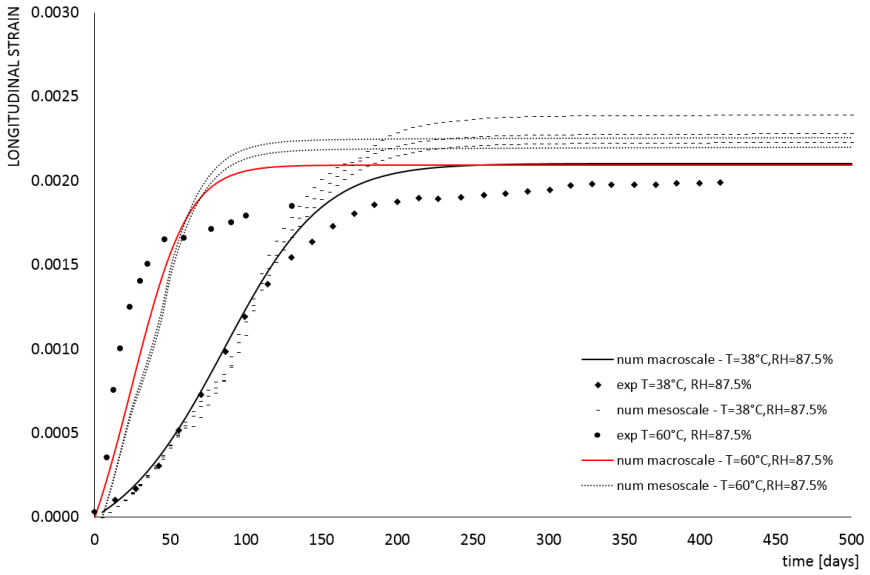

Figure 8. Comparison experimental-numerical strains curves at the macro-scale and meso-scale levels (T=38ºC/ 60ºC and RH=87.5%).

CONCLUSION

Concrete degradation mechanism due to ASR was examined at the meso-scale of heterogeneous concrete. At this level of investigation concrete becomes a composite material, where each component presents its own hygro-thermo-mechanical characteristics, allowing to evaluate the internal residual stresses in the medium which are not visible via homogenized macro-scale simulations.

3D meso-scale models were developed to fully capture the localized degradation introduced by gel formation.

The rate of ASR process exhibits strong dependence on temperature and relative humidity; the effect of humidity determines the level of chemical reaction due to ASR process, while the temperature determines the rate of the process (accelerated chemical aging).

REFERENCES

Baggio, P., Majorana, C.E., and Schrefler, B.A. (1995). "Thermo-hygro-mechanical analysis of concrete." *International Journal for Numerical Methods in Fluids* 20, 573-595.

Bažant, Z.P. and Baweja, S. (2000). "Creep and shrinkage prediction model for analysis and deign of concrete structures: Model B3." in *Adam Neville Symposium: Creep and Shrinkage – Structural Design Effects*, ACI SP – 194, 1-83.

Comi, C., Kirchmayr, B., and Pignatelli, R. (2012). "Two-phase damage modeling of concrete affected by alkali–silica reaction under variable temperature and humidity conditions." *International Journal of Solids and Structures*, 49(23-24), 3367-3380.

Dron, R. and Brivot, F. (1992). "Thermodynamic and kinetic approach to the alkali-aggregate reaction. Part 1: concepts." *Cem. Concr. Res*., 22(5), 941-948.

Larive, C. (1998). “Apports combinés de l’expérimentation et de la modélisation à la comprehénsion de l’alcali réaction et de ses effets mécaniques.” Monograph LCPC, OA28, Laboratoire Central des Ponts et Chaussées, Paris.

Mazars, J. (1986). “A Description of Micro and Macro-scale Damage of Concrete structures.” *Engineering Fracture Mechanics*, 25 (5-6), 729-737.

Pesavento, F., Gawin, D., Wyrzykowski, M., Schrefler, B.A., and Simoni, L. (2012). “Modeling alkali–silica reaction in non-isothermal, partially saturated cement based materials.” *Comput. Methods Appl. Mech. Engrg*., 225 (228), 95-115.

Stanton, T. E. (1940). “Expansion of concrete through reaction between cement and aggregate” *Proc. ASCE* 66, 1781-1811.

Steffens, A., Li, K., and Coussy, O. (2003). “Ageing approach to water effect on alkali-silica reaction.” *Degradation of Structures, Journal of Engineering Mechanics,* 129, 50-59.

Ulm, F.J., Coussy, O., Kefei, L., and Larive, C. (2000). “Thermo-chemo-mechanics of ASR expansion in concrete structures.” *Journal of Engineering Mechanics*, 126, 233-242.

Wu, T., Temizer, I., and Wriggers, P. (2014). “Multiscale hydro-thermo-chemo-mechanical coupling: application to alkali-silica reaction.” *Computatioanl Materials Science*, 84, 381-395.

Xotta, G., Salomoni, V.A., and Majorana, C.E. (2013). “Thermo-hygro-mechanical meso-scale analysis of concrete as a viscoelastic-damaged material.” *Engineering Computations*, 30 (5), 728-750.

Effects of Internal Cracking and Drying Shrinkage on the Corrosion Processes of RC Beam Specimens

K. Kawaai[1]; I. Ujike[1]; and I. Nakai[1]

[1]Department of Civil and Environmental Engineering, Ehime University, 3, Bunkyocho, Matsuyama, Ehime 790-8577, Japan. E-mail: kkawaai@cee.ehime-u.ac.jp

Abstract

Internal cracking tend to arise from the edge of knots present in deformed bars embedded in tension zone of reinforced concrete structure when loaded up to 100 N/mm^2. This could be further exacerbated by drying shrinkage depending on types of aggregate used in concrete mixtures under dry environment. The objective of this study was to examine the durability performance of internally cracked RC beam specimens cast using aggregate including crushed limestone and sandstone with different absorption capacity obtained in regional resources. Based on accelerated chloride-induced corrosion tests carried out via a cycle of 3-day wet and 11-day dry until the age of 1 year, although corrosion tended to occur severely in the cracked parts with higher chloride content depending on the drying shrinkage of concrete specimens, the results showed that internal cracking could trigger localized corrosion initiated especially at the knots of deformed steel bar.

1. INTRODUCTION

Corrosion of steel bars embedded in concrete owing to chloride attack or carbonation are major durability issues, resulting in a reduction in durability of reinforced concrete (RC). It is widely known that the durability performance of RC structure is adversely affected by the presence of cracks owing to early age cracking, bending moment, drying shrinkage and etc., which leads to less resistance against ingress of harmful substances including chloride ions especially in marine environment. Many studies have been carried out for examining the effects of such cracks on the corrosion processes in concrete (e.g., Beeby, 1978, 1983). Besides such cracks appeared on the surface of cover concrete, Goto and Otsuka (1980) reported that internal cracks tend to arise from the edge of knots present in deformed steel bars owing to tensile stresses increased up to 100 N/mm^2 when loaded under service conditions. This may have a significant impact on the durability performances pertaining to corrosion processes of steel bars if present (Ujike et al., 2013). The corrosion processes occurring in the presence of internal cracks could be further exacerbated by drying shrinkage depending on types of aggregate with different absorption capacity used in concrete mixtures under dry environment. These effects on the corrosion processes of steel bars in RC member were not comprehensively investigated in past research. Therefore, the objective of this study was to examine the durability performance of internally cracked RC beam specimens cast using

various types of aggregate including crushed limestone and sandstone obtained in regional resources.

2. EXPERIMENTAL PROGRAM

2.1. Materials and mixes

Table 1 shows the mix proportions of concrete mixtures used in this study. Water-to-cement ratio was chosen as 40% and cement used was high early strength Portland cement with a specific gravity of 3.14. In order to investigate the effect of drying shrinkage on the corrosion processes occurring in internally cracked RC beam specimens, three types of aggregate were used as summarized in Table 2. The maximum size of coarse aggregate was 20mm for each case.

Table 1. Mix proportion.

Specimen	W/C (%)	s/a (%)	Unit weight (kg/m^3)				AE (C×%)	AE-WRA (C×%)	SP (C×%)	Slump (cm)	Air (%)
			W	C	S	G					
F40	40	44	175	437	809	883	0.5	1.5	-	4	4
S40	40	43	175	437	822	910	0.5	-	0.45	5	4
C40	40	43.5	175	437	825	907	0.25	1.5	-	11	3.5

Table 2. Properties of aggregate.

Specimen	Fine aggregate (S) Coarse aggregate (G)	Types	Specific gravity (SSD)	Absorption capacity (%)	Fineness modulus
F40	S1	Crushed sand obtained from sandstone	2.61	1.06	2.88
C40	S2	Crushed sand obtained from limestone	2.66	1.02	2.74
S40	S3	Crushed sand obtained from sandstone	2.65	1.72	2.80
F40	G1	Crushed sandstone	2.63	0.68	-
C40	G2	Crushed limestone	2.70	0.36	-
S40	G3	Crushed sandstone	2.71	0.66	-

2.2. Testing procedures

Reinforced concrete specimens used in this study were of cross section 250 mm by 100 mm, and length 1800 mm as shown in Figure 1. In order for visual observations made on the evolution of internal cracks initiated at the edge of knots present in deformed steel bars (D22), the ribs were slightly exposed from the cover concrete as shown in the figure. After demolding at the age of 3 days, initial water curing was carried out using saturated coverings until the age of 7 days. According to past research, internal cracking can be observed in surrounding concrete around embedded deformed bars at stresses below 100 N/mm^2 (Goto and Otsuka, 1980). In this study, preliminary experiment was carried out to determine the stresses in facilitating the evolution of internal cracking, which suggested that internal cracks were visually confirmed at stresses corresponding to 500μ in strain measured using

strain gauge. Thus, the strain in reinforcement steel was targeted when the RC specimens were continuously loaded in four-point bending setup where the loading span was 500 mm as shown in Figure 2 during chloride-induced corrosion tests.

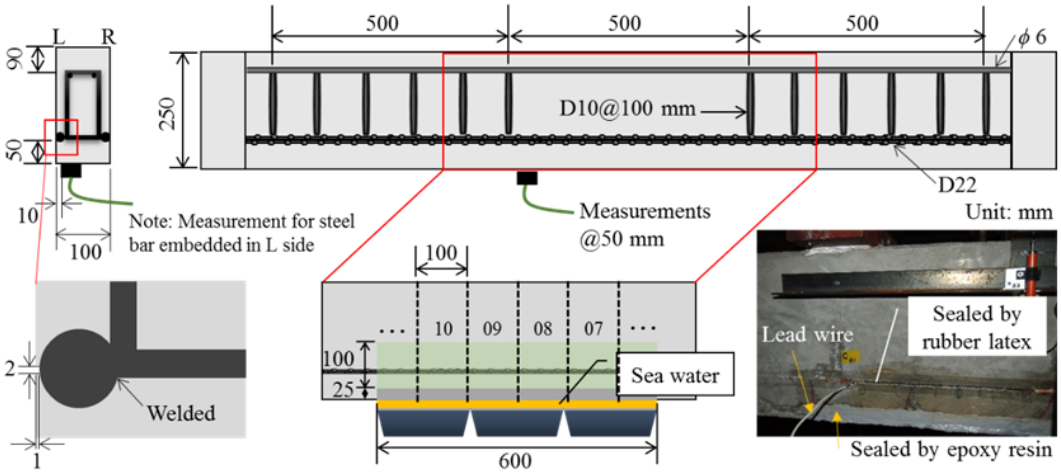

Figure 1. Schematic of RC beam specimens.

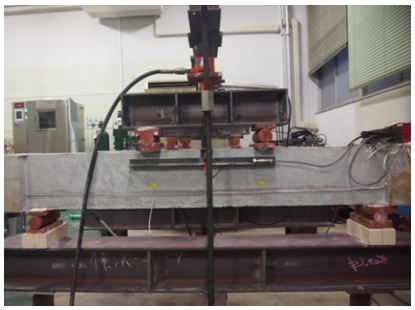

Figure 2. Four-point bending setup.

The chloride-induced corrosion tests were carried out via dry and wet cycles using sea water. The durations in which dry and wet conditions were kept under room conditions controlled at 20°C were 11 days and 3 days respectively. Although shorter dry duration was not necessarily sufficient in facilitating the drying shrinkage of concrete, it was confirmed that the cycle led to distinguishable drying shrinkage of prism concrete specimen carried out by preliminary experiments. The wet conditions were kept using a sponge containing sea water from the bottom surface of the RC specimens. This is intentional to facilitate the ingress of chloride ions via capillary action though pores and cracks. It is noted that the surface on the both sides of concrete specimens was sealed with epoxy resin and rubber latex in order to prevent harmful substances penetrating into the concrete.

Corrosion of steel bars were measured via AC impedance method using CM-SE1 (Nippon Steel Technoreserch) and Ag/AgCl as a reference electrode. The measurements were carried out at the intervals of 50 mm from the bottom surface where the counter electrode was placed through the medium of saturated material.

Based on the results obtained by the tests, corrosion current density was estimated based on the Stern-Geary constant taken as 0.026V. The severity of corrosion of steel bars were assessed based on the references reported by CEB (1997). Each measurement was carried out at the same location for more than three times to confirm the consistency. After the testing was continued until the age of 1 year, loading equipment was dismantled and the RC beam specimens were cut into smaller specimens by dry cutting. The specimens in 100 mm long as shown in Figure 1 were subsequently split into smaller specimens with each single steel bar. Chloride penetration depth was measured using 0.1N silver nitrate solution sprayed on freshly split surfaces (Otsuki et al., 1992). Besides the depth of chloride ions present in the specimens, total chloride content was calculated based on chloride ion concentration measured via the coulometric titration.

3. RESULTS AND DISCUSSION

3.1. Compressive strength and modulus of elasticity

Compressive strength was determined in accordance to JIS A 1108 using cylindrical specimens with a diameter of 100 mm and height of 200 mm. Modulus of elasticity was calculated based on stress-strain relationship obtained in accordance to JIS A 1149 in measuring displacement of concrete specimens parallel to the loading direction using compressometer. As summarized in Table 3, the compressive strength was higher in the case of the F40 mixture compared to the C40 mixture by a factor of 1.3. Although the compressive strength of the C40 mixture using the limestone was the smallest among the mixtures tested, the modulus of elasticity was higher than other two mixtures.

Table 3. Compressive strength and modulus of elasticity.

Specimen	*Compressive strength*	*Modulus of elasticity*
F40	69.0 N/mm^2	32.5 kN/mm^2
S40	65.3 N/mm^2	32.2 kN/mm^2
C40	54.1 N/mm^2	36.8 kN/mm^2

3.2. Drying shrinkage strain

Figure 3 shows drying shrinkage strains measured using dial gauges in prism specimens with dimensions of 100×100×400 mm under room conditions controlled at 20^{o}C. The specimens were cured in water tank until the age of 7 days after casting and subsequently tested under the dry environment for 18 weeks. As can be seen in the figure, the magnitude of those shrinkage strains measured for the F40, S40 and C40 specimens was 833μ, 1070μ and 469μ respectively. It was confirmed that the development of the drying shrinkage measured in the concrete specimens highly depends on the types of aggregates used. The smallest shrinkage strain was observed in the case of the concrete specimens cast using the limestone, which could be attributed to the lower absorption capacity and higher modulus of elasticity.

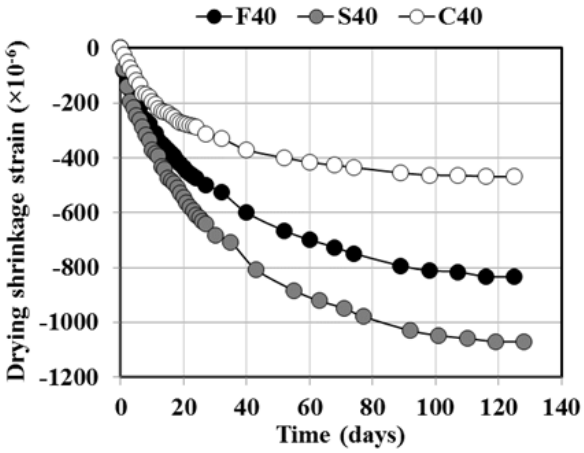

Figure 3. Drying shrinkage strain of prism specimens.

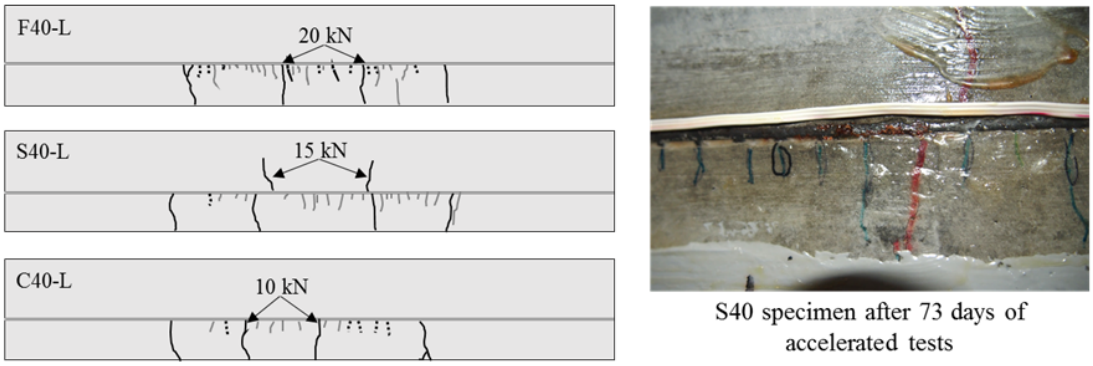

Figure 4. Sketch of flexural and internal cracks.

3.3 Observation of flexural and internal cracks

A significant advantage of the specimens used in this study was the surface treatment using rubber latex in the parts of reinforcement steel embedded slightly exposed in order for the visual observations made on the cracks evolution when loaded. Flexural cracks in the region subjected to uniform bending moment were observed at the loads as indicated as black color in Figure 4. It is noted that the evolution of cracks observed in the R side of the specimens was similar to those observed in the L side. Besides those cracks developed from the bottom surface of concrete specimens to the reinforcement steel, internal cracks were clearly observed as shown in the figures. It is noted that the solid line in gray color indicates the cracks developed before loading, and the dotted line in black color indicates cracks developed internally after loading. The results showed that those cracks tended to form majorly underneath the reinforcement steel. Since those cracks arose from the edge of knots present in deformed steel bars embedded, it was postulated that the cracks should be also initiated around the edges of knots present on the circumference including the regions embedded in the surrounding concrete, which can be confirmed only when the specimens were split.

The crack width measured for the flexural cracks on the bottom surface of the specimens using a microscope was shown in Figure 5. It is noted that the measurements were made using the specimens subjected to the dry and wet cycles for 1 year. Based on the experimental setup used for the three specimens including the cover depth, the type of steel bars and tensile strains initially exerted, the effects of creep and drying shrinkage are significant factors contributing to the flexural crack width. The largest crack width was observed in the S40 specimen, which could be attributed to the larger drying shrinkage strains measured in the prism specimens. This was aggravated owing to drying processes of the testing accounting for 11 days in a cycle. On the other hand, the crack widths measured in the C40 specimen were relatively smaller, which is consistent with the results of drying shrinkage strains measured in prism specimens. Thus, the resistance against the ingress of harmful substances including sea water and oxygen into the concrete leading to corrosion of steel bars was essentially modified by the presence of those cracks, which will be discussed in subsequent sections.

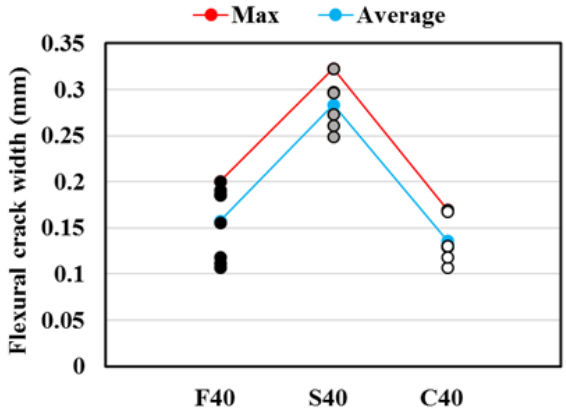

Figure 5. Flexural crack width of the F40, S40 and C40 specimens after 1-year exposure tests.

3.3 Corrosion current density (AC impedance method)

Figure 6 shows the corrosion current density estimated based on the polarization resistance measured in the specimens. The results showed that the corrosion current density increased owing to the presence of flexural cracks compared to the regions with internal cracks. In particular, higher corrosion current density at the maximum of 1.6 $\mu A/cm^2$ was observed in the F40 and S40 specimens tested. Although these specimens had a significant difference with respect to the flexural crack widths, the results seemed to suggest that corrosion processes taking place in the cracked parts as anodic region would be similar between the two specimens tested. In addition, the corrosion current density was relatively smaller in the case of the C40 specimen ranging from 0.2 to 1.3 $\mu A/cm^2$ tested in this study.

On the other hand, the corrosion current density measured in the regions with internal cracks as shown in Figure 6(b) was comparable among the specimens in terms of the average values. It was assumed that when the testing was continued for

longer periods, the corrosion processes could be similar to those observed in the regions with flexural cracks. The results seemed to suggest that the testing period about 1 year may not be sufficient for investigating the effects of drying shrinkage of concrete specimen on the corrosion occurring in the vicinity of internal cracks developed in the surrounding concrete covering the reinforcement steel.

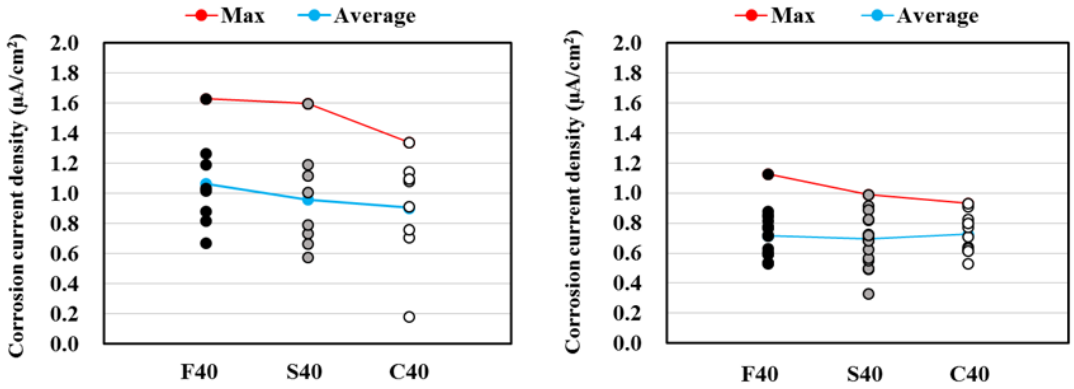

Figure 6. Corrosion current density measured in the presence of (a) flexural crack and (b) internal crack.

3.4 Chloride penetration depth and total chloride content

The chloride penetration depth was measured using 0.1N silver nitrate solution sprayed on the split surface of concrete specimens. In the regions without flexural cracks but with internal cracks, chloride penetration depth owing to capillary action of pores formed reached to the depth of 15 mm from the exposed surface. Since the maximum length of internal crack was at most 20 mm from the edges of exposed deformed steel bars, the results suggested that the ingress of chloride ions from the exposed surface was not major passage resulting in the corrosion of steel bars. The main passage leading to chloride-induced corrosion was assumed to be the penetration of chloride ions through flexural cracks reaching to the depths of 100, 120 and 70 mm for the F40, S40 and C40 specimens respectively. Besides the crack width observed in the specimens, the chloride penetration depth was observed to increase in the specimens with larger drying shrinkage strains especially along the flexural cracks.

As can be seen in Figure 7, the RC specimens were dismantled via dry cutting and splitting and the smaller specimens with each reinforcement steel were used for the chemical analysis in determining chloride content in concrete. In addition, corroded steel bars were carefully taken out from the specimens and then examined with respect to corrosion formation occurring in the vicinity of flexural and/or internal cracks. Table 4 summarizes notation of specimens with flexural and/or internal cracks for the three specimens tested.

Table 4. Specimens with flexural and/or internal cracks

Specimen	*Flexural cracks*	*Internal cracks*
F40	FL07, FL09	FL08, FL10
S40	SL07, SL10	SL08, SL09
C40	CL08, CL10	CL07, CL09

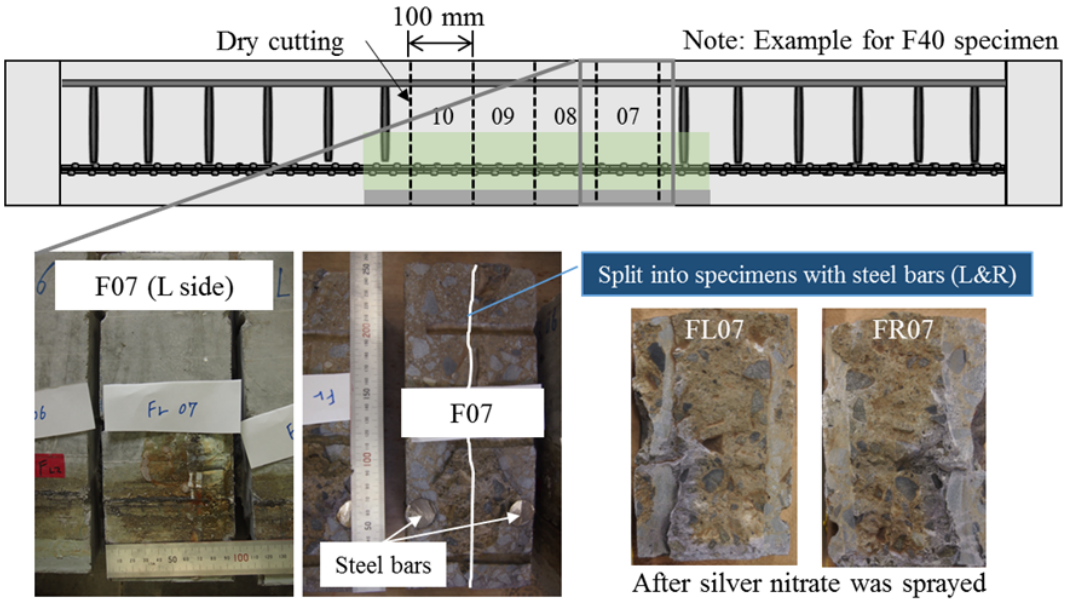

Figure 7. Dismantlement of RC specimens.

Figure 8 shows distribution of total chloride content estimated using coulometric titration in the presence of flexural and/or internal cracks. As can be seen in the Figure 8(a), the total chloride content exceeded the threshold value i.e. 1.2 kg/m^3 up to the depth of 100 mm from the exposed surface, which is consistent with the results of corrosion current density in the presence of flexural cracks. On the other hand, the total chloride content in the presence of internal cracks was likely to increase with increasing depth of cover concrete up to 75 mm as shown in Figure 8(b). In particular, the content at the depth of 75 mm in the case of SL09 specimen exceeded 1.2 kg/m^3. Based on the results obtained, it seemed that the chloride ions penetrated deeper zones in such a way that internal cracks could trigger the widespread chloride ions in the vicinity of flexural cracks. Thus, the results suggested that corrosion could occur not only underneath the steel bars but also over the steel bars. Besides the processes pertaining to the ingress of chloride ions, one significant observation made was that the corrosion tended to localize especially at the knots of deformed bars as shown in the Figure 9. This is highly detrimental to the durability and structural integrity with respect to composite action between deformed steel bars and the surrounding concrete.

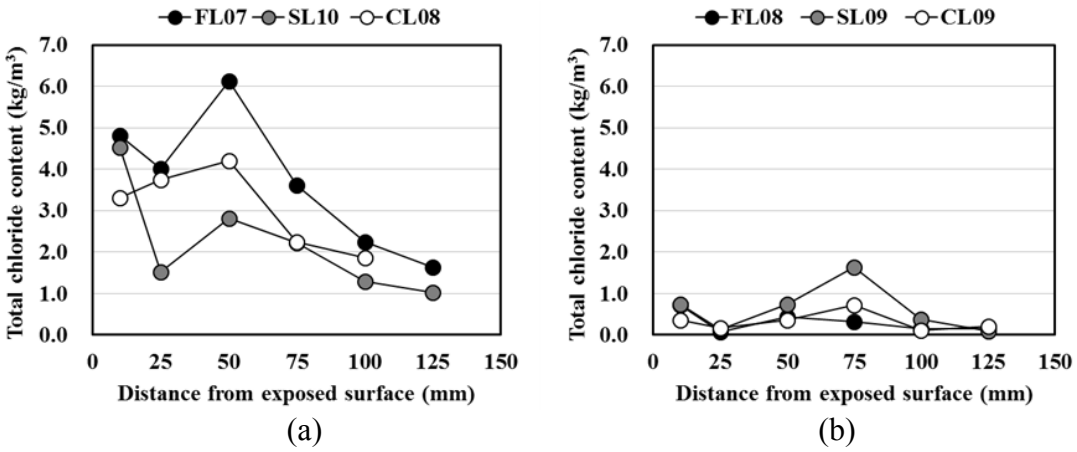

Figure 8. Total chloride content in the presence of (a) flexural crack and (b) internal crack.

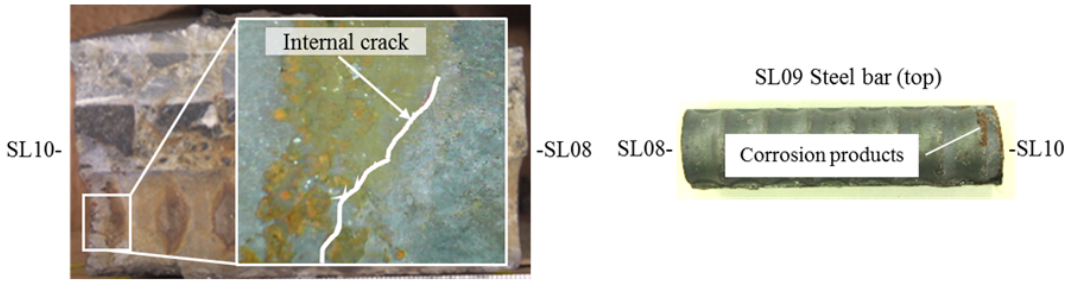

Figure 9. Corrosion formation in the presence of internal cracking.

CONCLUSION

Based on the results obtained, it was confirmed that total chloride content measured along flexural cracks increased in concrete specimens with larger drying shrinkage strains. Corrosion of steel bars formed in the cracked parts tended to be severe especially in the presence of flexural cracks. It was found that corrosion current density was not dependent on flexural crack width, however those measured in the presence of flexural cracks seemed to be relatively smaller in the case of concrete specimen cast using the limestone with smaller drying shrinkage strains. Although it was not clear that drying shrinkage of concrete specimens had an influence on the corrosion processes occurring in internally cracked parts in concrete, it was found that the presence of internal cracks formed in the vicinity of flexural cracks led to widespread chloride ions and induced localized corrosion initiated especially at the knots of deformed steel bars.

ACKNOWLEDGEMENTS

This research was supported by Grant-in-Aid for Scientific Research (A): 21246071, the author would like to express his sincere appreciation.

REFERENCES

Beeby, A.W. (1978) Cracking, cover, and corrosion of reinforcement. Concrete International, 5(2), pp. 35-40.

Beeby, A.W. (1983) Corrosion of reinforcing steel in concrete and its relation to cracking. The Structural Engineer, Vol. 56A, No. 3, pp. 77-81.

CEB, Working Party V/4.1 (1997) Strategies for Testing and Assessment of Concrete Structures Affected by Reinforcement Corrosion, 27-30BRI-CSTC-WTCB.

Goto, Y. and Otsuka, K. (1980) Experimental Studies on Cracks Formed in Concrete around Deformed Tension Bars. Journal of Japan Society of Civil Engineers, No. 294, pp. 85-100.

Otsuki, N., Nagataki, S. & Nakashita, K. (1992) Evaluation of $AgNO_3$ solution spray method for measurement of chloride penetration into hardened cementitious matrix materials. ACI Materials Journal, Vol. 89, No. 6, pp. 587-592.

Ujike, I., Okazaki, S., and Sato, R. (2013) Experimental Study on Effect of Internal Cracking on Corrosion Rate of Reinforcement in Concrete. Mechanics and Physics of Creep, Shrinkage, and Durability of Concrete: pp. 277-284.

Multiscale modeling of chloride diffusion in cementitious materials

T. Wu[1], L. De. Lorenzis[1] and P. Carrara[1]

[1] Institut für Angewandte Mechanik, Technische Universität Braunschweig, Bienroder Weg 87, 38106 Braunschweig, Germany; email: taowu@tu-braunschweig.de, l.delorenzis@tu-braunschweig.de,p.carrara@tu-braunschweig.de.

ABSTRACT

The motivation of this contribution is to apply computational diffusion homogenization to the microscale and mesoscale of concrete sequentially, while taking into account both physical and chemical bindings. The effective diffusivity of cement paste obtained by homogenization at the microscale is considered as the input for diffusion homogenization at the mesoscale, thereby establishing the link between three length scales of concrete. Comparisons between numerical results of each step of the diffusion homogenization and experimental data from the literature are reported and discussed.

1 Introduction

Cementitious materials suffer from the interaction of diffusion processes combined with chemical reactions, such as the attack of chloride ions. Moreover, the micro- and macrocracks induced by reaction-diffusion processes cause that attack processes of chloride ions are accelerated since low-resistance pathways for chloride ions are formed. For example, chloride-induced corrosion of the reinforcing steel is one of the main causes of deterioration of reinforced concrete structures. Not only the dependency of diffusion of chloride ions on the microstructure of the material but also the difficulty in measuring diffusion properties at the microscale through conventional experiments underline the need to develop numerical multiscale models for analyzing the diffusion of chloride ions in cementitious materials.

Over the past 20 years, a number of works have contributed to predict the diffusivity of chloride ions of cement paste or concrete by using multiscale approaches. Most recently, Zhang et al. [1][2] adopted a hybrid lattice Boltzmann-finite element method to estimate the effective diffusivity to chloride ions of cement paste and concrete, where the microstructure and mesostructure of concrete were generated with HYMOSTRUC3D. Nilenius et al. [3] predicted the effective diffusivity of concrete, which is comprised of cement paste, aggregates and interfacial transition zone (ITZ). In this model, the consideration of the anisotropy of ITZ results in the dependency of the diffusivity tensor on the normal to the aggregate surface.

The comprehensive understanding of the complex heterogeneity of concrete at different length scales plays a significant role in developing multiscale models for analyzing the diffusion of chloride ions (Figure 1). At the macroscale, concrete is assumed

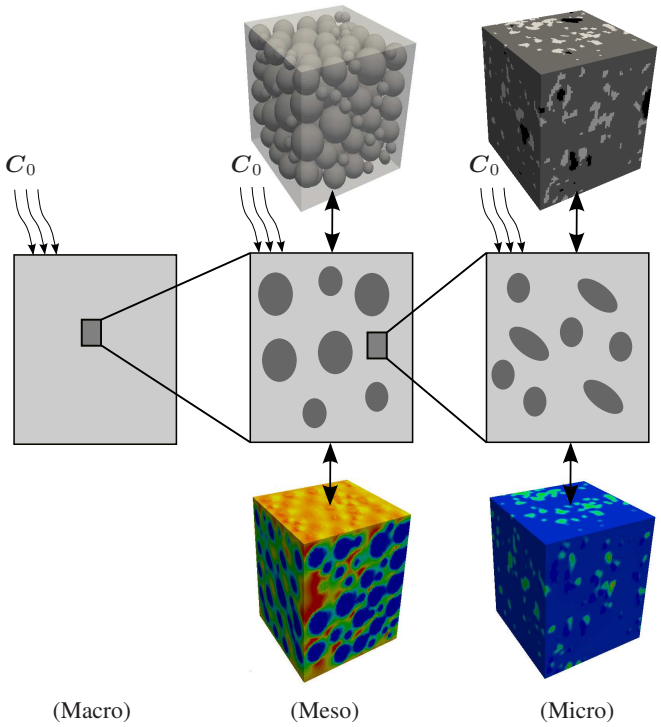

Figure 1. Representations of concrete at different length scales and the framework of the multiscale model for diffusion.

to be a homogeneous material. The mesoscale consists of hardened cement paste (HCP) and aggregates. At the microscale, the HCP is comprised of hydration products, unhydrated residual clinker and micropores. One scale lower, CSH and CH are the main hydration products. The unhydrated residual klinker contains C3S, C4AF, C2S and C3A.

In this work, the microstructure of the HCP is obtained through three-dimensional micro-CT scans with a resolution of 1 μm per voxel dimension [4][5]. The mesoscale of concrete is represented by randomly distributed spheres in the homogenized cement paste by using the Take-and-Place approach [4]. This contribution is initialized by homogenization at the microscale of HCP, where physical and chemical bindings are accounted for based on models from [1][2]. The obtained effective diffusivity from the microscale is considered as input for diffusion homogenization at the mesoscale. This approach thus establishes the link between the micro, meso and macro scales of concrete.

2 Binding

As discussed in [6], the binding mechanisms affecting the diffusion of chloride ions can be generally classified into chemical binding and physical binding. The chemical binding refers to the reaction between chloride ions and C3A and C4AF, forming Friedel's salt. The physical binding is concerned with the absorption of chloride ions by the CSH.

The diffusion of chloride ions can be described by

$$\frac{\partial c}{\partial t} = -\nabla \cdot \boldsymbol{j} \quad , \tag{2.1}$$

where c is the concentration. $\boldsymbol{j}$ indicates the diffusion flux which is obtained by Fick's constitutive law $\boldsymbol{j} = -D\nabla c$, where D is the scalar diffusivity for the case of isotropic diffusion. Concrete is a porous medium, such that the diffusion process is not only affected by the pore structure of concrete but also influenced by the presence of other types of species in the pore solution [1]. Therefore, the total concentration of chloride ions c_t is the sum of the concentrations of bound chloride ions c_b and free chloride ions c_f

$$c_t = c_f + c_b \quad . \tag{2.2}$$

Bound chloride ions refer to results of chemical and physical binding. Note that only the free chlorides c_f can dissolve in the pore solution and diffuse through the pore solution. Equation (2.2) leads to

$$\frac{\partial c_t}{\partial t} = \frac{\partial c_f}{\partial t} + \frac{\partial c_b}{\partial t} = \Big(1 + \frac{\partial c_b}{\partial c_f}\Big)\frac{\partial c_f}{\partial t} \quad . \tag{2.3}$$

Combining Equations (2.1), (2.3) and Fick's constitutive law yields

$$\frac{\partial c_f}{\partial t} = \frac{D}{1 + \frac{\partial c_b}{\partial c_f}}\Delta c_f = D_\alpha \Delta c_f \quad , \tag{2.4}$$

where Δ is the Laplace operator and

$$D_\alpha(c_f) = \frac{D}{1 + \frac{\partial c_b}{\partial c_f}} \quad . \tag{2.5}$$

In this model, the binding is only taken into account in micropores of HCP, hence, D_α denotes the apparent diffusivity of micropores which is a function of the diffusivity of micropores D and chloride binding capacity $\frac{\partial c_b}{\partial c_f}$. The chloride binding capacity $\frac{\partial c_b}{\partial c_f}$ used in [1] is given by

$$\frac{\partial c_b}{\partial c_f} = 21.84 \cdot \frac{2.65}{(1 + 2.65 c_f)^2} \cdot X_{\mathrm{CSH}} + 48.88 \cdot 0.58 \cdot c_f^{-0.42} \cdot X_{\mathrm{AFm}} \quad . \tag{2.6}$$

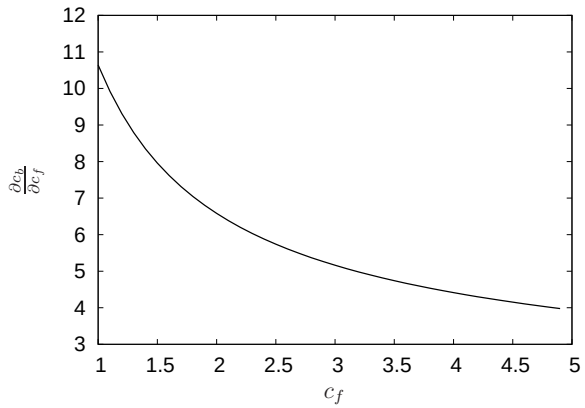

Figure 2. Relationship between chloride binding capacity $\frac{\partial c_b}{\partial c_f}$ and c_f.

This equation is in turn taken from Hirao et al. [7] and matches very well the experimental results over a wide range of chloride concentration from 0 to 5 mol/l. X_{CSH} and X_{AFm} denote the contents of CSH and AFm in the cement paste [1], which are expressed by

$$X_{\mathrm{CSH}} = 1.007 \cdot \alpha_{\mathrm{C3S}} \cdot X_{\mathrm{C3S}} + 1.335 \cdot \alpha_{\mathrm{C2S}} \cdot X_{\mathrm{C2S}} \quad , \tag{2.7}$$

$$X_{\mathrm{AFm}} = 2.307 \cdot \alpha_{\mathrm{C3A}} \cdot X_{\mathrm{C3A}} + 1.305 \cdot \alpha_{\mathrm{C4AF}} \cdot X_{\mathrm{C4AF}} \quad , \tag{2.8}$$

where X_{C3S}, X_{C2S}, X_{C3A} and X_{C4AF} represent the mass fraction of each component respectively, and α_{C3S}, α_{C2S}, α_{C3A} and α_{C4AF} denote the corresponding degrees of hydration.

As visible from Equation (2.6), $\frac{\partial c_b}{\partial c_f}$ is determined not only by the free chloride concentration c_f, but also by the microstructure of cementitious materials. The analytical relationship between chloride binding capacity $\frac{\partial c_b}{\partial c_f}$ and c_f is shown in Figure 2, where the free chloride concentration c_f is from 0 to 5 mol/l. More information about this model can be found in [1][2].

3 Computational diffusion homogenization

The objective of computational homogenization is to characterize the macroscopic behavior of an heterogeneous material by identifying a statistically representative volume element (RVE). This is a sample from the heterogeneous material which is small enough compared to the dimensions of the upper length scale, yet includes sufficient statistical information about the microstructure so as to accurately represent the response that the heterogeneous material exhibits on the upper scale [8].

In terms of the procedure of computational diffusion homogenization, the effective diffusivity D^* for the isotropic case is determined by minimizing a least-square

function

$$\Pi := [\langle \boldsymbol{j} \rangle - \boldsymbol{j}^*(\langle \nabla c \rangle)]^2 \quad \rightarrow \quad \min \quad , \tag{3.1}$$

in which the effective constitutive equation for diffusion is defined by

$$\boldsymbol{j}^*(\langle \nabla c \rangle) = -D^* \langle \nabla c \rangle \quad . \tag{3.2}$$

where $\langle \bullet \rangle$ is the volume averaging operator. Differentiation of Equation (3.1) with respect to D^* leads to

$$\frac{\mathrm{D}\Pi}{\mathrm{d}D^*} \stackrel{!}{=} 0 \quad . \tag{3.3}$$

Thus, the isotropic effective diffusivity is obtained through

$$D^* = -\frac{\langle j \rangle_1 \langle \nabla c \rangle_1 + \langle j \rangle_2 \langle \nabla c \rangle_2 + \langle j \rangle_3 \langle \nabla c \rangle_3}{\langle \nabla c \rangle_1^2 + \langle \nabla c \rangle_2^2 + \langle \nabla c \rangle_3^2} \quad . \tag{3.4}$$

with j_1, j_2 and j_3 as the scalar components of $\boldsymbol{j}$.

Boundary conditions for diffusion homogenization are chosen as

$$c = \boldsymbol{C}_0 \cdot x \ \text{ on } \ \partial \mathcal{B}_\mathrm{t} \ , \tag{3.5}$$

where $\boldsymbol{C}_0 = \langle \nabla c \rangle$ is a constant prescribed average concentration gradient, and $\partial \mathcal{B}_t$ is the surface of the RVE.

3.1 Homogenization at the microscale

Component	Diffusivity ($10^{-9}\mathrm{m}^2/\mathrm{s}$)
Hydration product	0.0051 [1]
Unhydrated clinker	0.0051 [1]
Micropore	2.05 [1]

Table 1. Diffusivity of components in HCP.

Table 1 illustrates the diffusivity of the components in the HCP. The boundary conditions given in Equation (3.5) are prescribed on the surface of the RVE of HCP for diffusion homogenization. In this work, an RVE with the size of $64 \times 64 \times 64 \mu m^3$ is chosen. The proof that the chosen size of RVE satisfies the Hill's criterion can be found in [9]. Figure 3 shows the diffusion flux of chloride ions in HCP, where cases are investigated with binding and without binding. It is clearly observed that the diffusion flux is decreased when the binding is accounted for.

Theoretically, it is desirable to choose an RVE including entirely realistic information of the microstructure, such that the obtained effective response is independent

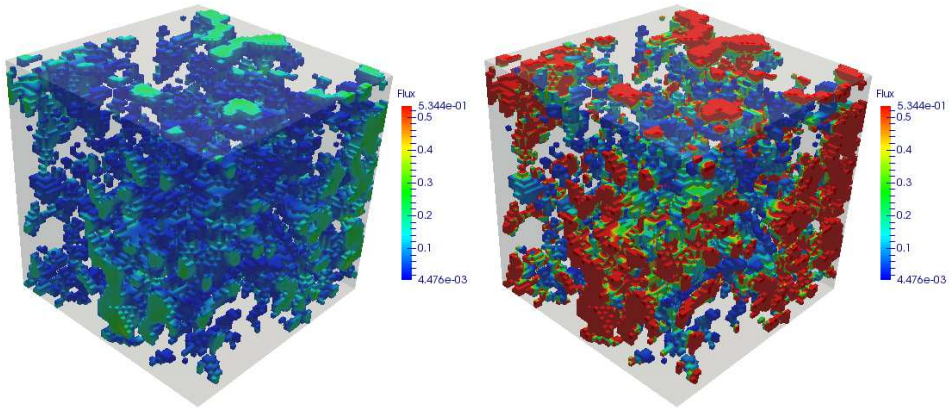

(a) (b)

Figure 3. Diffusion flux of chloride ions in HCP (a) without binding (b) with binding.

of the type of boundary conditions, yet the computational cost is high. Therefore, realistically a sample slightly smaller than the ideal RVE is typically chosen. The approximate RVE is a randomly chosen sample from a much larger micro-CT scan of HCP. In this work, 200 randomly obtained RVEs from a micro-CT scan were tested. Table 2 presents the average value of these 200 statistical tests without binding and with binding. Equation (2.4) is a non-linear diffusion equation which thus requires a non-linear homogenization procedure. The fully non-linear problem will be solved in future. In this work, linear homogenization is performed by assuming c_f in Equation (2.6) to be a constant. Results in Table 2 are given for different values of the assumed constant c_f in the range of the experimental validation [1][2]. The obtained effective diffusivity with binding is smaller than the one without binding. Moreover, as the assumed constant c_f is increased, the obtained effective diffusivity of HCP is increased as well.

	Diffusivity ($10^{-9}\mathrm{m}^2/\mathrm{s}$)
Without Binding	0.0932
With Binding c_f=1 mol/l	0.0104
" " c_f=2 mol/l	0.0110
" " c_f=3 mol/l	0.0113
" " c_f=4 mol/l	0.0115
" " c_f=5 mol/l	0.0116

Table 2. Effective diffusivity of HCP for 200 statistical tests.

Figure 4 illustrates comparisons between numerical results and experimental

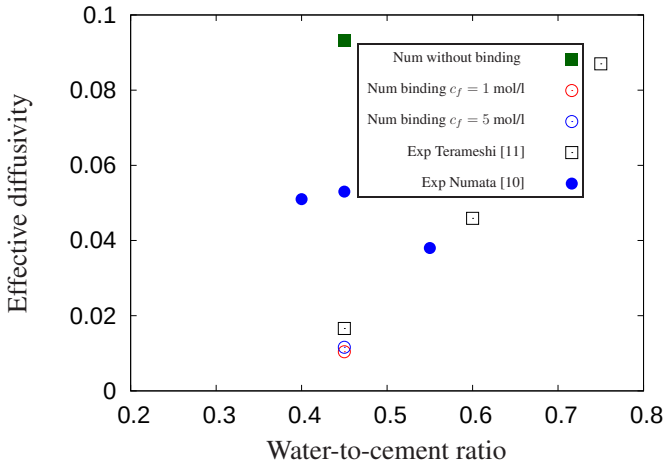

Figure 4. Comparison between numerical results and experimental data of HCP.

data. The obtained effective diffusivity taking into account binding provides better agreement with the experimental data. The difference between numerical results and experimental data [10] could be attributed to: (1) hydration degree and other sample properties of cement paste used in the experiment [10] are different from those in the cement paste sample for CT-scan (2) micropores are assumed to be fully saturated for simulation, however, in reality they are only partially saturated.

3.2 Homogenization at the mesoscale

The effective diffusivity of cement paste obtained by homogenization at the microscale of concrete is considered as the input for diffusion homogenization at the mesoscale. The diffusivity of aggregates $D = 0.308 \cdot 10^{-12}\mathrm{m}^2/\mathrm{s}$ at the mesoscale of concrete is obtained from [12]. Figure 5 illustrates the diffusion flux at the mesoscale of concrete. It is clearly observed that the diffusion flux in aggregates is much smaller than that in the cement paste due to small diffusivity of aggregates.

Table 3 shows the calculated effective diffusivity of concrete, where not only different volume fractions of aggregates but also the calculated effective diffusivity of the cement paste with different assumed values c_f in the binding equation are investigated. The effective diffusivity of concrete is decreased as the volume fraction of aggregates is increased, and is increased as c_f rises. Comparisons between numerical results and experimental data from [13] can be found in Figure 6. When binding is taken into account, the calculated effective diffusivity of concrete provides better agreement with the experiment.

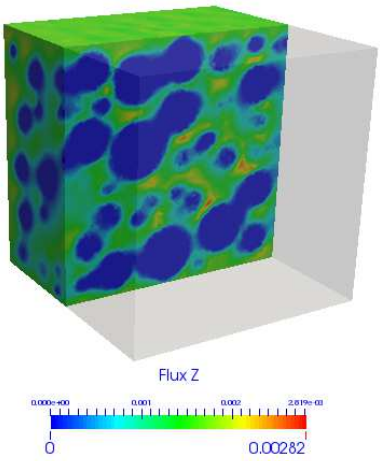

Figure 5. Diffusion flux at the mesoscale of concrete.

-	30% ($10^{-9}\mathrm{m}^2/\mathrm{s}$)	40% ($10^{-9}\mathrm{m}^2/\mathrm{s}$)	60% ($10^{-9}\mathrm{m}^2/\mathrm{s}$)
Without Binding	0.058017	0.038816	0.035697
With Binding c_f=1 mol/l	0.006611	0.004532	0.004192
" " c_f=2 mol/l	0.004420	0.004780	0.004420
" " c_f=3 mol/l	0.007170	0.004904	0.004535
" " c_f=4 mol/l	0.007295	0.004987	0.004611
" " c_f=5 mol/l	0.007357	0.005029	0.004649

Table 3. Calculated effective diffusivity of concrete for various volume fractions of aggregates.

4 CONCLUSIONS

Diffusion of chloride ions relying on the microstructure of cementitious materials underlines the need to develop multiscale models for analyzing the diffusion of chloride ions in cementitious materials. In this contribution, 3D micro-CT scan of hardened cement paste (HCP) and aggregates with a random distribution embedded in a homogenized HCP are used to represent the microscale and mesoscale of concrete respectively.

Taking into account chemical and physical bindings in HCP, numerical diffusion homogenization is implemented on a representative volume element of HCP for calculating the effective diffusivity of HCP. In order to obtain reliable results, a sufficient number of statistical samples are chosen for diffusion homogenization.

The effective diffusivity of cement paste obtained by homogenization at the

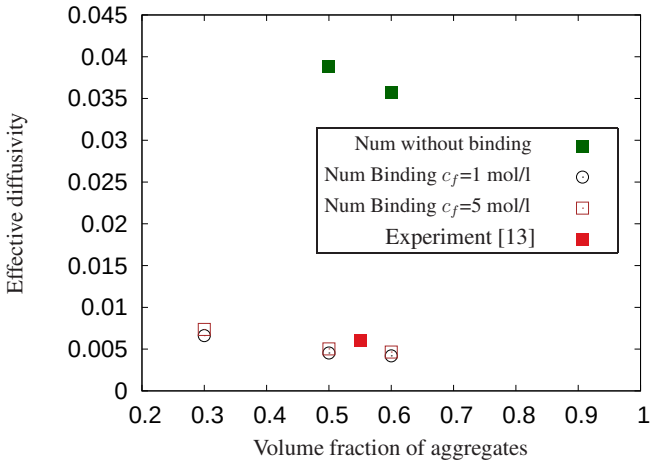

Figure 6. Comparison between numerical results and experimental data of concrete.

microscale of concrete is considered as the input for diffusion homogenization at the mesoscale, where various volume fractions of aggregates are taken into account. Each step of diffusion homogenization is compared with available experimental data.

Due to the dependency of the chloride binding capacity $\frac{\partial c_b}{\partial c_f}$ on the free chloride concentration, which is used for calculating the effective diffusivity of HCP, a nonlinear homogenization procedure will be implemented in future work.

References

[1] M. Z. Zhang, Y. Guang, and K. van Breugel. Multiscale lattice boltzmann-finite element modelling of chloride diffusivity in cementitious materials. part I: Algorithms and implementation. *Mechanics Research Communications*, 58:53–63, 2014.

[2] M. Z. Zhang, Y. Guang, and K. van Breugel. Multiscale lattice boltzmann-finite element modelling of chloride diffusivity in cementitious materials. part II: Simulation results and validation. *Mechanics Research Communications*, 58:64–72, 2014.

[3] F. Nilenius, F. Larsson, K. Lundgren, and K. Runesson. Computational homogenization of diffusion in three-phase mesoscale concrete. *Computational Mechanics*, In press, 2014.

[4] T. Wu, İ. Temizer, and P. Wriggers. Computational thermal homogenization of concrete. *Cement and Concrete Composites*, 35:59–70, 2013.

[5] T. Wu, İ. Temizer, and P. Wriggers. Multiscale hydro-thermo-chemo-mechanical coupling: Application to alkali-silica reaction. *Computational Materials Science*, 84:381–395, 2014.

[6] D. P. Bentz and E. J. Garboczi. A computer model for the diffusion and binding of chloride ions in Portland cement paste. *NISTIR 5125*, 45:528–535, 1993.

[7] H. Hirao, K. Yamada, H. Takahashi, and H. Zibara. Chloride binding of cement estimated by binding isotherms of hydrates. *Journal of Advanced Concrete Technology*, 3:77–84, 2005.

[8] T. I. Zohdi and P. Wriggers. *An Introduction to Computational Micromechanics*. Springer Verlag, 2008.

[9] M. Hain and P. Wriggers. Numerical homogenization of hardened cement paste. *Computational Mechanics*, 42:197–212, 2008.

[10] S. Numata, H. Amano, and K. Minami. Diffusion of tritiated water in cement materials. *Journal of Nuclear Materials*, 171:373–380, 1990.

[11] T. Yamaguchi, K. Negishi, S. Hoshino, and T. Tanaka. Modeling of diffusive mass transport in micropores in cement based materials. *Cement and Concrete Research*, 39:1149–1155, 2009.

[12] K.L. Vasconselos, A. Bhasin, D.N. Little, and R.L. Lytton. Experimental measurement of water diffusion through fine aggregate mixtures. *Journal of Materials in Civil Engineering*, 23:445–452, 2011.

[13] G. de Vera, M. A. Climent, E. Viqueira, C. AntÃşn, and C. Andrade. A test method for measuring chloride diffusion coefficients through partially saturated concrete. part ii: The instantaneous plane source diffusion case with chloride binding consideration. *Cement and Concrete Research*, 37:714–724, 2007.

Durability Performance of Polymer-Concrete Composites in a Diffusion-Dominated Process

F. Nabavi[1]

[1]Xypex Australia Company, 45 Union Rd., Albury, NSW 2641, Australia. E-mail: farhadn@xypex.com.au

Abstract

Durability of the concrete depends on the mass transfer properties of the concrete. This paper investigates the chloride diffusion in polymer-concrete composites subjected to pure diffusion process for 720 days. Chloride profiles for all types of concrete were obtained and then chloride diffusion coefficients were calculated. Extensive experimental program showed a significant enhancement of concrete durability by means of polymer-concrete composites. Reducing numbers and size of cracks and blocking the interconnected pores in concrete can enhance the durability of concrete. The results of this experimental study revealed that utilising both synthetic fibres and polymers in concrete improved durability of the concrete significantly.

INTRODUCTION

The subject of the reinforced concrete structures durability has extensively been studied and investigated for the last four decades. But, premature deterioration of reinforced concrete structures is still widely recognized problem in the world. According to the vast investigations, it is found out that the dominant factor of this process is chloride-induced corrosion of the steel reinforcement in concrete (Shaker et al., 1997, Costa and Appleton, 1999, Zornoza et al., 2009, Ann et al., 2009, Song and Kwon, 2009).

Chloride diffusion into the concrete occurs through the interconnected pores and cracks in concrete. Increasing the number and the width of cracks will not only accelerates the diffusion process but also enhances the probability of the steel corrosion which consequently decreases the service life of structures. When the concentration of chloride ions around the steel reinforcement surface reaches to chloride threshold level (CTL), depassivation of high alkaline protective layer leads to corrosion initiation (Alonso et al., 2000, Angst et al., 2009, Ann and Song, 2007, Deb, 2012, Koleva et al., 2007).

Increasing the ductility and tensile strength of the concrete in order to reduce the cracks from one side and to reduce the permeability of concrete by blocking the interconnected pores from the other side can definitely increase the durability and service life of the structure. In this study, polymer-concrete composites were investigated as a practical solution to increase the concrete durability.

POLYMER-CONCRETE COMPOSITES

Composite materials are produced by combining two or more distinct phases and materials to achieve properties far superior than each of the base materials. The properties of the composites not only depend on the properties of each individual material, but also on the interfacial zone properties of them (Li, 2003).

This investigation concentrates on synthetic fibres and especially on polypropylene (PP) fibres and also, dispersion aqueous polymers especially styrene butadiene rubber (Latex).

PP fibers have several unique properties that make them especially suited for using in the concrete. They are chemically inert and stable in the alkaline environment of concrete with a relatively high melting point and low cost. They do not absorb water due to a hydrophobic surface which prevents any chemical adhesion with the concrete matrix; they are non-corrosive and compatible with all types of cements and admixtures. They do not affect concrete mix design, pumpability, placing, setting time and finishing surface characteristics (Geleji et al., 1977, Brandt, 2008).

Crack control plays a crucial role in the performance life of the concrete structure. This is because the settlement and plastic shrinkage cracks may pass through fresh concrete, thus forming planes of weakness and lowering the integrity of the structure of concrete (Song et al., 2005). PP fibers mitigate plastic and early drying shrinkage by increasing the tensile property of concrete and bridging the forming cracks (Toutanji, 1999). PP fibre is introduced in the mix to minimize brittleness of the matrix thereby reducing the susceptibility to cracking of a concrete. It is also reported that PP fiber was effective in resisting the development of cracks caused by drying shrinkage (Toutanji et al., 1998, Huang, 2001).

Polymer modified concrete (PMC) is normal Portland cement concrete with a polymer as an admixture. The polymer and the cement hydration products comingle and create two interpenetrating matrices working together which results the improvement of the material properties of conventional concrete (Kardon, 1997, Fowler, 1999, Knapen and Van Gemert, 2009).

Latex modified concrete (LMC) is the most common type of PMC because latex is relatively simple to incorporate in mortar or concrete. It is added with the other ingredients during the mixing of the fresh concrete. The water portion of the latex must be considered in the overall mix design of the concrete. Latexes are suspensions in the water of solid monomers or polymers (Zhong and Chen, 2002). For solidification of latex, it must be suspended in water, and then give up that water. As the proportion of water in the latex drops below a critical fraction, the polymer particles suspended in the water begin to coalesce into a solid. On the other hand, cement requires water in order to carry out the hydration process. When an aqueous latex and cement are mixed together, the water in the latex is taken up by the cement hydration process. In this case, two materials tend to form solids in an interlacing skeleton (Su et al., 1991, Silva and Monteiro, 2006). The hydrated cement phase and polymer phase interpenetrate, and aggregates are bound by this co-matrix phase (Ma et al., 2011).

MATERIALS AND MIX DESIGN

Materials properties. The properties of the materials used in this investigation are expressed as follows:

- Portland cement type General Purpose (GP) based on Austalian Standard (ASTM C150 Type (I)).
- Crushed coarse aggregate with maximum size of 20 mm, specific gravity of 2710 kg/m^3, and water absorption capacity of 1.48%.
- Natural fine aggregate with maximum size of 4.75 mm, specific gravity of 2620 kg/m^3, and water absorption of 1.67%.
- Polypropylene (PP) fibres with length of 19 mm, nominal diameter of 24 μm, specific gravity of 0.91 g/cm^3, modulus of elasticity of 3.5 GPa, and tensile strength of 0.47 GPa.
- Styrene Butadiene Rubber (SBR, Latex) with spherical particles with diameter range variety from 0.05 to 0.50 μm, and 50% of solid content.

Mix design. In order to obtain high quality of conventional concrete as reference concrete, the following assumption were considered to design the concrete mix:
Mean compressive strength of 60 MPa, water to cement ratio (w/c) of 0.35, cement content of 400 kg/m^3, and slump of 65 ± 10 mm.

Types of Concrete. Conventional concrete (CC) as reference concrete and polymer-concrete composites with different proportions of PP fibres and latex were cast as shown in Figure 1.

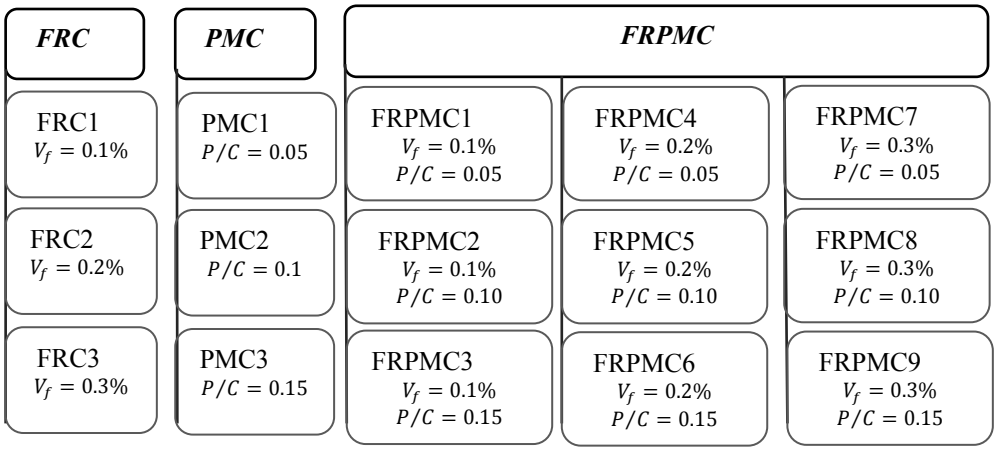

Figure 1. Characteristics of polymer-concrete composites

Since chloride diffusion into the concrete is the dominant factor in concrete structures deterioration, chloride profile can be used to estimate the residual corrosion-free service life of the structure. The chloride profile is attained by measuring the concentration of chloride in different depth of the concrete cover in a certain time. By using the chloride profile, initiation time of corrosion can be predicted. Chloride profile can be used as a criterion to assess the durability of the

concrete. In this experimental study, chloride content has been measured as durability assessment of different type of concretes.

PURE DIFFUSION TEST METHOD (CHLORIDE PROFILE)

All steady-state and non-steady-state diffusion tests are time consuming and therefore not suitable for use in quality control. However, they can be used in laboratory experiments and they also have the advantage of yielding a meaningful value of chloride ion diffusivity.

Among the long-term diffusion tests like Diffusion Cell, Ponding Test and Bulk Diffusion Test, Bulk Diffusion Test (NT Build 443) is claimed to be the most accurate as it measures pure diffusion (Stanish et al., 1997).

To conduct the Bulk Diffusion test, cube specimens were cured for 28 days. After curing period, they were coated on five sides with epoxy resin and left for 24 hours for the epoxy to cure. Then, they were immersed in water and weight gain of each cube was recorded every day. The immersion in water was continued until the weight gain was less than 0.01% of the sample weight per day to make sure that the concrete was fully saturated. They were then immersed in salt solution (NaCl) with concentration of 16.5% for diffusion test as shown in Figure 2.

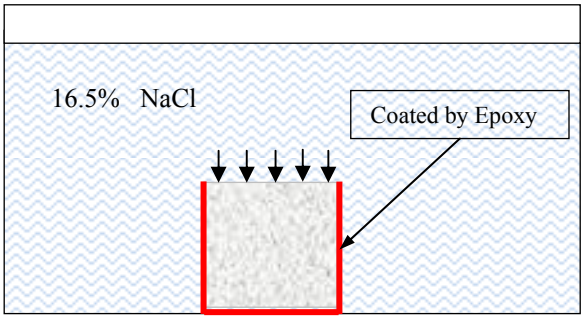

Figure 2. Exposure condition for pure diffusion test

The test method to obtain chloride content in the sample was conducted based on RILEM TC178-TMC, 'Analysis of Total Chloride Content in Concrete'.

RESULTS AND DISCUSSION

In this section the results of compressive strength as a mechanical properties and chloride diffusion into concrete as a durability criterion are investigated.

As a general trend, FRCs showed slightly higher compressive strength than CC. FRCs compressive strength increases by increasing the proportion of PP fibres (Figure 3-a). PMCs indicated lower compressive strength than CC. The strength reduction was correspondence with polymer cement ratio increment (Figure 3-b). Although, the compressive strength test results of PMCs are less than CC strength they are still in acceptable range of target strength which was assumed as 60 MPa and can be categorised as a structural concrete. Figure 3 presents the effects of PP fibres and latex proportions on concrete compressive strength, respectively. The graphs

show that compressive strength changes linearly with proportions of PP fibres and latex in the concrete.

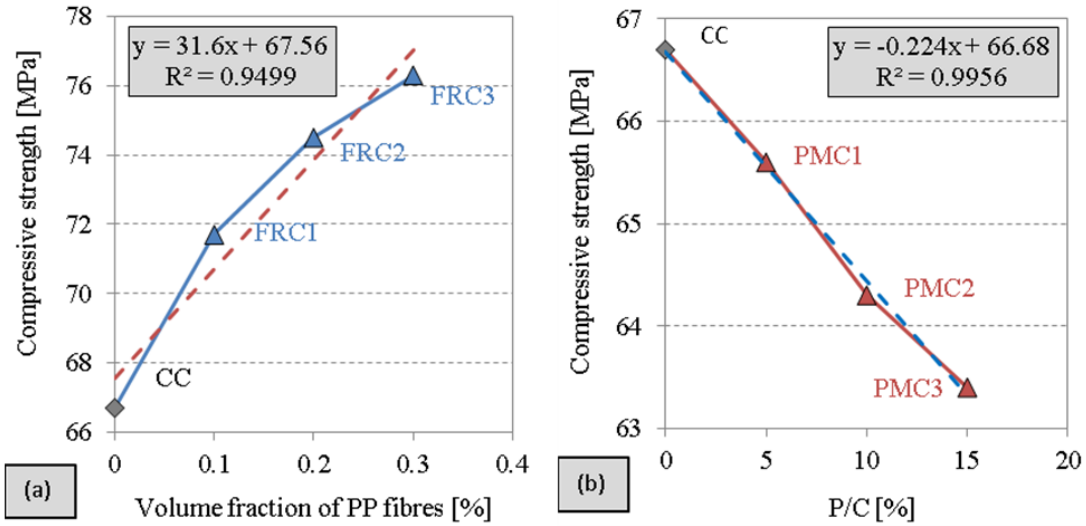

Figure 3. The effect of PP fibres (a) and latex (b) on concrete compressive strength

Figure 4 confirms that using PP fibres improves compressive strength of PMC. For instance; Compressive strength of PMC3, with P/C of 0.15, is 63.4 MPa. The correspondent concrete types to PMC3 are FRPMC3 (0.1% of PP fibres), FRPMC6 (0.2% of PP fibres), and FRPMC9 (0.3% of PP fibres) with the same proportion of latex improve the compressive strength of 4.73%, 7.89%, and 11.2%, respectively.

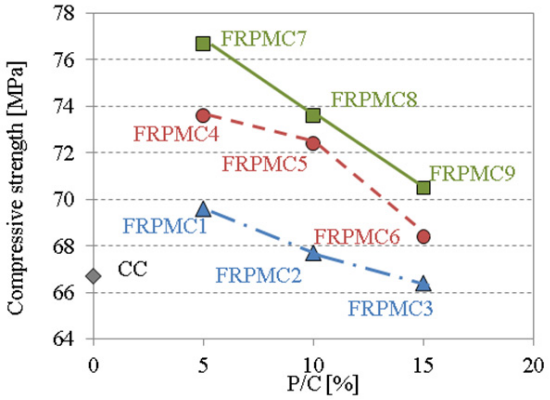

Figure 4. Compressive strength of FRPMCs

As discussed earlier, specimens were maintained in pure diffusion conditions (always submerged) and subjected to 16.5% concentration of chloride solution for 24 months. In time intervals of 1, 5, 9, 13, 17, 21, and 24 months, chloride measurement at different depths. In following presented graphs the average depth has been used as 10, 20, 30, 40, and 50 mm. For each concrete type two measurements were carried

out and average value has been reported. The first 5 mm of the depth of each specimen was removed to reduce the skin effect factor on the chloride content which consequently decreases the error in estimations. Chloride content up to depth of 5 mm was measured in abovementioned time intervals and considered as surface chloride concentration (C_s).

The chloride profiles for all types of concrete are presented in Figure 5 to Figure 12.

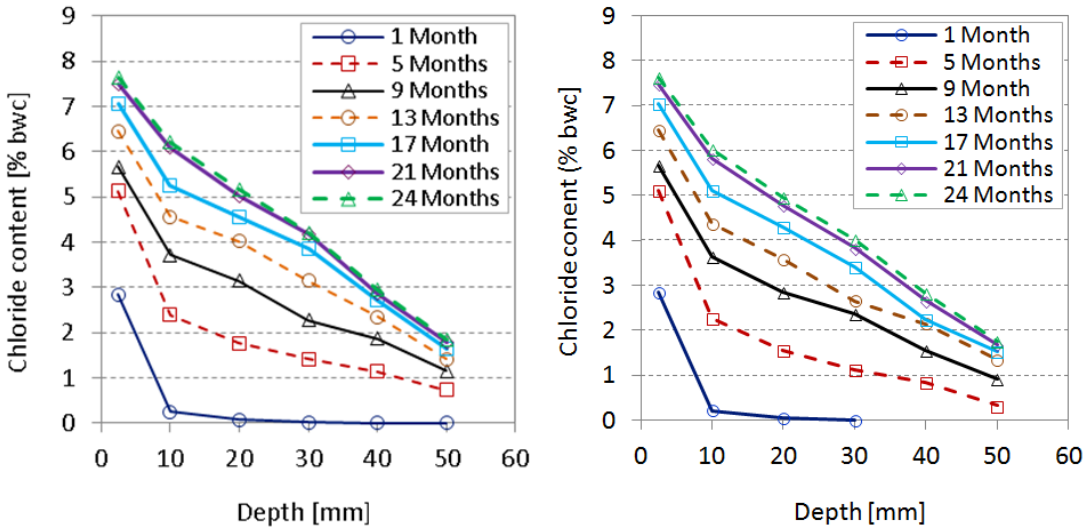

Figure 5. Chloride profiles for CC and FRC1

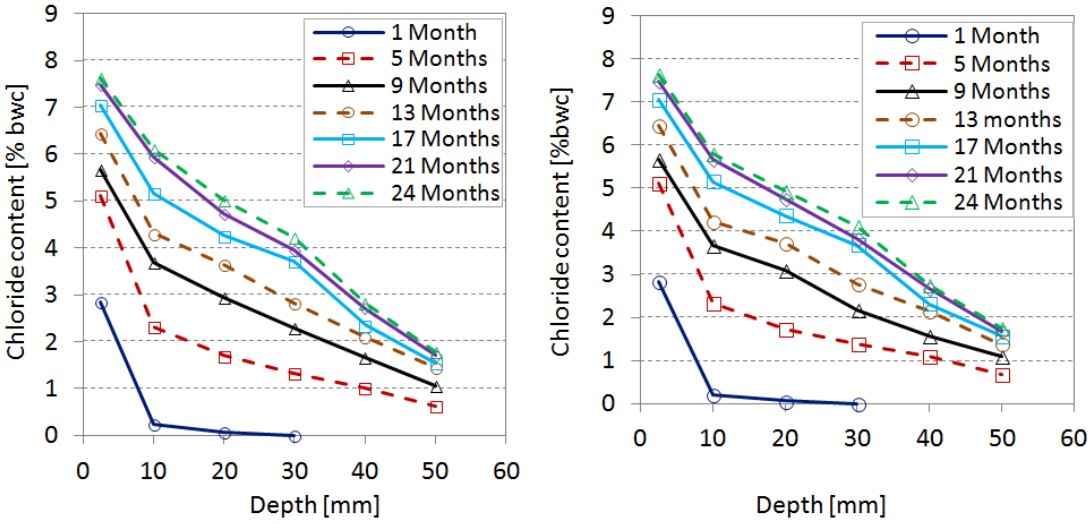

Figure 6. Chloride profiles for FRC2 and FRC3

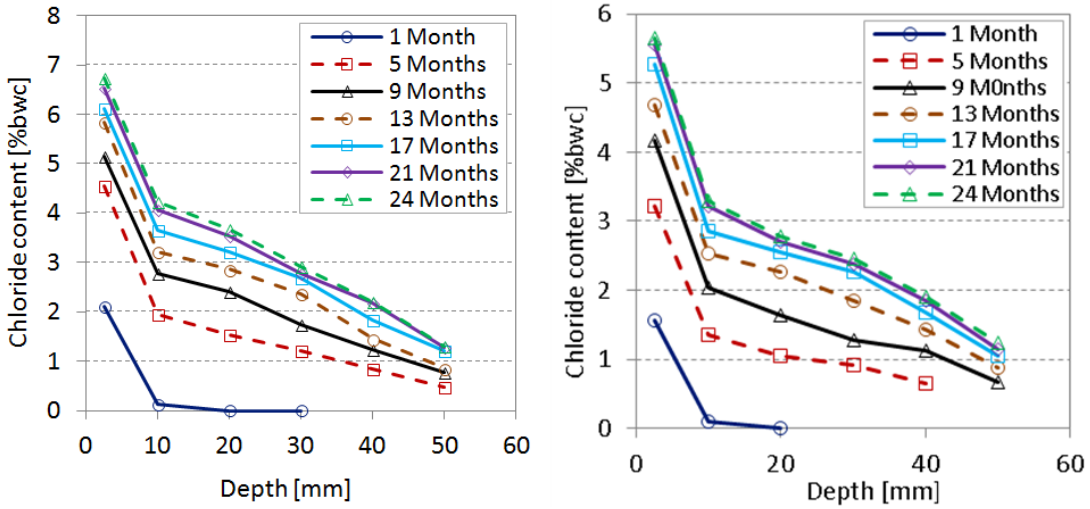

Figure 7. Chloride profiles for PMC1 and PMC2

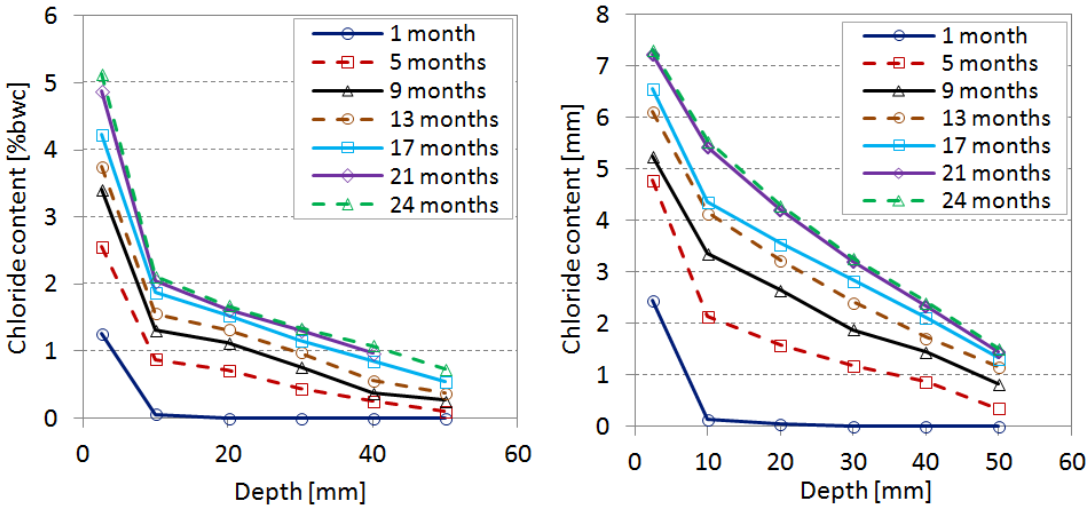

Figure 8. Chloride profiles for PMC3 and FRPMC1

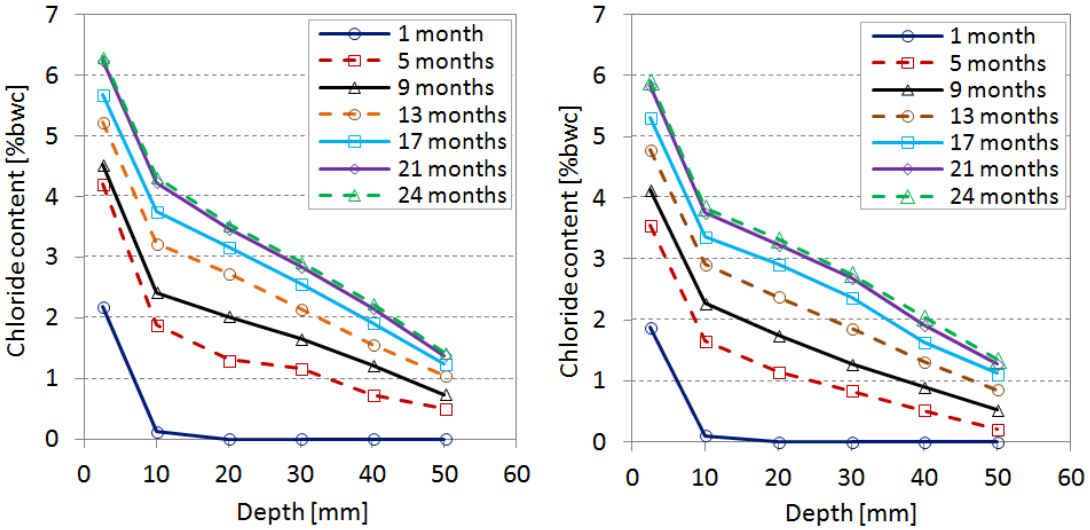

Figure 9. Chloride profiles for FRPMC2 and FRPMC3

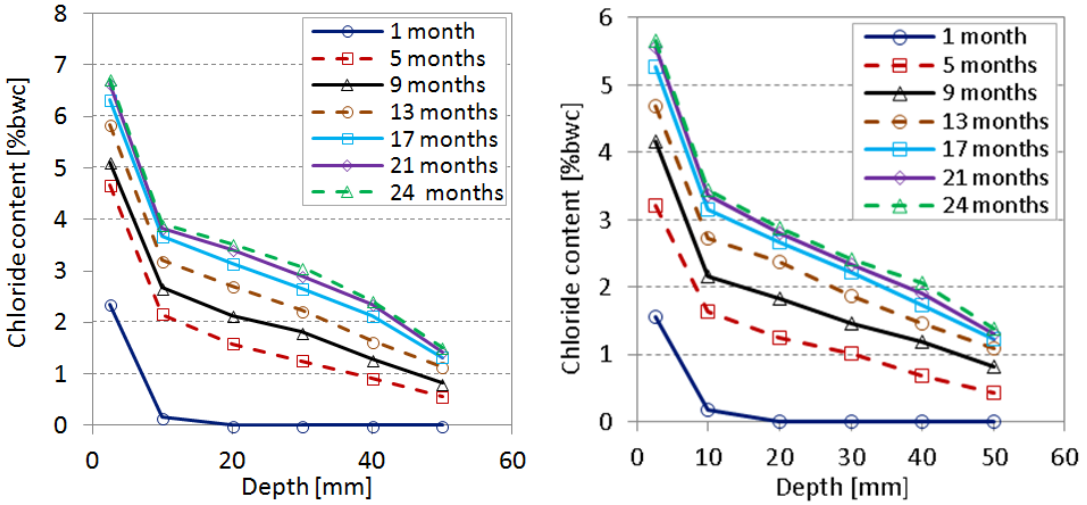

Figure 10. Chloride profiles for FRPMC4 and FRPMC5

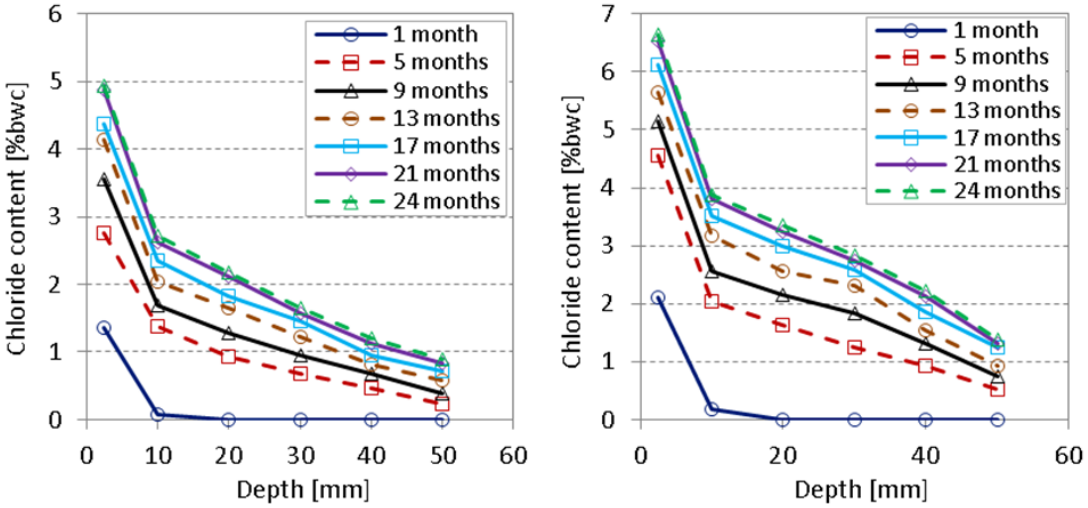

Figure 11. Chloride profiles for FRPMC6 and FRPMC7

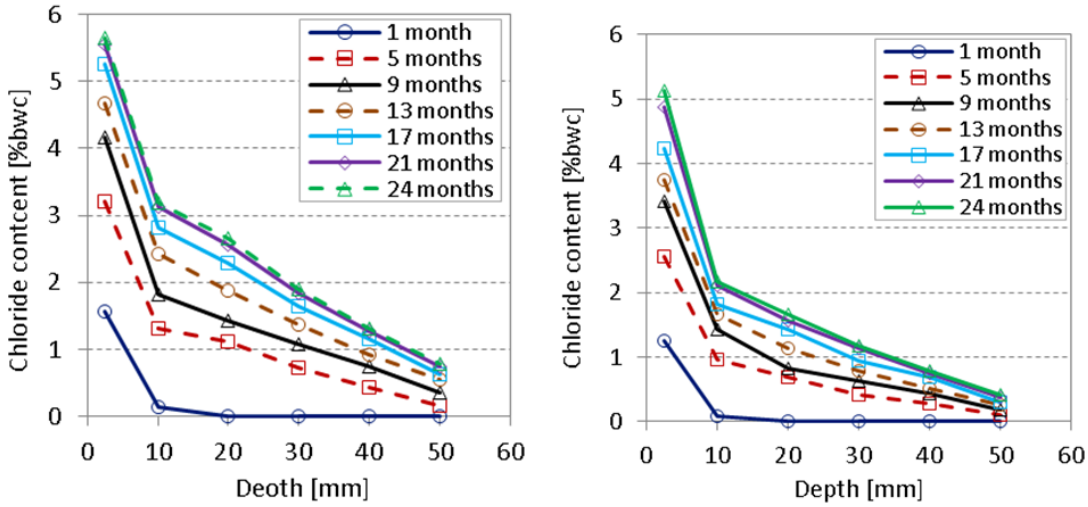

Figure 12. Chloride profiles for FRPMC8 and FRPMC9

The results show that all types of polymer-concrete composites can reduce the rate of chloride diffusion into concrete. Among all polymer-concrete composites PMC3, FRPMC6, FRPMC8, and FRPMC9 have consistently shown the most chloride resistance compared to the other type of polymer-concrete composites investigated in this study. FRPMC9 has the minimum chloride diffusion rate among the other types of concrete and shows approximately 75% reduction of chloride content in various depths compared to CC.

CONCLUSION

Chloride-induced corrosion is the dominant factor in deterioration of RC structures. By reducing the chloride diffusion rate, service life of the RC structures can be definitely extended. The results of this study revealed that polymer-concrete composites can be used as structural concrete. Polymer-concrete composites showed an excellent resistance to chloride diffusion into concrete. Reducing chloride diffusion coefficient can enhance the durability of the concrete and extend the service life of RC structures significantly. Generally, PMC improves the durability of the concrete more than FRC. But, combination of PP fibres and latex makes ultra-high performance concrete.

References

ALONSO, C., ANDRADE, C., CASTELLOTE, M. & CASTRO, P. 2000. Chloride threshold values to depassivate reinforcing bars embedded in a standardized OPC mortar. *Cement and Concrete Research,* 30**,** 1047-1055.

ANGST, U., ELSENER, B., LARSEN, C. K. & VENNESLAND, Ø. 2009. Critical chloride content in reinforced concrete — A review. *Cement and Concrete Research,* 39**,** 1122-1138.

ANN, K. Y., AHN, J. H. & RYOU, J. S. 2009. The importance of chloride content at the concrete surface in assessing the time to corrosion of steel in concrete structures. *Construction and Building Materials,* 23**,** 239-245.

ANN, K. Y. & SONG, H.-W. 2007. Chloride threshold level for corrosion of steel in concrete. *Corrosion Science,* 49**,** 4113-4133.

BRANDT, A. M. 2008. Fibre reinforced cement-based (FRC) composites after over 40 years of development in building and civil engineering. *Composite Structures,* 86**,** 3-9.

COSTA, A. & APPLETON, J. 1999. Chloride penetration into concrete in marine environment—Part I: Main parameters affecting chloride penetration. *Materials and Structures,* 32**,** 252-259.

DEB, S. 2012. Critical Chloride Content in Reinforced Concrete. *The Materbuilder***,** 9.

FOWLER, D. W. 1999. Polymers in concrete: a vision for the 21st century. *Cement and Concrete Composites,* 21**,** 449-452.

GELEJI, F., KÓCZY, L., FÜLÖP, I. & BODOR, G. Properties of polypropylene fibers made from polymer homologue mixtures. Journal of Polymer Science: Polymer Symposia, 1977. Wiley Online Library, 253-273.

HUANG, W.-H. 2001. Improving the properties of cement–fly ash grout using fiber and superplasticizer. *Cement and Concrete Research,* 31**,** 1033-1041.
KARDON, J. B. 1997. Polymer-modified concrete: Review. *Journal of Materials in Civil Engineering,* 9**,** 85.
KNAPEN, E. & VAN GEMERT, D. 2009. Cement hydration and microstructure formation in the presence of water-soluble polymers. *Cement and Concrete Research,* 39**,** 6-13.
KOLEVA, D. A., HU, J., FRAAIJ, A. L. A., VAN BREUGEL, K. & DE WIT, J. H. W. 2007. Microstructural analysis of plain and reinforced mortars under chloride-induced deterioration. *Cement and Concrete Research,* 37**,** 604-617.
LI, V. C. 2003. On Engineered Cementitious Composites (ECC)
A Review of the Material and Its Applications. *Journal of Advanced Concrete Technology,* 1**,** 215-230.
MA, H., TIAN, Y. & LI, Z. 2011. Interactions between Organic and Inorganic Phases in PA-and PU/PA-Modified-Cement-Based Materials. *Journal of Materials in Civil Engineering,* 23**,** 1412-1421.
SHAKER, F. A., EL-DIEB, A. S. & REDA, M. M. 1997. Durability of Styrene-Butadiene latex modified concrete. *Cement and Concrete Research,* 27**,** 711-720.
SILVA, D. A. & MONTEIRO, P. J. M. 2006. The influence of polymers on the hydration of portland cement phases analyzed by soft X-ray transmission microscopy. *Cement and Concrete Research,* 36**,** 1501-1507.
SONG, H.-W. & KWON, S.-J. 2009. Evaluation of chloride penetration in high performance concrete using neural network algorithm and micro pore structure. *Cement and Concrete Research,* 39**,** 814-824.
SONG, P. S., WU, J. C., HWANG, S. & SHEU, B. C. 2005. Statistical analysis of impact strength and strength reliability of steel–polypropylene hybrid fiber-reinforced concrete. *Construction and Building Materials,* 19**,** 1-9.
STANISH, K., HOOTON, R. & THOMAS, M. 1997. Testing the chloride penetration resistance of concrete: a literature review. *FHWA contract DTFH61***,** 19-22.
SU, Z., BIJEN, J. M. J. M. & LARBI, J. A. 1991. Influence of polymer modification on the hydration of portland cement. *Cement and Concrete Research,* 21**,** 242-250.
TOUTANJI, H., MCNEIL, S. & BAYASI, Z. 1998. Chloride permeability and impact resistance of polypropylene-fiber-reinforced silica fume concrete. *Cement and Concrete Research,* 28**,** 961-968.
TOUTANJI, H. A. 1999. Properties of polypropylene fiber reinforced silica fume expansive-cement concrete. *Construction and Building Materials,* 13**,** 171-177.
ZHONG, S. & CHEN, Z. 2002. Properties of latex blends and its modified cement mortars. *Cement and Concrete Research,* 32**,** 1515-1524.
ZORNOZA, E., GARCÉS, P., PAYÁ, J. & CLIMENT, M. A. 2009. Improvement of the chloride ingress resistance of OPC mortars by using spent cracking catalyst. *Cement and Concrete Research,* 39**,** 126-139.

Viscoelasticity of UHPC - Computation of Maxwell chain relaxation spectra based on creep experiments

T. Stengel[1]

[1]Dr.-Ing. Thorsten Stengel, Ingenieurbüro Schießl Gehlen Sodeikat GmbH, Landsbergerstr. 370, 80687 München, Germany, PH (0049) 89-546372927, FAX (0049) 89-546372910, email: stengel@ib-schiessl.de

ABSTRACT

The present paper gives an overview of creep data of UHPC and an appropriate creep function based on this data which was used to compute age-dependent relaxation spectra, i.e. Maxwell chain parameters. The relaxation spectra computed was validated with the help of cracking frame tests. The numerically obtained relaxation spectra enables mechanical studies of members made from UHPC taking into account the age-dependent viscoelastic behavior.

INTRODUCTION

The excellent properties of ultra high performance concrete (UHPC) are due to an optimized particle packing, a high volume of binder and a very low water to binder ratio. Therefore UHPC exhibits high autogenous and chemical shrinkage during hydration which may lead to restraint stress. The magnitude of restraint stress, i.e. the risk of cracking depends mainly on the degree of restraint, the magnitude of shrinkage and the viscoelasticity of the UHPC in use. In order to a priori evaluate risk of cracking of UHPC members age dependent mechanical properties and viscoelasticity has to be known. Therefore a study on creep tests covering the last 20 years of research and in total 34 creep curves with age of loading between $1d$ and $360d$ was done. Based on this study an appropriate creep function was chosen as well as relaxation curves and Maxwell chain parameters were computed. The relaxation spectra was validated with the help of a cracking frame test.

REVIEW OF CREEP DATA

Creep tests (performed under compression) publicated by (Anders and Müller 2014), (Burkart and Müller 2009), (Cheyrezy and Behloul 2001), (Fehling et al. 2005), (Kamen 2007), (Loukili and Richard 1995), (Loukili and Richard 1998), (Matsuda, Kawakami and Nishimoto 2009) and (Tue et al. 2006) were taken into consideration within this study. Having screened all creep tests best fit of all 34 creep curves was obtained using an approach with creep parameters φ^*, a and b based on (Bažant 1972) and (Bažant and Wu 1974). Deviation of fit-curves from test results is in most cases

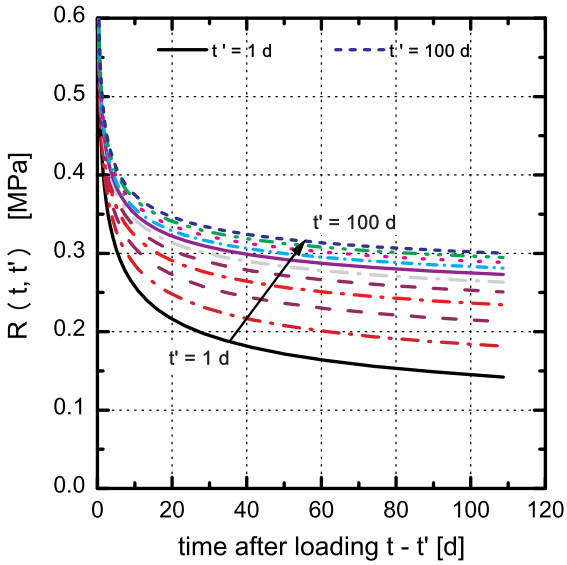

Figure 1. Relaxation curves of a typical UHPC.

well below 10%. For computation of relaxation functions 95% quantile values were taken for φ^*, a and b, see equation (1).

$$\varepsilon'_{tot}(t,\ t') = J(t,\ t') = \frac{1}{E(t')} \cdot \left[1 + 3.43 \cdot 1,25 \cdot t'^{-0.049} \cdot \frac{(t-t')^{0.45}}{10 + (t-t')^{0.45}}\right] \qquad (1)$$

COMPUTATION OF RELAXATION SPECTRA

Taking into account equation (1) relaxation curves were computed with the help of a framework given in (Bažant 1972a) and (Bažant and Ashgari 1974). Relaxation curves at $t' = 1d$, $1.6d$, $2.5d$, $4d$, $6.3d$, $10d$, $15.8d$, $25.1d$, $39.8d$, $63.1d$ and $100d$ are shown in Figure 1 exemplarily for a typical UHPC based on Ordinary Portland cement and silica fume ($680kg/m^3$ OPC, $204kg/m^3$ silica fume, w/c $= 0.27$). Maxwell chain parameters were computed using an algorithm given in (Bažant and Ashgari 1974). The relaxation function $R(t,\ t')$ is given by equation (2).

$$R(t,\ t') = \sum_{i=1}^{n} E_i(t') \cdot \exp(-(t-t')/\tau_i) \qquad (2)$$

A Maxwell chain consisting of $n = 6$ elements and relaxation times $\tau_i = 0.1h$, $1h$, $10h$, $100h$, $1,000h$ and 10^5h was used for this study. Applying aforementioned algorithm relaxation spectra i.e. E_i for various ages of loading t' (starting with $t' = 1d$) can be computed.

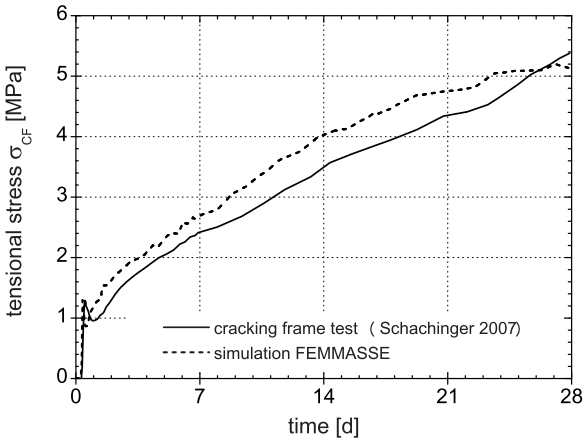

Figure 2. Results of cracking frame test and FEMMASSE simulation.

VALIDATION OF RELAXATION SPECTRA

To validate the resultant relaxation spectra the cracking frame tests given in (Schachinger 2007) were modeled using FEMMASSE© software package. Time dependent concrete properties as publicated by (Schachinger 2007) were used as input parameters for the calculations. The creep test based relaxation spectra is valid for ages of loading of $24h$ and beyond. To estimate relaxation within the first $24h$ a trial-and-error study for $t' = 8h$, $14h$ and $24h$ has been done. The results - both from the experiment and the calculations - are shown in Figure 2. Using aforementioned approach for viscoelasticity the calculated restraint stress is in good accordance with stress measured during the experiment.

CONCLUSION

The present paper briefly summarizes creep data for UHPC and gives an appropriate creep function. Maxwell chain parameters are computed based on these creep function and the resulting relaxation spectra is validated with the help of a cracking frame test. Using aforementioned approach for creep and relaxation the restraint stress measured during experiment can be well simulated with the help of e.g. FEMMASSE© software package.

REFERENCES

Anders, I., and Müller, H. S. (2014). "Material Laws on the Time-Dependent Stress-Strain Behaviour of Ultra-High Performance Concrete." *Sustainable Building with Ultra-High Performance Concrete,* kassel university press, Kassel.

Bažant, Z. (1972). "Prediction of concrete creep effects using age-adjusted effective modulus method." *ACI Journal Proceedings*, 69(4), 212-219.

Bažant, Z. (1972a). "Numerical determination of long-range stress history from

strain history in concrete." *Materials and Structures,* 5(3), 135-141, http://dx.doi.org/10.1007/BF02539255, ISSN 1359-5997.

Bažant, Z., and Wu, S. (1974). "Rate-type creep law of aging concrete based on maxwell chain." *Materials and Structures,* 7(1), 45-60, http://dx.doi.org/10.1007/BF02482679, ISSN 1359-5997.

Bažant, Z., and Ashgari, A. (1974). "Computation of age-dependent relaxation spectra." *Cement and Concrete Research,* Vol. 4, 567-579, ISSN 1359-5997.

Burkart, I., and Müller, H. S. (2009). "Creep and shrinkage characteristics of ultra high strength concrete (UHPC)." *Proceedings of the CONCREEP 8 conference,* Taylor & Francis Group.

Cheyrezy, M., and Behloul, M. (2001). "Creep and shrinkage of Ultra-High Performance Concrete." *Proceedings of the CONCREEP 6 conference,* Elsevier.

Fehling, E. et al. (2005). "Development, Durability and Calculation of Ultra-High Performance Concrete (UHPC)." (in German) *Structural Materials and Engineering Series No. 1,* kassel university press, Kassel.

Kamen, A. (2007). "Comportement au jeune âge et différé d'un BFUP écrouissant sous les efets thermomécaniques." *Dissertation No. 3827, École Polytechnique Fédérale de Lausanne (EPFL),* Lausanne.

Loukili, A., and Richard, P. (1995). "Creep and shrinkage of ultra high-performance steel fibre reinforced concrete." *Proceedings of the International Conference on Concrete under Severe Conditions CONSEC 95,* E & FN Spon.

Loukili, A., and Richard, P., and Lamirault, J. (1998). "A study on delayed deformations of an ultra high strength cementitious material." *Proceedings of the Fourth CANMET/ACI/JCI Conference: Advances in Concrete Technology*.

Matsuda, T., and Kawakami, H., and Nishimoto, Y. (2009). "Influence of loading condition on creep properties of ultra-high strength concrete." *Proceedings of the CONCREEP 8 conference,* Taylor & Francis Group.

Schachinger, A. I. (2007). "The Production of Crack-free Structural Components using Ultra High Performance Concrete with High Ductility." (in German) *Dissertation, Technische Universität München*.

Tue, V. N. et al. (2006). "Creep of Ultra-High Performance Concrete." (in German) *Bautechnik,* 83(2), 119-124, http://dx.doi.org/10.1002/bate.200610012, ISSN 1437-0999.

Creep of Bulk C–S–H: Insights from Molecular Dynamics Simulations

M. Bauchy,[1] E. Masoero,[2] F.-J. Ulm[3,4] and R. Pellenq[3,4,5]

[1]Physics of AmoRphous and Inorganic Solids Laboratory (PARISlab), Department of Civil and Environmental Engineering, University of California, Los Angeles, CA 90095, United States; PH (310) 825-9991; email: bauchy@ucla.edu
[2]School of Civil Engineering and Geosciences, Newcastle University, Newcastle upon Tyne, NE1 7RU, United Kingdom; PH (+44) 191 208 7686; email: enrico.masoero@ncl.ac.uk
[3]Concrete Sustainability Hub, Department of Civil and Environmental Engineering, Massachusetts Institute of Technology, 77 Massachusetts Avenue, Cambridge, MA 02139, United States; PH (617) 253-3544; email: ulm@mit.edu
[4]MIT-CNRS joint laboratory at Massachusetts Institute of Technology, 77 Massachusetts Avenue, Cambridge, MA 02139, United States; PH (617) 253-7117; email: pellenq@mit.edu
[5]Centre Interdisciplinaire des Nanosciences de Marseille, CNRS and Aix-Marseille University, Campus de Luminy, Marseille, 13288 Cedex 09, France; PH (+33) 6 62 92 28 33; email: pellenq@cinam.univ-mrs.fr

ABSTRACT

Understanding the physical origin of creep in calcium–silicate–hydrate (C–S–H) is of primary importance, both for fundamental and practical interest. Here, we present a new method, based on molecular dynamics simulation, allowing us to simulate the long-term visco-elastic deformations of C–S–H. Under a given shear stress, C–S–H features a gradually increasing shear strain, which follows a logarithmic law. The computed creep modulus is found to be independent of the shear stress applied and is in excellent agreement with nanoindentation measurements, as extrapolated to zero porosity.

INTRODUCTION

Creep is a major limitation of concrete. Indeed, it has been suggested that creep deformations are logarithmic, that is, virtually infinite and without asymptotic bound, which raises safety issues (Bažant et al., 2011). The creep of concrete is generally thought to be mainly caused by the viscoelastic and viscoplastic behavior of the cement hydrates (Acker, 2004). While secondary cementitious phases can show viscoelastic behavior (Nguyen et al., 2012), the rate and extent of viscoelastic deformations of such phases is far less significant than that calcium–silicate–hydrate (C–S–H), the binding

phase of the cement paste (Acker, 2004). As such, understanding the physical mechanism of the creep of C-S-H is of primary importance.

Despite the prevalence of concrete in the built environment, the molecular structure of C–S–H has just recently been proposed (Pellenq et al., 2009; Abdolhosseini Qomi et al., 2014a), which makes it possible to investigate its mechanical properties at the atomic scale. Here, relying on the newly available model, we present a new methodology allowing us to simulate the long-term creep deformation of bulk C–S–H (at zero porosity, i.e., at the scale of the grains). Results show an excellent agreement with nanoindentation measurements (Vandamme et al., 2010).

SIMULATION DETAILS

To describe the disordered molecular structure of C–S–H, Pellenq et al. (Pellenq et al., 2009) proposed a realistic model for C–S–H with the stoichiometry of $(CaO)_{1.65}(SiO_2)(H_2O)_{1.73}$. We generated the C–S–H model by introducing defects in an 11 Å tobermorite (Hamid, 1981) configuration, following a combinatorial procedure. Whereas the Ca/Si ratio in 11 Å tobermorite is 1, this ratio is increased to 1.71 in the present C–S–H model, through randomly introducing defects in the silicate chains, which provides sites for adsorption of extra water molecules. The REAXFF potential (Manzano et al., 2012), a reactive potential, was then used to account for the reaction of the interlayer water with the defective calcium–silicate sheets. More details on the preparation of the model and its experimental validation can be found in Ref. (Abdolhosseini Qomi et al., 2014a) and in previous works (Bauchy et al., 2014b; Pellenq et al., 2009; Abdolhosseini Qomi et al., 2013, 2014b; Bauchy et al., 2014e,c,a,d, 2015).

We simulated the previously presented C–S–H model, made of 501 atoms, by molecular dynamics (MD) using the LAMMPS package (Plimpton, 1995). To this end, we used the REAXFF potential (Manzano et al., 2012) with a time step of 0.25fs. Prior to the application of any stress, the system is fully relaxed to zero pressure at 300K.

RESULTS

The relaxation of C–S–H, or of other silicate materials, takes place over long periods of time (years), which prevents the use of traditional MD simulations, which are limited to a few nanoseconds. To study the long-term deformations of C–S–H, we applied a method that has recently been introduced to study the relaxation of silicate glasses (Yu et al., 2015). In this method, starting from an initial atomic configuration of glass, formed by rapid cooling from the liquid state, the system is subjected to small, cyclic perturbations of shear stress $\pm\tau_p$ around zero pressure. For each stress, a minimization of the energy is performed, with the system having the ability to deform (shape and volume) in order to reach the target stress. These small perturbations of stress deform the energy landscape of the glass, allowing the system to jump over energy barriers. Note that the observed relaxation does not depend on the choice of τ_p, provided that this stress remains sub-yield (Yu et al., 2015). This method mimics the

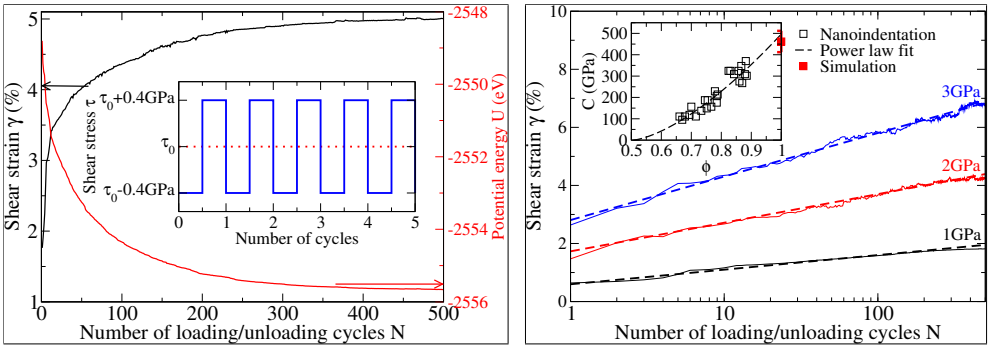

(a) (b)

Figure 1: (a) Shear strain and potential energy with respect to the number of loading/unloading cycles. The inset shows the shape of the applied shear stress. (b) Shear strain with respect to the number of loading/unloading cycles, under a constant shear stress of 1, 2, and 3 GPa. The inset shows the creep modulus C with respect to the packing fraction ϕ obtained from nanoindentation (Vandamme et al., 2010), compared with the computed value at $\phi = 0$.

artificial aging observed in granular materials subjected to vibrations (Richard et al., 2005).

Here, in order to study creep deformation, we add to the previous method a constant shear stress τ_0, such that $\tau_p < \tau_0$ (see the inset of Figure 1a). When subjected to shear stresses of different intensities, C–S–H presents a shear strain γ that: (1) increases logarithmically with the number of cycles N (Figure 1a) and (2) is proportional to the applied shear stress (see Figure 1b).

DISCUSSION

The creep of bulk C–S–H can then be described by a simple logarithmic law $\gamma(N) = (\tau_0/C)\log(1 + N/N_0)$, where N_0 is a constant analogous to a relaxation time and C is the creep modulus. A careful look at the internal energy shows that the height of the energy barriers, through which the system transits across each cycle, remains roughly constant over successive cycles. According to transition state theory, which states that the time needed for a system to jump over an energy barrier E_A is proportional to $\exp(-E_A/kT)$, we can assume that each cycle corresponds to a constant duration Δt, so that a fictitious time can be defined as $t = N\Delta t$ (Masoero et al., 2013).

We note that the computed creep moduli C does not show any significant change with respect to the applied stress τ_0. As such, it appears to be a material property that can directly been compared to nanoindentation results extrapolated to zero porosity (Vandamme et al., 2010). As shown in the inset of Figure 1b, we observe an excellent agreement, which suggests that the present method offers a realistic description of the creep of C–S–H at the atomic scale. This result also suggests that, within the linear regime (i.e., for sub-yield stresses, when C remain constant), deformations

due to cyclic creep and basic creep, with respect to the number of stress cycle or the elapsed time, respectively, should be equivalent.

CONCLUSION

We reported a new methodology based on atomistic simulation, allowing us to successfully observe long-term creep deformations of C–S–H. Creep deformations are found to be logarithmic and proportional to the applied shear stress. The computed creep modulus shows an excellent agreement with nanoindentation data, which suggests that the present methodology could be used as a predictive tool to study the creep deformations of alternative binders.

ACKNOWLEDGMENTS

MB acknowledges partial financial support for this research provisioned by the University of California, Los Angeles (UCLA). This work was also supported by Schlumberger under an MIT-Schlumberger research collaboration and by the CSHub at MIT. This work has been partially carried out within the framework of the ICoME2 Labex (ANR-11-LABX-0053) and the A*MIDEX projects (ANR-11-IDEX-0001-02) cofunded by the French program "Investissements d'Avenir" which is managed by the ANR, the French National Research Agency.

References

M. J. Abdolhosseini Qomi, K. J. Krakowiak, M. Bauchy, K. L. Stewart, R. Shahsavari, D. Jagannathan, D. B. Brommer, A. Baronnet, M. J. Buehler, S. Yip, F.-J. Ulm, K. J. Van Vliet, and R. J.-M. Pellenq. Combinatorial molecular optimization of cement hydrates. *Nature Communications*, 5, September 2014a.

Mohammad Javad Abdolhosseini Qomi, M. Bauchy, R. J-M. Pellenq, and F-J. Ulm. Applying Tools from Glass Science to Study Calcium-Silicate-Hydrates. In *Mechanics and Physics of Creep, Shrinkage, and Durability of Concrete: A Tribute to Zdenek P. Bazant: Proceedings of the Ninth International Conference on Creep, Shrinkage, and Durability Mechanics (CONCREEP-9), September 22-25, 2013 Cambridge, Massachusetts*, pages 78–85. ASCE Publications, September 2013.

Mohammad Javad Abdolhosseini Qomi, Mathieu Bauchy, Franz-Josef Ulm, and Roland J.-M. Pellenq. Anomalous composition-dependent dynamics of nanoconfined water in the interlayer of disordered calcium-silicates. *The Journal of Chemical Physics*, 140(5):054515, February 2014b.

P. Acker. Swelling, shrinkage and creep: a mechanical approach to cement hydration. *Materials and Structures*, 37(4):237–243, May 2004.

M. Bauchy, Mohammad Javad Abdolhosseini Qomi, R. J. M. Pellenq, and F. J. Ulm.

Is cement a glassy material? *Computational Modelling of Concrete Structures*, page 169, 2014a.

M. Bauchy, Mohammad Javad Abdolhosseini Qomi, F.-J. Ulm, and R. J.-M. Pellenq. Order and disorder in calcium–silicate–hydrate. *The Journal of Chemical Physics*, 140(21):214503, June 2014b.

M. Bauchy, H. Laubie, M. J. Abdolhosseini Qomi, C. G. Hoover, F.-J. Ulm, and R. J.-M. Pellenq. Fracture toughness of calcium-silicate-hydrate grains from molecular dynamics simulations. *arXiv:1410.2915 [cond-mat]*, October 2014c.

M. Bauchy, M. J. Abdolhosseini Qomi, C. Bichara, F.-J. Ulm, and R. J.-M. Pellenq. Topological Origin of Fracture Toughening in Complex Solids: the Viewpoint of Rigidity Theory. *arXiv:1410.2916 [cond-mat]*, October 2014d.

Mathieu Bauchy, Mohammad Javad Abdolhosseini Qomi, Christophe Bichara, Franz-Joseph Ulm, and Roland J.-M. Pellenq. Nanoscale Structure of Cement: Viewpoint of Rigidity Theory. *The Journal of Physical Chemistry C*, 118(23):12485–12493, June 2014e.

Mathieu Bauchy, Mohammad Javad Abdolhosseini Qomi, Christophe Bichara, Franz-Josef Ulm, and Roland J.-M. Pellenq. Rigidity Transition in Materials: Hardness is Driven by Weak Atomic Constraints. *Physical Review Letters*, 114(12):125502, March 2015.

Zdenek P. Bažant, Mija H. Hubler, and Qiang Yu. Excessive creep deflections: An awakening. *Concrete International*, 33(8):44–46, 2011.

Sa Hamid. The Crystal-Structure of the 11-a Natural Tobermorite Ca2.25[si3o7.5(oh)1.5].1h2o. *Zeitschrift Fur Kristallographie*, 154(3-4):189–198, 1981.

Hegoi Manzano, Sina Moeini, Francis Marinelli, Adri C. T. van Duin, Franz-Josef Ulm, and Roland J.-M. Pellenq. Confined Water Dissociation in Microporous Defective Silicates: Mechanism, Dipole Distribution, and Impact on Substrate Properties. *Journal of the American Chemical Society*, 134(4):2208–2215, 2012.

E. Masoero, H. Manzano, E. Del Gado, R. Pellenq, F.J. Ulm, and S; Yip Kinetic simulation of the logarithmic creep of cement. *Mechanics and Physics of Creep, Shrinkage, and Durability of Concrete: A Tribute to Zdenk P. Bazant*, pages 166–173. ASCE Publications, September 2013.

Dan-Tam Nguyen, R. Alizadeh, J. J. Beaudoin, and L. Raki. Microindentation creep of secondary hydrated cement phases and C–S–H. *Materials and Structures*, 46(9): 1519–1525, December 2012.

Roland J.-M. Pellenq, Akihiro Kushima, Rouzbeh Shahsavari, Krystyn J. Van Vliet, Markus J. Buehler, Sidney Yip, and Franz-Josef Ulm. A realistic molecular model of cement hydrates. *Proceedings of the National Academy of Sciences*, 106(38): 16102–16107, September 2009.

S. Plimpton. Fast parallel algorithms for short-range molecular dynamics. *Journal of computational physics*, 117(1):1–19, 1995.

Patrick Richard, Mario Nicodemi, Renaud Delannay, Philippe Ribière, and Daniel Bideau. Slow relaxation and compaction of granular systems. *Nature Materials*, 4(2):121–128, February 2005.

Matthieu Vandamme, Franz-Josef Ulm, and Philip Fonollosa. Nanogranular packing of C-S-H at substochiometric conditions. *Cement and Concrete Research*, 40(1): 14–26, January 2010.

Yingtian Yu, Mengyi Wang, Dawei Zhang, Bu Wang, Gaurav Sant, and Mathieu Bauchy. Stretched Exponential Relaxation of Glasses at Low Temperature. *arXiv:1503.07242 [cond-mat]*, March 2015.

Fracture Toughness of Synthetic C-S-H Using Nanoindentation

S. H. Aboubakr[1]; E. M. Soliman[2]; and M. M. Reda Taha[3]

[1]Department of Civil Engineering, University of New Mexico, MSC 01 1070, Albuquerque, NM 87131-0001.E-mail: aboubakr@unm.edu
[2]Department of Civil Engineering, Assuit University, Assuit, Egypt 71516. E-mail: eslam.soliman@eng.au.edu.eg
[3]Department of Civil Engineering, University of New Mexico, MSC 01 1070, Albuquerque, NM 87131-0001. E-mail: mrtaha@unm.edu

Abstract

Calcium Silicate Hydrate gel (C-S-H) is the basic product of the cement hydration process responsible for strength and durability of concrete. Synthetic C-S-H was synthesized by mixing Calcium oxide (CaO denoted as C) and silicate (SiO_2 denoted as S) with a C/S mixture ratio of 1.5. C-S-H powder was filtered, and dried to a relative humidity of 11% and then compacted at 400 MPa. Nanoindentation tests incorporating time-dependent effect (creep) were performed on polished C-S-H specimens using Berkovich indenter tip. The reduced elastic modulus and creep compliance of C-S-H specimens were extracted from nanoindentation measurements. An innovative approach is suggested to extract cracking energy. A viscoelastic-plastic finite element model was developed to simulate the nanoindentation of C-S-H incorporating creep and cracking. The finite element model was used to isolate the viscoelastic from the cracking energy components. The proposed approach enabled estimating fracture toughness of C-S-H.

INTRODUCTION

Calcium Silicate Hydrate (C-S-H) is the main binding agent that makes up two-thirds of Portland cement paste by volume (Taylor 1997, Jennings 2000). As the main binding material, C-S-H governs some key characteristics of concrete such strength, durability, creep and shrinkage. Significant research investigations examined the different chemical, physical and mechanical aspects of C-S-H in the last few decades (Beaudoin and Feldman 1986, Alizadeh et al. 2010). It was demonstrated that the chemical composition of C-S-H, represented by variation in CaO to SiO_2 (C/S) ratio, is strongly correlated to its physical and mechanical characteristics (Beaudoin and Feldman 1986). It was also reported that the final product of C-S-H is strongly dependent on the conditions of mixing and curing including temperature, pressure and humidity (Kim et al. 2014). The above list of factors add complexity to characterization of C-S-H and makes it difficult to identify its physical or mechanical characteristics with high certainty.

Taylor (1997) concluded that there are two types of C-S-H, identified as C-S-H (I) and C-S-H (II), while classifying C-S-H (I) to a similar structure of 1.4 nm

tobermorite and C-S-H (II) to a jennite like composition. Jennings (2000) categorized C-S-H as Low Density (LD) and High Density (HD), having a volume fraction of 30 and 70%, respectively. It is believed that two-thirds of C-S-H is comprised of LD C-S-H, while the HD C-S-H phase encompasses the rest. Classification of C-S-H from hydrated cement is challenging because of its mix with other hydration phases such as calcium hydroxyl (CH) and calcium aluminate trisulfate hydrate (ettringite). Statistical methods were used to characterize C-S-H and identify its different submicron phases after performing a relatively large number of nanoindentation measurements of cement paste (Constantinides and Ulm, 2004).

Another approach was recently suggested is to synthesize C-S-H powder outside cement (Sugiyama 2008; Alizadeh et al. 2010; Foley et al. 2012). The synthetic C-S-H was compacted and the compacted powder was then mechanically characterized. Two methods were used in the synthesis process; Beaudoin and Feldman (1986) mixed aqueous solutions of sodium meta-silicate and calcium oxide with various ratios to produce C-S-H. Sugiyama (2008), Alizadeh et al. (2010) and Foley et al. (2012) synthesized C-S-H with C/S ratios ranging from 0.6 to 2.0 by mixing calcium oxide with amorphous silica and distilled water together continuously for 7 days. Lodeiro et al. (2009) synthesized C-S-H by continuously mixing $Ca(NO_3)_2 \bullet 4H_20$ and NaOH solutions at temperature of 5 ^oC. The resultant gel of all the above methods was then dried using varying drying methods such as D-Drying and using Lithium Chloride to reach 11% relative humidity (Taylor 1997). Microstructure of the different synthetic C-S-H with varying C/S ratios was observed using different microstructural techniques such as X-ray diffraction analysis (XRD), scanning electron microscopy (SEM) and other methods (Beaudoin and Feldman 1986; Lodeiro et al. 2009; Alizadeh et al. 2010 and Foley et al. 2012). Different techniques such as dynamic mechanical analysis (DMA) and nanoindentation were used to mechanically characterize C-S-H (Alizadeh et al. 2010 and Foley et al. 2012).

There has been considerable research investigations examining elastic material properties using nanoindentation (Fisher-Cripps, 2004). Moreover, nanoindentation of cementitious materials were also reported (Constantinides and Ulm 2004, Foley et al. 2012). Significant investigations were reported on extracting creep characteristics of materials using nanoindentation (Kumar and Narasimhan 2004). There have also been significant efforts to extract fracture characteristics of materials using micro and nanoindentation (Anstis et al. 1981; Rosenfeld et al. 1990; Field et al. 2003). For instance, Harding et al. (1995) suggested that fracture toughness of thin films can be measured using nanoindentation. In this method, a large radial cracks in the range of 100 μm in length were produced using Vickers microindenter with a load of 1000 gm. Fracture toughness K_c was then calculated as a function of other material properties including its elastic modulus, E, hardness, H, and the geometry of the indentation with the load.

$$K_c = \alpha\left(\frac{E}{H}\right)^n\left(\frac{P}{c^{3/2}}\right) \tag{1}$$

where, P is the applied indentation load, α is an empirical constant that is related to the geometry of the indenter used and c is the radial crack length corresponding to the applied load. This method proved difficult to implement due to propagation of cracks within the thin film rather than in a radial fashion.

An interesting approach was that suggested by Chen and Bull (2007). In this approach, the total energy during indentation can be decomposed to elastic, plastic, fracture and other negligible energies. The total and elastic energies can be computed from the nanoindentation load-indentation curve. The plastic and fracture energies combined represent the irreversible energy which can be computed as the difference between the elastic and total energy. The plastic energy corresponds to the plastic deformation and therefore it can be estimated as a function of the residual to total indentation depth ratio using Equation 2.

$$\frac{W_p}{W_t} = (1+\gamma)\frac{h_f}{h_m} - \gamma \tag{2}$$

where W_p is the plastic work or energy, W_t is the total work, h_f is the residual indentation, h_m is the maximum indentation, and γ is constant dependent on the indenter geometry. Once the plastic energy is computed, the fracture energy U_f can be computed as the difference between the irreversible energy and plastic energy. Thus, the fracture toughness K_c can be computed as

$$K_C = \sqrt{\frac{U_f E}{(1-\upsilon^2)A_{fra}}} \tag{3}$$

A_{fra} is the total interfacial fracture area as a function of the radial crack length.

PROPOSED METHOD

We suggest that fracture toughness of quasi-brittle viscoelastic cementitious materials, here C-S-H can be extracted from nanoindentation data if a method to separate the energy components can be developed. We suggest that finite element method can perform this task by simulating a nanoindentation test incorporating a dwell time. The reason for using dwell time loading is to enable steady crack growth. To extract the cracking energy, two FE models shall be developed. In the first model, a viscoelastic-plastic material model is assigned to the material to fit the loading-unloading nanoindentation data. This model considers the three components of strain (elastic, plastic, and creep). In the second model, a viscoelastic material model is assigned to the material to simulate the elastic and creep strains only. In cementitious materials, the plastic energy corresponds to plastic deformation can be considered negligible compared with the cracking energy. Therefore, we hypothesize here that the difference in total energy of both FE models represents the cracking energy necessary to propagate equivalent elastic cracks. By determining the cracking energy and the associated crack area from indentation geometry, fracture toughness can be estimated using principles of linear elastic fracture mechanics.

EXPERIMENTAL METHODS

Calcium oxide, fumed silica, and deionized water were combined with CaO/SiO_2 molar mixture ratio of 1.5. The mixture was placed under nitrogen and resulted in gel-like slurry structure that was mixed for 7 days. The slurry was then carefully removed and placed into a filtration system using a vacuum for removal of

excess water for 24 hours and the C-S-H gel was then dried to 11% Relative Humility (RH) in accordance with ASTM Standard E 104-02 as shown in **Figure 1**. C-S-H powder was then compacted under 400 MPa. Loads were applied under a constant load rate of 1% maximum load per second and held at maximum load for three minutes before unloading. Compaction pressure was selected based on prior work by Alizadeh et al. (2010) to produce micro porosity of 30-40% similar to that observed in cement with 0.4 water/cement ratio.

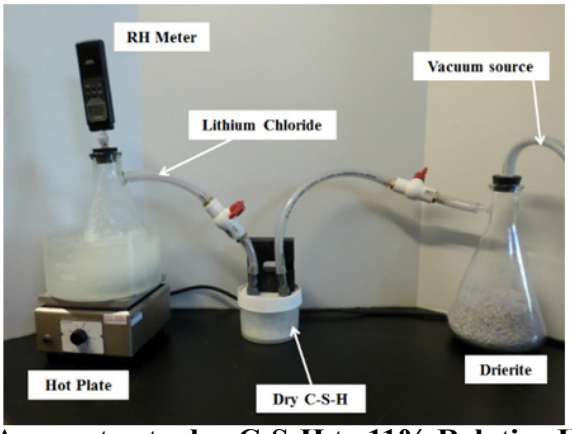

Figure 1. Apparatus to dry C-S-H to 11% Relative Humidity.

Nanoindentation specimens were prepared by casting compacted C-S-H samples in a fast set acrylic. Next, the specimens were polished on a Buehler Ecomet 3 auto-polisher. Specimens were polished until a flat and smooth mirror-like surface was obtained using 125-micron, 70-micron, 30-micron, 9-micron, and 1-micron diamond pads. In between polishing stages, specimens were placed in an ultrasonic bath for 2 minutes to remove dust and diamond particles left on the surface. Nanoindentation was performed using the NanoTestTM 600 indenter system from Micro Materials, Inc. Berkovich indenter tip was used with a loading and unloading rate of 0.0125 mN/sec, initial load of 0.05 mN, and maximum load of 0.6 mN. The maximum load was held constant for a dwell time of 120 seconds. Four nanoindentations were performed and spaced at 200 micrometer. The recorded load-indentation data was analyzed using Oliver and Pharr (1992) method to extract the reduced elastic modulus while creep compliance *J(t)* was evaluated using Equation 4 after Lu et al. (2003)

$$J(t) = \frac{4h^2(t)\tan\alpha}{\pi(1-\nu)P_0} \tag{4}$$

Where, *h(t)* is nanoindentation depth varying with time, ν is Poisson's ration, α is the indenter surface angle with the vertical axis, and P_0 is the maximum applied load.

FINITE ELEMENT SIMULATION

Two two-dimensional axisymmetric finite element models were developed under ANSYS® APDL modeling environment to simulate the nanoindentation experiment and determine different types of strain energies. In the axisymmetric model, Berkovich indenter was modeled as a conical tip with effective cone angle of 70.3º as suggested by Fisher-Cripps (2004) since it would have same contact area as

Berkovich pyramidal indenter with semi angle of 65.27º. A 10 µm × 10 µm substrate represents the C-S-H bulk material was modeled as shown in **Figure 2**. The size of the substrate in the simulation has been made large enough (≈ 50 times) compared to the maximum indentation depth observed experimentally to avoid edge or restrains effects. Appropriate symmetric boundary conditions were applied at the axis of symmetry in the left edge of the model. In addition, the base of the C-S-H substrate was restrained from vertical and horizontal directions. Load controlled simulation was performed similar to the nanoindentation experiment. A four-noded PLANE182 element type was assigned to the indenter and the C-S-H substrate. This element type supports important features required for nanoindentation simulations including axisymmetric and large strain capabilities. In addition, it supports wide range of material models including elastic, plastic, and viscous models. CONTA172 and TARGE169 were employed at the contact lines of the indenter and C-S-H for contact detection and control during the simulation. Appropriate refinement for the mesh is made near the contact lines to ensure accuracy and convergence of the simulation.

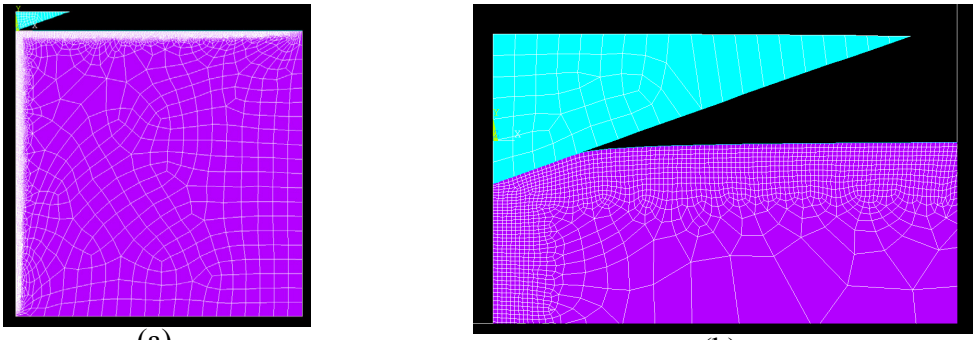

(a) (b)

Figure 2. (a) Finite element model for nanoindentation and (b) close view of the indentation deflection showing refinement of elements near the indented surface

We hypothesize here that the strain components are additives and uncoupled. This assumption enables us to isolate and distinguish between them as

$$\varepsilon_{Total} = \varepsilon_{elastic} + \varepsilon_{plastic} + \varepsilon_{creep} \tag{5}$$

We therefore implement an implicit time hardening law for modeling primary creep to simulate the viscous behavior of C-S-H. In the creep law, the creep strain rate $\dot{\varepsilon}_{creep}$ is defined as a function of time t, stress σ, and temperature T as

$$\dot{\varepsilon}_{creep} = C_1 \sigma^{C_2} t^{C_3} e^{-C_4/T} \tag{6}$$

where C_1, C_2, C_3, and C_4 are the model coefficients. In this study, temperature dependency is not considered and therefore C_4 is set to zero. The remaining three coefficients were determined by fitting the experimental data of the creep strain rate $\dot{\varepsilon}_{creep}$ for the dwell period as a function of time. The experimental creep strain rate $\dot{\varepsilon}_{creep}$ beneath the indenter is determined using Equation 7 as suggested by Mayo and Nix (1988) and reported recently by Hasnine et al. (2014)

$$\dot{\varepsilon} = \frac{1}{h}\frac{dh}{dt} \tag{7}$$

where $\frac{dh}{dt}$ is the experimentally measured deformation rate and depth h is the indentation depth. Although Equation 7 is based on uniform stress underneath the indenter, it provides reasonable initial guess for the model coefficients to fit the creep experimental data. Finally, the indenter tip was modeled as linear elastic material with diamond's Young's modulus of 1400 GPa and Poisson's ratio of 0.2. Other elastic and plastic material properties for C-S-H were determined iteratively so that the load-indentation simulated by the finite element method closely fits the one observed experimentally. In this context, Young's modulus and Poisson's ratio for C-S-H were defined as 5.0 GPa and 0.15 respectively. For cracking, bilinear plastic model with Yield stress of 3.0 MPa and tangent modulus of 2.0 GPa was assigned to C-S-H.

RESULTS, ANALYSIS AND DISCUSSION

Figure 3 shows the load-indentation depth of the four nanoindentations performed on synthetic C-S-H. In addition, the reduced modulus and creep compliance for the four nanoindentations are listed in **Table (1)**.

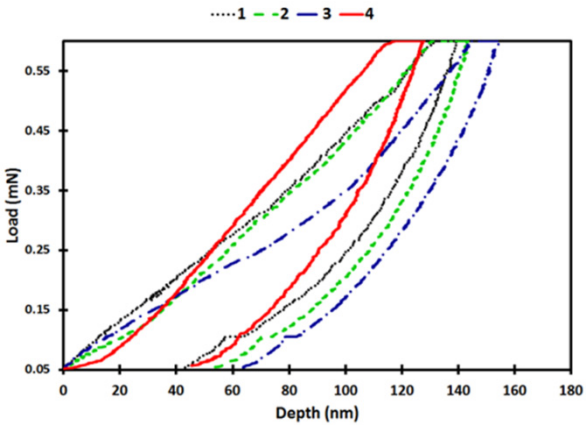

Figure 3. Load displacement during nanoindentations of synthetic C-S-H

Table (1): Reduced modulus and creep compliance of different nanoindentations

Indentation No.	Reduced modulus (GPa)	Creep compliance (1/Pa)
Test No. 1	19.34	4.18E-11
Test No. 2	18.28	7.69E-11
Test No. 3	17.09	6.51E-11
Test No. 4	18.14	9.07E-11
Mean	18.21	6.863E-11
Standard Deviation	±0.920	±2.072E-11

The mean reduced modulus and creep compliances for synthetic C-S-H where 18.21 GPa and 6.863 × 10^{-11} 1/Pa respectively. Based on the standard deviation, the table shows that a little coefficient of variation (COV) for reduced modulus is

observed (only ±5%) while a large COV of ±30% is observed for the creep compliance. Such large variation in creep compliance can be attributed to the roughness of the specimens and the existing of different densities for C-S-H.

Test No. 2 is chosen as a median specimen in terms of reduced modulus, creep compliance, and strain energy to examine the proposed method to extract fracture toughness for synthetic C-S-H. **Figure 4** shows comparison for load-displacement of nanoindentation between the experiment and the two FE models. The figure shows good agreement between the experimental data and the viscoelastic-plastic FE model. This is expected since the FE model accounts for the three components of strain (elastic, plastic, and viscous components). On the other hand, the viscoelastic model demonstrates relatively lower displacements than of that observed experimentally since it accounts for two components of strains (elastic and viscous components).

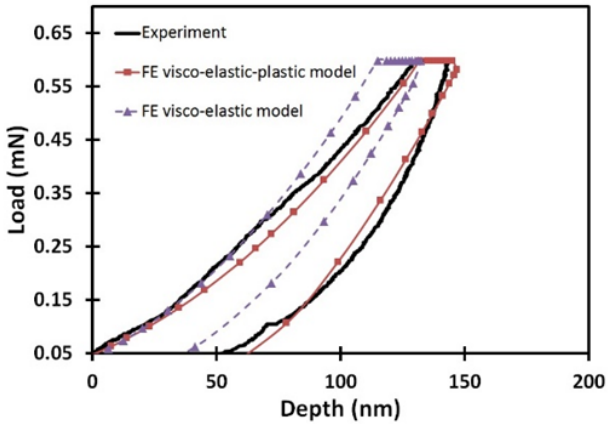

Figure 4. Load displacement response of median nanoindentation

A time hardening creep law, presented in Equation 8, was used in the model

$$\dot{\varepsilon}_{creep} = 10^{7}\left(\frac{\sigma}{t}\right) \tag{8}$$

where stress σ and time t are in MPa and seconds respectively. The creep law is used to fit the show the nanoindentation displacement-time response for the experimental data during the dwell/creep period as shown in **Figure 5**.

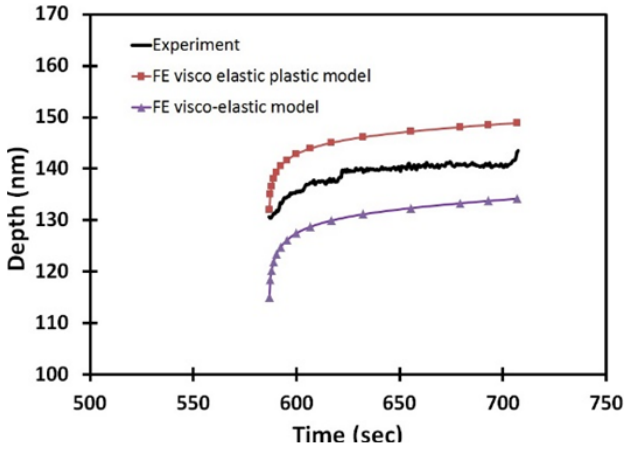

Figure 5. Deformation at dwell/creep period.

While the viscoelastic model significantly underestimates the displacements, the viscoelastic-plastic model slightly overestimates the displacements. We believe that there are two factors could be used to improve the fitting of the experimental data. First, to consider the time dependent viscous/creep effect during the loading and unloading of the nanoindentation process. This is because of the relatively long duration and the relatively high stresses of the loading and unloading stages. Second, by considering the viscous effect in the loading stage, the creep during the dwell period may be better described as a secondary creep rather than a primary creep. Therefore, a mathematical model that accounts for both primary and secondary creep would be more appropriate. Further research is ongoing to improve this model.

The difference in the load-displacement response between the two models is used to extract information about the cracking of the C-S-H. It is assumed here that cracking occurs due plastic strains and therefore plastic energy can be used to predict fracture toughness. The effect of cracking can also be observed by comparing the loading and unloading curves for each model. In the viscoelastic model, the loading and unloading curves are almost parallel while in the viscoelastic-plastic model, the loading is steeper than the unloading due to the presence of plastic/cracking strain in the loading curve only. The total strain energy for the viscoelastic-plastic model and viscoelastic models can be expressed in Equations 9 and 10 respectively as follows.

$$\left[U_{Total}\right]_{viscoelastic-plastic} = U_{elastic} + U_{plastic} + U_{creep} \tag{9}$$

$$\left[U_{Total}\right]_{viscoelastic} = U_{elastic} + U_{creep} \tag{10}$$

The analysis method is based on the energy approach originally introduced for ductile materials by Cheng et al. (2002). The total and elastic energies for the experimental data and the two FE models are presented in **Table (2)**. The total energy is computed as the area under the load-displacement curve up to the end of dwell period while the elastic energy is computed as the area under the unloading curve. It can be observed that the total energy for the experimental data and the viscoelastic-plastic model are fairly close while the total energy for the viscoelastic model is less. The difference here can be attributed to the plastic or fracture energy. The fracture energy in this case can be obtained from Equation 11.

$$U_{fra} = \left[U_{Total} - U_{elastic}\right]_{viscoelastic-plastic} - \left[U_{Total} - U_{elastic}\right]_{viscoelastic} \tag{11}$$

The critical energy release rate G_c can then be determined by dividing the cracking energy by the cracked area as follows

$$G_c = \frac{\partial U_{fra}}{\partial A} = \frac{U_{fra}}{A_m} \tag{12}$$

where $A_m = 24.5h_{max}^2$ is the maximum crack area given for Berkovich indenter based on the maximum indentation depth h_{max} assuming stable crack growth under

nanoindentation load. The fracture stress intensity factor K_c can be computed from the energy release rate G_c and reduced modulus E_r following Equation 13.

$$K_c = \sqrt{G_c E_r} \tag{13}$$

The above computational approach yields a fracture toughness of 0.45 MPa $m^{1/2}$. The analytical fracture toughness is in agreement with fracture toughness of cement determined experimentally by Shah (1988) who showed that fracture toughness of cement paste ranges between 0.3-0.5 MPa $m^{1/2}$. It is important to note that the above method for computing fracture toughness is computed considering only one representative nanoindentation curve. Nanoindentation curves of C-S-H in **Figure 4** show some variation in the material properties and strain energies which would affect the estimated fracture toughness. The variation is attributed to the existence of C-S-H with wide range of densities.

Table (2): Total and elastic energies for the experimental data and FE models

	Experimental data	Viscoelastic-plastic model	Viscoelastic model
Total Energy (nJ)	45.7×10^3	46×10^3	42.55×10^3
Elastic Energy (nJ)	24.4×10^3	25.1×10^3	27.8×10^3

CONCLUSION

Calcium Silicate Hydrate gel (C-S-H) with C/S mixture ratio of 1.5 was synthesized and tested using nanoindentation. Time-dependent (creep) test was performed using Berkovich indenter tip and the creep measurements were employed to determine the fracture toughness. A two dimensional finite element model was developed and used to separate the fracture energy from other types of strain energies using energy conservation approach. Implicit time hardening creep law was implemented to describe the viscoelastic behavior of C-S-H. The fracture toughness of C-S-H was then calculated from the obtained fracture energy. The fracture toughness of 0.45 MPa $m^{1/2}$ were determined for C-S-H and were found to be in range with fracture toughness of cement paste reported in the literature.

REFERENCES

Alizadeh, R. Beaudoin, J.J. Raki, L. Mechanical properties of calcium silicate hydrates, Materials and Structures, Vol. 44, 2010, pp. 13–28.

Anstis G.R., Chantikul, P., Lawn, B.R. and Marshall, D.B., A critical evaluation of indentation techniques for measuring fracture toughness: I, Direct crack measurements. *J. American Ceramics Society*, Vol. 64, 1981, pp. 533–538.

ASTM Standard E 104-02: Standard Practice for maintaining Constant Relative Humidity by Means of Aqueous Solution. ASTM International, 2007.

Beaudoin, J.J., Feldman, R.F., Dependence of degree of silica polymerization and intrinsic mechanical properties of C-S-H on C/S ratio, 8th International Congress on the Chemistry of Cement, Brazil, 3, 1986, pp. 337–342.

Chen, J., and Bull, S.J., Indentation fracture and toughness assessment for thin optical coatings on glass. Journal of Applied Physics, Vol. 40, 2007, pp. 5401–5417.

Cheng, Y.T., Li, Z.Y. and Cheng, C.M., Scaling, relationships for indentation measurements. Philosophical Magazine A, Vol. 82, 2002, pp.1821–1829.

Constantinides, G., and Ulm, F.J. 2004. The effect of two types of C-S-H on the elasticity of cement based materials: results from nanoindentation and micro modeling. Cement and Concrete Research, Vol. 34, 2004, pp. 67–80.

Field, J.S., Swain, M.V., and Dukino, R.D., Determination of fracture toughness from the extra penetration produced by indentation-induced pop-in. Journal of Materials Research, Vol.18, 2003, pp. 1412–1419.

Fisher-Cripps, A.C., Nanoindentation, Springer, New York, 2004.

Foley, E.M., Kim, J.J., Reda Taha, M.M. Synthesis and nano-mechanical characterization of C-S-H with a 1.5 C/S ratio, Cement and Concrete Research, Vol. 42, 2012, pp. 1225–1232.

Harding, D.S., Oliver, W.C., and Pharr, G.M., Cracking during nanoindentation and its use in the measurement of fracture toughness. Materials Research Symposium. 1995, Houston, USA, pp. 663–668.

Hasnine, M., Mustafa, M., Suhling, J. C., Prorok, B. C., Bozack, M. J., and Lall, P., Nanomechanical characterization of lead free solder joints. In MEMS and Nanotechnology, Springer International Publishing, Vol. 5, 2014, pp. 11-22.

Jennings, H.M., A model for the microstructure of calcium silicate in cement paste, Cement and Concrete Research, Vol. 30, 2000, pp. 855–863.

Kim, J.J., Foley, E.M., Reda Taha, M.M. Nano-mechanical characterization of synthetic calcium–silicate–hydrate (C–S–H) with varying CaO/SiO2 mixture ratios, Cement and Concrete Composites, Vol. 36, 2013, pp. 65–70.

Kumar, R., and Narasimhan, R., Analysis of spherical indentation of linear viscoelastic materials. Current Science, Vol. 87, 2004, pp. 1088-1095.

Lodeiro, I.G., Macphee, D.E., Palomo, A., Fernández-Jiménez, A. Effect of alkalis on fresh C–S–H gels. FTIR analysis, Cement & Concrete Research, Vol. 39, 2009, pp. 147–153.

Lu, H., Wang, B., Ma, J., Huang, G., Viswanathan, H., Measurement of creep compliance of solid polymers by nanoindentation, Mechanics of Time-Dependent Materials, Vol. 7, 2003, pp. 189–207.

Mayo, M. J., and Nix, W. D., A micro-indentation study of superplasticity in Pb, Sn, and Sn-38 wt% Pb. Acta Metallurgica, Vol. 36, 1988, pp. 2183-2192.

Oliver, W. C., Pharr, G.M., An improved technique for determining hardness and elastic modulus using load and displacement sensing indentation experiments, Journal of Materials Research, Vol. 7, 1992, pp. 1564–1583.

Rosenfeld, L.G., Ritter, J.E., Lardner, T.J., and Lin, M.R. Use of the microindentation technique for determining interfacial fracture energy. Journal of Applied Physics, Vol. 67, 1990, pp. 3291–3296.

Shah, S.P., Fracture toughness of cement-based materials. Materials and Structures, Vol. 21, 1988, pp. 145–150.

Sugiyama, D. Chemical alteration of calcium silicate hydrate (C-S-H) in sodium chloride solution, Cement and Concrete Research, Vol. 38, 2008, pp. 1270–1275.

Taylor, H.F.W. Cement Chemistry, second ed., Thomas Telford Publishing, 1997.

Cement Setting Is Not Just Smooth Anymore: Insight from the Physics of Jamming

Henri Van Damme[1,2,3] and Sidney Yip[4,5]

[1]Department of Civil and Environmental Engineering, Massachusetts Institute of Technology, 77 Massachusetts Ave., Cambridge, MA 02139-4307. E-mail: henrivd@mit.edu
[2]MIT-CNRS Joint Laboratory, 77 Massachusetts Ave., Cambridge, MA 02139-4307.
[3]Centre Interdisciplinaire des Nanosciences de Marseille, CNRS and Aix-Marseille Université, Campus de Luminy, 13288 Marseille Cedex 09, France.
[4]Department of Material Science and Engineering, 77 Massachusetts Ave., Cambridge, MA 02139-4307. E-mail: syip@mit.edu
[5]Department of Nuclear Science and Engineering, Massachusetts Institute of Technology, 77 Massachusetts Ave., Cambridge, MA 02139-4307.

Abstract

A wide variety of fluid systems including organic liquids, mineral melts, colloidal suspensions and granular materials, undergo a dynamical arrest transition when the temperature is lowered, or the density is increased, or the applied stress is decreased. This is known as the glass transition in the first case and as the jamming transition in two latter cases. The purpose of this paper is to show that the coagulation and the setting of cement pastes share with these systems several key attributes which bring them under the same umbrella.

INTRODUCTION

The simplest way to define what a glass is, in popular terms, is probably to say that it is a liquid that has lost its ability to flow [Angell, 1995]. This seemingly trivial statement is deeper than it seems because it emphasizes correctly two key features of glasses. The first is the structural resemblance – if not similitude – between a glass and the liquid it was before becoming a solid. Both exhibit only short range order and may be qualified as amorphous. The second feature – of which the arrest of flow is just one manifestation – is the dramatic slowing down of the structural relaxations as the liquid crosses the transition temperature.

As first pointed out by Liu and Nagel (1998), this feature is shared by several other rigidity transitions in dense systems, such as the flow arrest of complex fluids when the flow inducing stress drops below some critical value (the yield stress σ_y), or the jamming of granular media when the particle volume fraction reaches a critical packing fraction (Figure 1).

The case of colloidal suspensions of attractive particles is particularly interesting because it introduces a competition between the attractive energy W and

thermal energy k_BT, which leads to consider the ratio k_BT/W rather than T or k_BT alone (Trappe et al., 2001).

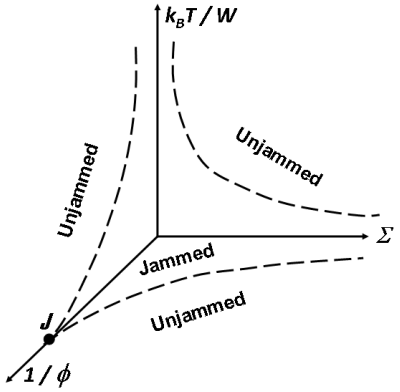

Figure 1. Jamming phase diagram (adapted from Trappe et al., 2001).

The purpose of this contribution is to revisit cement setting under the light of the jamming transition. As will be shown, there is conclusive evidence that cement behavior does indeed fit into the general frame of jamming.

GELATION and SETTING

Setting is the property which has made the success of cement and which justifies the surname "liquid stone". Setting is a crossover from a soft and viscous or viscoelastic state to a hard, elastic, and brittle state. It stems from the hydration reaction of the anhydrous cement which, on the average, transforms one volume of anhydrous minerals into two volumes of hydrates, the most important being the self-adhesive C-S-H. Quite naturally, setting is often interpreted as the result of this volume increase, which is supposed to lead to overlap and links between the hydration products around the initial cement grains. Percolation theory with a hard core – soft shell model is a priori the right framework to describe this process and attempts have been made to use it in order to fit quantitatively the modulus rise beyond the onset of setting (Scherer et al., 2012). A critical-like behavior is observed, as expected (modulus scaling as the distance to the percolation point to some scaling exponent), but the value of the exponent does not agree with the expectations.

Here we suggest that the fluid to solid transition induced by the reaction of cement with water can be described as a two-step jamming process. Each step exhibits critical-like behavior with a power law increase of modulus with respect to time ($G^* \sim t^{\upsilon}$), as illustrated in Figure 2. The first step, which could be called the "gelation" phase, is the transition from a dispersed or weakly coagulated initial slurry to a more strongly coagulated slurry within a matter of minutes, due to the onset of strong non van der Waals attractive interactions (ion correlation forces or direct electrostatic forces) between cement grains. More exactly, due to the universal nano- and mesoscale roughness of mineral particles, the attraction would develop between the micro- and/or nano-asperities in the contact zone between cement grains. Gelation is occurring at zero hydrate content, but the surface chemistry of the cement grains at this stage is probably very close to that of C-S-H (Nachbaur et al., 1998). Hence, the

forces between asperities should be very similar to those between C-S-H nanoparticles. As illustrated in Figure 2, the amplitude of the modulus jump due to gelation is very sensitive to the solid volume fraction and to the measurement frequency.

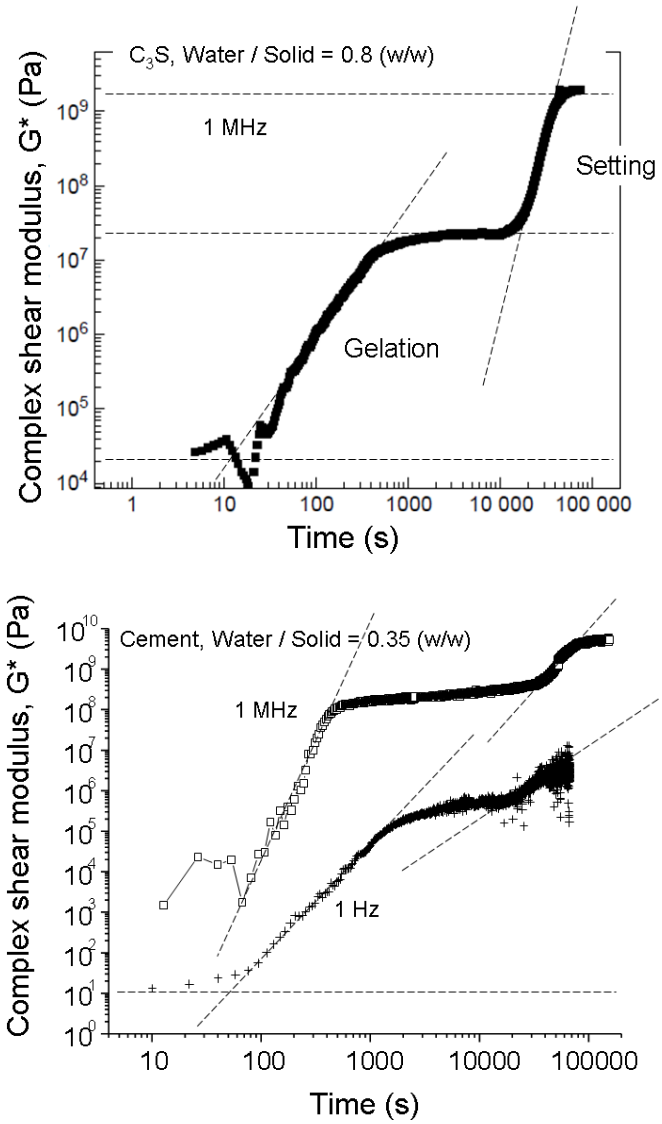

Figure 2. Evolution of the complex shear modulus, in the linear regime, of a tricalcium silicate (C3S) paste prepared at a water/solid ratio of 0.8 (top, adapted from Lootens et al., 2004) and a cement paste prepared at a water/solid ratio of 0.35 (bottom). Measurements made using an ultrasonic method at 1 MHz or a dynamic rheometry (plane-plane) method at 1 Hz.

The second step, which corresponds to the usual "setting" phase, is occurring in this strongly coagulated medium, in conditions where the degree of hydration is very small (a few %) and where the overall solid volume fraction is still well below the loose random packing limit. Hence, the increase of shear modulus can indeed hardly be interpreted in terms of a significant solid volume fraction increase. Yet, the

increase of shear modulus which is due to this very small volume fraction of hydrates is able to induce a jump of about two orders of magnitude in G* (Figure 2). As already suggested (Nachbaur et al., 2001), this may be related to the preferential precipitation of hydrate nanoparticles in the contact region between cement grains. Once again, the mesoscale roughness of the grains may be important in this process. Covering the rough cement grains surface with nanoparticles in the contact zone would simply amount to increase the contact area between cement grains or, equivalently, the effective strength of the attractive interaction W between cement grains. Note that W is a time- and hydration rate (α) - dependent interaction, $W(\alpha)$. In terms of structural relaxation time,

$$\tau \propto \exp\left(-W(\alpha)/k_B T\right),$$

this would lead to an evolution very close to that observed for viscosity in glass-forming liquids as the glass transition temperature is approached from above.

CONCLUSION

We showed that the gelation and setting of cement constitute one additional example of the highly non linear mesoscale-based character of soft or hard "glassy" materials (Yip & Short, 2013). It would be interesting to investigate to what extent the flow (after gelation) and creep (after setting) behaviors confirm this conclusion (Fan et al., 2013).

REFERENCES

Angell, C. A. (1995). "Formation of Glasses from Liquids and Biopolymers." *Science*, 267, 1924-1935.

Fan, Y., Yildiz, B., and Yip, S., (2013). "Analogy between glass rheology and crystal plasticity: Yielding at high strain rate". *Soft Matter*, 9, 9511-9514.

Liu, A. J., and Nagel, S. R. (1998). "Jamming is not just cool any more". *Nature*, 396, 21-22.

Lootens, D., Hebraud, P., Lecolier, E., and Van Damme, H. (2004). "Gelation, Shear-Thinning, and Shear-Thickening in Cement Slurries". *Oil & Gas Sci. Technol*., 59(1), 31-40.

Nachbaur, L., Nkinamubanzi, P.C., Nonat, A., and Mutin, J.C., (1998). "Electrokinetic Properties which Control the Coagulation of Silicate Cement Suspensions during Early Age Hydration". *J. Coll. Interf. Sci.*, 202, 261-268.

Nachbaur, L., Mutin, J.C., Nonat, A., and Choplin, L., (2001). „Dynamic mode rheology of cement and C3S pastes from mixing to setting". Cem. Concr. Res., 31, 183-192.

Scherer, G. W., Zhang, J., Quintanilla, J. A., and Torquato, S., (2012). "Hydration and percolation at the setting point". *Cem. Concr. Res.*, 42, 665-672.

Trappe, V., Prasad, V., Cipelletti, L., Segre, P. N., and Weitz, D. A., (2001). "Jamming phase diagram for attractive particles". *Nature*, 411(14 June), 772-775.

Yip, S., and Short, M.P. (2013). "Multiscale materials modelling at the mesoscale". *Nature Mater.*, 12, 774-777.

Creep of Clay: Numerical Results at the Scale of a Layer and Experimental Results at the Scale of Thin Self-Standing Films

B. Carrier[1], M. Vandamme[1], R. J.-M. Pellenq[2,3,4], H. Van Damme[2,3,4]

[1]Université Paris-Est, Laboratoire Navier (École des Ponts ParisTech, IFSTTAR, CNRS), 6-8 Av. B. Pascal, 77420 Champs-sur-Marne, France; PH (+33) 1 64 15 37 04; FAX (+33) 1 64 15 37 41; emails: matthieu.vandamme@enpc.fr, benoit.carrier@polytechnique.edu
[2]<MSE>2, UMI 3466, CNRS-MIT, 77 Massachusetts Avenue, Cambridge, Massachusetts 02139, emails: pellenq@mit.edu, henrivd@mit.edu
[3]Department of Civil and Environmental Engineering, Massachusetts Institute of Technology, 77 Massachusetts Avenue, Cambridge, Massachusetts 02139
[4]Centre Interdisciplinaire des Nanosciences de Marseille, CNRS (UPR 7251), Campus de Luminy, 13288 Marseille Cedex 09, France

ABSTRACT

This work focuses on the creep of clay-based materials, which exhibit significant analogies with cement-based materials. Here, we studied the creep of clay at two scales and with two techniques: numerically (with molecular simulations) at the scale of a clay layer (nm), and experimentally at the scale of thin self-standing clay films (few dozen μm). At the scale of the clay layer, numerical simulations showed that the shear rate was constant over time and an affine function of the shear stress. Creep experiments showed that, after a transient period, the creep function of our thin self-standing clay films was a logarithmic function of time. A comparison of the results obtained at the two scales shows that the origin of the logarithmic feature of clay creep must at least partly originate from a scale greater than that of an individual clay layer. By analogy, such result is likely to hold for cementitious materials, which are also known to creep logarithmically with respect to time in the long term: the origin of this logarithmic feature is likely to stem at least partly from a scale greater than the scale of an individual C-S-H layer.

INTRODUCTION

Cementitious materials creep, i.e., slowly deform under the application of a sustained load. But creep is also observed for a variety of materials relevant for civil engineering applications, in particular clays. Clays and cementitious materials have a lot in common, both from a microstructural and from a mechanical point of view. For instance, mechanically, both clays and cementitious materials are known to creep logarithmically with respect to time after a transient period. Also, from a microstructural

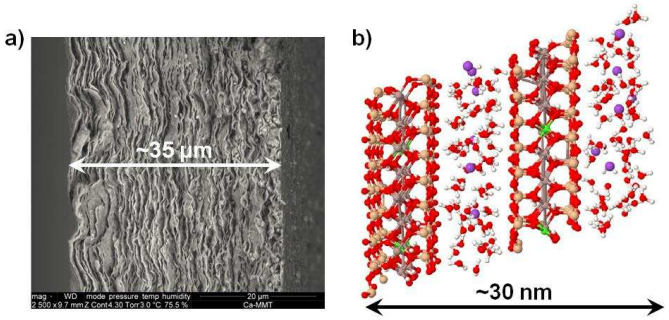

Figure 1. a) ESEM image of the edge of a self-standing film used during the experiments (Ca-montorillonite at a 76% relative humidity). The image was acquired in collaboration with L. Wang at LMS (Ecole Polytechnique). b) Typical simulation cell used during the molecular simulations of montomorillonite.

perspective, for both materials, their basic building units (i.e., calcium silicate hydrates (C-S-H) for cementitious materials and clay minerals for clays) are microporous and layered, consisting of solid layers stacked parallel to each other, with a few layers of interlayer water molecules in-between them.

This work focuses on the creep of clay-based materials. Here, we study the creep of clay at two scales (see Fig. 1) and with two techniques: numerically (with molecular simulations) at the scale of a clay layer, and experimentally at the scale of thin clay films.

EXPERIMENTS ON THIN CLAY FILMS

Materials and methods

We manufactured thin self-standing films of montmorillonite clay. Details of the experimental methods to prepare the films can be found elsewhere (Carrier et al., 2013) and are only summarized here. We used the Swy-2 clay, which is a commercially available montmorillonite. The clay fraction was isolated by centrifugation and purification was performed, so that we obtained both a montmorillonite with sodium interlayer cations only (which we note Na-montmorillonite) and a montmorillonite with calcium interlayer cations only (which we note Ca-montmorillonite). The films were made from a slurry deposited on a substrate, which after evaporation led to a self-standing film which could be peeled off the substrate. The thickness of the resulting films was a few dozen microns. The films were cut into rectangles which were 9.3-mm-wide by 80-mm-long.

We performed a tensile creep experiment on each manufactured film. To do so, one end of the film was fixed and the other end was attached to a mobile ball slide which could move linearly on a rail. The sample was loaded with a weight attached to a string, which itself was attached to the mobile ball slide. The whole creep apparatus was located in a chamber which was at room temperature, and in which we could control the relative humidity at various levels.

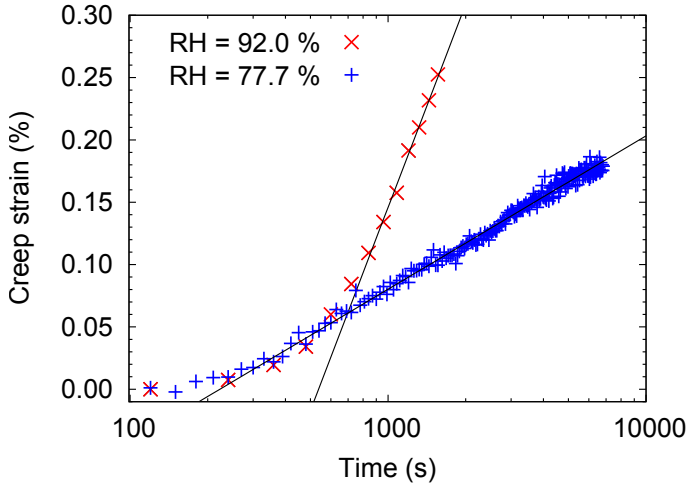

Figure 2. Creep strain observed on a thin self-standing film of Ca-montmorillonite clay, at 2 relative humidities.

We measured strains by using digital image correlation (DIC), which is a contact-free technique that consists in comparing an image of the deformed sample with an image of the sample in its state of reference. Images of the surface of the samples were acquired continuously by a video camera and were then analyzed by DIC.

Results

An example of result from tensile creep experiments is given in Fig. 2, for 2 films of Ca-montmorillonite tested at different relative humidities. Clearly, after a transient period (i.e., in these specific experiments, after a few hundreds of seconds), the creep strain was a logarithmic function of time. We also observe that creep was more important at higher than at lower relative humidity. For some experiments (e.g., for the experiment performed at a relative humidity of 92% in Fig. 2), after some time the sample failed. For other experiments (e.g., for the experiment performed at a relative humidity of 77.7% in Fig. 2), we stopped the experiment before failure.

The qualitative feature of a creep strain that evolved logarithmically with time after a transient period was observed for all clay films tested, independent of the interlayer cation (Ca or Na) or of the relative humidity (for relative humidities higher than 50%). Given this feature, for each experiment performed, from how the creep strain ε evolved after the transient period, we calculated a creep coefficient $d\varepsilon/d\log(t)$ (where t is the time), as this parameter is constant when creep is a logarithmic function of time. Performing tensile creep experiments at various levels of load suggested that this creep coefficient was proportional to the load, so that we eventually introduced a creep compliance κ defined as $\kappa = (b/F)d\varepsilon/d\log(t)$, where b is the width of the sample (i.e., 9.3 mm in our case) and F is the force applied per clay layer.

For the two types of clay films manufactured, we studied how the intro-

duced creep compliance depended on the hygric state. Given that the water adsorption isotherms of the manufactured films were available (Carrier et al., 2013), this dependence could as well be expressed as a function of water content or of relative humidity. For both types of films, on the whole range of relative humidities considered (i.e., from about 55% to about 95%), the creep compliance was an increasing function of the relative humidity. For the films made of Na-montmorillonite, from a relative humidity of 60% to a relative humidity of 92%, the creep compliance increased by 2 orders of magnitude. For the films made of Ca-montmorillonite, from a relative humidity of 51% to a relative humidity of 99%, the creep compliance increased by more than 2.5 orders of magnitude. At any water content, the creep compliance of the films made of Na-montmorillonite was 0.5 to 1 order of magnitude greater than that of the films made of Ca-montmorillonite.

MOLECULAR SIMULATIONS AT SCALE OF CLAY LAYER

Numerical methods

We also investigated the creep of clay-based materials at the nanometric scale. To do so, we performed full-atomistic molecular dynamics simulations of clay layers subjected to a constant shear force in the plane of the layer. We simulated a montmorillonite clay as described elsewhere (Carrier et al., 2014). We ran simulations with either sodium or calcium counterions. Three water contents were considered, which corresponded to 1, 2, and 3 layers of interlayer water.

Periodic boundary conditions were used and the cell contained 2 clay layers and therefore 2 interlayer spaces. We used the CLAYFF force field and the LAMMPS package. Simulations were run in the isobaric-isothermal ensemble, at a temperature of 300 K. All cell parameters were free to evolve. For each simulation, the cell was first equilibrated under the action of an isotropic compressive stress equal to 0.1 MPa. Then, to this isotropic compressive stress was added a shear stress τ parallel to the clay layers. We monitored the shear strain γ over time.

Results

For all simulations performed, we observed that the shear strain γ evolved linearly with time. Therefore, from each simulation, a shear strain rate $\dot{\gamma}$ could be calculated.

Figure 3 displays how the shear strain rate $\dot{\gamma}$ evolved with the shear stress τ for a layer of montmorillonite with calcium counterions. For all shear stresses considered, increasing the water content increased the shear strain rate. Interestingly, especially at the lowest water content considered, the shear strain rate was not proportional to the shear stress, i.e., the layer did not behave in a Newtonian manner. Such features were also observed in the simulations of montmorillonite with sodium counterions.

A quite representative model of the observed dependence of the shear strain

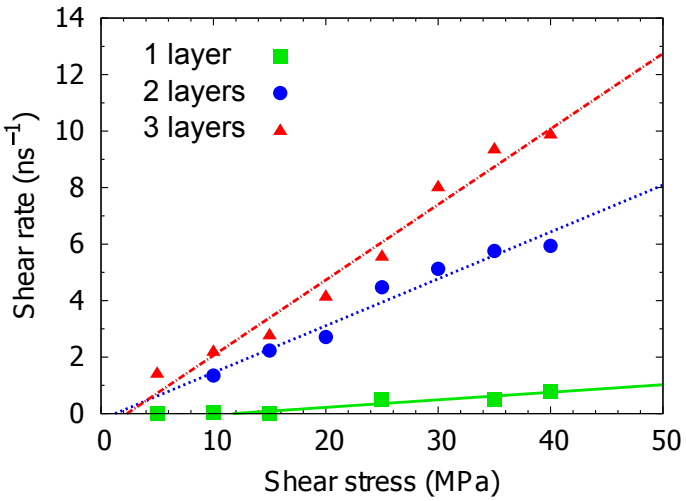

Figure 3. Dependence of shear strain rate with respect to shear stress for a layer of montmorillonite with calcium counterions, at 3 water contents.

rate on the shear stress would be that of a Bingham fluid, to which can be associated a viscosity η and a yield stress τ_c such that $\dot{\gamma} = 0$ if $\tau < \tau_c$ and $\dot{\gamma} = (\tau - \tau_c)/\eta$ if $\tau > \tau_c$.

DISCUSSION

Numerical results at the scale of the clay layer and experimental results at the scale of the clay films were very different qualitatively: at the scale of the nanometric clay layer, creep was linear with time while, at the scale of the dozens-of-microns-thick clay films, creep was linear with the logarithm of time. Such strong qualitative difference suggests that logarithmic creep in clay does not originate from the scale of an individual clay layer only, but must at least partly originate from a greater scale, i.e., from a mesoscale of an assembly of clay layers.

By analogy, it is likely that the fact that, in the long term, cementitious materials creep logarithmically with respect to time, originates at least partly from a scale greater than that of the individual C-S-H layer.

CONCLUSIONS

The conclusions of this work are several:

- Self-standing clay films with a thickness of a few dozen microns, when subjected to a tensile load, creep logarithmically with respect to time after a transient period. The greater the water content, the more the films creep.
- At the scale of a clay layer, creep is a linear function of time. With respect to the applied shear stress, the clay layers exhibit a Bingham-type behavior. The greater the water content, the more the clay layer creeps.

- The creep behavior of the clay layers differs qualitatively from the creep behavior of the clay films, as the clay layers creep linearly with time, while the clay films creep linearly with the logarithm of time (after a transient period). This quantitative difference suggests that the logarithmic feature of long-term creep must originate at least partly from a scale greater than the scale of the individual clay layer.
- By analogy, for cementitious materials, it is likely that the fact that their long-term creep is a logarithmic function of time must originate at least partly from a scale greater than the scale of the individual C-S-H layer.

REFERENCES

Carrier, B., Wang, L., Vandamme, M., Pellenq, R. J.-M., Bornert, M., Tanguy, A., and Van Damme, H. (2013). "ESEM study of the humidity-induced swelling of clay film." *Langmuir: The ACS Journal of Surfaces and Colloids*, 29(41), 12823-33.

Carrier, B., Vandamme, M., Pellenq, R. J.-M., and Van Damme, H. (2014). "Elastic properties of swelling clay particles at finite temperature upon hydration." *The Journal of Physical Chemistry C*, 118(17), 8933-8943.

A creep-damage model for mesoscale simulations of concrete expansion-degradation phenomena

Alain B. Giorla[1] and Yann Le Pape[1]

[1]Oak Ridge National Laboratory, One Bethel Valley Road, Oak Ridge, TN 37831, USA; email: giorlaab@ornl.gov; lepapeym@ornl.gov

ABSTRACT

Long-term performance of aging concrete in nuclear power plants (NPPs) requires a careful examination of the physical phenomena taking place in the material. Concrete under high neutron irradiation is subjected to large irreversible deformations as well as mechanical damage, caused by a swelling of the aggregates. Mesoscale numerical simulations are performed to separate the underlying mechanisms and their interactions. The cement paste creep-damage model accounts for the effect of the loading rate on the apparent damage properties of the material and uses an event-based approach to capture the competition between creep and damage. The model is applied to the simulation of irradiation experiments from the literature and shows a good agreement with the experimental data.

INTRODUCTION

In the recent years, aging and long-term performance of concrete have become a subject of renewed interest for NPPs in the United States, as a significant number of plants are envisioning extended operations beyond 60 years. Hence, it is critical to understand the long-term behavior of concrete in the environmental and operational conditions of these structures to ensure continued safe and cost-effective electricity generation. One aspect of the long-term operation of NPPs is the degradation of concrete caused by irradiation, and is one of the research priority of the U.S. Department of Energy Light Water Reactor Sustainability program (Field et al., 2015; Le Pape et al., 2015).

Several experimental studies have shown that concrete under neutron irradiation suffers large irreversible deformations as well as mechanical damage, caused by a high swelling of the aggregates (e.g., Elleuch et al., 1972), hereafter referred to as Radiation-Induced Volumetric Expansion (RIVE) (Field et al., 2015). The application of the experimental results obtained under accelerated condition in test reactors to the operational and structural conditions is a crucial question, as the environmental conditions differ widely between test reactors and actual structures, and several effects are competing one against another. The influences of temperature, humidity, neutron fluence, creep and damage might be strongly coupled, and require the development of adequate numerical tools.

In this paper, we briefly present a damage algorithm for the simulation of concrete at its mesoscale, followed by an application to irradiated concrete. The model is integrated using space-time finite elements (Giorla et al, 2014) and implemented in the C++ finite element framework AMIE (Dunant and Scrivener, 2010).

CREEP-DAMAGE ALGORITHM

We use an event-based approach to characterize the creep-damage coupling in the material. This approach is an extension of the saw-tooth algorithm of (Rots and Invernizzi, 2004) to visco-elastic materials. On a single time step from t_0 to t_{max} the algorithm can be simply described as follow:

1. Solve the system between t_0 and t_{max} using the initial conditions $\mathbf{u}_0$ and assuming that there is no additional damage in the material.
2. Find t_1 the first instant at which at least one element reaches its failure surface and $\mathbf{u}_1$ the displacements at that instant.
3. Re-assemble the system between t_1 and t_{max} considering the damage in the element found at step 2. has increased, using $\mathbf{u}_1$ as the new initial conditions.
4. Iterate on steps 1-3 until no elements reach its failure surface.

With this algorithm, we construct a series of events at which damage increases. Between these damage events, the material behaves as a linear visco-elastic solid as it remains below its failure surface. In this way, the relaxation mechanisms are accounted for without additional modifications to the model. The algorithm can use failure surfaces that depend on time or the advancement of other phenomena like hydration or drying. The damage model is made non-local by using averaged values for the strain and stress when calculating the instant at which an element reaches its failure surface (step 2). The use of space-time finite elements reduces the re-assembly (step 3) to the multiplication of the elementary matrices by the appropriate scalar (except for the elements that have been damaged) (formal proof in Giorla 2014), while more common finite difference schemes (e.g., Zienkiewicz et al., 1968) require the recalculation of the elementary matrices and associated nodal forces for all visco-elastic elements, as these depend non-trivially on the time step.

SIMULATION OF IRRADIATED CONCRETE

As an example, we simulate the irradiation experiments of Elleuch et al. (1972). The histories of the temperature, neutron fluence and relative humidity are summarized in Figure 1 (left). The material is pre-dried (thermal pre-treatment) in order to limit the presence of water (and thus, radiolytic hydrogen production) during the irradiation experiment. The material properties of the serpentine aggregates, aluminous cement paste, and resulting concrete were measured before pre-treatment, between the pre-treatment and the irradiation, and after the cool-off period.

The material model accounts for the creep of the cement paste using a simplified B3 model (Bažant and Baweja, 2000), including the influence of temperature and relative humidity on creep. The RIVE in assumed to take place homogeneously in

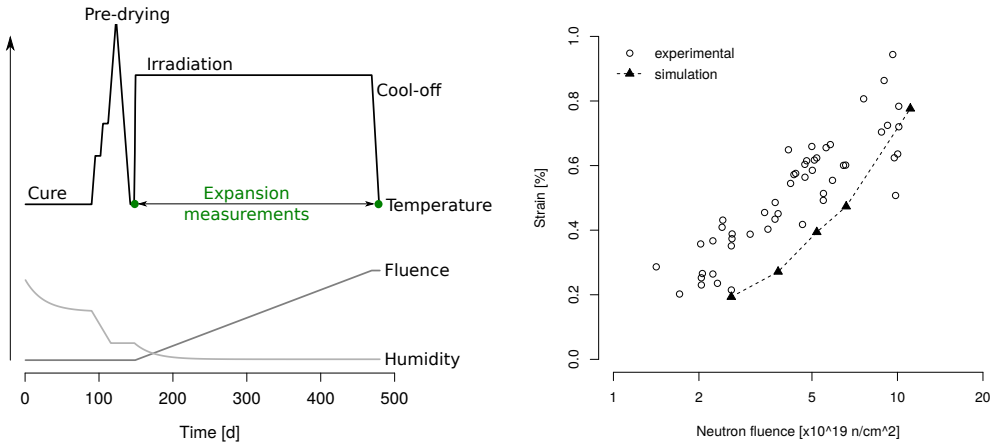

Figure 1. Temperature, relative humidity and neutron fluence history (left), Experimental and numerical RIVE of concrete (right).

the aggregates, and is governed by an S-shape curve, intially proposed by (Zubov and Ivanov, 1966) for quartz:

$$\epsilon_{\text{RIVE}} = \frac{\kappa\, \epsilon_{\max} \left(e^{\delta \cdot \Phi} - 1\right)}{\epsilon_{\max} + \kappa\, e^{\delta \cdot \Phi}}$$

with Φ the fast-neutron fluence, $\epsilon_{\max}$, κ and δ material parameters calibrated on irradiation experiments made on the same aggregates (Le Pape et al., 2015). The thermal pre-treatment phase allows us to calibrate mechanical properties that were not measured, such as the fracture energy of the cement paste.

Figure 1 (right) shows the concrete RIVE as a function of the neutron fluence, using a simplified microstructure containing only 50% of aggregates for preliminary calculations (66% in the experiments). The simulated expansion variation is measured between the two instants, i.e., pre- and post-irradiation assessment, as shown in Figure 1 (left). The computed dimensional changes show the appropriate trend, but remain below the experimental expansions. This underestimation could be attributed to the lower amount of aggregates in the numerical sample, or a debonding of the aggregates during the cool-off phase following the the irradiation experiment.

CONCLUSION AND PERSPECTIVES

We presented an event-based algorithm to simulate degradation in materials with coupled creep and damage. The algorithm is applied to the study of concrete subject to neutron irradiation in test reactors. The model provides the same trend as the experimental data from (Elleuch et al., 1972), in which all phases of the experiments were simulated. In future work, the model will be applied to the simulation of concrete exposed to conditions more representative to NPPs, notably in terms of material properties, relative humidity, temperature and neutron fluence history and rate.

The algorithm can be applied to other phenomena where creep-damage competition occurs, including long-term expansion-degradation such as alkali-silica reaction or delayed ettringite formation, as well as materials for which the failure surface

changes with time or the advancement of other processes.

ACKNOWLEDGEMENTS

This research is sponsored by the U.S. Department of Energy (DOE) Light Water Reactor Sustainability Program. This manuscript has been authored by UT-Battelle, LLC under Contract No. DE-AC05-00OR22725 with the U.S. Department of Energy. The United States Government retains and the publisher, by accepting the article for publication, acknowledges that the United States Government retains a non-exclusive, paid-up, irrevocable, world-wide license to publish or reproduce the published form of this manuscript, or allow others to do so, for United States Government purposes. The Department of Energy will provide public access to these results of federally sponsored research in accordance with the DOE Public Access Plan (`http://energy.gov/downloads/doe-public-access-plan`).

REFERENCES

Bažant, Z.P., and Baweja, S. (2000). "Creep and shrinkage prediction model for analysis and design of concrete structures: Model B3." *Special Publication of The American Concrete Institute,* 194, 1-84.

Dunant, C.F., and Scrivener, K.L. (2010). "Micro-mechanical modelling of alkali-silica-reaction-induced degradation using the AMIE framework" *Cement and Concrete Research,* 40(4), 517-524.

Elleuch, L.F., and Dubois, F., and Rappeneau, J. (1972). "Effects of neutron radiation on special concretes and their components." *Special Publication of The American Concrete Institute,* 43, 1071-1108.

Field, K.G., and Remec, I., and Le Pape, Y. (2015). "Radiation Effects on Concrete for Nuclear Power Plants, Part I: Quantification of Radiation Exposure and Radiation Effects" *Nuclear Engineering and Design,* 282, 126-143.

Giorla, A.B., and Scrivener, K.L., and Dunant, C.F. (2014). "Finite elements in space and time for the analysis of generalised visco-elastic materials" *International Journal for Numerical Methods in Engineering,* 97(6), 454-472.

Le Pape, Y., and Field, K.G., and Remec, I. (2015). "Radiation Effects on Concrete for Nuclear Power Plants, Part II: Perspective from Micromechanical Modeling" *Nuclear Engineering and Design,* 282, 144-157.

Rots, J.G., and Invernizzi, S. (2004). "Regularized sequentially linear saw-tooth softening model" *International Journal for Numerical Methods in Engineering,* 28(7-8), 590-614.

Zienkiewicz, O.C., and Watson, M., and King, I.P. (1968). "A numerical method of visco-elastic stress analysis" *International Journal of Mechanical Sciences,* 10(10), 807-827.

Zubov, V.G., and Ivanov, A.T. (1966). "Expansion of quartz caused by irradiation with fast neutrons" *Soviet Physics Crystallography,* 11(3), 372-374.

Confined Transport in Multiscale Porous Materials: From the Pore Scale to the Pore Network

P. Levitz

Université Pierre et Marie Curie, CNRS, Phenix Laboratory, 75252 Paris Cedex 5, France.
E-mail: pierre.levitz@upmc.fr

Abstract

Current advances in micro and nano X-ray tomography allow to image multiscale porous materials with spatial resolutions up to about 10 nm. This is particularly the case of natural or industrial geo-materials like sedimentary rocks, shale or cement pastes. These experiments reveal complex multiscale morphologies and raise the question to couple these various length scales with some functional properties such as the transport of gas or liquid in strong confinement. In this conference, we focus on the diffusive transport of molecule in porous media where adsorption and geometrical confinement at different time and length scales are observed. We propose some possible ways to quantitatively decouple the fluid confinement within "elementary pores", involving adsorption, intermittent dynamics, and the long distance exploration, sensitive to the porous network connection.

INTRODUCTION

Porous materials, concentrated colloidal suspensions are example of confining systems developing large specific surface, presenting a rich variety of shapes and exhibiting complex and irregular morphologies on a large length scale. Such a confinement strongly influences the molecular dynamics of embedded fluids and plays a crucial role in various transport phenomena in nature and industry (Sahimi-1995).

Current advances in micro and nano X-ray tomography allow to image multiscale porous materials with spatial resolutions up to about 10 nm. This is particularly the case of natural or industrial geo-materials like sedimentary rocks (Han-2009), shale or cement pastes (Brisard-2012, Jackson-2013). These experiments reveal complex multiscale morphologies and raise two questions: first, how to chose tools allowing simplifying the morphological analysis; second, how to relate these observed complex morphologies at different length scales with some functional properties such as the dynamics of gas or liquid in strong confinement.

In this work, we focus on the diffusive transport of molecule in porous media where adsorption and geometrical confinement at different time and length scales are observed. In the first part, we discuss some properties of the pore network topological

graphs (PNTG) [Pothuaud-2000; Levitz-2012).We show that the PNTG allows an operational definition of what is usually called "the elementary pore" within a complex structure. Finally, we show how these topological graphs can be used to analyze diffusive molecular transport in porous media. We propose a possible way to decouple the local scale fluid confinement where adsorption and intermittent dynamics (Levitz-2013) dominate (confinement within “elementary pores”) and the long distance scale exploration, sensitive to the porous network connection. For this presentation, we focus on one example of porous medium: a Vycor-like matrix [Levitz-1998] having a nanometer pore scale and a porosity of 0.5. A snapshot of this material is shown in Fig 1. This matrix was reconstructed using a threshold correlated Gaussian field [Levitz-1998]. Generalization of our analysis to disordered carbon membranes, cement pastes and polydisperse granular media will be published elsewhere.

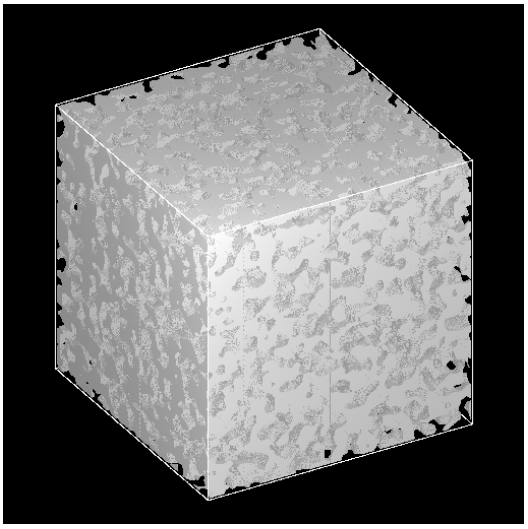

Figure 1:3D configuration of a Vycor-like porous matrix. The cube is 300 nm large. The porosity is 0.5.

I/ DECOUPLING THE PORE GEOMETRY

I-1/ The pore network topological graph (PNTG)

A powerful tool to characterize the topology is the pore network topological graph (Barett-1970, Cohen-1982,Pothuaud-2000). This graph is obtained by progressively narrowing the pore space starting from the internal surface. This thinning retraction must satisfy both the invariance of the three first Betti numbers (Barett-1970) and some morphological constraints in order to get a PNTG statistically centered in the pore network. A difficult step is to reduce the numerical PNTG in terms of a simple graph made of vertices connected by edges and having the same topological properties that the initial set. In this paper, we use a numerical scheme proposed some years ago (Pothuaud-2000). An example of this “skeletonisation” is shown in

Figure 2 where dangling bonds (the so-called termini) are eliminated under a continuous retraction.

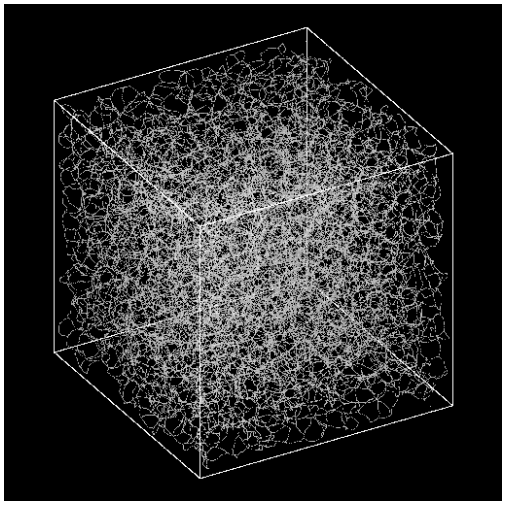

Figure 2: The pore network topological graph of the porous medium shown in Fig 1

I-2/ Possible definition of an "Elementary" Pore

As discussed elsewhere (Pothuaud-2000), the pixels belonging to a defined edge of the pore network topological graphs can be labeled with a specific index. The segmentation of the binary pore network in a set of so-called "elementary pores" consists of giving to all pixels of the initial pore network an index equal to the index of the nearest pixel belonging to the set of edges. In such a condition, each "elementary pore" is attached to a specific edge. The application of this algorithm allows to get a complete set of "elementary pores" topologically equivalent to a portion of a tube and having two opposite entrance surfaces. A snapshot of a sub set of "elementary pores" is shown in Fig 3.

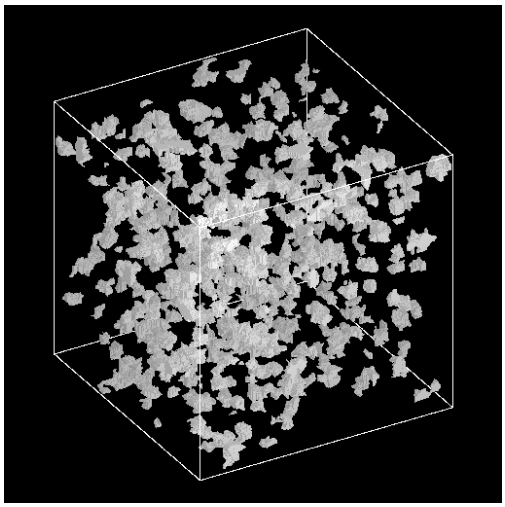

Figure 3: A sub-set of "elementary pores"

It is then possible to analyze the morphology of each "elementary pore" and to compute the statistical distribution of various geometrical properties such as the pore size distribution in volume or the Entrance pore size distribution. These two distributions are shown in Fig 4.

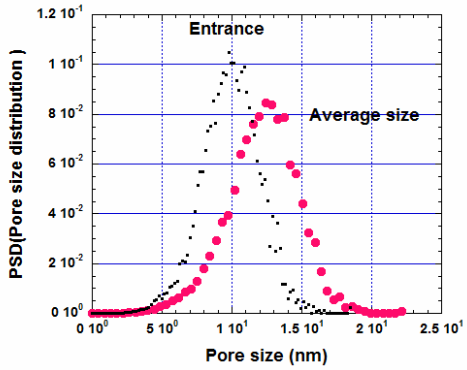

Figure 4: Pore size distributions of the "elementary pores" set.

II/ BULK RELOCATION AND ADSORPTION IN THE PORE

As shown in Fig 5, the confined dynamics of a molecule inside a pore is an intermittence of adsorption steps near the interface and excursions in the confined bulk (Levitz-2013). The time evolution can be described using an indicator function I(t) equals to one in the adsorption state and zero in the confined bulk. This random signal is associated to two probability distribution functions (p.d.f), $\Psi_B(t)$ and $\Psi_A(t)$. $\Psi_A(t)$ characterizes the way an adsorbed molecule is released in the bulk. $\Psi_B(t)$ provides the time distribution spent in the bulk before returning to the surface. The first moment of $\Psi_B(t)$ noted τ_B is the average time spent in the confined bulk during the relocation from one point to another of the adsorption region. Similarly, the first moment of $\Psi_A(t)$, τ_A, is the average time spent in the adsorption region between a first entry and the consecutive exit. The analytical evolution of $\Psi_B(t)$ is dependent of the roughness of the pore surface (Levitz-2006), the dimensional confinement of the pore and the interaction potential between the molecule and the pore wall (Levitz-2013)

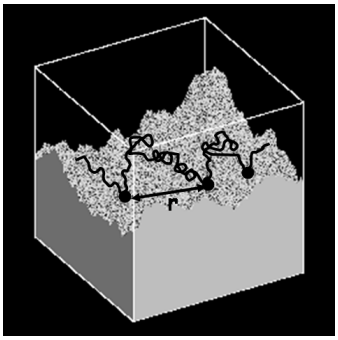

Figure 5: Intermittent Dynamics near a pore wall.

III/ MOLECULAR DIFFUSION: FROM THE PORE TO THE PORE NETWORK

III-1/ Role of the adsorption

We have simulated the Brownian diffusion of a molecule inside the pore network of the Vycor-like porous medium. We have added the possibility of a localized adsorption defined by an exponential distribution of adsorption time. Looking at the evolution of the mean square displacement at long time and more especially its time first derivative, we have computed the evolution of the self diffusion coefficient $D(\tau_A)$. The ration $D_0/ D(\tau_A)$ is defined as the so-called tortuosity $T(\tau_A)$ where D_0 is the unconfined bulk self diffusion coefficient (taken as $D_0=2\ 10^{-9}\ m^2/s$) . As shown in Fig 6, the numerical simulation shows a linear evolution of $T(\tau_A)$ with τ_A. We were able to show that the theoretical evolution of $T(\tau_A)$ can be written as:

$$T(\tau_A) = T(\tau_A = 0)(1 + \frac{\tau_A}{\tau_B}) \qquad \text{Eq(1)}$$

The tortuosity is the product of the tortuosity without adsorption and of a second factor directly related to the local intermittent dynamics with adsorption and relocation.

As shown in Fig 6, a very good agreement is observed between the numerical simulation and the prediction of Eq(1). However, Eq(1) does not clearly separate the dynamics at the pore scale and the long range transport. In fact $T(\tau_A=0)$ mixes the two contributions.

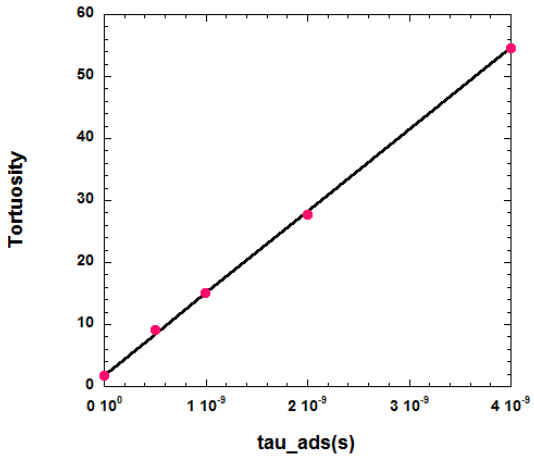

Figure 6: Evolution of the tortuosity associated to an intermittent Brownian dynamics inside the Vycor-like porous medium as the average localized adsorption

time increases. Full points: The numerical simulation. The full line: evolution predicted by Eq(1).

III-2/ Diffusion on the topological graph and in pore network

As shown in the former paragraph, it is necessary to decouple the fluid confinement within "elementary pores", involving adsorption, intermittent dynamics, and the long distance exploration, sensitive to the porous network connection. For this, we have compared the self diffusion a molecule during an intermittent Brownian dynamics with τ_A=0 ns inside the pore space and the Brownian dynamics on the pore network topological graph. The evolutions of the two associated square displacements are shown in Fig 7. Let first consider the diffusion inside the pore network. At very short time, the mean square displacement follows the curve $6D_0t$. At early time; the molecule does not feel the presence of pore walls. After some transient time, the asymptotic comportment is reached with $T(\tau_A=0)=1.82$. The Brownian dynamics on the pore network topological graph shows some interesting features. First, a 1D dynamics along the branches are observed at early time, up to a mean square displacement of 2.0 $10^{-16}m^2/s$. The square root of this value is on the same order of magnitude that the average pore size shown in fig 4. Moreover, the average escaping time τ_{branch} from a statistical branch is estimated to 5 10^{-8} s. At longer time, an asymptotic comportment is reached allowing to estimated the associated graph tortuosity $T_{graph}(\tau_A=0)=1.6$. The difference between $T(\tau_A=0)$ and $T_{graph}(\tau_A=0)$ is a direct estimation of the average sojourn time of a molecule inside a statistical "elementary pore" according to the relation:

$$T(\tau_A = 0) = T_{graph}(\tau_A = 0)\frac{\tau_{sejourn}}{\tau_{branch}} \qquad \text{Eq(2)}$$

Association of of Eq(1) and Eq(2) reads as

$$T(\tau_A) = \left[\frac{T_{graph}(\tau_A = 0)}{\tau_{branch}}\right]\left[\tau_{sejourn}(1+\frac{\tau_A}{\tau_B})\right] \qquad \text{Eq(3)}$$

Eq(3) allows to decouple in a multiplicative way, the fluid confinement within "elementary pores", involving adsorption, intermittent dynamics, and the long distance exploration, sensitive to the porous network connection.
The computation of the average sojourn time is related to first passage statistics (Benichou-2010) and will be discussed elsewhere.

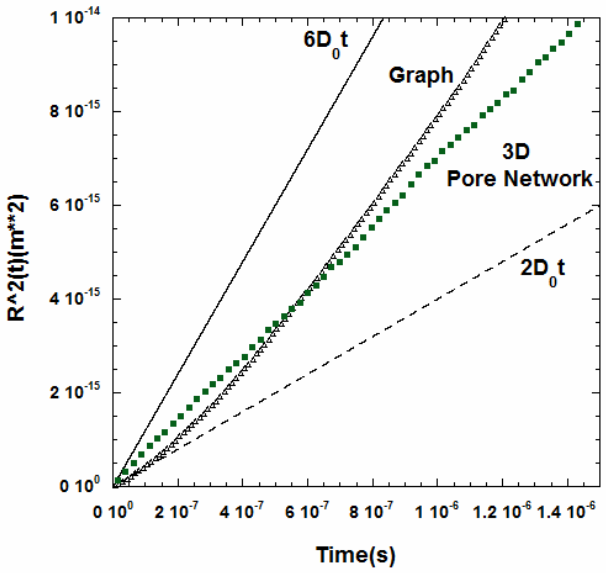

Figure 7: full square: Mean square displacements of a molecule during an intermittent Brownian dynamics inside the pore network (with τ_A=0 ns). Open triangle: Brownian dynamics on the pore network topological graph. The full line: the unrestricted 3D diffusion regime (with D_0=2 10^{-9} m^2/s). The dot line: the unrestricted 1D diffusion regime (with D_0=2 10^{-9} m^2/s).

CONCLUSION

Based on 3D reconstructions of disordered porous media, we have focused on the diffusive transport of fluid in porous material where adsorption and geometrical confinement at different time and length scales are observed. We first discuss the intermittent dynamics of the confined fluid at the scale of pore where the adsorption plays a central role. In order to upscale the analysis of the fluid dynamics, we present some properties of pore network topological graphs. We discuss their interest in describing the connection properties. We show how the topological graphs can be used to decouple in one hand, the fluid confinement within "elementary pores" involving adsorption, intermittent dynamics and in another hand, the long range exploration, sensitive to the porous network connection. Finally, we have proposed a multiplicative expression of the tortuosity taking into account this decoupling.

REFERENCES

Barrett L.K.and Yust C.S.(1970) “Some fundamental ideas in topology and their application to problems in metallography” Metallography, 3, 1

Cohen C. and C. Lin C. (1982) “Topology, geometry, and physical properties of porous rocks” in Macroscopic Properties of Disordered Media” Lecture Note in Physics 152, 74-84.

Bénichou O., Grebenkov D., Levitz P., Loverdo C. and Voituriez R. (2010) “Optimal reaction time for surface-mediated diffusion”. Phys. Rev. lett 105, 150606.

Brisard, S; Chae, RS; Bihannic, I; Michot, L; Guttmann, P; Thieme, J; Schneider, G ; Monteiro, PJM ; Levitz, P (2012). Morphological quantification of hierarchical geomaterials by X-ray nano-CT bridges the gap from nano to micro length scales. *American Mineralogist*, 97, 480-483.

Brisard S. and Levitz P (2013) “Small-angle scattering of dense, polydisperse granular porous media: computation free of size effects” *Phys. Rev. E* 87, 1, 013305.

Jackson M. D, Moon J , Gotti E., Taylor R., Chae S. R., Kunz M., Emwas A. H., Meral C., Guttmann P., Levitz P., Wenk H. R. and Monteiro P. (2013) ”Material and Elastic Properties of Al-Tobermorite in Ancient Roman Seawater Concrete” J. Am. Ceram. Soc., 1, 9.

Han M, Youssef S, Rosenberg E, Fleury M and Levitz P (2009) “Deviation from Archie's law in partially saturated porous media: Wetting film versus disconnectedness of the conducting phase” Phys. Rev E, 79, 031127.

P. Levitz P (1998) “Off lattice reconstruction of porous media: Critical evaluation, Geometrical confinement and molecular transport”.. Advances in Colloid and Interface Science. 76-77, 71-106.

Levitz P, Grebenkov DS, Zinsmeister M, K. Kolvankar and B. Sapoval (2006) “Brownian flights over a fractal nest and first-passage statistics on irregular surfaces” ” Phys. Rev. lett 96, 180601.

Levitz, P , Tariel, V , Stampanoni P., Gallucci, E (2012) “Topology of evolving pore networks” European Physical Journal-AP, 60, 24202

Levitz P., Bonnaud P.A., Cazade P-A, Pellenq R J-M and Coasne B (2013)“Molecular intermittent dynamics of interfacial water: probing adsorption and bulk confinement” Soft Matter, 9, 8654–8663.

Pothuaud L., Porion P., Lespessailles E., Benhamou C.L., and Levitz P. (2000) “A new method for three-dimensional skeleton graph analysis of porous media: application to micro-architecture characterization of trabecular bone” Journal of Microscopy 199, 149.

M. Sahimi, Flow and transport in porous media and fractured rock, VCH , 1995.

Evolution of the Strength of Polymer Fiber-Reinforced SCC during Early Hydration

L. K. Mettler; F. K. Wittel; R. J. Flatt; and H. J. Herrmann

Institute for Building Materials, ETH Zurich, Stefano-Franscini-Platz 3, HIF, 8093 Zurich, Switzerland. E-mail: fwittel@ethz.ch

Abstract

Novel fabrication techniques for non-standard concrete structures rely on the interplay of robotic fabrication with the evolution of the material performance, mainly during early hydration. When the material transforms from a yield stress fluid to a cohesive frictional material, detailed knowledge on the evolution of the strength envelope becomes essential. This is even truer, as the dead weight acting on the previously fabricated zones increases with the size of the fabricated structures. A set of non-standard mechanical tests for compression, tension and shear, particularly suited for measuring failure from early hydration states on, exhibits two distinct scaling regimes. The first one is characteristic for large local plastic deformations, followed by the transition to the second regime with material behavior dominated by crack growth. Finally we condense all test results to a limit surface in principal stress space and discuss its evolution with the advancing state of hydration.

INTRODUCTION

The strength evolution during early hydration is of increasing importance for new technologies in concrete fabrication such as robotic slip-forming of concrete pillars with variable cross-sections by flexible actuated formworks. It is significantly smaller than the structures produced and the material leaves the mold during the ongoing early hydration process, while it is still deformable and yet able to provide the strength necessary to sustain its own weight. The trade-off between deformability and strength during hydration restricts the time for active shaping. It is crucial to precisely predict the rheological properties of the material during the early phase of its transition from a complex yield stress fluid to a solid material. We focus on self-compacting concrete (SCC) with and without polymer fibers in an accelerated mixture. Two types of failure constrain the design window: (1) breakdown of the micro-structure due to motion of the formwork caused by the thixotropic nature of SCC, resulting in sudden local liquefaction and following structural collapse and (2) appearance of surface cracks due to forming, caused by the rapid increase in yield stress with respect to the current tensile strength. For such a demanding process, the strength evolution needs to be continuously monitored by means of simple on-line rheological measurements that are related to the known scaling behavior of the failure envelope for the SCC material during early hydration.

To assess the early regime with mechanical tests at diverse stress states, “non-standard” mechanical tests were performed within the described bounds of liquefaction and fracture localization. This work presents results from 4 different test setups on SCC, followed by the discussion of the respective results and their condensation to a set of failure criteria evolving with the advancing state of hydration.

EXPERIMENTAL FINDINGS

The SCC used throughout this study was heavily retarded by means of a sucrose solution (2.7g/l) and subsequently accelerated (60 g/l BASF X-Seed 100). The concrete mixture comprises CEM I 52.5 R Portland cement (981.73g/l Holcim Normo 5R), sand aggregates of up to 4mm in diameter (740.34 g/l), two mineral admixtures fly ash (164.67 g/l Holcim Hydrolent) and silica fume (92.89 g/l Elkem Microsilica Grade 971 U), as well as a superplasticizer (4 g/l BASF Glenium ACE30) as a water reducing admixture and water (371 g/l). Mixtures with and without PVA fiber reinforcement of 6 mm (13 g/l) and 12 mm (13 g/l) were compared. The slump diameter obtained by a Hagermann cone is typically 20- 22 cm and the density of the mixture amounts to 2350 kg/m^3. Special attention was also given to maintaining a uniform mixing procedure for all tests. 5-10 min after completing the mixing with a rotating pan mixer (Zyklos ZK 50 HE), all samples were cast into the respective molds and put to rest. Note that already the short time span of the mold filling makes a noticeable difference in strength evolution due to the thixotropic structural buildup at rest, calling for a correction procedure.

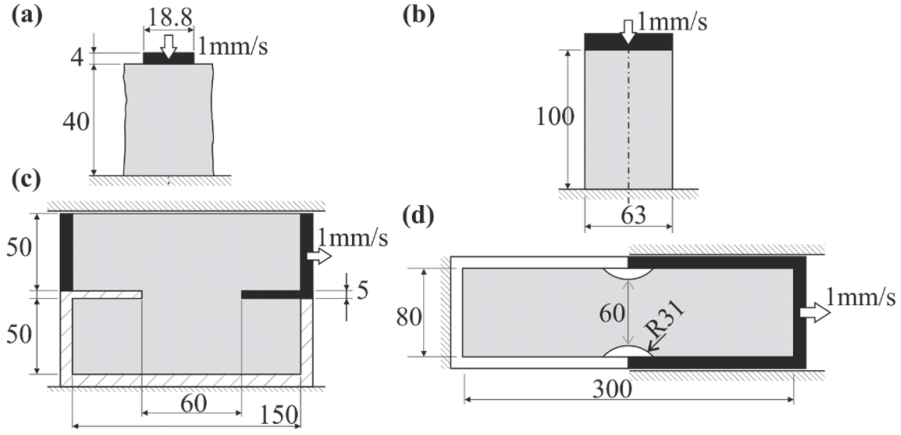

Figure 1: Test setups: (a) penetration of a cylinder into a concrete basin; (b) cylinder compression; (c) shear cell of 60mm depth; and (d) tensile sample of 60mm depth. All dimensions in mm. Moving parts are black, concrete is shaded grey.

Samples were stored and tested at 50%RH/20°C for a period of up to 6 hours after mixing using a triaxial table and a universal testing machine (Zwick 1454). Measurements started as soon as possible with respect to each of the 4 test setups (see Figs. 1a-d), namely: **Test (a) – Penetration** of a rigid cylinder into a basin of concrete similar to ASTM C403/ C403M-08. **Test (b) - Compression** of cylindrical samples, **test (c) - Shear** strength measurements inside molds, in a setup similar to the Jenike shear cell (ASTM D6128-14), as well as **test (d) - Tension** testing inside a mold of two separable parts with a notch. The shear force transmission at the walls of the mold for tests **c** and **d** is assured by several rows of pins along the box walls. Unfortunately, due to the fresh state, an accurate determination of the degree of hydration through calorimetry or other means proved to be unfeasible. A displacement rate of 1mm/s attested to minimize rate effects.

Typical load-displacement curves and identified ultimate load values are shown in Figs. 2 a-d for polymer fiber reinforced concrete (FRC). By normalization with the

respective reference areas of the tests, time dependent strength values are obtained. However to correct for differences in the onset of the evolution e.g. due to different molding times or between different series, each set is corrected to obtain the data collapse shown in Figs. 2A,B. For comparison, the curves for plain SCC without fibers are added. Corrections are based on the observation that penetration data (test a) from within one mixture follows approximately an exponential evolution law $S=a\cdot exp(bt)$ between 0.01-1MPa with similar exponents in between sets. Hence all data form a master curve that can be used for mapping the evolution. Also gravitational loads are added to the measured force.

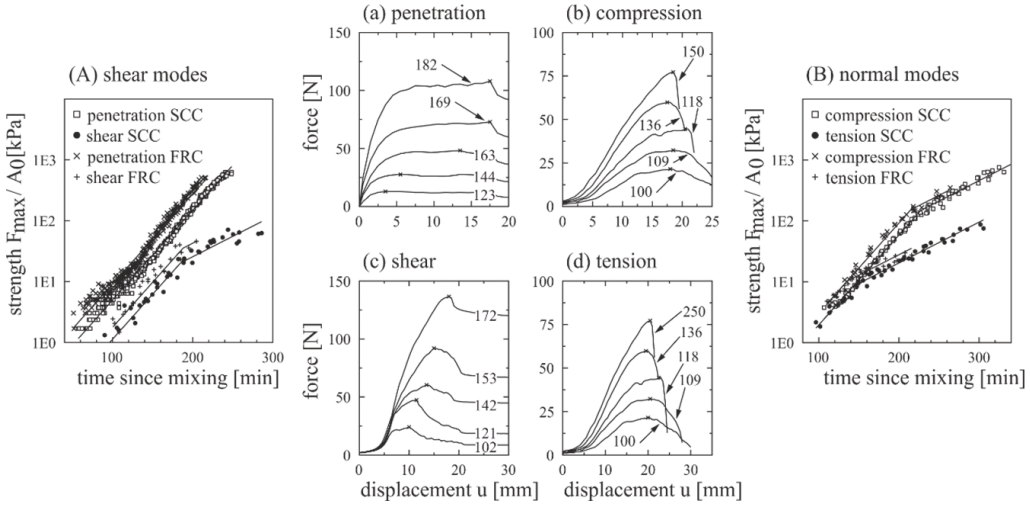

Figure 2: Exemplary force-displacement curves (a-d) and corrected time dependent strength evolution for shear mode (A) and normal mode (B) failure.

Two principal regimes seem to govern the strength evolution: A first one, where material is deformed in a ductile way and shear, compressive and tensile strengths are well-represented by the Mises criterion. An identical exponent of b=0.033min^{-1} and pre-factor a=0.07kPa describes this regime. In the second regime cracks begin to prevail (see Fig. 3b), and failure is increasingly dependent on the hydrostatic component of stress, as seen e.g. by the divergence between compressive and tensile strengths. The exponents b are around 0.014min^{-1}, but the main differences between tensile and compressive strength originates from differences in transition time between the two regimes.

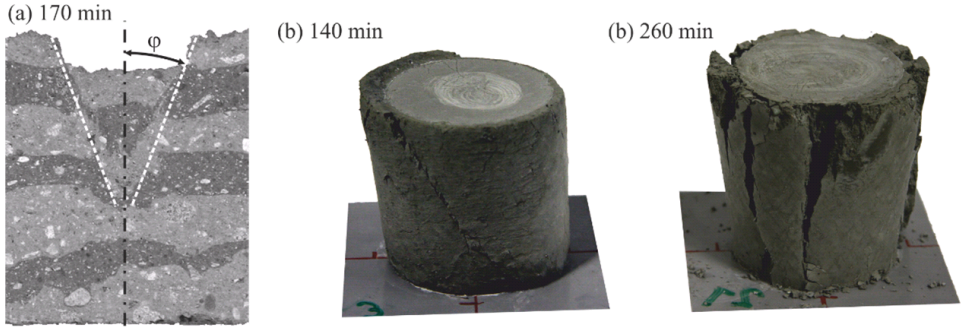

Figure 3: Compression cone test (a), crack patterns test (b) at different times.

CONCLUSIONS

Our study captures the strength evolution of the initially ductile material to a point where failure is brittle and starts to become dependent on hydrostatic stress. We find two scaling regimes of strength that are also evident in the constructed failure envelopes in the principal stress space in Fig. 4. The isochronous limit curves follow thermodynamic principles and material symmetry. At early times a von Mises type behavior fits the experimental data best, while at later times a pressure sensitive behavior emerges due to the different times of regime change of each test setup. The effect of the fibers is shown by comparing FRC to SCC. As expected FRC values are higher throughout the evolution. Note that strength values for shear are corrected by a factor of 1.4 to account for strength increase due to the unsuitability of the shear cell when cohesive properties become increasingly important.

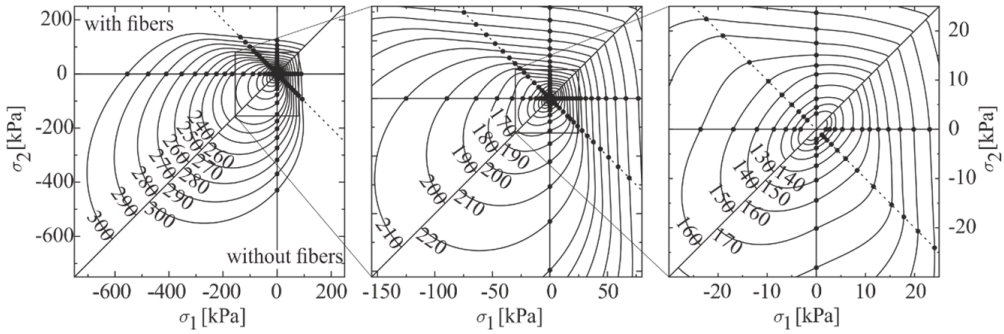

Figure 4: Fitted isochronous failure envelopes with time in minutes from mixing. The upper left envelopes represent FRC, while the lower right ones are fitted to data obtained on SCC without fiber reinforcement.

The time frame of this study was chosen to be up to 6 hours after mixing, keeping the technological design window of the adaptive slip casting process in mind. For such processes it is crucial to precisely predict the rheological and mechanical properties of the material during the early phase of its transition from a non-Newtonian yield stress fluid to a cohesive frictional material.

ACKNOWLEDGEMENT

We acknowledge the support by the ETH Zurich under ETHIIRA grant no. ETH-13 12-1 “Smart Dynamic Casting”.

REFERENCES

[1] Bullard, J. W., Jennings, H. M., Livingston, R. A., Nornat, A., Scherer, G. W., Schweitzer, J. S., Scrivener, K. L., and Thomas, J. J. (2011). “Mechanisms of cement hydration.” *Cem. Concr. Res*. 41, 1208-1223.

[2] Lloret, E., Shahab, A. R., Mettler, L. K., Flatt, R. J., Gramazio, F., Kohler, M., and Langenberg, S. (2014). “Complex concrete structures merging existing casting techniques with digital fabrication.” *Comput. Aided Design* 60, 40–49.

[3] Lootens, D., Jousset, P., Martinie, L., Roussel, N., and Flatt, R. J. (2009). "Yield stress during setting of cement pastes from penetration tests." *Cem. Concr. Res.* 39, 401-408.
[4] van Mier, J. G. M. (1997). *Fracture Processes of Concrete*. CRC Press.

Kinetic simulations of cement creep: mechanisms from shear deformations of glasses

E. Masoero[1], M. Bauchy[2], E. Del Gado[3], H. Manzano[4], R.M. Pellenq[5,6,7], F-J. Ulm[5,6], and S. Yip[8]

[1]School of Civil Engineering and Geosciences, Newcastle University, NE1 7RU, Newcastle upon Tyne, United Kingdom; PH (+44) 191 208 7686; email: enrico.masoero@newcastle.ac.uk
[2]Physics of AmoRphous and Inorganic Solids Laboratory (PARISlab), Department of Civil and Environmental Engineering, University of California, Los Angeles, CA 90095, United States; PH (310) 825-9991; email: bauchy@ucla.edu
[3]Department of Physics, Georgetown University, Washington D.C. 20057, United States; PH (202) 687-5984; email: ed610@georgetown.edu
[4]Molecular Spectroscopy Laboratory, Basque Country University, UPV/EHU, 48940 Leioa, Vizcaya, Spain ; email: hegoi.manzano@ehu.es
[5]Concrete Sustainability Hub, Department of Civil and Environmental Engineering, Massachusetts Institute of Technology, 77 Massachusetts Avenue, Cambridge, MA 02139, United States; PH (617) 253-3544; email: ulm@mit.edu
[6]MIT-CNRS joint laboratory at Massachusetts Institute of Technology, 77 Massachusetts Avenue, Cambridge, MA 02139, United States; PH (617) 253-7117; email: pellenq@mit.edu
[7]Centre Interdisciplinaire des Nanosciences de Marseille, CNRS and Aix-Marseille University, Campus de Luminy, Marseille, 13288 Cedex 09, France; PH (+33) 6 62 92 28 33; email: pellenq@cinam.univ-mrs.fr
[8]Department of Nuclear Science and Engineering, Massachusetts Institute of Technology, 77 Massachusetts Avenue, Cambridge, MA 02139, United States; PH (617) 253-3809; email: syip@mit.edu

ABSTRACT

The logarithmic deviatoric creep of cement paste is a technical and scientific challenge. Transition State Theory (TST) indicates that some nanoscale mechanisms of shear deformation, associated with a specific kind of strain hardening, can explain the type of deviatoric creep observed experimentally in mature cement pastes. To test this possible explanation, we simulate the shear deformations of a colloidal model of cement hydrates at the nanoscale. Results from quasi-static simulations indicate a strain hardening analogous to that postulated by the TST approach. Additional results from oscillatory shear (fatigue) simulations show an increase of deformation with number of loading cycles that is consistent with the observed creep. These findings indicate

that nanoscale simulations can improve our current understanding of the mechanisms underlying creep, with potential to go beyond the logarithmic creep and explore the onset of failure during tertiary creep.

INTRODUCTION

The creep of metals and amorphous materials evolves generally through three regimes (see Figure 1.a). During the initial transient regime, the rate progressively decreases until stabilizing to a constant value, at the onset of steady state creep. Then the accumulation of deformation eventually leads to damage which marks a new increase of rate at the onset of tertiary creep. Many materials though, and especially quasi-brittle materials like cement paste and concrete, evolve from initial transient directly into tertiary regime, without experiencing a steady state between them (see Figure 1.b). In this cases, a comforting scenario of years-long decreasing rate can turn relatively rapidly into a regime of damage accumulation, exponentially increasing deformations, and structural collapse, like in the case of the Palau bridge (Bažant et al., 2012). To cope with such risk, it is particularly important to understand the microstructural evolution that accompanies the macroscopic transient creep, in order to interpret correctly any signal indicating that damage and failure are beginning to develop.

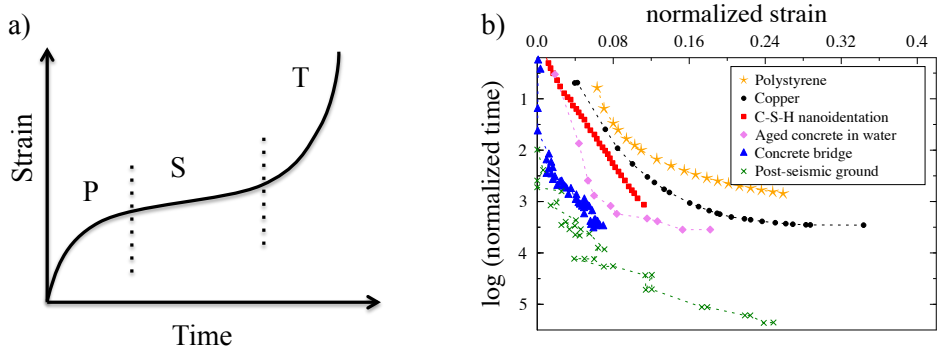

Figure 1. a) The three regimes of creep: P – primary; S – steady state; T – tertiary. (b) Creep in various materials, in semi-log scale (the axes are scaled by constants because the entity of the deformation and the their time-scale can vary significantly from one material to another. For concrete in particular, the rate of creep grows rapidly as soon as the initial logarithmic transient regime is over. The data in (b) are from (Münstedt, 1975; Bažant and Osman, 1976; Savage et al., 2005; Vandamme and Ulm, 2009; Bažant et al., 2012; Sandström, 2012)

Experimental observations of the long-term (years), basic (constant relative humidity), transient, deviatoric creep of cement paste and concrete indicate a behaviour

that can be described by (see, e.g., Vandamme and Ulm, 2009):

$$\varepsilon_c = \frac{\sigma_0}{C} \log\left(\frac{t_c}{\tau} + 1\right) \quad . \tag{1}$$

ε_c is the creep strain, σ_0 is the externally applied load, C is a material's constant known as the creep modulus (units of pressure), t_c is the time elapsed after the application of the load, and τ is another material's constant. Equation 1 is valid only if the load σ_0 is held constant after being applied to a mature paste, with no hydration reaction going on anymore. Equation 1 comes with important technical implications. In particular, the $\log(t)$ trend indicates that the deformations under constant load increase indefinitely, until damage and tertiary creep occur (no asymptotes).

The logarithmic creep can be rationalized in the framework of the exhaustion theory, which dates back to the 1950's (Mott and Nabarro, 1948; Smith, 1948; Cottrell, 1952; Wyatt, 1953; Nabarro 2001). Mott pointed out how the exhaustion theory contained and extended the previous strain hardening theory of logarithmic creep, proposed by Orowan (Mott, 1951; Orowan, 1946). Strain hardening means that the energy to activate a mechanism of deformation increases with the amount of strain accumulated. In addition to strain hardening, the exhaustion theory can account also for stress redistributions triggering avalanches of deformation mechanisms, which lead to Andrade's and steady state creep regimes, and for the regeneration of creep sites too (Cottrell, 1996). However, Cottrell confirmed that also within the exhaustion theory a significant strain hardening is needed for logarithmic creep to develop (Cottrell, 1996).

In this paper, we first show that not all types of strain hardening can lead to the creep behaviour in Equation 1. We show that a logarithmic strain hardening leads to Equation 1 whereas, for example, a simple linear strain hardening would not capture the dependence on σ_0. Then we show that a recent colloidal model of cement hydrates (Masoero et al., 2012; Masoero et al., 2014) predicts indeed a logarithmic strain hardening during quasi-static shear simulations. However we recognize that the sampling of the potential energy surface (PES) during quasi-static simulations is very limited. Therefore, we test further the same model configurations of cement hydrates using oscillatory shear, which mimics a fatigue test and improves the sampling of the PES. In this case the simulation results, combined with a linear relationship between number of cycles and time, lead to creep curves that can be fitted by Equation 1 yielding a creep modulus C that agrees with experimental measurements from nanoindentation (Vandamme and Ulm, 2009).

STRAIN HARDENING

The creep regimes in Figure 1 can be rationalized using Transition State Theory (TST) (Vineyard, 1957) and considering that the activation energy $U_a(\varepsilon)$ of the microscopic mechanisms of deformations change as a function of the accumulated strain. According

to TST:

$$\frac{d\varepsilon}{dt} = \nu \exp\left[-\frac{U_a(\varepsilon)}{k_B T}\right] \quad . \tag{2}$$

where ε stands for total strain (elastic + creep), ν is a characteristic vibrational frequency related to the activated complex associated with the mechanism (e.g. Lasaga, 2014), k_b is the Boltzmann's constant, and T is the temperature in degrees Kelvin. Equation 2 is the starting point to show that an activation energy that increases with strain leads to a decreasing rate, whereas a constant activation energy with strain leads to a steady-state creep regime.

Here we will start from Equation 2 and discuss under what condition a logarithmic transient creep of the type in Equation 1 emerges. Rearranging and integrating Equation 2 between the time of load application and the generic time t yields:

$$t_c = t - t_0 = \nu^{-1} \int_0^{\varepsilon_c} \exp\left[\frac{U_a(\varepsilon) - U_a(\varepsilon_0)}{k_B T}\right] d\varepsilon \quad , \tag{3}$$

where t_0 is the time of application of the external stress σ_0, and ε_0 is the corresponding instantaneous strain. In Equation 3 we made the implicit assumption that the baseline energy level reached immediately after the application of σ_0, viz. $U_a(\varepsilon_0)$, is maintained constant during the evolution of creep.

The strain-dependence of U_a in Equation 3 incorporates the strain hardening an determines the type of creep. For example, it one can easily see that a linear relationship $U_a = k\varepsilon$ would capture the $\log(t)$ trend but would miss the linear dependence on σ_0 in Equation 1. Differently, we show hereafter that a logarithmic relationship between U_a and ε can lead indeed to Equation 1. To this end, consider:

$$U_a(\varepsilon) = B \log(\varepsilon) + c \quad , \tag{4}$$

where B and c are constants (material's properties). One should not worry about the singularity of $U_a(\varepsilon \to 0)$ because the activation of irreversible deformation mechanisms normally requires a minimum finite amount of total strain $\varepsilon_{min} > 0$. Equation 3 thus becomes:

$$t_c = \nu^{-1} \int_0^{\varepsilon_c} \exp\left[\frac{B \log(\varepsilon/\varepsilon_0)}{k_B T}\right] d\varepsilon \quad . \tag{5}$$

For small creep deformations ($\varepsilon_c = \varepsilon - \varepsilon_0$), we can linearize $\log(\varepsilon/\varepsilon_0)$ near ε_0. Also, we can assume that that the material is in linear elastic regime under the applied stress σ_0, viz. $\varepsilon_0 = \sigma_0 \mu$, where μ is the shear modulus. Overall this leads to:

$$\begin{aligned} t_c &= \nu^{-1} \int_0^{\varepsilon_c} \exp\left[\frac{B\mu}{\sigma_0 k_B T}\varepsilon - \frac{B}{k_B T}\right] d\varepsilon = \\ &= \nu^{-1} \exp\left(-\frac{B}{k_B T}\right) \frac{\sigma_0 k_B T}{B\mu} \left[\exp\left(\frac{B\mu}{\sigma_0 k_B T}\varepsilon_c\right) - 1\right] \quad . \end{aligned} \tag{6}$$

Taking the logarithm of both sizes, changing base from natural to 10, and rearranging opportunely, one recovers indeed Equation 1, where now τ and C can be expressed as:

$$\tau = \nu^{-1} \exp\left(-\frac{B}{k_B T}\right) \frac{\sigma_0 k_B T}{B\mu} \quad ,$$
$$C = \frac{B\mu \log(e)}{k_B T} \quad , \tag{7}$$

where e is simply Napier's constant, and the logarithm is in base 10.

QUASI-STATIC COLLOIDAL SIMULATIONS

The previous section showed that a strain hardening with activation energies U_a increasing logarithmically with the strain ε could explain the type of logarithmic creep observed experimentally in cement paste and concrete. In this section we test whether a recent nanoscale model of cement hydrates (Masoero et al., 2012) could predict such a relationship between U_a and ε. The model represents the cement hydrates as dense aggregates of polydisperse nanoparticles (see Figure 2.a), held together by strong cohesive forces that match interactions at the molecular scale (Pellenq et al., 2004; Pellenq et al., 2009; Masoero et al., 2013; Ioannidou et al, 2014; Abdolhosseini Qomi et al., 2014, Del Gado et al., 2014).

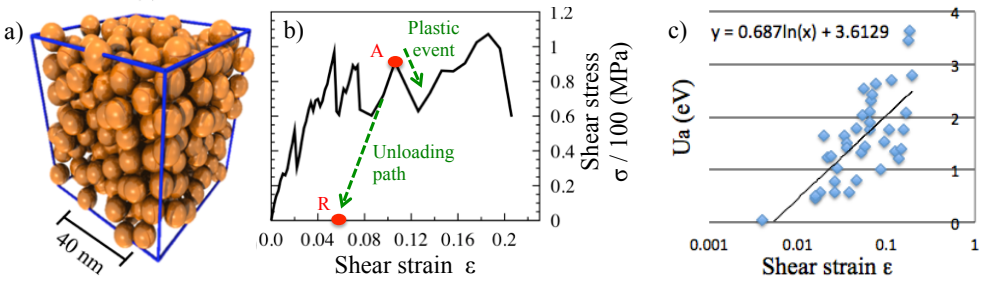

Figure 2. a) Snapshot from colloidal simulations of cement hydrates. b) Shear stress-strain curves simulated with the colloidal model. c) Activation energies of shear deformation mechanisms against shear strain.

The model configurations used in this work are made of particles that are monodisperse in size and are packed to the limit of random close packing, i.e. packing density (solid volume fraction) of 0.64. The configurations are subjected to a sequence of increments of shear strain, and the corresponding shear (virial) stress is computed, leading to the curve in Figure 2.b. Each configuration corresponding to a stress-strain pair on the curve is then taken separately and relaxed to zero shear stress. Some configurations, after relaxation, end up being equivalent in terms of particle position, residual strain, and energy. From time to time though, two successive configurations, after relaxation to zero stress, end up in different state. This indicates that a plastic event,

viz. a deformation mechanisms, has taken place between these two configurations. In Figure 2.b, the point marked with A corresponds to a configuration just before one such plastic event. A more detailed explanation on how plastic events are recognized is given in (Masoero et al., 2014). The mechanical activation energy for a plastic event is obtained from the difference in interaction energy U between the deformed configuration just before the mechanism takes place, and the corresponding configuration relaxed to zero stress. With respect to the mechanism at point A in Figure 2.b, the energy for mechanical activation is obtained as $U(A) - U(R)$, where R indicates the configuration relaxed starting form A. This procedure to obtain the mechanical activation energy was originally proposed in (Masoero et al., 2013).

The energies for mechanical activation can be much larger than those for thermal activation. In particular, quasi-static tests lead to energies for mechanical activation that are extensive, i.e. increasing with the size of the system, while thermal activation energies should be weakly dependent on the size of system. Therefore, in a rough first approximation, we estimate the thermal activation energies U_a as the mechanical ones computed before divided by the number of particles in the system. This takes us to Figure 2.c, where the estimated thermal activation energies are plotted against the shear strain at which the mechanism takes place. The increasing $U_a(\varepsilon)$ trend is evident. The results shown in Figure 2.c come from two independent tests on statistically equivalent configurations, akin to that in Figure 2.a. The large scattering could be due to the small size of the system. However, attempting a logarithmic fitting provides a value of $B = 0.687/\log(e) = 1.58$ eV. Inserting this value in Equation 7 and taking shear modulus $\mu = 6$ GPa (Masoero et al., 2014) and temperature $T = 25$ Celsius leads to $C = \frac{1.58 \cdot 6 \cdot \log(e)}{0.0257} = 160$ GPa. This value is in the correct order of magnitude, but still about twice as large as experimental values from nanoindentaion on C–S–H with packing density of 0.64 (Vandamme and Ulm, 2009). However, it is remarkable that the simulations indicate indeed an increase of activation energies with strain that can be described with a logarithmic relationship, and therefore could underlie the experimentally observed load-linear, time-logarithmic creep of cement paste.

OSCILLATORY SHEAR SIMULATIONS

It was quite predictable that the quasi-static simulations would have returned a large value of C. In fact, quasi-static simulations provide a very limited sampling of the potential energy surface compared to the many direction sampled by random thermal fluctuations. The values could be even larger if one considers the effect of our rough assumption of dividing the energy of mechanical activation by the number of particle, in order to estimate U_a. One might even question whether a better sampling would preserve the logarithmically increasing trend of activation energies wit strain in Figure 2.c, which is the key to connect to the experimentally observed type of creep. In order to address some of these questions, we have tested the same configuration under oscillatory shear, which improves the sampling of the potential energy surface.

The oscillatory shear tests start by applying and maintaining a constant stress σ_0 on the system, and then minimizing the interaction energy. In response to the stress, the system develops an equilibrium strain ε_0. At this point, one could just impose a certain temperature (canonical ensamble) and wait for the system to develop progressively additional shear deformations in time. This is what happens in reality, but the timescale of such deformations would not be accessible by nanoscale simulations. Therefore, instead of using temperature, we subject the system to a sequence N of stress fluctuations $\Delta\sigma \pm 10$ MPa around σ_0. This mimics the action of rare thermal fluctuations, and connects the modelling of creep with that of fatigue. More details about this methodolocy can be found in an accompanying paper (Bauchy et al, 2015).

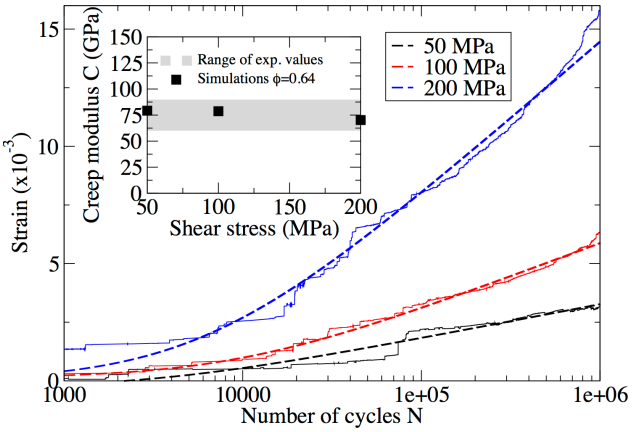

Figure 3. Strain accumulation during oscillatory shear test on the model configurations of cement hydrates in Figure 2.a. The simulation results are the solid lines, while the dashed lines are fitting curves based on the equation $\varepsilon = K\log(\alpha N + 1)$. The inset shows the creep moduli at different stress levels, obtained as K/σ_0.

The oscillatory shear tests display a logarithmic accumulation of shear strain with the number of cycles N, which is plotted in Figure 3. A linear linkage between a cycle and a constant time step can be argued on the basis of TST (see Equation 2), taking the increase of strain energy produced by $\Delta\sigma$ as a measure for U_a. Figure 3 therefore implies that the simulations would predict also a logarithmic increase of strain with time, as observed experimentally. Furthermore, the quite constant values of creep modulus with σ_0 indicate that the simulations also predict a load-linear type of creep. This confirms the results obtained from the quasi-static simulations, indicating that the improved sampling probably does not remove the salient features of activation energy evolution with strain that lead to the qualitative agreement between simulations and experiments. Furthermore, the improved sampling leads actually to better quantitative agreement between simulations and experiments, with creep moduli being now in the range of the experimental results from (Vandamme and Ulm, 2009).

CONCLUSION

We have shown that the long-term basic creep of cement paste and concrete can be explained by a strain hardening where the thermal activation energies for shear deformations increase logarithmically with the accumulated strain. Quasi-static simulations on a colloidal model of cement hydrates show that this type of strain hardening may emerge from the collective response of the system to shear strain. This extends and complements other theories that relate the logarithmic creep of cement paste with molecular-scale processes (private communication with M. Vandamme and Z.P. Bažant). Oscillatory shear simulations on the same colloidal model confirm the qualitative trends emerging from the quasi-static tests and, probably because of the better sampling of the potential energy surface, improve the quantitative agreement with experimental results. This encouraging results shows that nanoscale modelling and simulations have the capability to shed light onto the fundamental mechanisms that control the creep of cementitious materials. It is now timely to investigate in detail the mechanisms emerging from such simulations, in order to identify the chemical and structural features that control the evolution and activation energy of the deformations. Overall this outlines a new approach to predicting the long-term creep of concrete and other disordered materials, toward an improved risk management of structural collapse induced by uncontrolled creep deformations.

REFERENCES

Abdolhosseini Qomi, M., Krakowiak, K.J., Bauchy, M., Stewart, K.L., Shahsavari, S., Jagannathan, D., Brommer, D.B., Barronet, A., Buehler, M.J, Yip, S., Ulm, F.-J., Van Vliet, K.J., and Pellenq, R. J. (2014). "Combinatorial molecular optimization of cement hydrates." *Nature Comm.* 5.

Bažant, Z.P., and Osman, E. (1976). "Double power law for basic creep of concrete." *Mater. Constr.* 9(1), 3-11.

Bažant, Z.P., Yu, Q., and Li, G.H. (2012). "Excessive long-time deflections of prestressed box girders. I: Record-span bridge in Palau and other paradigms." *J. Struct. Eng.* 138(6), 676-686.

Bauchy, M., Masoero, E., Ulm, F.J., and Pellenq, R.J.M. (2015). "Creep of Bulk CSH: Insights from Molecular Dynamics Simulations" *CONCREEP-10*, Vienna, Austria, 21-23 Sept.

Cottrell, A.H. (1952). " The time laws of creep." *J. Mech. Phys. Solids* 1(1), 53-63.

Cottrell, A.H. (1996). "Criticality in Andrade creep." *Phil. Mag. A* 74(4), 1041-1046.

Del Gado, E., Ioannidou, K., Masoero, E., Baronnet, A., Pellenq, R.J.-M., Ulm, F.-J., ans Yip, S. (2014) "A soft matter in constructionStatistical physics approach to formation and mechanics of CSH gels in cement" *Europ. Phys. J. Special Topics* 223(11), 2285-2295.

Ioannidou, K., Pellenq, R.J.-M., and Del Gado, E. (2014). "Controlling local packing and growth in calcium–silicate–hydrate gels" *Soft Matter* 10, 1121-1133.

Lasaga, A.C. (2014)."Section 2: Transition state theory." *Kinetic theory in the earth sciences,* Princeton University Press, 152

Manzano, H., Masoero, E., Lopez-Arbeloa, I., and Jennings, H.M. (2013). "Shear deformations in calcium silicate hydrates." *Soft Matter* 9(30), 7333-7341.

Masoero, E., Del Gado, E., Pellenq, R.M., Ulm, F.J., and Yip, S. (2012). "Nanostructure and nanomechanics of cement: polydisperse colloidal packing." *Phys. Rev. Lett.* 109(15), 155503.

Masoero, E., Manzano, H., Del Gado, E., Pellenq, R.J.M., Ulm, F.J., and Yip, S. (2013). "Kinetic simulation of the logarithmic creep of cement." *Mechanics and Physics of Creep, Shrinkage, and Durability of Concrete: A Tribute to Zdenk P. Bazant*, 166-173.

Masoero, E., Del Gado, E., Pellenq, R.J.M., Yip, S., and Ulm, F.J. (2014). "Nano-scale mechanics of colloidal CSH gels." *Soft Matter* 10(3), 491-499.

Mott, N.F., and Nabarro, F.R.N. (1948). "Report on strength of solids." *Phys. Soc. Lon.*, 221-233.

Mott, N.F. (1951). "The mechanical properties of metals." *Proc. Phys. Soc. Section B* 64(9), 729.

Münstedt, H. (1975). "Viscoelasticity of polystyrene melts in tensile creep experiments." *Rheologica Acta* 14(12), 1077-1088.

Nabarro, F.R.N. (2001). "The time constant of logarithmic creep and relaxation." *Mater. Sci. Eng.: A* 309, 227-228.

Pellenq, R.J.M., and Van Damme, H. (2004). "Why does concrete set?: The nature of cohesion forces in hardened cement-based materials." *MRS Bull.* 29(05), 319-323.

Pellenq, R.J.M., Kushima, A., Shahsavari, R., Van Vliet, K.J., Buehler, M.J., Yip, S., and Ulm, F. J. (2009). "A realistic molecular model of cement hydrates." *Proc. Natl. Acad. Sci.* 106(38), 16102-16107.

Orowan, E. (1946). "The creep of metals." *J. West Scotland Iron Steel Inst.* 54, 45-53.

Sandström, R. (2012). "Basic model for primary and secondary creep in copper." *Acta Mater.* 60(1), 314-322.

Savage, J.C., Svarc, J.L., and Yu, S.B. (2005). "Postseismic relaxation and transient creep." *J. Geophys. Res.: Solid Earth (19782012)* 110(B11).

Smith, C.L. (1948). "A theory of transient creep in metals." *Proc. Phys. Soc.* 61(3), 201.

Vandamme, M., and Ulm, F.J. (2009). "Nanogranular origin of concrete creep." *Proc. Nat. Acad. Sci.* 106(26), 10552-10557.

Vineyard, G.H. (1957). "Frequency factors and isotope effects in solid state rate processes." *J. Phys. Chem. Solids* 3(1), 121-127.

Wyatt, O.H. (1953). "Transient creep in pure metals." *Proc. Roy. Soc. Section B* 66(6), 459.

Hydration kinetics and gel morphology of C-S-H

K. Ioannidou[1,2], E. Masoero[3], P. Levitz[4], R. J.-M. Pellenq[1,2,5] and E. Del Gado[6,7]

[1]Department of Civil and Environmental Engineering, Massachusetts Institute of Technology, Cambridge, USA; emails: hekate@mit.edu; pellenq@mit.edu
[2]MIT-CNRS Joint Laboratory, Massachusetts Institute of Technology, Cambridge, USA
[3]School of Civil Engineering and Geosciences, Newcastle University, Newcastle upon Tyne, Newcastle, UK; email: Enrico.Masoero@newcastle.ac.uk
[4]PHENIX Laboratory, CNRS and University Pierre et Marie Curie, Paris, France; email: pierre.levitz@upmc.fr
[5]CINaM, CNRS and Aix-Marseille University, Marseille, France
[6]Department of Physics and Institute for Soft Matter Synthesis & Metrology, Georgetown University, Washington DC, USA; email:ed610@georgetown.edu
[7]Department of Civil, Environmental and Geomatic Engineering, ETH Zurich, Zurich, Switzerland

ABSTRACT

Calcium-silicate hydrate (C-S-H) is the main binder in cement and concrete. It starts forming from the early stages of cement hydration and it progressively densifies as cement sets. C-S-H nanoscale building blocks form a cohesive gel, whose structure and mechanics are still poorly understood, in spite of its practical importance. Here we review a statistical physics approach recently developed, which allows us to investigate the C-S-H gel formation under the out-of-equilibrium conditions typical of cement hydration. Our approach is based on colloidal particles, precipitating in the pore solution and interacting with effective forces associated to the ionic environment. We present the evolution of the space filling of C-S-H with different particle interactions and compare them with experimental data at different lime concentrations. Moreover, we discuss the structural features of C-S-H in the mesoscale in terms of the scattering intensity. The comparison of our early stage C-S-H structures with small angle neutron scattering (SANS) experiments shows that long range spatial correlations and structural heterogeneties that develop in that early stages of hydration persist also in the hardened paste.

INTRODUCTION

C–S–H is the most abundant hydration product of cement and the main responsible for cement strength. The reaction of anhydrous cement with water forms an

amorphous solid which is soft in the first hours and turns into a stone-like material during cement setting [1, 2]. From the early stages of cement hydration, C-S-H hydrates progressively precipitate in the capillary pore solution and assemble in a heterogeneous complex gel structure that glues together the solid products [2–5]. C-S-H gel structure displays a disordered and heterogeneous mesoscale organization made of structural units of few nm [2, 6, 7]. The organisation of the nanoscale units is influenced by the out-of-equilibrium conditions and the effective interactions. During the early stages of hydration the cohesion between the nanoscale units arises due to ion-correlation forces [8, 9].

Starting from this information, we developed a model for C-S-H precipitation based on colloidal spherical units interacting with forces found in experiments and simulations [8, 10]. Here, we review the mesoscale model for C–S–H precipitation, discuss the hydration kinetics and their comparison to experiments. Moreover, we discuss the mesoscale structure of C–S–H, present the computation of scattering intensity and compare it to SANS data.

MESOSCALE MODEL FOR C–S–H PRECIPITATION

We used a statistical physics approach to investigate the formation of C-S-H structure at the mesoscale, i.e. $5nm - 500nm$, during the early stages of hydration. Our model consists of colloids representing the nanoscale C-S-H units of size $5 - 10nm$ which precipitate in the simulation box that corresponds to a small volume in the pore solution. The C-S-H particles interact with cohesive effective potentials arising from experiments and simulations [8, 10] and form gels networks that progressively densify due to further precipitation. The rate of hydrate precipitation controls the far-from-equilibrium conditions in the development of the C-S-H structure [11]. The structure that the particles form at different stages of the hydration process is not pre-imposed and arises from the interactions and the interplay of the out-of equilibirum conditions with the underlying thermodynamics.

The simulations of C–S–H precipitation in the early stages of cement hydration were implemented by combining Grand-Canonical Monte Carlo (GCMC) and Molecular Dynamics (MD) [11]. A GCMC cycle consists of N_{MC} attempts of particle insertions or deletions followed by $N_{MD} = 100$ MD steps. The rate $R = N_{MC}/N_{MD}$ of hydrate production is controlled by the chemistry of the system. We explored R values between 0.2 and 4, with monodisperse spherical particles that correspond to nano-scale units of $5nm$. The effective interactions consist of a generalized Lennard-Jones attractive well and a long range Yukawa repulsion and are based on forces measured in [10], which represent the early age conditions in the experiments [11]. The potentials we investigated are defined as

$$V(r) = 4\epsilon \left[\left(\frac{\sigma}{r}\right)^{24} - \left(\frac{\sigma}{r}\right)^{12} \right] + A\frac{e^{-\kappa r}}{r} , \quad (1)$$

where r is the inter-particle distance, ϵ is the well depth between two particles with size

diameter σ, κ is the inverse screening length and A is a constant [12]. We investigated two cases, $A = 12$ and $\epsilon = 2.4$ (S1) and $A = 4$ and $\epsilon = 1.5$ (S2), in both cases $\kappa^{-1} = 0.5\sigma$. Both S1 and S2 have a short-range attractive well and long range repulsion. S1 is more repulsive and according to Ref. [10] corresponds to low lime concentration. Increasing the lime concentration reduces the repulsion of the interaction, then the potential S2 is more appropriate to describe such chemical environment. The results shown here refer to box sizes $300nm < L < 630nm$ and number of particles $2900 \lesssim N \lesssim 23000$. Averages have been performed over at least 3 independently generated samples and we used the sample-to-sample standard deviation to evaluate error bars, which are smaller than the line width.

Hydration kinetics

Fig. 1 shows the evolution of the volume fraction ϕ of colloidal C-S-H hydrates during the precipitation as function of the MD time at precipitation rate $R = 1$ for S1 (top) and S2 (bottom) respectively. The volume fraction is defined as $\phi = NV_p/V_{box}$, where N is the number of particles, $V_p = 4\pi(\sigma/2)^3/3$ is the volume of a spherical particle with diameter σ and V_{box} is the volume of the simulation box.

The simulation data (dashed lines) of both S1 and S2 display the characteristic sigmoidal time dependence that it is also observed in hydration experiments [13]. In the experiments of Ref. [13], the degree of hydration of dilute $C3S$ systems under constant lime concentrations is measured. To compare our simulation data to the experiments [13], we rescale the simulation time into the real time by considering that each GCMC cycle lasts finite time τ_s and that τ_s increases linearly with the simulation time. Hence, the real time corresponds to the logarithm of the simulation MD time [11]. Moreover, the volume fraction of precipitated C–S–H particles is proportional to the degree of hydration. We use for both S1 and S2 potentials the same arbitrary multiplication constants to rescale the x- and y-axis and compare with experimental data (dots) of Ref. [13] of low and high lime concentration respectively. Our simulation data agree qualitatively with the experiments. The fact that the same arbitrary factors fit different sets of simulation and experimental data indicates that our precipitation model with varying potentials according to the lime concentrations describes the underlying mechanisms of C-S-H precipitation in varying lime concentrations. Reducing the repulsion in our simulations (from S1 to S2) results to faster densification as it occurs in the experiments by increasing the lime concentration [11].

MESOSCALE STRUCTURE OF C–S–H

The C-S-H gels morphologies formed in the precipitation simulations are shown in Fig. 2. Instead of the spherical particles, the bonds between the particles are depicted by lines coloured according to the number of nearest neighbours. Two particles have a bond if their distance is smaller or equal to a cutoff distance r_C, which is defined by the first minimum of the radial distribution function $g(r)$ [14]. The gel

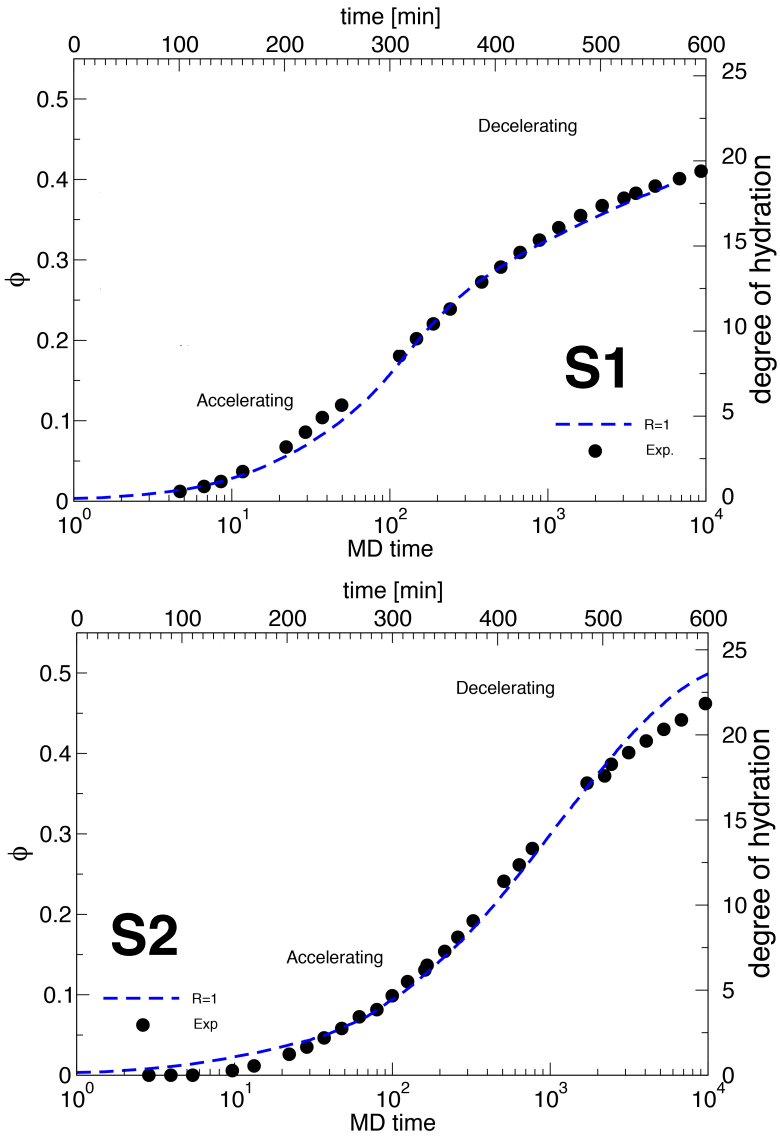

Figure 1. Evolution of volume fraction ϕ for S1 (top) and S2 (bottom) over the simulation MD time at precipitation rate $R = 1$. The black dots are data from experimental measurements of the degree of hydration in Ref. [7] corresponding to low (top) and high (bottom) lime concentration.

structures of C-S-H are influenced by the interaction potentials and the out of equilibrium conditions, controlled through the precipitation rate R. In Fig. 2, the left snapshot

corresponds to S1 and the right to S2.

The effect of the effective interactions is shown as both snapshots were taken at the same precipitation rate $R = 0.2$ and volume fraction $\phi = 0.25$. By reducing the repulsion, from S1 (left snapshot) to S2 (right snapshot), the gel branches become thicker, the local packing of the particles changes (more red lines in S2) and the conjugate void space organises in fewer and larger pores. S1 forms an open network of thin branches of width ranging from 1-3 particles, where S2 forms a network of thick branches consisting of optimally packed particles surrounded by 9-12 neighbours indicating local crystalline order [11]. Due to the different local and mesoscale organisation of the particles in the S2 C-S-H gel, the pore sizes are larger than in S1. Tuning the effective interaction by changing the lime concentration of the pore solution provides a way to control pore size, branch thickness and local packing in the early stages of hydration.

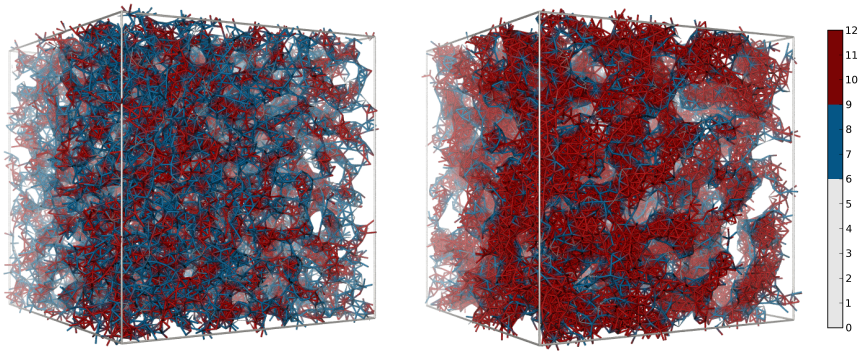

Figure 2. Snapshots of C-S-H gels, with S1 (left) and S2 (right) at volume fraction $\phi = 0.25$ produced by the particle precipitation. Only the bonds between the particles are depicted using line. The color code corresponds to the amount of nearest neighbors.

Scattering Intensity

The small angle neutron scattering (SANS) intensity $I(q)$ is computed from the particle coordinates in the amorphous assemblies obtained in the simulations using the method as described in Refs. [15, 16]. The scattering intensity is computed as

$$I(q) = \phi V^2 \Delta\rho^2 P(q) S(q) \tag{2}$$

where $q = 2\pi/r$ is the modulus of the scattering vector, ϕ is the volume fraction, V is the volume of a particle, $\Delta\rho$ is the scattering contrast, $P(q)$ is the form factor of spherical particles and $S(q)$ is the structure factor. $S(q)$ is the Fourier transform of the radial distribution function $g(r)$ and can be computed directly from the particle

coordinates r_i

$$S(q) = \left\langle \frac{1}{N} \sum_{i,j} e^{-iq(r_i - r_j)} \right\rangle \tag{3}$$

where N is the number of particles [17]. To comply with the periodic boundary conditions used in the simulation the q vectors are chosen as: $q = \{n_x 2\pi/L_x, n_y 2\pi/L_y, n_z 2\pi/L_z\}$, where n_x, n_y, and n_z are integers > 0 and L_x, L_y, and L_z are the sizes of the rectangular simulation box. Assuming that the system is isotropic, we perform an average over all q vectors with same modulus q. The form factor P(q) accounts for the contribution to the scattering intensity of a single particle, which is basically determined by its size and shape. For spherical particles the form factor is:

$$P(q) = \left[3 \frac{\sin(qR) - qR\cos(qR)}{(qR)^3} \right]^2 . \tag{4}$$

The scattering contrast between the C–S–H particles and the water surrounding them is $3.1 \cdot 10^{-4}\,\mathrm{nm}^{-2}\mathrm{sr}^{-1}$ [2].

Fig. 3 shows the data from simulations for low and high volume fraction plotted together with experimental data. The low volume fraction configuration was produced during the early stages by the precipitation simulations with $R = 0.2$ and S2. Here, we also used size polydispersity ranging from minimum $\sigma_m = 3.2$ nm to maximum particle diameter $\sigma_M = 8$ nm. The high volume fraction configuration represents the dense packed branches of the C–S–H gel in the hardened cement paste and it was produced as described in Ref [18].

The scattering intensity detected at a given q is directly related to the spatial correlations in density fluctuations over length scales $\simeq 2\pi/q$. At high q values, $q \geq 2\mathrm{nm}^{-1}$, the scattering intensity probes length scales in the order of the nanoscale units. In this regime, the scattering intensity increases by decreasing q following a Porod law $I(q) \propto q^{-4}$ due to the interface between particles. The size polydispersity of the particles suppresses the strong oscillations that are typically observed in assemblies of monodisperse spherical particles [16]. Our simulation data of both low and high packing density correctly capture this regime.

At intermediate q values, between $q \approx 0.3$ nm^{-1} and $q \approx 1$ nm^{-1}, the experimental data display a $I(q) \sim q^{-2}$ regime. This q dependence is usually attributed to fractal organization produced by diffusion limited cluster aggregation [19–21] or to dense packings of anisotropic particles [16]. Fig. 3 shows that our simulations on very dense and highly polydisperse systems ($\phi = 0.76$) start to display a q^{-2} regime consistent with the experiments.

At low q values, from $q \approx 0.02$ nm^{-1} up to $q \approx 0.3$ nm^{-1}, SANS data show a dependence $I(q) \propto q^{-3}$. Our data of low volume fraction configurations, produced in the early stages of hydration, show such a dependence for a limited q range. This is most likely due to the large mesoscale pores. The upturn of the scattering intensity indicates significant spatial long range correlations and structural heterogeneities that are likely

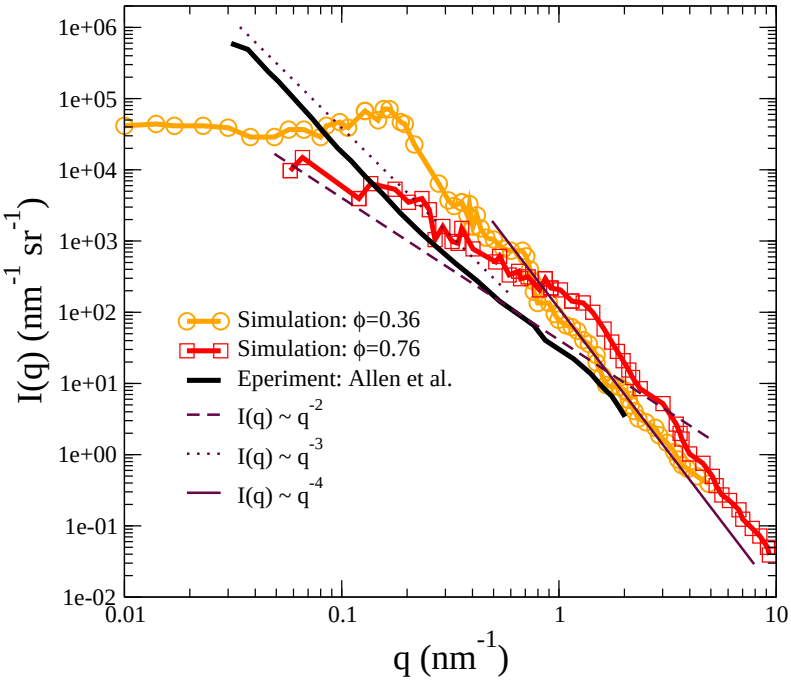

Figure 3. Small angle neutron scattering intensity $I(q)$ vs. wave number q of particle size polydisperse simulations at low packing density $\phi = 0.36$ and at high packing density $\phi = 0.76$ and some particle size polydispersity (see Method section) and of experiment on hardened cement. Typical power law regimes are also indicated. the experimental curve of Ref. [2].

to extend over a few hundreds of nanometers. This regime is still not fully understood. It has been suggested that it might be related to the presence of relatively rough interfaces between different phases or to correlations present in the spatial distribution of the gel pores [22]. Although these simulation data do not capture the full q range of this regime, they give indications that the structural disorder that develops in the early stages of hydration also persists in the hardened cement paste.

CONCLUSIONS

We presented recent advancements on mesoscale modelling of C–S–H. Our model for C–S–H precipitation captures the basic mechanisms that control the hydration kinetics and mesoscale structure of C–S–H gels. It provides a connection between the hydration kinetics and the changes of the C–S–H gel morphology through the different effective interactions. Moreover, the comparison with the SANS data indicates that the structural heterogeneities developed in the early stages of hydration can be the reason of the long range strong correlations in the hardened cement paste. This high-

lights the importance of the morphology of C–S–H gels formed during the early stages in the structural and mechanical properties of hardened cement paste.

AKNOWLEDGMENTS

The authors acknowledge support from Schlumberger (SDR Cambridge, U.S./SRPC Clamart, France), the CSHub at MIT and the Swiss National Science Foundation (SNSF) (Grants No. PP00P2_150738).

References

[1] J. W. Bullard, H. M. Jennings, R. A. Livingston, A. Nonat, G. W. Scherer, J. S. Schweitzer, K. L. Scrivener, and J. J. Thomas. Mechanisms of cement hydration. *Cem. Concr. Res.*, 41:1208–1223, 2011.

[2] A. J. Allen, J. J. Thomas, and H. M. Jennings. Composition and density of nanoscale calcium-silicate-hydrate in cement. *Nat. Mater.*, 6:311–316, 2007.

[3] A. Nonat. The structure and stoichiometry of C-S-H. *Cem. Con. Res.*, 34(9):1521–1528, 2004.

[4] I.G. Richardson. The calcium silicate hydrates. *Cem. Con. Res.*, 38(2):137–158, 2008.

[5] J. J. Thomas and H. M. Jennings. A colloidal interpretation of chemical aging of the C-S-H gel and its effects on the properties of cement paste. *Cem. Con. Res.*, 36(1):30–38, 2006.

[6] W.-S. Chiang, E. Fratini, P. Baglioni, D. Liu, and S.-H. Chen. Microstructure determination of calcium-silicate-hydrate globules by small-angle neutron scattering. *J. Phys. Chem. C*, 116(8):5055–5061, 2012.

[7] S. Garrault, E. Finot, E. Lesniewska, and A. Nonat. Study of C-S-H growth on C3S surface during its early hydration. *Mater. Struct.*, 38(4):435–442, 2005.

[8] M. Pellenq, R. J and H. Van Damme. Why does concrete set?: The nature of cohesion forces in hardened cement-based materials. *MRS Bull.*, 29(5):319–323, 2004.

[9] R.J.-M. Pellenq, N. Lequeux, and H. van Damme. Engineering the bonding scheme in C-S-H: The iono-covalent framework. *Cem. Con. Res.*, 38(2):159–174, 2008.

[10] Cedric Plassard, Eric Lesniewska, Isabelle Pochard, and André Nonat. Nanoscale Experimental Investigation of Particle Interactions at the Origin of the Cohesion of Cement. *Langmuir*, 21(16):7263–7270, 2005.

[11] K. Ioannidou, R. J-M Pellenq, and E. Del Gado. Controlling local packing and growth in calcium–silicate–hydrate gels. *Soft Matter*, 10:1121–1133, 2014.

[12] J. N. Israelachvili. *Intermolecular and Surface Forces, Second Edition: With Applications to Colloidal and Biological Systems (Colloid Science)*. Academic Press, 1992.

[13] S. Garrault, T. Behr, and A. Nonat. Formation of the CSH layer during early hydration of tricalcium silicate grains with different sizes. *J. Phys. Chem. B*, 110:270–275, 2006.

[14] E. Del Gado and K. Ioannidou. Nanoscale numerical study of C-S-H precipitation and gelation. *Conference proceedings ASCE, Mechanics and Physics of Creep, Shrinkage, and Durability of Concrete*, pages 30–39, 2013.

[15] Sebastien Brisard, Rosie S Chae, Isabelle Bihannic, Laurent Michot, Peter Guttmann, Jürgen Thieme, Gerd Schneider, Paulo JM Monteiro, and Pierre Levitz. Morphological quantification of hierarchical geomaterials by X-ray nano-CT bridges the gap from nano to micro length scales. *American Mineralogist*, 97(2-3):480–483, 2012.

[16] Sébastien Brisard and Pierre Levitz. Small-angle scattering of dense, polydisperse granular porous media: Computation free of size effects. *Physical Review E*, 87(1):013305, 2013.

[17] J.P. Hansen and I.R. McDonald. *Theory of Simple Liquids: with Applications to Soft Matter*. Elsevier Science, 2013.

[18] E Masoero, E Del Gado, R J-M Pellenq, F-J Ulm, and S Yip. Nanostructure and nanomechanics of cement: Polydisperse colloidal packing. *Physical Review Letters*, 109(15):155503, 2012.

[19] Richard A Livingston. Fractal nucleation and growth model for the hydration of tricalcium silicate. *Cement and concrete research*, 30(12):1853–1860, 2000.

[20] T Mazumdar, S Mazumder, and D Sen. Temporal evolution of mesoscopic structure of some non-Euclidean systems using a Monte Carlo model. *Physical Review B*, 83(10):104302, 2011.

[21] R González-Teresa, JS Dolado, A Ayuela, and Jean-Christophe Gimel. Nanoscale texture development of CSH gel: A computational model for nucleation and growth. *Applied Physics Letters*, 103(23):234105, 2013.

[22] P. Levitz. Off-lattice reconstruction of porous media: critical evaluation, geometrical confinement and molecular transport. *Advances in Colloid and Interface Science*, 76–77(0):71–106, 1998.

Micromechanics of hydrating cement pastes considering C-S-H gel densification

M. Königsberger[1], Bernhard Pichler[1], and Christian Hellmich[1]

[1]Institute for Mechanics of Materials and Structures, Vienna University of Technology (TU Wien) Karlsplatz 13/202, A-1040 Vienna, Austria
e-mail: markus.koenigsberger@tuwien.ac.at

ABSTRACT

C-S-H gel densifies progressively during hydration. Consideering that the available precipitation space may be the key parameter driving gel densification, we here use NMR relaxometry data in combination with basic stoichiometric relations of hydration chemistry, in order to develop a model for the evolution of C-S-H gel density as well as the phase volume fractions of hydrating cement pastes. Then, we combine the hydration model with a multiscale microstructural representation of cement paste. Considering full anisotropy of solid C-S-H crystals, we are able to predict the experimentally determined stiffness increase during proceeding hydration.

INTRODUCTION

Cement paste is a hierarchically organized heterogeneous material. At early ages, the chemical reaction between cement clinker and water produces several types of crystals, including most importantly Calcium Silicate hydrates (C-S-H). Remaining water fills capillary porosity and the smaller gel porosity, whereby the latter is located in between solid C-S-H crystals. Gel pores together with solid C-S-H crystals form the so-called *C-S-H gel*. Powers and Brownyard [9] stated that from 24h after mixing onwards, the newly formed gel always binds the same amount of water (constant gel porosity), leading to their famous and widely used (see e.g. [8, 10]) hydration model. Recent nuclear magnetic resonance (NMR) measurements [6], however, revealed that gel porosity decreases with proceeding hydration – in other words, the C-S-H gel densifies .

Relating the measured densification behavior to space which is available for new hydrates to precipitate, we first generalize the C-S-H gel densification behavior observed for a *specific* composition, in order to predict gel densities for pastes of *any* composition and of any maturity state. Densification behavior and chemical equations of hydration stoichiometry allow us to predict phase volume evolutions (of clinker, portlandite, solid C-S-H, gel water, capillary water and air voids), which are validated against experimental results, thereafter. Next, we incorporate this hydration

model into a multiscale continuum micromechanics model. We resolve the heterogeneous microstructure of cement paste on three observation scales and thus are able to upscale the stiffness of the nanometer-sized solid C-S-H particles to the macroscopic stiffness of cement paste. Experimental validation corroborates the predictive capabilities of the model.

HYDRATION INDUCED Ddensification OF C-S-H GEL

Experimental data from NMR and X-Ray diffraction

Combining ^{1}H nuclear magnetic resonance (NMR) relaxometry with Rietveld analyses of X-ray diffraction patterns, Muller et. al. [6] carried out early-age characterization of a white cement paste with initial water-to-cement mass ratio $w/c = 0.40$, curing at a constant temperature of 20°C. Based on the measurement principle that the detectable relaxation times of water molecules are the larger, the more bound (i.e. the less mobile) the molecules are, NMR relaxometry delivered the amounts (i) of chemically bound water in portlandite or ettringite crystals, (ii) of chemically bound water in solid C-S-H, (iii) of water filling gel pores, and (iv) of water filling capillary pores. Rietveld analyses, in turn, delivered hydration degrees ξ quantifying the fraction of hydrated clinker volume divided by the initial clinker volume. This way, Muller et. al. [6] showed that the density of the C-S-H gel increases from $\rho_{gel} = 1.777\,\text{g/cm}^3$ at a hydration degree of 40 percent up to $\rho_{gel} = 2.085\,\text{g/cm}^3$ at a hydration degree of 89 percent, see Fig. 1 (a). The best linear fit of these data, providing a vanishing "square-root of sum of squares error", reads as

$$\rho_{gel}(\xi) = 1.522\,\text{g/cm}^3 + \xi \times 0.595\,\text{g/cm}^3 \tag{1}$$

We are interested in the C-S-H gel densification behavior for any cement paste composition. This generalization will be done based on Eq. (1), as presented next.

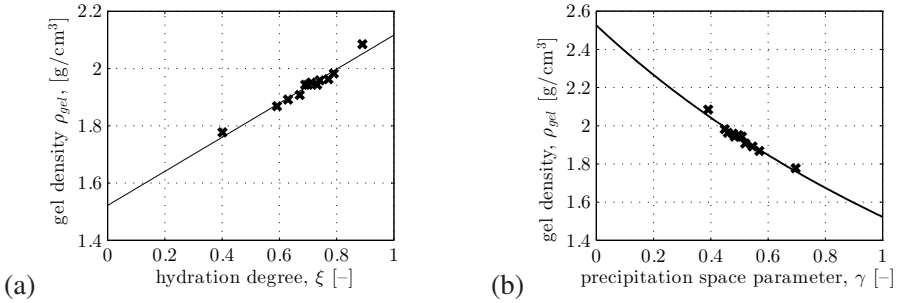

(a) (b)

Figure 1. Evolution of the density of solid C-S-H as a function (a) of hydration degree ξ and (b) of precipitation space parameter γ

Derivation of a model for C-S-H gel densification

Herein, we develop a model quantifying the C-S-H gel densification as a function of the available precipitation space, i.e. envisioning that the density of the C-S-H gel becomes the larger, the smaller the space which is available for precipitation of new hydration products [5]. In this context, we envision a *C-S-H foam* consisting of solid C-S-H crystals as well as gel *and* capillary pores, and we introduce a precipitation space parameter γ which is equal to the overall porosity of this C-S-H foam. Denoting the volume occupied by solid C-S-H crystals as V_{sCSH}, the volume occupied by gel porosity as V_{gpor}, and the volume occupied by capillary porosity as V_{cpor}, the precipitation space parameter reads at any hydration degree ξ as

$$\gamma(\xi) = \frac{V_{gpor}(\xi) + V_{cpor}(\xi)}{V_{sCSH}(\xi) + V_{gpor}(\xi) + V_{cpor}(\xi)} \,. \tag{2}$$

The sought relationship between the C-S-H gel density and the precipitation space parameter will be identified by linking the hydration degrees in Fig. 1 (a) to γ. To this end, we need to model the phase volume evolutions involved in Eq. (2), and this calls for a characteristic hydration stoichiometry, discussed next.

As for the hydration stoichiometry, we first recall the notation in cement chemistry: C=CaO, S=SiO_2, H=H_2O, CH=$Ca(OH)_2$. We consider typical Portland cement clinker to consists of 70 % (per mass) alite (C_3S) and 30 % belite (C_2S).[1] It is assumed that the standard alite and belite reactions take place simultaneously and at constant proportions, i.e. C_3S and C_2S are consumed proportional to their initial mass fractions. Thus, a combined chemical reaction accounting for cement paste hydration of of alite and belite with water, forming C-S-H and portlandite (CH) reads as (corresponding mass and volume balance equations are included, the former follow directly from molar masses, the latter are based on mass densities as given in [6])

$$\begin{array}{ccccccccccc}
\begin{matrix}0.6377\,\mathrm{C_3S}\\ 0.3623\,\mathrm{C_2S}\end{matrix} & + & 2.738\,\mathrm{H} & \Rightarrow & \mathrm{C_{1.7}SH_{1.8}} & + & 0.938\,\mathrm{CH} & + & \text{voids} & 100\,\% \\
208.0 & & 49.32 & & 187.8 & & 69.48 & & 0 & \text{g/mol} \\
\underbrace{65.30}_{V_{m,cem}} & & \underbrace{49.32}_{V_{m,H_2O}} & & \underbrace{68.81}_{V_{m,sCSH}} & & \underbrace{31.58}_{V_{m,CH}} & & \underbrace{14.24}_{V_{m,void}} & \text{cm}^3\text{/mol}
\end{array} \tag{3}$$

where $V_{m,cem}$, V_{m,H_2O}, $V_{m,sCSH}$, $V_{m,CH}$, $V_{m,void}$ denote molar volumes. They can be interpreted as phase volume changes per consumption of one mole of unhydrated cement.

Reaction stoichiometry (3) allows us to derive volume evolution functions involved in the precipitation space parameter definition, see $V_{gpor}(\xi)$, $V_{cpor}(\xi)$, $V_{sCSH}(\xi)$ in Eq. (2). They will be expressed as functions (i) of hydration degree ξ, (ii) of the

[1] Separate aluminate clinker phases are not considered explicitly herein, as they are morphologically and mechanically sufficiently similar to the other hydration phases.

initial water-to-cement mass ratio w/c, and (iii) of the molar volumes given in (3), see [5] for details. To this end, we recall that hydration degree ξ is defined as the volume of hydrated cement, $V_{cem}(\xi=0) - V_{cem}(\xi)$, divided by the initially available volume of cement $V_{cem}(\xi=0)$, $\xi = \frac{V_{cem}(\xi=0)-V_{cem}(\xi)}{V_{cem}(\xi=0)}$ which yields

$$V_{cem}(\xi) = (1-\xi)\, V_{cem}(\xi=0) \tag{4}$$

The phase volume evolutions of solid C-S-H, portlandite, and shrinkage-related voids follow from the linear hydration stoichiometry (3) as

$$V_i(\xi) = \frac{V_{m,i}}{V_{m,cem}}\, \xi\, V_{cem}(\xi=0) \qquad i \in [sCSH,CH,void] \tag{5}$$

Given our focus on hydration under sealed conditions, the sum of gel and capillary porosity, see (2), is simply equal to volume occupied by water

$$V_{gpor}(\xi) + V_{cpor}(\xi) = V_{H_2O}(\xi)\,. \tag{6}$$

The total water volume at any hydration degree ξ follows from the definition of the water-to-cement mass ratio $w/c = \frac{\rho_{H_2O}\, V_{H_2O}(\xi=0)}{\rho_{cem}\, V_{cem}(\xi=0)}$ and from the hydration equation (3) as

$$V_{H_2O}(\xi) = \left(w/c\, \frac{\rho_{cem}}{\rho_{H_2O}} - \frac{V_{m,H_2O}}{V_{m,cem}}\, \xi \right) V_{cem}(\xi=0) \tag{7}$$

Combining the gel-densification approximation function (1), the precipitation space parameter γ, see (2), as well as the phase volume evolutions of water (7) and of solid C-S-H (5), we find the sought relationship between the C-S-H gel density and the precipitation space parameter as

$$\gamma(\xi) = \frac{w/c\, \frac{\rho_{cem}}{\rho_{H_2O}} - \frac{V_{m,H_2O}}{V_{m,cem}}\, \xi}{w/c\, \frac{\rho_{cem}}{\rho_{H_2O}} + \frac{V_{m,sCSH} - V_{m,H_2O}}{V_{m,cem}}\, \xi} \tag{8}$$

The reciprocal relationship of (8), i.e. the hydration degree ξ expressed as a function of the precipitation space parameter γ, allows for replacing hydration degree ξ in the approximation function (1) by the precipitation space parameter γ. Notably, in the resulting expression, w/c has to be specified for 0.40, since the underlying experimental data refer to a cement paste with an initial water-to-cement mass ratio amounting to 0.40. This delivers the sought relationship between the C-S-H gel density and the precipitation space parameter, see Fig. 1 (b). It can be expressed as a function of hydration degree ξ and initial water-to-cement mass ratio w/c reading as

$$\rho_{gel}(w/c\,,\, \xi) = 1.522\,\text{g/cm}^3 + \frac{\xi}{w/c} \times 0.238\,\text{g/cm}^3 \tag{9}$$

Validation of hydration model

Herein, we check the predictive capabilities of C-S-H gel densification model (9) by deriving related phase volume fraction functions and comparing them with experimental data from Muller et. al. [6]. They combined ^{1}H nuclear magnetic resonance relaxometry, Rietveld analyses of X-ray diffraction patterns, and thermal gravimetric analysis (TGA), for identification of phase volume evolutions of cement pastes exhibiting initial water-to-cement mass ratios amounting to 0.32, to 0.40, and to 0.48, respectively.

While model-predicted phase volume evolutions for cement, water, solid C-S-H, portlandite, and voids are already derived [see (4), (7), and (5)], we need corresponding expressions for gel pores and for capillary pores, disussed next. For low w/c-pastes, a transition hydration degree, labeled as ξ_{trans}, exists at which all water in capillary pores is consumed. Continued hydration of cement involves water stemming from gel pores [6]. As for partitioning of water to gel and capillary pores, two regimes have to be distinguished, in regime $\xi < \xi_{trans}$ capillary porosity volume $V_{cpor} > 0$ and regime $\xi > \xi_{trans}$ exhibits $V_{cpor} = 0$. First, we focus on the hydration stage, where capillary water still exists. Since the C-S-H gel consists of solid C-S-H crystals and water-filled gel pores, knowledge on the gel density evolution, such as given in (9), allows for determination of the gel porosity evolution, $V_{gpor}(\xi)$, as described next. As an alternative to (9), the gel density can be expressed as the masses of solid C-S-H and gel pores, divided by their volumes, whereby the masses can be expressed as products of mass densities times volumes, i.e.

$$\rho_{gel}(w/c\,,\,\xi) = \frac{\rho_{sCSH}\,V_{sCSH}(\xi) + \rho_{H_2O}\,V_{gpor}(\xi)}{V_{sCSH}(\xi) + V_{gpor}(\xi)} \tag{10}$$

Solving (10) under consideration of solid C-S-H volume evolution $V_{sCSH}(\xi)$ given in (5) for $V_{gpor}(\xi)$ yields,

$$\begin{aligned} \forall \xi < \xi_{trans} \qquad & V_{gpor}(\xi) = \left(\frac{\rho_{sCSH} - \rho_{gel}(w/c\,,\,\xi)}{\rho_{gel}(w/c\,,\,\xi) - \rho_{H_2O}} \right) \frac{V_{m,sCSH}}{V_{m,cem}}\,\xi\,V_{cem}(\xi{=}0) \\ & V_{cpor}(\xi) = V_{H_2O}(\xi) - V_{gpor}(\xi)\,, \end{aligned} \tag{11}$$

whereby the capillary pore volume, in turn, follows from (6). Notably, $\rho_{gel}(w/c\,,\,\xi)$ appearing in Eqs. (11) stands for the C-S-H gel densification model (9). The transition hydration degree ξ_{trans} follows, under consideration of the densification model (9), from the solution of $V_{cpor} = 0$, see (11), as linear function of w/c. As for the second regime with vanishing capillary porosity, (6) implies

$$\forall \xi \geq \xi_{trans} \qquad V_{gpor}(\xi) = V_{H_2O}(\xi) \quad \text{and} \quad V_{cpor}(\xi) = 0\,. \tag{12}$$

As for the comparison of model predictions to experiments, phase volume *fractions* are calculated. Cement paste-related phase volume fractions of all material

phases, f_i^{cp}, are defined, at any hydration degree ξ, as the phase volume $V_i(\xi)$ over the total cement paste volume $V_{cp}(\xi)$

$$f_i^{cp}(\xi) = \frac{V_i(\xi)}{V_{cp}(\xi)} \qquad i \in [cem\,,\ shyd\,,\ gpor\,,\ cpor\,,\ void] \tag{13}$$

whereby f_{shyd}^{cp} denotes the volume fraction of all solid hydrates (i.e. the sum om solid C-S-H and of CH). Total cement paste volume is, for the sake of simplicity, traditionally set equal to its initial value. Thus, it reads as

$$V_{cp}(\xi) \approx V_{cem}(\xi{=}0) + V_{H_2O}(\xi{=}0) = \left(1 + w/c\,\frac{\rho_{cem}}{\rho_{H_2O}}\right) V_{cem}(\xi{=}0) \tag{14}$$

Comparing model predictions regarding phase volume fractions of unhydrated cement, solid hydrates, gel porosity, capillary porosity, and voids with experimental data from Muller et. al. [6] underlines satisfactory predictive capabilities of the developed model (Fig. 2). It is particularly appealing that the model reliably foresees hydration degrees ξ_{trans} at which water stemming from capillary pores is completely consumed by the chemical reaction, such that the continued hydration of cement involves water stemming from gel pores [5].

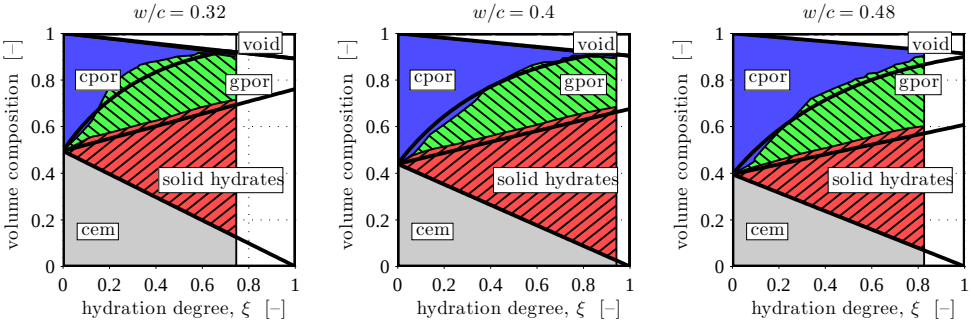

Figure 2. Comparison of model predicted phase volume fraction evolutions (thick black lines) with experimental data from Muller et. al. [6] (colored areas)

MULTISCALE MICROMECHANICS MODEL

Microstructural representation

Inspired by existing successful micromechanics approaches [1, 8, 10, 13], a multiscale poromechanics model involving three observation scales is developed for hydrating cement pastes, see Fig. 3, with microstructural features described as follows. At the scale of several nanometers, solid C-S-H crystals are represented as oblate ellipsoids, as evidenced recently by experimental methods such as small angle neutron/X-ray scattering [2]. Moreover, aspect ratios of the crystals are considered to be a function

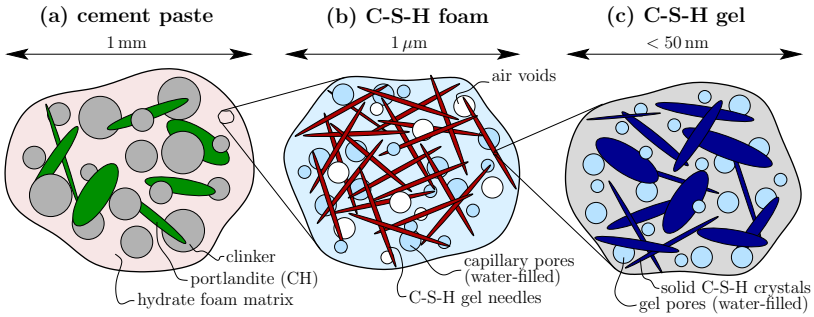

Figure 3. Three-scale representation of cement paste

of the available precipitation space. In more detail, the earlier the crystals precipitate, the closer is their shape to plates; the later they precipitate, the closer is their shape to spheres. Solid C-S-H crystals, intermixed with nanometer-sized and water-filled gel pores, form the *C-S-H gel* at the scale of one micron. At the next scale of observation, a porous polycrystal called *C-S-H foam* is introduced. It consists of a highly disordered mixture of C-S-H gel needles with capillary pores. The C-S-H foam together with embedded spherical clinker grains and plate-like portlandite crystals finally represents *cement paste*.

Homogenization of elastic properties of cement paste

Homogenization is based on (i) the described hierarchical representation of cement paste, (ii) the novel hydration model accounting for C-S-H gel densification, and (iii) a continuum micromechanics approach. Considering a heterogeneous composite material comprising n material phases ($i=1,2,\ldots,n$), the homogenized stiffness tensor $\mathbb{C}^{hom}$ can be found by upscaling based on knowledge of phase volumes fractions f_i, phase stiffness tensors $\mathbb{C}_i$, and phase strain concentration tensors $\mathbb{A}_i$ (which can be estimated based on on matrix inclusion problems [3]) as

$$\mathbb{C}^{hom} = \sum_{i=1}^{n} f_i \mathbb{C}_i : \mathbb{A}_i \,. \tag{15}$$

Given the multiscale organization of the cement paste microstructure, see Fig. 3, homogenization of elastic properties according to Eq. (15) is carried out step by step, as discussed next.

We start to homogenize the *C-S-H gel* stiffness at the smallest scale of observation, where solid C-S-H crystals – orientated randomly in all directions – are intermixed with spherical gel pores. The layered structure of the C-S-H crystal [2, 6] implies an intrinsic anisotropy of the elastic phase behavior. The stiffness tensor of solid C-S-H crystals is identified by means of atomistic modeling [7]. Given the polycrystalline

RVE, the self consistent scheme is relevant for consideration of phase interactions. Applying Eq. (15) for this scale yields the homogenized gel stiffness.

On the *C-S-H foam* scale, we envision needle-shaped gel elements (again orientated in all space directions) to be in mutual interaction with spherical capillary pores and with spherical air voids. By analogy to the C-S-H gel scale, the self consistent scheme is used to represent phase interactions. Applying Eq. (15) for this 3-phase RVE yields the homogenized C-S-H foam stiffness.

Finally, we deal with the RVE of cement paste. A matrix phase of C-S-H foam is envisioned to host plate-like portlandite crystals (orientated randomly in all space directions) and spherical clinker grains. Phase interaction in this matrix-inclusion-type RVE are considered according to the Mori-Tanaka scheme. Elastic phase properties of clinker (isotropic) and portlandite (anisotropic) are taken from experimental results available in the open literature [11, 12]. Applying Eq. (15) provides access to the sought stiffness tensor of hydrating cement paste. This way, we are able predict the elastic stiffness of cement pastes for any given combination of the composition parameter w/c and maturity parameter ξ.

Model Validation

Herein, experimentally determined stiffness evolutions with respect to the hydration degree, measured by mechanical testing at TU Wien – Vienna University of Technology [4], are compared to corresponding model predictions, see Fig. 4. Predicted Young's moduli agree with the experimentally determined almost linear stiffness increase during hydration very well.

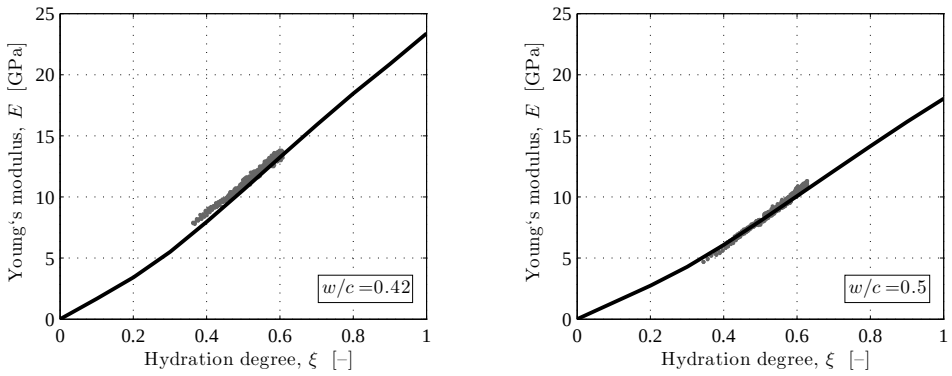

Figure 4. Comparison of experiments from mechanical testing experiments [4] (points) to model predictions for cement pastes exhibiting water cement ratios w/c=0.42 (left) and w/c=0.50 (right)

SUMMARY AND OUTLOOK

Recent nuclear magnetic resonance applied to cement paste allows for differentiating water filling the gel pores, from water filling the much larger capillary pores. Based on these experimental data, we here present an update of the Powers' hydration model, by consideration of C-S-H gel densification. The resulting model allows for reliably predicting evolutions of phase volume fractions of hydrating cement pastes, as a function of the initial water-to-cement mass ratios and the maturity.

Using the new hydration model in the framework of a micromechanics multiscale approach allows us to predict the stiffness of hydrating cement paste. Thereby, we bridge the scale from the anisotropic stiffness of individual solid C-S-H crystals, recently identified by atomistic modeling, to the material scale of cement paste. Successful validation of the micromechanics model by independent experimental results corroborates the presented model.

In order to account for water pressures developing – upon fast loading – both in gel and capillary pores, an extension towards a poroelastic model for hydrating cement paste is developed in a next step. In addition, the detailed resolution of the microstructure of cement paste allows for studying stress concentration characteristics, and they are a prerequisite for future strength predictions.

REFERENCES

[1] O. Bernard, F.J. Ulm, and E. Lemarchand. A multiscale micromechanics-hydration model for the early-age elastic properties of cement-based materials. *Cement and Concrete Research*, 33(9):1293–1309, 2003.

[2] W.-S. Chiang, E. Fratini, P. Baglioni, D. Liu, and S.-H. Chen. Microstructure determination of calcium-silicate-hydrate globules by small-angle neutron scattering. *The Journal of Physical Chemistry C*, 116(8):5055–5061, 2012.

[3] J.D. Eshelby. The determination of the elastic field of an ellipsoidal inclusion, and related problems. *Proceedings of the Royal Society London, Series A*, 241(1226):376–396, 1957.

[4] P. Karte, M. Hlobil, R. Reihsner, W. Dörner, O. Lahayne, J. Eberhardsteiner, and B. Pichler. Unloading-based stiffness characterisation of cement pastes during the second, third and fourth day after production. *Strain*, 51(2):156–169, 2015.

[5] M. Königsberger, B. Pichler, and C. Hellmich. Densification of cement hydration products is mainly driven by available precipitation space - arguments from a new mathematical model integrating data from NMR experiments. *Cement and Concrete Research*, 2015. In preparation.

[6] A.C.A. Muller, K.L. Scrivener, A.M. Gajewicz, and P.J. McDonald. Densification of C–S–H measured by 1H NMR relaxometry. *The Journal of Physical Chemistry C*, 117(1):403–412, 2012.

[7] R.J.-M. Pellenq, A. Kushima, R. Shahsavari, K.J. Van Vliet, M.J. Buehler, S. Yip, and F.-J. Ulm. A realistic molecular model of cement hydrates. *Proceedings of the National Academy of Sciences*, 106(38):16102–16107, 2009.

[8] B. Pichler and C. Hellmich. Upscaling quasi-brittle strength of cement paste and mortar: A multi-scale engineering mechanics model. *Cement and Concrete Research*, 41(5):467–476, 2011.

[9] T.C. Powers and T.L. Brownyard. Studies of the physical properties of hardened Portland cement paste. *American Concrete Institute Journal Proceedings*, 18(2–8):101–992, 1946–1947.

[10] J. Sanahuja, L. Dormieux, and G. Chanvillard. Modelling elasticity of a hydrating cement paste. *Cement and Concrete Research*, 37(10):1427–1439, 2007.

[11] S. Speziale, H.J. Reichmann, F.R. Schilling, H.R. Wenk, and P.J.M. Monteiro. Determination of the elastic constants of portlandite by brillouin spectroscopy. *Cement and Concrete Research*, 38(10):1148 – 1153, 2008.

[12] K. Velez, S. Maximilien, D. Damidot, G. Fantozzi, and F. Sorrentino. Determination by nanoindentation of elastic modulus and hardness of pure constituents of Portland cement clinker. *Cement and Concrete Research*, 31(4):555–561, 2001.

[13] N. Venkovic, L. Sorelli, B. Sudret, T. Yalamas, and R. Gagné. Uncertainty propagation of a multiscale poromechanics-hydration model for poroelastic properties of cement paste at early-age. *Probabilistic Engineering Mechanics*, 32:5–20, 2013.

Modeling the Influence of Micro-Structure and Permeability on Water Freezing in Cementitious Materials

D. Gawin[1]; P. Konca[1]; M. Koniorczyk[1]; and A. Marciniak[1]

[1]Department of Building Physics and Building Materials, Łódź University of Technology, Al. Politechniki 6, 90-924 Łódź, Poland. E-mail: dariusz.gawin@p.lodz.pl; piotr.konca@p.lodz.pl; marcin.koniorczyk@p.lodz.pl; alicja.marciniak@p.lodz.pl

Abstract

Cyclic water freezing/thawing in concrete is a major cause of civil engineering infrastructure deterioration in cold climates. Ice exerts some additional pressure on the skeleton, causing its damage, which is dependent on the material microstructure. The total open porosity, pore size distribution, contribution of ink-bottle pores, capillary suction coefficient and strength properties were experimentally investigated for the virgin cement mortar and after 25 and 50 freezing cycles. The results indicate that the narrowest throats between larger pores are broken by frost damage, causing increase of the material permeability. A mathematical model of coupled heat and water transport in deformable, fully saturated porous materials, accounting for the kinetics of water/ice phase change, is developed and validated experimentally. The kinetics of water freezing - ice thawing is described with non-equilibrium Thermodynamics. The average crystallization pressure is determined for the measured parameters of the frost-deteriorated microstructure of cement mortar. The model equations are solved numerically with FE and FD methods. Considering the evolution of material microstructure allows for modeling the progress of frost induced damage in cementitious materials at low temperatures.

INTRODUCTION

Many civil engineering structures, made of concrete, are exposed to a combined action of climatic conditions and other factors varying in time. They may possibly cause the deterioration and degradation of the service properties of these structures. Frost damage, due to repeated freeze/thaw cycles of water in the pores of concrete, is a main reason jeopardizing durability of the structures in cold climates. For this reason, frost resistance was subject of intensive scientific research, both experimental and theoretical, starting from the famous works of Powers (1945) and Everett (1961), up to recent publications of Scherer (1999, 2005), Setzer (2001), or Coussy (2005, 2008), among others. In this paper, a mathematical model of coupled heat and moisture transfer and frost deterioration is formulated by means of mechanics of porous media for a fully water saturated porous material exposed to freezing/thawing cycles. The crystallization pressure exerted by frozen water and

possible material deterioration are considered. The kinetics of phase change is modelled with a non-equilibrium approach.

MODELING KINETICS OF FREEZING - THAWING PROCESS

The water freezing in a porous material is modelled as non-equilibrium process (but close to thermodynamic equilibrium), the rate of which may be described by the linear evolution law, obtained by Koniorczyk et al. (sumitted) from the second law of Thermodynamics in the following form,

$$\dot{\eta}_C = A_{L\to C} / RT\tau_{fr}, \tag{1}$$

where τ_{fr} is the characteristic time of freezing, R the universal gas constant, T the absolute temperature, and the process affinity, $A_{L\to C}$, is given by (Setzer 2001),

$$A_{L\to C} = \mu_L(T, p^L) - \mu_C(T, p^C).$$

μ_κ means the chemical potential of κ–phase of water and p^κ the pressure of κ–phase (κ= L, C), where L and C concern liquid and crystallized water (ice), respectively.

After some transformations, the process affinity may be expressed as follows (Koniorczyk et al. submitted),

$$A_{L\to C} = (s_L - s_C)(T_m - T) + v_L(p^L - p^{atm}),$$

where s_κ and v_κ ($\kappa = L, C$) mean molar entropy and molar volume of κ–phase, T_m is the melting temperature of water at the atmospheric pressure, p^{atm}. During freezing the actual and equilibrium pressure difference on the ice - liquid water interface, $(p^L - p^C)_{fr}$ and $(p^L - p^C)_{eq}$, are equal to (Setzer 2001),

$$\begin{aligned}(p^L - p^C)_{fr} &= 2\gamma_{CL} / r_{pore} = \Delta p_{fr}(\eta_L),\\ (p^L - p^C)_{eq} &= -(s_L - s_C)(T_m - T) = \Delta p_{eq}^{L/C}(T),\end{aligned} \tag{2}$$

where γ_{CL} is the surface tension of the ice - liquid water interface, r_{pore} is the actual pore entrance radius during intrusion of ice into a water saturated pore, corresponding to the actual water saturation degree, η_L, and p^C is assumed to be equal to p^{atm}.

Finally, the freezing rate, $\dot{\eta}_C$, is given by (Koniorczyk et al. submitted),

$$\dot{\eta}_C = \frac{v_L}{RT}\frac{\Delta p_{eq}^{L/C}(T) - \Delta p^{fr}(\eta_L)}{\tau_{fr}}. \tag{3}$$

The ice thawing in a porous material is described by the similar relationship as eq. (1), but taking into account different value of characteristic time, τ_m, and different pressure difference at the water – ice interface during melting due to the different value of interface curvature, $\Delta p^m(\eta_L) = \gamma_{CL} / r_{pore}$, see (Setzer 2001),

$$\dot{\eta}_C = \frac{v_L}{RT}\frac{\Delta p_{eq}^{L/C}(T) - \Delta p^{m}(\eta_L)}{\tau_{m}}. \tag{4}$$

Freezing of water proceeds when $\Delta p_{eq}^{L/C}(T) > \Delta p^{fr}(\eta_L)$, and it stops when water reaches thermodynamic equilibrium with ice in the pores. Similarly, melting of ice occurs when $\Delta p_{eq}^{L/C}(T) < \Delta p^{m}(\eta_L)$. Since $\Delta p^{m}(\eta_L) > \Delta p^{fr}(\eta_L)$, hence at a given temperature the liquid water content during freezing is higher than the value during

melting of ice, see (Setzer 2001). This is also confirmed by the results of calorimetric test presented in the next section and shown in Figure 3.

During freezing of water in a saturated porous material, pressure, p^B, is exerted on the pore walls by liquid water and ice crystals. It is usually assumed that the isotropic pressure in the crystal is controlled by the interface between liquid and ice crystal in equilibrium. Considering the difference in the chemical potential of small and large crystals of cylindrical shape, Everett (1961) derived the following equation:

$$p^C = p^L + p^B = p^L + 2\gamma_{CL}\left(\frac{1}{r_{eq}} - \frac{1}{r_B}\right),$$

where r_{eq} is the equilibrium pore radius, associated with the overcooling temperature T, see eq. (2), r_B is the pore side radius.

Assuming that the advancing ice front is hemispherical, the volume averaged pressure exerted by ice on the solid walls reads as follows (Coussy 2005):

$$\left\langle \eta_C p^B \right\rangle = \frac{\gamma_{CL}}{n}\int_{\infty}^{r_{eq}}\left(\frac{2}{r_{eq}} - \frac{2}{r}\right)\frac{dV(r)}{dr}dr, \tag{5}$$

where n means the material porosity, $V(r)$ is the cumulative pore size distribution curve, and r_{eq} at temperature T is calculated using Gibbs-Thomson's equation,

$$r_{eq} = \frac{\gamma_{CL}}{(s_L - s_C)(T_m - T)}.$$

MATHEMATICAL MODEL

Water saturated porous materials exposed to freezing are modeled as multi-phase porous media, composed of the solid skeleton, the voids of which are filled with liquid water and ice, where $\eta_L + \eta_C = 1$. The chosen state variables of the model are: liquid water pressure, p^L, temperature, T, and displacement vector, $\mathbf{u}$. The internal variables are ice saturation degree, η_C, and mechanical damage parameter, d.
The mass balances of liquid water, ice and solid skeleton have the following form,

$$\frac{D^S\left(n\eta_L\rho^L\right)}{Dt} + div\left(n\eta_L\rho^L\mathbf{v}^{LS}\right) + n\eta_L\rho^L div\mathbf{v}^S = -\dot{m}_{L\to C}, \tag{6}$$

$$\frac{D^C\left(n\eta_C\rho^C\right)}{Dt} = \dot{m}_{L\to C}, \tag{7}$$

$$\frac{D^S\left(1-n\right)\rho^S}{Dt} + \left(1-n\right)\rho^S div\mathbf{v}^S = 0, \tag{8}$$

where D^κ/Dt ($\kappa = S, L, C$) means the material derivative with respect to κ-phase, $\mathbf{v}^\kappa$ and $\mathbf{v}^{LS}$ the velocity of κ-phase and velocity of liquid water with respect to solid skeleton, ρ^κ the real density of κ-phase ($\kappa = S, L, C$), $\dot{m}_{L\to C}$ the volumetric mass source of ice due to water phase change.

After summing up equations (6) and (7), introducing constitutive relationships for the densities of liquid water, ice and solid skeleton, and deriving the material derivative of porosity, one obtains the mass balance equation for water.

The energy conservation equation for the multi-phase medium, after neglecting convective heat transfer, and considering the kinetics of water/ice phase change and the energy sink/source related to that transformation, reads,

$$\left(\rho C_P\right)_{ef} \frac{D^S T}{Dt} = \nabla \cdot \left(\lambda_{ef}\, grad\, T\right) + \dot{m}_{L\to C} \Delta H_{fr}\,, \tag{9}$$

where $(\rho C_p)_{ef}$ and λ_{ef} are the effective values of thermal capacity and thermal conductivity of the multiphase material and ΔH_{fr} is the volumetric latent heat of water freezing.

The linear momentum conservation equation for the multiphase medium, after neglecting the inertial terms, has the following form (Koniorczyk et al. submitted),

$$div\,\mathbf{t}^{\text{total}} + \mathbf{g}\left[(1-n)\rho^S + n\eta_L \rho^L + n\eta_C \rho^C\right] = 0\,. \tag{10}$$

The total stress, $\mathbf{t}^{\text{total}}$, of a saturated material consists of the effective stress, $\mathbf{t}$', transfer-red by the solid skeleton and a part, which accounts for the solid pressure P^S,

$$\mathbf{t}^{\text{total}} = \mathbf{t}' - bP^S\mathbf{I}\,,$$

where $b = 1 - K_T/K_S$ is Biot's coefficient, with K_T the bulk modulus of the porous material and K_S the bulk modulus of solid skeleton. The pressure exerted by the phases occupying pores on the solid skeleton might be given in the simplified form as, $p^S = \eta_L p^L + \eta_C p^C$. The two forms of the solid pressure are related by, $p^S = bP^S$.

Material damage, d, due to external load and/or internal one (e.g. crystallization pressure) is described here by means of delayed damage model proposed by Allix and Deu (1997). The rate form of the model has the following form,

$$\dot{d} = \frac{1}{\tau_c}\left[1 - \exp\left(-a\left\langle g(\kappa) - d\right\rangle\right)\right], \tag{11}$$

where τ_c is the characteristic time, representing the inverse of the maximum damage rate, a is a second parameter of the model, and $g(\kappa)$ has the following form,

$$g(\kappa) = \begin{cases} 0 & if\ \kappa \le \varepsilon_0, \\ 1 - \dfrac{\varepsilon_0}{\kappa}\exp\left(-\dfrac{\kappa - \varepsilon_0}{\varepsilon_f}\right) & if\ \kappa \ge \varepsilon_0, \end{cases}$$

where $\kappa(t) = \max_{\tau \le t} \tilde{\varepsilon}(\tau)$ is the maximum strain reached in the loading history up to the given time t (Mazars and Pijaudier-Cabot 1989), ε_0 the strain in the elastic limit, ε_f the parameter controlling the post-peak slope of stress-strain curve. The delayed damage model must be supplemented with the initial condition, usually $d(t=0) = 0$.

Hence, finally the mathematical model consists of three balance equations: for water mass, eqs. (6) + (7), linear momentum, eq. (10), and energy of the whole medium, eq. (9), and two evolution equations: for water freezing, eqs. (3) or (4), and mechanical damage, eq. (11). The model equations, after introducing the constitutive relationships, and space discretization with Finite Element Method, e.g. (Lewis and Schrefler 1998), may be written in the matrix form as follows (Koniorczyk et al. submitted),

$$\begin{bmatrix} C_{LL} & C_{LT} & C_{L\mathbf{u}} \\ C_{TL} & C_{TT} & 0 \\ 0 & 0 & 0 \end{bmatrix} \begin{Bmatrix} \dot{\overline{\mathbf{p}}}_L \\ \dot{\overline{\mathbf{T}}} \\ \dot{\overline{\mathbf{u}}} \end{Bmatrix} + \begin{bmatrix} K_{LL} & 0 & 0 \\ 0 & K_{TT} & 0 \\ K_{\mathbf{u}L} & K_{\mathbf{u}T} & K_{\mathbf{uu}} \end{bmatrix} \begin{Bmatrix} \overline{\mathbf{p}}_L \\ \overline{\mathbf{T}} \\ \overline{\mathbf{u}} \end{Bmatrix} = \begin{Bmatrix} f_L \\ f_T \\ f_{\mathbf{u}} \end{Bmatrix}, \tag{12}$$

where the terms of the above matrices are given in detail in (Koniorczyk et al. submitted).

After applying the fully implicit Finite Difference Method to approximate the time derivatives in eq. (12), the set of governing equations may be written in the compact form as,

$$\mathbf{C}_{ij}(\mathbf{x}_{n+1}) \frac{\mathbf{x}_{n+1} - \mathbf{x}_n}{\Delta t} + \mathbf{K}_{ij}(\mathbf{x}_{n+1})\, \mathbf{x}_{n+1} - \mathbf{f}_i(\mathbf{x}_{n+1}) = \mathbf{0}, \tag{13}$$

where $i, j = L, T, \mathbf{u}$; $\mathbf{x} = [\overline{\mathbf{p}}_L, \overline{\mathbf{T}}, \overline{\mathbf{u}}]$, subscript n means the number of time step, Δt the time step length. The nonlinear equation set (13) is solved by means of a monolithic Newton-Raphson type iterative procedure. On the basis of the above described numerical model, the research computer code HMTRA-FREEZE was developed.

EXPERIMENTAL RESULTS

The laboratory tests were performed for the cement mortar made of CEM 1 32.5R, with the water / cement / sand mass ratios equal to 1:2:6. The total open porosity, pore size distribution and contribution of ink-bottle type pores were investigated by means of the MIP technique for the virgin cement mortar and after 25 and 50 freezing cycles (after 100 cycles the specimens were completely damaged), see Table 1 and Fig. 2. Moreover, the changes of capillary suction coefficient and strength properties, due to cyclic freezing of water were measured, see Table 1.

The test results indicate that the cement mortar micro-structure is deteriorated due to frost damage. The narrowest throats between larger pores are broken by freezing water due to crystallization pressure. This is manifested by the increase of the pores volume, usually with diameter of 100 nm – 10 μm (Figure 1a) and decrease of the ink-bottle pores contribution (Figure 1b). The mortar porosity and capillary suction coefficient increase and the strength properties significantly decrease, with the progress of ice-induced damage.

Using the MIP results from Figure 1a, the average crystallization pressure at different temperatures was calculated by means of eq. (5), for the cement mortar sample after 0, 25 and 50 freeze – thaw cycles, i.e. with the damage parameter $d = 1 - E/E_0$, equal to 0, 0.55 and 0.72 (E_0 and E are initial and final Young moduli values), see Figure 2.

Table 1. Main material properties of the investigated mortar.

Parameter	*Unit*	*Number of freeze - thaw cycles*		
		0	*25*	*50*
Total pore area	m^2/g	5.94	8.75	8.44
Bulk density	g/ml	2.03	2.04	1.88
Apparent density	g/ml	2.51	2.57	2.49

Porosity	%	19.04	20.70	24.51
Compressive strength	MPa	57.98	30.76	21.77
Bending strength	MPa	9.98	1.04	0.39
Young modulus of elasticity	GPa	24.46	11.00	6.85
Capillary suction coefficient	$kg/(h^{0.5}m^2)$	1.983	2.723	8.254

The cylindrical sample of water saturated cement mortar (with diameter of 4 mm and height of 1 mm) was also tested in the Differential Scanning Calorimeter during cooling to the temperature of -18°C and heating back to 0°C. The change of ice content at different temperatures was determined during the processes, see broken lines in Figure 3. As one can observe, at a given temperature, the ice content is higher during melting than during freezing process, what is in agreement with the experimental results of Coussy and Monteiro (2008) and theory presented in the second section.

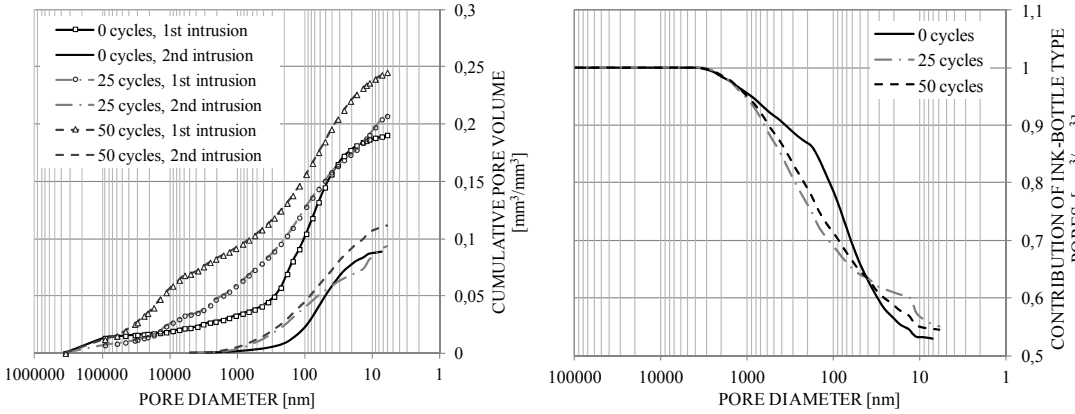

Figure 1. Cumulative pore volume (a) and contribution of ink-bottle pores (b) after 0, 25 and 50 freeze-thaw cycles.

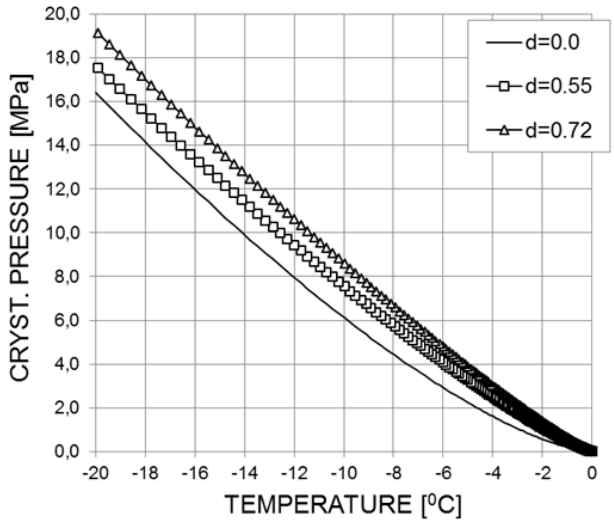

Figure 2. Average crystallization pressure at different temperature calculated for the cement mortar after 0, 25 and 50 freeze-thaw cycles.

NUMERICAL EXAMPLE

To validate the mathematical model and the numerical code HMTRA-FREEZE, the DSC test, described in the previous section, was numerically simulated. The problem was modelled as an axisymmetric one. The cylindrical sample with diameter equal to 4mm and 1mm high was considered. The calculations were performed for one half of the specimen cross-section, modelled by means of 75, 8-noded finite elements. The mesh density was increased in the vicinity of the boundary. On the external surface convective (Robin) BCs were assumed for heat transport with surface transfer coefficient h_c= 8W/(m^{2}K). The ambient temperature was decreasing from the initial value, T_{up}= 10^{o}C, to the temperature T_{low}=-20^{o}C with the rate of 15K/h (i.e. during 2 hours), maintained constant at the value of -20^{o}C for 2 hours, then increased to the value T_{up}= 10^{o}C with the rate of 15K/h (i.e. during next 2 hours), and finally maintained constant at the value of 10^{o}C during last hour. A constant liquid pressure, equal to the atmospheric one, was assumed on external surfaces of the sample. This slightly differs from the real test conditions but enables an undisturbed water flow across the boundary.

The main material parameters were assumed as follows: total porosity n= 15%, thermal conductivity λ_{ef}= 1.1W/(m·K) and intrinsic permeability $k = 10^{-20}$ m^2. An important parameter of the model is the water relative permeability, k_{rl}, which depends only on the saturation with liquid phase. Here, the relationship of van Genuchten, adjusted for different types of concrete by Baroghel-Bouny et al. (1999), was assumed,

$$k^{rl} = \sqrt{\eta_L}\left[1-\left(1-\eta_L^{1/m}\right)^m\right]^2 \quad . \tag{14}$$

In order to analyze the effect of permeability of the evolution of water freezing, the simulations were performed for three different values of the parameter m, equal to 0.3, 0.5 and 0.8 (marked in Figure 3 as simulation 1, 2 and 3). The results concerning the evolution of ice content in the sample central point during the whole freezing – thawing cycle are presented in Figure 3 and compared to the DSC experimental data. As can be observed, the relative permeability relation to the water saturation has a visible influence of the evolution of water phase change in the fully saturated cement mortar. The best agreement with the experimental results was obtained for m= 0.5, but for all the cases a significant hysteresis during the freezing – thawing cycle was observed.

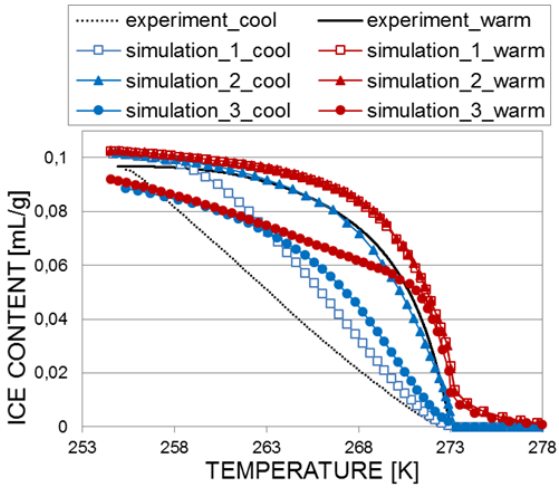

Figure 3. Comparison of the DSC data and simulation results for the ice content in the center of cement paste specimen, for different values of *m* in eq. (14).

CONCLUSIONS

A mathematical model of coupled hydro-thermo-mechanical phenomena in fully saturated porous materials exposed to water freezing/melting processes was developed. The crystallization pressure, exerted by phase changes, and induced material frost damage are considered. The kinetics of phase transformation is modelled by means of a non-equilibrium approach. A kinetic description of phase transformations allows avoiding numerical problems due to the strong sources of heat/mass accompanying the processes. The frost deterioration is modelled by means of an isotropic nonlocal delay-damage theory. The model equations are solved numerically by means of finite element and finite differences methods. A numerical example was solved to validate the model by comparison to experimental results. The performed laboratory tests of a cement mortar exposed to cyclic freezing – thawing show that the microstructure and physical properties of cementitious materials deteriorate significantly during the process.

ACKNOWLEDGEMENTS

The research was partly funded by within the grant of National Science Center – Poland, No. UMO-2011/03/B/ST8/05963 entitled "*Degradation of material properties due to development of expanding phases in building composites with a microstructure*" realized at the Lodz University of Technology in years 2012-2015.

REFERENCES

Allix, O., and Deu, J.F. (1997). “Delay-damage modelling for fracture prediction of laminated composites under dynamic loading”, *Eng Trans*, 45, 29–46.

Baroghel-Bouny, V., Mainguy, M., Lassabatere. T., and Coussy, O. (1999). “Characterization and identification of equilibrium and transfer moisture properties for

ordinary and high-performance cementitious materials". *Cement and Concrete Research*, 29, 1225-1238.
Coussy, O. (2005). "Poromechanics of freezing materials", *Journal of the Mechanics and Physics of Solids*, 53, 1689–1718.
Coussy, O., and Monteiro, P.J.M. (2008). "Poroelastic model for concrete exposed to freezing temperatures", *Cement and Concrete Research*, 38, 40–48.
Everett, D.H. (1961). "The Thermodynamics of Frost Damage to Porous Solids" *Transactions of the Faraday Society*, 57, 1541-1551.
Koniorczyk, M., Gawin, D., and Schrefler, B.A. (submitted). "Modelling evolution of frost damage in fully saturated porous materials exposed to variable hygro-thermal conditions", *Comput. Methods Appl. Mech. Engrg.*
Lewis, R.W., and Schrefler, B.A. (1998). *The Finite Element Method in the Static and Dynamic Deformation and Consolidation of Porous Media, 2nd edition*. John Wiley & Sons, Chichester.
Mazars, J., and Pijaudier-Cabot G. (1989). "Continuum damage theory – application to concrete", *ASCE J Eng Mech*, 115, 345-65.
Powers, T.C. (1945). "A working Hypothesis for Further Studies of Frost Resistance of Concrete", *Journal of American Concrete Institute*, 41 (4), 245- 272.
Scherer, G.W. (1999). "Crystallization in pores", *Cement and Concrete Research*, 22, 1347-1358.
Scherer, G.W., and Valenza, J.J. (2005). "Mechanisms of frost damage", in: J. Skalny, F. Young (Eds.), *Materials Science of Concrete, vol. VII*, ACS, 209–246.
Setzer, M.J. (2001). "Micro-Ice-Lens Formation in Porous Solid", *Journal of Colloid and Interface Science*, 243, 193–201.

Modeling Strains of Concrete Induced by Delayed Ettringite Formation in Variable Hygro-Thermal Conditions

M. Januszkiewicz[1]; F. Pesavento[2]; W. Grymin[1]; and D. Gawin[1]

[1]Department of Building Physics and Building Materials, Łódź University of Technology, Al. Politechniki 6, 90-924 Łódź, Poland. E-mail: marta.j.90@gmail.com; witold.grymin@p.lodz.pl; dariusz.gawin@p.lodz.pl
[2]Department of Civil, Environmental and Architectural Engineering, University of Padova, Marzolo 9, 35131 Padova, Italy. E-mail: francesco.pesavento@dicea.unipd.it

Abstract

Delayed Ettringite Formation is a type of chemical degradation of moist concrete exposed at early ages to heating up to temperature of about 70-80°C. The material deterioration is caused by expanding phases produced by the ettringite reaction. A phenomenological, rate-type model of the DEF strains, considering effect of the temperature and duration of heat-treatment of concrete at early ages, and the evolution of ambient temperature and relative humidity, on the development of strains is introduced into the mathematical model of heat and moisture transport in deformable porous media. The model equations are solved numerically by means of finite element, finite difference and Newton-Raphson methods. The computer code was developed and used for the model validation by comparing its' results with the published experimental data.

INTRODUCTION

Delayed Ettrigite Formation (DEF) is the reaction resulting in formation of ettringite within a cementitious material that begins several months (or even years) after its' setting and without any contribution of any external sulphate (Taylor et al. 2001). Most commonly it arises in concrete elements, cured in an autoclave at elevated temperature at early age, or in massive concrete elements, temperature of which exceeded the threshold of 65-70°C due to the self-heating during cement hydration process. In the both cases, the structure must be later subjected to high humidity or be in direct contact with water. The term 'delayed' refers to the fact that ettringite is not formed during cement hydration, but after complete material hardening. This phenomenon, often occurring together with swelling strains due to alkali-silica reaction (Martin 2010), was discovered in early 1980's, when many cases of cracking precast concrete railroad ties were reported, mostly in Germany and the United States.

The chemistry of the Delayed Ettringite Formation is now quite well recognized and the reaction in the abbreviated notation may be described as follows (Taylor et al. 2001),

$$3\ CaO{\cdot}Al_2O_3 + 3\ CaSO_4{\cdot}2\ H_2O + 26\ H_2O = 3\ CaO{\cdot}Al_2O_3{\cdot}3\ CaSO_4{\cdot}32\ H_2O$$

According to the present knowledge, see e.g. (Collepardi 2003, Pavoine 2006, Brunetaud et al. 2007, Escadeillas et al. 2007, Flatt and Scherer 2008, Martin 2010), to initiate the DEF reaction and support the further expansion and damage of concrete, a combination of the following parameters is needed,

- presence of sufficient amount of moisture – all the DEF related problems have arisen in areas exposed to water (bridges, dams, rail ties, etc.);
- internal temperature of element exceeding ca. 70°C during casting – result of the high heat of cement hydration in massive concrete components or to the steam curing of concrete (precast products);
- presence of sulfates and aluminates (coming from cement, aggregate or mixing water);
- a high alkalis content in the concrete – they play a significant role for the stability of ettringite at high temperature;
- the presence of pre-existing micro-cracks in the material.

Based on the aforementioned findings, a rate-type phenomenological model, describing the development of DEF-induced strains in concrete exposed to variable hygro-thermal conditions, considering effect of the temperature and duration of heat-treatment of the material at early ages, is proposed in this paper. The DEF strains are introduced into the mathematical model, based on porous media mechanics, previously proposed for heat and moisture transport in building materials by Gawin and Schrefler (1996). The proposed, extended model is experimentally validated by comparison with the results of experimental tests performed by Martin (2010) and by Flatt and Scherer (2008).

MODEL OF STRAINS CAUSED BY DELAYED ETTRINGITE FORMATION

The evolution of DEF strains in time has a similar shape as for the ASR strains, hence the proposed here description has an alike form as the mathematical model of ASR developed by Pesavento et al. (2012). The rate of DEF strains, $\dot{\boldsymbol{\varepsilon}}_{DEF}$, is assumed to be proportional to the reaction rate,

$$\dot{\boldsymbol{\varepsilon}}_{DEF}(t) = \beta_{DEF}(S_w, T_{ht}, t_{ht})\,\dot{\Gamma}_{DEF}(t)\cdot \mathbf{I}, \tag{1}$$

$$\beta_{DEF}(S_w, T_{ht}, t_{ht}) = \beta_{DEF,0}(T_{ht}, t_{ht})\cdot(A_{DEF}\cdot S_w + B_{DEF})$$

$$\beta_{DEF,0} = (A_{ht}\cdot T_{ht} - B_{ht})\cdot(C_{ht}\cdot t_{ht} + D_{ht})$$

where $\beta_{DEF,0}$ is the material parameter, equal to the final value of the ASR strain, which is dependent on the actual water saturation degree, S_w, as well as the temperature, T_{ht}, and duration, t_{ht}, of heating treatment of concrete at early ages. The latter two parameters may also correspond to the conditions arising inside the massive concrete structures during their maturing period. A_{ht}, B_{ht}, C_{ht} and D_{ht} are the model parameters.

The reaction rate, $\dot{\Gamma}_{DEF}$, is given by,

$$\dot{\Gamma}_{DEF} = \frac{1-\Gamma_{DEF}}{t_r}, \tag{2}$$

with the characteristic time of reaction, t_r, described by the following relationship, similar to that for the ASR (Pesavento et al. 2012),

$$t_r = \tau_r(T) \cdot \frac{1+\exp\left[-\tau_L/\tau_r\right]}{\Gamma_{DEF}+\exp\left[-\tau_L/\tau_r\right]}, \tag{3}$$

where $\tau_L(S_w,T)$ is the latency time, related to the time until the beginning of the swelling process,

$$\tau_L\left(S_w,T\right) = \tau_{L0} \cdot \exp\left[U_L \cdot \left(\frac{1}{T}-\frac{1}{T_0}\right)\right] \cdot \left(A_L \cdot S_w + B_L\right), \tag{4}$$

and $\tau_r(T)$ is the reaction time, corresponding to the rate of development of the swelling,

$$\tau_r\left(S_w,T\right) = \tau_{r0} \cdot \exp\left[U_r \cdot \left(\frac{1}{T}-\frac{1}{T_0}\right)\right] \cdot \left(A_r \cdot S_w + B_r\right). \tag{5}$$

τ_{r0} and τ_{L0} are the reaction and latency time constants at the temperature T_0, U_L and U_r, while A_L, B_L, A_r and B_r are the model parameters.

MATHEMATICAL MODEL

The equations (1) – (5) clearly indicate that the evolution and final value of the ASR strain depend on the hygro-thermal state of concrete during the whole process. For this reason the strains description should be introduced into a mathematical model of heat and moisture transport in porous materials. Here, for this purpose the mathematical model of coupled heat, mass and linear momentum transport in capillary-porous deformable media, originally proposed by Gawin and Schrefler (1996), is used.

In the model a porous material is composed of the solid skeleton, the voids of which are partly filled with liquid water and partly with moist air. The model consists of four macroscopic balance equations, the water mass balance, the dry air mass balance, the heat balance and the linear momentum balance. They are valid in Representative Elementary Volume (REV), where one can measure experimentally all necessary coefficients and material properties, e.g. the apparent density of materials, the permeability, the diffusivity coefficients and thermal properties. Here we present only the final form of the balance equations. The detailed derivation of the equations is presented in (Gawin and Schrefler 1996).

The mass balance equation of the dry air includes both diffusive and advective components of the mass fluxes:

$$\begin{aligned} & n\frac{\partial}{\partial t}\left(S_g\rho^a\right) - \beta_s S_g \rho^a \left(1-n\right)\frac{\partial T}{\partial t} + div\left(\mathbf{J}_g^a\right) + S_g\rho^a div\left(\frac{\partial \mathbf{u}}{\partial t}\right) \\ & + div\left(nS_g\rho^a \mathbf{v}^{gs}\right) = 0, \end{aligned} \tag{6}$$

where t means time, β_s the cubic thermal expansion coefficient of the solid skeleton, $\mathbf{v}^{gs}$ the gas velocity relative to the solid skeleton, $\mathbf{J}_g^a$ the diffusive flux of the dry air, ρ the density of the phase matched by the subscripts: w for the liquid phase, a the

dry air, *v* the vapour, *s* the solid skeleton, *p* the precipitated salt, and *g* the gas phase. S_g is the pores' saturation with the gaseous phase given by, $S_g = 1 - S_w$.

The mass balance of liquid water and vapour, which are summed together to eliminate the source term related to the evaporation-condensation or adsorption-desorption phase transitions, form the mass balance equation of water species,

$$n\frac{\partial}{\partial t}\left(S_w\rho^w\right)-\beta_s\left(1-n\right)\left(S_g\rho^v+S_w\rho^w\right)\frac{\partial T}{\partial t}+n\frac{\partial}{\partial t}\left(S_g\rho^v\right)+div\left(\mathbf{J}_g^v\right)$$
$$+\left(S_w\rho^w+S_g\rho^v\right)div\left(\frac{\partial\mathbf{u}}{\partial t}\right)+div\left(nS_w\rho^w\mathbf{v}^{ws}\right)+div\left(nS_g\rho^v\mathbf{v}^{gs}\right)=0, \tag{7}$$

where $\mathbf{v}^{ws}$ is the fluid phase velocity relative to the solid skeleton, $\mathbf{J}_g^v$ the diffusive flux of water vapour.

The enthalpy conservation equation of the multi-phase medium, which was obtained by summing the corresponding balance equations for the constituents includes the heat effects due to phase change of the water and the DEF reaction, as well as the convective and latent heat transfer,

$$\left(\rho C_p\right)_{ef}\frac{\partial T}{\partial t}+\left(\rho^w C_p^w\mathbf{v}^{ws}+\rho^g C_p^g\,\mathbf{v}^{gs}\right)\cdot grad\ T-div\left(\lambda_{ef}\,grad\ T\right)$$
$$=-\dot{m}_{vap}\,\Delta H_{vap}, \tag{8}$$

where $(\rho C_p)_{ef}$ is the effective thermal capacity, C_p the isobaric specific heat, λ_{ef} the effective thermal conductivity, ΔH_{vap} the specific enthalpy of phase change of the water, $\dot{m}_{vap}$ the mass source or sink of vapour related to the evaporation / condensation process.

Introducing Bishop's stress tensor $\mathbf{t}^e$, called also the effective stress tensor, the linear momentum conservation equation of the whole medium is given by (Lewis and Schrefler 1998),

$$div\left(\mathbf{t}^e-\alpha\mathbf{I}\left(p^g-S_w p^c\right)\right)+\mathbf{g}\left((1-n)\rho^s+nS_w\rho^w+nS_g\rho^g\right)=0, \tag{9}$$

where **I** is the unit second order tensor, α Biot's coefficient, and **g** the acceleration of gravity.

The constitutive relations of the mathematical model, given by equations (6) – (9), as well as the numerical methods used for solution of its' governing equations are described in detail in (Gawin and Schrefler 1996). Into the model equations the description of the DEF strains has been introduced. On the basis of the above described numerical model, the research computer code HMTRA-DEF was developed and used in simulations, the results of which are presented here.

MODEL VALIDATION

First the model and computer code validation was performed by comparison the simulation results with the DEF strains measured by Martin (2010) for the specimens (cylinders with diameter of 11cm and height of 22cm), made of concrete with w/c= 0.45, exposed to different heat-treatment during maturing at early ages:

- heated to temperature T= 80°C for 3 days, and then stored in different humidity conditions, i.e. kept in water (Sat.= 100%) or above the water surface (Sat.= 99.50%), see Figure 1;
- for three different durations, 1 (1D 80°C), 3 (3D 80°C) or 5 days (5D 80°C) of heating treatment at 80°C, see Figure 2;
- heated for 3 days to three different temperatures,70°C (3D 70°C), 80°C (3D 80°C) and 85°C (3D 85°C), Figure 3.

Considering the axisymmetry of the problem, the 2-D mesh of 200 (10 × 20) 8-noded finite elements (5.5mm × 5.5mm) was assumed in the simulations. The time step was variable, dependent on the stage of process. The convective boundary conditions for heat and moisture exchange were assumed, with the heat exchange coefficient α_c= 5.0 W/m^{2}K, ambient temperature T_a= 311.15 K, moisture exchange coefficient β_c= 0.05 m/s, and ambient relative humidity according to the case considered.

The main material parameters assumed in the simulations were as follows: τ_{r0}= 13 days, τ_{L0}= 85 days, U_L=1361.9 J/mol, U_r=1940.8 J/mol, A_L=1.001, B_L=-1.001, A_r= 1.001, B_r=-1.001, A_{DEF}=20.0, B_{DEF}=-19.0, A_{ht}= 0.000554 K^{-1}, B_{ht}= 0.184, C_{ht}= 0.00093 h^{-1} and D_{ht}= 0.0046.

As may be observed in Figures 1-3, the simulation results are in a good agreement with the experimental data, measured by Martin (2010).

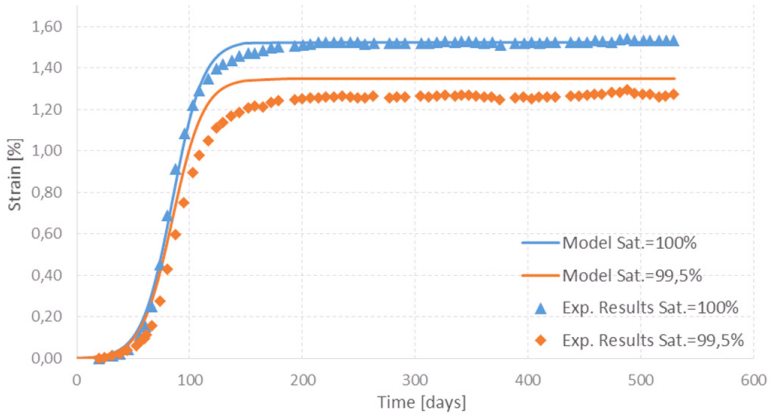

Figure 1. The comparison the simulation results for 2 different moisture states of specimens with the experimental data (Martin 2010).

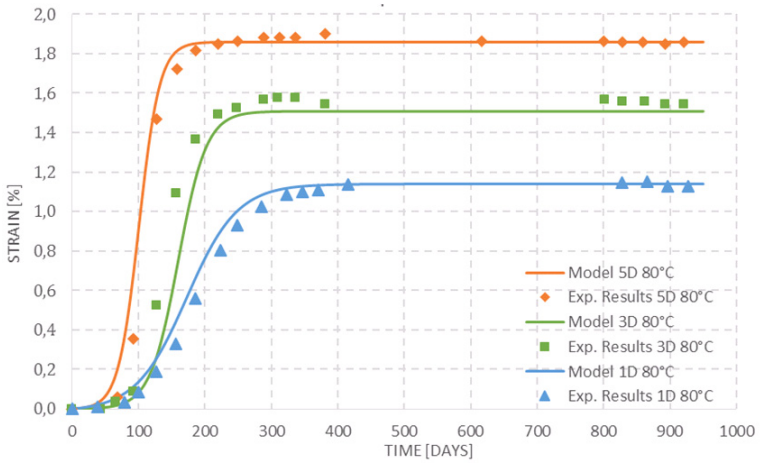

Figure 2. The comparison of simulation results for 3 different durations of heat treatment with the experimental data (Martin 2010).

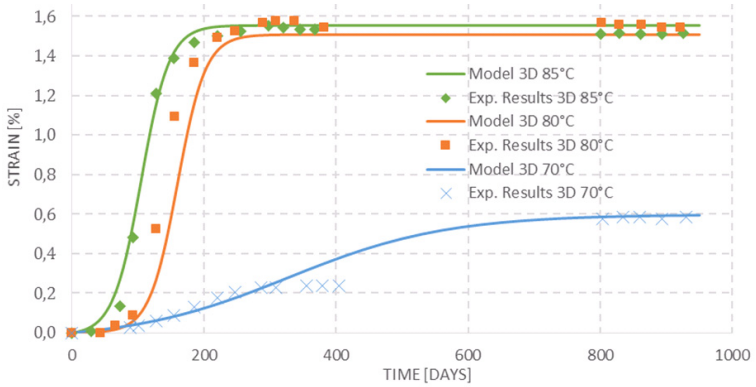

Figure 3. The comparison of simulation results for 3 different temperatures of heat treatment with the experimental data (Martin 2010).

The second example, used for the model validation, is based on the experiments performed by Flatt and Scherer (2008). They analysed the role of storage temperature on the evolution of DEF-expansion. The measurements were done on the bars (16mm ×16mm×160mm), made of mortar with water/cement/sand ratio, w:c:s= 1:2:6. The bars were casted, then put in plastic bags into the water and precured for 4h at the temperature of 20°C. Next the bars were cured at 90°C for 12h and finally left to cool down naturally at 20°C for about 5h. After demolding the samples were stored in water at temperature of 20°C or 38°C for 400 days. The example was modelled with the mesh of 32 (1×32) 8-noded finite elements of equal size. The time step of calculations was variable, dependent on the stage of the process. The same material parameters were used in the simulations, except of τ_{r0}= 17 days, τ_{L0}= 120 days, $\beta_{DEF,0}$= 0.127 at 20°C and $\beta_{DEF,0}$= 0.1065 at 38°C.

In Figure 4 the results of simulations are compared with the experimental data of Flatt and Scherer (2008), showing a good agreement, sufficient for practical applications.

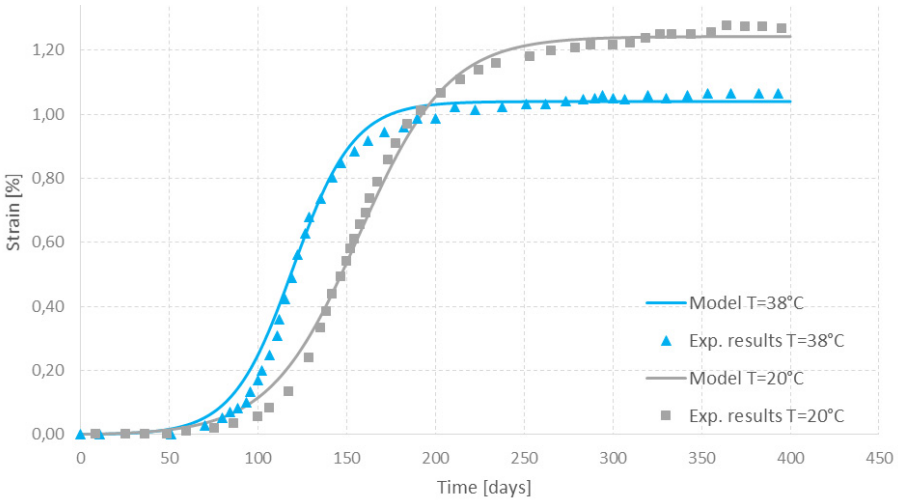

Figure 4. The comparison of simulation results for 2 different temperature of DEF process with the experimental data (Flatt and Scherer 2008).

NUMERICAL EXAMPLE

To demonstrate the model application for a real concrete structure exposed to variable in time hygro-thermal conditions, a retaining wall made of precast concrete is analyzed. The material parameters, assumed in the simulations, are the same as those used for Martin's experiment, corresponding to the case of 1-day accelerated maturing at 80°C. Simulation concerns 2.5 years of service life, with a sinusoidal variation of temperature and relative humidity, corresponding to average weather conditions of Lodz (Poland) with the temperature between -2^{o}C and 18^{o}C, and the relative humidity between 70 %RH and 90 %RH, shifted in phase by 4 months. The relative humidity of the ground was assumed to be constant and equal to 95 %RH. The geometry of the retaining wall and the mesh used in the simulations (930, 8-noded FE with 2997 nodes) are presented in Figure 5. The simulations results, concerning distribution of the temperature, relative humidity and DEF-induced strains after 6 and 9 months are presented in Figures 6 and 7. Additionally, the ASR-strains after 12, 15 and 30 months are presented in Figure 8.

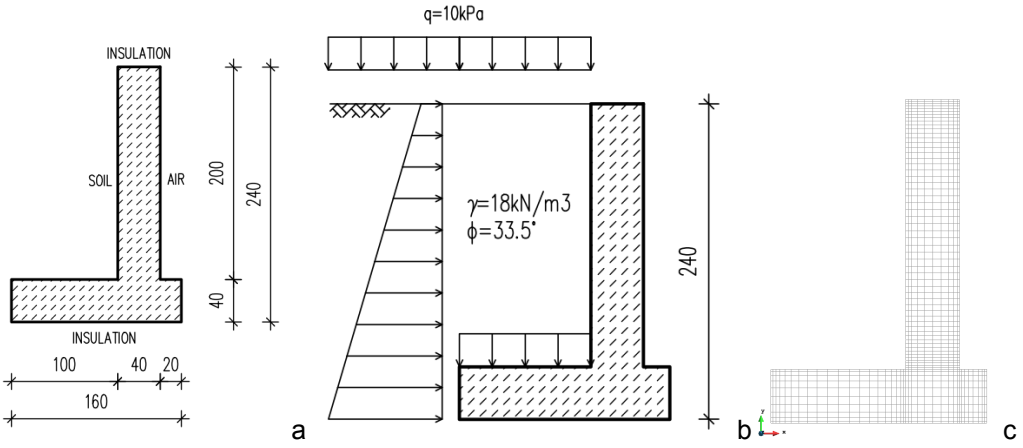

Figure 5. The geometry (dimensions in cm) (a), assumed load (b) and the FE mesh used in simulations (c) of the analyzed retaining wall.

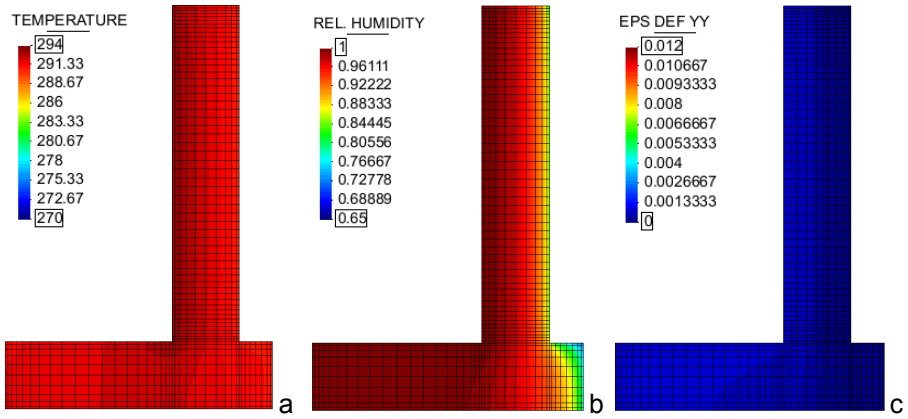

Figure 6. The distribution of temperature (a), relative humidity (b) and DEF-induced strains in the analyzed retaining wall at time instant 3 months.

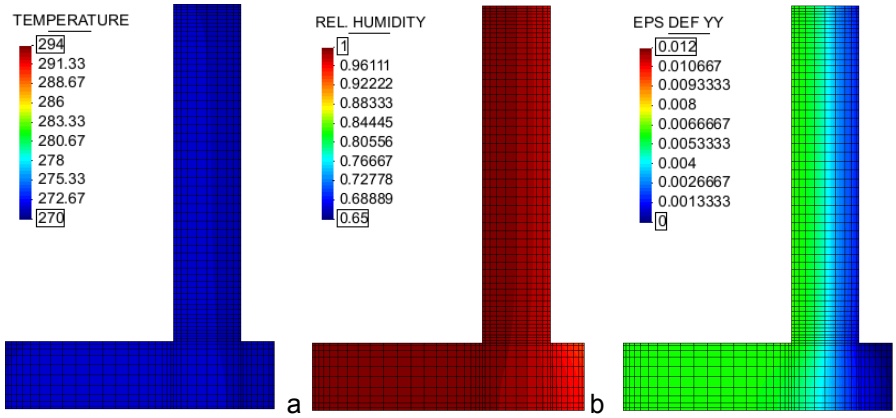

Figure 7. The distribution of temperature (a), relative humidity (b) and DEF-induced strains in the analyzed retaining wall at time instant 9 months.

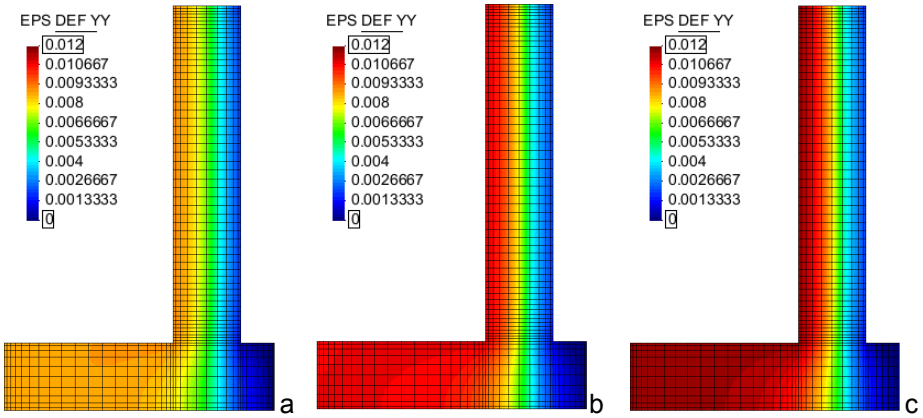

Figure 8. The distribution of DEF-induced strains in the analyzed retaining wall at time instant: 12 months (a), 15 months (b) and 30 months (c).

As may be seen in Figures 6 – 8, the presented mathematical model of DEF-induced strains evolution allows for numerical analyses of 2-D concrete structures exposed to variable hygro-thermal conditions. The numerical performance of the computer code is satisfactory, and the obtained results seem to be reasonable.

CONCLUSIONS

A mathematical, rate type model of the chemical strains due to the Delayed Ettringite Formation in cement based materials in different hygro-thermal conditions was developed. This is a phenomenological type model, the parameters of which should be determined experimentally for the analyzed material. The model validation with the published experimental data showed that the model is capable to describe the evolution of DEF-induced strains of materials, exposed during their maturing to heat-treatment of different temperature and duration, and then stored in different hygro-thermal conditions. Thanks to its' rate form, the model can be used for analyses in variable hygro-thermal conditions, e.g. described by the real hourly weather data.

ACKNOWLEDGEMENTS

The research was partly funded by within the grant of National Science Center – Poland, No. UMO-2011/03/B/ST8/05963 entitled "*Degradation of material properties due to development of expanding phases in building composites with a microstructure*" realized at the Lodz University of Technology in years 2012-2015.

REFERENCES

Brunetaud, X., Linder, R., Divet, L., Duragrin, D., and Damidot, D. (2007) "Effect of curing conditions and concrete mix design on the expansion generated by delayed ettringite formation", *Materials and Structures*, 40, 567–578.

Collepardi, M. (2003). "A state-of-the-art review on delayed ettringite attack on concrete", *Cement and Concrete Composites*, 25, 401-407.

Escadeillas, G., Aubert, J.-E., Segerer, M., and Prince W. (2007). “Some factors affecting delayed ettringite formation in heat-cured mortars”, *Cement and Concrete Research*, 37, 1445-1452.

Flatt, R.J., and Scherer, G.W. (2008). “Thermodynamics of crystallization stresses in DEF”, *Cement and Concrete Research*, 38, 325-336.

Gawin, D., and Schrefler, B.A. (1996). “Thermo- hydro- mechanical analysis of partially saturated porous materials”. *Engineering Computations*, 13(7): 113-143.

Lewis, R.W., and Schrefler, B.A. (1998) *The Finite Element Method in the Static and Dynamic Deformation and Consolidation of Porous Media, 2nd edition*. John Wiley & Sons, Chichester.

Martin, R.-P. (2010). *Analyse sur structures modèles des effets mécaniques de la réaction sulfatique interne du béton (PhD thesis)*, Ecole Nationale des Ponts et Chausses, Paris.

Pesavento, F., Gawin, D., Wyrzykowski, M., Schrefler, B.A., and Simoni, L. (2012). “Modeling alkali–silica reaction in nonisothermal, partially saturated cement based materials”, *Comput. Methods Appl. Mech. Engrg*., 225-228, 95-115.

Pavoine A., Divet L., and Fenouillet S. (2006). “A concrete performance test for delayed ettringite formation: Part I optimization”, *Cement and Concrete Research*, 36, 2138-2143.

Taylor, H.F.W., Famy, C., and Scrivener, K.L. (2001), “Delayed Ettringite Formation”, *Cement and Concrete Research*, 31, 683-693.

Study on the Effect of Water Migration and Visco-Elastic Behavior on Creep Deformation

Hideki Oshita[1]
[1]Professor, Department of Civil and Environmental Engineering, Chuo University, Tokyo, Japan. E-mail: oshita@civil.chuo-u.ac.jp

Abstract

A quantitative influence of the water migration in pores of a cement-based material on the creep phenomenon was estimated in a viewpoint of micromechanics and then the effect of the pore water pressure as a disjoining pressure, the friction resistance between water and pore walls due to the water migration and the viscoelastic behavior of the solid phase on the creep phenomenon were mutually discussed. At first, the coupled model of the liquid and solid phase of a cement-based material as a porous permeable material developed by authors, which simultaneously satisfies the force equilibrium equation and the mass conservation law of pore water, was expanded so as to be taken the diffusion phenomenon and seepage phenomenon for pore water and the viscoelastic behavior of the solid phase into account. Secondary, an experimental apparatus, which can reproduce the creep phenomenon due to the water migration in micro pores, was developed.

1. INTRODUCTION

A creep phenomenon for a cement-based material is not only influenced by deformational behavior of a solid phase, but also by a stress state of pore water and water migration. Namely, water migration in a cement-based material is a very important factor for a creep phenomenon and a representative theory is a seepage theory which is related to the diffusion of liquid and vapor phase existing in the gel and capillary pores. Regarding to this theory, a creep strain becomes higher as a gradient of humidity between inside and outside of a material. However, there is a lot of real phenomenon which cannot be explained by this theory, for example, a creep strain for a specimen, which is dried in an air environment, subjected to continuously loading in a water environment is about two times higher than that of cured in a water environment and so on. Namely, a creep phenomenon for a cement-based material can't be explained by only one theory, but by a unified theory of various theories. Moreover, it seems that a detailed modeling for each theory, which is related to a creep phenomenon, hasn't been established until now.

From the above all, the modeling related to the water migration in a cement-based material has been performed by authors based on the experimental results in which the pore water pressure occurs with an order of MPa due to the external loading. In this study, it was pointed out that the sudden increase of the creep strain occurs due to the water migration inside the specimen and after the water migration reaches a

steady state, a creep phenomenon ceases at last of which phenomenon is not corresponding to the experimental results such that the gradual increase of the creep strain occurs. Namely, the outflow of water from inside to outside of the specimen continuously occurs nonetheless the water migration reaches a steady state and the friction resistance occurring between such outflow of water and the wall of micro pores seems to be a great influence on the creep phenomenon.

In this study, a quantitative influence of the water migration in pores of a cement-based material on the creep phenomenon was estimated in a viewpoint of micromechanics and then the effect of the pore water pressure as a disjoining pressure, the friction resistance between water and pore walls due to the water migration and the viscoelastic behavior of the solid phase on the creep phenomenon were mutually discussed. At first, the coupled model of the liquid and solid phase of a cement-based material as a porous permeable material developed by authors, which simultaneously satisfies the force equilibrium equation and the mass conservation law of pore water, was expanded so as to be taken the diffusion phenomenon and seepage phenomenon for pore water and the viscoelastic behavior of the solid phase into account. Secondary, an experimental apparatus, which can reproduce the creep phenomenon due to the water migration in micro pores, was developed. And finally, the relationship between the water behavior and the creep phenomenon was discussed in detail experimentally and analytically.

2. COUPLED ANALYTICAL MODEL WITH LIQUID AND SOLID PHASE

2.1. Modeling of Concrete by Saturated Porous Two Phase Material

In the analysis which is a coupled model with liquid and solid phase of concrete structure developed by authors, concrete is regarded as a porous material which is composed of aggregate, cement paste and water. Aggregate is considered as perfectly elastic material while cement paste is assumed to behave as an elasto-plastic permeable material.

(a) Formulation of equilibrium equation

With the presence of pore water pressure p, the relation of effective stress $\{\sigma'\}$ and total stress $\{\sigma\}$ will become

$$\{\sigma\} = \{\sigma'\} - \{m\}p \tag{1}$$

where the sign of tensile stress is taken as positive and $\{m\} = \{\,1\;1\;1\;0\;0\;0\,\}^T$.

The incremental effective stress-strain relation for concrete can be written as

$$d\{\sigma'\} = \left[D_s^{ep}\right]\left(d\{\varepsilon^t\} - d\{\varepsilon^{pr}\} - d\{\varepsilon^h\} - d\{\varepsilon^{cr}\}\right) \tag{2}$$

where $[D_T^{ep}]$ is the elasto-plastic stiffness matrix of concrete where voids are not saturated with water, and $d\{\varepsilon^{pr}\}$ is the incremental strain of solid phase resulted from the incremental pore water pressure $d\{p\}$. Elasto-plastic stiffness of concrete can be written with the use of average elasto-plastic stiffness matrix of solid phase $[D_S^{ep}]$ and porosity ξ as follows.

$$[D_T^{ep}] = (1-\xi)[D_S^{ep}], \qquad d\{\varepsilon^{pr}\} = -D[D_S^{ep}]^{-1}\{m\}dp \tag{3}$$

Then by using the principle of virtual work and appropriate shape function, the equilibrium equation can be written in differential form as

$$K_T \frac{d\{\bar{u}\}}{dt} - L\frac{d\{\bar{p}\}}{dt} - \frac{d\{\bar{f}\}}{dt} = 0 \tag{4}$$

where matrices K_T and L are the tangential stiffness and effect of both pore water pressure and volume change of solid phase, respectively. The vector $\{f\}$ denotes the effect of external force on displacement. These notations can be defined as follows.

$$K_T = (1-\xi)\int_\Omega B^T D_s^{ep} B\, d\Omega \quad , L = \xi\int_\Omega B^T\{m\}\bar{N}\, d\Omega \quad , \{\bar{f}\} = \int_\Omega N^T\{b\}d\Omega + \int_\Gamma N^T\{t\}d\Gamma \tag{5}$$

where N and $\bar{N}$ are the shape functions for displacement, the pore water pressure ,while B is the strain-displacement matrix.

(b) Formulation of Flow Continuity Equation

Water head h can be written as

$$h = z + \frac{p}{\gamma} \tag{6}$$

where z is the vertical coordinate of the point which is positive for upward direction, γ is the specific gravity of fluid. From the mass conservation law, the volume change in a unit volume ΔV is equal to the difference of the amount of inflow q and outflow from this volume, which can be written as

$$\Delta V = q - \nabla^T\{v\} \tag{7}$$

where v is the flow velocity, which is considered to follow Darcy's law. The factors which contribute to the volume change can be summarized as follows.

Due to total strain change

Due to the change of volume of particles caused by changes of hydrostatic pressure

Due to the change of fluid volume

Due to the change of particle size by effective stresses

Substituting these factor into Eq. (7) and applying the Galerkin's method, Eq.(7) becomes in differential form as

$$H\{\bar{p}\} + S\frac{d\{\bar{p}\}}{dt} + L^T\frac{d\{\bar{u}\}}{dt} - \{f_p\} = 0$$

,

$$H = \int_\Omega (\nabla\bar{N})^T k'\nabla\bar{N}d\Omega, \quad S = \int_\Omega \bar{N}^T s\bar{N}d\Omega, \quad L^T = \int_\Omega \bar{N}^T\{m\}^T B d\Omega, \tag{8}$$

$$\{f_p\} = \int_\Omega \bar{N}^T q d\Omega - \int_\Omega (\nabla\bar{N})^T k'\nabla\gamma z d\Omega + \int_{\Gamma_m} \bar{N}^T(\{v\}^T n)d\Gamma_m,$$

$$s = \frac{\xi}{k_f}, \quad k' = \frac{k}{\gamma}.$$

(c) Formulation of Coupled Equations

The coupled equations which satisfy the force equilibrium and continuity condition can be written in the next matrix form.

$$\begin{bmatrix} [K_T] & -[L] \\ -[L]^T & -\Delta t[H]-[S] \end{bmatrix}\begin{Bmatrix}\{\Delta\bar{u}\}\\ \{\Delta\bar{p}\}\end{Bmatrix} = \Delta t\left[\begin{Bmatrix}\dfrac{d\{f\}}{dt}\\ -\{f_p\}\end{Bmatrix} - \begin{bmatrix}[0] & [0]\\ [0] & -[H]\end{bmatrix}\begin{Bmatrix}\{\bar{u}\}_i\\ \{\bar{p}\}_i\end{Bmatrix}\right] \tag{9}$$

where $\{\bar{u}\}_i$ is the nodal displacement and $\{\bar{p}\}_i$ is the nodal pore water pressure at the previous step.

2.2. Seepage phenomenon for pore water at the seepage boundary

Seepage for pore water at seepage boundary can be expressed as follows Eq. (10).

$$f_{out} = \int_{\Gamma_m} \bar{N}^T \left(\{v\}^T n\right) d\Gamma_m \tag{10}$$

where f_{out} is the seepage for pore water, n is normal vector at seepage boundary and Γ_m is surface area at seepage boundary. Then, $\{v\}$ is the seepage velocity for pore water at seepage boundary and can be written by the following equation according to Darcy's law.

$$\{v\} = -[k]\nabla h \tag{11}$$

where k is permeation coefficient [m/s]. Then, the boundary condition at seepage boundary can be expressed as follows Eq. (12).

$$\{v\}^T n = -k\nabla h \; n = -m\left(h - h_\infty\right) \tag{12}$$

where m is called the permeation coefficient [m/s], in case pore water move through the same material. However, in this study, m is called the seepage coefficient [m/s] when the pore water is moving from inside the concrete to the atmosphere. Naturally, the permeation and the seepage coefficient are different. Finally, Eq. (12) becomes as follows by the pore water pressure and ambient pressure.

$$\{v\}^T n = -m\left(\frac{p - p_\infty}{\rho_w}\right), \quad \text{boundary is} \quad \Gamma_m. \tag{13}$$

Ultimately, the creep model, which is capable of evaluating the diffusion and seepage phenomenon for the pore water, was constructed by substituting Eq. (13).

2.3. Modelling of Water Migration which is capable of Evaluating the Diffusion and Seepage Phenomenon

The creep model, which is capable of evaluating the diffusion and seepage phenomenon for the pore water, becomes as follows.

$$\begin{bmatrix} [K_T] & -[L] \\ -[L]^T & -\Delta t\{[H]-[M]\}-[S] \end{bmatrix} \begin{Bmatrix} \{\Delta\bar{u}\} \\ \{\Delta\bar{p}\} \end{Bmatrix} = \Delta t \begin{bmatrix} \begin{Bmatrix} \dfrac{d\{f\}}{dt} \\ -\{f_p\} \end{Bmatrix} - \begin{bmatrix} [0] & [0] \\ [0] & [M]-[H] \end{bmatrix} \begin{Bmatrix} \{\bar{u}\}_i \\ \{\bar{p}\}_i \end{Bmatrix} \end{bmatrix}, \quad M = \int_{\Gamma_m} \bar{N}^T \frac{m}{\rho_w} \bar{N} d\Gamma_m,$$

$$\{f_p\} = \int_\Omega \bar{N}^T q d\Omega - \int_\Omega \left(\nabla\bar{N}\right)^T k \nabla\gamma z d\Omega - \int_{\Gamma_m} \bar{N}^T \frac{m}{\rho_w} \bar{N} d\Gamma_m \{\bar{p}_\infty\} \tag{14}$$

where M is the matrix and f_p is vector on the seepage of the pore water at the seepage boundary.

The ambient pressure, which represents the degree of dryness or wetness on concrete surface, was taken into account by Eq. (14). As it has been mentioned above, it has become possible to evaluate influence of drying or wetting of the surface on the creep properties. Here, determination of ambient pressure was decided based on the Bazant's study.

3. CREEP EXPERIMENT UNDER CONSTANT LATERAL PRESSURE

3.1. Layout of the experiment

A device of loading of constant lateral pressure is shown in **Fig. 1** and the detailed layout of the cell is shown in **Fig.2**. Water is filled the space between the cell and the specimen, and the pressure is applied by hydraulic press. Here, the water cement ratio of the specimen is 60% and it is carried out at 3 days and 7days. The mix proportion of concrete and the strength are shown **Table 1** and **Table 2**.

3.2. Method of sustained pressure loading

At first, prior experiment was carried to measure the failure loading pressure σ_{ru}. The specific method is pressuring the water between the cell and the specimen directly at the speed of 0.1MPa/sec. Then, the pressure loaded on the side surface at the speed of 0.1MPa/sec and the lateral water pressure kept by jack.

3.3. Experimental parameters

The parameters adopted in the experiment are shown in **Table 3**, including sustained pressure and loading days. Moreover, to prevent the water flow into the specimen, it was covered with rubber sleeve and tested it.

3.4. Measured item

The measured item includes longitudinal and hoop strain of concrete and the pore pressure. The measure method of pore pressure, ϕ 1mm steel pipe was cast in the concrete and filled with water, then was set to a water pressure gauge at the tip. The pipe was set in the 3 locations at 2.5cm, 5cm and 7.5cm from the surface (**Fig. 3**).

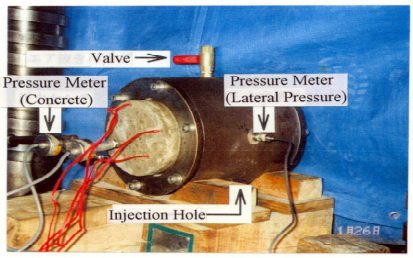

Fig.1: A device of loading of constant lateral pressure.

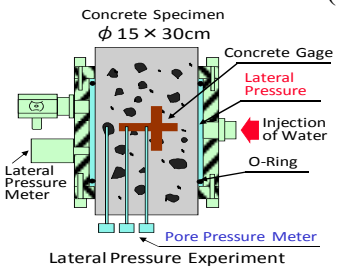

Fig.2: The detailed layout of the cell.

Table.1: Mix proportion of concrete.

SL (cm)	Air (%)	W/C (%)	s/a (%)	Unit weight (kg/m^3)			
				W	C	S	G
10±2	2.5±1	60	54	226	337	906	732

Table.2: Strength properties.

Age	Compressive (Mpa)	Tensile (Mpa)	Elastic modulus (Gpa)
The 3rd	17.2	1.7	22.4
The 7th	25.0	2.6	25.5

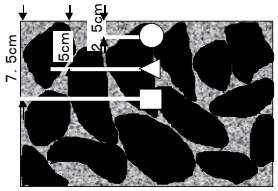

Fig.3: Locations of measurement of the water pressure.

Table.3: Experimental parameters.

Specimen	Age(day)	Value of constant lateral pressure (Mpa)	Rubber sleeve
Ⅲ-50	3	$0.5\times\sigma_{ru}$	No
Ⅲ-70	3	$0.7\times\sigma_{ru}$	No
Ⅶ-50	7	$0.5\times\sigma_{ru}$	No
Ⅶ-70	7	$0.7\times\sigma_{ru}$	No
Ⅶ-70-G	7	$0.7\times\sigma_{ru}$	Yes

σ_{ru} (Material age 3 days)=4.2Mpa
σ_{ru} (Material age 7 days)=5.6Mpa

3.5. Deformation of concrete under sustained pressure

(a) State of pore water

The specimen Ⅲ-50 was used to clarify the state of pore water as shown in **Fig. 4**. **Figure 4** represents relation between the history of pressure of pore water caused by sustained pressure and the cost time. In the figure, ○, △ and □ represent the pore pressure at location 2.5cm (surface), 5cm (middle) and 7.5cm (center).

At first, water on the side surface was loaded, in 3min, the surface, 6min middle, 18mim center, pore pressure increased, and then about 32min, the pressure in the 3 locations are 50% of the loading pressure and kept. Moreover, about 20min, a drop of water appeared on the surface. It means that water dispersed to the center, then diffused and exuded to the place with lower pressure. The phenomenon that pore water diffused and exuded to the outside was confirmed by the experiments.

(b) Effect evaluation of days on deformation

As shown in **Fig. 5** and **Fig. 6**, specimen Ⅲ-50, Ⅶ-50 and Ⅲ-70, Ⅶ-70 sustained pressure loading longitudinal strain. In the figure, ● and ○ represent the result 3days and 7days.

First, sustained pressure is half failure pressure in **Fig. 5**, each day early loading stage the concrete creep are almost the same, increased at a certain degree, increased gradually. However, creep causes failure (split failure) about 60μ and 3 days specimen earlier stage of sustained pressure caused creep is larger than 7 days. Because, the permeation coefficient is large due to the porous material and appeared pore pressure distribution is large pore water from inner of the specimen diffused to the outside phenomenon is continuous. In other words, the strain becomes large by water flow into and exuded phenomenon happened continuously. In case permeation coefficient is large, in the specimen, pressure transferred quickly, and then from early stage sustained pressure loading, the pore water diffused main reason. that is, specimen with 3 days, drop appeared on the surface, specimen with 7 days, there is no drop, dry state up and sown surface see by eye it is possible. On the other hand, 20min after sustained pressure loading, increase degree of strain are almost the same in spite of the ages. About the specimen whose age is 3 days, the pore water exuded to the outside continuously. However, in the specimen whose age is 7 days, there is almost no pore water exuded to the outside, thus, it can be concluded that the pore water has no effect.

Then, when the sustained pressure up to the 70% of failure pressure, the creep strain increased linearly no matter the age as shown in **Fig. 6**. Compared to the time past 40min in **Fig. 5**, only the value of sustained pressure is different. Thus in case the sustained pressure up to the 50% of failure pressure, the creep mechanism is the same.

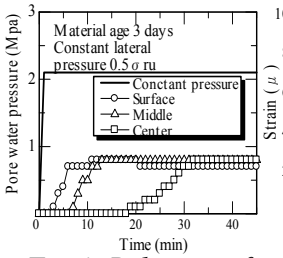

Fig.4: Behavior of pore pressure.

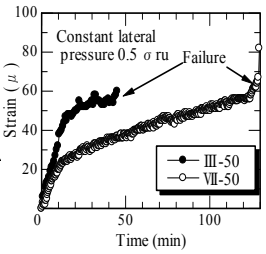

Fig.5: Lateral pressure $0.5\sigma_{ru}$.

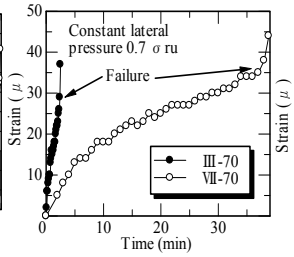

Fig.6: Lateral pressure $0.7\sigma_{ru}$.

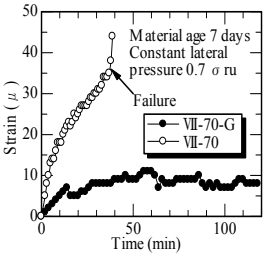

Fig.7: Creep strain.

That is to say, the larger the sustained pressure, the larger the friction of the frame, as shown in **Fig. 5** on the later loading stage and the creep strain increased significantly. Thus, it can be conclude that till the pore pressure disappears, the changing of pore pressure is very large.

(c) Effect evaluation of impress on deformation

It is to evaluate the effect of impress of water from outside on deformation. The experiment in former, the specimen surface is immersed in water directly, and the water impressed inside to compare the specimen covered with rubber sleeve is also conducted. **Fig. 7** is the sustained pressure loading longitudinal strain specimen Ⅶ-7 (below, no rubber) and specimen Ⅶ-70-G (below, with rubber) with sustained pressure. In the figure, ● and ○ represent the result specimen Ⅶ-70-G (below, with rubber) and specimen Ⅶ-70 (below, no rubber).

The specimen without rubber, the longitudinal creep strain happened because the diffusion phenomenon of the pore water. On the other hand, in the specimen with rubber, after sustained pressure applied, strain remains at a constant value. As the specimen with rubber, the increase creep at the earlier stage is less than that of specimen without rubber, and it kept constant. This phenomenon means that the diffusion phenomenon in not so serious, due to the less pore pressure. Thus, the pore pressure inner the specimen is near to zero.

It can be inferred from the experimental result that the difference between with and without rubber sleeve is that the water is impressed into the specimen. It can be judged that pore pressure is the driving force, the less the low pressure, the longitudinal creep appeared due to the pore water diffuses or exudes.

3.6. Creep mechanism of concrete suffering sustained lateral water pressure

In case the side surface of concrete is suffered sustained pressure directly, it is cleared that creep deformation formed in longitudinal direction by experiment. diffusion phenomenon of pore water affect this kind of creep property, compare the result of the specimen in the experiment with rubber sleeve by visualization, it can be conclude that it is very large. Thus in this chapter, effect of diffusion phenomenon and seepage phenomenon of pore water on this kind of creep property is numerically analyzed, at the same time, experiment and numerical analysis are carried creep mechanism.

In the process of analysis, the model of analysis, boundary condition, the mechanical properties of concrete and the pore water are needed. The mechanical properties of concrete are derived forms experiment. Moreover, the bulk modulus of pore water is 2.2kN/mm^2, permeation coefficient, specimen about Ⅲ-50, 70 are 60×10^{-8} cm/sec, specimenⅦ-50, 70 are 3.30×10^{-10} cm/sec, seepage coefficient of pore water from boundary is $1.0\times10^{-9}\sim5.0\times10^{-9}$ cm/sec and the atmosphere is 1atm.

(a) Specimen Ⅲ-50 and Ⅲ-70

Fig. 8 and **Fig. 9** compared the experimental result of specimen Ⅲ-50 and specimen Ⅲ- 70, ○ represents the experimental result, and solid line is the analysis result. Moreover, in each **Fig. (a)**, relation between longitudinal creep strain and the time, in each **Fig. (b)** is the relation between seepage water form boundary and the time. First, the accuracy of analysis is very good, about creep strain of specimen Ⅲ-50 increased significantly, and then it increased gradually. About creep strain of specimen Ⅲ-70

increased significantly, this tendency is accurately simulated.

Then, each **Fig. (b)** shows relevance of mass of pore water seepage analysis result and the creep strain. In specimen Ⅲ-50, 10min after sustained loading, increased significantly, and almost the same time the mass of pore water seepage increased significantly. Moreover, after then increased gradually, and almost the same time the mass of pore water seepage increased gradually. Based on this conclusion, in the process of heavy diffusion of pore water after sustained pressure, the friction of concrete frame become large and thus the creep strain increased significantly. In the process of slight diffusion of pore water after sustained pressure, the friction of concrete frame becomes less and thus the creep strain increased gradually. This kind of phenomenon, after loading of sustained pressure, distribution of pressure of pore water becomes steady state, the pore water in the specimen, diffused and exuded to the outside heavily. And then it can be considered that pore water diffused and exuded in the pore pressure kept constant.

(b) Specimen Ⅶ-50 and Ⅶ-70

Fig. 10 and **Fig. 11** show the comparison of analysis and experimental result of specimen Ⅶ-50 and Ⅶ-70 respectively. ○ represents the experimental result, and solid line is the analysis result. Then, **Fig. 10** and **Fig. 11** represent relation between

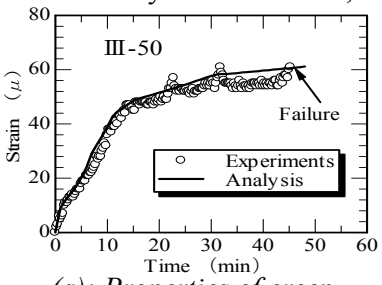

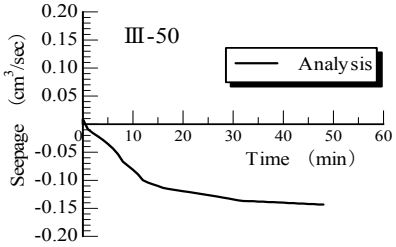

(a): Properties of creep. *(b): Seepage.*

Fig.8: Properties of creep and seepage (Ⅲ-50).

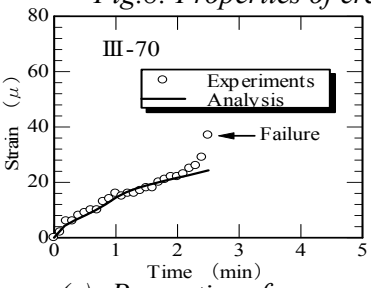

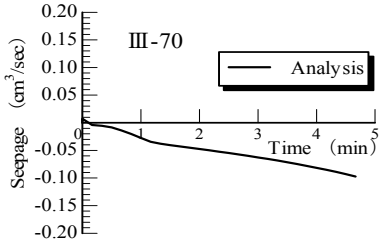

(a): Properties of creep. *(b): Seepage.*

Fig.9: Properties of creep and seepage (Ⅲ- 70).

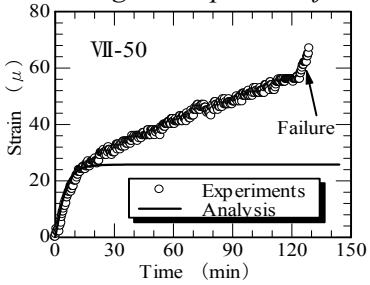

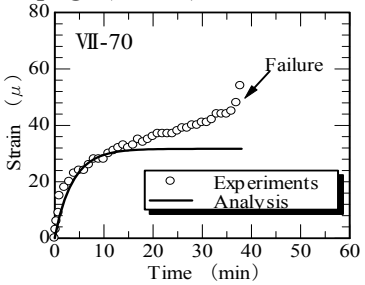

Fig.10: Properties of creep (Ⅶ-50). *Fig.11: Properties of creep (Ⅶ-70).*

longitudinal creep strain and the time. Here, mass of pore water analysis seepage is zero for Ⅶ-50 and Ⅶ-70 in spite of the time.

First, about both specimen Ⅶ-50 and Ⅶ-70, creep strain of experiment increased significantly, and then it increased gradually. About the analysis result, creep strain increased significantly, and then kept a constant. The phenomenon that the tendency of increasing significantly after loading accord with analysis is well, however in the next loading stage, the tendency is different, because the water seepage is zero. After the loading, the diffusion of the pore water in the specimen become large gradually, and thus the creep strain increase significantly. Then the pressure of pore water is up to a certain value. The concrete become compactness and the pore water do not diffused. As a result, the pore water does not seepage. Then the creep strain does not increase. Thus, permeation coefficient becomes less, the strength of concrete frame become stronger. It can be considered effect of diffusion phenomenon on creep properties only act at the moment of loading.

Here, force equilibrium equation in the longitudinal direction, it can be shown below.

$$\sigma = \sigma' - p \tag{16}$$

where σ is total stress, σ' is effective stress and p is pressure of pore water, rule of sign, about the stress, tension is positive, pressure of pore water, compressive is positive.

In longitudinal direction, stress of concrete frame (effective stress) equal to pressure of pore water because no external force act, and stress of concrete frame is tension stress and the pressure of pore water is compressive force.

That is to say, concrete frame and pressure of pore water kept the equilibrium equation. Thus, pressure of pore water which act on pore water was considered to be disjoining pressure. On this background, specimen Ⅲ-50 and Ⅲ-70 are porous material, thus pore water is easy to diffuse by gradient of the pore water to longitudinal. Specimen Ⅶ-50 and Ⅶ-70 are close, thus diffusion of pore water is not so easy and pressure of pore water as disjoining pressure acts on the frame.

Now, it is assumed that the concrete frame becomes large and creep strain appeared by the disjoining pressure. The pore pressure and visco-elastic item ware considered by introducing this hypothesis. Moreover, the visco-elastic behavior is taken into account when there is no effect of pore water.

Fig. 12 and **Fig. 13** show the experimental result of specimen Ⅶ-50 and Ⅶ-70 respectively compared the analysis result. ○ represents the experimental result, dot

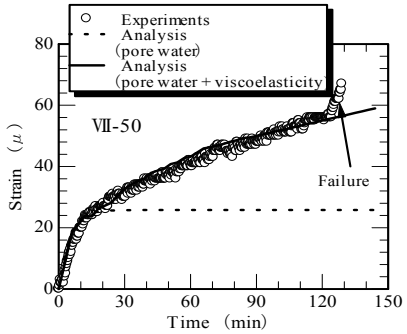

Fig.12: Creep mechanism (Ⅶ-50).

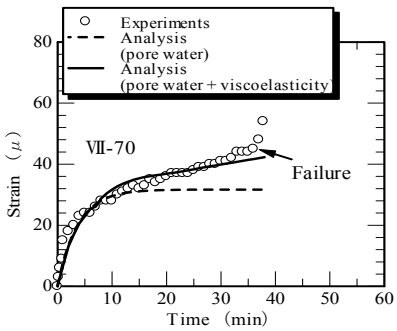

Fig.13: Creep mechanism (Ⅶ-70).

line and solid line are the analysis result only effect of pore water was taken into account and the analysis result effect of pore water and visco-elastic behavior are taken into account.

First, in the two specimen, the result considered the effect of visco-elastic behavior, accorded to experiment well. About the experiment result and the analysis result considered the effect of visco-elastic behavior, the moment loading, due to diffusion phenomenon of pore water, creep strain increased significant, this tendency happened till there is no diffusion of pore water. Then, the positive pore pressure in equilibrium stress state becomes disjoining pressure and concrete frame enlarged gradually due to effect of the visco-elastic behavior, the creep strain increased gradually. That is to say, the difference between solid line and dotted line is the pore pressure as disjoining pressure and is showing the visco-elastic ingredient.

Thus, when the permeation coefficient is little, the strength of concrete frame is comparable large, the creep mechanism is that the pore water diffused in the inner on the moment loaded by sustained pressure, and then the pressure of pore water disjoining pressure act on concrete frame happened due to the visco-elastic behavior, which is clarified by both experiment and analysis.

4. CONCLUSIONS

As a result, the following findings were observed.

(1) The creep model, which is capable of evaluating the diffusion and seepage phenomenon for the pore water, was constructed. Moreover, the visco-elastic item of cement paste was taken into account.

(2) The phenomenon that pore water diffused and exuded to the outside was confirmed by the experiments.

(3) It can be judged that pore pressure is the driving force, the less the low pressure, the longitudinal creep appeared due to the pore water diffuses or exudes.

(4) The creep mechanism of concrete in the young material age, which the permeation coefficient has relatively a big, was controlled by behavior of the water movement in the pore.

(5) The permeation coefficient is little, the strength of concrete frame is comparable large, the creep mechanism is that the pore water diffused in the inner on the moment loaded by sustained pressure, and then the pressure of pore water disjoining pressure act on concrete frame happened due to the visco-elastic behavior, which is clarified by both experiment and analysis.

REFERENCE

Oshita, H., and Tanabe, T. (2000) “Water migration phenomenon model in cracked concrete. Ⅰ:Formulation.” J. Engrg. Mech, ASCE, 126(5), 539-543.

Oshita, H., and Tanabe,T. (2000). “Water migration phenomenon model in cracked concrete. Ⅱ:Calibration.” J. Engrg. Mech, ASCE, 126(5), 544-549.

Oshita, H., Ishikawa, Y. and Tanabe, T. (1993) “Creep Mechanism of Early Age Concrete Modeling with Two Phase Porous Material”, *Proc. of the Fifth International RILEM Symposium*, pp.465-470.

Modelling Damage from the Nano-Scale Up

C. T. Davie[1] and E. Masoero[1]

[1]School of Civil Engineering and Geosciences, Newcastle University, Newcastle upon Tyne, Tyne and Wear NE1 7RU, U.K. E-mail: colin.davie@ncl.ac.uk

Abstract
In the light of the developing use of cementitious materials in safety critical, high temperature applications associated with energy industries (nuclear, oil and gas) this work looks to the nano-scale to consider the origins of macro-scale phenomena. It enables a first comparison of nano-scale results with macro-scale observations, toward the inclusion of physico-chemico-mechancial processes in models at larger scales and a move away from phenomenological models. Assuming the development of nano-scale porosity to be the principal effect of temperature at the nano-scale, comparisons are here developed between nano-scale measurements, simulations and macro-scale experimental results. The results suggest that the effect of temperature on the nano/micro mechanical properties of cementitious materials might be responsible for a significant part of the experimentally observed trends at the macro-scale, although more work is required to understand scaling of fracturing. It is concluded that modifying the nano-scale material response to temperature gradients could eventually impact the engineering performance of structures at elevated temperatures.

INTRODUCTION

With the ever increasing demand for energy worldwide, nuclear power is experiencing a resurgence in popularity with several countries looking again to it as a reliable, plentiful and low carbon supply of electricity (Committee on Climate Change 2011, Parliamentary Office of Science and Technology 2011) including China, India and the UK recently approving the development of new build plants, and several operators extending the lives of existing plants. Similarly, oil and gas production continues at a high level with new fields being opened in evermore challenging environments around the world.

Key to both of these energy industries are cementitious materials (used for the power plant structures themselves and for well bore cements) and in both applications these materials experience high temperatures and high pressures/stresses that could induce deformations and degradation, ultimately leading to the possibility of fracturing.

With continued concerns over safety, following events such as those at the Fukushima Dai-ichi plant in Japan, where a loss of cooling led to the overheating of several reactors and the release of radioactive material (IAEA 2011), and the Deepwater Horizon oil-spill, where a failure in the well liner led to a fire resulting in 11 deaths and a subsequent oil spill that cost ~$40b to mitigate (Cleveland 2010), and

with continuing threats from militant groups and terrorists, understanding, assessing and analysing damage to these safety critical materials is ever more important. To do this efficiently, complex numerical models are required to consider the chemo-hygro-thermo-mechanical processes at work in these multi-phase porous materials.

To determine the most appropriate macro-scale interpretations and in order to allow a move from a phenomenological representation to a mechanistic or physical one, this work looks to the nano-scale to consider the origins of macro-scale phenomena and enables a first comparison of nano-scale results with macro-scale observations, toward incorporation in models at larger scales.

MACRO-SCALE

Considering macro-scale modelling approaches to these types of problem, state-of-the-art models adopt multi-phase coupled, hygro-thermo-chemo-mechanical frameworks and often address the thermo-mechanical evolution of the material via a damage mechanics approach (Gawin, Majorana et al. 1999, Davie, Pearce et al. 2010). In these models the traditional mechanical damage formulation is modified to include a thermal damage parameter that acts multiplicatively with the mechanical damage as below:

$$\sigma' = (1-\chi)(1-\omega)\mathbf{D}_0 : \boldsymbol{\varepsilon}^{\mathrm{e}}$$

Where, σ' is the Bishop's stress, χ is the thermal damage parameter, ω is the mechanical damage parameter, $\mathbf{D_0}$ is the initial elasticity tensor and $\boldsymbol{\varepsilon}^{\mathbf{e}}$ is the elastic strain tensor.

In the model by (Davie, Pearce et al. 2010) the thermal damage parameter, χ, is related directly to the degradation of the stiffness of the material as a result of temperature and, following (Peerlings, de Borst et al. 1998), a modified Mazar's type criterion is employed for the mechanical damage parameter, ω.

$$\chi = 1 - \frac{E(T)}{E_0}; \qquad \omega = 1 - \frac{\kappa_0^{md}(T)}{\kappa^{md}} \mathrm{e}^{-\gamma(T)\left(\kappa^{md} - \kappa_0^{md}(T)\right)}$$

Where, E_0 is the elastic modulus, $\kappa_0^{md} = f_t(T)/E(T)$ defines the threshold for onset of damage, where $f_t(T)$ is the tensile strength, and $\kappa^{md} = \max\{\kappa_0^{md}, \max(\bar{\varepsilon})\}$ is a measure of the maximum strain experienced to date, where $\bar{\varepsilon}$ is the equivalent strain measure. $\gamma(T) = l_c(1-\chi)f_t(T)/\mathrm{G_f}(T)$ is the ductility parameter and is a function of the fracture energy release rate, $\mathrm{G_f}$, and a length scale parameter l_c.

It should be noted that, at these scales, the material under consideration is typically concrete, or at least mortar; i.e. a composite consisting of cement paste and various sizes of aggregate and the macro-scale properties measured therefore reflect the behaviour of these composites.

As can be seen in the model above the key properties under consideration are the tensile strength, elastic modulus and fracture energy release rate, all of which are

temperature dependent. Various phenomenological relationships for these properties derived from experimental work can be found in the literature and some normalised examples are given in Figure 1. As can be seen for tensile strength and elastic modulus (Figure 1a & b) the trends are broadly similar and show degradation with increasing temperature to a total loss of strength and stiffness around 600-800°C, where upon both thermal and mechanical damage parameters will approach 1, i.e. total damage. However, the evolution of the damage criteria with temperature is also dependent on the ratio of these two properties and the combined thermal and mechanical aspects of their individual phenomenological behaviours are not well quantified (Davie, Zhang et al. 2012). The development of ductility via fracture energy release rate is even less well quantified and what little data exists can be contradictory, as shown in Figure 1c.

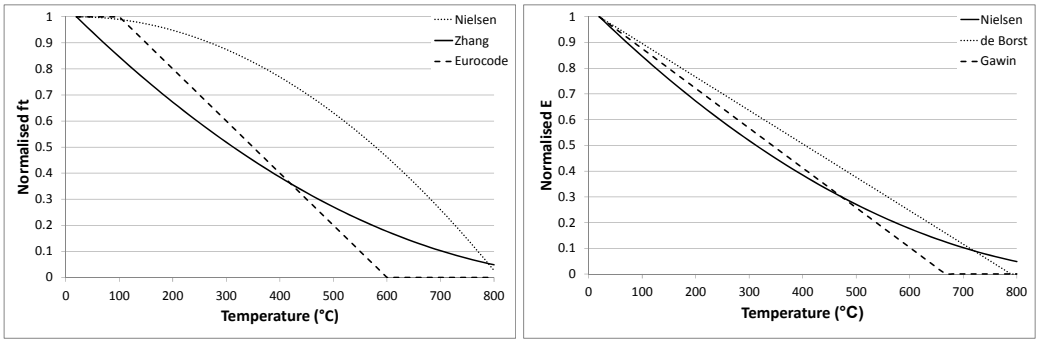

a) b)

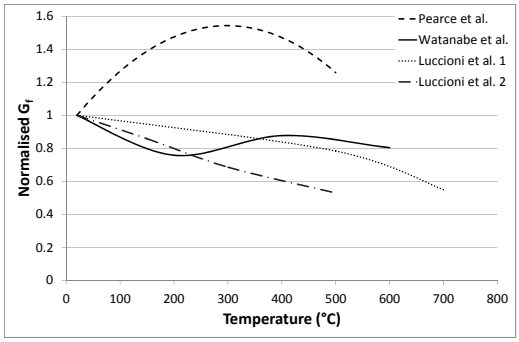

c)

Figure 1. Macro-scale temperature dependent relationships for a) tensile strength, b) elastic modulus & c) fracture energy release rate of concrete [(de Borst and Peeters 1989, Gawin, Majorana et al. 1999, Nielsen, Pearce et al. 2002, Luccioni, Figueroa et al. 2003, CEN 2004, Pearce, Nielsen et al. 2004, Davie, Zhang et al. 2010)]

It is recognised that the observed trends in these properties are a function of physico-chemical processes seated in the cement paste phase of the composite material. A first step in including more of the individual material behaviours is to carry out meso-scale modelling where the cement and aggregate phases are represented separately. However, there have been comparatively few attempts at this in the literature with notable work by e.g. (Fu and Li 2011, Zhao, Zheng et al. 2014) and the material behaviours again tend to be based on macro-scale experimental work albeit on individual materials rather than composites. Temperature dependent trends for the mechanical properties of cement paste are also very difficult to find in the literature. An example of compressive strength (which may be related to tensile strength) and two examples of elastic modulus are shown in Figure 2.

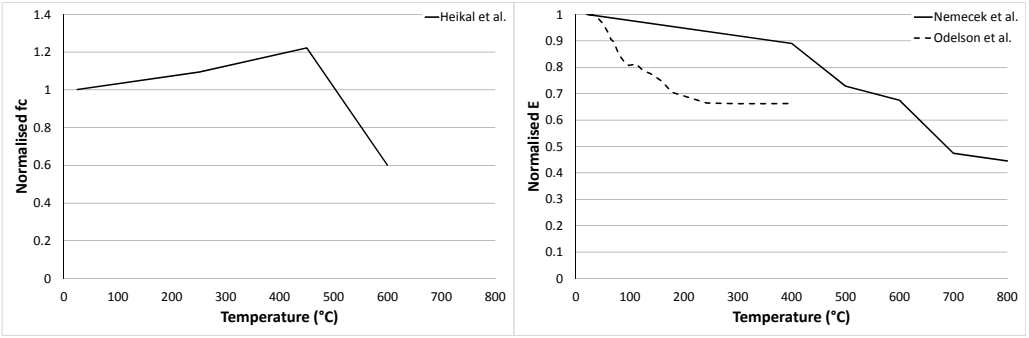

a) b)

Figure 2. Macro-scale temperature dependent relationships for a) compressive strength, b) elastic modulus of cement paste [(Němeček, Kopecký et al. 2004, Odelson, Kerr et al. 2007, Heikal, El-Didamony et al. 2013)]

As can be seen, these relationships show similar trends to those for concrete, although there are clear differences such as the compressive strength initially increasing before degrading and the elastic modulus retaining at least 40% of its original value even at 800°C. This implies less damage than suggested for concrete but would allow meso-scale interactions between paste and aggregate to be inherently captured. However, the physico-chemical processes are still represented only phenomenologically.

NANO-SCALE

The relationships between material properties and temperature shown in the previous section indicate the variety of results that can be found in the literature (see e.g. the results for G_f of concrete (Figure 1c)). These properties are in fact expected to depend on a multitude of factors, including mix design variables (e.g. water to cement and aggregate to cement ratios), age, and environmental conditions (e.g. humidity). Given the reliance of damage models on the material properties discussed here, we propose that it is timely to attempt a new bottom-up approach that can consider the above factors explicitly and provide predictions of material properties based on them.

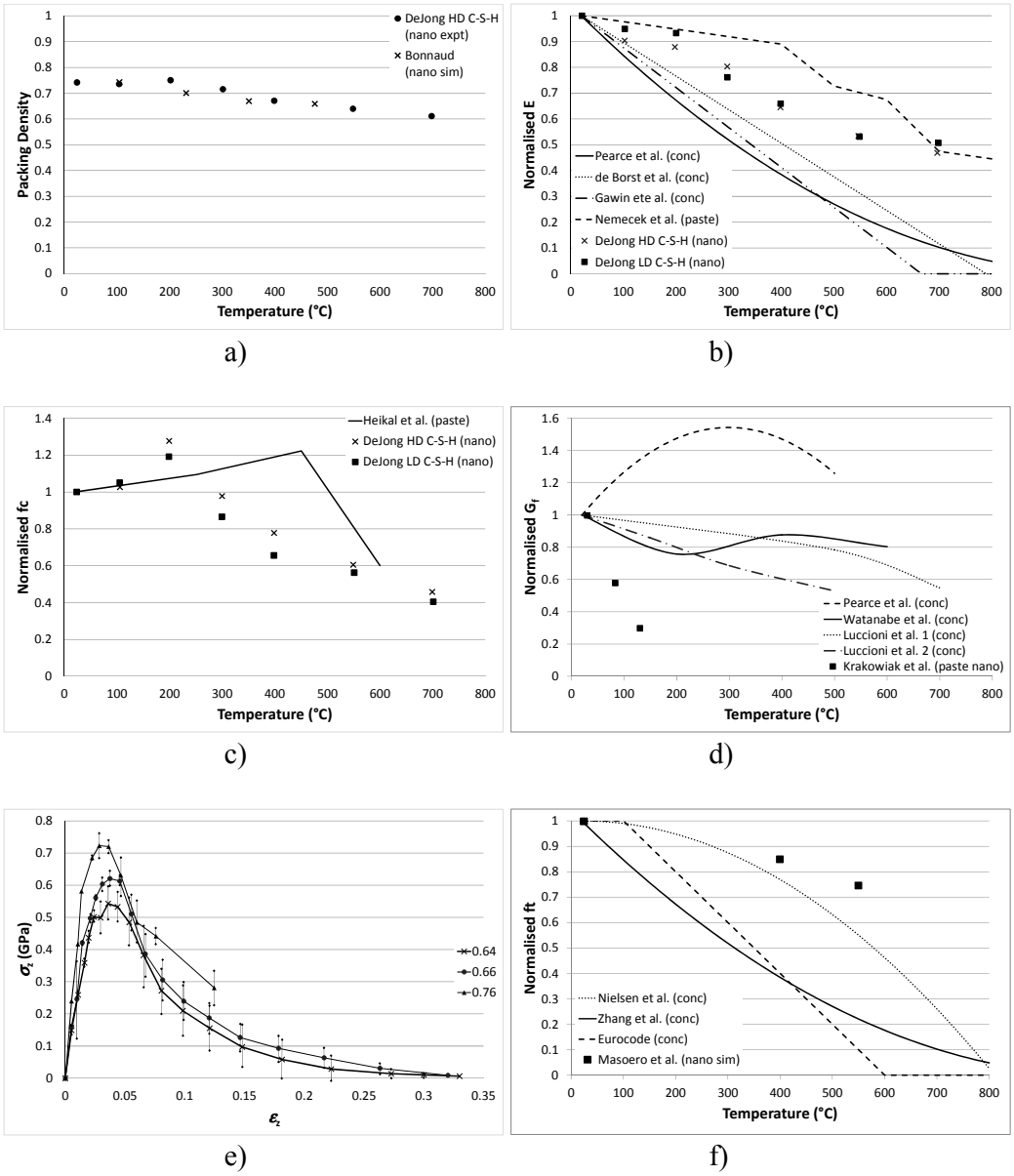

Figure 3. Nano-scale temperature dependent relationships for a) packing density in C-S-H gel, b) elastic modulus, c) compressive strength, d) fracture energy release rate, e) tensile stress-strain curves from nano-particle simulations, f) tensile strength (where LD and HD are low and high density; two types of C-S-H typically found in cement pastes) [(de Borst and Peeters 1989, Gawin, Majorana et al. 1999, Luccioni, Figueroa et al. 2003, Němeček, Kopecký et al. 2004, Pearce, Nielsen et al. 2004, DeJong and Ulm 2007, Masoero, Del Gado et al. 2012, Bonnaud, Ji et al. 2013, Heikal, El-Didamony et al. 2013, Watanabe, Bangi et al. 2013, Krakowiak, Thomas et al. 2015)].

The observed effect of temperature on material properties is likely to develop at multiple length scales. At the macro-scale, one important factor would be the spatial heterogeneity of mechanical properties (e.g. thermal dilation coefficients and elastic constants) that can generate eigenstresses. These properties can be accounted for in typical design codes, e.g. via statistical distributions of mechanical properties in a Finite Element based program. Other effects however develop at much smaller scales and can be considered inherent temperature-dependent properties of the cement paste. In this section we collect some recent data from nano-scale experiments and simulations that allow qualitative trends, akin to those in Figures 1 and 2, to be extracted from bottom-up extrapolations.

The linkage between temperature and mechanical properties of cement paste at the nano-scale can be traced in two steps. First, we assume that a major effect of temperature is to alter the amount of nano-pores in the C-S-H gel, which is the main binding phase in ordinary cement pastes. We also assume that the change in larger capillary pores induced by temperature gradients is much smaller and therefore negligible. These assumptions are supported by experimental measurements from nano-indentaiton (DeJong and Ulm 2007) and by molecular simulation results (Bonnaud, Ji et al. 2013), which quantify the relationship between nano-scale porosity and temperature as indicated in Figure 3a. In particular, we refer to the packing density, which is the volume fraction of solid C-S-H or, one minus the volume fraction of pores (i.e. the porosity).

The second step is then to relate the packing density with the mechanical properties of the material. Nano-indentation measurements on C-S-H from (DeJong and Ulm 2007) provide the dependence of indentation modulus M and hardness H on temperature, via the link with packing density. M is related to the elastic modulus $E = M / (1-\nu^2)$, where ν is the Poisson's ratio of the C-S-H gel (approximately 0.2). H is related to the shear strength of the material τ_{max}. However, a simplified relationship, which is strictly valid only for perfectly plastic materials, often provides a good approximation: $\tau_{max} = H/(3^{0.5})$. In turn, τ_{max} can be related approximately to the compressive strength f_c via Mohr's circles, which provides: $f_c = 2\ \tau_{max}$. Based on the above, we can state that the normalised trends of E and f_c with T should be similar to the trends of M and H measured directly by nano-indentation, which we report in Figures 3b and 3c and compare with the macroscopic experimental trends from Figures 1 and 2.

In addition to compressive strength and elastic moduli, recent experimental results from micro-scratching have provided a relationship between temperature, specific surface area of the C-S-H gel, and fracture toughness K_c (Krakowiak, Thomas et al. 2015). Here we convert fracture toughness to energy release rate $G_f = K_c^2/E$ using $E(T)$ from Figure 3b. The resulting fracture energies are compared to the macro-scale trends in Figure 2 (Figure 3d).

The tensile strength of the C-S-H is still difficult to characterize via nano-scale experiments. However, a recent computer model of the C-S-H gel based on strongly cohesive polydisperse particles (Masoero, Del Gado et al. 2012, Masoero,

Del Gado et al. 2014) allows simulating tensile stress-strain curves for C-S-H gels with different packing densities, here shown in Figure 3e. The tensile strengths f_t read from the stress-strain curves and combined with the information in Figure 3a, lead to the trends of f_t with T in Figure 3f.

CONCLUSIONS

From this nano/micro - macro comparison it appears that the effect of temperature on the nano/micro mechanical properties of cement paste might be responsible for a significant part of the experimentally observed trends at the macro-scale. The mechanical property that shows the worst micro-macro correlation is the fracture energy, which indicates that more work is currently needed to understand the scaling of fracture and to draw correlations between nano/micro-scale and macro-scale experimental measurements.

In this study, the change in packing density of the nano-scale cement hydrates is what controls the response to temperature gradients. This means that improving the nano-scale response to temperature gradients, e.g. in terms of reduced loss of packing density/increase in nano-porosity, has the potential to lead to improvements at all scales and to eventually impact the engineering performance of structures at elevated temperatures.

REFERENCES

Bonnaud, P. A., Q. Ji and K. J. Van Vliet (2013). "Effects of elevated temperature on the structure and properties of calcium-silicate-hydrate gels: the role of confined water." Soft Matter **9**(28): 6418-6429.

CEN (2004). BS EN 1992-1-2:2004 Eurocode 2: Design of concrete structures - Part 1-2: General rules - Structural fire design. London.

Cleveland, C. (2010). "Deepwater Horizon oil spill." Retrieved 9th December 2014.

Committee on Climate Change (2011). The Renewable Energy Review. London, UK, <http://www.theccc.org.uk/reports> Last accessed 28 Aug 2012.

Davie, C. T., C. J. Pearce and N. Bicanic (2010). "A Fully Generalised, Coupled, Multi-Phase, Hygro-Thermo-Mechanical Model for Concrete." Materials and Structures **43**(Sup. 1).

Davie, C. T., H. L. Zhang and A. Gibson (2010). Investigation of a Continuum Damage Model as an Indicator for the Prediction of Spalling in Fire Exposed Concrete. Proceedings of the 18th Annual Conference of the Association for Computational Mechanics in Engineering, Southampton.

Davie, C. T., H. L. Zhang and A. Gibson (2012). "Investigation of a continuum damage model as an indicator for the prediction of spalling in fire exposed concrete." Computers & Structures **94-95**: 54-69.

de Borst, R. and P. Peeters (1989). "Analysis of Concrete Structures under Thermal Loading." Computer Methods in Applied Mechanics and Engineering **77**(3): 293-310.

DeJong, M. J. and F.-J. Ulm (2007). "The nanogranular behavior of C-S-H at elevated temperatures (up to 700 degrees C)." Cement and Concrete Research **37**(1): 1-12.

Fu, Y. F. and L. Li (2011). "Study on mechanism of thermal spalling in concrete exposed to elevated temperatures." Materials and Structures **44**(1): 361-376.

Gawin, D., C. E. Majorana and B. A. Schrefler (1999). "Numerical Analysis of Hygro-Thermal Behaviour and Damage of Concrete at High Temperature." Mech of Cohesive-Frictional Mat. **4**: 37-74.
Heikal, M., H. El-Didamony, T. M. Sokkary and I. A. Ahmed (2013). "Behavior of composite cement pastes containing microsilica and fly ash at elevated temperature." Construction and Building Materials **38**: 1180-1190.
IAEA (2011). Mission Report: The Great East Japan Earthquake Expert Mission - IAEA International Fact Finding Expert Mission of the Fukushima Dai-Ichi NPP Accident Following the Great East Japan Earthquake and Tsunami. Tokyo, IAEA, Division of Nuclear Installation Safety, Department of Nuclear Safety and Security.
Krakowiak, K. J., J. J. Thomas, S. Muss, S. James, A.-T. Akono and F.-J. Ulm (2015). "Nano-chemo-mechanical signature of conventional oil-well cement systems: Effects of elevated temperature and curing time." Cement and Concrete Research **67**: 103-121.
Luccioni, B. M., M. I. Figueroa and R. F. Danesi (2003). "Thermo-mechanic model for concrete exposed to elevated temperatures." Engineering Structures **25**(6): 729-742.
Masoero, E., E. Del Gado, R. J. M. Pellenq, F. J. Ulm and S. Yip (2012). "Nanostructure and Nanomechanics of Cement: Polydisperse Colloidal Packing." Physical Review Letters **109**(15).
Masoero, E., E. Del Gado, R. J. M. Pellenq, S. Yip and F.-J. Ulm (2014). "Nano-scale mechanics of colloidal C-S-H gels." Soft Matter **10**(3): 491-499.
Němeček, J., L. Kopecký and Z. Bittnar (2004). Heat influence on micromechanical properties of cement pastes. Ia-FraMCos.
Nielsen, C. V., C. J. Pearce and N. Bicanic (2002). "Theoretical model of high temperature effects on uniaxial concrete member under elastic restraint." Magazine of Concrete Research **54**(4): 239-249.
Odelson, J. B., E. A. Kerr and W. Vichit-Vadakan (2007). "Young's modulus of cement paste at elevated temperatures." Cement and Concrete Research **37**(2): 258-263.
Parliamentary Office of Science and Technology (2011). Carbon Footprint of Electricity Generation.
Pearce, C. J., C. V. Nielsen and N. Bicanic (2004). "Gradient enhanced thermo-mechanical damage model for concrete at high temperatures including transient thermal creep." International Journal for Numerical and Analytical Methods in Geomechanics **28**(7-8): 715-735.
Peerlings, R. H. J., R. de Borst, W. A. M. Brekelmans and M. G. D. Geers (1998). "Gradient-enhanced damage modelling of concrete fracture." Mechanics of Cohesive-Frictional Materials **3**(4): 323-342.
Watanabe, K., M. R. Bangi and T. Horiguchi (2013). "The effect of testing conditions (hot and residual) on fracture toughness of fiber reinforced high-strength concrete subjected to high temperatures." Cement and Concrete Research **51**(0): 6-13.
Zhao, J., J.-j. Zheng, G.-f. Peng and K. van Breugel (2014). "A meso-level investigation into the explosive spalling mechanism of high-performance concrete under fire exposure." Cement and Concrete Research **65**(0): 64-75.

The effects of long term behavior of both concrete and prestressing tendons on the delayed deflection of a prestressed structure

J.-F. Barthélémy[1], J.-P. Sellin[1] and J.-M. Torrenti[2]

[1]CEREMA/DTecITM, 110 rue de Paris, BP 214, 77487 Provins Cedex, France; email: jf.barthelemy@cerema.fr, jean-philippe.sellin@cerema.fr
[2]IFSTTAR, 14-20 boulevard Newton, Cité Descartes, Champs sur Marne, F-77447 Marne la Vallée Cedex 2, France; email: jean-michel.torrenti@ifsttar.fr

ABSTRACT

This work aims at putting in evidence the coupled effects of both delayed deformations of concrete and relaxation of prestressing steel on the long term behavior of long span bridges. After recalling the possible origins of delayed deformations of prestressed concrete structures, the example of the Savines bridge is presented. This 65-year-old bridge shows excessive deflections at mid-spans which can not be predicted by the current Eurocode 2 creep laws, unless artificial coefficients are adjusted. Then a simplified prestressed cantilever beam is considered allowing to quasi-analytically address the problem of interaction between concrete creep and steel relaxation. The resolution of this problem with ageing material laws which are adapted from Eurocode 2 highlights the importance of the evolution of steel tendons after decades and allows to question the validity of laws used in models and the difficulty to identify the contributions of concrete and steel in the evolution of the deflection.

INTRODUCTION

Many examples of long span prestressed segmental box girders showing excessive deflections continuously increasing with time have been reported in the literature (Bažant et al., 2011). Nevertheless, although many progress have been made in the past years to increase the knowledge about materials such as concrete and steel, it remains difficult today to accurately predict the level reached by these deflections after a long time. In particular, standard concrete constitutive laws developed for engineering purposes may suffer from a lack of experimental validation since the duration of experiments is in general too short and some physical mechanisms responsible for the delayed deformations at the microscopic scale are still being debated among the scientific community.

The first part of this paper focuses on some published results about the possible origins of delayed deformations of prestressed concrete structures. The second part is then dedicated to the assessment of the Eurocode 2 ability to predict the evolution of the deflection of the Savines Bridge. Finally the third part presents the resolution of a

simplified structure in order to analyze the interaction between concrete creep and steel relaxation.

ORIGINS OF THE DELAYED DEFORMATION OF PRESTRESSED CONCRETE STRUCTURES

The delayed deformations occuring in a prestressed long span bridge may have several origins : shrinkage and creep of concrete (Acker and Ulm, 2001) and relaxation of prestressing steel (Muller and Zetterholm, 2002) as well as the interaction between these phenomena.

Concrete shrinkage, defined as the delayed deformation produced independently of any macroscopic loading, is mainly due to chemical, thermal and hygral process as recalled in (Acker and Ulm, 2001). Shrinkage will not be considered in the simplified model since its long term variation is assumed to be of lesser amplitude than creep if long-cycle variations of thermal and hygral conditions over decades can be neglected. Concrete creep corresponds to the delayed deformation in response to a macroscopic loading. It is usually decomposed into two parts: desiccation creep related to drying and basic creep in absence of water exchange with the exterior. The former exhibits a characteristic time depending on water transfer properties of concrete and the local notional size of the structure. Neglecting once again long-cycle variations of hygral conditions, its effect should stabilize with time such as shrinkage and will therefore not been considered in the simplified model.

The long term behavior of concrete remains a relatively open issue in the scientific community. The most often mentionned mechanisms in the literature are the solidification theory (Carol and Bažant, 1993) related to internal water movements and hydration process at short term and microcracking (Rossi et al., 2012) or viscous slippage between hydrate layers possibly in relation to microprestress variations (Bažant et al., 1997) at longer term. The actual behavior of concrete may result from a combination of those mechanisms at the small scale but it remains difficult to clearly identity each contribution. However an overall long term trend of the creep compliance law of any concrete is needed for structure calculation and the issue of the existence of a superior bound in the law is raised. Experimental results at the macroscopic scale (Brooks, 2005) as well as at the microscopic scale (Vandamme and Ulm, 2013) tend to argue in favor of a logarithmic time function representing the basic creep compliance law for large times. In order to compute the evolution of structures such as concrete bridges, several macroscopic laws of basic creep can be found in the literature as well as in standard codes. Let us for example cite the *B3* model (Bažant and Baweja, 2000) or the recent *fib* Model Code 2010 (*fib*, 2013) which provide a logarithmic trend of basic creep whereas compliance laws proposed in Eurocode 2, (NF EN1992-1-1, 2005) and (NF EN1992-2, 2006), exhibit an asymptotic trend tending towards a finite value for large times.

As regards steel relaxation, several models have been reported in the literature:

for example Eurocode 2-1-1 proposes a power law function whereas a bilogarithm function is derived from $42\ \mathrm{year}$ experiments in (Muller and Zetterholm, 2002). Besides, the steel relaxation function may also be limited by a possible bound from a given time. This point is discussed later in the simplified model.

Even if deflection measurements on prestressed concrete bridges suggest applying logarithmic concrete creep laws (Bažant et al., 2011), the interaction with the steel tendons still deserves to be questioned, especially concerning old tendons with an initial high tension. Indeed, the relaxation in this case could be rather high and could also explain a continuously growing deflection. The issue is now to know whether a deflection history is sufficient to identify the long term trend of both concrete creep and steel relaxation.

MODELLING THE LONG TERM BEHAVIOR OF THE SAVINES BRIDGE

Built at the end of the 60's, the Savines bridge belongs to the first generation of post-tension prestressed concrete bridges built in France by the free cantilever method. Each cantilever is linked with its adjacent counterpart thanks to an horizontal sliding hinge ideally transferring only shearing forces. A numerical model using the latter assumption is used in order to simulate the bridge as a cantilever using ST1 beam software (CEREMA (Structural Calculation and Software Division), 2015). The rather low number of available long term measurements of existing structures makes the Savines bridge an exceptional ressource for comparison of experimental data with models as defined in standards. Indeed, since the first findings of span sagging, vertical deformations are measured by levelling[1].

The deflection measured for a span as well as models computed according to the Eurocode 2 standards and the recent *fib* Model Code are plotted against time in Fig. 1. In-situ measurements far exceed computed deflections from any standard. These discrepencies might come from a non appropriated model used for the simulation, unknown characteristics or unadapted constitutive laws. That is why, in order to predict the evolution of deflection, it is proposed to reach in-situ measurements by means of an adaptation of compliance functions thanks to weighting coefficients. This approach requires to identify the parameters to which the deflection shows the highest sensitivity. In the present case, optimization parameters are the loss by relaxation of steel at $1000\ \mathrm{h}$, the specific weight of concrete and some additional weighting coefficients in the compliance function, either simple multiplicative coefficients acting on the basic creep or the desiccation creep terms or a coefficient allowing to modify the kinetics of the basic creep (see (Sellin et al., 2014) for more details).

Although this method makes it possible to reach the level of in-situ measure-

[1]Since the reference measurement baseline has changed several times without information cross-referencing, the deflections are defined up to an unknown translation from one dataset period to another. Consequently, for some dates, manual corrections are required in order to estimate likely values of absolute deflections and two trends are therefore imagined.

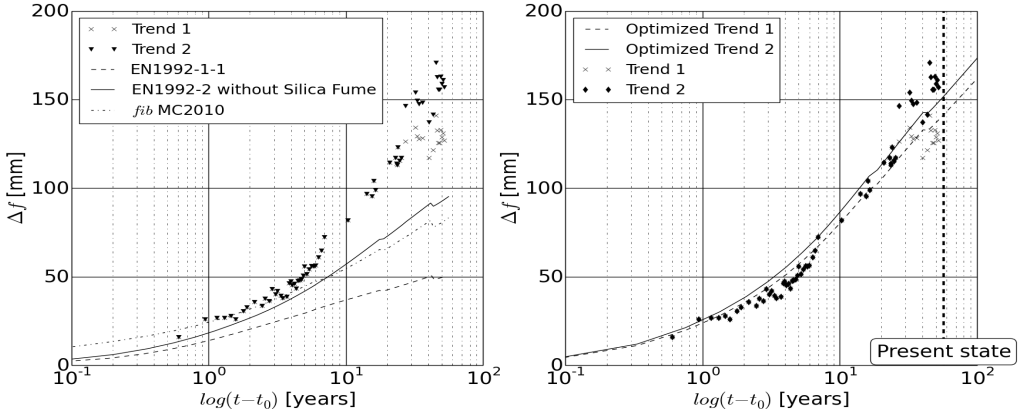

Figure 1. Comparison of the computed deflections with in-situ measurements before and after optimization.

ments, the analysis of the deflection raises several questions. Indeed Fig. 1 shows no stagnation of the deflection or even no change of curvature. This finding actually highlights the decisive role of steel relaxation, especially considering the fact that concrete shrinkage or creep laws from Eurocode 2 present asymptotic behaviors such that the evolution of the deflection would be expected to slow down before the end of the interval represented in Fig. 1. The evolution of relaxation as written in Eurocode 2-1-1 and as implemented in models presented in Fig. 1 follows a power law function of time. Nevertheless, Eurocode 2 offers the possibility to use the value of this function at 500000 h (about 57 years) for a rough assessment of the contribution of long term deformations at the end of service life. It is not really clear whether this value should be used as a bound when the entire evolution has to be calculated. This bound has not been introduced in the models presented in Fig. 1 but it is expected that such an initiative would affect the future evolution of the models and their predictive potential. Moreover the question of whether the deflection measurements alone bring enough information to quantify the contributions of concrete and steel and adapt the laws is also raised. This interrogation is the starting point for the following simplified analysis where the interaction between creep of concrete and relaxation of steel is regarded on a simple cantilever beam presenting geometrical characteristics close to those of the Savines bridge.

ANALYSIS OF THE COUPLED EFFECTS OF CONCRETE CREEP AND STEEL RELAXATION THROUGH A SIMPLIFIED MODEL

Let us consider in this paragraph a simplified model of prestressed cantilever concrete beam of length L oriented along x-axis (see Fig. 2). For the sake of simplicity, the prestress is assumed external and applied by steel tendons all located along the same

straight line at $y = h$ and subjected to an initial tension F at $t = t_0^-$. The beam is then loaded at $t = t_0$ by its own weight defined as a uniform lineic density P oriented downwards y-axis.

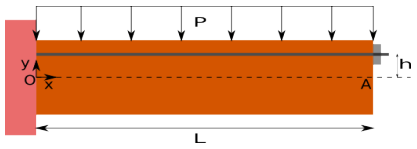

Figure 2. Prestressed cantilever beam

Resolution of the coupled viscoelastic problem

Let $N_c(x,t)$, $M_c(x,t)$ and $N_s(x,t)$ respectively denote the normal force and the bending moment supported by the concrete part of the beam and the normal tension within the whole set of steel tendons. The simplifying hypothesis of external prestressing implies that N_s is uniform along the beam and only depends on time t. According to stress free boundary conditions at $x = L$ and the balance law of the structure, it comes that (with the notation $H_{t_0}(t) = 1$ if $t \geq t_0$ and 0 if $t < t_0$)

$$N_c(t) = -N_s(t) \quad \text{and} \quad M_c(x,t) = N_s(t)h - H_{t_0}(t)P(L-x)^2/2 \tag{1}$$

The area A_c and the moment of inertia I_c around z-axis (see Fig. 2) of the concrete cross-section as well as the total area of the steel cross-section A_s are uniform along the beam. The displacement components and the axial strain of the neutral axis are denoted by $\xi_x^c(x,t)$, $\xi_y^c(x,t)$ and $\varepsilon_c = \partial \xi_x^c / \partial x$. The cross-section rotation $\theta_c(x,t)$ and its derivative $\chi_c = \partial \theta_c / \partial x$ are also introduced. The longitudinal displacement and strain of the steel tendons are respectively denoted by $\xi_x^s(x,t)$ and $\varepsilon_s = \partial \xi_x^s / \partial x$. At each time, any concrete cross-section is assumed to remain planar and orthogonal to the current neutral axis (Navier-Bernoulli condition). This implies that the rotation writes $\theta_c = \partial \xi_y^c / \partial x$ and $\chi_c = \partial^2 \xi_y^c / \partial x^2$ is the current curvature of the beam. The section at $x = 0$ corresponds to a fixed support, which means that $\theta_c(0,t) = 0$ and $\xi_x^c(0,t) = \xi_y^c(0,t) = 0$. Both concrete and steel are assumed to follow linear viscoelastic laws written for plane curvilinear structures as shown in (Salençon, 2009)

$$\varepsilon_c = J_c \circ N_c / A_c \quad ; \quad \chi_c = J_c \circ M_c / I_c \quad ; \quad \varepsilon_s = J_s \circ N_s / A_s \tag{2}$$

where $J_c(t,t')$ and $J_s(t,t')$ are respectively the concrete and steel uniaxial compliance laws, $E_c(t) = 1/J_c(t,t)$ and $E_s(t) = 1/J_s(t,t)$ are the instantaneous moduli and $\circ$ denotes the so-called Volterra operator which can be expressed by means of the Stieltjes integral (3) between time functions (Salençon, 2009)

$$Y = f \circ X \quad \Leftrightarrow \quad Y(t) = \int_{t_0}^{t} f(t,t') \, \mathrm{d}X(t') \quad \text{if} \quad X(t') = 0 \text{ for } t' < t_0 \tag{3}$$

In the following, the notations $J_c^{t_0}(t) = J_c(t, t_0)$ and $J_s^{t_0}(t) = J_s(t, t_0)$ are used.

Although the influence of the anchorage seating g may be minor in such a case of an external prestressing, it is easy to consider it in the expression of the initial normal force applied to tendons

$$N_s^0 = N_s(t = t_0) = F - E_s^0 A_s g/L \quad \text{with} \quad E_s^0 = E_s(t_0) \tag{4}$$

The expressions of the displacement and rotation fields at time t_0^-, i.e. just after the anchorage of steel tendons but before the application of the own weight, write thanks to (1), (2) and (4) with $E_c^0 = E_c(t_0)$

$$\begin{array}{l} \xi_x^c(x, t_0^-) = -N_s^0 x/(E_c^0 A_c) \quad ; \quad \theta_c(x, t_0^-) = N_s^0 hx/(E_c^0 I_c) \\ \xi_y^c(x, t_0^-) = N_s^0 hx^2/(2E_c^0 I_c) \quad ; \quad \xi_x^s(x, t_0^-) = N_s^0 x/(E_s^0 A_s) \end{array} \tag{5}$$

After applying the own weight, those fields (functions of t and x) become at $t \geq t_0$

$$\begin{array}{l} \xi_x^c = -J_c \circ N_s x/A_c \quad ; \quad \theta_c = J_c \circ N_s hx/I_c + J_c^{t_0} PL^3\big((1 - x/L)^3 - 1\big)/(6I_c) \\ \xi_y^c = J_c \circ N_s hx^2/(2I_c) + J_c^{t_0} PL^4\big(-(1 - x/L)^4 - 4x/L + 1\big)/(24I_c) \\ \xi_x^s = J_s \circ N_s x/A_s \end{array} \tag{6}$$

The consistency between the kinematics of the concrete beam and the tendons is obtained by equality of the relative horizontal displacements at the anchorage point

$$\xi_x^s(L, t) - \xi_x^s(L, t_0^-) = \xi_x^c(L, t) - h\theta_c(L, t) - \big(\xi_x^c(L, t_0^-) - h\theta_c(L, t_0^-)\big) \tag{7}$$

Introducing (5) and (6) in (7) allows then to deduce the tension N_s and the deflection $D = -\xi_y^c(x = L)$ as the following time functions

$$N_s = K^{\circ -1} \circ \big(H_{t_0} K_0 N_s^0 + J_c^{t_0} PhL^2/(6I_c)\big) \; ; D = \big(J_c^{t_0} PL^2/4 - J_c \circ N_s h\big)\, L^2/(2I_c) \tag{8}$$

with

$$K = J_s/A_s + J_c/\tilde{A}_c \quad ; \quad K_0 = 1/(E_s^0 A_s) + 1/(E_c^0 \tilde{A}_c) \quad ; \quad \tilde{A}_c = \big(A_c^{-1} + h^2/I_c\big)^{-1} \tag{9}$$

and $K^{\circ -1}$ inverse in the sense of the Volterra operator (3) of the kernel K (9).

Application to modified Eurocode 2 laws

In this section, specific concrete and steel viscoelastic laws are considered. As at least the concrete law is assumed of the ageing type, it is not possible to resort to the Laplace-Carson transform to achieve the determination of the evolutions of N_s and D in (8). Nevertheless, the latter can be obtained through a numerical integration strategy allowing to estimate the Volterra integral operators appearing in (8). An algorithm based on the trapezoidal rule has been proposed in (Bažant, 1972) also recently exploited in (Sanahuja, 2013). It relies on a given (not necessarily linearly distributed) time discretization between t_0 and a final time. Any time variable in (8) is seen as

a vector which components correspond to its values at the successive discretization times. Moreover the Volterra operators become matrix multiplications in which matrices are derived from the kernels J_c, J_s, their combination K (9) or inverse (simple matrix inversion) thanks to the procedure presented in (Sanahuja, 2013).

Assuming that the origin of time $t = 0$ is taken at concrete casting of the whole beam, the concrete basic creep compliance law (including the instantaneous elastic part) proposed in Eurocode 2-2 (NF EN1992-2, 2006) writes

$$J_c(t,t') = \frac{1}{E_c(t')} + \frac{\varphi_{b0}(t')}{E_c^*} \frac{\sqrt{t-t'}}{\sqrt{t-t'} + \beta_{bc}(t')} \quad \text{with} \quad E_c^* = 1.05\, E_c(28\,\text{days}) \tag{10}$$

The instantaneous modulus $E_c(t)$ needed in (10), depending on the time elapsed since concrete casting, is related in Eurocode 2-2 to the instantaneous mean compressive strength $f_{cm}(t)$ by

$$E_c(t) = A\ \left(f_{cm}(t)/B\right)^{0.3} \text{ with } A = 22 \text{ GPa and } B = 10 \text{ MPa} \tag{11}$$

in which $f_{cm}(t)$ writes with respect to the characteristic compressive strength f_{ck} at 28 days and a coefficient s depending on the cement type (see Eurocode 2-2) as

$$f_{cm}(t) = (f_{ck} + f_0) \exp\left[s\left(1 - \sqrt{\frac{\tau_c}{t}}\right)\right] \text{ with } f_0 = 8 \text{ MPa and } \tau_c = 28 \text{ days} \tag{12}$$

The functions $\varphi_{b0}(t)$ and $\beta_{bc}(t)$ have two definitions in Eurocode 2-2 depending on the presence or not of silica fume. It will be considered in the following that the concrete does not contain any, which corresponds to

$$\varphi_{b0}(t) = 1.4 \quad ; \quad \beta_{bc}(t) = \beta_{bc}^0 \exp\left(3.1 \frac{f_{cm}(t)}{f_{ck}}\right) \text{ with } \beta_{bc}^0 = 0.4\sqrt{\text{ days}} \tag{13}$$

The steel relaxation function $R_s(t,t')$, defined as the inverse of $J_s(t,t')$ in the sense of the Volterra operator (3) is built here from an adaptation of the expression proposed in Eurocode 2-1-1

$$R_s(t,t') = E_s^0 \left(1 - k_1 \rho_{1000} e^{k_3 \mu} \left(\frac{t-t'}{\tau_s}\right)^{0.75(1-\mu)}\right) \text{ with } \tau_s = 1000 \text{ h} \tag{14}$$

where μ is the ratio between the tensile stress at time t' and the steel tensile strength but is considered here as a positive constant (lower than 1) in order to remain in the linear viscoelastic framework. The constants k_1, k_3 and the tensile loss by relaxation at 1000 h denoted by ρ_{1000} depend on the class of steel tendons. Three classes corresponding to intervals of ρ_{1000} are defined in Eurocode 2-1-1. Although $R_s(t,t')$ continuously decreases with t, Eurocode 2-1-1 suggests using the value at 500000 h to assess the long term contribution of the steel relaxation to the behavior of the structure without

calculating the whole structure history. But the issue whether this value should also play the role of a bound when the whole structure history is sought or whether the relaxation goes on following the power law trend (14) even after 500000 h is not really resolved in Eurocode 2-1-1.

Two first models are built to analyze the effect of bounding the relaxation. Both are based on the concrete compliance law (10) and the steel relaxation (14) but, in the first one denoted by **M1**, the relaxation function is assumed to remain constant when $t-t'$ exceeds 500000 h whereas the second one **M2** is characterized by the power law (14) at any time. The numerical values required in the calculations are gathered in Tab. 1 and the deflection and steel tension evolutions are plotted against time in Fig. 3.

Table 1. Numerical values

Variable	Value	Variable	Value	Variable	Value
t_0	28 days	L	36 m	h	1 m
A_c	5 m^2	I_c	8 m^4	$\tilde{A}_c$	3.08 m^2
A_s	360 cm^2	F	46.8 MN	g	6 mm
P	125 kN/m	E_s^0	190 GPa	E_c^0	35.2 GPa
f_{ck}	40 MPa	s	0.2	ρ_{1000}	10 %
k_1	$5.39\,10^{-5}$	k_3	6.7	μ	0.8

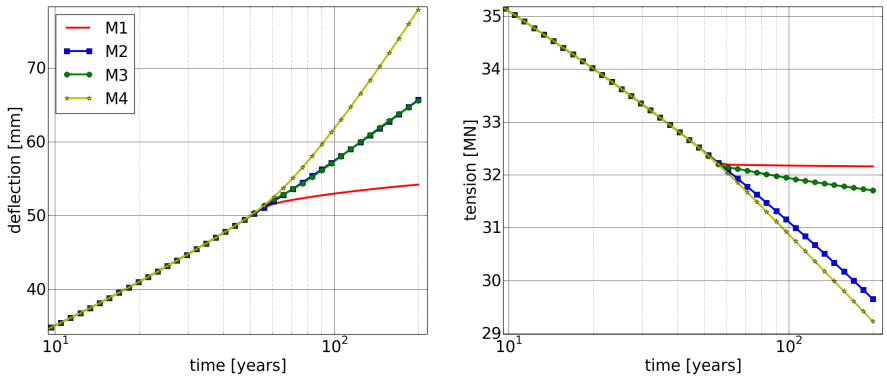

Figure 3. Evolution of the beam deflection and the prestressing tension

As it can be noticed in Fig. 3, **M1** is impacted by the limitation of steel relaxation after 500000 h (about 57 years) together with the asymptotic constant branch of concrete creep. On the contrary, both deflection and tendon tension in **M2** follow the same trends as before 500000 h. It is now interesting to consider the case of a bounded steel relaxation and an unbounded concrete compliance and examine whether the same deflection as in **M2** can be obtained with this new combination. A new concrete law is thus built by adding a $\log$ term to (10) activated only if $t-t' \geq \tau$. The proposed new law ensuring the continuity of the compliance function as well as its derivative

with respect to t in $t = t' + \tau$ is given in (15). Three constants τ, a and b have to be optimized in order to minimize the difference with the deflection provided by **M2** through a least-square method. The obtained model in which $a = 0.35$, $b = 2.43$, $\tau = 44.4$ years is called **M3** and the deflection and tendon tension are plotted in Fig. 3.

$$J_c(t,t') = \frac{1}{E_c(t')} + \frac{\varphi_{b0}(t')}{E_c^*}\frac{\sqrt{t-t'}}{\sqrt{t-t'}+\beta_{bc}(t')} + a\frac{\log\left(1+b\left(\frac{t-t'}{\tau}-1\right)^2\right)}{E_c^*}H_\tau(t-t') \quad (15)$$

Starting from **M1** as a reference, Fig. 3 shows that **M2** undergoes a much higher loss of steel tension than **M3** while both models equally increase the deflection. Although both concrete creep and steel relaxation have a high influence on the deflection, it seems that the tension in tendons is more impacted by releasing the bound constraint on the steel relaxation than by adding a $\log$ term into the concrete creep law. Finally a last model **M4** is built with the same creep concrete law as in **M3** but without any bound on the steel relaxation. Comparing **M3** and **M4** in Fig. 3 clearly puts again in evidence the great effect of steel relaxation on both the deflection and the tension.

CONCLUSION

After analyzing in details the deflection of the Savines Bridge, a synthetic simplified model has been built in order to examine the effects of concrete creep, steel relaxation and their coupling on a structure response in terms of deformation and prestressing tension. Standard creep and relaxation laws may fail to explain the evolution of the deformation of old long span prestressed bridges. It becomes then necessary to adapt these laws by taking advantage of in-situ measurements. The latter remain the most precious source of long term information since laboratory tests lasting for several decades as well as techniques to speed up time-dependent processes seem out of reach. Nevertheless, the example of Savines has pointed out the importance of the completeness of gathered data as well as the preservation of a reliable reference point for levelling data. The synthetic model has allowed to perform simple calculations involving various creep and relaxation laws in order to put in evidence their coupled effects. One of the major findings has been the insufficiency of the deflection history alone to determine the actual trend of the concrete creep law. It has indeed proved impractical to distinguish the contribution of concrete creep and that of steel relaxation from the sole observation of a logarithmic trend of beam deflection since two different combinations of laws have led to the same result. In contrast, any information about the evolution of the prestressing tension, by means for example of the crossbow method, could usefully complement the available data and make it possible to adjust more reliably the creep and relaxation laws. Another more ambitious way of identifying long term material behaviors consists in improving and justifying upscaling techniques based on a fine analysis and characterization of the microscopic origins of delayed deformations ((Bažant et al., 1997), (Sanahuja and Dormieux, 2010), (Sanahuja, 2013), (Vandamme and Ulm, 2013)).

References

Acker, P. and Ulm, F. J. (2001). Creep and shrinkage of concrete: Physical origins and practical measurements. *Nucl. Eng. Des.*, 203(2-3):143–158.

Bažant, Z. P. (1972). Numerical determination of long-range stress history from strain history in concrete. *Matériaux Constr.*, 5(1):135–141.

Bažant, Z. P. and Baweja, S. (2000). Creep and Shrinkage Prediction Model for Analysis and Design of Concrete Structures : Model B3. In Al-Manaseer, A., editor, *Adam Nevill Symp. Creep Shrinkage - Struct. Des. Eff.*, volume 83, pages 1–83, Farmington Hills, Michigan. ACI SP-195.

Bažant, Z. P., Hauggaard, A. B., Baweja, S., and Ulm, F.-J. (1997). Microprestress-Solidification Theory for Concrete Creep I: Aging and Drying Effects. *J. Eng. Mech.*

Bažant, Z. P., Hubler, M. H., and Yu, Q. (2011). Excessive Creep Deflections : An Awakening. *Concr. Int.*, pages 44–46.

Brooks, J. (2005). 30-year creep and shrinkage of concrete. *Mag. Concr. Res.*, 57(9):545–556.

Carol, I. and Bažant, Z. P. (1993). Viscoelasticity with Aging Caused by Solidification of Nonaging Constituent. *J. Eng. Mech.*

CEREMA (Structural Calculation and Software Division) (2015). ST1 structural software, website: http://www.setra.fr/html/logicielsOA/logiciels.htm.

fib (2013). *fib* Model Code for Concrete Structures 2010.

Muller, H.-R. and Zetterholm, S. (2002). Results of Extreme Long Duration of a Relaxation Test (42 years) on Prestressing Steel. In *Proc. first fib Congr.*, pages 8–385–8–390, Osaka.

NF EN1992-1-1 (2005). Eurocode 2: Design of concrete structures - Part 1-1: General rules and rules for buildings.

NF EN1992-2 (2006). Eurocode 2: Design of concrete structures - Part 2: Concrete bridges - Design and detailing rules.

Rossi, P., Tailhan, J.-L., Le Maou, F., Gaillet, L., and Martin, E. (2012). Basic creep behavior of concretes investigation of the physical mechanisms by using acoustic emission. *Cem. Concr. Res.*, 42:61–73.

Salençon, J. (2009). *Viscoélasticité pour le calcul des structures*. Ecole Polytechnique.

Sanahuja, J. and Dormieux, L. (2010). Creep of a C-S-H gel: A micromechanical approach. *An. Acad. Bras. Cienc.*, 82:25–41.

Sanahuja, J. (2013). Effective behaviour of ageing linear viscoelastic composites: Homogenization approach. *Int. J. Solids Struct.*, 50(19):2846–2856.

Sellin, J.-P., Barthélémy, J.-F., Torrenti, J.-M., and Bondonet, G. (2014). Delayed deformations of segmental prestressed concrete bridges: the case of the Savines Bridge. In van Breugel, K. and Koenders, E., editors, *Proc. 1st Ageing Mater. Struct. 2014 Conf.*, number 217062, pages 266–273, Delft, The Netherlands.

Vandamme, M. and Ulm, F. J. (2013). Nanoindentation investigation of creep properties of calcium silicate hydrates. *Cem. Concr. Res.*, 52:38–52.

On the Very Long-Term Delayed Behavior of Biaxially Prestressed Structures: The Case of the Containments of Nuclear Power Plants

F. Benboudjema[1] and J. M. Torrenti[2]

[1]LMT-Cachan/ENS-Cachan/CNRS/Université Paris Saclay. E-mail: farid.benboudjema@ens-cachan.fr
[2]IFSTTAR, Department Materials and Structures, Université Paris-Est. E-mail: jean-michel.torrenti@ifsttar.fr

Abstract

The typical French reactor building consists of two concentric containments. The outer containment is made with reinforced concrete. The inner containment is biaxially prestressed, from 80 to 120 cm thick, and designed to withstand an internal pressure of 0.5 MPa (absolute) in case of an accident. In order to avoid tensile stresses in concrete, a prestress is applied, corresponding to compressive stresses in concrete of about 8.5 MPa and 12 MPa along vertical and tangential directions, respectively. In order to maintain enough prestressing in the structure, the delayed behavior of concrete on the very long term should be correctly assessed. The measurements of the very long term deformations of larges bridges and of nuclear containments seem to indicate that, on the very long term, creep strains are function of the logarithm of time. In particular, the measurements of delayed strains in the containment wall show two distinct kinetics:

- the difference between tangential and vertical strains, which exhibits a fast kinetics and becomes almost constant after 500 days,
- the average of tangential and vertical strains undergoes a slow kinetics. If vertical and tangential strains rates are equal (despite different values of the prestressing), this means that the long term biaxial creep deformations are only sensible to the mean stress and independent of deviatoric ones.

In the recent Model Code 2010 creep is expressed as a combination of an asymptotic and a logarithmic function. The logarithmic function corresponds to basic creep while drying creep is asymptotic. Using this model for delayed strains, and adding the possibility to adjust the parameters of the relations proposed by MC2010 on experimental results, the evolution of the strains is calculated and compared to in situ measurements. We finally discuss the set of adjusted possible parameters.

INTRODUCTION – BASIC CREEP OF CONCRETE

The typical French reactor building consists of two concentric containments (fig. 1). The outer containment, designed to sustain external aggressions, is made with reinforced concrete. The inner containment is biaxially prestressed, from 80 to 120 cm thick, and designed to withstand an internal pressure of 0.5 MPa (absolute) in case of an accident. In order to avoid tensile stresses in concrete, a prestress is applied,

corresponding to compressive stresses in concrete of about 8.5 MPa and 12 MPa along vertical (zz) and tangential (θθ) directions, respectively. In the previous generation of French Nuclear Power Plant (NPP), there was no metallic liner inside the internal containment. So the tightness of the containment in case of an accident is only assured by concrete. To limit leakage, cracking should be avoided and, so, tensile stresses should remain below the tensile strength of concrete. That is why the evolution of prestressing forces during time is critical for the NPP operation and why a good prediction of the evolution of delayed strains of the containment is needed.

To predict the evolution of prestressing forces with time, the delayed behavior of the constitutive materials (relaxation for steel and creep and shrinkage for concrete) has to be modelled precisely on the long term. In this paper only creep of concrete is considered and two problems are discussed: is the very long term creep asymptotic or not and how to deal with biaxial stresses?

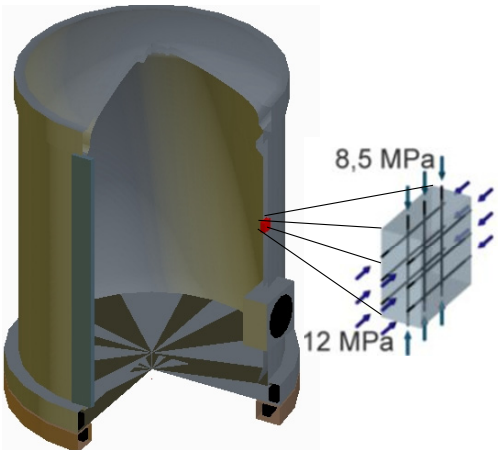

Figure 1. Simplified diagram of the containment and its prestressing.

IS THE VERY LONG TERM CREEP ASYMPTOTIC?

Laboratory tests

Classical creep tests in laboratory last generally less 2 or 3 years (and sometimes less). With such duration it is possible using these tests to fit as well an asymptotic or a logarithmic evolution of strains. There are nevertheless some basic creep tests performed by Brooks (Brooks, 2005) with a duration of 30 years, Troxell (Troxell, 1958) and Russell (Russel, 1989) with a duration of 20 years. These tests performed on concretes with different water to cement ratio and with different aggregates types, show that basic and total creep are not asymptotic (figure 2). It should be emphasized that, the specimens are either tested under water (Brooks, 2005) or tested under autogeneous conditions (Troxell, 1958; Russel, 1989). Thus, it means in the latter case, it is not sure that the specimens are not undergoing some parasite drying.

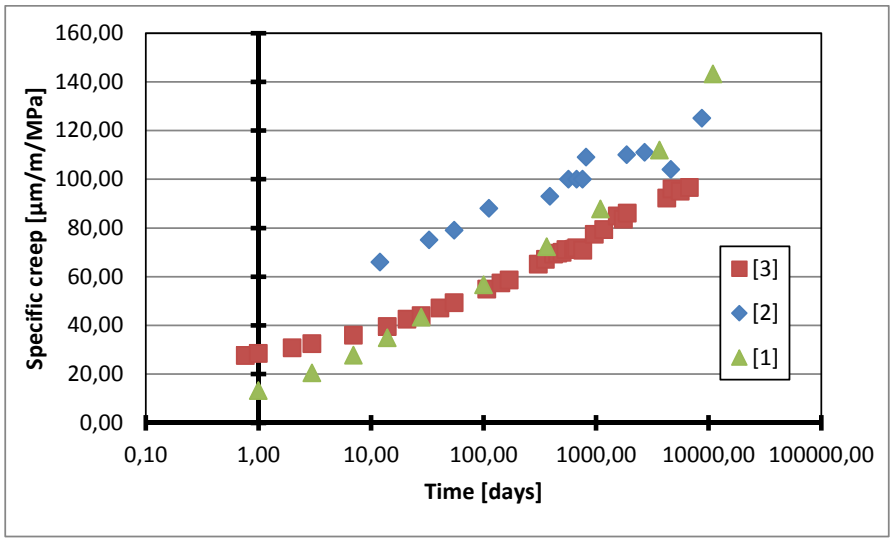

Figure 2. Basic creep of concrete; [1]=(Brooks, 2005), [2]=(Troxell, 1958) and [3]=(Russel, 1989)

Long term deformations of prestressed structures

The observation of the deflections of several bridges built by means of prestressed box girders indicates rather clearly that long term deflections are not asymptotic (Bazant et al., 2011) (Vitek and Křístek, 2000) (Sellin et al., 2015). In the case of NPP, thanks to a large monitoring of the behavior of the containment, global and local deformations are measured. Figure 3 presents the evolution of the deformations of the central part of the containment of three French NPP. The long term behavior in the two directions of the prestressing is not asymptotic and seems in accordance with a logarithmic evolution with time. Note that in the global behavior of the structure, the effects of drying shrinkage and relaxation of the prestressing tendons are included in the delayed strains.

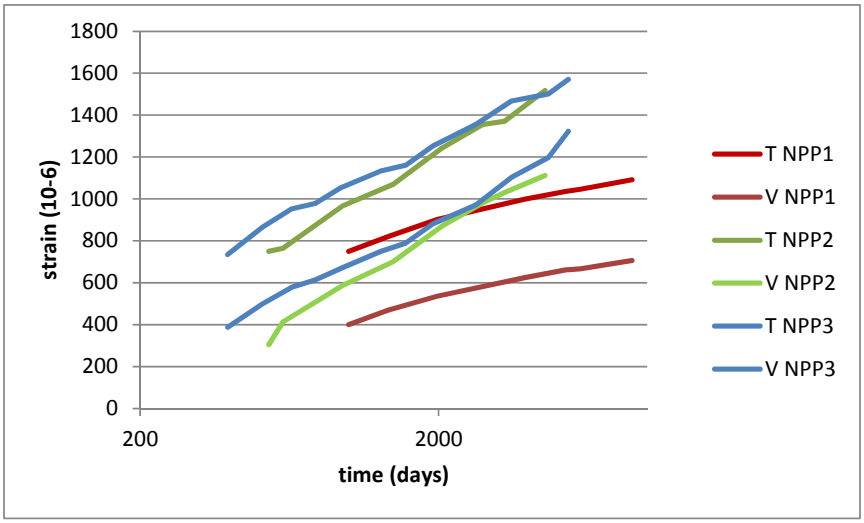

Figure 3. Evolution of the deformations in the central part of the containment of 3 NPP (V=vertical strains, T=tangential strains)

Consequences in codes

In the actual Eurocode 2 (EN1992-1-1, 2005), creep is calculated by means of an asymptotic hyperbolic function (equation 1) while in the recent Model Code 2010 creep is expressed as a combination of an asymptotic and a logarithmic function (equation 2) (Muller et al., 2013). In the latter case the logarithmic function corresponds to basic creep while drying creep is asymptotic.

$$\varepsilon = \frac{\sigma}{Ec}\, a\, f_1(h) \left(\frac{t-t0}{b\, g_1(h)+(t-t0)}\right)^c \qquad \text{[eq. 1]}$$

$$\varepsilon = \frac{\sigma}{Ec}\left[a\, f_2(h) \left(\frac{t-t0}{b\, g_2+(t-t0)}\right)^c + d \ln\left(1 + e(t-t0)\right)\right] \qquad \text{[eq. 2]}$$

where a, b, c, d and e are fitted constants. f_1, f_2, g_1 and g_2 are functions of the notional size h and the relative humidity RH. These functions are given by Eurocode 2 and MC2010.

Using these equations, it is possible to adjust the parameters on experimental results obtained in the laboratory by Granger (Granger, 1995). Figure 4 shows that it is possible to find a set of parameters that could fit the experimental results (at least on the long term which is the most important), for a sample with a diameter of 16cm stored in a relative humidity RH=50%, despite the fact that the used equations are very different.

The creep models being optimized on a sample, it is possible to predict the creep deformations of a larger structure. In our case, a structure with a notional size h=800mm and loaded under a constant uniaxial stress of 12MPa and a RH of 50% is considered. Figure 5 shows that in this case at very long term large differences occur despite a good calibration of the model on the same test. This is of course due to the differences in the nature of the equations (asymptotic or not) and it shows the importance of the physical manner to model the very long term behaviour of concrete structures. It indicates also that the observation of the behaviour of a sample, even during 3 years, is not enough to predict the correct behaviour of a structure during several decades.

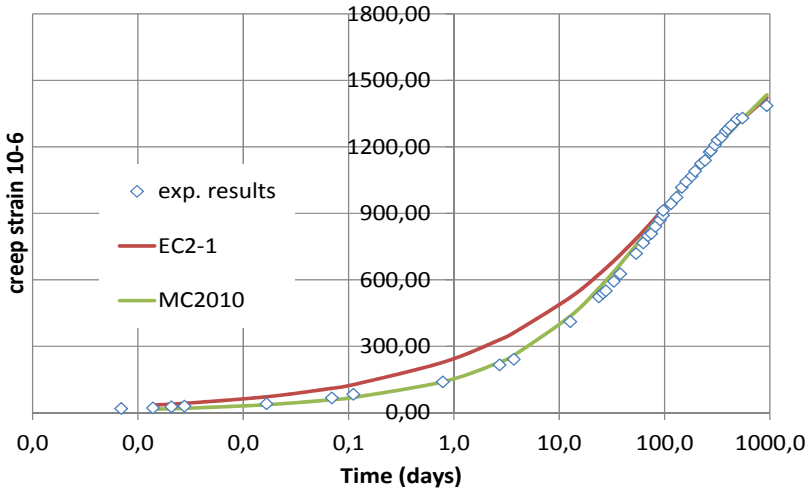

Figure 4. Comparison of experimental results [8] and models corresponding to equations 1 and 2. σ=12MPa, RH=50%, h=80mm.

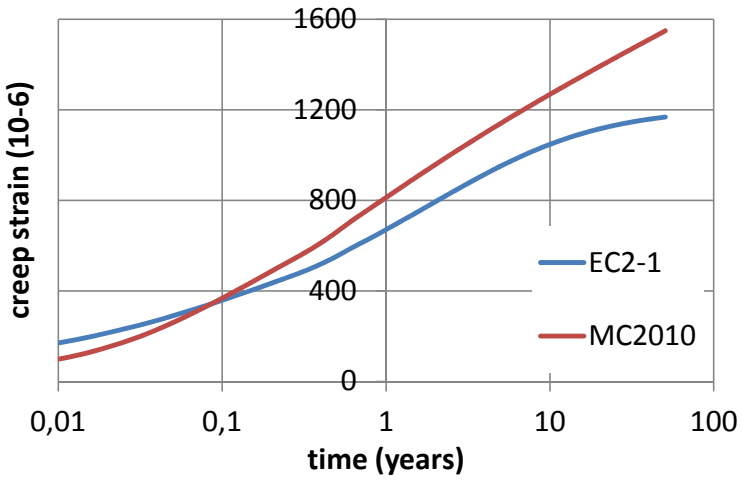

Figure 5. Comparison of the estimated creep strains using equations 1 and 2, parameters fitted on laboratory experiment, σ=12MPa, RH=50%, h=800mm

LONG TERM DEFORMATIONS OF A NPP

Analysis of the behavior of containment vessels

In Figure 3, the evolution of the biaxial deformations during times in a NPP was presented. From these deformations one can express the evolutions of the average and the difference of the vertical and tangential strains. These evolutions are presented figures 6 for the same three NPPs (Barré et al., 2014). It can be seen that the delayed strains in the containment wall follow two distinct kinetics:

- the difference between tangential and vertical strains, which exhibits a fast kinetics and becomes almost constant after 500 days,

- the average of tangential and vertical strains, which corresponds to a slow kinetics. If vertical and tangential strain rates are equal despite different values for the prestressing, this means that in the long term biaxial creep deformations are only sensible to the mean stress and independent of deviatoric ones. If biaxial creep is expressed using a tangent Poisson ratio, this is equivalent to a Poisson ratio equal to -1. This is what is proposed actually in Eurocode 2 part 1 (French national annex) for drying creep (NF EN 1992-2, 2005), as for basic creep it is proposed to use a Poisson ratio equal to the elastic one. It could be explained for instance if one assumes that drying creep is only an amplification of drying creep due to the loading (as proposed in (Sellier and Buffo-Lacarrière, 2009). In fact, the behavior of the containment vessel is also affected by other phenomena like drying shrinkage and relaxation of the prestressing. So a more complete modelling is needed.

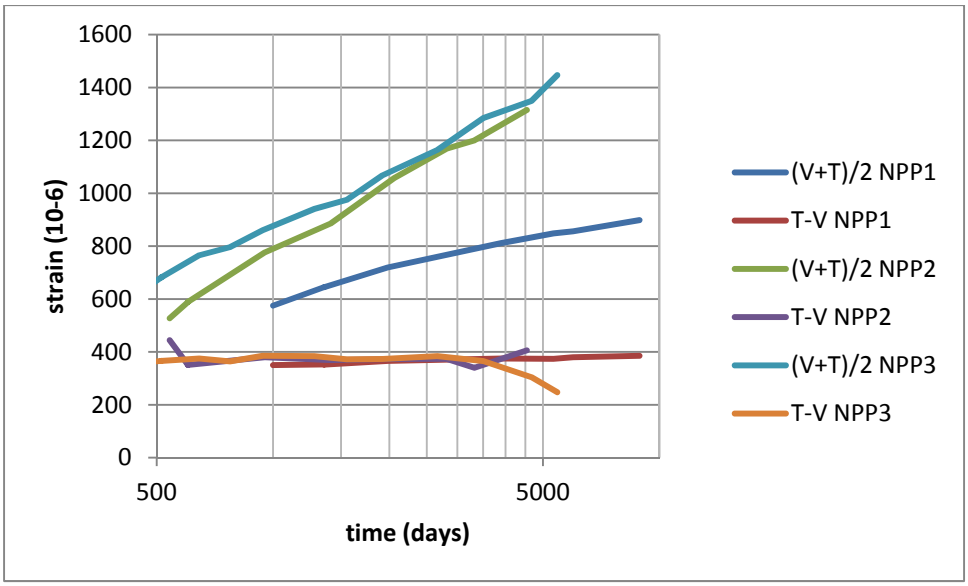

Figure 6. Evolutions of the tangential (T) and vertical (V) deformations in the central part of the containment of the three NPPs – same data as in figure 3.

Modelling

To model the biaxial behavior of the containment the following assumptions are made:

- Free boundary conditions are assumed (no structural effect),
- Boltzmann superposition principle is used,
- MC2010 relations are used for drying shrinkage, basic and drying creep of concrete and for steel relaxation,
- Kinetics and amplitude of drying shrinkage, basic and drying shrinkage could be adjusted by means of 6 parameters (see eq.2) to experimental results (laboratory tests or in-situ measurements),
- Uniaxial relations for creep are extended to 3D by means of two constant Poisson ratio for basic and desiccation creep – see (Aili et al., 2015) for a discussion about Poisson ratio for creep,
- The vertical prestressing corresponds to a vertical stress of 8,5MPa and a tangential stress of 12MPa.

To limit the number of parameters when adjustments are made Poisson ratio is taken equal to 0,35 for basic creep (Galenne et al., 2013) and -1 for drying creep (as recommended in the French national annex of Eurocode 2 part 1). Then, three scenarii are tested:

- 1st scenario: MC2010 relations are directly used
- 2nd scenario: MC2010 relations are adjusted to laboratory data (like in figure 4)
- 3rd scenario: MC2010 relations are adjusted to in-situ measurements

Figure 7 shows the comparison between experimental results and the modellings following the three different scenarii. One can see that:

- MC2010 relations underestimate the delayed deformations (scenario 1),
- with adjustment of the MC2010 relations for creep on laboratory tests, delayed strains are closer of the measured ones but still underestimated (scenario 2),
- it is possible to adjust MC2010 relations to obtain a good agreement with in-situ measurements (scenario 4). Figure 8 shows the results of the modelling following this scenario and measurements corresponding to figure 6 (difference between tangential and vertical strains). These results indicate that it is possible to predict the behavior of the containment on a reasonable period of time.

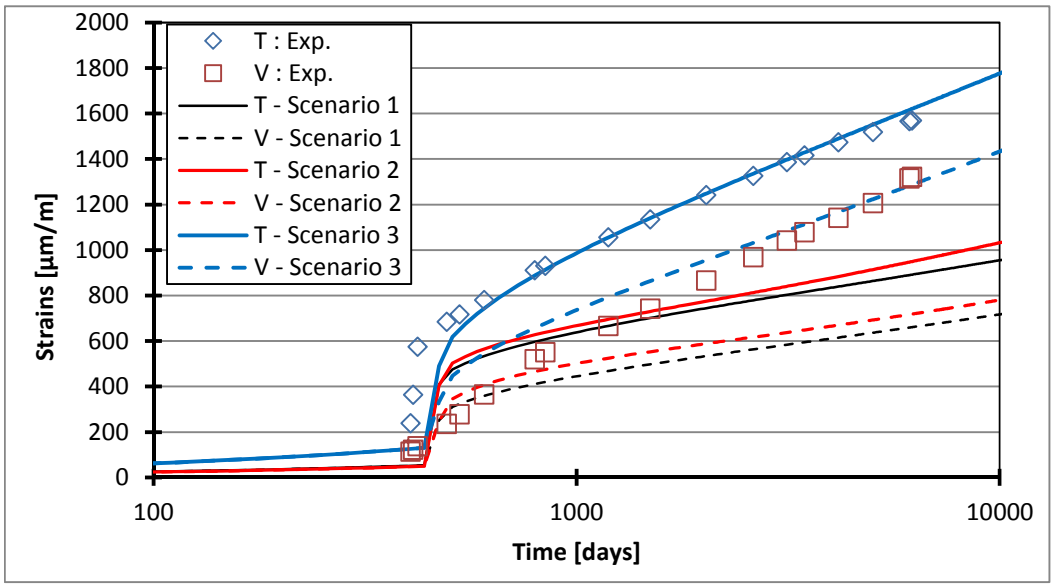

Figure 7. Comparison between in-situ measurements of tangential and vertical strains and modelling following the three scenarii

It should be emphasized that due to the large number of unknown factors when using only measurements on structures (at least 10 parameters: Young modulus; elastic, basic creep and drying creep Poisson ratio; amplitude and kinetic correction factor related to drying shrinkage, basic and drying creep), it is possible to find by inverse analysis a large number of material parameters allowing for reproducing rather correctly the experimental measurements. The analysis of the possible sets of parameters is actually conducted. Besides, the vertical and tangential prestress is supposed to be applied instantaneously. In reality, the duration of the prestress application last approximatively 3 and 7 months for the tangential and vertical prestress, respectively. It explains partially that it is difficult with here to capture the beginning of the vertical strain evolution.

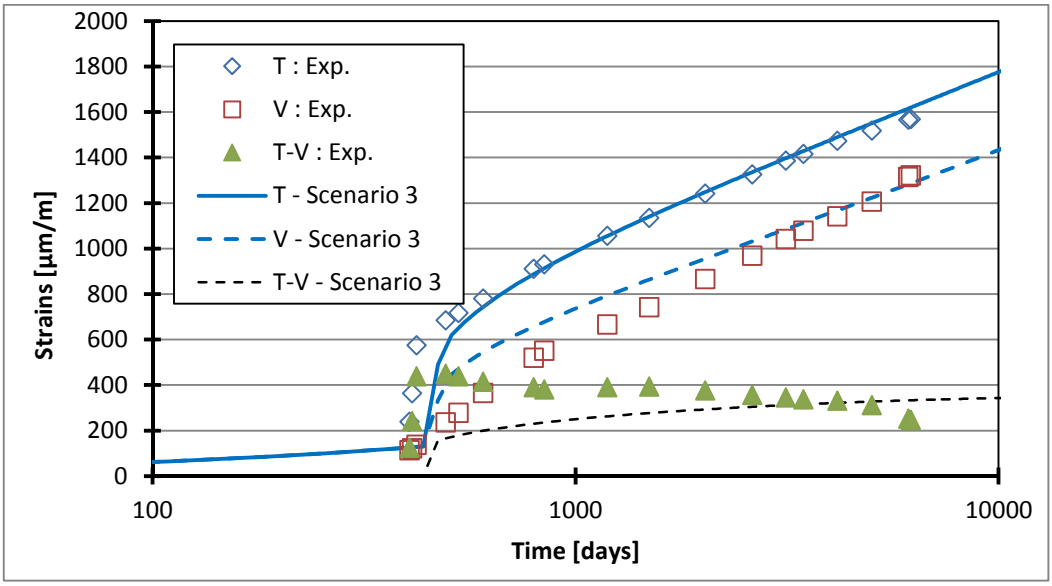

Figure 8. Comparison between in-situ measurements of tangential and vertical strains and of the difference between theses strains and modelling following the scenario 3.

Table 1. set of parameters for the three scenarii of figure 7.

		Scenario 1	Scenario 2	Scenario 3
Drying shrinkage	Amplitude	1	0.95	2.4
	kinetics	1	1.05	0.95
Basic creep	Amplitude	1	2.71	3.2
	kinetics	1	0.063	0.73
Drying creep	Amplitude	1	1.28	2.3
	kinetics	1	0.43	1.93

CONCLUSION

The main conclusions of this work are the following ones:

- Very long term creep in laboratory or of real structures seems to be non-asymptotic
- Using a long test (3 years) in a laboratory is not enough to assess the long term behavior of a massive structure for several decades. We need physical relations for creep in codes in order to predict correctly the delayed behavior of massive structures!
- Biaxial creep of nuclear power plant could be modelled using data of the structure itself. This would allow to predict the delayed behavior of these structures. Further work is needed to improve the prediction in the design phase.

In short-term perspective, effect of temperature will be investigated (the service temperature in a NPP is around 40°C), since it will increase delayed strains and prestress relaxation. In mid-term perspective, numerical simulations will be

undertaken (Benboudjema and Torrenti, 2014; Hilaire et al., 2014), and compared in order to investigate the structural effects such as gradients of shrinkage and restraint (dome and raft foundation).

REFERENCES

Aili A., Vandamme M., Torrenti J.-M., *Difference Between Creep And Relaxation Poisson's Ratios: Theoretical And Practical Significance For Concrete Creep Testing,* Concreep10 conference, 2015.

Barré F., Chauvel D., Coste J.-F., Ragouin R., Rospars C., Torrenti J-M., *Enhancement of the assessment of the concrete creep and shrinkage strains*, colloque TINCE 2014, Paris, 2014.

Bažant, Z. P., Hubler, M., Yu, Q., Excessive creep deflections: An awakening. *Concrete international*, n°33(8), pp 44-46, 2011.

Benboudjema F., Torrenti J.-M., Modelling desiccation shrinkage of large structures, European Physics Journal Conferences. Volume 56, 2013

Brooks J. J., 30-Year creep and shrinkage of concrete. *Mag. Concr. Res*., 57(9), 545–556, 2005.

EN1992-1-1, Eurocode 2, *Calcul des structures en béton*, Partie 1-1 : Règles générales et règles pour les bâtiments, octobre 2005.

Galenne E., Foucault A., Hamon F., *Prediction of Delayed Strain of Nuclear Containment Building: from laboratory tests to an industrial mock-up*, TINCE 2013, Paris.

Granger L., *Comportement différé du béton dans les enceintes de centrales nucléaires : analyse et modélisation*, thèse de l'Ecole nationale des ponts et chaussées, 1995.

Hilaire A., Benboudjema F., Darquennes A., Berthaud Y., Nahas G., Modeling basic creep in concrete at early-age under compressive and tensile loading. *Nuclear Engineering Design*, Volume 269, 2014, pages 222-230, 2014

Muller H., Anders I., Breiner R., Vogel M., Concrete: treatment of types and properties in MC 2010, *Structural concrete*, Volume 14, Issue 4, pages 320–334, 2013

NF EN 1992-2, Eurocode 2 - *Calcul des structures en béton - Partie 2: Ponts en béton - Calcul et dispositions constructives*, octobre 2005.

Russel, H.G., Larson, S.C. Thirteen Years of Deformations in Water Tower Place. *ACI Structural Journal* Vol. 86, No. 2, (1989) 131-145.

Sellier A., Buffo-Lacarrière L., Vers une modélisation simple et unifiée du fluage propre, du retrait et du fluage en dessiccation du béton, *REGC*, Vol 13, n°10, 2009

J.P. Sellin, J.B. Barthelemy, G. Bondonnet, B. Cauvin, J.M. Torrenti, *Delayed deformations of concrete structures: the Savines bridge and the Cheviré bridge,* MSLB15 conference, Porto, 2015

Troxell, G.E., Raphael, J.E., Davis, R.W., "Long-time creep and shrinkage tests of plain and reinforced concrete," *Proc. ASTM* 58 (1958), 1101-1120.

Vítek, J., Křístek, V. (2000) *Deflections and Strains of Prestressed Concrete Bridges*, 16th congress of IABSE, Lucerne, 2000.

Stress Redistribution in Prestressed Concrete Bridges Built with Ultra-Thin Precast Girders

Dominik Suza[1] and Johann Kollegger[2]

[1]Vienna University of Technology, Institute for Structural Engineering, Karlsplatz 13/E212-2, 1040 Vienna, Austria. E-mail: dominik.suza@tuwien.ac.at
[2]Vienna University of Technology, Institute for Structural Engineering, Karlsplatz 13/E212-2, 1040 Vienna, Austria. E-mail: johann.kollegger@tuwien.ac.at

Abstract

The balanced lift method for bridge construction proposes to build the bridge girders in a vertical position and to rotate them into the final horizontal position with the aid of compression struts. During the construction process, when the bridge girders are rotated from the initial vertical position into the final horizontal position, it is of utmost importance for an economic application of the balanced lift method that the structural members are as light as possible. In a test beam (length = 30.02 m, height = 1.44 m, width = 0.7 m) the actual filling process with concrete was carried out. Subsequently, the longitudinal strains on the outside of the beam were monitored over a period of four years in order to investigate the creep behaviour. Due to creep, the initially high stresses in the prefabricated outer shell are gradually reduced and the in-fill concrete is subjected to axial compressive stresses.

INTRODUCTION

In the conventional bridge construction methods the production of the bridge superstructure is carried out in horizontal position. By using the balanced lift method, developed at Vienna University of Technology, the bridge girders are erected next to the pier in a vertical position and are subsequently rotated into the final horizontal position (Kollegger & al. 2014). In order to rotate the bridge girders, additional structural elements (compressions struts or tension ties) are required. These elements then become an integral part of the finished bridge. The rotation of the bridge girders functions similarly to the opening of an umbrella, which is displayed in (Fig. 1) for the example of a bridge with compression struts.

Figure 1. Balanced lift method for bridge with high pier.

The example displayed in (Fig. 1) is suited for a valley bridge with high piers. The application of balanced lift method for bridges with piers of small height is possible, if an auxiliary pier is used as is shown in (Fig. 2).

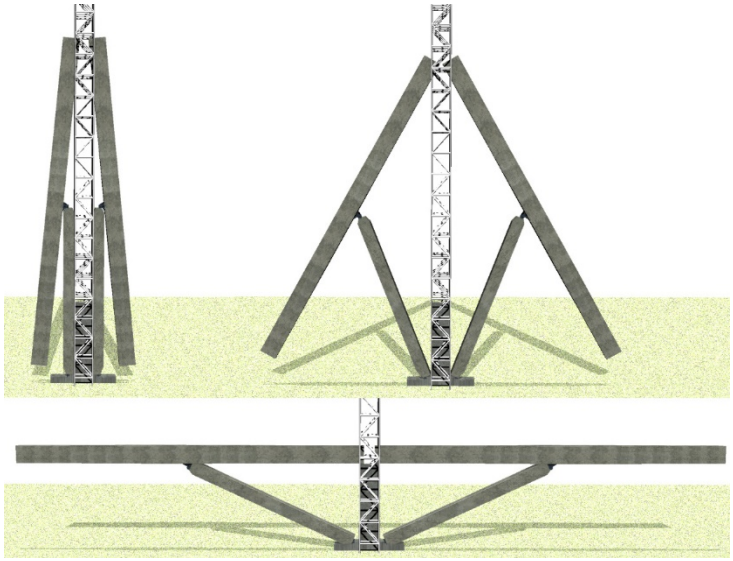

Figure 2. Balanced lift method for bridge with low pier, compression struts and auxiliary pier.

During the construction process, when the bridge girders are rotated from the initial vertical position into the final horizontal position, it is of utmost importance for an economic application of the balanced lift method that the structural members are as light as possible. It was therefore suggested to produce the bridge girders and the compression struts using thin prefabricated concrete elements. In building construction, lattice girder floor slabs have been successfully used for years. These precast elements of 50 to 70 mm thickness serve as permanent formwork for the subsequently added in-situ concrete. The advantages of this construction method are planned to be applied in bridge construction as well. A research project was implemented at the Institute of Structural Engineering at Vienna's University of

Technology in collaboration with the Association of Austrian Concrete and Precast Plants, Austrian National Railways (ÖBB), and the Austrian Expressway and Highway Financing Company (ASFINAG). In this research project the application of precast elements for bridge structures was investigated (Wimmer 2013). The objective was the development of precast concrete girders light enough for transport and erection by conventional transport and lifting equipment. The trough-shaped precast elements are intended to be used as formwork for the filler concrete and will be cast at the construction site to considerably reduce the use of formwork and scaffolding (Fig. 3).

The required reinforcement and the ducts for the tendons can be installed at the precast plant (Fig. 5). It is also possible to supplement the appropriately cast girders with a conventional roadway slab, similar to steel-concrete composite bridges. The advantages that can be gained through the use of precast girders are very promising: Industrialized prefabrication, which is independent of the weather, considerably reduced construction time at the site as well as for the periods during which traffic must be rerouted. Apart from the minimized cost and time required for installing the reinforcement and for building the formwork at the site, the good concrete quality achieved in precast plants is another advantage for this construction method. Other than with composite steel-concrete construction, the connection between web and roadway slab can be established with conventional connecting reinforcement and obviates the need for expensive, welded-on head-bolt dowels.

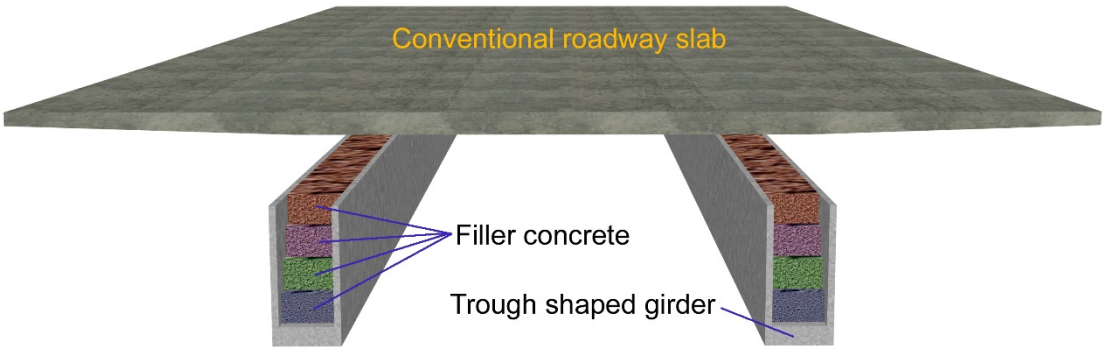

Figure 3. Schematic sketch of bridge with trough shaped precast girders.

PRODUCTION OF 30 m BEAM FOR STRESS REDISTRIBUTION EXPERIMENT

In order to demonstrate the feasibility of building bridges with thin precast concrete elements, a field test was realized with the aim of testing the behaviour of the thin-walled elements under the load of the cast in-situ concrete and, at a later stage, of measuring the stress redistribution between prefabricated girder and filler concrete due to creep.

A longitudinal section of the left half of the 30,02 m long test beam is shown in (Fig. 4). Transverse beams, each with a length of 3 m, were built at both ends of the test beam. The test beam consisted of three prefabricated parts, namely two 6,02 m long end sections with transverse end beams and a 17,98 m long central section.

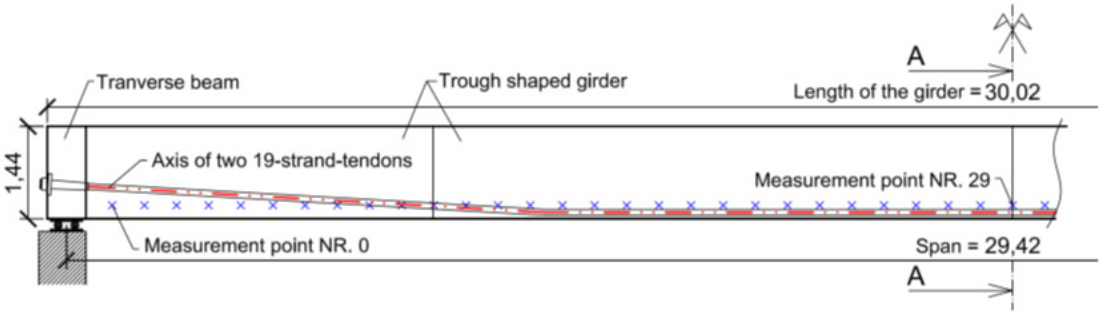

Figure 4. Longitudinal section of test beam.

The thickness of the wall elements was equal to 70 mm and the bottom plate had a thickness of 200 mm. The overall dimensions of the section amounted to a width of 700 mm and a height of 1440 mm. The photograph in (Fig. 5) shows an interior view of a pre-fabricated end part. The steel ducts for the two 19-strand-tendons as well as the lattice girders (consisting of two reinforcement bars, diameter 6 mm, placed in the wall elements, one reinforcement bar, diameter 10 mm, placed at the inside of the beam and diagonal bars with a diameter of 7 mm) are clearly recognizable.

Figure 5. Interior view of the prefabricated end part.

The three pre-fabricated parts were transported to the test site, placed on temporary supports, the ducts were connected and the 20 mm wide joints were filled with a high-strength grout. In the next step the two tendons were stressed to 1500 kN each, which resulted in an upward movement of the central part of the test beam. Due to the upward movement the self weight of the beam (g=7,84kN/m) was carried over the distance of 29,42 m between the load cells by the beam itself.

Within a time difference of 24 hours, the filling concrete was placed in four layers with a thickness of 0,31m (Fig. 6, Fig. 7 and Fig. 8). During the pouring of the concrete, the post-tensioning force was increased stepwise up to 5300kN. Details of the manufacturing procedure can be found in (Table 1).

Table 1. Production sequence of test beam.

Day	*Time*	*Activity*
1		Casting of bottom slabs of prefabricated parts of the girder
29		assembly of prefabricated parts on temporary supports and filling of joints with high-strength grout
30		Stressing of post-tensioning tendons P = 1 500kN
	11:05	increase tendon force to P = 2 500kN
	11:10	casting of filler concrete layer 1
31	11:34	increase tendon force to P = 3 000kN
	12:00	casting of filler concrete layer 2
	12:10	end of casting
	9:50	increase tendon force to P = 4 500kN
	10:25	casting of filler concrete layer 3
32	10:38	end of casting
	10:46	increase tendon force to P = 5 300kN
	11:25	casting of filler concrete layer 4
	11:40	end of casting

The 28-day compressive strength of concrete for the precast elements as well as for the filler concrete was determined using concrete cubes. The 28-day strength for the precast elements and the filler concrete was equal to 43,2 MPa and 41,9 MPa, respectively (Kromoser 2011).

The filling of the test beam with in-situ concrete is shown in (Fig. 6). The hydraulic jack positioned at the stressing anchorage can be seen at the end of the beam. There was a second jack placed at the other end of the test beam since the stressing of the two tendons was carried out simultaneously. A more detailed description of the production of the test beam is contained in (Kromoser 2011 and Wimmer 2015).

Figure 6. Filling of 30m test beam with in-situ concrete.

NUMERICAL SIMULATION AND COMPARISON WITH EXPERIMENT

The test beam was modelled using 44 beam elements. The specified concrete strength was equal to C30/37 and the material parameters were chosen according to Eurocode 2.

An important feature of the numerical analyses was the modelling of the incremental production of the test beam. Also the increase of the modulus of elasticity of concrete and the time dependent creep behaviour was taken into account.

The calculated stresses in the centre of the beam (section A-A of Fig. 4) at the top and bottom of the precast girder are shown in (Fig. 7 and Fig. 8). It can be seen that the central cross-sections of the test beam is always in a compressed state. This fact is of utmost importance at the joints between the individual precast elements since no longitudinal reinforcement is provided at these locations.

During the production of the beam compressive stresses are calculated for the first and second concrete layer for the time equal to 32 days, because the strength of these concrete layers (age equal to 1 day) is taken into account in the numerical calculations (Fig. 7 and Fig. 8).

Although the concrete compressive stresses are quite high during the filling of the test beam with in-situ concrete, it can be noted that these stresses are quite reduced for the final state (time equal to 100 years) according to the results shown in (Fig. 8). The redistribution of stresses between the prefabricated girder and the filler concrete is important for the economic application of this construction method, because the stress limitation of Eurocode 2 have to be observed.

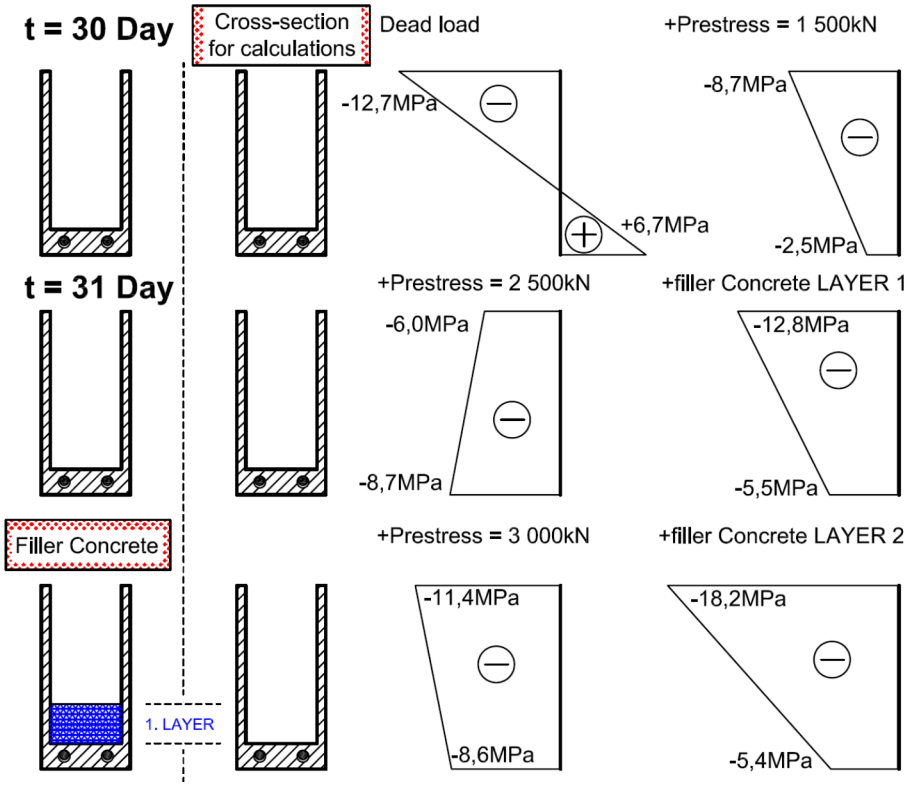

Figure 7. The calculated stresses in the centre of the beam (section A-A – Fig. 4).

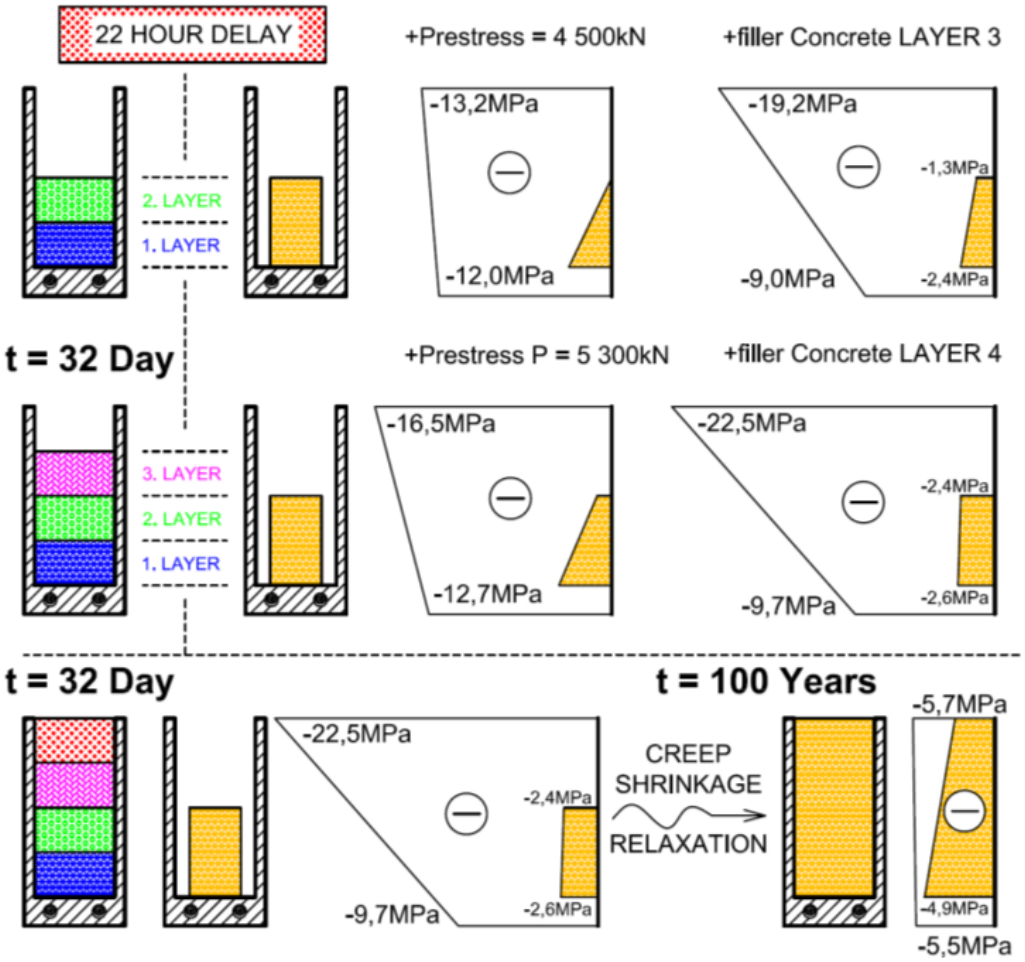

Figure 8. The calculated stresses in the centre of the beam (section A-A – Fig. 4).

A comparison of measured concrete strains and calculated concrete strains was carried out in order to assess the quality of the numerical simulation of the test beam. 58 measurement points had been fixed close to the bottom fibre in the longitudinal direction of the test beam (Fig. 4). With the aid of an extensometer the relative displacement between the measurement points could be determined. The results of the strain measurements from October 2010 to August 2014 are shown in (Fig. 9). The calculated strains are also shown in (Fig. 9) with solid lines. A good correlation of measured and calculated strains can be noted from the results displayed in (Fig. 9).

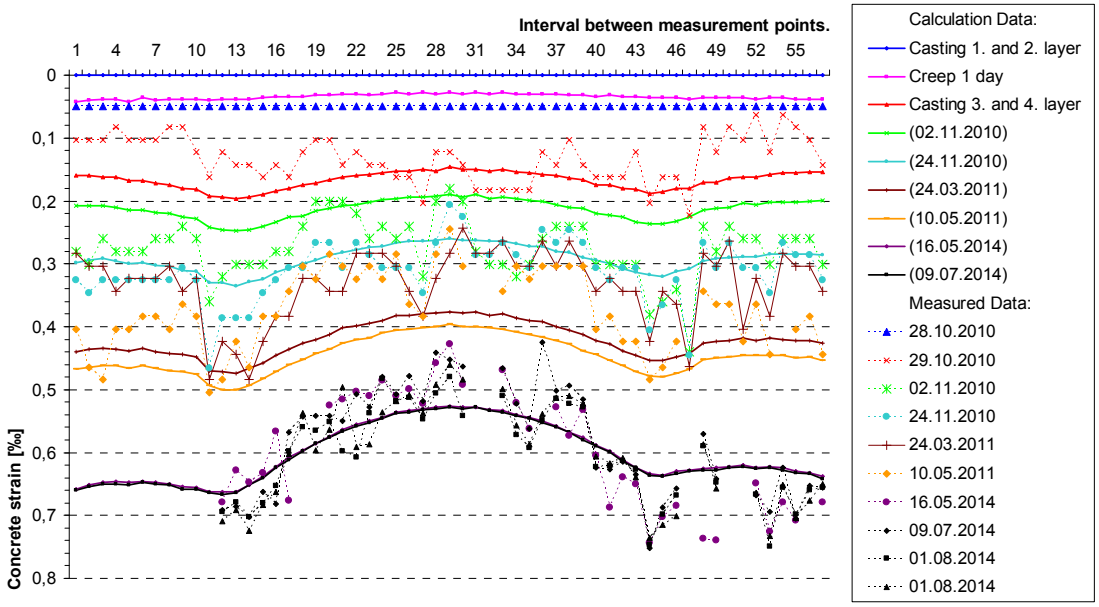

Figure 9. Comparison of measured and calculated concrete compressive strain of test beam.

CONCLUSION

The balanced lift method is a new bridge building method, which enables the construction of elegant and economical valley bridges. A careful and meticulous analysis of the different construction stages is required for designs based on this method, because light structural elements are used during the balanced lift. These light elements are subsequently filled with in-situ concrete, which leads to many different construction stages and structural elements with changing cross-sections. It could be shown in this paper that a considerable redistribution of concrete stresses does occur, which should be taken into consideration in the design calculations for economic reasons.

REFERENCES

Kollegger, J., Foremniak, S., Suza, D., Wimmer, D. & Gmainer, S. (2014), "Building bridges using the balanced lift method", *Structural Concrete: Journal of the fib*, Vol. 15, No. 3, pp. 281-291.

Wimmer, D. (2013), "Thin-walled precast concrete girder for bridges construction and civil engineering", *Concrete Plant + Precast Technology*, Vol. 79, pp. 44-51.

Kromoser, B. (2011), „Brückenbau mit Fertigteilen – Großversuch zur Herstellung und zum Torsionswirkungsverhalten". Masterthesis – Vienna University of Technology.

Wimmer, D. (2015), „Entwicklung eines neuen Brückenbauverfahren durch die Kombination von dünnwandigen Betonfertigteilen und Vorspannung". Doctor thesis – Vienna University of Technology.

Evaluation of a Cracking Load Considering the Internal Stress Caused by the Shrinkage and Creep of Mortar

Yuto Ohno[1] and Ken Watanabe[2]

[1]M.E., Concrete Structures, Structures Technology Division, Railway Technical Research Institute, 2-8-38, Hikaricho, Kokubunji, Tokyo 185-8540, Japan. E-mail: ono.yuto.47@rtri.or.jp
[2]Ph.D., Concrete Structures, Structures Technology Division, Railway Technical Research Institute, 2-8-38, Hikaricho, Kokubunji, Tokyo 185-8540, Japan. E-mail: watanabe.ken.08@rtri.or.jp

Abstract

Evaluation of the internal stress will be a key for understanding the cracking potential of concrete structures. One of the reasons for generation of internal stress in concrete is the volume change of cementitious material such as shrinkage and creep in the vicinity of aggregates and reinforcements in concrete. To overcome the complexity of concrete as a heterogeneous material, stress generation needs to be evaluated by the effect of difference in stiffness between materials. The objective of this research is to evaluate the internal stress of concrete in an early age through the measurement of strain. Image analysis will be helpful in clarifying the development and the quantity of strain. In order to have the various potential of internal stress, specimens with different restrained conditions were prepared in the experiment. Furthermore, the difference of cracking load was explained by the development of internal stress with age of concrete.

INTRODUCTION

Cracks and deformation of concrete structures occur by the application of external force and restriction of concrete volume change. One of the reasons of concrete volume change is the shrinkage of cement paste and aggregates by moisture evaporation (Neville 1996; Moon 2005). Stress and strain are not generated uniformly in the reinforced concrete (RC) members, because the difference in shrinkage causes the stress at the interface between cement paste and aggregate. The distribution of stress is important for analyzing the internal stress in RC member.

The objective of this paper is to evaluate the internal stress of the mortar by measuring the strain. Specifically, a mortar plate specimen with a steel-ring at its center was subjected to the drying test, and the internal stress was evaluated by the strain measured on the side surface and the inner surface of the steel-ring of the mortar plate specimen. And then, the relation between the cracking load and the evaluated internal

stress was examined. The strain increasing non-uniformly on the surface of the specimen was measured by using the digital image correlation method (Chu 1985; Choi 1997).

EXPERIMENTAL OUTLINE

Specimens outline. Figure 1 shows three specimens having the dimensions of 100×100×10-mm. A cylinder of 30-mm in diameter, made by Styrofoam, or by a steel-ring with 1-mm in thick, or by a steel-ring with 3-mm in thick was provided at the middle of each specimen. The weight ratio of water, cement, and fine aggregate in mortar was equal to 2:5:10.

The drying test and the loading test. Figure 2 shows the drying test. The specimen was casted in the mold and demolded after 24-hours, and cured on Teflon-sheet placed inside the chamber by keeping the temperature at 20-degree Celsius and the relative humidity at

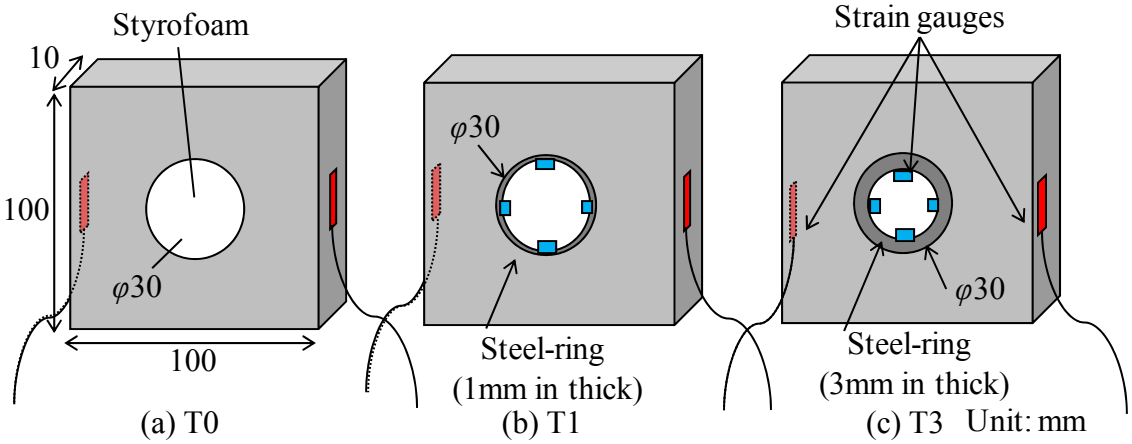

Figure 1 Details of specimens.

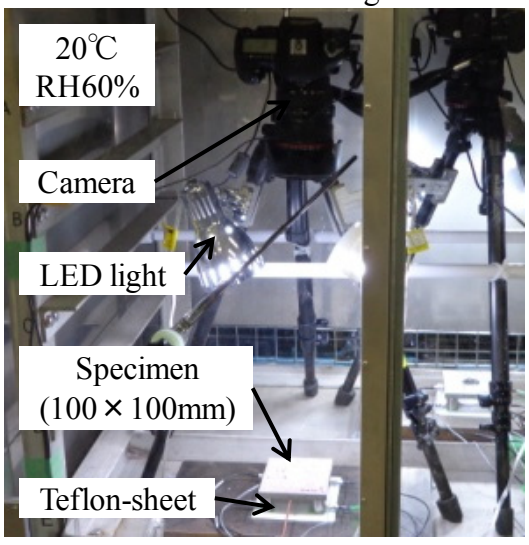

Figure 2 The drying test.

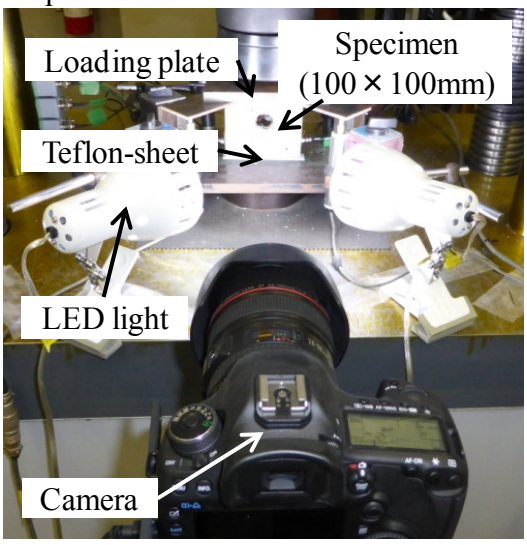

Figure 3 The loading test.

60 % for 28-days. The specimen was loaded after 28-days of curing (Figure 3). Teflon-sheets were set between the loading plates and the specimen for reducing friction caused by loading.

Measurement. During the drying test and the loading test, strains on the inner surface of steel-rings in the circumferential direction, and on the side surface of the mortar plate were measured by using strain gauges. In addition, strains generated on the surface of specimens were measured by the digital image correlation method.

Figure 4 shows the outline of the digital image correlation method. A digital image consists of pixels having brightness value. The digital image correlation method can calculate a strain distribution by the difference in the brightness pattern between two digital images. The initial-image and the target-image are prepared. The subset of pixels in the initial-image is set. And then, the location having the high degree of correlation about the brightness pattern with the initial-image is searched in the target-image. The displacement of the subset is determined by the coordinates of the centers of subsets in the initial-image and the target-image. The strain of arbitrarily-defined point is calculated by the displacements of plural subsets in the area in the vicinity of the point. The strain distribution in the whole area of the target-image can be obtained by interpolation of strain of each point.

In this paper, the subset size was set at 100×100 pixels; the searched area, at 100×100 pixels; the subset interval, at 50 pixels; and the pitch of the point, at 2mm. The digital single-lens reflex cameras (5760×3840 pixels, 5616×3744 pixels) were used for taking pictures of high resolution. LED (light-emitting diode) lights were used in shooting for reducing light flicker on the surface of the specimen. The digital images were corrected with respect to distortion. The surface of the specimens was sprayed with color for getting brightness gradation. The image prepared after six hours from being

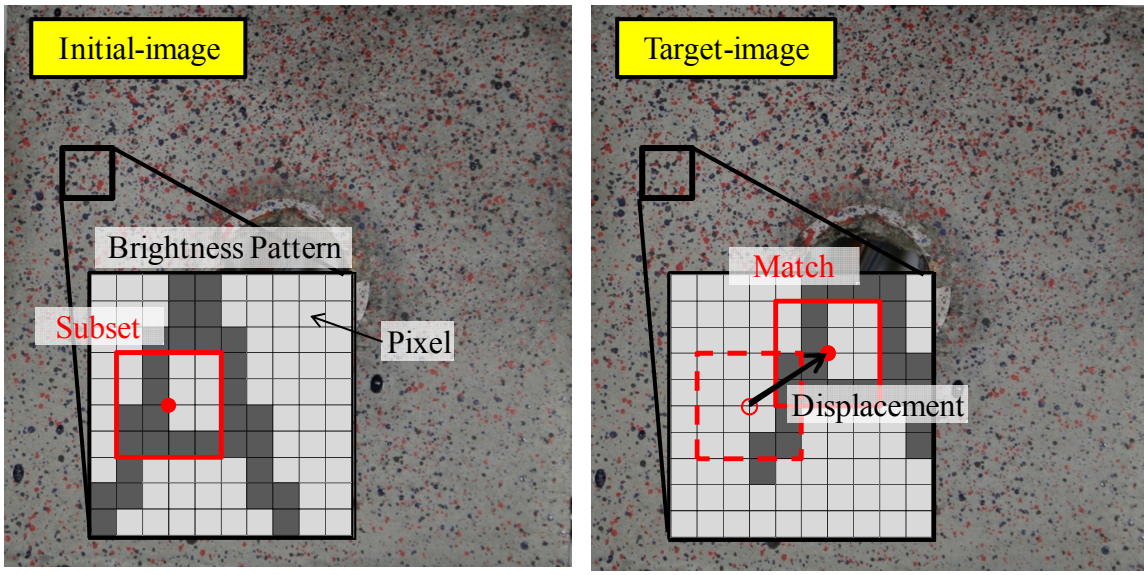

Figure 4 Outline of the digital image correlation method.

demolded was decided as the initial-image, because the drying of six hours changed the brightness pattern on the surface of the specimens drastically.

Mechanical properties. Figures 5 and 6 show compressive strength, tensile strength and Young's modulus against age. These values were measured by using φ50×100-mm cylinders. The cylinders were made of the same mortar, and cured in the same condition as the specimens. Equations (1),(2),(3) were the approximation formulas obtained by the method of the least squares.

$$f_c'(t) = \frac{t - 0.37}{0.92 + 0.90 \times (t - 0.37)} \times 50.7 \quad (1)$$

$$f_t(t) = 0.24 \times f_c'(t)^{0.69} \quad (2)$$

$$E_m(t) = 6351 \times f_c'(t)^{0.37} \quad (3)$$

where t, is time from casting; $f'_c(t)$, compressive strength at t-age; $f_t(t)$, tensile strength at t-age; $E_m(t)$, Young's modulus at t-age.

RESULT OF THE DRYING TEST

Examination of the creep property of mortar by using strain gauges. Figures 7 and 8 show the strain variations with age, which were measured on the inner surface of the

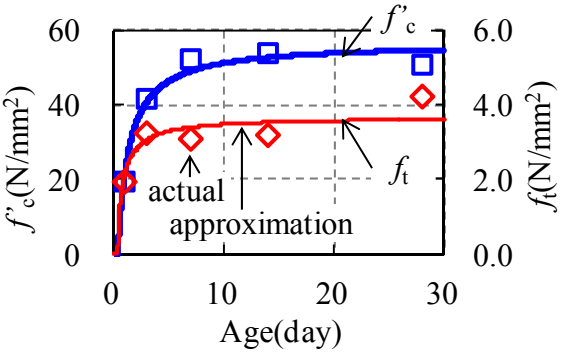

Figure 5 Compressive and tensile strength.

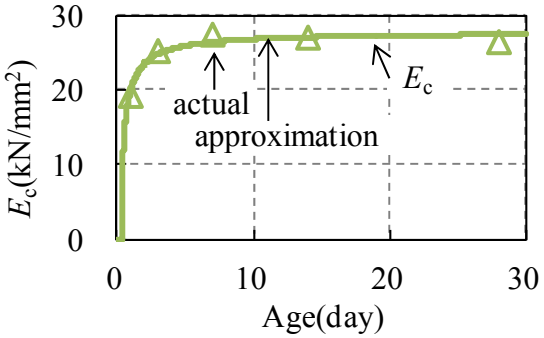

Figure 6 Young's modulus.

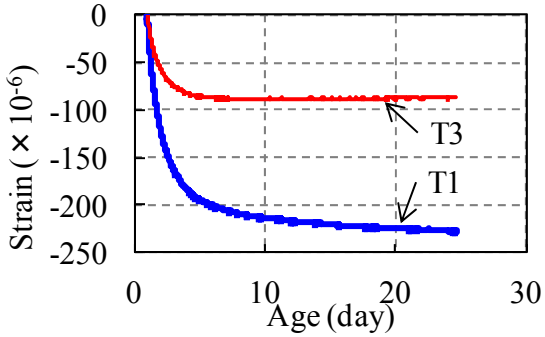

Figure 7 Strain on the internal surface of steel-ring.

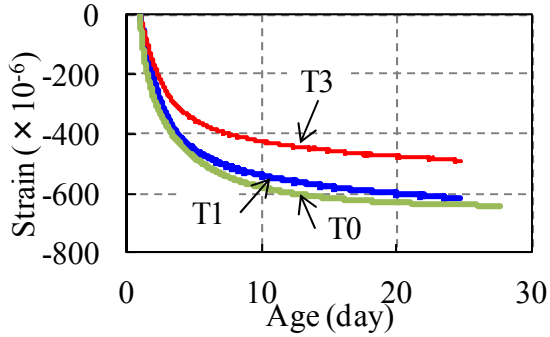

Figure 8 Strain on the side of mortar.

steel-ring and the side surface of the mortar specimen. The magnitude of strain of the mortar specimen was increased with the increment of restriction by steel-rings. The theory (Timoshenko 1996) for calculating the stress distribution of a hollow cylinder subject to uniform pressure on the inner and the outer surface was applied to calculation of the strain and stress in a circumferential direction ($\varepsilon_{m\theta}(x)$, $\sigma_{m\theta}(x)$) by Equations (4),(5) as follows.

$$\sigma_{m\theta}(x) = -\frac{(b^2+c^2)(b^2-a^2)}{2b^2(c^2-b^2)} \cdot E_s \cdot \varepsilon_{s\theta}(a) \quad (4)$$

$$\varepsilon_{m\theta}(x) = \frac{a^2+b^2}{2b^2}\varepsilon_{s\theta}(a) \quad (5)$$

where a is, radius of inner diameter of the steel-ring (=14mm for T1, =12mm for T3); b, radius of outer diameter of the steel-ring (=15-mm); c, a half of specimen length (=50-mm); Es, stiffness of the steel-ring (=200-kN/mm^2). Figure 9 shows stress tensile-strength ratio ($\sigma_{m\theta}(x)_{x=b}$ / $f_t(t)$) of the mortar specimen. The value of $\sigma_{m\theta}(x)_{x=b}$/ $f_t(t)$ of T1 approached to 1.0; on the other hands, the value of T3 reached 1.0 at 3-day age. Invisible cracks seemed to be generated around the steel-ring in T3. Subtracting $\varepsilon_{sh}(x)$, the shrinkage strain from $\varepsilon_{m\theta}(x)$, the component of strain caused by sustained loading, the effective strain ($\varepsilon_{eff\theta}(x)$= $\varepsilon_{m\theta}(x) - \varepsilon_{sh}(x)$), is calculated which is plotted in Figure 10 as a function of age. The value of $\sigma_{m\theta}(x)$ is expressed as a function of $\varepsilon_{eff\theta}(x)$ and Young's modulus E_m as follows.

$$\sigma_{m\theta}(x) = E_{eff\theta}(t) \cdot \varepsilon_{eff\theta}(x) = \varphi(t) \cdot E_m(t) \cdot (\varepsilon_{m\theta}(x) - \varepsilon_{sh}(x)) \quad (6)$$

where $\varphi(t)$ is, the reduction coefficient of Young's modulus; and $E_{eff\theta}(t)$, the effective Young's modulus (=$\varphi(t)\times E_m(t)$). The value of $\varepsilon_{eff\theta}(x)_{x=b}$ is expressed as a function of stress $\sigma_{m\theta}(x)_{x=b}$ as shown in Figure 11. The relationship between $\sigma_{m\theta}(x)_{x=b}$ and $\varepsilon_{eff\theta}(x)_{x=b}$ is nearly linear until the end in the case of T1, however, in the case of T3, $\sigma_{m\theta}(x)_{x=b}$ takes a constant value beyond 3.5-N/mm^2, the tensile strength f_t of mortar at age of 4-day. In case where the strain $\varepsilon_{eff\theta}(x)_{x=b}$ consists of elastic strain $\varepsilon_{el}(x)_{x=b}$ (=$\sigma_{m\theta}(x)_{x=b}$/ $E_m(t)$) and the creep strain $\varepsilon_{cr}(x)_{x=b}$, the linear relationship between the stress and the effective strain implies that the creep strain is increased in proportion to $\sigma_{m\theta}(x)_{x=b}$ as well as $\varepsilon_{el}(x)_{x=b}$. On the other hands, this cannot be applied to the flat region of T3 where the generation of micro-cracking is expected as discussed in Figure 9.

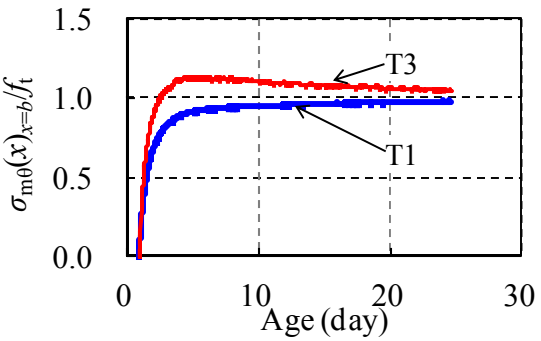

Figure 9 Tensile stress-strength ratio.

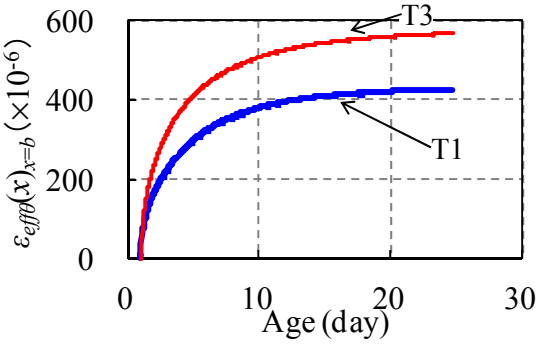

Figure 10 Effective strain.

Examination of the distribution of internal stress by using image correlation method. In Figure 12, the magnitudes of the maximum principal strains measured on the surface of the specimens during the drying test are shown. The magnitudes of strains are changed by age and the thickness of the steel-ring. The strains in the circumference direction $\varepsilon_{m\theta}(x)$ were estimated from Figure 12. The specimen was shrunk uniformly with age in the case where there was no steel-ring such as the case of T0. The distribution of strain in the case of T3 indicates an increase of strain of the steel-ring surface compared with that on the side surface, which implies the generation of stress by restriction of the steel-ring. The stress was calculated by Equation (6), and plotted in Figure 13. Tensile stress of the average of 4.1-N/mm^2 was generated at 2-day age in the case of T1, and that was decreased to 3.0-N/mm^2 at 20-day age. On the other hands, tensile stress in the case of T3 was the same as that of T1 at 2-day age, and that was less than 2.0-N/mm^2 at 20-day age. This may be caused because the stress was released according to the micro-cracks as discussed above in the case of T3.

RESULT OF THE LOADING TEST

Figure 14 shows the comparison of the load-displacement relationships of three

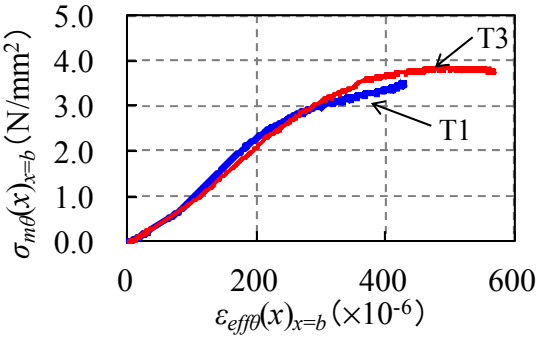

Figure 11 Stress-effective strain relationship.

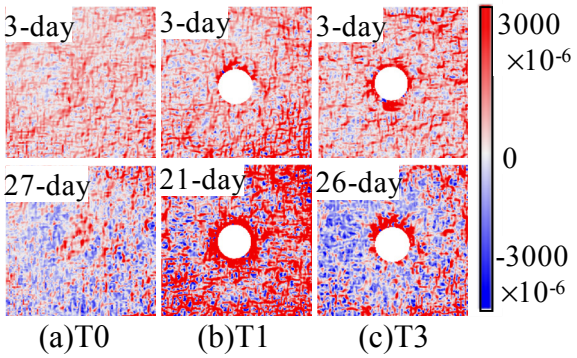

Figure 12 Maximum principal strain distribution during the drying test.

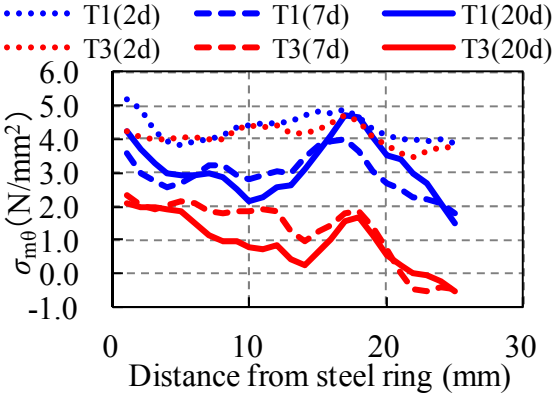

Figure 13 Internal strain varied by age.

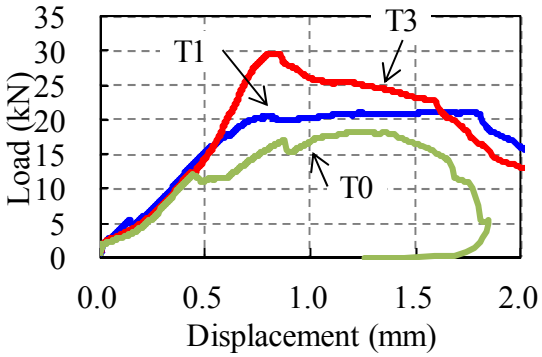

Figure 14 Load-displacement relationship.

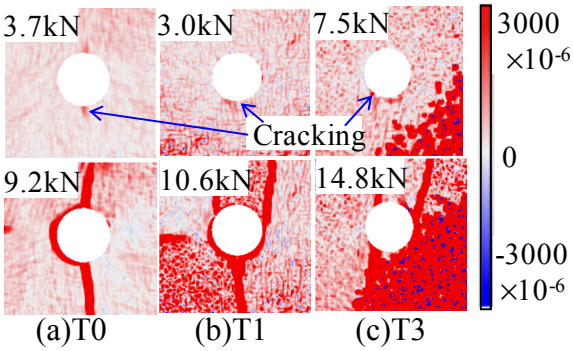

Figure 15 Maximum principle strain distribution during the loading test.

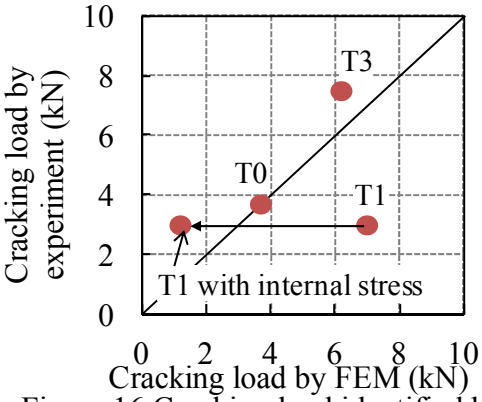

Figure 16 Cracking load identified by experiment and analysis.

specimens subjected to uniaxial loading. Figure 15 shows the variation of maximum principal strain measured by the digital image correlation method during the loading test. The specimen happened to move on the loading plate during the load, which made the results in the cases of T1 and T3 deteriorated. The cracking load of the specimen was defined as that to cause the strain of mortar on the outer surface of the steel-ring to be 1000×10^{-6} in tension. In the finite element method (FEM), the cracking load in the cases of T0 and T3 was defined as that to cause the maximum principal stress $\sigma_m(x)$ of mortar at the surface of steel-rings to reach the tensile strength $f_t(t)$. Mechanical properties of mortar changing by the age were expressed by Equations (1),(2),(3). Comparison of the cracking loads obtained by the experiment and the FEM calculation in Figure 16 indicates that the experimental cracking loads in the cases of T0 and T3 are corresponding to the calculated cracking loads in the case where the internal stress was not considered in the calculation. This means that there was no initial stress in both the specimens in the cracked area, because there is no restriction in the case of T0 or the stress was released due to micro-cracking in the case of T3. On the other hands, the cracking load in the experiment was decreased by around 4.0-kN compared with that by the calculation made without consideration on internal stress in the case of T1. In order to make the effect of the internal stress be reflected on the cracking loads in the FEM in the case of T1, the initial stress caused by the shrinkage, 3.0-N/mm^2 (Figure 13), was referred to. The cracking load in the case of T1 obtained by FEM was modified as 1.2-kN, which was close to the experimental cracking load (=3.0-N/mm^2).

CONCLUSION

The above discussion was summarized as follows. The reduction coefficient of Young's modulus $\varphi(t)$ in Equation (6) was calculated by using gauges attached to the inner surface of the steel-ring. The strain distribution can be obtained by the digital image correlation method. The value of $\varphi(t)\times E_m(t)$ transferred the elastic and the creep strains into the stress distribution generated in the specimens. The reduction of cracking load was explained exactly by using the internal stress generated around the steel-ring by

the shrinkage of mortar. This paper concludes that the examination of internal stress caused by the shrinkage and the creep, is important for predicting the generation of cracks as well as fracture of concrete.

This work was supported by JSPS KAKENHI (24246078).

REFERENCES

Choi, S. and Shah, S. P. (1997): "Measurement of Deformations on Concrete Subjected to Compression Using Image Correlation", *Experimental Mechanics*, Vol.37 No.3, pp.307-313.

Chu, T. C., Ranson, W. F., Sutton, M. A. and Peters, W. H. (1985): "Application of Digital-Image-Correlation Techniques to Experimental Mechanics", *Experimental Mechanics*, Vol.25, No.3, pp.232-244.

Moon, J. H., Rajabipour, F., Pease, B., and Weiss, J. (2005): "Autogenous Shrinkage, Residual Stress, and Cracking in Cementitious Composites", *The Influence of Internal and External Restraint*, Fourth International Seminar on Self-desiccation and Its Importance in Concrete Technology.

Neville, A. M. (1996): "Properties of Concrete Fourth Edition", John Wiley & Sons.

Timoshenko, S. P. and Goodier, J. N. (1970): "Theory of Elasticity Third Edition", McGraw-Hill International Editions.

Creep and Shrinkage in Fastening systems

I. Boumakis[1], M. Marcon[1], Lin Wan[1,2], and R. Wendner [1]

[1] Christian Doppler Laboratory LiCRoFast, Institute of Structural Engineering, University BOKU, Vienna, Austria, roman.wendner@boku.ac.at
[2] Northwestern University, Evanston, IL, USA

ABSTRACT

The efficient and permanently safe design of fastening systems requires a thorough understanding of all involved load carrying mechanisms and their potential change in course of time due to deterioration and material aging. The latter are determined by the involved materials - concrete, steel, and, depending on the system, the mortars. In this contribution we focus on concrete cone failure, the critical failure mechanism for bonded as well as mechanical anchors under pre-dominant tension loading. Both mechanical as well as chemical anchors undergo an approval process during which their performance is certified. These tests are performed according to strict guidelines and for concretes of a specified composition and age range. Nonetheless, differences between laboratories, the age of concrete at testing, the storage conditions, the coarse aggregate type exist. In this contribution we attempt to quantify the effect of testing age in combination with storage conditions on obtained pull-out loads. We will present the numerical framework that is able to model the coupled problem of heat- and moisture transport, hydration, aging of material properties, shrinkage and creep in a rate–type, point–wise form. The framework will be calibrated based on an experimental study of creep and shrinkage on a typical C25/30. The mechanical model is calibrated and validated on standard tests for uniaxial compression, three point bending as well as pull-out tests. Afterwards, the calibrated framework is applied in a purely predictive way to fastenings under sustained loads.

Introduction

Fastening technology including post-installed mechanical and chemical anchors plays an important role in structural engineering. It's importance can be highlighted by the need to connect structural elements, assemble precast elements, and attach non-load bearing components not only during construction but especially during strengthening and retrofitting. Therefore, fastenings are important for any adaption of existing infrastructure and for the life-cycle design of new structures. The economic significance of fastenings is indicated by the fact that the potential damage caused by failed fastening elements can be by several orders of magnitude higher than the value

of the products themselves. Thus the necessity of an accurate prediction of the long term behavior of fastenings systems is a crucial characteristic of their safe design.

In order to have a thorough understanding of the long term behavior of fastenings, it is required to take into account the deterioration of the involved materials — concrete, steel, and the mortars — as a function of time. More specifically and regarding concrete, which is the objective of this study, time dependent deformations, potentially accompanied by damage, due to creep and shrinkage have to be considered. Consequently, the need of developing a robust framework emerges, capable of describing appropriately the mechanisms of the aforementioned phenomena. In the present paper the effect of creep and shrinkage on the load capacity of fastenings systems is studied using the hygro-thermo-chemical (HTC) model (Di Luzio et Cusatis, 2009), which can simulate the moisture transport, hydration, as well as the temperature evolution of concrete specimens, and the micro-prestress solidification theory (MPS) (Bažant et al. 1997), which links the evolution of internal state variables to shrinkage and creep strains in a rate-type, point-wise form. The accurate description of damage is ensured by a well established discrete particle model called LDPM (Cusatis et al. 2015, Alnaggaar et al. 2015).

The goal of this investigation is a quantification of the effect of concrete creep and shrinkage on the performance of anchors systems. For two selected concrete classes C25/30 and C50/60 a full experimental characterization of the material properties, accompanied by pull-out test of headed studs, and shear–loaded headed studs at different ages, is carried out. The main material properties are obtained from standard cubes and prisms at various ages between 2 days and 56 days, providing cylinder compressive strength $f_c(t)$, Young's modulus $E_c(t)$, indirect tensile strength through three point bending and Brazilian splitting tests $f_t(t)$, and fracture energy $G_F(t)$ as functions of time. The anchor tests are carried out at days 3, 7, and 28. Using both types of data the age dependent constitutive model LDPM can be calibrated and validated. Starting at the time of casting the internal humidity and temperature evolution have been measured in two cubes of 20 cm edge length. This information is essential for calibrating the HTC parameters. For the calibration and validation of the MPS type creep and shrinkage model a series of creep and shrinkage tests are running. These include cylinders for autogenous shrinkage starting at time of demolding after 24 hours, drying shrinkage starting after 3,7,28 days, and creep loaded at 3,7,28 days including sealed and unsealed specimens. As these tests are still running in a first approximation data from the NU database for creep and shrinkage (Hubler et al. 2015a) are adopted as a surrogate for the preliminary phase of this project. Particularly, data sets of (Brooks 1984) are used for the case of concrete class C25/30. The selected dataset is relatively close in composition and provides relatively long experimental data for both cases of drying and basic creep, as well as autogenous and drying shrinkage.

Formulation

The MPS theory formulates the time dependent strain in concrete accepting the superposition principle, which decomposes the total strain into different contributions according to the rheological model of Figure 1. In this formulation, the elastic deformation is described by an elastic non-aging spring, while the short-term creep strain is calculated using the solidifying Kelvin chain, and the long-term creep strain can be described by the aging dashpot, that is dependent on solidification. The shrinkage and thermal strains are represented by the last two units in Figure 1.

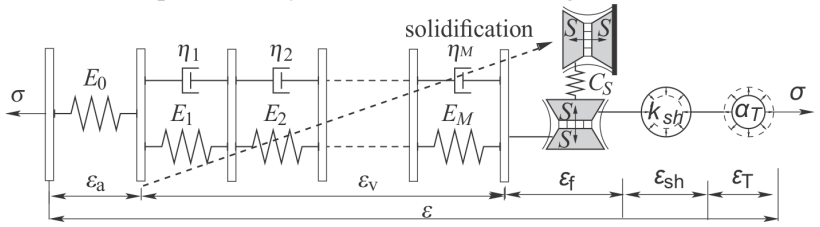

Figure 1. Rheological scheme of concrete strains (Havlásek and Jirásek 2012)

The total strain can be described as a summation of the different individual components of the rheological model, as

$$\epsilon_{tot} = \epsilon_a + \epsilon_v + \epsilon_f + \epsilon_{sh} + \epsilon_T \tag{1}$$

where ϵ_{tot} is the total strain, $\epsilon_a = \frac{\sigma}{E_0}$ is the elastic response, as a fraction of stress, σ over instantaneous elastic modulus E_0, ϵ_v is the viscoelastic creep strain, ϵ_f is the purely viscous creep strain, ϵ_{sh}, is the shrinkage strain, and ϵ_T is the thermal strain, due to temperature changes. The stress σ is constant in series system. The shrinkage and thermal strains can be described as incrementally linear functions of humidity and temperature (Bažant et al. 2004),

$$d\epsilon_{sh} = k_{sh} \cdot dh \tag{2}$$

$$d\epsilon_T = \alpha_T \cdot dT \tag{3}$$

The creep compliance function of MPS, can be derived using e.g. the B3, or it's successor B4 (Wendner et. al 2015a, Wendner et. al 2015b), formulation (Bažant et al. 1997),

$$J(t,t') = q_1 + q_2 \int_{t'}^{t} \frac{ns^{-m}}{s - t' + (s-t')^{1-n}} ds + q_3 ln[1 + (t-t')^n] + q_4 ln\frac{t}{t'} \tag{4}$$

where t and t' are current time and time at loading, n and m are constants with 0.1 and 0.5 respectively, while the parameters q_1, q_2, q_3 and q_4, are corresponding to the different units of rheological model, concerning creep strains, of Figure 1. Specifically, q_1 represents the compliance of the elastic spring, $\frac{1}{E_0}$,q_2 and q_3 the Kelvin chain, and q_4

is the parameter of the dashpot $\eta_f(t) = t/q_4$. All of them have to be calibrated for each concrete composition in order to fit to experimental data. The B3 model is formulated under constant humidity and temperature, while the strength of MPS is the extension to environment of non constant humidity and/or temperature. This could be achieved by replacing the dependence of η_f on time by the dependence on the microprestress S, which is the stress, in microscale, due to the volume changes during hydration process. The rate of microprestress is given by

$$dS + \psi_S(T,h)c_o \cdot S^2 = k_1 \left| d(Tlnh) \right| \tag{5}$$

where S microprestress, T temperature, h relative humidity, c_o, k_1 constant parameters, and the non-constant factor ψ_S, represents the dependence of microprestress relaxation on humidity and temperature as

$$\psi_S(T,h) = \exp\left(\frac{Q_S}{R}\left(\frac{1}{T_0} - \frac{1}{T}\right)\right)\left(\alpha_s + (1-\alpha_s)\,h^2\right) \tag{6}$$

where Q_S is the activation energy, R Boltzman's constant, T_0 room temperature in Kelvin, and a_s a parameter, with $a_s = 0.1$ and $Q_S/R = 3000K$ (Bažant et al. 1997a, Bažant et al. 1997b). Therefore the dashpot viscosity η_f can be formulated as

$$\eta_f = \frac{1}{cS} \tag{7}$$

and thus the viscous flow of the third unit of the rheological model can be written as

$$\sigma = \eta_f d\epsilon_f \tag{8}$$

where c is a parameter directly related to q_4, and c_o. Finally the solidifying Kelvin chain, the second unit of rheological model, can be expressed approximately, in numerical applications, using Dirichlet series (Bažant et al. 1997a, Di Luzio and Cusatis 2013), while for the viscous flow, and also shrinkage and thermal strains, information about the temperature, and relative pore humidity is necessary. Hence, a robust formulation, being able to catch the problem of moisture transport, thermal evolution and aging degree evolution, in concrete, is requisite. Such a strong model for that purpose is the hygro-thermo-chemical model (Di Luzio and Cusatis 2009a, Di Luzio and Cusatis 2009b). In its framework h and T evolution is represented, by

$$\nabla \cdot (D_h \nabla h) - \frac{\partial w_e}{\partial h}\frac{\partial h}{\partial t} - \frac{\partial w_e}{\partial \alpha_c}\dot{\alpha}_c - \frac{\partial w_e}{\partial \alpha_s}\dot{\alpha}_s - \dot{w}_n = 0 \tag{9}$$

and

$$\nabla \cdot (\lambda_t \nabla T) - \rho c_t \frac{\partial T}{\partial t} + \dot{\alpha}_c c \tilde{Q}_c^{\infty} + \dot{\alpha}_s s \tilde{Q}_s^{\infty} = 0 \tag{10}$$

with D_h, moisture permeability, w_e evaporable water, a_c and a_s, the degree of hydration and silica fume reaction respectively, $\dot{w}_n$ is the time derivative of non-evaporable water,

ρ is concrete density, c_t is isobaric heat capacity, λ_t is heat conductivity, c and s are cement and silica fume content, $\tilde{Q}_c^\infty$ is cement hydration enthalpy and $\tilde{Q}_s^\infty$ is latent heat of silica fume reaction. For further information on the presented formulation see Bažant et al. (1997a,1997b), Di Luzio and Cusatis (2013), and a companion paper at this conference (Alnaggaar et al. 2015).

Calibration and Validation

As it is already mentioned, in order to calculate the effect of creep and shrinkage on fastenings systems, for concrete reference class C25/30, a calibration of both models' parameters is required. For that reason, data sets for autogenous and drying shrinkage, and basic and drying creep are taken from the extended creep and shrinkage database of Northwestern University (Hubler et al. 2015a). It is essential to use only part of the available experimental data for calibration so that the predictive capabilities of the model can also be validated. The chosen experimental data (Brooks 1984) use cylindrical specimens with radius $r = 38$mm and length, $l = 255$mm for sealed, $h = 100\%$ and unsealed condition, $h = 60\%$, exposed (t_0) or loaded at $\sigma = 10\% \cdot f_{c28}$, after $t' =$14 days. Some of the material properties of specimens can be found in Table 1.

Table 1. Material Parameters

Water to cement ratio, w/c	0.58
Aggregate to cement ratio, a/c	4.75
Cement conctent, c (kg/m ^{3})	337
Cement Hydration enthalpy (kJ/kg)	500

The strategy of calibration can be summarized as follows: In a first step the HTC model parameters describing the kinetics of the hydration reaction have to be determined, coupled with the parameters for moisture diffusion and heat transfer. Autogenous shrinkage data provides insight into the progress of self-desiccation while the difference to a drying specimen allows the determination of the transport parameters. In a similar fashion the creep parameters can be sequentially calibrated determining first the pure basic creep related parameters, followed by those determining the increase in creep deformation due to drying. The calibrated parameters of the HTC model are shown in Table 2, while in Table 3 the used default HTC parameters are listed.

Table 2. HTC Calibrated Parameters

D_0 (m^2/h)	$2.4 \cdot 10^{-3}$
D_1 (m^2/h)	3.22
n	3.25
g_1	1.5
kvg_c	0.18

Table 3. HTC Default Parameters

Density, ρ (kg/m^3)	2400
Isobaric Heat Capacity, c_t (J/kg ^{o}C)	1100
Heat Conductivity, λ_t (W/m ^{o}C)	2.3
Cement Hydration enthalpy (kJ/kg)	500
Hydration activation energy/R (K)	5000
Diffusivity activation energy/R (K)	9700
Polymerization activation energy/R (K)	6000
Hydration threshold for polymerization	0.1

Table 4 presents the MPS parameters for creep and shrinkage of C25/30. The experimental and simulated creep and shrinkage curves are shown in Figure 2.

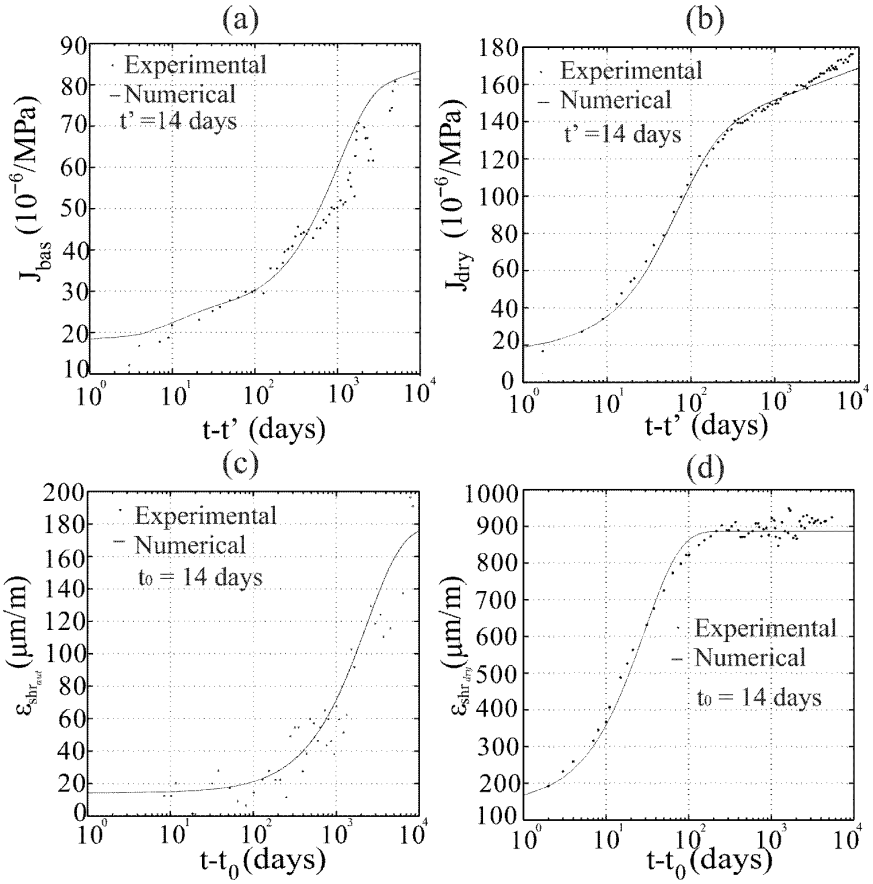

Figure 2. Simulated versus measured creep and shrinkage response: (a) basic and (b) drying creep compliance, (c) autogenous and (d) drying shrinkage strain

Table 4. Creep and Shrinkage Parameters

q_1 (10^{-5}/MPa)	3.2
q_2 (10^{-5}/MPa)	1.55
n_α	1.9
q_4 (10^{-5}/MPa)	1.6
c_0 (MPa^2 days)$^{-1}$	10^{-2}
κ_1 (MP/K)	5
k_{sh}	$2.3 \cdot 10^{-3}$

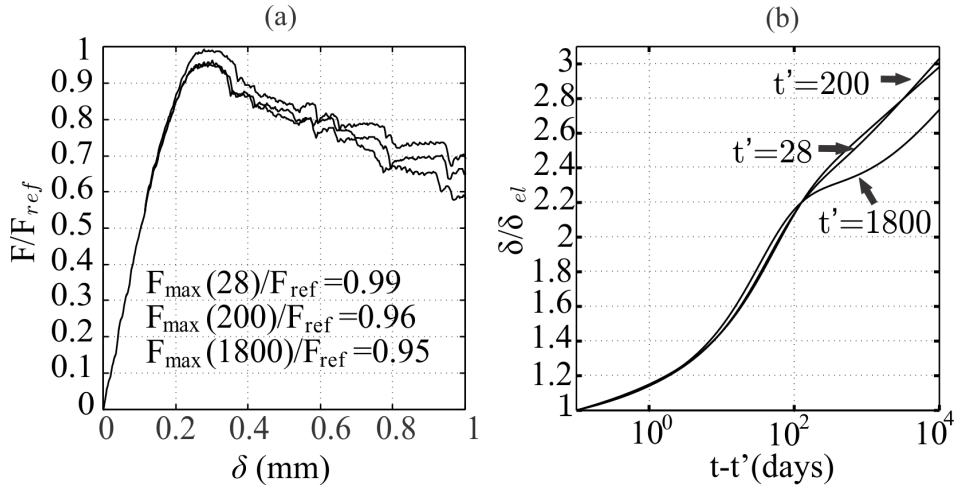

Figure 3. Simulated effect of creep and shrinkage: (a) relative load displacement curves for different simulated ages considering the evolution of shrinkage damage, (b) increase in total deformation due to concrete creep for 3 ages of load application as ratio between elastic deformation δ_{el} and long-term deformation

Application to fastenings

Once the parameters of the models are calibrated, the long-term effects of shrinkage and creep on anchor systems can be studied in a predictive way. Experimental data on the system response (pullout tests) serves as partial validation. Specifically a concrete slab of class C25/30 with dimensions $100 \times 100 \times 30$ cm is simulated first in HTC in order to obtain the evolution of the internal state variables for 10 years. The ambient environment as boundary condition is modeled as $h = 50\%$ relative humidity and $T = 20°C$. The mechanical problem is given by a headed stud anchor with a shaft radius, $r = 6$mm, at embedment depth of 60mm. The headed stud is ignored in the HTC model. Three types of simulations are carried out, (a) pure shrinkage and thermal

strains, (b) pullout tests at three different ages, $28, 200$, and 1800days, and (c) shrinkage and thermal strains followed by sustained load applied at the above listed three ages. In order to minimize the effects of the particle placement all simulations are run with the same seed.

For this preliminary study the required LDPM material parameters are taken from a list of suggested default values provided by Cusatis et al. (Cusatis et al. 2011b) for concrete with the same properties. The boundary conditions for the mechanical problem during the pull-out tests have been set up to reproduce the low confinement given by a tripod configuration with feet distance of 17 cm. For the creep simulations a sustained load corresponding to approximately 40% of the anchor's capacity in concrete of the given mix design and properties at the age of loading is assumed. Using the results of the simulated temperature, humidity and reaction degree fields the effects of creep and shrinkage on the performance of a headed stud can be quantified. The results of the simulations for the three different "pullout" tests and the three different "ages of loading" are shown in Figure 3 for this preliminary case study and specific configuration.

From this analysis it can be concluded that at least for the investigated case the effect of shrinkage on the maximum pullout load for this anchor configuration is noticeable but not significant while the post-peak response is affected clearly. The loss of load carrying capacity, solely by shrinkage, is 1%, 4% and 5% at 28, 200 and 1800 days, respectively, as compared to the reference simulation without consideration of shrinkage.

On the other hand, after almost 30 years the total long-term deformation due to concrete creep reaches almost three times the level of the short-term elastic deformation for loading at $t' = 28, 200$ days, and 2.6 times for loading at $t' = 1800$days. For the purpose of this analysis the elastic deformation is defined as deformation caused by a sustained load after approximately 1.5 minutes following the approximate relationship between compliance function and engineering modulus $E(t) \approx J(t, t' + 0.001)$ (Wendner et al. 2015a).

Conclusions

The safety and cost-efficient maintenance of our infrastructure, including also fastenings systems, demands more accurate longterm predictions taking into account all relevant phenomena. These models should be able to quantify the effects of all relevant deterioration mechanism that can affect a structure's life time and performance. In the present study the effects of concrete shrinkage and creep on the long-term behavior of headed studs are investigated. First results clearly prove notable effects that have to be investigated systematically. The currently ongoing full characterization of two concretes for fastening applications will provide the necessary inputs for calibrated and validated parameter studies.

Acknowledgements

The financial support by the Austrian Federal Ministry of Economy, Family and Youth and the National Foundation for Research, Technology and Development is gratefully acknowledged.

References

Alnaggar, M., Boumakis, I., Abdellatef, M., Wendner, R., "Lattice Discrete Particle Modeling for coupled concrete creep and shrinkage using Solidification Microprestress Theory". submitted in CONCREEP 2015.

Alnaggar, M., Cusatis, G., and Di Luzio, G. (2013). "Lattice discrete particle modeling (LDPM) of alkali silica reaction(ASR) deterioration of concrete structures." *Cement and Concrete Composites*, 41, 45–59.

Bažant, Z. P., D., Cusatis, G., and Cedolin, L. (2004). "Temperature effect on concrete creep modeled by microprestress solidification theory." *Journal of Engineering Mechanics*, 130 (6), 691–699.

Bažant, Z. P., Baweja, S. (2000). "Creep and shrinkage prediction model for analysis and design of concrete structures: Model B3." *ACI SPECIAL PUBLICATIONS 194*, 184.

Bažant, Z. P., Hauggaard, A. B., Baweja, S., and Ulm, F. (1997a). "Microprestress solidification theory for concrete creep. I: aging and drying effects." *Journal of Engineering Mechanics*, 123 (11), 1188–1194.

Bažant, Z. P., Hauggaard, A. B., and Baweja, S. (1997b). "Microprestress solidification theory for concrete creep. II: Algorithm and verification." *Journal of Engineering Mechanics*, 123 (11), 1195–1201.

Brooks, J. J. (1984). "Accuracy of estimating long term strains in concrete." *Magazine of Concrete Research*, 36, 131–145.

Cusatis, G., Pelessone, D., and Mencarelli, A. (2011a). "Lattice Discrete Particle Model (LDPM) for failure behavior of concrete. I: Theory." *Cement and Concrete Composites*, 33 (9), 881–890.

Cusatis, G., Mencarelli, A., G., Pelessone, D., and Baylot, J. (2011b). "Lattice Discrete Particle Model (LDPM) for failure behavior of concrete. II: Calibration and validation." *Cement and Concrete Composites*, 33 (9), 891–905.

Di Luzio, G., and Cusatis, G. (2013). "Solidification-microprestress-microplane (SMM) theory for concrete at early age: Theory, validation and application." *International Journal of Solids and Structures*, 50 (6), 957–975.

Di Luzio, G., and Cusatis, G. (2009a). "Hygro-thermo-chemical modeling of high performance concrete. I: Theory." *Cement and Concrete Composites*, 31 (5), 301–308.

Di Luzio, G., and Cusatis, G. (2009b). "Hygro-thermo-chemical modeling of high performance concrete. II: Numerical implementation, calibration, and validation." *Cement and Concrete Composites*, 31 (5), 309–324.

Di Luzio, G. (2009). "Numerical model for time-dependent fracturing of concrete." *Journal of engineering mechanics*, 135 (7), 632–640.

Havlásek, P. and Jirásek, M. (2012). "Modeling of Concrete Creep Based on The Microprestress-solidification Theory." *Acta Polytechnica*, 52 (2), 34–42.

Hubler, M. H., Wendner, R., and Bažant, Z. P. (2015a). "Comprehensive database for concrete creep and shrinkage: analysis and recommendations for testing and recording." *ACI Materials Journal*.

Hubler, M. H., Wendner, R., and Bažant, Z. P. (2015b). "Statistical justification of Model B4 for drying and autogenous shrinkage of concrete and comparisons to other models." *Materials and Structures*, 48 (4), 797–814.

Wendner, R., Hubler M. H., and Bažant, Z. P. (2015a). "Statistical justification of model B4 for multi-decade concrete creep using laboratory and bridge databases and comparisons to other models." *Materials and Structures*, 48 (4), 815–833.

Wendner, R., Hubler M. H., and Bažant, Z. P. (2015b). "Optimization method, choice of form and uncertainty quantification of Model B4 using laboratory and multi-decade bridge databases." *Materials and Structures*, 48 (4), 771–796.

Progressive Drying and Shrinkage of Concrete

Marek Vinkler[1] and Jan L. Vítek[2]

[1]Ph.D. Student, Faculty of Civil Engineering, Czech Technical University in Prague, Thákurova 7, 166 29 Praha 6 – Dejvice. E-mail: marek.vinkler.1@fsv.cvut.cz
[2]Professor, Faculty of Civil Engineering, Czech Technical University in Prague and Metrostav, a.s., Koželužská 2450/4, 180 00 Praha 8. E-mail: vitek@metrostav.cz

Abstract

The paper deals with drying and shrinkage of concrete specimens. Drying of concrete was measured first on small concrete cubes (edge length 200 mm), which were sealed on all with exception of one side (top side). The pore relative humidity was measured in different depth from the surface exposed to the environment (the top side, which were not sealed). The pore humidity is recorded at the moment for a period of about 14 months. After a good experience with the measurements, the experimental program was extended. The segments of walls of the thickness 200 mm, 400 mm and 800 mm were cast. Four sides were sealed in order to simulate the drying of the infinite walls of different thicknesses. The relative pore humidity is measured in different distances from the surface of individual walls. The elements are equipped with vibrating wire strain gauges which measure strains inside the elements. The strains in vertical as well as in horizontal directions are recorded. Additional tests are executed. The concrete compression strength is measured on cubes and uniaxial shrinkage is measured on standard cylinders using embedded vibrating wire strain gauges. The cylinders are stored in both, in laboratory conditions and in water.

INTRODUCTION

The crack development in concrete elements and structures reduces their durability; therefore it is of primary importance to investigate the processes in concrete and to improve the prediction of strain development on concrete structures. The experimental data are necessary for i) better understanding of the strain development and ii) development of the numerical procedures for their prediction.

Drying of concrete is a major phenomenon influencing shrinkage of concrete. Due to progressive drying of concrete the non-uniform shrinkage develops in concrete elements. The compatibility of elements prevents free shrinkage, which results in the development of eigenstresses even in elements which are completely free to deform. In order to evaluate such stresses it is essential to investigate mutual relations between drying of concrete, shrinkage, creep, etc. [Bažant et al; 1992], [Havlásek; 2014].

Moisture diffusion in concrete is a complex process affected by numerous effects, particularly concrete composition, age of concrete, environmental conditions

and local temperature and humidity in individual points of the concrete member [Bažant, Najjar; 1972], [Xi et al; 1994]. It influences maturing of concrete and subsequently shrinkage, creep and other parameters necessary for correct analysis of stresses in concrete elements. The paper addresses two issues:

1. Experimental program where the progressive drying is measured,
2. Experimental program where concrete drying and shrinkage is measured.

EXPERIMENTAL PROGRAM

Pilot experiment. Initial lack of experience with direct measurement of drying process in concrete required to design a simple experimental program, which would be able to verify the functionality of the methods of measurement of the moisture variation in concrete. The layout of the pilot experiment is shown in Figure 1. Concrete cubes with edge length of 200 mm were selected for simplicity of their production and low costs. The device measuring the relative moisture content in concrete is equipped with the gauge which comes to contact with concrete. In order to measure pore relative humidity in various depths, plastic tubes of various lengths from 20 to 100 mm were embedded in concrete. The applied method measures humidity in depths in the range from 30 to 100 mm. In order to ensure drying in one direction, cubes were sealed with plastic foil over 5 sides. This arrangement allowed for considering the problem as one dimensional and thus the experiment could simulate drying of 400 mm thick concrete slab from both surfaces or 200 mm thick concrete slab from one surface.

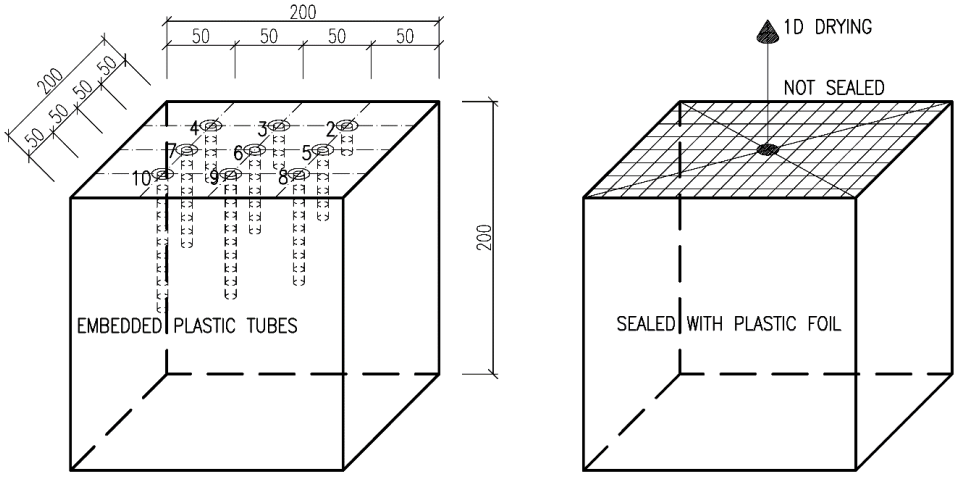

Figure 1. Layout of the Pilot Experiment.

Concrete mixture was provided by concrete mixing plant. Monitoring tests of compression strength on 3 concrete cubes were carried out in order to verify concrete quality. After pouring concrete mix into the steel mould and after embedding plastic tubes, the concrete cubes were covered with plastic foil and left to harden for one day. Then cubes were removed from the moulds and cured in water for next four days. The water temperature was 20°C. On the fifth day cubes were taken out from the water and surface water were wiped. Then 5 sides were sealed with plastic foil and

cubes were left to dry. The environment conditions were not controlled. Measurements were carried out for 271 days. Good experience with the measurements allowed for extension of the experimental program.

Drying and shrinkage of concrete wall segments. Three wall segments with the thicknesses of 200 mm (refereed as ST1), 400 mm (refereed as ST2) and 800 mm (refereed as ST3) were cast into prepared wooden formworks. Individual segments had the same longitudinal size 800 x 800 mm. Plastic tubes of different lengths were embedded in concrete wall segments in order to measure pore relative humidity in various depths. Each tube had airtight closure and as such provided space for water vapour to reach equilibrium with pore relative humidity of concrete in corresponding depth. Four vibrating wire strain gauges were embedded into each segment (two in horizontal direction and two in vertical direction) for measurements of shrinkage of concrete. As an example, layout of the wall segment ST2 with thickness 400 mm is provided below (see Figure 2).

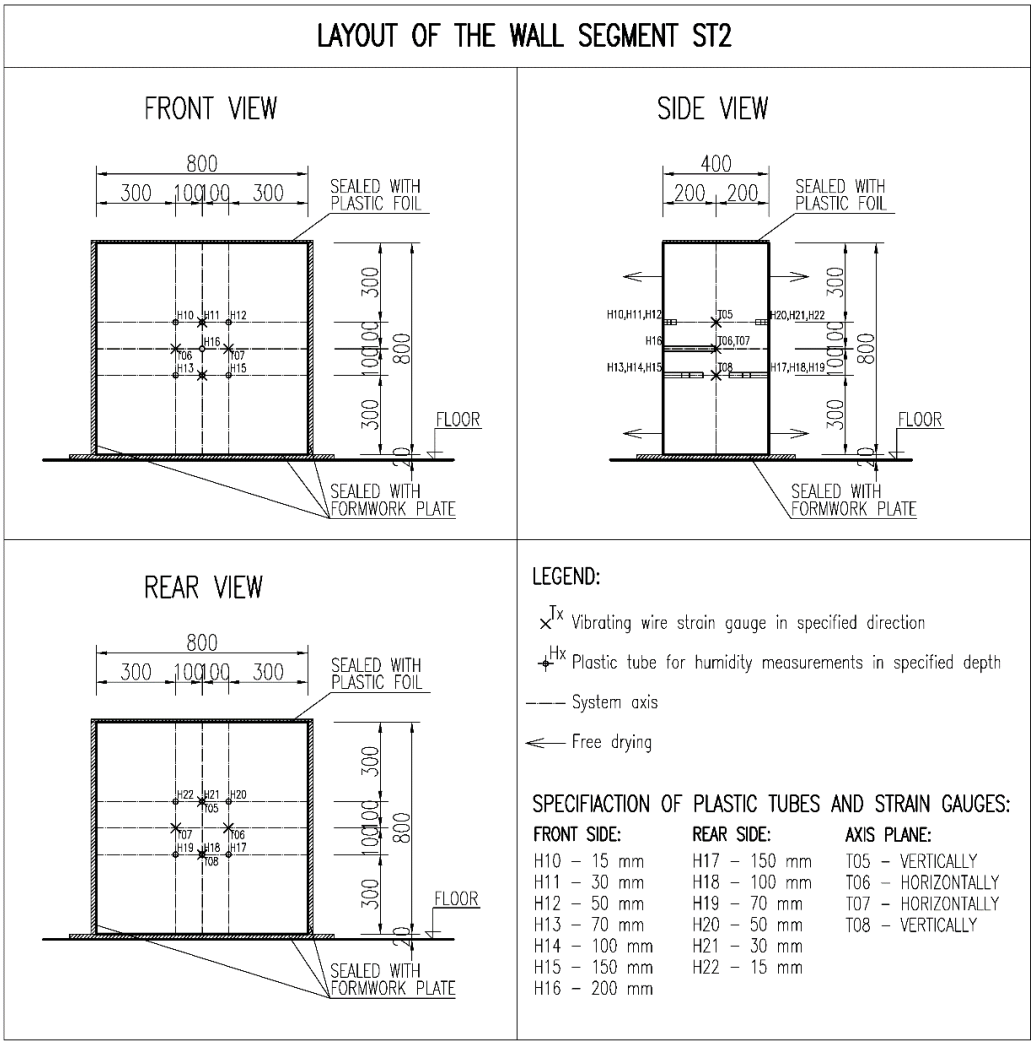

Figure 2. Layout of the Wall Segment ST2.

Segments were equipped with the auxiliary steel reinforcement placed in axis plane of the wall segments. Auxiliary reinforcement functioned as an anchorage member for vibrating wire strain gauges and also as a transport hanger. Four sides of the wall segments were sealed to simulate one dimensional drying of the infinite walls of different thicknesses. Plenty of additional test were also carried out (see below).

A typical concrete mix was provided by the professional concrete producer TBG Metrostav, Ltd. The concrete strength class C30/37 was selected because of the most frequent production. The measured parameters of concrete are slightly better than those required by the code for the concrete strength class. The measured compression cube strength at 28 days was about 55 MPa.

Measurements of strains in concrete started few hours after concreting, measurements of pore relative humidity of concrete started 10 days after concreting. Measurements are still in progress in the laboratory of the Department of concrete and masonry structure at the Faculty of Civil Engineering CTU in Prague. Here, the data till the age of 62 days of the wall segments are shown. The values of pore relative humidity were measured in the corresponding depths for each drying surface of each segment (15, 30, 50, 70, 100, 150, 200, 300, 400 mm). The environmental relative humidity and temperature were recorded closely with time step of 5 minutes using datalogger. Both relative humidity and temperature of the specimens were measured with Hygropin moisture meter. Photos from the experiment are shown (see Figures 3-4).

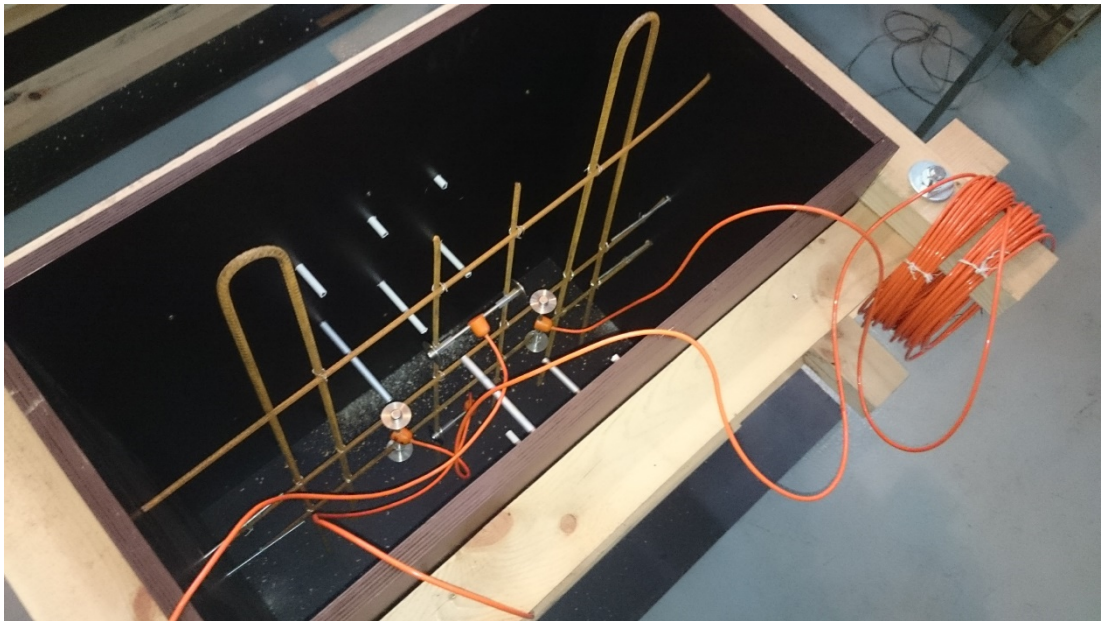

Figure 3. Formwork of the Wall Segment ST2 Prepared for Concreting.

Figure 4. Final Placement of the Wall Segments.

Additional tests. Experimental program was supplemented with additional measurements in order to provide better support for interpretation of the measured data. All the specimens were made at the same time, from the same concrete mix and had the same curing conditions as the wall segments. Additional tests were grouped as follows:

1. Measurements of shrinkage on 6 concrete cylinders. Each specimen had one embedded vibrating wire strain gauge in vertical direction. Standard cylinders of the diameter 150 mm and the height 300 mm were used. Cylinders were divided into three groups of two specimens and placed in different environmental conditions: first group (refereed as V1-V2) was located in the same room as the wall segments, second group (refereed as V3-V4) was stored in controlled room with 65 % relative humidity and the third group (refereed as V5-V6) was stored in controlled room with 100 % relative humidity. Different curing conditions allowed for determination of autogenous shrinkage and for comparison of shrinkage measured in cylinders and in large concrete elements.

2. Measurements of pore relative humidity and weight loss on 4 concrete cubes. Cubes with the edge length 200 mm were produced (same as in the pilot experiment). Plastic tubes for measurements of pore relative humidity were embedded into concrete in various depths from 15 to 100 mm (same as in the wall segments). Weight loss of the specimens was also measured using laboratory scales. Cubes were divided into two groups of two specimens and placed in the same room as the wall segments. First group (refereed as K1-K2) was sealed over 5 sides and the last side was left to dry. Second group (refereed as K3-K4) was sealed over 4 sides and 2 opposite sides were left to dry. By this set-up, first and second group can simulate drying from both surfaces of 400 mm and 200 mm thick walls respectively. This test allows for determination whether the pore relative humidity measured in concrete cubes and that measured in large concrete elements are comparable. Provided that this assumption is met, measured weight loss could be extrapolated to

the wall segments and also further measurements of pore relative humidity could be carried out on smaller specimens such as mentioned cubes rather than on bigger ones. It could lead to simplification of future experiments.

3. Measurements of self-dessication on 2 concrete cubes. Cubes were made with the edge length 150 mm and were left in the moulds with the upper surface sealed with plastic foil in order to guarantee that no drying occurs. One plastic tube for measurements of pore relative humidity was embedded in the middle of each specimen. This test enables to trace the difference between the humidity drop caused by self-dessication from the one caused by drying.

The additional specimens may be seen also in Figure 4.

EXPERIMENTAL RESULTS

The experimental program was started early this year and all the measurements are in progress. Some results illustrating the initial experience (measurements 62 days after casting) are presented in this paper.

Drying of the wall segments. Relative humidity profiles have a typical convex shape (see Figures 5 and 6). Only small difference can be found in relative humidity development in the same depth in each wall segment (also Figures 7 and 8). More significant difference is expected to be seen after longer time period of drying.

Weight loss of the cubes K1-K4. The weight loss measured on the cubes reached about 130 g in cubes K1 and K2 (5 sides sealed) and about 180 g in cubes K3 and K4 (4 sides sealed). The evaporation is not proportional to the area exposed to drying.

Shrinkage of the wall segments ST1-ST3 and the cylinders V1-V6. Shrinkage in wall segments is plotted in Figure 9. As expected the thicker element shrinks less due to slower drying. Comparing to shrinkage of cylinders (Figure 10), the strains in walls are smaller. It shows that the strains measured on laboratory specimens cannot be directly used for assessment of shrinkage in larger elements, which unfortunately sometimes happen in design practice. The autogenous shrinkage was not observed. The reason may be found in the composition of concrete. The cement content is only about 360 kg per m^3 of concrete.

Environmental conditions. The environmental conditions in the laboratory were carefully recorded. The measurements of temperature and relative humidity of the air are taken every 5 minutes. The average relative humidity within the initial period (62 days) was 25%, while the average temperature was 21.7 deg. C. The dry environment is a result of heating during the winter period. In summer more humidity may be expected.

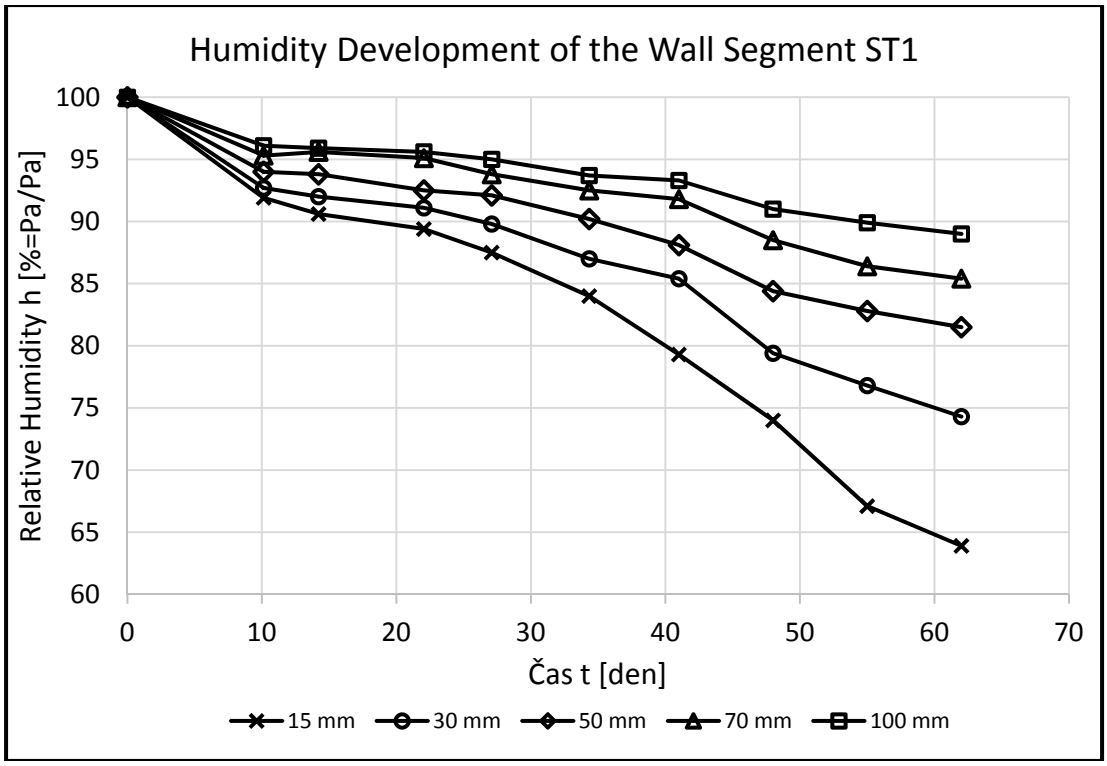

Figure 5. Humidity Development of the Wall Segment ST1

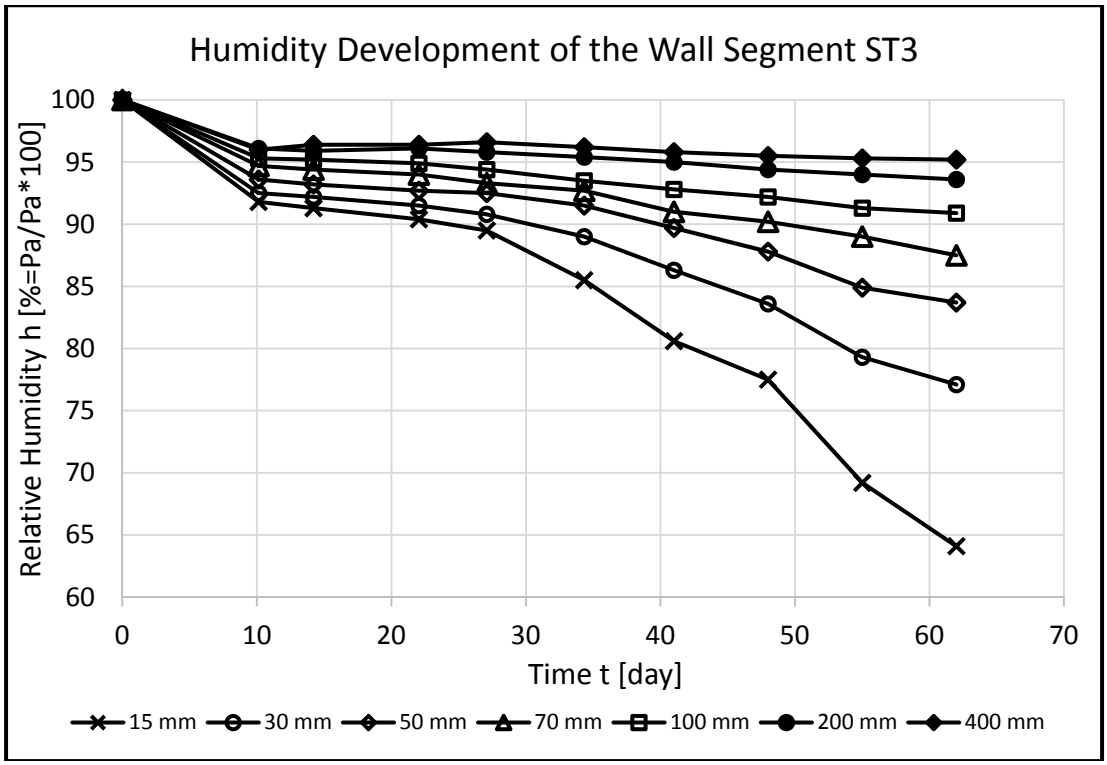

Figure 6. Humidity Development of the Wall Segment ST3

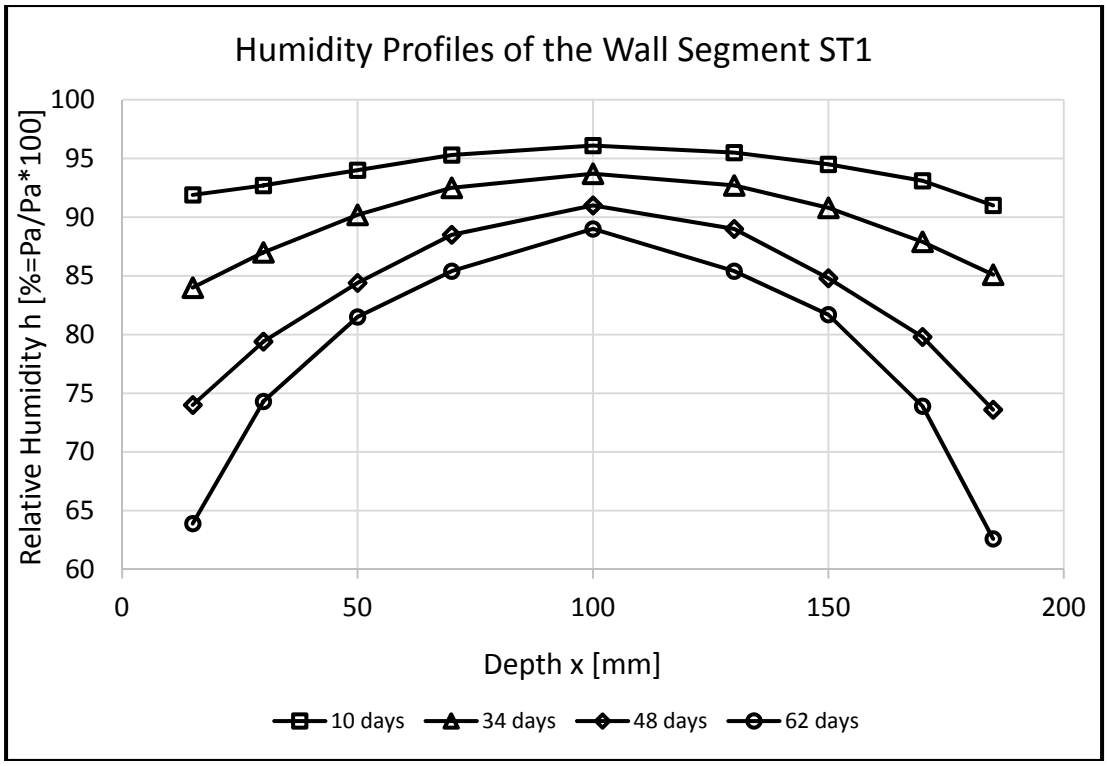

Figure 7. Humidity Profiles of the Wall Segment ST1

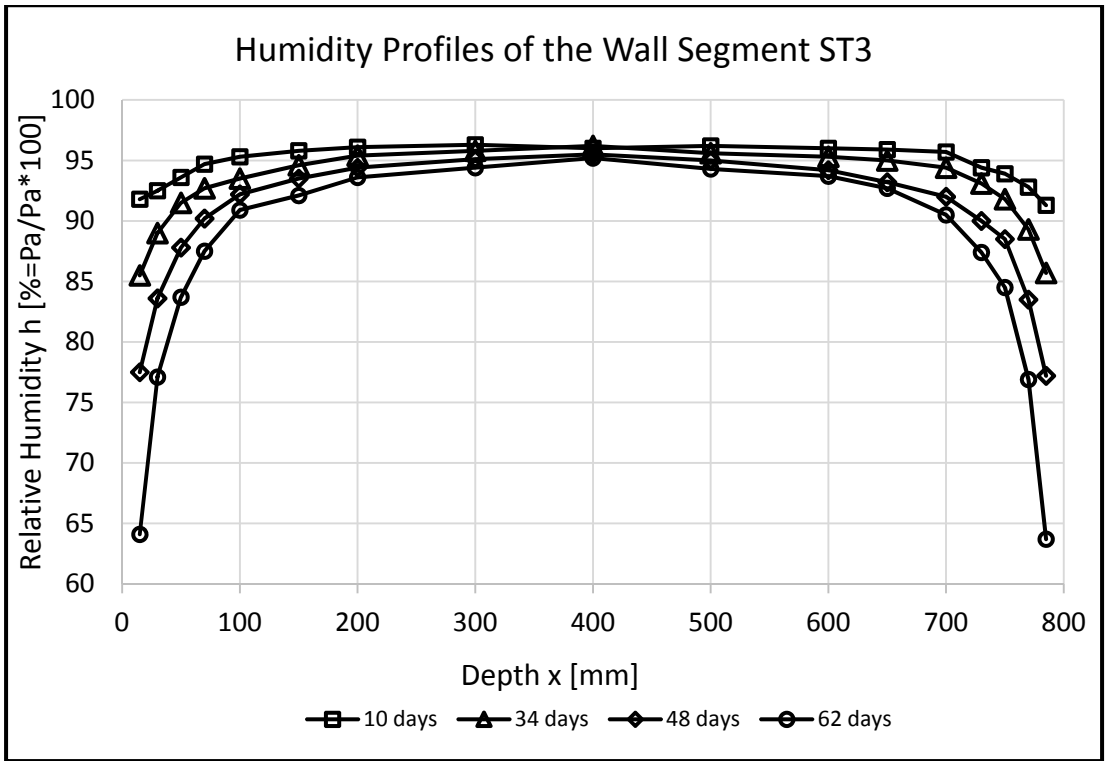

Figure 8. Humidity Profiles of the Wall Segment ST3

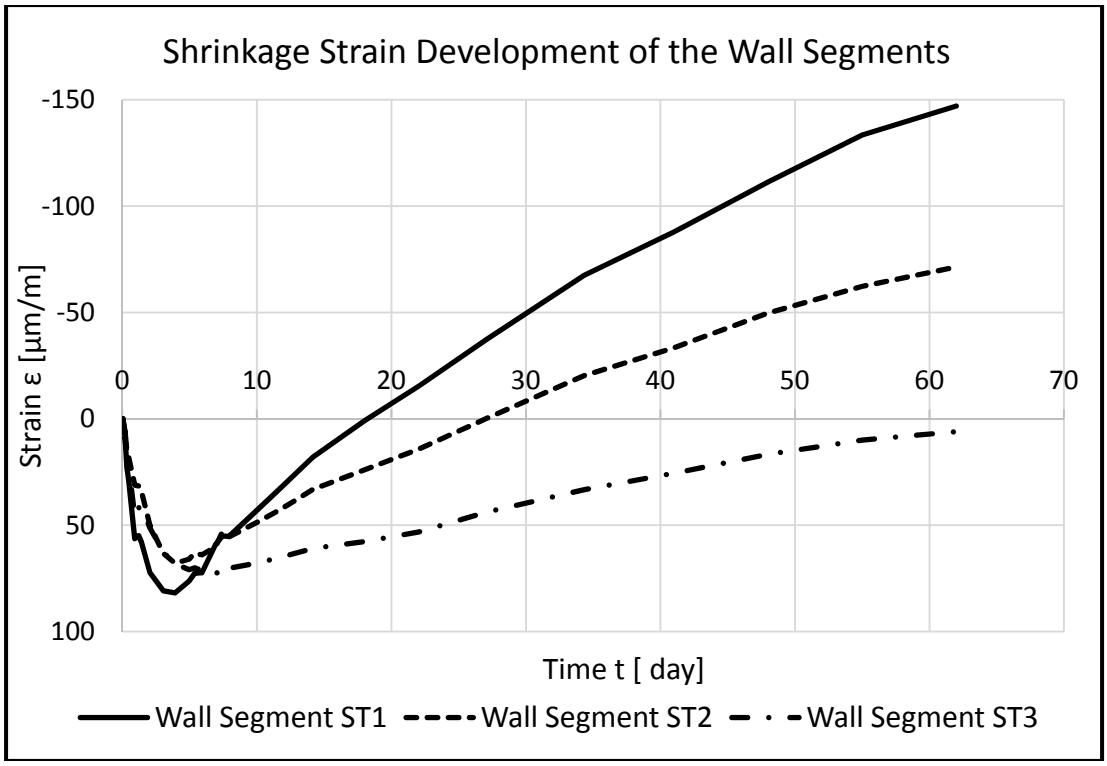

Figure 9. Shrinkage Strain Development of the Wall Segments.

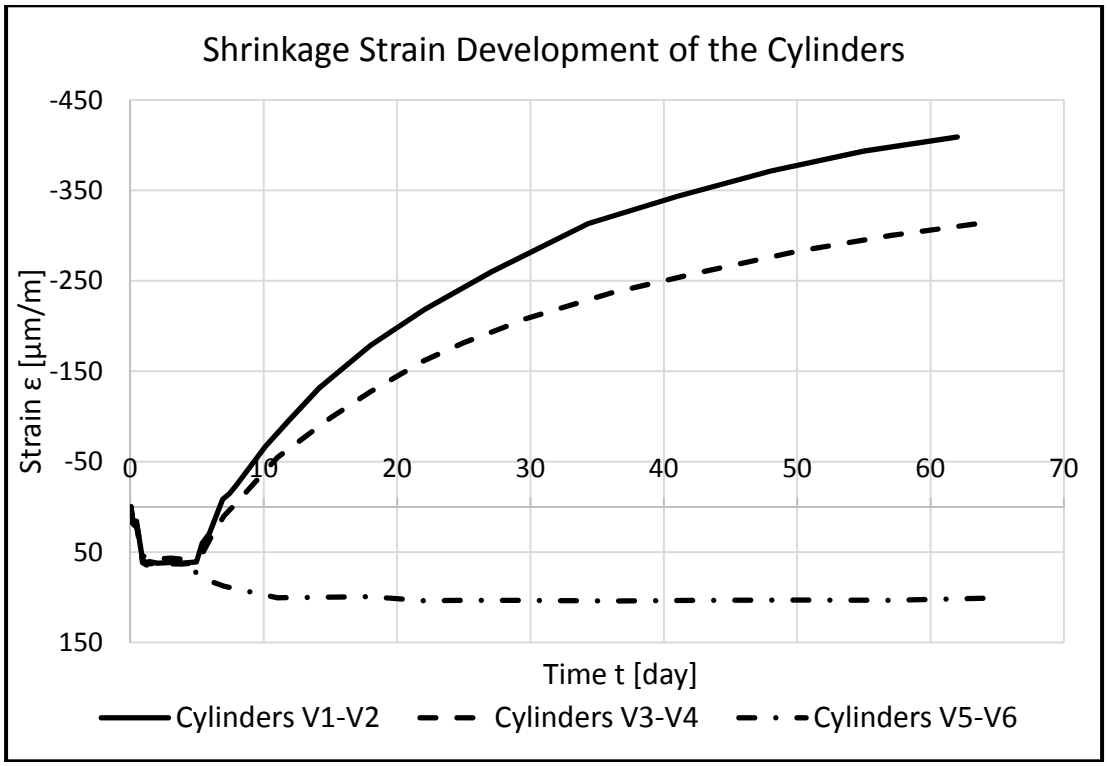

Figure 10. Shrinkage Strain Development of the Cylinders.

CONCLUSIONS

The initial results of the experimental program were presented. The measured relative humidity in individual specimens (cubes and wall elements) shows that the program was started successfully and that the measured values recorded in individual specimens are mutually in accordance. The shrinkage strains measured in larger elements are smaller than those measured in smaller elements, which confirms the long term experience. The formulas for prediction of shrinkage strain taking the size of the elements into account may be verified using the presented results.

The experimental program will continue in the future years and the numerical models will be modified or developed using the measured results.

ACKNOWLEDGEMENTS

The experimental program is a long term activity. The production of specimens was supported by the Ministry of Industry and Trade (Project no. FR-TI3/531) and the measurements are supported by the SGS grant SGS15/032/OHK1/1T/11and by the Technological Agency of the Czech Republic (Project No. TE 01020168). All the supports are gratefully acknowledged.

REFERENCES

Bažant, Z. P.; Najjar, L. J. (1972). *Nonlinear Water Diffusion in Nonsaturated Concrete*. Materials and Structures, Vol. 5, pgs. 3-20.

Bažant, Z. P., Křístek, V., Vítek, J. L. (1992). *Drying and Cracking Effects in Box – Girder Bridge Segment*. Journal of Structural Engineering, Vol.118, No.1.

Havlásek, P. (2014). *Creep and Shrinkage of Concrete Subjected to Variable Environmental Conditions*. Ph.D. Thesis, CTU in Prague.

Xi, Y.; Bažant, Z. P.; Molina, L.; Jennings, H. M. (1994). *Moisture Diffusion in Cementious Materials: Adsorption Isotherms*. Advanced Cement Based Materials.

Xi, Y.; Bažant, Z. P.; Molina, L.; Jennings, H. M. (1994). *Moisture Diffusion in Cementious Materials: Moisture Capacity and Diffusivity*. Advanced Cement Based Materials.

Study on the Shrinkage of a Full-Scale Wall Made with Blast Furnace Slag Fine Aggregates

Tomiyuki Kaneko[1]; Keiichi Imamoto[2]; Chizuru Kiyohara[3];
Akio Tanaka[4]; and Ayuko Ishikawa[5]
6-3-1 Niijuku Katushika-ku, Tokyo, Japan. E-mail: tomiyuki3123@gmail.com
[1,2,3,5]Tokyo University of Science. [4]Hachiyo Consultant Corporation.

Abstract
The purpose of this study is to clarify shrinkage of full-scale wall made with Blast Furnace Slag Fine Aggregate (BFS). Authors investigated the influence of BFS on strength properties, drying shrinkage, uni-axial restraint stress, tensile creep and drying shrinkage cracking of full-scale wall. Following findings were obtained. The concretes with BFS had high shrinkage cracking resistance. The shrinkage stress could be calculated with incremental effective young's modulus method. This analytical approach also indicated that the shrinkage cracking resistance of concrete with BFS was good enough.

INTRODUCTION

Shrinkage cracking of concretes is one of the factors that affects durability of concrete structures. It has been reported that the use of BFS reduces the drying shrinkage of concretes (Saito et al., 2009). It would be expected that the use of BFS contributes effective reuse of industrial by-product. However, there are no studies on shrinkage cracking properties of full-scale specimens made with BFS. The purpose of this study is to clarify the drying shrinkage of full-scale wall made with BFS.

OUTLINE OF TESTS

Table1. shows test items. Strength tests, drying shrinkage tests, tensile creep tests, uni-axial restraint stress tests, drying shrinkage cracking tests and full-scale wall tests were performed to clarify drying shrinkage cracking properties of concrete with BFS. Table2. shows properties of fine and coarse aggregate used in this study. And table.3 shows mixtures of the concretes in this study. 50% of full fine aggregates was replaced with BFS. Target strength of concrete was 25.2N/mm^2. The concretes were mixed at ready mixed concrete and 2 mixing trucks were used for casting of concrete.

Table1. Test items

Test item		JIS Number	Curing condition	Specimens dimension (mm)	Number	Test age (days)
Fresh properties (slump, air content)		A 1101 A 1128	-	-	-	-
Compressive strength (modulus of elasticity) Splitting tensile strength		A 1108 A 1149 A 1113	Indoor And outdoor	φ100×200	3	*1
Drying shrinkage		-		100×100×400	2	4,7
Drying shrinkage cracking		-	indoor	100×100×1100	2	7
Uni-axial restraint stress		-		100×100×1000	1	7
Tensile creep		-		100×100×1000	1	7
Shrinkage of full-scale wall	Full-scale wall	-	outdoor	400×1800×2300	1	4/7
	Dummy wall	-		200×900×1200	1	7
	Dummy upper beam	-		400×400×800	1	7
	Dummy lower beam	-		400×400×800	1	4

*1 Indoor:3,7,14,28,56,91 outdoor:7,28,91 standard:28

Table2. Properties of aggregates

Symbol	Types of aggregate	Maximum sieve size (mm)	Density in saturated surface-dry condition (g/cm^3)	Absorption (%)
SC	Crushed sand	5.0	2.58	2.87
SL	Limestone crushed sand	5.0	2.66	0.89
SP	Mountain sand	5.0	2.80	1.23
SB	Blast Furnace Slag Fine Aggregate	5.0	2.64	1.88
GC	Crushed coarse sand	20.0	2.61	2.76
GL	Limestone crushed coarse sand	20.0	2.68	0.65

Table3. Mixture proportions

Types of concrete	s/a (%)	Unit content (kg/m^3)							
		W	C	SC	SL	SP	SB	GC	GL
N	48.4	182	298	427	171	255	-	459	471
BFS	47.4	182	298	-	171	252	436	466	479

s/a : sand - total aggregate ratio , W:water, C : cement(Ordinary portland cement , density:3.16g/cm^3)

Test method in the room

Specimens were prepared in air conditioning room with temperature and humidity of 20±2°C and 60±5%, respectively. Molds of the specimens were removed at 4 or 7 days after placement of the concrete. (Indoor curing)

Strength test. Cylindrical specimens with φ100×200mm were used. Compressive strength tests, modulus of elasticity and splitting tensile strength tests were performed according to JIS A 1108, 1149 and 1113, respectively. JIS stands for Japanese

industrial standards. The molds were removed at 7 days after placement of concrete. In addition, the specimens cured in water (temperature 20°C) for 28 days were used.

Measurement of drying shrinkage. Specimens with 100×100×400mm were used and shrinkage strains were measured with embedded gauges. In order to keep the same drying condition with the wall, the sides of specimens (100×400mm) were sealed with alminum foil tape.

Drying shrinkage cracking test. Figure1. shows the details of the specimens. Specimens were prepared according to "test method for shrinkage cracking of concrete" proposed by Japan Concrete Institute (JCI, 2010). To provide restraining, a longitudinal steel bar(φ32) was inserted at the center of the specimen as shown in Figure1. Within 300mm length of the center of the bar, the surface was shaved and strain gauges were attached to the central portion of the bar. In order to keep the same drying condition with the wall, the sides of specimens (100×1100mm) were sealed with alminum foil tape.

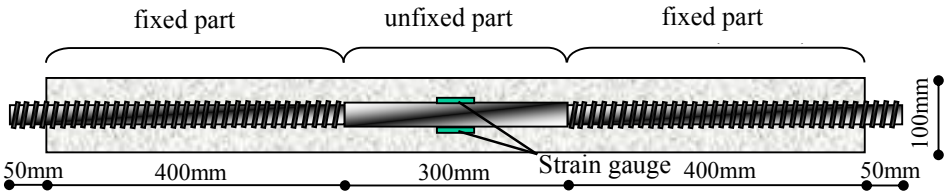

Figure1. Details of the drying shrinkage cracking specimens

Uni-axial restraint stress tests. This device can control the restrained degree of concrete shrinkage (Hamanaga,Y et al.,2007). In order to keep the same drying condition with the wall, the sides of specimens (100×1000mm) were sealed with alminum foil tape.

Measurement of tensile creep. Creep strains were measured with embedded gauge using 100×100×1000mm specimens at same condition with drying shrinkage test. Age of concrete at application of load was 7 days and applied load was 30% of tensile strength of concrete. In order to keep the same drying condition with the wall, the sides of specimens (100×1000mm) were sealed with alminum foil tape.

Tests method for exposure

The specimens were prepared in outdoor condition and exposed to actual environment. The molds were removed at 4 or 7 days after placement of the concrete. (Outdoor curing)

Measurement of drying shrinkage. Specimens with 100×100×400mm were used for the test and shrinkage strains were measured with embedded gauges. In order to keep the same drying condition with the wall, the sides of specimens (100×400mm) were sealed with alminum foil tape.

Shrinkage of full-scale wall. Figure2. shows the details of the specimens. Full-scale wall was made of two components. Lower beam of the wall was made at 1st placement (I) . After 12 days, walls, columns and upper beams were constructed at 2nd placement (II) . The molds of lower beam and upper parts were removed at 4 and 7 days, respectively. At the same time, dummy specimens that have same cross sections and re-bar arrangements to RC member were produced. Dummy specimens were sealed with almnium foil tape to be same drying conditions to RC member.

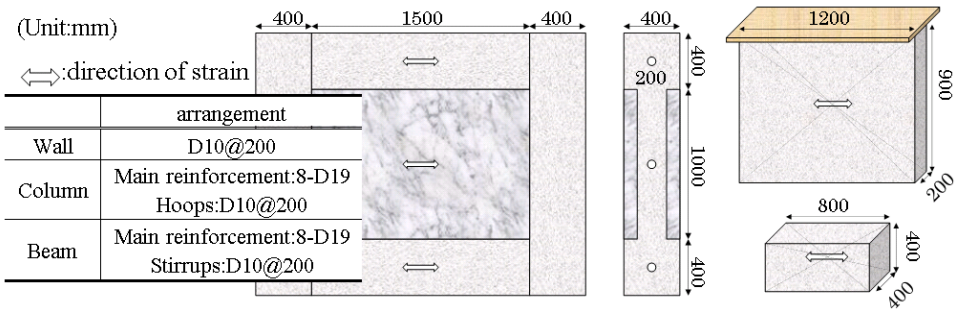

	arrangement
Wall	D10@200
Column	Main reinforcement:8-D19 Hoops:D10@200
Beam	Main reinforcement:8-D19 Stirrups:D10@200

Figure2. Full-scale wall, dummy wall and dummy beam

TEST RESULTS and DISCUSSIONS

Fresh properties of concrete. Table4. shows fresh properties of concrete at the times of placement. Because BFS tended to increase air bubble in concrete, antifoaming agent was used to reduce the air content of concrete with BFS. The slump was settled within 20±2.0cm, and the content of air was settled within 4.5±1.0%.

Table4. Fresh properties of concretes

Types of concrete	Concrete placing	Unit content of mixing agent (kg/m^3) (C×%)			Slump (cm)	Air content (%)
		Water reducing agent	Air entraining agent	Antifoaming agent		
N I	I	1.1	0.002	-	18.5	5.3
N II	II				18.0	5.3
BFS I	I			0.01	19.0	4.5
BFS II	II				21.0	4.2

Strength properties. Strength tests results of standard test specimens at 28 days are shown in Figure3. The strength of all specimens at 28 days were higher than designed strength. However increment of strength were not remarkable. It has been reported that early age strength development of concrete with BFS was relatively low (AIJ, 2010). In this study, the strength development of both concretes with natural and BFS were close in spite of their curing conditions. Although the strength of specimens under actual environmental condition were lower than that under room condition at 7 days, the both strength were close at 28 days. It was confirmed that the strength of concretes with BFS was close to normal concrete.

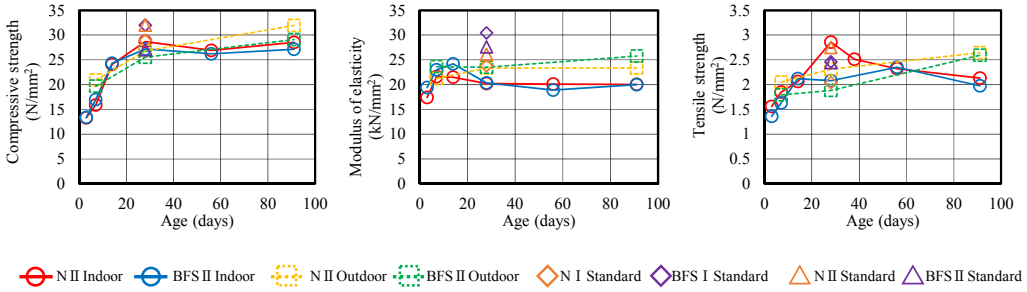

Figure3. Results of strength tests

Drying shrinkage properties. Figure4. shows changes of drying shrinkage strains and outdoor weather with removing days. Outdoor specimens repeated expansion and shrinkage within a day with change of temperature and humidity. After the rain, the strains moved to expansion due to the supply of water. Regardless of placing time and curing condition, magnitudes of the drying shrinkage strains of concrete with BFS were decreased. At 100 days after form removal, indoor and outdoor shrinkages of the concretes members with BFS were smaller about 9% and 13% than that of reference concrete, respectively. It was confirmed that BFS is effective to reduce the shrinkage under real environment.

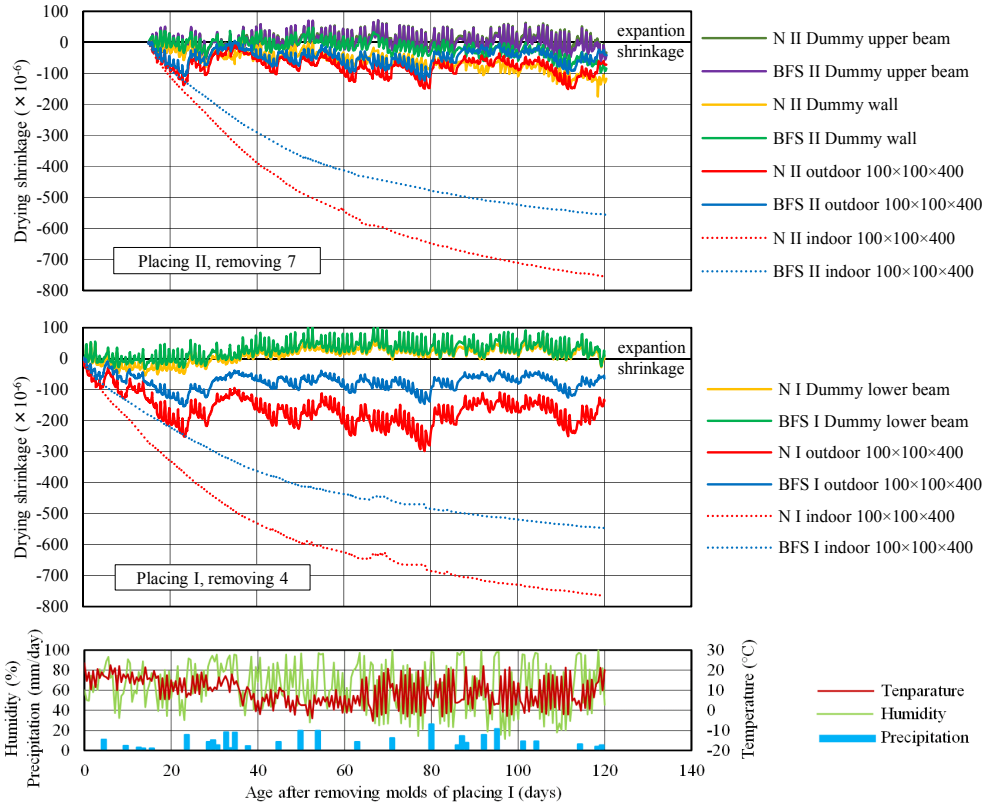

Figure4. Changes of drying shrinkage and weather

Drying shrinkage cracking test. Figure5. shows the changes of shrinkage induced stress of concrete with time. The cracking age was detected the moment that stress fell down rapidly. Although the specimens of the concretes with BFS hasn't cracked at 120 days, that of reference concrete was cracked at 21 days after drying. The stress strength ratio is the value that divided the stress at cracking age by tensile strength of concrete. It was thought that BFS has higher cracking resistance because the stress strength ratio of the specimens of the concrete with BFS were higher than that of reference concretes.

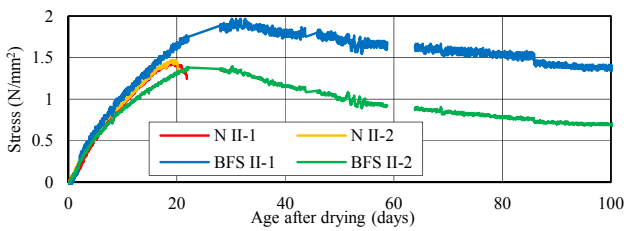

Figure5. Changes of shrinkage induced stress

Uni-axial restraint stress tests. Figure6. shows relation of restraint strain and induced stress. It was considered that tangent of stress-strain curvature is effective modulus of elasticity under sustained stress. The induced stress of BFS was smaller than that of reference concretes.

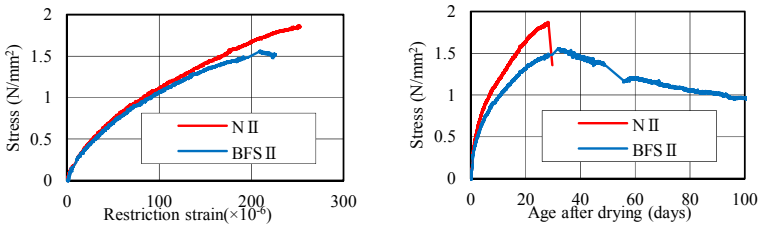

Figure6. Relation of restraint strain and induced stress

Tensile creep. Figure7. shows tensile creep strain and creep strain calculated of uni-axial restraint test. The creep strains were calculated using Eq.1.

$$\varepsilon_{cr}=(\varepsilon_f-\varepsilon_m)-\varepsilon_e \quad (1)$$

Where,

ε_{cr} : Creep strain ($\times 10^{-6}$)
ε_f : Free shrinkage strain ($\times 10^{-6}$)
ε_m : Actual strain ($\times 10^{-6}$)
ε_e : Elastic strain ($\times 10^{-6}$)

Elastic strain was calculated by using logarithm approximation of the result of strength tests. Because the calculated creep strain of the reference concretes was closed to tested tensile creep strain, it was considered that both creep strains might be close. The calculated creep strain of the concretes with BFS was about 5% lower than that of the reference concretes. Therefore, tensile creep strain of the concretes with BFS was estimated as 0.95 of that of the reference concrete.

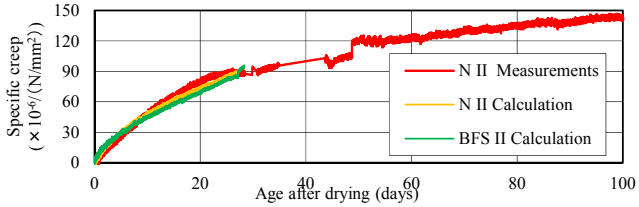

Figure7. Tested tensile creep strain and creep strain calculated

Shrinkage of full-scale wall

Drying shrinkage. Figure8. shows changes of drying shrinkage strains of full-scale wall and dummy specimens. Deference of strains between full-scale wall and dummy wall was due to restriction by surrounding members. Regarding the each beam, the shrinkage strains of the member were higher than that of the dummy specimens. Because V/S of walls of RC member was smaller than that of beams, the shrinkage strains of wall of RC member were higher than that of beams hence, stress of the beam would be compression and on the other hand, that of the wall would be tension.

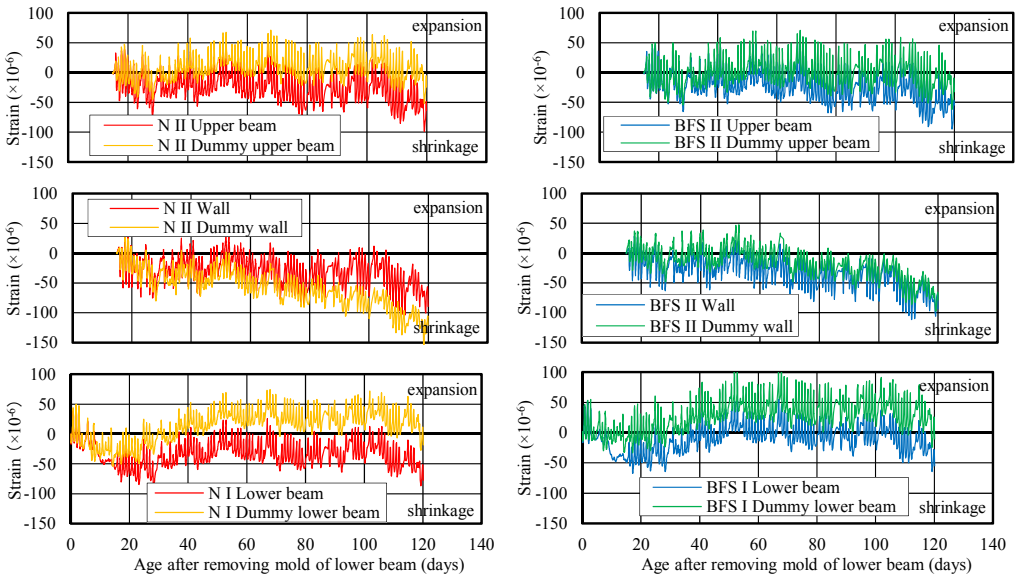

Figure8. Change of strain of full-scale wall and dummy specimens

Restrain stress. Figure9. shows changes of the shrinkage stress. The shrinkage stress was estimated considering the effective modulus of elasticity of concrete. The cracking strength was estimated by logarithm approximation of the tensile strength and the stress strength ratio of the concrete evaluated based on the drying shrinkage cracking test. It was observed that the cracking strength increased with age. However, shrinkage strain progressed slowly due to rain, and hence, the clack did not occur. Regarding cracking strength and restriction stress ratio, that of concrete with BFS was higher than that with reference aggregate. This mean that the full-scale wall of concrete with BFS has higher shrinkage cracking resistance than that with reference concrete.

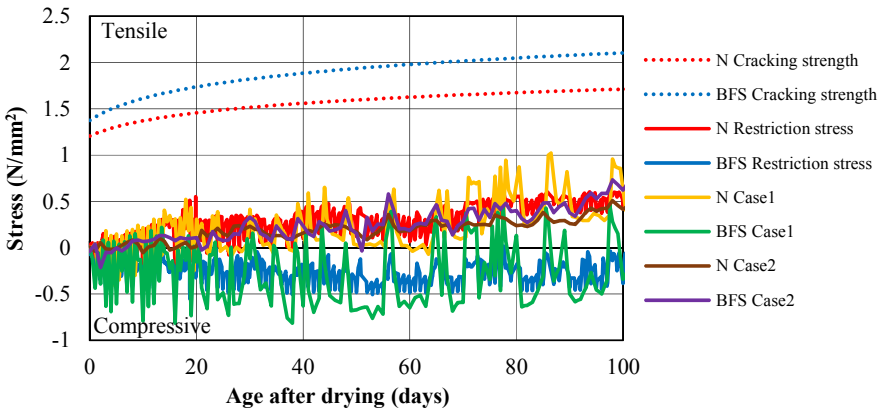

Figure9. Restriction Stress and cracking strength

STRESS ANALYSIS

The shrinkage stress was calculated by incremental effective young's modulus method shown in Eq.2. (AIJ, 2006). Mechanical properties of concrete used in this study was obtained from the data described previous study. The influence of the temperature and rain on the stress was not considered in this analysis.

$$\sigma(t) = \sum_{t'}^{t} \frac{E(t')}{(1+\phi(t,t'))} \Delta\varepsilon(t') \qquad (2)$$

Where,

t : Age (days)
t' : Age at loading (days)
$\sigma(t)$: Stress at time t (N/mm²)
$E(t')$: Elastic modulus at time t' (N/mm²)
$\Delta\varepsilon(t')$: Increment of restraint strain between t'-1 and t'
$\phi(t,t')$: Creep coefficient at time t for age at loading t'

Difference of strains between RC wall and dummy specimens due to as the restriction of surrounding members were used for calculation in Case1. The strains of dummy wall and beams were used for calculation in Case2. The development of elastic modulus of lower beam was calculated by using the model codes of compressive strength by "CEB-FIP1990" and Japanese RC standard formula. Elastic modulus of upper beam and wall of RC member were calculated by using logarithm approximation of the testedt strength. The total specific creep at time t at loading of t' was evaluated as 0.95 of the reference concrete, considering V/S.

Figure9. shows the changes of stresses of concretes. Although, in Case1, analysis

indicated good precision, the analysis did not exhibit not good in Case2. Further research should be needed in near future.

CONCLUSION

The purpose of this study is to clarify shrinkage behavior of full-scale concrete wall made with Blast Furnace Slag Fine Aggregate (BFS). Authors investigated the influence of BFS on strength properties, drying shrinkage, uni-axial restraint stress, tensile creep, drying shrinkage cracking of full-scale wall with BFS. The following findings were obtained.

1) Strength of BFS concrete was close to normal aggregate concrete.
2) Shrinkage of BFS concrete was lower than that of normal aggregate concrete under the real environmental condition.
3) It was observed that the full-scale wall of concrete with BFS has high shrinkage cracking resistance.

Acknowledgement

Authors thank to Nippon Steel Association for carrying out and to Akio Tanaka(HCC), Takumi Warino(TUS) and Tomoki Taniuchi(TUS) for working. Drying shrinkage cracking test devices were supplied by Yoshitaka Ishikawa(J-POWER EPDC) and Yasuhiro Dan(Nippon Steel & Sumikin Blast Furnace Slag Cement Co.,Ltd).

References

1) Saito,K., Kinoshita,M., Ihara,T., Yoshizawa,C., (2009) “Property of durable improvement concrete with Blast Furnace Slag Fine Aggregate.” JCI Annual Convention, 32(1),139-144.(in Japanese)
2) Japanese Concrete Institute (JCI). (Sep. 2010) Committee of Shrinkage cracking reduction and the durable improvement considered admixture. (in Japanese)
3) Hamanaga,Y., Sato,Y., Ueda,K., Kiyohara,C., (Jun.2007) “DEVELOPMENT OF A NEW APPARATUS FOR SHRINKAGE CRACKING TEST OF CONCRETE” Transactions of AIJ (Architectural Institute of Japan). Journal of structural and construction engineering, 616,1-7.(in Japanese)
4) Architectural Institute of Japan (AIJ). (Feb. 2013) “Recommendation for Practice of Concrete with Blast Furnace Slag Fine Aggregate.” (in Japanese)
5) Architectural Institute of Japan (AIJ). (Feb. 2006) “Recommendations for Practice of Crack Control in Reinforced Concrete Buildings (Design and Construction)” (in Japanese)

Effect of Lime Stone Aggregate on Drying Shrinkage and Shear Strength of an RC Beam

Kenichiro Nakarai[1]; Ryoichi Sato[2]; Yuko Ogawa[3]; and Kenji Kawai[4]

[1]Associate Professor, Structural Engineering Laboratory, Department of Civil and Environmental Engineering, Institute of Engineering, Hiroshima University, 1-4-1 Kagamiyama, Higashi-Hiroshima, Hiroshima 739-8527, Japan. E-mail: nakarai@hiroshima-u.ac.jp
[2]Specially Appointed Professor, Institute of Engineering, Hiroshima University, 1-4-1 Kagamiyama, Higashi-Hiroshima, Hiroshima 739-8527, Japan. E-mail: sator@hiroshima-u.ac.jp
[3]Assistant Professor, Structural Materials and Concrete Structures Laboratory, Department of Civil and Environmental Engineering, Institute of Engineering, Hiroshima University, 1-4-1 Kagamiyama, Higashi-Hiroshima, Hiroshima 739-8527, Japan. E-mail: ogaway@hiroshima-u.ac.jp
[4]Professor, Structural Materials and Concrete Structures Laboratory, Department of Civil and Environmental Engineering, Institute of Engineering, Hiroshima University, 1-4-1 Kagamiyama, Higashi-Hiroshima, Hiroshima 739-8527, Japan. E-mail: kkawai@hiroshima-u.ac.jp

Abstract

In this study, we investigated the drying shrinkage and fracture energy of concrete with lime stone and other aggregates and their effect on the shear strength of RC beams. The results of material experiments showed that the use of the lime stone aggregate having large aggregate crushing value decreased the fracture energy and drying shrinkage compared to the other aggregates. The results of structural experiments showed that the measured shear strength of RC beam with the lime stone aggregate was smaller than that with rhyolite aggregate, while it reduced internal stress of RC beams caused by the shrinkage of concrete. It was suggested that the decrease in the shear strength was caused by the small fracture energy and characteristic length of the concrete with the lime stone aggregate.

INTRODUCTION

Shrinkage of concrete may affect the mechanical performance of concrete structures as well as the durability with shrinkage cracks. The effect of the shrinkage on the flexural cracking capacity, width and stiffness has already been investigated by many researchers such as Tanimura et al. (2005). In addition, the recent studies by Sato and Kawakane (2008) revealed that the shrinkage can decrease the shear strength of concrete structures using high strength concrete. They also showed that the decrease in the shear strength of RC beams caused by high autogenous shrinkage can be reproduced by their proposed method based on the concept of equivalent tension reinforcement ratio. In addition, the applicability of this concept for

evaluating the effect of drying shrinkage of normal strength concrete has been verified by Nakarai et al. (2014).

The shrinkage of concrete was significantly affected by properties of aggregates in concrete. In Japan, the standard specification for concrete structures by Japan Society of Civil Engineers (JSCE) recently modified the equation predicting the shrinkage so as to consider the effect of aggregate. To reduce the shrinkage, the use of lime stone aggregates is increasing. However, there are few studies to discuss the effect of fracture property of the lime stone aggregate on the mechanical performance of concrete structures. Because the lime stone aggregate generally shows large aggregate crushing value (ACV), the use of lime stone aggregate may have negative impact on the shear performance of concrete structures.

In this study, we firstly investigated the drying shrinkage and fracture energy of concrete with various type of aggregate (lime stone aggregate and others). Then, we conducted the loading tests to discuss the effect of shrinkage and fracture energy on the shear strength of RC beams.

OUTLINE OF MATERIAL EXPERIMENTS

Materials. To investigate the effect of aggregate on drying shrinkage and fracture energy of concrete, material properties of concrete such as strength, drying shrinkage, fracture energy as well as aggregate crushing value were measured. In these tests, 5 kinds of aggregates (quartz porphyry, hornfels, tight sands, rhyolite and lime stone) shown in **Table 1** were used for concrete. The used cement was ordinary Portland cement (OPC) and the water-to-cement ratio (W/C) was 50% in all concrete.

Table 1. Properties of aggregates.

Types of aggregate	*Fine aggregates (density, water absorption)*	*Coarse aggregates (density, water absorption)*	*Aggregate crushing value*
QP (quartz porphyry)	2.52 g/cm^3, 1.33 %	2.63 g/cm^3, 0.49 %	9.9
HF (hornfels)	2.66 g/cm^3, 1.55 %	2.72 g/cm^3, 0.54 %	11.7
TS (tight sands)	2.64 g/cm^3, 1.75 %	2.72 g/cm^3, 0.39 %	8.6
LM (lime stone)	2.67 g/cm^3, 1.26 %	2.71 g/cm^3, 0.62 %	20.0
RY (rhyolite)	2.62 g/cm^3, 1.76 %	2.65 g/cm^3, 0.56 %	-

Table 2. Mix proportions of concrete

Types of concrete	*W/C (%)*	*W (kg/m^3)*	*C (kg/m^3)*	*S (kg/m^3)*	*G (kg/m^3)*	*Ad (kg/m^3)*	*AE (g/m^3)*
QP	50	175	350	781	944	4.550	7.0
HF	50	175	350	830	971	1.575	19.3
TS	50	175	350	829	965	1.400	0
LM	50	175	350	833	968	2.980	0
RY	50	175	350	789	976	2.630	21.0

W: Water, *C*: Ordinary Portland cement, *S*: Fine aggregate, *G*: Coarse aggregate, *Ad*: AE water reducing agent, *AE*: Air entraining agent

Table 2 shows the mix proportions of concrete. The concrete specimens were exposed to the drying condition (20 °C and 60 %RH) after 7 days water curing.

Testing method. Drying shrinkage was measured based on JIS A 1129-2 (Methods of measurement for length change of mortar and concrete. − Part 2: Method with contact-type strain gauge.). The length change of prism specimen (100 × 100 × 400 mm) was measured after the age of 7 days in the control room (20 °C and 60 %RH). Compressive strength was measured at the age of 28 days based on JIS A 1108 (Method of test for compression strength of concrete) using cylindrical specimens (ϕ100 × 200 mm). Fracture energy was measured at the age of 91 days based on JCI-S-001-2003 (Method of test for fracture energy of concrete by use of notched beam). The three-point loading test was performed for the prism specimen (100 × 100 × 400 mm) having notch of 50 mm depth at the middle of the span. Then, the fracture energy was calculated from the relationship between load and crack opening displacement at the notch.

RESULTS AND DISCUSSION OF MATERIAL EXPERIMENTS

Drying shrinkage. Figure 1 shows time histories of measured drying shrinkages of concrete specimens. Because the relative humidity in the room was not controlled between 131 and 136, 160 and 181 days, the approximate curves calculated by the following equation (JSCE 2012) were also plotted.

$$\varepsilon'_{sh}(t,7) = \{\varepsilon'_{sh,inf} \cdot (t-7)\}/\{\beta + (t-7)\} \quad (1)$$

where, $\varepsilon'_{sh}(t,7)$: shrinkage strain at the age of t, $\varepsilon'_{sh,\mathrm{inf}}$: ultimate shrinkage strain at the infinite time, β: parameter to show time-dependency. The drying shrinkage was significantly affected by the type of aggregate in concrete. The concrete with lime stone aggregate showed relatively low shrinkage while the concrete with rhyolite and tight sands showed relatively large shrinkage.

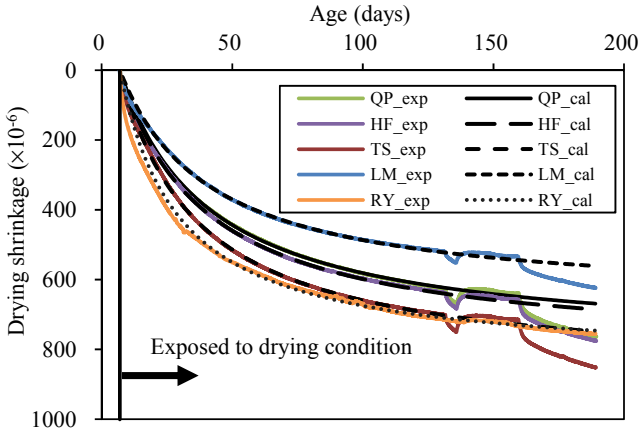

Figure 1. Time histories of drying shrinkage of concrete.

In the JSCE Standard Specification for Concrete Structures (2012), the effect of aggregate on the drying shrinkage is considered by the using water contents in the aggregate in the following equation.

$$\varepsilon'_{sh,cal} = 2.4\left\{W + \frac{45}{-20+30\cdot C/W}\cdot\alpha\cdot\Delta\omega\right\} \quad (2)$$

where, $\varepsilon'_{sh,cal}$: the estimated shrinkage strain at the age of 182 days ($\times 10^{-6}$), W: the unit water content of concrete (kg/m^3) (W≤175kg/m^3), C/W: the cement-to-water ratio, α: the parameter considering the quality of aggregate (4~6) , $\Delta\omega$: the water content in the aggregate (kg/m^3). **Figure 2** shows the shrinkage strains at the age of 182 days calculated from the approximate curve shown in Eq.(1) and the JSCE prediction model shown in Eq. (2). They showed good agreement so that the applicability of the prediction model in JSCE code was verified.

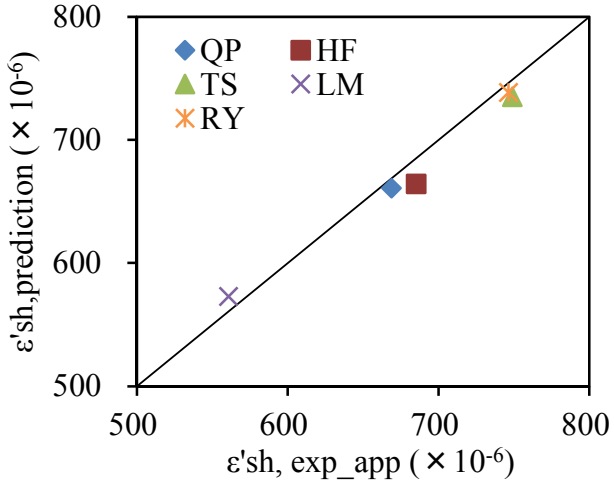

Figure 2. Relationship between shrinkages from experiment and JSCE code.

Strength and fracture energy. Table 3 shows the measured compressive strength, elastic modulus, tensile strength, fracture energy. In addition, the characteristic length was calculated by the following equation. The concrete with lime stone aggregate showed much smaller fracture energy and characteristic length than the other concrete. It can be explained by the large aggregate crushing value (ACV) of lime stone aggregate shown in **Table 1**.

$$l_{ch} = 1000E_c \cdot G_f / {f_t}^2 \quad (3)$$

where, l_{ch}: the characteristic length, E_c: the elastic modulus, G_f: the fracture energy, f_t: the tensile strength of concrete.

Table 3. Strength and fracture energy of concrete

Types of concrete	*Compressive strength (N/mm^2)*	*Elastic modulus (kN/mm^2)*	*Tensile strength (N/mm^2)*	*Fracture energy (N/mm)*	*Characteristic length (mm)*
QP	46.5	36.3	2.97*	0.245	1010
HF	47.9	32.0	3.03*	0.227	791
TS	45.3	35.3	2.92*	0.284	1180
LM	36.6	33.5	3.12	0.117	457
RY	38.1	30.5	2.95	0.235	824

* The tensile strength was estimated from the compressive strength.

OUTLINE OF STRUCTURAL EXPERIMENTS

Specimens. To investigate the effect of the drying shrinkage and fracture energy of concrete on the shear performance of RC structures, RC beams with size of 200 × 320 × 2300 mm were prepared by using 2 kinds of concrete with lime stone (LM) and rhyolite (RY) aggregates, which were the same as those used for the material experiments. The outline of the RC beam specimen was shown in **Figure 3**. The tensile reinforcement ratio in the RC beam specimen was 0.8% and high strength deformed bars were used as tension reinforcement to cause shear failure. The beam specimens were exposed to drying condition after sealed curing for 7 days and the changes in strains of reinforcements caused by shrinkage of concrete were measured during the curing. Two RC beam specimens were prepared for each conditions.

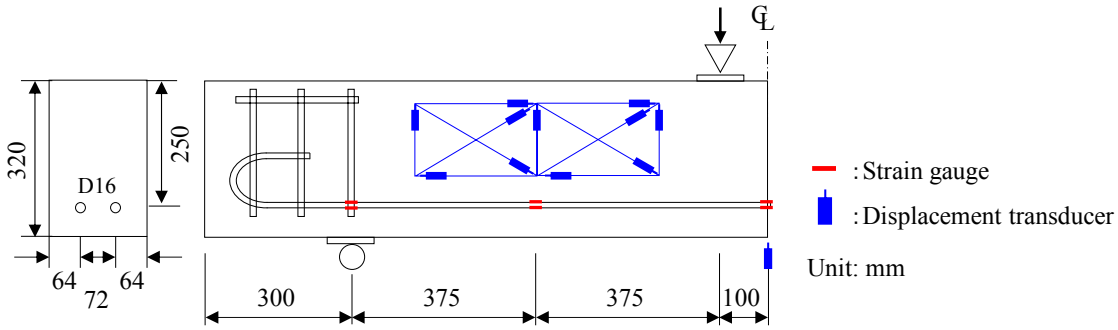

Figure 3. Outline of RC beam specimen.

Loading tests. At the age of around 3 months, the loading tests on the RC beams were conducted as shown in **Figure 3**. The shear span to effective depth ratio (a/d) was fixed to 3.0. Deflections at the center section and shear displacements of the RC beams were measured by displacement transducers installed at the center of span and the shear span, respectively. The load and crack patterns were also recorded during loading tests.

RESULTS OF STRUCTURAL EXPERIMENTS

Measurement of strain of reinforcement. Figure 4 shows the time histories of strain of reinforcements embedded in RC beam specimens during the curing. Drying

shrinkage of concrete caused compressive strain of the reinforcements. The measured strains of reinforcement in RC beams with the rhyolite and lime stone aggregates were about 110 and 20 $\times$ 10^{-6} in compression at the age of around 3 months, respectively. It means that the lime stone aggregate reduced the internal stress because of decreasing the shrinkage of concrete.

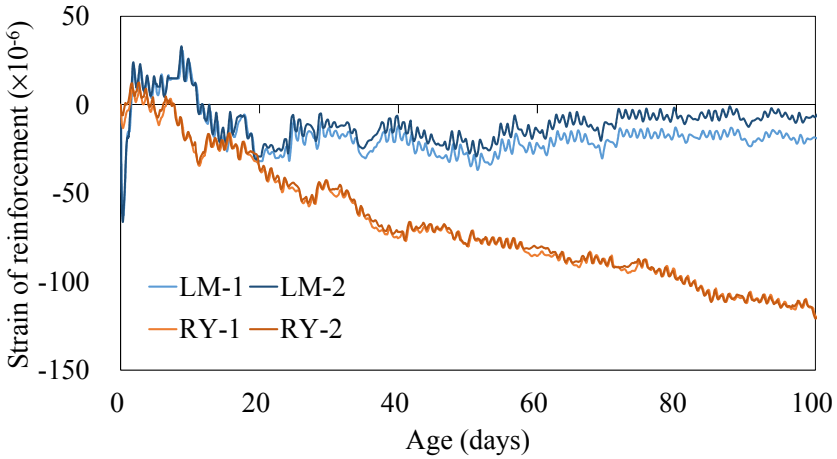

Figure 4. Time histories of strain of reinforcement in RC beam specimen.

Loading tests. Figure 5 shows the relationship between load and deflection at the center of span of RC beam. **Figures 6** show the crack patterns at the failure. The diagonal cracking, which caused the shear failure, was shown by bold lines. **Figures 7** and **8** show the relationship between load and vertical and shear displacements at the shear span. The vertical and shear displacements crossing the diagonal cracking were plotted in these figures. In all specimens, the loads was increased after diagonal cracking because of the arch effects with the crack propagation under the loading plates. Since the diagonal cracking loads were not clear from the load-deflection curves, they were determined from the sudden increase in the vertical or shear displacement at the shear span. In **Figures 5**, **7** and **8**, the diagonal cracking loads were indicated by the circles. In the case of LM-1 and RY-1, the diagonal cracking loads were determined from the vertical displacement, while, in the case of LM-2 and RY-2, they were determined from the shear displacement. In **Table 4**, the diagonal cracking loads and maximum loads of RC beams specimens were shown with the compressive and tensile strengths and elastic modulus of concrete specimens prepared together with the beam specimens.

The experimental results showed that the measured diagonal cracking loads and shear strengths of RC beams with rhyolite (RY) aggregate was higher than those with lime stone (LM) aggregate. The maximum load became higher when the diagonal cracking progressed relatively close to the middle of span. However, the crack patterns were not affected by the type of aggregates.

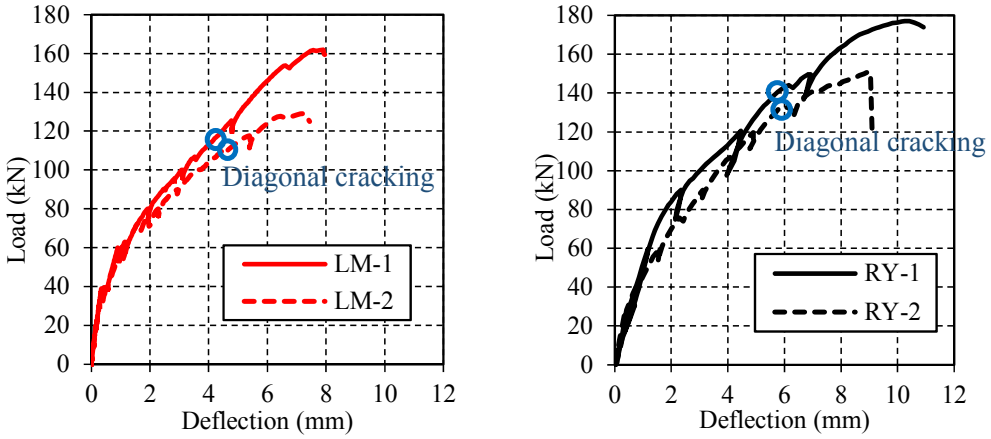

Figure 5. Relationship between load and deflection at the center of span. (Left: Beam with lime stone, Right: Beams with rhyolite)

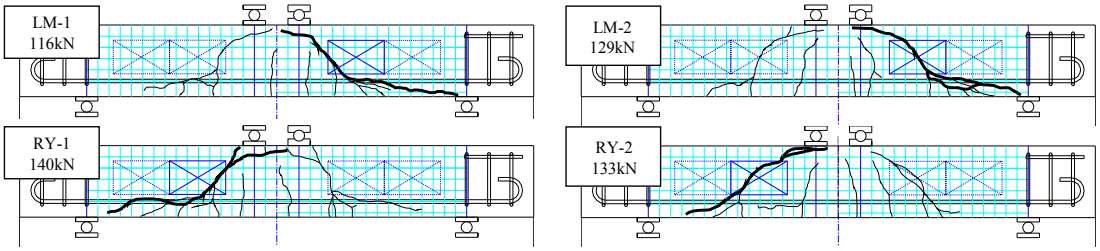

Figure 6. Cracking patterns of RC beams at the failure.

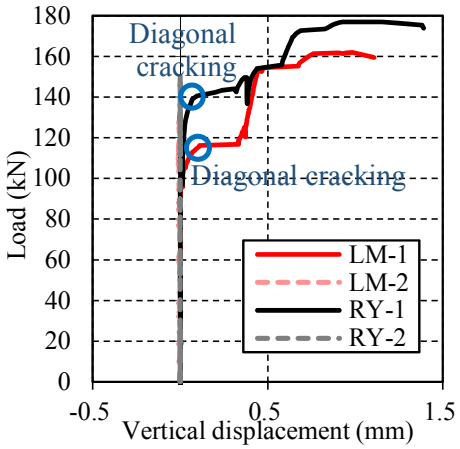

Figure 7. Vertical displacement.

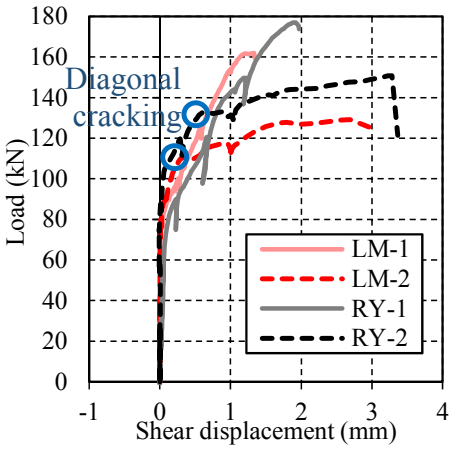

Figure 8. Shear displacement.

Table 4. Material strength of concrete and shear capacity of RC beams

Specimens	*Compressive strength (N/mm^2)*	*Elastic modulus (kN/mm^2)*	*Tensile strength (N/mm^2)*	*Diagonal cracking load (kN)*	*Shear strength (N/mm^2)*	*Maximum load (kN)*
LM-1	36.3	31.9	3.1	116	1.06	162
LM-2	34.6	31.5	3.0	111	1.11	129
RY-1	36.8	28.3	2.8	140	1.40	177
RY-2	35.2	27.0	2.8	133	1.33	151

EFFECTS OF SHRINKAGE AND FRACTURE ENERGY ON SHEAR STRENGTH OF RC BEAMS

In the civil engineering field in Japan, the following equation proposed by Niwa et al. (1986) is widely used. The design equation in the standard specification for concrete structures published by JSCE was established based on Niwa's equation with neglecting the term for shear span to effective depth ratio (a/d).

$$V_c = 0.2\sqrt[3]{f_c'}\sqrt[3]{100p_s}\sqrt[4]{1000/d}\left(0.75+\frac{1.4}{a/d}\right)b_w d \quad (4)$$

where, V_c is the shear capacity of slender beam (N), f'_c is the compressive strength (N/mm^2), p_s is the longitudinal tensile reinforcement ratio, d is the effective depth (mm),a is the shear span (mm), b_w is the breath of web (mm). This Niwa's equation was formulated based on the statistical analysis of the experimental data (around 300 results). Here, the effect of the shrinkage was not explicitly considered.

For considering the effect of the autogenous shrinkage of high strength concrete, Sato and Kawakane (2008) have proposed a new evaluation method based on the concept of strain change in tension reinforcement due to shrinkage of concrete. Here, they used the following equivalent tensile reinforcement ratio.

$$p_{s,e} = \frac{\varepsilon_s}{\varepsilon_s - \varepsilon_{s0,def}} p_s \quad (5)$$

where, $p_{s,e}$ is the equivalent tensile reinforcement ratio, ε_s is the tension reinforcement strain at the section 1.5d distant from loading section in shear span at the diagonal cracking, $\varepsilon_{s0,def}$ is the tension reinforcement strain when concrete stress at the depth of reinforcement is zero, which is positive in tension and negative in compression. They installed this concept on the equation for evaluating shear capacity of high strength concrete, which was formulated based on the fracture energy. Then, they showed that their proposed new evaluation method well reproduced the shear capacities of the high strength concrete showing high and low autogenous shrikage.

In this study, our target was the normal strength concrete. Therefore, we proposed to install the concept proposed by Sato and Kawakane (Eq. (5)) on the Niwa's equation (Eq. (4)) by replacing the definition of the tensile reinforcement ratio as following.

$$V_c = 0.2\sqrt[3]{f_c'}\sqrt[3]{100p_{s,e}}\sqrt[4]{1000/d}\left(0.75+\frac{1.4}{a/d}\right)b_w d \quad (6)$$

Table 5 shows the experimental and calculated shear strength with the measured strain of reinforcement for the calculation by Eq. (6). **Table 6** also shows the average shear strengths for each concrete and their comparisons.

Since the compressive strengths of LM and RY were almost same in this experiment, the calculated shear strength by using Niwa's equation of Eq. (4) showed no significant differences between LM and RY. When the effect of shrinkage of concrete was considered by using the concept of the equivalent tensile reinforcement ratio in Eqs. (5) and (6), the calculated shear strength was decreased. The decreasing

ratio of the calculated shear strength was larger in the RC beam specimens with RY because the concrete with RY showed relatively large drying shrinkage. The calculated shear strengths were larger than the measured strength in the experiments. It can be explained by the differences in dimensions of RC beams. That is, the thick cover concrete of RC beams in this study might increase the measured shear strength. The detail will be discussed in the future study. Here, we focused on the effect of aggregate by their comparison.

The measured shear strength, τ_{exp}, and the shear strength ratio, $\tau_{exp}/\tau_{cal(4)}$, of the RC beams with LM was smaller than those with RY, as the above discussion. By considering the effect of shrinkage, the shear strength ratio, $\tau_{exp}/\tau_{cal(6)}$, of the RC beams with LM became more smaller than those with RY. This suggested that the smaller fracture energy and characteristic length of LM decreased the shear strength of RC beams. Gustafsson and Hillerborg (1988) explained that the ratio of the shear strength of RC beam to the tensile strength of concrete could be proportional to one-fourth power of the ratio of the characteristic length to the effective depth. It means that the shear strength of RC beams could decrease with the decrease in the characteristic length of concrete. The results of this study qualitatively agreed with their proposal although the exponent was one-third in this study.

Table 5. Experimental and calculated shear strength of RC beams

Specimens	*Measured strain of reinforcement at the loading* ($\times 10^{-6}$)	*Measured shear strength,* τ_{exp} (N/mm^2)	*Calculated shear strength by Eq. (4),* $\tau_{cal(4)}$ (N/mm^2)	$\tau_{exp}/\tau_{cal(4)}$	*Calculated shear strength by Eq. (6),* $\tau_{cal(6)}$ (N/mm^2)	$\tau_{exp}/\tau_{cal(6)}$
LM-1	-25	1.16	1.06	1.10	1.05	1.11
LM-2	-17	1.11	1.04	1.07	1.03	1.08
RY-1	-96	1.40	1.06	1.32	1.03	1.36
RY-2	-131	1.33	1.04	1.27	1.00	1.33

Table 6. Average shear strength and their comparison

	Average measured shear strength, τ_{exp_ave} (N/mm^2)	*Average calculated shear strength by Eq. (4),* $\tau_{cal(4)\_ave}$ (N/mm^2)	$\tau_{exp\_ave}/\tau_{cal(4)\_ave}$	*Average calculated shear strength by Eq. (6),* $\tau_{cal(6)\_ave}$ (N/mm^2)	$\tau_{exp\_ave}/\tau_{cal(6)\_ave}$
LM	1.14	1.05	1.08	1.04	1.09
RY	1.37	1.05	1.30	1.02	1.35
LM/RY	0.83	1.00	0.83	1.02	0.81

CONCLUSION

In this study, we firstly investigated the drying shrinkage and fracture energy of concrete with various type of aggregate (lime stone aggregate and the others). Then, we conducted the loading tests to discuss the effect of shrinkage and fracture energy on the shear strength of RC beams. The followings are the findings in this study.

The results of material experiments showed that the use of the lime stone aggregate having large aggregate crushing value decreased the fracture energy and drying shrinkage compared to the other aggregates. The shrinkage behaviors of concrete with various kinds of aggregates were well predicted by considering the water absorption ratios of aggregates in the equation of JSCE.

The results of structural experiments showed the use of lime stone aggregate reduced the internal stress caused by shrinkage of concrete in RC beams. However, the results also showed that the measured shear strength of the RC beam with the lime stone aggregate was smaller than that with rhyolite aggregate. It was suggested that the decrease was caused by the small characteristic length of the concrete with the lime stone aggregate. Based on the calculation by the concept of the equivalent tension reinforcement ratio, it was indicated that the shear strength of RC beams might be decreased in proportion to one-third power of the characteristic length of concrete.

ACKNOWLEDGEMENTS

This study was financially supported by JSPS KAKENHI Grant Numbers 24246077. The authors also appreciate the contribution on the experimental work by Ms. Nao Kawai, Mr. Yuto Sakamoto, Mr. Kohei Sasada, Mr. Kazuya Miyamoto and the other students of Hiroshima University.

REFERENCES

Gustafsson, P.J. and Hillerborg, A. (1988), "Sensitivity in Shear Strength of Longitudinally Reinforced Concrete Beams to Fracture Energy of Concrete", *ACI Structural Journal*, Vol.85, Issue 3, pp.286-294.

JSCE (Japan Society of Civil Engineers) (2012), *Standard Specification for Concrete Structures 2012, Design*, JSCE

Nakarai, K., Matsushita, S, and Morito, S., (2014), "Effect of volume change of concrete on shear capacity of RC beam and its evaluation", *Fourth international fib congress 2014*, Mumbai, India.

Niwa, J., Yamada, K., Yokozawa, K., and Okamura, H. (1986), "Revaluation of the equation for shear strength of reinforced concrete beams without web reinforcement", *Journal of Materials, Concrete Structures and Pavements*, Japan Society of Civil Engineers, No.372/V-5, pp.167-176. (in Japanese)

Sato, R. and Kawakane, H. (2008), "A New Concept for the Early Age Shrinkage Effect on Diagonal Cracking Strength of Reinforced HSC Beams", *Journal of Advanced Concrete Technology*, Vol. 6, No. 1, pp.45-67

Tanimura, M., Suzuki, M., Maruyama, I. and Sato, R. (2005), "Improvement of Time-Dependent Flexural Behavior in RC Members by Using Low Shrinkage-High Strength Concrete", *Proceedings of the Seventh International Symposium on the Utilization of High Strength/High Performance Concrete*, Volume II, SP-228, ACI, Washington, D.C., USA, pp.1373-1395

Prestress Loss and Uncertainty in Concrete Box Girder Creep

L. Kadlec[1] and V. Křístek[2]

[1]CTU in Prague, Faculty of Civil Engineering, Dept. of Concrete and Masonry Structures, Thákurova 7, 166 29 Prague 6, Czech Republic.
E-mail: lukas.kadlec@fsv.cvut.cz
[2]CTU in Prague, Faculty of Civil Engineering, Dept. of Concrete and Masonry Structures, Thákurova 7, 166 29 Prague 6, Czech Republic.
E-mail: kristek@fsv.cvut.cz

Abstract

The paper is directed to the cross section warping effect and to the warping induced long term prestress loss due to creep of concrete, which is analyzed deterministically and stochastically. The statistical variability of material creep parameters and environmental factors has a significant effect on the statistical scatter of the calculated prestress loss. In order to obtain the real development of concrete creep it is important to use a model with strong theoretical basis. Sophisticated model B4 provides very accurate concrete creep and shrinkage prediction. The statistical randomness of boundary and environmental conditions is solved by application of Monte Carlo – Latin hypercube sampling method. It is shown that the severity of cross section warping can be of fundamental importance, particularly in the case of unevenly distributed and isolated tendons in cross-section and in the case of short spans. Both the 3D effects and the statistical variability of creep must be taken into account if a reliable design of box girder bridges from the viewpoint of long-term serviceability should be achieved.

INTRODUCTION

One of the most important factors which provide perfect function of prestressed concrete structures (serviceability, loading carrying capacity, durability) is real and correct assessment of prestressing – i.e. development of prestress losses. It is possible to divide prestress losses to two basic groups. The first one – short-term (technological) losses (e.g. losses due to friction, movement of tendons in anchorages) appeared between the time of prestressing and time of anchoring. To the second group belong long-term prestress losses appearing between the time of anchoring and the analysed time, and the final time of the operation life (e.g. losses due to creep, shrinkage, and steel relaxation). It is evident that due to long-term character of this type of losses, their correct prediction has to be based on the true mathematical models for description of rheological properties of materials – concrete (creep and shrinkage) and steel (relaxation).

Prestress losses - significantly affecting the prestress magnitude - play significant role for the reliable design of prestressed concrete structures. Results confirm the essential importance of the effects of creep and cross section warping for reliable determination of prestress loss [7]. A lump estimate of the final prestress loss was generally used in the design practice - the prestress loss was commonly calculated not by the 3D analysis but by simple formulas based on the theory of beam bending, in which the cross sections are assumed to remain plane. This is why formulas for prestress loss according to textbooks and standards are inadequate and dangerously misleading. The prestress loss in box girders can be two to three times higher than predicted by simple textbook formulas, lump estimates or than recommended by standards [3].

The modern bridge girders are of plated character for which the beamtype analysis is inadequate [2]. Three-dimensional approach applying advanced computational analyses must be used to obtain the true 3D structural performance stresses and strains in the singular regions, warping of cross-sections and other significant consequences like shear lag, shear deformation of webs, etc.. So, it is inevitable that the cross section warping effect with the associated creep-induced longitudinal deformations necessitates 3D simulations.

The increase of long-term prestress loss due to creep is driven by non-linearly distributed stress over the cross-section in anchorage regions. The statistical variability of material creep parameters and environmental factors has a significant effect on the statistical scatter of the calculated prestress loss. In order to obtain the real development of concrete creep it is important to use a model with strong theoretical basis [8]. The new B4 model provides very accurate concrete creep and shrinkage predictions [10].

Results of experimental studies on real structures and their analysis confirm, that present methods for evaluation of prestressing losses due to concrete creep are not realistic, prestressing losses are extremely underestimated. Importance of prestress losses due to creep taking into account cross section warping has been confirmed by the complex and expensive computational analysis of the collapsed bridge Koror – Babelthuap in Palau [1], [3].

The concrete creep deformation may be characterized by one of the existing prediction models for the compliance function defined as the total strain at age t caused by a sustained uniaxial stress applied at age t_0. Application of creep models that realistically describe the real developments is essential; the B4 model [10], which has a strong theoretical basis and which gives realistic multidecade predictions, is proved as the best choice.

There the effects of humidity and temperature variations and of the self-eqi1ibrated nonuniform stress distribution across the plate thickness which they produce will be left out of consideration, even though they may cause extensive cracking or strain softening and make the average creep properties of the cross section dependent on the size and configuration of the cross section. Due to the strong nonuniformity of the stress distribution across the plates of the cross section, which is caused by humidity and temperature effects, only the stress average over the plate thickness is practically meaningful if the foregoing effects are disregarded in the

analysis. Therefore, the prestress loss will be evaluated from the stresses at the middle of the plate thicknesses.

DETERMINISTIC ANALYSIS

Cross-section corresponding to a real bridge segment (Fig.1), having cross section as in Fig.2, was chosen for the study presented in [9]. Straight unbonded post-tensioned cables were considered in this study. A deterministic analysis was carried out in the usual manner using the mean values of all input parameters as specified in Table 1.

Figure 1. Bridge segment

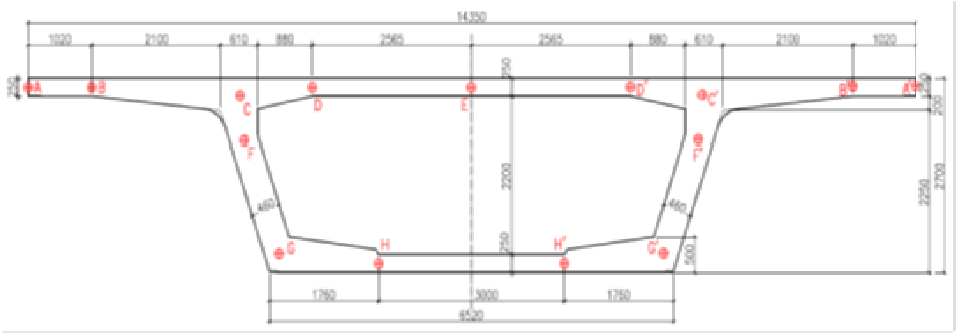

Figure 2. The layout of cables

Figs. 3, 4, 5 show the warping patterns of the girder end cross-section due action of prestress forces applied at various location in the end cross-section of a box girder (Figs. 1, 2) of span length of 30 m. The dominant role of warping, exceeding dramatically the planar component of longitudinal displacements, is clearly seen. Applied prestress forces manifest themselves differently according to their different locations – prestress acting in cantilever (points B,B´) or at the midwidth of the top slab (point E) produce warping of much higher intensity than prestress located at the box corner areas (points C,C´ and G,G´).

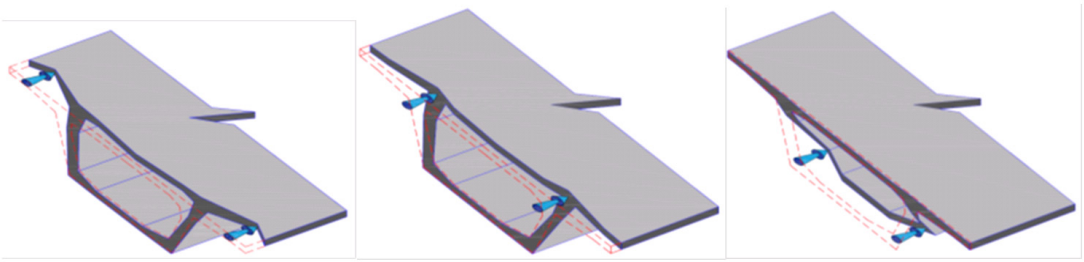

Figure 3. The warping pattern due to forces applied at points B, B´
Figure 4. The warping pattern due to forces applied at points C, C´
Figure 5. The warping pattern due to forces applied at points G, G´

The intention was to analyse significance of the cross-section warping in comparison with deformations calculated by the elementary theory of beam bending, in which the cross sections are assumed to remain plane and to investigate the ratio of the prestress loss caused by creep of concrete due to the cross-section warping and the prestress loss evaluated by the elementary theory of beam bending in which the cross sections are assumed to remain plane (commonly used in design practice). It was found that this ratio depends strongly upon location of the cable in the cross section and upon the span length.

Evaluating the prestress loss caused by creep of concrete due to the cross-section warping , it was clearly proved that location of the cable in the cross section plays dominant role: the cables located in the bulky regions at corners of cross section (i.e. at points C-C´, D-D´, F-F´, G-G´) near to intersections of slabs and webs, exhibit much less contribution to prestress loss induced by warping than the cables located in the cross section cantilevers (points A-A´) or at the midspan of the slab (point E). This is fully intelligible taking into account much higher stiffness of the corner regions in comparison with stiffness of wide and thin slabs. This is also one of reasons why bridge designers locate prestressing cables in the cross section corner areas (see locations of tendon ducts in Fig. 1).

For very short spans, the component of the creep induced prestress loss corresponding to cross section warping can - for some cable locations - be more than three times higher than the component of the creep induced prestress loss predicted by common design calculations.

The significance of prestress loss caused by creep of concrete due to the cross-section warping in relation to the prestress loss evaluated by the elementary theory strongly depends upon the length of prestressed section of the bridge girder (i.e. upon the cable lengths).

RESPONSE STATISTICS

Along with shrinkage, creep is the most uncertain mechanical property of concrete. Therefore, the stochastic nature of creep ought to be taken into account in the design of bridges [4]. Due to the notorious statistical variability of creep

predictions, structures should be designed for certain extreme effects exceeded with a specified small probability, such as 5%, rather than for the mean effects as is customary at present. Both the 3D performance and the statistical variability of creep must be taken into account if a reliable design of box girder bridges from the viewpoint of long-term serviceability should be achieved.

The statistical randomness of the studied problem is solved by application of Monte Carlo – Latin hypercube sampling method. The procedure of calculation need not be repeated here. It suffices to say that the Latin hypercube sampling is a method to randomly generate, according to the specified probability distributions of the random parameters affecting creep, a finite set of parameter samples of equal probability. For each such set, a deterministic structural creep analysis, in our case with consideration of the prestress loss, is carried out. From the responses obtained one can then estimate not only the mean value but also the standard deviation of any response quantity.

The random parameters affecting creep are considered to consist of environmental relative humidity h [%], temperature of the environment during curing T_{cur} [^{0}C], the cement content c (mass per 1 m^3 of concrete) [kg/m^3], the water-cement ratio w/c (by weight), the sand-cement ratio s/c (by weight), and the design value of the standard cylinder strength of concrete f_c [MPa]. It is assumed that all variables are distributed normally. In previous studies of creep effects it was approved to be a relatively good assumption. All these stochastic input parameters are listed in Table 1, (in order to describe the random character of variables the mean value, standard deviation and coefficient of variation is introduced).

Table 1. Stochastic input parameters assumed in B4 model

	μ	σ_N	CV
h	0.7	0.1	0.14
T_{cur}	10	3	0.3
c	390	39	0.1
w/c	0.45	0.045	0.1
a/c	4.6	0.46	0.1
f_c	45	6.75	0.15

However, some input parameters affecting creep according to B4 model were taken with constant value. Namely it is volume/surface ratio V/S [mm], age at the start of environmental exposure (time of curing) t_0 [day], temperature of the environment T [^{0}C], type of cement: R, geometry: infinite slab (see Table 2). It is obvious that nature of these parameters is steady and they have to be considered deterministically.

Table 2. Deterministic input parameters assumed in B4 model

V/S	172
t_o	5
T	10
Cement	*R*
Geometry	infinite slab

A certain number of different random parameter samples, chosen as 10, may then be generated according to the method of Latin hypercube sampling (LHS). The moderate correlation between *w/c* with *fc* and *c* with *fc* was assumed. Other input parameters were considered to be independent. Moreover, during LHS sampling the undesired correlation can be introduced between random variables. In order to avoid this possibility - the desired correlation matrix was prescribed and subsequently the input parameters were generated with use of optimization method. Realized correlation matrix between individual input parameters are shown in Table 3. Generated input parameters are listed in table 4.

Table 3. Realized correlation coefficients between sampled input variables

	h	T_{cur}	***c***	***w/c***	***a/c***	***fc***
h	1.000	-0.005	0.033	0.045	0.001	-0.012
T_{cur}	-0.005	1.000	-0.006	0.003	0.006	0.015
c	0.033	-0.006	1.000	-0.028	0.024	0.492
w/c	0.045	0.003	-0.028	1.000	0.003	-0.523
a/c	0.001	0.006	0.024	0.003	1.000	0.010
fc	-0.012	0.015	0.492	-0.523	0.010	1.000

Table 4. Sampled input parameters

Sample	***c***	***w/c***	***a/c***	***fc***	***h***	T_{cur}
1	363.6	0.4443	4.912	40.43	0.5245	12.03
2	374.9	0.4195	3.793	44.15	0.5955	4.74
3	416.4	0.4326	4.120	56.85	0.6323	15.27
4	349.3	0.4557	5.407	47.61	0.6614	7.97
5	458.4	0.5290	4.658	45.85	0.6874	6.87
6	430.7	0.3710	5.081	49.57	0.7126	9.62
7	405.1	0.4674	4.542	37.95	0.7387	13.13
8	321.6	0.4970	4.288	33.15	0.7677	11.16
9	394.9	0.4805	4.778	42.39	0.8045	10.38
10	385.1	0.4030	4.422	52.05	0.8755	8.84

These random samples are all of equal probabilities. For the set of material parameter values for each sample, i.e., for each of the row of Table 4, the solution is calculated deterministically. Shrinkage and creep was evaluated by B4 model in

certain times (see Table 5). Mean value and sample standard deviation of shrinkage strain ε_{sh}, compliance function J and creep coefficients ϕ was calculated from results obtained in time 100 years. These statistic characteristics of creep and shrinkage enable to determine 0.025 and 0.975 quantile of observed variables (see Table 6). It was assumed that both variables are normally distributed.

Table 5. B4 model results of creep and shrinkage determined at time 365 days, 10 years and 100 years

	t = 365 days			t = 10 years			t = 100 years		
No.	ε_{sh} [*10^{-6}]	J [*10^{-12}/Pa]	ϕ	ε_{sh} [*10^{-6}]	J [*10^{-12}/Pa]	ϕ	ε_{sh} [*10^{-6}]	J [*10^{-12}/Pa]	ϕ
1	311.5	109.1	1.7	515.5	171.3	3.3	569.5	206.7	4.2
2	383.8	105.2	1.8	602.7	160.7	3.2	666.8	194.3	4.1
3	341.8	103.6	2.1	544.5	153.3	3.6	601.2	182.9	4.5
4	256.1	104.8	1.9	416.5	147.6	3.0	457.5	171.9	3.7
5	256.1	142.9	2.8	464.0	192.9	4.2	518.0	225.7	5.1
6	360.1	78.3	1.2	486.1	112.0	2.1	518.4	129.3	2.6
7	260.1	116.5	1.8	422.2	157.3	2.8	465.8	182.7	3.5
8	238.4	134.0	2.1	400.8	177.6	3.0	446.5	206.7	3.7
9	217.1	118.5	2.1	345.6	155.4	3.0	379.4	179.1	3.6
10	276.5	90.4	1.6	355.3	119.7	2.4	376.8	136.8	2.9
						μ	500.0	181.6	**3.784**
						σ_{N-1}	93.76	30.19	0.72

Table 6. 0.025 and 0.975 quantile for shrinkage strain, compliance function and creep coefficients evaluated in time 100 years

t = 100 years		
$\varepsilon_{sh\_0.025}$[*10^{-6}]	316.2	
$\varepsilon_{sh\_0.975}$[*10^{-6}]	683.8	
$J_{0.025}$[*10^{-12}/Pa]	122.4	
$J_{0.975}$[*10^{-12}/Pa]	240.8	
$\phi_{0.025}$	**2.374**	**62.7%**
$\phi_{0.5}$	**3.784**	**100%**
$\phi_{0.975}$	**5.193**	**137%**

Concrete creep directly affects the long-term prestress loss. Creep coefficient represents multiplier of instantaneous strain, so the random scatter of creep coefficient is the same also for prestress loss produced by creep. The LHS method put into practice enable to determine 95% confidence limits for prestress loss. The lower margin of prestress loss is 62.7% of mean (deterministic) prestress loss. The upper margin of prestress loss is 137% of mean (deterministic) prestress loss. Both percentage results are valid for the input parameters and boundary conditions assumed in this study. The variability such as this may seriously influence the

performance of the structure. To assure the prescribed good long-term serviceability it seems reasonable to require that the design of box girder bridges should be based on these limits. Figure 6 depicts the long-term prestress loss ratio between results determined by 3D stochastic analysis and deterministic beamtype analysis. We see that the spread of the results for the warping induced long term prestress loss due to creep of concrete is very large.

Figure 6. Prestress loss due to creep determined by stochastic analysis (95% confidence limits) respecting warping related to deterministic beamtype analyses (cables location D-D´)

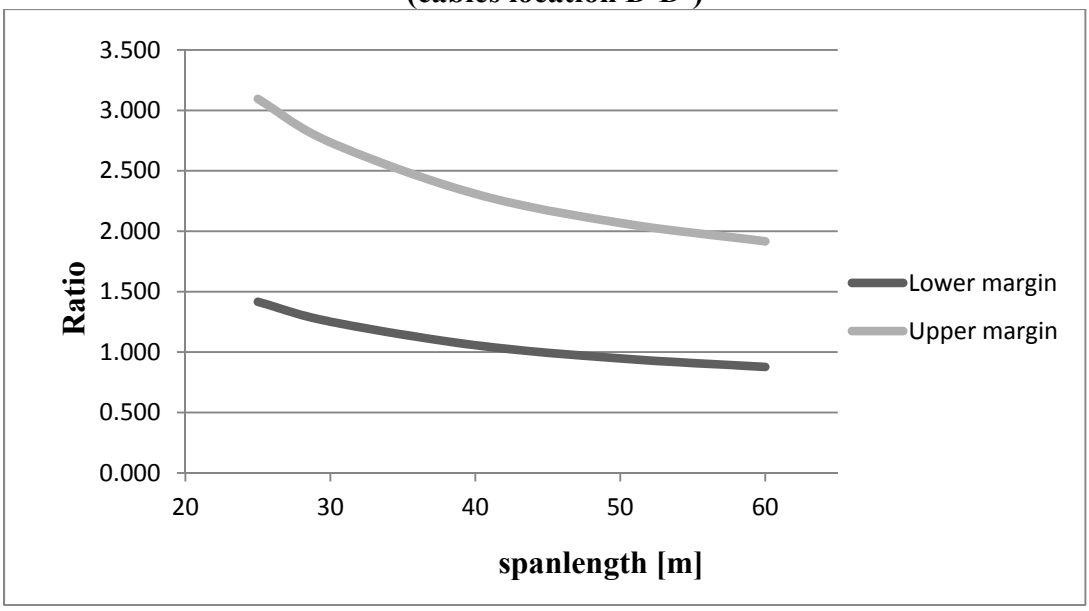

CONCLUSION

Accuracy in calculating the prestress loss is crucial because the responses of prestressed structures are small differences of two large statistically uncertain, variable quantities, of two opposite actions, in the downward direction caused by external loads, and in the upward deflection caused by prestress. Small percentage errors in each will result in a far larger percentage error in the total performance. The uncertainties concern in particular the estimation of the prestressing action in the prediction of its evolution along the time as affected by prestress losses.

It may be concluded that the main causes of underestimation of prestress loss due to creep of concrete are as follows:

(i) Beam-type analysis instead of a full 3D analysis – the elementary presumption that cross sections remain planar and normal to the deflection curve after deformations is not acceptable. The warping of cross sections cannot be realistically captured by the classical concept. Since beam-type analysis is inadequate for the structural arrangement of bridge girders, the three-dimensional analysis must be used.

(ii) Poor material prediction model for creep. This is why the real development of concrete creep must be predicted– application of the B4 model [10], which has a strong theoretical basis, is proved as the best choice. In the creep prediction model, the drying creep should be separated from the basic creep, because the former is thickness-dependent and approaches a finite terminal value, whereas the latter is thickness-independent and unbounded. Model B4 has this feature [10]. The rheological non-homogeneity of cross sections should also to be taken into account – the moisture diffusion process, which causes that the drying creep is significantly affected by thickness differences among the webs and the top and bottom slabs of cross sections [5]. This leads to nonuniform creep properties throughout the cross section, manifested as differential drying creep compliances.

The problem of prestress loss due to creep of concrete is essential for the understanding the real structural performance and for reliable design of prestressed concrete structures. It is proved that the severity of cross section warping is of fundamental importance, particularly in the case of isolated and unevenly distributed cables in cross-section and in the case of short spans of plated prestressed concrete structures. Thus it will be appropriate to introduce a new component of the prestress loss – the prestress loss due to creep of concrete induced by cross section warping.

ACKNOWLEDGEMENTS

Financial support from the Technological Agency of the Czech Republic, through the project CESTI, Grant No. TE01020168, is gratefully acknowledged.

REFERENCES

[1] Bažant, Z. P., Yu, Q., Li, G.-H., Klein, G., and Křístek, V. (2010). “Excessive deflections of record-span prestressed box girder: Lessons learned from the collapse of the Koror-Babeldaob Bridge in Palau.” Concr. Int., 32(6), pp. 44–52.

[2] Bažant, Z. P., Yu, Q., Křístek, V., Kim, K.T., Hubler, M., Šmilauer,V., Vráblík, L., Lepš, M. (2011). “Excessive Multi-decade Deflections of Prestressed Concrete Bridges” fib Symposium ISBN 978-80-87158-29-6, pp. 827-831

[3] Bažant, Z.P., Yu Q., and Li, G.-H. (2012). „Excessive Long-Time Deflections of Prestressed Box Girders. I: Record-Span Bridge in Palau and Other Paradigma”, Journal of Structural Engineering, ASCE / June 2012

[4] Křístek, V., and Bažant, Z. P. (1987). “Shear lag effect and uncertainty in concrete box girder creep.” J. Struct. Eng., 113(3), pp. 557–574.

[5] Křístek, V., Bažant, Z. P., Zich, M., and Kohoutková, A. (2006). “Box girder deflections: Why is the initial trend deceptive?” ACI Concr.Int., 28(1), pp. 55–63.

[6] Křístek, V., Vráblík, L., Bažant, Z. P., Li, G.-H., and Yu, Q. (2008). "Misprediction of long-time deflections of prestressed box girders: Causes, remedies and tendon lay-out effect." Proc., 8th Int. Conf. Creep, Shrinkage and Durability Mechanics of Concrete and Concrete Structures (CONCREEP-8), Ise-Shima, Japan, R. Sato, K. Maekawa, T. Tanabe, K. Sakata, H. Nakamura and H. Mihashi, eds., Taylor & Francis, London

[7] Vráblík, L., Loško, J, Křístek, V. (2011). " Prestress loss due to creep and shrinkage in singular regions of concrete members", fib Symposium, ISBN 978-80-87158-29-6

[8] Vráblík, L., Křístek, V., Teplý, B. (2012). "Application of B3 prediction model to analyse prestress loss in prestressed concrete members", IALCCE 2012,Vienna, Oct. 3-6

[9] Křístek, V., Kadlec, L. (2014). "The cross-section warping effect with the associated creep-induced deformations, Advances in Engineering Software", Elsevier Science, Oxford , ISSN: 0965-9978 ., http://dx.doi.org/10.1016/j.advengsoft.2013.06.015

[10] Wendner , R., Hubler M. H., Bažant, Z.P. (2015). Optimization method, choice of form and uncertainty quantification of Model B4 using laboratory and multi-decade bridge databases, Materials and Structures" 48:771–796, DOI 10.1617/s11527-014-0515-0

Creep and Shrinkage of Fibre-Reinforced Concrete and a Guide for Modeling

Alena Kohoutková[1]; Jan Vodička[2]; and Vladimír Křístek[3]

[1]CTU in Prague, Faculty of Civil Engineering, Dept. of Concrete and Masonry Structures, Thákurova 7, 166 29 Prague 6, Czech Republic. E-mail: akohout@fsv.cvut.cz

[2]CTU in Prague, Faculty of Civil Engineering, Dept. of Concrete and Masonry Structures, Thákurova 7, 166 29 Prague 6, Czech Republic (corresponding author). E-mail: vodicka@fsv.cvut.cz

[3]CTU in Prague, Faculty of Civil Engineering, Dept. of Concrete and Masonry Structures, Thákurova 7, 166 29 Prague 6, Czech Republic. E-mail: kristek@fsv.cvut.cz

Keywords: Concrete; Creep; Fibre reinforced concrete; Prediction models.

Abstract

A robust advanced model for creep and shrinkage of fibre reinforced concrete is presented; the influence of various types of fibres, their shapes and bonding to the matrix is respected in the models. The intention is to present a method for better understanding rheological performance of fibre reinforced concrete, to improve conventional calculation methods and to offer suitable design tool for practice. The prediction models will create instruments enabling efficiency of materials and offer objective and effective tools increasing in the same time the level of reliability, durability and efficiency of fibre reinforced concrete structural members.

Introduction

The viscous behavior of concrete awakened the attention of researchers already from the first employments of the reinforced concrete technique. The long-term performance of concrete structures is significantly influenced by the time-dependent behaviour of the material. Along with shrinkage, creep is the most uncertain mechanical property of concrete [2]. A realistic evaluation of the influence of delayed deformations of concrete on the structural behaviour represents an important aspect of the design and performance assessment process, and requires, on the one hand, the definition of reliable models for the prediction of creep and shrinkage phenomena (a material properties problem) and, on the other hand, the development of reliable computational methods for the evaluation of the structural effects of these phenomena, with an accuracy degree appropriate to the specific case (a structural analysis problem) [4], [5].

Modeling of the structural effects of creep and shrinkage has achieved significant progresses in the last years [1], [3],[9]. The intention was to achieve an agreement about prediction models which are, on the one hand, sufficiently anchored to the physics of the material, the mechanisms of which, although today better understood, certainly still require other in-depth examinations, and on the other hand adequately controlled in their

phenomenological responses with respect to data banks that cover sufficiently extended time periods. The ultimate purpose is to arrive to define appropriate tools for evaluating the response of the structures to the delayed phenomena during their service life.

The creep and shrinkage analyses are often conducted in a rather simplified way. It usually relies on the material models recommended by the standards which grossly underestimate multidecade creep, give unrealistic shapes of creep and shrinkage curves and unrealistic effects of drying, and assume the creep to terminate at some fixed upper bound, for which no experimental support exists.

The concrete creep deformation may be characterized by one of the existing prediction models for the compliance function defined as the total strain at age t caused by a sustained uniaxial stress applied at age t_0.

Application of creep models that realistically describe the real developments is essential; the B4 model [9], which has a strong theoretical basis and which gives realistic multidecade predictions, is proved as the best choice. Model B4 [9] stems from the solidification theory, which is important from a fundamental theoretical point of view, is scientifically justified by the known physical mechanisms of creep and shrinkage, fits optimally the relevant test data available in the literature, agrees with all the required simple asymptotic trends, and offers the widest choice of input parameters covering the entire practical range, and agrees with the theory of moisture diffusion theory including diffusion based parameters for slab thickness.

Creep and shrinkage of fibre reinforced concrete

The interest in FRC (the fibre reinforced concrete), namely in SFRC (the steel fibre reinforced concrete), generated by the efforts to use the FRCs in the design of load carrying concrete structures, dictates the necessity to study the creep and shrinkage phenomena also for these composites [3]. Presently, there appears a rather complex problem due to the added component - fibers - in the concrete composite. In addition, this component is dispersed in the concrete matrix randomly, which further contributes to the complexity of the problem. The nature of fibers (fibers of different origins, shapes and types) also multiplies the complexity.

Several prediction models for creep and shrinkage of concrete were proposed in the past in scientific literature and/or in technical guidance documents of national and international associations, but no any model for creep and shrinkage prediction of a new, very perspective composite material – the fibre reinforced concrete (FRC) - is presently available.

The aim of the paper is to present a suitable creep and shrinkage prediction model representing physical phenomena and performance of the fibre reinforced concrete and to identify the decisive input information. The results of the long term experimental measurements, performed by authors, represent a database allowing to develop the model for the creep and shrinkage prediction for various SFRCs of different composition.

Very wide experimental program was performed [6], [7], [8]; series of cubes of the edge of 150 mm of the fibre reinforced concrete, on the one hand, and cubes of the plain concrete (with the same size and composition, but without fibres) were made on the other hand, and subjected to long-term tests (the mean values of results are plotted in Fig. 1).

Mix composition with synthetic fibres FERRO FORTA - Example:

Cement:	CEMH 32,5R	340 kg
Sand:	fraction 0-4	980 kg
Coarse aggregate:	fraction 8-16	890 kg
Water:		170 kg
Plasticizer:		2.4 kg
Fibres:	Ferro Forta (1 %)*	9.1 kg
Fibres:	Ferro Forta (0,5%)*	4.5 kg

Mix composition with steel fibres (parameters length/thickness 60 mm 10.60 mm) - Example:

Cement:	CEMU 32,5 R	491 kg
Fine aggregate/Sand:	fraction 0-8	791 kg
Coarse aggregate:	fraction 8-16	198 kg
Coarse aggregate:	fraction 16-22	745 kg
Water:		167 kg
Plasticizer:	Umaform SM	4.9 kg
Fibres:	Steel fibres (1%)*	78.5 kg
Fibres:	Steel fibres (0,5%)*	39.2 kg

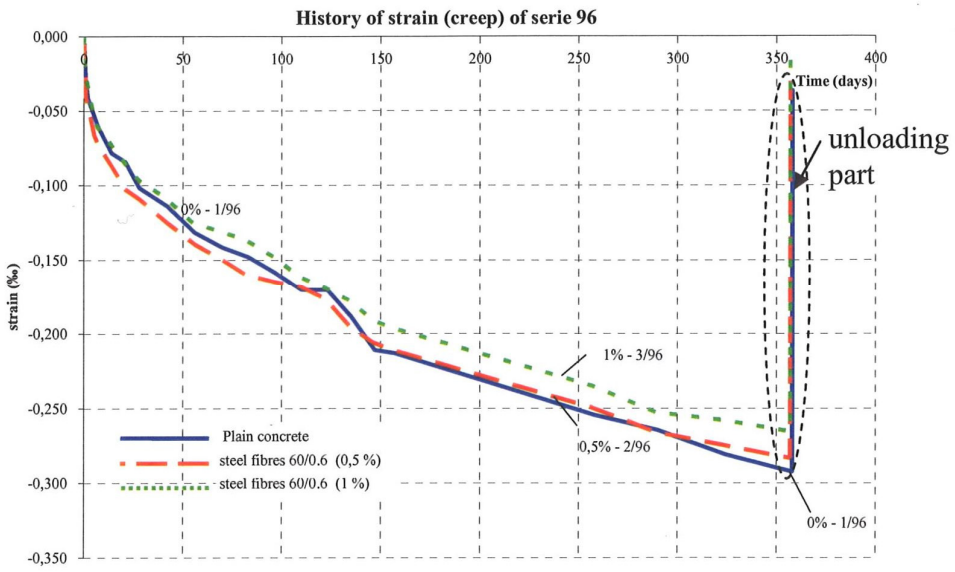

Figure 1. Creep strain recorded during 1 year measurements of series 1/96 (plain concrete), 2/96 (0.5% steel fibres) and 3/96 (1.0% steel fibres).

The ratio of basic strengths of FRCs vs. plain concrete with identical cement matrix composition (compressive strength and splitting tensile strength) was found as the decisive factor. The advantage of application of these basic strengths is that they are measured on the same forms of specimens like the plain concrete, typically on cubes of 150 mm. The main advantage of the prediction model for FRCs is that the determined strengths reflect the complete FRC technology, which - in comparison with the plain concrete - is much more complex (mix design, maintaining of the homogeneity, etc.).

No significant influence of fluctuations of environmental humidity and temperature (example - Fig. 2) on the development of creep strain was identified (Fig.l); this allowed to simplify the prediction model - it was possible to calculate the creep strain taking into account the weighted average of humidity during test period.

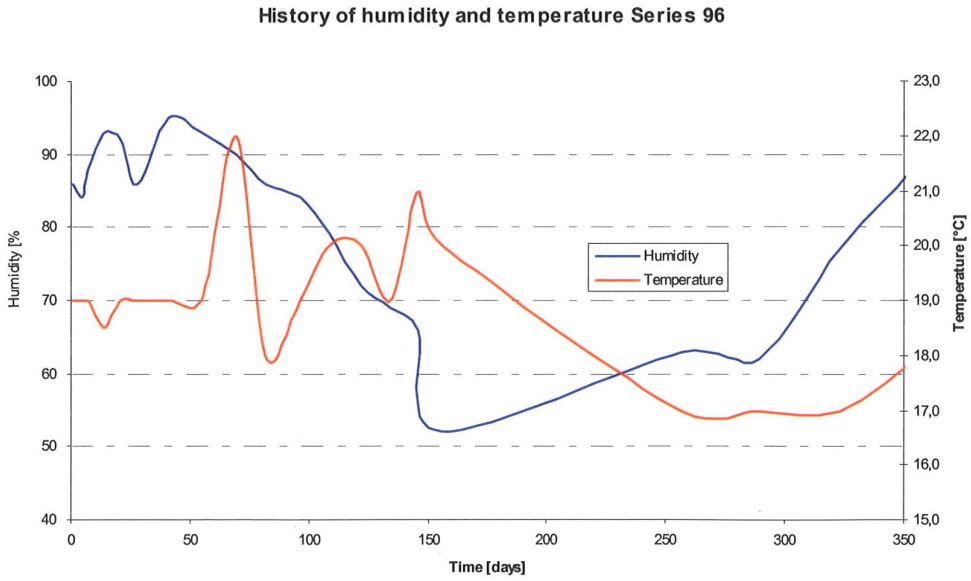

Figure 2. Humidity and temperature variations recorded during tests

Results of the study clearly proved that the relations of basic strength characteristics play the decisive role in prediction of time variation of long term deformations of the fibre reinforced concrete.

The model was developed on the basis of test results of the creep and shrinkage. The experimental program covered a wide variety of different types of fibres. The model for creep and shrinkage prediction of FRCs consists of two parts. The first part reflects the fact that the main role of creep and shrinkage is related to the composition of cement matrix that determines the volume changes of plain concrete. The influence of fibre reinforcement forms the second part of the prediction model.

The compliance function in the proposed model for creep of the fibre reinforced concrete is based on a sound prediction model (e.g. on Model B4) modified by relations of the mentioned basic strength characteristics: it has been proved that the creep strain of FRC may be predicted

as the creep strain of the plain concrete modified by the ratio of the compressive strength of plain concrete to the compressive strength of SFRC as follows

$$\varepsilon_{f,creep} = \varepsilon_{c,creep} \frac{f_c}{f_f}$$

Similarly, it can be written for shrinkage

$$\varepsilon_{f,sh} = \varepsilon_{c,sh} \frac{f_{ct,spl}}{f_{ft,spl}}$$

where:

$\varepsilon_{c,creep}$ strain-creep of plain concrete

$\varepsilon_{f,creep}$ strain-creep of FRC

$\varepsilon_{c,sh}$ strain-shrinkage of plain concrete

$\varepsilon_{f,sh}$ strain-shrinkage of FRC

f_c compressive strength of plain concrete

f_f compressive strength of SFRC

$f_{ct,spl}$ splitting tensile strength of plain concrete

$f_{ft,spl}$ splitting tensile strength of SFRC.

Table. 1 Selected results of series 96 and series 03 with very good agreement between measured and calculated (by authors model) creep values

Series	Reinforced	Compressive strength (cube specimen) at age 28 days (MPa)	Ratio of compressive strength of plain concrete and SFRC (cube specimen)	Creep total without instantaneous (‰)	
				experiment	calculated
1/96	Plain concrete	50.10	1.000	-0.293	-0.293
2/96	Steel fibres 60/0.6 - 0.5%	55.40	0.905	-0.283	-0.265
3/96	Steel fibres 60/0.6 - 1.0%	57.60	0.870	-0.265	-0.254
4/03	Plain conerete	40.40	1.000	-0.315	-0.315
1/03	Ferro Forta - 0.5%	38.50	1.049	-0.307	-0.331
2/03	Ferro Forta - 1%	39.10	1.033	-0.308	-0.325

The test results presented in example - Table 1 show that the material and shapes of fibres can significantly affect the time dependent strain; the steel fibre concrete is produced properly (with high standard properties: good homogeneity without agglomerating of steel fibres, good compaction and low porosity, minimum dispersion of mass density) in comparison with concrete with synthetic fibres where these conditions are not fulfilled (problems with lower compaction or porosity than with steel fibres); this is why increase in creep strain with the volume of fibers can be expected (see Tab. 1 - series 2/96 (0,5%) and 3/96 (1.0%).)

Improved formulae were obtained to predict the parameters of the compliance function for creep of fibre reinforced concrete from concrete composition parameters, including fibre contents, fibre types, the water-cement and aggregate cement ratios, cement content and type and admixtures. Comparisons with measured values and their time variations served as an essential check to validate the form of the proposed prediction creep and shrinkage models.

The calculation of the strain for several selected SFRCs is summarized in Tab. l. The tables include also the ratio between the calculated and measured strain to assess the accuracy of the prediction models.

The proposed model for calculation of creep strain may be applied for steel fibre reinforced concrete and also for the fibre reinforced concrete with synthetic fibres.

It is seen that the strain is increasing when the synthetic fibres are used in a large volume; these effects are possible to find in the compressive strength of fibre concrete. Therefore, the compressive strength which this reality predestines was accepted like a basic quantity in the model which expressed strain of fibre concrete.

SUMMARY AND CONCLUSIONS

The intention of the paper was to present a method for better understanding rheological performance of FRC, to improve conventional calculation methods and to offer suitable design tool for practice. Robust advanced models for medium/long-term strain predictions were established which respect the influence of various types of fibres, their shapes and bonding to the matrix and quality of production.

The principal significance of the presented study consists in that the results of the performed experimental research will help to create the advanced tools for full understanding all phenomena pertinent to long term structural performance of the fibre reinforced concrete.

The modified prediction models will create instruments enabling efficiency of materials and offer objective and effective tools increasing in the same time the level of reliability, durability and efficiency of fibre reinforced concrete structural members. The achieved results will help to avoid long-time serviceability problems.

During 15 year tests [6], [7], [8] good agreement between calculated and measured creep and shrinkage strains proved that the proposed model can be used for design the FRC structures.

ACKNOWLEDGEMENTS

This work was initiated during cooperation with Warsaw Technical University and supported by Czech Grant Agency under grant contract No. 14-17636S.

REFERENCES

[1] ACI 209.3R-XX, Analysis of Creep and Shrinkage Effects on Concrete Structures, Final Draft, Chiorino M.A. (Chairm. of Edit. Team), ACI Committee 209, March 2011, 228 pp

[2] Bažant, Z.P., and Li, G.-H., Comprehensive database on concrete creep and shrinkage, *ACI Materials Journal* Vol. 105, No. 6, Nov.-Dec. 2008, pp. 635-638.

[3] Chiorino, M.A., Carreira, D.J.: Factors affecting creep and shrinkage of hardened concrete and guide for modelling, The Indian Concrete Journal, December 2012, Volume 86, Number 12.

[4] Chiorino M.A. and Lacidogna G. (1999a), *General Unified Approach for Creep Analysis of Concrete Structures,* Revue Française de Génie Civil, Vol. 3, N° 3- 4, pp. 173-217.

[5] Chiorino M.A. (2005), A Rational Approach to the Analysis of Creep Structural Effects, in: J. Gardner and J. Weiss eds., Shrinkage and Creep of Concrete, *ACI American Concrete Institute SP-227*, 2005, pp. 107-141.

[6] Krátký, J., Trtík, K., Vodička, J., Spůra D., Abramowicz, M. „Determination of Creep and Shrinkage of Steel Fibre Reinforced Concrete". Proceedings of the Sixth International Symposium on BMC6, Warsaw, Poland, October. 2000, pp 352-356.

[7] Spůra D., Vodička, J., Krátký, J., Abramowicz, M. „Method of Determination of Creep and Shrinkage of SFRC ". Proceedings of the Seventh International Symposium on Brittle Matrix Composites (BMC7), Warsaw, Poland, October. 2003, pp 515-521.

[8] Spůra D., Krátký, J., Vodička, J. „Model for Calculation of Creep and Shrinkage of Fibre Reinforced Concrete". Proceedings of the Sixth International RILEM Symposium on Fibre-Reinforced Concretes , BEFIB 2004, Varenna, Italy, October. 2004, pp 895-902.

[9] Wendner , R., Hubler M. H., Bažant, Z.P.: Optimization method, choice of form and uncertainty quantification of Model B4 using laboratory and multi-decade bridge databases, Materials and Structures (2015) 48:771–796, DOI 10.1617/s11527-014-0515-0

Investigation of the Initiation and Propagation of Shrinkage Cracking in a Restrained Elliptical Ring Test

Wei Dong[1]; Xiangming Zhou[2]; and Zhimin Wu[3]
[1]State Key Laboratory of Coastal and Offshore Engineering, Dalian University of Technology, Dalian 116024, P.R. China. E-mail: dongwei@dlut.edu.cn
[2]Department of Mechanical, Aerospace and Civil Engineering, Brunel University, London UB8 3PH, U.K.; and State Key Laboratory of Coastal and Offshore Engineering, Dalian University of Technology, Dalian 116024, P.R. China. E-mail: Xiangming.Zhou@brunel.ac.uk
[3]State Key Laboratory of Coastal and Offshore Engineering, Dalian University of Technology, Dalian 116024, P.R. China. E-mail: wuzhimin@dlut.edu.cn

Abstract

The restrained ring test has been used to assess the potential for early-age cracking of concrete and other cement-based materials. Recently, a novel elliptical ring test method is proposed to replace the circular ring test method for the purpose of shortening test duration and more conveniently examining crack evolution in restrained concrete rings. In order to explore the mechanism of this test method, a numerical model is developed to analyze crack propagation process in restrained concrete rings, in which the effect of concrete shrinkage is simulated by a fictitious temperature drop applied on concrete causing the same strain as that induced by shrinkage. Finite element analysis is carried out to simulate the evolution of SIF in restrained concrete rings subject to circumferential drying. It is found that the failure mechanism of concrete rings changed with the increase of concrete ring wall thickness. Elliptical rings with appropriate geometry can enable crack initiation much earlier than circular rings in the case that crack is caused by the restraint of the central steel ring.
Keywords: Ring test; Restraint shrinkage; Elliptical ring; Initial fracture toughness.

INTRODUCTION

As a standard test method, circular ring test is first approved by the American Association of State Highway and Transportation (AASHTO) for the determination of the cracking tendency of restrained concrete specimens which consists of a concrete ring with an inner diameter of 305 mm, and a wall thickness and height of 75 and 150 mm, respectively, surrounding a restraining steel ring with an outer diameter of 305 mm and a wall thickness of 12.5 mm. Later, the circular ring test is also recommended by ASTM to determine the age at cracking and induced tensile stress characteristics of mortar or

concrete specimens under restrained shrinkage condition. Different from AASHTO, ASTM recommends thin rings with a reduced wall thickness of 37.5 mm to enable cracking to initiate at an earlier age to shorten the duration of ring test. On the other hand, novel elliptical ring geometries were adopted to replace circular ring geometries for investigating shrinkage cracking of mortar and concrete under restrained condition (He et al (2004), Ma et al (2007), Zhou et al (2014), Dong et al (2014)). It is generally regarded that, due to stress concentration caused by geometry effect, cracks initiate earlier in elliptical ring specimens than in circular ones though this has yet been validated in those studies.

Moreover, it is believed that the thickness of a concrete ring wall has a significant effect on the stress development in concrete under restrained shrinkage. AASHTO PP34-99 recommends thick rings with the concrete wall thickness of 75 mm while ASTM C1581/C1581M-09a recommends thin rings with the concrete wall thickness of 37.5 mm. Therefore it is necessary to investigate how a concrete mixture may exhibit different cracking behaviors in thin and thick ring specimens respectively, i.e., AASHTO PP34-99 and ASTM C1581/C1581M-09a may yield different results in cracking potential of a concrete mixture. Experiments have indicated that thicker concrete sections exhibited higher resistance to cracking than thinner ones, which suggests that the age of cracking of concrete is different in structures with different thickness (Weiss (1999)). In order to characterize stress development with the consideration of the effect of ring geometry and drying direction, analytical models were developed to assess residual stress in restrained ring specimens (Weiss (1999), Hossain and Weiss (2006), Moon and Weiss (2006), Moon et al (2006)). But it should be noted that those analytical models were developed for circular ring specimens only and they may not be appropriate for elliptical ones.

In line with this, a numerical model is developed in this study to analyze evolution of stress/stress intensity factor and to predict cracking age, position and/or propagation in a series of circular and elliptical concrete ring specimens subject to restrained shrinkage. The effects of ring geometry on cracking age, position and/or propagation on concrete rings under restrained shrinkage are also discussed.

EXPERIMENTAL

In this study, two series of circular and elliptical concrete ring specimens, with the concrete wall thicknesses of 37.5 mm quoted as “thin rings” and 75 mm quoted as “thick rings”, respectively, were subject to circumferential drying under restrained shrinkage to investigate the initial cracking age, position and crack propagation in concrete rings. The shapes and notations of geometries of the circular and elliptical rings are shown in Figure 1. The mix proportion of the concrete for making those specimens was 1:1.5:1.5:0.5 (cement: sand: coarse aggregate: water) by weight with the maximal coarse aggregate size of 10 mm, which represents a normal weight and normal strength concrete.

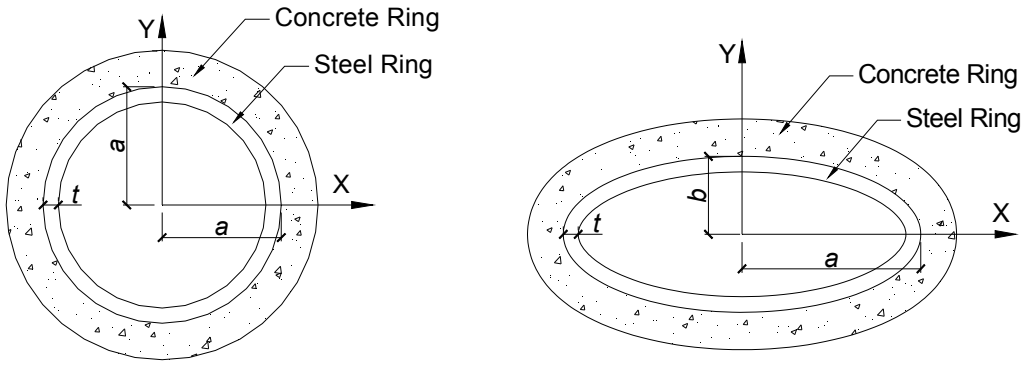

(a) Circular ring (b) Elliptical ring

Figure. 1. Notations of geometries of ring specimens

Thin ring tests were performed conforming to ASTM C1581/C1581M-09a. Five different ring geometries, with the inner major radius a equal to 150 mm but the inner minor radius b varying from 150, 125, 100, 75 to 60 mm and two rings for each geometry were tested subject to restrained shrinkage under the drying environment of 23°C and 50% RH. The wall thickness, t, of the restraining steel rings and concrete rings was as 12.5 and 37.5 mm, respectively. The height of the rings was 75 mm. Thick ring specimens with a 75 mm-thick wall, which was recommended by AASHTO PP34-99, were also tested under restrained shrinkage. Five different ring geometries were prepared with their geometries listed in Table 1.

It can be seen from table 1, that the thin elliptical rings with a geometrical factor $a/b<2$, i.e. those with a=150 mm, and b=125, or 100 mm, did not crack earlier than the circular ones with a=150 mm, suggesting that these elliptical ring geometries do not provide the expected higher degree of restraint than the circular ones do. However, for the elliptical ring specimens with $a/b\geq2$, i.e. those with a=150 mm, and b=75 or 60 mm, they cracked earlier than the circular ones. The circular thick ring specimens with a=125 mm cracked at about an age of 22 days. For elliptical ring specimens, with the increase of the geometrical factor a/b, i.e. minor semi-axis b decreased from 125, 100, 75 to 60 mm, average cracking ages are around 21, 22, 18, and 20 days, respectively, as observed from experiment. It seems that the effects of elliptical shape on shortening cracking age in thick rings is not as significant as that in thin ones.

Table 1: Cracking ages (in days) obtained from numerical analyses and experiment

$a\times b$ mm^2	Concrete ring wall thickness					
	37.5 mm			75 mm		
	Num.	Exp.		Num.	Exp.	
150×150	18	15	14	16	—	—
125×125	—	—	—	18	19	25
150×125	20	15	14	17	20	21
150×100	17	15	14	18	21	22
150×75	11	10	10	21	18	18
150×60	12	11	15	—	21	19

NUMERICAL

Fictitious temperature filed In this numerical approach, shrinkage effect of concrete was represented by a fictitious temperature field applied on concrete ring specimens. There is an assumption adopted in numerical analyses, i.e. free shrinkage is the same for concrete elements with the same A/V ratio but maybe different geometries/shapes. In case of a thin ring wall, concrete shrinkage can be regarded uniform across the wall. Based on the derived fictitious temperature drop and the corresponding A/V ratio for concrete prisms, the relationship between fictitious temperature drop and A/V ratio for thin concrete elements at various ages can be obtained. The corresponding A/V ratios of the circular and elliptical thin ring specimens were calculated based on the geometry of rings and the sealed condition. Figure 2, as the outcome of this analysis, showed the fictitious temperature drop for the elliptical ring with $a \times b$=150×60 mm^2.

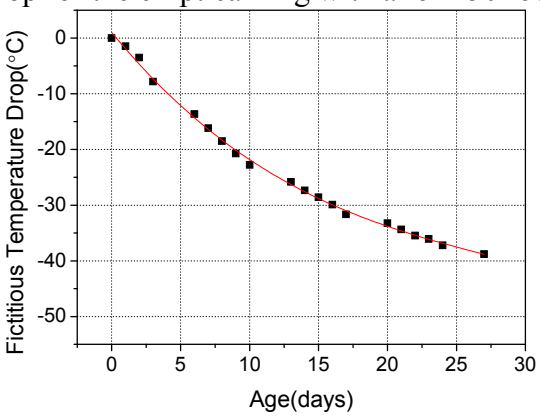

Figure. 2. Fictitious temperature drop for a thin elliptical ring ($a \times b$=150×60 mm^2)

With the increase of the thickness of a concrete element, the influence of moisture gradient across the thickness becomes more and more significant and cannot be neglected. It is therefore believed that the assumption of a uniform moisture loss, consequently uniform shrinkage, therefore uniform fictitious temperature field, across the thickness of the ring wall adopted for analysing thin rings is not appropriate for thick rings. The temperature distribution across a thick ring wall should correspond to the moisture distribution in a 75 mm-thick concrete wall with only one side surface exposed for drying. According to the experimental investigation conducted by Weiss (1999), the humidity in a normal strength concrete specimen at any age and position can be calculated by the following equation:

$$H(x,t) = H_{INTERNAL} - (H_{INTERNAL} - H_{EXPOSED})\left(10^{-(A_1 D + A_2) t^{(B_2 + B_1 \ln(D))} \frac{x}{D}}\right) \quad (1)$$

Where, $H(x,t)$ is the relative humidity at the depth x from the drying surface, $H_{INTERNSL}$ is the internal humidity if the specimen was completely sealed (in this paper $H_{INTERNAL}$ was assumed to be 100%), $H_{EXPOSED}$ is the relative humidity at the exposed surface of the specimen. The coefficients A_1, A_2, B_1, and B_2 in Equation (1) was

determined as 0.2007, -1.0455, 0.0865 and -0.9115, respectively, for normal strength concrete. *D* is the overall depth of a concrete specimen, which was 75 mm in this study. Figure 3 presents an example of relative humidity profiles, calculated based on Equation (1), across the wall of a thick concrete ring at various ages when subject to circumferential drying. Figure 4 presents the fictitious temperature drop at the exposed surface of thick ring with age.

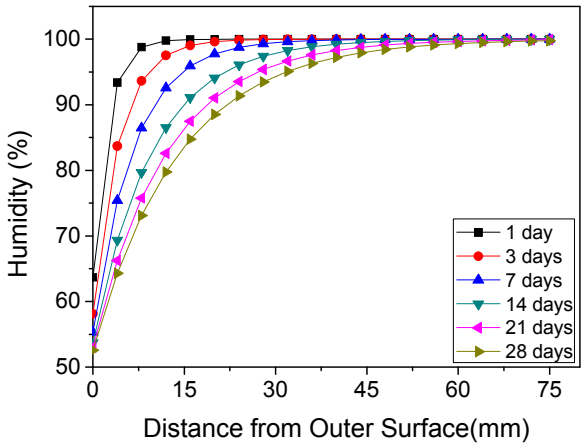

Figure. 3. Humidity distribution across the wall of a thick concrete ring

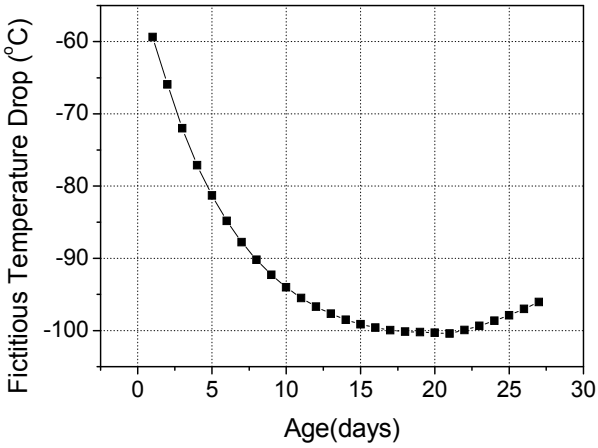

Figure. 4. Fictitious temperature drop at the exposed surface of a thick concrete ring

Numerical analysis In numerical analyses, concrete shrinkage effect was simulated by fictitious temperature fields applying on ring specimens. For thin rings with a 37.5 mm-thick wall, a uniform temperature field with zero gradient across concrete ring wall was adopted. For thick ring specimens with a 75 mm-thick wall, considering the effect of moisture gradient across the wall, different fictitious temperature drops were applied across the ring wall. As aforementioned, maximal circumferential tensile stress criterion was employed for predicting cracking position and cracking age in thin ring specimens. In case of thick rings, a fracture mechanics-based cracking criterion was adopted for

determining cracking age. For this purpose, a pre-crack with 2 mm long is set on the outer circumference of a thick elliptical ring along its minor axis, in which the maximum circumferential tensile stress occurs as per elastic analysis results which will be elaborated later. The fictitious crack model is introduced in the fracture analysis through establishing softening stress (σ)-crack opening displacement (w) relationship of concrete. In this paper, the bilinear expression for σ-w is chosen in the proposed numerical approach. σ_s, w_s and w_0 can be determined as follows:

$$\sigma_s = f_t / 3 \tag{2}$$

$$w_s = 0.8 G_F / f_t \tag{3}$$

$$w_0 = 3.6 G_F / f_t \tag{4}$$

Where w_0 is the displacement of the terminal point of σ-w curve beyond which no stress can be transferred, i.e. the stress-free crack width, w_s and σ_s is the displacement and stress, respectively, corresponding to the break point in the bilinear σ-w relationship. These parameters and the σ-w relationship can be derived given the fracture energy G_F and the tensile strength f_t. Here, f_t is obtained from experiment and G_F is from the formula recommended by CEB-FIP model code 2010.

In this study, a crack propagation criterion (Dong et al (2013)) is introduced to analyze crack initiation and propagation in concrete rings subject to the restrained shrinkage. This criterion can be described as following: crack begins to propagate when the difference, between the stress intensity factors K_{I}^{S} caused by the applied load and K_{I}^{σ} by the cohesive stress, exceeds the initial fracture toughness K_{IC}^{ini} of concrete. The notched concrete beams were tested under three-point bending to measure the initial fracture toughness, K_{IC}^{ini}, of concrete. Based on the results of regression analyse, the initial fracture toughness, K_{IC}^{ini} of the concrete at early ages can be predicted using Equation (5):

$$\begin{aligned} K_{IC}^{ini} &= 0.0011t^3 - 0.0574t^2 + 1.016t + 10.04 \quad (t<14) \\ &= -0.002t^2 + 0.1429t + 14.3 \quad (14 \le t \le 28) \end{aligned} \tag{5}$$

RESULTS AND DISCUSSION

Crack position According to experimental results, for elliptical rings with $a \times b = 150 \times 75$ mm^2 (see Figure 5(a)), cracks initiated close to the vertices on the major axis of the inner elliptical circumference. It can be seen from the circumferential stress contour (see Figure 5 (b)) that the stress concentration is significant in elliptical concrete rings with 150×75 mm^2. Figure 6 presents crack position in thick ring specimen observed from experiment. It can be seen that, different from the scenario observed from thin ring specimens, crack (see Figure 6(a)) occurred between the major and minor axes and they were not in the vertices on the major or minor axis of the outer elliptical circumference. This can be explained based on numerical results as following. According to the circumferential stress contour (see Figure 6(b)) from numerical analysis of a thick ring, the variation of circumferential stress along the radial direction is not sharp and stress concentration is not significant either.

(a) crack position (b) circumferential stress contour at 11th day

Figure. 5. Crack and circumferential stress contour of thin ring ($a \times b$=150×75 mm^2)

(a) crack position (b) circumferential stress contour at 7th day

Figure. 6. Crack and circumferential stress contour of thick ring ($a \times b$=150×75 mm^2)

Cracking age and evolution of stress/SIF Figure 7 presents the maximum circumferential tensile stress developed in various thin rings obtained from numerical analyses. The maximum circumferential tensile stress was chosen from the mid-height section of a concrete ring specimen. When the maximum circumferential tensile stress developed in a concrete ring reaches the tensile strength of concrete, crack initiates and the age at the meeting point gives the cracking age. Figure 8 presents the evolution of SIF caused by shrinkage effect and cohesive stress with respect to age in a series of thick concrete rings.

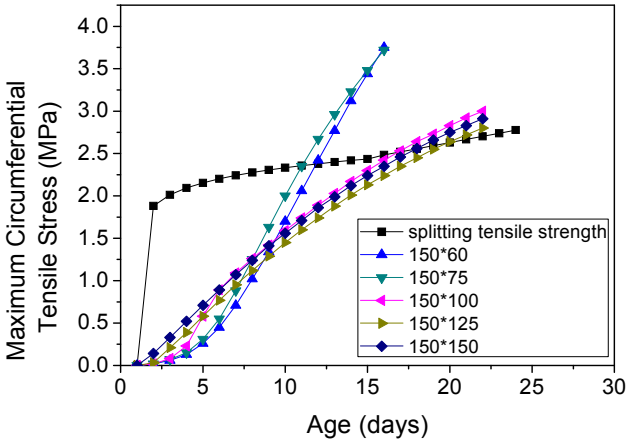

Figure. 7. Maximal circumferential tensile stress in thin rings with respect to age from numerical analysis

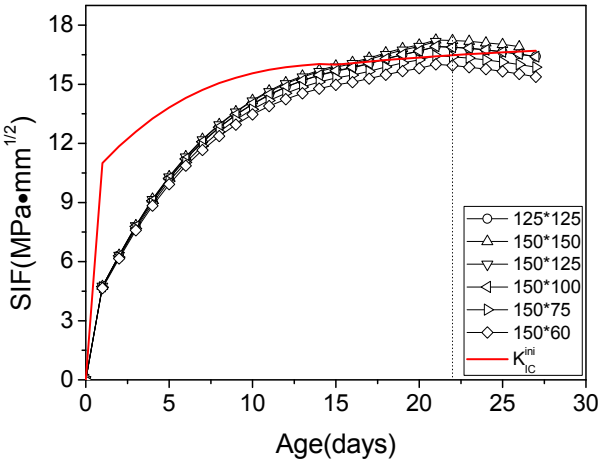

Figure. 8. SIF in thick concrete rings with respect to age

Figure 9 presents evolution of SIF with respect to crack length for various thick rings at cracking age *t*. According to Hossain and Weiss (2006), the circumferential tensile stress in concrete in a restrained ring specimen subject to drying shrinkage consists of two parts: (1) caused by self-restraint in a concrete wall and (2) caused by the central steel ring in the radial direction. In numerical analyses of thick rings, the first part circumferential tensile stress can be calculated through analysing a concrete ring with nonlinear free shrinkage without any external restraint. The second part circumferential tensile stress, which is caused by the central steel ring, can be calculated by applying restraining pressure on the inner circumferential surface of a concrete ring enforced by the central steel ring. Thus, the SIF caused by drying shrinkage and restraint shrinkage can be obtained through finite element analyses.

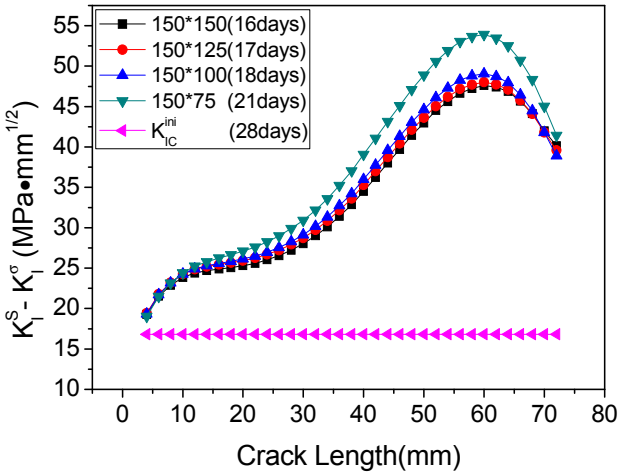

Figure. 9. Evolution of SIF with crack propagation in thick rings

As an example of such analysis, Figure 10 presents the evolution of SIF with respect to crack propagation in a circular concrete ring with $a \times b$=150×125 mm^2. It can be seen

from Figure 10 that the SIF caused by self-restraint keeps stable with respect to crack length, i.e. remains almost no change when the distance between crack tip and the outer circumferential surface of the steel ring is greater than 15 mm.

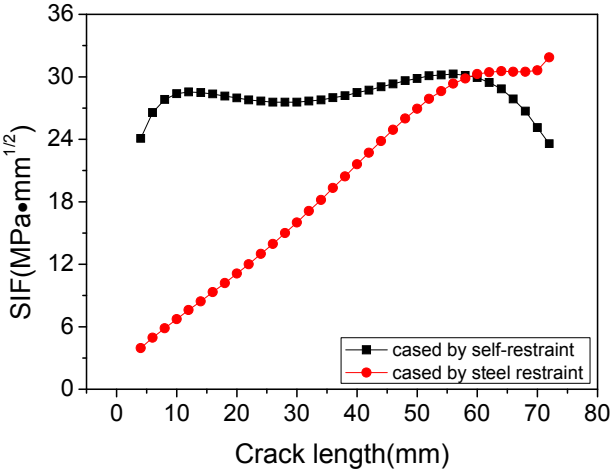

Figure. 10. Evolution of SIFs caused by various restraining effects with crack propagation in the 150×125 mm^2 thick ring

COCLUSION

A series of circular and elliptical concrete rings were tested subject to restrained shrinkage to investigate the effect of ring geometry and concrete wall thickness on evolution of stress/stress intensity factor in concrete rings. A numerical model, by introducing fictitious temperature fields to represent the mechanical effect of shrinkage of concrete, was developed for predicting stress/SIF development and cracking initiation in concrete rings subject to restrained shrinkage. The following conclusions can be drawn:

(a) Based on experimental results, the thin elliptical ring with the geometrical factor *a*/*b* between 2 to 3 is recommended to replace traditional circular rings for restrained shrinkage test. With the increase of concrete ring wall thickness, the restraining effect provided by the inner steel ring on surrounding concrete decreases, which marks down the advantage of using thick elliptical ring specimens to replace circular ring specimens in shortening restrained shrinkage ring test period.

(b) In thin elliptical rings, the maximum circumferential tensile stress occurred in the two vertices on the major axis of the inner elliptical circumference, resulting in that crack initiated in these zones and propagated towards the outer one. In thick elliptical rings, the maximum circumferential tensile stress occurred in the two vertices on the minor axis of the outer elliptical circumference resulting in that crack initiated in these zones and propagated towards the inner circumference.

(c) The restraint effect mainly comes from self-restraint from surrounding concrete due to non-uniform shrinkage caused by nonlinear moisture movement across a

thick concrete ring wall. The external restraint effect from the central steel ring is relatively weak at the onset of crack propagation. Crack will propagate very quickly throughout thickness of a ring wall once it starts to propagate.

ACKNOWLEDGEMENT

The financial support of the National Natural Science Foundation of China under the grant of NSFC 51478083, the fundamental research funds for the Central Universities under the grant of DUT14LK06 and the Engineering and Physical Sciences Research Council under the grant of EP/I031952/1 is gratefully acknowledged.

REFERENCES

Dong, W., Wu, Z. M., Zhou, X. M. (2013) "Calculating crack extension resistance of concrete based on a new crack propagation criterion", *Constr. Build. Mater*, 38(1), 879-889.

Dong, W., Zhou, X. M., Wu, Z. M. (2014) "A Fracture Mechanics-based Method for Prediction of Cracking of Circular and Elliptical Concrete Rings under Restrained Shrinkage", *Eng. Fract. Mech*, 131(12), 687-701.

He, Z., Zhou, X. M., Li, Z.J. (2004). "New experimental method for studying early-age cracking of cement-based materials." *ACI Mater. J.*, 101(1), 50-56.

Hossain, A. B., Weiss, J. (2006). "The role of specimen geometry and boundary conditions on stress development and cracking in the restrained ring test." *Cement. Concrete. Res*., 36(1),189-199.

Ma, G. B., Wang, X. G., Liang, W. Q., Li, X. G., He, Z. (2007). "Study on early-age cracking of cement-based materials with superplasticizers" *Constr. Build. Mater*, 21(11), 2017-2222.

Moon, J.H., Weiss, J. (2006). "Estimating residual stress in the restrained ring test under circumferential drying." *Cement. Concrete. Comp.,* 28(5), 486-496.

Moon, J. H., Pease, B., Weiss, J. (2006). "Quantifying the influence of specimen geometry on the results of the restrained ring test." *J. ASTM. Int.,* 3(8), 1-14.

Zhou, X. M., Dong, W., Oladiran, O., (2014) "Assessment of Restrained Shrinkage Cracking of Concrete Using Elliptical Ring Specimens: Experimental and Numerical", *ASCE J. Mater. Civil. Eng*.,, 26(12), 871-878.

Weiss, W. J. (1999). "Prediction of early-age shrinkage cracking in concrete." *Ph.D Dissertation*, Northwestern University.

Updated Temperature-Stress Testing Machine (TSTM): Introductory Tests, Calculations, Verification, and Investigation of Variable Fly Ash Content

Anja Estensen Klausen[1,2]; Terje Kanstad[2]; and Øyvind Bjøntegaard[3]

[1]SINTEF, Building and Infrastructure, Richard Birkelandsvei 3, 7034 Trondheim, Norway. E-mail: anja.klausen@sintef.no
[2]Department of Structural Engineering, NTNU, Richard Birkelandsvei 1A, 7491 Trondheim, Norway. E-mail: terje.kanstad@ntnu.no
[3]The Norwegian Public Roads Administration (NPRA), Abels gate 5, 7030 Trondheim. E-mail: oyvind.bjontegaard@vegvesen.no

Abstract

The Temperature-Stress Testing Machine (TSTM) System at NTNU is well established, but the software for logging and management is new. The degree of restraint can now be varied in the range between 0 and 100%, and thus the real temperature- and stress history of critical positions in large concrete structures can be experimentally investigated. Introductory tests, calculations and evaluations are on-going, and the test equipment gives reliable results and good reproducibility. The verification of the TSTM System includes comparisons of test results with three different calculations approaches: Excel, CrackTeSt COIN and DIANA. Tests conducted in the TSTM show that the restrained stress development is reduced when increasing the concrete fly ash content. However, this has to be considered in combination with the simultaneously reduced tensile strength. The performed restrained stress tests and appurtenant calculations show that good knowledge regarding the creep/relaxation behavior of the concrete in question is of major importance. In addition, the obtained results indicate a correlation between temperature history and the magnitude of the E-modulus for fly ash concretes. A mechanical test series of concretes with varying fly ash content has been carried out, and the determined material properties: E-modulus, tensile strength and compressive strength, were all found to be decreasing with an increasing amount of fly ash content. The described activities have been a part of the COIN-project «Crack free concrete structures».

INTRODUCTION

Hydration reactions in concrete during the hardening phase always cause volume changes, and these volume changes are proven to be a considerable challenge. If these movements are restrained by the subgrade and/or adjoining structural parts, stresses will build up in the hardening concrete, which again may lead to cracking. In the literature, autogenous deformation and thermal dilation are shown to be the major

driving forces to stress generation and cracking in real concrete structures. The amount of stress generated by autogenous deformation and thermal dilation in a given time interval is dependent on the degree of restraint and the visco-elastic properties of the concrete.

The Temperature-Stress Testing Machine (TSTM) System at NTNU is well established (Bjøntegaard 1999), and consists of a Dilation Rig and a TSTM, Figure 1. The Dilation Rig measures free deformation, i.e. thermal dilation and autogenous deformation, while the TSTM is constructed to measure the stress generation of concrete through the hardening phase. During the years 2009-2013, the software for logging and management of the TSTM has been updated. In addition, the instrumentation system has been improved to achieve the necessary accuracy and robustness of the system. The degree of restraint can now be varied in the range between 0 and 100 %, and thus the real temperature- and stress history of critical positions in large concrete structures can be experimentally investigated. In addition, the concrete E-modulus can be determined based on the measured data, providing an E-modulus development over time for the concrete in question. The system can also be used for creep testing in tension and compression under prescribed temperature histories. Introductory tests, calculations and evaluations are on-going to verify the test equipment and reproducibility.

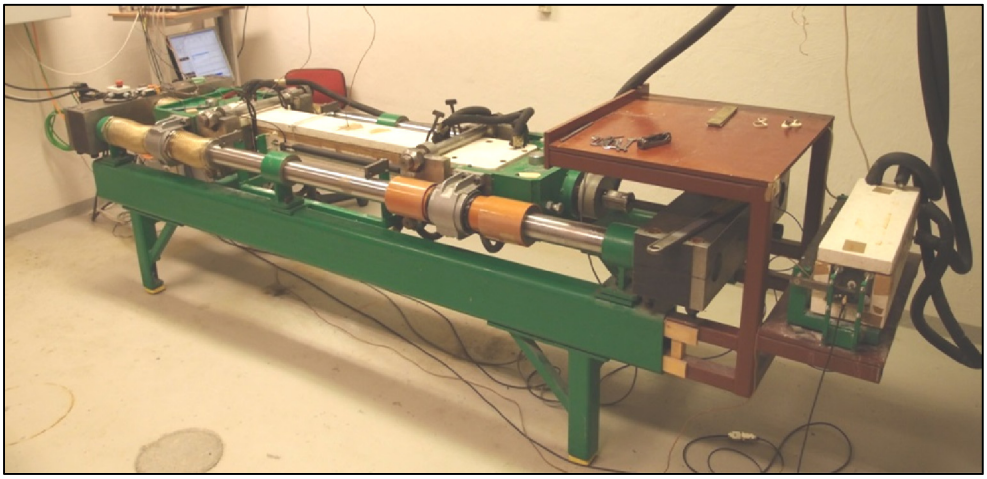

Figure 1 – The TSTM system at NTNU: consisting of the TSTM (left) and the Dilation Rig (right)

EXPERIMENTS

The TSTM introductory tests are conducted with a series of four concretes designed within the COIN-project «Crack free concrete structures». The concretes contain Portland cement, and they have a water-to-binder ratio of 0.4. The given concretes contain a varying amount of fly ash: 0 %, 20 %, 28 % and 36 %, respectively. This article focuses on the results from the two concretes most thoroughly investigated during the introductory tests: the reference concrete without fly ash, *ANL Ref.*, and the concrete with the highest fly ash content (36 %), *ANL +36% FA*.

A minimum of two tests have been conducted in the TSTM System for each concrete. In one of the tests, the TSTM concrete specimens were fully restrained and subjected to isothermal conditions with a constant temperature of 20 °C. In the other test, the TSTM concrete specimens were applied a degree of restraint of 50 % and a realistic temperature history. The Dilation Rig (the «dummy») always follows the same temperature history as the TSTM. The applied realistic temperature histories were found by heat-development calculations based on semi-adiabatic calorimeter tests for the given concretes. The calculated temperature represents the average temperature in a selected section of an 800 mm thick and 4200 mm high wall structure exposed to Norwegian summer conditions (20 °C). Results from the tests performed with realistic temperature histories (semi-adiabatic tests) are presented in the following.

In addition to the tests in the TSTM System, a parallel mechanical test series (20 °C standard curing) was carried out to identify the model parameters needed for the theoretical approach regarding the TSTM stress calculations. The mechanical test series is reported in (Kjellmark and Klausen, 2015).

Due to results obtained from calculations of the restrained stress tests in the TSTM System, supplementary creep tests were initiated for the concrete *ANL +36% FA*. The creep tests were conducted in the TSTM System at a constant temperature of 20 °C: one test measuring creep in compression and one test measuring creep in tension. For a more realistic approach with regard to the TSTM stress calculations, the creep tests were realistically adjusted to match the nature of the actual measured restraint stress curve for the given concrete. The load, 1 MPa, was applied and removed from the concrete specimen according to the stress development curve previously obtained from the TSTM, Figure 2.

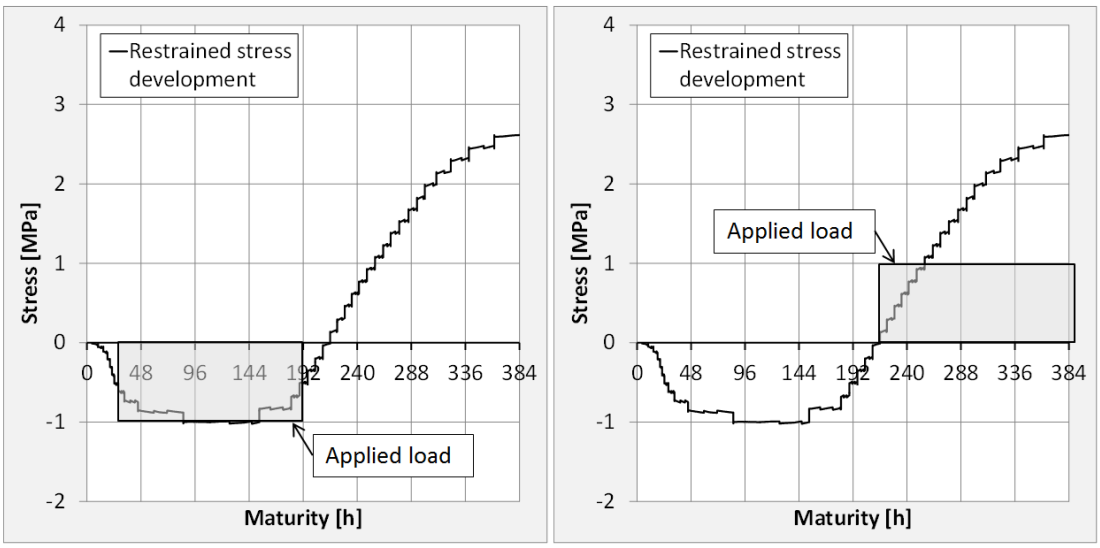

Figure 2 – Applied load during TSTM creep tests designed according to the actual restrained stress for the given cocnrete: Creep in compression (a) Creep in tension (b)

CALCULATION APPROACHES

As a part of the verification of the TSTM System, measured restrained stress results have been compared with calculated stress developments calculated by different calculation approaches. These calculations of the restrained stress development in the TSTM are based on:

- Parallel free deformation measurements in the Dilation Rig
- The degree of restraint
- Temperature measured in the TSTM
- Material parameters determined from parallel mechanical testing

While most of the material parameters were found from mechanical testing, the applied creep parameters were based on previous experience with corresponding concretes (Bjøntegaard and Kjellsen, 2012).

Three different calculation approaches were used for the TSTM stress calculations:

- A specially designed 1D calculation program performed with Excel and Visual Basic, based on linear visco-elasticity with age adjusted effects
- The special-purpose 2D program CrackTeSt COIN
- The multi-purpose 3D FE program DIANA

In the specially designed program performed with Excel, the visco-elastic behaviour of the concrete is described with linear superposition method and the «Double power law». In CrackTeSt COIN however, the visco-elastic behaviour is described by a Maxwell chain model. In DIANA, both «Double power law» and Maxwell chains are available when describing the creep/relaxation behavior of the concrete. For the calculations where the creep/relaxation behavior is described by Maxwell chains, the given creep parameters were transformed to relaxation data by the program RELAX (Jonasson et al, 2001).

Due to the obtained deviations between the measured and calculated restrained stress development in the TSTM, the specially designed program run in Excel was modified to open for a more comprehensive calculation routine with regard to the visco-elastic behavior. The modified stress calculation differentiates between creep in compression, creep recovery and creep in tension. The appurtenant sets of creep parameters (creep in compression, creep recovery and creep in tension) were determined based on the dedicated creep tests in the TSTM System discussed in the previous chapter.

RESULTS

The model parameters used in the TSTM back-calculations for *ANL Ref.* and *ANL +36% FA* are presented in Table 1. The model parameters were determined based on the previously mentioned mechanical test series. The material properties: E-modulus,

tensile strength and compressive strength, were all found to be decreasing with an increasing amount of fly ash.

Table 1. Model parameters determined from mechanical testing (20 °C curing)

	E-modulus E_{28} - [GPa]	**Tensile strength** f_{t28} - [MPa]	**Compressive strength** f_{c28} - [MPa]
ANL Ref.	32.3	3.9	78.8
ANL +36% FA	27.8	3.1	67.9

Several introductory tests have been performed in the TSTM System. Both isothermal and semi-adiabatic tests show very good reproducibility for both the Dilation Rig and the TSTM. All stress developments from the TSTM tests have been calculated using the previously described calculation approaches. Figure 3 presents the restrained stress development for the reference concrete *ANL Ref*. The test is conducted with a degree of restraint of 50 % and a realistic temperature history, and the specimen develops failure in tension after approximately seven days. Figure 3 also shows the stress developments calculated by two of the calculation approaches: the specially designed program performed with Excel and the special-purpose program CrackTeSt COIN. The calculation approaches give very good agreement, both with each other as well as with the measured stress development in the TSTM. In the following, only the stress calculations performed with Excel are presented.

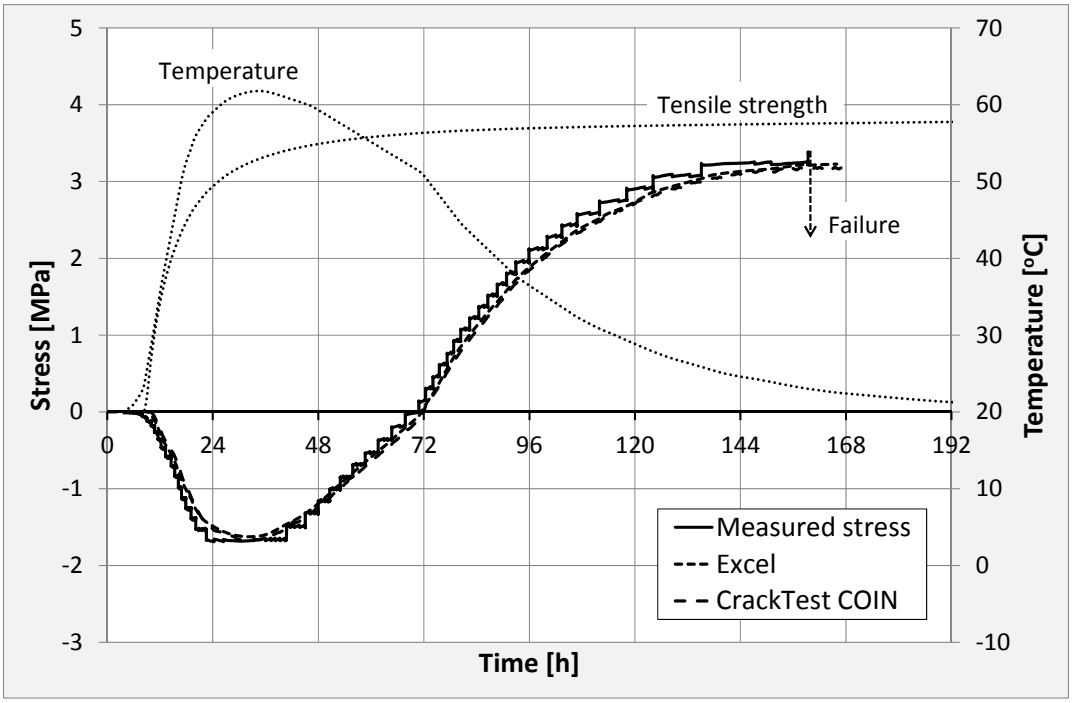

Figure 3 – Measured vs. calculated restrained stress in the TSTM, *ANL Ref.*

Figure 4 shows measured and calculated restrained stress development for *ANL +36% FA*. The test is conducted with a degree of restraint of 50 % and a realistic

temperature history. It can be seen that the match between measured and calculated stress is rather poor. This result is in line with the other tests (not discussed) in the way that the difference between measured and calculated stress is found to be increasing with an increasing amount of fly ash content. Due to this observation, a series of creep tests were initiated in the TSTM System as described in the previous chapters. The new sets of creep parameters, combined with a more comprehensive calculation routine in Excel, provided a calculated restrained stress as given in Figure 5. As can be seen, the new stress calculation gave better agreement with the measured stress in the TSTM. There is however still some deviation. The stress calculations use model parameters found from mechanical testing, however the incremental E-modulus achieved from the given TSTM test is found to be higher than the E-modulus found from mechanical testing. The original mechanical test program (giving the values in Table 1) was performed at 20 ^{o}C isothermal conditions. In the calculations theses data are expressed by a continuous function, and the time domain is adjusted by the use of the maturity concept to give the relevant time development according to the actual temperature history in the given TSTM test. Possible effects of temperature on the final properties (final strength, final E-modulus) is not handled by the maturity concept. Any such temperature effects will then be reflected in the incremental E-modulus values from the TSTM (semi-adiabatic temperature), but not in standard 20 ^{o}C mechanical tests.

Figure 6 shows a calculation with both new creep parameters and an E-modulus development obtained from the given semi-adiabatic TSTM test. As can be seen from Figure 6, the stress calculations now give very good agreement with the measured restrained stress development.

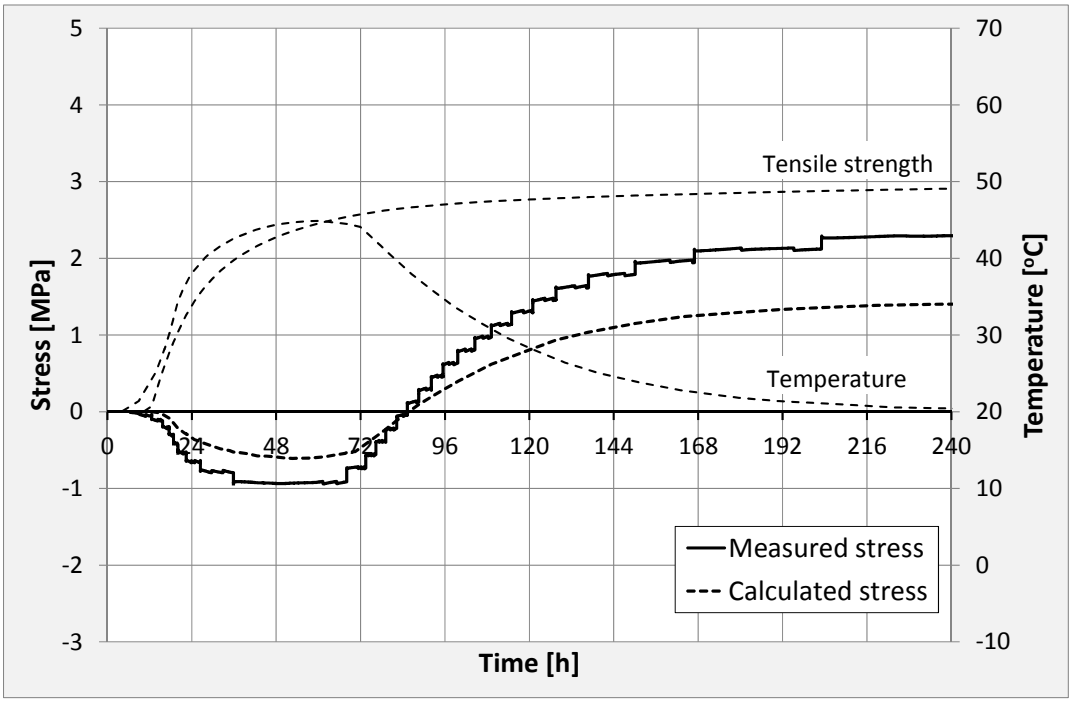

Figure 4 – Restrained stress development in the TSTM, *ANL +36% FA*

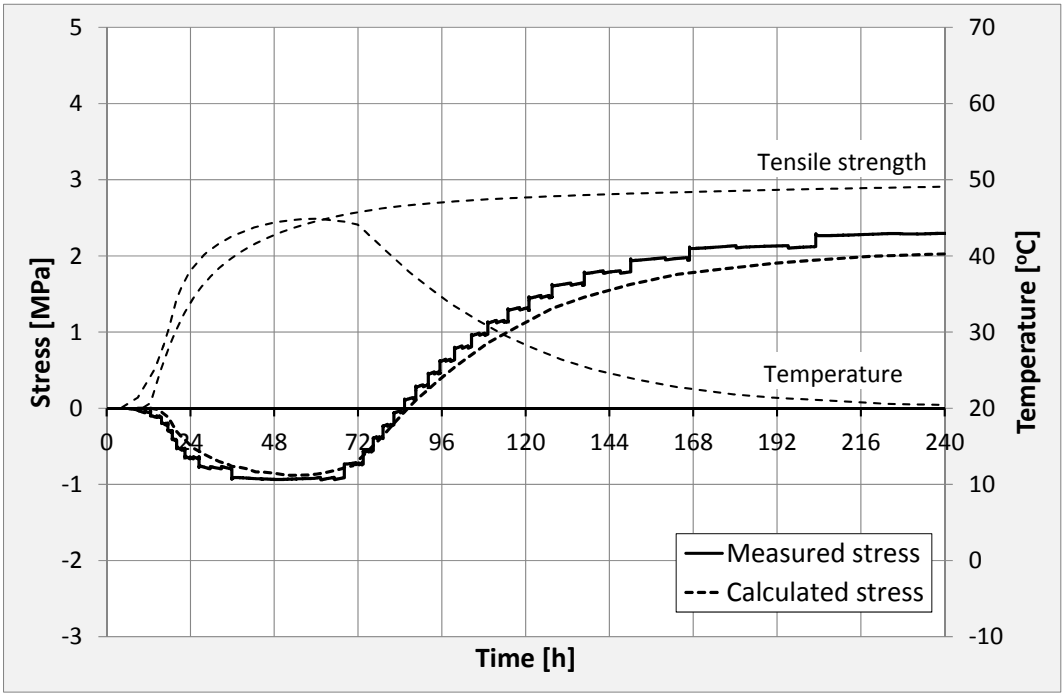

Figure 5 – Stress development in the TSTM, *ANL +36% FA*, new creep data

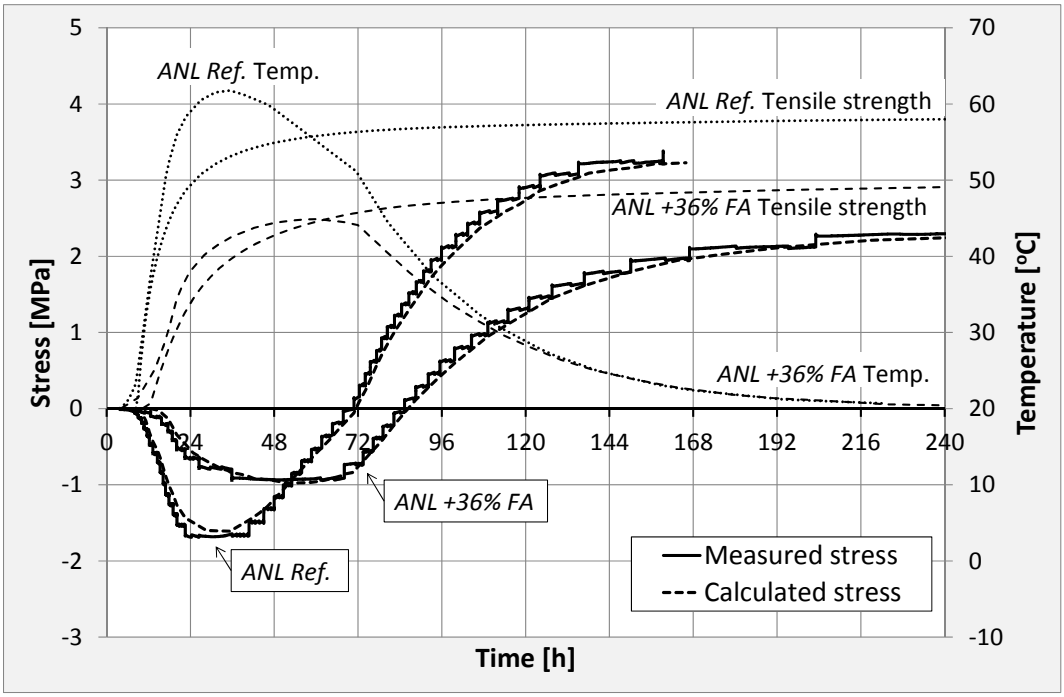

Figure 6 – Stress development in the TSTM, *ANL Ref.* and *ANL +36% FA*

Several semi-adiabatic TSTM tests indicate that *ANL +36% FA* has an higher E-modulus during testing in the TSTM than determined by mechanical testing (cured at

20 °C). It appears that the magnitude of the E-modulus for fly ash concrete is influenced by temperature. This assumption is currently being investigated further, and a mechanical test series with semi-adiabatic curing conditions is presently in progress. Preliminary test results indicate that the E-modulus for fly ash concrete is indeed higher for specimens exposed to semi-adiabatic curing conditions than for specimens exposed to standard 20 °C isothermal curing conditions.

Figure 6 shows the restrained stress development for the two given concretes: both subjected to a realistic temperature history which is relevant for each concrete when used in an 800 mm thick wall as previously described. The stress development is decreasing with an increasing amount of fly ash. However, the tensile strength is also decreasing with an increasing amount of fly ash, which has to be considered as the risk of cracking is dependent on the restrained stress/tensile strength – ratio. The temperature effect on the tensile strength is also presently investigated further.

CONCLUSION

Results from mechanical testing (20 °C standard curing) show that the determined material properties (E-modulus, tensile strength and compressive strength) are all decreasing with an increasing amount of fly ash content. In addition, heat development and thus thermal dilation is decreasing with an increasing amount of fly ash. Restrained stress development is consequently also reduced when increasing the fly ash content, but this has to be considered in combination with the reduced tensile strength. In the given case (800 mm wall and summer conditions), fly ash addition has a positive effect when it comes to reducing the cracking tendency.

The obtained deviation between restrained stress measured in the TSTM and calculated stress development for the concrete containing fly ash was partly caused by insufficient information of the creep parameters for the given concretes. Applying new creep parameters determined by dedicated creep tests have a major impact on the calculated stress development, and thus illustrates the importance of good knowledge regarding the creep/relaxation behavior of the concrete in question. With new creep parameters, there was still a deviation between measured and calculated restrained stress development. The remaining deviation is believed to be caused by a fundamental temperature influence on the E-modulus (and possible also tensile strength) for fly ash concretes. This assumption is currently being investigated further.

ACKNOWLEDGEMENTS

The paper is based on the work performed in COIN - Concrete Innovation Centre (www.coinweb.no) - which is a Centre for Research based Innovation, initiated by the Research Council of Norway (RCN) in 2006. The Centre is directed by SINTEF, with NTNU as a research partners and with the present industrial partners: Aker Solutions, Norcem, Norwegian Public Roads Administration, Rescon Mapei, Skanska, Spenncon, Unicon, Veidekke and Weber Saint Gobain.

REFERENCES

Bjøntegaard, Øyvind (1999): *Thermal Dilation and Autogenous Deformation as Driving Forces to Self-Induced Stresses in High Performance Concrete.* PhD Thesis. The Norwegian University of Science and Technology (NTNU), Trondheim, Norway

Bjøntegaard, Øyvind and Knut O. Kjellsen (2012): *Property development and cracking tendency in hardening concrete: Effect of cement type and fly ash content.* COIN Project Report 40, SINTEF Building and infrastructure, Norway

JEJMS Concrete AB (2009-2012): *ConTeST Pro (Now CrackTeSt COIN) Manual, Version 1.2*, Luleå, Sweden

Jonasson, Jan-Erik and Westman, Gustaf (2001): *RELAX - Conversion of creep data to relaxation data by the program RELAX.* Luleå University of Technology, Luleå, Sweden

Kjellmark, Gunrid and Anja Estensen Klausen (2015): *Mechanical properties and calculation of model parameters for concrete with variable fly ash content.* COIN Project Report - draft, SINTEF Building and infrastructure, Norway

Microsoft Office (2010): *Microsoft Excel, Version: 14.0.6123.5001*

TNO DIANA BV (2010): *Manual -- Release 9.4.3*

Numerical Simulation of the Long-Term Behaviour of Long Span Prestressed Concrete Bridges

Lukas Vrablik[1] and Milan Holy[1]

[1]CTU in Prague, Faculty of Civil Engineering, Department of Concrete and Masonry Structures, Thakurova 7, 166 29 Prague 6, Czech Republic.
E-mail: lukas.vrablik@fsv.cvut.cz

Abstract

The design of structures is more and more directed towards the entire lifetime design with multiple concurrent objectives. Apart from durability, the most important factor in the whole life design of reinforced and, in particular, prestressed concrete bridges, is the Service Limit State. From this point of view, prestressed concrete bridges are very sensitive to long-term increase of deflections. A survey of many bridges monitored in various countries showed that all of them have experienced similar deflection histories. The intention of the paper is to describe methods and mathematical models which should be used for reliable prediction of long-term behaviour of prestressed concrete bridges. The comparisons between results of numerical simulations and measurement data will be also mentioned.

INTRODUCTION

The long-term deflection behaviour of long-span prestressed concrete box girder bridges has often deceived engineers monitoring the deflections. This phenomenon has paramount importance for serviceability, durability and long-time reliability of such bridges. Due to excessive deflections, several bridges had to be either closed or repaired well before the end of their initially projected lifespan. The cost of reduced service life of structures is tremendous for society, the owners and users. In fact, it greatly exceeds, in strictly economic terms, the cost of catastrophic failure due to mispredicted safety margin.

DEFLECTION OF LONG SPAN CONCRETE BRIDGES

Six different causes of the deflection problems may be discerned:

- Design based on an obsolete, oversimplified and unrealistic model for predicting creep and shrinkage properties of concrete, or of cross sections of concrete girders.
- Obsolete and unrealistic method of time-dependent analysis of structural effects of creep and shrinkage, based, for instance, on assuming the creep and shrinkage properties to be homogeneous throughout the cross section and ignoring the effects of differences of shrinkage and drying creep between the top and bottom slabs of the box girder, which result from differences in drying half-times engendered by differences principally in slab thickness and secondarily in temperature history.

- Lack of updating of the long-time creep and shrinkage predictions by means of short-time (1 month) creep and shrinkage tests and water loss tests of the particular concrete to be used.
- Absence of statistical deflection predictions, ignoring the large random scatter in concrete creep and shrinkage effects, and especially the fact that the total observed deflection is the difference of two large numbers - the deflection due to external loads, and the deflection due to prestress (a difference of large numbers is greatly sensitive to a small change in one of these numbers and may thus result in a significant change of the difference, i.e., in a significant change of the total deflection value).
- Incorrect and harmful tendon layout - some tendon layouts benefiting the stress state can at the same time be harmful from the deflection viewpoint. Therefore, bridge design should be performed on two different levels: not only the common stress analysis, but also optimization of prestressing tendon layout to minimize deflections.
- An oversimplified structural model - particularly the use of the classical mechanics of beam bending, based on the Bernoulli-Navier hypothesis of cross sections remaining plane, while the true behavior is three-dimensional, with a strong shear lag, due to large shear deformations in the webs and plates.
- Underestimated prestressing losses due to steel relaxation and concrete creep and shrinkage.

CASE STUDIE - BRIDGE OVER LABE IN MELNIK (CZECH REPUBLIC)

Let us now present an example from practice the bridge structure with time increasing deflections. The example is the bridge over the river Labe (Elbe) in Mělník - three-span tapered continuous box girder (with spans 72.05 + 146.2 + 72.05 m), built in 1992 in Central Bohemia and erected using the cantilever technology. We are interested to identify possible reasons for time increasing midspan deflections and also to compare measurements results with mathematical simulations (studies of deflection causes).

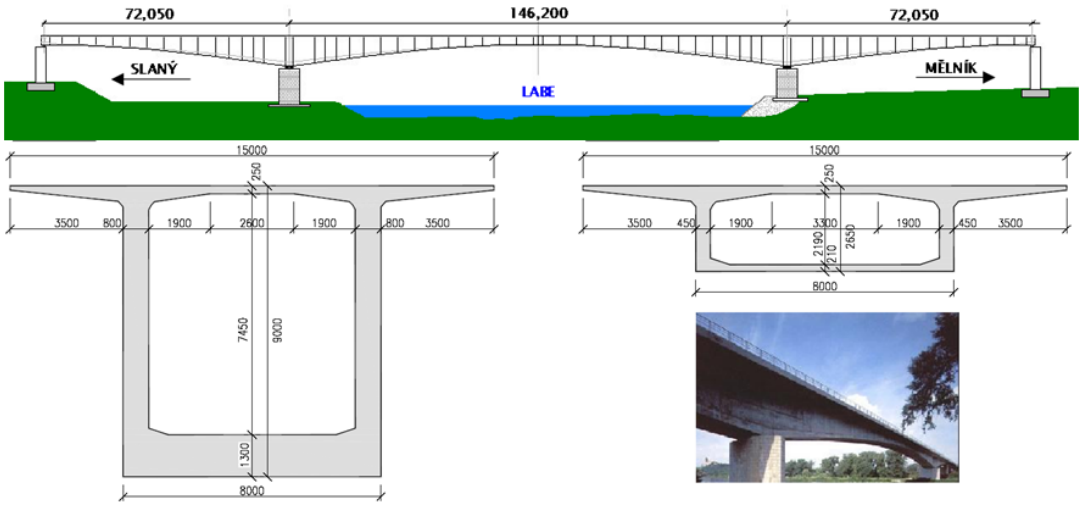

Figure 1. Bridge over Labe river in Melnik - basic structure arrangement, cross sections

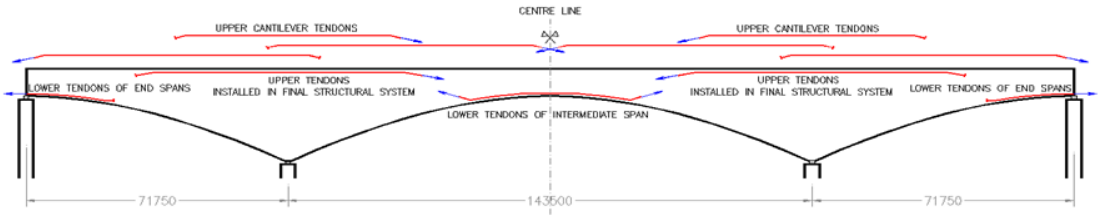

Figure 2. Arrangement of prestressing

NUMERICAL SIMULATION

For the mathematical simulation computational model including time dependant analysis was used.

The default option model ("Model 1") was considered material specifications according to the current standards EN 1992-1-1 and EN 1992-2. Concrete of superstructure was specified as C35 / 45 with modulus of elasticity of 34.1 GPa, tendon 1770-∅15,5 mm and modulus of elasticity 195 GPa, prestressing stress 1440 MPa. Relaxation behavior of class 1 according to EN 1992-1-1 was chosen - it means tendons with normal relaxation behaviour. Average humidity was set 70%. Sectional characteristics were considered without taking into account the effect of shear deformation of walls and shear lag.

Due to shear effect, we have to reduce cross section stiffness. Shear effect typical for box girder cross section is shear deformation of walls and shear lag. If we used mathematical models based on beam element it is necessary to reduce cross section parameters. For the box girder structures is possible to use method based on the reduction of cross-section shear areas (sectional area of the walls) that achieve nearly the same results as using the accurate calculations based on 3D models. Reduction of cross sections parameters is specified by the presence of the gradient and shears forces and thus respects the load distribution on the structure and boundary conditions.

In "Model 2" was simple reduction in shear areas used for all sections (to study this effect by 50%). The graph in Figure 3 shows that the modification does not modify the deflection prediction in "Model 2" according to "Model 1" and measurement.

According to design criteria, concrete B400 standard value modulus is 36 GPa. When considering concrete being pumped to consider reducing its size by 15% to 30.6 GPa. The "Model 4" reduce value of modulus of elasticity is applied in computational prediction.

Computational program allows analysing creep and shrinkage based on standard recommendations. The effect of creep and shrinkage can be changed, for example, by adjusting the humidity. In the "Model 3" was increased average humidity from 10% to 80% in the "Model 5" humidity was reduced to 60%. It is clear that at higher humidity means lower deflections growth. It would be interesting to specify different humidity for main span and end span of the bridge. The main span of the bridge is over water and therefore probably also in environment with different humidity.

Other parameter that significantly affects the behaviour of prestressed structures is the relaxation of the prestressing steel. Relaxation behaviour could be defined manually; it could be modified according to the contractor documentation. However, it was found that the use prestressing tendon shows a much worse relaxation properties compare to original calculation analysis. The "Model 7" was therefore considered relaxation value than twice the normal relaxation according to Eurocode. Line defined time deflection developments approximates the measured values.

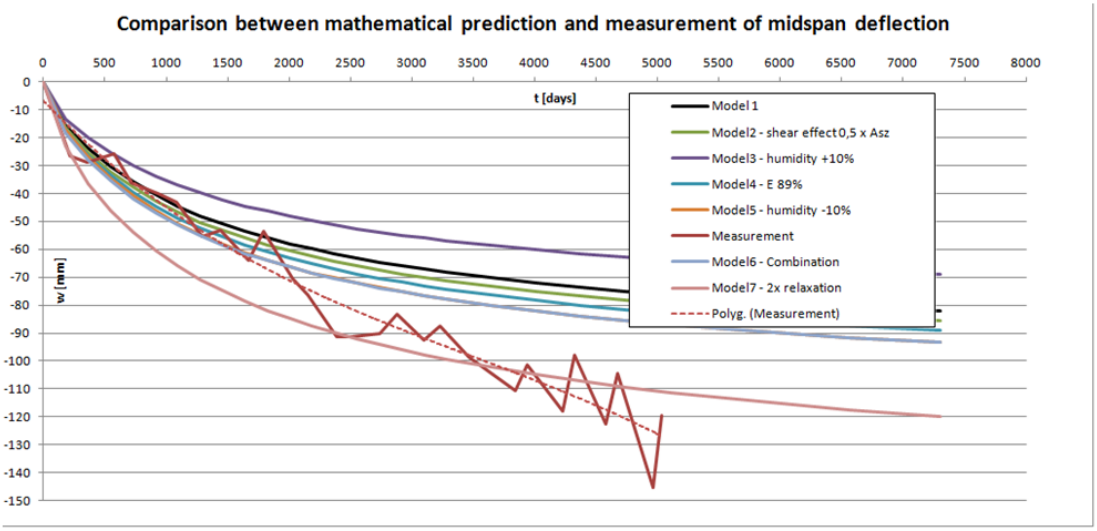

Figure 3. Midspan deflection - prediction and measurement

CONCLUSION

The prestressed box girder bridges typically exhibit only a portion of deflections during the first period and then continue to deflect. Extensive monitoring on many bridges confirms these observations.

The research on this problem is important, not only to avoid excessive deflections resulting in long-term serviceability impairments. It also should be noted that a wrong prediction of the development of deflections means that also prediction of the distribution of internal forces, particularly in bridges changing the structural systems, can be far from reality. Lessons from assessment of existing bridges can be learnt: bridge design should be performed on two different levels, including two equivalent parts – not only common stress analysis, but also optimization of prestressing tendon layout should be compulsorily performed to reach acceptable deflection variations.

Presented results can enable increase of economy of materials, energy and costs and their better utilisation and offer objective and effective tools increasing the level of serviceability, durability and efficiency of prestressed concrete box girder bridges. The achieved results will enable not only to avoid excessive deflections resulting in long-time serviceability problems, but also possibly other impairments.

REFERENCES

Kristek V. & Vrablik, L. 2005 To deflection control of prestressed concrete bridges (in Czech), *BETON No. 4, July 2005*

Vráblík, L., Loško, J., Křístek, V."To determination of prestressing in prestressed concrete elements and structures (in Czech)", BETON No. 4, July 2009

Experimental Investigation on Shrinkage in High Strength Fiber-Reinforced Concrete and Its Influence on the Shear Capacity of RC Beams Having Shear Reinforcement

Tomohiro Miki[1]; Kosuke Kita[2]; and Katsuya Kono[3]

[1]Department of Civil Engineering, Kobe University, 1-1 Rokkodai, Nada, Kobe 657-8501, Japan. E-mail: mikitomo@port.kobe-u.ac.jp
[2]Department of Civil Engineering, Kobe University, 1-1 Rokkodai, Nada, Kobe 657-8501, Japan.
[3]Central Research Laboratory, Taiheiyo Cement Corporation, Minato, Tokyo, Japan. E-mail: katsuya_kono@taiheiyo-cment.co.jp

Abstract

The present study includes the experimental investigation on the structural mechanism of reinforced concrete (RC) beams using high strength reactive powder concrete (RPC) and containing high-strength steel short fibers. The steel fiber reinforced high-strength RPC beams was design lightly reinforced with shear reinforcement but to still fail in shear in the loading tests. The parameter was set as shear reinforcement ratio (0, 0.3%, and 0.6%), volume fraction of fiber (0, 1%, and 2%) and volume change due to mainly shrinkage which was controlled by the water dissipation during the curing with drying or sealed sequences until the loading test for the beams. The strains of the concrete and reinforcing bars in the RC beams and the strain in the reference specimen were measured during the curing. In the loading test, an image analysis using a digital image correlation method was carried out in order to detect the micro- and macro-cracks in the RC beams. We have confirmed from the loading experiments that the increase in the shear capacity of the RC beams by containing the shear reinforcement and steel fibers even when the amount of shear reinforcement was set close to the minimum requirement. The interval of the diagonal cracks in the RC beams at the ultimate stage was changed according to the amount of the shear reinforcement and the volume fraction of fiber. In addition, the results of loading tests indicate that the initiation and propagation of a diagonal crack in the RC beams was changed and finally the shear capacity of the beams was influenced by the parameters, especially in the case of high shrinkage condition.

INTRODUCTION

Ultra high strength fiber reinforced concrete (UFC) shows high compressive strength and excellent deformation performance due to steel fiber reinforcement. The UFC shows large autogenous shrinkage because of the contents of large amount of binder. Therefore the design guideline for the construction of the UFC recommends no reinforcing bars are used in the structural members. There is a possibility however that shear failure which leads brittle failure in the member can be prevented by using

the shear reinforcing bars in the UFC member. In other words, if cracking due to restraining by steel rebar can be controlled an applicability of the UFC may be extend to more general practice. Few studies for the effect of shear reinforcing bars to investigate the effectiveness of UFC in improving the shear strength of beams are currently conducted. The purpose of this study is to investigate the effect the fiber mixing ratio, shear reinforcing bars ratio on the shear strength of the UFC beam. In this study, the loading test for the UFC beams was carried out where the amount of shrinkage was taken as a parameter. Here the amount of shrinkage was controlled by curing conditions.

TEST PROGRAM

Materials. Specimens used for experiments were prepared according to formulation shown in **Table 1**, using a commercially available pre-mix powder. In this study, no incorporation of steel fibers (hereinafter referred to as the specimen name F0), fiber volume fraction F_{vol} 1% (same F1) and 2% (same F2), was provided. After checking the flow of fresh mix satisfying the flow value of 260 ± 15 mm was used for casting specimens. For curing methods, in order to vary the amount of shrinkage, age up to 12 hours and after then were changed over. Here, curing conditions were set as a sealed curing and an air curing. In the sealed curing, the implantation surface of the specimen until removing the formwork, after removal from the mold the entire surface of the specimen was covered with a plastic sheet. In the name of the specimen shown in **Table 1**, SD corresponds to specimens in which curing is 12 hours and DS corresponds to specimens where curing is more than 12 hours. It should be noted that the relatively large shrinkage strain of the UFC specimens for SD case at the age of about a week were observed. The air curing was performed in a room with 20°C, after removal of the formwork at 48 hours and then specimens were cured at a constant temperature and humidity chamber set at RH 60% humidity.

Table 1. Mix proportion of UFC

ID	F_{vol} (%)	Unit weight (kg/m^3)			
		W	P*1	F*2	SP*3
F0	0	157	2212	0	23
F1	1	157	2212	78.5	23
F2	2	157	2212	157	23

*1 Premixed binder, *2 Steel short fiber, length 15mm, diameter 0.2mm, tensile strength 2700N/mm^2,
*3 Superplasticizer

Table 2. Experimental cases

Specimen	F_{vol} (%)	r_w (%)	Curing condition*1
F0SD-0	0	0	SD
F0DS-0	0	0	DS
F0SD-3	0	0.3	SD
F0SD-6	0	0.6	SD
F1SD-0	1	0	SD
F1DS-0	1	0	DS
F1SD-3	1	0.3	SD
F1DS-3	1	0.3	DS
F1SD-6	1	0.6	SD
F2SD-0	2	0	SD

*1 SD: Sealed curing until the age of 12 hours and then air curing is conducted, DS: Air curing until the age of 12 hours and then sealed curing is conducted

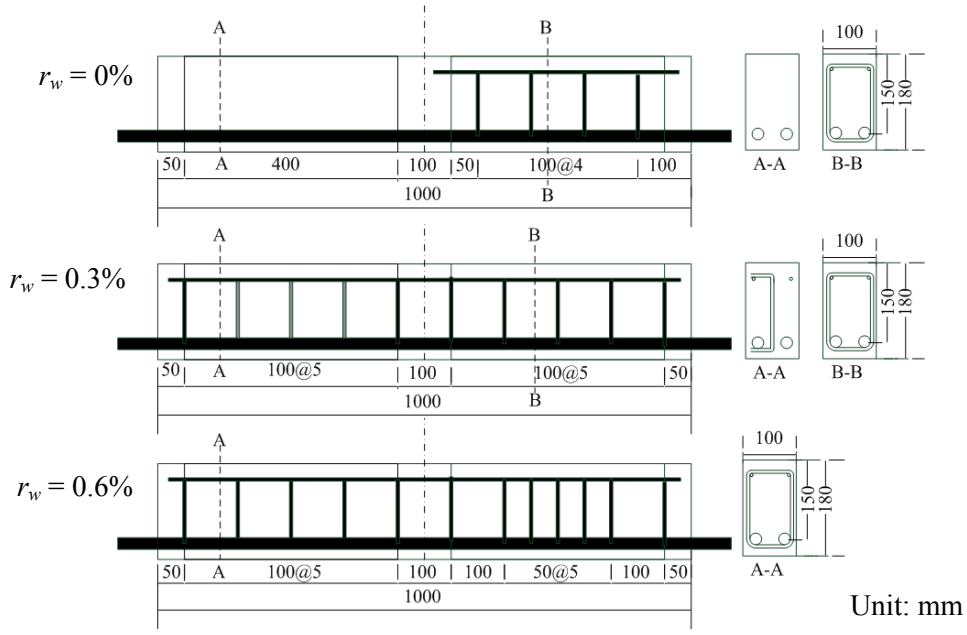

Figure 1. Specimen outlines

RC beams. The specimen dimensions are summarized in **Figure 1**. In this study, in order to confirm the effect of shrinkage and shear reinforcing effect of shear reinforcement rebar in RC beams using the UFC, volume fraction of the fiber mixed F_{vol}, shear reinforcement ratio r_w (= A_w /($b_w \times s$) are considered, where, A_w: cross-sectional area of shear reinforcement rebar, b_w: web width, s: shear reinforcement spacing). In the experiment the amount of shrinkage was set as a parameter. The experimental cases are shown in **Table 2**. F_{vol} was set as 0, 1% and 2%. The shear reinforcement ratio was set as relatively small values of 0, 0.3%, and 0.6%.

The dimensions of the specimens correspond to main rebar PC steel bar with D22, SBPD1080 (a yield strength 1026 N/mm^2), the shear reinforcement rebar is D6, SD295A (a yield strength N/mm^2). The ends of the longitudinal bars are extended by projecting the steel rod from the specimen in the RC beams, and to ensure a fixation by bolts. Also, in the specimens in order to facilitate observation of cracks in one side that cause shear fracture more closely spaced shear reinforcement bars were placed in one side.

UFC prisms. To confirm an effect of steel reinforcing bars on the shrinkage, five prismatic specimens of 100 × 100 × 400 mm for shrinkage strain measurement were prepared. Specimens here were F0SD, F0DS, F1SD, F1DS, and F2SD respectively.

Measurement items in the loading test. Two points of concentration loading was performed targeted for the simple support RC beam by a loading test. A hydraulic pressure system 2000 kN testing machine was used for loading. The loading point and the location of the fulcrum are at the 50 mm, 450 mm respectively from the center. Horizontal reaction force by a restriction at the supports was removed by inserting a Teflon sheet between the support and the test piece. The measurements are

Table 3. Results of material tests, shrinkage strain in the RC beam and results of loading tests

Specimen	f_c'	f_v	age	Shrinkage strain($\times 10^{-6}$)		Diagonal cracking		At maximum	
	N/mm²	N/mm²	days	7 days	At loading	P_c kN	V_c kN	P_{max} kN	V_{max} kN
F0SD-0	93.8	3.4	17	-495	-578	78.8	39.4	78.8	39.4
F0DS-0	110.2	4.0	12	-195	-239	62.8	31.4	62.8	31.4
F0SD-3	52.7	4.2	10	-812	-846	56.0	28.0	121.0	60.5
F0SD-6	100.3	3.2	13	-651	-709	70.0	35.0	226.6	113.3
F1SD-0	95.2	8.3	11	-364	-404	130.0	65.0	279.8	139.9
F1DS-0	91.7	14.1	20	-214	-387	120.0	60.0	258.0	129.0
F1SD-3	62.1	7.2	14	-284	-341	120.0	60.0	301.2	150.6
F1DS-3	120.6	14.3	11	-63	-85	90.0	45.0	302.6	151.3
F1SD-6	83.2	6.9	11	-331	-367	130.0	65.0	346.5	173.3
F2SD-0	78.7	12.7	9	-285	-305	150.0	75.0	329.0	164.5

a load, vertical displacement on the span center and the support, the steel strain at the center of reinforcing bars, the shrinkage strain inside both RC beams and prisms, the temperature and the humidity. The strain gauge was installed in the location of the height center of the respective test piece span center. The temperature in the room and the humidity were measured every 1 hour until the loading test.

EXPERIMENTAL RESULTS AND DISCUSSION

Results of Material tests. A cylindrical specimen of ϕ50 mm × 100 mm were used for the materials testing. Each cylinder specimens was cured in the same environment as corresponding RC beams. The average values of strength for the three specimens are shown in **Table 3**. The compressive strength at 7 days was small as compared to the previous studies (Kawaguchi et al. 2014) in which 124 N/mm^2 of the compressive strength and 7.4 N/mm^{2}of cracking strength, where a similar material of the UFC was used while F_{vol} = 2% were used and the sealed curing in a room of 20°C were performed. Looking at the curing conditions, with or without the incorporation of steel fibers, it is found that the case of DS indicates a larger compressive strength than that of the SD case. This tendency can be seen as for the tensile strength.

Effect of shrinkage on the beam before loading. The shrinkage strain aging of the prismatic specimens from the age of 12 hours to the 7 days (168 hours) is shown in **Figure 2**. Although figure shows for all specimens at the age of seven days, the shrinkage strain was measured in RC beams just before loading. Here the condensation start time of the UFC was around 12 hours from pouring water during mixing. Shrinkage strain at the age of 7 days was measured with a prism specimens where -1498×10^{-6} for F0SD, -583×10^{-6} for F0DS, -819×10^{-6} for F1SD, -415×10^{-6} for F1DS, -661×10^{-6} for F2SD, respectively. On the other hand, when comparing the shrinkage strain values at age of 7 days measured in the RC beams, the amount of

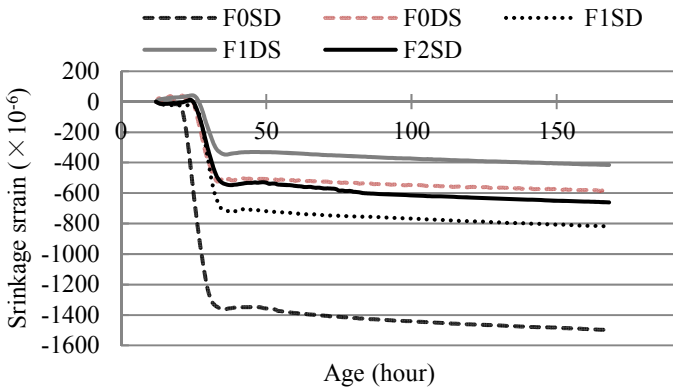

Figure 2. Shrinkage strain in the UFC prism specimens

shrinkage was larger than that of prism specimen. From this, it can be confirmed that the RC beams including the steel reinforcing bars has been restrained shrinkage.

Effect of fiber contents on the amount of shrinkage. Shear reinforcement ratio r_w = 0%, in the curing conditions of cases SD, strain contraction and a large steel fiber contamination rate is found to be small. This trend was the same in the other curing conditions.

Effect of curing conditions on the amount of shrinkage. In the case of a prismatic specimen, it has been confirmed that the shrinkage strain in SD strain shows larger than that in the curing conditions DS, and this tendency can be seen in the case of the RC beams. However, in the cases of r_w = 0%, when 1% steel fiber volume fraction was mixed, the difference in amount of shrinkage becomes smaller. This was similar in prismatic specimens.

Shear carrying capacity of RC beams. The load and deflection at a center of the span are indicated in **Figure 3**. The shear carrying capacity of the RC beams without the shear reinforcement increase as increase in the volume fraction of the fiber. As for

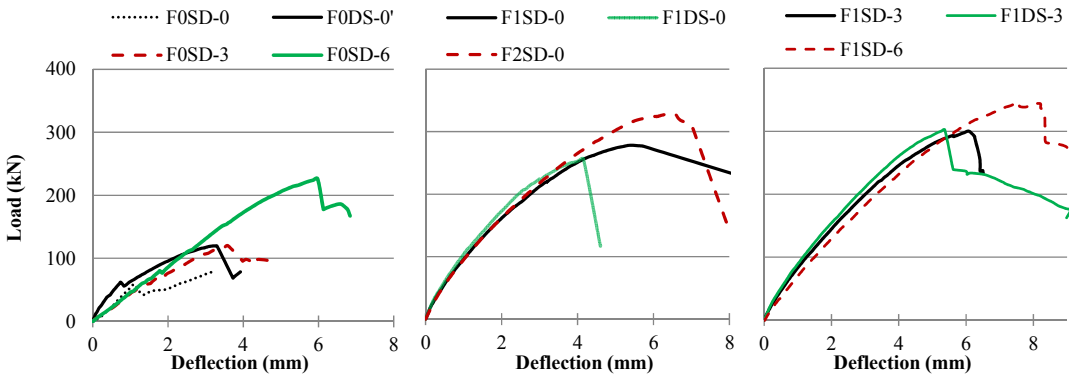

(1) no-fiber (2) F_{vol} = 1% and 2% (3) F_{vol} = 1% with shear reinforcement

Figure 3. Load-midspan deflection curves

the effect of shear reinforcement, the shear carrying capacity of the RC beams having shear reinforcement becomes larger than that without shear reinforcement which is similar to the ordinary reinforced concrete beams. As can be confirmed in **Table 3**, it is found that the shear carrying capacity of F1SD-6 indicated to be larger than that of F2SD-0. This means that we have confirmed the effect of combination between the fiber reinforcement and shear reinforcing bars.

The comparison between the capacities of F1SD-3 and F1DS-3 in **Figure 3** indicates that the capacity of F1DS-3 in which the amount of shrinkage is relatively small shows larger than that of F1DS-3 while smaller in the case of DS for the other cases. The factor which indicated such behavior is described in the following section.

Crack development. Image analysis was performed based on an image correlation method in order to confirm a crack development in the RC beams having the different amount of the shrinkage. An example of the distribution of the maximum principle strain obtained by the image analysis is indicated in **Figure 4**. The load when diagonal crack was occurred was defined based on the image analysis is indicated in **Table 3**. The domain of a target for the image analysis was set as around 180 mm × 400 mm in the left span in **Figure 1**. The resolution of the picture for the target domain was 0.11-0.16 mm/pix.

The brittle failure in shear was observed in the cases of F0SD-0 and F0DS-0. The shear carrying capacity for these cases corresponds to the load when a dominant diagonal crack was occurred. As for the F0SD-6, although the load when the diagonal crack was visibly observed was 85 kN the load of diagonal cracking based on the image analysis was 70 kN as shown in **Figure 4 (1)**. This reveals that the fine

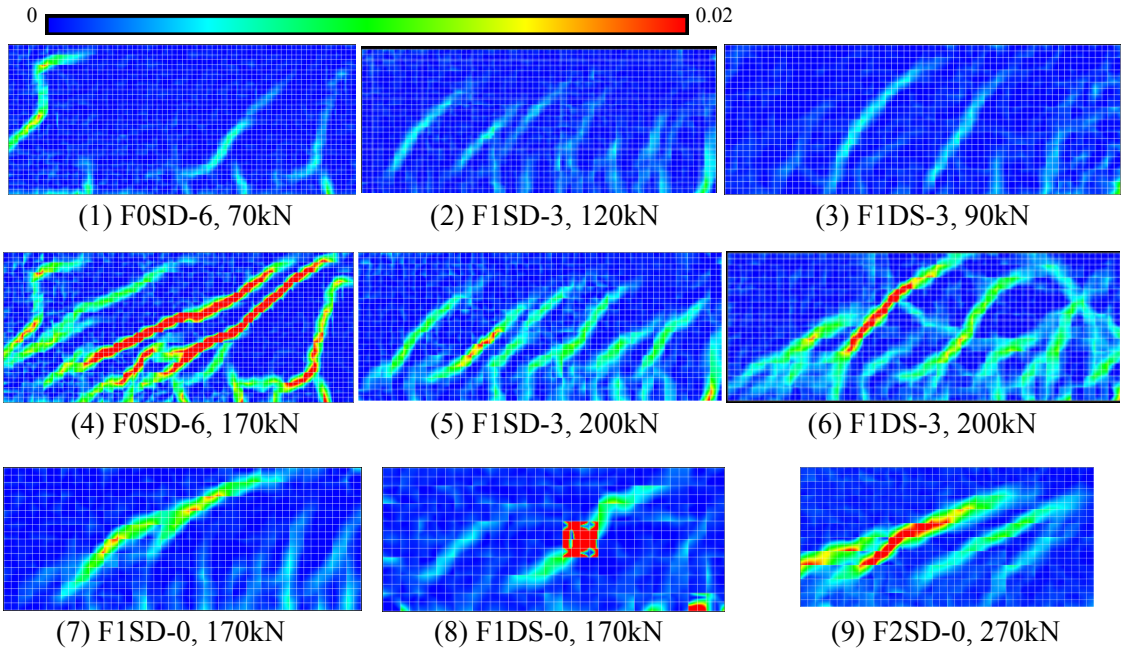

Figure 4. Distribution of maximum principle strain in tension obtained by the image analysis

diagonal cracks in the reinforced UFC beams containing steel fiber or having the shear reinforcing bar were observed by using the image analysis.

It is found that the number of diagonal crack that was occurred at the failure in shear increased in the case SD as compared with case DS in which the amount of the shrinkage was small. In other view point for the case DS the diagonal cracks was distributed in the RC beams as compared with the case of SD. Consequently, the tensile strain which was obtained by the image analysis has concentrated into one diagonal crack and this diagonal crack opened widely and consequently the shear carrying capacity decreased.

CONCLUSIONS

The loading test was performed for the RC beams in which the volume fraction of steel fiber, the stirrup ratio and the amount of the shrinkage that was controlled by changing the curing condition were varied in this research. The following conclusions can be draw.

(1) The shrinkage strain which was measured in RC beam became small as increase in the volume fraction of fiber and it resulted in the increase in the shear carrying capacity.
(2) It was confirmed that the shear capacity becomes larger in particular shear strengthening effect of F1SD-6 indicated stiffening effect slightly bigger than the shearing stiffening effect when mixing fiber 2%, of F2SD-0.
(3) The fine diagonal cracks in the reinforced UFC beams containing steel fiber or having the shear reinforcing bar were observed by using the image analysis.
(4) When the amount of shrinkage is small controlled by changing the curing condition, the number of diagonal cracks that is occurred at the failure in shear decreases and the tensile strain has concentrated into one diagonal crack, and consequently the shear carrying capacity decreases.

REFERENCES

JSCE (Japan Society of Civil Engineers). (2004) *Recommendations for Design and Construction of Ultra High Strength Fiber Reinforced Concrete Structures-Draft*

Kawaguchi, T., Kono, K. and Eduardo, D. (2014) *Study on Several Properties of PRC-type Ultra High Strength Fiber Reinforced Concrete cured in the room temperature,* Journal of JCI (Japan Concrete Institute), Vol.36, No.1, pp.274-279

Modelling of Long-Term Loading Tests on Reinforced Concrete Beams

N. Reybrouck; P. Criel; R. Caspeele; and L. Taerwe

Magnel Laboratory for Concrete Research, Department of Structural Engineering, Ghent University, Ghent, Belgium. E-mail: Robby.Caspeele@UGent.be

Abstract

During the period 1967-1985 the Magnel Laboratory for Concrete Research participated in an extensive Belgian research campaign with respect to the influence of creep and shrinkage on the long-term behaviour of reinforced and prestressed concrete beams. This research campaign, jointly conducted at several Belgian research institutes, comprised the investigation of concrete and reinforced concrete beams (phase 1), prestressed concrete beams (phase 2) and partially prestressed concrete beams (phase 3). The main aim of the research campaign was the determination of the long-term behaviour subjected to permanent loads, considering the influence of the magnitude of the loads, different reinforcement ratios and/or prestressing degrees and/or different cross-sectional shapes. These results were obtained by a joint collaboration of 4 Belgian research institutes, each focussing on a different reinforcement ratio and reinforcement arrangement. With respect to the reinforced concrete beams (phase 1), at each institute 12 beams were tested in a 4-point bending configuration, namely 2 static tests at 28 days and 10 long-term tests with a duration of 2 to 4 years, considering different loading levels. In this contribution some results of the reinforced concrete beams (phase 1) will be documented and analysed, comprising the results obtained on 48 reinforced beam specimens with a length of 3.4 m (span of 2.8 m) and cross-section of 0.28 m x 0.15 m. A cross-sectional calculation tool developed at our department – incorporating the current creep and shrinkage models in standards and guidelines – will be employed in order to investigate the accuracy of the available models with respect to their ability to predict the structural behaviour of the documented reinforced concrete beams.

INTRODUCTION

During the period 1967-1985, in Belgium a large set of concrete beams was tested with respect to the influence of creep and shrinkage on the long-term behaviour of reinforced and prestressed concrete beams. Several research institutes participated in this Belgian research campaign, including: Ghent University (UGent), the Vrije Universiteit Brussel (VUB), l'Université Libre de Bruxelles (ULB), KU Leuven, l'Université Catholique de Louvain (UCL) and l'Université de Liège (ULG). The main aim of this large research campaign was the determination of the long-term behaviour of concrete beams under permanent loads, considering the influence of the magnitude of the permanent loads (as a percentage of the ultimate load), different

reinforcement ratios and/or prestressing degrees and/or different cross-sectional shapes (Lambotte, Van Nieuwenburg, & Taerwe, 1988).

In this contribution some results of the reinforced concrete beams (phase 1) will be documented and analysed, comprising the results obtained on 48 reinforced beam specimens. These results were obtained by a joint collaboration of 4 Belgian research institutes. Each of these research institutes focussed on a different reinforcement ratio and reinforcement arrangement. The cross-sectional shape was the same for each research institute. One purchase was made for the reinforcement steel and the materials for the concrete to minimize the variation of the material characteristics. Afterwards the materials were distributed between the participating research institutes.

At each institute 12 beams were tested, namely 2 static tests at 28 days and 10 long-term tests. More specifically, the evolution of the deflections due to creep and shrinkage at mid-span, the deformations of the concrete cross-section and the evolution of the cracks were closely monitored during the period of the experiment. The ultimate load was experimentally obtained from the 2 static tests. The reinforcement ratio and arrangement for the different cross-section were chosen so that the beam specimens would fail due to yielding of the reinforcement steel (cross-sections I, II and IV) or by (theoretically) simultaneous yielding of the steel and crushing of the concrete (cross-section III).

Due to the high load levels considered in this first phase of the research campaign the stresses in the concrete will exceed 40% of the concrete strength. Such high stresses relative to the concrete strength have as a consequence that the time-dependent behaviour of concrete cannot be regarded as linear with the concrete stress. Hence adjustments of the creep coefficient will be required.

TEST PROCEDURE

The total length of each beam is 3.4m. Each beam is placed on two supports 2.8 m apart. One of these two supports allows free horizontal movement so that the creep and shrinkage deformations are not restricted by the supports. The beams are loaded by means of a 4-point bending test in which the point loads are placed at respectively one third and two thirds of the span. For the long-term measurements the beams are placed in pairs in a steel frame in such manner that they do not need to be supported by a reaction floor (except for the unloaded beams). To determine the ultimate loading, a traditional test setup was used. Additionally, for each beam type, a beam was placed on its supports without loading to measure the effects of shrinkage. The test setup for both the long-term test as for the static test is illustrated in Figure 1.

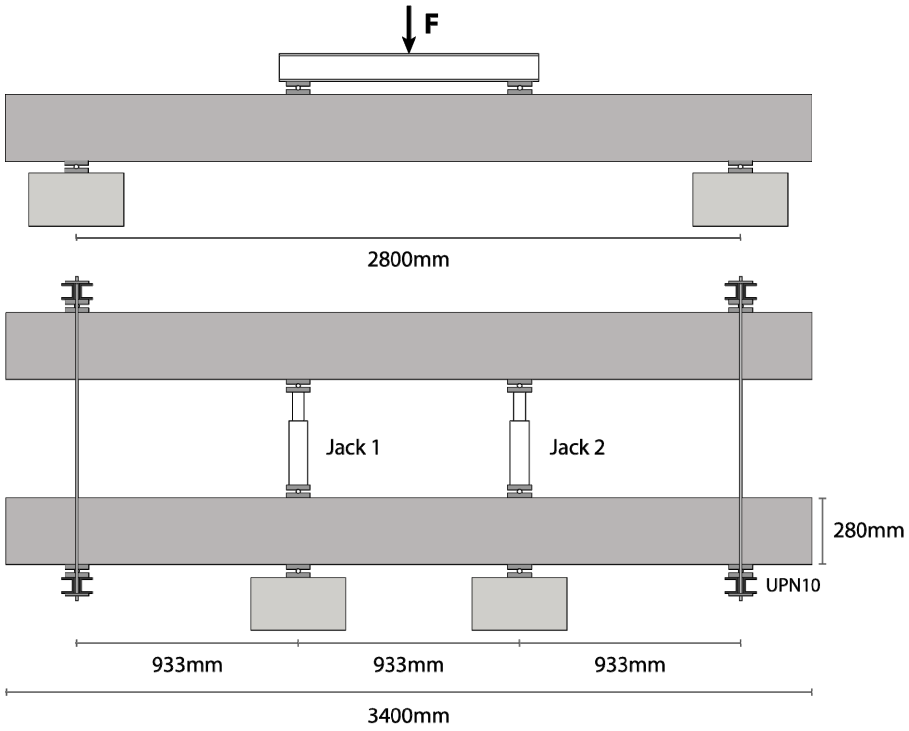

Figure 1 Test setup for the (a) static and (b) long-term tests

Four reinforcement schemes were considered in this experimental programme (part of a the larger research campaign). The first three types consist only of tensile reinforcement, while the last scheme also has some compressive reinforcement steel present. All reinforcement bars have a diameter of 14mm and have a characteristic yield strength of 400MPa. These reinforcement schemes are given in Figure 2.

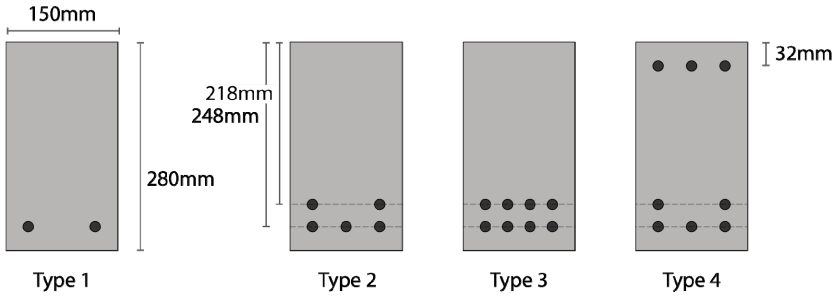

Figure 2 Dimensions and reinforcement schemes for the different beam types

Static tests

The beams are loaded in four equal steps up to the theoretical service load. Subsequently the load is completely removed. This procedure is then repeated to reach the service load again. Subsequently the load is increased by steps of 5% of the theoretical ultimate load until failure occurs.

The following ultimate moments $M_{u,0}$ were obtained from the static loading tests for each reinforcement arrangement respectively: (I) 29.9kNm, (II) 65.1kNm,

(III) 97.8kNm and (IV) 72.8kNm. Reinforcement arrangement III exhibits the highest ultimate load.

Long-term tests

The long-term tests start when the concrete age is equal to 28 days. As illustrated above, each testing frame contains two beams, which are mirrored. In a first loading phase, the beams were loaded in the same manner as described for the static tests. After complete unloading the load is increased to the theoretical service load and subsequently increased in steps of 5% of the theoretical ultimate load up to 40-60%, 70%, 80% and 90% of the observed ultimate load obtained from the static tests. Two additional beams for each reinforcement arrangement remained unloaded in order to measure the shrinkage behaviour of the beams.

Accumulation vessels are used to sustain the pressure in the hydraulic jacks, hence keeping the load constant. All long-term tests were executed under constant environmental conditions of 20°±1° C and 60% ± 5% relative humidity.

MEASUREMENTS

A summary of the instantaneous deflection measurements and the time-dependent deflections for 30 beams (each result given is the average of the measurements of the two beams in the loading frame) is given in Table 1.

Table 1 Summary of the time-dependent deflections for the different reinforcement schemes and load levels

Type 1

$M_s/M_{u,0}$	a_0 [mm]	a_t [mm]	*Duration [days]*
0.58	-	-	1450
0.72	6,02	10,29	1638
0.81	7,39	11,98	1372
0.91	8,94	15,02	1342

Type 2

$M_s/M_{u,0}$	a_0 [mm]	a_t [mm]	*Duration [days]*
0.52	7,27	13,49	1426
0.59	7,69	14,10	1569
0.70	9,36	17,56	1499
0.80	10,72	20,24	1513
0.90	13,10	24,23	1519

Type 3

$M_s/M_{u,0}$	a_0 [mm]	a_t [mm]	*Duration [days]*
0.43	7,08	14,51	1600
0.67	10,58	23,88	1600
0.77	13,84	28,74	1600

Type 4

$M_s/M_{u,0}$	a_0 [mm]	a_t [mm]	*Duration [days]*
0.52	5,98	10,52	800
0.70	8,80	13,90	800
0.80	11,16	16,96	1000
0.90	12,85	19,28	1000

a_0 indicates the instantaneous deflection due to the application of the load at 28 days, while a_t is the deflection after the duration of each test specifically.

Measurement results at 28 days for the concrete strength and modulus of elasticity for each beam type are available. The average concrete strength for each type is: (I) 35.5 MPa, (II) 31.5 MPa, (III) 36.3 MPa and (IV) 33.9 MPa. The secant

moduli of elasticity for the beam types are: (I) 35.5 GPa, (II) 31.0 GPa, (III) 27.8 GPa and (IV) 29.2 GPa.

CROSS-SECTIONAL CALCULATION PROCEDRUE

The deflection of the beam as function of time is calculated based on a cross-sectional approach using the Age Adjusted Effective Modulus Method (Bažant, 1972; Ghali & Favre, 2011; Gilbert & Ranzi, 2010). A general procedure was used as briefly described in the next paragraph in order to determine the deflection while taking into account the effects of creep and shrinkage and the effect of restraining by the reinforcement.

Concrete subjected to a sustained load deforms gradually as a result of creep and free shrinkage. However, these deformations of the concrete are partly restrained by the reinforcement. In order to asses this behaviour, the free shrinkage and creep are restrained by an artificial restraining stress. The resultant forces (ΔN and ΔM) are calculated by integrating the artificial restraint stress of the area of the cross-section. The opposite force $-\Delta N$ and $-\Delta M$ is introduced on the cross-section using transformed sectional properties to remove the restraint, resulting in additional stress, strain and curvature of the cross section.

The instantaneous curvature κ_0 and the strain ε_0 caused by a moment M can be determined by:

$$\begin{bmatrix}\varepsilon_0\\ \kappa_0\end{bmatrix} = \left(\frac{1}{EA \cdot EI - ES^2}\right)\begin{bmatrix}-ES\\ EA\end{bmatrix} M$$

in which EA, ES and EI are respectively the area, the first moment of area and the second moment of area of the transformed cross-section multiplied with a reference modulus of elasticity of concrete, which is equal to the modulus of elasticity measured at an age of 28 days. These cross-section properties are calculated relative to a random but fixed reference fibre. The centroid of the compressive zone is chosen for this reference fibre. The transformed cracked cross-section properties are given by:

$$EA = E_c(t_0) W x_{cr} + E_s \sum_i^n A_{s,i}$$

$$ES = E_s \sum_i^n \left[A_{s,i} \cdot \left(\frac{x_{cr}}{2} - y_{s,i}\right)\right]$$

$$EI = E_c(t_0)\frac{W \cdot {x_{cr}}^3}{12} + E_s \sum_i^n \left[A_{s,i} \cdot \left(\frac{x_{cr}}{2} - y_{s,i}\right)^2\right]$$

with $E_c(t_0)$ the modulus of elasticity at time of loading t_0, E_s the modulus of elasticity of steel, x_{cr} the height of the compressive zone, y_s the location of the reinforcement relative to the reference fibre, W the width of the beam, A_s and A_c the steel area of steel of steel and concrete, respectively. The total steel area is the sum of the area of each individual reinforcement bar $A_{s,i}$.

Based on the principle of superposition, the total curvature can be written as the sum of the instantaneous curvature and an additional curvature due to concrete creep and shrinkage (Khor et al., 2001).
The additional curvature caused by creep and shrinkage effects is given as:

$$\kappa_t = \frac{-ES \cdot N_{cr,sh} + EA \cdot M_{cr}}{EA \cdot EI - ES^2}$$

in which the restraining forces due to the shrinkage and creep effects are defined by:

$$N_{cr,sh} = \bar{E}_{\mathrm{c}}(t_e, t_0) A_{c0} [\varepsilon_O \phi_k(t_e, t_0) + \varepsilon_{sh}(t_e, t_0)]$$

$$M_{cr} = \bar{E}_{\mathrm{c}}(t_e, t_0) I_{co} \phi_k(t_e, t_0) \kappa_O$$

t_e is the duration of the long-term test expressed in days and $\bar{E}_{\mathrm{c}}(t_e, t_0)$ is the age adjusted effective modulus as defined by:

$$\bar{E}_{\mathrm{c}}(t_e, t_0) = \frac{E_c(t_0)}{1 + \chi \phi(t_e, t_0)}$$

χ is the ageing coefficient and $\phi(t_e, t_0)$ is the creep coefficient. A constant value of 0.8 is assumed for the ageing coefficient (Bažant, 1972, 1988). In the following calculations the creep coefficient given in Eurocode 2 is used (CEN, 2004).

For concrete stresses exceeding $0.45 f_{ck}$, the non-linear behaviour of creep is defined as (CEN, 2004):

$$\phi_k(t, t_0) = \phi(t, t_0) \exp\big(1.5(k_\sigma - 0.45)\big)$$

in which k_σ is the ratio between the concrete strength and the average concrete stress at the time of loading.

If the curvature is known, the deflection of the beam can easily be found by integration. The deflection in function of the curvature at mid-span and the position of the point loads is given by:

$$\delta_M = \left(\frac{3L^2 - 4a^2}{24EI}\right) \kappa$$

a is the distance between the point-loads and the supports, L is the length of the beam.

RESULTS

The cross-sectional approach described above is applied on the described beam tests.

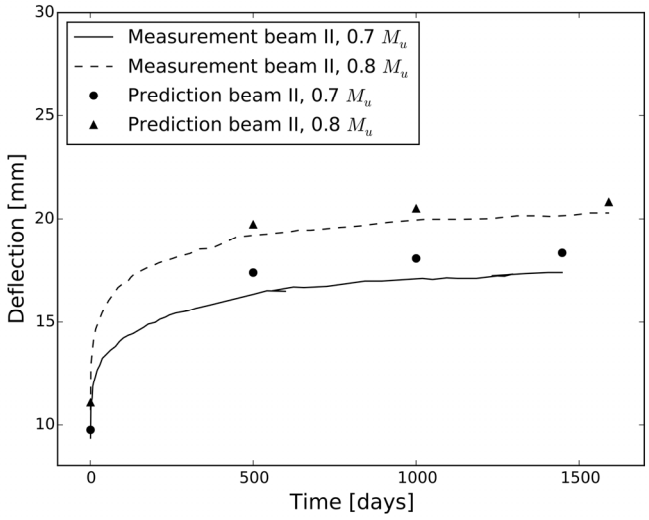

Figure 3 Measurements of the type II beams loaded with 0.7 M_u and 0.8 M_u and the predicted results.

Both the measurements and the predicted values for the beams of type II, respectively loaded with 70% and 80% of the ultimate moment are given in Figure 4.

An overview of all predicted values versus the measurements is given in Figure 4. The black-filled markers indicate the instantaneous deflections, while the white-filled markers indicate the deflection after the duration of each experiment individually.

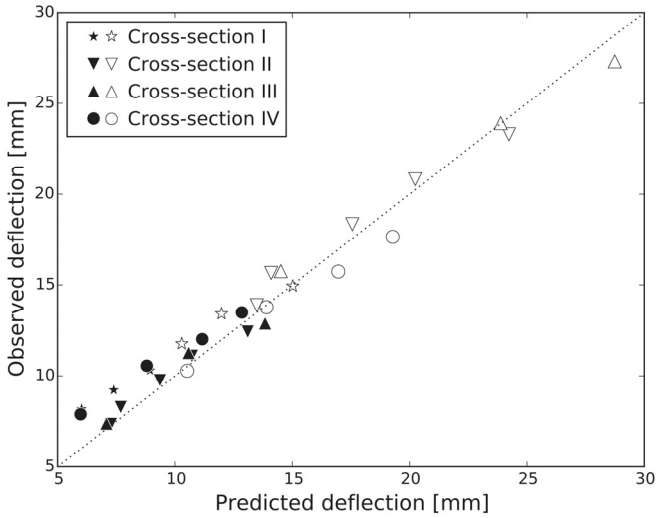

Figure 4 Measured and observed deflection after application of the loads (black-filled markers) and after the duration of the tests (white-filled markers)

The average ratio between the predicted and the observed instantaneous deflection is equal to 0.92 with a standard deviation of 0.10. The average ratio between the predicted and observed deflection after the duration of the tests is equal to 0.99 with a standard deviation of 0.07.

A slight underestimation of the predicted results is observed in both the instantaneous deflection and the deflection after creep. It is noted that this approach should be regarded as an approximation. First, a constant value for the ageing coefficient is assumed. Second, this approach makes no attempt to capture the shape of the creep curve under high stresses. It merely represents a simplification of the non-linear creep-stress relation since the general creep coefficient is just increased by a factor.

CONCLUSIONS

Phase 1 of an extensive Belgian research campaign with respect to the influence of creep and shrinkage on the long-term behaviour of reinforced, partial prestressed and prestressed concrete beams is presented. 48 beams were manufactured and tested divided over several Belgian research institutes, each focussing on a particular subset of the experimental programme. From the experiments and the analysis following conclusions can be drawn.

- The interpolation factor for tension stiffening ζ is larger than 0.97 for all the considered beams. As a consequence the effect of tension stiffening can be neglected due to the overall cracking behaviour. Hence, only a small portion of the beam is uncracked near the supports and their effect seems negligible with respect to the predicted deflections.

- The Age Adjusted Effective Modulus Method is a suitable method for fast calculations.
- High concrete stresses can be accounted for using an exponential correction factor for non-linear creep as defined in EN1992-1-1. This correction factor is reduced to only the part of the cross-section where concrete stresses exceed 0.45 f_{ck}.

REFERENCES

Bažant, Z. P. (1972). Prediction of Concrete Creep Effects Using Age-Adjusted Effective Modulus Method. *Journal Proceedings, 69*(4). doi: 10.14359/11265

Bažant, Z. P. (1988). *Mathematical Modeling of Creep and Shrinkage of Concrete*. New York: John Wiley & Sons.

CEN. (2004). EN 1992-1-1: Eurocode 2: Design of concrete structures - Part 1-1: General rules and rules for buildings. Brussels.

Ghali, A., & Favre, R. (2011). *Concrete Structures: Stresses and Deformations: Analysis and Design for Sustainability, Fourth Edition*: Taylor & Francis.

Gilbert, R. I., & Ranzi, G. (2010). *Time-Dependent Behaviour of Concrete Structures*: Taylor & Francis.

Lambotte, H., Van Nieuwenburg, D., & Taerwe, L. (1988). *Cracking and Crack Widths of Partially Prestressed Concrete Members*. Paper presented at the European Conference on Cracking of Concrete and Durability of Constructions, AFREM-CCE, Saint-Remy-Les-Cheveuse.

Modeling and Prediction of Time-Dependent Deformations of the I-35W St. Anthony Falls Bridge

Brock D. Hedegaard[1], Catherine E.W. French[2], and Carol K. Shield[3]

[1] Assistant Professor, University of Wisconsin – Madison, Department of Civil and Environmental Engineering, 1415 Engineering Drive, Madison, WI 53706-1691; PH (608) 890-3276; email: hedegaard@wisc.edu
[2] CSE Distinguished Professor, University of Minnesota, Department of Civil, Environmental, and Geo- Engineering, 500 Pillsbury Drive S.E., Minneapolis, MN 55455-0116; PH (612) 625-3877; email: cfrench@umn.edu
[3] Professor, University of Minnesota, Department of Civil, Environmental, and Geo- Engineering, 500 Pillsbury Drive S.E., Minneapolis, MN 55455-0116; PH (612) 625-5835; email: ckshield@umn.edu

ABSTRACT

To properly identify anomalous data in a structural monitoring system, the expected behavior of the structure under changing environmental conditions must be accurately determined. The St. Anthony Falls Bridge, a post-tensioned concrete box girder bridge, was examined as a case study for testing a data normalization scheme for temperature- and time-dependent deformations of an in situ structure. A methodology based on linear regression was developed to extract time-dependent behavior from the measured data. An Arrhenius-adjusted time was proposed to correct for the slowing and accelerating creep and shrinkage rates during the winter and summer, respectively. The extracted time-dependent deformations were compared to estimates using the finite element method. Bayesian regression was used to update the finite element model predictions using the measured data, substantially narrowing the expected bounds and facilitating anomaly detection.

INTRODUCTION

The ultimate goal of structural monitoring is to provide tools for owners and engineers that facilitate informed decision making for continued structural operation. At a basic level, the structural monitoring system must first accurately identify anomalous data. Anomalies, any data outside of expected bounds, might be caused by damage but could also be due to non-damage related factors, sensor failure, or otherwise spurious readings. As indicated by Sohn (2007), non-damage related factors such as temperature often impact monitoring data in ways that could mask changes caused by damage, and thus pose a significant challenge for accurate diagnostics regarding structural condition.

Data normalization is the process of isolating a behavior of interest from other expected behavioral changes, and can be used to reduce anomalies due to non-damage related factors (i.e., false positives) with respect to damage-related anomalies. The purpose of this paper is to present a data normalization technique for investigating the time-dependent behavior of post-tensioned concrete bridges. Predictions of concrete creep and shrinkage have high uncertainty. Therefore, finite element modeling and Bayesian regression are proposed to create upper and lower bounds facilitating the identification of damage-related anomalies in the extracted time-dependent behavior.

The I-35W St. Anthony Falls Bridge, a post-tensioned concrete box girder bridge in Minneapolis, Minnesota, USA, was used as a case study for examining the time-dependent behavior of an in situ structure. The St. Anthony Falls Bridge was constructed as two parallel four-span structures for northbound and southbound traffic. A profile view of the St. Anthony Falls Bridge indicating span labels and typical cross sections is shown in Figure 1. The behavior of the bridge was measured for the first five years of service life using a monitoring system that included vibrating wire strain gages, thermistors, and linear potentiometers, documented in French et al. (2014).

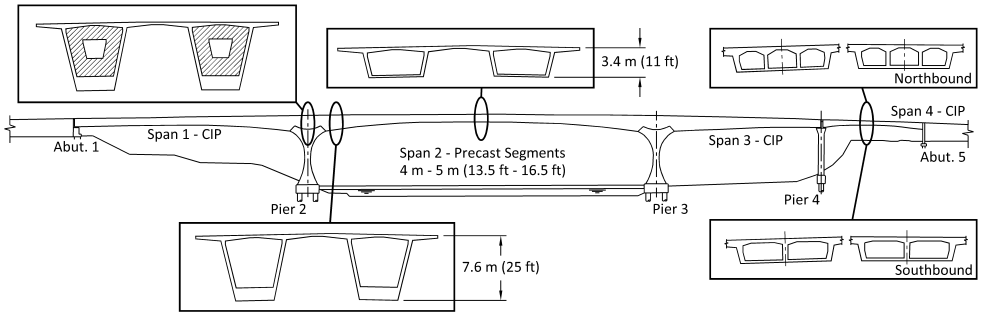

Figure 1. Elevation view of St. Anthony Falls Bridge with typical cross sections (Hedegaard et al. 2013a, © ASCE)

EXTRACTING TIME-DEPENDENT BEHAVIOR FROM MONITORING DATA

Long-term monitoring data collected from the vibrating wire strain gages and linear potentiometers installed in the St. Anthony Falls Bridge were largely affected by the bridge temperature and time-dependent behavior. Linear regression was used to extract the time-dependent and temperature dependent components. First, the collected data, y, was fit using the following regression function:

$$y = \alpha_1 \frac{\int T \, \mathrm{d}A}{T_{ref} A} + \alpha_2 \frac{\int T^2 \, \mathrm{d}A}{T_{ref}^2 A} + \alpha_3 \frac{\int zT \, \mathrm{d}A}{T_{ref} I_x / L_{ref}} + \alpha_4 \ln \left[1 + \left(\frac{t - t_0}{t_{ref}} \right)^{0.1} \right] + \alpha_5 + \delta$$

where the α-coefficients were the fitting coefficients for the linear regression, and δ was the residual, which aside from random noise in the data may also contain unex-

pected anomalies or systemic inaccuracies of the regression model. The first term was related to the average temperature of the bridge. Temperature readings were limited to the midspan of Span 2 of the southbound bridge, as sufficient sensors were not installed at other locations. Temperatures T were integrated over the cross section at midspan of Span 2 with area A, and non-dimensionalized using reference temperature $T_{ref} = 1°\text{C}$. The second term was necessary because the coefficient of thermal expansion, according to investigation of the measured data given in French et al. (2014), varied linearly with temperature. The third term was related to the thermal gradient, i.e., the variation of temperature through the depth z of the cross section with moment of inertia I_x measured at midspan of Span 2. Non-dimensionalization required division by the reference temperature T_{ref} and a reference length $L_{ref} = 1$ m. A quadratic form for the thermal gradient was tested but ultimately discarded, as it did not noticeably improve the linear regression fit. Effects of moving live loads on the measurements were expected to be minor, and thus were considered as part of the residual.

The fourth term in the linear regression is the log-power curve, intended to approximate all time-dependent behavior from initial loading at t_0 (assumed to be July 25, 2008, the time when the final closure pour was placed in the St. Anthony Falls Bridge) to time of interest t. The time was non-dimensionalized using reference time $t_{ref} = 1$ day. Because the objective of the linear regression procedure was to extract the time-dependent behavior, the chosen time-dependent curve was only necessary so that the regression coefficients for the temperature-dependent terms could be accurately computed. Five forms of the time-dependent curve were investigated for the fourth term, but the regression coefficients for temperature were not sensitive to the chosen time-dependent curve (French et al. 2014). Because all measured data only captured relative motion (either deflections or strains since beginning of measurement), addition of a constant α_5 coefficient was necessary for fitting the data, but the specific value did not have a physical basis.

Using the α-coefficients computed from linear regression on data y, the time-dependent behavior TD was extracted as follows:

$$TD + \delta = y - \alpha_1 \frac{\int T \, \mathrm{d}A}{T_{ref} A} - \alpha_2 \frac{\int T^2 \, \mathrm{d}A}{T_{ref}^2 A} - \alpha_3 \frac{\int zT \, \mathrm{d}A}{T_{ref} I_x / L_{ref}} - \alpha_5$$

The time-dependent behavior extracted from the linear potentiometer data, which measured the longitudinal deflections at the expansion joints located at Abutment 1 (denoted Span 1 expansion joint) and between Spans 3 and 4 at Pier 4 (denoted Span 3 expansion joint), using the linear regression procedure is shown in Figure 2. For monitoring purposes, examination of the time-dependent deflections at the expansion joints might reveal anomalies related to bearing lockup or unexpected acceleration in the time-dependent rates. The rates of the time-dependent deformations varied with the ambient temperature, such that creep and shrinkage slowed during the winter and accelerated in the summer.

To account for the temperature-dependent rates of the time-dependent behavior,

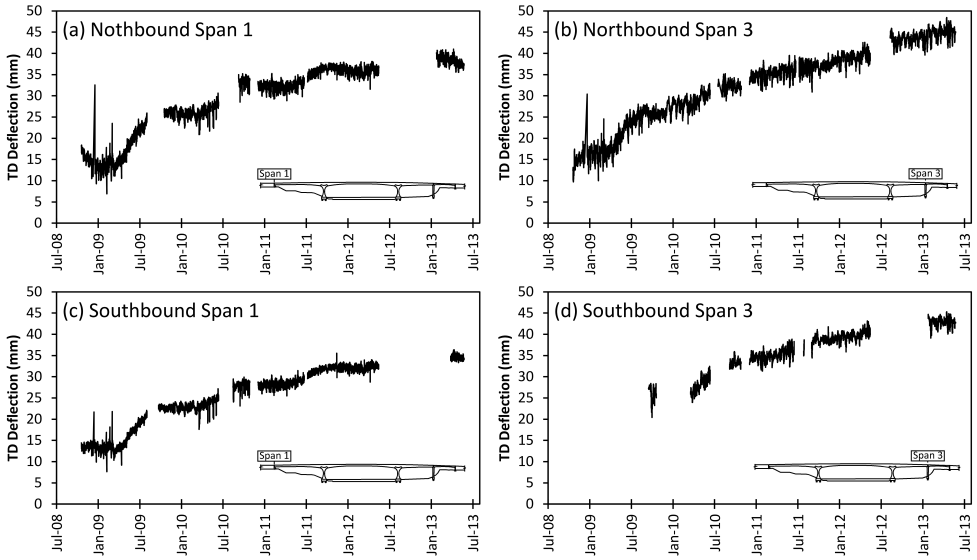

Figure 2. Time-dependent longitudinal deflection extracted from linear potentiometer data by linear regression

the Arrhenius equation was used to compute an "adjusted time" t_{adj} corresponding to an equivalent time at a constant reference temperature:

$$t_{adj} = \int_{t_0}^{t} e^{\left[\frac{Q}{R}\left(\frac{1}{T_0} - \frac{1}{T(t')}\right)\right]} \mathrm{d}t'$$

where the start time for the integration t_0 is July 25, 2008 when the midspan closure pour was placed, t is the unadjusted time in days of the time of interest, Q/R is the activation energy constant, T_0 is the reference temperature equal to 293 K (20°C), $T(t')$ is the temperature history specified in Kelvin, and time t' is specified in days. Because creep and shrinkage could not be separated in the measured data, the value of Q/R represented an aggregate activation energy for all time-dependent behavior. This value was chosen to be 7360 K using the expression for activation energy for basic creep from Bažant and Baweja (1995) with the nominal material properties for the superstructure concrete of the St. Anthony Falls Bridge.

The time-dependent behavior from the linear potentiometers, plotted with respect to real time in Figure 2, is plotted with respect to logarithm of the Arrhenius-adjusted time in Figure 3. Application of the Arrhenius-adjusted time smoothed the data, such that the resulting plots resembled a typical time-dependent curve for a structure in a controlled environment. Furthermore, the data approximately followed a line with respect to the logarithm of adjusted-time, indicating that no asymptotic bound was

witnessed during the first five years of data collection.

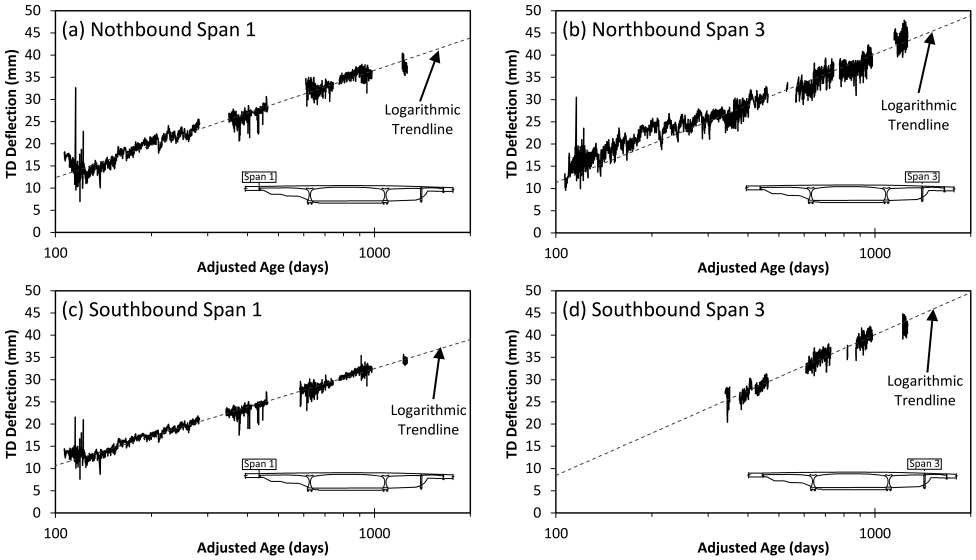

Figure 3. Time-dependent longitudinal deflection extracted from linear potentiometer data by linear regression and plotted with respect to Arrhenius-adjusted time (semilog plot)

TIME-DEPENDENT FINITE ELEMENT MODELING

Time-dependent behavior extracted from the measured data and normalized to the Arrhenius-adjusted time were compared to results from finite element models. Six time-dependent models were investigated: ACI-209 (1992), B3 (Bažant and Baweja 1995), 1978 and 1990 CEB/FIP Model Codes, GL2000 (Gardner and Lockman 2001), and the AASHTO LRFD (2010) provisions modified to include the strength gain equations from ACI-209 (1992).

The finite element model included geometry for the continuous Spans 1 through 3 and supporting Piers 2 and 3 of the southbound bridge. The full construction sequence for the bridge was modeled to properly capture the stresses at the end of construction. Time-dependent results were computed for a duration of 150 Arrhenius-adjusted age years past completion of construction, or approximately 200 real years given typical temperatures in Minnesota. Material properties and other details of the model construction are given in French et al. (2014). Time-dependent deformation of Span 4 caused deflection at the top of Pier 4, impacting the Span 3 expansion joint linear potentiometer readings. Because Span 4 was not modeled, the top deflection of Pier 4 was assumed to be equal to the hand-calculated time-dependent axial contraction of Span 4.

The procedure employed for creep modeling was the rate-type creep model de-

veloped for the solidification theory of concrete creep by Bažant and Prasannan (1989). Further discussion of this methodology, including an extension to incorporate the composite action between the concrete and embedded mild steel reinforcement, is provided in Hedegaard et al. (2014). Shrinkage strains were applied in an equivalent manner as thermal dilation, as both are volumetric strains dissociated with stress changes.

Each of the examined provisions for time-dependent behavior returned notably different estimates for the long-term behavior. As an example, Figure 4 compares the longitudinal deflections at the Span 1 and Span 3 expansion joints computed using the finite element model with the time-dependent behavior extracted from the linear potentiometers installed on the southbound bridge. The changes in deflection from the finite element models were set equal to the measured results at 10:00 AM CST on May 16, 2010 (adjusted age equal to 400 days) for purposes of the comparison, as linear potentiometer data from the Span 3 expansion joint were not available prior to this time.

The AASHTO and ACI-209 models appeared to provide accurate estimates of relative deflections from 100 adjusted-age days until 400 adjusted-age days, or approximately the first 1.5 real years after completion of the bridge. After this time, these models approached their asymptotic bounds and began to underestimate the measured changes in deflection. All other considered time-dependent provisions overestimated the measured change in longitudinal deflection. The B3 model provided the largest estimates of time-dependent behavior, which were nearly 2.5 times the measured changes in longitudinal deflection over the 5-year duration of data collection. Comparisons between the estimated and measured changes in longitudinal strain were similar, and are presented in French et al. (2014).

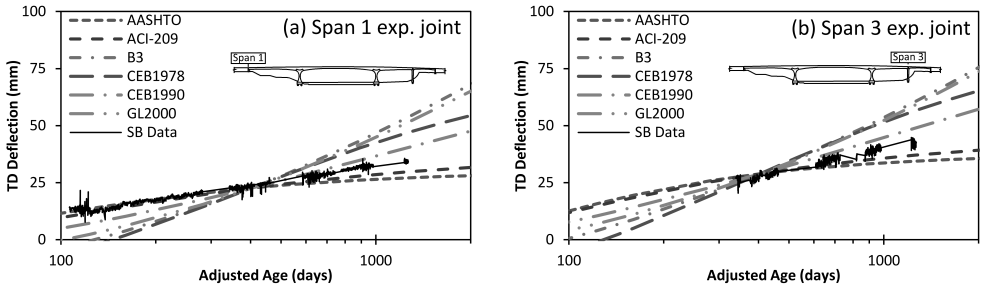

Figure 4. Comparison of FEM-estimated changes in longitudinal deflection with extracted time-dependent behavior from linear potentiometer data from southbound bridge

BAYESIAN REGRESSION FOR LONG-TERM PREDICTION

As evinced by comparison of the time-dependent finite element model predictions with the measured data from the St. Anthony Falls Bridge, the prediction of long-

term behavior of concrete structures is subject to significant uncertainty. Several studies have examined the variation of creep and shrinkage models with respect to measured data. Bažant and Li (2008), Gardner (2004), and Keitel and Dimmig-Osburg (2010) each concluded that, in comparison with the RILEM or updated NU-ITI creep and shrinkage database, the B3 and GL2000 models consistently had the lowest coefficients of variation, equal to approximately 25%. Other examined models typically had coefficients of variation at or above 33%. The B3 model was calibrated using the entire RILEM database and the GL2000 model was calibrated using a subset of the database, while the other models used different datasets for calibration. Thus, the reduced coefficient of variation for these two models in comparison to RILEM results was not unexpected.

A Bayesian statistical framework provides the means for considering the uncertainty of a model given a set of assumptions and prior knowledge, then updating the uncertainty given some new information, typically measured data. The initial uncertainty of the predictions are captured by the prior distribution which, after updating via the measured data, is transformed to the posterior distribution. The additional information used to build the posterior distribution narrows the expected bounds, ideally making anomaly detection feasible.

The prior distribution describing the time-dependent behavior of the St. Anthony Falls Bridge was assumed to be Gaussian with mean equal to the finite element model results and coefficient of variation equal to 25% for the GL2000 and B3 models and 33% for the remaining models. The measured data was assumed to have Gaussian noise with precision (i.e., inverse of variance) equal to a which could be estimated from the residual term δ from the linear regression procedure for extracting time-dependent behavior. The measured data was given by $\mathbf{D}$, a vector of length n, and was termed the training set. The future data not used in the Bayesian updating was $\hat{\mathbf{D}}$, a vector of length q, and was called the test set. The goal of the anomaly detection system was to compute the posterior distribution $p(\hat{\mathbf{D}}|\mathbf{D})$, meaning the probability of measuring a new set of data $\hat{\mathbf{D}}$ given existing data $\mathbf{D}$. If the latest test set of measured data was outside the credible bounds defined by $p(\hat{\mathbf{D}}|\mathbf{D})$ using training data $\mathbf{D}$, then the test set was classified as anomalous. Though this did not guarantee that the anomaly was related to damage, removal of the temperature dependency in the data was believed to make false positives less likely.

The training set $\mathbf{D}$ and test set $\hat{\mathbf{D}}$ were assumed to follow linear models

$$\mathbf{D} = \mathbf{A}\mathbf{w} + \epsilon \quad \text{and} \quad \hat{\mathbf{D}} = \hat{\mathbf{A}}\mathbf{w} + \epsilon$$

The matrices $\mathbf{A}$ and $\hat{\mathbf{A}}$ were the design matrices, where the first column was the finite element results computed at the times corresponding to the measured or expected readings and the second column had all entries equal to one to capture any constant offset between the data and the FEM predictions. Vector $\mathbf{w}$ with length 2 contained the fitting parameters to be computed using Bayesian regression. Vector ϵ was the Gaussian error term with zero mean and precision a.

The prior distribution of $\mathbf{w}$ was given by precision $\mathbf{B}$ and mean μ defined by

$$\mathbf{B} = \begin{bmatrix} 1/{C_{TD}}^2 & 0 \\ 0 & 1/v_2 \end{bmatrix} \quad \text{and} \quad \mu = \begin{bmatrix} 1 \\ \mu_2 \end{bmatrix}$$

The coefficient of variation C_{TD} of the time-dependent model was assumed to be either 25% for B3 and GL2000 or 33% for all other considered provisions. The variance v_2 of the constant parameter in $\mathbf{w}$ was specified to be very large. This ensured that the prior estimate for the mean μ_2 had no impact on the posterior distribution of $\mathbf{w}$, such that the constant offset term was effectively fit by linear regression.

Applying Bayesian regression, the posterior distribution of the fitting parameters $\mathbf{w}$ described by the variance $\mathbf{V_w}$ and mean $\mathbf{m_w}$ were equal to

$$\mathbf{V_w} = \left(a\mathbf{A}^T\mathbf{A} + \mathbf{B}\right)^{-1} \quad \text{and} \quad \mathbf{m_w} = \mathbf{V_w}\left(a\mathbf{A}^T\mathbf{D} + \mathbf{B}\mu\right)$$

Because all statistical processes were assumed to be Gaussian, then the posterior distribution $p(\hat{\mathbf{D}}|\mathbf{D})$ was also Gaussian, and was defined by variance $\mathbf{V}$ and mean $\mathbf{m}$:

$$\mathbf{V} = \hat{\mathbf{A}}\mathbf{V_w}\hat{\mathbf{A}}^T + \frac{1}{a}\mathbf{U} \quad \text{and} \quad \mathbf{m} = \hat{\mathbf{A}}\mathbf{m_w}$$

where $\mathbf{U}$ was a q x q matrix with all entries equal to one.

An example of the prior and posterior distributions for the time-dependent longitudinal displacement at the Span 1 expansion joint of the southbound bridge using the 1990 CEB/FIP Model Code provisions is given in Figure 5. The given prior distribution mean is the FEM results, with the 95%-credible bounds derived from the coefficient of variation equal to 33%. The posterior distribution $p(\hat{\mathbf{D}}|\mathbf{D})$, with mean and variance computed as given above and 95%-credible bounds plotted, was computed using a training set $\mathbf{D}$ containing the first three real-time years of collected data. Two real-time years of data after the termination of the training set $\mathbf{D}$ comprised the test set $\hat{\mathbf{D}}$. The test set data was found to lie within the 95%-credible bounds for $p(\hat{\mathbf{D}}|\mathbf{D})$. The posterior bounds, approximately ±2.5 mm regardless of adjusted-age, were greatly reduced from the prior distribution bounds, ±14 mm at the end of the training set and increasing at later times, providing useful limits for detecting anomalous data in the test set.

The posterior distribution was based on the assumption that the shape of the time-dependent curve was given in advance. Consequently, different time-dependent provisions provided different posterior distributions. The 1990 CEB/FIP Model Code, B3, and GL2000 models provided the most consistent estimates for various training and test sets taken from the time-dependent behavior extracted from the linear potentiometer data, implying that these models would minimize the incidence of false positives.

SUMMARY AND CONCLUSIONS

A method based on linear regression was proposed to separate the time-dependent and temperature-dependent behaviors in monitoring data taken from the St.

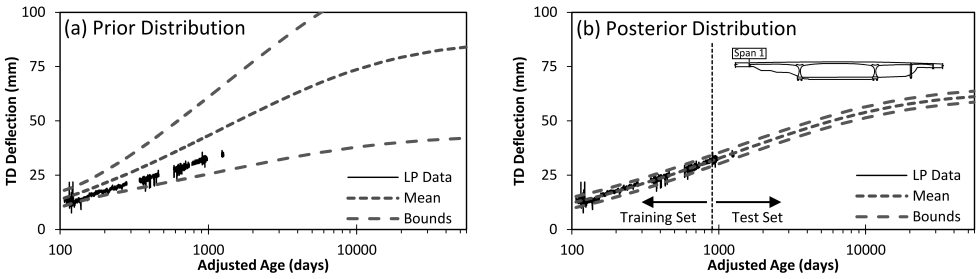

Figure 5. Prior and posterior distributions for time-dependent longitudinal deflections at Span 1 expansion joint of southbound bridge using 1990 CEB/FIP Model Code provisions

Anthony Falls Bridge. Terms accounting for uniform temperature changes through the section, including the effects of the linearly changing coefficient of thermal expansion, and thermal gradients were subtracted from the measured data to extract the creep and shrinkage deformations of the bridge. The rates of the time-dependent behavior were found to depend on the ambient temperature, accelerating in the summer and slowing in the winter. An Arrhenius-adjusted time was proposed. Plotting the extracted time-dependent behavior with respect to the adjusted age resulted in a line in semilog space.

The time-dependent behavior of the bridge was estimated using finite element models and creep and shrinkage provisions from ACI-209 (1992), B3 (Bažant and Baweja 1995), 1978 and 1990 CEB/FIP Model Codes, GL2000 (Gardner and Lockman 2001), and the AASHTO LRFD (2010). The ACI-209 and AASHTO models approached their asymptotic limits before any such limit was witnessed in the measured data. All other examined models overestimated the time-dependent behavior, by as much as 2.5 times in the case of the B3 model.

Long-term predictions of time-dependent behavior could not be reliably computed using just the finite element results because of the wide credible bounds, so Bayesian regression was used to combine the uncertainty inherent in the creep and shrinkage predictions with the measured data. Compared to the prior distribution taken from the finite element model results, the updated posterior distribution represented an order-of-magnitude reduction in credible bounds, allowing the posterior distribution to be useful for identifying anomalous data collected by the monitoring system.

ACKNOWLEDGMENTS

The authors would like to acknowledge the support of the Minnesota Department of Transportation. Numerical computations were performed using resources provided by the University of Minnesota Supercomputing Institute. The opinions expressed herein represent those of the authors and not necessarily those of the sponsors.

REFERENCES

American Association of State Highway and Transportation Officials (2010). *AASHTO LRFD Bridge Design Specifications*, Fifth Edition, Washington, DC.

ACI Committee 209 (1992). *ACI 209R-92 Prediction of Creep, Shrinkage, and Temperature Effects in Concrete Structures*, American Concrete Institute, Detroit, MI.

Bažant, Z.P., and Baweja, S. (1995). "Creep and Shrinkage Prediction Model for Analysis and Design of Concrete Structures Model B3," *Mat. and Struct.*, Vol. 28, pp. 357-365.

Bažant, Z.P., and Li, G.-H. (2008). "Unbiased statistical comparison of creep and shrinkage prediction models," *ACI Materials J.*, Vol. 105, No. 6, pp. 610-621.

Bažant, Z.P., and Prasannan, S. (1989). "Solidification Theory for Concrete Creep. I: Formulation," *J. Eng. Mech.*, Vol. 115, No. 8, pp. 1691-1703.

Comité Euro-International du Béton (CEB) and the Fédération International de la Précontrainte (FIP) (1978). *1978 CEB-FIP model code*.

Comité Euro-International du Béton (CEB) and the Fédération International de la Précontrainte (FIP) (1990). *1990 CEB-FIP model code*.

French, C.E.W., Shield, C.K., Stolarski, H.K., Hedegaard, B.D., and Jilk, B.J. (2012). "Instrumentation, Monitoring, and Modeling of the I-35W Bridge," *Report MN/RC 2012-24*, Minnesota Dept. of Transportation, St. Paul.

French, C.E.W., Shield, C.K., and Hedegaard, B.D. (2014). "Modeling and Monitoring the Long-Term Behavior of Post-Tensioned Concrete Bridges," *Report MN/RC 2014-39*, Minnesota Dept. of Transportation, St. Paul.

Gardner, N.J. (2004). "Comparison of prediction provisions for drying shrinkage and creep of normal-strength concretes," *Canadian J. Civil Eng.*, Vol. 31, No. 5, pp. 767-775.

Gardner, N.J., and Lockman, M.J. (2001). "Design Provisions for Drying Shrinkage and Creep of Normal-Strength Concrete," *ACI Materials J.*, Vol. 98, No. 2, pp. 159-167.

Hedegaard, B.D., Shield, C.K., and French, C.E.W. (2014). "Smeared-bar model for viscoelastic analysis of uncracked reinforced concrete structures," *J. Struct. Eng.*, published online.

Keitel, H., and Dimmig-Osburg, A. (2010). "Uncertainty and sensitivity analysis of creep models for uncorrelated and correlated input parameters," *Eng. Struct.*, Vol. 32, No. 11, pp. 3758-3767.

Sohn, H. (2007). "Effects of environmental and operational variability on structural health monitoring," *Philosophical Transactions of the Royal Society A*, Vol. 365, pp. 539-560.

Life-time prediction under sustained load and extreme events

Alexios E. Tamparopoulos[1] and Roman Wendner[2] and Konrad Bergmeister[3]

[1] Christian Doppler Laboratory, Institute of Structural Engineering, University of Natural Resources and Applied Life Sciences; Peter-Jordan-Strasse 82, A-1190, Vienna, Austria; email: alexios.tamparopoulos@boku.ac.at
[2] Christian Doppler Laboratory, Institute of Structural Engineering, University of Natural Resources and Applied Life Sciences; Peter-Jordan-Strasse 82, A-1190, Vienna, Austria; email: roman.wendner@boku.ac.at
[3] Christian Doppler Laboratory, Institute of Structural Engineering, University of Natural Resources and Applied Life Sciences; Peter-Jordan-Strasse 82, A-1190, Vienna, Austria; email: konrad.bergmeister@boku.ac.at

ABSTRACT

The efficient and permanently safe design of fastening systems requires a thorough understanding of all involved load-carrying mechanisms and their potential change in the course of time, due to deterioration and material ageing. The latter effects are mainly ruled by the involved materials: concrete, steel, and, depending on the system, the mortars. Considering the required extrapolation in time that is necessary for e.g. a 50 year design life-time and the required low failure probabilities, especially for the ultimate limit case, a suitable framework for prediction and assessment as well as accurate modelling concepts for all involved elements and processes with a quantification of the associated modelling and prediction uncertainties are paramount. Within this contribution we will present the framework for predicting the life-time of a (fastening) system subjected to a sustained load as well as extreme events following a stochastic process. For this formulation it is clear that any damage resulting from an early occurrence of the extreme event will influence the behaviour under sustained load. Conversely, the behaviour during an extreme event will be influenced by the sustained load effect up to this point in time. The stochastic ageing nature of concrete, which is the source of changes in mechanical properties, further complicates the analysis.

INTRODUCTION

Anchorages are very important for strengthening, retrofitting, and integrating precast elements. They allow the connection of new load bearing structural members with existing elements, as well as the installation of new, not structurally relevant, elements. Therefore, fastenings are important for any adaptation of existing infrastructure, and for the life-cycle design of new structures. The economic significance of fastenings is indicated by the fact that the potential damage caused by failed fastening

elements can be by several orders of magnitude higher than the value of the products themselves. It is also highlighted by the use of fastenings as key-elements of critical infrastructure, such as power plants, hospitals, and utility line systems. In the present paper, the requirements of an integrated life-cycle robustness design and application framework, focusing on fastening systems are discussed, the major challenges of this concept are briefly reviewed, and the main expected prospects that arise from the application to fastening systems are outlined (Wendner and Tamparopoulos 2014). Finally, computational aspects of life-cycle evaluation and robust design of fastening systems are presented.

The concept of life-cycle robustness borrows ideas from safety, sustainability and cost-efficiency of infrastructure, in an effort to include highly uncertain and unforeseen events. It can be defined as the ability of a component or a whole system to maintain its intended function and required safety level in spite of damage, ageing, extreme events, or changes in usage throughout its life-cycle. Each robustness perspective (installation, operation, demolition, recycling) faces different challenges, as it is subjected to different actions and variations. As the level of detail increases, more challenges and uncertainties are revealed, and weaknesses of commonly adopted assumptions are disclosed.

Any life-cycle robustness approach on fastenings begins with the requirements that should be addressed. Design requirements aim at formulating consistent design codes through experimentation and verification. Development of construction materials with unknown long-term behaviour require testing methods for investigating the effect of geometrical and material properties, including ageing. Installation requirements, particularly in critical infrastructure, need to take into account geometrical tolerances, variations, and possible human errors. Safety and reliability requirements should also include secondary consequences, progressive damage and disproportional failure effects over the intended lifespan. Apart from the need for optimised products, and accelerated production processes for existing ones, there are several cost-related requirements, such as experimentation, intervention, optimised maintenance planning, rehabilitation, renovation, repair, replacement, and sustainability.

In the study of robustness in time, challenges mostly arise due to temporal effects (processes, actions, influences, uncertainties) that develop differently in time. Further diversity emerges from variations in the formulation of components, failure modes, geometry, reinforcement type, loading type, base materials, and intended applications. Different uncertainties with often nonlinear effects are confined in the mechanical properties of materials, as well as in geometrical tolerances and installation variations, extreme events, environmental influences, and degradation processes. In the regime of low target failure probabilities, where performance is typically assessed, the influence of uncertainties can be decisive.

There are several prospects of developing an integrated approach of life-cycle robustness of fastenings. Recent advances in research on concrete behaviour (creep, shrinkage) can lead to much more refined prediction models. Stochastic models for

input variables in space and time in conjunction with uncertainty importance analyses can indicate the parameters that mostly influence the performance of fastenings in time. Thus, research efforts can be efficiently allocated to base material properties, time effects, loading scenarios, fracture development, testing procedures, and representation of spatial or other variations. Construction planning can take great advantage of realistic evaluations of system performance and cost efficiency since installation, maintenance, repair, and replacement can be studied within a unified framework. Thus, fast and automated construction techniques can be developed, and future market demands can be captured. Adequate assessment of existing fastening systems could significantly reduce cost and increase the reliability of complex systems.

TOWARDS A LIFE-CYCLE ROBUSTNESS QUANTIFICATION FRAMEWORK FOR FASTENING SYSTEMS

A fastening system is an arrangement of anchors and other structural members formed into a broader structure. Thus, the performance of the system is determined by the performance of its individual components, and by the arrangement layout. In order to realistically assess the performance of an individual anchor, and to formulate models for its life-cycle robustness, several time-dependent processes, which alter the initially assumed mechanical characteristics, need to be taken into account. Those effects do not necessarily develop monotonically or deterministically in time. Environmental influences may occur due to concrete carbonation, chloride effects, steel corrosion, UV radiation, and freeze-thaw cycles. Concrete creep may have significant influence on the long term performance (Wendner et al. 2015), while random actions (imposed by fatigue, fire, earthquakes, explosions, traffic accidents) can yield excessive loads and lead to complex loading scenarios. A life-cycle robustness quantification framework should include all these action, along with their uncertainties, properly quantified and integrated.

When the goal of the analysis is to predict the future and not to merely explain the past and current behaviour of the system, the distinction between actions and uncertainties is often hardly evident. At any point in time, the effect of applied loads depends on the system state, which depends on the load history. However, inherent variabilities and heterogeneities usually cannot be quantified in advance, but only through their long-term effects. In fact, the heterogeneity of concrete at lower scale is linked to a variety of macroscopic effects during failure. Since concrete fracture initiates at a very low scale, monitoring and model updating can be challenging. Further uncertainties arise from geometrical tolerances and installation inaccuracies. In general, the mechanical properties of materials and members after many years of operation are largely unknown.

Therefore, in order to simulate the behaviour of the system, one needs to simulate the expected loading scenario, and iteratively generate the development of material properties and damage state, with proper inclusion of respective uncertainties. For ev-

ery simulated case, the damage development can be traced until the system reaches the defined failure point, and the corresponding lifetime can be evaluated.

QUANTIFICATION OF PERFORMANCE

A quantification framework for life-cycle robustness primarily aims to devise a model that describes the performance of fastening systems with changing properties, subjected to uncertain load scenarios (sustained load and accidental events). The analysis begins with the basic requirement that resistance is not smaller than action, $R \geq S$. However, this condition is not straightforward to solve in order to analytically obtain failure probabilities. Firstly, both resistance $R(t)$ and action $S(t)$ are time-dependent. In addition, at any given time t, the system state (thus, the resistance R) depends on the load history. This interdependence between $R(t)$ and $S(t)$ can be particularly demanding, in terms of sampling and simulation (Bergmeister et al. 2009). Further complexity can be induced by nonlinearities of the system behaviour, and effective load event combination requirements. Moreover, the development of individual properties in time is not deterministic. The system state (reflected mainly as a result of ageing and degradation) is governed by largely unknown stochastic processes in concrete, steel or other materials.

To emphasise that the resistance R is not merely a deterministic function of time, but rather a random variable dependent on the variable mechanical properties and the load history, one can write:

$$R = R(t|L(t)) = R(t|\tilde{x}(t), S^{t}_{\tau=0})$$

where $L(t)$ is the system state at time t, the vector $\tilde{x}(t)$ represents the mechanical properties at time t, and $S^{t}_{\tau=0}$ expresses the complete load history. The vector of random mechanical properties $\tilde{x}$ exhibits statistical variability (described e.g. by proper distributions and possibly a correlation matrix), and spatial variability (described e.g. by a random field). Moreover, as mentioned earlier, it is time-dependent, since the properties change over time, while degradation occurs due to variable environmental influences.

In terms of remaining lifetime, the reliability of the system can be defined as the probability that it will perform its intended function under specified design limits (Pham 2006). If T is the random variable denoting the time-to-failure, with probability function $F(t)$, then the reliability of the system is $\bar{F}(t) = P(T > t), t \geq 0$. Properly calibrated damage models can introduce information on the lifetime T by describing the state of damage of the system at a given time t as a random variable D_t (Aven and Jensen 2013). Then:

$$T = \inf \{t > 0 : D_t \geq D_u\}$$

Therefore, the lifetime is defined as the first time the (total) damage reaches a given level D_u. Here, D_u can be a constant or, more general, a random variable independent of the damage process. In that case, the observed damage process does not carry the

entire information about the failure state. Damage can be viewed as a cumulative hazard affecting the system, and thus be described as a non-decreasing stochastic process (Singpurwalla 2006). This compound process can be viewed as a composition of three processes: (1) a process $X_t^{(1)}$, representing the occurrence of extreme loads, (2) a process $X_t^{(2)}$, representing the damage evolution between $X_t^{(1)}$ events, and (3) a process $X_t^{(3)}$, representing the damage owing to the occurrence of a $X_t^{(1)}$ event at time t.

For $X_t^{(1)}$, a counting process with constant appearance rate λ (e.g. a Poisson process) can be used to express the occurrence of events in time. In the case of the system of concern, one can assume more than one independent processes, in place of $X_t^{(1)}$, to account for the different event types (wind, extreme traffic load, snow, earthquake, etc.) In any case, the occurrence times are given by an increasing sequence $(t_j), j = 1, 2, ...$ of random variables, where each point corresponds to a random mark D_j describing the additional damage induced by the j-th load event.

For $X_t^{(2)}$, the damage evolution between events (under sustained load) can be modelled as e.g. a gamma process, where the independent nonnegative increments $X_t - X_s$ are assumed to be distributed as gamma distributions (Phadia 2013). Gamma processes have an infinite number of increments in a finite interval of time, and are therefore suitable for describing wear caused by continuous use (Singpurwalla 2010).

For $X_t^{(3)}$, the damage amounts D_j induced by the random events in the simplest case can be modelled as i.i.d. random variables. However, D_j depends also on the current state of the system, and possibly on the entire load history, thus:

$$D_j(t) = D_j(t|\tilde{x}(t), S_{\tau=0}^t)$$

The simulation of the aforementioned compound process can be described as follows: At the time $t = 0$ the system has a residual damage capacity D_u when it begins to operate under sustained load and undergoes wear e.g. due to ageing, described by a stochastic process of the $X_t^{(2)}$ type. The parameters of the process depend on the initial state of the system. At time $t = t_1$, given by a process of the $X_t^{(1)}$ type, an excessive load event occurs; at this point, the system state has suffered a damage D_{01} due to ageing, and it has a residual damage capacity $D_u - D_{01}$. The extreme event induces a random damage D_1 that depends on the system state. The system undergoes a deterioration D_{12} until the next point t_2 where the next load event occurs, inducing an additional damage, and so on. The process continues as long as the residual damage capacity is greater than the ultimate level D_u, until failure.

A Monte Carlo simulation of this system can yield the distribution of lifetimes. The availability of the lifetime distribution that includes all types of loading scenarios can allow for estimating safe values, in the sense of statistical quantiles, with a desired confidence level. The described framework yield a computational process that can be updated and refined, in the light of any additional information relevant to the applied loads, the system state, or the damage development.

CONCLUSION

The current state of fastening technology reflects only 25 years of systematic research. So far, practice has been limited to simplified methods for estimating lifetimes, to the assumption of unreinforced concrete, and to mere addition—as opposed to realistic combination—of safety factors. In recent years, steadily increasing budgetary constraints have led to a strengthened awareness regarding the importance of life-cycle performance and cost considerations. A multidisciplinary approach is needed in order to develop an efficient life-cycle robustness framework. In the present paper, some important aspects of a desired framework for life-cycle robustness of fastening systems were outlined.

Acknowledgements

The financial support by the Austrian Federal Ministry of Economy, Family and Youth and the National Foundation for Research, Technology and Development is gratefully acknowledged.

REFERENCES

Aven, T. and Jensen, U. (2013) *Stochastic Models in Reliability,* Springer, second edition.

Bergmeister, K., Novák, D., Pukl, R. and Červenka, V. (2009). "Structural assessment and reliability analysis for existing engineering structures, theoretical background." *Structure and Infrastructure Engineering*, 5(4), 267–275.

Pham, H. (2006). *Springer Handbook of Engineering Statistics,* Springer.

Phadia, E.G. (2013). "Prior Processes and Their Applications: Nonparametric Bayesian Estimation." Springer.

Singpurwalla, N.D. (2006). "Reliability and Risk: A Bayesian Perspective." Wiley.

Singpurwalla, N.D. (2010). "A new perspective on damage accumulation, marker processes, and Weibull's distribution." In Nikulin, M.S., Limnios, N., Balakrishnan, N., Kahle, W. and Huber-Carol, C. (editors), *Advances in Degradation Modeling: Applications to Reliability, Survival Analysis, and Finance*, pages 241–249. Springer.

Wendner, R., Hubler, M.H. and Bažant, Z. P. (2015). "Statistical justification of model B4 for multi-decade concrete creep using laboratory and bridge databases and comparisons to other models." *Materials and Structures*, 48, 797–814.

Wendner, R. and Tamparopoulos, A.E. (2014). "Life–cycle robustness: prospects and challenges." In *6th International Conference on Reliable Engineering Computing (REC)*.

Creep of Concrete in Bridge Standards

J. Hołowaty[1] and D. Jurkowski[2]

[1]West Pomeranian University of Technology Szczecin, Department of Civil Engineering and Architecture, al. Piastów 50, 70-311 Szczecin. E-mail: janusz.holowaty@zut.edu.pl
[2]PPDM, ul. Wilków Morskich 6/9, 71-063 Szczecin. E-mail: dajurny@wp.pl

Abstract

As structural concrete is a continuously-developing material, evolution in the estimation of its material properties can be seen with the development of concrete technology. The paper reviews methods for predicting concrete creep in bridge structures. The principal variables that influence creep are outlined. Code-related procedures have been drawn up in recently-used models for concrete creep with a higher range of concrete grades. This enables a more realistic estimation of delayed deformations and prestress losses in bridge structures.

INTRODUTION

Time-dependent deformations in concrete bridges have become of great interest in recent decades, as they cause gradual changes in stresses and strains which sometimes become too excessive. Delayed stresses and deformations in reinforced and prestressed concrete bridges may be several times higher than instantaneous deformations measured at the first loading. Numerous papers and reports have observed excessive deformations and deflections on cantilever prestressed concrete bridges in almost every country worldwide (Bažant et al. 2009; 2011). Excessive deformation usually results in problems with the serviceability of the structures; however, their safety is not compromised provided the stresses in the concrete are within the serviceability limit. When other concomitant issues arise, their combined effects on a structure may be deadly. A growing deflection in a prestressed concrete bridge is the first sign and warning that a prestressing force in the structure is decreasing due to excessive deformations or a failure in the prestressing system etc.

The precise determination of concrete structure deformations is still difficult as many influencing parameters need to be taken into account, including concrete shrinkage and creep, dimensions of a member and the amount and distribution of reinforcement (ACI 2009b; Bažant et al. 2009; Ghali et al. 2012, Gilbert et al. 2011). Concrete creep and shrinkage are time-dependent deformations which are interdependent. They are affected by humidity and stress history. Many models have been developed over the years to describe the time-dependent behavior of structural concretes (ACI 2009a; 2009b). Structural methods for time-dependent analysis were introduced to take into account of when delayed deformation influences the design of

a bridge. New models for the behavior of structural concrete are designed using code-type formulas and including wider ranges of concrete (CEN 2004; 2008; *fib* 2013). Prestressed concrete bridges are structures where the estimation of delayed deformation and loss of initial prestress is essential when designing the serviceability limit (Gilbert 1988; Ghali et al. 2012). Bridge designers use a range of simplifications to predict time effects in concrete structures, as detailed analysis is often too complex. The time-dependent analysis of concrete bridges is usually more complicated since construction in stages is applied. Where there are many construction and prestressing stages involved, the analysis is further complicated, especially for creep of concrete.

In bridge codes, there are different simplified procedures for the reasonable calculations of prestress losses or time-dependent deformations, as well as models for concrete properties. For basic structures, simple procedures allow final prestress losses at the end of the bridge's lifespan to be estimated. Where necessary, more detailed procedures may be used for predicting prestress losses over time. To express concrete creep in codes, a creep coefficient is generally used as a well-understood parameter in the delayed deformation of concrete under loading. For more complex problems, some codes suggest the use of compliance or relaxation functions.

Structural concretes are continuously developing materials; as a result, an evolution in the estimation of their material properties can be seen with the development of concrete technology. This is followed in structural codes for concrete structures which adopt different models for describing the creep properties of concretes (CEN 2004; 2008). In the paper, the prediction procedures or models for creep in cement concrete included in some bridge standards and *fib* Model Code 2010 are described and briefly compared. The description attempts to reflect both older approaches and also modern standards such as *fib* Model Code 2010 or the AASHTO specifications. Over the years, concrete models have evolved to code-type procedures for easy adoption at the design stage and to cover a higher range of concrete grades. In bridge codes, the adopted procedures have usually allowed the final values of creep deformation in addition to its development over time to be calculated. The progressively evolving concrete models and their implementation in bridge standards now give a practical and accurate method for the prediction of creep and shrinkage effects. Modern bridge standards also give recommendations on time-dependent analysis in the staged construction of concrete bridges.

CREEP DEFORMATION

Creep deformation in a concrete structure under load is a part of total deformation and now includes both initial plastic flow and time-dependent components. At constant temperature, the total concrete strain at time t, $\varepsilon_c(t)$ is expressed as the sum of the instantaneous strain $\varepsilon_{ci}(t)$, creep strain $\varepsilon_{cc}(t)$ and shrinkage strain $\varepsilon_{cs}(t)$. Creep strain $\varepsilon_{cc}(t,t_0)$ of concrete at time t due to the constant compressive stress of σ_c applied at concrete age t_0 is calculated as:

$$\varepsilon_{cc}(t,t_0) = \varphi(t,t_0)\left(\frac{\sigma_c}{E_c}\right)$$

where, $\varphi(t,t_0)$ is the creep coefficient and E_c is the tangent modulus of the concrete.

Creep coefficient is defined as the ratio of creep strain to instantaneous elastic strain, which are both proportional to stress. In the codes, creep coefficient is usually determined as a function of several parameters such as the stress range, the age of the concrete at the time of first loading, mean ambient humidity, the composition of the concrete mix or the concrete compressive strength, and the dimensions of members. Many codes introduce final (ultimate) values of creep coefficients for the assumed lifespan or its reliable estimation.

When a structure requires more detailed time-dependent analyses, it is recommended that the total stress-produced strain be calculated using a compliance (creep) function $J(t,t_0)$, which expresses the strain, measured at time t under the sustained unit stress applied at time t_0. For the reverse effects, under a sustained unit strain applied at time t_0, the relaxation function $R(t,t_0)$ is used.

EUROPEAN CODES

European standards implemented the progressively evolving CEB-FIP models from the 1970 recommendations up to CEB-FIP Model Code 1990, which was adapted in the Eurocodes (CEN 2004; CEN 2008). Two European bridge standards, British (BS 1990) and Polish (PKN 1992), which have been in use for many years, implemented the CEB-FIB 1970 recommendations with a simplification within the Polish bridge standard of ultimate creep coefficients. This results in the estimation of higher creep strains in the Polish codes (Figure 1).

At the time of implementation, the CEB-FIP 1970 recommendations gave simple procedures for the evaluation of the final values of time-dependent deformation in concrete and the possibility to take development over time into account. The formulas were calibrated for Portland cement concretes of ordinary quality in normal conditions. Concrete composition characteristics are used in describing delayed concrete deformation, so for the same concrete grades but with different compositions, the estimated values of delayed deformations may be different. The final creep is predicted for 30 years.

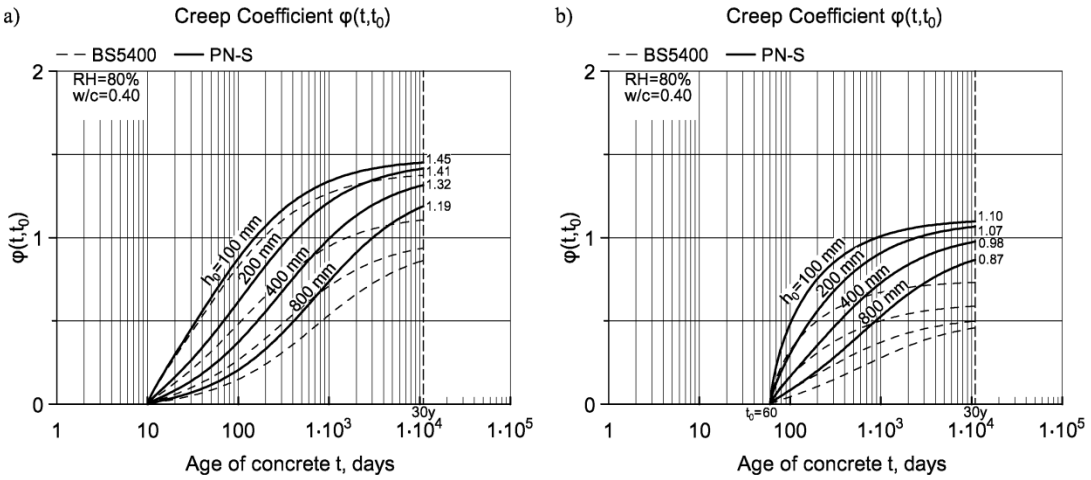

Figure 1. Creep coefficients $\varphi(t, t_0)$ versus notional size h_0 when f_{ck} = 40 MPa; humidity RH = 80%; the age of loading: (a) t_0 = 10 days, (b) t_0 = 60 days.

The comparison of concrete creep with time was performed to Polish and British codes for normal ambient humidity RH = 80%, with the age of concrete at loading t_0 = 10 days and 60 days and characteristic compressive strength of concrete at 28 days f_{ck} = 40 MPa. For this concrete, the following composition characteristics are used: cement class CEM I 42.5R, water-cement ratio w/c = 0.4 and cement content c = 370 kg/m^3. For the comparison of creep deformation with time versus the notional size h_0, the creep coefficients are employed (Figure 1). In the American standards, parameter h_0 is replaced by $V/S = h_0/2$. In the comparisons, creep values are higher for the Polish code despite the use of the same time formulas from the CEB-FIB 1970 recommendations, but the notional creep coefficients are established with higher values. Creep deformation curves, according to relative humidity RH = 40, 60 and 80%, are shown in Figure 2. The final creep coefficient values are still higher for the Polish code, but for lower ages at loading the differences are smaller.

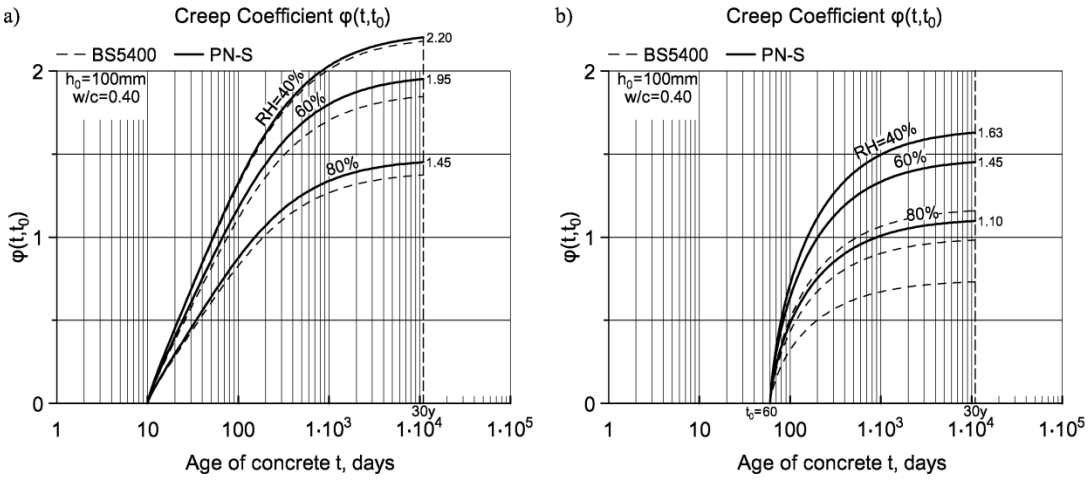

Figure 2. Creep coefficients $\varphi(t, t_0)$ versus humidity RH when f_{ck} = 40 MPa; notional size h_0 = 100 mm; the age of loading: (a) t_0 = 10 days, (b) t_0 = 60 days.

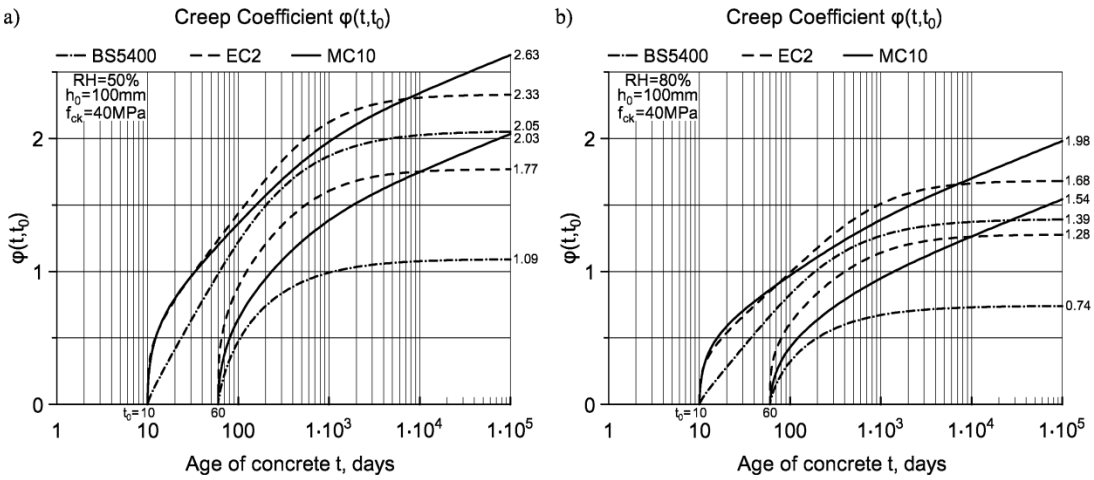

Figure 3. Creep coefficients $\varphi(t, t_0)$ when f_{ck} = 40 MPa; age of loading t_0 = 10 and 60 days; relative humidity: (a) RH = 50%, (b) RH = 80%.

A further description of creep is made for the concrete models included in Eurocode 2 (CEN 2004) and *fib* Model Code 2010 (*fib* 2013). These models use code-type formulas in which the concrete composition characteristics are omitted and replaced by the compressive strength of the concrete. The *fib* Model Code 2010 (MC10) introduced a new and improved formulation to describe creep effects as the sum of basic and drying creep deformations. In the description, the same parameters of the concrete are used (normal strength). The final creep coefficient values are established at different ages for each model, but for comparison with time they are omitted. The comparison of creep for the three models is shown in Figure 3. Lower values of creep for BS5400 are characteristic for the CEB-FIP model included in this code and in the Polish code (Hołowaty 2013). For the British code and Eurocode 2, the creep reaches asymptotic values, while as for *fib* MC 2010, creep does not reach ultimate values. The shapes of the creep curves indicate that an initial plastic deformation is not included in the creep deformations in BS5400. The effects of decreasing the creep values with increasing relative humidity is clearly visible.

AMERICAN CODES

American requirements for bridge structures are included in the AASHTO LFRD Bridge Design Specifications (AASHTO 1998, 2007; Barker et al. 2007). The evaluation of creep strain is based on parameters available at the design stage, so the compressive strength of concrete is used as a correction factor for creep. The early editions of the specifications gave simple procedures for calculating loss of prestress for normal strength concretes. As the procedure for creep grossly overestimated long-term deformation, it was corrected for higher concrete grades from the 2005 edition (AASHTO 2007; Al-Omaishi et al. 2009). The ultimate creep coefficient for standard conditions was changed from 2.3 to 1.9. The concrete strength correction factor accounts for the effect that creep decreases with higher concrete grades. The specifications also allow the use of the CEB-FIB or ACI 209 models in the calculation of creep.

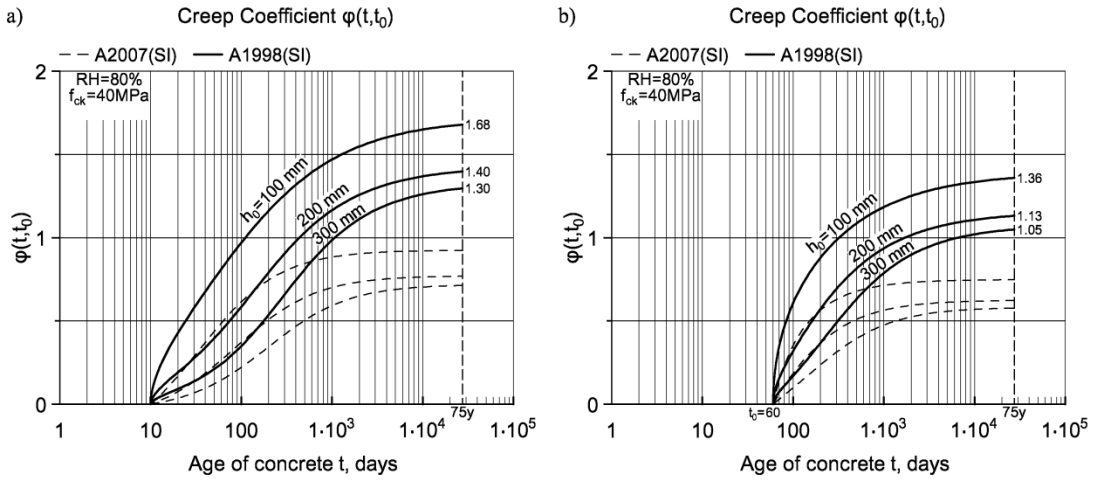

Figure 4. Creep coefficients $\varphi(t, t_0)$ versus notional size h_0 when f_{ck} = 40 MPa; humidity RH = 80%; the age of loading: (a) t_0 = 10 days, (b) t_0 = 60 days.

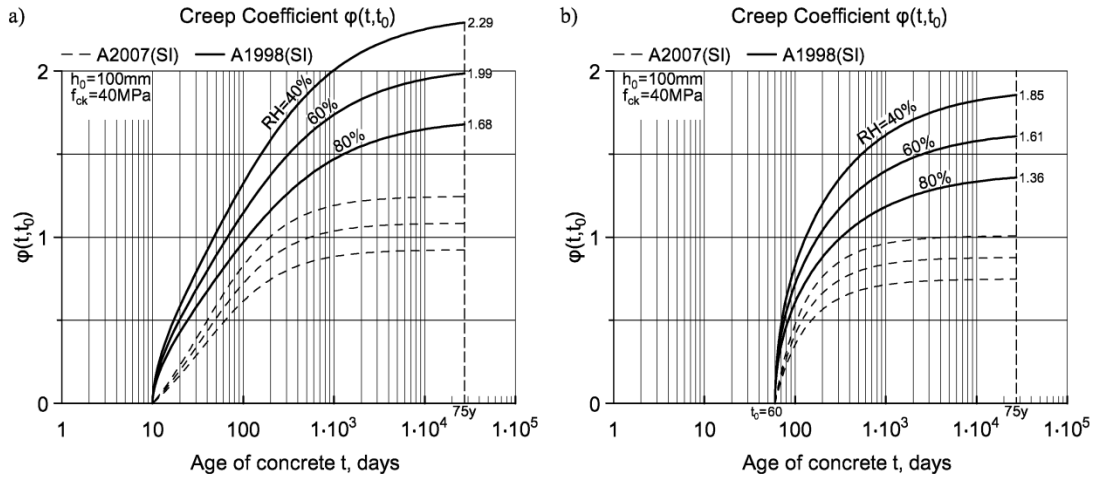

Figure 5. Creep coefficients $\varphi(t, t_0)$ versus humidity RH when f_{ck} = 40 MPa; the age of loading: (a) t_0 = 10 days, (b) t_0 = 60 days.

The calculation of concrete creep development over time for the two approaches in the AASHTO LFRD specifications are shown in Figures 4 and 5, using the same parameters as in the previous section. Final creep is predicted for 75 years. In describing member sizes, the AASHTO specifications, along with other American codes, use the volume-surface ratio V/S which is equal to $h_0/2$ in the European codes. The maximum value of V/S ratio used in the AASHTO formulas is 150 mm (h_0 = 300 mm). The final creep coefficient values are overestimated in the old approach in the AASHTO specifications. However, both approaches are still in error by ±50%. In both formulas, concrete creep though decreasing with time reaches its ultimate value.

The AASHTO specifications give some guidance on the estimation of prestress losses, deflection and camber. Recommendations when approximate, refined and time-step methods for estimation of time-dependent losses in prestressed concrete bridge are given.

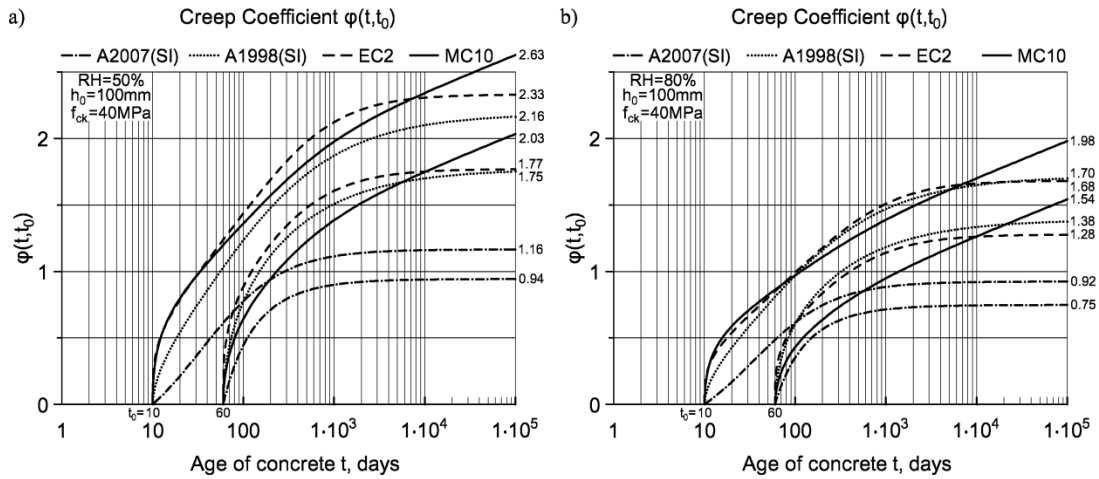

Figure 6. Creep coefficients $\varphi(t, t_0)$ when f_{ck} = 40 MPa; the age of loading t_0 = 10 and 60 days; relative humidity: (a) RH = 50%, (b) RH = 80%.

The time-step method supported by test results is required when a more precise calculation of prestressed losses is necessary. For segmental bridges with a span longer than 75 m, elastic structural analysis results should be evaluated with a consideration of the changing time-dependent properties of concrete. The requirements for different types of staged construction for concrete superstructures are also given in Eurocodes 2 (CEN 2008).

To simply compare creep development with time and final values in the AASHTO specifications, Eurocode 2 and fib Model Code 2010, the creep curves for the same parameters as in the previous section are shown in Figure 6. A wide range of creep values is obtained with final values for the AASHTO and EC 2 creep prediction models. Further comparison for the three models is made for the final values of creep coefficients depending on the parameters selected. The final values of creep coefficients versus the age of loading t_0 after casting are shown in Figure 7, and versus concrete strength in Figure 8.

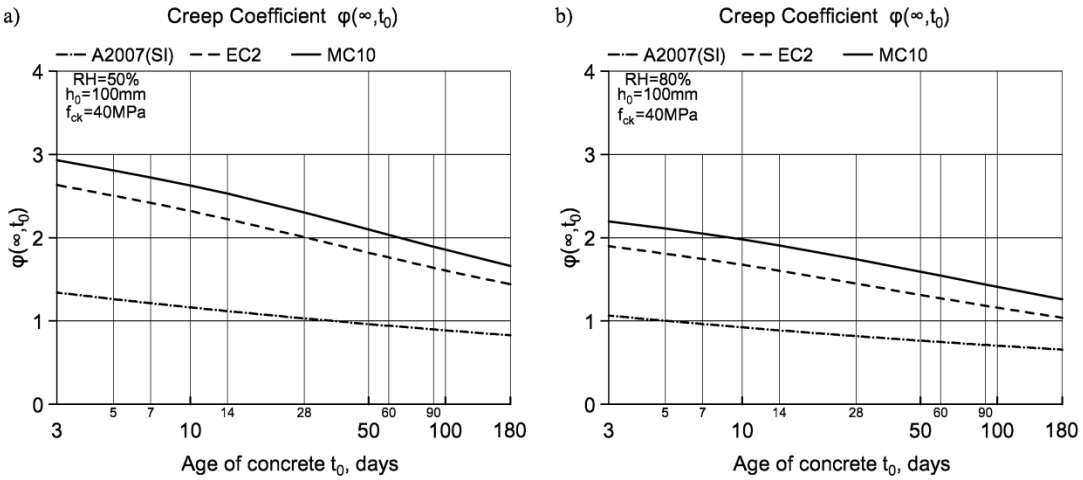

Figure 7. Final creep coefficients $\varphi(\infty, t_0)$ versus the age of loading t_0 when f_{ck} = 40 MPa; relative humidity: (a) RH = 50%, (b) RH = 80%.

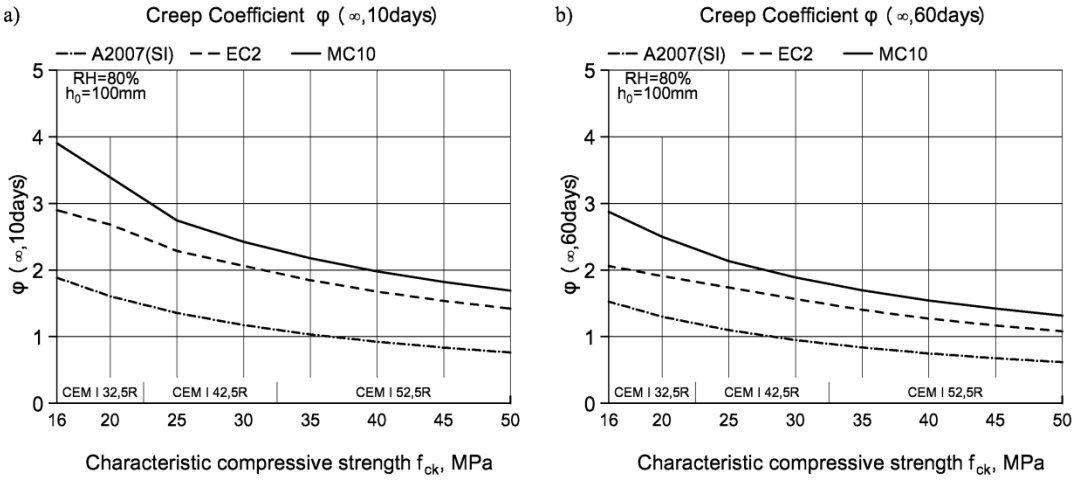

Figure 8. Final creep coefficients $\varphi(\infty, t_0)$ versus compressive strength f_{ck} when humidity RH = 80%; the age of loading: (a) t_0 = 10 days, (b) t_0 = 60 days.

A comparison is made for normal strength concretes i.e. with the strength class f_{ck} < 55 MPa according to Eurocode 2. Lower values of creep for loading at older concrete ages are pronounced in every model. Creep values also decline as concrete strength increases. Higher creep values are found in lower concrete strengths which are not used in prestressed concrete bridges. The tendency of declining creep with increasing concrete strength is also maintained for high-strength concretes (*fib* 2013; Hołowaty 2015). This means that the use of high-strength concretes in bridge construction may significantly reduce problems of creep in bridge structures, but also that by increasing deformation rigidity, there will be a reduction in relaxation capability.

SUMMARY

Creep of concrete is treated more precisely in bridge standards than other time-dependent deformations, because it may influence the behavior of some types of concrete bridges. Contemporary creep models adopted in bridge standards use code-type formulas for easy adoption at the design stage. Different, simplified procedures have been drawn up for reasonable calculations of prestress losses or time-dependent deformations, in addition to concrete material property models. For typical bridges with standard precast girders, the simplified procedures allow the final prestress losses at the end of the bridge's lifespan to be estimated. When necessary, more detailed methods may be used for predicting prestress losses with time.

Bridge standards include some guidance on time-dependent analyses, which are necessary for different concrete bridge construction techniques. However, modeling for creep and shrinkage in concrete bridges is still approximate, due to the great number of both variable and uncertain parameters. The methods for time-dependent analysis given in the literature and codes are sometimes too simplified, leading to misunderstandings in the real-time behavior of concrete structures. Many variable parameters induce significant differences in the deformations estimated, and lead to serviceability problems if they are treated too crudely.

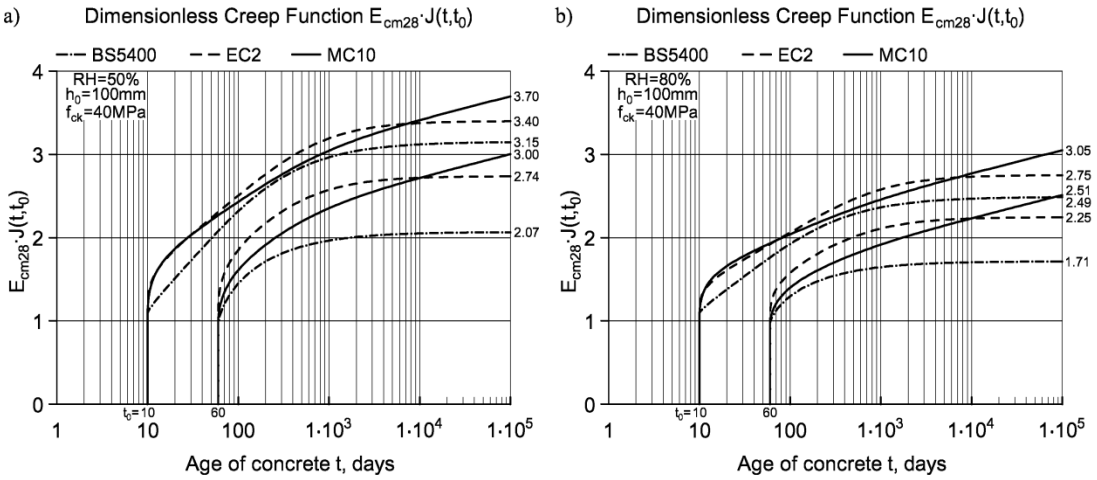

Figure 9. Dimensionless creep functions $J(t, t_0)$ when f_{ck} = 40 MPa; the age of loading t_0 = 10 and 60 days; relative humidity: (a) RH = 50%, (b) RH = 80%.

Possible variations in predicted values are still very wide, so in order to improve the estimations for an individual bridge, the bridge standards recommend that predictions be made on the basis of results measured over a short time frame. To express creep of concrete in the codes, a creep coefficient is usually used as a well-understood parameter of the delayed deformation of concrete under loading. For more complex problems, some codes suggest using compliance or relaxation functions. The compliance function is said to give a better description of the total deformation of a structure under load. The compliance functions for BS 5400, Eurocode 2 and *fib* Model Code 2010 are described for two ages at loading: at t_0 = 10 and 60 days after casting for C40 concrete grade, at relative humidity 50 and 80%, and for notional member size h_0 = 100 mm. Creep coefficient values predicted to be higher by MC10 than in Eurocode 2 are clearly visible. Figure 9 briefly shows the development in the assessment of creep deformations according to the CEB-FIP models. For high strength concretes, only *fib* Model Code 2010 is recommended.

CONCLUSION

Structural concrete is a continuously-developing material, with a higher range of concrete grades introduced over the last few decades, especially in bridge construction. The evolution in the estimation of the properties of concrete can be seen with the development of concrete technology. This is followed in the structural codes for bridge structures which adapt different models for describing the creep properties of concrete. In the paper, the procedures and models for creep in cement concrete included in some bridge standards are briefly described. The description reflects both older approaches along with modern standards such as *fib* Model Code 2010 or the AASHTO specifications. Over the years, concrete models have evolved into code-type procedures for easy adoption at the design stage. In bridge codes, the procedures adopted allow the estimation of final creep deformation values for simple calculations as well as its development with time for more complex problems. The evolving concrete models and their implementation in bridge standards give quite practical and generally accurate procedures for the prediction of time-dependent effects. In all the modern bridge standards, recommendations are given for time-dependent analysis in the staged construction of concrete bridges.

REFERENCES

ACI (American Concrete Institute) Committee 209. (2009a). *Guide for Modeling and Calculating Shrinkage and Creep in Hardened Concrete,* ACI 209.2R-08. ACI Manual of Concrete Practice*,* ACI, Farmington Hills.

ACI (American Concrete Institute) Committee 209. (2009b). *Prediction of Creep, Shrinkage and Temperature Effects in Concrete Structures*, ACI 209.2R-92 (Reapproved 2008). ACI Manual of Concrete Practice, ACI, Farmington Hills.

Al-Omaishi N., Tadros, M.K. and Seguirant, S.J. (2009). "Elasticity modulus, shrinkage, and creep of high-strength concrete as adopted by AASHTO." *PCI Journal,* 54(2), 44-63.

AASHTO (American Association of State Highway and Transportation Officials). (1998). *AASHTO LRFD Bridge Design Specification*. SI Units, second edition. AASHTO, Washington, DC.

AASHTO (American Association of State Highway and Transportation Officials). (2007). *AASHTO LRFD Bridge Design Specification*. SI Units, fourth edition. AASHTO, Washington, DC.

Barker, R.M., and Puckett, J.A. (2007). *Design of Highway Bridges: An LRFD Approach.* Second edition. John Wiley & Sons, Hoboken and New Jersey.

Bažant, Z. P., Li, G. H., and Yu, Q. (2009). "Prediction of Creep and Shrinkage and Their Effects in Concrete Structures: Critical Appraisal." *Proc. Eighth International Conference on Creep, Shrinkage and Durability Mechanics of Concrete and Concrete Structures,* CRC Press, Leiden, 1275-1289.

Bažant, Z. P., Hubler, M. H., and Yu, Q. (2011). "Excessive Creep Deflections: An Awakening. Data from numerous long-span prestressed segmental box girders show alarming trend" *Concrete International,* 33(8), 44-46.

BS (British Standard Institution. (1990). *BS 5400: Part 4. Code of practice for design of concrete bridges. British Standard.* Third edition. BS, London.

CEB-FIB (Euro-International Concrete Committee- International Federation for Prestressing). (1970). *CEB-FIP International Recommendations for the Design and Construction of Concrete Structures,* CEB, Paris and London.

CEN (European Committee for Standardization). (2004). *EN 1992-1-1, Eurocode 2: Design of Concrete Structures. Part 1-1: Generals Rules and Rules for Buildings.* European Standard. CEN, Brussels.

CEN (European Committee for Standardization). (2008). *EN 1992-2, Eurocode 2: Design of Concrete Structures. Part 2: Concrete Bridges—Design and Detailing Rules.* European Standard. CEN, Brussels.

fib (International Federation for Structural Concrete). (2013). *fib Model Code for Concrete Structures 2010*, Ernst & Sohn, Berlin.

Ghali, A., Favre, R., and Elbadry, M. (2012). *Concrete Structures: Stresses and Deformations: Analysis and Design for Serviceability.* Fourth edition, Spon Press, London and New York.

Gilbert, R. I. (1988). *Time Effects in Concrete Structures.* Elsevier, Amsterdam.

Gilbert, R. I., and Ranzi, G. (2011). *Time-Dependent Behaviour of Concrete Structures.* Spon Press, London and New York.

Hołowaty, J. (2013). "Comparison of Eurocode 2 and Polish Bridge Standards for Creep and Shrinkage of Concrete—Necessity for Implementation." *Proc. 9th Central European Conference on Concrete Engineering CCC 2013: Concrete Structures in Urban Areas,* DWE, Wrocław, 76-79.

Hołowaty, J. (2015). "Conventional Models For Creep in Normal- and High-Strength Concrete." *Architecture, Civil Engineering, Environment*, in press.

PKN (Polish Committee for Standardization). (1992). *PN-91/S-10042. Bridges. Concrete, Reinforced Concrete and Prestressed Concrete Structures.* Polish Standard. PKN, Warsaw (in Polish).

On Site Monitoring for Studying the Effects of Environmental Loads on the Corrosion Rate

F. Binder[1] and A. Strauss[2]

[1]Asset Management, ASFiNAG Service GmbH, Modecenterstraße 16/7, Vienna 1030. E-mail: fritz.binder@asfinag.at
[2]Department of Civil Engineering and Natural Hazards, Institute of Structural Engineering, University of Natural Resources and Life Sciences, Vienna, Peter-Jordan-Straße 82, Vienna 1190. E-mail: alfred.strauss@boku.ac.at

Abstract

Among the approximately 5,000 bridges which are maintained by the infrastructure operator ASFiNAG a total number of 1,500 objects are overpasses. Particularly their substructures are subject to increased chloride contamination due to the application of de-icing salt on the road. Sooner or later this results in damage to the infrastructure and, hence, in a reduced service life. This paper provides a critical discussion of data collected from an on-site monitoring and from weather stations. It reveals important interrelations and dependencies to the corrosion rate. The monitored time variant corrosion rate indicates a significant mathematical detectable periodicity. In particular, the paper focuses on the interactions between environmental loads and corrosion rates of the reinforcement of concrete columns. Finally a temperature compensated empirically model for prediction of the corrosion rate by using environmental and monitoring data will be proposed.

INTRODUCTION

A considerable part of the existing infrastructure has a high importance for a prosperous society. The Austrian motorway and expressway-financing company ASFiNAG ensures a significant contribution in this regard, by supplying an attractive traffic network. There are extensive tasks for ensuring the motorway network availability and safety. One of the core tasks is the inspection, the monitoring and the maintenance of the structures over the entire service life. In this context, it needs to be mentioned that the infrastructure net and the number of bridges is steadily growing, and hence the service effort. Reinforced concrete structures, which have a significant proportion in the infrastructure network, are often affected by degradation processes, such as corrosion, due unfavorable environmental conditions. For instance, chlorides which mainly originates from de-icing salts are mainly responsible for corrosion processes in traffic related reinforced concrete structures. The costs for operation and maintenance of the existing network and for repairing corrosion associated damages are high and will increase considerably in the future. For example, the structural maintenance costs of the ASFiNAG road network were 341

million € in 2013, which showed an increase of 11.9 % with respect to 2012 (Asfinag 2013).
A corrosion process is complex and is influenced by various environmental conditions or exposition. In particular, the exposition can be characterized by numerous parameters which are more or less correlated with each other and which are highly dependent on hand on the material and structural properties and on the other hand on the local climatic conditions. Nonetheless, the essential parameters for corrosion are the temperature, humidity and the presence of chlorides and oxygen. Hence this contribution presents findings with respect to environmental loads and associated corrosion rates based on monitored weather data and monitored corrosion activities in columns next to highway motorways.

ENVIRONMENTAL DATA

There is a net of meteorological weather stations around the world (Gattringer 2013) that allows the recording of global and regional climate conditions (e.g. air temperature, wind speed and direction, air pressure, air humidity, Precipitation (rain and snow) and cloud cover) and the characterization of environmental conditions in the vicinity of structures. Nevertheless, for the road environmental climatic parameters, it is essential to have also information e.g. about the composition and frequency of the traffic (traffic measurements) and about associated quantities such as the amount of used de-icing salt and its spreading on the structure. For the investigations which are undertaken in this paper, data from a weather station in the vicinity of the structure was used (Unfried 2014). Thereby, the data of the precipitation, the air humidity and temperature, as shown in Fig.1 are of particular interest, because they help to interpret the changes of the concrete resistivity or corrosion density currents (DuraCrete 1999). Fig. 1 portrays in particular the temperature, relative humidity and precipitation as well as the used de-icing salt for an exemplary annual cycle.

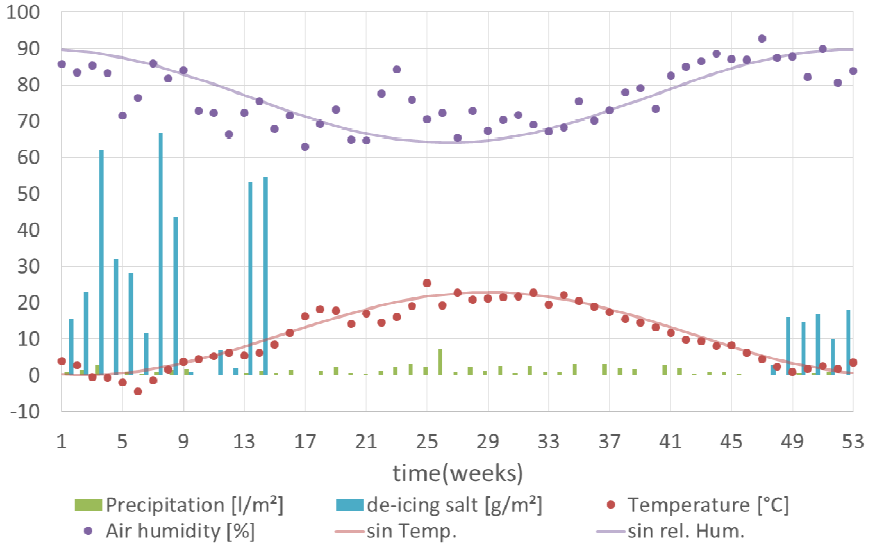

Figure 1. Environmental quantities for an exemplary annual cycle.

The application of smart statistical tools helps in recovery following findings: The temperature has an expected wave shaped cyclic seasonal behavior and varies between -12.5 and 30.5°C. The maximum temperature differences during a day were around 10°C and appeared in summer during a precipitation period. The relative air humidity does not have those significant seasonal variations as the temperature. As can be seen in Fig. 1 (a) the average relative air humidity was around 77% within a range between 36% and 100%, and (b) the relative air humidity is higher in winter than in summer. It is also obviously that the humidity is correlated with the temperature. There is a difference between air and concrete temperature but it amounts only 0.2°C in average. The differences are higher below the freezing point ($\Delta T \sim -4.3°C$) and lower ($\Delta T \sim +1.5°C$) above. The frequently mentioned time delay between air and concrete temperature could not be observed in this research.

DE-ICING SALT ENVIRONMENT

De-icing environment areas are around roads and parking lots (DuraCrete 1999) and are caused by thaw salting of e.g. roads. Roads in Austria are strewn with thaw-salt as soon as the freezing point is passed and pre-defined thresholds in the air humidity are exceeded. Recordings of winter services of motorway operator such as ASFINAG provide very interesting insights in physical processes. Such records include in general, a timestamp (t), location and applied density [g/m²] of de-icing salt and the name of motorway. A correlation between weather data, such as the temperature and the relative humidity with the winter service records allows to characterize the beginning of the winter service season. For instance the investigated records showed it begins in week 40 and ends after 31 weeks in week 18. As can been seen in Fig.3 the de-icing salts (Na Cl) had been applied for temperatures below 3°C combined with a high relative air humidity. Figure 2 also portrays for the analyzed 182 days winter period a 30 to 70 times de-icing salt service with 30-75 g/m²d salt.

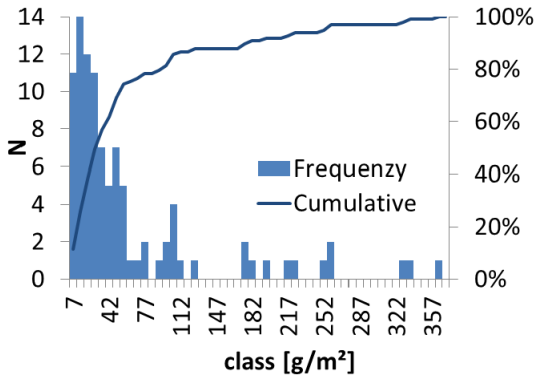

Figure 2. Histogram of de-icing salt services.

It has to be mentioned, that only 20 and 63% of the de-icing salt applied on the road will be transported due to wind and passing cars to structures and its components. The air transported salt is general deposited in a distance of 2–40 m to the road on the ground (Blomqvist and Johansson 1999). The passing vehicle velocity has a significant influence on the deposit rate and distance (McBean and Al-Nassri 1987). According to (Polder and Hug 2000), there is an indication of a relationship between the frequency of de-icing salt exposure and the chloride penetration. The deicing salts

are transported into the concrete by convection and diffusion in particular in the spray zone region it causes serious corrosion processes. As mentioned before, the frequency and amount of the salt feed on the concrete surfaces are decisive for corrosion processes. Nevertheless, there is no standard with respect to acceptable amount and frequency (Jung et al. 2003) of deicing salt. Hence it was of interest in this research to analyze possible relationships between corrosion rate and the resistivity of concrete.

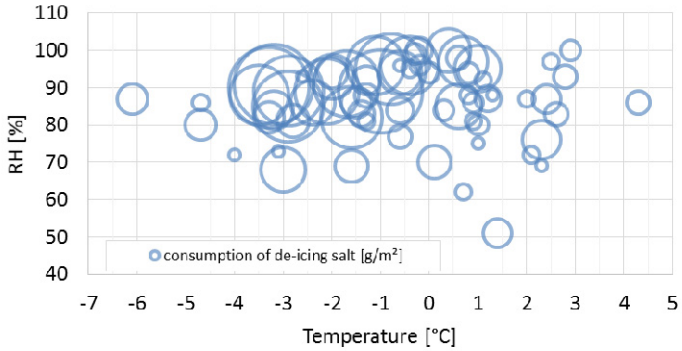

Figure 3. De-icing salt service in relation to temperature and relative humidity.

MONITORING DATA

For an in situ determination of the corrosion of the reinforcement, the existing environmental impact has to be monitored. Such a monitoring system was installed on columns in different heights on an overpass located in the Austrian motorway network of ASFiNAG. More details about sensors and measuring details can be found in (Binder and Pruckner 2014). The corrosion rate had been determined by the linear polarization resistance (LPR), see (Andrade and Alonso 1996).

The corrosion current density can be calculated as follows:

$$i_{corr} = \frac{B}{R_p} \quad (1)$$

where i_{corr} is the corrosion current density in mA/cm^2, R_p the electrical polarisation resistance and B=26 mV for corroding steel in concrete. The values of i_{corr} are average values referred to the overall reinforcement surface. The integration of these values over the exposure time allows estimating an average penetration of corrosion. The corrosion rate (CR) expressed as a diameter-loss per year [µm/a] is calculated from the corrosion current density using of the following formula:

$$CR = 11.6 \cdot i_{corr} \quad (2)$$

The corrosion rate is usually expressed as the penetration rate and is measured in µm/a. Especially in laboratory tests, but also in case of field observations, the corrosion rate is measured in electrochemical units, i.e. in mA/m² or in µA/cm² (Andrade and Alonso 2001).The annual variations of the monitored values can be modelled with a sinus approach.

$$y(t) = y_0 \cdot \sin(\omega t + \varphi_0) + \bar{y} \quad (3)$$

where $\omega = 2\pi/T$ is the radian frequency, T the observed time period in weeks, y_0 the amplitude, φ_0 the phase shifting and $\bar{y}$ the deflection.

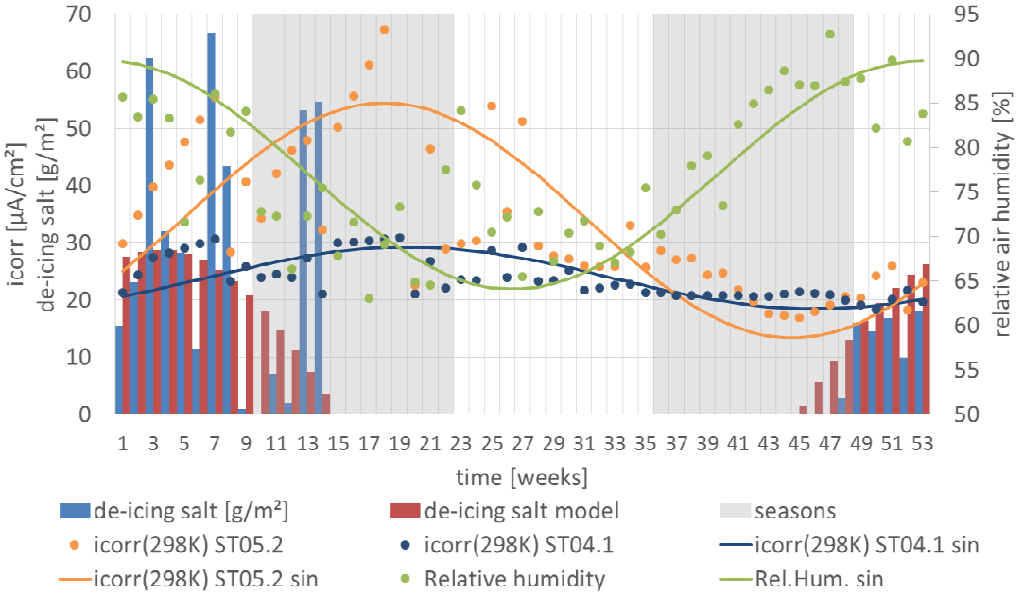

Figure 4. Annual variations of environmental and monitoring data.

As a first approach there is the possibility to model the de-icing service as a positive sinus wave as shown in Fig. 4. The approach can be verified with fitting parameter of R^2=0.975, It is also obvious in the graph that the temperature compensated corrosion current density shows a maximum at the end of spring in week 20. The maximum seems to have a high correlation to the application of the de-icing salt. It is, however, very difficult to generalize the effect of the de-icing salts because of the non-periodic application.

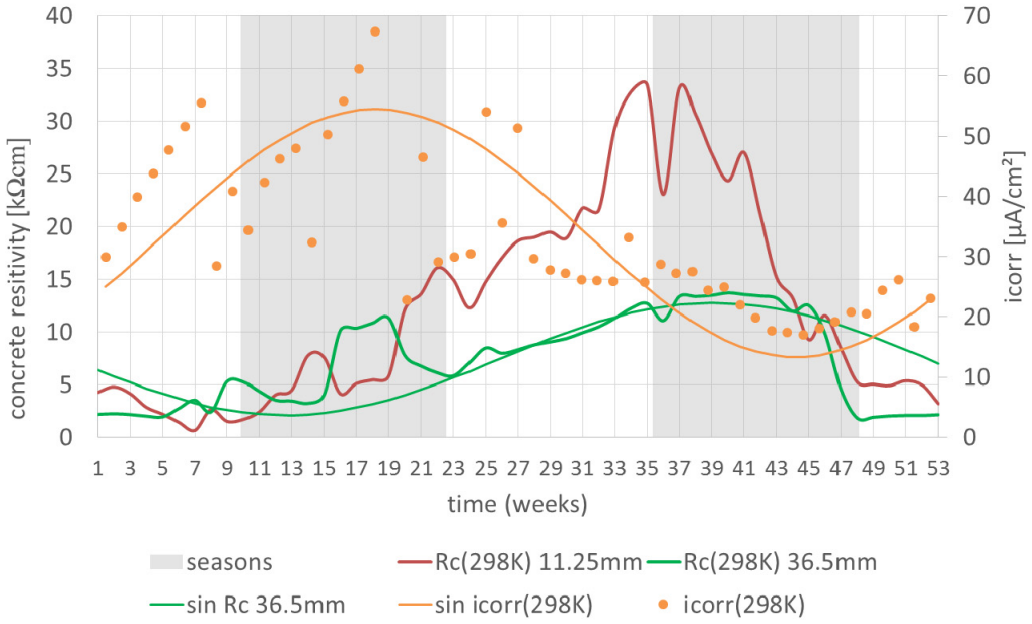

Figure 5. Concrete resistivity with respect to the corrosion current density.

The effect of the local climate on the concrete resistivity is apparent. In particular, the concrete resistivity shows dependences to the temperature and the relative air humidity. For instance, the resistivity decreases with increasing temperature and vice versa. In addition, the recorded data shows a continuously increase in the concrete resistivity in the surface layers (0-15 mm) with increasing dry periods. The range of variation range of the concrete resistivity during one season is up to two scales. These dehydration effects are not so distinctive in the deeper concrete layers, where the concrete resistivity is mostly controlled by season long term effects. For instance, the highest measured resistivity was at the beginning of autumn for a period of one year. At the end of autumn the concrete resistivity drops rapidly. At the same time the application of de-icing salt starts. If the concrete resistivity decrease, the corrosion rate increase.

PARAMETERS INFLUENCEING THE CORROSION RATE

As shown in the previous chapter the temperature has a significant effect on the corrosion rate of steel in concrete. The corrosion rate increases with temperature showing a linear correlation between the logarithm of i_{corr} and the reciprocal temperature. The effect of temperature on the corrosion current densities can be compensated by the Arrhenius function.

$$i_{corr}(298K) = i_{corr}(T) \cdot \exp\left[-\frac{E_A}{R} \cdot \left(\frac{1}{T} - \frac{1}{298K}\right)\right] \quad (4)$$

In Equation (4) $i_{corr}(298K)$ [µA/cm²] is the corrosion density at temperature 298 K (25° C), icorr(T) the current density at measured temperature, E_A the activation energy for the corrosion reaction (33.4 [kJ/mol]) (Pruckner 2001), R the gas constant (8,314 [J/molK]),and T the temperature (in degrees Kelvin).

The influence of the temperature on the electrical resistivity of concrete has successively been modeled by the use of the so-called Arrhenius equation (Chrisp et al. 2001):

$$R_C(298K) = R_C(T) \cdot \exp\left[\frac{E_A}{R} \cdot \left(\frac{1}{298K} - \frac{1}{T}\right)\right] \quad (5)$$

In Equation (5) Rc (298K) [Ω m] is the concrete resistivity and E_A (kJ/mole) the activation energy of resistivity. It was found that in this equation, the values of activation energy E_A for concrete is dependent on the saturation degree, e.g. 39 kJ/mol (for 55% saturation) and 27 kJ/mol (for 100% saturation) (Pruckner 2001). For studying the dominance of other parameters the following relations are done with temperature compensated values.

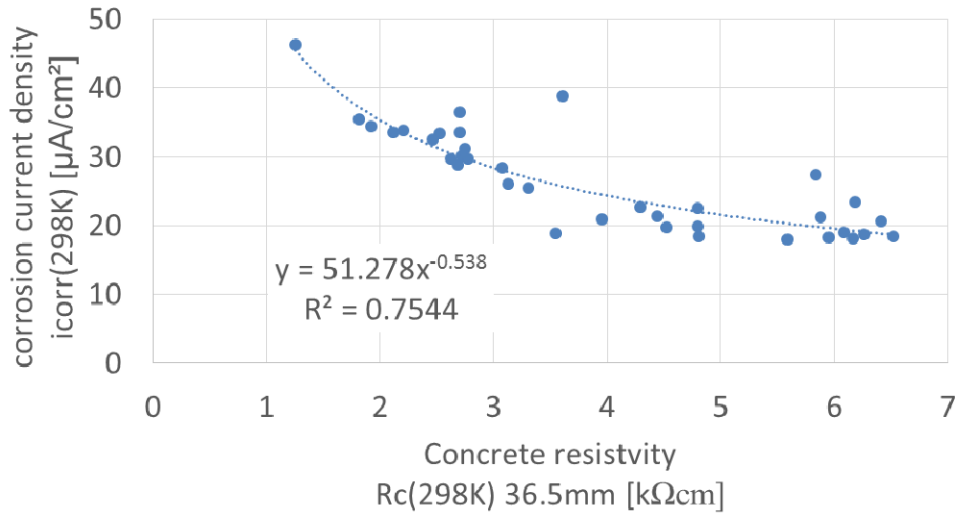

Figure 6. Measured concrete resistivity vs. corrosion rate.

From the electrochemical nature of the corrosion process, a relationship may be expected between the resistivity of concrete and the corrosion rate of reinforcement in the progression phase. Using a simplified approach based on the work of Bazant, the corrosion rate of corroding steel in concrete should be inversely proportional to the resistivity of the concrete (Bazant 1979). In this case, within a given structure, it is likely that areas with low resistivity will have a higher corrosion rate than areas with high resistivity. Figure 6 shows the comparsion of the resitivity with the corrosion rate. A power function was fitted to the monitoring data. It should be mentioned, that additionally to the relative humidity and the temperature, other factors, such as the presence of chlorides, w/c-value or the cement type, can also affect the concrete resistivity.

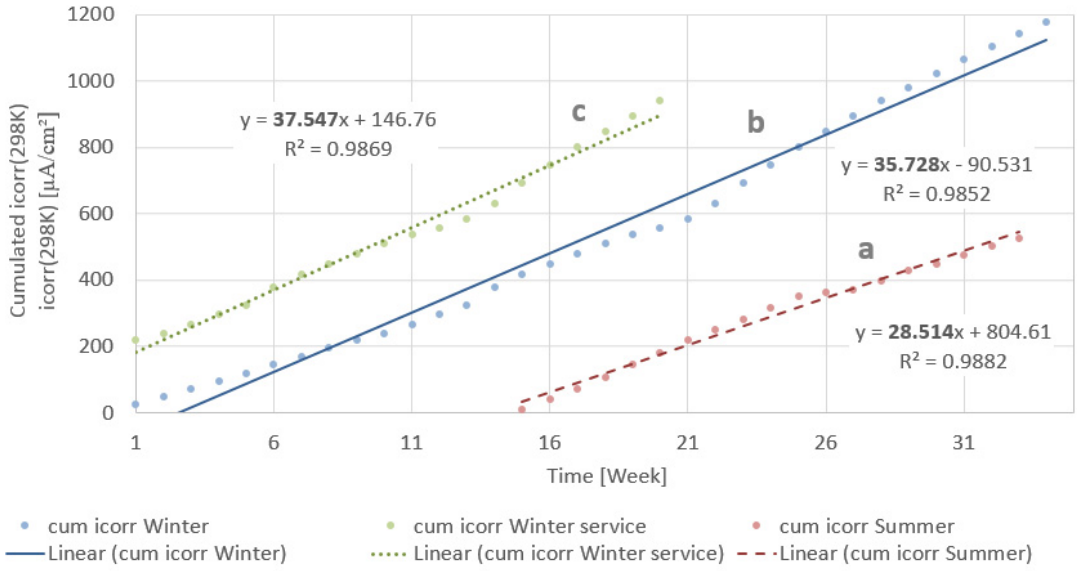

Figure 7. Time variant corrosion rate, (a) summer period "broken line", (b) winter period "continuous line", and (c) winter service "dotted line".

Figure 7 portrays the monitored dynamic corrosion process with respect to distinctive time periods: (a) during the summer period (week 21 to 40) the lowest gradient of the cumulated corrosion rate is observed. This is due to the high concrete resistance level as presented in Figure 4; (b) during the winter period (week 41 to 20) and especially during the winter service period (week 48 to 14) a higher gradient is prevalent.

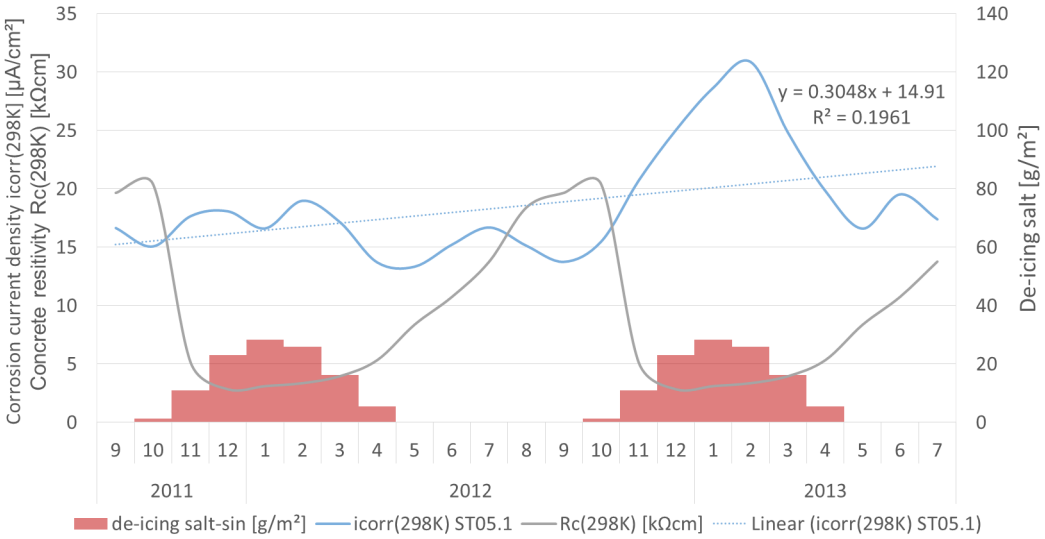

Figure 8. Time variant temperature compensated corrosion rate.

Another interesting result of the monitoring campaign is shown in Figure 8.
It shows the progressive evolution of the corrosion current density together with two periods of winter service. The ascending tendency of the temperature compensated corrosion rate is displayed by the linear slope presented in Figure 8. Lower levels of the temperature compensated corrosion current density can observed during the summer period and are attributed to the higher concrete resistance during this period.

EMPIRICAL MODEL

Corrosion of steel in concrete is an electrochemical process which is governed by several factors. Therefore prediction models are often derived empirically (Liu and Weyers 1998) (Jung et al. 2003) (Morinaga et al. 1990) (Lu et al. 2008) (Vu and Stewart 2000).
Three main parameters have been identified, namely the concrete resistivity, the chloride content of concrete, the humidity and the temperature in the concrete. For taking the allocation of de-icing salt in terms of the chloride content near the reinforcement into account, the model requires an additional increasing term.

$$i_{corr(298K)(t)} = i_{corr(298K)(0)} + A_{(t)} \cdot t^{b} + B \cdot \mathrm{Rc}_{(298K)(t)} \quad (6)$$

The evolution of i_{corr} over time can be explained by considering in the addition of 3 terms: an initial corrosion rate gained from the monitored data or condition assessment, an increasing term accounting the influence of the chloride content and a term for considering the actual resistivity of the concrete. The initial corrosion rate considering the duration of corrosion until the structure is monitored. This is especially the initial chloride content, the chloride contend due to the prior application of deicing salt and the carbonation of the concrete. This parameter can be

evaluated by a condition assessment. The increasing term is taking into account the additional loading of de-icing salt. As can be seen in Figure 5 the resistivity is following a periodic sine wave shaped curve during a time period of one year.
Therefore, it is recommended to consider this behavior in the last term of the model:

$$B \cdot \mathrm{Rc}_{(298K)(t)} = B \cdot \mathrm{Rc}_{(298K)} \cdot \sin\left[\left(\frac{2\pi}{53\mathrm{Weeks}}\right) \cdot (\mathrm{t} + \varphi)\right] + \bar{R}c_{(298K)} \quad (7)$$

The implementing of seasonal variations enable an increased accurate prediction of the corrosion current density in connection with climate exposure conditions. In addition to that, the use of this method may allow to reducing the number of expensive laboratory test or in situ measurements that are necessary to determine the corrosion rate of actively corroding concrete structures.
The next steps in this research will focus on the influences of material properties such as the w/c-value, the concrete cover or cracks in order to implement them in the presented model.

CONCLUSIONS

Environmental action on the corrosion rate of embedded reinforcements exposed to de-icing salt condition were assessed through an in-situ monitoring and weather data. Mean values for every week during a time period of 3 years were used in order to derive a relationship between the corrosion rate and concrete resistance and temperature. As expected, the rebar corrosion process depends on three factors, namely the environmental exposure conditions, the concrete resistivity and the chloride concentration. The resistivity decreases at increasing temperature and vice versa. The concrete resistivity is increasing continuously in longer dry phases at the concrete surface. The corrosion rate increases if the concrete resistivity decreases. Apart from the dominating influence of the concrete resistivity to the corrosion rate, the monitored data indicates a qualitative relation to the application of de-icing salt. The greatest increases of the temperature compensated corrosion rate is observed in January, whereas the highest temperature compensated corrosion rate was observed in February and March. The proposed model enables a more accurate prediction of the time variant corrosion rate due to the implementing of a sine term.

REFERENCES

Andrade, C., and Alonso, C. (1996). "Corrosion rate monitoring in the laboratory and on-site." *Construction and Building Materials*, 10(5), 315-328.

Andrade, C., and Alonso, C. (2001). "On-site measurements of corrosion rate of reinforcements." *Construction and Building Materials*, 15(2), 141-145.

Asfinag (2013). "Consolidated Balance Sheet." <http://gb1.asfinag.at/geschaeftsbericht2013/en/consolidated-balance-sheet.html>. (13.04.2015).

Bazant, Z. P. (1979). "Physical model for steel corrosion in concrete sea structures - theory." *Proc. Am. Soc. Civ. Eng., J. Struct. Div., 105(ST6), 1137-1153, (1979)*

Binder, F., and Pruckner, F. "Korrosionsrate und Korrosionsfortschritt an stark Chlorid belasteten Stützen." *Proc., Beurteilung, Ertüchtigung und Instandsetzung von Brücken : 1. Kolloquium*, Techn. Akad. Esslingen, 550.

Blomqvist, G., and Johansson, E.-L. (1999). "Airborne spreading and deposition of de-icing salt — a case study." *Science of The Total Environment*, 235(1–3), 161-168.

Chrisp, T. M., Starrs, G., McCarter, W. J., Rouchotas, E., and Blewett, J. (2001). "Temperature-conductivity relationships for concrete: An activation energy approach." *Journal of Materials Science Letters*, 20(12), 1085-1087.

DuraCrete (1999). "Models for Environmental Actions on Concrete Structures : Brite EuRam III ; Contract BRPR-CT95-0132, Project BE95-1347, Document BE95-1347/R3, March 1999." A. Lindvall, ed., CUR, Gouda, 273 S.

Gattringer, O. (2013). "AWEKAS-Automatisches Wetterkarten system." <www.awekas.at>. (2015.04.13).

Jung, W.-Y., Yoon, Y.-S., and Sohn, Y.-M. (2003). "Predicting the remaining service life of land concrete by steel corrosion." *Cement and Concrete Research*, 33(5), 663-677.

Liu, T., and Weyers, R. W. (1998). "Modeling the Dynamic Corrosion Process in Chloride Contaminated Concrete Structures." *Cement and Concrete Research*, 28(3), 365-379.

Lu, Z.-H., Zhao, Y.-G., and Yu, K. (2008). "Stochastic modeling of corrosion propagation for service life prediction of chloride contaminated RC structures." 195-201.

McBean, E., and Al-Nassri, S. (1987). "Migration pattern of de-icing salts from roads." *Journal of Environmental Management*, 25(3), 231-238.

Morinaga, S., Irino, K., Ohta, T., and Tsuchimoto, Y. (1990). "Life Prediction of Reinforced Concrete Structures determined by Corrosion." *Concrete Research and Technology*, 1(1), 177-189.

Polder, R. B., and Hug, A. (2000). "Penetration of chloride from de-icing salt into concrete from a 30 year old bridge." *Heron*, 45(2), 109-124.

Pruckner, F. (2001). "Corrosion and protection of reinforcement in concrete measurements and interpretation." *Corrosion and protection*.

Unfried, P. (2014). "private Wetterstation Weidling." <http://www.unfried.or.at/Wetter/wetterstationweidling.htm>. (2015.04.13, 2015).

Vu, K. A. T., and Stewart, M. G. (2000). "Structural reliability of concrete bridges including improved chloride-induced corrosion models." *Structural Safety*, 22(4), 313-333.

Diffusion-Based Model for Predicting Chloride Ingress into Road Structures

G. Kapteina[1]

[1]Schießl Gehlen Sodeikat Consulting Engineers, Landsbergerstraße 370, 80687 Munich, Germany. E-mail: kapteina@ib-schiessl.de

Abstract

Chloride transport mechanisms into road structures are multifarious. Because the current level of knowledge is not sufficient to model all relevant transport mechanism, the approach chosen to model chloride ingress should capture the decisive mechanisms involved. Based on this idea, Fick's 2nd law of diffusion has been selected as the basic physical approach. With this approach the apparent diffusion coefficient is one of the key variables. To improve the accuracy of the approach this variable has been adapted empirically. As for concrete exposed to intermittent splash water the profile may have a maximum content inside, Fick's 2nd law of diffusion cannot be applied without restrictions. The two published approaches regarding this issue will be discussed and assessed. For the selected approach, the empirical adaptation of the apparent chloride diffusion coefficient has been carried out by evaluation of chloride profiles. The regression variables derived have been quantified stochastically to enable a full-probabilistic calculation of the predicted chloride profile. Finally, an example calculation has been carried out to demonstrate the application of this model within the framework of service life design.

Introduction

During winter, chloride-containing de-icing salt is spread on roads. Chlorides will penetrate into the concrete of surrounding structures and may cause corrosion of the reinforcement. To predict chloride ingress and thus enable a service life design, a model for chloride transport into concrete of road structures is required. The selected approach should enable the calculation of chloride profiles of sufficient complexity and also simultaneous consideration for the existing variation.

1. Chloride Transport Mechanisms into Road Structures Concrete

In completely water-saturated concrete the chloride transport takes place solely by diffusion. As concrete exposed to road environment conditions is not completely water saturated, the concrete is able to absorb water as a result of a water impact (e.g. splash water). Depending on the climatic conditions, the absorption can either take place by capillary suction or by the micro-ice-lens-pump. In the case of absorbed water containing chloride ions, chloride transport by convection takes place because the chloride ions are drawn in with the penetrating water. The depth affected by this convective uptake of chlorides is usually restricted to the outer layer near the surface. After the uptake, the chloride ions diffuse further into the concrete, thereby reaching

deeper layers. Due to intermittent moisture conditions in the outer concrete layer, a redistribution of chloride ions back to the surface may also take place. The effectiveness of the redistribution and subsequent removal (e.g. by rain events) depends on the binding capacity of the concrete, which is affected by leaching and carbonation. For concrete with vertically orientated surfaces located near the road, relevant chloride transport mechanisms can be roughly divided into: (1) uptake - predominantly due to convention and (2) redistribution - predominantly due to diffusion, see Fig. 1.

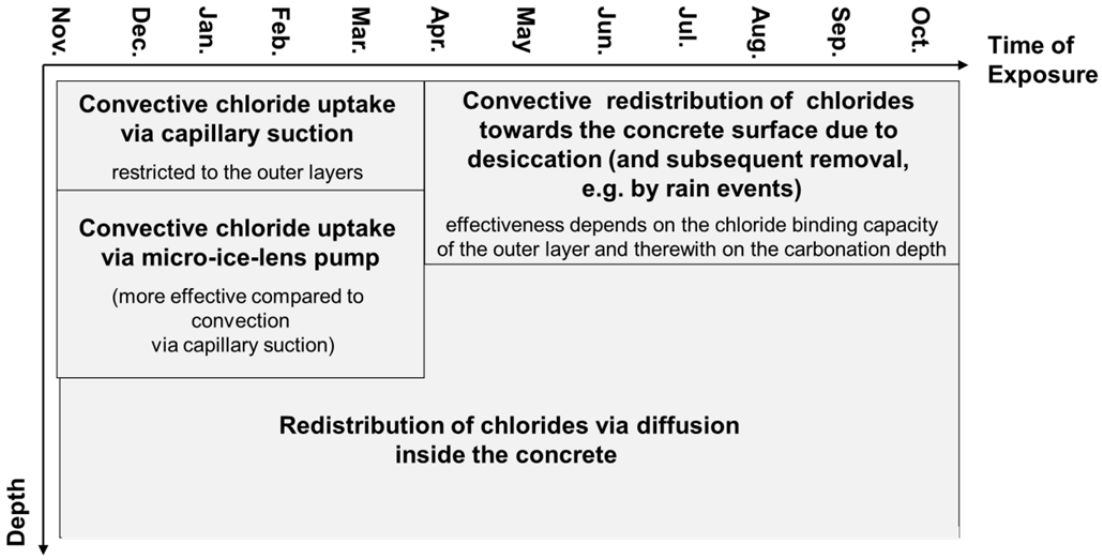

Figure 1. Chloride transport mechanisms involved over one year within the first years of exposure

Associated with the transport of chloride ions in concrete, it has to be taken into account that non-carbonated concrete is able to bind chloride ions. As bound chlorides are immobile, so too does the binding capacity of concrete have a major influence on the chloride penetration depth. In general, the binding capacity depends on the cement type and the hydroxide (OH^-) concentration, which can be influenced by exposure conditions.

2. Approach for Chloride Ingress into Road Structures

2.1 Basic Model, Fick's 2nd Law of Diffusion

Due to the multitude of mechanisms involved, a physical ingress model for structures exposed to splash water caused by traffic would be highly complex. Based on initial studies by Li & Tang (2008) and Ungricht (2004), it has to be assumed that the micro-ice-lens-pump has a decisive contribution on chloride ingress. Chloride ingress via micro-ice-lens-pump takes place only while the concrete is thawing and only if, at the same time, water on the concrete surface is present containing chlorides. For the time being the current level of knowledge of this transport mechanism is not sufficient to model the chloride ingress considering road conditions. Taking into account that even the number of freeze-thaw-cycles show a large variation within one structure (Siebel et al. (2005)) and can hardly be predicted

beforehand, it seems questionable if a physical model may be targeted specifically for the issue raised.

Usually a service life design includes a prediction of the chloride content at the reinforcement level (concrete cover in the range of 40 mm to 70 mm) after more than 50 years of exposure times. With longer exposure time and increasing penetration depth, diffusion becomes the controlling chloride transport mechanism. The choice to use Fick's 2nd law of diffusion is confirmed by most chloride profiles attained from road structures. These show a hyperbolic-shaped decrease of chloride content with increasing penetration depth, which is typical for a diffusion-controlled transport. The apparent chloride diffusion coefficient D_{app} is the governing variable for this approach. In case the chloride transport is solely controlled by diffusion, this variable characterises the inverse resistance of the material against chloride transport, hereby also considering the binding capacity of the concrete. For road structures, the adaptation D_{app} becomes necessary because other transport mechanisms provoked by exposure conditions also influence this variable, see Fig. 1.

The adaptation has been carried out empirically by evaluating chloride profiles from existing structures or specimens exposed to road environment conditions. The apparent chloride diffusion coefficient has been derived by a curve fitting procedure which yields two regression variables (starting chloride content and apparent chloride diffusion coefficient).

2.2 Approaches Based on the 2nd Law of Diffusion Considering the Convection Zone

Practical observations have shown that the approach of Fick's 2nd law of diffusion may not be applied without restrictions for intermittent chloride impact. Close to the surface the concrete is exposed to frequent changes between wetting and subsequent evaporation. This zone is usually referred to as the "convection zone", see Gehlen (2000).

Due to the changes in the moisture content within the convection zone, transport mechanism back to the concrete surface may also be activated. The accumulated chloride ions near the surface can be removed from the concrete through a subsequent water impact (e.g. by rain). As a result, the chloride content near the surface decreases and maximum chloride content inside the concrete increases. Hence, the chloride content in the outer layer cannot be calculated with the 2nd law of diffusion. To simplify matters, this zone with deviating chloride contents regarding the 2nd law of diffusion is also be referred to as "convection zone" and titled with Δx. Principally, two different approaches have been found in literature. These will be briefly introduced and discussed with regard to the applicability for concrete exposed to splash water caused by traffic. To illustrate the difference between the approaches, the least square fitting procedure has been applied to given chloride profiles to yield regression values for the apparent chloride diffusion coefficient and for the starting chloride content defined in a certain depth.

Approach [I] for deriving the apparent chloride diffusion coefficient ($D_{app,I}$): Within this approach the chloride content in the convection zone Δx will be neglected within the fitting procedure, see Lindvall et al. (2000) and Nilsson et al. (2000). For a

given chloride profile linked to a certain exposure time t_{exp} the fitting procedure will generally result in the regression values: $C_{S,a}$, $D_{app,\,I}$. Due to the applied procedure the value $C_{S,a}$ is defined as the chloride content at the surface x = 0, which is a theoretical value determined by extrapolation of the fitted chloride profile, see Fig. 2.

Approach [II] for deriving the apparent chloride diffusion coefficient ($D_{app,II}$): Within this approach the chloride content in the convection zone Δx will be excluded via transformation of the x-axis by a value of Δx, see e.g. Gehlen (2000) and Schießl & Lay (2003). For a given chloride profile liked to a certain exposure time t_{exp} the fitting procedure will result in the regression values: $C_{S,\Delta x}$, $D_{app,II}$. Due to the applied procedure, the value $C_{S,\Delta x}$ is defined as the chloride content at the substitute surface layer Δx mm, see Fig. 2.

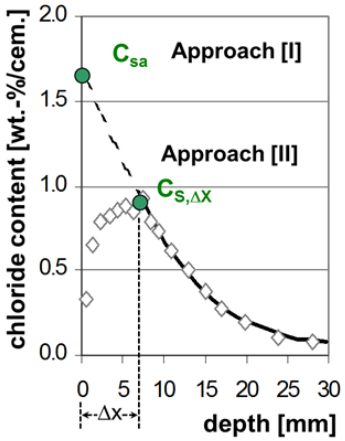

Approach [I]:
Neglecting the chloride content in the convection zone Δx within the fitting procedure (regression values: $C_{S,a}$, $D_{app,I}$)

$$C(x,t_{exp}) = C_{S,a}\left[1 - erf\frac{x}{2\cdot\sqrt{D_{app,I}(t_{exp})\cdot t_{exp}}}\right]$$

$C_{S,a}$: Chloride content at the surface x = 0 mm, theoretical value determined by extrapolation [wt.-%/cem.]
$D_{app,I}(t_{exp})$: Apparent chloride diffusion coefficient linked to the exposure time t_{exp} [mm^2/a]

Approach [II]:
Exclusion of the depth layer Δx by transformation of the x-axis (regression values: $C_{S,\Delta x}$, $D_{app,II}$)

$$C(x,t_{exp}) = C_{S,\Delta x}\left[1 - erf\frac{x-\Delta x}{2\cdot\sqrt{D_{app,II}(t_{exp})\cdot t_{exp}}}\right]$$

$C_{S,\Delta x}$: Substitute chloride content at depth Δx [wt.-%/cem.]
$D_{app,II}(t_{exp})$: Apparent chloride diffusion coefficient linked to the exposure time t_{exp} [mm^2/a]
Δx: depth layer near the surface, with deviating chloride content in relation to the 2nd law of diffusion [mm]

Figure 2. Main characteristics of the different approaches with regard to the treatment of the convection zone Δx, see Kapteina (2013)

The difference between these approaches becomes obvious when applying the curve fitting procedure to achieve input variables for the starting chloride content (either $C_{S,a}$ or $C_{S,\Delta x}$) and the apparent diffusion coefficient (either $D_{appI,}$ or $D_{app,II}$). For a given chloride profile linked to a certain exposure time (here: t_{exp} = 4.6 a) Approach [I] leads to higher values for the starting chloride concentration, which is a logical result due to the definition of this variable. But also the value for the apparent chloride diffusion coefficient turns out to be considerably higher for Approach [I] compared to Approach [II], in this example about 30 %, see Fig. 3.

Although both approaches lead to comparable values for chloride contents in depths x > Δx, there are still some differences. By definition the starting value of the chloride content is constant over the exposure time. This implies that for Approach [I] in a depth x = Δx the chloride content increases with increasing exposure time whereas by Approach [II] this value is constant. Another difference is the influence of the "convection zone" on the regression variables $D_{app,I}$ and $D_{app,II}$.

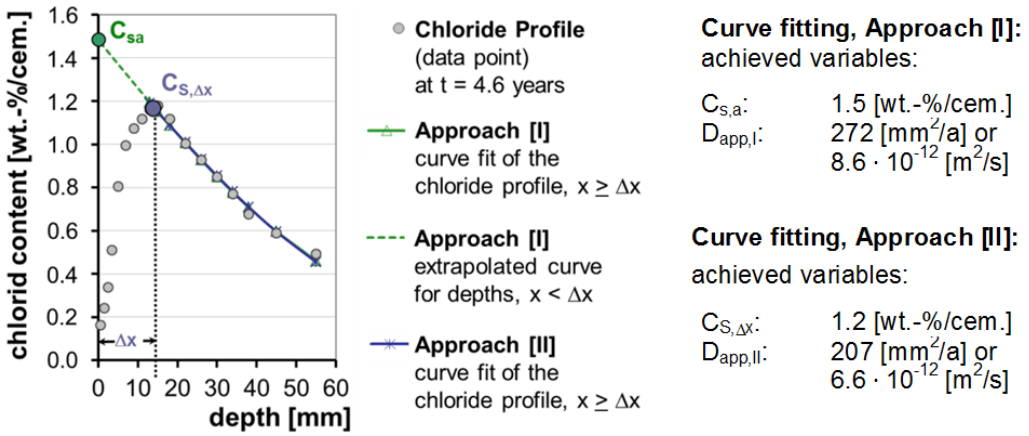

Figure 3. Comparison of regression variables derived by the fitting procedure according to Approaches [I] and [II], see Kapteina (2013)

A very pronounced scattering of the convection zone has been recorded for road structures; see Schießl & Lay (2003). Therefore the influence of varying Δx values within the chloride profiles has been examined for both approaches as part of an example calculation. In the first step, the apparent diffusion coefficient has been derived by adopting the fitting procedure for both approaches. For the next step the convection zone has been increased, whereas the chloride content at depths $x \geq \Delta x$ stayed unchanged. The apparent diffusion coefficients have then been determined once again for these modified chloride profiles. The example shows that the derived diffusion coefficients $D_{app,II}$ decrease inversely proportional with Δx for Approach [II], whereas for Approach [I] $D_{app,I}$ remains constant, see Fig. 4.

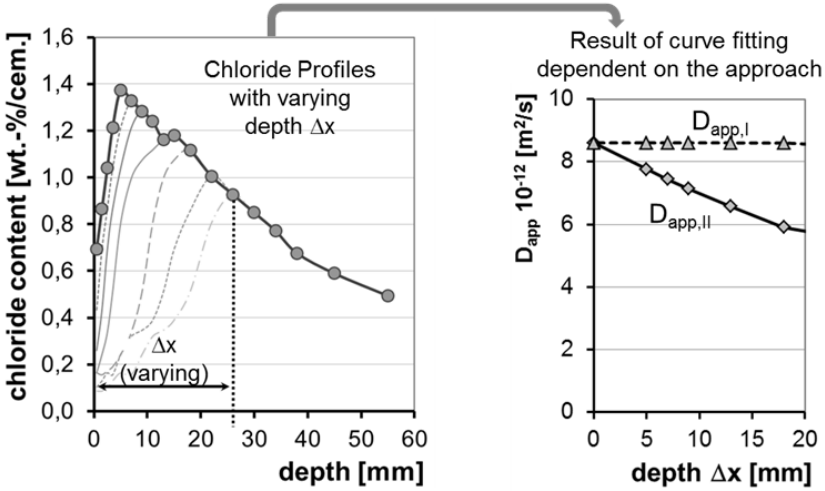

Figure 4. Apparent chloride diffusion coefficients obtained from chloride profiles with varying depth Δx according to Approaches [I] and [II], Kapteina (2013)

The reason for the deviating results within both approaches is given by the gradient of the fitted chloride profile, as the absolute value for the normalized gradient for a given value x and t_{exp} corresponds directly to D_{app}. At the starting point of the chloride profile ($x = 0$ or $x = \Delta x$ depending on the approach) an inverse

correlation exists between the absolute values of the normalized gradient and the apparent diffusion coefficient. This means for decreasing absolute values of the normalized gradient the derived apparent diffusion coefficient increases. Depending on the chosen approach the normalized gradient at the starting point ($x = 0$ for Approach [I] and $x = \Delta x$ for Approach [II] respectively) deviates in case $\Delta x > 0$. For Approach [I] the normalized gradient of the chloride profile within the starting point is independent of Δx, whereas for Approach [II] the absolute value of the normalized gradient increases with increasing values of Δx, which results in smaller values for the apparent diffusion coefficient.

2.3. Assessment of the Approaches Considering the "Convection Zone"

Ideally the apparent chloride diffusion coefficient should describe the material characteristics linked to chloride ingress (inverse material resistance). From a physical point of view it is not justifiable that this variable depends on the convection zone, which is strongly influenced by the exposure conditions. This is particularly important for road structures, as a more pronounced scattering of the convection zone has been recorded compared to marine structures. Although the apparent chloride diffusion coefficient of concrete subjected to road environment conditions includes influences of the exposure conditions due to the different transport mechanism being activated, the chosen approach should have the objective of reducing the environmental influences as much as possible. In light of this, a dependency of the chloride diffusion coefficient on the convection zone Δx should be prevented. For this reason, Approach [I] has been chosen for modelling chloride ingress under the prevailing exposure conditions, because this approach takes the ideal conception of the apparent diffusion coefficient being a material variable into account.

3. Apparent Chloride Diffusion Coefficient

3.1 Evaluation

The adaptation of the apparent chloride diffusion coefficients for concrete exposed to road environment conditions (in this case $D_{app,R}$) becomes necessary as other transport mechanism provoked by exposure conditions influence this variable. Hence this variable has to be generally regarded as a transport variable. The apparent diffusion coefficient $D_{app,R}$ has been determined by evaluating published chloride profiles (primarily from Germany and Sweden) with the least square fitting procedure. Data from OPC concrete has been considered, whose mainly vertically orientated surface is exposed to road environment conditions, see Kapteina (2013) for survey of data used. By the application of this procedure, the derived $D_{app,R}$ is an integral mean value over the time span from first chloride impact up to the considered point in time, in the following called exposure time t_{exp}. This implies that $D_{app,R}$ is affected by the entire impact history up to the considered exposure time.

The equation describing the time-dependent development of $D_{app,R}(t_{exp})$ is generally divided into two parts, see Fig. 5. The first part describes the starting point and the second part the decrease over the time of exposure. The starting point has been defined based on the non-steady state rapid chloride migration coefficient $D_{RCM,0}$, see DuraCrete (2000) and Gehlen (2000). Compared to the non-steady state diffusion coefficients derived from immersion tests, the duration of a migration test is

rather short, whereas $D_{RCM,0}$ can be considered an instantaneous variable. Due to different test conditions the binding capacity reached during immersion tests is not comparable to the ones reached during migration tests. Nevertheless, for a young concrete age, $D_{RCM,0}$ and the chloride diffusion coefficient derived from immersion testing showed a very good correlation, wherefore the testing variable k_t for converting accelerated test conditions linked to diffusion can be quantified as $k_t = 1$, see Gehlen (2000). For road structures, regression analysis has been used to determine the shift of the starting point of $D_{app,R}$ compared to the diffusion coefficient derived from immersion tests at 20°C (k_R) and the time-dependent decrease (age exponent a_R). In Fig. 5 the time-dependent decrease of $D_{app,R}$ according to the presented approach is outlined. Furthermore the respective quantiles for submerged concrete (e.g. parts of marine structures) according to Gehlen (2000) are given.

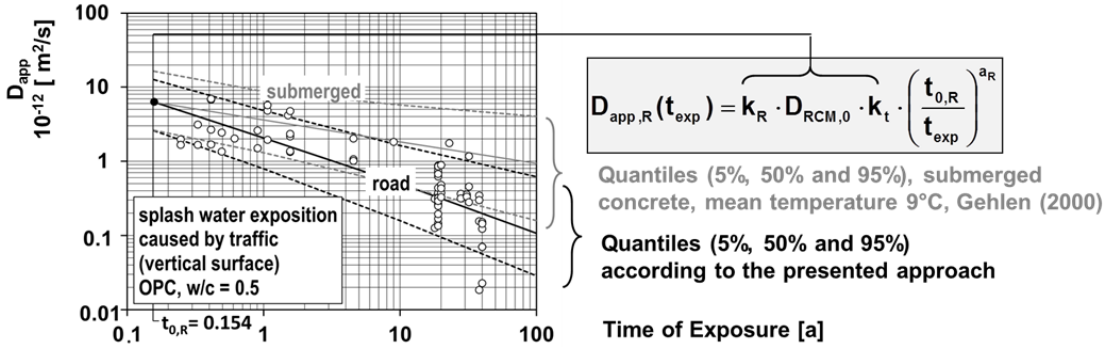

Figure 5. Time-dependent $D_{app,R}$ of OPC exposed to splash water caused by traffic, see Kapteina (2013)

3.2 Influences on the Apparent Chloride Diffusion Coefficient

In order to estimate the influence of chloride transport mechanisms and other governing boundary conditions evoked by road environment conditions on the apparent diffusion coefficient, a comparative consideration has been carried out.

- **Chloride Ingress via Convection**

Chloride ingress via convection leads to a much deeper penetration depth compared to diffusion-controlled ingress. It has to be assumed that this applies especially for convection initiated by the micro-ice-lens-pump. Therefore the analysis of the chloride profile will lead to an underestimation of the concrete resistance against chloride ingress when assuming solely diffusion-induced ingress. When applying the fitting procedure on such a profile, the achieved $D_{app,R}$ is significantly higher compared to a diffusion-controlled chloride profile. This effect is predominant especially within the first years of exposure. Furthermore, the intermittent chloride impact with subsequent desiccation leads to an accumulation of chlorides near the surface. This in turn causes chloride profiles with a comparably high normalized gradient near the surface, resulting in an overestimation of the resistance against chloride ingress. When applying the fitting procedure $D_{app,R}$ decreases due to the accumulation of chlorides. During the following spring season, the accumulated chloride ions are to some extent re-moved by rain, whereby the effect described becomes reversed leading to increasing apparent chloride diffusion coefficients over the following spring and

summer. Depending on the season of sampling, this effect leads particularly to an increased variation in the derived $D_{app,R}$. Because after the first years of exposure the maximum chloride concentration is usually established inside the concrete, the influence of this effect on the apparent diffusion coefficient decreases afterwards.

- **Diffusion**

The diffusion of chlorides into road structures concrete takes place in partially saturated concrete, whereby the chloride supply is transient during the time of exposure. Due to these boundary conditions, the chloride transport is decelerated leading to lower apparent chloride diffusion coefficients compared to water saturated concrete with a steady chloride supply. With increasing exposure time, the impact of diffusion controlled chloride ingress becomes more decisive regarding the shape of the chloride profile and with that the resulting apparent chloride diffusion coefficient. As the predominant chloride transport mechanisms and their respective velocities change over the time of exposure (from rather fast to slow), the aging behaviour of $D_{app,R}$ is affected, leading to a larger value for the aging exponent a_R compared to totally submerged concrete.

- **Concrete Age at First Exposure**

For road structures such as bridges and tunnels, the time span between casting and first exposure of the concrete to de-icing salt may vary strongly and can take up to several years. Due to the time-dependent increase in concrete resistance against chloride ingress, the influence of the concrete age at first exposure on the apparent chloride diffusion coefficient can be recorded, see Lindvall (2002) and Kapteina (2013). Systematic investigations linked to this issue are not available for the time being; therefore an adaptation of $D_{app,R}$ cannot be carried out. Information concerning the concrete age during first exposure has not been made available for the data set used for quantification of $D_{app,R}$. Ignoring this fact may contribute to the large coefficient of variation derived from the variable $D_{app,R}$.

Based on the given reasoning it is not surprising that beside the fact that concrete is a non-homogeneous material, the variable $D_{app,R}$ shows a large variation. To capture this variation the application of a probabilistic approach is strongly recommended, see also the DuraCrete (2002) regarding marine structures.

4. Example Calculation for Service Life Design (SLD)

In the following, a brief example calculation for service life design is given which enables a reliability-based assessment of a structural element. In the first instance a limit state function g(X) has to be formulated to describe the adverse event which is relevant for decision making. The reliability index can be calculated by evaluating the respective limit state equation fully-probabilistically. In this case study, the limit state function considers the depassivation of the reinforcement due to chloride ingress, which marks the end of the initiation period.

$$g\left(C_{crit}, C(d_c, t_{exp})\right) = C_{crit} - \left\{ (C_{Sa} - C_i) \cdot \left[1 - \operatorname{erf} \frac{d_C}{2 \cdot \sqrt{\left(k_R \cdot D_{RCM,0} \cdot k_t \cdot \left(\frac{t_{0,R}}{t_{exp}} \right)^{a_R} \right) \cdot t_{exp}}} \right] + C_i \right\}$$

In the given example, the parts of bridge columns exposed to splash water have been considered, located approx. 1.0 m from the roadside. The equation given above has been evaluated with the program Strurel, see RCP (1995). The reliability index at the end of service life has been calculated by taking into account the quantities of the variables as given in **Table 1**.

Table 1. Quantification of variables for SLD (depassivation of reinforcement), OPC, (w/c =0.45) exposed to splash water caused by traffic, vertically orientated

Variable	*Quantification source*	*Quantification*[1)]
$\mathbf{C_{crit}}$: chloride threshold level, [wt.-%/cem.]	Gehlen (2000)	betaD ($0.2 \leq C_{crit} \leq 2$, m = 0.6, s = 0.15)
$\mathbf{C_{Sa}}$: notional chloride content at the surface, [wt.-%/cem.]	see Kapteina (2013) based on Schießl (2003)	logD (m = 2, s = 1.5)
$\mathbf{C_i}$: initial chloride content, [wt.-%/cem.]	Lay (2006)	logD (m = 0.055, s = 0.028)
$\mathbf{d_c}$ concrete cover, [mm]	German NA EN 1992-1-1	ND (m = 55, s = 8 mm)
$\mathbf{D_{RCM,0}}$: chloride migration coefficient, [mm^2/a]	compliance test result concrete age t = 28 d	ND (m = 316, s = 63)
$\mathbf{k_t}$: transfer variable to convert D_{RCM}, [-]	Gehlen (2000)	D (value: 1)
$\mathbf{t_{0,R}}$: time of reference, [a]	Kapteina (2013)	D (value: 0.154),
$\mathbf{k_R}$: regression variable [-]	Kapteina (2013)	ND (m = 0.45, s = 0.12)
$\mathbf{a_R}$: regression variable[-]	Kapteina (2013)	betaD ($0 \leq a_R \leq 1$, m = 0.6, s = 0.12)
$\mathbf{t_{exp}}$: time of exposure, [a]	target service life	D (value: 80)

[1)] Distributions: D-deterministic, ND-normal, logD-lognormal, betaD-beta

It has been assumed that the owner predefines a target minimum reliability for these areas of $\beta_0 = 1.5$ over a target service life of 80 years. This example calculation cannot be applied to the bases of columns, where chloride-containing water can accumulate directly at their surface. This might be the case if the surrounding area exhibits a slope towards the base of the column. In such a case, the influence of convective uptake of chloride ions increases, which may lead to more significant chloride ingress as considered within the presented model.

The calculation based on the stated assumption results in a reliability index of $\beta = 1.6$ after 80 years linked to chloride-induced depassivation of the reinforcement. This calculated reliability can be compared to the predefined target minimum. The maintenance planning procedure can also be optimized based on this comparison.

CONCLUSION

The introduced full-probabilistic model enables the calculation of chloride profiles of sufficient complexity and with simultaneous consideration for the existing variation. The model can be implemented as part of a service life design linked to chloride-induced depassivation of reinforcement. However, due to the empirical adaptation of the apparent diffusion coefficient, the applicability to other concrete

binder compositions is restricted. Therefore a further differentiation of the apparent diffusion coefficient (and thus the regression variables a_R and k_R) concerning different binder compositions and varying concrete ages at first exposure would be helpful to expand the presented approach for other boundary conditions. Furthermore the influence of the micro-ice-lens-pump on chloride uptake should be examined under different exposure conditions to enable a more differentiated prediction. Current research deals with modeling corrosion rates of depassivated reinforcement. Because the prediction of events linked to reinforcement corrosion requires a precise prediction of the initiation phase, depassivation models will also play a major role for limit states within the propagation period. For this reason, further research on this topic is still important and necessary.

REFERENCES

DuraCrete – Probabilistic Performance Based Durability Design of Concrete Structures (2002). Deterioration Modelling. Report No.: BE 95-1347, Brussels: European Union - Brite EuRam, 1997. Contract BRPR-CT95-0132.

Gehlen, C. (2000). „Probabilistische Lebensdauerbemessung von Stahlbetonbauwerken – Zuverlässigkeitsbetrachtungen zur wirksamen Vermeidung von Bewehrungskorrosion“, issue no. 510 of DAfStb, Beuth-Verlag, Berlin.

Kapteina, G. (2013) „Modell zur Beschreibung des Eindringens von Chlorid in Beton von Verkehrsbauwerken“, issue no. 607 of DAfStb, Beuth-Verlag, Berlin.

Lay, S. (2006). „Abschützung der Wahrscheinlichkeit tausalzinduzierter Bewehrungskorrosion - Baustein eines Systems zum Lebenszyklusmanagement von Stahlbetonbauwerken, issue no. 568 of DAfStb, Beuth-Verlag, Berlin.

Li, B.; Tang, L. (2008) “The effects of mineral additions on chloride penetration into concrete under frost action”; in: Life-Cycle Engineering - Biondini & Frangopol (eds), Taylor and Francis Group, London, pp. 189-194.

Lindvall, A.; Andersen, A.; Nilsson, L.-O. (2000). “Chloride ingress data from Danish and Swedish road bridges exposed to splash from de-icing salt”. Chalmers University of Technology, Department of Building Materials.

Lindvall, A. (2002) “Chloride ingress in a Swedish road environment – five years exposure for three concrete compositions”, Chalmers University of Technology, report P-02:04, Goteborg.

Nilsson, L.O.; Andersen, A.; Luping, T.; Utgennant, P. (2000) “Chloride ingress data from field exposure in a Swedish road environment”. Department of Buildings and Materials; Chalmers University of Technology, P-00:5, Goteborg.

RCP Consulting (1995) “STRUREL, A Structural Reliability Analysis Program System”, Munich.

Schießl, P.; Lay, S. (2003): Dauerhaftigkeitsbemessung von Stahlbetonkonstruktionen. Forschungsbericht, AiF 12525 N, DBV 225, München, 2003.

Siebel, E. et al. (2005). „Übertragbarkeit von Frost-Laborprüfungen auf Praxisverhältnisse – Sachstandsbericht“. in publication series of the DAfStb, issue no. 560, published by Beuth-Verlag, Berlin.

Ungricht, H. (2004). „Wasserhaushalt und Chlorideintrag in Beton - Einfluss der Exposition und der Betonzusammensetzung“, Eidgenössische Technische Hochschule ETH Zürich, published by the author, Zürich.

New Analysis Method for the Accurate Determination of Chloride Content in the Cement Phase of Concrete

Andreas Limbeck[1]; Armin Eitzenberger[1]; Maximilian Bonta[1]; and Stefan Burtscher[2]

[1]Vienna University of Technology, Institute of Chemical Technologies and Analytics, Getreidemarkt 9/164-IAC, 1060 Vienna, Austria.
[2]Technische Versuchs- und Forschungsanstalt GmbH, Vienna University of Technology, Gutheil-Schoder-Gasse 17, 1230 Vienna, Austria (corresponding author). E-mail: stefan.burtscher@tvfa.at

ABSTRACT

Corrosion of reinforcing steel in concrete is on one hand a major security problem and on the other a cost driver, which is very often not appropriately considered. Corrosion induced by chloride leads to localized corrosion phenomena, which reduces the cross section rapidly. Already corroded steels have to be replaced. When the initiation of the corrosion can be predicted accurately, the reinforcing steels can be prevented from corrosion and a comparatively small rehabilitation measure is sufficient. The cost for rehabilitation, which is necessary approximately every 20 years, can be reduced to half the costs. For an approximate structure lifetime of 100 years this leads to enormous cost savings. Accurate measurements are the basis for understanding and defining the process of Cl-ingress into concrete structures. In this paper, the deficiencies of the standard methods are demonstrated and a new evaluation method is applied. The calibration process as well as real life applications on retaining walls are presented and discussed.

INTRODUCTION

The longevity of reinforced concrete itself is in most cases determined by the protection against corrosion of the steel reinforcements. Together with oxygen and an electrolyte (wet concrete), the steel reinforcements may corrode. While oxygen and an electrolyte are in most cases available, the protection against corrosion is accomplished by the natural alkalinity of the concrete, which is generally provided by the alkalinity of the surrounding cement paste. This alkalinity is mainly determined by the amount of cement in the concrete and can be reduced by a number of factors, one of them being the chloride content due to uptake from the environment.
Completely chloride-free concrete constituents cannot be gained economically; therefore, a low “natural chloride content” is present, which should not lead to corrosion and is accepted by the standards. On motor highways, de-icing salts are used during the winter season. Those de-icing salts contain chlorides which are mobilized by water and carried into the concrete and towards the reinforcements. As a

result, the chloride content increases during the lifetime of the structure. The chloride-induced corrosion is defined in standards (e.g., ÖNORM B 4706), to start above a chloride to cement ratio of about 1.0 m%.
After the exposure of concrete to chloride, it is only a question of time until the critical chloride to cement ratio is reached. Chloride-triggered corrosion leads to a pitting corrosion phenomenon which reduces the cross section of the steel reinforcements in relatively short time. This leads to a structural safety problem. A retrofitting action where only the alkalinity has to be re-established (e.g., new concrete cover) is approximately half of the cost of replacing the reinforcements. Thus, there is an ideal point in time for the retrofit measure, which is shortly before the reinforcements start to corrode. For the determination of this optimal point, appropriate evaluation techniques are essential.
Currently, the standards suggest determination of the chloride content from borehole cuttings by titration. The problem with this method is that the chloride content of the entire borehole cuttings are analyzed and calculated with an assumed cement content of the sample. The fraction of aggregates in the borehole cutting sample is usually not representative for the concrete, as the sampled volume of concrete may contain a higher or lower content of aggregates. These variations lead to a result that is subject to high scatter. Due to the low number of samples, the result has to be considered as not accurate enough to assess or predict any danger of corrosion.
Additionally, the aggregates may contain chlorides which will not be mobilized under natural (non-acidic) conditions and therefore will not contribute to corrosion effects. However, these chlorides falsify the evaluation suggested by the standards.
Because of these shortcomings a new method (LA-ICP-MS, Laser ablation inductively coupled plasma mass spectroscopy) was applied for that purpose. The advantages of the method presented in this paper are:

- The chloride content can be determined selectively in the cement phase.
- Aggregates and cement phase can be distinguished.
- Depth-profiles of the chloride content in the cement phase can be determined at a very high resolution, which makes a reliable assessment easier.
- The specimen preparation is strongly simplified and less prone to errors.

A forecast model can be derived and calibrated from the data (future work). The profile determined from borehole cuttings is too coarse for such purposes.

EXPERIMENTAL

Collection and preparation of the samples

Drilled cores were sampled from a highway bridge in Vienna. The samples were taken at four different heights with 6 cores sampled at each height. The drilled cores had a diameter of 45 mm, and were 100 mm in length. Before analysis, the samples were cut in two halves to enable LA-ICP-MS analysis in the center of the cores. Dry cutting was performed, to prevent mobilization of chloride.

Instrumentation

The presented experiments were performed using an iCAP Q quadrupole ICP-MS (ThermoFisher Scientific, Bremen, Germany). For direct solid sampling experiments, an NWR213 laser ablation unit (ESI, Fremont, CA) was connected to the ICP-MS

device using PTFE tubing. For sample ablation, the ablation chamber was purged with helium, which was also used as carrier gas to transport the generated aerosol particles to the ICP-MS. Before introduction of the ablation stream into the plasma, argon was admixed (make-up gas) to create more stable plasma conditions. The instrumental conditions were optimized on a daily basis using a reference material (NIST 612, trace elements in glass, National Institute of Standards and Technology, Gaithersburg, MD). Instrument tuning was performed for highest signal intensity for $^{115}In^{+}$, while keeping the ratio of formed oxides (monitored by $^{140}Ce^{16}O^{+}/^{140}Ce^{+}$) below 1.9%. Typical instrumental parameters are listed in Table 1. Using test samples, the optimal laser parameters for sample investigation were determined. Wherever possible, less abundant isotopes were used for analysis in the case of bulk constituents.

Table 1. Typical instrumental parameters for the LA-ICP-MS measurements.

laser ablation		*ICP-MS*	
wavelength	213 nm	plasma power	1550 W
pulse duration	4 ns	cool gas flow	14.0 $Lmin^{-1}$
laser repetition rate	10 Hz	auxiliary flow	0.8 $Lmin^{-1}$
laser beam diameter	250 µm	cones	Ni
laser energy	1.38 mJ	scanning mode	peak hopping
laser scan speed	40 µm s^{-1}	dwell time per isotope	10 ms
laser beam geometry	circular	monitored isotopes	$^{25}Mg^{+}$, $^{27}Al^{+}$, $^{29}Si^{+}$, $^{35}Cl^{+}$, $^{42}Ca^{+}$, $^{49}Ti^{+}$, $^{57}Fe^{+}$
He gas flow	0.4 L min^{-1}	mass resolution	300 m/Δm
Ar make-up flow	0.8 L min^{-1}		

Quantification of LA-ICP-MS signals and LA-ICP-MS measurements

The sample surfaces were cleaned using pressurized air prior to analysis. Before LA-ICP-MS measurement of the samples, the ablation chamber was purged with helium gas for 20 minutes to reduce background signals to a minimum. Qtegra software, as provided by the manufacturer of the instrument, was used for recording of the time resolved intensity data for the selected isotopes. Each sample was analyzed using 24 scanned lines with a distance of 3.3 mm between the lines. Scanning direction was perpendicular to the drilling axis to obtain depth profiles from the chloride distribution.

Quantification of the chloride content in the concrete samples was performed using external calibration. Pressed pellets were prepared from cement with known chloride concentrations (certified reference materials). Homogenization of the material was performed using an ultrasonic swing mill; 300 mg sample material were pressed using a pneumatic press for 30 s at 10 bar. The chloride contents of the reference materials were 0.022, 0.040, 0.057, and 0.077 m%, respectively. To manufacture matrix-matched standards with higher chloride concentrations, pure sodium chloride was mixed with the previously described reference materials. Homogeneity of those standards was tested using LA-ICP-MS; standards with 0.23, 0.49, and 1.01 m% chloride were obtained.

RESULTS

Signal quantification using LA-ICP-MS

Analyte signals obtained from the pressed pellet standards were used for signal quantification of the samples with unknown chloride content. Two calibration functions (for low and high concentration) were calculated. Both calibrations yielded correlation coefficients above 0.9990. As calcium is main constituent of the cement, the $^{42}Ca^{+}$ signal was used as internal standard to compensate for instrumental drifts as well as possible matrix variations. For the calibration functions, a limit of detection (LOD) of 0.008m% and a limit of quantification (LOQ) of 0.021m% chloride were obtained. The pressed pellet from the reference material containing 0.077 m% chloride was used for validation of the calibration and is therefore not included in the linear regression. The external validation resulted in a calculated chloride content of 0.072 ± 0.006m% (α=0.95, n=4), underlining the reliability of the calibration model.

Quantification of chloride in the cement phase

Using LA-ICP-MS, reliable and fast analysis of the chloride concentration in the analyzed samples is possible. In comparison to titrimetric or other wet chemical methods, LA-ICP-MS allows for much more detailed resolution in the resulting depth profiles.

DISCUSSION

The depth profiles obtained by LA-ICP-MS measurement are based on the mean value calculated from single measurements across a line perpendicular to the drilling direction. The line measured is approximately 30 mm long; measurements on the aggregates are neglected and therefore not taken into consideration for the chloride determination. In contrast to the strongly varying values obtained by titration of the borehole cuttings, using LA-ICP-MS much more reliable results can be obtained by sampling a large number of measurement points

Figure 1 shows depth profiles of drilled cores taken from four different height levels. It shows that the maximum chloride content at lower heights (Fig. 1a, and 1b) is higher, and becomes lower for higher sample heights. At depths higher than 60 or 70mm the chloride content appear to approach the “natural chloride content” which is in this case slightly lower than 0.1m%.

It is interesting to see that the maximum chloride content is not on the surface, but in most cases at depths of 10 to 20mm. We assume that this is a consequence of chloride being washed away from the surface during the drying process. Thus, under completely wet conditions the chloride content should be even higher in this depth range.

As we can see here, the depth profile needs to be fine to identify the maximum of the chloride content as well as to determine the shape of the chloride distribution. By application of titration of the borehole samples, often only depth resolutions of 20mm are achieved. Especially by the depth profile shown in Fig. 1a, this averaging process would strongly lower the maximum value and the information about the real chloride distribution is lost.

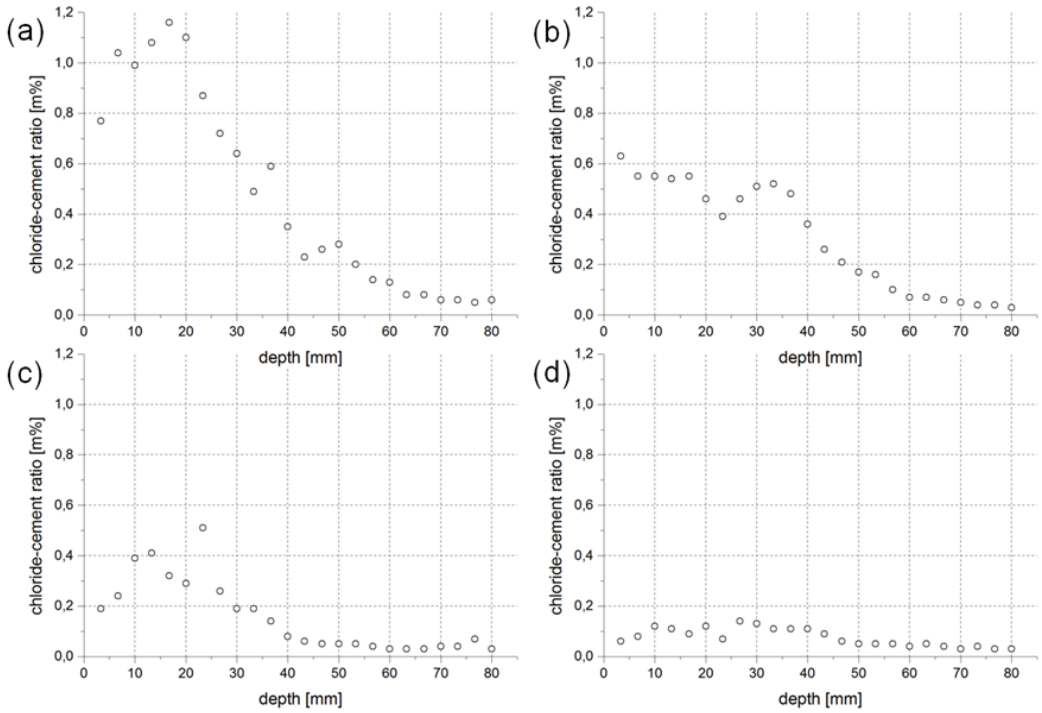

Figure 1. Depth profiles from drilled core samples taken at different heights as ratio of chloride in cement [m%]: 0.8 m above street level (a), 1.8 m above street level (b), 2.6 m above street level (c), and 4.6 m above street level (d).

CONCLUSION

The standard method for the determination of the critical chloride value is the titration of borehole cuttings. This method suffers on one hand from high scatter in combination with a low number of replicates (in fact one for each borehole depth). The scatter is mostly a result of the strongly varying amount of aggregates in the sample, on the other hand by falsification of the results by taking the chloride content of the aggregates into account. In contrast, LA-ICP-MS represents a fast and reliable method for the analysis of chloride in concrete samples. Besides omitting tedious wet chemical analysis, depth profiles with very high resolution can be generated. This allows deeper insight into diffusion processes of chloride in the cement phase, accurate measurements, and the basis for a forecast model.

Cracking Behaviors Caused by the Corrosion of Reinforcing Bars in RC Columns

H. Maruyama[1]; Y. Gakuhari[2]; and Y. Shinohara[3]

[1]Department of Environmental Science and Technology, Tokyo Institute of Technology, G5-5, 4259 Nagatsutacho, Yokohama-City, Kanagawa. E-mail: maruyama.h.ae@m.titech.ac.jp
[2]Kajima Corporation, 3-1 Motoakasaka 1-chome, Minatoku.
[3]Structure Engineering Research Center, Tokyo Institute of Technology, G5-5, 4259 Nagatsutacho, Yokohama-City, Kanagawa. E-mail: yshinoha@serc.titech.ac.jp

Abstract

Cracking and transverse bars strain behaviors of reinforced concrete (RC) columns induced by expansive pressure of corrosion products around corroding reinforcement were investigated through an accelerated corrosion test. Ten full-scale specimens which were element of RC columns having a dimension of 600 x 600 x 300mm were prepared. To get closer to actual phenomenon of chloride attack, a different amount of current was given into the longitudinal and transverse bars in response to the diffusion progresses of chloride ions depending on their cover thickness. Variable factors were concrete strength, bar arrangement and cover thickness. Test results indicated that concrete strength affects reinforcing bar strain and surface crack width growth considerably. A corrosion product generated in high strength concrete with less pores does not diffuse and concentrates into a crack. A specimen of smaller cover thickness (20mm) increased surface crack width and transverse bars strain was small compared with basic cover thickness specimen (40mm). On the other hand, bar arrangement didn't show a remarkable effect on cracking behaviors and strain of transverse bar.

INTRODUCTION

The corrosion of reinforcing bar is an important problem on the deterioration of RC structures because it may induce cracking of concrete cover as well as bond degradation. Cracking of concrete cover caused by corrosion product expansion of a steel bar is one of the main factors in determining durability performance and service life of RC structures. There have been a large number of experimental studies such as Kitsutaka et al. (2011) and Toongoenthong and Maekawa (2005) to evaluate the cracking behaviors (e.g. crack initiation and propagation) of concrete under corrosion of reinforcing bar for past years. However, most of their specimens have single bar installed in concrete prism or cylinder without any transverse bar. This bar arrangement may not represent the actual boundary condition of RC structural members.

The present study is intended to investigate the influence of actual confinement provided by surrounding concrete and transverse bar on the cover cracking behaviors induced by corrosion product expansion, and to obtain a general tendency on crack propagation, crack width and stress behavior of transverse bar using an element of full-scale RC columns. Furthermore, the corrosion process is given as a function of a time. The main purpose is to estimate the corrosion level of reinforcement in concrete from crack width of concrete surface which can be measured easily.

CORRODED EXPERIMENTAL PROGRAM

Specimen details. Ten specimens assuming an element cut from RC columns were designed to investigate the relationship between cracking behaviors induced by corrosion and variable factors including concrete strength and cover thickness. Figure 1 shows the bar arrangement of each specimens and strain gage points which are shown in black marker.

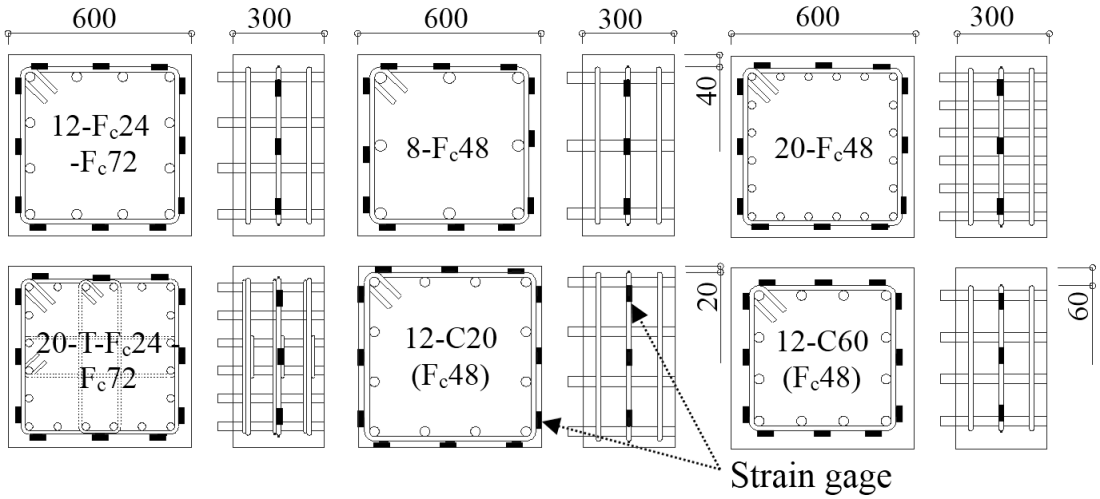

Figure 1. Bar arrangements and strain gage point of each specimens.

Table 1. Specimen Properties.

Specimen designation	Compressive strength (N/mm^2)	Longitudinal bars	Transverse bars		Cover thickness (mm)
		Bar property	Bar property	Inter. Bar property	
12-F_c48	44.7	12-D32	D16@100	-	40
12-F_c24	22.3				
12-F_c72	59.0				
8-F_c48	44.7	8-D32			
20-F_c48		20-D25			
20-T-F_c24	22.3		D13@100	D10@100	
20-T-F_c48	44.7				
20-T-F_c72	59.0				
12-C20	44.7	12-D32	D16@100	-	20
12-C60					60

Test specimens have a large cross section of 600×600 mm, cutoff height of 300 mm, longitudinal bars of p_g=2.7%, and transverse bars of p_w=0.66%. The variable factors of specimens are concrete strength (Fc24, Fc48, Fc72), longitudinal bar arrangement (20-D25, 12-D32, 8-D38), transverse bar arrangement (D16@100, D13+D10@100) and cover depth (20, 40, 60 mm) (Table 1). The proportion of concrete mixture and measured material properties are summarized in Table 2 and Table 3.

Table 2. Mixture proportions.

Design Strength	w/c (%)	Cement (kg/m^3)	Water (kg/m^3)	Fine aggregate (kg/m^3)	Coarse aggregate (kg/m^3)	Admixture (kg/m^3)
F_c24	63.5	290	184	891	901	2.90
F_c48	43.7	389	170	822	923	3.89
F_c72	34.1	499	170	804	891	5.49

Table 3. Mechanical properties of materials.

Mechanical properties	Concrete			Steel bar					
	F_c24	F_c48	F_c72	D10	D13	D16	D25	D32	D38
Compressive strength (N/mm^2)	22.3	44.7	59	-	-	-	-	-	-
Tensile strength (N/mm^2)	2.83	3.96	4.06	486	493	493	553	611	641
Yield strength (N/mm^2)	-	-	-	351	349	340	380	439	447
Young's Modulus (×10^{5}N/mm^2)	0.24	0.30	0.36	1.93	1.83	1.82	1.91	1.89	1.91

Accelerated corrosion procedures. All specimens were cured for 28 days before an accelerated corrosion test was applied. Figure 2 shows the system of accelerated corrosion test. All specimens were placed into a tank containing 3% of NaCl solution. To avoid penetration of NaCl solution, each surfaces on the top and the bottom were coated by epoxy resin with one millimeter thickness two times. A direct-constant voltage of 10 V was basically given into each reinforcing bar.

To considered diffusion progress of chloride ions depending on a difference of between longitudinal bars and transverse bars of cover thickness, a switch was installed in a circuit of longitudinal bars. The switch was changed based on (1), (2) equations by Miyazato et al. (2011) which shows the density of chloride ions from cover concrete

$$\mathrm{C} = (C_0 - C_{ini})\left\{erfc(\frac{x}{2\sqrt{Dt}})\right\} + C_{ini} \quad (1)$$

$$\log_{10} D = -3.9(w/c)^2 + 7.2(w/c) - 2.5 \quad (2)$$

where C is density of chloride ion (kg/m^3), C_0 is amount of surface chloride ion (kg/m^3), C_{ini} is density of initial chloride ion (kg/m^3), D is assumption diffusion

coefficient, x is distance of reinforcing bar and concrete surface, t is test period (s), w/c is water-cement ratio.

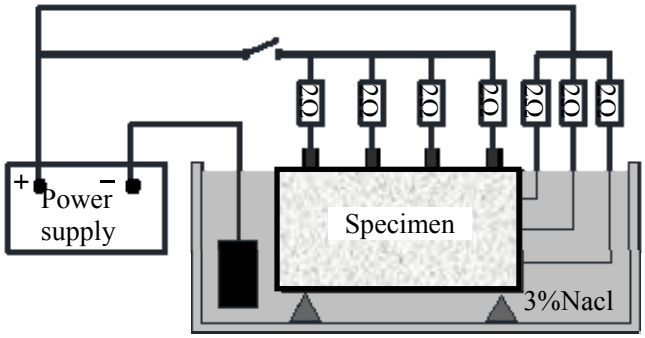

Figure 2. Accelerated corrosion test setup.

The measurement factors are the strain of transverse bar, surface crack width, and current amount. To measure current amount hourly, 2Ω resistance was set between reinforcing bar and power supply and connected to a data logger. The reinforcing bar weight loss by accelerated corrosion test was evaluated from current amount by using a Faraday's law, and predicted value of it was calculated using an equation(3)

$$Corr.\ rate\ = \frac{J_{corr} M_{Fe} t}{Fn} \qquad (3)$$

where *Corr. rate* is the amount of reinforcing bar weight loss; F is Faraday's constant (96485C/mol); n is valence of iron (= 2); J_{corr} is corrosion current density (mA/cm^2); M_{Fe} is atomic mass of iron (55.8 g/mol); and t is test period (s). The transverse bar strain were also measured hourly using date logger.

The transverse bar strain were recorded hourly using date logger. The cracks on the surface of cover were visually observed and the crack width at certain locations was frequently measured using digital microscope having resolution of 0.01mm to monitor the crack width increment.

To accurately determine the corrosion rate of reinforcing bar, after accelerated corrosion test, the reinforcing bars were removed from these specimens, chemically and mechanically cleaned based on JCI-SC Committee (1991) and measured the weight loss.

EXPERIMENTAL RESULT AND CONSIDERATION

Corrosion rate of reinforcing bars. Table 4 shows measured corrosion rate of reinforcing bar for each specimen. The weight loss of four corner bars, four to sixteen intermediate bars and three transverse bars are shown on average. The specimen having 60mm cover thickness is under the accelerated corrosion test. The weight loss of transverse bars was higher ratio than the estimated weight loss based on Faraday's law. On the other hand, the weight loss of longitudinal bars was the lower than the estimated weight loss by Faraday's law. This may be because that most of electric current flowed into the transverse bars due to its lower resistance.

Table 4. Average Corrosion amount in weight loss (mg/cm^2).

Specimen	Longitudinal bar						Transverse bar		
	Conner bar			Intermediate bar					
	W_{loss}	W_{cal}	W_{loss}/W_{cal}	W_{loss}	W_{cal}	W_{loss}/W_{cal}	W_{loss}	W_{cal}	W_{loss}/W_{cal}
12-F_c48	55	104	0.53	18	114	0.16	128	84	1.51
12-F_c24	49	125	0.39	38	99	0.38	140	63	2.21
12-F_c72	38	119	0.32	26	62	0.42	102	92	1.10
8-F_c48	43	131	0.33	28	111	0.25	117	84	2.10
20-F_c48	45	170	0.27	44	111	0.13	120	76	1.68
20-T-F_c24	81	90	0.90	53	110	0.48	192	59	3.25
20-T-F_c48	110	174	0.64	49	81	0.60	199	108	1.84
20-T-F_c72	59	144	0.41	31	75	0.41	122	78	1.57
12-C20	47	189	0.25	16	131	0.12	156	61	2.57

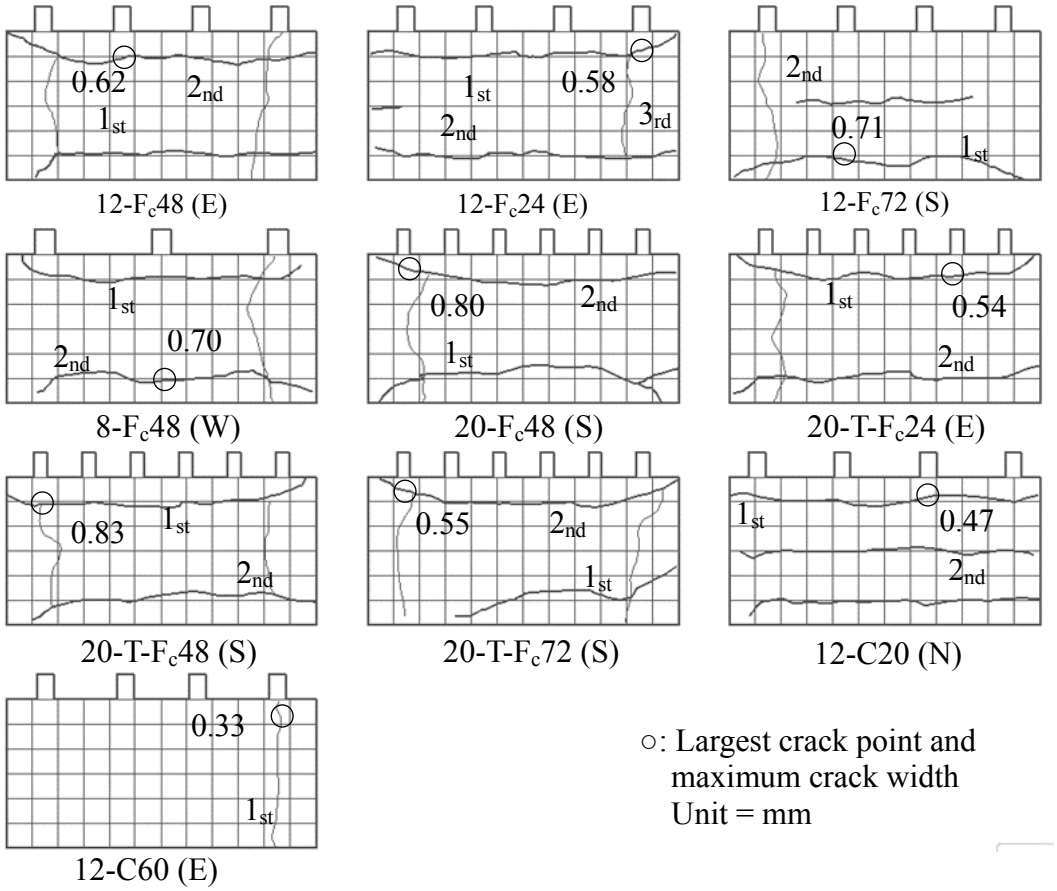

Figure 3. Crack patterns at final stages.

Cracking behavior. Figure 3 shows crack patterns of each specimen at final stage. A corrosion cracking is most early appeared on the surface parallel to transverse bar of the specimen having 20mm cover thickness. Although the appearance of corrosion cracking in high strength concrete specimens (F_c72) is later than other specimens (F_c24 and F_c48), the crack width is rapidly increasing compared with specimens having lower concrete strength. This may be due to the lower porosity in higher

concrete strength, because it may be difficult for the corrosion product to penetrate or to diffuse in the cement paste for high strength concrete. As a result, most of corrosion product concentrate in a crack. The maximum crack width was observed on parallel to transverse bars which showed higher corrosion ratio compared with longitudinal bars. But the specimen having 60mm cover thickness, it was early observed on parallel to longitudinal bars. This indicates lateral crack grows between cover concrete and transverse bar. The difference in bar arrangement did not show a significant influence on the crack width.

Figure 4 shows appearance of specimen having variable factors about concrete strength and cover thickness after 40 days from the start of accelerated corrosion test. For low strength concrete (Fc24) and small cover thickness (20mm) specimens, more corrosion products are leaking comparison with high strength concrete (Fc72, Fc48) and large cover thickness (40, 60mm) specimens. This tendency shows that the more specimen has high strength concrete and large cover thickness, the more specimens can prevent form penetration of chloride ions.

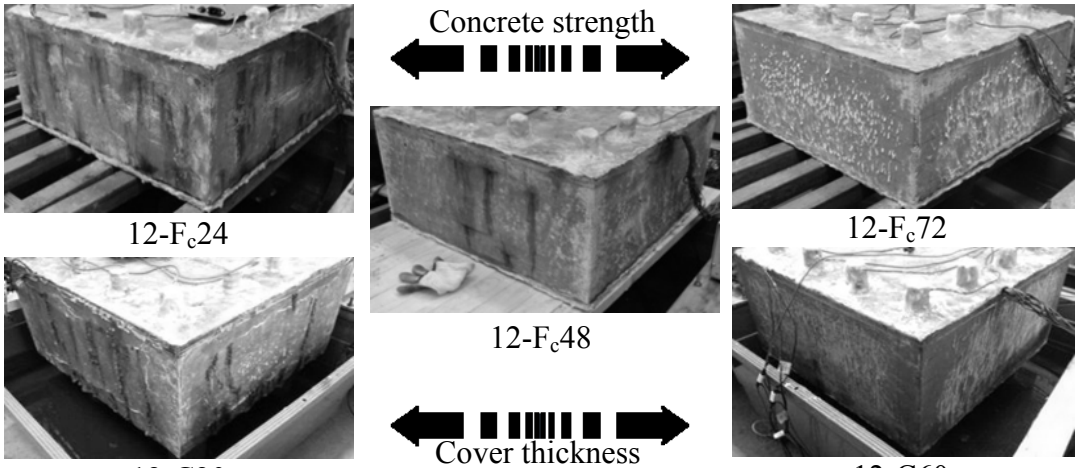

Figure 4. Comparison at 40 days passed on accelerated corrosion.

Figure 5 shows relationship between average surface crack width and calibrated corrosion rate which was modified by multiplying W_{loss}/W_{cal} in Table 4 by corrosion rate in equation (3). The effect of concrete strength is shown in Figure 5 (a). High strength concrete shows that the crack width is larger than specimens having low concrete strength at similar level. Tanaka (2001) reported the porosity of hardened cement paste increase with of w/c ratio, so lots of corrosion products accumulated around reinforcing bars in high strength concrete which prevents the corrosion products to penetrate within the pores of hardened cement paste. The effect of bar arrangement is shown in Figure 5 (b). The tendency of increasing crack width about two specimens (12-F_c48, 20-F_c48) is almost same due to same concrete strength, but the specimen (8-F_c48) occurred initial crack later than other specimen because it has large diameter longitudinal bars which requires more electric current to obtain the same corrosion level.

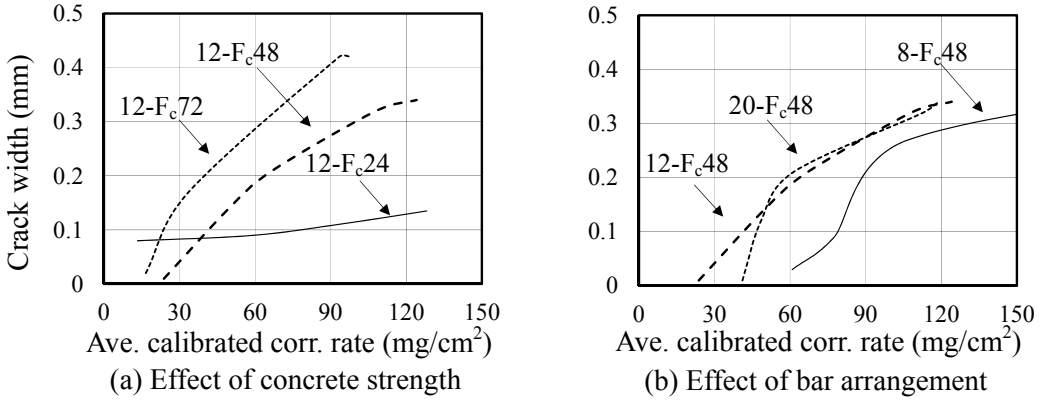

Figure 5. Average surface crack width along with lateral bar.

Transverse bar strain behavior. Aryanto and Shinohara (2014) indicated that transverse bars will increase confinement level around corroded longitudinal bar. Half of strain gages were not able to measured transverse bar strain during accelerated corrosion test because of damage, so Figure 6 shows the relationship between calibrated corrosion rate and the maximum transverse bar strain each specimens. Higher strain at transverse bar was observed for specimen with high concrete strength (12-F_c72). Maximum strain generated in 12-F_c72 is about 470μ or 25% of yield stress. In the low w/c ratio concrete, corrosion products concentrate in a crack, and crack width increased.

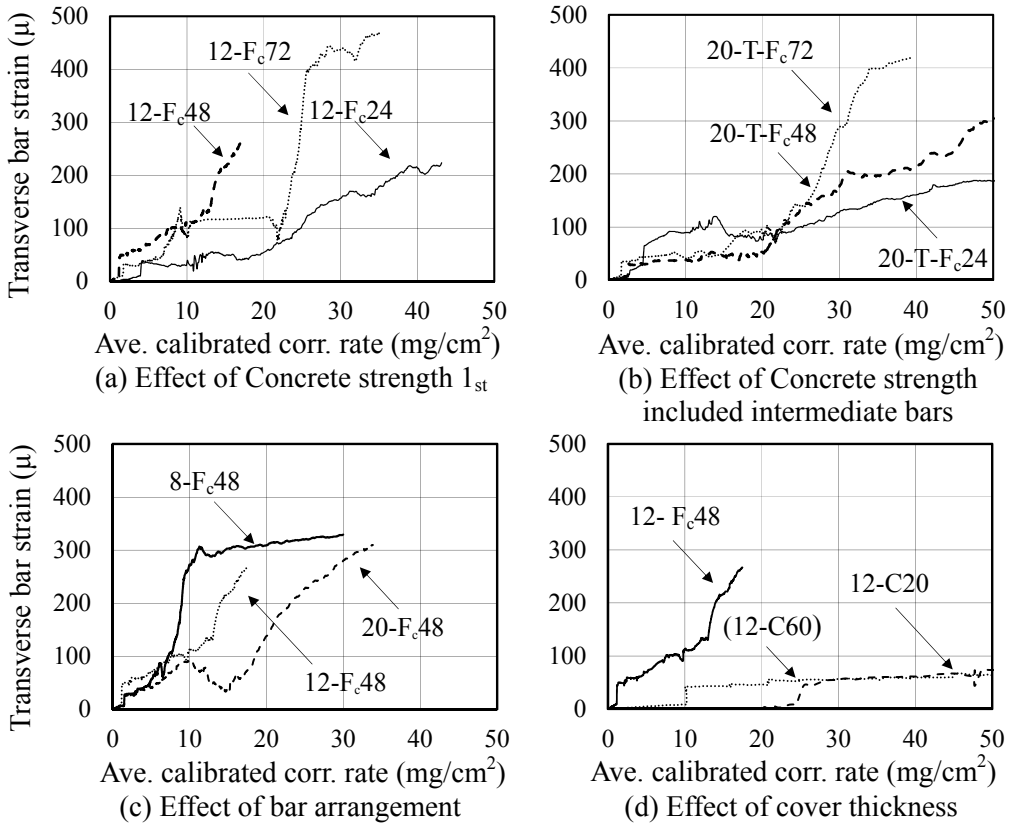

Figure 6. Maximum transverse strain.

In Figure 5(c), the large diameter longitudinal bar (8-F_c48) induce increasing of transverse bars strain rapidly compared with small one at initial crack. But in final stage, the strain of transverse bars reached to the same level because the surface crack greatly developed and most of corrosion product leaked.

In Figure 5(d), the strain of small cover thickness specimen (12-C20) did not increased. Because ring tension stress surrounding longitudinal bar was smaller and initial crack occurred earlier than any other specimen. The calibrated corrosion rate of large cover thickness specimen (12-C60) was used date of measured by data logger due to under test.

Relationship between internal cracking and reinforcing bar corrosion. After accelerated corrosion tests, cover concrete was removed to observe the internal cracking induced by corrosion and the stain of corrosion products. Corrosion products were observed between cover concrete and transverse bars, especially, along with vertical layer throughout the three transverse bars as shown in Figure 6. The transverse bars were greatly corroded compared with the longitudinal bars. On the other hand in the core concrete, any corrosion product was not observed.

(a) Removed cover concrete

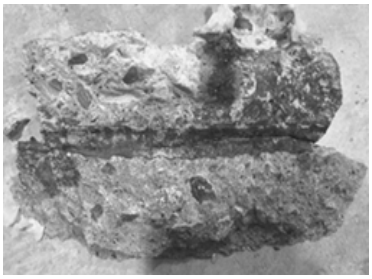

(b) Brittle crack surface

Figure 7. Internal cracking surfaces and corrosion products migration.

Proposed Equation to estimate the limits of the possible in corrosion. Figure 8 shows the relationship between calibrated corrosion and the ratio of cover thickness to diameter of reinforcement and using test results when the crack width reached to approximately 0.1mm crack width. In Figure 8, black-painted makers show longitudinal bar, and white-painted makers show transverse bars. An equation proposed by JSCE (2000) is also shown

$$W_{cr} = 10(c/d) \quad (4)$$

where W_{cr} is corrosion rate of reinforcing bar, c is cover thickness, d is diameter of reinforcing bar. The test results vary widely. In this study, so this paper proposes an equation considering effect of *w/c*.

$$W_{cr} = 10(c/d + 28)\{-0.00146 \cdot (w/c)^2 + 0.154(w/c) - 2.87\} \quad (5)$$

Equation (5) can estimate the limits of the possible in corrosion rate.

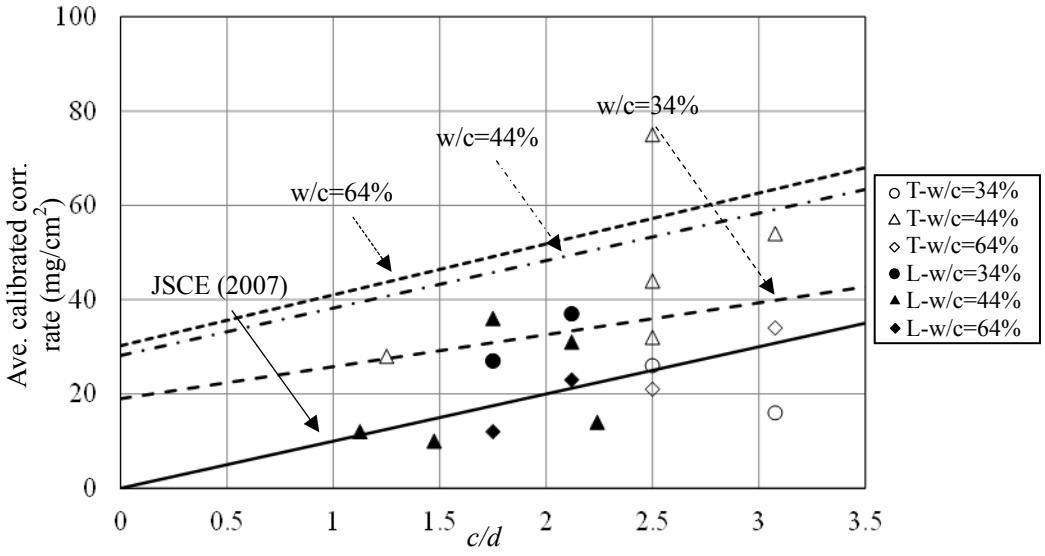

Figure 8. c/d vs W_{cr} and proposed equations.

CONCLUSIONS

This experimental study investigated the relationship between cracking behavior and reinforcing bar corrosion under closer actual condition of corrosion environment in RC column. The main conclusions are as follow:

1. The measured corrosion rate of transverse bars is higher than calculated values W_{cal} by 1.1 to 3.3 times. On the other hand, longitudinal bar's corrosion rate is lower than a calculated values by 0.1 to 0.9 times.
2. The initial crack is appeared in the direction of parallel to transverse bars, and the maximum crack width was also observed on the same location.
3. The high-strength concrete delays the occurrence of crack compared with low strength concrete. But crack width rapidly increases after cracking.
4. The specimen having small cover thickness causes crack early and generate much corrosion product in comparison with large cover thickness one.
5. Corrosion products were observed along with vertical layer throughout the three transverse bars, but it was not observed in core concrete.
6. An equation to estimate the limit of the corrosion is proposed by considering w/c about relationship between c/d and W_{cr}.

ACKNOWLEGEMENTS

The authors acknowledge the supports of Nuclear and Industrial Safety Agency (NISA) as a part of the project on enhancement of Ageing Management and Maintenance of Nuclear Power Stations.

REFERENCES

Kitsutaka, Y., Le, P. N., Tukakoshi, M. and Matsuzawa, K. (2011) "Investigation the Amount of Reinforcing Bar Corrosion when the Crack Generates on Reinforced Concrete Surface". *Proceeding of the Japan Concrete Institute,* Vol.33, No1, 1145-1150.

Toongoenthong, K. and Maekawa, K. (2005). "Simulation of Coupled Corrosive Product Formation, Migration into Crack and Propagation in Reinforced Concrete Section" *Journal of Advanced Concrete Technology* Vol.3, No.2, 253-265.

Miyazato, S., Noguchi. T. and Takekawa, K. (2011). "Long Term Performance Control Technology of the Concrete Structure" *Concrete journal* Vol.49, No.5, 21-24.

JCI-SC Committee. (1991). "Corrosion of Concrete structure – Standards Test Method for Corrosion protection" *Japan Concrete Institute*.

Tanaka, K. and Kurumisawa, K. (2009). “Development of Technique for Observing Pores in Hardened Cement Paste” *Journal of Structural and Construction Engineering AIJ*, No.532, 21-26.

Aryanto, A. and Shinohara, Y. (2014). “Effect of Confinement and Concrete Strength Induced by Corrosion Product Expansion for Reinforced Concrete Members” Journal of Structural and Construction Engineering AIJ, No.696, 305-313.

JSCE (2002). “Standard Specification for Concrete Structure” Structure Performance collation, No.696, 27-28.

Quantitative Determination of Chloride-to-Cement Content of Concrete by Laser-Induced Breakdown Spectroscopy (LIBS)

G. Wilsch[1]; Thorsten Eichler[2]; Steven Millar[1]; and Cassian Gottlieb[1]

[1]BAM Federal Institute for Materials Research and Testing, Unter den Eichen 87, 12200 Berlin, Germany. E-mail: Gerd.Wilsch@bam.de
[2]CORR-LESS Isecke und Eichler Consulting GmbH & Co. KG, Kurfürstendamm 194, 10707 Berlin, P.O. Box 450307, 12137 Berlin, Germany. E-mail: Eichler@corr-less.de

Abstract

Laser-induced breakdown spectroscopy (LIBS) is a combination of plasma generation on the sample surface by a high power laser pulse and optical emission spectroscopy (OES). It is a direct measurement method without an extensive sample preparation. Concrete is a multi phase system. With LIBS it is possible to distinguish the different phases and based on that to correlate the chloride content to the cement mass. This is done by scanning the surface with a resolution of up to 0.1 mm. The high measurement frequency of 100 Hz or even higher allows the in-situ visualization of the chloride content over the measured area. With a calibration a quantification of chloride concentration is possible. As an example the LIBS measurement on a 50 mm by 70 mm area with a resolution of 0.5 mm and the visualization of the chloride distribution takes only 10 minutes. Additionally it is possible to evaluate the carbonation depth from the same measurement. Examples of practical application to determine the chloride-to-cement-content on concrete samples are presented. The possibilities and the limitations of LIBS are discussed.

Introduction

Reinforced concrete structures are generally dimensioned in consideration of a specific expected life time. For usual structures in civil engineering as e.g. multi store parking decks or bridges a minimum life time of approximately 50 years is expected. In some cases, the assessed life time is not attainable and ageing of specific structures happens far more quickly than expected. Environmental factors, influenced by weather, location or general exposition may cause the access of harmful species like SO_4^{--}, Na^+, CO_2 or Cl^-, etc. to the structure and accelerate the ageing process due to deterioration of concrete and/or reinforcement. Laser Induced Breakdown Spectroscopy (LIBS) can be applied as a fast and reliable method in order to identify harmful reagents and accompanying damage processes.

The LIBS technique shows a quick development at the moment, induced by progress in laser development for industrial applications and ongoing research projects. It may be applied for the investigation of gases, liquids or solids. Typical

fields of applications are process control in steel or glass fabrication, waste sorting, quality assurance of industrial and pharmaceutical products and also forensic and biomedical investigations (Hahn2012, Noll2012).

LIBS is principally able to detect all elements, in particular hydrogen, lithium or sodium which are difficult to detect by other well established techniques like XRF. Sample preparation is limited to few easy routines. The pulsed laser hits the optical accessible surface and if the power density in the focal point exceeds a certain value plasma is formed. It holds all information about the chemical composition of the evaporated material. During plasma expansion and cooling an element specific radiation is emitted and analyzed by spectroscopic methods.

The laser wavelength, the pulse duration, the pulse energy and the focus conditions are important parameters which influence the plasma properties and thus the analytical performance. Also the spectroscopic system has to be adapted for the measurement. The spectrometer type (single or multi element), the detector type (CCD, ICCD or CMOS) and the delivery of the plasma emission to the spectrometer have to be considered. After calibration based on reference samples quantitative concentrations are obtained.

LIBS is able to scan the surface of a sample with a resolution of some micrometer and frequencies of 100 Hz or even higher. Thus the heterogeneity of the material can be taken into account. For the multiphase system concrete the element content can be related to the cement mass.

At BAM the possibilities of LIBS have been investigated for several years. It has been shown that LIBS is able to measure all elements which may be influence the service lifetime, e.g. Cl, S, C, N, Na, Li and K. Also the cement type and the aggregates maybe identified (Wilsch2005, Weritz2006, Wilsch2011).

The challenge of separating aggregates and cement-matrix for investigating element distributions of concrete based materials was solved with a scanning system (see figure 1, left) for LIBS. Taking the heterogeneity of concrete into account is necessary and elementary, because the main transport-processes occur in the cement-matrix via pores. Wet chemistry analysis can not solve this particular problem.

Measurement

A photo of typical LIBS set-up as used for the investigation of building materials is shown in figure 1, left. During the measurement the measuring head is moved line by line in a plane parallel to the sample surface. The head includes both the focusing and also the collecting optics.

Figure 1. Right: Translation stage with measuring head and a core cut in the middle to do measurements on the cross section. During the measurement the head is moved line by line in a plane parallel to the sample surface. Left: Detailed view – showing the plasma on the sample surface

The radiation of a pulsed NdYAG-laser (λ = 1064 nm, pulse rate 10 to 100 Hz, energy per pulse 3 to 400 mJ, pulse duration = some ns) is focused to an area of less then a square millimeter to evaporate a small amount of the surface under investigation (some micrograms). Due to the high power density in the focus area plasma ignites and radiates for some microseconds (see figure 1, right). The plasma radiation is guided by an optical fiber to a spectrometer, which breaks the radiation into its spectral components. At the exit of the spectrometer the light intensities as function of the wavelength are detected by a CCD-camera. The focal length of the focusing lens or mirror is adjusted to the surface roughness and the target spot size. The volume around the plasma can be purged with air or helium to remove dust and enhance the results for the detection of some elements. The detection of chlorine and sulfur is more sensitive if helium is used as a process gas.

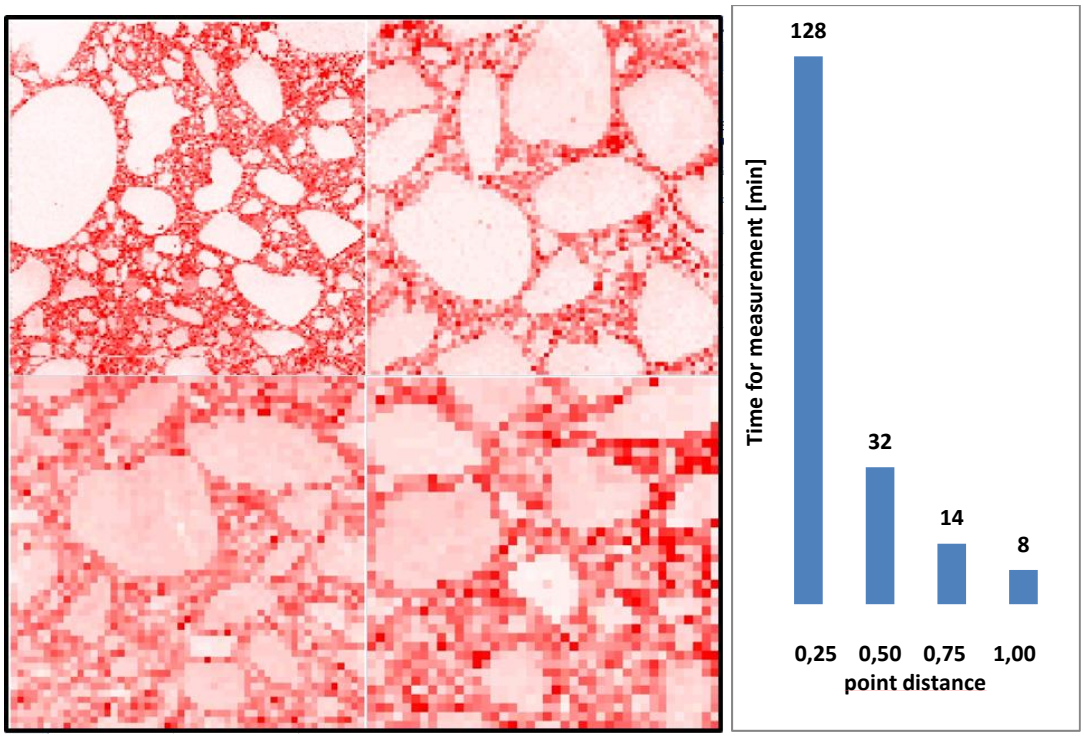

Figure 2. Right: Result of scanning of a 10 cm by 10 cm area on a concrete specimen using four different resolutions for each 5 cm by 5 cm subarea. Color coded is the intensity of the chlorine spectral line. Left: Time for measurement of a subarea in correlation to resolution (point distance) at 10 Hz.

The setup is controlled by customized LABVIEW software. An automated measurement procedure minimizes errors and enables fast analysis of samples.

The possible output of the measurement is the distribution of a specific element on the surface under investigation or, if the measurements are averaged per line, a gradient of element content.

Due to the ability of multi-element analysis the measurement of trace elements as well as the differentiation between cement and aggregates is possible. At BAM also a mobile LIBS set-up is available and was successfully tested at several on-site tests.

Figure 2 shows an example obtained at concrete specimen using different resolution (point distance). The measured intensity of the chlorine spectral line is shown in color coding.

A 10 cm by 10 cm area was divided in four subareas of 5 cm by 5 cm each. The subareas were scanned with a different point distance (0.25 mm, 0.5 mm, 0.75 mm and 1 mm). The time for the measurement is increasing from 8 minutes (0.25 mm point distance) to 128 minutes (1 mm point distance), but also more details were obtained with lower point distance.

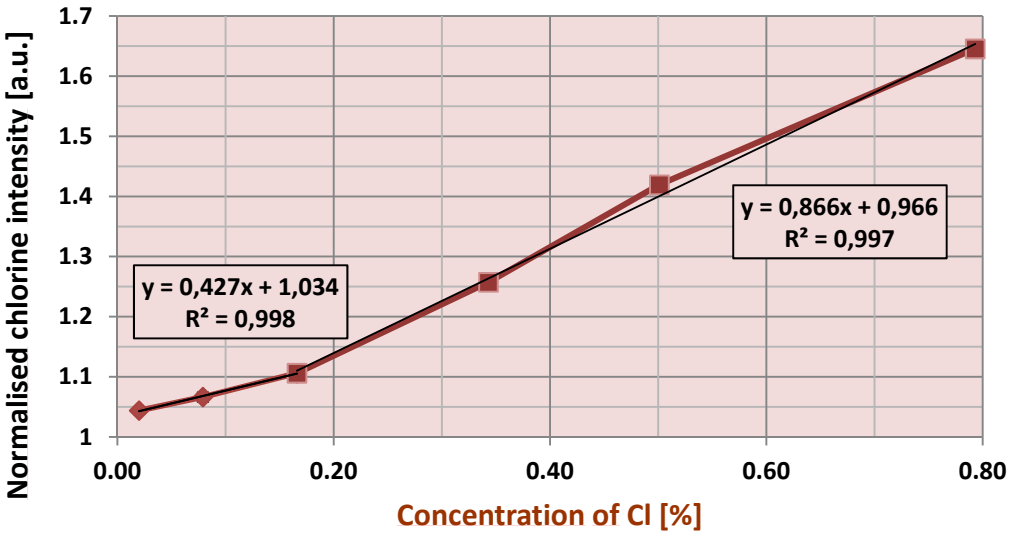

Figure 3. Calibration curve for chlorine obtained based on reference samples. The concentration is correlated to the evaporated mass.

LIBS can be seen as a semi quantitative method, because it gives normalized intensity values for different elements. After a calibration based on well investigated reference samples, quantitative values are obtained. As an example the calibration curves for the evaluation of quantitative concentrations of chloride in correlation to the evaporated mass is shown in figure 3.

Results

In figure 4 the results of a LIBS measurement at the cross section (40 mm × 70 mm) of a concrete core taken from a highway are shown. The chlorine concentration on the cross section is color coded (red), dark red means high chlorine intensity (figure 4, left).

With the help of elements that rather occur in the cement-matrix than in the aggregates or vice versa, it is possible to exclude the coarse aggregates. These elements could be e.g. calcium, hydrogen and/or oxygen, which are detected simultaneous with chlorine in the same measurement. See figure 4, middle, the large aggregates are indicated by black color. To which size the aggregates can be excluded depends on the chosen focal size and spatial resolution (see figure 2).

In figure 4, right, the quantitative ingress profile, determined by LIBS with excluding large aggregates is compared with the qualitative ingress profile obtained by µXRF. The spatial resolution (line interval/point distance) is 0.5 mm × 0.5 mm. With a laser pulse frequency of 10 Hz the measurement of 11200 points takes less than one hour and with a pulse frequency 50 Hz only about 12 minutes.

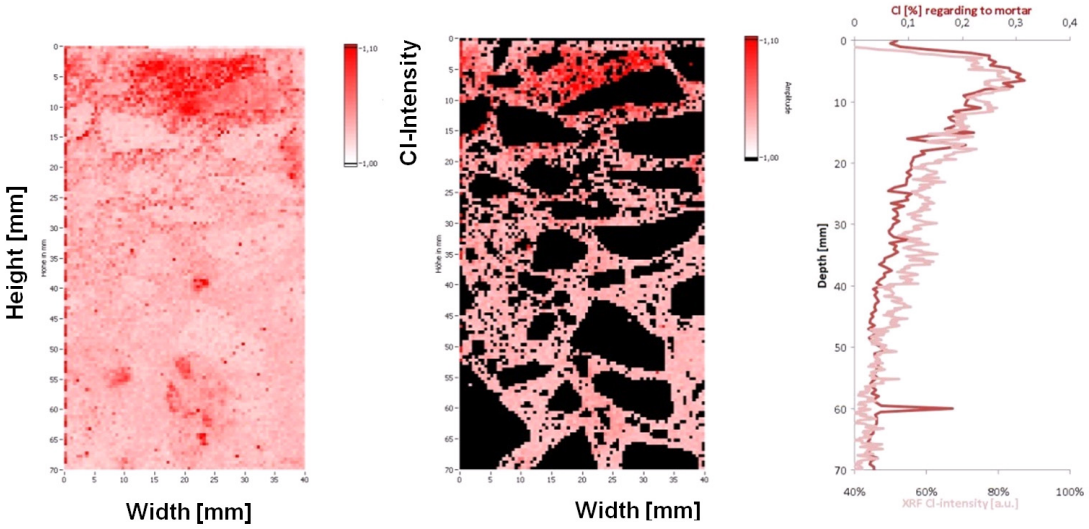

Figure 4. Left: Color coded chlorine intensity on the cross section of a concrete core; dark red represents high chlorine content. Middle: LIBS result excluding the measurements on aggregates from the data set, indicated by black color. Right: Depth profile of chlorine ingress measured by LIBS (dark red) in comparison with ingress profile measured by µXRF.

In damaged concrete the transport processes can be supported by cracks. In collaboration with TU Delft BAM investigated a set of concrete cores containing cracks of different width (Savija2014). As an example in figure 5, left, a photo of the cross section of a cracked concrete core (140 mm x 140 mm) with a crack width of 305 µm is shown. The core was loaded with NaCl-solution from the top. The result of scanning measurement on that cross section by LIBS with a resolution of 1 mm x 1 mm is shown in figure 5 right. The chlorine intensity is color coded and plotted on the cross section. Dark red means high chlorine intensity. The aforementioned scanning technique LIBS is able to image the transport of harmful ions by cracks.

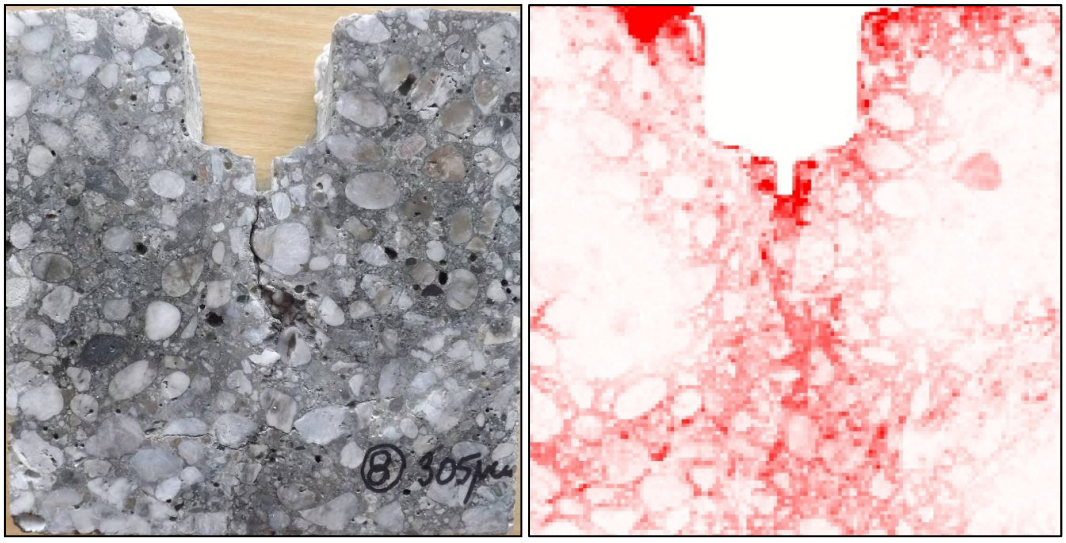

Figure 5. Left: Photo of the cross section of a cracked concrete specimen; sample-size 140 mm × 140 mm; crack width 305 µm. Ingress of NaCl-solution from the top. Right: Color coded chlorine intensity on same specimen; dark red represents high chlorine content.

CONCLUSION

The following conclusions may be drawn from the investigations exemplarily shown above:

- With LIBS it is possible to measure directly on the accessible sample surface. In comparison to the standard methods normally used in civil engineering only a minimum of sample preparation is necessary.
- The method is able to take the heterogeneity of the material into account. Coarse aggregates can be excluded (to which size depends on the chosen focal size and the spatial resolution) by evaluating elements that rather occur in the cement-matrix than in the aggregates or vice versa, e.g. calcium or oxygen. Finally it should be possible to correlate the concentration of an element to the cement mass.
- With the use of reference samples quantitative results can be derived.
- Automated LIBS measurements are fast and save time and man power.
- The possibility to detect several elements at the same time enables the engineer to make statements about different damage processes or their probability with just one measurement. Especially for the assessment of corrosion endangered reinforced concrete buildings LIBS may have a significant advantage because it can detect the chloride ingress and the carbonation front simultaneously.
- The technique is currently progressing from a pure laboratory application to an on-site analysis technology. The mobile system (with the appropriate detector) is able

to give quantitative results, comparable to the lab-system. First measurements under rough weather conditions are successful completed.

REFERENCES

Hahn, D. W. and N. Omenetto (2012). "Laser-Induced Breakdown Spectroscopy (LIBS), Part II: Review of Instrumental and Methodological Approaches to Material Analysis and Applications to Different Fields." Appl. Spectrosc. 66(4): 347-419.

Noll, R., Laser-induced Breakdown Spectroscopy - Fundamentals and applications, 2012, Springer Verlag, Berlin Heidelberg.

Savija, B., E. Schlangen, et al. "Chloride ingress in cracked concrete: a laser induced breakdown spectroscopy (LIBS) study." Journal of Advanced Concrete Technology 12(10): 425-442.

Weritz F, Schaurich D, Taffe A, and Wilsch G (2006) Effect of heterogeneity on the quantitative determination of trace elements in concrete, Anal Bioanal Chem 385: 248-255.

Wilsch G, Weritz F, Schaurich D, and Wiggenhauser H (2005) Determination of chloride content in concrete structures with laser-induced breakdown spectroscopy, Constr Build Mater 19:724-730.

Wilsch, G., D. Schaurich, et al. (2011). Imaging Laser Analysis of Building Materials - Practical Examples. Review of Progress in Quantitative Nondestructive Evaluation, Vols 30a and 30b 1335: 1315-1322.

Mechanical Behavior of Recycled Aggregate Concrete under Uniaxial Loading-Unloading Cycles

M.-D. Nguyen[1]; G. Wardeh[2]; and E. Ghorbel[3]

[1]University of Cergy-Pontoise, 5 Mail Gay LUSSAC, 95031 Neuville-sur-Oise.
E-mail: nguyenminhduc.gtvt@gmail.com
[2]University of Cergy-Pontoise, 5 Mail Gay LUSSAC, 95031 Neuville-sur-Oise.
E-mail: George.Wardeh@u-cergy.fr
[3]University of Cergy-Pontoise, 5 Mail Gay LUSSAC, 95031 Neuville-sur-Oise (corresponding author). E-mail: Elhem.Ghorbel@u-cergy.fr

Abstract

The paper presents the results of an experimental program related with the damage behavior of Recycled Aggregate Concrete (RAC) under uniaxial loading-unloading cycles. To this purpose, the effect of the percentage of recycled aggregates (RA) on the compressive mechanical properties of concrete was investigated. Eight mixes with C25/30 and C35/45 target class of compressive strength were prepared using normal or recycled coarse aggregates. For both series, a target S4 class of workability has been chosen. Cylindrical specimens were fabricated with different RCA replacement percentages of 0%, 30%, 100% fine and coarse RA and 100% of coarse RA. Uniaxial loading-unloading compression tests were performed using controlled displacement rate of 0.5 mm/min. From the obtained stress-strain curves, the scalar damage is quantified as the variation of the elastic modulus. Based on the experimental results, it was found that the damage depends on the replacement percentage of recycled aggregates and increases when the replacement ratio is high.

Keywords: Recycled aggregate; Concrete; Mechanical properties; Uniaxial loading; Damage.

INTRODUCTION

This work is part of the French project ANR VBD 2013 (ECOREB 2012) which is closely related to the French national project RECYBETON (RECYBETON 2012). The main aim of these two projects is the reuse of recycled aggregates, RA, in concrete structures. The project ANR is particularly interested on the study of the short and the long term behavior as well the durability of two series of recycled aggregate concretes developed in the framework of RECYBETON by the French laboratory IFSTAAR (RECYBETON 2012; Sedran 2013). The two series correspond to two classes of compressive strength (C25/30 and C35/45) and S4 class of flowability (slump between 160 and 210 mm).

The main objective is to study the influence of recycled gravel on the mechanical properties of concrete and particularly on the behavior under monotonically and cyclic uniaxial compression.
Numerous studies in the literature have developed mixing methods of concrete with recycled aggregates, and studied physical and mechanical properties, as well as their indicators of durability (Xiao, Li et al. 2005; Etxeberria, Vazquez et al. 2007; Evangelista and de Brito 2007; Belén, Fernando et al. 2011; Wardeh, Ghorbel et al. 2014). These studies have shown that recycled aggregate concretes may have mechanical properties similar to those of concrete mixed with natural aggregates, NAC, (Xiao, Li et al. 2005; Evangelista and de Brito 2007; Wardeh, Ghorbel et al. 2014). However, few studies have focused on the cyclic behavior and the damage evolution of RAC. These points are considered in the present work.

MATERIALS AND METHODS

Materials

All raw materials have been provided by the national project RECYBETON to associated partners (RECYBETON 2012).
Cement type CEM II/A-L 42.5, provided by Holcim, was used in this investigation. The natural aggregate used throughout this study was natural sand with a maximum size of 5 mm, and two types of crushed limestone gravel 4/10 mm and 6.3 / 20 mm.
The recycled aggregates were prepared in a platform of recycling into 3 classes 0/4, 4/10 and 10/20 mm. All aggregates were transported to the laboratory in big-bags and they were characterized to verify their conformity with the materials delivered to the other project partners.
For all mixes, limestone fillers, known by Betocarb HP-OG, manufactured by OMYA SAS and a MC PowerFlow 3140 superplasticizer were used.

Concrete mix proportions

Two series of concrete with target compressive strength classes C25/30 and C35/45 were designed. For both series a target S4 class of workability is specified where slump is comprised between 160 and 210 mm. Each Series includes four concretes: a control concrete and three RAC concretes with various replacement ratios. The nomenclature used is the following C25/30-xR yR-or C35/45-xR yR where xR represents the replacement ratio of sand by the total weight of sand and yR represents the replacement ratio of gravel by the total weight of gravel. Recycled aggregates were saturated during 24h before mixing with water equivalent to their absorption capacity plus 1%. The water absorption was taken equal to:

- 9.9% for recycled sand,
- 6.6% for recycled 4/10 gravel,
- 6.8% for recycled 10/20 gravel.

The concrete mix proportions, optimized by Ifsttar (Sedran 2013), are given in Table 1. From this table, it can be noticed that water to binder (cement + filler) ratio and paste volume are not constants. Furthermore, the cement content increases when the replacement ratio increases in order to achieve the target compressive strengths.

Test specimens

220x110 diameter and 320x160 diameter concrete cylinders were manufactured and cured in water to determine the compressive strength, splitting tensile strength and both dynamic and static modulus of elasticity. Uniaxial compressive and splitting tensile tests were performed on 220x110 mm specimens using a servo-hydraulic INSTRON machine with a capacity of 3500 KN. Experiments were performed at a stress rate of 0.5 MPa/s. Other tests were carried out by performing loading-unloading cycles up to failure at a displacement rate of 0.5 mm / min. Axial strains were measured using strain gauges and an extensometer with 3 LVDTs mounted along the circumference of the tested 320x160 mm cylinders. This instrumentation allowed the values of the static modulus of elasticity and the full stress-strain curve in compression to be determined. Finally, the dynamic modulus of elasticity is determined finally using E-Meter MK II device.

Table 1. Mix proportions of concrete mixtures.

Constituents (kg/m^3)	C25/30-0R-0R	C25/30-30R-30R	C25/30-0R-100R	C25/30-100R-100R	C35/45-0R-0R	C35/45-30R-30R	C35/45-0R-100R	C35/45-100R-100R
Total water	188	158	244	303	185	220	238	284
Effective water	180	185	189	199	175	179	185	184
Cement	270	277	282	326	299	321	336	381
Fillers	45	31	31	50	58	44	53	70
Natural sand	780	519	806	-	771	491	782	-
Recycled sand	-	241	-	673	-	214	-	663
Natural gravel (4/10)	267	173	-	-	264	168	-	-
Recycled gravel (4/10)	-	156	163	304	-	142	158	299
Natural gravel (6.3/20)	820	556	-	-	810	542	-	-
Recycled gravel (10/20)	-	179	701	442	-	164	682	435
Superplasticizer	1.31	1.08	1.26	1.18	1.89	1.64	1.83	2.18
Effective water/Binder (W/B)	0.57	0.60	0.61	0.53	0.49	0.49	0.48	0.41
Paste volume (m^3)	0.28	0.29	0.29	0.32	0.29	0.30	0.31	0.33

EXPERIMENTAL RESULTS

Each characterization test was repeated at least three times and the following results are the average of measurements.

Mechanical properties

The mechanical properties of studied materials are summarized in table 2. The replacement ratio is defined as the ratio between the weight of recycled aggregates and the total weight of aggregates in the mixture. It is given by Equation 1.

$$\Gamma = \frac{\sum M_{RA}}{\sum M_{(NA+RA)}} \quad \text{Equation 1}$$

where M_{RA} and $M_{(NA+RA)}$ are the weight of recycled aggregates and the total weight of natural and recycled aggregates respectively. Hence $\Gamma=1$ when both sand and recycled gravels are used.

The results show that for the same class of compressive strength the introduction of recycled aggregates leads to a decrease in the tensile strength and the elastic modulus. Similar observation is reported in the literature and the reduction is attributed to the higher porosity of recycled aggregates, the lower modulus of elasticity of recycled aggregates than that of natural aggregates and to the weaker interfaces between the recycled aggregates and old / new cement mortars (Xiao, Li et al. 2005; Casuccio, Torrijos et al. 2008; Wardeh, Ghorbel et al. 2014).

Table 2. Characteristics of concrete at 28 days.

	f_{cm} (MPa)	f_t (MPa)	E (GPa)	Γ (replacement ratio)
C25-0R-0R	33.8±1.4	3.1±0.9	36.9±2.2	0.0
C25-30R-30R	33.5±0.9	3.3±0.2	29.5±0.4	0.3
C25-0R-100R	32.5±1.0	3.4±0.2	28.1±1.0	0.5
C25-100R-100R	28.6±0.7	2.8±0.3	25.5±0.2	1.0
C35-0R-0R	41.5±1.2	3.6±0.2	42.1±1.7	0.0
C35-30R-30R	40.3±1.4	3.7±0.2	35.7±1.5	0.3
C35-0R-100R	38.1±2.2	3.4±0.4	31.8±0.4	0.5
C35-100R-100R	37.3±1.3	3.4±0.1	30.7±0.5	1.0

Peak and ultimate strains

The peak strain is the strain corresponding to the maximum compressive stress. The evolution of this strain as a function of replacement ratio is shown in Figure 1.a. It can be seen that the peak strain increases when the replacement ratio increases. These results are in agreement with the results reported in the literature (Xiao, Li et al. 2005; Belén, Fernando et al. 2011; Wardeh, Ghorbel et al. 2014). The increase in the peak strain is a consequence of the use of recycled aggregates which are characterized by a reduced elastic modulus compared to natural aggregates.

The influence of the recycled aggregates content on the ultimate strain was also investigated. It was evaluated in the descending branch of the stress-strain curve at a value of 0.6 of the maximum compressive strength. The results are presented in Figure 1.b. where it can be seen that the value of this strain increases when the replacement ratio increases.

Figure 2 illustrates the relationship between the ultimate and the peak strains for each concrete mixture. It can be noticed that $\varepsilon_{cu}/\varepsilon_{c1}$ increases with the recycled aggregates

content. This increase means that under the same loading conditions, the deformation capacity of RAC is higher than that of NAC and therefore recycled aggregate concretes are more ductile. These results are in good agreement with those of Wardeh et al (Wardeh, Ghorbel et al. 2014). However, they are inconsistent the conclusion of Xiao et al who found that this ratio decreases when the replacement ratio increases (Xiao, Li et al. 2005).

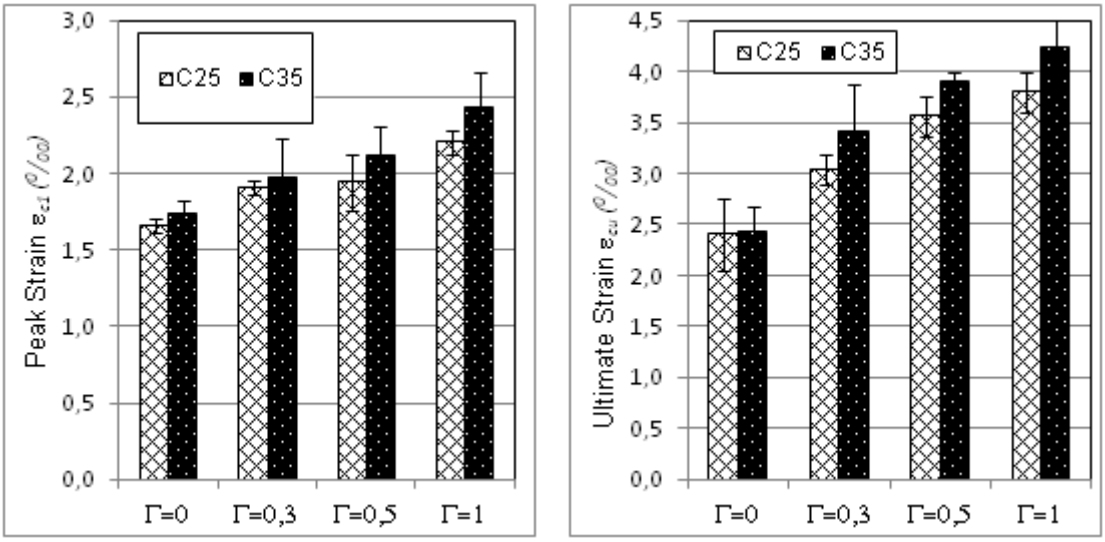

a) Peak strain

b) Ultimate strain

Figure 1. Peak and ultimate strains

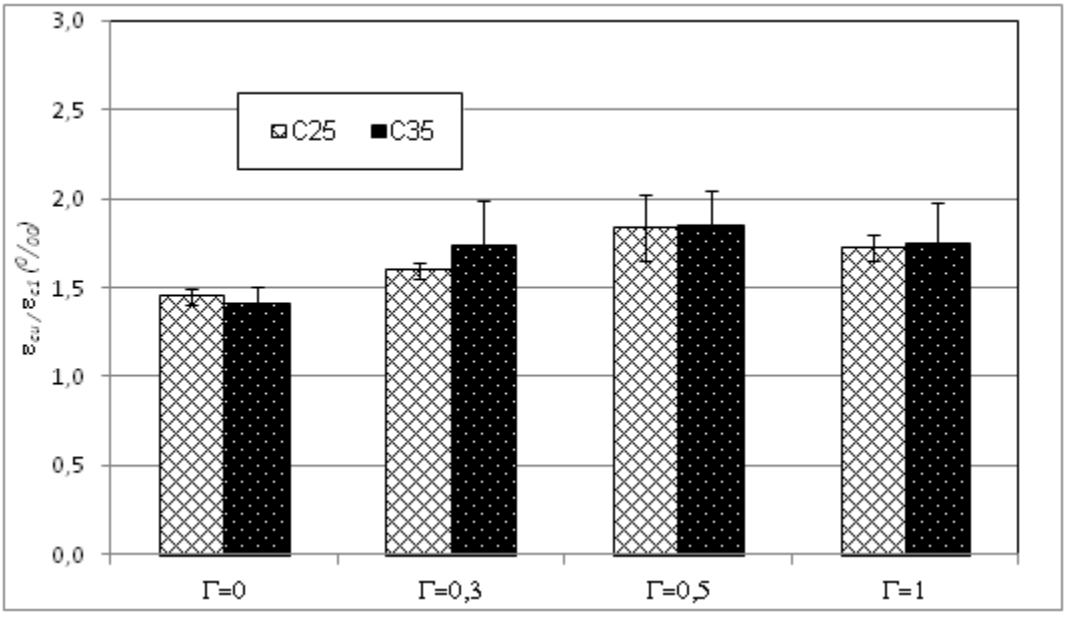

Figure 2. Relationship between ultimate and peak strains.

Proposed analytical models for mechanical properties and stress-strain curve

Design codes provide empirical expressions to relate the elastic modulus of elasticity and the tensile strength to the compressive strength. Moreover, the design codes simplify the stress–strain models. The main parameters of these curves are the initial tangent modulus of elasticity, the strain corresponding to the maximum stress, and the shape of the descending branch. In the following the necessary modifications to take into account the effect of recycled aggregates are provided. In addition to the experimental results of the present study, other results from published investigations in the literature have been considered in order to allow a better optimization of the proposed expressions (Etxeberria, Vazquez et al. 2007; Evangelista and de Brito 2007; Domingo-Cabo, Lazaro et al. 2009; Martinez-Lage, Martinez-Abella et al. 2012; Wardeh, Ghorbel et al. 2014).

- *Elastic modulus*

To predict the elastic modulus of recycled aggregate concretes, the relationship initially proposed by EC2 was modified as follows:

$$E_{cm} = \frac{22000}{1+\alpha\Gamma}\left(\frac{f_{cm}}{10}\right)^{0,30} \quad \text{Equation 2}$$

with α=0.6 this expression predicts the experimental results with a correlation coefficient $R^2 = 0.69$.

- *Tensile strength*

The following expression allows predicting the experimental data with a correlation coefficient R^2=0.77 for α=0.06.

$$f_{ctm} = \frac{0.34}{1+\alpha\Gamma}(f_{cm})^{0,06} \quad \text{Equation 3}$$

- *Peak and ultimate strain*

The following relationships are proposed to predict the peak and ultimate strains based on the compressive strength, f_{cm}, and the replacement ratio Γ.

$$\varepsilon_{c1} = x(\alpha f_{cm} + \beta)^{y}\left(1+\frac{\Gamma}{a\Gamma^2+b\Gamma+c}\right) \quad \text{Equation 4}$$

x	y	α	β	a	b	c	R^2
0,5	0,351	0,629	23,00	871,20	-1055,79	321,18	0,42

$$\varepsilon_{cu} = \left(0,00298 - 0,0625\left\langle\frac{50-f_{cm}}{100}\right\rangle^{4}\right)(1+0,2\Gamma) \text{ for } f_{cm} \le 50(MPa) \quad \text{Equation 5}$$

- *Stress-strain relationship*

In this study the models proposed by EC2 (Eurocode2 2004), Carreira and Chu (Carreira and Chu 1985) and Xia et al. (Xiao, Li et al. 2005) were extended to recycled aggregate concretes (RAC) using equation 2 for the prediction of elastic modulus and equation 4 for the prediction of the peak strain. A comparison between experimental curves and those obtained by the means of three models is shown in

Figure 3. It can be noticed that the modified model of Carreira and Chu (Carreira and Chu 1985) is the most suitable to predict the post-peak behavior of RAC.

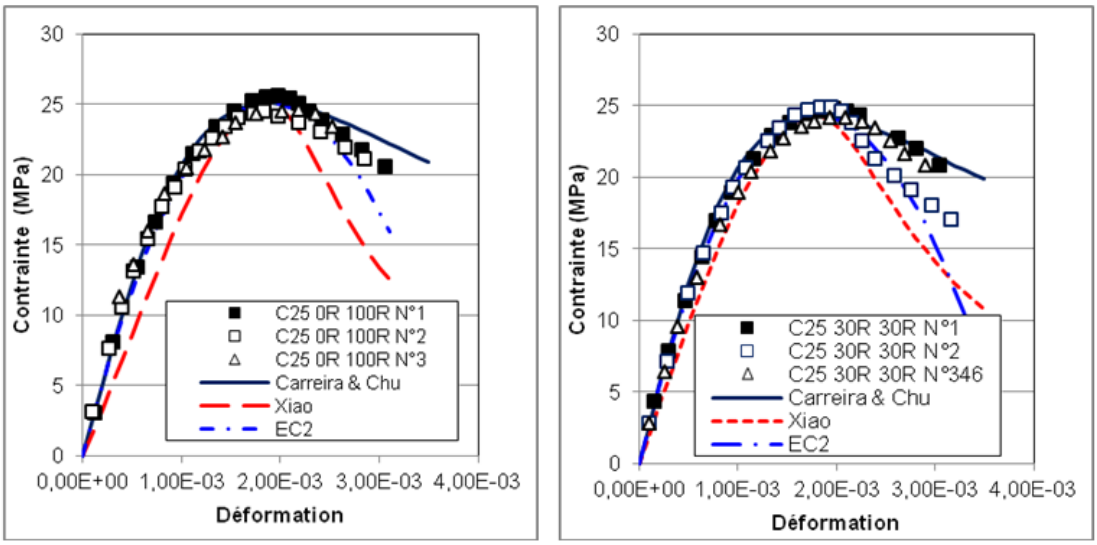

a) C25-0R-100R b) C25-30R-30R

Figure 3. Stress-strain relationship for studied concretes.

Behavior of concrete under cyclic axial compression

The behavior of studied concrete under cyclic axial loading-unloading conditions is illustrated in Figure 4. The analysis of the curves shows that:

- All obtained curves have the same shape,
- The behavior is elastic up to about 40% of the maximum stress. According to the study Mehta (Mehta 1986) a microcraking mechanism is activated at the paste-aggregate interfaces for 30% of the maximum stress,
- The behavior becomes nonlinear up to the peak stress. According to the studies reported in the literature, the non linearity is related to microcracks propagation mechanism in the mortar embedding the coarse grains. When the loading continues, microcracks form a network of connected microcracks in the cement paste,
- Beyond the peak stress, concrete shows compressive softening because macroscopic localized cracks open and propagate leading to the failure of the material,
- Recycled aggregates generate more dissipative behavior, probably, by a more gradual and diffuse damage due to the nature of aggregate and by their porosity which is higher than the porosity of natural aggregates.

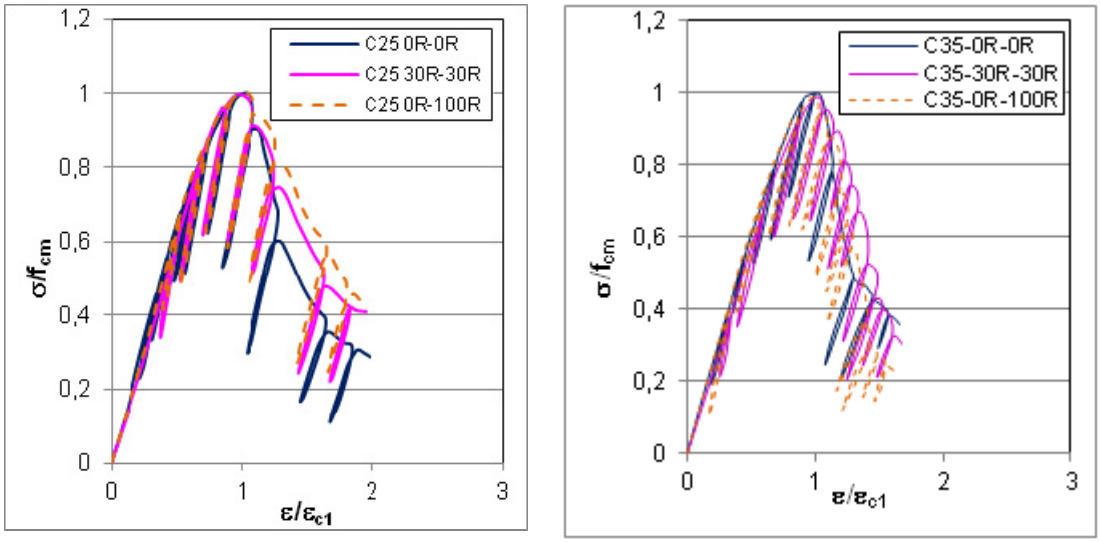

a) series C25 b) series C35

Figure 4. Behavior of concrete under cyclic axial compression.

Damage evolution of studied concretes

The damage variable, named d, characterizes the progressive degradation of the material due to mechanical loading preceding the failure. In the most likely case where cracks are randomly distributed in the concrete, the damage is defined through a scalar which expresses the variation of elastic modulus:

$$d = 1 - \frac{E}{E_0} \qquad \text{Equation 6}$$

where E and E_0 are respectively the elastic modulus of damaged material and the initial one. A value d=0 corresponds to the undamaged material while d=1 represents a completely damaged one. The elastic modulus considered in equation 6 are the secant ones obtained from loading-unloading curves.

The evolution of damage as a function of strain is illustrated in Figure 5. The experimental results show that the damage is about 0.33 at the ultimate strain ε_{cu}. Moreover, its evolution is linear with the applied strain with a correlation factor R^2 which varies between 0.92 and 0.97.

A general expression for the evolution of the damage can be written as:

$$d = \alpha\langle \varepsilon - \hat{\varepsilon} \rangle \qquad \text{Equation 7}$$

In this expression α appears as the damage rate while $\hat{\varepsilon}$ appears as a threshold at which damage occurs. The variation of these parameters for the concretes studied in this work is given in Table 3. Based on the obtained results, it can be observed that the damage rate is lower for RAC than for NAC. Moreover, the damage rate is lower for C35 than C25. With regard to $\hat{\varepsilon}$, its value oscillates around 0.05%.

Table 3. Variation of α and $\hat{\varepsilon}$

	α	$\hat{\varepsilon}$ (%)	R^2
C25-0R-0R	177.5	0.05	0.92
C25-30R-30R	119.9	0.04	0.97
C25-0R-100R	120.4	0.06	0.96
C25-100R-100R	88.1	0.03	0.93
C35-0R-0R	113.1	0.02	0.96
C35-30R-30R	99.3	0.09	0.94
C35-0R-100R	98.6	0.03	0.95
C35-100R-100R	98.5	0.06	0.98

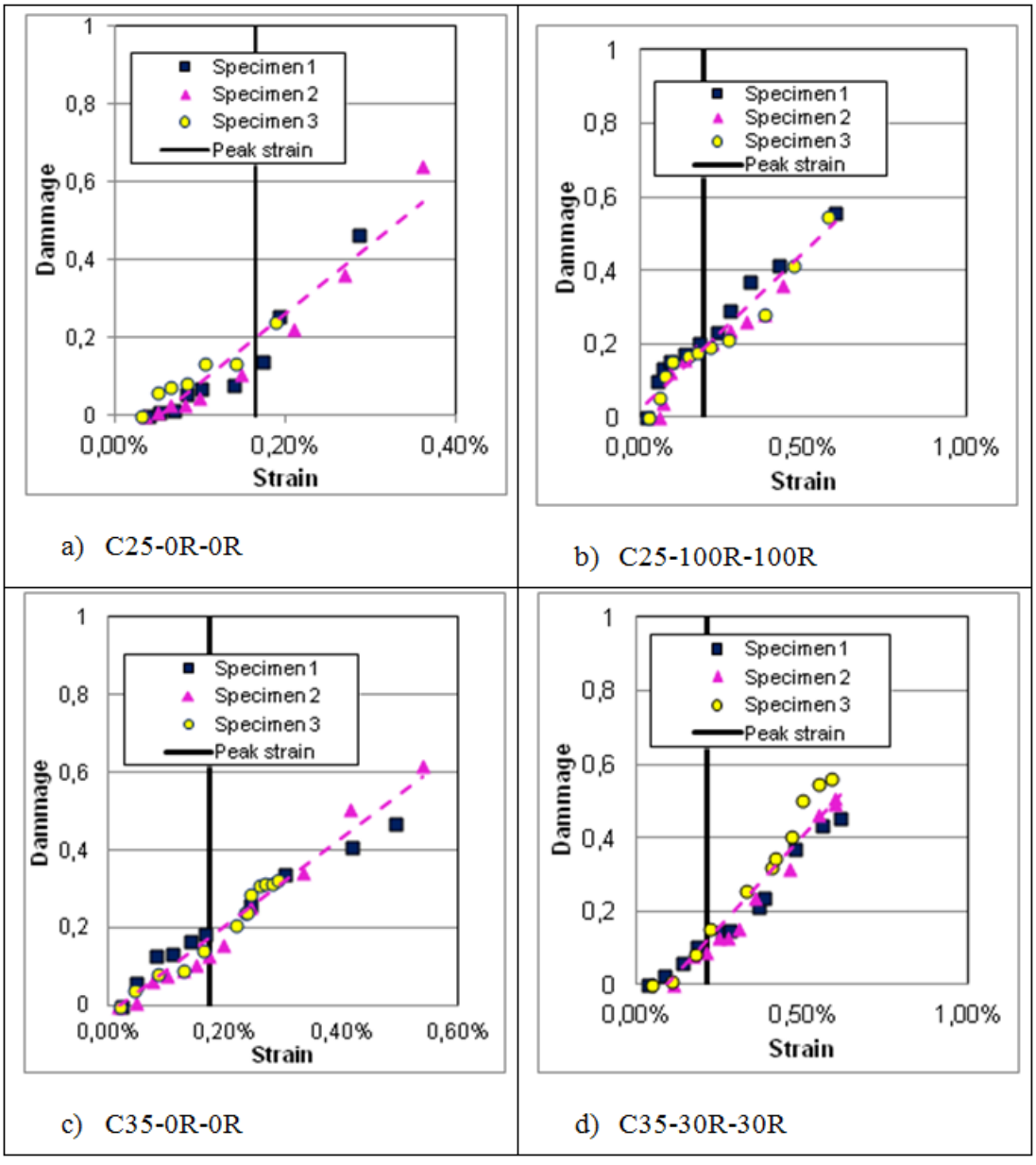

Figure 5. Damage evolution with axial strain.

CONCLUSIONS

In this work the experimental results for the mechanical properties and the damage evolution of recycled aggregate concretes are presented and discussed. Eight mixes with C25/30 and C35/45 classes of compressive strength and S4 class of workability were studied. Based on experimental results, the main conclusions are:

- For the same class of compressive strength, the introduction of recycled aggregates results in a decrease in both tensile strength and elastic modulus,
- The peak and ultimate strains increase by increasing the recycled aggregates content,
- Damage related to the peak stress increases by increasing the replacement ratio of recycled aggregates,
- The rate of damage is lower for concrete with recycled aggregates compared to natural aggregate concrete.
- Proposed analytical expressions reproduce satisfactory experimental results.

ACKNOWLEDGEMENTS

The authors wish to acknowledge the French national research agency (ANR) for the financial support.

REFERENCES

Belén, G.-F., M.-A. Fernando, et al. (2011). "Stress-strain relationship in axial compression for concrete using recycled saturated coarse aggregate."onstruction and Building Materials 25(5): 2335-2342.

Carreira, D. J. and K.-H. Chu (1985). " Stress-Strain Relationship for Plain Concrete in Compression." ACI Materials Journal 82(6): 797-804. Casuccio, M., M. C. Torrijos, et al. (2008). "Failure mechanism of recycled aggregate concrete." Construction and Building Materials 22(7): 1500-1506.

Domingo-Cabo, A., C. Lazaro, et al. (2009). "Creep and shrinkage of recycled aggregate concrete." Construction and Building Materials 23(7): 2545-2553.

ECOREB (2012). "Ecoconstruction par le Recyclage du Béton. http://ecoreb.fr/."

Etxeberria, M., E. Vazquez, et al. (2007). "Influence of amount of recycled coarse aggregates and production process on properties of recycled aggregate concrete." Cement and Concrete Research 37(5): 735-742.

Eurocode2 (2004). Design of concrete structures_Part 1-1 General rules and rules for buildings. Paris.

Evangelista, L. and J. de Brito (2007). "Mechanical behaviour of concrete made with fine recycled concrete aggregates." Cement and Concrete Composites 29(5): 397-401.

Martinez-Lage, I., F. Martinez-Abella, et al. (2012). "Properties of plain concrete made with mixed recycled coarse aggregate." Construction and Building Materials 37(0): 171-176.

Mehta, P. K. (1986). Concrete. Structure, properties and materials. New Jersey,

RECYBETON (2012). "projet national recybeton . http://www.pnrecybeton.fr."

Sedran, T. (2013). Mise au point des formules de béton de référence: 37.

Wardeh, G., E. Ghorbel, et al. (2014). "Mix Design and Properties of Recycled Aggregate Concretes: Applicability of Eurocode 2." International Journal of Concrete Structures and Materials DO - 10.1007/s40069-014-0087-y: 1-20 LA - English.

Xiao, J., J. Li, et al. (2005). "Mechanical properties of recycled aggregate concrete under uniaxial loading." Cement and Concrete Research 35(6): 1187-1194.

Physical and Mechanical Properties of Recycled Demolition Gravels Submitted to Freeze/Thaw in Comparison to Natural Ones

Safiullah Omary[1]; Elhem Ghorbel[2]; and George Wardeh[3]

[1]University of Cergy-Pontoise, 5 Mail Gay LUSSAC, 95031 Neuville-sur-Oise. E-mail: safiullah.omary@etu.u-cergy.fr

[2]University of Cergy-Pontoise, 5 Mail Gay LUSSAC, 95031 Neuville-sur-Oise. E-mail: Elhem.Ghorbel@u-cergy.fr

[3]University of Cergy-Pontoise, 5 Mail Gay LUSSAC, 95031 Neuville-sur-Oise. E-mail: george.wardeh@u-cergy.fr

Abstract:

Nowadays, there is a significant increase in researches of concretes based on recycled aggregate. In this study, the recycled aggregates are provided from demolition waste. This work aims to characterize recycled gravels (RG) and to estimate their deterioration after their exposure to freezing and thawing cycles. The main objective is to determine the quality and suitability of RG by comparison to natural ones (NG) in manufacturing concretes dedicated to buildings, in particular when they are exposed to freeze/thaw. For each granular type, sieving, water absorption, porosity (n), Los Angeles (LA) and Micro-Deval (MDE) tests were conducted before and after their exposure to freezing/thawing in water according to European standards. The coefficient of water absorption, WA, was evaluated by three different methods. Results show that the law of mixtures can be used to predict all the studied properties of gravels mixes (natural and recycled gravels) except for MDE. Relationships are established between WA-density, LA-WA and LA-density on the basis on the results of this work and those of literature. Good correlation between the Micro-Deval (MDE) and the WA, as well as between MDE and LA was found. The analysis of the durability performance allowed concluding that, RGs are less resistant to freeze/thaw than NGs but their degradation, estimated through WA, n and MDE, is not significant.

.

INTRODUCTION

Development in many sectors has negative environmental effects. In construction sector, there are millions tones of construction and demolition waste (CDW) every year. CDW has significant damage on the environment and may endanger its durability and sustainability. To find a conceivable solution for CDW and to preserve the natural resources, particularly the non-renewable ones, worldwide researches on recycled aggregates have been raised in order to investigate revalorizing possibility of CDW in concretes.

In Europe Union, France, Germany and United Kingdom produce 39% of all waste. France, with a ratio of 5.5 tons of waste/person per year, is at the higher level. Moreover, 2.6 million tons of fresh concrete is considered as waste and should be recycled in France [UNPG 2009]. As many developed countries, France also has introduced legislation and strategies to reduce the environmental effects of CDW. Corresponding to problem of CDW, there is a national project [PN-RECYBETON 2013] that leads about how to manufacture concretes for building field using aggregates provided from CDW.

Aggregates represent about 70-80 % of concrete components, accordingly the properties of concretes are directly depending on the physical and mechanical properties of aggregates. This paper presents a detailed research on physical and mechanical properties of natural aggregates, called NA, and recycled ones, designed as RA.

The most of the researches deal with the influence of the partially or totally substitution of natural aggregates by recycled ones on the characteristics of concretes [Etxeberia M. 2007]. Few of them attempt to propose relations that link the properties of RA to the strength of recycled aggregate concrete (RAC) [Khaleel H. Younis 2013] or to examine the effect of attached cement mortar content on the properties of recycled aggregates [De Juan MS 2009].

This research aims to study the physical and mechanical properties of RA and NA and to establish relationships between physical and mechanical properties of aggregates on the basis of experimental data obtained in this study and those of literature so that proposed models will cover a wide range of sources of aggregate. This work is done in the framework of the national French project ANR-VBD2012-ECOREB [ECO 2012].

MATERIALS AND EXPERIMENTAL METHODS

The NA and RA were provided by PN-Recybeton [8]. Natural aggregates are classified as coarse gravels (NG2 6.3/20), fine-coarse gravels (NG1 4/10) and sand (NS 0/4). The recycled aggregates were prepared in a platform of recycling. Three granular fractions are considered (RS 0/4, RG1 4/10 and RG2 10/20). All aggregates were transported to the laboratory in big-bags

In order to determine the physical properties of aggregates, all fractions of NA and RA were separately subjected to granulometrey, density, water absorption and porosity tests.

To define the size distribution of NA and RA, the sieving was carried-out according to NF EN 933-11. It has been observed that, both NG and RG have approximately the similar size distribution. However, grading curves prove that recycled sand is too rich in fine fraction (<2 mm sieve). This can be critical for the concrete mix design.

Water absorption (WA) is an important physical property of aggregates. Hence, it was determined by means of three methods. The first one is the pycnometer method according to standard NF EN 1097-6, method allowing measuring WA, porosity and specific gravity of aggregates. The second one is the method of Hydrostatic Weighing Continuously (HWC) used to follow the evolution of mass change of aggregates immersed in water. The balance is linked to a computer so that

the evolution of the mass is recorded continuously. The third method obeys to the French standard NF P 18-459 in which measurements must be done after the gravels exposure to vacuum for 4hours.

To assess the mechanical properties of gravels, Los Angeles test according to NF EN 1097-2 have been conducted in order to determine their resistance to fragmentation and Micro-Deval test according to NF EN 1097-1 to check the resistance to wear of coarse aggregates and therefore their quality.

The durability of gravels regarding to freezing/thawing cycles was considered according NF EN 1367-1. The mass loss F of the different fractions of gravels that, submitted to freezing/thawing test was measured by the equation $F(\%) = \frac{M_1 - M_2}{M_1}$ where, M_1 is the dried mass of sample before test; M_2 is the dried mass of sample retained on the sieve proposed by the mentioned standard.

EXPERIMENTAL RESULTS

Density: Bulk density of the NA $\rho_{rd}^{NG(orNS)}$ and recycled ones $\rho_{rd}^{RG(orRS)}$ were determined according to standard NF EN 1097-6. The evolution of bulk density as a function of the soaking time is illustrated in Figure 2a. It can be concluded that, the density of recycled aggregates is lower than this of natural ones. This is mainly due to the existence of the old cement paste attached to NA in RA [Silve R.V. 2014]. The analysis of the results shows that, the soaking period to determine RA's bulk density should be longer than 24h (the recommended period by standard). The final soaking time required is about 7 days for RG and 48 hours for the other aggregates.

The granular skeleton in concretes is composed of a mixture of NA and recycled ones. The effect of substitution NG by RG has been characterized. The ratio of substitution is defined as $r_m^G = \frac{M^{RG}}{M^{RG} + M^{NG}}$ where M^{RG} and M^{NG} are the mass of RG and NG respectively. Experimental results illustrated in Figure 2b, reveal that, the law of mixtures predicts well the bulk density of the gravel mixtures (Equation 1)

$$\rho_{rd}^{G} = r_m^G \rho_{rd}^{RG} + \left(1 - r_m^G\right) \rho_{rd}^{NG} \quad [1]$$

Water absorption: Water absorption (WA) is an important parameter that has a key role on concrete's mix design. The coefficient of WA of NA and RA is measured by three methods. The method of pycnometer was applied according to standard NF EN 1097-6 longer than the time recognized by the standard (24h). The measurement of WA by the method according to standard NF P 18-459 was carried out under vacuum pressure for 1, 2 and 7 soaking days. The last method was hydrostatic weighing continuously performed until a period of 7 days.

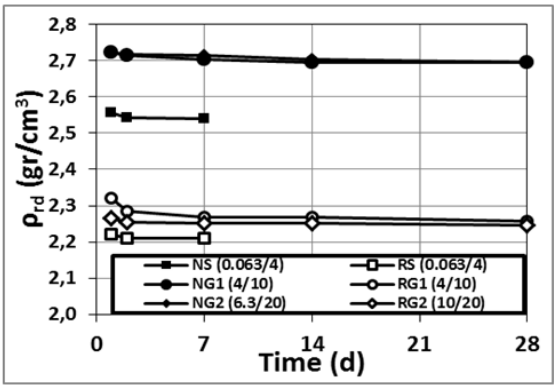

Figure 2a. Evaluation of density in terms of time.

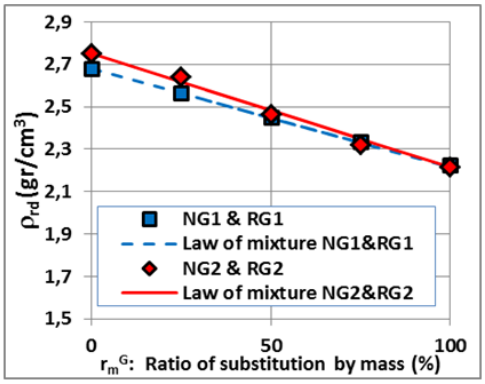

Figure 2b. Density of granular mixes

To check the applicability of the standard to recycled gravels regarding to the determination of the water absorption coefficient at 24 hours, an index of water absorption is calculated, $i_{WA} = \frac{WA_{t(h)}}{WA_{24h}}$, and plotted against the soaking duration (Figure 3b). The experimental results indicate that 24h soaking duration is insufficient to determine the RG's coefficient of WA.

Water absorption coefficient obtained by HWC method is compared the obtained values by the pycnometer method. It can be concluded that HWC and pycnometer methods lead to quite similar measurements (Table 1) while the method according to standard NF P 18-459 leads to higher values for recycled gravels.

Linear Relationship between bulk density and coefficient of WA is established (Figure 5) on the basis of the obtained experimental results and those of the literature concerning more than 40 types of aggregates from different CDW plants [PN-RECYBETON 2013, Etxeberia M. 2007, Khaleel H. Younis 2013, De Juan MS 2009, Silve R.V. 2014, Dilbas H. 2014, Çakır Ö. 2014, Thomas C. 2013, Wardeh G 2013, Kou Shi-Cong 2013].

$$WA_{24} = 13,4\left\langle 2,72 - \rho_{rd}^{G} \right\rangle \text{ and } WA_{24} = 0 \text{ if } \rho_{rd}^{G} \geq 2,72 \qquad [2]$$

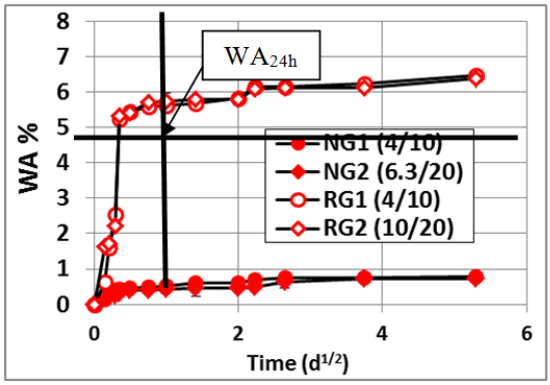

Figure 3a. The evaluation of WA by method of pycnometer.

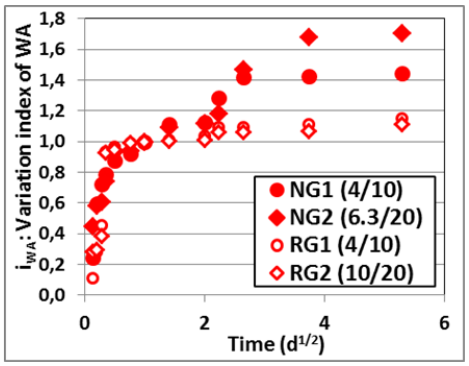

Figure 3b. The variation index of WA by method of pycnometer.

Table 1 – The experimental results of WA and porosity of aggregates.

Method		*RG1*		*RG2*		*RS*		*NG1*		*NG2*		*NS*	
Soaking duration		24h	48h	24h	48h	24h	48h	24h	48h	24h	48h	24h	48h
Pycnometer [NF EN 1097-6]	WA	$5.6^{\pm0.2}$	$5.7^{\pm0.1}$	$5.7^{\pm0.2}$	$5.8^{\pm0.2}$	$7.3^{\pm0.1}$	$7.7^{\pm0.2}$	$0.5^{\pm0.1}$	$0.6^{\pm0.1}$	$0.4^{\pm0.1}$	$0.5^{\pm0.2}$	$1.3^{\pm0.1}$	$1.5^{\pm0.2}$
	n_p^G	$13.0^{\pm.,2}$		$12.7^{\pm0.2}$		$16.1^{\pm0.1}$		$1.4^{\pm0.1}$		$1.1^{\pm0.1}$		$2.2^{\pm0.2}$	
Under vacuum [NF P 18-459]	WA	$6.1^{\pm0.1}$	$6.4^{\pm0.1}$	$6.2^{\pm0.1}$	$6.2^{\pm0.1}$	-	-	$0.6^{\pm0.1}$	$0.7^{\pm0.1}$	$0.5^{\pm0.1}$	$0.6^{\pm0.1}$	-	-
	n_v^G	$13.4^{\pm0.2}$		$13.7^{\pm0.2}$		-		$1.6^{\pm0.1}$		$1.2^{\pm0.1}$		-	
HWC	WA^G	$5.4^{\pm0.2}$	$5.7^{\pm0.1}$	$5.6^{\pm0.0}$	$5.6^{\pm0.1}$	$7.3^{\pm0.1}$	$7.8^{\pm0.1}$	$0.5^{\pm0.1}$	$0.6^{\pm0.0}$	$0.4^{\pm0.0}$	$0.5^{\pm0.0}$	$1.3^{\pm0.1}$	$1.4^{\pm0.1}$

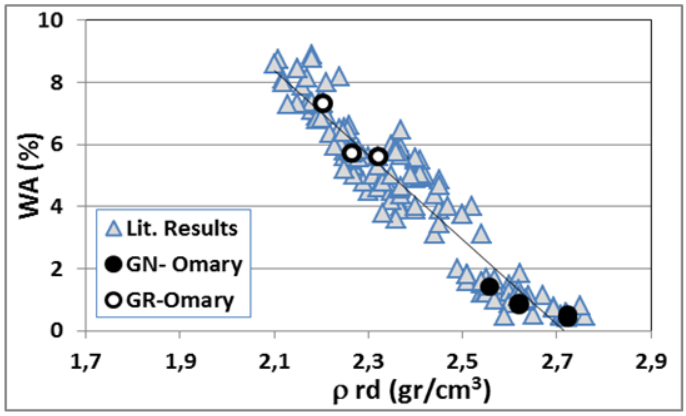

Figure 5. Relationship between WA and reel density of aggregates.

Porosity: The water porosity of NG and RG was measured according to both standards NF EN 1097-6 and NF P 18-459. Obtained results are summarized in Table 1. It is observed that both methods provide quite similar values for porosity of gravels. Recycled aggregates are much porous than natural ones. Moreover, it can be pointed out that fine recycled aggregates are characterized by a higher porosity than coarse ones. This can be explained mainly by the presence of old paste cement, which is more important for fine aggregates, assumption in accordance with the literature [Silve R.V. 2014].

The porosity and water absorption of the different gravel mixtures are linked to the ratio of substitution. Results show that, the law of mixtures predicts well the porosity and the WA of gravels mixes (equation 3 and 4).

$$n_v^G = r_m^G n_v^{G_R} + \left(1 - r_m^G\right) n_v^{G_N} \quad [3]$$

$$WA_{24} = r_m^G WA_{24}^{G_R} + \left(1 - r_m^G\right) WA_{24}^{G_N} \quad [4]$$

Los Angeles: The test of Los Angeles (LA) was applied according to standard NF EN 1097-2. This standard describes that, after 500 tours of machine, the gravels are then separated into material passing the 1.6 mm sieve and material retained on the 1.6 mm sieve (M2). In this work, the mass of material passing the 63 µm sieve (named M4), was determined to find out the quantity of fines generated by the test. The experimental results are plotted in Figure 7a & 7b.

It appears that RG has a significantly greater LA coefficient than this of NG $\left(\frac{LA_{RG}}{LA_{NG}} \cong 2\right)$. However these values are acceptable and are in accordance with the requirements of the standards (LA ≤ 30 for NG and LA ≤ 40 for RG if $f_{ck} \geq 36$ MPa). The mass retained on the sieve of 63 µm and passing the sieve 1. 6mm (named M3) and mass of fines (M4) are more important for recycled gravels by comparison to natural ones due probably to the old cement paste which is less resistant to fragmentation.

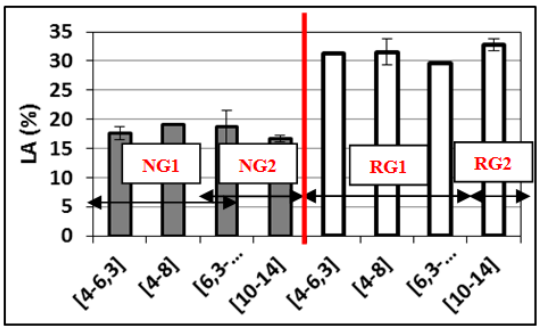

Figure 7a. LA coefficient for NG and RG.

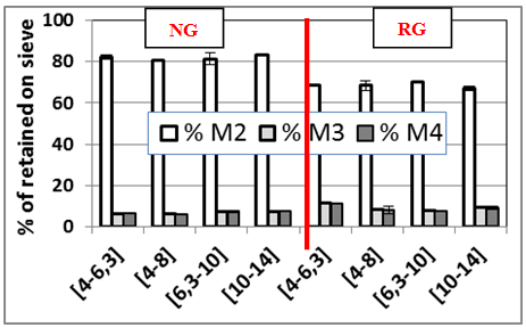

Figure 7b. Retained masses and fines

LA abrasion tests are, also, conducted on the selected granular fractions [4-8] and [10-14] of the gravel mixes. Experimental results, illustrated in Figure 8a, show that the laws of mixtures (Equation 5) well predict the LA of the gravels mixes.

$$LA\ (\%) = r_m^G LA_{graviers\_recyc} + \left(1 - r_m^G\right) LA_{graviers\_nat} \quad [5]$$

The evolution of LA as a function of the porosity (Figure 8b) reveals that gravels wit low porosity are characterized by a greater resistance to fragmentation.

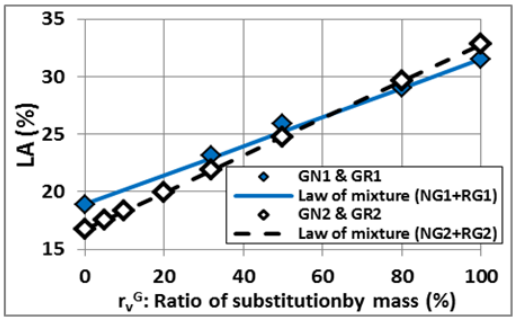

Figure 8a. Coeff. of LA for mixes.

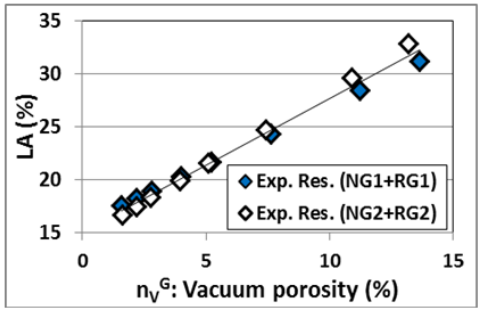

Figure 8b. Coeff. of LA versus Porosity.

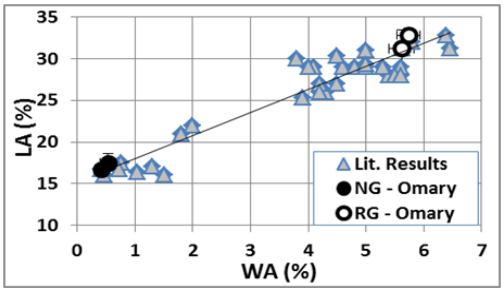

Figure 9a. Coeff. of LA versus WA

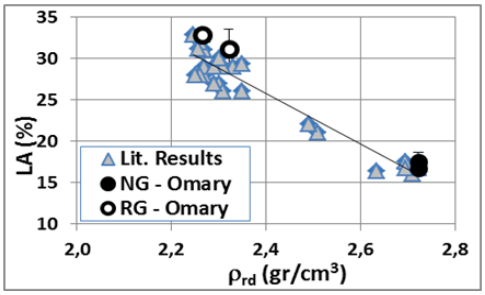

Figure 9b. Coeff. of LA versus density

Moreover, experimental results of this work and those of literature highlight the effect of WA_{24}, related to the porosity, on their abrasion resistance. Increasing the porosity induces an increase of WA and therefore an increase of LA (equation 7).

$$LA = 2,73WA_{24} + 15,58 \quad [7]$$

Furthermore, as the porosity rises the density decreases leading subsequently to the LA coefficient increase. This assumption has been confirmed by means of the results of this work and those of literature [PN-RECYBETON 2013, Khaleel H. Younis 2013, Dilbas H. 2014, Çakır Ö. 2014, Thomas C. 2013]. The relationship between these two parameters is established (equation 8).

$$LA(\%) = 28,72\left\langle 3,31 - \rho_{rd}^{G} \right\rangle \text{ with } R^2=0,91 \quad [8]$$

Micro-Deval: The test of Micro-Deval was carried out according to European French standard NF EN 1097-1 to determine the resistance to wear of NG and RG. It has been performed at wet condition (MDE). To find out the quantity of produced fine, the gravel masses passing the 63 µm sieve (M4), retained on 1.6mm sieve (M2) and passing 1.6mm and retained on 63 µm sieve (M3) are weighed. The experimental results (Figure 10a) reveal that, the coefficient of MDE of RG is slightly greater than this of NG ($\frac{MDE_{RG}}{MDE_{NG}} \cong 1.4$ for 10/14 mm size fraction). Testing 4/6 mm and 6.3/10 mm size fractions produces MDE coefficient in accordance with the requirements of the European standard $(MDE \le 20$ for $f_{ck} \ge 36MPa)$.

Moreover, it must be noted that increasing the size fraction leads to a decrease of the wear resistance of the natural gravel while such effects are not observed for recycled ones, probably due to the fact that they are coated by old cement paste having the same resistance to wear. Furthermore, the production of fines is more important for recycled aggregates, phenomenon related to the old paste surrounding natural aggregates which is less resistant to wear than rocky materials (Figure 10b).

Micro-Deval test was carried out on natural and recycled gravels mixes. It appears clearly that the law of mixtures cannot be used to predict the MDE of the gravel mixes. This can be explained by the fact that wear resistance of gravels is mainly governed by the aggregate mineralogical composition and in a lesser degree by the particle shape

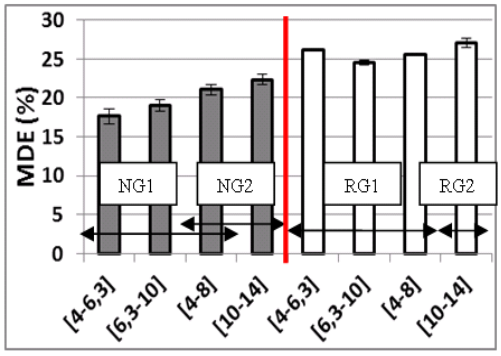

Figure 10a. Experimental coefficient of MDE for NG and RG.

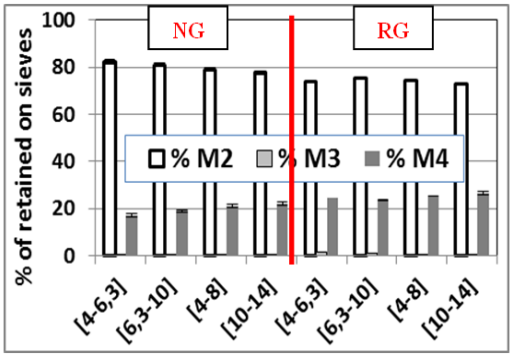

Figure 10b. masses of retained gravels on the different sieves and of fines

Freezing/thawing: The durability of aggregates was measured by means of freezing/thawing cycles in water according to the standard NF EN 1097-1. The coefficient of mass loss (F) was calculated after 10 cycles as recommended by the standard. Experimental results are given in Table 2. It can be pointed out the effect of fraction size on this parameter which decreases for coarse fraction sizes for both NG and RG. As expected the durability of RG under freezing/thawing cycles in water is lower than that of NG. The coefficient of WA for all fractions of freezing thawing is summarized in Table 2. It appears that aggregates with higher WA are less frost resistant. In addition, it seems that the source of the gravels as well as their chemical composition play an important role on their resistance to frost. Hence for RA, processed from crushed concretes blocks resulting from the building demolition, it can be expected that the old cement paste contains micro-cracks due to the crushing phenomenon and subsequently the freezing/thawing resistance of RA is diminishing.

Table 2. Effects of freezing/thawing cycles on characteristics of the gravels.

		Mass loss	***Before freezing/thawing***			***After freezing/thawing***		
	Fraction (mm)	**F (%)**	WA (%)	n_v^G(%)	MDE (%)	WA (%)	n_v^G(%)	MDE (%)
NG	4/8	$\mathbf{2.7^{\pm 0.4}}$	$0.75^{\pm 0.01}$	$2.0^{\pm 0.11}$	-	$0.90^{\pm 0.02}$	$2.4^{\pm 0.11}$	-
	8/16	$\mathbf{2.3^{\pm 0.5}}$	$0.55^{\pm 0.01}$	$1.5^{\pm 0.10}$	-	$0.79^{\pm 0.01}$	$2.2^{\pm 0.01}$	-
	16/25	$\mathbf{1.8^{\pm 0.1}}$	$0.50^{\pm 0.02}$	$1.4^{\pm 0.13}$	-	$0.76^{\pm 0.01}$	$2.1^{\pm 0.02}$	-
	10/14	**-**	-	-	$22.4^{\pm 0.7}$	-	-	$26.4^{\pm 0.5}$
RG	4/8	$\mathbf{4.1^{\pm 0.5}}$	$6.4^{\pm 0.1}$	$14.2^{\pm 0.3}$	-	$5.9^{\pm 0.1}$	$13.6^{\pm 0.2}$	-
	8/16	$\mathbf{3.5^{\pm 0.4}}$	$6.0^{\pm 0.2}$	$13.6^{\pm 0.2}$	-	$5.5^{\pm 0.1}$	$12.7^{\pm 0.2}$	-
	16/25	$\mathbf{3.4^{\pm 0.1}}$	$5.9^{\pm 0.2}$	$13,2^{\pm 0.2}$	-	$5.5^{\pm 0.1}$	$12.7^{\pm 0.2}$	-
	10/14	**-**	-	-	$27.1^{\pm 0.4}$	-	-	$22.9^{\pm 0.2}$

The grain size distribution of granular fractions submitted to freezing/thawing cycles is illustrated in Figure 11a & 11b. The curves show that, the granular distribution changes after freezing/thawing cycles for RG while it is almost the same for NG. Freezing/thawing cycles have damaged more severely RG than NR. Subsequently, more fine particles have been produced due to the degradation of the old cement paste surrounding RA that has been separated from the natural aggregate because of frost. RAs collected after frost are the most resistant (Figure 12).

Such degradation can explain that MDE coefficient of RG after freezing thawing test decreases to reach the value of NG before frost while it increases for NG (Table 2). It can be concluded that if the cohesion between the old paste and the natural granular is strong than the old paste protects natural granular against frost. Freezing thawing cycles affects NG more severely than RG.

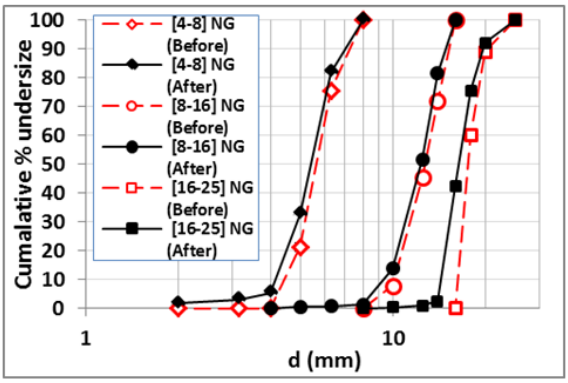

Figure 11a. Particle size distribution of NG before and after freezing/thawing cycles.

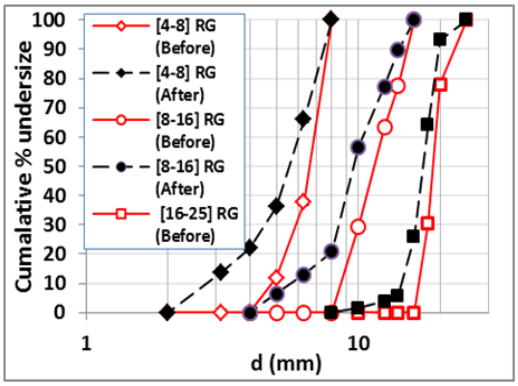

Figure 11b. Particle size distribution of RG before and after freezing/thawing cycles.

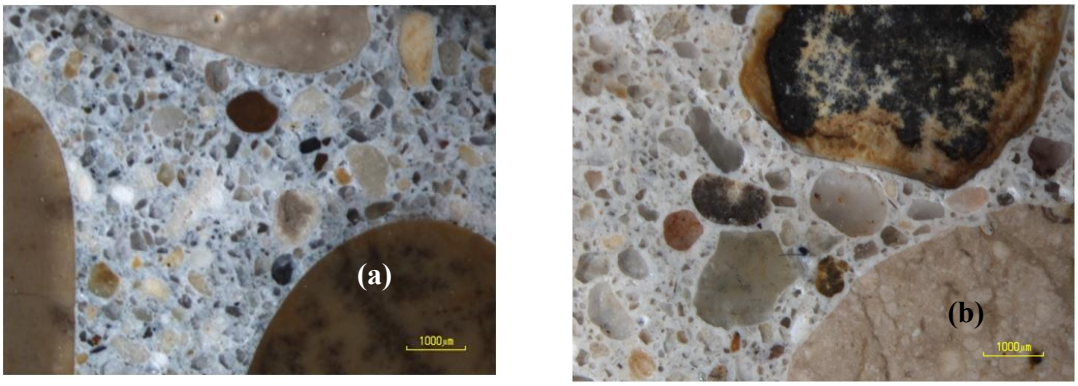

Figure 12. Microscopic observation of RAs before (a) and after 10 freezing/thawing cycles (b).

CONCLUSION

This work is related to the study of some physical and mechanical properties of natural aggregates and recycled aggregates provided from waste construction materials. These aggregates are used for preparation of concrete for building structures applications. The main objective is to analyze in detail the characteristics of the aggregates (natural and recycled) in order to promote their use in concrete construction applications. Results point out that, the WA and the porosity of RA are higher than those of NA but their resistance to abrasion is slightly less important. In contrast the MDE is significantly greater for RA than that of NA as well as the resistance to freezing/thawing cycles.

The old cement paste present in RA contains micro cracks due the crushing process of old concrete blocks. It is responsible of porosity's rise then the WA increase and therefore the decrease of density, wear resistance, abrasion resistance and frost resistance independently of RA's sources. However, it seems that this old cement paste protects natural granular against frost and therefore freezing thawing cycles affects NG more severely than RG.

In this work, we attest that, the law of mixtures can be used to predict all the studied properties of gravels mixes (natural and recycled gravels) except for MDE.

ACKNOWLEDGEMENTS

The authors wish to acknowledge the French National Research Agency ANR (ANR-VBD2012-ECOREB) for the financial support.

REFERENCES

Çakır Ö. "*Experimental analysis of properties of recycled coarse aggregate (RAC) concrete with mineral additives*" Construction and Building Materials 68 (2014) 17-25.

De Juan MS, Gutierrez PA. *Study on the influence of attached mortar content on the properties of recycled concrete aggregate*. Construction and Building Materials 2009;23:872-7.

Dilbas H., M. Şimşek, Ö. Çakır "*An investigation on mechanical and physical properties of recycled aggregate concrete (RAC) with and without silica fume*" Construction and Building materials 61 (2014) 50-59.

ECOREB (2012). "*Ecoconstruction par le Recyclage du Béton*. http://ecoreb.fr/."

Etxeberia M, Vaguez E, Mari A, Barra M. *Influence of amount of recycled coarse aggregates and production process on properties of recycled aggregate concrete.* Cement Concrete Res 2007;37:735-42.

Kou Shi-Cong, Chi-sun Poon. *Long term mechanical and durability properties of recycled aggregate concrete prepared with the incorporation of fly ash*. In: Cement & Concrete Composites 37 (2013) 12-19.

PN-RECYBETON R13RECY003 – '*Theme 0 - Mise au point des formules de reference du beton*' and 'Rapport Ifsttar formules de référence V2' - TSEDRAN - IFSTTAR - LC12RECY14.

Silva R.V., J. de Brito, R.K. Dhir. *Properties and composition of recycled aggregates from construction and demolition waste suitable for concrete production*. In: Construction and Building Materials 65 (2012) 201-217.

Soares D., J. De Brito, J. Ferreira, J. Pacheco. *Use of coarse recycled aggregates from precast concrete rejects: Mechanical and durability performance*. In: Construction and Building Materials 71 (2014) 263-272.

Symonds Group Ltd. (ed.), ARGUS, (1999) Consulting Engineers and Planners and PRC Bouwcentrum. Report to DGXI: *Construction and Demolition Management Practices and their Economic Impacts*, Symonds Group, Brussels, Belgium.

Thomas C., J. Setien, J.A. Polanco, P. Aljaejos, M. Sanchez de Juan, "*Durability of recycled aggregates concrete*" Construction and Building Materials, 40 (2013) 1054-1063.

UNPG, *Union Nationale des Producteurs de Granulats*. http://www.unpg.fr/.

Wardeh George, E. Ghorbel, H. Gomart. "*Mix Design and Properties of Recycled Aggregate Concretes: Applicability of Eurocode 2*", International Journal of Concrete Structures and MaterialsVol.9, No.1, pp.1–20, Mar2015.

Younis Khaleel H., Kypros Pilakoutas. *Strength prediction model and methods for improving recycled aggregate concrete*. Construction and Building Materials 49 (2013) 688-701.

Epoxy Resin/Recycled Sand Mortars' Resistance to Chloride Ions Diffusion

Amal Bourguiba[1]; Elhem Ghorble[2]; and Wadia Dhaoui[2]

[1,2]Mechanics and Civil Engineering Materials Laboratory, University of Cergy Pontoise, 5Mail Gay-Lussac, Neuville sur Oise, 95031, Cergy Pontoise Cedex.
[1]E-mail: bourguibaamal@hotmail.com
[2]E-mail: elhem.ghorbel@u-cergy.fr
[3]Unit of Applied Mineral Chemistry, Faculty of Science of Tunis, Tunis El Manar University, Le Campus Universitaire, Tunis El Manar, 2092 Tunis, Tunisie.
E-mail: wadia.ammar@planet.tn

Abstract

This work aims to study the possibility of using recycled sand to prepare an epoxy resin mortar mechanically resistant and resistant against chloride ions diffusion. Comparative studies were performed on standardized hydraulic mortar and epoxy / standardized sand. The effect of the incorporation of a thinner, methyl octanoate, on the workability, mechanical properties and durability of the epoxy resin mortar is analyzed. It appears from this study that investigated mortars have a workability which is improved with the increase in the percentage of resin and with the addition of thinner. The total substitution of standardized sand by recycled sand alters this property. The resin mortar have a lower porosity than the hydraulic mortar, better mechanical properties and better resistance to chloride ions diffusion regardless of sand nature. The total substitution of standardized sand by recycled sand does not significantly affect the mechanical properties of resin mortars having the same binder percentages (20%). However, it causes a slight decrease in the resistance to chloride ions diffusion attributed to a higher total porosity accessible to water for recycled sand mortar. Similarly, the migration of these ions into mortar decreases with increasing the resin percentage, decrease attributed to the lowering of total porosity. Thinner addition affects the apparent diffusion coefficient.

INTRODUCTION

Sustainability is one of the key concerns in the design, construction or maintenance of civil engineering works. The corrosion is the main cause of deterioration of reinforced concrete structures leading to the highest costs in terms of repair. The penetration of aggressive agents in concrete, in particular chloride ions, is responsible of the initiation and the development of the corrosion process.
This phenomenon represents a technological, economic and scientific issue requiring finding effective solutions to extend the service life of structures and therefore to optimize maintenance and repair costs. The use of mortars based on polymers for structures confinement or repairing is a solution. This method requires the study of the durability of such mortars. Two categories of mortars based on polymers can be listed: polymer-modified mortars and resin mortars [Emberson, 90], [Morgan, 96]. In this work, several epoxy mortars were formulated by varying the percentage of resin and sand type (standardized sand and recycled sand). A thinner was introduced into mortar compositions in order to improve their workability. In the hardened state mechanical strength, porosity accessible to water and resistance to chloride ions diffusion were studied as a function of mortar composition. The results were compared to those of standardized hydraulic mortar.

MATERIALS AND EXPERIMENTAL METHODS

Materials. The epoxy resin used in this work was a bi-component epoxy-amine system (Eponal 371) provided by BOSTIK (France). The blend consists of a DGEBA-type epoxy resin and a hardener based on aliphatic amine. These components were mixed at a ratio of 100:60 by weight (resin : hardener) according to the manufacturer recommendations.

The thinner used to reduce the viscosity of the resin and thus to improve the mortar workability is methyl octanoate (Aldrich). It was added with a weight percentage of 5% relative to the total mass of mortar [Bourguiba 14].

Two types of sands were used for the formulation of resin mortars: standardized sand and another recycled (supplied by the PN Recybeton). The particle size distribution of these inorganic fillers is shown in Figure 1.

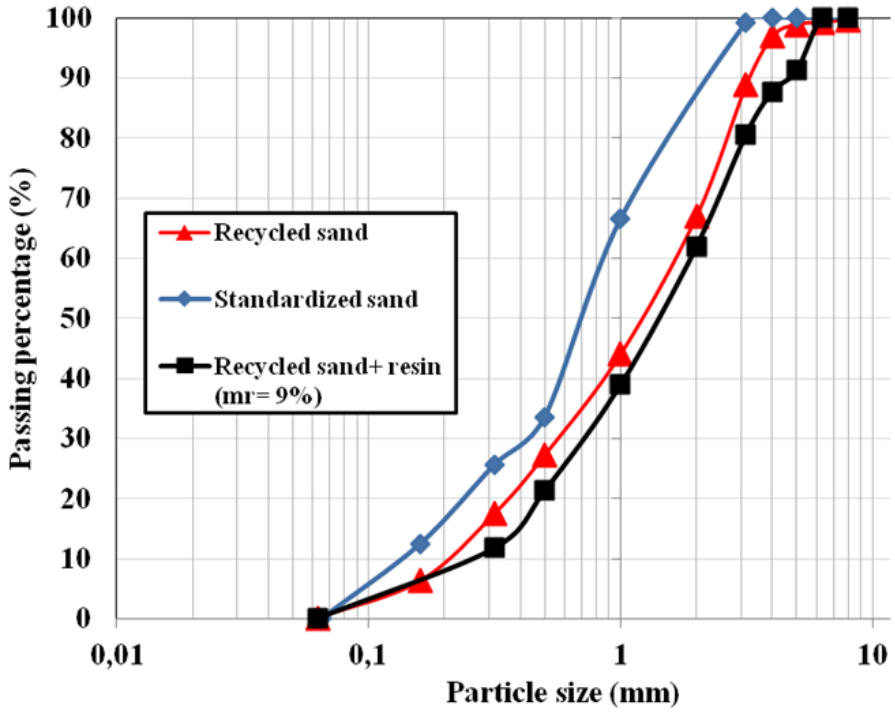

Figure1. Granulometric analysis of standardized and recycled sand.

Different mortar formulations were studied by varying the resin percentage $m_r = \frac{M_{resin}}{M_{mortar}}$ (9%, 12% and 20%) and the type of sand.

A standardized hydraulic mortar was, also, manufactured according to EN 196-1 standard in order to compare its resistance to chloride ions diffusion with those of resin mortars.

EXPERIMENTAL METHODS

Water porosity measurement. This study requires a ventilated oven maintained at a temperature of (105 ± 5) °C, a vacuum apparatus (desiccator + pump) that can reduce and maintain the pressure at less than or equal to 25 mbar and a hydrostatic balance with an accuracy of 0.01% of the test body mass and allowing the weighing in water and in air. The test consists of putting the samples under vacuum for 4 h, gradually introduce the imbibition

liquid (for a period of 15 min) and to maintain this reduced pressure for 44 hours. At the end of this step, a hydrostatic weighing of samples is carried out, followed by weighing in air (saturated dry surfaces mass). To determine the dry mass, the samples were kept at 105 °C until a constant mass. The value of porosity is obtained by the following formula [1]:

$$P = \frac{M_{sds} - M_d}{M_w} \text{ [1]}$$

Where M_{sds} saturated dry surfaces mass, M_d dry mass and M_w mass in water.

Non steady state chloride ions diffusion (NT Build 492, [NTBuild192, 99]). The resistance of resin mortar to chloride ions diffusion was performed on cylindrical specimens (diameter=110 mm and thickness= 50 mm) at the age of 28 days. The test consists in placing samples in the vacuum container for vacuum treatment (4 hours). These samples are then saturated, under vacuum with an NaOH solution (12g / L) for 44h. After saturation, the samples are inserted in chloride ions diffusion cells. These cells are composed of two compartments: the upstream compartment, connected to the anode, is filled with a solution of NaOH (12g / L) and the downstream compartment, connected to the cathode, is filled with a solution of NaCl (112 g / L). The attack by the Cl^- ions is carried for 24 hours by imposing a potential difference between the two electrodes. These ions migrate from the cathode to the anode. The experimental device is shown in Figure 2.

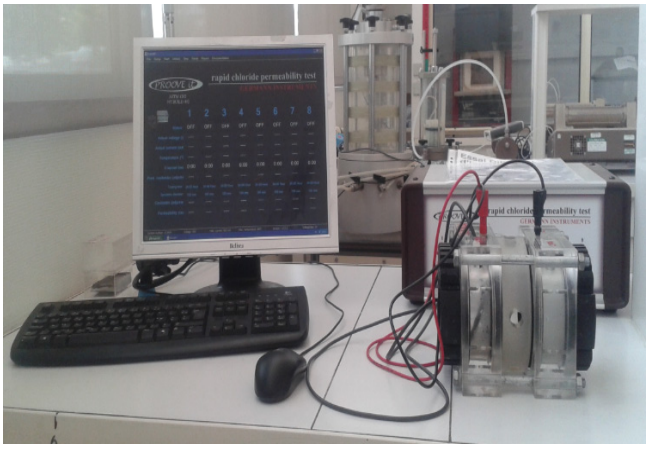

Figure 2. Experimental setup of the chloride ions diffusion.

Thereafter, the specimens are cut into two and then sprayed with silver nitrate (0.1 M). The formation of a white precipitate of AgCl on specimen surface enables the measure of chloride ions migration depth "Xd" inside the sample. This distance is used to calculate the migration coefficient according to the following equation:

$$D_{nssm}\left(10^{-12} m^2/s\right) = \frac{0{,}0239(273+T)L}{(U-2)t}\left(X_d - 0{,}0238\sqrt{\frac{(273+T)LX_d}{U-2}}\right) \text{ [2]}$$

Where D_{nssm} designates the non-steady-state migration coefficient, U the absolute value of the applied voltage, $T(°C)$ the mean initial and final temperatures of the anolyte solution, $L(mm)$ the sample thickness, $X_d(mm)$ the average penetration depth and $t(h)$ test duration.

RESULTS AND DISCUSSION

Resin mortars workability. Workability of mortars was investigated using a mini cone open at both ends (D=100 mm, d = 70 mm, h = 51 mm) and a shaking table. The cone is placed in the center of the table and filled with mortar. After 15 shocks, the mould is carefully lifted vertically upwards, so as not to disturb the mortar and slump is measured.

Different formulations were designed differing by the resin percentage (m_r) as well as by the sand type. The obtained results are shown in Figure 3. It should be noted that by increasing the percentage of resin, the slump of standardized mortars increases and the workability is improved. Beyond 20%, a bleed phenomenon is observed. For mortars made with recycled sand, workability tests were conducted only for mortars made with a resin percentage higher than 12%. In fact, below 12% a non cohesive mixture is obtained (sand with agglomerates). For m_r = 9% the obtained mixture (recycled sand + resin) is a sand with a grain size distribution illustrated in Figure 1. The measure of water absorption coefficient,WA24, after 24 hours soaking and of porosity according to EN 1097- 6 standard indicates that adding low ratios of resin to recycled sand has coating effect. The recycled sand becomes less porous and therefore characterized by a lower absorption coefficient (Table 1). It can be concluded that part of the resin is absorbed and / or adsorbed by recycled sand which generates a decrease of workability.

Table 1. Water absorption and porosity of the different types of sand

Sand type	*WA (%)*	*Porosity (%)*
Standardized sand	0,15	0,38
Recycled sand	7,9	16 ,1
Recycled sand + 9% resin	3,44	7,76

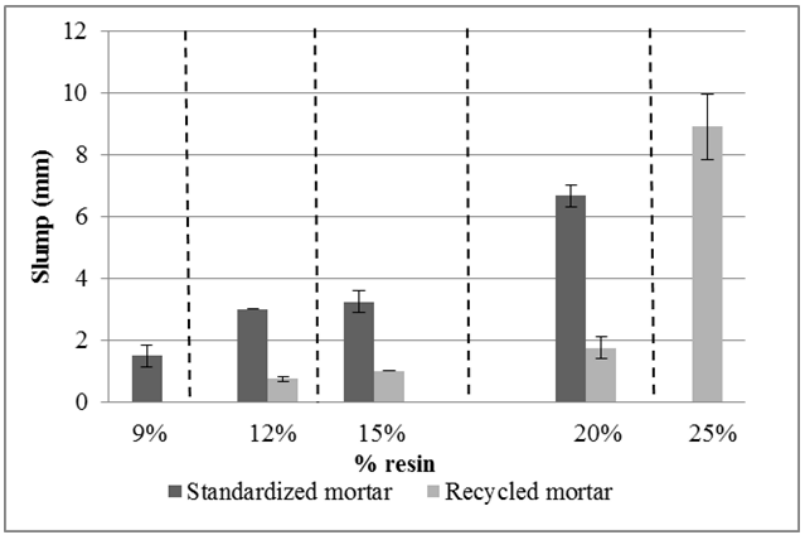

Figure 3. Slump evolution as function of resin percentage and sand type

Methyl octanoate was added to resin mortar composition in order to improve the workability. Previous studies [Bourguiba14] show that adding 5% of thinner by the total mass of mortar is an optimal ratio. Figure 4 shows that the slump is more important when thinner is added. Workability improvement with the introduction of the methyl octanoate is very remarkable for the standardized sand mortar formulated with 20% of resin.

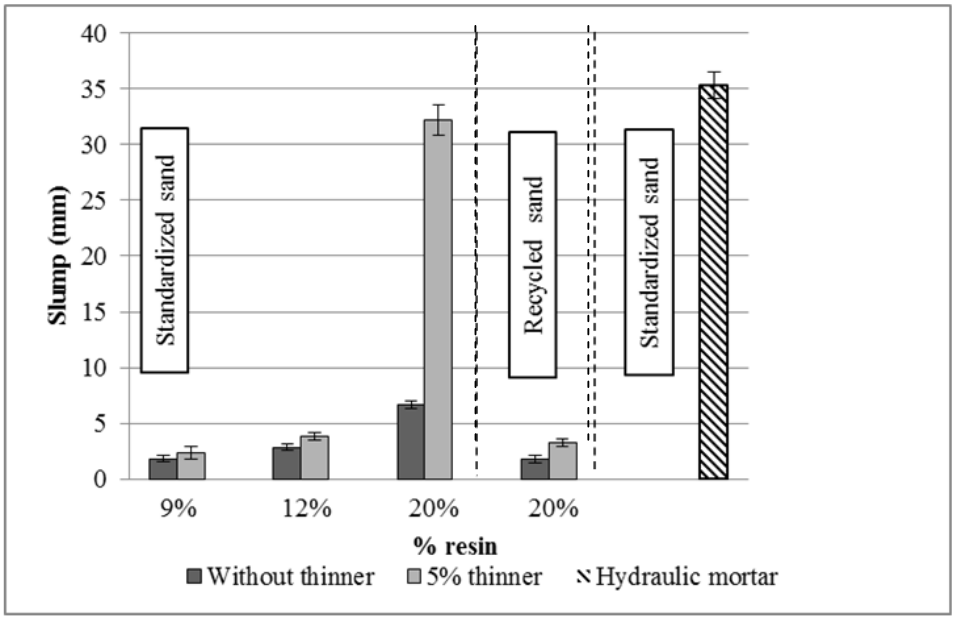

Figure 4. Slump evolution as function of resin percentage, methyl octanoate percentage and sand type

Water porosity. Durability properties such as resistance to corrosion and to chloride ions diffusion are closely related to the material porous structure [Bagel 97]. Porosity is considered as an indicator of sustainability. The porosity accessible to water of mortars at 28 days age is shown in Figure 5.

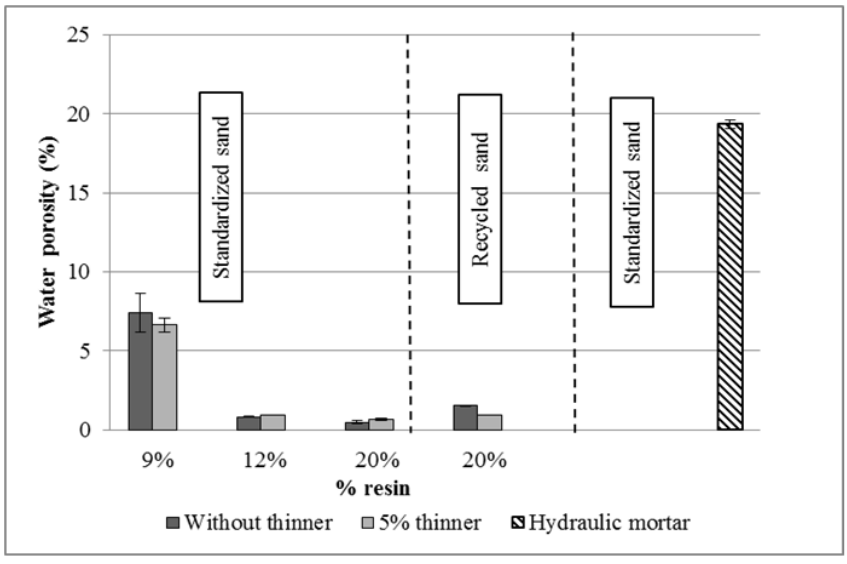

Figure 5. Water porosity evolution as a function of resin percentage, thinner percentage and sand type.

The results show that high resin ratios lead to lower the porosity values. Porosity varies from 7.4% for mr=9% to 0.5% for mr=20%. The same evolution was observed by Haidar [Haidar 11] when measuring polymer mortar porosity by mercury intrusion

porosimeter. The addition of methyl octanoate has no significant effect on this property. Moreover, it should be noted that the total substitution of standardized sand by recycled sand increases the porosity of mortar made with 20% of resin to achieve 1.5%. Porosity values of resin mortars remain remarkably lower than that of standardized hydraulic mortar which is equal to 19.5%.

Mechanical resistances. Flexure and compression tests were carried out on 4x4x16 cm^3 samples, according to NF EN 196-1 standard, at different maturation ages (3, 7, 4 and 28 days). The conservation of test specimens was carried out at a temperature of 30 °C and a humidity of 48% RH. The obtained results are shown respectively in Figures 6 and 7.

Increased mechanical strengths with maturity age are observed for all studied compositions. Histograms show that strengths increase by increasing the resin ratio. Substitution of standardized sand (named SS) by recycled one (called RS) for the mortar formulated with 20% of resin causes a reduction of flexure and compressive strengths. Hence, at 28 days, the flexure strength falls from 30.58 MPa (m_r=20% and SS) to 22.55 MPa (m_r=20% and RS) while compressive strength diminishes from 114 MPa (m_r=20% and SS) to 101.5 MPa (m_r=20% and RS). The addition of methyl aoctanoate in mortars composition causes a decrease in these strengths. Thus, at 28 days the compressive strength of mortar (for m_r = 12%) initially of 87 MPa is reduced to 61.24 MPa with the addition of 5% of thinner. This decrease can be explained by the fact that thinner plasticizes the epoxy resin three-dimensional network at cured state. Thereby the rigidity and strength of the epoxy binder are reduced while its ductility is increased. However, it is important to note that mechanical strengths of resin mortars are much higher than those of hydraulic mortar especially for flexure strength. This result was also obtained by other others [Elalaoui 12] [Haidar 11].

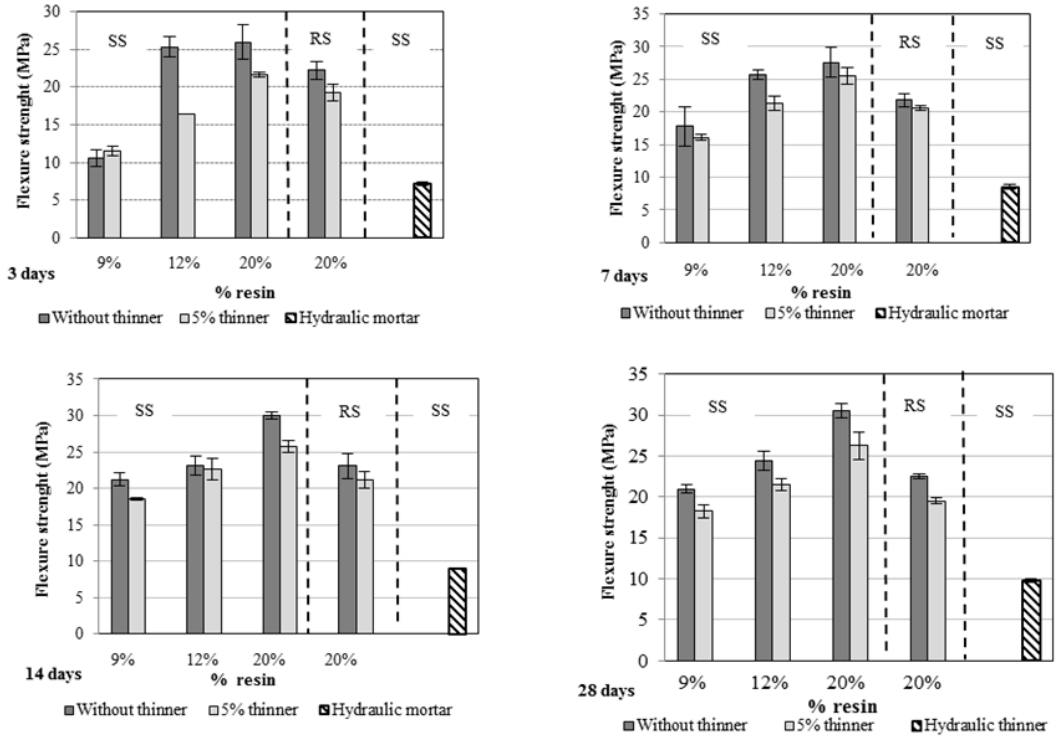

Figure 6. Evolution of flexure strenght as function of resin percentage, thinner percentage, sand type.

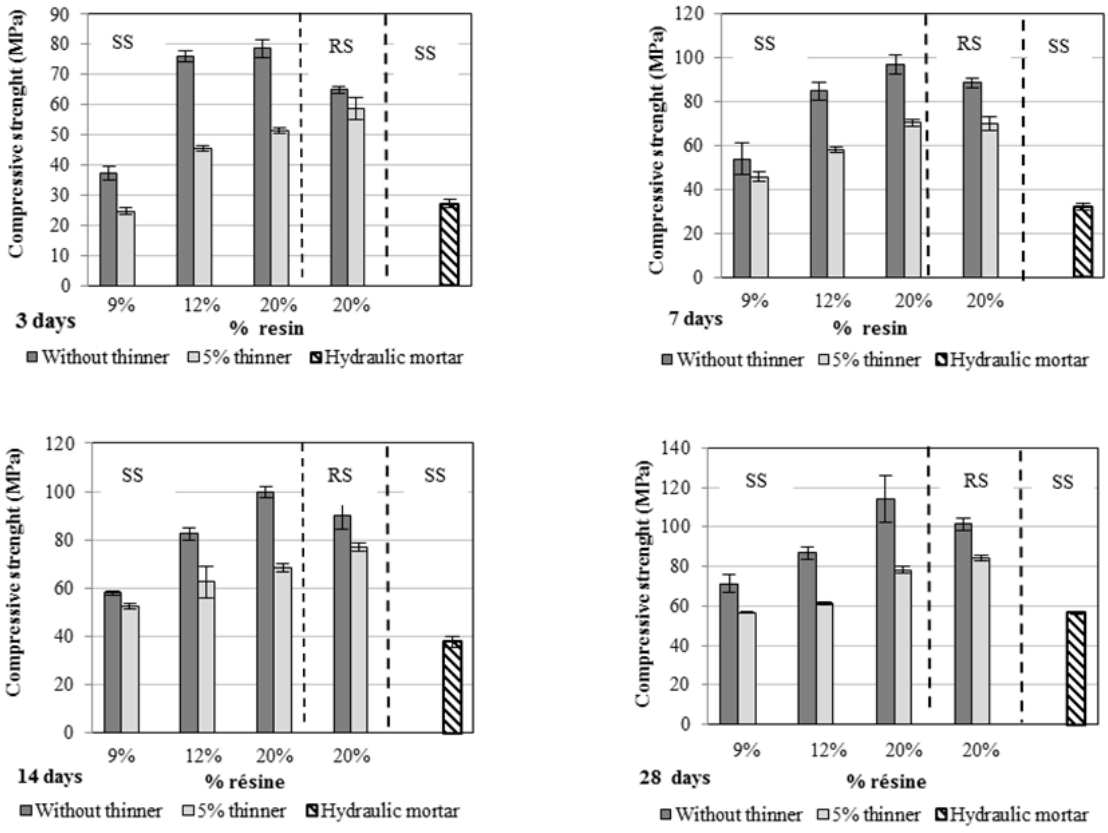

Figure 7. Evolution of compressive strength as function of resin percentage, thinner percentage and sand type.

Chloride ions diffusion. In order to study the resistance of resin mortars to chloride ions diffusion, transient migration test (Non Steady State Migration) was conducted on te different formulations of mortars. This test, developed by Tang and Nilsson [Tang 92], has the advantage of providing a result after 24 hours. It allows calculating the apparent diffusion coefficient D_{nssm}. The evolution of this coefficient was studied as a function of resin percentage m_r, type of sand and thinner (methyl octanoate) percentage. Figure 8 shows that the increase of the resin ratio conducts to the decrease of the diffusion coefficient of the chloride ions. For $m_r = 20\%$ and the use of standardized sand in epoxy resin mortar $D_{nssm} = 0,11x10^{-12} m^2 / s$ while when the standardized sand is substituted by recycled one, $D_{nssm} = 0,75\times10^{-12}\ m^2 / s$. In contrast, the addition of methyl octanoate in the mortar composition has no significant influence on chloride ions migration in epoxy resin mortars. These results were compared with those obtained for the standardized hydraulic mortar for which diffusion coefficient is equal to $10.66x10^{-12}$ m^2/s. This comparison shows that all the resin mortars have a much higher resistance to chloride ions diffusion than that of hydraulic mortar. Figure 9 shows the depth of chlorides ions diffusion on hydraulic and resin mortar made with 9% of resin.

Many authors studied the evolution of chloride ions diffusion into polymer-modified mortars as a function of polymer percentage. Aggarwal [Aggarwal, 07] stated that adding an acrylic polymer (designed by P) to cement paste (designed by C) with a P/C ratio of 20% reduced by 40% the depth of chlorides penetration. Saija [Saija, 95] also obtained a reduction of penetration depth with the increase of the P/C ratio for an acrylic polymer-modified mortar.

Gao [Gao, 02] studied the influence of P/C and silica fume on the effective chloride diffusion coefficient, the polymer was a polyacrylic ester (PAE). The results showed a decrease in the effective chloride diffusion coefficient with increasing P/C ratio and the addition of silica fume. Yang [Yang, 09] obtained the same results with an SBR polymer. No investigations deal with the effect of using a resin binder on the chloride ions penetration depth. The results illustrated in figure 8 show that increasing the epoxy resin ration decreases significantly the penetration depth which is drastically lower than this of hydraulic mortar.

Chloride ions diffusion in mortars is closely related to porosity [Bagel 97]. Figure 10 shows the evolution of D_{nssm} as a function of water porosity. It should be noted that the higher the porosity is, the more the ability of chloride ions to diffuse into the mortar is important. This statement is observed regardless of mortar formulation as long as the physicochemical nature of the binder is the same (with and without a thinner for epoxy binder).

The studies made on polymer-modified mortars related also the chloride ions diffusion to the porous structure. In fact, porosity tends to decrease with an increase in the P/C and a decrease in W/C ratio [Ohama, 91]. Studies conducted by Yang [Yang, 09] have shown that for a P/C greater than or equal to 10%, the microstructure of a SBR modified mortar becomes denser, the pore size and porosity is reduced.

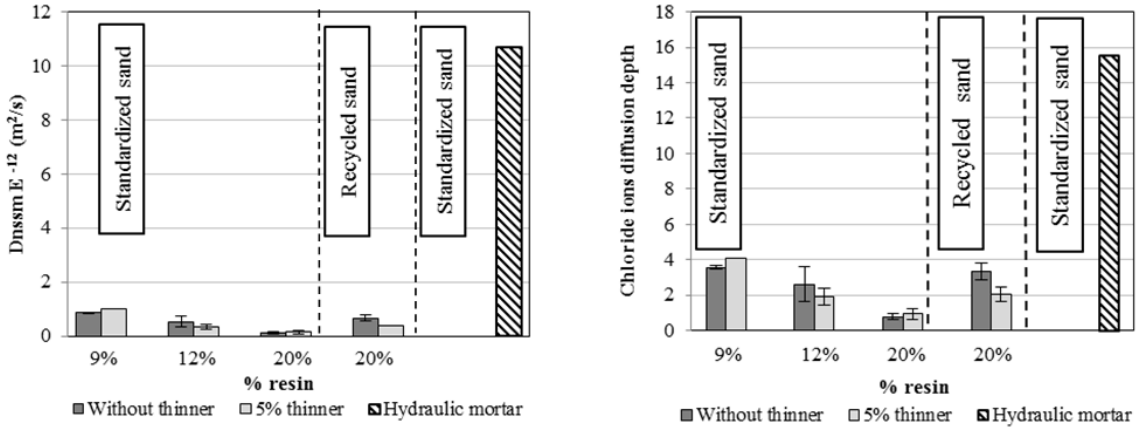

Figure 8. Evolution of chloride ions diffusion coefficient and diffusion depth as a function of resin percentage, thinner percentage and sand type.

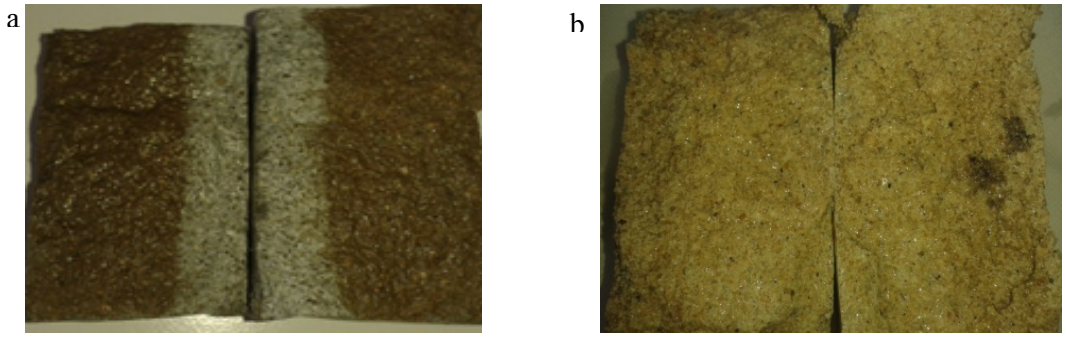

Figure 9. Pictures of hydraulic mortar sample (a) and resin mortar sample (rm= 9%) (b).

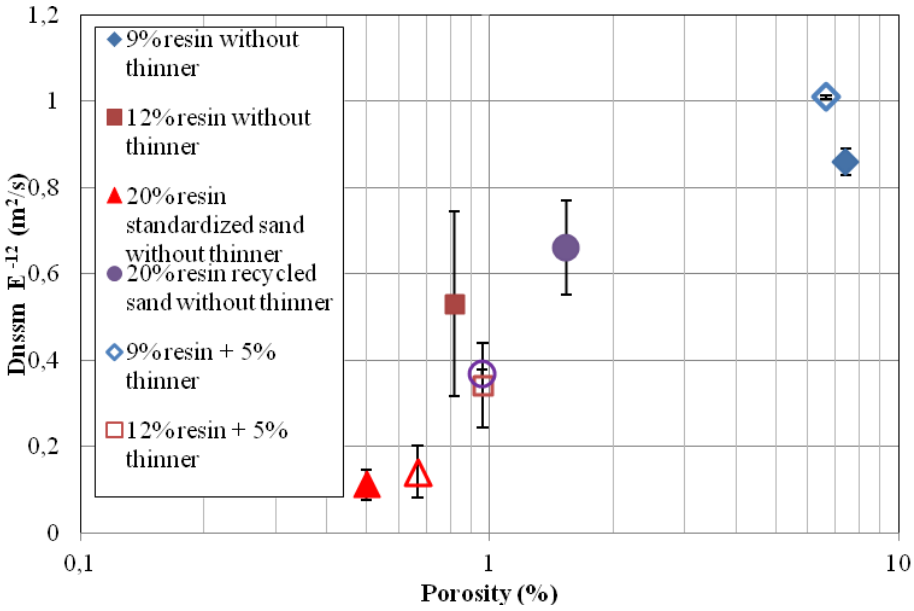

Figure 10. Evolution of chloride ions diffusion coefficient as a function of porosity.

CONCLUSION

It appears from this study that epoxy resin mortars have a workability which can be improved with the increase of resin ratio and with the addition of methyl octanoate. Substitution of standardized sand by recycled sand modifies the mortar workability which becomes poor. The mortar formulated with 20% of resin and standardized sand exhibits the best workability. At the cured state, the mechanical strengths were determined. The results showed that the mortar made with 20% of resin and standardized sand has the highest mechanical strengths. Epoxy resin mortars sustainability indicators were assessed at the age of 28 days. It was found that the porosity decreases with increasing resin content and therefore the resistance to chloride ions diffusion increases. The mortar made with 20% of resin and recycled sand has a lower resistance to chloride ions diffusion than the standardized sand epoxy mortar. The D_{nssm} values of epoxy resin mortars are lower than those of the standardized hydraulic mortar. This study allows concluding that the best epoxy resin mortar for repair is formulated with 20% of resin and standardized sand. However, the valorization of recycled sand in epoxy resin mortar manufacturing seems promising.

REFERENCES

Aggarwal L.K., Thapliyal P.C., Karade S.R. (2007). «Properties of polymermodified mortars using epoxy and acrylic emulsions». Construction and Building Materials, 21, 379-383.

Bagel L., Kivica V. (1997), «Relationship between pore structure and permeability of hardened cement mortars: on the choice of effective pore structure parameter», Cement and Concrete Research, 27, 1225-1235.

Bourguiba A., Ghorbel E., Dhaoui W. (2014), «Effets de l'introduction d'un diluant sur les propriétés physiques et rhéologiques des mortiers à base de résine époxyde», 32èmes rencontres de l'AUGC, Orléans 4 au 6 juin 2014.

Elalaoui O. Ghorbel E. , Mignot V. , Ben Ouezdou M. (2012). «Mechanical and physical properties of epoxy polymer concrete after exposure to temperatures up to 250 °C», Construction and Building Materials, 27, 415–424.

Embersons N. K., Mays G.C. (1990), «Significance of property mismatch in the patch repair of structural concrete, part I: properties of repair systems», Cement and Concrete Research, 19, 147-160.

Gaoa J.M., Qiana C.X., Wanga B., Morino K. (2002). «Experimental study on properties of polymer modified cement mortars with silica fume», Cement and Concrete Research, 32, 41-45, 2002.

Haidar M., Ghorbel E., Toutanji H. (2011). «Optimization of the formulation of micro-polymer concretes», Construction and Building Materials, 25, 1632–1644.

Morgan D.R. (1996), «Compatibility of concrete repair materials systems». Construction and Building Materials, 10, 51-61.

NF P 18-459, Béton, Essai pour béton durci, Essai de porosité et de masse volumique, 2010.

NT Build192, Concrete, mortar and cement based repair materials: chloride migration coefficient from non steady state migration experiments. Nordtest, 1999.

Ohama Y., Demura K.(1991). «Pore size distribution and oxygen diffusion resistance of polymer-modified mortars», Cement and Concrete Research, 21, 309-315.

Saija L.M.(1995). «Waterproofing of Portland cement mortars with a specially designed polyacrylic latex», Cement and Concrete Research, 25, 503-509.

Tang, L., Nilsson, L. O. (1992). «Rapid determination of chloride diffusivity in concrete by applying an electrical field», ACI Materials Journals, 89 (1), 49-53.

Yang Z., Shi X., Creighton A. T., Peterson M.M.(2009). «Effect of styrenebutadiene rubber latex on the chloride permeability and microstructure of portland cement mortar», Construction and Building Materials, 3, 2283-2290.

Mesoscale Modelling of Concrete with Recycled Aggregates

G. Mazzucco[1]; G. Xotta[1]; B. Pomaro[1]; C. E. Majorana[1];
F. Faleschini[1]; and C. Pellegrino[1]

[1]Department of Civil, Architectural and Environmental Engineering (DICEA), University of Padova, via F. Marzolo 9 35131, Padova, Italy.
E-mail: gianluca.mazzucco@dicea.unipd.it; giovanna.xotta@dicea.unipd.it; beatrice.pomaro@dicea.unipd.it; carmelo.maiorana@dicea.unipd.it; flora.faleschini@dicea.unipd.it; carlo.pellegrino@dicea.unipd.it

Abstract

In recent years new concrete types have been investigated, which include in the mix design a certain percentage of recycled aggregates, in view of a reduction of the production costs. Notably the re-use of material looks like an attractive alternative to landfill disposal and goes towards a more sustainable approach in the construction process. The present work addresses the realistic modelling of such a concrete mix design, focusing on both the geometric and constitutive aspect of the composite material, which is investigated at a mesoscale level, i.e. distinguishing concrete into its single components: matrix (cement paste) and coarse aggregates. A specific procedure for geometrically modelling such a kind of aggregates in a realistic way within a trial mix design is shown. The comparison between numerical and experimental results is in progress, to prove the goodness of the suggested approach, but here the challenging features represented by recycled aggregates in concrete from the point of view of numerical modelling, namely the geometric issue and the one related to the mechanics of the constituent materials are disclosed.

INTRODUCTION

Although traditional engineering studies consider concrete as a homogeneous material, idealized as a continuum medium with average properties (macroscopic approach), concrete is a highly heterogeneous material and its composite behavior is exceedingly complex.

A meso-scale approach will be followed here, which provides a more realistic description of concrete than the macro-scale, influenced by the geometry and the properties of its components. This could be expected, being the observed macroscopic behavior a direct consequence of the phenomena, which take place at the level of the material heterogeneities. Many mesoscopic models of concrete can be found in literature for the study of the influence of material composition on the overall behavior; here mesoscopic continuum models will be adopted, since through this approach mechanical and non-mechanical properties can be more realistically simulated for concrete with different compositions. Concrete at this level of study becomes a mixture of cement paste and aggregates of different sizes.

In this work the presence of a percentage of recycled aggregates (RAs) in the mix design will be considered, i.e. recycled materials from construction and demolition activities (C&D W - Construction and Demolition Waste). This is in

accordance with a growing attention to environmental issues by the UE, i.e. a reduced use of natural aggregates (NAs), being raw materials limited, and, at the same time, more and more restrictive regulations for the management of landfill waste.

The main issue with recycled aggregates is their peculiar geometry: due to their origin from demolition of pre-existing structures, they look quite irregular in shape and somehow difficult to characterize in which amount they are composed by NAs or old mortar connecting them.

The mortar coming from past concrete is known to be chemically stable during the hydration process but, at the same time, responsible for the global decay in the strength of concrete, due to its poor mechanic performance and the insufficient cohesion with the new cement paste (Faleschini et al., 2014).

Therefore, the complex nature of RAs must highly influence the overall hydro-mechanical behavior of the composite, based on the NA/mortar ratio, i.e. the quality of the RA itself. In this sense, the great heterogeneity of the RAs is worth a careful evaluation of the mix design of concrete and a deep knowledge of the constitutive relation among its components (Kou et al., 2011).

A specific procedure for geometrically modelling such a kind of aggregates in a realistic way within a mix design is shown here. Coarse aggregates are considered for the mix design after granulometric considerations, and only realistic NA/mortar ratios are taken into account. A random distribution into the matrix has been adopted, which well agrees with the volumetric curves of the companion mixture used in the experiments. The initial effort is paid on the aggregates topology reconstruction; indeed, the high irregularity of RAs does not allow any simplification in geometry (such as into spherical elements), as generally admitted in a mesoscale approach (Xotta et al., 2013; Xotta et al. 2015). In addition, mortar material around NAs, which takes origin from grinded old concrete, cannot be neglected in the modelling phase without compromising the adhesion between RAs and the cement paste. At this purpose the 3D laser scanning technique has been adopted to acquire, with a fairly good approximation, the external irregular surfaces of RAs. Starting from the external surface the whole inner volume has been subsequently distinguished into NA or mortar, based on continuity requirements for the splines describing the external surfaces. Three-dimensional models have been extracted and FE analyses on concrete samples made of such a kind of aggregates are carried out.

The modelling phase is aimed at a finite element discretization, to numerically investigate the mechanical behavior of RAs-made concrete under compression loads. To each component a specific constitutive behavior is assigned. To evaluate the brittle fracture behavior occurring in concrete at the overcoming of the elastic range under the applied loads, a specific damage-plasticity formulation has been developed able to reproduce the softening behavior during the deterioration process.

CONCRETE MIX DESIGN

A concrete mix design has been produced following the grading curve reported in Figure 1. This curve was obtained reproducing as well as possible a Bolomey ideal grading curve:

$$P = \frac{A - C + (100 - A)(d/D_{\max})^{1/2}}{100 - C} \cdot 100 \quad (1)$$

where P is the cumulative passing (%) for each size fraction d, D_{max} is the maximum size of the aggregates (in this case 22.4 mm), A is the Bolomey parameter depending on the shape of the aggregates and on the required consistency class to be reached (in this case $A=12$), and C is the percentage value of the cement content, expressed in weight as:

$$C = \frac{c}{c + i} \cdot 100 \quad (2)$$

c and i are respectively cement dosage and aggregate content, expressed in kg/m^3.

Cement dosage is 350 kg/m^3, w/c ratio is equal to 0.45, and i is equal to 1978 kg/m^3. The global volume of aggregates (RAs + gravel + sand) is distributed respectively in the following way: 9.2%, 39.8% and 51%.

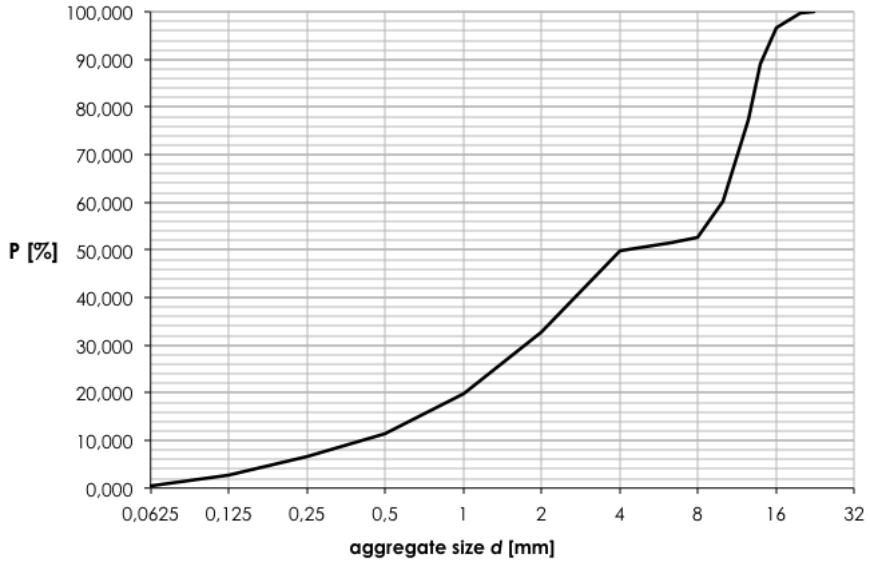

Figure 1. Grading curve adopted for the concrete mix design.

In a mesoscale approach only the coarse aggregates can be explicitly represented, with a diameter larger than 5 mm (RAs + gravel), while the smaller aggregates (sand) are considered into the matrix as a homogeneous material.

Assuming the cement and the water densities respectively equal to ρ_c=3000 kg/m^3 and ρ_w=1000 kg/m^3, the volumes of these two concrete components for each m^3 are V_{cement} = 350/3000 ≈ 0.12 m^3/m^3 and V_{water} = 157/1000 ≈ 0.16 m^3/m^3. The volume of the aggregates for each m^3 of concrete is evaluated as V_{aggr} = 1-V_{cement}-V_{water} ≈ 0.73 m^3/m^3.

Therefore, the volume of coarse aggregates has been assumed equal to $V_{agg,coarse}$ $=(9.8\%+39.2\%)V_{aggr} \approx 0.36 m^3/m^3$.

AGGREGATES GEOMETRICAL ISSUES

Taking into account how the RAs are obtained (by grinding old concrete elements), the topology of the aggregates results various and is not possible to simplify their shape as spherical elements, as generally done in a mesoscale approach. These types of elements are highly irregular and generally composed with different materials, i.e. one or two NAs connected to each other by old mortar.

In Figure 2 it is reported a typical recycled aggregate; as can be noticed the main problems for the numerical representation of this type of aggregates are related to their irregular shape and to the determination of the interface surfaces between the aggregate and mortar, and those between the matrix and recycled aggregates.

To solve the first problem, i.e. the representation of the geometric shape of the aggregates, 3D scanners have been used to obtain the virtual representation of the external surfaces (Rumpf and Wardetzky, 2014). The sequence of the process is shown in Figure 3. A geometry such as the one in Figure 3c), made with 545 surfaces, is easily convertible to a solid to obtain the numerical model.

Figure 2. Configuration of a typical RA from previous demolition.

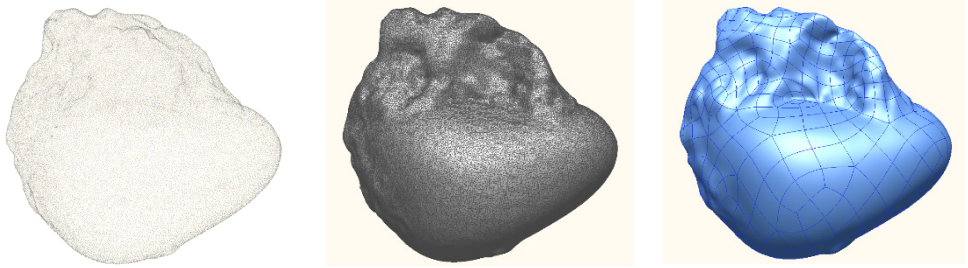

a) **b)** **c)**

Figure 3. 3D laser scanner output (cloud points) a); graphic elaboration into surfaces (tessellation) b); external surfaces c).

Being these surfaces very distorted the degree of discretization of the mesh results very dense; this can be problematic with the idea to create models with more aggregates within the matrix.

RAs reconstruction

The adoption of the three-dimensional scanning technique to obtain the geometry of the recycled aggregates does not allow diversifying the different

materials that can be present in these types of aggregates (mortar and stones). Indeed the scanning procedure allows to obtain only the external surface of the scanned object, while the internal surfaces between the materials remain unknown (see Figure 4 a)).

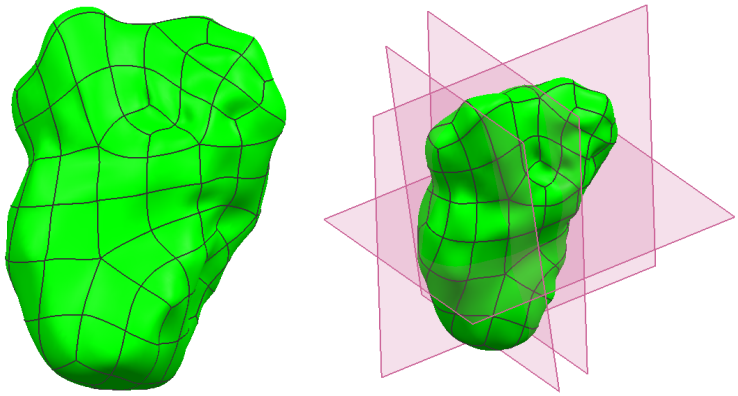

a) b)

Figure 4. Three-dimensional surfaces a); characteristics cut planes b).

The reconstruction has been obtained identifying in the scanned surfaces the aggregates and the mortar parts and subsequently, starting from the external aggregate surface, the reconstruction of the interfaces between mortar and stone have been carried out identifying some characteristic cut planes in the geometry (see Figure 4 b)).

For each plane, the external perimeter of the RA has been defined (see Figure 5a)) and the surfaces of the stones are obtained closing the external parts with *C0* (continuous) and *C1* (with first continuous derivative) lines (see Figure 5b)). Following this procedure for all the cut planes the three dimensional aggregate outlines have been determined (see Figure 5c)).

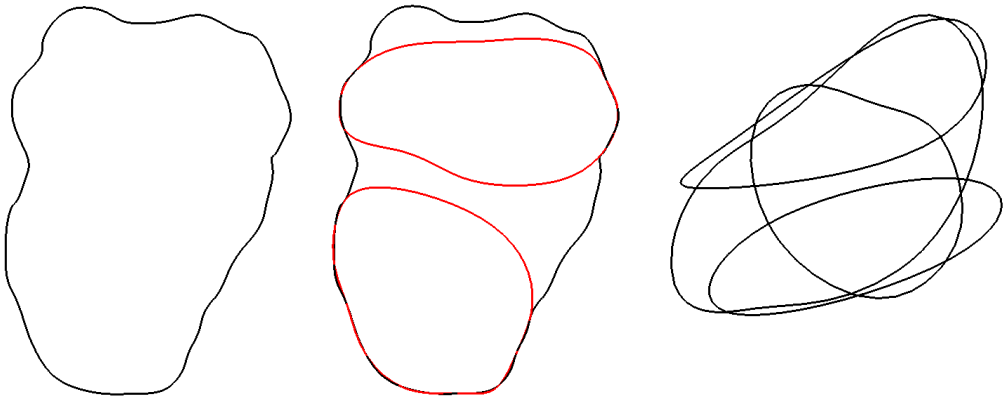

a) b) c)

Figure 5. External perimeter in a characteristic plane a); Stone perimeter b); Aggregate edge c).

Closing the outlines with appropriate surfaces the reconstructed aggregate has been obtained (see Figure 6 a)).

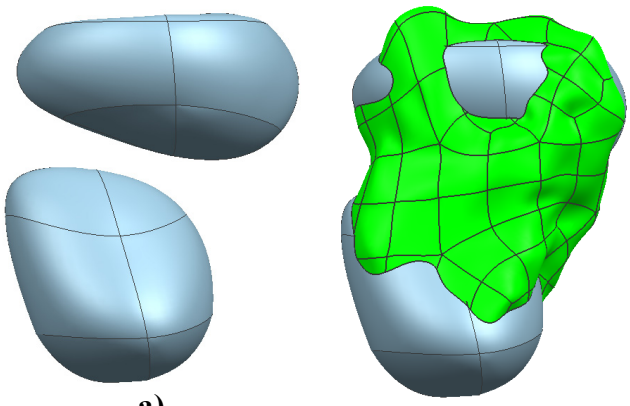

a) b)

Figure 6. Reconstructed aggregates a); new geometry with mortar and aggregates b).

RANDOM DISTRIBUTION PROCEDURE

A simplified random distribution algorithm has been adopted to obtain the concrete sample in a mesoscale approach (Torquato, 2002). Starting from the grading curve employed in the mix design, the random algorithm considers that each aggregate is surrounded by a "virtual" sphere (see Figure 7a)) with a diameter equal to the diameter of the passing present in the grading curve and the number of spheres that has been evaluated in relation to the percentage of volume.

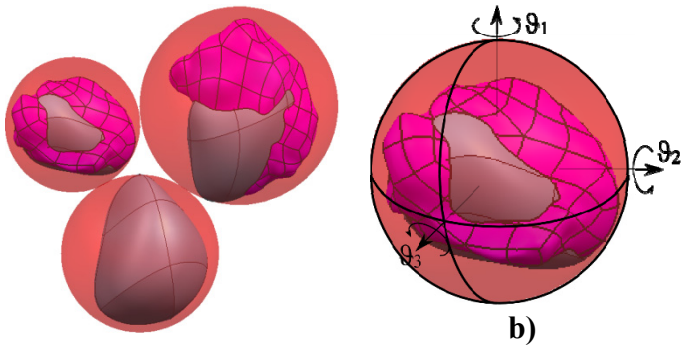

a) b)

Figure 7. Aggregates surrounded by virtual spheres a); three-dimensional rotational angle b).

Taking into account the interference between the spheres (the sphere cannot penetrate) the numerical procedure evaluate a minimum distance between the aggregates d_{min} and the effective distance d as:

$$d_{\min} = R_1 + R_2 + O \quad (3)$$

where R_i is the radius of the sphere i and O is the possible offset between the two spheres.

The effective distance between the two spheres is:

$$d = \sqrt{\sum_{j=1}^{3} \left(x_{2,j} - x_{1,j} \right)^2}$$
(4)

where $x_{i,j}$ is the j-th coordinate of the sphere i. This distance allows to evaluate the interference between two different aggregates. The position of the sphere's center **x** has been defined with a random function:

$$\mathbf{x}(j) = rand(j)$$
(5)

The iterative procedure to obtain the random aggregates distribution starts by defining a trial center position $\mathbf{x}^{Tr}$ of the sphere (equation (5)) and for each aggregate already inserted in the volume evaluates d_{min} and d. If $d > d_{min}$ the sphere penetrates and $\mathbf{x}^{Tr}$ should be rejected; otherwise a new aggregate is inserted with a center $\mathbf{x}=\mathbf{x}^{Tr}$. Considering the irregular form of the aggregates (see for example Figure 2) a random rotation angle has been defined:

$$\theta(j) = rand(j)$$
(6)

where j are the directions of the local axes (see Figure 7 b)).
An example of random distribution has been reported in Figure 8 for a concrete sample of size 35×35×70mm. The 36% of the concrete volume is characterized by coarse aggregates where the 80% are NAs and the 20% are RAs.

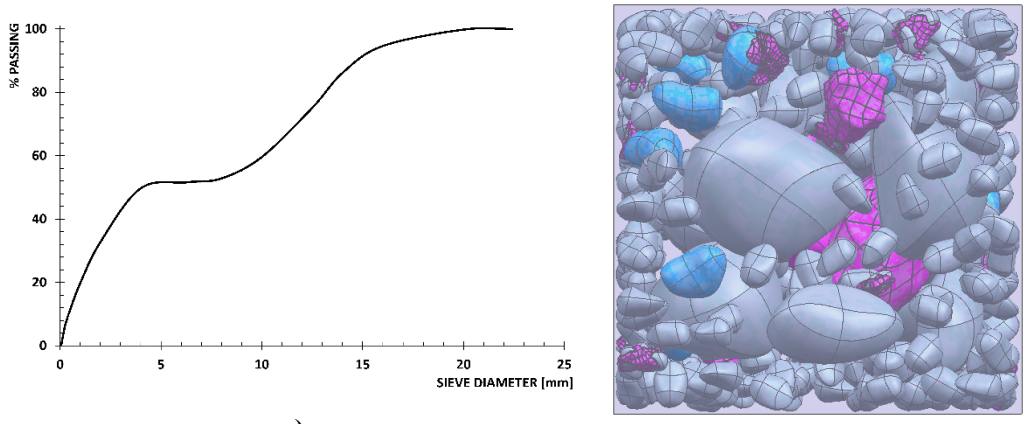

a) **b)**

Figure 8. Grading curve a); Plane view of the numerical random distribution b).

CONSTITUTIVE BEHAVIOUR OF CONCRETE

Once the different concrete sample models have been obtained at the meso-level, containing a random distribution of NAs and RAs, their mechanical behavior under a compression load has been numerically investigated.

To each component a specific constitutive behavior has been assigned; in specific, NAs have been considered to behave elastically while for "old" mortar and matrix a damage-plasticity formulation has been considered.

The coupled damage-plasticity model has been numerically implemented in Fortran and has been connected to ABAQUS (ABAQUS 6.12-1, 2012) finite element software in the form of a user subroutine (UMAT) for the numerical investigations.

As regards plasticity, the Drucker-Prager (1952) yield criterion has been adopted:

$$f_p\left(\boldsymbol{\sigma}, \boldsymbol{\varepsilon}_\mathbf{p}\right) = \alpha I_1 + \sqrt{J_2} - k \tag{7}$$

where $\boldsymbol{\sigma}$ is the stress tensor; I_1 and J_2 are respectively the first invariant of the stress tensor and the second invariant of the deviatoric stress tensor; α and k are a measure of the internal material friction and cohesion and are function of the plastic strain $\boldsymbol{\varepsilon}_\mathbf{p}$.

As regards damage, the Mazars' scalar damage model (Mazars and Pijaudier-Cabot, 1989) has been considered and combined with plasticity. The damage function governing the response of the material takes the following form:

$$f_d\left(\boldsymbol{\varepsilon}, \mathbf{D}_\mathbf{e}, K_0\right) = \tilde{\varepsilon} - K(D) \tag{8}$$

where $\boldsymbol{\varepsilon}$ is the strain tensor; $\mathbf{D}_\mathbf{e}$ is the stiffness material tensor; D is the damage parameter; $\tilde{\varepsilon}$ is the equivalent strain; $K(D)$ is the hardening/softening parameter initially equal to K_0.

More in specific, the damage parameter D is expressed as:

$$D = 1 - \frac{(1-A)K_0}{\tilde{\varepsilon}} - \frac{A}{\exp[B(\tilde{\varepsilon} - K_0)]} \tag{9}$$

where K_0, A and B are parameters determinable form experimental tests.

THREE-DIMENSIONAL NUMERICAL MODELS

A prismatic sample $35 \times 35 \times 70$mm, characterized by 36% of the concrete volume by coarse aggregates (80% NAs and 20% RAs), has been modeled via 950000 tetrahedral elements with linear shape functions and 200000 nodes. The imposed displacement of 0.1mm has been applied in Z direction to the top of the sample.

In the Table 1, reported below, the material properties are summarized in terms of elastic modulus E; Poisson's ratio v; compression and tension strength (f_c and f_t respectively) for each component: NAs, mortar and matrix:

Table 1. Material properties.

	NAs	Mortar	Matrix
E [MPa]	40000	9000	20000
v	0.15	0.15	0.15
f_c *[MPa]*	-	6.0	15.0
f_t *[MPa]*	-	1.0	1.5

The interfacial transition zones (ITZ) are thin layers between the aggregates and the matrix and, considering a single RA, they locate between the mortar and the stones (Scrivener et al., 2004). These zones are a product of concrete hydration; indeed, around the aggregates an accumulation of water occurs that increases the matrix porosity and reduces the mechanical characteristics of the paste. These zones have been modeled via a contact algorithm. The penalty coefficients have been reduced in order to represent the limited stiffness in these areas.

Numerical results

The evolution of damage in the matrix is reported in Figure 9. The damage-plasticity algorithm leads to first evidences of damage close to the biggest central RAs, where the maximum value is envisaged right at 60% of the analysis, while further regions into the matrix are involved at 70% and 80% of the analysis.

This is explained by the lower stiffness of the old mortar with respect to the surrounding matrix and the NAs. This allows damage to start at the weakest point and evolve into the matrix. The cracking is then expected to start at the peak values for damage and consequently spread within the sample.

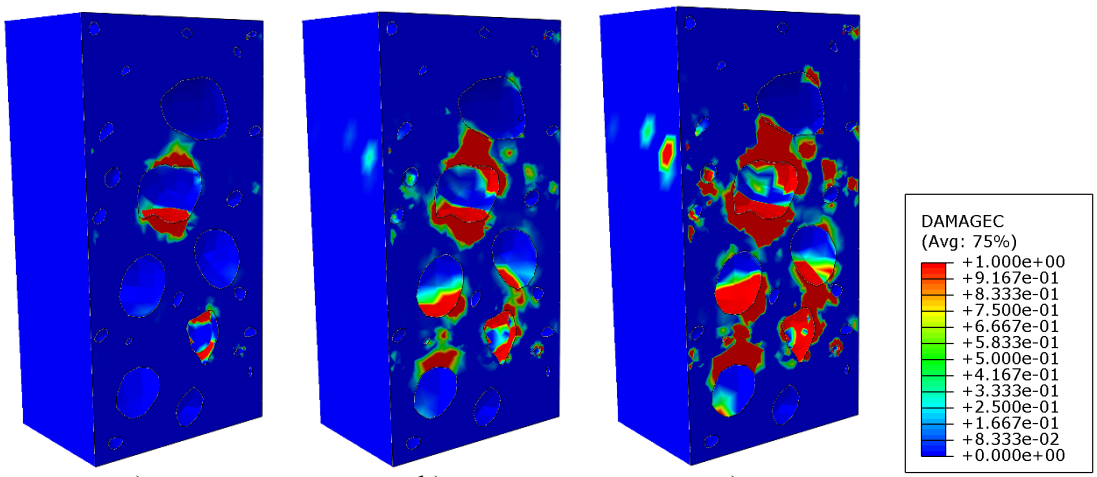

a) b) c)

Figure 9. Damage evolution in the sample matrix at 60% a); 70% b); 80% c) of the analysis.

CONCLUSION

The challenging aspects of the modelling of recycled aggregates from demolition waste in concrete mixtures is presented in this paper and a formalized

procedure is suggested to model such a complex composite material.

An accurate reproduction of the geometry of these aggregates has been achieved via the use of a 3D laser-scanning technique; the obtained geometry has been reasonably simplified with CAD programs in order to unburden the computational effort, then enriched by the geometry of the aggregate-mortar contact surface to handle the object with FEM analyses. A realistic concrete-mix has been defined, partially composed of natural aggregates, and partially of recycled aggregates, thanks to an ad-hoc random algorithm satisfying the volume ratio for aggregates of a given mix. Only the coarse fraction of aggregates have been modelled in ABAQUS environment, which is a reasonable choice when modelling concrete at the mesoscale.

A specific damage-plasticity formulation has been developed and assigned as constitutive behaviour to the mortar and the matrix and qualitative contour maps of damage evolution are obtained, which are being checked against a companion experimental test soon. Overall, the critical aspects for geometrically modelling concrete with recycled aggregates were overcome with the technique here illustrated, which can be extended to any kind of irregular composite material.

ACKNOWLEDGEMENTS

The authors gratefully acknowledge Prof. G. Concheri and his research group, Dept. ICEA – University of Padova, for providing the 3D scanner equipment and for the support during the acquisition process. His valuable comments during the work were really appreciated.

REFERENCES

ABAQUS Version 6.12-1 (2012). *ABAQUS 6.12-1 Documentation*, Dassault Systémes, Simulia Corporation, Providence, RI, USA.

Drucker, D.C. and Prager, W. (1952). “Soil mechanics and plastic analysis or limit design.” *Quarterly of Applied Mathematics*, 10, 157-165.

Faleschini, F, Jiménez, C., Barra, M., Aponte, D., Vázquez, E., and Pellegrino, C. (2014). “Rheology of fresh concretes with recycled aggregates.” *Construction and Building Materials*, 73, 407–416.

Kou, S., Poon, C., and Agrela, F. (2011). ”Comparisons of natural and recycled aggregate concretes prepared with the addition of different mineral admixtures.” *Cement & Concrete Composites*, 33, 788–795.

Mazars, J. and Pijaudier-Cabot, G. (1989). “Continuum damage theory – application to concrete.” *Journal of Engineering Mechanics*, 115(2), 345-365.

Rumpf, M. and Wardetzky, M. (2014). “Geometry processing from an elastic perspective.” GAMM-Mitt, 2, 184-216,

Scrivener, K.L., Crumbie, A.K., and Laugesen, P. (2004). “The interfacial transition zone between cement paste and aggregate in concrete.” *Interface Science*, 12, 411-421.

Torquato S. (2002). *Random Heterogeneous Materials:Microstructure and Macroscopic Properties*. New York, Springer-Verlag.

Xotta, G., Salomoni, V.A., and Majorana, C.E. (2013) "Thermo-hygro-mechanical meso-scale analysis of concrete as a viscoelastic-damaged material." *Engineering Computations*, 30(5), 728-750.

Xotta, G., Mazzucco, G., Salomoni, V.A., Majorana, C.E., and Willam, K.J. (2015). "Composite behavior of concrete materials under high temperatures", *International Journal of Solids and Structures*, doi:10.1016/j.ijsolstr.2015.03.016.

Influence of the Proportion of Recycled Gravel on Shrinkage and Cracking Risk: Early Age and Long-Term Behavior

A. Z. Bendimerad[1]; E. Rozière[1]; and A. Loukili[1]

[1]Institut de Recherche en Génie Civil et Mécanique (GeM), UMR-CNRS 6183, Centrale Nantes, France. E-mail: ahmed.bendimerad@ec-nantes.fr

Abstract

This paper presents the results of experimental research on recycled concrete at early age and long term. It consists in studying the effect of the proportion of recycled gravel (RG) on shrinkage and cracking risk. Three mixtures were investigated to study the effect of substitution of natural gravel (NG) by the recycled gravel (0% RG, 30% RG and 100% RG). A stress/strength approach was used to quantify the risk of cracking at early age. It is based on experimentally assessed parameters. At long term ring tests were performed to assess the cracking sensitivity induced by drying shrinkage. At early age the results indicate RG affected the properties of the recycled concrete and increase the potential risk of cracking. At long term, the effect of substitution of the recycled gravel on drying shrinkage was not significant. However, the three concrete showed different cracking sensitivity, thus shrinkage-induced cracking was influenced by the evolution of stiffness and relaxation. Finally, compared to the conventional concrete recycled concrete showed higher cracking sensitivity at early age and long term, but the effect was not proportional to the proportion of recycled gravel. 30% RG actually showed higher cracking sensitivity than 100% RG.

INTRODUCTION:

The use of construction waste obtained from building demolition as aggregates for the production of new concrete has become more common for the last decade. In many urban areas, a critical shortage of natural aggregates is detected. At the same time, increasing quantities of demolished concrete from old structures are generated as waste material in these same areas. In France, 300 million tons of building wastes are produced per year **(IREX 2011)**; only a part is used for recycled concrete, mainly for road works. Sustainable development has become a strategic issue and affects construction materials in terms of CO_2 emission, energy consumption and the use of natural raw materials. As a consequence, ready-mix concrete producers are forced to use natural aggregates with relatively high porosity (2%<water absorption<4%) and recycled aggregates (RA).

Replacing natural aggregates with recycled aggregates affects plastic shrinkage, long-term drying shrinkage and cracking. The main parameters that influence cracking actually depend on the proportion of recycled concrete. Recycled aggregates include old cement paste **(Belin 2014)** thus their use is likely to produce an increase in drying shrinkage and creep **(Domingo 2009 and Asamoto 2008)**. Natural aggregates are stiffer than cement paste, thus replacing natural aggregates

with recycled aggregates results in a decrease in elastic modulus **(Stock 1979; Hansen 1983 and Xiaoa 2005)**. The tensile strength of concrete made of recycled aggregates is generally lower than the strength of natural aggregate concrete. However it is not easy to conclude on the effect of replacing natural aggregates with recycled aggregates on restrained shrinkage cracking, as the parameters act in opposite ways, for instance drying shrinkage and elastic modulus.

The aim of the present experimental study is to assess the influence of the recycled concrete aggregates proportion on plastic shrinkage, long-term shrinkage and cracking risk of concrete.

The first part of the study deals with early age behavior. To quantify the cracking risk of recycled concrete the experimental study is based on the monitoring of the evolution of plastic shrinkage, ultrasonic Young modulus and direct tensile strength. An elastic approach based on stress/strength is then used.

The second part of the experimental work aimed at assessing the influence of recycled concrete aggregates proportion on drying shrinkage induced cracking of concrete. The experimental program consisted in a comprehensive study of the evolution of parameters involved in cracking tendency, namely: strength, autogenous and drying shrinkage, elastic modulus, and relaxation using ring test.

EXPERIMENTAL PROGRAM:

Three mixtures (Table 1) were designed to investigate the effect of substitution of natural gravel (NG) by recycled gravel (RG).

Table 1. Admixtures of natural and recycled concrete

	0% RG	30% RG	100% RG
NG 6,3/20 (kg/m^3)	820	462	
RG 10/20 (kg/m^3)		296	701
NG 4/10 (kg/m^3)	267	228	
RG 4/10 (kg/m^3)			163
NS 0/4 (kg/m^3)	780	813	806
Cement, C (kg/m^3)	270	276	282
Limestone, L (kg/m^3)	45	31	31
Superplasticizer SP (kg/m^3)	0.747	0.861	0.798
W_{eff}	180	185	189
W_{tot}	194.6	212.3	241.0
W_{eff}/B_{eq}	0.64	0.65	0.65
Volume of paste (l/m^3)	285	287	293
Gravel/Sand	1.39	1.21	1.07
Slump (mm)	195	193	195
Packing density g*	0.785	0.781	0.777
MPT (mm)	0.80	0.82	0.89

The study was dived into two parts. The first deals with early age and the second with long term behavior. At early age, the plastic shrinkage development was measured using a steel mold (7x7x28) cm^3 **(Turcry 2006)**, the evolution of elastic properties of concrete at early age was monitored by the *FreshCon* system which

measures the velocity of ultrasonic p and s waves **(Reinhardt 2004),** and the assessment of direct tensile strength using specific tests developed in GeM Laboratory at Ecole Centrale de Nantes **(Roziere 2015)**. At long term, mass loss, total and autogenous shrinkage were measured on prisms (7x7x28) cm^3. Finally, ring test was used to estimate the cracking sensitivity for the natural and recycled concrete. All the tests were conducted in an air-conditioned room, with controlled temperature (20°C±1) and relative humidity (50%±5) and all the aggregates were used in this study at saturated surface dry state (SSD).

RESULTS AND DISCUSION:

Early age behavior

The measurement of plastic shrinkage began 30 min after mixing. The graph on (Figure 1) shows the influence of the proportion of recycled gravel on plastic deformation. There was a difference of 21% after a period of 8 hours when the concrete with 100% recycled gravel was used compared to conventional concrete.

The plastic shrinkage of 30% RG and 100% RG concretes were the same. When the RG mixtures are compared with the conventional concrete mixture (red curve), the difference is significant but relatively low. This can be explained by a physical parameter called Maximal Paste Thickness (MPT). The MPT corresponds to the distance between two coarse aggregates. It is the highest gap between two particles, in such a uniform dilation process **(De Larrard 1994 and 1997)**. By using the software BETONLAB **(De Larrard 2007)**, the MPT was calculated for the three mixtures and the results show a quasi-constant MPT (Figure 2), knowing that the shrinkage of concrete can be summed up in the free shrinkage of the MPT. The recycled concrete 0RS-100RG has the highest value of MPT (0.89 mm) compared with the other recycled mixtures and it actually showed relatively high plastic shrinkage.

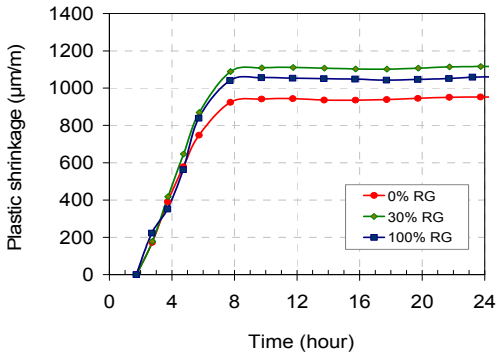

Figure 1. Effect of substitution rate on plastic shrinkage.

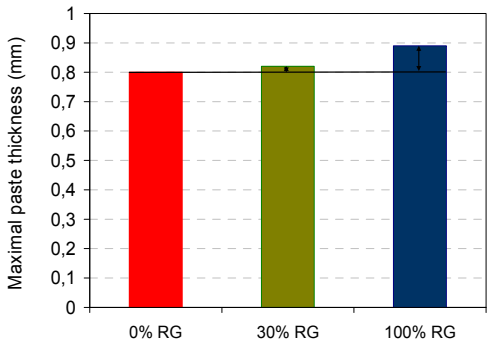

Figure 2. Effect of substitution rate on MPT.

Moreover, the evolution of the early age deformation can be correlated to the increase of the elastic modulus. At the end of setting, when the modulus reached

approximately 2 GPa, the plastic shrinkage stopped increasing. The most significant plastic shrinkage concerns concrete with 30% RG (Figure 3) which showed the highest development of the ultrasonic Young modulus.

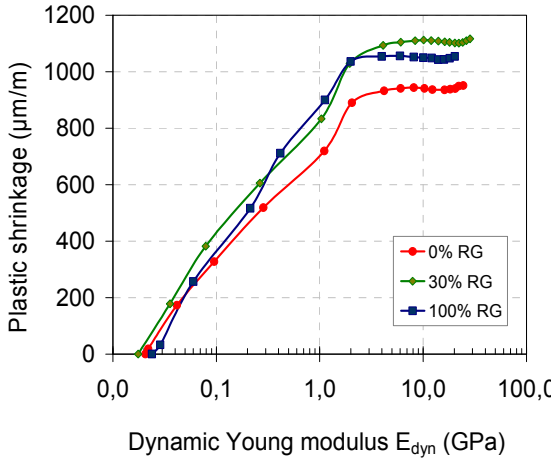

Figure 3. Plastic shrinkage vs. ultrasonic Young modulus.

In the present experimental study, the objective is to quantify the shrinkage-induced cracking risk of recycled concrete at early age, based on monitoring of the evolution of stress and strength. Previous works actually showed that failure occurs when the restraining stress exceeds the tensile strength **(Hammer 2001 and Ravina 1968)**. Plastic shrinkage is likely to generate such restraining stress. The evolution of plastic shrinkage and tensile strength has already been assessed using specific tests. An elastic approach based on stress/strength was used to assess the cracking risk. The approach was based on an elastic model and the time evolutions of the properties of concrete (Eq. 1):

$$\sigma(t) = \varepsilon(t) \times E(t) \tag{1}$$

Where: $\varepsilon(t)$ is plastic shrinkage deformation, $E(t)$ is Young modulus evolution and $\sigma(t)$ is the estimated stress of concrete noted as (stress S). The concrete tensile strength, noted as (resistance R), was experimentally assessed at 24 hours after mixing using direct tensile test.

The percentage of substitution of recycled gravel significantly affects the mechanical properties, e.g. elastic modulus and tensile strength (Table), and early age deformation (Figure 4 and Figure 5), causing a higher cracking sensitivity. The concrete 30% RG is characterized by a higher stress development due of the fast increase of elastic modulus and plastic deformation respectively which implies a higher S/R ratio. Consequently, the risk of cracking of this concrete is higher compared to the other concretes.

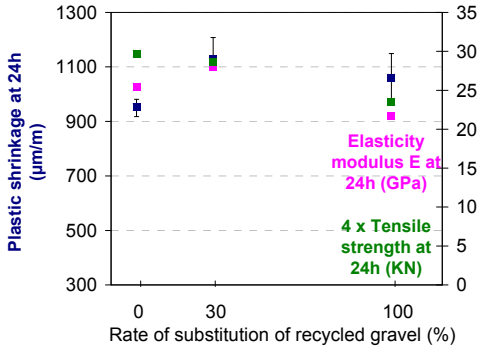

Figure 4. Correlation between plastic shrinkage, Young modulus and tensile strength at 24h.

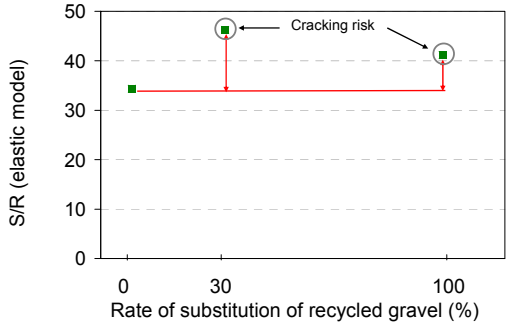

Figure 5. Effect of substitution rate on potential cracking risk.

Long term behavior

The natural and recycled concrete specimens are then subjected to compressive strength, splitting tensile strength tests, having reached ages of 1, 2, and 28 days. The Young's modulus is measured on cylindrical specimens (11x22 cm²) in compression at 1, 2, and 28 days (see Table 2).

Table 2. Mechanical properties and shrinkage indicators

	0% RG	30% RG	100% RG
fc (Mpa)			
1 day	7.2	6.2	5.7
2 day	13.1	12	10.1
28 day	32	29.8	26.8
ft (Mpa)			
1 day	1.3	1.14	1.01
2 day	1.41	1.38	1.26
28 day	2.48	2.47	2.28
E (Gpa)			
1 day	26.5	21.2	19.2
2 day	32	27,.1	23.7
28 day	43.5	39.7	33.5
Shrinkage			
Shrinkage half-time Ns (day)	21.9	21.7	25.4
Ultimate shrinkage ε_∞ (µm/m)	598	663	613

All the specimens were demolded 24h after mixing concrete and the shrinkage measures began. The drying shrinkage strain was calculated by the difference between the sealed and the total shrinkage strains. The graph on (Figure 6) shows that the curves of the three concretes (conventional and recycled concrete) are close, and

after 60 days of measurement the drying shrinkage of 100 % RG concrete keeps increasing and exceeds the conventional concrete.

A typical weight loss due to water evaporation was measured. The drying shrinkage was plotted as a function of mass loss (see Figure 7). Two stages can be distinguished. The first one corresponds to mass loss without drying shrinkage. This stage is more significant for the mixtures having higher total water, such as recycled concrete (see Table 1). During the second stage, all the curves have the same slope. This means that for the same water loss, the same drying shrinkage was generated.

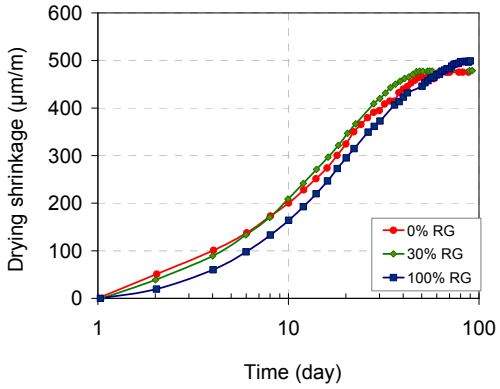

Figure 6. Drying shrinkage vs. age for natural and recycle concrete.

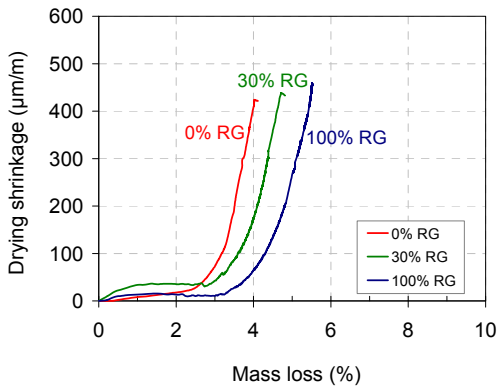

Figure 7. Drying shrinkage vs. Mass loss.

The strain that developed on the inner face of the steel ring was monitored during the test. The Figure 8 shows that cracking occurred in concrete with 30% RG and 100% RG at 35 days and 95 days respectively. However, the three concretes showed approximately the same shrinkage, but the conventional concrete and the concrete with 30% RG had higher elastic modulus than the 100% RG concrete which implies a significant stress development and a higher cracking sensitivity.

The stresses development in the conventional concrete began to decrease suggesting that micro-crack may have caused relaxation of stresses at 35 days. This corresponds to the age of cracking of concrete with 30% RG.

Compared to the conventional concrete the evolution of the cracking sensitivity at long term as a function of the proportion of RG is similar to that observed at early age.

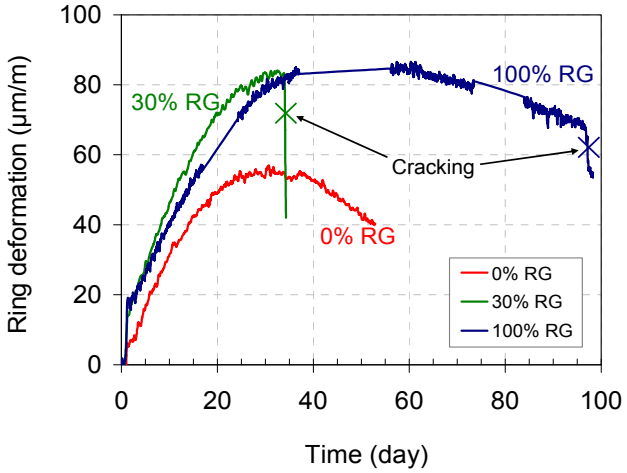

Figure 8. Tangential strain of the ring vs. age for natural and recycled concrete

CONCLUSION

The proportion of recycled gravels (RG) affects the early age as well as the long-term behavior and shrinkage-induced cracking sensitivity of concrete.

Recycled concrete mixtures and conventional concrete showed relatively low differences in terms of deformations. This can be explained by the Maximum Paste Thickness concept (MPT). The results showed a quasi-constant MPT. The shrinkage of concrete is actually mainly due to the free shrinkage of cement paste in the MPT.

At early age, the stresses were calculated from plastic shrinkage and elastic modulus. The concrete with 30% RG is characterized by a higher stress development due to the faster increase of elastic modulus and early age deformation respectively which implies a high stress-to-strength ratio and a higher potential risk of cracking.

At long term, the curves of drying shrinkage are close. The higher rate of water loss for the mixture with 100% RG may be explained by larger pores in the structure at early age and higher total water. The increase in cracking sensitivity is observed when the stiffness of concrete is higher.

At early age and long term, the evolutions of the cracking sensitivity as a function of the proportion of recycled aggregates are consistent, but the influence is not proportional to the proportion of recycled gravel.

REFERENCES

Asamoto S, Ishida T, Maekawa K (2008) Investigation into volumetric stability of aggregates and shrinkage of concrete as a composite. J Adv Concr Technol 6(1):77–90.

Belin P, Habert G, Thiery M, Roussel N (2014), Cement paste content and water absorption of recycled concrete coarse aggregates. Mater Struct 47(9):1451–1465.

Bendimerad A. Z., Roziere E., Loukili A. (2014), Combined experimental methods to assess absorption rate of natural and recycled aggregates, Materials and Structures, October.

De Larrard F. and Sedran T. (1994), Optimisation of ultra-high-performance concrete by the use of a packing model, Cement and Concrete Research vol 24 n° 6, pp. 997-1009.

De Larrard F., Belloc A. (1997), The Influence of Aggregate on the Compressive Strength of Normal- and High-Strength Concrete, ACI Materials Journal n°94, pp. 417-425.

De Larrard F., Sedran T. (2007), Le logiciel BetonlabPro 3 : Bulletin des laboratoires des ponts et chaussées, BLPC n°270-271, In French.

Domingo-Cabo A., Lázaro C., López-Gayarre F., Serrano-López M.A., Serna P., Castaño-Tabares J.O. (2009), Creep and shrinkage of recycled aggregate concrete, Construction and Building Materials 23, pp. 2545-2553.

Hammer T.A. (2001), On the strain capacity and cracking mechanisms of high strength concrete on very early age, Elsevier Science.

Hansen T.C., Narud H. (1983), Strength of recycled concrete made from crushed concrete coarse aggregate, Concrete International, 1983, p. 79-83.

IREX : Institut pour la recherche et l'expérimentation en génie civil (2011), Rapport PN-RECYBETON, (RECYclage complet des BETONs), In French, 45 p.

Ravina. D., and Shalon R. (1968), Plastic shrinkage cracking, ACI Journal, vol 65, n°22, pp. 282-294.

Reinhardt HW, Grosse CU. (2004), Continuous monitoring of setting and hardening of mortar and concrete, Construction and Building Materials 18, pp.145–154.

Roziere E., Cortas R., Loukili A. (2015), Tensile behaviour or early age concrete: New methods of investigation, Cement and Concrete Composites 55, pp. 153-161.

Stock A.F., Hannant D.J. and Williams R.I.T. (1979), The effect of aggregate concentration upon the strength and modulus of elasticity of concrete, Mag Conc Res, No 109, pp 225-34.

Turcry Ph., Loukili A. (2006), Evaluation of plastic shrinkage cracking of self-consolidationg concrete, ACI Materials Journal, n° 103, pp. 272-279.

Xiaoa J., Lia J., Zhang Ch. (2005), Mechanical properties of recycled aggregate concrete under uniaxial loading, Cement and Concrete Research 35 1187–1194.

Nanostructure of Cement/Polymer Fiber Interfaces

Faezeh Shalchy[1] and Nima Rahbar[2]

[1]Gaduate Student, Department of Civil and Environmental Engineering, Worcester Polytechnic Institute, 100 Institute Rd., Worcester, MA 01609. E-mail: fshalchy@wpi.edu

[2]Assistant Professor, Department of Civil and Environmental Engineering, Worcester Polytechnic Institute, 100 Institute Rd., Worcester, MA 01609. E-mail: nrahbar@wpi.edu

Abstract

Concrete is the most used materials in the world. It is also one of the most versatile while complex materials which human have used for construction. However, concrete is weak in tension. Therefore, over the past thirty years many studies were focused to improve the tensile properties of concrete (cement-based composites) using a variety of physical and chemical methods. One of the most successful attempts is to use polymer fibers in the structure of concrete to obtain a composite with high tensile strength and ductility. However, a thorough understanding of the mechanical behavior of fiber reinforced concrete requires the knowledge of fiber/matrix interfaces at the small scale. In this study, experimental techniques have been used to study the nanostructure of fiber/matrix interfaces. Based on Scanning Electron Microscopy (SEM) and Energy-dispersive X-ray spectroscopy (EDX) analysis, the calcium-silicate-hydrate (C-S-H)/fiber interfaces of two different polymer fibers, polyvinyl alcohol and polypropylene, was numerically studied at the atomistic level.

INTRODUCTION

As the most used materials in the world, concrete possess excellent compressive strength but weak tensile properties. The cement-based matrix of the concrete has a complex structure that makes concrete an undeveloped material in terms of material properties such as tensile strength and toughness. Therefore, over the past thirty years many studies were focused to improve the tensile properties of concrete (cement-based composites) using a variety of physical and chemical methods [1-3]. One of the most successful attempts is to use polymeric materials in the structure of concrete to obtain a composite with high tensile strength and ductility [4]. Improving the performance of polymer fiber-reinforced cement composites can also increase the durability of concrete structures and decrease the production of carbon dioxide [4, 5]. However, understanding the mechanical behavior of fiber-reinforced concrete requires the thorough knowledge of the fiber/matrix interface structure. While, a large body of macroscopic studies have been performed on the interfaces present in fiber-reinforced cement based composites [6], the nanostructure of interfaces between cement and polymer fiber has not been thoroughly investigated. This understanding is needed to fully predict and improve the mechanical behavior of fiber-reinforced cement based composites.

In Portland cement, the raw materials are limestone and clay. Hence, a typical composition of a clinker is about 67% CaO and 22% SiO_2 with mainly alite (C_3S) and belite (C_2S) molecules. After the hydration of the clinker is complete, the main components formed are portlandite (CH) and C–S–H gel. The C–S–H gel is up to 70% of the final volume and is responsible for the cohesion and strong mechanical properties of cement pastes [7]. During the past decade the principal new data bearing on the structure of polymer/cement interface have been on compositions, determined by X-ray microanalysis, and on silicate anion structures [8, 9].

An understanding of the nature of chemical reactions occurring in C-S-H is also necessary in modeling the mechanical properties of concrete. In order to understand the chemical reactions in C-S-H, many researches have previously tried to characterize the structure of C-S-H gel at the atomistic level [10, 11]. In a more recent study, Qomi et al. (2014) investigated the effect of C/S ratio on the molecular structure of C-S-H using MD simulation technique [12]. In this paper, Scanning Electron Microscopy (SEM) and Energy Dispersive X-Ray (EDX) analysis techniques were used to characterize the C-S-H interface with polymeric materials.

MATERIALS AND METHOD

In this study, we would like to achieve a better understanding the complex C-S-H gel, particularly at the fiber/matrix interface based on SEM/EDX analysis. Two polymer fibers with different side chains were investigated in this study to demonstrate the effect of the functional group on the properties of the polymer/cement interface. Side chains or functional groups are a chemical group of atoms or bonds within molecules that is attached to a core part of a molecule called main chain. The side chain is responsible for the characteristic chemical reactions of those molecules. The same functional group will undergo the same or similar chemical reaction(s) regardless of the size of its molecule. The first polymer fiber type in this study is Polyvinyl alcohol (PVA). PVA is one of the most popular fibers that have been used in fiber-reinforced cement composites. PVA is from the alcohol group that has hydroxyl side chain. The alcoholic functional group has just one oxygen atom that contributes to hydrogen bonding. Oxygen atoms in hydroxyl group are hydrogen bond acceptor and/or donor. The second polymer that was chosen is from the alkane group. Alkanes have little intermolecular association because the carbon-hydrogen bond is non-polar. Alkanes are essentially non-polar molecules and insoluble in water. Polypropylene is the polymer that was chosen from this group for this study. The monomers of both polymers are shown in Fig. 1. All of the fibers were provided by Forta Corporation Company (Grove City, PA).

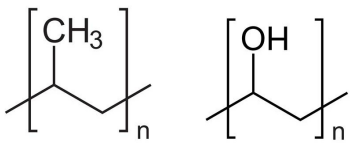

a) b)

Figure 1- The monomer structure of a) polypropylene and b) polyvinylalohol.

The fiber-reinforced cement paste composites evaluated in this study were prepared by mixing polymer fibers, water and cement powder to obtain mixtures with a specific concentration of fibers for a specific composition of cement. The composition of the cement type used in this study is shown in Table 1.

The cement pastes ingredients were mixed with a blender and sealed at 23 ± 1 C for curing at a curing room. All samples had 1% wt of polymeric fibers. At the age of 24 ± 1 h, the cylinder samples were demolded. Any excess of moisture on the surface was removed with a towel and the specimens were sealed in plastic bags at 23 ± 1 C until the age of testing. Since the curing reaction of cement pastes is generally completed by 28 days, all specimens were tested after 28 days of curing. After curing, the samples were cut using a diamond cutter and polished to be prepared for the SEM/EDX analysis.

Table 1: Typical Constituents of Portland Cement

Cement	*Cement chemists notation (CCN)*	*Mass %*
Calcium oxide, CaO	C	61–67%
Silicon dioxide, SiO2	S	19-23 %
Aluminum oxide, Al2O3	A	2.5-6 %
Ferric oxide, Fe2O3	F	0-6 %
Sulfate	$\overline{S}$	1.5-4.5 %

RESULTS AND DISCUSSION

A typical SEM image of the PVA reinforced concrete sample is shown in Fig. 2. This figure clearly shows that there is a transition zone between the polymer fibers and cement paste. This figure shows that the interfacial layer between fiber and matrix has a thickness of about 1-5 μm around the fiber. Regions of fiber, cement matrix, unhydrated clinkers and fiber/matrix interface are indicated in the figure.

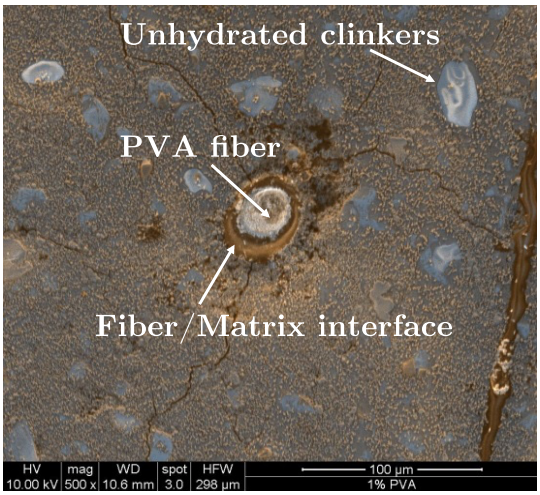

Figure 2- A typical SEM image of PVA/C-S-H interface. Regions of PVA fiber, interface and unhydrated clinkers are indicated in the image.

The EDX results for two different fiber/cement interfaces are shown in Fig. 3. The X-ray mapping was used to investigate the distribution and density of existing elements such as Si, and Ca in an area surrounding each fiber. The X-ray mapping of Si and Ca elements in PVA fibers clearly shows the accumulation of Calcium at fiber/matrix interface. However, this phenomenon was not observed in the samples of polypropylene fibers. Moreover, the EDX was performed on ten spectra of the fiber/matrix interface and ten spectra of regular C-S-H gel. The numerical EDX results show that the ratio of C/S in the interfacial zone significantly changes for PVA fibers, while it remains almost constant for polypropylene fibers. This is due to the polarity of different fibers caused by the functional groups on their molecular structure. This polarity enhances the absorption of water molecules and the positive ions, such as Ca^{2+} solved in it, to the fiber molecules during hardening.

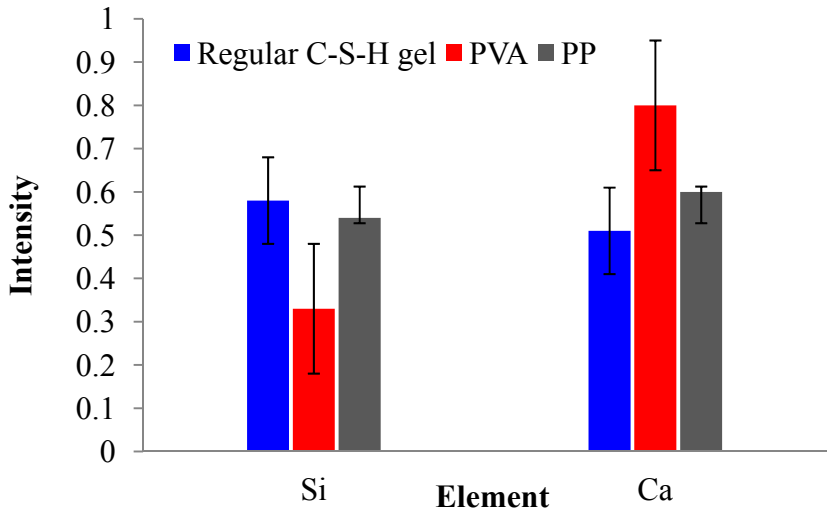

Figure 3- Results of EDX analysis on the samples for ten different spectra. First ten typical points were chosen on the C-S-H gel zone of the samples, and the other ten points were chosen on the fiber/matrix interface for two different fibers.

CONCLUSION

Across the globe, polymer fibers are added to concrete to enhance the tensile properties and ductility of concrete. While there is a large body of data on this subject, the nanostructure and nanomechanical properties of polymer fiber/cement interface is not completely known which is pivotal in the design of robust polymer reinforced concrete. This study presents a SEM/EDX analysis to investigate the nanostructure of the cement/fiber interfaces. In this study, two different polymer fibers were chosen based on different polarity of their functional groups. The electron microscopy results show that the ratio of C/S changes in the fiber/matrix interface for the two types of polymer fiber studied. This is due to the different polarities of the polymer molecules. Using SEM/EDX analysis, it is shown that the C/S ratios in PVA/C-S-H interfaces are higher than that in Polypropylene/C-S-H interface. This is mainly a result of high polarity of hydroxyl and amide functional groups. The authors

believe that the functional group in the molecular structure of polymers affects the overall adhesion energy between the fiber and matrix, primarily, by changing the C/S ratio of the C-S-H at the interface, and further, by absorbing additional positive ions in the C-S-H structure. The implications of these results are significant in further development of fiber reinforced cement composites.

REFERENCES

1. Balaguru, P.N. and S.P. Shah, *Fiber-reinforced cement composites*. 1992.
2. Sakulich, A.R., *Reinforced geopolymer composites for enhanced material greenness and durability.* Sustainable cities and society, 2011. **1**(4): p. 195-210.
3. Sharifi, N.P. and A. Sakulich. *Application of Phase Change Materials in Structures and Pavements*. in *Proceedings of the 2nd International Workshop on Design in Civil and Environmental Engineering*. 2013. Mary Kathryn Thompson.
4. *Global Cement Report (International Cement Review, London, ed. 9, 2011).*
5. Van Vliet, K., et al., *Set in stone? A perspective on the concrete sustainability challenge.* MRS bulletin, 2012. **37**(04): p. 395-402.
6. Sakulich, A.R. and V.C. Li, *Nanoscale characterization of engineered cementitious composites (ECC).* Cement and Concrete research, 2011. **41**(2): p. 169-175.
7. Dolado, J.S., M. Griebel, and J. Hamaekers, *A molecular dynamic study of cementitious calcium silicate hydrate (C–S–H) gels.* Journal of the American Ceramic Society, 2007. **90**(12): p. 3938-3942.
8. Yu, P., et al., *Structure of calcium silicate hydrate (C-S-H): Near-, Mid-, and Far-infrared spectroscopy.* Journal of the American Ceramic Society, 1999. **82**(3): p. 742-748.
9. Soyer-Uzun, S., et al., *Compositional evolution of calcium silicate hydrate (C–S–H) structures by total x-ray scattering.* Journal of the American Ceramic Society, 2012. **95**(2): p. 793-798.
10. Hamid, S., *The crystal structure of the 11 Ä natural tobermorite Ca2. 25 [Si3O7. 5 (OH) 1.5]· 1H2O.* Zeitschrift für Kristallographie-Crystalline Materials, 1981. **154**(1-4): p. 189-198.
11. Taylor, H., *Nanostructure of C- S- H: Current status.* Advanced cement based materials, 1993. **1**(1): p. 38-46.
12. Qomi, M.A., et al., *Combinatorial molecular optimization of cement hydrates.* Nature communications, 2014. **5**.

Effect of Nano Seeds in C-S-H Gel Formation: Simulation Study from the Colloidal Point of View

Achutha Prabhu[1]; Jean-Christophe Gimel[2]; Andres Ayuela[3]; and Jorge Sanchez Dolado[1]

[1]Tecnalia Research and Innovation, Derio, Spain.
[2]LUNAM Université, ISERM U1066 Micro et Nanomédecines Biomimétiques, Angers, France.
[3]Centro de Física de Materiales CFM-MPC, Centro Mixto CSIC-UPV/EHU, and Donostia Internacional Physics Center, San Sebastián, Spain.

Abstract

The addition of external nanoparticles, mainly nano silica during the hydration of cement is a field of investigation in high performance cements. The added particles act as seeds and initiate early nucleation and subsequent growth of C-S-H gel. Nucleation is triggered very early, before enough clinker grains are dissolved or in other words, before the super saturation condition is attained. Hence, depending on the amount of added seed, the morphology and the mechanical properties of the product differ. Experimental studies in this area are less favored due to economic reasons and simulation studies are rare in the literature. An earlier work by some of the authors introduced a Monte Carlo model which dealt with the kinetics of the hydration process at early ages. The colloidal model incorporated random nucleation in the bulk, followed by an Avramian style layer by layer growth of 5nm sized C-S-H particles. The model was based on a Random Sequential Addition scheme and enabled a satisfactory rationalization of the early growth of C-S-H gel. In the present study, we extend this model for the addition of extra seeds and for different water to cement ratios.

INTRODUCTION

The hydration of cementitious materials is considered to take place via an initial dissolution phase followed by a dissolution-precipitation process (Bullard, et al., 2011). The early hydration period is established to occur though a nucleation and growth process. Hence, Avrami-type nucleation and growth models are usually used to fit the calorimetric data from experiments, assuming that the hydration reaction is purely a space filling process. Even though this model gives a

good description of the initial part, it fails at larger times. Another analytical model by Cahn proposing the preferential nucleation at grain boundaries was found to give a better description (Scherer, et al., 2012). In this context, simulations studies become important, since they could be used to verify the analytical results. Also, they could provide us with a visual description of the process, which helps to identify some physical processes, usually unnoticeable in the analytical models.

The present work is a continuation of the previous work from our group (González-Teresa, et al., 2013). It basically described a nucleation and growth model, taking in to account the colloidal point of view (Jennings, 2008) (Thomas & Jennings, 2006) and the characteristic 5nm sized calcium silicate hydrate (C-S-H) particles found in the hydrated cement (Allen & Thomas, 2007) (Ficker, et al., 2011). In the present study, we further improve this model and explore the effects of the grain surfaces and also the effect addition of extra seeds.

MODEL AND SIMULATION TECHNIQUES

Our model is based on the typical 5nm sized (diameter) C-S-H particles, and hence it is chosen as the characteristic size in our system. All lengths we present in this work are in multiples of this characteristic length denoted by *d*.

The simulation box is modeled to mimic the pore space in the cement paste and is constructed as follows. We start by placing a cubic box of edge length L in the space. From the center of this this cube, a random direction is chosen and a sphere (corresponding to cement grains) of a given radius $R > \sqrt{3}/2 \cdot L$, is placed at a random distance $d_g\left(\sqrt{3}/2 \cdot L < d_g < \sqrt{3}/2 \cdot (L+R)\right)$. If any part of the sphere lies inside the cube and if it does not overlap with previously placed spheres, we record the position of the sphere. Otherwise, we ignore it and repeat the process until no more cement grains could be placed due to excluded volume restrictions. After, we check the volume of the box occupied by the grains. If it corresponds to the required volume fraction, we accept the system. Otherwise the whole process is repeated from the beginning until the required volume fraction is obtained. The schematic of this procedure is given in figure 1.

The cubic box with the part of the spheres intersecting it constitutes the simulation box. From the volume fraction occupied by the cement grains ϕ_g, we could calculate the local water to cement (w/c) weight ratio of the system using the relation $w/c = (1-\phi_g)/(3.15 \cdot \phi_g)$, where 3.15 g cm^{-3} is the assumed density of the cement. The system at hand with the length scale in nanometers is a much localized part of a macroscopic system with the characteristic length scale of the order of the size of the cement grains (usually in microns). Here we make a crude assumption that the grain positions we obtain belong to a well relaxed hard sphere system. Using this approximation, the properties of the grain system could be elucidated from the average distance to the nearest neighboring cement grains (Torquato, 1995). Thus, we

could approximate the packing fraction of the macroscopic system which in turn gives its w/c ratio.

For simplicity, we consider all the intended number of nuclei (the ones intrinsic to the system and the added seeds) to be present from the beginning. In Avramian description, this corresponds to the "site saturated" case. However, the existence of a characteristic nucleation time could be easily implemented. Every nucleus and the growth of C-S-H particles around it are modeled using hard spheres of the characteristic size. We also calculate the approximate surface area exposed by the grains inside the system such that we could calculate and use the surface density of the nuclei. We begin by trying to distribute the intrinsic nuclei randomly on the grain surfaces such that the desired surface density is achieved. For each nucleus to be added, we select randomly a grain surface and try to place the nuclei such that it does not overlap with any of the other particles (intrinsic nuclei, added seeds or the already grown C-S-H particles in case we use a delayed nucleation model) in the system and the grain surfaces. Also, the center of the spheres should lie inside the simulation box. This excluded volume constraint is valid for all particles in the system. No periodic boundary condition is considered for the present study. If we fail to place the nuclei in a certain number of trials (of the order of 10^4), we ignore it and move to the next. In the case of added seeds, we try to place them in the bulk (anywhere in the box volume) instead of the grain surfaces in a similar way, keeping all the previous excluded volume constraints. After the nucleation step, we note down the number of nuclei actually placed in the box, N_{nuc}.

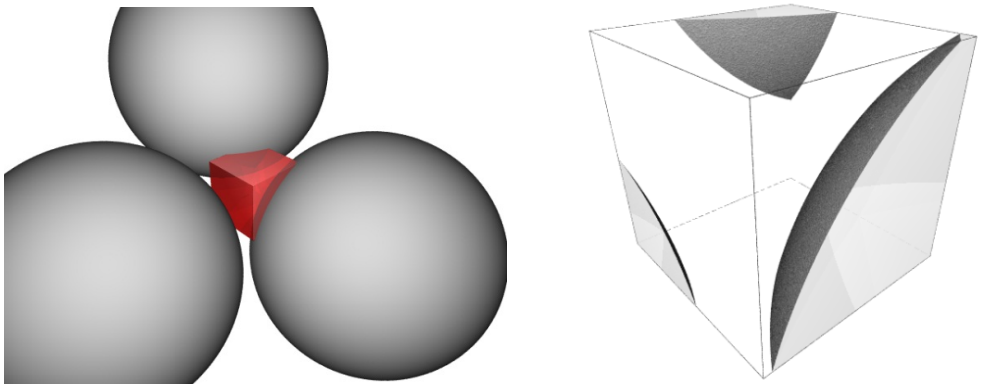

Figure 1: Creation of the grain boundaries: (Left) The bulk system containing the cement grains depicted in grey, which intersect the simulation box depicted in red. (Right) an enlarged picture of the simulation box, showing the intersecting parts of the cement grains.

A cluster construction procedure is then carried out to link the nuclei or in other words, the growing clusters to form bigger virtual clusters. For this, we define a small distance range of 10% of the particle diameter as a contact distance. When any two particles belonging to different growing clusters are within this distance, we link them

to form a bigger virtual cluster. They are called virtual because the growing clusters retain their growth identity and the linking is done only in a visual sense based on their proximity. This means that different parts of the virtual cluster grow at different times, depending on the nuclei they belong to.

From here onwards, we repeat the following until a desired number steps is reached. Select N_{nuc} times randomly a growing cluster and grow a layer of C-S-H particles around it. For this, we consider every particle belonging to the growing cluster at that point and try to place C-S-H particles around it subject to our excluded volume constraints. The selection of new particles is done in such a way that they are uniformly distributed in the spherical shell formed by the contact distance around the particle under consideration. When all the growing clusters have grown a layer around it in average, we perform the cluster construction procedure. A typical snapshot of the simulation for the seeded and non-seeded case is shown in figure 2. (Details of the simulation as follows)

For a simple study, we arbitrarily set the size of the box to be 20d (100nm) and the grain diameter to be 80d (400nm). We keep the surface density of the intrinsic nuclei a constant 0.0287 nuclei/d^2 (11.5×10^{-4} nuclei/nm^2).We choose two different w/c ratios,

Case1: Average grain occupation fraction in the box 0.43, which gives a w/c ratio 0.41 for the simulation box. From the average distance between the cement grains, the estimated bulk w/c ratio is 0.74. The surface area calculation gives in average 30 nuclei on the grain surface.

Case 2: Average grain occupation fraction 0.65, which gives a local w/c ratio 0.17. The bulk w/c ratio is estimated to be 0.49. The surface area calculation gives in average 33 intrinsic nuclei in the simulation cell.

Case 3: Same as case 1, but we add some extra nuclei/seeds in the bulk. The seed density is 0.0287 seeds/d^2 (17.5×10^{-6} seeds/nm^3), which give about 10 seeds in the simulation cell.

Figure 2 depicts snapshots of simulations of cases 1 and 3.

RESULTS AND DISCUSSION

Our model is supposed to give a better insight in to the cement hydration process in the nanopores of cement paste. The first thing to consider for this kind of simulation is the volume fraction of the hydration products. Figure 3 shows the evolution of the volume fraction of the grown C-S-H particles, ϕ (including that of the nuclei and added seeds, corrected for volume occupied by the grains) as a function of simulation steps. When we compare the increase for the two different w/c ratios (cases 1 and 2), we see that the appearance of hydration product is slightly faster for case2, but the final volume occupied being the same. This is an illusion coming from the fact that we consider the available volume instead of the total volume of the simulation cell.

However, the final occupation fraction around 0.4 in the available volume is consistent with previous observations (González-Teresa, et al., 2013).

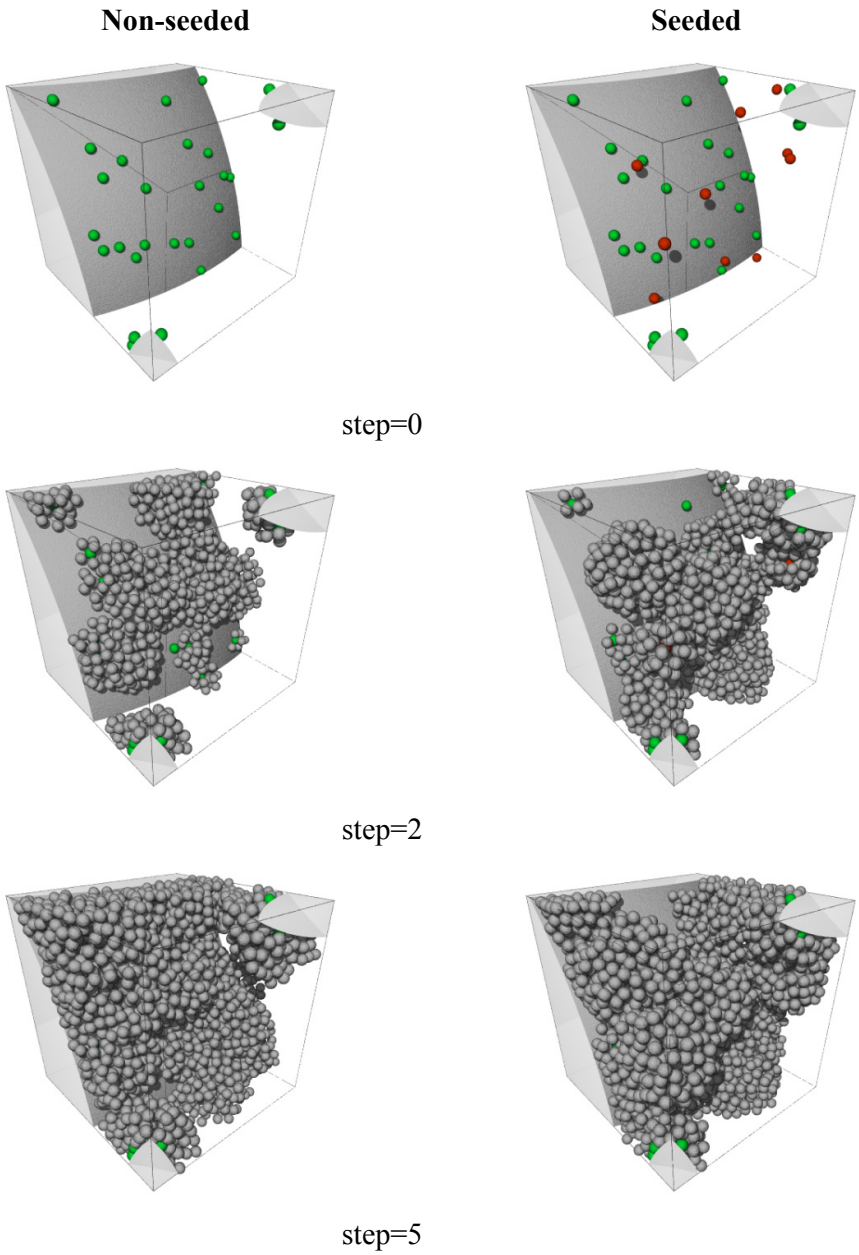

Figure 2: Snapshots of a simulation showing the characteristics of a seeded (right) and non-seeded (left) case at various simulation steps. The intrinsic nuclei are colored in green the added seeds in red for clarity and the C-S-H particles are colored in grey. For the seeded case, notice how the growing seeds form bridges and connect the cement grains (step 2). See text for details.

The addition of extra seeds (case 3) in the simulation cell shows a faster evolution for ϕ when compared to its non-seeded counterpart (case 1). Since these are having the similar w/c ratios, they could be directly compared. The faster increase is because of the increase in the number of growth sites due to the added seeds and their increased degree of freedom for growth. While the growth of surface nuclei is restricted by the grain surface, the added seeds the bulk can grow in all directions. This is clearly seen in figure 2, where the added seeds grow and link the cement grains, leading to an earlier connectivity and early strength development. We also notice that the final volume fraction of the hydrate is slightly higher for the seeded case, which is also experimentally observed (Thomas, et al., 2009) (Thomas, et al., 2009).

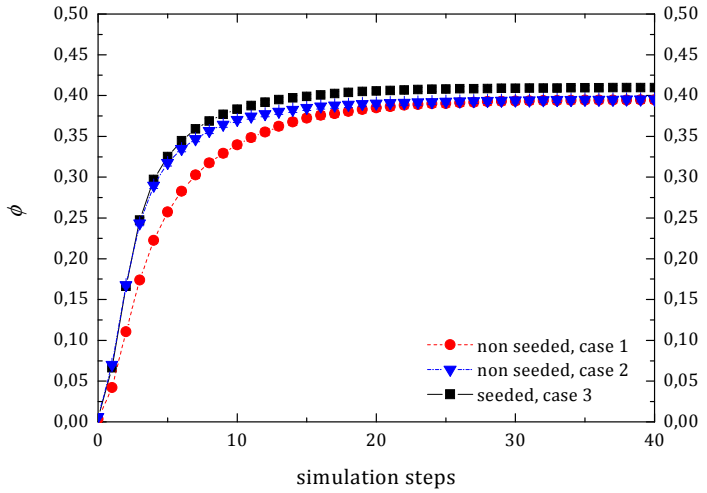

Figure 3: Evolution of the occupied volume fraction of the C-S-H gel as a function of simulation steps for the three samples.

In figure 4(a), we compare the rate of appearance of the hydration products ($d\phi/dt$) for case 3 (with bulk w/c ~ 0.49), with the experimental calorimetric curve of heat flow obtained for the hydration of pure Alite with a w/c ratio 0.5. In order to do this comparison, we first calculate $d\phi$/d(simulation step) and the resulting data is shifted and scaled such that it has the same peak value as in the calorimetric curve. Even though the shifting and scaling parameters are completely arbitrary, we see considerable similarities in the initial deceleration regime, while it fails to capture the behavior at large times. The difference at larger times could be due to the usage of the site saturation case in our simulations, which is far from the reality.

It is well known that the accelerated growth regime of the calorimetric curve could be fitted with a space filling model, and the rate equation could be explained in general

using an Avrami type equation. In these theoretical and analytical models, the w/c ratio is not considered. But, our model is built to account for the w/c ratio. A comparison of the w/c ratio effects on the rate curve is given in figure 4(b). For the comparison, we use case 3 as the reference and employ the same shifting and scaling parameters used in creating figure 4(a). The comparison shows a slower deceleration for case 1, over a longer time range. This is because of the increased pore space due to higher w/c ratio, where the hydrates continue to grow. While for case 2, the growth is slowed down very soon due to quicker filling of the smaller pores. This is also one of the reasons for the initial increase in the rate compared to case 1, the other being the slightly increased number of surface nuclei.

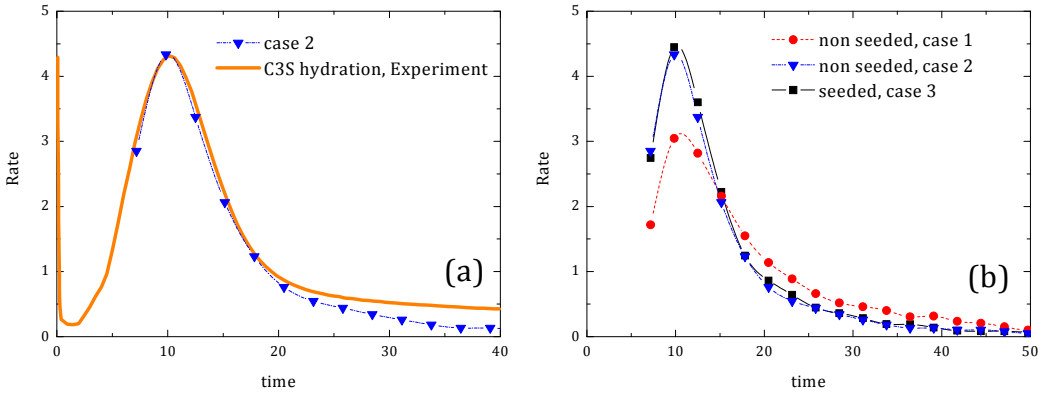

Figure 4: (a) Shifted and rescaled rate curve of case 3 compared with experimental data for Alite at a w/c ratio of 0.5 (Data extracted from (Thomas, 2007)**). (b) Comparison of cases with two different w/c ratios and seeding effect. In (b) all curves are shifted and scaled using the same parameters obtained from creating the simulation curve in (a). The lines/dotted lines in the simulation curves are a guide to the eye.**

Figure 4(b) also compares the effect of seeding for a given w/c ratio of 0.74. The curve corresponding to seeded case (case 3) is also scaled using the same parameters used for case 2. We see that the rate curve is quite different for the seeded case, where the growth rate is initially much higher and then follows a faster deceleration compared to the non-seeded one. As noted before, the added seeds have an increased degree of freedom for growing a layer of C-S-H particles around it. This difference, when combined with the relative increase in the number of growth sites contribute to the higher initial rate. However, after a short while when the added seeds have grown a considerable size, they start to obstruct the growth of the intrinsic nuclei and other seeds. This causes the growth to slow down, while in the non-seeded case, this happens very late. Also due to the uniformity in the growth (all nuclei being on the grain surface) a more gradual decrease is observed. This behavior is visible in figure 2 (step5), where we can still see some exposed grain surface in the seeded case due to

the blocking effect of the seeds. Whereas the in the non-seeded case, the grain surface is more or less uniformly covered by C-S-H particles and the nuclei are growing away from the surface. The similarity of the growth curve of case 2 with case 3 is a mere coincidence arising from the decrease in the available space for case 3 compensating for the growth rate.

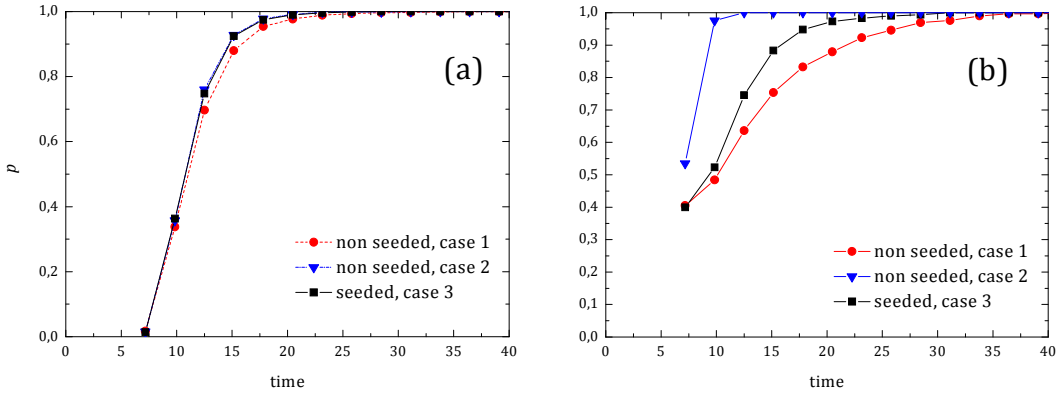

Figure 5: (a) Degree of clustering and (b) maximum number of grain links obtained for a virtual cluster normalized to the number of grains plotted as a function of the rescaled time.

Considering the nuclei/seeds as growing clusters gives us the degree of clustering $p = 1 - N_v / N_{nuc}$, where N_v is the number of virtual clusters at a given simulation step. At small times, when the clusters are far apart, we get p=0. As the growing clusters come in to contact, p increases and at large time when there exists only a single cluster, p=1. Figure 5 shows p plotted as a function of the rescaled time we obtained while constructing figure 4b. From this, we get an idea of how fast the clusters merge and in turn a qualitative idea about the cement setting. We believe this quantity is quite unreliable, unless strict comparisons are made with experiments. As seen from figure 5(a), the increase in p is almost identical for all the presented cases. Case 1 however is slightly delayed. This actually comes from the difference in the cement grain distribution. For higher w/c ratio, the possibility of having more cement grains around a pore is higher. For example, in figure 2 there are three grain surfaces present inside the simulation cell. Initially when growth occurs on the surface, the clusters on the surface merge. However, to reach the clusters on the grains across the simulation cell, they have to grow for longer times and hence the lag. While for the lower w/c ratio, the proximity of grains and for the seeded case, the seed growth causes a slightly faster increase.

Another quantity of interest is the maximum number of grain links (the number of cement grains a virtual cluster is connected to) obtained at a given time normalized to the number of grain surfaces in the simulation cell (figure 5(b)). This is a measure of

the connectivity of the grains. This quantity reaching 1 means that there is at least one cluster, which has contact with all of the grain surfaces. This could also be qualitatively linked to the setting and strength development during cement hydration. The variation of this quantity as a function of w/c ratios and due to the seed could be clearly understood using the same concepts as before.

CONCLUSION AND PERSPECTIVES

The present work introduces an improved method for the study of cement hydration, taking in to account the colloidal nature of the C-S-H particles and w/c ratio. The preliminary results appear to be quite promising and the model is able to capture the development of C-S-H gel formation at earlier ages. Also, preliminary efforts to investigate the setting and strength development under various cases seem to be qualitatively agreeable. This model could be easily extended to explore other properties, while also providing comparison with analytical results.

REFERENCES

Allen, A. J. & Thomas, J. J., 2007. Analysis of C–S–H gel and cement paste by small-angle neutron scattering. *Cement and Concrete Research,* 37(3), pp. 319-324.

Bullard, J. W. et al., 2011. Mechanisms of cement hydration. *Cement and Concrete Research,* 41(12), pp. 1208-1223.

Ficker, T., Len, A. & Martišek, D., 2011. A remark on nano-particle stability of cement C-S-H gel. *Central European Journal of Physics,* 9(2), pp. 553-557.

González-Teresa, R., Dolado, J. S., Ayuela, A. & Gimel, J.-C., 2013. Nanoscale texture development of C-S-H gel: A computational model for nucleation and growth. *Applied Physics Letters,* 103(23), p. 234105.

Jennings, H. M., 2008. Refinements to colloid model of C-S-H in cement: CM-II. *Cement and Concrete Research,* 38(3), pp. 275-289.

Lootens, D., Hébraud, P., Lécolier, E. & Van Damme, H., 2004. Gelation, Shear-Thinning and Shear-Thickening in Cement Slurries. *Oil & Gas Science and Technology - Rev. IFP,* 59(1), pp. 31-40.

Scherer, G. W., 2012. Models of confined growth. *Cement and Concrete Research,* 42(9), pp. 1252-1260.

Scherer, G. W., Zhang, J. & Thomas, J. J., 2012. Nucleation and growth models for hydration of cement. *Cement and Concrete Research,* 42(7), pp. 982-993.

Thomas, J. J., 2007. A New Approach to Modeling the Nucleation and Growth Kinetics of Tricalcium Silicate Hydration. *Journal of the American Ceramic Society,* 90(10), pp. 3282-3288.

Thomas, J. J., Allen, A. J. & Jennings, H. M., 2009. Hydration Kinetics and Microstructure Development of Normal and CaCl2 Accelerated Tricalcium Silicate Pastes. *The Journal of Physical Chemistry C,* 113(46), pp. 19836-19844.

Thomas, J. J. & Jennings, H. M., 2006. A colloidal interpretation of chemical aging of the C-S-H gel and its effects on the properties of cement paste. *Cement and Concrete Research,* 36(1), pp. 30-38.

Thomas, J. J., Jennings, H. M. & Chen, J. J., 2009. Influence of Nucleation Seeding on the Hydration Mechanisms of Tricalcium Silicate and Cement. *The Journal of Physical Chemistry C,* 113(11), pp. 4327-4334.

Torquato, S., 1995. Nearest-neighbor statistics for packings of hard spheres and disks. *Phys. Rev. E*, Volume 51, pp. 3170-3182.

Structural and Dynamical Studies of C-S-H Gel Synthesized with Nano-Silica Particles and Amine Functionalized Silica Nanoparticles

Silvina Cerveny[1]; Juan J. Gaitero[2]; Edurne Erkizia[3]; Manuel Monasterio[4]; and Jorge S. Dolado[5]

[1]Centro de Fisica de Materiales (CSIC, UPV/EHU)-Materials Physics Center (MPC), Paseo Manuel de Lardizabal 5, 20018, San Sebastián, Spain (corresponding author). E-mail: scerveny@ehu.es
[2]Tecnalia Research & Innovation, Materials, Sustainable Construction Division, c/ Geldo, Edificio 700, Parque Tecnológico de Bizkaia, Derio, Spain. E-mail: juanjose.gaitero@tecnalia.com
[3]Tecnalia Research & Innovation, Materials, Sustainable Construction Division, c/ Geldo, Edificio 700, Parque Tecnológico de Bizkaia, Derio, Spain. E-mail: edurne.erkizia@tecnalia.com
[4]Centro de Fisica de Materiales (CSIC, UPV/EHU)-Materials Physics Center (MPC), Paseo Manuel de Lardizabal 5, 20018, San Sebastián, Spain. E-mail: monasterio@ehu.es
[5]Tecnalia Research & Innovation, Materials, Sustainable Construction Division, c/ Geldo, Edificio 700, Parque Tecnológico de Bizkaia, Derio, Spain. E-mail: jorge.dolado@tecnalia.com

Abstract

In this work we have studied the dynamics of water confined in C-S-H gel and C-S-H gel synthesized with the addition of nano-silica (SiO_2) and aminopropyl (-$(CH_2)_3$-NH_2,) functionalized silica nanoparticles. Structural characterizations showed that the addition of nanoparticles increases the average length of the silicate chains in C-S-H gel. The dynamics of water confined in the microstructure of C-S-H with and without the addition of nanoparticles is altered and it can be related to a different porous structure in these materials.

INTRODUCTION

Water molecules play a significant function in both the structure and properties of cement like materials. Water molecules in C-S-H gel are adsorbed on the surface of solid phases and they can also be located in small cluster in the gel pores of the CSH network. These water molecules are considered as confined by the rigid material. To probe the state of water in this type of materials some experimental technique including broadband dielectric spectroscopy (BDS) (Cerveny, 2011), quasi-elastic neutron scattering (QENS, Ridi, 2009) and nuclear magnetic resonance (NMR, Korb, 2007) can be used. In previous works (Cerveny, 2011; Monasterio 2013), we analyzed the dynamical properties of water molecules confined in C-S-H gel of different water contents by BDS in the temperature range of 110–230 K. In particular, we found different relaxation processes which are related to water located in small nanometric pores (<1 nm) and water located in larger pores (3–10 nm).

On the other hand, the addition of nano-silica has been used to improve the performance of the cement-based materials (Richardson, 2004; Björnström 2004). Some authors have also studied the incorporation of organic compounds/moieties in the C-S-H gel structure in order to improve its properties (fracture toughness and durability (Minet, 2006; Franceschini, 2007) by trying to incorporate the properties of the organic material as it is seen in natural bio-composites (Minet 2006, Franceschini 2007; Beaudoin 2009; Raki, 2010; Sanchez, 2010).

In this work, we analyze the change of the dynamics of water confined in CSH gel due to structural differences promoted by the addition of two different nano-particles.

EXPERIMENTAL SECTION

Nanoparticles: Colloidal amorphous Silica (NyasilTM 20 – Nyacol Nano Technologies, Inc) and amine functionalized silica nanoparticles (Stoga) were used.
Synthesis of C-S-H gel: Three different samples were prepared in this study by hydration of tricalcium silicate (C_3S) in excess of water: a) pure C-S-H gel, b) C-S-H gel with colloidal amorphous Silica (NyasilTM-20), and c) C-S-H with amine functionalized silica nanoparticles (Stoga). The pure C-S-H gel was prepared by hydration of 2.5 g of pure C_3S with 704 g of distilled water. After 33 days of continuous stirring at room temperature, the dispersion was filtered and the obtained solid material was dried in an oven at 60 ºC for an hour. The C-S-H gels with nanosilica were prepared in the same way but also adding Stoga (1.2 gr) or NyasilTM (1.3 gr) nano-particles.

Characterization techniques. Thermogravimetry analysis was carried out on a TA Instrument Q500 thermogravimetric analyzer whereas calorimetric measurements (DSC) were carried out in a Q2000 TA Instruments to determine thermal events on all the samples analyzed. Structural characteristics were analyzed by means of solid State ^{29}Si NMR spectroscopy (Bruker Advance III 400 MHz spectrometer). To measure the dynamics of water we have used a Novocontrol Alpha-N to measure the complex dielectric permittivity $\varepsilon^*(\omega) = \varepsilon'(\omega) - i\,\varepsilon''(\omega)$, $\omega = 2\pi f$, in the frequency range $10^{-1} - 10^6$ Hz. To analyze the complex permittivity (ε^*), the imaginary part ε'' was fitted by the use of symmetric Cole-Cole functions

$$\varepsilon^*(\omega) = \varepsilon_\infty + \frac{\Delta\varepsilon}{1+(i\omega\tau)^\alpha} \quad (1)$$

where $\Delta\varepsilon$ is the dielectric strength ($\Delta\varepsilon = \varepsilon_s - \varepsilon_\infty$, ε_∞ and ε_s are the unrelaxed and relaxed values of the dielectric constant), τ is the relaxation time and α is the stretching parameter of each relaxation process and $\omega = 2\pi f$ is the angular frequency.

RESULTS AND DISCUSSION

Structural characterization of C-S-H and C-S-H with nano-particles: We analyze the structural aspects of these materials by means of ^{29}Si MAS-NMR. In particular we

will discuss the Q_n structures (Duchet, 2005), where Q-species is one in which the silicone atoms are bonded to four oxygen atoms (see an scheme in Figure 1a).
Figure 1b shows the NMR spectrum of C-S-H gel in which three chemical shifts at -81.30 (Q_1), -84.0 ppm (Q_2B) and -87.05 (Q2) ppm are observed similar to that observed in previous works (Richardson, 1999; Jonsson, 2004; Ayuela, 2007). For CSH-Stoga and CSH-Nyasil, we can observe a shift of all these signals to more negative values. This shift is particularly noticeable in the case of CSH-Stoga and it indicates that the degree of silicate polymerization is much more obvious with the addition of amino-propyl functionalized nanoparticles. In addition, the lack of Q_0 in all the samples is a strong indication that C_3S in these samples was fully hydrated.
The components of the spectrum of C-S-H gel obtained from the deconvolution process are also shown in Figure 1b. With the relative area of each component (Q_1, Q_2B and Q_2), the average degree of connectivity n_c can be calculated from the areas using the next equation (Le Saout, 2006):

$$\boldsymbol{n_c = \frac{Q_1+2Q_2+T_1}{Q_1+Q_2+T_1}} \quad (2)$$

Similarly, the average chain length L (number of silicates bound together in a chain) can be calculated as:

$$\boldsymbol{L = 2\left(1+\frac{Q_2}{Q_1+T_1}\right)} \quad (3)$$

Table 1 shows both n_c and L where it is easy to see that both values increases with the addition of nanoparticles. Thus, the silicate chains developed by CSH when adding the nanoparticles during hydration of C_3S, are longer than in the case of ordinary CSH, being this effect more important in the case of aminopropyl functionalized nanoparticles.

Table 1. Samples analyzed in this work, c_w represents the water content obtained by TGA, L is the average chain length, n_c is the average degree of connectivity and Ca/Si represents the Calcium/Silicon ratio obtained by fluorescence.

Sample	c_w	n_c	L	*Ca/Si*
CSH	21.3	1.54	3.45	1.30
CSH-Nyasil	21.8	1.72	7.14	0.98
CSH-Stoga	21.3	1.78	9.21	0.96

In the following we focus on the effect of the addition of the nanoparticles on the water dynamics of the C-S-H gel. In particular we want to explore whether this structural change affects the dynamics of water in this matrix.

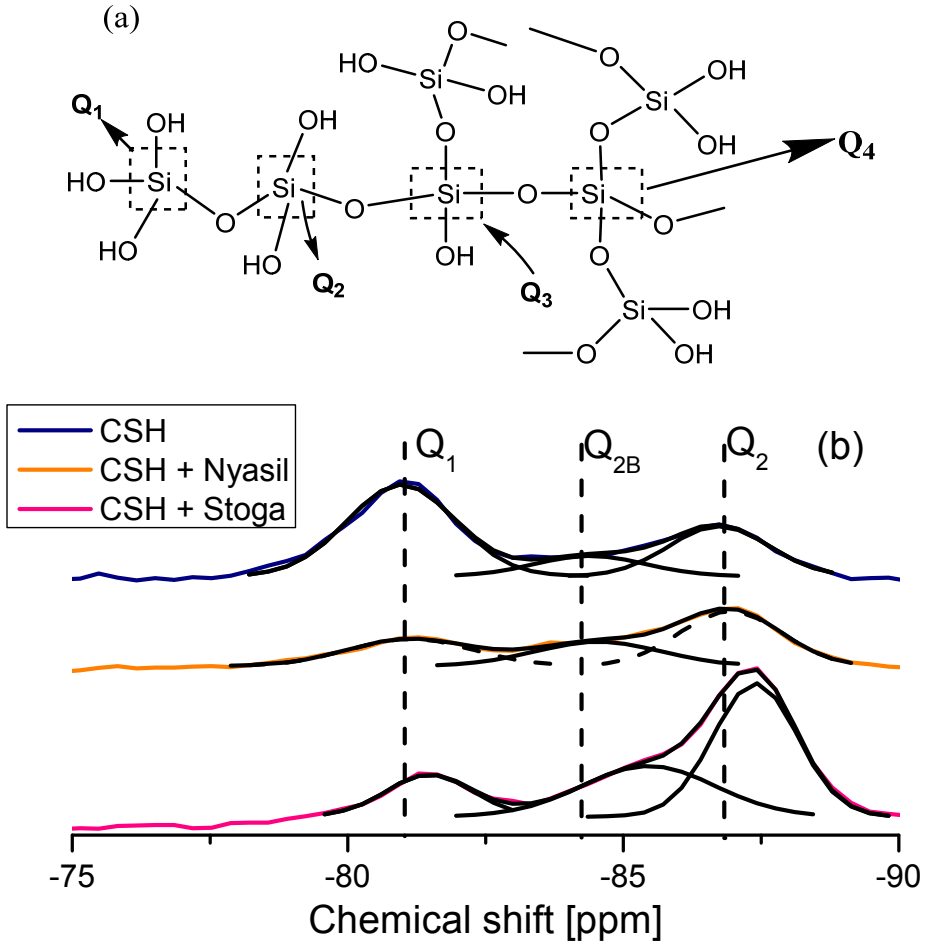

Figure 1. (a) Schematic representation of a silicate chain where Q_n (n = 1 to 4) species are showed in the picture. (b) ^{29}Si NMR spectrum of CSH, CSH-Nyasil and CSH-Stoga. The solid line is the superposition of three peaks (Q_1, Q_2 and Q_2B).

Water dynamics in CSH, CSH-Nyasil and CSH-Stoga

The rotational properties of water molecules confined in C-S-H gel at different water contents were analyzed by BDS at temperatures from 110 to 230 K. Previously, the thermal behavior was characterized by calorimetric measurements to observe that water remains amorphous in the whole temperature range analyzed.

For C-S-H and CSH-Nyasil, we found three dielectric relaxation (processes 1, 2 and 3) related to water confined in the structure developed during hydration similar to that found in C-S-H gel analyzed at a different water content (Cerveny, 2011; Monasterio, 2013). In contrasts, for CSH-Stoga we found the same processes 1 to 3 in well correspondence with the processes visible in CSH and CSH-Nyasil. However, between processes 2 and 3 we found an extra relaxation which is labeled as 2*. Thus,

the dielectric response of CSH-Stoga shows four different relaxations in this temperature range. As the origin of process 2* is not clear, we mainly focus on the behavior of processes 1, 2 and 3. All the relaxations were fitted using the Cole-Cole function for each relaxation process.

Figure 2 shows the temperature dependence of the relaxation times as obtained from the dielectric experiments. The time scale of the main relaxations 1, 2, and 2* exhibits Arrhenius-type temperature dependence ($\tau = \tau_0 \exp(E_a / kT)$, where E_a represents the activation energy and $\log(\tau_0)$ is a pre-exponential factor. Process 3 shows a Vogel-Fulcher-Tamman (VFT) temperature dependence ($\tau = \tau_0 \exp (D\, T_0/(T - T_0))$) indicating that the nature of both processes (2 and 3) is different.

The relaxation time of process 1 follows an Arrhenius behavior in the entire temperature range and for all the three samples analyzed. The relaxation time of this process does not change with the addition of nanoparticles although the intensity of the dielectric signal increases for CSH-Nyasil and CSH-Stoga. On average, the activation energy has a value of (0.24 ± 0.20) eV for all the samples which is close to the energy required to break a single hydrogen bond (0.22 eV). In a previous work (Monasterio, 2013), we showed that the fast process 1 could be attributed to the non-removable and dielectrically active hydroxyl groups on the surface of the C-S-H gel. Therefore, we do not expect changes in this process under changes in the structure of the samples.

Process 2 was previously attributed (Cerveny, 2011) to the relaxation of structural water (water extremely confined in small pores (~1 nm)) adsorbed on the neighboring calcium silicate sheets. The activation energy is similar for all the three samples (E_a = 0.44 eV), indicating that the environment seen for the water molecules is comparable in all the cases and its value supports that this type of water is chemically bound water. However, in spite of the fact that all the samples have the same water content, the relaxation time for both CSH-Stoga and CSH-Nyasil becomes faster (one decade) compared with the water dynamic in C-S-H. As previously observed by NMR for CSH-Stoga and CSH-Nyasil, the silicate chains are longer than in ordinary C-S-H and therefore at same water content, water molecules are more scattered in the interlayer space than in CSH. For this reason water dynamics is faster in CSH-Stoga and CSH-Nyasil compared to ordinary CSH. In other words, as the silicate chains are longer and more active sites for water interactions are available, surface-water interactions are more relevant in CSH-Stoga and CSH-Nyasil than in CSH gel, and this is compatible with the acceleration in the water dynamics. Another implication of this result is that the nano-porous structure in CSH-Nyasil and CSH-Stoga seems to be bigger than in ordinary CSH gel. This is also in agreement with a larger basal spacing found in CSH-Stoga in comparison to CSH (Monasterio, 2015).

Process 3 is significantly slower than process 2 and therefore it should arise from a different population of water molecules. As we previously studied in ordinary C-S-H (Cerveny, 2011; Monasterio 2013), this process corresponds with water molecules located in the big gel pores of C-S-H gel. These water molecules are forming small

clusters (i.e. water molecules are connected by more than a single hydrogen bond) and they are involved in cooperative motions as seen in the non-Arrhenius behavior of the temperature dependence of the relaxation times. The water dynamics reflected by process 3 becomes slower in CSH-Stoga and CSH-Nyasil compared with that in ordinary C-S-H (see Figure 2). This behavior contrasts with that of process 2, where the dynamics become faster. This is not surprising as these two processes reflect the behavior of water molecules in different environments. For CSH-Stoga and CSH-Nyasil it has been shown above that the silicate chains are longer than in ordinary C-S-H and therefore a densification of the structure is expected which in turn retards the relaxation of water molecules in the interior of the pore structure. This suggests that the size of the big gel pores is, on average, smaller in CSH-Stoga and CSH-Nyasil than in ordinary C-S-H.

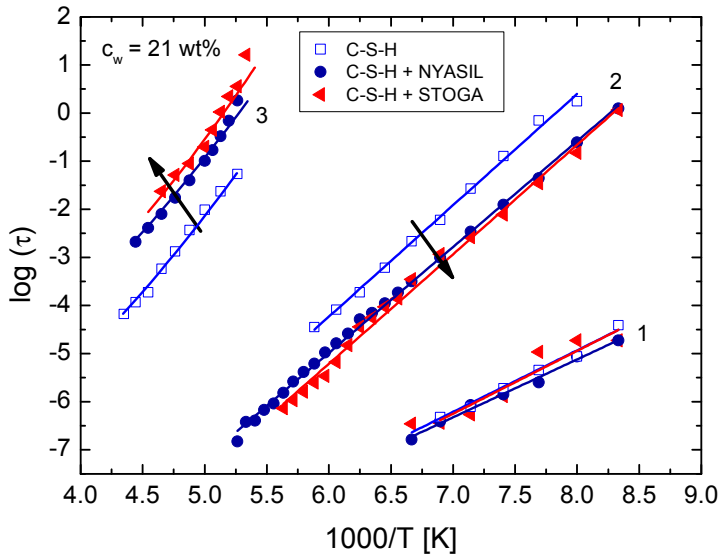

Figure 2. Temperature dependence of the relaxation time τ (T) for the three samples analyzed at c_w = 21 wt%. Process 1 is independent on the structure whereas processes 2 and 3 become faster and slower respectively when increasing the silicate chain where water is confined.

CONCLUSION

The addition of nanoparticles during the synthesis of CSH gel increases the lengths of the silicate chains. Water dynamics revealed by broadband dielectric spectroscopy, indicate that the microstructure of C-S-H gel changes appreciably with the addition of nanoparticles. These results suggest that in CSH-Stoga and CSH-Nyasil there are more water-surface interactions and smaller gel pores than in C-S-H.

REFERENCES

Ayuela A., J.S. Dolado, I. Campillo, Y.R. de Miguel, E. Erkizia, D. Sanchez-Portal, A. Rubio, A. Porro, P.M. Echenique. (2007) *J Chem. Phys.*127, 164710.

Beaudoin, J.; Dramé, H.; Raki, L.; Alizadeh, R. "2009) "Formation and properties of C-S-H–PEG nano-structures". Materials and Structures, 42 (7), 1003-1014.

Björnström J., A. Martinelli, A. Matic, L. Börjesson, I. Panas, Chemical Physics Letters 392 (2004) 242.

Cerveny, S.; Arrese-Igor, S.; Dolado, J. S.; Gaitero, J. J.; Alegria, A.; Colmenero, J. (2011) "Effect of hydration on the dielectric properties of C-S-H gel". *J Chem. Phys.,* 134 (3), 034509.

Franceschini, A.; Abramson, S.; Mancini, V.; Bresson, B.; Chassenieux, C.; Lequeux, N. (2007). "New covalent bonded polymer-calcium silicate hydrate composites". *J. Mat. Chem.*, 17 (9), 913-922.

Jonsson B., H. Wennerstrom, A. Nonat, B. Cabane, *Langmuir* 20 (2004) 6702.

Korb, J.; McDonald, P.; Monteilhet, L.; Kalinichev, A.; Kirkpatrick, R. (2007). *Cem. Concr. Res.*, 37, 348

Le Saout G., E. Lécolier, A. Rivereau, H. Zanni. (2006). "Chemical structure of cement aged at normal and elevated temperatures and pressures". *Cem. Concr. Res.* 36 (2006) 71.

Minet, J.; Abramson, S.; Bresson, B.; Franceschini, A.; Van Damme, H.; Lequeux, N. (2006) "Organic calcium silicate hydrate hybrids: a new approach to cement based nanocomposites". *J. Mat. Chem.*, 16 (14), 1379-1383.

Monasterio, M.; Jansson, H.; Gaitero, J. J.; Dolado, J. S.; Cerveny, S. (2013). "Cause of the fragile-to-strong transition observed in water confined in C-S-H gel". *J Chem. Phys.*, 139 (16), 164714.

Monasterio, M.; Gaitero, J. J.; Erkizia, E.; Guerrero Bustos, A. M.; Miccio, L. A.; Dolado, J. S.; Cerveny, S. (2015) "Effect of addition of silica- and amine functionalized silica-nanoparticles on the microstructure of calcium silicate hydrate (C–S–H) gel". *J. Colloid and Interface Science***,** *450*, 109-118.

Raki, L.; Beaudoin, J.; Alizadeh, R.; Makar, J.; Sato, T. (2010). "Cement and Concrete Nanoscience and Nanotechnology". *Materials*, 3 (2), 918-942.

Richardson I.G, (1999) "The nature of C-S-H in hardened cements". *Cem. Concr. Res.* 29 1131.

Richardson I.G., Cement and Concrete Research 34 (2004) 1733.

Ridi, F.; Luciani, P.; Fratini, E.; Baglioni, P. (2009). **"**Water Confined in Cement Pastes as a Probe of Cement Microstructure Evolution". *J. Phys. Chem. B***,** *113* (10), 3080-3087.

Sanchez, F.; Sobolev, K. (2010) "Nanotechnology in concrete – A review". *Construction and Building Materials*, 24 (11), 2060-2071.

Energy Efficient Cement-Based Building Materials

E. Goiti*; M. Ocejo; and M. Cano

Materials Area, Sustainable Construction Division, TECNALIA, Parque Científico y Tecnológico de Bizkaia, C/Geldo, Edif. 700, Derio, 48160 Bizkaia, Spain.
*E-mail: eunate.goiti@tecnalia.com

Abstract

Energy plays a key role in the technological, industrial, economical and societal development. The energy-intensive building construction sector accounts for approximately 42% of the total EU final energy consumption and is responsible for approximately 36% of EU CO_2 emissions. The building construction sector is considered to be the one with the biggest cost effective energy-saving potential impact. Consequently, there is a strong need for implementing: *i)* Quick low-cost energy efficient retrofitting solutions to adapt the non-efficient residential European building stock to present energy regulation and *ii)* Low-cost & low-energy new buildings in line with the "nearly zero energy buildings" standards. The building envelope is the key element to address, in a building, in order to achieve the best improvements in terms of energy efficiency while maintaining the indoor environment quality. Therefore, the development of new lightweight materials and components for the building envelope with outstanding properties is terms of high thermal performance is a must that is being addressed in this work. These new materials and components will not only reduce considerably the heating and cooling demands but will maintain the indoor comfort of the buildings. The general objective of this work is to design and synthesize high thermal insulating cement-based products by incorporation of superinsulating aerogel-like materials. The develop materials will be lightweight, with a low value for the thermal conductivity while maintaining their mechanical properties.

INTRODUCTION

New requirements for energy efficiency in the market for rehabilitation and new buildings entail a trade-off between insulation performance and minimization of thicknesses. Conventional insulation materials (polyurethane, fiberglass, mineral wool, etc) require higher thickness values to meet the current transmittance requirements, which are not always feasible due to exterior space limitations, restraints in loads or aesthetic and visual considerations. Similarly, for the interior part of the walls, the insulation solutions yielding high thicknesses are undesirable for various reasons: reductions of interior space, reset points of light and heating installations in interior insulation. In addition to this, there is another associated disadvantage, long execution-times required by most of the current conventional solutions. In such conditions demanding slim solutions, aerogels and aerogel-based products constitute an interesting alternative for the replacement of conventional thermal insulators due to their very low thermal conductivity at room temperature. Silica Aerogels are well established nanoporous materials on the labscale. In the 30s

Kistler[i] succeeded in converting gels with sparse solid backbone into a dry gel without destroying the filigree silica network by applying supercritical drying. Silica aerogels with hydrophobic inner surfaces are especially interesting for thermal insulation since thermal conductivities (λ) down to 0.012 W/(m K) can be achieved[ii] (being the lowest thermal conductivity for solids at ambient conditions); this is due to their high porosity (above 90%)[iii] in combination with their pore sizes below 60 nm[iv]. Due to the exceptional properties of these materials they are the excellent candidates for different application fields where the market demands products with enhanced thermal insulation,

Several attempts have been made so far to develop novel building products based on aerogel but there are still relevant challenges to achieve more mechanically rigid and durable products which minimize the release of dust and make them more compatible with other building conventional materials like cement based materials, gypsum based products, etc.

OBJECTIVE

The objective of this work was the preparation of aerogel-based cementitious materials for the development of lightweight mortars. Different types of aerogels have been employed for the preparation of the cement-based composites.

EXPERIMENTAL PART

Aerogel synthesis: Two types of aerogel granules were prepared employing tetraethoxysilane (TEOS) and methyltrimethoxysilane (MTMS) precursors. Silica alcogels were prepared by a two-step, acid-base, catalyzed sol gel process (combination of acid-catalyzed hydrolysis and base-catalyzed condensation). The first aerogel was prepared from TEOS and the second one from TEOS and MTMS in a molar ration equal to 0.6.

In the first step the general procedure was as follows: the precursors were mixed with a weighed amount of isopropanol and H_2O by stirring on a magnetic stirrer. To this solution a weighed amount of 0.1 M hydrochloric acid was added and the solution was kept at 60^oC for 1.5 hours.

The molar ratio H_2O/OR was kept in 1 (one water molecule for each hydrolyzable Si-OR bond) and isopropanol/Si molar ratio was kept in 4.

In the second step, a weighed amount of base NH_4OH (0.5 M) was added dropwise to promote the condensation reaction. After 5 minutes stirring at room temperature, the sol was transferred to silicone molds for gelation and they were aged at 50^oC for 24 h to strengthen the network structure.

After aging the alcogels were immersed in hexane for 24 hours in order to exchange the solvent of the pore before the surface modification treatment.

Surface modification was carried out by immersion of the gels in mixtures of hexamethyldisyloxane (HMDSO): hexane and a catalytic amount of HCl at 50^oC. Reaction time and ratios of HMDSO: hexane were varied in order to optimize this process.

After the surface modification of the gels, they were washed with hexane to remove the unreacted HMDSO. The gels were dried by ambient pressure drying yielding aerogels. Figure 1 shows the image of aerogel samples prepared.

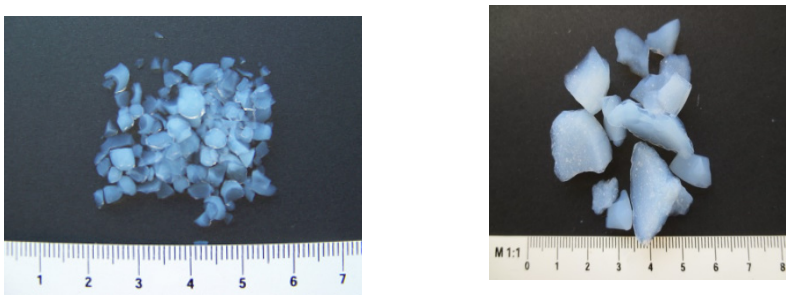

Figure 1. *Image of aerogel samples. On the left the one prepared from TEOS and on the right prepared from TEOS-MTMS.*

Aerogel-based cementitious materials preparation:
The aerogel samples were mixed with cement, water and superplastisizer employing the amounts described in Table 1. The composites samples were left 28days for curing.

Table 1. Recipes employed for the preparation of aerogel-based cement materials.

Samples	White cement 32,5 N (g)	Standard sand (g)	Aerogel (g)	Water (g)	Superplastisizer Auracast 280 (g)
Reference	200	600	-	80	1,15
A-TEOS	200	-	25,6	60	1,96
A-TEOS/MTMS	200	-	25,6	60	1,96

Characterization methods:
The specific surface areas, pore volume, average pore diameter of aerogels were determined by nitrogen sorption isotherms with Brunauer Emmitt-Teller (BET).
The packing densities were calculated from weight of cylindrical column of known volume filled with of the silica aerogels pieces.
Surface modification was confirmed by IR spectroscopy. The spectra were acquired using the KBr pellet method in the range of 400 to 4000 cm^{-1}.
Thermal properties of aerogels and aerogel-based cement materials were evaluated by the Hot-wire technique which yields the value of thermal conductivity (λ).

RESULTS and DISCUSSION

The aerogel samples were characterized and the main properties are shown in Table 2.

Table 2. Properties of ambient dried aerogels

Sample	Surface Area (m^2/g)	Average pore diameter (nm)	Pore volume (cm^3/g)	Density (g/cm^3)
TEOS	776	14.25	2.76	0.101
MTMS:TEOS	1035	9.05	2.34	0.123

In both cases, these ambient dried aerogels exhibit low values for density. The measured value of the thermal conductivity for both type of aerogel is lower than 0.018W/mK.
The figure 2 shows the image of some of the aerogel-based cement composite materials that were prepared.

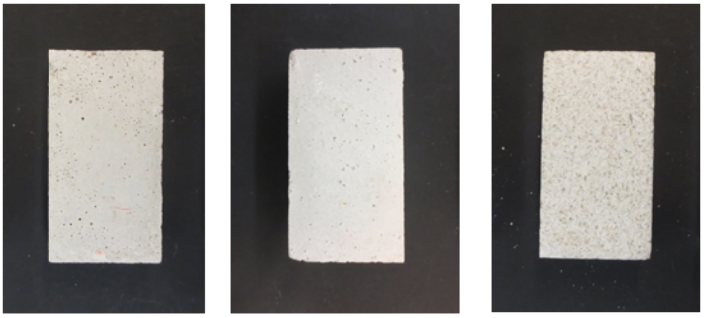

Figure 2. *Images of the aerogel-based cement samples: from left to right: reference, A-TEOS, A-TEOS/MTMS.*

Table 3 summarises the density and the thermal conductivity values obtained for these composites. It can be observed that the addition of aerogels allows a decrease in the density and an important reduction in the value of the thermal conductivity.

Table 3. Density values for aerogel-based cement composites.

Sample	Density (g/ml)	Thermal conductivity (W/mK)
Reference	2.22	2.97
A-TEOS	1.06	1.06
A-TEOS/MTMS	1.05	0.708

These results look promising and further research is underway in order to further reduce the thermal conductivity of aerogels synthesise by means of a cost-effective process. The employment of these aerogels in the preparation of cement based composites will allow the development of cost-effective high thermal insulation products.

REFERENCES

[i] S.S. Kistler, Coherent Expanded Aerogels and Jellies, Nature 127 (1931) 741-741 and S.S. Kistler, The Relation between Heat Conductivity and Structure in Silica Aerogel, J. Phys. Chem. 39 (1935) 79 – 86.
[ii] CJ Brinker, GW Scherer, (1990), Sol–gel science: The physics and chemistry of sol–gel processing. San Diego: Academic Press.
[iii] A Emmerling, J Fricke, "Scaling properties and structure of aerogels", Journal of Sol-Gel Science and Technology 8 (1997) 781.
[iv] H.-P. Ebert, Thermal properties of Aerogels, in: M.A. Aegerter, N. Leventis, M.M. Koebel (Eds.) Aerogels Handbook, Springer Science+Business Media, New York, 2011, pp. 537-564.

The Role of Water on C-S-H Gel Shear Strength Studied by Molecular Dynamics Simulations

H. Manzano[1]; E. Duque-Redondo[1]; E. Masoero[2]; and I. López-Arbeloa[1]

[1]Molecular Spectroscopy Laboratory, Basque Country University, UPV/EHU, 48940 Leioa, Vizcaya, Spain. E-mail: hegoi.manzano@ehu.eus
[2]School of Civil Engineering and Geosciences, Newcastle University, Newcastle upon Tyne NE1 7RU, U.K. E-mail: enrico.masoero@newcastle.ac.uk

Abstract

The properties of the cement paste are defined to a high extend by those of the C-S-H gel, and irreversible deformations such as creep and shrinkage are not an exception. It is believed that molecular scale processes play an important role on the stress accumulation and relaxation, and molecular dynamics simulation a great tool to identify and quantify those mechanisms. In this work, we use NEMD simulation to investigate first the effect of the temperature and shear rate on the shear strength, Then, we study the stress development on a C-S-H interface with an increasing distance between adjacent particles. We discuss the results in terms of water, and we define a limiting distance, 1 nm, at which the shear strength is lost.

INTRODUCTION

The C-S-H gel is the main constituent of cement paste, up to the 70% of the final material. It is the phase that gives cohesion to the material and the main responsible for its properties, including creep and shrinkage (Masoero et al. 2013; Jennings et al. 2013). The C-S-H gel can be broadly defined as a material composed of short silicate chains held together by calcium oxide regions, forming layered clay-like particles, with strongly confined water within and between the particles (Richardson 2008; Abdolhosseini Qomi et al. 2014). Understanding the mechanical properties within the C-S-H particles and between adjacent particles, and how the gel responds to applied load, is therefore of vital importance for the design of the new generation of Portland Cement (Masoero et al. 2012; Gonzalez-Teresa et al. 2010; Ioannidou et al. 2014; González-Teresa et al. 2013). Molecular simulation is a key technique to investigate the forces and processes that govern creep and shrinkage.

In this work we will focus on the interfacial strength between C-S-H nanoparticles under shear strain. We assume a colloidal nature of the C-S-H gel (Thomas & Jennings 2006; Jennings 2008; Masoero et al. 2012), and we suggest that the interface between particles could range between two limiting cases, see figure 1. The first case is that of an ideal interface where the interparticle contact is similar in

separation and composition as the interlayer space within a particle. The interfacial properties will be equal to the bulk intraparticle ones. The second case is that of a non-ideal interface where the separation between particles is larger than the interlayer space and will be saturated by water in an operational relative humidity range (r.h. > 0.2) (Bonnaud et al. 2012; Muller et al. 2012; Jennings et al. 2013). The interfacial cohesion is then expected to decrease as a function of the distance between the particles. The primary aim of this work is to determine the dependence of the shear strength with the distance, and to identify the limit where the tangential cohesion is lost.

In both the ideal and non-ideal interfaces (see figure 1) the stress relaxation under a shear deformation could be ascribed to a stick-slip phenomenon, in which the layers slide over each other without internal deformation. The water in the interlayer spaces controls the mechanical response in terms of yield strength, buildup of pressure during shear deformations, and magnitude of stress drops at large strain. Indeed, molecular simulation have identified this type of mechanism in layered materials like clays (Hantal et al. 2014; Duque-Redondo et al. 2014), tobermorite (Hegoi Manzano et al. 2013), and the C-S-H (Pellenq et al. 2009; Hegoi Manzano et al. 2013), and also indicate the presence of interfacial friction at the nanoscale (Bhushan et al. 1995; Yue et al. 2013). The objective here is to use these existing methodologies to assess how the shear response of the interparticle interface changes with the thickness of the water layer between them, going from an ideal to a non-ideal configuration.

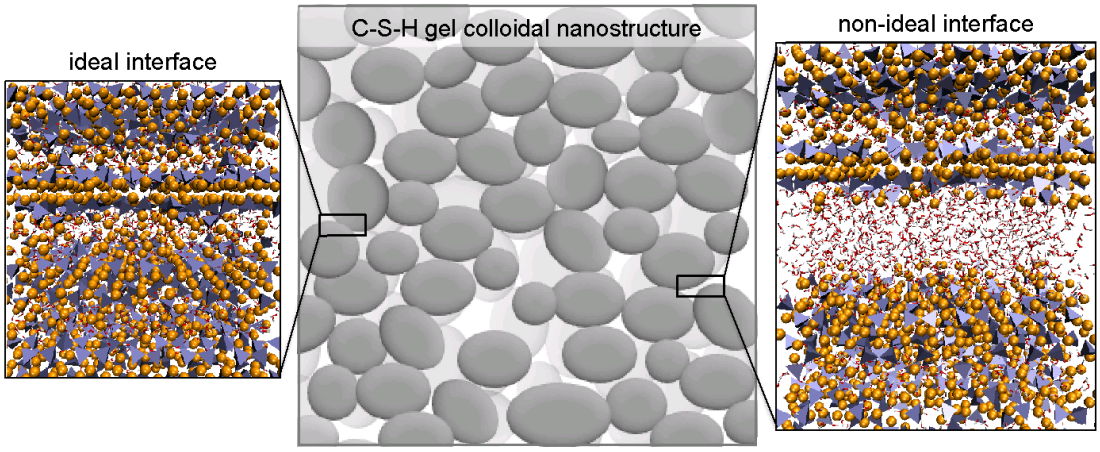

Figure 1. Representation of the model assumed for the C-S-H gel nanostructure. The gel is formed by polydisperse nanoparticles that percolate randomly, leading to multiple interfaces. The suggested limiting cases are an ideal interface with perfect contact, and non-ideal interfaces with a separation larger than the ideal one.

METHODOLOGY

We have constructed a C-S-H system with C/S=1.7 following the method described by Pellenq et al. (Pellenq et al. 2009), ending in a glass like material with the archetypal disordered structure calcium silicate hydrate gel. Then, the central interlaminar space has been increased to 0.25, 0.5, and 1 nm, and has been saturated with water. These configurations were then relaxed via molecular dynamics (MD) simulation in the NPT ensemble at room temperature and pressure. The generated systems represent possible distances between C-S-H particles in the cement paste, as depicted in figure 1.

The shear test were performed using non-equilibrium molecular dynamics (NEMD) simulations in the NVT ensemble at room temperature and pressure using the SLLOD equations of motions within the Nose/Hoover thermostat (Daivis & Todd 2006) to avoid velocity artefacts generated due to the deformation of a periodic box. The shear was imposed in a plane perpendicular to that of the calcium silicate layers, where the triggering of deformation requires minimum stress (Manzano et al. 2009; Manzano et al. 2007; Shahsavari et al. 2011; Hou et al. 2014). In all the simulation, the integration time step was 0.2 fs, and the thermostat and barostat constants were 20 and 100 ps respectively. The interatomic forces were computed using the well-tested ReaxFF parameters from refs. (Fogarty et al. 2010; Manzano, Pellenq, et al. 2012; Manzano, Moeini, et al. 2012).

RESULTS AND DISCUSSION

1. Effect of temperature and shear rate

The failure of the C-S-H gel molecular model under shear has been previously studied using a quasi-static approach, i.e., using a 0K approach where the kinetic energy and the strain rate are neglected (Hegoi Manzano et al. 2013; H Manzano et al. 2013; Pellenq et al. 2009). However, under quasi-static conditions the system explores a very limited region of the potential energy surface (PES), compared to the accessible PES at finite temperature. The lack of sampling implies that possible mechanisms of deformation will be exclueded, one of which could be the Hbond formation-disruption. Indeed, the quasi-static studies already highlighted the role of water as a lubricant agent that reduces the strength between surfaces, despite the contribution to the cohesion due to the formation of a strong hydrogen bond (Hbond) network (Duque-Redondo et al. 2014) could lead to an overestimation of the shear strength. First, the Hbond strength is small, and thermal energy at room temperature is sufficient to break the hydrogen bonds. For example, Carrier et al. demonstrated

that the out of plane elastic coefficient of montmorillonite at 300K decreases to ~1/3 of the 0K approximation. Second, the Hbond lifetime is short enough to be spontaneously broken before the strain affects them (Keutsch & Saykally 2001; Grabowski 2004).

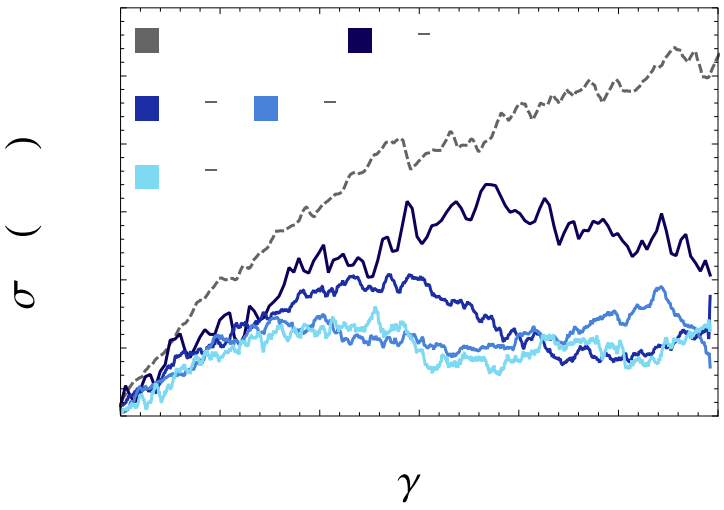

Figure 2. Stress-strain curves for the ideal contact interface under shear strain computed using quasiestatic deformation (dashed line) and NEMD at 4 different strain rates from 10^{-4} to 10^{-7} fs^{-1}

To address the limitations of 0K approaches mentioned above, here we perform NEMD simulations at room temperature and we compare them with results at 0K. Figure 2 shows such a comparison for an ideal contact interface, alongside the effect of shear rate on stress buildup (see figure 2). The stress-strain curves are qualitatively similar, with intermitting stress increases and drops even even at very small strain levels. The yield strength point is not well defined and the transition to the plastic regime is smooth, as in ductile disordered materials. The consideration of finite temperature leads to a decrease of yield strength compared to the 0K case, already at very high strain rates. The quasi-static yield stress and strain are about 4 and 3 times higher respectively than the value at the lowest strain rate investigated (10^{-7} fs^{-1}), probably, because the the temperature is dismissing the cohesion given by the hydrogen bond network. Further than the yield stress (which was quite expected), we found out that also the yield strain decreases when the strain rate is reduced. This is due to a lack of time to relax the internal stresses at high strain rate (Lau et al. 2010). The curves in figure 2 seem become statistically equivalent at strain rates smaller that ~10^{-6} fs^{-1}. This supports our suggestion that the Hbond plays a central role in the relaxation of C-S-H under shear. In fact, the lifetime of an Hbond is ~20 ps in bulk water, and can increase up to 100 ps due to confinement in the C-S-H

(Youssef et al. 2011). Therefore, a strain rate of 10^{-7} fs^{-1} provides enough time for Hbond spontaneous relaxation independent of the deformation.

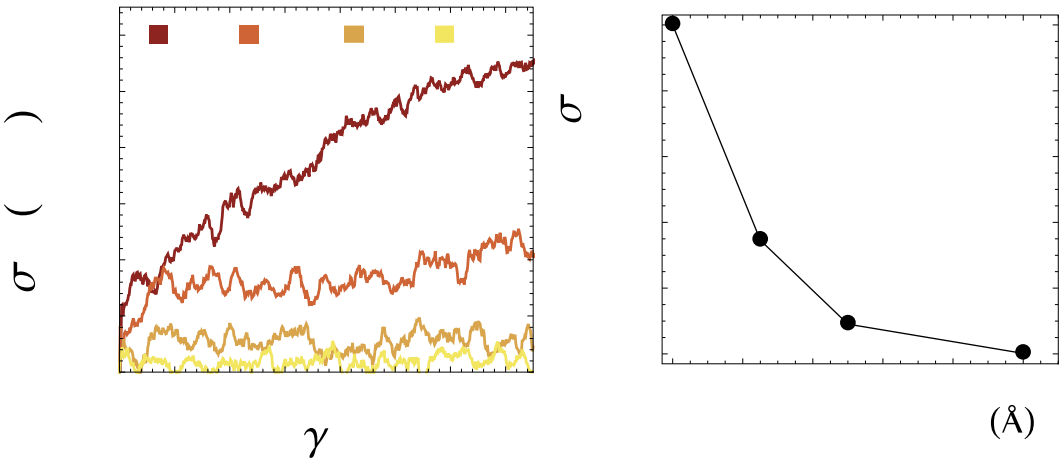

Figure 3. (a) Shear stress evolution as a function of the applied strain for the studied systems. (b) Decrease of the shear stress as a function of the distance between surfaces.

2. Shear strength as a function of the interparticle distance

Figure 3 shows the stress buildup as a function of the aplied strain for the ideal contact case (labeled as 0.0, which indictest the extra distance between surfaces compared to the ideal case) and adding up to 1nm interfacial distances. All the simulationsin figure 3 are performed at a strain rate of 10^{-7} fs^{-1}. In all the cases, the true elastic region is negligible, and there are multiple stress acumulation and relaxation events, consistent with the the stick-slip mechanism. The stress-strain curves clearly show a remarkable decrease of the the yield strenght as the distance between surfaces increases, as shown in figure 3b. An increase of the interfacial distance of just 2.5 Å from the ideal contact case reduces the shear strenght from ~0.75 GPa to less than 0.2 GPa. The decrease of the strain at which the onset of plastic flow is reached is even more pronounced, going down from ~10% to 1% as the interfacial distance increases. We must remark that the interfacial space is saturated with water, and no cavitation effect is present. At 5 Å, the shear strenght has dropped to as much as 10% of the ideal contact case, and the system loses all the cohesion under shear strain at 1 nm separation. It is interesting to note that for such a small distance the water is considered to present confined dynamics, with lower mobility than bulk water (Bonnaud et al. 2010; Hou et al. 2015). However, in terms

of cohesion, that amount of water screens the long-range coulombic interaction between the charged surfaces, and cannot form a Hbond netwrok strong enough to provide cohesion to the system. The results agree with investigation of the pore fluid components contribution to the interparticle pressure by Bonnaud et al. (Bonnaud et al. 2012).

CONCLUSION

In this work we used non-equilibrium molecular dynamics (NEMD) simulations at the atomic scale to investigate the cohesion of calcium silicate hydrates (C-S-H) interfaces under shear strain. We suggest that such interfaces may have a structure akin to that of the interlaminar space: a water-rich region with calcium ions that counterbalance the surface charge. Under this assumption, we discussed two limiting cases: a perfect contact interface with maximum cohesion, and the maximum interfacial distance when the cohesion is lost. We determined that the loss of cohesion under shear occurs already at distances of just 1 nm.

The suggestion that thick layers of interlaminar water can be regarded effectively as interfaces between particles nanoparticles is consistent with a number of concepts that can be found in the literature on creep. For instance, “creep sites” have been defined to indicate water-rich regions with low local stiffness, where slipping occurs preferentially (Jennings 2004; Bazant et al. 1997). According to our results, as the contact distance between particles increases they will present lower stiffness, and will have lower activation energy. Currently, we are working on the quantification of those activation energies to characterize the time dependence of creep as a function of time via transition state theory (Masoero et al. 2013). This work sets the limit of cohesion < 1 nm, above which particles cannot accumulate shear stress.

Two final comments must be done regarding the limitations of these simulations. First, C-S-H particles at an interfacial contact point could be misaligned, could have different orientations, or different C/S ratios. However, we expect that as far as water plays a central role in the cohesion (e.g. in absence of significant cross-links between the surfaces), the results presented here will be at least qualitatively correct. This is especially true at moderate distances (> 0.5 nm), when the behavior of bulk water is almost recovered. Second, we acknowledge that the macroscopic mechanical behaviour of the C-S-H gel is unlikely to be just a direct product of molecular scale processes. Other features that affect the macroscopic behaviour will likely emerge at larger scales, for example mesoporosity, particle packing fraction and size polydipersity (Masoero et al. 2014) number of contact points between C-S-H nanoparticles or “creep sites” and their relative distribution. Nevertheless, our results

address some fundamental mechanisms underlying creep of C-S-H, and provide useful information for models at larger scales.

REFERENCES

Abdolhosseini Qomi, M.J. et al., 2014. Combinatorial molecular optimization of cement hydrates. *Nat Commun*, 5.

Bazant, Z.P. et al., 1997. Microprestress-solidification theory for concrete creep. I: Aging and drying effects. *Journal of Engineering Mechanics*, 123(11), pp.1188–1194.

Bhushan, B., Israelachvili, J.N. & Landman, U., 1995. Nanotribology: friction, wear and lubrication at the atomic scale. *Nature*, 374(6523), pp.607–616.

Bonnaud, P.A. et al., 2012. Thermodynamics of Water Confined in Porous Calcium-Silicate-Hydrates. *Langmuir*, 28(31), pp.11422–11432.

Bonnaud, P.A., Coasne, B. & Pellenq, R.J.M., 2010. Molecular simulation of water confined in nanoporous silica. *Journal of Physics: Condensed Matter*, 22(28), p.284110.

Daivis, P.J. & Todd, B.D., 2006. A simple, direct derivation and proof of the validity of the SLLOD equations of motion for generalized homogeneous flows. *The Journal of chemical physics*, 124(19), p.194103.

Duque-Redondo, E. et al., 2014. Molecular Forces Governing Shear and Tensile Failure in Clay-Dye Hybrid Materials. *Chemistry of Materials*, 26(15), pp.4338–4345.

Fogarty, J.C. et al., 2010. A reactive molecular dynamics simulation of the silica-water interface. *Journal of Chemical Physics*, 132(17), p.10.

Gonzalez-Teresa, R. et al., 2010. Structural models of randomly packed Tobermorite-like spherical particles: A simple computational approach. *Materiales de Construcción*, 60(298), pp.7–15.

González-Teresa, R. et al., 2013. Nanoscale texture development of CSH gel: A computational model for nucleation and growth. *Applied Physics Letters*, 103(23), p.234105.

Grabowski, S.J., 2004. Hydrogen bonding strength—measures based on geometric and topological parameters. *Journal of Physical Organic Chemistry*, 17(1), pp.18–31.

Hantal, G. et al., 2014. Atomic-scale modelling of elastic and failure properties of clays. *Molecular Physics*, (May), pp.1–12.

Hou, D. et al., 2014. Mechanical properties of calcium silicate hydrate (C–S–H) at nano-scale: A molecular dynamics study. *Materials Chemistry and Physics*, 146(3), pp.503–511.

Hou, D. et al., 2015. Water transport in the nano-pore of the calcium silicate phase: reactivity, structure and dynamics. *Physical Chemistry Chemical Physics*, 17(2), pp.1411–1423.

Ioannidou, K., Pellenq, R.J.-M. & Del Gado, E., 2014. Controlling local packing and growth in calcium-silicate-hydrate gels. *Soft Matter*, 10(8), pp.1121–1133.

Jennings, H. et al., 2013. Water Isotherms, Shrinkage and Creep of Cement Paste: Hypotheses, Models and Experiments. In *Mechanics and Physics of Creep, Shrinkage, and Durability of Concrete*. American Society of Civil Engineers, pp. 134–141.

Jennings, H.M., 2004. Colloid model of C-S-H and implications to the problem of creep and shrinkage. *Materials and Structures*, 37(265), pp.59–70.

Jennings, H.M., 2008. Refinements to colloid model of C-S-H in cement: CM-II. *Cement and Concrete Research*.

Keutsch, F.N. & Saykally, R.J., 2001. Water clusters: Untangling the mysteries of the liquid, one molecule at a time. *Proceedings of the National Academy of Sciences*, 98(19), pp.10533–10540.

Lau, T.T., Kushima, A. & Yip, S., 2010. Atomistic simulation of creep in a nanocrystal. *Physical Review Letters*, 104(17), p.175501.

Manzano, H., Moeini, S., et al., 2012. Confined Water Dissociation in Microporous Defective Silicates: Mechanism, Dipole Distribution, and Impact on Substrate Properties. *Journal of the American Chemical Society*, 134(4), pp.2208–2215.

Manzano, H., Pellenq, R.J.M., et al., 2012. Hydration of Calcium Oxide Surface Predicted by Reactive Force Field Molecular Dynamics. *Langmuir*, 28(9), pp.4187–4197.

Manzano, H. et al., 2013. Mechanical Behaviour of Ordered and Disordered Calcium Silicate Hydrates under Shear Strain Studied by Atomic Scale Simulations. In *Mechanics and Physics of Creep, Shrinkage, and Durability of Concrete*. American Society of Civil Engineers, pp. 86–97.

Manzano, H. et al., 2007. Mechanical properties of crystalline calcium-silicate-hydrates: comparison with cementitious C-S-H gels. *Physica Status Solidi a-Applications and Materials Science*, 204(6), pp.1775–1780.

Manzano, H. et al., 2013. Shear deformations in calcium silicate hydrates. *Soft Matter*, 9(30), pp.7333–7341.

Manzano, H., Dolado, J.S.S. & Ayuela, a., 2009. Elastic properties of the main species present in Portland cement pastes. *Acta Materialia*, 57(5), pp.1666–1674.

Masoero, E. et al., 2013. Kinetic Simulation of the Logarithmic Creep of Cement. In *Mechanics and Physics of Creep, Shrinkage, and Durability of Concrete*. American Society of Civil Engineers, pp. 166–173.

Masoero, E. et al., 2014. Nano-scale mechanics of colloidal C-S-H gels. *Soft Matter*, 10(3), pp.491–499.

Masoero, E. et al., 2012. Nanostructure and Nanomechanics of Cement: Polydisperse Colloidal Packing. *Physical Review Letters*, 109(15), p.155503.

Muller, A.C.A. et al., 2012. Densification of C–S–H Measured by 1H NMR Relaxometry. *The Journal of Physical Chemistry C*, 117(1), pp.403–412.

Pellenq, R.J.M. et al., 2009. A realistic molecular model of cement hydrates. *Proceedings of the National Academy of Sciences of the United States of America*, 106(38), pp.16102–16107.

Richardson, I.G., 2008. The calcium silicate hydrates. *Cement and Concrete Research*, 38, pp.137–158.

Shahsavari, R. et al., 2011. Empirical force fields for complex hydrated calcio-silicate layered materials. *Physical chemistry chemical physics : PCCP*, 13(3), pp.1002–11.

Thomas, J.J. & Jennings, H.M., 2006. A colloidal interpretation of chemical aging of the C-S-H gel and its effects on the properties of cement paste. *Cement and Concrete Research*, 36(1), pp.30–38.

Youssef, M., Pellenq, R.J.M. & Yildiz, B., 2011. Glassy Nature of Water in an Ultraconfining Disordered Material: The Case of Calcium-Silicate-Hydrate. *Journal of the American Chemical Society*, 133(8), pp.2499–2510.

Yue, D.-C. et al., 2013. Tribochemistry of Phosphoric Acid Sheared between Quartz Surfaces: A Reactive Molecular Dynamics Study. *The Journal of Physical Chemistry C*, 117(48), pp.25604–25614.

Determination of Nanomechanical Properties of Cementitious Materials Using an Energy-Based Approach

K. Jha[1]; N. Suksawang[2]; and A. Agarwal[3]

[1]Former Doctoral Student, Department of Civil and Environmental Engineering, Florida International University, 10555 West Flagler St., Miami, FL 33174. E-mail: kjha001@fiu.edu
[2]Associate Professor, Department of Civil Engineering, Florida Institute of Technology, 150 West University Blvd., Melbourne, FL 32901-6975. E-mail: nsuksawang@fit.edu
[3]Professor, Department of Mechanical and Materials Engineering, Florida International University, 10555 West Flagler St., Miami, FL 33174. E-mail: agarwala@fiu.edu

Abstract

Nanoindentation is increasingly being used for the determination of nanomechanical properties of cementitious materials. The method is based on elastic punch theory to extract mechanical properties of interest from experimental load-displacement data. This theory requires initial unloading stiffness and contact area to be known. In this study, we propose a simplified method for the evaluation of stiffness and contact area based on more accurate and realistic interpretation of the load-displacement data. Such interpretation allows us to evaluate both the initial unloading stiffness and the contact area directly as a function of normalized elastic work. The area function derived herein may be used to compute contact area whenever the ratio of indenter tip to maximum penetration depth ratio is in the range of 0.1-1.67. Indentation moduli obtained using these expressions are in good agreement with those obtained by the Oliver and Pharr method for all the phases of hardened cement paste.

INTRODUCTION

Characterizing materials at nanoscale has broken ground into the study of concrete materials (Acker, 2001; Velez et al, 2001; Constantinides et al, 2003, 2007; Mondal et al., 2008; Nemecek, 2009; Vandamme and Ulm, 2009). One promising and relatively easy method is the nanoindentation experiment. This experiment is based on contact mechanics where the elastic modulus and hardness are determined by analyzing a load-displacement curve. The theory, introduced by Oliver and Pharr (1994, 2004), makes use of initial unloading stiffness and requires analysis of unloading portion of the load-displacement curves. An independent measurement of area of contact (between the indenter and the specimen) and slope of the curve (initial unloading stiffness) immediately upon unloading are required.

Although the Oliver and Pharr method works well for hard homogeneous materials, there are two main issues associated with it. First, an unloading curve may

not be suitably described by a power law as its parameters varies greatly even within a material due to the effect of residual stress (Gong at al., 2004; Marx and Blake, 1997). As a result, the values for the power-law exponent usually fall beyond the range of 1.2-1.6 for a Berkovich indenter and thus disprove the concept that it characterizes an indenter type. Second, the indenter tip requires to be calibrated each time at the start of a test to account for the tip bluntness in the area function, which is often time-consuming.

Based on the analysis of simulated nanoindentation data, we have recently shown that the normalized indentation work can be used to describe an indenter geometry and response of a material (Jha et al., 2013b). For instance, the total energy constant quantifies bluntness at the tip of an indenter; it is equal to 1.5 for an ideally sharp Berkovich indenter. It decreases with the increase in tip radius to maximum penetration depth ratio and is independent of material type when this ratio is less than or equal to 2. Again, a blunt indenter behaves like a sharp one if maximum penetration depth is very large in comparison to tip radius (Hainsworth et al, 1996). In this situation, the calibration of indenter tip is not required for the determination of area function. These observations lead us to believe that a universal area function could be formed and may be used to compute the contact area between an indenter and material. On the other hand, the elastic energy constant can be used to characterize response of a material to indentation; it varies in the range 1- ∞, where lower value represents the hardest material. In this study, we propose a simple method for the determination of indentation modulus by expressing contact area and initial unloading stiffness as a function of elastic energy constant. This method requires input parameters that are readily available from the experimental load-displacement curves.

METHODOLOGY

Nanoindentation experiment was carried out on cement paste samples. The cement paste samples were prepared using type I Portland cement with water-to-cement ratios (w/c) of 0.30, 0.40, and 0.50. The samples were prepared in accordance with ASTM C 305 using cylindrical rubber mold with internal diameter and height of 25 mm. After the samples were cured in water for 28 days, the sample surfaces were prepared in accordance to the best practices to ensure that they were smooth surface. Rough surface may yield spurious values of mechanical properties and damage the indenter tip permanently.

Nanoindentation tests were performed at random locations in a grid of 3 by 3. Grid indentation technique over representative area is preferred for nanoindentation in case of cementitious materials (Constantinides et al, 2003). Since the objective is to analyze individual nanoindentation curve corresponding to each phases of cement paste and not the determination of volume fraction of each phases, performing grid indentation over a large area is not required. Nanoindentation tests were also performed using a Berkovich tip of radius 50nm at several locations to capture the load-displacement curves corresponding to each of these four phases of cement paste sample with varying maximum applied load ranging from 250-1250 μN. This gives the ratio of tip radius to maximum depth of penetration in the range 0.13-1.67.

PROPOSED METHOD

The method described in this paper to compute indentation modulus for cementitious materials is very much straightforward. In order to apply the theory of elastic punch for this purpose, one needs to evaluate the initial unloading stiffness and the area of contact. Both of these quantities may be expressed as a function of elastic energy constant (v_E). Referring to Figure 1, the elastic energy constant is defined as a ratio of the absolute work of indentation (W_{S2}) to the elastic energy (W_E) recovered upon unloading such that $v_E = \frac{W_{S2}}{W_E}$; where $W_{S2} = 0.5 P_{\max} h_{\max}$ (Jha et al., 2012).

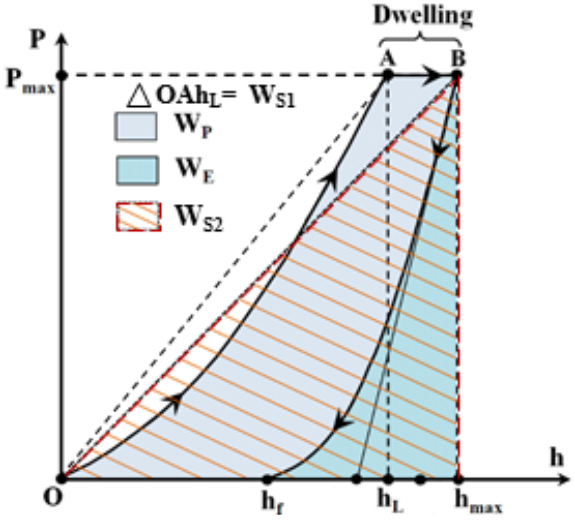

Figure 1. Schematic nanoindentation load-displacement curves

Jha et al. (2013a) derived a closed form solution for the computation of the initial unloading stiffness which may be written as:

$$S_E = \alpha_s \varepsilon (2v_E - 1)\frac{P_{\max}}{h_{\max}}$$

where ε is known as geometric constant and is equal to 0.75 for Berkovich indenter. α_s is a stiffness correction factor due to the proximity between maximum and contact depths, which can be determined from $\alpha_s = 1.23 - 0.38\log(v_E)$

Analysis of the nanoindentation test results revealed that the plot between the contact depth (h_c) and contact area (A_c) can be fitted by a cubic equation in the following form:

$$A_c = 776.2h_c + 24.58h_c^2 - 0.0008h_c^3$$

where

$$h_c = \frac{2(v_E - 1)}{(2v_E - 1)} h_{\max}$$

The elastic energy constant can be approximated, without the loss of accuracy, using the relation given below.

$$v_E = -3.33 \ln\left(\frac{h_f}{h_{\max}} - 0.0658\right)$$

Finally, the indentation modulus is given by

$$E_r = \frac{1}{2} S_E \sqrt{\frac{\pi}{A_c}}$$

Results, shown in Figure 2, indicate that the indentation modulus determined by the proposed method and the Oliver and Pharr method (denote as measured E_r) are in reasonably good agreement as the majority of data points fall on or near to the line of perfect equality for all phases of hardened cement paste considered in this study.

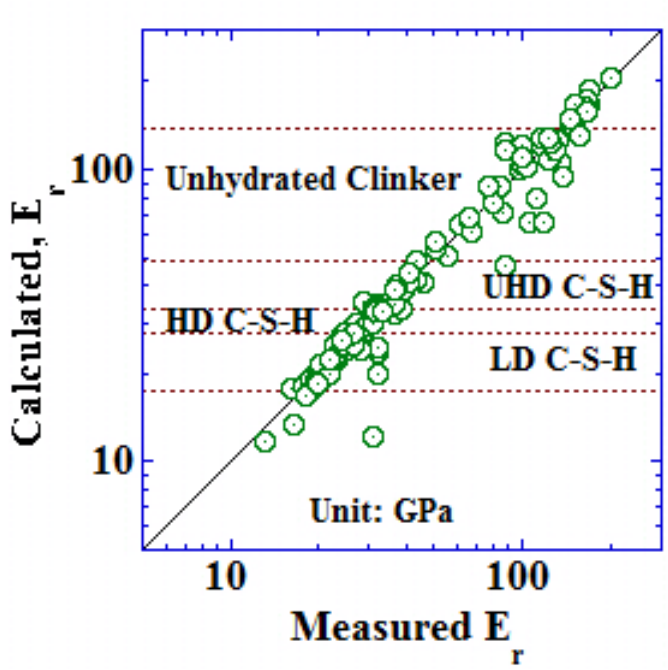

Figure 2. Comparison of computed and measured indentation moduli

CONCLUSION

By analyzing nanoindentation test data from hardened cement paste samples, we show that the initial unloading stiffness and contact area can be expressed as a function of normalized elastic work called elastic energy constant. The cubic equation proposed for the computation of contact area in this study can be considered universal as it is obtained by considering different indenter tip radius to maximum penetration depth ratio. These expressions give rise to the development of a simple method for the computation of indentation modulus and hardness of cementitious materials using Sneddon's solution for the indentation of elastic half space by a rigid indenter. Method described herein requires three input parameters: peak indentation load, maximum penetration depth and residual depth. These parameters can be read off from the nanoindentation load-displacement curves.

REFERENCES

Acker, P. (2001) "Micromechanical Analysis of Creep and Shrinkage Mechanism," *CONCREEP 6.*

Constantinides, G., Ulm, F.-J., and Van Vliet, K. (2003) "On the use of Nanoindentation for Cementitious Materials," *Materials and Structures*, V. 36, pp. 191-196.

Constantinides, G., Ravi Chandran, K.S., Ulm, F. J., and Van Vliet, K. J. (2007) "Grid Indentation Analysis of Composite Microstructure and Mechanics: Principles and Validation," *J. Mechanics and Physics of Solids*, V. 55, pp. 64-90.

Gong, J., Miao, H., and Peng, Z. (2004) "Analysis of the nanoindentation data measured with a Berkovich indenter for brittle materials: effect of the residual contact stress", *Acta Mater*, V. 52, pp. 785-793.

Hainsworth, S. V., Chandler, H. W., and Page, T. F. (1996) "Analysis of Nanoindentation Load-displacement Loading Curves", *J. Materials Research*, V. 11, no. 8, pp. 1987-1995.

Jha, K. K., Suksawang, N., Lahiri, D., and Agarwal, A. (2012) "Energy-based Analysis of Nanoindentation Curves for Cementitious Materials," *ACI Materials Journal*, V. 109, no.1, pp. 81-90.

Jha, K. K., Suksawang, N., Lahiri, D., and Agarwal, A. (2013a) "Evaluating Initial Unloading Stiffness from Elastic Work-of-indentation Measured in a Nanoindentation Experiment," *J. Materials Research*, V. 26, no.6, pp. 789-797.

Jha, K. K., Zhang, S., Suksawang, N., Wang, T., and Agarwal, A. (2013b) "Work-of-indentation as a Means to Characterize Indenter Geometry and Load-displacement Response of a Material," *J. Physics D: Applied Physics*, V. 46, pp. 415501- 415511.

Marx, V., and Blake, H. (1997) "A Critical Investigation of the Unloading Behavior of Sharp Indentation," *Acta Materialia*, V. 45, no. 9, pp. 3791-3800.

Mondal, P., Shah, S.P., and Marks, L.D. (2008) "Nanoscale Characterization of Cementitious Materials," *ACI Materials Journal*, V. 106, no. 2, pp. 174-179.

Nemecek, J., (2009) "Creep Effects in Nanoindentation of Hydrated Phases of Cement Pastes," *Material Characterization*, V. 60, pp. 1028-1034.

Oliver, W. C., and Pharr, G. M. (1992) "An Improved Technique for Determining Hardness and Elastic Modulus using Load and Displacement Sensing Indentation Experiments," *J. Material Research*, V. 7, pp. 1564-1583.

Oliver, W. C., and Pharr, G. M. (2004) "Measurements of Hardness and Elastic Modulus by Instrumented Indentation: Advances in Understanding and Refinements to Methodology," *J. Material Research*, V. 1, pp. 3-20.

Vandamme, M., and Ulm, F.-J. (2009) "Nanogranular Origin of Concrete Creep," *Proceedings of the National Academy of Sciences*, V. 106, pp. 10552-10557.

Velez, K., Maximilien, S., Demidot, D., Fantozzi, G., and Sorrentino, F. (2001) "Determination by Nanoindentation of Elastic Modulus and Hardness of Pure Constituents of Portland Cement Clinker," *Cement and Concrete Research*, V. 31, pp. 555-561.

Molecular Dynamics Simulations of Graphene Pull-Out from Calcium Silicate Hydrate

Chen Yang Li[1]; Shu Jian Chen[2]; Ye Lu[3]; and Wen Hui Duan[4]

[1]Department of Civil Engineering, Monash University, Clayton, VIC 3800, Australia. E-mail: chenyang.li@monash.edu
[2]Department of Civil Engineering, Monash University, Clayton, VIC 3800, Australia. E-mail: shujian.chen@monash.edu
[3]Department of Civil Engineering, Monash University, Clayton, VIC 3800, Australia. E-mail: ye.lu@monash.edu
[4]Department of Civil Engineering, Monash University, Clayton, VIC 3800, Australia. E-mail: wenhui.duan@monash.edu

Abstract

In recent years, the additions of nanomaterials as reinforcements for cement have attracted great interests. However, the understanding of the interfacial properties between these nanomaterials and the cement matrix is still limited. In this study, molecular dynamics (MD) simulations are conducted to investigate the graphene pull-out from calcium silicate hydrate (C-S-H). The jennite is simulated to model the structure of C-S-H. The graphene sheet is pulled out from the jennite matrix by 5 Å each time. The pull-out energy is found to increase linearly with the pull-out displacement. The pull-out force keeps constant (0.538N/m) throughout the pull-out process. This reinforcing mechanism is different with that of the microfibers (or macrofibers) and further research is needed to understand the role of nanomaterials in cement composites.

INTRODUCTION

The advancements in nanotechnology have opened new opportunities to improve the performance of cement with the inclusion of nanomaterials. Since the earler attempt by Campillo, Dolado et al. (2004), the one-dimensional carbon nanotubes (CNTs) have been incorporated into cement to improve the engineering properties of cement composites. It has been found that the addition of CNTs could improve compressive and flexural strength, fracture toughness, and Young's modulus of the composite (Chen, Collins et al. 2011). More recently, the two-dimensional graphene and its derivatives (e.g. graphene oxide) have been exploited as the nanofillers in cement composites (Chuah, Pan et al. 2014).

These carbon based nanomaterials are attractive for their high aspect ratio, which provides large interfacial area with the cement matrix. However, the understanding about the interfacial properties between the graphene surfaces and cement matrix is still limited. Chan and Andrawes (2010) estimated the average shear strength at the interface of CNTs and cement matrix using finite element methods. Chen, Zou et al.

(2014) extended the microfiber model (C. Li 1992) to CNT/cement composites. In these methods, the interfacial properties between nanofillers and cement matrix were estimated by using the macro-scale experimental results. As an alternative and more straightforward way, molecular dynamics (MD) simulations can directly calculate the interfacial properties at nanoscale.

Calcium silicate hydrate (C-S-H) is the main hydration product of cement. It is widely accepted that C-S-H has a layered structure akin mostly to that of tobermorite and jennite minerals (Shahsavari, Buehler et al. 2009). Therefore, the tobermorite and jennite minerals have been used as the crystal models to simulate the C-S-H structure. Compared with tobermorite, the Ca/Si ratio of jennite (1.5) is closer to that of C-S-H gel (1.7) as proposed by Allen, Thomas et al. (2007).

In this study, MD simulations of the graphene pull-out from C-S-H are conducted. The jennite is adopted as the structure of C-S-H. The graphene sheet is pulled out from the jennite matrix. The pull-out energy at different pull-out displacement is calculated, by which the pull-out force can be estimated. The reinforcing mechanism of the nanoscale graphene sheet is discussed.

METHODOLOGY

The crystal structure of jennite reported in Bonaccorsi, Merlino et al. (2004) is adopted in the simulation model, shown as Figure 1 (a). The charge of each atom is assigned based on the bond valence to reach the charge balance. This periodic jennite unit cell has the lattice parameters of $a = 10.576$ Å, $b = 7.265$ Å, $c = 10.931$ Å, $\alpha = 101.30^{\circ}$, $\beta = 96.98^{\circ}$ Å, and $\gamma = 109.65^{\circ}$ Å. A supercell containing 4 × 4 × 2 crystallographic unit cell is created.

To insert a graphene sheet into the jennite matrix, a gap was generated by cleaving the unit cell surface, which is parallel to the (001) crystallographic plane. A graphene sheet with a length of 29.520 Å and a width of 19.884 Å, shown as Figure 1 (b), is placed into the gap. The edge of the graphene sheet was saturated with the –OH groups.

The condensed-phase optimized molecular potentials for atomistic simulation studies (COMPASS) force field is adopted, which has been successfully employed to simulate the cement materials (Wu, Al-Ostaz et al. 2011, Duan, Chen et al. 2013).
After the graphene sheet being placed into the jennite matrix and water molecules being packed, a geometry optimization is conducted to minimize the total energy of the structure. A Smart minimization algorithm combining the Steepest Descent, Conjugate Gradient and Newton methods is adopted, and the convergence level for force is set to be 0.5kcal/mol/Å. Subsequently, a NPT ensemble (a constant number of particles, constant pressure and temperature dynamics simulation) is employed to optimize the shape of the supercell. The temperature is set to 298K with a temperature control method Nosé-Hoover thermostat; the pressure is set to be 0.11

MPa with a pressure control method Berendsen Barostat. The time step is set to be 1.0fs.

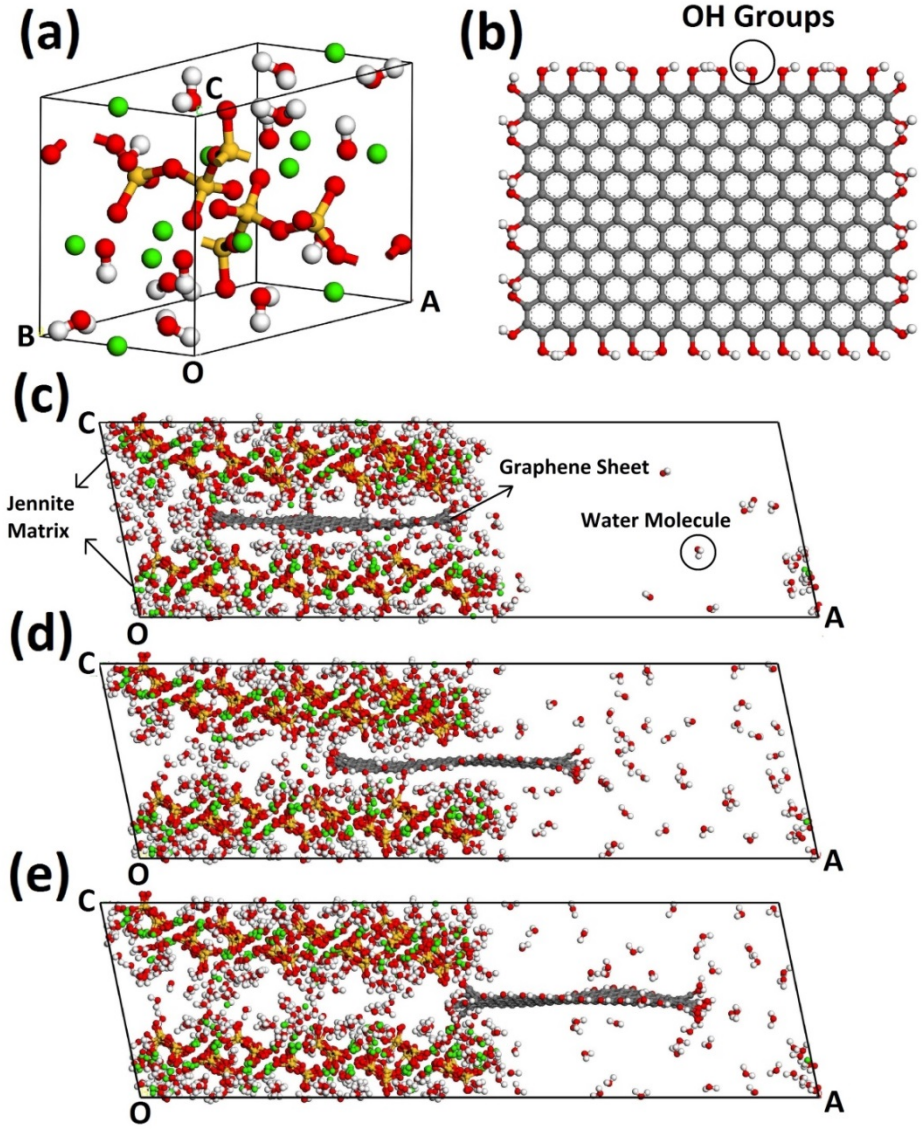

Figure 1. (a) Crystal structure of jennite: the green, yellow, red and white spheres represent calcium, silicon, oxygen, hydrogen atoms, respectively; (b) graphene sheet; (c) dynamics simulation with pull-out displacement 0; (d) dynamics simulation with pull-out displacement 1.5nm; (e) dynamics simulation with pull-out displacement 3nm.

The graphene sheet is pulled out by 5 Å at each step. Interaction energy between the jennite matrix and the graphene sheet is calculated as:

$$E_I = E_{total} - (E_{matrix} + E_{graphene}) \quad (1)$$

where E_{total} is the total energy of the composite structure; E_{matrix} and $E_{graphene}$ are the energies of the jennite and graphene sheet, respectively.

RESULTS AND DISCUSSION

The interaction energy between the jennite matrix and the graphene sheet at different pull-out displacement, as well as their standard deviations, are shown in Table 1. It can be seen that the interaction energy keeps decreasing along with the pulling out of graphene sheet. When the graphene sheet is fully pulled out, the interaction energy approaches to zero.

By calculating the energy difference at the initial state and the pulled out state, the energy spent in the pulling out can be obtained, namely, the pull-out energy (E_p), as listed in Table 1.

Table 1. Interaction energy, standard deviation and pull-out energy for different pull-out displacement.

Pull-out displacement δ (nm)	Interaction energy (10^{-18}J)	Standard deviation	Pull-out energy (E_p) (10^{-18}J)
0.0	-5.539	0.041	0.000
0.5	-3.990	0.073	1.549
1.0	-3.424	0.082	2.115
1.5	-2.370	0.037	3.169
2.0	-2.384	0.029	3.155
2.5	-1.282	0.047	4.257
3.0	-1.254	0.012	4.285
3.5	-0.460	0.020	5.079
4.0	-0.335	0.022	5.204

The pull-out energies vs. pull-out displacements are plotted in Figure 2. It can be found that, in general, the E_p-δ curve shows a linear increase pattern. By regression analysis, a linear trendline is illustrated in Figure 2. The R-squared value is 0.961, which is a good fit of the line to the data.

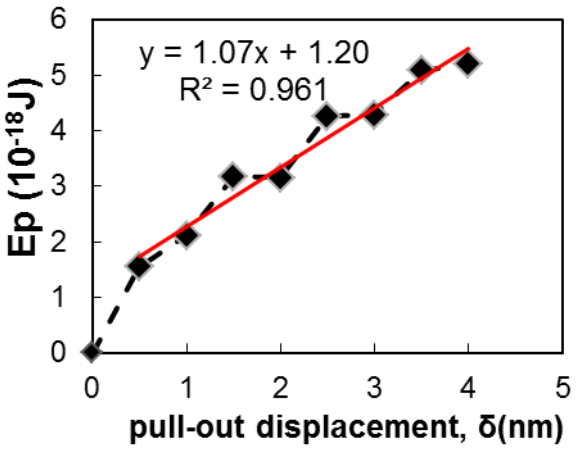

Figure 2. Pull-out energy at different pull-out displacement.

The linear increase of pull-out energy along with the pull-out displacement indicates that the pull-out force remains constant throughout the pull-out process. Because the interaction area between the graphene sheet and the jennite matrix decreases with the pull-out displacement, it means that the pull-out force is independent with the pull-out displacement. Based on the slope 1.07 of the trendline, the pull-out force (N per meter width of graphene sheet) can be calculated as 0.538N/m. This pull-out force predicted at nanoscale can be linked with the macro-scale mechanical properties by modifying the existing models for fiber reinforced cementitious composites, e.g. Li's model (C. Li 1992). The interfacial behaviors between graphene and cement matrix will be useful to understand the effect of nanomaterials on the durability of cement and concrete composites.

CONCLUSION

The pull-out behavior of a graphene sheet from cement matrix is investigated by molecular dynamics simulations. The interaction energy decreases with the pulling out of graphene sheet and approaches to 0 when the graphene sheet is fully pulled out. The pull-out energy shows a linear increase with the pull-out displacement, indicating the pull-out force remains constant (0.538 N/m) throughout the pull-out process. This reinforcing mechanism is different with that of the microfibers (or macrofibers).

ACKNOWLEDGMENT

Authors are grateful for the financial support provided by the Australian Research Council to conduct this study.

REFERENCES

Allen, A. J., J. J. Thomas and H. M. Jennings (2007). "Composition and density of nanoscale calcium–silicate–hydrate in cement." Nature materials **6**(4): 311-316.
Bonaccorsi, E., S. Merlino and H. Taylor (2004). "The crystal structure of jennite, Ca 9 Si 6 O 18 (OH) 6· 8H 2 O." Cement and Concrete Research **34**(9): 1481-1488.
C. Li, V. (1992). "Postcrack scaling relations for fiber reinforced cementitious composites." Journal of Materials in Civil Engineering **4**(1): 41-57.
Campillo, I., J. Dolado and A. Porro (2004). "High-performance nanostructured materials for construction." SPECIAL PUBLICATION-ROYAL SOCIETY OF CHEMISTRY **292**: 215-226.
Chan, L. Y. and B. Andrawes (2010). "Finite element analysis of carbon nanotube/cement composite with degraded bond strength." Computational Materials Science **47**(4): 994-1004.
Chen, S., F. Collins, A. Macleod, Z. Pan, W. Duan and C. Wang (2011). "Carbon nanotube–cement composites: A retrospect." The IES Journal Part A: Civil & Structural Engineering **4**(4): 254-265.

Chen, S. J., B. Zou, F. Collins, X. L. Zhao, M. Majumber and W. H. Duan (2014). "Predicting the influence of ultrasonication energy on the reinforcing efficiency of carbon nanotubes." Carbon **77**: 1-10.
Chuah, S., Z. Pan, J. G. Sanjayan, C. M. Wang and W. H. Duan (2014). "Nano reinforced cement and concrete composites and new perspective from graphene oxide." Construction and Building Materials **73**: 113-124.
Duan, W. H., S. J. Chen and M. Hubler (2013). Water Sorption Hysteresis in Cement Nano Slits. Proceedings of the Ninth International Conference on Creep, Shrinkage, and Durability Mechanics (CONCREEP-9), September 22-25, 2013 Cambridge, Massachusetts, ASCE Publications.
Shahsavari, R., M. J. Buehler, R. J. M. Pellenq and F. J. Ulm (2009). "First-principles study of elastic constants and interlayer interactions of complex hydrated oxides: Case study of tobermorite and jennite." Journal of the American Ceramic Society **92**(10): 2323-2330.
Wu, W., A. Al-Ostaz, A. H.-D. Cheng and C. R. Song (2011). "Computation of elastic properties of Portland cement using molecular dynamics." Journal of Nanomechanics and Micromechanics **1**(2): 84-90.

Efficiency of an Innovative Self-Healing System in Ultra-High-Strength Concrete under a Salt Spray Test

G. Pérez[1]; J. L. García Calvo[1]; P. Carballosa[1]; V. Rodríguez Allegro[1]; J. J. Gaitero[2,3]; E. Erkizia[2,3]; and A. Guerrero[1,3]

[1]Institute for Construction Sciences "Eduardo Torroja", CSIC, Serrano Galvache, 4, E-28033 Madrid, Spain. E-mail: gperezaq@ietcc.csic.es; jolgac@ietcc.csic.es; carballosa@ietcc.csic.es; allegro@ietcc.csic.es; aguerrero@ietcc.csic.es
[2]Tecnalia, Materials Sustainable Construction Division, Geldo, Edificio 700, Parque Tecnológico de Bizkaia, E-48160 Derio, Spain. E-mail: juanjose.gaitero@tecnalia.com; edurne.erkizia@tecnalia.com
[3]MATCON, Associated Unit CSIC-Tecnalia.

Abstract

Ultra-high strength concretes (UHSC) with self-healing system based on the combined action of two additions have been developed in order to seal developing cracks, thus improving their long-term durability. The present work evaluates the efficiency of the self-healing system in aggressive environmental conditions with chloride attack. UHSC with and without the addition of the self-healing system were fabricated and cracked at 28 days of curing considering two crack width. Once cracked, the specimens were subjected to a salt spray test during 90 days and, after that, they were characterized by means of capillarity tests and colorimetric methods (chloride penetration evaluation). Unlike in the concretes without the self-healing system, the initial water absorption rate of the cracked specimens of self-healing concretes is similar to that of the corresponding un-cracked samples and almost insensitive to the crack width, thus confirming a robust self-healing mechanism that even limits chloride penetration.

INTRODUCTION

Chloride penetration promotes the generation of a lot of damage for constructions in marine environments. Moreover, during the service life of structures, cementitious materials are subjected to several actions that can promote the formation of cracks, thus accelerating chloride penetration in the concrete matrix and limiting the durability of reinforced concrete structures. Concretes have certain autogenous self-healing ability mainly attributed to two mechanisms: hydration of unhydrated cement particles and dissolution and subsequent carbonation of $Ca(OH)_2$ (Ramm, 1998; Yang, 2009). However, this ability is not enough to completely heal the formed cracks and this is more evident in severe environmental conditions as the one considered in this paper (chloride attack). As repair is usually costly and sometimes even impossible due to inaccessibility, a promising solution to minimise the

mentioned problem is to control and/or repair the cracks at the earliest stage. As a consequence, preventive technologies, like those based on "self-healing" concepts, are very interesting (Wu, 2012; Mihashi, 2012; Van Tittelboom, 2013).

Most of the developed self-healing technologies have not been already tested in aggressive media. Nevertheless, recent preliminary studies have indicated a promising reduction of chloride penetration into the concrete matrix when encapsulated self-healing mechanisms are used (Maes, 2014). In the present work, an innovative cementitious material in which the self-healing mechanism is based on the combined action of two additions is used. On the one hand, silica microcapsules containing an epoxy compound (CAP) are added to the paste and get bound to the matrix as it hardens. On the other hand, amine functionalised silica nanoparticles (NS) are also added to react with the clinker during the hydration process in order to generate an amine functionalised cementitious matrix. Upon the formation of a microcrack, some microcapsules break releasing the epoxy which spreads along the crack. The epoxy then comes into contact with the amine groups in the matrix which cure the epoxy thus sealing the crack. The efficacy/capacity of this system in sealing the cracks formed has been already demonstrated (García Calvo, 2014). Therefore, the main objective of the present study is the evaluation of the efficiency of the self-healing system in aggressive environments with high chloride content. Moreover, the possible increase of the resistance against chloride penetration promoted by the developed self-healing mechanism is also preliminary tested. In this sense, as chloride penetration in cracked concretes strongly depends on the crack width (Jacobsen, 1996), two different crack mouth opening displacements (CMOD) are considered: 150μm and 300μm.

EXPERIMENTAL

Materials. Two different ultra-high strength concretes (UHSC) have been considered, one without the self-healing system (REF) and the other with it (SH). This system consists of silica microcapsules (CAP) and amine-functionalized nanosilica particles (NS). Silica microcapsules containing the epoxy sealing compound (Epothin® from Buehler) and amine-functionalised nanosilica particles were synthesised by a sol-gel method described elsewhere (Kaltzakorta, 2010; Berriozabal, 2010). As shown in Table 1, both UHSC have similar compositions but in SH concrete the silica fume content is partially substituted by the corresponding amount of CAP and NS.

Cylindrical specimens of 100 mm in diameter and 25 mm thick were fabricated with a water/cement ratio of 0.3. For the fabrication of the specimens, the silica fume Elkem Grade 940-U undensified (SF), the microcapsules encapsulating the epoxy (CAP), the aggregates, the limestone powder and the cement were mixed slowly (according to UNE-EN 196-1) for one minute. The amine-functionalized nanosilica (NS), previously dispersed for 5 minutes in distilled water with the superplastizicer Structuro 351 from Fosroc using an ultrasonic probe, was then added to the solids. The mix was mixed 1 minute at slow rate, 3 minutes fast and then mixing was halted for 2 minutes. The mixing proceeded fast for two more minutes and then half of the steel fibers (OL13/0.16) were added and mixed fast for 1 minute followed by the addition of the other half and fast mixing for another minute. The

specimens were stored for 24 hours in a controlled chamber at 20±1 ºC and 100 % relative humidity and after that time they were unmolded and cured under water at 20±1 ºC, according to UNE-EN 196-1.

Table 1. UHPC compositions.

Components (g)	*REF*	*SH*
CEM I 52.5N	680	680
Water	204	204
Siliceous aggregates (∅<1mm)	510	510
Limestone powder (∅<0.5mm)	510	510
Silica Fume	170	91
CAP	-	34
NS	-	45
Superplastizicer	27.2	27.2
Fibers	119	119

Experimental Program. At 28 days of curing, four cylindrical specimens of each matrix were cracked to a specified crack mouth opening displacement (CMOD) of 150 μm and four to 300 μm using the Brazilian splitting tension test. The CMOD was measured with an extensometer placed between two steel plates stuck on one face of the specimen and the tests were performed at a constant crack mouth opening rate of 0.5 μm/s. It must be remarked that the remaining final crack width was lower than the CMOD specified in each case as in the splitting tension test, when the load was removed, there was a crack relaxation with the subsequent decrease of width. Regarding the final CMOD of 150 μm, the remaining crack width had a mean value of 60 μm in the REF samples and of 85 μmin the SH ones. Regarding the final CMOD of 300 μm, the remaining crack width had a mean value of 190 μm in the REF samples and of 235μmin the SH ones. Taking into account that in this study the self-healing capacity was evaluated by measuring the water absorption rate of the cracked samples, these differences in the remaining crack opening displacement might be detrimental to the efficient evaluation of the self-healing system.

Once cracked, the specimens were weighed before placing them in a climatic chamber to be subjected to the salt spray test as defined in the UNE-EN-ISO9227-2007 standard during a period of 90 days. Un-cracked specimens of each material were also placed in the same chamber to be used as references. The samples were weighed and visually observed periodically. After the salt spray test, the samples were dried at 50ºC up to constant weight as a preconditioning procedure for the measurement of water absorption rate and capillary suction coefficient by means of capillarity test based on the standard UNE 83982. This test was considered in order to evaluate the autonomous healing capacity of the fabricated UHPC. The specimens were then placed in a receptacle with a water level of 5mm, putting in contact with the water only one of the faces of the sample. Test specimens were periodically weighed in order to determine the water absorption rate.

Moreover, for comparison reasons the water absorption rate and capillary suction coefficient by means of capillarity test were also measured in un-cracked and cracked specimens after a healing time of 28 days at 20ºC. During this period,

samples were wrapped in retractable film with the aim of not allowing moisture exchange between the UHPCs and the environment.

At last, after the salt spray test some samples were reloaded until they split into two halves in order to evaluate their resistance to chloride penetration. This phenomenon was visually analyzed by means of the colorimetric method that implies to spray an $AgNO_3$ solution in the concrete failure surfaces. After the solution spraying, a dark colored surface indicates no chloride penetration and pale purple surface indicates the opposite.

RESULTS AND DISCUSSION

Behavior of the UHPC during the salt test. After the specific crack formation, the specimens were placed in the climatic chamber to be subjected to the salt test conditions. As previously mentioned, un-cracked specimens of each material were also placed in the same chamber to be used as references. During the 90 days of the salt test, the specimens were periodically weighed and visually inspected in order to detect possible damages associated to the severe exposure conditions. Figure 1 shows images of samples with a CMOD = 150μm before and after the salt test and Figure 2 the weight gain measured during the 90 days (mean values).

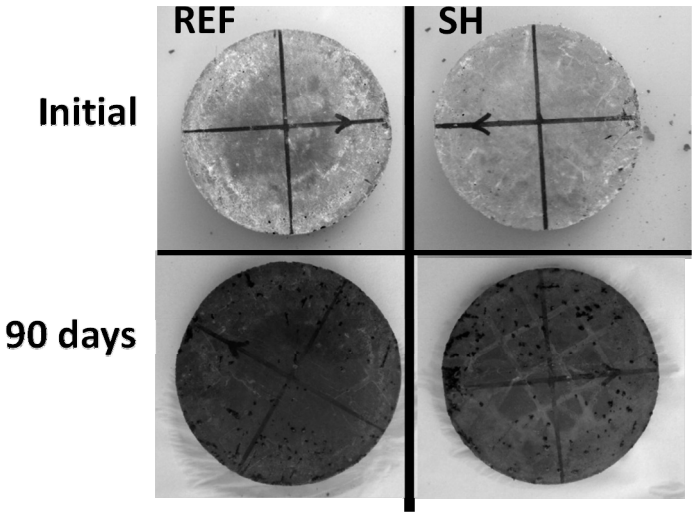

Figure 1. Sample with CMOD=150μm before and after the salt test. Left: REF; right: SH.

No significant external damage was noticed in the concrete matrix of the specimens during the test, neither significant visual differences, except for darker surface in the center of the REF samples after the test. This darker tonality could be related to a higher and faster saline solution penetration in the REF samples. In all the cases, the steel fibers of the concrete surfaces were oxidized after the test period. In fact, in Figure 2 a clear increase of the measured weight with the test time is observed in the case of the cracked samples that was attributed to the formation of corrosion products in the used fibers and also to penetration of the pulverized saline solution. This weight increase is also detected in the un-cracked samples in the long-term but

in a significantly lower degree. Regarding the cracked samples, important differences are detected between samples REF and SH in the short-term. At 7 days, the weight increase is 60% higher in REF samples regardless of the CMOD considered. Certainly, this fact must be related with the efficiency of the self-healing mechanism that limits or delays the penetration of the pulverized saline solution. However, the final weight gain is very similar in SH and REF. Moreover, in SH samples there are no difference observed as a function of CMOD considered. The results suggest that the similar final weight change detected should be mainly related to formation of corrosion products in the fibers placed in the surface since, during the splitting test, concrete scaling was more important in the SH samples; thus leaving more fibers exposed to corrosion.

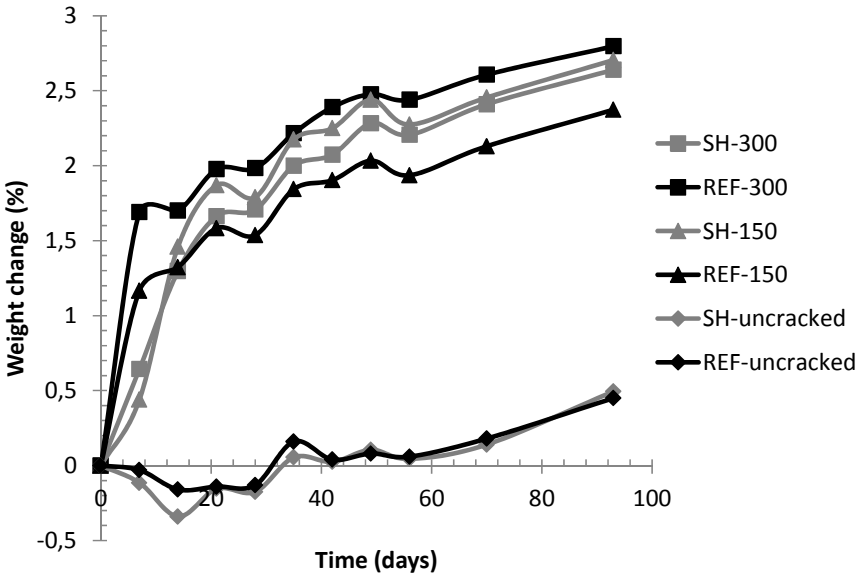

Figure 2. Weight change of specimens during the salt spray test.

Influence of the severe exposure conditions in the self-healing mechanism. In this study, the self-healing capacity has been evaluated by measuring the water absorption rate and capillary suction coefficient. First of all, in order to evaluate if the severe conditions considered limit the UHPC performance, Figure 3 shows the water absorption rate and the capillary suction coefficients of the REF and SH concretes measured after 28 days at 20ºC (without water exchange) and after the salt spray test. No significant difference is detected between the results obtained in both environments but it is remarkable that the capillary suction coefficient is always lower in the SH concrete, suggesting a denser matrix in this material. Then, considering that the capillary suction coefficient is a durability indicator, it can be concluded that the inclusion of the self-healing mechanism does not limit the durability performance of the UHPC developed.

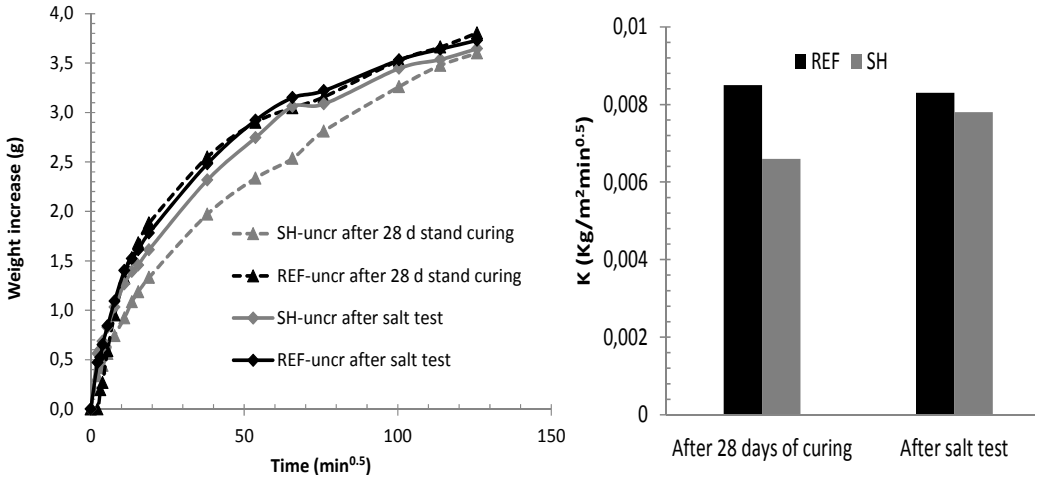

Figure 3. Water absorption rate (left) and capillary suction coefficient (right) of the UHPC after 28 days of standard curing and after the salt spray test.

Figure 4 and Figure 5 show the water absorption rate of the samples with a final CMOD of 150 μm and 300 μm respectively, both after the salt spray test (ST samples) and after 28 days of curing at 20ºC. The results of the un-cracked samples are also shown for comparison reasons. Moreover, Figure 6 presents the capillary suction coefficients obtained in each case. Regardless of the final CMOD, in the cracked REF samples a clear increase in the initial slope of the water absorption curve with respect to un-cracked specimens is detected. On the contrary, the initial absorption rate of the SH samples is very similar to that measured in the un-cracked corresponding specimens for both CMOD, although the final weight increase is higher in cracked specimens. In any event, it is worth noting that the obtained results in cracked SH samples after the salt spray test and in those samples maintained for 28 days at 20ºC (without water exchange) are very similar, thus confirming the little or no influence of the chloride attack in the self-healing efficacy. Consequently, the obtained results confirm the self-healing capacity of the SH samples even in the aggressive environment considered in this study.

It is also interesting to note that in the REF samples, for the higher CMOD (Figure 5), both the initial slope of the water absorption curve and the final weight increase are lower in the samples subjected to the salt spray test. This must be related to secondary hydration of the unhydrous cement particles by the water infiltration from the salt solution that partially heals the cracks. Thus, according to the results obtained for CMOD = 300μm, it is evident that the UHPC developed have a significant autogenous self-healing capacity.

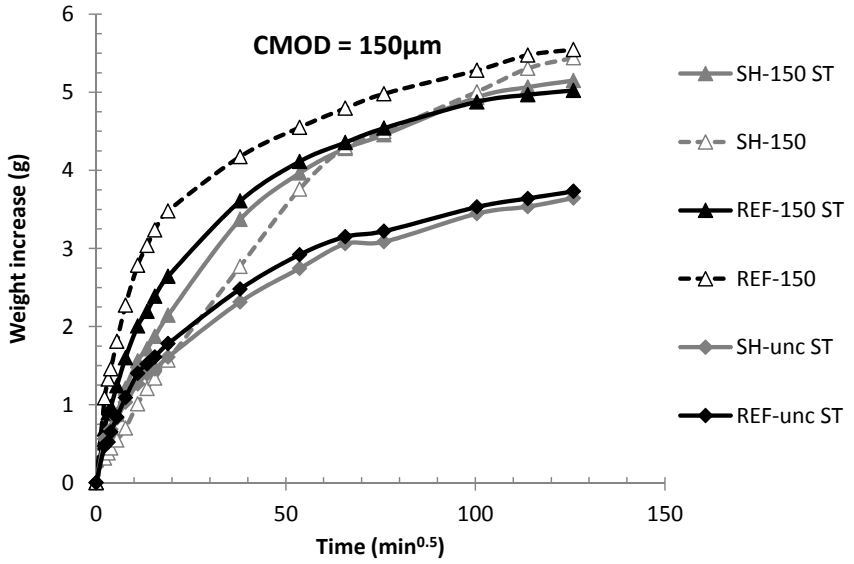

Figure 4. Water absorption rate of the samples with a CMOD=150µm. unc = uncracked samples; ST = the test was made after 90 days in the salt spray chamber.

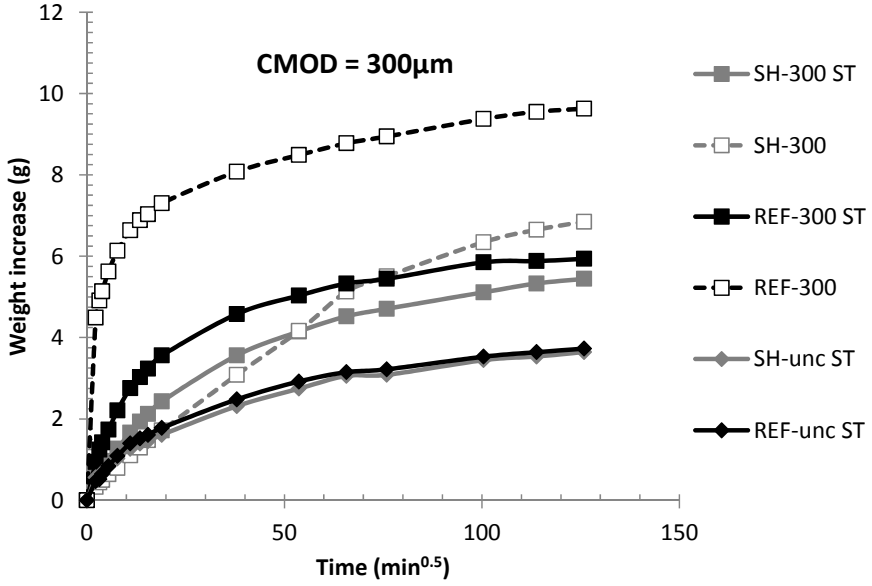

Figure 5. Water absorption rate of the samples with a CMOD=300µm. unc = uncracked samples; ST = the test was made after 90 days in the salt spray chamber.

Obviously, the obtained capillary suction coefficients confirm the results mentioned above. It is remarkable that this parameter remains almost constant in the SH samples for all the considered conditions and regardless of the CMOD specified. Thus, the self-healing mechanism developed is robust enough to resist the external chloride attack. Moreover, the existence of an autogenous self-healing mechanism is again confirmed as the coefficients obtained in the REF samples after the salt spray test are lower than those calculated after 28 days without water exchange. In fact, the higher the CMOD considered, the higher the decrease in the obtained coefficient in humid conditions.

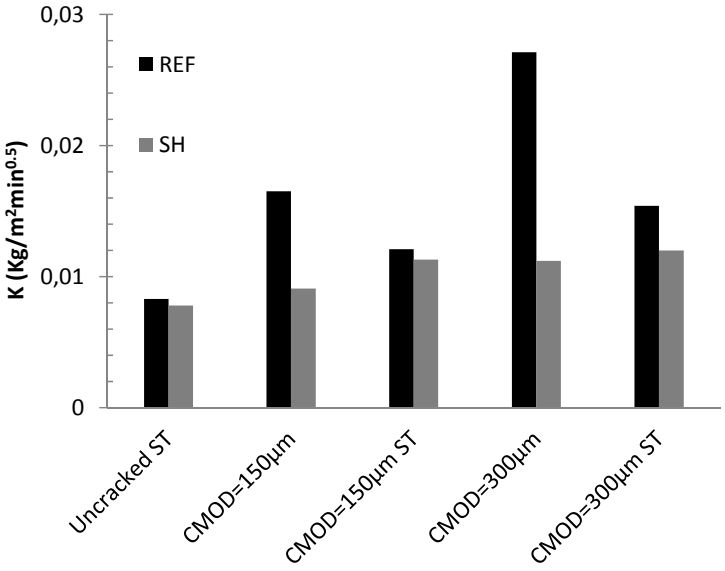

Figure 6. Capillary suction coefficients of the tested samples. ST = the test was made after 90 days in the salt spray chamber.

Therefore, the obtained results suggest a higher efficiency of the self-healing UHPC developed in the severe conditions simulated during the salt spray test because of the synergetic effect of the self-healing additions and the autogenous healing capacity of the concrete.

Influence of the self-healing mechanism in the chloride penetration. After the salt spray test, some samples were split into two halves in order to visually determine chloride penetration by means of the colorimetric method. Figure 7 shows two examples of REF and SH samples with a CMOD of 300µm, after 90 days testing and after the $AgNO_3$ solution spraying. In the pictures showed in Figure 7, it is evident that the surface of SH sample is darker than the one of REF sample which presented many pale purple patches. This indicates significant higher chloride penetration in cracked REF samples, thus the self-healing mechanism developed has also high potential protection against chloride penetration. This reduction of the chloride ingress into the concrete matrix involves a fast self-healing system (Maes, 2014).

Since the colorimetric method is a qualitative technique, further tests will be made in order to quantitatively determine the chloride penetration within the concrete matrix and the subsequent protection promoted by the autonomous self-healing mechanism developed. Anyway, according to the obtained preliminary results it can be remarked that the self-healing mechanism developed is not only robust enough in aggressive chloride environments but also provides resistance to chloride penetration for the cracked concrete matrix.

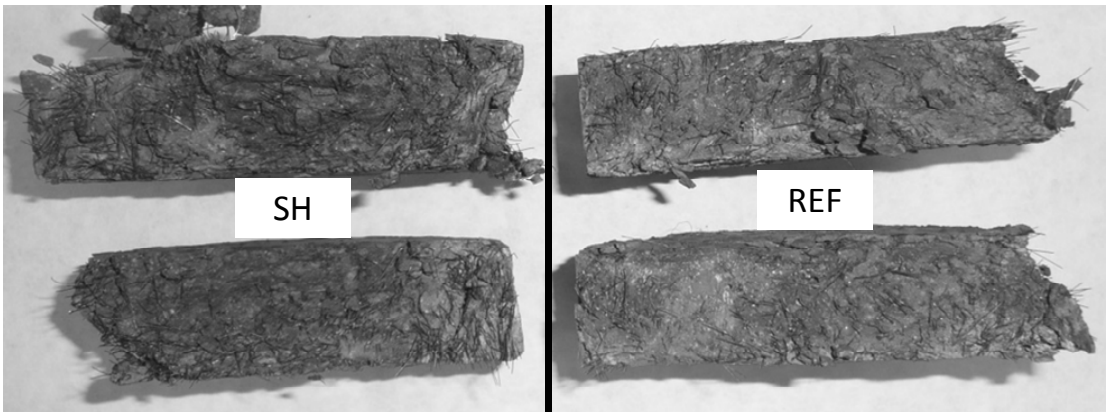

Figure 7. Visual evaluation of chloride penetration of the samples with CMOD=300μm after the salt spray test.

CONCLUSIONS

In this paper, the efficacy and the robustness of the self-healing system of the UHPC developed has been tested in chloride containing environments. During the exposure to these severe conditions, no significant external damage was noticed in the concretes but only an increase of the measured weight with the test time in cracked samples that was attributed to the corrosion of the fibers and to penetration of the pulverized saline solution. This weight increase was slower in the SH samples because the self-healing mechanism limited the penetration of the pulverized saline solution.

Regarding the capillary suction coefficients measured in the un-cracked samples, it can be concluded that the inclusion of the self-healing system improved the durability of the UHPC developed. Moreover, the self-healing mechanism developed is robust enough to resist the external chloride attack and to effectively heal the formed microcracks in the severe exposure conditions considered. In fact, in the UHPC developed self-healing is favored in humid conditions by the existence of an autogenous self-healing mechanism.

Finally, according to the preliminary results obtained with the colorimetric method, high potential protection against chloride penetration can be deduced for the self-healing UHPC studied.

AKNOWLEDGEMENTS

The authors would like to acknowledge the financial support of the BIA2011-29234-C02-01 Project, funded by the Spanish Government (Ministerio de Economía y Competitividad) as well as the funding from the Basque Government through the PI2012-23 Project and Nanoiker Project (Grant No. E11-304) within the Etortek program and under the umbrella of Baskrete.

REFERENCES

Berriozabal, G., and de Miguel, Y.R. (2010). "Synthesis and characterisation of silica nanoparticles bearing different functional groups obtained via a two-stage method." *Physica Status Solidi C*, 7(11-12), 2692-2696.

García Calvo, J.L., Carballosa, P., Perez, G., Erkizia, E., Gaitero, J.J., and Guerrero A. (2014). "Effect of Self-Healing Nano-Additions on the Performance and the Durability Properties of Ultra-High Strength Concretes." *1st Concrete Innovation Conference*. Oslo, 2014.

Jacobsen, S., Marchand, J., and Boisvert, L. (1996). "Effect of cracking and healing on chloride transport in OPC concrete." *Cem. Concr. Res.* 26, 869–881.

Kalzakorta, I., and Erkizia, E. (2010). "Study on the effect of sol-gel parameters on the size and morphology of silica microcapsules containing different organic compounds." *Physica Status Solidi C*, 7(11-12), 2697-2700.

Maes, M., Van Tittelboom, K., and De Belie, N. (2014). "The efficiency of self-healing cementitious materials by means of encapsulated polyurethane in chloride containing environments." *Constr. Build. Mat.* 71, 528-537.

Mihashi, H., and Nishiwaki, T. (2012). "Development of Engineered Self-Healing and Self-Repairing Concrete – State of the Art Report." *J. Adv. Concr. Technol.* 10, 170-184.

Ramm, W., and Biscoping, M. (1998). "Autogenous healing and reinforcement corrosion of water-penetrated separation cracks in reinforced concrete." *Nucl. Eng. Des.* 179, 191–200.

Van Tittelboom, K., Snoeck, D., Wang, J., and De Belie, N. (2013). "Most recent advances in the field of self-healing cementitious materials." *Proc. ICSHM2013 Fourth In. Conf. Self-Healing Mat.*, Nele De Belie, Sybrand van der Zwaag, Eike Gruyaert, Kim van Tittelboom, Brenda Debbaut (ed.), Ghent, Belgium, 406-413.

Wu, M., Johannesson, B., and Geiker, M. (2012). "A review: Self-healing in cementitious materials and engineered cementitious composite as a self-healing material." *Constr. Build. Mat.* 28, 571-583.

Yang, Y., Lepech, M.D., Yang, E.-H., and Li, V.C. (2009). "Autogenous healing of engineered cementitious composites under wet-dry cycles." *Cem. Concr. Res.* 39, 382–390.

Creep of early age concrete under variable stress

Wibke Hermerschmidt[1] and Harald Budelmann[1]

[1]Institute for Building Materials, Concrete Construction and Fire Protection (iBMB), TU Braunschweig, Beethovenstr. 52, D-38106 Braunschweig, Germany; PH (+49) 531-3915508; FAX (+49) 531-3915900; email: w.hermerschmidt@tu-bs.de

ABSTRACT

This contribution aims at describing the creep behaviour of early age concrete with particular focus on the hardening process and the stress history.

The influence of the hardening process on basic creep behaviour is investigated through tensile creep tests at different loading ages under constant stress. Influences of preloading are analysed through creep tests with several different stress histories. Creep tests with a stepped stress change are performed to check the applicability of superposition principle. Tests with slow and continuous stress application are targeted at describing the influence of loading velocity.

The modelling of the viscoelastic behaviour is done using a rheological approach in terms of a generalized Maxwell model with aging spring stiffnesses and dashpot viscosities. The results show a good correlation for all investigated stress histories. This implies that the viscoelastic behaviour of early age concrete in tension can be described by theory of linear viscoelasticity.

1 INTRODUCTION

Modelling approaches for predicting the viscoelastic behaviour of early age concrete are of particular importance for the calculation of the stress development and the cracking risk caused by heat of hydration in hardening concrete structures. Early age concrete shows a very intense viscoelastic behaviour which decreases continuously with progression of the hardening process. There are several models that describe the influence of the hardening process in different ways. Models which define a function for the creep coefficient in which the parameters depend on the degree of reaction at loading were proposed e.g. by Gutsch (2002) and De Schutter and Taerwe (1997). Another way to describe the influence of the hardening process is to define a factor depending on the equivalent age at loading and connect it with a function defining the time dependent evolution of the creep coefficient (Westman 1999, Anders and Müller 2013).

If the behaviour under non constant load is described by means of creep coefficients, the creep strain is calculated assuming the validity of superposition principle.

This approach is only valid for linear viscoelastic behaviour and the analysis of complex stress histories produces high computational costs. Material models which use an incremental formulation are therefore more suitable for application to variable stresses and implementation in numerical simulations. Most of these models use rheological modelling approaches in terms of Kelvin bodies and dashpots with parameters that depend on degree of hydration or equivalent age (Briffaut et. al. 2012, Hauggaard-Nielsen 1997, De Schutter 1999).

The material model presented in this contribution is based on a generalized Maxwell model with aging parameters. The main advantage of this model is that it includes the description of the instantaneous strain at loading in contrast to other rheological models which mostly describe the instantaneous strain through an additional spring which leads to a higher number of parameters. The model is calibrated using creep tests under constant stress. For verification an appropriate number of tests with different stress histories is carried out to show the applicability to increasing and decreasing stress histories at several loading ages and stress levels.

2 EXPERIMENTAL PROGRAM

2.1 Concrete properties

For the experimental investigations a typical mass concrete is defined as reference, the composition and properties are summarised in table 1.

Table 1. Composition and properties of reference concrete

cement type	[-]	CEM III/A 32,5 N		
cement content	[kg/m^3]	300		
w/c-ratio	[-]	0.48		
slump	[cm]	45		
density	[kg/m^3]	2410		
compressive strength 2 d / 7 d / 28 d	[N/mm^2]	15.5	36.7	57.8
tensile strength 2 d / 7 d / 28 d	[N/mm^2]	1.5	2.9	3.9
Young's modulus (tension) 2 d / 7 d / 28 d	[N/mm^2]	26 700	35 600	41 300

2.2 Experimental equipment

A temperature stress testing machine (TSTM) is used to characterise the viscoelastic properties. The functional principle of the TSTM is illustrated in figure 1. The specimens have a cross section of 100 x 100 mm^2. The strains are measured using embedded strain gauges with a length of 60 mm (type PMFL-60). The bone shaped specimen is loaded in tension via the movable cross head. Since the fresh concrete is

filled directly into the temperature controlled moulds of the TSTM, creep testing can start at very early ages and under well known curing conditions. The strain of an unloaded specimen that can deform totally free on a layer of PTFE is measured to separate the shrinkage strain from the creep strain.

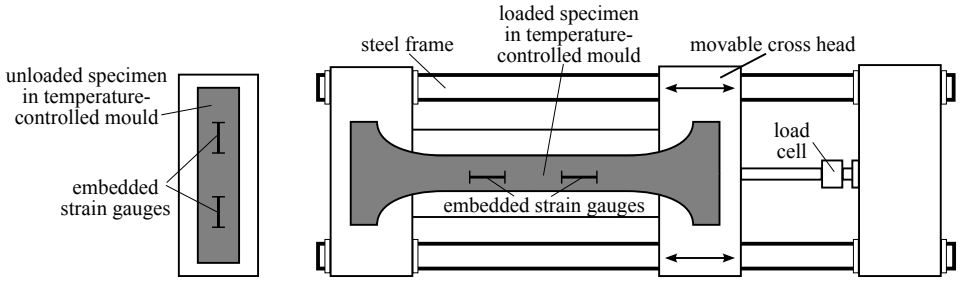

Figure 1. Functional principle of temperature stress testing machine

2.3 Conception of creep tests

Creep tests with constant stress are performed at loading ages of 2, 3, 4 and 7 days to describe the basic creep of aging concrete. For each loading age at least two stress levels between 20% and 65% of the tensile strength at loading are investigated to prove the linearity of tensile creep.

Creep tests with stepwise stress increase or decrease are performed to check the applicability of superposition principle. The points for application and change of stress correspond with the loading ages used in the basic creep tests. Overall, 14 different combinations of stepwise loading and unloading are investigated.

The influence of the loading velocity on creep is studied by tests with a slow loading velocity. The stress is increased or decreased linearly to its final value over a time period of 12 hours. In parallel, the same stress history is applied in 12 small steps (1 step per hour) to check the difference between continuous and stepped loading.

All tests are carried out at a constant temperature of 20°C and under sealed moisture conditions.

3 RESULTS AND MODELLING

3.1 Basic principle of modelling

The chosen rheological modelling approach consists of four Maxwell units and one single spring in parallel (fig. 2). The stiffness of the single spring E_0 and the viscosities of the dashpots η_i increase with increasing concrete age t_e to describe the influence of the hardening process on the viscoelastic behaviour. Their values are found via least squares fitting of the mean strains from the basic creep tests, table 2 summarises the parameters.

Table 2. Parameters for rheological model

f_1	2.81·10^4	[MPa]	f_2	-1.95	[-]	f_3	-1.26	[-]
$d_{1,1}$	2.47·10^2	[MPa·d]	$d_{1,2}$	8.58·10^2	[MPa·d]	$d_{1,3}$	3.24·10^3	[MPa·d]
$d_{1,4}$	4.94·10^7	[MPa·d]	d_2	0.64	[-]	E_1	2.90·10^3	[MPa]
t_k	1	[d]						

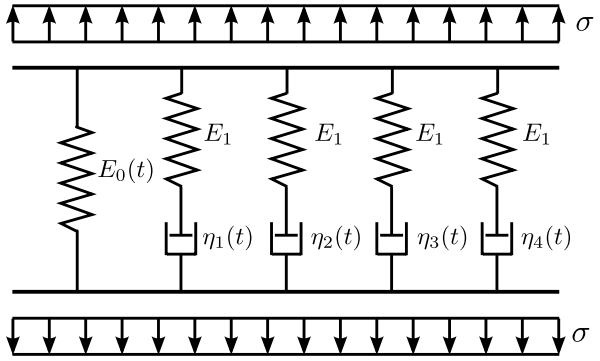

$$E_0(t) = f_1 \cdot \exp\left(f_2 \cdot \left(\frac{t}{t_k}\right)^{f_3}\right)$$

$$\eta_i(t) = d_{1,i} \cdot \left(\frac{t}{t_k}\right)^{d_2}, \quad i = 1 \ldots 4$$

Figure 2. Rheological modelling approach

The constitutive behaviour is described by the following differential equation:

$$a_0 \cdot \sigma + a_1 \cdot \frac{\partial \sigma}{\partial t} + a_2 \cdot \frac{\partial^2 \sigma}{\partial t^2} + a_3 \cdot \frac{\partial^3 \sigma}{\partial t^3} + a_4 \cdot \frac{\partial^4 \sigma}{\partial t^4} = b_0 \cdot \varepsilon + b_1 \cdot \frac{\partial \varepsilon}{\partial t} + b_2 \cdot \frac{\partial^2 \varepsilon}{\partial t^2} + b_3 \cdot \frac{\partial^3 \varepsilon}{\partial t^3} + b_4 \cdot \frac{\partial^4 \varepsilon}{\partial t^4}$$

The coefficients a_0 to a_4 and b_0 to b_4 are functions of the spring stiffnesses E_0 and E_1 and dashpot viscosities η_1 to η_4, the exact definition can be found in (Findley et al. 1989). The equation is solved numerically using the solver 'ode23s' provided by MATLAB, which is a one-step solver based on a modified Rosenbrock formula (Shampine and Reichelt 1997). For an abrupt loading with a stress increment $\Delta\sigma$ at time t_0 the initial conditions are (Boley and Weiner 1997):

$$\begin{aligned}
\varepsilon(t_0) &= \frac{a_4}{b_4} \cdot \Delta\sigma \\
\frac{\partial \varepsilon(t_0)}{\partial t} &= \frac{1}{b_4} \cdot (a_3 \cdot \Delta\sigma - b_3 \cdot \varepsilon(t_0)) \\
\frac{\partial^2 \varepsilon(t_0)}{\partial t^2} &= \frac{1}{b_4} \cdot \left(a_2 \cdot \Delta\sigma - b_2 \cdot \varepsilon(t_0) - b_3 \cdot \frac{\partial \varepsilon(t_0)}{\partial t}\right) \\
\frac{\partial^3 \varepsilon(t_0)}{\partial t^3} &= \frac{1}{b_4} \cdot \left(a_1 \cdot \Delta\sigma - b_1 \cdot \varepsilon(t_0) - b_2 \cdot \frac{\partial \varepsilon(t_0)}{\partial t} - b_3 \cdot \frac{\partial^2 \varepsilon(t_0)}{\partial t^2}\right)
\end{aligned}$$

If an additional stress increment is applied, the initial conditions for the next phase are derived from superposition of the new and the previous loading phase, which means that the initial conditions for the new stress increment like defined above are added to the strain and its derivatives at the end of the previous phase.

3.2 Creep under constant stress

Fig. 3 shows the basic creep behaviour for the different loading ages in terms of a creep compliance which is defined as:

$$J(t) = \frac{\varepsilon(t)}{\sigma(t)}$$

The creep compliance illustrates the linearity of tensile basic creep for the investigated stress levels. The comparison of the different loading ages shows the influence of the hardening process on basic creep. As expected the concrete shows the largest deformation when loaded after 2 days. The magnitude of strains decreases quickly with increasing loading age. The largest decrease occurs between loading at 2 days and 3 days which can be explained by the fact that the largest growth in stiffness occurs in this time period.

The rheological model describes the aforementioned facts with good accuracy.

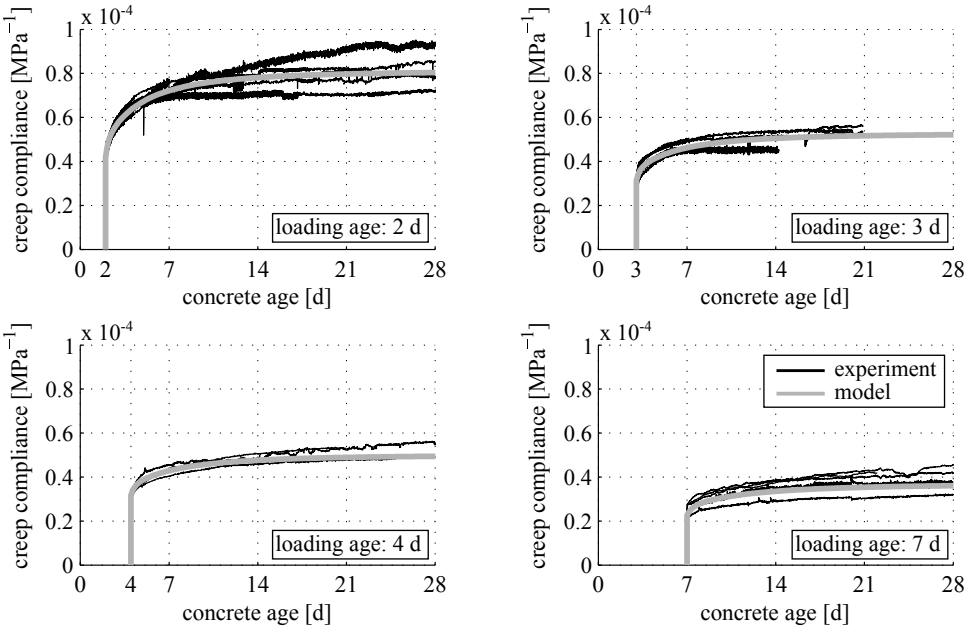

Figure 3. Influence of loading age on basic creep behaviour

3.3 Creep under stepwise changing stresses

Fig. 4 shows three examples for measured and calculated strains under stepwise changing stresses. In these tests the concrete is loaded at an age of 2 days to a stress level of 65% of the tensile strength (first phase), at an age of 4 days it is partially or totally unloaded (second phase) and at an age of 7 days loaded again to a stress level

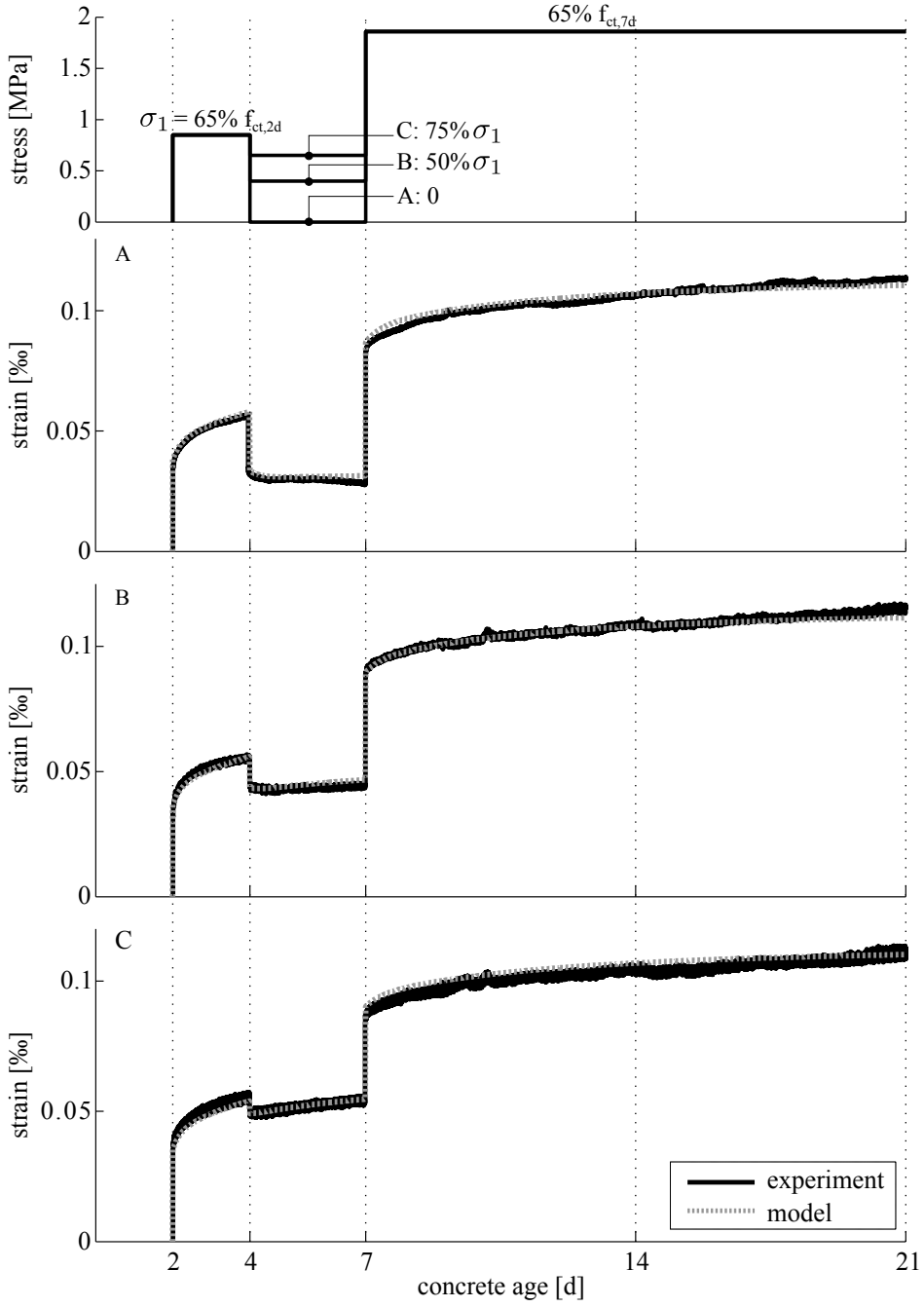

Figure 4. Measured and calculated strains under stepwise changing stresses

of 65% of the current tensile strength (third phase). From the comparison of the three tests the influence of the loading history on the creep behaviour can be recognised. If the concrete is totally unloaded in the second phase (test A), there first is a small back creep and after that the strain remains nearly constant. If the stress is reduced to the half of its value in the second phase (test B), there is also a small back creep but then there is a slow tensile creep again. If the stress is reduced only a little bit in the second phase (test C), there is no noticeable back creep but an ongoing tensile creep with a reduced creep velocity. The creep in the third phase depends on the creep velocity at the end of the second phase and the additionally applied stress increment. In the tests shown here the highest creep velocity at the end of the second phase is combined with the smallest additional stress increment and vice versa. This leads to a nearly identical strain evolution in the third phase for all the three tests. The rheological model is able to describe the strain evolution in every phase with good accuracy which implies that the superposition principle is valid for stepped stress increase and decrease.

3.4 Creep under continuously changing stress

Fig. 5 shows the results from creep tests with slow loading and unloading. The stress is increased and decreased to its final value over a time period of 12 hours. In test A the stress is applied and removed with a constant velocity, in test B the stress is applied and removed in 12 small steps (1 step per hour). The specimen in test B failed at the last load step of the third phase which is a result of the high stress level and the naturally high variance of direct tensile strength of concrete. The results for the first and second loading phase show that the strain evolution is nearly the same for both loading procedures. Hence, complex loading histories may be devided in small stress increments for testing and calculation. The agreement of modeled and measured strains is again very good which proves the applicability of the model for continuously changing stresses.

4 CONCLUSIONS AND OUTLOOK

An experimental program was carried out with the aim to describe the creep behaviour of early age concrete under constant and variable stress. A rheological model in terms of a Maxwell model with age dependent spring and dashpot parameters is chosen to model the creep behaviour. Creep tests with stepped stress changes and the comparison with the modeled results show the validity of the superposition principle. Creep tests with slow and continuous stress application and with stress application in small steps show nearly equal results and a good agreement with the modeled results for both cases. The differential formulation of the model makes it possible to implement the viscoelastic behaviour of early age concrete efficiently into numerical simulations for the prediction of the temperature and stress development in hardening concrete structures.

As all tests have been carried out under tensile stresses, further research will aim

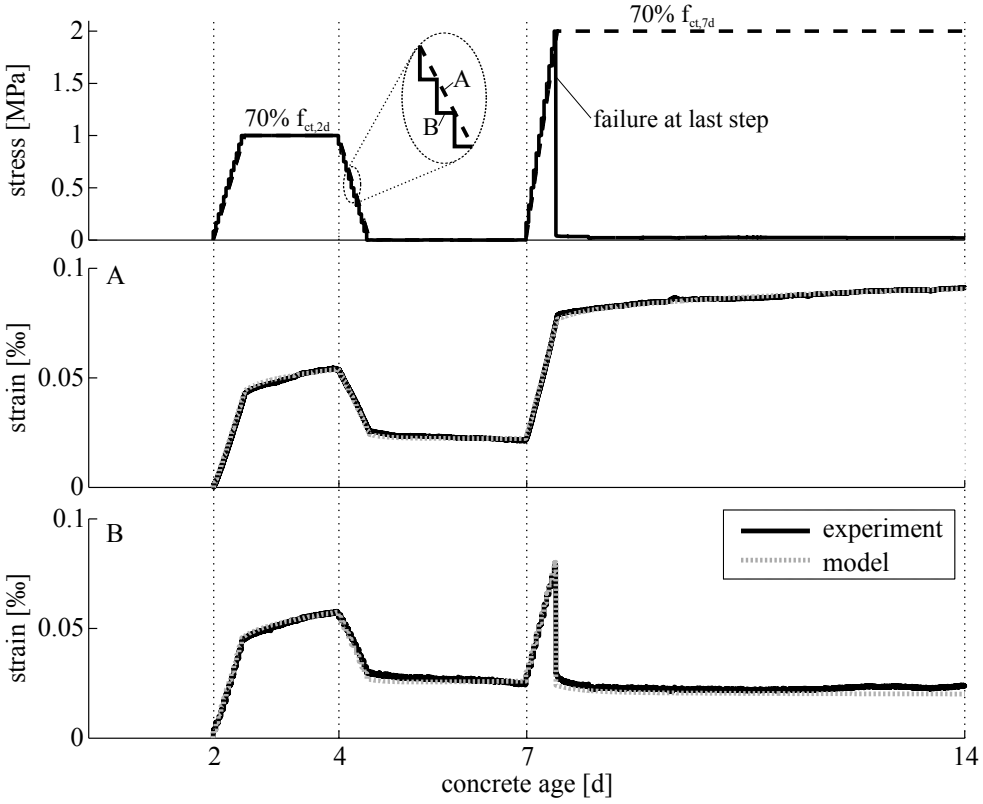

Figure 5. Measured and calculated strains under continuously changing stress

at checking the investigated facts for compressive creep with focus on nonlinearities and their description in rheological models.

Another point for further research is the investigation of different concrete mixes to check the applicability of the rheological model for arbitrary concrete mixes and to find dependencies between the model parameters and concrete properties such as Young's Modulus, compressive strength and composition parameters.

ACKNOWLEDGEMENTS

The authors thank the German Research Foundation (DFG) for the financial support of the present research within the project NO 886/1-1.

REFERENCES

Anders, I. and Müller, H. S. (2013). "Material Law on the Time-dependent Stress-strain Behavior of Young Concretes." *Proc., Mechanics and Physics of Creep, Shrinkage, and Durability of Concrete (CONCREEP-9)*, ASCE, Reston, VA,

467-474

Boley, A. and Weiner, J. H. (1997). *Theory of thermal stresses.* Dover Publications, New York, 502-508

Briffaut, M., Benboudjema, F., Torrenti, J. M. and Nahas, G. (2012) ”Concrete early age basic creep: Experiments and test of rheological modelling approaches.” *Constr. Build. Mater.,* 36, 373-380

Findley, W. N., Lai, J. S. and Onaran, K. (1997) *Creep and relaxation of nonlinear viscoelastic materials.* Dover Publications, New York, 64-77

Gutsch, A.-W. (2002). ”Properties of early age concrete - Experiments and modelling.” *Mater. Struct.,* 35(2), 76-79

Hauggaard-Nielsen, A. B. (1997). *Mathematical modelling and experimental analysis of early age concrete.* Doctoral Thesis, Department of Structural Engineering and Materials, Technical University of Denmark.

Schutter, Geert de and Taerwe, L. (1997). ”Towards a more fundamental non-linear basic creep model for early age concrete.” *Mag. Concr. Res.,* 49(180)

Schutter, Geert de (1999). ”Degree of hydration based Kelvin model for the basic creep of early age concrete.” *Mater. Struct., 32(4),* 260265

Shampine, L. F. and Reichelt, M. W. (1997). ”The MATLAB ode suite.” *SIAM J. Sci. Comput.,* 18(1), 1-22

The Hybrid Approach in Constitutive Modelling of Tension Stiffening Accounting for the Shrinkage Effect

G. Kaklauskas[1] and V. Gribniak[2]

[1]Professor, Head of Department of Bridges and Special Structures, Vilnius Gediminas Technical University, Vilnius LT-10223, Lithuania. E-mail: Gintaris.Kaklauskas@vgtu.lt
[2]Senior Researcher, Head of Research Laboratory of Innovative Building Structures, Vilnius Gediminas Technical University, Vilnius LT-10223, Lithuania. E-mail: Viktor.Gribniak@vgtu.lt

Abstract

Shrinkage, restrained by reinforcement or structural supports, induces tensile stresses in the concrete that might significantly affect the cracking resistance and short-term deformations of reinforced concrete (RC) elements. Incorrect assessment of this effect might result in noticeable errors of constitutive modeling. Recently the authors proposed a methodology for eliminating the shrinkage effect from short-term moment-curvature and tension stiffening relationships. However, due to rather complex issues of convergence and numerical integration, this approach was difficult to apply in practice. To simplify the methodology, the authors introduce a new concept of tension stiffening, the *hybrid* approach. Similar to the reinforcement-attributed approach, it assumes that tension stiffening stresses act in the area equivalent to the area of reinforcement. As in the concrete-related concept, tension stiffening is attributed to the material having the ability to shrink. The constitutive modeling based on the hybrid concept has become straightforward and easily performed by hand that is illustrated using experimental data of RC beam tested by the authors.

INTRODUCTION

The necessity to assess shrinkage influence on deformation behavior of cracked RC members has been recognized in the second half of XX century by Lash (1953), L'Hermite (1955), and other researchers who had conducted comprehensive experimental studies on deformation behavior of reinforced concrete (RC). In the engineering practice, shrinkage along with creep is taken into account in long-term deformation analysis. However, even at first loading, restrained shrinkage of concrete might significantly affect cracking resistance and short-term deformations. Shrinkage, restrained by stiff reinforcement or structural supports, induces tensile stresses in concrete that might significantly affect the cracking resistance and short-term deformations of RC elements.

For decades, development of numerical tools has resulted in extended application of computers in structural design. However, calculation results are always

dependent on the assumed material laws. Though generally neglected, the shrinkage effect may be of high significance in the constitutive modeling, particularly, when it is based on tests of reinforced concrete members (Gribniak et al. 2013b). Application of inadequate constitutive models may cause significant errors in design of RC structures. To prevent the undesirable outcomes, an engineer should recognize, at least, importance of the restrained shrinkage effect on the structural behavior.

Until nowadays, concrete shrinkage along with cracking provides one of the major concerns to the designers because of the inaccuracies and unknowns that surround those (Gribniak et al. 2013a). Tension stiffening is another complicated physical phenomenon in the behavior of RC. Its interdependence with shrinkage to a significant effect contributes to the complexity of the modeling. Recently the authors proposed a methodology for eliminating the shrinkage effect from the short-term moment-curvature and tension stiffening relationships (Kaklauskas and Gribniak 2011). However, due to rather complex issues of convergence and numerical integration (Gribniak et al. 2012), this approach was difficult to apply in practice. The present study proposes an improvement making the methodology a transparent and mechanically sound tool for the analysis. The study introduces a new concept of tension stiffening, the *hybrid* approach. Similar to the reinforcement-attributed approach, it assumes that tension stiffening stresses act in the area equivalent to the area of tensile reinforcement. As in the concrete-related concept, tension stiffening is attributed to the material having the ability to shrink.

Following the idea of simplification reported elsewhere through the closed-form solutions, the authors set up a task of proposing such a solution for the constitutive (inverse) analysis problem. The assumptions taken in the present work made both the inverse analysis technique and the whole methodology of shrinkage elimination much simpler. Assuming the *hybrid* concept of tension stiffening with a single "layer" of tensile concrete and elastic properties for compressive concrete, the inverse analysis has become straightforward. It does not require iterative computations and can be performed by hand.

The proposed methodology can be used not only to remove shrinkage, but also to take into account this effect on short-term deformations of cracked RC members assuming any value of the shrinkage strain. Realization of the proposed methodology is very simple from the numerical point-of-view – an inexperienced user can apply it by means of unsophisticated software. To ease application of the methodology, it is illustrated using experimental data of RC beam tested by the authors.

HYBRID CONCEPT OF TENSION STIFFENING

With a proposed *hybrid* concept of tension stiffening, a closed form solution for the inverse problem has been obtained. This has become possible after reducing a multiple number of concrete layers (with different deformation properties) to two layers, one compressive and one tensile, each of them having homogeneous deformation characteristics. Assumption of the elastic properties allows the reduction of the number of layers of the compressive concrete to a single layer. This permits easy finding of the respective resultant forces and theirs position in the section.

The proposed *hybrid* concept, similarly to the reinforcement-attributed approach, assumes that the tension stiffening stresses are concentrated in the area equivalent to the area of the tensile reinforcement. However, the tension stiffening effect is attributed to the concrete, but not to the reinforcement, assuming that the area of the concrete has the same centroid as the reinforcement (Figure 1). It is supposed that both the elastic and the tension stiffening stresses are carried by the tensile concrete with modified deformation characteristics (in the current study defined by the *inverse* technique). The respective secant deformation modulus E_{ts} is hereafter termed the *equivalent deformation modulus*.

Tension Strain Components

The inverse analysis using the proposed *hybrid* and the original *reinforcement-related* approaches of tension stiffening will result in identical output. However, the original concept is not capable of taking into account the shrinkage effect in the deformation analysis. This important feature of the *hybrid* concept can be explained analyzing strain components in the tensile zone. Due to strain compatibility, reinforcement strain and the *total* strain in the tensile concrete are equal:

$$\varepsilon_{s1} = \varepsilon_{ct,tot}. \tag{1}$$

The total strain in concrete can be split into the components of shrinkage strain ε_{cs} and the strain induced by stress ε_{ct}:

$$\varepsilon_{ct,tot} = \varepsilon_{cs} + \varepsilon_{ct}. \tag{2}$$

Then, for the deformation analysis accounting the shrinkage effect

$$\varepsilon_{s1} = \varepsilon_{cs} + \varepsilon_{ct}. \tag{3}$$

The original *reinforcement-related* approach is unable to evaluate the above equation (as reinforcement material is unable to shrink). Consequently, Equation (3) reads as

$$\varepsilon_{s1} = \varepsilon_{ct}. \tag{4}$$

Assumptions

The proposed concept is based on following assumptions: 1) the smeared crack approach; 2) linear strain distribution within the depth of the section; 3) linear-elastic behavior of reinforcement and compressive concrete; 4) the tensile concrete with modified characteristics shrinks the same amount as the compressive concrete; and 5) creep in concrete due to the long-term effect of restrained shrinkage is neglected.

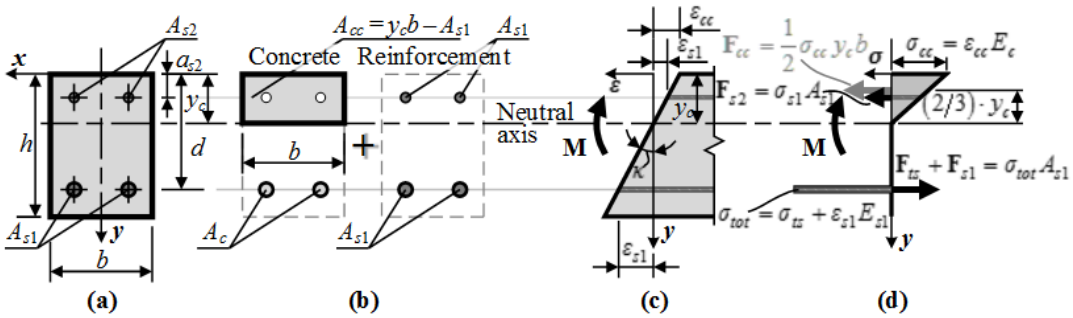

Figure 1. RC section (a) and the hybrid model of the section (b); strain profile (c); stresses and respective internal forces (d) in the section subjected to bending.

Governing Equations for Deformation Analysis

The deformation analysis aims at predicting moment-curvature response of a RC member with a specified material law of tension stiffening. The technique takes into account the influence of shrinkage occurring prior to the flexural loading **M**. Following Kaklauskas et al. (2009), the shrinkage effect is modeled by means of *fictitious* axial force $\mathbf{N}_{cs}$ related to axial stiffness of the concrete section:

$$\mathbf{N}_{sc} = \varepsilon_{cs}\left(E_c\left[y_c b - A_{s2}\right] + E_{ts}A_{ct}\right), \quad A_{ct} = A_{s1}. \tag{5}$$

Here E_c is the elastic modulus of concrete; A_{ct} is the localization area of the tensile concrete; other notations are evident from Figure 1. It is important that the shrinkage strain ε_{cs} is taken negative.

If the centroids of concrete and RC sections do not coincide (in the case of asymmetrically reinforced members or start of cracking of bending members), force $\mathbf{N}_{cs}$ acts with eccentricity exerting bending upon the member:

$$\mathbf{M}_{sc} = \mathbf{N}_{sc}\left(y_{c,c} - y_c\right). \tag{6}$$

Here $y_{c,c}$ is the distance between the top edge and centroid of the concrete net-section.

The centroid of RC section y_c can be found from the condition of equilibrium of the first moments of area (Figure 1d):

$$\frac{1}{2}y_c^2 bE_c + \left(E_{s2} - E_c\right)A_{s2}\left(y_c - a_{s2}\right) - \left(E_{s1} + E_{ts}\right)A_{s1}\left(d - y_c\right) = 0. \tag{7}$$

This equation can be rearranged as a square polynomial with coefficients

$$C_2 = \frac{1}{2}bE_c; \quad C_1 = \left(E_{s2} - E_c\right)A_{s2} + \left(E_{s1} + E_{ts}\right)A_{s1}; \tag{8}$$
$$C_0 = \left(E_{s2} - E_c\right)A_{s2}a_{s2} + \left(E_{s1} + E_{ts}\right)A_{s1}d.$$

Indexes of the coefficients are related to the power of the variable y_c in the polynomial. From the condition $0 < y_c \le h$, the solution is

$$y_c = -\frac{C_1 - \sqrt{C_1^2 - 4C_2C_0}}{2C_2}. \tag{9}$$

The centroid of concrete net-section $y_{c,c}$ can be calculated as

$$y_{c,c} = \frac{E_c\left(y_c^2 b/2 - A_{s2}a_{s2}\right) + E_{ts}A_{s1}d}{E_c\left(y_c b - A_{s2s}\right) + E_{ts}A_{s1}}. \tag{10}$$

Curvature κ (Figure 1b) is determined as

$$\kappa = \frac{\mathbf{M} + \mathbf{M}_{cs}}{[EI]}. \tag{11}$$

Taking into consideration relation (1), the total strain in the tensile concrete $\varepsilon_{c,tot}$ and strain in the tensile reinforcement ε_s can be found as

$$\varepsilon_s \left[= \varepsilon_{c,tot} \right] = \frac{\mathbf{M} + \mathbf{M}_{cs}}{[EI]} (d - y_c) + \frac{\mathbf{N}_{cs}}{[EA]} = \kappa (d - y_c) + \frac{\mathbf{N}_{cs}}{[EA]}. \tag{12}$$

In Equations (11) and (12), flexural $[EI]$ and axial $[EA]$ stiffnesses are determined as

$$\begin{gathered} [EI] = \frac{1}{3} E_c y_c^3 b + (E_{s2} - E_c) A_{s2} (y_c - a_{s2})^2 + (E_{s1} + E_{ts}) A_{s1} (d - y_c)^2, \\ [EA] = E_c y_c b + (E_{s2} - E_c) A_{s2} + (E_{s1} + E_{ts}) A_{s1}. \end{gathered} \tag{13}$$

CONSTITUTIVE MODELING OF THE HYBRID TENSION STIFFENING

The deformation analysis procedure, described above, requires specification of a proper material model for tensile concrete. In this manuscript, the hybrid tension stiffening is modeled using experimental data of RC beam tested by the authors with the help of the modified numerical procedure (Kaklauskas et al. 2011).

The constitutive (inverse) analysis is based on the equations of equilibrium and strain compatibility, derived for an experimental moment-curvature relation assuming geometrical characteristics of the section (Figure 1) and elastic properties (moduli of elasticity) of the materials. The equilibrium equation of axial forces can be written as

$$\begin{gathered} \mathbf{F}_{ts} + \mathbf{F}_{s1} - \mathbf{F}_{cc} - \mathbf{F}_{s2} = 0, \\ \mathbf{F}_{ts} = \sigma_{ts} A_{s1}; \quad \mathbf{F}_{s1} = \sigma_{s1} A_{s1}; \quad \mathbf{F}_{cc} = \frac{1}{2} \sigma_{cc} y_c b; \quad \mathbf{F}_{s2} = \left(\sigma_{s2} - \sigma_{cc} \left[1 - \frac{a_{s2}}{y_c} \right] \right) A_{s2}. \end{gathered} \tag{14}$$

Here σ_{ts} is the equivalent tension stiffening stress in tensile concrete; other notations are evident from Figure 1. The equilibrium equation of bending moments in respect to the centroid of the tensile is follow

$$\mathbf{F}_{cc} \left(d - \frac{y_c}{3} \right) + \mathbf{F}_{s2} (d - a_{s2}) - \mathbf{M} = 0. \tag{15}$$

Expressing stresses in compressive reinforcement σ_{s1} and compressive concrete σ_{cc} through the strains, Equations (14) and (15) read as

$$\begin{gathered} (\sigma_{ts} + \varepsilon_{s1} E_{s1}) A_{s1} - \varepsilon_{cc} E_c y_c b / 2 - \varepsilon_{s2} (E_{s2} - E_c) A_{s2} = 0, \\ \frac{1}{2} \varepsilon_{cc} E_c y_c b \left(d - \frac{y_c}{3} \right) + \varepsilon_{s2} (E_{s2} - E_c) A_{s2} (d - a_{s2}) - \mathbf{M} = 0. \end{gathered} \tag{16}$$

For given curvature κ, the characteristic strains (Figure 1c) can be expressed through the conditions of strain compatibility:

$$\varepsilon_{cc} = y_c \kappa, \quad \varepsilon_{s2} = (y_c - a_{s2}) \kappa, \quad \varepsilon_{ct} = \varepsilon_{s1} = (d - y_c) \kappa. \tag{17}$$

Using the above expressions, the equilibrium equation of bending moments (16) can be rearranged as

$$\frac{1}{2} E_c y_c^2 b \left(d - \frac{y_c}{3} \right) \kappa + (E_{s2} - E_c) A_{s2} (d - a_{s2}) (y_c - a_{s2}) \kappa - \mathbf{M} = 0 \tag{18}$$

and expressed as a third order polynomial (assuming position of the neutral axis y_c as variable) with coefficients

$$C_3 = \frac{1}{6} bE_c\kappa; \quad C_2 = \frac{1}{2} bE_c d\kappa; \quad C_1 = (E_{s2} - E_c) A_{s2} (d - a_{s2})\kappa; \\ C_0 = -(E_{s2} - E_c) A_{s2} (d - a_{s2}) a_{s2}\kappa - \mathbf{M}. \tag{19}$$

Indexes of the coefficients are related to the power of the variable y_c in the polynomial. From the condition $0 < y_c \le h$, the proper solution is

$$y_c = -\frac{2\sqrt{C_2^2 - 2C_3C_1}}{3C_3} \sin\left(\frac{1}{3}\arcsin\left[\frac{9C_3C_2C_1 - 27C_3^2C_0 - 2C_2^3}{2\{C_2^2 - 2C_3C_1\}^{3/2}}\right]\right) - \frac{C_2}{3C_3}. \tag{20}$$

The equivalent tension stiffening stress is calculated from the equilibrium equation of axial forces (16) using expressions (17):

$$\sigma_{ts} = \left[E_c y_c^2 b/2 + (E_{s2} - E_c) A_{s2} (y_c - a_{s2})\right]\kappa \Big/ A_{s1} - E_{s1} (d - y_c)\kappa. \tag{21}$$

The corresponding equivalent deformation modulus (needed for the deformation analysis) is assessed as

$$E_{ts} = \sigma_{ts} / \varepsilon_{ct}. \tag{22}$$

A NUMERICAL EXAMPLE

This section presents examples of application of the *Microsoft Excel* data tables for constitutive modeling of the hybrid tension stiffening and deformation analysis accounting for the shrinkage effect. The numerical examples use the data of beam *S1-4* tested by the authors. The beam had 3000 mm span and rectangular section reinforced with two 22 mm bars. Concrete mix proportion of C35/45 grade was used. The water/cement and aggregate/cement ratios by weight were taken as 0.42 and 2.97, respectively. The beam was kept for 68 days in the laboratory conditions under average humidity of 70% that resulted in the free shrinkage strain $\varepsilon_{cs} = -225$ μstrains. It was tested under a four-point-bending scheme with 1000 mm pure bending zone.

Constitutive Modeling: Deriving the Hybrid Tension Stiffening Relation

A fragment of the *Excel* worksheet with data tables for the constitutive analysis is shown in Figure 2. The table "Input Parameters" represents geometric and material properties. In this table, h and b are the height and the width of the section; d, A_{s1}, and E_{s1} are the distance from the top edge of the section to the tensile reinforcement, its area and elastic modulus, respectively; a_{s2}, A_{s2}, and E_{s2} are the same parameters for the compressive reinforcement; E_c is the elastic modulus of the concrete. Other data are the experimental moment-curvature relations (Figure 3a), specified in the cell range D4:E58. The cells I4:M58 contain formulas, described in Table 1. The analysis results in the equivalent tension stiffening stress-strain σ_{ts}-ε_c relations (Figure 3b) and the equivalent deformation modulus E_{ct} (Figure 3c).

Deformation Analysis: Deriving the Shrinkage-Free Moment-Curvature Diagram

A fragment of the *Excel* worksheet that contains the data tables for the deformation analysis is shown in Figure 4. The table "Input Parameters" represents the same geometric and material data as described above (Figure 2). In addition, cells B11 and B12 indicate a negative (shrinkage) and a positive (expansion) strain of concrete. Negative values are used in the deformation analyses (accounting for shrinkage), whereas positive ones are taken in the cases when the shrinkage-free constitutive laws are derived. The hybrid tension stiffening relation (determined at the previous stage) is specified in the cell range D4:E58; the target loads – in the cells G4:G58.

The deformation analysis requires to perform a simple iterative computation as the equivalent deformation modulus varies with strain. It is important to note that, by default, *Excel* does not permit iterative calculations; thus, the *Enable Iterative Calculation* box must be activated in the *Formulas* section of the *Excel Options* dialog window. The *Array Formula* manages a numerical expression of the tension stiffening stress-strain relationship (Walkenbach 2013). Table 2 presents the formulas used in the deformation analysis. The moment-curvature diagram with the eliminated shrinkage effect (*shrinkage-free*) is shown in Figure 3a along with the experimental relationship. The modified curvatures can be used for obtaining the *shrinkage-free* tension stiffening law (Kaklauskas and Gribniak 2011).

	A	B	C	D	E	F	G	H	I	J	K	L	M
1	**Input Parameters**			**Experimental Data**							**Tension Stiffening Model**		
2	h	0.300 m		**Moment**	**Curvature**	**Coefficients**				**Heigth**	**Strain**	**Stress**	**Modulus**
3	b	0.280 m		**M**, MNm	κ, 1/m	C_0	C_1	C_2	C_3	y_c, m	ε_{ct}	σ_{ts}, MPa	E_{ts}, MPa
4	d	0.267 m		0	0	0	0	0	0	0.1575	0	0	1.299E+6
5	A_{s1}	7.600E-4 m²		3.147E-3	1.181E-4	-3.154E-3	3.092E-4	0.1559	-0.1949	0.1575	1.289E-5	16.74	1.299E+6
6	E_{s1}	1.993E+5 MPa		4.117E-3	1.546E-4	-4.126E-3	4.045E-4	0.2039	-0.2550	0.1575	1.686E-5	21.90	1.299E+6
7	a_{s2}	0.024 m		5.207E-3	1.955E-4	-5.219E-3	5.115E-4	0.2579	-0.3225	0.1575	2.133E-5	27.70	1.299E+6
8	A_{s2}	5.732E-5 m²		6.132E-3	2.302E-4	-6.146E-3	6.024E-4	0.3038	-0.3798	0.1575	2.512E-5	32.62	1.299E+6
9	E_{s2}	2.235E+5 MPa		7.307E-3	2.743E-4	-7.324E-3	7.179E-4	0.3620	-0.4525	0.1575	2.993E-5	38.87	1.299E+6
10	E_c	3.539E+4 MPa		8.147E-3	3.058E-4	-8.166E-3	8.004E-4	0.4036	-0.5046	0.1575	3.337E-5	43.33	1.299E+6
11				8.992E-3	3.376E-4	-9.013E-3	8.834E-4	0.4454	-0.5569	0.1575	3.683E-5	47.83	1.299E+6
12				1.035E-2	3.884E-4	-1.037E-2	1.016E-3	0.5125	-0.6408	0.1575	4.237E-5	55.04	1.299E+6
13				1.131E-2	4.375E-4	-1.134E-2	1.145E-3	0.5773	-0.7218	0.1548	4.891E-5	59.37	1.214E+6
14				1.209E-2	4.852E-4	-1.212E-2	1.270E-3	0.6402	-0.8004	0.1516	5.580E-5	62.37	1.118E+6
15				1.301E-2	5.313E-4	-1.304E-2	1.390E-3	0.7011	-0.8766	0.1501	6.191E-5	66.56	1.075E+6
16				1.432E-2	6.031E-4	-1.435E-2	1.578E-3	0.7958	-0.9949	0.1475	7.183E-5	72.19	1.005E+6
17				1.525E-2	6.813E-4	-1.529E-2	1.783E-3	0.8989	-1.124	0.1427	8.441E-5	74.67	8.845E+5
48				7.129E-2	1.036E-2	-7.194E-2	2.711E-2	13.67	-17.09	0.07512	1.984E-3	-7.107	-3.582E+3
49				7.350E-2	1.071E-2	-7.417E-2	2.803E-2	14.13	-17.67	0.07502	2.052E-3	-8.698	-4.239E+3
50				7.556E-2	1.106E-2	-7.625E-2	2.895E-2	14.60	-18.25	0.07483	2.122E-3	-11.48	-5.410E+3
51				7.751E-2	1.134E-2	-7.821E-2	2.967E-2	14.96	-18.70	0.07486	2.174E-3	-11.24	-5.171E+3
52				7.958E-2	1.167E-2	-8.031E-2	3.053E-2	15.39	-19.24	0.07478	2.238E-3	-12.74	-5.695E+3
53				8.129E-2	1.194E-2	-8.204E-2	3.124E-2	15.75	-19.69	0.07471	2.291E-3	-14.03	-6.124E+3
54				8.333E-2	1.228E-2	-8.409E-2	3.214E-2	16.20	-20.26	0.07457	2.358E-3	-16.51	-7.001E+3
55				8.513E-2	1.263E-2	-8.592E-2	3.305E-2	16.67	-20.84	0.07430	2.429E-3	-20.93	-8.619E+3
56				8.606E-2	1.280E-2	-8.686E-2	3.348E-2	16.88	-21.11	0.07422	2.462E-3	-22.47	-9.128E+3
57				8.921E-2	1.327E-2	-9.004E-2	3.473E-2	17.51	-21.90	0.07419	2.554E-3	-23.71	-9.283E+3
58				9.107E-2	1.361E-2	-9.192E-2	3.561E-2	17.95	-22.45	0.07402	2.621E-3	-27.01	-1.031E+4

Figure 2. A fragment of *Excel* data table for the constitutive analysis.

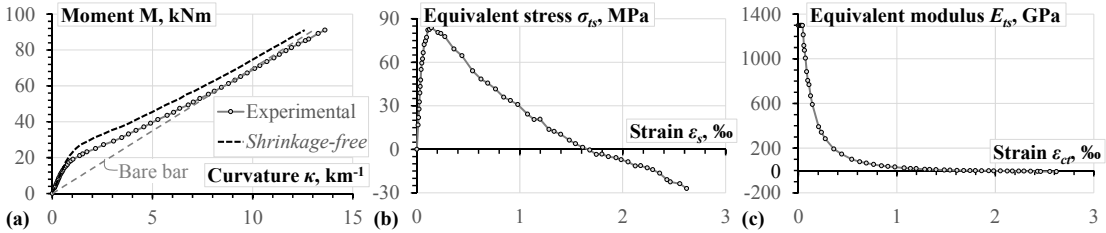

Figure 3. Experimental and *shrinkage-free* moment-curvature diagrams (a), the equivalent tension stiffening stresses (b) and deformation modulus (c).

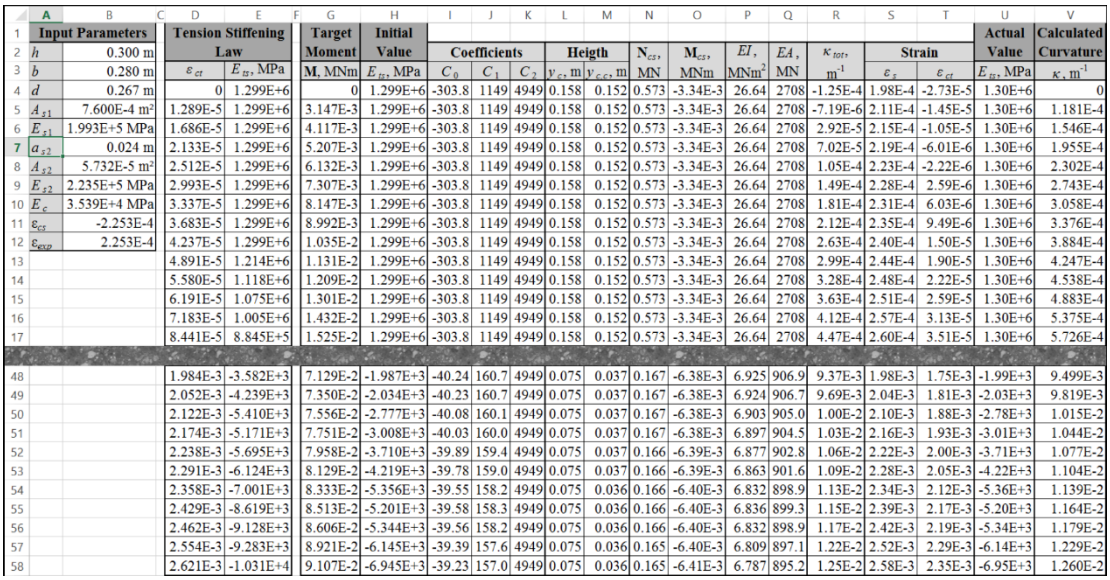

	A	B	C	D	E	F	G	H	I	J	K	L	M	N	O	P	Q	R	S	T	U	V
1	Input Parameters			Tension Stiffening Law			Target Moment	Initial Value	Coefficients			Heigth		N_{cs},	M_{cs},	EI,	EA,	κ_{tot},	Strain		Actual Value	Calculated Curvature
2	h	0.300 m																				
3	b	0.280 m		ε_{ct}	E_{ts}, MPa		M, MNm	E_{ts}, MPa	C_0	C_1	C_2	y_c, m	$y_{c.c}$, m	MN	MNm	MNm^2	MN	m^{-1}	ε_s	ε_{ct}	E_{ts}, MPa	κ, m^{-1}
4	d	0.267 m		0	1.299E+6		0	1.299E+6	-303.8	1149	4949	0.158	0.152	0.573	-3.34E-3	26.64	2708	-1.25E-4	1.98E-4	-2.73E-5	1.30E+6	0
5	A_{s1}	7.600E-4 m^2		1.289E-5	1.299E+6		3.147E-3	1.299E+6	-303.8	1149	4949	0.158	0.152	0.573	-3.34E-3	26.64	2708	-7.19E-6	2.11E-4	-1.45E-5	1.30E+6	1.181E-4
6	E_{s1}	1.993E+5 MPa		1.686E-5	1.299E+6		4.117E-3	1.299E+6	-303.8	1149	4949	0.158	0.152	0.573	-3.34E-3	26.64	2708	2.92E-5	2.15E-4	-1.05E-5	1.30E+6	1.546E-4
7	a_{s2}	0.024 m		2.133E-5	1.299E+6		5.207E-3	1.299E+6	-303.8	1149	4949	0.158	0.152	0.573	-3.34E-3	26.64	2708	7.02E-5	2.19E-4	-6.01E-6	1.30E+6	1.955E-4
8	A_{s2}	5.732E-5 m^2		2.512E-5	1.299E+6		6.132E-3	1.299E+6	-303.8	1149	4949	0.158	0.152	0.573	-3.34E-3	26.64	2708	1.05E-4	2.23E-4	-2.22E-6	1.30E+6	2.302E-4
9	E_{s2}	2.235E+5 MPa		2.993E-5	1.299E+6		7.307E-3	1.299E+6	-303.8	1149	4949	0.158	0.152	0.573	-3.34E-3	26.64	2708	1.49E-4	2.28E-4	2.59E-6	1.30E+6	2.743E-4
10	E_c	3.539E+4 MPa		3.337E-5	1.299E+6		8.147E-3	1.299E+6	-303.8	1149	4949	0.158	0.152	0.573	-3.34E-3	26.64	2708	1.81E-4	2.31E-4	6.03E-6	1.30E+6	3.058E-4
11	ε_{cs}	-2.253E-4		3.683E-5	1.299E+6		8.992E-3	1.299E+6	-303.8	1149	4949	0.158	0.152	0.573	-3.34E-3	26.64	2708	2.12E-4	2.35E-4	9.49E-6	1.30E+6	3.376E-4
12	ε_{exp}	2.253E-4		4.237E-5	1.299E+6		1.035E-2	1.299E+6	-303.8	1149	4949	0.158	0.152	0.573	-3.34E-3	26.64	2708	2.63E-4	2.40E-4	1.50E-5	1.30E+6	3.884E-4
13				4.891E-5	1.214E+6		1.131E-2	1.299E+6	-303.8	1149	4949	0.158	0.152	0.573	-3.34E-3	26.64	2708	2.99E-4	2.44E-4	1.90E-5	1.30E+6	4.247E-4
14				5.580E-5	1.118E+6		1.209E-2	1.299E+6	-303.8	1149	4949	0.158	0.152	0.573	-3.34E-3	26.64	2708	3.28E-4	2.48E-4	2.22E-5	1.30E+6	4.538E-4
15				6.191E-5	1.075E+6		1.301E-2	1.299E+6	-303.8	1149	4949	0.158	0.152	0.573	-3.34E-3	26.64	2708	3.63E-4	2.51E-4	2.59E-5	1.30E+6	4.883E-4
16				7.183E-5	1.005E+6		1.432E-2	1.299E+6	-303.8	1149	4949	0.158	0.152	0.573	-3.34E-3	26.64	2708	4.12E-4	2.57E-4	3.13E-5	1.30E+6	5.375E-4
17				8.441E-5	8.845E+5		1.525E-2	1.299E+6	-303.8	1149	4949	0.158	0.152	0.573	-3.34E-3	26.64	2708	4.47E-4	2.60E-4	3.51E-5	1.30E+6	5.726E-4
48				1.984E-3	-3.582E+3		7.129E-2	-1.987E+3	-40.24	160.7	4949	0.075	0.037	0.167	-6.38E-3	6.925	906.9	9.37E-3	1.98E-3	1.75E-3	-1.99E+3	9.499E-3
49				2.052E-3	-4.239E+3		7.350E-2	-2.034E+3	-40.23	160.7	4949	0.075	0.037	0.167	-6.38E-3	6.924	906.7	9.69E-3	2.04E-3	1.81E-3	-2.03E+3	9.819E-3
50				2.122E-3	-5.410E+3		7.556E-2	-2.777E+3	-40.08	160.1	4949	0.075	0.037	0.167	-6.38E-3	6.903	905.0	1.00E-2	2.10E-3	1.88E-3	-2.78E+3	1.015E-2
51				2.174E-3	-5.171E+3		7.751E-2	-3.008E+3	-40.03	160.0	4949	0.075	0.037	0.167	-6.38E-3	6.897	904.5	1.03E-2	2.16E-3	1.93E-3	-3.01E+3	1.044E-2
52				2.238E-3	-5.695E+3		7.958E-2	-3.710E+3	-39.89	159.4	4949	0.075	0.037	0.166	-6.39E-3	6.877	902.8	1.06E-2	2.22E-3	2.00E-3	-3.71E+3	1.077E-2
53				2.291E-3	-6.124E+3		8.129E-2	-4.219E+3	-39.78	159.0	4949	0.075	0.037	0.166	-6.39E-3	6.863	901.6	1.09E-2	2.28E-3	2.05E-3	-4.22E+3	1.104E-2
54				2.358E-3	-7.001E+3		8.333E-2	-5.356E+3	-39.55	158.2	4949	0.075	0.036	0.166	-6.40E-3	6.832	898.9	1.13E-2	2.34E-3	2.12E-3	-5.36E+3	1.139E-2
55				2.429E-3	-8.619E+3		8.513E-2	-5.201E+3	-39.58	158.3	4949	0.075	0.036	0.166	-6.40E-3	6.836	899.3	1.15E-2	2.39E-3	2.17E-3	-5.20E+3	1.164E-2
56				2.462E-3	-9.128E+3		8.606E-2	-5.344E+3	-39.56	158.2	4949	0.075	0.036	0.166	-6.40E-3	6.832	898.9	1.17E-2	2.42E-3	2.19E-3	-5.34E+3	1.179E-2
57				2.554E-3	-9.283E+3		8.921E-2	-6.145E+3	-39.39	157.6	4949	0.075	0.036	0.165	-6.40E-3	6.809	897.1	1.22E-2	2.52E-3	2.29E-3	-6.14E+3	1.229E-2
58				2.621E-3	-1.031E+4		9.107E-2	-6.945E+3	-39.23	157.0	4949	0.075	0.036	0.165	-6.41E-3	6.787	895.2	1.25E-2	2.58E-3	2.35E-3	-6.95E+3	1.260E-2

Figure 4. A fragment of *Excel* data table for the deformation analysis.

Table 1. Formulas for solving the constitutive analysis problem.

Cell	*Formula*	*Eqn.*
F5	=–E5*(B$9–B$10)*B$8*B$7*(B$4–B$7)–D5	(19)
G5	=E5*(B$9–B$10)*B$8*(B$4–B$7)	(19)
H5	=E5*B$10*B$3*B$4/2	(19)
I5	=–E5*B$10*B$3/6	(19)
J5	=–2*SQRT(H5^2–3*I5*G5)/3/I5*SIN(ASIN(–(27*I5^2*F5–9*I5*H5*G5+2*H5^3)/2/(H5^2–3*I5*G5)^(3/2))/3)–H5/3/I5	(20)
K5	=E5*(B$4–J5)	(17)
L5	=E5/B$5*(B$10*J5^2*B$3/2+(B$9–B$10)*B$8*(J5–B$7))–K5*B$6	(21)
M5	=L5/K5	(22)

Comments

1. The above equations specified in the cells of Line 5 can be copy-pasted (as "formulas") in the Lines 6 to 58.
2. In Line 4, the cells contain "0" value with the exception of the cells J4 and M4, which refer to the cells of Line 5, i.e. "=J5" and "=M5", respectively.

Table 2. Formulas for the deformation analysis accounting the shrinkage effect.

Cell	*Formula*	*Eqn.*
H4	=U4	–
I4	=–B$8*B$7*(B$9–B$10)–B$5*B$4*(B$6+H4)	(8)
J4	=B$8*(B$9–B$10)+B$5*(B$6+H4)	(8)
K4	=B$10*B$3/2	(8)
L4	=–(J4–SQRT(J4^2–4*K4*I4))/2/K4	(9)
M4	=(B$10*(L4^2*B$3/2–B$7*B$8)+B$4*B$5*H4)/(B$10*(L4*B$3–B$8)+H4*B$5)	(10)
N4	=B$12*(B$10*(B$3*L4–B$8)+H4*B$5)	(5)
O4	=N4*(M4–L4)	(6)
P4	=B$10*L4^3*B$3/3+(B$9–B$10)*B$8*(L4–B$7)^2+(B$6+H4)*B$5*(B$4–L4)^2	(13)
Q4	=B$10*L4*B$3+(B$9–B$10)*B$8+(B$6+H4)*B$5	(13)
R4	=(G4+O4)/P4	(11)

S4	=R4*(B$4–L4)+N4/Q4	(12)
T4	=S4–B$12	(2)
U4	{=IF(T4<D$4;E$4;IF(T4<D$58;SUM(IF(NOT(D$4:D$57>T4);1;0)*IF(D$5:D$58>T4;1;0)*((E$4:E$57+(E$5:E$58–E$4:E$57)*(T4–D$4:D$57)/(D$5:D$58–D$4:D$57))));E$58))}	–
V4	=R4–R$4	–

Comments

1. The above equations specified in the cells of Line 5 can be copy-pasted (as "formulas") in the Lines 6 to 58.
2. The reference to the cell 'U4', entered in the cell 'H4', is termed the "Circular Reference". It controls the iterative calculations (enabled using the Excel Options dialog window).
3. The cell 'U4' contains the so-called 'Array Formula' – it is entered by pressing 'Ctrl+Shift+Enter' (but do not typing the curly brackets).
4. The cell 'V4' contains the formula that shifts the shrinkage-free moment-curvature diagram into the origin of the coordinates.

CONCLUSIONS

Based on the earlier researches, the authors propose a simplified methodology accounting for shrinkage in the short-term deformation and constitutive analyses of RC elements in flexure. The study highlighted that:

1. Assuming elastic properties for compressive concrete and the innovative *hybrid* concept of tension stiffening with a single "layer" of tensile concrete, the constitutive analysis has become straightforward. It does not require iterative computations and can be performed by hand.
2. The proposed methodology can be used not only to remove the shrinkage effect, but also to take into account its influence on short-term deformations of cracked RC members subjected to flexure.

ACKNOWLEDGEMENT

The authors gratefully acknowledge the financial support provided by the *Research Council of Lithuania* (Project No. MIP–050/2014).

REFERENCES

Gribniak, V., Kaklauskas, G., Kacianauskas, R., and Kliukas, R. (2012). "Improving Efficiency of Inverse Constitutive Analysis of Reinforced Concrete Flexural Members." *Sci. Res. Essays*, 7(8), 923-938.

Gribniak, V., Kaklauskas, G., Kliukas, R., and Jakubovskis, R. (2013a). "Shrinkage Effect on Short-Term Deformation Behavior of Reinforced Concrete – When it Should Not be Neglected." *Mater. Des.*, 51, 1060-1070.

Gribniak, V., Torres, L., Kaklauskas, G., Daniunas, A., Kacianauskas, R., and Jakubovskis, R. (2013b). "Prediction of Concrete Shrinkage Occurring Prior to External Loading and Effect on Short-Term Constitutive Modeling and Design." *Adv. Structural Eng.*, 16(6), 1061-1080.

Kaklauskas, G. and Gribniak, V. (2011). "Eliminating Shrinkage Effect from Moment-Curvature and Tension-Stiffening Relationships of Reinforced Concrete Members." *J. Struct. Eng.*, 137(12), 1460-1469.

Kaklauskas, G., Gribniak, V., Bacinskas, D., and Vainiunas, P. (2009). "Shrinkage Influence on Tension Stiffening in Concrete Members," *Eng. Struct.*, 31(6), 1305-1312.

Kaklauskas, G., Gribniak, V., Salys, D., Sokolov, A., and Meskenas, A. (2011). "Tension-Stiffening Model Attributed to Tensile Reinforcement for Concrete Flexural Members," *Procedia Eng.*, 14, 1433-1438.

Lash, S.D. (1953). "Ultimate strength and cracking resistance of lightly reinforced beams", *ACI J. Proc.*, 49(2), 573-582.

L'Hermite, R. (1955). *Idées actuelles sur la technologie du béton. Collection de l'Institut technique du bâtiment et des travaux publics*, Documentation technique du bâtiment et des travaux publics. Paris, France (in French).

Walkenbach, J. (2013). *Excel 2013 Formulas*. John Wiley & Sons, Hoboken, NJ.

CEOS.FR Experiments for the Crack Control of Concrete at an Early Age

L. Buffo-Lacarrière[1] and J. M. Torrenti[2]

[1]Université de Toulouse; UPS, INSA; LMDC (Laboratoire Matériaux et Durabilité des Constructions); 135, avenue de Rangueil; F-31 077 Toulouse Cedex 04, France.
[2]CEOS.FR Program Partners (www.ceosfr.org); and Université Paris-Est, IFSTTAR, Department Materials and Structures. E-mail: jean-michel.torrenti@ifsttar.fr

Abstract

Within the CEOS.FR national research project, several experiments on massive concrete structures were conducted in order to improve the knowledge on the cracking phenomenon and, at last, to provide the designers with reliable crack design codes, able to give a reasonable appreciation of crack width and spacing for these structures as well as for classical ones. In this paper, experiments where deformations at early age are restrained are presented. Three restrained shrinkage testing bodies that are I-shaped, with a central part which has a cross-section of 0.80 mx0.50 m were tested. Two largely dimensioned steel struts (diameter equal to 32.3 cm and thickness of 4 cm) are placed laterally between the two transverse heads to prevent almost any shrinkage. They are equipped with strain gauges to know the level of restraint and to obtain the forces generated in the struts. Examples of the evolution of temperature, strains and forces are given. A first analysis of the cracking process shows that the cracks could appear for stresses below the tensile strength. With mainly strain information, global strain and local strain in concrete and on rebars, the force and then the stresses in concrete and rebars could be deduced. From numerical simulation and more simple elastic approach, state in each beam section could be obtained, and thus concordance between all the measures established. This huge amount of data allows verifying the phenomenology of the concrete in such boundary conditions. Various hypotheses were analyzed to explain strain measured and the corresponding forces in each component (concrete, rebars and struts) during specific period of early age. A particular attention was paid on the early age before the occurrence of the first crack. A realistic scenario is then proposed to explain the measurements. These hypotheses are done using a complementary numerical modelling and measurement analysis.

INTRODUCTION – THE CEOS.FR PROJECT

According to current practice and considering crack control, structural design is based either on a formula as in the fib model Code 2010, EC 2-1-1 or ACI 318 design codes, or on detailed procedures. Experience has shown that this approach is not accurate and is sometimes misleading for thick slabs, walls and other massive structures. Therefore, the French concrete construction community initiated the CEOS.FR national research project, which brought together more than 41 research

organizations and companies, including infrastructure owners, construction companies, engineering companies, and private or public research centers, with the support of the French Ministry of Sustainable Development. The aim of CEOS.fr was to improve understanding of the cracking phenomenon and, in the longer term, to provide designers with reliable crack design codes, able to give a reasonable appreciation of crack width and spacing, and applicable to a greater number of structures. With a total funding budget of 7 million Euros, the project lasted five years, from 2008 to 2013.

It was organized on a cross theme approach. Three types of situations involving cracking were identified: static and monotonous loading, cyclic or seismic loading and thermo-hydro-mechanical (THM) loading (restrained shrinkage). For all these loading situations, structural analysis and design, scientific modelling and experimental testing were performed (Demilecamps, 2010). This paper presents the THM experimental part of the work and a part of its results.

After a description of the concrete structures tested and the instrumentation used, the results are analyzed in terms of temperatures, strains, global forces and crack analysis.

PRESENTATION OF THE EXPERIMENTAL PROGRAM

Geometry and reinforcement of the structures tested

The restrained shrinkage testing bodies were massive I-shaped reinforced beams composed of a central part (5.1 m long, 50 cm wide and 80 cm high) and two massive heads (90 cm long, 2.2 m wide and 90 cm high), (figure 1). Two largely dimensioned steel struts (diameter 32.4 cm and thickness 5.5 cm) were placed laterally between the two transverse heads to prevent almost all shrinkage. They were equipped with vibrating wire gauges to measure the forces generated in the struts and to deduce the exact level of restraint. Three test bodies were made: RG8, the reference; RG9, with reduced reinforcement; and RG10, with increased cover (see table 1). Figure 2 gives the reinforcements that were used in the central section.

Instrumentation

All specimens were fully instrumented, externally and internally. The exact position of all the sensors is available on the site where the results of this project are stored (see corresponding section) but the kind of sensors used is summarized below:

- 9 points for internal temperature probes (Pt 100 Ω type sensors)

-16 vibrating wire extensometers (VWE) for local internal micro deformation measurement + 6 to measure the forces in the struts (2 self-sustaining reading coils)

- 3 internal long-base optical-fiber displacement sensors (Michelson type) (except for RG10 test)

- 6 electrical strain gauges (resistance type) placed on reinforcement bars (except for RG10 test).

Boundary conditions

The structures were placed outside for the THM test and all the environmental conditions were been recorded in the field from the time of casting. The thermal characteristics of the formworks and the variations of external temperature, relative humidity, wind speed and solar radiation (on a horizontal sensor) for the three tests

are available in the database Cheops (https://cheops.necs.fr) with all the results of the tests.

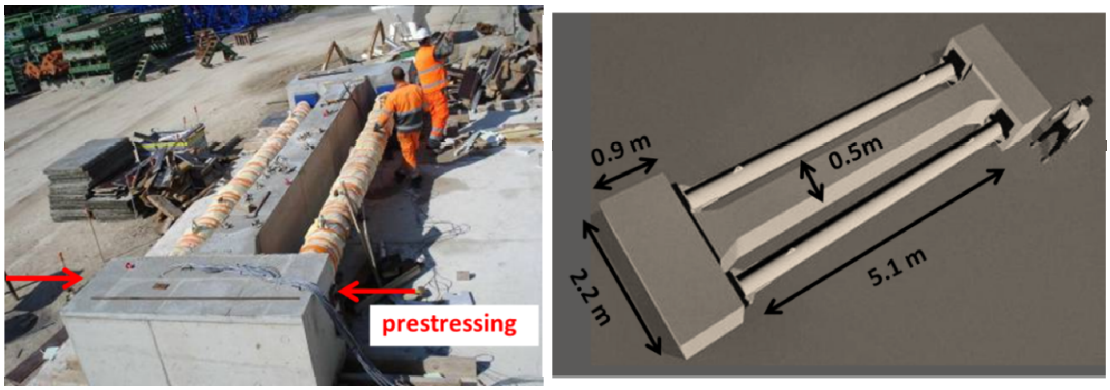

Figure 1. Geometry of the RG specimen

Table 1. Reinforcement of the central part of specimens RG8, RG9 and RG10.

	RG8	RG9	RG10
% of longitudinal reinforcement	2%	0.56%	2%
Cover	30 mm (50 mm for longitudinal rebars)	30 mm (50 mm for longitudinal rebars)	50 mm (70 mm for longitudinal rebars)

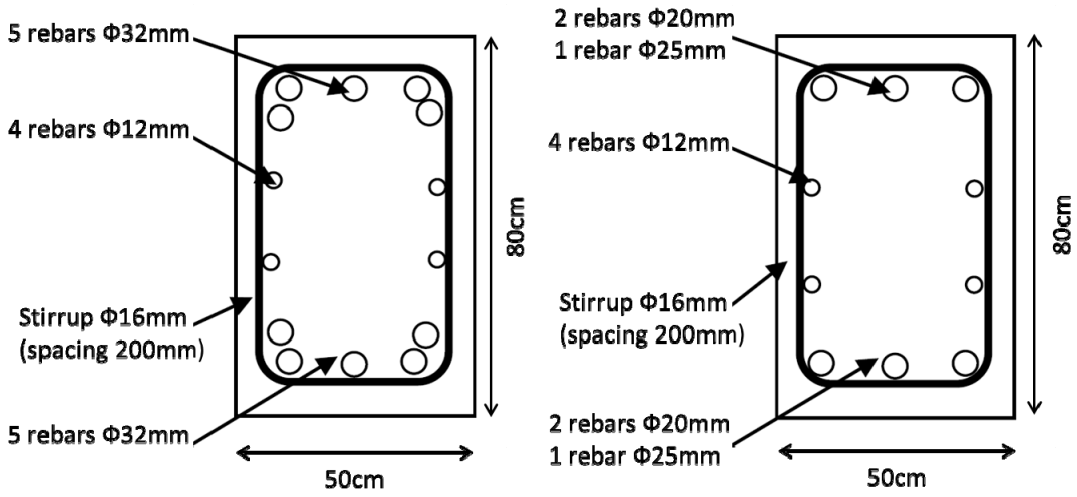

Figure 2. Reinforcement of the central parts of specimens

Concrete composition

The concrete composition of the CEOS.fr experimental campaign was characterized by a Portland cement CEM I 52.5 N and two different fractions of aggregates (0/4 and 4/20). Its water-cement ratio (w/c) was 0.46 and its cement content was 400 kg/m³. The admixture (Cimfluid Adagio 4019) used was a

polycarboxylate type superplasticizer. The amount of this admixture was equal to 1.35% of the cement content.

Evolution of mechanical properties at early age

Concrete compressive and tensile strengths and Young modulus were measured at 1, 2, 7 and 28 days. The cracking energy Gf was also measured at 1, 2 and 28 days by means of three points bending tests (Kolani 2012). Using a hydration model (Buffo-Lacarrière et al. 2007; Kolani et al. 2012), the hydration degree of each specimen tested was determined at the ages of testing. The evolution of the mechanical characteristics could thus be presented according to a variable independent of the experimental conditions (casting temperature for instance) (Figure 3). From these experimental results, the evolution of these parameters could be predicted (Figure 3) using the relation proposed by de Schutter (Schutter and Taerwe 1996):

$$\frac{X(\alpha)}{X(\infty)} = \left(\frac{\alpha-\alpha_0}{1-\alpha_0}\right)^n$$

where

- α is the hydration degree
- $X(\alpha)$ is the value of the mechanical property for the hydration degree α
- α_0 is the hydration degree for the development of a significant strength (percolation threshold) (Stefan et al. 2010)
- X_∞ is the theoretical value of the mechanical property for a total hydration (fitted on experimental results)
- n is a constant fitted using the experimental results

The fitting parameters obtained for each mechanical property are summarized in Table 3.

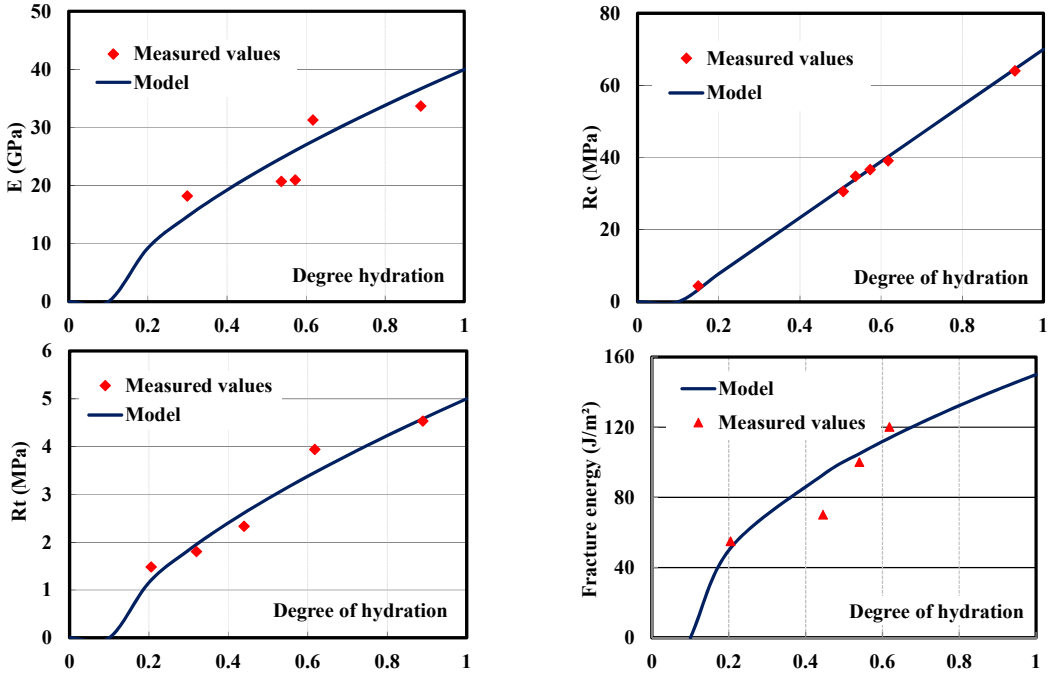

Figure 3. Evolution of instantaneous characteristics according to hydration development (experimental results from (Kolani 2012))

Table 3. Fitting parameters for mechanical properties of CEOS concrete (Buffo-Lacarriere et al. 2014).

	E	Rc	Rt	Gf
X_∞	41 GPa	70 MPa	5.4 MPa	138 J/m²
n	0.667	1	0.667	0.46
α_0		0.1		

Other characteristics

Other tests were performed: creep and shrinkage, adiabatic temperature rise… The results of these tests are also available in the database Cheops.

ANALYSIS OF THE RESULTS

Temperature variations

The main result in terms of thermal evolution was the core temperature. The mechanical loading of this kind of structure is restraint by the struts of the thermal strains induced by the global cooling of the structure after the formwork is removed.

The cooling accelerated after the formwork removal led to a dependence of the structure temperature (even at the core, as can be seen in Figure 4) to the variation of external temperature. We also note that the impact of solar radiation was considerable and can be observed on the core temperature for RG8, where the temperature is higher than the external temperature even after a long time.

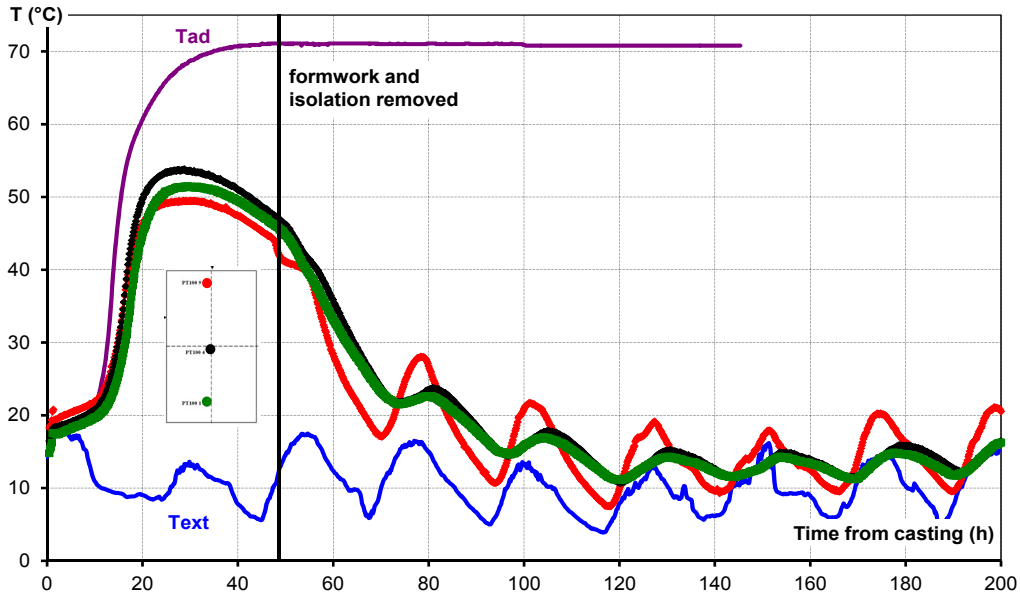

Figure 4. Evolution of temperature in RG8 at core and on upper and lower faces compared to the evolution of external temperature and adiabatic temperature

Strain evolutions

As explained previously, strains were measured by local vibrating wire extensometers at different cross sections. Figure 5 presents the evolution of longitudinal strains in the central cross section at core for the RG8 structure. The

results obtained show that the structure first exhibited extension during the heating and then a progressive contraction induced by the global cooling. The relatively large effect of the environmental conditions on RG8, which was not protected from solar radiation, can also be noted; it led to daily variation of strains of around +/- 75 µm/m.

In Figure 6, these strains obtained at the core for RG8 are compared with the thermal strain that would be obtained in a free structure subjected to the same thermal history. A comparison is made with optical fibers embedded in the concrete in three sections of the beams.

The restraining effect of the struts can be estimated using this comparison during the cooling (from 30 hours). For RG8, the restraining effect before the first crack appeared (observed around 70 hours after casting) led to approximately 30% of strain reduction.

In Figure 6, the results obtained by vibrating wires are also compared with the mean strain deduced from the relative displacements measured by optic fibres (2.5m long). We note that the optical fibers were not able to follow the strain properly at very early age (underestimation of the strain before 20 hours). A marked dispersion can also be observed for these sensors before the mechanical percolation of concrete (when concrete did not exhibit mechanical properties according to shear stresses). The results in terms of displacement are therefore presented after 10 hours and measurements before this time are neglected.

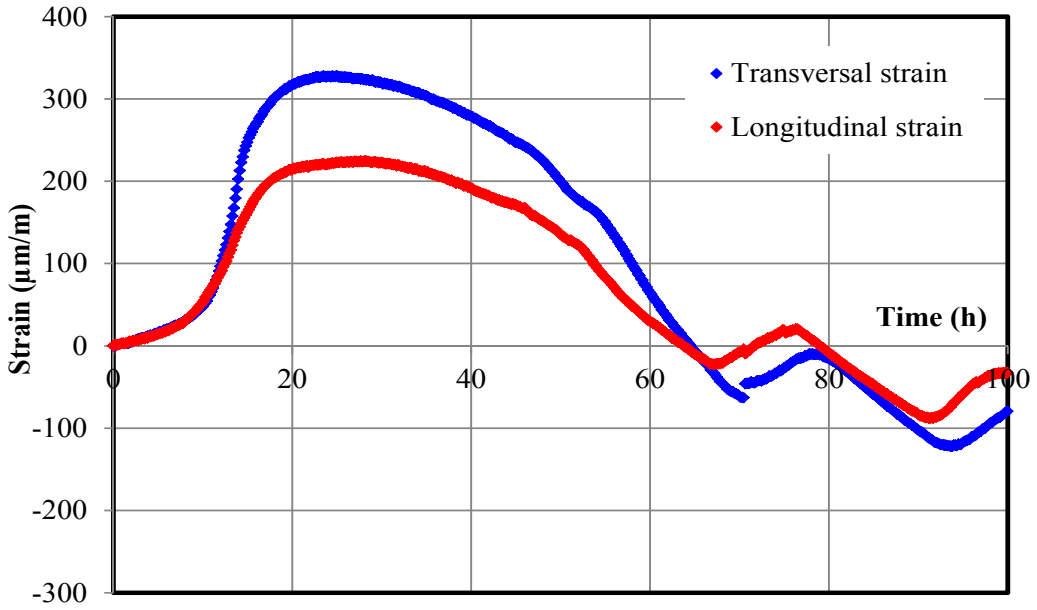

Figure 5. Evolution of longitudinal and transversal strains at core of the central section for RG8 structure

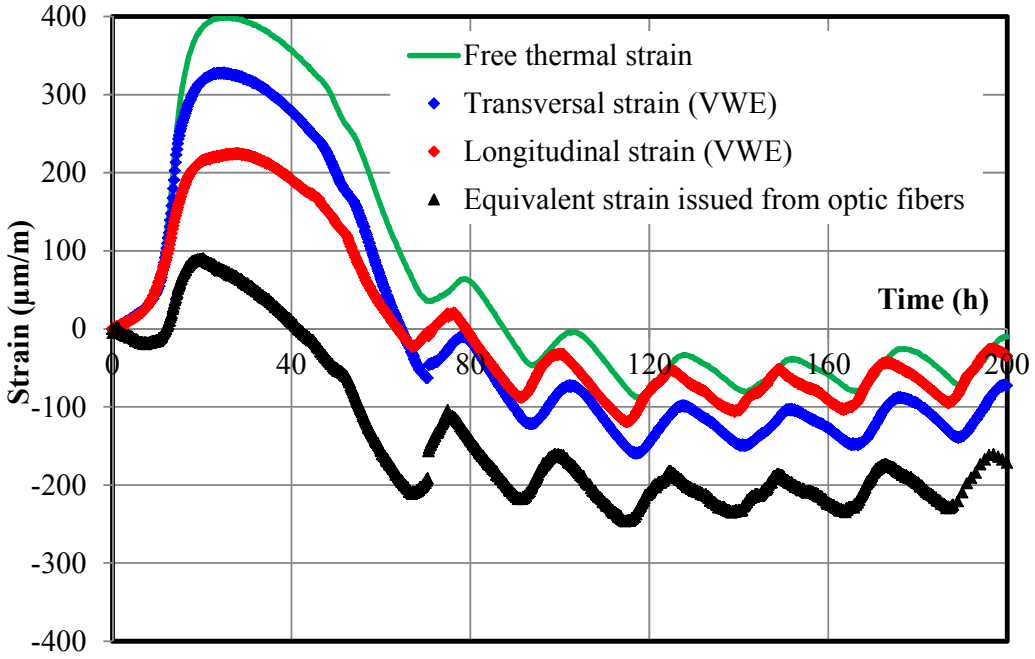

Figure 6. Comparison of strains recorded by local vibrating wire extensometers (VWE) and optical fibers with the thermal strain for a free sample

Processed measurements are presented in Figure 7 for optical fibres located at the core and near the two surfaces (upper and lower faces) for 2.5 m in the central part of the RG8 structure.

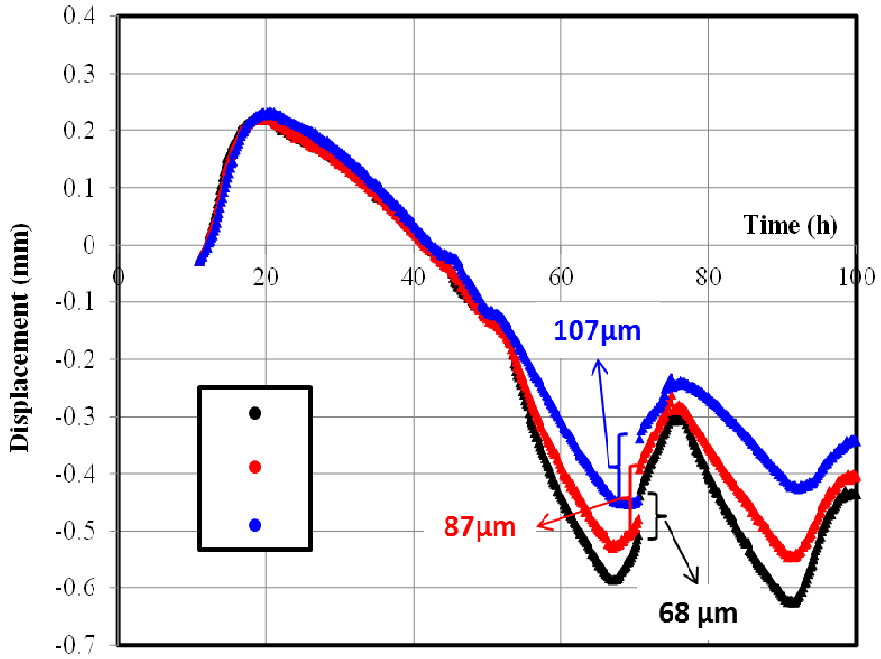

Figure 7. Relative displacement in RG8 structure measured by optic fibers.

In the particular case of RG8 (Figure 7), the first crack occurred in the optical fibres measurement zone, and was clearly detected 72 hours after casting. The displacement jump of the 3 curves indicates the instantaneous crack opening occurring in the measurement zone. We observe a non-homogenous opening in the section with a crack more open in the lower surface. This can be explained by (i) the specificity of the thermal history of RG8, which was not protected from solar radiation and the upper face of which reached higher temperatures than at the core, and (ii) the effect of dead weight (see next section).

Estimation of stresses

The behaviour of the longitudinal steel reinforcement of RG8 is analysed below. Three sections of this brace were instrumented with resistive gauges glued on the top and bottom Ø32 mm rebars. The strains were recorded in central section and in two other sections situated symmetrically at 80 cm from the central one. The resistive gauges measured the mechanical strain, which could be directly used to assess the longitudinal stresses in the top and bottom bars from the classical elastic stress-strain relationship. Typical stress profiles deduced from the strain state in rebars, with Es=210 GPa, are illustrated in Figure 8. The stress gradient of 10MPa between the upper and the lower bars is induced by the dead weight.

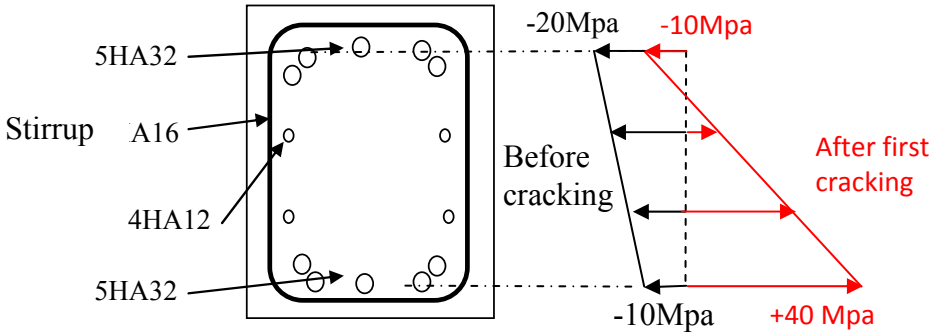

Figure 8: Stresses in reinforcement of the central section of RG8 72h after casting, just before and after the first cracking (tensile stresses positive)

Analysis of the RG8 test

The concrete force just before cracking corresponds to the compressive force in the struts (-61 tons) and the force in the rebars (-14 tons) and it corresponds to a tensile stress of +1.9 MPa in the concrete. This tensile strength of 1.9MPa is lower than the mean tensile strength supplied by the split tests carried out in the laboratory for this concrete, which was close to 4MPa for the hydration degree reached at 72h. The difference can be explained by several causes:

- A probabilistic scale effect (Rossi et al. 1994; Sellier and Millard 2014): compared to the volume of a sample used in a splitting test cracking in a real structure concerns a larger volume. This implies a probabilistic reduction of the tensile strength;
- The non-homogeneous stress profile in the central section of this brace, since as explained above, the dead weight induced a stress of +5MPa in the low steel corresponding to +0.8MPa in the low concrete part of the brace;
- Another cause of tensile stress heterogeneity could be the temperature gradient in the section during hydration, which is not perfectly homogeneous

and leads to self-equilibrated stresses in this section;

- Damage due to a coupling with creep could also be involved: when stresses are sustained damage evolves and cracking could occur at a lower value than the tensile strength (Briffaut et al. 2011; Torrenti et al. 2011)
- The last possible cause of differences is the number of sensors and associated wires accumulated close to this section, which could slightly perturb the stress profile and accelerate crack initiation.

CONCLUSION

These results are part of a huge amount of data obtained from various massive tests at full scale designed to study the effect of restrained conditions on massive beams. To analyse thermo-hydro-mechanical effects, I-shaped beams were designed so as to create restrained shrinkage on the central part of the beam. A full set of measurements were used to investigate phenomena occurring inside these beams at early age. Optical long base fibres gave information on the relative displacement along their length (2.5 m). These long base optical fibres were situated in the central part of the beams and embedded in the concrete at 3 different levels. Local measurements were taken in the concrete by means of Vibrating Wire Extensometers placed in 3 vertical positions, and in various horizontal sections in order to give local information on the strain in the concrete. Gauges on rebars produced data on the strain in the rebars of the first reinforcement layer, and the force in the struts was monitored.

With mainly strain information (global strain and local strain in concrete and on rebars), we have deduced the force and then the stresses in the concrete and rebars. This huge amount of data allows the phenomenology of the concrete to be verified in such boundary conditions. Various hypotheses were analysed to explain the strain measured and the corresponding forces in each component (concrete, rebars and struts) during a specific period of early age. Particular attention was paid to the early age before the occurrence of the first crack. A realistic scenario was then proposed to explain the measurements. All these experimental results are stored in a database and can be used for benchmarking. A complementary study of massive beams without restraining struts has also been carried out. It gives complementary results on the effect of early age strain resulting from the size of the specimens.

Acknowledgements
The investigations and results reported here were supported by the French national program CEOS.fr. The authors also thank VINCI Construction (L. Demilecamps and F. Cussigh) for the management of the technical aspects of the tests.

REFERENCES

Briffaut, M., Benboudjema, F., Torrenti, J. M., and Nahas, G. (2011b). “Numerical analysis of the thermal active restrained shrinkage ring test to study the early

age behavior of massive concrete structures." *Engineering Structures*, 33(4), 1390–1401.

Buffo-Lacarrière, L., Sellier, A., Escadeillas, G., and Turatsinze, A. (2007). "Multiphasic finite element modeling of concrete hydration." *Cement and Concrete Research*, 37(2), 131–138.

Buffo-Lacarriere, L., Sellier, A., and Kolani, B. (2014). "Application of thermo-hydro-chemo-mechanical model for early age behaviour of concrete to experimental massive reinforced structures with strain-restraining system." *European Journal of Environmental and Civil Engineering*, 18(7), 814–827.

Demilecamps, L. (2010). "*Reliable shrinkage and crack design: CEOS.fr french national research program, experimental aspects*." Third International fib Congress, Washington, DC, USA, 4888–4902.

Kolani, B. (2012). "*Comportement au jeune âge des structures en béton armé à base de liants composés aux laitiers*." PhD, Université de Toulouse, Université Toulouse III - Paul Sabatier.

Kolani, B., Buffo-Lacarrière, L., Sellier, A., Escadeillas, G., Boutillon, L., and Linger, L. (2012). "Hydration of slag-blended cements." *Cement and Concrete Composites*, 34(9), 1009–1018.

Rossi, P., Wu, X., Lemaou, F., and Belloc, A. (1994). "Scale Effect on Concrete in Tension." *Materials and Structures*, 27(172), 437–444.

Schutter, G. D., and Taerwe, L. (1996). "Degree of hydration-based description of mechanical properties of early age concrete." *Materials and Structures*, 29(6), 335–344.

Sellier, A., and Millard, A. (2014). "Weakest link and localisation WL2: a method to conciliate probabilistic and energetic scale effects in numerical models." *European Journal of Environmental and Civil Engineering*, 18(10), 1177–1191.

Stefan, L., Benboudjema, F., Torrenti, J.-M., and Bissonnette, B. (2010). "Prediction of elastic properties of cement pastes at early ages." *Computational Materials Science,* 47(3), 775–784.

Torrenti, J. M., de Larrard, T., and Benboudjema, F. (2011). "*Tertiary Creep: A Coupling Between Creep and Damage - Application to the Case of Radioactive Waste Disposal*." Damage Mechanics of Cementitious Materials and Structures, Gilles Pijaudier-Cabot et Frédéric Dufour, 183–202.

Experimental Investigation on Short- and Long-Term Deformations of Cracked Reinforced Concrete Ties

E. Gudonis[1,2]; G. Kaklauskas[1]; D. Bacinskas[1]; V. Gribniak[1,2]; R. Ramanauskas[1]; and V. Tamulenas[1]

[1]Department of Bridges and Special structures, Vilnius Gediminas Technical University, Sauletekio ave. 11, Vilnius LT-10223. E-mail: bridge@vgtu.lt
[2]Research Laboratory of Innovative Building Structures, Vilnius Gediminas Technical University, Vilnius LT-10223, Lithuania. E-mail: Viktor.Gribniak@vgtu.lt

Abstract

The current study reports the test results on deformations of cracked reinforced concrete (RC) ties. Four ties were tested under short- and long-term loading for 315 days. To perform the long-term tests, four testing rigs were constructed. The experimental results were compared with the Model Code 2010 predictions. It was revealed that the code overestimates the cracking load by 65-90%, and it is most likely due to the neglect of the shrinkage effect. It has been shown that 30-45% of the strain increment due to the long-term loading occurred during the first two-three days. The deformations of RC ties have practically stabilized after almost 300 days. The code quite accurately predicted the ultimate long-term strains. However, the prediction model was found to be too simplified to assess the increment of the long-term deformations.

INTRODUCTION

Structures are designed to satisfy both strength and serviceability requirements. In consequence of the extensive studies, the ultimate load behavior of reinforced concrete (RC) flexural members is well understood. Nevertheless, due to the use of refined ultimate state theories as well as higher strength materials, resulting in structures with longer spans and smaller depths, control of deformations is often the governing design criterion. Adequate modelling of cracking and, particularly, post-cracking behavior, as one of the major sources of physical nonlinearity, is the most important and difficult task of structural mechanics.

Complex physical phenomena, such as concrete creep, shrinkage, and cracking greatly contribute to deformation increments: the long-term deformations might increase up to 3-4 times above the initial values (Gribniak *et al*. 2013). Most of the studies of the long-term deformations of RC members were dedicated to the investigation of bending members and only a few experimental programs were devoted to RC ties (Jaccoud 1987, Beeby and Scott 2005, Wu and Gilbert 2008, Vilanova *et al*. 2014). To fill this gap, the current study reports experimental results of four RC ties tested under short-term and under sustained load for a period of 315 days. The results gathered from the short-term experiments were compared to the deformations predicted by the Model Code 2010.

EXPERIMENTAL PROGRAM

The experimental program involved four RC elements. The concrete strength f_{cm} and reinforcement ratio p (around 1.1%) were similar for all specimens. Geometrical properties of the elements were also identical: 1500 mm in length and with a nominal cross-section of 100 × 100 mm (Figure 1). High-strength deformed steel bars of 12 mm diameter were used as reinforcement. Identical concrete mixture was used for all the specimens. Mechanical properties of the concrete, determined at age of 28 days, are: the mean compressive strength f_{cm} = 33.6 MPa and the modulus of elasticity E_{cm} = 35.9 GPa. Reinforcement steel bar properties were determined from four samples. 700MPa and 190GPa values were obtained (based on nominal diameter) from tests for ultimate stress f_u and modulus of elasticity, respectively.

The reinforced concrete elements were moisture cured from 2 days after casting until loading of the element at t_0 = 52 days. The loaded specimens were kept under controlled environmental conditions: the ambient average relative humidity (RH) was 64%, average temperature – 19°C. The applied tensile load was 57% of the ultimate load bearing capacity for DT-14, DT-15 elements and 65% for DT-12, DT-13 elements.

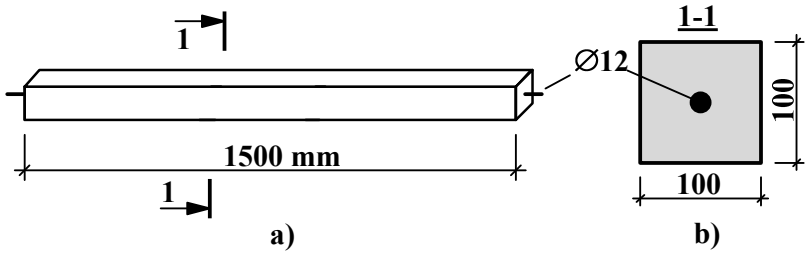

Figure 1. Geometrical properties of the specimens (a), cross-section (b).

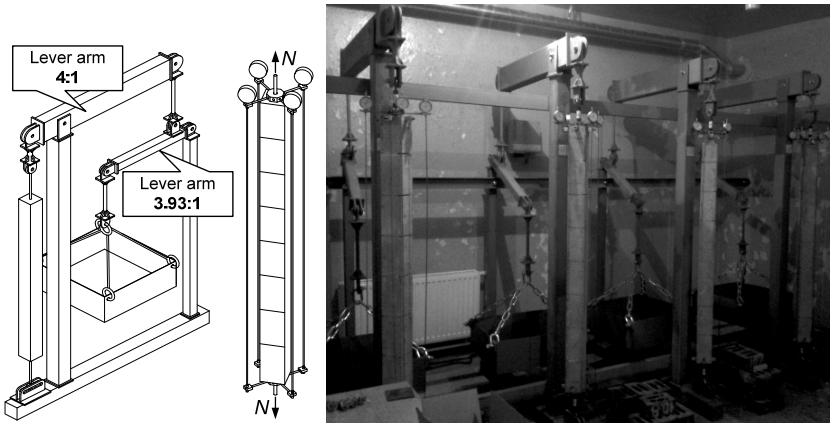

Figure 2. The experimental setup.

Four test frames based on a double lever system were designed to sustain the applied load for these long-term experiments (Figure 2). Mechanical gauges of 0.001 mm accuracy were used and deformations were measured along the base of

1520 mm. The load was applied by means of the double lever system achieving a 16:1 load ratio. Loading was gradually applied using 1.5 and 5kg weights. In order to determine the crack initiation stage, the load was applied in smaller increments when approaching the cracking load. Readings were taken during the short pause after each load step. The short-term test took on average 1 hour and required 30 load increments, whereas the long-term loading tests were performed over 315 days.

COMPARATIVE DEFORMATION ANALYSIS

In this section, the experimental results were compared with the Model Code 2010 (MC 2010) predictions. According to the MC 2010, the average short-term strains of a tie ε_m are obtained by interpolating between uncracked and fully cracked section strains (Figure 3a).

During the long-term experiment a tensile load P is gradually applied up to the target sustained load level. In Figure 3b, the idealized deformation behavior from this loading is depicted by the black solid line (OAB). From point B the diagram represents the deformational behavior under sustained loading. Thus, the long-term deformations $\varepsilon_m(t, t_0)$ are composed from the short-term deformations $\varepsilon_m(t_0)$ and the long-term increment $\Delta\varepsilon_m(t, t_0)$ over the loading period $t–t_0$. These deformation components are given in Table 1. In contrast to short-term modeling, the prediction of deformation at time t (point B_1 in Figure 3b) is the only adequate output in long-term analysis by using MC 2010. The grey solid line ($OA_1A_1'B_1$) in Figure 3b represents this prediction. Theoretical and experimental deformations are compared in Table 1.

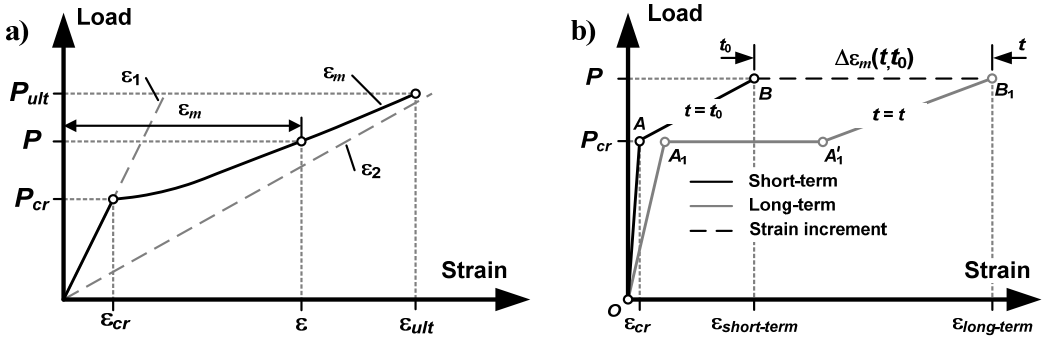

Figure 3. Load-average strain diagram for short-term loading by MC 2010 (a) and comparison of short- and long-term deformations (b).

Table 1. Comparison of experimental (Exp.) and theoretical (Th.) strains.

Specimen	*Short-term strains,* $\varepsilon_m(t_0)\times10^{-4}$			*Long-term strains,* $\varepsilon_m(t,t_0)\times10^{-4}$			*Strain increments,* $\Delta\varepsilon_m(t,t_0)\times10^{-4}$		
	Exp.	*Th.*	*Exp./Th.*	*Exp.*	*Th.*	*Exp./Th.*	*Exp.*	*Th.*	*Exp./Th.*
DT-12	14.8	10.6	1.40	17.4	14.6	1.19	2.55	4.08	0.63
DT-13	16.8	10.7	1.57	19.2	14.6	1.32	2.43	3.93	0.62
DT-14	14.2	7.05	2.01	16.9	11.6	1.46	2.71	4.51	0.60
DT-15	12.9	6.99	1.84	16.2	11.5	1.41	3.32	4.52	0.73

The experimental and theoretical curves of tie DT-13 are given in Figure 4. The difference between theoretical and experimental cracking limits is evident for the short-term loading case. Most probably, this might be related to the shrinkage effect reducing the cracking resistance (Kaklauskas and Gribniak 2011). Consequently, the relative short-term strain prediction errors varied from 1.4 to 2.0 (Table 1). The cracking load determined by the MC 2010 is overestimated by 65–90%. Despite the long-term effects, which should complicate the analysis, the long-term strains were underestimated with 1.2-1.5 relative errors (see Table 1 and Figure 4c).

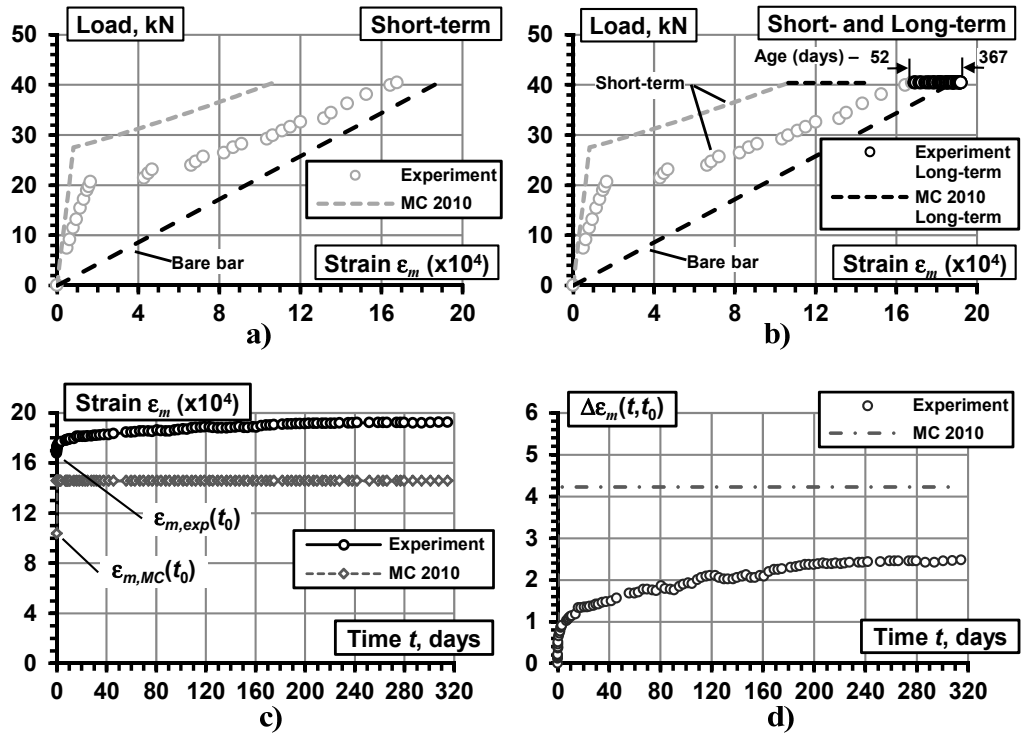

Figure 4. Comparison of experimental and theoretical diagrams: short-term (a), short- and long-term (b) loading; change of long-term strains (c) and long-term strains increment (d) over time.

In contrast to the strains, relative increments $\Delta\varepsilon_m(t,t_0) / \Delta\varepsilon_{m,\mathrm{MC}}(t,t_0)$ varied from 0.60 to 0.73 (Table 1). An example of this increment is also presented in Figure 4d. It is evident that the increase of theoretical strains occurs immediately after applying the sustained load which remains constant over time, whereas the experimental increment is gradually increasing. A noticeable increase of the deformations is observed during the first 2-3 days and reaches 30-45% of the ultimate value. The strain increment has stabilized after 300 days.

Two tendencies can be identified from the analysis. On the one hand, the MC 2010 underestimates the short-term strains $\varepsilon_m(t_0)$ significantly. On the other hand, the long-term strain increment $\Delta\varepsilon_m(t,t_0)$ is considerably overestimated as well. Due to the opposite sign of these errors, the resultant behavior is evaluated with improved accuracy. However, the theoretical long-term strains $\varepsilon_m(t,t_0)$ should still be adjusted.

CONCLUSIONS

The following conclusions can be drawn from this study:

- The Model Code 2010 overestimates the cracking load by 65-90 %, most likely due to the neglect of the shrinkage effect.
- During the first two-three days, the strain increment under sustained load reaches 40 % of the ultimate load value. The experimental deformations have stabilized after about 300 days of sustained loading.
- The Model Code 2010 underestimated the ultimate long-term strains by 20-50%. Thus, the deformation model needs to be improved.

ACKNOWLEDGMENT

The authors gratefully acknowledge the financial support provided by the Research Council of Lithuania (Research project No. MIP-093/2015).

REFERENCES

Beeby, A.W. and Scott, R.H. (2005). "Long-term tension-stiffening effects in concrete." *ACI Struct. J.*, 102(1), 31–39.

Gribniak, V., Bacinskas, D., Kacianauskas, R., Kaklauskas, G., and Torres, L. (2013). "Long-term deflections of reinforced concrete elements: accuracy analysis of predictions by different methods." *Mech. Time-Dependent Mat*., 17(3), 297-313.

Jaccoud J.-P. (1987). *Minimum reinforcement for control of cracking in concrete structures*. PhD Thesis, Swiss Federal Institute of Tecnology, Lausanne, Switzerland. (in French).

Kaklauskas, G., Gribniak, V. (2011). "Eliminating shrinkage effect from moment-curvature and tension-stiffening relationships of reinforced concrete members." *J. Struct. Eng. ASCE*, 137(12), 1460-1469.

Vilanova, I., Torres, L., Baena, M., Kaklauskas, G., Gribniak, V. (2014). "Experimental study of tension stiffening in GFRP RC tensile members under sustained load." *Eng. Struct.,* 79, 390-400.

Wu, H. Q., Gilbert, R. I. (2008). *An experimental study of tension-stiffening in reinforced concrete members under short-term and long-term loads*. UNICIV Report No. R-449. University of South Wales, Sydney, Australia.

RILEM TC 195-DTD (2002-2006): Round Robin Test Program on Free Deformation Rigs; Planning, Test Results, and Statistical Evaluation

Ø. Bjøntegaard[1] and T. A. Martius-Hammer[2]

[1]Ph.D, Senior Principal Engineer, Norwegian Public Roads Administration, the Road Directorate, Tunnel and Concrete Section, Abels Gate 5, 7030 Trondheim, Norway. E-mail: oyvind.bjontegaard@vegvesen.no
[2]Senior Scientist, SINTEF Building and Infrastructure, Rich. Birkelands vei 1c, 7034 Trondheim, Norway. E-mail: Torarne.hammer@sintef.no

Abstract

In order to evaluate concretes in terms of crack sensitivity in the hardening phase it is essential to quantify thermal dilation (TD) and autogenous deformation (AD) in laboratory tests. Many laboratories performed such tests using different techniques for linear and volumetric measurements. The paper presents the results from a RR-program performed within the RILEM committee TC 195-DTD where 10 laboratories were represented and totally 30 Dilation Rig tests (linear test set-ups) were performed. For simplicity the nominal test condition for the RR was 20 ^{o}C isothermal temperature; i.e. the scope was to measure only the effect of AD. The results showed that fresh concrete properties varied significantly in the various laboratories and this, amongst others, appears to have contributed to variations in the measured AD. The coefficient of variation (COV) of AD is significantly larger than for mechanical properties.

INTRODUCTION

Massive concrete structures may develop significant volume changes during the hardening phase due to heat of hydration (casing thermal dilation, TD) and chemical shrinkage (causing autogenous deformation, AD). In a restraint case, the two types of self-generated volume changes (TD and AD) are the driving forces to stress generation in hardening concrete; and so-called “thermal cracking” is too often the result of such stresses.

Quantification of TD and AD in laboratory tests in Dilation Rigs (linear test set-ups) is a prerequisite for evaluation/simulation of the stress generation and cracking tendency of hardening concrete structures. In the following, the work of the previous RILEM Technical Committee TC195-DTD (2002-2006) is summarized. For more details see (Bjøntegaard et al. 2015), (Bjøntegaard et al. 2006), (Hammer et al. 2006) and (Krauss et al. 2006). The committee’s three letter short term “DTD” was the

above described AD and TD, and the full name of the committee was "Recommendation for test methods for AD and TD of early age concrete".

Many laboratories perform tests on TD and AD using different techniques for linear and volumetric measurements. The motive for establishing the committee was that results in the literature showed great differences for quite similar concretes and even in Round-Robin (RR) tests on nominally identical concretes (Morabito et al. 2001). The main assignments for the committee were the following:

- Gather experience on variation in earlier Round Robin (RR) test programs.
- Establish an overview of the various linear Dilation Rig set-ups for measuring AD and TD among the participants.
- Planning and execution of a RR test program: The main RR-test was to measure AD on a given concrete composition during 20 ^{o}C isothermal conditions (i.e. sealed conditions to prevent any external drying).
- Evaluate the 20 ^{o}C AD-results statistically.
- Come up with a recommendation on a test procedure on how to measure TD and AD.

MATERIALS AND MIX DESIGN OF A STABLE CONCRETE MIX

Trial mixtures were made at SINTEF/NTNU in Trondheim, Norway. The main idea was to make the mix design simple with as few part materials as possible (experience from earlier RR-programs implied that this was sensible). The chosen RR mix was a concrete with maximum grain size of 8 mm and a water-to-cement ratio (w/c) of 0.35. The RR concrete mix contained only three part materials (plus local water):

- a given cement (CEM I), available in 40 kg bags
- a given 0 - 8 mm sand, packed in plastic bags
- a given superplasticizer, available in plastic cans

It was seen during the trial mixtures that the chosen low w/c concrete was stable and did not develop any bleed water on the top surface during the first hours after casing. No bleeding is fortunate since if bleed water collects on the top surface it will be sucked back into the specimen during the first hours after setting. Such reabsorption of bleed water is seen to generate a swelling of the concrete specimen, see (Bjøntegaard 1999). After that the degree of saturation of the pore system will probably to a certain extent be permanently affected (higher) by the early reabsorption where the magnitude is likely to depend on the amount of bleed water reabsorption. Hence, the AD (and TD) results may be affected also on longer terms. The point is that a concrete mix that has low stability (i.e. with bleeding and segregation tendency) may produce different amount of bleeding when mixed in different laboratories and, thus, be a source of variation in RR Dilation Rig tests.

The part materials were sent out by the Norwegian cement producer Norcem to the participants of the RR. The mortar mix proportions, see Table 1, were submitted as an Excel spreadsheet were the only optional changes for each participants were the

desired mixing volume and the measured total moisture content of the sand. A detailed mixing procedure was also provided.

Table 1. RR concrete composition (1 m^3)

Constituent	*kg / m^3*
Cement CEM I 42.5 R	522
Water added	188
Sand 0 - 8 mm (SSD)	1729
Superplasticizer, SP	10.4

The water absorption of the aggregate is 0.8% (SSD-condition), therefore 13.8 ltr of water of the total added water (188 ltr) is absorbed and not regarded in the w/c-ratio. The SP contains 82% water, meaning 8.6 ltr. It follows then that: w/c=(188-13.8+8.6)/522) = 0.35

PARTICIPANTS, RR TEST PROGRAM AND CONCRETE MIXING

Participants and RR test program

The part materials were distributed to 10 laboratories (Canada, Denmark, France, Germany, Japan, The Netherlands, Norway, Sweden and USA, see section Acknowledgements, and (Bjøntegaard et al. 2015), hence the RR-concrete were mixed by each participant. As discussed, AD measured at 20 ^{o}C isothermal condition was the main study of the RR and totally 30 Dilation Rig tests on AD were carried out. In addition some supporting tests were also performed such as fresh concrete properties and 28-days strength, and for some partners: hydration heat, relative humidity and restraint stress in Temperature-Stress testing machines. The testing also involved a smaller RR on a w/c=0.35 cement paste (involving only three participants). All RR-results were submitted to the first author of this paper. It is notable that TD was not investigated directly in the RR (only isothermal tests), but both AD and TD were of course treated in the final test procedure recommendation, see (Hammer et al. 2006).

Prescribed mixing procedure

The following mixing procedure was prescribed to all participants:

- Add the superplasticizer to the water prior to mixing
- Mix sand and cement for 1 minute
- Add the mixture of superplasticizer and water and mix for 2 minutes (included the time of adding)
- Stop the mixer and let rest for 2 minutes
- Mix for 1 minute - end

The following fresh concrete measurements were prescribed:

- Slump, preferably according to EN 12350-2 (cone: bottom ø200 mm, top ø100 mm, height 300 mm)
- Air content, preferably according to EN 12350-7 (“pressure method”)
- Density, preferably according to EN 12350-6
- Control whether bleeding occur on the top surface in a separate sample every hour the first five hours. If bleed water occurred, it was suggested to remove all

bleed water from the top surface of the Dilation Rig specimen with the use of drying paper or a drying cloth (and then seal the specimen again afterwards).

Prescribed Dilation Rig procedure; casting and reporting of results

The following framework for the Dilation Rig test was described:

- Target test temperature: 20 ^{o}C isothermal conditions
- Protect the concrete against moisture loss between mixing and casting.
- Cast the mortar in the Dilation Rig within 45 minutes after mixing (remember the lining to avoid direct contact between specimen and mould)
- Describe the method used for compaction
- Insert a thermo-couple in the center of the specimen for continuous temperature registration
- Seal the specimen
- Start the measurement as soon as possible (before setting)
- Measure over at least two weeks

All information and all Dilation Rig test results in raw-data format (no data processing) were submitted to the organizer. An own excel spread sheet was distributed containing demands for the following information: Test laboratory, name of person submitting the data, batch number, temperature history, description of mixer, volume of batch, initial concrete temperature, slump, slump test method, fresh concreter density, density test method, fresh concrete air content, air content test method.

The excel spread sheet also contained empty columns ready to be filled in with the continuous measurements from each Dilation Rig test, having the following headlines:

- Time axis (time after mixing)
- Measured specimen temperature
- Measured free length change (microstrain, 10^{-6})
- Bleeding (if observed)

THE DILATION RIGS

Detailed description of the participating 10 Dilation Rigs is given in (Bjøntegaard et al. 2015). All rigs were so-called linear set-ups; nine rigs were horizontal oriented and one rig was vertical. Six rigs had active temperature-control while four had not (only climate room control). Some rigs measured the length change on both sides of the specimen using two LVDTs, while others only on one side using one LVDT. One rig measured the length change using two cast-in rods that went through the cross section, sticking out on both sides, and used one LVDT on each side of the specimen. One rig measured the length change from the top surface using a LVDT connected to two “forks”. And finally, one rig made use of a cast-in strain gauge in the center of the specimen. In other words, a variety of Dilation Rig designs were represented in the RR. An example of a Dilation Rig set-up with active temperature-control is shown

in Figure 1. This particular rig is located at the Norwegian Univ. of Sc. and Tech. and was a part of the RR. The rig (slightly modified since the RR) is today used in an on-going PhD-work presented at this mini-seminar by (Klausen et al. 2015).

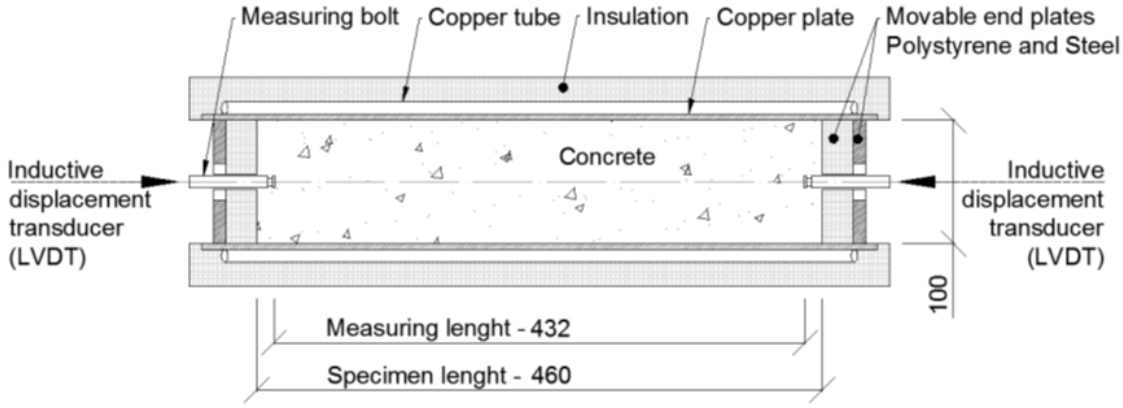

Figure 1. Example of Dilation Rig set-up (Klausen et al. 2015)

RR-RESULTS AND STATISTICAL EVALUATION

Dilation Rig test results (target temperature 20 ^{o}C)

As can be seen from the measured raw data from the Dilation Rig tests, the results deviated quite markedly, see Figure 1 (all data up to 24 hours) and Figure 2 (zeroed at 10 hours, and up to 336 hours). The fresh concrete temperatures varied from about 16 ^{o}C to around 24 ^{o}C, and a hydration heat generated temperature increase was observed in some tests due to lack of temperature control. On longer times there were also some differences in the test temperature.

Not surprisingly there are great deviations in the measured length change during the very first hours after mixing/first hours after starting the tests. This is due to the fact that the concrete is fresh and there may be settlement and movements of measuring devise in the more or less liquid specimen. Setting time was around 8 hours for the tested concrete (though some variations were also seen for setting time, for instance from hydration heat measurements), so from this point it is reason to believe that the concrete is stiff and measuring devises should be well fixed/bonded to the specimen.

The results in Figure 1 and 2 have not been compensated for the variations in the in test temperatures. For the tests that experienced temperature changes during the test and/or test temperature deviation from 20 ^{o}C, a temperature compensation would include both elimination of the effect of TD from the result (by assuming a value for the coefficient of thermal expansion) as well as a time-shift (maturity transformation). Such compensation was done during the statistical evaluation of the results, see following section.

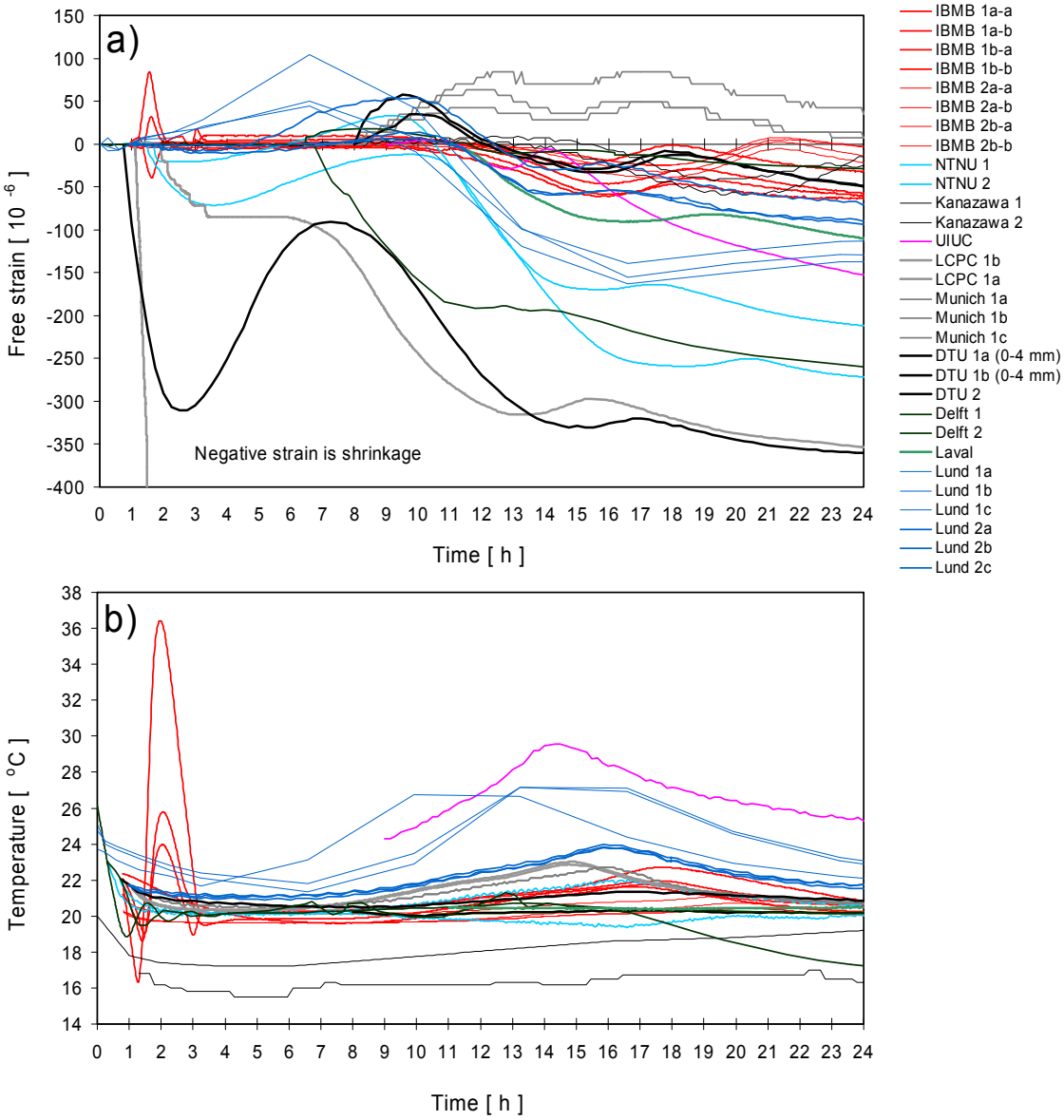

Figure 2. RR Dilation Rig test results, all data up to 24 hours. Measured length change (negative values are contraction) (a) and specimen temperature (b).

Statistical evaluation of the Dilation Rig test results

The statistical evaluation of the results was performed by Matias Kraus, Tech. Univ. of Braunschweig, (Krauss et al. 2006) and (Krauss 2004). It was shown that AD is a lognormal distributed random variable. No outliers were detected among the 30 Dilation Rig measurements at significant levels of 5% and 20%. According to the registrations at the various laboratories some errors occurred during the test program. The main deviations were wrong w/b-ratio (extra mixing water was used in one case to obtain workability), test temperature was to high (26 °C) or to low (16 °C),

malfunction of temperature control, wrong aggregate size (4 mm used in one case instead of 8 mm), low amount of superplasticizer, and bleeding.

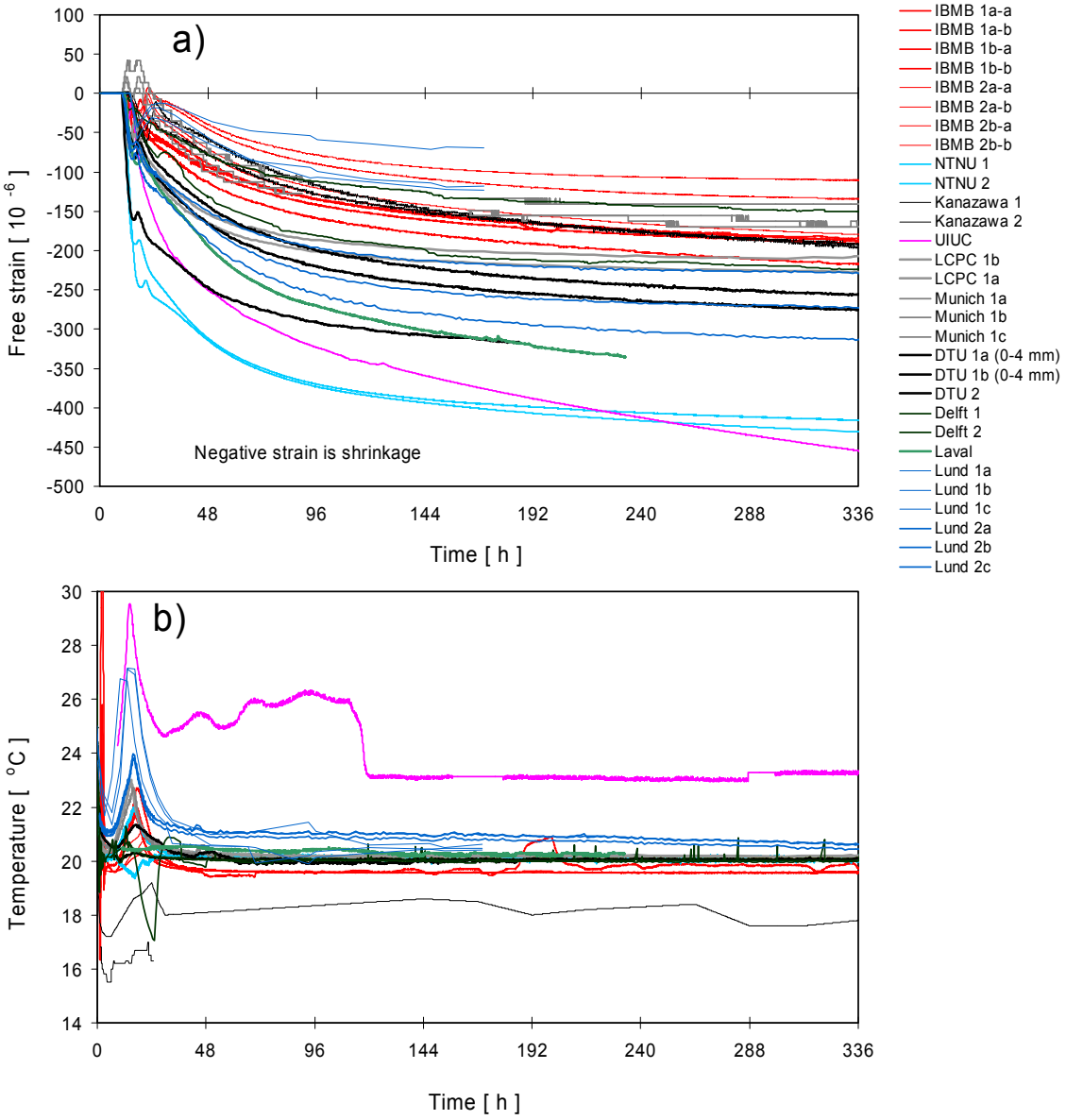

Figure 3. RR Dilation Rig test results, up to 336 hours. Measured length change (negative values are contraction), zeroed at 10 hours (a) and specimen temperature (b).

The data were divided into some subsets (group 1 to 6) which pool the data of non-outliers candidates, where the data removed in each group varied. Hence the number (N) of AD-results varied in the groups. In Table 1 the 6 groups are described together with the corresponding median value MED, mean value MEAN, standard deviation SD and coefficient of variation COV for AD after 7 days maturity time t_e. Table 2 shows the statistical attributes for all data (N=30) at different times, also including

Q05 and Q95 which are the 5% and 95% quantile, respectively. For t_e = 14 days the number (N) of AD-results is only 17 since only 17 tests lasted this long.

Table 1. Statistical attributes of AD data for all groups for t_e = 7 days.

GROUP	REMOVED DATA	**N**	MED [10^{-6}]	MEAN [10^{-6}]	SD [10^{-6}]	**COV [%]**
1	No data removed, i.e. all tests	**30**	-186	-225	110	**48**
2	Wrong mixing procedure, high test temperature, high temperature maximum	**25**	-174	-215	111	**52**
3	Additional to group 2: low superplasticizer, dosage, lack of information, bleeding	**19**	-158	-159	42	**26**
4	Additional to group 3: One particular laboratory was taken out	**16**	-155	-147	31	**21**
5	All tests with high air content > 2.5 %	**13**	-163	-169	39	**23**
6	All tests with low air content ≤ 2.5 %	**14**	-205	-238	115	**48**

Table 2. Calculated statistical attributes of AD for different ages – all partners.

t_e [days]	**N**	MIN	MAX	MED	MEAN	Q05	Q95	SD	**COV**	***COV*) [%]***
1	**30**	-358	46	-57	-94	-353	13	104	**111**	***77***
2	**30**	-414	-22	-110	-149	-411	-44	106	**72**	***54***
3	**30**	-442	-51	-144	-180	-438	-70	108	**60**	***46***
5	**30**	-469	-74	-170	-209	-387	-117	109	**52**	***41***
7	**30**	-481	-92	-186	-225	-471	-104	110	**48**	***38***
14	**17**	-474	-99	-221	-254	-457	-122	118	**46**	***35***

*) These COV-values come out after compensating for temperature, i.e. the effect of thermal strains (TD) have been approximated and subtracted from the measured results.

SUMMARY AND CONCLUSION

The results from the Round Robin (RR) tests in the Dilation Rigs on autogenous deformation (AD) performed at nominally 20 °C isothermal temperature can be summarized as follows:
A literature review showed that the time-dependent coefficient of variation (COV) of AD is around 3-4 times larger than for mechanical properties. The present analysis confirms this trend.

In the analyses the measured results have been compensated for test temperatures deviating from 20 ^{o}C, which was the case in several tests. The COV for AD after 7 days was then determined to be 38% for the whole sample of 30 tests (N=30) (corresponding COV was 48% when not compensating for temperature). The fresh concrete characteristics appear to have a very large influence on the AD in the early stages. An partitioning of the entire sample into the subsets "small air void content" and "high air void content" showed that the COV of the group "small air void content" (N=13, COV=10%) is approximately half of the COV of the group "high air void content" (N=14, COV=21%). The air void effect remains even in later ages due to memory character of the void structure, while the influence of the variations in fresh concrete temperature is not so strongly pronounced at later ages.

The sample contains values from faulty measurements. A reduction of the sample from these measurements did not bring improvements of the computed COV. Outliers test confirms that no unusual values are contained in the available sample. The large scatter cannot be explained thereby. Therefore more tests (larger sample) are necessary.

With a significance level of 20% it implies that 8 individual measurements on one particular concrete are needed in each lab. The batch-to-batch variation between laboratories was large (seen as variation in fresh concrete properties) whereas the within-laboratory variation was less. This implies that the necessary number of individual measurements in each laboratory can be reduced (to around five individual measurements).

Possible pitfalls attached to each test set-up may be: friction between specimen and mould, unwanted movement of measuring points, reabsorption of top surface bleed water into the specimen after setting, malfunction/lack of temperature control, and temperature increase due to hydration heat, moisture loss between mixing and casting and during the measuring period.

Possible disturbing factors in RR-programs may be: initial aggregate moisture state (some dried the aggregate before mixing, some did not), wrong mixing proportions, the mixing energy, amount of superplasticizer, varying test procedure, varying reference time, varying initial temperature and test temperature (here: 16-26 ^{o}C), uncertain degree of data processing before submission of data to administrator.

ACKNOWLEDGMENTS

The statistical analysis performed by Matiass Krauss, Tech. Univ. of Braunschweig, is greatly acknowledged. So are the participants in the RILEM TC195-DTD Round Robin test program: Tech. Univ. of Braunschweig, Delft Univ. of Tech., Tech. Univ. of Denmark, Kanazawa Univ., Laval Univ., Lab. Central des Ponts et Chaussées, Lund Inst. of Tech., Tech. Univ. of Munich, The Norwegian Univ. of Sc. and Tech., SINTEF Building and Infrastr., Univ. of Illinois at Urbana-Champaign, Norcem AS.

REFERENCES

Bjøntegaard Ø., Martius-Hammer T.A., Krauss M. and Budelmann H. (2015) *Round Robin documentation report: Program, test results and statistical evaluation, RILEM TC 195-DTD Recommendations for test methods for AD and TD of early age concrete*, RILEM State-of-the-art Reports, Vol.16, ISBN 978-94-017-9265-3, Springer, 93 p

Bjøntegaard Ø. and Hammer T.A. (2006) *RILEM Technical Committee 195-DTD: Motive and technical content*. Proc. of the Int. RILEM conference on Volume Changes of Hardening Concrete: Testing and Mitigation, 20-23 Aug. 2006, Tech. Univ. of Denmark, Lyngby, Denmark, pp.357-366

Bjøntegaard Ø. (1999) *Thermal Dilation and Autogenous Deformation as Driving Forces to Self-Induced Stresses in High Performance Concrete*. Doctoral thesis, NTNU, Dept. of Structural Eng., Dec. 1999, ISBN 82-7984-002-8.

Hammer T.A. and Bjøntegaard Ø. (2006) *Testing of autogenous deformation (AD) and thermal dilation (TD) of early age mortar and concrete – recommended test procedure*. Proc. of the Int. RILEM conference on Volume Changes of Hardening Concrete: Testing and Mitigation, 20-23 Aug. 2006, Tech. Univ. of Denmark, Lyngby, Denmark, pp.341-346

Klausen A., Kanstad T. and Bjøntegaard Ø. (2015) *Updated Temperature-Stress Testing Machine (TSTM): Introductory tests, calculations, verification and investigation of variable fly ash content*, Proc. of the mini-symposium of COST Action TU1404: Towards the next generation of standards for service life of cement-based materials and structures, as part of the CONCREEP-10 Conference, September 21-23, 2015, Vienna, Austria

Krauss. M. (2004) *Probabilistic concept for the validation of the effectiveness of measures against early age cracking in massive concrete structures*. Doctoral-thesis. TU Braunschweig. (in German).

Krauss M., Bjøntegaard Ø. and Hammer T.A. (2006) *Statistical evaluation of autogenous deformation test results performed in the RILEM Technical Committee 195-DTD framework*. Proc. of the Int. RILEM conference on Volume Changes of Hardening Concrete: Testing and Mitigation, 20-23 Aug. 2006, Tech. Univ. of Denmark, Lyngby, Denmark, pp.347-356

Morabito P., Bjøntegaard Ø., van Breugel K., Dalmagioni P., Gram H.-E., Gutsch A., Hedlund H., Jonasson J.-E., Kanstad K., Lura P., Pellegrini R., Rostasy F. and Sellevold E. (2001) *Round Robin Testing Program. Equipment, testing methods, test results*, IPACS report, Ed. by P.Morabito, TU Luleå, Sweden, ISBN 91-89580-42-7, 110 pages

COST Action TU1404—Recent Advances of WG1: Testing of Cement-Based Materials

Gregor Trtnik[1] and Marijana Serdar[2]

[1]IGMAT Building Materials Institute, Polje 351c, 1260 Ljubljana, Slovenia. E-mail: grega.trtnik@igmat.eu
[2]Faculty of Civil Engineering, University of Zagreb, Fra Andrije Kacica-Miosica 26, 10000 Zagreb, Croatia. E-mail: mserdar@grad.hr

Abstract

Work Group 1 (WG1) of COST Action TU1404 entitled "Testing of cement based materials" deals with determination of different properties of early age and hardened cement based materials with the following main objectives: (1) to recommend new advanced standard techniques which have been developed during the last years to become standard in the (near) future, (2) to test the ability of using different waste, recycled, and by-products as raw materials to design sustainable concrete mixture, and (3) to prepare a database of concrete mixtures which could serve designers and engineers to better predict lifespan, durability, and serviceability of concrete mixtures and structures. The paper describes organization and strategic view of WG1, presents its main objectives and gives important details about Round Robin Test, as a main tool that will be employed within WG1.

OVERVIEW OF WG1

In current design standards (*e.g.* Eurocode, fib Model codes) design and quality control during construction are based on classification of structural materials according to strength classes, with most of the other material properties being practically dependent only on strength classes, which is feasible for Ultimate Limit State purposes. Nowadays, it is clear that this approach is not sufficient; creating a need for performance-based methodology based on different parameters (Bjegovic et al. 2014), relevant for the structural and environmental application and strongly depended on modelling / prediction of cement-based materials (CBM) behavior. This is especially the case when considering incorporation of by-products and waste materials in CBM to preserve the raw materials in Europe and to decrease the environmental impact of the production of cement. Most of the requirements prescribed in nowadays standards are limiting the utilization of alternative CBM and/or cannot be applied directly to concrete incorporating alternative CBM.

Furthermore, the inclusion of new additional materials in CBM frequently induces changes in performance that need to be taken into account by designers.

In order to successfully apply performance-based approach, data on different properties of different types of CBMs need to be known and validated and a database of material properties established. This database needs to incorporate not only concrete prepared with cements currently available on the European market, but needs to take into account different scientifically proven efficient materials, which can be used as a substitute of ordinary Portland cement. Additionally, there are numerous advanced techniques continuously being developed, that can give answers to questions raised by modelling and limit the need for assumptions and uncertainties in current models. But to step out of the research framework and come to the wider practice, these techniques have to be validated on European significant level.

WG1 of COST Action TU1404 is entitled "Testing of cement based materials" and deals with determination of different properties of early age and hardened CBMs with the following main objectives: (1) to recommend new advanced standard techniques which have been developed during the last years to become standard in the (near) future, (2) to test the ability of using different waste, recycled, and by-products as raw materials to design sustainable concrete mixture, (3) to prepare a database of concrete mixtures which could serve designers and engineers to better predict lifespan, durability, and serviceability of concrete mixtures and structures, and (4) to provide input data needed for modelling phase of the Action (WG2). In order to achieve these objectives, one of the main instruments employed by this WG is Round Robin Testing (RRT), organized among numerous European laboratories.

ROUND ROBIN TESTING (RRT)

The main objectives of RRT are twofold. The first objective is to provide better understanding of the CBM themselves (database of properties), especially high-performance and eco-concrete. This will offer new opportunities to simulation/predictive models both in terms of validation of modelling assumption/strategies and opportunities for the validation of simulation results. The second objective is the mutual validation of advance, non-standardised experimental techniques developed in European laboratories. This will highlight the validity and added value of newly developed techniques, and lead to standardization of more precise and property targeted methods for testing CBM.

In order to adequately achieve the above objectives, the organization of RRT is divided in the following three different ways (see figue 1):

- In two different phases according to main objectives of RRT ("in the following division 1 – DIV1")
- In three different levels according to the materials used to perform necessary experiments ("in the following division 2 – DIV2"),
- In two different types according to the interest of the participants ("in the following division 3 – DIV3")

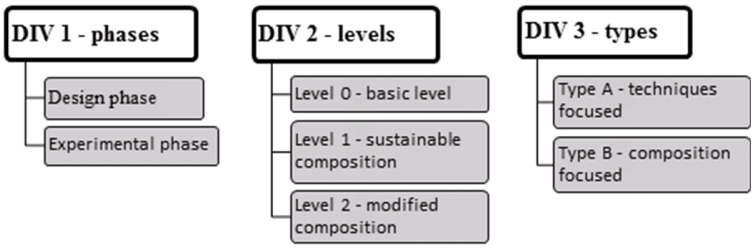

Figure 1 Organization of Round Robin Testing program within WG 1.

Different phases of RRT – DIV1

According to its nature, RRT can be divided into the following two phases: i) design phase and ii) experimental phase. Design phase is aimed to prepare a detailed plan of RRT procedure, namely: (1) to define testing laboratories, (2) to define experimental materials (i.e. basic materials and mixtures), (3) to define mixing procedure and curing conditions, (4) to define testing methods and (5) to prepare detailed experimental plans for each GP1. Experimental phase can be further divided into the following two sub-phases: (1) main phase, and (2) additional phase. During the main phase, a vast majority of RRT procedure will be performed used to achieve main objectives of RRT. Additional phase will be performed on the basis of the results of main phase and also on basis of the results of the numerical benchmarking.

Different levels of RRT

According to type of experimental materials, RRT be divided into three different levels. Level 0 is the basic level of RRT which deals with two reference concrete mixes, i.e. ordinary concrete (in the following "OC") and modified ordinary concrete (MOC) with a decreased water/cement ratio in order to emphasize the effect of the amount of available water for hydration in the mix". Both OC and MOC use the same basic materials, namely Portland cement with clinker and crushed natural aggregate, and have therefore strong environmental effect.

Level 1 is focusing on sustainable and innovative CBM compositions. The idea of this level is to propose mixes with lower environmental effect and compare their properties with basic reference mixes from level 0. These mixes are called "ECO concrete mixtures" (ECOC) and can be formed by substituting part of the constituting material with a more sustainable alternative and/or by using a different type of constituting materials. Here the highlight should be given to locally available materials and mixes originally developed by a participating laboratory. Consequently, each participating laboratory is encouraged to use its own supplementary materials.

Level 2 is the level in which participants can modify reference mixes to obtain desired variations, necessary for validation of their experimental techniques. In that case, participants can propose mixes that suit their experimental technique, but are still based on the reference mixes and use the same constituting materials (changes in w/c ratio, aggregate content, curing conditions, initial concrete temperature, etc. are some of the typical examples).

Different types of RRT

RRT can be divided into the following two categories according to the main interest of the participants included in RRT. Type A participants are interested in

using advanced, non-standardized experimental techniques developed or used in their laboratories. Their aim would be to use this RRT to perform validation and benchmark of experimental technique. They can choose to use their experimental program on all three levels of RRT.

Type B participants are interested in testing their innovative, more advanced mixes with improved properties. Their aim would be to perform validation and benchmark of mixes, comparing behavior of alternative mix to basic reference mix. They can perform test using their own methods or can propose to another participant (e.g. through STSM tool) to perform test using their advanced experimental technique.

GROUP PRIORITIES

Due to the complexity of the RRT described above, the following six Group Priorities (GP1), managed by experienced and highly competent GP1 leaders, have been defined to adequately achieve the objectives of WG1:

GP1a - Fresh properties and setting,
GP1b - Chemical and microstructural characterization,
GP1c - Transport properties and boundary effects,
GP1d - Mechanical properties and creep,
GP1e - Volume stability and
GP1f - Fracture properties and cracking.

GP1a: Fresh properties and setting

Cement hydration is a complex chemical process that involves a progressive change in the state of the material from a fluid state into a porous solid state as a result of dissolution of cement grains and nucleation of solid phases of hydration products such as calcium silicate hydrates (C-S-H), calcium hydroxide (CH), monosulfoaluminate (AFm), and ettringite (AFt). This complicated process can be monitored using various standard and advanced techniques, e.g. monitoring heat output or ultrasonic (US) wave propagation. Additionally, output from these techniques can be used to predict various macro scale properties of hardened CBMs, such as the time evolution of the early age compressive strength *fc*, Figure 2.

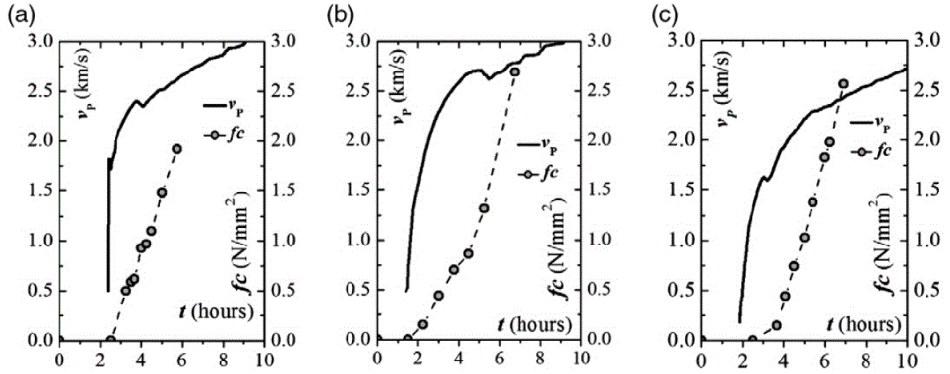

Figure 2 Relationship between vP–t and fc–t curves for concretes with different w/c ratio; a) w/c= 0.35, b) w/c = 0.40, c) w/c= 0.45 (Trtnik & Gams, 2015)

Due to the importance of fresh concrete state on the later concrete properties, many efforts have been employed to develop advanced methods and protocols used to obtain valuable information at the early ages of matrix (Trtnik & Gams, 2015, Mikulic et al. 2013, Gams & Trtnik, 2013, Gabrijel et al. 2011, Azehna et al. 2010, Figueiras et al. 2014). However, for a more routine application of these techniques in the practice, they have to be validated on a European significant level. The main objective of this GP1 is therefore to provide a platform for mutual validation of advance, non-standardised experimental techniques developed in European laboratories. Some of the techniques that will be included are:

- Heat of hydration
- Ultrasonic testing
- Rheology tests.

The main anticipated outcome is to evaluate efficiency and accuracy of considered advanced techniques to obtain certain parameters of concrete at early ages, as well as their repeatability and reproducibility.

GP1b: Chemical and microstructural characterization

Both chemical and microstructural analyses are frequently used in concrete research to evaluate the influence of different added materials on hydration progress (Van Tuan et al. 2011, Cizer et al. 2012, Gao et al. 2015) or of different aggressive exposures on initial matrix (Maes & De Belie, 2014, Chappex & Scrivener, 2012). Most of the microstructural analyses, such as scanning electron microscope (SEM), X-ray diffraction (XRD), thermogravimetric analysis/differential scanning calorimetry (TGA/DSC) or Mercury intrusion porosity (MIP) are complex methods and their utilization on CBMs is not standardized. Many laboratories have established their own protocol for performing most of these techniques and analyzing obtained results. An example below shows the use of XRD to qualitatively follow the hydration progress of lime-metakaolin paste (a) and quantitative XRD analysis of hydrated activated stainless steel refining slag at different ages (b).

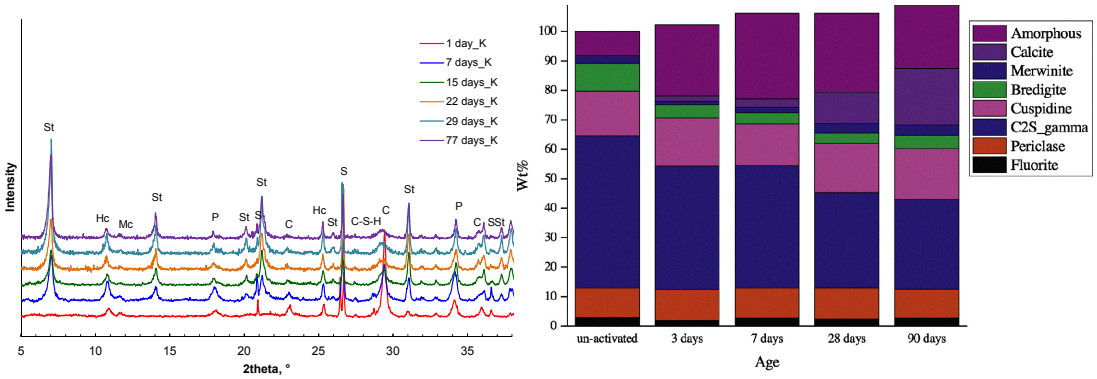

Figure 3 a) XRD analysis of solid phases during hydration of lime-calcined kaolinite paste and b) QXRD analysis of hydrated SSR 45 at different ages activated with Na-silicate and 5M NaOH in 50:50 ratio (Salman et al. 2015)

The main objective of this GP1 is to provide a platform for comparison of different protocols used in different participating laboratories for evaluating microstructural properties of CBM. Following techniques are planned to be included:

- Thermogravimetric analysis/differential scanning calorimetry (TGA/DSC)
- SEM-BSE image analysis
- Selective dissolution (to identify unreacted SCMs by XRD analysis)
- Mercury intrusion porosity (MIP)
- X-ray computed microtomography (X-CT).

The main anticipated outcome is better understanding of the hydration and microstructure development of CBM in particular when SCMs such as conventional materials (blast furnace slag, fly ash, limestone) and new materials (locally available by-products and residues according to a specific interest of each country) are incorporated in the binder system to create eco-concrete mixtures (Level 1). The ultimate target is to build up reliable database through a set of complementary experimental techniques (standardized, non-standardized, advanced, novel) in European laboratories as input data for simulation models in WG2 for service life predictions.

GP1c: Transport properties and boundary effects

Transport of fluids and aggressive substances through the porous structure of hardened cement paste is the controlling parameter of the potential durability of a reinforced concrete structure. Microstructure and the percolation are known to control the inflow and outflow (transport) of ions and substances in porous building materials. The driving force for the flow is often the external environment and as such is termed as the boundary condition. Nowadays, many testing procedures for testing penetrability properties of concrete are standardized or have already been used for long periods, and have proven to have satisfactory precision (Elahi et al. 2010, Alexander et al. 2001). Example here shows the application of air permeability to evaluate progress of hydration beyond 28 days. A comparison of the various mixes between 44 and 91 days clearly shows a decrease in air permeability, which is considered to be due to the continued hydration of the CBMs.

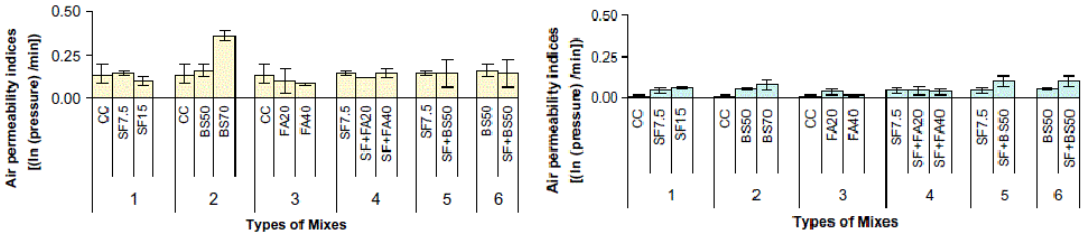

Figure 4 Air permeability of various mixes at 44 and 91 days (Elahi et al. 2010)

The aim of this work package is twofold: (1) to determine the transport properties that can be linked to a deterioration mechanism with emphasis to standard error and scope, and (2) to outline the boundary conditions, so that transport properties can be linked to models for predicting future behavior as identified in WP2.

GP1d: Mechanical properties

Mechanical properties present one of the first and most important information about concrete mixes. Since there are numerous research and practical experience with mechanical behavior of concrete during several decades, most of the current standards in civil engineering practice are based almost solely on them. In the present RRT they will be represented by following properties:

- Compressive strength
- Bending strength
- Tensile strength
- Young's modulus and Poisson's ratio.

Most of these methods are standardized and performed routinely in most of the participating laboratories. Nevertheless, there is still potential for improving repeatability and reproducibility of these methods and initiatives for their customization, which is the main objective of GP1d.

GP1e: Volume stability

Volume instability of concrete as the hydration of cement goes on and the cement paste starts hardening is strongly influencing cracking, deflection and prestress loss in concrete structures later on during service life. This is especially the case when considering different types of concrete mixes with different or unknown interaction of stress and strain, such (ultra)-high strength concrete (UHSC) (Lura et al. 2003), self-consolidating concrete (SCC) (Leemann et al. 2011) or concrete with alternative binders used as SCMs (Darquennes et al. 2011). Measuring shrinkage at the beginning of reaction between water and cement can give valuable information about the hydration process, define need for external or internal curing and determine the risk of formation of cracks that could significantly influence serviceability of concrete structure. Examples presented below show how significant difference can be in autogenous shrinkage when by-products from waste industry are used as a partial replacement of cement (here L-lime, Q-quarry dust, R-red mud and F-fly ash) a) and how influential is the amount of cement paste in the concrete on total shrinkage during long term b).

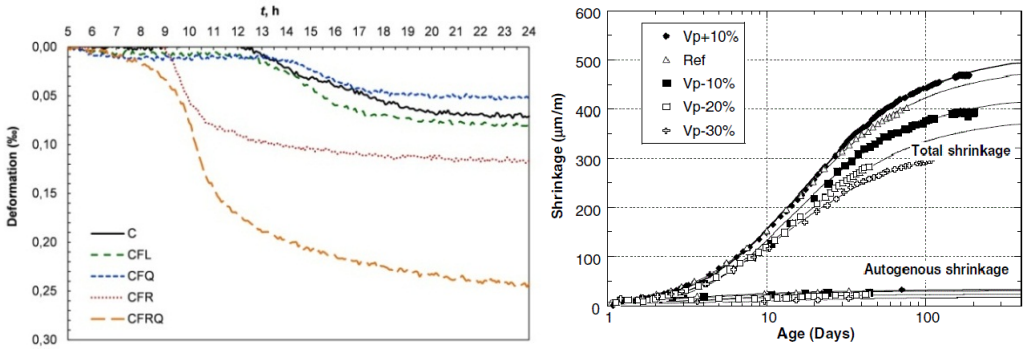

Figure 5 a) Comparison of autogenous shrinkage of mixtures with different SCMs during 24 hours (Serdar et al. 2015) and b) total shrinkage and autogenous shrinkage of the concrete mixes with different amount of cement paste (Roziere et al. 2007)

Even if the phenomena involved in autogenous and restrained shrinkage and creep are well researched, the experimental assessment of these volume deformations

has not come to such a consensus between research teams because of many practical difficulties. Numerous methods for evaluating volume stability have been developed for the last two decades. Following techniques are planned to be included in the RRT:

- Autogenous shrinkage
- Restrained shrinkage (dog-bone/TSTM, ring test)
- Creep or relaxation
- Thermal dilation.

The main benefit of RRT is to give a platform where all of the developed methods can be compared and validated under controlled conditions.

GP1f: Fracture properties and cracking

Cracking in concrete used in civil structures has been a worldwide critical issue in the field of engineering. Characterization of the cracking mode in cementitious materials allows evaluations concerning the remaining life of the structure since in general, shear-like phenomena occur after tensile cracking (Aggelis et al. 2013). Therefore, predicting cracking, defining limiting conditions where there is a risk of cracking and developing non-destructive methods to monitor cracking are only few aims of research in this field. Nowadays there are vast possibilities of advanced non-destructive methods used as a part of the structural health monitoring, and acoustic emission surely presents one of the most promising ones (Mpalaskas et al. 2014). These non-destructive techniques become even more beneficial when applied to concrete elements with improved cracking resistance, such as fiber reinforced concrete. Examples here shows the correlation of one of the parameters of acoustic emission, AE hits, with fracture behavior of fiber reinforced concrete mix (Figure 6 a) and beneficial effect of fibers (I-industrial, R-recycled, G-rubber) on fracture behavior (Figure 6 b).

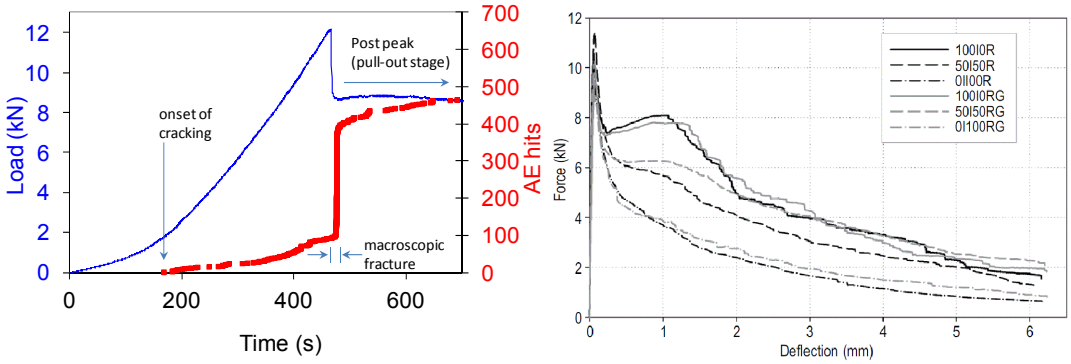

Figure 6 a) Comparison of fracture behavior of different fiber reinforced concrete mixes showing effect of fiber quantity and dimensions and b) comparison of fracture behavior and simultaneous monitoring od acoustic emission events (Bjegovic et al. 2014)

In the present RRT following tests will be included:

- Fracture toughness, KI
- Fracture energy
- Bending strength
- Fracture toughness index $T_{100,2.0}$

Fracture behavior of ordinary concrete and fiber reinforced concrete will be monitored, to highlight the applicability and benefits of standardized and non-standardised non-destructive methods.

CONCLUSION

In the paper, some basic principles and objectives of Round Robin Test as a main mechanism within WG1 of COST TU1404 Action is presented. Due to the high complexity of the subject, associated with large number of interested participants from numerous European organizations and various properties of cement based materials which significantly influence durability, sustainability, and long term performance of the materials and concrete structures, special emphasis was put on defining organization of Round Robin procedure.

The presented paper was prepared on a basis of the first Round Robin Testing document developed by Core Group members of COST TU1404 Action and GP leaders of WG1. Large number of highly motivated participants together with their recently developed advanced testing techniques and complex experimental equipment guarantee high quality of the project and important, accurate, and highly influential experimental results.

REFERENCES

Aggelis, D. G., Mpalaskas, A., Matikas, T. E. Investigation of Different Fracture Modes in Cement-Based Materials by Acoustic Emission, Cement and Concrete Research, vol. 48, pp. 1-8 (2013).

Alexander, M. G., Mackechnie, J. R. and Ballim, Y., Use of durability indexes to achieve durable cover concrete in reinforced concrete structures. In Materials science of concrete, Vol. VI, J. P. Skalny and S. Mindess (Eds.), American Ceramic Society, pp 483–511, 2001.

Azenha, M., Magalhães F., Faria, R., Cunha, A. Measurement of concrete E-modulus evolution since casting: A novel method based on ambient vibration, Cement and Concrete Research 40 (2010) 1096–1105

Bjegovic, D., Baricevic, A., Lakusic, S., Damjanovic, D., Duvnjak, I. Positive interaction of industrial and recycled steel fibres in fibre reinforced concrete, Journal of Civil Engineering and Management, 2013, (Supplement 1): S50–S60

Bjegovic, D.; Beushausen, H.; Serdar, M. Proceedings of the RILEM International workshop on Performance-based specification and control of concrete durability / Zagreb : RILEM Publications S.A.R.L., 2014

Chappex, T., Scrivener, K. Alkali fixation of C–S–H in blended cement pastes and its relation to alkali silica reaction, Cement and Concrete Research 42 (2012) 1049–1054

Cizer, Ö., Van Balen, K., Elsen, J., Van Gemert, D. Real-time investigation of reaction rate and mineral phase modifications of lime carbonation, Construction and Building Materials 35 (2012) 741–751

Darquennes, A., Khokhar, M.I.A., Rozière, E., Loukili, A., Grondin, F., Staquet, S. Early age deformations of concrete with high content of mineral additions, Construction and Building Materials 25 (2011) 1836–1847

Elahi, A., Basheer, P.A.M., Nanukuttan, S.V., Khan, Q.U.Z. Mechanical and durability properties of high performance concretes containing supplementary cementitious materials, Construction and Building Materials 24 (2010) 292–299

Figueiras, H., Nunes, S., Coutinho, J.S., Andrade, C. Linking fresh and durability properties of paste to SCC mortar, Cement & Concrete Composites 45 (2014) 209–226

Gabrijel, I., Mikulić, D., Milovanović, B. Application of Ultrasonic Measurements for Determination of Setting and Hardening in Cement Paste. // Journal of Civil Engineering and Architecture. 5 (2011) , 3; 278-283

Gams, M., Trtnik, G. A new US procedure to determine setting period of cement pastes, mortars, and concretes Cement and Concrete Research 53 (2013) 9–17

Gao, X., Yu, Q.L., Brouwers, H.J.H. Reaction kinetics, gel character and strength of ambient temperature cured alkali activated slag–fly ash blends, Construction and Building Materials 80 (2015) 105–115

Leemann, A., Lura, P., Loser, R. Shrinkage and creep of SCC – The influence of paste volume and binder composition, Construction and Building Materials 25 (2011) 2283–2289

Lura, P., Jensen, O.M., van Breugel, K. Autogenous shrinkage in high-performance cement paste: An evaluation of basic mechanisms, Cement and Concrete Research 33 (2003) 223 – 232

Maes, M., De Belie, N. Resistance of concrete and mortar against combined attack of chloride and sodium sulphate, Cement & Concrete Composites 53 (2014) 59–72

Mikulić, D., Milovanović, B., Gabrijel, I. Analysis of thermal properties of cement paste during setting and hardening // Nondestructive testing of materials and structures / Büyüköztürk, Oral ; Taşdemir, Mehmet Ali ; Güneş, Oğuz ; Akkaya, Yılmaz (ur.). Dordrecht : Springer, 2013. Str. 465-471.

Mpalaskas, A. C., Thanasia, O., Matikas, T. E., Aggelis, D.G. Mechanical and Fracture Behavior of Cement-Based Materials Characterized by Combined Elastic Wave Approaches, Construction and Building Materials, vol. 50, pp. 649-656 (2014).

Roziere, E., Granger, S., Turcry, Ph., Loukili, A. Influence of paste volume on shrinkage cracking and fracture properties of self-compacting concrete, Cement & Concrete Composites 29 (2007) 626–636

Salman, M., Cizer, Ö., Pontikes, Y., Snellings, R., Vandewalle, L., Blanpain, B., Van Balen, K. Cementitious binders from activated stainless steel refining slag and the effect of alkali solutions, Journal of Hazardous Materials 286 (2015) 211–219

Serdar, M., Biljecki, I., Bjegovic, D. Beneficial addition of aluminium slag and quarry dust to high-volume fly ash concrete, 2015 (submitted for publishing)

Trtnik, T., Gams, M. Ultrasonic assessment of initial compressive strength gain of cement based materials, Cement and Concrete Research 67 (2015) 148–155

Van Tuan, N., Ye, G., van Breugel, K., Copuroglu, O. Hydration and microstructure of ultra-high performance concrete incorporating rice husk ash, Cement and Concrete Research 41 (2011) 1104–1111

Experimental Assessment of Autogenous Shrinkage

E. Roziere[1]; B. Delsaute[2]; A. Loukili[1]; and S. Staquet[2]

[1]Institut de Recherche en Génie Civil et Mécanique, GeM-UMR CNRS 6183, Centrale Nantes, 1 rue de la Noe, BP 92101, F-44321 Nantes Cedex 3, France. E-mail: emmanuel.roziere@ec-nantes.fr
[2]Service BATir, Université Libre de Bruxelles, 87, A. Buyl Ave. CP194/4, 1050 Brussels, Belgium. E-mail: sstaquet@ulb.ac.be

Abstract

The study presented in this paper deals with the influence of the measurement technique on autogenous shrinkage. A state of the art shows that many setups based on different techniques have been designed to measure autogenous deformations. In this experimental study, four different setups and setting devices were gathered in the same laboratory. All the methods were found to fulfill the criteria for reliable assessment of autogenous deformation. The different methods showed good repeatability and consistent evolutions of autogenous shrinkage. The autogenous shrinkage was initialized at the time of minimum shrinkage rate. Good correlations could be found between the times of minimum and maximum shrinkage rate, the evolutions of ultrasonic velocities, and the times of maximum temperature.

1. STATE OF THE ART

In a homogeneous and isotropic cementitious system, autogenous shrinkage is theoretically an isotropic deformation, so volumetric measurements as well as linear methods may be used to assess autogenous deformation of early age concrete. Due to the improvement of measurement techniques, numerous test setups have been designed and experimental studies have been published (Bjøntegaard & Hammer, 2006). (Jensen & Hansen, 2001) have pointed out the need for round robin tests to conclude on the relevance of different measurement techniques. Round robin tests involving ten laboratories have been realized (Bjøntegaard et al., 2006). A statistical evaluation of tests results has been published (Krauß et al., 2006). Estimations of the coefficient of variation of autogenous shrinkage have been given. They showed the influence of the fresh concrete characteristics like the air content.
To reduce the influence of properties of fresh concrete, the study presented in this paper deals with measurements of autogenous deformations that took place in the same time in one laboratory. Four different setups and the users were gathered in the same place. The test methods all consist in linear measurements but the configurations of the test rigs are different: horizontal and vertical, with rigid or flexible moulds. They were chosen because they fulfill the main criteria to measure autogenous deformation (Hammer & Bjøntegaard, 2006). Specimens are totally sealed to avoid any moisture exchange.

Friction between the specimen and the frame is limited. The maximum temperature increase in concrete was measured and it did not exceed 2°C. All the setups were equipped with automatic data logging.

The experimental study aims at providing autogenous deformation to assess autogenous shrinkage and the influence of the test method. The first section deals with a state of the art of measurement techniques. Then, the experimental program and the test methods are presented. The last section gives the methods used to analyse autogenous deformation and their correlations with setting kinetics assessed from ultrasonic monitoring and standard tests.

Even if the phenomena involved in autogenous shrinkage are now well known, the experimental assessment of autogenous shrinkage has not come to such a consensus between research teams because of many practical difficulties. Several artefacts actually have to be avoided to measure autogenous shrinkage as defined in the previous section.

The specimen must be perfectly sealed to avoid any external drying or water uptake. The temperature must be kept constant, which requires external control because the hydration of cement releases heat. The test rig should be designed to limit the friction with the specimen.

Numerous methods have been developed and can be divided into two groups: volumetric and linear measurements. Whereas volumetric methods are mainly used on cement pastes and mortars linear methods have been used on concrete. Horizontal and vertical setups have been designed. Both methods can be divided into two groups: rigid moulds and flexible moulds. Rigid moulds have been reported to underestimate the magnitude of autogenous shrinkage because of friction between the specimen and the mould (Barcelo et al., 1999, Eppers, 2008. Moreover a membrane, such as plastic foil with talcum powder, is often added to minimize the friction. Flexible moulds are often named corrugated tubes. Such methods can be improved by controlling the temperature through a bath (Jensen and Hansen, 1995), by reducing the stiffness of the mould (Boulay, 1993), and by using displacement transducers without contact. An ASTM standard has been published (ASTM C 1698, 2009).

The assessment of autogenous shrinkage is not only influenced by the test procedure but also by the time when the measures are initialized, which is often referred to as time-zero. Irrelevant time-zero is likely to result in giving different behavior for a given material (Sant et al., 2006). Initializing the strain at the time of mixing includes the chemical shrinkage. Setting time is often chosen for time-zero. There is not a clear agreement on choosing the initial (Tazawa et al., 2000, Cusson et al., 2007) or final setting time (Turcry et al., 2002, Sant et al., 2006). Moreover different assessments of the setting of concrete result in different setting times (EN 196-3, ASTM C403, Reinhardt, 2004, Robeyst, 2007). The determination of time-zero through the minimum of the shrinkage rate can be a simple solution as no additional test is required (Eppers 2008). Moreover Eppers et al. (2008) have shown that this time corresponds to the time when stresses are generated in ring tests due to restrained shrinkage.

2. EXPERIMENTAL PROGRAM

2.1 MATERIALS AND MIXTURES

The Portland cement used in UHSC was produced in Germany and conformed to the European standard EN 197-1. It is referred to as cement 'A', a CEM I 52.5 R-HS/NA. One type of ground-granulated blast furnace slag was used. It conformed to the European standard EN 15167. One type of silica fume powder was used, conforming to the European standard EN 13263. The superplasticizer was polycarboxylate ether based and had a solids content of approximately 35.0 mass-percent. Quartz sand and quartz powder were used as aggregates. The nominal particle size of the quartz sand ranged from 0.125 mm to 0.5 mm, whereas the quartz powder contained particles up to a diameter of 0.125 mm. The compositions of UHSC mixtures are given in Table 1.

Table 1. UHSC mixtures.

(kg/m^3)	**Portland**	**BFS 75%**
Sand 0/0.5 mm	1015	1015
Quartz powder	220	220
Silica fume	130	130
Cement	800	200
GGBFS	0	600
Water	168	176
Superplasticizer Sp1	24	13
Effective water W_{eff}	186	186
W_{eff}/Binder	0.20	0.20
Sp1/C (%)	3.0	1.6
fc,2d (MPa).	99	24
fc,28d (MPa).	161	135

2.2 ASSESSMENT OF AUTOGENOUS SHRINKAGE

Prisms

The development of plastic shrinkage was measured using a prism-shaped steel mould device (70 x 70 x 280 mm^3) covered with PTFE to limit the friction between the concrete and the mould (Turcry, 2006). The concrete was poured into an envelope built using two PVC plates (70 x 68 x 5 mm^3) also used as reflecting plates and a plastic sheet (Figure 1). The sample temperature was controlled using water circulation in both side walls and the steel mould bottom (Figure 1). In this study isothermal tests were performed at 20°C.

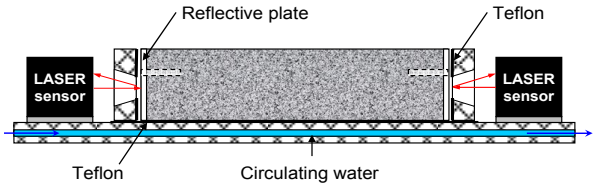

1a. Prism.

1b. Corrugated tubes

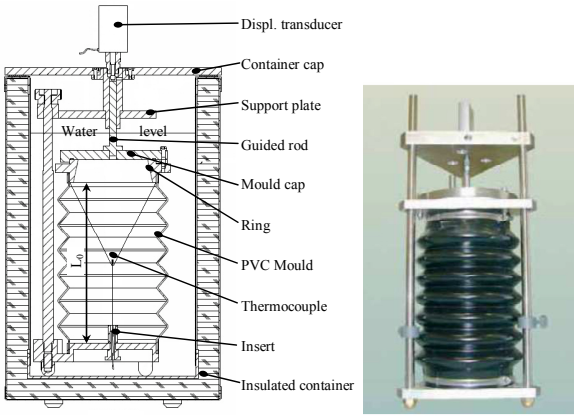

1c. BTJADE.

1d. Cone.

Figure 1. Autogenous measurement techniques.

Corrugated tubes

The basic setup described in the ASTM standard C1698 consists of the following items: (a) a corrugated tube mold made of plastic with a length of 420mm and an outer diameter of 29 mm; (b) a testing frame ('dilatometer bench') on which the filled corrugated mold is placed; (c) a measuring gauge with a minimum resolution of 2.5µm/m and a measuring range of at least 10mm. The tubes, having an inlet diameter of approximately 20 mm, were filled with the help of an applicator gun to facilitate the procedure. The concrete was filled into the apposite cartridge and pressed into the tube through a long rubber hose. The tubes were fixed vertically to a stand which was placed on a vibrating table during the process of filling. Digital feather touch spring push probes with extra-low tip force (0.18 N) were used to avoid compression of the tubes.

BTJADE

The autogenous deformation measurements of the studied concretes were carried using a BTJADE device. This latter is composed by a corrugated PVC mould (Boulay, 1993) in which the concrete is casted. The stiffness of the mould is assumed to be negligible. As shown in Figure 3, a thermocouple is inserted into the concrete specimen. The base length (L_0 = 250 mm) gives scale. The sample and the mould are maintained vertically by

means of a metal frame. The deformation is measured by means of an external displacement sensor. The device is completely immersed inside a temperature controlled bath and totally surrounded by water to insure isothermal conditions. The autogenous deformations can be corrected with the thermal variations (Staquet, 2008). The thermal deformation is computed by assuming a constant specimen thermal expansion coefficient after setting (Laplante, 1994).

Cone

The shrinkage cone originally had been developed for measuring the plastic shrinkage (Kaufmann, 2004). The method underwent some modifications which partly were described in (Eppers, 2009). The basic setup consists of a laser unit which is mounted on a stand, and a cylindrical jar which forms a cone on the inside. The jar used here is recommended for paste or concrete up to a maximum particle size of 2mm. The nominal height of the inner cone is 100mm; the diameter of the opening is approx. 115mm. The nominal volume is 350ml. The temperature of the material can be controlled by a coolant that flows through the jar. In addition, the manufacturer provides cone-shaped protection sheets which minimize friction, and reflector pads made of plastic (Figure 4). Pads made of concrete were used instead of the plastic pad to ensure a more neutral behavior in terms of thermal expansion. Diameter and height of the pads were 3 mm and 18 mm, respectively. Before being used the pads were stored for at least one week to minimize the influence of shrinkage of the pad.

2.3 ULTRASONIC MONITORING OF SETTING AND HARDENING

The *FreshCon* device which was developed at the University of Stuttgart was used to monitor the early age behavior of concrete using ultrasonic waves (Reinhardt and Grosse, 2004). This device is composed of two polymethacrylate (PMMA) walls which form a U-shaped mould. The U-shaped mould has high damping properties in order to absorb the waves passing trough the mould and moving around the concrete sample (concrete volume: 450 cm^3). The test was carried out in an air-conditioned room and the concrete sample was protected from desiccation by the use of a plastic foil. A data logging system allowed obtaining the ultrasonic velocity, the energy and the frequency spectrum evolution.

4. RESULTS AND DISCUSSION

4.1 ANALYSIS OF AUTOGENOUS DEFORMATIONS

This part shows how rough autogenous deformation data were analyzed to determine the autogenous shrinkage and correlate the evolutions of concrete properties. Figure 5 deals with Portland mixture at 20°C and BTJADE device. Autogenous shrinkage starts when concrete sets. However setting rather refers to a period and it depends on the

experimental procedure. The minimum of the shrinkage rate $t_{s,min}$ was chosen here as the time when autogenous shrinkage is initialized.

This is consistent with the assumptions on the mechanism of self-desiccation. As the stiffness of concrete starts increasing the chemical shrinkage slows down after a maximum $t_{s,max1}$ (Figure 5.a.). As long as voids and menisci have not been created in cement paste, self-desiccation does not develop. Thus the shrinkage rate goes through a minimum. Then as voids and capillary depression appear the shrinkage rate increases until a maximum $t_{s,max2}$ then it decreases. Hydration rate actually decreases and concrete becomes stiffer.

In order to confirm these assumptions shrinkage data were correlated with the data from the other tests, namely: the velocity of ultrasonic waves (Figures 5.b), setting from ASTM tests (Figure 5.c), and temperature (Figures 5.d). The maximum of the first derivative of ultrasonic velocity $t_{usI,max}$ is used to determine the initial setting time, whereas the time when it has decreased by 80% $t_{usI,max-80\%}$ or the minimum of the second derivative $t_{usII,min}$ were reported to correspond to the final setting time (Robeyst, 2007).

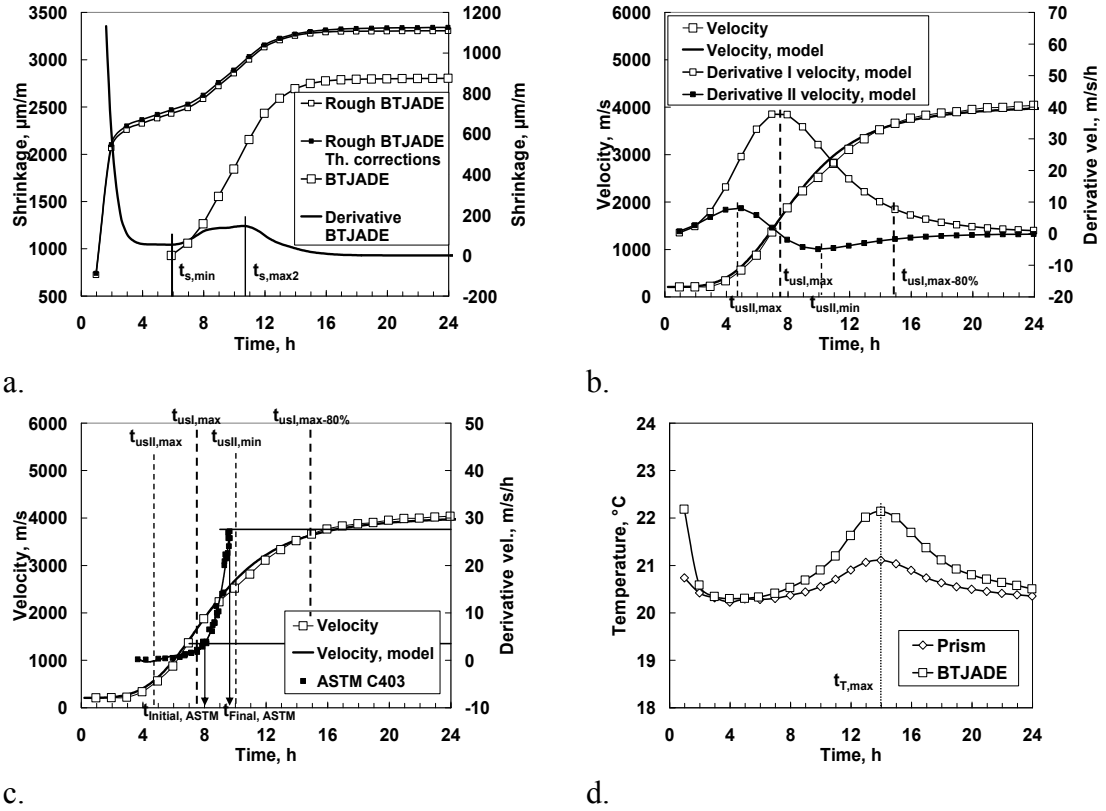

Figure 5. Assessment of autogenous shrinkage and times for correlation of properties. Portland UHSC mixture.

The specific times deduced from different shrinkage measurements and other tests have been correlated in figures 6 and 7. The minimum of the shrinkage rate $t_{s,min}$ was generally comprised between $t_{usII,max}$ and $t_{usI,max}$ (Figure 6). The initial setting time from Vicat test (EN standard) was closer but slightly higher.

Figure 7 shows a good correlation between the maximum of the shrinkage rate $t_{s,max2}$ and $t_{usII,min}$. $t_{usI,max-80\%}$, which can be correlated with the final setting time (Robeyst et al., 2007), was usually higher. Figure 7 also shows a good correlation between $t_{s,max2}$, $t_{usII,min}$, and the final setting time t_{final}, ASTM from ASTM tests.

As a consequence, even if the initialization of the autogneous shrinkage curves at the time of minimum shrinkage rate was provided by a mathematical analysis, it actually corresponds to specific stages of the physical evolution of the studied concrete mixtures.

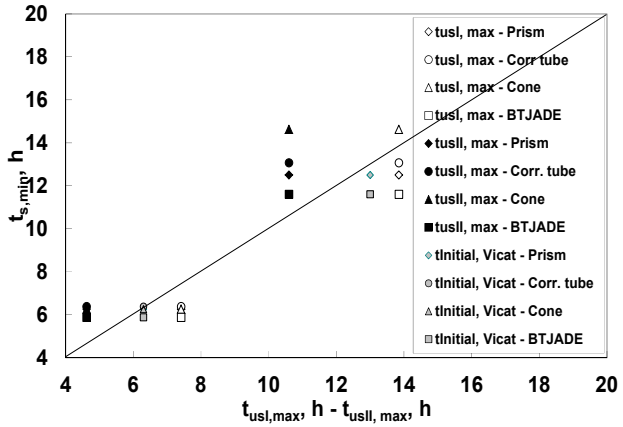

Figure 6. Correlations between minimum shrinkage rate and properties of ultrasonic waves.

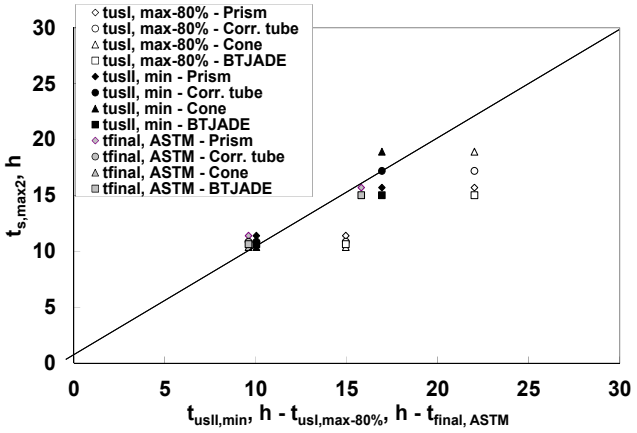

Figure 7. Correlations between maximum shrinkage rate, properties of ultrasonic waves, and ASTM final setting times.

4.2 INFLUENCE OF THE MEASUREMENT TECHNIQUE

In Figure 8, shrinkage curves are initialized at the minimum of the shrinkage rate. Each curve is the average of two tests (prism and cone) or three tests (BTJADE and corrugated tubes). The scatter of individual measurements is given at the end of the curve.

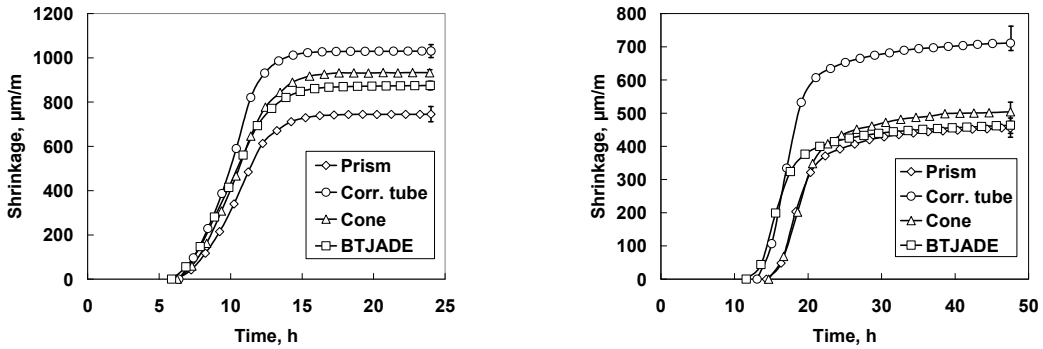

Portland **BFS 75%**

Figure 8. Autogenous shrinkage of UHSC.

Each method generally showed a good repeatability. However significant differences could be observed. The prisms showed lower shrinkage than BTJADE. The corrugated tubes and the cones gave the highest values. Whatever concrete mixture the ranking of shrinkage magnitudes was the same, thus the methods used in this study had intrinsic effects on shrinkage magnitude. This was not due to the direction of measurement since both horizontal measurements namely prisms and corrugated tubes respectively produced the lowest and the highest magnitudes. The measures could have been influenced by the temperature increase in the specimen, but this is not consistent with the trends observed here. BTJADE specimens actually showed higher temperature increase than prisms (Figure 5.d) but higher shrinkage magnitude.

CONCLUSION

Experimental methods were used to determine autogenous deformations to assess the influence of the measurement technique on autogenous shrinkage. Four different setups were gathered in the same laboratory. All the tests including ultrasonic monitoring were performed on the same batch of concrete. The following conclusions can be drawn:

• In spite of significant differences between the shrinkage magnitudes, all the methods showed good repeatability.

• Different sets of autogenous shrinkage data showed the same ranking of magnitudes as a function of the test method, namely: 1. Corrugated tubes, 2. Cones, 3. BTJADE, 4. Prisms.

• The time-zero used to initialize the autogenous shrinkage was based on the time of minimum autogenous deformation rate.

• The time of maximum autogenous shrinkage rate showed good correlations with the final setting time from ASTM, the minimum of second derivative of ultrasonic velocity, and the maximum temperature.

ACKNOWLEDGEMENTS

Data measurements corresponding to the corrugated tube and the cone have been obtained in the framework of the research stay of Sören Eppers at ULB who was highly appreciated and was funded by FNRS which is acknowledged too.

REFERENCES

Barcelo, Boivin, S., Rigaud, S., Acker, P., Clavaud, B., Boulay, C., 1999, “Linear vs. volumetric autogenous shrinkage measurement: Material behavior or experimental artifact?”, Self-desiccation and its importance in concrete technology, Proceedings of the Second International Research Seminar, 18 Juin, Lund, Edité par Persson, B., et Fagerlund, G., pp.109-125

Bjøntegaard, O., Hammer, T.A. 2006. RILEM Technical Committee 195 DTD: Motive and technical content. In O.M. Jensen et al. (eds), Volume Changes of Hardening Concrete: Testing and Mitigation; Proceedings of the In-ternational RILEM Conference, Lyngby, Denmark, 20-23 August 2006. Bagneux, France: RILEM Publications.

Bjøntegaard, Ø., Hammer, T.A. and Krauss, M., 'RILEM TC195-DTD Documentation report: Round Robin test results, statistical evaluation and test method proposal', RILEM report, 2006.

Boulay, C., Paties, C., 1993, “Mesure des déformations du béton au jeune âge”, Materials and Structures, 26, pp.307-311.

Cusson, D., Hoogeveen, T., 2007, “An experimental approach for analysis of early-age behaviour of high-performance concrete structures under restrained shrinkage”, Cement and Concrete Research, 37, pp.200-209.

Eppers, S., Mueller C.: Autogenous shrinkage and time-zero of UHPC determined with the shrinkage cone. In: Proceedings of Concreep 8, Ise-Shima, Japan, 2008, pp. 709-714.

Eppers, S., Müller, C.: On the examination of the autogenous shrinkage cracking propensity by means of the restrained ring test with particular consideration of temperature influences. In: beton 5/2009 pp. 227-230 (part 1) and beton 6/2009 pp. 283-289 (part 2).

Hammer, T.A., Bjøntegaard, Ø., 2006, “Testing of autogenous deformation and thermal dilation of early age mortar and concrete – Recommended test procedure”, Volume Changes of Hardening Concrete: Testing and Mitigation, International RILEM Conference, 20-23 Août, Lyngby, Danmark, Edited by Jensen, O.M., Lura, P., et Kovler, K., pp.341-346.

Jensen O.M. and P.F. Hansen. (1995), A dilatometer for measuring autogenous deformation in hardening Portland cement paste, Material and Structures, vol. 28 (181), p.406-409.

Jensen O. M. & Hansen P. F., Autogenous deformation and RH-change in perspective, Cement and Concrete Research, Vol. 31, No. 12, 2001, pp. 1859-1865.

Kaufmann, J., Winnefeld, F., Hesselbarth, D.: Effect of the addition of ultrafine cement and short fiber reinforcement on shrinkage, rheological and mechanical properties of Portland cement pastes. In: Cement & Concrete Composites 26 (2004), pp. 541-549.

M. Krauß, Ø. Bjøntegaard, and T. A. Hammer, Statistical evaluation of autogenous deformation – Test results performed in the RILEM TC195-DTD framework, International RILEM Conference on Volume Changes of Hardening Concrete: Testing and Mitigation, 20-23 August 2006, Technical University of Denmark, Lyngby, Denmark.

Laplante, P., Boulay, C., Evolution du coefficient de dilatation thermique du béton en fonction de sa maturité aux tout premiers âges, Materials and Structures, 27 (1994) 596 – 605.

Reinhardt H.W., Grosse C.U. 'Continuous monitoring of setting and hardening of mortar and concrete', Construction and Building Materials, 18 (2004), 145–154.

Robeyst, N., Gruyaert, E., De Belie, N., 2007, Ultrasonic monitoring of setting and hardening behaviour of concrete and mortar with blast-furnace slag cement, Douzième Congrès International de la Chimie du Ciment, 8-13 Juillet, Montréal, Canada, 11p.

Sant, G., Rajabipour, F., Lura, P., Weiss, J., 2006, "Examining time-zero and early age expansion in pastes containing shrinkage reducing admixtures (SRA'S) ", 2nd International Symposium on Advances in Concrete through Science and Engineering, 11-13 Septembre, Québec city, Canada, Edité par Marchand, J., Bissonnette, B., Gagné, R., Jolin, M., et Paradis, F., 11p.

S Staquet C Boulay N Robeyst, N De Belie, Ultrasonic monitoring of setting and autogenous shrinkage development of high performance concrete, Creep, Shrinkage and Durability Mechanics of Concrete and Concrete Structures, Tanabe et al. (eds), proc. of the 8th International Conference on Creep, Shrinkage and Durability of Concrete and Concrete Structures (CONCREEP 8), (Sept. 30th – Oct. 2nd, 2008, Ise-Shima, Japan) 321-327.

Tazawa, E., Sato, R., Sakai, E., Miyazawa, S., 2000, "Work of JCI committee on autogenous shrinkage", Shrinkage 2000, Proceedings of the International RILEM Workshop, PRO17, 16- 17 Octobre, Paris, France, Edité par Baroghel-Bouny, V., et Aïtcin, P.C., pp.21-40.

Ph. Turcry, A. Loukili, L. Barcelo, J.M. Casabonne Can the maturity concept be used to separate the autogenous shrinkage and thermal deformation of a cement paste at early age? Cement and Concrete Research 32 (2002) 1443–1450.

Turcry, P., Loukili, A., 'Evaluation of plastic shrinkage cracking of self-consolidating concrete'. ACI Mater J 103 (4) (2006) 272–9.

Numerical Experimentation on Thermo-Hydro Mechanical Behavior of Massive Reinforced Concrete Structures at an Early Age

L. Buffo-Lacarrière[1] and A. Sellier[1]

[1]Université de Toulouse, UPS, INSA, LMDC (Laboratoire Matériaux et Durabilité des Constructions), 135, Ave. de Rangueil, F-31 077 Toulouse Cedex 04, France. E-mail: buffo-lacarriere@insa-toulouse.fr

Abstract

The work presented here was performed in the context of the French national project CEOS.fr. The study is part of the second axis of the project dealing with the concrete behavior under thermo-hydro-chemo-mechanical (THCM) loads. One of the objectives of this component was to construct some massive structures with strain restraint in order to test and validate THCM model for predicting the early-age cracking of concrete structures. Once validated, this THCM model is used in the last part of the project to perform some numerical parametric studies and a more precise analysis of the effect of the reinforcement on the crack pattern of massive structures at early age.

INTRODUCTION

In the international literature, several recent studies have focused on the finite element modeling of this early-age behavior of massive concrete structures. However, many of them are more concerned with validating a thermal model and propose a purely numerical analysis of mechanical aspects, used to identify some characteristic features of early-age behavior aspects (Azenha et al. 2011; Lackner and Mang 2004; De Schutter 2002). In a few studies on restrained shrinkage structures that will be subjected to early age cracking, crack patterns are also compared (Benboudjema and Torrenti 2008; Bertagnoli et al. 2011; Buffo-Lacarriere et al. 2011; Faria et al. 2006) but, as instrumentation of "real case" massive structures is difficult to carry out, mechanical results at early age (strains) are not usually compared (Azenha et al. 2009).

In this context, the French national project CEOS.fr proposes to study three massive reinforced concrete beams cast in "industrial conditions". A strain restraining system was used in order to study the early age cracking of this kind of structures and more especially the effect of reinforcement on the cracking pattern. The beams were highly instrumented so as to record local temperature and strains (in concrete and on the reinforcement), global response, and cracking pattern in order to use them in the validation of the models developed or improved in the project. More details about the experimental results are available in (Buffo-Lacarrière and Torrenti 2015 p. -).

The first part of this paper will demonstrate the applicability of recent models developed in our laboratory to predict early-age cracking on a real massive reinforced structure.

The massive structures cast in the framework of the CEOS project are thus used in this objective. The second part of this paper will expose complementary numerical experimentation performed to study the influence of key phenomena on the early age cracking pattern: creep and shrinkage of concrete and reinforcement ratio.

PRELIMINARY VALIDATION OF THCM MODEL ON CEOS RESULTS

The model used in this numerical experimentation study has been previously validated on the field experimental results of French national project CEOS.fr (Buffo-Lacarriere et al. 2014). The restrained shrinkage testing bodies were massive I-shaped reinforced beams composed of a central part (5.1 m long, 50 cm wide and 80 cm high) and two massive heads (90 cm long, 2.2 m wide and 90 cm high), (**Figure 1**). Two largely dimensioned steel struts (diameter 32.4 cm and thickness 5.5 cm) were placed laterally between the two transverse heads to prevent almost all shrinkage.

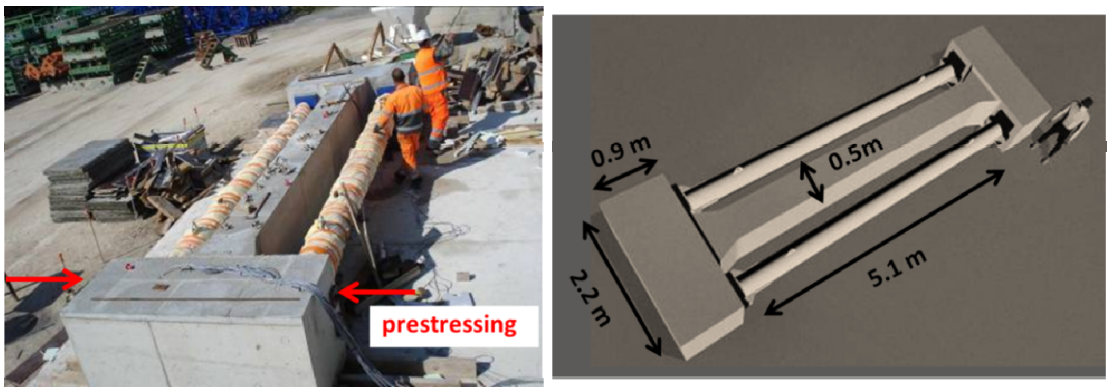

Figure 1. Geometry of the RG specimens

Three test bodies were made: RG8, the reference; RG9, with reduced reinforcement; and RG10, with increased cover (see **Table 1**). More information about these tests is available in (Buffo-Lacarrière and Torrenti 2015 p. -).

Table 1. Reinforcement of the central part of specimens RG8, RG9 and RG10

	RG8	RG9	RG10
% of longitudinal reinforcement	2%	0.56%	2%
Cover	30 mm (50 mm for longitudinal rebars)	30 mm (50 mm for longitudinal rebars)	50 mm (70 mm for longitudinal rebars)

The early age behavior of these structures was modeled using a THCM model adapted to early age behavior. Its validation can be found in (Buffo-Lacarriere et al. 2014) and only the general principles of the modeling are recalled here.

First the thermal behavior of concrete structure was predicted using a multiphasic hydration model. This model is able to reproduce the hydration of composed binders and its consequences for in situ conditions and is based on the coupling between hydration, water content and temperature (Kolani et al. 2012).

The consequence of the temperature variation is the thermal strain imposed to the concrete. In order to evaluate the induced stress, we use a rheological model which reproduces the visco-elastic behavior of concrete at early age. The model is divided in 3 levels: first an elastic level for the instantaneous behavior, then a visco-elastic level for the reversible part of the creep and a non-linear viscous level for the irreversible part of the creep. The non-linearity is obtained by introducing a consolidation to affect the viscosity. Next, the consequence of the consumption by hydration of water is the autogenous shrinkage. In our approach it is modeled as the strain induced in the creep module by the application on the solid of the capillary pressure induced by water consumption (Sellier and Buffo-Lacarrière 2009). To be applied to early age behavior, all the mechanical properties are expressed according to hydration degree development (Schutter and Taerwe 1996) and numerical implementation is adapted (Buffo-Lacarrière and Sellier 2011). Once the effective stress induced by temperature and water content variations is determined, the apparent stress and crack state are evaluated using a damage model. It is based on a unilateral damage tensor. In compression the variable is isotropic and the criterion used is inspired of Drucker-Prager. In tension, the damage is anisotropic, uses a Rankine criterion and takes into account of the possibility of crack closure (Sellier et al. 2013).
The steel-concrete bond is modeled using a 3D viso-plastic law adapted to early age behavior (evolution of mechanical characteristics of the bond).
The results obtained with the model for RG8 and RG9 are presented in **Figure 2** and **Figure 3** and successfully compared to the experimental results.

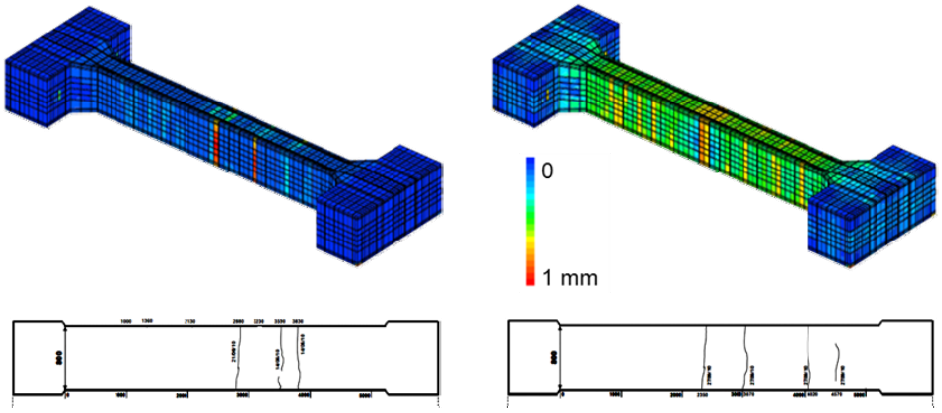

Figure 2. Numerical and experimental crack pattern for RG8 and RG9

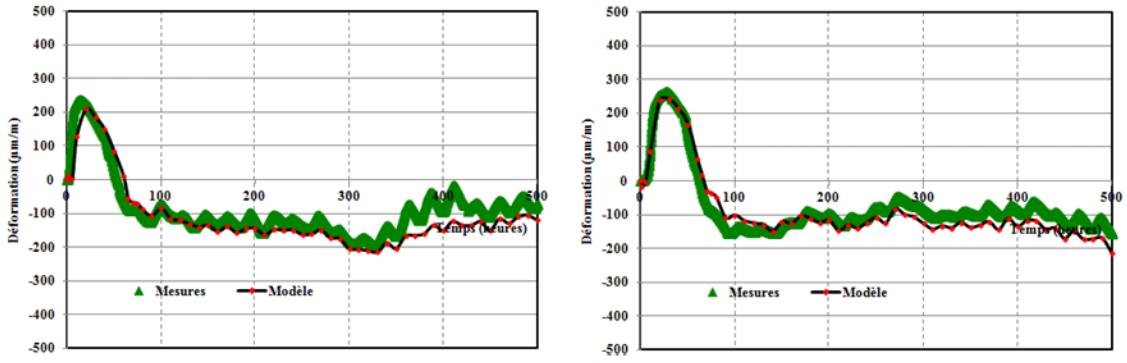

Figure 3. Numerical and experimental strain variations for RG8 and RG9

NUMERICAL EXPERIMENTATIONS

Principle of the numerical study

In order to complete the results obtained on the field, it was decided to perform a numerical experimental study able to highlight the influence of some "key" parameters of early age cracking risk: (i) creep and shrinkage of creep (its effect cannot be evaluated experimentally because concrete always exhibits delayed strains), (ii) reinforcement ratio. The effect of reinforcement ratio was partially identified with on the field results (by comparing RG9 and RG10 only because the thermal behavior of RG8 was different) but as RG10 was less instrumented the influence on crack opening and steel behavior was not investigated.
The virtual numerical tests were performed on simplified structures presented in **Figure 4**. The mechanical restraint imposed by the two metallic struts was replaced by a perfect restraint on the two vertical faces identified in **Figure 4**.

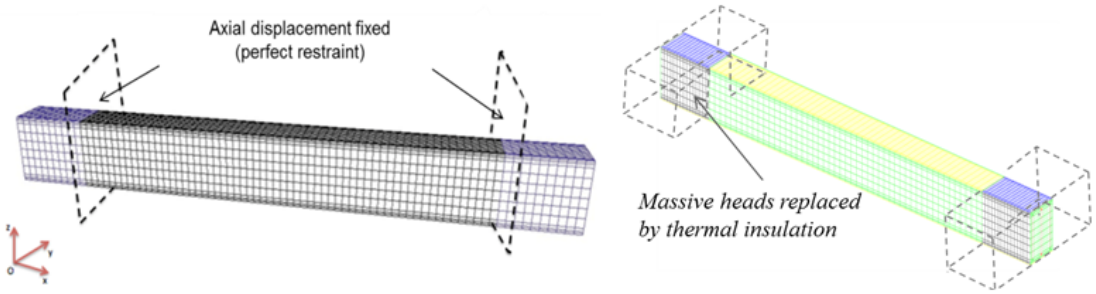

Figure 4. Simplified geometry and boundary conditions for virtual tests

The two massive heads was neglected and their thermal effect on central part was modeled by imposing no thermal transfer on the lateral faces of the extremities of ties (**Figure 4** right).
Two numerical tests were performed on virtual structures associated the real ones: the reference one RG8v using the simplified geometry with the reinforcement present in RG8 (2%) and RG9v which uses the simplified geometry with the reinforcement present in RG9 (0.6%). For the reference one (RG8v), the numerical test was performed with and without taking delayed behavior into account.
The thermal loading was also simplified by neglecting the daily variation of external temperature. Moreover similar boundary conditions were considered in each faces (no solar radiation). These simplifications would allow easier analysis of the effect of both key parameters tested (creep of concrete and reinforcement ratio).
The global mechanical response for the reference virtual test (RG8v) is presented in **Figure 5** through the force developed by the restraint of thermal strains.

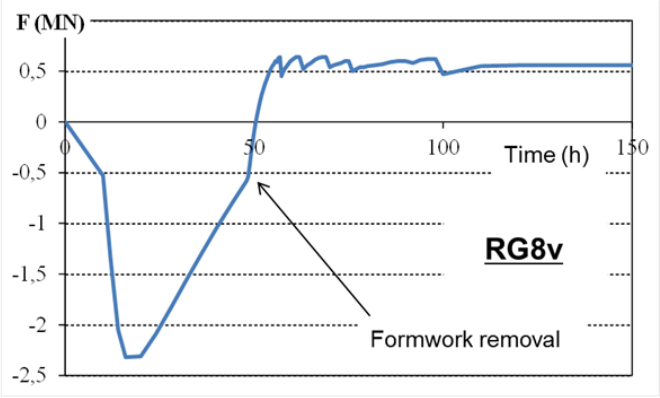

Figure 5. Force developed by the restraint in the reference virtual test RG8v

The classical behavior of restrained structures at early age can be observed: first compressive stresses induced by the dilation restraint during heating phase and then progressive tensile stresses during cooling phase. When tensile stresses reach the tensile strength, a crack has been observed and the force was relaxed.

The numerical simulation also allows analyzing the development of stresses in the reinforcement. Stress profile in one longitudinal bar is plotted in **Figure 6** from casting to the occurrence of the first crack (figure on the left) and then to 100 hours (figure on the right).

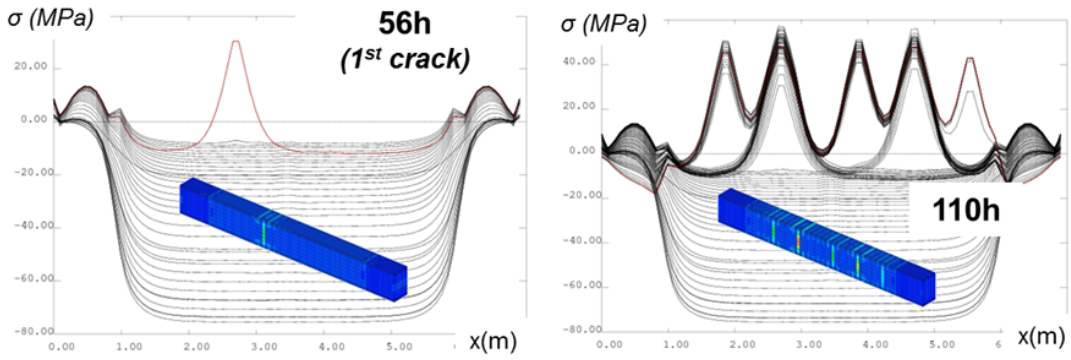

Figure 6. Stress in the steel from casting to the 1st crack and then to 110h

It is note that even during the cooling phase, steel developed compressive stresses in the central part of the beam (between restraint surfaces). Tensile stresses were observed in the entire bar only for important crack density. This is explained by the fact that the bars are anchored in the extremity of concrete ties which developed higher temperature (due to less heat transfer in massive heads, see **Figure 4**). Hydration is developed faster than in the central part of the tie and steel strains in this part were partially restraint.

Effect of delayed behavior of concrete

The effect of delayed behavior of concrete was investigated by a simulation made using only the elastic part of the rheological model. This simulation took account of the autogenous shrinkage and thermal strain induced by heating development. The effect can be observed on the global force and on the cracking pattern (**Figure 7**).

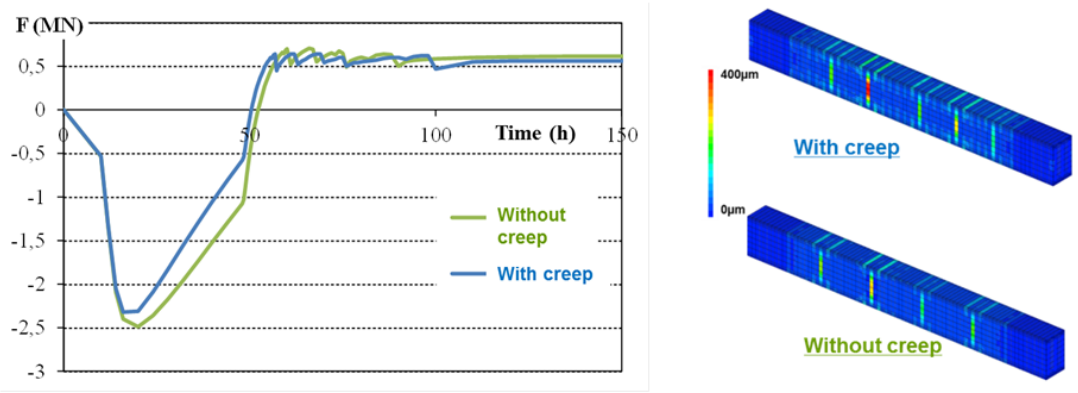

Figure 7. Influence of creep on the force and the cracking pattern

Contrary to what could be expected, neglecting creep led in this simulation to a non-safe calculation. Indeed, when creep was neglected, cracking was occurring later and led to a slight lower crack opening (as can be seen with more details in **Figure 8**).

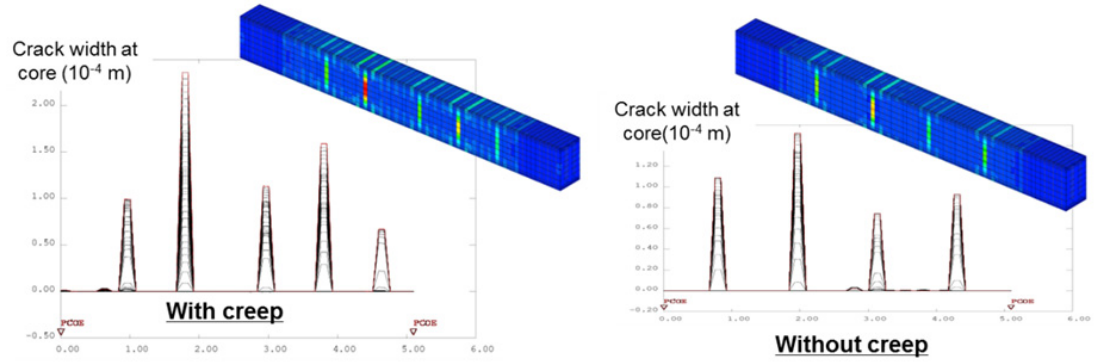

Figure 8. Influence of creep on crack opening 150 hours after casting

To understand why neglecting creep leads to a delay in crack occurring, the stress development in concrete (with creep) is plotted in **Figure 9** and compared to the theoretical elastic stress developed due to the perfect restraint of thermal strains.

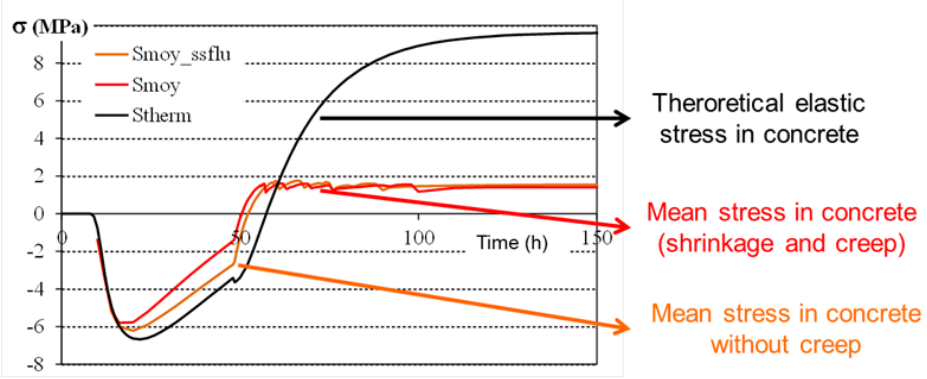

Figure 9. Development of stresses with and without creep and shrinkage

It is note that when neglecting creep, the compressive stress developed during the heating phase was over-estimated (black curve for elastic response). This overestimation led to a delay in the development of tensile stress and thus in the first crack occurring.

In **Figure 9**, the stress developed when autogenous shrinkage was not neglected is also plotted (orange curve). The corresponding curve is obtained with the numerical model taking account of autogenous strain but with only the elastic part of the rheological model. It shows that considering autogenous strain in an elastic approach (with damage) reduced the delay in crack occurring.

Effect of the reinforcement ratio

The effect of reinforcement ratio is studied comparing the numerical results obtained on the virtual test RG8v versus RG9v. Reinforcement are similar to the real structures RG8 and RG9 (**Table 1**).
The results in terms of global force are presented in **Figure 10** with a zoom between 50 and 150h (right graph), period which correspond to tensile stress development in concrete.

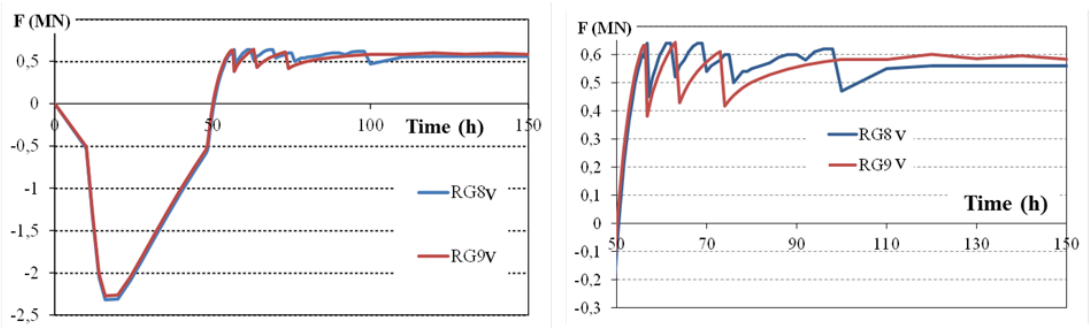

Figure 10. Effect of reinforcement ratio (red curve = low ratio)

Any effect of reinforcement ratio is observed during heating phase and cooling phase before the first crack occurring (around 55h). The difference resides in the number of crack, the lower reinforced structure (RG9v) exhibiting (as expected) lower cracks (red curve in **Figure 10**). **Figure 11** confirms this result and shows that the cracks were more open in the case of low reinforcement ratios. The results were thus similar to the one observed in the real structures of CEOS project.

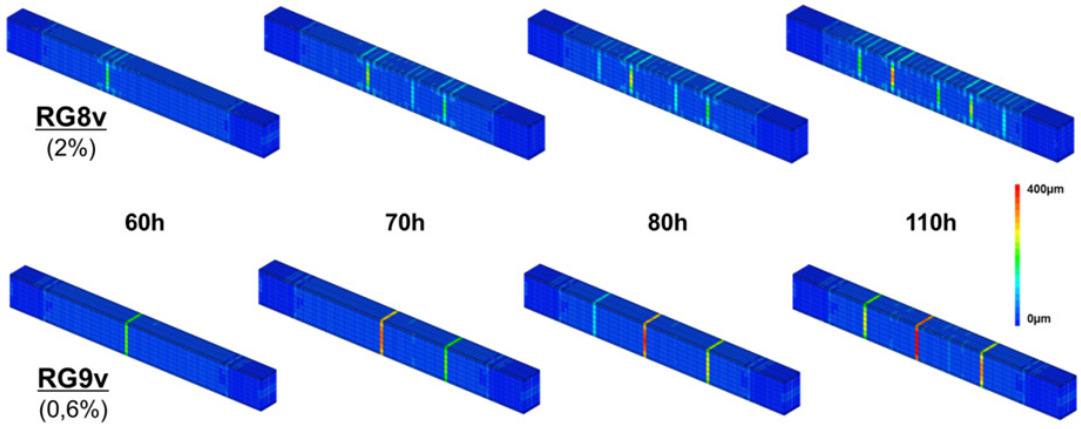

Figure 11. Cracking pattern for both virtual structures

Using this numerical experimentation, it was possible to evaluate more precisely the influence of reinforcement ratio on the crack opening.

It is note in **Figure 12** that the major crack opening in the case of lower reinforcement ratio (0.6%) was quite 50% higher than the one of larger reinforcement (2%).

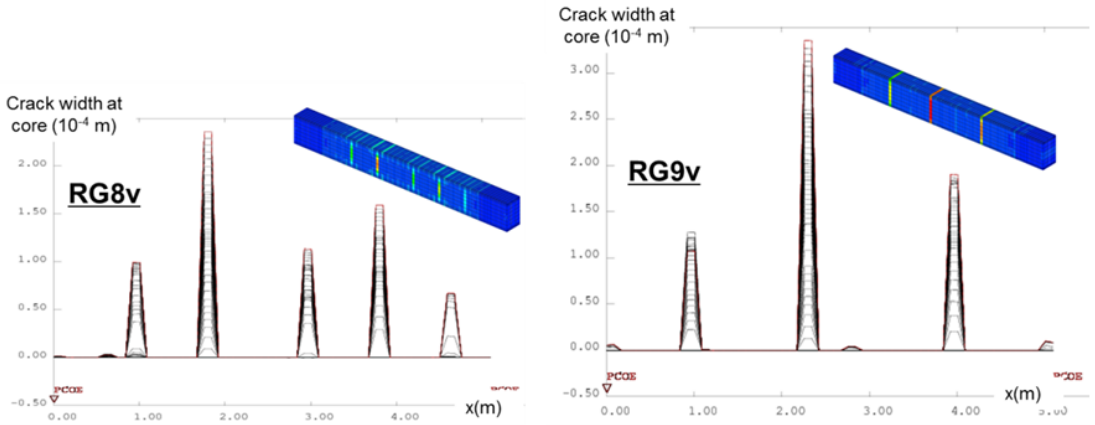

Figure 12. Crack opening for RG8v and RG9v (150h after casting)

The difference between both reinforcement ratios was also note on the shear stress profile along the longitudinal bars (**Figure 13**).

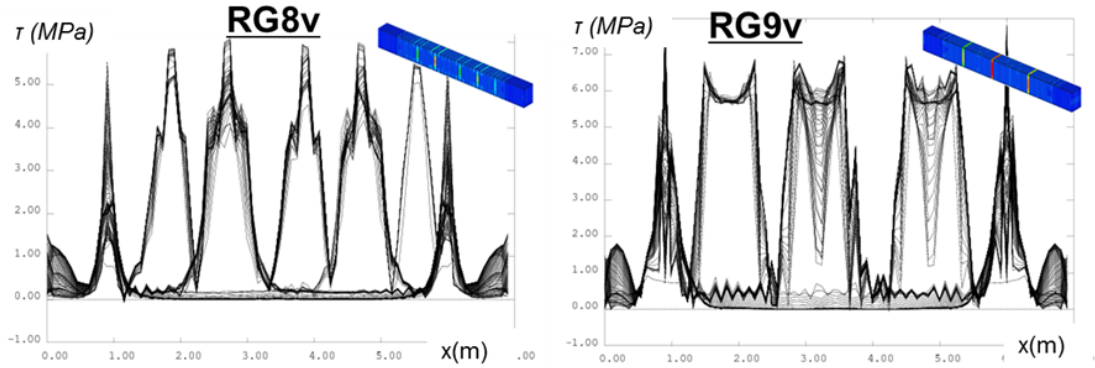

Figure 13. Shear stress profile in the reinforcement (150h after casting).

For the more reinforced structure, the steel-concrete bond remained in the elastic domain and the shear stress varied linearly near the crack. On the contrary, for the lower reinforced structure, the plastic plateau was reached by the shear stresses near the crack and the shear stress was constant in the anchorage length.

CONCLUSION

The paper presents a numerical study that complete the huge experimental program performed in the French national program CEOS.fr. The simulations were performed using a THCM model for early age behavior of concrete validated on the experimental on the field results of CEOS.fr program. In this numerical experimentation, the effect of two key parameters was more precisely investigated (creep of concrete and reinforcement ratio effect).

Numerical results show that if creep and shrinkage were neglected (and more especially compressive creep during heating period), the occurrence of cracking was delayed and the crack opening was slightly decreased.

Results on the parametric study concerning the reinforcement highlight that the less reinforced structure exhibited lower cracks but cracks more open (crack opening quite 50% higher for a reinforcement ratio decreasing from 2% to 0.6%). It also show different distribution of the shear stresses around the reinforcement bars after the first crack depending on the reinforcement ratio.

ACKNOLEDGEMENTS

The investigations and results reported here were supported by the French national program CEOS.fr. We are also grateful to CEA/DEN/DM2S/SEMT for providing the finite element code CASTEM.

REFERENCES

Azenha, M., Faria, R., and Ferreira, D. (2009). “Identification of early-age concrete temperatures and strains: Monitoring and numerical simulation.” *Cement & Concrete Composites*, 31(6), 369–378.

Azenha, M., Sousa, C., Faria, R., and Neves, A. (2011). “Thermo-hygro-mechanical modelling of self-induced stresses during the service life of RC structures.” *Engineering Structures*, 33(12), 3442–3453.

Benboudjema, F., and Torrenti, J. M. (2008). “Early-age behaviour of concrete nuclear containments.” *Nuclear Engineering and Design*, 238(10), 2495–2506.

Bertagnoli, G., Mancini, G., and Tondolo, F. (2011). “Early age cracking of massive concrete piers.” *Magazine of Concrete Research*, 63(10), 723–736.

Buffo-Lacarrière, L., and Sellier, A. (2011). “Chemo-Mechanical Modeling Requirements for the Assessment of Concrete Structure Service Life.” *Journal of Engineering Mechanics*, ASCE-AMER SOC CIVIL ENGINEERS, 137(9), 625–633.

Buffo-Lacarriere, L., Sellier, A., and Kolani, B. (2014). “Application of thermo-hydro-chemo-mechanical model for early age behaviour of concrete to experimental massive reinforced structures with strain-restraining system.” *European Journal of Environmental and Civil Engineering*, 18(7), 814–827.

Buffo-Lacarriere, L., Sellier, A., Turatsinze, A., and Escadeillas, G. (2011). “Finite element modelling of hardening concrete: application to the prediction of

early age cracking for massive reinforced structures." *Materials and Structures*, 44(10), 1821–1835.
Buffo-Lacarrière, L., and Torrenti, J.-M. (2015). "CEOS.fr experiments for crack control of concrete at early age." *Concreep 10*, Vienna, Austria.
Faria, R., Azenha, M., and Figueiras, J. A. (2006). "Modelling of concrete at early ages: Application to an externally restrained slab." *Cement & Concrete Composites*, 28(6), 572–585.
Kolani, B., Buffo-Lacarrière, L., Sellier, A., Escadeillas, G., Boutillon, L., and Linger, L. (2012). "Hydration of slag-blended cements." *Cement and Concrete Composites*, 34(9), 1009–1018.
Lackner, R., and Mang, H. A. (2004). "Chemoplastic material model for the simulation of early-age cracking: From the constitutive law to numerical analyses of massive concrete structures." *Cement & Concrete Composites*, 26(5), 551–562.
De Schutter, G. (2002). "Fundamental study of early age concrete behaviour as a basis for durable concrete structures." *Materials and Structures*, 35(245), 15–21.
Schutter, G., and Taerwe, L. (1996). "Degree of hydration-based description of mechanical properties of early age concrete." *Materials and Structures*, Springer Netherlands, 29(6), 335–344.
Sellier, A., and Buffo-Lacarrière, L. (2009). "Towards a simple and unified modelling of basic creep, shrinckage and drying creep of concrete." *European Journal of Environmental and Civil Engineering*, 13(10), 1161–1182.
Sellier, A., Casaux-Ginestet, G., Buffo-Lacarrière, L., and Bourbon, X. (2013). "Orthotropic damage coupled with localized crack reclosure processing. Part I: Constitutive laws." *Engineering Fracture Mechanics*, PERGAMON-ELSEVIER SCIENCE LTD, 97, 148–167.

From Testing and Modeling to Guidelines and Standards: The Case of Restrained Volume Changes in Concrete Structures at Early Ages

F. Toutlemonde[1]; T. Kanstad[2]; F. Benboudjema[3]; and M. Wyrzykowski[4]

[1]IFSTTAR, Paris-Est University, Materials & Structures Department, 77447 Marne-la-Vallée Cedex 2, France. E-mail: francois.toutlemonde@ifsttar.fr
[2]Department of Structural Engineering, The Norwegian University of Science and Engineering (NTNU), Trondheim, Norway. E-mail: terje.kanstad@ntnu.no
[3]LMT-Cachan/ENS-Cachan/CNRS/Université Paris Saclay, Cachan, France. E-mail: farid.benboudjema@ens-cachan.fr
[4]Empa, Swiss Federal Laboratories for Materials Science and Technology, Duebendorf, Switzerland. E-mail: mateusz.wyrzykowski@empa.ch

Abstract

Restrained volume changes in concrete structures at early age may be concomitant with mechanical loadings and lead to cracking. If this is not precisely addressed in service-life design, long-term consequences on the serviceability, the durability and the structural behavior of concrete structures may occur. Qualification of advanced models and development of appropriate standards and specification are two main target points of a recently launched COST Action. The main features of the program and objectives of the related working groups are detailed in this paper.

INTRODUCTION AND MOTIVATION

An adequate justification of the service life of concrete structures in conformity with the specified expected value may require an appropriate evaluation and analysis of imposed strains (mainly thermal strains possibly induced by hydration, creep and shrinkage), and control of their induced effects in combination with (usual mechanically loading) actions. Although this has been recognized as a principle in section 2 of Eurocode 2 (CEN, 2004), accepted reliable methods to address these combined effects are not currently available, and thus have not been described in present standards, although the consequences of possibly induced cracking (especially widely-open early-age cracks and induced water and ions transfer) may impair the expected service life in a more critical way than common material ageing mechanisms known as “durability-related” (carbonation, sulfate attack, chloride penetration etc.).

Technological national provisions, dealing e.g. with the spacing of expansion joints in current buildings (AFNOR, 2007), tend to bypass in such common cases the necessity of a detailed study. For special structures however, such as large rafts, large

industrial facilities (Labbé & coll., 2015), structures with tightness requirements, composite structures (Kretz & coll., 1995; Pascu & Toutlemonde, 2003) where concrete parts may be subject to restraint (Fig. 1), large structures built in successive lifts, and numerous structural retrofitting projects including restrained cast-in-situ concrete parts, it is necessary to explicitly address the combined effects of early age restraints and further service loads. Moreover, even in the case of ordinary buildings or structures, several in-service problems have been observed even when current regulations are strictly followed (underground parking slabs, e.g.).

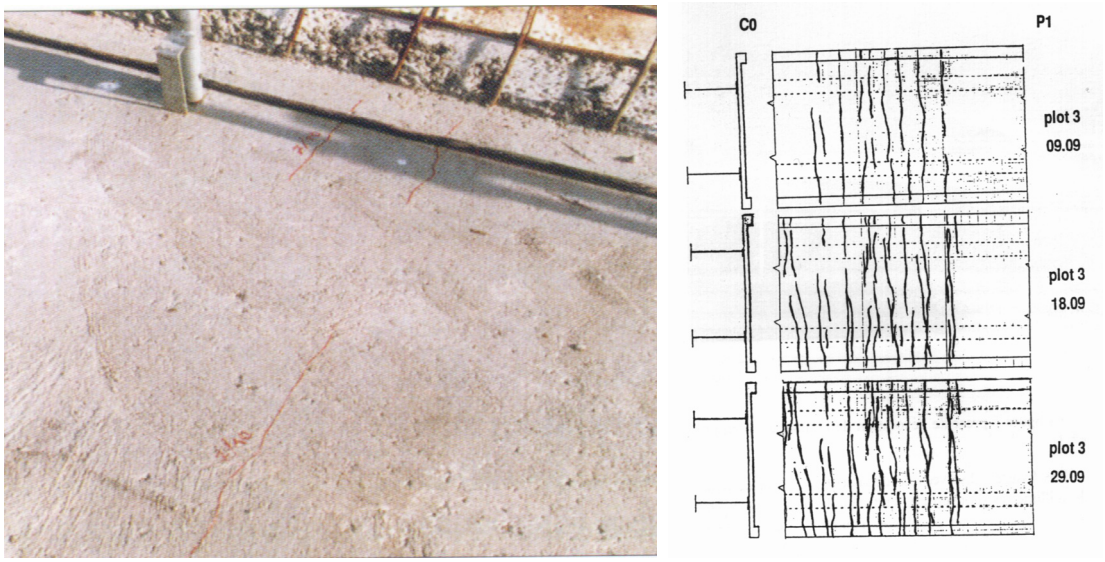

Figure 1: Example of through-going transversal cracks in composite bridge decks due to insufficiently consideration of restrained shrinkage.
a) Visual evidence on site.
b) Crack pattern evolution during the first four weeks of a bridge deck.

Therefore, improved models making it possible to rationally analyze the concrete behavior and crack development under such effects are required, as well as subsequently updated and rationally-based codes and standards provisions, which shall lead to more sustainable and effective solutions for concrete structures at both economical and environmental levels.

Predicting cracking due to restrained shrinkage is quite a difficult task. Indeed, it involves for the determination of input data a number of experimental tests (calorimetry, measurements of autogenous shrinkage, mechanical properties, creep in tension etc.) which are not readily available industrial practice. Besides, special attention is required in experiments since all phenomena occur simultaneously and separation is not straightforward in some cases due to couplings (e.g. thermal and autogenous strain). The heterogeneity of concrete complicates the analysis of experimental data: e.g. shrinkage occurs only in cement paste and is restrained locally by aggregates and size effects must be considered carefully (decreasing tensile

strength with the size of structures, gradients of temperature). Therefore, in order to extrapolate measured experimental results to concrete structures, numerical models are required. They have to be based on physical mechanics (often necessarily simplified or bypassed by empirical approaches, e.g. description of creep) in order to get rid of all aforementioned issues.

Following various research efforts as documented in (Toutlemonde & Torrenti, 2012), it has been decided to federate and coordinate actions at the European level, and the COST TU 1404 action was able to be launched (Azenha *et al.*, 2014). Within this frame, the tasks of consolidating and qualifying advanced models in terms of their usability for service-life related analyses, and preparing improved codes and standards, are taken in charge by the Working groups WG2 and WG3 of this COST TU 1404 action. This initiative is supported by 93 participants (individuals or institutions) from 23 countries for WG2 and by 77 participants from 22 countries for WG3. The WG1 is devoted to the determination of different properties of early age and hardened cement based materials, and a strong coordination with WG2 dedicated on modeling is obviously required, so that input for computational analysis can be reliably determined. Moreover, in order to enable adopting the most recent modeling approaches into practical recommendations and software tools, a strong interaction between the WG3 and WG2 shall be reached.

The planned work consists of analyzing the different models and their prediction capacities, with respect to relevant benchmark studies, drawing general lessons and proposing a standard methodology compatible with the Eurocode standard format to address thermo-hydro-chemo-mechanical coupled effects in serviceability design, including transient construction phases. Based on the rational understanding of these effects, it is also intended to provide quantitative and enhanced ways of considering curing, release of hydration heat and induced temperature development, restraint to deformations and visco-elastic effects in the service life predictions, addressing associated material specifications in the material standards and execution provisions in the relevant standards.

CONSOLIDATION OF ADVANCED MODELS FOR SERVICE-LIFE RELATED ANALYSES

The description of concrete behaviour has proven a very challenging task due to a complex material microstructure and various phenomena of chemo-physical nature taking place during material setting and hardening and due to its interaction with environment. In order to cover different aspects of concrete behaviour, modeling approaches exist at various scale levels of concrete microstructure, from atomistic models that focus on molecular size, to structural models that describe the behaviour of concrete elements, structures and buildings. Application of complex modeling for predictions of service-life of cement-based materials is usually not required in standards. Instead, simple empirical approaches are used. One of the major reasons for the absence of a commonly accepted methodology regarding application of advanced modeling in standard design practice is due to the great diversity of

modeling approaches (some couplings and phenomena are neglected or not), with various assumptions related to mechanisms of delayed strains, variety of input parameters and different qualities regarding robustness and predictive power.

With the specific issue of restrained volume changes in concrete structures at early ages, sometimes combined with mechanical loadings, most critical challenges include:

- accurate prediction of the temperature field (evolution of thermo-physical parameters with temperature and hydration, heat generation due to hydration coupled with boundary conditions), which requires appropriate materials inputs (Torrenti, 2010);
- accurate prediction of the (temperature and hydration dependent) fields of water saturation, and coupled visco-elastic effects (thermal, autogenous and drying shrinkage which may be restrained); especially when tensile creep is considered, a review of the literature shows a large discrepancy in experimental results, see Fig. 2);
- accurate description of the concrete mechanical behaviour during its hardening phase, as well as bond strength development between concrete and reinforcement, which has turned out to be a key point (Labbé & coll., 2015);
- adequate representation of mechanical effects (strains, stresses, crack depth and openings) in relation with control criteria for the engineer (Balázs *et al.*, 2013).

Basically, it is in fact necessary to unveil the mechanisms at the origin of shrinkage and creep. As long as capillary pressure is generally assumed to drive autogenous shrinkage and also drying shrinkage at higher RH levels, e.g. (Lura *et al.*, 2003, Gawin *et al.*, 2008), no consensus exists regarding other possible mechanisms. For creep, it is even worse, since several mechanisms are proposed: migration of water, sliding of the C-S-H etc. It is crucial since predictive models can be proposed only if mechanisms are known. It needs relevant experiments and observations, as well as multi-scale modeling: namely, at 50 % RH, pores of a few nanometers diameters are concerned, while shrinkage and creep are restrained by aggregates (size going from 100 μm up to 2 cm usually).

The models should take into account all dependencies found by experiments (e.g. temperature and hydration effects on thermal conductivity, autogenous shrinkage etc.). Nevertheless, numerical simulations can also improve or orientate experiments:

- for verification that there are no artifacts in the tests (like edge effects);
- for determination by means of sensitivity analysis (Gaspar *et al.,* 2014) of the material parameters which have the most significant impact on the prediction of the risk of cracking (e.g. see in Fig. 3 the effect of basic tensile creep in a massive wall).

In turn, numerical analysis of experiments will help simplifications in justifying the possibility to disregard some couplings or some dependencies (e.g., is the effect of hydration degree on the coefficient of thermal expansion significant?). Consolidation of available advanced modeling methods will thus be carried out within the Working Group 2 of COST TU1404 Action on the basis of benchmarks, among which the most recent 1/3 scaled containment structure built by the French power company EDF (Masson, 2013).

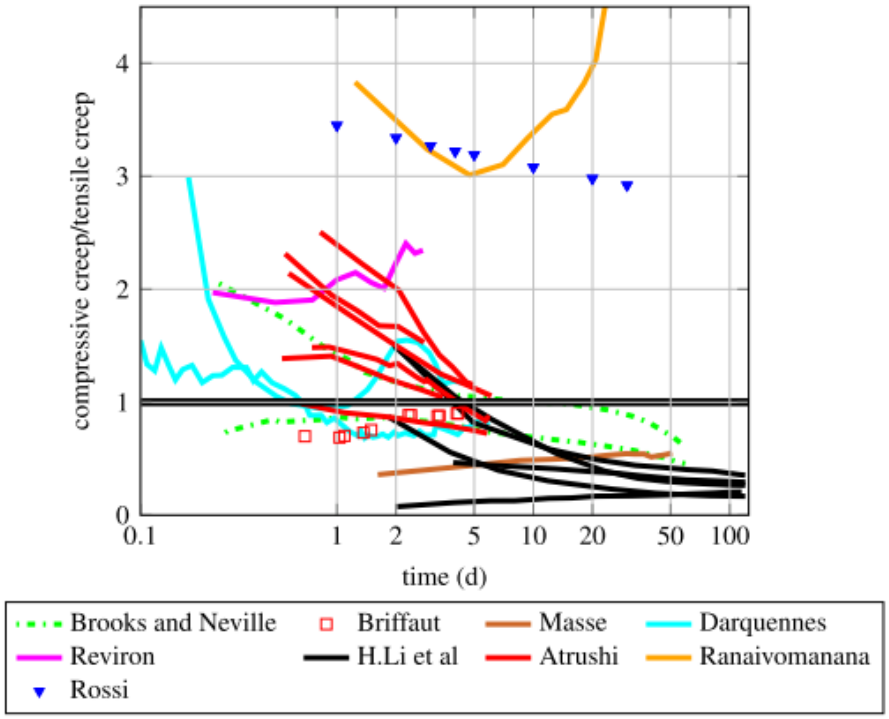

Figure 2: Evolution of the ratio of the basic compressive creep divided by tensile creep (Hilaire *et al.*, 2014)

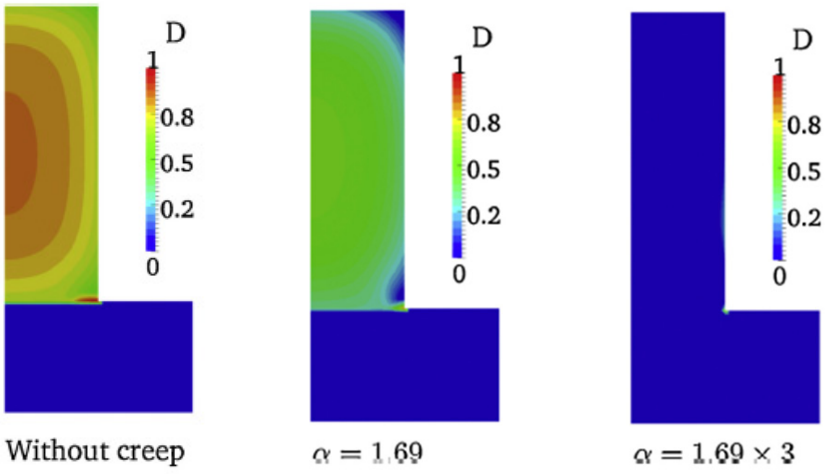

Figure 3: Effect of tensile creep on the prediction of damage by thermal and autogenous shrinkage in a massive concrete wall (Hilaire *et al.*, 2014). α is the ratio between basic tensile and basic creep.

PRODUCTS AND STANDARDS TO BE IMPROVED AND HOW TO PROCEED?

As a result of the WG2 benchmark examples associated to the prediction of temperature fields, deformations, cracks and stresses in concrete structures at early age resulting from prescribed physic-chemical strains as well as possible concomitant external loadings, it is expected that the main principles of satisfactory computational methods can be drawn and exemplified. It is deemed as a significant benefit for engineering to have access to such a recommended methodology, which could constitute a framework for software development or qualification. With respect to the development effort of such advanced software, major issues are:

- documented reliability of the predicted output (temperature, strains and displacements, stresses and cracks),
- user-friendliness, limited cost,
- probabilistic analysis to determine the safety factors,
- appropriate parameters used as input and detailed precautions associated to input values determination: as an example, duration of the dormant period before hydration for some ultra-high performance concrete mixes which may have a strong influence on the cracking risk (Sorelli *et al.*, 2012)).

A specific group priority in WG3 of COST TU1404 Action has thus been dedicated to software development and qualification.

Fair comparison of the software ability to predict relevant output values requires consistent use of input characteristics. Definition of such characteristics shall address the following aspects:

- relevance,
- absence of bias,
- limited uncertainty (repeatability)
- ease to handle, limited cost of the measuring protocol,
- documented qualification of the dedicated material / measurement method.

Another specific group priority in WG3 of COST TU1404 Action has been dedicated to devices development and qualification, which is also related to the development of recommendations or pre-standard measurement methods. Technical exchanges and round robin tests within the WG1 of COST TU 1404 Action help to optimize and validate measurement protocols in determining associated scatter and uncertainties, which make the task of pre-standards writing feasible. Main efforts should be focused on the determination of thermal expansion coefficient, autogenous shrinkage development with time (as an example, the BTJADE device described in Staquet et al., 2008, is illustrated on Fig. 4), moisture diffusion coefficient and its evolution with progressive hydration, etc.

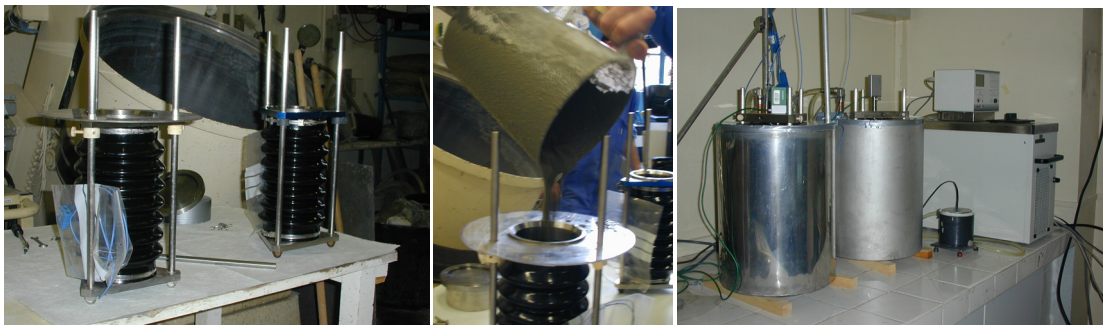

Figure 4: BTJADE device developed at IFSTTAR for the determination of autogenous shrinkage at early age

Controlling cracking or excessive deformations or stresses which could impair serviceability could thus be related to controlling the relevant physically-based input parameters. In such a context, the associated test results can be considered as possible specified values according to a performance-based updated standard for material specification (AFNOR, 2014; J.O., 2015). Discussions should progress for establishing such possible specifications, either using direct physical results, or classes, after a step of benchmarking. Based on clarification of the scientific issues stated above, the WG3 of the COST TU1404 Action is thus aimed to develop guidelines and establish protocols for improving existing standards in the context of combination of imposed / restrained deformations and service loads so as to control serviceability and durability of concrete structures effectively. Although these considerations have sometimes been deemed as secondary for ordinary buildings, they are important for synthesizing the different parts of Eurocode 2 in a future unified standard. In such a perspective, autogenous shrinkage, heat generation associated to the concrete mix, or induced cracking risk in a standardized test (possibly a type of ring test, for example), should deserve the main attention of the specific group priority dedicated to recommendations and proposals for Standards evolution in WG3 of COST TU1404 Action.

While improvements and developments of test standards, of concrete specification standards and of computational methods addressed in the standard for design of concrete structures are thus expected, it also appears necessary to clarify the reasonable combination of loads and imposed or initial strains to be addressed in the general reliability format of structures verification.

Namely, based on the risk of impaired serviceability for structures having a tightness requirement, it can be considered that the opening of possible cracks produced at early age due to restrained thermal or desiccation shrinkage, mechanical loadings during the execution phases, as well as the crack opening due to further service loading(s) associated to the tightness verification scenarios should be added and their sum should be lower than the maximum design crack opening.

Conversely, for structures where the control of cracking mainly aims at limiting the stress variations in the reinforcement and ensuring durability, aspect

preservation and continuity in the structural behavior, the reinforcing bars should help controlling cracks at three successive stages which could be considered as independent, thus no additive combination of these scenarios should be carried out. The underlying assumption is that if cracking is sufficiently controlled at each step, relaxation can occur but the continuous behaviour of the structure is maintained and the induced compliance is not due to localized cracks modifying the further behaviour. Such a simplified vision may remain questionable due to the continuous development of autogenous shrinkage; however it has simplicity advantages for the designer. These three successive stages are:

1. From concrete placement to the end of the period associated to setting and heat generation,
2. From the construction to delivery of the structure to the client, before operation,
3. After long-term operation of the structure.

Discussion of such proposals for standards updating certainly exceeds the mandate of a COST action and requests debates in the appropriate CEN committees. However, diffusion of such possible ideas and preliminary technical instruction of the consequences and benefits of such proposals is of interest within the frame of such a group representing over 20 European member States.

CONCLUSION

Advanced modeling and appropriate standard accounting of restrained volume changes in concrete structures at early ages in possible concomitance with mechanical loadings deserves joint efforts within the frame of the recently launched COST TU1404 Action, which shall complete its ambitious program by the end of 2017. The main features of the program and objectives of the related working groups (WG) have been detailed in this paper. Modelling of the behavior of cement based materials and structures with regard especially to the mechanisms that may impair service life will be addressed within WG2 of the Action. The efforts will in particular focus on describing restrained deformations and cracking. In addition to the synergies resulting from joining the modeling efforts between the different groups within WG2, a number of benchmarking campaigns will be run. This will enable proving the robustness and predictive power of different models and will help establishing the general guidelines for the required input data and the expected results. At the same time, the COST Action will promote creation of recommendations and pre-standard regulations that will enable appropriate assessment of service life of cement based materials and structures. These assets will be a main objective of WG3 of the Action. In order to promote adopting the new modeling approaches into practice, WG3 will focus on development and qualification of both experimental techniques and software tools that address the problems related to impaired service life.

ACKNOWLEDGEMENTS

The authors would like to acknowledge the contribution and networking support of the COST Action TU1404 “Towards the next generation of standards for service life of cement-based materials and structures”, 2014-2017.

REFERENCES

AFNOR (French Association for Standardization), (2007) *Annexe nationale à la NF EN 1992-1-1:2005*, NF EN 1992-1-1/NA, French National Annex to NF EN 1992-1-1

AFNOR (French Association for Standardization), (2014) *Béton: spécification, performance, production et conformité*, NF EN 206/CN, French standard for concrete specification

Azenha M. *et al.* (2014) *Memorandum of Understanding for the implementation of a European Concerted Research Action designated as COST Action TU1404: Towards the next generation of standards for service life of cement-based materials and structures*, http://www.cost.eu/COST_Actions/tud/Actions/TU1404

Balázs G. *et al.* (2013) Design for SLS according to fib Model Code 2010, *Structural Concrete* (*fib* Journal), vol. **14** n°2, pp. 99-123

CEN (European Committee of Standardization), (2004) *Eurocode 2* (EN 1992-1-1, 2004 Design of concrete structures – Part 1-1: General rules and rules for buildings)

Gaspar A. *et al.* (2014) Methodology for a probabilistic analysis of an RCC gravity dam construction. Modelling of temperature, hydration degree and ageing degree fields, *Engineering Structures*, n°65, pp. 99-110.

Gawin, D., Wyrzykowski, M., Pesavento, F. (2008) Modeling Hygro-thermal Performance and Strains of Cementitious Building Materials Maturing in Variable Conditions, J. Build. Phys., 31, 301-318.

J.O. (Official Publications of the French Republic), *Fascicule 65 du CCTG, Exécution des ouvrages de génie civil en béton*, version dated November 2014, to be published in 2015.

Kretz, T. & coll. (1995) *Ponts mixtes. Recommandations pour maîtriser la fissuration des dalles*, Sétra, Bagneux (now Cerema, Bron), France.

Hilaire, A. *et al.* (2014) Modeling basic creep in concrete at early-age under compressive and tensile loading, *Nuclear Engineering Design*, n°269, pp. 222-230.

Labbé, P. & coll. (2015) *Comportement et évaluation des ouvrages spéciaux vis-à-vis de la fissuration et du retrait. Recommandations pour la maîtrise des phénomènes de fissuration*, guide technique, projet CEOS.fr, Paris, 2015.

Lura, P., Jensen, O.M., van Breugel, K. (2003) Autogenous shrinkage in high-performance cement paste: An evaluation of basic mechanisms, Cem. Concr. Res., 33, 223-232.

Masson B. (2013) *Démarche industrielle de compréhension des phénomènes de transferts dans les parois en béton*, keynote lecture, 31èmes rencontres de l’AUGC, ENS de Cachan, 29-31 May.

Pascu, I. R. & Toutlemonde, F. (2003) Modeling of initially cracked reinforced concrete bridge decks, in *Computational Modelling of Concrete Structures*, Bicanic et al. (eds), proc. Euro-C 2003, pp. 847-854.

Sorelli L. *et al.* (2012) Analysis of early-age cracking for UHPFRC elements (cast-in place or prefabricated) based on experience of Glenmore / « Passerelle des Anges » footbridges, in *Crack control of mass concrete and related issues concerning early-age of concrete structures*, RILEM PRO 85, pp. 211-222.

Staquet S., Boulay C., Robeyst N. & De Belie N. (2008) Suivi ultrasonique de la prise et mesure du développement du retrait endogène d'un béton à hautes performances, GEODIM'08, *Variations dimensionnelles des géomatériaux*, Saint-Nazaire (France), Abstracts. pp. 23-24

Torrenti, J.-M., ed. (2010) Chaleur d'hydratation des bétons – Mesures et exemples d'application, *Bulletin des laboratoires des Ponts et Chaussées*, Special issue, **278**, LCPC, Paris (now IFSTTAR, Marne-la-Vallée), France.

Toutlemonde, F. & Torrenti, J.-M. eds, (2012) *Crack control of mass concrete and related issues concerning early-age of concrete structures*, RLEM PRO 85, proceedings of the RILEM-JCI international Workshop ConCrack 3, March 15-16, 2012, Paris (France).

Verification of an Inkbottle Pore and a Continuative Pore Determined by a Step-by-Step Mercury Intrusion Porosimetry Test

Ryo Yohida[1]; Kohei Mizuno[1]; and Toshiharu Kishi[2]

[1]Department of Civil Engineering, Nagoya Institute of Technology, Gokiso-Cho, Showa-ku, Nagoya 466-8555, Japan. E-mail: yoshida.ryo@nitech.ac.jp
[2]Department of Human and Social Systems, Industrial Institute of Science, University of Tokyo, 4-6-1, Komaba, Meguro-ku, Tokyo 153-8505, Japan. E-mail: kishi@iis.u-tokyo.ac.jp

Abstract

The quantitative verification of an inkbottle pore and a continuative pore determined by mercury intrusion porosimetry (MIP) was conducted by comparing the volume of air obtained through the linear-traverse method (image analysis) with the mass change due to water absorption and drying. The c pore had a high correlation with the volume of air voids and the continuative pore with the amount of rapid water absorption and drying up to 3 hours from the start of the test.

1. INTRODUCTION

Mehta et al. showed that the threshold pore diameter and the total pore volume measured through MIP have a high correlation with the coefficient of permeability of concrete [1]. However, it is stated that the evaluation of pore structure by MIP is not reliable, because there have been problems that the overestimation of small pores due to the inkbottle effect or the deformation of samples by the excessive pressure [2].

On the other hand, a hysteresis curve, when the incompressible mercury is pressed again into pores, has a strict regularity of following the previous hysteresis curve. Applying this regularity, a unique technique for separation of continuative pores and inkbottle pores was proposed [3]. In this technique the overlapping portion of the hysteresis curve (envelope) is determined as a continuative pore and the difference branched from the envelope when updating the pressure as an inkbottle pore, which are obtained from the intrusion hysteresis when repeating the intrusion to pores with progressively updating maximum experienced pressures. In addition, it is possible using this method to determine the appropriate measurement pressure range based on the fact that the hysteresis curve deviates from the envelope when an overpressure is applied.

This study aims to examine the relationship of hardened mortar with the volume of air voids using the linear-traverse method for the volume of inkbottle pores and its relationship with the amount of water absorption and drying for the volume of continuative pores in order to verify physical properties of inkbottle pores and continuative pores that are separated with the proposed (step-by-step MIP) method.

2. OUTLINE OF THE EXPERIMENT

In this study, the following two series of experiments are provided for quantitative verification of inkbottle pores (section 2.1) and continuative pores (section 2.2) obtained through the step-by-step mercury intrusion porosimetry method.

2.1 The relationship between the volume of inkbottle pores and air voids (Experimental series 1)

2.1.1 Preparation of specimen

Mortar was prepared with water-to-cement (W/C) of 0.50, using ordinary Portland cement, limestone crushed sand, and tap water. The size of entrained air was adjusted using three kinds of air entraining (AE) agents: alkyl ether sulfate-based agents (M), rosin salt-based agents (L), and alkyl phosphate ester-based agents (S) (size series). The size of entrained air is in the order L > M > S. In addition, before casting, the target air volume of refresh mortar was adjusted with the addition amount of AE agent: 3.5 %, 6 %, and 7.5 % for AE agent M and 6 % for AE agents L and S (amount series). Table 1 shows the relationship between the specimen type and the volume of air. A cylindrical specimen (φ 100 × 200 mm) was prepared, cured in water until the age of 28 days.

2.1.2 Test and measurement methods

The central portion of the cylindrical specimen of φ 100 × 200 mm was cut to prepare a specimen with a thickness of approximately 40 mm, and then the surface

Table 1. AE agent types and amount of air

Mixture	W/C	AE agent		Air (%)		Air void spacing factor (μm)
		type	dosage (C * %)	fresh mortar	hardened mortar	
50M3.5	0.5	M	0.01	3.8	3.5	570
50M6.0			0.004	5.9	4.3	317
50M7.5			0.02	7.4	5.9	316
50N		-	-	3	2.4	852
50L6.0		L	0.005	5.6	4.7	348
50S6.0		S	0.012	6.3	4.4	332

Table 2. Material properties

Material	Property [density(g/cm^3)]
OPC	Ordinary portland cement [3.15]
MPC	Moderate heat portland cement [3.21]
BFS	Blast furnace slag (4200 cm^2/g) [2.88]
FA	Fly ash (4420 cm^2/g) [2.28]
SF	Silica fume (18.7 m^2/g)[2.20]
W	tap water
S	crushed sand [2.68]
G	crushed gravel (G_{max} = 20 mm) [2.71]
SP	super plasticizer
A	antiforming agent

Table 3. Mix-proportion

Mixture	W/B	quantity of material per unit volume (kg/m^3)								Agent (g/m^3)		Slump	Air	concrete
		W	O	M	S	G	BFS	FA	SF	SP	A	(cm)	(%)	temp.(℃)
OPC50	50	165	330	-	907	1034	-	-	-	2640	23	8.0	1.0	21.5
MPC50			-	330			-	-	-	2310	20	10.0	1.8	24.7
BFS30-50			231	-			99	-	-	1815	36	10.0	1.0	23.0
BFS45-50			182	-			149	-	-	1650	30	10.0	1.9	22.9
BFS65-50			116	-			215	-	-	1320	23	10.0	1.4	22.3
FA10-50			297	-			-	33	-	2805	26	11.0	1.7	22.5
FA30-50			231	-			-	99	-	2145	20	10.0	1.6	22.2
SF10-50			297	-			-	-	33	4290	40	11.0	1.9	23.0
SF15-50			281	-			-	-	50	3300	40	10.0	1.9	20.4
SF30-50			231	-			-	-	99	4290	50	3.0	2.0	21.4

was polished. The volume of air was calculated by applying the linear-traverse method using this specimen.

The measurement of pore structures was performed with a pressure cycle of 0 → 1 → 0.3 → 4 → 0.3 → 13 → 0.3 → 25 → 0.3 → 87 → 0.3 → 406 → 0.3 [MPa] using the step-by-step MIP method. The total amount of intruded mercury was treated as a "total pore," the amount of mercury being left behind in the sample at the time of depressurization as an "inkbottle pore," and the difference between the total pore and the inkbottle pore as a "continuative pore." AutoPore3 manufactured by Micromeritics, Inc. was used for measurements, and the contact angle $\theta = 130°$ and the surface tension of mercury $\gamma = 484$ dyn/cm were used in the Washburn equation for calculating pore diameters.

Two measurements were performed per mixture and their average value was adopted as test results. If two measured pore volume curves were different, however, additional measurements were performed and the average of the additional measurements of which pore volume curves were nearly identical was defined as the test result.

For making samples, the above disc samples were crushed to about 5 mm square with a chisel and a hammer, soaked in acetone for 24 hours, and then vacuum-dried in a desiccator laid with soda lime at a relative humidity (R.H.) of 30% for one month.

2.2 The relationship between the amounts of continuative pores and water absorption and drying (Experimental series 2)

2.2.1 Used materials and mix-proportion

Materials used are shown in Table 2, and the compounding and fresh properties are shown in Table 3. Concretes specimens with different types of cement and mineral admixture were prepared. The substitution of mineral admixture was performed with the range of types A, B, and C that are respectively defined in JIS. The unit water content of 165 kg/m^3, the water-to-binder (W/B) ratio of 0.50, the amount of fine aggregate, and the amount of coarse aggregate were constant among the mix-proportions. Super plasticizer and antifoaming agents were added such that the slump was 10 ± 2 cm, and that the volume of air was 2% or less in fresh concrete.

As mortar samples, cubes of approximately 8 mm each side were prepared from the mortar part of the cylindrical 28-days-age concrete specimen of φ 100 × 200 mm. Before water absorption tests and the MIP test, samples were soaked in acetone for 24 hours and subsequently vacuum-dried in a desiccator at a R.H. of 11% for 7 days.

2.2.2 Measurement of water absorption and drying

The amount of water absorption was determined with the Archimedes method in 1, 3, 12, and 24 hours after samples were immersed in pure water. In addition, the samples after the water was absorbed were placed gently in a desiccator at a R.H. of 11 % and the amount of their drying was determined in a drying period of 1, 3, 12, and 24 hours. Three measurements were performed for each mixture, and the average of two measurement results or more that showed a similar tendency was adopted as the test result.

2.2.3 Measurement of pore structures

While the sample size is approximately 8 mm, other conditions are the same as the Step-by-Step MIP method in section 2.1.2.

3 RESULT OF EXPERIMENT

3.1 Comparison between inkbottle pores determined through the step-by-step MIP and air voids obtained through the linear-traverse method (Series 1)

Figures 1 and 2 show the distribution of air voids diameters obtained through the linear-traverse method. It was found that the number of air voids, mainly of 0.01 mm - 0.30 mm, increases with increase in the amount of addition, when using the same AE agent M. On the other hand, for three kinds of specimens for which the target volume of air was set to 6 % and the size of air voids was varied with the type of the AE agent, a trend was observed that the number of air voids of 0.05 - 0.25 mm relatively increased in samples using the AE agent L.

Figure 3 shows cumulative pore volume curves of four types of specimens for which the dosage of the AE agent M was varied. Compared to a no-AE agent specimen as a reference, the volume of total pores increased with the dosage. On the other hand, the volume of continuative pores is substantially constant irrespective of the dosage of the AE agents.

Figure 4 shows cumulative pore volume curves for three types of specimens for which the target air volume was set to 6 % and the size of air voids was varied with the type of the AE agent. Both the volume of total pores and the volume of continuative pores are nearly constant regardless of types of the AE agents. This result indicates that the size of air voids and the distribution of diameters of air voids confirmed through the image analysis could not be determined by the MIP method.

Figure 5 shows intrusion curves at each stage of intrusion of 50N and 50M7.5. As described above, continuative pore curves of both samples match with each other. And it can be seen that there is a difference in the pore volume of the added AE agents 50M7.5 and 50N in each stage of intrusion. As there is only the difference in the amount of AE agent dosage in the specimen specifications of the two samples, it is considered that the difference in air volume has appeared as the above difference in the volume of inkbottle pores.

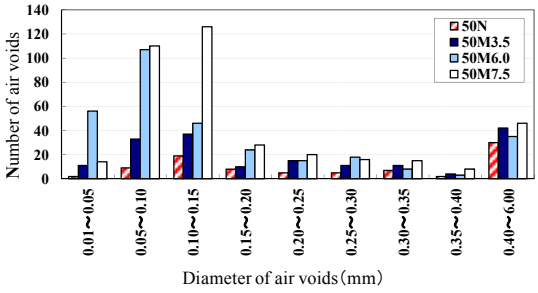

Figure 1. Relationship between AE agent dosage and air voids diameter obtained with the linear-traverse method

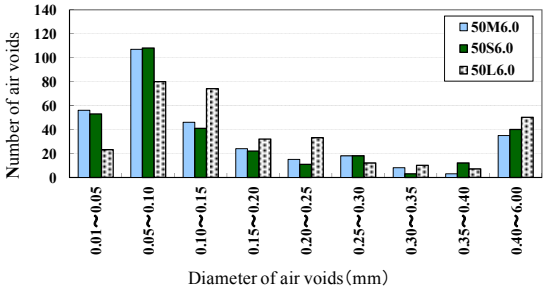

Figure 2. Relationship between AE agent type (size) and air voids diameter obtained with the linear-traverse method

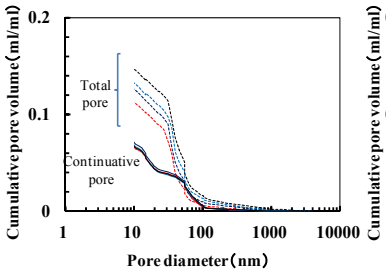

Figure 3. Difference of air voids amount in cumulative pore volume curves

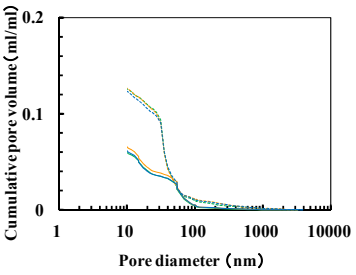

Figure 4. Difference of air voids size in cumulative pore volume curves

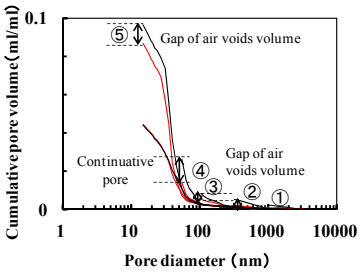

Figure 5. Gap of air voids volume in each intrusion steps

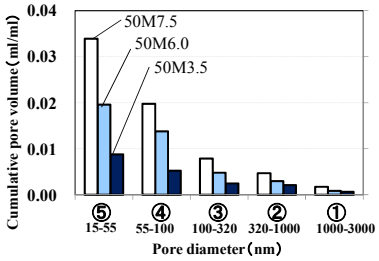

Figure 6. Difference of air voids amount in each intrusion steps

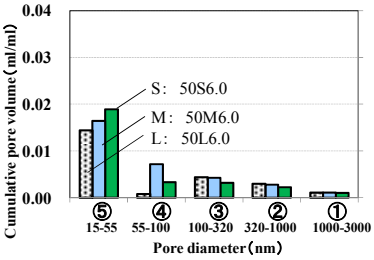

Figure 7. Difference of air voids size in each intrusion steps

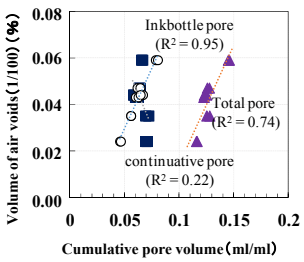

Figure 8. Relationship between air voids volume obtained with the linear-traverse method and pore volume determined with the step-by-step MIP

Values calculated by subtracting through setting 50N as a reference are regarded as the volume of inkbottle pores caused from air voids, shown in Figures 6 and 7. When focusing on the specimens with the use of the AE agent M, it is found that the volume of inkbottle pores (air voids) also increases with increase in AE agent dosage. In addition, a tendency was found that air voids appear as the volume of inkbottle pores at higher intrusion steps.

On the other hand, among the three types of specimens for which the target air volume was fixed to be 6 % and the size of air voids were varied with types of AE agents, the volume of inkbottle pores were smaller in 50L6.0, which has a larger air void size, than in 50M6.0 and 50S6.0.

Figure 8 shows the correlation between the volume of air volume obtained through the linear-traverse method and the cumulative volume of pores obtained through the step-by-step MIP. When seeing coefficients of determining pore volumes obtained by the MIP in the figure, it is found that the coefficient (R^2) of the continuative pore volume is 0.22 with almost no correlation found; R^2 of the total pore volume has a slightly high value of as much as 0.74; and R^2 of the inkbottle pore volume is 0.95, showing a very high correlation. This result shows the possibility of evaluating air voids with inkbottle pores obtained through the MIP.

4 The relationship between the continuative pore volume and water absorption and drying (Series 2)

4.1 Water absorption and drying phenomena in hardened mortar

Figure 9 shows a change in the amount of water absorption, and Figure 10 shows a change in the amount of drying. The largest increase is observed an hour after the starting of water absorption in all samples. The curves of the water absorption amount after 1 hour show gentle slopes at the time of 1 - 12 hours for BFS30-50 and BFS45-50, whereas generally horizontal straight lines are drawn for other samples after 1 hour. On the other hand, the largest slope of a linear straight line can be identified in 1 hour from the start of drying, and the slightly larger amount of drying can be identified up to 3 hours after that. The drying curve becomes almost horizontal after 3 hours. It can be verified from these result that the time necessary for

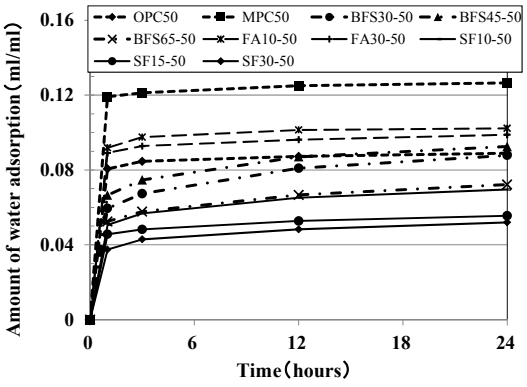

Figure 9. Change in the amount of water adsorption

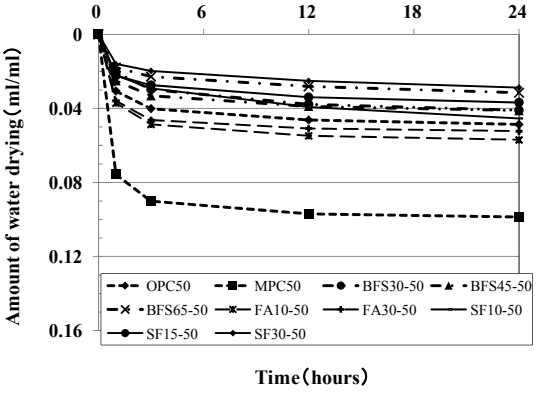

Figure 10. Change in the amount of water drying

Table 4. Summary of cumulative pore volume

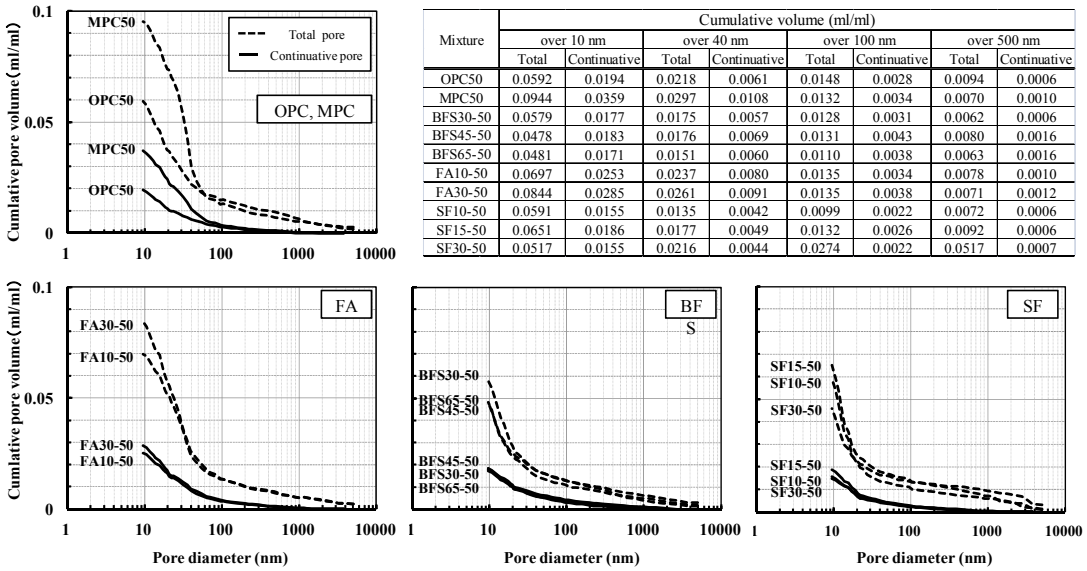

Mixture	Cumulative volume (ml/ml)							
	over 10 nm		over 40 nm		over 100 nm		over 500 nm	
	Total	Continuative	Total	Continuative	Total	Continuative	Total	Continuative
OPC50	0.0592	0.0194	0.0218	0.0061	0.0148	0.0028	0.0094	0.0006
MPC50	0.0944	0.0359	0.0297	0.0108	0.0132	0.0034	0.0070	0.0010
BFS30-50	0.0579	0.0177	0.0175	0.0057	0.0128	0.0031	0.0062	0.0006
BFS45-50	0.0478	0.0183	0.0176	0.0069	0.0131	0.0043	0.0080	0.0016
BFS65-50	0.0481	0.0171	0.0151	0.0060	0.0110	0.0038	0.0063	0.0016
FA10-50	0.0697	0.0253	0.0237	0.0080	0.0135	0.0034	0.0078	0.0010
FA30-50	0.0844	0.0285	0.0261	0.0091	0.0135	0.0038	0.0071	0.0012
SF10-50	0.0591	0.0155	0.0135	0.0042	0.0099	0.0022	0.0072	0.0006
SF15-50	0.0651	0.0186	0.0177	0.0049	0.0132	0.0026	0.0092	0.0006
SF30-50	0.0517	0.0155	0.0216	0.0044	0.0274	0.0022	0.0517	0.0007

Figure 11. Cumulative pore volume determined with the step-by-step MIP

the changes in water absorption amount and drying amount to become very small in mortar samples of 8 mm square would be 1 hour and 3 hours, respectively.

4.2 The pore structure of the mortar hardened body

Cumulative pore volume curves obtained using the step-by-step MIP method is shown in Figure 11. The pore diameter at which a cumulative pore volume curve starts to rise from the horizontal axis as mercury is intruded inside the sample is called “threshold pore diameter”. Types of cement, types of mineral admixtures, and compounding conditions on substitution rates are different among ten mortar samples measured in this study, but no differences in the threshold pore diameter can be identified among them. The difference in compounding conditions can be identified by the positions of bending points that appeared at 100 nm or less and cumulative pore volumes. In addition, when a minimum pore diameter is set to 10, 40, 100, or 500 nm, cumulative values above each minimum pore diameter are summarized in Table 4. The bend point is a point at which a curve has the maximum curvature. The bending point appears below 100 nm in the mortar sample as well as in hardened cement paste.

When comparing bending points with respect to the difference in mix-proportion, they appear at 40 - 50 nm in OPC, at 50 - 60 nm in MPC, at 20 - 30 nm in BFS, at 50 - 60 nm in FA, and at 20 - 30 nm in SF, which are considered to reflect also the type of cements, the reactivity of mineral admixture, and the difference in particle size.

Then cumulative pore volumes are compared. It is found that cumulative pore volumes are large in MPC and FA that had bending points at relatively large diameters while they are small in BFS and FS that had bending points at small diameters.

In the next section, the relationship between the volume of cumulative pores and the amount of water absorption and drying are examined to discuss how pores

obtained through MIP are involved in the capillary water absorption and drying phenomena.

4.3 The relationship between water absorption and drying properties and pore structures obtained through MIP in hardened mortar

Figures 12 and 13 show the relationship between the amount of water absorption and total (of continuative and inkbottle) pores or continuative pores determined through the step-by-step MIP method, and Figures 14 and 15 show the relationship between the amount of drying and total pores or continuative pores. The relationship between the amount of water absorption and pore volumes at the time of 1, 3, 12, and 24 hours is shown from the left side of the figures in order. Cumulative pore volumes where the minimum diameter is 10, 40, 100, or 500 nm each were compared in these figures.

First, the relationship between the amount of water absorption and the volume of total pores shown in Figure 12 is explained. The maximum value of the coefficient of determination R^2 indicated in the legend of the graph is 0.66 which shows the relationship with the pore volume of over 40 nm in the figure of 1 hour after water absorption. A close value of 0.64 is also shown for the total pore volumes of over10

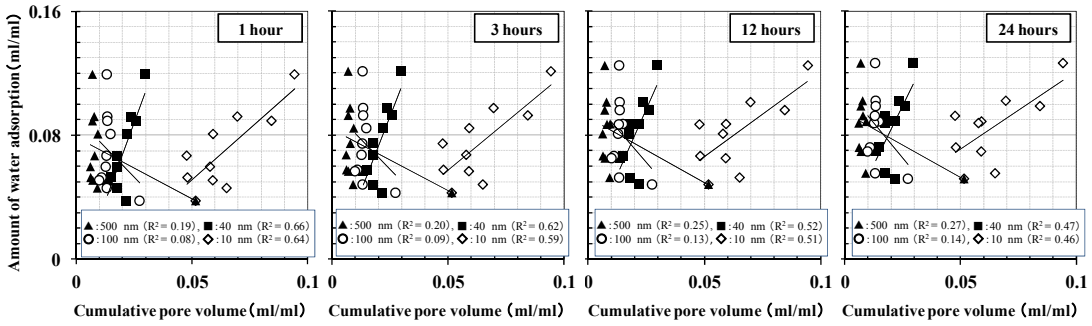

Figure 12. Relationship between amount of water adsorption and cumulative pore volume (total pore)

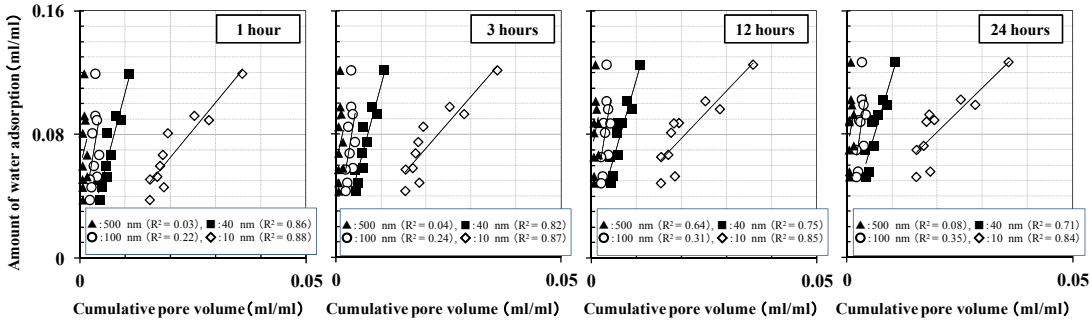

Figure 13. Relationship between amount of water adsorption and cumulative pore volume (continuative pore)

nm in the same figure. The figure also shows that R^2 between the water absorption amount and the total pore volumes of over 100 nm and over 500 nm is small,

suggesting their weak relationship therebetween. Furthermore, when looking at the relationship between the amount of water absorption and the total pore volume at each absorbing time, R^2 is decreasing after it reaches the peak in 1 hour. At each of the time, as described above, a relatively stronger relationship between the water absorption amount and the pore volumes of 10 nm and 40 nm is shown compared to that of over 100 nm.

Next, the relationship between the amount of water absorption and the continuative pore volume in Figure 13 is explained. Similarly to the total pore volume, the highest R^2 was obtained for the continuative pore volumes of over 10 nm and over 40 nm in 1 hour of water absorption. The resulting R^2 was 0.88, slightly higher for the continuative pores of over 10 nm. Similarly to the case of total pores, no relationship is found between the cumulative pore volume of over 100 nm and the amount of water absorption in the continuative pores as well. At any absorbing time, higher R^2 are obtained with the relationship between the amount of water absorption and the continuative pore volume than the relationship between the amount of water absorption and the total pore volume.

The relationship between the amount of drying and the total pore volume is shown in Figure 14. The maximum value of R^2 is 0.74 in the total pore volume of

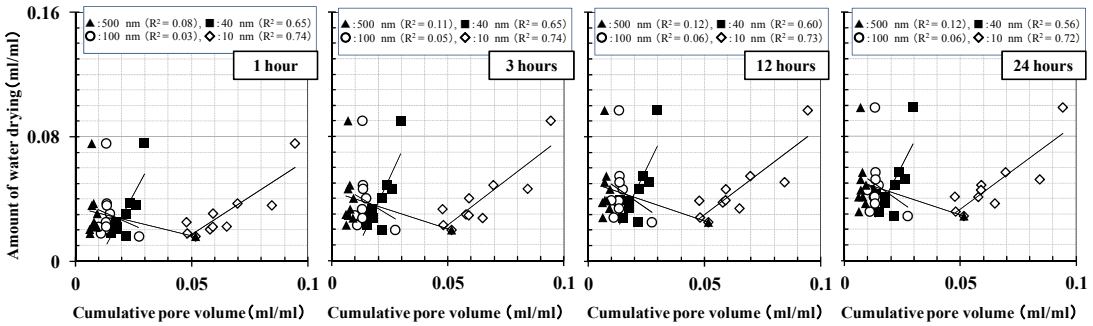

Figure 14. Relationship between amount of water dryinf and cumulative pore volume (total pore)

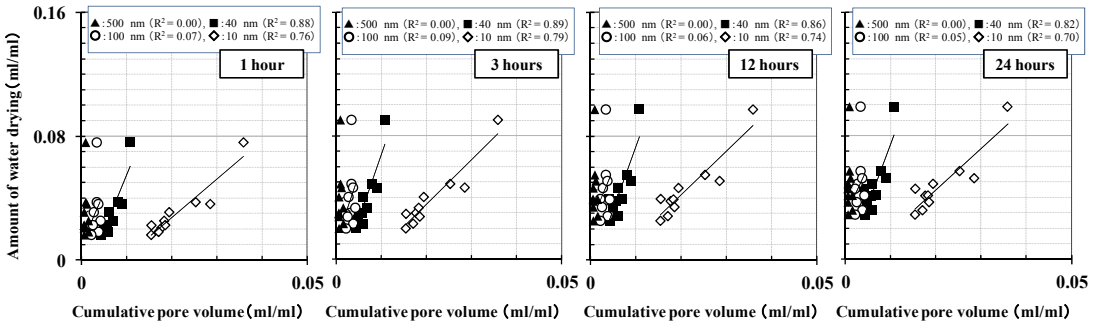

Figure 15. Relationship between amount of water drying and cumulative pore volume (continuative pore)

over 10 nm in 1 hour and 3 hours. Similarly to the relationship with the water absorption, no relationship was found with the total pore volume of over 100 nm.

When looking at the relationship between the amount of drying and the continuative pore volume in Figure 15, the highest R^2 of 0.89 is obtained for the continuative pore volumes of over 40 nm in 3 hours. Moreover, it is shown that there is almost no relationship between the continuative pore volume of over 100 nm and the amount of drying.

The relationship with the amount of drying was stronger than that with the amount of water absorption in both of the total pores and the continuative pores. This is considered to be attributed to the result that the amount of moisture wetting poresfiner than capillary pores that can be measured in the mercury intrusion test is contained in the amount of water absorption. It is seemed that the higher correlation can be obtained in respect with the amount of water absorption by conditioning the moisture to a relative humidity R.H. of more than 11%.

The highest coefficient of determination was obtained with the cumulative pore volume in 1 hour for the amount of water absorption and in 3 hours for the amount of drying. As shown in section 4.1, changes in the amount of water absorption and drying began to decrease at the times. It was suggested from the results of the above examination that pore structures measured by the step-by-step MIP method would be the pores absorbed within 1 hour after the start of water absorption and dried within 3 hours after the start of drying.

5 SUMMARY

The relationship between the air volume obtained through the linear-traverse method and the amount of water absorption or drying was verified for the inkbottle pore volume and the continuative pore volume obtained through the step-by-step MIP method.

With regard to the relationship between the inkbottle pore volume and the continuative pore volume obtained through the step-by-step MIP method, the relationship between the air volume obtained through the linear-traverse method and the amount of water absorption and drying was examined.

As for the relationship between inkbottle pores obtained through the step-by-step MIP method and air voids, the possibility of evaluate the information on air voids volume and size calculated through the liner-traverse method was examined using hardened mortar obtained by adjusting their amount and size. Although it is not possible to obtain the information on the size of air voids using the method proposed this time, a high correlation was confirmed between the volume of inkbottle pores and the volume of air voids.

As for continuative pores obtained through the step-by-step MIP method, their relationship with the behavior of liquid water movement in the phenomena of water absorption and drying in mortar samples was verified. In the water absorption phenomena in samples of about 8 mm each side, a rapid water absorption until about 1 hour after the start of soak and the continuation of slight water absorption until 24 hours after that could be verified. In the drying phenomenon, moreover, the rapid drying proceeds up to 1 hour after the start of the test, and then the relatively larger amount of drying was confirmed up to 3 hours, and a slight amount of drying was measured from 3 hours until 24 hours. For continuative pores obtained through the step-by-step MIP method, a strong correlation could be found with the amount of

water absorption in 1 hour for the water absorption phenomenon and the amount of drying in 3 hours for the drying phenomenon.

ACKNOWLEDGEMENTS

We sincerely appreciate Kazuhide Saito (Takemoto oil & fat CO. LTD) for his advice about AE agents and the linear-traverse method.

REFERENCES

[1] P.K.Mehta and D.Manmohan.(1980). “Pore size distribution and permeability of hardened cement paste” ICCC-7

[2] S.Diamond.(2000). “Mercury porosimetry: An inappropriate method for the measurement of pore size distributions in cement-based materials” Cement and Concrete Research, Vol.30, pp.1517-1525.

[3] R.Yoshida and T.Kishi.(2008). “Proposal of a new approach for determination of pore continuity and suitable intrusion pressure based on step-by-step mercury intrusion porosimetry test.” 1st International conference on Microstructure Related Durability of Cementitious Composites, Vol.2, pp.1455-1464.

From micromechanisms to mechanical behaviour: an application to ageing creep of a cement paste

J. Sanahuja[1] and M. Di Ciaccio[2]

[1]EDF lab, Site des Renardieres, Route de Sens, Ecuelles, 77250 Moret sur Loing, France; PH +33 1.60.73.79.92; FAX +33 1.60.73.65.59; email: julien.sanahuja@edf.fr
[2]formerly at EDF lab, Site des Renardieres

ABSTRACT

Due to chemical hydration processes, cementitious materials exhibit a strong evolution of their physical (mechanical, transport, etc...) properties as a function of time. More precisely, as hydration proceeds, phase transformations occur, such as dissolution of anhydrous phases and precipitation of hydrates. The microstructure strongly evolves. Micromechanics can be used to translate this time-dependent microstructure into mechanical properties evolution. This is straightforward when the investigated behaviour does not involve time by itself, such as elasticity. The case of creep is much more complex, as another time scale steps in, through the intrinsic delayed behaviour of hydrates. Taking advantage of recent works on ageing viscoelastic homogenization of random media, and on a micromechanical extension of Bažant's solidification theory, a simplified model of cement paste ageing basic creep is proposed. Assuming an evolving morphological model with three phases (anhydrous, hydrates and capillary porosity), the effective ageing creep of the paste is estimated.

INTRODUCTION

Taking advantage of recent works on ageing viscoelastic homogenization of random media [Sanahuja, 2013], the solidification theory of Bažant [Bažant, 1977] has been micromechanically extended to investigate more realistic precipitation scenarii [Sanahuja, 2014].

This contribution proposes a first application to cementitious materials. The aim is to investigate the influence of the ongoing hydration process on effective creep. To ease the presentation of the approach, several aspects of the model are simplified: hydration and kinetics, local behaviours, and the evolving morphological model.

A SIMPLIFIED MODEL OF EVOLVING CEMENT PASTE

A simplified view of a cement paste is adopted: both anhydrous and hydrates are not detailed but considered as single phases. Thus, only three phases are present: anhydrous (subscript a), hydrates (subscript h) and capillary pores (subscript p). The drained behaviour is sought, thus capillary water is disregarded.

Chemistry and kinetics

The volume fractions are estimated as a function of the hydration degree α using the classic Powers model:

$$f_a(\alpha) = \frac{0.32(1-\alpha)}{w/c + 0.32}\,, \quad f_h(\alpha) = \frac{0.68\alpha}{w/c + 0.32} \quad \text{and} \quad f_p(\alpha) = \frac{w/c - 0.36\alpha}{w/c + 0.32} \tag{1}$$

w/c being the water to cement mass ratio. As viscoelastic behaviours are considered here, these volume fractions need to be related to time. To do so, an simple empirical kinetic model is considered:

$$\alpha(t) = \frac{(t/\tau_{kin})^4}{1 + (t/\tau_{kin})^4}\alpha_{max} \quad \text{where} \quad \alpha_{max} = \min\left(\frac{w/c}{0.42}, 1\right) \tag{2}$$

τ_{kin} being a kinetics characteristic time, and where the maximum reachable hydration degree α_{max} is also estimated from the Powers model.

The volume fractions evolution is plotted on figure 1 left, for $w/c = 0.4$.

Phases behaviour

In a hydrated cement paste, only C-S-H exhibit significant creep. Here, anhydrous are considered as elastic, while hydrates are, once precipitated, non ageing linear viscoelastic. For the sake of simplicity, a Maxwell model is used, with the same characteristic time τ_h for both bulk and shear behaviours. The relaxation tensor of hydrates thus writes:

$$\mathbb{C}_h(t-t') = \left(\frac{1}{1-2\nu_h}\mathbb{J} + \frac{1}{1+\nu_h}\mathbb{K}\right) E_h \mathrm{e}^{-\frac{t-t'}{\tau_h}} \mathrm{H}(t-t') \tag{3}$$

E_h and ν_h being the Young's modulus and Poisson's ratio characterizing the elastic part of the Maxwell model, and H being the Heaviside function.

The stiffness parameters come from nano-indentation measurements: $E_a = 135$ GPa, $\nu_a = 0.3$ and $E_h = 31$ GPa, $\nu_h = 0.24$. The hydrates creep characteristic time is defined relative to the kinetics characteristic time, and arbitrarily taken as: $\tau_h/\tau_{kin} = 3$.

Morphology of composite and its evolution

For the sake of simplicity, the cement paste is considered as a polycrystal-like assemblage. Each cell of the latter is thus occupied by either anhydrous, hydrates or capillary pores. The hydration reaction transforms anhydrous into hydrates, with a volume increase: the capillary porosity decreases as a function of time. Thus, a part of the initial anhydrous phase is progressively transformed into hydrates. And a part of the initial capillary porosity is progressively invaded by hydrates. At the scale of the individual cell, these transformations are assumed to occur instantly.

To take into account these two processes, the transforming materials are replaced by fictitious ageing linear viscoelastic materials, as presented in [Sanahuja, 2014] for solidification. Thus, at the polycrystal scale, the domain occupied by anhydrous grains that are progressively transformed to hydrates is split into a number N of fictitious phases. Each fictitious phase is transformed at a time t_t depending on the volume fractions evolution (figure 1 left). The domain occupied by pores progressively invaded by hydrates is treated in the same way.

Then homogenization of these fictitious ageing phases is performed resorting to a self-consistent scheme, with spherical particles, as detailed in [Sanahuja, 2013].

Fictitious behaviour for cells transformed to hydrates, from pores or anhydrous

Hydrates solidifying at time t_t into capillary porosity are replaced by a fictitious phase whose relaxation tensor writes (as in [Sanahuja, 2014]):

$$\mathbb{C}_{p\to h}(t,t') = \mathbb{C}_h(t-t')\mathrm{H}(t'-t_t) \tag{4}$$

The case of the fictitious phase replacing the anhydrous transforming into hydrates is new here. To simplify, an instant phase transform process involving complete dissolution then massive precipitation is assumed at the scale of the cell. That is, hydrates precipitate in a zero stress-state. The fictitious relaxation tensor is thus:

$$\mathbb{C}_{a\to h}(t,t') = \mathbb{C}_a(t-t')\mathrm{H}(t_t-t)\mathrm{H}(t_t-t') + \mathbb{C}_h(t-t')\mathrm{H}(t'-t_t) \tag{5}$$

RESULTS

Effective uniaxial creep functions, for $w/c = 0.4$, are plotted on figure 1 right, as plain lines. Dotted lines represent the evolution of the instantaneous elastic compliance (inverse of the effective Young's modulus), estimated from the usual elastic self-consistent scheme, taking into account the current morphology at time t. The instantaneous elastic compliance estimated from the ageing model is clearly consistent with these "reference" predictions of elasticity. Even if the behaviour of each individual phase is non ageing, the hydration process (transformation of anhydrous into hydrates, and solidification of hydrates into pores) clearly yields an ageing effective behaviour.

CONCLUSION

This contribution proposes a first model to estimate the effect of ongoing hydration on the ageing basic creep of a cement paste. Each part of the model has been chosen as simple as possible to focus on the presentation of the approach. To be able to compare model estimates to experimental results, improvements are required on several aspects: taking into account the different anhydrous and hydrates phases, using a more realistic viscoelastic behaviour for hydrates, improving the morphological model (for example adapting models which have been successfully used to estimate elasticity, such as [Bernard et al., 2003, Sanahuja et al., 2007]). As the proposed approach is

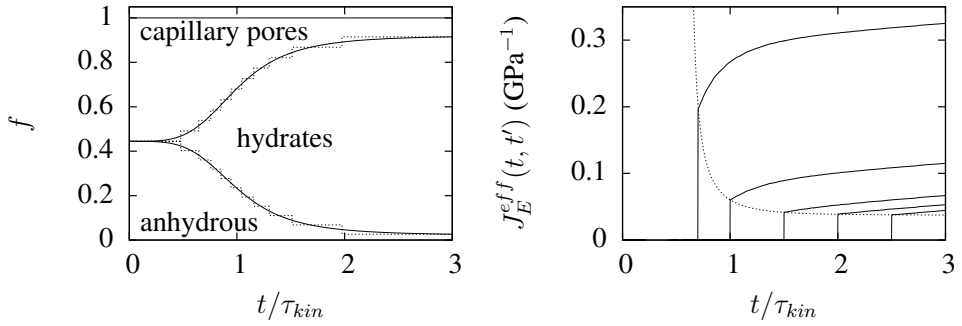

Figure 1. Left: cumulative volume fractions, and as a dotted line the discretized volume fractions as considered by the micromechanical approach (for $N = 10$ fictitious ageing phases used to model the part of anhydrous, resp. pores, transformed to hydrates). Right: estimated effective uniaxial creep functions ($N = 100$).

modular, each of these prospects can be considered independently. Some of these will be addressed in the companion paper [Sanahuja and Di Ciaccio, 2015].

REFERENCES

[Bažant, 1977] Bažant, Z. (1977). Viscoelasticity of solidifying porous material—concrete. *Journal of the Engineering Mechanics Division*, 103:1049–1067.

[Bernard et al., 2003] Bernard, O., Ulm, F.-J., and Lemarchand, E. (2003). A multiscale micromechanics-hydration model for the early-age elastic properties of cement-based materials. *Cement and Concrete Research*, 33(9):1293–1309.

[Sanahuja, 2013] Sanahuja, J. (2013). Effective behaviour of ageing linear viscoelastic composites: Homogenization approach. *International Journal of Solids and Structures*, 50:2846–2856.

[Sanahuja, 2014] Sanahuja, J. (2014). Homogenization of solidifying random porous media: application to ageing creep of cementitious materials. In *RILEM international symposium on concrete modelling*, Tsinghua University, Beijing, China.

[Sanahuja and Di Ciaccio, 2015] Sanahuja, J. and Di Ciaccio, M. (to be submitted in 2015). Micromechanical modelling of ageing creep of hydrating cementitious materials. *Journal of Nanomechanics and Micromechanics*.

[Sanahuja et al., 2007] Sanahuja, J., Dormieux, L., and Chanvillard, G. (2007). Modelling elasticity of a hydrating cement paste. *Cement and Concrete Research*, 37(10):1427–1439.

Nano-Indentation Testing and Modelling of Cement Paste

E. Schlangen[1]; M. Lukovic[1]; B. Šavija[1]; and O. Copuroglu[1]

[1]Delft University of Technology, Faculty of Civil Engineering and Geosciences, Stevinweg 1, 2628 CN Delft, The Netherlands. E-mail: erik.schlangen@tudelft.nl

Abstract

Nano-indentation is used to study the mechanical properties of cement paste. A method is developed to prepare small cement paste cubes (100 μm). These samples are loaded to failure with a Berkovich indenter to obtain the global mechanical properties of the material. Local mechanical properties are obtained by standard nan-indentation measurements on the same material. These local properties are used as input parameters for a lattice-type model to simulate the failure of heterogeneous microstructures. With the model the failure of the small cement paste cubes is simulated and the outcome of test and simulation is compared. The proposed technique forms the basis for upscaling of modelling techniques and validating the results on every scale.

INTRODUCTION

Nano-indentation is becoming a popular method to measure micro-mechanical properties of cement paste. It provides local properties like stiffness and hardness of the different reaction products in the material (Constantinides and Ulm, 2004). These values can be used as input to perform simulations of mechanical tests and performance of the material on a larger scale (Çopuroğlu and Schlangen, 2008, Lukovic et al. 2014). The scatter in the results is big and it is debated in literature whether this method can be used at all for heterogeneous materials like cement paste or even concrete. Reason for this is that you actually never indent in a single phase, but always hit a composite made up of different phases by indenting the material with a diamond tip, although the tip-radius is very small. Furthermore, when dealing with a cement paste, which is a 3D heterogeneous material, the indentation outcome is always influenced by the underlying material, which can be stiffer and harder or just the opposite (Lukovic et al. 2015).

In this paper a new method is proposed to study the failure under indentation loading of small scale specimens of cement paste. The method for making the specimens as well as the loading procedure are explained in the next section. To study the damage that is made by performing an indent and to relate this damage to the local properties obtained from the tests a modelling procedure is proposed. Fracture simulations with a lattice model are performed on small scale specimens. In the simulations the nano-indentation loading is mimicked as accurate as possible. The results of the simulation are fracture patterns and indentation curves. The results of

the simulations are compared with tests performed on specimens of the same scale that are produced with the newly developed technique.

EXPERIMENTAL PROCEDURE AND RESULTS

The cement paste was a standard grade OPC CEM I 42.5 N paste with 0.4 water-to-cement ratio. Cylindrical specimens (diameter, 24 mm, height 39 mm) were cast. The specimens were cured for 28 days in sealed conditions at room temperature of 20°C. After 28 days, the sample was cut with a diamond saw into slices with a thickness of 8 mm. In order to stop hydration, solvent exchange by isopropanol was used. The sample was immerged five times and taken out for a period of one minute in order to enable faster water-solvent exchange. Afterwards, it was placed for 72 hours in isopropanol and subsequently taken out, and solvent was removed by evaporation at ambient conditions.

In order to make the thickness of the specimens equal to 100 μm and even and uniform, a thin sectioning machine was used for cutting and grinding of the specimen. Samples were not impregnated with epoxy resin prior to slicing. An object glass was glued on the sample and it was cut with a diamond saw. Afterwards, all samples were ground in the thin section machine in several passes and polished on a lapping table. After every step, an optical microscope was used to check the effectiveness of grinding and polishing. The samples were soaked into an ultrasonic bath to remove any residue from the surface. Samples were kept in a desiccator under vacuum until further cutting and testing.

Next step in the process is to create small cubes from the 100 μm thin slice. For this process a diamond dicing saw for semiconductor wafers was used. By running this precise saw with a 400 μm wide blade in two directions over the thin section small cubes as shown in Figure 1a were obtained. To prevent chipping of the edges of the small cement paste cubes while cutting, a thin layer of nail-polish was applied on the surface of the thin section, which was later removed by soaking the specimen for a short time in acetone. The dicing saw machine was set in such a way that the saw was cutting a few micrometres into the glass plate in order to make sure that the cement paste cubes have the required dimensions and that also the glue between cement paste and glass was sliced. The final cubes are all at the dimension of 100x100x100 ± 3 μm (Figure 1b).

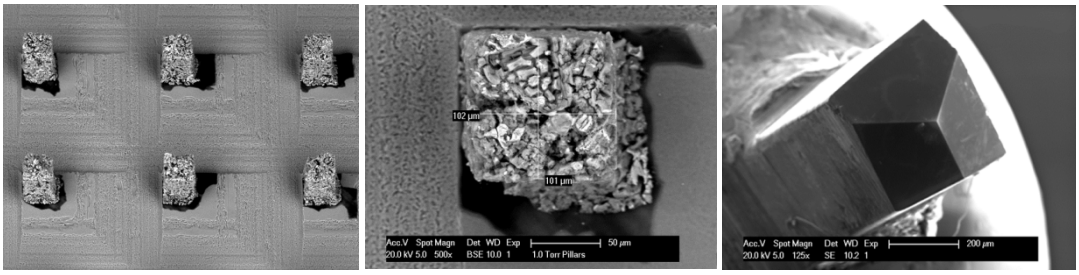

Figure 1: a) Small cement paste cubes on glass plate b) Single cube with dimensions c) Diamond Berkovich tip.

The small cubical cement paste samples on the glass plate were placed in an Agilent G200 nano-indenter and were tested with a Berkovich tip (Figure 1c). A displacement controlled test was performed by using the CSM (Continuous Stiffness Method). The loading procedure is discussed in more detail in Poelma et al (2014) in which carbon nano tube bundles are loaded to failure with a nano-indenter. Different loading depths were applied. This made it possible to obtain crack patterns at various depths as shown in Figure 2. The typical failure mechanism obtained is crushing of the material under the tip and three main cracks running to the sides of the cubes, starting from the three edges of the Berkovich tip. Indenting the tip further into the specimen results in complete crushing of the sample as can be seen in the ESEM image in Figure 2c.

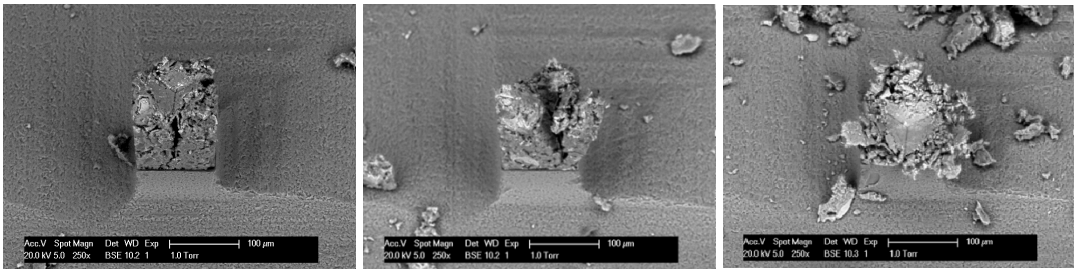

Figure 2: Three stages in the nano-indentation loading process of small cubes observed in ESEM.

MODELLING PROCEDURE AND RESULTS

For the modelling a 3D lattice network model is used. As starting point for the simulations a 3 dimensional hydrated cement paste specimen is constructed using the HYMOSTRUC3D model. A cement paste with water-to-cement ratio of 0.4 and age of 28 days was simulated. More details on the construction of these 100 μm cubes and the implementation of local material properties can be found in Qian et al. (2011). The 3D domain is divided into a number of cubic cells with linear dimension 2 μm. In each cell, a random location for a lattice node is selected. Voronoi tessellation of the cubical domain is performed. Nodes with adjacent Voronoi cells are connected by lattice elements. In order to take material heterogeneity into account, different material properties are ascribed to elements representing the different phases (un-hydrated cement, hydration products and pores) in the cement paste. The properties are obtained from local nano-indentation tests. The different colours in Figure 3a represent the different phases. For the boundary conditions in the simulation it was assumed that the displacement of the nodes at bottom surface was fixed in all directions to represent the glued sample on the glass plate. A vertical displacement in 4 nodes in the centre of the top surface was applied to mimic the indenter load.

The result of one of the simulations is presented in Figure 3s as deformed and cracked specimen. Figure 3b and c show the cracked elements from different viewpoints. It can be clearly seen that a lot of damage occurs under the loading points and that the final crack pattern results in three main cracks under angles of 120º.

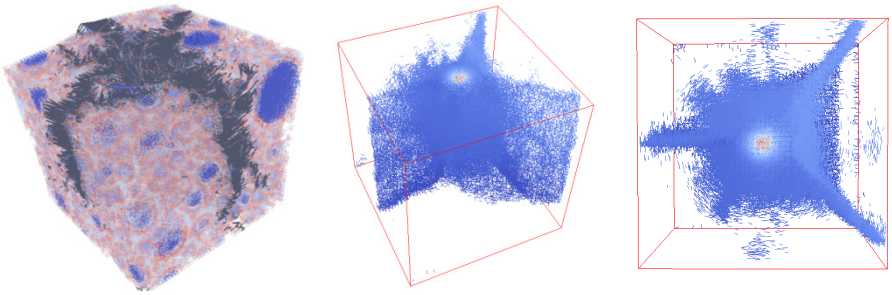

Figure 3: Simulation of nano-indentation on a 3D cube; a) deformed and cracked sample, b) crack pattern, showing 3 localized main cracks, c) top view.

CONCLUSIONS

In this paper a combination of experimental technique using nano-indentation and a modelling technique using 3D discrete lattice model simulations is applied to study the failure mechanism in cement paste specimens at micro-scale. The input for the simulation are mechanical properties for the local lattice elements, which can be obtained from local nano-indentation measurements in single phases of the heterogeneous composite. However, these properties cannot be used directly, because they depend on the size of the elements used in the model and should be transferred to model-parameters. Fitting of these local scale properties for the elements is possible when an experiment on specimen size is available. With the method presented in this paper the framework for such fitting and validation of the modelling is created. This method forms also a basis for upscaling of the modelling and validation on every scale.

REFERENCES

Constantinides, G. and Ulm, F.J. The effect of two types of CSH on the elasticity of cement-based materials: Results from nanoindentation and micromechanical modeling. *Cement and Concrete Research*, 2004. 34(1): p. 67-80.

Çopuroğlu O, Schlangen E. Modeling of frost salt scaling. *Cement and Concrete Research*. 2008;38(1):27-39.

Lukovic, M., Savija, B., Dong, H., Schlangen, E., Ye, G.. Micromechanical study of the interface properties in concrete repair systems. *Journal of Advanced Concrete Technology*, 2014; 12: 320-339.

Lukovic, M., Schlangen, E., Ye, G. Combined experimental and numerical study of fracture behaviour of cement paste at the microlevel. *Cement & Concrete Research,* 2015; 73:123–135.

Poelma, R.H., Morana, B., Vollebregt, S., Schlangen, E., van Zeijl, H.W., Fan, X. and Zhang, G. Tailoring the Mechanical Properties of High-Aspect-Ratio Carbon Nanotube Arrays using Amorphous Silicon Carbide Coatings, *Advanced Functional Materials*, 2014; 24, 36: 5737-5744.

Qian, Z., Ye, G., Schlangen, E., Van Breugel, K. 3D lattice fracture model: Application to cement paste at microscale (2011) *Key Engineering Materials*, 2011;452-453: 65-68.

Evolution of Microstructure and Transport Properties of Cement Pastes Due to Carbonation under a CO_2 Pressure Gradient—A Modeling Approach

Q. T. Phung[1,2,a]; N. Maes[2,b]; D. Jacques[2,c]; G. De Schutter[1,d]; and G. Ye [1,3,e]

[1]Magnel Laboratory for Concrete Research, Ghent University, B9052 Ghent, Belgium. E-mail: [a]QuocTri.Phung@sckcen.be; [d]Geert.DeSchutter@ugent.be
[2]EHS Institute, Belgian Nuclear Research Centre (SCK•CEN), Boeretang 200, B2400 Mol, Belgium. E-mail: [b]Norbert.Maes@sckcen.be; [c]Diederik.Jacques@sckcen.be
[3]Microlab, Delft University of Technology, P.O. Box 5048, 2600 GA Delft, The Netherlands. E-mail: [e]G.Ye@tudelft.nl

Abstract

Most carbonation models only account for diffusion as the main transport mechanism rather than advection. Nevertheless, in the case of concrete used for underground waste disposal facilities, concrete may be subjected to a high hydrostatic pressure and the surrounding environment may contain a high dissolved CO_2 concentration. Therefore, a combination of diffusion and advection should be taken into account. This is also the case in accelerated carbonation where a high CO_2 pressure gradient is applied in which advection in the gas phase has a significant contribution to the carbonation process. This study aims at developing a model to predict the evolution of the microstructure and transport properties of cement pastes due to carbonation under accelerated conditions in which a pressure gradient of pure CO_2 is applied. The proposed model is based on a macroscopic mass balance for carbon dioxide in gaseous and aqueous phases. Besides the prediction of the changes in transport properties (diffusivity, permeability), the model also enables to predict the changes in microstructure. Data from accelerated tests were used to validate the model. Preliminary verification with experimental results shows a good agreement.

1. INTRODUCTION

The carbonation process in cement-based materials is a deterioration phenomenon. Carbonation results in a pH decrease. The development of lower alkaline environment accelerates the corrosion of reinforcing bars in concrete because of dissolution of the thin oxide passive layer protecting the steel bars from corrosion (Glasser et al. 2008). On the other hand, carbonation also results in beneficial effects. It is generally believed that carbonation decreases transport properties and refines pore structure of Portland cement-based materials. However the extent of modification in transport properties and microstructure significantly depends on carbonation conditions and cement types. The reduction of transport properties is the result of the precipitation of carbonation products in the pore structure. This leads to a significant reduction of the total porosity and transport properties.

In general, it is thought that the carbonation mechanism is determined by the inward diffusion of CO_2 in normal conditions. Nevertheless, in the case of concrete used for underground waste disposal purposes, concrete is almost fully saturated and subjected to a high hydrostatic pressure and the surrounding environment may contain a high bicarbonate concentration. Therefore, a combination of diffusion and advection should be taken into account when one considers the carbonation mechanism. However, so far as the authors are aware, none of published studies considers the contribution of advection to the carbonation modelling.

A number of models have been proposed based on Fick's law for diffusion. Almost all models relate the carbonation depth with square root of time. However, a sharp front is not always observed. Instead of giving an explicit formula to predict the carbonation depth, a large number of models have been developed in order to solve the carbonation problem numerically (Bary and Sellier 2004; Muntean et al. 2011). These approaches are mainly based on conservation laws and can capture most important factors influencing the carbonation process. As carbonation of cement-based materials under atmospheric conditions is a slow process; a number of accelerated carbonation methods have been proposed. A common way is to put concrete samples in a controlled chamber with a specific CO_2 partial pressure and an optimized relative humidity (50-70%) to speed up carbonation. An alternative method has been proposed in a companion paper (Phung et al. 2015) in which a high pressure gradient of pure CO_2 is applied to samples at controlled initial internal relative humidity. Interpretation of such accelerated carbonation experiment requires a 1-D reactive transport model accounting for advective flow as a consequence of the applied CO_2 pressure gradients. Contrary to the existing models, the proposed model accounts for both advective and diffusive transports. Besides the prediction of the carbonation depth, the model also enabled to predict the change in permeability, diffusivity, and porosity due to carbonation.

2. MODEL DEVELOPMENT

The proposed model was based on a macroscopic mass balance for CO_2 in gaseous and aqueous phases. A simplified solid-liquid equilibrium curve was used to relate the Ca contents in aqueous and solid phases. The model only considers the carbonation of portlandite (CH) and calcium silicate hydrates (C-S-H). Initial hygrothermal conditions were accounted for and their evolutions during carbonation are also considered. It is assumed that the hydration of concrete is not changed when the carbonation process starts.

2.1. Theory

2.1.1. Mass conservation of CO_2

The mass balance equation for CO_2 is given as:

$$\partial c/\partial t + \partial J/\partial x = -Q \tag{1}$$

where c is the total concentration of CO_2 in the porous media [kg/m^3]; J is the total flux of CO_2 [kg/m^2.s]; Q is the reaction rate of CO_2 [kg/m^3.s], t is time [s] and x is the spatial distance [m]. The total concentration of CO_2 in the porous media is the sum of the amounts of CO_2 in the gaseous c_g and aqueous c_l phases [kg/m^3]:

$$c = \phi(1-S)c_g + \phi S c_l \tag{2}$$

where ϕ is porosity [-] and S is water saturation degree [-]. The total flux of CO_2 includes both the CO_2 fluxes in the gaseous J_g and aqueous J_l phases. Accounting for diffusion and advection results in following equation:

$$J = J_g + J_l = -\left[c_g v_g + D_g(\partial c_g/\partial x)\right] - \left[c_l v_l + D_l(\partial c_l/\partial x)\right] \tag{3}$$

where D_g and D_l are effective diffusion coefficients of gaseous and aqueous phase, respectively [m^2/s]; v_g and v_l are the volumetric flux densities [m/s] of gaseous and aqueous phases due to a pressure gradient, respectively, which are obtained via Darcy's law for the aqueous and gaseous phases as:

$$v_l = -(k_l(\phi,S)/\mu_{H_2O})(\partial P_l/\partial x) \qquad k_l(\phi,S) = k_{l0}(\phi)k_l(S) \tag{4}$$

$$v_g = -(k_g(\phi,S)\beta(P_a)/\mu_{CO_2})(\partial P_g/\partial x) \qquad k_g(\phi,S) = k_{g0}(\phi)k_g(S) \tag{5}$$

where μ_{H_2O} and μ_{CO_2} denote the dynamic viscosity of water and CO_2 gas, respectively [Pa.s]. $k_{g0/l0}(\phi)$ is intrinsic permeability [m^2] which depends on porosity; and $k_{g/l}(S)$ is the function accounting for the effect of saturation degree on the intrinsic permeability of gaseous/aqueous phase, respectively. P_g and P_l [Pa] denote the pressure of gaseous phase and pore solution, respectively

The relationships between permeability and saturation degree are expressed by invoking the relation of (van Genuchten 1980) and (Wardeh and Perrin 2006) for the aqueous and gaseous phases, respectively:

$$k_l(S) = S^p\left[1-(1-S^{1/q})^q\right]^2 \qquad k_g(S) = (1-S)^p\left(1-S^{1/q}\right)^{2q} \tag{6}$$

where p [-] and q [-] are empirical coefficients. In order to establish the relationship between permeability and pore structural parameters, we explored well-known Kozeny-Carman relation.

$$k = \chi\phi^3/(1-\phi)^2 \qquad \chi = \left(\tau^2 S_a^2 F_s\right)^{-1} \tag{7}$$

where χ [m^2] is a function of tortuosity, τ [-]; specific surface of pores, S_a [m^2/m^3]; and shape factor, F_s [-]. Both parameters τ and F_s are very difficult to quantify because of the complex pore system of hardened cement paste. However, the lumped term $\Omega = 1/\tau^2 F$ [-] can be determined with the knowledge of intrinsic permeability, total porosity and specific surface of pores. Numerical calculation of Ω performed on carbonated and reference samples (Phung et al. 2015) shows that the average value of Ω for sound materials is one order of magnitude higher than one for carbonated materials. Therefore, we assume that the lumped term Ω linearly decreases as a function of carbonation degree as follows:

$$\Omega = \Omega_0 - (\Omega_0 - \Omega_c)d_c = \Omega_0(1-0.9d_c) \tag{8}$$

where subscript 0 and c denote for sound and carbonated materials; Ω_0 can be calculated from porosity, specific surface area and intrinsic permeability of reference sample; d_c is the carbonation degree (see Section 2.2.1).

The $\beta(P_a)$ function is introduced to account for the slip effect on gas permeability known as the Klinkenberg effect and is written as:

$$\beta(P_a) = (1+\lambda/P_a) \tag{9}$$

where λ is a saturation dependent parameter (Abbas et al. 1999) $\lambda = 3.37 - 0.036S$ [atm] and P_a denotes the mean pressure [atm]. We use the empirical formula proposed by (Papadakis et al. 1991) to calculate the diffusivity of gaseous CO_2:

$$D_g = D_0\phi^{1.8}(1-RH)^{2.2} \tag{10}$$

The effective diffusivity calculated in Eq. (10) is actually applied for large pores (molecular diffusion). However, in carbonated/carbonating material, of which the pore size range is shifted to smaller size, Knudsen diffusion should be considered together with molecular diffusion. In this case, the (bulk) effective diffusivity is smaller as reported by (Houst and Wittmann 1994). In a simplified approach, we take into account this effect by changing D_0 to $10^{-d_c}D_0$, and $\phi^{1.8}$ to $\phi^{1.8+k_1 d_c}$, where d_c is the carbonation degree; and k_1 is in range 0.5 – 1. The value of k_1

may be determined if the gas diffusivity of carbonated cement paste is known. For dissolved CO_2, we account for the effects of porosity, tortuosity, and saturation degree as the proposed following equation to estimate effective diffusivity of dissolved CO_2:

$$D_l = D_{l0} \times k_D(\phi,\tau) \times k_D(S) \tag{11}$$

where $k_D(\phi,\tau)$ [-] accounts for the contributions of porosity and tortuosity. This relation was proposed by (Garboczi and Bentz 1992):

$$k_D(\phi,\tau) = 0.001 + 0.07\phi_c^2 + 1.8H(\phi_c - 0.18)(\phi_c - 0.18)^2 \tag{12}$$

where and $H()$ is the Heaviside function; $k_D(S)$ [-] accounts for the effect of saturation degree (Thiéry 2005):

$$k_D(S) = \left(1 + 625(1-S)^4\right)^{-1} \tag{13}$$

Eq. (12) was originally developed for sound materials. As carbonation proceeded, the precipitation of calcium carbonate does not only reduce the porosity but also increase the tortuosity. Therefore, with the same porosity drop, the reduction of diffusivity is expected to be faster for carbonation compared to hydration. Experimental results (Phung 2015) shows that the relative diffusivity of carbonated zone is about 70% smaller than the relative diffusivity of sound material with the sample capillary porosity. As a first estimation, Eq. (13) is adapted for carbonating materials as:

$$k_D^*(\phi,\tau) = \left(1 - 0.7d_c\right)k_D(\phi,\tau) \tag{14}$$

The saturation degree is related to the internal relative humidity by combining Kelvin-Laplace equation and van Genuchtens relation (van Genuchten 1980):

$$S = \left[1 + \left(-\alpha \ln(RH)\right)^{\frac{1}{1-\beta}}\right]^{-\beta} \tag{15}$$

where α and β are experimental fitting parameters.

Evolution of porosity due to carbonation

The change in porosity is estimated by comparing the volume of new products (solid) produced by the carbonation of portlandite and C-S-H.

$$Ca(OH)_2 + CO_2 = CaCO_3 + H_2O \qquad \Delta\phi_{CH} = \left(C_{CH0} - C_{CH}\right)/M_{CH}\left(V_{CH} - V_{CC}\right) \tag{16}$$

y_0CaO•SiO$_2$•z_0H$_2$O + (y_0-y)CO$_2$ = yCaO•SiO$_2$•zH$_2$O + (y_0-y)CaCO$_3$ + (z_0-z)H$_2$O

$$\Delta\phi_{CSH} = C_{CSH0}/M_{CSH0}\left[\left(y_0 - y\right)V_{CC} - \left(V_{CSH0} - V_{CSH}\right)\right] \tag{17}$$

where $\Delta\phi_{CH}$ and $\Delta\phi_{CSH}$ are porosity changes [-] due to portlandite and C-S-H carbonation, respectively; y and z are the average Ca/Si ratio and stoichiometric ratio of H_2O in C-S-H, respectively; C_{CH} and C_{CSH} are portlandite and C-S-H contents [kg/m^3], respectively; M_{CH} and M_{CSH} [kg/mol] are molar masses of portlandite and C-S-H, respectively; V_{CH}, V_{CC} and V_{CSH} [m^3/mol] are molar volumes of portlandite, calcite and C-S-H, respectively. Subscript 0 denotes initial condition. Data for molar volume of C-S-H is still scarce and it is supposed to be stoichiometry-dependent parameter. Recent experimental study (Morandeau et al. 2014) showed that the molar volume of C-S-H is in direct proportion to Ca/Si ratio as:

$$V_{CSH0} - V_{CSH} = \omega\left(1 - y/y_0\right) \tag{18}$$

where $0.02 < \omega < 0.04$ [l/mol]. By comparing the porosity of carbonated and uncarbonated samples, we find that $\omega = 0.04$ [l/mol] gives the best fit. The total porosity of sample during carbonation is simply expressed as follows:

$$\phi = \phi_0 + \Delta\phi_{CH} + \Delta\phi_{CSH} \quad (19)$$

where ϕ_0 is initial total porosity which is determined experimentally or can be calculated as follows (Hansen 1986):

$$\phi_0 = (w/c - 0.17m)/(w/c + 0.32) \quad (20)$$

in which m denotes the degree of hydration. The change in capillary porosity is mainly due to the carbonation of portlandite. However, C-S-H carbonation might partially contribute to the capillary porosity change, especially in accelerated conditions which is expressed by coefficient υ ($0 \le \upsilon \le 1$) as follows. The value of υ is set to be 0.5 in this study, which gives a good fit with capillary porosity change determined by MIP.

$$\phi_c = \phi_{c0} + \Delta\phi_{CH} + \upsilon\Delta\phi_{CSH} \quad (21)$$

where ϕ_{c0} is initial capillary porosity which is either determined by experiment or calculated as follows (Hansen 1986):

$$\phi_0 = (w/c - 0.36m)/(w/c + 0.32) \quad (22)$$

Reaction kinetics

As mentioned before, we only take into account the carbonation of CH and C-S-H. Instead of separately modelling the carbonation reactions of CH and C-S-H, we combine both reactions as a single reaction between Ca^{2+} (dissolved from CH and C-S-H) and CO_3^{2-} ions:

$$Ca^{2+}(\text{total}) + CO_3^{2-} \rightarrow CaCO_3 \quad (23)$$

We consider that the reaction (23) is of the first order with respect to Ca^{2+} and CO_3^{2-}. The rate of the combined carbonation reaction, r [mol/s.m^3], is written as follows:

$$r = -Q/(\phi M_{CO_2}) = -\partial[CH]/\partial t - \partial[C-S-H]/\partial t = k_C f(S) k_r (C_{Ca}/M_{Ca})(C_{CO_3}/M_{CO_3}) \quad (24)$$

where k_C [m^3/mol.s] is the reaction rate coefficient, which is temperature dependent, expressed via the Arrhenius' equation:

$$k_C = \psi.\exp(-E_0/RT) \quad (25)$$

in which ψ is prefactor [m^3/mol.s] and E_0 is activation energy [J/mol]. C_{Ca} and C_{CO_3} [kg/m^3] are total concentration of Ca^{2+} in solution and concentration of CO_3^{2-}, respectively. M_{Ca} and M_{CO3} [kg/mol] are molar masses of Ca^{2+} and CO_3^{2-}, respectively. The concentration of CO_3^{2-} can be related to the concentration of dissolved CO_2 by considering the equilibrium of CO_2 in solution. The function $f(S) = S^n$ (n = 3.7 (Papadakis et al. 1991)) is introduced in Eq. (24) in order to account for the effect of saturation degree on the carbonation reaction rate. The carbonation products are mainly formed surrounding CH/C-S-H which will reduce the reaction rate because CO_2 has to diffuse through the product layer. Therefore, a retardant factor is added into Eq. (24) as follows:

$$k_r = (C_{Ca}^s / C_{Ca0}^s)^2 \quad (26)$$

where C_{Ca}^{s} [mol/m^3] is total concentration of solid Ca except for Ca in calcium carbonate, subscript 0 denotes the initial concentration. Finally, we obtain the following expression of the mass balance of dissolved CO_2:

$$\frac{\partial\left(\left[\phi(1-S)\frac{K_{CO_2}^{H}}{RT}+\phi S\right]c_l\right)}{\partial t}-\frac{\partial\left(\left[\frac{K_{CO_2}^{H}}{RT}v_g+v_l\right]c_l\right)}{\partial x}-\frac{\partial\left(\left[\frac{K_{CO_2}^{H}}{RT}D_g+D_l\right]\frac{\partial c_l}{\partial x}\right)}{\partial x}=-f(S)\phi k_c k_r\frac{C_{Ca}}{M_{Ca}}\frac{C_{CO_3}}{M_{CO_3}}M_{CO_2} \tag{27}$$

Each term in Eq. (27) corresponds to a different mechanism. The first term on the left hand side describes the exchanging rate of CO_2 concentration in aqueous phase. The second term is called the advection term and obeys Darcy's law. The last term involves the diffusion, following Fick's law. The right hand side of Eq. (27) is responsible for chemical reaction of CO_2 in which the total concentration of Ca^{2+} is determined by solving a separate reaction-transport Eq. of Ca^{2+} (Section 2.1.2). The initial and boundary conditions are:

$$\begin{cases} c_l(x,0)=c_{l0} & x\geq 0 \\ c_l(0,t)=c_l^{in} & t>0 \\ c_l(L,t)=c_l^{out} & t>0 \end{cases} \tag{28}$$

where c_l^{in} and c_l^{out} are the concentration of dissolved CO_2 at inlet and outlet, respectively; c_{l0} are the initial concentration of dissolved CO_2; L is the length of the sample [m]. The problem is numerically solved by using the COMSOL program.

2.1.2. Mass conservation of calcium ion

In the same way as CO_2, the mass balance equation for total Ca^{2+} is given as:

$$\partial(\phi SC_{Ca})/\partial t-\partial(v_l C_{Ca})/\partial x-\partial(D_{Ca}(\partial C_{Ca}/\partial x))/\partial x=-\phi r(M_{Ca}/M_{CO_2})+r_d \tag{29}$$

where D_{Ca} [m^2/s] is the effective diffusivity of calcium ion in the porous media (cement/concrete); r_d is the dissolution rate of CH and C-S-H [kg/m^3.s] which is calculated from the mass balance equation of total amount of Ca in solid CH and C-S-H as follows:

$$(\partial C_{Ca}^{s}/\partial t)M_{Ca}=-r_d \tag{30}$$

In order to establish a relation between concentration of calcium ion in solution and concentration of Ca in solid phases, we propose a solid-liquid equilibrium curve of Ca based on the experimental data collected by (Berner 1992) as expressed in Eq. (31).

$$C_{Ca}^{s}=\begin{cases}(d/a)C_{Ca} & C_{Ca}\leq a \\ d+((e-d)/(b-a))(C_{Ca}-a) & a<C_{Ca}\leq b \\ e+((f-e)/(c-b))(C_{Ca}-b) & b<C_{Ca}\leq c\end{cases} \tag{31}$$

The values of a, b and c are well-defined in literature. Therefore, we use fixed values: a = 2 [mol/m^3], b = 19 [mol/m^3] and c = 22 [mol/m^3] for numerical modelling. The Ca fraction in CH and C-S-H can be estimated from the hydration of minerals (C_2S, C_3S) in cement which can be estimated by the Bouge calculation. Whereas the critical value d where C-S-H starts sharply decalcifying is determined by multiplying the amount of SiO_2 in C-S-H with the corresponding Ca/Si ratio (0.85) (Berner 1992).

By substituting Eqs. (30) and (31) to Eq. (29), with initial and boundary (Neumann) conditions (32) we can determine the concentration of calcium in solution which is needed for the sink term of Eq. (27).

$$\begin{cases} C_{Ca}(x,0) = c & x \geq 0 \\ \partial C_{Ca}(0,t)/\partial x = 0 & t > 0 \\ \partial C_{Ca}(L,t)/\partial x = 0 & t > 0 \end{cases} \tag{32}$$

2.2. Derivation of auxiliary variables

2.2.1. Carbonation degree

The term "carbonation depth" is commonly used to quantify the carbonation of concrete. It is experimentally determined by the de-colouring of phenolphthalein indicator in carbonated zone. The question is how to mathematically define the carbonation depth? In the present study, we combine the carbonation reaction of CH and C-S-H. Therefore, it is logical to relate the carbonation depth to total concentration of Ca in the solid phases. Here we define the carbonation depth as the position at which X_{Ca} percentage of total Ca is carbonated. By comparing with carbonation depth determined by phenolphthalein, it is found that X_{Ca} is roughly 20%. The carbonation degree, d_c, is then formulated as:

$$d_c = \begin{cases} 1 & C_{Ca}^s < X_{Ca} f \\ (f - C_{Ca}^s)/((1 - X_{Ca}/100) f) & C_{Ca}^s \geq X_{Ca} f \end{cases} \tag{33}$$

2.2.2. Evolution of saturation degree during carbonation

As mentioned, the carbonation reactions release water. Therefore, the saturation degree (thereby RH) will change during carbonation. This change can be estimated based on the reactions of CH and C-S-H with CO_2 shown in Eqs. (16) and (17). The calculation of released water for CH carbonation is straightforward. However, for C-S-H carbonation y mol of Ca in C-S-H will release z mol H_2O. The stoichiometry values of y and z are only slightly different (Allen et al. 2007). Therefore, we assume that ratio $y/z = 1$. It is then possible to calculate the amount of released water, m_{wr} [kg], based on the change of total Ca in solid phase.

$$m_{wr} = \left(f - C_{Ca}^s\right) M_w F dx \tag{34}$$

where M_w is molar weight of water [kg/mol], F denotes surface area of sample [m^2]. The total water in domain Fdx can be computed as follows:

$$m_w = \left(f - C_{Ca}^s\right) M_w F dx + S_0 \phi_0 \gamma_w F dx \tag{35}$$

Finally, the saturation degree can be calculated as:

$$S = V_w/V_p = \left(\left(f - C_{Ca}^s\right)(M_w/\gamma_w) F dx + S_0 \phi_0 F dx\right)\Big/(\phi F dx) = \left(\left(f - C_{Ca}^s\right)(M_w/\gamma_w) + S_0 \phi_0\right)\Big/\phi \tag{36}$$

where V_w and V_p [m^3] are volumes of water and pore in domain Fdx, respectively.

2.2.3. Changes in permeability and diffusivity under saturated condition

The permeability of carbonating material varies along the depth of sample. In order to calculate the composite (or overall) permeability coefficient of the sample, the sample depth is divided into small layer Δx. The permeability of each layer is assumed to be constant. The series model is applied to calculate the composite permeability. The fluxes in each layer and the overall flux must be the same because each layer is connected together in series.

$$J_1 = J_2 = \ldots = J_n = (k_n/\eta)(\Delta p_n/\Delta x) = (k_{com}/\eta)(P/L) \tag{37}$$

where J_n, Δx and Δp_n denote the flux, thickness and pressure gradient of layer n, respectively; k_{com} denotes the composite intrinsic permeability coefficient of the sample. Additionally, the total pressure drop on each layer must be equal to gradient pressure applied on the sample. Therefore, the overall permeability can be derived as:

$$k_{com} = L \Big/ \sum_{i=1}^{n} \frac{\Delta x}{k_i} \simeq L \Big/ \int_0^L \frac{dx}{k(x)} \tag{38}$$

where $k(x)$ is intrinsic permeability at distance x. With the same approach, the composite diffusivity, D_{com} [m^2/s], of carbonated materials is written as:

$$D_{com} = L \Big/ \sum_{i=1}^{n} \frac{\Delta x}{D_i} \simeq L \Big/ \int_0^L \frac{dx}{D(x)} \tag{39}$$

where $D(x)$ [m^2/s] is effective diffusion coefficient at distance x.

3. MODELING RESULTS AND VERIFICATIONS

Experiments were performed on cement pastes with w/c ratio of 0.425. Type I ordinary Portland cement (CEM I 52.5 N) was used. Details of the setup and experimental procedure were described in (Phung et al. 2015). A pure CO_2 pressure gradient of 6 bar was applied in order to accelerate the carbonation process. A single carbonation test was performed for a period of 4 weeks.

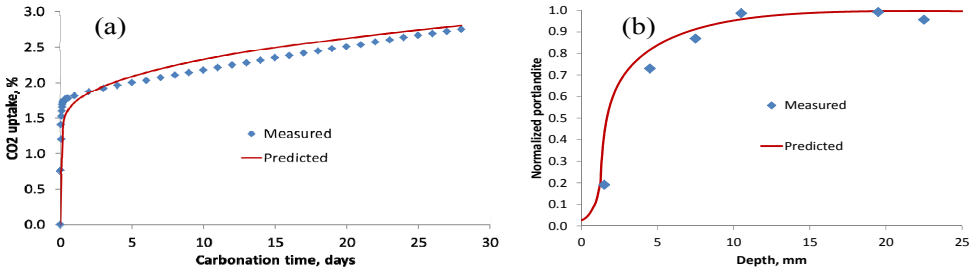

Fig. 1. CO_2 uptake (a) and portlandite profile after 28-day carbonation (b)

Fig. 1a compares the predicted CO_2 uptake with the measurement. Except for a slight difference at the transition between initial and residual stages, the predicted CO_2 uptakes are in good agreement with the measured ones. In the initial stage, CO_2 uptake rapidly increases but the uptake rate is significantly decreased in the residual stage because of porosity decrease and saturation degree increase. Fig. 1b shows the comparison of predicted portlandite profile with the one obtained by TGA measurements. The predicted value is in line with the measured one. The measured portlandite content at the downstream (not in contact with pure CO_2) is relatively smaller than the predicted value. The difference is attributed to the atmospheric carbonation which could occur during sample preparation for carbonation test or/and TGA measurements.

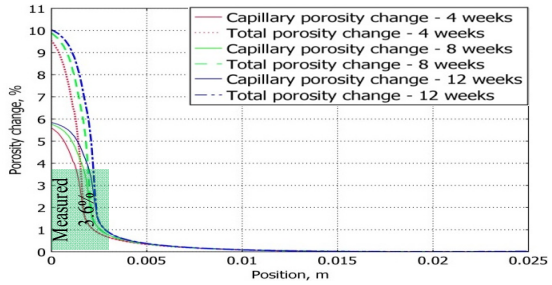

Fig. 2. Reduction of porosity (absolute value) at different carbonation time

The capillary and total porosities relatively decrease due to carbonation as shown in Fig. 2. The decrease in total porosity can mainly be attributed to the portlandite carbonation. However, in well-carbonated zone (near reacted surface), C-S-H carbonation may contribute up to 45% of

total porosity reduction. The average capillary porosity change, determined by MIP up to a depth of 3 mm from the exposed surface, compares well with the predicted capillary porosity change.

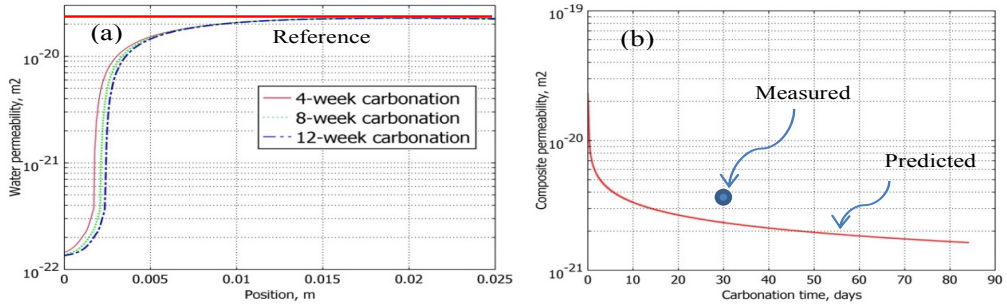

Fig. 3. Water permeability over the depth (a) and composite permeability decrease as a function of carbonation time (b)

Permeability of carbonated zone significantly decreases as shown in Fig. 3a. After 4-week carbonation, the alteration in permeability is not significant when carbonation proceeds further. The permeability coefficient decreases 2 orders of magnitude in the zone near the exposed surface. The composite permeability is dominated by the permeability of the carbonated zone despite its limited carbonation depth compared to the sample length. Therefore, a significant decrease in composite permeability is also observed as presented in Fig. 3b. The composite permeability rapidly decreases in the first few days of carbonation. It is then slightly reduced as carbonation proceeds. After 28-day carbonation, the predicted composite permeability is 2.5×10^{-21} m^2 which is a bit lower compared to the measurement (3.6×10^{-21} m^2).

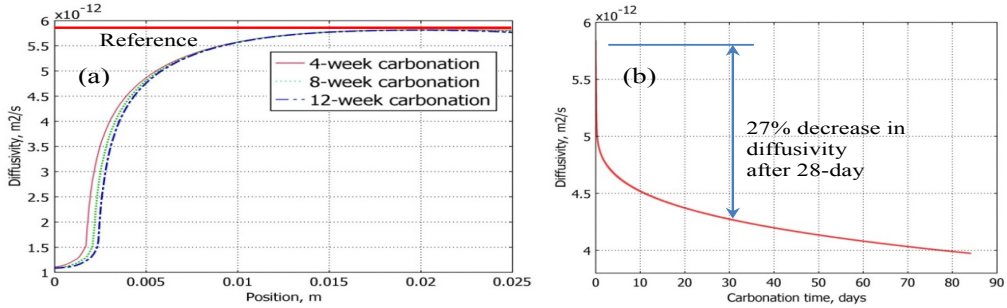

Fig. 4. Change in Ca diffusivity over the depth of at different carbonation time - (a) and composite Ca diffusivity decrease as a function of carbonation time (b)

The modification of diffusivity over the depth of sample due to carbonation is shown in Fig. 4a. The diffusivity of the carbonated zone is significantly decreased similar to the decrease in permeability. However, the magnitude of the reduction is less pronounced than for permeability. After 4 weeks of carbonation, the saturated Ca diffusivity decreases by a factor of 5 for the zone near the exposed surface which is consistent with the estimation from experimental result (4.92 times (Phung 2015)). The evolution of composite diffusivity is shown in Fig. 4b. As permeability, the composite diffusivity rapidly decreases in the first few days of carbonation. In the later stage, the diffusivity slightly decreases over carbonation time. The measured composite diffusivity of dissolved He is decreased by 30% after 28-day carbonation (Phung 2015), which is quite similar to the predicted Ca diffusivity decrease (27%). Note that the change in diffusion property of Ca and He due to carbonation may be

differed from each other because of its differences in molecular size, electrical force and binding effect.

4. CONCLUSIONS

A one-dimensional reactive transport model coupled advection and diffusion to simulate the carbonation under controlled CO_2 pressure has been developed. The model enables to predict a variety of important parameters including the CO_2 uptake, porosity change and variation of transport properties. The model helps to better interpret the experimental observations and understand the phenomena behind such as the formation of a gradual carbonation front. Primary verification with accelerated carbonation experiments gives a good agreement even though more experimental data is still required to validate and improve the model, especially to better predict the changes in transport properties.

REFERENCES

Abbas, A., Carcasses, M., and Ollivier, J. P. (1999). "Gas permeability of concrete in relation to its degree of saturation." *Mater Struct*, 32(215), 3-8.

Allen, A. J., Thomas, J. J., and Jennings, H. M. (2007). "Composition and density of nanoscale calcium-silicate-hydrate in cement." *Nat Mater*, 6(4), 311-316.

Bary, B., and Sellier, A. (2004). "Coupled moisture-carbon dioxide-calcium transfer model for carbonation of concrete." *Cement and Concrete Research*, 34(10), 1859-1872.

Berner, U. R. (1992). "Evolution of pore water chemistry during degradation of cement in a radioactive waste repository environment." *Waste Manage*, 12(2–3), 201-219.

Garboczi, E. J., and Bentz, D. P. (1992). "Computer simulation of the diffusivity of cement-based materials." *J Mater Sci*, 27(8), 2083-2092.

Glasser, F. P., Marchand, J., and Samson, E. (2008). "Durability of concrete - Degradation phenomena involving detrimental chemical reactions." *Cement and Concrete Research*, 38(2), 226-246.

Hansen, T. (1986). "Physical structure of hardened cement paste. A classical approach." *Mater Struct*, 19(6), 423-436.

Houst, Y. F., and Wittmann, F. H. (1994). "Influence of porosity and water content on the diffusivity of CO2 and O2 through hydrated cement paste." *Cement and Concrete Research*, 24(6), 1165-1176.

Morandeau, A., Thiéry, M., and Dangla, P. (2014). "Investigation of the carbonation mechanism of CH and C-S-H in terms of kinetics, microstructure changes and moisture properties." *Cement and Concrete Research*, 56(0), 153-170.

Muntean, A., Bohm, M., and Kropp, J. (2011). "Moving carbonation fronts in concrete: A moving-sharp-interface approach." *Chem Eng Sci*, 66(3), 538-547.

Papadakis, V. G., Vayenas, C. G., and Fardis, M. N. (1991). "Experimental Investigation and Mathematical-Modeling of the Concrete Carbonation Problem." *Chem Eng Sci*, 46(5-6), 1333-1338.

Papadakis, V. G., Vayenas, C. G., and Fardis, M. N. (1991). "Physical and Chemical Characteristics Affecting the Durability of Concrete." *Aci Mater J*, 88(2), 186-196.

Phung, Q. T. (2015). "Effects of Carbonation and Calcium Leaching on Microstructure and Transport Properties of Cement Pastes."PhD thesis, Ghent University, Belgium.

Phung, Q. T., Maes, N., Jacques, D., Bruneel, E., Van Driessche, I., Ye, G., and De Schutter, G. (2015). "Effect of limestone fillers on microstructure and permeability due to carbonation of cement pastes under controlled CO2 pressure conditions." *Constr Build Mater*, 82(0), 376-390.

Thiéry, M. (2005). "Modélisation de la carbonatation atmosphérique des matériaux cimentaires: prise en compte des effets cinétiques et des modifications microstructurales et hydriques."PhD thesis, Laboratoire central des ponts et chaussées, Paris.

van Genuchten, M. T. (1980). "A Closed-Form Equation for Predicting the Hydraulic Conductivity of Unsaturated Soils." *Soil Sci Soc Am J*, 44(5), 892-898.

Wardeh, G., and Perrin, B. (2006). "Relative permeabilities of cement-based materials: Influence of the tortuosity function." *J Build Phys*, 30(1), 39-57.

Influence of the Alkali-Dolomite Reaction on the Mechanical Properties of Concrete

P. Štukovnik[1]; M. Marinšek[2]; and V. Bokan Bosiljkov[1]

[1]University of Ljubljana, Faculty of Civil and Geodetic Engineering, SI-100 Ljubljana, Jamova 2, Slovenia. E-mail: petra.stukovnik@fgg.uni-lj.si; violeta.bokan-bosiljkov@fgg.uni-lj.si
[2]University of Ljubljana, Faculty of Chemistry and Chemical Technology, SI-1000 Ljubljana, Večna pot 113, Slovenia. E-mail: marjan.marinsek@fkkt.uni-lj.si

Abstract

This paper deals with the process of non-expansive alkali-carbonate reaction (ACR) in cement mortar prepared with specific dolomite aggregate. ACR was studied for one year in accelerated conditions. Results obtained at microstructural level show that ACR is progressive with time and reflects in the process of aggregate grains' dedolomitisation, the formation of secondary calcite in binder and the formation of new reaction products rich in Mg, Al and Si atoms along the dedolomitised parts of the grains. Observed mineralogical and microstructural changes reflect in relatively high increase in compressive strength of the mortar over time. On the other hand, its modulus of elasticity started to decrease already after five months of the exposure and was gradually decreasing until one year of the exposure.

INTRODUCTION

For certain dolomite rock used as the aggregate source we observed unusually fast increase in compressive strength of concrete over time [Štukovnik et al., 2014], unlike other mixtures, despite identical composition of all mixtures, apart from the aggregate source applied. Detailed study of this concrete's microstructure was carried out and it revealed the presence of ACR [Prinčič et al., 2013; Štukovnik et al., 2014].

In order to observe the process of ACR reaction in cement mortar between hydroxyl ions from the binder and the dolomite aggregate grains in more detail, we exposed newly prepared cement mortar specimens to different normal and accelerated exposure conditions: water at 20 °C and 60 °C, 1M NaOH solution at 20 °C and 60 °C. In this paper only results obtained for the most accelerated exposure conditions (1M NaOH at 60 °C) are presented up to 1 year of the exposure in order to show possible long-term extent of alterations to the mortar's microstructure due to ACR and their influence to the mechanical properties of concrete.

MATERIALS AND SPECIMENS

The used aggregate's parent rock is lower Triassic age dolomite. The result of mineralogical quantitative X-Ray analyses shows that dolomite represents 97 % of the mineral content of the aggregate, and calcite represents 3%. The water absorption

of the used dolomite aggregate fraction (0/4) is 0.48 % and its density is 2850 kg/m^3. The cement binder used was ordinary cement CEM I 42.5R (EN 197-1) with a Blain specific surface area of 3760 cm^2/g and density equal to 3.05 g/cm^3, and with alkali content of 1.0% (Na_2O equivalent). Producer of the cement is different from that in [Prinčič et al., 2013; Štukovnik et al., 2014]. The water-to-cement ratio of the mortar was 0.45. The mixing of the mortars, the casting of the mortar bars (40x40x160 mm^3) and the curing were completed according to the procedures given in EN 1015-11. The mortar bars were cured for 28 days and after that exposed to the 1M NaOH solution at 60 °C for different time intervals, up to 1 year. The time of exposure was marked as time zero ("0").

TESTING AND TEST RESULTS

Dynamic modulus of elasticity (E_{dyn}) was determined using GrindoSonic apparatus. Before the test was carried out the mortar bars had been cooled down to 20 °C, while the saturated state of the bars was maintained. Compressive strength was determined according to the standard EN 1015-15.

For the examination of thin sections a polarizing optical microscope with transmitted light, NIXON Eclipse E 200, was used. A Scanning electronic microscope, FE-SEM Zeiss Ultra Plus microscope equipped with EDS (Oxford X-Max SDD 50 mm2 106 detector and INCA 4.14 X-ray microanalysis software), was used in order to detect the process of dedolomitization on polished thin sections.

Compressive strength and modulus of elasticity

After exposure of the mortar bars to the accelerated conditions, compressive strength stayed unchanged for the first month. However, at longer exposure times considerable increase in compressive strength of the mortar with time was observed (Figure 1), by 20 MPa after 6 months and by 30 MPa after 1 year of exposure. This was not the case for the mortar prepared by inert limestone aggregate, where the same conditions resulted in the drop of compressive strength to the values lower than at time "0".

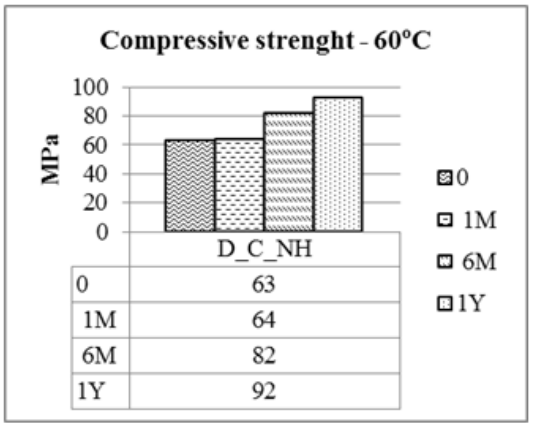

Figure 1. Compressive strength increase of cement mortar

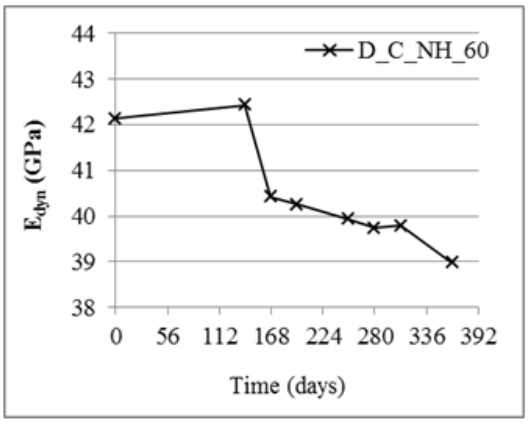

Figure 2. Change in E_{dyn} over time

However, continuous measurements of E_{dyn} carried out on mortar bars (Figure 2) revealed that alterations to the mortar's microstructure, due to ACR, influenced this elastic property of the mortar. The modulus stayed almost unchanged during the first five months of the exposure. However, already after six months we observed the first drop in E_{dyn} and further on the modulus was decreasing with time. Alteration of dolomite aggregate grains, due to ACR, was identified as the source of the observed behaviour. Therefore, we present below photographic micrographs and SEM/EDS images, to illustrate the identified reactions in the cement mortar microstructure.

Microstructure of cement mortar

Photomicrograph in Figure 3 presents the microstructure of the samples after 6 months of exposure. In Figure 3 thick (about 200 μm) reaction rim at the edge of a 1 mm dolomite aggregate grain can be observed, as well as progressive process of recrystalisation along the pre-existing cracks. Aggregate grains that are smaller than 0.3 mm had been recrystallized completely.

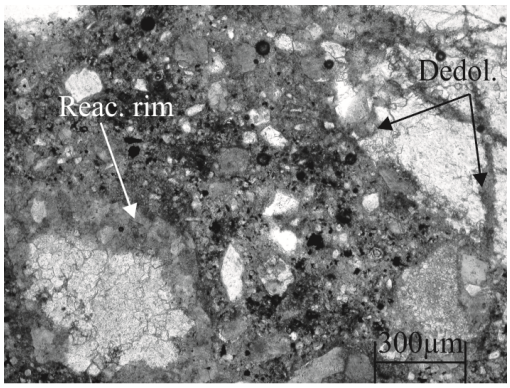

Figure 3. Sample D_C_NH_60 after 6 months of exposure

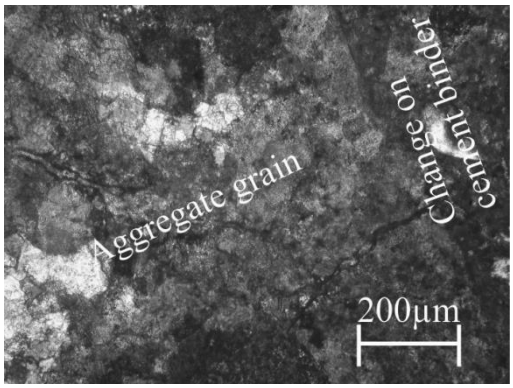

Figure 4. Sample D_C_NH_60 after 1 year of exposure

After 1 year of the exposure (Figure 4) dolomite grains with diameter up to about 2 mm recrystallized completely and the alteration of the cement binder along the grain was also observed.

SEM/EDS analyses after 1 year of exposure (Figure 5) revealed that alterations observed under polarizing microscope are due to dedolomitisation that had occurred within the reaction rims and along pre-existing cracks. Dedolomitisation is visible as characteristic fine grained myrmekitic texture observed already by [Katayama, 2004], which is characterised by mixed, but separated concentration of calcium and magnesium atoms. In the binder, next to the dedolomitised parts of aggregate grains, a high concentration of calcium atoms can be observed, which is evidence of secondary calcite formation, and is known as a "carbonate halo" [Katayama, 2004]. Along the edges of the recrystalisation areas of the aggregate, Si and Al atoms are concentrated in the same areas where the increased concentration of Mg atoms and at the same time decreased concentration of Ca atoms were detected (Figure 5). We can conclude that the formation of an Mg-Si-Al phase occurred.

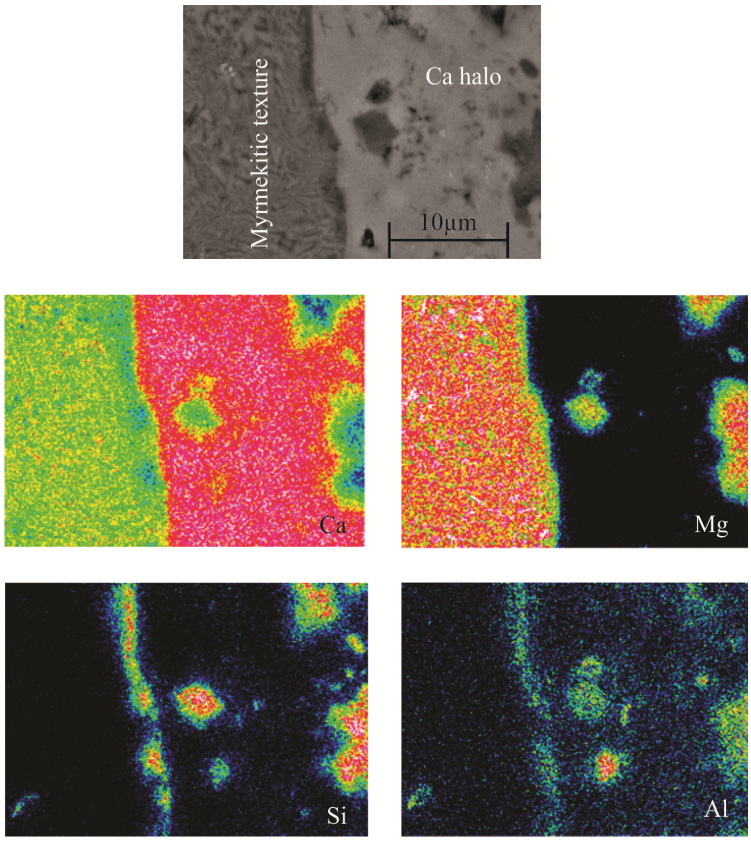

Figure 5. SEM/EDS image of sample D_C_NH_60 after 1 year of exposure (top) with concentrations of Ca, Mg (middle) and Si, Al (bottom) atoms.

CONCLUSIONS

Gradual decrease in E_{dyn} that was detected after five months and followed until one year of the exposure was attributed to the dedolomitisation process and the formation of new pores inside the dedolomitised parts of aggregate grains [Štukovnik et al., 2014]. Observed relatively high increase in compressive strength of the cement mortar over time (up to one year) was attributed to the secondary calcite formation and the formation of the Mg-Al-Si phase. Change in the source of the CEM I seems not to influence the process of ACR.

REFERENCES

Prinčič, T., Štukovnik, P., Pejovnik. S., De Schutter, G., and Bokan Bosiljkov, V. (2013). "Observations on dedolomitization of carbonate concrete aggregates, implications for ACR and expansion". *Cem. Con. Res.* 54(12):151–60.

Štukovnik, P., Prinčič, T., Pejovnik, R.S., Bokan Bosiljkov, V. (2014). "Alkali-carbonate reaction in concrete and its implications for a high rate of long-term compressive strength increase". *Con. Build. Mat.* 50:699-709.

Katayama T. (2004). "How to identify carbonate rock reactions in concrete". *Mat. Char.* 53:85-104.

The Influence of Leaching on the Ion Adsorption Ability of Hardened Cement Paste

Kiyofumi Kurumisawa[1]; Haruka Abe[2]; and Toyoharu Nawa[3]

[1]Faculty of Engineering, Hokkaido University, Kita 13, Nishi 8, Kita-ku, Sapporo, Hokkaido, Japan. E-mail: kurumi@eng.hokudai.ac.jp
[2]Faculty of Engineering, Hokkaido University, Kita 13, Nishi 8, Kita-ku, Sapporo, Hokkaido, Japan. E-mail: aharuka0329@gmail.com
[3]Faculty of Engineering, Hokkaido University, Kita 13, Nishi 8, Kita-ku, Sapporo, Hokkaido, Japan. E-mail: nawa@eng.hokudai.ac.jp

Abstract

The durability of the concrete structure is determined by transport properties of concrete. The transport of chloride ions greatly changes by the amount of adsorption by hydrates. However, there are few studies on change of the amount of adsorption with the calcium leaching. In this study, the purpose is to investigate a change of the amount of adsorption of the chloride ion with the calcium leaching of hardened cement pastes. The amount of chloride ion adsorption increased with the increase of the replacement ratio of the blast furnace slag. We established an equation to predict the amount of chloride ion adsorption on C-S-H and Afm. It was clarified that the amount of chloride ion adsorption on C-S-H of leached hardened cement paste depends on Ca/Si and Al/Si.

INTORODUCTION

Concrete is used for disposal of radioactive waste as artificial barrier in Japan. It is necessary for the radioactive waste to keep it safely for tens of thousands of years. Therefore, the durability of concrete is also needed for tens of thousands of years. When concrete contacts with groundwater, a calcium in concrete might leach out. The durability of the concrete decreases by calcium leaching. Therefore it is necessary to evaluate calcium leaching from concrete exactly (Heukamp,2001, Carde, 1996). Calcium leaching is influenced by the transport properties of concrete. Transport properties of several ions concrete is influenced by its adsorption (Elakneshwaran, 2010). It was clarified in previous reports that the adsorption ability is changed with the calcium leaching of concrete during service life. It was also reported that the adsorption ability of the C-S-H is depended on its Ca/Si (Kurumisawa, 2013). However, it is the report only for hardened white cement paste (WPC). In this study, cement mixed with blast furnace slag (BFS) was used for clarifying the effect of BFS on the adsorption ability of cement-based materials is investigated. Because it was difficult to use a radionuclide for adsorption, we investigated the adsorption of the chloride ion.

EXPERIMENTAL

Hardened cement paste was used for experiment. White cement (density: 3050kg/m^3, blaine surface area: 3440cm^2/g) was used for experiment because of NMR measurement. Water to binder ratio is 0.4, and replacement ratio of BFS (density: 2910kg/m^3, blaine surface area:4050cm^2/g) is 0(WPC), 0.5(BFS50) and 0.7(BFS70). 2.5-5mm crushed specimen was used for immersion (Abe, 2014). Ammonium nitrate solution (NH_4NO_3 6M) was used to accelerate the deterioration of hardened cement paste, and the degree of the deterioration of the hardened cement paste was changed by the immersion period of ammonium nitrate solution (Kamali, 2003). It was possible to produce hardened cement pastes with different CaO/SiO_2 by varying the immersion period of ammonium nitrate solution. The Chloride ion adsorption isotherms was measured for the determination of adsorption ability of hardened cement paste (Luping, 1993). The microstructure of hardened cement paste was observed by backscattered electron image, and Ca/Si and Al/Si ratio of C-S-H was determined by energy dispersive electron spectroscopy (EDX). Specimen for observation is immersed in epoxy resin, and polished the surface. Surface area of specimen was determined by water adsorption. And the mineral composition in leached cement pastes was determined by X-ray diffraction with Rietveld analysis. The chemical state of silicate chain of C-S-H in hardened cement paste was measured by ^{29}Si-NMR. Q^0, Q^1, Q^2(1Al), Q^2, Q^3(1Al) and Q^3 were assigned at -71, -74.5, -78, -80.5, -90 and -95ppm, respectively (Puertas, 2011).

RESULTS AND DISCUSSIONS

Ca/Si and Al/Si ratio. Figure 1 shows the change of Ca/Si ratio in C-S-H with NH_4NO_3 immersion period. Ca/Si ratio in C-S-H decreased with long immersion period. Ca/Si ratio of WPC showed the highest value in every period. Figure 2 shows the change of Al/Si ratio in C-S-H with NH_4NO_3 immersion period. Contrary to Ca/Si, Al/Si ratio in C-S-H increased with long immersion period (Miroslav,2012).

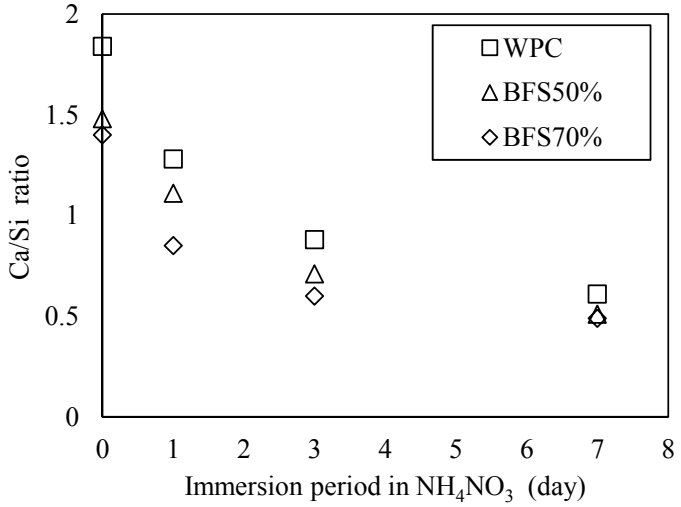

Figure 1. Change of Ca/Si ratio in C-S-H with NH_4NO_3 immersion period.

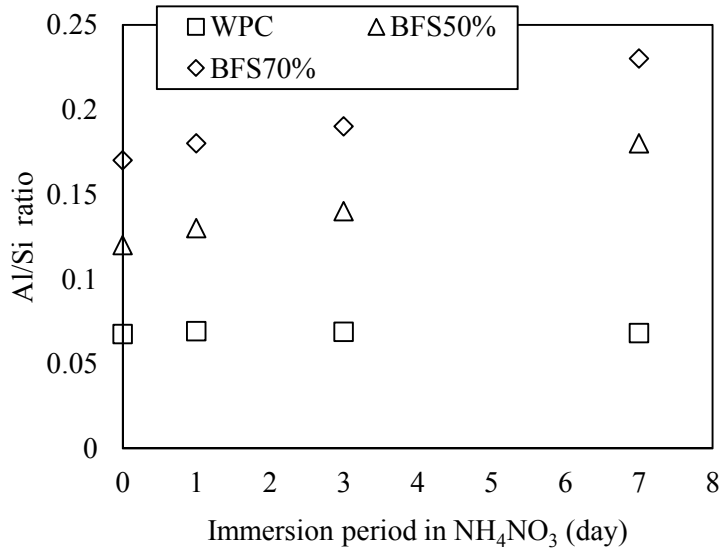

Figure 2. Change of Al/Si ratio in C-S-H with NH_4NO_3 immersion period.

Al/Si ratio of BFS showed the highest value in every period. It was possible to produce different composition of C-S-H in hardened cement paste.

Adsorption of chloride. Figure 3 shows the chloride adsorption isotherm of hardened cement paste without leaching. This result was similar to the result by Luping (Luping, 1993). The amount of chloride adsorption of BFS50 is higher than that of other specimen as reported by previous report. Figure 4 shows the chloride adsorption isotherm of hardened cement paste with calcium leaching by NH_4NO_3 immersion in 7day. The amount of chloride adsorption of BFS50 is also higher than that of other specimen.

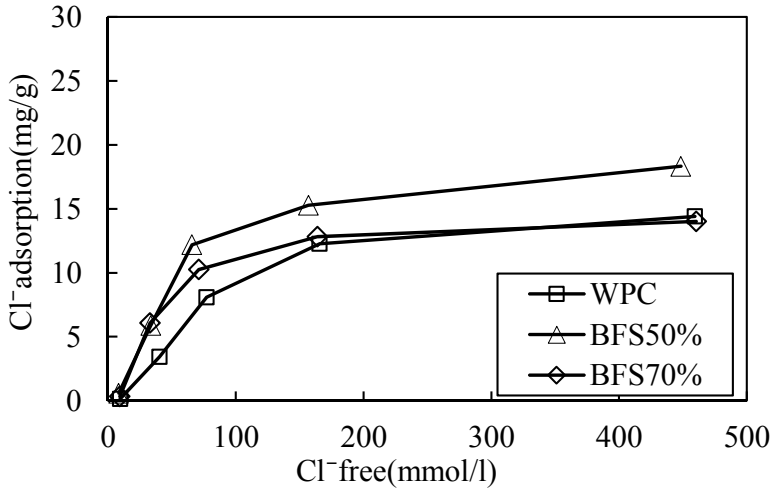

Figure 3. Chloride adsorption isotherm of hardened cement paste without leaching.

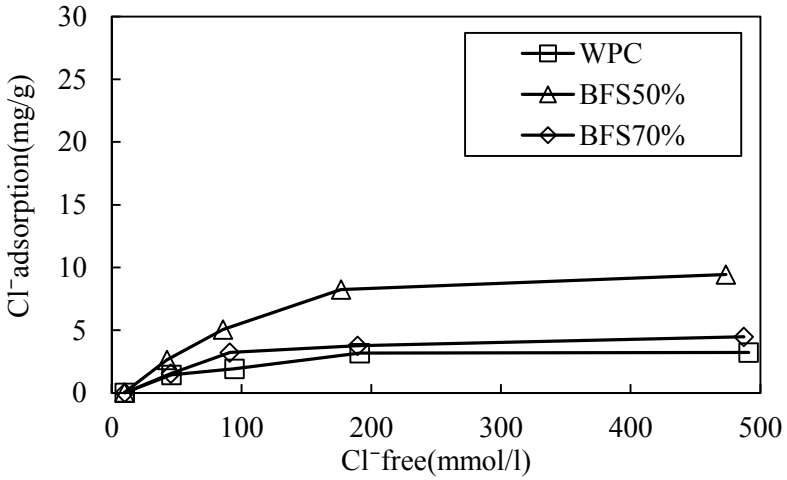

Figure 4. Chloride adsorption isotherm of hardened cement paste with leaching immersion in 7day.

Effect of properties of C-S-H on chloride adsorption. Figure 5 shows the plot of Ca/Si ratio and Cl adsorption to C-S-H at 200mM NaCl solution. The amount of adsorption of C-S-H was determined by the difference of the amount of adsorption of monosulfoaluminate (Afm) and hardened cement paste as shown in Figure 3 and 4. The amount of adsorption by Afm was determined by the report of Hirao (Hirao, 2005). As a result, the amount of chloride adsorption of C-S-H decreased with the decrease of Ca/Si ratio. This result was consistent with the result of previous report (Beaudoin, 1990). Figure 6 shows the plot of Al/Si ratio and Cl adsorption to C-S-H at 200mM NaCl solution. The tendency of the amount of adsorption to C-S-H of BFS was different from that of WPC. The Al/Si of WPC did not greatly change, and the amount of adsorption decreased. However, the amount of adsorption of BFS

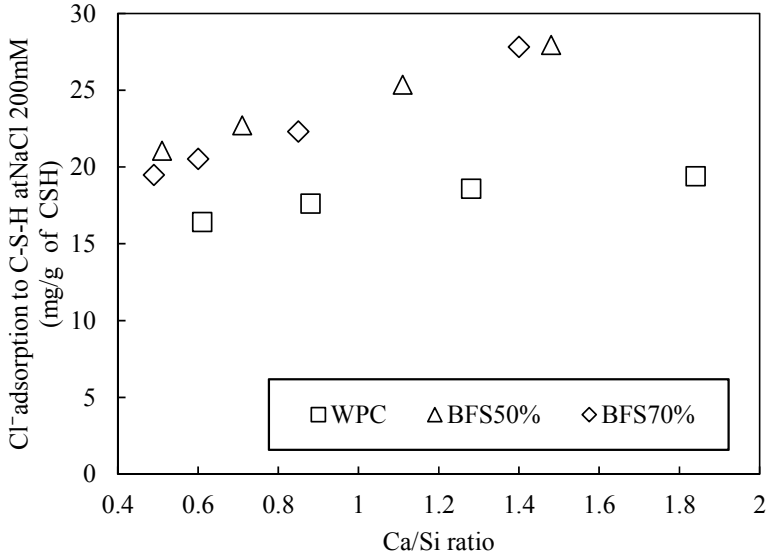

Figure 5. The plot of Ca/Si ratio and Cl adsorption to C-S-H at 200mM NaCl solution.

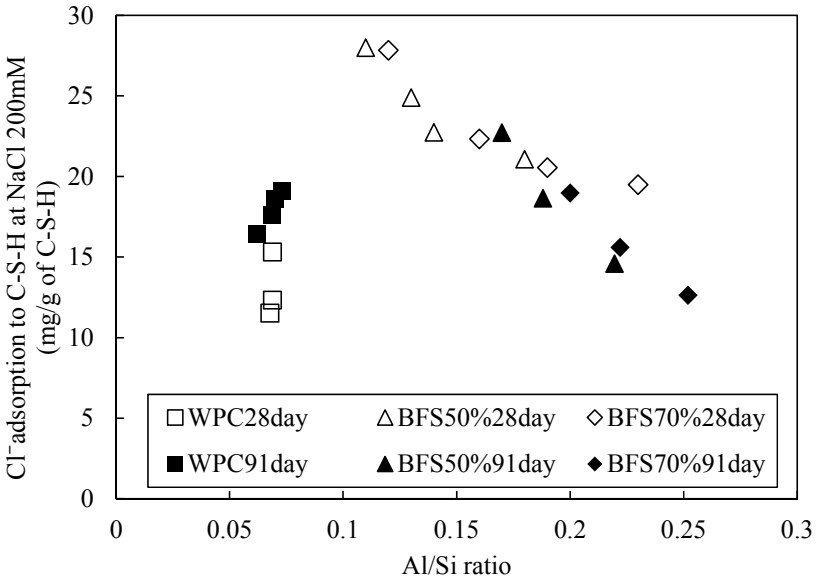

Figure 6. The plot of Al/Si ratio and Cl adsorption to C-S-H at 200mM NaCl solution.

decreased with the increase of Al/Si of BFS. Therefore, it is sufficient to consider Ca/Si in the case of pure C-S-H, but it is necessary to consider Al/Si in the case of C-A-S-H.

It was clarified that the adsorption ability of C-S-H is dependent on its Ca/Si and Al/Si of C-S-H. Therefore, we established the prediction equation of the chloride adsorption ability using Ca/Si and Al/Si of C-S-H based on equation proposed by Hirao as shown in following,

Al/Si≦0.1

$$y = \left\{0.55 \times \frac{12.8x}{1+12.8x} \times \frac{a}{100} \times \frac{\frac{Ca}{Si}}{1.8} + 0.859x^{0.58} \times \frac{1000}{623} \times \frac{b}{100}\right\} \times 35.5$$

Al/Si>0.1

$$y = \left\{\left(1.76 - 4.51 \times \frac{Al}{Si}\right) \times \frac{12.8x}{1+12.8x} \times \frac{a}{100} \times \frac{\frac{Ca}{Si}}{1.8} + 0.859x^{0.58} \times \frac{1000}{623} \times \frac{b}{100}\right\} \times 35.5$$

where y: amount of chloride adsorption of hardened cement paste(mg/g), a: amount of C-S-H(%), b: amount of Afm(%), x: chloride concentration(mol/l).

Figure 7 shows change of surface area measured by water adsorption. Surface area increased with longer immersion period. Therefore, it was shown that the surface area does not affect the amount of adsorption. Figure 8 shows the plot of $Q^2Al/(Q^1+Q^2+Q^3)$ and Cl adsorption to C-S-H at 200mM NaCl solution. The amount of chloride adsorption to C-S-H increased with the increase of fraction Q^2Al in C-S-H. It was shown that the chloride adsorption to C-S-H is greatly affected by the

substitution of Aluminum of the Si. However, investigations are not enough, a further study will be necessary in future.

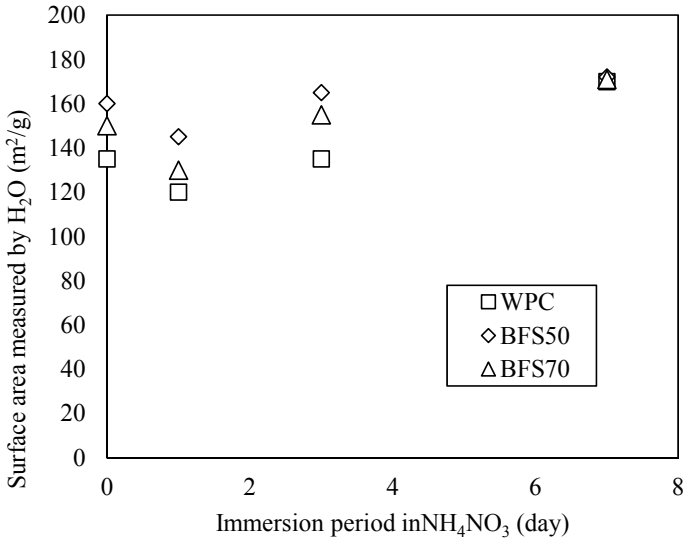

Figure 7. Change of surface area measured by water adsorption.

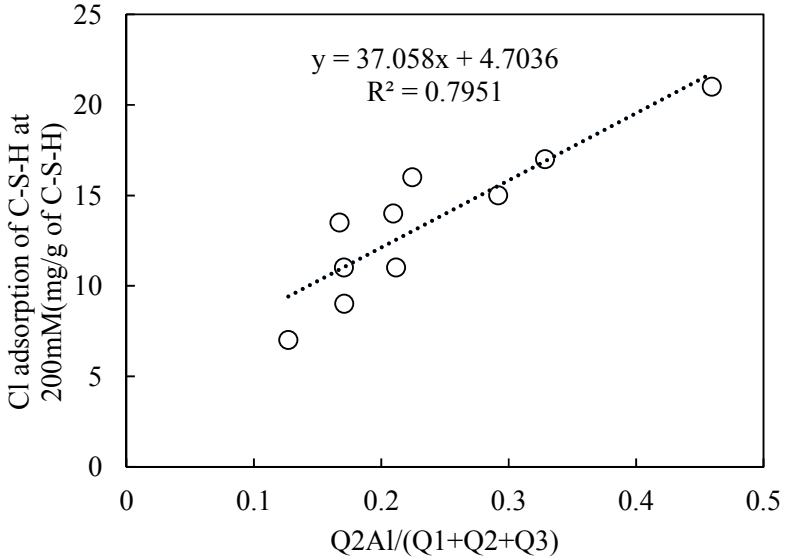

Figure 8. The plot of $Q^2Al/(Q^1+Q^2+Q^3)$ and Cl adsorption to C-S-H at 200mM NaCl solution.

CONCLUSION

It was shown that Ca/Si and Al/Si of C-S-H in specimen mixed with BFS changed with calcium leaching. And it was cleared that both of Ca/Si and Al/Si of C-S-H in specimen mixed with BFS had influence on the chloride adsorption ability.

The chloride adsorption ability of C-S-H was shown to be correlated with the quantity of Q^2Al in C-S-H from results of the ^{29}Si-NMR. Finally, we established a prediction equation of the chloride adsorption ability using Ca/Si and Al/Si of C-S-H.

ACKNOWLEDGMENTS

This research is partially supported by JSPS Kakenhi No. 25420565. And we also thank Mr. Awamura of Hokkaido University for help with the measurements.

REFERENCES

Abe H., et al. (2014). “Adsorption ability of the hardened slag cement paste.”, *Cement Science and Concrete Technology*, 68, (in press)

Beaudoin, James Joseph., Vangipuram Seshachar Ramachandran., and Raouf F. Feldman. (1990). "Interaction of chloride and CSH." *Cement and Concrete Research,* 20, 6, 875-883.

Carde C., Francois R. (1997). “Effect of the leaching of calcium hydroxide from cement paste on mechanical and physical properties.” *Cement and Concrete Researc*h, 27, 539-550.

Elakneswaran, Y., et al. (2010). "Ion-cement hydrate interactions govern multi-ionic transport model for cementitious materials." *Cement and Concrete research*, 40.12, 1756-1765.

Heukamp F. H., et al. (2001).”Mechanical properties of calcium-leached cement pastes Triaxial stress states and the influence of the pore pressures.” *Cement and Concrete Research*, 31, 767-774.

Hirao H. et.al. (2005).”Chloride Binding of Cement Estimated by Binding Isotherms of Hydrates.” *Journal of Advanced Concrete Technology,* 3(1), 77-84

Kamali S. et al. (2003).”Modeling the leaching kinetics of cement-based materials-influence of materials and environment.” *Cement and Concrete Composites*, 25, 451-458.

Kurumisawa K., et al. (2012). “The effect of the calcium leaching on capacity for chloride ion binding of the hardened cement paste.”, *Cement Science and Concrete Technology*, 67, 1,137-143.

Luping, Tang., and Lars-Olof Nilsson. (1993). "Chloride binding capacity and binding isotherms of OPC pastes and mortars." *Cement and concrete research* 23, 2, 247-253.

Miroslav et al. (2012). “Decalcification resistance of alkali activated slag.” *Journal of Hazardous Materials*, 233, 112-121.

Puertas F.et al. (2011). “A model for the C-A-S-H gel formed in alkali activated slag cements.” *Journal of the European Ceramic Society*, 31,2043-2056.

Multiscale Estimation of the Viscoelastic Properties of Cementitious Materials at an Early Age: A Combined Analytical and Numerical Approach

T. Honorio[1,2]; B. Bary[1]; and F. Benboudjema[2]

[1]CEA, DEN, DPC, SECR, Laboratoire d'Etude du Comportement des Bétons et des Argiles, F-91191 Gif-sur-Yvette, France. E-mail: tulio.honoriodefaria@cea.fr
[2]LMT (ENS Cachan, CNRS, Université Paris Saclay) 94235 Cachan, France.

Abstract

We propose an investigation combining numerical and analytical tools to estimate the ageing viscoelastic properties of cementitious materials within a multiscale framework. With analytical homogenization the properties at the cement paste and mortar scale are estimated by a combination of Generalized Self-Consistent (GSC) and Mori-Tanaka (MT) schemes. With numerical homogenization the effective properties at the concrete scale are estimated. Numerical homogenization has the advantage of allowing to assess local information as well as to study more complex geometries. This combined strategy constitutes a promising tool to investigate how different mechanisms leading to ageing at the hydrate products scale, as well as other features of cement-based materials such as the Interfacial Transition Zone (ITZ), affect the viscoelastic behavior at superior scales. In this context, we study the solidification of non-ageing constituents as the mechanisms leading to the ageing behavior. Relaxation and creep results at different scales are presented.

INTRODUCTION

Homogenization techniques have been widely used to estimate different properties of concrete. The estimation of elastic properties is of current use, and due to the Mandel (1966) correspondence principle, the estimation in non-ageing viscoelasticity is straightforward. More recent investigations have dealt with the ageing cases in which Mandel correspondence principle does not hold anymore (Masson et al. 2012; Sanahuja 2013a; Scheiner and Hellmich 2009). Different mechanisms are reported as potentially leading to the ageing behavior (Carol and Bažant 1993; Thomas and Jennings 2006; Vandamme and Ulm 2009). Moreover, other features of cement-based materials, such as the presence of an ITZ and the mismatch of properties of different phases may affect the overall response.

We propose an investigation combining numerical and analytical tools to estimate the ageing viscoelastic properties of cementitious materials within a multiscale framework. We are interested in the behavior at the mesoscale, defined here as the concrete (or coarse aggregate) scale but without neglecting the multiscale character of cement-based materials, especially some relevant aspects of some phases at the lower scales, such as, for instance, solidification or phases with viscoelastic

behavior. Some details of the analytical and numerical analysis are presented in the following. This work is a contribution towards the development of tools to investigate the mechanisms leading to ageing and how they affect the macroscopic response of the material.

ANALYTICAL HOMOGENIZATION

Analytical homogenization is used to estimate the properties at the cement paste and mortar scale (Figure 1). Two-coated sphere morphology is used to represent the cement paste and mortar microstructures, as proposed e.g. by Stora et al. (2009). Regarding the cement paste, the hydrating particle is embedded in a high density products layer which is, in turn, embedded in a low density products layer. Regarding the mortar, the sand particle is embedded in an ITZ layer which is, in turn, embedded in a cement paste layer. The GSC scheme is used to obtain the homogenized properties of the cement paste and mortar. MT scheme is used to estimate the properties within each coat. This representation of the microstructure was recently applied by the authors to estimate the elastic properties of concrete (Honorio et al. 2014). Here, both homogenization schemes are developed in an ageing viscoelastic framework, based on the derivation by Sanahuja (2013) for the MT scheme and on a specific formulation developed by the authors for the GSC (Honorio et al. submitted paper). These schemes are derived in a division algebra in which the non-commutative Volterra integral operator is defined. The resulting lengthy equations are not presented here for conciseness. As in Sanahuja (2013), a numerical solution following Bažant (1972) proposition is used to compute the time integrals.

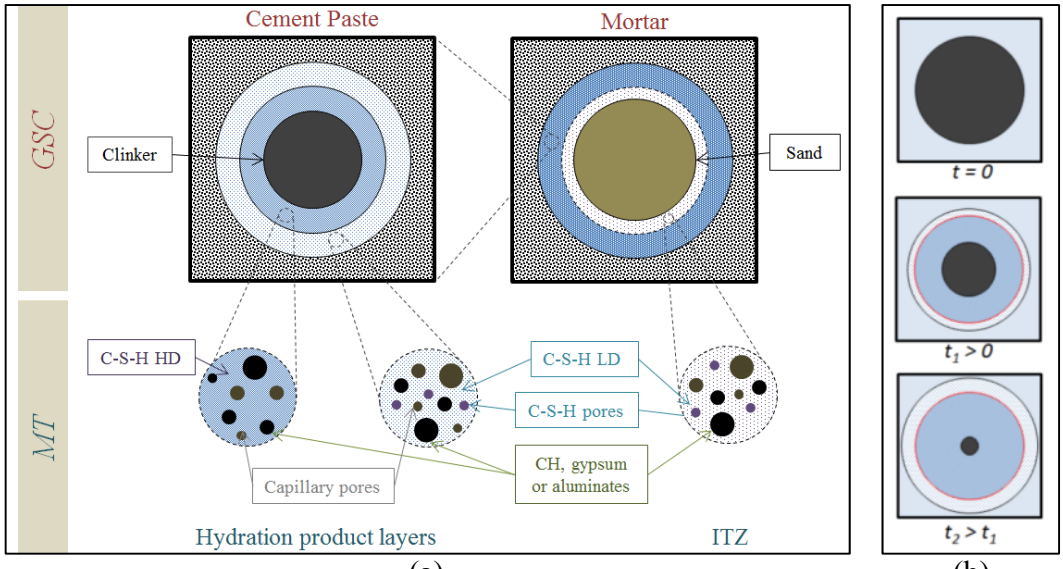

Figure 1. Microstructure representation (a) and solidification mechanism (b)

Precipitation/solidification mechanism

For the analytical part, we propose a scenario in which solidification of a non-ageing phase lead to the ageing behavior (Carol and Bažant 1993). Other scenarios in

which, for example, an intrinsically ageing phase undergoes solidification will be studied in a future contribution. Solidification is represented following Carol and Bažant (1993) solidification theory defined in a tensorial form (Sanahuja 2013b), which allows writing the relaxation tensor for a given phase solidifying at time t' by:

$$\mathbb{R}_i(t,t') = \mathbb{R}_s(t-t')\,\mathrm{H}(t'-t_i) \quad (1)$$

where $\mathrm{H}(.)$ is the Heaviside function and $\mathbb{R}_s(t-t')$ is the relaxation tensor of the solidified material. We adopted Maxwell rheological model to write $\mathbb{R}_s(t-t')$.

An ageing function is attributed to each phase present in the paste according to the hydration kinetics model of cement proposed by Honorio et al. (submitted paper). The evolution of volume fractions, as presented in Figure 2, is estimated by means of Tennis and Jennings (2000) balance equations. A non-ageing viscoelastic behavior is attributed to C-S-H phases; the other phases are assumed to behave elastically. In this paper the C-S-H behaviors are represented by Maxwell generalized rheological model with the parameters presented in Table 1. Such a behavior seems adequate regarding the effective behavior obtained confronted to experimental data. However, further investigations are needed to define C-S-H behavior at early-age. The elastic properties of the phases are the same as in Honorio et al. (2014). The repartition of the products in High Density (HD) and Low Density layers and in ITZ is performed following also Honorio et al. (2014).

Estimation of mortar properties

ITZ volume and composition are established as in Honorio et al. (2014). Differently of the cement paste scale, the volumes of the three phases in the coated sphere morphology at the mortar scale remain the same.

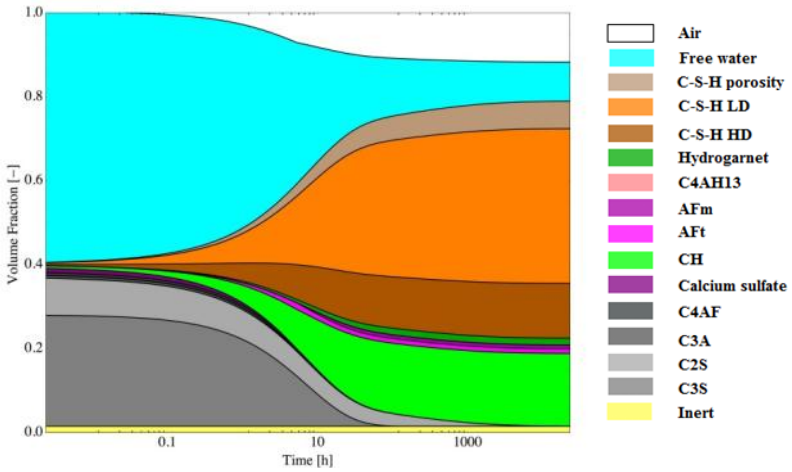

Figure 2. Evolution of volume fractions of hydration products and reactants

Table 1. Behavior of C-S-H for the shear and bulk modulus based on Maxwell generalized model: $\chi = \chi_0 + \sum \chi_i \, exp[-(t-t')/\tau_i]$

	E [GPa]	*ν*	τ_1 *[days]*	τ_2 *[days]*	τ_3 *[days]*	χ_0	χ_1	χ_3	χ_4
LD	29.4	0.24	0.1	1	10	0.2	0.4	0.2	0.2
HD	21.7	0.24	0.1	1	10	0.2	0.4	0.2	0.2

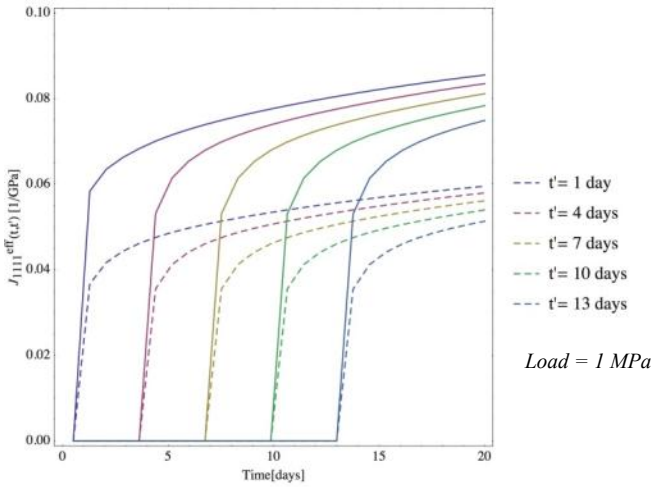

Figure 3. Creep functions (uniaxial) of cement paste (full lines) and mortar (dashed lines) estimated by analytical homogenization

Results

Bulk and shear moduli were obtained by analytical homogenization. With these properties, the compliance tensor can be computed by inversion of the stiffness tensor in the Volterra integral operator formalism. Figure 3 shows the uniaxial creep function obtained by analytical homogenization for the cement paste and mortar. With the behavior attributed to the phases, a not very well pronounced ageing character is observed at the cement paste and mortar scale. As expected, the creep in the cement paste is more accentuated than in the mortar paste, even if the ITZ creep (not shown for conciseness) is more elevated than cement paste creep.

NUMERICAL HOMOGENIZATION

Numerical homogenization is used to estimate the properties at the concrete scale. Here, we use a specific procedure associated with the Finite Elements code (Cast3m) to generate and compute 3D microstructures (de Larrard et al. 2013). With numerical homogenization, local information regarding the stresses and strains repartition in the heterogeneities and in definite regions of the matrix can be assessed. This is an advantage compared to analytical schemes which generally provide accurate estimations only on averaged fields. With the local information, the zones in which stresses are localized can be more precisely identified. Previous results showed that a considerable dispersion of the averaged stresses within the inclusions and matrix subvolumes is observed (Bary et al. 2014). Additionally, numerical homogenization allows testing more complex geometries and constitutive models.

The representative elementary volume (REV) tested is shown in Figure 4. The total volume fraction of the 556 inclusions is 40.0%.The matrix is divided in 125 elements in the local evaluation. Kinetic uniform boundary condition is adopted.

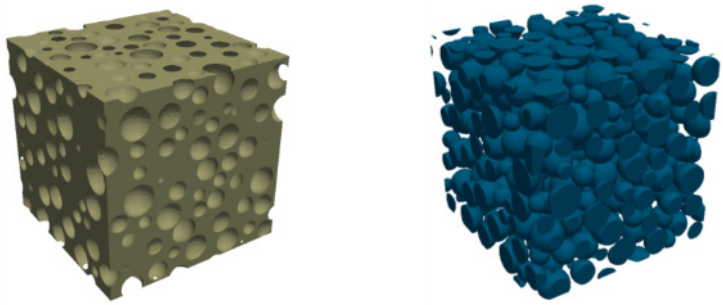

Figure 4. REV with matrix (left) and spherical inclusions (right) used in FEM simulations

Results

At the concrete scale, the behavior of the mortar is fitted on the macroscopic one obtained by analytical homogenization by means of Prony series multiplied by and ageing function. Figure 5 shows the effective creep function for concrete obtained by the numerical homogenization. With the mortar behavior computed in the last section, only a moderate ageing effect is observed in the period of the analysis.

Figure 6 shows an example of dispersion of the average strains within aggregates and matrix subvolumes for a given loading time. A more pronounced dispersion is observed within the inclusions. A part of this effect is due to the edge effects occurring in the inclusions near the boundaries where the loading is applied (Bary et al. 2014). Figure 7 shows an example of the longitudinal strain distribution in the material for two given times and a loading time of 4 days. In this figure it is possible to observe that the strains evolve differently within the matrix and the inclusions: they tend to decrease on average in the matrix while they increase in the aggregates. Further investigations are needed to study the effects of the aggregate shape on the dispersion of strains and stresses.

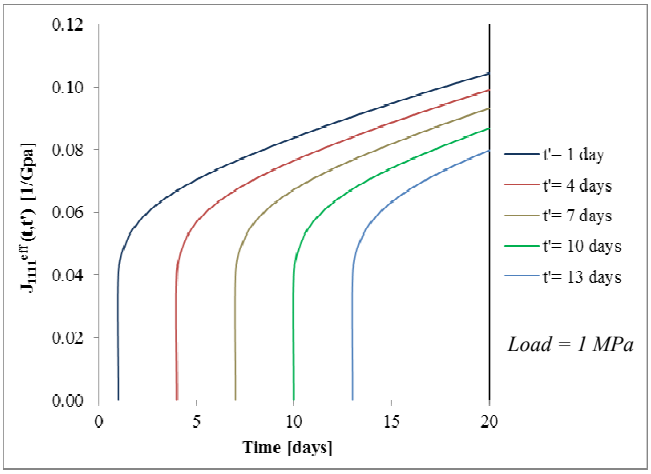

Figure 5. Overall uniaxial creep function of concrete obtained by combined numerical and analytical homogenization

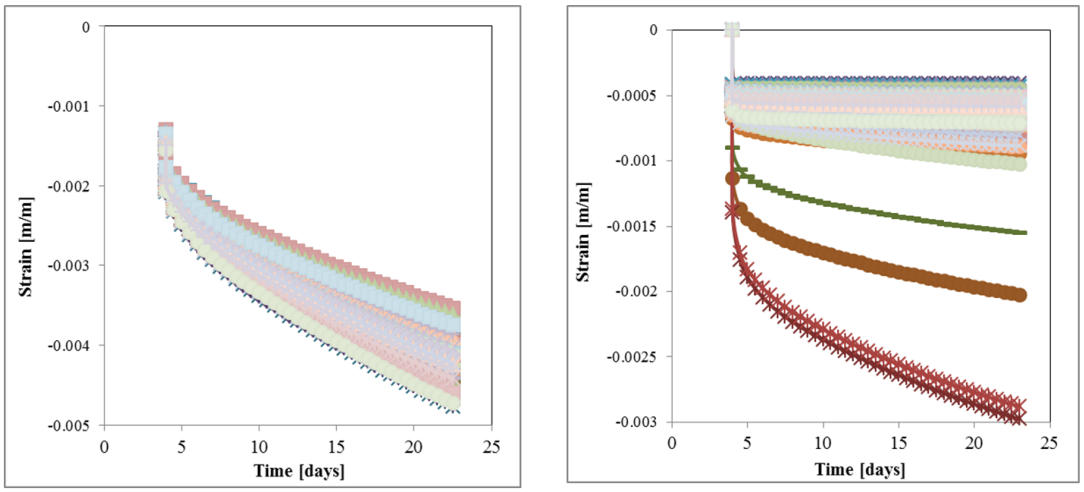

Figure 6. Dispersion of the uniaxial strain within the matrix (left) and the aggregates (right) and for t' = 4 days

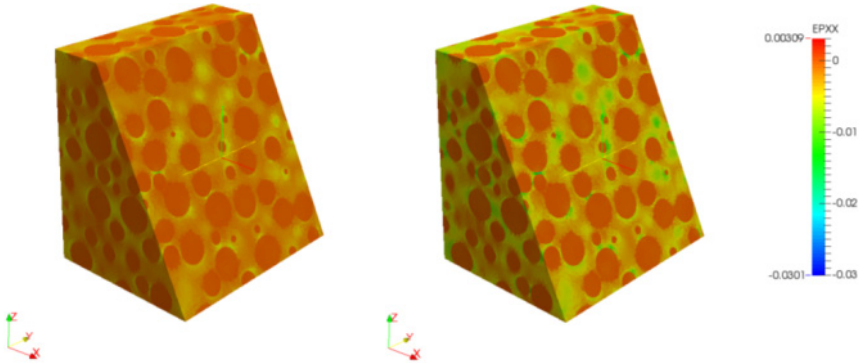

Figure 7. Strains within aggregates and mortar matrix at different ages for t' = 4 days: t = 6.5 days (left); t = 20 days (right)

CONCLUSIONS AND PERSPECTIVES

A strategy combining analytical and numerical homogenization is proposed to investigate the ageing viscoelastic behavior of cement-based materials at early-age in a multiscale framework. Analytical schemes derived in an ageing linear viscoelasticity background are used to estimate the properties at the cement paste and mortar scales. Numerical homogenization is used to study the concrete scale. This work provides a promising first attempt in the investigation of the factors affecting the ageing viscoelastic behavior. Further developments including other aspects important for early age analysis will be considered in future contributions.

- The approach develop here allows to investigate different propositions of mechanisms leading to an ageing behavior. In future communications, phases with intrinsically ageing behavior will be studied. Further developments include also an improved description of C-S-H viscoelastic behaviour (e.g. Sanahuja and Dormieux 2010; Smilauer and Bazant 2010; Vandamme and Ulm 2009).

- The estimations of the creep response are in agreement with the usual values obtained experimentally for similar concretes. Experimental validation in a multiscale background is foreseen.
- Strategies to account for the existence of a percolation threshold are to be developed. Also an improved description of the ITZ accounting, for example, for the interpenetration of the ITZ of neighboring particles, a more precise composition of the ITZ and a definition of a fixed ITZ volume independent of the size of the particle are aspects to be considered.
- According to the homogenized behavior of the mortar, different microstructures (with spherical, Voronoi and oblate inclusions) will be studied numerically in future contributions.

Acknowledgements

This present work has been performed as part of the project on disposal of LILW-SL that is carried out by ONDRAF/NIRAS, the Belgian Agency for Radioactive Waste and enriched Fissile Materials.

REFERENCES

Bary, B., Gélébart, L., Adam, E., and Bourcier, C. (2014). "Numerical analysis of linear viscoelastic 3D concrete specimens." *Computational Modelling of Concrete Structures*, CRC Press, 373–381.

Bažant, Z. P. (1972). "Numerical determination of long-range stress history from strain history in concrete." *Matériaux et Construction*, 5(3), 135–141.

Carol, I., and Bažant, Z. (1993). "Viscoelasticity with Aging Caused by Solidification of Nonaging Constituent." *Journal of Engineering Mechanics*, 119(11), 2252–2269.

Honorio, T., Bary, B., and Benboudjema, F. (in preparation). "Effective properties of n-coated composite spheres in an ageing viscoelastic framework."

Honorio, T., Bary, B., and Benboudjema, F. (2014). "Estimation of Elastic Properties of Cement based Materials at Early Age based on a Combined Numerical and Analytical Multiscale Micromechanics Approach." *RILEM International Symposium on Concrete Modelling*, Beijing, China.

Honorio, T., Bary, B., Benboudjema, F., and Poyet, S. (submitted paper). "Modelling hydration kinetics based on boundary nucleation and space-filling growth in a fixed confined zone."

De Larrard, T., Bary, B., Adam, E., and Kloss, F. (2013). "Influence of aggregate shapes on drying and carbonation phenomena in 3D concrete numerical samples." *Computational Materials Science*, 72, 1–14.

Mandel, J. (1966). "Cours de mécanique des milieux continus."

Masson, R., Brenner, R., and Castelnau, O. (2012). "Incremental homogenization approach for ageing viscoelastic polycrystals." *Comptes Rendus Mécanique*, Recent Advances in Micromechanics of Materials, 340(4–5), 378–386.

Sanahuja, J. (2013a). “Effective behaviour of ageing linear viscoelastic composites: Homogenization approach.” *International Journal of Solids and Structures*, 50(19), 2846–2856.

Sanahuja, J. (2013b). “Efficient Homogenization of Ageing Creep of Random Media: Application to Solidifying Cementitious Materials.” American Society of Civil Engineers, 201–210.

Sanahuja, J., and Dormieux, L. (2010). “Creep of a C-S-H gel: a micromechanical approach.” *Anais da Academia Brasileira de Ciências*, 82(1), 25–41.

Scheiner, S., and Hellmich, C. (2009). “Continuum microviscoelasticity model for aging basic creep of early-age concrete.” *Journal of engineering mechanics*, 135(4), 307–323.

Smilauer, V., and Bazant, Z. P. (2010). “Identification of viscoelastic CSH behavior in mature cement paste by FFT-based homogenization method.” *Cement and Concrete Research*, 40(2), 197–207.

Stora, E., Bary, B., He, Q.-C., Deville, E., and Montarnal, P. (2009). “Modelling and simulations of the chemo–mechanical behaviour of leached cement-based materials: Leaching process and induced loss of stiffness.” *Cement and Concrete Research*, 39(9), 763–772.

Tennis, P. D., and Jennings, H. M. (2000). “A model for two types of calcium silicate hydrate in the microstructure of Portland cement pastes.” *Cement and Concrete Research*, 30, 855–863.

Thomas, J. J., and Jennings, H. M. (2006). “A colloidal interpretation of chemical aging of the C-S-H gel and its effects on the properties of cement paste.” *Cement and Concrete Research*, 36(1), 30–38.

Vandamme, M., and Ulm, F.-J. (2009). “Nanogranular origin of concrete creep.” *PNAS*.

Uniaxial Restraint Tests under High-Stress Conditions and a Chemo-Hygral Model for ASR Expansion

Y. Takahashi[1]; K. Shibata[2]; M. Maruno[2]; and K. Maekawa[2]

[1]Department of Civil Engineering, The University of Tokyo, Hongo 7-3-1, Bunkyo-Ku, Tokyo 113-8656, Japan (corresponding author). E-mail: takahashi@concrete.t.u-tokyo.ac.jp
[2]Department of Civil Engineering, The University of Tokyo, Hongo 7-3-1, Bunkyo-Ku, Tokyo 113-8656, Japan.

Abstract

For evaluating damages of structural concrete by ASR, an analytical platform to rationally deal with the complex interaction of multi-scale chemo-physics events is being developed. For experimental verification of the predictive model proposed, ASR expansion tests under several magnitudes of confinement are conducted and the results are compared with the multi-scale simulation. It is experimentally found that the highly deviatoric compression may bring about isotropically confined ASR expansion. The poro-mechanics based multi-phase modeling can simulate this nonlinearity by considering the quasi-hydro static pressure of created ASR gels in concrete composites and its injection into the micro-pores.

INTRODUCTION

Although alkali silica reaction (ASR) is one of the major deteriorations of concrete and has been intensively studied in the past decades, practical methods to simulate structural performances of ASR deteriorated concrete are under investigation owing to its complexity of solid concrete and ASR gel's kinematics inside pores. The authors have been developing a model for ASR reaction and its mechanistic actions based upon Biot's solid-liquid interaction model as shown in Figure1 (Takahashi et al. 2014). The gel product is thought to be an agent to migrate inside micro pores and cracks, and the concrete constitutive law of sparse cracking is integrated with the motion of ASR gels (Maekawa et al. 2008). Here, the pressure dependent absorption

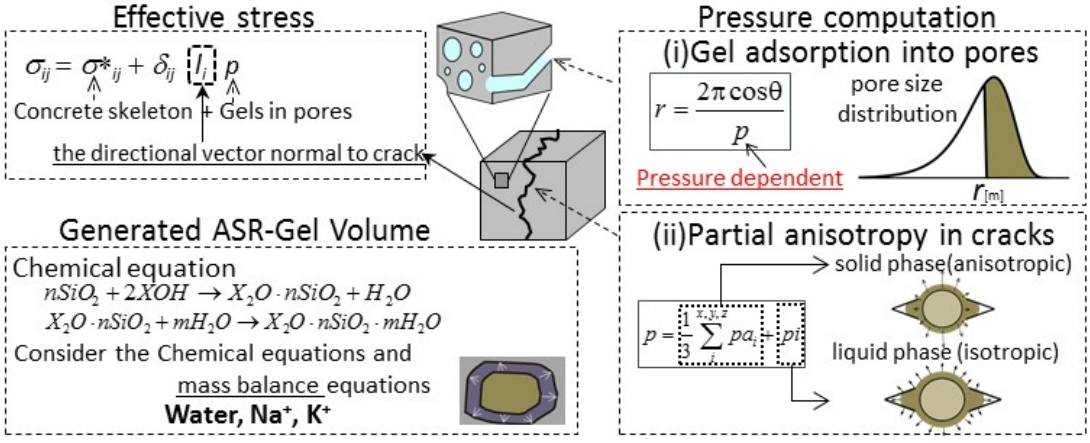

Figure 1. Models for ASR deterioration

of gels into cement micro-pores is focused on for consideration of the complex anisotropy of confined concrete with ASR. ASR expansion tests under several grades of confinement are reported in this study and their results are used for experimental verification of the ASR modeling proposed for structural concrete.

EXPERIMENT

Objective and test conditions. ASR-induced expansion tests were conducted in order to investigate the anisotropy of the expansions. Prism specimens were made in the size of 10*10*40cm (Figure 2) with the aggregate, which is reactive with alkali and additional sodium hydroxide was applied to accelerate ASR. The mix proportion is shown in Table 1. The reactive aggregates were originally evaluated as harmless. After 28days sealed curing, specimens were subjected to three levels of restraints. The first is free expansion case, the second is the one with restraint by a steel bar, and the last is the case with 6.2 MPa of additional stress by pre-stressing. After inducing these restraints, specimens were stored inside the ASR-activated environments, i.e., the temperature is kept constant at 40°C and the specimens were wrapped by wet clothes in order to supply enough water which may be consumed through ASR. Under these conditions, strains on the surfaces of the specimens and weight change were measured periodically. By using a contact-type strain gauge with chip targets attached on the specimens, space averaged strain were measured in both longitudinal and vertical directions (Figure 1).

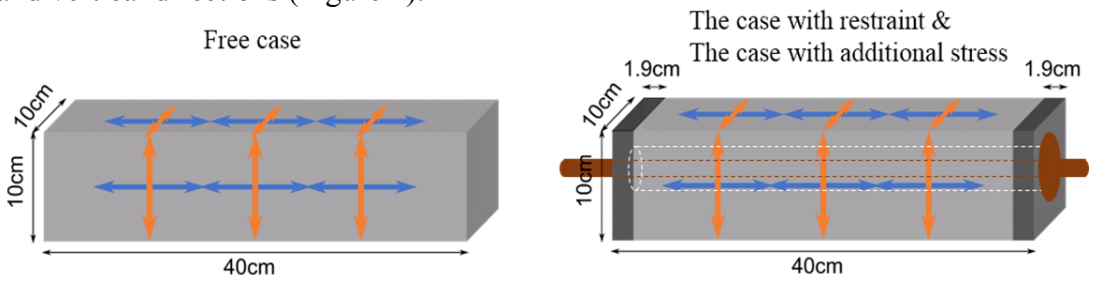

Figure 2. Dimensions of specimens.

Table 1. Mix proportion

W/C	W	C	S	G	Na_2Oeq
55%	170 kg/m^3	309 kg/m^3	853 kg/m^3	983 kg/m^3	6.1 kg/m^3

Test results. Figure 3 shows the weight changes of the specimens. The results of 3 specimens are almost the same. It means that the water adsorption from wet clothes mostly coincides with each other. Then, the degree of ASR and the corresponding moisture states are thought to be similar among these cases. Figure 4 shows the development of the

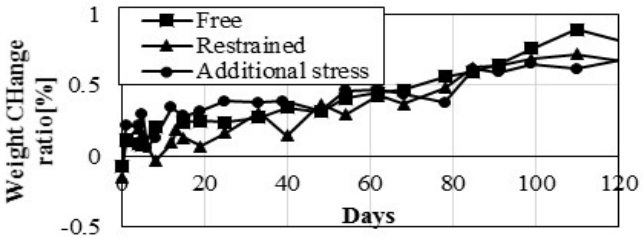

Figure 3. Weight change of specimens.

strains in both longitudinal and transverse directions. The isotropic free expansion case indicates approximately 800μ by volume.

Significant anisotropy in expansion was observed in the case with restraint as shown in Figure 4(ii). The absolute expansion is smaller than that of the free case in the longitudinal direction, while it is larger than the free case in the vertical direction. It is due to the restraint by steel bar and such a behavior is well-known as anisotropic effect caused by liquidity of ASR gel.

The response of the case with additional compressive stresses (Figure 4(iii)) differs from the simple restraint case. Not only in the longitudinal direction but also in the vertical one, the expansion is considerably decreased in comparison with other cases. This fact cannot be simply explained only by the change of the ASR-gel movement directions. It appears that some of the generated ASR-gel is not obviously active but firmly fixed on the aggregates. The gel adsorption into the pores of concrete mixture leads to less expansion in such a large stress conditions.

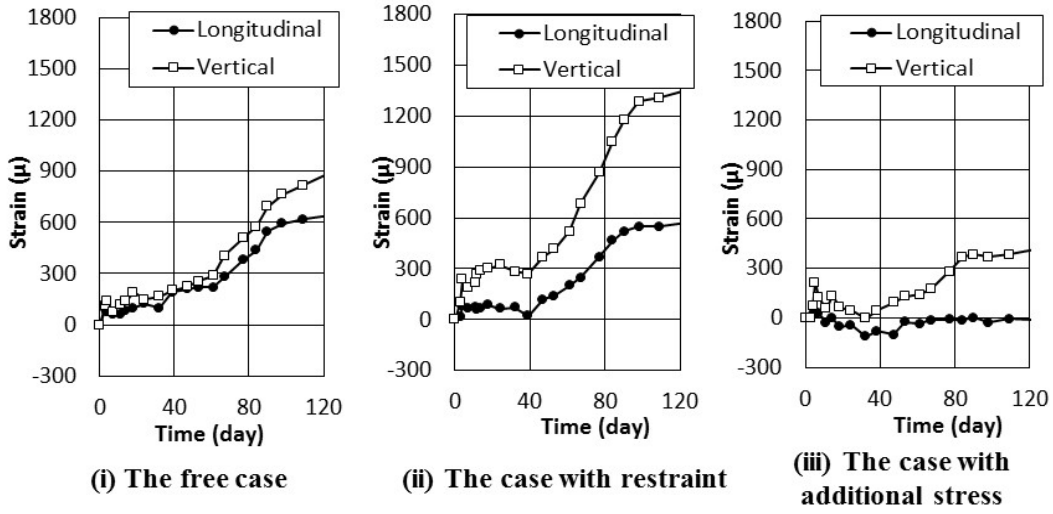

Figure 4. Measured expansion in each restraint condition

Comparative analysis. Figure 5 shows the analytical results which simulate the uniaxial restraint experiments. Reactivity of aggregate or physical properties of ASR-gel cannot be modeled precisely, so those variables are determined by sensitivity analyses using the experimental data for the free case. The applicability of the models can be confirmed with comparing the behaviors in restraint conditions.

For the case with additional stress, the analysis successfully reproduced the expansion behavior in both longitudinal and transverse directions. Without modeling the gel absorption considering the gel pressure, such like behaviors cannot be simulated. Focusing on the amount of gel absorption in the computation (the graph is shown in Figure 6), the absorbed amount at day 120 is about 25% larger in the additional stress case than the free case. Such difference in adsorbed amount can create the significant behavior change in expansion. It is confirmed that analytical model of pressure dependency of gel absorption is needed for ASR-induced expansions.

For the case with simple restraint, the anisotropic expansion (Figure 4(ii)) is not well simulated (Figure 5(ii)), while such like anisotropy in uniaxial restraint experiments can be reproduced with current models in past research by Takahashi et

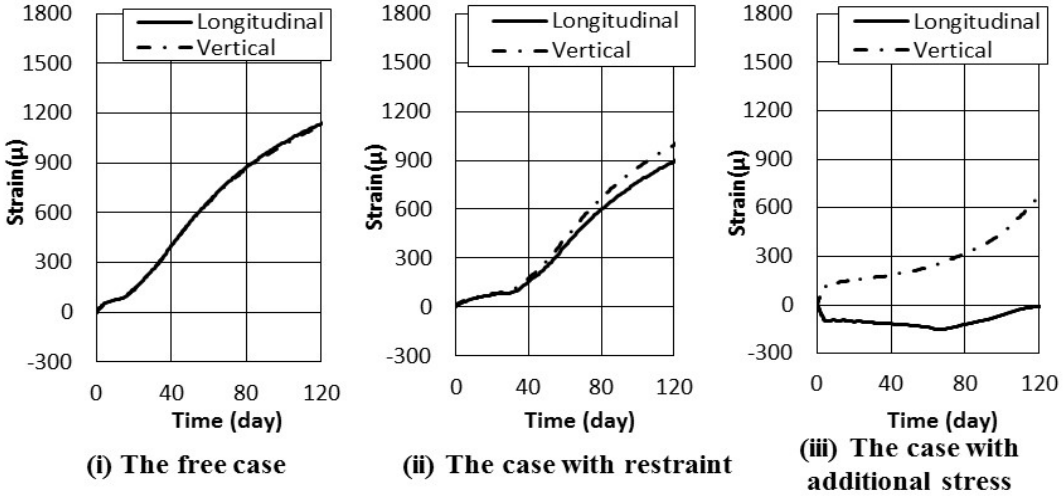

Figure 5. Simulated expansion in each restraint condition

al.. The difference between past and this research is the final expansion amount of free cases; 3500μ in past research and 800μ in this research. Further research about the gel properties focusing on such a moderate ASR expansion cases seems to be needed.

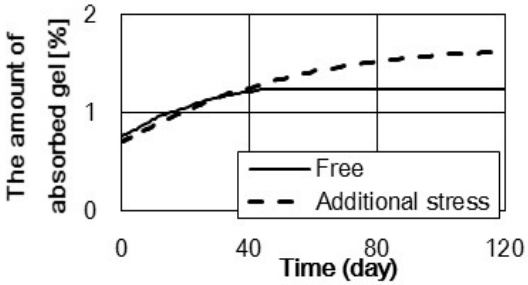

Figure 6. Gel absorption to pores

CONCLUSIONS

ASR expansion and the uniaxial confinement experiment by steel rods are conducted for experimental verification of the ASR modeling based upon the multi-scale formulation. The significant anisotropic expansion in restraint conditions was experimented. In the case where additional stress is applied further on the pre-expanded concrete, the characteristic expansion was observed and the experimental isotropic and anisotropic deformation is fairly simulated especially by considering the absorption into pores according to the ASR-gel pressure.

REFERENCES

Maekawa K., Ishida T. and Kishi T. (2008). Multi-Scale Modeling of Structural Concrete, Taylor and Francis

Meakawa K. and Fujiyama C. (2013). Rate-dependent model of structural concrete incorporating kinematics of ambient water subjected to high-cycle loads, Engineering Computations, Vol. 30, Iss: 6, 825-841

Takahashi, Y., Shibata, K., Maekawa, K. (2014). Chemo-hygral modeling and structural behaviours of reinforced concrete damaged by alkali silica reaction, Proceedings of ACF2014, pp.1274-1281

Tsukada T., Koga H., Hayakawa T., Watanabe H. and Kimura Y. (2010). Basic study about expansion and restriction of structural concrete deteriorated with alkali silica reaction, Proceedings of JSCE, V-276, 551-552 (in Japanese).

Experimental and analytical study of creep and shrinkage in early-age concrete

Inamullah Khan[1], Angus Murray[2], Arnaud Castel[3] and Raymond Ian Gilbert[4]
[1] Research Associate, [2] PhD Student, [3] Associate Professor, [4] Emeritus Professor
Centre for Infrastructure Engineering and Safety, School of Civil and Environmental Engineering, UNSW Australia, Sydney, NSW, Australia

ABSTRACT

The magnitude and rate of development of early-age deformation of concrete is often not known reliably and restraint to shrinkage is often poorly modelled in structural design. In order to accurately quantify the early-age deformational characteristics of Australian concrete, including shrinkage and tensile creep, a comprehensive experimental program is underway at the Centre for Infrastructure Engineering and Safety at UNSW Australia, where a series of experiments have been performed to quantify the early-age properties of concrete. A restrained cracking test was devised and reinforced concrete prisms were tested in tension under sustained loading to measure tensile creep and restrained shrinkage. Free shrinkage was measured on companion unreinforced prism specimens. Dog-bone shaped specimens were also tested in direct tension in portable creep rigs. All the specimens were tested at a stress-strength level of 50 % of the tensile strength of concrete at the age of 2 days.

It was found that RC prisms cracked with time under sustained tension before reaching the instantaneous tensile strength of concrete. A strength reduction factor of 0.7 and 0.87 was observed based on split tensile strength and direct tensile strength, respectively. Tensile creep coefficients calculated from tension prisms agree well with the tensile creep coefficients of dog-bone shaped specimens.

Keywords: Concrete, tensile creep, restrained shrinkage, creep coefficient.

INTRODUCTION

Concrete is prone to volumetric changes due to thermal and moisture related shrinkage at early ages. If concrete is allowed to shrink freely, shrinkage causes only a reduction in volume. However, if there is restraint, and concrete is prevented from shrinking freely, tensile stresses develop in the restrained concrete and, because of its low tensile strength, particularly at early ages, these stresses often exceed the tensile strength of concrete and cause cracking in the young concrete. The restraint may be external to the concrete, imposed by the supports or adjacent parts of the structure, or may be internal, imposed by embedded steel reinforcement or by non-uniform shrinkage gradients. The shrinkage induced tensile stresses are relaxed by tensile creep of concrete and it is therefore important to accurately quantify the early-age tensile creep and shrinkage of concrete.

In the literature, there is limited information on the tensile creep of concrete loaded in direct tension at early ages. Accurate measurements of tensile creep are difficult to obtain. Because of the necessarily low stress levels, the tensile strains to be measured in a tensile creep test are small. When the concrete is also shrinking, the specimen in direct tension may actually be shortening and the measured strains will be

compressive. Even in specimens where drying is prevented, autogenous shrinkage will be taking place in the first few days and weeks after casting, thus rendering the measurement of tensile creep in early-age concrete problematic. The large variability of shrinkage and creep from specimen to specimen in concrete at early ages further complicates the issue. Because of these difficulties, some researchers [1-4] have used uniaxially restrained shrinkage tests to indirectly measure the tensile creep characteristics of concrete. Relatively few experimental programs [5-7] have been conducted where tensile creep was measured in direct tension tests. In this paper, an experimental program to measure early-age tensile creep using uniaxial direct tensile loading tests is described. Tests were also performed on RC prisms internally restrained by steel reinforcement and subjected to various levels of sustained tension at early ages. Free shrinkage was measured on companion plain concrete prisms. Dog-bone shaped specimens were also subjected to direct tensile loading. Tensile creep, shrinkage and creep coefficients were measured and results obtained from both test were compared.

EXPERIMENTAL PROGRAM

A single concrete mix was used for all tests – a 32 MPa normal class concrete (with GP cement and a water-cement ratio of 0.55). Further testing is currently underway to determine the effects of varying the type of cement, the type and grade of aggregate and the water-cement ratio. The tests were carried out in a temperature-humidity control room at a constant temperature of 23^{o}C and a relative humidity of 50 %.

Concrete mix:

The mix proportions used in the experimental program are shown in Table 1. A sufficient number of cylinders and prisms were cast and tested to determine the evolution of compressive strength, tensile strength and elastic modulus, with tests performed at the ages of 0.75, 1, 2, 3, 7 and 28 days. For each material test, three specimens were tested in order to assess the statistical variation and this practice was repeated for each concrete batch.

Compressive strength, elastic modulus and indirect tensile strength tests were conducted on cylinders in accordance with AS 1012.9: 2014 [8] and AS 1012.10: 2000 [9] and the modulus of rupture tests were conducted on prisms in accordance with AS 1012.11: 2000 [10]. The evolution of concrete mechanical properties is presented in Table 2.

Creep test prototype and setup:

Restrained cracking test:

Reinforcement embedded in a concrete member provides restraint to shrinkage leading to compressive stresses in reinforcement and tensile stresses in the concrete. In these tests, reinforced concrete prisms having dimensions 60 x 60 x 400 mm containing a single 12 mm diameter steel reinforcement bar located centrally on the longitudinal axis of the prism were tested. Three types of specimens were tested: reinforced concrete prisms under sustained loading to measure the tensile creep of

Table 1. Mixture proportions of concrete (kg/m^3)

Components	*GP Cement*	*Sand*	*Gravel (10mm Basalt)*	*Water*
Mass	380	545	1265	210

Table 2. Mechanical characteristics of concrete

Age (days)	*Compressive strength (MPa)*	*Modulus of rupture (MPa)*	*Indirect tensile strength (MPa)*	*Elastic modulus (GPa)*
0.75	13.18	2.57	1.20	18.35
1	15.28	3.11	1.40	20.35
2	21.55	3.79	2.10	22.05
3	24.64	4.03	2.54	22.70
7	32	4.56	2.94	27.78
28	37	4.84	3.47	28.58

concrete; reinforced concrete prisms subjected to no external loading to measure the restrained shrinkage; and plain concrete prisms to measure free shrinkage. The geometry of these specimens is shown in Figure 1.

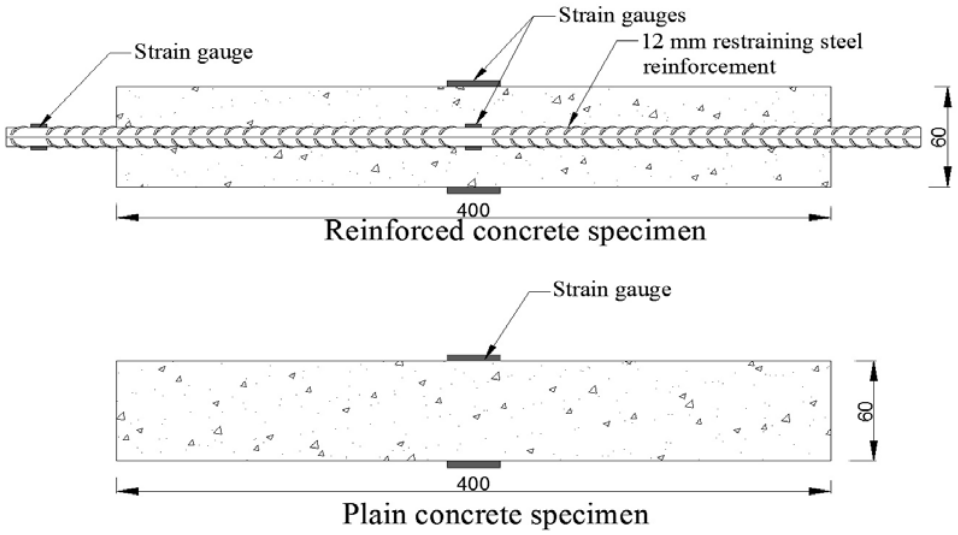

Figure 1. Specimens for restrained cracking test

Loading arrangement of the specimens and a typical creep rig capable of testing three specimens simultaneously is shown in Figure 2. The reinforcing bar protruding from the ends of each RC prism was connected to high strength threaded bar by means of female threads made in the steel bar at both ends prior to casting. These high strength threaded bars were then passed through the holes made at top and bottom of the creep rig where the bottom bar was tightened with a nut. Load cells were placed on the top of each specimen to monitor the load. Load was applied from the top by tightening the nut on high strength threaded bar and a spring was used maintain a constant load.

Dog-bone test:
In order to measure tensile creep, a slight modification to the restrained cracking rig was made to test dog-bone specimens loaded in direct tension. The dimensions of the dog-bone specimens were 200 x 300 x 35 mm and the loading arrangement is shown in Figure 3.

Figure 2. Restrained cracking rig

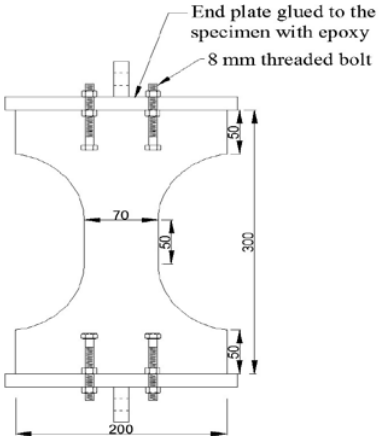

a.

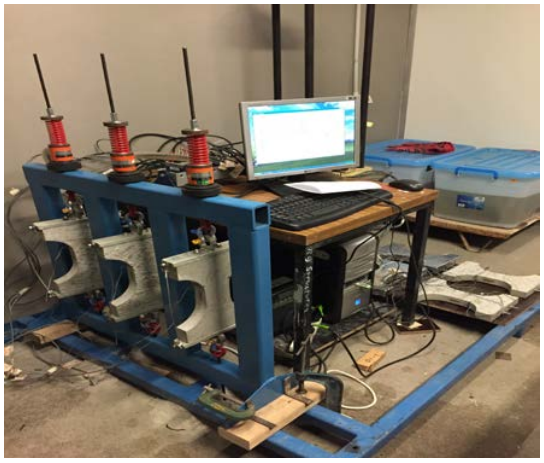

b.

Figure 3. (a) Dog bone specimen (b) loading of dog-bone specimen

The dog-bone specimens were fixed into the creep rig by means of two steel plates glued to each end of the specimen with high strength epoxy. Two threaded bolts are also cast in the specimen and are further connected to the steel plates at each end as shown. The purpose of gluing steel plates to the specimen is to ensure an even stress distribution from the applied tensile load. All specimens were loaded to the same stress level representing 50% of the tensile strength measured at an age of 2 days.

All specimens were covered with wet burlap and polyethylene during a 24-hour period after casting. They were then removed from their moulds and left in laboratory ambient conditions.

Instrumentation:
For the RC prisms, strain evolution was measured with the help of strain gauges which were attached to the specimens at different locations. Strain gauges were attached at the mid-height on two opposite faces of the specimens on both the steel and concrete surfaces in the locations shown in Figure 1. For the specimen subjected to loading, two strain gauges were attached to the reinforcing bar on the length protruding from the concrete prism in order to measure initial applied stress which was further verified by load cells mounted on the creep rig. The strains were recorded at regular intervals with a data acquisition system.

For the dog-bone specimens, strain gauges were attached to each 35 mm thick face of the dog-bone specimen at the centre positon at mid-height where the width of the specimen is 70 mm.

TEST RESULTS AND DISCUSSIONS

Restrained cracking test
Stresses due to shrinkage in a RC member can be derived on the basis of equilibrium and compatibility of strains assuming that perfect bond exists between concrete and steel. This is a perfectly reasonable assumption before the onset of cracking. The axial force applied to the RC prism is partly taken by steel and partly taken by concrete:

$$F_{total} = F_C + F_S = \sigma_{conc} A_c + \varepsilon_s E_s A_s \quad (1)$$

and, provided the steel strain and the applied load are known, the concrete stress at any time can be determined from:

$$\sigma_{conc} = \left(F_{total} - \varepsilon_s E_s A_s\right) / A_c \quad (2)$$

where F_{total} is the total force applied on the specimen, F_C is the force in concrete, F_S is the force in steel bar, σ_{conc} is stress in concrete, ε_s is strain in steel measured from strain gauges, E_s is the elastic modulus of steel, A_s is cross-sectional area of steel and A_c is cross-sectional area of concrete. Elastic strain in concrete, which varies with the time due to the gradual change in the concrete stress due to restraint provided by the steel bar, can be calculated as:

$$\varepsilon_e = \sigma_{conc} / E_c \quad (3)$$

where ε_e is the elastic strain in concrete and E_c is the elastic modulus of concrete at the age of first loading. Total strain in a uniaxially loaded specimen at constant temperature may be expressed as the sum of instantaneous or elastic, creep and shrinkage strain components:

$$\varepsilon(t) = \varepsilon_e(t) + \varepsilon_c(t) + \varepsilon_{sh}(t) \quad (4)$$

where $\varepsilon(t)$ is total strain, $\varepsilon_c(t)$ is creep strain and $\varepsilon_{sh}(t)$ is the shrinkage strain. Total strain was measured on the loaded specimens, shrinkage strains were recorded on

plain concrete specimens and elastic strains are determined from Equation 3. The unknown creep strain $\varepsilon_c(t)$ can easily be determined using Equation 4.

Due to the varying stress history and concrete time-dependent properties, the analysis is complicated by interdependence between stress history and creep strain. The Trost-Bazant method [11], [12] and [13], also called the age-adjusted effective modulus method [13], gives a simple procedure for computing a strain under a varying stress. The method introduces the ageing coefficient $\chi(t,\tau_o)$ which takes into account the fact that the stress $\sigma(t,\tau_o)$ gradually applied from time τ_o to t will cause smaller strain than the stress $\sigma(t,\tau_o)$ instantly applied at time τ_o and kept constant until time t. For the shrinkage analysis of an uncracked member assuming zero initial stress at time τ_o, creep strain in concrete can be expressed as follows:

$$\varepsilon_c(t) = \frac{\sigma(t,\tau_o)}{E_c(\tau_o)}\chi(t,\tau_o)\varphi(t,\tau_o) \tag{5}$$

where $\varphi(t,\tau_o)$ is the creep coefficient. For an axially loaded uncracked member subjected to an initial tensile stress σ_o at time τ_o, the stress gradually increases with time t due to the gradually applied stress $\Delta\varphi(t,\tau_o)$ caused by the restraining force. Creep strain is expressed as:

$$\varepsilon_c(t) = \frac{\sigma_0}{E_c(\tau_o)}\varphi(t,\tau_o) + \frac{\Delta\sigma(t,\tau_o)}{E_c(\tau_o)}\chi(t,\tau_o)\varphi(t,\tau_o) \tag{6}$$

Creep coefficient $\varphi(t,\tau_o)$ can be calculated using Equation 6 as follows:

$$\varphi(t,\tau_o) = \frac{\varepsilon_c(t)}{\dfrac{\sigma_o}{E_c(\tau_o)} + \dfrac{\Delta\sigma(t,\tau_o)}{E_c(\tau_o)}\chi(t,\tau_o)} \tag{7}$$

For concrete loaded at early ages (τ_o < 20 days), the recommended value of final ageing coefficient is taken as 0.80 for relaxation problems [14].

All the three initially loaded RC specimens cracked at the age of 24 days. The initially applied stress on the concrete (1.0 MPa) was about 50 % of the instantaneous tensile strength. Due to shrinkage-induced stresses, the initially applied stress increased from 1 MPa at day 2 to 2.4 MPa at day 24 and at this stress all the specimens cracked. The ratio of final or cracking stress to split tensile strength was 0.7. The stress development in all three specimens is shown in Figure 4.

Altoubat and Lange [15] found a cracking stress to split cylinder strength ratio of 0.64 for a concrete with w/c ratio of 0.5. However, they reported that the use of split cylinder tensile strength in creep analysis may not be accurate in the early age and they suggested that the direct tensile strength of concrete is 80 % of the split cylinder tensile strength for concrete age greater than 100 hours. Using their proposed relationship, the cracking stress value of the RC prisms tested here corresponds to 87 % of direct tensile strength of concrete at the age of 24 days.

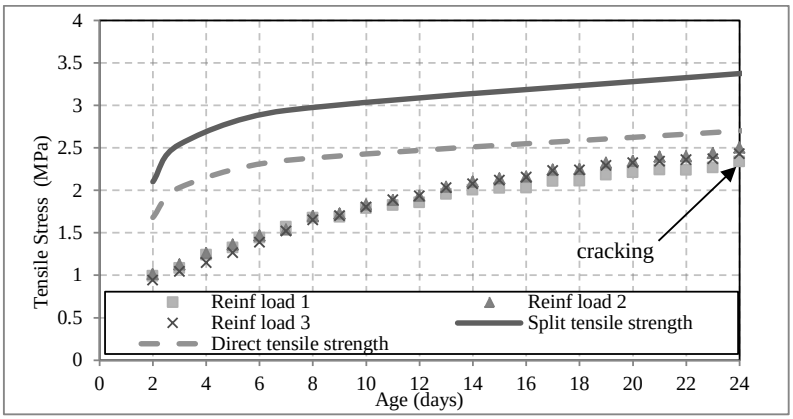

Figure 4. Tensile stress and strength evolution

It is important to note that the sustained stress at which cracking occurs is lower than the tensile strength of the concrete. Altoubat and Lange [15] suggested that the reduction is related to static fatigue and internal damage accumulation under sustained stress. Thus it is essential that when concrete is subjected to sustained load, a strength reduction factor should be applied for predicting the time of first cracking. Altoubat and Lange [15] further reported that the magnitude of the tensile stress at the time of cracking of a restrained concrete member depends on the stress history at very early ages. The RC prisms were subjected to relatively high tensile stresses at a very early age perhaps causing some permanent damage at the micro-level and leading to cracking of the sample earlier than expected.

Concrete creep strains and elastic strains for the three loaded specimens are calculated using Equations 2-4 and are presented in Figure 5. The initial elastic strain due to applied load was 42 micro-strains for each specimen and the elastic strain gradually increased to about 100 micro-strains due to shrinkage-induced stresses. Figure 5(b) shows the development of creep strains as a function of age. For all the three specimens creeps strains increase steadily with the age as expected. The creep strain

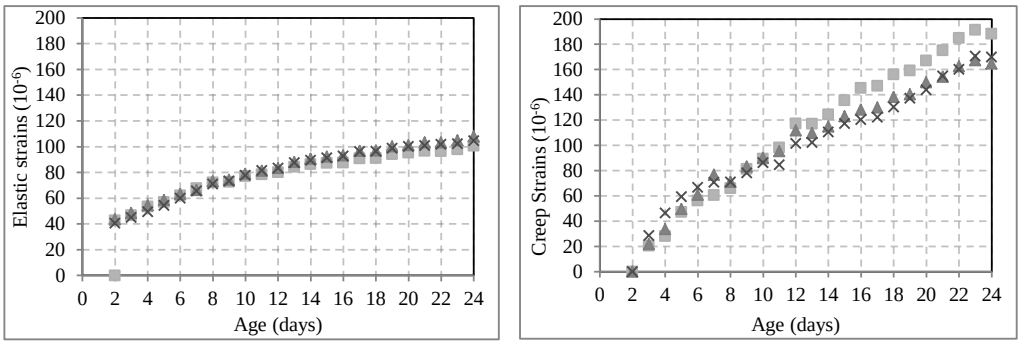

a. Elastic strains b. Creep strains

Figure 5. Elastic and creep strains of loaded RC specimens

at the time of cracking reached an average of value of 174 micro-strains which corresponds to 37 % of the magnitude of the total free shrinkage value recorded on the plain concrete specimens at the same age. Tensile creep coefficients are calculated using Equation 7 and are presented in Figure 6a. The average value of the creep coefficient at the age of cracking was 1.89. Figure 6b shows a comparison of restrained shrinkage and free shrinkage. The difference between the two curves is the sum of the tensile elastic and creep strains caused by the restraining force.

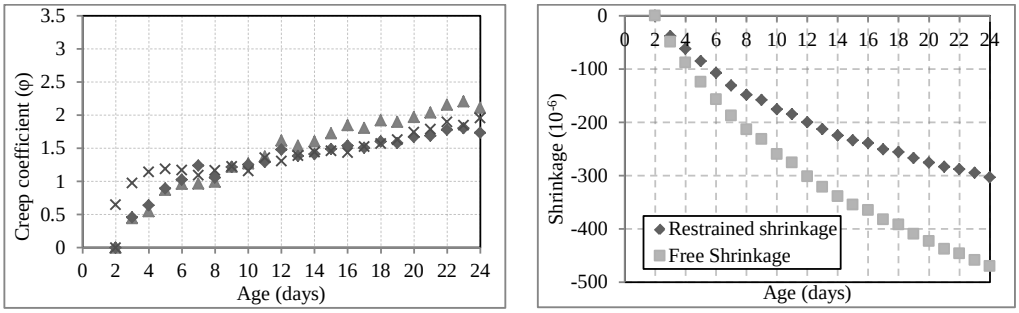

a. b.

Figure 6. (a)Tensile creep coefficients of loaded RC specimens (b) Free and restrained shrinkage

Dog-bone test

Total strains were recorded on each dog-bone specimen and creep strains were calculated using Equation (4). Shrinkage strains were recorded on the companion specimens. Evolution of creep strains and creep coefficients are presented in Figures 7a and 7b. It can be seen that creep strains and creep coefficients follow the similar trends as in the case of restrained shrinkage test. The average value of the creep coefficient at the age of 24 days was 1.70, which is close to the value 1.89 calculated from the RC prisms. A comparison of average creep coefficients of the dog-bone specimens and RC prisms is presented in Figure 8a. It can be seen that the tensile creep coefficients measured in both types of tests were in reasonable agreement. Contrary to the RC prisms, none of the dog-bone specimens cracked under sustained tension.

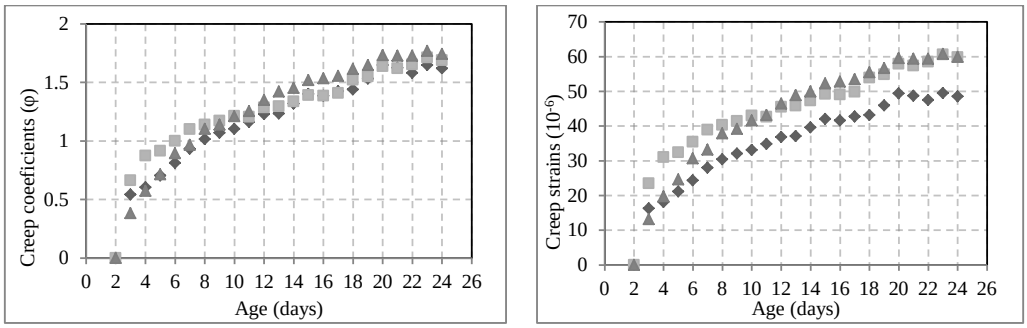

a. b.

Figure 7. Evolution of (a) creep coefficients and (b) creep strains in dog-bone specimens

This was because shrinkage in the dog-bone specimens was not restrained and no additional tension developed with time.

In order to compare the total shrinkage strains measured on both types of specimens, i.e. the dog-bone specimens and prisms, the hypothetical thicknesses t_h as defined in AS3600-2009 [16] has been calculated for both specimens as follows:

$$t_h = 2A/u \tag{8}$$

where A is the cross-sectional area of the specimen and u is the perimeter of the specimen exposed to the atmosphere. Excellent agreement between the total shrinkage strains measured on the dog-bone specimens and those measured on the prisms is obtained if the prism strains are modified using Equation 9. This comparison is shown in Figure 8b.

$$(\varepsilon_{sh})_{\text{dogbone}} = \frac{(t_h)_{\text{prisms}}}{(t_h)_{\text{dogbone}}} * (\varepsilon_{sh})_{\text{prisms}} \tag{9}$$

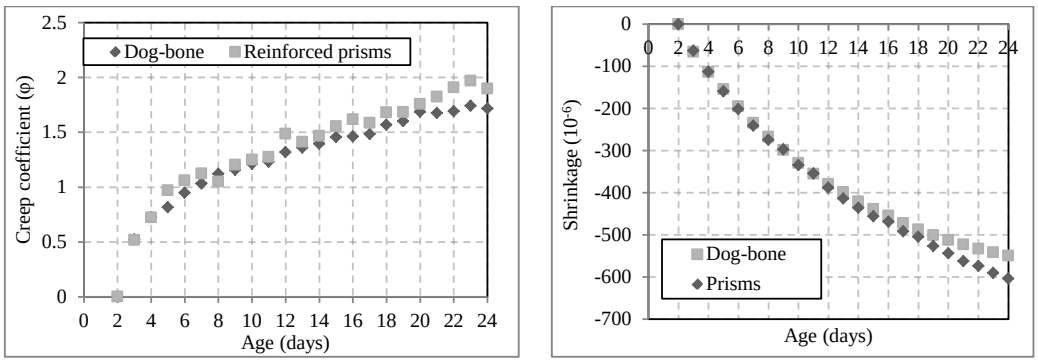

a. b.

Figure 8. Comparison of (a) creep coefficients and (b) free shrinkage of dog-bone and RC prisms specimens

CONCLUSIONS

An experiment program has been carried out to quantify early-age tensile creep of concrete (made with ordinary Portland cement and with a water-cement ratio of 0.55). It was found that early-age tensile creep plays an important role in reducing shrinkage strains and relaxing stresses produced from restraint. RC specimens cracked before attaining the maximum instantaneous concrete tensile strength indicating that the tensile strength under sustained stress is typically lower than its short-term value and a strength reduction factor must be applied to specimens under sustained loading to predict the time to first cracking.

These experiments form a part of a more comprehensive research program to quantify the early-age properties of concrete. These results, together with the results of future experiments, will be used to accurately model the early-age cracking of concrete.

Acknowledgement: This research was supported by the Australian Research Council's Discovery Project funding scheme (project number DP130102966).

REFERENCES

1. Kovler K. “Testing system for determining the mechanical behavior of early age concrete under restrained and free uniaxial shrinkage.” Materials and Structures, 1994, 27, No. 170, 324–330.
2. Lennart Østergaarda, David A. Langeb, Salah A. Altoubatb, Henrik Stanga “Tensile basic creep of early-age concrete under constant load.” Cement and Concrete Research 31 (2001) 1895 – 1899
3. T. Aly and J. G. Sanjayan, “Shrinkage cracking properties of slag concretes with one-day curing”, Magazine of Concrete Research, 2008, 60, No. 1, 41–48.
4. Ya Wei and Will Hansen. "Tensile Creep Behavior of Concrete Subject to Constant Restraint at Very Early Ages." Journal of Materials in Civil Engineering, 2013, 25(9): 1277-1284.
5. Pierre Rossi, Jean-Louis Tailhan, Fabrice Le Maou (2013). "Comparison of concrete creep in tension and in compression: Influence of concrete age at loading and drying conditions." Cement and Concrete Research 51: 78-84.
6. G. M. Ji, T. Kanstad ,Ø. Bjøntegaard , E. J. Sellevold, “Tensile and compressive creep deformations of hardening concrete containing mineral additives”, Materials and Structures (2013) 46:1167–1182
7. Matthieu Briffauta, Farid Benboudjemab, Jean-Michel Torrentic, Georges Nahasd. "Concrete early age basic creep: Experiments and test of rheological modelling approaches." Construction and Building Materials, 2012, 36: 373-380.
8. AS 1012.9: 2014. Methods of testing concrete – Compressive strength tests – concrete, mortar and grout specimens. Standards Australia: Sydney. 2014.
9. AS 1012.10: 2000. Methods of testing concrete – Determination of indirect tensile strength of concrete cylinders (‘Brazil’ or splitting test). Standards Australia: Sydney. 2000.
10. AS 1012.11: 2000. Methods of testing concrete – Determination of the modulus of rupture. Standards Australia: Sydney. 2000.
11. Trost, H. 1967. ‘Auswirkungen des Superpositionsprinzips auf Kriech- und Relaxations Probleme bei Beton und Spannbeton’. Beton- und Stahlbetonbau 62, I 230-8, 261-9.
12. Dilger, W. and Neville, A.M. 1971. Method of Creep Analysis of Structural Members. ACI SP 27-17, pp 349-379.
13. Bazant ZP. “Prediction of concrete creep effects using age-adjusted effective modulus method.” ACI Journal, 69 (4) (1972), pp. 212–217
14. Gilbert, R. I., and Ranzi, G. (2011). “Time-Dependent Behaviour of Concrete Structures.” Spon Press, London.
15. Salah A. Altoubat and David A. Lange, “Creep, Shrinkage, and Cracking of Restrained Concrete at Early Age”, ACI Materials Journal, V. 98, No. 4, July-August 2001.
16. AS3600-2009, “Australian Standard for Concrete Structures”, Standards Australia, 2009.

Experimental Study of Temperature Effects on Water Vapour Sorption and Moisture Transport Phenomena

James M. de Burgh[1]; Stephen J. Foster[2]; and Hamid R. Valipour[3]

[1]Ph.D. Candidate, School of Civil and Environmental Engineering, UNSW Australia, Sydney, NSW 2052, Australia. E-mail: j.deburgh@unsw.edu.au
[2]Professor and Head of School, School of Civil and Environmental Engineering, UNSW Australia, Sydney, NSW 2052, Australia. E-mail: s.foster@unsw.edu.au
[3]Senior Lecturer, School of Civil and Environmental Engineering, UNSW Australia, Sydney, NSW 2052, Australia. E-mail: h.valipour@unsw.edu.au

Abstract

Water vapour sorption isotherms (WVSIs) provide a relationship between the mass of adsorbed water within pores and the prevailing relative humidity; they are a reflection of the material microstructure. One aspect of cementitious material WVSIs that has not been firmly established is the effect of elevated temperatures. In this paper, two newly developed multi-chamber WVSI testing apparatus are described. These apparatus have been used to study the adsorption and desorption isotherms and kinetics of HCP and concrete at various temperatures. Results show a two-stage equilibrium process in desorption studies, where the initial stage is associated with diffusive moisture transport, and the second appears associated with a time-dependent loss of hysteresis moisture.

INTRODUCTION

Water vapour adsorption/desorption experiments have been used extensively over the last half century to help understand the material micro-structure and moisture transport of cementitious materials at ambient temperatures. The classical research of Powers and Brownyard (1946) involved extensive adsorption experiments, and these observations were largely responsible for the development of gel and capillary porosity designations. More recently, WVSI isotherms have been revisited as an essential component in the durability assessment of concrete structures (Baroghel-Bouny 2007).

Many studies on cementitious WVSI behaviour have involved only powdered or granulated specimens; the high surface area to volume ratio of such specimens generally enables tests to progress at a relatively rapid rate. Indeed, modern automatic WVSI machines are used to rapidly evaluate an isotherm within a day or two, where non-granulated specimens may take weeks or years to equilibrate (De Belie et al. 2010). One significant advantage, however, of studying non-powdered specimens (with known geometry) is that they can provide additional quantitative information on drying/wetting kinetics. This kinetic information has been used to predict

important moisture transport properties, such as the humidity dependent water vapour diffusivity (Baroghel-Bouny 2007b).

Significant questions still exist in the literature around the effect of temperature on WVSI behaviour of HCP and concrete materials. Maekawa et al. (2009), Poyet (2009) and others have gone some way towards investigating this material behaviour, but more accurate data is required to develop better models.

An experimental programme was undertaken to better understand the kinetics of adsorption, desorption and scanning behaviour of hardened cement paste (HCP) specimens. Test apparatus was designed to provide a temperature (from 5°C to 85°C) and humidity regulated environment, facilitating an improved understanding of moisture interactions.

DESCRIPTION OF TESTS

Materials and sample preparation

Cement paste specimens having a 0.45 mass ratio of water to GP cement (OPC with 7.5% limestone mineral addition) were prepared using a planetary type mixer and cast into cylindrical moulds of 100 mm diameter and 200 mm length. Curing and storage were performed at 23°C ± 2°C. After one day the specimens were de-moulded and sealed in aluminium foil to minimise any moisture loss and ensure uniform hydration. After a minimum of 100 days sealed curing, specimens were removed from foil immediately prior to wet sawing into discs of approximately 3 mm to 8 mm thickness (depending on the test). After sawing, discs were placed immediately into saturated limewater for 3 to 6 weeks prior to testing.

Test preparation

Both initially saturated (desorption) and initially dry (adsorption) tests were performed. For desorption tests, the discs were weighed in a saturated surface dry (SSD) condition, measured for geometry and then placed into the test apparatus. For adsorption tests, the discs were weighed in an SSD condition, before placing into a desiccator with fan circulation and reconditioned Molecular Sieve. After approximately 2 months of drying, the sample mass loss was less than 0.0002g/g per day; at this point, the samples were removed and immediately weighed before placing into the test apparatus.

Experimental apparatus

A pair of experimental testing apparatus have been developed to facilitate the study of medium to long term adsorption, desorption and scanning kinetics of cementitious samples (see Figure 1). Each apparatus contains 8 stainless steel chambers of approximately 230 mm × 230 mm × 260 mm; these are jacketed with continuously circulating water and maintained at a set temperature within ±0.1°C in the long term (a Pt100 platinum resistance type thermometer is used for temperature regulation). Individual chambers have removable tempered glass lids seated on firm silicone seals, covered by removable 60 mm PIR insulation blocks.

Humidity regulation was achieved using reagent grade salts prepared in a saturated solution with distilled water, in accordance with ASTM E104-02 (2012). Individual salt solutions sat within Pyrex dishes covering almost the entire base of each chamber such that the maximum recommended volume/surface area of ASTM

E104 is met. A “dry” condition was achieved using reconditioned Molecular Sieve type 4Å. Each chamber was provided with an internal 80 mm electric fan giving 15.8 CFM of circulating airflow (fans were pointed away from specimens, to avoid any direct airflow impingement effects). Constant monitoring of the actual environment within individual chambers was achieved using additional Sensirion SHT7x digital sensors (temperature and humidity) suspended near to the sample location.

Figure 1. Overview of the two WVSI testing apparatus, weighing rails visible.

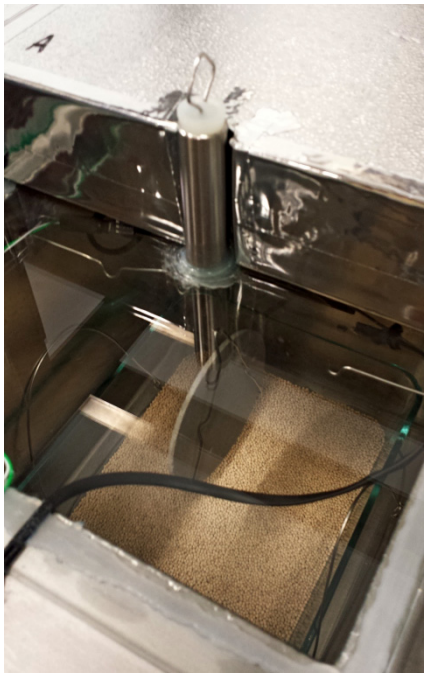

Figure 2. Inside a typical chamber (with Molecular Sieve for dry state); the front top insulation panel has been removed to expose a specimen inside.

While achieving a stable and constant environment within each chamber is important, it is equally important to be able to assess the quantity of adsorbed or desorbed water within specimens without disrupting the environment. For this purpose, a small port is provided centrally on each chamber – a stainless steel wire hook passes permanently through this, suspending the test sample. Gravimetric assessment of the adsorbed water is performed rapidly using a precision scientific

balance (0.001g accuracy), placed on fixed weighing rails. The individual chamber fan is momentarily turned off when assessing the sample weight inside that chamber.

Experimental program

An extensive test program was performed at temperatures of 23°C, 40°C, 60°C and 80°C, with desorption, adsorption and scanning increments. Specifically discussed below are Tests 1L, 1R and 2R. Tests 1L and 1R are desorption (from saturation) tests performed at 40°C using discs nominally 3 mm thick; these demonstrated close repeatability of experimental results. Test 2R had nominally 8 mm thick discs; the edge of these discs was sealed using adhesive aluminium tape to ensure 1-dimensional moisture transport (see Figure 3).

RESULTS AND DISCUSSION

Performance of test equipment

Using the individual chamber temperature and humidity sensors, it was found that temperature regulation was stable within the accuracy of sensors (±0.1°C). The humidity was found to be very stable, although a small amount of drift (typically less than 0.5% over several months) was observed in some cases.

During the first set of tests (Test 1L and 1R) an issue with electrostatic attraction between weighing hook and sample chambers generated additional scatter in the experimental data; this was fixed for all subsequent tests. Test disc weights were approximately 40g to 120g, and repeatability of balance measurements was 0.001g – giving a measurement precision of around 2×10^{-5} g/g dry.

Effect of temperature on WVSIs and kinetics

The effect of temperature on desorption isotherms was found to be generally consistent with that published in the literature. With an increasing temperature the desorption isotherm reduces in magnitude – giving less retained moisture at a given relative humidity. The adsorption isotherm was found to also reduce, to a significantly greater extent, with a consequent reduction in observed hysteresis. Unlike the proposal of Maekawa et al. (2007), the hysteresis moisture is not found to decay continuously toward the adsorption isotherm (with the rate merely increasing with temperature). Rather, a stable magnitude of WVSI hysteresis is found, although this reduces with temperature. With increasing temperature, diffusion kinetics increase and pseudo-equilibrium is reached faster, as expected.

Two-stage equilibrium process in desorption

Among other methods to experimentally assess the moisture diffusivity of samples experiencing 1-dimensional transport, one established approach is to use the final rate of sorption/desorption. Crank (1975) describes that in the later stages of diffusion we should find:

$$\frac{d}{dt}\{\ln\,(M_\infty - M_t)\} = -\frac{D\pi^2}{t^2} \quad (1)$$

Thus, an exponential decay curve should fit the experimental mass variation, and the exponent should be proportional to the inverse of sample thickness, squared. Curiously, this was not observed in the WVSI testing of HCP samples. As shown in Figure 4 (obtained by fitting an exponential curve to data from 13 days onwards), the

exponential decay constant was indistinguishable across specimens having greater than a factor of two difference in thickness, providing strong evidence that the latter part of kinetics is not controlled by a diffusion process. Only the initial kinetics (see Figure 3) is diffusion controlled for specimens of this type. Similar results are found across all temperatures, and for concrete specimens; R^2 values for this fit are typically > 0.99.

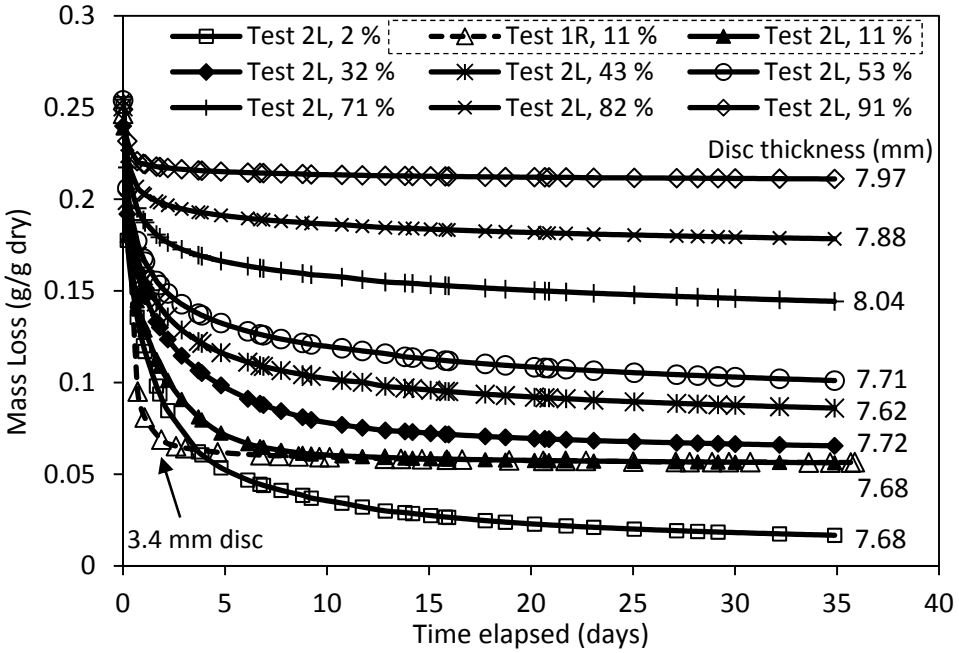

Figure 3. Moisture loss kinetics (nominally 8mm disc desorption tests at 40°C).

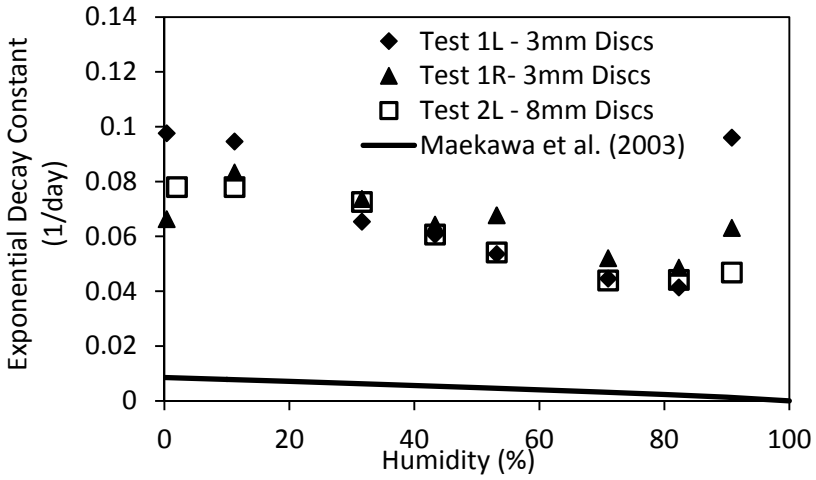

Figure 4. Observed exponential decay constant (desorption tests at 40°C).

A recent study by Wu et al. (2014) on OPC concrete specimens cut into thin discs (1 mm to 3 mm thick and 37.5 mm in diameter) also observed that, following apparent 'mass stabilisation', the thickness had no clear influence on the mass variation. However, their study did not provide sufficient environmental control to facilitate a quantitative examination of this effect.

CONCLUSIONS AND OUTLOOK

A new experimental apparatus for assessing the effect of temperature on the water vapour adsorption, desorption and scanning behaviour of cementitious materials has been described. By tightly regulating environmental variables, accurate WVSI data and kinetics have been measured. A two-stage or two-part equilibrium process in water vapour desorption experiments has been observed. In the specimens studied, an initial diffusion process scales with the thickness of specimen, whereas a later time dependent loss of hysteresis moisture does not. This has implications in the numerical modelling of moisture transport in cementitious materials. It also helps explain significant differences observed between long term and rapid WVSI measurements, and the scatter in diffusivity estimations made using non-steady state drying tests.

REFERENCES

ASTM. (2012) *Standard Practice for Maintaining Constant Relative Humidity by Means of Aqueous Solutions*, Standard ASTM E104-02 (Reapproved 2012). ASTM International, West Conshohocken, PA.

Baroghel-Bouny, V. (2007). "Water vapour sorption experiments on hardened cementitious materials: Part I: Essential tool for analysis of hygral behaviour and its relation to pore structure" *Cement and Concrete Research*, 37(3), 414-437.

Baroghel-Bouny, V. (2007b). "Water vapour sorption experiments on hardened cementitious materials: Part II: Essential tool for assessment of transport properties and for durability prediction" *Cement and Concrete Research*, 37(3), 438-454.

Crank, J. (1975). *The Mathematics of Diffusion, Second Edition*. Oxford University Press, London, Great Britain.

De Belie, N., Kratky, J. and Van Vlierberghe, S. (2010). "Influence of pozzolans and slag on the microstructure of partially ccarbonate cement paste by means of water vapour and nitrogen sorption experiments and BET calculations" *Cement and Concrete Research*, 40(12), 1723-1733.

Maekawa, K., Ishida, T. and Kishi, T. (2009). *Multi-Scale Modeling of Structural Concrete*. Taylor & Francis.

Powers, T. C. and Brownyard, T. L. (1946). "Studies of the Physical Properties of Hardened Portland Cement Paste" *Journal of the American Concrete Institute*, 18(2-8), 101-992.

Poyet, S. (2009). "Experimental investigation of the effect of temperature on the first desorption isotherm of concrete" *Cement and Concrete Research*, 39(11), 1052-1059.

Wu, Q., Rougelot, T., Burloin, N. and Bourbon, X. (2014) "Experimental investigation of the first desorption isotherm of a high performance concrete with thin sliced samples" *Construction and Building Materials*, 72, 389-397.

Effect of the Incorporation of Mineral Admixtures and Shrinkage-Mitigating Ingredients on the Plastic Shrinkage of Concrete

Moghul Sirajuddin[1] and Ravindra Gettu[2]

Department of Civil Engineering, Indian Institute of Technology Madras, Chennai 600036, India. E-mail: [1]moghul.uddin786@gmail.com; [2]gettu@iitm.ac.in

Abstracts

In recent years there has been a rapid increase in the use of supplementary cementitious materials, such as fly ash and ground granulated blastfurnace slag, for high performance and durable concrete, as well as to reduce clinker requirement. Such materials being fine and not as reactive as cement, increase the setting time and water demand, and reduce bleeding in concrete. If the rate of evaporation is high enough, plastic shrinkage cracking occurs in slabs and other elements that have high surface area to volume ratios. Such premature surface cracks may accelerate the ingress of harmful agents, and impair durability and serviceability of the structures. The present study has two objectives: firstly, to investigate the influence of supplementary cementitious materials on plastic shrinkage cracking, in hot and dry environmental conditions; and secondly, to control plastic shrinkage cracks using fibers and shrinkage reducing admixtures. Four synthetic fibers – polyacrylonitrile, polyester, glass and polypropylene fibers at commonly-used dosages are evaluated. The results indicate that the addition of supplementary cementitious materials increases the cracking potential as the dosage increases. The incorporation of fibers and shrinkage reducing admixtures reduce crack widths, suggesting that they are viable solutions for combating plastic shrinkage cracking in concretes with supplementary cementitious materials.

INTRODUCTION

Supplementary cementitious materials (SCMs) are being extensively used in concrete either as a replacement for portland cement or in blended cements. The use of materials, such as fly ash and ground granulated blast furnace slag (GGBS), in concrete is promoted for producing better performance, as well as for environmental concerns (i.e., reduction of carbon footprint of cement and better exploitation of the clinker). Incorporation of these materials into concrete usually modifies its properties in both fresh and hardened states. Generally, in the fresh state, SCMs retard the setting of concrete, and reduce bleeding and early-age strength (Johari et al. 2011). When concretes with SCMs are used in structures with extensive surface areas, such as pavements, slabs, bridge decks, tunnel linings, etc., there is a serious concern for plastic shrinkage cracking, especially in hot and dry conditions (Dias 2003). Such

premature surface cracks may accelerate the ingress of harmful agents, and impair the durability and serviceability of the structures.

The incorporation of short synthetic fibers into concrete has been a highly effective technique for minimizing or preventing plastic shrinkage cracking (Balaguru 1994; Berke & Dallaire 1994; Soroushian & Ravanbakhsh 1999; Wang et al. 2002; Banthia & Gupta 2006) Some of the commonly used synthetic fibers are nylon, polyester, glass, polypropylene, cellulose, etc., at volume fractions below 0.5% (Naaman et al. 2005;Sivakumar & Santhanam 2007; Pelisser et al. 2010).Another viable solution for tackling plastic shrinkage cracking is by reducing the surface tension of the water through the incorporation of a shrinkage reducing admixture (SRA). Extensive studies have been conducted on the effects of using SRAs on hardened concrete (e.g., Folliard & Berke 1997; Roncero et al. 2003; Gettu & Roncero 2005) while studies on its influence on plastic shrinkage are limited (Lura et al. 2007; Mora et al. 2009; Saliba et al. 2011; Leemann et al. 2014).

RESEARCH SIGNIFICANCE

Supplementary cementitious materials are advantageous for improving the performance and durability of concrete, as well as for decreasing the clinker consumption. However, plastic shrinkage cracking is often a undesired consequence of SCM usage. Since data on the influence of SCMs on plastic shrinkage cracking is meager, this study aims at quantifying the influence of fly ash and slag. Furthermore, the efficiency of shrinkage reducing components (i.e., fibers and SRAs) is also evaluated in order to provide solutions for mitigating plastic shrinkage cracking.

EXPERIMENTAL PROGRAM

Materials used

Commercially available 53 grade ordinary portland cement conforming to IS 12269, and fly ash (FA) and slag (SG) obtained from the North Madras Power Plant and Jindal Steel Works, respectively, were used for the concrete mixtures. Two different fractions of crushed granite (20–10 and 10–4.75 mm in the proportions of 65:35) were used as coarse aggregates while river sand was used as fine aggregates. A sulfonated naphthalene formaldehyde based superplasticizer (Daracem 811 supplied by W.R.Grace & Co) was used to attain a slump of 100–120 mm. Eight shrinkage reducing components (four types of fibers and three SRAs) were incorporated. The four synthetic fibers were polyacrylonitrile (PAN), polypropylene (PP), glass (GS) and polyester (PE), incorporated at the dosages recommended by the corresponding suppliers. Some of the properties and dosages of the fibers are listed in Table 1.It should be noted that the volume fractions and the total number of fibres incorporated per unit volume differ from one fiber to the other. The glycol-based SRAs (denoted as BM, BT, and GE) were incorporated at dosages of 2% with respect to binder content, by weight, replacing an equivalent weight of water.

Table 1. Properties of fibers

Fibre	Length (mm)	Diameter (μm)	Tensile strength (GPa)	Elastic modulus (GPa)	Specific gravity	Dosage(kg/m^3)	Volume fraction (%)
PAN	12	14.4	0.69	12.0	1.17	0.45	0.04
PP	12	20	0.55	6.8	0.92	0.90	0.10
GLS	12	14	1.70	72.0	2.68	0.60	0.02
PE	12	20	0.50	>5.0	1.34	0.90	0.07

Mix proportioning

Normal 35 MPa strength concrete with a water-to-binder ratio of 0.55 and binder content of 340 kg/m^3 was selected for the study. Fly ash and slag are incorporated at replacement levels of 15% and 30%, by weight of cement. For compensating the increase in volume of binder due to the difference in densities of the SCMs from cement, the total aggregate content was altered based on absolute volume calculations. However, the relative proportions of the different aggregate fractions were maintained. The mix proportions of all the concretes are provided in Table 2.

Table 2. Mix proportions of concrete mixes

Constituents	Control Mix	Fly Ash Mixes		Slag Mixes	
	CM	FA15	FA30	SG15	SG30
Cement	340	289	238	289	238
Mineral admixture	0.0	51	102	51	102
Coarse aggregate (20 – 10 mm)	703	696	689	702	700
Coarse aggregate (10 – 4.75 mm)	377	374	370	377	376
Fine aggregate	796	788	780	794	792
Water	187	187	187	187	187

Specimen configuration and environmental conditions

A procedure conforming to ASTM C1579-13 was adopted to analyze the plastic shrinkage behavior of the concretes. The configuration consists of a slab (560 × 355 × 100 mm) with two end restraints of 32 ± 1 mm height, placed at 90 ± 2 mm from both the ends, as shown in Figure 1. Additionally, a stress riser of 63.5 ± 1 mm height is placed at the center to induce cracking. This configuration can be used to evaluate the effects of settlement, evaporation and early autogenous shrinkage (Lura et al. 2007; Leemann et al. 2014). The specimens were exposed to a hot and dry environment within a specially designed chamber, shown in the Figure 2. The conditions maintained in the chamber in the present tests are: temperature of

42 ± 1°C, relative humidity of 35 ± 2% and wind velocity of 4.5 ± 0.2 m/s; the consequent rate of evaporation of water is about 0.9 kg/m^2/hr.

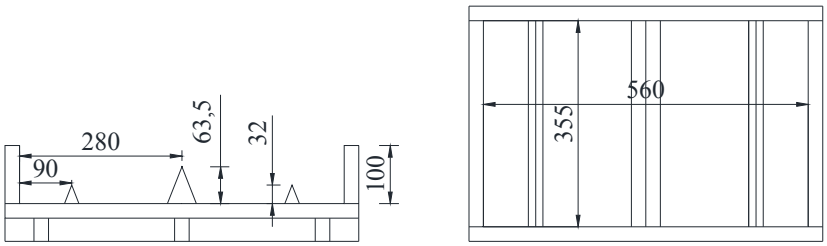

Figure 1. Plastic shrinkage test configuration

Figure 2. Environmental chamber

Test procedure and programme

The control mix (CM) and the mixes with SCMs (FA15, FA30, SG15 and SG30) were first tested and the mix with the highest potential for plastic shrinkage cracking was selected to investigate the efficiency of shrinkage reducing components. Three slabs were cast for each concrete and exposed to the above mentioned environmental conditions for 24 hours. The cracked specimens were later allowed to cool for 24 hours. The crack lengths were measured by getting the length of a thread placed along the cracks while the widths were measured at regular intervals of 1 cm along the crack using a hand held microscope. From the measured data, cracking potential is quantified in terms of crack area, length, and maximum and mean widths. For obtaining the crack initiation time, the slabs were visually inspected at intervals of 30 minutes.

RESULTS

Influence of SCMs on plastic shrinkage

Figures 3(a) to 3(e) show the different crack parameters of the control concrete and those incorporating SCMs. Compared to the control mix, significant

increases in crack dimensions was observed in the concretes with SCMs, clearly indicating the higher cracking potential due to plastic shrinkage. The average crack area in the control mix was 100 mm^2, and with a 30% replacement of cement by fly ash and slag, the areas increased to 138 mm^2 and 402 mm^2, respectively. The maximum crack width in the control mix was 0.6-0.7 mm, which increased to 1.65-1.9 mm with 30% of slag. The cracks were initiated about 30 minutes earlier in the SCM mixes than in the control mix. Overall, SG30 was found to be most prone to plastic shrinkage cracking, and considered further on as the benchmark mix for the crack mitigation studies.

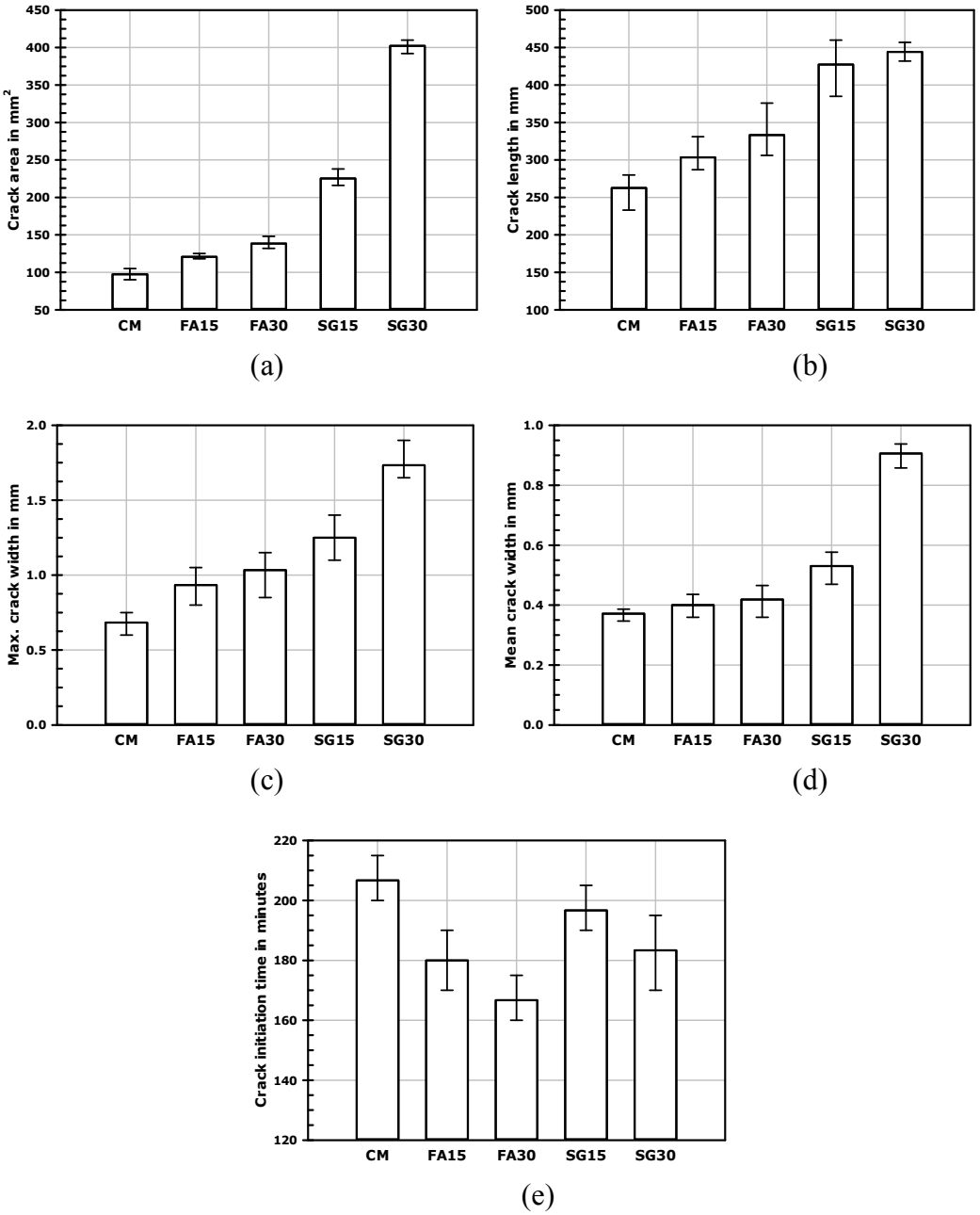

Figure 3. Crack properties: (a) area, (b) length, (c) maximum width, (d) mean width, (e) initiation time.

Influence of fibres in mitigating cracking

The presence of fibers in the concrete has a substantial influence in mitigating plastic shrinkage cracking. Out of all the fiber reinforced concretes (i.e., SG30 with polyacrylonitrile - PAN, polypropylene - PP, glass - GS and polyester - PE fibers), SG30-PP and SG30-PE did not exhibit any cracking. The results of the cracked mixes are summarized in Table 4. The results indicate that the PAN and GLS fibers were beneficial in the reducing the severity of cracking but were not as effective as the PP and PE fibers, probably due to the low dosages used.

Table 4. Summary of test results

Mix ID	Crack initiation time (min)	Crack properties				Reduction in crack area	Reduction in mean crack width
		Length (mm)	Max. width (mm)	Mean width (mm)	Area (mm^2)		
SG30	185	444	1.7	0.9	400	-	-
SG30-PAN	225	365	0.7	0.4	130	67%	60%
SG30-GLS	230	240	0.5	0.2	55	86%	75%

Influence of SRAs on the mitigation of cracking

When the concretes with SRAs were tested, SG30-BT and SG30-GE did not show any cracking, indicating much better performance than SG30-BM. The crack data for SG30-BM are compared with those of SG30 in Table 5. It is evident that all SRAs, though they may belong to the same generic chemical family (glycols in this case), need not behave similarly. This confirms the observations of previous researchers, such as Mora et al. (2000), on ordinary portland cement concretes with SRAs.

Table 5. Summary of test results

Mix ID	Crack initiation time (min)	Crack properties				Reduction in crack area	Reduction in mean width
		Length (mm)	Max. width (mm)	Mean width (mm)	Area (mm^2)		
SG30	185	444	1.7	0.9	400	-	-
SG30-BM	215	378	0.9	0.4	150	62%	56%

DISCUSSION AND CONCLUSIONS

Considering the results obtained here, it is clear that the use of SCMs increases the risk of plastic shrinkage cracking. The reasons can be due to higher maximum capillary pressures, and delay in setting and strength gain. Moreover, the addition of SCMs, increases the binder surface area and consequently the water

demand, which reduce the workability and bleeding. As a result, in hot and dry conditions, the rate of evaporation exceeds the rate of bleeding earlier in the concretes with SCMs, thus increasing the plastic shrinkage cracking potential. Incorporation of shrinkage reducing components (i.e., fibers and SRAs) was found to be significantly effective in mitigating plastic shrinkage cracking in the concretes with SCMs.

From the results obtained, the following specific conclusions can be drawn:

- The intensity of plastic shrinkage cracking due to the incorporation of supplementary cementitious materials increases with higher cement replacement levels.
- Among the synthetic fibers evaluated at the dosages recommended by the suppliers, polyester and polypropylene fibers performed better than glass and polyacrylonitrile, in terms of crack mitigation.
- At a dosage of 2%, two glycol-based shrinkage reducing admixtures (BT &GE) completely eliminated cracking while one did not perform as well. This reiterates the fact that commercial SRAs can differ significantly in performance though they are of the same generic chemical family.

REFERENCES

ASTM Standard Designation C1579-13, Standard test method for evaluating plastic shrinkage cracking of restrained fiber reinforced concrete,West Conshohocken, Pennsylvania, USA.

Balaguru, P., 1994. Contribution of fibers to crack reduction of cement composites during the initial and final setting period. ACI Materials Journal, 91(3), pp.280–288.

Banthia, N. & Gupta, R., 2006. Influence of polypropylene fiber geometry on plastic shrinkage cracking in concrete. Cement and Concrete Research, 36(7), pp.1263–1267.

Berke, N.S. & Dallaire, M.P., 1994. The effect of low addition rates of polypropylene fibers on plastic shrinkage cracking and mechanical properties of concrete. in: Fiber reinforced concrete: Development and innovations; ACI SP-142-2, American Concrete Institute, pp. 19–41.

Dias, W.P.S.Ã., 2003. Influence of mix and environment on plastic shrinkage cracking. Magazine of Concrete Research, 55(4), pp. 385–394.

Folliard, K.J., & Berke, N.S., 1997. Properties of high-performance concrete containing shrinkage-reducing admixture. Cement and Concrete Research, 27(9), pp. 1357–1364.

Gettu, R. & Roncero, J., 2005. On the long-term response of concrete with a shrinkage reducing admixture, in: R.K. Dhir, P.C. Hewlett and M.D. Newlands (Eds.), Admixtures – Enhancing Concrete Performance (Proc. Intnl. Conf., Dundee, UK), Thomas Telford, London, pp. 209–216.

Indian Standard Designation, IS 12269-2013, Specification for 53 grade ordinary portland cement, Bureau of Indian Standards, New Delhi, India.

Johari, M.A., Brooks, J.J., Kabir, S. & Rivard, P., 2011. Influence of supplementary cementitious materials on engineering properties of high strength concrete. Construction and Building Materials, 25(5), pp. 2639–2648.

Leemann, A., Nygaard, P. & Lura, P., 2014. Impact of admixtures on the plastic shrinkage cracking of self-compacting concrete. Cement and Concrete Composites, 46, pp.1–7.

Lura, P., Pease, B.J., Mazzotta, G., Rajabipour, F., & Weiss, J., 2007. Influence of shrinkage-reducing admixtures on development of plastic shrinkage cracks. ACI Materials Journal, 104(2), pp. 187–194.

Mora-Ruacho, J., Martín, M.A., Gettu, R., Aguado, A., 2000. Study of plastic shrinkage cracking in concrete and the influence of fibers and a shrinkage reducing admixture, in: V.M. Malhotra (Ed.), Proc. Fifth CANMET/ACI Intl Conf on Durability of Concrete (Barcelona, Spain), Supplementary Papers, pp. 469–483.

Mora-Ruacho, J., Gettu, R., & Aguado, A., 2009. Influence of shrinkage-reducing admixtures on the reduction of plastic shrinkage cracking in concrete. Cement and Concrete Research, 39(3), pp. 141–146.

Naaman, A.E., Wongtanakitcharoen, T. & Hauser, G., 2005. Influence of different fibers on plastic shrinkage cracking of concrete. Cement and Concrete Research, 36(7), pp.1263–1267.

Pelisser, F., Santos Neto, A.B.S., Rovere, H.L., Pinto, R.C.A., 2010. Effect of the addition of synthetic fibers to concrete thin slabs on plastic shrinkage cracking. Construction and Building Materials, 24(11), pp. 2171–2176.

Roncero, J., Gettu, R., & Martín, M.A., 2003. Evaluation of the influence of a shrinkage reducing admixture on the microstructure and long-term behavior of concrete, in: V.M. Malhotra (Ed.), Proc. Seventh CANMET/ACI Intnl. Conf. on Superplasticizers and Other Chemical Admixtures in Concrete (Berlin), Supplementary papers, pp. 207–226.

Saliba, J.,Rozière, E., Grondin, F., Loukili, A., 2011. Influence of shrinkage-reducing admixtures on plastic and long-term shrinkage. Cement and Concrete Composites, 33(2), pp.209–217.

Sivakumar, A. & Santhanam, M., 2007. A quantitative study on the plastic shrinkage cracking in high strength hybrid fibre reinforced concrete. Cement and Concrete Composites, 29(7), pp.575–581.

Soroushian, P. & Ravanbakhsh, S., 1999. Control of plastic shrinkage cracking with specialty cellulose fibers, ACI Materials Journal, 95(4), pp. 429–435.

Wang, K., Shah, S.P. & Phuaksuk, P., 2002. Plastic shrinkage cracking in concrete materials – Influence of fly ash and fibers, ACI Materials Journal, 98(6), pp. 458–464.

Numerical Analysis of Concrete Creep on Mesoscopic 3D Specimens

B. Bary[1]; C. Bourcier[2]; and T. Helfer[3]

[1]CEA, DEN, DPC, SECR, Laboratoire d'Etude du Comportement des Bétons et des Argiles, Bât. 158, F-91191 Gif-sur-Yvette, France. E-mail: benoit.bary@cea.fr
[2]CEA, DEN, DM2S, Laboratoire de Génie Logiciel et de Simulation, Bât. 454, F-91191 Gif/Yvette, France. E-mail: christophe.bourcier@cea.fr
[3]CEA, DEN, DEC, SESC, Laboratoire de Simulation du comportement des Combustibles, Bât. 151, 13108 St. Paul lez Durance, France. E-mail: thomas.helfer@cea.fr

Abstract

In this paper we investigate analytically and numerically the creep behavior of concrete at mesoscale. The simulations are carried out with the finite element (FE) code (Cast3M) on 3D concrete specimens consisting in about 4600 polyhedral aggregates of various size and shapes randomly distributed in a box. Both matrix and Interfacial Transition Zone (ITZ) are considered as linear viscoelastic materials while the aggregates are elastic. Specific interface finite elements are introduced between the aggregates and the matrix to model the ITZ. The overall and intra-phase response of the numerical specimens when subjected to classical creep loadings is investigated, and then compared to the results of analytical estimations obtained with classical mean-field approximation schemes. These schemes are applied in the Laplace-Carson (LC) space, and the effects of the ITZ are accounted for via appropriate interface models. The results obtained for different ITZ thicknesses are analyzed so as to evaluate their respective influence on mortar and concrete materials.

INTRODUCTION

Two main functions are devoted to concrete structures in the nuclear context (containment building, waste storage structures…): containment and protection against radionuclide migration. The constitutive material must then meet high requirements in terms of performance and durability. In particular, loss of containment abilities due to long-term creep and induced development of cracks shall be prohibited. Concrete is a heterogeneous material made up at the mesoscale of linear elastic aggregates distributed in a mortar matrix whose behavior is time-dependent. Besides, the presence of an ITZ between the aggregates and the matrix is known to also influence the overall behavior (see e.g. (Lavergne et al. 2015; Lutz et al. 1997; Scrivener et al. 2004)). It is then of particular importance to correctly characterize the respective role and impact of both phases and ITZ regarding the creep strains, since the initiation and propagation of cracks are strongly related to the local stresses and strains states as well as their history.

In this paper we investigate analytically and numerically the creep behavior of concrete at mesoscale. The simulations are carried out on 3D concrete specimens generated by means of python scripts using the functionalities of the integration platform Salome (Bourcier et al. 2013; Salome). They consist in about 4600 polyhedral aggregates of various sizes and shapes obtained by a Voronoi space decomposition, and randomly distributed in a box. Only the coarser aggregates representing a volume fraction of 50% are considered in order to generate mesostructure meshes of reasonable size. Then, unstructured periodic meshes with tetrahedral elements are generated, and computations are carried out in the finite element code (Cast3M). The matrix and ITZ are considered as linear viscoelastic materials ruled by different generalized Maxwell models. Specific interface elements are introduced between the aggregates and the matrix to model the ITZ.

One purpose of the study is to analyze the overall and intra-phase response of the numerical specimens when subjected to classical creep loadings. In particular, the evolutions of averaged stresses and strains in the matrix and aggregate phases will be reported and compared to analytical estimations obtained with classical mean-field approximation schemes. These schemes will be applied in the Laplace-Carson (LC) space via the well-known elastic – linear viscoelastic correspondence principle. The effects of the ITZ will be accounted for via interfaces modelled with the linear-spring model (LSM) (see e.g. (Duan et al. 2007)) in the LC space. The influence of the ITZ thickness on the overall and local response of the specimens is studied. Further, an analysis regarding the evolutions of the mean stresses and strains in each aggregate and in matrix subvolumes is performed so as to quantify their fluctuations. Finally, the impact of the aggregate shape on both local and macroscopic response is analyzed through different mesostructures with flat and elongated particles.

MESOSTRUCTURE GENERATION

The procedure for constructing the numerical cubic samples is detailed in (Bourcier et al. 2013; de Larrard et al. 2013). The open-source python library Combs (Bourcier et al. 2013) based on the Computer-Aided Design code (Salome) is used to generate both geometry and meshes of the mesostructures. To improve the placement procedure time, the GJK 3D algorithm has been implemented in Combs for fast polyhedrons distance computation (see e.g. http://www.dyn4j.org/2010/04/gjk-distance-closest-points). The geometries considered in this paper are obtained by randomly distributing in a box polyhedral aggregates of various sizes and shapes obtained by a classical Voronoi space decomposition (de Larrard et al. 2013). To limit the FE computation time and the placement procedure, the choice of 4627 coarse aggregates has been retained, for a total volume fraction of 0.50. Their number and volume are defined to match the ones of the corresponding spheres assembly according to the sieve curve described in (de Larrard et al. 2013). The total number of aggregates in the samples is greater than the prescribed one since the aggregates overlapping the surfaces of the mesostructures are cut and the remaining parts are placed on the opposite faces to ensure periodicity. To evaluate the effects of the aggregates shape, three mesostructures are generated, one with the initial Voronoi aggregates (denoted as ‘isotropic’ in the following), another with flat ones and the

third with elongated inclusions. These flat and elongated aggregates are obtained by applying a scale transform of 3 on the initial aggregates along one or two perpendicular axes randomly defined. The Figure 1 presents a sample realization with isotropic (left) and flat (right) particles.

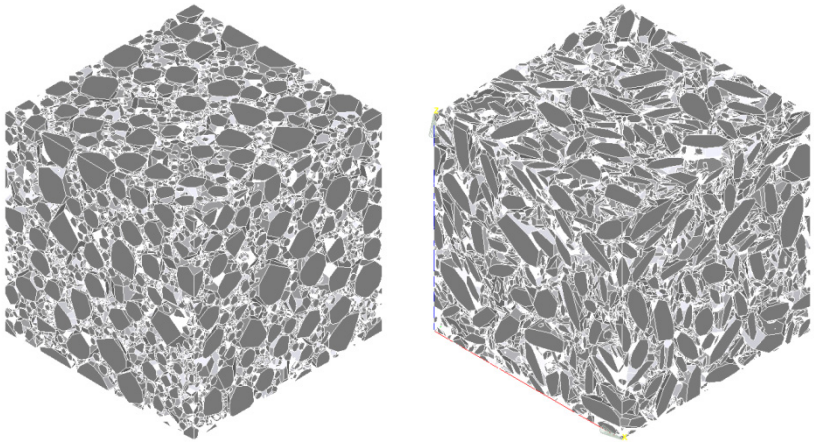

Figure 1. Sample with isotropic (left) and flat (right) aggregates.

For the numerical results to be comparable, the meshes are constrained to have a similar size. Here the number of linear tetrahedral finite elements ranges from 3.71 to 4.21×10^6.

MODELLING

As mentioned above, the behavior of the matrix material is assumed to be linear viscoelastic, with bulk $k^m(t)$ and shear moduli $\mu^m(t)$ ruled separately by a generalized Maxwell model with 4 elements (the element labeled as 0 is only composed of a spring) as:

$$k^m(t) = k_0^m + \sum_{i=1}^{3} k_i^m e^{-t/\tau_i^m}, \quad \mu^m(t) = \mu_0^m + \sum_{i=1}^{3} \mu_i^m e^{-t/\tau_i^m}$$

in which k_i^m and μ_i^m with $i \in \{0,3\}$ are the elastic moduli of the Maxwell elements, τ_j^m are the relaxation times. It is well-known that in the case of linear viscoelasticity the time-dependent problem may be equivalently reformulated as a linear elastic problem in the Laplace-Carson space (Mandel 1966), allowing to applying classical upscaling techniques. It is shown in (Thai et al. 2014) that in the particular case of the MT scheme and spherical particles, exact or semi-analytical solutions of the inversion problem can be derived. We choose here to apply this simplified methodology. The macroscopic behavior may then take the general form of a linear viscoelastic material:

$$\boldsymbol{\sigma}(t) = 3\int_{0^-}^{t} k^{MT}(t-\tau)\frac{d\epsilon}{d\tau}d\tau\,\mathbf{1} + 2\int_{0^-}^{t} \mu^{MT}(t-\tau)\frac{d\boldsymbol{e}}{d\tau}d\tau$$

with $\boldsymbol{\sigma}(t)$, $\epsilon = 1/3\,\mathrm{tr}(\boldsymbol{\varepsilon})$ and $\boldsymbol{e}$ the macroscopic stress tensor, bulk and deviatoric part of the strain tensor $\boldsymbol{\varepsilon}$, respectively; k^{MT} and μ^{MT} are the homogenized bulk and

shear moduli, which take the general form of Dirichlet series. The Young modulus of the aggregates is taken as E = 70 GPa and its Poisson ratio as ν = 0.3. The parameters of the Maxwell models are identified on a classical concrete creep test realized by (Ladaoui 2010) (see (Bary et al. 2014)). To simplify, the relaxation times are chosen a priori, in accordance with the duration of the creep tests (300 days). The behavior of the interface between the aggregates and the matrix is also assumed to be ruled by generalized Maxwell models. As in concrete the mechanical properties of the ITZ are known to be more compliant than the ones of the mortar matrix and aggregates, we chose to apply the LSM in the LC space to simulate the interface effects. The interface conditions for the LSM are (e.g., (Duan et al. 2007; Hashin 1991)):

$$[\tilde{\boldsymbol{\sigma}}].\boldsymbol{n} = 0, \tilde{\mathbf{k}}.[\boldsymbol{u}] = \tilde{\boldsymbol{\sigma}}.\boldsymbol{n}$$

where $\boldsymbol{n}$, $\tilde{\mathbf{k}}$, $\boldsymbol{u}$ are the unit normal vector to the interface, the second order tensor characterizing the elastic parameters in the LC space (the 'tilde' notation designates the properties expressed in the LC space), and the displacement; $[\cdot]$ denotes the jump of the corresponding quantities. In the case where the interface is thin and compliant with respect to the inclusion, i.e. $h \ll R_I$, $E_c \ll E_I$ and $\mu_c \ll \mu_I$ with h the thickness of the interphase, R_I the radius of the spherical inclusion, E_c and μ_c the Young and shear moduli of the interphase, E_I and μ_I the Young and shear moduli of the inclusion, the tensor $\tilde{\mathbf{k}}$ can be expressed as $\tilde{\mathbf{k}} = \tilde{\mathrm{k}}_n \boldsymbol{n}\otimes\boldsymbol{n} + \tilde{\mathrm{k}}_t \boldsymbol{s}\otimes\boldsymbol{s} + \tilde{\mathrm{k}}_t \boldsymbol{t}\otimes\boldsymbol{t}$ with

$$\tilde{\mathrm{k}}_n = \frac{2\tilde{\mu}_c(1-\tilde{\nu}_c)}{h(1-2\tilde{\nu}_c)}, \tilde{\mathrm{k}}_t = \frac{\tilde{\mu}_c}{h}$$

in which $\boldsymbol{s}$ and $\boldsymbol{t}$ are the two orthogonal unit vectors in the tangent plane of the interface and $\tilde{\nu}_c$ is the Poisson ratio of the interphase. In the following, we will retain this model for characterizing the viscoelastic properties of the interfaces in the FE simulations, providing k_n and k_t are expressed in the time space. Further, we propose to estimate the overall properties of the heterogeneous material by making use and extending the approach due to (Duan et al. 2007), based on a replacement procedure. In this approach, the elastic composite inclusions composed of the aggregates and their surrounding interfaces are replaced by equivalent homogeneous spherical inclusions. The expressions of the moduli for these equivalent particles depend then on both inclusion and interphase properties; as they are lengthy, they are not recalled here, see (Duan et al. 2007) for details. Since these formulas are established in an elastic framework, they are applied here in the LC space. Once the composite inclusions are substituted by equivalent homogeneous ones, the MT scheme may be applied to obtain the overall properties of the concrete material.

SIMULATION RESULTS

We propose to perform the simulations in the FE code Cast3M with the different following values of interphase thickness h=1, 10, 50, 100 and 250 μm. A calculation with no interfaces between aggregates and matrix is also carried out to control the accuracy of the results with smaller thicknesses. Note that the higher values of thickness considered are unrealistic for concrete, but are representative for mortars, provided the aggregates are regarded as sand particles. The loading corresponds to a typical creep test, defined by a constant normal stress

of -25.8×10^6 Pa applied on the sample boundaries in the direction 1 and zero stress on the other faces, via uniform stresses boundary conditions (BC). Such BC are preferred as they give results close to the periodic ones, for a much lower computation time (Bary et al. 2014). The computations are performed on standard Linux machine with 20 cores and 128 Go RAM. The total simulated time is 300 days, reached in 32 time steps. The computation time is about 10-12 hours, and additional 10-12 hours are needed for post-processing the results (i.e. calculating the average stresses and strains in all inclusions and matrix subvolumes for all time steps). The mechanical properties of the interphase are supposed to be half those of the matrix (e.g. (Neubauer et al. 1996)). The mechanical models for both matrix and interphase materials have been implemented via the Mfront code generator developed at CEA (MFront).

Figure 2 presents the evolutions of the creep longitudinal and transversal strains obtained numerically by FEM (symbols) and analytically (lines) for the different interface thicknesses and the isotropic aggregate case. We observe as expected that the magnitude of strains progressively increases for higher values of thickness. The differences are negligible between h=1 and 10 µm, and are about 6, 14 and 33% between h=1 and 50, 100 and 250 µm, respectively. Note that the results with no interface are omitted as they are superposed with the h=1 thickness ones. One may conclude that the presence of ITZ, whose typical thickness is around 20-25 µm (Scrivener et al. 2004) in concrete at mesoscale (i.e. considering the matrix as mortar), is not significant regarding the estimation of macroscopic response of the material. By contrast, for mortars which correspond approximately to the case of a thickness of 250 µm with respect to the aggregate sizes, they appear very influential and should not be neglected. Note that all the results shown here may be somewhat moderated since ITZ are modelled as idealized interfaces with very low mechanical properties, which may not be totally realistic.

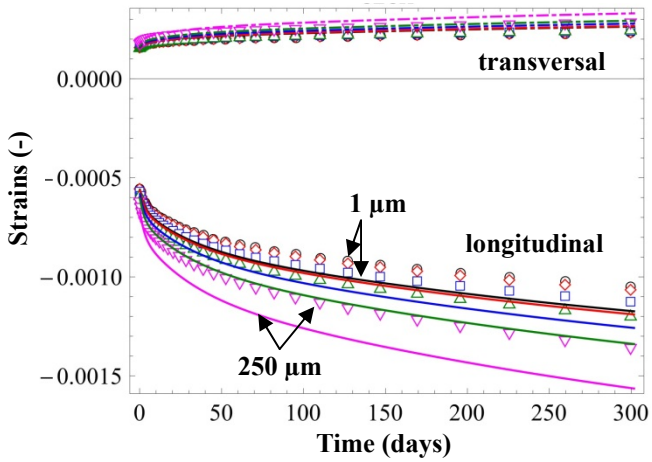

Figure 2. Longitudinal and transversal creep strains obtained numerically (symbols) and analytically (lines) for interface thicknesses of 1, 10, 50, 100 and 250 µm.

We also observe that the strains estimated by the model overestimate in magnitude the numerical ones for all interface thicknesses. Several causes may explain these discrepancies: one is due to the inherent use of the MT scheme whose application domain should not in principle exceed about 30% of inclusion volume fraction; another lies in the inclusion shape considered, spherical for the model and polyhedrons for the FE. Biases introduced by the insufficiently fine meshes and the considered BC are also well-known sources of inaccuracies. Figure 3 shows the evolutions of average stresses (left) and strains (right) in the aggregates and matrix in the direction of creep loading, obtained numerically (symbols) and analytically (lines) for the different interface thicknesses. It should be noted that the average strains in the aggregate phase (contrary to the average stresses in the case of LSM) cannot be directly obtained via the estimation of the strain concentration tensor since in the approach of (Duan et al. 2007) the MT scheme is applied to the material exhibiting equivalent homogeneous inclusions in replacement of the composite sphere-interface ones. This Figure indicates that an increase of the interface thickness tends to reduce the magnitude of the stress in the aggregates and to augment it in the matrix; this is the reverse for the strain: it increases in the matrix and decreases in the aggregates. Again, the model provides estimations relatively close to the FE simulations.

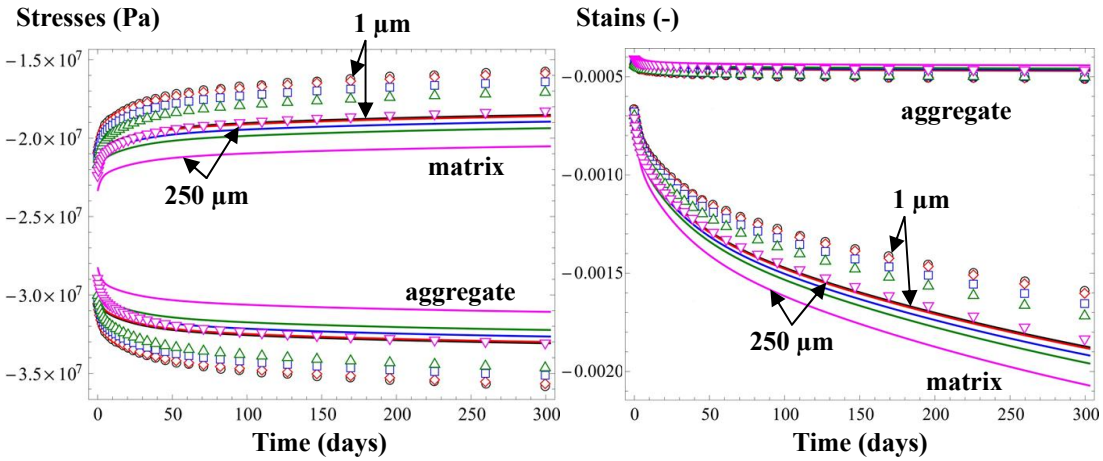

Figure 3. Average stresses (left) and strains (right) in both aggregate and matrix phase, obtained numerically (symbols) and analytically (lines) for different interface thicknesses ranging from 1 to 250 µm.

Figure 4 presents the probability distribution functions (PDF) of the longitudinal average stress in the aggregates and matrix subvolumes for the interface thicknesses of 1 (left) and 250 (right) µm, and at 0.38, 24.5 and 300 days. The matrix subvolumes are obtained by dividing the matrix with a voxel-type procedure. Here the dimension of a voxel is chosen as 1/20 of the edge dimension of the initial box (i.e. 8000 subvolumes are expected). We observe that the stress in the aggregates is more dispersed than in the matrix subvolumes, in particular in the case of the smaller interface thickness. This dispersion tends to reduce for higher thickness (Figure 4 right). Moreover, in all cases the PDF are more dispersed at later ages. These results indicate that the presence of interfaces affects notably the mean stress in both matrix

and aggregate phases, but also the dispersion essentially in the inclusive phase. Besides, the relatively high dispersion proves that important stress concentrations arise locally, meaning that microcracking is likely to occur in particular in the matrix and ITZ phases, whose strength is in general weaker than in the aggregate one.

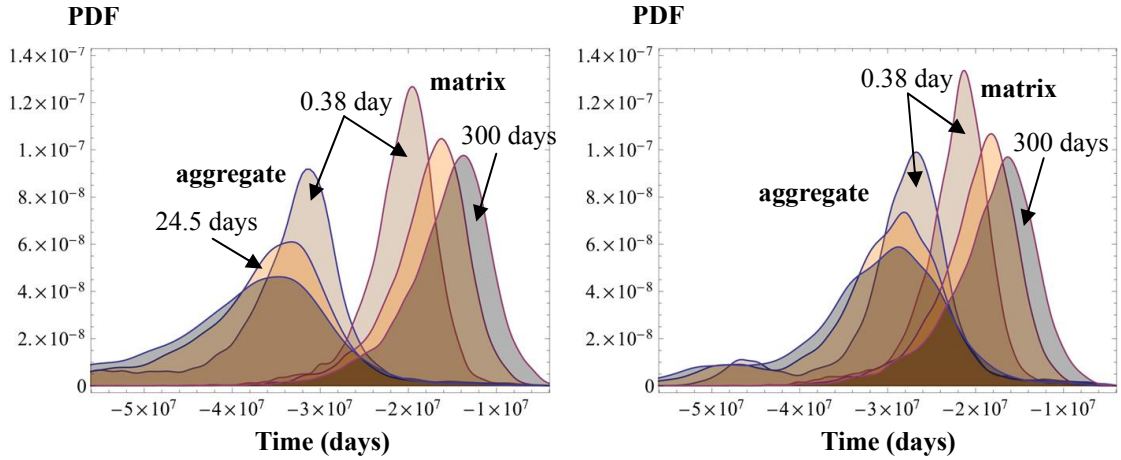

Figure 4. FE Probability Distribution Function for the average longitudinal strain in both matrix subvolumes and aggregates for the 1 µm (left) and 250 µm (right) interface thickness and at 0.38, 24.5 and 300 days.

Finally, we compare on Figure 5 the longitudinal creep strain obtained in the cases of isotropic, flat and elongated aggregates, and for the interface thickness of 1, 100 and 250 µm. The curve obtained for a mesostructure containing 1052 spherical particles representing a volume fraction of 50% is also depicted. We note that the effects of the aggregate shape as considered here (i.e. polyhedrons with different aspect ratios) are not important regarding the macroscopic creep response, whatever the interface thicknesses. This aspect is in agreement with results reported in e.g. (Lavergne et al. 2015).

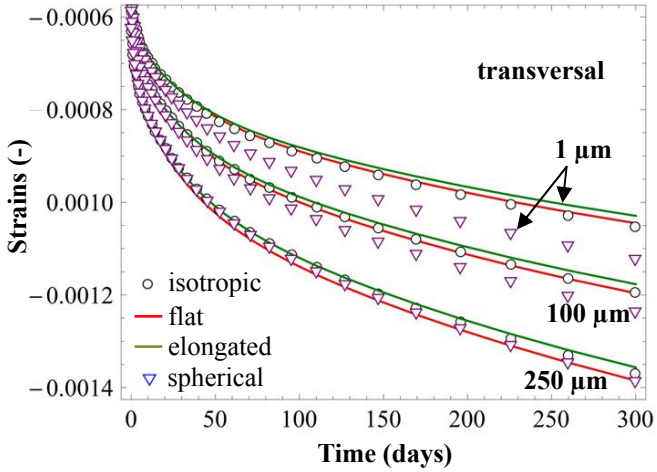

Figure 5. Longitudinal creep strain obtained numerically for different aggregate shapes and 3 interface thicknesses.

By contrast, significant discrepancies are observed between spherical and non-spherical aggregates for lower ITZ thickness, which tend to reduce and even cancel for higher ones. However, it should be noted that the mesostructure with spherical particles has much less inclusions and then interfaces than the ones with polyhedrons. This was imposed to obtain meshes of similar size, due to the fact that curved surfaces necessitate a much finer discretization than plane ones. Consequently, the results may only be compared cautiously in particular for high ITZ thicknesses.

CONCLUSION

In this paper, we have analyzed analytically and numerically the viscoelastic behavior of concrete at mesoscale. FE simulations have been carried out on 3D concrete specimens with 4600 polyhedral aggregates randomly distributed in a box and representing a volume fraction of 50%. Both matrix and ITZ behaviors have been considered as linear viscoelastic and the aggregates one as elastic. Specific FE interface elements have been introduced to model the ITZ, assumed to be more compliant than the matrix. The overall and intra-phase responses in the numerical specimens have then been investigated when subjected to classical creep loading, and compared to the analytical estimations obtained with classical mean-field approximation schemes accounting explicitly for ITZ and applied in the LC space. The results obtained show that typical ITZ thicknesses for concrete of 20-25 μm do not affect significantly the macroscopic and intra-phase response, contrary to the case of mortars whose behavior is comparatively notably influenced. As expected, increasing the ITZ thickness leads globally to a rise of the creep strains magnitude, i.e. the material becomes more compliant. Moreover, it implies a reduction (in magnitude) of the stresses in the aggregates and an increase of both stresses and strains in the matrix phase. A significant dispersion has been observed in the average creep stress per aggregate and per matrix subvolumes, indicating potentially important local stress concentrations. Higher ITZ thicknesses tend to slightly reduce this dispersion. The effects of the aggregate shape (i.e. flat or elongated polyhedrons with aspect ratio of 3) are weak on the macroscopic response, whatever the interface thickness. More important discrepancies are observed with spherical particles.
Future works will focus on the introduction of a more realistic ITZ behavior discarding the hypothesis of very low mechanical properties. Coupling with damage will also be a challenging aspect to study both analytically and numerically.

REFERENCES

Bary, B., Gélébart, L., Adam, E., and Bourcier, C. (2014). “Numerical analysis of linear viscoelastic 3D concrete specimens: Comparison between FE and FFT methods.” *Computational Modelling of Concrete Structures*, St. Anton am Arlberg, Austria, 373–381.

Bourcier, C., Dridi, W., Chomat, L., Laucoin, E., Bary, B., and Adam, E. (2013). “Combs: open source python library for RVE generation. Application to microscale diffusion simulations in cementitious materials.” Paris.

Cast3M. *www-cast3m.cea.fr*.

Duan, H. L., Yi, X., Huang, Z. P., and Wang, J. (2007). "A unified scheme for prediction of effective moduli of multiphase composites with interface effects: Part II—Application and scaling laws." *Mechanics of Materials*, 39(1), 94–103.

Hashin, Z. (1991). "Thermoelastic properties of particulate composites with imperfect interface." *Journal of the Mechanics and Physics of Solids*, 39(6), 745–762.

Ladaoui, W. (2010). "Etude expérimentale du comportement Thermo-Hydro-Mécanique à long terme des BHP destinés aux ouvrages de stockage des déchets radioactifs." Université de Toulouse, Université Toulouse III-Paul Sabatier.

De Larrard, T., Bary, B., Adam, E., and Kloss, F. (2013). "Influence of aggregate shapes on drying and carbonation phenomena in 3D concrete numerical samples." *Computational Materials Science*, 72, 1–14.

Lavergne, F., Sab, K., Sanahuja, J., Bornert, M., and Toulemonde, C. (2015). "Investigation of the effect of aggregates' morphology on concrete creep properties by numerical simulations." *Cement and Concrete Research*, 71, 14–28.

Lutz, M. P., Monteiro, P. J. ., and Zimmerman, R. W. (1997). "Inhomogeneous interfacial transition zone model for the bulk modulus of mortar." *Cement and Concrete Research*, 27(7), 1113–1122.

Mandel, J. (1966). *Cours de mécanique des milieux continus*. Gauthier-Villars.

MFront. *www.tfel.sourceforge.net*.

Neubauer, C. M., Jennings, H. M., and Garboczi, E. J. (1996). "A three-phase model of the elastic and shrinkage properties of mortar." *Advanced Cement Based Materials*, 4(1), 6–20.

Salome. *www.salome-platform.org*.

Scrivener, K. L., Crumbie, A. K., and Laugesen, P. (2004). "The interfacial transition zone (ITZ) between cement paste and aggregate in concrete." *Interface Science*, 12(4), 411–421.

Thai, M.-Q., Bary, B., and He, Q.-C. (2014). "A homogenization-enriched viscodamage model for cement-based material creep." *Engineering Fracture Mechanics*, 126, 54–72.

Experimental Study of the Water Desorption and Drying Shrinkage of Cement-Based Materials with Thin Slices

Qier Wu[1]; Thomas Rougelot[1]; Nicolas Burlion[1]; and Xavier Bourbon[2]

[1]Laboratoire de Mécanique de Lille, Polytech Lille, Cité Scientifique, Ave. Paul Langevin, 59650 Villeneuve d'Ascq, France.
[2]ANDRA, 1-7 Rue Jean Monnet, 92298 Châtenay-Malabry Cedex, France.

Abstract

The aim of the present study is to experimentally investigate the water vapor desorption and drying shrinkage of cement-based materials during a step-by-step desorption process, with the objective to link drying shrinkage to water desorption. Water vapor desorption isotherms of two cement pastes and two mortars (with water-to-cement ratio of 0.5 and 0.8) were studied using thin slices with three thicknesses 1 mm, 2 mm and 3 mm. Drying shrinkage was measured with 2 mm slices for each material. The slice thickness has an impact on the relative mass variation, but the difference between 2 mm slices and 3 mm slices is very small or even negligible. The results obtained in the present study are compared with a former study on larger prismatic beams. The curing condition influences the water desorption isotherm: the water content in the present study is always higher at each relative humidity after a longer curing period with thin slices. The size effect is pronounced for drying shrinkage: the drying shrinkage obtained with slices is always bigger than larger prismatic beams. The correlation between drying shrinkage and water mass loss shows two almost linear parts with different slopes for both cement pastes and exhibits three characteristic phases for both mortars.

1. Introduction

The importance of durability of cement-based materials is well known in practice. Drying shrinkage is probably one of the most disadvantageous properties of cement-based materials. It is the reduction in volume caused principally by the water loss during the drying process. Drying shrinkage could impair the mechanical behavior of cement-based materials structures. Cracks generated by differential shrinkage could increase the permeability of materials and act as a preferential path for aggressive species, and hence lead to overall durability and serviceability decreases. It is of great interest to understand the drying shrinkage phenomenon in order to predict and even control the strains.

The major mechanisms to explain the shrinkage of hardened cement-based materials have been summarized by Kovler and Zhutovsky (2006). The shrinkage at relative humidity above 40% is usally attributed to the capillary tension (Wittmann 1968). Most researchers attribute the shrinkage at relative humidity below 40% to the

variation in the surface enerny (Powers 1968). The variation of the disjoning pressure is considered as another mechanism for the shrinkage at relative humidity above 40% (Powers 1968). Feldman and Sereda (1970) suppose that the movement of interlayer water could be responsible for the shrinkage at relative humidity below 35%.

The variation of relative humidity leads to the varation of water content of cement-based materials, which could be associated to the drying shrinkage. Rougelot et al. (2009) investigated the water desorption and drying shrinkage of two types of cement-based materials (cement paste and mortar) with two W/C (water-to-cement) ratios using prismatic specimens of 20×20×160 mm^3. The drying of cement-based materials is a slow process leading to moisture gradients in the specimens. The moisture gradients are mainly dependent on the pore structure of materials, as well as the specimen shape and specimen size. Hence, the assessment of drying shrinkage exhibits a size effect (Miyazawa and Tazawa, 2000). Using thin slices to carry out water vapor desorption and drying shrinkage experiment allows on the one hand, considering that one-dimensional moisture transport takes place in the slices and on the other hand, obtaining moisture equilibrium more quickly (Baroghel-Bouny et al. 1999). When few-millmeter thick slices are submitted to a step-by-step drying process with small relative humidity steps, a quite homogeneous moisture distribution can be ensured in the slices, allowing a reliable measurment of drying shrinkage.

In this work, water desorption and drying shrinkage of two cement pastes and two mortars (with W/C ratios of 0.5 and 0.8) were studied using thin slices. The size effect on the mass variation kinetics is analyzed. The present experimental results are then compared with a former study (Rougelot et al. 2009), in order to clarify the effects of specimen size and curing condition. The correlation between drying shrinkage and relative humidity, as well as that between drying shrinkage and relative mass variation are also analyzed.

2. Experimental program

2.1 Materials

Two cement pastes and two mortars based on a common Portland cement CEM II/B 32.5 R were tested in this study: cement paste C05 with W/C ratio 0.5, cement paste C08 with W/C ratio 0.8, normalized mortar M05 with W/C ratio 0.5 and normalized mortar M08 with W/C ratio 0.8. The sand used to prepare the mortars is normalized sand from Leucate (France, norm EN 196-1) with a maximum diameter of 2 mm. The sand-to-cement ratio is 3. The mixture compositions are given in Table 1. They are the same to the materials tested by Rougelot et al. (2009).

Table 1. Mixture compositions.

Material	*Sand/cement*	*Water/cement*
C05	-	0.5
C08	-	0.8
M05	3	0.5
M08	3	0.8

2.2 Sample preparation

The materials were poured into cylindrical molds with a diameter of 37 mm and a height of 100 mm. Plastic sheets were used to cover the surfaces before demoulding in order to avoid early desiccation. After 24 hours, all the cylinders were demoulded and cured for 1 year in lime-saturated water at 20 °C. 3 cylinders of each material were sawed by a diamond wire saw into thin slices with 3 different thicknesses 1 mm, 2 mm, and 3 mm, and were then cured for 10 additional months in lime-saturated water at 20 °C until the start of the experiment. The tolerance of slice thickness is ±0.05 mm.

Both coring and sawing were carried out under water, so it could be assumed that no desiccation occurred during sample preparation. Considering that the experiment started after nearly 22 months' curing, the evolution of cement hydration and associated autogenous shrinkage were negligible during the experiment.

During the preparation of cylinders of C08, a considerable amount of bleed water appeared at the upper surface of cylinders due to a very high water-to-cement ratio. Therefore, the effective water-to-cement ratio of C08 was smaller than 0.8.

2.3 Experimental procedure

In order to ensure that experimental results can be statistically considered representative for the materials, 6 slices of 3 mm, 9 slices of 2 mm and 18 slices of 1 mm were chosen from 3 different cylinders to perform the water desorption experiment for each material. 2 slices of 2 mm were used to measure drying shrinkage for each material. During the experiment, the initially water-saturated slices were submitted to decreasing relative humidity steps at a fixed temperature $T = 20°C$. A range of relative humidity was imposed successively with RH = [95%; 90%; 80%; 65%; 50%; 30%; 12%]. Both temperature and relative humidity were controlled by a climatic chamber.

In order to avoid frequent and significant disturbances to the environment in the climatic chamber, every time a box of 8 or 9 slices was removed from the climatic chamber for mass monitoring. Every time one slice was taken out from the climatic chamber for diameter measurement and mass monitoring. As soon as the slices were weighted, they were immediately replaced in the climatic chamber. Sample mass monitoring was carried out with a balance with a resolution of 0.1 mg. The diameter variations of slices were assessed by means of a retractometer (resolution 1 μm). All the measurements were carried out under controlled conditions ($T = 20±2$ °C, RH = 40±5%). A continuous injection of nitrogen into the climatic chamber is maintained during the whole experiment to limit the carbonation, which can influence the sample mass and total shrinkage. Furthermore, additional nitrogen is injected into the climatic chamber after each series of measurement.

The initial water-saturated sample mass was measured after surface drying with clean tissues. The dry state was obtained by an oven-drying at 60 °C and then 90 °C successively until the sample mass remained constant.

3. Results and discussions

3.1 Mass variation kinetics

Figure 1 presents the average relative mass variation of two cement pastes C05 and C08 as a function of time during the step-by-step desorption process for different slice thicknesses. The evolution of the relative mass variation confirms that drying is a very slow process for cement pastes. Even thought very thin slices are tested here, the time required to obtain moisture equilibrium is considerably long, especially at lower relative humidity. The slice thickness has a great impact on the relative mass variation of C05. As can be seen, the thinner slices have a bigger relative mass variation once the mass stabilization is obtained at each relative humidity. However, compared to the difference between 1 mm slices and 2 mm slices, the difference between 2 mm slices and 3 mm slices is much smaller or even negligible. The dispersion of relative mass variation is also evident at high relative humidity among different thicknesses for C08. The thinner slices of C08 also have a bigger relative mass variation at high relative humidity. However, the decrease of relative humidity can weaken or even reverse the size effect of C08. Compared to C05, the size effect is much weaker for C08.

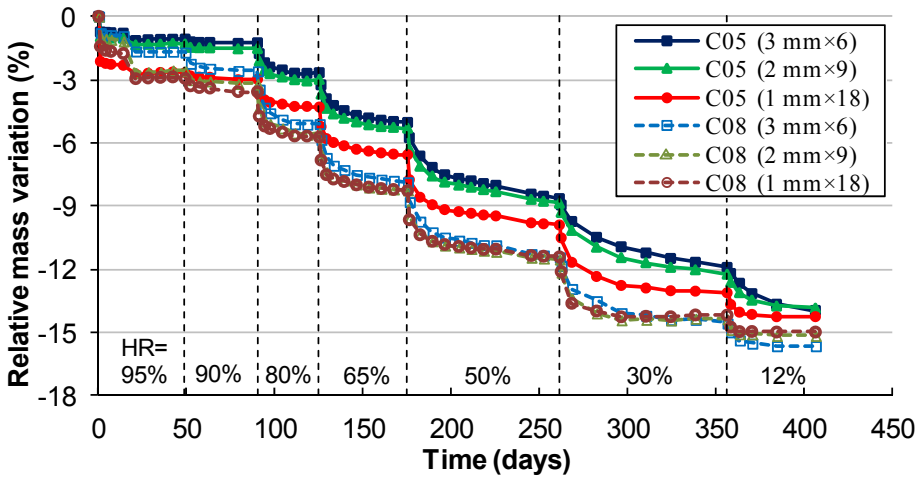

Figure 1. Evolution of average relative mass variation of two cement pastes for different slice thicknesses during a step-by-step desorption process at $T = 20°C$.

The evolution of average relative mass variation of two mortars M05 and M08 for different slice thicknesses is plotted in Figure 2. The time required for mass stabilization of mortars is much shorter than cement pastes with the same water-to-cement ratio. The acceleration of drying for mortars due to a lower volume fraction of cement matrix could also be associated with the presence of the interfacial transition zone more porous and the microcracks generated by the presence of aggregate (differential deformations between cement matrix and aggregates). The slice thickness has an unexpected influence on the relative mass variation of M05: the 1 mm slices always have a smaller relative mass variation, in contrast to C05. In addition, the difference between 1 mm slices and other slices increases as the relative humidity decreases. However, the difference between the 2 mm slices and 3 mm

slices is negligible. No clear effect of the slice thickness can be concluded according to the evolution of average relative mass variation of M08.

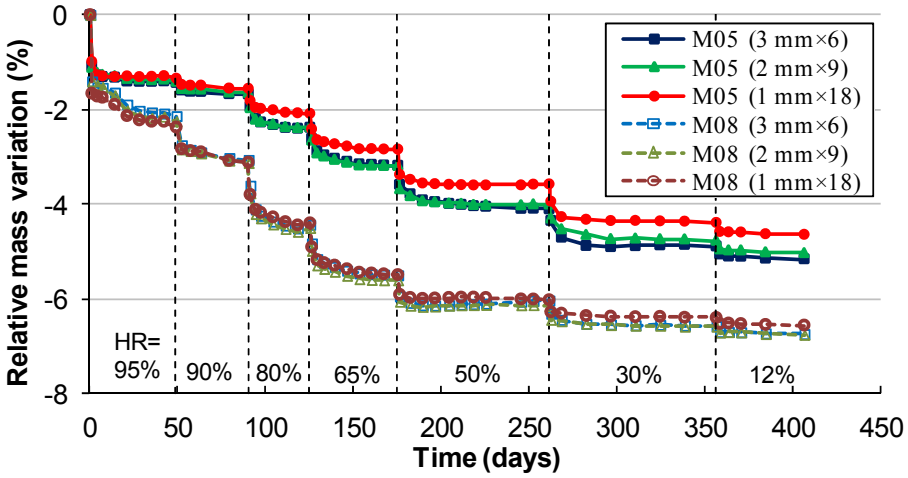

Figure 2. Evolution of average relative mass variation of two mortars for different slice thicknesses during a step-by-step desorption process at T = 20°C.

3.2 Water vapor desorption isotherm

As mentioned above, the effect of slice thickness has an impact on the relative mass variation of cement pastes and mortars. However, the difference in relative mass variation becomes smaller as the slice thickness increases. As shown in Figure 1 and Figure 2, the difference in relative mass variation between 2 mm slices and 3 mm slices is very small or even negligible. Hence, the water vapor desorption isotherms presented here are calculated from the average relative mass variation of all the 2 mm slices and 3 mm slices tested for each material.

The water vapor desorption isotherms of two cement pastes C05 and C08 in terms of water content are presented in Figure 3, together with the results of Rougelot et al. (2009) (obtained with prismatic beams of 20×20×160 mm^3 after 5 months' curing). Similar to their results, compared to C05, C08 has bigger water content at very high relative humidity (above 90%) though smaller one for other relative humidity in the present study, indicating that the cement paste with a higher W/C ratio has a higher proportion of large pores. In comparison with C08 in their study, C08 in the present study has slightly higher water content at fully water-saturated state (RH = 100%) though much higher water content at other relative humidity. C05 in the present study always has higher water content than their C05 at each relative humidity. Due to the creation of new surfaces of slices and an increase in porous connectivity, a further hydration and saturation process could occur during the curing after sawing (Wu et al. 2014). The slices in the present study are more water-saturated than their prismatic beams after curing. The water filled the additional accessible pores led to an increase in water content at fully water-saturated state. The further cement hydration made the pore network finer. Hence, the slices, containing more small pores than the prismatic beams, retain more water at low relative humidity and consequently have higher water content.

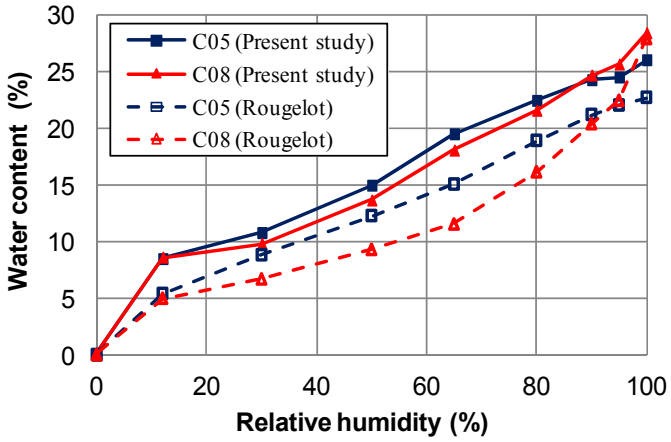

Figure 3. Comparison of water vapor desorption isotherms for two cement pates at T = 20°C with the results of Rougelot et al. (2009).

Figure 4 presents the water desorption isotherms of two mortars M05 and M08, as well as the results of Rougleot et al. (2009). The results obtained in the present study are very close to theirs. The water content is always a bit higher in the present study, which could be attributed to the water filled the additional accessible pores and the finer pore network due to further hydration and saturation process during the curing after sawing of slices, as mentioned before. Using thin slices can provide reliable water desorption isotherm for mortars.

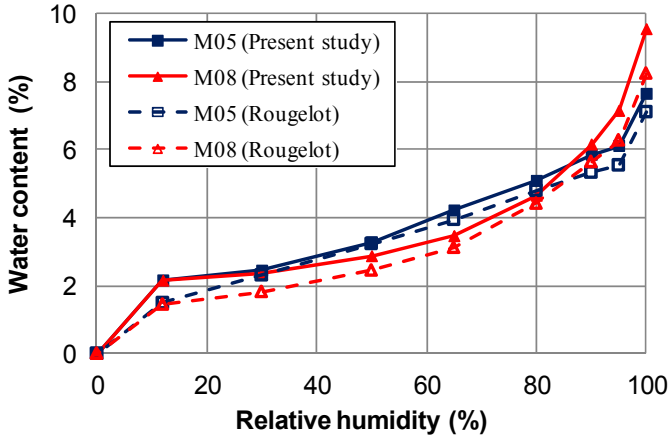

Figure 4. Comparison of water vapor desorption isotherms for two mortars at T = 20°C with the results of Rougelot et al. (2009).

3.3 Drying shrinkage

The evolution of drying shrinkage illustrated in Figure 5 represents the mean values calculated from 2 slices of 2 mm for each material. The cement paste (and mortar) with a higher W/C ratio exhibits a bigger drying shrinkage, since the elevation of W/C ratio leads to an increase in porosity and a decrease in rigidity. The mortar exhibits a smaller drying shrinkage than the cement paste with the same W/C ratio due to the presence of aggregates, which rigidify the matrix skeleton and reduce the paste volume (Bissonnette et al. 1999).

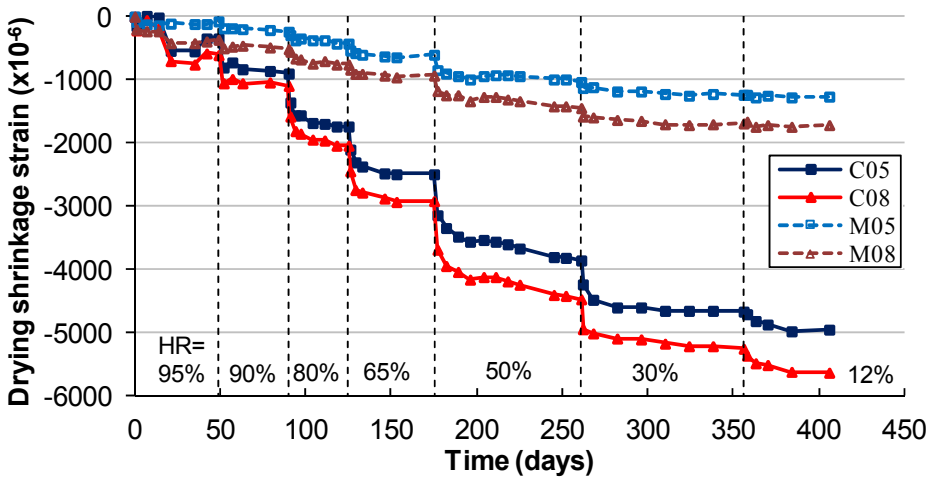

Figure 5. Evolution of drying shrinkage of cement pastes and mortars during a step-by-step desorption process at $T = 20°C$.

3.4 Correlation between drying shrinkage and relative humidity

The correlation between drying shrinkage and relative humidity is presented in Figure 6 for two cement pastes, together with the results of Rougelot et al. (2009). The ratio of the volume to the exposure surface area (V/A) is 0.9 mm in the present study and 4.7 mm in their study. The smaller V/A ratio and smaller specimen size ensure a more homogeneous moisture distribution and weaker moisture gradients in the slices during the drying process and consequently lead to fewer microcracks. The induced microcracks may hinder the shrinkage (Bažant et al. 1986) and lead to a smaller drying shrinkage in their study. The slopes of the curves decrease gradually as relative humidity decreases in their study. A different evolution of the slopes of two curves can be seen in the present study: they decrease as the relative humidity decreases gradually to 65%, increase as the relative humidity decreases from 65% to 50% and then decrease again with the relative humidity.

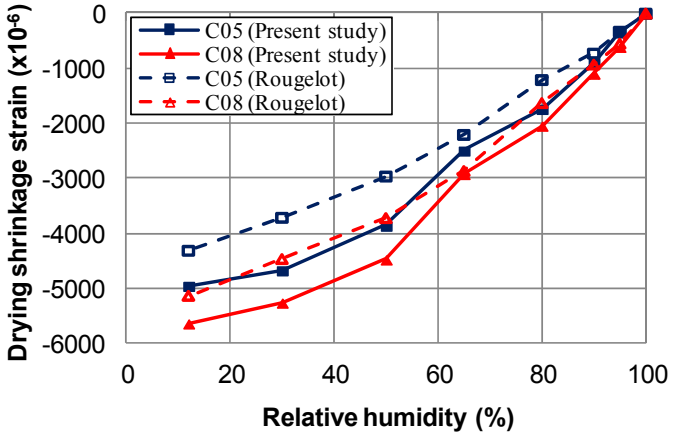

Figure 6. Comparison of the correlation between drying shrinkage and relative humidity for two cement pastes with the results of Rougelot et al. (2009).

The correlation between drying shrinkage and relative humidity is presented in Figure 7 for two mortars and is compared with the results of Rougelot et al. (2009). Similar to cement pastes, the mortars in the present study exhibit a bigger drying shrinkage due to a smaller V/A ratio and a smaller specimen size. The tendency of evolution of the slopes of curves for mortars is very similar to that for cement pastes.

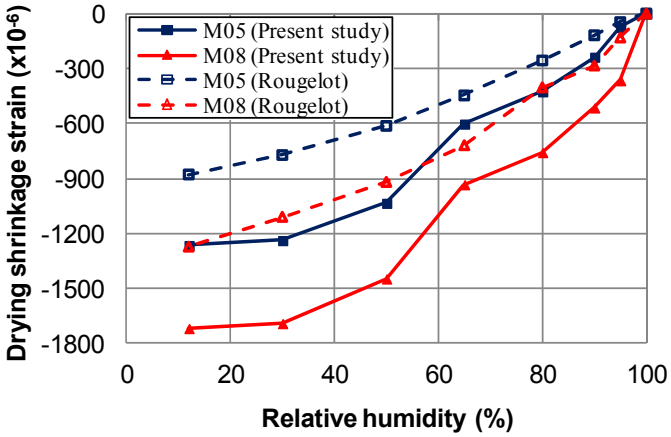

Figure 7. Comparison of the correlation between drying shrinkage and relative humidity for two mortars with the results of Rougelot et al. (2009).

3.5 Correlation between drying shrinkage and relative mass variation

Figure 8 presents the correlation between drying shrinkage and relative mass variation of two cement pastes. The last point of each curve, denoted "dried sample", corresponds to the drying shrinkage measured after oven-drying at 90 °C until mass stabilization. The curves consist in two almost linear parts with different slopes for both cement pastes: a smaller slope for RH > 30% and a bigger slope for RH < 30%.

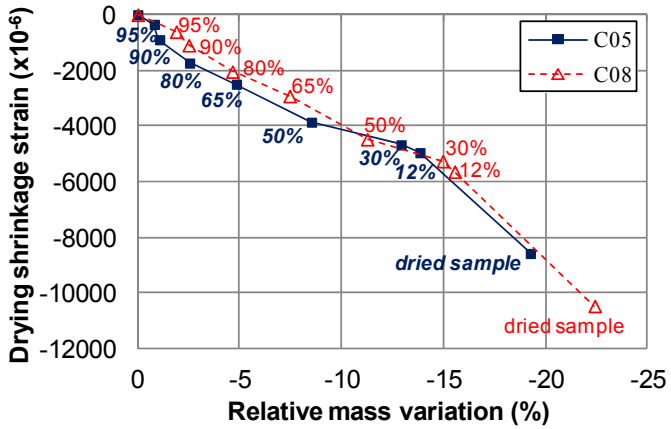

Figure 8. Correlation between drying shrinkage and relative mass variation for two cement pastes.

The correlation between drying shrinkage and relative mass variation of two mortars is given in Figure 9. Three distinct characteristic phases can be observed for M05, similar to the observations of Yurtdas et al. (2004). In the first phase (RH > 95%), the

water mass loss causes little shrinkage, since this water mainly comes from large capillary pores. In the second phase (50% < RH < 95%), the drying shrinkage is approximately proportional to the water mass loss with a much bigger slope than the first phase, which could be mainly attributed to the contraction of solid skeleton induced by capillary depression (Coussy et al. 2004). The third phase corresponds to a weaker drying shrinkage in spite of high water mass loss, which can be explained either by a nonlinear mechanical behavior of mortar (Meftah et al. 2000), or by the appearance of microcracks generated by the presence of aggregates and desiccation. The induced microcracks may promote the water mass loss and hinder the shrinkage (Bažant et al. 1986). Three phases can also be observed for M08: a smaller slope for RH > 65%, a bigger slope for 30% < RH < 65% and a smaller slope for RH < 30%.

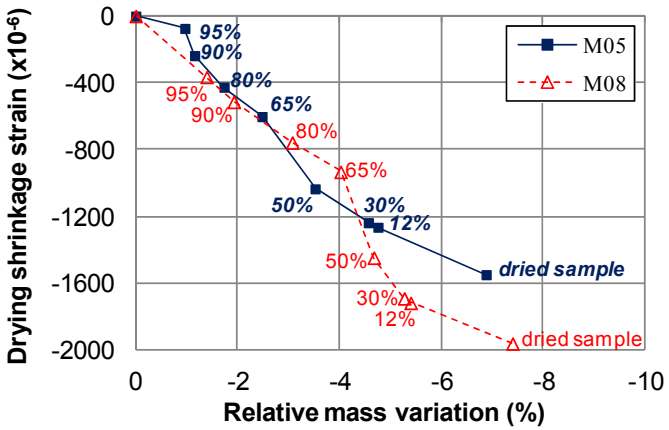

Figure 9. Correlation between drying shrinkage and relative mass variation for two mortars.

4. Conclusions

The main experimental results are summarized as follows:

(i) The slice thickness has an impact on the relative mass variation for some materials, but the difference between 2 mm slices and 3 mm slices remains very small or even negligible.

(ii) The results of water vapor desorption isotherms in the present study compare well with a former study on larger prismatic beams: the shape and the tendency of isotherms are very similar. However, the curing condition influences the water desorption isotherm: the water content in the present study is always higher due to the creation of new surfaces of slices, an increase in porous connectivity and a much longer curing period, allowing further hydration and saturation of slices.

(iii) The size effect is pronounced for drying shrinkage of materials tested: the drying shrinkage obtained with slices is always bigger than larger prismatic beams due to a smaller V/A ratio and a smaller specimen size.

(iv) The correlation between drying shrinkage and water mass loss demonstrates two almost linear parts with different slopes for both cement pastes: a smaller slope for RH > 30% and a bigger slope for RH < 30%. It exhibits three characteristic phases for both mortars, in agreement with the commonly assumed drying shrinkage mechanism. The first phase presents a small drying shrinkage despite the water mass loss. In the second phase, the drying shrinkage is globally linear to the water mass loss. The third phase shows a small drying shrinkage with further water mass loss.

4 References

Baroghel-Bouny, V., Mainguy, M., Lassabatere, T. and Coussy, O. (1999). "Characterization and identification of equilibrium and transfer moisture properties for ordinary and high-performance cementitious materials." *Cem. Concr. Res.*, 29, 1225-1238.

Bažant, Z.P., Sener, S. and Kim, J.K. (1986). "Effect of cracking on drying permeability and diffusivity of concrete." *ACI Mater. J.*, 7, 351-357.

Bissonnette, B., Pierre, P. and Pigeon, M. (1999). "Influence of key parameters on drying shrinkage of cementitious materials." *Cem. Concr. Res.*, 29, 1655-1662.

Coussy, O., Dangla, P., Labassatère, T. and Baroghel-Bouny, V. (2004). "The equivalent pore pressure and the swelling and shrinkage of cement-based materials." *Mater. Struct.*, 37, 15-20.

Feldman, R.F., and Sereda, P.J. (1970) "A new model for hydrated cement and its practical implementations." *Eng. J.*, 53, 53–59.

Kovler, K. and Zhutovsky, S. (2006). "Overview and Future Trends of Shrinkage Research." *Mater. Struct.*, 39, 827-847.

Meftah, F., Torrenti, J. M., Nechnech, W., Bendoudjema, F. and de Sa, C. (2000). "An elasto-plastic damage approach for the modeling of concrete submitted to the mechanical induced effects of drying." *International RILEM Workshop on Shrinkage of Concrete (shrinkage 2000)*, Paris, France, 341-354.

Miyazawa, S. and Tazawa, E. (2000). "Influence of specimen size and relative humidity on shrinkage of high-strength concrete." *International RILEM Workshop on Shrinkage of Concrete (shrinkage 2000)*, Paris, France, 233-246.

Powers, T.C. (1968). "The thermodynamics of volume change and creep." *Mater. Struct.*, 1(6), 487–507.

Rougelot, T., Skoczylas, F. and Burlion, N. (2009). "Water desorption and shrinkage in mortars and cement pastes: Experimental study and poromechanical model." *Cem. Concr. Res.*, 39, 36-44.

Wittmann, F. (1968). "Surface tension, shrinkage and strength of hardened cement paste." *Mater. Struct.*, 1(6), 547–552.

Wu, Q., Rougelot, T., Burlion, N. and Bourbon, X. (2014). "Experimental investigation of the first desorption isotherm of a high performance concrete with thin sliced samples." *Constr. Build. Mater.,* 72, 389-397.

Yurtdas, I., Burlion, N. and Skoczylas, F. (2004). "Triaxial mechanical behaviour of mortar: Effects of drying." *Cem. Concr. Res.*, 34, 1131-1143.

Crack Initiation and Length Change in Modified Alkali Activated Slag Mortars

V. Bílek Jr.[1]; I. Havlíková[2]; L. Topolář[2]; P. Schmid[2]; H. Šimonová[2]; P. Frantík[2]; and Z. Keršner[2]

[1]Brno University of Technology, Faculty of Chemistry, Purkyňova 464/118, 612 00 Brno, Czech Republic. E-mail: xcbilekv@fch.vutbr.cz
[2]Ditto, Faculty of Civil Engineering, Veveří 331/95, 602 00 Brno, Czech Republic. E-mail: havlikova.i@fce.vutbr.cz; topolar.l@fce.vutbr.cz; schmid.p@fce.vutbr.cz; simonova.h@fce.vutbr.cz; kitnarf@centrum.cz; kersner.z@fce.vutbr.cz

Abstract

The aim of this paper was to quantify crack initiation and length change of ordinary Portland cement-based mortar and three types of alkali activated slag mortars: reference one that only slag was used as binder, the second one with same amount of slag and with shrinkage reducing admixture in amount 1 % weight of slag and the third one with 5 % weight of slag replaced by fluidized bed combustion fly ash. Czech standard sand consisting of three different fractions (fulfilling requirements of ČSN EN 196-1) was used in all mixtures. The sand to binder ratio was 2:1 and water to binder ratio was 0.40 in all mixtures. Curing and length change testing of the specimens were based on ASTM C596-07 and ASTM C490-7. After demolding and three days of water curing mortar prisms were placed in air storage for 24 days. During this period length change (shrinkage) was measured. After that the three point bending test was performed on these specimens at the age of 28 days to obtain the fracture parameters, which was determined via Double-*K* fracture model. The initiation of cracks during the fracture tests was also monitored by the acoustic emission method. For comparison, specimens cured in water until the age of 28 days were tested in the same manner.

INTRODUCTION

Binders based on ordinary Portland cement (OPC) are the most commonly used in concrete production. However, manufacturing process of cement significantly contributes to the global emissions of CO_2. On average approximately one tonne of CO_2 is liberated per tonne of cement produced (Aïtcin and Mindess 2011). As a consequence, there has been an increasing effort to develop some alternative binders like alkali activated slag (AAS) during the recent decades.

Materials based on AAS can be similar or ever better than materials based on OPC in terms of mechanical properties (Collins and Sanjayan 1999), durability in aggressive environments (Bakharev et al. 2003; Bakharev et al. 2002) and resistance to elevated temperatures (Wang et al. 2014). On the other hand use of conventional chemical admixtures for workability improvement is complicated in the case of AAS (Palacios and Puertas 2011). Another big challenge is to deal with high shrinkage of

AAS, which was reported to be significantly higher than that of OPC and is considered as one of the main limitations for AAS use in practice (Melo Neto et al. 2008).

In order to reduce shrinkage, many less or more successful attempts including utilization of fibres (Alcaide et al. 2007), shrinkage reducing admixtures (Palacios and Puertas 2007) or mineral admixtures (Aydin 2013) etc. have been done. Yuan et al. (2014) investigated influence of expanding agent containing anhydrite and quick lime for compensating shrinkage of AAS. Drying shrinkage decreased as content of expanding agent increased. Despite the absence of portlandite in the hydration products of neat AAS, they concluded that, when expanding agent was used, formation of portlandite was shrinkage compensating mechanism, while ettringite was not detected.

The aim of this study was to investigate the influence of fluidized bed combustion (FBC) fly ash and shrinkage reducing admixture (SRA) on shrinkage and fracture parameters of AAS.

EXPERIMENTAL DETAILS

Materials and specimens preparation. Granulated blast furnace slag from Czech production with specific surface 380 m^2/kg was used as a reference binder. Slag consisted of amorphous phase with traces of melilite and merwinite. Slag binder was modified (partially replaced) by FBC fly ash (5 %). Phase composition of fly ash was determined by X-ray diffraction. Main phases found in fly ash were anhydrite, quartz, glassy phase, free lime, portlandite and calcite. Moreover, commercial SRA designed for OPC systems, based on 2-methyl-2,4-pentandiol, was added to the reference binder at dosage 1 % by mass of slag. Waterglass with silicate modulus equal to 1.85 was used as an activator. Na_2O/slag ratio was 0.042 by mass. Czech standard siliceous sand (fulfilling requirements of ČSN EN 196-1) was used as a fine aggregate. Mortar specimens were prepared with a mass proportion of binder:sand:water of 1:2:0.40. After the four minutes of mixing the mortar was cast into the steel moulds for preparation of prisms with dimensions 25×25×285 mm.

Based on the composition mentioned above, prepared specimens were as follows: six specimens from Portland cement mortar (marked by PC), six (reference) specimens, in which only slag was used as binder (marked by R), six specimens with same amount of slag and with 1 % of SRA (marked by S1), and seven specimens with partially replacement of slag by FBC fly ash (marked by L).

Fracture tests. Quantification of mechanical fracture parameters was performed using the three-point bending tests, which were conducted on beams with a central edge notch. The geometry of a specimen used in this test is shown in Figure 1 (left), where D is the specimen depth, B the width, L the length, S the span; a_0 is the initial notch length, H_0 the thickness of the edge of the holder clip on the extensometer and $CMOD$ the crack mouth opening displacement at load P. Specimens were cut from origin beams, the nominal dimensions of the specimens were 25×25×200 mm; span length was equal to 150 mm. The initial notch was made by a diamond blade saw. Note that the depth of the notches was about 1/3 of the specimen depth. Specimen's

age was 28 days. Fracture tests were carried out using a Heckert FP 10/1 testing machine within the range of 0–400 N. Load versus crack mouth opening displacement (*P–CMOD*) diagrams and also acoustic emission signals were recorded during the fracture tests.

METHODS

Measurement of length change. 24 hours after the mixing, mortar prisms were demoulded and immersed in water. After the three days of water curing, three specimens from each mixture (four specimens in the case of mixture L) were taken out and air cured at approximately 50 % relative humidity and 25 °C until the age of 28 days. Another three specimens were stored in water for the whole time. During this air/water curing length change were recorded in accordance with ASTM C490 (2011). Length change tests were performed every weekday.

Double-*K* fracture model. The mechanical fracture parameters of the tested materials were determined using Double-*K* fracture model (Kumar and Barai 2011). From above mentioned *P–CMOD* diagrams were deducted input data for this model, namely maximum load P_{max} and its corresponding critical crack mouth opening displacement $CMOD_c$, and load P_i deducted from the linear part of diagram and its corresponding crack mouth opening displacement $CMOD_i$, see Figure 1 (right).

The Double-*K* model combines the concept of cohesive forces acting on the faces of the effective crack increment with a criterion based on the stress intensity factor. The unstable fracture toughness K_{Ic}^{un} was determined first, followed by the cohesive fracture toughness K_{Ic}^{c}. When both of these values were known, the following formula was used to calculate the initiation fracture toughness K_{Ic}^{ini}:

$$K_{Ic}^{ini} = K_{Ic}^{un} - K_{Ic}^{c}.$$

Details regarding the calculation of both unstable and cohesive fracture toughness can be found in numerous publications e.g. in Kumar and Barai 2011.

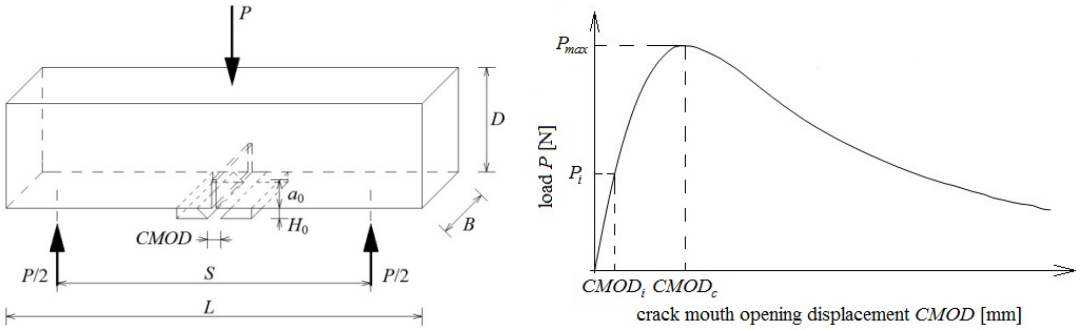

Figure 1. Three-point bending fracture test geometry (left), deduction of input data for the Double-*K* model from the *P–CMOD* diagram.

Finally, the value of the load P_{ini} was determined according to following equation. This value can be defined as the load level at the beginning of stable crack propagation from the initial crack/notch:

$$P_{ini} = \frac{4WK_{Ic}^{ini}}{SF_1(\alpha_0)\sqrt{a_0}}, \text{ where } F_1(\alpha_0) = \frac{1.99 - \alpha_0(1-\alpha_0)(2.15 - 3.93\alpha_0 + 2.7\alpha_0^2)}{(1+2\alpha_0)(1-\alpha_0)^{3/2}},$$

W is section modulus determined as $W = 1/6BD^2$, B is the specimen width, D is the specimen depth, S is the load span, $F_1(\alpha_0)$ is geometry function, α_0 is the ratio a_0/D, and a_0 is the initial notch length.

Acoustic emission method. Acoustic emission (AE) is the term for the noise emitted by material and structures when they are subjected to stress. Types of stresses can be mechanical, thermal or chemical. This emission is caused by the rapid release of energy within a material due to events such as crack formation, and the subsequent extension occurring under an applied stress, generating transient elastic waves which can be detected by piezoelectric sensors. AE method can monitor change in materials behaviour over a long time and without moving one of its components i.e. sensors. This makes the technique quite unique along with the ability to detect crack propagation occurring not only on the surface but also deep inside the material. The AE method is considered to be a "passive" non-destructive technique, because usually identifies defects while they are developing during the test (Grosse and Ohtsu 2008).

RESULTS AND DISCUSSION

Length change and fracture parameters. Mean values (and coefficients of variation) of the length change and selected fracture parameters obtained using Double-K fracture model are summarized in Table 1: relative length change at the age of 14 and 28 days $\Delta l_{14\ \text{days}}$ and $\Delta l_{28\ \text{days}}$, respectively; elasticity modulus E; effective crack elongation $a_c - a_0$; fracture toughness K_{Ic}^{un}; and the K_{Ic}^{ini}/K_{Ic}^{un} ratio, i.e. the ratio expressing the resistance to stable crack propagation.

As can be seen from Table 1, all the air-cured specimens showed negative relative deformation values, which indicated that they shrank. This is also true for all the alkali activated specimens submerged in water, although the extent of shrinkage was much lower than that of air-cured specimens. Only PC mortar cured in water expanded very slightly and absolute value of this expansion was 2–5 times lower than the absolute values of shrinkage of the alkali activated mortars cured at the same conditions. This is in contrast with some results mentioned in the state of the art report (Provis and van Deventer 2014), where slight expansion of AAS mortar specimens was observed compared to a slight shrinkage in OPC-based materials.

When air-cured, the mortar containing FBC fly ash exhibited very similar shrinkage values to those of the reference mortar, while when the SRA was used, shrinkage was reduced by 85 %. However, SRA also significantly reduced the fracture toughness in comparison with the reference mortar. In the case of PC mortar, the same shrinkage as for the S1 mortar was detected. The other two AAS mortars exhibited more than six times higher drying shrinkage than PC mortar.

Water curing of AAS based mortars resulted in increase of most of the fracture parameters, which indicates that water curing provides better conditions for the binder evolution than air curing. Modulus of elasticity and fracture toughness were more sensitive to the type of curing for both L and S1 mortar than for R mortar.

The PC composites showed opposite behaviour in terms of curing type to the alkali activated composites, i.e. its fracture parameters generally decreased when cured in water as compared to the air curing. The differences in the evaluated parameters regarding the type of curing were lower for PC mortars than for AAS based mortars. Therefore, AAS based materials are likely more sensitive to the proper curing that PC based materials.

Table 1. Mean values of selected parameters (coefficients of variation in %).

parameter	type of curing	R	L	S1	PC
$\Delta l_{14\ \mathrm{days}}$ [%]	air	−0.641 (1.0)	−0.667 (2.0)	−0.068 (11.6)	−0.082 (1.8)
	water	−0.005 (6.8)	−0.024 (2.1)	−0.019 (1.0)	0.004 (0.0)
$\Delta l_{28\ \mathrm{days}}$ [%]	air	−0.726 (0.1)	−0.696 (1.7)	−0.110 (7.0)	−0.111 (7.0)
	water	−0.012 (19.1)	−0.020 (4.1)	−0.025 (2.3)	0.005 (9.4)
E [GPa]	air	7.15 (20.5)	6.56 (2.1)	7.72 (22.2)	28.46 (12.8)
	water	13.32 (23.6)	18.87 (4.0)	19.63 (8.8)	24.22 (9.5)
$a_c - a_0$ [mm]	air	2.51 (4.8)	2.76 (10.5)	2.08 (7.8)	2.15 (21.0)
	water	2.20 (20.7)	3.49 (11.1)	3.18 (19.8)	2.76 (14.9)
K_{Ic}^{un} [MPa·m$^{1/2}$]	air	0.364 (5.5)	0.290 (5.5)	0.170 (1.8)	0.794 (2.8)
	water	0.677 (6.1)	0.610 (7.5)	0.600 (7.0)	0.682 (11.9)
K_{Ic}^{ini}/K_{Ic}^{un} [–]	air	0.230 (35.4)	0.191 (16.8)	0.555 (4.4)	0.686 (4.4)
	water	0.499 (12.9)	0.235 (27.4)	0.410 (16.2)	0.603 (3.1)

Signals of Acoustic emission method measured during the fracture tests. For selected specimens the records of three-point bending test (*P–CMOD* diagrams) coupled with AE results (AE counts) and outputs from Double-*K* fracture model (load P_{ini}) are shown in the following Figures 2 to 12.

CONCLUSIONS

The aim of this study was to quantify the influence of fluidized bed combustion (FBC) fly ash and shrinkage reducing admixture (SRA) on the length change and fracture parameters of alkali activated slag (AAS) mortar and their comparison with those of PC mortar cured at the same conditions.

In case of water curing, both 5 % of FBC fly ash and 1 % of SRA increased the modulus of elasticity and effective crack elongation of AAS mortar and decreased its fracture toughness.

In case of air curing, SRA reduced shrinkage by about 85 %, while FBC fly ash did not affect it. PC mortar showed more than 6 times lower drying shrinkage than AAS mortar and significantly higher elasticity modulus value for both air and water curing. Fracture toughness value of air cured PC mortar was two times higher than that of reference AAS mortar, while for the water cured samples it was practically the same.

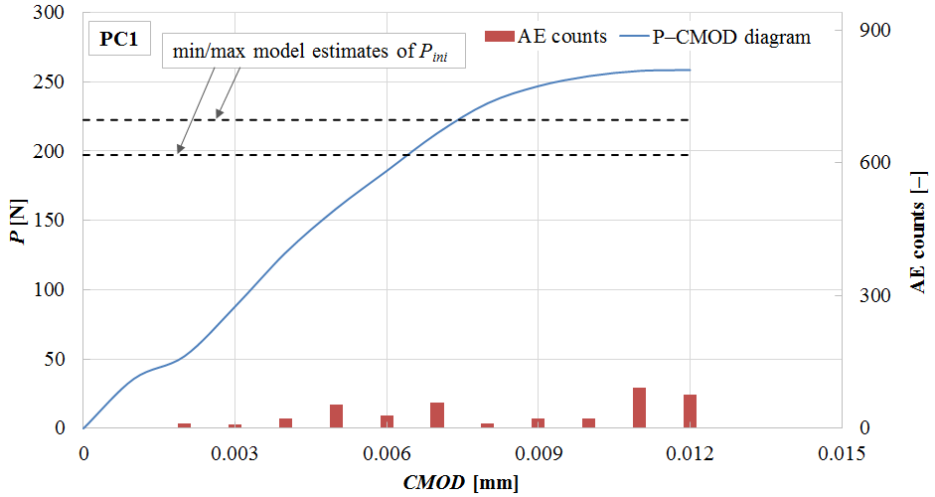

Figure 2. *P–CMOD* diagram with acoustic emission (AE) counts and load P_{ini} obtained using Double-*K* model for specimen PC1.

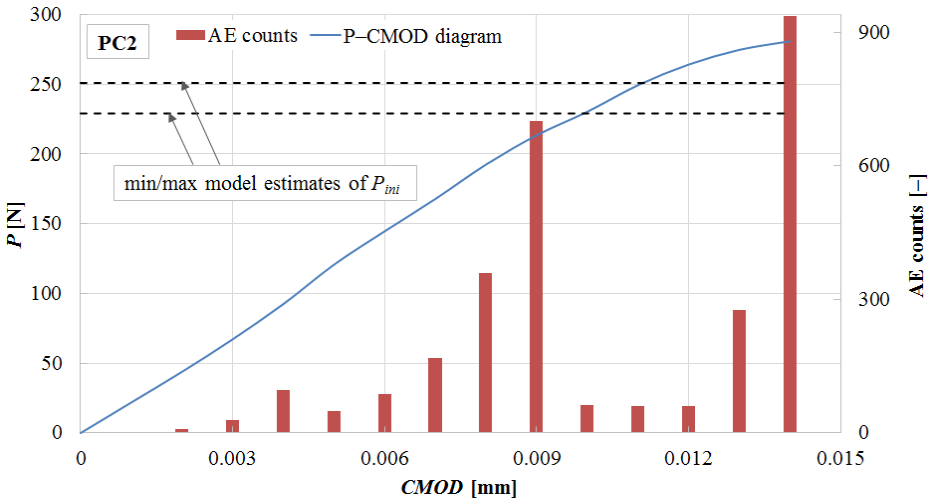

Figure 3. *P–CMOD* diagram with AE counts and load P_{ini} for specimen PC2.

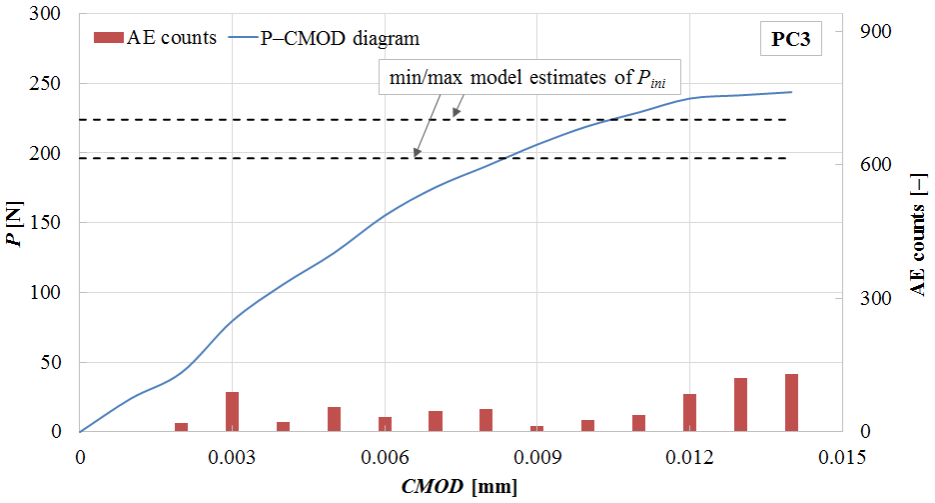

Figure 4. *P–CMOD* diagram with AE counts and load P_{ini} for specimen PC3.

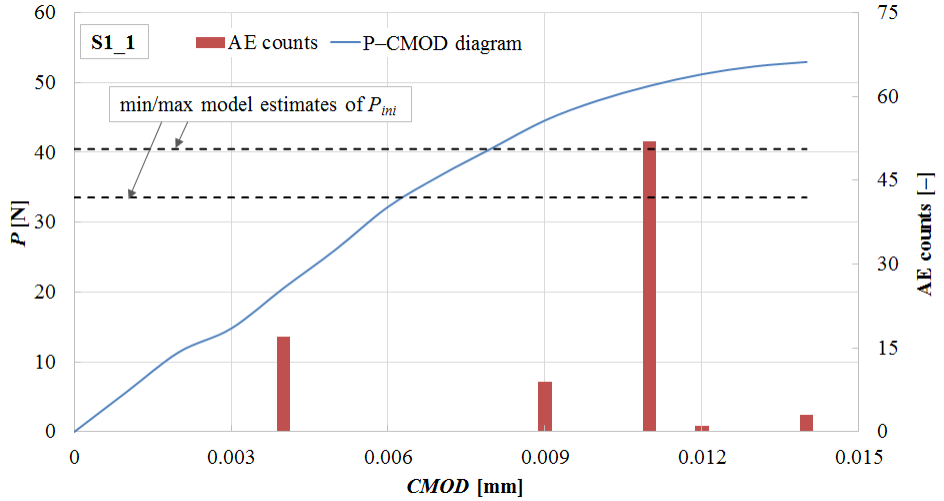

Figure 5. *P–CMOD* diagram with AE counts and load P_{ini} for specimen S1_1.

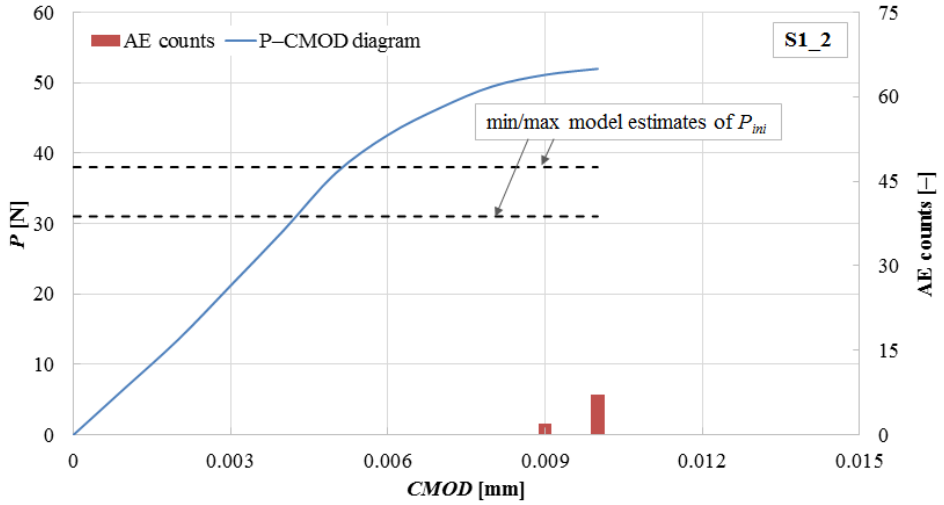

Figure 6. *P–CMOD* diagram with AE counts and load P_{ini} for specimen S1_2.

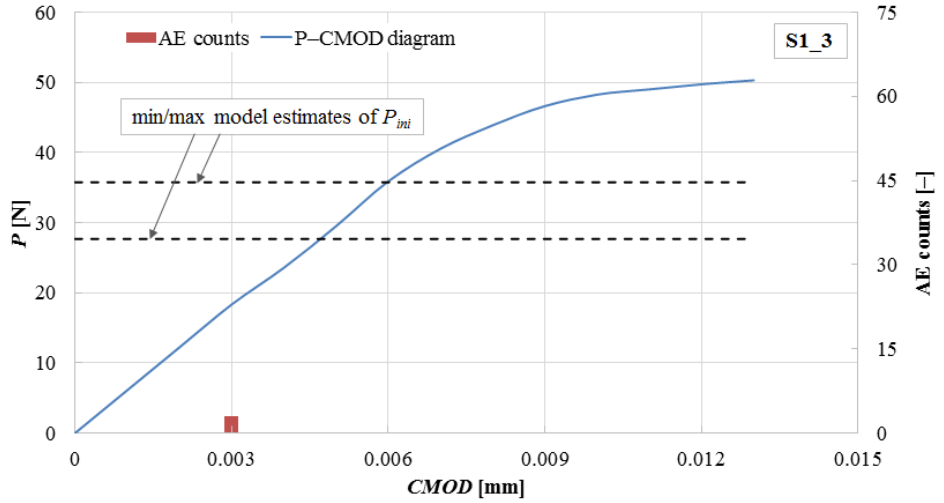

Figure 7. *P–CMOD* diagram with AE counts and load P_{ini} for specimen S1_3.

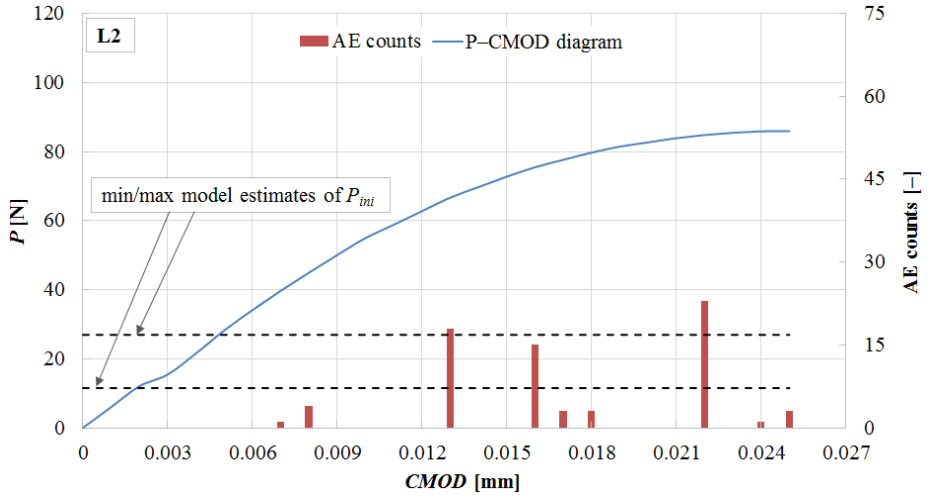

Figure 8. *P–CMOD* diagram with AE counts and load P_{ini} for specimen L2.

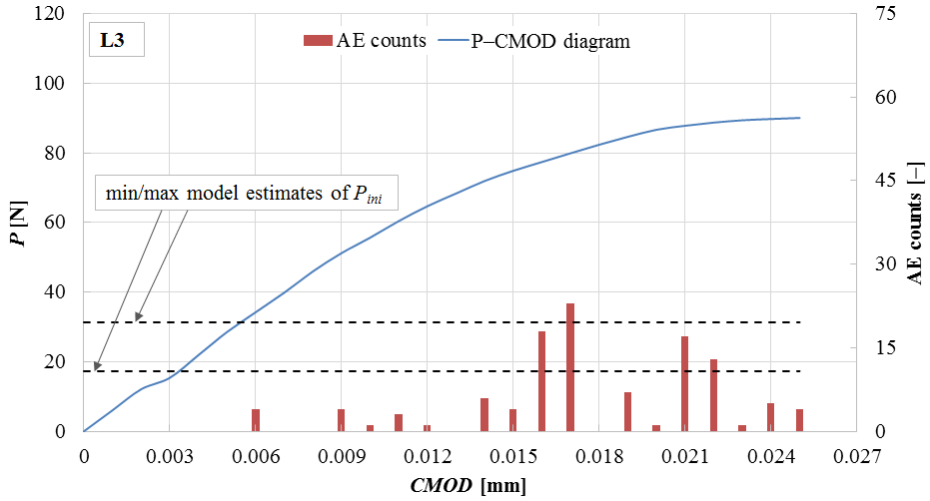

Figure 9. *P–CMOD* diagram with AE counts and load P_{ini} for specimen L3.

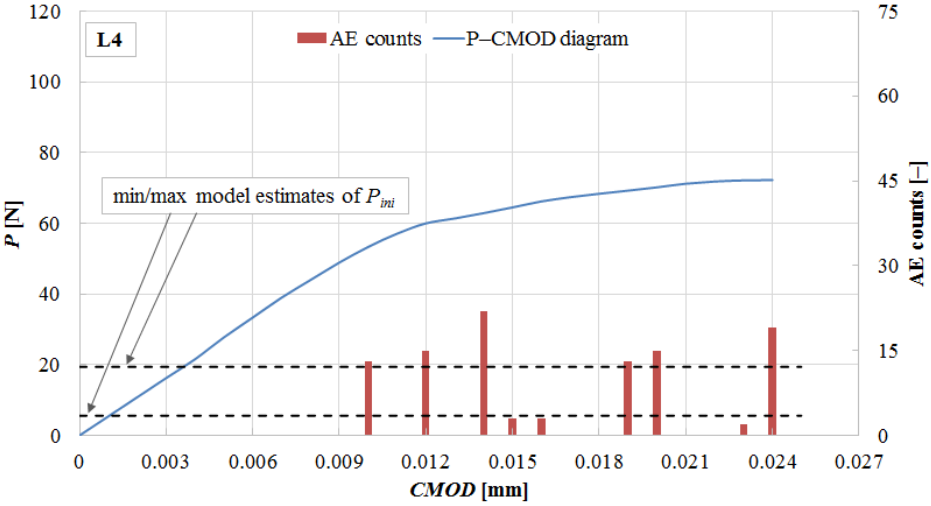

Figure 10. *P–CMOD* diagram with AE counts and load P_{ini} for specimen L4.

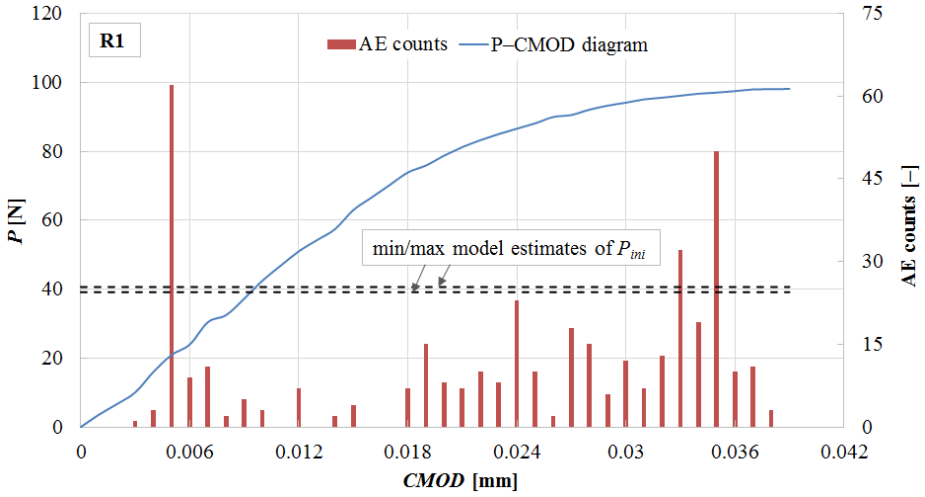

Figure 11. *P–CMOD* diagram with AE counts and load P_{ini} for specimen R1.

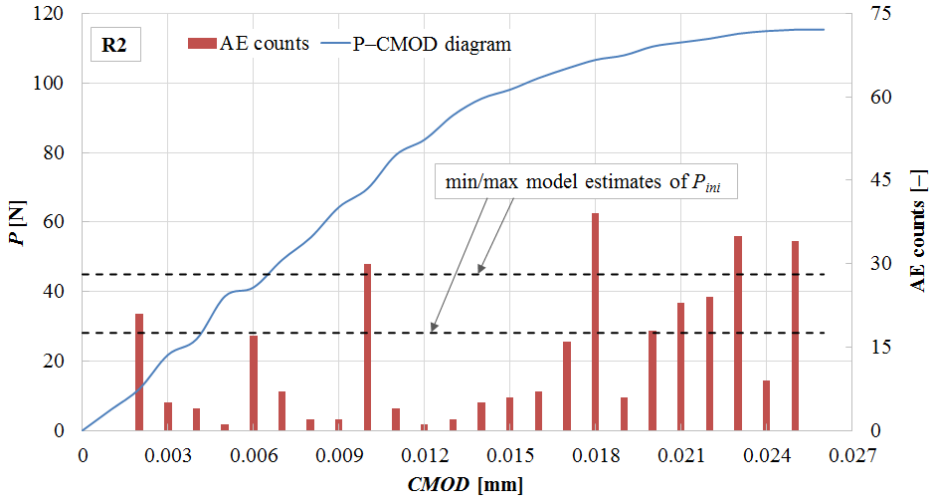

Figure 12. *P–CMOD* diagram with AE counts and load P_{ini} for specimen R2.

Curing method had a greater impact on the fracture parameters of AAS based mortars than on PC mortar. Fracture parameters of AAS were significantly higher in the case of water curing as compared to air curing (after the three days of water curing), while for PC based composites water curing for the entire time led to a slight decrease of fracture parameters in comparison with air curing.

From acoustic emission (AE) results is evident, that during first higher number of counts begins the stable crack propagation from the initial crack/notch. That means, this moment should correspond to the value of load P_{ini} – we can see in the above mentioned Figures that it is not agree exactly. This may be caused by incorrect parameter values of Double-*K* fracture model. So using AE results it will be possible to fit these parameters.

ACKNOWLEDGMENT

This outcome has been achieved with the financial support of the standard specific research program at Brno University of Technology, project No. FCH-S-15-2813, and

the project No. LO1408 "AdMaS UP – Advanced Materials, Structures and Technologies", supported by Ministry of Education, Youth and Sports under the „National Sustainability Programme I".

REFERENCES

Aïtcin, P.-C., and Mindess, S. (2011). *Sustainability of concrete*. New York: Spon Press, xxv, 301 p. Modern concrete technology, 17. ISBN 978-0-415-57196-8.

Alcaide, J. S., Alcocel, E. G., Puertas, F., Lapuente, R., and Garcés, P. (2007). "Carbon fibre-reinforced, alkali-activated slag mortars." *Materiales de Construcción*., 57(288), 33–48.

ASTM C490-07. Standard Practice for Use of Apparatus for the Determination of Length Change of Hardened Cement Paste, Mortar, and Concrete, ASTM International, West Conshohocken, PA.

ASTM C596-07. Standard Test Method for Drying Shrinkage of Mortar Containing Hydraulic Cement, ASTM International, West Conshohocken, PA.

Aydin, S. (2013). "A ternary optimisation of mineral additives of alkali activated cement mortars." *Constr. Build. Mater*., 43, 131–138.

Bakharev, T., Sanjayan, J. G., and Cheng, Y.-B. (2003). "Resistance of alkali-activated slag concrete to acid attack." *Cem. Concr. Res.,* 33(10), 1607–1611.

Bakharev, T., Sanjayan, J. G., and Cheng, Y.-B. (2002). "Sulfate attack on alkali-activated slag concrete." *Cem. Concr. Res*., 32(2), 211–216.

Collins, F. G., and Sanjayan, J. G. (1999). "Workability and mechanical properties of alkali activated slag concrete." *Cem. Concr. Res*., 29(3), 146–175.

Grosse, Ch. U., and Ohtsu, M. (2008). *Acoustic Emission Testing*, Springer-Verlag: Berlin, ISBN 978-3-540-69895-1, DOI 10.1007/978-3-540-69972-9.

Kumar, S., and Barai, S. V. (2011). *Concrete Fracture Models and Applications*, Berlin: Springer, 406 p.

Melo Neto, A. A., Cincotto M. A., and Repette W. (2008). "Drying and autogenous shrinkage of pastes and mortars with activated slag cement." *Cem. Concr. Res*., 38(4), 565–574.

Palacios, M., and Puertas F. (2011). "Effectiveness of Mixing Time on Hardened Properties of Waterglass-Activated Slag Pastes and Mortars." *ACI Mater. J*., 108(1), 106-145.

Palacios, M., and Puertas, F. (2007). "Effect of shrinkage-reducing admixtures on the properties of alkali-activated slag mortars and pastes." *Cem. Concr. Res*., 37(5), 691–702.

Provis, J. L., and van Deventer J. S. J., eds. (2014). *Alkali activated materials: state-of-the-art report, RILEM TC 224-AAM,* Dordrecht: Springer 388 p. ISBN 978-94-007-7671-5.

Wang, W. Ch., Wang, H. Y., and Lo, M.-H. (2014). "The engineering properties of alkali-activated slag pastes exposed to high temperatures." *Constr. Build. Mater*., 68, 409–415.

Yuan, X. H., Chen, W., Lu, Z. A., and Chen, H. (2014). "Shrinkage compensation of alkali-activated slag concrete and microstructural analysis". *Constr. Build. Mater.,* 66, 422–428.

Influence of Formwork Duration on the Shrinkage, Microstructure, and Durability of Cement Based Materials

H. Samouh[1]; E. Rozière[1]; and A.Loukili[1]

[1]Institut de Recherche en Génie Civil et Mécanique (GeM), UMR-CNRS 6183, Centrale Nantes, France. E-mail: hamza.samouh@ec-nantes.fr

Abstract

The quality of curing is a significant initial condition, which changes regularly during construction. A longer sealed curing results in higher strength and stiffness of concrete. It also provides a better durability and a lower carbonated depth. However, few studies deal with the influence of the duration of sealed curing on the long-term drying shrinkage and cracking sensitivity. In this paper, one self-consolidating concrete and one vibrated concrete, referred to as SCC and VC respectively are tested to study the effect of sealed curing duration on the long-term behaviour of concrete. The corresponding specimens were demolded after three different curing durations: 16, 24, and 48 hours. Total and autogenous shrinkages and mass-loss evolutions were monitored. Mercury intrusion porosimetry was performed in the three cases. The carbonated depth was measured after 6 months and one year. A long curing period actually gives more time to the cement to hydrate without water loss, and the pores become finer under these conditions. The application of the Kelvin-Laplace equation results in a higher stress for finer capillary pores. The experimental results confirmed this theoretical assumption, for a higher drying shrinkage for concrete associated with a longer sealed period. The experimental cracking sensitivity also increases with this duration owing to higher stiffness and shrinkage.

INTRODUCTION:

The study on the influence of boundary and initial conditions on long-term behaviour of cement based materials has two objectives: firstly understanding the influence of the actual construction site conditions on the long-term drying behaviour of concrete, and secondly figuring out how laboratory tests can be accelerated by changing the external relative humidity. The influence of formwork duration on shrinkage, microstructure, and durability of cement-based materials are studied here.

After a longer sealed curing concrete shows higher compressive and tensile strengths and stiffness owing to the better hydration of cement [1] [2] [3]. Based on these results and on the better durability for the concrete with a longer sealed curing [4], it is advised to keep the formwork or other curing as long as possible. Unfortunately, this approach does not take into account drying shrinkage and cracking sensitivity, which can be explained by the existing lack in published data on the subject.

Long formwork duration allows a good hydration of cement and a decrease in the free water content. Thus capillary pores became finer and the water that can be lost when concrete is exposed to drying decreases [5]. This paper deals with an experimental investigation on the influence of this initial condition on the concrete microstructure and long-term shrinkage and cracking sensitivity.

EXPERIMENTAL PROGRAM:

Two concrete compositions are studied, namely: one self-consolidating concrete (SCC) and one vibrated concrete (VC) presented in Table 1. Both series of specimens were demolded after 16, 24, and 48 hours in an air-conditioned room, with controlled temperature (20±1°C) and relative humidity (50±5%). Then the SCC specimens were subjected to compressive strength, splitting tensile strength tests, at ages of 16 h, 24 h, 48 h, 7 d, and 28 d. The static Young's modulus was measured in compression on cylindrical specimens (11x22 cm²) at 16 h, 24 h, 48 h, and 7 d (Table 2). Ring test was used to estimate the cracking sensitivity of the SCC. Finally, mass-loss, total and autogenous shrinkage of both concrete were measured on cylindrical specimens (7.8x28 cm²).

Table 1 Concrete mixtures

kg/m³	***SCC***	***VC***
Gravel (Amphibolite) 10/14 (G)	*290*	*875*
Gravel (Amphibolite) 6/10 (G)	*550*	*211*
Sand 0/4 (S)	*780*	*855*
Cement (C)	*330*	*303*
Limestone filler (A)	*210*	-
Superplasticizer	*2.8*	-
Water (W)	*205*	*182*
V_G/V_S	*0.92*	*1.1*
W/C	*0.62*	*0.60*
W/(C+A)	*0.38*	*0.60*
Paste volume (l/m^3)	*391*	*280*

Table 2 Influence of formwork duration on SCC strength

Test time	16 h			24 h			48 h			7 j			28 j		
formwork duration	f_c	f_t	E	f_c	f_t	E	f_c	f_t	E	f_c	f_t	E	f_c	f_t	E
16 h	9.7	1.0	18.2	12.2	x	20.5	20.5	2.0	29.0	28.9	3.0	34.1	34.5	2.6	x
24 h	-	-	-	16	1.8	21.8	23.2	2.2	28.8	31.3	2.9	33.7	35.7	2.9	x
48 h	-	-	-	-	-	-	21.5	2.0	29.3	32.3	3.0	37.9	34.5	3.6	x
Test time	10	1.2	12.8	17.4	1.7	22.0	24.4	2.4	24.7	x	x	x	35.4	4.0	31.4

Mercury intrusion porosimetry measurements were performed on 1.5-cm^3 samples of the material from the centre and the edge of the cylindrical specimens, which were exposed to drying for 6 months (the three study cases were considered). To tackle the durability issue, the carbonation depth was measured with phenolphthalein [6] after 6 months and 1 year of exposure.

EXPERIMENTAL RESULTS AND DISCUSSION

Free and restrained drying shrinkage:

The mechanical properties can be indicators of the influence of the formwork duration on hydration and microstructure evolution. Before 7 days, the Young's modulus value did not change for the three durations considered. However values were significantly higher after t_0 = 48 h. No considerable change was observed for compressive and splitting tensile strengths. These results can be explained by opposite effects of high water saturation and better hydration conditions on strength.

The results of water loss are predictable, since the specimens demolded after a shorter period of time loose a higher amount of capillary water [5] [7], as the drying starts during the hydration of cement. In the drying conditions of the study, the free water was released in an irreversible manner. A gap may remain at long-term between the mass-losses associated to the different formwork durations (Figure 1).

The beginning of the drying process influences the amount of water available for hydration. The longer the formwork duration the higher the hydration degree and the lower the water content available for drying.

The ultimate mass-loss of each specimen represents a part of the free water content of concrete, which cannot be used for the cement hydration because of evaporation. The ultimate mass-loss corresponds to the equilibrium between liquid and gaseous phases. It depends on the external relative humidity and the pore radius, according to Kelvin-Laplace equation. If specimens are demolded at different times, the final mass-loss is not the same. Specimens, which were demolded earlier showed higher mass-loss, correspond to higher free water content.

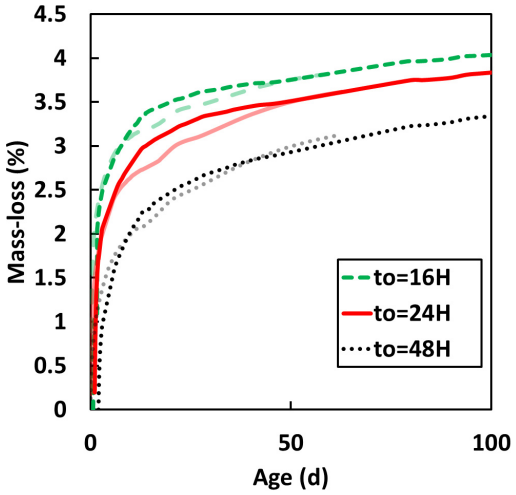

Figure 1 Mass-loss vs. Age for SCC

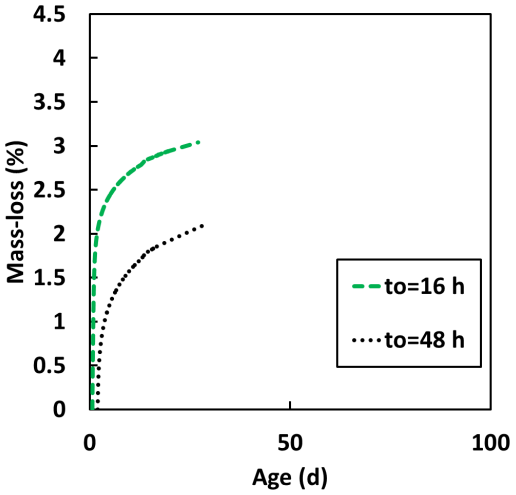

Figure 2 Mass-loss vs. Age for VC

The shrinkage measurements have been conducted twice on the same SCC mixture, and once on the vibrated concrete to get more reliable results. Whatever the data series, the long-term drying shrinkage was higher for specimens demolded after a longer time. This result can be surprising at first glance, as it is always recommended to keep the formwork or curing as long as possible to get better strength and durability. The shrinkage was not taken into account in these recommendations, and there is a lack of published results on this issue.

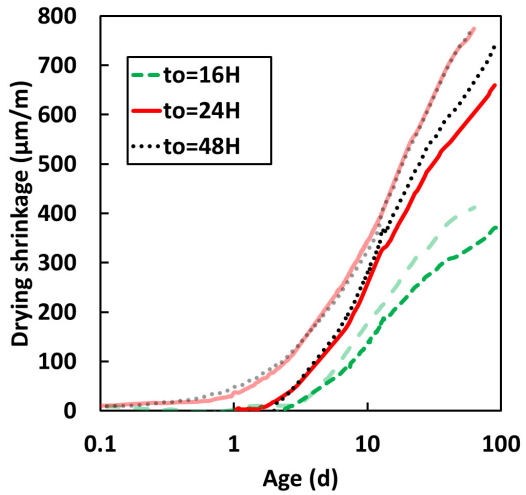

Figure 3 Drying shrinkage vs. Age for SCC

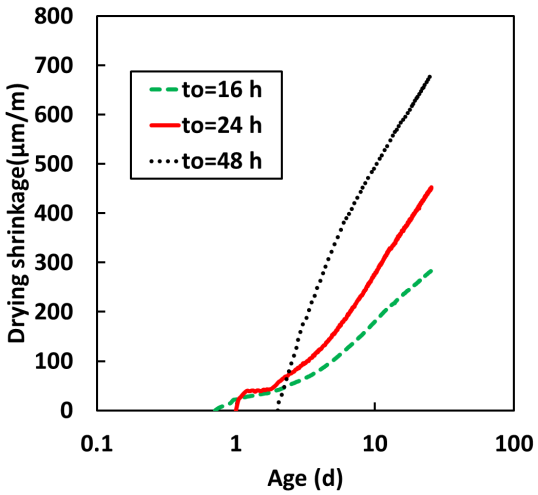

Figure 4 Drying shrinkage vs. Age for VC

Longer formwork duration of "48 h" specimens allowed a development of the porous network towards a finer porous microstructure. For a given water departure, finer pores lead to a higher capillary depression with Laplace equation (1), and thus to a higher drying shrinkage. From this point of view, it is consistent to get a higher

drying shrinkage for specimens demolded after longer formwork duration. This is confirmed by drying shrinkage vs. mass-loss curves plotted in Figures 5 and 6.

The first stage of the curves in Figures 5 and 6, which corresponds to the mass loss not inducing drying shrinkage, is shorter for specimens, which were kept for a longer time in formworks. For a sufficiently delayed formwork removal and a more mature material, this first stage seems to disappear.

$$\sigma_{cap} = \frac{2\sigma}{r} \cos \alpha_m \quad \textbf{(1)}$$

σ: surface tension of gas-liquid interface (σ = 72,75.10^{-3} N.m^{-1} for water) [N.m^{-1}], r: pore radius [m], and α_m: wetting angle [rad].

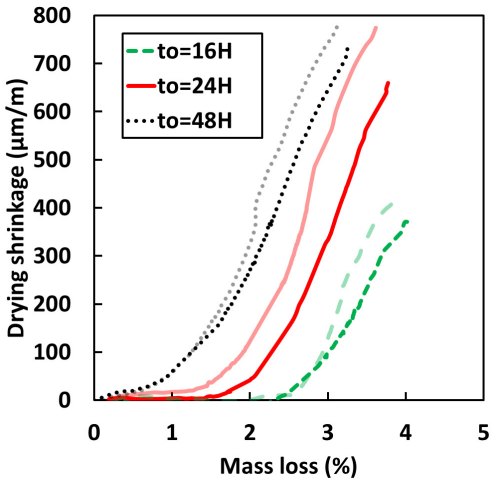

Figure 5 Drying shrinkage vs. mass-loss for SCC

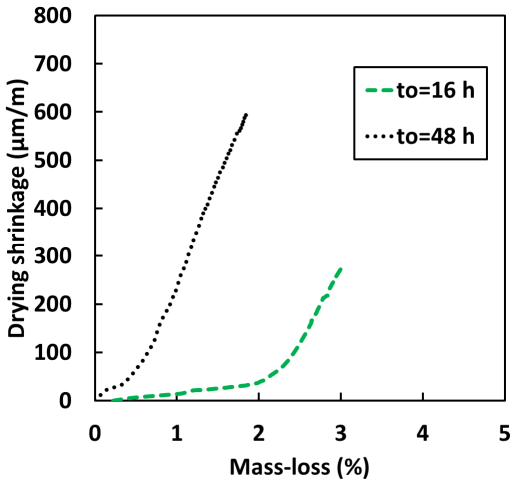

Figure 6 Drying shrinkage vs. mass-loss for VC

Cracking sensitivity

Figure 7 shows that cracking first occurs for the specimen demolded after 48 h, before specimen demolded after 24 h. No cracking was observed in the 16-h ring during the 4-month monitoring. The calculated stresses for the three cases are very close, and do not allow a clear distinction to classify concrete according to their cracking sensitivity. The influence of higher shrinkage due to delayed formwork removal was reinforced by the increase of stiffness due to better hydration, thus it resulted in increased cracking sensitivity.

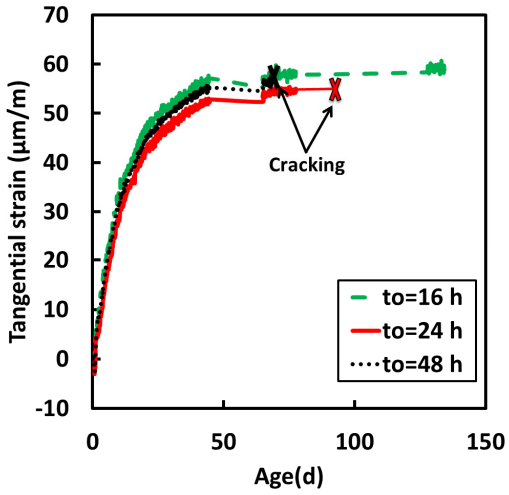

Figure 7 Strain of the ring vs. age for SCC

Microstructure and durability:

These last results seemed interesting, and could suggest that early formwork removal is the appropriate choice. However, this first part of the study does not take into account the durability issues. The phenomena leading to low drying shrinkage actually involve a relatively high carbonation risk. The measurements of the carbonated depths at 6 months or 1 year showed a 30% higher depth for t_0=16 h in comparison with t_0=48 h (Figures 8 and 9). Between 6 months and 1 year, a 6-mm increase of the carbonation depth was observed.

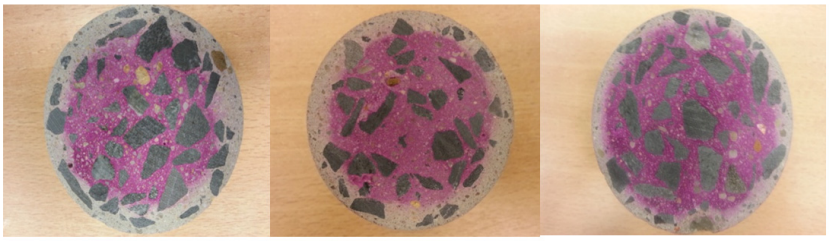

Figure 8 Carbonated depths after 6 months of exposure, from left to right: 16h, 24h and 48h

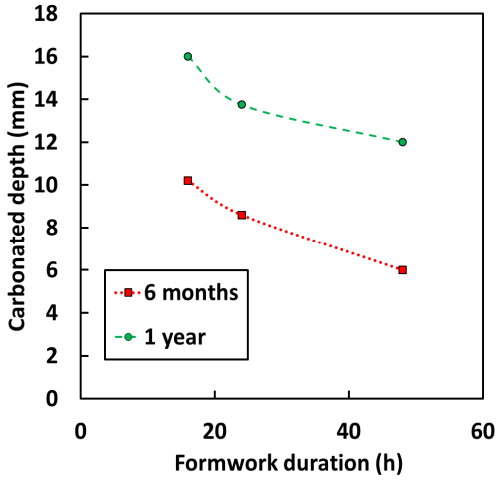

Figure 9 Carbonated depths vs. formwork duration for SCC

Mercury intrusion porosimetry was used to study the pore size distribution of the three sets of specimens. Small samples were picked from the middle and the edge of the cylinder. Two modes were observed (see figures 14 and 15). The first one concerns the finest porosity of less than 20 nm. It was not affected by the sealed curing duration. A longer drying time is actually needed to drain the smallest pores, and this long period favours the formation of small pores. The second mode corresponding to larger pores is clearly affected by the formwork duration even in the centre of the specimen (Figure 10). The longer the sealed curing duration is the more uniform the pores sizes become. This could be explained by the time taken by the drying to reach the centre of the cylinder. The modal peak then becomes thinner.

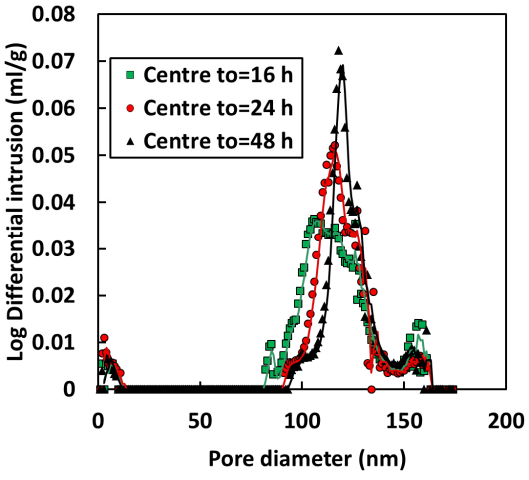

Figure 10 Differential mercury intrusion vs. pore diameter in the center of specimen for t_0 equal to 16h, 24h and 48h (SCC)

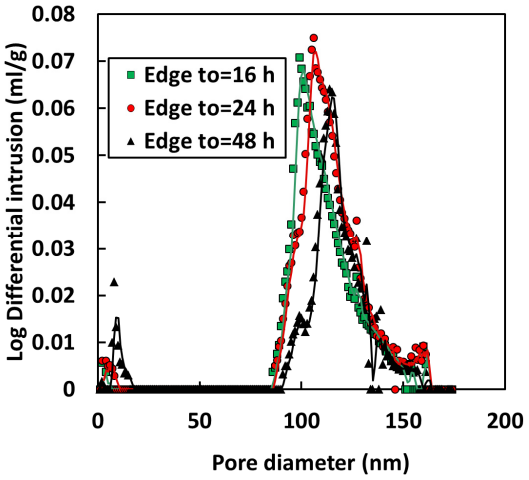

Figure 11 Differential mercury intrusion vs. pore diameter in the edge of specimen for t_0 equal to 16h, 24h and 48h (SCC)

The results of the samples taken from the edge are different. The first mode was actually affected by the sealed curing duration. For t_0=16h, a greater peak was noted, because the fine pores have more time to form. For the second mode, the area under the curve t_0=48 h is smaller, meaning a decrease in the pore volume. A decrease of the volume of pores with a diameter of less than 100 µm was observed.

The median pore diameter gives global quantitative information about the porosity and confirms this last result. Its value actually decreased with the formwork duration in both series at the edge and the centre of specimens (Figure 12). The median pore diameter is smaller in the centre where the hydration is less affected by drying. The shape of the two curves reminds us of the drying depth carbonation curve (Figure 9), thus the carbonation depth was plotted as a function of the median pore diameter in Figure 13. A linear increasing curve is observed between these two parameters in the centre and the edge of specimens after 6 months and 1 year.

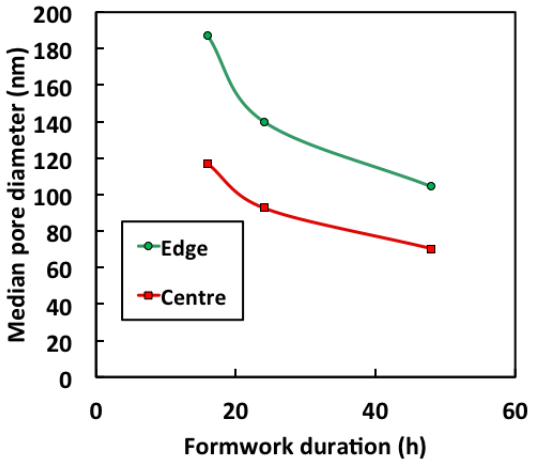

Figure 12 Median pore diameter vs. formwork duration in the centre and the edge of specimen

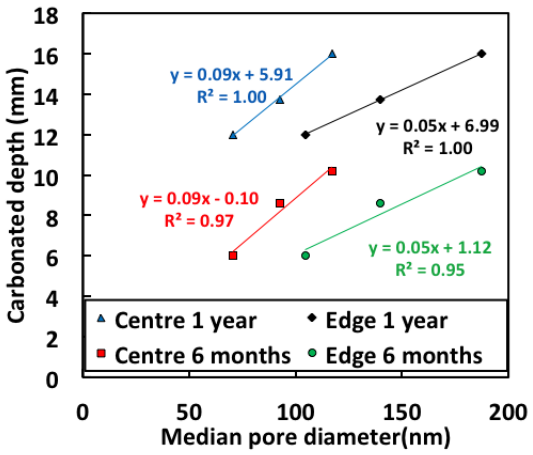

Figure 13 Carbonated depth vs. median pore diameter in the centre and the edge of specimen after 6 months and 1 year

The earlier the removal of formworks, the lower the degree of hydration is. Thus the free water content is higher, which leads to a more significant mass loss. If specimens are exposed to drying earlier, the hydration conditions are different between the middle and the edge and significant differences can be observed for the pore diameter in these two positions. For the same reasons, median pore diameter is bigger when the sealed curing duration is low, which can also explain the low drying shrinkage and cracking sensitivity. Table 3 shows the influence of the demolding time on the general concrete behaviour. The consequences of early demolding can be summarized as follows:

- Higher carbonation depth,
- Lower capillary stresses, as described by Laplace's law, inducing a lower drying shrinkage,
- Lower cracking sensitivity.

Table 3 Influence of the formwork duration on global behaviour of SCC

Formwork duration	*Drying shrinkage*	*Mass-loss*	*Median pore diameter*	*Carbonation depth*	*Difference for the median pore diameter: middle & edge*	*Young's modulus*	*Cracking sensitivity*
16 h	+	+++	+++	+++	+++	+	+
24 h	++	++	++	++	++	++	++
48 h	+++	+	+	+	+	+++	+++

CONCLUSIONS & PERSPECTIVES

Longer formwork duration provides concrete with a better strength, a higher stiffness, lower mass-loss and measured carbonation depth, after 6 months and one year in drying conditions. Prima facie these results are positive, but they do not take into account drying shrinkage and cracking sensitivity. The obtained experimental results show a higher shrinkage for a longer formwork duration (t0=48h), which can be explained through mercury intrusion porosimetry tests. After a longer casting duration the porosity network actually becomes finer due to the further progress of the cement hydration. For a given water loss, the resulting drying shrinkage can be higher as shown in the shrinkage vs. mass-loss curves. This shrinkage can induce cracking. The cracking sensitivity is all the more high that the stiffness is greater when the specimen is demolded after 48 h. The median pore diameter and the carbonation depth are affected in the same way by the formwork duration, and a linear correlation can be found between these two parameters. The increase in cracking sensitivity with the casting duration has been proven experimentally for the studied SCC. Accelerating the ring test by delayed demolding allows a cheaper solution in comparison with placing the ring under lower humidity in a climatic chamber. Finally, the same concrete mixture with different initial conditions can lead to several concrete microstructures with varying long-term behaviours.

REFERENCES

[1] Balayssac, Détriché, and Diafat, “Influence de la durée d’une cure humide sur les caractéristiques mécaniques de bétons d'usage courant (Effect of wet curing duration upon mechanical properties of commonly-used concretes),” *Mater. Struct.*, vol. 30, no. June, pp. 284–292, 1997.

[2] Al-Ani Samir H. and A.-Z. M. A.K., “The effect of curing period and curing delay on concrete in hot weather,” *Mater. Struct.*, vol. 21, pp. 205–212, 1988.

[3] I. Soroka, A. Bentur, and H. Jaegermann, “Short-term steam-curing and concrete later-age strength,” *Matériaux Constr.*, vol. 11, no. 62, pp. 93–96.

[4] *Cahier des clauses techniques générales applicables aux marchés publics de travaux. Fascicule N°65. Exécution des ouvrages de génie civil en béton armé ou précontraint*. 2012.

[5] Q. City, T. Adam, O. Kroggel, and P. Gruebl, "Influence of the relative humidity on the hydration kinetics of concrete," in *2nd International Symposium on Advances in Concrete through Science and Engineering 11-13 September 2006, Quebec City, Canada*, 2006, no. September.

[6] E. Rozière, A. Loukili, and F. Cussigh, "A performance based approach for durability of concrete exposed to carbonation," *Constr. Build. Mater.*, vol. 23, no. 1, pp. 190–199, Jan. 2009.

[7] B. Bissonnette, P. Pierre, and M. Pigeon, "Influence of key parameters on drying shrinkage of cementitious materials," *Cem. Concr. Res.*, vol. 29, no. July, pp. 1655–1662, 1999.

Chloride Penetration Profile of Polyvinyl Alcohol (PVA) Treated Oil Palm Shell (OPS) Concrete

C. C. Thong[1]; D. C. L. Teo[2]; and C. K. Ng[3]

Faculty of Engineering, Universiti Malaysia Sarawak, 94300 Kota Samarahan, Sarawak, Malaysia.
[1]E-mail: thong_cc38@hotmail.com
[2]E-mail: tdelsye@feng.unimas.my
[3]E-mail: ckng@feng.unimas.my

Abstract

Oil palm shell (OPS) is the hard endocarp which surrounds the palm kernel and received as crushed pieces during the extraction of palm oil. It is an agricultural waste and can be found in abundance in Malaysia. Economic and environmental benefits as well as decreasing the use of natural resources can be achieved if OPS can be utilised as a building material. Promising results showed that OPS has good potential to be used as coarse aggregate replacement in making structural lightweight concrete. It has also been previously established that polyvinyl alcohol (PVA) can be used to improve the properties of OPS concrete. Chloride induced reinforcement corrosion is an important area of study which needs to be investigated, especially for concrete structures exposed to marine environments. Therefore, this paper presents an experimental study on the chloride penetrability of PVA treated OPS concrete in comparison to that of raw OPS concrete using the 90-day salt ponding test. The effects of different curing conditions (full water curing, air-dry curing and site curing) on the chloride penetration resistance of PVA treated OPS concrete and raw OPS concrete were also studied. Both PVA treated OPS and raw OPS concrete surface were ponded with 3% sodium chloride solution up to 90 days, and the chloride profiles were measured by analysing concrete dust samples extracted from different depth intervals from the chloride exposed concrete surface. Subsequently, chloride diffusion coefficients were determined by fitting the experimental data to Fick's second law of diffusion. From the test results, it was found that PVA treated OPS concrete had high surface chloride concentration as compared to raw OPS concrete. However, PVA treated OPS concrete showed higher resistance to chloride penetration as compared to raw OPS concrete as indicated from the chloride diffusion coefficient. The results indicated that curing conditions also have a significant influence on the chloride resistance of PVA treated OPS concrete and raw OPS concrete.

INTRODUCTION

The high demand for concrete in building construction consumes large amounts of natural aggregates, such as gravel and granite, which has drastically reduced the stone deposits and caused a serious impact to the environment (Short & Kinniburgh, 1978). Therefore, there is a need to explore alternative materials (i.e. solid waste or by-product from different industries) that could be used to substitute the conventional coarse aggregates in concrete making.

Oil palm shell (OPS) is an agricultural solid waste generated from the palm oil industry. It is the hard endocarp that surrounds the palm kernel and received as crushed pieces during the extraction of palm oil (Chandra & Berntsson, 2003). It was reported that the oil palm planted area and the fresh fruit bunches (FFB) yield in Malaysia reached 5.23 million hectares and 19.02 tonnes per hectare respectively in 2013 (Malaysia Palm Oil Board, 2013). Chandra and Berntsson (2003) estimated that the weight of OPS waste generated is about 5.5% of the total weight of FFB yield. Consequently, it is approximated that 5.5 million tonnes of OPS waste is generated in Malaysia alone. Normally, this waste material is stockpiled and dumped which subsequently causes storage problems in the vicinity of the palm oil mills. This disposal method also pollutes the environment and may ultimately affect human health. Therefore, to preserve the environment from being polluted by this waste, researchers have taken an initiative to utilise OPS as coarse aggregate for concrete production (Alengaram et al., 2010; Mahmud et al., 2009; Mannan & Ganapathy, 2004; Okafor, 1988; Okpala, 1990; Shafigh et al., 2011; Teo et al., 2006; Yew et al., 2014).

Previous researches (Mannan & Ganapathy, 2004; Shafigh et al., 2011; Teo et al., 2006) have shown that OPS concrete has potential to be used in practical applications as it satisfies the minimum requirements in terms of compressive strength for structural lightweight concrete as recommended by ACI 213R-03. The mechanical strength of OPS concrete is dependent on various factors such as cement, water, sand and OPS aggregate content (Okafor, 1988; Okpala, 1990) and the size of OPS aggregate used (Alengaram et al., 2010). However, some researchers found that the strength of OPS concrete is governed by the strength of the OPS aggregate (Mahmud et al., 2009; Okafor, 1988) and the bond between the OPS aggregate and the paste (Okpala, 1990). Yew et al. (2014) reported that the strength of OPS aggregate is governed by its species (thickness and size) and Okpala (1990) found that the smooth surface textures of OPS aggregate is the factor that causes the bond failure of OPS aggregate and the paste. Therefore, several pre-treatment methods have been applied to improve the properties of OPS aggregate and consequently the resulting concrete (Kupaei et al., 2014; Mannan et al., 2006).

Polyvinyl alcohol (PVA) is a water soluble sythethic polymer and has been widely used in various applications, such as in textile sizing, paper processing, food additive, and also in the building industry. Mannan et al. (2006) reported that the physical properties and chemical resistance of OPS aggregate pre-treated with PVA

was significantly improved. The better adhesion between the PVA treated OPS aggregate and the paste can also be observed which results in the improvement of compressive strength (Mannan et al., 2006). Chai et al. (2014) also reported that the water absorption of PVA treated OPS concrete registered an improvement of up to 32.06% as compared to the raw OPS concrete. Therefore, the incorporation of PVA in concrete making could yield advantages in its durability performance.

Chloride induced reinforcement corrosion is a major cause that can lead to deterioration of reinforced concrete structures and a subsequent reduction in its strength and serviceability. This research aims to investigate the chloride penetrability of PVA treated OPS concrete under three different curing conditions. The chloride contents obtained from the 90-day salt ponding test were used to plot the chloride penetration profiles and subsequently the diffusion coefficient was determined by fitting the experimental data into Fick's second law of diffusion.

EXPERIMENTAL PROGRAM

Materials, Mix Proportion and Curing Conditions

The materials used in this study were ASTM Type 1 Portland cement, river sand, OPS (specific gravity: 1.32, maximum size: 12.5 mm) and water. The concrete mix proportion consists of 485 kg/m^3 cement, 786 kg/m^3 sand, 415 kg/m^3 OPS and water-cement (w/c) ratio of 0.42. The amount of polycarboxylate ether-type superplasticiser used was 1.3 l/ 100 kg which is within the recommended range provided by the manufacturer. In this study, OPS aggregates were used to fully substitute the conventional stone aggregates to produce concrete. Two forms of OPS aggregates were used which were raw OPS (untreated) and treated OPS aggregate with 5 % of PVA (PVA treated OPS).

The effect of curing conditions on the PVA treated OPS concrete and raw OPS concrete was also studied in this research. The three curing conditions adopted in this research were full water curing (CW), air-dry curing (CA) and site curing (CS). Immediately after casting, the concrete samples were covered with plastic sheet for 24 $\pm$ 4 hours to prevent excessive evaporation. After 24 $\pm$ 4 hours, all the concrete samples were demoulded and transferred to the respective curing conditions until the age of testing. CW is the normal type of curing practiced in the laboratory where the demoulded concrete samples were fully submerged in water (temperature =26 $\pm$ 2^{o}C). CA is the air-dry curing where the concrete samples were left in ambient laboratory conditions (temperature=26-32^{o}C, relative humidity=58-90%) immediately after demoulding until the age of testing. CS is to simulate the site curing conditions. For this curing condition, the demoulded concrete samples were covered with plastic sheet for two additional days at the exposure site, after which, the plastic sheet was removed and the concrete samples were left at the exposure site (temperature=26-49 ^{o}C, relative humidity= 26-99 %) until the age of testing.

Testing Regimes

The 90-day salt ponding test was conducted in accordance with AASHTO T 259-02. Concrete slab panels with dimensions of 350 mm (length) x 250 mm (width) x 75 mm (depth) were produced and cured in the respective curing conditions up to 28 days. After the specified curing period, the concrete slabs were removed from their curing environments and subjected to continuous ponding with 3% (w/v) of sodium chloride (NaCl) to a depth of 20 mm from the casting surface.

After 90 days of exposure, powdered samples were collected from the concrete slabs at depth intervals of 5 mm. The collected powdered samples were allowed to dry at 100 $\pm$ 5^{o}C until constant mass was obtained and then sieved passing through 300 μm before being used for chloride analysis. The sieved powdered samples were first digested using concentrated nitric acid and subsequently the chloride concentrations were determined by spectrophotometric method using mercuric thiocynate and the ferric ion solution as adopted by Herald et al. (1992). The chloride content (expressed in percentage by weight of cement) versus the depth intervals was plotted to obtain the chloride penetration profile. An approximate conversion of chloride by weight of concrete to chloride by weight of cement was done by direct proportioning the cement to concrete as outlined by Erdoğdu et al. (2004) and Roy et al. (1993). The obtained chloride profile was used to determine the coefficient of chloride diffusion using Fick's second law of diffusion from Equation 1.

$$\frac{C_x}{Cs} = 1 - \text{erf}\left\{\frac{x}{2\sqrt{D_e t}}\right\} \qquad \text{Eqn. (1)}$$

Where, C_x is the chloride concentration at distance x (%), C_s is the surface chloride concentration (%), x is the depth from concrete surface (cm), t is the time (s), D_e is the effective diffusion coefficient (cm^2/s), and erf is the Gaussian error function.

RESULTS AND DISCUSSION

Chloride Penetration Profiles

The chloride penetration profiles of PVA treated OPS concrete and raw OPS concrete under different curing conditions are shown in Figures 1 (a) and (b) respectively. It can be observed that the surface chloride concentration for PVA treated OPS concrete was higher than that of the raw OPS concrete. However, it can be seen that the chloride content of PVA treated OPS concrete drastically decreased with increasing depth intervals from the ponded concrete surface. Therefore, by comparing the trend of chloride penetration profiles, a steep chloride profile was obtained for the PVA treated OPS concrete, while a more gradual chloride profile was evident for the raw OPS concrete due to the gradual decrease in chloride content with increasing depth intervals. This trend existed for all curing conditions.

PVA treated OPS concrete cured under CS and CA conditions accounted the least amount of penetrated chloride, with 0.147% and 0.175% at 35-40 mm depth

interval respectively. However, the chloride concentration of PVA treated OPS concrete under CW condition was 1.25 times greater than that of CS condition at 35-40 mm depth interval. For raw OPS concrete, the chloride concentration at 35-40 mm depth interval was found approximately 1.16, 1.11 and 1.84 times higher as compared to the PVA treated OPS concrete under CW, CA and CS conditions respectively. These results show that for PVA treated OPS concrete there was an improvement in the resistance towards chloride penetrability, even though the surface chloride concentration was higher.

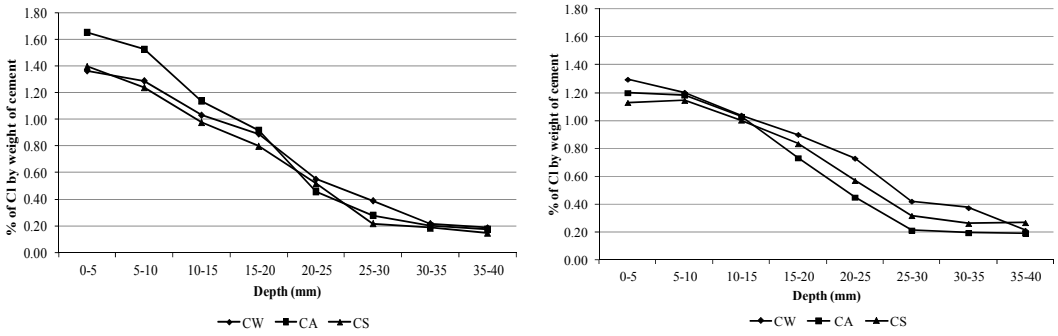

(a) (b)

Figure 1. The chloride penetration profile (a) PVA treated OPS concrete; (b) raw OPS concrete under different curing conditions.

Diffusion Coefficients

Diffusion is a common way of transport for chloride into concrete. It is caused by the movement of fluid from one part of a system to another part of the system due to the differential concentration of chloride (Neville, 1995). Therefore, diffusion coefficient is a parameter used to measure the effective rate of chloride ion penetration in concrete structures. The surface chloride concentration (C_s) obtained from the nonlinear curve fitting of chloride penetration profiles was used in the analysis of diffusion coefficient (D_e) by using Equation 1. The values of those parameters are presented in Table 1.

The analysis shows that the diffusion coefficients for PVA treated OPS concrete were in the range of 2.6695 to 4.72829 x 10^{-7} cm^2/s and for raw OPS concrete they were in the range of 4.21339 to 9.60153 x 10^{-7} cm^2/s respectively. This indicates that PVA treated OPS concrete had better resistance towards chloride penetration as compared to raw OPS concrete under all types of curing conditions. These results are also consistent with the results reported by Kou and Poon (2010) in which the resistance of chloride-ion penetration was significantly increased with the incorporation of the PVA-imprenagted recycled aggregate in the concrete mixes. From literature, the interfacial transition zone (ITZ) between the paste and the aggregate is identified as the preferential path for chloride ingress, as it is the most porous phase in concrete (Villagrán Zaccardi & Taus, 2011). Wan et al. (2006) reported that the thickness of the interfacial transition zone (ITZ) between the cement paste and the recycled aggregate treated with PVA at age 28 days was reduced.

Therefore, this may have been the case for PVA treated OPS concrete, where the reduced thickness of the ITZ in between the paste and PVA treated OPS aggregate, resulted in the improvement of chloride penetration resistance of PVA treated OPS concrete.

It has also been found that conventional concretes subjected to continuous ponding with 3.0% NaCl solutions for 90 days have diffusion coefficients in the range of 1.540 to 1.649 x 10^{-7} cm^2/s, 2.300 to 2.387 x 10^{-7} cm^2/s and 2.796 to 2.997 x 10^{-7} cm^2/s for concretes with w/c ratio of 0.45, 0.55 and 0.65 respectively (Yang, 2005). The results showed that the diffusivity for PVA treated OPS concrete is comparable to the conventional concrete subjected to continuous ponding with 3.0% NaCl solutions.

The rate of chloride penetration is also influenced by different curing conditions. The test results showed that the CA curing account for the lowest values of diffusion coefficients, followed by CS curing and CW curing for both PVA treated OPS concrete and raw OPS concrete. This may be due to the dry condition of the CA curing which promotes the film formation of PVA, and consequently increases the resistance of chloride ion diffusivity.

Table 1. The surface concentration and diffusion coefficient for PVA treated OPS concrete and raw OPS concrete under different curing conditions.

Concrete samples	*Curing conditions*	*Surface concentration, C_s (%)*	*Regression coefficient, R^2*	*Diffusion coefficient, D_e ($\times 10^{-7}$ cm^2/s)*
PVA treated OPS concrete	CW	1.6690	0.9783	4.72829
	CA	2.1676	0.9726	2.66950
	CS	1.7563	0.9786	4.38237
Raw OPS concrete	CW	1.4728	0.9848	9.60153
	CA	1.5702	0.9413	4.21339
	CS	1.3934	0.9392	6.10352

CONCLUSIONS

Based on the experimental investigation on the chloride penetration of PVA treated OPS and raw OPS concrete through the 90-day salt ponding test, the following conclusions can be drawn:

i. PVA treated OPS concrete registered higher surface concentration as compared to raw OPS concrete. However, a steep chloride profile was obtained for the PVA treated OPS concrete, while a more gradual chloride profile was evident for the raw OPS concrete.

ii. PVA treated OPS concrete registered lower diffusion coefficients as compared to raw OPS concrete under all curing conditions.

iii. Both PVA treated OPS and raw OPS concrete perform better in terms of chloride resistance under CA condition, followed by CS condition and CW condition.

ACKNOWLEDGEMENTS

The authors gratefully acknowledge the funding provided by Ministry of Education Malaysia under Fundamental Research Grant Scheme (FRGS) grant No. FRGS/TK04(01)/972/2013(13). The first author is supported by Zamalah Siswazah UNIMAS.

REFERENCES

AASHTO T 259-02. (2002). S*tandard method of test for resistance of concrete to chloride ion penetration*, American Associations of State Highway and Transportation Officials, Washington, DC.

ACI 213R-03. (2003). *Guide for structural lightweight-aggregate concrete*, American Concrete Institute, Detroit.

Alengaram, U. J., Mahmud, H., Jumaat, M. Z., and Shirazi, S. M. (2010). "Effect of aggregate size and proportion on strength properties of palm kernel shell concrete." *Int. J. Phys. Sci.*, 5(12), 1848–1856.

Chai, W. W. S., Teo, D. C. L., and Ng, C. K. (2014). "Improving the properties of oil palm shell (OPS) concrete using polyvinyl alcohol (PVA) coated aggregates." *Adv. Mater. Res.*, 970, 147–152.

Chandra, S., and Berntsson, L. (2003). *Lightweight aggregate concrete science, technology and application*, Noyes, Norwich, New York.

Erdoğdu, Ş., Kondratova, I. L., and Bremner, T. W. (2004). "Determination of chloride diffusion coefficient of concrete using open-circuit potential measurements." *Cem. Concr. Res.*, 34(4), 603–609.

Herald, S. E., Henry, M., Al-qadi, I. L., Richard, E. W., Feeney, M. A., Howlum, S. F., and Cady, P. D. (1992). *Condition evaluation of concrete bridges relative to reinforcement corrosion, volume 6 : method for field determination of total chloride content,* No. SHRP-S-328, Strategic Highway Research Program*,* National Research Council, Washington.

Kou, S. C., and Poon, C. S. (2010). "Properties of concrete prepared with PVA-impregnated recycled concrete aggregates." *Cem. Concr. Compos.*, 32(8), 649–654.

Kupaei, R. H., Alengaram, U. J., and Jumaat, M. Z. (2014). "The effect of different parameters on the development of compressive strength of oil palm shell geopolymer concrete." *Sci. World J.*, 2014, Article ID 898536, 16 pages.

Mahmud, H. Bin, Jumaat, M. Z., and Alengaram, U. J. (2009). "Influence of sand/cement ratio on mechanical properties of palm kernel shell concrete." *J. Appl. Sci.*, 9(9), 1764–1769.

Mannan, M. A., Alexander, J., Ganapathy, C., and Teo, D. C. L. (2006). "Quality improvement of oil palm shell (OPS) as coarse aggregate in lightweight concrete." *Build. Environ.*, 41(9), 1239–1242.

Mannan, M. A., and Ganapathy, C. (2004). "Concrete from an agricultural waste-oil palm shell (OPS)." *Build. Environ.*, 39(4), 441–448.

Malaysia Palm Oil Board (MPOB). (2013). "Overview of the Malaysian oil palm industry 2013". <http://bepi.mpob.gov.my/images/overview/Overview_of_Industry_2013.pdf> (Jan. 20, 2015).

Neville, A. M. (1995). *Properties of concrete*, 4th ed., Longman, London.

Okafor, F. O. (1988). "Palm kernel shell as a lightweight aggregate for concrete." *Cem. Concr. Res.*, *18*(6), 901–910.

Okpala, D. C. (1990). "Palm Kernel Shell as a Lightweight Aggregate in Concrete." *Build. Environ.*, 25(4), 291–296.

Roy, S. K., Liam, K. C., and Northwood, D.O. (1993). "Chloride ingress in concrete as measured by field exposure tests in the atmospheric, tidal and submerged zones of a tropical marine environment." *Cem. Concr. Res.*, 23(6), 1289–1306.

Shafigh, P., Jumaat, M. Z., Mahmud, H. Bin, and Alengaram, U. J. (2011). "A new method of producing high strength oil palm shell lightweight concrete." *Mater. Des.*, 32(10), 4839–4843.

Short, A., and Kinniburgh, W. (1978). *Lightweight concrete,* 3rd ed., Applied Science Publishers, London.

Teo, D. C. L., Mannan, M. A., and Kurian, V. J. (2006). "Influence of site curing on bond properties of reinforced lightweight concrete." *J. Civ. Eng. Res. Pract.*, 3(1), 9–19.

Villagrán Zaccardi, Y. A., and Taus, V. L. (2011). "Approximation by finite element method to the preferential chloride diffusion through interfacial transition zone in concrete." *Lat. Am. Appl. Res.*, 41(3), 285–290.

Wan, H. W., Yang, L. Y., and Shui, Z. H. (2006). "Modificatin of ITZ structure and properties of regenerated concrete." *J. Wuhan Univ. Technol.*, 21(2), 128–132.

Yang, C. C. (2005). "A comparison of transport properties for concrete using the ponding test and the accelerated chloride migration test." *Mater. Struct.*, 38(3), 313–320.

Yew, M. K., Bin Mahmud, H., Ang, B. C., and Yew, M. C. (2014). "Effects of oil palm shell coarse aggregate species on high strength lightweight concrete." *Sci. World J.*, 2014, Article ID 387647, 12 pages.

Evaluation of the Thermal Expansion Coefficient Using Non-Destructive Testing

Semion Zhutovsky[1] and Konstantin Kovler[2]

[1]Department of Civil Engineering, University of Toronto, 35 St. George St., Toronto, ON, Canada M5S 1A4. E-mail: semionz@yahoo.com
[2]Faculty of Civil and Environmental Engineering, Technion - Israel Institute of Technology, Haifa 32000, Israel. E-mail: cvrkost@technion.ac.il

Abstract

Coefficient of thermal expansion of concrete is an essential part of cracking risk analysis. A formula for coefficient of thermal expansion based on the theory of poromechanics was derived. This formula utilizes ultrasonic pulse velocity measurements. To validate the formula, ultrasonic pulse velocity and free shrinkage of cement paste with water to cement ratio of 0.33 were measured starting from the casting. A good agreement was found between the calculated values and the data found in the literature. In addition, the calculated coefficient of thermal expansion was applied for decoupling of thermal and autogenous shrinkage of cement paste. Decoupled linear autogenous shrinkage was compared to the measured volumetric autogenous shrinkage.

INTRODUCTION

Thermal deformations play significant role in early-age cracking sensitivity of concrete, especially for high-performance concrete (HPC), which has a high content of cementitious materials (Kovler and Zhutovsky 2006). Thus, determination of coefficient of thermal expansion (CTE) of concrete is a vital part of cracking risk analysis. Another important type of deformations in HPC is autogenous shrinkage.

Autogenous shrinkage received special attention, in recent years, in view of the increased research interest to the HPC, because autogenous shrinkage is considered by most researchers and practitioners as the Achilles heel of high-performance concrete (Kovler and Jensen 2005). Autogenous shrinkage is defined as isothermal macroscopic volume reduction during hydration of cementitious materials after the initial setting. Autogenous shrinkage does not include the volume change due to loss or ingress of substances, temperature variation, and application of external force or restraint. One of the most challenging issues in the research of autogenous shrinkage is how to separate it from thermal deformations. While it is relatively simple to prevent drying during shrinkage measurements, it is almost impossible to completely eliminate temperature changes of concrete in time and thermal gradients in a concrete cross-section. Decoupling of thermal and autogenous strains is a complicated task in view of considerable variation of CTE at early ages, and especially in the proximity of setting time. Monitoring of early-age changes of CTE is a complicated procedure, associated with a variety of technical problems. Thus, a

simplified approach to assess CTE is required. In the present paper, an approach to estimate CTE, using poromechanics theory and non-destructive testing, is suggested.

Modern poromechanics takes its origin from the pioneering works of Terzaghi on soil mechanics and the theory of poroelasticity of Biot. Recently, a number of researchers successfully applied poromechanics to ce mentitious materials (Coussy O. 2004, Coussy et al. 2004, Coussy and Brisard 2009). Poromechanics allows predicting the behavior of porous body based on the properties of the solid phase, pore fluid and porosity. A formula for coefficient of thermal expansion based on the theory of poromechanics was derived. This formula utilizes basic measurements that may be obtained by non-destructive testing such as ultrasonic pulse velocity measurements.

To validate the formula, ultrasonic pulse velocity and free shrinkage of cement paste with water to cement ratio of 0.33 were measured starting from the casting. Based on ultrasonic pulse velocity measurements, a dynamic bulk modulus was calculated and coefficient of thermal expansion was evaluated and compared to the literature data. A good agreement was found between the calculated values and the literature data. The calculated coefficient of thermal expansion is applied for decoupling of thermal and autogenous shrinkage of cement paste. Decoupled linear autogenous shrinkage was compared to the measured volumetric autogenous shrinkage.

THEORETICAL BACKGROUND

In order to assess cracking risk, determination of thermal and autogenous deformations is required. For this purpose, CTE has to be determined. At early ages, CTE of cement paste changes significantly. Thus, CTE of concrete cannot be just taken as a constant value for evaluation of thermal deformations. For this reason, the development of a method for the assessment of CTE of cement paste and concrete is an important research task.

Direct measurement of coefficient of thermal expansion is a difficult task. The use of buoyancy method is reported by several researchers for successful measurement of volumetric CTE (Loukili et al. 2000, Turcry et al. 2002, Loser et al. 2010, Wyrzykowsky and Lura 2013). Special equipment, such as high-precision temperature controlled bath, is required for this purpose. The temperature dependence of buoyancy liquid, thermal gradient across a sample of cement paste and the effect of temperature on the reaction of cement hydration are additional complicating factors. Finally, using of buoyancy method for CTE measurements is problematic, because it utilizes small specimens of paste or mortar sealed in a condom, and, thus, the results cannot be directly extended for concrete.

Here a novel approach to evaluate the linear CTE based on the measurements of dynamic bulk modulus by means of ultrasonic pulse velocity is suggested. This approach relies on the theory of poroelasticity and the assumption that the dynamic bulk modulus is the undrained bulk modulus of cement paste. Poroelastic properties are considered undrained when a porous body is treated as a closed system made of the porous solid and the saturating fluid, which means the fluid is not allowed to escape from the pores (Coussy O. 2004). Indeed, the velocity of ultrasound waves in cement paste is very high and permeability of cement paste is very low. Thus,

dynamic properties of cement paste, including immediate response to the change of temperature, i.e. CTE, should be considered undrained.

Let us recall some fundamental relationships from the poroelasticity (Detournay and Cheng 1993) or (Coussy O. 2004). One of the most important properties of a porous body in poromechanics is Biot's coefficient (b). It represents the portion of the volumetric deformation produced by the variation of porosity (ϕ) when fluid can freely escape from the pores, i.e. pore pressure is absent. It can be expressed using the ratio of the bulk modulus of the porous body and the bulk modulus of the solid phase:

$$b = 1 - \frac{K}{K_s} \tag{1}$$

Another important characteristic in poroelasticity is Biot's modulus (M). It takes into account the coupling effect between the porous body and the filling fluid:

$$\frac{1}{M} = \frac{b - \phi_0}{K_s} + \frac{\phi}{K_f} \tag{2}$$

where ϕ_0 is the undeformed porosity; K_s and K_f are the bulk moduli of solid and fluid phase, respectively. By these means the undrained bulk modulus (K_u) of a porous body can be calculated as follows:

$$K_u = K + b^2 M \tag{3}$$

Now let us discuss a porous body subjected to temperature changes. First, we consider the drained properties, when pore fluid can freely escape from the pores and no pressure is exerted on the pore walls. The CTE value of the porous body (α), in this case, will be equal to that of the solid phase (α_s):

$$\alpha = \alpha_s \tag{4}$$

However, in case of a porous body with very low permeability, such as cement paste, pore fluid cannot easily leave the pores. As a result of significantly higher CTE of pore fluid, pressure is built up in the pores and, because of low permeability, released very slowly. In this case, the immediate response of the porous body to the temperature changes is governed by undrained CTE (α_u), which is calculated in the following way:

$$3\alpha_u K_u = 3\alpha K + 3\left(\alpha_\phi + \phi\alpha_f\right) Mb \tag{5}$$

where α_f is linear CTE of the pore fluid, and α_ϕ is linear CTE related to the porosity and is defined as follows:

$$\alpha_\phi = \alpha_s (b - \phi_0) \tag{6}$$

Substituting the expressions (1) - (4) into the equation (5) and assuming small deformations ($\phi \approx \phi_0$), the following expression for the undrained coefficient of linear thermal expansion can be obtained:

$$\alpha_u = \frac{K_s\left(K_u - K_f\right)\alpha_s + K_f\left(K_s - K_u\right)\alpha_f}{K_u\left(K_s - K_f\right)} \tag{7}$$

It can be seen that using equation (7) and assuming that CTE and bulk modulus of fluid and solid phases, and the undrained bulk modulus of the porous body are known, it is possible to calculate the undrained CTE. Undrained bulk

modulus is, in fact, equal to the dynamic bulk modulus, that can be obtained from the ultrasonic pulse velocity measurements.

In this work, the ultrasonic pulse velocity in cement paste was measure starting from the casting, and CTE of cement paste using the derived equation (7) was assessed and compared to the literature data. The calculated value of CTE was used to decouple thermal and autogenous deformations. The autogenous shrinkage of large 70×70×1000 mm prism, obtained in this way, was compared to the autogenous shrinkage measured by volumetric method, where temperature changes were less than 1 °C.

MATERIALS AND METHODS

Cement paste of water to cement ratio of 0.33 was prepared using a pan mixer. Cement was Portland cement of CEM I 52.2 N type with the loss on ignition was 4.12 % by weight and the specific surface area of 421.7±40 m^2/kg. The dynamic modulus of elasticity was measured by means of ultrasonic pulse velocity on the top surface of the beam specimens with dimensions of 70×70×280 mm. The measurements started immediately after casting. The resonance ultrasonic transducers of 60 kHz were used. The specimens were demolded at 1 day, and cured in sealed conditions at 30±2 °C. Four twin specimens for the testing of dynamic elasticity modulus were used. For ultrasonic pulse velocity, standard deviation reached a maximum of 5% at the time of setting, though at later ages it did not exceed 1%.

Linear shrinkage tests were conducted using the testing apparatus similar to that described in (Kovler 1994). This system is characterized by complete automation and high accuracy of measurement. It allows starting deformation measurement immediately after the casting. The apparatus consists of detachable steel molds mounted horizontally on laboratory tables, allowing carrying over the molds to a vibration table. The specimens had size of 70×70×1000 mm. Both ends of the specimen were free, and displacements in each end were measured independently by a linearly variable displacement transducer (LVDT) connected to the computerized measuring system. Each displacement measuring cycle consisted of 1000 measurements during 1 ms and the result was averaged. By this means, high accuracy and reproducibility were achieved, not worse than 0.0001 mm. To minimize friction between the mold and the specimen, a teflon sheet was placed in between. The specimens were cured in sealed conditions in a room at a constant temperature of 30±1 °C. The sealing was provided with polyethylene sheets, which covered the concrete by at least five layers. Temperature development due to heat of hydration was measured by means of three thermocouples, which were imbedded into the concrete at the time of casting. The maximum temperature gradient across the section of concrete sample was about 3 °C.

The procedure of volumetric measurement of autogenous shrinkage involved monitoring the weight of the cement paste sample in elastic membrane submerged in paraffin oil. The test method for volumetric autogenous shrinkage used in current research is similar to the method described by P. Lura and O. M. Jensen (Lura and Jensen 2007). The weight of the samples submerged in paraffin oil was measured by a balance connected to a logging device. The accuracy of volumetric strain measurements was about 3-4 microstrain considering the typical sample sizes and

precision of weighing. The cement paste sample was suspended in a 7 liter steel cylindrical container filled with paraffin oil. For temperature stability, the container was placed in a large water bath. The test was carried out in a temperature-controlled room at 30±1 °C. A maximum temperature increase of 1.0 °C was measured in the samples by means of thermocouples.

RESULTS AND DISCUSSION

The dynamic bulk modulus calculated for the cement paste with a w/c ratio of 0.33, using ultrasonic pulse velocity measurements, is given in Figure 1. For the calculations of the linear thermal expansion coefficient and the corresponding thermal deformations, a continuous function is required. For this reason, the following mathematical function was used for curve fitting of the dynamic bulk modulus, after setting:

$$K_u(t) = a \cdot t^b + c \cdot t + d \tag{8}$$

where t is the age of the cement paste from the water addition, and a, b, c and d are fitting parameters. Before setting, ultrasonic pulse velocity remained constant, and the time, when the first increase of ultrasonic pulse velocity was registered, is considered as the setting time or "time zero" (Sant et al. 2009). "Time zero" is important for considering shrinkage as a factor for the induction of stresses. The fitted curve for the dynamic bulk modulus is shown in Figure 1 by dotted line.

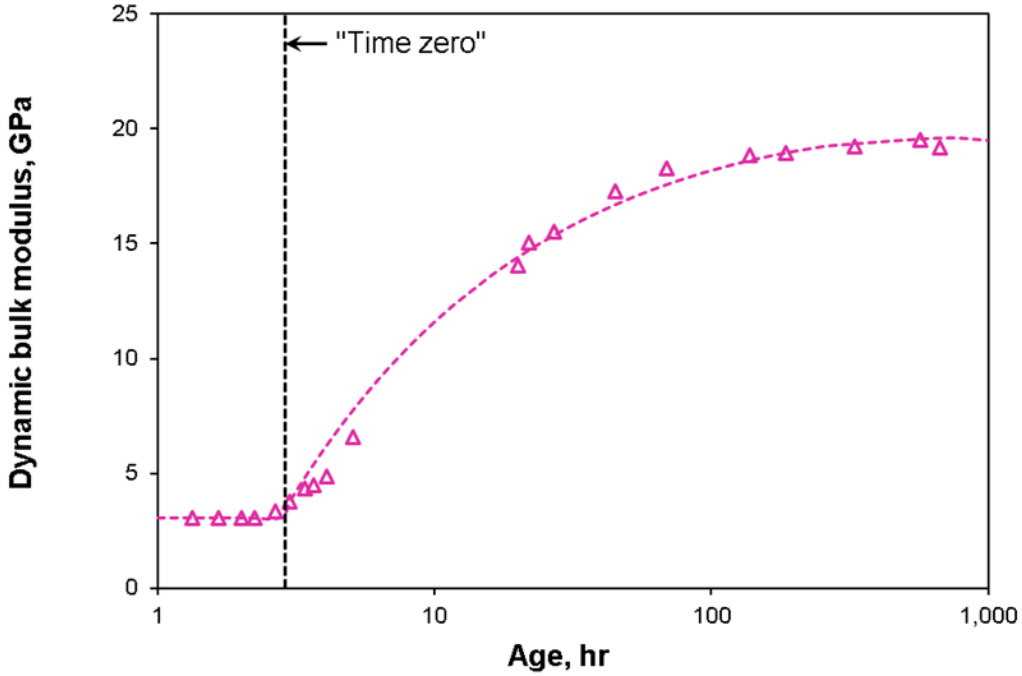

Figure 1 Experimental values and fitted curve for dynamic bulk modulus for cement paste with w/c ratio of 0.33.

The linear coefficient of thermal expansion calculated according to equation (7) and using the values of dynamic bulk modulus, which is shown in Figure 1, are plotted in Figure 2. For the linear coefficient of thermal expansion of solid matrix, the

characteristic value of silicates α_s=8·10^{-6} (°C)$^{-1}$ was used (Jahangirnejad et al. 2009). The volumetric thermal expansion coefficient of pore liquid was taken as the volumetric thermal expansion coefficient of water at 30 °C: $3\alpha_f$=302.6·10^{-6} (°C)$^{-1}$ (Eisenberg and Kauzmann 1969). The bulk modulus of the solid phase was taken K_s=44 GPa (Helmuth and Turk 1966, Lura et al. 2003). The bulk modulus of the liquid phase was taken as the inverse of water compressibility K_f=2.2 GPa (Eisenberg and Kauzmann 1969).

For the comparison, the experimental data and fitting curves from the literature (Loukili et al. 2000), (Turcry et al. 2002, Loser et al. 2010) are given in Figure 2. It can be seen that the kinetics of the development of the linear coefficient of thermal expansion is similar to the data in the literature. The initial values almost did not change, because the cement paste did not set yet.

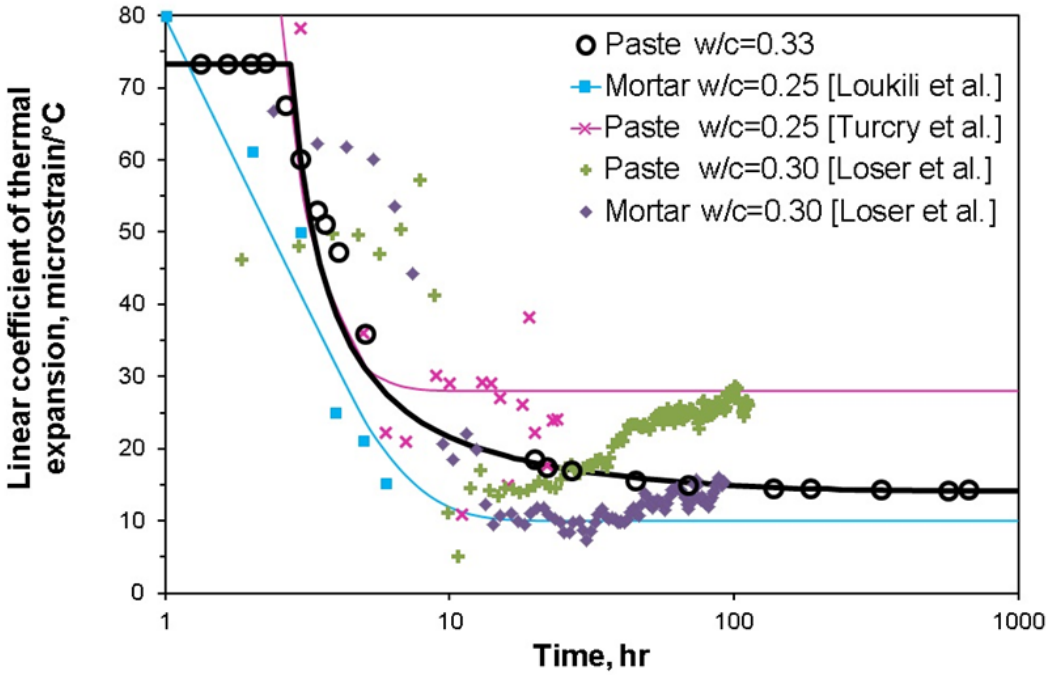

Figure 2 The calculated linear coefficient of thermal expansion compared with the literature data.

Generally, the linear thermal expansion coefficient calculated by equation (7) agrees well with the literature data and reflects well the hydration kinetic and setting time of the tested cement pastes. The calculated CTE value does not reflect a small increase due to self-desiccation, at a later age, such as seen in the measurements of Loser et al. (Loser et al. 2010). Obviously, two phase model of fully saturated cement paste is not capable of self-desiccation simulation. In order to model self-desiccation, further development of the model is required in order to introduce gaseous phase. Yet, the simple model presented by equation (7) gives a good estimation of CTE during the early age for assessment of thermal deformations.

Free shrinkage measured by means of linear and volumetric methods is shown in Figure 3. The free shrinkage measured by volumetric method is presented in Figure 3 as a linear deformation for the comparison. In the linear shrinkage sample, the

temperature increased by almost 15 °C, after casting. The temperature measured in the sample during the linear shrinkage test is given in Figure 6. As can be seen in Figure 5, the temperature peak is also reflected in the measurements of linear shrinkage. Now, let us subtract thermal deformations from the linear shrinkage curves.

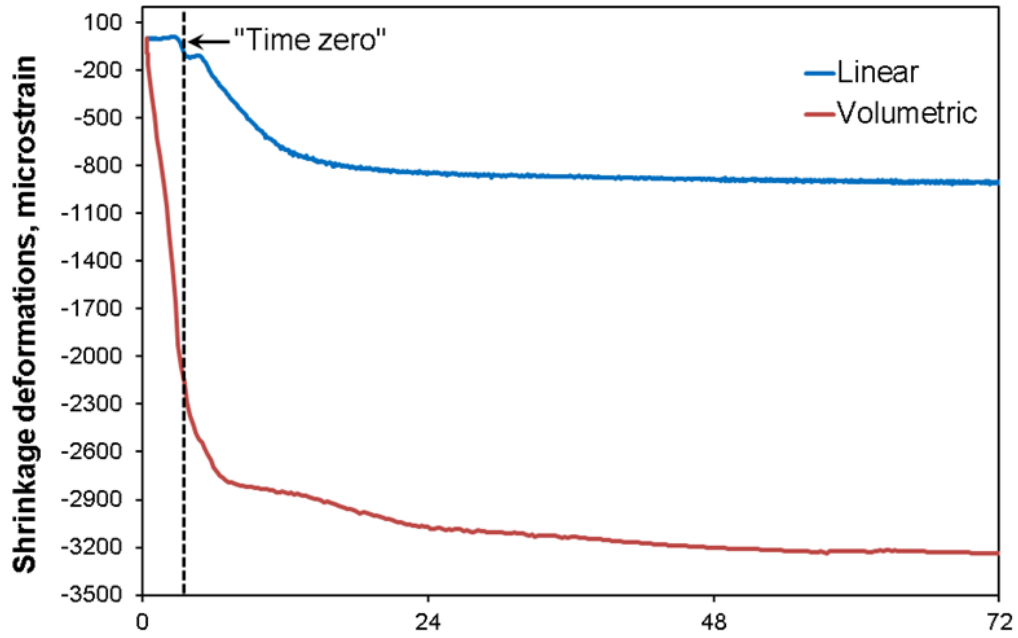

Figure 3 Measured linear and volumetric free shrinkage.

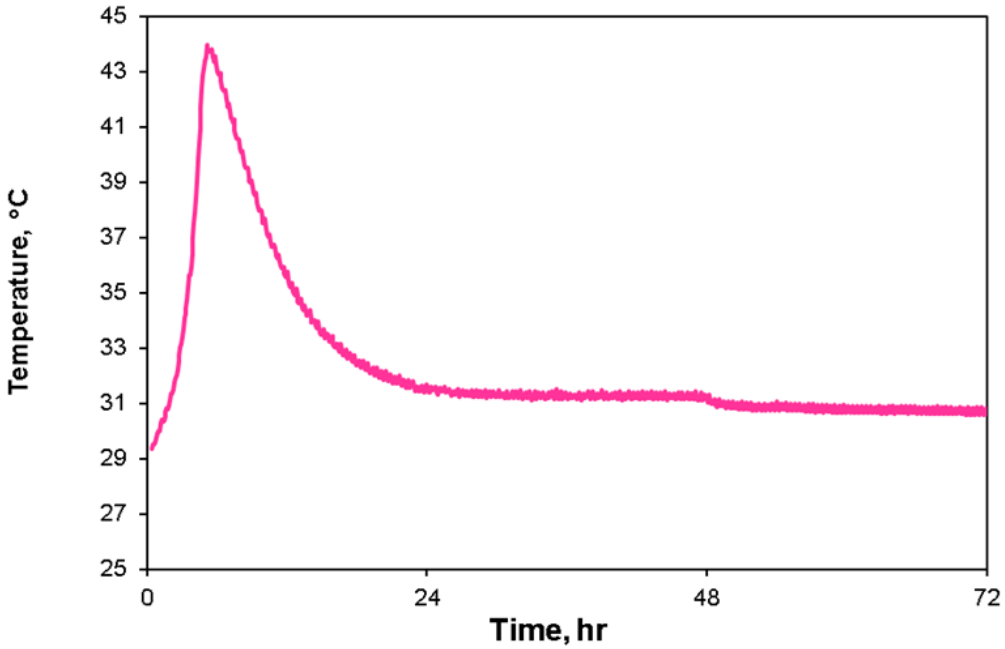

Figure 4 The temperature measured in the sample during linear shrinkage test.

Disregarding the coupling effect of temperature and autogenous shrinkage, at this stage, the only parameter that essentially depends on the temperature used in the

equation (7) is the CTE value of water. In order to take into account this dependence, the polynomial fitting curve, which is given in Figure 5, was used. The polynomial fit, in Figure 5, is based on the data of Kell (Kell 1967) on the temperature dependence of CTE of water. The linear coefficient of thermal expansion, calculated by this way, was used for evaluation of the thermal deformations during free shrinkage tests. The autogenous deformations were obtained by subtracting the calculated thermal deformations from the total free shrinkage curve given in Figure 6. These curves start just after the casting and include part of the deformations prior to setting time. Generally, for the analysis of the effect of autogenous shrinkage on the generated restrained stresses, the autogenous shrinkage is taken since "time zero". For this reason, the part of deformation preceding "time zero" was cut off. The resulting curves for autogenous shrinkage are shown in Figure 6.

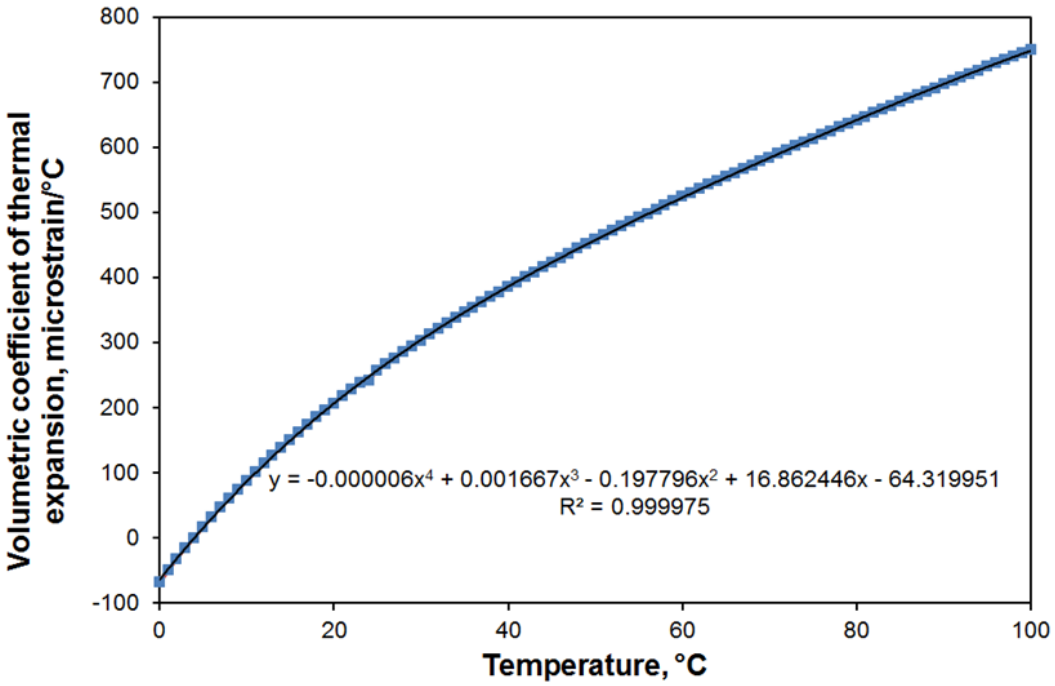

Figure 5 The volumetric coefficient of thermal expansion of water as a function of temperature.

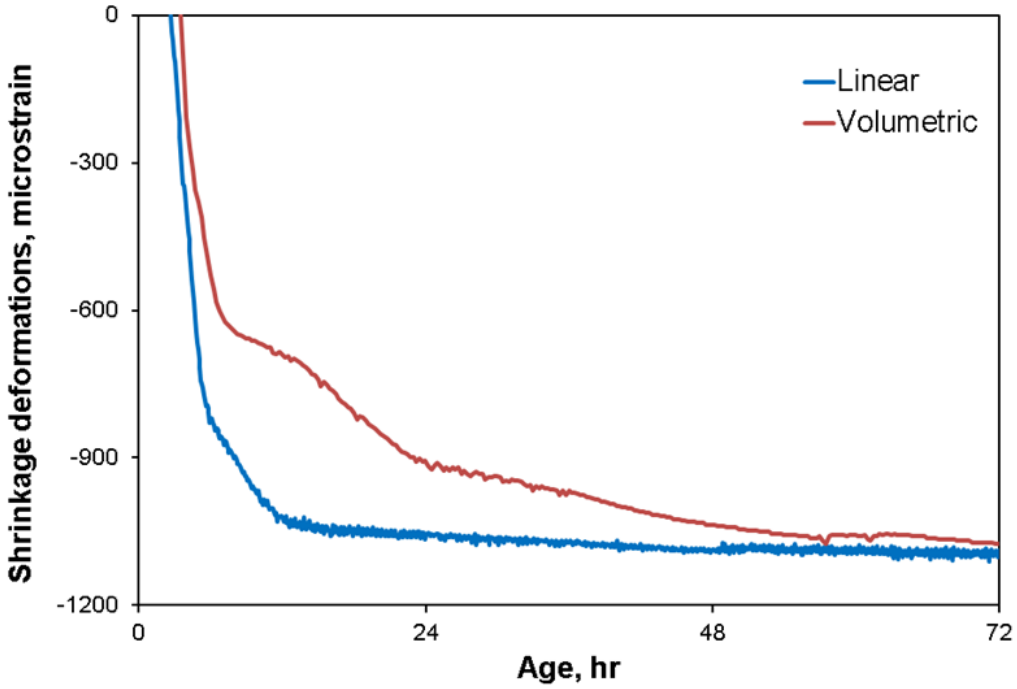

Figure 6 Comparison of shrinkage data obtained by linear and volumetric measurements for cement pastes with a w/c ratio of 0.33.

It can be seen in Figure 6 that there is a gap between volumetric and linear measurements at a very early age, probably because of small temperature changes during volumetric test. However, the final values of shrinkage agree well between volumetric and linear measurements.

CONCLUSION

A new approach to evaluate CTE of cementitious materials at early ages using ultrasonic pulse velocity measurements was proposed. The results are in agreement with the literature data and can be successfully used for separation of thermal and autogenous deformation. Further development to include gaseous phase is needed in order to predict the effect of self-desiccation.

REFERENCES

Coussy, O. (2004). "Poromechanics." Chichester, West Sussex, England: John Wiley & Sons Ltd.

Coussy, O., and Brisard, S. (2009). "Prediction of drying shrinkage beyond the pore isodeformation assumption." Journal of Mechanics of Materials and Structures, 4(2), 263-279.

Coussy, O., Dangla, P., Lassabatere, T., and Baroghel-Bouny, V. (2004). "The equivalent pore pressure and the swelling and shrinkage of cement-based materials." Materials and Structures, 37(1), 15–20.

Detournay, E., and Cheng, A.-D. (1993). "Fundamentals of poroelasticity." In C. Fairhurst (Ed.), Comprehensive Rock Engineering: Principles, Practice and Projects (Vols. Vol. II, Analysis and Design Method, 113-171). Pergamon Press.

Eisenberg, D., and Kauzmann, W. (1969). "The Structure and Properties of Water." Oxford, UK: Oxford University Press.

Helmuth, R., and Turk, D. (1966). "Elastic moduli of hardened Portland cement and tricalcium silicate pastes: effect of porosity." Symposium on structure of Portland cement paste and concrete (special report 90), Highway Research Board: Washington, DC 135–144.

Jahangirnejad, S., Buch, N., and Kravchenko, A. (2009). "Evaluation of Coefficient of Thermal Expansion Test Protocol and Its Impact on Jointed Concrete Pavement Performance." ACI Materials Journal, 106(1), 64-71.

Kell, G. S. (1967). "Precise representation of volume properties of water at one atmosphere." Journal of Chemical Engineering Data, 12(1), 66–69.

Kovler, K. (1994). "Testing System for Determining the MechanicBehavior of early age concrete under restrained and free uniaxial shrinkage." Materials & Structures, 27, 324-330.

Kovler, K., and Jensen, O. M. (2005). "Novel technologies of concrete curing." Concrete International, 27(9), 39-42.

Kovler, K., and Zhutovsky, S. (2006). "Overview and Future Trends of Shrinkage Research." Materials and Structures, 39(9), 827-847.

Loser, R., Münch, B., and Lura, P. (2010). "A volumetric technique for measuring the coefficient of thermal expansion of hardening cement paste and mortar." Cement and Concrete Research, 40(7), 1138-1147.

Loukili, A., Chopin, A., Khelidj, A., and Le Touzo, J.-Y. (2000). "A new approach to determine autogenous shrinkage of mortar at an early age considering temperature history." Cement and Concrete Research, 30(6), 915–922.

Lura, P., and Jensen, O. (2007). "Measuring techniques for autogenous strain of cement paste." Materials and Structures, 40(4), 431-440.

Lura, P., Jensen, O. M., and van Breugel, K. (2003). "Autogenous shrinkage in high-performance cement paste: An evaluation of basic mechanisms." Cement and Concrete Research, 33(2), 223–232.

Sant, G., Dehadrai, M., Bentz, D., Lura, P., Ferraris, C. F., Bullard, J. W., and Weiss, J. (2009). "Detecting the Fluid-to-Solid Transition in Cement Pastes,." Concrete International, 31(6), 53-58.

Turcry, P., Loukili, A., and Barcelo, L. (2002). "Casabonne, J.M. Can the maturity concept be used to separate the autogenous shrinkage and thermal deformation of a cement paste at early age." Cement and Concrete Research, 32(9), 1443-1450.

Wyrzykowsky, M., and Lura, P. (2013). "Controlling the coefficient of thermal expansion of cementitious materials – A new application for superabsorbent polymers." Cement and Concrete Composites, 35(1), 49–58.

Cracking Behaviour of FRC Beams under Long-Term Loading

L. Candido[1]; F. Micelli[1]; E. Vasanelli[2]; M. A. Aiello[1]; and G. Plizzari[3]

[1]Department of Engineering for Innovation, University of Salento, P.O. Box 73026, Lecce, via per Arnesano. E-mail: leandro.candido@unisalento.it
[2]Institute for Archeological and Monumental Heritage (CNR-IBAM), via per Monteroni, 73100 Lecce, Italy. E-mail: e.vasanelli@ibam.cnr.it
[3]Dept. of Civil Engineering, Architecture, Land and Environment, University of Brescia, Via Branze 43, 25123 Brescia, Italy.

Abstract

The extensive research activity carried out over the last decades on fibre-reinforced concrete (FRC) has shown that such material has enhanced mechanical and durability properties compared to plain concretes. The presence of short fibres in the concrete mass allows to control cracking and have moderate time-dependent effects. Compared to plain concrete, FRC flexural members show a higher number of cracks with reduced mean width. The experimental study presented herein discusses the mechanical behavior of FRC flexural beams subjected to sustained service load and environmental exposure for 72 months. The effects of different short fibers (polyester and steel), sustained loading and aging were investigated. A comparison with the results of a previous research is shown, with reference to the same kind of beams exposed for 17 months under the same conditions. The results show the beneficial effects of the fibers in terms of reduced crack width and increased flexural stiffness. The mechanical tests also highlighted how the presence of short structural fibers could play an effective role in mitigating creep effects in the concrete elements.

INTRODUCTION

The dispersion of short fibres - made of steel, polymers, carbon, etc. - in the concrete mass brings in a 'crack bridging' effect, which controls and delays cracking (Di Prisco et al. 2009; NRC; Fib Model Code 2010) and allows moderate time-dependent effects (Tan et al. 1995; Altoubat and Lange 2003; Vasanelli et al. 2013). FRC develops toughness and ductility which improve the structural performance of members, not only under static and fatigue loading, but also under dynamic and seismic loading. Compared to plain concrete, FRC members show a higher number of cracks but reduced mean width. Therefore the material may develop an enhanced protection against water and contaminants, which are responsible for corrosion of reinforcing steel and potential deterioration of concrete. Such behavior offers the perspective of a longer service life, especially in aggressive environments.

At the moment, there are limited experimental data concerning crack width and spacing in FRC structural elements under sustained bending loads, thus reliable analytical models are not fully developed yet (Tan et al. 1995; Vasanelli et al. 2014). Similarly to the case of plain concrete, a crack width relationship for FRC elements is desirable for designers and engineers involved in the design of FRC members. The development of important technical design codes, such as RILEM TC 162 TDF and Model Code (MC) 2010 is currently embracing this idea. However, further validation of these models by means of experimental results is still needed. On the other hand, the study of the influence of long-term loading on crack width in presence of short fibres reinforcement is an almost unexplored topic and a crucial issue at the same time. This research addresses the cracking behavior of FRC concrete beams reinforced with both traditional steel bars and short fibres, presenting the results of an experimental campaign, which involves a given number of full-scale FRC beams tested under long-term bending loadings. The experimental program includes the measurements of crack width and flexural displacement . The results presented in the paper show that the addition of fibres in concrete reduces flexural displacements, crack widths and modify the long term behavior of FRC members compared.

EXPERIMENTAL PROGRAM

The experimental campaign reported in this paper is the continuation of the research study published by Vasanelli et al. (2013). The work aimed at understanding the effects of long term loads on the performance of RC/FRC members. Thirteen full scale beams were casted and left in laboratory for one year. The first group including three reinforced concrete beams casted respectively with plain concrete, steel fiber reinforced concrete and polyester fiber reinforced concrete was tested in laboratory (_L). These beams were used as reference specimens. The remaining beams were placed outside and exposed to natural weathering (_E) and contemporarily subjected to sustained loads in order to simulate real service conditions. They can be distinguished into two sets of five beams: the first were tested after 17 months (_17), the last were tested in the long-term after about 6 years (_72). Both these two sets consisted of one beam casted with plain concrete (_PC), two beams casted with steel fiber reinforced concrete (_ST) and two beams casted with polymeric fiber reinforced concrete (_POL). Table 1 reports the details of these beams such as IDs and time of exposition and testing in months.

During the exposure time, the evolution of the crack patterns for each beam (namely position, width and length of cracks) was monitored according to a regular time scheduling. The two sets of five beams were then unloaded and tested in laboratory, respectively after seventeen months and seven years, for the determination of the mechanical behavior.

The investigation of the long-term effects consisted of two steps besides the material characterization. A first step consisted in field-tests aimed at detecting the cracking evolution of the exposed beams. This step was performed for 17 months. A second laboratory phase involved four point bending tests performed on beams up to their failure.

Table 1. Beam IDs and time of exposition and testing [in months]

Beam ID	*Exp./ load time*	*Testing time*
PC_L / ST_L / POL_L	-	12
PC_E_17/ST_E_17/POL_E_17	17	29
PC_E_72/ST_E_72/POL_E_72	72	84

The beams were 3000 mm long, with square cross section 250x250 mm. Three and two ϕ14 mm bars were respectively used as longitudinal reinforcement in tension and compression side of the beams. In the transverse direction, 8 mm diameter stirrups were spaced 140 mm in the central part of the member and 70 mm close to the supports. The two loading frames at the exposure site are depicted in Figure 1. The loading scheme represents a four point bending condition with a span of 280 cm and a distance of 90 cm between the two loading points.

Table 2 reports the average mechanical properties of longitudinal bars and stirrups adopted in the beams; they were measured according to UNI EN ISO 15630-1 by testing three samples for each diameter.

Figure 1. The two exposure loading frames.

Table 2. Experimental mechanical properties of steel rebars.

Reinforcing element	*Diameter (mm)*	*Yield strength (MPa)*	*Ultimate strength (MPa)*	*Elongation at rupture (%)*
Longitudinal bar	14	520	614	12.2
Stirrups	8	567	600	4.8

Two different types of fibers were used: polyester fibers (Graminflex PE30 furnished by La Matassina Technology) and steel fibers (La Gramigna 060x30 furnished by La Matassina Technology). The aspect ratios (length/diameter) were equal 50 and 66 respectively for steel and polyester fibers. All geometrical and mechanical properties of the short fibers as measured by the manufacturer are summarized in Table 3. Therefore, three different concrete mixes were prepared: a reference mix without fibers (PC), a concrete mix with a volume fraction of 0.6% of steel fibers (ST) and a concrete mix with 0.9% of polyester fibers (POL). The fiber volume fractions were decided according to the results obtained by a previous

research (Vasanelli et al. 2008) considering the best compromise in terms of mechanical properties and workability of concrete. All the mixes had a water-cement ratio equal to 0.65, a cement type 32.5R II-A/LL (UNI EN 196-1) (Table 4) and a workability class S5. Four cubes (150 x 150 x 150 mm) for each mix (PC, ST and POL) were cast for quality control; the values of the compressive strength obtained after 28 days from casting are reported in Table 5. The compressive strength of ST mix was comparable to that of POL mix and both were slightly lower than that evaluated for PC. This was probably due to a higher content of entrapped air in the mix as it was found in a previous research carried out by the authors (Vasanelli et al. 2008). The influence of fibers on compressive strength can be considered negligible, especially for low fiber volume contents (ACI Committee 544).

Table 3. Geometrical and mechanical characteristics of the short fibers.

Type	*Shape*	*Diameter (μm)*	*Length (mm)*	*L/D*	*Tensile strength (MPa)*	*Elastic modulus (kN/mm^2)*
Steel	Hooked	600	30	50	> 1150	210
Polyester	Waved	450	30	66	400-800	11.3

Table 4. Concrete mix.

	ST	*POL*	*PC*
CEM 32.5R II-A/LL (kg/m^3)	300	300	300
Superplasticizer CRTV-L *(kg/m^3)*	1.59	2.5	1.77
Sand (0-4) *(kg/m^3)*	1028	1023	1037
Gravel (4-10) *(kg/m^3)*	704	701	710
Water/Cement ratio	0.65	0.65	0.65

Table 5. Cubic cylindrical compressive strength.

Beam IDs	*Average cubic strength (MPa)*	*COV (%)*
PC	25.8	4
ST	21.4	8
POL	23.2	8

The reinforced concrete beams were designed according to the Eurocode 2, on the basis of the loading scheme reported in Figure 2 (a). The reinforcement ratio was chosen to have a bending failure of the beam, with concrete crushed after steel yielding of the tension bars. Vertical stirrups were designed to prevent premature shear failure. Figure 2 (a) shows the geometry of the beams as well as the reinforcement details, while Figure 2 (b) show the actual experimental set-up.

The two loading frames were located in Brindisi (Italy), in an industrial area which is 600 m far from the sea. The site has a high relative humidity rate (>70%) and presence of chlorides in the air. According to EN 206-1, the exposition class of the site is XC3 for corrosion induced by carbonation, and XS1 for corrosion induced by chlorides. Five beams were loaded in each frame by means of a screw jack. A service limit state load of about 50 kN has been applied during the exposure time,

accounting for about 50% of the ultimate design load. Due to relaxation effects of the loading system, the beams were periodically reloaded in order to keep the initial value. During the exposure time a handheld digital microscope with 200x magnification was used to measure crack width at the bottom edge of the beams.

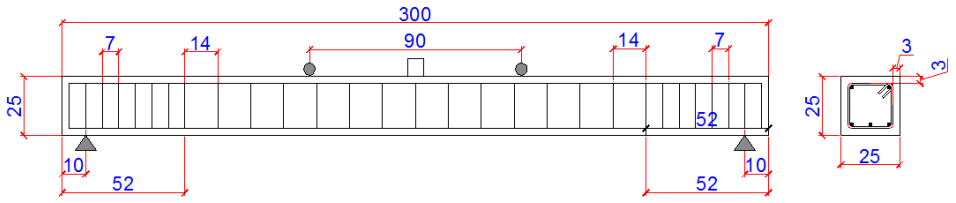

(a)

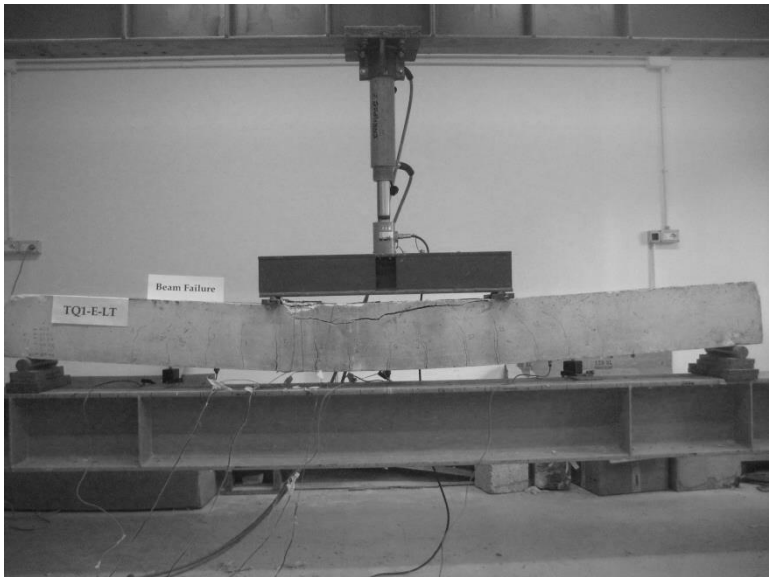

(b)

Figure 2. (a) Beam details (cm) and (b) experimental set-up.

After one year from casting, the laboratory beams were tested according to the four point scheme represented in Figure 2. During the test, deflections at midspan and at quarter points of the beams and crack widths were continuously monitored respectively by means of three Linear Variable Differential Transducers (LVDTs) and a digital microscope. Tests were performed under load control; a load cell having a capacity of 30 ton was used to measure the applied force. The crack pattern of the exposed beams (number of cracks, crack widths and crack lengths) was recorded at five load steps: Step 1=20kN; Step 2=30kN; Step 3=50kN; Step 4=80kN; Step 5=100kN. Beams in long term were tested after 29 and 84 months respectively, according to the same protocol adopted for laboratory beams.

EXPERIMENTAL RESULTS AND DISCUSSION

Experimental results of the tests carried out on beams exposed for 17 months are already presented in Vasanelli et al. (2013). The authors confirmed that the presence

of fibers helps reducing the long-term crack growth, as already found by Tan et al. (1995, 2005). Vasanelli et al. found that crack widths measured on FRC beams were lower than those measured on PC beams and crack widths seemed to be stabilized after ten months of exposure. Furthermore, the authors confirmed that despite the higher modulus of steel fibers, steel and polyester fibers had quite the same effect on the cracking behavior of the beams. The authors also showed that - under short term loading -analytical predictions of deflections made according to Model Code 2010 are conservative if compared to the experimental values, especially for low values of the load.

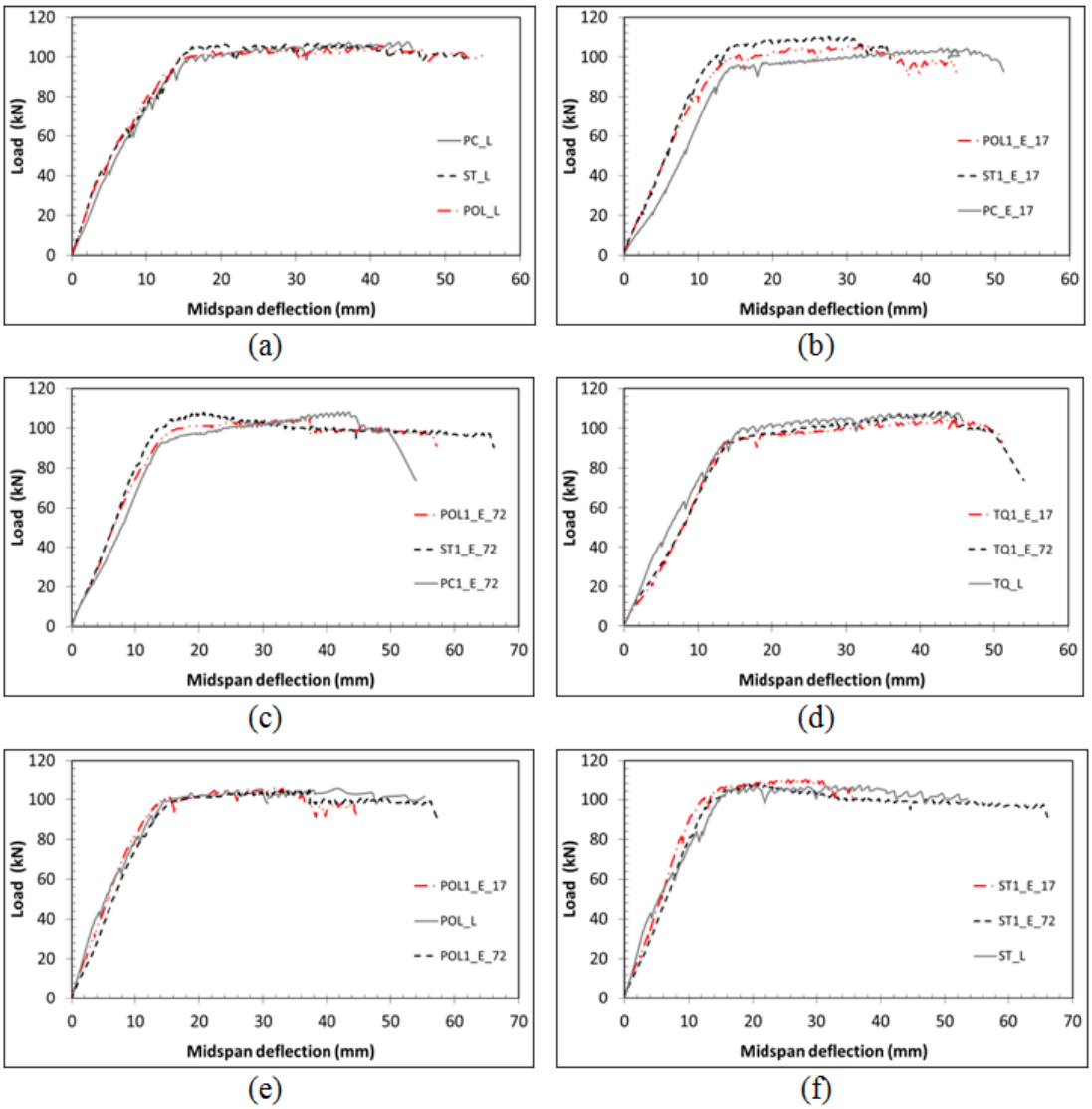

Figure 3. Load vs midspan deflection curves: comparisons among beams. (a) laboratory (b) 17 months (c) 72 months (d) PC (e) Polyester FRC (f) Steel FRC

During the four-point testing phase, as expected, all the thirteen beams failed by concrete crushing after yielding of tensioned steel bars, just as designed by the

authors; PC beams showed the most extensive concrete damage in the upper side at failure. Figure 3 shows the load – midspan deflection curves of the tested beams compared by mix type and time of exposure. To better evidence the general trend Figure 3 reports only the results of ST1 and Pol1 specimens, since they fairly represent all the other samples, for long term conditions.

It can be observed that the flexural behavior of beams tested under short time conditions was very similar, showing a typical pseudo bi-linear curve. As expected the influence of fibers is negligible in terms of bearing capacity, even if it is important to see the behaviour under service loads. In terms of ultimate load , the steel FRC beams showed the best mechanical performance (Fig.3(a)). After 17 months of sustained loading and external exposure, FRC beams show an improved mechanical performance compared to that of plain concrete beam (Fig.3(b)). In fact a 10% increase of ultimate load has been registered. After 72 months of sustained loading, instead, there is a limited difference in the global performance of the beams (Fig.3(c)) in terms of ultimate limit state, but there are important implications under service conditions. In this case the trend of Fig.3(b) is confirmed, by showing that the flexural stiffness of FRC beams is strongly higher than PC beams in the range of service loads. In any case steel FRC beams present a better performance in terms of bending capacity and stiffness compared to the other beams, especially when loading is lower than the sustained applied load. Figure 3(d) shows the behavior of PC reference beams. In this case the effects of applied sustained loads in aggressive environment are pronounced. Exposed beams show reduced stiffness - until the testing load reaches the value of about 80 kN - and a lower steel yielding load. The effects of creep and sustained applied loading in PC beams seem to be exhausted after 17 months of sustained laoding. In fact, the load-deflection curves in diagram representing 17 and 72 months of sustained loading overlap. For FRC specimens the effect of sustained applied load is far less pronounced, as it can be seen in Fig.3(e)-(f). Therefore the presence of fibers guarantees a limited loss of stiffness. In any case the presence of fibers limits the effects of time-dependent phenomena and of sustained loading, as already found in Vasanelli et al. (2013) for the beams tested after 17 months of exposure.

On-site measurements on beams undergoing sustained loading showed that crack widths were lower in FRC beams than in the PC beam (Vasanelli et al. 2013). In fact, after 17 months of sustained loading, PC beams had a crack opening equal to 0.24 mm while FRC beams had a crack opening ranging between 0.13 and 0.18 mm. Furthermore, at 20 kN PC1-E beam showed an average crack opening equal to 0.24 mm, very similar to the average crack opening value measured after 17 months of exposure. In FRC beams the average crack width at 20kN was about 0.10 mm, namely 23% less than that measured on the exposure site. Thus, it was observed that the presence of fibers helped in reducing residual crack openings after unloading of the beams.

Figure 4 reports crack openings during the four-point bending test for all the exposed beams. The beams tested in long term conditions are depicted on the left and on the right respectively. Independently from the exposure time and from the applied load, FRC beams show a remarkable reduction of crack width compared to PC beams. PC beams show comparable mean crack widths after both 17 and 72 months of sustained

loading, confirming the global behaviour of Fig.3(d). The results of the four point bending test on both PC and FRC beams exposed for 72 months under sustained loading are comparable with those obtained for beams exposed and loaded for 17 months. By the way, the greatest variance in terms of crack openings is obtained for steel FRC beams.

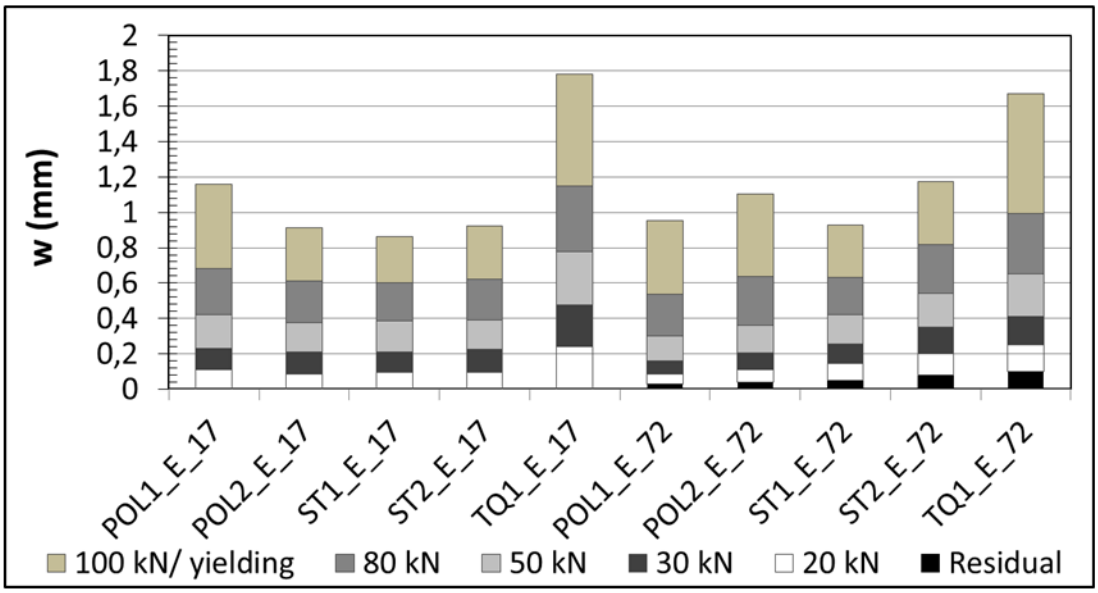

Figure 4. Mean crack width in the for exposed beams at each load step.

CONCLUSIONS

The present work aimed at understanding the effects of long term loading on the performance of RC/FRC structural members exposed to natural weathering. The results of an experimental study were presented and discussed. Ten RC beams, casted with and without fibers, were tested after several months of exposition to natural agents under sustained load, in addition to the three reference unconditioned beams. The exposed beams were unloaded and brought to laboratory for bending test after 17 and 72 months of exposition, respectively. The cracking pattern and displacements were accurately detected during exposure and during the tests at different loading steps until failure of the beams.

The results confirmed that the presence of fibers helps in reducing crack width and in increasing bending stiffness of the beams. Under service loads the slope of the load vs midspan displacement curves increases when the fibers are present into the concrete matrix, as expected. The effects of the sustained loads and exposure were detrimental for all kind of beams even if the presence of the fibers mitigated these effects. Further research is needed in the field in order to calibrate analytical models which may take into account the reduced stress in the concrete matrix due to the presence of short fibers, which produces reduced strain in the long period, as found in the experimental tests.

REFERENCES

Abrishami, H.H., and Mitchell, D. (1997). "Influence of steel fibers on tension stiffening". ACI Struct. J. (94), 769-775.

Altoubat, S.A. and Lange, D.A. (2003) "A new look at tensile creep of fiber reinforced concrete". *ACI Special Publication.* (216), 143–160.

ACI Committee 222. *Corrosion of Metals in Concrete*. ACI Journal 1985; 82, 1: 3-32

ACI Committee 224. *Control of Cracking of Concrete Structures*. ACI Special Publication 224R-01.

ACI Committee 544 . *Measurement of Properties of Fiber Reinforced Concrete*. ACI Report 544.2R-89, American Concrete Institute, Farmington Hillis.

Balazs, G.L., and Kovacs, I. (2004). "Effect of steel fibers on the cracking behaviour of RC members". *Proc. of 6th RILEM Symp. on Fiber-reinforced Concretes* – BEFIB, 20-22 September 2004, Varenna, Italy.

Bishoff, P.H. (1993). "Tension stiffening and cracking of steel fiber reinforced concrete". *J. of Mater. in Civ. Eng.* March-April, 174-182.

CEB (Comite Euro-International du Beton). (1993) *CEB-FIP Model Code 1990 Bullettind'Information, No. 203-205*, Thomas Telford, London, UK,.

Chiaia, B., Fantilli, A.P., and Vallini, P. (2008). "Crack Patterns in Reinforced and Fiber Reinforced Concrete Structures". *The Open Construction and Build. Technology J.*, (2), 146-155.

Collepardi, M. (1995). "Quick method to determine free and bound chlorides in concrete". *RILEM International Workshop on Chloride penetration into concrete*, Saint Rèmy-les-Chevreuse, 15-18 Oct., 10-16.

Di Prisco, M., Plizzari, G., Vandewalle, L. (2009) "Fibre reinforced concrete: new design perspectives". *Mater. Struct.* (42),1261–1281.

Eurocode 2. (2004) *Design of concrete structures - Part 1-1: General rules and rules for buildings*. EN 1992-1-1:2004.

FIB Model Code. (2010). *First complete draft, vol 2, chaps (7–10) in fib Bulletin* 562010, ISBN 978-2-88394-096-3.

Leutbecher, T., Fehling, E. (2008). "Crack Width Control for Combined Reinforcement of Rebars and Fibres exemplified by Ultra-High-Performance Concrete". In fib task group 8.6 "UHPFRC", Varenna.

Minelli, F., Tiberti, G. and Plizzari, G. (2010). "Durability and cracking in fibrous R/C elements: a broad experimental study". *Atti del Convegno Le Nuove Frontiere del Calcestruzzo Strutturale*, Università degli Studi di Salerno – ACI Italy Chapter, 22-23 Aprile.

National Research Council. (2007) *Guide for the design and construction of fiber-reinforced concrete structures.* ROME, CNR.

NTC. (2008) *Norme tecniche per le costruzioni.* D.M. 14/01/2008.

Oh, B.H. (1992). "Flexural analysis of reinforced concrete beams containing steel fibers". *J. of Struct. Eng.*, (118), 2821-2836.

Tan, K.H., Paramasivam, P., and Tan, K.C. (1995). "Cracking characteristics of reinforced steel fiber concrete beams under short and long-term loadings". *Adv. Cem. Based Mat.,* (2), 127-137.

Tan, K.H., and Saha, M.K. (2005) “Ten-year study on steel fiber-reinforced concrete beams under sustained loads”. *ACI Struct.l J.,* 102-(3), 472-472.

UNI EN 196-1. (2007) *Cement - Part 1: Composition, specifications and conformity criteria for common cements. Italian Board of Standardization* (UNI).

UNI EN 206-1. (2010) *Concrete - Specification, performance, production and conformity. Italian Board of Standardization* (UNI), 2001.

UNI EN ISO 15630-1. *Steel for the reinforcement and pre-stressing of concrete - Test methods - Part 1: Reinforcing bars, wire rod and wire. Italian Board of Standardization* (UNI).

UNI 9944. (1992) *Corrosione e protezione dell'armatura del calcestruzzo. Determinazione della profondità di carbonatazione e del profilo di penetrazione degli ioni cloruro nel calcestruzzo*. Italian Board of Standardization (UNI).

Vandewalle, L. (2000). “Cracking behavior of concrete beams reinforced with a combination of ordinary reinforcement and steel fibers”. *Mat. and Struct.*, (33), 164-170.

Vandewalle, L. (2000). RILEM TECHNICAL COMMITTEES - Recommendations of RILEM TC 162-TDF: Test and design methods for steel fibre reinforced concrete. *Mat. and struct.*, 33(225), 3-5.

Vasanelli, E., Micelli, F.,.Aiello, M.A and Plizzari, G. (2008) “Mechanical characterization of fiber reinforced concrete with steel and polyester fiber”. *Proc. of the BEFIB 2008, 7th RILEM Int. Symp. on Fibre Reinforced Concrete*, Chennai India, 537-546.

Vasanelli, E., Micelli, F., Aiello, M.A. and Plizzari, G. (2013) "Long term behavior of FRC flexural beams under sustained load", *Eng. Struct.*, (56), 1858-1867.

Vasanelli, E., Micelli, F., Aiello M.A. and Plizzari, G. (2014). “Crack width prediction of FRC beams in short and long term bending condition”. *Mat. and Structures*. (47)1-2, 39-54.

Influence of Mineral Admixtures (Metakaolin, Slag, Fly Ash) on the Plastic, Free, and Restrained Shrinkage of SCCs

D. Niknezhad[1]; S. Kamali-Bernard[1]; and C. Garand[1]

[1]Laboratory of Civil Engineering and Mechanical Engineering LGCGM, National Institute of Applied Sciences (INSA), 20, Ave. des Buttes de Coësmes, CS 70839, 35708 Rennes cedex 7. E-mail: Davood.nik-nezhad@insa-rennes.fr; Siham.Kamali-Bernard@insa-rennes.fr

Abstract

Because of their high volume of paste, self-compacting concretes (SCCs) cost more expansive than ordinary concrete and exhibit more shrinkage values which increases their susceptibility to cracking and may alter their durability performances. For economical and environmental considerations, many studies were done these last years on the use of mineral admixtures as filler in SCCs. The aim of this paper is to contribute to the characterization and the understanding of shrinkage of SCCs where Portland cement is partially substituted by slag, fly ash or metakaolin. The shrinkage from casting to 360 days of aging of four SCC mixtures based on CEM I 52.5N, CEM III/A 52.5L (slag cement), CEM V 42.5N (blended cement containing fly ash and slag) and CEM I + 15% of metakaolin is investigated. Experimental tests include plastic, autogenous, free drying and restrained shrinkage. Results show that shrinkage depends on the mineral admixture type and more particularly on the developed microstructure. Replacing 15% of Portland cement by metakaolin increases the shrinkage at the plastic state and decreases it significantly at the hardened state in free drying conditions. The use of CEM III instead of CEM I involves an inverse behavior. In restrained conditions, mineral admixtures seem to reduce the age of crack initiation. However, the crack opening is reduced by at least a factor of 2. The results are in a good agreement with water porosity, mass loss, compression strength and thermal measurements.

INTRODUCTION

Self-Consolidating Concrete is a highly flowable, non-segregating concrete that can flow into place, fill the formwork, and encapsulate the reinforcement without any mechanical consolidation. Because of their high volume of paste, self-compacting concretes (SCCs) cost more expansive than ordinary concrete and exhibit more shrinkage values which in turn increases their susceptibility to cracking and may lead to durability problem. For economical and environmental considerations, many studies were done these last years on the use of mineral admixtures as filler in SCCs. Most of them deal with the rheology of these materials at the fresh state and the development of their strength. However, few studies were done on the shrinkage of these materials from the fresh state to the hardened one. It is well known that concrete shrinks at the plastic state (plastic shrinkage) and then at the hardened one. There is little information concerning the study of plastic shrinkage in self

compacting concrete. The main difficulties are caused by the lack of appropriate tests to obtain correct measurements. Long-term shrinkage often refers to the shrinkage of hardened concrete, typically from 24 h. Although free shrinkage measurements are useful in comparing different mixture compositions, they do not provide sufficient information to determine if the material will crack in service. Thus, shrinkage tests in restrained conditions are useful. The purpose of this research is to determine the shrinkage from casting to 360 days of aging and cracking potential of self-consolidating concrete when Portland cement is partially replaced by slag cement (CEM III), blended cement (Slag and fly ash cement) and by 15% of metakaolin. Sealed and drying conditions are investigated.

MATERIALS AND METHODS

Materials and mix proportions

A granular class 0/4 sand (S) with a density of 2.6 t/m³ and limestone gravel (G) with 6.3/10 granular class, 2.66 t/m^3 of density were used in this study. Three cements according to European standard EN 197-1: CEM I 52.5N (Portland cement), CEM III/A 52.5L (slag cement) and CEM V 42.5N (blended cement containing slag and fly ash); limestone filler (LF) and metakaolin (MK) were tested.

Table1. Composition and physical properties of cements and mineral additions

Name	*CEM I*	*CEM III*	*CEM V*	*LF*	*MK*
Clinker content (% in mass)	98	36	54	_	_
Slag content (% in mass)	_	62	25	_	_
Fly ash content (% in mass)	_	_	20		
Specific Surface Blaine (cm²/g)	3649.9	4263	4250	4190	17000
Specific gravity (g/cm³)	3.15	2.98	2.85	2.7	2.4

Table 2.Mix proportions and physical properties at the fresh state

Composition (kg/m³)	*SCC CEM I*	*SCC CEM I/MK*	*SCC CEM III*	*SCC CEM V*
Aggregate 6.3/10	760	760	760	760
Sand 0/4	780	780	780	780
CEM I	330	280.5	-	-
CEM III	-	-	330	-
CEM V	-	-	-	330
Limestone filler	240	240	240	240
Metakaolin	-	49.5	-	-
Water	210	210	210	210
Superplasticizer	2.8	4.4	2	2.5
w/b	0.368	0.368	0.368	0.368
Slump (cm)	66	67	69	68
bleeding (%)	8.1	7	9.6	7.9
L-Box (H_2/H_1)	0.83	0.82	0.87	0.84

Their composition and properties are given in Table 1. A total of four SCCs mixtures with a constant water-to-binder ratio (w/b) of 0.368 and a total binder content of 570 kg/m³ were investigated. Designations, mix proportions and physical properties at the fresh state of the different SCCs are given in Table2.

Methods:

Water porosity, evaporable and non-evaporable water content measurements: thermal tests were performed on binder pastes with w/b ratio of 0.4 cured during 28 days in water. Both evaporable (25°C to 105°C) and non-evaporable (105°C to 1000°C) water contents were deduced. The water porosity based on the evaporable water content at 105°C after water saturation of the specimens was measured according to NF P 18-459 standard.

Compressive strength measurement: compression strength was measured on six half-samples obtained after bending test on 70 x 70 x 280 mm specimens. The mechanical tests were carried out on concrete samples at 1, 7, 28, 90 and 360 days of hardening at 20°C and 95% of relative humidity.

Plastic shrinkage testing: plastic shrinkage was measured using a specific device closed to the one developed in (Turcry et al 2004). The designed device enables the measurement of horizontal deformation of fresh concrete specimens as well as its vertical settlement as illustrated in figure 1.

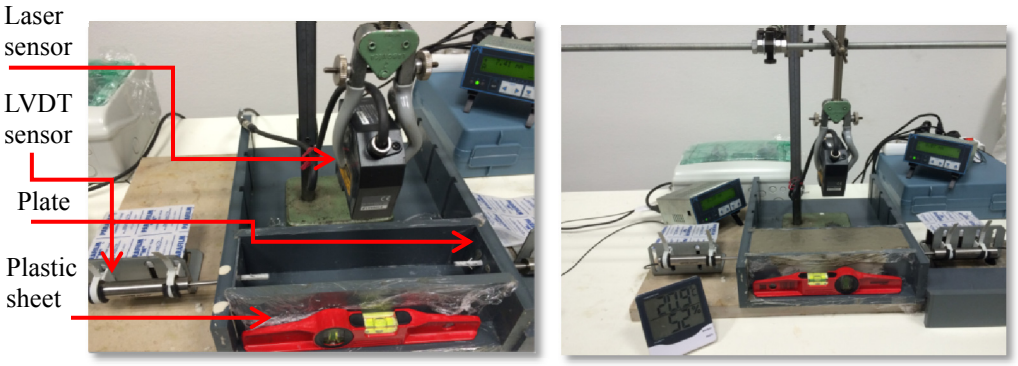

Figure 1. Plastic shrinkage device used in this study

It consists of a prism-shaped PVC mould (70 mm x 70 mm x 280 mm) where the internal sides were covered with a "plastic sheet" to reduce friction between concrete and the mould. Two LVDT sensors were used to monitor and measure the horizontal displacement, at mid-height of the specimen, of the plates dragged along by the concrete while shrinking. These sensors have an accuracy of 2µm.Plastic shrinkage was then deduced. A thermocouple was placed in the middle of the sample to allow thermal monitoring of the concrete during the test. Tests were performed in an air-conditioned room with a temperature of 20±1 °C and relative humidity of 50±2%. Plastic shrinkage tests were realized in two environmental conditions: (1) Sealed conditions where the top surface of the specimen was covered by a plastic sheet to prevent drying. In this case, the measured shrinkage corresponds to the autogenous one that is only caused by cement hydration. (2) Free and dry conditions

where the top surface was allowed to dry. In this case, shrinkage is caused by both drying and cements hydration. Mass loss measurements were carried out on cylindrical specimens with a diameter of 100 mm and 70 mm of height, placed on electronic balances. Evaporation E is defined by the ratio: $E(\mathbf{t}) = [m_0 - m(\mathbf{t})]/S$, where m_0 is the initial mass of the sample, m(t) the mass of the sample at time t and S is the evaporation surface area.

Measure of shrinkage: The measure of shrinkage was performed according to NF P 15-433 standard on prismatic specimen (70 mm x 70 mm x 280 mm). The measurements started just after demoulding using a digital comparator with an accuracy of 0.001 mm. Mass losses of the specimen were monitored in order to investigate the relationship between the variation in mass and drying shrinkage of each mixture.

Restrained shrinkage testing: The restrained shrinkage test was performed in accordance with AASHTO PP34-98 standard practice for estimating the trend of concrete cracking. The concrete was cast around a steel ring that had an inner diameter (r_1) of 260 mm and an outer diameter of 310 mm (r_2). The concrete ring had an diameter of 380 mm (r_3) and a height of 140 mm. The geometry of the ring is described in Figure 2. Three strain gauges are glued at mid-height outer surface of the steel ring to control the deformation in the steel ring caused by the shrinkage of concrete. Other three strain gauges are glued at mid-height on the outside surface of the concrete ring to measure the restrained shrinkage of concrete as shown in figure 2. As the concrete shrinks, a compressive stress is produced in the steel ring, which is balanced by a tensile stress in the concrete. When cracking occurs in the concrete, the stress and thus the strain in the steel ring is released. Strain gauges were connected to a computer. The deformation values were recorded every 5 minutes for 40 days. Measurements of crack opening were also recorded every 5 minutes using a crack sensor. Specimens were then placed in a air-controlled environment of $20\pm1°C$ and $50\pm2\%$ relative humidity. In order to ensure a radial drying, the top surfaces of the concrete rings are protected from drying by a double layer of aluminum adhesive.

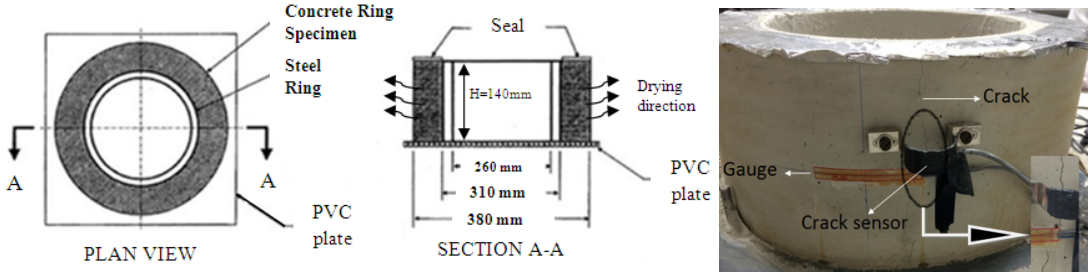

Figure 2. Restrained ring specimen geometry and device.

Calculation of residual stress in the rings: The ring test was used to measure the restrained shrinkage and predict cracking in cementitious materials (mortar, concrete). This test may also give information about the residual stresses present after cracking that develop in these materials at the interface with the ring. Indeed, must be considered the concrete ring as a cylinder exposed to uniform pressure on its internal

surface, while the metal ring is exposed to the same pressure on its outer surface. The residual stress can be calculated thanks to an analytical approach proposed by Yuan Gao and Jun Zhang (2013). According to this approach, one can calculate the maximum residual stress developed in the concrete according to the deformation measured by the strain gauges placed on the concrete rings. These stresses were calculated according to this equation $\sigma_{eff}(t) = \sigma_{tot}(t) - \sigma_R(t)$ where $\sigma_{eff}(t)$ is the effective stress due to the shrinkage; $\sigma_{tot}(t)$ is the total stress measured by the strain gauges and $\sigma_R(t)$ the stress due to creep. $\sigma_{eff}(t)$ is calculated using the equation $E\varepsilon_{eff}(t) = E\varepsilon_{sh}(t) - E\varepsilon_{creep}(t, t_0)$ where ε_{sh} is effective shrinkage strain that actually be used for generation of shrinkage stress in the concrete ring, t and t_0 are loading end and the load start time respectively and E is elastic modulus of concrete. ε_{creep} is the creep strain after loading period of (t, t_0). The creep strain may relate with the effective shrinkage strain by a so-called creep coefficient factor φ: $\varphi(t, t_0) = \frac{\varepsilon_{creep}(t,t_0)}{\varepsilon_{eff}(t,t_0)}$. Different models exist for the prediction of creep coefficient of concrete, in this study the CEB-FIP 1990 model for estimating the creep coefficient is used. From calculating the creep coefficient, one can obtain effective shrinkage strain by:

$$\varepsilon_{eff}(t) = \varepsilon_{sh}(t)\left[1 - \frac{\varphi(t,t_0)}{1+\varphi(t,t_0)}\right] \quad \text{Eq. [1]}$$

After considering creep of concrete, the interfacial pressure stress generated from concrete shrinkage should be reduced. Yuan Gao and Jun Zhang (2013) obtained the interfacial pressure stress after considering creep relaxation for varied loading history as:

$$q = \frac{-\frac{2}{r_3^2 - r_2^2}\sum_{i=1}^{n}\left[1-\frac{\varphi(t,t_i)}{1+\varphi(t,t_i)}\right]\int_{r_2}^{r_3}\varepsilon_{shi} r dr}{\frac{1}{E_1}\frac{(1-\mu_1)r_2^2+(1+\mu_1)r_3^2}{r_3^2+r_2^2}+\frac{1}{E_2}\frac{(1-\mu_2)r_1^2+(1+\mu_2)r_2^2}{r_2^2+r_1^2}} \quad \text{Eq. [2]}$$

On the other hand, the interfacial stress q can be related to the inner surface strain on the steel ring, ε_θ:

$$q = -[1 - \left(\frac{r_1}{r_2}\right)^2]E_2\varepsilon_\theta \quad \text{Eq. [3]}$$

The strain ε_θ is measured from experiments by the gauges on the steel ring.

RESULTS AND DISCUSSION

Microstructure analysis

Table 3 shows the results regarding to evaporable and non-evaporable water content for the four binder pastes. The results show a higher content of bound water (non-evaporable water) in the SCC-CEM I/MK compared to the other blends, which indicate its greater hydration and thus the likely development of a greater amount of

hydrates. The SCC based on CEM V has the highest free water content (evaporable water) close to that of SCC-CEMIII.

Table 3. Water porosity, evaporable and non-evaporable water content values

Mixtures	*SCC CEM I*	*SCC CEM III*	*SCC CEM V*	*SCC CEMI/MK*
Evaporable water content (%)	22.3	23.9	23.1	22.0
Non-evaporable water content (%)	25.3	24.7	24.4	25.7
Water porosity at 28 days	19.1	20.7	20.3	18.0

These results are in a good agreement with the measures of water porosity which shows a lower porosity for the SCC containing metakaolin compared to the reference SCC. SCC-CEM III has a higher porosity compared to SCC-CEMV.

Compressive strength

The compressive strength of the different mixtures at different ages is shown in Figure 3. As can be expected the compressive strength of all the studied SCCs enhanced by the age of concrete. The experimental results show that the replacement of Portland cement by 15% of MK involves a significant decrease of the compressive strength at very early ages. At one day of hardening, compared to the reference SCC, a decrease of 18% is obtained. However, at 7 days, this decrease drops to 6% and at 28 days of hardening, SCC with MK exhibits higher compressive strength value than reference SCC.

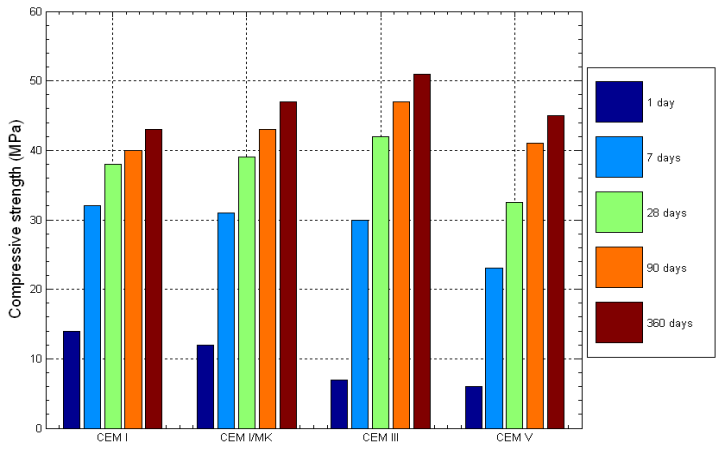

Figure 3. Evolution of compressive strength of SCCs mixtures with age

This result suggests that MK have an important effect on the development of hydrates even before 28 days of aging probably due to its pozzolanic reactivity and to nucleation sites that it offers (Khatib et al 2005). This remark is consistent with both non-evaporable water content and water porosity experimental results. Compared to SCC with MK, SCCs with CEM III and CEM V exhibit lower compressive strength at early ages particularly due to the well-known slow hydration kinetics of slag. However, at long term, SCC with CEM III presents the highest compressive strength (17% higher than reference SCC at 360 days).

Plastic shrinkage

The measures of horizontal plastic shrinkage and settlement of concrete samples are given in Figure 4.

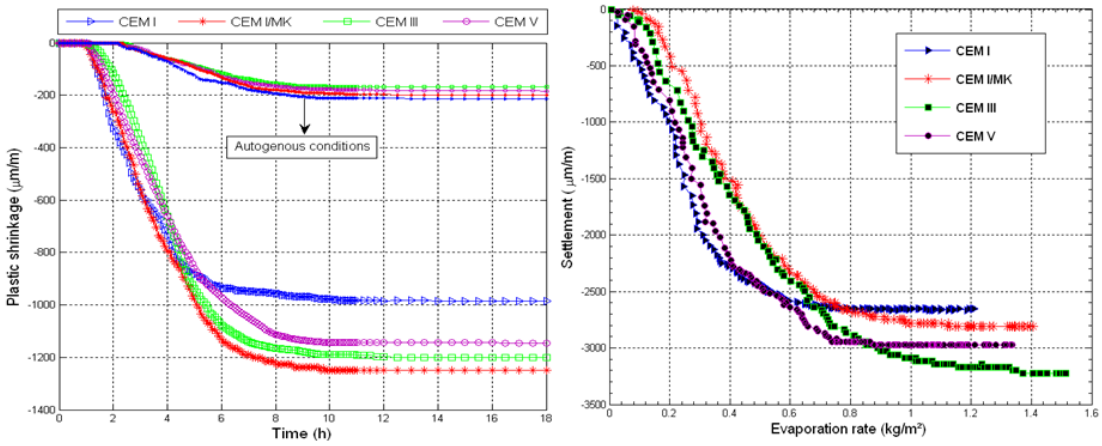

Figure 4. Measures of plastic shrinkage with evaporation rate

Results show that SCCs with mineral admixtures present higher plastic shrinkage than reference SCC. SCC with MK exhibits the highest plastic shrinkage (1250 µm/m at 18 hours) followed by CEM III and then CEM V. Results of settlement vs. mass loss are shown in Figure 4. All curves present an important decrease followed by a plateau. SCC-CEM III shows the highest settlement: 17.8% and 9% greater than SCC-CEM I and SCC-CEM V respectively. Mixture with metakaolin exhibits a moderate settlement 7% higher than the one of the reference SCC at 15 hours. In the reference SCC, settlement stopped at 3 hours after casting, while in the SCCs with minerals admixtures, settlement stopped later. Thus, the value of the settlement depends on the nature of the mineral addition.

Drying and Autogenous shrinkage

The strain developments versus time of the total and autogenous shrinkage of the studied SCCs are illustrated in figure 5. From the results obtained at long-term, free shrinkage of reference SCC (711 µm/m) is closed to the one of CEM V-SCC (741 µm/m) and both are lower than the one obtained with CEM III-SCC (1007 µm/m) at 400 days. The relatively greater mass loss of the CEM III-SCC seems to support this explanation. The replacement of 15% of Portland cement by metakaolin decreases the amplitude of total shrinkage by 20%. This reduction can be explained by the low mass loss recorded for SCC-CEM I/MK as shown in Figure 5. Results obtained in the sealed conditions show that deformation of SCCs with CEM III and CEM V are characterized by the expansion of cement matrix at early age. This is important because it delays the autogenous shrinkage. This phenomenon was also observed by other authors (Lura et al 2003, Aly et al 2008). The expansion of slag cement SCCs is related to the formation of hydration products which apply crystalline pressures on the pore surfaces against which the growing rigidity of the cement matrix cannot compete at early age. According to our experimental results, SCC based on CEM III and CEM V exhibit a lower autogenous shrinkage than the one of

reference SCC during the six weeks and a higher autogenous shrinkage by 18% and 13% respectively at 400 days.

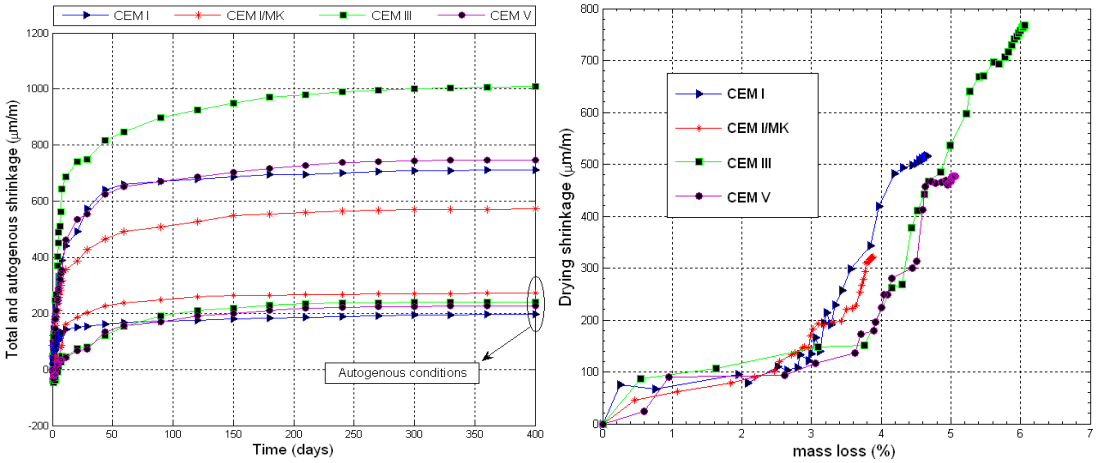

Figure 5. Measures of total, autogenous, drying shrinkage and mass loss

At long term, the use of 15% of MK increases the autogenous shrinkage by 28%. The use of suitable content of MK makes a cement paste have finer pore structures. The more the refinement process leads to the formation of finer pores, the more the self-desiccation shrinkage induced is larger (Brooks et al 2001). Self-desiccation shrinkage development is intimately related to fine pores known as the critical pore-size population and to the threshold pore radius. The finer the pore network, the more self-desiccation shrinkage is accentuated. Indeed, due to the refinement of pore size distribution, capillary tension increases faster, leading to an increase in autogenously shrinkage and to decrease drying shrinkage as shown in Figure 5.

Restrained shrinkage and stress calculated in the steel and SCC rings

Figure 6 shows the effect of admixtures on restrained shrinkage due to drying until 40 days. The effect of MK occurs only after 9 days with a slight decrease of shrinkage. In the long term, the presence of MK reduces the shrinkage of SCC-CEM I/MK concrete by 17% compared to SCC-CEM I. By comparing the development of shrinkage for the three types of cements, we find that CEM III concrete has a greater shrinkage by 26% and 21% relative to SCC-CEM I and SCC-CEM V respectively. The amplitudes of restrained shrinkage in CEM I and CEM V concrete are comparable: -610µm/m and -650µm/m respectively at 40 days. The shrinkage stresses developed in the interface of the steel and concrete ring is calculated from measure of strain concrete by the gauges. These stresses are calculated according to the equation [2] and strain measurements the figure 6 presents the residual stress calculated from the deformation of the concrete ring. SCC based on CEM III show greater shrinkage kinetics and low strength at early age compared to SCC-CEM I and SCC-CEM V which causes reach earlier at the threshold of elasticity and therefore crack earlier. Figure 6 gives also the stresses measured due to steel ring deformation. In these curves, stress falls to almost zero showing age of cracking which corresponds to the drop of deformations. The stress curves of the steel ring show that the SCC based on

MK seems to be subjected to lower stress compared to the SCC reference. However, the interface pressure and the residual stress that developed in metakaolin specimen were slightly lower. This may be due to a lower shrinkage in metakaolin mixtures.

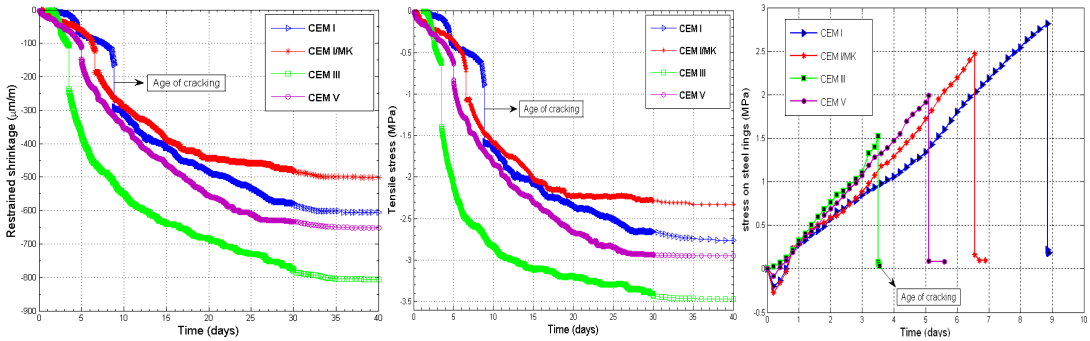

Figure 6. Development of strain and stress in concrete and steel (right) rings

Indeed the concrete may not result in a uniform deformation of the outside steel ring along its height (Z direction) and as a result, the strain measured at the mid-height of the ring may be higher than the strain that develops at the top and bottom of the ring. By comparing the three types of cements, we concluded that the SCC based on CEM III shows a higher stress in the interface of the concrete-steel ring before cracking due to a greater shrinkage at early age. After cracking, the concrete ring relaxes its stress and then, it comes down to zero and a fall in the curves of stress occurs that shows the age of cracking.

Crack initiation and propagation in SCC rings

Cracking age due to of a restrained shrinkage was determined by strain gauges. Figure 7 provides the age of cracking initiation of each mixture.

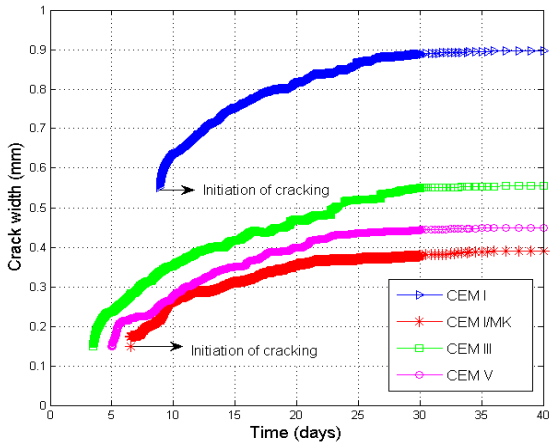

Table 4.Width and age of crack initiation

References	*Age of crack (days)*	*Crack width (mm)*
SCC-CEM I	8.83	0.9
SCC-CEM I/MK	6,56	0,39
SCC-CEM III	3.5	0.57
SCC-CEM V	5.1	0.46

Figure 7. Measured crack opening with time

The age of crack initiation was given by the abrupt drop on the deformation curves as shown in figure 6. The initiation point of crack opening was measured by a micrometer microscope and then crack width was monitored using a crack sensor. Figure 7 shows that SCCs with admixtures have cracked earlier than reference SCC. However the crack opening is lower and its propagation is limited when MK is used. The SCC-CEM I/MK exhibit a lower crack opening, 2.3 times lower than the one of

SCC-CEM I. This reduction can be attributed to the fine porosity involved by of the use of MK. The findings of the current study agree with the observations of Guneyisi et al 2012. They concluded that the incorporation of metakaolin into concrete can reduce the restrained shrinkage cracking width.

CONCLUSION

Based on the findings of this study, the following conclusions may be drawn:

- At very early age, SCCs using CEM III, CEM V or CEM I + 15% of metakaolin exhibit a higher free plastic shrinkage and settlement than SCC based on portland cement. However, in autogenous conditions, the plastic shrinkage is lower for SCCs with mineral admixtures. This can be linked to their slow hydration kinetics.
- In restrained and drying conditions, one crack was developed on the different mixtures at different ages: first in the CEM III-SCC, then in CEMV-SCC followed by SCC with CEM I+15% of MK and finally in CEM I-SCC, showing the sensibility of SCCs with mineral admixtures to early cracking. However, the crack opening is reduced by at least a factor of 2. This is due to their higher content of evaporable water and their lower mechanical performances at early ages.
- At long term and in free drying conditions, shrinkage of SCC-CEM V is closed to the one of SCC-CEM I and both are lower than the one obtained with CEM III cement. However, SCC with metakaolin presents the best resistance to free drying shrinkage. Substituting portland cement by 15% of metakaolin involves a significant decrease on the total shrinkage by 20% at 400 days.

REFERENCES

Aly, T. and Sanjayan, JG. (2008). "Shrinkage cracking properties of slag concretes with one day curing."*Mag Concr Res*; 60:41–8.

Brooks, JJ. And Johari, MA. (2001). "Effect of métakaolin on creep and shrinkage of concrete."*Cement Concrete Comp;* 23(6):495–502.

GuneyisiEr. (2012). "Strength, permeability and shrinkage cracking of silica fume and metakaolin concretes."Mermerdas. *Construction and Building Materials* 34 120–130

Khatib, JM. and HIBBERT, J.J. (2005). "Selected engineering properties of concrete incorporating slag and Métakaolin."*Construction and Building Materials* 19, 460 472

Lura P. (2003). "Autogenous deformation and internal curing of concrete."DTU, The Netherlands, PhD thesis; 180p.

Poon, CS. Lama L, Koua SC, Wonga YL, Wong R. (2001). "Rate of pozzolanic reaction of métakaolin in high performance cement pastes." *Cement Concrete Res*;31(9):1301–6.

Turcry P., Loukili A. (2006)."Evaluation of plastic shrinkage cracking of self consolidating concrete."*ACI Materials journal*, 2006, *Res*; P: 272-279.

Yuan G., Jun Z., and Po H. (2013)."Determination of stress relaxation parameters of concrete in tension at early-age by ring test" *Construction and Building Materials* 41 152–164.

Experimental Study on the Effects of Aggregates Restraint on the Delayed Behavior of Cementitious Materials

M. Malbois; A. Darquennes; C. De Sa; and F. Benboudjema

LMT-Cachan/ENS-Cachan/CNRS/Université Paris Saclay, 61 Ave. du Président Wilson, 94230 Cachan. E-mail: malbois@lmt.ens-cachan.fr; darquennes@lmt.ens-cachan.fr; de-sa@lmt.ens-cachan.fr; benboudjema@lmt.ens-cachan.fr

Abstract

The drying of concrete induces surface microcracking due to hydric gradients, and intern microcracking due to drying shrinkage incompatibilities between cement paste and aggregates. The difficulty of separating each size effect on concrete cracking makes it hard to quantify aggregates effects with classical experiments. An ongoing parametrical experimental study aims at quantifying the impact of drying and of inclusions by using morphologically controlled materials. In these materials, the aggregates size and volume fraction is set. The samples are then submitted to drying and regularly controlled for mechanical and transport properties. Also, microcracks development is followed using X-Ray tomography. The first results indicate the low impact of aggregates size, whereas the one of volume fraction is significant. The study is to be enhanced of several results: different formulations and tests to assess the evolution of mechanical and transport properties at several ages are currently undertaken.

INTRODUCTION

ANR MOSAIC. The French project ANR MOSAIC is a collaboration between four French laboratories all recognized for their expertise within the field of cement-based materials durability: LML (Lille, France), LMT Cachan (Cachan, France), LMDC (Toulouse, France) and IFSTTAR (Marne-la-Vallée, France).
This project investigates, experimentally and numerically, the effect of drying and delayed ettringite formation but also their coupling, at a mesoscopic scale.

First, this project plans to set up an experimental methodology based on studying the two types of pathologies on two classes of materials:

- Materials where the mesoscale morphology is completely controlled : “morphologically controlled” materials
- Materials where the mesoscale morphology is uncertain : “real” materials

The study of the morphologically controlled materials aims at easily uncoupling the influent parameters (as aggregates size or aggregates distribution) on the global behavior of the concrete.

In order to assess the role of the morphology within the pathologies development, but also to allow the gathering of results of all the members of the

project, these materials must be built from the same components: cement, aggregates, water to cement ratio.

In a second time, the MOSAIC project aims at developing a predictive way of modeling the consequences of the two phenomena at a mesoscopic scale.

Drying. Drying consists in water departure from the structure due to the imbalance with the environment. The water loss leads to drying shrinkage strains and stresses gradients that may lead to superficial microcracking. These microcracks are perpendicular to the surface of the structure. Besides it is mostly the cement paste that shrinks – the aggregates are generally inert regarding drying – therefore, it leads to strains and stresses gradients between cement paste and aggregates due to the restraint of drying shrinkage of cement paste by the aggregates (Figure 1). This phenomenon induces the debonding at the cement paste - aggregates interfaces (circumferential cracks) and the development of inter-granular cracks (radial cracks) ([Lagier et al., 2011], [Bisschop et al, 2002, a], [Hearn, 1999], [Goltermann, 1995]). These two types of cracking may change in a significant manner mass transfer properties, which are of major importance for durability aspects and when trying to ensure a well-controlled confinement of the structure (e.g. problematic of nuclear waste storage). Many papers deal with the structural effects of drying, reporting qualitative and quantitative experimental ([Bisschop et al, 2002, a&b], [Burlion et al, 2003], [Burlion et al, 2005], [Torrenti, 1987]) and numerical studies ([Burlion et al, 2005] [De Sa et al, 2008]). Few works have been devoted to cement paste and aggregates strain incompatibilities. This lack of numerical and experimental knowledge dealing with this heterogeneity effect can be associated to the difficulty of separating each size effect on concrete cracking. Moreover, a lot of parameters are linked to aggregates effects on a drying concrete specimen (e.g. shapes, size distribution, aggregates type, surface rugosity and interfacial transition zone), which experiments is an important challenge.

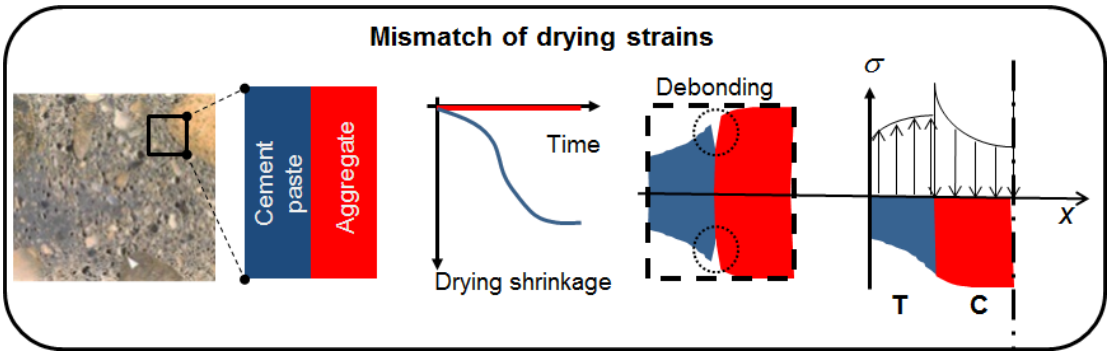

Figure 1 - Figure 1 – Cracking mechanism: restraint of drying shrinkage of cement paste by the aggregates [De Sa, 2007]

Some recent works [Lagier et al., 2011] have investigated the experimental decoupling of macroscopic and mesoscopic effects, studying more particularly the influence of concrete heterogeneity on cracking due to drying. These preliminary works, based on 2D digital image correlation experiments on morphologically controlled materials, have shown the ability quantifying cracking due to drying and

the impact of the heterogeneities (Figure 2). Numerically, several strategies can be considered to study drying effects. The literature ([Grassl et al., 2010], [Lagier et al., 2011]) has already underlined the interest of working at mesoscopic scale to describe the effects of heterogeneity. Yet, those works have not demonstrated the entire predictive feature of mesoscopic models.

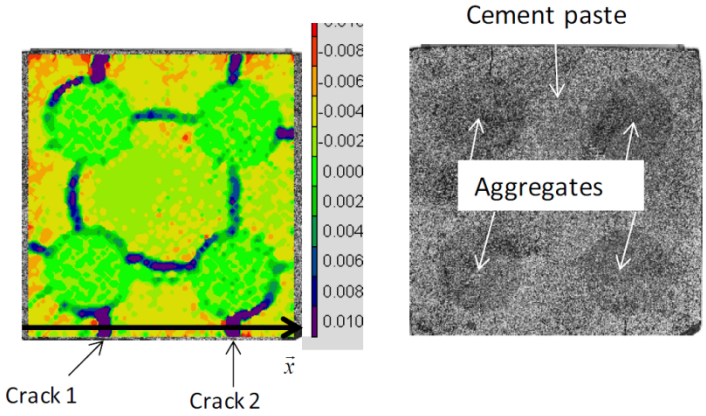

Figure 2 - 2D digital image correlation study on morphologically controlled materials investigating cracking due to drying incompatibilities between cement paste and aggregates. [Lagier et al., 2011]. Trace of the strain tensor.

In this paper we will focus on the ongoing experimental study led in the LMT Cachan dealing with the drying phenomenon and its impact on morphologically controlled materials. First, we will present the different materials studied, with the optimization process followed to set the different formulations. Then we will take interest in the different technics to assess the macroscopic effects of drying and the morphology impact. We will finally present and discuss the results.

MATERIALS

Formulation. As mentioned before, it is important that the laboratories all use the same concrete formulation. An internship led in the LMT Cachan was dedicated to determine it and adapt it for the morphologically controlled materials.
Calcia cement Airvault (42.5 MPa) has been used, since several studies dealing with drying in the LMT Cachan [Hilaire, 2014] have been undertaken and calcareous aggregates (Boulonnais aggregates) has been chosen, since it has been used several times at IFSTTAR.
Then the requirements of the formulation are:

- water to cement ratio : 0.57
- maximal diameter of aggregates : 12.5 mm

The reference formulation was obtained by modifying an existing formulation, provided by the LMDC (see Table 1).

The main objective is to perform a parametric study on drying of morphologically controlled materials:

- Inclusions sizes: aggregates diameter between 6.3 and 8mm and between 10 and 12.5mm.

- Inclusions volume fractions: 30% and 50% of the total volume.

This morphologically controlled materials lack most of the granular skeleton that would have insured a homogeneous distribution of the aggregates in the sample. The risks of segregation between the aggregates and the cement paste are thus significant. An adjustment and optimization of the reference composition needed to be performed. With this objective, the most unfavorable parametrical sets regarding the risk of segregation were chosen to improve the formulations tested and to select the best one: aggregates size of 10-12.5 mm, in a volume fraction of 30% of the total sample volume.

Two parameters were identified as influent on the segregation:

- Thickness of the cement paste, that can be modified by the use of additive
- Vibration of the sample

Table 1 – Existing and reference compositions for 1m3

Materials	Existing composition	Reference composition
Cement	400 kg	350 kg
Water	171 kg	201 kg
Sand (0-5 mm)	858 kg	858 kg
Aggregates (5-12.5mm)	945 kg	945 kg
Plasticizer	10 kg	0 kg
W/C	0,43	0,57
A/S	1,10	1,10
Volumetric mass	2384	2354

A first “Marsh cone” test was performed, to assess the evolution of a cement paste thickness when modifying the dose of additive. An optimal amount of 0.8 % of cement mass of additive was found, which correspond to the lowest flow of the cement paste.

In second time, the aggregates were added. Several samples were made to test the optimal value and the impact of vibration. The sections of samples revealed that all the vibrated samples (Figure 3) and the non-vibrated samples with the 0.8 % amount of additive (Figure 4, sample 1bis) presented segregation. The amount of additive was doubled and, without vibration, the section presented a satisfying distribution of aggregates (Figure 4, sample 2bis).

Once the components doses optimized, samples of the first three compositions of morphogically controlled materials were made.

These compositions are:

- Cement paste with 6-8 mm inclusions in a 50% volume fraction
- Cement paste with 10-12.5 mm inclusions in a 50% volume fraction
- Cement paste with 10-12.5 mm inclusions in a 30% volume fraction

They will allow us to assess the impacts of volume fraction and aggregate size.

They will then later be completed by three other compositions:

- Cement paste
- Mortar
- Cement paste with 6-8 mm and 10-12.5mm inclusions in a 50% volume fraction

We will now see by which means we will assess the different effects of drying and of aggregates.

Figure 3 - Vibrated samples for 0.8 and 1.6% of additive

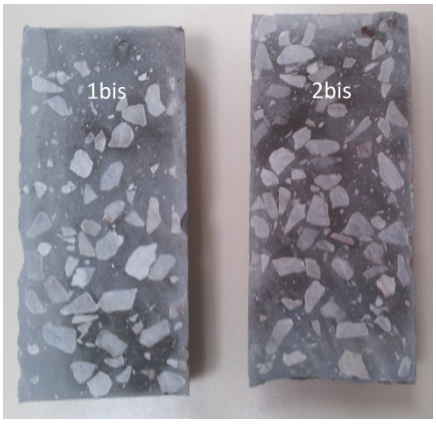

Figure 4 - Non vibrated samples for 0.8 and 1.6% of additive

EXPERIMENTAL PROCEDURE

Tomography. A campaign of accelerated drying was conducted to conclude on the possible visualization and quantification of internal microcracks using a X-Ray microtomograph. X-ray microtomography is a nondestructive imaging technic allowing the access to the structure of a sample by numerically reconstructing a 3D volume using hundreds of 2D radiographies without needing to damage the samples by making cuts or impregnating them with revealing products (Bisschop and van Mier, 02). A X-Ray microtomograph is composed of X-Ray source, a rotary platform on which the sample is placed and a detector screen connected to a computer. 2D projections of the X-Ray absorption level of the sample are taken at many different angles. They are then mathematically reconstructed to produce a 3D map of the X-ray absorption of the sample. The X-Ray absorption level can be directly linked to the structure of studied object.

Mechanical tests. 3 points flexural test. 3 points flexural tests are performed at several deadlines: at 28 days, after the autogenous cure, and at the end of the drying period. The tests are performed on 3 70*70*280 mm prims for each composition, and charge operated at a 0,5mm/s speed. An apparatus was set up to ensure that no

punching phenomenon appears, and also to measure the sample exact maximum deformation (Figure 5).

Drying. Drying is studied on 70*70*280 mm prims. For each formulation, 3 samples are made. They are removed of their mold after 24h and immediately packed with two layers of aluminum foil. They are kept during 28 days under sealed conditions. Then, they are unwrapped to begin a drying phase, in a room controlled in temperature, 25 ± 1°C, and relative humidity, 30 ± 5%HR. To guaranty a unilateral drying, layers of aluminum foil are applied on the superior and inferior square faces of the prisms. The samples are regularly controlled for mass loss and shrinkage.
The latest is measured by the device presented in Figure 6. The prisms have an embedded apparatus made of brass, allowing the positioning of sample between a fixed support and a comparator. To have an access to the desiccation shrinkage, 3 prisms of each composition are also studied under sealed conditions.

Figure 5 – 3 points flexural test

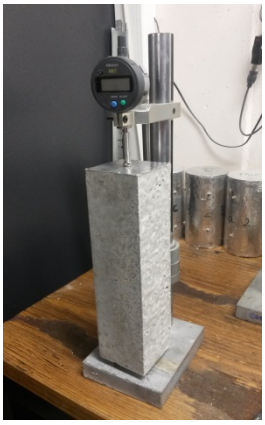

Figure 6 - Measurement of drying shrinkage

RESULTS AND DISCUSSION

Macroscopic effects of drying.

Development of cracking. Internal microcracking has an average opening of 1µm whereas the superficial one is around 50µm. Figure 8 shows a 2D projection of a 70*160 cylindrical sample, containing 30% of 10 to 12mm inclusions, obtained during the campaign of accelerated drying. The resolution of the image is 42µm and is an average of 30 projections taken at the same angle. It is possible to clearly observe the microcraks around the aggregates and connecting them. We then used the reconstruction software to reconstruct a smaller volume of the sample (300*300*300 pixel) and to isolate the microcracks as shown in Figure 7 ([Bouterf, 2014]). The internal microcracking has an average opening of 1µm, and the best resolution achieved was 42µm. The residual noise is the same size of the cracking, it was impossible to achieve a precise quantification of cracking. Nonetheless, the improvement of the images resolution could lead to a correct quantification, by using sample with a smaller diameter and changing the parameters of the tomograph.

Mechanical properties. On this day, only two compositions were tested after the first deadline. Results are gathered in Table 2.

Comparing the Young Modulus, the inclusions size doesn't appear to have an impact for samples in autogenous conditions. Tests will be performed to test the impact of volume fraction of inclusions, and of drying when the samples are mature. Some of these new results will be presented during the presentation.

Table 2 – Results of the 3 points flexural test on two compositions

Composition *Inclusions*	Maximum Charge	Tensile Resistance	Young Modulus
6-8mm – 50 %	5896 N	3,347 MPa	23,35 GPa
10–12 mm – 50%	5038 N	2,776 MPa	24,17 GPa

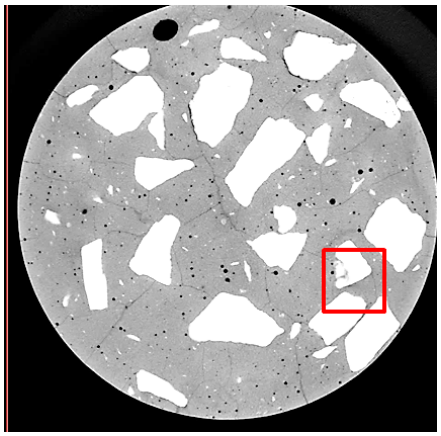

Figure 7 - Internal cracks after accelerated drying – 1700*1700 pixels - 42µm resolution

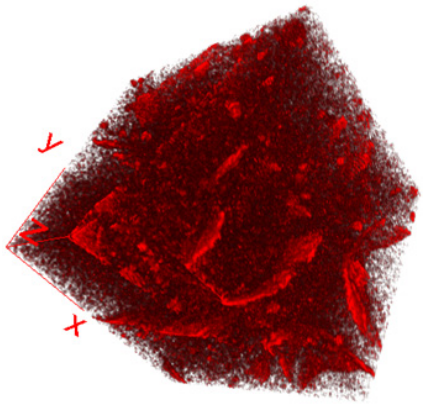

Figure 8 - Numerical reconstruction of the cracks of the cropped area (300*300 pixels)

Morphology effects: impact of size and volume fraction of aggregates

Shrinkage. Figure 9 presents the global evolution of mass loss on the first 70 days of the drying period. As expected, the mass loss curves display a decrease of mass loss for higher aggregates volume fractions. Moreover, Figure 9 presents the evolution of mass loss of samples under sealed conditions. The autogenous mass loss can be neglected face to the total mass loss.

As said before, we make the hypothesis that the water departure is due to the cement paste and thus depends on its volume fraction. To validate this hypothesis, Figure 10 presents the relative mass loss normed by the cement paste fraction. The curves are very similar in this case. This confirms that the aggregates do not influence the mass transfers within the concrete and that potential difference in term of cracking does not have a significant impact on water transport properties. Future test on cement paste only will unveil in a more relevant way the effects of aggregates.

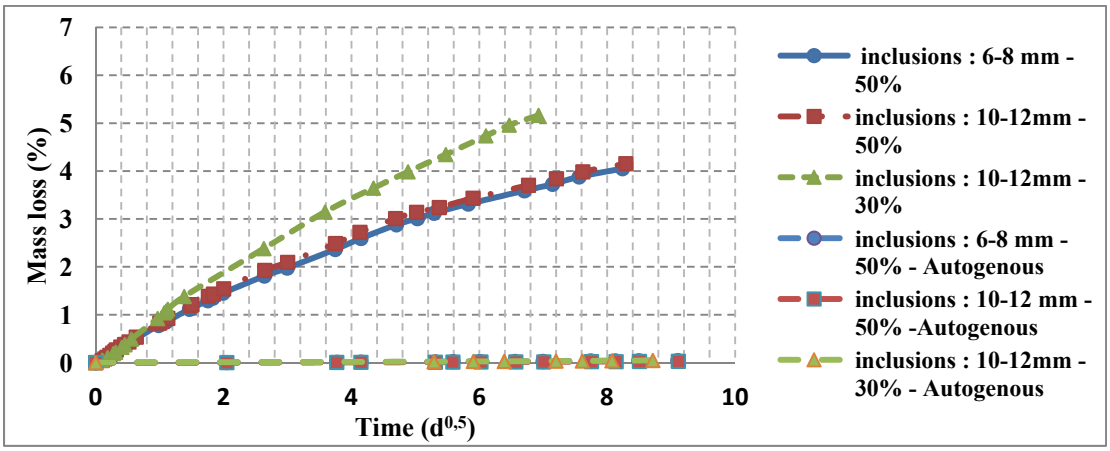

Figure 9 - Mass loss evolution of different compositions with time under drying and autogenous conditions

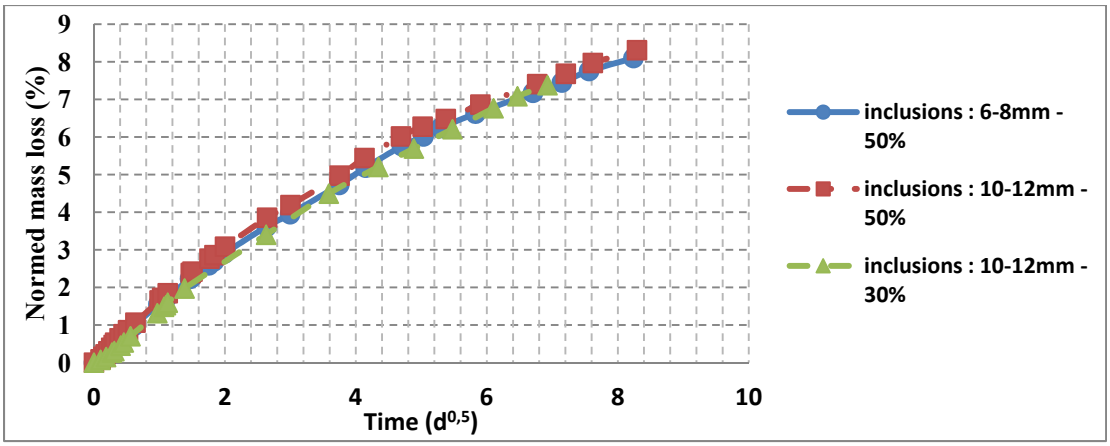

Figure 10 - Evolution of mass loss normed by cement paste volume fraction with time under drying conditions

Total shrinkage of the different composition is displayed on Figure 11, under drying conditions, and Figure 12, under sealed conditions. Under drying conditions, we expected to observe a decrease of apparent shrinkage with the increase of the volume fraction of aggregates and that the size of inclusions has no significant influence. At this time (the test are in progress), the separation of the composition is not clear but these first results seem to indicate that it will appear with higher mass loss. Figure 12 indicates, that even after 28 days, autogenous shrinkage still occur, but remains limited and would not explain the lack of separation between compositions. It should be emphasized that we have intentionally chosen to plot total shrinkage, and not drying shrinkage, since Figure 12 indicates clearly some parasite drying. Some numerical simulations are currently undertaken to separate autogenous and drying shrinkage.

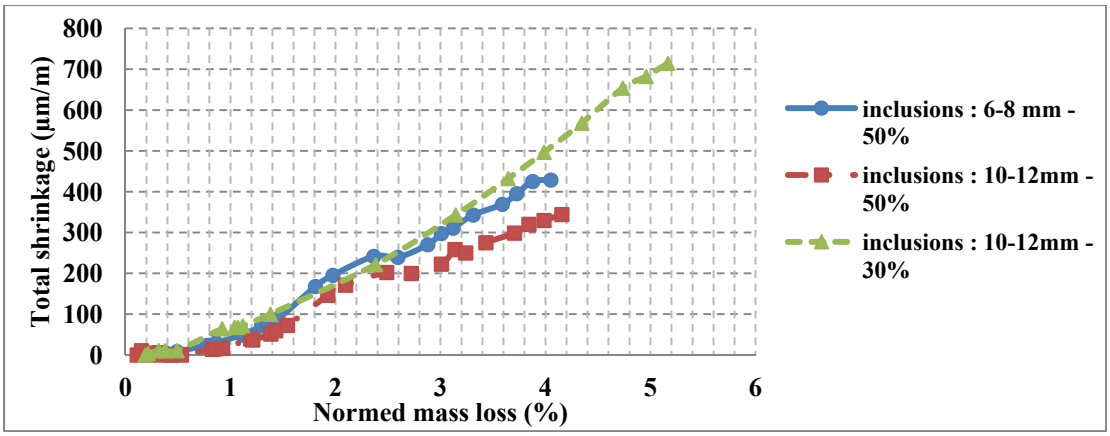

Figure 11 - Total shrinkage of different mesostructures versus relative mass loss percentage under drying conditions

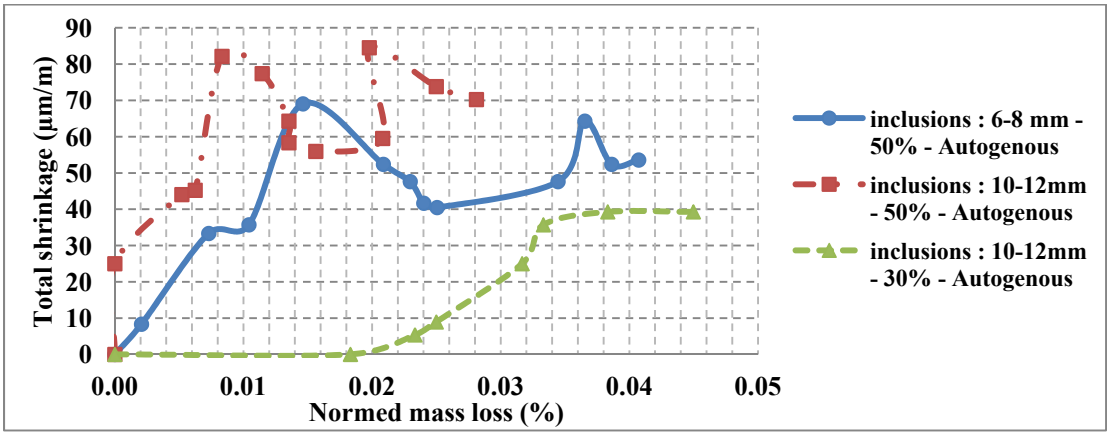

Figure 12 - Total shrinkage of different mesostructure versus relative mass loss under autogenous conditions (with parasite drying)

CONCLUSION

The results presented in this paper are the first of a more enhanced experimentation campaign. Within the next months, they will be completed by mechanical tests: compressive tests, and the end of the flexural tests; but also by several tests to conclude on the evolution of the transport properties (after potential drying cracks): water porosity, air permeation, chloride diffusion.

Moreover, three other formulations are to be tested: cement paste, mortar and "real" concrete, which will allow us to conclude more precisely on the effect of aggregates in concrete.

ACKNOWLEDGEMENT

This research was achieved in the framework of the French research Project ANR MOSAIC. The authors would like to extend their appreciation and gratitude for the financial support provided by the French National Research Agency.

REFERENCES

Bisschop, J. and van Mier, J.G.M. (2002). "Effect of aggregates on drying shrinkage microcracking in cement-based composites." *J. Materials and Structures*, Vol.30, September-October 2002, 453-461.

Bisschop, J. and van Mier, J.G.M. (2002). "How to study drying shrinkage microcracking in cement-based materials using optical and scanning electron microscopy." *J. Cement Concrete Res.*, 32, 279-287.

Bouterf, A., (2014) "Comportement mécanique de la plaque de plâtre étudié par tomographie et essais mécaniques in-situ." (In French), PhD thesis, Cachan, Ecole Normale Supérieure de Cachan.

Burlion, N., Yurtdas, I., Skoczylas F. (2003), "Comportement mécanique et séchage de matériaux à matrice cimentaire." (In French), Revue Française de Génie Civil, Vol.7(2), 145-165.

Burlion, N., Bourgeois F., Shao J.-F. (2005). "Effects of desiccation on mechanical behaviour of concrete." *J. Cement Concrete Compos*, 27, 367-379.

De Sa, C., (2007). "Etude hydro-mécanique et thermos-mécanique du béton",(In French), PhD thesis, Cachan, Ecole Normale Supérieure de Cachan.

De Sa, C., Benboudjema F., Thiery M., Sicard J., (2008). "Analysis of microcraking induced by differential drying shrinkage." *J. Cement Concrete Compos*, 30, 947-956.

Goltermann, P. (1995), "Mechanical predictions of concrete deterioration – Part 2: classification of crack patterns.", *ACI Mater. J.*, 92(1), 58-63.

Grassl, P., Wong, H.S., Buenfeld, N.R., (2010) "Influence of aggregate size and volume fraction on shrinkage induced micro-cracking of concrete and mortar", *J. Cement Concrete R.*, 40(1), 85-93.

Hilaire, A. (2014) "Étude des déformations différées des bétons en compression et en traction, du jeune âge au long terme", (In French), PhD thesis, Cachan, Ecole Normale Supérieure de Cachan.

Hearn, N. (1999), "Effect of shrinkage and load-induced cracking on water permeability of concrete.", *ACI Mater. J.*, 96(2), 234-241.

Lagier, F., Jourdain, X., De Sa, C., Benboudjema F., Colliat J.-B., (2011) "Numerical strategies for prediction of drying cracks in heterogeneous materials: Comparison upon experimental results", *J. Engineering Struct.*, 33(3), 920-931.

Torrenti, J.-M. (1987), "Comportement multiaxial du béton : aspects expérimentaux et modélisation." (In French), PhD thesis, Marne-la-Vallée, Ecole Nationale des Ponts et Chaussées.

Creep and Mechanical Properties of Concrete after Exposure to Elevated Temperatures

M. Guerrieri[1] and Sam Fragomeni[2]

[1]CESARE, College of Engineering, Victoria University, Werribee Campus, Melbourne 3030, Australia. E-mail: maurice.guerrieri@vu.edu.au
[2]College of Engineering, Victoria University, Footscray Park Campus, Melbourne 3011, Australia. E-mail: sam.fragomeni@vu.edu.au

Abstract
This paper discusses key processes and phenomena that occur when concrete is exposed to elevated temperatures up to 800 degrees Celsius which is of significant importance to high fire risk infrastructures such as Nuclear power plants. The majority of research in this field to date has concentrated on the mechanical properties of concrete such as compressive strength at elevated temperatures. In order to fully develop accurate computational analyses of the performance of concrete in fire, the long-term deformation of concrete known as creep at elevated temperature must be included. This is particular important since high fire risk infrastructures are designed for operation for a very long period of time and therefore their long-term deformation under elevated temperatures is of significant concern to design engineers. This paper presents a brief state of the art literature review regarding the mechanical properties of concrete and creep of concrete after exposure to elevated temperatures.

INTRODUCTION

Historically, the introduction of a type of concrete for construction purposes dates back to the Phoenician masons about 1500 BC and was later used during the Roman Empire (Hertz 2003). Today, over 3500 years since the invention of ancient concrete, and 150 years since the invention of Portland cement based concrete, concrete is the most widely used material in the construction industry. Its ease of placement and excellent structural performance makes it the most cost effective and efficient material to use for the construction of slabs, roads, bridges, beams, columns and other various construction applications. Over the past 100 years, concrete engineering continues to diversify with applications becoming ever more sophisticated, new structural forms are conceived and the requisite theories are formulated (Bazant 1996). A new development has been the application of concrete in various high temperature environments, for example, in the chemical and mechanical industry, in nuclear reactor structures and in the fire protection lining of walls and floors (Bazant 1996). These applications have resulted in the need to obtain knowledge of the performance of concrete at elevated temperatures. This has led many researches conducting extensive investigations on the fire performance of cement paste and concrete.

When exposed to fire, concrete deteriorates, as evidenced by progressive, and sometimes sudden, breakdown of the cement gel structure and therefore, consequential loss in its load bearing capacity (Lea and Stradling 1922). Research on the fire behavior of concrete began in the early 1920s (Lea and Stradling 1922) and since then, a number of studies have summarized the properties of cement paste and concrete under elevated temperature exposure, although primarily based on Ordinary Portland cement paste/concrete (OPCP/OPCC) (Schneider 1986, Phan 1996, Phan and Carino 1998, Phan and Carino 2001, Phan, Lawson et al. 2001). OPC materials are generally considered to have adequate fire resistance for most applications; however at elevated temperatures exceeding 105ºC, the mechanical properties of the cement paste and concrete deteriorate due to chemical and physical changes that occur in the hydrated phases of the binder, and therefore, some form of additional passive fire protection may be required.

In addition to strength loss, OPC materials are prone to spalling in fire (Phan 1996, Phan and Carino 1998, Phan, Lawson et al. 2001), which can reduce the concrete section thickness and expose the steel reinforcement to fire. Concrete spalling due to fire has received worldwide attention since the 1990s as the advent of high strength concrete in the 1980s and the consequent widespread use of high strength concrete in major constructions. The high risk of spalling in high strength concrete compared to normal strength concrete has also been identified (Sanjayan and Stocks 1993). Research of spalling of concrete in fire also received attention because of the three major accidents in Europe causing fire and spalling of high strength concrete, namely, Channel Tunnel in 1996, Mount Blanc Tunnel in 1999, and the St. Gotthard Tunnel in 2002 (Khoury, Majorana et al. 2002).

Over the last three decades, literature on the fire performance of cement pastes and concretes and the issue of concrete spalling has grown exponentially. However, due to the differences in concrete properties, design requirements and testing procedures and standards between countries, the research results have been scattered over a wide range of reporting media including journal publications, conference proceedings and various sections of books of broader scope (Bazant 1996).

In addition to strength loss, concrete materials are prone to undergo long-term deformation of concrete known as creep. Under elevated temperatures, the creep phenomenon is accelerated and becomes both time and temperature dependent. In order to fully understand the performance of concrete under elevated temperatures, it is important to understand the interdependent relationship between the mechanical properties and creep of concrete when exposed to fire. To date, many experimental works have been carried out which examine these interdependent parameters individually which have provided insight into the mechanisms which are occurring under the testing conditions, however there has only been limited works which link these interdependent parameters together.

Strength loss due to chemical decomposition: influence of the composition and structure of the hardened Portland cement paste

The microstructure of hardened Portland cement and the chemical composition of the hydration products have a direct bearing on the strength properties of Portland cement paste at elevated temperatures (Bazant 1996). Brouwers (2004) acknowledged that Powers and Brownyard (1947) were the first to study the reaction of water with cement to produce cement paste. At any stage of hydration, the major hydration products of the hardened cement are calcium-silicate-hydrate (C-S-H) and calcium hydroxide $Ca(OH)_2$ in addition to anhydrous cement, gel pores and capillary pores (Powers and Brownyard 1947, Bazant 1996, Brouwers 2004). The amount and nature of the water content in the gel and capillary pores is dependent upon the saturation conditions of the hardened cement paste (Bazant 1996). Under saturated conditions, water in the pores exists as capillary water (free water), absorbed water (gel water) and chemically bound water. When exposed to elevated temperatures, the hydration products and the water content state are altered (Bazant 1996) which causes strength loss of hardened Portland cement paste. These strength loss mechanisms can be categorized into the following components which have been derived by thermal analysis techniques involving thermogravimetric analysis (TGA) and differential thermal analysis (DTA): evaporation of free water, calcium-silicate-hydrate decomposition, calcium hydroxide decomposition and decarbonation of calcium carbonate. These mechanisms are described in detail below.

Evaporation of free water

At temperatures of up to 105°C, all water that can be evaporated in the hardened cement paste is considered to be evaporable water and consists of the free water in the capillaries and the absorbed water in the gel pores (Bazant 1996). Depending on numerous factors (including water cement ratios, moisture contents and duration of

drying exposure) strength gains in the order of 5% usually occur. Phan (1996) labeled this phenomenon as "dry hardening" with strength increases resulting from further hydration of the binders. This phenomenon has also been believed to be caused by strengthening due to confinement as a result of the evaporation of the free water. This leads to greater Van der Waal's forces as a consequence of the cement gel layers moving nearer to each other (Dias, Khoury et al. 1990, Khoury 1992, Xu, Wong et al. 2001).

Calcium-silicate-hydrate decomposition

Between 105 ºC and 800ºC, the dehydration of the C-S-H increases continuously and decomposes mainly into β-dicalcium silicate (β-C_2S), β-wollastonite (β-CS) and water (Harmathy 1970, Khoury 1992, Bazant 1996, Alarcon-Ruiz, Platret et al. 2005). Between 105ºC and 400ºC, water loss from the gel pores also occurs (Bazant 1996). Harmathy (1970) estimated the degree and rate of decomposition of the C-S-H with the aid of TGA and DTA of an idealized cement paste (Bazant 1996). At 500ºC, 50% of the decomposition of C-S-H is completed whilst at about 800ºC, the C-S-H is completely dehydrated. The rate of reaction is most rapid at around 200ºC as observed by Harmathy (1970). Based on the work of Buckle and Taylor (1959) who studied data from TGA and DTA investigations, Bazant (1996) has given a representative DTA of hardened Ordinary Portland cement paste and states that there is a narrow endotherm which peaks at about 110ºC and coincides with the release of free water. The C-S-H decomposition is represented by a broad endotherm which seems to commence at around 110ºC and asymptotes at around 800ºC (Harmathy 1970, Khoury 1992, Bazant 1996, Alarcon-Ruiz, Platret et al. 2005).

Calcium hydroxide decomposition

Between 450ºC and 550ºC, $Ca(OH)_2$ dehydrates to calcium oxide (CaO) which then rehydrates during cooling forming back $Ca(OH)_2$ according to the following equation:

$$Ca(OH)_2 \leftrightarrow CaO + H_2O \qquad \textbf{Equation 1}$$

Conversion of calcium hydroxide into calcium oxide causes chemically bound water to be gradually released and become evaporable water. The rehydration is accompanied by a volume increase which initiates cracks and disintegrates the concrete and thus decreases the compressive strength (Lea and Stradling 1922, Bazant 1996, Alarcon-Ruiz, Platret et al. 2005, Mendes, Sanjayan et al. 2008a). The conversion starts at around 400ºC and is completed at around 600ºC. The decomposition of the $Ca(OH)_2$ is related to the prominent endotherm at around 520ºC.

Decarbonation of calcium carbonate

The differential thermal analysis of Portland cement paste demonstrates a slight endotherm occurring at around the 800ºC mark. This is related to the decarbonation of calcium carbonate ($CaCO_3$) according to the following chemical equation (Bazant 1996, Alarcon-Ruiz, Platret et al. 2005):

$CaCO_3 \rightarrow CaO + CO_2$ **Equation 2**

The presence of calcium carbonate, although in small quantities is suggested to be present as a result of the carbonation by atmospheric carbon dioxide (CO_2) of the $Ca(OH)_2$ (Bazant 1996, Alarcon-Ruiz, Platret et al. 2005).

Strength loss due to physical mechanisms: thermal-incompatibility between Portland cement paste and aggregate:

Besides the chemical considerations leading to strength loss, Lea and Stradling (1922) proposed that the strength loss of OPCC at elevated temperature was a result of the thermal-incompatibility between concrete components (TICC) arising from unequal volumetric changes between aggregates and paste. The thermal-incompatibility phenomenon leads to internal micro stresses and micro cracking that can lead to strength reductions. This is due to the paste contracting at elevated temperatures relative to the aggregate. A number of authors have supported the thermal-incompatibility theory which is detailed in the literature review presented by Venecanin (1990).

The influence of various aggregates on the compressive strength of the concrete at elevated temperatures was studied by Chakrabarti and Jain (1999) who found that discrepancies in residual strength performances can be attributed to the competition between simultaneous thermal shrinkage of the paste and expansion of the aggregate which induces micro cracks and thus reduces the compressive strength. They concluded that the coefficient of thermal expansion of the aggregates is an important aspect to consider for the fire performance of concrete. However, the amount of thermal contraction of the paste must also be evaluated.

Mechanical Properties of Concrete at Elevated Temperatures

Mechanical properties of concrete at elevated temperatures are of primary interest in fire resistance design. The major mechanical property of interest of concrete exposed at elevated temperature is compressive strength. A brief literature review is presented below.

A detailed literature review regarding the compressive strength of concrete after exposure to elevated temperatures has been detailed in literature (Kodur 2014). Figures 1 and 2 respectively illustrate the variation of compressive strength of normal strength concrete (NSC) and high strength concrete (HSC) between all reported data in literature.

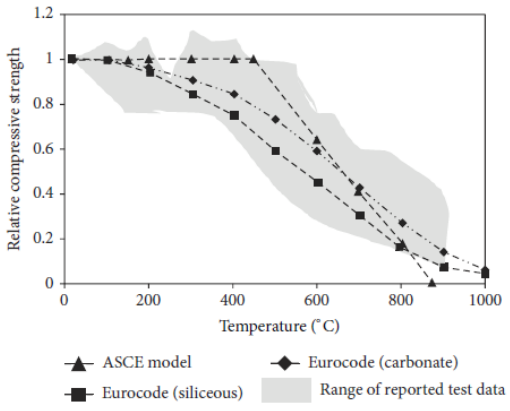

Figure 1: NSC Residual compressive strength strength Modified from Kodur (2014)

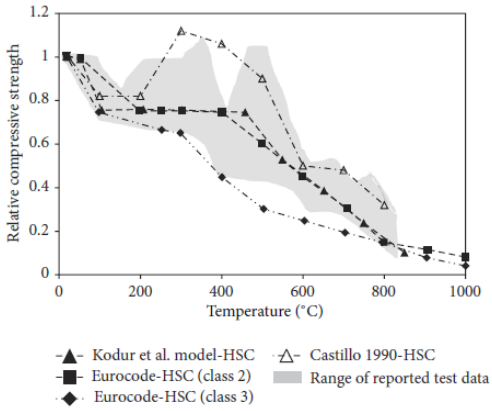

Figure 2: HSC Residual compressive Modified from Kodur (2014)

For comparative reasons, also plotted in these figures is the variation of compressive strength obtained using Eurocode (1992) Kodur (2008) and ASCE (1992). As pointed by Kodur (2014), there is more less variability in data for the HSC data above 500˚C. A plausible suggestion for this is that above 500˚C, fewer data points are available due to the occurrence of spalling or due to the limits of the furnace apparatus.

Among the factors that directly affect compressive strength at elevated temperatures include initial curing, moisture content at the time of testing, and the addition of admixtures of admixtures and silica fume to the concrete mix (Kodur 2014). As has been well been documented in literature (Phan 1996, Phan and Carino 1998), another main factor which influences results is the use of different testing conditions (unstressed tests vs stressed tests) and loading rates which is due to a lack of a standardized test method (Kodur 2014)

Deformation Properties of Concrete at Elevated Temperatures

Nuclear power plants are usually designed to remain in operation for a very long period of time and therefore their long-term deformation under elevated temperatures is of significant concern to design engineers. Under elevated temperatures, the creep phenomenon is accelerated and becomes both time and temperature dependent under compressive stresses (Kodur 2014). Under elevated temperatures, creep is accelerated due to the moisture movement out of the concrete matrix, moisture dispersion and loss of bond strength in the cement gel (C-S-H).

Neville (1983) summarized the creep of concrete under elevated temperatures. At 50˚C, creep strain was found to be approximately two to three times greater than at temperatures between 19-24˚C. Between 50-100˚C, Neville (1983) concluded the creep strain increases up to four to six times than that experiences at room temperature. From their experiments, Nasser and Neville (1965) found that the rate of creep at 70°C is 3.5 times greater than at 23°C. Creep test data obtained by Arthananari and Yu (1967) concluded that at 80°C, the creep is about two times greater than at 20°C. In this temperature range, Arthananari and Yu (1967) found that

there is no change in the fundamental creep mechanisms and the the creep strain is simply accelerated by the elevated temperatures.

Under exposure to significant temperature, the mechanisms causing creep may change given the chemical phase changes that occur in the microstructure of the cement paste these elevated temperatures (Mendes, Sanjayan et al. 2008a). Cruz (1968) conducted tests to investigate the elastic and inelastic properties of concrete exposed to high temperatures up to 650˚C for a period of five hours. The results of these tests are summarized in Table 1.0.

Temperature	Tests	Ratio of creep as a multiple of creep at 23˚C
(˚C)	#	
23	21	1
150	3	3.3
425	4	6.4
480	5	14.9
650	5	32.6

Table 1.0: Creep of concrete under various temperatures. Modified from Cruz (1968)

From Table 1, the creep at 480°C is about 15 times of the creep at room temperature, and the creep at 650°C is more than 30 times. Similar findings have been reported by Marechal (1972) who found that the creep strains at 480°C is also about 15 times of the creep at room temperature.

At elevated temperatures, it is postulated that the occurrence of creep occurs under completely different mechanisms under elevated temperatures compared to room temperature tests. Similar to the mechanical properties of concrete, chemical phase changes and deformations are occurring (Mendes, Sanjayan et al. 2008a). In order to design concrete structures that are prone to high temperature environments, for example, nuclear power stations, it is essential that calculations for long term creep deformations take into account the creep mechanisms at elevated temperatures.

Anderberg and Thelandersson (1976) developed constitutive models for creep and transient strains in concrete at elevated temperatures. These equations for creep and transient strain at elevated temperatures as suggested by Anderberg and Thelandersson (1976) are

$$\varepsilon_{cr} = \beta_1 \frac{\sigma}{f_{c,T}} \sqrt{t} e^{d(T-293)} \qquad \textbf{Equation 3}$$

$$\varepsilon_{tr} = k_2 \frac{\sigma}{f_{c,20}} \varepsilon_{th} \qquad \textbf{Equation 4}$$

where ε_{cr} = creep strain, ε_{tr} = transient strain, $\beta_1 = 6.28 \times 10^{-6} s^{-0.5}$, $d = 2.658 \times 10^{-3} K^{-1}$, T = concrete temperature (˚K) at time t (s), $f_{c,T}$ = concrete strength at temperature T, σ = stress in the concrete at the current temperature, k_2 = a constant ranges between 1.8 and 2.35, ε_{th} = thermal strain, and $f_{c,20}$ = concrete strength at room temperature.

CONCLUSION

When concrete is subjected to elevated temperatures, it undergoes significant chemical changes. These changes are detrimental to concrete as they can lead to reduced strength, concrete spalling and accelerated creep strains. Hence, the design of high fire risk concrete structures such as nuclear power stations need to take into account both the mechanical properties of concrete at elevated temperatures and sustainably, the long term deformation properties of concrete after exposure to elevated temperatures. These two mechanisms are interdependent as they both are related to chemical phase changes under elevated temperatures.

This paper presented a brief literature review of how fire exposure effects the mechanical and long term deformation parameters of concrete at elevated temperatures. The results from literature regarding the residual strength of concrete after fire exposure are available in substance, however, there is minimal data on the creep of concrete after exposure to elevated temperatures. The literature suggests that creep is accelerated after fire exposure, however, it remains unclear of the mechanism which generate this acceleration. It is postulated that the water mass loss of concrete during heating is the cause of the creep acceleration as it causes loss of bond strength in the cement gel (C-S-H).

REFERENCES

Eurocode 2, General rules—structural fire design, in: prEN1992-1-2: design of concrete structures, Part 1–2, Comité Europeén de Normalisation (CEN), Brussels, 2004.

(1992). ASCE, Structural Fire Protection, ASCE Committee on Fire Protection, Structural Division, American Society of Civil Engineers. New York, NY, USA, .

Alarcon-Ruiz, L., G. Platret, E. Massieu and A. Ehrlacher (2005). "The use of thermal analysis in assessing the effect of temperature on a cement paste." Cement and Concrete Research 35(3): 609-613.

Anderberg, Y. and s. Thelandersson (1976). "Stress and Deformation Characteristics of Concrete at High Temperatures. 2. Experimental Investigation and Material Behaviour Model." Bulletin 54, Lund Institute of Technology, Lund, Sweden.

Arthananari, S., and Yu, C.W. (1967). "Creep of Concrete Under Uniaxial and Biaxial Stresses at Elevated Temperatures " Magazine of Concrete Research, 19(60): 7.
Bazant, Z. (1996). Concrete at high temperatures - material properties and mathematical models. England, Longman Group Limited.
Brouwers, H. (2004). "The work of Powers and Brownyard revisited: Part 1." Cement and Concrete Research 34(9): 1697-1716.
Buckle, E. and H. Taylor (1959). "Hydration of tricalcium and beta dicalcium silicates in pastes under normal and steam curing conditions." Journal of Applied Chemistry 9(3): 163-172.
Chakrabarti, S. and A. Jain (1999). "Strength properties of concrete at elevated temperature - a review." Indian Concrete Journal 73(8): 495-501.
Cruz, C. R. (1968). " Apparatus for Measuring Creep of Concrete at Elevated Temperature." J. of PCA Research and Development Laboratories, PCA Research and Development Bulletin 225, Portland Cement Associations, 10(3).
Dias, W., G. Khoury and P. Sullivan (1990). "Mechanical properties of hardened cement paste exposed to temperatures up to 700°C (1292°F)." ACI Materials Journal 87(2): 160-166.
Harmathy, T. (1970). "Thermal properties of concrete at elevated temperatures." Journal of Materials 5(1): 47-74.
Hertz, K. (2003). "Limits of spalling of fire-exposed concrete." Fire Safety Journal 38(2): 103-116.
Khoury, G. (1992). "Compressive strength of concrete at high temperatures: a reassessment." Magazine of Concrete Research 44(161): 291-309.
Khoury, G., C. Majorana, F. Pesavento and B. Schrefler (2002). "Modelling of heated concrete." Magazine of Concrete Research 54(2): 77-101.
Kodur, V. (2014). "Properties of Concrete at Elevated Temperatures." ISRN Civil Engineering 2014: 15.
Kodur, V. K. R., M. M. S. Dwaikat and M. B. Dwaikat (2008). "Hightemperature properties of concrete for fire resistance modelingof structures." ACI Materials 105(5): 10.
Lea, F. and R. Stradling (1922). "The resistance to fire of concrete and reinforced concrete." Engineering 114(2959): 341-344.
Marechal, J. C. (1972). "Creep of Concrete as a Function of Temperature. In Int. Seminar on Concrete for Nuclear Reactors,
Detroit, 547-564." ACI Special Publication 34(1).
Mendes, A., J. Sanjayan and F. Collins (2008a). "Phase transformations and mechanical strength of OPC/Slag pastes submitted to high temperatures." Materials and Structures/Materiaux et Constructions 41(2): 345-350.
Nasser, K. W., and Neville, A.M. (1965). "Creep of Concrete at Elevated Temperatures." J. of ACI 62: 12.
Neville, A. M. (1983). Creep of Plain and Structural Concrete. London, Construction Press.
Phan, L. (1996). Fire performance of high-strength concrete: a report of the state of-the-art. Gaithersburg, Maryland, Building and Fire Research Laboratory, National Institute of Standards and Technology.

Phan, L. and N. Carino (1998). "Review of mechanical properties of HSC at elevated temperature." Journal of Materials in Civil Engineering 10(1): 58-64.
Phan, L. and N. Carino (2001). Mechanical properties of high strength concrete at elevated temperatures. Gaithersburg, Maryland., Building and Fire Research Laboratory, National Institute of Standards and Technology.
Phan, L., J. Lawson and F. Davis (2001). "Effects of elevated temperature exposure on heating characteristics, spalling, and residual properties of high performance concrete." Materials and Structures 34(2): 83-91.
Powers, T. and T. Brownyard (1947). "Studies of the physical properties of hardened Portland cement paste, Bull. 22, Res. Lab. of Portland Cement Association, Skokie, IL, U.S.A., reprinted from J. Am. Concr. Inst. (Proc.), vol. 43 (1947). pp. 101– 132, 249– 336, 469– 505, 549– 602, 669– 712, 845–880, 933–992.": 101-132.
Sanjayan, J. and L. Stocks (1993). "Spalling of high-strength silica fume concrete in fire." ACI Materials Journal 90(2): 170-173.
Schneider, U. (1986). "Concrete at high temperatures - a general review." Fire Safety Journal 13(1): 55-68.
Venecanin, S. (1990). "Thermal incompatibility of concrete components and thermal properties of carbonate rocks." ACI Materials Journal 87(6): 602-607.
Xu, Y. Wong, C. Poon and M. Anson (2001). "Impact of high temperature on PFA concrete." Cement and Concrete Research 31(7): 1065.

Analogy between Sustained Loading and Strain Rate Effects on the Nonlinear Creep Response of Concrete

Darko Tasevski[1]; Miguel Fernández Ruiz[1]; and Aurelio Muttoni[1]

[1]Structural Concrete Laboratory, School of Architecture, Civil and Environmental Engineering, Swiss Federal Institute of Technology Lausanne, EPFL IBETON, Station 18, CH-1015 Lausanne, Switzerland. E-mail: darko.tasevski@epfl.ch

Abstract

This paper investigates the uniaxial compression behaviour of concrete under different strain rates and its relation to sustained loading. The aim is to observe the strain rate effect on the pre- and post-peak behaviour of concrete. In particular, the development of nonlinear creep strains for different strain rates has been investigated and compared to the sustained load behaviour. The development of creep strains is in accordance with the progress of cracking as observed by acoustic emissions. An analogy is found between the concrete compression behaviour under various strain rates and the concrete compression behaviour under sustained loads at different stress levels.

INTRODUCTION

A reliable prediction of the time-dependent elastic and inelastic behaviour of concrete subjected to high levels of sustained loads is essential to understand the internal stress redistributions and the potential long-term failures occurring in structural concrete members. This behaviour is usually referred to as the time-dependent response of concrete, which is found to be nonlinear for stresses higher than 40% of the short-term concrete strength. Levels of stress above this threshold imply the development of inelastic creep strains (Fernández Ruiz et al. 2007), leading to redistribution of stresses occurring at different strain rates and at different locations in r/c structural members.

Previous research on elevated sustained loads has shown that the delayed creep effects do not only concern the serviceability of concrete structures but also their load-bearing capacity (Kaltakci et al. 2007). Failure under a sustained load can occur in a period of several minutes to several months after loading, depending on the degree of loading (σ/f_c). This phenomenon was initially investigated by Rüsch (1960), who concluded the existence of a critical degree of loading at which concrete is able to sustain over time without failing. He established the term "sustained load strength" referring to the stress at the critical degree of loading. According to Rüsch (1960), for a sustained load below the critical degree of loading concrete would reach the so called creep limit that is a maximal value of strain which could be obtained

depending on the degree of loading. Above the critical degree of loading, concrete would fail after a certain time again depending on the degree of loading.

Most of the researchers have found that the sustained load strength of normal strength concrete amounts around 70 % to 75 % of the short term strength (Rüsch (1960); Ngab et al. (1981); Smadi et al. (1982)). According to the experimental evidence of Rüsch (1960), the sustained load strength should be independent of the concrete short term strength, but Ngab et al. (1981), Smadi et al. (1982) and Iravani et al. (1998) observed that for high strength concrete, the sustained load strength is about 80 - 90% of the short term strength. Smadi et al. (1982) and Iravani et al. (1998) have also investigated the time of failure under high leves of sustained strain. For concrete with short-term strength of 35-40 MPa, Smadi et al. (1982) observed failure of several specimens under a sustained load of 75% of the short-term strength after 49 days, whereas several other specimens didn't fail during 6 months. Similarly, Iravani et al. (1998) observed failure of high strength concrete (short-term strength of 65 MPa) after 30 days and 7 days for specimens under sustained load of 75% and 80% of the short term strength respectively.

As for the influence of loading and strain rates on concrete compressive behaviour, most of the research in the last decades has been focused on high strain rates in order to understand the influence of impact loads. However, not many studies could be found on the influence of low strain rates apart of the work of Rüsch (1960). Some phenomenological studies on the effect of loading rate on the concrete compressive behaviour have been performed by Fernández Ruiz et al. (2007). Fischer et al. (2014) studied the loading rate effect on the behaviour of cement paste at young age, but these results cannot be taken as a reference for mature concrete.

This paper investigates the uniaxial compression behaviour of concrete under different strain rates and its relation to sustained loading. The aim is to observe the strain rate effect on the pre- and post-peak behaviour of concrete. In particular, the development of nonlinear creep strains for different strain rates has been investigated and compared to the sustained load behaviour.

EXPERIMENTAL STUDY

For the study of the influence of different strain rates on the uniaxial concrete behaviour of concrete, the Structural Concrete Laboratory of the Swiss Federal Institute of Technology in Lausanne is equipped with a Schenck Hydroplus servo-hydraulic testing machine with capacity of 2.5 MN and a custom-made steel frame which enhances the stiffness of the test setup. The testing machine is placed in a room with controlled temperature of 21±0.5 °C and a relative humidity of 52±3 %. The tests are performed on concrete cylinders of size øxh = 160x320 mm. The longitudinal strain ε_3 is measured with three omega strain gages fixed on two steel rings with a distance of 250 mm. The transversal strain ε_1 is measured with a steel ribbon dilatometer equipped with a linear variable differential transformer (LVDT).

A set of specimens was tested under constant strain rates from $2 \cdot 10^{0}$ [‰/s] to $2 \cdot 10^{-6}$ [‰/s] (time to failure from 1 second to ca. 12 days), using concrete cylinders with a mean 28-day compressive strength of 30.6 MPa (tested with the reference strain rate of $2 \cdot 10^{-2}$ [‰/s], i.e. test duration about 100 seconds). The age of the concrete at the time of testing was about 10 months (refer to Table 1 for the strength of concrete tested at the reference strain rate of $2 \cdot 10^{-2}$ [‰/s]). The general stress-strain behaviour is presented in Figure 1 and the results are presented in Table 1:

Table 1. Main experimental results.

$\dot{\varepsilon}_{pilotage}$ [s^{-1}]	$t_{u,expected}$ [s]	f_c [MPa]	ε_{3u} [‰]	t_u [s]	t_u [-]	$\dot{\varepsilon}$ [s^{-1}]
2E+00	1	41.8	1.88	0.85	1sec	2.2E+00
2E-01	10	40.5	2.03	9.26	10sec	2.2E-01
2E-02	100	38.7	2.01	98.6	100sec	2.0E-02
2E-03	1‘000	37.8	2.07	1‘010	17’	2.0E-03
2E-04	10‘000	37.1	2.36	11‘800	3h 17’	2.0E-04
2E-05	100‘000	36.5	2.61	113‘000	1d 7h	2.3E-05
2E-06	1‘000‘000	34.3	2.75	1‘050‘000	12d 4h	2.6E-06

$\dot{\varepsilon}$…strain rate, t_u…time at failure, f_c…compressive strength, ε_{3u}…longitudinal strain at failure

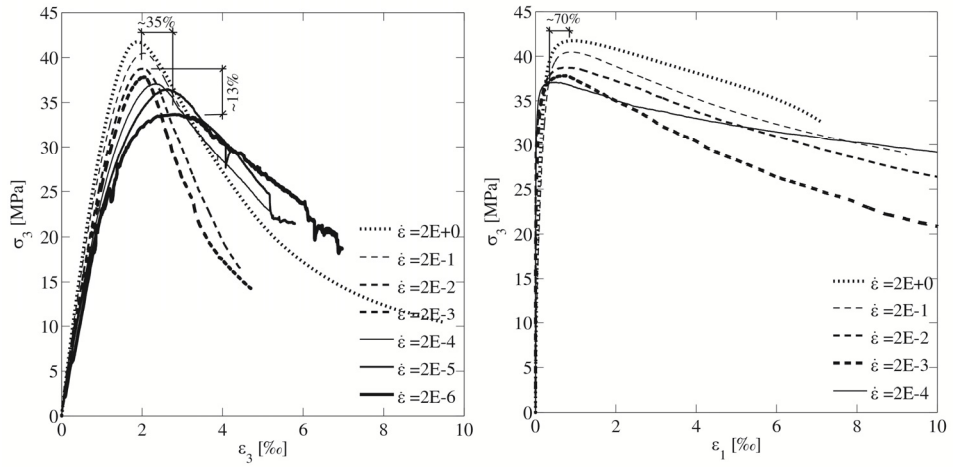

Figure 1. Stress-strain curves for longitudinal (left) and transversal strain (right).

The results of the experimental programme show that, with decreasing strain rate, the concrete strength reduces by about 13% (between the reference test of 100s and the slowest test of ca. 12 days). The associated strain at failure in the longitudinal direction follows an increase of about 35% with decreasing strain rate. As for the transversal strain, a decrease is observed for decreasing strain rate. In addition, a less brittle behaviour of concrete is observed after peak load for decreasing strain rates (lower slopes at the post-peak softening branch).

Acoustic Emission analysis was also performed during the tests in order to detect the development of cracks. An AE device with two piezoelectric sensors (frequency 100-1000 kHz) was used. The sensors were placed according to Figure 2. A pre-amplifier with a gain of 40dB was used to amplify the signal. The detection threshold was set to 60 dB in order to filter the high environmental noise caused by the hydraulic testing machine. The AE results are presented in Figure 3.

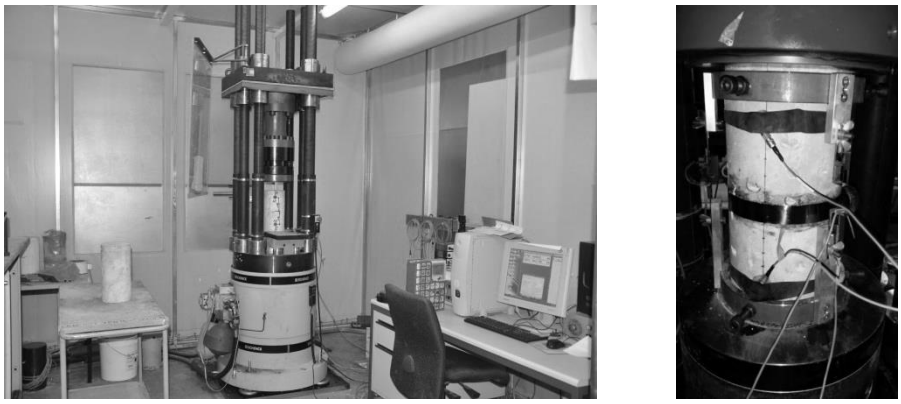

Figure 2. Servohydraulic testing machine (left). Position of the AE sensors (right).

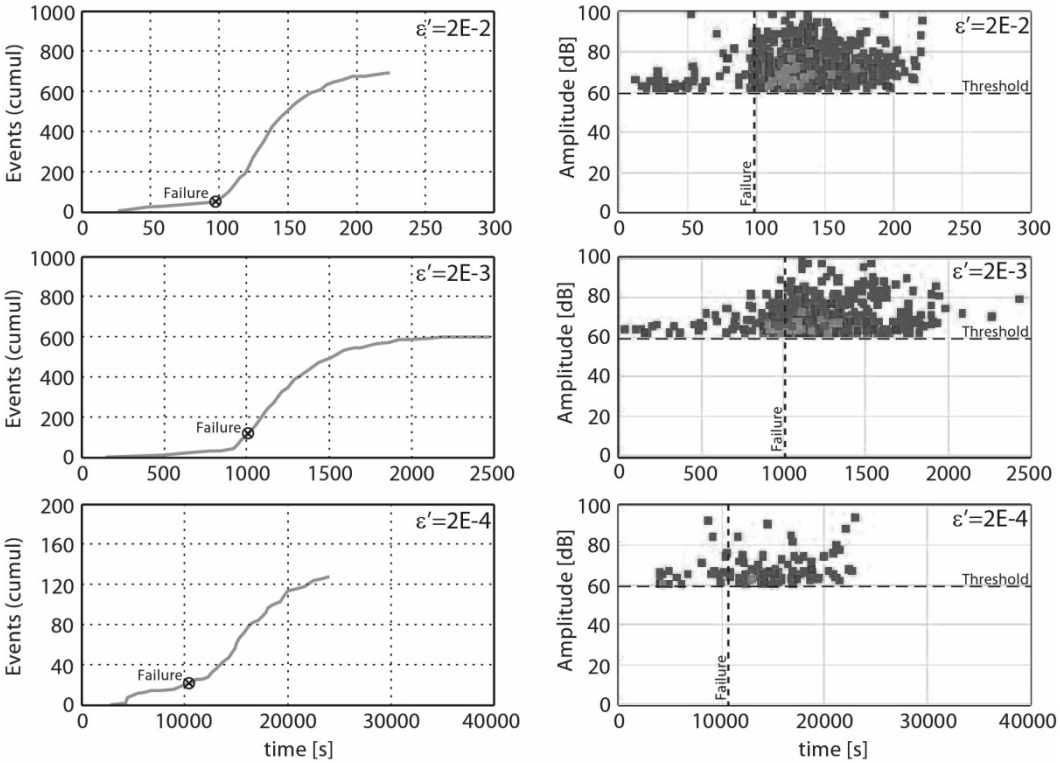

Figure 3. AE cumulative events and event amplitude distribution with time.

The development of creep strains is in accordance with the progress of cracking as observed by acoustic emissions (measurements performed on the specimens). The AE

results indicate that for lower strain rates the rate of micro-cracking increases more rapidly. Especially in the domain of elevated stresses (near to failure) a significant increase in the cracking rate and the corresponding amplitudes of the observed events is detected.

DISCUSSION OF RESULTS

The decrease of strength for lower strain rates can be linked to the fact that for lower strain rates, the time to failure is larger and thus larger nonlinear creep strains can potentially develop (concrete is subjected to higher levels of stress during larger periods of time). Consequently, more micro-cracks can develop in the material leading to damage of the internal structure and reduction of the strength. A similar behaviour has been also observed by Fernández Ruiz et al. (2007), who found that the cracks at lower loading rates have enough time to open and to propagate similarly to pure creep tests.

As observed by the AE measurements, the increase in propagation of micro-cracks for elevated levels of stress seems to be in accordance with the development of nonlinear creep strains. Consistent with the explanation of Fernández Ruiz et al. (2007), the three different phases of nonlinear creep strain development could be observed, namely the crack formation, the stable crack growth and uncontrolled crack propagation up to failure associated with tertiary creep. The first two phases are indicated by the changes of inclination of the cumulative event curve for the tests with lower strain rates (Figure 3 left). The increase in the amplitude of the corresponding acoustic signals is associated with the acoustic energy dissipated at crack propagation. The increase of the amplitude indicates the increase of the cracking rate at the initiation of the third phase for elevated stress levels (Figure 3 right). Similar behaviour was observed by Rossi et al. (1994) for compressive creep and by Denarié et al. (2006) for tensile creep. Rossi et al. (1994) found that the basic creep strain is proportional to the number of micro-cracks created in the material. Denarie et al. (2006) indicated that the internal damaged caused by creep-induced micro-cracking should be taken into account when evaluating the long term benefits of concrete viscoelastic behaviour.

Finally, an analogy is found in the phenomenological compressive behaviour of concrete under various strain rates and under sustained loads at different levels. An ultimate strength envelope for the varying strain rate could be clearly observed from the experimental evidence, consistently to the sustained load strength envelope observed under sustained loads at different levels as shown by Rüsch (1960). Thanks to this analogy, the phenomenon of failure under sustained load can be investigated. However, further experimental observations are necessary in order to better understand the correlation between the behaviour of concrete under these two types of loading.

CONCLUSION

This paper presents an experimental investigation on the influence of the strain rate on the uniaxial compressive behaviour of concrete. The main conclusions of this investigation are:

- Strain rate has a significant influence on the compressive strength and associated deformations of concrete.
- The concrete compressive strength decreases for decreasing strain rates.
- The longitudinal strain at peak load increases for decreasing strain rates.
- The transversal strain at peak load decreases for decreasing strain rates.
- The brittleness of concrete (defined as the area under the stress - longitudinal strain curve) after peak load increases for decreasing strain rates.
- Acoustic emissions confirm that the development of tertiary creep strains is related to the development of micro-cracking in concrete.

ACKNOWLEDGEMENT

The authors acknowledge the financial support from the Swiss Federal Roads Office.

REFERENCES

Denarié, E., Cécot, C. and Huet, C. (2006). “Characterization of creep and crack growth interactions in the fracture behavior of concrete”, *Cem. Concr. Res.*, vol. 36, no. 3, pp. 571–575, Mar. 2006.

Fernández Ruiz, M., Muttoni, A. and Gambarova, P. G. (2007). “Relationship between nonlinear creep and cracking of concrete under uniaxial compression,” *J. Adv. Concr. Technol.*, vol. 5, no. 3, pp. 383–393, 2007.

Fischer, I., Pichler, B., Lach, E., Terner, C., Barraud, E. and Britz, F. (2014). “Compressive strength of cement paste as a function of loading rate: Experiments and engineering mechanics analysis”, *Cem. Concr. Res.*, vol. 58, pp. 186–200, Apr. 2014.

Iravani, S. and MacGregor, J. G. (1998). “Sustained load strength and short-term strain behavior of high-strength concrete”, *ACI Materials Journal*, vol. 95, no. 5, pp. 636–647, Sep.-Oct. 1998.

Kaltakci, M. Y., Arslan, M. H. and Ozturk, M. (2007). "Results and Lessons Learnt from the Buildings which Failed under their own Weight in Turkey. "*Structural Engineering International*, vol. 17, no. 2, May 2007, pp. 159-165

Ngab, A. S., Nilson, A. H. and Slate, F. O. (1981). “Shrinkage and Creep of High-Strength Concrete,” *ACI Journal, Proceedings*, vol. 78, no. 4, pp. 255–261, July-Aug. 1981.

Rossi, P., Godart, N., Robert, J. L., Gervais, J. P. and Bruhat, D. (1994). “Investigation of the Basic Creep of Concrete by Acoustic Emission”, *Materials and Structures*, vol. 27, no. 9, 510-514, Nov. 1994.

Rüsch H. (1960). “Researches Toward a General Flexural Theory for Structural Concrete,” *ACI Journal, Proceedings*, vol. 57, no. 1, pp. 1-28, July 1960.

Smadi, M. M., Slate, F. O. and Nilson, A. H. (1982). “Time-Dependent Behavior of High-Strength Concrete under High Sustained Compressive Stresses”, *Research Report*, no. 82-16, Department of Structural Engineering, Cornell University, Ithaca, NY, 264 pp., Nov. 1982.

Study on the Modeling of Microscopic Water Migration Depending on the C/S Ratio and Volumetric Changes

Naoki Takahashi[1] and Hideki Oshita[2]

[1]Bachelor, Department of Civil and Environmental Engineering, Chuo University, Tokyo, Japan. E-mail: n-takahashi@civil.chuo-u.ac.jp
[2]Professor, Department of Civil and Environmental Engineering, Chuo University, Tokyo, Japan. E-mail: oshita@civil.chuo-u.ac.jp

Abstract

The volumetric change is a very important problem e.g. the cracking of concrete. Therefore, the evaluation of the detailed water migration mechanism and the accurate predicted model of the volumetric change are indispensable. In this study, the diffusion model depending on the pore diameter was constructed by introducing the dominant substance transfer forms in each diameter of pore focusing on the water migration in a microscopic viewpoint. Moreover the proposed model was expanded by considering the ratio of CaO to SiO_2 (hereafter C/S ratio) in C-S-H that is a main cement hydrate. Furthermore the volumetric changes, which occur in the state during the dehydration from inside to outside of the specimen and in the state after the finish of dehydration, were modeled. Finally, the comparisons between the experimental and analytical results for the volumetric change of the cement paste due to the drying were performed and then the applicability of the proposed model was confirmed.

1. Introduction

The volumetric change of the cement-based materials was closely related to the characteristic of C-S-H gel and the pore structure because it is a porous permeable material containing multi-scale pores and water inside existing as a liquid and vapor which changes depending on the environmental condition. In particular, the volumetric change is a very important problem e.g. the cracking of concrete and therefore the evaluation of the detailed water migration mechanism and the accurate predicted model of the volumetric change are indispensable.

In the past studies regarding the water migration, the coefficient of diffusivity, which has been obtained by the experiment in a macroscopic viewpoint, has been treated as a material property of cement based material. In recent years by using Nuclear Magnetic Resonance (NMR), however, it is pointed out that the molecular motion of the water confined in nanospaces is inhibited compared with bulk water existed in macro space. It can be presumed that there is a closely relationship with the intermolecular interaction. As a result, the coefficient of the water diffusivity in nanospaces became smaller compared with a bulk flow. In addition, it was pointed out that the influence both the interaction and the potential energy greatly was

dependent on the diameter of pores. Namely, it is worthwhile considering about the water diffusivity in a microscopic viewpoint.

In this study, the dominant substance transfer forms in each diameter of pore were taken into consideration, focusing on the water migration in a microscopic viewpoint. Moreover, the proposed model was expanded by introducing the Kinetic Theory of Gases and by considering the C/S ratio. Furthermore, the volumetric changes, which occur in the state during the dehydration from inside to outside of the specimen and in the state after the finish of dehydration, were modeled.

2. Model of diffusion depended on the pore size

Cement-based materials are porous permeable material having pore size of the multi-scale order. Therefore, it is necessary to clarify the mechanism of water migration in micro pore, in order to grasp water diffusive property in concrete.

When the water molecules pass through pores, relatively small pores have a strong effect on the force acting between the molecules and the walls (hereafter wall effect). On the other hand, relatively large pores have a little effect. Therefore, gas molecular movement in the pores was divided into three diffusive forms depending on the pore size as shown **Fig.1**. Firstly, it has been governed by the influence of wall effect (a). Secondly, it has been governed by the influence of collision between water molecules (b). Finally, it has been governed by both of such influence (c). In this chapter, the diffusivity of each diffusive form based on kinetic theory of gases is determined. Moreover the proposed model was expanded by considering the hydrogen bond between water molecules as shown **Fig.2** and the C/S ratio of C-S-H that is a main cement hydrate.

2.1. Diffusivity model depending on the pore size

(a) Governed diffusion by the influence of wall effect

At first, the diffusion model of the water molecules was constructed. These water molecules are moving inside the cylindrical pore having the same diameter in the axial direction of a cylinder. In the proposed model, the Van der Waals force and the Coulomb force as the potential between the molecule and pore walls were taken into account. When the molecule is in the distance z from the pore wall, a potential $\phi(z)$ is

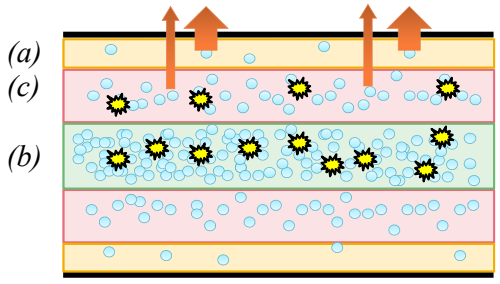

Fig. 1: Schematic of diffusive forms;
(a) Governed by the influence of wall effect,
(b) Governed by collision between molecules,
(c) Governed by both of influence.

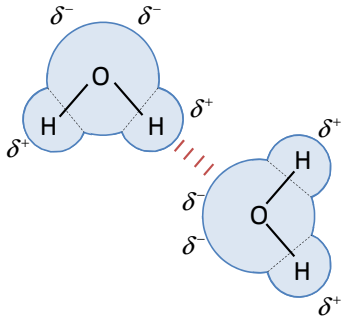

Fig. 2: Conceptual view of hydrogen bond water molecules.

expressed as a summation of the Coulomb potential U and Lennard-Jones potential E. This is given by

$$\phi(z) = E(z) + U(z) \tag{1}$$

$$E(z) = 4\pi\varepsilon N_A \sigma^2 \left\{ -\left(\frac{\sigma}{z}\right)^4 + \left(\frac{\sigma}{z}\right)^{10} \right\}, \quad U(z,\theta) = \sum \frac{q\mu\cos\theta}{4\pi\varepsilon_0 z^2},$$

where ε is the deeper the well depth, N_A is the atomic density in-plane, σ is the molecular diameter, ε_0 is the permittivity of vacuum, q is the electric charge of charged particles of cement material and the specific values are $\varepsilon = 4.323 \times 10^{-20}$[J], $\sigma = 0.3$[nm], $\varepsilon_0 = 8.85 \times 10^{-12}$[C^2/J$\cdot$m] and $q = 1.6 \times 10^{-19}$[C].

Equation (1) shows the potential energy at distance z from the wall. In this study, the average potential energy of each pore was assumed to be the potential $\phi(d)$ between the water molecules and the pore walls surface with the pore diameter d as shown in Eq. (2).

$$\phi(d) = \int_{\omega}^{d-\omega} \phi(z)dz \tag{2}$$

where ω is the thickness of the adsorption. Moreover, the diffusivity D_k is calculated from three-dimensional equation of the Brownian movement derived by Einstein, as shown in Eq.(3). This equation is composed of two variables which are distance x and time t. Where x is migration distance and t is elapsed time, until the molecules given the initial velocity have been adsorbed on the pore wall by the potential energy.

$$D_k = \frac{< x^2 >}{6t} \tag{3}$$

(b) Governed diffusion by collision between molecules

In the relatively large size of pores, the frequency of collisions between molecules becomes high. In other words, the diffusion becomes to be governed by the influence of the collision between water molecules. Therefore, the diffusion is independent of the pore size because the effect of the pore wall surface on water molecules decreases. Here, the average distance (mean free path λ), which molecules fly until the collisions, is essential. Mean free path can be written by the following equation according to the Kinetic Theory of Gases.

$$\lambda = \frac{kT}{\sqrt{2}\alpha h P_0} \tag{4}$$

where α is the collision cross section[m^2], P_0 is the saturated vapor pressure[Pa], k is the Boltzmann's constant[J/K], T is the temperature[K] and h is the relative humidity. From the change in momentum, the diffusivity D_n is given by Eq. (5)

$$D_n = \frac{1}{3}\lambda\bar{v} \tag{5}$$

where $\bar{v}$ is the average speed of the molecules[m/s].

(c) Governed diffusion by both of influence

The diffusion of the area between (a) and (b) was affected by both wall effect and collision. Therefore, in order to determine the intermediate diffusivity, a composition diffusivity model was constructed. The specific method was the use of series model. The small pores and the large pores are assumed to be connected in series.

Then, the intermediate diffusivity D_c can be expressed as follows Eq. (6).

$$\frac{1}{D_c} = \frac{1}{D_k} + \frac{1}{D_n} \tag{6}$$

(d) Apparent diffusivity

As it has been mentioned above, the diffusivity governed by the influence of collisions between molecules, the wall effect and the both of such (hereafter D_n, D_k and D_c) were shown. In this section, in order to determine the apparent diffusivity, the degree of influence of each diffusive form was considered. In this study, the area of each diffusive form was determined by using the Knudsen number. The apparent diffusivity D_s was calculated by multiplying the length of each area as the weight function. The Knudsen number K_n in the case of circular tube can be expressed as follows Eq. (7).

$$Kn = \frac{kT}{\sqrt{2}\alpha P d} \tag{7}$$

where d is the characteristic length[m].

2.2. Consideration of the hydrogen bond between water molecules

Figure 2 shows a conceptual view of hydrogen-bond water molecules. Electrostatic power acts on water molecules and forms hydrogen-bond, because a water molecule is a polar molecule. Generally, it is said that the water molecule of gas does not bond due to the distance between molecules is far. However, it is assumed that the water molecules form hydrogen-bond at very short time because the movement of the water molecule in the pore is confined by strongly receiving the wall effect.

In this study, it is taken into consideration of the influence of the hydrogen-bond according to the energy conservation law. The specific method is comparison with hydrogen-bond energy and kinetic energy when the selected molecules collide. It is assumed that the molecules form hydrogen-bond and move until adsorption if the kinetic energy is less than the hydrogen-bond energy. Here, the initial velocity of the water molecule was determined by using the Maxwell's velocity distribution as the weight function.

2.3. Consideration of the variety of C/S ratio

In the past study, when the C/S ratio of C-S-H decreases, it is confirmed that specific surface area increases by an experiment. As a result, the relation equation between the C/S ratio and specific surface area of C-S-H was proposed. This is given by Eq. (8).

$$S = 269.3 - 325.1 \cdot \log(C/S) \tag{8}$$

where S is specific surface area [m^2/g] and C/S is the ratio of CaO to SiO_2 of C-S-H. Equation (8) was constructed by least squares method using specific surface area in each C/S ratio calculated by BET theory. Moreover, Eq. (8) shows a good agreement with the experiment results within the C/S ratio range of 1.0-1.5.

It is assumed that the domain of the wall surface acting on a water molecule changes owing to the different specific surface area. In other words, the wall effect changes due to the varying ratio of C/S, as shown in **Fig.3**. Therefore, the water migration property changes because the number of wall surface molecule acting on a water molecules changes.

In this study, Eq. (8) was applied to the range of C/S ratio of 0.5-2.5 and the model diffusion depended on the C/S ratio was constructed. The specific method defined the specific surface area that became the smallest value at the C/S ratio 2.5 as a standard S_0. Moreover, the specific area at the C/S ratio 2.0, 1.5, 1.0 and 0.5 were defined as $S_{2.0}$, $S_{1.5}$, $S_{1.0}$ and $S_{0.5}$. It is inferred that the potential between the pores wall and the water molecules became larger due to increase the specific surface area. Therefore, the diffusivity depended the C/S ratio was calculated in terms of the specific area by multiplying the potential $\phi(d)$ by these ratios as influence rate $K(= S_i/S_0)$.

2.4. Characteristic of the constructed diffusivity model

Figure 4 shows the apparent diffusivity D_s at the relative humidity of 60% in each C/S ratio. **Figure 4** (a) and (b) show the result with a relatively small pore diameter of below 100nm and with the whole pore diameter of below 300nm, respectively. Here, the value of the diffusivity at the C/S ratio 2.5 was the analysis value that did not consider an influence rate. The diffusion was prevented if the C/S ratio becomes small, regardless of a pore diameter. Namely, it is assumed that motion of the water molecule was suppressed due to the number of wall surface molecules acting on a water molecule increases if the specific surface area becomes large. On the other hand, the diffusivity at the relative humidity of 40% and 80% also showed a similar tendency. Namely, it was confirmed that the diffusion was prevented if the specific surface area becomes large, regardless of relative humidity.

Figure 5 shows the diffusivity at the C/S ratio of 0.5 and 2.5 that the difference of the specific surface area becomes biggest. It was confirmed that the smaller the C/S ratio was the smaller the diffusion coefficient irrespective of the relative humidity. This finding indicates that physical properties are significant such as the specific surface area for the microscopic water migration.

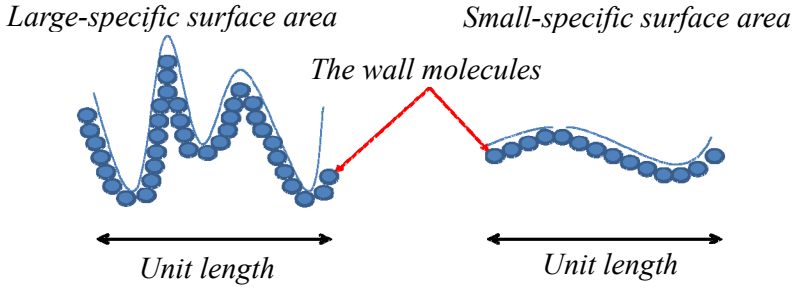

Fig. 3: Difference of the wall domain.

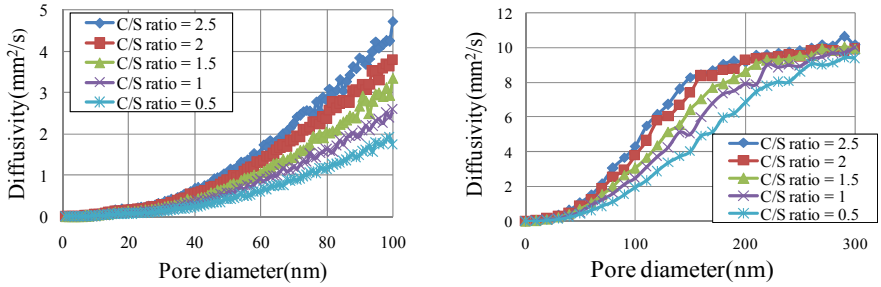

(a) Small-diameter area *(b) Large-diameter area*

Fig. 4: Diffusivity of each pore size (RH. =60%).

2.5. Comparison with experimental result

(1) Micro diffusivity

A comparison of diffusivity depending on pore size with experiments was performed. In past study, the relaxation times (1/T1) of the confined water molecules in artificial nano pore were examined by using Nuclear Magnetic Resonance (NMR). The 1/T1 values at bulk of H_2O were normalized to unity, and the relative 1/T1 values in nano spaces $1/T1_{nano}/1/T1_{bulk}$ were measured. This ratio can be expressed as $1/D_s/1/D_n$ in this study. Here, D_s and D_n are the values at the C/S ratio 2.5.

Figure 6 shows $[1/T1_{nano}/1/T1_{bulk}]$ and $[1/D_s/1/D_n]$. These analytical results showed a good agreement with the experimental results. Namely, wall effect can be qualitatively grasped by the proposed model.

(2) Macro diffusivity

A comparison of calculated average diffusivity by the proposed model with measured macro diffusivity was performed. Furthermore, **Fig.7** shows the measured pore size distribution. In the proposed model, the average diffusivity was calculated at the C/S ratio 2.5 by multiplying the diffusivity of the each diameter by this distribution as the weight function.

Figure 8 shows the diffusivity coefficient of the analytical and the experimental result. These analytical results showed a relatively good agreement with the experimental results. Moreover, it should be noted that in the proposed model the qualitative coefficient of the diffusivity can be evaluated each ages.

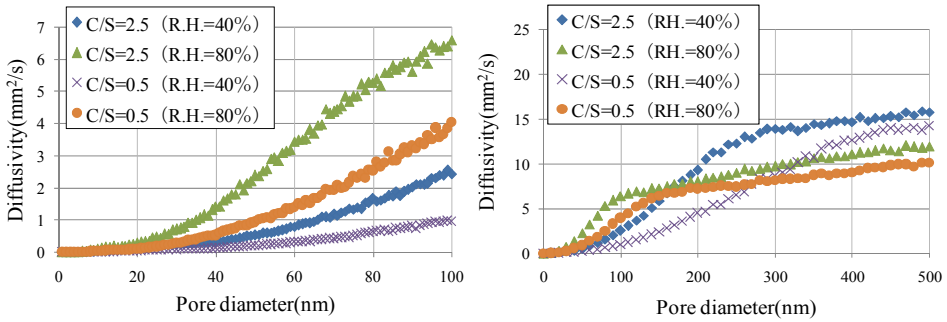

(a) Small-diameter area *(b) Large-diameter area*

Fig. 5: Diffusivity of each pore size.

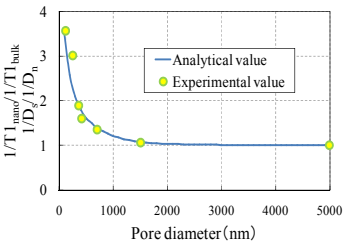

Fig. 6: Comparison of diffusivity depending on pore size with experiments.

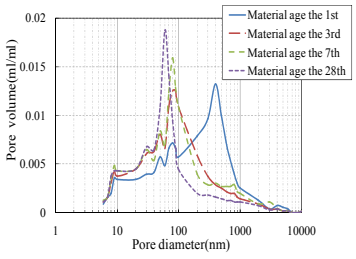

Fig. 7: Measured pore size distribution.

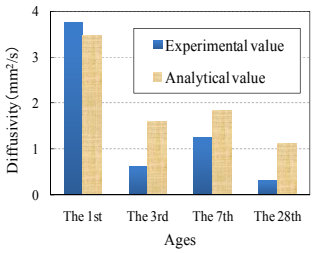

Fig. 8: Comparisons between the experimental and analytical results.

3. Modeling of the volumetric change mechanism

In the past study, dry shrinkage had been assumed in close contact with dehydration. However, in recent years as shown in **Fig.9**, it was pointed out by authors that the shrinkage strain continuously increased after the finish of the dehydration. Namely, it can be said that this phenomenon has two stages mechanism as shown in **Fig.10**. In the first stage, the dehydration progresses to outside of the hardened body and the dehydration cause shrinkage. In the second stage after having disappeared of the dehydration, the vapor diffusion occurs from large pores to small pores inside materials, namely the capillary condensation occurs between micro pores with different diameters.

In this chapter, the modeling of the volumetric changes which was caused by the vapor diffusion from inside in the material to outside and by the vapor diffusion only in the materials inside was developed. The former phenomenon is called as "First stage" and the latter as "Second stage" in this study.

3.1 Volumetric change mechanisms at first stage

The volumetric change mechanism of the first stage was assumed to follow the "surface energy theory" and "capillary tension theory". In the past study, the analysis was performed using the three-dimensional governing equation about the volumetric change by the surface energy change based on the thermodynamics. This equation is written as Eq. (9).

$$\int_A \frac{\Delta\gamma}{\{\Delta u\}} = \int_V [B]^T [D][B] dV \{\Delta\bar{u}\} = A\left(\gamma \frac{\partial\{\varepsilon\}}{\partial\{u\}}\{\delta\} + \Delta\gamma \frac{\partial\{\varepsilon\}}{\partial\{u\}}\{\delta\}\right), \quad A = \frac{\pi V_0}{r_{\min}} \left[\sum_{k=1}^{n} \frac{\alpha^k r^{k\beta+4} e^{-\alpha r^\beta}}{\left(k+\frac{4}{\beta}\right)!} \right]_0^\infty \tag{9}$$

where $[B]$ is the strain-displacement matrix, $[D]$ is the elastic matrix, $\{\bar{u}\}$ is the Nodal displacement vector, $\{\varepsilon\}$ is the strain vector, $\{\delta\}$ is the Kronecker delta, α and β are the material constant to express the difference in water-binding materials ratio.

Moreover, the tensile stress caused by the capillary tension is given from Young-Laplace equation and the Kelvin equation. This equation is written as Eq. (10).

$$\Delta P = \frac{2\gamma}{r} = \frac{RT\rho}{M} \ln \frac{P}{P_0} \tag{10}$$

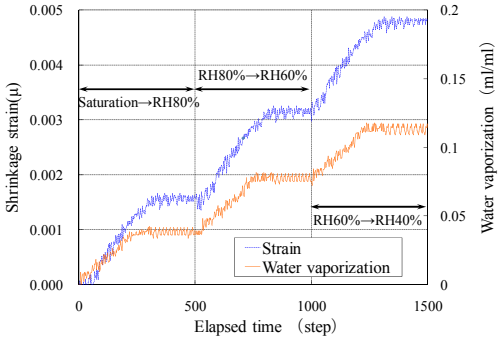

Fig. 9: Water vaporization and Shrinkage strain;the vertical dashed line marks the stop time of dehydration.

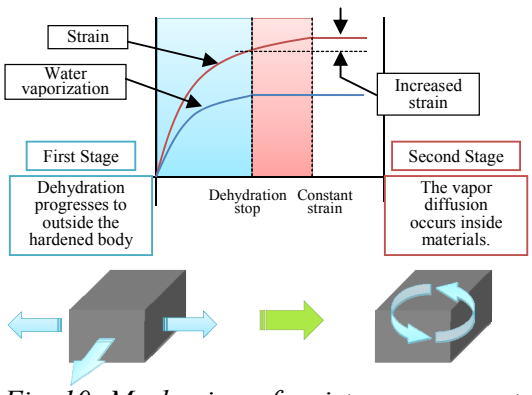

Fig. 10: Mechanism of moisture movement.

where γ is surface tension of water [N/m], r is a pore radius [m], P is vapor pressure [N/m^2], P_0 is saturated vapor pressure [N/m^2], R is gas constant [N・mm/K・mol] and ρ is water density [g/mm^3].

3.2 Volumetric change mechanisms at second stage

It seems that the increase of the strain may correlate strongly with an ink-bottle pore. **Figure 11** shows a conceptual view of an ink-bottle pore. Immediately after the first stage was completed (State.2), water seeks a steady state, and moves in order to condense into a small pores (State.3). At this time, shrinkage was caused by capillary tension since the meniscus was formed inside the micro pores. This phenomenon corresponds to the shrinkage mechanisms of the second stage.

Therefore, in this study, the maximum pore diameter, which could form a meniscus in any relative humidity, was calculated. Moreover, the strain of the whole hardened body was obtained by using the strain caused by capillary tension and the pore size distribution. (Here, the pore size distribution is required. In this study, the pore size distribution density function is used.)

The region of pore size which was re-condensed in the second stage was determined as below. Minimum pore size r_{min} was equivalent to be total adsorption thickness which was decided by free energy of Gibbs as shown **Fig.12**. Maximum pore size r_{max} was defined by a Kelvin equation. Furthermore, all strain of the hardened body was obtained by summing up strain of each pore.

3.3 Examination on the applicability of the volumetric change mechanism model

The comparison with the experimental results was performed in order to confirm the applicability of the proposed model.

(1)Experiment outline

In the experiments, the used cements were ordinary portland cement, high early strength portland cement and low heat portland cement (notated as N, H and L). Moreover, N and H were replaced by the mass of 20% silica fume (notated as N+SF and H+SF). In addition, the water cement ratio was 50% and the specimens were cured in water with the 20℃ for two years. The experiment was performed in chamber at a constant temperature and relative humidity. The water adhered to the surface was removed, and the specimens were set under the environment RH80% until the weight of the specimen did not change. Thereafter, the specimens were set under the RH60% and RH40% sequentially.

(2) Comparison of experimental and analysis results

Figure 13 shows the pore size distribution of each specimen calculated by the pore structured model. According to the pore size distribution, the average diffusivity at

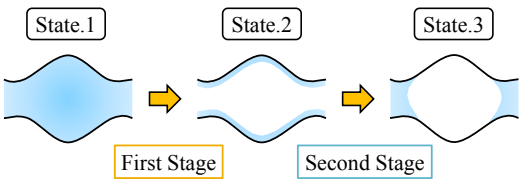

Fig. 11: Schematic illustration of an ink-bottle pore.

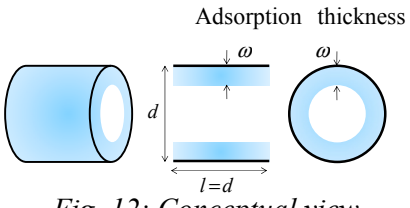

Fig. 12: Conceptual view of hydrogen-bond adsorption thickness.

the first stage and the re-condensed pore volume at the second stage was determined.

Figure 14 shows the experimental and analytical results of the process of drying from RH60% to RH40% of each specimen. Analytical results were good agreement with the measured values of the strain.

Figure 15 shows the relation between the strain of second stage and the water vaporization. The values showed in this figure represent the incremental strain at the second stage. Here, the values for the incremental strain obtained by the analysis were: N=129μ, H=230μ, L=215μ, N+SF=189μ and H+SF=320μ. These results show a good agreement with measured values. It should be noted that the values of H and H+SF were higher than other specimens. It has considered that shrinkage strain has increased because of the effect of the capillary tension strongly caused by containing the small diameter such as a nano-pore. As it has been mentioned above, it has shown the usefulness of the proposed model.

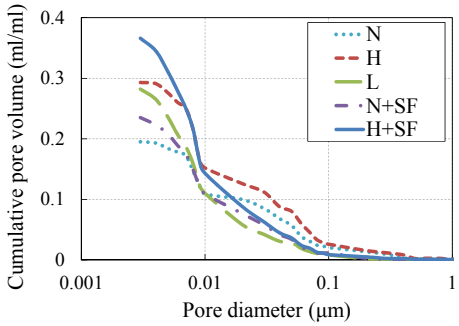

Fig. 13: The pore size distribution by the past model.

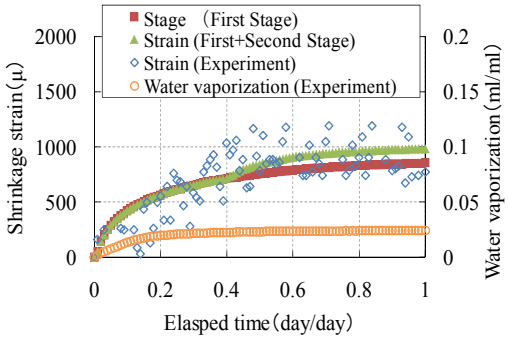

(a) N

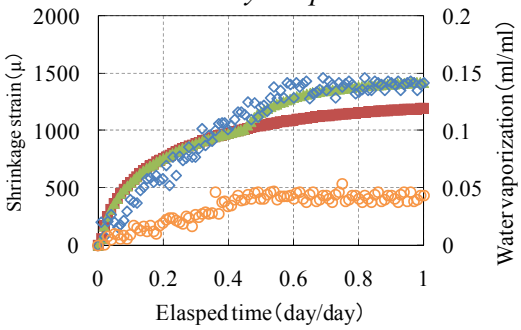

(b) H

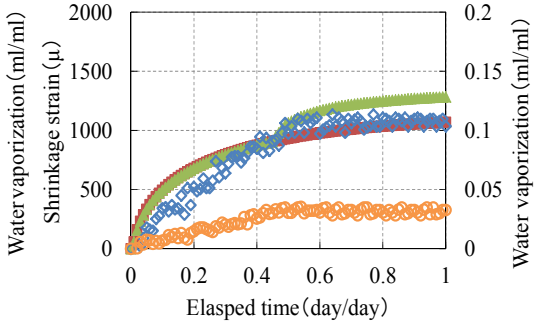

(c) L

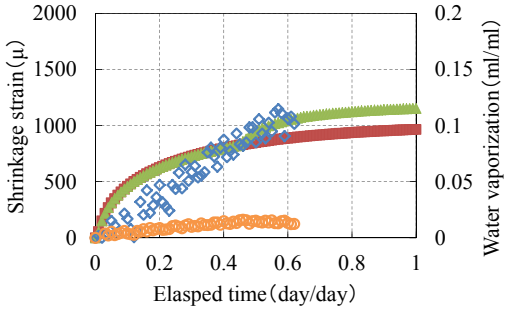

(d) N+SF

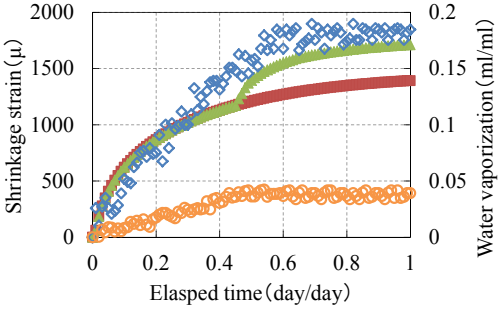

(e) H+SF

Fig. 14: Analysis results of each specimen;Shrinkage strain (Left-hand scale) and amount of dehydration (Right-hand scale).

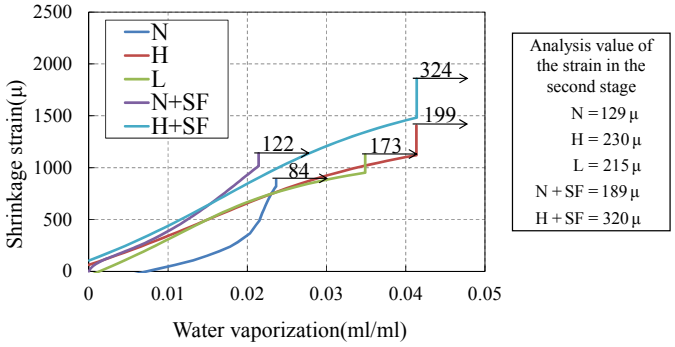

Fig. 15:Increasing rate of water vaporization and shrinkage strain.

4. Conclusions

As a result, the following findings were observed.

(1) The diffusion model of the water molecules depending on pore size was built. The constructed model is possible to calculate the average diffusivity if given the pore size distribution in advance.

(2) It was confirmed that the smaller the C/S ratio is the smaller the diffusion coefficient, regardless of the relative humidity and the pore diameter.

(3) Mechanism of volumetric changes was divided into two stages and each mechanism was modeled. The proposed model can be applicable due to the comparison of the experimental results.

Reference

Dan, Y., Iyoda, T., Ohtsuka, Y., Sagawa, Y. and Hamada, H. (2009) "The Relationship between Curing Condition and Durability on Concrete Using Blast-Furnace Slag Cement." Journal of JSCE, Vol.65, No. 4, pp. 431-441.

Fujikura, Y. and Oshita, H. (2010) "Pore Structure Model of Cement Hydrates Based on Hydration and Change of Particle Size of Constituent Phase." Journal of JSCE, Vol.66, No.1, pp.38-52.

Koizumi, R., Fujikura, Y., Yokoyama, S. and Oshita, H. (2011) "Study on the Correlation of Water Vaporization and Length Change of Cement Paste Due to the Humidity Change." JSCE Technical presentation abstracts Collection, Vol.66, pp.883-884.

Suda, Y.,Tsuchida, S. and Saeki, T.(2011)."Study on Specific Surface Area of Hydration Products in Hardened Cement Paste." Cement Science and Concrete Technology, No.65, pp.103-110

Tsukahara, T., Mizutani, W., Mawatari, K. and Kitamori, T. (2009) "NMR Studies of Structure and Dynamics of Liquid Molecules Confined in Extended Nanospaces." Journal of Physical Chemistry B, 113, 10808 – 10816.

Tsunoda, H. and Oshita H. (2004)"Study on the Volumetric Change Due to Change of Dry and Wet Cement Paste Based on Surface Energy Theory Considering Temperature History." Proceedings of the Japan Concrete Institute, Vol.26, No. 1, pp. 525-531.

Numerical Simulation of Sorption-desorption Isotherme for Cement based materials

March 31, 2015

M. Hosseini[1] , J.-B. Colliat[1] and N. Burlion[1]

[1]Laboratoire de Mecanique de Lille, Universite Sciences et Technologies Lille 1, CNRS, Ecole Centrale de Lille, Arts et Metiers ParisTech Boulevard Paul Langevin, Cite Scientifique, 59655 Villeneuve d'Ascq Cedex, FRANCE. Email: ms.hosseini@ed.univ-lille1.fr

Abstract

One of the most important issues in civil engineering about structures is their durability. A structure during his lifetime faces different environmental situations, like different relative humidities, and different cycles of drying and saturation will be imposed on it, so it is very critical to characterize materials behavior against these changes. Some informations are needed to predict it, one of these informations is desorption and sorption isotherm. In cement based materials just as cement paste, there remain generally extremely fine pores, consequently obtaining isotherms experimentally is considered as a substantially time-consuming experience. Therefore, it is of interest to model the isotherm from a numerical point of view. This physical phenomenon has been a field of study of intense researches, however, there are not many models relying on true physical effects which take place during drying and saturation.
In the present work, in order to model a porous media, a numerical morphology of the geometry of the porous media has been presented by means of a random field excursion through the selection of a random field and a threshold. Random field parameters are defined based on experimental values. Once the porous media has been reproduced, the morphological analysis must be done in order to model water transfers.

Introduction

Water activity in a porous media depends essentially on water content and temperature. The graph representing the variation of water content regarding relative humidity at a given temperature of an equilibrium environment is called an isotherm. Water sorption isotherms are used to characterize the hydraulic behavior of cement based materials. In isothermal conditions, variation of relative humidity is the only factor leading the material to dry. Analysing water sorption isotherm also allows characterizing the microstructure of the material, including porosity distribution through Kelvin Laplace equation [1].

A hysteresis is noticeable between two curves of sorption and desorption. Looking closely at the curves, one could note that for a given relative humidity, two different water contents are distinguished. This phenomenon is related to the structure of the porous network. Pores of a certain diameter are not equally accessible. This phenomenon is referred to as ink-bottle effect. It has been shown throughout different researches [2] [3] that it strongly depends on particular details of the pores geometry. This physical phenomenon with such complicated effects makes complications in the modelling of isotherm hysteresis. Moreover, there are several physical phenomenon which are intervening together, for example capillarity, permeation and diffusion. Capillarity is the most important one and it is considered as the key acting physical phenomenon of this study.

It should be mentioned that in present study there is no assumption on the pore shapeand it is the original point of this modelling . In other studies often they consider the pores as cylindrical or spherical elements which will be a simplified model of real porous network.

Morphological modelling of porous media

Initial step of this study is to model the morphology of porous media as a heterogeneous material. The most common representation of heterogeneities is often performed using objects with simple geometrical definitions such as spheres or ellipsoids, but to have a more similar model to real porous network it is better to turn to morphological models with a more important underlying random aspect such as excursion sets [4]. Consequently, initial morphologies are generated with Gaussian correlated Random Fields.

A random field is defined as a random function $f(x)$ over a parameter space M that takes values in $\mathbb{R}$. f will always be taken as a specific isotropic and stationary Gaussian random field with zero mean and $\sigma^2 = 1$ as variance.

In the presented framework, random field is defined over a three-dimensional space ($M \subset \mathbb{R}^3$) using the program 'R' (figure 1).

An excursion set is defined as the resulting subset of correlated random field thresh-

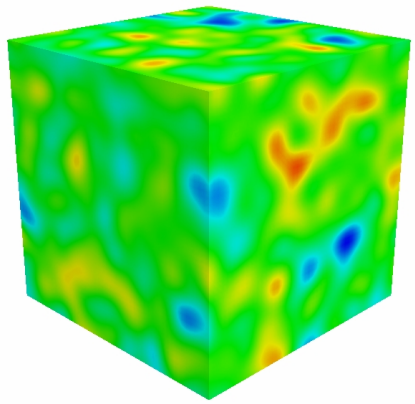

Figure 1: Realisation of a correlated random field

olding. This operation transforms a continuous field to a binary one, creating randomly shaped morphologies. Herein, excursion sets, noted A_D are the morphologies of the subsets M, defined by thresholding realisations of random fields, creating various randomly distributed shapes. Let $f(x)$ be a realisation of random field $f(x)$ defines as above and $D \subset \mathbb{R}$ a given hitting set. The excursion set A_D is defined by the subset of M where f takes its values in D, A_D is also defined by equation 1.

$$A_D \triangleq \{x \in M | f(x) \in D\} \tag{1}$$

Examples of three dimensional excursions are given in figure 2 for two different level sets.

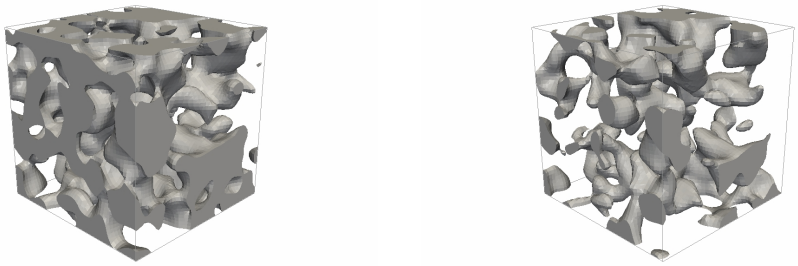

Figure 2: Two excursion sets of the same realisation with different level sets

As shown in figure 2, Level set value has clearly an important impact on the resulting morphology. Playing with this parameter gives a wild range of morphologies which could be similar to pores or connected components in porous media.

Morpho-mathematical operations

Mathematical morphology (MM) is a theory and technique for the analysis and processing of geometrical structures. It is most commonly applied to binary images treated as sets and generated a large number of binary operators and techniques: dilation, erosion, opening, closing [5].
Morphological operations transform the image. The most basic morphological operations are that of erosion and dilation. Suppose A is a set (a binary image or part of it) and D is a structuring element then erosion is denoted $A \ominus D$ and dilation is denoted $A \oplus D$. Applying erosion or dilation to a binary set could Respectively compress or enlarge that as the size of structuring element.
In the continue of morphological operations, another widely used operation is opening. Opening is an erosion followed by a dilation. Figure 3 shows the effect of opening. It has had the effect of removing small black features in the white area of the image, it is equivalent to vanish the speckles smaller than the structuring element.

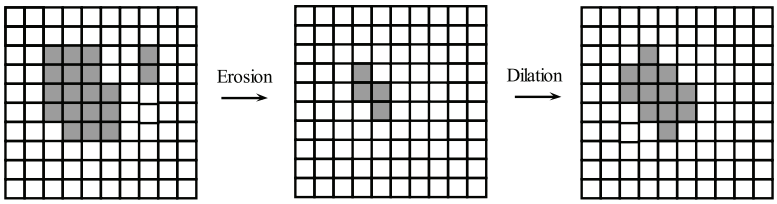

Figure 3: Opening process

Opening could be performed with different sizes of structuring element, and it measure the size distribution of objects in an image. This is known as granulometry.
To achieve the purpose of this study for modelling the water transfer using the morphological model, the connected volume outwards is needed and to access this volume another morpho-mathematical operation should be applied which called geodesic reconstruction. This operation lets to specify this connected volume outwards.

Application to sorption-desorption isotherm

Based on previous sections a morphological model using correlated random field excursion sets has been introduced, two phases material is modelled, pores and matrix. And primarily result, the porous network, is illustrated in figure 4. The bases of the

numerical model proposed in this study, and the experimental values needed during the simulation, were established from the results of mercury intrusion.

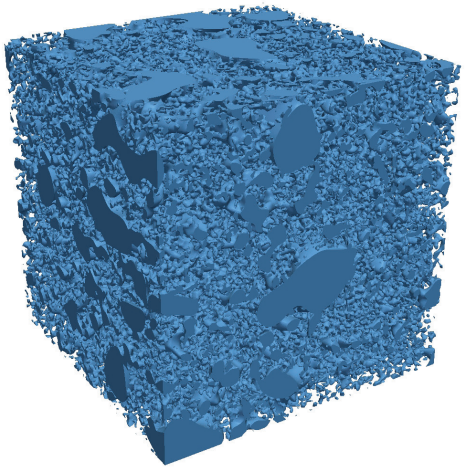

Figure 4: Total porosity of simulated morphology

To verify the quality of the simulated morphology, the pore distribution is obtained by using opening operation and the numerical result is compared to the result of mercury intrusion (figure 5).
In the continue, this numerical morphology will be used to simulate desorption and sorption isotherm. As explained above, isotherm is representing the variation of water content regarding relative humidity at a given temperature. Toward its simulation, initially it is necessary to explain internal circumstance of porous medium by variation of relative humidity.
In desorption it starts with a completely saturated porous medium. Decreasing relative humidity, according to Kelvin-Laplace equation, corresponding to each level of relative humidity, certain radius of pore (after here reference radius) could be obtained and pores larger than this reference radius are emptied earlier than larger radius pores. Knowing that, for simulating isotherm, it is necessary to have the volume of the porous medium which is filled with water, consequently the volume of all the smaller pores than the reference radius must be calculated. Hence, the morpho mathematical operations as opening and geodesic reconstruction is applied to find this volume.
In order to represent sorption isotherm, the material will be resaturated. But it should be mentioned that the pores are not filled in the same order that they drained and this will reproduce hysteresis in isotherm.

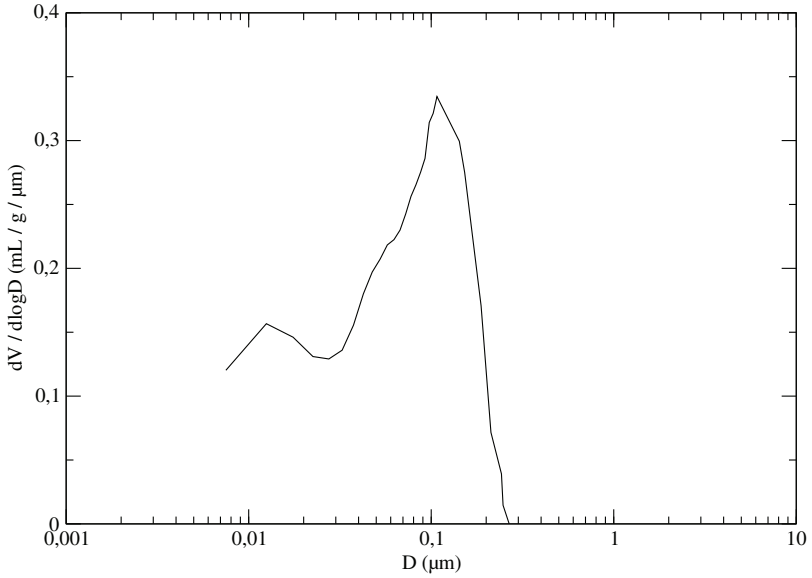

Figure 5: Pore ditribution

Regarding the simulated morphology of cement paste calculated isotherm with simulation hysteresis between desorption and sorption cycle is shown in graph figure 6 as numerical result.

Conclusion

In presented work porous network of a cement paste is modelled based on the correlated random field excursion sets and there is no assumption on the pores shape in this morphological modelling. Following Kelvin-Laplace law, the more relative humidity decrease, the smaller pores are drained, and in this study the numerical simulation based on fine geometrical data. The morpho-mathematical operations are applied on the numerical model to simulate sorption and desorption isotherm in numerical point of view.

References

[1] Rougelot T. Etude exprimentale multi-chelles des couplages hydriques, mcaniques et chimiques dans les matriaux cimentaires, Universite des Science et Technologies de Lille, France, 2008.

[2] V. Baroghel Bouny. Caracterisation des pates de ciment et des betons : Methodes, analyse, interpretations. PhD thesis, Ecole Nationale des Ponts et Chaussees, 1994.

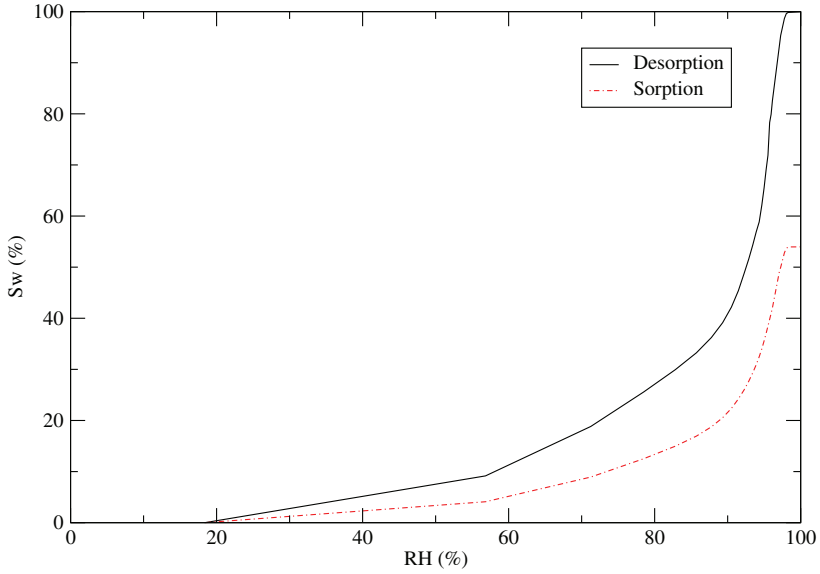

Figure 6: Numerical sorption-desorption isotherm

[3] V. Baroghel Bouny. Water vapour sorption experiments on hardened cement based materials, part i: essential tool for analysis of hygral behaviour and its relation to pore structure. Cement and Concrete Research, 37:414437, 2007.

[4] E. Roubin. Modelisation EF et morphologique de milieux heterogenes a l'echelle mesoscopique : applications aux materiaux a matrice cimentaire. PhD thesis, Ecole Normale Superieure de Cachan, 2013.

[5] G.W. Horgan C.A. Glasbey. Image analysis for the biological sciences. Wiley, 1995.

Multiscale micromechanical damage model for compressive strength based on cement paste microstructure

M. Hlobil[1], V. Šmilauer[1], and G. Chanvillard[2]

[1]Department of Mechanics, Faculty of Civil Engineering, Czech Technical University in Prague, Thákurova 7, 166 29 Praha 6; PH (00420) 22435 4489; email: michal.hlobil@fsv.cvut.cz; vit.smilauer@fsv.cvut.cz
[2]Lafarge Centre de Recherche, 95 rue du Montmurier BP 15, 38291 Saint-Quentin Fallavier Cedex - France; email: gilles.chanvillard@pole-technologique.lafarge.com

ABSTRACT

Compressive strength is one of the most important and tested mechanical properties of cement paste. This paper presents a new four-level micromechanical model for compressive strength applicable on both pure and blended cement pastes. The model assumes that intrinsic tensile strength of C-S-H globules governs the compressive strength of cement paste. Crack propagation on all hierarchical levels starts once tensile stresses on a randomly inclined ellipsoidal inclusions within C-S-H exceed cohesive stress. The inclusion of unhydrated clinker, supplementary cementitious materials, other hydration products, or entrapped (or entrained) air further decreases the compressive strength of cement paste.

The multiscale model uses volume fractions of principal chemical phases as input parameters as well as introduces a spatial gradient of C-S-H between individual grains which has a pronounced impact on predicted compressive strength. Calibration of the model on 95 experimental compressive strength values shows that the intrinsic tensile strength of C-S-H globule amounts to 320 MPa. Principal factors influencing compressive strength evolution are "C-S-H/space" ratio, volume of entrapped (entrained) air, and the spatial gradient of C-S-H.

INTRODUCTION

Evolution of compressive strength is one of the fundamental and tested parameters for concrete. Due to its multiscale nature, spanning the range from sub-nanometer to meters and its heterogeneous microstructure, several factors on different scales of observation (including time-dependent phenomena) influence its compressive strength: evolution of chemical phases spanning from hydration of the binder, mineral additions, aggregate type and its interfacial transition zone, and air content (Neville, 1997).

Removing aggregates reduces concrete to cement paste which consists of binder and water. Traditionally, ordinary Portland cement was used as a binder. However,

since the mid-twentieth century, supplementary cementitious materials (SCMs) such as ground granulated blast-furnace slag, fly ash, limestone or silica fume, began to substitute part of cement clinker due to, mostly, economical and ecological reasons. Blended binders exhibit altered chemistry due to the delayed pozzolanic reaction spanning from the hydration of SCMs.

Relation between cement paste micrustructure and compressive strength was established by Powers (Powers, 1948) using the "gel/space" ratio as a microstructural descriptor. This was developed for pure Portland-based cements and needs several adjustements when considering blended binders (Lam, 2000). Identification of a unique relation between cement paste microstructure and compressive strength, applicable for both pure and blended binders motivates the development of the presented multiscale model.

DAMAGE MATERIAL MODEL

The presented material model assumes that a crack starts to propagate as soon as the cohesive stress is exceeded on a critically inclined ellipsoidal inclusion within the material. For loading by uniaxial tension, this cohesive stress corresponds to the tensile strength of a material. Using equivalent strain, $\tilde{\varepsilon}$, to describe the evolution of damage yields a Rankine criterion for tensile loading as

$$\tilde{\varepsilon} \;=\; \frac{\sigma_1}{E},\ \sigma_1 > 0 \tag{1}$$

where E is the elastic modulus and σ_1 is the maximum positive effective principal stress on undamaged-like material.

For loading by uniaxial compression, cementitious specimens fail by tensile microcracking on randomly inclined directions (Bazant,1998). This behaviour can be interpreted as tensile stresses which appear on inclined ellipsoidal voids (even under uniaxial compressive loading) as described in (Griffith, 1924). The equivalent strain, $\tilde{\varepsilon}$, for compressive loading then takes the form of a Griffith criterion as

$$\tilde{\varepsilon} = \frac{1}{E} \cdot \frac{-(\sigma_1 - \sigma_3)^2}{8(\sigma_1 + \sigma_3)} \tag{2}$$

where σ_3 is the minimum effective principal stress on undamaged-like material.

The equivalent strain may arise either from Rankine or Griffith criterion, see Eq. (1) or Eq. (2), respectively, depending on macroscopic loading. However in both cases, the material fails due to tensile failure on the microscale.

FINITE ELEMENT MODEL FOR MULTISCALE ANALYSIS

Finite element analysis with implemented Griffith-Rankine constitutive laws, see Eqs. (1), (2), is used for the multiscale model. The microstructure at each homogenization level, see Figure 1, is discretized by finite elements. Level 1 (C-S-H foam)

uses a three dimensional uniform mesh consisting of $20\times20\times40$ brick elements with linear displacement interpolations and the resolution of 0.25 μm/voxel. Level 2 (cement paste) and level 3 (cement paste with air) both use a two dimensional uniform mesh composed of 100×100 and 50×50 quadrilateral elements with linear interpolations with a resolution of 1 μm/pixel and 20 μm/pixel for levels 2 and 3, respectively.

Table 1 shows intrinsic elastic and fracture properties assigned to relevant phases. Elastic properties were determined by nanoindentation. The tensile strength of C-S-H globules was identified by model validation on 95 experimental results.

Table 1. Intrinsic elastic and fracture properties of relevant chemical phases.

Phase	Elastic modulus (GPa)	Poisson's ratio (-)	Tensile strength (MPa)	Fracture energy (J/m^2)	Reference
C-S-H globule	57.1	0.28	320	2^a	(Termkhajornkit, 2014)
C-S-H$_{LD}$	21.7	0.24	66^b	5^a	(Constantinides, 2004)
C-S-H$_{HD}$	29.4	0.24	107^b	5^a	(Constantinides, 2004)
Water-filled porosity	0.001	0.499924	-	-	(Smilauer, 2006)
CH	38.0	0.31	-	-	(Constantinides, 2004)
AFt	22.4	0.25	-	-	(Haecker, 2005)
AFm	42.3	0.32	-	-	(Haecker, 2005)
Clinker minerals	139.9	0.30	-	-	(Pichler, 2013)
Cement paste	-	-	-	15	-

^{a}) Higher fracture energy leads to the same material strength
^{b}) Calculated from packing of C-S-H globules

MULTISCALE MODEL FOR CEMENT PASTE

The multiscale model for cement pastes consists of four hierarchival levels, see Figure 1. Level 0 describes how packing density of C-S-H globules determines mechanical properties of C-S-H. Level 1 (C-S-H foam) contains C-S-H together with capillary porosity. To mimic an uneven distribution of C-S-H within grains, C-S-H foam exhibits a spatial gradient. Level 2 ads remaining phases (i.e. unhydrated clinker, SCMs, and remaining hydration products) into a homogenized matrix of C-S-H foam. Level 3 captures the effect of entrained / entrapped air.

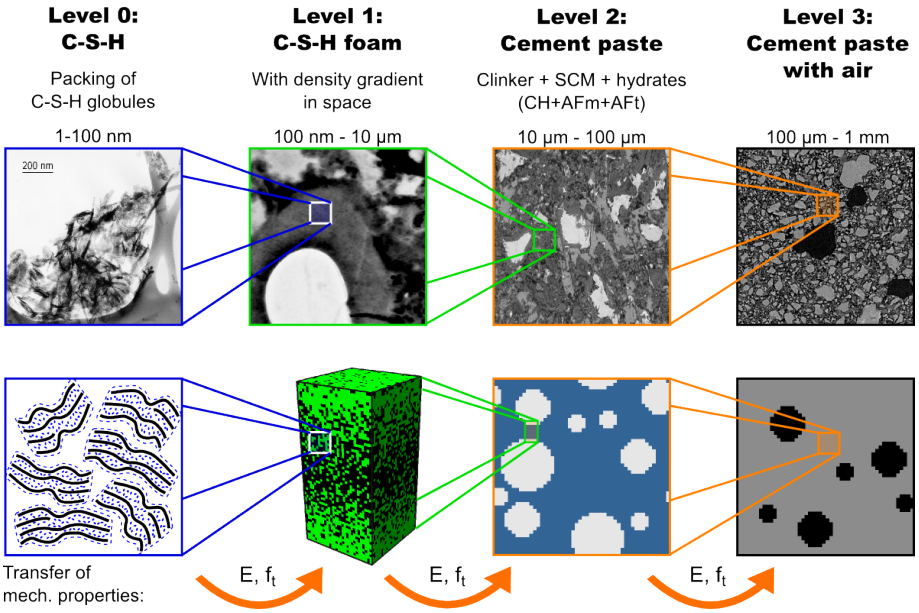

Figure 1. Four-level hierarchical multiscale model. TEM/SEM images from left to right: Eric Lachowski, S.Y. Hong, and F.P. Glasser (e.lachowski@abdn.ac.uk, http://publish.illinois.edu/concretemicroscopylibrary/transmission-electron-microscopy-tem/); L. Kopecký (CTU in Prague); Paul Stutzman (NIST, http://publish.illinois.edu/concretemicroscopylibrary/magnification-progression-series-1000x/); D. P. Bentz, et al. (Visible Cement Dataset: http://visiblecement.nist.gov).

Transfer of elastic modulus and tensile strength ensures coupling between hierarchical levels. Tensile strength, f_t is obtained from compressive strength, f_c, using Griffith's criterion, see Eq. (2), under the assumption of $f_c/f_t = 8$.

During hydration C-S-H precipitates unevenly in proximity to clinker grains. This manifests in a spatial gradient which can be approximated in the proposed model by a probability density function ρ as

$$\rho(x, \beta) = \frac{1}{\beta} \exp\left(-\frac{x/\ell_{UC}}{\beta}\right) \tag{3}$$

where x stands for the distance from clinker grain surface, β is a scaling parameter of the exponential distribution and ℓ_{UC} is the characteristic length of the unit cell (UC). Low values of the scaling parameter ($\beta < 0.6$) indicate a high gradient of C-S-H in space; the majority of C-S-H precipitates preferentially around clinker grain surface and not much C-S-H expand into capillary space whereas high values ($\beta > 0.6$) describe a more uniform distribution of C-S-H in space.

RESULTS AND DISCUSSION

Four-level hierarchical model aims to predict the compressive strength of cement pastes. It contains two inputs that need to be calibrated from experimental results: (i) the intrinsic tensile strength of C-S-H globule and (ii) an optimal scaling parameter describing the exponential distribution of C-S-H in space.

Level 0: C-S-H

Two C-S-H morphologies (low- and high density, or outer and inner product) emerge from different packing density of C-S-H globules. Constantinides and Ulm (Constantinides, 2004) identified limit packing densities as $\eta_{\text{C-S-H}_{\text{LD}}} = 0.63$ and $\eta_{\text{C-S-H}_{\text{HD}}} = 0.76$ for low- and high density C-S-H as well as elastic moduli $E_{\text{C-S-H}_{\text{LD}}} = 21.7$ and $E_{\text{C-S-H}_{\text{HD}}} = 29.4$ GPa using nanoindentation.

The presented model does not arbitrarily differentiate between low and high density C-S-H in terms of morphology or mechanical properties but rather considers a single type of C-S-H with properties depending on actual globule packing density. This density stems from the ratio of actual volume of C-S-H_{HD} within C-S-H which can be estimated from CEMHYD3D hydration model with implemented confinement algorithm (Šmilauer, 2006) based on initial water-to-binder ratio and capillary porosity, see Figure 2(a). The actual packing density of globules, η_{glob}, can then be linearly interpolated between the bounding values for $\eta_{\text{C-S-H}_{\text{LD}}}$ and $\eta_{\text{C-S-H}_{\text{HD}}}$.

Finite element simulation in analogy to Level 1 allowed to predict tensile strength based on a given packing density for a uniform distribution of globules in C-S-H. Extrapolation to single C-S-H globule yields the intrinsic tensile strength as $f_{t,glob} = 320$ MPa, see Figure 2(b).

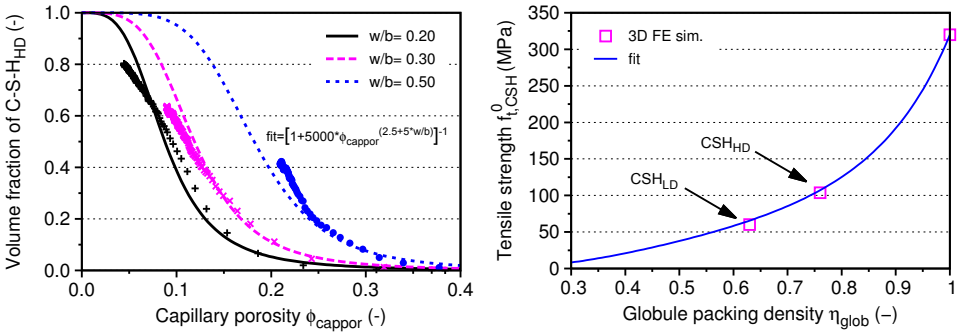

Figure 2. Evolution of the volume fraction of C-S-H_{HD} within C-S-H (left); identification of tensile strength of C-S-H globule depending on packing density (right).

Level 1: C-S-H foam

C-S-H foam describes the region between individual clinker grains. Uneven precipitation of C-S-H manifests in a spatial gradient which has a pronounced impact on compressive strength of cement paste. Increasing the gradient of C-S-H by lowering β yields lower compressive strength, see Figure 3 (left).

Level 2: Cement paste

Remaining hydration products are merged together with unhydrated clinker and SCMs into a solid homogeneous inclusion, which is the inserted into a homogenized matrix of C-S-H foam. Homogenization using a self-consistent scheme provides access to the elastic properties of such inclusion. Stiff inclusions divert stress trajectories from compressive loading during finite element simulations which results in stress concentration in diluted areas, decreasing the load bearing capacity of the material, see Figure 3 (middle).

Level 3: Cement paste with air

Experiments show that the presence of entrained (or entrapped) air significantly influences mechanical properties of cement paste. Finite element simulations capture this behaviour as compressive strength is reduced overlinearly with increasing air content, see Figure 3 (right).

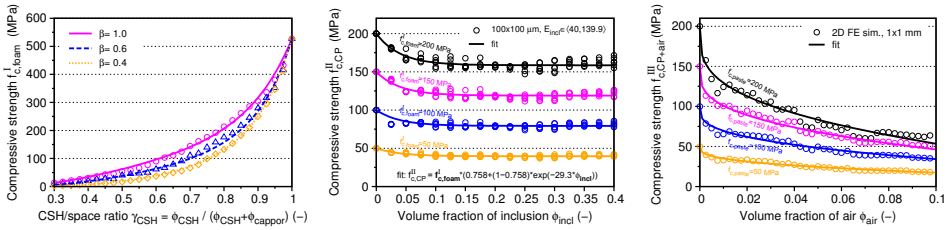

Figure 3. Model-predicted compressive strength on level 1: C-S-H foam (left), on level 2: cement paste (middle) and on level 3: cement paste with air (right).

Calibration of model inputs

The proposed multiscale model contains two independent variables that need to be calibrated from experimental data: the intrinsic tensile strength of C-S-H globules, $f_{t,glob}$, and the spatial gradient of C-S-H, described by the scaling parameter β.

To obtain highest possible values of compressive strength from the multiscale model, the scaling parameter was set to $\beta = 1$ for numerical simulations. This signalizes a nearly perfectly uniform distribution of C-S-H within capillary pores. We

then identified the intrinsic strength of C-S-H globules as $f_{t,glob} = 320\,\text{MPa}$ by back-analysis from 95 experimental results of compressive strength on both pure and blended cement pastes.

Introducing a spatial gradient into C-S-H (by means of lowering the scaling parameter) decreases the model-predicted compressive strength. The range of $\beta \in (0.4, 1)$ can accommodate all experimental results, however the value $\beta = 0.6$ seems to be an optimal value, see Figure 4.

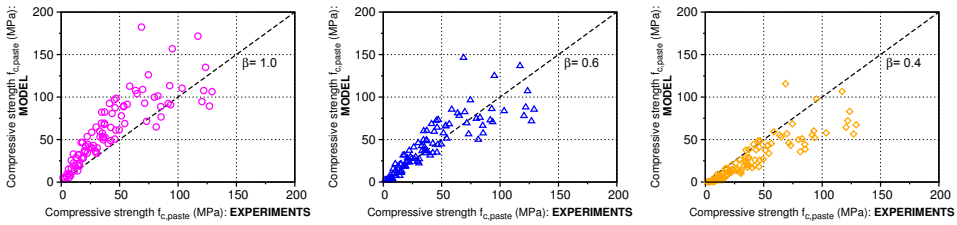

Figure 4. Validation of model-predicted compressive strength with experiments for $\beta = 1.0$ (left), $\beta = 0.6$ (middle), $\beta = 0.4$ (right).

CONCLUSION

This paper describes a four-level micromechanical model for compressive strength of cement pastes. The model uses a "C-S-H/space" ratio as a microstructural descriptor instead of the traditional "gel/space" ratio as coined by Powers (Powers, 1948). This extends the practical applicability of the model also on blended cement under the assumption that C-S-H emanating from hydration of SCMs exhibit identical mechanical properties such as elastic modulus, Poisson's ratio and tensile strength as those from ordinary Portland cement.

Intrinsic tensile strength of C-S-H globule was identified as $f_{t,glob} = 320\,\text{MPa}$. Although there is no direct experimental evidence of this tensile strength, for a cohesive brittle material the tensile strength f_t is related to elastic modulus, E, through surface energy. Typical estimates (Feldbeck, 1984) for $f_t \in (0.01 - 0.1)E$, which gives a range for $f_{t,glob} \in (571 - 5710)\,\text{MPa}$. Our value for tensile strength of C-S-H lies near the bottom range of the theoretical limit value, indicating a presence of defects within the globule.

Precipitating C-S-H exhibits a spatial gradient between clinker grains which has a strong impact on compressive strength. Densification of the microstructure, either by decreasing water-to-binder ratio or providing additional surfaces for C-S-H to precipitate onto, leads to a more uniform C-S-H formation as well as higher compressive strength.

ACKNOWLEDGEMENT

The authors gratefully acknowledge "NANOCEM" funding within Core Project 10 "Micromechanical Analysis of Blended Cement-Based Composites" and discussions with Bernhard Pichler (TU Wien), and Klaus-Alexander Rieder (WR Grace). Support from CTU grant SGS15/030/OHK1/1T/11 and Technology Agency of the Czech Republic (TACR), project Centre for Effective and Sustainable Transport Infrastructure (No. TE01020168) are acknowledged.

REFERENCES

Bažant, Z. P., Planas, J. (1998). *Fracture and Size Effect in Concrete and Other Quasibrittle Materials*, CRC Press.

Constantinides, G., Ulm, F.-J. (2004). "The effect of two types of C-S-H on the elasticity of cement-based materials: Results from nanoindentation and micromechanical modeling", *Cement and Concrete Research*, 34(1), 67-80.

Felbeck, D. K., Atkins, A. G. (1984). *Strength and Fracture of Engineering Solids*, New Jersey, Prentice-Hall.

Griffith, A. A. (1924). *Theory of rupture*, in: C. Biezeno, J. Burgers (Eds.), First International Congress for Applied Mechanics, Delft, 55-63.

Haecker, C.-J., Garboczi, E. J., Bullard, J. W., Bohn, R. B., Sun, Z., Shah, S. P., Voigt, T. (2005). "Modeling the linear elastic properties of portland cement paste", *Cement and Concrete Research*, 35(10), 1948-1960.

Lam, L., Wong, Y., and Poon, C. (2000). "Degree of hydration and gel/space ratio of high-volume fly ash/cement systems", *Cement and Concrete Research*, 30(5), 747-756.

Neville, A. M. (1997). *Properties of Concrete*, John Wiley & Sons, Inc.

Pichler, B., Hellmich, C., Eberhardsteiner, J., Wasserbauer, J., Termkhajornkit, P., Barbarulo, R., Chanvillard, G. (2013). "Effect of gel-space ratio and microstructure on strength of hydrating cementitious materials: An engineering micromechanics approach", *Cement and Concrete Research*, 45(0), 55-68.

Powers, T. C., Brownyards, T. L. (1948). "Studies of physical properties of hardened portland cement paste", *Bulletin 22*, Research Laboratories of the Portland Cement Association.

Šmilauer, V., Bittnar, Z. (2006). "Microstructure-based micromechanical prediction of elastic properties in hydrating cement paste", *Cement and Concrete Research*, 36(9), 1708-1718.

Termkhajornkit, P., Vu, Q. H., Barbarulo, R., Daronnat, S., Chanvillard, G. (2014). "Dependence of compressive strength on phase assemblage in cement pastes: Beyond gel-space ratio - experimental evidence and micromechanical modeling", *Cement and Concrete Research*, 56(0), 1-11.

Difference Between Creep And Relaxation Poisson's Ratios: Theoretical And Practical Significance For Concrete Creep Testing

Abudushalamu Aili[1], Matthieu Vandamme[2], Jean-Michel Torrenti[3] and Benoit Masson[4]

[1]Université Paris-Est, IFSTTAR, 14 Boulevard Newton, F-77420 Champs-sur-Marne, France; email: abudushalamu.aili@enpc.fr
[2]Université Paris-Est, Laboratoire Navier (UMR 8205), CNRS, ENPC, IFSTTAR, F-77455 Marne-la-Vallé, France; PH: (33) 1 64 15 37 04; FAX:(33)1 64 15 37 41; email: matthieu.vandamme@enpc.fr
[3]Université Paris-Est, IFSTTAR, 14 Boulevard Newton, F-77420 Champs-sur-Marne, France; email: jean-michel.torrenti@ifsttar.fr
[4]EDF-DIN-SEPTEN, Division GS - Groupe Enceintes de confinement, 12-14 Avenue Dutriévoz, F-69628, Villeurbanne, France; email: benoit.masson@edf.fr

ABSTRACT

The viscoelastic Poisson's ratio is an important parameter for assessing the multiaxial creep behavior of concrete. However, its definition in viscoelasticity can generate some ambiguity: at least five different ways of defining a viscoelastic Poisson's ratio are presented in the literature. As to their difference either in theory or in practice, little is known. In this work, we focus on the most intuitive two ways of defining a viscoelastic Poisson's ratio, which we call "relaxation Poisson's ratio" and "creep Poisson's ratio". First, we derive the analytical expressions of the two Poisson's ratios and a relationship between them. We show that their initial values are identical, and that their asymptotic values when time tends towards infinity as well. We also show that such is the case for their derivatives with respect to time. Then, considering concrete as a non-aging linear viscoelastic material, the results of multiaxial basic creep tests on concrete available in the literature are analyzed to compare the relaxation and the creep Poisson's ratios. The results show that the difference between the two Poisson's ratios is rather small but does exist in some cases. In such cases, whether this difference is significant should be considered with respect to the application considered.

INTRODUCTION

The delayed behavior of nuclear containment is an important question when the service life of these structures is discussed. The containment vessel is a biaxially prestressed structure. In this case, the viscoelastic Poisson's ratio is an important parameter for assessing the multiaxial creep behavior of concrete.

However, the definition of the time-dependent Poisson's ratio in linear viscoelasticity can generate some ambiguity: at least five different ways of defining a time-dependent viscoelastic Poisson's ratio are presented in the literature (Hilton, 2001). In this work, we focus on two ways of defining a viscoelastic Poisson's ratio that are based directly on the ratio of lateral strain $\varepsilon_l(t)$ over axial strain $\varepsilon_a(t)$. The first one, which we call relaxation Poisson's ratio ν_r, can be measured directly in the uniaxial relaxation test where the axial strain $\varepsilon_a(t)$ is kept constant, i.e., $\varepsilon_a(t) = \varepsilon_{a0}$:

$$\nu_r(t) = \frac{\varepsilon_l(t)}{\varepsilon_{a0}} \tag{1}$$

The second one, which we call creep Poisson's ratio ν_c, can be measured directly in the uniaxial creep test where the axial stress $\sigma_a(t)$ is kept constant, i.e., $\sigma_a(t) = \sigma_{a0}$:

$$\nu_c(t) = \frac{\varepsilon_l(t)}{\varepsilon_a(t)} \tag{2}$$

Hilton (2001), Tschoegl et al. (2002) and Lakes & Wineman (2006) showed that the two Poisson's ratios are not equal. How much they differ from each other has not been studied yet.

The main objective of the present study is the difference between the two Poisson's ratios. First, we derive the analytical expressions of the two Poisson's ratios as well as a relation between them. Then, we compare their initial and long-time asymptotic values. In the end, their difference during their evolution with respect to time is studied for cementitious materials by analyzing multiaxial creep test results available in literature.

POISSON'S RATIOS IN THEORY

Theoretical derivation

We restrict ourselves to non-aging linear isotropic viscoelastic materials. The general constitutive relation through which the stress tensor $\underline{\underline{\sigma}}$ (decomposed into the volumetric stress $\sigma_v = \mathrm{tr}(\underline{\underline{\sigma}})/3$ and the deviatoric stress tensor $\underline{\underline{s}} = \underline{\underline{\sigma}} - \sigma_v \underline{\underline{1}}$) is linked to the strain tensor $\underline{\underline{\varepsilon}}$ (decomposed into the volumetric strain $\varepsilon_v = \mathrm{tr}(\underline{\underline{\varepsilon}})$ and the deviatoric strain tensor $\underline{\underline{e}} = \underline{\underline{\varepsilon}} - (\varepsilon_v/3)\underline{\underline{1}}$) reads (Christensen, 1982):

$$\sigma_v(t) = K(t) \otimes \dot{\varepsilon}_v(t) \tag{3a}$$
$$s_{ij}(t) = 2G(t) \otimes \dot{e}_{ij}(t) \tag{3b}$$

where $\otimes$ holds for the convolution product defined as $f \otimes g = \int_{-\infty}^{t} f(t-\tau)g(\tau)d\tau$ and $\dot{f}$ holds for derivative with respect to time such as $\dot{f} = df(t)/dt$. Those state equations can equivalently be written (Christensen, 1982):

$$\varepsilon_v(t) = J_K(t) \otimes \dot{\sigma}_v(t) \tag{4a}$$

$$e_{ij}(t) = \frac{1}{2} J_G(t) \otimes \dot{s}_{ij}(t) \tag{4b}$$

where $J_K(t)$ and $J_G(t)$ are the bulk creep compliance and the shear creep compliance, respectively. Relaxation moduli and creep compliances are linked through $\widehat{K}\widehat{J_K} = \widehat{G}\widehat{J_G} = 1/s^2$ (Christensen, 1982), where s is the Laplace variable and $\widehat{f}(s)$ represents the Laplace transform of the function $f(t)$.

By combining Eq. 1 with Eq. 3 and solving them in Laplace domain for a uniaxial relaxation test, the relaxation Poisson's ratio ν_r is found:

$$\widehat{\nu_r}(s) = \frac{3\widehat{K}(s) - 2\widehat{G}(s)}{2s(3\widehat{K}(s) + \widehat{G}(s))} \tag{5}$$

Similarly, combining Eq. 2 with Eq. 4 and solving them directly in time domain for a uniaxial creep test, the creep Poisson's ratio ν_c is found:

$$\nu_c(t) = \frac{3J_G(t) - 2J_K(t)}{2(3J_G(t) + J_K(t))} \tag{6}$$

The elastic-viscoelastic correspondence principle (Christensen, 1982) states that by replacing the elastic parameters in an elastic relation by the s-multiplied Laplace transform of the corresponding viscoelastic parameters, one can obtain the relation between viscoelastic parameters. Applying this principle to the relation between elastic Poisson's ratio ν_0 and elastic moduli K_0 and G_0 yields Eq. 5, not Eq. 6. This means the corresponding viscoelastic parameter of elastic Poisson's ratio is the relaxation Poisson's ratio ν_r, not the creep Poisson's ratio ν_c, i.e., the elastic-viscoelastic correspondence principle can be applied only to the relaxation Poisson's ratio ν_r.

We introduce the uniaxial creep compliance $J_E(t)$ defined such that, in any uniaxial test, $\varepsilon_a(t) = J_E(t) \otimes \dot{\sigma}_a(t)$. For a uniaxial creep test, evaluating the ratio of the Laplace transform $\widehat{\varepsilon}_l(s)$ of the lateral strain over the Laplace transform $\widehat{\varepsilon}_a(s)$ of the axial strain and comparing with Eq. 2 gives:

$$\nu_c(t) J_E(t) = \nu_r(t) \otimes \dot{J}_E(t) \tag{7}$$

This formula, although derived by considering the specific case of a uniaxial creep test, is in fact generic.

Comparison of the two Poisson's ratios at initial and large times

This section is devoted to compare the two Poisson's ratios at initial time and large times. At initial time $t = 0$, the initial values of the relaxation moduli and creep

compliances are equal to their elastic values: $K(t=0)=K_0$, $G(t=0)=G_0$, $J_K(t=0)=J_{K0}=K_0^{-1}$, $J_G(t=0)=J_{G0}=G_0^{-1}$. By using the initial value theorem (Auliac et al., 2000) on Eq. 5, and comparing the result with the value of Eq. 6 at $t=0$, one finds that the two Poisson's ratios are equal to the elastic Poisson's ratio ν_0:

$$\nu_r(0)=\nu_c(0)=\frac{3K_0-2G_0}{6K_0+2G_0}=\frac{3J_{G0}-2J_{K0}}{6J_{G0}+2J_{K0}}=\nu_0 \tag{8}$$

At very large times, i.e., $t\to\infty$, the bulk and shear relaxation moduli tend toward K_∞ and G_∞, respectively. Then, by using the final value theorem, the asymptotic values of creep compliances can be deduced: $J_K(t\to\infty)=1/K_\infty$, $J_G(t\to\infty)=1/G_\infty$. By using the final value theorem on Eq. 5, and comparing the result with the limit value of Eq. 6 at $t\to\infty$, one finds that the two Poisson's ratios are equal to a same asymptotic value ν_∞:

$$\nu_r(\infty)=\nu_c(\infty)=\frac{3K_\infty-2G_\infty}{6K_\infty+2G_\infty}=\nu_\infty \tag{9}$$

As to the derivative with respect to time, simplifying the heredity integral on the right side of Eq. 7, then deriving Eq. 7 with respect to time and evaluating the result at $t=0$, one finds their derivatives with respect to time are equal $\dot{\nu}_r(0)=\dot{\nu}_c(0)$. At large times, as the Poisson's ratios tend toward a finite value ν_∞, their derivatives with respect to time tend towards 0, i.e., $\dot{\nu}_r(\infty)=\dot{\nu}_c(\infty)=0$.

In conclusion, both at initial time $t=0$ and at very large times $t\to\infty$, the two Poisson's ratios are equal to each other, respectively. So are their derivatives with respect to time.

POISSON'S RATIOS IN CREEP TESTS ON CEMENTITIOUS MATERIALS

This section is devoted to compare the two Poisson's ratios from experimental creep test results that are available in literature (Bernard et al., 2003; Jordaan & Illson, 1969; Parrott, 1974). Only the "basic" creep is considered, which is the difference between the strain that takes place under autogenous condition under load and the autogenous shrinkage (Neville, 1995).

Under the assumption of linear viscoelasticity, the stress-strain relation for a multiaxial creep test can be written using either the relaxation Poisson's ratio $\nu_r(t)$ or the creep Poisson's ratio $\nu_c(t)$:

$$\varepsilon_i(t)=J_E(t)\sigma_{i0}-(\sigma_{j0}+\sigma_{k0})\nu_r(t)\otimes\dot{J}_E(t),\ \text{where } i\neq j\neq k\in\{1,2,3\} \tag{10a}$$

$$\varepsilon_i(t)=J_E(t)\sigma_{i0}-(\sigma_{j0}+\sigma_{k0})\nu_c(t)J_E(t),\ \text{where } i\neq j\neq k\in\{1,2,3\}. \tag{10b}$$

where σ_i and ε_i are the principal (constant) stresses and principal (time-dependent) strains, respectively, with $i=1,2,3$;

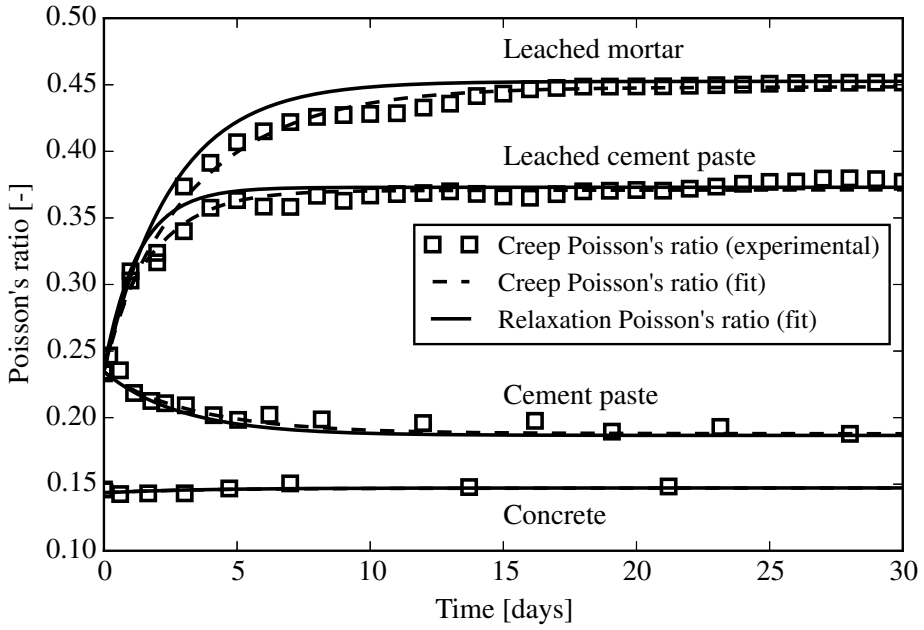

Figure 1. Experimental data of multiaxial creep tests on cementitious materials (data from (Bernard et al., 2003; Jordaan & Illson, 1969; Parrott, 1974))

One observes by comparing Eq. 10a and Eq. 10b that the creep Poisson's ratio ν_c is easier to compute from experimental results, as it does not require the calculation of a convolution integral. This explains why the creep Poisson's ratio ν_c is used more widely in the back analysis of creep experimental data than the relaxation Poisson's ratio ν_r (Jordaan & Illson, 1969, Benboudjema, F. 2002; Torrenti, J. M. et al., 2014; Hilaire, A. 2014). Using Eq. 10b, we compute experimental values of the creep Poisson's ratio ν_c and of the uniaxial creep compliance J_E. Fitting an analytical expression to the uniaxial creep compliance J_E and combining it with Eq. 7, we obtain the Poisson's ratios, which are compared to each other.

Figure 1 displays experimental data on concrete, cement paste and leached mortar and cement paste. The Poisson's ratio shows different trends for different tests. We focus on the difference between the two Poisson's ratios. The test on concrete is a biaxial creep test on a cubic sample (Jordaan & Illson, 1969): The two Poisson's ratios are almost equal during all times. The test on cement paste is a uniaxial creep test on a cuboid cement paste (Parrott, 1974): The maximum difference between the two Poisson's ratios is 0.004. The tests on leached cement paste and mortar are triaxial tests on cylindrical samples (Bernard et al., 2003): the difference between the two Poisson's ratios reaches 0.017 and 0.025 for leached cement paste and mortar, respectively. From these curves, it is observed that the difference between the two Poisson's ratios is very small when the Poisson's ratios vary little over time. On the contrary, when the variation over time is large, the difference between the two Poisson's ratios does exist but

remains still rather small.

CONCLUSIONS

Two Poisson's ratios are defined for non-aging linear isotropic viscoelastic materials. Several conclusions are drawn on their difference:

- The two Poisson's ratios are material properties independent of the loading mode. They are linked to each other through Eq. 7.
- The relaxation Poisson's ratio ν_r is more convenient for solving analytically a viscoelastic problem by means of the elastic-viscoelastic correspondence principle.
- The creep Poisson's ratio ν_c is more favored in the back analysis of creep experimental data, because it can be calculated easily.
- The initial values of the two Poisson's ratios are equal, and so are their long-time asymptotic values. Similarly, the initial values of derivative with respect to time of the two Poisson's ratios are equal, and so are their long-time asymptotic values.
- Multiaxial creep test results show that the difference between the two Poisson's ratios is not significant if the Poisson's ratio varies little over time. In contrast, when variations over time are significant, a difference does exist but remains still rather small.

REFERENCES

Auliac, G., Avignant, J., Azoulay, É. (2000) *Techniques mathématiques pour la physique,* Ellipses, Paris.

Benboudjema, F. (2002) *Modélisation des déformations différées du béton sous sollicitations biaxiales. Application aux enceintes de confinement de bâtiments réacteurs des centrales nucléaires,* PhD thesis, Université de Marne-la-Vallée.

Bernard, O., Ulm, F.-J., Germaine, J. T. (2003) "Volume and deviator creep of calcium-leached cement-based materials." *Cement and Concrete Research,* 33(8):1127–1136.

Christensen, R. (1982) *Theory of viscoelasticity: an introduction,* Elsevier, Mineola, New York.

Hilaire, A. (2014) *Étude des déformations différées des bétons en compression et en traction, du jeune âge au long terme,* PhD thesis, École Normale Supérieure de Cachan.

Hilton, H. H. (2001) "Implications and constraints of time-independent Poisson ratios in linear isotropic and anisotropic viscoelasticity." *Journal of Elasticity,* 63:221–251.

Jordaan, I. J., Illson, J. M. (1969) “The creep of sealed concrete under multiaxial compressive stresses.” *Magazine of Concrete Research,* 21(69):195–204.

Lakes, R. S., Wineman, A. (2006) “On Poisson’s ratio in linearly viscoelastic solids.” *Journal of Elasticity,* 85(1):45–63.

Neville, A. M. (1995) *Properties of concrete,* Pearson Education Limited, Essex, England.

Parrott, L. J. (1974) “Lateral strain in hardened cement paste under short- and long-term loading.” *Magazine of Concrete Research,* 26(89):198–202.

Tschoegl, N. W., Knauss, W. G., Emri, I. (2002) “Poisson’s ratio in linear viscoelasticity - a critical review.” *Mechanics of Time-Dependent Materials,* 7(6):3–51.

Torrenti, J.-M., Benboudjema, F., Barré, F., Gallitre, E. (2014) “On the very long term delayed behaviour of concrete,” *Proceedings of the International Conference on Ageing of Materials & Structures,* 218885.

A Coupled Creep-Damage Model for Hardening Concrete

M. Farah; F. Grondin; and A. Loukili

LUNAM Uuniversité, Ecole Centrale de Nantes, Institut de Recherche en Génie Civil et Mécanique (GeM), UMR-CNRS 6183, 1 rue de la Noé, F-44321 Nantes. E-mail: mounia.farah@ec-nantes.fr;frederic.grondin@ec-nantes.fr; ahmed.loukili@ec-nantes.fr

Abstract

In order to understand the interaction between creep and damage, some experimental methods were developed to follow the microcracking evolution during creep tests as the acoustic emission technique. However, these techniques are unable to analyze the real coupling between creep and damage. In fact, the creep deformations lead to the damage which in turn modifies the creep deformations. Thanks to the modeling, we can take in consideration the microscopic mechanisms to better evaluate the creep deformations of young concrete. For this, a multi-scale creep model was developed to calculate the viscoelastic parameters at the concrete scale from those of hydrates. Then, the creep model was coupled to an isotropic damage model to understand the interaction between creep and damage during creep tests and to evaluate its effect on the mechanical behavior after creep. Finally, the coupled model was used to simulate the interaction creep-damage of pre-damaged materials in order to assess the effect of an initial damage on the creep deformations and on the residual capacity.

1. Introduction

The study of the cementitious materials loaded at early ages is very interesting because it allows assessing the interaction between creep deformations, damage and hardening. There are different scenarii for concrete subjected to creep at early ages. For example, the concrete in contact with reinforcements or the pre-stress cables in reinforced and pre-stressed concretes is locally submitted to high stresses due the restrained shrinkage. These stresses increase with the hydration process of the young concrete and lead to a stress redistribution in the nearby zones and thus to the creep deformations which induce microcracking. In addition, the concrete underground structures (tunnels for example) are subjected during construction phase to the soil pressure which can be considered constant and which leads to significant creep deformations.

The most existing creep models were developed at the structure scale taking into account only the implicit effects which requires a calibration of several parameters (Bazant and Prasannan 1989; Briffaut et al. 2012; De Schutter 1999). Besides, the creep models are, in most case, of a constant stress levels and do not take in consideration the evolution of the strength with age for concretes loaded at early ages. In fact, the hydration process continues to evolve under creep and consequentially the mechanical parameters, thus the stress levels decrease with ages

for young concretes loaded at early ages; especially during the first month of loading where hydration is still evolving.

Experimental investigations showed an interaction between creep and microcracking (Rossi et al. 1993; Saliba 2012). In these investigations, the authors observe an increase of the creep deformations with the microcracking density. However it is impossible to determine if the microcracking is the cause or the consequence of the creep deformations. Also, experiments were conducted for high load levels. As a result, to better understand the real coupling between the creep deformations and microcracking during creep tests, some models were recently developed coupling the creep and damage models. This coupling has been established either by the use of empirical coefficients to weight the part of the viscoelasticity on the damage evolution (Briffaut 2010; Reviron et al. 2007; J. M. Torrenti et al. 2008) or by adding an additional inelastic strains from microcracking of the material under load (Ruiz et al. 2007). To take in consideration the part of the paste-aggregates interface effects on the creep deformations, (Saliba et al., 2012) proposed a coupling between creep and damage at the mesoscopic scale.

In this paper, we presents a validation of the multi-scales creep model presented in (Farah et al., 2013) coupled with a damage model at the concrete scale (Saliba et al., 2012). This model is then used for the analysis of the experimental results presented in (Farah et al., 2015).

2. Local viscoelastic problem

The local problem is defined over a representative elementary volume (REV). We consider a volume V formed by two distinct phases: a matrix Vm and n inclusions Vi (i=1,n). The matrix has a visco-elastic behaviour while the inclusions have an elastic behaviour. The volume is subjected to a load $\bar{F}$ on the border (Γ_1) according to the unit normal vector $\bar{n}$. The displacements are zero on the border (Γ_2). These efforts imply local displacements fields $\bar{u}(t,\bar{y})$, strains $\bar{\bar{\varepsilon}}(t,\bar{y})$ equal to the sum of elastic deformations $\bar{\bar{\varepsilon}}^e(\bar{y})$ and viscoelastic ones $\bar{\bar{\varepsilon}}^v(t,\bar{y})$, and stresses $\bar{\bar{\sigma}}(t,\bar{y})$ on each point $\bar{y}$ of the volume V. The viscoelastic problem is written as follows:

$$\overline{div}\left(\bar{\bar{\sigma}}(t,\bar{y})\right) = \bar{0}\ \forall\ \bar{y}\ \in V \tag{1}$$

$$\bar{\bar{\sigma}}(t,\bar{y}) = \bar{\bar{\bar{\bar{C}}}}(t,\bar{\bar{\varepsilon}}(\bar{y}),\bar{y}) : \left(\bar{\bar{\varepsilon}}(\bar{y}) - \bar{\bar{\varepsilon}}^v(t,\bar{y})\right)\ \forall\ \bar{y}\ \in V \tag{2}$$

$$\bar{\bar{\varepsilon}}(t,\bar{y}) = \frac{1}{2}\left(\bar{\bar{\nabla}}\bar{u}(t,\bar{y}) + {}^t\bar{\bar{\nabla}}\bar{u}(t,\bar{y})\right)\ \forall\ \bar{y}\ \in V \tag{3}$$

$$\bar{F} = \bar{\bar{\sigma}}.\bar{n}\ \forall\ \bar{y}\ \in\ \Gamma_1 \tag{4}$$

$$\bar{u} = \bar{0}\ \forall\ \bar{y}\ \in\ \Gamma_2 \tag{5}$$

where $\bar{\bar{\bar{\bar{C}}}}(t,\bar{\bar{\varepsilon}}(\bar{y}),\bar{y})$ represents the secant stiffness tensor depending on time, the local strains and damage. The chosen damage model is the isotropic model developed by Fichant et al. (1997). It allows to represent the unilateral effect and to obtain objective results independently of the length of the finite elements by controlling the fracture energy. This model is a simplified version of the microplan model of Bazant and Ozbolt (1990) and is based on the relation between the total stress and the effective stress $\underline{\underline{\tilde{\sigma}}}(\underline{y})$:

$$\underline{\underline{\sigma}} = (1-d)\underline{\underline{\tilde{\sigma}}} \tag{6}$$

where d is the scalar value of the isotropic damage (Saliba et al., 2013).
The viscoelastic behaviour of the matrix was modeled by the Kelvin-Voigt model with three units (Figure 3.1).

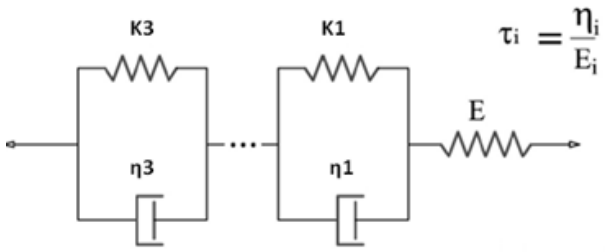

Figure 2.1. Generalized bounded Kelvin-Voigt model

3. Simulation of creep tests

The simulation of the creep tests have been performed on concrete beams with the same conditions as in the experimental tests. The mesh of the beam and the boundary conditions are given in Figure 3.1 (Farah et al., 2015). A mesoscopic mesh is generated at the center of the beam to take into account the heterogeneity of concrete. The rest of the beam is meshed homogeneously having the mean macroscopic properties of concrete.

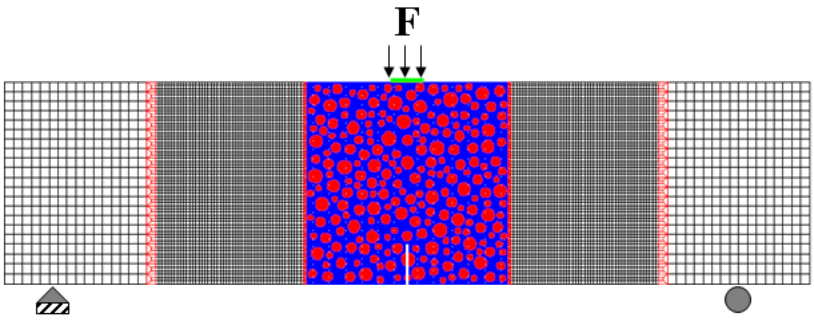

Figure 3.1. Mesh of the beam and boundary conditions

For the creep model, the viscoelastic parameters of mortar and concrete have been calculated by a numerical homogenization method (Farah et al. 2013) while they were given for aggregates (Saliba et al., 2013). Two tests were simulated: on concrete beams submitted to a load equal to 30% of the flexural strength at 24h, on pre-damaged concrete beams submitted to a load equal to 30% of the residual flexural strength at 24h.

3.1. Simulation of creep for the undamaged beams

At early ages, the beam's weight has a major effect on the creep displacement and the internal state of the loaded material. Thus, the simulation of the creep displacement of young concrete requires taking into account the weight effect. Experimentally, the beams of series IV presented an important displacement under the free flexion (the beams were placed on the supports without application of load) as given in Figure 3.2.

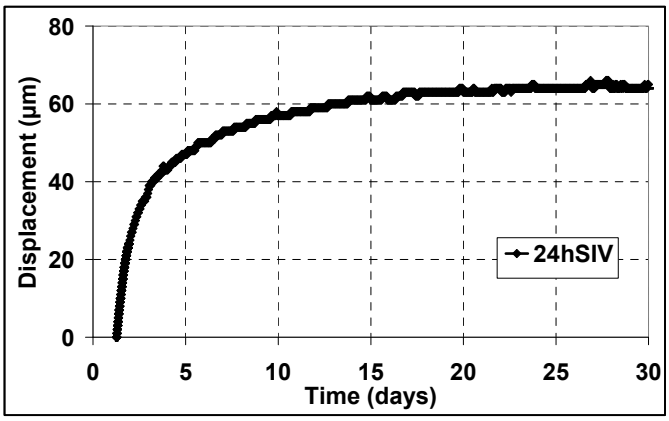

Figure 3.2: Creep displacement measurement under free flexion

First of all, we introduced the weight in the calculation; however, the obtained result shows that it does not influence the displacement magnitude. It means that the flexural displacement is not entirely due to the weight. There are internal forces which drive this displacement (shrinkage, microcracks, water flow in capillaries, etc.). The model does not take into account these phenomena. So, it has been chosen to add a virtual loading force corresponding to this free displacement:

$$F = \frac{48EIf}{l^3} \tag{7}$$

where E represents the young modulus, I the moment of inertia, f the measured displacement and l the distance between supports.

This load was applied at the center of the upper surface of the beam and taken evolving with time until the age of three days, for which the creep kinetic decreases to become zero after, and then it was taken constant. This load was added to that applied during creep tests to simulate the creep displacement under a constant creep load (series I) as given in the Figure 3.3 and under an increasing creep load (series II) as illustrated in the Figure 3.4. These results validate the model approach presented in (Farah et al., 2013).

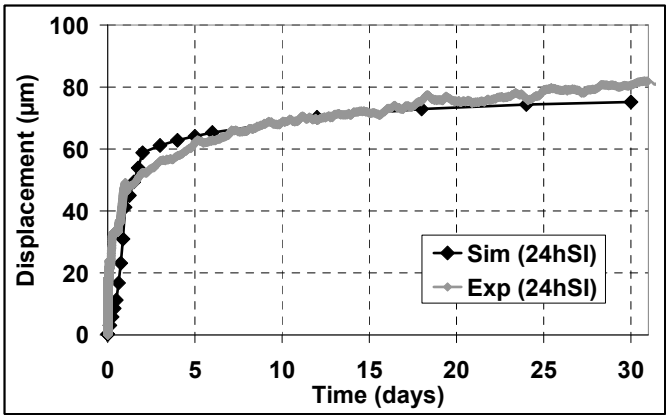

Figure 3.3: Simulation of creep displacement under a constant load

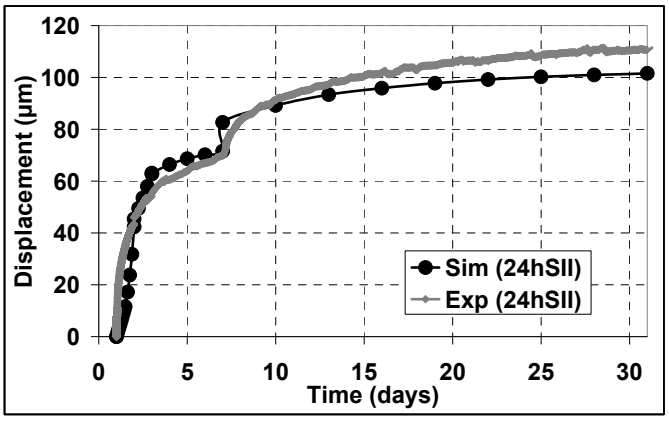

Figure 3.4: Simulation of the creep displacement under an increasing creep load

The main objective of this work is the checking of the microcracking of the concrete beams suggested in the experimental part of this study (Farah et al., 2015). The Figure 3.5 shows that the mechanical behaviour after creep of the two series I and II are identical while a slight decrease of the flexural strength, also observed in the experiments for the beams of the series II. In fact, in spite of the importance of the damage after creep for the beams of the series II (Figure 3.6), the damage is diffuse and it is located at the aggregates paste interface without forming macrocracks. That is why there is no influence of damage on the simulated mechanical behaviour.

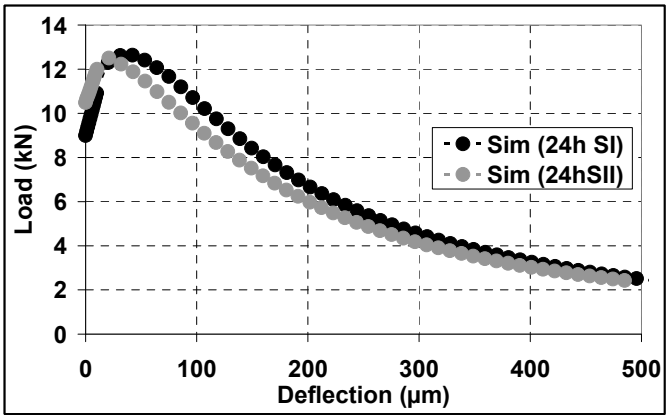

Figure 3.5: Mechanical behavior after creep of the series I and II

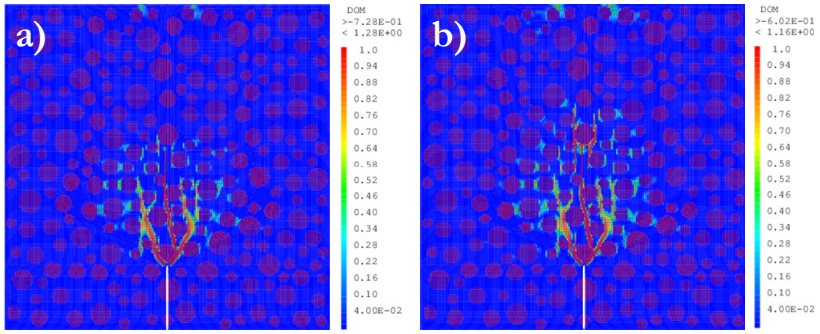

Figure 3.6: Damage state after one month of loading a) constant load b) increasing creep load

3.2. Simulation of creep for pre-damaged beams

The creep tests on the partially damaged beams (series III) are given in detail in the experimental part of this study (Farah et al., 2015). Usually, the elastic part of the behaviour is removed to consider only the viscoelatic part in the comparison. But in the case of pre-damaged beams this method is not adapted. To analyze the creep of the serie III we removed the creep displacement of the two first days in the same way of the experimental analysis. The simulated creep displacement is compared to the experimental one in Figure 3.7. We observe that the calculated displacement is in good agreement with the measurement.

The comparison between the mechanical behaviours after creep of the series I and III (Figure 3.8) shows that there is an effect of the pre-damage on the stiffness of the beams with a negligible effect on the flexural strength. This decrease is related to the damage state after creep for the beams of series III (Figure 3.9). It can be observed that damage increase highly during the creep period.

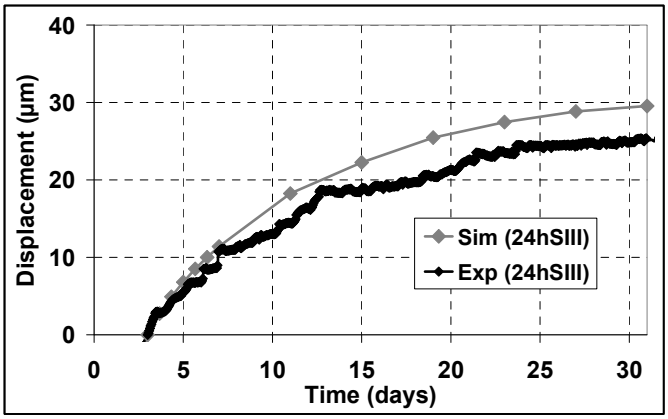

Figure 3.7: Comparison between the creep displacements obtained by simulation and experimentation

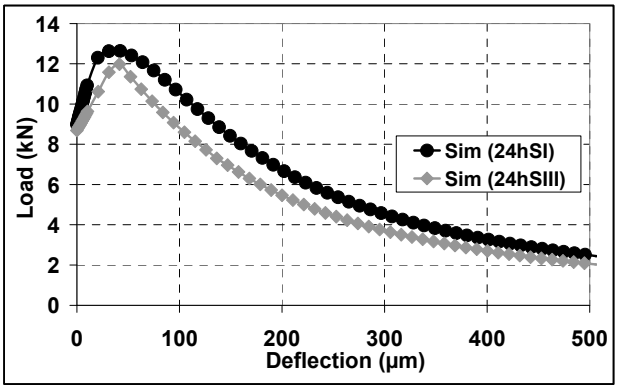

Figure 3.8: Comparison between the mechanical behaviors after creep of the pre-damaged and undamaged beams

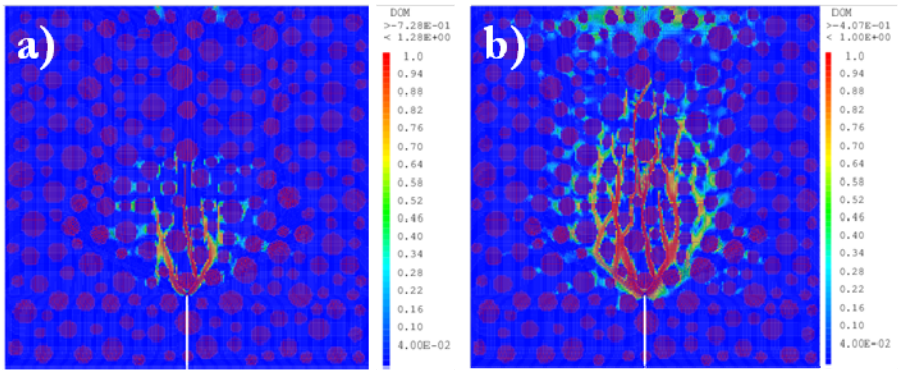

Figure 3.9: Damage state after one month of loading a) undamaged beams b) pre-damaged beams

4. Conclusion

The coupled creep-damage model allowed reproducing practically the creep displacements measured in experiments. The consideration of the internal micromechanisms in the simulation of the creep displacement at early ages had a major importance to well reproduce the creep and the damage of concrete beams. Indeed, the associated internal forces lead to a high displacement of the concrete beams. The model was also used to simulate the failure after creep. The damage field observation allows concluding that the creep leads to micro-cracking even for low loads. These results confirm this assumption given in the experimental study.

REFERENCES

Bazant, Z. P., and Prasannan, S. (1989). "Solidification theory for concrete creep: I. Formulation." *Journal of Engineering Mechanics*, 115(8), 1691-1703.

Briffaut, M. (2010). "Étude de la fissuration au jeune âge des structures massives en béton: influence de la vitesse de refroidissement, des reprises de bétonnage et des armatures." *Thèse de Doctorat, ENS Cachan, France*.

Briffaut, M., Benboudjema, Farid, Torrenti, Jean-Michel, and Nahas, Georges. (2012). "Concrete early age basic creep: Experiments and test of rheological modelling approaches." *Construction and Building Materials*, Elsevier Ltd, 36, 373-380.

Farah, M., Grondin, F., Matallah, M., Loukili, A., and Saliba, J. (2013). "Multi-scales Characterization of the Early-age Creep of Concrete." *CONCREEP-9, September 22-25, Cambridge, Massachusetts*, 211-218.

Farah, M., Loukili, A. and Grondin, F. (2015). "Experimental investigation of the creep-damage interaction effect on the mechanical behaviour of hardening concrete." *CONCREEP-10, September 23-25, Vienna, Austria*.

Reviron, N., Benboudjema, F., Torrenti, J.-M., Nahas, G., and Millard, A. (2007). "Coupling between creep and cracking in tension." *In: The Sixth Int. Conf. in Frac. Mech. of Concr. and Concr. Struct. (Framcos-6), Catania, Italy, June 17–22*.

Rossi, P., Godart, N., Robert, J. L., Gervais, J. . P., and Bruhat, D. (1993). "Investigation of the basic creep of concrete by acoustic emission." *in Proceedings of the Fifth International RILEM Symposium on Creep and Shrinkage of Concrete, Barcelona, Spain, pp. 33-38*.

Ruiz, M. F., Muttoni, A., and Gambarova, P. G. (2007). “Relationship between nonlinear creep and cracking of concrete under uniaxial compression.” *Journal of Advanced Concrete Technology*, 5(3), 1-11.

Saliba, J. (2012). “Apport de l’émission acoustique dans la compréhension et la modélisation du couplage fluage-endommagement du béton.” *Thèse de Doctorat à l’Ecole Centrale de Nantes*.

Saliba, J., Grondin, F., Matallah, M., Loukili, A. and Boussa, H. (2013). "Relevance of a mesoscopic modelling for the coupling between creep and damage in concrete". Mechanics of Time-Dependent Materials, 17(3), 481-499.

De Schutter, G. (1999). “Degree of hydration based Kelvin model for the basic creep of early age concrete.” *Materials and Structures*, 32(4), 260-265.

Torrenti, J. M., Nguyen, V. H., Colina, H., Le Maou, F., Benboudjema, F., and Deleruyelle, F. (2008). “Coupling between leaching and creep of concrete.” *Cement and Concrete Research*, 38(6), 816-821.

Drained and Undrained Creep of Hardened Cement Paste under Isotropic Loading

Siavash Ghabezloo[1]; Jean Sulem[1]; and Manh-Huyen Vu[2]

[1]Université Paris-Est, Laboratoire Navier-CERMES, Ecole des Ponts ParisTech, 6-8 av. Blaise Pascal, Cité Descartes, 77455, Marne la Vallée Cedex 2.
E-mail: siavash.ghabezloo@enpc.fr
[2]CurisTec, 1bis allée de la Combe, 69380 Lissieu, France.

Abstract

The experimental results of isotropic compression tests performed at 20°C and 90°C on a class G hardened cement paste (Ghabezloo et al., 2008, Cem. Conc. Res. 38, 1424-1437) have been revisited considering time-dependent response. Within the frame of a viscoplastic model, the non-linear responses of the volumetric strains as observed in drained and undrained tests and of the pore pressure in undrained tests are analysed. The calibration of model parameters based on experimental data allows to study the effect of the test temperature on the time-dependent response of hardened cement paste.

INTRODUCTION

For cementing an oil well, the cement slurry is pumped into the annular space between the casing and the rock around the well. This cement sheath plays a very important role during the life of the well particularly for zonal isolation and separation of different fluids in the reservoir. It supports also the casing and protects it against corrosion (Bois et al., 2013). The knowledge of the poromechanical and time-dependent behavior of the cement paste is thus essential for prediction of the well performance. Ghabezloo et al. (2008, 2009a, 2009b) studied experimentally the thermo-poro-mechanical behavior of a hardened oil-well cement paste. They performed an experimental study of drained, undrained and unjacketed isotropic compression tests, as well as permeability evaluation tests on hardened class G cement paste. The tests have been performed at 20°C and 90°C on hardened cement pastes hydrated at 90°C for several months. The experimental results permitted the evaluation of a complete set of thermo-poro-elastic parameters of the tested cement pastes. These results have been then extrapolated to other cement pastes with various w/c ratio or chemical compositions by using micromechanical modeling and homogenization method (Ghabezloo 2010, 2011a, 2011b). The experimental results show a highly nonlinear response and hysteresis loops during unloading–reloading cycles of isotropic compression tests, reflecting the viscous behavior of the material. Creep tests under isotropic stress show that the creep is more pronounced at higher stress and higher temperature. These observations highlight the importance of time dependent deformations for oil well cement sheath at great depth. A degradation of the interface between the cement sheath and the rock can induce the formation of a

micro-annular around the well. This micro-annular allows leakage of gas and fluid, which can affect the performance and the safety of the well.

One purpose of the present paper is therefore to study the time dependent behavior of the hardened cement paste under high stresses and temperature. Emphasis is given on the effect of test temperature on the time-dependent behavior considering drained and undrained isotropic tests on hardened cement paste hydrated at 90°C. A rheological model is proposed and calibrated on drained isotropic compression tests data. The validation of the model is performed by simulation of other tests: a drained compression test with different back pressure, a creep test and an undrained isotropic compression test. A discussion on the effect of the test temperature on the parameters of the model is presented. The results of this work have already been presented in more details by Vu et al. (2012).

EXPERIMENTAL RESULTS AND OBSERVATIONS

In the experimental study of Ghabezloo et al. (2008), a class G cement was used to prepare the cement paste with a water to cement ratio w/c=0.44. After 3 months of hydration at 90°C, cylindrical specimens with 38mm diameter and 76mm length were fabricated. Drained and undrained isotropic compression tests as well as an unjacketed compression test were performed at 20°C. Drained triaxial compression tests were also performed at 90°C (Ghabezloo, 2008). For all tests, few loading-unloading cycles were performed at different stress levels (around 20 MPa, 40 MPa and 60 MPa). The loading rate was 0.025 MPa/min and 0.10 MPa/min for drained tests and undrained tests respectively.

The stress-strain response of drained tests is presented in Figure 1. for samples hydrated at 90°C and tested at 20°C and 90°C. We can observe the non-linear response of the hardened cement paste under isotropic compression. The unloading-reloading cycles show a hysteresis which is more pronounced at higher Terzaghi effective stress level. Under higher stress, one can see that the volumetric strain continues to increase at the beginning of the unloading parts. This clearly reflects the viscous behavior of the material under isotropic compression. The non-elastic strains at the end of unloading are quite small (<0.3%) when the Terzaghi effective stress level at the beginning of the unloading is lower than about 43 MPa and 25 MPa for the tests Tt20 and Tt90 respectively. The volumetric strain increases with a much higher rate and the non-elastic strains become much higher beyond these stress levels. This suggests that an additional mechanism, such as microcrack development or collapse of the Large Gel Pores (LGP), i.e. with a size between 3nm and 12nm, is activated when the stress is high enough and accelerates the development of volumetric strain. This mechanism occurs at lower stress levels when test temperature is higher. The sample tested at 90°C exhibits a lower tangent elastic modulus. Moreover, the volumetric strain is larger and the viscous effects are more pronounced for this test temperature.

For the undrained test performed at 20°C, the maximal pressure reached 58.0 MPa and the pore pressure reached 26.5 MPa that corresponds to a Terzaghi effective stress of 31.5 MPa (Figure 2). The non-elastic strains remain small which is consistent with a maximal Terzaghi effective stress lower than the stress threshold

(43 MPa). The pore pressure-confinement pressure curve in Figure 2 shows that the reloading phases are quite linear whereas the unloading phases are highly non-linear. One observes that in the beginning of the unloading phases, the decrease of the pore pressure is delayed. At 12 MPa, the pore pressure becomes equal to the confinement pressure. In triaxial cells, in this situation the pore fluid infiltrates between the specimen and the jacket and in consequence the decrease of the pore pressure until the end of the unloading phase is pursued with a slope of 1:1. The slope of linear part of reloading phases, equal to 0.4, was chosen by Ghabezloo et al. (2008) as Skempton coefficient. However, the delayed decrease of the pore pressure at the beginning of unloading phases cannot be explained in in the framework of poro-elasticity theory.

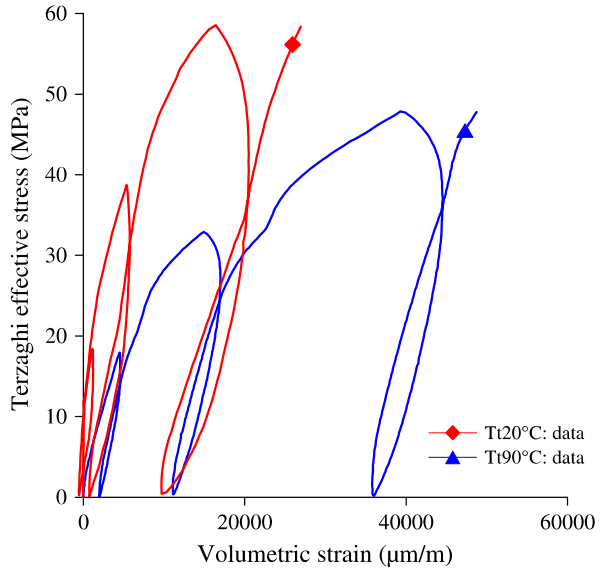

Figure 1. Drained isotropic compression tests: Volumetric strain-Terzaghi effective stress (Tt is the test temperature) (Ghabezloo, 2008; Ghabezloo et al., 2008)

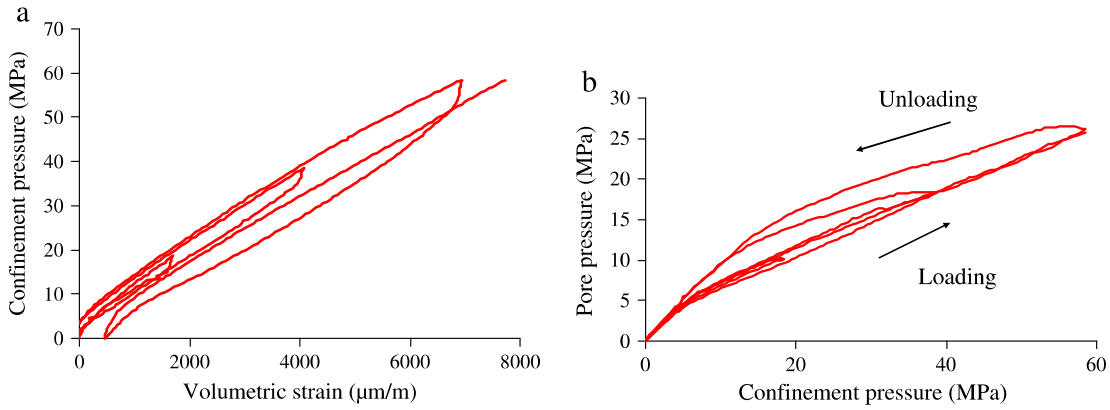

Figure 2. Undrained isotropic compression test at Tt=20°C (Ghabezloo et al., 2008): (a) volumetric strain response, (b) pore pressure response

VISCOELASTIC MODELING

As mentioned above, the unloading-reloading cycles under drained isotropic compression exhibit a degree of hysteresis, which increases with the stress level. This phenomenon reflects the viscous behaviour of the material. Moreover, the volumetric strain and viscous effects are enhanced at higher stress and depend upon the test temperature. One can consider that under low stress level, time dependent deformation has a viscoelastic nature (primary creep) and at higher stresses, an additional irreversible component is triggered and viscoplastic strains develop beyond a stress threshold (secondary creep).

Drained isotropic compression

The response of the material is described by the rheological model depicted in Figure 3. The model contains two groups of elements: a viscoelastic Kelvin element which represents the viscoelastic part and a Maxwell element in parallel with a sliding friction element which represents the irreversible part of the deformation. In the Kelvin element, the linear spring (bulk modulus K_0) represents the time independent volumetric strain, and the Voigt element with a linear spring (bulk modulus K_1) and a dashpot (viscosity η_1) in parallel represents the primary creep deformation. The viscoplastic component includes a sliding frictional element which is activated only for stresses exceeding a given Terzaghi effective stress threshold σ_s and results in time dependent volumetric deformation which develops at constant rate under constant load (bulk modulus K_2, and viscosity η_2). The six parameters of the rheological model are assumed to be constant for a given test temperature.

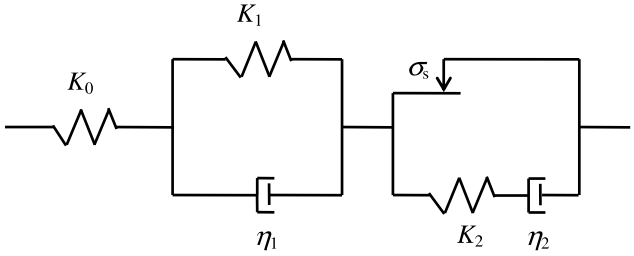

Figure 3. Rheological model

The overall volumetric strain under a Terzaghi effective stress σ_d is written as the sum of the viscoelastic part and the viscoplastic part $\varepsilon = \varepsilon_{ve} + \varepsilon_{vp}$:

$$\dot{\varepsilon}_{\mathrm{ve}} = \dot{\varepsilon}_0 + \dot{\varepsilon}_1 = \frac{\dot{\sigma}_d}{K_0} + \frac{1}{\eta_1}\left(\sigma_d - K_1\varepsilon_1\right) \tag{1}$$

$$\dot{\varepsilon}_{\mathrm{vp}} = \left(\frac{\dot{\sigma}_d^{\mathrm{vp}}}{K_2} + \frac{\sigma_d^{\mathrm{vp}}}{\eta_2}\right)\mathrm{H}\left[\frac{\dot{\sigma}_d^{\mathrm{vp}}}{K_2} + \frac{\sigma_d^{\mathrm{vp}}}{\eta_2}\right] \quad ; \quad \sigma_d^{\mathrm{vp}} = \left(\sigma_d - \sigma_s\right)\mathrm{H}\left[\sigma_d - \sigma_s\right] \tag{2}$$

where H is the Heaviside function. It is worth to note that in the beginning of the unloading phase, the viscoplastic strain continues to increase until $\left(\dot{\sigma}_d^{\mathrm{vp}}/K_2 + \sigma_d^{\mathrm{vp}}/\eta_2\right)$ becomes negative. Then the rate of viscoplastic strain is nil and

the sliding friction element is blocked. The viscoelastic strain can be found using Laplace transformation. For an arbitrary function f, the Laplace transform $\mathcal{L}$, denoted as $\overline{f}$ is defined as $\overline{f}(s)=\int_0^\infty f(t)e^{-st}\,dt$. In the Laplace transform domain, the viscoelastic strain is written as:

$$\overline{\varepsilon}_{\text{ve}}=\left(\frac{1}{K_0}+\frac{1}{K_1+\eta_1 s}\right)\overline{\sigma}_d \tag{3}$$

The viscoplastic part of the model exhibits a different response in loading and unloading due to the presence of the sliding frictional element. No general closed-form solution can be derived and a numerical solution is required. For this purpose a finite difference scheme is used. The evolution in time of the applied stress during the experiment, presented in Figure 4, is expressed as:

$$\sigma_d(t)=V_0 t+\sum_{i=1}^{n}(-1)^i\left(V_{i-1}+V_i\right)\left(t-t_i\right)\mathrm{H}\left[t-t_i\right] \tag{4}$$

where the parameters t_i are the times at which the sign of the loading rate V_i is changed. Equation (4) is written in the Laplace transform field as:

$$\overline{\sigma}_d=\frac{1}{s^2}\left[V_0+\sum_{i=1}^{n}(-1)^i\left(V_{i-1}+V_i\right)e^{-t_i s}\right] \tag{5}$$

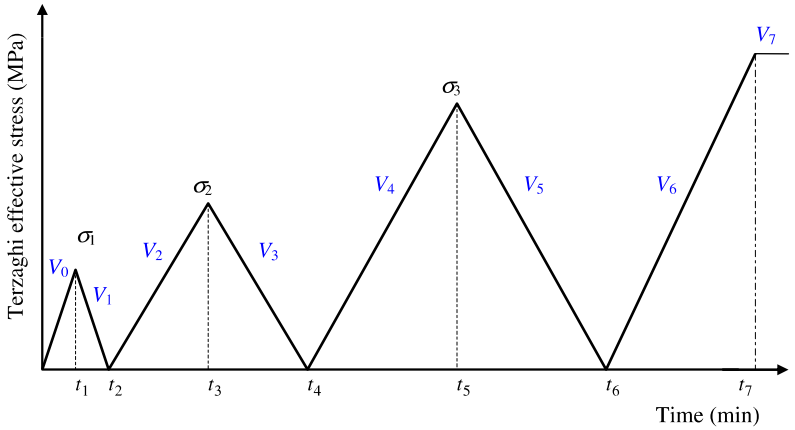

Figure 4. Loading-unloading cycles

Replacing equations (4) and (5) in equation (3) and inverting the Laplace transform, the analytical solution of the viscoelastic part ε_{ve} of the volumetric strain for drained isotropic compression is obtained as:

$$\begin{aligned}\omega(t)=&\frac{V_0}{a_3^2}\left[a_3a_1+\left(a_2a_3-a_1a_4\right)\left(1-e^{-\frac{a_3}{a_4}t}\right)\right]\\&+\frac{1}{a_3^2}\sum_{i=1}^{n}(-1)^i\left(V_{i-1}+V_i\right)\mathrm{H}\left[t-t_i\right]\left[a_3a_1\left(t-t_i\right)+\left(a_2a_3-a_1a_4\right)\left(1-e^{-\frac{a_3}{a_4}\left(t-t_i\right)}\right)\right]\end{aligned} \tag{6}$$

Note that the above relation is written in a general form which will be used later for the material response in undrained conditions. For the case of the drained isotropic compression test $\omega(t)=\varepsilon_{ve}^{d}(t)$ and the coefficients a_1, a_2, a_3 and a_4 are given in Table 1.

Undrained isotropic compression

The correspondence principle between poro-elasticity and poro-viscoelasticity is used here to calculate the poro-viscoelastic parameters. For solid materials under isotropic loading, the relationship between the applied confinement pressure and volumetric strain can be expressed by the hereditary integral $\sigma(t)=\int_{-\infty}^{+\infty}\hat{K}(t-t')\dot{\varepsilon}\,dt'$ (Schapery, 1984), where $\hat{K}(t-t')$ is the relaxation modulus at instant t'. By using the principle of superposition and in the same way one can write the equivalent expressions for a poro-viscoelastic material under isotropic loading as (Abousleiman et al., 1996):

$$\sigma_c(t)-\int_{-\infty}^{+\infty}\hat{\alpha}(t-t')\dot{p}\,dt'=\int_{-\infty}^{+\infty}\hat{K}(t-t')\dot{\varepsilon}\,dt' \tag{7}$$

$$p_f(t)=\int_{-\infty}^{+\infty}\hat{N}(t-t')\dot{\phi}\,dt'-\left[\int_{-\infty}^{+\infty}\hat{K}_s(t-t')\dot{\varepsilon}\,dt'+\phi_0\int_{-\infty}^{+\infty}\hat{N}(t-t')\dot{\varepsilon}\,dt'\right] \tag{8}$$

where N is the Biot modulus; $\sigma_c(t)$ and $p_f(t)$ are confinement pressure and pore pressure respectively; $\hat{\alpha}(t-t')$ is a coefficient corresponding to the variation of confinement pressure over a unit of pore pressure change at time t' when the volumetric strain is maintained constant. By writing equations (7) and (8) in the Laplace transform domain and knowing that $\int_{-\infty}^{+\infty}f(t)\dot{g}(t)dt=s\overline{f}\times\overline{g}$, one obtains:

$$\overline{\sigma}_c-\tilde{\alpha}\overline{p}_f=\tilde{K}_d\overline{\varepsilon} \tag{9}$$

$$\overline{p}_f=\tilde{N}\overline{(\phi-\phi_0)}-\left(\tilde{K}_s\overline{\varepsilon}+\phi_0\tilde{N}\overline{\varepsilon}\right) \tag{10}$$

$$\tilde{\alpha}=s\overline{\hat{\alpha}}\quad;\quad\tilde{K}_d=s\overline{\hat{K}}_d\quad;\quad\tilde{K}_s=s\overline{\hat{K}}_s\quad;\tilde{N}=s\overline{\hat{N}} \tag{11}$$

For isotropic undrained compression tests with a constant loading rate V, the confinement pressure is written in the Laplace transform domain as:

$$\overline{\sigma}_c=\frac{1}{s^2}\left[V_0+\sum_{i=1}^{n}(-1)^i\left(V_{i-1}+V_i\right)e^{-t_i s}\right] \tag{12}$$

The equations of poro-viscoelasticity written in the Laplace transform domain are formally similar to those of poro-elasticity. From equation (3), the expression of the drained bulk modulus in the Laplace transform domain is given as:

$$\tilde{K}_d=\frac{1}{1/K_0+1/\left(K_1+\eta_1 s\right)} \tag{13}$$

By performing an unjacketed test at 20°C, Ghabezloo et al. (2008) found that the solid phase of hardened cement paste behaves elastically and that its compression modulus K_s is constant and equal to 21.0 GPa, hence $\tilde{K}_s = K_s$. For undrained isotropic compression tests, the followed expressions can be written:

$$\overline{p}_f = \tilde{B}\overline{\sigma} \quad ; \quad \varepsilon_{\mathrm{ve}}^{\mathrm{u}} = \frac{\overline{\sigma}}{\tilde{K}_u} \tag{14}$$

One can evaluate the coefficients $\tilde{K}_u$ and $\tilde{B}$ as (Abousleiman et al., 1996):

$$\tilde{K}_u = \frac{\tilde{K}_d}{1-\tilde{B}\left(1-\tilde{K}_d / K_s\right)} \quad ; \quad \tilde{B} = \frac{1/\tilde{K}_d - 1/K_s}{\left(1/\tilde{K}_d - 1/K_s\right)+\phi\left(1/K_f - 1/K_s\right)} \tag{15}$$

where $\tilde{K}_d$ is expressed by equation (13). The coefficients $\tilde{K}_u$ and $\tilde{B}$ are functions of K_0, K_1, η_1, K_f, K_s and ϕ. Replacing equations (12) and (15) in equations (14) and inverting the Laplace transform, the pore pressure p_f and the volumetric strain $\varepsilon_{\mathrm{ve}}^{\mathrm{u}}$ are calculated. The solutions are written under the form given in equation (6), where ω can be the volumetric strain $\varepsilon_{\mathrm{ve}}^{\mathrm{u}}$ or the pore pressure p_f. The coefficients a_1, a_2, a_3 and a_4 are given in Table 1.

Table 1. Parameters of equations (6) for drained and undrained tests

$\omega(t)$	$\varepsilon_{\mathrm{ve}}^{\mathrm{d}}$	$\varepsilon_{\mathrm{ve}}^{\mathrm{u}}$	p_f
a_1	$K_0 + K_1$	$\frac{K_0+K_1}{\eta_1}a_2 - K_f K_0^2$	$K_f\left(K_0K_s - K_0K_1 + K_1K_s\right)$
a_2	η_1	$K_fK_s\eta_1\left(-1+\phi+\frac{K_0}{K_s}-\phi\frac{K_s}{K_f}\right)$	$K_f\eta_1\left(K_s-K_0\right)$
a_3	K_1K_0	$\frac{K_1}{\eta_1}a_4 - K_0K_fK_s^2$	$a_1+\phi K_0K_1\left(K_s-K_f\right)$
a_4	$K_0\eta_1$	$K_fK_0K_s\eta_1\left(1+\phi-\frac{K_s}{K_0}-\phi\frac{K_s}{K_f}\right)$	$a_2+\phi K_0\eta_1\left(K_s-K_f\right)$

MODEL CALIBRATION AND VERIFICATION

The parameters K_0, K_1, η_1, K_2 and η_2 are calibrated on the drained compression tests. Theses values are then validated for others tests performed at the same temperature. The evaluated parameters at 20°C are used to analyse the viscoelastic response under undrained isotropic loading.

Drained isotropic compression tests

Calibration of the model parameters is done as follows. The stress threshold σ_s is first estimated as the stress level above which the strain rate changes

significantly. The parameters of the viscoelastic part (K_0, K_1, η_1) are evaluated for the part of the stress-strain curves corresponding to $\sigma \leq \sigma_s$ and the two parameters of the viscoplastic part (K_2, η_2) are calibrated then for $\sigma > \sigma_s$. The model parameters are evaluated using the least-square method by. The computed parameters are listed in Table 2. The computed curves are compared in Figure 5 with the experimental results and show a good compatibility. We also note that at 20°C the viscosity η_1 of the viscoelastic element is found equal to 46×10^5 MPa.mn. This value is comparable with the one evaluated by Ghabezloo et al. (2009b) (from 26×10^5 to 39×10^5 MPa.mn) from back analysis of transient permeability tests.

Table 2- Calibration of model parameters for a cement paste hydrated at 90°C (Th90) and tested at 20°C and 90°C (Tt20, Th90)

T_h (°C)	T_t (°C)	σ_s (MPa)	K_0 (MPa)	K_1 (MPa)	K_2 (MPa)	η_1 (MPa.mn)	η_2 (MPa.mn)
90	20	43	8000	5500	7000	46.0×10^5	12.0×10^5
	90	25	5000	3000	4300	22.0×10^5	8.5×10^5

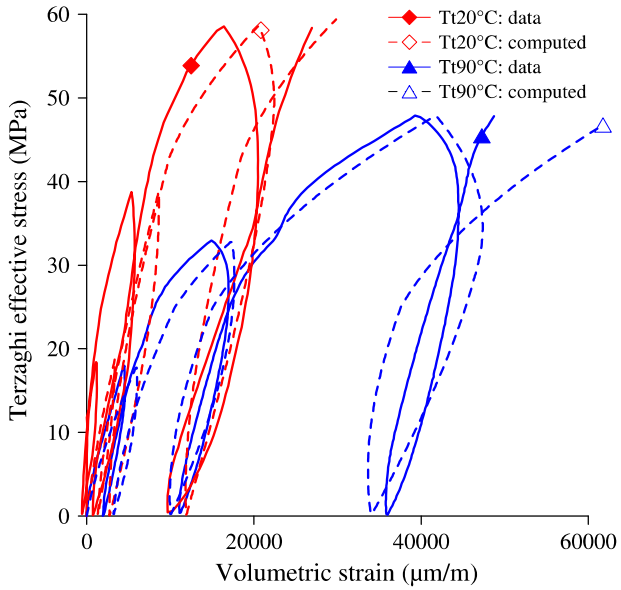

Figure 5- Computed and experimental stress-strain curves under isotropic compression

Using the calibrated model parameters, an isotropic compression test, which is not used for model calibration is simulated. This test corresponds to a sample hydrated at 90°C and tested at 20°C. The comparison of the simulated stress-strain curve and the experimental result in Figure (6a) shows a good compatibility. Moreover this test contains a creep phase at 36 MPa. The model correctly reproduces the creep phase as shown in Figure (6b).

Undrained isotropic compression test

The parameters K_0, K_1 and η_1 calibrated on drained tests for the test temperature of 20°C are used to validate the model by simulation of the undrained test presented above. The unjacketed modulus K_s is equal to 21.0 GPa, the total porosity is 0.39 and the bulk modulus of water K_f is 2.2 GPa at 20°C. The parameters are summarized Table (3) and the simulation results are presented in Figure (7) showing a very good agreement between the model predictions and the measurements of volumetric strain and pore pressure. Note that the part of the simulated pore pressure-confinement pressure curve in which the pore pressure exceeds the confinement pressure is disregarded in this analysis, because this situation cannot occur in a triaxial cell. One can see that the non-linear response of the pore pressure during the unloading phase is indeed well described by the model.

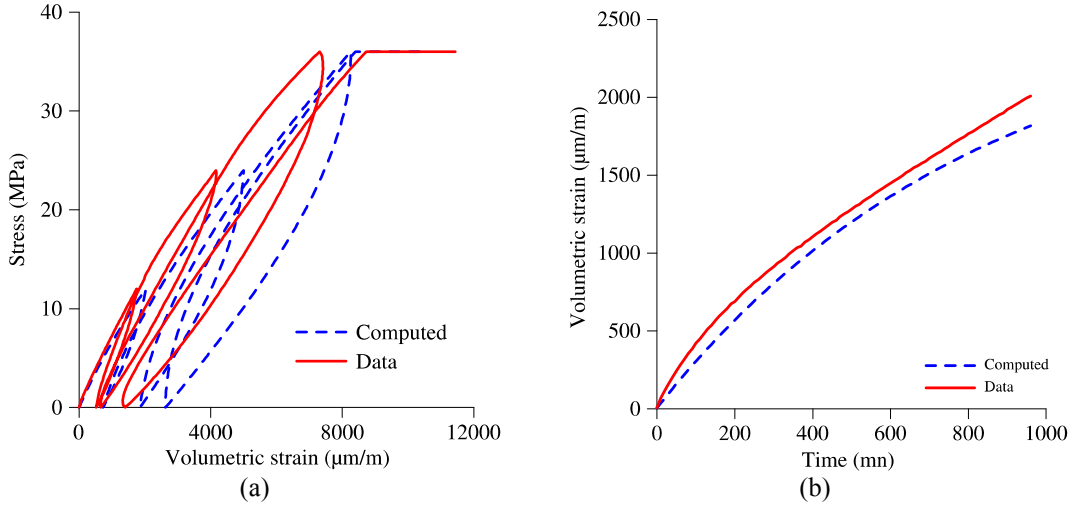

Figure 6- Isotropic compression test at 20°C on a sample hydrated at 90°C (a) loading-unloading phase (b) creep phase under 36 MPa

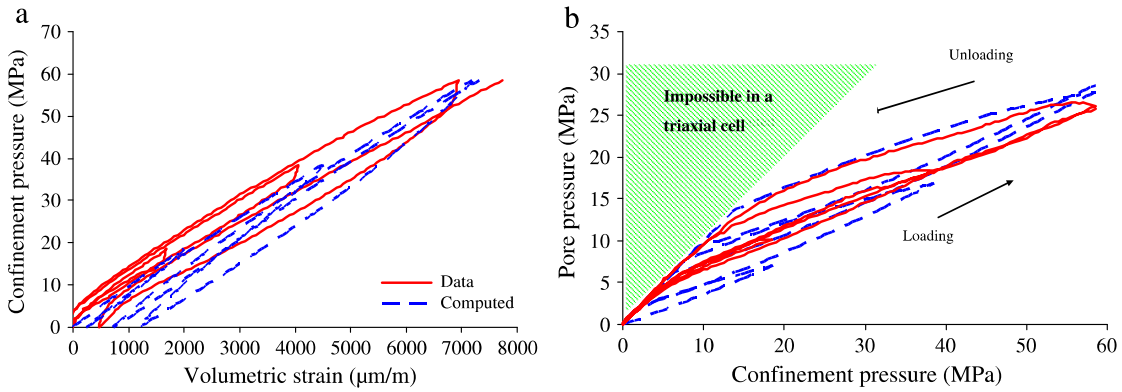

Figure 7- Comparison of experimental results and model prediction for undrained isotropic compression test, (a) volumetric strain response, (b) pore pressure response

CONCLUSIONS

Revisiting the isotropic compression tests on a hardened class G cement paste hydrated at 90°C in (Ghabezloo 2008, Ghabezloo et al., 2008), we analyse in this paper the time dependent response. A viscoplastic model is proposed and calibrated on the experimental data. The model describes the non-linear response of the volumetric strain for both drained and undrained compression tests as well as the delayed response of the pore pressure in undrained tests. The parameters of the model reflect the effect of the test temperature on the viscoplastic properties of the hardened cement paste. It is shown that the creep of the material is more pronounced at higher test temperature.

REFERENCES

Abousleiman Y., Cheng A. H.-D., Jiang C., Roegiers J.-C. (1996) Poroviscoelastic analysis of borehole and cylinder problems, Acta Mechanica 119, 199-219.

Bois A.-P., Vu M.-H., Ghabezloo S., Sulem J. (2013) Garnier A., Laudet J.-B., Cement Sheath Integrity for CO_2 Storage – An Integrated Perspective, Energy Procedia. 37, 5628–5641.

Ghabezloo S., Sulem J., Guedon S. (2008) Martineau F., Saint-Marc J., Poromechanical of hardened cement paste under isotropic loading. Cement and Concrete Research 38(12) 1424-1437.

Ghabezloo S. (2008) Comportement thermo-poro-mécanique d'un ciment pétrolier, PhD Thesis, Ecole Nationale des Ponts et Chaussées, France.

Ghabezloo S., Sulem J., Saint-Marc J. (2009a) The effect of undrained heating on a fluid-saturated hardened cement paste. Cement and Concrete Research 39(1) (2009) 54-64.

Ghabezloo S., Sulem J., Saint-Marc J. (2009b) Evaluation of a permeability-porosity relationship in a low-permeability creeping material using a single transient test, International journal of Rock Mechanics and Mining Sciences, 46(4) (2009), 761-768.

Ghabezloo S. (2010) Association of macroscopic laboratory testing and micromechanics modelling for the evaluation of the poroelastic parameters of a hardened cement paste, Cement and Concrete research, 40(8), 1197-1210.

Ghabezloo S. (2011a) Micromechanics analysis of thermal expansion and thermal pressurization of a hardened cement paste, Cement and Concrete Research 41(5), 520-532.

Ghabezloo S. (2011b) Effect of the variations of clinker composition on the poroelastic properties of hardened class G cement paste, Cement and Concrete Research 41(8) 920-922.

Vu M.-H., Sulem J., Ghabezloo S., Laudet J.-B., Garnier A., Guédon S. (2012) Time-dependent behaviour of hardened cement paste under isotropic loading, Cem. Concr. Res. 42, 789–797

Schapery R.A. (1984) Correspondence principles and a generalized J-integral for large deformation and fracture analysis of viscoelastic media, Int. J. Fracture, 25(1) 95-223.

Bond Deterioration Mechanism and Its Modeling for Reinforced Concrete Subjected to Freezing-Thawing Action

T. Kanazawa[1] and Y. Sato[2]

[1]Laboratory of Engineering for Maintenance System, Division of Engineering and Policy for Sustainable Environment, Graduate School of Engineering of Hokkaido University, Kita 13, Nishi 8, Kita-ku, Sapporo, Hokkaido 060-8628, Japan. E-mail: takeru-kanazawa@eng.hokudai.ac.jp
[2]Laboratory of Engineering for Maintenance System, Division of Engineering and Policy for Sustainable Environment, Faculty of Engineering of Hokkaido University. E-mail: ysato@eng.hokudai.ac.jp

Abstract

A new bond model for reinforced concrete members considering material deterioration induced by freezing-thawing action has been developed. The developed model with the extensive applicability from non-damaged to severely damaged members can reasonably describe deterioration mechanism between steel bar and concrete.

INTRODUCTION

It is quite difficult to assess remaining structural performance of existing structures deteriorated by freezing-thawing action. This is because the deterioration mechanism caused by the action is extremely complex, and furthermore, the influences of the material deterioration on the member behaviour are still unresolved.

To solve the problem above, the authors are planning to employ a nonlinear finite element analysis, which can apply various damage level to each element, and simulate the overall structural behaviour after the deterioration.

Several constitutive models considering the material deterioration must be prepared so as to conduct the analysis. In this paper, as a first step in developing the models, bond between steel bar and concrete is discussed, that is, a new bond model considering bond deterioration caused by freezing-thawing action is proposed. The proposed model can take the damage at steel bar-concrete interface quantitatively into account as the change of the mechanical properties of concrete: compressive strength (f'_C), elastic modulus (E_C), and tensile strength (f_t). This involves the bond deterioration mechanism based on experimental observations of uniaxial tension members subjected to freeze-thaw cycles.

BOND DETERIORATION MECHANISM CAUSED BY FREEZING-THAWING ACTION

Experimental outline and results. Figure 1 shows the specimens, which are prismatic elements with a single reinforcing bar at the center in the cross-section. The experimental parameters are the absence/presence of water, the number of fr-

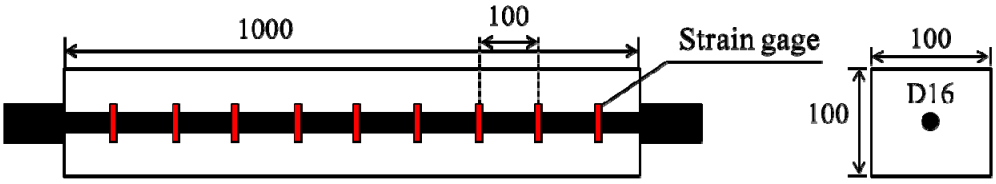

Figure 1. Specimen Dimensions. (mm)

Table 1. Experimental Parameters.

Specimen	*Number of Freeze-thaw Cycles*	*Water Provision*	*Pre-crack*
N0	0	×	×
N100	100	×	×
PN100	100	×	○
PW100	100	○	○

eeze-thaw cycles, and absence/presence of pre-cracks as shown in Table 1.

Figure 2 shows the average bond stress and average tensile strain (τ-ε) of rebar observed in the uniaxial tensile test. The effect of freezing-thawing action obviously results in the smaller average bond stress. The significant bond stress deterioration is observed especially in the specimen PW100 with a pre-crack under water provision.

Bond deterioration mechanism. Fig. 2 indicates that only temperature change is sufficient to cause a deterioration at the interface. This is because the average bond stresses observed in N100 and PN100 were smaller than that of N0 (undamaged specimen). In particular, PN100 (pre-cracked specimen) showed the significant tendency. Concrete and steel have the same coefficient of linear expansion whereas they have the different specific heat, and the interior temperatures differ from each other. This situation imposes a relative displacement on the interface. As a result, the slip-strain (S-ε) relationships change as shown in Figure 3.

All the above-mentioned results imply that there are two kinds of bond deterioration mechanisms: the concrete cover deterioration due to external factors such as water penetration from surface, and interface deterioration due to different thermal properties between steel and concrete. Therefore, appropriate modeling can be achieved by considering those deterioration mechanisms.

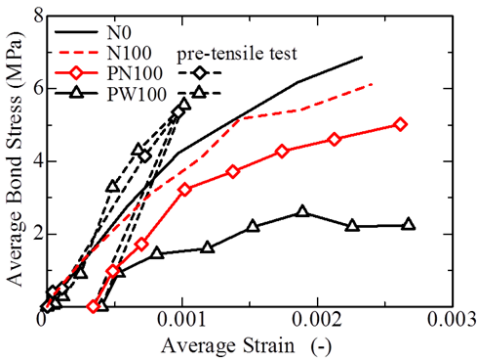

Figure 2. Average Bond Stress-Strain Relationships.

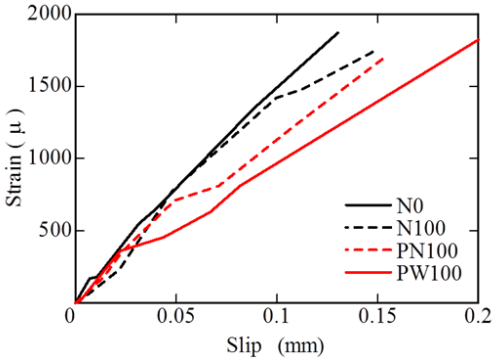

Figure 3. Slip-Strain Relationships.

MODELING

Basic models for modeling. Firstly, in order to discuss the change of S-ε relationship, we introduce the bond stress-slip-strain (τ-S-ε) relationship proposed by Shima et al. (1987), which can consider the change of S-ε relationship:

$$\tau = k \cdot f'_c \cdot \ln \{ 1 + 5 \cdot (1000\, S / D) \}^3 / g(\varepsilon) \quad (1)$$

where $k = 0.73$; S = slip; D = bar diameter; $g(\varepsilon) = 1 + \varepsilon \cdot 10^5$ (strain function)

An important feature of Shima model is to explain the influence of boundary conditions by incorporating the strain function into bond stress-slip (τ-S) relationship. Additionally, this is very advantageous to nonlinear analysis because of easy installation.

According to previous studies, freezing-thawing action causes change of stress-strain (σ-ε) relationship of concrete as well as reduction of compressive strength. In this study, therefore, Bigaj model (1996) is introduced because the model can take into account σ-ε relationship of concrete. Combining these two models enables us to reasonably describe the bond and deterioration mechanisms.

Object scope. Figure 4 shows the scheme to obtain the bond stress, slip, and strain profiles along reinforcing bar under the condition that no slip and zero strain were obtained at the free end.

Shima model is applicable to massive concrete. By contrast, Bigaj model can cover both massive concrete and concrete with small cover.

Figure 5 shows the τ-S relationships derived from the two models. The τ-S relationship derived from Bigaj model presents the softening behaviour when C/D, namely cover normalized by bar diameter, becomes less than 2.3. In this study, a bond model for the case of C/D $\geq$ 2.3 will be discussed.

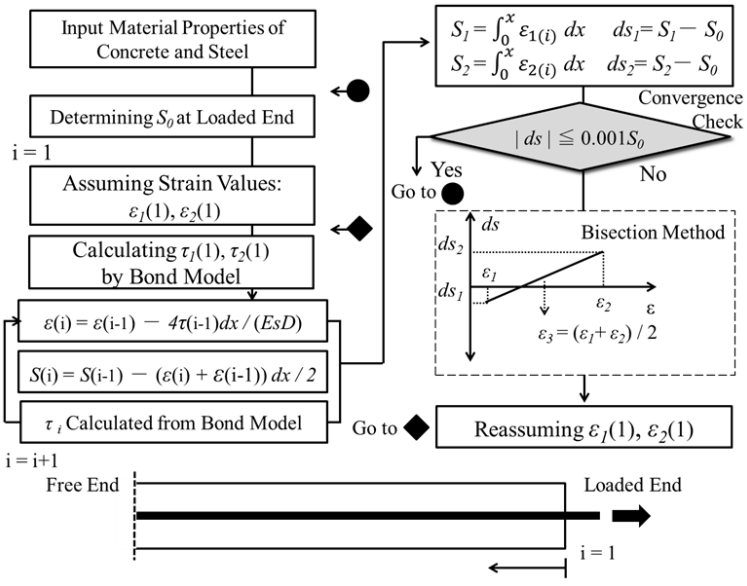

Figure 4. Scheme to Obtain Bond Stress, Slip, and Strain Profiles.

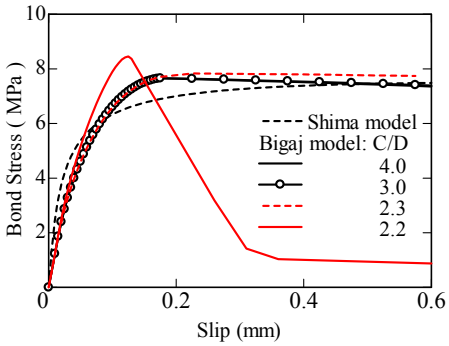

Figure 5. Bond Stress-Strain Relationships with different C/D.

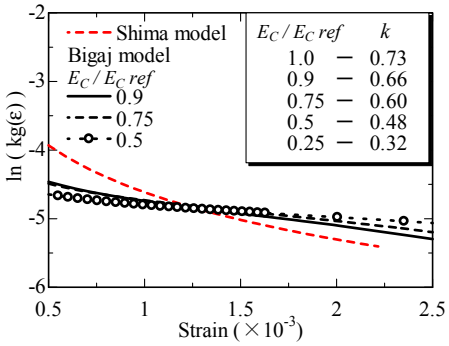

Figure 6. Relationships between $k \cdot g(\varepsilon)$ and ε .

Modeling of concrete cover deterioration. It seems that the concrete confinement effect would be weakened after the cover deterioration. The influence is considered by changing concrete stiffness in the proposed model. Figure 6 shows the relationships between $k \cdot g$ (ε) and ε on logarithmic scale calculated from τ, S, and ε values derived from Bigaj model with different elastic moduli. When Eq. (2) is introduced in the Shima model, the tendency becomes close to Bigaj model:

$$f_1(E_C) = \left(\frac{E_C}{E_C ref}\right)^{0.56} \tag{2}$$

where f_1 = elastic modulus function; E_C = damaged elastic modulus due to freezing-thawing action; $E_C ref$ = reference elastic modulus

Modeling of interface deterioration. Figure 7 shows $g(\varepsilon)$ calculated from Eq. (1) with τ, S, and ε values derived from Bigaj model with different tensile strengths. It also shows that smaller tensile strength results in more significant effect of the strain function on bond stress. Because of simplicity, Eq. (3) is obtained from the linear regression of the gradients shown in Fig. 7.

$$f_2(f_t) = \left(\frac{f_t}{f_t ref}\right)^{-0.13} \tag{3}$$

where f_2 = tensile strength function; f_t = damaged tensile strength due to freezing-thawing action; $f_t ref$ = reference tensile strength

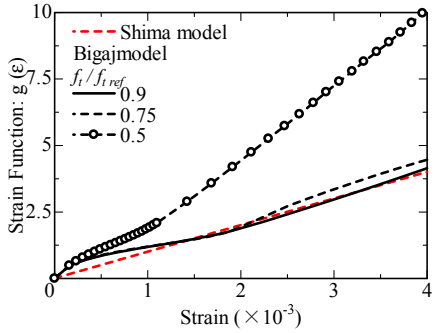

Figure 7. relationships between $g(\varepsilon)$ and ε .

Finally, the following model is proposed.

$$\frac{\tau}{f'_c} = \frac{0.73 f_1(E_c) \cdot \ln\{1 + 5 \cdot (1000 S/D)\}^3}{1 + f_2(f_t) \cdot \varepsilon \times 10^5}$$

Verification of proposed model. The validity of the proposed model is confirmed by the comparison with the experimental results. The compressive strength of the specimens was derived from uniaxial compressive tests of the cylindrical specimens, which were suffered to the same freezing-thawing environment as the uniaxial tension specimens. According to previous studies, material properties of damaged concrete can be related to Relative Dynamic Elastic Modulus (*RDEM*). In this study, therefore, the tensile strength and elastic modulus after freeze-thaw cycles were determined based on the relationships between *RDEM* and reduction of compressive strength reported by Hayashida and Sato (2012) and Matsumura et al. (2003). The properties are shown in Table 2.

Figure 8 shows the comparison of experimental and analytical average τ-ε relationships. The analytical results show a good agreement with all of the experimental ones regardless of damage level.

Table 2. Material Properties of Damaged Concrete.

Number of Freeze-thaw Cycles	f'_c (*MPa*)	$f'_c/f'_c ref$ (%)	*RDEM* (%)	$E_c/E_c ref$ (%)	$f_t/f_t ref$ (%)
0	38.7 ($f'_c ref$)	100	100	100	100
100 (without water)	35.6	92	87	79	87
100 (with water)	30.4	79	80	60	85

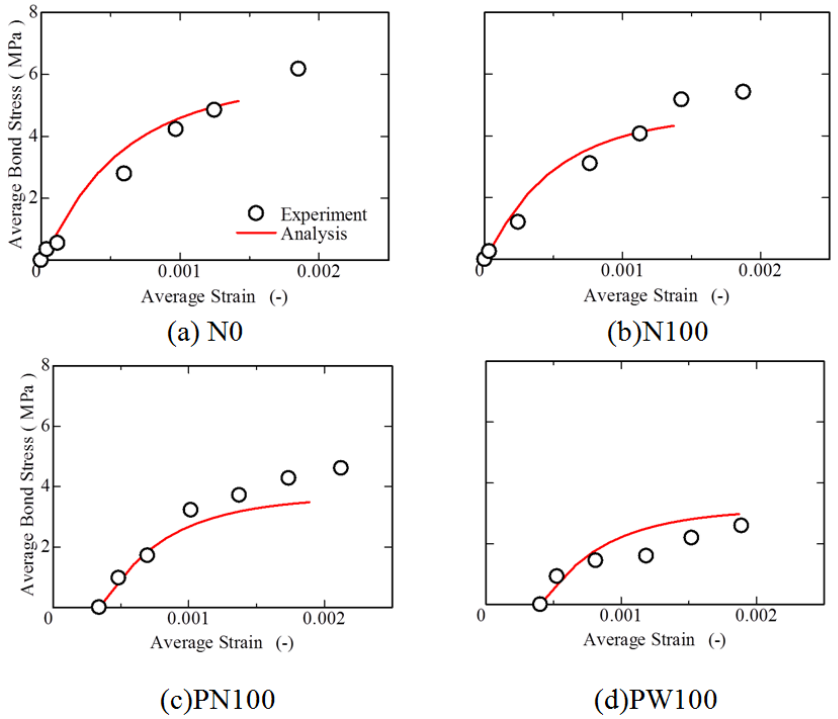

Figure 8. Comparison of Experimental and Analytical Average Bond Stress-Strain Relationships.

CONCLUSIONS

The following conclusions are drawn in this study.

- The bond deterioration due to freezing-thawing action consists of the two mechanisms: the one is the cover deterioration originated by moisture penetration from concrete surface, and the second one is the interface deterioration originated by water passing through the interface from a crack.
- In the proposed model, the cover and interface deterioration are incorporated as the change of elastic modulus, and the effect of the concrete confinement on the strain function, into the τ-S-ε relationship, respectively.
- The proposed model shows a good agreement with the experimental average τ-ε relationships.

REFERENCES

Den Ujil, J. A. and Bigaj, A. J. (1996). "A bond model for ribbed bars based on concrete confinement", *HERON*, Vol.41, 201-226

Hayashida, H. and Sato, Y. (2012). "Fundamental study on tensile strength of concrete subjected to freezing and thawing", *2012 JSCE Annual Meeting* (*CD-ROM*), JSCE, Tokyo (in Japanese)

Matsumura, T., Katsura, O., and Yoshino, T. (2003). "Properties of frost damaged concrete and the estimation of the degree of frost damage", *J. Struc. Constr. Eng.*, Vol.563, 9-13 (in Japanese)

Shima, H., Chou, L., and Okamura, H. (1987). "Micro and macro models for bond in reinforced concrete", *J. Fac. Eng. Univ. Tokyo*, vol.39, No.2, 133-194

Meso-Scale Analysis of the Mechanical Properties of Chemically-Deteriorated Mortar

Y. Sato[1]; T. Miura[2]; and H. Nakamura[3]

[1]Laboratory of Engineering for Maintenance System, Division of Engineering and Policy for Sustainable Environment, Hokkaido University, Kita 13, Nishi 8, Kita-ku, Sapporo 060-8628, Japan. E-mail: ysato@eng.hokudai.ac.jp
[2]Concrete Laboratory, Division of Civil Engineering, Nagoya University, Furo-cho, Chikusa-ku, Nagoya 464-8603, Japan. E-mail: t.miura@civil.nagoya-u.ac.jp
[3]Concrete Laboratory, Division of Civil Engineering, Nagoya University, Furo-cho, Chikusa-ku, Nagoya 464-8603, Japan. E-mail: hikaru@cc.nagoya-u.ac.jp

Abstract

How volume change of the cement hydrates affects mechanical characteristics of mortar after calcium leaching are discussed and prediction equations for elastic modulus, tensile strength, fracture energy and shear strength are proposed. Furthermore an analysis of mass transfer with chemical reaction based on a finite volume method is developed and is coupled with a mechanical analysis based on the RBSM. The validity of the coupled analytical method is discussed.

INTRODUCTION

Concrete would be deteriorated by various factors in severe environment. In fact there are several deterioration mechanism such as, calcium leaching, salt corrosion, chemical erosion, frost damage and fatigue. Among those deterioration mechanisms, calcium leaching and chemical erosion are very important mechanism for durability design of underground and hydraulic concrete structures.

The calcium components in concrete are gradually dissolved in water when concentration difference between external solution and pore solution is in existence. There are many reports on those issues with physical, chemical, and mechanical point of views. However, investigations with mechanical point of view are very limited (C. Le Bellego, 2000).

In this study, mechanical characteristics of meso-scale mortar, whose size is 70 mm in length, 3 mm in thick, and 30 mm in width, deteriorated by calcium leaching are discussed. That is, the relationships between mechanical properties and physico-chemical properties are examined qualitatively. Furthermore an analysis of mass transfer with chemical reaction based on finite volume method is developed and coupled with the Rigid Body Spring Method (RBSM) for simulating mechanical performance of mortar. Finally the validity of the analysis method is discussed by comparing with the experimental results.

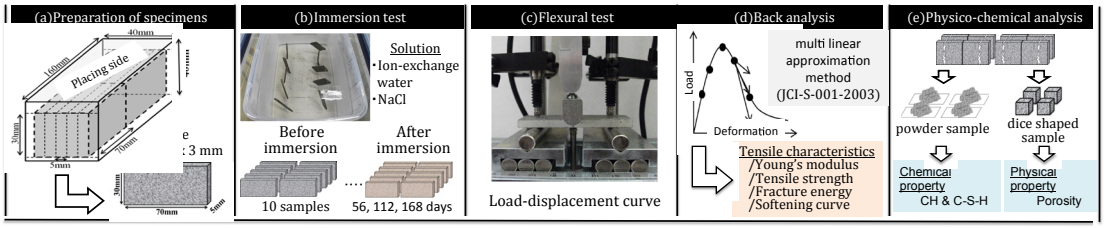

Figure 1. Flow of experiments.

OUTLINE OF EXPERIMENTS

Materials and specimens. Normal Portland cement and normal fine aggregates that passed through a 1.0 mesh sieve were used. The mass ratio among water, cement and fine aggregates was 1 : 2 : 3.3. Mortar prisms whose size was 40 mm wide by 40 mm high by 160 mm length were firstly made and were cured in water for 120 days. Just before the tests, thin specimens with 3 mm in thick, 30 mm in width, and 70 mm length were hewed out from the mortar prisms as shown in Fig.1(a).

Immersion test. Immersion condition is shown in Table 1. Ion-exchanged water and NaCl solution were used. Ten meso-scale specimens were drooped in 15 L poly container using a corrosive-resistant string as shown in Fig.1(b). The containers were left at rest at 20 $°C$ in temperature-controlled room. The solution in each container was replaced by fresh solution every 14 days so as to keep the concentration constant.

Flexural test. Three point bending test was carried out after immersion as shown in Fig.1(c). In the test, LVDTs were placed at the center and supporting points of the specimen. The beam span and the loading speed were set to 50 mm and 0.0001 mm/sec, respectively. The tension softening curves were obtained from the observed load-displacement curves using the program JCI-S-001-2003 (JCI, 2003), adapting multi linear approximation method.

Chemical and physical analysis. After the immersion test and the bending test, chemical analyses were carried out in order to determine cement hydrates variation with time as shown in Fig.1(d). Dice shaped samples for porosity measurement were taken from the thin specimens broken after the flexural test. In this study, porosity was measured by the Archimedes method. The remaining parts were crushed with a hummer and reduced to a fine powder using a ball mill for chemical analysis. Specially, amount of calcium hydroxide (CH) in each specimen was measured by TG/DTA, while the amount of calcium silicate hydrate (CSH) was measured by a heavy liquid separation method and salicylic acid-methanol method.

Table 1. Condition of immersion test.

Specimen	Solution	Immersing period (day)
NM	Ion-exchange water	0, 56, 112, 168
CM	NaCl Cl^- 20g/L	0, 56, 112, 168

EXPERIMENTAL RESULTS

Changes of physico - chemical properties. Changes of CH, C-S-H, and porosity are shown in Fig.2. CH quickly decreases and almost vanishes at 56 days and then C-S-H tends to decrease after 50 days. The porosity steadily increases with the immersing period.

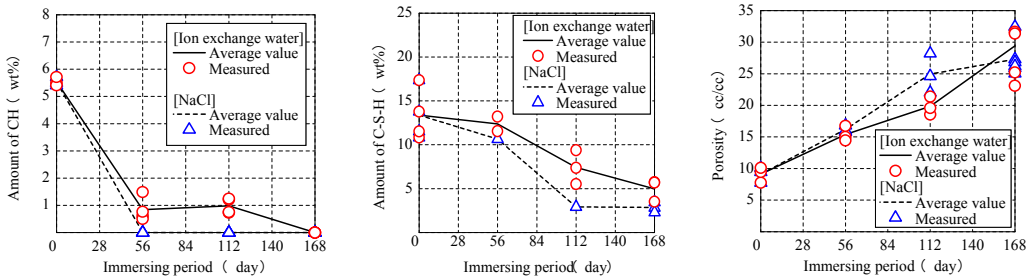

(a)CH (b) C-S-H (c)porosity

Figure 2. Change of CH, C-S-H, porosity observed in the experiment.

Changes of mechanical characteristics. Figure 3 shows relationships between flexural stress and mid-span deflection. Flexural strength and stiffness are remarkably reduced with the exposure time. Tension softening curves obtained from load-displacement curves are shown in Fig.4. The reduction in tensile strengths is clearly observed as immersing period increases.

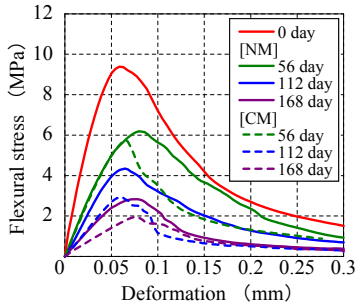

Figure 3. Flexural stress – deformation curves.

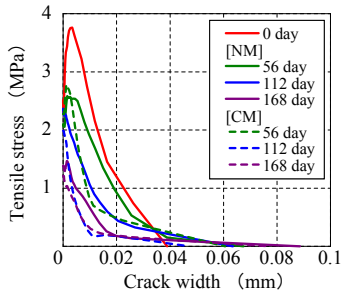

Figure 4. Tensile stress – crack width curves

Relationships between mechanical and physico-chemical characteristics. Through the experiments, we found there were strong association between the change in mechanical characteristics and the change in physico-chemical property. Especially, the increment of porosity was strongly related in each mechanical behavior as shown in Fig.5.

In this study, therefore, the following prediction equation of elastic modulus, tensile strength, fracture energy and shear strength for mortar deteriorated by calcium leaching is proposed.

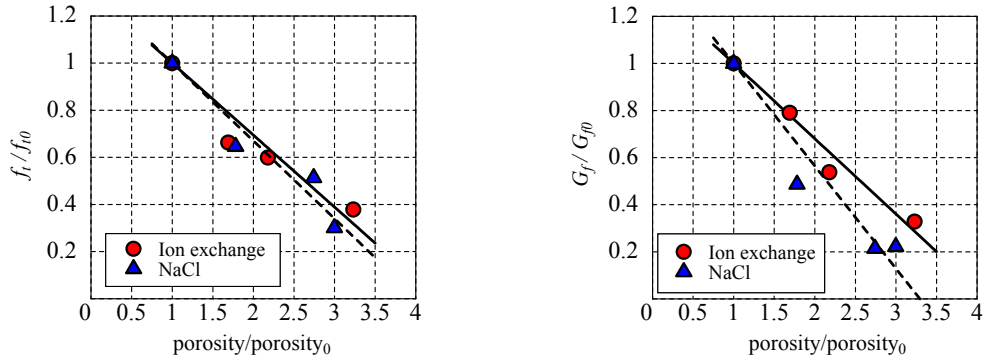

(a) Tensile strength **(b) Fracture energy**

Figure 4. Relationships between mechanical characteristics and porosity.

$$\frac{F}{F_0} = a \cdot \exp\left(-k \cdot \frac{\Delta p}{p_0}\right) \tag{1}$$

where F is mechanical property of deteriorated mortar. F_0 is mechanical property of non-damaged mortar. p is porosity after deterioration. p_0 is porosity of non-damaged mortar (ml/ml). a is a coefficient that including the effect of aggregate amount, maximum aggregate size and size effect, k is a coefficient that directly affects mechanical behavior.

Table 1 shows the coefficient value a and k of each mechanical behavior. In this study, in both cases of mortar immersed in demineralized water and NaCl solution, the deterioration mechanism that is Ca leaching is same, therefore, these coefficient values should be same in both cases. Then, the coefficient values are determined by the results of mortar immersed in demineralized water and they are also applied to the model in the case of mortar immersed in NaCl solution.

Table 2. Coefficient in the prediction equations.

	E	*ft*	*Gf*	*fs*
k	12.1	4.8	5.3	4.9
a	3.0	1.5	1.6	1.6

OUTLINE OF CHEMICAL ANALYSIS

In this study, Ca leaching was modeled by a finite volume method to describe the diffusion behavior and dissolution of cement hydrates. Basic equations adapted in mass transfer / chemical reaction analysis (T. Miura, 2014) are shown below.

Law of the conservation of mass of different coexisting ions. In this analysis, the diffusion of different coexisting ions in the liquid phase was described as shown in the following equation.

$$\frac{\partial\left(p \cdot C_{liquidi}\right)}{\partial t} = \frac{\partial}{\partial x}\left(\sum_{j=1}^{n} D_{ij}^{eff} \frac{\partial\left(p \cdot C_{liquidj}\right)}{\partial x}\right) \tag{2}$$

where C_{liquid}: the concentration of Ca ions at the liquid phase (mol/l), D^{eff} : the effective diffusion coefficient (mm^2/sec), p: the porosity of cement paste, and n: the type of ionic species.

Mutual ion diffusion coefficient model. In this analysis, the diffusion behavior of various ions was modeled by the concept of mutual ion diffusion coefficients to evaluate the behavior of various ions other than a Ca ion. The mutual diffusion coefficient was expressed by the following equations.

$$D_{ij} = \delta_{ij} \cdot D_i^0 \cdot \left(1 + \frac{\partial \ln \gamma_i}{\partial \ln C_{liquidi}}\right) - \left\{\frac{z_i \cdot D_i^0 \cdot C_{liquidi}}{\sum_{k=1}^{n} z_k^2 \cdot D_k^0 \cdot C_{liquidk}} \cdot z_j \cdot D_j^0 \left(1 + \frac{\partial \ln \gamma_j}{\partial \ln C_{liquidj}}\right)\right\} \tag{3}$$

$$D_{ij}^{eff} = \frac{p}{\tau^2} D_{ij} \tag{4}$$

where D_{ij}: the mutual diffusion coefficient (mm^2/sec), δ_{ij}: the Kronecker delta function (=1 when $i=j$, 0 when $i \neq j$), D^0: the tracer diffusion coefficient (mm^2/sec), z_j: the valence number of the jth ionic species, γ_i: the mean activity coefficient of the ith ionic species, which is derived by the Debye-Huckel theory, and τ: the tortuosity of concrete.

The dissolution of cement hydrate. When a chloride ion exists in the pore solution, the solubility product of CH increases. In this analysis, this phenomenon was considered by the following formulas.

$$CaL0 = \frac{1}{2}\sqrt[3]{2K_{spcl}} \tag{5}$$

$$K_{spcl} = K_{sp} + \left(0.00075\left[Cl^-\right]^2 - 0.0005\left[Cl^-\right]^3\right) \tag{6}$$

where $CaL0$: the maximum concentration of Ca ions at the pore solution, K_{sp}: the solubility product of CH, K_{spcl}: the solubility product of CH in the case that chloride ions exist, and Cl^-: the concentration of chloride ions.
Moreover, to consider the chemical equilibrium of the outer solution, the concentration of Ca ions of the outer solution was forcibly increased as a function of soaking periods.

$$Ca_{out} = Ca_{total} \cdot \frac{T}{T_{equili}} \tag{7}$$

where Ca_{out}: the concentration of Ca ions in the outer solution, Ca_{total}: the average concentration of Ca ions at the analytical object, T: the soaking time until the solution exchange, and T_{equili}: the period at which Ca_{out} is equal to Ca_{total} (=5 days).

Calculation of porosity. Porosity is simply calculated by the following equation.

$$p_{cal} = p_0 + \frac{(CH_0 - CH)}{\rho_{CH}} + \frac{(CSH_0 - CSH)}{\rho_{CSH}} \tag{8}$$

where p_{cal}: the calculated porosity (cm^3/cm^3), p_0: the initial porosity (cm^3/cm^3), ρ_{CH}: the density of CH (=2.24 g/cm^3), ρ_{CSH}: the density of C-S-H (=1.90 g/cm^3), CH, CSH: the amount of CH and C-S-H, and CH_0, CSH_0: the initial amount of CH and C-S-H.

OUTLINE OF MECHANICAL ANALYSIS

Outline of RBSM. A rigid body spring method (RBSM) (K. Nagai, 2004) is used. Analyzed model is divided into polygonal elements interconnected along their boundaries by normal and shear springs as shown in Fig.5. A random geometry is introduced using a Voronoi diagram as shown in Fig.6.

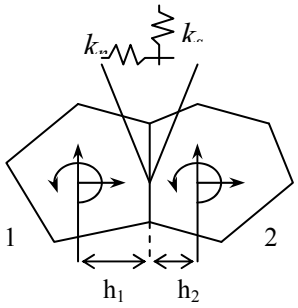

Figure 5. Rigid body with springs

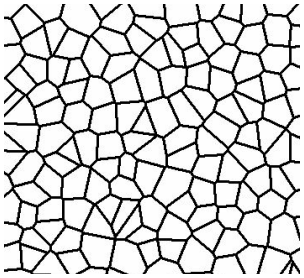

Figure 6. Voronoi diagram

Constitutive models. Tension and shear models adapted are shown in Fig.7. The strengths and stiffness required in the models are given by Eq.(1) in which the porosity calculated by mass transfer – chemical reaction analysis is used.

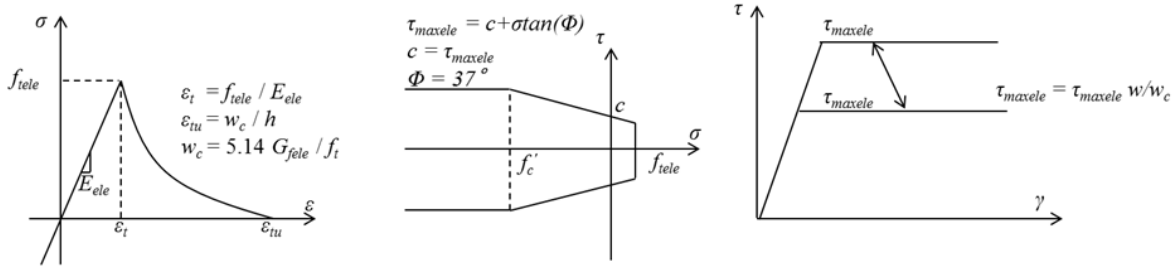

(a)Tension **(b) Failure criteria** **(c)Shear**

Figure 7. Constitutive models.

VERIFICATION OF THE ANALYSIS

Analytical specimen. Analytical specimen is shown in Fig.8. In the analysis of mass transfer with chemical reaction, all faces were contacted with ion exchange water or NaCl. In the mechanical analysis, both supporting points can move horizontally like experimental condition.

(a) Boundary condition in mass transfer / chemical reaction analysis

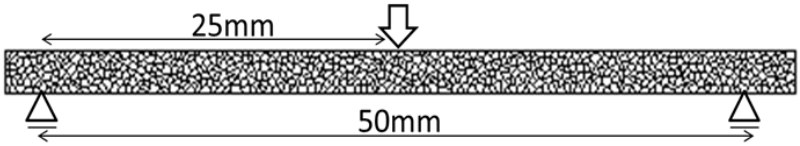

(b)Boundary condition in mechanical analysis

Figure 8. Analytical specimen.

Analytical results and discussions. Change of CH, C-S-H, and porosity are shown in Fig.9. On the other hand, Fig.10 shows flexural stress and deformation curves. The analysis can simulate the experimental results reasonably. However the accuracy of the porosity and the flexural strength prediction degrades as the immersing period becomes longer. This discrepancy must be improved.

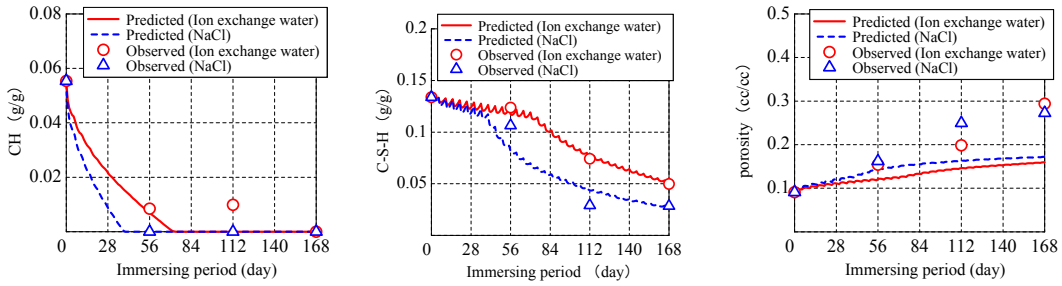

(a)C-H **(b)C-S-H** **(c)Porosity**

Figure 9. Results predicted by the mass transfer / chemical reaction analysis.

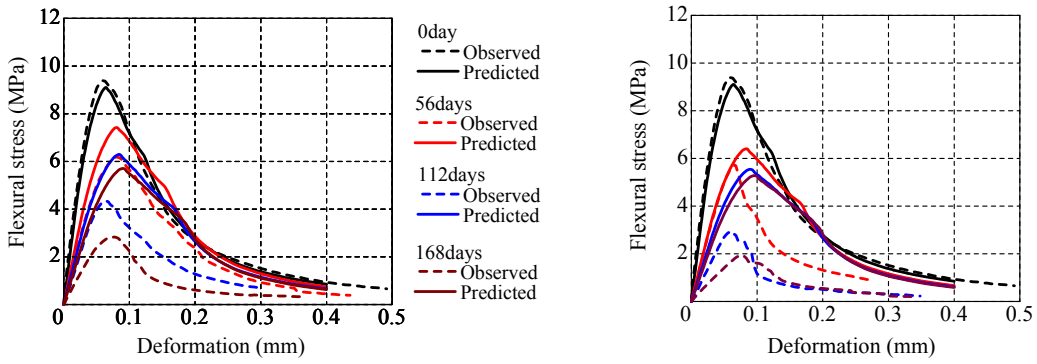

(a) Ion exchange water **(b) NaCl**

Figure 10. Results predicted by the mass transfer / chemical reaction analysis.

CONCLUSIONS

- The mechanical characteristics are remarkably reduced by calcium leaching.
- Each mechanical characteristic is strongly related to amount of cement hydrate and porosity change.
- The coupled analysis method that composes of mass transfer with chemical reaction and mechanical analysis is developed.
- The coupled analysis can simulate the experimental results reasonably.

REFERENCES

C. Le Bellego, B. Gerard, and G. Piijaudier-Cabot, (2000). "Chemo-mechanical Effects in Mortar Beams Subjected to Water Hydrolysis," *Journal of Engineering Mechanics*, 266-272.

JCI, (2003)."Method of test for fracture energy of concrete by use of notched beam." http://www.jci-web.jp/jci_standard/img/JCI-S-001-2003-e.pdf

K. Nagai, Y. Sato, T. Ueda, (2004). "Mesoscopic Simulation of Fracture of Mortar and Concrete by 2D RBSM, " *Journal of Advanced Concrete Technology*, Vol.2, No.3, 359-374.

T. Miura, Y. Sato, and H. Nakamura, (2014) "Modeling of physic-chemical property and mechanical characteristics of meso-scale mortar deteriorated by Ca leaching." (2013). Proceedings of Fourth International Symposium on Life – Cycle Civil Engineering, CD-ROM

Local Response in Concrete and Other Composite Material Structures Using the Embedded Unit Cell Approach

M. Grigorovitch[1] and E. Gal[2]

Department of Structural Engineering, Ben-Gurion University of the Negev, Beer-Sheva 84105, Israel. E-mail: [1]shuhman@gmail.com; [2]erezgal@bgu.ac.il

Abstract

In this paper we are presenting the development of a new concept, the embedded unit cell (EUC) approach, used to calculate local responses in elastic media. In addition, the suggested formulation provides homogenization and multi scale analysis of composite materials, structures and domains; where the classical theory of homogenization does not valid. The EUC approach is based on a multi-scale formulation of the asymptotic homogenization theory to evaluate structure response in several special cases, such as response of non-periodic domains or local/micro response at zones that are expected to develop stress concentrations. The suggested approach is based on the zone-adapted unit cell, restricted by alternative boundary conditions and surrounded by micro scale domain that represents non periodic features of the macroscopic structure. By using the alternative boundary conditions, the periodic assumption of unit cell response that is essential in the classical theory, is no longer required yet preserving an accurate micro-scale response evaluation. This approach offers a reduced computational cost model of the macroscopic/global problem however the precision of the microscale problem solution is retained. The EUC concept broadens the applicability of multiscale analysis techniques, used to evaluate mechanical response of variety of composite materials, in particular highly heterogeneous materials (i.e. concrete, etc.), which are widely used in modern construction industry.

1 INTRODUCTION

In the recent years, constructions are required to sustain constantly increasing geometrical complexity as well as structure durability to variety of loads. Using the advanced knowledge and production techniques of composite materials [Gibson 2011, Hashin 1962], modern complex structures are preprogrammed and simulated, so that specific requested engineering performance can be achieved.

At the beginning of the 21st century, civil engineers face the often-contradictory demands for designing larger, safer, and more durable structures at lower cost and

shorter time. To adhere to this challenge, it is necessary to employ novel materials together with new structural concepts and construction methods. High performance cement-based composites can be named as a typical representative of these modern materials. With the help of micromechanical models and optimization techniques it is now possible to design concrete structures to meet requirements for both feasible production and superior failure behavior.

The inhomogeneous structure of composite materials often appears in more than one material scale, which makes influence on material properties. One of the main difficulties in computational mechanics is the model complexity due to microscopic accuracy demand, which requires extensive computing time.

A practical method for evaluating the mechanical response of structures that are based on composite materials is Finite Element Method (FEM) [Chen and Hou 2003, Feyel 2003, Novak, Kaczmarczyk 2012, Zahavi 1992]. The analysis using FEM is numerical technique to solve differential equations that evaluate the requested mechanical variables, such as stress and displacement fields. If the material scale solution is required, the finite elements model should include the material scale elements. Such model is often not applicable in a single scale solution due to limited computing resources. Computational method that significantly reduces the complexity of the model by reducing the number of degrees of freedom is Multi Scale Analysis [Gonella 2007, Oskay and Fish 2008, Zeman, Novak 2008].
One of the methods used during the Multi Scale analysis is homogenization theory [Allaire 1992, Babushka 1976, BabuSka 1976, Mei and Vernescu 2010]. The generalized homogenization is based on replacement of heterogeneous microscopic structure by homogeneous statistically representative volume element with equivalent material properties. There are many different ways to define that repetitive volume element, also called Unit Cell, which become more complicated with increasing level of inhomogeneity in concrete and other composite materials.

In general, the classical homogenization is restricted to solution of structures with periodic material matrix. There are numerous research efforts to find adaptations to classical theory in order to avoid periodic restrictions and to use homogenization for highly heterogeneous materials without proper periodic material matrix, such as concrete [Dujc, Brank 2010, Gal, Ganz 2008, Wu, Yuan 2010], by defining representative unit cell with satisfied accuracy.

Moreover, neither of the classical homogenization formulations allows finding precise structure response at zones that are not periodic in respect to the rest of the body. The lack of periodicity can be geometrical, such as in the boundaries of the macroscopic domain; as well as in the zones with local non periodic material response, such as in damage zones, where stress concentration is expected.
In this research we are suggesting the Embedded Unit Cell multi-scale approach in order to obtain solution for some of those problems.
In the suggested formulation we are adjusting the theory of homogenization to be used in a domain decomposing scheme. In this research, the multi scale analysis is used to evaluate the macroscopic and microscopic response of heterogeneous

materials, by avoiding the assumption of periodic response required for the classic homogenization theory to be valid.

The formulation is based on the asymptotic homogenization theory without periodic assumption by dividing the problem into pair of independent models which are coupled using a unit cell having alternative boundary conditions by mean of an interface zone (surrounding domain) between the microscopic and the macroscopic models. The EUC model is used in a multi-scale scheme to homogenize the microscopic domain and up-scale its properties to the macro-scale (structural) model. Consequently, instead of solving one demanding problem, we are solving two much less demanding problems while preserving the accuracy.

2 PERIODIC MATHEMATICAL FORMULATION

At first, the classical periodic homogenization theory is described; latter the non-periodic formulation is developed.

Let assume that macroscopic body is formed by heterogeneous microscopic structure with local periodicity set by unit cell.

The displacement field $u_i^{\zeta}(x,y)$ can be described by the following asymptotic expansion

$$u_i^{\zeta}(x,y) = u_i^{(0)}(x,y) + \zeta u_i^{(1)}(x,y) + \zeta^2 u_i^{(2)}(x,y) + \ldots$$

where ζ is ratio between the scales that denotes the periodicity rate of $u_i^{\zeta}(x,y)$.

Subsequently deriving the asymptotic expansion (10), and using the set of equations that define the problem (physical and constitutive rules, essential and natural boundary conditions), we obtain the set of equilibriums equations, according to the power of ζ :

$$O(\zeta^m): \qquad \frac{\partial \sigma_{ij}^{(m)}}{\partial x_j} + \frac{\partial \sigma_{ij}^{(m+1)}}{\partial y_j} = 0 \quad (m \geq 1)$$

The classical homogenization assumes periodic unit cell response for the solution of the set of equilibriums equations.

The solution of ζ^{-2} equation imposes that $u_i^{(0)}(x,y) = u_i^{(0)}(x)$, which means that the average displacement change over macroscopic domain is not fluctuated inside the microscopic domain Y.

The solution of ζ^{-1} equation represents the unit cell problem (Yuan et al [30]), to evaluate the equivalent material properties C_{ijkl}^{*} of the unit cell as:

$$C_{ijmn}^{*} = \frac{1}{|Y|}\int_Y C_{ijkl}\left(\frac{\partial \chi_k^{mn}}{\partial y_l} + I_{klmn}\right) dY$$

3 NON-PERIODIC MATHEMATICAL FORMULATION

In order to develop the EUC approach, we are suggesting that the solutions of these equilibrium equations will be obtained without using the periodicity assumption of the unit cell response.

Let consider the solution of the ζ^{-2} equation without applying the periodicity assumption. Integrating it over the unit cell domain, we obtain that:

$$\frac{\partial}{\partial y_j}\sigma_{ij}^{(-1)}(x,y)=\frac{\partial}{\partial y_j}\left(C_{ijkl}\frac{\partial u_i^{(0)}}{\partial y_j}\right)=0$$

In order to satisfy the last equation, one of the terms inside parentheses shall vanish. Since C_{ijkl} is the material properties tensor and cannot be equal to zero, we conclude that $\frac{\partial^2 u_i^{(0)}}{\partial y_j}=0$ should be valid. It implies that $\frac{\partial u_i^{(0)}}{\partial y_j}=const$.

Therefore, we have the alternative boundary condition:

$$\frac{\partial u_i^{(0)}}{\partial y_j}=const=\sigma_{ij}^{(-1)} \quad \rightarrow \quad \int_{\partial Y} u_i^{(0)} n_j d\Gamma=0$$

In cases where scale separation can not be applied, such as in local-global problems, we assume that $u_i^0(x,y)$ on the boundary is equal to $\varepsilon_{jk}^{(0)}(x)\chi_i^{jk}(y)$, since unit cell rigid body displacement along the unit cell boundaries shall vanish. The application of this equation for the suggested unit cell approach is described in the next section.

The EUC formulation based on the solution of the ζ^{-1} equilibrium equation describing the unit cell problem subjected to alternative boundary conditions

$$\int_{\partial Y} u_i^{(0)} n_j d\Gamma=0 \tag{1}$$

4 EMBEDDED UNIT CELL APPROACH

The purpose of this method is the solution of composites materials with local global problems or solution for the macroscopic problem, where classical homogenization does not provide a valid solution due to non-periodic response.

This approach can be considered as a domain decomposition approach, since it separates the solution of a demanding problem into a coarse (global/macro) and fine (local/micro) problems. Let assume a macroscopic domain Ω containing small domains Θ_{Yi} where their microscopic response is required (Figure 1); or alternatively boundary zones Θ_{Yi} (Figure 2). In order to correctly separate this demanding problem into a set of macro and micro scale problems, we have to define the boundary conditions of the small domains (unit cells) Θ_{Yi}, based on its surrounding. In the EUC formulation, eq. (1) is applied to the boundary Γ_{Yi}. Yet it is not enough, since in order to appropriately describe the physical response at Θ_{Yi} using the

suggested EUC approach, we have to define a surrounding domain Θ_{Si} for each unit cell. By doing so, Γ_{Yi} are the boundaries where the alternative boundary conditions (1) are prescribed and Γ_{Si} are the boundaries where the boundary conditions have to be specified for each macroscopic problem.

Using the above definitions, we allow the use of multi-scale techniques to solve these problems. First, the macroscopic material properties of the domains Θ_{Yi} are evaluated by solving the micro-scale problem for each domain by applying the relevant boundary conditions through the appropriate definitions of Θ_{Si} and Γ_{Si}. Then, we can solve a macro-scale problem over Ω, where the domains Θ_{Yi} are replaced by domains having equivalent properties, that were calculated using the embedded unit cell problems. Finally, the macroscopic deformation gradients are applied to the EUC micro-scale problems to obtain the local response at Θ_{Yi}.

Important to note, that the surrounding domain is essential and should fairly represent the stiffness of the entire structure around the hole.

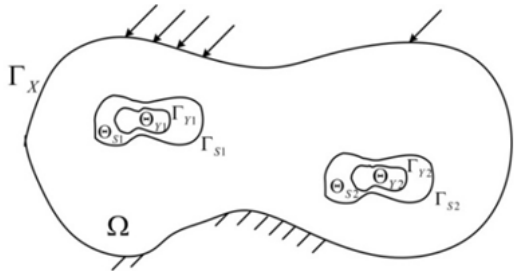

Figure 1. Embedded unit cell for stress concentration problems

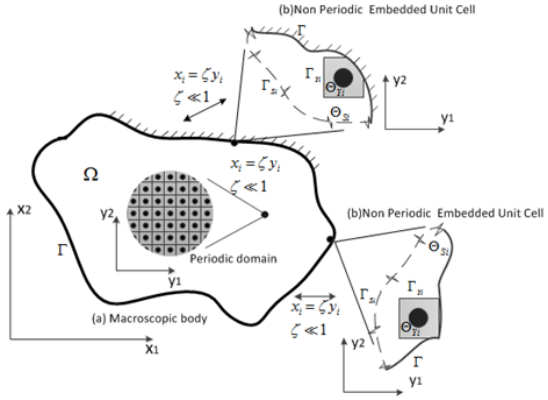

(a) The macroscopic heterogeneous body with homogeneous micro structure (Θ_{Yi}). (b) The Embedded unit cell for different zone (Θ_{Yi} and Θ_{Si}).

Figure 2. The macroscopic heterogeneous body

Moreover, the definitions of EUC boundary conditions for evaluation of the effective material properties are the same as for evaluation of the microscopic strain and stress fields. Both processes require the same alternative boundary conditions for Γ_{Yi} and proper boundary condition for Γ_{Si}.

5 NUMERICAL IMPLEMENTATION OF THE EMBEDDED UNIT CELL APPROACH USING MULTISCALE TECHNIQUES

In this research the suggested EUC approach implemented using finite element software ABAQUS. Various models were selected for verification of this method, some of which are shown below.

The model selected to implement the solution of Local Global problem first model is plate with stress concentration in the vicinity of small hole.

The model selected to implement the solution of the geometric edge problems is one side fixed plate with homogeneous micro structure which contains two materials. Figure 3 and Figure 4 contain the multiscale analysis models involved in the evaluation procedure, such as classical FE model (for reference purpose), the EUC and the reduced macroscopic model.

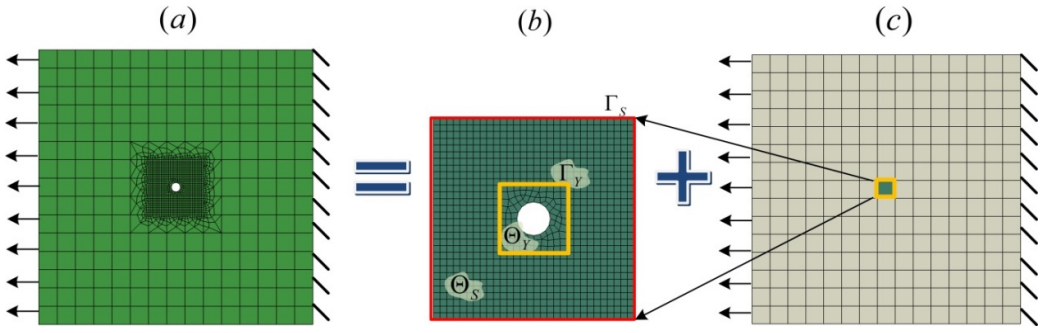

Figure 3. (a) Finite element model of a plate with a small hole; (b) The embedded unit cell, micro scale finite element model; (c) The macro scale finite element model

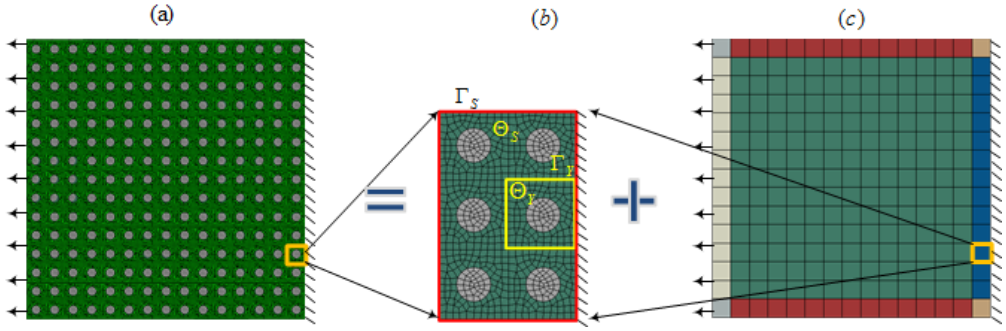

Figure 4. (a) Finite element model of a plate includes to materials; (b) The embedded unit cell, micro scale finite element model; (c) The macro scale finite element model

In order to imply EUC approach on the geometric edge problems, it is necessary to generate a considerable number of appropriate embedded unit cells to fit different geometry of boundary zones (Figure 5a). Optimization of the unit cell evaluation

procedure is achieved by defining new finite element model (Figure 5b) of the internal unit cell domain Θ_{Yi} only and substituting the surrounding domain Θ_{Si} and its boundary conditions on Γ_{Si} with equivalent-stiffness springs. The stiffness of the springs is evaluated as the force obtained due to unit displacement applied on the internal boundary Γ_{Yi}. The reactions forces obtained in the previous step are converted to springs. Figure 5b depicts embedded unit cell including equivalent springs instead of the surrounding area. In order to use the embedded unit cell for various boundary zones, we defined zone groups according to their locations, where some springs are replaced by the appropriate boundary condition of the macroscopic problem, as shown in Figure 5c.

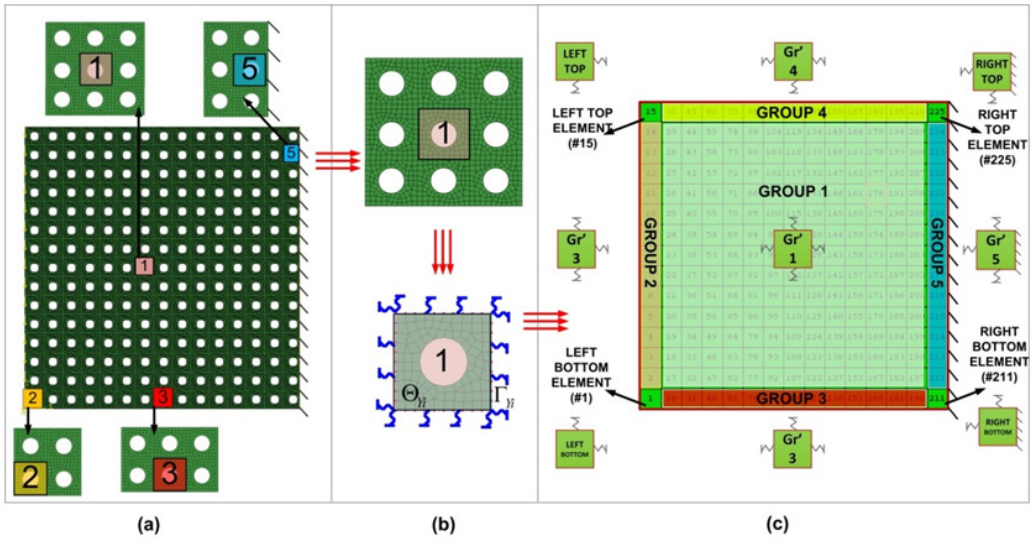

Figure 5. (a) Groups of EUC types according to various boundary domains (b) EUC optimization procedure (c) the optimized EUC

The next step of the procedure is calculation of macroscopic material properties tensor of each domain, using the resulted stress influence functions, solving the macroscopic model with equivalent material properties.
Finally, the stress fields at the microscopic level (EUC) are evaluated using the strain components resulted from the macroscopic level.

6 VERIFICATION STUDIES

In order to verify the implementation of EUC method, several examples with different geometry and boundary conditions were evaluated by Abaqus software, as described on the following figures.

The results of EUC method were compared to those achieved by classical homogenization and full reference model with high density mesh.

The following figure describes the Local Global problem example:

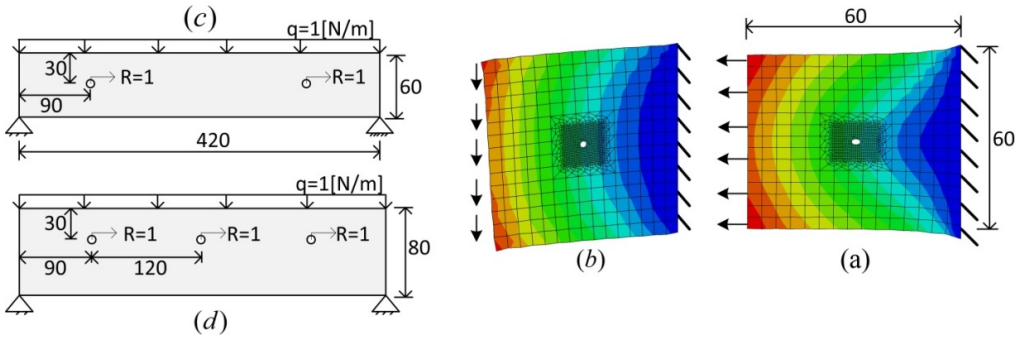

Figure 6. FE models for stress concentration problem

As expected, the results obtained using the classical homogenization theory are not satisfying compared to the reference solution since the assumption of periodic response of the unit cell is not valid for this problem, while the EUC method results and the reference FEM model are in good agreement.

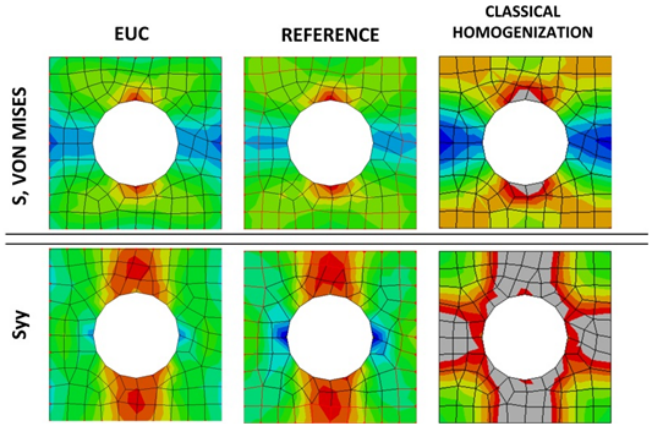

Figure 7. Stress fields results for stress concentration problem – center element

The following figure describes the example of homogenization problem at boundary zone example:

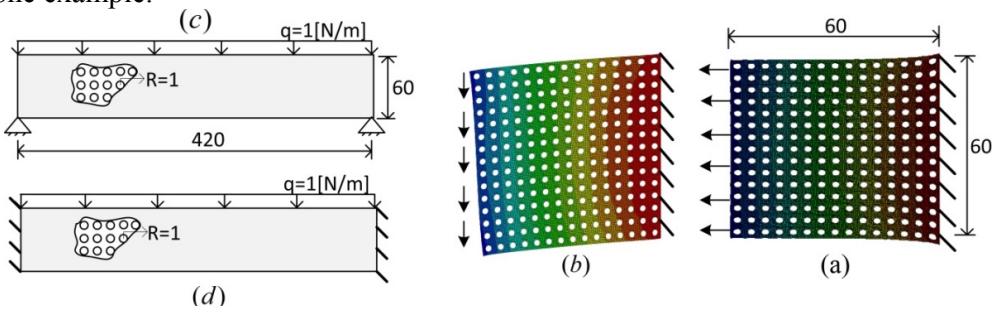

Figure 8. FE models for homogenization problem

As for previous example, the EUC method results and the reference FEM model are in good agreement.

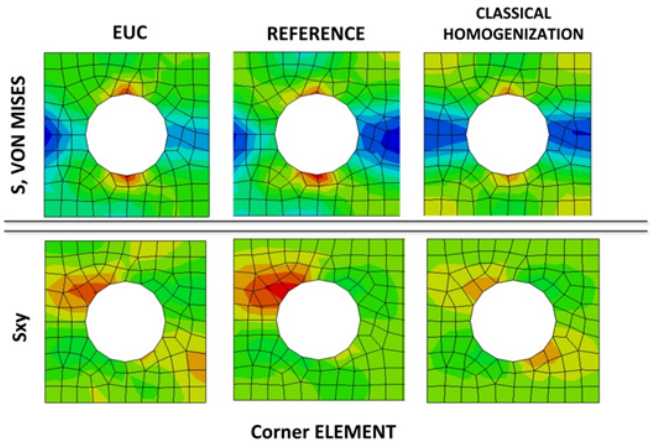

Figure 9. Stress fields results for stress concentration problem – corner element

7 CONCLUSION

This paper presents the embedded unit cell (EUC) approach for analyzing local-global problems using multi-scale technics. The mathematical theory of homogenization was extended to evaluate non-periodic responses of the unit cell and to represent the global structural effects on small, local domains that have compound responses.

This approach provides a reduced order model of the macroscopic problem by means of multiscale homogenization techniques. Moreover, it broadened the applicability of multiscale analysis techniques to analyze local-global problems through domain decomposition. This type of problems is widely used in engineering systems, for example, stress concentration in the vicinity of small holes.

A numerical study to verify the suggested formulation showed very good agreement comparing to the FE reference solutions.

The proposed EUC approach can be extended to be used for homogenization of non-periodic materials and for problems where scale separation can't be applied. In addition, the suggested EUC approach can be extended to obtain the nonlinear responses of damaged domains for concrete structures.

REFERENCE LIST

Allaire G. Homogenization and two-scale convergence. SIAM Journal on Mathematical Analysis. 1992;23(6):1482-518.
Babushka I. Solution of interface problems by homogenization. I. SIAM Journal on Mathematical Analysis. 1976;7(5):603-34.
BabuSka I. Homogenization and its application. Mathematical and computational problems. Numerical solution of partial differential equations. 1976:89-115.
Chen Z, Hou T. A mixed multiscale finite element method for elliptic problems with oscillating coefficients. Mathematics of Computation. 2003;72(242):541-76.
Dujc J, Brank Bt, Ibrahimbegovic A, Brancherie D. An embedded crack model for failure analysis of concrete solids. Computers & Concrete. 2010;7(4):331-46.
Feyel F. A multilevel finite element method (FE2) to describe the response of highly non-linear structures using generalized continua. Computer Methods in applied Mechanics and engineering. 2003;192(28):3233-44.
Gal E, Ganz A, Hadad L, Kryvoruk R. Development of a concrete unit cell. International Journal for Multiscale Computational Engineering. 2008;6(5).
Gibson RF. Principles of composite material mechanics: CRC Press; 2011 2011.
Gonella S. Homogenization and bridging multi-scale methods for the dynamic analysis of periodic solids. 2007.
Hashin Z. The elastic moduli of heterogeneous materials. Journal of Applied Mechanics. 1962;29(1):143-50.
Mei CC, Vernescu B. Homogenization methods for multiscale mechanics: World scientific; 2010 2010.
Novak J, Kaczmarczyk L, Grassl P, Zeman J, Pearce CJ. A micromechanics-enhanced finite element formulation for modelling heterogeneous materials. Computer Methods in Applied Mechanics and Engineering. 2012;201:53-64.
Oskay C, Fish J. On calibration and validation of eigendeformation-based multiscale models for failure analysis of heterogeneous systems. Computational Mechanics. 2008;42(2):181-95.
Wu W, Yuan Z, Fish J. Eigendeformation-based homogenization of concrete. International Journal for Multiscale Computational Engineering. 2010;8(1).
Zahavi E. The finite element method in machine design: Prentice Hall; 1992 1992.
Zeman J, Novak J, Sejnoha M, Sejnoha Jù. Pragmatic multi-scale and multi-physics analysis of Charles Bridge in Prague. Engineering Structures. 2008;30(11):3365-76.

Properties of Creep Compliance Functions and their Relation to Retardation Spectra

M. Jirásek

Department of Mechanics, Faculty of Civil Engineering, Czech Technical University in Prague, Czech Republic; PH +420-224354481; FAX +420-224310775; email: Milan.Jirasek@fsv.cvut.cz

ABSTRACT

This contribution examines how the properties of a viscoelastic model are affected by the choice of the creep compliance function and by the properties of the corresponding continuous retardation spectrum. Attention is paid to the phenomenon called divergence of creep curves, which arises for certain types of models but is questionable or even unacceptable from the physical point of view. Divergence occurs when the distance between creep curves (plotted for different ages at loading as a function of current age) increases, and its consequence is that, if the principle of superposition is accepted, the recovery of strain after unloading becomes non-monotonic. Analysis of this undesirable phenomenon is performed for creep models recommended by major design codes (ACI, CEB, *fib*, JSCE), and for simple as well as advanced models developed by researchers (DPL, LDPL, B3/B4, GL2000). The ranges of ages at loading and load durations for which divergence occurs are detected and illustrated by graphs. It is suggested that the origin of divergence could be explained by examining the corresponding continuous retardation spectra.

INTRODUCTION

At low and moderate stress levels, the time-dependent behavior of concrete is usually described by models based on the theory of linear viscoelasticity with aging, and this formulation is also the basis of more advanced models that take into account nonlinear phenomena such as cracking or crushing. The mechanical properties of a linear viscoelastic material are uniquely characterized by the creep compliance function, which reflects the growth of strain in a creep test at constant stress. The specific form of the compliance function must be chosen carefully, in order to reflect the true physical behavior of the material and to avoid various questionable or non-physical effects. Many different analytical forms of creep compliance functions for concrete have been proposed by researchers and some of them have been adopted by design codes.

For numerical implementation of the stress-evaluation algorithm based on a rate-type formulation, it is useful to approximate the compliance function by Dirichlet

series. This can be achieved by an ad-hoc optimization of the Dirichlet series parameters or, more systematically, using the concept of retardation spectrum and representing the compliance function by an integral closely related to the Laplace transform.

MONOTONIC RECOVERY AND NON-DIVERGENCE CONDITION

Consider a linear viscoelastic material with aging, i.e., with the compliance function $J(t,t')$ expressed as a function of two variables—the current time t and the time at load application t', both measured from the set of concrete. According to the principle of superposition, the evolution of strain in a specimen loaded by constant stress $\bar{\sigma}$ from time t_1 to time $t_2 > t_1$ and then unloaded is, for times $t > t_2$, given by

$$\varepsilon(t) = \bar{\sigma}\ [J(t,t_1) - J(t,t_2)] \tag{1}$$

The behavior of the unloaded specimen corresponds to recovery of the reversible strain, and it is natural to require that this recovery be monotonic, with non-decreasing strain rate. Differentiating (1), we can write the condition of monotonic recovery as

$$\dot{\varepsilon}(t) = \frac{\partial}{\partial t}\left(\bar{\sigma}\ [J(t,t_1) - J(t,t_2)]\right) = \bar{\sigma}\left[\frac{\partial J(t,t_1)}{\partial t} - \frac{\partial J(t,t_2)}{\partial t}\right] \leq 0 \tag{2}$$

For sufficiently smooth compliance functions we have

$$\frac{\partial J(t,t_2)}{\partial t} = \frac{\partial J(t,t_1)}{\partial t} + \int_{t_1}^{t_2} \frac{\partial^2 J(t,t')}{\partial t \partial t'} \mathrm{d}t \tag{3}$$

Thus, if the mixed second partial derivative of compliance function is non-negative for all t and t', inequality (2) is always satisfied. If the mixed derivative is negative for a certain range of arguments, there exist situations in which the recovery proceeds in a non-natural way.

The condition

$$\frac{\partial^2 J(t,t')}{\partial t\ \partial t'} \geq 0 \qquad \text{for all } t > t' \tag{4}$$

which is sufficient to guarantee monotonic recovery for all possible combinations of times t, t_1 and t_2, is called the non-divergence condition, because of its geometric interpretation: The compliance curves plotted as functions of the current time t for two different times at loading, t_1 and t_2, do not diverge from each other.

ANALYSIS OF NON-DIVERGENCE CONDITION

Solidification Theory and B3/B4 Models

If the creep model is constructed within the framework of the solidification theory (Bažant and Prasannan, 1989a,b), the rate of the compliance function is given by

$$\frac{\partial J_{\mathrm{v}}(t,t')}{\partial t} = \frac{\dot{\Phi}(t-t')}{v(t)} \tag{5}$$

where $\Phi(t-t')$ is interpreted as the compliance function of a non-aging solidifying constituent and $v(t)$ is an non-decreasing function reflecting the evolution of the solidification process. Differentiating (5) with respect to t', we get

$$\frac{\partial^2 J_{\mathrm{v}}(t,t')}{\partial t \partial t'} = -\frac{\ddot{\Phi}(t-t')}{v(t)} \tag{6}$$

Since $v(t)$ is always a positive function, condition (4) is satisfied if and only if $\ddot{\Phi}(t-t') \leq 0$. Thus the sufficient and necessary condition for non-divergence of compliance curves generated by the solidification theory is that the compliance function of the non-aging constituent be concave. In other words, the rate of creep must monotonically decrease in time, or remain constant, but must never increase. This is a very natural condition, easy to satisfy, and it is satisfied by the function

$$\Phi(t-t') = q_3 \ln\left(1 + \left(\frac{t-t'}{\lambda_0}\right)^n\right) \tag{7}$$

used by the B3 model (Bažant and Baweja, 1995) as well as by the B4 model (Hubler et al., 2015), with positive parameters q_3 and λ_0 and with exponent n between 0 and 1 (typically $\lambda_0 = 1$ day and $n = 0.1$).

Strictly speaking, the compliance function of models B3/B4 is the sum of a constant asymptotic compliance $1/E_0$, viscoelastic compliance $J_{\mathrm{v}}(t,t')$ and flow compliance $J_{\mathrm{f}}(t,t')$. The flow compliance, defined as

$$J_{\mathrm{f}}(t,t') = \int_{t'}^{t} \frac{\mathrm{d}s}{\eta(s)} \tag{8}$$

always satisfies the non-divergence condition (4), for any age-dependent viscosity $\eta(t)$, because its rate $\partial J_{\mathrm{f}}(t,t')/\partial t = 1/\eta(t)$ does not depend on t' and thus the mixed second derivative of J_{f} vanishes.

So far we have considered only the basic creep compliance. It can be shown that, for models B3/B4, the drying creep compliance satisfies the non-divergence condition, too.

Double-Power Law, ACI, CEB and JSCE Models

The compliance functions used in various codes and recommendations often have the general form

$$J(t,t') = \frac{1}{E(t')} + c\,\frac{f(t-t')}{g(t')} \tag{9}$$

in which $E(t')$ is the aging elastic modulus, c is a positive constant (independent of t and t', but possibly dependent on the concrete properties and environmental conditions), $f(\hat{t})$ is an increasing function describing the shape of the creep curve, and $g(t')$ is an increasing function that reflects aging (lower creep if the concrete is loaded at a

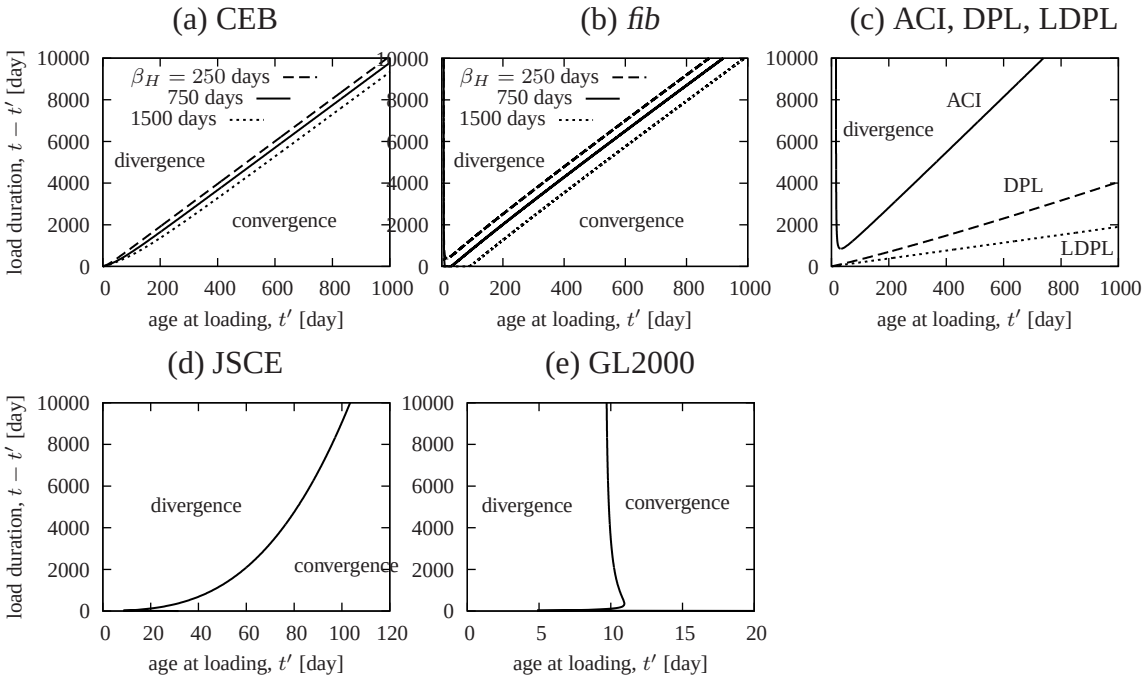

Figure 1. Critical load duration after which divergence of creep curves occurs, plotted as function of the age at loading for (a) CEB Model Code with various values of parameter β_H, (b) *fib* Model Code with various values of parameter β_H, (c) ACI model, double-power law (DPL) and log-double-power law (LDPL), (d) JSCE model, (e) Gardner-Lockman model (GL2000)

higher age). With specific choices of c, f and g, equation (9) gives the double-power law (Bažant and Osman, 1976), or the formulae recommended by ACI Committee 209 (1971), CEB Model Code (Comité Euro-International du Béton, 1991), or Japan Society of Civil Engineers (2010). Differentiation of (9) yields

$$\frac{\partial J(t,t')}{\partial t} = c\,\frac{\dot{f}(t-t')}{g(t')} \tag{10}$$

$$\frac{\partial^2 J(t,t')}{\partial t \partial t'} = c\,\frac{-\ddot{f}(t-t')g(t') - \dot{f}(t-t')\dot{g}(t')}{g^2(t')} \tag{11}$$

and since $c > 0$, the non-divergence condition $\partial^2 J(t,t')/\partial t \partial t' \geq 0$ is violated if

$$\ddot{f}(t-t')g(t') + \dot{f}(t-t')\dot{g}(t') > 0 \tag{12}$$

For simplicity, dots over f and g denote derivatives of these functions, no matter whether the argument is denoted as $t-t'$ or t'. Since $\dot{f}$ and g are positive functions, the last condition can be rewritten as

$$\frac{\ddot{f}(t-t')}{\dot{f}(t-t')} > -\frac{\dot{g}(t')}{g(t')} \tag{13}$$

The left-hand side of this inequality depends only on the load duration, $t - t'$, and the right-hand side only on the age at loading, t'. Therefore, for each value of t' we can evaluate the range of values of $t - t'$ in which divergence occurs. Typically, this happens when the load duration $t - t'$ exceeds a certain limit, which can be computed from (13) if the inequality sign is replaced by equality.

The compliance function stipulated by the CEB Model Code (Comité Euro-International du Béton, 1991) has the form (9) with

$$f(\hat{t}) = \left(\frac{\hat{t}}{\beta_H \beta_T + \hat{t}} \right)^{0.3}, \qquad g(t') = 0.1 + t'^{0.2} \tag{14}$$

where β_H and β_T are parameters. Parameter β_T depends on the temperature and at $20°$C is equal to 1. Parameter β_H depends on the compressive strength, environmental humidity, and equivalent thickness of the member. For concrete of mean compressive strength 35 MPa it must be in the range from 250 to 1500 (days). Figure 1a shows the critical load duration $t - t'$ after which divergence occurs as a function of the age at loading t' for the extreme values of β_H and for an intermediate value $\beta_H = 750$. It is clear that the specific value of β_H has only a marginal influence, and that in general divergence occurs when the load duration exceeds the age at loading by a factor of 10, for younger concrete even less than that.

A pathological consequence of divergent creep curves combined with the principle of superposition is non-monotonic recovery, illustrated for the CEB Model Code in Figure 2a.

A similar analysis can be performed for the ACI model (ACI Committee 209, 1971), which has the form (9) with $f(\hat{t}) = \hat{t}^{\psi}/(d + \hat{t}^{\psi})$ and $g(t') = t'^{m}/\sqrt{b + a/t'}$; see Bažant and Kim (1978). For standard parameters $m = 0.118$ (moist curing), $\psi = 0.6$, $a = 4$, $b = 0.85$ and $d = 10$, the results are plotted in Figure 1c by the solid curve. Divergence occurs for those combinations of t' and $\hat{t} \equiv t - t'$ that lie above the curve.

The double-power law (Bažant and Osman, 1976) has the form (9) with $f(\hat{t}) = \hat{t}^{n}$ and $g(t') = 1/\left(t'^{-m} + \alpha\right)$. This model violates the non-divergence condition (4) for $t - t' > (1-n)(1+\alpha t'^{m})t'/m$ (Bažant and Kim, 1978). For standard parameter values $n = 0.1$, $m = 1/3$ and $\alpha = 0.05$, this happens if the load duration $t - t'$ exceeds the age at loading t' approximately 3 to 4 times; see the dashed curve in Figure 1c.

The basic creep compliance function of the JSCE Model (Japan Society of Civil Engineers, 2010) has the form (9) with $f(\hat{t}) = 1 - \exp\left(-0.09\,\hat{t}^{0.6}\right)$ and $g(t') = (\ln t')^{0.67}$. The divergence condition (13) can be transformed into the inequality

$$\frac{1}{t - t'} + \frac{0.135}{(t - t')^{0.4}} < \frac{1.675}{t' \ln t'} \tag{15}$$

The regions of divergence and convergence are graphically presented in Figure 1d. For instance, for loading at age $t' = 28$ days, divergence occurs for load durations $t - t'$ exceeding 280 days.

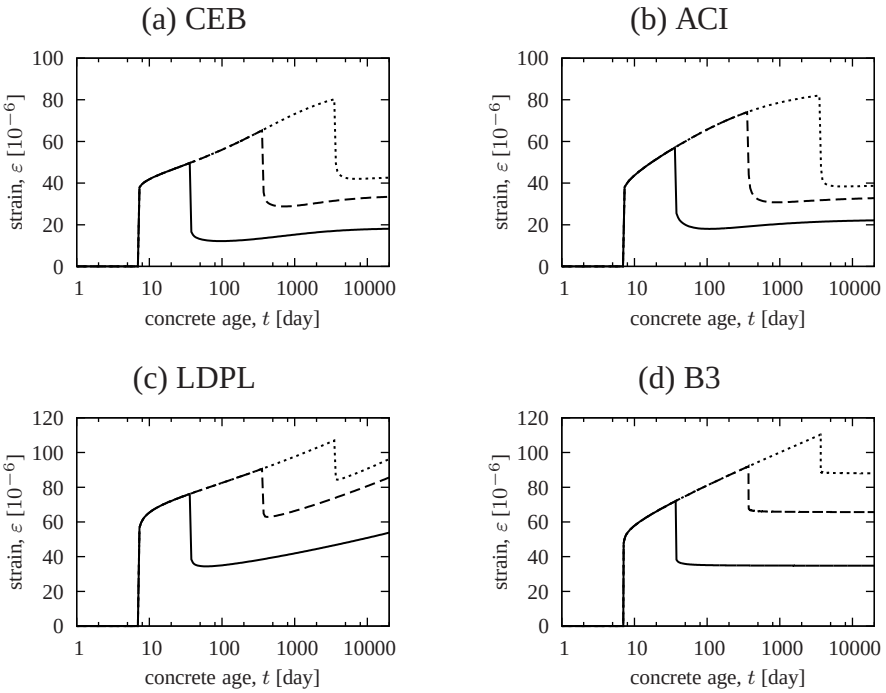

Figure 2. Strain recovery obtained by the principle of superposition for concrete loaded by stress 1 MPa from age 7 days, with stress removed after 1 month, 1 year or 10 years, as predicted by the (a) CEB model, (b) ACI model, (c) log-double-power law, (d) B3 model

Log-Double-Power Law

The log-double-power law (Bažant and Chern, 1985) uses the compliance function

$$J(t,t') \,=\, \frac{1}{E(t')} + q_s \ln\left[1 \,+\, \psi\,\left(t'^{-m} + \alpha\right)(t-t')^n\right] \tag{16}$$

with typical values of model parameters $n = 0.1$, $m = 0.5$, $\alpha = 0.001$, $\psi = 0.3$ and $q_s = 11.4/E_{\rm c}$, where $E_{\rm c} =$ conventional elastic modulus. For this model, the analysis is somewhat more tedious because the compliance function does not have the form (9). Nevertheless, it is still possible to analyze the non-divergence inequality and show that it is violated for $t - t' > (t'^{1+m}/m)(\alpha + t'^{-m})[1 - n + \psi(\alpha + t'^{-m})(t-t')^n]$. This condition is implicit, because t appears also on the right-hand side, but for standard parameter values n = 0.1, m = 0.5, α = 0.001 and ψ = 0.3 the term with $(t-t')^n$ is negligible. Except for very early ages, the critical load duration is very close to $t'(1-n)/m$, which is just $1.8\,t'$; see the dotted curve in Figure 1c.

Figure 2b presents examples of non-monotonic recovery for the ACI model and Figure 2c for the log-double-power law. For the B3 model, which satisfies the non-divergence condition, monotonic recovery is guaranteed, as confirmed by Figure 2d.

GL2000

The compliance function of model GL2000, proposed by Gardner and Lockman (2001), can be considered as a generalized version of (9), given by

$$J(t,t') = \frac{1}{E(t')} + c\left[\frac{f(t-t')}{g(t')} + h(t-t')\right] \tag{17}$$

The analysis becomes more tedious, nevertheless the condition of divergence can again be established. Divergence occurs if

$$\ddot{h}(t-t')g^2(t') + \ddot{f}(t-t')g(t') + \dot{f}(t-t')\dot{g}(t') > 0 \tag{18}$$

Equation (17) covers the case of basic creep. For the specific form of function

$$g(t') = \sqrt{t'} \tag{19}$$

used by Gardner and Lockman (2001), condition (18) can be rewritten as

$$2\ddot{h}(t-t')\,t'^{3/2} + 2\ddot{f}(t-t')\,t' + \dot{f}(t-t') > 0 \tag{20}$$

With $t-t'$ considered as given, condition (20) is a cubic inequality in terms of $\sqrt{t'}$. For the functions

$$f(t-t') = \sqrt{\frac{7(t-t')}{t-t'+7}} \tag{21}$$

$$h(t-t') = \frac{2(t-t')^{0.3}}{(t-t')^{0.3}+14} \tag{22}$$

used by Gardner and Lockman (2001), the results are plotted in Figure 1e. It turns out that condition (20) is never satisfied for $t' > 11$ days, and for $t' < 9$ days it is satisfied for virtually all load durations. This means that the GL model exhibits divergence only for loading at young age, and in that case divergence occurs almost immediately.

fib Model Code 2010

The recently approved *fib* Model Code 2010 (Fédération internationale de béton, 2013) uses the compliance function in the form

$$J(t,t') = \frac{1}{E(t')} + c_1 \ln\left(1 + \left(0.035 + \frac{30}{t'}\right)^2 (t-t')\right) + \frac{c_2}{0.1 + t'^{0.2}}\left(\frac{t-t'}{\beta_H + t - t'}\right)^{\gamma(t')} \tag{23}$$

where constants c_1 and c_2 depend on the compression strength and c_2 also depends on the ambient relative humidity. The second term on the right-hand side of (23) represents the basic creep compliance and the third term represents the drying creep compliance.

It can be proven that the basic creep compliance function always satisfies the non-divergence condition. The drying creep compliance function has a similar form to the previous CEB Model Code 1990, see (9) and (14), but the fixed exponent 0.3 is replaced by the function

$$\gamma(t') = \frac{1}{2.3 + \dfrac{3.5}{\sqrt{t'}}} \tag{24}$$

Evaluation of the second mixed derivative of the drying creep compliance function leads to the non-divergence condition

$$\frac{1.75\,\gamma(t')}{t'^{1.5}} - \frac{1}{5(t' + 0.1\,t'^{0.8})} \geq \frac{(\gamma(t') - 1)\,\beta_H}{(\beta_H + t - t')(t - t')} - \frac{2}{\beta_H + t - t'} \tag{25}$$

which is violated for certain combinations of age at loading t' and load duration $t - t'$; see Figure 1b.

RELATION TO RETARDATION SPECTRUM

The compliance function of a non-aging linear viscoelastic material can be split into a jump at $t = t'$ and a continuously growing part, and expressed as

$$J(t, t') = \frac{1}{E_0} + \Phi_0(t - t') \tag{26}$$

where $E_0 = 1/J(t, t)$ is the instantaneous modulus and $\Phi_0(0) = 0$. The continuous part can be represented as

$$\Phi_0(t - t') = \int_{\tau=0}^{\infty} L_0(\tau) \left[1 - \exp\left(-\frac{t - t'}{\tau}\right)\right] \,\mathrm{d}(\ln \tau) \tag{27}$$

where $L_0(\tau)$ is the continuous retardation spectrum, which is closely related to the inverse Laplace transform of function $\Phi_0(\hat{t})$; see e.g. Bažant and Xi (1995) and Jirásek and Havlásek (2014) for a detailed explanation.

The foregoing equations can be generalized to aging linear viscoelasticity by setting

$$J(t, t') = \frac{1}{E(t')} + \Phi(t - t', t') \tag{28}$$

$$\Phi(t - t', t') = \int_{\tau=0}^{\infty} L(\tau, t') \left[1 - \exp\left(-\frac{t - t'}{\tau}\right)\right] \,\mathrm{d}(\ln \tau) \tag{29}$$

By double differentiation we obtain the mixed second derivative

$$\frac{\partial^2 J(t, t')}{\partial t \partial t'} = \int_{\tau=0}^{\infty} \frac{1}{\tau^2} \left(L(\tau, t') + \tau \frac{\partial L(\tau, t')}{\partial t'}\right) \exp\left(-\frac{t - t'}{\tau}\right) \,\mathrm{d}(\ln \tau) \tag{30}$$

which should be non-negative if the divergence of compliance curves is to be excluded.

As shown by Jirásek and Havlásek (2014), the spectral values L are positive for virtually all compliance functions proposed for concrete. In the absence of aging, $L(\tau, t') \equiv L_0(\tau)$ does not depend on t' and the derivative $\partial L(\tau, t')/\partial t'$ vanishes. In that case, positive spectrum results into positive value of the integral in (30) and divergence cannot occur.

On the other hand, for models with aging, the sign of the integrand in (30) is given by the sign of the expression $L(\tau, t')+\tau\partial L(\tau, t')/\partial t'$. For a fixed retardation time τ, the spectral content typically decreases with increasing age t', and so the derivative $\partial L(\tau, t')/\partial t'$ is negative and the whole expression may become negative. Of course, divergence occurs only if the integral (30) over all retardation times is negative.

To get an insight, consider the compliance function in the form (9), with the retardation spectrum described by

$$L(\tau, t') = \frac{c}{g(t')} L_f(\tau) \tag{31}$$

where $L_f(\tau)$ is the retardation spectrum of function $f(\hat{t})$ interpreted as a non-aging compliance function. In this case we have

$$L(\tau, t')+\tau\frac{\partial L(\tau, t')}{\partial t'} = \frac{c}{g(t')} L_f(\tau) - \tau\frac{c\dot{g}(t')}{g^2(t')} L_f(\tau) = \frac{c}{g(t')} L_f(\tau) \left(1 - \tau\frac{\dot{g}(t')}{g(t')}\right) \tag{32}$$

For each age t', the ratio $T_g(t') = g(t')/\dot{g}(t')$ is positive and corresponds to a certain characteristic time of the aging process. Thus the negative contribution to the integral in (30) is provided by all retardation times $\tau > T_g(t')$. On the other hand, for very large retardation times, the magnitude of the integrand is strongly reduced by the factor $1/\tau^2$, while for retardation times much smaller than the load duration $t - t'$, the magnitude is reduced by the exponential term $\exp(-(t - t')/\tau)$.

Based on the knowledge of the specific form of retardation spectra for individual models, it is possible to analyze the interplay between the characteristic time of the aging process the age at loading and the duration of loading, and explain why divergence of compliance curves occurs for certain combinations of t' and $t - t'$. Due to space limitations, a detailed explanation is left for a full journal paper.

ACKNOWLEDGMENT

This research has been financially supported by the Czech Science Foundation (GAČR) under project 13-18652S.

References

ACI Committee 209 (1971). Prediction of creep, shrinkage and temperature effects in concrete structures. In *Designing for the Effects of Creep, Shrinkage and Temperature*, Number SP-27, pp. 51–93. Farmington Hills, Michigan: American Concrete Institute.

Bažant, Z. P. and S. Baweja (1995). Creep and shrinkage prediction model for analysis and design of concrete structures – model B3. *Materials and Structures 28*, 357–365. RILEM Recommendation, in collaboration with RILEM Committee TC 107-GCS, with Errata, Vol. 29 (March 1996), p. 126.

Bažant, Z. P. and J. C. Chern (1985). Concrete creep at variable humidity: Constitutive law and mechanism. *Materials and Structures 18*, 1–20.

Bažant, Z. P. and S. Kim (1978). Can the creep curves for different loading ages diverge? *Cement and Concrete Research 8*, 601–612.

Bažant, Z. P. and E. Osman (1976). Double power law for basic creep of concrete. *Materials and Structures 9*, 3–11.

Bažant, Z. P. and S. Prasannan (1989a). Solidification theory for concrete creep: I. Formulation. *Journal of Engineering Mechanics, ASCE 115*, 1691–1703.

Bažant, Z. P. and S. Prasannan (1989b). Solidification theory for concrete creep: II. Verification and application. *Journal of Engineering Mechanics, ASCE 115*, 1704–1725.

Bažant, Z. P. and Y. Xi (1995). Continuous retardation spectrum for solidification theory of concrete creep. *Journal of Engineering Mechanics, ASCE 121*, 281–288.

Comité Euro-International du Béton (1991). *CEB-FIP Model Code 1990: Design Code*. London: Thomas Telford. also published in 1993 by Comité Euro-International du Béton (CEB), Bulletins d'Information No. 213 and 214, Lausanne, Switzerland.

Fédération internationale de béton (2013). *fib Model Code for Concrete Structures 2010*. Ernst & Sohn, Berlin.

Gardner, N. J. and M. J. Lockman (2001). Design provisions for drying shrinkage and creep of normal strength. *ACI Materials Journal 98*, 159–167.

Hubler, M. H., R. Wendner, and Z. P. Bažant (2015). Model B4 for creep, drying shrinkage and autogenous shrinkage of normal and high-strength concretes with multi-decade applicability. *Materials and Structures 48*, 753–770. RILEM Technical Committee TC-242-MDC.

Japan Society of Civil Engineers (2010). *Standard Specifications for Concrete Structures – 2007 "Design"*. Tokyo, Japan: Japan Society of Civil Engineers. JSCE Guidelines for Concrete No. 15.

Jirásek, M. and P. Havlásek (2014). Accurate approximations of concrete creep compliance functions based on continuous retardation spectra. *Computers and Structures 135*, 155–168.

Study on Prediction of Behavior of Shrinkage with Volume Change of Concrete in Early Age

T.Mizobuchi [1], J. Arai[2] and R. Senba[3]

[1] Department of Civil and Environmental Engineering, Hosei University, 2-33Tamachi, Ichigaya Shinjuku-ku TOKYO JAPAN; PH +81-3-5228-1450; FAX +81-3-5228-1408; email: mizobuch@hosei.ac.jp
[2] Department of Civil and Environmental Engineering, Hosei University, 3-7-2 Kajino-cho Koganei-city TOKYO JAPAN; PH +81-42-387-6276; FAX +81-42-387-6214; email: arai@retec.co.jp
[3] Department of Civil and Environmental Engineering, Hosei University, 3-7-2 Kajino-cho Koganei-city TOKYO JAPAN; PH +81-42-387-6276; FAX +81-42-387-6214; email: ryouta.senba.3f@stu.hosei.ac.jp

ABSTRACT

In this study, for the purpose of improving the prediction technique of cracking with volume change of concrete structures, it is to develop the system which can simulate shrinkage stress with volume change of concrete in the laboratory. For the behavior of shrinkage of concrete at early age, it was carried out to compare the data measured in the existing structures with experimental results using the equipment (TSTM) in which it is possible to simulate the behavior of thermal stress, autogenous stress and creep stress of existing structures in the laboratory. As the results of experiments, it was confirmed that it was possible to comparatively reproduce the stress in concrete at the good accuracy by using TSTM. By comparing the direct tensile strength with experimental results, it was possible to acquire the useful data in which it was possible to evaluate cracking using direct tensile strength.

INTRODUCTION

Shrinkage stress with volume change of concrete in early age causes cracks in the concrete according to the size of the structure or the kind of concrete used in the structure. As the factors of the shrinkage cracking with volume change in the early age, thermal stress, autogenous shrinkage stress, drying shrinkage stress and creep stress are related. The inhibition of shrinkage cracking due to shrinkage stress with volume change of concrete in concrete structures is an important research topic. Shrinkage cracking may occur due to many factors such as size, shape, concrete placement period, materials, mix proportions and environmental conditions of the structure being constructed. Shrinkage cracking may occur even if the same materials and mix proportions are used, if the placement period or the shape of the structure differs. On the other hand, such cracks may not occur, or even if they do occur, the width or the number of cracks may vary. In short, it is extremely difficult to predict shrinkage cracking.

Extensive research has been carried out and various proposals have been made until now on methods for evaluating the possibility of occurrence of shrinkage cracking. However, as autogenous shrinkage strain is smaller than thermal strain and dry shrinkage strain, autogenous shrinkage strain has not considered until now in the design within the shrinkage strain with the volume change. Though, since high performance would be required for the concrete structures recently, the applications of high strength concrete and self-compacting concrete increase. The autogenous shrinkage strain of concrete cannot be disregarded, since the unit-cement content used by the application of such concrete increases. Then, Studies on mechanism and control method of the autogenous shrinkage strain of concrete are recently reported in large numbers. The strain calculated in the prediction formula of the autogenous shrinkage strain of concrete is deducted the thermal strain from the strain measured under the condition for fixed temperature (20^{o}C) and under the condition for receiving the effect of high-temperature with hydration of cement. The thermal strain multiplied the temperature change by the thermal expansion coefficient. In past studies, though the autogenous shrinkage strain of concrete is quickly as the temperature rise with the hydration of cement is bigger, it is reported that it is possible to evaluate the effect of temperature in the autogenous shrinkage strain of concrete by using the temperature adjusted age of concrete. However, it is necessary to exclude the effect of thermal strain by the assumption of the thermal expansion coefficient of concrete for measuring the autogenous shrinkage strain of concrete in existing structure. Therefore, prediction formula of the autogenous shrinkage strain excluded the effect by the thermal strain as much as possible is necessary. It seems that the prediction formula which can be evaluated using the age without using the temperature adjusted age of concrete is higher on the applicability.

On the other hand, the amount of actually measured data is not many because it is difficult to measure thermal stresses in the actual structure. In addition, mechanical properties such as Young's modulus, tensile strength and creep of materials in early age are not fully known. In view of the above, it is extremely difficult to quantitatively evaluate beforehand the crack initiation stress, the crack width and the number of cracks after crack initiation.

In this study, for the purpose of improving the prediction technique of cracking with volume change of concrete structures, it is to develop the system which can simulate shrinkage stress with volume change of concrete in the laboratory. For the behavior of shrinkage of concrete at the early age, it was carried out to compare the data measured in the existing structures with experimental results using the thermal stress testing machine (TSTM) in which it is possible to simulate the behavior of thermal stress, autogenous stress and creep stress of existing structures in the laboratory. As the results of the experiments, it was confirmed that it was possible to comparatively reproduce the stress in the concrete at the good accuracy by using the TSTM. By comparing the direct tensile strength with experimental results, it was possible to acquire the useful data in which it was possible to evaluate the cracking using the direct tensile strength. In addition, from the results which the splitting tensile strength compared with the experimental results, it was possible to confirm a

case in which the splitting tensile strength was connected for the evaluation in the danger side. Furthermore, the method for evaluating the autogenous shrinkage strain from the relationship between the factor in terms of the rate of the autogenous shrinkage strain and age under the temperature constancy condition in the age was examined.

In this report, in order to improve estimation accuracy of the prediction of cracking, by individually evaluating the prediction of a series of behaviors of shrinkage with volume change obtained by carrying out to the experiment of autogenous shrinkage using TSTM and the direct tensile strength test, the results of evaluation with the limit to cracking are reported.

OUTLINE OF STUDY

Investigation on behavior of autogenous shrinkage considering dependence on temperature. In this study, the experiment for the purpose of comprehending the behavior only of autogenous shrinkage strain except for the effect of thermal strain and dry shrinkage strain was carried out using TSTM and the prediction formula of the autogenous shrinkage strain considering with dependent on temperature was proposed.

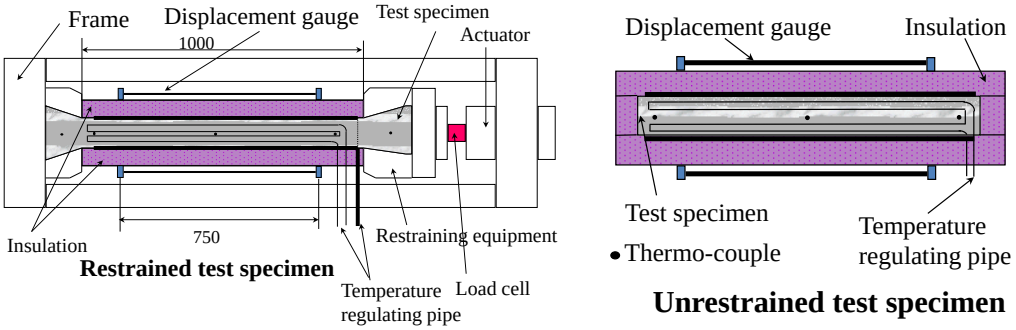

Figure 1. Overview of thermal stress testing machine.

This simulator was designed such that it could be used to control flexibly the temperature rise and the temperature drop due to heat of hydration of cement near the center of members in mass concrete structures from the start of concrete placement. A displacement control mechanism consisting of an actuator was installed so that the thermal expansion due to the heat of hydration and contraction due to the drop in temperature could be controlled under arbitrary restraint conditions. Test specimens used in the thermal stress simulator were of two kinds – a specimen with arbitrary degree of restraint as shown in Figure 1 and a specimen in the unrestrained condition. The restrained specimen was of size 150 × 150 × 1500 mm. The length of the specimen gripped in the restraining equipment is the effective length for the test. This length was 1000 mm. To minimize the pullout or slip in the area under tension in the part gripped by the restraining equipment, the width at the ends of the specimen was fanned out by 20º and tapered to a gradual curve so as to prevent stress concentration at the boundary of the gripped

area and the restraining equipment. The test specimen was covered with sheet to prevent dissipation of water before performing the tests.

In this study, only autogenous shrinkage strain which took way the effect of thermal strain and drying shrinkage strain was measured by keeping temperature fixedly and conducting sealed curing at the plastic sheet for preventing the drying using the specimen with the unstrained condition in TSTM. Table 1 shows the cases studied. The initial setting time was decided at the start of the test in case of 20 ^{o}C and the time in which the temperature of concrete cast at 20^{o}C reached that of the target was decided the start of the test in the cases of 30^{o}C to 60^{o}C.

Table 1. Case studied

Case	Type of cement	Water to cement ratio W/C	Condition of temperature (^{o}C)
1	Portland blast furnace slage cement type B	0.50	20
2			30
3			40
4			50
5			60

Investigation on strength in cracking. In this study, characteristics of tensile and deformation in concrete using various kinds of cement were investigated by carrying out direct tensile strength test using the specimen whose shape was the dog-bone. The equipment of direct tensile test shows Figure 2. In turn, the effect of test method and curing condition on strength at the limit to cracking was investigated by comparing with the results of the uniaxial constraint test of giving the preset historical curve of temperature using TSTM, while the splitting tensile strength is compared with the direct tensile strength. Used cement was the normal Portland cement, high strength Portland cement, blast furnace slag cement type B, low heat Portland cement, low heat blast furnace slag cement and moderate-heat Portland cement. Water to cement ratios were four levels from 0.30 to 0.60.

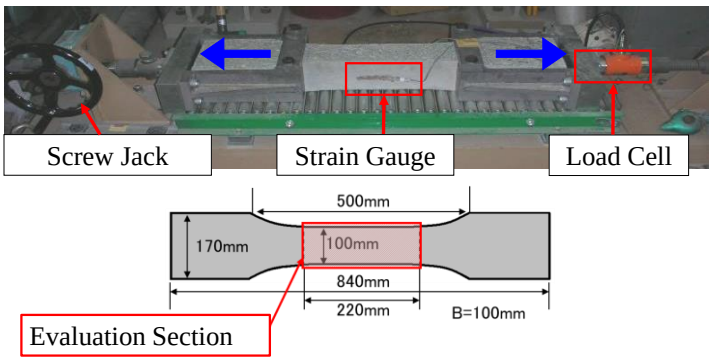

Figure 2. Overview of Direct tensile strength test equipment.

Investigation on limit to cracking of concrete received historical curve of temperature. In this study, the hysteresis of thermal expansion coefficient except for effect of the autogenous shrinkage strain under the temperature history condition on the assumption of the existing structure was investigated using the prediction

formula of mentioned autogenous shrinkage strain. Next, the investigation on stress and strain in the cracking was carried out, while a series of behaviors of shrinkage with volume change caused in concrete under the temperature history condition on the assumption of existing structure was comprehended. The degree of restraint of restraint in the test was set 1.0 (fully restrained). If the crack occurred, the testing time was taken as the time of initiation of crack. The preset historical curve of temperature using TSTM shows Figure 3.

Figure 3. Preset historical curve of temperature.

RESULTS OF EXPERIMENTS AND DISCUSSIONS

Investigation on behavior of autogenous shrinkage considering dependence on temperature. The results of the measurement of strain obtained from this experiment were shown in Figure 4. As shown in Figure 4, rate of progress of autogenous shrinkage strain tended to increase with rise in curing temperature. As well, in curing temperature from 30°C to 60°C, the progress of autogenous shrinkage strain tended to be stagnant around 90 μ and the autogenous shrinkage strain tended to progress again after passing through prescribed period. Furthermore, start age of this stagnation tended to accelerate and the stagnant period tended to be shortened with rise in curing temperature. On this stagnation phenomenon, reported studies are yet little, though the tendency has been confirmed in past researches. Also, as this stagnation phenomenon occurs in the early age in which various mechanical and thermal properties of concrete greatly change, it seems that this phenomenon may be one of factors which influence the analytical results in the prediction of cracking caused by shrinkage with change volume. Therefore, in this study, the prediction formula considering with the stagnation phenomenon should be constructed.

In this study, in order to express this stagnation phenomenon, autogenous shrinkage strain was stagnated for the first time and the point of time in which the autogenous shrinkage strain developed afterwards again was defined as the point of inflection. Then, the prediction formula was composed of defining the interval before inflection point as the interval 1 and the interval after inflection point as the interval 2. The outline of the prediction formula of autogenous shrinkage strain is shown in Figures 5. The prediction formula is shown referring to past researches using following equation (1) to (3).

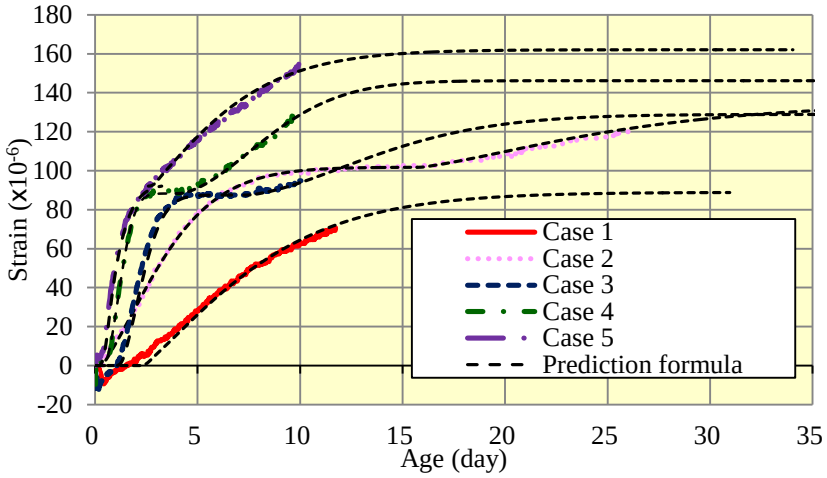

Figure 4. Measurement and prediction of strain obtained from TSTM.

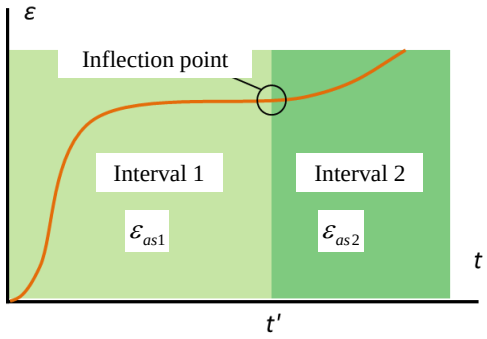

Figure 5. Overview of interval in prediction formula.

$$\varepsilon_{as} = \varepsilon_{as1} + \varepsilon_{as2} \tag{1}$$

$$\varepsilon_{as1} = \frac{1}{\left[1+\alpha\times e^{(-\alpha\times(t-t_0))}\right]}\times\varepsilon_{sh\infty}\times\left(1-e^{\{-\beta(t-t_0)\gamma\}}\right) \tag{2}$$

$$\varepsilon_{as2} = \frac{1}{\left[1+\alpha'\times e^{(-\alpha'\times(t-t'))}\right]}\times\varepsilon'_{sh\infty}\times\left(1-e^{\{-\beta'(t-t')\gamma'\}}\right) \tag{3}$$

Where, ε_{as} = autogenous shrinkage strain ($\times10^{-6}$), ε_{as1} =autogenous shrinkage strain in interval 1 ($\times10^{-6}$), $(t_0 \le t \le t')$, ε_{as2} =autogenous shrinkage strain in interval 2 ($\times10^{-6}$), $(t' < t)$, t' = age at inflection point (day), t= age (day), t_0= initial setting time (day), $\varepsilon_{as\infty}$ = ultimate value of autogenous strain in interval 1 ($\times10^{-6}$), $\varepsilon'_{as\infty}$ = ultimate value of autogenous strain in interval 2 ($\times10^{-6}$), α, β, γ = constants in interval 1, α', β', γ' = constants in interval 2.

In equation (1), the optimization of the prediction formula was attempted so that square residual sum of experimental value and calculated value may be minimum. In the optimization, the method called "Particle Swarm Optimization" (PSO) was used.

PSO was one of the fields called Swarm Intelligence proposed by J. Kennedy et al. and it is that the algorithm searches the solution for obtaining the optimum value of objective function, while large number of particles move the multidimensional space.

The results of comparing the optimized predictive values with measured values are shown in Figures 4. From Figures 4, the predictive values by each temperature condition are possible to sufficiently estimate experimental values. The prediction formula of autogenous shrinkage strain considering dependence on temperature was proposed using each identified constant. However, since the curing condition of 60°C constant tends to be different from another curing condition, the application range of this prediction formula was changed to 50°C from 20°C.

Investigation on strength in cracking. On the relationship between splitting tensile strength and direct tensile strength of concrete using various kinds of cement, in almost all cases, splitting tensile strength is 20 to 30 % stronger than direct tensile strength. As the reason why the splitting tensile strength was stronger than the direct tensile strength, it seems that cracks are caused in the part in which cross section is the weakest in the direct tensile strength test, while the cross section which causes crack has been limited to some extent in the splitting tensile strength test.

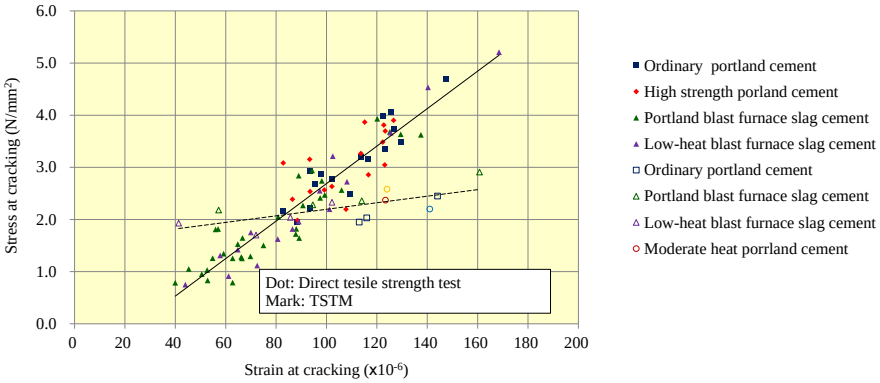

Figure 6. Relationship between stress and strain at cracking.

Next, relationship between stress and strain at cracking in the direct tensile strength test and TSTM test is shown in Figure 6. As shown in Figure 6, relationship between stress and strain was almost linear without relating to the difference between cement in both tests and the tensile strength increased with increase in the strain at cracking. When the relationship between stress and strain at cracking is compared in type of cement, the strain at cracking was from 40×10^{-6} to 100×10^{-6} in the case of Portland blast furnace slag cement type B and Low-heat blast furnace slag cement, while the strain at cracking was about 80 $\times10^{-6}$ to 130×10^{-6} in the case of Ordinary portland cement and Low-heat portland cement, and the strain at cracking in the case of Blast furnace slag cement type B and Low-heat blast furnace slag cement tended to decrease in comparison with Ordinary portland cement. The similar result was shown in past researches, and the strain at cracking of concrete seemed to decrease by containing blast-furnace slag fine powder. From results of the experiment using TSTM, for example, on the case using Portland blast furnace slag cement type B, the

relationship between the stress history in the restrained specimen after placing concrete and the estimation of tensile strength development is shown in Figure 7. The temperature adjusted age is determined by the equation shown in the following.

$$t_e = \sum_{i=1}^{n} \Delta t_i \times e^{\left(13.65 - \frac{4000}{273 + \frac{T(\Delta t_i)}{T_0}}\right)} \tag{4}$$

Where, t_e=temperature adjusted age of concrete (day), Δt_i =period of constant temperature continuing in concrete (day), $T(t_i)$=concrete temperature for Δt_i (^{o}C), T_0=1^{o}C.

When the stress at cracking was evaluated in temperature adjusted age, it was shown that the stress at cracking in the experiment using TSTM was almost equivalent to the estimation of direct tensile strength at cracking. The strength at cracking in existing structures should be evaluated in temperature adjusted age, and it seems that it is possible to more appropriately evaluate by using the direct tensile strength.

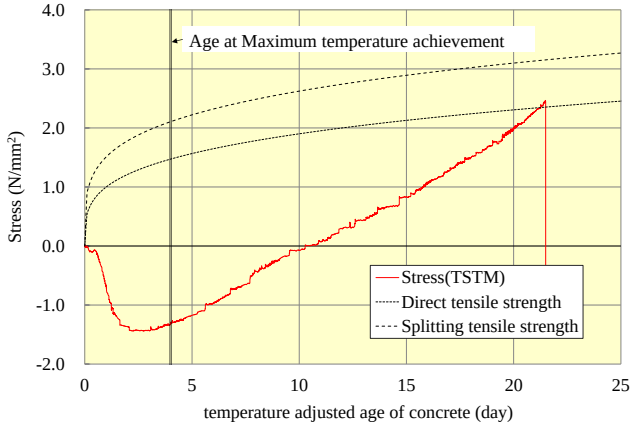

Figure 7. Stress history.

Investigation on limit to cracking of concrete received historical curve of temperature. On the basis of prediction formula and data obtained until now, the investigation on the limit to cracking of concrete under the condition of temperature history was carried out. The autogenous shrinkage strain was calculated by Step by step method which summed up difference of the autogenous shrinkage strain which received effects of temperature to unit time. The result is shown in Figure 8.As shown in Figure 8, it was possible to show the tendency in which the progress of the autogenous shrinkage strain stagnates by using the Step by step method in about ages 4 days. Furthermore, thermal expansion coefficient was estimated thermal strain by deducting the estimate of autogenous shrinkage strain obtained by the Step by step method from experimental results of strain of the specimen in the unrestrained condition. The thermal expansion coefficient calculated from the Step by step

method is shown in Figure 9. As shown in Figure 9, it was shown that the thermal expansion coefficient greatly changed by ages 2 days in the early age.

The creep strain was used creep estimation method in past researches. Figure 10 shows the hysteresis of stress multiplied Young's modulus estimated from experimental result by the total strain which added each calculated strain. As shown in Figure 10, when evaluated in temperature adjusted age considering temperature effects, the stress estimated at cracking agreed comparatively well with the result of experiment using TSTM.

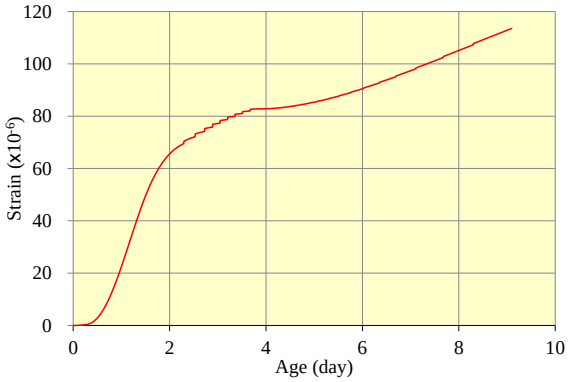

Figure 8. Estimation curve of autogenous shrinkage strain.

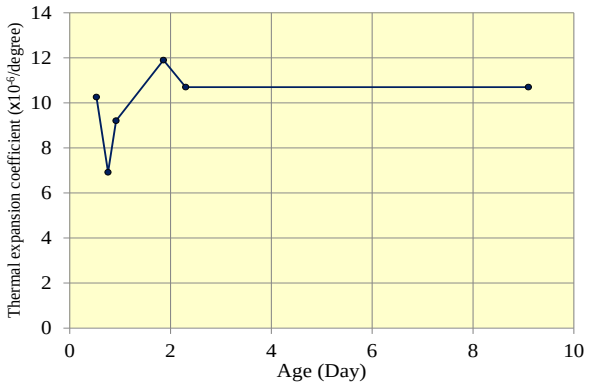

Figure 9. Thermal expansion coefficient history.

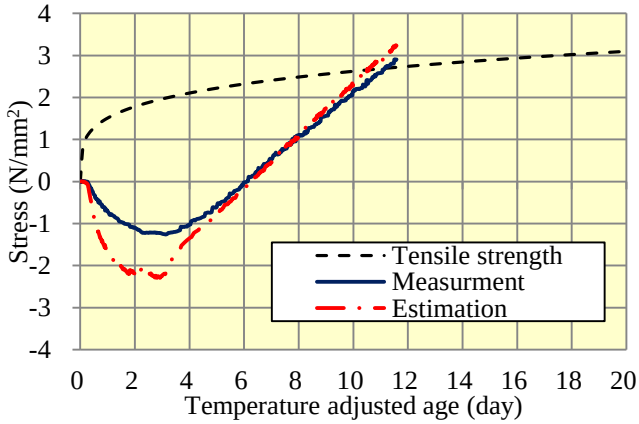

Figure 10. Comparison between measurement and estimation.

CONCLUSIONS

In this study, for the purpose of prediction of shrinkage with volume change under conditions of existing concrete structures and evaluation of limit to cracking limit of concrete, investigation using TSTM and the equipment of direct tensile strength test was carried out. Knowledge obtained in this study is shown in the following.

As the results of experiment using TSTM in the condition of fixed temperature, it was confirmed that the autogenous shrinkage strain was stagnated in a point of time and that the period of stagnation possessed the dependence on temperature. Furthermore, as the result of observation using scanning electron microscope (SEM) for the purpose of the clarification of this stagnation phenomenon, it was confirmed that the hydration product of concrete differed in curing temperature and age.

It was confirmed that splitting tensile strength was about 20% stronger than the direct tensile strength and that the strain at cracking decreased by containing blast-furnace slag fine powder. Furthermore, by comparison with the results of experiment using TSTM, the possibility of estimating limit to crack using direct tensile strength test by considering the dependence on temperature effects was shown.

In proposed prediction formula, it seems that it is possible to evaluate the behavior of shrinkage with volume change under the hysteresis of temperature in concrete.

REFERENCES

Atsushi T. and Ippei M. (2008). "Temperature dependent Behavior of Autogenous Shrinkage of Cement Paste Containing Silica Fume with Low W/B Ratio", *Proc. of 8th International Symposium on Utilization of High-Strength and High-Performance Concrete*, 141-147.

Keishiro I., Tatsuya H. and Hidetaka U. (1998). "Study on Characterization of Compressive and Tensile Creep Behavior for Early aged Concrete". *Journal of JSCE* (*Japan Society of Civil Engineering*), No.599/V-40, 105-117.

Mitsuo O., Ryouhei K., Katsumi K and Hiroaki M (2000). "Study on Creep Properties of High Strength Concrete at Early Ages" *Proceeding of Japan Concrete Institute*, Vol.22, 631-636.

Technical Committee on Autogenous Shrinkage. (1996). *Report of Technical Committee on Autogenous Shrinkage*, JCI(Japan Concrete Institute).

Technical Committee on Revision of JCI Guidelines for Control of Cracking of Mass Concrete .(2008). *Guidelines for Control of Cracking of Mass Concrete 2008*, JCI.

Toshiyuki T., Hideki N., Kozaburo Y. and Seishi G. (1996). "Influence of Hydration on Autogenous Shrinkage of Cement Pastes", *Concrete Research and Technology*, Vol. 7, No. 2, 137-142.

Thermal Crack Estimation of Dam Concrete Considering the Influence of Autogenous Shrinkage

H. Sato[1]; S. Miyazawa[2]; and A. Yatagai[3]

[1]Kumagai Gumi Co., Ltd., 2-1 Tsukudo-cho Shinjuku-ku, Tokyo 162-8557, Japan. E-mail: hsatoh@ku.kumagaigumi.co.jp
[2]Department of Civil Engineering, Ashikaga Institute of Technology, 268-1 Ohmae, Ashikaga 326-8558, Japan. E-mail: smiyazaw@ashitech.ac.jp
[3]DC Co., Ltd., Parele Mitsui Bldg., 8 Higashida-cho, Kawasaki-ku, Kawasaki 210-0005, Japan. E-mail: yatagai_atsushi@dccorp.jp

Abstract

Thermal stress in a gravity concrete dam was simulated by three dimensional FEM analyses taking autogenous shrinkage of concrete with full-sized aggregate into account. It is proved from experimental results that external concrete with blast-furnace slag Portland cement exhibits autogenous shrinkage of 130×10^{-6} at one year after casting, which is much larger than moderate-heat Portland cements with and without fly ash. Calculated thermal stress in upstream-downstream direction at the center of the concrete blocks near foundation rock is increased by autogenous shrinkage if concrete with large autogenous shrinkage is used. Thermal stresses in dam-axis direction at upstream and downstream surfaces are increased by the difference in autogenous shrinkage strains between internal and external concretes, if blast-furnace slag Portland cement is used. It can be said that autogenous shrinkage which simultaneously occurs with thermal strain should be taken into account in order to control thermal cracking during construction period which can adversely affect the stability, water tightness and durability of concrete gravity dams.

INTRODUCTION

In the design and the construction of concrete dams, it is well known that the control of thermal cracking caused by heat of cement hydration is very important to secure the stability, the water tightness and the durability of the dam. Verifications of the possibility of thermal cracking in concrete dams have generally been conducted so that harmful cracks should not occur at the central portion of the concrete blocks casted in layers when thermal equilibrium has been essentially achieved. It is also important to control thermal cracking during the construction period which can occur at the central portion of the concrete blocks and at the upstream and the downstream surfaces of the dam.

It has been reported that not only thermal strain but also autogenous shrinkage strain should be taken into account for control of thermal cracking in general mass concrete structures (Tazawa et al. 1994). Experimental studies on autogenous shrinkage of dam concrete were carried out by some researchers (Davis 1940; Uvan

et al. 1969) and autogenous shrinkage has been referred in some guidelines as a type of volume changes which occurs in dam concrete (ACI 2005; ICOLD 2009). However, there are few researches in which autogenous shrinkage of concrete with full-sized aggregate was measured, and the influence of autogenous shrinkage on thermal cracking in concrete dams has not quantitatively been understood.

One of the authors has recently demonstrated from experimental results on dam concrete with full-sized aggregate that autogenous shrinkage of dam concrete could be so large depending on the type of cement that it should be taken into account for control of thermal cracking (Sato and Hirano 1998). The purpose of this study is to investigate the influence of autogenous shrinkage of concrete on thermal cracking in concrete gravity dams during the construction period. Restraint stress caused by temperature change and autogenous shrinkage was estimated by finite element method for a model of a model dam constructed by Extended Layer Construction Method (ELCM). In constructions of dams by ELCM, which has often been applied to constructions of concrete gravity dams in Japan, conventional dam concrete with slump of about 3 cm is extended in horizontal layers and it is compacted with internal vibrators.

In order to obtain concrete properties to be used as input data for numerical simulations, adiabatic temperature rise and autogenous shrinkage of typical mixtures of dam concrete with maximum size of aggregate of 150 mm were measured. In order to study the effect of cement type, moderate-heat Portland cement with and without fly ash, and blast-furnace slag Portland cement were used. Compressive strength, splitting tensile strength and Young's modulus were measured with the specimens, which were prepared after aggregate larger than 40 mm was removed from concrete with full-sized aggregate by screening the wet concrete. In these experiments, the specimens were prepared for internal and external concretes, since concrete mixes for concrete dams are generally classified into internal concrete and external concrete. Internal concrete, which is used inside the dam, is very lean concrete with low cement content to reduce heat of hydration. External concrete is used at the upstream and downstream surfaces of the dam to obtain water-tightness and high durability.

EXPERIMENTAL PROCEDURES

Materials and mix proportions of concrete. Three types of cement; moderate-heat Portland cement (M), moderate-heat Portland cement with 30 % replacement of fly ash (MF) and moderate-heat Portland with 55 % replacement of blast-furnace slag (BB) were used in the experiments. Coarse aggregate with the maximum size of 150 mm was used. Retarding type air-entraining and water-reducing agent was used. The properties of the materials are shown in Table 1.

Mix proportions of concrete with full-sized aggregate, which were prepared to make concrete specimens, are shown in Table 2.

Water-cement ratio of external concrete is lower than that of internal concrete in order to obtain water-tightness and durability at upstream and downstream surface of the dam. Cement content was about 190 kg/m^3 in external concrete, and about 130 kg/m^3 in internal concrete. Water content was adjusted in order to obtain the specified slump of 3 ± 1 cm and air content of 3 ± 1 %.

Table 1. Materials.

		Density (g/cm^3)	Specific surface area (cm^2/g)	Replacement ratio (%)
Cement (C)	Moderate heat Portland cement (M)	3.21	3,850	—
	Moderate heat fly-ash cement (MF)	2.85	3,800	30
	Blast-furnace slag cement (BB)	3.00	4,010	55
		Density (g/cm^3)	Adsorption (%)	Fineness modulus
Fine aggregate (S)	pit sand	2.65	1.03	2.74
Coarse aggregate (G)	150 - 80 mm (crushed stone)	2.73	0.22	-
	80 - 40 mm (crushed stone)	2.72	0.37	-
	40 - 20 mm (crushed stone)	2.74	0.40	-
	20 - 5 mm (crushed stone and gravel)	2.64	0.66	-

Table 2. Mix proportion of concrete.

Cement	Category of concrete	$\frac{W}{C+F}$ (%)	$\frac{s}{a}$ (%)	Unit content (kg/m^3)					
				W	C	S	G	Ad-1	Ad-2
BB	Internal	66.9	24	87	130	534	1728	0.324	0.016
	External	47.6	23	90	189	498	1704	0.473	0.076
M	Internal	64.6	24	84	130	538	1738	0.325	0.016
	External	46.3	23	88	190	502	1715	0.474	0.076
MF	Internal	63.8	24	83	130	535	1730	0.326	0.052
	External	46.3	23	88	190	497	1700	0.474	0.284

W : water, s/a : sand-total aggregate ratio by volume

Ad-1 : Air-entraining and water-reducing agent, retarding type, Ad-2 : Air-entraining agent

Experimental procedures. Adiabatic temperature rises of external concrete and internal concrete with full-sized aggregate were measured using an air circulation type adiabatic temperature rise apparatus, in which the quantity of concrete sample was 40 liters.

Compressive strength, splitting tensile strength and Young's modulus were measured on sieved concrete with maximum size of aggregate of 40 mm. The specimens were stored under water at 20 ºC until the tests which were conducted at the age of 7 days, 28 days, 91 days and 1 year.

Autogenous shrinkage strain of concrete with full-sized aggregate was measured with cylindrical specimens with a diameter of 500 mm and a height of 1000 mm, as shown in Figure 1. Teflon sheet with 1 mm in thickness was

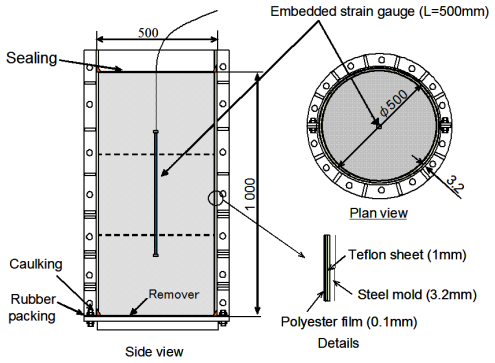

Figure 1. Measurement of autogenous shrinkage of concrete with full-sized aggregate.

Table 3. Properties of fresh concrete and setting time

Type of cement	Category of concrete	Slump (cm)	Air content[1] (%)	Temperature at casting (ºC)	Time of setting[2] (h-m)	
					Initial	Final
BB	Internal	2.0	2.6	16.5	8-55	15-50
	External	3.5	2.9	15.5	11-05	15-00
M	Internal	4.0	3.0	20.0	8-00	11-00
	External	4.0	3.2	21.5	9-20	12-15
MF	Internal	4.0	2.7	20.5	8-30	12-40
	External	4.0	3.2	22.0	9-15	13-15

1) Converted into air content of concrete with full-sized aggregate
2) Cured at temperature of 20 ºC

put on the inside of the mold in order to eliminate the restraint by the molds. After casting concrete, the top surface of the specimens was sealed to prevent evaporation. The specimens were stored in a room at 20 ± 2 ºC throughout the test periods without stripping the molds. Longitudinal strain of the specimens was measured with strain gauges with measuring length of 500 mm and modulus of elasticity of 1000 N/mm^2 which were embedded at the center of the specimens. The reason why the strain gauge with very low rigidity is to measure the strain form early ages when concrete has not hardened yet. Autogenous shrinkage of sieved concrete, in which aggregate larger than 40 mm was removed by wet screening, was also measured with cylindrical specimens with a diameter of 150 mm and a height of 300 mm. The increase in temperatures of the specimens due to heat of cement hydration was less than 4 ºC during the measurement of autogenous shrinkage. Autogenous shrinkage strain was determined by subtracting thermal strain from the observed total strain, where the thermal expansion coefficients of the concretes were assumed to be 10×10^{-6}/ ºC.

RESULTS AND DISCUSSIONS

Fresh and setting properties of concrete. Test results for slump, air content, setting time and concrete temperature at casting are shown in Table 3. Air content was measured with the sieved concrete and the observed values of air content were converted into those of concrete with full-sized aggregate taking the volume fraction of aggregate into account.

Adiabatic temperature rise. Test results of adiabatic temperature rise of concrete with full-sized aggregate are shown in Figure 2. For any type of cement, temperature rise of the external concrete was larger than that of the internal concrete since the cement content in the external concrete was much larger. It can also be seen that temperature rise of concrete with BB was larger than those with M and MF.

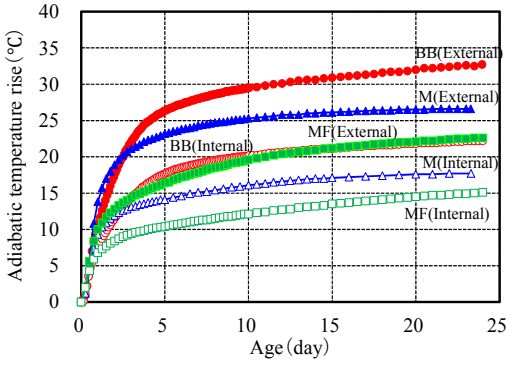

Figure 2. Adiabatic temperature rise of concrete with full-sized aggregate.

Autogenous shrinkage. The test results for autogenous shrinkage of concrete with full-sized aggregate are shown in Figure 3. In this figure, the start point of autogenous shrinkage is taken to be the time at which early-age expansion is maximized. It can be seen from the experiments that the start point, which was dependent on type of cement, was about one day after casting. In Figure 3, autogenous shrinkage of concretes was observed for the external concretes and was predicted for the internal concretes. It was reported in a published paper that autogenous shrinkage of dam concrete with full-sized aggregate can be roughly predicted from the observed value on the sieved concrete with maximum aggregate size of 40mmn, taking the volume fraction of aggregate into account (Sato et al. 2011).

It is seen from Figure 3 that autogenous shrinkage significantly increased until about the age of one or two months and after that it continued to increase gradually until one year. In case of BB, autogenous shrinkage of the external concrete was much larger than M and MF and was as much as 130×10^{-6} at the age of one year. In case of M and MF, autogenous shrinkage of the external concrete ranged between 50×10^{-6} and 60×10^{-6} at the age of one year, which was less than the half of BB. It is proved from the experimental results that autogenous shrinkage of external concrete can be considerably large, depending on type of cement. On the other hand, autogenous shrinkage of internal concretes, which have higher water-cement ratios than external concretes, was relatively small regardless of cement type. As a result, the difference in autogenous shrinkage of external concrete and internal concrete can be large depending on the type of cement.

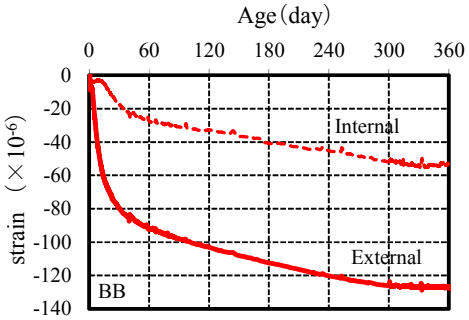

(a) Cement BB

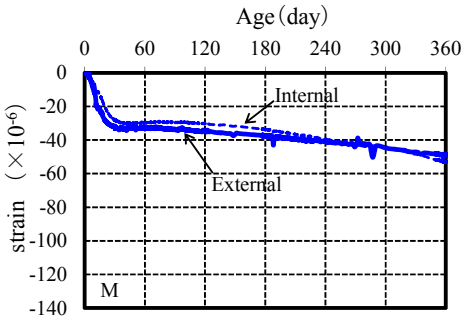

(b) Cement M

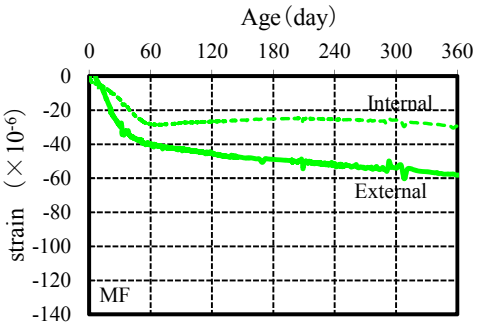

(c) Cement MF

Figure 3. Autogenous shrinkage of concrete with full-sized aggregate.

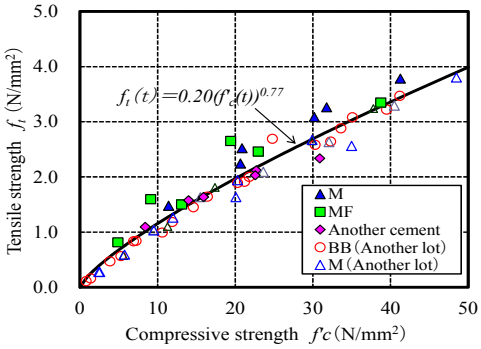

Figure 4. Relation between compressive strength and Young's modulus of concrete.

Mechanical properties of concrete.
Young's modulus and splitting tensile strength of concrete are generally obtained as functions of compressive strength. It was found from the experimental results that the development of compressive strength with time $f_c'(t)$ could be approximated with the equations (see Table 4). Test results of Young's modulus $E_c(t)$ and splitting tensile strength $f_t(t)$ which are plotted against compressive strength $f_c'(t)$ are shown in Figure 4 and Figure 5, respectively. It can be seen that $E_c(t)$ and $f_t(t)$ can be approximately estimated as the functions of $f_c'(t)$ shown in the figure.

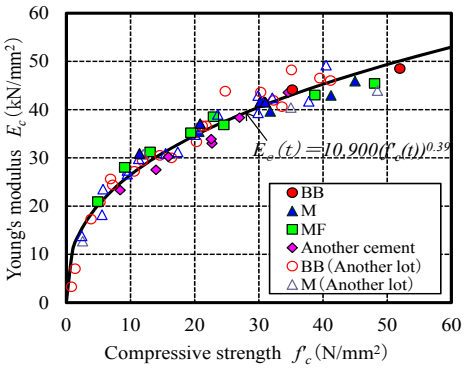

Figure 5. Relation between compressive strength and Young's modulus of concrete.

A Dam Model for Thermal Stress Analyses. In concrete dams, volume change of concrete caused by heat of cement hydration and ambient temperature change is externally restrained by the foundation rock and the other concrete layers and is internally restrained in the cross section due to temperature gradient.

As is earlier mentioned, autogenous shrinkage strain can be added to thermal strain, which can result in increase in external and internal restraint stresses. In this study, the restraint stress caused by both thermal strain and autogenous shrinkage strain, which will develop in a model concrete dam (see Figure 6) during the construction period, was numerically simulated.

In order to simulate thermal cracking, which can occur at the central part of the concrete block and at the surficial portions of upstream and downstream surfaces (see Figure 7), three-dimensional FEM analyses were conducted. As shown in Figure

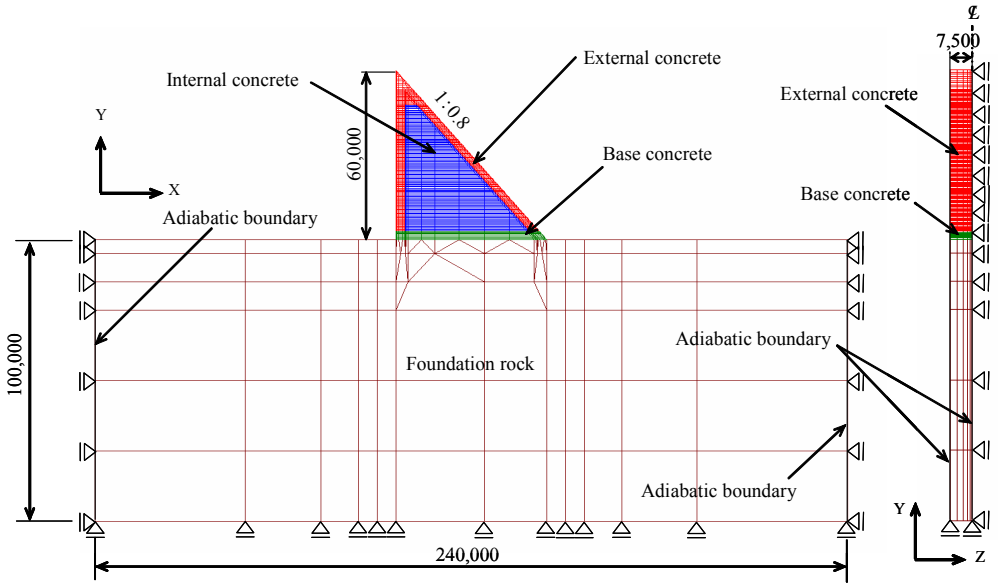

Figure 6. Concrete dam model for thermal stress analyses.

6, the model is a typical concrete gravity dam which is constructed by ELCM (Extended Layer Construction Method), in which construction block is 15 m in width, and 0.75 m in height. Four lifts on the foundation rock are base concrete. The depth of external concrete at upstream and downstream surfaces is 3 m.

In thermal analyses, the transient heat transfer analyses were carried out. In thermal stress analyses, autogenous shrinkage strain was added to thermal strain and linear elastic analyses were carried out, in which stress relaxation due to creep of concrete was taken into account by using effective Young's modulus proposed by Japan Concrete Institute (JCI 2008). Adiabatic temperature rise, autogenous shrinkage,

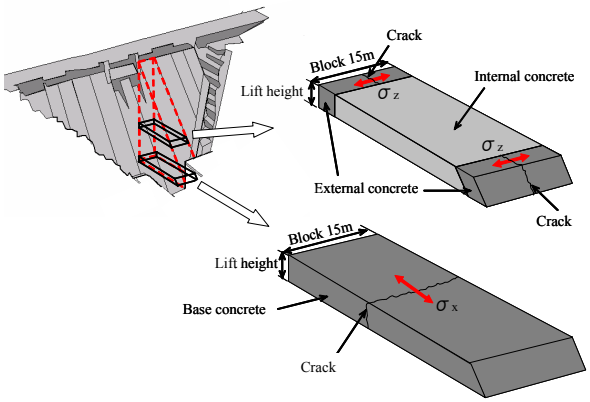

Figure 7. Typical crack patterns in concrete dams

Table 4. Conditions of thermal stress analysis.

		Internal concrete			External concrete Base concrete		
Thermal properties	Specific heat (kJ/kg ºC)	0.871			0.871		
	Thermal conductivity (W/m ºC)	2.88			2.88		
	Density (kg/m^3)	2,483			2,488		
Adiabatic temperature rise (ºC) $Q(t)= a\cdot\{1-exp(bt)\}$			*a*	*b*		*a*	*b*
		BB	21.0	-0.37	BB	31.9	-0.43
		M	15.7	-0.68	M	24.9	-0.65
		MF	14.6	-0.27	MF	22.1	-0.24
Mechanical properties	Compressive strength (N/mm^2) $f'_c(t)= log(M)-b$		*a*	*b*		*a*	*b*
		BB	14.1	40.6	BB	18.9	50.2
		M	13.3	37.1	M	17.3	42.8
		MF	12.2	41.0	MF	21.2	66.0
	Autogenous shrinkage	Observed data (Figure 3)					
	Tensile strength (N/mm^2)	$f'_t(t)=0.13(f'_c(t))^{0.89}$			$f'_t(t)=0.15(f'_c(t))^{0.83}$		
	Young's modulus (N/mm^2)	$E_c(t)=7{,}838(f'_c(t))^{0.52}$			$E_c(t)=9{,}326(f'_c(t))^{0.44}$		
	Effect Young's modulus of elasticity $E_e(t)= \varphi E_c(t)$	Until the age of 2 days φ=0.42 After the age of 3 days φ=0.65 From 2 days to 3 days : Linear interpolation					
	Coefficient of thermal expansion (×10^{-6}/ ºC)	10					
Initial condition	Concrete temperature at casting (ºC)	T_{air}+2					
Boundary conditions	Coefficient of heat transfer (W/m^2 ºC)	14 (Upstream and downstream surfaces, Horizontal construction joint)					
	Ambient temperature (ºC)	$T_{air}=12.34+12.40sin\{2\pi(t+154)/365\}$ *t*: elapsed time after casting concrete (days)					

compressive strength and Young's modulus, which were determined on the basis of the experimental results, were used as input data (see Table 4).

The start of placing concrete was taken to be October 1st and the interval of lifting was taken to be 5 days. A seasonal variation of ambient temperature in a typical region in Japan was taken into account. It was assumed that the concrete temperature at casting was taken to be within the ranges between 5 ºC and 25 ºC, since specifications generally limit the maximum and minimum placing temperatures.

Results of thermal stress analyses. Calculated values of restraint stress of concrete in the upstream-downstream direction (σ_x) at the center of the blocks near the dam-foundation interface are shown in Figure 8. The restraint stress σ_x shown in this figure, which correspond to the third lift, is caused mainly by external restraint. It can be seen from the figure that tensile stress in the base concrete is significantly increased by autogenous shrinkage of concrete with BB, which has larger autogenous shrinkage that those with M and MF. Tensile stress significantly increases during a

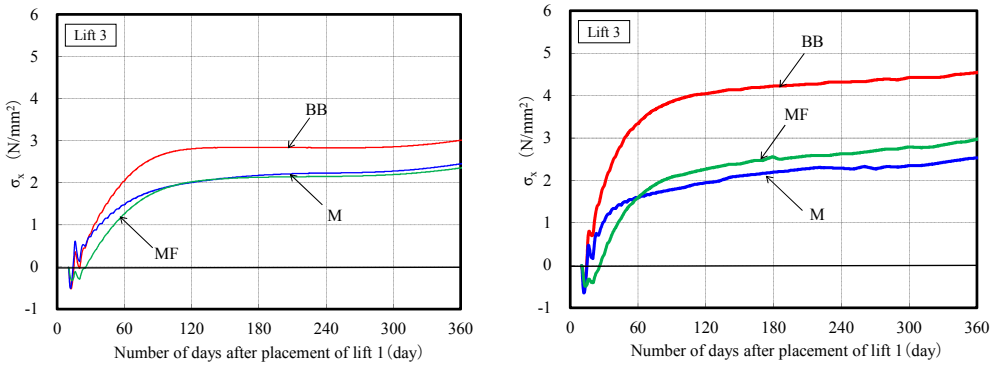

(a) without autogenous shrinkage (b) with autogenous shrinkage

Figure 8. History of thermal stress in upstream-downstream direction at the center of block near bedrock.

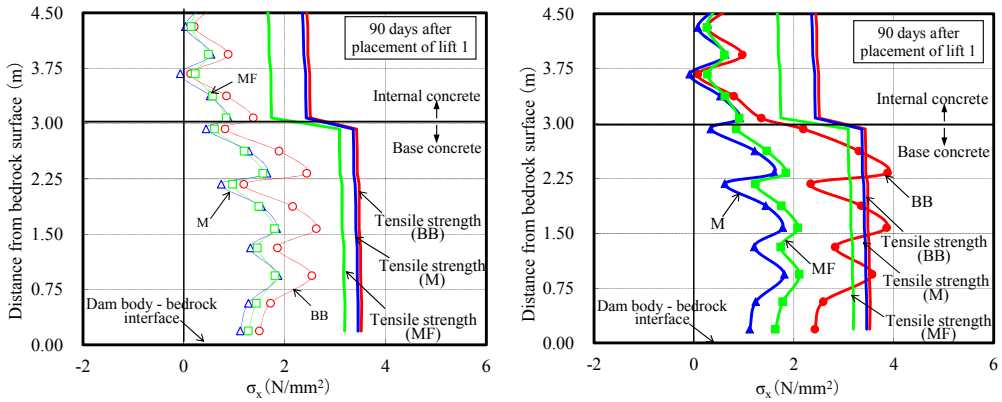

(a) without autogenous shrinkage (b) with autogenous shrinkage

Figure 9. Vertical distribution of thermal stress in upstream-downstream direction at the center of block near bedrock.

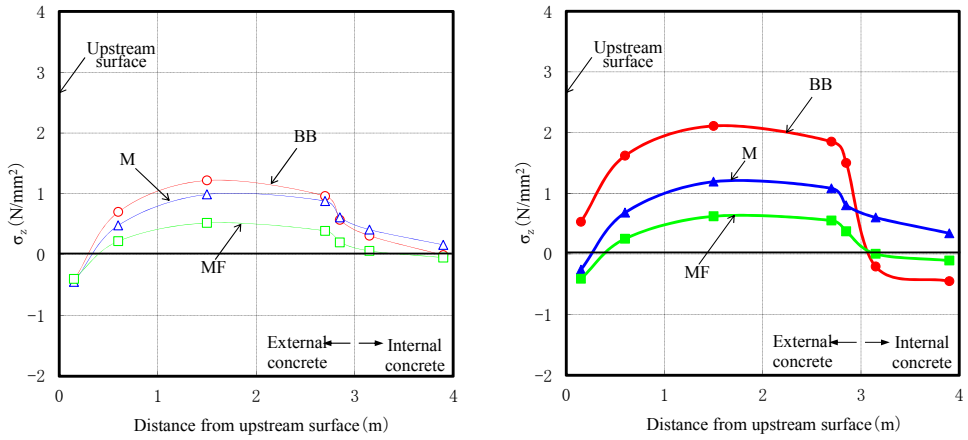

(a) without autogenous shrinkage (b) with autogenous shrinkage

Figure 10. Horizontal distribution of thermal stress in dam-axis direction at the center of block near upstream surface.

few months after casting concrete that the possibility of cracking can be increased in base concrete during construction period. On the other hand, restraint stress is hardly affected by autogenous shrinkage when concretes with M and MF are used.

The vertical distributions of the calculated values of σ_x at 90 days after the first lift placement are shown in Figure 9 with tensile strength of concrete at the same age. It can be seen from the figure that the values of σ_x in concrete with BB can be larger than tensile strength in large portion of base concrete, when autogenous shrinkage strain is taken into account. It can also be seen that the portion in which tensile stress is increased by autogenous shrinkage is limited to the lifts within 3 m from the foundation rock which corresponds to the base concrete. On the other hand, tensile stress of base concrete was slightly increased for MF concrete and was not increased for M concrete when autogenous shrinkage was taken into account. Therefore, not only thermal strain but also autogenous shrinkage strain can be a cause of cracking in base concrete which has adversely influence on water tightness and stability of concrete dams when concrete with large autogenous shrinkage is used.

The horizontal distributions of the calculated values of restraint stress in the dam-axis direction (σ_z) at about one month after casting concrete are shown in Figure 10. In this figure, the calculated values of σ_z in 46th lift (35 m above the foundation rock), which is not affected by external restraint of the foundation rock, are shown. It can be seen from this figure that tensile stress is increased in the external concrete and is decreased in the internal concrete by autogenous shrinkage. When BB is used, tensile stress is increased by about 1 N/mm^2 in almost full depth of the external concrete. It should be noted that autogenous shrinkage of external concrete is much larger than internal concrete when BB was used (see Figure 3). Therefore, the difference in autogenous shrinkage strain between the internal concrete and the external concrete can increase the restraint stress in the external and it can be a cause of cracking during construction period which can have adversely influence on water tightness and durability of the dam.

CONCLUSIONS

Thermal stress in a gravity concrete dam was simulated by three dimensional FEM analyses taking autogenous shrinkage of concrete with full-sized aggregate into account. Findings in this study are as follows.

(1) Autogenous shrinkage of dam concrete is dependent on type of cement. External concrete with blast-furnace slag Portland cement exhibits autogenous shrinkage of 130×10^{-6} at one year after casting, which is much larger than moderate-heat Portland cements with and without fly ash.

(2) Thermal stress in upstream-downstream direction at the center of the concrete blocks near foundation rock is increased by autogenous shrinkage if concrete with large autogenous shrinkage is used.

(3) Thermal stresses in dam-axis direction at upstream and downstream surfaces are increased by the difference of autogenous shrinkage strains between internal and external concretes, if blast-furnace slag Portland cement is used.

(4) In concrete gravity dams, autogenous shrinkage which simultaneously occurs with thermal strain should be taken into account in order to control thermal cracking during construction period which can adversely affect the stability, water tightness and durability of dams.

REFERENCES

American Concrete Institute (ACI) (2005). Chapter 3 in *Guide to Mass Concrete*. ACI 207. 1R-05. Reported by ACI Committee 207, 12-19.

Davis, H. E. (1940). "Autogenous Volume Changes of Concrete." Proc. of ASTM, 40, 1103-1110.

Japan Concrete Institute (JCI) (2011). Chapter 4 in *Guidelines for Control of Cracking of Mass Concrete* 2008. 25-49.

Sato, H. and Hirano, A. (1998). "Effect of Curing Temperature on Autogenous Shrinkage of Dam Concrete." Proceedings of the 53rd Annual Meeting, Japan Society of Civil Engineers, Tokyo, Japan, 762-763. (in Japanese)

Sato, H., Miyazawa, S. and Yatagai, A. (2011). “Autogenous shrinkage of dam concrete and its influence on thermal stress.” International Conference on Advances in Construction Materials through Science and Engineering. RILEM Bagneux, France.

Tazawa, E. et al. (1994). "Effect of Autogenous Shrinkage on Self Stress in Hardening Concrete." Proceedings of the International Symposium on Thermal Cracking in Concrete at Early Ages, E &FN SPON, London UK, 221-228.

The International Commission on Large Dams (ICOLD) (2009). Chapter 6 in *The Specification and Quality Control of Concrete for Dams*. 51-54

Uvan, E. H. et al. (1969). "Studies of Autogenous Volume Change in Concrete for Dworshak Dam." ACI Journal, 560-568.

Serviceability and Stability of Unreinforced Mass Concrete Structures – EC 2 Compatible Design Concept Derived from Comprehensive FE-Studies on Real Structural Behaviour

P. J. Heinrich[1], D. Schlicke[2], N. V. Tue[3]

[1,2,3]Institute for Structural Concrete, Graz University of Technology, Austria, 8010 Graz, Lessingstraße 25/I; PH +43 (0)316 873-6691; email: peter.heinrich@tugraz.at

ABSTRACT

Many existing mass concrete structures are unreinforced because of economic aspects. Based upon the fact that no national or international standards for the design of such structures are available, each of them has to be treated as individual case. This often leads to safety concerns or concerns of reliability. An efficient design of unreinforced mass concrete structures needs a realistic evaluation of any crack formation to be expected. This calls for a realistic quantification of the decisive stress-distribution. This contribution shows first results of a preliminary study to develop a new design concept for unreinforced mass concrete structures that is in accordance with the design philosophy of Eurocode 2 (ÖNORM B 1992-1-1, 2011). This contribution also deals with the development of a new, efficient time-step FEM-based approach for the consideration of viscoelasticity in order to allow a comprehensie parametric study on the restraint behaviour of mass concrete structures.

INTRODUCTION

Eurocode 2 considers a concrete structure as an unreinforced structure if its containing reinforcement is less than the required minimum reinforcement. This design method is often used because of economic aspects, especially if large dimensions are needed due to structural stiffness requirements. This is the reason why many practical cases of unreinforced concrete structures are mass concrete applications such as large bridge foundations or hydraulic structures. However, the shape of unreinforced mass concrete members usually do not correspond to the geometric conditions of a slab or a wall.

Motivation

Until today, the dimension of residual stresses caused by hardening and their interaction with additional restraint due to seasonal temperature change have not been investigated systematically. However, this information is essential for a reliable design of unreinforced mass concrete structures in order to achieve a realistic superposition

of restraint stresses with stresses aroused by load. Since this question has not been answered yet, contrary opinions regarding the influence of restraint stresses on the structures serviceability or stability remain. They often lead to safety concerns or concerns of reliability. As a result, this leads to interminable discussions, which can cause delays in construction progress. Also extra costs may arise. This situation is very unsatisfying for the employer as well as for the contractor.

State of the Art

A comprehensive literature study on national and international standards showed that the present design rules for unreinforced mass concrete structures are mainly based upon experience (Heinrich and Schlicke, 2014). The main rule is the limitation of tensile stress in order to avoid cracking at all. Furthermore, regulations exist ranging from concrete technology to constructive aspects. This includes minimal post-curing-durations and limited temperatur gradients in the cross-section, as well as the provision of geometric boundary conditions such as maximum length to heigth ratios and/ or the requirement of sliding-layers between the restraining structures.

Requirements

An efficient design of unreinforced mass concrete structures calls for a realistic evaluation of any crack formation to be expected. In detail, the type of cracking due to hardening restraint (separating cracks, bending cracks or micro-cracks due to residual stresses) has to be confirmed depending on material properties, structural dimensions and surrounding conditions. Besides, a reliable quantification of the decisive stress-distribution in the structure also requires the superposition of restraint stresses caused by hardening and further restraint stresses that occur within the lifetime, as well as stresses due to loading. However, this superposition has to consider that the relevant structures are usually thick and further restraint stresses that occur within the lifetime are already partly included in the restraint stresses caused by hardening. The development of restraint stresses and the influence of different boundary conditions on the structure should be investigated in a comprehensive time-step FE-based parametric study. To conduct such a study as efficiently as possible, a preliminary FE-study must be performed. The following sections show and discuss the set-up for these studies and present some general, important results that could have been concluded from them.

FE-MODEL

The preliminary studies use a 3D FE-model. This model is generated in the modular FE-framework SOFiSTiK, its mesh is illustrated in figure 1. The mesh is finer at the structure edges because of the expected higher influence of the ambient temperature.

The included module SOFIMSHA uses the geometric node-definitions to gen-

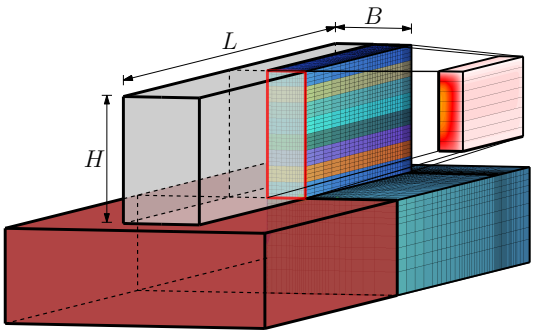

Figure 1: FE-structure.

erate a regular mesh. Later, the module HYDRA is used to determine the temperature-field in the structure for each time-step. The module ASE follows the procedure and calculates the resulting stresses, taking It takes the temperature-field directly from HYDRA as thermal loading. The module SOFILOAD applies additional loads, e.g. further deformation impact from shrinkage.

Structural Idealization

The whole model consists of several 3D elements (8 nodes with linear shape functions). It represents only a quarter ($\frac{L}{2}, \frac{B}{2}, H$) of the whole structure. This reduces the complexity of the calculation and increases the speed of the simulation. Appropriate boundary conditions consider the symmetry as well as bedding and thermal conditions. In the temperature-field calculation, the modelled soil acts as heat storage. Just before the stress calculation, it changes into a non-linear compression-spring-bedding. In the bedding plane, 2D elements (4 nodes with linear shape functions) with changeable stiffness represent the soils horizontal support.
The dimensions of the structure are fully variable in every direction; each surrounding condition can be altered and furthermore it is possible to investigate different types of construction-methods (e.g. concreting in layers).

Material Model

The hardening process of the concrete is considered consistantly for all related properties on base of the so-called *effective concrete age*. The effective concrete age is a state variable that takes the influence of the real concrete temperature in the structure on the speed of the hardening itself into account (ARRHENIUS function). Based on this sate variable the release of hydration heat is simulated by the JONASSON approach. The simultaneously developing strength properties of the hardening concrete are described by the WESCHE approach.

Furthermore, the shrinkage impact (mainly autogenous shrinkage) are also

modelled on the base of the effective concrete age. The considered absolute values are taken from Eurocode 2.

The consideration of the viscoelastic behaviour of concrete (creep as well as relaxation due to restrained creep) can be achieved by a deformation based approach developed at the Institute for structural concrete at Graz University of Technology (Schlicke, 2013). The advantage of this model is a very clear input data definition, derived from the strength class of concrete and the surrounding conditions of the structure.

PRELIMINARY STUDIES

To perform a coherent comprehensive parametric study, it is necessary to discuss the efficiency of the FE-model and the material approaches employed in advance. Here, this is done with a preliminary study. On one hand, this study is intended to show the main influencing factors to obtain information whether the structures mesh is fine enough. On the other hand this study is intended to provide a better understanding of the behaviour of mass concrete structures whose shapes are normally neither walls nor slabs. Since the upcoming parametric study is very extensive, the preliminary study should also indicate whether there is a necessity, or at least some potential available to speed up the whole calculation process.

In the preliminary study, the method of construction (monolithic; concreting in sections/layers), the bedding situation and the influence of climatic surrounding conditions were varied. The following main results were gained from the study which confirms the findings of (Schlicke, 2014) and (Schlicke and Tue, 2012):

- The hydration of concrete as a highly exothermic reaction is an important design criteria. Therefore it is necessary to accurately determine its temperature development.
- Centric restraint as well as bending restraint is of minor importance in the case of the investigated mass structures.
- Considerable residual stresses occur because of a huge temperature difference between the structures core with almost adiabatic environmental conditions and the surface that is exposed to ambient air.
- Due to the restraint condition of a plane cross-section, the resulting residual stresses lead to cracks in the surface zone that cannot be prevented. The cracks can easily reach depths of up to several meters due to the large dimension of the structure, although they remain in the surface zone.
- The effects of viscoelasticity are not negligible since they highly influence the stress distribution in the considered cross section.

- When it comes to structural failure, the negligence of viscoelasticity leads not to safe side results in general.

A weak point of the deformation based approach used for the consideration of viscoelasticity was its costly routine (computation time). The reason is the process of reading and writing in the SOFiSTiK database because of the stress-recording (stress-history). However, if the creep behaviour of the concrete to be investigated is very well known, a speeding up of the whole simulation process is possible by the usage of rheological based models for the consideration of viscoelasticity. Those models do not need stress-recording, and therefore no database access at all.

CONSIDERATION OF VISCOELASTICITY

Recently, a new model for the consideration of viscoelasticity has been developed at the Technical University of Braunschweig (Hermerschmidt and Budelmann, 2014). In general, this model uses some rheological elements to formulate the constitutive strain-stress-relation. Over the last few years, different types of such rheological models have been published. One weak point of the larger part of these models is that their material parameters are calibrated by the sole use of a few load cases. In addition, this means that it is not possible to prove their applicability to arbitrary boundary conditions. The model that should be used in the parametric study to describe the viscoelastic behaviour is calibrated using (TSTM) creep tests (age 2, 3, 4 and 7 days) under constant load. At the Technical University of Braunschweig, an appropriate number of tests with different boundary conditions have been performed to show the applicability of the model. If the model uses an incremental formulation of its strain-stress-relation, it is more suitable for application and no stress-recording is needed. This means that the whole calculation process could be sped up because the mentioned database access is not required anymore.

Basic principle

The rheological body to describe the viscoelastic behaviour is a so-called *generalized* MAXWELL-*model* (also known as ZENER$_m$-*body*). It consists of four parallel Maxwell-elements (a series of a HOOKEan spring and a NEWTONian dashpot) and a parallel single Hookean spring, see figure 2. The material properties of each dashpot (η_i) and the single spring (E_0) are both functions of the effective age t_{eff}. This is necessary to take the effects of temperature into account.

The fourth-order differential equation eq. (1) describes the strain-response $\epsilon(t)$ under a random stress $\sigma(t)$ impact.

$$b_0 \cdot \epsilon + b_1 \cdot \dot{\epsilon} + b_2 \cdot \ddot{\epsilon} + b_3 \cdot \dddot{\epsilon} + b_4 \cdot \ddddot{\epsilon} = a_0 \cdot \sigma + a_1 \cdot \dot{\sigma} + a_2 \cdot \ddot{\sigma} + a_3 \cdot \dddot{\sigma} + a_4 \cdot \ddddot{\sigma} \quad (1)$$

a_n, b_n are functions that depend on the specific material parameters: dashpot viscosities and spring stiffnesses. These viscosities and the spring stiffness of the first

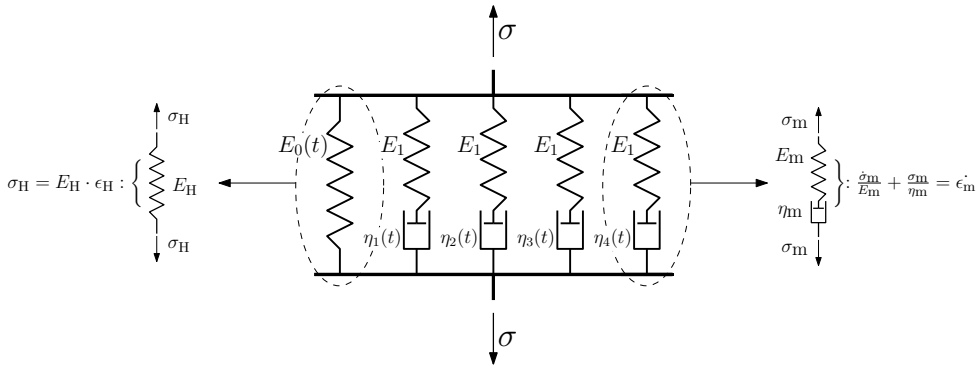

Figure 2: Used rheological body with equations of its basic-elements.

spring are time dependent. They are described by form functions whose parameters have been determined by least square fits of the gained experimental data.

In most of the commercial FE-frameworks it is not possible to implement such constitutive laws directly. However, if a time-step restraint-stress-analysis is performed, then one can a determine deformation-increment as additional load for each time-step (load case). In general, an additional deformation-increment caused by viscoelasticity depends on an elastic stress increment $\Delta\sigma_i^{\text{el}}$ and on the actual total stress state σ_i^{tot}. The elastic stress increment $\Delta\sigma_i^{\text{el}}$ for each time-step is the difference between the resulting total elastic stress of the actual time-step and a previous time-step: $\Delta\sigma_i^{\text{el}} = \Delta\sigma_i^{\text{el}} - \Delta\sigma_{i-1}^{\text{el}}$. If this increment is then applied to the rheological model, the model responds with a strain-increment. This strain-increment includes an *immediate elastic* response that occurs at the point of loading as well as a *viscous* part that is zero at the point of loading ($t = t_i$) and that changes with increasing time ($t > t_i$).

The size of the immediate elastic response depends on the models age and on the occuring elastic stress increment $\Delta\sigma_i^{\text{el}}$. The viscous part's size also depends on the elastic stress increment $\Delta\sigma_i^{\text{el}}$ and on the length of the considered time-step and furthermore on the concrete's age at the loading point as well as on the degree of restraint. The resulting strain-increment at the end of a time-step is the additional deformation for the FE-calculation of the new total stress state. For a better understanding, eq. (2) describes the determination of the remaining (viscoelastic) stress of a fully restrained 1D element – see also figure 3 for more details.

$$\sigma_i^{\text{visc}} = \sigma_i^{\text{tot}} - \underbrace{\overbrace{\Delta\epsilon\big[(t_{i+1}, t_i); \Delta\sigma_i^{\text{el}}; \sigma_i^{\text{tot}}\big]}^{\epsilon_{\text{cc},i}} \cdot E_c(t_i)}_{\Delta\sigma_i^{\text{visc}}} \qquad \text{and} \quad \sigma_i^{\text{tot}} = \sigma_{i-1}^{\text{visc}} + \Delta\sigma_i^{\text{el}} \tag{2}$$

Simplification and Implementation in FE-Framework

Because the parameters a_n, b_n of the differential equation given in eq. (1) are time-dependent, it is not possible to solve the equation analytically. As a result, numerical methods have to be used. The problem with a numerical method is that because of their iterative processes, it is often costly to obtain a solution. Another issue is the question of dealing with non-convergence after a finite number of iterations. One can increase the number of iterations, but as mentioned above, the whole procedure should be contained. Therefore, the following assumptions have to be made:

- The time-steps in the restraint analysis are so small that a change of the material-properties within a single step is negligible.
- The total stress state that acts on the model remains constant during a time-step.

These assumptions turn the problem into a stepwise consideration of "creep under constant load" with changing load for each time-step. Figure 3 shows the basic idea of this procedure. Notice that it is not possible to determine σ_i^{visc} at the same point in time as σ_i^{el}.

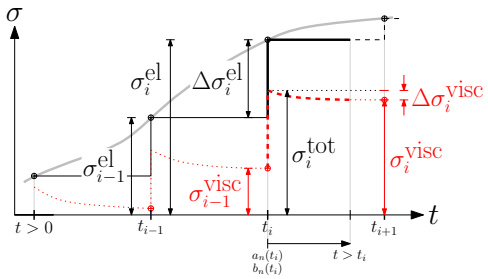

Figure 3: Schematic visualization of the time-step-method.

This has the effect of simplifying the differential equation eq. (1) to eq. (3).

$$b_0 \cdot \epsilon + b_1 \cdot \dot{\epsilon} + b_2 \cdot \ddot{\epsilon} + b_3 \cdot \dddot{\epsilon} + b_4 \cdot \ddddot{\epsilon} = a_0 \cdot \sigma \tag{3}$$

Eq. (3) is also considered in time-steps. It is now possible to solve it analytically, if one uses correct initial and transitional conditions for every step $t_i - t_{i-1}$, see (Boley and Weiner, 1997). The viscoelastic stress redution $\Delta\sigma_i^{\text{visc}}$ must also be considered for the formulation of the transition conditions for the following time-step. Finally, this leads to a 4x4 system of linear equations. For a solution, there are well-established algorithms available. Here, the GAUSSian elimination with pivoting leads to results with good accuracy. Because there exist always an exact solution for the system of linear equations, it is possible to specify its solution directly. Therefore, no solution-algorithm is needed and this increases also calculation speed.

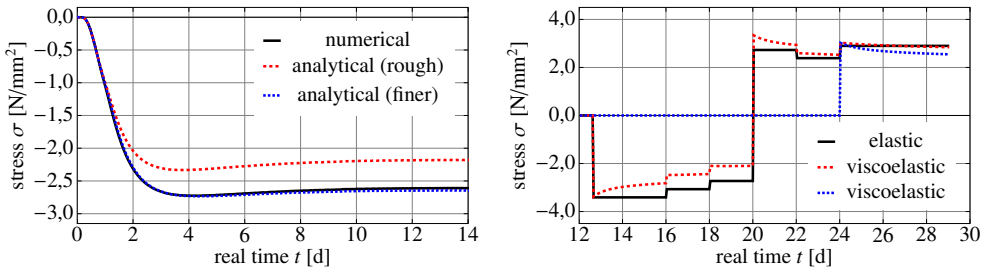

(a) Analytical vs. numerical solution (b) Stepwise creep-test

Figure 4: 1d stress calculation (full restraint).

Figure 4(a) shows a comparison of the "simplified" time-step-analytical solution and a numerical result from a Runge-Kutta method (Rosenbrock-Wanner) for a hardening full restraint concrete beam in the first 14 days. For the analytical solution, there is – as assumed – no change of the material properties possible within a single time-step, whereas for the numerical solution, the material properties can change. Both solutions assume that the stress-impacts remain constant in each step. The calculation uses fixed time-steps of $\Delta t = 1$ h. One can see that the results correlate well, especially if the number of steps is increased in the first 2.5 days ($\Delta t = 25$ min) for the analytical solution. This is comprehensible if one takes in mind that in the first few hours the concrete's creeping-behaviour is quite distinctive, but it decreases rapid with progressive time. This means that the time-steps of $\Delta t = 1$ h imply a too high stress-reduction in the concrete's early age and therefore there remains less stress at the end of one single step, compared to the smaller time-steps of $\Delta t = 25$ min.

Figure 4(b) illustrates the effectiveness of the model for a stepwise temperature-loading on an older fully restrained concrete beam. This temperature leads to an elastic stress (black line) that acts on the rheological model. The dashed red line marks the corresponding viscoelastic solution. Besides, the dotted blue line shows the stress-response if a constant elastic stress of the same size as the red solution at $t = 24$ h is applied. This scenario assumes a constant Young's modulus of $E_c = 31400$ Nmm^2. Figure 4(b) also shows that the behaviour of the presented model is qualitatively the same as the one that could be investigated with the model used previously, see (Schlicke, 2014).

The procedure explained above was derived by considerating only one direction. Through the usage of the FE-framework, it is not difficult to adapt it for a 3D simulation. Therefore, the whole procedure has to be done for every element, in each direction (x, y, z), depending on the actual stress-state in the considered direction. This leads to an additional deformation in the regarded direction that has to be put back into the FE-structure. The resulting stress is then calculated by the usage of the FE-framework.

CONCLUSION AND OUTLOOK

A preliminary parametric study for the investigation of unreinforced mass concrete structures showed that a realistic evaluation of any crack formation to be expected calls for a precise determination of the stress distribution in the structure. This precise determination of the stress distribution is only possible if the effects of viscoelasticity are not neglected. At the moment, not many models exist that allow the estimation of viscoelastic stresses in a realistic way. One of these models has been developed at the Institute for Structural Concrete at Graz University of Technology. Besides its advantage of very clear input data derived from the strength class of concrete and the surrounding conditions, a disatvantage of this model is that it requires a sophisticated mesh and time-step control in order to avoid computation-time costly calculations.For this reason, a new model that is based upon rheological elements was implemented with a commercial FE-framework. First calculations showed that the calculation speed increased remarkable with this new model. Hence it is more suitable for a prospective parametric study that should be done for the development of a Eurocode 2 compatible ULS and SLS design concept for unreinforced mass concrete structures.

REFERENCES

Boley, B. A., and Weiner, J. H. (1997). "Theory of Thermal Stresses." Unabridged Dover (1997) republication of the edition published by Robert F. Krieger Publishing Company, Malabar, Florida, 1985.

ÖNORM B 1992-1-1 (2011). "Eurocode 2 – Bemessung und Konstruktion von Stahlbeton- und Spannbetontragwerken – Teil 1-1: Allgemeine Bemessungsregeln und Regeln für den Hochbau." German Version, Österreichisches Normungsinstitut, Vienna, 2011.

Heinrich, P. J., and Schlicke, D. (2014). "Normative Regelungen zur unbewehrten Ausführung von massigen Betonbauteilen." *Nachhaltig Bauen mit Beton: Werkstoff und Konstruktion,* 2. Grazer Betonkolloquium, Graz, 281-288.

Hermerschmidt, W., and Budelmann, H. (2014). "Constitutive Law for the Viscoelastic Behaviour of Early Age Concrete in Massive Structures." RILEM International Symposium on Concrete Modelling, Bejing, 183-189.

Schlicke, D., and Tue, N. V. (2012). "Restraint impacts during Hardening Period for the Piers of Botlek Bridge; NL." Feasibility Study (unreleased), Institute for Structural Concrete. Graz, University of Technology.

Schlicke, D., and Tue, N. V. (2013). "Consideration of Viscoelasticity in Time Step FEM-Based Restraint Analyses of Hardening Concrete." *Journal of Modern Physics 4*, SCIRP, 9-14.

Schlicke, D. (2014). "Mindestbewehrung zwangbeanspruchter Betonbauteile unter Bercksichtigung der erhrtungsbedingten Spannungsgeschichte und der Bauteilgeometrie." PhD-Thesis. Graz, University of Technology.

Computational Fatigue Life Assessment of Corroded Reinforced Concrete Beams

Y. Tanaka[1]; Y. Takahashi[2]; and K. Maekawa[3]

[1]Department of Human and Social Systems, Institute of Industrial Science, The University of Tokyo, 4-6-1, Komaba, Meguro-ku, Tokyo 153-8505. E-mail: yasuxi@iis.u-tokyo.ac.jp
[2]Concrete Laboratory, Department of Civil Engineering, The University of Tokyo, 7-3-1, Hongo, Bunkyo-ku, Tokyo 113-8656. E-mail: takahashi@concrete.t.u-tokyo.ac.jp
[3]Concrete Laboratory, Department of Civil Engineering, The University of Tokyo, 7-3-1, Hongo, Bunkyo-ku, Tokyo 113-8656. E-mail: maekawa@concrete.t.u-tokyo.ac.jp

Abstract

Remaining performance of corroded reinforced concrete beams is numerically evaluated by means of poro-mechanics approach. Corrosion substance is treated as the combined phases of liquid and solid gels. The static loading experiment of corroded reinforced concrete beams is fairly simulated by the multi-directional fixed crack model combined with corrosion gel migration. Further, fatigue life of corroded reinforced concrete beams is studied numerically. Even if static shear strength is not reduced so much, remaining fatigue life could be shortened significantly due to the cyclic degradation of cracked cover concrete around expanded steel bars.

INTRODUCTION

Aged bridges in service of more than 50 years are increasing over the world and many of them are deteriorated due to steel corrosion located close to the sea shores. For maintaining these infrastructures as a social asset, quantitative assessment of life-extending effect by repair work is crucial. Not only the static capacity for safety performance but also the service-life related to fatigue shall be encompassed in maintenance planning. In this study, the coupled issue of steel corrosion and mechanistic fatigue loads are discussed as an engineering target. RC beams and decks of which bridges consist are subjected to high cycle repetition of dynamic loads. Herein, it is of great importance to estimate the remaining service-life. This study aims at corroded RC beams and guarders under fatigue actions by simulating steel corrosion with poro-mechanics approach.

NUMERICAL MODELING

Remaining fatigue life is assessed by multi-scale chemo-physical simulation in this study. Logarithmic-integral scheme (Maekawa and Fujiyama, 2013a) is

applied in case where compression, shear and tensile fatigue models are combined into the multi-directional fixed crack model (Maekawa et al. 2003) as summarized in Figure 1. Time-dependent deformation is also considered by the evolution law of the damage parameter K_c.

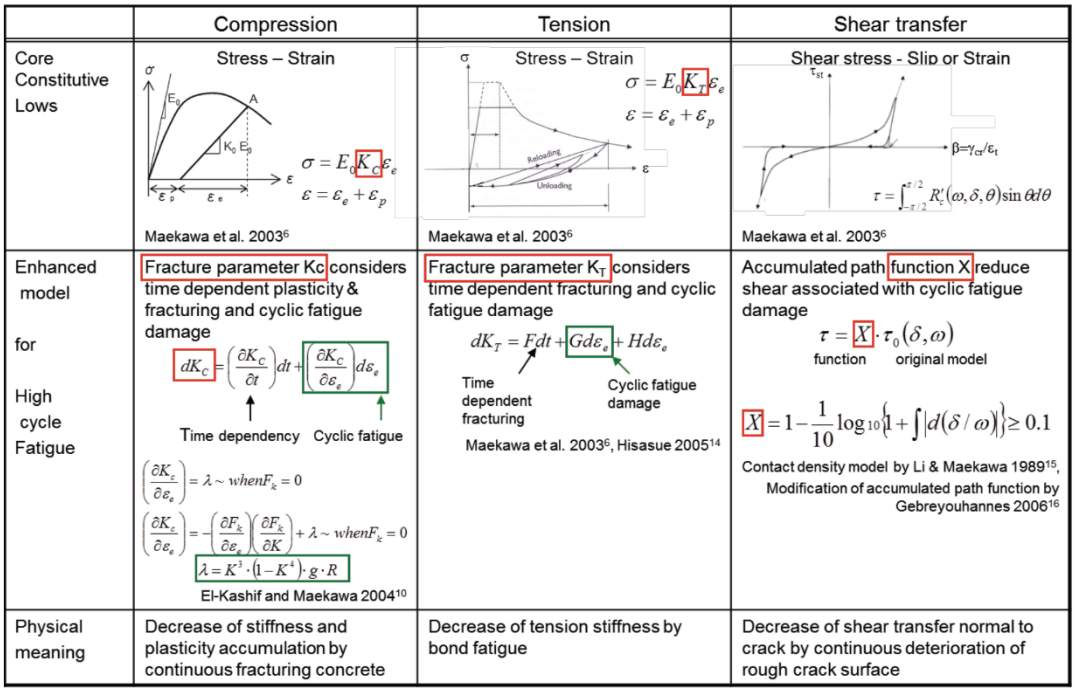

Figure 1. Constitutive laws for high cycle fatigue (Maekawa et al. 2003)

The authors pay their attention to the location of corrosion and the deteriorated bond through the cracked cover concrete. Here, poro-mechanics modeling (Maekawa and Fujiyama, 2013b) of corrosion gel substances is coupled with solid skeleton based on Biot's theory. Original governing equation for isotropic soil-pore system is described as follows.

$$\sigma_{ij} = \sigma^*_{ij} + \delta_{ij} p \tag{1}$$

where, σ_{ij} is total stress, σ^*_{ij} is effective stress and p is pore pressure. Effective stress of skelton phase is calculated from the constitutive laws as shown in Figure 1, while the substantial linear stiffness is assumed for pore pressure as,

$$p = \overline{K_f}\left(w_{ii} + \varepsilon_{ii}\right) \tag{2}$$

$$\overline{K_f} = \left(\frac{1-n}{K_c} + \frac{n}{K_g}\right)$$

where, K_c and K_g are bulk stiffness of concrete matrix and corrosion gel, $w_{ii}+\varepsilon_{ii}$ is volumetric strain of corrosion gel inside cracked concrete and n is constant to represent the effect of porosity. As to volumetric strain of corrosion gel, volumetric expansion ratio of corrosion substances is assumed as 5.0. While this two phase model was originally developed for concrete-pure water interaction, corrosion gel is the mixture of liquid and solid. Therefore, part of corrosion product is assumed as

crystalline solid, while the rest is assumed as liquid. Ratio of the crystalline phase is simply assumed to be 30 % in this study. The Darcy law is used to consider the flow of liquid phase of the corrosion gels. The permeability of corrosion gel in capillary pores κ^* is assumed as 10^{-12} m/s, which is significantly smaller than that of pure condensed water (10^{-7} m/s).

In cracked concrete, the authors apply anisotropy by assuming that pore water pressure acts perpendicular to the crack plane as,

$$\sigma_{ij} = \sigma^*_{ij} + \delta_{ij} l_i p \tag{3}$$

where, l_i is the unit directional vector normal to crack plane (Figure 2). The permeability of cracked concrete is estimated as a function of crack width.

$$\kappa_i = \kappa^* \left\{ 1 + \left(\frac{\varepsilon_{jj} + \varepsilon_{kk}}{a} \right)^4 \right\} \tag{4}$$

$\varepsilon_{jj}+\varepsilon_{kk}$ is the transverse in-plane strain. a is material constant where $1.0E^{-4}$ is assumed tentatively.

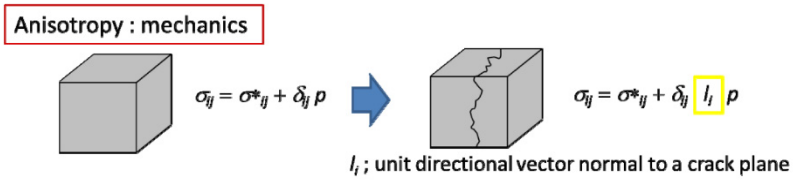

Figure 2. Anisotropy of cracked concrete

BOND DEGRADATION IN STATIC BEAM TEST

The flexural-shear experiment of RC beams with corrosion along longitudinal bars (Kanaduka *et al*. 2011) is simulated numerically. Figure 3 shows the dimensions of the targeted beam specimens. Cover depth, which is the main parameter in this experimental series, is 40 mm (C40) or 60 mm (C60). Entire length of the longitudinal bars was forced to be corroded electrochemically until the cross sectional area was reduced by 8 % on average. The compressive strength of concrete is 33N/mm^2. The high-strength reinforcing bars, which yield strength is 750N/mm^2, are used not to fail in flexure.

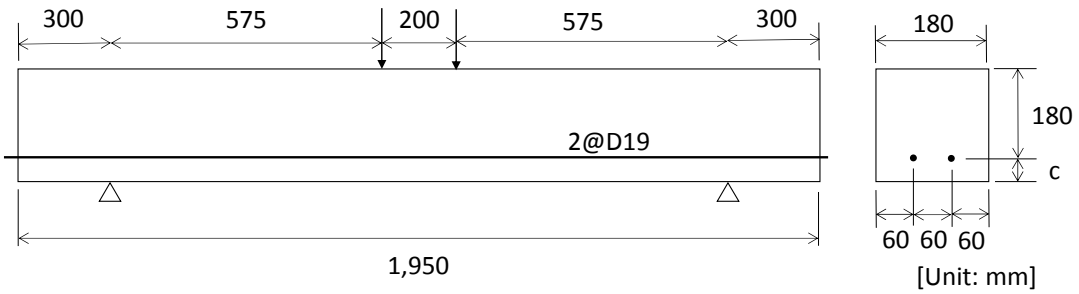

Figure 3. Dimensions of beam specimen (Kanaduka *et al.* 2011)

After the accelerated corrosion experiment, those simply supported beams were loaded concentrically. The shear span to effective depth ratio (a/d) is 3.19 while the development length is selected as 300 mm (15.8D).

As shown in Figure 4, corrosion cracks were induced along the reinforcing bars. In the case of 60 mm of the concrete cover depth (C60), corrosion cracks appeared on both sides of the beam and the bottom face. On the contrary, corrosion cracks were observed only on the bottom face in the case of 40 mm (C40). In loading, few flexural cracks were observed due to the reduction of macroscopic bond strength associated with cracked damage of cover concrete. The diagonal crack was formed near by the loading points and it propagated along with the longitudinal bars. Failure occurred when a diagonal shear crack reached the end of specimen.

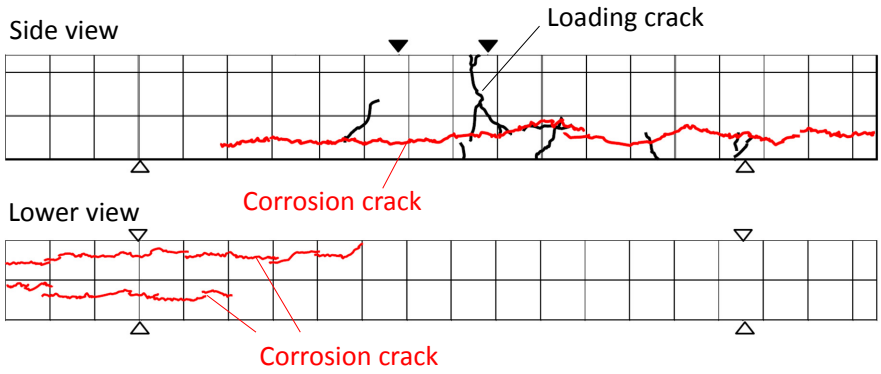

Figure 4. Crack patterns observed in experiment (C60)

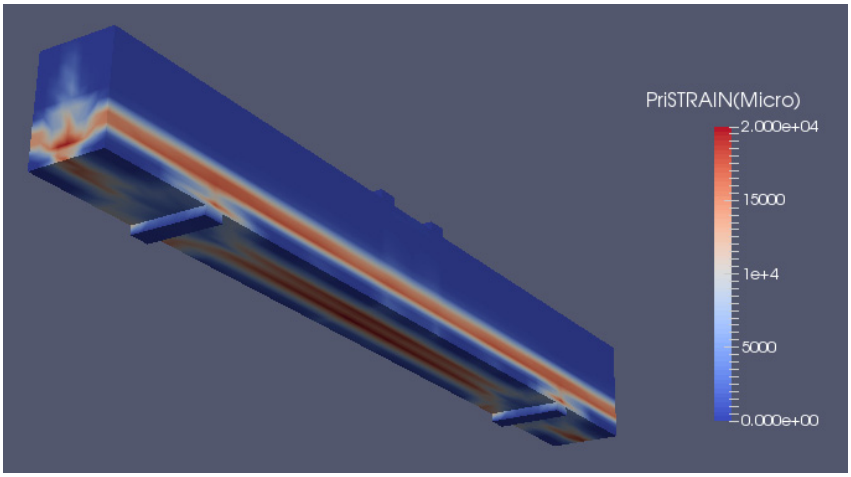

(a) Corrosion cracks before the loading (Bottom perspective view)

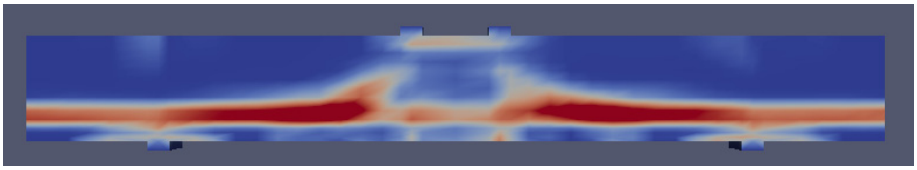

(b) After loading (Side view)

Figure 5. Post-loading crack patterns estimated by the analysis (C60)

Figure 5 shows estimated cracks before and after the loading. It is obvious that numerical simulation may capture both corrosion crack before loading and those induced by the external loading. Diagonal crack formed near loading plate and its propagation caused failure. Figure 6 shows the load - deflection relations of analyzed specimens. Numerical simulation is able to estimate lower loading capacity of C40 specimen which has smaller cover depth. This is because resultant restriction force of cracked cover concrete is naturally calculated by applying the chemo-mechanics model. Otherwise, we need to set up bond-slip model between reinforcement and concrete by considering corrosion cracks, cover concrete, envelop re-bars and so on. In many cases, the bond strength and bond-slip relations are not material properties but the resultant of the mechanistic damage of the beam. Then, the apparent bond-slip relation is not unique but different according to the damage patterns of cover concrete and their location. The bond deterioration is not the unique characteristics but to be computed value.

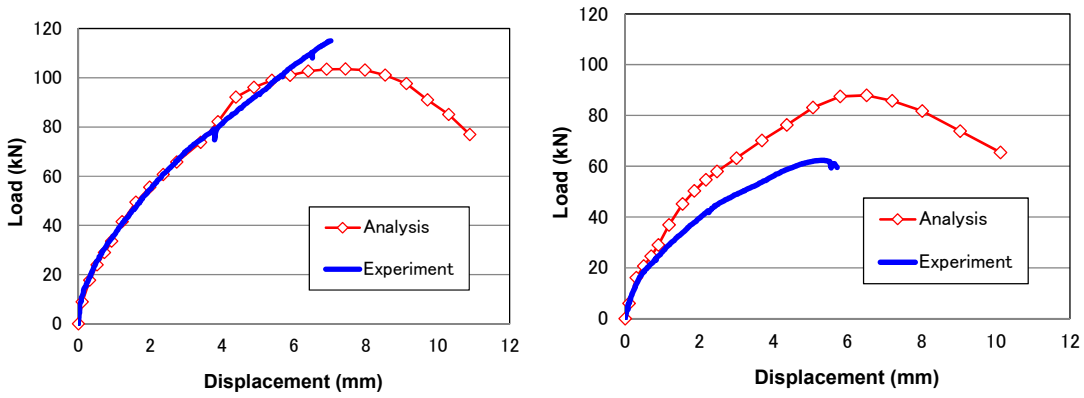

(a) C60 (Cover depth = 60 mm) **(b) C40 (Cover depth = 40 mm)**

Figure 6. Load-displacement relation at the center span

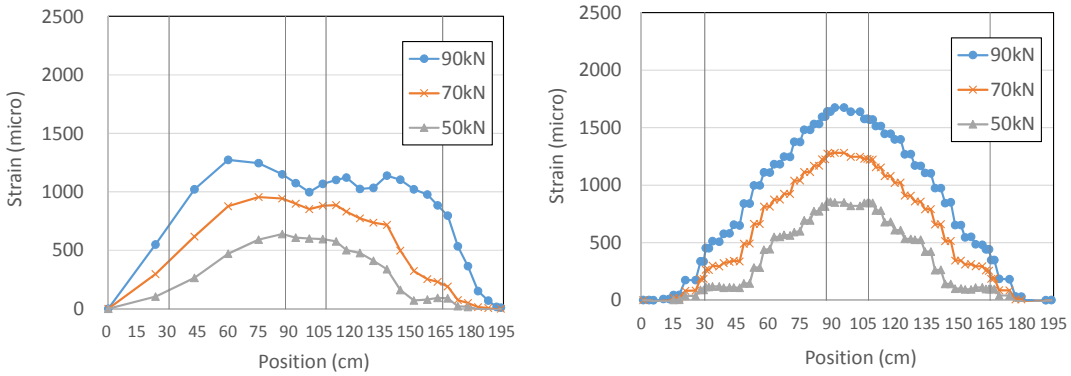

(a) Experiment **(b) Analysis**

Figure 7. Steel strain distribution along the beam axis (C60)

Figure 7 shows the steel strain distribution along the main reinforcement in several load levels. In experiment, steel strain is constant beyond constant moment span due to the weakened bond strength. Pretty high steel strain is observed at

supporting point as the load increases. Even though the numerical analysis simulates developed strain profile in anchorage, smaller de-bonding effect is expected compared with experiment. Within the constant moment span, constant strain is calculated in lower load such as 50kN. In contrast, inclined strain profile is achieved in higher load level (70kN and 90 kN) because damages are induced asymmetrically. Figure 8 shows numerical result of steel strain distribution in case the amount of corrosion substance increases double. Increase of corrosion product results in the higher steel strain distribution. Because steel strain profile is somewhat different from that of experiment, there is a room for improvement of our model.

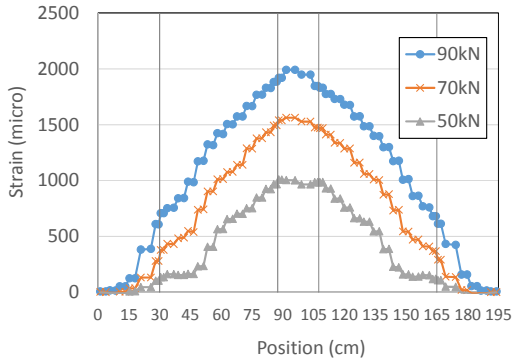

Figure 8. Numerical result of steel strain distribution in case of 16 % of weight loss due to corrosion

FATIGUE ANALYSIS

Sensitivity analysis is carried out regarding fatigue strength of corroded reinforcing beam. In this study, direct pass integral scheme is applied to simulate the progress of fatigue damage. Figure 9 shows the numerical results of center span deflections. However static shear strength of corroded beam is barely reduced, failure cycle of fatigue load decreases significantly. Compared with sound beam, fatigue life is shortened especially in case of lower repeated load as shown in Figure 10. This is because corrosion product is weak against cyclic slip. Kuroda *et al*. (2014) and Kivell *et al*. (2014) found the bond strength of corroded reinforcing bar drops drastically under

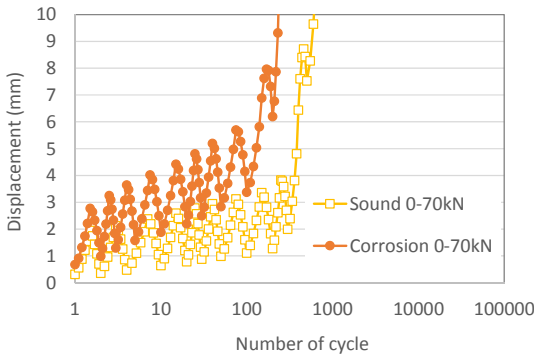

(a) 0 ~ 70 kN

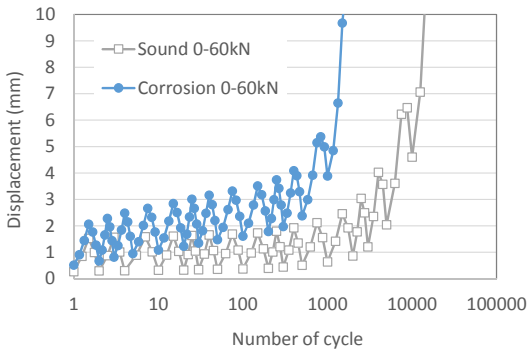

(b) 0 ~ 60 kN

Figure 9. Progressive displacement at the span center under the high cycle repetition of loads.

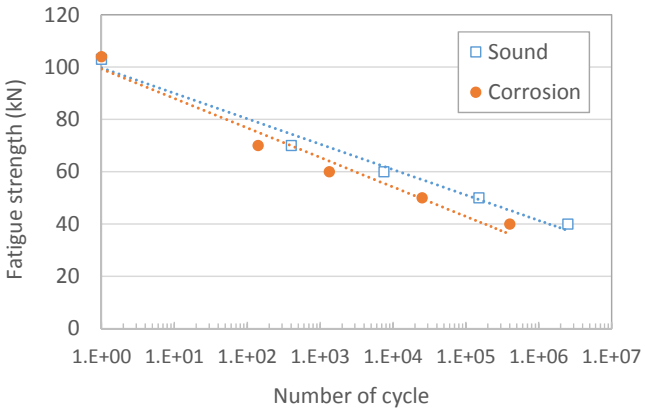

Figure 10. S – N diagram

the cyclic load in pull out test. Corrosion product easily migrates into crack under cyclic load condition. With use of poro-mechanics scheme, this phenomenon is consistently taken into account in the numerical simulation (Maeshima *et al*. 2014).

CONCLUSION

In this study, remaining performance of corroded reinforced concrete beams are numerically simulated with Poro-mechanics approach. By considering corrosion substance as the combination of liquid and solid phases, bond deterioration and remaining shear strength of corroded reinforced concrete beams are simulated successfully. Results of fatigue analysis pointed out that even if static shear strength is barely reduced, remaining fatigue life could be shortened significantly due to the degradation of bond strength under cyclic deformation.

ACKNOWLEDGEMENT

Authors appreciate Dr. Murakami who provided us the experimental data. This work was supported by Council for Science, Technology and Innovation (CSTI), Cross-ministerial Strategic Innovation Program (SIP), “Maintenance, renewal and management of infrastructure” (Funding agency: JST).

REFERENCES

Coronelli, D. and Gambarova, P. (2004). “Structural assessment of corroded reinforced concrete beams: Modeling guidelines” *J. Structural Engineering*, 130(8), 1214-1224.

Kallias, A. N. and Rafiq, M. I. (2010). “Finite element investigation of the structural response of corroded RC beams” Engineering Structures, 32(9), 2984-2994.

Kanaduka, T., Ogawa, K. and Murakami, Y. (2011). *Proceedings of JCI*, 33(1), 833-838.

Kivell, A., Palermo, A. and Scott, A. (2014). "Complete model of corrosion-degraded cyclic bond performance in reinforced concrete" *J. Struct. Eng.*, ASCE, 04014222-1-9.

Kuroda, (2014). "Bond behavior of corroded re-bars under alternative loads" Proc. the 15th JSMS symposium on concrete structure, 655-660.

Maekawa, K., Pimanmas, A. and Okamura, H. (2003). "Nonlinear mechanics of reinforced concrete" Spon press

Maekawa, K. and Fujiyama, C. (2013a). "Crack Water Interaction and Fatigue Life Assessment of RC Bridge Decks" *Poromechanics V*, ASCE, 2280-2289.

Maekawa, K. and Fujiyama, C. (2013b). "Rate-dependent model of structural concrete incorporating kinematics of ambient water subjected to high-cycle loads" *Engineering computations*, 30(6), 825-841

Maeshima, T., Koda, Y., Tsuchiya, S. and Iwaki, I. (2014) "Influence of corrosion of rebars caused by chloride induced deterioration on fatigue resistance in RC road deck" *J. JSCE E2*, 70(2), 208-225.

Tran, K. K., Nakamura, H., Kawamura, K. and Kunieda, M. (2011). "Analysis of crack propagation due to rebar corrosion using RBSM" *Cement & Concrete Composite*, 33, 906-917.

Simulation of Long-Term Stress and Deflection of Concrete Structures Based on Precise Considerations of Environmental Action

T. Shimomura

Department of Civil and Environmental Engineering, Nagaoka University of Technology, Nagaoka, Niigata 940-2188, Japan. E-mail: takumi@nagaokaut.ac.jp

Abstract

A numerical simulation system for long term stress and deflection of concrete structures is developed. Environmental actions on structures, which are temperature, humidity, rain fall, sunlight and their time-dependent changes, are precisely considered. Time-dependent behaviour of concrete member is calculated by the moisture transport and drying shrinkage model based on pore structure of concrete. Coupled transport model of heat, vapour and liquid water in concrete pore structure is employed. In addition, capillary suction from the surface, condensation of vapour on the surface and acceleration of evaporation by direct sunlight are taken into account. Automated Meteorological Data Acquisition System provided through Internet is utilized to evaluate climatic action. It is demonstrated that time-dependent change of moisture content, free shrinkage of concrete specimen and deflection in prestressed concrete beam under natural environmental action and sustaining load can be adequately simulated.

INTRODUCTION

In order to predict long term stress and deflection of concrete structures rationally, time-dependent moisture loss and associated shrinkage of concrete and their spatial distribution under the given service condition should be evaluated. In particular, to precisely predict moisture content in actual concrete structures under natural condition, it is significant to evaluate time-dependent hydrothermal conditions adequately. For instance, temperature and humidity varies daily and seasonally. Drying on the top surface of structure is accelerated by sunlight. On the other hand, the surface subjected to rainfall absorbs water by capillary suction. When atmospheric temperature rapidly changes, condensation of water takes place on the concrete surface, which makes concrete wet. Therefore, to evaluate drying and wetting behaviour of concrete under natural environment, these effects should be adequately taken into account in the calculation.

A methodology to model environmental action on structures was developed in the previous study, considering hydrothermal actions including time-dependent temperature, humidity, rain fall and solar radiation (Shimomura 2014). The developed environmental action model can create input data for calculation of time-dependent behaviour of concrete member by means of the moisture transport and drying

shrinkage model based on pore structure of concrete (Shimomura 1993, 1997). In addition, capillary suction from the surface, condensation of vapour on the surface and acceleration of evaporation by sunlight were taken into account (Thynn 2009).

To generally predict long term behaviour of actual concrete structures, environmental action on the target structure at the service location should be adequately considered. In other words, it is necessary to assess environmental action on the structure and transform them into the boundary condition to be adopted in numerical analysis of the structure. In this study, Automated Meteorological Data Acquisition System (AMeDAS), which is provided by Japan Meteorological Agency (JMA) through Internet, is utilized to create environmental action model.

ANALYTICAL METHOD

Outline of the computational system. Figure 1 shows outline of the developed computational system for long term moisture transport and drying shrinkage of concrete structure under real environment. The system consists of moisture transport and drying shrinkage model within concrete, model for local hydrothermal conditions of structure and model for climatic action.

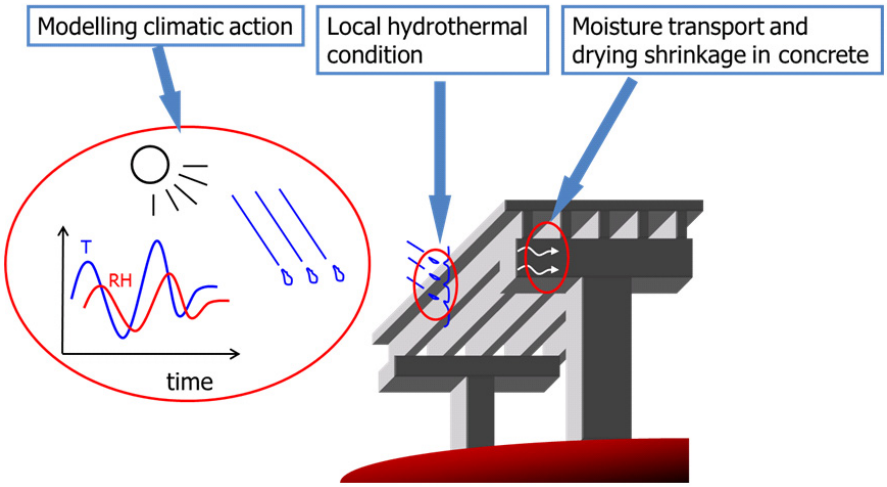

Figure 1. Outline of the computational system.

Moisture transport and drying shrinkage model for concrete. Time-dependent moisture content and drying shrinkage of concrete structural member is calculated by the computational model, whose outline is shown in Figure 2. Transport of water in concrete pore structure, drying shrinkage of cement paste and mechanical interaction between cement paste and aggregate in concrete are considered. The core model for moisture transport and drying shrinkage in nonsaturated concrete under ordinary atmosphere is on the basis of pore structure of concrete and thermodynamic behaviour of vapour and liquid water (Shimomura 1993, 1997). In addition, capillary suction from the surface was also taken into account (Thynn 2009). When concrete surface is exposed to the air, transport of vapour through the boundary surface is driven by hydrothermal gradient between the exposed surface and the atmosphere and transport of water within concrete was calculated by diffusion model in nonsaturated

concrete. When concrete surface directly contacts with liquid water due to rainfall, capillary suction from the surface becomes dominant. Then, transport of liquid water through the boundary surface and within concrete was calculated by the capillary suction model in partially saturated concrete instead of diffusion model. Cyclic drying and wetting behaviour of concrete under natural environment can be simulated by alternatively using the diffusion model and the capillary suction model.

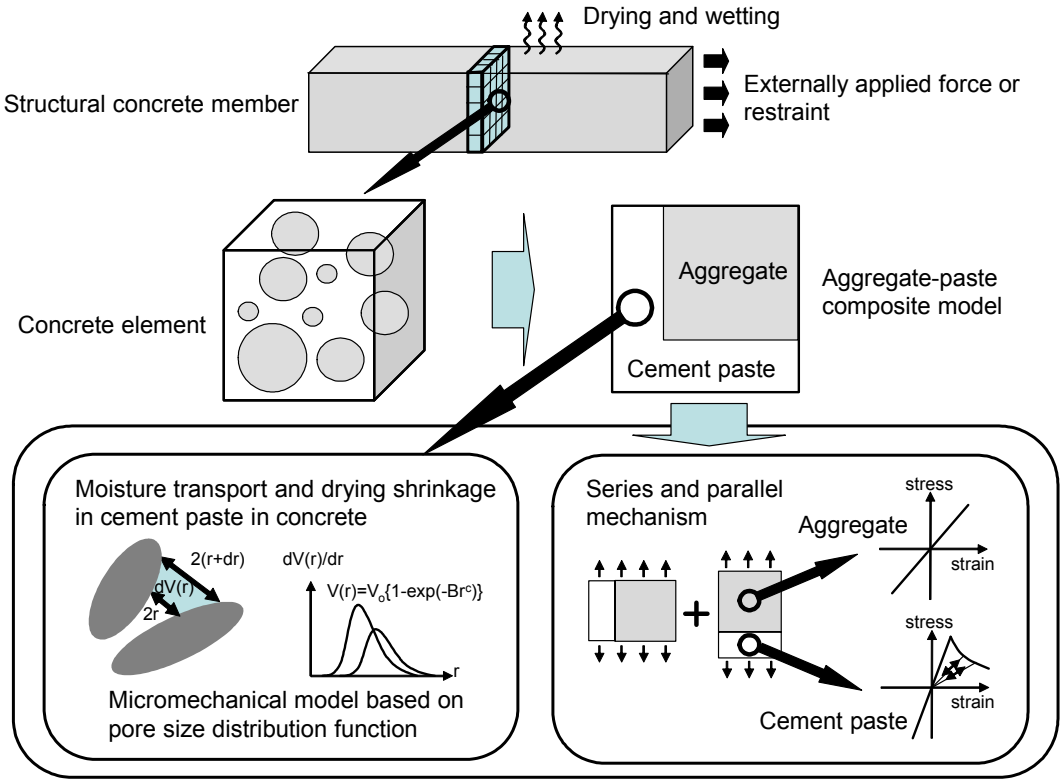

Figure 2. Moisture transport and drying shrinkage model for concrete.

Unrestrained drying shrinkage of cement paste in concrete is calculated according to moisture content. Stress and deformation analysis of structural member is carried out based on aggregate-cement paste composite model (Obata 1999, Shimomura 2013). Aggregate in concrete plays both roles to resist shrinkage and deformation of cement paste and to reduce shrinkage and deformation of concrete according to its volume fraction in concrete. The former is parallel mechanism and the latter is series one. To express both mechanisms are effective in shrinkage problem, series-parallel composite model was employed. Aggregate is treated as linear elastic material. Tensile strain softening of cement paste is considered.

Modelling local hydrothermal condition. Concrete under natural environment is subjected to rainfall, sunlight in addition to time-dependent change of atmospheric temperature and humidity. The effect of rainfall can be expressed in terms of capillary suction from the concrete surface during raining. The sunlight and time-dependent change of the atmospheric temperature and humidity influence dying and wetting behaviour of concrete by changing local hydrothermal condition near the surface of

concrete as following mechanisms. The surface temperature of concrete under natural environment does not always correspond with the atmospheric temperature. Since the saturated partial pressure of vapour depends on absolute temperature, local relative humidity near the concrete surface can be estimated as following equation.

$$RH_s = \frac{p_v}{p_{vos}} = RH_a \times \frac{p_{vo}}{p_{vos}} \quad (1)$$

where RH_s is relative humidity near the concrete surface, p_v is partial pressure of vapour, p_{vos} is saturated partial pressure of vapour near the surface, RH_a is atmospheric relative humidity and p_{vo} is saturated partial pressure of vapour of the atmosphere.

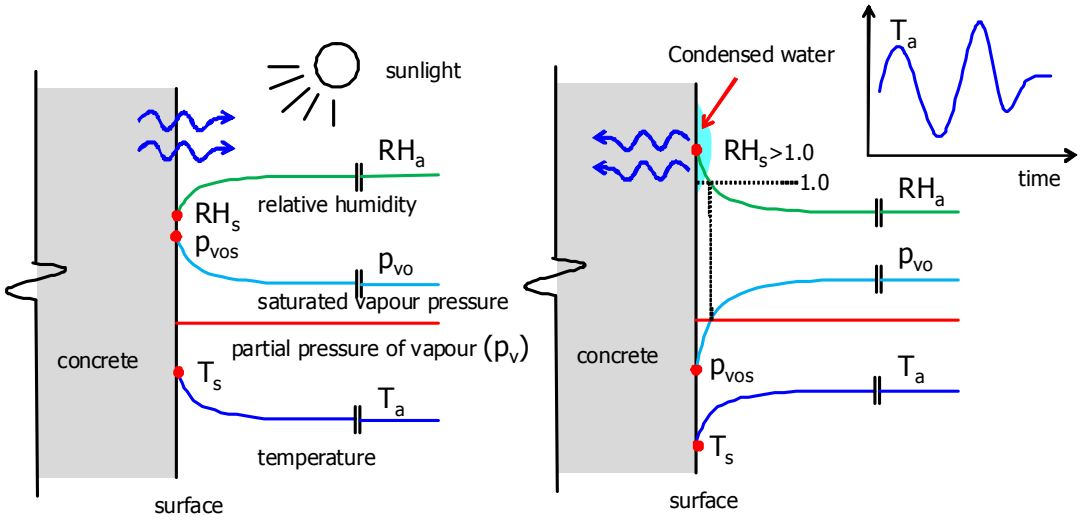

(a) Drying is accelerated by rising of surface temperature (b) Wetting with condensed water on the surface

Figure 3. Local hydrothermal condition near the concrete surface.

When the surface temperature of concrete becomes higher than the atmospheric temperature by heating effect by sunlight as illustrated in Figure 3 (a), relative humidity near the concrete surface becomes lower than the atmospheric relative humidity and consequently drying of concrete is accelerated than estimated from the atmospheric relative humidity. On the contrary, when the surface temperature becomes lower than the atmospheric temperature due to the time-dependent change of atmospheric temperature, relative humidity near the concrete surface becomes higher than the atmospheric relative humidity and consequently drying of concrete is retarded or adsorption is accelerated. In particular, when the evaluated relative humidity near the concrete surface becomes over 100% as in Figure 3 (b), condensation of water takes place on the surface and concrete become wetting. The condensed water is considered to be absorbed into concrete by capillary suction mechanisms.

As discussed above, surface temperature of concrete is important to calculate drying and wetting behaviour of concrete under natural environment because local hydrothermal condition near the concrete surface is dependent of the surface temperature. However, in case of real structure, surface temperature is generally

unknown. Therefore, surface temperature of structure is estimated by heat transfer analysis. Boundary condition considering the effect of global solar radiation is:

$$\kappa \frac{\partial T}{\partial n} = -m(T_s - T_a) + R_n \quad (2)$$

where T is temperature, κ is thermal conductivity of concrete, T_s is surface temperature, T_a is atmospheric temperature and R_n is global solar radiation. Atmospheric temperature and solar radiation are either measured by a weather meter or given as public meteorological data.

Modelling climatic action. In Japan, real time meteorological data, as well as previous data, including atmospheric temperature and relative humidity, wind direction and speed, precipitation and global solar radiation at each measurement point every hour are provided through Internet from Automated Meteorological Data Acquisition System (AMeDAS) by Japan Meteorological Agency (JMA). Over 1300 measurement points are located about every 20km. Making use of this, a climatic action model to be adopted as input data for moisture transport analysis is created.

Temperatures, relative humidity, global solar radiations every hour in a day are averaged during one month. It is assumed that averaged hourly temperature is repeated every day in the month. In predicting drying and wetting behaviour in future, averaged hourly temperature calculated based on previous data is used. On the other hand, the length of time of raining is sensitive on the wetting behaviour of concrete, adequate length of drying-wetting cycle is determined based on sensitivity analysis (Shimomura 2014). The length of one cycle is determined so that raining time in each cycle shall be one hour.

EXPERIMENTAL VERIFICATION

Free shrinkage of concrete under natural environment. The size of specimen is 100x100x400 mm. Water cement ratio of concrete is 50 %. Specimens were cured for 49days within plastic bags. To investigate the sensitivity of influence of environmental action on unrestraint shrinkage of concrete, specimens were exposed to three environmental conditions: temperature controlled room, field exposure under roof and field exposure without roof. The characteristic of these three test conditions are shown in Table 1. During the field test, temperature, relative humidity and solar radiation were measured and recorded by a weather station equipped in the test field. The exposure test started in May 2014, the beginning of summer season.

Table 1. Test Conditions.

Test condition	Temperature	Humidity	Rainfall	Sunlight
Temperature controlled room	Constant 20 deg	Constant 60%RH	Not affects	Not affects
Field exposure (under roof)	Naturally changes	Naturally changes	Not affects	Not affects
Field exposure (without roof)	Naturally changes	Naturally changes	Affects	Affects

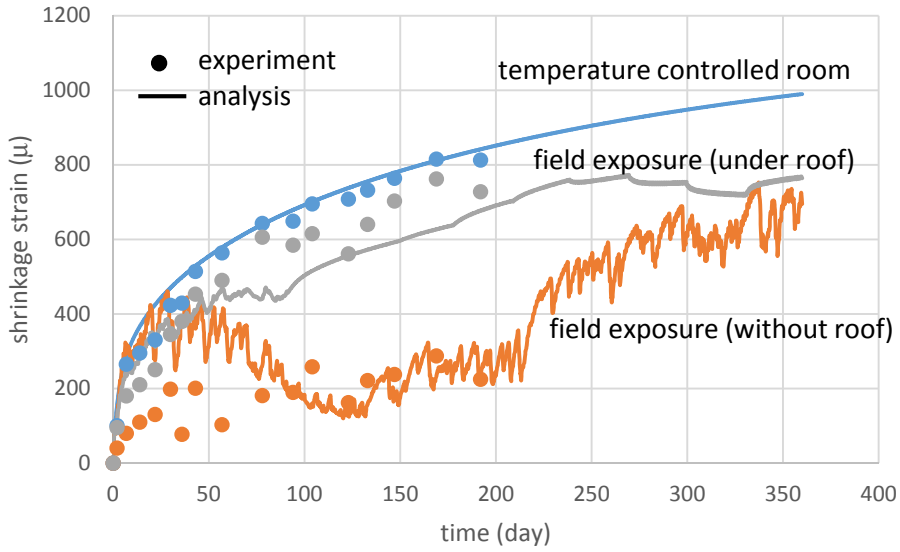

Figure 4. Shrinkage of unrestraint specimens.

Figure 4 shows experimental and analytical results of shrinkage strain of unrestraint concrete specimens. It is clear that shrinkage of concrete depends on local hydrothermal condition. Compared with temperature controlled room, shrinkage of concrete under natural environment is small. Shrinkage of the specimen without roof showed fluctuation due to wetting by rainfall and did not increase in winter, while it was accelerated in summer because of much snow in winter in the test location.

Sustaining loading test of PC beam under natural environment. Pretentioned prestressed concrete beam, whose size is 100x100x3000 mm with PC tendon (ϕ2.9x3) in the centroid of the cross section, was subjected to sustaining load and natural weather action. Figure 5 and 6 show setup of loading test. Applied sustaining load was controlled by weight of steel plates. Time-dependent deflection, strain of concrete and strain of PC tendon were measured. Temperature, relative humidity and solar radiation were measured and recorded by a weather station.

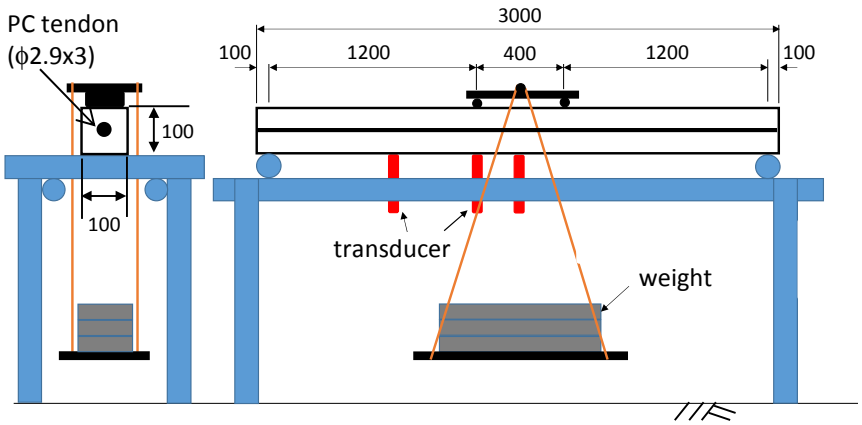

Figure 5. Setup of sustaining loading test of PC beam.

Figure 6. Sustaining loading test of PC beam under natural environment.

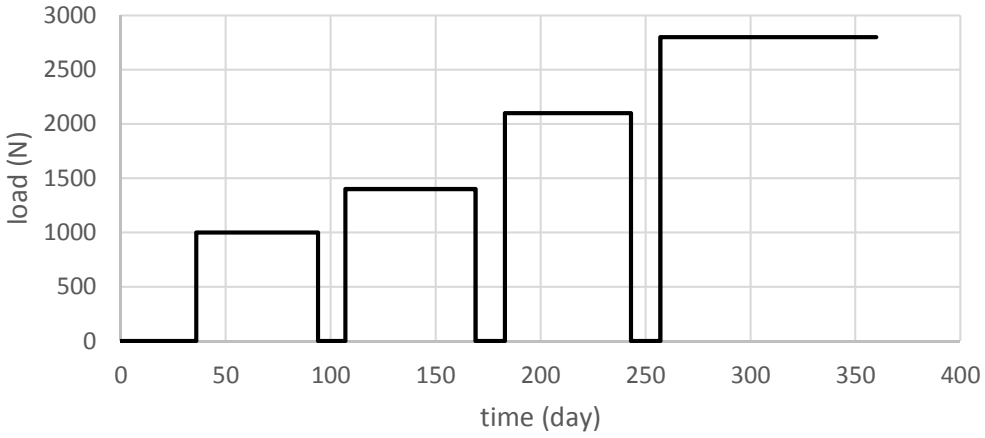

Figure 7. Loading path of PC beam.

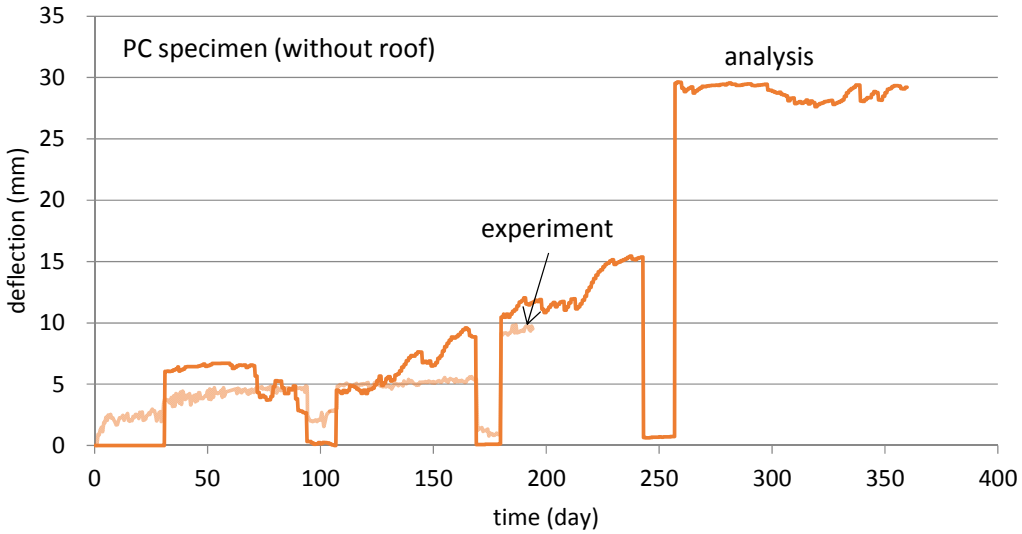

Figure 8. Deflection of PC beam.

Figure 7 shows loading path. Figure 8 shows experimental and analytical results of deflection at the mid span of the PC beam. Deflection of the beam gradually increased even during the applied load was kept constant. This is attributable to creep and shrinkage of concrete. Analytical results can adequately simulate experimental results of time-dependent deflection taking into account of actual hydrothermal action on the PC beam including temperature, relative humidity, rainfall and solar radiation.

CONCLUSION

The significance of considering actual environmental action on the structure in predicting shrinkage related behaviour of concrete structure was discussed in this paper. Computational system of moisture transport and shrinkage of concrete structure based on precise consideration of hydrothermal action was proposed. The adequateness of the proposed analytical method was demonstrated through simulation of experimental results of time-dependent deflection of PC beam subjected to sustaining load and natural weather action.

ACKNOWLEDGEMENT

The author expresses his gratitude to K. Onoya and T. Shiga, graduate students of Nagaoka University of Technology, for their contribution to this work. This work was supported by JSPS Grants-in-Aid for Scientific Research, Grant Number 25289131.

REFERENCES

Obata, H. and Shimomura, T. (1999), "Time-dependent stress analysis of concrete member by aggregate-paste composite model", *Transactions of the Japan Concrete Institute*, (21), 135-142.

Shimomura, T. and Maekawa, K. (1993) "Micromechanical model for drying shrinkage of concrete based on the distribution function of porosity", *Proceedings of the Fifth International RILEM Symposium on Creep and Shrinkage of Concrete*, 133-138.

Shimomura, T. and Maekawa, K. (1997) "Analysis of the drying shrinkage behaviour of concrete using a micromechanical model based on the micropore structure of concrete", *Magazine of Concrete Research*, 49 (181), 303-322.

Shimomura, T, Aoki, Y. and Obata, H. (2013) "Simulation of time-dependent tensile behavior of concrete under various loading and drying path". *Proceedings of the 9th International Conference on Creep, Shrinkage and Durability Mechanics*, CONCREEP-9, 421-428.

Shimomura, T. Onoya, K. and Thynn Thynn H. (2014) "Modelling of environmental action for simulation of long term variation of moisture content in concrete structures", *Proceedings of the 1st International Conference on Aging of Materials and Structures*, 416-423.

Thynn Thynn H. and Shimomura T. (2009) "Hybrid computational method for capillary suction and nonsaturated diffusion in concrete", *Proceedings of the 4th International Conference on Construction Materials*, 1075-1080.

Anomalies of Shrinkage and Tensile Creep of Concrete

H. W. Reinhardt

Department of Construction Materials, University of Stuttgart, Pfaffenwaldring 4, 70569 Stuttgart, Germany. E-mail: reinhardt@iwb.uni-stuttgart.de

Abstract

Experiments have shown that shrinkage of concrete is larger in those specimens which are loaded in tension compared to non-loaded specimens. The hypothesis is that this is a consequence of microcracking and increase of water diffusivity. Water diffusivity is indeed increased by tensile loading as several researchers have demonstrated. That shrinkage is increased by tensile loading is in contradiction to other theories which state that surface cracking is caused by eigenstresses during drying and thus the shrinkage strain is reduced. Several experimental series have been carried out on concretes with various strength and composition which have confirmed the phenomenon. Another phenomenon has been observed on concrete which was mixed with superabsorbent polymers (SAP). Super-absorbent polymers are a new class of admixture. They absorb a manifold of water compared to the own weight. Mixed in concrete, they store the water and release it during the hydration of cement. They can be used for internal curing of high-performance concrete, further, they can heal cracks and can make concrete more impervious. Tensile creep tests have been performed on dogbone shaped specimens. It appeared that tensile creep of SAP modified concrete was considerably reduced while shrinkage was not. The reason for this behavior is attributed to self-healing of microcracks. Results will be shown and discussed.

INTRODUCTION

Shrinkage of concrete is a well investigated phenomenon. There are several causes for shrinkage: chemical shrinkage is the consequence of the smaller volume of hydration products compared to the original volume of cement and water, autogenous shrinkage is mainly due to self-desiccation of hydrating cement paste, carbonation shrinkage takes place when the hydrated cement paste takes up carbon dioxide from the ambient air and carbonates, and finally, drying shrinkage follows from the loss of water during drying. Only drying shrinkage will get attention in this contribution. Drying is a time dependent diffusion process and, thus, also dependent on the size of the specimen or structural member. A large member will dry slower and will exhibit large differences of moisture content between the surface and the core. The consequence are eigenstresses with tension at the surface and compression at the core. The tensile stresses can be so large that cracking occurs which has been

discussed by Rossi and Acker (1988), Wittmann (1993), Alvaredo (1994) and others. Surface cracks reduce the measured shrinkage. Bažant and Chern (1985) postulate that shrinkage decreases linearly with tensile stress.

However, tensile creep tests have revealed another phenomenon, i.e. shrinkage of loaded specimens appeared to be larger than shrinkage of non-loaded specimens. This phenomenon will be discussed in the following. Moreover, concrete with superabsorbent polymers (SAP) has been investigated in creep and shrinkage experiments. They show a distinct influence of the water which is stored in the SAP.

EXPERIMENTAL EVIDENCE

The first publication which addresses the load-induced drying was by Alexandrovsky and Desov (1968) who have noted that the moisture loss in loaded specimens was larger than in unloaded specimens. The authors have compared the moisture loss of free shrinkage specimens with the moisture loss of specimens which were restrained at the ends. Due to shrinkage, tensile stresses build up in the restrained specimens. The stressed specimens showed a moisture loss which was about 10% larger than that of non-loaded specimens after 60 days (Fig. 1). Unfortunately the authors did not indicate concrete composition and strength and specimen cross-section. The only value they gave is the tensile strength of 1.96 MPa and the tensile stress which developed gradually from zero to 1.8 MPa after 60 days.

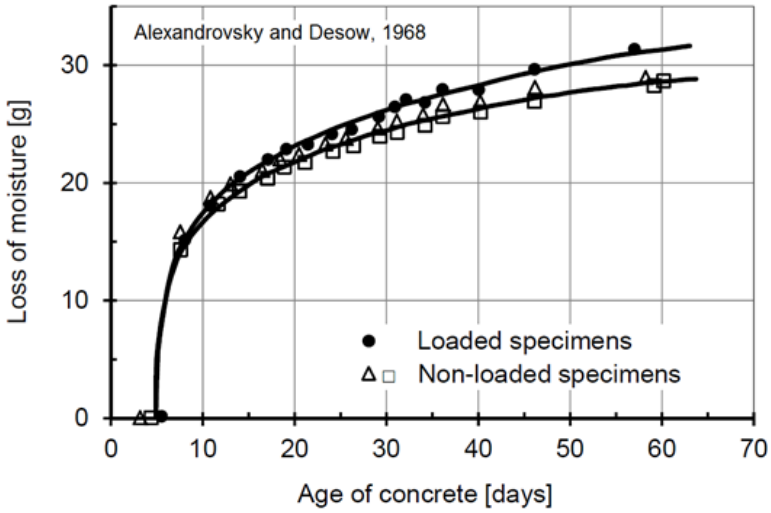

Figure 1. Moisture loss of loaded (top) and non-loaded specimens (bottom) (Alexandrovsky & Desov 1968)

Reinhardt and Rinder (2006) carried out tensile creep tests on high-strength concrete. They found that loaded concrete specimens exhibited a large reduction of strain during the first 200 days of loading, i.e. larger negative strains (contraction) than positive strains (extension). Fig. 2 shows results of three types of concrete which were wrapped in foil in order to prevent quick drying. The test should simulate a thick-walled structure.

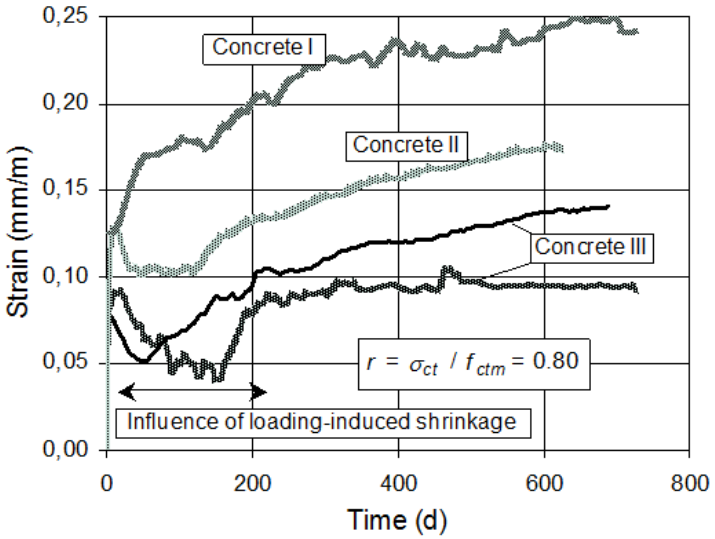

Figure 2. Total strain minus free shrinkage (Reinhardt & Rinder 2006)

The plotted strain is the total measured strain minus shrinkage strain which has been measured on non-loaded companion specimens in the same climate controlled room also wrapped in foil. The applied stress amounted to 80 % of the mean tensile strength. Concrete I (f_{cm} = 80 MPa) exhibits continuously increasing strain which is due to creep. The strain at origin conforms to the initial strain at loading on 28 days. Concrete II (f_{cm} = 95 MPa) and III (f_{cm} = 107 MPa) reveal a distinct bump between 0 and 200 days which can only be explained by excessive shrinkage.

Wüstholz and Reinhardt (2007) and Reinhardt and Wüstholz (2009) performed similar tests on self-compacting concrete with stress/strength ratios of 55 and 69 % and mean compressive strength between 41 and 78 MPa, resp. on wrapped specimens. An example of the test results is shown in Fig. 3.

The figure shows the total strain of the loaded specimen and the strain of non-loaded companion specimen as measured. One can see that the total strain, which comprises elastic, creep and shrinkage strain, is positive (elongation) up to 100 days. Thereafter, the total strain becomes negative. In order to estimate the shrinkage part of the loaded specimen the creep part has been calculated with the formulas given in *fib* Model Code (2010) under the assumption that tensile creep is equal to compressive creep, except the sign (which is discussed contradictorily in the scientific community (Hilaire et al. 2013). Since the humidity in der wrapping has been measured which varied between 50 and 80 % three values were calculated. Fig. 3 shows in the upper part the progress of ($\varepsilon_{el} + \varepsilon_{cr}$) which should be equal to ($\varepsilon_{tot} - \varepsilon_{s}$). There is a great discrepancy. Subtracting ($\varepsilon_{el} + \varepsilon_{cr}$) from the measured ε_{tot} one observes that the shrinkage part comes out to be considerably larger than the measured shrinkage on non-loaded specimens. That means that the loaded specimen shrinks more. This effect is called stress-induced shrinkage.

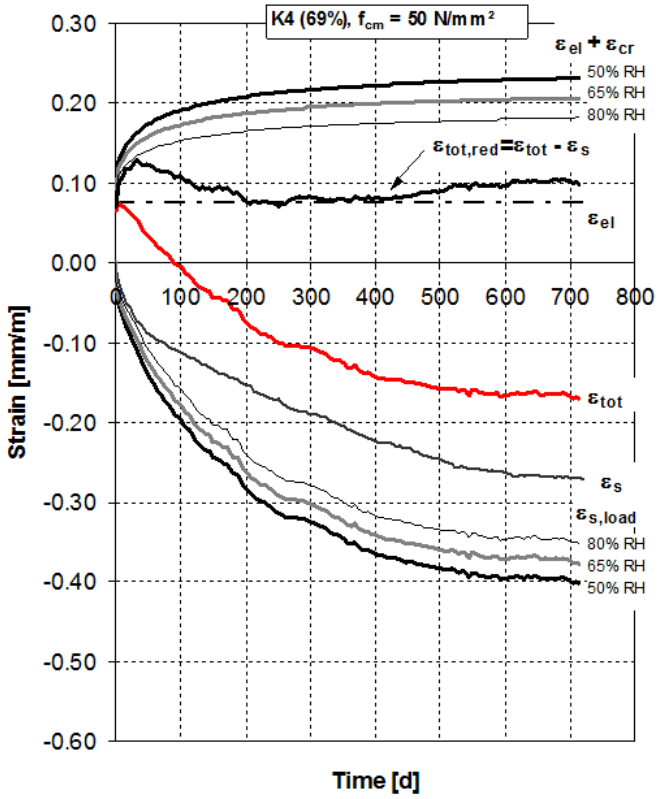

Figure 3. Development of strains of specimen K4 vs. time (Wüstholz & Reinhardt 2007)

POSSIBLE EXPLANATION OF STRESS INDUCED SHRINKAGE

The assumption is made that tensile loading promotes the movement of water in concrete and, in consequence, promote shrinkage. To this end, a few relevant publications will be cited. Gérard (1996) reports on tests in which the water permeability has been investigated in the so-called BIPEDE device (Bresse et al. 1994). The device allows to control tensile strain up to 1.3E-3. Of course, cracking occurs at such a high strain, however, if the first part of the diagram is evaluated one observes that the permeability increases from beginning of strain when only micro-cracks can form. The tests by Reinhardt, Rinder and Wüstholz had a tensile strain in the creep tests which ranged between 0.06 and 0.12E-03. The tests by Gérard showed an increase of permeability between non-loaded specimens and specimens strained with 0.1E-03 of a factor of about 80. Of course, water permeability is not equal to diffusivity which governs the movement of water in concrete but there is an empirical relation coupling both properties. Nilsson and Tang (1995) have evaluated literature data and found a power law between permeability and diffusivity in the sense that the diffusivity decreases when permeability decreases. For water vs. water vapor, the power was established to 1.8. Gaber (1988) suggested a power of 2.3. With the sake of simplicity, one can state that there is a quadratic relation between permeability and diffusivity K and the diffusivity D:

$$K \sim D^2 \tag{1}$$

The tests by Gérard mean that the diffusivity has increased by a factor of $80^{½}$ when the permeability increased by a factor of 80.

Tests on bending beams have been performed by Feng et al. (2005) where the chloride penetration in the uncracked tensile zone has been measured. The authors found a power law between diffusivity and flexural stress which indicates its great influence. Wittmann (Wittmann & Zaytsev 2013) reported a decrease of diffusivity with compressive stress and an increase of diffusivity with tensile stress.

Although the findings give only an indication one must conclude that tensile strains promote the water movement in concrete. Rossi et al. (2012) have stated "…the assumption is made that basic creep of concrete is mainly due to microcracking which induces additional self-drying shrinkage". Rossi et al. (2012) have followed tensile creep by acoustic emission and they have proven that microcracking occurs during sustained loading. Most acoustic events occurred when the load was applied, i.e in the most wet state. When microcracks are formed the water is redistributed to the microcracks (Rossi et al. 2012, Rossi & Tailhan 2013). This has been two consequences: first, the water can escape from the concrete easier due to the larger diffusivity and, second, the microcracks generate new surfaces in unhydrated cement grains which hydrate. Both aspects have been measured in (Reinhardt & Rinder 2006).

The load induced shrinkage occured in the first 200 days of creep tests which is a confirmation of the proposed mechanism.

SHRINKAGE AND TENSILE CREEP OF SAP MODIFIED CONCRETE

When superabsorbent polymers (SAP) are mixed in concrete they absorb water in the fresh state and release it during hydration (Mechtcherine & Reinhardt 2012). One can assume that the presence of this water will influence the water migration and also the microcracking of concrete. This should have a measurable impact on shrinkage and creep.

Tests have been carried out on concrete with and without SAP (details are given in (Assmann & Reinhardt 2014). The reference composition had a water/cement ratio of 0.42 and 0.36 resp. while the SAP modified concrete had a basic w/c of 0.36 and a water entrainment of 0.06, i.e. the total w/c was 0.42. The 28 d cube strength amounted to 62.8, 75.3 and 63.4 MPa resp. while the tensile strength was 4.38, 4.99 and 4.42 MPa, resp. The creep specimens were loaded to 60 % of 28 d tensile strength. One group of the specimens was wrapped in PE foil to simulate gentle drying while the other group was sealed with aluminum foil. The first specimens would give results on autogenous shrinkage + drying shrinkage + basic creep + drying creep and the second would lead to autogenous shrinkage + basic creep. Non-loaded companion specimens were used for shrinkage measurements. Fig.4 shows the results.

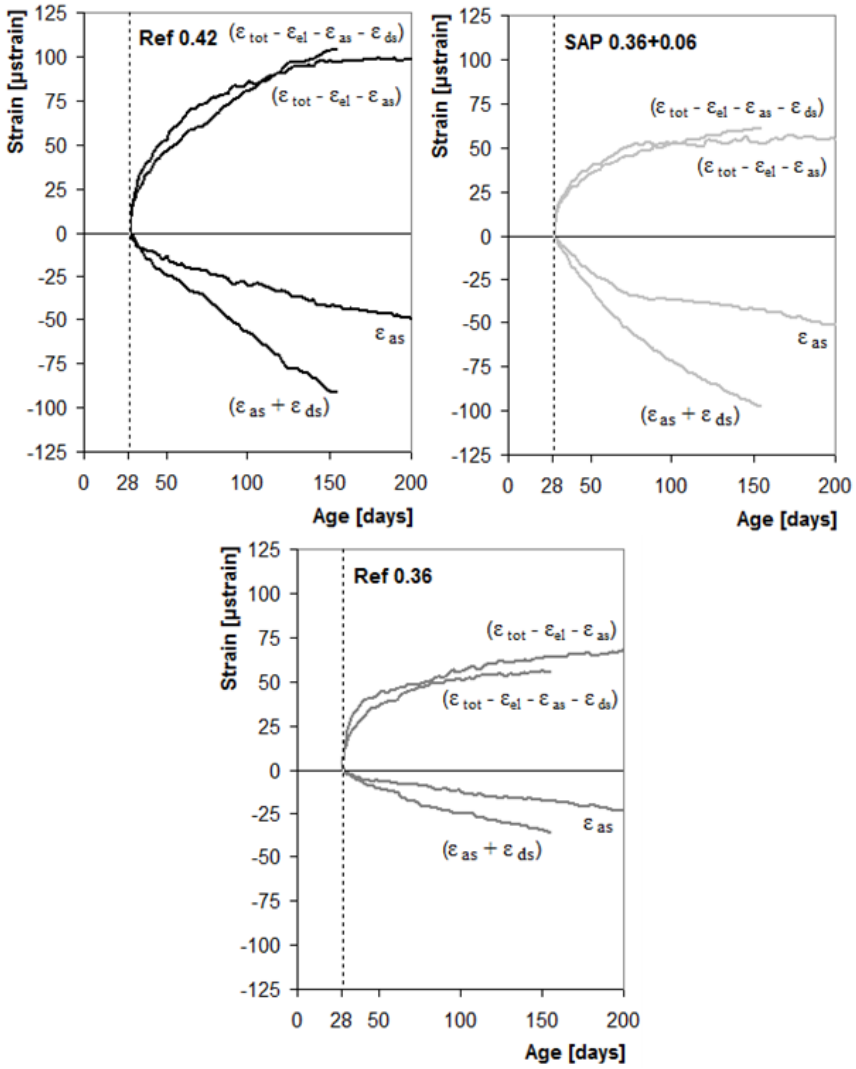

Figure 4. Creep and shrinkage strain vs. age zeroed at loading (Assmann & Reinhardt 2014)

The diagrams contain the strains after loading without the initial strain and without shrinkage strain before loading. The creep strains show little difference between the sealed and wrapped concrete. The gentle drying did cause only a small contribution to the strain. However, it seems that the wrapped specimens would lead to larger creep at longer times because the gradient is steeper. The top right figure for SAP 0.36 + 0.06 shows similar progress of shrinkage as Ref 0.42. The water content of both concretes is the same. A large difference occurs for creep. The SAP 0.36 + 0.06 concrete creeps much less than the Ref 0.42 concrete although the strength is almost the same. The creep strains of Ref 0.36 (bottom figure) are the smallest as expected since the strength is the highest. The creep strains of Ref 0.36 and SAP 0.36 + 0.06 are similar while the shrinkage is rather different.

This behavior is attributed to the avoidance of microcracking due to SAP. SAP creates a water reservoir in concrete which is emptied during hydration when the free water has been taken up. This water can counteract self-desiccation. On the other

hand if microcracks would occur the water can promote self-healing which has been shown by Snoek et al. (2012). Their experiments have shown that SAP can heal cracks up to 130 µm within 30 days. They found an average healing rate of 5 µm/d, i.e. a microcrack of 5 µm width would heal within about one day.

One can conclude that creep is governed by the basic water/cement ratio while shrinkage depends on the total w/c. Stress-induced shrinkage has not been observed with these tests. Both observations support the assumption that microcracking is one important cause of excessive shrinkage due to higher diffusion on the one hand and reduction of tensile creep on the other due to self-healing.

CREEP AND CRACKING

Previous researchers have also discussed the role of cracking on creep and shrinkage, they came to different conclusions. Ward and Cook (1969) state that "microcracking creep" increase the tensile creep rate. Microcracking is attributed to the effect of shrinkage when specimens are stored from wet to dryer environment. It is also mentioned that differential shrinkage can be the cause for larger creep rate. Bissonnette et al. (2007) could not confirm the presence of microcracks although they loaded the specimens to 50 % of tensile strength. Altoubat and Lange (2002) investigated the so-called Pickett effect, i.e. the increase of creep due to drying. They separated the stress induced shrinkage from microcracking. However, the case they treated refers to surface cracking due to eigenstresses. This is not the same as what has been shown above. Rossi et al. (2012) state that "basic creep strain is proportional to the total number of microcracks created in the material" and "basic creep is mainly an additional self-drying shrinkage under stress". So, it is postulated that creep and cracking occur at the same time and cannot be separated.

CONCLUSIONS

1) There is strong experimental evidence that specimens which are loaded in tension shrink more than non-loaded companion specimens.
2) Literature data confirm the presence of microcracks in tensile members.
3) These microcracks lead to large increase of water permeability and vapor diffusivity.
4) Loaded specimens can dry out faster and exhibit extra shrinkage. This additional shrinkage is called stress-induced shrinkage.
5) Tensile creep tests on concrete with superabsorbent polymers (SAP) have shown that the extra water which is stored in the SAP reduces tensile creep considerably. It is assumed that microcracks can heal and that continuing hydration takes place.
6) The findings support the assumption by Rossi et al. that microcracking is an important aspect of tensile creep.
7) More experiments are necessary to validate the data. It is recommended to investigate the influence of strength class of concrete on stress-induced shrinkage and the effect of superabsorbent polymers on compressive creep.

ACKNOWLEDGEMENT

The author is indebted to his former students T. Rinder, T. Wüstholz and A. Assmann for their valuable contributions.

REFERENCES

Alexandrovsky, S.W., Desov, A.E. *Some characteristic properties of wet strains in concrete*. RILEM Symp. "The shrinkage of hydraulic concretes", III-G, Madrid, March 1968, pp. 1-33

Altoubat, S.A., Lange, D.A. *The Pickett effect at early age and experiment separating its mechanisms in tension*. Materials & Structures 35(2002), No. 5, pp. 211-218

Alvaredo, A.M. *Drying shrinkage and crack formation*. ETH Building Materials Reports No. 5, Aedificatio Freiburg 1994

Assmann, A., Reinhardt, H.W. *Tensile creep and shrinkage of SAP modified concrete*. Cement and Concrete Res. 58 (2014), pp. 179-185

Bazant, Z.P., Chern, J.C. *Concrete creep at variable humidity: constitutive law and mechanism*. Materials and Structures 18 (1985), No. 103, pp. 1-20

Bissonnette, B., Pigeon, M., Vaysburd, A.M. *Tensile creep of concrete. Its sensitivity to basic parameters*. ACI Materials Journal 104 (2007), No. 4, pp.360-368

Bresse, D., Gérard, B., Lasne, M. *An experimental device to study cracking and deterioration of concrete*. 3rd CANMET/ACI Int. Conference on duralility of concrete, Nice 1994, pp. 5-1994

Feng, X., Leng, F.-g., Feng, N.-q. *Chloride diffusivity of plain concrete subjected to sustained flexural loading*. Proc. Int. Workshop CMCL, Quingdao, China 2005, pp. 133-137

fib Model Code 2010, Bulletin 55, Vol. 1, Lausanne 2010

Gaber, K. *Influence of mix proportions and components on the diffusion coefficient and permeability of concrete*. Darmstadt Concrete 3 (1988), pp. 39-48

Gérard, B. *Contribution of mechanical-chemical-transfer couplings for long term storage facilities for radioactive waste* (in French), PhD thesis LMT Cachan, ENS/CRNS, Univ. Paris 6, 1996

Hilaire, A., Benboudjema, F., Darquennes, A., Bertaud, Y., Nahas, G. *Analysis of concrete creep in compression, tension and bending: Numercal modeling*, In F.-J. Ulm, H.M Jennings, R. Pellenq " (Eds.) Mechanics and physics of creep, shrinkage, and durability of concrete" (Concreep-9), ASCE, Reston 2013, pp. 348-355

Mechtcherine, V., Reinhardt, H.W. "Application of superabsorbent polymers (SAP) in concrete construction". RILEM State-of-the-Art Reports Vol. 2, Springer, Dordrecht 2012

Nilsson, L.-O., Tang, L. *Relations between different transport parameters*. In Kropp, J., Hilsdorf, H.K. (Eds.) Performance criteria for concrete durability, RILEM Report 12, E&FN SPON, London 1995, pp. 15-32

Reinhardt, H.-W., Rinder, T. *Tensile creep of high-strength concrete*. J. Advanced Concrete Technology 4 (2006), No. 2, pp. 277-283

Reinhardt, H.W., Wüstholz, T. *Stress induced shrinkage of concrete in tension*. In Tanabe, T.-a., Sakata, K., Mihashi, H., Sato, R., Maekawa, K., Nakamura, H. (Eds.) Creep, shrinkage and durability mechanics of concrete structures. Francis & Taylor, London 2009, pp. 65-71

Rossi, P., Acker, P. *A new approach to the basic creep and relaxation of concrete*. Cement and Concrete Res. 18 (1988), pp. 799-803

Rossi, P., Tailhan, J.-L., Le Maou, F., Gaillet, L., Martin, E. *Basic creep behavior of concretes investigation of the physical mechanisms by acoustic emission*. Cement and Concrete Res. 42 (2012), No.1, pp. 61-73

Rossi, P., Tailhan, J-L. *Macrocrack propagation in a concrete specimen subjected to a sustained loading: Influence of tensile creep*. In " Mechanics and physics of creep, shrinkage, and durability of concrete" (Concreep-9), ASCE, Reston 2013, pp. 332-339

Snoek, D., Van Tittelboom, K., De Belie, N., Steuoeraert, S, Dubruel, P. *The use of SAP as a crack sealing and crack healing mechanism in cementitious materials*, in M.G. Alexander, H.-D. Beushausen, Dehn, F., Moyo, P. (Eds.) Concrete repair, rehabilitation and retrofitting III, CRC Press 2012, pp. 58-59 and disc

Ward, M.A., Cook, D.J. *The mechanism of tensile creep in concrete*. Magazine of Concrete Research 21 (1969), No. 68, pp.151-158

Wittmann, F.H. *On the influence of stress on shrinkage of concrete*. In Z.P. Bazant and I. Carol (Eds.) Creep and shrinkage of concrete, E&FN SPON London 1993, pp. 151-157

Wittmann, F.H., Zaytsev, Y.V. *Application of fracture mechanics to investigate durability of concrete under load*. FraMCoS-8, CIMNE 2013, pp. 36-42

Wüstholz, T., Reinhardt, H.-W. *Deformation behaviour of self-compacting concrete under tensile loading*. Materials and Structures 40 (2007), No. 9, pp. 965-979

Decrease of Tensile Creep Response under Realistic Restraint Conditions in Structures

D. Schlicke[1]; K. Turner[2]; and N. V. Tue[1]

[1]Institute of Structural Concrete, Graz University of Technology, Lessingstraße 25/I, A-8010 Graz, Austria. E-mail: dirk.schlicke@tugraz.at
[2]Federal Waterways Engineering and Research Institute (BAW), Kußmaulstraße 17, D-76187 Karlsruhe, Germany. E-mail: katrin.turner@baw.de

Abstract

The creep behavior of concrete members is of major importance for their serviceability. Besides its negative influence on deflections under load impact, creep strains are supposed to positively reduce the hardening induced restraint stresses after temperature equalization - which is an essential assumption for today's design practice of neglecting the superposition of hardening induced restraint stresses with later restraint stresses during life time. A number of different experimental studies, however, have indicated that the assumed positive effect of creep is highly overestimated. This can mainly be explained by disproportionately diminishing tensile creep responses after relaxation under the maximum of all ever experienced tensile stresses. Based on detailed information on the experimental studies with passive restraint frames as well as comparative tensile creep tests, this contribution presents new insights on tensile creep behavior under realistic conditions in concrete structures.

PROBLEM DEFINITION AND OBJECTIVE

Different experimental studies indicated that the reduction of hardening induced restraint stresses by ongoing creep after temperature equalization is very limited. Today's common design practice of neglecting the superposition of hardening induced restraint stresses with later restraint stresses during service life may therefore not generally lead to results that are on the safe side, as schematically shown in Figure 1.

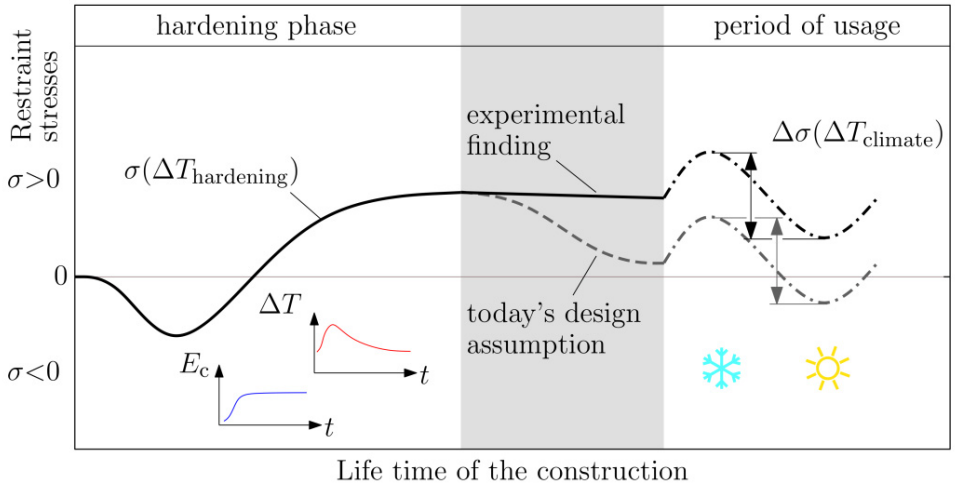

Figure 1. Stress history of a restrained concrete member.

As a result of this, structural damage often occur - especially in form of leaking cracks in watertight constructions. The reliable service life design of concrete structures therefore requires an all-embracing understanding of this context. This refers not only to pure material tests to quantify the difference between creep under compression and tension but also to the investigation of the real relaxation under realistic conditions of (always) only partially restrained concrete members.

State of knowledge

In the context of structural behavior, the creep response to restraint stresses leads to a decrease in the total stress level. In detail, the theoretical creep response of any restraint stresses is also restrained. And due to its reverse orientation compared to the initial restrained deformation impact the restrained creep leads to relaxation. Even though the total stress level decreases steadily, the member is still under stress and the creep response is assumed to continue. The quantity of the upcoming creep response, however, decreases progressively in relation to the total stress decrease. This slows the whole process down.

Intensive efforts have been made through until today to quantify the creep response in concrete mixtures. The experimental testing for this is mainly carried out for concrete under compression, largely due to the comparably simple procedure involved. The creep response under tension is usually assumed to be approximately identical to the creep response under compression (e.g. EC2). However, this was only confirmed by few experiments, e.g Kordina (2000).

With respect to the importance of tensile creep on the reduction of hardening induced restraint stresses, there is a current increase in the number of creep tests being carried out to compare the creep response under compression as well as under tension (e.g. THAILHAN ET. AL). The underlying experiments were usually carried out as pure material tests, performed by monitoring the deformation increase under a constant stress level. Furthermore, recent investigations by SCHLICKE (2014) indicated a significant importance of the influence of realistic restraining conditions on the relaxation to be expected in real concrete members.

Hypothesis

The creep behavior of concrete differs fundamentally for partial unloading under compression and tension. Partial unloading under compression leads to a decreasing of the creep responses, but they will still continue according to the remaining total stress level and loading duration. In contrast, the creep responses under tension diminish disproportionately when the total stress level falls below the maximum of all the tensile stresses that are ever experienced. Figure 2 provides a schematic impression of this.

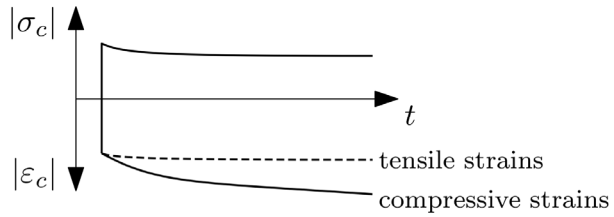

Figure 2. Hypothesis of creep strains to be expected after partial unloading.

The reason for this behavior is presumed to originate in (at least) partially different driving forces for creep under compression and tension. Creep under compression is well known as an effect mainly resulting from movement of unbound water in the cement paste in compressed concrete. However, creep under tension is not totally explicable with considerations of this kind, since the concrete volume increases under tension. Therefore, micro-cracking comes more likely into question as the main reason for tensile creep.

This hypothesis can explain the observed behavior of restrained concrete, in which a considerable part of the hardening induced tensile stresses remain in the structure, even if they have an absolute size of up to 60% of the long term tensile strength. Independent from the absolute size of the tensile stress level reached after temperature equalization, the tensile creep always appears to end after a minimal relaxation. In detail, the micro-cracks created during former tensile creep are assumed to partially close due to the first small relief experienced at the beginning of relaxation. This stops the ongoing process of micro-cracking and tensile creep discontinues.

Objective

This contribution aims at a preliminary presentation of the experimental findings and discusses their importance for the service life design of concrete structures on base of hypothetical considerations.

EXPERIMENTAL STUDIES

The experimental studies consist of the two different set-ups with passive restraint frames as well as suspended cylindrical specimens. All the experiments were carried out with the same conventional normal strength concrete. This reference concrete has a strength class of C 35/45 according to EC2 and due to the blast furnace cement it is suitable for mass concrete applications.

Table 1. Mix design of the reference concrete.

Parameter	*Value*	*Unit*
CEM III / A 32.5 N Holcim	300	kg/m³
Water	145	kg/m³
Aggregates 0/16	2000	kg/m³
BV ViscoCrete-1051 PCE	3	kg/m³

Passive restraint frames with a realistic stress history due to hardening.

In order to investigate the stress history of restrained concrete members, two steel frames were specifically designed at Graz University of Technology. Each steel frame restrains a 3.7 m long concrete specimen (cross section 25 x 25 cm, reinforcement 4 Ø 14 mm) which was cast horizontally hanging between the frame cross girders. The restraining starts on the setting of the concrete and the stiffness of the frame represents a realistic restraint condition over time.

The developing restraint force is recorded with load cells arranged in the steel frame. At the same time, the concrete temperature of the specimen as well as the deformation along the longitudinal axis are monitored so that the correctness of the measurement system can be verified by a compatibility check. Additionally the crack width movement, concrete strain between cracks and indoor climate is measured. Next to this, comprehensive investigations on complementary specimens were conducted to determine the thermal and mechanical material properties of the concrete composition used. Figure 3 gives an impression of this experimental set-up.

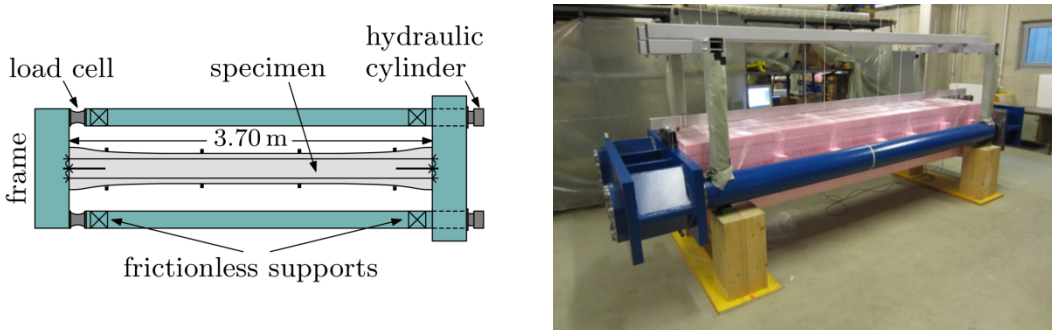

Figure 3. Passive restraint frames for realistic stress history due to hardening.

Besides detailed results for the hardening phase, which are shown in TURNER ET. AL., this set-up shows the development of the restraint stresses after temperature equalization, given in Figure 4. Punctual increases in the stresses of series 3 result from additional deformation impacts generated by the hydraulic cylinders, which can be added at one cross girder as shown in Figure 3.

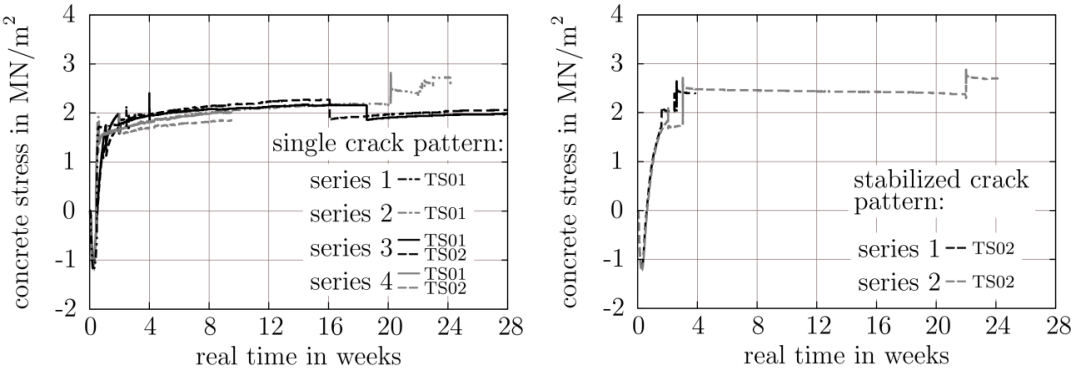

Figure 4. Influence of drying shrinkage and bond creep depending on the crack formation: single crack pattern (left side) or stabilized crack pattern (right side)

Independent of the crack pattern, all experiments showed not the expected decrease of restraint stresses after temperature equalization. On the contrary, all specimens with a single crack pattern even show increasing restraint stresses since ongoing shrinkage is decisive.

Tensile creep monitoring of partially unloaded concrete.

To investigate the unexpected behavior observed with the restraint frames, simple tensile creep monitorings on hanging cylindrical specimens were carried out. The loading of the specimens was provided by suspended weights, which can be partially removed in order to simulate a partial reduction of the total tensile stresses.

The specimens have a diameter of 10 cm and a length of 1.0 m. They were casted in plastic tubes and covered with aluminum foil directly after stripping, so that serious influences due to drying can be excluded further on. The mounting of the head plates for installation was achieved by an epoxy based glue. Figure 5 gives an impression of this experimental set up.

Figure 5. Hanging cylindrical specimens with suspended load for tensile creep monitoring under changing stress level.

The strains were measured with 3 strain transducers at each specimen to provide at least the minimum required number for conclusions on the average elongation of the specimen. The special feature of these experiments is the very long measuring length of around 0.9 m to allow a very precise detection of the very small strains to be expected under tensile creep. The adjustment for influences arising out of autogenous shrinkage and indoor air temperature changing was carried out with the simultaneously measured strains of an additional specimen, which was treated equally but left unloaded.

To allow a simple preliminary study on the effect of unloading on tensile creep, the weights were partially removed at one point. The insights result from a comparison of two parallel conducted experiments with different stress histories. The theoretical result to confirm the hypothesis is shown in Figure 6 by a comparison of well-known creep behavior under compression with the experimentally simulated creep behavior under tension. The shown stress levels in this illustration are exemplary for one certain investigated case, for which the results were provided afterwards.

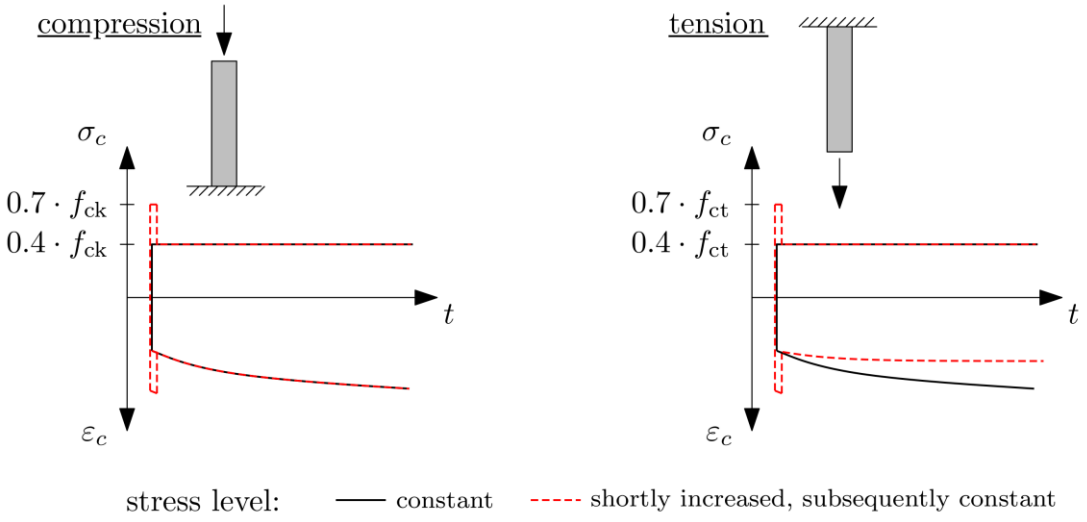

Figure 6. Behavior to be detected in the experiments to confirm the hypothesis

The real detected behavior of one preliminary test is given in Figure 7. This test specimens had an effective concrete age at loading of seven days. The underlying stress history is in accordance of the stress history in Figure 6 and the duration of the briefly increased high stressing was five minutes. Unloading was carried out manually step by step and lasted for another twenty minutes. To still allow a direct comparison of the results, the measured creep strain is expressed by a creep strain to stress level ratio.

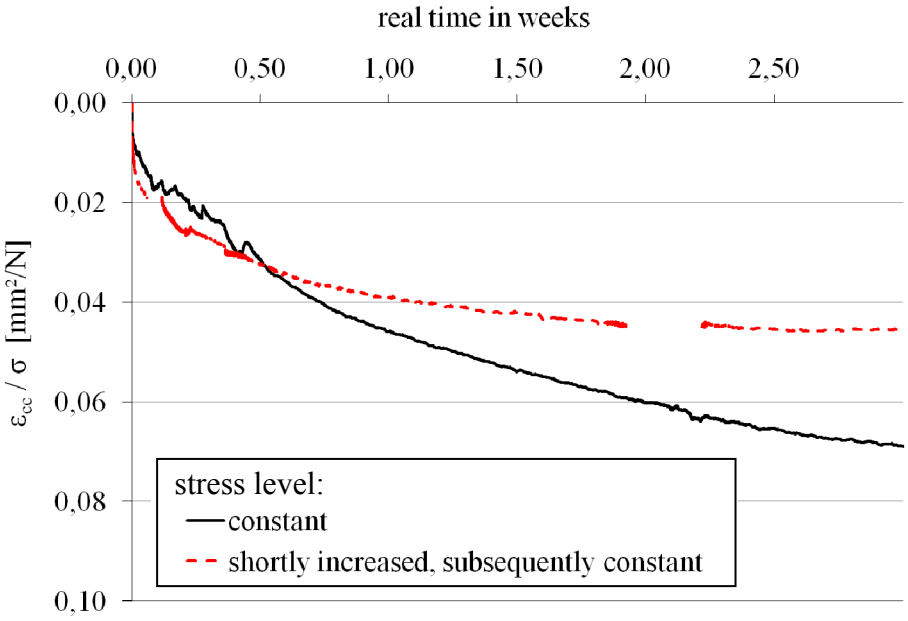

Figure 7. Measured creep strain / stress level ratio according to stress history in Figure 6 (effective concrete age of the specimens at loading was 7 days).

In sum all results of the preliminary test consisting of four series showed the hypothesized behavior, where the creep responses under tension diminish disproportionately when the total stress level falls below the maximum of all the tensile stresses ever experienced.

And even if this preliminary study was carried out on a single partial unloading at one point, it confirms the hypothesis. Finally this may explain, why experiments on hardening induced tensile stresses under realistic restraint conditions did not show the expected (and in daily design assumed) behavior of a considerable relaxation of such stresses by time.

CONCLUSION

This contribution showed preliminary results to confirm a unexpected observation of realistically restrained concrete members regarding its creep under tension. After the point, where the stress level already decreases due to relaxation no further considerable reduction of the hardening induced restraint stresses could be detected.

To explain this complex behavior a hypothesis was formulated, which could be simulated by simple creep monitoring of hanging and additionally loaded specimens. The hypothesis could be confirmed and from that it can be concluded, that today's common design practice of neglecting the superposition of hardening induced restraint stresses with later restraint stresses during service life may not generally lead to results on the safe side.

Even if the preliminary test was carried out for only one specific reference concrete with a specific concrete age at loading as well as a very specific (un-)loading history, the results are suitable for a general identification of this effect.

Further investigations are needed and already in the process of planning in order to allow a reliable quantification of this context for further considerations in the service life design of concrete structures.

REFERENCES

EN 1992-1-1:2004 + AC:2008: EUROCODE 2: Design of concrete structures - Part 1-1: General rules and rules for buildings.

Kordina, K., Schubert, L. and Troitzsch, U. (2000). "Kriechen von Beton unter Zugbeanspruchung". Heft 498 Deutscher Ausschuss für Stahlbeton.

Schlicke, D. (2014). “Mindestbewehrung für zwangbeanspruchten Beton.” Verlag der Technischen Universität Graz. *print: ISBN: 978-3-85125-363-4, E-Book: ISBN: 978-3-85125-365-8*.

Tailhan, J. L., Boulay, C., Rossi, P., Maou, F. L. und Martin, E. (2013)."Compressive, tensile and bending basic creep behaviour related to the same concrete." *Structural Concrete 14*, pp.124-130. Wilhelm Ernst & Sohn, Berlin.

Turner, K., Schlicke, D. and Tue, N.V. (2015). “Restraint and crack width development during service life regarding hardening caused stresses.” *Proceedings of fib 2015 symposium in Copenhagen.*

Experimental Studies on an Effective Creep Coefficient in a Prestressed Concrete Girder

Y. Ogawa[1]; S. Kameta[2]; R. Sato[3]; K. Nakarai[3]; and K. Kawai[3]

[1]Department of Civil and Environmental Engineering, Hiroshima University, 1-4-1 Kagamiyama, Higashi-hiroshima City, Hiroshima, Japan. E-mail: ogaway@hiroshima-u.ac.jp
[2]Narita International Airport Corporation.
[3]Department of Civil and Environmental Engineering, Hiroshima University, 1-4-1 Kagamiyama, Higashi-hiroshima, Hiroshima, Japan.

Abstract

A new concept for creep coefficient defined as effective creep coefficient was proposed. This concept was derived based on strain in prestressing strand directly measured in a prestressed concrete slab-girder as well as shrinkage strain of concrete specimen, which were made of ultra high strength concretes containing a molten slag fine aggregate and both the molten slag fine aggregate and roof tile waste coarse aggregate. The effective creep coefficient was verified by comparing the prestress loss obtained using the effective creep coefficient with that obtained using experiment as well as that by the creep coefficient obtained from the conventional creep test. The results showed that the stress losses obtained using effective creep coefficients agreed with experimentally obtained stress better than those obtained using creep coefficients from the conventional creep test.

INTRODUCTION

As creep of concrete under varying stress is one of the major targeted topics in concrete technologies, many studies have been performed on the mechanism of creep as well as the creep analysis for stress and deformation of concrete and concrete structures. However, creep analysis for concrete under varying stress is comparatively complicated, resulting in numerical creep analysis. Probably in order to solve this problem, Trost and Bazant proposed a simple creep analysis method by applying a so-called aging coefficient derived based on a step-by-step procedure, which is simple and widely used in design. The step-by-step procedure based on the superposition principle is known to overestimate the strain when concrete is unloaded in a step-by-step manner and subsequently subjected to a constant stress for a certain period on each step (Neville A. M. et al. 1983).

On the other hand, in prestressed concrete, compressive stress in concrete is lost with time just after the prestress is introduced. Although the superposition principle has been used to design the prestress loss because of its simplicity, as mentioned above, it should produce a certain level of prediction error. Furthermore,

one creep coefficient is applied for both constant compressive stress and varying stress loss.

For the reason mentioned above, the present study proposes a new concept of an effective creep coefficient derived from measurement of strain in prestressing strands in prestressed concrete slab-girder in which there exists a constant compressive stress mixed with stress loss in concrete with time and verifies the validity of the effective creep coefficient by comparing the stress loss calculated using the effective creep coefficient with that obtained by conventional creep test for two types of ultra high strength concretes.

EFFECTIVE CREEP COEFFICIENT

A practical method expressed by Eq. (1) was proposed by Trost and later improved by Bazant in order to predict creep strain simply under varying stress in concrete (Dilger W. H. 1982). Assuming that stress loss at the time is considered, creep strain is calculated by applying an aging coefficient and a creep coefficient. The aging coefficient is obtained based on step-by-step procedure in which variations of stress and Young's modulus in concrete with time, and creep coefficient depending on age at loading are considered.

$$\varepsilon_{c,cr}(t_t,t_0)=\left\{\frac{\sigma_c(t_0)}{E_c(t_0)}+\frac{\sigma_c(t_t)-\sigma_c(t_0)}{E_c(t_0)}\chi(t_t,t_0)\right\}\varphi(t_t,t_0) \tag{1}$$

where, $\varepsilon_{c,cr}(t_t,t_0)$ = creep strain generated between t_0 and t_t; $\sigma_c(t_0)$ and $\sigma_c(t_t)$ = stresses in concrete at prestressing and the time considered; $E_c(t_0)$ = Young's modulus of concrete at prestressing; $\chi(t_t,t_0)$ = aging coefficient between t_0 and t_t.

Unlike the above concept, the present study proposes Eq. (2) to obtain directly the effective creep coefficient to predict the prestress loss in prestressed concrete in which there exists a constant compressive stress mixed with stress loss with time. In Eq. (2), all of creep strain on the left-hand side, Young's modulus $E_c(t_0)$ and stress in concrete $\sigma_c(t_0)$ at prestressing, and stress of concrete $\sigma_c(t_t)$ at time t_t considered on the right-hand side are obtained experimentally. The elastic strain in concrete varying with time under stress loss is obtained by averaging varying stress loss of concrete with respect to time. The effects of variations of stress and Young's modulus in concrete with time, and creep coefficient depending on age at loading are comprehensively included in the creep strain on the left-hand side. Calculating the elastic strain in concrete considering change in Young's modulus with time, the effective creep coefficient may be more reliable.

$$\left\{\varepsilon_{c,cr}(t_t,t_0)\right\}_{meas.}=\left\{\frac{\sigma_c(t_0)}{E_c(t_0)}+k_m\frac{\sigma_c(t_t)-\sigma_c(t_0)}{E_c(t_0)}\right\}\varphi_{eff}(t_t,t_0) \tag{2}$$

$$k_m=\frac{\Delta\sigma_{c,m}}{\sigma_c(t_t)-\sigma_c(t_0)} \tag{3}$$

where, $\{\varepsilon_{c,cr}(t_t,t_0)\}_{meas.}$ = measured creep strain; $\phi_{eff}(t_t,t_0)$ = effective creep strain; k_m = the ratio of averaged stress to stress loss between t_0 and t_t; $\Delta\sigma_{c,m}$ = average of stress loss.

EXPERIMENTAL PROGRAM

Materials. The properties of materials used in this study are shown in Table 1. A low-heat portland cement premixed with 9.7% silica fume in mass was used as a binder. Two types of ultra high strength concretes were made with water to binder ratio of 0.17 as shown in Table 2. One contained molten slag fine aggregate derived from municipal waste and the other contained both molten slag fine aggregate and porous ceramic coarse aggregate, which is a waste roof tile material. The replacement ratios of the molten slag fine aggregate and the porous ceramic aggregate were 30% and 20% by volume, respectively. Table 3 shows properties of prestressing steels. Prestressing strands and bars were used for girders and creep test specimens, respectively.

Table 1. Properties of materials

Material	Type	Symbol	Density (g/cm^3)	Specific surface area (cm^2/g)	Water absorption (%)
Binder	Low-heat Portland cement premixed 9.7% of silica fume by mass	SFLC	3.08	6250	-
Fine aggregate	Crushed sand	S	2.59	-	1.36
	Molten slag	MS	2.75	-	0.82
Coarse aggregate	Crushed stone	G	2.62	-	0.72
	Porous ceramic coarse aggregate	PCCA	2.25	-	9.15
Chemical admixture	Polycarboxylate superplasticizer	SP	-	-	-

Table 2. Mix proportions.

Name	W/SFLC	Air content (%)	Unit content (kg/m^3)					
			W	SFLC	S	MS	G	PCCA
MS	0.17	2.0	155	912	370	171	849	0
MS+PCCA	0.17	2.0	155	912	370	171	679	146

Table 3. Properties of prestressing steels.

Specimen	Type	Nominal diameter (mm)	Area of section (mm^2)	Breaking load (kN)	Load at 0.2% permanet elongation (kN)	Young's modulus (kN/mm^2)
Girder specimen	7 wire strand (SWPR7BL)	12.7	98.71	183	175	193.3
Creep test specimen	Steel bar	32	804.2	1037	869	200.0

Specimens and measurement. A girder specimen having a length of 4,550 mm and a cross section as shown in Figure 1 (a) was prepared for each mixture. Strands were arranged at three depths; “Upper” was at the depth of 70 mm, “Middle” was 205 mm, and “Lower” was 260 mm, from the top surface. Strain in strands at each depth was measured using wire strain gages to obtain stress in concrete, in which stress relaxation in the strand has to be calculated.

A creep test specimen with the same cross section as that of the girder was also prepared for each concrete to investigate creep strain and creep coefficient with

the conventional test method. The left half of Figure 1 (b) shows the detail of half of the cross section of creep test specimen with the length of 1,800 mm. Creep strains at the same three depths as those of the girder specimen were measured using embedded strain gauges with Young's modulus of 400 N/mm^2. A target prestressing force for each arranged bar was measured using load cell and controlled to be 560±17kN, which resulted in 10.1±0.3 N/mm^2 in prestress in concrete.

A specimen for measuring free deformation of each concrete was also prepared, which has the same cross section as shown on the right half of Figure 1 (b) and the same length as those of the creep test specimen as shown on the right half of Figure 1 (b). The free deformations including thermal deformations at three depths were also measured using embedded strain gauges.

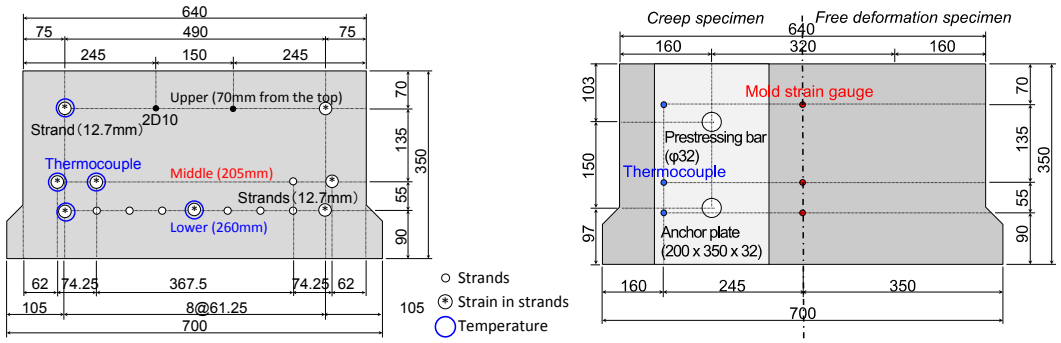

(a) PC slab-girder specimen (b) Creep and free deformation specimen

Figure 1. Cross section of specimen

Testing procedures and instrumentations. Compressive strength and Young's modulus were measured at the age of 24 hours, 40 hours, 2, 3, 7, 28, 56, 91, 182 days. Those for specimen cured in water of 20 °C were also measured at the age of 28 and 91 days. In addition, splitting tensile strength test was carried out at the ages of 2, 28, 91 and 182 days. Strain with time in concrete and prestressing strands were measured automatically using data loggers.

Curing condition. All specimens were steam cured. The ambient temperature was raised up to 40 °C at a rate of 5 °C/hour after 20 hours of initial curing at 20 °C and 60%R.H.. After maintaining the ambient temperature at 40 °C for 15hours, the specimens were allowed to cool naturally to 20 °C. The girder specimens and creep specimens were prestressed after steam curing was completed and then all specimens were demoulded at the age of 2 days. They were then stored in a room without any temperature control. The ends of specimens for creep strain and free deformation tests were sealed just after demoulding so that the deformation could develop uniformly in the longitudinal direction.

RESULTS AND DISCUSSION

Properties of concrete. Compressive strength and Young's modulus are shown in Figures 3 (Ogawa Y. et al. 2014). The data is expressed as a function of temperature adjusted concrete ages calculated based on Arrenius concept (fib 2012). Hereafter, the

temperature adjusted age is expressed as TA-age. As shown in Figure 2, compressive strengths of MS and MS+PCCA were more than 60 N/mm^2 at the age of 1 day and more than 150 N/mm^2 at the TA-age of around 180 days. The compressive strengths of MS+PCCA are almost the same as those of MS. On the other hand, Young's moduli of MS+PCCA are about 5 % less than those of MS due to Young's modulus of PCCA being lower than that of natural coarse aggregate.

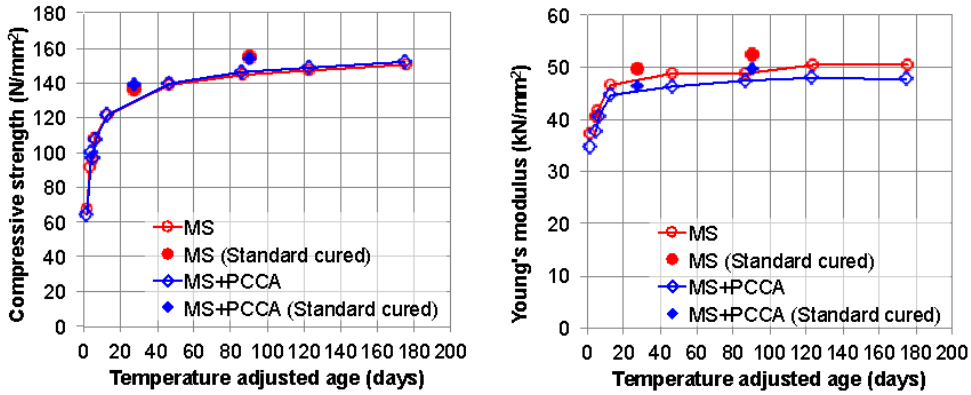

Figure 2. Compressive strength and Young's modulus. (Ogawa Y. et al. 2014)

Shrinkage strain of concrete. The thermal expansion coefficient of each concrete was obtained using the relationship between temperature and free deformation measured in specimen for 28 days after the TA-age of 500 days, because the shrinkage after this TA- age hardly increased as shown in Figure 3. The averages of MS and MS+PCCA are 11.1x10^{-6}/ºC and 11.5x10^{-6}/ºC, respectively. Figure 3 shows shrinkage strain obtained using the thermal expansion coefficient. From Figure 3, shrinkage strain of MS+PCCA are about 30 % smaller than those of MS at the TA-age of around 535 days shown which is the last measured value in the figure, and therefore it can be said that PCCA is effective in reducing shrinkage strain of ultra high strength concrete.

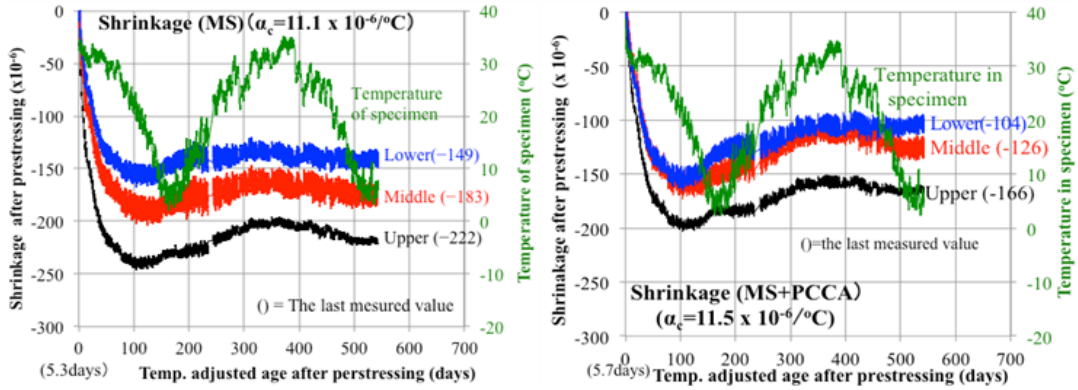

Figure 3. Shrinkage strain of concrete based on α_c obtained experimentally. (Left=MS (α_c=11.1 x 10^{-6}/ºC), Right=MS+PCCA (α_c=11.5 x 10^{-6}/ºC))

Strain in strands of PC girder specimen. As shown in Figure 4, strains in strands at all depths are almost the same except for that at the upper depth in the case of MS. As the effect of temperature was compensated using apparent strain based on strain

gauge test data, all strains in specimen MS varied negligibly, though the seasonal temperature change was significant, while the strain change was observed in MS+PCCA depending on the seasonal temperature change. The reason for this is difficult to explain as of now.

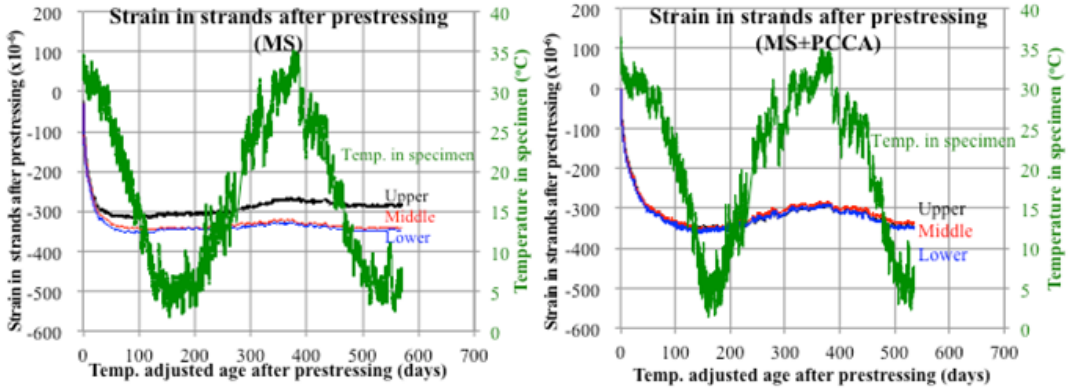

Figure 4. Strain in strands. (Left=MS, Right=MS+PCCA)

Stress in concrete. Figure 5 shows stress in concrete at each depth. Stress losses at three depths in concrete were calculated using Eq. (4), which was derived based on strain compatibility between concrete and steel after prestressing. It is observed that stress loss in concrete at the upper, middle and lower depth reached 0.32, 0.65 and 0.78 N/mm^2 by the TA-age of 100 days, respectively. Thereafter, the stress changes with time were negligible and there were almost no differences between the two concrete.

$$\begin{Bmatrix} \Delta\sigma_{cpe,1}(t_e) \\ \Delta\sigma_{cpe,2}(t_e) \\ \Delta\sigma_{cpe,3}(t_e) \end{Bmatrix} = -\begin{bmatrix} p_1\gamma_{11} & p_2\gamma_{21} & p_3\gamma_{31} \\ p_1\gamma_{12} & p_2\gamma_{22} & p_3\gamma_{32} \\ p_1\gamma_{13} & p_2\gamma_{23} & p_3\gamma_{33} \end{bmatrix} \begin{Bmatrix} \Delta\sigma_{pe,1}(t_e) \\ \Delta\sigma_{pe,2}(t_e) \\ \Delta\sigma_{pe,3}(t_e) \end{Bmatrix}, \gamma_{ji} = 1 + \frac{(d_i - c_g) - (d_j - c_g)}{I_c / A_c} \quad (4)$$

where, $\Delta\sigma_{cpe,i}$ and $\Delta\sigma_{pe,i}$ = stress loss in concrete and in strands; p_j = ratio of cross-sectional area of strands to that of concrete; d_i = depth of the strands; c_g = depth of centroid of net concrete section; I_c = second moment of area of net concrete section; A_c = cross-sectional area of net concrete; suffixes j and i = j-th and i-th depth of prestressing steel from the top surface.

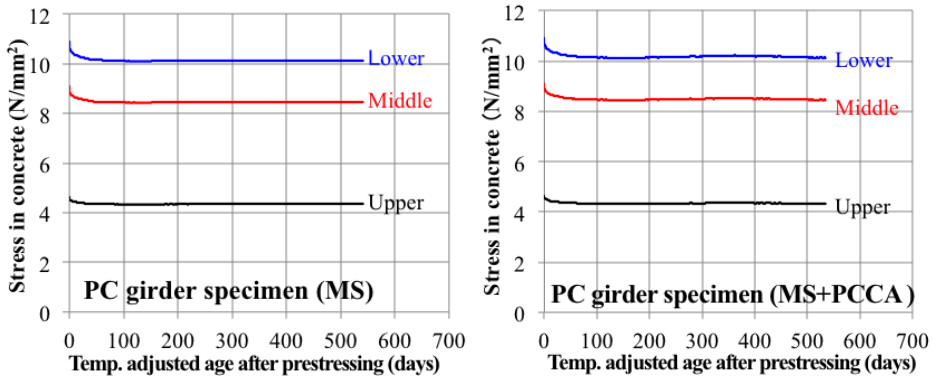

Figure 5. Stress in concrete. (Left=MS, Right=MS+PCCA)

Creep strain. Figures 6 and 7 show comparison between creep strain of PC girder specimen and creep specimen in the case of MS and MS+PCCA, respectively. As shown in Figure 6, in the case of MS, it can be observed that creep strain in PC girder specimen increased at a steep rate up to the TA-age of 20 days, then gradually increased up to 100 days, and thereafter negligibly increased or decreased, whereas creep strains in creep specimen increased at roughly the same rate as that in the girder up to 100 days, but thereafter increased gradually even after the TA-age of 500 days. On the other hand, as shown in Figure 7, in the case of MS+PCCA, creep strains in the girder specimen showed seasonal variation and the creep strain just after 500 dasys increased slightly compared to that at about 200 days, while creep strain in the creep specimen continued to increase after 100 days in the same way as MS and the magnitude of increase after 200 days was larger than that of the girder specimen.

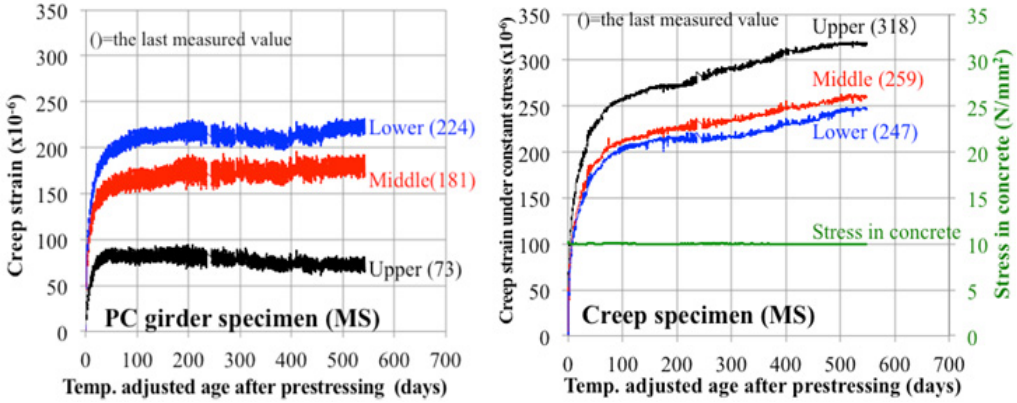

Figure 6. Creep strain in MS. (Left= PC girder, Right= creep specimen)

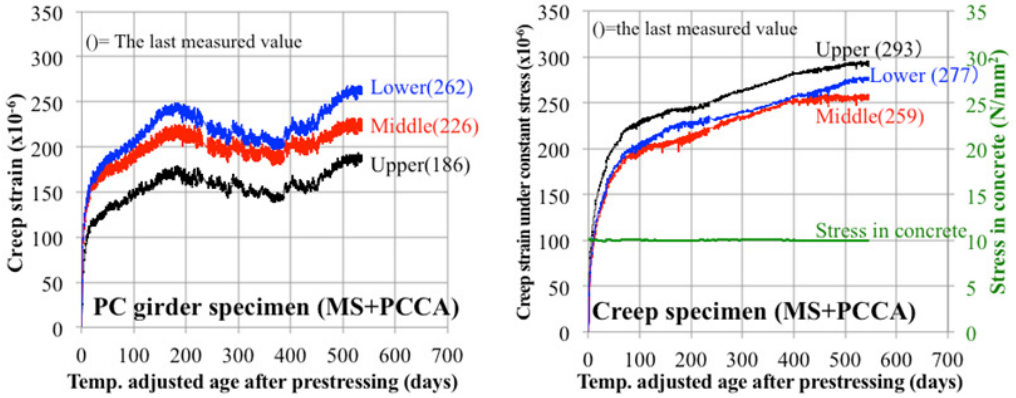

Figure 7. Creep strain in MS+PCCA. (Left= PC girder, Right= creep specimen)

Effective creep coefficient. Effective creep coefficients and creep coefficients obtained from the conventional creep test (hereafter, the conventional creep coefficient) in the case of MS are shown in Figure 8, and those in the case of MS+PCCA are in Figure 9. In addition, both creep coefficients at the TA-age of around 535 days are listed in Table 4. It should be noted that Young's modulus of each concrete cured in water at 20 ^{o}C for 28 days were used to calculate each creep coefficient, and the value of MS and MS+PCCA is 49.7 kN/mm^2 and 46.2 kN/mm^2, respectively. Therefore, the relationship between the effective creep coefficient ($\varphi_{eff,28}$) and that obtained using Eq.(2) (φ_{eff}) can be described as follows.

$$\varphi_{eff,28} = \frac{E_{c,28}}{E_c(t_0)}\varphi_{eff} \tag{5}$$

The tendencies of increases of both effective and conventional coefficients are similar to creep strain shown in Figure 6 and Figure 7, independent of the type of concrete. Table 4 lists the effective creep coefficients at the upper, middle and lower depths compared with the conventional creep coefficients for both concretes. According to the table, the effective creep coefficients of MS and MS+PCCA at the lower depth are 11 % and 8 % smaller than the conventional creep coefficient at the day the last values were measured.

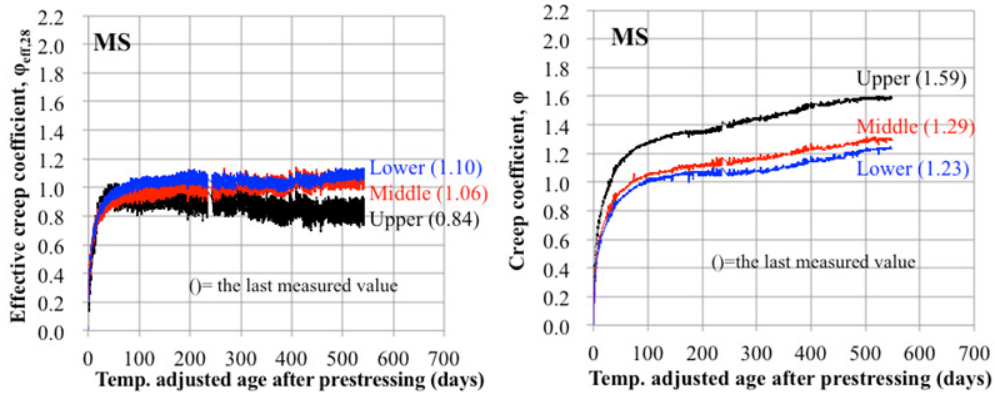

Figure 8. Effective creep coefficient and creep coefficient in MS.

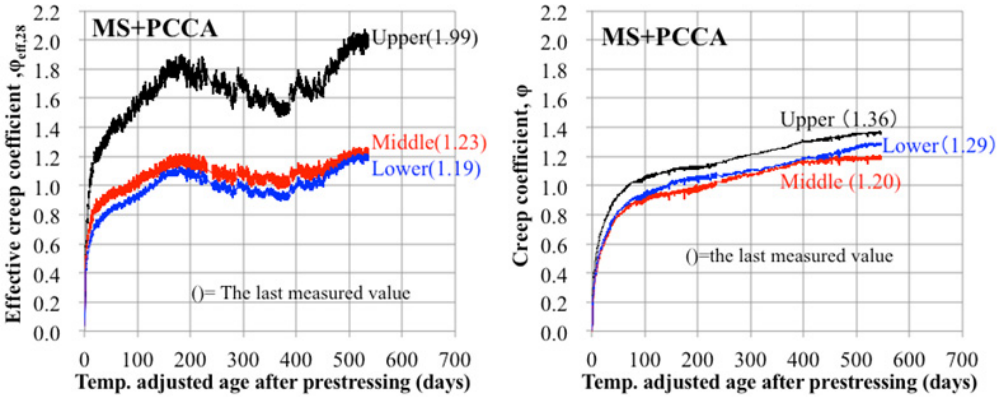

Figure 9. Effective creep coefficient and creep coefficient in MS+PCCA.

Table 4 Effective creep coefficient and creep efficient at the TA-age of 535 days.

Mix proportion	Position	PC girder spcimen		Creep specimen		
		Effective creep coefficient $\varphi_{eff,28}$	Elastic strain ($x10^{-6}$)	Creep coefficient φ	Elastic strain ($x10^{-6}$)	$\varphi_{eff,28}/\varphi$
MS	Upper	0.84	87	1.59	200	0.53
	Middle	1.06	170	1.29	200	0.82
	Lower	1.10	203	1.23	200	0.89
MS+PCCA	Upper	1.99	94	1.36	215	1.46
	Middle	1.23	183	1.20	215	1.03
	Lower	1.19	219	1.29	215	0.92

Estimation of stress loss. Eq.(7) for calculating prestress losses in steel at three depths due to creep and shrinkage are formulated based on strain compatibility between concrete and steel after prestressing given by Eq.(6) below.

$$-\frac{\Delta\sigma_{cpe,i}}{E_{c,28}}+\frac{\sigma_{cpe,i}(t_0)-\chi\Delta\sigma_{cpe,i}}{E_{c,28}}\varphi_i+\frac{\sigma_{cd,i}}{E_{c,28}}\varphi_i+\varepsilon_{sh,i}=-\frac{\Delta\sigma_{pe,i}}{E_{c,28}} \tag{6}$$

where, E_p = Young's modulus of steel; $\sigma_{cd,i}$ = stress in concrete due to dead load; $\varepsilon_{sh,i}$ = shrinkage strain of concrete; $\sigma_{cpi,i}$ = stres in concrete at prestressing; $\Delta\sigma_{cpi,i}$ and $\Delta\sigma_{pe,i}$ = stress losses in concrete and prestressing steel. Both stress and strain are used as positive values regardless of compression or tension.

$$\begin{Bmatrix}\Delta\sigma_{pe,1}\\ \Delta\sigma_{pe,2}\\ \Delta\sigma_{pe,3}\end{Bmatrix}=[K]^{-1}\begin{Bmatrix}\varphi_1\sigma_{cpi,1}+E_p\varepsilon_{sh,1}\\ \varphi_2\sigma_{cpi,2}+E_p\varepsilon_{sh,2}\\ \varphi_3\sigma_{cpi,3}+E_p\varepsilon_{sh,3}\end{Bmatrix} \tag{7}$$

where, $$[K]=-\begin{bmatrix} n(1+\chi\varphi_1)p_1\gamma_{11}+1 & n(1+\chi\varphi_1)p_2\gamma_{21} & n(1+\chi\varphi_1)p_3\gamma_{31}\\ n(1+\chi\varphi_2)p_1\gamma_{12} & n(1+\chi\varphi_2)p_2\gamma_{22}+1 & n(1+\chi\varphi_2)p_3\gamma_{32}\\ n(1+\chi\varphi_3)p_1\gamma_{13} & n(1+\chi\varphi_3)p_2\gamma_{23} & n(1+\chi\varphi_3)p_3\gamma_{33}+1\end{bmatrix} \tag{8}$$

The stress losses in strands in the PC girder specimens were estimated using the initial stresses in concrete and shrinkage strain of concrete at three depths, where the effect of dead load was ignored. Table 5 shows the stress losses in prestressing strands due to creep and shrinkage estimated using the effective creep coefficient and the conventional creep coefficient compared with measured losses on the assumption that the aging coefficient was 0.8. Focusing on the stress losses at the lower depth, which have the strongest impact on prestress at the bottom fiber, because the prestressing strand at the lower depth is considerably heavier and has the longest eccentricity between the centroid of net concrete and that of the prestressing strands, the prestress losses evaluated by the effective creep coefficient in the case of MS and MS+PCCA are 5 % (=70/74) and 6 % (=68/72) smaller than those by the conventional creep coefficient. Consequently, the effective creep coefficient and the conventional creep coefficient overestimate experimentally obtained stress loss by 3 % and 9 % for MS and by 28% and 36% for MS+PCCA, respectively.

Table 5 Estimation of stress loss in steel (χ=0.8).

Depth	Shrinkage, ε_{sh} (10^{-6})	Measured loss, $\Delta\sigma_{pe,meas.}$ (N/mm^2)	Effective creep coefficient		Conventional creep coefficient	
			Estimated loss, $\Delta\sigma_{pe}$ (N/mm^2)	$\Delta\sigma_{pe}/\Delta\sigma_{pe,meas.}$	Estimated loss, $\Delta\sigma_{pe}$ (N/mm^2)	$\Delta\sigma_{pe}/\Delta\sigma_{pe,meas.}$
Upper	222	69	57	0.83	69	1.00
Middle	183	62	69	1.11	77	1.24
Lower	149	68	70	1.03	74	1.09
Upper	166	62	68	1.10	57	0.92
Middle	126	57	67	1.18	66	1.16
Lower	104	53	68	1.28	72	1.36

CONCLUSION

A new concept for creep coefficient defined as effective creep coefficient was proposed, which was derived based on strain in prestressing steel directly measured in the girder and shrinkage strain in concrete. The effective creep coefficient was verified by comparing the prestress loss obtained using the effective creep coefficient with that obtained experimentally using ultra high strength concretes containing molten slag (MS) and containing both molten slag and roof tile waste aggregates (MS+PCCA), as well as using the creep coefficient obtained from the conventional creep test. The major conclusions obtained in the present study are as follows;

The stress loss obtained using effective creep coefficients were 5% and 6% smaller than in the case where creep coefficients obtained from the conventional creep test was used.

The stress loss obtained by effective creep coefficients overestimated experimentally obtained stress loss by 3% for MS and by 28 % for MS+PCCA, while those where creep coefficients obtained from the conventional creep test were used overestimated by 9% and 36%, respectively.

ACKNOWLEDGMENT

The authors are grateful to Dr. Suzuki and others for assistance in the experiment.

REFERENCES

Dilger W. H. (1982). " Chapter 9: Methods of Structural Creep Analysis (Dilger, W. H.)." *Creep and Shrinkage in Concrete Structures,* edited by Bazant Z. P. and Wittmann F. H., John Wiley and Sons, 305-339.

BSI (British Standards Institute) (2008). "Section 5.10.6: Time dependent losses of prestress for pre- and post-tensioning" *Eurocode 2: Design of concrete structures, Part 1-1,* BSI, 80.

fib (International Federation for Structural Concrete) (2012). "Section 5.1.10.2 Maturity." *fib Model code for concrete structures 2010,* Wilhelm Ernst & Sohn, 94.

Ghali A., Favre R. and Eldbadry M. (2002). "Chapter 1: Creep and Shrinkage of Concrete and relaxation of steel." *Concrete Structures – Stresses and Deformation- third edition*, Spon Press, 8-11.

JSCE (Japan Society of Civil Engineers). (2013). "Title 8: Prestressed Concrete." *Standard Specifications for Concrete Structures-2012, Design,* JSCE, 390-399.

Neville M. A., Dilger H. W. and Brooks J. J. (1983). "Chapter 13: Prediction of stress and strain under varying history, and relaxation of stress." *Creep of plain and structural concrete,*" Construction Press, 207-215.

Ogawa Y., Suzuki M., Sato R., Ohta S. and Kameta S. (2014). "Applicability of Waste Aggregates Derived from Municipal and Ceramic Roof Tile Wastes to Ultra-High-Strength Concrete." *Proc. of Concrete Innovation Conference*, Oslo, Norway, 11pages. (in UFD)

Mini-Beam Test for Assessing the Creep Trend of Paste, Mortar, and Concrete

C. H. Un[1]; J. G. Sanjayan[1]; R. San Nicolas[1]; and J. S. J. van Deventer[2]

[1]Centre for Sustainable Infrastructure, Swinburne University of Technology Hawthorn, VIC 3122, Australia. E-mail: cun@swin.edu.au
[2]Zeobond Pty. Ltd. and Department of Chemical & Biomolecular Engineering, The University of Melbourne, VIC 3010, Australia. E-mail: jannie@zeobond.com

Abstract

A mini-beam test has been designed to assess the flexural creep and shrinkage behaviors of paste and mortar samples. It is a four-point bending test carried out on a plate sample of 350 mm long. In total seven sets of samples, pastes and mortars made of ordinary Portland cement (OPC) and geopolymer were tested. Test results of OPC and geopolymer pastes and mortars from this test showed agreement with the general long-term performance of OPC and geopolymer concretes from the literature. The mini-beam test can be performed under various environmental conditions, such as high temperature and sealed condition, to assess the environmental effects on the samples. Furthermore, prediction of long-term behavior of OPC mortar and concrete can be done by using the developed models from the literature, based on the long-term behavior of OPC paste obtained from the mini-beam test.

Keywords:

Creep; Shrinkage; Flexural; Bending test; Deflection; Paste; Mortar; Geopolymer.

INTRODUCTION

Creep testing for concrete specimens is usually carried out on concrete cylinders of 100 mm or 150 mm diameter in compression by using a creep loading rig specified in the standards, such as ASTM C512 (American Society for Testing and Materials 2010) and AS1012.16 (Standards Australia 1996). Load adjustment is required regularly to ensure constant loads on the samples at all time during test period. On the other hand, tensile creep testing can only be done on custom designed loading rigs (Bissonnette, Pigeon et al. 2007, Rossi, Tailhan et al. 2013). In such case difficulty is experienced in both the equipment setup and sample preparation. The tensile creep measured from the direct tensile creep test can be affected by damage from microcracking and additional shrinkage. This leads to a contracting tendency if the shrinkage from the companion specimens is used. One of the ways to overcome this problem is to obtain tensile creep from the flexural creep test, since it would give a better result as the above effects are less (Ranaivomanana, Multon et al. 2013a). Therefore, flexural creep tests have been carried by a number of researchers for the

investigation of creep of concrete (Arango, Serna et al. 2012, Tailhan, Boulay et al. 2013). Ranaivomanana, Multon et al. (2013b) suggested that the basic creep strains were the same in compression and tension in the bending specimens under sealed condition.

The paste content in concrete and mortar, as the major binder materials, is mainly responsible for effects of creep and shrinkage. This is due to the diffusion of water and other molecules along pore networks in the gel microstructure of C-S-H (Bažant 1972). A study of paste samples would give the fundamental information on the long-term behavior of concrete and mortar. Therefore, a new type of flexural creep test has been designed for paste samples of small size to accelerate the investigation of creep of concrete.

Specimens of paste and mortar made of ordinary Portland cement (OPC) and geopolymer were tested by using the proposed min-beam test method and the results are presented in this paper. The effects of drying and temperature, and the relationship between the long-term behavior OPC paste and mortar are discussed.

TEST PROCEDURES

Test setup

The test specimen used in this study is a plate specimen, or so called mini-beam. The size of the mini-beam sample is of 350 mm long, 50 mm wide and 10 mm deep. The shape aspect ratio of width to depth is chosen as 5:1 as Valenza II and Scherer (2004) suggested the aspect ratio of the plate of saturated porous material equal or greater than this value can be considered effectively “infinitely wide”. The mini-beam sample is supported over a span of 300 mm for flexural creep test. Loads are applied in the middle 100 mm apart in this four-point-bending test. Due to the thin property of this mini-beam, it only requires small test area and light sustained loads. An illustration of the test setup is shown in Figure 1. A dial gauge with accuracy of 1 μm is set to measure the long-term mid-span deflection.

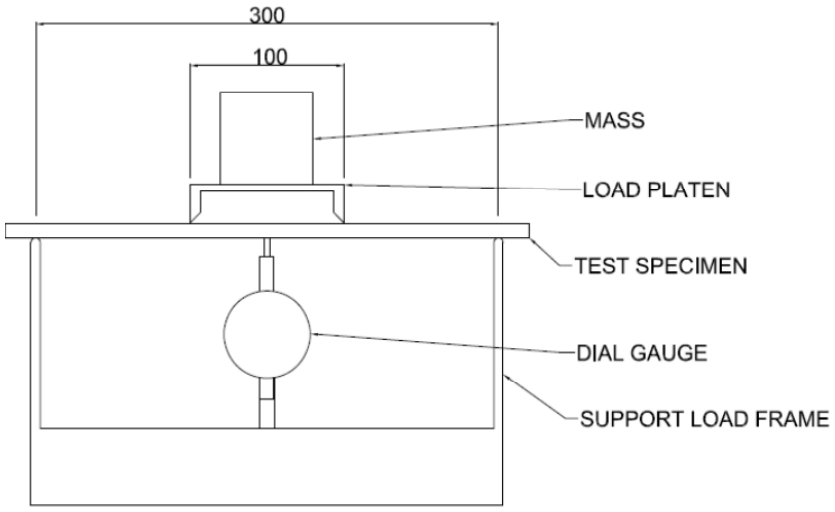

Figure 1. Detail of flexural creep test.

For each batch of test specimens, a minimum of six mini-beam samples are made for two creep test samples, two companion samples and two samples for destructive testing. The companion samples are made for testing shrinkage effects, with no load being applied on these samples. Measurement of shrinkage is done by using a demountable mechanical digital gauge (demec gauge) of 200 mm gauge length. Since the sample under mini-beam testing is subjected to drying at all surfaces, the companion sample is stored with the short side standing to allow drying at most surfaces. Because it is important to ensure the uncracked condition of the creep samples under load, the four-point-bending test is done on samples from the same batch to determine the failure load. The sustained load on the creep samples is then applied at no more than 40% of this failure load.

Creep and shrinkage

The creep of the specimen can be measured from the deflection from mid-span. Based on the uncracked condition for the whole length of the mini-beam, the deflection at mid-span is:

$$\Delta(t) = -\frac{W/_2 \times L/_3}{24E_e(t)I}\left(3L^2 - \frac{4}{9}L^2\right) = -\frac{23WL^3}{1296E_e(t)I} \quad \text{Eq. 1}$$

and $$M = \frac{\sigma I}{y} = \frac{\varepsilon(t)E_e(t)I}{y} = \frac{WL}{6} \quad \text{Eq. 2}$$

Therefore, $$\Delta(t) = -\frac{23L^2}{216y}\varepsilon(t) \quad \text{Eq. 3}$$

When $t = 0$, $$\Delta(0) = -\frac{23L^2}{216y}\varepsilon(0)$$

Hence, $$\frac{\Delta(t)}{\Delta(0)} = \frac{\varepsilon(t)}{\varepsilon(0)} = 1 + \phi(t) \quad \text{Eq. 4}$$

Where Δ(t) and Δ(0) are the mid-span deflection at time t and immediately after loading, W is the applied load, L is the span length, $E_e(t)$ is the age-adjusted effective modulus, I is the moment of inertia, M is the maximum bending moment, σ is the maximum compressive stress on the top surface, y is half the depth, ε(t) and ε(0) are the strain at time t and immediately after loading, and Φ(t) is the creep coefficient.

The creep coefficient during the test period can be derived in this case. When the mini-beam sample is sealed, the creep coefficient due to basic creep can be obtained for both compressive and tensile creep.

Because the mini-beam sample is thin, symmetric and not reinforced, the shrinkage strain is assumed to be uniform with gradient. Therefore, the effect of shrinkage does not affect the deflection of the specimen. The total shrinkage strain is measured from the specimens subjected to drying, while the autogeneous shrinkage strain is measured from the specimens in sealed condition. The drying shrinkage strain is calculated by subtraction of the autogeneous shrinkage strain from the total shrinkage strain.

Experimental program

Paste and mortar specimens are made of OPC and geopolymer separately as the binder materials. The detail of mix design is shown in Table 1. The water/binder ratio is 0.4 for all mixes and the aggregate/binder ratio is 1.575 for mortar mixes. The silica sand with a specific gravity of 2.55 and water absorption of 0.90% was used as fine aggregate. Commercial sodium silicate was used as activator in geopolymer samples, with a chemical composition of 50.5 wt% Na_2O and 46.0 wt% SiO_2.

For OPC paste, the binder material is mixed in a mixer with water added in gradually for two minutes; while for geopolymer paste the activator is blended into the wet mix and mixed for five minutes. For mortar mixes, the binder material is first well mixed with the aggregates, and then follows the same procedures as paste mixes.

Table 1. Mix designs for paste and mortar.

Raw materials	*OPC paste*	*Geopolymer paste*	*OPC mortar*	*Geopolymer mortar*
OPC	1500	/	760	/
Blasted furnace slag (BFS)	/	1368	/	722
Fly ash (FA)	/	70	/	38
Sand	/	/	1197	1197
Water	600	576	304	304
Alkali activator	/	144	/	76

Test samples are cast in mini-beam moulds of 350 mm long × 50 mm wide × 10 mm deep and 50 mm cubic moulds. Each set of samples contains six mini-beam samples and six cubic samples of 50 mm for compressive strength testing according to ASTM C109/C109M (American Society for Testing and Materials 2013). All samples are demoulded and tested at 1 day. The immediate mid-span deflection of the creep samples is recorded and the long-term deflection, together with the shrinkage results from the companion samples, are recorded hourly until 6 hours, then daily until one week, then weekly until one month, then at 56 days, similar to the recording procedures by AS1012.16 (Standards Australia 1996). In total seven sets of sample of paste and mortar were tested, with details listed in Table 2.

Table 2. Details of test samples.

Sample set	*Test condition*
Paste	
OPC paste	23 °C temperature and 50% relative humidity
OPC paste sealed	23 °C temperature in sealed condition*
OPC paste heat	50 °C temperature and 50% relative humidity
Geopolymer paste	23 °C temperature and 50% relative humidity
Geopolymer paste sealed	23 °C temperature in sealed condition*
Mortar	
OPC mortar	23 °C temperature and 50% relative humidity
Geopolymer mortar	23 °C temperature and 50% relative humidity

* Sample is sealed by wrapping adhesive aluminum foil

RESULTS AND DISCUSSION

Strength of test materials at 1 day

The results of compressive strength and failure load under four-point-bending testing are shown in Table 3. At 1 day, the compressive strength of geopolymer was higher than that of OPC in both paste and mortar samples, but has the opposite trend in flexural failure load. This is likely due to the fast reaction of slag-based geopolymer, so it usually results in high early compressive strength. However, surface microcracking occurs when subjected to drying conditions (Collins and Sanjayan 2001), which reduces the tensile capacity of the geopolymer samples and thus resulted in low flexural strength.

Table 3. Compressive strength and flexural failure load of test samples at 1 day

Test samples	*Compressive strength (MPa)*	*Flexural failure load (N)*
OPC paste	31.2	93.9
Geopolymer paste	50.5	41.9
OPC mortar	32.4	136.1
Geopolymer mortar	49.9	37.9

Results from mini-beam test

The creep coefficient of the test samples was computed from the deflection measured from the mini-beams (see Figure 2 for test setup) and is shown together with the shrinkage measurement in Figure 3. Test results for geopolymer paste could not be obtained throughout the test period due to high drying shrinkage causing cracking on the mini-beams in the first day. Also, its total shrinkage strain was more than the measurement capacity of the demec gauge.

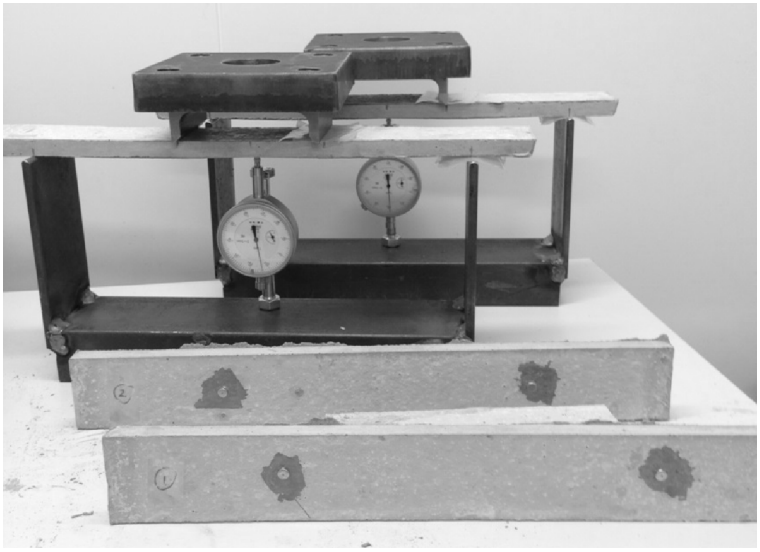

Figure 2. Picture of mini-beam test

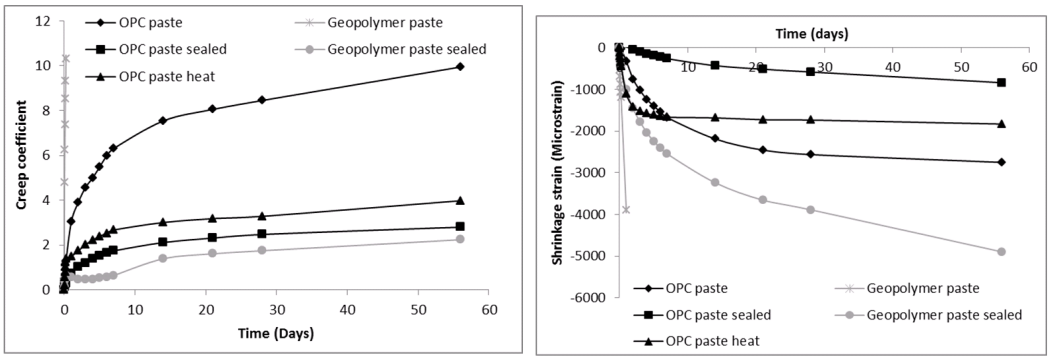

(a) (b)

Figure 3. Test results for OPC and geopolymer paste: (a) Creep coefficient; and (b) Shrinkage strain

Unlike the geopolymer paste, the geopolymer mortar samples did not crack during the test period because of the restraint by the aggregates. Figure 4 shows the test results for mortar samples. It can be seen from these results that geopolymer paste had higher creep and shrinkage effects than OPC paste, and so did geopolymer mortar. This differences between OPC and geopolymer generally agreed with the finding by Collins and Sanjayan (1999) on OPC and geopolymer concrete.

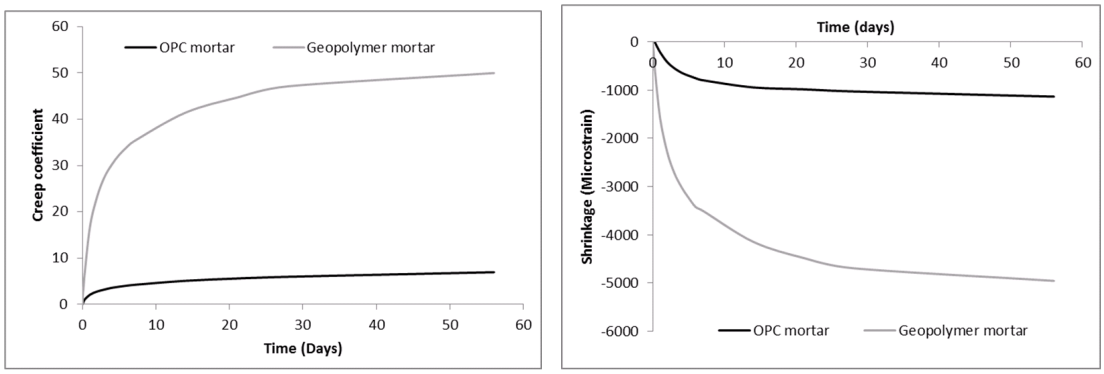

(a) (b)

Figure 4. Test results for OPC and geopolymer mortar: (a) Creep coefficient; and (b) Shrinkage strain

Thermal effect on cement paste

The OPC samples heated at 50 °C during the test exhibited less creep and shrinkage than the standard OPC samples stored at 23 °C at 56 days. They showed similar creep behavior in the early age but diverged after 1 day. However, the heated OPC samples exhibited more shrinkage than the standard OPC samples in the first day, but the growth reduced thereafter. The shrinkage of the standard OPC samples surpassed the heated OPC samples at 7 days and kept increasing. The total shrinkage strain of the standard OPC samples at 56 days was 2752 microstrains, while that of the heated samples was 1832 microstrains.

External heat provided to OPC concrete at early accelerates the degree of hydration of OPC and has an influence on the microstructure (Kjellsen 1996). Therefore, most of the shrinkage of the heated OPC samples is due to autogeneous shrinkage during accelerated hydration. And since the microstructure of the heated OPC samples changed and there was less free water in the pore structure, this sample exhibited less creep and drying shrinkage than the standard OPC samples.

Drying effect on paste samples

Drying has a significant impact on the long-term behaviors of OPC and geopolymer paste samples. The paste samples in sealed condition exhibited less creep and shrinkage effects than the standard samples. Measurement of creep on geopolymer paste became feasible under sealed condition. The basic creep values measured from the sealed samples of OPC and geopolymer paste at 56 days are 2.80 and 2.24, respectively. Since the total creep coefficient of OPC paste at 56 days is 9.94, the drying creep of that sample is the difference between the total creep and the basic creep, which is 7.14.

The basic creep of geopolymer paste was smaller than that of OPC paste but it was out of measurement when exposed to atmosphere. The drying shrinkage of geopolymer paste also exceeded the measurement capacity in this study. This indicates that drying had more influence on geopolymer paste than on OPC paste. It can be explained that the geopolymer paste has a finer pore network than OPC paste, so the capillary tensile force is higher at the meniscus and this causes higher drying shrinkage (Collins and Sanjayan 2000). Therefore, the drying creep is also affected.

Relationship between paste and mortar

Comparison of OPC paste and mortar shows that the creep and shrinkage of the former were higher than that of the latter (see Figure 5). This is because the portion of aggregates in the mortar does not exhibit creep, so generally more creep occurs in the binder-aggregates composite with more paste proportion.

The long-term behavior of mortar or concrete can be predicted based on the behavior of paste. Hobbs (1971) proposed some simple equations on prediction of properties of composite upon aggregate volume concentration,

$$\frac{\varepsilon_{cm}(t)}{\varepsilon_{cp}(t)} = \frac{1-D_a}{1+D_a} \quad \text{Eq. 5}$$

$$\varepsilon_{sm}(t) = \varepsilon_{sp}(t) - \frac{\varepsilon_{sp}(t) D_a \cdot 2k_a}{k_p + k_a + D_a(k_a - k_p)} \quad \text{Eq. 6}$$

where ε_{cm} and ε_{cp} are the creep strain of mortar and paste, D_a is the aggregate volume concentration, ε_{cm} and ε_{cp} are the shrinkage strain of mortar and paste, and k_a and k_p are the bulk modulus of aggregates and paste.

Eq. 5 estimates the creep strain of mortar but it assumed both mortar and paste with the same creep coefficient. Another function was proposed by Bažant (1993) based on the combined series-parallel model for creep interaction of aggregates and mortar matrix. This was originally developed for concrete but it can be applied to the creep prediction of mortar, based on the creep of paste (Granger and Bažant 1995). This model is applied with the age-adjusted effective modulus method.

$$J_m(t,t_0) = \frac{\beta}{\alpha E_a + (1-\alpha)E_p(t_0)}\left[1 + (1-\alpha)\frac{E''_p}{E''_m}\Phi_p(t,t_0)\right] + (1-\beta)J_p(t,t_0) \quad \text{Eq. 7}$$

$$\Phi_m(t,t_0) = E_m(t_0)J_m(t,t_0) - 1 \quad \text{Eq. 8}$$

where J_m and J_p are the creep compliance function of mortar and paste, α and β are the section parameter and the length parameter ($\alpha\beta = D_a$), E_a, E_p and E_m are the Young's modulus of aggregates, paste and mortar, respectively, E''_p and E''_m are the age-adjusted effective modulus of paste and mortar, and Φ_p and Φ_m are the creep coefficient of paste and mortar.

With the E_a = 72 GPa, E_p = 29.2 GPa estimated from compressive strength of paste samples (Boumiz, Vernet et al. 1996), D_a = 0.416, and an assumption of Poisson's ratio, ν = 0.2 for both paste and aggregates, the creep coefficient of mortar was predicted by using Eq. 7 and 8 and the shrinkage strain of mortar was predicted by using Eq. 6. The results are shown in Figure 5.

The predictions show generally good agreement with the test result of OPC mortar but there are some variations. This can be due to the presence of interfacial transition zone (ITZ) between the aggregates and the hydrated paste. ITZ has weaker properties compared to cement paste and aggregates and this can affect the long-term behavior (Neubauer, Jennings et al. 1996).

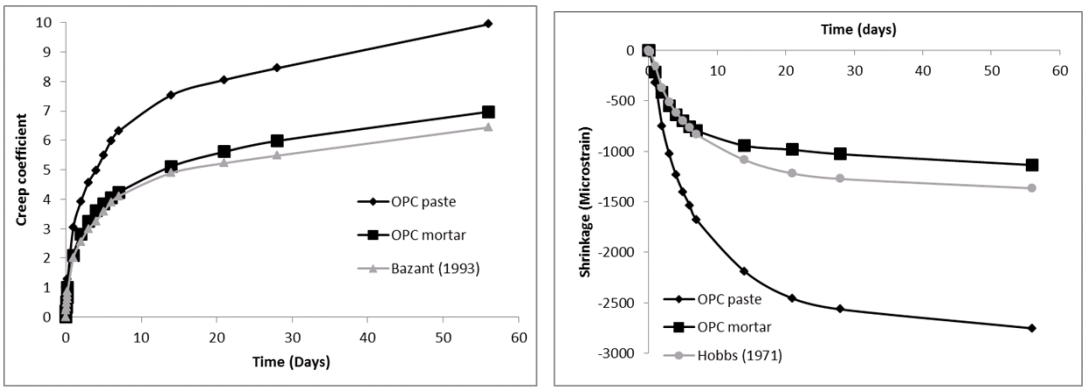

(a) (b)

Figure 5. Prediction of long-term behaviors of OPC mortar: (a) Creep coefficient; (b) Shrinkage strain

CONCLUSION

A flexural creep mini-beam test has been designed to assess the creep and shrinkage behavior of paste and mortar samples. The test setup requires less space and lighter applied loads than the conventional creep test, and thus ease of handling. Furthermore, it can be performed under various environmental conditions, such as high temperature, depending on the measuring method. When the test sample is sealed, basic creep can be measured.

The mini-beam test results of OPC and geopolymer pastes and mortars agreed with the general long-term performance of OPC and geopolymer concretes from the literature. The recorded creep and shrinkage of geopolymer paste and mortar were higher than that of OPC paste and mortar. This would be caused by drying since the

sealed geopolymer paste samples exhibited less creep than those subjected to drying. With addition of aggregates, both creep and shrinkage of the mortar samples reduced compared to the paste samples, due to restraint provided by the aggregates.

The long-term behavior of OPC mortar can be predicted based on the long-term behavior of OPC paste. Prediction of the creep coefficient of OPC mortar shows good agreement with the test results. Therefore, when the properties of aggregates and paste are known, the mini-beam test result on paste samples can be used to estimate the long-term behavior of OPC mortar and even concrete, without further tests on large samples.

REFERENCES

American Society for Testing and Materials (2010), Standard test method for creep of concrete in compression, ASTM C512/C512M.

American Society for Testing and Materials (2013), Standard test method for compressive strength of hydraulic cement mortars (Using 2-in. or [50-mm] Cube Specimens) ASTM C109/C109M.

Arango, S. E., Serna, P., Martí-Vargas, J. R. and García-Taengua, E. (2012), "A test method to characterize flexural creep behaviour of pre-cracked FRC specimens." *Experimental Mechanics* 52(8): 1067-1078.

Bažant, Z. (1993), "Current status and advances in the theory of creep and interaction with fracture."

Bažant, Z. P. (1972), "Thermodynamics of interacting continua with surfaces and creep analysis of concrete structures." *Nuclear Engineering and Design* 20(2): 477-505.

Bissonnette, B., Pigeon, M. and Vaysburd, A. M. (2007), "Tensile creep of concrete: Study of its sensitivity to basic parameters." *ACI Materials Journal* 104(4): 360-368.

Boumiz, A., Vernet, C. and Cohen Tenoudji, F. (1996), "Mechanical properties of cement pastes and mortars at early ages." *Advanced Cement Based Materials* 3(3-4): 94-106.

Collins, F. and Sanjayan, J. G. (2000), "Effect of pore size distribution on drying shrinking of alkali-activated slag concrete." *Cement and Concrete Research* 30(9): 1401-1406.

Collins, F. and Sanjayan, J. G. (2001), "Microcracking and strength development of alkali activated slag concrete." *Cement and Concrete Composites* 23(4–5): 345-352.

Collins, F. G. and Sanjayan, J. G. (1999), "Workability and mechanical properties of alkali activated slag concrete." *Cement and Concrete Research* 29(3): 455-458.

Granger, L. P. and Bažant, Z. P. (1995), "Effect of composition on basic creep of concrete and cement paste." *Journal of engineering mechanics* 121(11): 1261-1270.

Hobbs, D. W. (1971), "The dependence of the bulk modulus, Young's modulus, creep, shrinkage and thermal expansion of concrete upon aggregate volume concentration." *Matériaux et Constructions* 4(2): 107-114.

Kjellsen, K. O. (1996), "Heat curing and post-heat curing regimes of high-performance concrete: Influence on microstructure and C-S-H composition." *Cement and Concrete Research* 26(2): 295-307.

Neubauer, C. M., Jennings, H. M. and Garboczi, E. J. (1996), "Three-phase model of the elastic and shrinkage properties of mortar." *Advanced Cement Based Materials* 4(1): 6-20.

Ranaivomanana, N., Multon, S. and Turatsinze, A. (2013a), "Tensile, compressive and flexural basic creep of concrete at different stress levels." *Cement and Concrete Research* 52(0): 1-10.

Ranaivomanana, N., Multon, S. and Turatsinze, A. (2013b), "Basic creep of concrete under compression, tension and bending." *Construction and Building Materials* 38: 173-180.

Rossi, P., Tailhan, J.-L. and Le Maou, F. (2013), "Comparison of concrete creep in tension and in compression: Influence of concrete age at loading and drying conditions." *Cement and Concrete Research* 51(0): 78-84.

Standards Australia (1996), Methods of testing concrete - Determination of creep of concrete cylinders in compression, Sydney, AS1012.16-1996.

Tailhan, J. L., Boulay, C., Rossi, P., Le Maou, F. and Martin, E. (2013), "Compressive, tensile and bending basic creep behaviours related to the same concrete." *Structural Concrete* 14(2): 124-130.

Valenza II, J. and Scherer, G. W. (2004), "Measuring permeability of rigid materials by a beam-bending method: V, isotropic rectangular plates of cement paste." *Journal of the American Ceramic Society* 87(10): 1927-1931.

Continuous Monitoring of Concrete Mechanical Properties since an Early Age to Support Construction Phasing

José Granja[1] and Miguel Azenha[2]

[1]Civil Engineering Department, School of Engineering, University of Minho, 4800-058 Guimarães, Portugal. E-mail: granja@civil.uminho.pt
[2]Civil Engineering Department, School of Engineering, University of Minho, 4800-058 Guimarães, Portugal. E-mail: miguel.azenha@civil.uminho.pt

Abstract

The assessment of concrete mechanical properties during construction of concrete structures is of paramount importance for many intrinsic operations. However many of the available non-destructive methods for mechanical properties have limitations for use in construction sites. One of such methodologies is EMM-ARM, which is a variant of classic resonant frequency methods. This paper aims to demonstrate the efforts towards in-situ applicability of EMM-ARM, as to provide real-time information about concrete mechanical properties such as E-modulus and compressive strength. To achieve the aforementioned objective, a set of adaptations to the method have been successfully implemented and tested: (*i*) the reduction of the beam span; (*ii*) the use of a different mould material and (*iii*) a new support system for the beams. Based on these adaptations, a reusable mould was designed to enable easier systematic use of EMM-ARM. A pilot test was successfully performed under in-situ conditions during a bridge construction.

INTRODUCTION

Concrete is a composite material which undergoes significant microstructural changes along cement hydration. Right after mixing, concrete behaves similarly to a Newtonian fluid that evolves gradually to a solid state. Knowing how the mechanical properties of concrete evolve at early ages is extremely important, particularly for predicting stresses and cracking risks in such time span. The importance of this knowledge is even wider if aspects related to construction are taken into account. In fact, many construction operations are conditioned by the evolution of concrete properties: prestress application, formwork removal, etc.

Given the importance of knowing the evolution of the mechanical properties of concrete since casting, many non-destructive methods have been developed over the years: wave transmission methods, dielectric methods, BTJASPE, TSTM, maturity method, among others (Voigt *et al.*, 2006, Beek, 2000, Boulay *et al.*, 2013). However they still have limitations for use in the construction sites that have prevented their widespread application in such context.

Based on the intent to overcome limitations associated to existing techniques for E-modulus assessment, the EMM-ARM (Elasticity Modulus Measurement through Ambient Response Method) has been developed for continuous measurement of the E-modulus of cement-based materials (Azenha *et al.*, 2010, Azenha *et al.*, 2012). The technique is based on modal identification of a composite beam of acrylic and concrete. By allowing continuous monitoring of the concrete stiffness evolution from the instant of casting, the information provided by this methodology can have an important impact on the work site as it enables to assist and anticipate the verification of the design specifications, providing technical and economic advantages.

This paper aims to demonstrate the in-situ implementation (construction of a bridge) of an experimental framework that allows the continuous monitoring of concrete E-modulus as to provide real-time information about estimated compressive strength and assist decision making in regard to prestress application. This objective was achieved through the implementation of EMM-ARM. However, for systematic application of EMM-ARM in the construction site some improvements to the testing technique had to be implemented. The main improvements to EMM-ARM consisted in: (i) reduction of the beam length to facilitate de casting operations and the handling of the beams, (ii) development of a new support system to eliminate potential uncertainties about the support conditions and (iii) a reusable mould for EMM-ARM has been devised, making it easier to prepare/perform, more reliable and less expensive. This paper presents the implementation of these improvements to the EMM-ARM methodology as well as a pilot experiment of in-situ test performed during the construction of the bridge.

EMM-ARM – DESCRIPTION OF THE ORIGINAL IMPLEMENTATION

The EMM-ARM is a variant of the classical resonance method and was originally proposed by Azenha *et al.* (2010). Through the modal identification of a composite beam (composed by the mould filled with the material to be tested) it is possible to obtain the evolution of the resonance frequency of the first mode of vibration. From this evolution, it is then possible to estimate the stiffness of the material inside the mould under testing. In the original implementation of the method applied to concrete, the mould was a 2 meters long acrylic tube with external/internal diameters of 100/92mm. After casting concrete inside the mould, it was placed horizontally over four concrete cubes supported by two horizontal rods (with 5mm in diameter) that trespassed the composite beam at its axis. This configuration, shown schematically in Figure 1, allows the structure to behave as a simply supported beam with a free span of 1.8m. Due to the length of the beam and potential tangential stresses caused by autogenous shrinkage (which might induce debonding between concrete and mould), 5 vertical connectors were disposed evenly spaced along the total length of the composite beam.

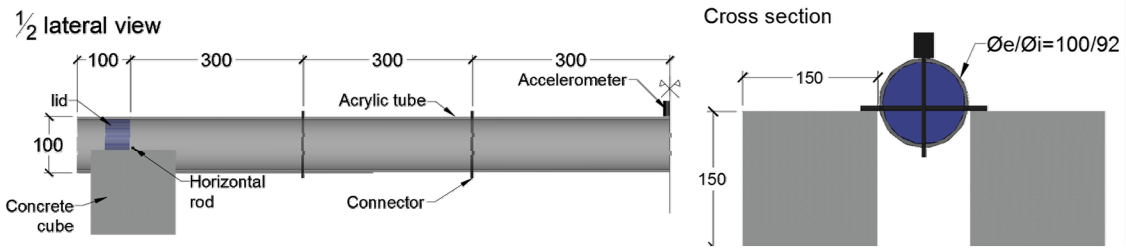

Figure 1. EMM-ARM original test apparatus.

The beam is then excited by the environmental noise (e.g.: wind, people walking, noises from construction site, etc.) that can be assumed as a white noise, i.e. a stochastic process with constant spectral intensity in all frequencies. The resulting vibrations are then acquired in the vertical direction through an accelerometer (PCB 393B12: sensitivity: 10V/g; range: ±0.5g) attached at mid span to the composite beam. In order to identify the natural frequency of the beam, the recorded accelerograms (in packets of 300 seconds) are converted to the frequency domain, through the Welch procedure (Welch, 1967), thus resulting in the normalized power spectrum density of each measured package of data – see further details in Azenha *et al.* (2012). The resonance frequencies of the first vibration mode are identified through the highest peak in each amplitude spectrum. In order to obtain a continuous evolution of the resonance frequency of the composite beam the whole process is repeated every 10 minutes.

Finally the stiffness evolution of the tested material (concrete) can be inferred with basis on the resonance frequency evolution of the composite beam using the equation of motion of a simply supported beam with a mass at mid span (detailed explanations in Azenha *et al.* (2010)).

Since the original implementation of EMM-ARM, a pilot experiment was made to change the testing mould. The attempt, reported by Azenha *et al.* (2012), aimed to make the method more suitable for in-situ applications, through the use of a mould made with a thin steel plate (1mm in thickness) that had two interesting characteristics: the mould could be reused and had an open section on the top of the beam (configuration in "U") making the casting and vibration operations easier. However, despite the very successful implementation, the mould proved to be impractical to systematic use due to its large size (2.6 meter span). Furthermore, due to the reduced thickness of the steel plate used, the mould had some localized deformation in the cross section after a few uses, that tended to compromise the accuracy of the stiffness estimations, resulting in erroneous values of the concrete E-modulus.

IMPROVEMENTS TO THE AMBIENT VIBRATION METHOD

Until now the EMM-ARM method has been applied mainly in laboratorial conditions with very good outcomes. However the method still has some points where improvements are required. The main limitations are related to the mould used in the tests that tends to pose some problems when a systematic application is considered: (*i*) the casting operations as well as the handling of the mould is complex due to its significant length (2.0m); (*ii*) the mould material (acrylic) together with the

vertical connectors along the tube disable the access of a vibrating needle to vibrate the concrete inside the mould and (*iii*) the beam supports are very sensible to the meticulousness of the test operator. The aforementioned limitations pose relevant difficulties to the practical application of EMM-ARM in systematic in-situ experimental programs.

Based on these limitations, the following sections present part of a laboratory study conducted for validation of various proposed adaptations to the mould, as to make the method more suitable for in-situ applications. It is noted that all the experiments presented in this section share the same type of accelerometer placed at mid-span of the tested beam (PCB 393B12), which is in turned connected to an NI 9233 acquisition system with 24bit resolution at a rate of 500Hz.

Original mould adaptations

The main drawback of the original mould to perform EMM-ARM tests is related to its geometry. Therefore, it was decided to adapt the mould by reducing its total length, which renders easier casting operations. However, it is necessary to take into account that the reduction of the beam span increases the overall stiffness of the system and thus decreases the amplitude of ambient-induced vibrations of the beam, making accelerations more difficult to detect.

Therefore a parametric study was made to optimize the beam span. In this study it was established that the maximum resonance frequency of the first vibration mode of the beam should be around 150Hz. This value, which was based on the accumulated experience of previous applications, should be appropriate to enable the identification of the beam vibrations by the accelerometer used in the tests and to prevent the test from reaching very high resonant frequencies that could lead the test in to a dynamic regime. Thus, given a typical modulus of elasticity of concrete (30GPa) and a corresponding typical density (2400kg/m^3), a beam with similar cross-sectional characteristics to the original implementation (see Figure 1), but with a span of 0.9m was found to fill the intended requirements. It should also be noted that this smaller span increases the method resolution by increasing the range of variation of the resonance frequencies, from a range between 7.4 and 38.6Hz (original implantation) to a range between 28.8 and 147.7Hz (span reduced to 0.9m), when the stiffness of concrete evolves from 0 to 30GPa. The new mould, resulting from this adaptation, is shown in Figure 2.

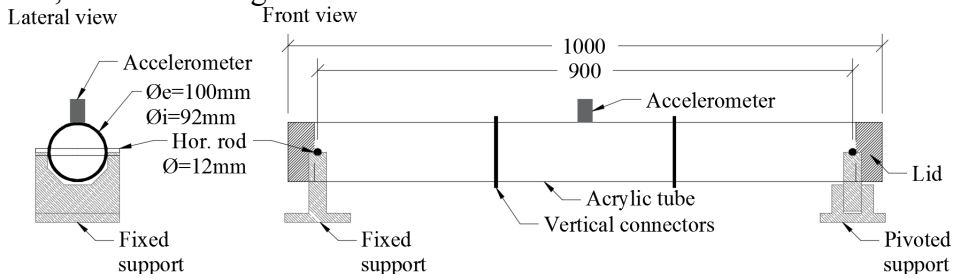

Figure 2. Scheme of the reduced span mould for EMM-ARM tests [units: mm].

In addition to the issues related to the vibrations identification, reducing the beam span strongly increases the sensitivity of the method to the stiffness of the beam

supports, and erroneous estimations of the concrete stiffness can be made as reported by Azenha *et al.* (2010). Therefore a further parametric study was conducted to verify the minimum acceptable vertical stiffness of the supports. For a beam with the geometry presented in the Figure 2, to estimate the concrete E-modulus with an error lower than 0.1% the vertical stiffness of the support should be at least 6GN·m. However, as mentioned, the supports of the original beam were very sensitive to the precision of the operator and to the adequate alignment of the horizontal rods. These issues can easily make the stiffness of the supports lower than the minimum acceptable and then the prediction of the real stiffness becomes a difficult task. So in attempt to eliminate this problem and increase the robustness of EMM-ARM, a new support system was designed. Figure 3 shows a photo of new EMM-ARM steel supports. These supports enable to control of the distance between the support and the tested beam and eliminate the effect of geometric imperfections of misalignments of the two horizontal rods that support the beam, by having a transversal bearing on one of the supports. In addition to the new steel supports, the diameter of the horizontal rods used to support the beam was increased from 5 to 12 mm as to increase the overall stiffness of the beam supports (see Figure 2).

Figure 3. New EMM-ARM steel supports.

In order to verify the viability of the proposed adaptations to the mould and support system, one test was performed with the beam shown in Figure 2. The concrete composition presented in Table 1 was used. In addition to the EMM-ARM beam, the modulus of elasticity of concrete was accessed through three cyclic compression tests (CC) performed after 7 days of curing according to standard LNEC E 397 (1993).

Table 1. Concrete composition.

Component	Mass (kg/m^3)
Fine sand	250
Medium sand	460
Gravel	1140
Cement CEM II/A-L 42.5R	218
Fly ash	112
Water	155
Admixture (Sikament 400+)	3.3

The resonant frequencies identified by EMM-ARM for the new beam (ACR-0.9-MS) are shown in Figure 4a. As it can be seen the range of frequencies covered during the test (34.1 to 153.6Hz) is much higher than range covered in the tests performed with the original beam (Typically 9 to 40Hz (Azenha *et al.*, 2010)). Nevertheless the evolution curve appears to be plausible, showing an initial dormant period after witch the frequency evolved significantly until approximately 24 hours of

curing period, followed by a dramatic reduction in the slope of frequency evolution. From these frequencies is possible to estimate the E-modulus evolution, as shown in Figure 4b. From observation of such figure, it can be seen that the modulus of elasticity results obtained at 7 days by EMM-ARM and CC tests showed a significant coherence allowing to confirm the viability of all the changes made in the EMM-ARM test mould.

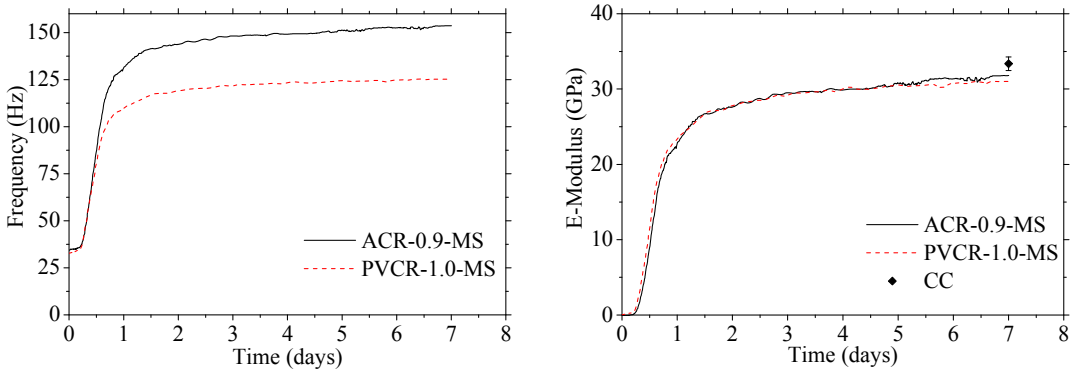

a) b)

Figure 4. EMM-ARM improvements test results: a) Frequency evolution; b) E-modulus evolution.

Development of a new reusable mould

Based on the previous developments, and taking into account the intention of making a reusable mould, a new PVC mould reinforced with aluminium rings, with the geometry shown in Figure 5, was tested. To enable the reuse of the PVC tube, the tube was sliced in two halves along its longitudinal direction through a vertical plane. The cut was made in this position as to avoid undermining the composite behaviour of the beam, as shear stresses are minimum in the top and bottom parts of the beam. In order to ensure constancy of geometry of the PVC mould, three lightweight aluminium rings were glued to the tube, which also ensure adequate connection between the two PVC halves.

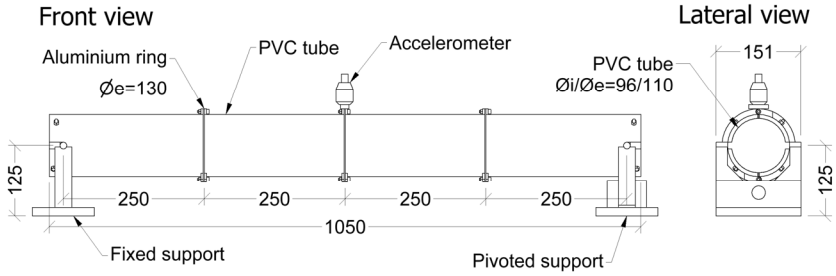

Figure 5. Scheme of the reusable mould for EMM-ARM tests [units: mm].

The combination of circular cross section of this mould, its span, thickness and material eliminates some of the problems observed for the steel U-shaped mould presented before. Indeed, the new mould allows better control of the geometry of the beam, while its smaller size, makes it more practical and easier to handle. This mould also has the advantage of not having connectors along its length, thus enabling the

access of a vibrating needle during casting operations. This new mould was tested with the same concrete of the previous reported experiment (shown in Table 1).

The evolution of the concrete elastic modulus monitored with this new beam (PVCR-1.0-MS) is shown in Figure 4b. There is a great coherence between the results obtained with the two different beams (acrylic and PVC), with deviations below 3% during the whole test. Furthermore, the results obtained by EMM-ARM beams and cyclic compression tests show only a shift of 1.25GPa (4%) thus validating the results of adapted EMM-ARM method.

IN-SITU MONITORING OF THE CONCRETE MECHANICAL PROPERTIES

The main objective of this work is the implementation of EMM-ARM methodology for continuous monitoring of the mechanical properties of concrete to serve as support to decision making in prestressing application during the construction of a bridge. The bridge where the study took place is located in the Dão river, and consists of three spans (120 m + 170 m + 100 m) supported by two intermediate columns. The deck consists of a prestressed concrete box girder, built by the balanced cantilever method. Each casting stage (4 to 5 meters long) is prestressed as soon as concrete reaches a prescribed minimum strength. Therefore, the use of a methodology that allows continuous estimates of the mechanical properties of concrete can be of significant usefulness to support decision-making processes for the prestress application. The next section presents a pilot study of the in-situ implementation of EMM-ARM to monitor the concrete curing process, providing real-time information on the mechanical properties. The concrete composition used in this bridge girder is shown in Table 2. It is noted that the maximum aggregate size is 22mm.

Table 2. Concrete composition

Component	Mass (kg/m^3)
Fine sand	330
Medium sand	560
Gravel 1	550
Gravel 2	440
Cement	220
Fly ash	130
Water	160
Plast.	2.10
Super.	2.45

In-situ validation of EMM-ARM

A pilot experiment was initially devised to perform the validation of EMM-ARM in the construction site. In this experiment, two different beams were tested: one acrylic beam with the same characteristics presented in the Figure 2 (ACR-0.9-MS-C) and one reusable PVC beam as presented in the Figure 5 (PVCR-1.0-MS-C). The test was carried out inside a container placed adjacently to the work area of the discharge of the concrete trucks. As the container did not have a

rigid floor, a small concrete slab was placed over the container's floor in order prevent adverse effects from the flexibility of the base on the resonance frequencies of the test beams. Accelerations were monitored by an accelerometer PCB 393B12 connected to a 24bit NI 4431 acquisition system at a rate of 500Hz. The samples were cured at room temperature.

The obtained results are shown in Figure 6a. It is remarked that, in addition to the EMM-ARM tests, cyclic compression tests (CC) were performed at 1, 2 and 7 days (three tests at each age) on test specimens casted on site and tested in the structures laboratory of the University of Minho, according to the standard LNEC E 397 (1993). By analysing the results of the EMM-ARM beams is possible to confirm that the kinetics of evolution of the elastic modulus of concrete has shape and magnitude consistent with typical results obtained in previous applications. It is also possible to observe a great coherence between the results obtained by the two EMM-ARM beams, with a maximum difference of 1.5GPa (3.5%). It should also be emphasized the congruence between the results obtained by the EMM-ARM and the classic cyclic compression method. This consistency in the results suggests that the EMM-ARM can be applied in construction site conditions. Despite these good results, a remark is made regarding the early age curing temperatures. In fact, due to the lack of temperature control in the tested specimens, they endured lower temperatures than those which were experienced in the actual structure. Therefore, some extent of discrepancy would be expectable within the first 1.5 days of curing, while hydration heat still had a relevant role. This limitation can however be easily overcome by imposing the temperatures recorded in the actual structure to the tested samples

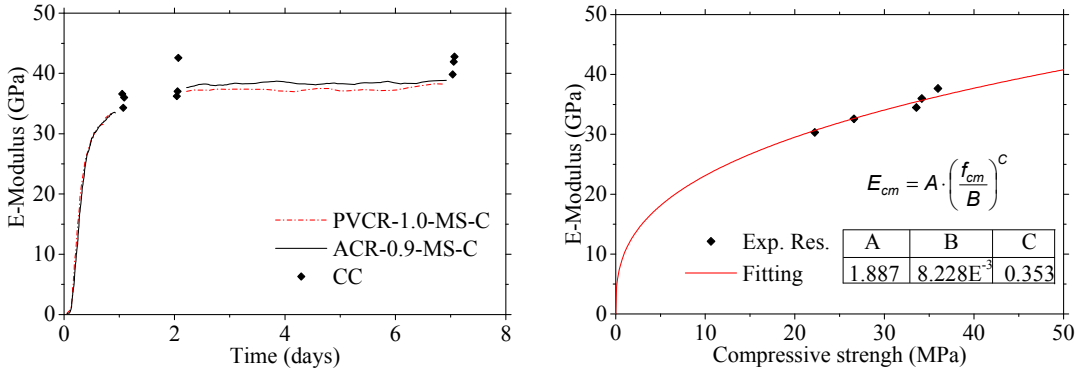

a) b)

Figure 6. a) E-modulus evolution of the EMM-ARM validation test; b) Relationship between compressive strength and elastic modulus.

After the in-situ validation of the EMM-ARM, it was necessary to devise a process that makes EMM-ARM results useful for the contractor to support prestress application decisions. For such purpose, the relationship between the concrete elastic modulus and compressive strength was assessed. For this purpose, in addition to the EMM-ARM beams and the cyclic compression tests presented above, compressive strength tests were conducted on concrete cubes, cured in the same conditions, in accordance with the standard EN 12390-3 (CEN, 2009), at 6 different ages: 0.58, 0.83, 1.33, 1.54, 1.71, and 28 days. The results of the compressive strength obtained

in these tests, compared to the corresponding average elastic modulus obtained through the EMM-ARM specimens at the same age are shown in the Figure 6b. A similar function to the one proposed by EN1992-2 (2010) was used to fit to the experimental data. The fitting was made through the minimization of the fitting error and the obtained coefficients (A, B and C) are shown in the table embedded in Figure 6b.

By applying the relation between the elastic modulus and the compressive strength is possible to estimate the evolution of compressive strength based on the results of the EMM-ARM tests. Figure 7 presents this estimation (average of the two EMM-ARM specimens) as well as the results of compressive strength of the tested cubes. As expected there is a great coherence between the results. To demonstrate that the EMM-ARM methodology can serve as a basis for decision-making in construction sites further tests will be performed and the same E vs f_{cm} relationship will be used. These further tests will encompass temperature matched curing to impose the same temperature of the real concrete structure to the EMM-ARM specimens, and thus obtain information that benefits from the acceleration of reactions induced by the temperature rises within the actual structure.

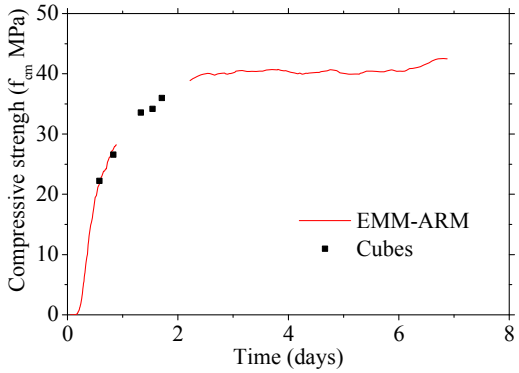

Figure 7. Estimation of the compressive strength of concrete.

CONCLUSIONS

This paper presents the optimization and application of EMM-ARM to construction sites as to support decision-making processes in prestress applications during the construction of a prestressed bridge. From the analysis of the experimental program where some improvements were suggested for EMM-ARM, the following conclusions can be drawn:

- In an attempt to make the method more suitable for in-situ applications, where the test procedures need to be as simple as possible, a set of changes to the EMM-ARM original mould has been successfully tested, in particular the reduction of the beam length and the development of a new support system. These adaptations have increased the robustness of the method and made the casting operations simpler.
- A reusable mould was designed to enable easier systematic use of EMM-ARM, reducing uncertainties between tests related to the use of newly fabricated moulds, which inherently have slight variations in geometrical and mechanical characteristics.

After the improvements made to EMM-ARM methodology a pilot test was made in the construction site of a bridge. This test allowed validating the adapted version of EMM-ARM in the context of in-situ environments.

It was also possible to show the potential that the methodology may have to serve as a support to decision-making in construction sites by providing real-time information on the mechanical characteristics of the concrete. However more tests need to be done to further validate this statement.

ACKNOWLEDGEMENTS

This work was supported by FEDER funds through the Operational Program for Competitiveness Factors - COMPETE and National Funds through FCT - Portuguese Foundation for Science and Technology under the project ViscoDyn EXPL/ECM-EST/1323/2013, as well to the Research Unit ISISE. The authors would like to thank all the companies that have been involved supporting and contributing for the development of this study, mainly, Grupo Casais, SA. The first author also acknowledges the PhD grant SFRH/BD/80338/2011 provided by FCT.

REFERENCES

Azenha, M., Magalhães, F., Faria, R. and Cunha, Á. (2010). Measurement of concrete E-modulus evolution since casting: A novel method based on ambient vibration. *Cement and Concrete Research,* 40 (7)**,** 1096-1105.

Azenha, M., Ramos, L. F., Aguilar, R. and Granja, J. L. (2012). Continuous monitoring of concrete E-modulus since casting based on modal identification: A case study for in situ application. *Cement and Concrete Composites,* 34 (7)**,** 881-890.

Beek, A. v. (2000). Dielectric properties of young concrete: non-destructive dielectric sensor for monitoring the strength development of young concrete. PhD Thesis, Delft University.

Boulay, C., Staquet, S., Azenha, M., Deraemaeker, A., Crespini, M., Carette, J., Granja, J., Delsaute, B., Dumoulin, C. and Karaiskos, G. (2013). Monitoring Elastic Properties of Concrete since Very Early Age by means of Cyclic Loadings, Ultrasonic Measurements, Natural Resonant Frequency of Composite Beam (EMM-ARM) and with Smart Aggregates. *In:* J.G.M. Van Mier, G. Ruiz, C. Andrade, R.C. Yu and X.X. Zhang (eds.) *VIII International Conference on Fracture Mechanics of Concrete and Concrete Structures. FraMCoS-8.* Toledo, Spain.

CEN (2009). Testing hardened concrete - Part 3: Compressive strength of test specimens. *EN 12390-3.* European Committee for Standardization.

CEN (2010). Eurocode 2: Design of concrete structures - Part 1-1: General rules and rules for buildings. *EN 1992-1-1.* Brussels, Belgium: European Committee for Standardization.

LNEC (Laboratório Nacional de Engenharia Civil) (1993). Betões - Determinação do módulo de elasticidade em compressão. *E 397.*

Voigt, T., Sun, Z. and Shah, S. P. (2006). Comparison of ultrasonic wave reflection method and maturity method in evaluating early-age compressive strength of mortar. *Cement and Concrete Composites,* 28 (4)**,** 307-316.

Welch, P. D. (1967). The use of Fast Fourier Transform for the Estimation of Power Spectra: a method based on time averageing over short, modified periodograms. *IEEE Transactions on Audio and Electroacoustics,* 15 (2)**,** 70-73.

Innovative Method for the Continuous Monitoring of Concrete Viscoelastic Properties since Early Ages: Concept and Pilot Experiments

M. Azenha[1]; J. Granja[1]; and R. Oliveira[1]

[1]Department of Civil Engineering, ISISE – Institute for Sustainability and Innovation in Structural Engineering, School of Engineering of the University of Minho, Campus de Azurém, 4800-058 Guimarães, Portugal. E-mail: miguel.azenha@civil.uminho.pt; granja@civil.uminho.pt; ricardobastosdeoliveira@gmail.com

Abstract

The experimental evaluation of viscoelastic properties of concrete is traditionally made upon creep tests that consist in the application of sustained loads either in compression or in tension. This kind of testing demands for specially devised rigs and requires careful monitoring of the evolution of strains, whereas assuring proper load constancy. The characterization of creep behaviour at early ages offers additional challenges due to the strong variations in viscoelastic behaviour of concrete during such stages, demanding for several testing ages to be assessed. The present research work aims to assist in reducing efforts for continuous assessment of viscoelastic properties of concrete at early ages, by application of a dynamic testing technique inspired in methodologies used in polymer science: Dynamic Mechanical Analyses. This paper briefly explains the principles of the proposed methodology and exhibits the first results obtained in a pilot application. The results are promising enough to encourage further developments.

INTRODUCTION

Even though the importance of concrete creep in structural behaviour is widely recognized, the existing design code approaches are relatively simplified, and research efforts still struggle with experimental difficulties both at very early ages of testing (less than 72h of age) and at very long term (several decades). In fact, it is probably due to current experimental limitations and relatively scarce comprehensive sets of data focused on these two opposing time spans, that the existing models for creep behaviour tend to exhibit limitations in such concern (Azenha, 2009, Bazant, 1988).

In view of the above identified research gap, the purpose of this paper is to describe an innovative testing procedure developed at the University of Minho that allows new insights into testing of the viscoelastic behaviour of concrete. The intent is to explore the possibility of using dynamic test approaches to assess viscoelastic properties of concrete, with the proposal of a new methodology termed VisCoDyn. Such innovative implementation can be achieved through the submission of a concrete specimen (e.g. a beam) to a known dynamic excitation and assessing the

corresponding response. According to the theory of viscoelasticity, the deflection response of the beam to the known excitation allows the identification of viscoelastic parameters. Even though similar experimental approaches have been mostly adopted in polymer science, with availability of commercial equipment for such purpose (DMA – Dynamic Mechanical Analyser), the reality is that very few polymer science works focus on the interpretation of DMA results in order to infer viscoelastic properties that can be related to those obtained in a classic creep test. Nonetheless, the underlying interconversion process is described in the literature (Park and Schapery, 1999).

In terms of concrete science, no references were found to focus in the subject of the present research, highlighting its innovative character. The paper focuses on the discussion of the hurdles that hinder the direct extrapolation of DMA techniques to concrete (e.g. those related to size and cement hydration processes), while showing the experimental setup that was developed for exploratory attempts, which involves a cylindrical specimen (100mm diameter and 1.0m long). Detailed descriptions are given in regard to the experimental setup that includes an electrodynamic shaker, a piezoelectric force/acceleration transducer and a laser displacement transducer. The experiment can be started right after casting. Then, sets of pre-programmed sinusoidal forces are applied, and the corresponding response of the beam is recorded. The experiment is fully automatic and requires no human intervention after it is begun.

A set of results is shown in this paper, highlighting the observed evolution of viscoelastic properties assessed through this method.

DYNAMIC CHARACTERIZATION OF VISCOELASTIC PROPERTIES

The dynamic characterization of viscoelastic properties is usual in polymer science. In such context, specifically devised equipment exists that allows to apply controlled excitations (normally sinusoidal) to the specimen under test and evaluate its response (Brinson and Brinson, 2008). This methodology is termed as ‘Dynamic Mechanical Analysis’ (DMA) and a functional scheme of a DMA experiment is shown in Figure 1. In the figure, the specimen is shown in its testing position, within the controlled environment chamber, and subject to simply supported conditions. The specimen typically has thickness of 5mm or less, whereas its length and width may reach approximately 50mm and 15mm, respectively (PerkinElmer, 2013). During testing, the specimen is subjected to a controlled dynamic load application at its mid-span (in case of a three-point bending configuration, as shown in Figure 1), with known amplitude and frequency, whereas the deformation of the specimen is recorded directly by instrumentation installed in the actuator.

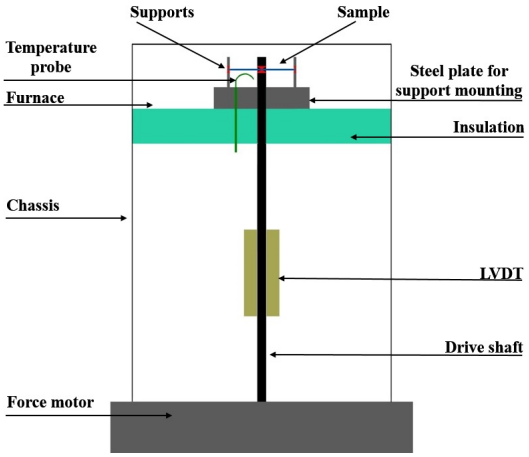

Figure 1. Functional scheme of a DMA apparatus [adapted from (NETZSCH, 2013)]

A typical input-output result of a DMA test is shown in Figure 2. The graphic shows an imposed sinusoidal force of amplitude $\pm\sigma_0$ and frequency f (1Hz in the depicted figure). The strain response of the tested specimen has the same frequency, with amplitude of $\pm\varepsilon_0$, but with a lag in the response as identified in the figure. This observed lag can be attributed to dissipative/viscoelastic processes in the material.

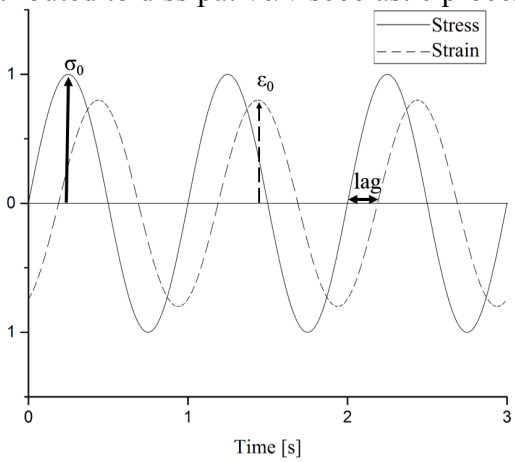

Figure 2. Typical input and output signal of a DMA test

Based on σ_0 (Pa), ε_0 and the lag (s) for a given frequency of testing (Hz), it is possible to quantify the phase angle of the material (δ), as well as the storage modulus *E'* (related to the elastic behaviour of the material) and the loss modulus *E''* (related to the viscous behaviour).

$$\delta = f * 360 * lag$$

$$E' = \frac{\sigma_0}{\varepsilon_0} \times \cos\delta$$

$$E'' = \frac{\sigma_0}{\varepsilon_0} \times \sin\delta$$

The storage and loss moduli correspond respectively to the real and imaginary part of the complex modulus, denoted by E^* as shown below:

$$E^* = E' + iE''$$

The DMA testing procedure that has just been described is usually conducted at several combinations of frequencies and temperatures in order to increase the quantity of information extracted from the experiment. An example of the storage modulus that is obtained upon testing at several temperatures and frequencies can be seen in Figure 3.

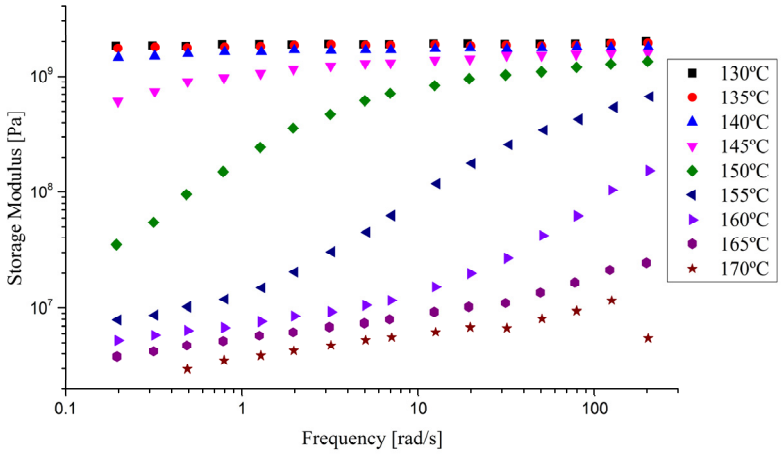

Figure 3. Storage modulus obtained for a DMA test conducted at several temperatures and frequencies [adapted from (Brinson, 2013)]

The observed behaviour in Figure 3 clearly shows that the tested material tends to show a stiffer response at lower temperatures and at higher frequencies of testing.

An important concept to be presented henceforward is the principle of time-temperature superposition. It basically consists in the interconversion of time and temperature through horizontal translation of the results represented in Figure 3, provided both axes (vertical and horizontal) are plotted in the logarithmic scale, and a reference temperature is defined (Dealy and Plazek, 2009). By applying such horizontal translation according to a predefined set of rules (Dealy and Plazek, 2009), it is possible to obtain a continuously chained curve, usually termed the Master Curve, that is shown in Figure 4. This curve allows describing the material behaviour at time scales that are far larger than those studied in the experiments. The application of this principle therefore allows to use experimental results obtained within the time scale of minutes to extrapolate the delayed behaviour at hours, days or even years. It is nonetheless remarked that the time-temperature superposition principles are only applicable to some materials (wide range of polymers), which are consequently classified as thermo-rheologically simple materials (Roylance, 2001).

Based on the data obtained from DMA testing, it is conceptually possible to perform mathematical interconversions that allow inferring the creep/relaxation parameters to describe the static delayed behaviour of the tested material through Prony/Dirichlet series (Park and Schapery, 1999, García-Barruetabeña *et al.*, 2013).

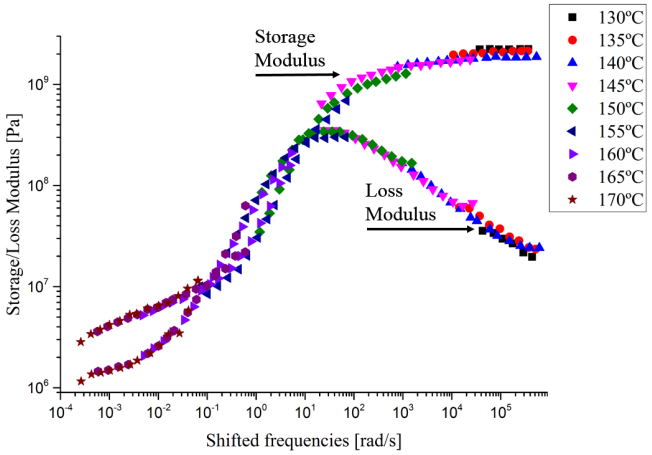

Figure 4. Master curve with values of E' and E" obtained after application of the time-temperature superposition principle [adapted from (Brinson, 2013)]

THE PROPOSED METHODOLOGY FOR CONCRETE

General overview

The literature review conducted in the scope of this research did not encounter any existing work that specifically focused in the application of dynamic testing principles (analogous to DMA) applied to the evaluation of viscoelastic properties of concrete at early ages. There are three main factors that are possibly contributing to this fact: (i) there is no evidence of the thermo-rheological simplicity of concrete in the literature; (ii) the hydration of cement brings chemical hardening to the material, thus further limiting the application of time-temperature superposition principles alone; (iii) the test setups are relatively difficult to deploy and require integration of know-how that is not usually available in concrete material scientists (structural dynamics, viscoelasticity, electronics). Even though conditions (i) and (ii) hinder direct applicability of DMA testing interpretation procedures, the condition (iii) was matched by the team at the University of Minho, particularly due to previous involvements in the development and improvements of the EMM-ARM technique (Azenha *et al.*, 2010), which relies on modal identification of a simply supported composite beam (filled with fresh concrete) in order to continuously infer the evolution of E-modulus of the tested concrete.

The team has thus embraced the challenge of producing an experimental setup inspired in DMA testing, that would be apt to continuously assess the dynamic response of a concrete beam since its early ages, and infer the evolution of δ, E' and E'' for a predefined set of testing frequencies, and at constant temperature (~20ºC).

The developed methodology is termed VisCoDyn, and it is intended to be applied in parallel with classical creep tests, as to infer potential synergies of these two methodologies, particularly in view of VisCoDyn filling gaps of information at ages in which classical creep tests are not possible (either due to problems with testing at very early ages, but also due to logistical issues).

VisCoDyn – Experimental setup and procedures

The pilot experiment of VisCoDyn had its setup strongly based on a recent implementation of EMM-ARM (Granja and Azenha, 2015). A longitudinal section of the experimental setup is shown in Figure 5 in order to support the description. The basic unit of the experiment is the acrylic beam of 1.0m length and 100mm outer diameter (92mm inner diameter). Concrete is casted into this acrylic mould through one of its extremities, with one of its lids already put into its final position in the opposite extremity. Upon completion of the casting process, the other extremity lid is fixed into position, and the specimen can be placed horizontally over steel supports that ensure structural operation as simply supported. These supports are actually in contact with horizontal rods that are placed into position before casting, and are aligned with the cross-sectional centre of gravity of the composite beam. The supporting rods are spaced by 900mm, which ends up being the actual free span of the beam. Additionally to the two horizontal rods, there are two further vertical rods that are placed at the thirds of the free span, acting as connectors between the acrylic and concrete as to ensure full composite behaviour.

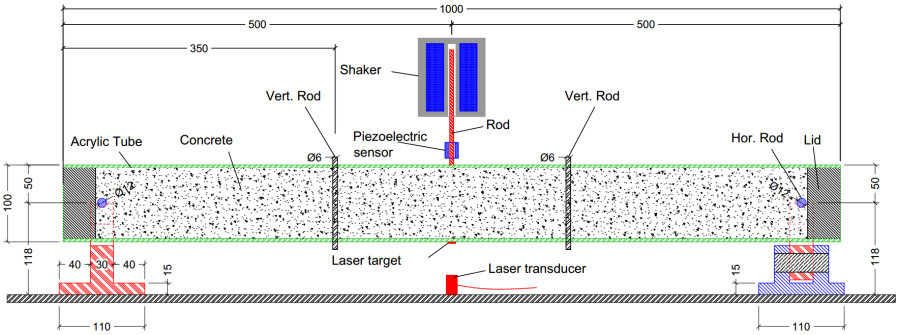

Figure 5. Schematic representation of the longitudinal section of the VisCoDyn setup (pilot experiment). Units: mm

The imposed force is applied by an electrodynamic shaker (Modal Shop 2025E), attached by a 2.5mm diameter steel rod to the top surface of the mid-span of the beam, and capable of exerting up to 58N at frequencies up to 9kHz. The actuator was suspended from a steel frame placed transversally over the beam.

The measurement of exerted forces and resulting acceleration was made with a piezoelectric sensor placed at the interface between the actuator rod and the beam itself. This piezoelectric sensor (PCB 288D01) has the capability to simultaneously monitor force and acceleration within the tested ranges. The devised setup also allows the measurement of displacements at the bottom of the tested beam through a non-contact technique based on a laser transducer (SICK OD25-01T1). However, the pilot experiments presented herein did not yet include such transducer.

The generation of excitation signals is made by a ±10V signal generator (NI 9269), whereas the force/acceleration measurement acquisition is made with a NI 9234 conditioner.

PILOT EXPERIMENTS

The first pilot experiment was conducted within a climatic chamber (20±1ºC) on a hardened specimen, which was 48 days age and had $f_{cm,28d}$=48MPa. A signal with 1V amplitude and fixed frequency (at a sampling rate of 25kHz) was sent to the amplifier as to attain 1 A intensity. The experiment was carried out at stretches of 60 seconds duration, each of which at a fixed excitation frequency of 40, 50, 60 and 100Hz. This strategy avoided potential resonance issues as the resonant frequency of the composite beam (determined in a preparatory experiment) was found to be 158Hz.

A second experiment was carried out by deploying a distinct strategy in regard to the actuator system. Instead of using the commercial shaker, a custom-built solution was built, based on a magnet combined with a coil, as shown in the photo of Figure 6. This alternative excitation technique has two interesting distinctive features in regard to the previous one: (i) it allows that the experiment is conducted without physical contact with the tested beam; (ii) the whole system is significantly cheaper due to the ease of construction of the coil/magnet. The second pilot experiment carried a further distinctive feature in regard to the first one, in the sense that the excitation was applied through frequency sweeps between 10 and 200Hz during 300 seconds, with peak-to-peak amplitude of 0.02N. The excitation signal was generated at a sampling rate of 20kHz.

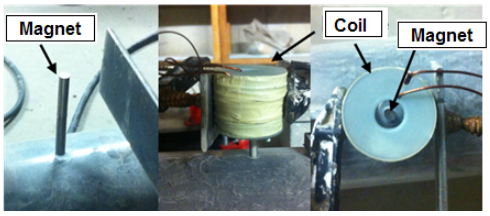

Figure 6. Photo of the actuator in the second pilot experiment

RESULTS AND DISCUSSION

As the pilot experiments did not include the actual measurement of displacements, the measurement of accelerations was used to evaluate the response delay. In fact, acceleration and displacement are shifted by 180º in regard to each other, thus their peaks coincide. All recorded forces in the several tested frequencies of the first pilot experiment had peak values in the range 8.4~9N, which are reasonably low values.

The force/acceleration diagram for pilot experiment 1 at 100Hz is shown in Figure 7. Firstly, it can be observed that the expected tendency of sinusoidal shape of both applied force and recorded accelerations was obtained. Furthermore, consecutive cycles exhibit remarkably similar behaviour, with the delay between imposed force and response acceleration being easy to identify, as shown in Figure 7b: the delay was 244μs, and the corresponding phase angle was 8.56º. Similar types of response were obtained in the other tested excitation frequencies, which are omitted here for the sake of brevity. Nonetheless, it is interesting to remark that higher frequencies of excitation led to smaller delays in the response, as expectable.

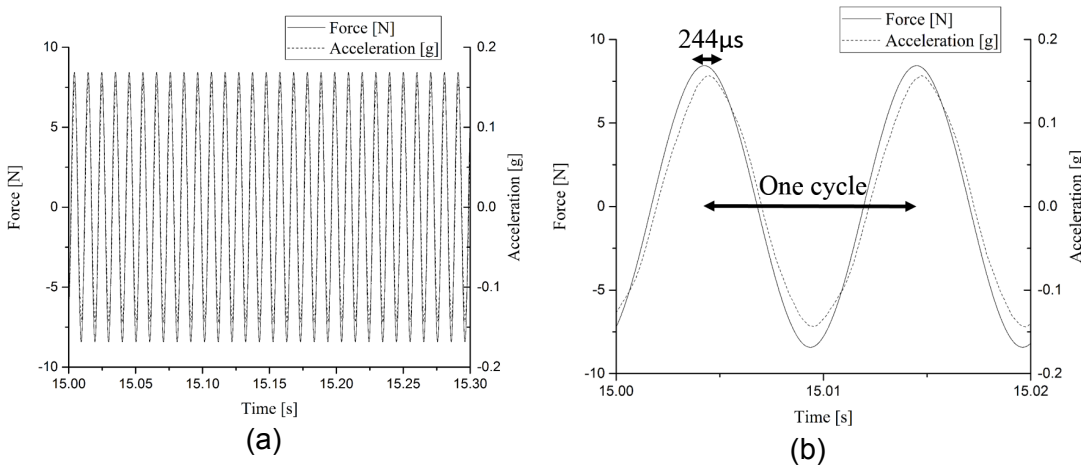

Figure 7. Results of the first pilot experiment at 100Hz: a) set of cycles; b) close-up of a single cycle

The second pilot experiment was conducted in frequency sweeps between 10 and 200Hz, allowing to obtain continuous representations of the variation in delay according to the excitation frequency, as shown in Figure 8. There is a consistent and continuous character of the decrease in delay as the excitation frequency increases. This points towards the feasibility of the adopted techniques and setups. However, the order of magnitude of the delay exhibited distinct values from those obtained in pilot experiment 1: at 100Hz, the delay recorded in pilot experiment 1 was 244μs, whereas that of pilot experiment 2 was 1066μs. Several factors may be contributing to this difference, one of which being the difference in stiffness and interaction possibility of both the testing systems. It is also worth remarking that the force level exerted by the coil/magnet in this second pilot experiment is much smaller than that of pilot experiment 1: 0.01 against ~8N. These aspects, among others, are still currently being studied.

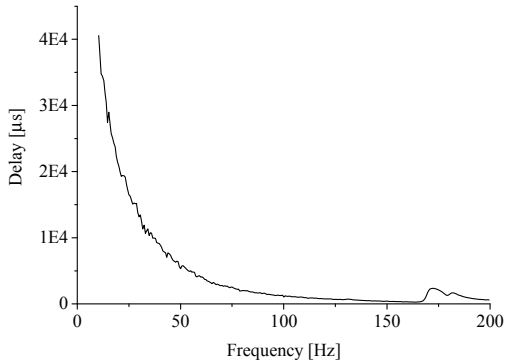

Figure 8. Pilot experiment 2: evolution of delay in the response of the tested beam, according to the excitation frequency

CONCLUSION

This paper has presented the conceptual principles and preliminary tests regarding a new method to evaluate viscoelastic properties of concrete since its early ages (termed VisCoDyn), with inspiration on methodologies that are normally applied in polymer science with very small specimens (DMA testing). Changing the scale of the experiment and introducing a complex material, such as concrete, raises several important challenges to the setup and procedures, but also to the interpretation of the results itself. The research work reported herein pertains to the first two pilot experiments applied to hardened concrete, before actually attempting to study hardening concrete samples. The results obtained have shown the feasibility of both test setup and procedures, allowing the evaluation of the delays and phase angles of the response of the specimen in regard to the applied excitation. Indeed, the relation between the excitation and response, as well as its dependency on excitation frequency have been coherent with the expectable trends for a viscoelastic material, such as concrete.

It is worth remarking that the second pilot experiment included a variant custom-built actuator (composed by a system coil/magnet). This lower cost alternative has demonstrated adequate performance levels that seem to be compatible with the expectable requirements for the VisCoDyn test.

Further experiments are now under way both on hardened specimens and also on hardening specimens, as to evaluate the true potential of applying the VisCoDyn method to infer the evolution of the viscoelastic properties of concrete. It is however remarked that the applications to hardening concrete are being applied to non-composite beams (i.e. without outside form), as to simplify the evaluation of results (i.e. avoiding the need to cancel the effects of the mould, which has a viscoelastic behaviour itself, as the case of acrylic).

ACNKOWLEDGMENTS

This work has been funded by FEDER funds (COMPETE program) and by National Funds through FCT (Portuguese Foundation for Science and Technology) in the scope of the Research Project EXPL/ECM-EST/1323/2013 and the individual PhD scholarship awarded to the second author (SFRH/BD/80682/2011). The authors also acknowledge the financial support of FCT to the research unit ISISE. The assistance of SECIL and CIMPOR is also gratefully mentioned in concern to the supply of materials for the tests here reported.

REFERENCES

Azenha, M. (2009). Numerical Simulation of The Structural Behaviour of Concrete Since its Early Ages. PhD, Faculdade de Engenharia da Universidade do Porto.

Azenha, M., Magalhães, F., Faria, R. and Cunha, Á. (2010). Measurement of concrete E-modulus evolution since casting: A novel method based on ambient vibration. *Cement and Concrete Research,* 40 (7)**,** 1096-1105.

Bazant, Z. P. (1988). Mathematical modeling of creep and shrinkage of concrete, John Wiley & Sons Ltd.
Brinson, F. H. and Brinson, L. C. (2008). Polymer engineering science and viscoelasticity: an introduction.
Brinson, L. C. (2013). Time-Temperature Superposition, McCormick School of Engineering - Northwestern University.
Dealy, J. and Plazek, D. (2009). Time-Temperature Superposition - A Users Guide. *Rheology Bulletin,* 78 16-31.
García-Barruetabeña, J., Cortés, F., Abete, J. M., Fernández, P., Lamela, M. J. and Fernández-Canteli, A. (2013). Relaxation modulus - Complex modulus interconversion for linear viscoelastic materials. *Mechanics of Time-Dependent Materials,* 17 (3)**,** 465-479.
Granja, J. and Azenha, M. (2015). Continuous monitoring of concrete mechanical properties since early age to support construction phasing. *In:* Mechanics and Physics of Creep, Shrinkage, and Durability of Concrete and Concrete Structures, 2015 Vienna, Austria.
NETZSCH (2013). Dynamic Mechanical Analysis - Method, Technique, Applications.
Park, S. W. and Schapery, R. A. (1999). Methods of interconversion between linear viscoelastic material functions. Part I—a numerical method based on Prony series. *International Journal of Solids and Structures,* 36 (11)**,** 1653-1675.
PerkinElmer (2013). DMA - A Beginner's Guide, PerkinElmer, Inc.
Roylance, D. (2001). Engineering Viscoelasticity, Massachusetts Institute of Technology.

EDF Study of 10-Years Concrete Creep under Unidirectional and Biaxial Loading: Evolution of Poisson Coefficient under Sealed and Unsealed Conditions

L. Charpin[1], Y. Le Pape[2], E. Coustabeau[3], B. Masson[4], and J. Montalvo[3]

[1]EDF R&D, Department of Mechanics and Materials of Components, Avenue des Renardières, Ecuelles, 77818 Morêt sur Loing Cédex, France; PH (+33) 160736647; email: laurent.charpin@edf.fr
[2]Oak Ridge National Laboratory, One Bethel Valley Road, Oak Ridge, TN 37831-6148, United States
[3]EDF DIN CEIDRE TEGG, 905 av Camp de Menthe, 13090 Aix en Provence, France
[4]EDF DIN SEPTEN, Division GS - Groupe Enceintes de Confinement, 12-14 avenue Dutriévoz, 69628 Villeurbane, France

ABSTRACT

The post-tensioned inner concrete containment building of nearly half of the French nuclear power plants has the role of barrier against potential radiological release, since these containments buildings have no metallic liner. Hence, the integrity of concrete and the stability of post-tensioning are of paramount importance. Since the variation of post-tensioning is partly due to concrete creep, EDF has been interested in the subject for more than two decades.

This article presents the results of experiments performed on a concrete similar to that of a concrete containment building, with an emphasis on the bidimensional nature of creep, on the basis of 1D and 2D tests that were performed at EDF. The evolution of the creep Poisson ratio is discussed as well as its use by different authors. Creep is then analyzed in terms of deviatoric and volumetric components. We show that assuming a constant Poisson ratio is a good assumption.

INTRODUCTION

Nearly half of the Nuclear Power Plants (NPPs) Concrete Containment Buildings (CCBs) in France were designed as double-containments: i.e., instead of placing a metallic liner, as commonly adopted for other Pressurized Water Reactors (PWRs) designs, a post-tensioned inner concrete containment creates a barrier against potential radiological release during a hypothetical accident. Although residual air leaks are collected and dynamically filtered in the air gap between the inner and the outer containments, the safety of the CCB is primarily dependent on the integrity of the concrete, which is tested periodically during the decennial Integrated Leak Rate Tests (ILRTs).

The air tightness of the post-tensioned CCB wall is largely dependent on the induced stress level, which decreases over the years as a result of concrete shrinkage

and creep. To prevent potential corrosion-induced brittle failure of the tendons, the tendon ducts are cement-grouted which does not make possible lift-off tests or subsequent re-tensioning procedures. Hence, the CCB deformations are permanently monitored using, in particular, embedded wire gauges. The need to predict the long-term creep deformations of the CCBs has conducted EDF to launch a comprehensive research program on the subject since the 90s.

MULTIAXIAL CREEP

Need for biaxial creep tests

In particular, a vast experimental program was developed in the early 2000s as a tentative approach to study the nature of biaxial creep, unaddressed question in Granger's pioneer work [Granger(1995)]. Since the CCB wall is post-tensioned in both vertical and circumferential directions, it is important to understand how a loading in one direction induces delayed strains in the other directions. The conducted experimental program includes shrinkage and creep tests on sealed and unsealed concrete specimen from the same batch; 1D-tests refers to concrete cylinders under vertical loading, while 2D-tests correspond to concrete rectangular prisms subjected to biaxial creep loading. The deformations of the 1D-test specimens are measured in the vertical and radial directions, while the deformations of the 2D-tests are measured in the three directions, which allows determining the actual creep Poisson Ratio (PR).

2D creep testing rigs

A specific 2D-testing rig was designed to reproduce the biaxial stress level obtained after post-tensioning the CBB prestressing system (see Figure 1). The magnitude of vertical and horizontal stresses are close to those developed in actual CBBs. To limit unwanted shear stresses, the biaxial loading is applied to the concrete specimens through a metallic-comb system. This system ensures that the applied stresses are effectively the principal stresses.

The creep Poisson ratio

The creep Poisson ratio (CPR) has been the subject of sustained research efforts in the past [Jordaan and Illston(1969), Gopalakrishnan et al.(1969), Parrott(1974), Bernard et al.(2003), Grasley and Lange(2007)], but remains largely unresolved. Assuming the elasticity theory of isotropic materials, its definition is unambiguous: it is the opposite of the ratio between transverse and axial strain in uniaxial compression. When viscoelasticity is assumed, the creep PR is obtained experimentally when the uniaxial stress is held constant, while a relaxation PR is obtained if the uniaxial strain is kept constant. Both these coefficients are equal to the elastic PR at the loading time, although their respective values can evolve differently over time [Hilton(2009)]. More-

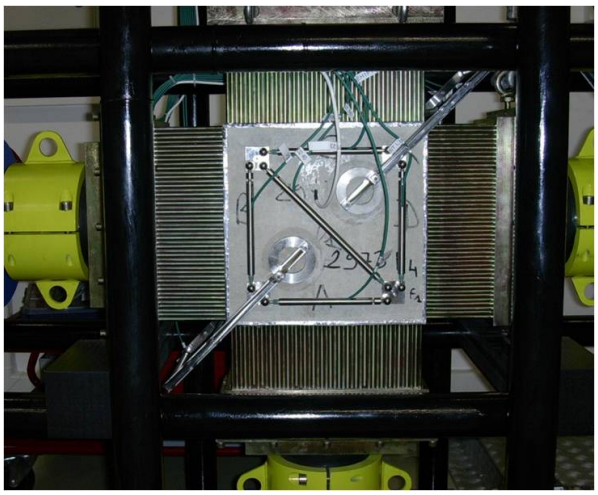

Figure 1. Close picture of the 2D rig and LVDT system used for strain monitoring

over, some authors have claimed that relaxation PR cannot be a decreasing function of time, which seems highly arguable, as pointed out by [Lakes and Wineman(2006)]. Adding even more confusion, the definition of the creep PR varies with the authors: e.g., [Gopalakrishnan et al.(1969)] derivation uses the creep strain only, after substracting the elastic part, which is questionable and makes the comparison difficult.

TEST RESULTS

In this section the creep compliance curves and the derived CPRs are presented both under sealed and unsealed (i.e., drying) conditions. It must be recognized that drying specimens are subjected to heterogeneous internal moisture content profiles, inducing varied local delayed strains and stresses causing an important micro-cracking and hence, heterogeneity of the sample [Bazant and Chern(1985), Benboudjema et al.(2005)]. All quantities computed on drying tests must therefore be considered as "apparent" properties rather than material properties.

Raw test results

We first show the results from the uniaxial tests. Two hydric conditions, respectively, sealed and unsealed (the room is kept at $T = 20 \pm 1$ °C and $RH = 50 \pm 10\%$), and two loading conditions, unloaded and loaded (the longitudinal stress is initially 12 MPa and decreases over 10 years by less than 10%) must be considered. 1D shrinkage and creep tests are performed on 16 cm diameter and 100 cm length specimens. The longitudinal strains shown on Figure 2 were measured by a single linear variable differential transformer (LVDT) displacement transducer, using 6 invar bars transmitting displace-

ments over a measuring length of 50 cm. Each test was performed on three samples in parralel. As a good agreement was found between the results of the three samples, two were stopped after 5 years, while a single test has been carried out for 11 years. After, the creep specimens were unloaded and a year of creep recovery was monitored. As it is found classically on samples of this size and this range of loading magnitude, the largest strains are found for the drying creep, followed by the sealed creep, the drying shrinkage, and finally the sealed shrinkage. Drying creep strains were almost, but never totally stabilized after two years. Sealed tests strains exhibited a gradual increase for the whole testing period, probably partly due to leaking of the sealant (two layers of aluminum foils for the 1D tests), but also because the mechanism of basic creep is instrinsically non-stabilizing. After 2-years, although the mass loss of unsealed samples is stabilized, the creep deformation induced by basic creep at 50% RH was still increasing. A similar observation was made on very-long-term creep experiments by [Troxell et al.(1958)].

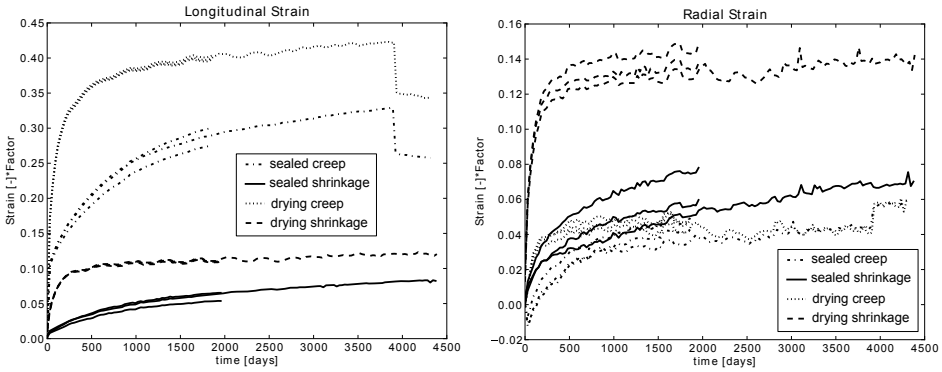

Figure 2. Left: longitudinal strain in the four 1D tests. Right: radial strain. Raw results multiplied by an unknown Factor for confidentiality purposes

The radial strain is measured by 3 LVDTs attached to an aluminum ring supported by the sample. The average radial strain is shown in Figure 2. The accuracy of the measurement is obviously less satisfactory than for the longitudinal strain for various reasons: (1) The reference distance is only 8 cm; (2) The magnitude of the radial strain is approximately a fifth of that of the longitudinal strain, and (3), the radial measurement is very sensitive to concret internal moisture loss close the contact point of the radial LVDTs with the sample.

The 2D-test raw results are not shown here due to space limitations, but the same comments could apply, except that due to the prismatic shape of the specimen and an improved measuring technology, the precision of the out-of-loading-plane-strain measurement was more satisfactory. The efficiency of sealing was also improved between the 1D and the 2D campaign, by placing four aluminum layers instead of two.

Discussion on the creep Poisson ratio

Definition chosen in this work To define the creep Poisson's ratio, we start with the multiaxial isotropic strain response to a stress increment $\underline{\underline{\sigma}}^0$ at time $t_0 = 90$ days, which we write in terms of the uniaxial compliance function $\overline{\overline{\mathcal{J}}}(t_0, t)$ and the creep Poisson ratio $\nu^c(t_0, t)$ as given by [Salençon(1983)]:

$$\underline{\underline{\varepsilon}}(t) = [1 + \nu^c(t_0, t)]\, \mathcal{J}(t_0, t)\underline{\underline{\sigma}}^0 - \nu^c(t_0, t)\mathcal{J}(t_0, t)\, \mathrm{tr}\, \underline{\underline{\sigma}}^0 \underline{\underline{1}} \tag{1}$$

For the 2D-creep tests, the stress and strain are defined by:

$$\underline{\underline{\sigma}}^0 = \begin{pmatrix} \sigma_v & 0 & 0 \\ 0 & \sigma_h & 0 \\ 0 & 0 & 0 \end{pmatrix},\ \underline{\underline{\varepsilon}}(t) = \begin{pmatrix} \varepsilon_v(t) & 0 & 0 \\ 0 & \varepsilon_h(t) & 0 \\ 0 & 0 & \varepsilon_w(t) \end{pmatrix} \tag{2}$$

Hence, inserting Eq. (2) into Eq. (1), the compliance function derived form the 2D test reads:

$$\mathcal{J}_{2D}(t) = \frac{\sigma_v \varepsilon_v(t) - \sigma_h \varepsilon_h(t)}{\sigma_v^2 - \sigma_h^2},\ \nu_{2D}(t) = \frac{\sigma_h \varepsilon_v(t) - \sigma_v \varepsilon_h(t)}{\sigma_v \varepsilon_v(t) - \sigma_h \varepsilon_h(t)} \tag{3}$$

The corresponding expressions for the 1D-creep test can be obtained by setting $\sigma_h = 0$ for instance.

These expressions lead to the derivation of the experimental Poisson ratio during a basic creep test (Figure 3). As mentioned by [Galenne et al.(2013)], and shown by [Torrenti et al.(2014)], the Poisson ratio, plotted here in a semi-logarithmic scale, slowly decreases from 0.35 to 0.25 over the 10 years of test in the 2D case, but decreases much faster in the 1D case, stabilizing around zero after about 1 year of testing. The CPRs derived from the 1D and 2D creep test show very different values. Can we conclude that the Poisson ratio has a different value depending on the kind of loading, as was concluded by some authors, e.g., [Gopalakrishnan et al.(1969)]? In our opinion the improvement of the quality of the sealing between the 1D and 2D tests makes them too different to conclude on this point. Note that the derived CPRs are decreasing functions of time, which is perfectly consistent with [Lakes and Wineman(2006)]. Relaxation PRs are also displayed, and are very close to the creep PR, due to their moderate variation in time. They were computed using and iterative inversion of the Laplace Transform as shown in [Sorvari and Malinen(2007)]. The Poisson ratio is now observed in the desiccation creep case (Figure 4). The removal of the shrinkage contribution in the drying creep measurement is made difficult by the fact that in the drying creep test, drying started at loading, i.e. 90 days, while in the drying shrinkage test, it started at 24h. Hence, we considered that the shrinkage contribution in the drying creep test at time t writes $\varepsilon^{es}(t) - \varepsilon^{es}(t - t_0) + \varepsilon^{ds}(t - t_0)$ where es stands for endogenous shrinkage while ds stands for desiccation shrinkage. We observe that the Poisson ratio is again slightly decreasing, from its elastic value, over the 11 years of the test. This time, the 1D and 2D tests give closer results.

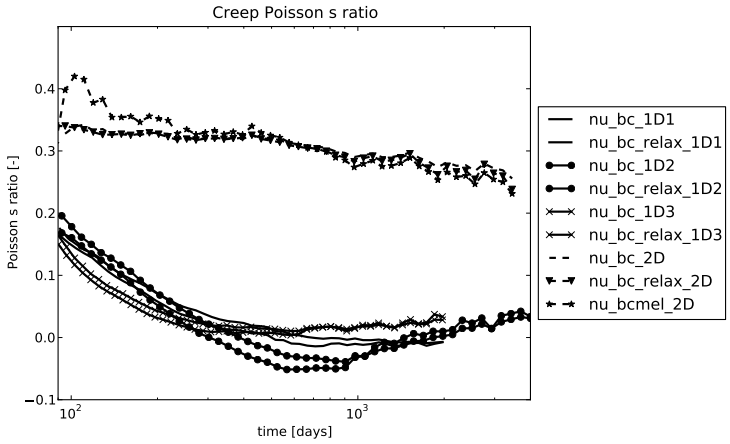

Figure 3. Creep and relaxation Poisson ratio for basic creep. Basic creep is here understood as the difference of the result of the sealed creep test and the sealed shrinkage test, except for nu_bcmel which was computed substracting the elastic strain.

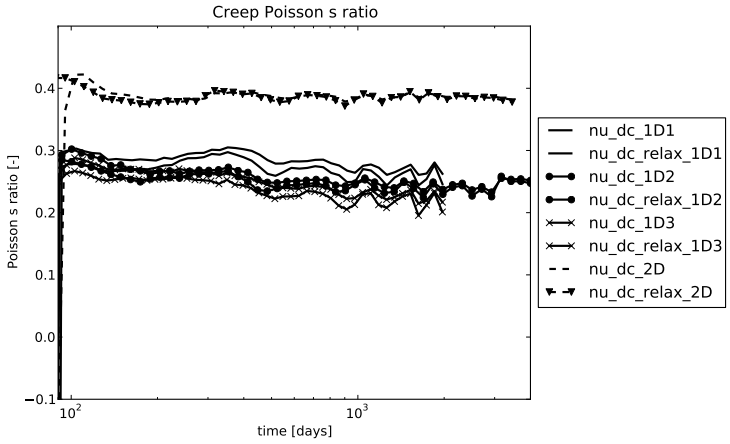

Figure 4. Creep and relaxation Poisson ratio for desiccation creep. Desiccation creep is here understood as the difference of the result of the drying creep test and the drying shrinkage test.

A point of surprise is the high value of the instantaneous Poisson ratio in 2D in both sealed and drying conditions, compared to usually admitted values of PRs for concrete. A possible explanation may be related to the loading rate that is know to increase the value of the instantaneous PR [Harsh et al.(1990)]. However, this does not

explain why the value of the CPR remains high after the application of the load. This question is still under investigation.

The main conclusion we can draw here is that in the 2D tests, for which the hydric conditions were best controlled, the Poisson ratio is almost constant. Let us now study the consequences of assuming a constant Poisson ratio.

Reconstruction of 1D tests from 2D tests, constant basic creep Poisson ratio In this paragraph, we use the compliances functions identified using the 2D results, and create a 1D response that we compare to the actual 1D tests (Figure 5). In terms of

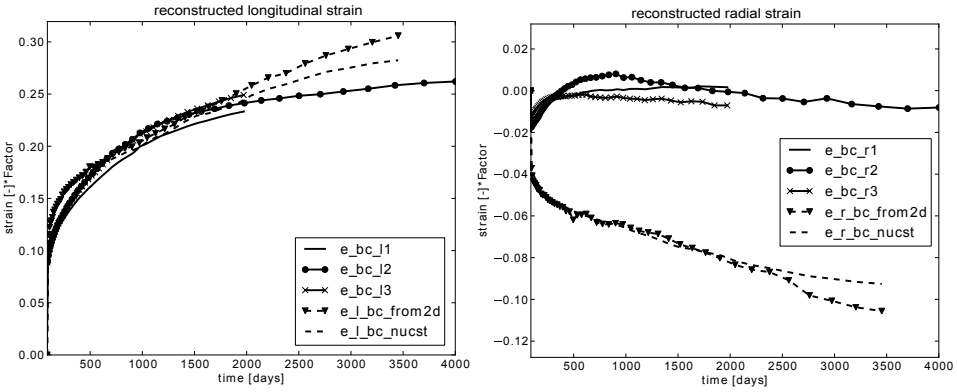

Figure 5. Comparison of longitudinal and radial strain computed from compliances identified on 2D tests to the actual 1D strains

longitudinal strains, the reconstructed strain (labeled "from2d" on Figure 5) is close to the 1D measured strain. This observation cannot be made regarding the radial strains. The reconstructed basic creep radial strain seems more physical that the measured one since it is a dilation rather than a contraction.

Finally we perform the same reconstruction, but instead of using the full value of the CPR determined on the 2D test, we replace it by its instantaneous value at loading. We can see that the reconstructed 1D response is very close. Our conclusion is that our 2D results show that assuming the CPR a constant equal to the elastic PR is a good approximation for modeling basic creep.

Comparison to PR not including elastic strain As Gopalakrishnan and, subsequently, a number of authors [Gopalakrishnan et al.(1969), Torrenti et al.(2014)] compute the creep PR not including the elastic strain, we also show the basic creep PR computed in this manner (Figure 3)

First, a singularity arises at the instant of loading, leading to high values of the CPR. Second, the initial value has no more reason to be equal to the elastic PR, which is inconvenient. However, for a moderately varying PR as in our case, the subsequent

evolution is close. Third, this definition is not compatible with the formalism of non-ageing viscoelasticity.

Given all these difficulties related to the definition and the derivation of the CPR, and even if our tests shows that it is almost constant, we suggest that this quantity should not be used to characterize multiaxial creep, but that volumetric and deviatoric creep functions are preferable. Hence, we present our results using these functions and discuss the results for the 2D-tests.

Volumetric and deviatoric creep strains

The strain response to a stress increment given in Equation 1 can also be written in terms of volumetric $\mathcal{L}(t_0,t)$ and deviatoric $\mathcal{I}(t_0,t)$ compliance functions.

$$\underline{\underline{\varepsilon}} = \mathcal{I}(t_0,t)\underline{\underline{\sigma}}^0_d + \frac{1}{3}\mathcal{L}(t_0,t)\,\mathrm{tr}\,\underline{\underline{\sigma}}^0\underline{\underline{1}} \tag{4}$$

Inserting the stress and strain tensors given in Eq, (2) into Eq. (4), one gets in the 2D case :

$$\begin{cases} \mathcal{L}_{2D}(t) = \dfrac{\varepsilon_v(t)+\varepsilon_h(t)+\varepsilon_w(t)}{\sigma_h+\sigma_v},\ \mathcal{I}^1_{2D}(t) = \dfrac{2\varepsilon_v(t)-\varepsilon_h(t)-\varepsilon_w(t)}{2\sigma_v-\sigma_h} \\ \mathcal{I}^2_{2D}(t) = \dfrac{2\varepsilon_h(t)-\varepsilon_v(t)-\varepsilon_w(t)}{2\sigma_h-\sigma_v},\ \mathcal{I}^3_{2D}(t) = -\dfrac{2\varepsilon_w(t)-\varepsilon_v(t)-\varepsilon_h(t)}{\sigma_v+\sigma_h} \end{cases} \tag{5}$$

Where the three expressions for the deviatoric strain are determined in each direction. The deviatoric and volumetric compliances for basic and drying desiccation creep are shown in Figure 6. The good agreement between the different deviatoric creep curves shows that the material remains isotropic. Recalling that the quality of the sealing of our tests was such that important water leakage occurred in the 1D tests, and that is was much more limited in the 2D tests, we can draw the conclusions that (1) the volumetric drying creep is much faster than volumetric basic creep, but it stops before the mass is stabilized, while the volumetric basic creep continues to increase; (2) the deviatoric drying creep kinetics is also much higher than that of the deviatoric basic creep, and continues as long as the mass loss continues.

CONCLUSION

In this article, we explain the need for 2D-creep tests in the context of the safety of Nuclear Power Plants. We provide information about the 2D creep rig that was developed at EDF for the purpose of better understanding the nature of multiaxial creep.

We compute the creep Poisson ratio in the manner that seemed the most rigorous and display these quantities for basic and desiccation creep. We show that, at least for the 2D-sealed-creep tests, their variation is moderately decreasing. We also show that assuming constant Poisson ratio is a good assumption and that the radial measurements in 1D are questionable.

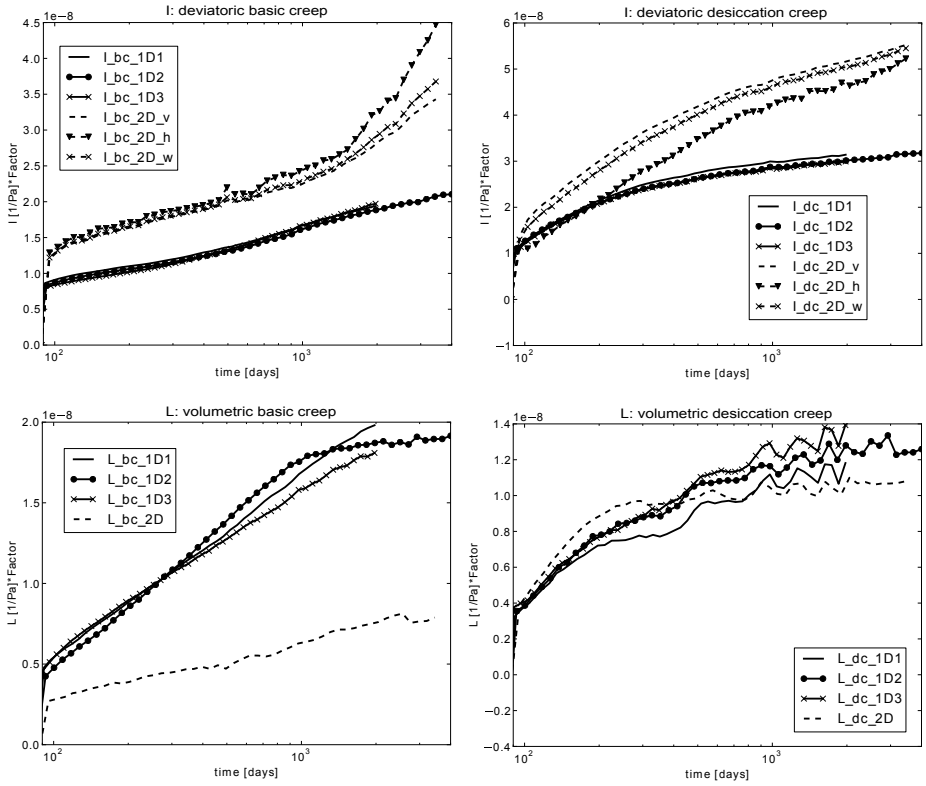

Figure 6. Volumetric and deviatoric, basic and desiccation creep.

Finally, we argue that, at least in the situations where the creep Poisson ratio is not constant, it is preferable to use the deviatoric and volumetric creep compliances, because their definition is unambiguous.

REFERENCES

[Bazant and Chern(1985)] Z.P. Bazant and J.C. Chern. Concrete creep at variable humidity: constitutive law and mechanism. *Materials and structures*, 18(1):1–20, 1985.

[Benboudjema et al.(2005)] F. Benboudjema, F. Meftah, and J.-M. Torrenti. Interaction between drying, shrinkage, creep and cracking phenomena in concrete. *Engineering structures*, 27(2):239–250, 2005.

[Bernard et al.(2003)] O. Bernard, F.-J. Ulm, and J.T. Germaine. Volume and deviator creep of calcium-leached cement-based materials. *Cement and concrete research*, 33(8):1127–1136, 2003.

[Galenne et al.(2013)] E. Galenne, A. Foucault, and F. Hamon. Prediction of delayed strain of nuclear containment building: from laboratory tests to a industrial mock-up. *Proceedings of TINCE 2013, Paris, France*, 2013.

[Gopalakrishnan et al.(1969)] K.S. Gopalakrishnan, A.M. Neville, and A. Ghali. Creep poisson's ratio of concrete under multiaxial compression. In *ACI Journal Proceedings*, volume 66. ACI, 1969.

[Granger(1995)] L. Granger. *Comportement différé du béton dans les enceintes de centrales nucléaires : analyse et modélisation*. PhD thesis, École Nationale des ponts et Chaussées, 1995.

[Grasley and Lange(2007)] Z.C. Grasley and D.A. Lange. The viscoelastic response of cement paste to three-dimensional loading. *Mechanics of Time-Dependent Materials*, 11(1):27–46, 2007.

[Harsh et al.(1990)] S. Harsh, Z. Shen, and D. Darwin. Strain-rate sensitive behavior of cement paste and mortar in compression. *ACI Materials Journal*, 87(5), 1990.

[Hilton(2009)] H. Hilton. The elusive and fickle viscoelastic poisson's ratio and its relation to the elastic-viscoelastic correspondence principle. *Journal of Mechanics of Materials and Structures*, 4(7):1341–1364, 2009.

[Jordaan and Illston(1969)] I.J. Jordaan and J.M. Illston. The creep of sealed concrete under multiaxial compressive stresses. *Magazine of Concrete Research*, 21(69): 195–204, 1969.

[Lakes and Wineman(2006)] R.S. Lakes and A. Wineman. On poisson's ratio in linearly viscoelastic solids. *Journal of Elasticity*, 85(1):45–63, 2006.

[Parrott(1974)] L.J. Parrott. Lateral strains in hardened cement paste under short-and long-term loading. *Magazine of Concrete Research*, 26(89):198–202, 1974.

[Salençon(1983)] J. Salençon. *Viscoélasticité*. Presses de l'Ecole Nationale des Ponts et Chaussées, 1983.

[Sorvari and Malinen(2007)] J. Sorvari and M. Malinen. On the direct estimation of creep and relaxation functions. *Mechanics of Time-Dependent Materials*, 11 (2):143–157, 2007. ISSN 1385-2000. doi: 10.1007/s11043-007-9038-1.

[Torrenti et al.(2014)] J.M. Torrenti, F. Benboudjema, F. Barré, and E. Gallitre. On the very long term delayed behaviour of concrete. *Proceedings of the International Conference on Ageing of Materials & Structures*, 2014.

[Troxell et al.(1958)] G.E. Troxell, J.M. Raphael, and R.E. Davis. Long-time creep and shrinkage tests of plain and reinforced concrete. In *ASTM Proceedings*, volume 58, pages 1–20, 1958.

Experimental Investigation of the Creep-Damage Interaction Effect on the Mechanical Behaviour of Hardening Concrete

M. Farah; A. Loukili; and F. Grondin

LUNAM Université, Ecole Centrale de Nantes, Institut de Recherche en Génie Civil et Mécanique (GeM), UMR-CNRS 6183, 1 rue de la Noé, F-44321 Nantes.
E-mail: mounia.farah@ec-nantes.fr; ahmed.loukili@ec-nantes.fr; frederic.grondin@ec-nantes.fr

Abstract

The creep behavior of concrete structures at long term depends on the initial state and therefore on an eventual damage of the main material. Most studies were interested in creep phenomenon of mature concrete while a few works were carried out on young concrete. However, the concrete structures may be solicited earlier as the tensioning of the pre-stress cables induces an early creep and an eventual cracking, thus reducing the structure capacity at the long term. An original device for creep tests has been developed to follow the evolution of the displacement, the force and the crack opening during creep since early ages for concrete beams. Creep tests were performed on concrete beams aged of 24h during 28 days. Results show that creep influences the rigidity and the strength when the load-to-strength ratio is maintained constant and if the beam is damaged before the creep test.

1. Introduction

The study of the earlier loaded materials is very interesting because it allows assessing the interaction between creep deformations, damage and hardening. There are different scenarii for concrete submitted to creep at early ages. For example, the concrete in contact with reinforcements or of the pre-stress cables in reinforced and pre-stressed concretes is locally submitted to high stresses due the restrained shrinkage. These stresses increase with the hydration process of the young concrete and lead to a stresses redistribution in the nearby zones and thus to the creep deformations which induce microcracking. In addition, the concrete underground structures (tunnels for example) are early submitted to the soil pressure which can be considered constant and which leads to significant creep deformations.

The creep tests of young concrete are generally performed in tension and compression (Atrushi 2003; Briffaut et al. 2012; Østergaard et al. 2001), but not in flexion. Indeed, the flexural creep tests have a particular interest in studying the interaction between creep deformations and damage (Saliba et al., 2012). In this type of solicitation, the cracks appear when the tensile strength in the lower fiber of the beam is reached; the propagation of the cracks is then blocked near of the neutral axis due to the weak stresses in this area. In addition, as mentioned before, the long term behavior of concrete depends on its initial state. So the creep loading of the pre-damaged material gives more information of the interaction between creep deformations and damage. To assess this interaction, Carpinteri and coworkers

(Carpinteri et al. 1997) have been studied the desiccation creep of mature pre-damaged specimens in tension and bending.

The early loaded materials are characterized by the evolution of their hydration degree during loading. This leads to an increase of the mechanical parameters as the Young's modulus and the strength. Thus, the stress level applied at the beginning does not remain constant but it decreases vs. the hydration degree (Jiang et al. 2014; Kovler et al. 1999). Some authors took into account this strength increase during loading by applying a stepwise increasing creep load (Hughes and Ash 1970; Jiang et al. 2014). However, the creep tests at early ages are, in most cases, for constant stress levels.

Rusch and coworkers (Rüsch H. 1960; Rüsch et al. 1958) were the first to reveal the damage of concrete under creep. Then, other authors (Omar et al. 2009) brought out the decrease of the residual strength, fracture energy and the fracture process zone due to creep. The evolution of the microcracking during loading has also been confirmed by the acoustic emission technique (Rossi et al. 1993; Saliba et al. 2012). The nonlinearity thresholds, beyond which the cracks start to develop, depend on the type of solicitation. For mature concretes the authors agree on the variation interval of these thresholds, but for young concretes these thresholds vary from an author to another.

The present work highlights the development of a new experimental approach in order to study the interaction between creep and damage at early ages by means of three-point-bending creep tests. For that, creep loadings were performed on initially sound concrete beams and partially damaged ones. Finally, to evaluate the effect of the creep loading history on the mechanical behavior, the beams were loaded up to failure without stress relaxation to obtain the residual capacity.

2. Experimental investigation

2.1. Materials

The studied concrete mixture is composed of Portland cement CEM I 52.5 N, crushed coarse aggregates of classes 6/10 and 10/14, having respectively an absorption coefficient of 0.41% and 0.31%, a marine sand of class 0/4 with an absorption coefficient of 2.19%. The densities and mass contents of the constituents are given in Table 1. This formulation is characterized by a water-to-cement ratio of 0.57, a compressive strength at 28 days (fc_{28}) of 37 MPa and a slump of 165 mm.

Table 1. Concrete mixture.

Constituents	*Dosage (kg/m^3)*	*Density (kg/m^3)*
Gravel 6/10	210	2980
Gravel 10/14	860	2990
Sand 0/4	824	2550
CEMI 52.5N	350	3140
Effective water	199	1000

2.2. Specimen preparation

The flexural failure and creep tests were performed on notched beams of prismatic geometry. The beam's dimensions are presented in Figure 1. The samples were cast in plastic moulds containing a metallic plate with a thickness of 1mm to create the notch. The upper surfaces of the moulds were covered by a double impermeable plastic sheet to avoid drying. The moulds were then stored in a room at a temperature of 20°C and a relative humidity 80%. The beams were demoulded two hours before the tests performed at 24h, 48h and 7d, while they were demoulded after 24h and then placed in a basin of saturated lime water for the tests performed at 28d.

To avoid desiccation during creep tests, a double layer of adhesive aluminum paper was glued on tested beams. The height of the notch is equal to 4 cm which represents 1/5 of the total height of the beam.

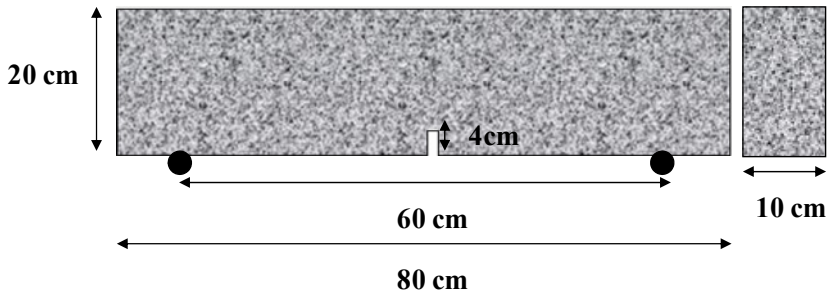

Figure 1. Geometry of the tested beams.

2.3. Experimental setup

The new three-point bending frames (Figure 2) allow performing failure tests as well as creep tests thanks to their double function (force and crack opening controls). In addition, these frames enable to realize creep tests on pre-damaged beams and load up to failure without stress relaxation.

The three-point bending failure and creep tests took place in a room at a temperature of 20°C (± 2°C) and relative humidity of 50% (± 5%). These devices are composed of an electromechanical press (Figure 2) with a capacity of 50 kN (± 5N). The failure tests were controlled by the Crack Mouth Opening Displacement (CMOD) with a speed of 3 µm and the creep tests by the force load. The deflection is measured in the beam's center by a LVDT gauge, having a measurement range of ±1mm and accuracy of 1µm. The crack opening is measured by a CMOD gauge, placed at the bottom of the beam, with a measurement range of (0mm, 5mm) and an accuracy of 0,1 µm.

The load was applied at the midspan with a cylindrical tip to ensure a point of load application. A rubber pad was placed between the press and the beam to avoid localized damage in the point of the load application.

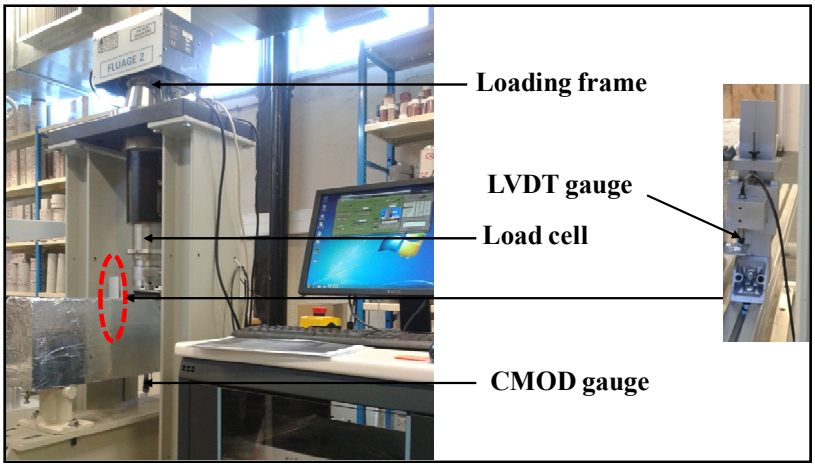

Figure 2. Components of the three-point bending frame for creep and failure.

2.4. Three-point-bending tests

Two series of three-point-bending basic creep tests were performed on undamaged notched concrete beams: the first one (serie SI) with a constant load and the second one with a stepwise increasing creep load (serie SII), which is done in an automatic way, to maintain the creep loading level constant. The creep test was done in two steps. At the first step, the desired load (30% of the strength at the loading age) was reached by the CMOD control. Then, the creep loading was controlled by the load. Finally, to assess the creep effect on the mechanical behavior, the beams of the two series were loaded up to failure.

The modeling of concrete damage is based on the softening behavior which is characterized by the decrease of the stress-carrying capacity and the increase of the deformation in the damage zone. Therefore, the interaction between creep and damage of the strain-softening materials loaded at early ages has been experimentally investigated. Two series of three-point bending basic creep tests were carried out on partially-damaged beams. Beams were loaded until a desired residual strength in the softening branch, corresponding to 90% of the maximum strength. Then they were unloaded and reloaded to 30% of the residual strength (serie SIII). After 28 days under creep, the beams were then loaded up to failure to determine the residual capacity. The load-deflection curves were used to assess the effect of the interaction creep-damage on concrete stiffness and residual strength.

3. Results and discussion

3.1. Case of the initially undamaged beams

The flexural strength values at the pre-defined ages are given in Table 2. These values allow following the evolution of the strength during loading by increasing the creep load in order to keep a constant load level (serie II).

Table 2. Flexural strength values at different ages

Age	*24h*	*48h*	*7d*	*28d*
Peak load (kN)	7.4±0.3	9.1±0.45	11.4±0.4	13.3±1

The creep displacements for the series I and II are shown on Figure 3 where the instantaneous displacement (obtained when the constant load has been reached) has been removed. The comparison of the creep displacements of the two series I and II shows the effect of the creep load increase on the magnitude of the displacement. This difference in amplitudes is due to stresses redistribution within C-S-H hydrates at the time of load increase which leads to additional deformations.

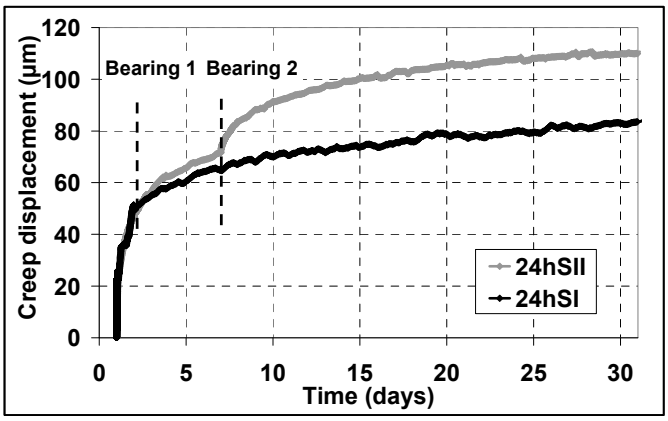

Figure 3. Comparison between the creep displacements of the series SI and SII.

Despite the importance of the creep displacement magnitude of the series II, the beams did not reach the failure after one month of loading. As a result, we loaded the beams up to failure in order to evaluate the effect of the creep loading history on the mechanical behavior. The Figure 4 shows the mechanical behavior after creep of the two series I and II. The flexural strength of SI is equal to that obtained for concrete beams at 28 days without creep (Table 2). But, we can observe a relative decrease of the residual flexural strength and a significant decrease of the stiffness for the beams of SII. This means that the material, under the stepwise increasing load, loses its mechanical capacities. Therefore, the material behavior is no longer linear which could be explained by the microcracks formation and then of an increase of a damaged zone.

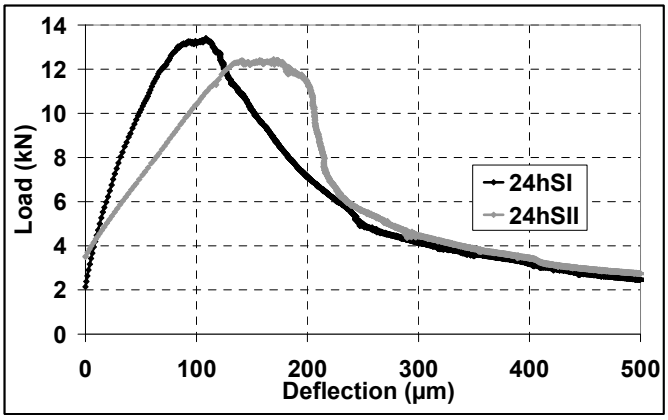

Figure 4. Effect of creep loading history on the mechanical behavior.

3.2. Case of the partially damaged beams

The Figure 5 shows the load-CMOD curves for the partially damaged beams SIII. The period between the two failure curves concerns the creep test which is discussed below.

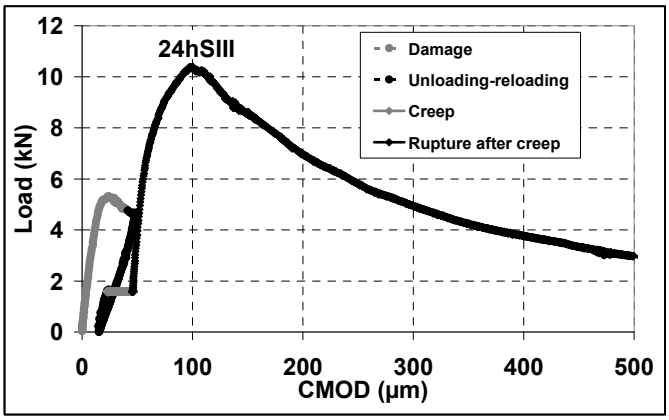

Figure 5. Failure tests for the serie SIII.

The Figure 6 shows the comparison between the creep displacement of the series I and III. For damaged beams the method retained below to remove the instantaneous displacement can not be applied, because during the reloading the displacement can not be considered as an elastic phase. That is why we have chosen to remove the displacement for the first day of the creep test. We observe that the creep displacements of the two series are equal which means that the pre-damage does not influence the creep evolution kinetic. This result can be explained by the fact that the material hardens during the creep period due to the hydration process and also by the low rate of loading which does not lead to a significant microcracking.

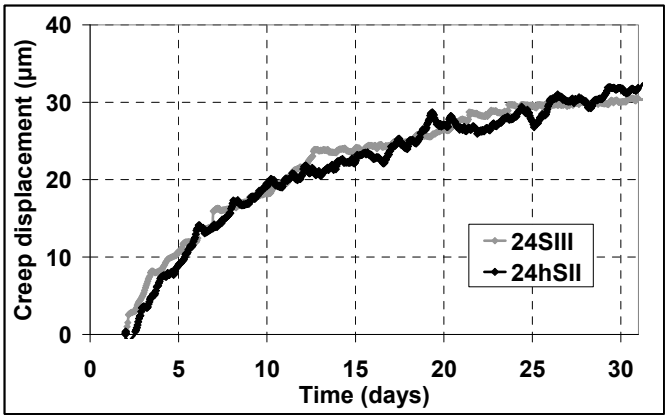

Figure 6. Comparison between the creep displacements of initially undamaged beams and partially damaged beams.

In order to assess the effect of the creep-damage coupling on the mechanical parameters after creep, we compare the mechanical behavior of the initially undamaged beams (SI) to that of the partially damaged beams (SIII). Results given in the Figure 7 show a significant decrease of the residual load and the stiffness of the partially damaged beams. Indeed, for the initial damage state made in these beams, the density of microcracks is very important and leads to an increase of the crack length at the tip crack equivalent to 22% of the ligament (area between the crack tip and the edge of the specimen) as approved by the digital image correlation technique (Alam 2011) performed on mature concrete beams with the same dimensions as the beams of the current study. Therefore, based on these results, the crack length at the crack tip for the beams of SIII at the time of loading is very important and could be greater than that observed for the mature concrete. So, in spite of the lower load level (30%) and the continuation of the hydration process in the pre-damaged beams loaded at early ages, the evolution kinetic of the mechanical parameters during the creep loading is very influenced by the creep-damage interaction. Then, the gain in mechanical properties of pre-damaged material is much less than that of the undamaged one.

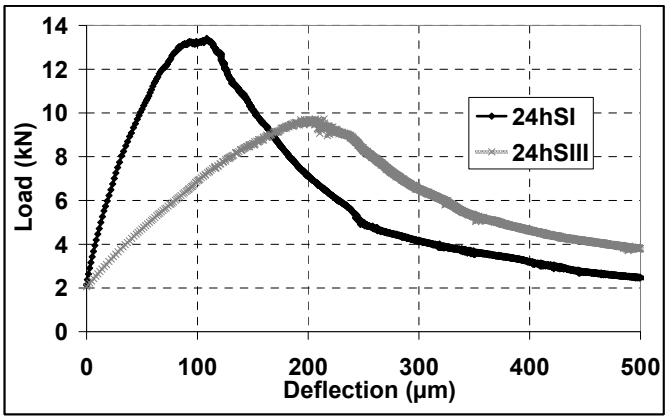

Figure 7. Comparison of the mechanical behavior of the series SI and SIII.

In comparison with the values at 28 days for uncreep beams, the decrease, in the mechanical properties of the serie SIII is mainly due to the first failure test. In the Figure 5 we see that the flexural strength after creep is higher than that obtained at 24h. So, the solidification of concrete with hydration overrides damage formed during creep.

4. Conclusion

We can deduce from the previous results that contrary to the mature concrete where the nonlinearity threshold of the three-point-bending creep tests is more important (about 70% of the peak load), the young concrete loaded at 24h loses this linearity by applying an increase creep load level equal to 30% of the maximum strength evolving during the creep loading. This result was approved by failure tests after the creep loading, showing a decrease in the residual capacity and the stiffness of the material submitted to a gradual increase creep load compared to that submitted to a constant creep load.

To evaluate the effect of the creep-damage interaction on the mechanical behavior after creep, we performed creep tests on the partially damaged beams. Then, to assess the pre-damage effect on the mechanical behavior after creep, we compared failure tests of initially undamaged beams and those of the partially damaged beams. Results showed a very significant decrease in the residual strength and the stiffness of the pre-damaged material.

REFERENCES

Alam, S. Y. (2011). “Experimental study and numerical analysis of crack opening in concrete.” *Ph.D. thesis, Ecole Centrale de Nantes*.

Atrushi, S. D. (2003). “Tensile and compressive creep of early age concrete: testing and modelling.” *Ph.D. thesis, Norwegian University of Science and Technology*.

Briffaut, M., Benboudjema, F., Torrenti, J.-M., and Nahas, G. (2012). “Concrete early age basic creep: Experiments and test of rheological modelling approaches.” *Construction and Building Materials*, Elsevier Ltd, 36, 373-380.

Carpinteri, A., Valente, S., Zhou, F., Ferrara, G., and Melchiorri, G. (1997). “Tensile and flexural creep rupture tests on partially-damaged concrete specimens.” *Materials and Structures*, 30(June), 269-276.

Hughes, B. P., and Ash, J. E. (1970). “Some factors influencing the long term strength os concrete.” *Materials & Design*, 3(2), 81-84.

Jiang, W., De Schutter, G., and Yuan, Y. (2014). "Degree of hydration based prediction of early age basic creep and creep recovery of blended concrete." *Cement and Concrete Composites*, Elsevier Ltd, 48, 83-90.

Kovler, K., Igarashi, S., and Bentur, A. (1999). "Tensile creep behavior of high strength concretes at early ages." *Materials and Structures*, 32(5), 383-387.

Omar, M., Loukili, A., Pijaudier-cabot, G., and Le Pape, Y. (2009). "Creep-Damage Coupled Effects : Experimental Investigation on Bending Beams with Various Sizes." *Journal of Materials in Civil Engineering*, (February), 65-72.

Rossi, P., Godart, N., Robert, J. L., Gervais, J. . P., and Bruhat, D. (1993). "Investigation of the basic creep of concrete by acoustic emission." *in Proceedings of the Fifth International RILEM Symposium on Creep and Shrinkage of Concrete, Barcelona, Spain, pp. 33-38*.

Rüsch, H., Sell, R., Rasch, C., and Stöckl, S. (1958). "Investigations on the Strength of Concrete under Sustained Load." *And, RILEM Symposium on the Influence of Time on the Strength Deformation of concrete, Munich*.

Rüsch H. (1960). "Research toward a general flexural theory for structural concrete." *ACI Journal*, 57(1), 1-28.

Saliba, J., Loukili, A., Grondin, F., and Regoin, J.-P. (2012). "Experimental study of creep-damage coupling in concrete by acoustic emission technique." *Materials and Structures*, 45(9), 1389-1401.

Østergaard, L., Lange, D. A., Altoubat, S. A., and Stang, H. (2001). "Tensile basic creep of early-age concrete under constant load." *Cement and Concrete Research*, 31(12), 1895-1899.

Analysis and Modelling of Basic Creep

J. M. Torrenti[1] and R. Le Roy[1,2]

[1]Université Paris-Est, IFSTTAR, Department Materials and Structures. E-mail: jean-michel.torrenti@ifsttar.fr
[2]ENSAPM, Paris. E-mail: robert.leroy@enpc.fr

Abstract

Basic creep of concrete is the part of the delayed deformation that occurs when concrete is loaded without drying. In this work results from the literature are analyzed: the derivative of the compliance function J of basic creep tests with different loading ages t_0 are compared. It has been observed that considering dJ/dt as a function of time t the long term behavior is a logarithmic one with the same slope. Here it is shown that if we consider dJ/dt as a function of the age since loading ($t-t_0$) a unique behavior is observed. This indicates that basic creep could be expressed as a logarithmic function in which the age of loading affects only the term $(t-t_0)$. In the recent Model Code 2010 basic creep is exactly expressed like that. Using the experimental data the parameters of the model are calculated for each test and compared with the values proposed by MC2010. It is shown that MC2010 gives a rather good set of values for the two parameters but it could be improved by adjusting some parameters on experimental results.

INTRODUCTION – BASIC CREEP OF CONCRETE

A good prediction of delayed deformations of concrete is an important issue for prestressed structures and a correct design of prestressing. In modern codes the delayed strains comprise four components: autogenous shrinkage, drying shrinkage, basic creep and drying creep - see for instance the last model code of the fib MC2010 (Muller et al., 2013). In this paper only basic creep is considered.

Basic creep is conventionally obtained from the deformation of a concrete sample charged under a constant stress σ and protected from desiccation. In laboratory it is obtained by protecting the concrete from drying. To obtain basic creep, autogenous shrinkage is measured in parallel, so that it can deduced from creep sample raw measurements. We define J - the compliance - whereby the mechanical deformation ε (deformation due to the applied load, that is total strain minus shrinkage) is equal to the product of this compliance by the applied stress: $\varepsilon = J\,\sigma$.

Acker et Ulm (2001), analyzing Le Roy's tests (1995), have expressed the derivative of the compliance dJ/dt. Considering different loading ages, they showed that this derivative tends to $1/Ct$ when t was large, with the same value of C for a given concrete regardless of the age of loading t_0 (see Figure 1). The conclusions of the authors were that two mechanisms were involved in basic creep: a short term one corresponding to a stress-induced water movement towards the largest diameter pores

and a long term mechanism corresponding to an irreversible viscous behavior, and related to viscous flow in the hydrates (slippage between layers of C-S-H).

We will show in this paper that considering Le Roy' tests and other tests from the literature, if one expresses the derivative of the compliance in relation to the time elapsed since the loading or $dJ/d(t-t_0)$, a single curve is obtained and therefore a single phenomenon is involved in basic creep. The integration of the derivative of the compliance allows then to obtain the expression of basic creep and shows that the relationship obtained is similar to that proposed in the MC2010 (Muller et al., 2013). The analysis of different results of the literature shows that it is quite possible to model these tests using the proposed relation and ultimately allows comparing the parameters proposed by the MC2010 with those deduced from experiences.

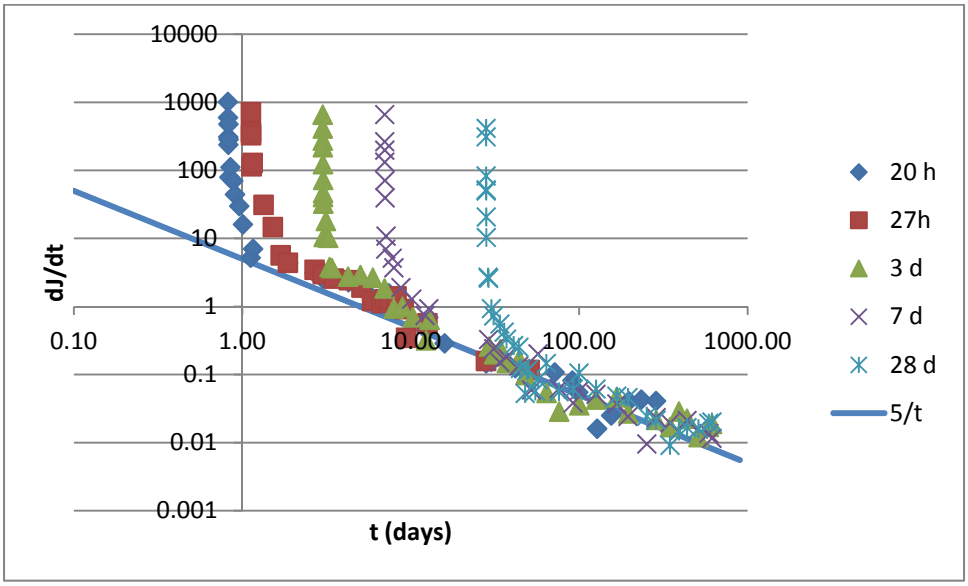

Figure 1. Derivative of the compliance with respect to time.

ANALYSIS OF LE ROY'S BASIC CREEP TESTS

Le Roy has performed basic creep on 10 different concretes varying loading age, proportion of water, silica fume and paste volume [Le Roy, 95]. Table 1 shows compositions and main properties of two of these concretes. Figure 2 gives an example of the strain evolution for concrete B0 and Figure 3 shows, for the same concrete, the derivative of the compliance with respect to $(t-t_0)$. We can see that in a log-log representation of the results, we obtain a line with a slope $1/Ct$ since the beginning. The same result is obtained with concrete B8 (Figure 4).

Table 1. Properties of concretes B0 and B8, differing only in the W/C ratio.

	W/C	*Cement type*	f_{cm28} [MPa]	$1/E_{28j}$ [10^{-6} MPa^{-1}]
B0	0,5	CEMI 52.5	43,5	25,5
B8	0,33	CEMI 52.5	67,2	20,6

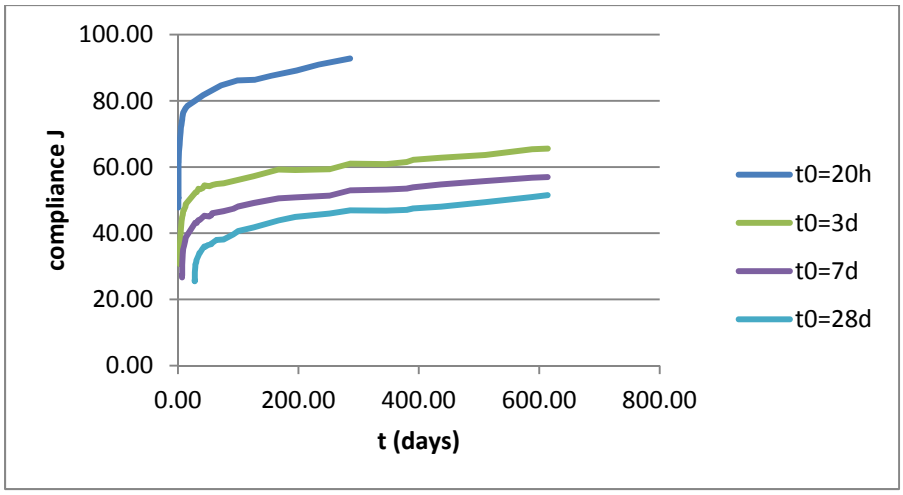

Figure 2. Evolution of the compliance with respect to time for different ages of loading – concrete B0.

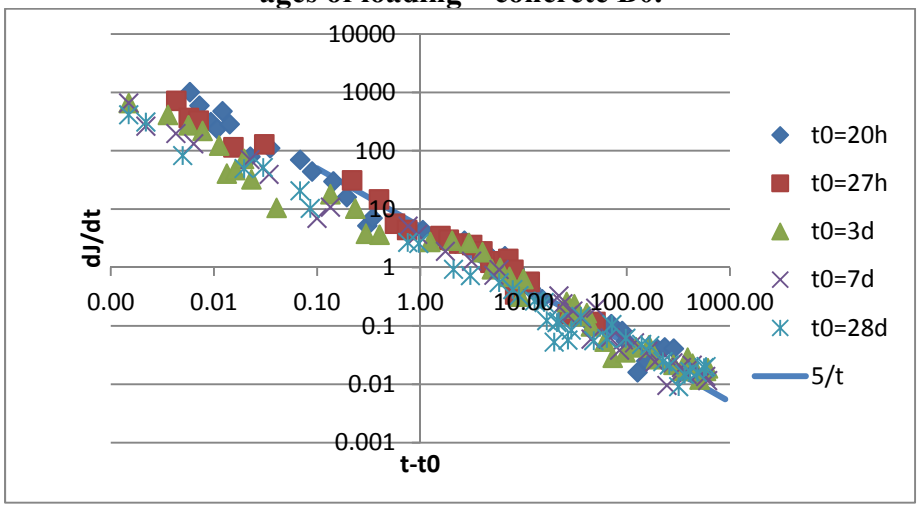

Figure 3. Derivative of the compliance with respect to time elapsed since the loading time for the B0 concrete; same tests as those of Figure 1 (log-log scale).

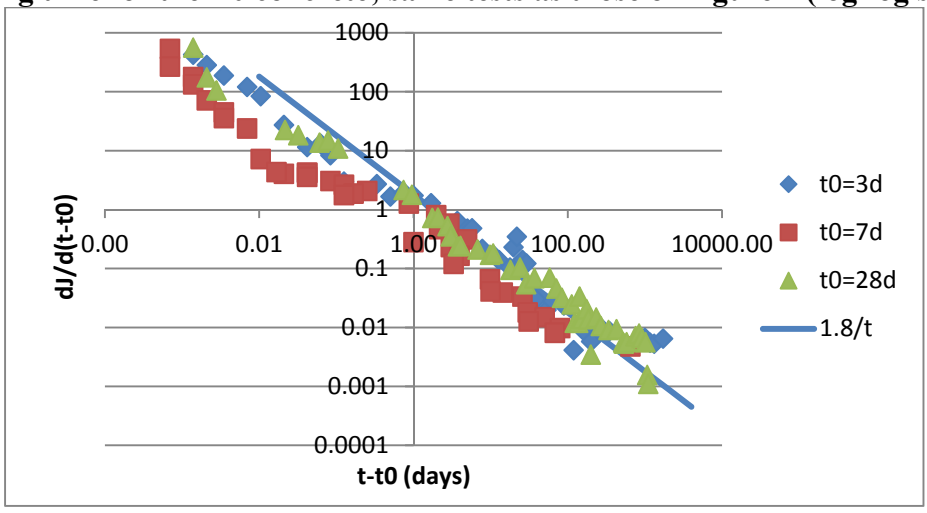

Figure 4. Derivative of the compliance with respect to time elapsed since the loading time for the B8 concrete (log-log scale).

CONSEQUENCES FOR BASIC CREEP

These results indicate that basic creep could be considered as a unique logarithmic function wherein the loading age affects only the term depending of $(t-t_0)$:

$$J=1/E+1/C\ log(1+(t-t0)/\tau(t0)) \qquad \text{[eq.1]}$$

with when $t\rightarrow\infty$ $dJ/dt\rightarrow 1/Ct$

This corresponds to the behavior observed on small samples by nanoindentation (Vandamme *et al*., 2013) but also on real structures (Bazant *et al.,* 2012), (Torrenti and Benboudjema, 2015) although in the case of structures there are other phenomena that should be considered (drying shrinkage and relaxation of prestressing for example).

We can compare this relationship with the test results taken from the NU database (http://www.civil.northwestern.edu/people/bazant/CreepShrinkData_131127.xlsx). Basic creep tests, where several different loading ages were tested, are considered. Table 2 shows the characteristics of the concrete used when these are available. Figures 2 to 11 show that by taking a constant coefficient C for a given concrete and by varying the parameter $\tau\ (t_0)$ for each loading age the proposed relationship is capable of representing the physical phenomena.

Table 2. Properties of the concretes considered in this study.

	W/C	*Cement type*	f_{cm28} [MPa]	E_{28j} [MPa]
Kawasumi (1982)	0,47	SL (slow)	33	21950
Shritharan (1989)	0,47	R (rapid)	50	29800
Hanson (1953)	0,56	SL	34	-
Nagamatsu (1986)	0,55	R	32	26650
Browne (1969)	0,42	-	50	-

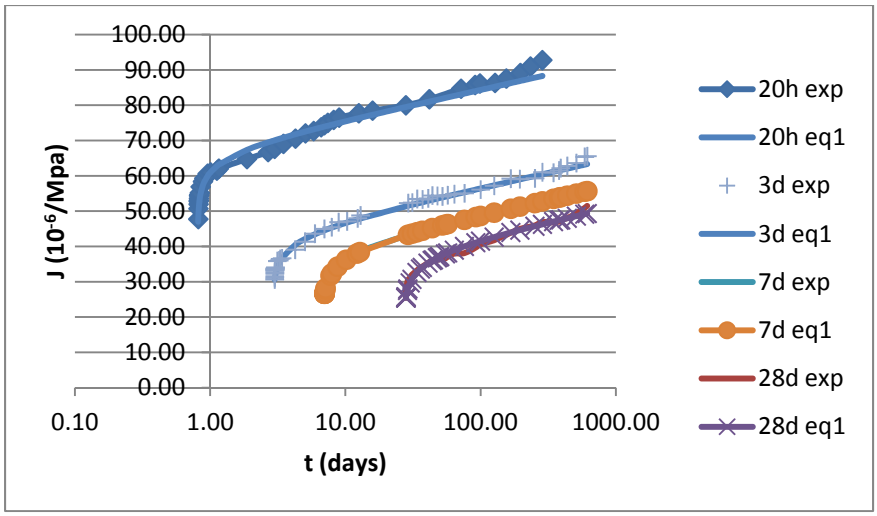

Figure 5. Comparison between experimental results and equation 1 – Le Roy's tests – B0 (Le Roy, 1995)

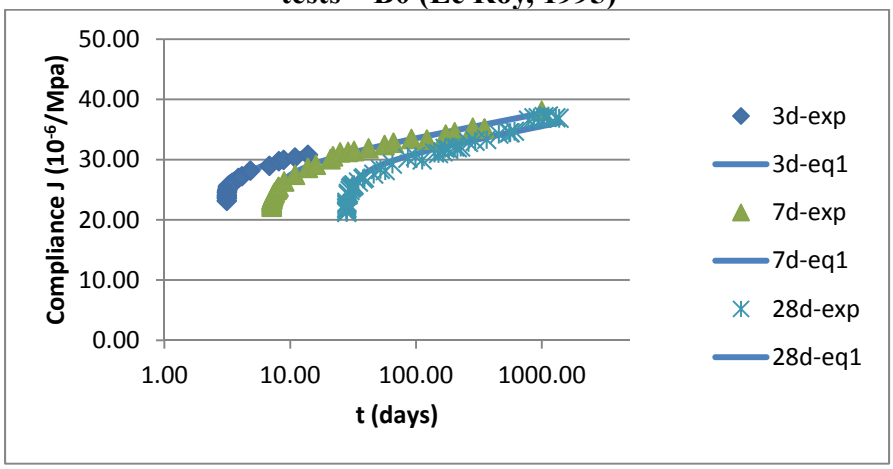

Figure 6. Comparison between experimental results and equation 1 – Le Roy's tests – B8 (Le Roy, 1995)

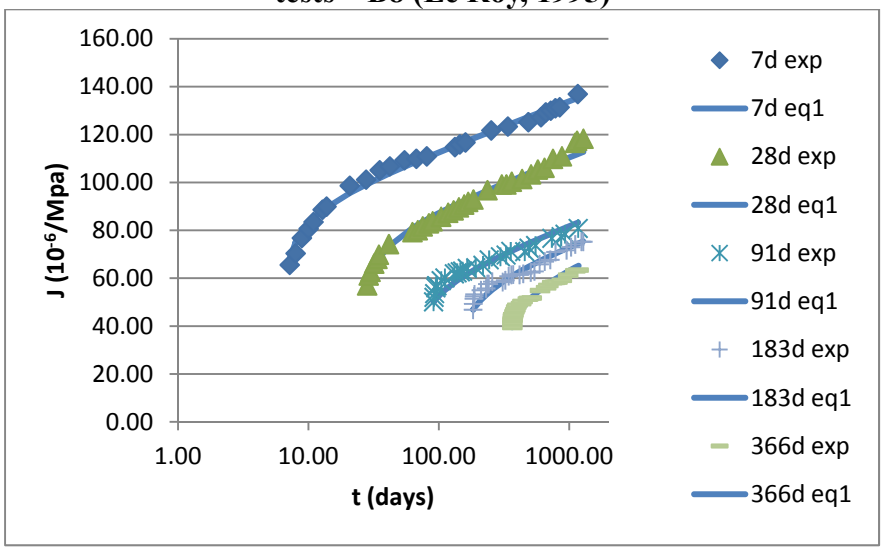

Figure 7. Comparison between experimental results and equation 1 – Kawasumi's tests (Kawasumi, 1982)

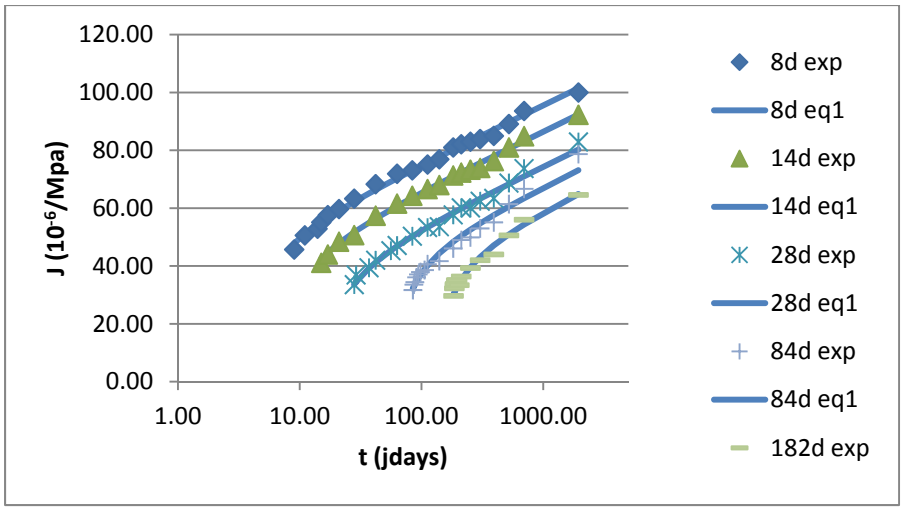

Figure 8. Comparison between experimental results and equation 1 – Shritharan's tests (Shritharan, 1989)

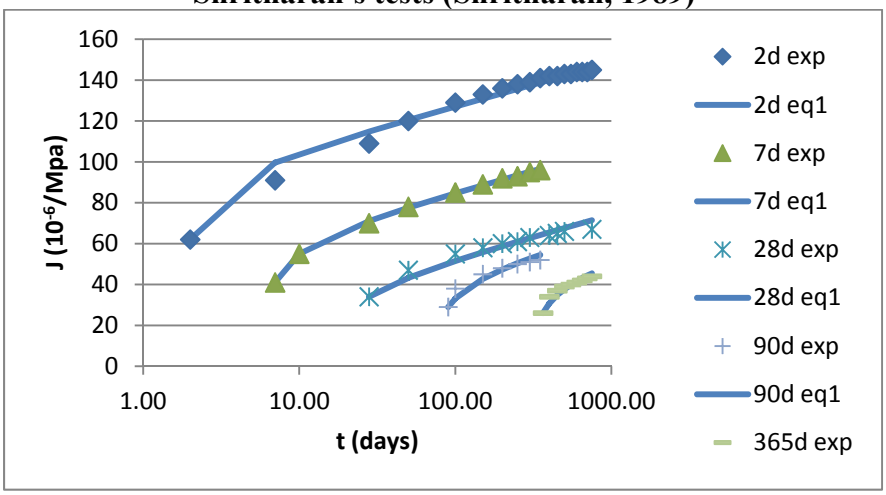

Figure 9. Comparison between experimental results and equation 1 – Hanson's tests (Hanson, 1953)

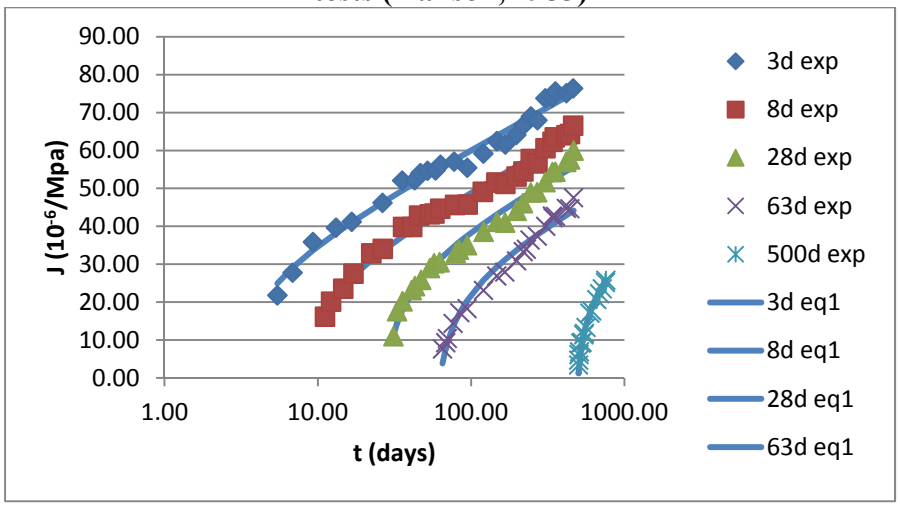

Figure 10. Comparison between experimental results and equation 1 – Hanson's tests (Nagamatsu, 1986)

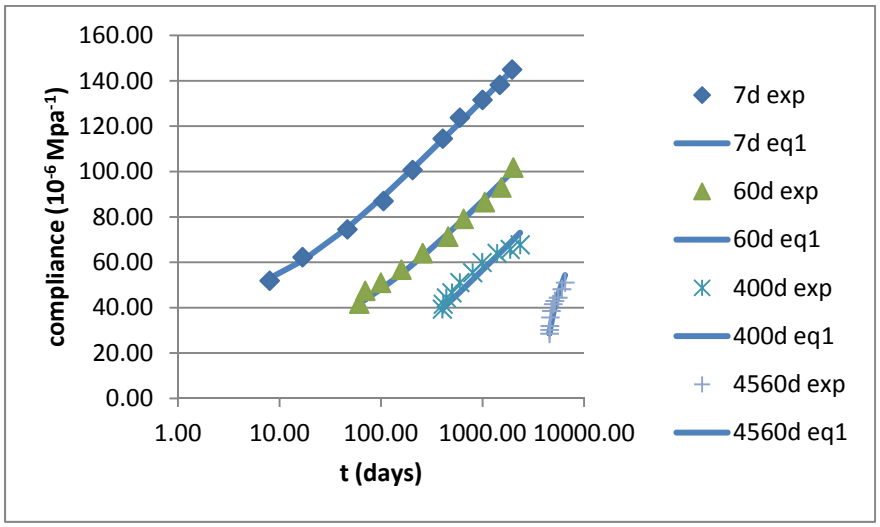

Figure 11. Comparison between experimental results and equation 1 – Browne's tests (Browne, 1969)

COMPARISON WITH MC2010

In the recent Model Code 2010, basic creep is expressed in the same manner as equation 1 (Muller et al., 2013):

$$\varepsilon_{bc} = \frac{\sigma}{E_{28}} \varphi_{0,bc} \beta_{bc}(t, t_0) \quad \text{[eq. 2]}$$

$$\text{with } \beta_{bc} = \ln\left(1 + (t - t_0)\left(0.035 + \frac{30}{t_{0,adj}}\right)\right)^2 \quad \text{[eq. 3]}$$

where $t_{0,adj} = t_0 \left(1 + \frac{9}{2+t_0^{1,2}}\right)^{\alpha}$ with $\alpha = -1$ for a cement CEM32.5N (or SL), 0 for a 32.5R or a 42.5N (or N) and +1 for 42.5R, 52.5N, 52.5R (or R)

Comparing with equation 1, one obtains the relations: $\frac{1}{C} = \frac{1}{E_{28}} \varphi_{0,bc} = \frac{1{,}8}{E_{28}\, f_{cm}^{0,7}}$ and $\frac{1}{\tau(t_0)} = \left(0.035 + \frac{30}{t_{0,adj}}\right)^2$

We can then compare the values obtained by fitting equation 1 on the experimental results with those proposed by the Model Code 2010. Figures 12a and 12b provide the comparisons for the parameter $\tau(t_0)$ respectively in the case of SL and R cements. Figure 13 shows the evolution of C versus strength. There is a proper agreement, but some variability of these parameters is observed when changing concrete. For the case of sensitive structures in which the prediction of creep is important, it will be important to calibrate these parameters on prior laboratory experiments.

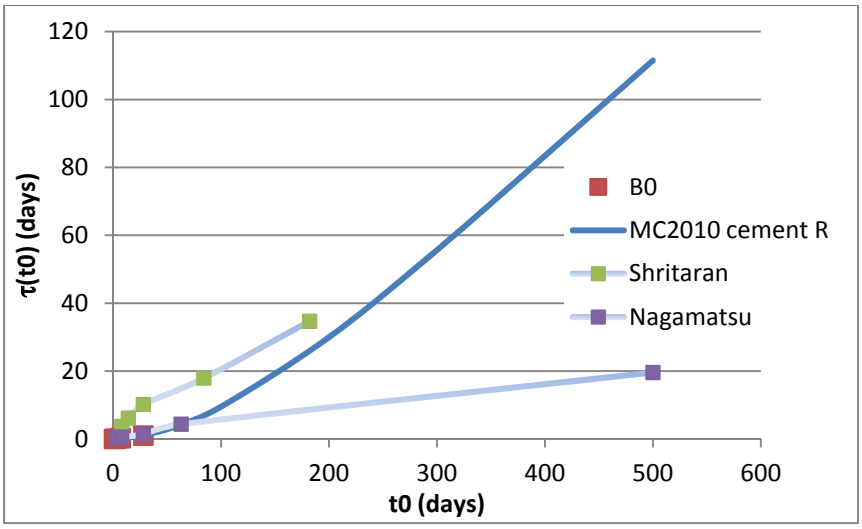

Figure 12.a Evolutions of $\tau(t_0)$ predicted by MC2010 and obtained by fitting of experimental results – case of cement type R

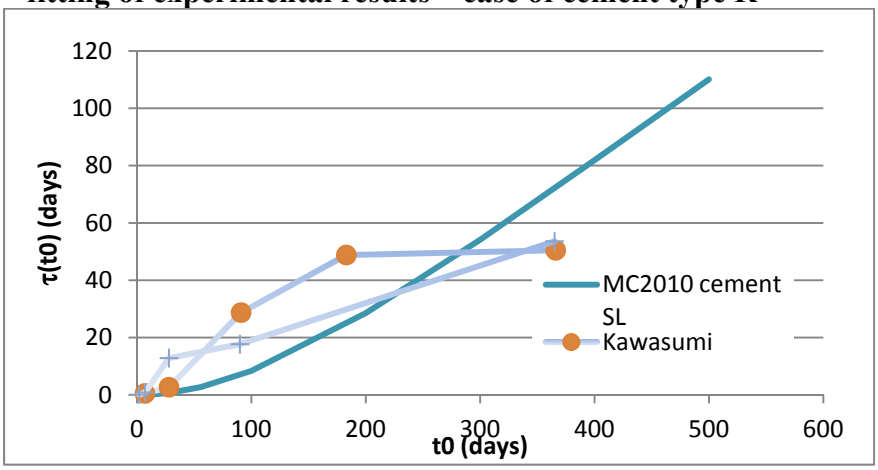

Figure 12.b Evolutions of $\tau(t_0)$ predicted by MC2010 and obtained by fitting of experimental results – case of cement type SL

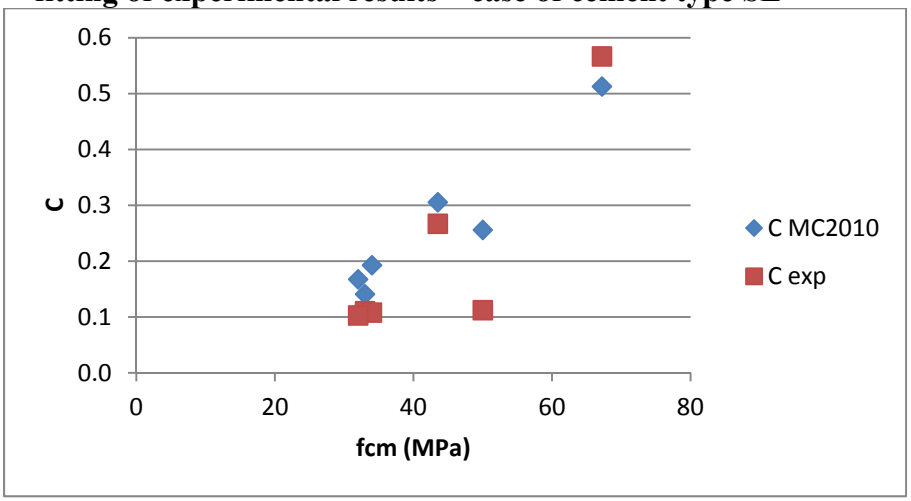

Figure 13. Comparison of predicted values of parameter C obtained with MC2010 and obtained by fitting of experimental results

CONCLUSION

The analysis of experimental results of basic creep of ordinary and high performance concretes shows that when expressed in function of the elapsed time since loading, the derivative of the compliance is linear in log-log scale. This result sheds a different light compared to the work of Acker and Ulm, which interpreted the experimental results over time (not time since loading), which led them to propose two characteristic times, so two different phenomena in the origins creep.

From the analysis presented here, the basic creep compliance is expressed as a logarithm function of time, involving two parameters - C and $\tau(t_0)$. The confrontation of this expression with a number of experiments in the literature, fixing the parameter C for a given concrete, and $\tau(t_0)$ for each loading age, shows that the basic creep temporal evolution of various concretes, at different loading ages, can be satisfactorily predicted, and in particular, the long-term magnitude. The comparison of the proposed expression of the MC2010 for basic creep shows that the parameters vary in a range similar to that observed experimentally, that means that an adjustment of the parameters from creep experiments is recommended for structures sensitive to creep.

REFERENCES

P. Acker, F. Ulm. « Creep and shrinkage of concrete: physical origins and practical measurements », *Nuclear Engineering and Design* 203 (2001) 143–158

Z.P. Bazant, Y. Qiang, L. Guang-Hua. « Excessive long-time deflections of prestressed box girders: I. Record-span bridge in Palau and other paradigms », *ASCE J. of Structural Engrg*. 138 (6), 2012, 676–686

Browne, R., Blundell, R. « The influence of loading age and temperature on the long term creep behaviour of concrete in a sealed, moisture stable state », *Materials and Structures* 2, (1969) 133-143.

Hanson, J.A. « *A ten-year study of creep properties of concrete* », Report No. SP-38, Concrete Laboratory, US Department of the Interior, Bureau of Reclamation, Denver (1953).

Kawasumi, M., Kasahara, K., Kuriyama, T. « *Creep of Concrete at Elevated Temperatures, Part 3, The Influence of Ages at Loading and Water/Cement Ratios.* » CRIEPI Report, No.382008, 1982

P. Laplante (1993) *Propriétés mécaniques des bétons durcissants : analyse comparée des bétons classiques et à très hautes performances*, Thèse de doctorat de l'ENPC, spécialité Matériaux et Structures

Le Roy R., *Déformations instantanées et différées des bétons à hautes performances – Etude paramétrique en fonction de la formulation – Proposition de modèles simplifiés*, Thèse de doctorat, Ecole nationale des ponts et chaussées, 1995, repris dans Etudes et Recherches des LPC, OA 22 (1996).

H. Muller, I. Anders, R. Breiner, M. Vogel, « Concrete: treatment of types and properties in fib Model Code 2010 », *Structural Concrete* 14 (2013), No. 4

Nagamatsu, S., Sato, Y., Takeda, Y., « Creep Function for Aging Concrete », *Fourth RILEM International Symposium on Creep and Shrinkage of Concrete: Mathematical Modeling* Ed. by Z.P. Bazant, 1986 pp.743-754

Shritharan, S. « Structural Effects of Creep and Shrinkage on Concrete Structures », M.E. thesis, Civil Engineer, University Auckland (1989).

J.M. Torrenti, F. Benboudjema. “On the very long term delayed behaviour of biaxially prestressed structures: the case of the containments of nuclear power plants”, *Concreep10*, 2015

M. Vandamme, F. Ulm, Nanoindentation investigation of creep properties of calcium silicate hydrates, Cement and Concrete Research 52 (2013) 38–52ASCE (American Society of Civil Engineers). (2014) *Minimim Design Loads for Buildings and Other Structures,* Standard ASCE/SEI 7-10. Third printing. ASCE, Reston, VA.

Adiabatic Temperature Rise Model of Ultra-High-Volume Fly Ash Conventional Dam Concrete and a FEM Simulation of the Temperature History Curve

Z. F. Zhao[1]; K. K. Mao[1]; S. W. Ji[2]; Z. Y. Zhang[3]; H. N. Zhu[1]; and W. L. Wang[4]

[1]College of Civil Engineering and Architecture, Zhejiang University of Technology, No. 18 Chaowang Rd., Hangzhou 310014, P.R. China. E-mail: zhaozhifang7@126.com
[2]Zhejiang Institute of Hydraulics & Estuary, No. 50 Fengqi East Rd., Hangzhou 310020, P.R. China. E-mail: jishunwen@126.com
[3]Gezhouba Group Testing Co., Ltd., No. 25 Qingbo Rd., Yichang 443002, P.R. China. E-mail: 664552055@qq.com
[4]Guangdong Provincial Key Laboratory of Durability for Marine Civil Engineering, Shenzhen University, Nanhai Ave. 3688, Shenzhen 518060, P.R. China. E-mail: wang_weilun@hotmail.com

Abstract

The adiabatic temperature rise model of concrete is very important in simulated computations of temperature field of mass concrete. A combination model from different kinds of function models of adiabatic temperature rise of concrete was proposed to fit the adiabatic temperature rise test data of Ultra-High-Volume Fly Ash Conventional Dam Concrete (UHVFACDC) to obtain a reasonable adiabatic temperature rise model. This model can improve a 3-D FEM simulation program for calculating the temperature field of a dam whose material is UHVFACDC (content of fly ash reaches up to 80%). The 1.2m×1.2m×1.2m large cubic specimen of UHVFACDC was tested to obtain the temperature history curve in the middle of the specimen. The temperature history curve obtained by the FEM simulation for the large specimen was compared with the tested one. The two results coincided to a substantial degree which revealed that the obtained model is valid. Thus, the temperature history curve of UHVFACDC can be achieved. This model can improve the precision of temperature field simulation for the dam. It provides the temperature history curve as input for the experimental study on temperature-stress testing machine test of UHVFACDC which is crucial for the evaluation of crack resistance performance at early age.

0. INTRODUCTION

From a sustainability standpoint, high-volume fly ash (HVFA) concrete not only significantly reduces consumption of Portland cement, but also results in a concrete of superior quality in many aspects when compared with that of conventional

concrete in regard to workability, strength and durability(ACI 232.3R-14, 2014). HVFA concrete is defined as having a large replacement by mass of Portland cement with fly ash. Malhotra defined HVFA concrete as concrete containing fifty percent (50%) or more fly ash by mass of total cementitious materials (ACI 232.3R-14, 2014).

As to the constructed conventional dam concrete (non-roller compacted dam concrete) dams around the world, the highest content of fly ash is less than 70% (fly ash accounts for 70% of the mass of total cementitious material). The highest content is 25% and 50%, respectively for the exterior and interior parts of such dams in America and 30% in Japan. This content varies from 20% to 50% in China's Three Gorges dam concrete. According to the Technical Specification of Fly Ash for use in Hydraulic Concrete (DL/T 5055-2007, 2007), the content of fly ash has to be less than 55%. However, with the development of concrete technique and engineering application, the content of fly ash increases. The American patent (Lisowski, et al., 2013) released in 2013 reveals that non-clinker high-volume fly ash cement for concrete has been successfully developed.

Some scholars (Ding, et al., 2011), utilizing the temperature-stress testing machine (TSTM), carried out research on crack resistance of two kinds of dam concrete at early age cured by three distinct modes: (a) adiabatic curing; (b) temperature match curing (TMC); and (c) 20 °C constant temperature curing. The results reveal that the concrete tensile stress developed faster and the cracking temperature was higher under the adiabatic curing mode. There are distinct difference in crack resistance behavior between the two kinds of concrete. Under the other two modes, the crack resistance equals. The start point of cooling was overestimated and the crack resistance capacity was underestimated under the adiabatic curing mode. The influence of compressive pre-stress on the crack resistance of concrete cannot be reflected if cured by the constant temperature mode and the cracking temperature is relatively lower than the true value. It has been showed that only the temperature match curing can objectively represent the influence of temperature history on the stress and cracking temperature of the real structures.

In this paper, conventional dam concrete with a content of fly ash of 35% (“reference concrete” for short) and ultra-high-volume fly ash conventional dam concrete with a content of fly ash of 80% (“UHVFACDC” for short) were employed for the study. The adiabatic temperature rise tests were carried out for these two kinds of concrete. The temperature of interior part of 1.2m×1.2m×1.2m large cubic specimen of UHVFACDC was measured by the test. Also, the temperature record of the interior part of the 210-meter-high dome dam “A”, which has been constructed with the reference concrete in practice was collected. Based on these tests data, an improved temperature rise model for the UHVFACDC was proposed to employ in the dam temperature field calculation. Thus the temperature history curve of UHVFACDC which has never been used to build a dam was obtained to investigate

the crack resistance of UHVFACDC at early age by TSTM.

1. EXPERIMENTS

1.1 Adiabatic temperature rise tests of the two kinds of dam concrete

The adiabatic temperature rise tests of the above-mentioned two kinds of dam concrete were accomplished by our research team.

1.1.1 Materials

The raw materials of these two kinds of dam concrete are the same as the materials adopted by the dome dam "A". Type I cement, class F fly ash, crushed gravel, crushed sand were used in both of the mixes. The water to binder ratio were 0.43 and 0.26 for the reference concrete and UHVFACDC respectively. The substitution rate of fly ash were 35% and 80% for the total binder content. The maximum size of crushed gravel is 40mm for all the mixes. Table 1 shows the concrete mix proportions.

Table 1 Mix proportions

fly ash binder ratio	Water binder ratio	Unit content (kg/m^3)						Water reducing agent (kg)	Air entraining agent (kg)
		Water	Cement	Fly ash	Sand	Gravel (5~20)mm	Gravel (20~40)mm		
35%	0.43	125	189	102	672	637	637	2.04	0.035
80%	0.26	89	69	277	670	636	636	3.46	0.242

1.1.2 Test procedure

The adiabatic temperature rise were tested according to Test Code for Hydraulic Concrete (DL/T 5150-2001, 2001).

1.1.3 Results of adiabatic temperature rise tests

Figure 1 shows the tested adiabatic temperature rise curves of the reference concrete and UHVFACDC.

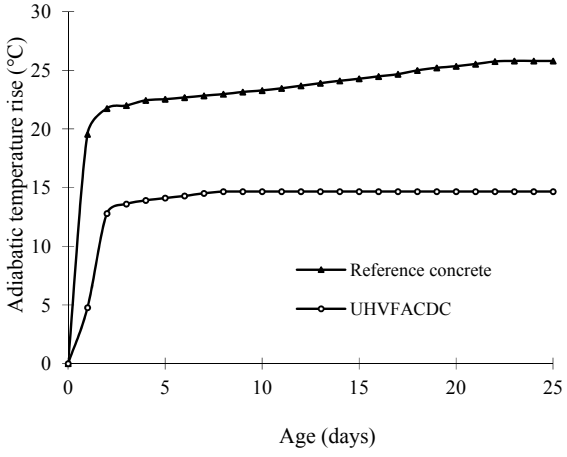

Fig.1 Tested adiabatic temperature rise curves of the two kinds concrete

The figure 1 reveals that the adiabatic temperature rise values of the two kinds of concrete differs with a range of 11.13 °C which indicates that fly ash has a noticeable influence on the adiabatic temperature rise.

1.2 Temperature measurement test of UHVFACDC by large cubic specimen

The points for measuring the temperature history of UHVFACDC were arranged at interior middle point of the 1.2m×1.2m×1.2m large cubic specimen and other suitable points, as well as the point outside of the specimen for measuring the ambient temperature.

The measured temperature history curve of the interior middle point of the 1.2m×1.2m×1.2m large cubic specimen is showed in Fig. 5.

2. ADIABATIC TEMPERATURE RISE MODELS

The exponential function, hyperbolic function and composite exponential function are usually adopted to express the adiabatic temperature rise of concrete (Zhu, 1999). Exponential function and hyperbolic function can simulate the adiabatic temperature rise curve of low-volume fly ash concrete well because the cement hydration releases the heat quickly. However, it is difficult to simulate the adiabatic temperature rise curve of UHVFACDC by these two functions and it may also bring a relatively high error. The combination functions based on the exponential function and hyperbolic function were proposed to express the adiabatic temperature rise of the two kinds of dam concrete as follows:

$$\theta(\tau)=\frac{p\tau}{m+\tau}+\frac{q\tau}{n+\tau} \qquad (1) \qquad\qquad \theta(\tau)=p(1-e^{-a\tau^{b}})+\frac{q\tau}{n+\tau} \qquad (2)$$

Where $\theta(\tau)$ --adiabatic temperature rise of concrete, °C;

τ --age of the concrete，days; m,n,p,q,a,b--undetermined coefficients

By adopting the formula (1) and (2), the related coefficients in these function expressions were determined by fitting test data of adiabatic temperature rise of the two kinds of concrete with these models. The results are listed in table 2(a) and 2(b).

Table 2(a) Related coefficients determined by fitting with two models for reference concrete

Formula	p	a	b	q	m	n
(1)	10.75	-	-	15.00	1.809	0.010
(2)	13.00	31.344	24.733	12.51	-	1.246

Table 2(b) Related coefficients determined by fitting with two models for UHVFACDC

Formula	p	a	b	q	m	n
(1)	7.77	-	-	7.91	0.857	0.857
(2)	7.622	0.020	7.108	7.305	-	0.580

By contrasting the fitting curve by different function expressions of adiabatic temperature rise with the tested one, the fitting curve corresponding to the reasonable adiabatic temperature rise model was obtained which is closest to the tested curve for

the two kinds of concrete. The fitting curves and tested ones can be found in Fig. 2 for the two kinds of concrete.

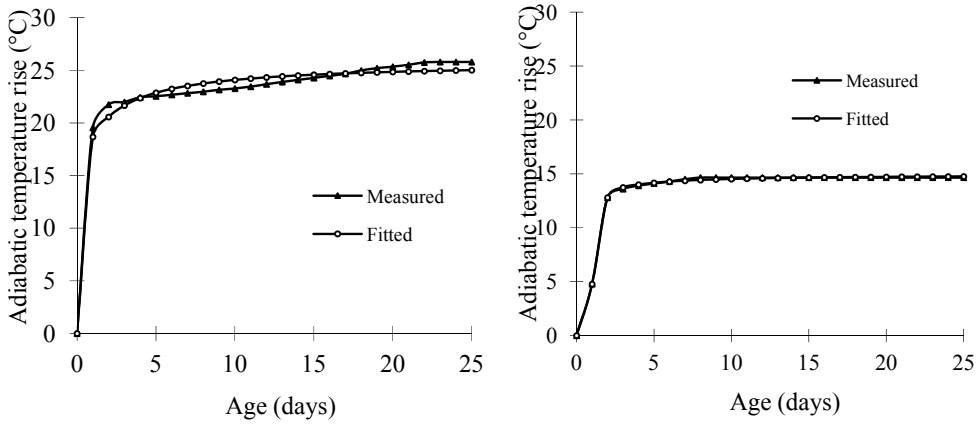

(a) reference concrete (b) UHVFACDC

Fig.2 Comparison between the fitting adiabatic temperature rise curve and tested one for the two kinds of concrete

Thus, the function expressions of adiabatic temperature rise model of the two kinds of concrete were achieved as follows:

For reference concrete: For UHVFACDC:

$$\theta(\tau)=\frac{10.75\tau}{1.809+\tau}+\frac{15.00\tau}{0.01+\tau} \quad (3) \qquad \theta(\tau)=7.622(1-e^{-0.02\tau^{7.108}})+\frac{7.305\tau}{0.58+\tau} \quad (4)$$

3. IMPROVED TEMPERATURE FIELD FEM SIMULATION PROGRAM OF DAM AND THE TEMPERATURE HISTORY CURVE OF UHVFACDC

3.1 Improved temperature field FEM simulation program

The Temperature Stress Simulation Program (Ji, 2009), which is written based on Fortran language, can simulate the temperature field and stress field of concrete specimens as well as concrete structures. The temperature field simulation program was improved by improving the adiabatic temperature rise model of concrete material.

The flow chart of improved temperature field FEM simulation is illustrated in Fig. 3.

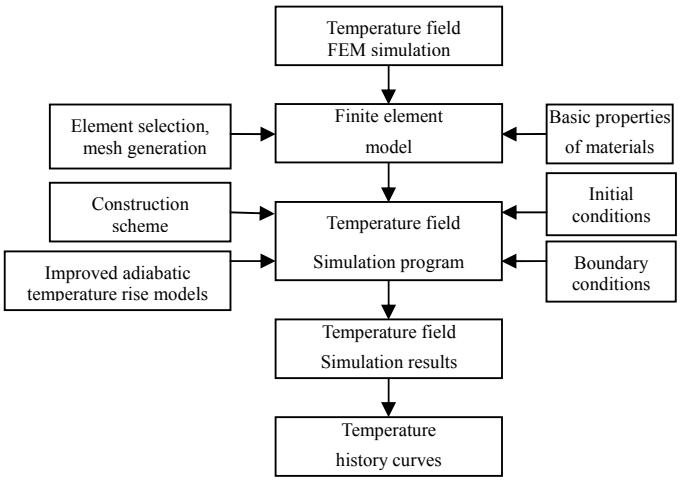

Fig.3 Flow chart of improved temperature field FEM simulation of dam

3.2 The temperature history curve of large cubic specimen of UHVFACDC was obtained by the improved temperature field FEM simulation program

The temperature history curve of the measuring point in interior middle of the 1.2m×1.2m×1.2m large cubic specimen of UHVFACDC was calculated by the improved temperature field FEM simulation program. The FEM model is showed in Fig.4.

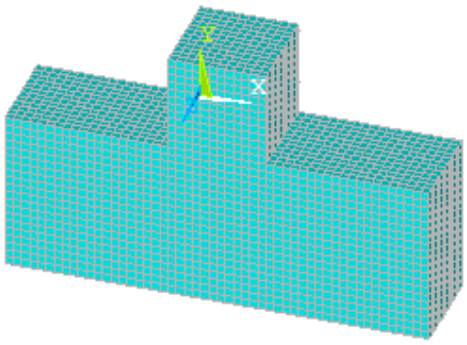

Fig.4 FEM model of large cubic specimen of UHVFACDC

In Fig. 4, the upper part of the FEM model is the 1.2m×1.2m×1.2m large cubic specimen of UHVFACDC and the lower part is the foundation needed to calculate heat conduction by the simulation program. The mesh generation adopted the hexahedron element with a side length of 10cm. The formula (4) for UHVFACDC was employed as the adiabatic temperature rise function in the FEM simulation. The comparison between the simulated temperature history curve of the measuring point and the tested one for the large cubic specimen of UHVFACDC is illustrated in Fig.5.

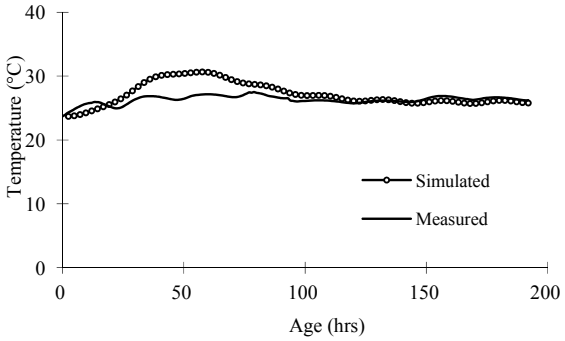

Fig.5 Comparison between the simulated temperature history curve and the tested one for the large cubic specimen of UHVFACDC

It shows that the simulated temperature history curve agrees with the tested curve for the large cubic specimen of UHVFACDC. The temperature rises to peak value during 2-3 days according to the simulation. However, the tested temperature curve tends to have no obvious temperature-rise period and temperature-fall period compared to the simulated one. The reason may attribute to the size of the cubic specimen which is not large enough to avoid the effect of fluctuation of ambient temperature. If the size of specimen is increased further, it may lead to a closer curve to the real temperature history curve of UHVFACDC.

3.3 Simulation of temperature history curve at interior point of the 16th monolith of the dome dam "A"

The reference concrete has been employed to build a real dam in China which is a 210-meter-high dome dam "A". The temperature measuring point was fixed at the point of 16th monolith which lies in the center of the 3m-height layer where it is 22.5m far away from the dam bottom and the temperature history was recorded by the thermometer internally set when this monolith was constructed. This measuring point was also set as the calculating point for the dam temperature field simulation. Fig.6 is the comparison between the calculated temperature history curve and the tested one of the reference concrete for 16th monolith of the dam.

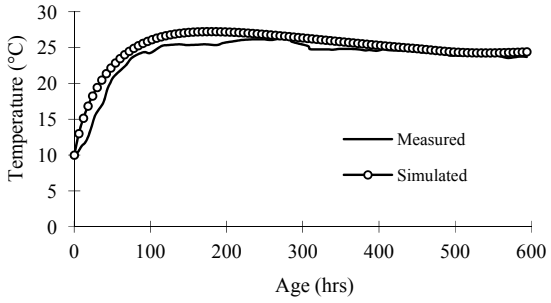

Fig.6 comparison between the calculated temperature history curve and the tested one of the reference concrete dam

It can be seen that the two temperature history curves are very close to each other and the trend are almost the same. The temperature at early age increased with the release of heat in the process of cement hydration. It reached to the peak value at an age of about 200 hours and decreased later. It is clearly showed in fig. 6 that the simulated and measured temperature history curves coincided to a substantial degree, which further indicates the rationality and precision of the temperature field simulation of the dam by this FEM simulation program.

The UHVFACDC has never been used to build any dam and expect to be put in the dam construction in the future for the sustainability. The temperature history curve of UHVFACDC was simulated by adopting the same dam model, construction scheme and ambient condition and so on as the actual dome dam "A" for the FEM simulation. The difference here is to employ different adiabatic temperature model because the actual dome dam "A" adopted reference concrete. The temperature history curves of the two kinds of concrete were achieved by the improved FEM simulation program of dam and showed in the Fig.7.

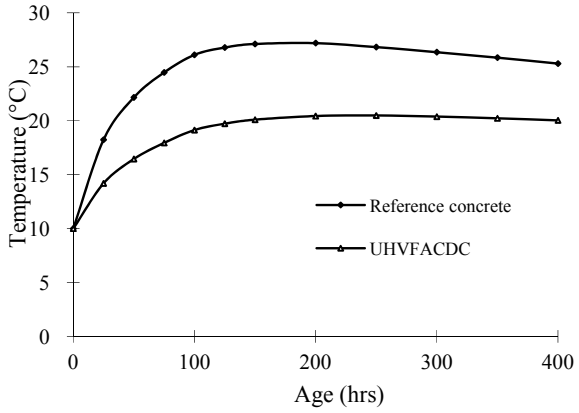

Fig.7 Temperature history curves of the two kinds of concrete by the improved FEM simulation of dam

From Fig. 7, it can be seen that the peak temperature is 27.2 °C and it took about 200 hours to reach the peak for the reference concrete. For the UHVFACDC, it took about 250 hours to reach the peak temperature 20.5 °C. It indicates that UHVFACDC can decrease the peak temperature as well as the rate of heat release during cement hydration, and delay the time when the peak temperature appears.

Both two kinds of concrete have an original casting temperature when they are poured. The original casting temperatures were all subtracted from the temperature history curves in order to conveniently compare with the adiabatic temperature rise curves for both two kinds of concrete, and as illustrated in the Fig. 8.

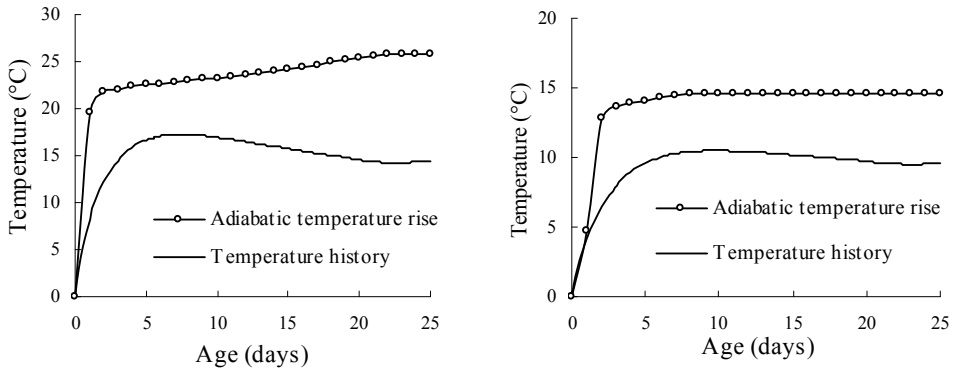

（a）Reference concrete （b）UHVFACDC

Fig.8 Comparison between the adiabatic temperature rise curve and simulated temperature history curve of the two kinds of concrete

The Fig.8 shows comparison between the adiabatic temperature rise curve and the simulated temperature history curve of the two kinds of concrete. It can be seen that the adiabatic temperature rise curve is higher than the temperature history curve.

3.4 Temperature history curve of UHVFACDC under the TMC mode

The guide temperature history curve for the TSTM test under TMC mode can be obtained by adding the casting temperature of TSTM test specimen to the temperature history curve of the UHVFACDC by FEM simulation. Thus, the crack resistance of UHVFACDC at early age can be studied by TSTM test.

4. CONCLUSIONS

1) Based on the adiabatic temperature rise tests data of these two kinds of dam concrete, combination models for the reference concrete and UHVFACDC were proposed and the related coefficients in these models were also determined.

2) For the 1.2m×1.2m×1.2m large cubic specimen of UHVFACDC, the obtained adiabatic temperature rise model was employed in the FEM simulation to calculate the temperature field of the interior point of this large cubic specimen. It shows that the calculated temperature history curve was in good agreement with that measured result. It demonstrates that this adiabatic temperature rise model is suitable for the FEM simulation of temperature field of UHVFACDC and can improve the FEM program.

3) For the monolith of a built dam made with reference concrete, the calculated temperature field by the improved FEM simulation program of the dam coincide with the temperature history record in the actual dam. Thus, the temperature history curve simulated by the improved FEM program of UHVFACD dam was obtained to serve as the temperature history curve for TSTM test to study the crack resistance of UHVFACDC at early age.

ACKNOWLEDGEMENTS

This work was supported by a grant from National Natural Science Foundation of China (NSFC, No. 51479178), Zhejiang Provincial Natural Science Foundation of China (No. LY14E090006), Zhejiang Provincial Science and Technology Project (No. 2013F20002) and Guangdong Provincial Key Laboratory of Durability for Civil Engineering, Shenzhen University (No. GDDCE14-01). They are gratefully appreciated.

REFERENCES

ACI (American Concrete Institute) Committee 232. (2014). "Report on High-Volume Fly Ash Concrete for Structural Applications". ACI 232.3R-14

Ding, J.T., Chen, B., Cai, Y.B. and Sun W. (2011). "Influence of temperature history on crack resistance of early age concrete ". Journal of Jiangsu University, 32(2), 236-240

Ji, S.W. (2009). "Study for causes of cracking and measures for crack prevention in construction and operation period of high arch dam". Nanjing ,China: College of Water Conservancy and Hydropower Engineering of Hohai University.

Lisowski et al. (2013). "Cementitious compositions and related system and methods". United States Patent, Patent No. : US 8,529,689 B2.

PRC National Development and Reform Commission. (2007). "Technical specification of fly ash for use in hydraulic concrete". Specification DL/T 5055-2007, Beijing, China: China Electric Power Press.

PRC National Economic and Trade Commission.(2001). "Test code for hydraulic concrete". Code DL/T 5150-2001, Beijing , China: China Electric Power Press.

Zhu, B.F. (1999). "Thermal stresses and temperature control of mass concrete". Beijing , China: China Electric Power Press.

Development, Calibration, and Validation of Lateral Displacement for a Concrete Uniaxial Compression Test

G. Sherzer; E. Marianchik; R. Cohen; and E. Gal

Abstract

This research presents a novel uniaxial compression test system for concrete specimens. The motivation for this development comes from the need to calibrate and validate multi-scale numerical methods for the analysis of concrete structures, a research field which requires new experimental systems for concrete. The aim of this study is to offer an experimental methodology and to develop an experimental uniaxial compression system which provides the results needed for the calibration and validation of multi-scale models. The uniqueness of the suggested experimental system is related to its ability to measure the lateral displacements of a specimen with a rectangular cross section. The main challenges to achieving reliable results using electro-mechanical means are concerned with attachment of the lateral gauges so that it can follow the targeted spot with progressing longitudinal deformation. The unique experimental system developed for this study was found to be accurate and was validated by comparing macroscopic experimental results such as: displacements, modulus of elasticity and Poisson's ratio with the literature on concrete and aluminum specimens.

Keywords (CE Database Subject Headings): Uniaxial compression test; Lateral displacement; Concrete; Mechanical properties of concrete; Multi-scale analysis; Modulus of elasticity; Poisson's ratio; Calibration; Validation.

INTRODUCTION

At present, there is no designated testing method for measuring the lateral deformation of rectangular cross section concrete specimens. Contact methods, which are used for cylinder specimens, are not suitable due to either the non-homogeneous shape of these specimens, the impossibility of attaching the measuring equipment to their surface, or the lack of adhesion in the case of the application of embedded strain gauges. This research presents a novel uniaxial compression test system for measuring lateral displacement of the concrete specimens. The motivation for this development comes from the need to calibrate and validate e.g. multi-scale numerical methods for the analyses of concrete structures e.g. see

(Cusatis et al. 2011 I; Cusatis et al. 2011 II; Gal et al. 2008; Gal and Kryvoruk 2011; Gal and Kryvoruk 2011; Gal et al. 2013).

Many experimental attempts have been made in the past to assess the difficulties associated with experimentally obtaining the full stress-strain curve of concrete in uniaxial compression (Ahmad 1979; van Mier 1986; Vonk 1992; Zisopoulos et al. 2000) Such experiments have generated conflicting evidence and considerable debate, especially regarding the post peak segment of the full stress-strain curve, which is influenced by such factors as the shape and size of the specimen, the slenderness (h/d) (or width for prisms) ratio, the stiffness of the testing machine, and the effect of the frictional forces between the loading platens and specimen. These factors were summarized by (Van Mier et al. 1997). Other articles represent the effect of the frictional forces between the loading platens and the specimen (Al-Chalabi and Huang 1974; Allen and Drauglis 1969; Boyd and Robertson 1945; Bridell 1991; Kotsovos 1983; Tarrant 1954; Vonk 1992; Vonk 1989; Zisopoulos et al. 2000) and other articles the size effect (di Prisco et al. 2004; Kim and Yi 2002; Markeset and Hillerborg 1995; Richart et al. 1928; Shin and Andrawes 2010).

(van Vliet and van Mier 1996) conducted a uniaxial compression test in which the experiment was tested on a prism specimen. It was noted that the measured lateral deformations was incomplete because of the non-perfect experimental design that caused rotation of the measuring points. In another study, (Colombo et al. 2010) displayed a mechanical characterization of steel fiber reinforced concrete (SFRC) used for prefabrication after thermal cycles at high temperature. In their research, three different tests were considered, of which uniaxial compression was one. They used a chain clamped on a cylinder specimen to measure circumferential relative displacement. Another article (Štemberk and Kohoutková 2005) investigated the experimental optical method, where an image is captured with a high-resolution CCD- (charge coupled device) camera for measuring the lateral deformation of solidifying and hardening concrete.

In this paper, an experimental methodology of measuring the lateral deformation of concrete specimen is described. The developed experimental system have been calibrated and validated and finally experimental results of lateral and longitudinal displacement components are presented.

UNIAXIAL COMPRESSION TESTS

Experiment Design

The compression tests that are described next were carried out in a uniaxial compression machine with a capacity of 2000 kN. This machine is controlled by a closed-loop servo hydraulic system and can act both under load or displacement controls. The press element transfers the pressing force uniformly to the specimen by using two surfaces, where there is contact between the specimen and the press element. However, the upper loading platen is free to rotate. In this way, the loading platen position can be adjusted to geometrical imperfections in the specimen. The loading rate in all experiments was 118.6 kPa/sec.

Specimens were instrumented by means of four linear variable differential transformer (LVDT) transducers: three disposed at 120° around the specimen, in order to measure the displacement between the press platens, these LVDTs were connected to magnetic bars attached to the bottom platen, and a fourth LVDT connected to a ring clamped onto the specimen to measure its circumferential relative displacement in the central region and transition it to the average displacement on concrete specimens using the following formula. The dimensions are shown in Figure 1:

$$\varepsilon_{specimen} = \frac{\Delta t}{\pi a} \tag{1}$$

Where:
a = the width of the specimen
Δt = addition to change the volume of the ring
Figure 1 shows the dimensions for calculating lateral strain:

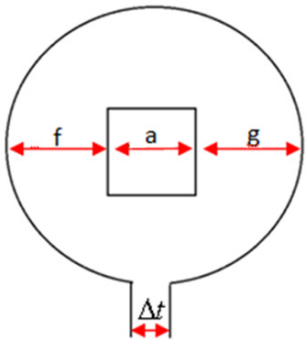

Fig. 1. Appropriate measurements to calculate lateral strain

The ring has four adjustable supports that enable it to be centered to the height of the specimen, using screws to hold the ring tight. This tightening allows the ring gravity to be balanced. It is possible for a specimen to have different geometric shapes—for example, a prisms, cylinder, hexagon, etc.—because simple adjustments can be made to the thread of the ring. The attachment of the ring to the specimen enables the use of specimens with variable slenderness with the location of the ring in the center of the specimen. The ring has a threshold that is dominated by four supporters, and is instrumented by lips to which the LVDT is fixed. The threshold variable during the experiment is measured by the measuring instrument. The specimen set-up in uniaxial compression is shown in Figure 2–3.

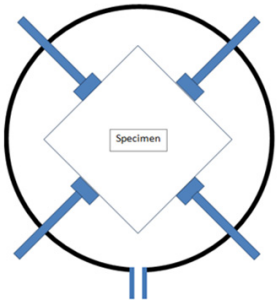

Fig. 2. **Experiment set-up-overall view**

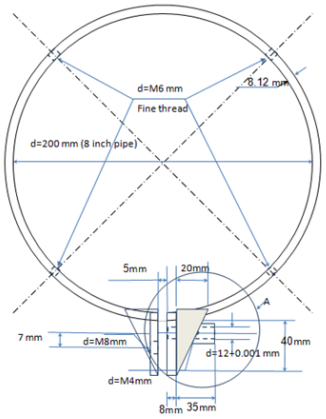

Fig. 3. Experiment set-up - design details

The benefits of this ring include:
a) Circumferential measurement capability providing solutions to irregular displacements of a prisms specimen;
b) Exclusion for measuring displacement of the rigid body;
c) Flexibility of the measurement device that can be adapted to the displacement of the specimen;
d) No obstacle exists to the transfer of information for the displacement measurement.

The development of a new prototype was completed in this study, and the results obtained during the experiments showed high reliability.

Boundary Conditions

In order to investigate the effect of boundary friction on the test results, two different boundary conditions were applied. Half of the tests were carried out with specimen and steel loading platens in direct contact with each other. This boundary condition will be referred to as high friction (HF) platens. In the remaining tests, a friction reducing interlayer was used between the specimen and loading platens, referred to as low friction (LF) platens. The interlayer comprised stearic acid (Bridell 1991).

MATERIALS AND SPECIMEN PREPARATION

A detailed manufacturing procedure was specified (Van Mier et al. 1997) Larger blocks were cast from which the prisms could be sawn or specimens could be cored, such that the direction of loading in the compression experiments would be perpendicular to the direction of casting. As shown before by (van Mier 1986) the direction of casting has a profound effect on the shape of the stress–strain diagram in compression. Micro-cracks caused by differential shrinkage, temperature gradients, and bleeding during the hardening of the concrete are the main reasons for the initial anisotropy, which cannot be neglected.

Uniaxial compression tests were carried out on prisms with a cross section of $100x100mm^2$ and lengths of *100* and *200mm*, respectively. Larger prisms of

100x100x400mm^3 were cast, and the specimens were sawn from the prisms to the desired size and polished on the loading surface sides. A further advantage of testing specimens that are sawn from large blocks is that the weak top layer is removed from the specimen. The weak casting layer can, in the worst case, lead to significant flexural stresses in the test specimen.

The specimen mixture was composed of: Portland Cement (CEM II 42.5 N/AM-SLV) *391 kg/m*^{3}*"* with a maximum aggregate size of *14mm* and Rotem quarry sand sifted through the sub-division distribution: *1.2-0.5 mm*, having an uptake ability of *0.9%* and weighing *779 kg/m*^{3} mixed together with a water-to-cement ratio of *0.567*. All aggregates were saturated (with dry surfaces), where the weight of the coarse aggregate was *661 kg/m*^{3}, and the fine aggregate was *220 kg/m*^{3}. This led to a compressive strength of *44-52 MPa*. The mix composition is shown in Table 1 below.

Table 1. Concrete Mix Composition

	GS-14-9.5"	GS-9.5-2.36"	Sand	PC	w/c
Amount (kg/m^3)	661	220	779	391	0.5687

GS: Grain size in mm', PC: Portland cement, and w/c: water-to-cement ratio

Methodology

For the purpose of experiments designed for the verification and validation of multi-scale numerical methods for the analysis of concrete structures, the methodology was based on that of Round Robin (Van Mier et al. 1997) in terms of vertical measurement, and it presents a prototype for lateral measurement.

1. ***Composition of the concrete mixtures*****:** Multi-scale analysis requires modeling of the concrete unit cell, which includes information relating to the concrete mixtures, so it was important to note the maximum aggregate size, the minimum aggregate size, the percentage of the volume of each type of aggregate (coarse or fine) from the overall mixtures, the w/c-ratio, the size of the sifted sand, and the degree of uptake.

2. ***Shape and size of the concrete specimen*****:** Casting the mixtures into larger scale prisms than desired and sawing to varying slenderness sizes was performed, removing the weak top layers that have different properties then the rest of the mixture. The specimens must have a variety of slenderness to produce the data required to calibrate the size effect.

3. ***Curing procedure*****:** The user may choose the procedure.

4. ***Grinding the specimen*****:** In this experiment, grinding the surfaces of the specimens was very important in order to avoid inaccurate measurements that would have created rotational displacement of the upper loading platen. The existence of the possibility of rotation of the loading platen movement was essential for creating a full contact area between it and the specimen. Grinding reduced the rotational movement

and was intended to prevent errors in measurement and inclusion stress, by reducing the bending that may result from the formation of the angle.

5. ***Testing between loading types*:** Testing had to be carried out between at least two different types of loading platens. The default was an experiment between rigid steel loading platens. The other systems to be used can be freely selected by the participant. The second system should preferably reduce the friction between the loading platen and specimen to a minimum. In this study, we used stearic acid.

6. ***Calibration results*:** In order to obtain satisfactory results for calibration, the recommended measurement system should be used. The minimum test program consisted of a series of uniaxial compression tests on either prisms or cylinders, loaded between two different types of loading platens. Two different slenderness ratios were tested using specimens of one concrete quality, with a repetition factor of three for each parameter combination.

7. ***Rigidity*:** The rigidity of the press element should be determined in order to facilitate the comparison of different contributions. Defining this rigidity is very important in order to isolate the effect of the measuring instrument from the measurement data of the specimen. In addition, the rigidity of the plates is a calibration parameter.

8. ***Degree of loading rate*:** The uniaxial compression test is based on quasistatic loading, while recording low rates for the parameters for calibration. This study was carried out at a loading rate of *118.6 KPa/s*.

9. ***Verification and validation of results*:** To verify and validate the results using the finite element software, it is necessary to consider the vertical deformation of the loading platens of the press element. Therefore, in order to verify the experimental results with finite element software more accurately and reliably and to overcome the effect of the press element, the modeling of the experimental set-up included a loading platen.

RESULTS

The experiment was conducted on four sets:

- First set—tested on specimens with a cross section of *100 x100mm*^{2} and a length of *100mm* with an HF boundary condition.
- Second set—tested on specimens with a cross section of *100 x100mm*^{2} and a length of *100mm* with an LF boundary condition.
- Third set—tested on specimens with a cross section of *100 x100mm*^{2} and a length of 200 mm with an LF boundary condition.
- Fourth set—tested on aluminum specimens with a cross section of *100 x100mm*^{2} and a length of *100mm*.

The stress—vertical strain curve is shown in Figure 4

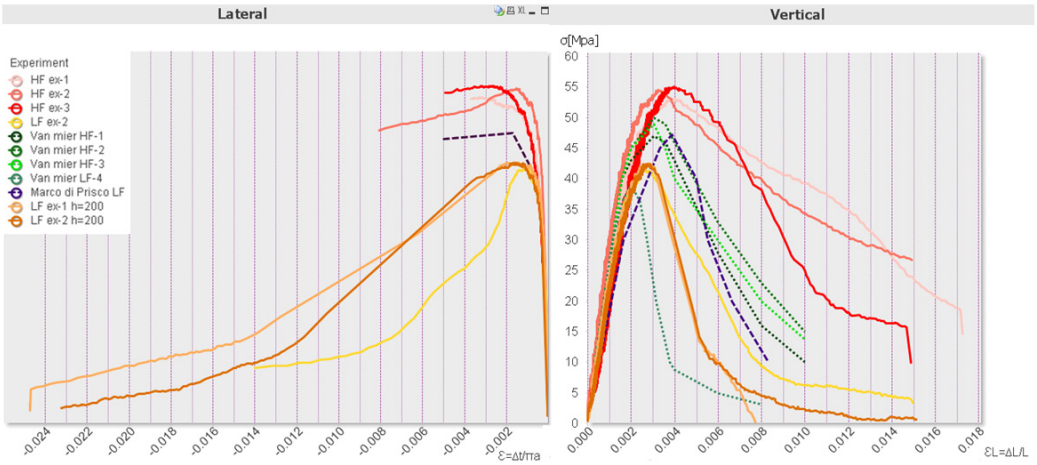

Fig. 4. Uniaxial compression test experimental results: average behaviors

In this figure, the nominal stress ($\sigma = P/A$ where A = the initial cross section area) is respectively plotted with respect to the normalized total vertical strain ($\varepsilon_{vertical} = \Delta L/L$) on the right side, and with respect to the normalized lateral strain on the left side. In the lateral case, when transferring the circumferential displacement of the ring to the specimen with average strain ($\varepsilon_{specimen} = \Delta t/\pi a$), the length of the specimen in this curve is *100mm*.

Figure 4 includes research results, as well as the results of similar studies that appear in the literature (Colombo et al. 2010; van Vliet and van Mier 1996), which are shown by the purple and green curves, respectively. In our comparison, we did not expect to see the same results because a different mixture was cast, but we did expect to see the same character of the curve reflected both in terms of the orders of magnitude of the values of lateral and vertical maximum strain, and of the mechanical properties of elastic modulus and Poisson ratio.

Validation of the Lateral Measurement

The scientific novelty of this study is the use of a ring, in which the change of its radius is relative to the lateral deformation of the concrete prisms specimen. The verification of this conversion method and quality of the measurement was done using an aluminum specimen.

The aluminum specimen remained in the elastic stage in the field of load in this study, and its mechanical properties are known. To achieve this, we carried out an experiment on the aluminum specimen that has the same cross section as the concrete specimen. For verification, we compared the value of the strain obtained from the test to the lateral that was calculated by using Hooke's Law as. By comparing the results of the calculation and the experiment results, it was found that the results are similar with a percent of error of 0.07756%. Therefore, it is possible to

determine that the lateral measurement accurately represents the deformation of the specimen.

CONCLUSIONS

Our method for measuring the lateral deformation of concrete yields the following conclusions:
Technically, it was found that this method requires only a standard loading system used for the uniaxial compression test, in which LVDTs are the measuring instrument, and a ring is clamped onto the specimen to measure its circumferential relative displacement in the central region, ensuring the accuracy of this method. As a result, this measuring system can be easily used in scientific testing. This measuring method was found to be precise and accurate, and this conclusion was reconfirmed using a validation process with an aluminum specimen. The test configuration has been shown, and the methodology formulation explained.

The experimental system developed for this study was validated by comparing its macroscopic experimental results, such as displacements, modulus of elasticity, and Poisson's ratio, with the literature on concrete and aluminum specimens. This measuring system provides a missing link for commencing a full analysis of multi-scale numerical models. The testing data was collected for a microscopic model, while the reliable test results can be compared to the macroscopic results of the numeric model.

This research opens up new horizons for researching the non-linear behavior of concrete specimens. Research flexibility is enhanced when using this measuring system and this method of testing was found to be relatively inexpensive.

REFERENCES

Ahmad, S. H. S. S. P. (1979). *Complete stress-strain curve of concrete and nonlinear design*, Dept. of Theoretical and Applied Mechanics, University of Illinois, [Urbana, Ill.].

Al-Chalabi, M., and Huang, C. L. (1974). "Stress distribution within circular cylinders in compression." *International Journal of Rock Mechanics and Mining Sciences & Geomechanics Abstracts*, 11(2), 45-56.

Allen, C., and Drauglis, E. (1969). "Boundary layer lubrication: monolayer or multilayer." *Wear*, 14(5), 363-384.

Boyd, J., and Robertson, B. P. (1945). *The Friction Properties of Various Lubricants at High Pressure*.

Bridell, J. M. (1991). *Reducing Frictional Constraint in Compression Testing Through Lubrication*, University of Minnesota.

Colombo, M., di Prisco, M., and Felicetti, R. (2010). "Mechanical properties of steel fibre reinforced concrete exposed at high temperatures." *Materials and Structures*, 43(4), 475-491.

Cusatis, G., Mencarelli, A., Pelessone, D., and Baylot, J. (2011). "Lattice Discrete Particle Model (LDPM) for failure behavior of concrete. II: Calibration and validation." *Cement and Concrete Composites*, 33(9), 891-905.
Cusatis, G., Pelessone, D., and Mencarelli, A. "Lattice Discrete Particle Model (LDPM) for failure behavior of concrete. I: Theory." *Cement and Concrete Composites*, 33(9), 881-890.
di Prisco, M., Felicetti, R., Lamperti, M., and Menotti, G. (2004). "On size effect in tension of SFRC thin plates." *Fracture mechanics of concrete structures. BL Schmick and AD Pollington, USA*, 1075-1082.
Gal, E., Ganz, A., Hadad, L., and Kryvoruk, R. (2008). "Development of a Concrete Unit Cell." 6(5), 499-510.
Gal, E., and Kryvoruk, R. (2011). "FRC Material Properties - a Multi-scale Approach." *Computers and Concrete*, 8(5).
Gal, E., and Kryvoruk, R. (2011). "Meso-scale analysis of FRC using a two-step homogenization approach." *Computers & Structures*, 89(11–12), 921-929.
Gal, E., Suday, E., and Waisman, H. (2013). "HOMOGENIZATION OF MATERIALS HAVING INCLUSIONS SURROUNDED BY LAYERS MODELED BY THE EXTENDED FINITE ELEMENT METHOD." 11(3), 239-252.
Kim, J.-K., and Yi, S.-T. (2002). "Application of size effect to compressive strength of concrete members." *Sadhana*, 27(4), 467-484.
Markeset, G., and Hillerborg, A. (1995). "Softening of concrete in compression—localization and size effects." *Cement and Concrete Research*, 25(4), 702-708.
Richart, F. E., Brandtzaeg, A., and Brown, R. L. (1928). "A study of the failure of concrete under combined compressive stresses."
Shin, M., and Andrawes, B. (2010). "Experimental investigation of actively confined concrete using shape memory alloys." *Engineering Structures*, 32(3), 656-664.
Štemberk, P., and Kohoutková, A. (2005). "Image-analysis-based measuring of lateral deformation of hardening concrete." *Materials Science (Medžiagotyra)*, 11(3), 292-296.
Tarrant, A. G. (1954). "Measurement of friction at very low speeds." *The Engr*, 262-263.
Van Mier, J., Shah, S., Arnaud, M., Balayssac, J., Bascoul, A., Choi, S., Dasenbrock, D., Ferrara, G., French, C., and Gobbi, M. (1997). "Strain-softening of concrete in uniaxial compression." *Materials and Structures*, 30(4), 195-209.
van Mier, J. M. (1986). "Multiaxial strain-softening of concrete." *Materials and Structures*, 19(3), 190-200.
van Vliet, M., and van Mier, J. (1996). "Experimental investigation of concrete fracture under uniaxial compression." *Mechanics of Cohesive-frictional Materials*, 1(1), 115-127.
Vonk, R. A. (1992). "Softening of concrete loaded in compression."
Vonk, R. A., Rutten, H.s, Van Mier, J.G.M. and Fijneman, H.J. (1989). *Influence of boundary conditions on softening of concrete loaded in compression*, Fracture of concrete and rock : recent developments, London ; New York : Elsevier Applied Science.

Zisopoulos, P. M., Kotsovos, M. D., and Pavlovic, M. N. (2000). "Deformational behaviour of concrete specimens in uniaxial compression under different boundary conditions." *Cement and concrete research*, 30(1), 153-159.

Monitoring and Behavior of an Instrumented Concrete Lining Segment of a TBM Excavation Experiment at the Meuse Haute-Marne Underground Research Laboratory (France)

J. Zghondi[1]; S. Carraretto[1]; A. Noiret[1]; and G. Armand[1]

[1]Andra R&D, French National Radioactive Waste Management Agency, Meuse/Haute-Marne Underground Research Laboratory, 55290 Bure, France.

Abstract

One of the main issues of the ongoing Andra's research program is the development of construction methods and optimization of radioactive waste structures of the disposal facility. A new method for tunnel construction was tested in the underground research laboratory (URL) using a TBM with segment emplacement technique. The lining is composed of reinforced concrete segments, backfilled with two types of grouting mortar: a classical and a compressible grout. The major objectives of this experiment are to check the technological feasibility, and to analyze the hydromechanical behavior of the host rock and of the lining. Different investigation methods were used; the host rock and the concrete lining were instrumented, and the different grouts and concrete used are being characterized. The global data analyses, underline an anisotropic loading, which is more pronounced on the classical mortar zone. The major radial loading is identified in the horizontal direction which is consistent with the existing drifts along this orientation.

INTRODUCTION

The French national radioactive waste management agency (Andra) started in 2000 to build the Meuse/Haute-Marne underground research laboratory (URL) at Bure (nearly 300 km East of Paris). The host formation consists of a claystone (Callovo-Oxfordian argillaceous rock – COX) lying between 420 m and 550 m in depth. The Callovo-Oxfordian claystone is overlain and underlain by poorly permeable carbonate formations.

Clay formations in their natural state exhibit very favorable conditions for repository of radioactive waste, as they generally have a very low hydraulic conductivity, small molecular diffusion and significant retention capacity for radionuclide. In 2005, Andra demonstrated the order to demonstrate the feasibility of repository in a deep claystone layer (Andra, 2005).

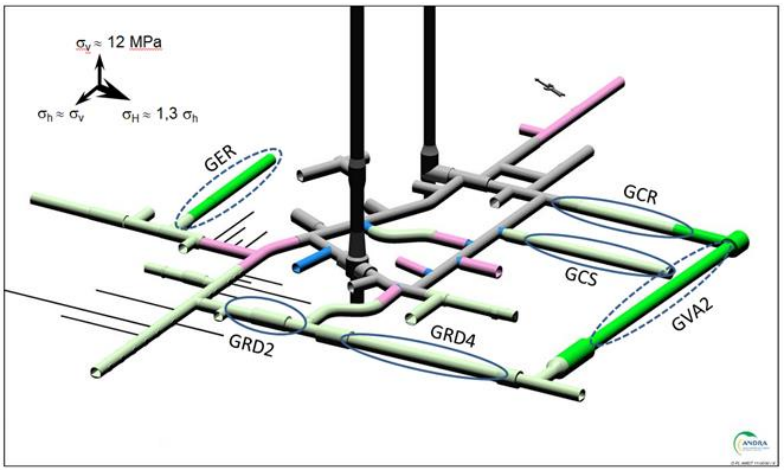

FIGURE 1. Meuse / Haute-Marne URL drifts network, (full line: already excavated, dashed line: to be excavated).

Since 2006, further researches are ongoing in the URL to increase the knowledge on the rock properties, particularly to study the excavated damaged zone (EDZ) and to test and optimize repository concepts at full scale on site.

One of the main issues of this program is the development of construction methods and optimization of structures of the disposal facility.

An important on-going program was launched to study the impact of different excavation and support techniques. Parallel drifts far enough from each other and with different construction methods and support structures are and will be constructed (Figure 1).

At main level of the URL, the anisotropic stress state of the claystone was determined by Wileveau et al. (2007). The major stress (Figure 1) is horizontally oriented at NE155°.

FIGURE 2. The four excavated drifts dedicated to structure influence study (parallel to the major in situ stress direction)

Figure 2 presents the excavated drift parallel to the major in situ stress direction.
The sequential construction program of parallel galleries (Figure 1) started with structures allowing the convergence of the ground (GCS), followed by rigid structures testing implemented at different times (GCR and GRD2 gallery).
GRD4 was the last method tested on that direction, using a tunnel boring machine road header associated with a segmental lining.

DESCRIPTION OF THE ACHIEVEMENT

Excavation process

The road header TBM used for this experiment was manufactured by Herrenknecht. The excavation of the gallery GRD4 lasted 6 months (June to November 2013) in 3 workstations 5 days weekly, with an average weekly advancement of 4,67 rings. Carraretto et al. (2014)

FIGURE 3. View of the TBM

The final inner diameter of the gallery is 5.10 m with a total length of 89 m, consisting of:

- 6 "false rings" of 0.80 m width;
- 93 rings of 0.80 m width including:
  - An area of 36 m grouted with a conventional mortar type,
  - A transition zone of 8 m long,
  - A 30.40 m zone with a compressible grouting mortar,

And finally a 10 m zone for the TBM disassembly.

Lining segments design

The segments and reinforcements were designed in a way to take into account the construction and the exploitation of the drift for a 20 years period (Figure 4).
The main characteristics of the segments are:

- Dimensions: width = 0.80 m / thickness = 0.45 m
- Weight: 1.9 t (except key segment)
- Concrete = C60/75 (C1 0.65)
- Steel reinforcement ratio = 150 kg / m3 (210 kg / m3 for the key segment)

FIGURE 4. Precast of an instrumented segment and assembly of a ring

Backfill grout mortar characteristics

Two types of filling mortar were injected, a classical mortar and a compressible mortar with polystyrene beads. The comparison of the two sections and the long term monitoring will help to optimize the lining thickness. The used mortar types are:

- A classical grouting mortar conventional type BRG2 from Socli (Italcementi Group),
- A compressible grouting mortar type DeCoGrout / Compex product of the partnership between Hochtief AG and Schretter & Cie based on polystyrene beads.

Backfilling process:
The formulation, mixing and grouting took place underground using a 1 m^3 mixer.
The grouting was injected through an embedded socket on the segments (70mm diameter). On each pumping intervention, different segments were grouted, mainly on three different levels (in strike right out of the shield tail, in the middle of the section at the middle of the backup train and in top at the end of the backup train), in a way to respect the identified mortar slope (25° for the compressible mortar and 30° for the classical mortar).
The short term behavior of the grout, his workability, drying period, pumpability, are important issues that condition the backfill quality and planning.
In terms of the injected volumes, a 10% overconsumption was estimated for the classical mortar, while overconsumption of compressible mortar was about 20% (due to its higher workability).

INSTRUMENTATION: STRATEGY & INSTALLATION

To understand the interaction between the rock and the lining segments and to characterize the excavation damaged zone (EDZ), several scientific instrumentations were used (Figure 5).

Different equipments were installed before, while and after excavating. Boreholes were instrumented to follow deformation and pore pressure evolution, taking in consideration the "lessons learned" from the different instrumentations performed in the underground laboratory (Noiret et al, 2011).

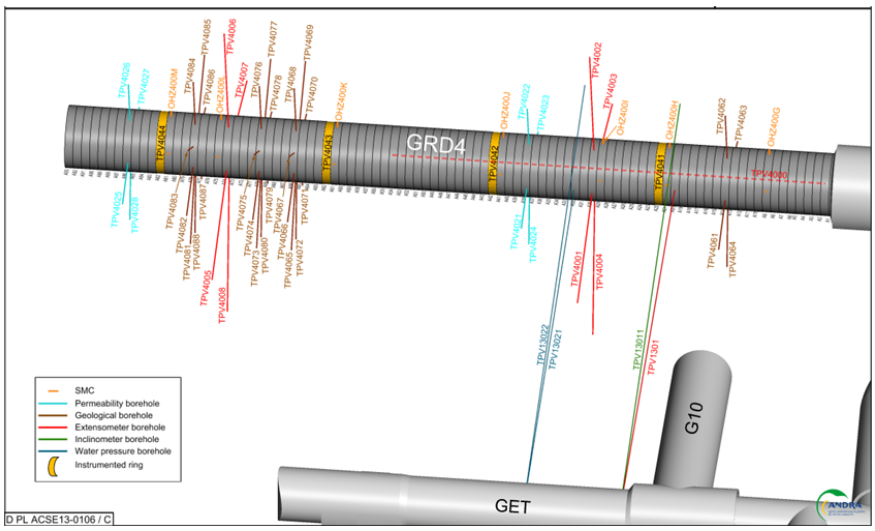

FIGURE 5. Instrumentation of the GRD4 drift

The mechanical behavior of the structure was followed, in particular strains and stresses in the concrete lining, as well as the compression of the backfill mortar.
Four rings (8 segments/ring - the key segment is not instrumented) have been equipped in Stradal's manufactory. Three total pressure cells and eight strain gages were installed on the reinforcement of each segment of the 4 monitored rings.

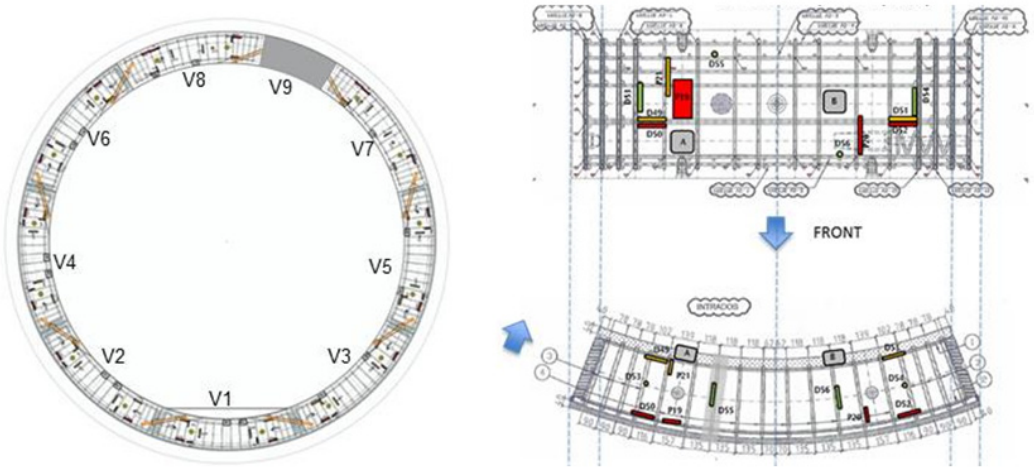

FIGURE 6. Instrumented ring; 64 strain gages, 24 total pressure sensors.

As shown on the Figure 6, pressure cells and strain gages were installed mainly on the intrados and extrados sides of the segment, in a way to follow the orthoradial behavior.

CONCRETE AND GROUT CHARACTERIZATION

The characterizations of the mechanical parameters as well as the creep and shrinkage behavior are essential to evaluate the loading of the ring due to the host rock convergence.

The backfill grouts as well as the lining segment concrete were characterized at different cases and stages of the projects:

- Formulation validation before and while grouting (compression strength, oedometric and workability tests),
- A laboratory testing program (characterization, creep, shrinkage)
- An instrumented segment dedicated to be deposed on the GRD4 drift but not to be installed on any ring (reference segment), as well as of 4 instrumented concrete test tubes (grouted and stocked respectively with each instrumented ring).

Only the mechanical behavior of the backfill compressive grout and the shrinkage of the concrete lining are presented on this article.

Concrete lining segment

One of the difficulties concerning the ring deformation analysis is to evaluate the different phenomena which have in impact that measurement, starting from shrinkage, creep, temperature and humidity influence.
Shrinkage was evaluated in different ways (autogeneous and drying), and on different sample sizes, the Figure 7 shows a comparison between:

- different sizes of samples monitored inside of an air conditioning unit that reproduce daily the climatic condition of the segments,
- instrumented reference segment,
- the four instrumented concrete test tubes.

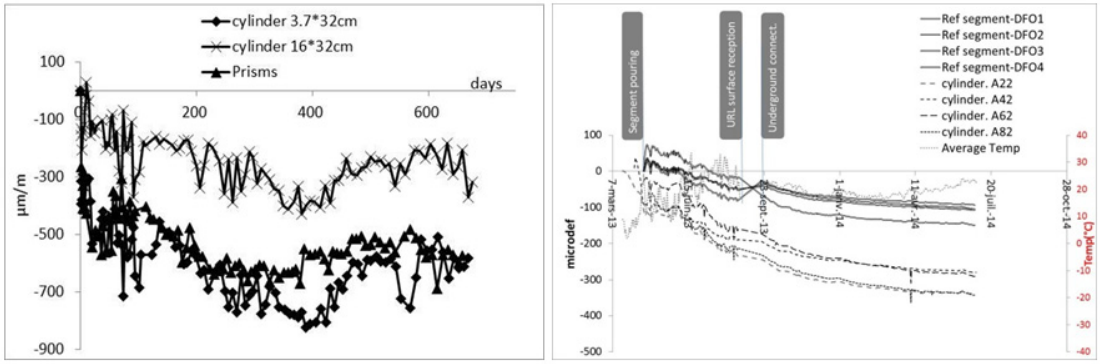

FIGURE 7. (a) Drying shrinkage measurement in 2 different cylinder sizes and prisms (b) Shrinkage measure by vibrating wires inside of the cylinder tubes, and the reference segment element.

Even if the evolution is similar, the drying shrinkage potential is the highest on the small diameter cylinder, and the lowest on the segment lining. That confirms the influence of the exchange surface and the reinforcement effect, and gives a first value of "shrinkage potential" around 800microdef.

Different characterizations are still ongoing in partner laboratories. The actual applied correction is based mainly on the reference segment. It consists on fitting to zero the deformations values, directly after grouting and before moving the segment underground (in a way to estimate the shrinkage of the segment during that period). After the ring installation, the measurements were corrected taking in account the "reference segment" evolution. That correction takes into account a large part of the shrinkage and climatic deformation.

Compressible grout mortar

The compressible potential of that grout is a major benefit; the convergence of the host rock apply a mechanical load on the backfill grout, which will deform easily, and transmit a maximum of 1 to 2 MPa to the lining.

Oedometric tests performed by the company in charge of construction as well as the laboratory complementary program confirm the compressive deformation which offers an optimization possibility for the lining.

Creep tests at 0.25MPa and 4MPa are ongoing with the partner laboratories. The shrinkage values of that grout are extremely high and not stabilized yet (about 2000 microdef in 460 days of monitoring).

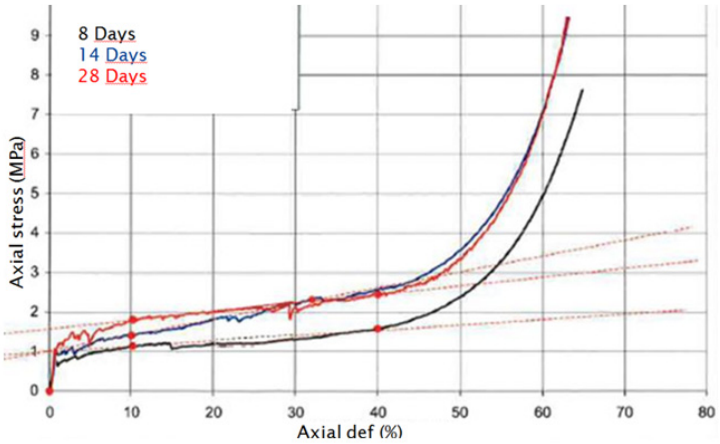

FIGURE 8. Oedometric tests on the compressible grout.

HOST ROCK MECHANICAL BEHAVIOR ANALYSIS

The analysis of the rock behavior, confirm what is observed on drifts having the same direction (Armand et al. 2013). Even though the drift direction is parallel to the major stress, the excavation work induces anisotropic fracturation networks around the drifts due to the semi-brittle behavior of the rock (even if cross section initial stresses are isotropic). That fracturation network induces an anisotropic convergence more marked on the horizontal direction (Figure 9). Highest convergence is observed where the extent of induced fractures is larger.

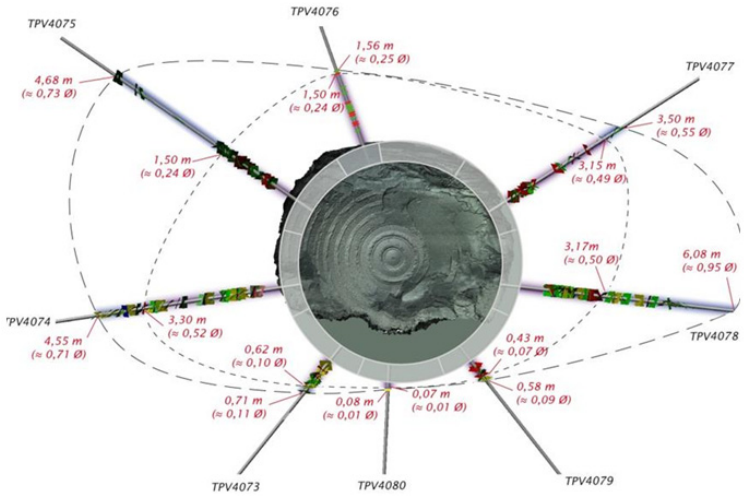

FIGURE 9. Extension of the shear and tensile fracture zones on the GRD4 drift.

LINING MECHANICAL BEHAVIOR ANALYSIS

Deformations and stresses of the instrumented lining are more significant on the classical backfill zone. Figure 10 shows an example of that behavior, it compares the total deformations (without correction) of two V4 segments one on the classical mortar (A22) and one in the compressible mortar (A62).

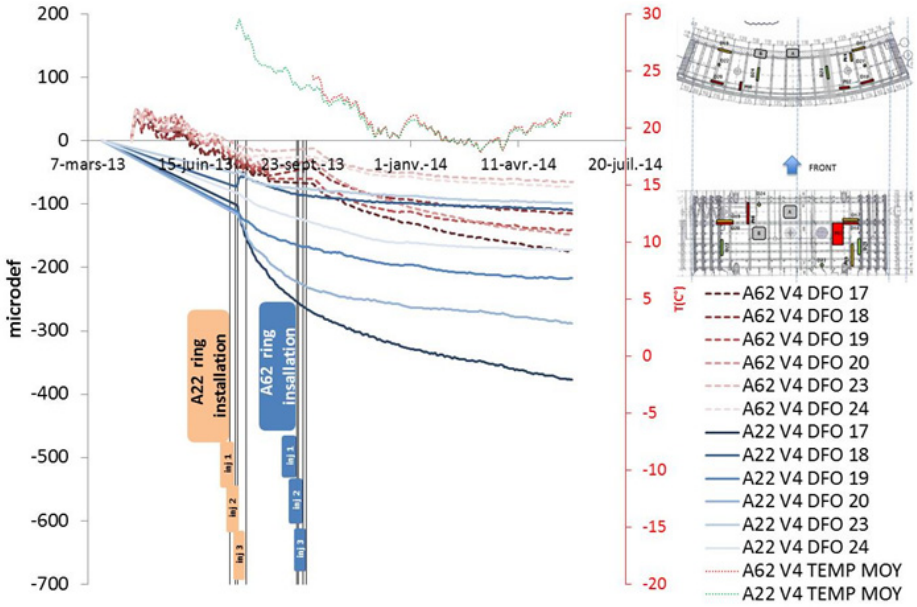

FIGURE 10. Comparison of deformations in the V4 segment lining for the two different backfill grout zones: A22 (classical grout zone) and A62 (compressible grout zone).

The Figure 11 presents the corrected deformations and stresses evolution on the lining section circumference; the results show an anisotropic loading signature with

opposite deformations and stresses between intrados and extrados. Anisotropic loading is observed from early age.
Loading and deformations on the two mortar zones have similar shape but they are more significant on the classical mortar zone. That behavior confirms the compressible mortar impact.

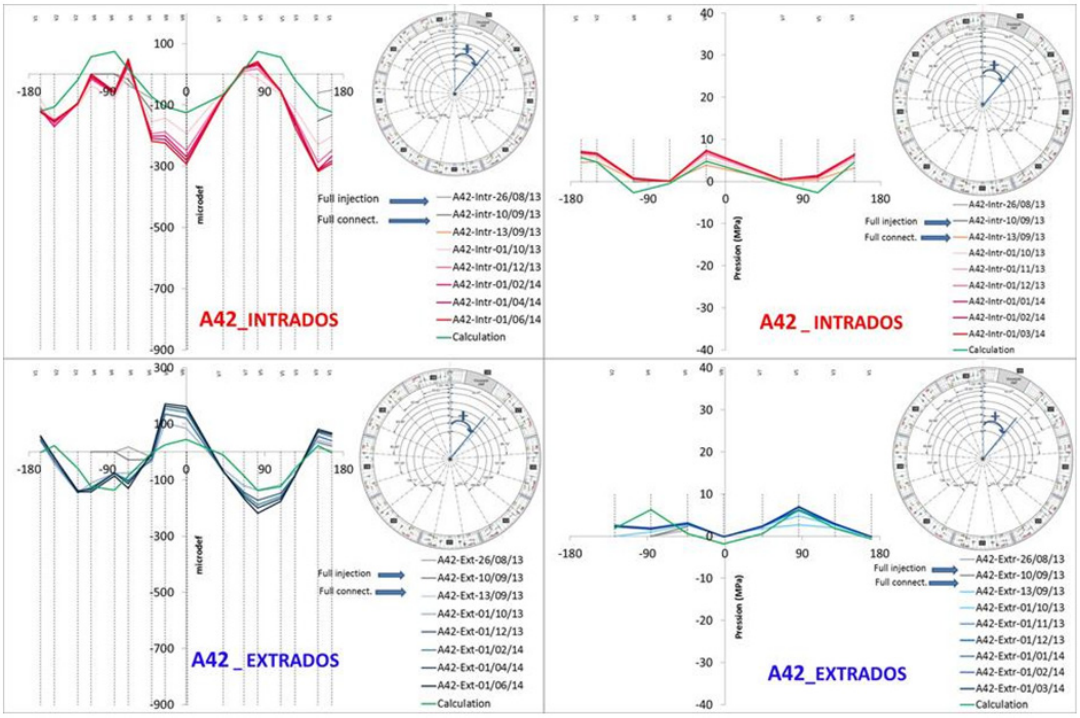

Figure 11 *Evolution of the circumferential strains (microdef.) and stresses (MPa) on the extrados and intrados of the A42 (classical mortar backfill zone) ring.*

Figure 11 shows also a comparison with a finite element calculation, taking in account a radial loading applied directly on the ring. Lining characteristics found in the partner laboratories, were taken into consideration on that calculation. Lining segment behavior was considered elastic, which is justified taken in account the actual level of stresses. The anisotropic loading that fit the best to the observed classical zone behavior is a radial loading of 0.2MPa in all the segments other than V4 and V5 with a 0.4MPa. These results confirm the host rock behavior and offer a global homogenous rock/structure behavior.

CONCLUSION

Lining deformations and stresses describe the same anisotropic loading applied on the two instrumented sections of each zone. Differences were noticed between the two zones of backfill mortar, lining is less loaded on the compressible zone. The potential of deformation of the compressible grout is clearly a major benefit to optimize the concrete lining.

REFERENCES

Andra 2005. Dossier 2005 Argile. "*Evaluation de la faisabilité du stockage géologique en formation argileuse profonde*". Rapport de synthèse, Juin 2005, Andra, www.andra.fr.

Wileveau, Y., Cornet, F.H., Desroches, J. & Blumling, P. 2007. "*Complete in situ stress determination in an argillite sedimentary formation.*" Physics and Chemistry of the Earth, vol. 32, 866-878.

Carraretto S., Noiret A., Zghondi J., Armand G., Richard-Panot L. (2014). "*TBM excavation in Underground Research Laboratory of Meuse Haute-Marne,* AFTES congress 2014, Tunnels and underground space.

Noiret A., Armand G., Cruchaudet M., Conil N. (2011). "*Mine by experiments in order to study the hydromechanical behavior of the Callovo-Oxfordian Claystone at the Meuse Haute-Marne underground research laboratory (France)",* 8th International Symposium on Field Measurements in Geomechanics, FMGM 2011, Berlin, Germany, September 12-16 2011.

Armand G., Noiret A., Zghondi J., Seyedi D. (2013). "*Short and long term behavior of drifts in the Callovo Oxfordian claystone at the Meuse Haute-Marne Underground research laboratory*", Journal of Roch Mechanics and Geotechnical Engineering, 2013,4(1).

Monitoring the Creep of Prestressed Concrete Girders Affected by the Thickness of a Cross Section

Ken Watanabe[1] and Yuto Ohno[2]

[1]Ph.D., Concrete Structures, Structures Technology Division, Railway Technical Research Institute, 2-8-38, Hikaricho, Kokubunji, Tokyo 185-8540, Japan. E-mail: watanabe.ken.08@rtri.or.jp
[2]M.E., Concrete Structures, Structures Technology Division, Railway Technical Research Institute, 2-8-38, Hikaricho, Kokubunji, Tokyo 185-8540, Japan. E-mail: ono.yuto.47@rtri.or.jp

Abstract

Even there are many influential parameters on both the shrinkage and the creep of concrete, one of the most important indices is the moisture movement that is affected by the concrete size as well as the relative humidity of environment surrounding the concrete. The objective of this study is to evaluate the difference of the creep coefficient of concrete by the location by monitoring used for the prestressed concrete (PC) girders of railway structures. Based on the monitored data, the value of creep coefficient was different according to the location: e.g. web, flange, and slab in PC girders.

INTRODUCTION

The properties of shrinkage and creep of concrete are important for predicting the deflection and the stress reduction of prestressed concrete (PC) girders. Even there are many influential parameters on both shrinkage and creep of concrete, one of the most important indices is the moisture movement that is affected by the relative humidity (*RH*) of environment surrounding the concrete. The value of *RH* has been set as an identical value when PC girders are designed, even the value has a potential of changing according to the location: e.g. web, flange, and slab in PC girders. Prestress-force and deformation generated in PC girders over time has been calculated based on the relaxation of PC cables, rebars distribution, the relative humidity (*RH*), restriction conditions, in particular, the creep and the shrinkage of concrete. The objective of this study is to evaluate the difference of the creep coefficient of concrete by the location based on monitoring used for the PC girders of railway structures.

OUTLINE OF MEASUREMENTS

Figure 1 shows the monitored PC girder. The PC girder had T-shape cross-section and 20-m in span, the early-strength cement with water-to-cement ratio of 0.40 was used for the concrete in order to introduce the prestress force at 5-day in

(a)Casting. (b)Installation. (c)Completion.

Figure 1. Measured PC girder.

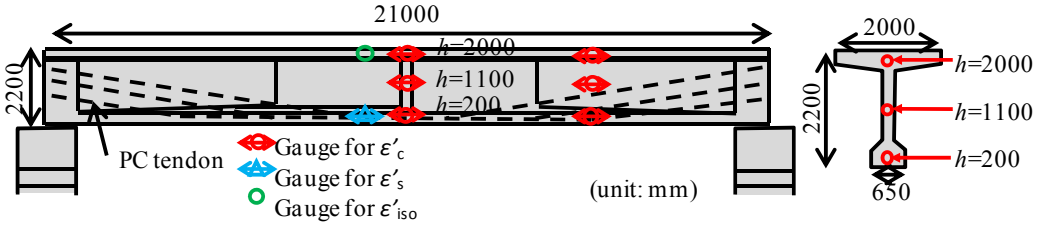

Figure 2. Location of measurement equipment.

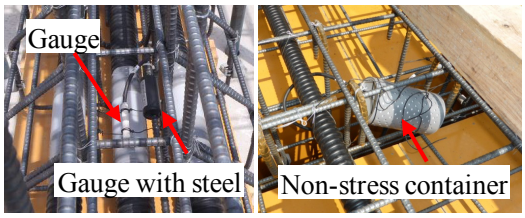

Figure 3. Setting detail of equipment.

Table 1. Contraction process.

Cast	0-day
Remolded	1-day
Installing of PC	5-day
Erection	23-day
Connection of girders	47-day
Casting of slab	505-day

age. Figure 2 indicates the dimension of PC-girder and the location of gauges for measurements. The PC girder monitored in this study was one of four girders in railway bridges. The averages in a year were the temperature of 16.9 in Celsius and the *RH* of 71%.

The cross-section in the middle span of PC girder was provided some gauges. The strain gauges with temperature measuring functions, which measures the total strain of concrete ε'_c including creep, shrinkage, strain caused by applied force, temperature change, etc., were installed at upper flange (h=2000-mm), web (h=1100-mm), bottom flange (h=200-mm). The reinforcing bar strain gauge with temperature measuring functions was set at the bottom flange to obtain ε'_s. In addition, the strain gauge with temperature measuring functions was embedded together with concrete in a non-stress container to measure the non-stressed strain ε'_{iso} (shrinkage strain). The setting detail of gauges were shown in Figure 3.

Table 1 lists the construction process. The PC girder was remolded at the age of 1-day, installed the prestress force at the age of 5-day, erected at 23-day on RC columns.

Nine prism-shape specimens were also cast and cured in different environment conditions as shown in Figure 4. Specimens suffered by rain and sun-light (rained specimen), specimen without rain and sun-light (no-rained specimen), and specimen perfectly covered by aluminum tape (sealed specimen). A mold-gauges (measured length: 60-mm) and thermocouples were provided at the center of each

(a)Raind specimens (b)No-rained, sealed specimens. (c) View.

Figure 4. Specimens cured near the PC girder.

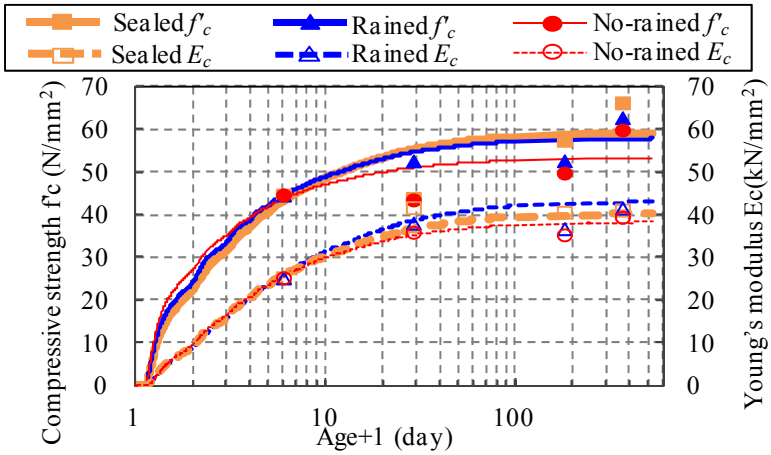

Figure 5. Material properties.

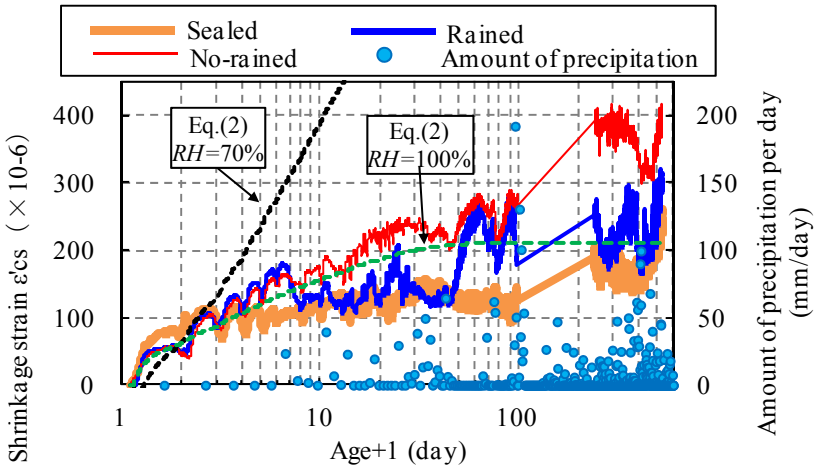

Figure 6. Shrinkage strain.

specimen for measuring strain and temperature. In addition, specimens with φ100×200-mm were also casted and cured in the same environment condition for measuring the compressive strength and Young's modulus of concrete at arbitral age.

Compressive strength and Young's modulus. Figure 5 shows the measurement results and predictions (JSCE 2010) of the compressive strength and Young's modulus at the age of 5, 28, 180, 365-day. Because of water evaporation, both

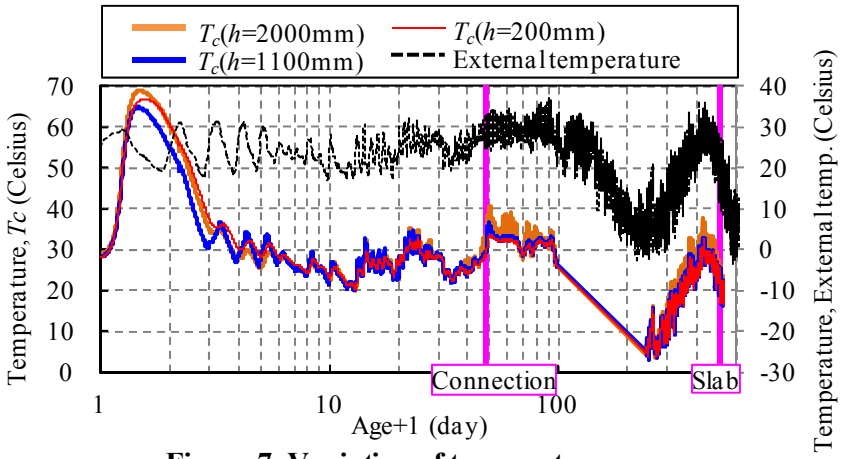

Figure 7. Variation of temperature.

measured values of no-rained specimen were around 10% smaller than those of the other specimens.

Shrinkage strain. Figure 6 compares the development of shrinkage strain by age depending on the cured method. The averaged value of three specimens at each curing method was selected, and the positive value indicates shrinking. The measured data seemed to be demonstrated by Eq. (1); the auto-generous shrinkage generated between the setting time of concrete t_s (day) and beginning of drying t_0 (day) is also evaluated as:

$$\varepsilon'_{cs}(t,t_s)=\varepsilon'_c(t,t_s)-\alpha\times\Delta T(t,t_s) \tag{1}$$

$$\varepsilon'_{cs\,cal}(t,t_0)=\varepsilon'_{dc}(t,t_0)+\varepsilon'_{ac}(t,t_0) \qquad 55<f_c'\le 80\text{N/mm}^2 \tag{2}$$

where, $\varepsilon'_{cs}(t,t_s)$: shrinkage strain from the setting time of concrete t_s (day) to its age t (day), $\varepsilon'_c(t,t_s)$: total strain from the setting time of concrete t_s (day), α: temperature coefficient of expansion of concrete ($=10\times10^{-6}$/Celsius), $\Delta T(t,t_s)$: temperature difference between the setting time and age t (Celsius), t_0 and t: temperature adjusted age (day) of concrete at the beginning of drying and during drying, $\varepsilon'_{ds}(t,\ t_o)$: dry shrinkage strain of concrete from the age of t_o to t, $\varepsilon'_{as}(t,\ t_o)$: autogenerous shrinkage strain of concrete from the age of t_o to t.

The shrinkage strain of no-rain specimen was largest at each age. Even there are some difficulty in finding the relationship between rained and no-rain specimens, the deference of the strain was generated at the age of 5-day when the first rainy day after casting. The strain obtained by the sealed specimen was good agreement with the value of autogenous shrinkage ($\varepsilon'_{as}(t,t_s)$).

The result implies that the shrinkage strain generated in RC and PC girders will be varied by the location, e.g. the rain makes top surface of flanges of girders wet, however, the web or the bottom surfaces of PC girders are sometimes dried. Because of these situation and the results of "rained specimen" or "no-rain specimen", the shrinkage strain at the age of t (day) will be increased at the dried

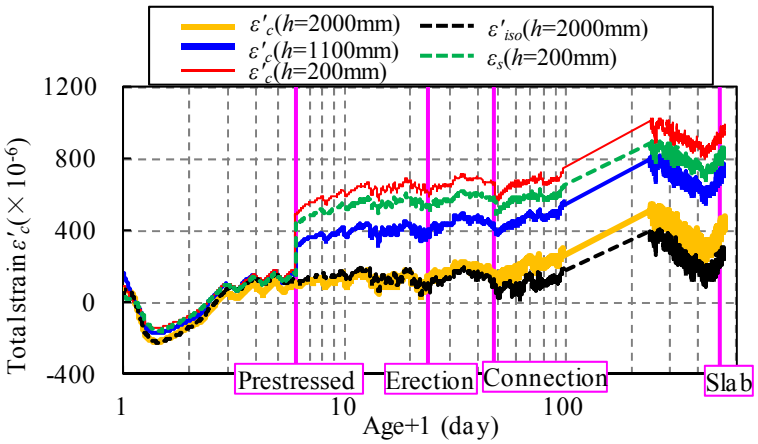

Figure 8. Total strain.

portion, even the magnitude of the value was smaller compared with the calculation by Eqs.(2).

MEASURED RESULTS OF PC GIRDER

Temperatures. Figure 7 shows the temperatures change measured at the cross-section of middle span of PC girder and a local meteorological observatory. The temperatures in the PC girders were suddenly increased just after casting, in particular, at the height of 2000-mm where the width was the largest at the upper flange. The he daily temperature also indicates the highest because of insolation, however, the magnitude of variation was smaller than that of ambient temperature.

Total strain. Figure 8 compares the time dependence of the total strain of concrete ε'_c (creep, shrinkage, strain caused by applied force, temperature change, etc.), the isolated strain ε'_{iso} (shrinkage), and strain in reinforcing bar ε'_s. Negative value indicates the expansion of concrete. The value of ε'_c were decreased (expanding) with heating and increased (shrinking) with cooling during hydration. It is also varied by the daily temperature. The difference between ε'_c and ε'_{iso} means the value of ε'_c captured the effect of loading at the age of 5-day.

Subtract $\alpha\times\Delta T(t,t_s)$ from ε'_{iso} was almost similar tendency with those of sealed specimen in Figure 6. Because the value of ε'_{iso} was measured at 100-mm from surface, the curing condition was identical with the sealed specimen during measuring, even the curing condition will change by age.

Deflections. The curvature distribution along the span was assumed as quadratic function with considering the total strain measured at the middle or the quarter of the span. The integral of curvature along the span gave the deflection of the PC girder as shown in Figure 9. Negative value indicates the upper direction. The deflection ate the middle span was increased as 8-mm in upper direction at installing the prestressed force. The deflection was gradually increased by age.

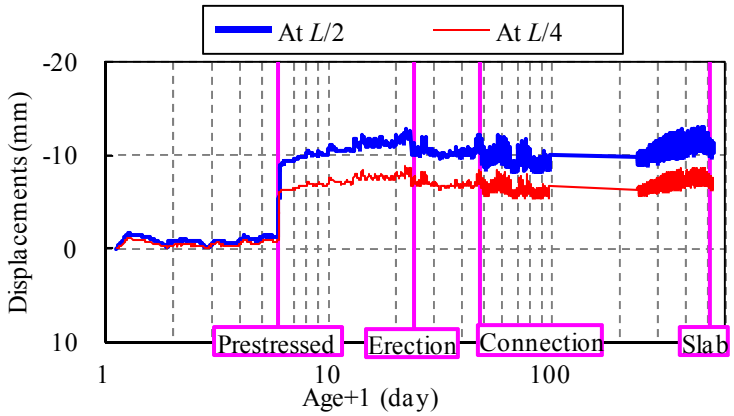

Figure 9. Deflection of PC girder.

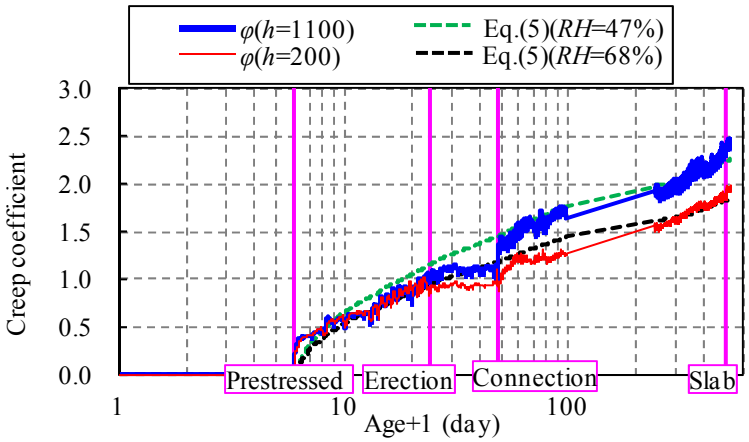

Figure 10. Creep coefficient.

Creep coefficient. Creep strain ($\varepsilon'_{cc}(t,t')$) and creep coefficient ($\varphi(t,t')$) generated between the ages of t' and t (day) are calculated by Eqs.(3)(4) as:

$$\begin{aligned}\varepsilon'_{cc}(t,t') &= \varepsilon'_{c}(t)-\varepsilon'_{cT}(t)-\varepsilon'_{cs}(t)-\sigma'_{c}(t)/E_{c}(t) \\ &= \varepsilon'_{c}(t)-\varepsilon'_{iso}(t)-\sigma'_{c}(t)/E_{c}(t)\end{aligned} \tag{3}$$

$$\varphi(t,t') = \varepsilon'_{cc}(t,t')\times E_{c}(t')/\sigma'_{c}(t') \tag{4}$$

where, $\varepsilon'_{c}(t)$: the total strain, $\varepsilon'_{cT}(t)$: the strain calculated by the coefficient of thermal expansion, $\varepsilon'_{cs}(t)$: the shrinkage strain, $\sigma_c'(t)/E_c(t)$: the elastic strain caused by loading, $\varepsilon'_{iso}(t)$: strain measured in the non-stress container.

Figure 10 plots $\varphi(t,t')$ at h=200-mm and 1100-mm. The magnitude of stress at the upper flange (h=2000-mm) was so small that the impact of $\sigma_c'(t)/E_c(t)$ on $\varphi(t,t')$ was significant. The results were not useful, and not involved in the following discussion. Even both $\varphi(t,t')$ showed the same value at installing the prestress force, however, there were some gaps by increasing its age. The value of $\varphi(t,t')$=2.5 with h=1100-mm and $\varphi(t,t')$=2.0 with h=200-mm at 526-day. The width of each height related to the distance for drying was 250-mm at h=1100-mm, or 650-mm at h=200-mm. The gap in Figure 10 seems to be the smaller width the larger creep coefficient.

One of the methods for predicting the creep (JSCE 2010) is Eqs.(5)(6) as:

$$\varphi_{\mathrm{cal}} = \frac{4W(1-RH/100)+350}{12+f'_{\mathrm{c}}(t')}\log_{\mathrm{e}}(t-t'+1)\cdot E_{\mathrm{ct}} \quad 55 < f_c' \le 80\text{-N/mm}^2 \qquad (5)$$

$$t,t' = \sum_{i=1}^{n}\Delta t_i \cdot \exp\left[13.65 - \frac{4000}{273+T(\Delta t_i)/T_o}\right] \qquad (6)$$

where, f_c': compressive strength of concrete at the loading age t' (N/mm^2), t' and t: temperature adjusted age (day) at the beginning of loading and during loading, respectively W: unit water content (kg/m^3) (130-kg/m^3 $\le W \le$230-kg/m^3), and RH: relative humidity (%) (40% $\le RH \le$ 90%), E_{ct}: Young's modulus of concrete at the loading age t' (N/mm^2), Δt_i: number of days when the temperature in T (Celsius), and T_o: 1 in Celsius.

The dependence of creep coefficient $\varphi(t,t')$ on the location would be caused by the cross-section width, rain, relative humidity of outside PC girder, therefore, the measured values would be expressed by Eq.(5) with controlled RH. Based on the data, Eq.(5) demonstrated the creep coefficient by setting RH=47% at h=1100-mm, or by setting RH=68% at h=200mm. The value of "setting RH" in this paper was involved some influences as stated in above, it should be corresponding to the relative humidity surrounding the PC girder. As stated in above, "setting RH" will be changed by age. The significance of difference in the shrinkage strain and the creep coefficient according to the location will be evaluated by monitored data.

CONCLUSION

The creep coefficient corresponding to the creep strain divided by elastic strain was calculated at the height of 2.0-m, 1.1-m, and 0.2-m. Even the stress condition was different among these heights, the measured creep coefficient was strongly depending on the height of cross section because the drying condition was changed. Based on the conventional equation, the creep coefficient at web was corresponding to the calculated value by the conventional equation with RH of 47%, and at the bottom flange was corresponding to the condition of RH=68%. The effect of beam thickness affected the creep behavior of concrete. This RH was not corresponding to the relative humidity of the environment surrounding the PC girder; however, it was useful for understanding the relationship between laboratory specimens and real structures. The creep behavior of PC beams, which was varied by location as well as drying condition, was evaluated according to the conventional model with controlled by the RH.

REFERENCES

Japan Society for civil engineers JSCE Concrete Committee (2010): Standard Specifications for Concrete Structures -2007 "Design".

Health Monitoring of Prestressed concrete structures based on finite element model updating with uncertainty

S. Biswal[1] and A. Ramaswamy[2]

[1]Civil Engineering Department, Indian Institute of Science, Bangalore, India; PH (+91) 9483709860; email: skbiswal@cistup.iisc.ernet.in
[2]Civil Engineering Department, Indian Institute of Science, Bangalore, India; PH (+91) 80-2293-2817 ; FAX (+91) 80-2360-0404; email: ananth@civil.iisc.ernet.in

ABSTRACT

A finite element model updating technique based on measured strain responses is used to monitor the health of prestressed concrete structures. In this work health corresponds to the existing prestressing force present and the associated stiffness properties of the structure. Measurements are taken on post-tensioned beams, both bonded and unbonded. The measured response is the total strain of the beams at predefined locations and the natural frequencies of the structures. In this work uncertainties in the measured data and those in the stiffness parameters are considered. The uncertainties are modeled using both Bayesian technique and interval analysis. The uncertain parameters in the finite element model are then estimated using Markov chain Monte Carlo technique in Bayesian framework and set inversion via interval analysis in interval analysis framework. The existing prestressing force estimated by both the mentioned techniques are then compared with the measured actual prestressing force present in the structure. To check the robustness of the proposed algorithm tests are conducted at different time spans corresponding to different prestress loss and different material stiffness.

INTRODUCTION

Prestressed concrete is widely used in civil engineering structures like bridges, nuclear power plants etc. But the prestressing structures are subjected to loss of prestress force and reduction in stiffness properties due to adverse environmental conditions. The major sources of losses are the structural deformation due to creep and shrinkage in concrete and relaxation in the prestressing strands. Hence it is necessary to estimate the long term prestress loss in the prestressed concrete structures. But the available models for the loss of prestress force are empirical in nature and it is necessary to evaluate their suitability in the short term prediction before taking any decision on the long term prestress loss estimation. Various nondestructive methods such as ultrasonic sound wave based methods, impedance based methods, change in magnetic flux based method are available for measuring the existing prestressing force. These

methods are not only very expensive but also need proper accessibility for the instrumentation. Therefore various semi-destructive methods are developed to measure the existing prestressing force. Among these semi-destructive methods, crack re-opening method is widely used. In this paper a nondestructive method based on the measured strain response and natural frequencies is proposed for the determination of existing prestressing force. The measured responses are assumed to contain uncertainties due to error in calibration of sensors, transmitting, recording and manipulating the measured quantities. Two types of methods are used to handle the measurement uncertainty one based on the probabilistic method and the other on interval analysis. In probabilistic based method Bayes rule is used to estimate the unknown parameters with respect to the uncertain measured responses whereas in interval analysis based method set inversion via interval analysis is used for the estimation of them. The estimated prestressing force is then compared with the actual prestressing force present in the structure measured using crack re-opening method.

This paper is organized as follows. Section 2 describes the proposed method in the finite element modeling of structures for the estimation of uncertain structural parameters. Section 3 presents the experimental set up and instrumentation of sensors. Section 4 explains the results and discussions. Section 5 includes the conclusion.

FINITE ELEMENT MODEL UPDATING

In this study a finite element model is employed to obtain the load deformation response prediction. But the responses obtained from the actual measurement on the structure and the predictions from the finite element analysis usually vary. Hence it is necessary to update the parameters of the finite element model so as to match the predicted response with the actual measurement data. In this study the existing prestressing force and the modulus of concrete in each element are taken as the unknown parameters. Two types of updating procedures used in this study are described below.

Probabilistic Approach

Updating models and their uncertainties in a statistical framework is given in [3]. Bayesian probabilistic approach is used in [4] for structural health monitoring. The algorithm proposed in the above article is used in this study for updating the parameters of the finite element model. If θ is the vector of random variables representing the unknown uncertain parameters and Z is the vector of measurement data the Bayesian estimation of the parameter vector is given by

$$\pi(\theta|Z) = \frac{p(Z|\theta) \times \pi_0(\theta)}{\int p(Z|\theta) \times \pi_0(\theta) d\theta}$$

Where,

$\pi_0(\theta)$ = prior distribution of parameter vector

$p(Z|\theta)$ = likelihood of measurement with respect to the given parameter vector

The evaluation of multivalued integral in the denominator of the equation.1 can be avoided by using Markov chain Monte Carlo based methods. In this study Metropolis Hastings algorithm [1] is used for the estimation of the posterior distribution of the output parameter vector and the steps involved are given below.

- set the number of simulations
- initialize the parameter vector θ^0
- for all the simulations
  - find the acceptance ratio α as given in [1] as the ratio of likelihood of the measurement given the parameters in the current simulation to the likelihood of the measurement given the parameter in the previous simulation.
  - accept the current sample with probability α

Interval Analysis Approach

In the interval analysis approach the unknown uncertain parameters are taken as closed intervals with their values bounded between the lower and the upper bounds. If θ is an interval then it is defined as $\theta = \{x|\underline{\theta} \leq x \leq \overline{\theta}\}$, where $\underline{\theta}$ is the lower bound of θ and $\overline{\theta}$ is the upper bound of θ.

The uncertain bounded parameters are obtained using the set inversion via interval analysis algorithm given in [2] and shown in Figure. 1. Set inversion is the estimation of the box X with respect to the measured responses carried by the box Z and is defined by

$$X = f^{-1}(Z) = \{x \in R^n \mid f(x) \in Z\}$$

EXPERIMENTAL TEST SET UP

Experiments are conducted in our laboratory to validate the proposed method. Two post-tensioned beams are cast one beam with bonded tendons whereas the other one with unbonded tendons. Bonding of tendons is achieved by grouting the prestressing tendon ducts with cement paste. Both of them have the same structural properties with length 2200 mm, width 250 mm and depth 250 mm. Four prestressing tendons are placed concentrically with an initial prestress force of 13.09 Tonnes in each of them. After the application of prestressing force they are kept inside the humidity chambers with constant relative humidity of 70% and temperature of 40^0C. The beams are removed after an interval of three months and after testing they are again put back into the humidity chamber. Beams are loaded using four point bending method with MTS(Material Testing System) which is a universal testing machine. Five strain gauges

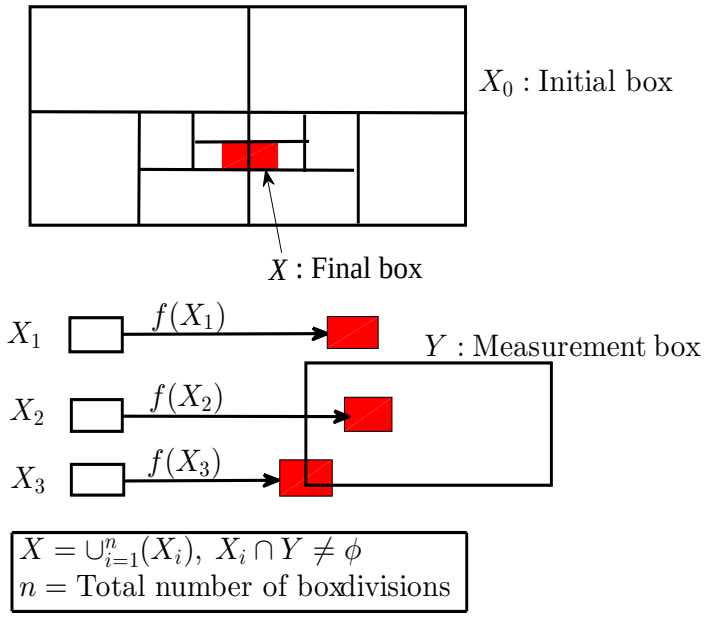

Figure 1. Set Inversion Via Interval Analysis.

are used for strain measurement and five LVDT's are used for measuring the displacements. The experimental set up is shown in Figure. 2.

Figure 2. Experimental set up.

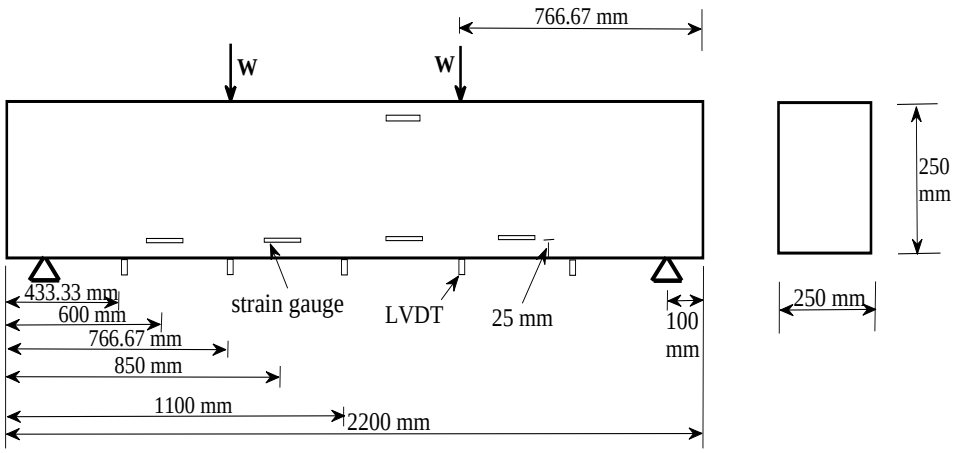

Figure 3. Beam dimension and sensor location.

The beam dimension and the location of sensors is shown in Figure.3. For measuring the natural frequencies an impact hammer and accelerometers are used. To know the actual prestress force existing in the beams crack reopening method is used. For crack reopening the beams are loaded till the crack occurs and then putting an LVDT across the crack the load versus the crack reopening displacement is obtained. Then using bending theory the existing prestressing force is calculated from the load at which the crack reopened.

RESULTS

The prestress loss and the stiffness losses are estimated using both the Bayesian analysis and interval analysis. Figure. 4 shows the Markov chain corresponding to a prestress loss of 20% and stiffness loss of 8%. The Markov chains are run till they reach stationary. The samples after the stationarity are used for the evaluation of probability densities of the parameters. The prior and posterior densities of the loss estimates are given in Figure. 5 and Figure. 6 respectively. The unknown parameters are represented as the mean of the probability density functions. Similarly for the prestress loss of 30% and stiffness loss of 15% the Markov chain is shown in Figure. 7. The corresponding prior and posterior density estimates are shown in Figure. 8 and Figure. 9 respectively. The comparison of losses and the load deformation responses estimated using Bayesian analysis and interval analysis is done against the measured responses and is reported in Table. 1 and Table. 2. From the results it is clear that the Bayesian analysis can estimate the unknown parameters when uncertainty is present in the measurement data but the most representative number is a crisp quantity whereas in interval analysis the estimated uncertain parameters are bounded by their lower and bounds.

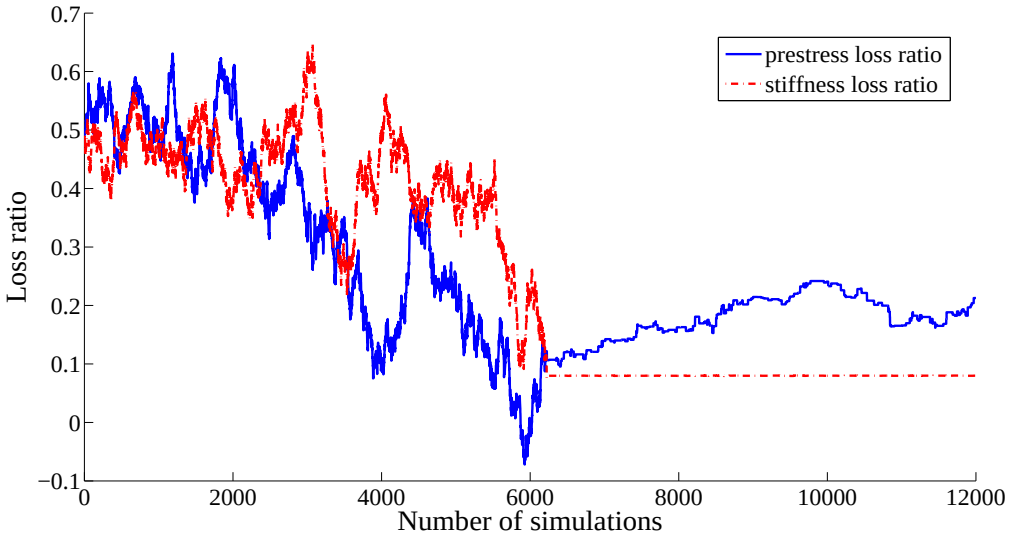

Figure 4. MCMC chain for prestress loss of 20% and stiffness loss 0f 8%

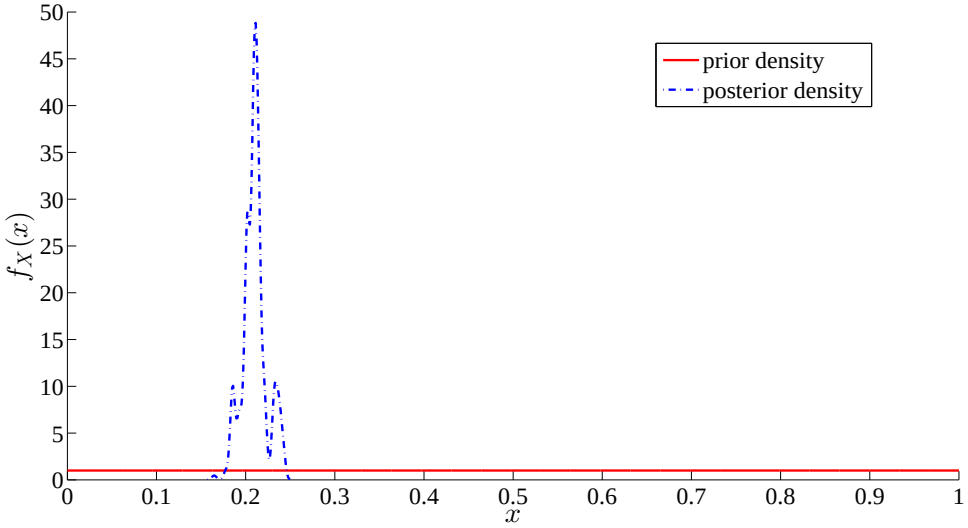

Figure 5. Prestress loss estimate for prestress loss of 20% and stiffness loss 0f 8%

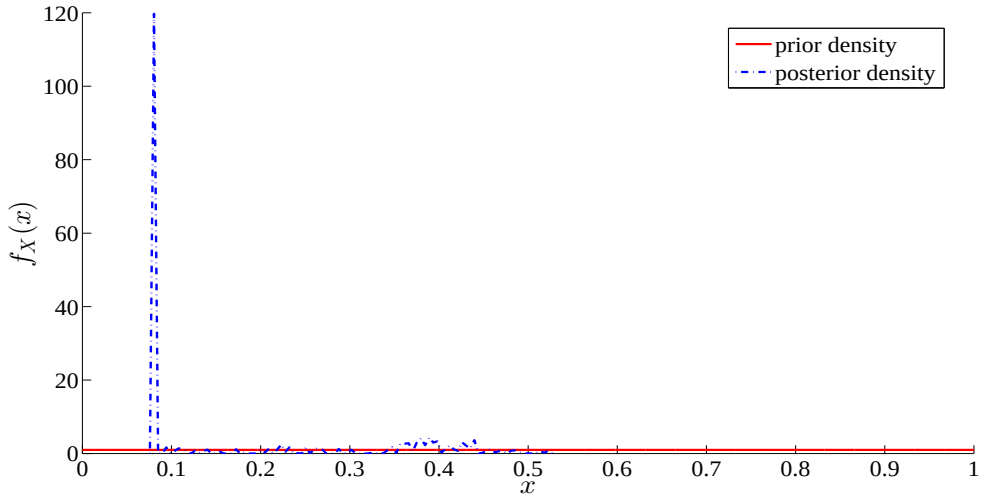

Figure 6. Stiffness loss estimate for prestress loss of 20% and stiffness loss 0f 8%

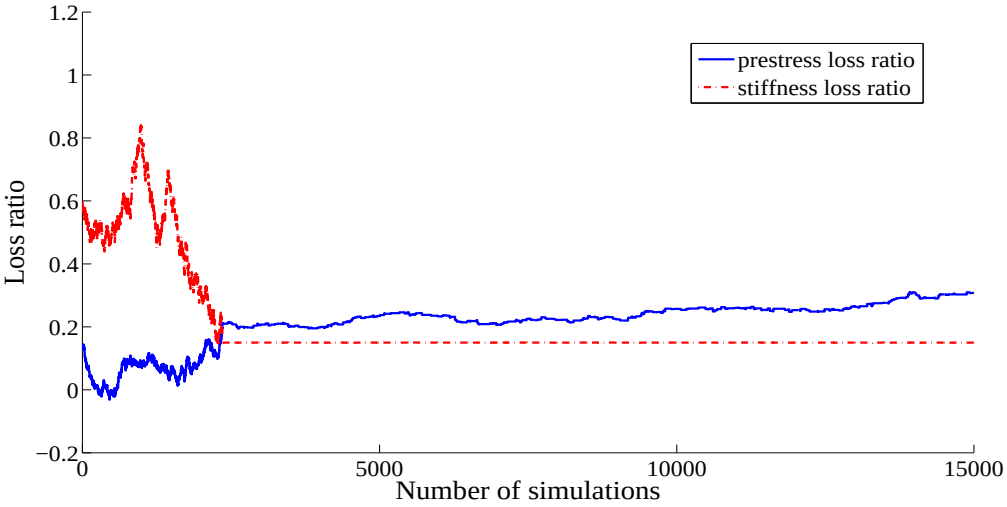

Figure 7. MCMC chain for prestress loss of 30% and stiffness loss 0f 15%

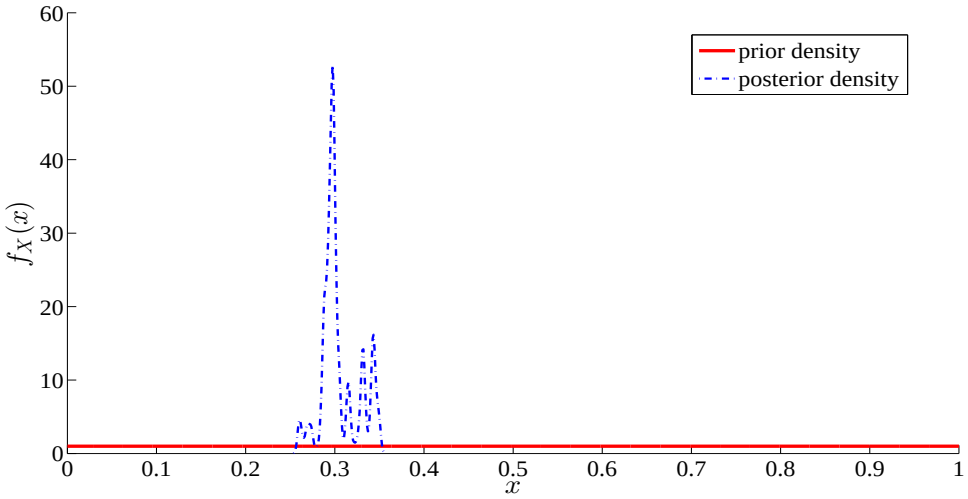

Figure 8. Prestress loss estimate for prestress loss of 30% and stiffness loss 0f 15%

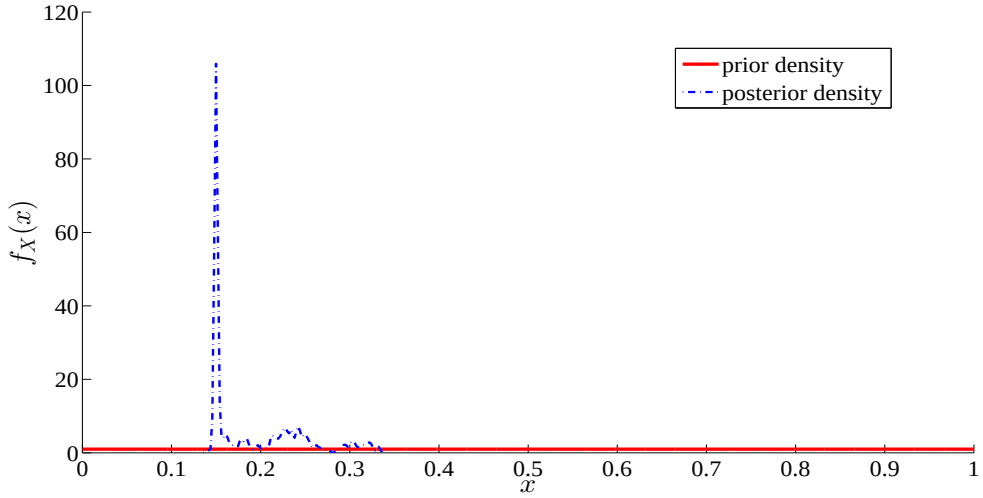

Figure 9. Stiffness loss estimate for prestress loss of 30% and stiffness loss 0f 15%

Table 1. Analysis vs Measurement w.r.t prestress loss 20% and stiffness loss 8%.

Response	Measurement	Bayesian Analysis (mean)	Interval Analysis	
			Lower Bound	Upper Bound
Prestress loss	20 %	20.95 %	17.5 %	24.5 %
LVDT:1	0.1215 mm	0.1215 mm	0.11195 mm	0.1234 mm
LVDT:2	0.1599 mm	0.1600 mm	0.1574 mm	0.1626 mm
LVDT:3	0.1734 mm	0.1733 mm	0.1706 mm	0.1762 mm
SG:1	91.7918 ms	91.8360 ms	90.3529 ms	93.3480 ms
SG:2	459.0293 ms	459.1801 ms	451.7647 ms	466.7403 ms
SG:3	550.9052 ms	551.0161 ms	542.1176 ms	560.0884 ms
Frequency:1st	205.7635 Hz	204.0985 Hz	207.4537 Hz	200.1129 Hz
Frequency:2nd	567.2813 Hz	562.7259 Hz	571.9769 Hz	551.7372 Hz
Frequency: 3rd	884.438 Hz	877.2088 Hz	891.6297 Hz	860.0789 Hz
Frequency:4th	1113.2184 Hz	1103.9078 Hz	1122.0555 Hz	1082.3510 Hz

Notes. mm-millimeter, ms-micro-strain, Hz-hertz.

Table 2. Analysis vs Measurement w.r.t prestress loss 30% and stiffness loss 15%.

Response	Measurement	Bayesian Analysis (mean)	Interval Analysis	
			Lower Bound	Upper Bound
Prestress loss	30 %	29.65 %	26.5 %	34.5 %
LVDT:1	0.1315 mm	0.1312 mm	0.1285 mm	0.1347 mm
LVDT:2	0.1732 mm	0.1728 mm	0.1692 mm	0.1773 mm
LVDT:3	0.1876 mm	0.1872 mm	0.1833 mm	0.1921 mm
SG:1	99.3882 ms	99.1549 ms	97.1034 ms	101.7831 ms
SG:2	496.9411 ms	495.7746 ms	485.5172 ms	508.9157 ms
SG:3	596.3294 ms	594.9296 ms	582.6207 ms	610.6988 ms
Frequency:1st	197.7994 Hz	198.0319 Hz	195.4584 Hz	200.1129 Hz
Frequency:2nd	545.3585 Hz	545.9997 Hz	538.9043 Hz	551.7372 Hz
Frequency: 3rd	850.1355 Hz	851.1351 Hz	840.0744 Hz	860.0789 Hz
Frequency:4th	1069.8379 Hz	1071.0958 Hz	1057.1767 Hz	1082.3510 Hz

Notes. mm-millimeter, ms-micro-strain, Hz-hertz.

CONCLUSION

Health monitoring of prestressed concrete structures is necessary in order to evaluate the current and future working state of them. In this study both Bayesian analysis method which is a probabilistic technique and interval analysis method which is a non-probabilistic technique are used for the estimation of existing prestress loss and the stiffness loss. Both the methods are capable of handling the measurement uncertainty in their own way. While in Bayesian analysis we get the distribution function of the parameters, still the most representative number is a crisp one. In interval analysis methods the lower and upper bound on the uncertain parameters are obtained which will result in bounded structural responses. Bayesian analysis is used when the sufficient information about the parameter is known so as to fit a prior distribution where as interval analysis is used when information about the uncertain parameters is vague. For taking decisions on long term deformations it is necessary to consider the uncertainty present in the structural parameters. For using empirical models for estimating long term deformations it is necessary to calibrate the models for the short term data. The present study can be used for updating the empirical models based on the short term measurement data on the structure.

REFERENCES

Hastings, W. K. (1970). "Monte Carlo sampling methods using Markov chains and their applications." *Biometrika.,* ASCE, 57, 97-109.

Jaulin, L., and Walter, E. (1996). *Applied Interval Analysis : With Examples in Parameter and State Estimation, Robust Control and Robotics,* Springer-Verlag, London.

Beck, J. L., and Katafygiotis, L. S. (1998). "Updating models and their uncertainties. I: Bayesian statistical framework." *Journal of Engineering Mechanics.,* ASCE, 124(4), 455-461.

Vanik, M. W., and Beck, J. L., and Au, S. K. (2000). "Bayesian probabilistic approach to structural health monitoring." *Journal of Engineering Mechanics.,* ASCE, 126(7), 738-745.

Friswell, M. I., and Mottershead, J. E., and Ahmadian, H. (2001). "Finite-element model updating using experimental test data: parametrization and regularization." *Phil. Trans. R. Soc. Lond. A.,* The Royal Society, 359, 169-186.

Moore, R. E., and Kearfott, B., and Cloud, M. J. (2009). *Introduction to interval analysis,* SIAM, Philadelphia.

Xia, B., and Yu, D. (2014). "Modified Interval and Subinterval Perturbation Methods for the Static Response Analysis of Structures with Interval Parameters." *Journal of Engineering Mechanics.,* ASCE, 140(5), 04013113.

Simplified Element-Based Model to Estimate Strain-Related Prestress Loss in Pretensioned Simply Supported Bridge Girders

J. Gallardo[1]; D. Garber[2]; D. Deschenes[3]; and O. Bayrak[4]

[1]Adjunct Professor, Technological University of Panamá. E-mail: jose.gallardo@utp.ac.pa
[2]Assistant Professor, Florida International University, Miami, FL. E-mail: dgarber@fiu.edu
[3]Research Associate, University of Texas at Austin, Austin, TX. E-mail: dean.deschenes@utexas.edu
[4]Professor, University of Texas at Austin, Austin, TX. E-mail: bayrak@mail.utexas.edu

Abstract

While models to study prestress losses based on cylinder data are valuable for their flexibility and ability to investigate micro-phenomena, calibration of models based on girder data is also valuable for some applications. More specifically, data obtained from the monitoring of girders captures the effects of physical phenomena taking place within a girder section, effects that are not accurately captured with cylinder testing (e.g. irregular sectional geometry and variable stress history). While general methods are aimed at a broad range of cases, it is intuitive that less complexity is necessary in a method aimed to a singular type of structure. The development of such a method, for use on pretensioned, simply-supported girders is briefly summarized herein. This model provides simple numerical estimates for strain-related prestress losses, and retains the transparency of basic creep and shrinkage models. The model was calibrated using full-scale structural test data.

INTRODUCTION

There are currently many available theoretically accurate procedures for estimating prestress loss, most of which have been developed on the basis of behavioral models for concrete creep and shrinkage. While the use of these models is necessary for complex structures, simplified models can be used for the estimation of losses in standardized elements, which are well understood and feature less variation. Furthermore, simplistic creep and shrinkage models for the estimation of prestress losses, based on the fundamentals of recent creep and shrinkage theories, are desirable and feasible. These models serve as a way to transfer knowledge from research into the engineering community.

The calibration and use of models based on cylinder test data is widely accepted, and such models have many advantages. First, there is abundant experimental evidence from cylinders currently available, which can contribute to the calibration of all-

encompassing models (to be used for any application). Additionally, the diverse amount of experimental results can be used to characterize many phenomena that are not easily extracted using girder instrumentation.

When calibrating empirical equations, it is beneficial to use the data that is most relevant to the given problem. In this sense, cylinders and prisms have several marked differences from girder specimens (e.g. shape of specimen, stress history and profile, thermal profile, moisture content profile, and environmental conditions).While general methods are aimed at a broad range of cases (and thus required to capture the effect of broad variations in several parameters), it is intuitive that less complexity is necessary in a method aimed to a singular type of structure. One example of a relevant parameter with limited variability, in pretensioned simply-supported girders, is the age at release, which typically falls within 0.5 and 3 days.

The development of a simplified method to estimate strain-related prestress losses, considering the basic mechanisms of creep and shrinkage (originally presented in Gallardo, 2014), is briefly summarized herein. In addition to providing numerical estimates to the prestress losses, this prestress loss model is intended to retain the transparency of many simple creep and shrinkage models. The display of these material models was aimed to educate the designers of the basic mechanisms that drive the occurrence of creep and shrinkage. This is necessary as there are a considerable number of recent findings regarding the creep and shrinkage of concrete that are not being utilized in the currently available methods for estimating prestress losses. Consideration of the contributions from these studies will promote a better understanding and improved estimation of prestress losses. The integration of this knowledge in a detailed estimation method is a valuable means to promote the transfer of knowledge in the topic of creep and shrinkage from research to the bridge designer, and into the practical estimation of strain-related prestress losses. The estimation of strand relaxation losses, and its effects is out of the scope of this study.

In this attempt, the most basic model that can capture the elastic, creep, and shrinkage deformations is used to estimate prestress losses. Such basic models are: (1) a spring subjected to internal water pressure used to model shrinkage and (2) a Burgers model, in series with the shrinkage spring, used to model creep. The stiffness of the springs, the viscosities of the dashpots and the magnitude of the internal water pressure used in this study are defined as functions of a few of the most relevant parameters. The formats of these functions are based on the main mechanisms at the origin of elastic deformations, creep, and shrinkage. Here, the deformation of concrete is idealized as the summation of elastic and viscous deformations. Such elements have been used in multiple configurations in an effort to simulate time-dependent deformation of concrete (Neville A. M., 1983). In summary, a simplified model of prestress loss developed on the basis of girder behavior is presented herein. This model is calibrated on the basis of girder behavior through the inclusion of girder-based sectional creep and shrinkage coefficients.

CREEP MODEL

The deformation of concrete can be idealized as the summation of elastic and viscous deformations. These girder deformations (including those in the concrete and strands) are driven by the action of an initial stress (σ_{ci}). For simplicity, the change in stress is not explicitly included; however, the calibration of coefficients based on representative, full-scale, girder specimens is aimed to capture the full relationship within the final strains (ε) and the initial stress (σ_{ci}). Springs and dashpots are the theoretical elements used to model these deformations. Such elements have been used in multiple configurations in an effort to simulate time-dependent deformation of concrete (Neville A. M., 1983).

The basic nature of creep can be summarized by two time-related mechanisms: short-term creep and long-term creep. Previous studies have used the Burgers model (Figure 1) to model creep strains. Within this model, the Kelvin-Voigt elements are used to capture the short-term creep, while the Maxwell element captures the long-term creep and the elastic deformation.

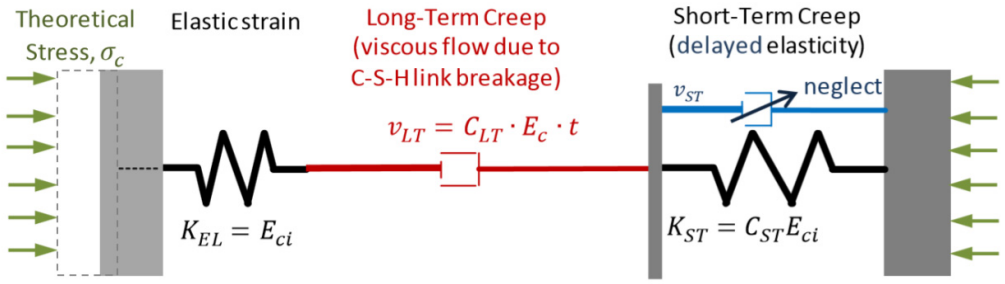

Figure 1: Burgers model with proposed stiffness and viscosities

The use of the Burgers model requires the definition of the properties of four elements: (1) the stiffness of the spring modeling the elastic strain, K_{EL} , (2) the viscosity of the long-term creep dashpot, v_{LT}, (3) the stiffness of the spring to capture short-term creep, K_{ST}, and (4) the viscosity of the dashpot for the short-term creep, v_{ST}.

The numerical values of the stiffnesses and viscosities within the model are set as dependent variables that are controlled by the concrete stiffness (E_c). This is due to the strong correlation between the long-term deformation and concrete stiffness. The use of concrete stiffness is also convenient because it is the only property that: (1) is obtained through the measurement of concrete deformation, and (2) can be easily measured in most concrete testing laboratories. In this sense, the stiffness of the elastic strain spring is simply defined as the initial concrete stiffness, i.e. $K_{EL} = E_{ci}$. Also, since the short-term creep is considered a "delayed elasticity", it is convenient and intuitive to make the stiffness of the short-term creep proportional to the concrete stiffness, i.e. $K_{ST} \propto E_{ci}$.

Considering that the short-term creep usually is almost developed in a few days (Ulm,

Maou, & Boulay (2000) and Neville A. M. (1983));in prestressed girders, for ages larger than a few days(e.g. a month) the stress in the short-term-creep dashpot has been almost dissipated, and all the stress is transmitted through the short-term-creep spring. For the ages of interest for this study (larger than a month) the dashpot can be considered as having zero force, and then it can be excluded with no detriment to the model.

As previously mentioned the parameters are defined in terms of the concrete stiffness. With this relationship in mind, the viscosity for the long-term creep was assumed to be proportional to the concrete stiffness ($v_{LT} \propto E_c$); an increase in the concrete stiffness will result in a reduction of creep and vice versa. This parameter is set to be proportional to the standard concrete stiffness (instead of the initial stiffness) because the long-term creep rate (which depends on v_{LT}) does not depend on the concrete age at loading; the use of the initial stiffness would give that impression.

The deformation of a standard viscous element is defined by its rate ($\dot{\varepsilon}$), which is proportional to the applied stress and inversely proportional to its viscosity. (e.g. for our model the rate of the long term creep would be defined as $\dot{\varepsilon} = \sigma_{ci}/v_{LT}$. The viscosity of the long-term creep dashpot should capture the always-increasing resistance of concrete to creep, which is explained as the consequence of a continuous depletion of creep potential by Bažant et al. (1997). In this sense, the creep rate is widely accepted to be inversely proportional to the age of concrete (Vandamme & Ulm, 2009). Such behavior is adequately modeled using a viscous element with viscosity proportional to the concrete age (t) as part of the Burgers model (Figure 1). This simplified function defining the viscosity shows the logarithmic development of creep: a basic idea of the most fundamental concepts found in commonly accepted creep and shrinkage theories. Finally, the viscosity for the long-term dashpot is proportional to both the concrete stiffness and the age (i.e. $v_{LT} \propto E_c \cdot t_{age}$)

Considering the above, two constants, C_{ST} and C_{LT}, are used as proportionality constants to define the stiffness of the spring for the short-term creep and the viscosity for the long-term creep respectively. Then the function defining the stiffness of the short-term spring, and the long-term creep viscosity are $K_{ST} = C_{ST}E_{ci}$ and $v_{LT} = C_{LT}E_c t_{age}$, respectively.

SHRINKAGE MODEL

The shrinkage model to be used is defined as follows. Generally, the ultimate magnitude of shrinkage is considered to be affected by concrete properties, girder reinforcement, environmental conditions, and many other factors; however, aiming for simplicity, a constant value for the ultimate shrinkage strain is proposed. Such strain is considered as a constant factor to be calibrated using data from representative girder specimens (see “calibration of coefficients of the model on basis of girder data”, below).

It is conventional to assume that the halftime of shrinkage is proportional to the square

of the distance the water has to travel to arrive at the surface (Bažant & Kim, 1991). This distance is commonly considered to be equivalent to the volume-to-surface area ratio. Simplistically, the half-shrinkage time can be expressed as Equation (1). Furthermore, it has been proposed that the development of drying shrinkage can be modeled as proportional to the hyperbolic tangent of the square root of the ratio of time to half-shrinkage time (τ_{SH}), (Bažant, 2000). The square root of the ratio of time to half-shrinkage time gives a conservative approximation of the mentioned function, and is used here for simplicity; the function is then used as presented in Equation (2). Such formulation represents the development of the hygral shrinkage; however, for simplicity, the development of the total sectional shrinkage is modeled using this function.

$$\tau_{SH} = 1day[(^{v}/_{s})/d_{\tau SH}]^2 \quad (1)$$

$$\varepsilon_{SH} = 0.5\varepsilon_{SH,final}\sqrt{t/\tau_{SH}} \leq \varepsilon_{SH,final} \quad (2)$$

CREEP AND SHRINKAGE OF CONCRETE WITHIN THE GIRDER SECTION

Non-uniform creep, shrinkage and elastic strains occur locally within the section of concrete elements and its distribution can be complex; however, the distribution of total sectional strains in a cylinder or a girder is simple. The creep and shrinkage strains experienced in the concrete within a cylinder or girder are govern by the global (sectional) behavior of it; which, in general, is not representative of the local behavior of the concrete within the girder. However, the global behavior has been successfully used to define the behavior of simple concrete elements.

The most basic form of commonly used models to estimate concrete strains is shown in Equation (3). A single creep coefficient (ψ) and a shrinkage strain (ε_{SH}) are used to represent the *sectional strain* (ε) of a cylinder as a function of the *sectional elastic strain* (ε_{ELA}) on the cylinder. If the stress (or elastic strain) is the only parameter varied, then the coefficients of the model (ψ and ε_{SH}) can be calibrated using two (or more) specimens under varied stress. The form of Equation (3) can be adopted as adequate to estimate the sectional behavior of girders. The total strain, in a given point of the girder, would similarly be a function of the elastic strain, in the point under consideration. For girders, the elastic strain changes linearly with depth within the girder section (instead of been constant as is the case within standard cylinders). The coefficients of the model can be calibrated using strains measured at two (or more) points, experiencing different elastic strains, within the section of a single girder. The coefficients for this approach are referred to as: *sectional creep coefficient* (ψ') and *sectional shrinkage coefficient* (ε'_{SH}), as used in Equation (4).

$$\varepsilon = \varepsilon_{SH} + \varepsilon_{ELA} + \varepsilon_{ELA} \cdot \psi \quad (3)$$

$$\varepsilon' = \varepsilon'_{SH} + \varepsilon'_{ELA} + \varepsilon'_{ELA} \cdot \psi' \quad (4)$$

ASSESSMENT OF LONG-TERM SECTIONAL CREEP COEFFICIENT AND SECTIONAL SHRINKAGE STRAIN

Although the local behavior is complex and the non-uniformity of local stresses, creep, and shrinkage cannot be measured, the sectional creep and shrinkage can be measured. The approach presented here to assess sectional creep and shrinkage, based on sectional strain measurements, implies assumptions commonly used in sectional design: (1) constant creep coefficient and shrinkage strain through the section, (2) creep and shrinkage strains are independent of each other, (3) linear distribution of stress, (4) superposition of creep is valid, (5) the elastic shortening is equal to the strain measured after release, and is the only non-zero elastic strain, and (6) there are no thermal strains.

Equation (5) is based on Equation (4) and the assumptions stated above. This equation can be used at any point on the girder. The use of this equation implies that many complex phenomena, (such as differential shrinkage), are neglected. While this is necessary to avoid complexity, it requires the calibration of the coefficients (ε'_{SH} and ψ') to be conducted using full-scale specimens to be representative of the structures under study.

$$\varepsilon' = \varepsilon'_{SH} + \varepsilon_{ES}(1 + \psi') \qquad (5)$$

In an instrumented section of a girder, the elastic shortening strain (ε_{ES}) and the long-term strain (ε') are measured at various points. A linear strain profile through the height of the cross-section can be established using the data from two or more gauges, as shown in Figure 2 (a). Also, a plot of ε' versus ε_{ES} can be constructed, as shown in Figure 2 (b). A linear regression, of the data from the gages, is used to find the solution for ε'_{SH} and ψ' coefficients. From the plot in Figure 2 (b), coefficients $\psi' = 0.66$, and $\varepsilon'_{SH} = 254\mu$ are obtained. Similar analysis where conducted in 20 girders to calibrate the coefficients, as presented in the next section. It is important to mention that negative shrinkage strains were obtained for a few of the specimens. These extension strains are believed to be a consequence of differential shrinkage, although further verification is needed.

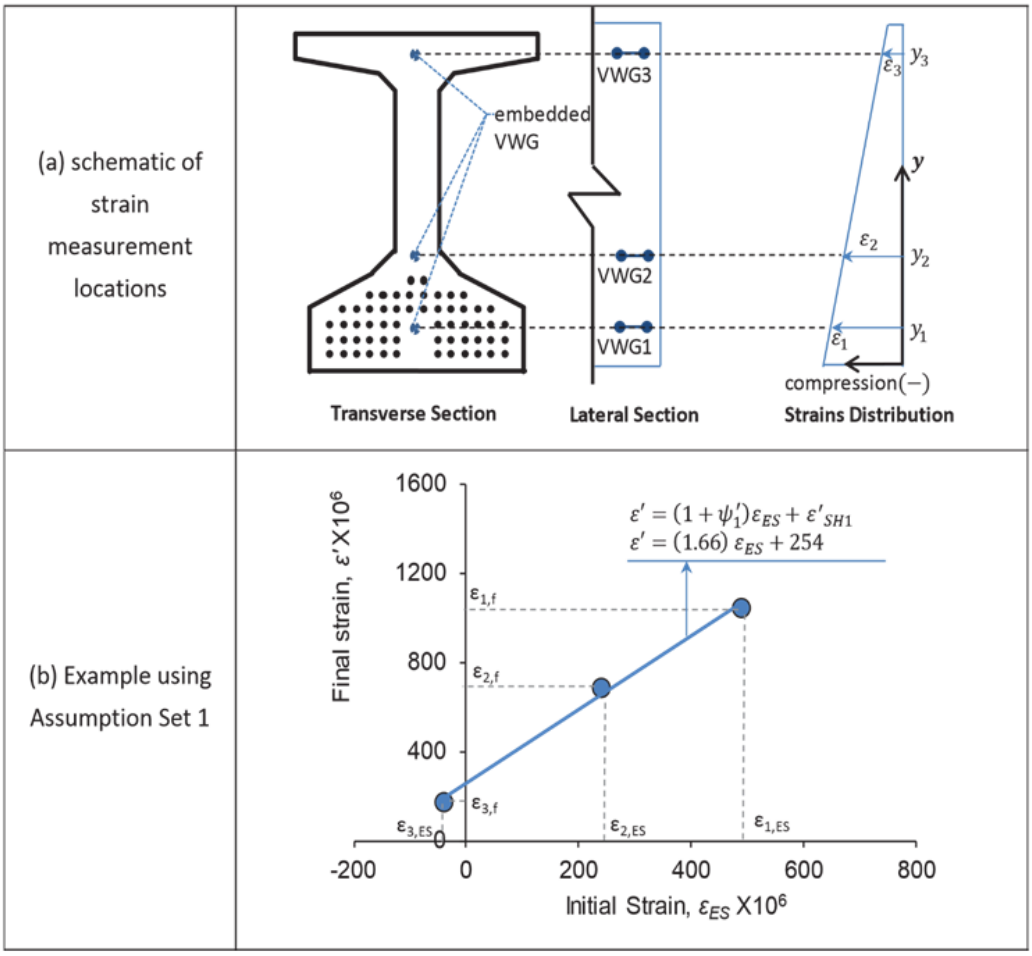

Figure 2. Determination of sectional coefficients for a girder from Gamble (1970).

CALIBRATION OF THE MODEL ON BASIS OF GIRDER DATA

As discussed above, the presented models require the calibration of four coefficients that are involved in the model to estimate creep strains (C_{ST} *and* C_{LT}) and shrinkage strains (ε'_{SHu} and $d_{\tau_{SH}}$). The initial and final strain profiles of 30 girders were studied (as described in the previous section) in order to calibrate the ultimate sectional shrinkage coefficient (ε'_{SHu}). The final age for the specimens ranged from 197 to 978 days. The average resulting *final* coefficients were $\psi'_f = 0.68$ and $\varepsilon'_{SH,f} = 140$ μ (Gallardo, 2014). The final sectional shrinkage $\varepsilon'_{SH,f}$ is considered representative of ultimate conditions; therefore it is used as the value of ε'_{SHu}. The girder-based calibration of $d_{\tau_{SH}}$ could not be achieved by the authors; a cylinder-based calibration of the model was conducted and adopted for the girder-based model. Such calibration resulted in $d_{\tau_{SH}} = 0.2in$ $(50.8\,mm)$. Details of the specimens and the cylinder-based calibration can be found in Garber et al., 2013 and Gallardo, 2014.

To calibrate the creep model coefficients C_{ST} and C_{LT}, sectional creep coefficients were obtained for various ages through an analysis of the sectional strains (as detailed above). A time-dependent expression for the creep coefficient was then formulated using these results. An expression of the total sectional creep coefficient ($\psi' = m_{LT} \cdot ln(t) + b$) was obtained separately for each specimen using a linear regression, as shown in the Figure 3. With this expression for the creep coefficient, the calibration coefficients could be determined. Such expressions were developed for 20 specimens within the UTPS-Loss Evaluation Database (Garber et. al, 2013) for which the strain profile history was discovered.

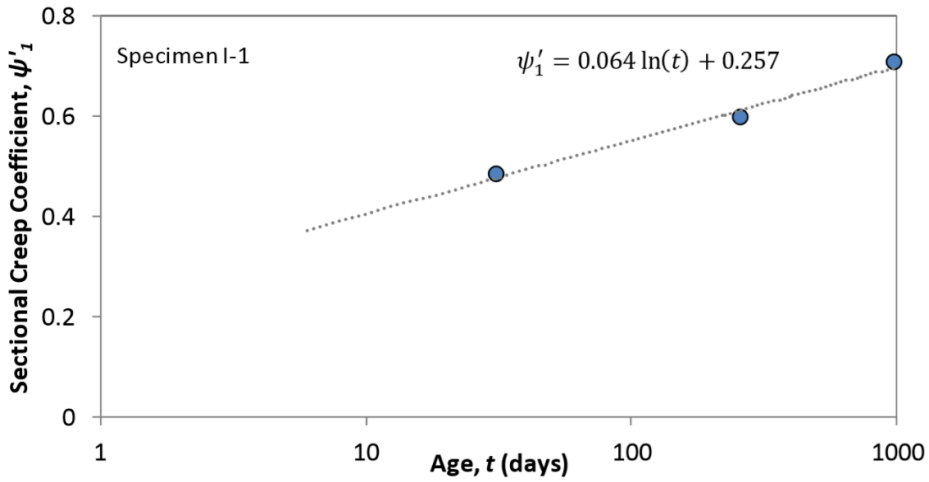

Figure 3: Time-development of effective creep coefficient for Specimen I-1

The creep coefficient is considered as the summation of two terms, the long term creep coefficient, ψ'_{LT}, and the short term creep coefficient, ψ'_{ST}, (see Equation (8)). The long term creep coefficient is the fraction of creep that increases linearly with the logarithm of time, (see Equation (10)). With this convention, the coefficient C'_{LT} is derived from the specimen data, as presented in Table 1 and shown in its final form in Equation (13).

Table 1. Derivation of $1/C'_{LT}$ from girder data

From specimen data (see figure 3)	$\psi'_1 = b + m_{LT} \cdot ln(t)$	(6)
Defining	$\varepsilon_{CR} = \varepsilon_{CR\|ST} + \varepsilon_{CR\|LT}$	(7)
	$\psi'_1 = \psi'_{LT} + \psi'_{ST}$	(8)
	$\varepsilon_{CR\|LT} = \frac{\sigma_{ci}}{E_{ci}} \cdot \psi'_{LT}$	(9)
	$\psi'_{LT} = m_{LT} \cdot [ln(t) - ln(t_i)]$	(10)
From the model (see figure 2) (viscuous deformation)	$\varepsilon_{CR\|LT} = \frac{\sigma_{ci}}{C'_{LT} E_c} [ln(t) - ln(t_i)]$	(11)
Plug (11) & (10) in (9)	$\frac{\sigma_{ci}}{C'_{LT} E_c} [\Delta\, ln(t)] = \frac{\sigma_{ci}}{E_{ci}} \cdot m_{LT} \cdot [\Delta\, ln(t)]$	(12)

Simplifying (12)	$\frac{1}{C'_{LT}} = \frac{E_c}{E_{ci}} \cdot m_{LT}$	(13)

The coefficient C'_{ST} is derived from the specimen data as presented in Table 2. Equation (20) is used to determine the parameter $1/C'_{ST}$ based on the coefficients of the equation of the sectional creep coefficient (b and m_{LT}), and the time at transfer t_i. The average behavior of the 20 specimens results in coefficients $C'_{LT} = 12$ and $C'_{ST} = 3.7$ (Gallardo, 2014). These coefficients are aimed to define the sectional behavior of prestressed simple-supported girders and are therefore not representative of cylinder behavior.

Table 2. Derivation of $1/C'_{ST}$ from girder data

From 0.5a	$\psi'_{ST} = \psi'_1 - \psi'_{LT}$	(14)
Plug 6 & 10 into (14)	$\psi'_{ST} = \{b + m_{LT} \cdot ln(t)\} - \{m_{LT} \cdot [ln(t) - ln(t_i)]\}$	(15)
Reducing (15)	$\psi'_{ST} = b + m_{LT} \cdot ln(t_i)$	(16)
Defining	$\varepsilon_{CR\|ST} = \frac{\sigma_{ci}}{E_{ci}} \cdot \psi'_{ST}$	(17)
From the model (see Figure 1)	$\varepsilon_{CR\|ST} = \frac{\sigma_{ci}}{C'_{ST} E_{ci}}$	(18)
Plug 18 and 16 in 17	$\frac{\sigma_{ci}}{C'_{ST} E_{ci}} = \frac{\sigma_{ci}}{E_{ci}} \cdot [b + m_{LT} \cdot ln(t_i)]$	(19)
simplifying	$\frac{1}{C'_{ST}} = b + m_{LT} \cdot ln(t_i)$	(20)

GIRDER-BASED PRESTRESS LOSSES ESTIMATION METHOD

Based on the time-dependent strain model developed above, a method to estimate losses is proposed, as shown in Figure 4 and Table 3. Aiming for simplicity, the time-dependent strains considered for the estimation of losses are: (1) short-term and long-term creep due to initial stress (2) sectional short-term creep due to deck-induced stress, and (3) sectional shrinkage strain. Sectional long-term creep due to deck-induced stress is neglected (for common ages at deck casting, the creep compliance rate is very small, as compared to the compliance at transfer times, and is assumed as zero).

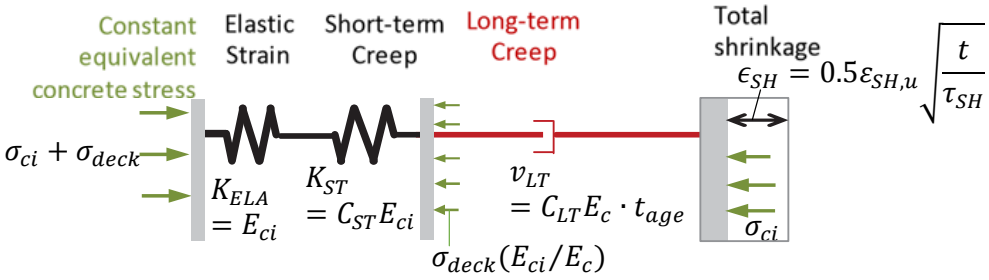

Figure 4. Scheme of proposed model to estimate long-term strain

This method is limited to pretensioned girders, because the calibration of the creep and shrinkage models was conducted using such types of elements. The calculation of the losses is based on mechanics of materials, assumptions aimed to simplify the model without hiding the main mechanisms underlying time-dependent strain origins, and coefficients calibrated for the specific use intended herein.

Table 3: Simplified Time-Dependent Prestress Losses Estimation

Stress conditions	$\sigma_{ci} = \mathrm{k_{fpi}} \cdot \mathrm{f_{pi}} A_p \left[1/A_g + e_p^2/I_g\right] - M_{sw}\, e_p/I_g$
	$\Delta\sigma_{cDECK} = -M_{deck}\, e_p/I_g$
Elasticity	$\varepsilon_{ELA} = \sigma_{ci}/E_{ci} + \Delta\sigma_{cDECK}/E_c$
Shrinkage at time *t*	$\tau_{SH} = 1day[(^{v}/_{S})/d_{\tau SH}]^2$ $\varepsilon_{SH} = 0.5\varepsilon_{SH,f}\sqrt{t/\tau_{SH}} \leq \varepsilon_{SH,f}$
Short-term Creep (delayed elasticity)	$\varepsilon_{CR\|ST} = \frac{\sigma_{ci} + \sigma_{cdeck}}{C'_{ST} E_{ci}}[ln(t) - ln(t_i)]$
Long-term Creep (irrecoverable)	$\varepsilon_{CR\|LT} = \frac{\sigma_{ci}}{C'_{LT} E_c}[ln(t) - ln(t_i)]$
Total Losses at time t	$\Delta f_{pe} = \left(\varepsilon'_{ELA} + \varepsilon'_{CR\|ST} + \varepsilon'_{CR\|LT} + \varepsilon'_{SH}\right)\mathrm{E_p}$
Calibrated Coefficients	$C'_{LT} = 12; C'_{ST} = 3.0; \varepsilon_{SH,f} = 140\mu$ $K_{fpi} = 0.7/0.75 = 0.93$ (based on Garber et al 2013) $d_{\tau SH} = 0.2\ in \approx 5\ mm$ (cylinder based calibration)

The performance of this method is evaluated using the UTPSC-Loss Strain Evaluation Database (Gallardo, 2014). The plot of estimated vs measured prestress loss is shown in Figure 5. The method shows good precision (CoV = 21%).

CONCLUSIONS

The long-term behavior of concrete is complex. However, the similitudes found within a specific type of structure limits the complexity of the problem. A girder-based model was developed to offer a simple, conservative method for the estimation of strain-related prestress losses. The approach considered for the development of the model included an experimental determination of sectional creep and shrinkage coefficients based on the measurement of girder strains. Such a technique condenses all the phenomena occurring within the girder into equivalent creep and shrinkage coefficients. Based on the statistical evaluation of the results, the developed method satisfactorily estimates prestress losses, with precision comparable to that of the methods currently being used. The method presented herein is a simplified technique developed for everyday use in the design of typical pretensioned bridge girders.

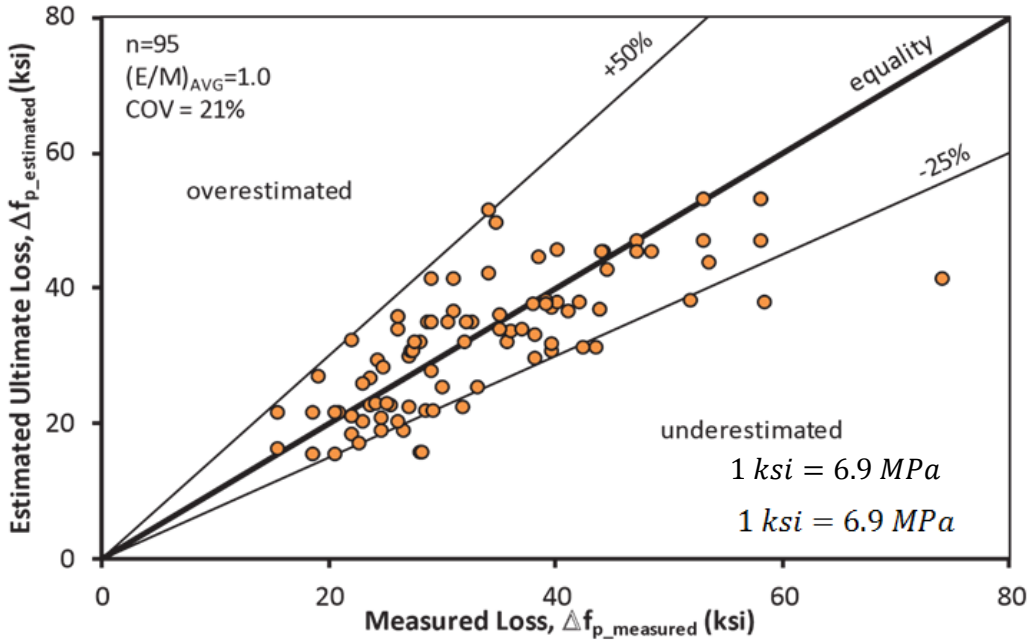

Figure 5 Performance evaluation of the girder-based loss estimation model.

REFERENCES

Bažant, Zdeněk P., and Joong-Koo Kim. "Consequences of diffusion theory for shrinkage of concrete." *Materials and structures* 24.5 (1991): 323-326.

Bazant, Zdenek P., et al. "Microprestress-solidification theory for concrete creep. I: Aging and drying effects." *Journal of Engineering Mechanics* 123.11 (1997): 1188-1194.

Bazant, Zdenek P. "Criteria for rational prediction of creep and shrinkage of concrete." *ACI Special Publication* 194 (2000).

Gallardo, J. M. "Model of Strain-Related Prestress Loss in Pretensioned Simply Supported Bridge Girders." (2014).

Gamble, William Leo. Field Investigation of a Continuous Composite Prestressed I-Beam Highway Bridge Located in Jefferson County, Illinois. No. Ihr-93. 1970.

Garber, David, et al. Effect of New Prestress Loss Estimates on Pretensioned Concrete Bridge Girder Design. No. FHWA/TX-12/0-6374-2. (2013).

Neville, Adam M., Walter H. Dilger, and Jeffery J. Brooks. *Creep of plain and structural concrete*. Construction Press, 1983. (Ulm, Maou, & Boulay (2000)

Vandamme, Matthieu, and Franz-Josef Ulm. "Nanogranular origin of concrete creep." *Proceedings of the National Academy of Sciences* 106.26 (2009): 10552-10557.

Investigation of Microstructure Properties and Early Age Behavior of Cementitious Materials Containing Metakaolin

Burcu Akcay[1] and Mehmet Ali Tasdemir[2]

[1]Civil Engineering Department, Kocaeli University, Umuttepe, 41380 Kocaeli, Turkey. E-mail: burcu.akcay@kocaeli.edu.tr
[2]Civil Engineering Department, Istanbul Technical University, Maslak, 34469 Istanbul, Turkey. E-mail: matasdemir@gmail.com

Abstract

Metakaolin is one of the most attracting gradients of high and ultra high performance concretes which are used in different types of buildings such as nuclear waste storages, impact-resistant military buildings, fire-resistant high-rise buildings and reinforced concrete bridges. The metakaolin induced concretes are very dense and more homogeneous than normal strength concrete. However, these properties cause significant increase in brittleness of hardened concrete and change of volume during the hardening of these materials. In this work, cement pastes were produced at three different water/binder (w/b) ratios of 0.42–0.35 and 0.28 for which cement has been replaced by metakaolin with at different weight fractions of 8%, 16% and 24%. 48 hours volumetric autogenous shrinkage measurements showed that in pastes with 0.42 w/b ratios autogenous shrinkage reduced with increasing metakaolin content. In mixtures with 0.35 and 0.28 w/b ratios, on the other hand, it has been seen that the autogenous shrinkage increased with increasing the amount of metakaolin. Using thermo-gravimetric analysis and mercury porosimetry measurements, it has been found that with increasing metakaolin content the amount of calcium hydroxide decreased and critical pore size reduced. It has been determined that as a result of the pozzolanic reaction the amount of fine gel pores increased and those of the coarser pores significantly decreased at 28 days. One year linear autogenous shrinkage measurements showed that in pastes with 0.42 w/b ratios the autogenous shrinkage increased with increasing metakaolin content, while it decreased in pastes with lower w/b ratios.

INTRODUCTION

One of the most important developments in concrete industry is the use of the industrial wastes or by products as partial replacement materials with cement. Because of their favorable engineering performances, fly ash, granulated blast furnace slag, and silica fume are frequently used in high strength and high performance concrete. On the other hand, being a relatively new mineral additive, metakaolin is not a byproduct of any industrial process; hence it is not completely natural. It is produced in a specific way; thus unlike other pozzolans with variable compositions, metakaolin can be produced for specific circumstances in desirable

particle size, mineralogical composition and whiteness (Brooks et al., 2000). Dehydroxylation of clay minerals by thermal activation in 600–900ºC temperature range forms highly reactive transition phases with break downing the crystal structure partially or totally. On the other hand, metakaolin ($Al_2O_3.2SiO_2$ or AS_2) is formed by calcinations of kaolin-rich clay ($Al_2Si_2O_5(OH)_4$) and soil at 500-600°C. If there is water, metakaolin reacts with calcium hydroxide (CH) to form calcium silicate hydrate gels along with calcium aluminate hydrates and calcium silicate aluminate hydrate crystalline productions such as C_2ASH_8-stratlingite, C_4AH_{13} and rarely C_3ASH6-hydrogarnet (Murat, 1983; Khatib et al., 1996).

In most cases, porosity of concrete with pozzolans are equal or smaller than that of Portland cement concrete which is an important parameter for high performance and strength. It is also well known that, in addition to the total porosity, pore size distribution is essential for durability and performance. Frias and Cabrera (2000) stated that with using metakaolin the total porosity increased at 14 days and gel porosity of metakaolin mixtures increases between 7-90 days, while the Portland cement mixtures remains practically constant. They concluded that it is necessary to add at least 15-20% of metakaolin to obtain important enhancement in porosity and to reduce the average pore diameter. On the other hand, Poon et.al. (2001) and Ambroise et al. (1994) found that total porosity can be reduced significantly using metakaolin. It is well known that the volume of production of hydrates is less than the volume of components involved in reaction. This situation is defined as chemical shrinkage (also called as Le Chatelier's contraction). If there is no external water source to cementitious micro-structure, chemical shrinkage will result with empty pores and cause decrease in internal relative humidity and consequently measurable autogenous shrinkage (Akcay, 2007). Autogenous shrinkage is one of the important parameters for especially high strength performance, and yet the effect of metakaolin addition on autogenous shrinkage has not been well detailed. Since metakaolin addition to the cementitious materials decreases total porosity and causes finer pore structure, water loss generally takes place with self desiccation instead of diffusion to the external media. Brooks and Megat Johari (2001) showed that because of finer pore structures the use of metakaolin increases autogenous shrinkage. However, 15% replacement of metakaolin with cement resulted in 65% decrease in autogenous shrinkage at 24 hours. Similarly, Justice and Kurtis (2007) reported an increase in autogenous shrinkage with adding metakaolin. On the other hand, Gleize et al. (2007) showed that at later ages, pastes with metakaolin exhibited less autogenous shrinkage than cement pastes and this effect is more significant for pastes with higher water/cement (w/c) ratios. Wild et al. (1998) and also Kinuthia et al. (2000) reported that addition of metakaolin at a rate of 10-15% caused an increase in autogenous shrinkage, while higher amount of replacement resulted in apparent decrease. It seems that there is a need more research in this subject.

In this work, cement paste samples were produced at three different water/binder (w/b) ratios: 0.42–0.35 and 0.28, and cement has been replaced by metakaolin at different weight fractions: 8%, 16% and 24%. The effect of metakaolin addition on autogenous shrinkage, pore structure and CH content were investigated.

EXPERIMENTAL WORKS

All mixtures were prepared using typical CEM 42.5R cement. Metakaolin used had 53% SiO_2 and 43.8% Al_2O_3 content with an average particle density of 1.3 μm and specific surface of 13m^2/g. Specific gravities of cement and metakaolin were 3.14 and 2.5 g/cm^3, respectively. To maintain the same workability, polycarboxylic ether based high-range water reducing admixture (HRWRA) were used in mixtures. The mix design and codes of the paste samples are given in Table 1.

Table 1. Mix proportions of paste samples (1 m^3).

Mix code	Cement, kg	Metakaolin, kg	Water, kg	HRWRA, kg
P42	1348	0	566	0
P42MK8	1240	108	566	0
P42MK16	1132	216	566	1.24
P42MK24	1024	324	566	2.32
P35	1513	0	529	0.42
P35MK8	1392	121	529	1.1
P35MK16	1271	242	529	2.44
P35MK24	1150	363	529	3.8
P28	1644	0	460	1.7
P28MK8	1512	132	460	2.9
P28MK16	1381	263	460	5.6
P28MK24	1249	395	460	8.94

The volumetric autogenous shrinkage measurement of samples was performed by weighing the volume change in buoyancy started after initial setting until 48 hours. The linear autogenous deformations were determined by measuring displacements on the sealed specimens 40×40×240 mm. For defining the pozzolanic effect of metakaolin, CH contents were determined using DTA/TGA (differential thermal analysis/thermo-gravimetric analysis). To calculate the CH content, the method proposed by Marsh and Day (1988) and used by Fernandez Lopez (2009) was employed. In addition, mercury intrusion porosimetry (MIP) have been used to evaluate meso and micro pore structure of cementitious materials.

EXPERIMENTAL RESULTS AND DISCUSSION

Autogenous Shrinkage

Figure 1 gives the volumetric and linear autogenous measurements of pastes with different w/b ratios. In the series with 0.42 w/b ratios, autogenous shrinkage of paste samples decreased with adding metakaolin. Since the filler effect of metakaolin addition resulted in denser inner structure, water loss was prevented and autogenous shrinkage was decreased. On the other hand, in the paste with 0.35 w/b ratio, another mechanism was operative because the water to be in reaction was interrupted between recently formed hydration products, causing in shrinkage in pores. This effect is more pronounced in pastes with lower w/b ratios.

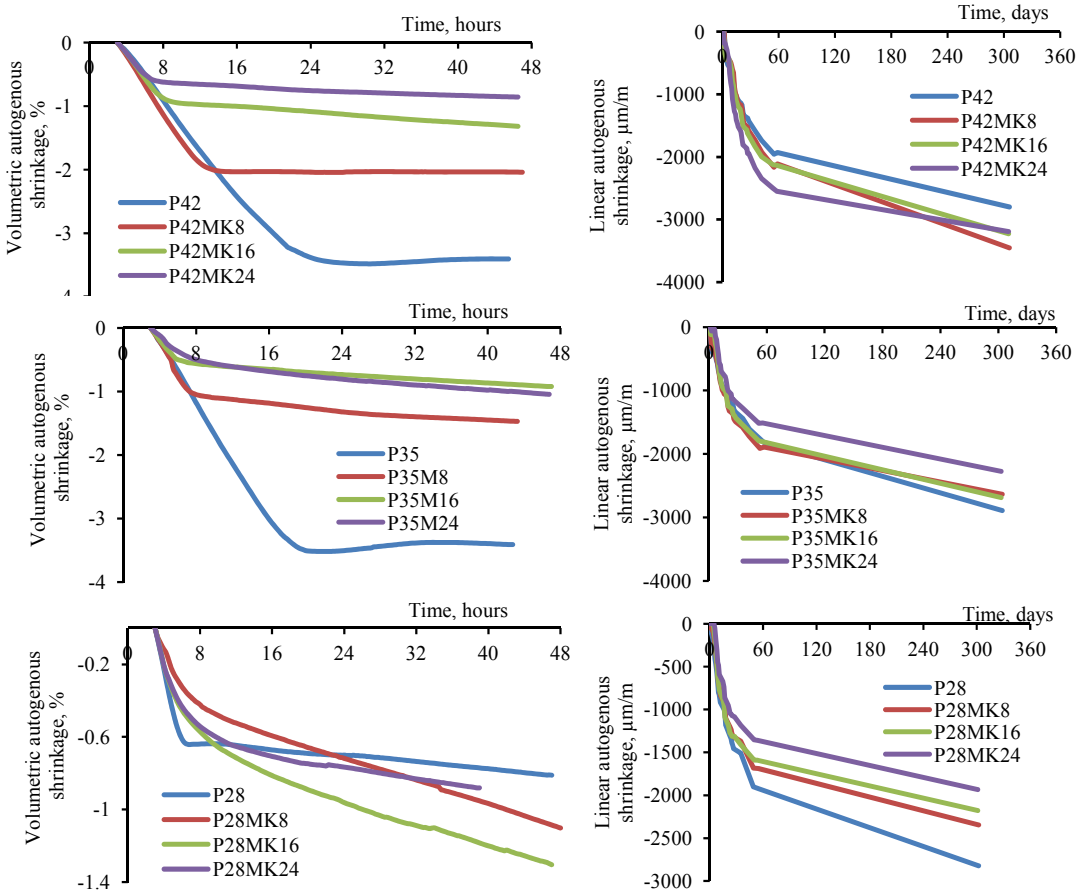

Figure 1. Volumetric and linear autogenous shrinkage measurements of paste samples.

Within the first hours, the magnitude of autogenous shrinkage decreased with increasing amount of metakaolin and decreasing cement content because of less amount of shrinking paste, while at later stages the production of CH initiates metakaolin pozzolanic reaction, resulting in higher magnitude of autogenous shrinkage. Similar effects are also seen in measurement of linear autogenous shrinkage in later ages.

Calcium Hydroxide Content

CH contents of paste samples obtained from TG analysis are presented in Figure 2. As expected, with ongoing hydration CH content increased in reference samples, while it decreased in pastes with low w/b ratios. With addition of metakaolin there is considerable decrease in CH contents. This effect is less significant in series with higher w/b ratios especially at early ages. There were slowdowns in the CH consumption ratios compared to the reference samples at 7 to 28 days. This is probably because of the preventive layers of reaction productions around metakaolin particles.

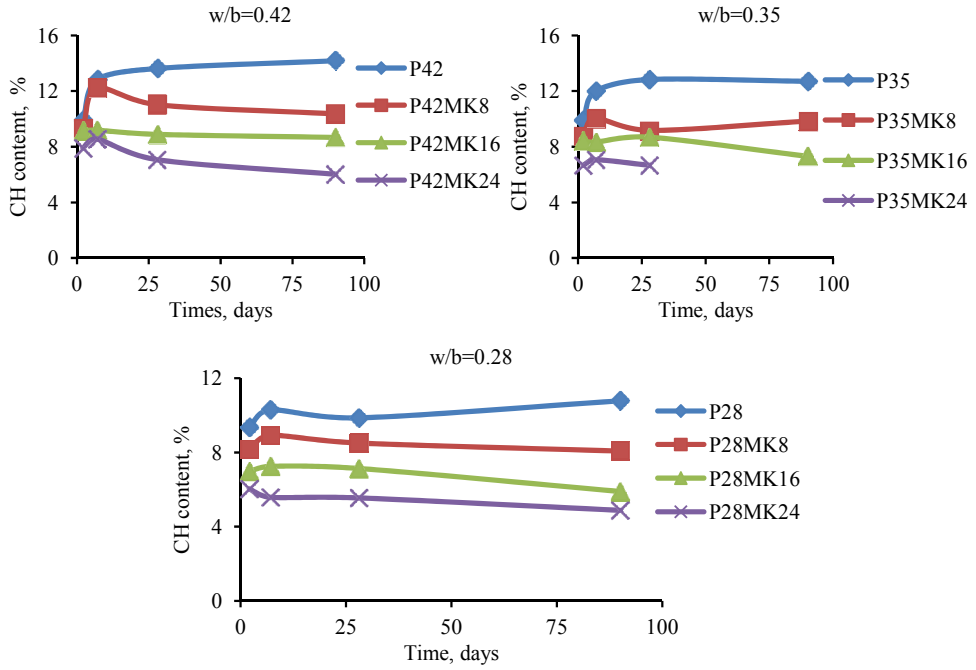

Figure 2. Variation of CH content of paste samples with different w/b ratios with time calculated using TGA.

Pore Structure Investigation with MIP

Porosity results of paste samples at 2 and 28 days obtained from MIP analysis are given in Table 2.

Table 2. Some porosity properties of paste samples at 2 and 28 days of ages obtained from MIP analysis.

	Cumulative intruded		Critical pore diameter,		Total porosity, %	
Time, days	2	28	2	28	2	28
P42	0.074	0.104	59.34	16.65	8.54	15.35
P42MK8	0.1239	0.0384	36.68	7.743	10.94	7.85
P42MK16	0.2419	0.0531	36.94	8.171	29.70	10.64
P42MK24	0.3082	0.0785	39.58	7.32	29.41	12.60
P35	0.1954	0.055	14.39	15.78	19.76	8.39
P35MK8	0.1308	0.0569	17.76	10.1	22.21	9.33
P35MK16	0.1222	0.0967	22.85	<6.711	21.81	9.64
P35MK24	0.1246	0.0427	23.87	<6.169	11.26	5.49
P28	0.0789	0.101	12.6	9.046	9.61	9.06
P28MK8	0.0879	0.0286	15.04	<7.16	12.48	3.90
P28MK16	0.0999	0.0047	7.49	<7.014	11.99	0.59
P28MK24	0.0586	0.0192	<6.77	<6.204	6.99	2.10

With increasing the amount of metakaolin in pastes, the critical pore diameter decreased, especially at 28 days of age. Total porosity was calculated from the ratio of total intruded mercury volume to the sample volume. These results showed that total porosity increased with the amount of metakaolin until 24% of replacement. This is because there was not enough CH to react with metakaolin especially at 2

days. It should also be noted that since metakaolin has finer particle it makes the microstructure denser. In the series with w/b ratios of 0.42 the effect of metakaolin on the critical pore diameter was observed even at 2 days. As is known, this parameter is very important for durability of cementitious materials.

Table 3 presents the pore size distribution of pastes at different ages calculated with normalizing the pore volume in cumulative intruded mercury volume curves. At 28 days of age, the amount of fine gel pores (<10 nm) increased, while that of larger pores decreased because of the pozzolanic reaction. The amount of fine capillary (10–100 nm) and coarse capillary (100–200 nm) pores decreased significantly with increasing amount of metakaolin especially in the series with 0.42 and 0.35 w/b ratios. Because of this effect, metakaolin becomes a requested pozzolan for cementitious materials.

Table 3. Pore size distributions of paste samples according to the porosity results (%).

		Pore size range			
	days	>200 nm	200-100 nm	100-10 nm	<10 nm
P42	2	0.35	0.70	3.62	3.86
	28	0.07	0.37	12.56	2.35
P42MK8	2	0.09	0.69	4.49	5.68
	28	0	0	6.99	0.86
P42MK16	2	0.96	1.82	17.80	9.12
	28	0	0	10.31	0.32
P42MK24	2	0.22	1.01	16.19	12.00
	28	0	0	6.07	6.53
P35	2	0.22	0.30	8.77	10.47
	28	0	0	6.70	1.69
P35MK8	2	0.07	0.68	19.19	2.28
	28	0	0	6.05	3.28
P35MK16	2	0	0.29	14.51	1.90
	28	0	0.39	2.35	6.90
P35MK24	2	0.24	0.28	5.13	5.61
	28	0	0	1.13	4.36
P28	2	0.26	0.01	5.74	3.61
	28	0	0.02	0.32	8.72
P28MK8	2	0	0	8.90	3.58
	28	0	0	0.49	3.41
P28MK16	2	0	0.23	4.75	7.01
	28	0	0	0.14	0.46
P28MK24	2	0.01	0.06	2.06	4.86
	28	0	0	0.05	2.05

CONCLUSIONS

Based on the tests conducted, following conclusions can be made:

1. It has been shown by volumetric autogenous measurement that metakaolin has different effects on autogenous shrinkage mechanisms of pastes with different w/b ratios. At early ages, with increasing amount of metakaolin, autogenous shrinkage decreased significantly in pastes with 0.42 w/b ratios. On the other hand in the series with 0.35 and 0.28 w/b ratios, formation of CH content and pozzolanic reaction with metakaolin dominated the autogenous shrinkage.

2. The reference pastes completed the important part of their volumetric autogenous shrinkage at 24 hours, while for the pastes with metakaolin there was no asymptotically stationary in shrinkage curves.

3. Measurement of linear autogenous shrinkage at later ages showed that autogenous shrinkage increased with addition of metakaolin to the paste with 0.42 w/b ratios, while decreased with the amount of metakaolin at lower w/b ratios.

4. The amount of CH decreased with metakaolin, but this effect is less prominent in the paste with higher w/b ratios.

5. Investigation of pore structures by MIP showed that critical pore size decreased with using metakaolin. Total porosity of samples decreased at 28 days compared to that at 2 days, and metakaolin addition made it more noteworthy. As a result of pozzolanic reaction, the amount of fine gel pore increased, while that of capillary pores decreased. Especially in the series with 0.28 w/b ratios, using metakaolin eliminated almost all the larger pores.

ACKNOWLEDGMENTS

This research was carried out in the Civil Engineering Department at Kocaeli University. The authors wish to acknowledge the financial support by TUBITAK (The Scientific & Technical Research Council of Turkey): Project:110R008.

REFERENCES

Akcay, B. (2007). “Effects of Lightweight Aggregates on Autogenous Deformation and Fracture of High Performance Concrete.” *PhD thesis, Istanbul Technical University, Civil Engineering Faculty.*

Ambroise J., Maximilien S. and Pera J. (1994). “Properties of metakaolin blended cements.” *Advanced Cement Based Materials*, 1(4), pp. 161-168.

Brooks J.J. and Megat Johari M.A. (2001). “Effect of metakaolin on creep and shrinkage of concrete.” *Cement and Concrete Composites*, 23, pp. 495-502.

Brooks J.J., Megat Johari M.A. and Mazloom M. (2000). “Effect of admixtures on the setting times of high-strength concrete.” *Cement and Concrete Composites*, 22, pp. 293-301.

Fernandez Lopez R. (2009). “Calcined Clayey Soils as a Potential Replacement for Cement in Developing Countries.” *PhD thesis, Ecole Polytechnique Federale de Lausanne.*

Frias M. and Cabrera J. (2000). “Pore size distribution and degree of hydration of MK-cement pastes.” *Cement and Concrete Research*, 30, pp. 561-569.

Gleize P.J.P., Cyr M. and Escadeillas G. (2007). “Effects of metakaolin on autogenous shrinkage of cement pastes.” *Cement and Concrete Composites*, 29, pp. 80–87.

Justice J.M. and Kurtis K.E. (2007). "Influence of metakaolin surface area on properties of cement-based materials." *ASCE Journal of Materials in Civil Engineering*, 19(9), pp. 762-771.

Khatib, J.M., Sabir, B.B. and Wild, S. (1996). "Some properties of metakaolin paste and mortar." *International Congress, Concrete in the Service of Mankind-Concrete for Environmental Enhancement and Protection, Theme 6-Waste Materials and Alternative Product*, University of Dundee. London E&FN Spon, pp: 637-644.

Kinuthia J.M., Wild S., Sabir B.B. and Bai J. (2000). "Self-compacting autogenous shrinkage in Portland cement-metakaolin-fly ash pastes." *Advanced Cement Research,* 12(1), pp. 35-43.

Marsh B.K. and Day R.L. (1988). "Pozzolanic and cementitious reactions of fly ash in blended cement pastes." *Cement and Concrete Research* (18), pp. 301-306.

Murat M. (1983). "Hydration reaction and hardening of calcined clays and related minerals." *Cement and Concrete Research*, 13, pp. 259–266.

Poon C.S., Lam L., Kou S.C., Wong Y.L. and Wong R. (2001). "Rate of pozzolanic reaction of metakaolin in high-performance cement pastes." *Cement and Concrete Research*, 31, pp. 1301-1306.

Wild S., Khatib J.M., and Roose L.J. (1998). "Chemical shrinkage and autogenous shrinkage of Portland cement metakaolin pastes." *Advances in Cement Research,* 10(3), pp. 109-119.

Shrinkage of Mortar Samples Made of Limestone-Rich Cements

Moien Rezvani[1]; Tilo Proske[1]; and Carl-Alexander Graubner[1]

[1]Institu für Massivbau, Technische Universität Darmstadt, Franziska-Braun-Str. 3, 64287 Darmstadt, Germany. E-mail: rezvani@massivbau.tu-darmstadt.de

Abstract

Shrinkage in concrete structures may lead to cracks which reduce the durability of concrete against aggressive mediums. In prestressed concrete elements shrinkage results in a significant loss of prestressing forces. Limestone-rich cements with limestone contents beyond the values of DIN EN 197-1 were developed in order to reduce the influence of cement production on environment. In this paper the shrinkage behavior of mortar and concrete samples made of limestone-rich cements up to 70 wt.% with different water/cement-ratios was analyzed. The results indicate that shrinkage of such cements is strongly dependent on the amount, chemical and physical properties and the mineral components of limestone. The mortar samples made of such cements had shown both higher or lower shrinkage than reference samples made of pure Portland cement (CEM I 52,5 R) depending on the used limestone type. Specific surface area measured by BET-method seems to play a key role on the shrinkage behavior by controlling the disjoining pressure between hydration products. Meanwhile, it was found that in contrary to reference samples the prolonged curing in water does not influence the shrinkage of specimens made of limestone-rich cements significantly.

INTRODUCTION

Limestone-rich cements

Concrete is known as the most widely used building material of our time. The major environmental impact of concrete comes from the CO_2 emissions during cement production, which is altogether responsible for more than five percent of global anthropogenic CO_2 release. In 2013 more than 4 billion tons of cement were produced and mainly used in the concrete industry (*U. S. Geological Survey, Mineral commodity summaries,* 2013). It is visible that the reduction of the Portland cement clinker content in cement will reduce the environmental impact of concrete.

For decades, Portland limestone cement is used widely in Europe in accordance with the European cement standard EN 197-1. For instance, in year 2012 near 27 % of total produced CEM II in Europe were Portland limestone cements. The use of cements with a limestone content up to 15 wt.-% is now allowed also in the US and Canada since 2013 and 2008, respectively (ASTM C595 / C595M, 2013; CAN/CSA-A3000-08, 2008). In Europe, the cement type CEM II/B-LL can even contain limestone up to 35 wt.-%. According to EN 197-1, the total organic carbon

(TOC) of limestone is limited to 0.2 wt.-%, and the content of clay minerals (obtained from methylene blue test) in limestone shall not exceed 1.2 wt.-%. The $CaCO_3$ content of the limestone is not allowed to be lower than 75 wt.-%. However, the use of such cements in concrete is restricted on national levels for severe environmental exposures. However, further reduction of clinker content as well as increase of limestone in Portland limestone cements beyond the current limits of EN 197-1 is environmentally and economically desirable. From the technical aspect of view, the performance of concrete made of Portland limestone cement with a limestone content above 20-35 wt.-% and common water/cement-ratios is reported to be critical (*Production and Application of Blended Cements - Research Activities, 5. Periodic Report,* 2005). Thus, desirable durability of the concrete made of cements with high limestone contents > 35 wt.-% cannot be achieved unless the water/cement-ratio is reduced. Principles for the development of such concrete with reduced clinker and water content are described in (Proske et al., 2013). This procedure suggests the use of high performance superplasticizer. Furthermore, the optimization of the packing density is advantageous. This allows the reduction of the water demand and therefore simultaneously the minimization of the Portland cement clinker content in the cement (Proske et al., 2013; 2014; Haist et al., 2014).

Shrinkage mechanisms of cementitious materials

Principally the drying shrinkage is quite similar to the autogenous shrinkage where both happen due to loss of moisture. For drying shrinkage, the humidity is transferred to the surrounding environment, whereas for autogenous shrinkage the moisture is used up with progress of hydration or transferred to the empty pores without mass change. This is known as self-desiccation. Drying shrinkage is defined as the time-dependent deformation due to loss of water at constant temperature and relative humidity (Hansen, 1987). When the free water is evaporated, the drying process continues by sucking gel water from cement paste in which the larger pores being first emptied (Koenders, E. A. B, 1997). Despite extensive investigation into the origin of shrinkage, this property is not well understood. The four most prominent shrinkage mechanisms that have been proposed are capillary tension (Feldman and Sereda, 1970; Bažant, 1972; Hansen, 1987; Powers, 1968), movement of interlayer water (Feldman and Sereda, 1968; Wittmann, 1973), surface free energy (Powers, 1968; Wittmann, 1977; Feldman and Sereda, 1970; Parrott and Young, 1982),and disjoining pressure (Power and Brownyard, 1947; Wittmann, 1977; Bažant, 1972). However, the range of validity of aforementioned mechanisms is quite various.

The capillary tension acts normally when the capillary and gel pores are almost filled with water or condensed water from vapor denoting the high RHs (> 65 %). On the other hand, some researchers mentioned that capillary tension is responsible for hygral deformation even in low ranges of RH. It is visible that the capillary tension rises when the curvature of meniscus increases. But the total force due to capillary tension acting on the hardened cement paste (HCP) surfaces reduces when their acting perimeter reduces by losing moisture. Surface tension can be defined as the results of asymmetry of attractive forces on atoms or molecules in the close vicinity of the solid surface. Increase of relative humidity from near zero to 40% results in increase of adsorbed water molecules on the surface of solid particles,

i.e. C-S-H sheets. At this moment, according to Eq. 1, which is known as Gibbs equation, the surface energy $\Delta\gamma$ will be decreased by increasing the vapor pressure. The reduction in surface energy causes C-S-H sheets distance from each other and swelling occurs. The reverse mechanism which accompanies with reduction of humidity leads to hygral contraction of the xerogel is called Bangham shrinkage and defined as follow:

$$\Delta\gamma = \gamma_0 - \gamma = -R \cdot T \cdot \int_0^p \Gamma \cdot d(\ln p) \qquad \textit{Eq. 1}$$

In above equation R stands for gaseous constant, T for the absolute temperature, Γ for the thickness of absorbed water, and p for the vapor pressure. Bangham and Fakhouri (Bangham et al., 1932) showed that the length change $\Delta l/l$ can be correlated linearly to change of surface energy $\Delta\gamma$ as follow:

$$\Delta l / l = \lambda \cdot \Delta\gamma \qquad \textit{Eq. 2}$$

In Eq. 2 the λ factor depending on the properties of colloid system denoting the stiffness of the xerogel.

Wittmann, Power and Bažant unanimously believed that the Bangham equation cannot approximate the volume change in RH range above 50% (Wittmann, 1977; Bažant, 1972; Power and Brownyard, 1947). They attributed this nonlinearity in swelling (by increasing water vapor pressure) to the disjoining pressure which was stablished first by Derjaguin (Derjaguin et al.). In a narrow space smaller than ten times of water molecule (about 2.6 nm) the interlayer water is in a hindered desorption condition. The adsorbed water builds up a repulsive disjoining pressure. Conversely, when drying the thickness of adsorbed reduces and the disjoining pressure will depress and distance between two layers will be reduced. This results in a sudden increase of overall shrinkage in RH above 40 %.

Influence of limestone on the shrinkage deformation was investigated in some studies. Espion concluded that shrinkage of ternary cements with 30 wt.-% limestone and 50 wt.-% GGBFS is lower than that of concrete with Portland cement (Espion et al., 2012). Higher limestone content could result a larger drying shrinkage deformation for self-compacting concrete with the same water content (Heirman et al., 2008). Esping showed that the higher BET-surface area of limestone leads to a higher autogenous shrinkage of self-compacting concretes (Esping, 2008).

The aim of the present study is to analyze the shrinkage behavior of mortar samples made of Portland limestone cements with high limestone content of up to 70 wt.-% for the production of sustainable concrete. This paper is basically divided into two parts. In the first part the influence of limestone content, curing age and the w/c-ratio on the shrinkage behavior of small mortar samples is investigated. The type of limestone was not changed. In the second part, the influence of limestone quality in studied. For this purpose the limestone content of cement was fixed to 50 wt.-%, w/c = 0.35 and the age of curing was 7 days.

EXPERIMENTAL PROGRAM

As was mentioned above in the first test series of this study, different cements with different limestone contents were prepared by mixing CEM I 52,5 R and various

contents of limestone LL1 from 0 up to 70 wt.-% namely CEM I 52,5 R, CEM (15% LL1), CEM (30% LL1), CEM (50% LL1) and CEM (70% LL1). Moreover, in this series two w/c-ratios of 0.60 and 0.35 as well as two curing durations of 1 and 7 days were considered for the experiments. In the test series, the type of limestone was varied. Three cements were composed of 50 wt.-% of different limestone, denote as CEM (50% LL1), CEM (50% LL2) and CEM (50% LL3). The w/c-ratio was 0.35. In both series the mortar specimens were produced according to EN 196-1 sand. The paste content (CEM I 52,5 R + limestone + water) was kept constant for all mixtures to 420 ml/l. The specimens were de-molded after 24 ± 2 hours and were stored in water at 20 ± 1 °C. Mortar compressive strength was determined on the samples after 7 days of curing.

The shrinkage measurement was carried out by means of an extensometer with an accuracy of 0.001 mm on 40×40×160 mm³ prisms. For this purpose, the measurement points were glued on two surfaces of each specimen just after demolding. Deformations were measured after demolding, shortly, 1, 3, 7, 14, 28, 56 and 84 days after water storage. The samples were stored in climate chamber under 20 ± 1°C and 65 ± 3% RH conditions. Two specimens were prepared for each mixture and each storage condition.

Chemical composition and physical properties of used cement and limestones are presented in **Table 1**.

Table 1. Some chemical and physical properties of cement and limestones

	Unit	*CEM I*	*Limestones*		
Properties		*52,5 R*	*LL1*	*LL2*	*LL3*
SiO_2	[wt.-%]	21.3	0.44	18.25	7.55
Al_2O_3	[wt.-%]	4.21	0.18	2.89	2.15
TiO_2	[wt.-%]	0.22	0.01	0.15	-
P_4O_{10}	[wt.-%]	0.12	0.05	0.11	-
Fe_2O_3	[wt.-%]	2.67	0.12	1.13	1.13
Mn_2O_3	[wt.-%]	0.07	0.04	0.03	-
MgO	[wt.-%]	0.96	0.41	0.49	0.86
CaO	[wt.-%]	64.6	54.1	42.17	48.6
SO_3	[wt.-%]	3.69	0.02	0.30	0.12
K_2O	[wt.-%]	0.57	0.01	0.59	0.53
Na_2O	[wt.-%]	0.19	0.00	0.12	0.06
Na-equivalent	[wt.-%]	0.57	0.01	0.51	0.41
Loss on ignition	[wt.-%]	0.76	43.8	34.28	38.1
Total organic carbon	[wt.-%]	-	-	0.12	-
Methylene blue value	[wt.-%]	-	0.03	0.37	-
$CaCO_3$ content	[wt.-%]	-	97.8	74.77	86.7
Blaine specific surface area	[cm²/g]	5508	4200	4600	5000
BET specific surface area	[cm²/g]	-	7790	63790	95520

RESULTS AND DISCUSSIONS

Compressive strength. The results of compressive strength of mortar specimens after 7 days of curing (1 day in mold and 6 days in water) are shown in **Figure 1**. It is obvious that for both w/c-ratios, the increase in limestone content of cement results in a decrease of compressive strength. However, a slight increase of compressive strength was observed by CEM (15% LL1).

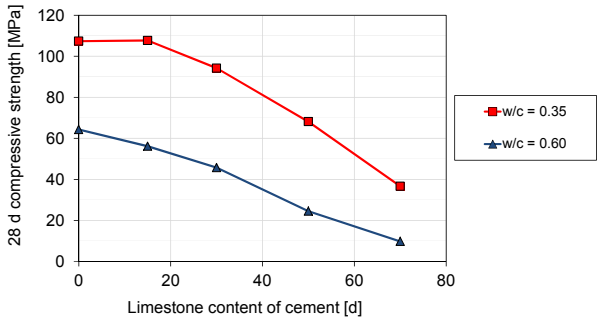

Figure 1. Compressive strength of mortar specimens made of LL1 limestone after 7 days of curing

Shrinkage and mass change. Figure 2 shows the results of shrinkage deformation of mortar samples up to 112 days. It is visible that the shrinkage deformation of specimens is highly dependent on the duration of curing and limestone content. In general, a lower w/c-ratio results in lower shrinkage values. This is more pronounced for samples made of lower limestone contents. No significant difference was observed for shrinkage values of specimens made of CEM (70% LL1) with different w/c-ratios, while the difference between mortars made of pure CEM I with different w/c-ratios was remarkable.

The sensitivity of shrinkage strain to curing time is decreased by increase of limestone content in cement, regardless to the w/c-ratio. It can be seen that for w/c = 0.35, increase of curing duration from 1 to 7 days, decreases the shrinkage deformations of mortars made of cements with limestone contents lower than 50 wt.-%. As **Figure 3** shows, longer curing period (from 1 to 7 days) had a negative influence on the shrinkage strain of samples with limestone higher than 50 wt.-%. It resulted that curing had no pronounced influence on the shrinkage behavior of mortar sample made of CEM (50% LL1). A similar trend was also observed for mixtures with w/c = 0.60, but with this difference that samples made of CEM (30% LL1) behaved neutral against curing length. The reason for this behavior could be progress of hydration by a prolonged curing period for cements with higher clinker contents. In this case, more calcium silicate hydrate (C-S-H) particles are formed. The very fine C-S-H phases as well as water moisture within C-S-H pores are the driving force for the shrinkage and swelling deformation of the cementitious matrixes. Moreover, in contrast to mixtures with high limestone content, more water will be available in the paste matrix due to lower porosity and lower diffusion of moisture to the environment. Hence, presence of water as well higher C-S-H particles increases the shrinkage potentials of such mixtures by increasing the disjoining pressure.

Although self-desiccation occurs in closed systems without moisture transport to environment, in mortar with high clinker content and w/c-ratio

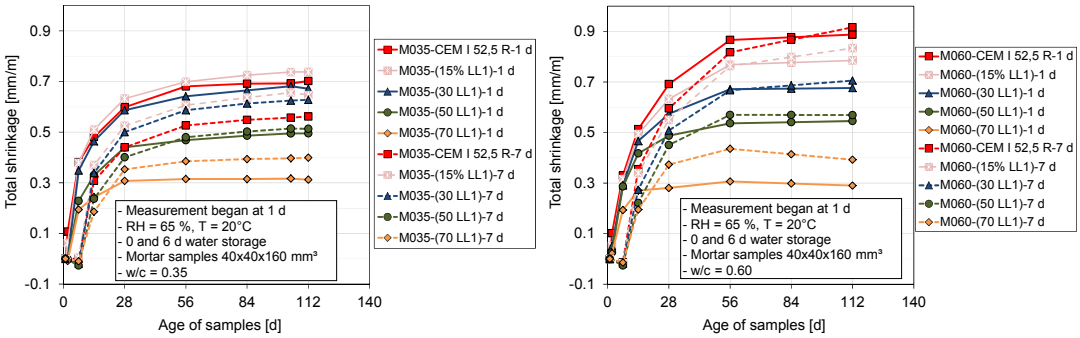

Figure 2. Shrinkage deformation of mortar samples with w/c = 0.35 (left) and 0.60 (right) after 1 and 7 days curing

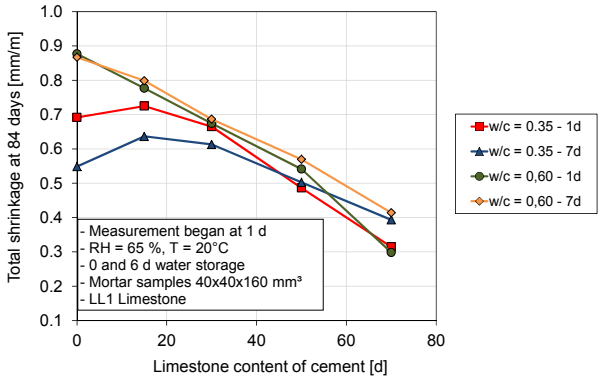

Figure 3. Shrinkage deformation and mass change of reference and mortar samples made cements with 50 wt.-% different limestones

Shrinkage strain and mass change of reference samples and samples made of cements with 50 wt.-% limestones are illustrated in **Figure 4**. It can be observed that the quality of limestone does influence the shrinkage behavior of mortar samples significantly. Limestone LL1 which is composed of 98 wt.-% $CaCO_3$ results in the lowest shrinkage values, whereas other limestones with lower $CaCO_3$ exhibited larger shrinkage deformations.

Comparison of the mass change of the specimens (which denotes the moisture loss by neglecting the amount of absorbed CO_2) reveals that shrinkage cannot be correlated to the moisture loss of specimens. All samples with 50 wt.-% limestone had approximately the same moisture loss but the shrinkage deformations were quite different. In this case mixture with LL3 limestone had the highest shrinkage strain about twice than that of LL1 limestone. The shrinkage behavior of LL2 limestone was also comparable to LL3. However, all these mixtures had lower shrinkage that the reference mixture with w/c = 0.60 but significantly higher than reference mixture with w/c = 0.35 (with the same paste content). The higher shrinkage rate of mixtures with LL2 and LL3 can be justified by presence of mineral impurities such as clay minerals. The presence of clay minerals can be proved by reviewing the methylene

blue values from **Table 1**. Considering the ambient relative humidity of 65%, it is expected that disjoining pressure to be the dominant driving force for shrinkage. The thickness of adsorbed water on the solid surface of HCP is one of the main parameter controlling the disjoining pressure between surfaces.

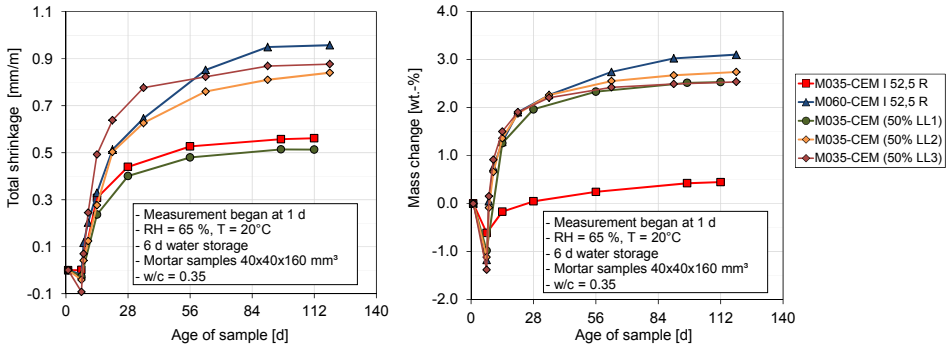

Figure 4. Shrinkage deformation and mass change of reference and mortar samples made cements with 50 wt.-% different limestones

Thickness of adsorbed water is governed by non-chemically bounded water (namely evaporable water) and total surface area of the HCP. Hardened cement paste – at a degree of hydration between 50 and 100% - is composed of anhydrate clinker phases, hydration products, limestone particles and pore water. Basically the total surface area of HCP is governed by the C-S-H crystal phases, due to their high specific surface area (> 100 cm²/g) which is obviously dominant to others. In the limestone-rich systems, the contribution of limestone to the total specific surface area comes into action when the limestone powder itself has a high specific surface area in comparison to other components of HCP. Within investigated limestones in this study, LL2 and LL3 have significantly high specific surface areas. Considering the high limestone content of the mixture, the total surface area will be remarkable (for instance in comparison with mixtures with limestone LL1).

On the other hand all the mixtures made of limestones LL1, LL2 and LL3 have approximately the same amount of free water but different total surface area. Thus it is expected that the thickness of adsorbed water to be notably different for these mixtures and consequently different shrinkage tendencies. Shrinkage strain as the function of BET-specific surface area of the limestone for the mortar samples made of same limestone content and w/c-ratio is shown in **Figure 5**.

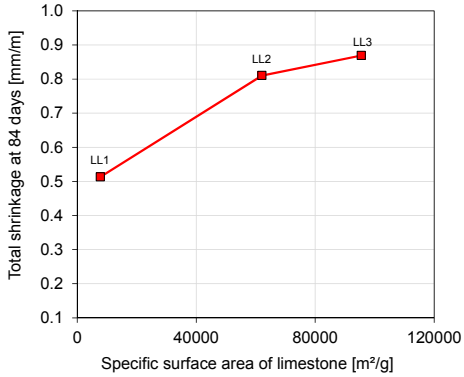

Figure 5. Relation between BET specific surface area of limestone and shrinkage strain of the mortar samples made of cements with 50 wt.-% limestone

CONCLUSION

In this paper shrinkage behavior of mortar samples made of limestone-rich cements with different limestone content, limestone quality, w/c-ratio and curing time was analyzed. Based on the results the following remarks can be given:

- Shrinkage deformation of the samples with different limestone content depends on the w/c-ratio. For mortar samples with w/c = 0.35 the largest shrinkage strain was observed for cement with 15 wt.-% limestone. Further increase of limestone LL1 resulted in lower shrinkage deformations.
- Effect of curing duration was remarkable for samples made of lower w/c-ratios. However, the sensitivity of shrinkage to curing duration was decreased by increase of limestone content of cement.
- The quality of limestone was shown to have a huge influence on the hygral deformation of mortar samples with w/c = 0.35, although the desorption process was identical.
- Different shrinkage strain of mortars could be attributed to the composition of the limestones, mainly presence of clay mineral by BET specific area.
- Extra attentions has to be paid when selection the limestone to be used as main component of cements with very high limestone contents.

REFERENCES

(2013) *U. S. Geological Survey, Mineral commodity summaries,* Virginia, USA.

(2005) *Production and Application of Blended Cements - Research Activities, 5. Periodic Report,* EUROPEAN CONSTRUCTION INSERVICE OF SOCIETY (ECOServe) CLUSTER 2.

ASTM C595 / C595M (2013) *Standard Specification for Blended Hydraulic Cements,* American Society for Testing and Materials (ASTM).

Bangham, D.H., Fakhoury, N. and Mohamed, A.F. (1932) 'The Swelling of Charcoal. Part II. Some Factors Controlling the Expansion Caused by Water, Benzene and Pyridine Vapours', *Proceedings of the Royal Society of London. Series A, Containing Papers of a Mathematical and Physical Character*, Vol. 138, No. 834, pp.162–183.

Bažant, Z.P. (1972) 'Thermodynamics of hindered adsorption and its implications for hardened cement paste and concrete', *Cement and Concrete Research*, Vol. 2, No. 1, pp.1–16.
CAN/CSA-A3000-08 (2008) *CAN/CSA-A3000-08: Cementitious Materials Compendium,* Canadian Standards Association.
Derjaguin, B.V., Churaev, N.V., Muller, V.M. and Kitchener, J.A. *Surface forces*.
Esping, O. (2008) 'Effect of limestone filler BET(H2O)-area on the fresh and hardened properties of self-compacting concrete', *Cement and Concrete Research*, Vol. 38, No. 7, pp.938–944.
Espion, B., Lebon, B., Pierre, C., Germain, O. and Hellebois, A. (2012) 'Characterisation of new ternary cements with reduced clinker content', *In: First International Conference on Concrete Sustainability*, pp.145–152.
Feldman, R.F. and Sereda, P.J. (1970) 'A new model for hydrated portland cement and its practical implications', *Engineering Journal*, Vol. 53, 8/9, pp.53–59.
Feldman, R.F. and Sereda, P.J. (1968) 'A model for hydrated portland cement paste as deduced from sorption-length change and mechanical properties', *Materials and Structures*, Vol. 1, No. 6, pp.509–520.
Haist, M., Moffatt, J.S., Breiner, R. and Müller, H.S. (2014) 'Entwicklungsprinzipien und technische Grenzen der Herstellung zementarmer Betone', *Beton- und Stahlbetonbau*, Vol. 109, No. 3, pp.202–215.
Hansen, W. (1987) 'Drying Shrinkage Mechanisms in Portland Cement Paste', *American Ceramic Society*, Vol. 70, No. 5.
Heirman, G., Vandewalle, L., van Gemert, D., Boel, V., Audenaert, K., Schutter, G. de, Desmet, B. and Vantomme, J. (2008) 'Time-dependent deformations of limestone powder type self-compacting concrete', *Engineering Structures*, Vol. 30, No. 10, pp.2945–2956.
Koenders, E. A. B (1997) *Simulation of volume changes in hardening cement-based materials,* Delft University Press, Delft.
Parrott, L.J. and Young, J.F. (1982) 'Shrinkage and Swelling of Two Hydrated Alite Pastes', *Fundamental Research on Creep and Shrinkage of Concrete*, pp.35–48.
Power, T.C. and Brownyard, T.L. (1947) 'Studies of the Physical Properties of Hardened Portland Cemenet paste (nine parts)', *Journal of American Concrete Institute, Research laboratories of the Portland cement association, Bulletin 22*, Vol. 43.
Powers, T.C. (1968) 'The thermodynamics of volume change and creep', *Matériaux et Constructions*, Vol. 1, No. 6, pp.487–507.
Proske, T., Hainer, S., Rezvani, M. and Graubner, C.-A. (2014) 'Eco-friendly concretes with reduced water and cement content – Mix design principles and application in practice', *Construction and Building Materials*.
Proske, T., Hainer, S., Rezvani, M. and Graubner, C.-A. (2013) 'Eco-friendly concretes with reduced water and cement contents — Mix design principles and laboratory tests', *Cement and Concrete Research*, Vol. 51, pp.38–46.
Wittmann, F.H. (1977) *Grundlagen eines Modells zur Beschreibung charakteristischer Eigenschaften des Betons. DAfStb., Heft 290,* Berlin.
Wittmann, F.H. (1973) 'Interaction of Hardened Cement Paste and Water', *Journal of the American Ceramic Society*, Vol. 56, No. 8, pp.409–415.

Modelling the Time-Dependent Pull-Out Behaviour of Hooked Steel Fibres

P. D. Nieuwoudt[1] and W. P. Boshoff[1,*]

[1]Civil Engineering Department, Stellenbosch University, Private Bag X1, Stellenbosch 7602, South Africa. E-mail: bboshoff@sun.ac.za

Abstract

Steel Fibre Reinforced Concrete (SFRC) is currently being used as a structural material even though little is known about the creep behaviour of SFRC, specially the cracked tensile creep. In recent studies it has been revealed that even though the tensile creep of SFRC is similar to that of ordinary concrete, the creep increased significantly after the SFRC had cracked. This phenomenon can be associated with time-dependent crack widening that is caused by fibre pull-out over time. Single fibre pull-out rate and sustained load tests were performed to investigate the time-dependent pull-out behaviour of hooked-end steel fibres. Four pull-out rates ranging from 2.5 mm/s to 0.00025 mm/s were considered. The sustained load varied from 30 % to 85 % of the maximum (short term) pull-out resistance. Finally, an analytical study was conducted to predict the time-dependent pull-out behaviour.

1 INTRODUCTION

The addition of randomly distributed steel fibres to concrete has been proven to improve the mechanical behaviour of the matrix (Kim 2009, Wang 2006). However, the benefit of the fibres only becomes obvious once the matrix starts cracking as the fibres bridging the crack transfer the stress between both faces of the crack. This phenomenon imparts a post-cracking strength to the composite. A single fibre pull-out test is often used to represent the effect that a single fibre has on a cement-based composite (Robins et al. 2002, Cunha et al. 2007, Wille and Naaman 2012). These studies are performed under short term loading conditions. It is a well-known fact that ordinary concrete is dependent on the duration of loading and therefore it is also expected that the fibre/matrix interface will be dependent on it. Babafemi and Boshoff (2015) performed single fibre sustained load tests on macro-synthetic fibres (MSF) and concluded that the pull-out displacement is dependent on the sustained applied load. The pull-out behaviour of hooked-end steel fibres is significantly different when compared to that of MSF.

Numerous studies have been performed on predicting the single fibre pull-out behaviour. Sujivorakul (2000) and Cunha et al. (2007) are the few that derived models that predict the pull-out force-displacement relationship for hooked-end steel fibres. According to the author's knowledge no literature is available on methods to predict the time-dependent pull-out behaviour of hooked-end steel fibres. The main

focus of this study is to assess and predict the time-dependent pull-out behaviour of hooked-end steel fibres.

2 EXPERIMETAL METHOD

Two different loading conditions were considered in this experimental program, namely single fibre pull-out rate and single fibre sustained load tests. Pull-out rate tests were conducted to investigate what effect the pull-out rate has on the pull-out behaviour whereas sustained load tests were conducted to investigate the long term pull-out behaviour. All these tests were performed in a climate controlled room with a temperature of 23 ± 1˚C and a relative humidity of 65 ± 5 %.

2.1 Mix Composition

The materials and proportions used in the mix composition are summarised in Table 1. Dynamon SP1 superplasticiser based on modified acrylic polymer supplied by MAPEI South Africa was used to adjust the workability of the mix. The fibres used in the single fibre pull-out tests were DRAMIX RC-65/60-BN hooked-end steel fibres, supplied by BEKAERT in Belgium.

Table 1. Mix composition

Material type	*kg/m^3*
Cement (CEM I 52.5N)	395
Water	190
Sand (Malmesbury)	990
Stone (6 mm Crushed Greywacke)	800
Superplasticiser (0.5% by weight of binder)	1.975

No fibres were added to the matrix during the mixing process. Once the specimens were cast the single fibre were carefully inserted vertically in the middle of each specimen to a depth of 15 mm. Thereafter the moulds were gently vibrated to remove any voids that formed between the fibre and the matrix. The specimens were kept in a climate controlled room for 24 hours where after they were removed from the moulds and placed in curing baths for an additional 27 days. The dimensions of the single fibre specimens are shown in Figure 1 b) and 2 b).

2.2 Single Fibre Pull-out Rate Tests

The pull-out tests were performed using a Zwick Z250 Universal Materials Testing Machine which has a capacity of 250 kN, see Figure 1 a). The single-sided specimen is gripped with hydraulic clamps. A fibre gripping setup was designed to ensure that the bond between the fibre and the matrix was not damaged during the gripping of the fibre. The pull-out force was recorded with a 500 kg load cell connected in series. The fibre pull-out displacement is measured by means of two Linear Variable Differential Transformers (LVDT's) that have a measuring range of 50 mm.

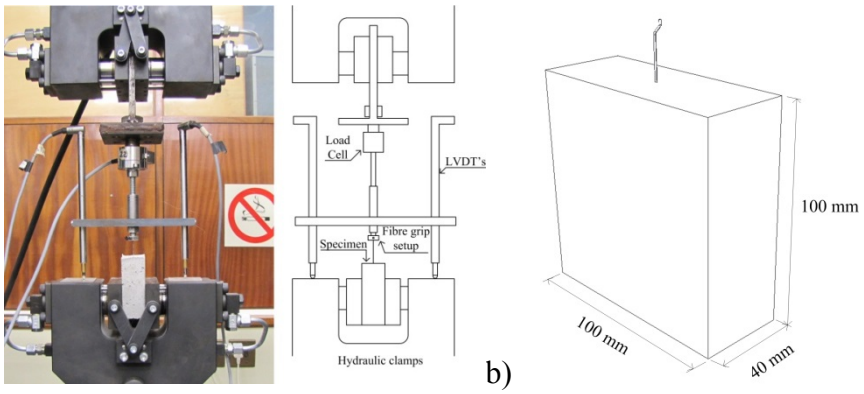

Figure 1. a) Pull-out rate test setup and b) specimen dimensions

Pull-out rate tests were performed on hooked-end steel fibres. A set of pull-out tests was also performed on straight steel fibres in order to establish the contribution made by the mechanical bond. Straight fibres were obtained by cutting the hooked-ends of the RC-65/60-BN fibres with pliers. Care was taken to ensure that no rough edges created after cutting the hooked-ends. For the straight single fibre pull-out tests seven specimens were tested at a pull-out rate of 2.5 mm/s. For the hooked-end single fibre pull-out rate tests, the pull-out rate was varied from 2.5 x 10^{-4} mm/s to 2.5 mm/s. Six specimens were tested at each pull-out rate.

2.3 Single Fibre Sustained Load Tests

A simple test setup was designed whereby the sustained load is applied by free hanging weights, see Figure 2 a). The specimens are anchored to the frames through the threaded bars that are embedded in the matrix on the opposite side of the protruding fibre. The gripping setup in Section 2.1 was modified in order that the free hanging weights can be applied to the fibre. The pull-out displacement was measured optically by taking digital images with a microscope incorporating a 3.1 Mega-pixel EC3 Leica camera. These images were scaled to the correct size using a fixed calibration plate.

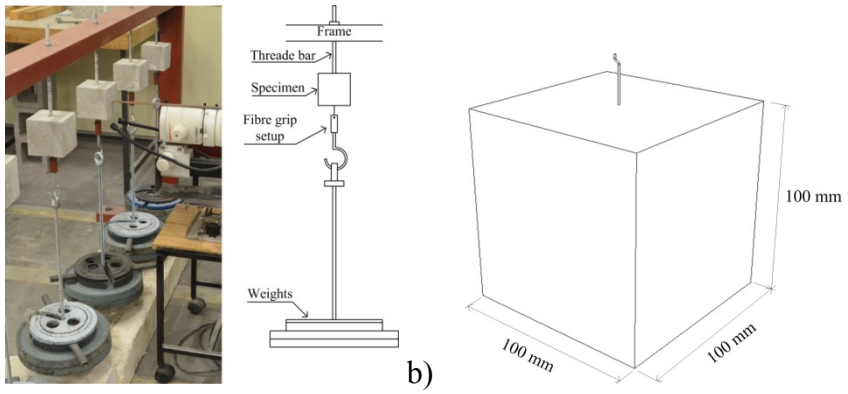

Figure 2. a) Sustained load test setup and b) specimen dimensions

The sustained load level was varied between 30% and 85% of the average maximum pull-out force (366.11 N) that had been determined from the results of the single fibre pull-out rate tests. Three specimens were tested for each load level.

3 EXPERIMENTAL RESULTS

3.1 Rate Pull-out Results

The results of the pull-out rates are shown in Figure 3. Graphs summarising the maximum force and the pull-out displacement at the maximum force for hooked-end fibres are shown in Figure 4. Minimum and maximum values are also shown to indicate the scatter of the values.

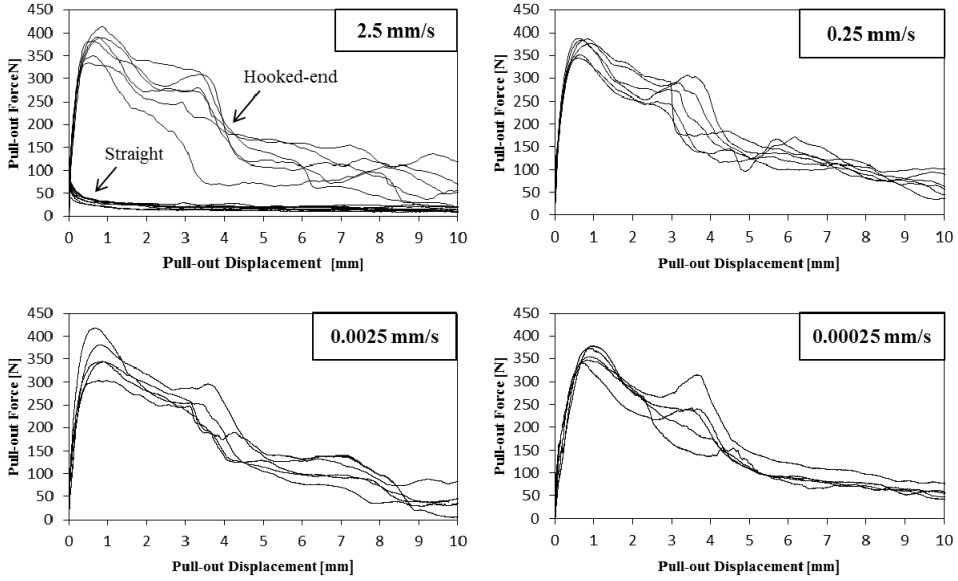

Figure 3. Single fibre pull-out rate results for hooked-end fibres.

At the tested pull-out rate range an insignificant change in maximum pull-out force was noticed. However, a remarkable rate effect on the pull-out displacement at maximum force was noticed. A decrease of 23.1 % from the lowest to the highest pull-out rate was found.

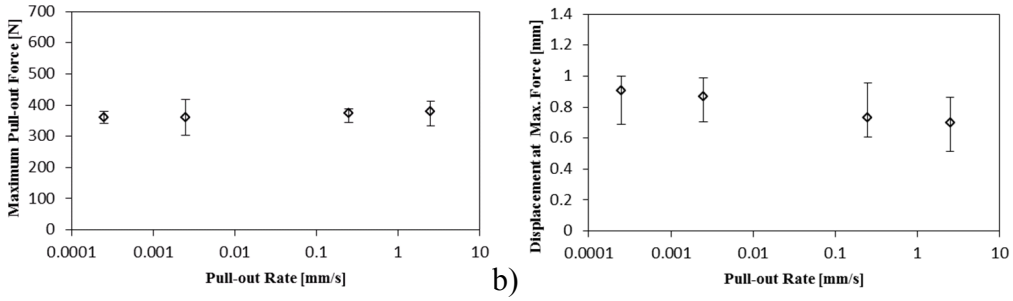

Figure 4. a) The average maximum pull-out force and b) the average pull-out displacement at the maximum force at different pull-out rates.

3.2 Sustained load Results

The pull-out displacement of the sustained loading tests was measured using the method of microscope as mentioned in Section 2.3. The average pull-out displacement over time for each loading percentage is presented in Figure 5 a). During the measured time period (186 days), none of the fibres pulled-out completely, even for sustained loads as high as 85 % of the average maximum pull-out force.

In Figure 5 b) the average pull-out displacement at the end of 186 days for each loading percentage are presented. The results show that the average pull-out displacement increases linearly up to a loading of 50 % of the average maximum pull-out force. An exponential increase in the pull-out displacement is observed for higher sustained loadings. The mechanisms causing the non-linear increase in the pull-out displacement are still unknown and further investigations are required.

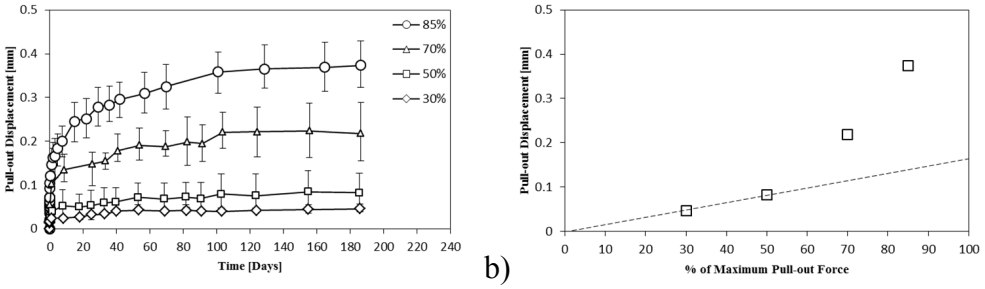

a) b)

Figure 5. a) The average pull-out displacement results b) The average pull-out displacement at the end of 186 days.

4 MODELLING THE TIME-DEPENDENT SINGLE FIBRE PULL-OUT BEHAVIOUR

The model developed by Cunha et al. 2007 is used to describe the single fibre pull-out behaviour. It was assumed that the increased time-dependent pull-out was insignificantly small at a pull-out rate of 2.5 mm/s. The experimental results of the 2.5 mm/s series were used to calibrate the model developed by Cunha et al. (2007). A linear visco-elastic component was added to incorporate the time-dependant pull-out behaviour.

4.1 Analytical Modelling of Fibre Pull-out (Cunha et al., 2007)

The pull-out problem is a complex three dimensional problem. However Cunha et al. (2007) simplified it to a two dimensional axisymmetric problem by simulating the adhesion and friction with a local bond displacement relationship and treating the end anchorage as a spring component. A detailed description of the mathematical equations presented in this paper can be found in Cunha et al. (2007).

4.1.1 Local bond-displacement relationship

The following second order differential equation describes the local bond phenomena between the fibre and matrix:

$$\frac{d^2 s}{dx^2} = \frac{P_f}{E_f A_f}\tau \tag{1}$$

where $\tau = \tau[s(x)]$ is the local bond shear stress between fibre and the concrete matrix, and s = pull-out displacement, i.e. the relative displacement between the fibre and concrete matrix surrounding the fibre. P_f, E_f, and A_f are the perimeter of the fibre, Youngs modulus and cross-sectional area, respectively.

4.1.2 Pull-out force-displacement relationship

The generic applied pull-out force for a hooked-end fibre can be determined as follow:

$$\overline{N} = N_{sp} + \sqrt{2E_f \cdot A_f \cdot P_f \int_{s_f}^{s(x=\bar{L}_b)} \tau(s)ds} \tag{2}$$

where N_{sp} is the spring component which simulates the hooked-end of the fibre. The bond stress-displacement relationship, $\tau(s)$, used in Equation 2 is defined as:

$$\tau(s) = \begin{cases} \tau_m \left(\dfrac{s}{s_m}\right)^{\alpha} & , s \le s_m \\ \tau_m \dfrac{1}{1+\left(\dfrac{s-s_m}{s_1}\right)^{\alpha'}} & , s > s_m \end{cases} \tag{3}$$

where τ_m and s_m are the bond strength and its corresponding pull-out displacement, respectively. Parameter α defines the shape of the pre-peak branch, whereas α' and s_1 defines the shape of the post peak branch of the curve.

The mechanical bond, N_{sp}, was acquired by subtracting the experimental average curve of the straight fibres from the experimental curves of the hooked-end fibres. An analytical relationship of the average contribution of the mechanical bond was obtained by non-linear fitting. In Figure 6 the analytical simulation of the hook contribution for the 2.5 mm/s rate series is presented.

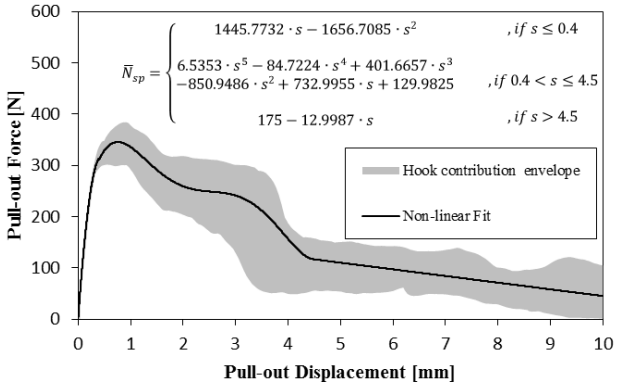

Figure 6. Analytical simulation of the hook contribution.

Equation 1 was solved numerically by obtaining the unknown parameters of the local bond stress-displacement relationship. To do this the algorithms and methods given by Cunha et al. (2007) were implemented.

4.1.3 Numerical simulations

The 2.5 mm/s experimental series envelope and numerical pull-out force-displacement relationship for hooked-end fibres are presented in Figure 7. The average values of the parameters defining the local bond stress-displacement relationship for hooked-end fibre are included in Table 2. Also included is the normalised error, ē, which was defined as the ratio between e and the area under the experimental curve; e is defined as the absolute difference between the area under the experimental and numerical curve.

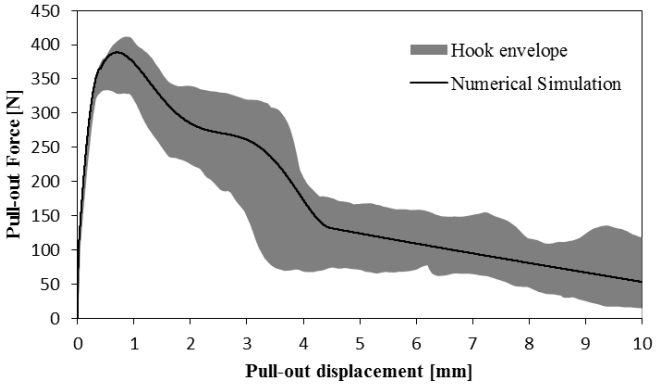

Figure 7. The 2.5 mm/s pull-out force-displacement relationship.

The values of the material and geometrical properties used in the numerical simulations were the following: a cross-sectional perimeter, P_f, of 2.827 mm, a Young's modulus, E_f, of 200 GPa and a cross-sectional area, A_f, of 0.636 mm^2.

Table 2. Parameters for the local bond stress-displacement relationship, determined using numerical strategy described by Cunha et al. (2007).

s_m [mm]	τ_m [Mpa]	α	α'	s_1 [mm]	ē [%]
0.018	1.797	0.830	0.917	0.958	1.740

The analytical model developed by Cunha et al. (2007) was able to simulate the experimental pull-out force-displacement results with high accuracy. This is evident in the relatively low value of the average normalised error.

4.2 Adapted Model to include Time-dependent Behaviour

A remarkable rate effect was found for the pull-out displacement at the maximum force. To model this behaviour a linear visco-elastic component was added in series with the analytical model developed by Cunha et al. (2007).

4.2.1 Mathematical derivation of Time-dependent Model

The generalised Kelvin-Voigt model (Reddy 2013) is used to represent the time-dependent behaviour and is expressed as follow:

$$s = N\sum_{i=1}^{r}\frac{1}{k_i}(1-e^{\frac{t}{\tau_i}}) \tag{4}$$

where k and τ are the spring stiffness and relaxation time, respectively. Equation 4 only counts for the conditions of constant force. The concept of superposition was used by Boshoff (2007) to derive a formulation that represents the complete force history over time without having to add a variable for each history point and is expressed as follow:

$$s_x = \sum_{i=1}^{r}\left[H_{1,i,x} + H_{2,i,x}\cdot e^{-\frac{t_{i,x}}{\tau_i}}\right], \text{ with } x \geq 1 \tag{5}$$

where,

$$H_{1,i,x} = H_{1,i,x-1} + \frac{(N_x - N_{x-1})}{k_i}$$

$$H_{2,i,x} = H_{2,i,x-1} + \frac{(N_{x-1} - N_x)}{k_i}e^{\frac{t_{x-1}}{\tau_i}}$$

This formulation will represent the single fibre pull-out rate effect. The applied force can change with time and the force history is only represented by two variables per Kelvin-Voigt element.

4.2.2 Implementation of the adapted Model

An iterative numerical method was used to find the required parameters for the formulation as described in Equation 5 so that it accurately predicts the pull-out rate effect. The values of the parameters defining the pull-out rate effect are included in Table 3.

Table 3. Time-dependent model parameters.

Element no.	*k [N/mm]*	*τ [Days]*
1	427731.033	305.802
2	2344.913	0.001859

In Figure 8 the average experimental and simulated pull-out displacements at maximum force for each pull-out rate are represented. The model is able to simulate the pull-out displacement at maximum force with high accuracy. This is evident in the relatively low normalised errors which are also presented in Figure 8. The normalised error is the ratio between e and the experimental average pull-out displacement at maximum force; e is the absolute difference between the experimental average pull-out displacement and modelled pull-out displacement at maximum force.

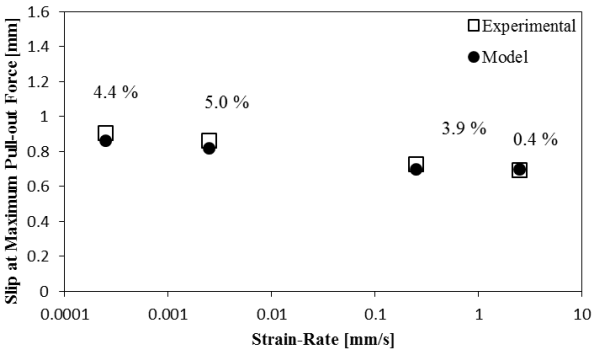

Figure 8. Simulated pull-out slips at maximum force at different pull-out rates.

4.2.3 Model Verification

The adapted model was verified with the experimental single fibre sustained load results. The time-dependent component of the adapted model was implemented using the obtained parameters in Table 3. In Figure 9 the average experimental and simulated pull-out displacement results are represented after 186 days. The model is able to simulate the sustained load results with a high degree of accuracy for sustained loads up to 50 % of the maximum pull-out force. However, for higher sustained loads the model fails to predict the results accurately. This is evident in the normalised errors also presented in Figure 9. The inaccurate simulation of the pull-out displacements for sustained loads higher than 50 % is because a linear visco-elastic component is added to predict the pull-out rate effect. Further investigation in this field is required to include the non-linear pull-out behaviour.

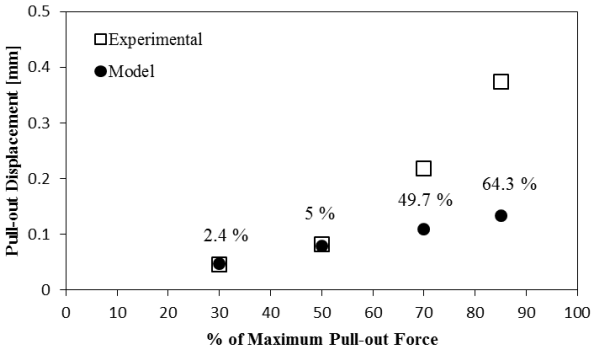

Figure 9. Sustained load simulated pull-out displacement at the end of 186 days.

5. CONCLUSIONS

Single fibre pull-out rate and sustained load tests were performed to investigate the time-dependent pull-out behaviour of steel fibres. An analytical study was performed on the prediction of the time-dependent behaviour. The following conclusion can be made from this study:

- The pull-out rate had no effect on the maximum pull-out force. However, an effect on the pull-out displacement at maximum pull-out force was observed.

- The sustained load tests showed that the pull-out displacement increases linearly up to a loading of 50 % of the average maximum pull-out force. For higher loadings the pull-out displacement increases exponentially.
- The proposed adapted model is insufficient to predict the non-linear time-dependent single fibre pull-out behaviour.

In this study a basis for modelling the time-dependent pull-out behaviour of hooked-end steel fibres is established. Further investigation in this field is required to include the non-linear time-dependent pull-out behaviour.

REFERENCES

Babafemi, A. & Boshoff, W., 2015. Tensile creep of macro-synthetic fibre reinforced concrete (MSFRC) under uni-axial tensile loading. *Cement & Concrete Composites,* Volume 55, pp. 62-69.

Boshoff, W. P., 2007. *Time-Dependant Behaviour of Engineered Cement-Based composites,* Stellenbosch: University of Stellenbosch.

Cunha, V. M., Barros, J. & Sena-Cruz, J., 2007. *Pullout behaviour of hooked-end steel fibres in self-compacting concrete,* University of Minho: Department of Civil Engineering.

Kim, D. j., 2009. *Strain rate effect on high performance fber reinforced cementitious composites using slip hardening high strength deformed fibers,* The University of Michigan: Deparment of Civil Engineering.

Reddy, J., 2013. Chapter 9: Linearized viscoelasticity. In: J. Reddy, ed. *An introduction to continuum mechanics.* New York: Cambridge University Press, pp. 389-423.

Robins, P., Austin, S. & Jones, P., 2002. Pull-out behaviour of hooked steel fibres. *Materials and Structures,* August, Volume 35, pp. 434-442.

Sujivorakul, C., Waas, A. & Naaman, A., 200o. Pullout response of a smooth fiber with an end anchorage. *Journal of Engineering Mechanics,* 126(9), pp. 986-993.

Wang, C., 2006. *Experimental investigation on behavior of steel fiber reinforced concrete (SFRC),* University of Canterbury: Department of Civil Engineering.

Wille, K. & Naaman, A. E., 2012. Pullout behavior of high-strength steel fibres embedded in ultra-high-performance concrete. *ACI MATERIALS JOURNAL,* 109(4), pp. 479-487.

Experimental Study of the Crack Widening Mechanisms in Polymer Fiber Reinforced Concrete

Rutger Vrijdaghs[1]; Els Verstrynge[2]; Marco di Prisco[3]; and Lucie Vandewalle[2]

[1]Doctoral Researcher, Department of Civil Engineering, KU Leuven, Kasteelpark Arenberg 40, Bus 2448, 3001 Heverlee, Belgium. E-mail: rutger.vrijdaghs@bwk.kuleuven.be
[2]Professor, Department of Civil Engineering, KU Leuven, Belgium.
[3]Professor, Department of Civil and Environmental Engineering, Politecnico di Milano, Italy.

Abstract

In fiber reinforced concrete, fibers are able to transmit forces across a crack. Macrofibers can be used in structural applications to arrest crack growth and increase the long-term durability of the structural element. However, time-dependent phenomena such as creep can gradually widen cracks. In fiber reinforced concrete, this time-dependent crack widening can be mainly attributed to two mechanisms, fiber creep and gradual fiber pull-out out of the concrete matrix. This paper presents the results of an experimental campaign into these two crack-widening mechanisms for polypropylene fiber reinforced concrete. Fiber creep is evaluated at different load levels. The tests show that creep fracture may occur after mere days to several months for high and low load levels, respectively. Furthermore, the total strain at failure can easily exceed 50 % for low load levels. Pull-out experiments have been done on the same polypropylene fiber at different embedded lengths. The results show that the maximum measured force is not linear dependent on the embedded length of the fiber. Furthermore, post-peak pull-out behavior can be related to the surface profile of the fiber.

INTRODUCTION

Fiber reinforced concrete (FRC) is a composite material in which fibers are added to the fresh concrete mix (Balaguru & Shah, 1992; Bentur & Mindess, 1990). These fibers are used to improve the properties of the concrete in the fresh or hardened state. In structural applications, fibers can partially or totally replace the traditional reinforcement. For these purposes, the fibers provide an enhanced post-cracking tensile strength in the hardened state by bridging crack faces (di Prisco, Plizzari, & Vandewalle, 2009). Commercially available fibers can be made from a number of different materials: steel, glass, synthetic and natural being the most common types (ACI Committee 544, 2002).

Until recently, the research effort has been focusing on the properties of FRC in the fresh and hardened state (Fibre-Reinforced Concrete; Fibre Reinforced Concrete: design and applications). It has been found that the inclusion of fibers

decreases plastic shrinkage cracking (Grzybowski & Shah, 1990) and flowability (Pasini, Garcia, Gettu, & Agullo, 2004) in the fresh state. In the hardened state, fibers provide a post-cracking strength as is shown in references (Barros, Cunha, Ribeiro, & Antunes, 2005; Buratti, Mazzotti, & Savoia, 2011; di Prisco, Ferrara, & Lamperti, 2013). However, investigations on the long-term structural properties of FRC have only recently become a research focal point. The recently published Model Code 2010 (fédération internationale du béton (fib), 2010) acknowledges that time dependent effects may significantly alter the behavior of structural elements, both in the serviceability limit state and in the ultimate limit state. In the former, creep may cause unwanted and unacceptable deflections of FRC beams (Kurtz & Balaguru, 2000; MacKay & Trottier, 2004), whilst in the latter, the residual load-bearing capacity of elements may be significantly lower than the design value based on the short-term strength assessment. However, the Model Code does not provide design rules to take long-term behavior into account. It is clear that further research on the long-term structural properties of FRC is required.

One of these time-dependent phenomena is creep. Creep deformations of cracked FRC elements are generally concentrated in the zones of the section subjected to tensile stresses. When an FRC element is loaded, a crack can widen due to two main mechanisms: pull-out creep and fiber creep. Pull-out creep is the mechanism in which the fiber gradually slides out of the concrete matrix (Li, Wang, & Backer, 1990; Zhao, Verstrynge, di Prisco, & Vandewalle, 2012). Fiber creep, on the other hand, is the time-dependent elongation of a stressed fiber itself. This fiber creep deformation is mainly a problem for synthetic and natural fibers (Drozdov & Christiansen, 2009; Sabuncuoglu, Acar, & Silberschmidt, 2011), but steel and glass fibers can exhibit creep behavior at high temperatures as well.

In this paper, experimental results into these two mechanisms are presented for a polypropylene fiber.

EXPERIMENTAL SETUP

Fiber creep setup

A straight polypropylene fiber used for structural concrete reinforcement is tested. The fiber has an equivalent diameter of 0.95 mm, making it a class II fiber, according to EN14889-2 (CEN, 2006). The initial length l_0 of the fiber is 200 mm. In total, 14 creep specimens have been tested. An overview of the creep tests is shown in Table 1. The load ratio is defined as the ratio of the applied load to the average fiber strength. The strength of the fiber is determined in a tensile test on 6 test specimens with a resulting average value of 274 N and a standard deviation of 7 N.

Table 1: fiber creep specimens

category	l_0	load ratio	# specimens	status
1	200 mm	53 %	6	Completed
2	200 mm	43 %	4	Completed
3	200 mm	36 %	4	Running

The creep specimen is placed in a creep frame in a climate controlled chamber at 20 °C and 60 % relative humidity. The creep frame is shown in Figure 1 (a). A photo of the actual creep frame is shown in Figure 1 (b). Optical laser sensors are used to contactlessly measure the fiber elongation. Measurements are taken at a rate of 1 Hz. The sensor has a maximum range of 250 mm, corresponding to a maximum measurable strain of 125 % and an accuracy of ± 0.1 mm. In the reported setup, iron plates are used as dead weight to apply the tensile load to the specimens.

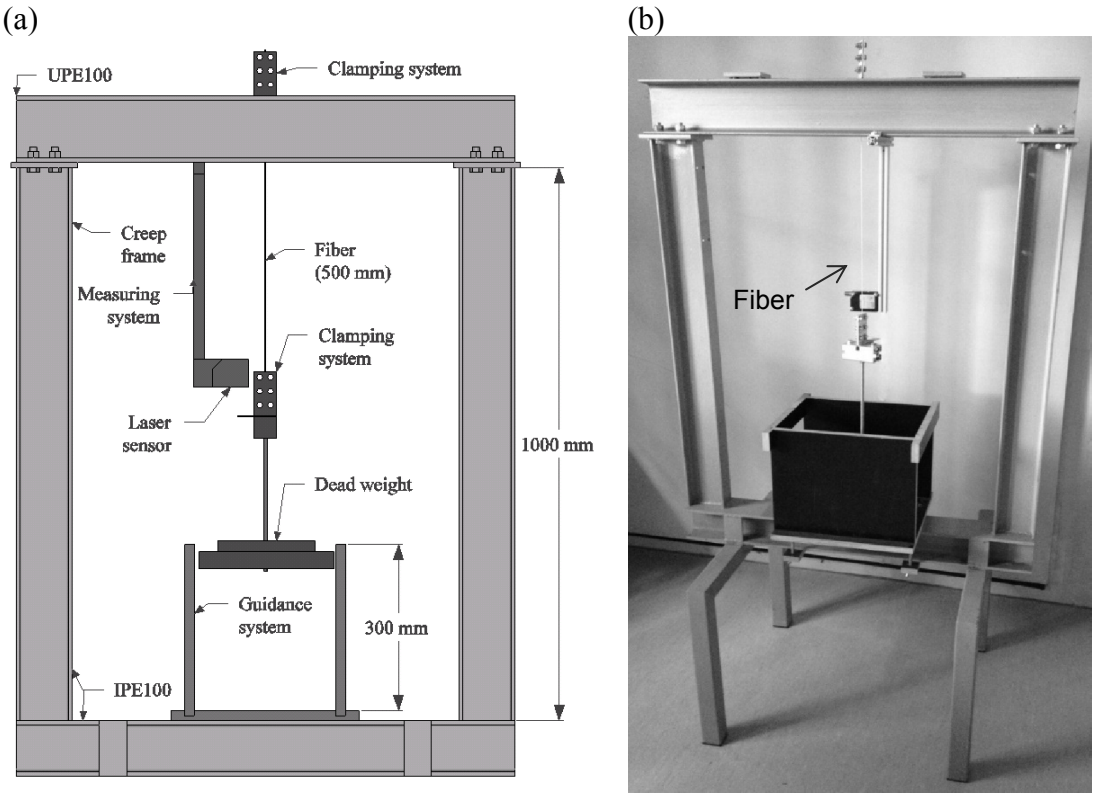

Figure 1: (a) drawing of the creep frame (b) picture of the actual creep frame

Pull-out setup

The same polypropylene fiber is subjected to pull-out tests from a concrete matrix as well. The concrete composition can be found in Table 2.

Table 2: concrete composition

component	amount [kg/m^3]
CEM I 42.5R HES	350
Water	175
Sand 0-4	835
Gravel 4-14	1099
Superplasticizer	1

The tests are performed on a universal test machine in a displacement controlled regime. The displacement rate is chosen to a relatively high value of 10 mm/min in order to minimize the effect of fiber creep on the measured deformation. The displacement is recorded by three LVDTs placed around the fiber. The LVDTs can measure displacements up to 30 mm with an accuracy of ± 0.01 mm. An external load cell with a capacity of 900 N measures the forces imposed on the fiber during the test. This load cell has a declared accuracy of ± 0.05 %. In Figure 2, (a) a simplified drawing and (b) a photo of the pull-out setup is shown.

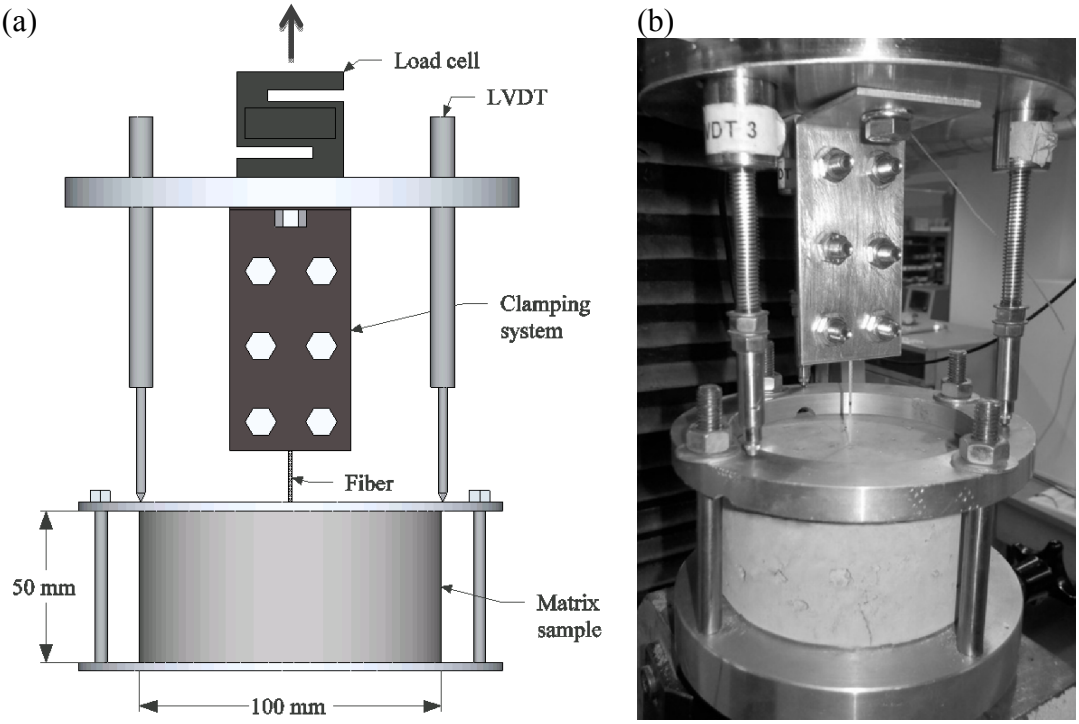

Figure 2: (a) simplified pull-out setup (b) picture of the actual pull-out setup

In total, 34 pull-out specimens have been tested. The fiber is embedded perpendicularly in the matrix, with embedded lengths of 10, 15, 20, 25 and 30 mm. During casting, the mold is filled in three layers, with manual compaction after every layer. All samples are demolded 1 day prior to testing at 7 days.

RESULTS

Fiber creep test

Out of 14 specimens, 10 failed due to creep failure and 4 specimens are still running. The experimental results are shown in Table 3. In this table, $t_{failure}$ denotes the average time to failure in seconds and $\varepsilon_{failure}$ the average total strain at failure as a percentage. The results from the creep tests are shown in Figure 3.

Table 3: experimental results for the fiber creep test

category	$t_{failure}$ [s] (#, *s*)	$\varepsilon_{failure}$ [%] (#, *s*)
1	1.86×10^5 (6, 3×10^4)	40.1 (6, 3.0)
2	4.06×10^6 (4, 2×10^6)	57.7 (4, 3.6)
3†	$> 8.06 \times 10^6$ (4, -)	> 42.5 (4, -)

† running experiment
# number of specimens
s standard deviation

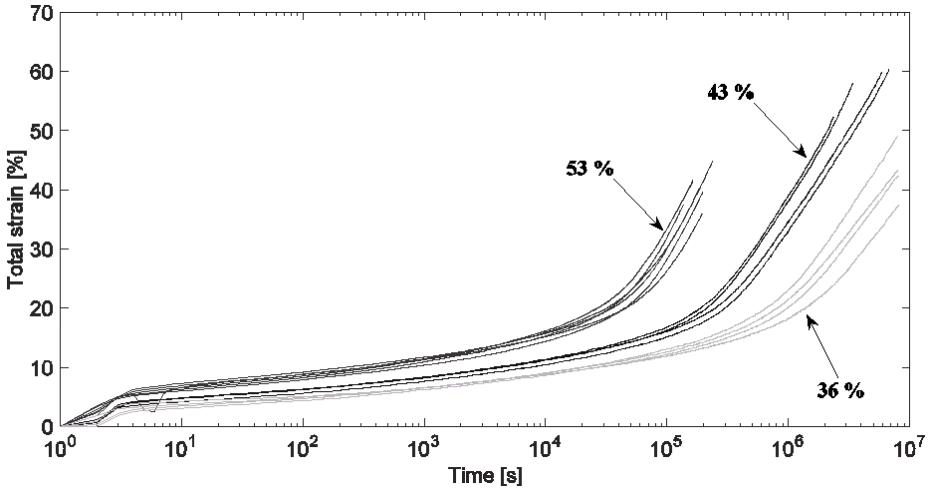

Figure 3: fiber creep deformations

Pull-out test

The maximum force F_{max} measured during the test is presented for different embedded lengths in Table 4. The force-displacement curves are shown in Figure 4. Note that two curves for each embedded length are presented, representing the pull-out specimen with the highest and lowest measured F_{max} for that specific length. The fiber strength is shown as a reference value.

Table 4: experimental results for pull-out tests

embedded length [mm]	average F_{max} [N]	standard deviation of F_{max} [N]	number of specimens [-]
30	227	31	6
25	203	17	6
20	186	23	9
15	178	19	7
10	114	23	6

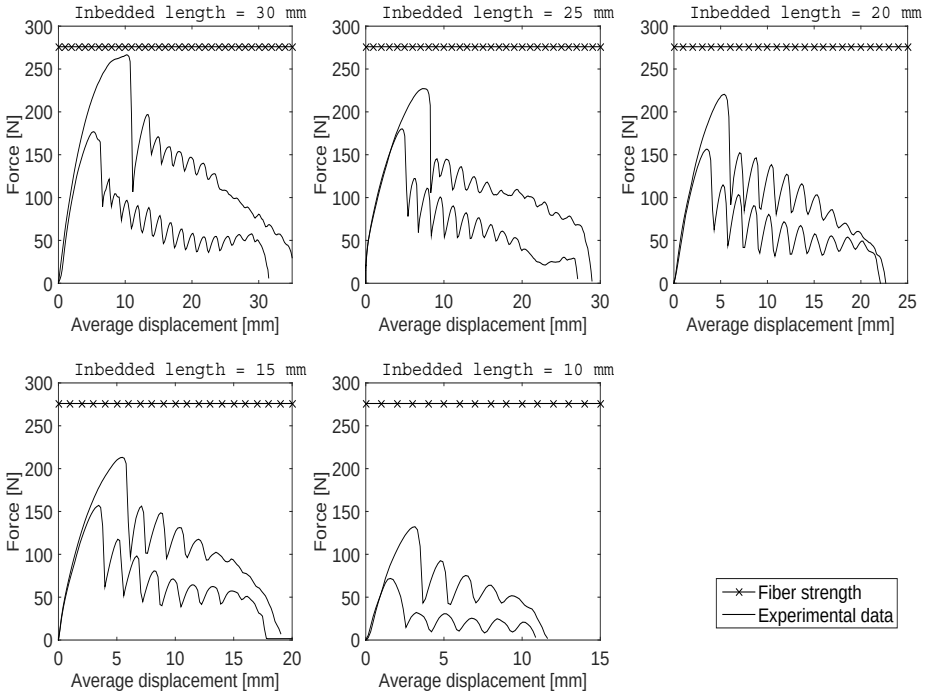

Figure 4: pull-out curves

DISCUSSION

Fiber creep

The creep compliance is defined as the ratio between the creep deformations and the applied stress. For the creep experiments considered, the average experimental creep compliance is shown in Figure 5. In an ideal viscoelastic material, the creep compliance is a material property, i.e. a function of time but not of the applied stress. Any deviation from this ideal behavior can be thought of as the onset of non-linear behavior, i.e. plastic deformations. The ideal behavior is indicated with a dashed line on Figure 5. It is clear that every specimen undergoes non-linear behavior after creeping for some time. The time to the onset of this non-linear behavior is called t_{plast}. t_{plast} can be related to the load ratio and the results lie on a power fitted curve, defined by:

$$t_{plast} = \left(\frac{127}{load\ ratio}\right)^{10.6}$$

with the load ratio expressed as a percentage. This power law intuitively holds asymptotically as well, with infinite times under zero load, and very short times near the failure load. The experimental results and the fitted line are shown in Figure 6.

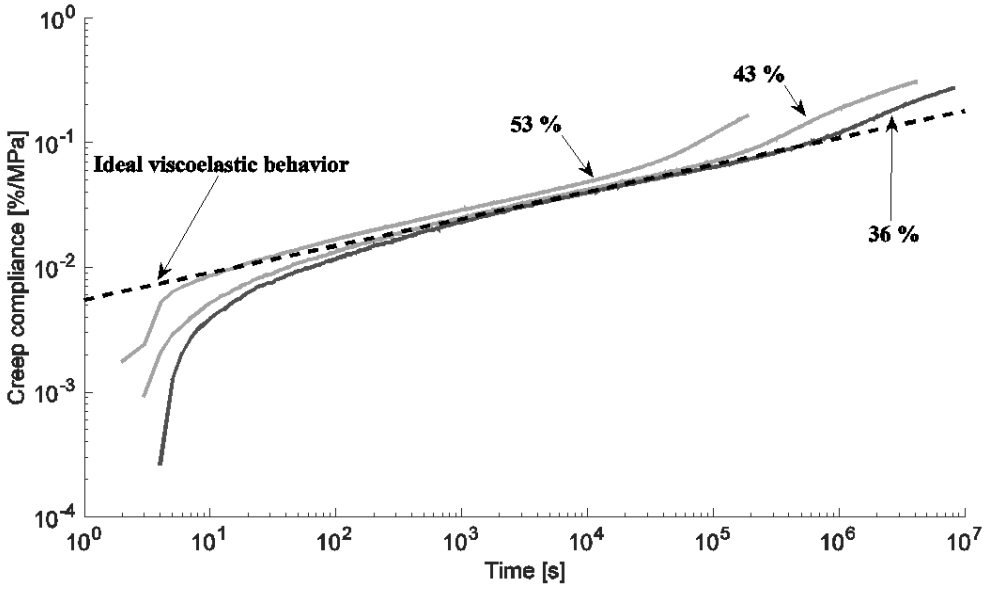

Figure 5: average creep compliance

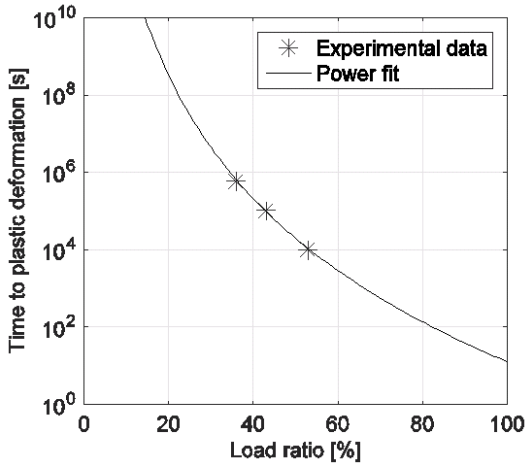

Figure 6: time to non-linear behavior fit

Pull-out test

The maximum measured pull-out force F_{max} does not vary linearly with the embedded length, as is shown in Figure 7. This might suggest that F_{max} is not only influenced by the elastic shear strength of the matrix. However, given the high coefficient of variation on these results, more tests are needed to confirm this. For all experiments, the force needed to initiate fiber pull-out is smaller than the fiber strength, and fiber pull-out is the dominant failure mechanism for the range of embedded lengths considered.

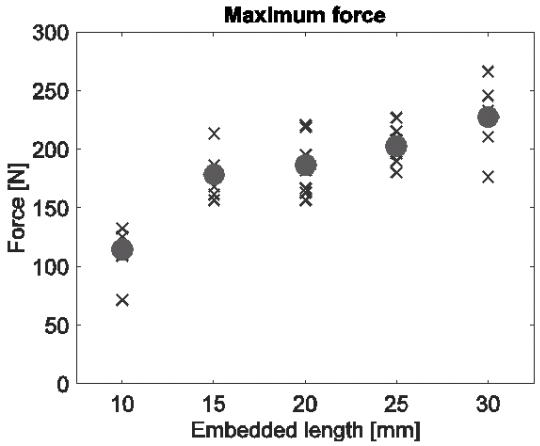

Figure 7: F_{max} at different embedded lengths
● indicates average value, × indicates individual results

Furthermore, all specimens exhibited an oscillating pattern after F_{max} was reached. This pattern has also been observed for nylon fiber pull-out tests from a cement matrix (Li et al., 1990), where it is suggested that the oscillating pattern is related to the fiber's surface profile with the wavelength of the oscillations being equal to the length between surface embossments. This observation seems to hold for this fiber as well, since the number of oscillations for an embedded length of 30 mm, 20 mm and 10 mm is around 15, 10 and 5, respectively.

CONCLUSION

Creep in FRC is not well understood, even though creep contributes to crack widening in FRC elements. This paper presents the results of an experimental campaign into two mechanisms that can cause crack widening: fiber creep and fiber pull-out. Fiber creep deformations are strongly dependent on the applied stress as lower loads increase the time to failure as well as the strain at failure. It is found that the fiber undergoes plastic deformations during the creep test. A power law is proposed to relate the onset of non-linear behavior to the load ratio. Fiber pull-out tests have shown that the maximum force depends, amongst other mechanisms, on the embedded length of the fiber. The observed oscillating pattern during pull-out can be related to the surface profile of the fiber, as the number of oscillations corresponds to the embedded length of the fiber.

REFERENCES

ACI Committee 544. (2002). State-of-the-Art Report on Fiber Reinforced Concrete. In J. I. Daniel (Ed.): American Concrete Institute.

Balaguru, P., & Shah, Surendra P. (1992). *Fiber-Reinforced Cement Composites*. Texas, USA: Mcgraw-Hill.

Barros, Joaquim, Cunha, V. M. C. F., Ribeiro, A. F., & Antunes, J. A. B. (2005). Post-cracking behaviour of steel fibre reinforced concrete. *Materials and Structures, 38*(1), 47-56. doi: 10.1007/BF02480574

Bentur, Arnon, & Mindess, Sidney. (1990). *Fibre Reinforced Cementitious Composites*. England: Elsevier Science Publishers LTD.

Buratti, Nicola, Mazzotti, Claudio, & Savoia, Marco. (2011). Post-cracking behaviour of steel and macro-synthetic fibre-reinforced concretes. *Construction and Building Materials, 25*(5), 2713-2722. doi: http://dx.doi.org/10.1016/j.conbuildmat.2010.12.022

CEN. (2006). EN 14889-2: Fibres for concrete - Part 2: Polymer fibres - Definitions, specifications and conformity: European Committee for Standardization.

di Prisco, Marco, Ferrara, Liberato, & Lamperti, Marco G. L. (2013). Double edge wedge splitting (DEWS): an indirect tension test to identify post-cracking behaviour of fibre reinforced cementitious composites. *Materials and Structures, 46*(11), 1893-1918. doi: 10.1617/s11527-013-0028-2

di Prisco, Marco, Plizzari, Giovanni, & Vandewalle, Lucie. (2009). Fibre reinforced concrete: new design perspectives. *Materials and Structures, 42*(9), 1261-1281. doi: 10.1617/s11527-009-9529-4

Drozdov, A. D., & Christiansen, J. deC. (2009). Creep failure of polypropylene: experiments and constitutive modeling. *International Journal of Fracture, 159*(1), 63-79. doi: 10.1007/s10704-009-9384-x

fédération internationale du béton (fib). (2010). Model Code 2010 First complete draft.

Fibre-Reinforced Concrete. Bagneux, France: RILEM Publications S.A.R.L.

Fibre Reinforced Concrete: design and applications. Bagneux, France: Rilem Publication S.A.R.L.

Grzybowski, Miroslaw, & Shah, Surendra P. (1990). Shrinkage Cracking of Fiber Reinforced Concrete. *ACI Materials Journal, 87*(2), 138-148.

Kurtz, S., & Balaguru, P. (2000). Postcrack creep of polymeric fiber-reinforced concrete in flexure. *Cement and Concrete Research, 30*(2), 183-190. doi: http://dx.doi.org/10.1016/S0008-8846(99)00228-8

Li, Victor C., Wang, Youjiang, & Backer, Stanley. (1990). Effect of inclining angle, bundling and surface treatment on synthetic fibre pull-out from a cement matrix. *Composites, 21*(2), 132-140. doi: Doi 10.1016/0010-4361(90)90005-H

MacKay, J., & Trottier, J. F. (2004). Post-crack creep behavior of steel and synthetic FRC under flexural loading *Shotcrete: More Engineering Developments* (pp. 183-192): Taylor & Francis.

Pasini, F., Garcia, T., Gettu, Ravindra, & Agullo, L. (2004). *Experimental study of the properties of flowable fiber reinforced concretes*. Paper presented at the 6th International RILEM Symposium on Fibre Reinforced Concretes.

Sabuncuoglu, Baris, Acar, M., & Silberschmidt, Vadim V. (2011). Analysis of Creep Behavior of Polypropylene Fibers. *Applied Mechanics and Materials, 70*(8), 410-415. doi: DOI 10.4028/www.scientific.net/.410

Zhao, Guanyu, Verstrynge, Els, di Prisco, Marco, & Vandewalle, Lucie. (2012). *Investigation on Single Fiber Pullout and Interfacial Debonding Mechanisms with Acoustic Emission Techniques*. Paper presented at the 8th RILEM International Symposium on Fibre Reinforced Concrete (BEFIB 2012), Guimarães, Portugal.

Early-Age Shrinkage of Ordinary Concrete and a Strain-Hardening Cement-Based Composite (SHCC) in the Conditions of Hot Weather Casting

Igor Serpukhov and Viktor Mechtcherine

TU Dresden, Institute of Construction Materials, 01062 Dresden, Germany.
E-mail: mechtcherine@tu-dresden.de

Abstract

The early-age shrinkage of concrete has a pronounced influence on the performance of the material during the whole service life. The casting of concrete in hot climatic conditions, which are harsh for early-age concrete, often lead to cracking which subsequently has an negative impact on various properties of the structural element, especially on its durability. The article at hand provides some additional insights on plastic and early-age shrinkage of two very different types of concrete: an ordinary concrete and a relatively new type of fiber-reinforced concrete – a strain-hardening cement-based composite (SHCC). These materials were produced and tested both without and with addition of a superabsorbent polymer (SAP), which was used as an internal curing agent for mitigating early-age shrinkage. Three climatic parameters were varied in a certain range: temperature of the surrounding air, its relative humidity and the wind velocity. The addition of SAP clearly reduces the capillary pressure within fresh concrete, which indicates the efficiency of its action as internal curing agent. The SHCC is able to successfully withstand the early-age shrinkage in the hot climatic conditions under investigation. In contrary, in the most cases a major crack developed in the ordinary through the entire height of the specimen and separated it in two parts.

INTRODUCTION

Early-age shrinkage of concrete may cause cracking which jeopardize the long time performance of structural elements in terms of durability and serviceability [1]. The danger of cracking is particularly high when concreting occurs in conditions of hot climate [2], since this causes pronounced plastic shrinkage due to the evaporation of water from fresh concrete [3, 4]. The plastic shrinkage increases with increasing content of fines and decreasing water content in concrete. External curing by spraying water and addition of fine polymeric fiber [5] have been proved to be efficient measures to mitigate the formation of cracks.

The article at hand focuses on plastic and early-age shrinkage of two very different types of concrete: an ordinary concrete and a relatively new type of fiber-reinforced concrete – a strain-hardening cement-based composite (SHCC). A special feature of SHCC is its containing only very fine sand as aggregate to ensure uniform distribution of the polymer fibers in the matrix; this helps achieve high ductility in the hardened material. The pronounced ductility and high strain capacity of SHCC give the material a remarkable potential for its use in various applications in which high non-elastic deformability is needed [6]. With respect to plastic shrinkage, on one hand an unfavorable behavior could be expected due to its very high content of fines. On the other hand, SHCC contains a high content of fine polymeric fibers, which might mitigate early-age cracking. Furthermore, the effect of the addition of

superabsorbent polymers (SAP) is included in the experimental program. This new additive proved to have multiple positive effects on properties of concrete [7]. Here, SAP is applied as an internal curing agent similarly as it has been successfully done for mitigating autogenous shrinkage of concretes with low w/c [7, 8].

The paper at hand presents the results of an investigation of plastic shrinkage of ordinary concrete and SHCC, both without and with addition of SAP and some extra water, in different climatic conditions.

MATERIALS AND EXPERIMENTAL METHODS

Materials

Table 1 gives the compositions of the ordinary concrete and SHCC under investigation. The ordinary concrete has a more or less typical composition of a multi-purpose concrete of the strength class C35. The composition of the SHCC was taken over from [9]. To produce the mixtures with SAP, this agent was added on top of the given mixture together water for internal curing. Subsequently, the real portions of solids as shown in Table 1 are slightly lower in the mixtures with SAP. In the case of the ordinary concrete 0.7 kg SAP and 17.5 kg of extra water per m³ of concrete were added for internal curing. In the case of the SHCC, these ingredients were 1.5 kg and 38 kg, respectively. The amount of extra water was chosen in the way, that the consistency of mixtures containing SAP were the same as without SAP.

Table 1. Compositions of concretes under investigation.

Component	OC [kg/m³]
CEM I 42.5 R-SR (Schwenk)	350
Quartz sand 0.06/0.2	56
Quartz sand 0/2	753
Quartz sand/gravel 2/4	169
Quartz sand/gravel 4/8	357
Quartz gravel 8/16	546
Superplasticizer Glenium ACE 30	2
Water	175

Component	SHCC [kg/m³]
CEM I 42.5 R-SR Schwenk	505
Fly ash H4	621
Quartz sand 0.06/0.2	536
PVA fibers Kuralon 15/ length 12 mm	26
Superplasticizer Glenium ACE 30	8
Stabilizer BASF	5
Water	338

The mixing was performed in the mixer ELBA, Germany. The spread of the standard cone of fresh ordinary concrete at the shocking table was 420±10 mm and the spread of the small cone of SHCC at Hägermann's shocking table was 160±20 mm; in none of the cases the materials showed any bleeding.

Measuring equipment

The measuring set-up with the forms for concrete was installed within a climatic chamber. It consisted of four boxes with internal dimensions of 300 mm x 300 mm x 100 mm and one dual restrained box, built according to ASTM C1579-13, with the internal dimensions of each section 500 mm x 120 mm x 75 mm. Fig. 1 shows the arrangement of the boxes and positions of sensors. Only selected results will be presented and discussed in this article. Another publication is in preparation.

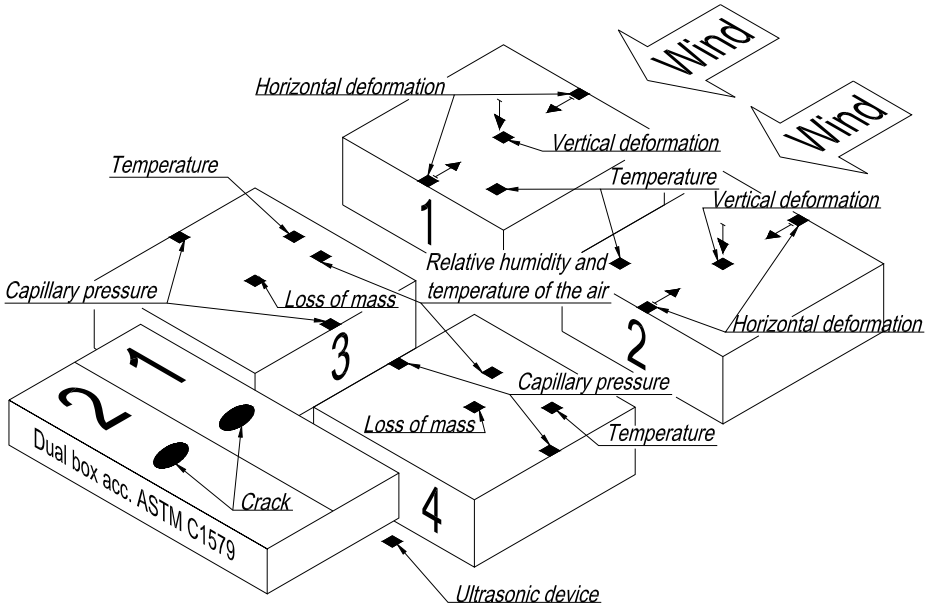

Figure 1. Schematic view of the arrangement of the measuring equipment.

The pair of boxes 1 and 2 (Fig. 2a) served for measuring the horizontal and vertical deformations as well as temperature of concrete. Boxes 3 and 4 (Fig. 2b) were equipped with tools for measuring capillary pressure, mass loss due water evaporation and temperature in concrete as well as relative humidity and temperature directly above concrete surface. The boxes were filled with concrete completely up to the brim, since it was found out in the preliminary tests that otherwise the relative humidity of the air above the concrete surface is considerably higher than that of the ambient air.

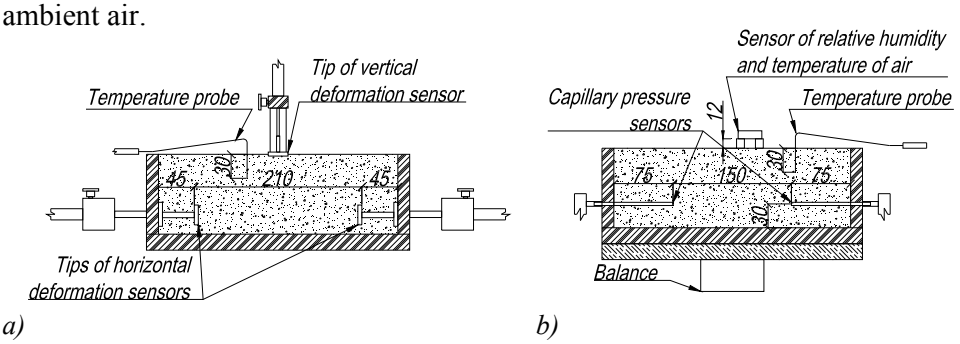

Figure 2. Schemamic view of the arrangement of the measuring equpment in: *a)* boxes 1 and 2, *b)* boxes 3 and 4.

The investigation also included the measurement of sonic speed through the concrete during the experiment for the detection of the moments of the beginning and the end of setting, as well as examination of the crack with the use of a dual restrained box with risers according to ASTM C1579-13, see Fig. 3. To achieve a better restraining effect, the box was modified with additional anchorages at its butt-

photographed on the surface, they were mostly well visible. In contrast, the specimens made of SHCC did not show any visible cracks at the surface and could be demolded without falling apart. They were processed for an examination under a light microscope.

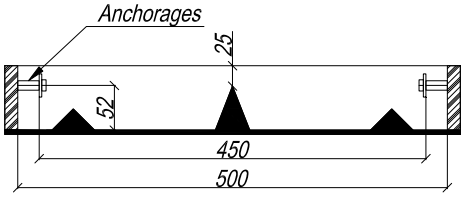

Figure 3. Restrained box acc. to ASTM C1579-13 modified with anchorages.

Climatic conditions

The variation of climatic conditions was based on three climatic parameters: temperature and relative humidity of the ambient air and wind speed. The investigation included the values of temperature 30 °C and 40 °C, relative humidity 40% and 60% and wind speed 5 m/s and 10 m/s in all possible combinations of them, i.e. the experimental program consisted of 8 individual cases of weather conditions. The machinery of climatic chamber kept the required climatic conditions automatically after the input of the parameters. Each experiment lasted for 18 to 22 hours, which was enough to record all the noteworthy processes related to plastic shrinkage and its transition into drying shrinkage.

RESULTS AND DISCUSSION

First, the case of ordinary concrete without addition of SAP will be presented for the climatic conditions with the air temperature of 40 °C, relative humidity of 40% and wind speed of 5 m/s. Fig. 4 shows the curves for the development of horizontal strain and capillary pressure over time. The negative values of capillary pressure indicate underpressure. During approximately the first three hours, the rise of the capillary pressure coincides with the increase in the horizontal strain, i.e., it can be assumed that the plastic shrinkage directly depends on the development of the capillary pressure at this period of time.

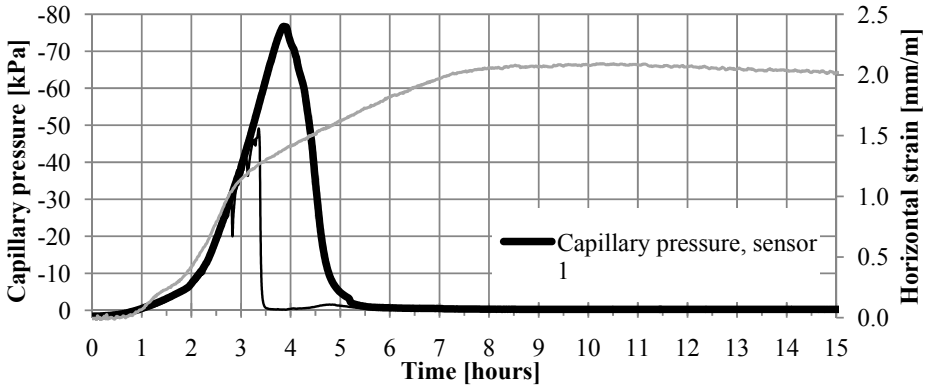

Figure 4. Development of capillary pressure and horizontal strain in ordinary concrete without SAP (temp. 40 °C, RH 40%, wind speed 5 m/s).

Three hours after the beginning of measurements the rate of shrinkage deformations significantly slows down and then remains constant even after the capillary (under)pressure breakdown. Thus, it can be supposed, that starting at the time of approximately three hours after the beginning of measurements the capillary pressure build up does not influence the development of the horizontal strain any longer, but rather some other factor starts to play a decisive role. Indeed, in Fig. 5a sharp increase of the sonic speed at the time point of three hours after the test start can be observed, which results from the beginning of setting of concrete. Based on that, it can be assumed, that the process of setting itself is the cause of shrinkage deformations at this stage.

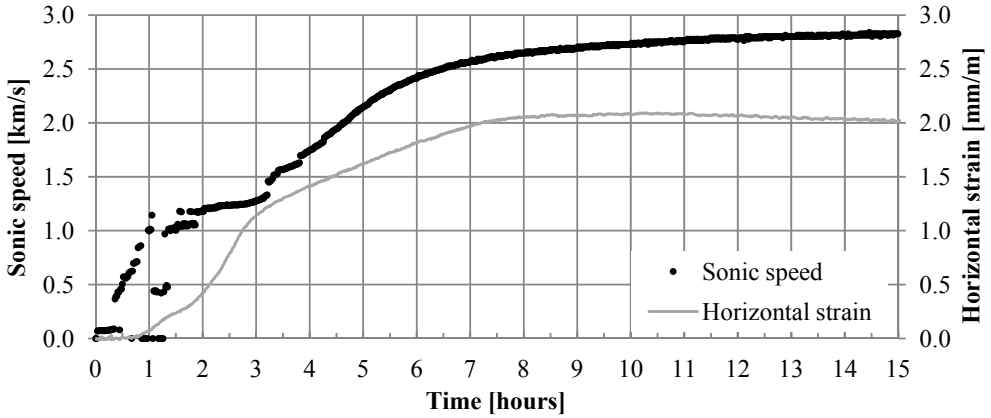

Figure 5. Development of sonic speed and horizontal strain in ordinary concrete without SAP (temperature 40 °C, RH 40%, wind speed 5 m/s).

The measurement of the concrete temperature supports the assumption concerning the beginning of setting, see Fig. 6. After the initial decrease, which is caused by the evaporation of water from concrete surface, the temperature starts to rise approximately three hours after the beginning of measurements. This increase in temperature can be traced back to the heat release due to hydration of cement.

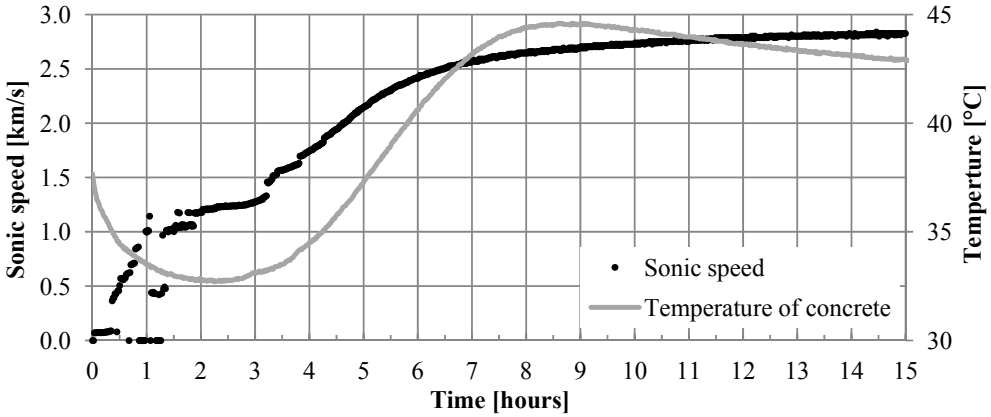

Figure 6. Development of sonic speed and temperature in ordinary concrete without SAP (temperature 40 °C, RH 40%, wind speed 5 m/s).

Fig. 7 shows the development of horizontal strain for all concrete compositions under investigation. SHCC exhibits clearly higher values than the ordinary concrete; this is due to the lack of coarse aggregates in SHCC. The addition of SAP results in lower horizontal strain values for both materials.

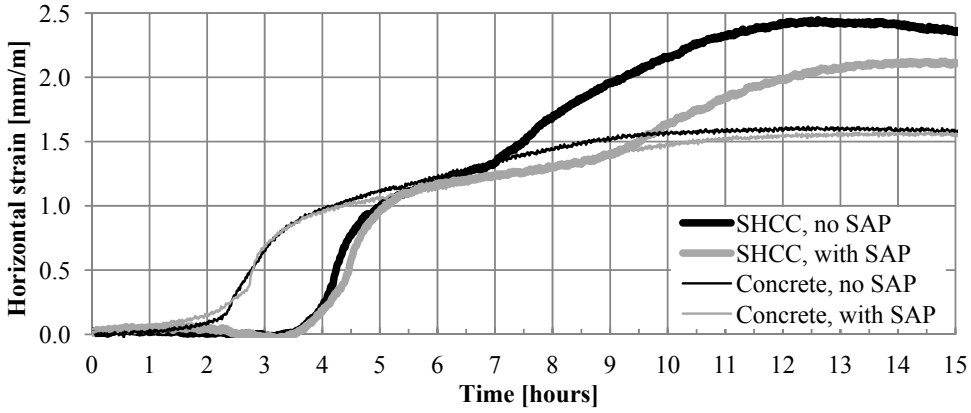

Figure 7. Development of horizontal strain in ordinary concrete and SHCC; Temperature 30 °C, relative humidity 40%, wind speed 5 m/s.

Summarizing the obtained results, it can be stated that relative humidity had the most pronounced influence on final values of horizontal shrinkage among the climatic parameters under investigation. The variation of temperature affected shrinkage to a lesser extent, while the variation of wind speed of wind exhibited the lowest impact on strain values. Fig. 8 presents the development of horizontal strains for the ordinary concrete with and without addition of SAP measured at various relative humidity (RH) but the constant temperature of 40 °C and wind speed of 10 m/s. The horizontal strain measured at RH of 40% was more than 0.5 mm/m higher than that observed at RH of 60%. The addition of SAP diminished the strains at the initial stage, approximately until the end of setting; at the later stage, the effect of SAP was less pronounced.

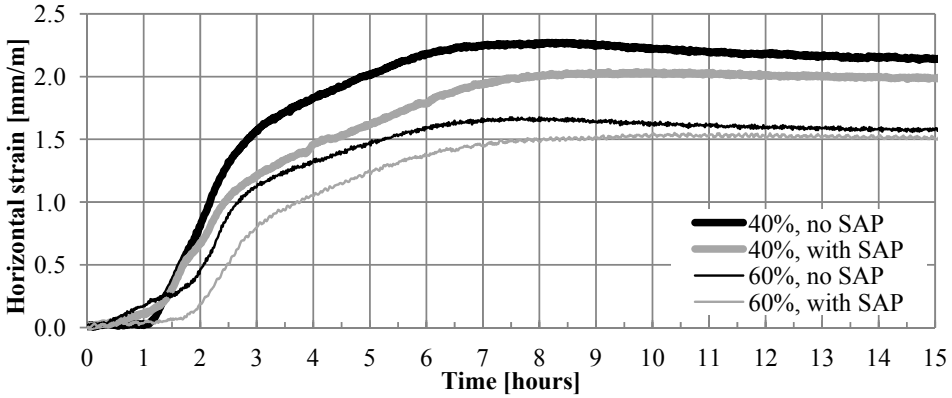

Figure 8. Development of horizontal strain in ordinary concrete at various relative humidity conditions (temperature 40 °C, wind speed 10 m/s).

Since the main cause of plastic shrinkage is the capillary pressure build up, it is important to know how the variation in climatic conditions and the addition of SAP affect this parameter. Fig. 9 shows the build-up of capillary pressure in ordinary concrete without SAP at various relative humidity conditions; the temperature was 40 °C and the wind speed was 10 m/s. Obviously, the variation of relative humidity resulted in change of the moment of the beginning of the capillary pressure build up: In harsher conditions the pressure starts to rise considerably earlier. Also the variation of the temperature and wind speed caused changes in the beginning of the capillary pressure build up.

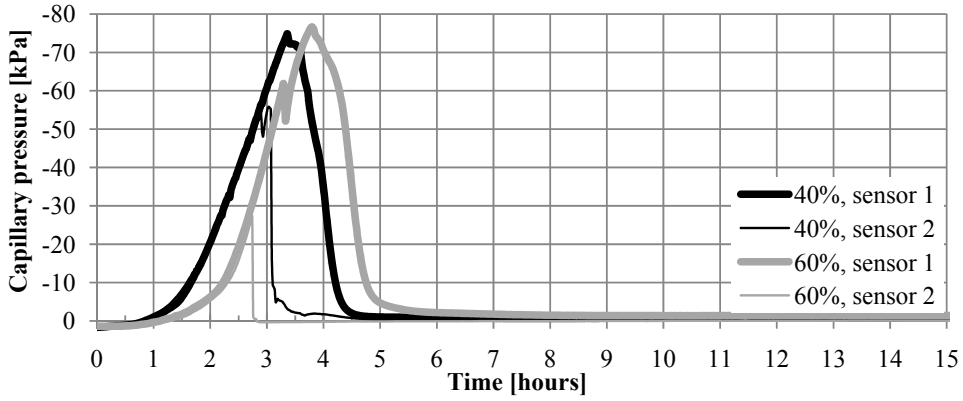

Figure 9. Development of capillary pressure in ordinary concrete without SAP at various relative humidity conditions (temperature 40 °C, wind speed 10 m/s).

The addition of SAP, however, slowed down the rate of the capillary pressure build-up. As an example, Fig. 10 shows the development of the capillary pressure in ordinary concrete with and without SAP at the temperature of 40 °C, relative humidity of 40% and the wind speed of 10 m/s. This phenomenon can be probably traced back the water release by SAP particles into surrounding matrix, thus causing some decrease in capillary pressure.

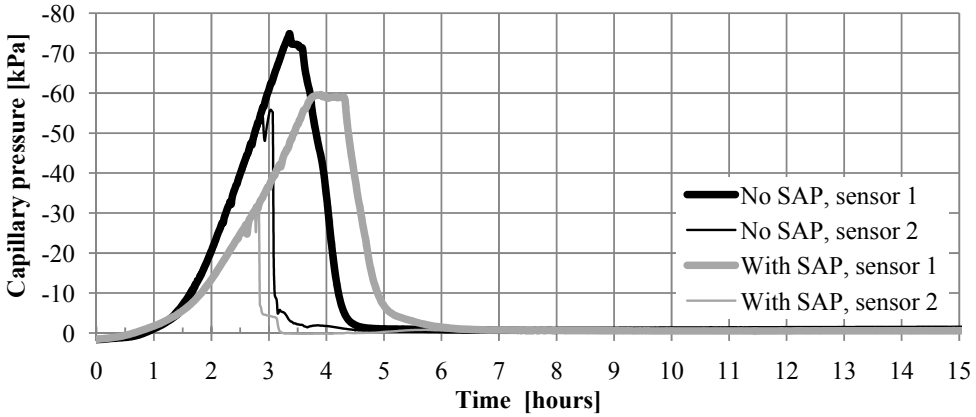

Figure 10. Development of capillary pressure in ordinary concrete with and without SAP (temperature 40 °C, RH 40%, wind speed 10 m/s).

Generally, the capillary pressure build-up in SHCC followed the same pattern as the corresponding process in ordinary concrete; however, there was a considerable difference in its development in SHCC with SAP. Fig. 11 presents the development of the capillary pressure in this material at the temperature of 30 °C, relative humidity of 40% and wind speed of 10 m/s. In the case of SHCC without SAP the increase of capillary pressure was faster, followed by an abrupt fall. For SHCC with SAP, however, a much slower increase in the capillary pressure was observed. In this case, very high pressure values were attained, but there was no abrupt breakthrough after reaching the maximum, but rather a gradual decrease in the capillary pressure. This effect was found to be more pronounced in the cases of lower temperature (here 30 °C); it probably can be explained by action of fibers in SHCC, which mitigated the development of cracks at the surface, thus hindering the air to enter into concrete and to cause an abrupt decrease in capillary pressure.

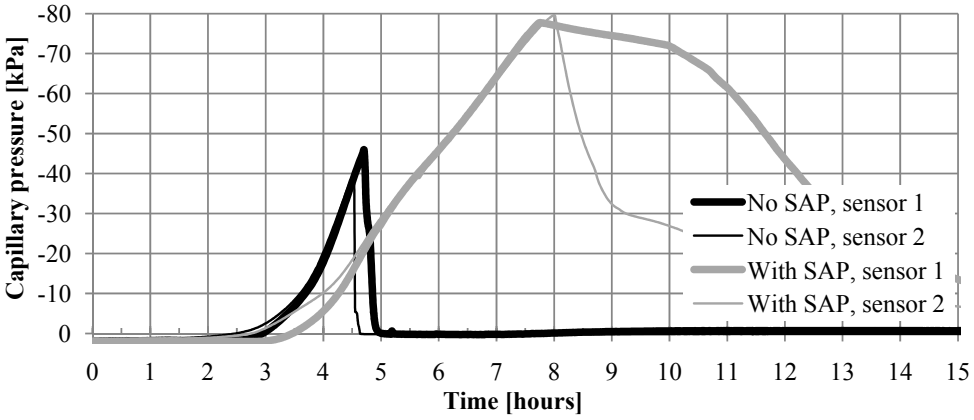

Figure 11. Development of capillary pressure in SHCC with and without SAP (temperature 30 °C, relative humidity 40% and wind speed 10 m/s).

The cracks in ordinary concrete as observed in the restrained box at the temperature of 30 °C, wind speed of 5 m/s are shown in Fig. 12 for varying relative humidity conditions. The cracks in concrete subject to more severe climatic conditions were wider, whereas the addition of SAP significantly diminished the crack width. Moreover, in the case of testing at the temperature of 30 °C, relative humidity of 60% and wind speed of 5 m/s, the specimen of ordinary concrete with SAP showed no obvious cracks at the surface and could keep its shape after taking out of the restrained box. The microscopic examination of the specimen cross-section showed that although the crack did not appear at the surface, it was present inside the concrete block. However, since the crack width was clearly below 0.1 mm, the concrete block did not fall apart due to the interlocking between the coarse aggregates and cement matrix.

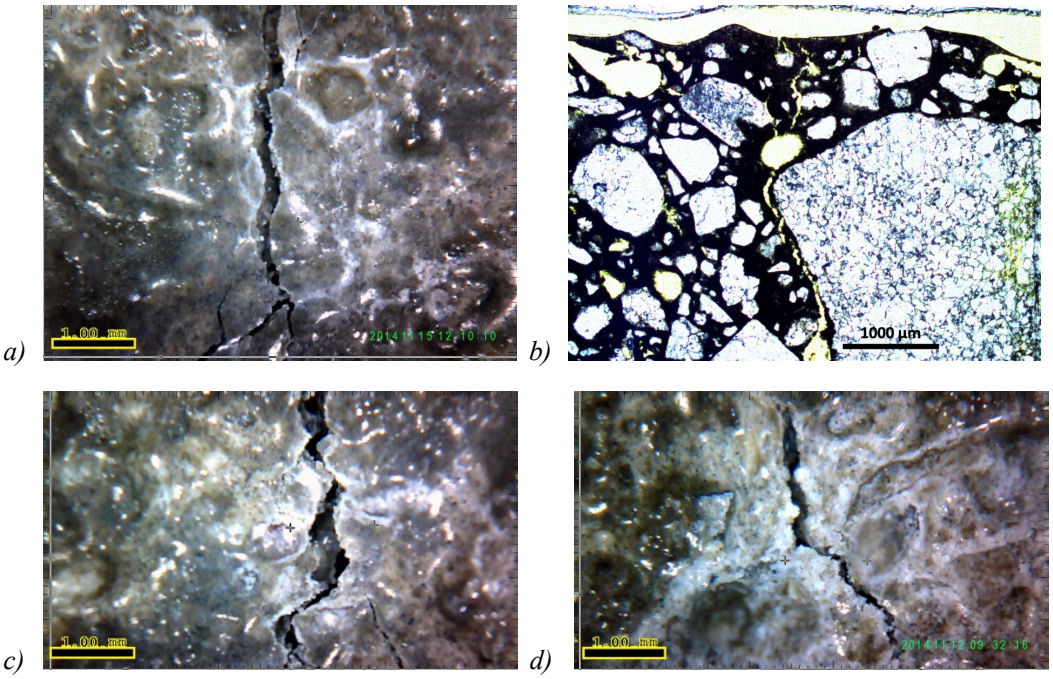

Figure 12. Surface cracks in ordinary concrete at various relative humidity, a) 60%, b) 60%, SAP, c) 40%, d) 40%, SAP (temperature 30 °C, wind 5 m/s)

In none of the tests performed with SHCC any surface cracks were visible, thus microscopic investigations on cut cross-sections were necessary. Fig. 13 presents the results some examples of the obtained crack images for the specimens tested at the temperature of 30 °C, relative humidity of 40% and wind speed of 10 m/s. In the most cases, especially in those when SHCC contained SAP, even using optical microscope no clear crack pattern could be found within SHCC, but rather some cluster of large pores in the vicinity of the tip of the central riser, which can be considered as "germs" of the future crack (see Fig. 13b, the region is outlined with a white dashed line). The lack of visible cracks can be explained by the action of fibers, which bridge the voids and prevent the development of cracks.

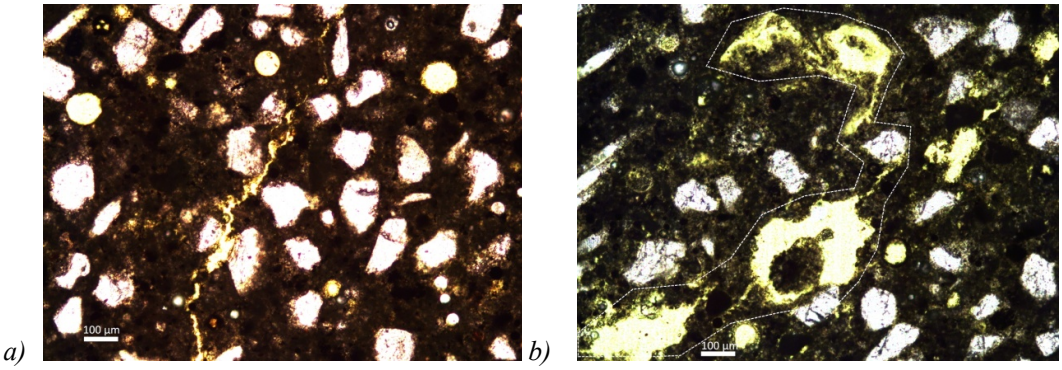

Figure 13. Cracks in the vicinity of the riser tip *a)* SHCC; *b)* SHCC with SAP.

CONCLUSIONS

The finding of the investigation at hand can be summarized as follows:

- Also SHCC exhibits a very pronounced plastic shrinkage, it has a very high resistance to cracking induced by this process.
- The addition of SAP slows down considerably the capillary pressure build-up, which results in decrease in plastic shrinkage and in related cracking of both ordinary concrete and SHCC.
- In the presented study, the magnitude of plastic shrinkage depended on the relative humidity in the first place. The effect of the temperature was less pronounced, whereas the wind speed showed the least impact on plastic shrinkage.

REFERENCES

[1] Holt, E. and Leivo, M. (2004). "Cracking risks associated with early age shrinkage." *Cement & Concrete Composites 26*, pp. 521–530.

[2] Al-Fadhala, M. and Hover, K.C. (2001). "Rapid evaporation from freshly cast concrete and the Gulf environment." *Construction and Building Materials 15*, pp. 1-7.

[3] Cohen, M.D., Olek, J. and Dolch, W.L. (1989). "Mechanism of Plastic Shrinkage Cracking in Portland Cement and Portland Cement-Silica Fume Paste and Mortar." *Cement and Concrete Research 20*, pp. 103-119.

[4] Slowik, V., Schmidt, M. and Fritzsch, R. (2008). "Capillary pressure in fresh cement-based materials and identification of the air entry value." *Cement and Concrete Composites 30*, pp. 557-565.

[5] Sivakumar, A. and Santhanam, M. (2007). "A quantitative study on the plastic shrinkage cracking in high strength hybrid fibre reinforced concrete." *Cement and Concrete Composites 29*, pp. 575–581.

[6] Mechtcherine, V. (2013). "Novel cement-based composites for the strengthening and repair of concrete structures." *Construction and Building Materials 41*, pp. 365–373.

[7] Mechtcherine, V. and Reinhardt, H. W., eds. (2012). "Application of superabsorbent polymers in concrete construction." RILEM State of the Art Reports 2, Springer.

[8] Schröfl, Ch., Mechtcherine, V. and Gorges, M. (2012). "Relation between the molecular structure and the efficiency of superabsorbent polymers (SAP) as concrete admixture to mitigate autogenous shrinkage." *Cement and Concrete Research 42,* pp. 865–873.

[9] Mechtcherine, V., Millon, O., Butler, M. and Thoma, K. (2011). "Mechanical behaviour of strain hardening cement-based composites under impact loading". *Cement and Concrete Composites 33*, pp. 1–11.

Early Age Drying Shrinkage Evaluation of Self-Compacting Concretes and Pastes with Mineral Additions

Gonzalo Barluenga[1]; Javier Puentes[1]; Irene Palomar[1]; and Olga Rio[2]

[1]Department of Architecture, University of Alcala, Calle Santa Ursula 8, Alcala de Henares. 28801-Madrid, Spain. E-mail: gonzalo.barluenga@uah.es (G. Barluenga); xmojica@hotmail.com (J. Puentes); Irene.palomar@uah.es (I. Palomar)
[2]Eduardo Torroja Institute of Construction Sciences, CSIC, Calle Serrano Galvache, 4, 28033-Madrid, Spain. E-mail: rio@ietcc.csic.es

Abstract

Early age (EA) drying shrinkage of cement based materials is a complex process because it comprises reaction evolution, microstructure development, stiffening and water evaporation due to environmental conditions. The occurrence of EA shrinkage can increase early age cracking risk which can compromise durability. Due to the larger amount of paste, moderate strength powder-type self-compacting concrete (SCC) is more prone to EA drying shrinkage than conventional concrete. To evaluate the effect of limestone filler, microsilica (MS), nanosilica (NS) and metakaolin (MK) on EA free drying shrinkage of cement pastes and SCC, an experimental program was carried out. Free shrinkage and mass loss were monitored on paste and SCC samples during 24 hours, subjected to surface desiccation to evaporate all the bled water during 6 hours, while temperature and Relative Humidity remained constant. It was observed that evaporation and free shrinkage were not related directly, although a physical relationship could be identified. Evaporation during EA shrinkage of pastes and SCC compositions showed similar values, while drying shrinkage depended on the presence of the aggregates. The effect of the paste components' amount and type, the volumetric fraction of aggregates and the evaporation were assessed and some equations were proposed to estimate EA drying shrinkage of moderate strength powder-type self-compacting pastes and concretes.

INTRODUCTION

Water evaporation from cement-based materials during Early age (EA) depends on the environmental conditions and the water availability on the exposed surface of the specimen (Uno, 1998). Water evaporation during setting can produce EA drying shrinkage, due to the lack of water and the subsequent intrusion of air inside the incipient pore network (Hammer, 2006). EA drying shrinkage is a consequence of the cement hydration, the microstructure development, the material stiffening and the environmental conditions (Barluenga, 2013). The period of time when the mechanical capacity develops, related to setting and initial hardening,

regarding the beginning of shrinkage can increase early age cracking risk which can compromise durability (Holt, 2003). However, the relation among evaporation, shrinkage and cracking at EA is not linear (Barluenga, 2007).

Although the main mechanisms involved in EA shrinkage of conventional cement based materials have been described (Hammer, 2006), the new self-compacting mixes, with larger amount of paste, show a different early age behavior (Bonen, 2005), as the paste phase is the primary responsible of shrinkage (Pickett, 1956). The EA behavior of Self-compacting concrete (SCC) depends on the different composition, characterized by the use of a high range water reducing admixture (HRWRA) (Leemann, 2014) and a large amount of mineral additions (Darquennes, 2011). The SCC composition is also responsible of its remarkable sensitiveness to environmental conditions (Turcry, 2006).

Among SCC, moderate strength powder-type with large amounts of filler combined with small amounts of active mineral additions (AMA) is an innovative approach which still needs to be studied (Barluenga, 2015). To evaluate the effect of different amounts of limestone filler combined with microsilica (MS), nanosilica (NS) and metakaolin (MK) on EA free drying shrinkage of cement pastes and SCC, an experimental program was carried out. Paste and SCC samples were subjected to forced evaporation, applying an airflow during the first 6 hours. Those compositions have shown no EA shrinkage when evaporation was inhibited by covering the samples with a plastic film (Barluenga, 2013). The aim was to identify the influence of the type and amount of addition, the amount of aggregate and the evaporation rate in order to adjust some equations to estimate EA drying shrinkage.

MATERIALS AND METHODS

SCC and pastes compositions. Table 1 summarizes the eleven concrete compositions considered in the study. A self compacting reference mixture (HREFG) with a cement type CEM I 42,5 R, designated according to UNE-EN 197-1:2000 and supplied by Cementos Portland Valderrivas, a high range water reducing admixture (HRWRA), Glenium® ACE 425 manufactured by BASF and a water to cement ratio in weight (w/c) of 0.36 was manufactured. Next, 25, 37.5 and 50 % of the cement was replaced by limestone filler (LF), Betocarb® P1-DA, supplied by Omya Clariana SL, producing a powder-type SCC (HCA). Afterwards, three AMA were included to the mixture, substituting part of the filler (2.5, 5 and 10 %): densified microsilica (MS), Meyco MS 610, and amorphous nanosilica suspension (NS), Meyco MS 685, both supplied by BASF Construction Chemicals España S.L., and metakaolin (MC), Optipozz®, manufactured by Burgess Pigment Company and supplied by Omya Clariana S.L. The water to fines ratio (w/f) remained 0.36 and the total volume of paste was constant. The spread diameter measured using the J-ring slump test was over 650 mm for all the mixtures. Table 2 records the paste compositions which corresponded to the concrete compositions without aggregates. To facilitate the comparison and therefore identify the effect of each component, only one component changed in each composition regarding to the previous.

Table 1. SCC compositions (kg/m^3).

	HREFG	HCA5	HCA75	HCA10	HCAMS25	HCAMS5	HCAMS10	HCANS25	HCANS5	HCAMC25	HCAMC5
Cement	700	466.5	400	350	350	350	350	350	350	350	350
Gravel (4-20)	790	790	790	790	790	790	790	790	790	790	790
Sand (0-4)	691	691	691	691	691	691	691	691	691	691	691
Filler	-	233.5	300	350	341.3	332.5	315	341.3	332.5	341.3	332.5
Micro-silica	-	-	-	-	8.75	17.5	35	-	-	-	-
Nano-silica	-	-	-	-	-	-	-	39.77	79.45	-	-
Metakaolin	-	-	-	-	-	-	-	-	-	8.75	17.5
Water (*)	199	202.5	203.5	204	204	204	204	173	142	204	204
HRWRA	10.5	7	6	5.25	5.25	5.25	5.25	5.25	5.25	5.25	5.25
W/c (**)	0.36			0.71	0.71	0.71	0.71	0.71	0.71	0.71	0.71
W/fines (**)	0.36	0.36	0.36	0.36	0.36	0.36	0.36	0.36	0.36	0.36	0.36

(*) Liquid water added.
(**)The amount of water included in the components (sand humidity 6.25 %, HRWRA and nano-silica) was also considered.

Table 2. Compositions of the fluid cement pastes (components in g)

	REF G	CA5	CA75	CA10	CAMS25	CAMS5	CAMS10	CANS25	CANS50	CAMC25	CAMC50
Cement	1700	1132	971	850	850	850	850	850	850	850	850
Filler	-	568	729	850	828.8	807.5	765	828.8	807.5	828.8	807.5
Micro-silica	-	-	-	-	21.25	42.5	85	-	-	-	-
Nano-silica	-	-	-	-	-	-	-	96.5	193	-	-
Metakaolin	-	-	-	-	-	-	-	-	-	21.25	42.5
Water (*)	581	590	592	594	594	594	594	518.6	443	594	594
HRWRA	25.5	17	14.60	12.75	12.75	12.75	12.75	12.75	12.75	12.75	12.75
w/c (**)	0.36	0.54	0.62	0.71	0.71	0.71	0.71	0.71	0.71	0.71	0.71
w/fines (**)	0.36	0.36	0.36	0.36	0.36	0.36	0.36	0.36	0.36	0.36	0.36

(*) Liquid water added.
(**)The amount of water included in the components (HRWRA and Nano-silica) was also considered.

Experimental methods. A free shrinkage apparatus with internal dimensions of 500 x 100 x 50 mm, subjected to an air flow of 3 m/s during 6 hours was used to simultaneously monitor Early Age (EA) free drying shrinkage and evaporation (Barluenga, 2015). The evaporation rate was calculated, measuring the mass loss of the samples by placing the shrinkage apparatus on a continuous recording scale.

EXPERIMENTAL RESULTS

Table 3 records the experimental results of EA drying shrinkage (in mm/m), the total time of EA shrinkage extent (in hours) and the evaporation rate (Kg/m^2 h) of

paste and SCC samples subjected to a 3 m/s airflow during the first 6 hours. EA shrinkage of pastes ranged from 2 to 5 mm/m, while SCC samples ranged between 0.5 and 2 mm/m. The largest shrinkage where recorded for samples with larger values of AMA. The extent of EA shrinkage ranged from1.5 to 3.67 hours and, as a general rule, the values were larger for pastes than for SCC. Evaporation rate values were from 0.35 to 0.6 kg/m^2 h and the values for pastes and SCC samples were very similar.

Table 3. Total Early Age (<6 hours) Shrinkage (*Shr*) (mm/m), Shrinkage time (t_{shr}), Evaporation rate (*Ev*), an volumetric fraction of aggregate (Vagg), cement (Vcem), filler (Vfill), microadditions (VmMA) and nanoadditions (VnMA) of pastes and SCC.

		Shr. (mm/m)	t_{shr} (h)	Ev_{rate} (kg/m^2 h)	*Vagg*	*Vcem*	*Vfill*	*VmMA*	*VnMA*
Pastes	REF G	2.42	2.5	0.35	-	0.47	-	-	-
	CA5	2.14	1.5	0.51	-	0.31	0.160	-	-
	CA75	1.96	2.33	0.57	-	0.27	0.200	-	-
	CA10	1.76	3.17	0.49	-	0.235	0.235	-	-
	CAMS25	2.36	2.83	0.53	-	0.235	0.229	0.006	-
	CAMS5	1.94*	2.66	0.55	-	0.235	0.223	0.012	-
	CAMS10	4.62	3	0.43	-	0.235	0.212	0.024	-
	CANS25	2.66	2.34	0.52	-	0.235	0.229	-	0.006
	CANS5	4.36	3.67	0.43	-	0.235	0.223	-	0.012
	CAMC25	2.38	2.83	0.53	-	0.235	0.229	-	0.006
	CAMC5	4.26	3.17	0.45	-	0.235	0.223	-	0.012
SCC	HREFG	0.58	1.66	0.38	0.525	0.188	-	-	-
	HCA50	0.42	2	0.43	0.525	0.124	0.064	-	-
	HCA75	0.96	2	0.42	0.525	0.108	0.080	-	-
	HCA10	1.38*	2.67	0.54	0.525	0.094	0.094	-	-
	HCAMS25	0.46	1.33	0.34	0.525	0.094	0.092	0.002	-
	HCAMS 5	0.88	1.67	0.44	0.525	0.094	0.089	0.005	-
	HCAMS10	1.6	2.16	0.45	0.525	0.094	0.085	0.009	-
	HCANS25	0.54	1.84	0.48	0.525	0.094	0.092	-	0.002
	H CANS5	1	2.16	0.41	0.525	0.094	0.089	-	0.005
	HCAMC25	0.8	2	0.45	0.525	0.094	0.092	-	0.002
	HCAMC5	1.6	2.66	0.42	0.525	0.094	0.089	-	0.005

* Not included in the analyses.

ANALYSIS AND DISCUSSION

The volumetric fraction of aggregate (*Vagg*), cement (*Vcem*), filler (*Vfill*), micro-additions (*VmMA*) and nano-additions (*VnMA*) included in the paste and SCC compositions are summarized in Table 3. It can be observed that the type and amount of filler and AMA modified the EA shrinkage recorded both for pastes and SCC.

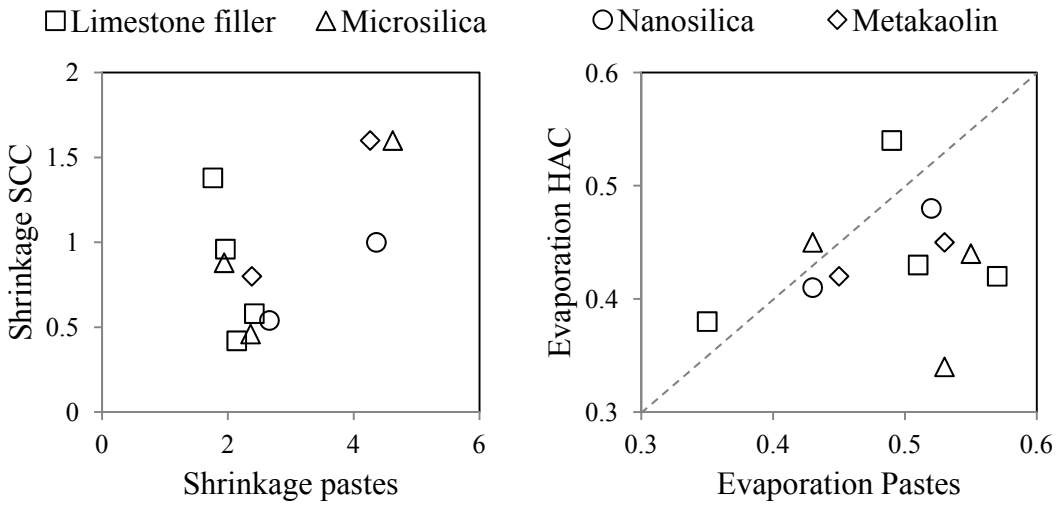

Figure 1. Drying Shrinkage (mm/m) and Evaporation rate (kg/m^2 h) of paste and SCC samples with the same type and amount of Mineral Addition at EA.

Figure 1 compares the experimental results of EA shrinkage and evaporation rate of paste and SCC samples with the same type and amount of filler and AMA. When SCC and pastes were compared, it was observed that the aggregate reduced the shrinkage as expected (Pickett, 1956). On the contrary, Evaporation rate was not affected by the aggregate, as SCC and pastes recorded very similar values. Although the evaporation is the main cause of EA drying shrinkage (Barluenga, 2013) no linear relationship between Evaporation and shrinkage could be found (Table 3).
Accordingly, three independent variables can be identified that affect EA shrinkage of the self-compacting pastes and concretes studied: the ***type and amount of the additions***, the ***aggregate*** and the ***evaporation***.

Effect of Mineral addition's type and amount. EA drying shrinkage of any composition can be related to the volumetric fraction of each component of the paste phase. The effectiveness of each component would depend on its physical and chemical performance, which can be related primarily to particle size and reactivity respectively. Accordingly, it can be considered that the expected shrinkage of a certain composition ($\varepsilon_{Sh,i}$) will be that of a reference mixture only with cement ($\varepsilon_{Sh,r}$) by the sum of the volumetric fraction of each component (V_{comp}) multiplied by a effectiveness coefficient (C_{comp}) and divided by the volumetric fraction of cement of the reference mixture ($V_{cem,r}$), as described in Eq. (1). A coefficient (k_1) has been included to adjust the estimated values to the experimental results.

$$\varepsilon_{Sh,i} = k_1 \cdot \varepsilon_{Sh,r} \cdot \frac{\left(\sum V_{comp} \times C_{comp}\right)}{V_{cem,r}} \quad (1)$$

The results reported in Table 3 were used to calculate the estimated EA drying shrinkage, considering as reference shrinkage ($\varepsilon_{Sh,r}$) and volumetric fraction ($V_{cem,r}$) those of REFG and HREFG, for pastes and SCC respectively.

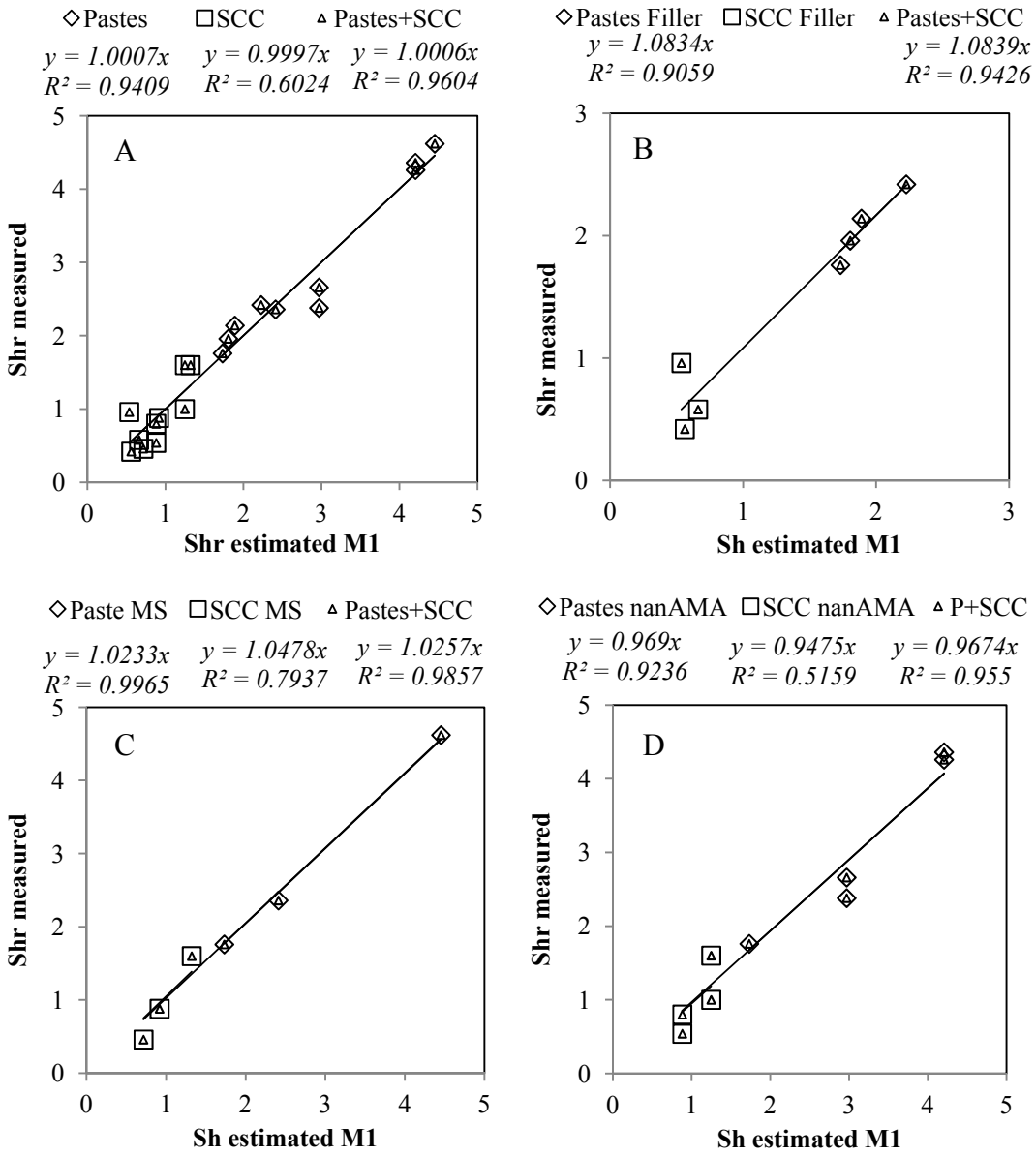

Figure 2. EA drying Shrinkage measured and estimated by Eq. (1) for: (A) all the pastes and SCC compositions, (B) the compositions only with filler, (C) with microsilica (MS) and (D) with nanosilica or Metakaolin (nanAMA).

The coefficients used to adjust the estimated to the measured values were: $k_{1,pastes}$=0.92; $k_{1,SCC}$=1.14; C_{cem}=1; C_{filler}=0.55; C_{MS}=25; C_{NS}=C_{MC}=45. The EA drying shrinkage measured and estimated according to Eq. (1) are plotted in Figure 2, considering: all the compositions, the compositions only with filler, those with MS and the mixtures with NS and MC and the values R^2 are reported for each combination.

Effect of Aggregates. According to Pickett (1956), shrinkage of a concrete can be estimated considering both the shrinkage of the paste and the volumetric

fraction of the aggregate. Eq. (2) incorporates the effect of both the paste shrinkage calculated with Eq. (1) and the effect of the aggregate described by Pickett.

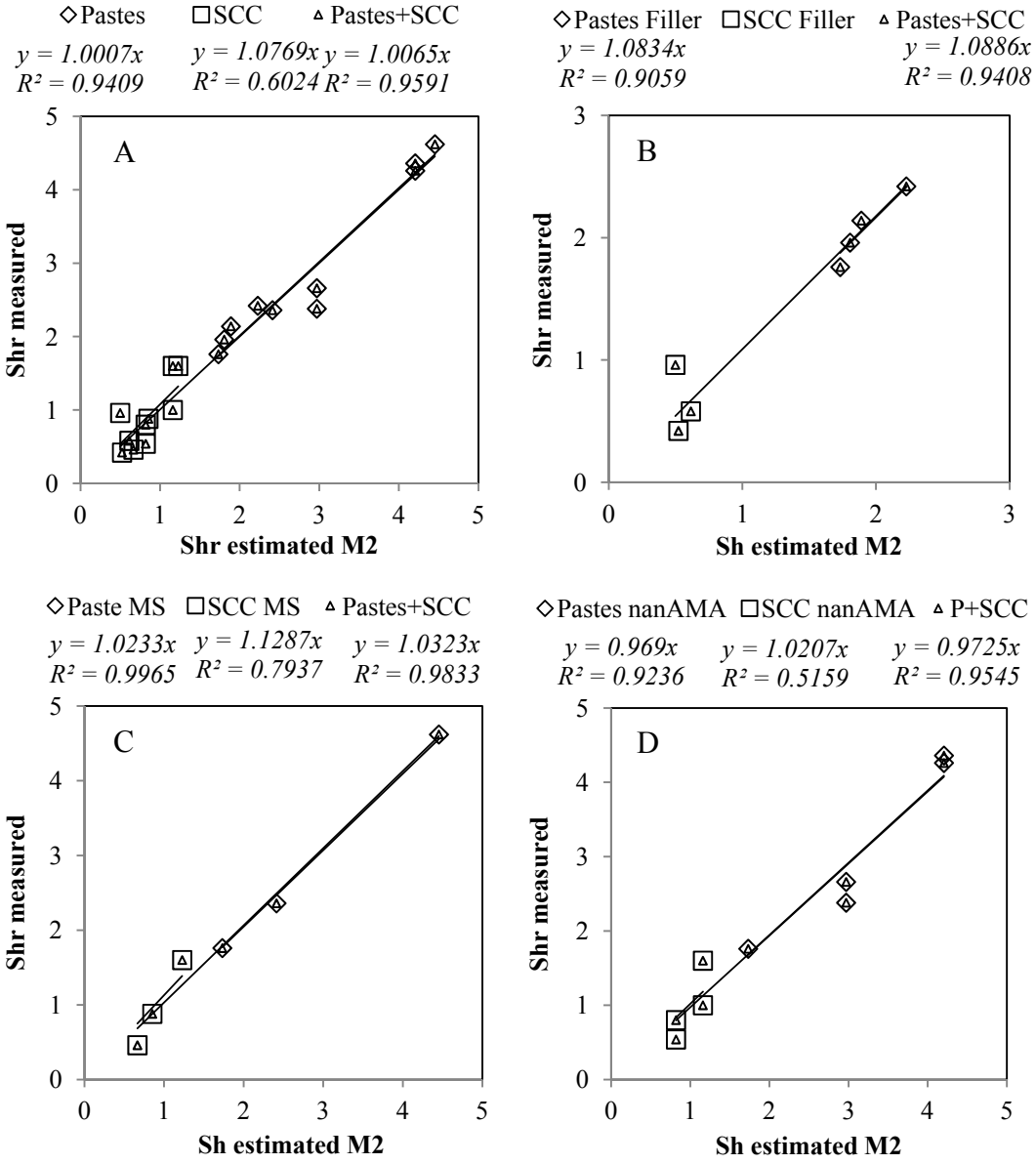

Figure 3. EA drying Shrinkage measured and estimated by Eq. (2) for: (A) all the pastes and SCC compositions, (B) the compositions only with filler, (C) with microsilica (MS) and (D) with nanosilica or Metakaolin (nanAMA).

$$\varepsilon_{Sh,i} = k_2 \cdot \varepsilon_{Sh,r} \cdot \frac{\left(\sum V_{comp} \times C_{comp}\right)}{V_{cem,r}} \cdot \left(1 - V_{agg}\right)^n \qquad (2)$$

In this case, the reference shrinkage and volumetric fraction were those of the reference paste REFG. The coefficients used to adjust the estimated to the measured values were: k_2=0.92; n=0.5 and those reported for Eq. (1). The EA drying shrinkage

measured and estimated according to Eq. (2) are plotted in Figure 3, considering all the compositions, the compositions only with filler, those with MS and the mixtures with NS and MC and the values R^2 are reported for each combination.

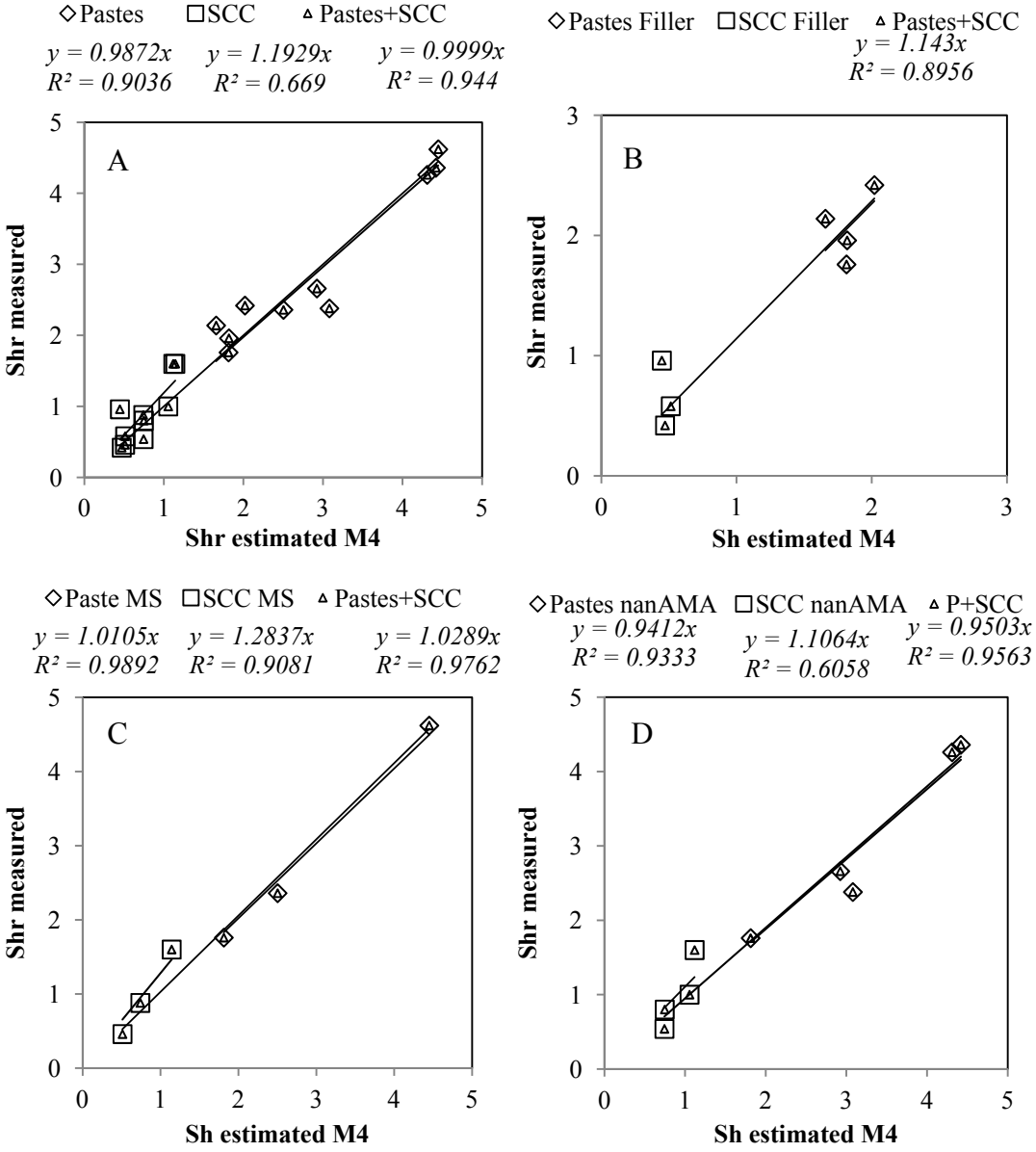

Figure 4. EA drying Shrinkage measured and estimated by Eq. (3) for: (A) all the pastes and SCC compositions, (B) the compositions only with filler, (C) with microsilica (MS) and (D) with nanosilica or Metakaolin (nanAMA).

Effect of Evaporation rate. Evaporation during EA depends on the environmental conditions and the water availability on the exposed surface of the sample (Uno, 1998) and is one the causes of EA shrinkage (Holt, 2003). It can be assumed that the larger the evaporation, the larger the EA drying shrinkage. The evaporation during EA shrinkage can be calculated as the product of evaporation rate (Ev_{rate} (kg/m2 h)) and Shrinkage extend (t_{shr} (h)) reported in Table 3. Accordingly, Eq.

(3) estimates EA drying shrinkage incorporating three factors: the effect of the paste composition, the aggregate amount and the ration between evaporation of a sample (Ev_i) and the evaporation of the reference composition (Ev_r). Although the environmental conditions applied to all the samples in this study were the same, Eq. (3) allows to estimate the EA drying shrinkage of different environmental conditions, even calculated using evaporation estimations (Uno, 1998).

$$\varepsilon_{Sh,i} = k_3 \cdot \varepsilon_{Sh,r} \cdot \frac{\left(\sum V_{comp} \times C_{comp}\right)}{V_{cem_r}} \cdot \left(1 - V_{agg}\right)^n \cdot \left(\frac{Ev_i}{Ev_r}\right)^m \quad (3)$$

As in Eq. (2), the reference shrinkage and volumetric fraction were those of the reference paste REFG. The coefficients used to adjust the estimated to the measured values were: k_3=1.14; m=0.25 jointly with those reported for Eq. (2). The EA drying shrinkage measured and estimated according to Eq. (3) are plotted in Figure 3, considering all the compositions, the compositions only with filler, those with MS and the mixtures with NS and MC and the values R^2 are reported for each combination.

CONCLUSIONS

A study on the effect of the paste components type and amount, the aggregate amount and the evaporation rate on Early Age (EA) drying shrinkage of pastes and Self-compacting concretes (SCC) with filler and active mineral additions (AMA) submitted to forced surface desiccation has been carried out. According to the experimental results, three independent variables were found to affect EA shrinkage: type and amount of mineral addition, amount of aggregate and evaporation during EA shrinkage. The effect of these factors was assessed and some equations were proposed to estimate EA drying shrinkage of moderate strength powder-type self-compacting pastes and SCC. It was observed that the larger the amount of AMA, the larger the shrinkage. On the other hand, the aggregate reduced the EA shrinkage. Finally, although there is a physical relationship between EA evaporation and free shrinkage, no direct relation could be identified. Evaporation during EA shrinkage of pastes and SCC compositions showed similar values, while drying shrinkage depended on the presence of the aggregates.

ACKNOWLEDGEMENTS

The financial support of projects **SCC_Pump (*BIA2013-48480-C2-2-R* and *BIA2013-48480-C2-1-R*)** funded by the *Spanish Ministry of Economy and Competitiveness* and ***PII-2014-022-P***, funded by the *Junta de Comunidades de Castilla La Mancha* is gratefully acknowledged.

REFERENCES

Barluenga, G., Hernandez-Olivares, F. (2007). "Cracking control of concretes modified with short AR-glass fibers at early age: Experimental results on standard concrete and SCC." *Cement and Concrete Research,* 37 (12), 1624-1638.

Barluenga G., Palomar I., Puentes J. (2013). "Early age and hardened performance of fluid cement pastes combining mineral additions". *Materials and Structures,* 46 (6), 921-941.

Barluenga, G., Puentes, J., Palomar, I. (2015). "Early age monitoring of self-compacting concrete with mineral additions." *Construction and Building Materials*, 77, 66-73.

Bonen, D., Shah, S.P. (2005). "Fresh and hardened properties of self-consolidating concrete". *Progress in Structural Engineering and Materials*, 7 (1), 14-26.

Darquennes, A., Khokhar, M.I.A., Rozière, E., Loukili, A., Grondin, F., Staquet, S. (2011). "Early age deformations of concrete with high content of mineral additions". *Construction and Building Materials*, 25, 1836–1847.

Hammer, T.A.,·Fossa, K.T. (2006). "Influence of entrained air voids on pore water pressure and volume change of concrete before and during setting." *Materials and Structures*, 39, 801–808.

Holt, E., Leivo, M. (2004). "Cracking risks associated with early age shrinkage." *Cement and Concrete Composites*, 26 (5), 521-530.

Leemann, A., Nygaard, P., Lura, P. (2014). "Impact of admixtures on the plastic shrinkage cracking of self-compacting concrete." *Cement and Concrete Composites*, 46, 1–7.

Turcry, P., Loukili, A. (2006). "Evaluation of Plastic Shrinkage Cracking of Self-Consolidating Concrete." *ACI Materials Journal*, 103, 272-279.

Uno, P. (1998). "Plastic Shrinkage Cracking and Evaporation Formulas." *ACI Materials Journal*, 95 (4), 365-375.

Pickett, G (1956). "Effect of Aggregate on Shrinkage of Concrete and Hypothesis Concerning Shrinkage." *Journal of ACI,* 52, 581-590.

Creep and Shrinkage in Concrete Containing Mineral Admixtures

D. Harinadha Reddy[1] and Ananth Ramaswamy[2]

[1]Department of Civil Engineering, India Institute of Science, Bangalore 560012, India. E-mail: harinadh@civil.iisc.ernet.in
[2]Department of Civil Engineering, India Institute of Science, Bangalore 560012, India. E-mail: ananth@civil.iisc.ernet.in

Abstract

A Predicting delayed strains (creep and shrinkage) in concrete proves to be critical to a large number of pre-stressed concrete structures, such as containment vessels of nuclear power plants, post-tensioned bridge girders, etc. These delayed strains include two components of shrinkage, namely, *Autogeneous shrinkage* and *Drying shrinkage* and two components of creep strains, namely, *Basic creep* and *Drying creep.* The present study focuses to predict the creep and shrinkage of Self Compacted Concrete (SCC) and High volume fly ash normal concrete experimentally. And a Hygro thermo chemo mechanical model (D.Gawin et al, 2006) is implemented to estimate gaseous pressure, capillary pressure and temperature and displacements which in turn varies with the hydration process. The Solidification theory proposed by Bazent (Bazant and Prasannan, 1989), is used to estimate the creep and shrinkage.

INTRODUCTION

Predicting delayed strains (creep and shrinkage) in concrete proves to be critical to a large number of pre-stressed concrete structures, such as containment vessels of nuclear power plants, post-tensioned bridge girders, etc. These delayed strains include two components of shrinkage, namely, *Autogeneous shrinkage* (deformation related to the water consumption during the hydration reaction in early-age concrete) and *Drying shrinkage* (deformation related to the moisture diffusion from the inner core to the outside of the concrete member) and two components of creep strains, namely, *Basic creep (a* time-dependent deformation of a loaded insulated specimen) and *Drying creep (*additional deformation that occurs due to drying in a loaded specimen (Pickett effect)).

One of the most important factors effecting time dependent deformations, both shrinkage and creep, is the relative humidity of the medium surrounding the concrete. For a given concrete, creep is higher when the relative humidity is lower. Concrete exhibiting high shrinkage also generally shows a high creep.

Creep in concrete is a function of both the state of the concrete composition and the magnitude of the imposed loads acting on the system (Bazant and Panula,

1979). A gradual removal of pore water with time under the action of loads results in 'drying' creep. Drying creep strains cannot be separated from other components of the delayed strains (Benboudjema et al 2001a). A drying test, a basic creep test and a total creep test need to be performed in order to get the drying creep strains. An elasto-plastic damage model approach together with the drying law has been employed to simulate the drying shrinkage and creep phenomena in both unloaded and loaded concrete specimen. Kovler (1997) has examined the phenomenon of drying creep in terms of an age adjusted effective modulus method. While creep and shrinkage in normal concrete has been researched extensively, both experimentally and through empirical models, in stark contrast, time dependent deformation estimates have not been deeply researched in self-compacting concrete. An exception is the work of Gawin et al 2006. Nevertheless parameters such as degree of hydration, water-binder ratio, aggregate strength and powder content have a strong influence on creep and shrinkage phenomenon. Drawing an inference that higher powder content results in higher shrinkage from studies on normal concrete to be applicable to self-compacting concrete would not be far from the mark, as SCC and high volume fly ash concretes contain a significant powder content.

The on-going research project aims to obtain results for creep and shrinkage measurements self- compacted concrete of different grades under different conditions of humidity, operating temperatures, age at loading that are envisaged to represent the conditions experienced by concrete in Indian nuclear power plants and then implemented in hydration based predictive model.

EXPERIMENTAL WORK

The experiments are carried out in a sustained environment with temperature 25 deg. celsius and relative humidity 70 percent. In this study, cylinder specimen was used to study to measure creep, while prism specimen were used to measure shrinkage. The mix for 70 MPa SCC and 45 MPa high volume flyash normal concrete based on weight proportions is shown Table 1.

Table 1. Details of Mix proportion of SCC and high volume fly ash concrete

Compressive strength (MPa)	*Cement (*kg/m^3)	Cement : Fine aggregates : Course aggregates : water/binder
70	498	1 : 1.68 : 1.37 : 0.30 (Silica Fume: 49 Kg/m^3 , Fly ash 98 Kg/m^3)
45	300	1 : 1.41 : 2.94 : 0.29 (Fly ash 200 Kg/m^3)

Specimen Preparation for creep and shrinkage

A standard cylinder specimen of 300 mm in height and 150 mm in diameter is used for measuring creep strain. The cylinders were cast and immediately the surface was sealed using plastic wrap and placed in the walk-in humidity and temperature controlled chamber. At an age of 24 hours, the specimens were demolded. The top and bottom surfaces were sealed to prevent drying. However, the lateral surfaces are exposed to controlled temperature and humidity in the chamber and were undergoing gradual drying. These specimens are cured under different relative humidity of 70%, with temperature of 25°C in controlled chambers until they were tested. These specimens has been loaded at different ages in days to assess the influence of concrete age on creep in concrete. The concrete specimen gains in strength as the age of concrete increases. Three specimen were placed one on top of the other in the creep frame for loading. Demec gauge pins were fixed on four lateral sides of each cylinder at a standard gage length (100mm), so that an average strain across each specimen could be reckoned from periodic measurements. The loading was applied through a jack and the load level measured by a load cell. Once the desired load level was reached, this was locked in using the locking nuts on each corner post of the reaction frame and the jack has been removed as shown in the fig 1. Different levels of loading is applied on these specimens. After application of desired load the instantaneous strain of the specimen is measured immediately by using Demec gauge (Strain gauge used for measuring the strains between two Demec points, the least count of the gauge is 0.0000157 m). The strain measurements are taken at each day after jacking to ensure constant load till the completion of the test.

Figure 1: Creep Experimental set up

Figure 2: Shrinkage Experimental set up

Shrinkage test has been conducted for the same mixes of concrete. The size of concrete prism specimens considered for this test is 100X100X500 mm as shown in the fig.2. These specimens are cured under 70% of relative humidity in walk-in chamber under constant temperature of 25°C. The specimens are demoulded after the 24hrs of casting. The top and bottom surfaces were sealed to prevent drying. The four lateral surfaces were allowed to dry in the controlled environment. The shrinkage strain measurements commenced immediately after demolding of the specimen by using Demmec strain measuring gauge with Demmec pins pasted on each of the four lateral surfaces at standard gage length, for obtaining an average strain.

Analytical work

In the present study A Hygro thermo chemo mechanical model (D.Gawin et al, 2006) is implemented to estimate gaseous pressure, capillary pressure and temperature and displacements which intern varies with hydration process.

The final form of equations are given here the details of the equations and description has given in the paper of D Gawin et. al. 2006. Table 2 shows the symbols that used in the analytical model.

Table2: The list of symbols used in the analytical model.

Symbol	Abbreviation and its unit
S_w	Saturation

β_s	cubic thermal expansion coefficient of solid (K^-1)
n	porosity
ρ^{ga}	Density of dry air (kg/m^3)
ρ^{g}	Density of gas(kg/m^3)
M_a	molar mass of dry air (kg/kmol)
M_w	molar mass of water vapor (kg/kmol)
D	Diffusivity Coefficient of vapor (m^2/s)
p^{ga}	capillary dry air pressure (Pa)
K	Intrinsic Permeability of concrete (m^2)
k^{rg}	relative permeability of gas phase
k^{rw}	relative permeability of liquid phase
g	acceleration due to gravity (m^2/s)
ρ^{gw}	density of vapor(kg/m^3)
m_{hydr}	density of hydrated water (kg/m^3)
β_w	cubic thermal expansion coefficient of water (K^-1)
ρ^{s}	density of concrete (kg/m^3)
μ^{g}	dynamic viscosity of gas phase (kg/m/s)
p^{gw}	Water vapor partial pressure (Pa)
μ^{w}	dynamic viscosity of water (kg/m/s)
ρC_p	effective thermal capacity of partially saturated medium(J/(m^3 K)
ρ^{w}	density of water (kg/m^3)
C_p^w	water specific heat (J/(kg K)
C_p^g	air specific heat (J/(kg K)
ΔH_{hydr}	latent heat of hydration (J/(kg)
ΔH_{vap}	latent heat of vaporization (J/(kg)
μ_{gv}	Water vapor dynamic viscosity (Pa.s)
μ_{ga}	Dry air dynamic viscosity (Pa.s)
p^{gws}	Water vapor saturation pressure (Pa)
β_ϕ	Experimental Coefficient in hydration equation
A_Γ	Normalized affinity
R	Universal gas constant(J/mol/K)
M_a	Molar mass of dry air (kg/kmol)
Γ_{hydr}	Hydration degree
ρC_p	Thermal capacity of partially saturated concrete (J/m^3.K)
α	Biots constant

λ_{eff}	Effective thermal conductivity (W/m/K)
ρ	effective density of concrete (kg/m^3)
$\frac{E_a}{R}$	activation energy(K)
β_{sw}	volume thermal dilatation of solid - water for incompressible solid grains

The mass balance equation for dry air

$$-n\frac{\partial S_w}{\partial p^c}\frac{\partial p^c}{\partial t}-\beta_s(1-n)(1-S_w)\frac{\partial T}{\partial t}+(1-S_w)\rho^{ga}div\frac{\partial u}{\partial t}-div\left[\rho^g\frac{M_aM_w}{M_g^2}D_d^{ga}\nabla\left(\frac{p^{ga}}{p^g}\right)\right]$$
$$+div\left[\rho^{ga}\frac{kk_{rg}}{\mu_g}\left(-\nabla p^g+\rho^g g\right)\right]+(1-S_w)n\left(\frac{\partial\rho^{ga}}{\partial T}\frac{\partial T}{\partial t}+\frac{\partial\rho^{ga}}{\partial p^c}\frac{\partial p^c}{\partial t}+\frac{\partial\rho^{ga}}{\partial p^g}\frac{\partial p^g}{\partial t}\right)$$
$$=\frac{\rho^{ga}}{\rho^s}(1-S_w)\frac{\partial m_{hydr}}{\partial t}$$

The mass balance equation for water vapor

$$-n\rho^{gw}\frac{\partial S_w}{\partial p^c}\frac{\partial p^c}{\partial t}-\beta_s(1-n)(1-S_w)\frac{\partial T}{\partial t}+(1-S_w)\rho^{gw}div\frac{\partial u}{\partial t}-div\left[\rho^g\frac{M_aM_w}{M_g^2}D_d^{ga}\nabla\left(\frac{p^{gw}}{p^g}\right)\right]$$
$$+div\left[\rho^{gw}\frac{kk_{rg}}{\mu_g}\left(-\nabla p^g+\rho^g g\right)\right]+(1-S_w)n\left(\frac{\partial\rho^{gw}}{\partial T}\frac{\partial T}{\partial t}+\frac{\partial\rho^{gw}}{\partial p^c}\frac{\partial p^c}{\partial t}\right)$$
$$=\frac{\rho^{gw}}{\rho^s}(1-S_w)\frac{\partial m_{hydr}}{\partial t}+\frac{\partial m_{vap}}{\partial t}$$

$$\frac{\partial m_{vap}}{\partial t}=-S_w\rho^w div\frac{\partial u}{\partial t}+\beta_{sw}\rho^w\frac{\partial T}{\partial t}-n\frac{\partial S_w}{\partial p^c}\frac{\partial p^c}{\partial t}$$
$$+div\left[\rho^w\frac{kk^{rw}}{\mu^w}\left(-\nabla p^g+\nabla p^c+\rho^g g\right)\right]=\frac{\rho^wS_w-\rho^s}{\rho^s}m_{hydr}$$

Enthalpy balance equation

$$\left(\rho C_p\right)_{eff}\frac{\partial T}{\partial t}+\rho_wC_p^w\left[\frac{kk^{rw}}{\mu^w}\left(-\nabla p^g+\nabla p^c+\rho^w g\right)\right].\nabla T$$
$$+\rho_gC_p^g\left[\frac{kk^{rg}}{\mu^g}\left(-\nabla p^g+\rho^w g\right)\right].\nabla T-div\left(\lambda_{eff}\nabla T\right)=-\frac{\partial m_{vap}}{\partial t}\Delta H_{vap}+\frac{\partial m_{hydr}}{\partial t}\Delta H_{hydr}$$

Momentum balance equation

$$div\left(\frac{\partial\sigma}{\partial t}-\alpha\frac{\partial p^s}{\partial t}I\right)+\frac{\partial\left[(1-n)\rho^s+nS_w\rho^w+n(1-S_w)\rho^g\right]}{\partial t}g=0$$

Hydration equation

$$\frac{\partial \Gamma_{hydr}}{\partial t} = A_{\Gamma}\left(\Gamma_{hydr}\right)\beta_{\varphi}(\varphi)\exp\left(-\frac{E_a}{RT}\right)$$

Where

$$A_{\Gamma}\left(\Gamma_{hydr}\right) = A_1\left(\frac{A_2}{k_{\infty}} + k_{\infty}\Gamma_{hydr}\right)\left(1-\Gamma_{hydr}\right)\exp\left(-\overline{\eta}\Gamma_{hydr}\right)$$

The above coupled equations the weighted residual method is applied to convert the equations in to weak form then a MATLAB and COMSOL platform is used to solve the above equations with appropriate boundary conditions specified in the paper Gawin et. al. 2006.

Creep

For modelling creep behavior here we have used micro prestress solidification theory proposed by Bazant et al.

$$J\left(t,t'\right) = \phi\left(t,t'\right) + \frac{1}{E} + cpS^{p-1}$$

Where $\phi(t-t')$ is viscoelastic compliance function which represented as with N finite number of kelvin units arranged in series. S is the microprestress, c and p are constants which considered as viscous term in compliance model.

Shrinkage

For modelling shrinkage behavior B3 model have used in this study.

$$\varepsilon_{sh}(\hat{t},t_0) = \varepsilon_{sh\infty}k_h S(\hat{t})$$

Where $\varepsilon_{sh\infty}$ is final shrinkage strain, k_h is a variable depends on humidity and S(t) is a time dependence factor.

According to the FEM model, the cylinder (150 mm dia and 300 mm length) modeled for creep and prism (100X100X100 mm) modeled for Shrinkage in MATLAB and COMSOL environment.

RESULTS AND DISCUSSION

Fig: 3 shows the simulation of degree of hydration using the hygro thermos mechanical model for the shrinkage specimen.it is seen that the hydration degree flatted after 150 days of age.

Fig: 4 shows the simulation of creep using the model with the high volume fly ash concrete (M45) experimental data. The prediction of strains by the model is seen to be in good agreement with the experimental data.

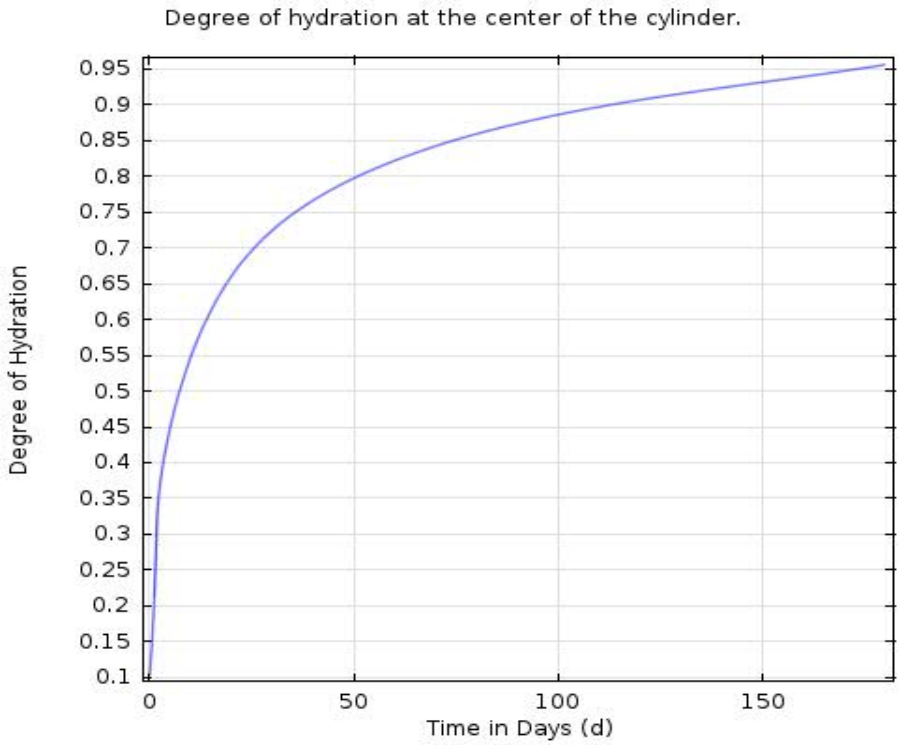

Figure3 : Degree of hydration for high volume fly ash concrete for shrinkage specimen

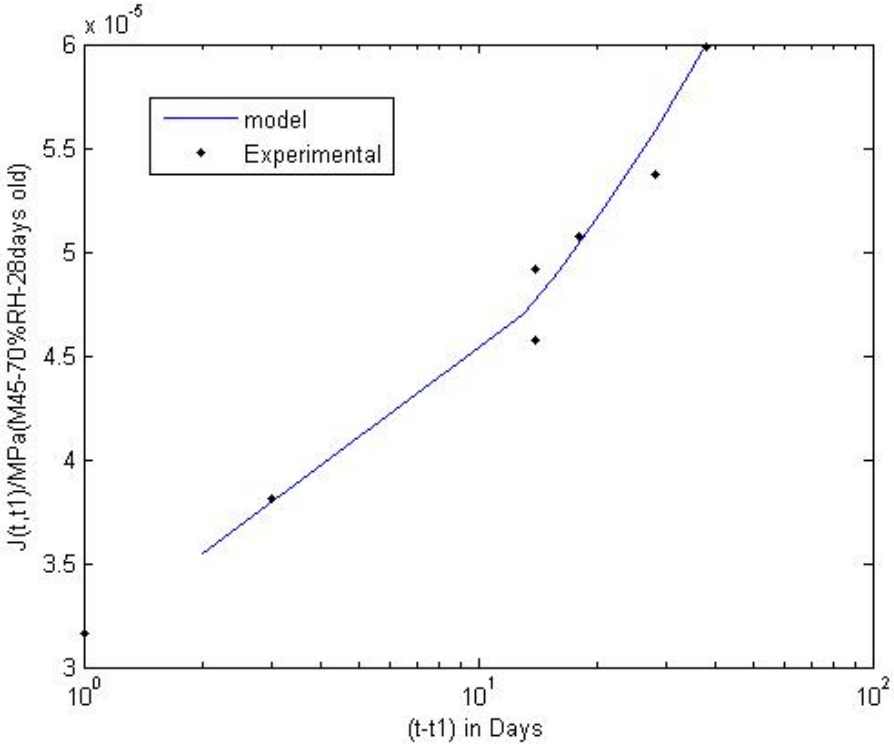

Figure4 : Creep strain for high volume fly ash concrete

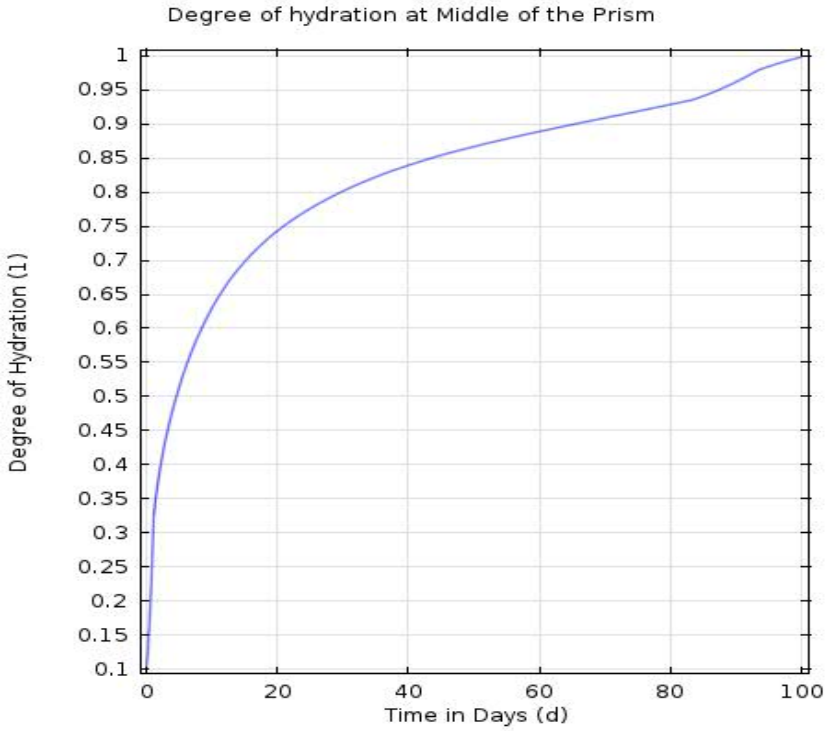

Figure5 : Degree of hydration for high volume fly ash concrete for shrinkage specimen

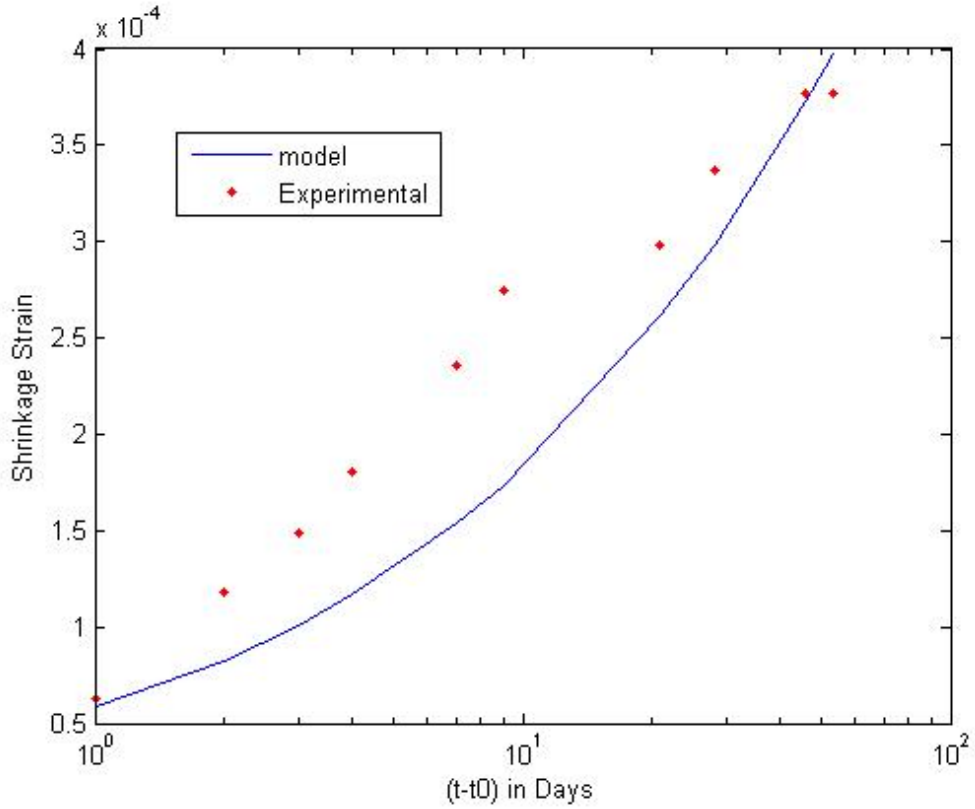

Figure6 : Shrinkage strain for high volume fly ash concrete

Fig: 5 shows the simulation of degree of hydration using the hygro thermo mechanical model for the creep specimen.

Fig: 6 shows the simulation of shrinkage using the B3 model with the high volume fly ash concrete (M45) experimental data. The prediction of initial strains by the model is seen to be some scatter with the experimental data but at later stage the model predictions improved.

Conclusions

From the present study, the following conclusions may be surmised:

(i) From a comparison of results from normal concrete and high volume fly ash of comparable strength it is seen that the high volume fly ash concrete specimen experience higher creep and shrinkage than the corresponding normal concrete specimen.

(ii) The analytical model is able to accurately predict the test results for creep and shrinkage.

REFERENCES

Bazant, Z. P., and Chern, J. C., 1985a, ‘‘Strain-softening with creep and exponential algorithm.’’ *J. Eng. Mech.,* 111, 391–415.

Bazant, Z. P., and Chern, J.-C., 1985b, ‘‘Concrete creep at variable humidity: Constitutive law and mechanism.’’ *Mater. Struct.,* 18, 1–20.

Bazant, Z. P., and Prasannan, S., 1989a, Solidification theory for concrete creep. I: Formulation.’’ *J. Eng. Mech.,* 115, 1691–1703.

Bazant, Z. P., and Prasannan, S., 1989b, ‘‘Solidification theory for concrete creep. II: Verification and application.’’ *J. Eng. Mech.,* 115, 1704–1725.

Benboudjema, F. Meftah, F., and Torrenti, J.M. (2001a) “Drying creep: An elastoplastic damage approach of the structural effect”, Fracture Mechanics of Concrete Structures, de Borst (ed.), 169-176, Swets Zeitlinger, France

Dariusz Gawin, Francesco Pesavento ans Bernhard A. Schrefler, 2006, “Hygro-thermo-mechanical modelling of concrete at early ages and beyond. Part I: Hydration and hygro-thermal phenomena” IJNME 67:299-331.

Dariusz Gawin, Francesco Pesavento ans Bernhard A. Schrefler, 2006, “Hygro-thermo-mechanical modelling of concrete at early ages and beyond. Part II: Shrinkage and creep of concrete” IJNME 67:332-363**.**

Kovler, K. (1997) “Drying creep of concrete in terms of age adjusted effective modulus method”, Magazine of concrete research, v49(181), 345-351.

Majorana,C., Salomoni V., Schrefler, B. (1998) “Hygrothermal and Mechanical model of concrete at high temperature”, Materials and structures, 31, 378-386.

Study on the Sulfate Resistance and Drying Shrinkage of Mortars Containing Scoria as a Cement Replacement

Aref Mohamad al-Swaidani[1] and Eng. Samira Dib Aliyan[2]

[1]Assistant Professor & Vice-Dean of Faculty of Architectural Engineering, Arab International University (AIU), Damascus, Syria (corresponding author). E-mail: aydlswaidani@yahoo.fr; a-swaidani@aiu.edu.sy
[2]Syria Arab Organization for Standardization and Metrology (SASMO), Damascus, Syria.

Abstract

Use of blended cements is growing rapidly in the construction industry due to economical, ecological and technical benefits. Syria is relatively rich in volcanic scoria. In the study, three types of cement were prepared; one plain Portland cement CEM I (control) and two blended cements: CEM II/A-P and CEM II/B-P (EN 197-1), each of them with three replacement levels of scoria: (10%, 15%, 20%) and (25%, 30%, 35%), respectively. Evaluation of sulfate resistance of mortars containing scoria-based cements was performed in accordance with ASTM C1012. Length measurements were performed up to 52 weeks after immersing the specimens into 5% Na_2SO_4 solution. Drying shrinkage has been evaluated using mortar bar method in accordance with ASTM C596. Lengths of mortar bars subjected to drying shrinkage were measured periodically up to 360 days. SRPC cement was employed for comparison in both tests. Test results revealed that the increase of scoria significantly improves the sulfate resistance of mortars. The expansion of scoria-based mortar bars decreased with the increase of scoria replacement level. Further, according to the expansion test results, CEM II/B-P can be used instead of SRPC in sulfate-bearing environments. The results of drying shrinkage showed that the CEM II/B-P-based mortar bars exhibited greater contraction when compared to the control mortar, especially at early ages. However, the long-term drying shrinkage of mortars was not influenced much by the addition of volcanic scoria.

Keywords: Sulfate attack; Drying shrinkage; Blended cement; Durability; Natural pozzolan; scoria.

INTRODUCTION

Use of natural pozzolan in production of blended Portland cements makes important effects on physical, chemical, mechanical and durability properties of mortar and concrete (Cavdar & Yetgin 2007; Ghrici et al. 2006; Hossain 2009; Rodriguez-Camacho & Uribe-Afif 2002; Senhadji et 2012; Turanli et al. 2005). In addition, since these materials enter the cement production after kiln process, they also provide important economical and ecological benefits (Mehta & Monteiro 2006). For this reason, a particular attention was recently given to the exploitation of natural pozzolan which is broadly abundant in Syria. More than 30000 km^2 of the country is covered by Tertiary and Quaternary-age volcanic rocks (General Establishment of Geology and Mineral Resources in Syria 2011), among which scoria occupies

important volume with estimated reserves of more than 600 million tones (General Establishment of Geology and Mineral Resources in Syria 2007).

In Syria, sulfate attacks on concrete structures have caused serious damage to these concretes. According to previous studies (Ghrici et al. 2006; Ramezanianpour et al. 2010; Rodriguez-Camacho & Uribe-Afif 2002), adding natural pozzolan led, through the pozzolanic reaction, to a refinement of the pore structure, resulting in a highly impermeable matrix. Further, A reduction in $Ca(OH)_2$ led to reductions in the formation of gypsum and ettringite. In addition, drying shrinkage which is regareded as "first natural enemy" of concrete durability (Yang 2015), is inevitable phenomenon in all cementitious products due to contraction of total mass upon loss of moisture. This phenomenon is largely influenced by mineral additions when used as partial cement replacement. According to (Itim et al. 2011), adding natural pozzolans as partial cement replacement involves an additional formation of CSH which generates more shrinkage. Many researchers (Massazza & Costa 1979; Mehta 1981; Shannag & Yeginobali 1995) showed that shrinkage of natural pozzolan-based cement was generally higher than that of ordinary Portland cement.

The objective of this paper is to report a part of the first detailed research in Syria on the effect of different amount of scoria when adding as cement replacement on some durability-related properties. Sulfate attacks and drying shrinkage have been particularly investigated in the study. Some chemical, physical and mechanical properties have also been reported. The study is of particular importance not only for the country but also for other areas of similar geology, e.g. Harrat Al-Shaam, a volcanic field covering a total area of some 40 000 km^2, third of which is located in the country. The rest is covering parts from Jordan and Saudi Arabia.

EXPERIMENTAL PROCEDURE

Scoria. The scoria used in the experiments was collected from Tal Dakwa' quarry, at 70 km southeast of Damascus as shown in Figure 1. The petrographical examination showed the scoria is consisted of amorphous glassy ground mass, vesicles, plagioclase and olivine with the following percentages (based on an optical estimate): 20%, 35%, 20% and 25%, respectively. Figure 2 shows thin sections of the used scoria.

Cement samples. Three types of binder were prepared, one plain Portland cement CEM I (control), and two blended cements: CEM II/A-P and CEM II/B-P (EN 197-1:2004), each of them with 3 replacement levels of scoria: (10%, 15% and 20%) and (25%, 30%, 35%), respectively. Chemical analysis of the scoria, clinker and gypsum used in the study is summerized in Table 1. This analysis was carried out by means of wet chemical analysis specified in EN 196-2:1989. All binders were interground by a laboratory grinding mill to a Blaine fineness 3200±50 cm^2/g. All replacements were made by mass of cement. Table 2 shows the chemical, physical and mechanical properties of the binders produced. CEM I (the control sample) was designated as C1, whereas blended cements were designated according to the replacement level. For instance, C2/10% and C7/35% refer to the blended cements containing 10% and 35% of scoria, respectively. In drying shrinkage and sulfate attack tests, sulfate-resisting Portland cement was employed for comparison. It was designated as C8.

a. Map of Harrat Al-Shaam and the studied area

b. The studied scoria quarry, some volcanic scoria cones are shown behind.

c. The studied scoria aggregate.

Figure 1. Map of Harrat Al-Shaam, photo of the studied quarry & the used scoria aggregate.

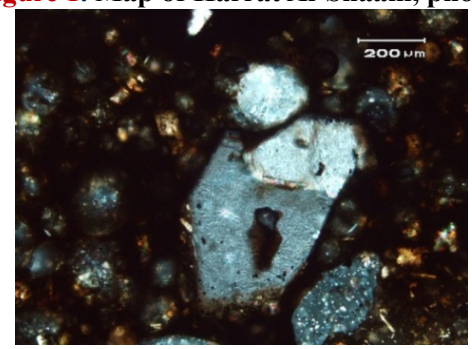

a.

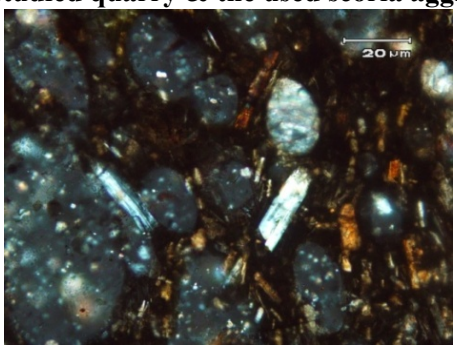

b.

Figure 2. Thin sections of the scoria. a). Microphenocryst of Olivine in volcanic glass matrix with vesicles, some of which are filled with white minerals. b). Microphenocrysts of elongated plagioclase in volcanic glass matrix with vesicles, some of which are filled with white minerals.

Mortar mixtures. Eight mortar mixtures were prepared using these binders and sand meeting the requirements of ASTM C 778. In all mixtures, binder: sand ratio was kept constant as 1:2.75 by weight. Mixtures containing CEM I and SRPC were prepared with a w/b ratio of 0.485. Mixtures containing scoria-based blended cements

were prepared by changing the w/b ratio in order to obtain a flow within ±5 of that of the CEM I mortar. For sulfate attack test, prismatic mortar bars and cubes were cast from each mixture in accordance with ASTM C 1012:2004. The compressive & flexural strength development was determined on 4×4×16 prismatic specimens, in accordance with ISO 4012, at ages of 2, 7, 28 and 90 days. The reported values represent the average of six readings for compressive strength test and the average of three readings for flexural tensile strength test.

Sulfate attack test. The evaluation of sulfate attack resistance of mortars was performed in accordance with ASTM C 1012-2004. Length measurements of the prepared prismatic specimens were performed at 1, 2, 3, 4, 8, 13, 15, 17, 26, 38, 52 weeks after immersing the specimens into the sulfate (5% Na_2SO_4) solution. The solution was renewed four times throughout the test; at 8, 17, 26 and 38 weeks.

Drying shrinkage test. Specimens of 25×25×285 mm^3 were prepared from each binder type. Each specimen was fitted with stainless steel studs at both ends. After casting for 24 h, the specimens were removed from the molds and cured in lime-saturated water for 1 day. After the age of 3 days, the specimens were removed from the water, wiped with damp cloth, and measured immediately to determine the initial length of the mortar specimens. The mortar specimens were subsequently placed in air storage with a controlled temperature of 23±2 ^oC and a relative humidity of 50±5% as prescribed by ASTM C596. The drying shrinkage measurements were recorded at 7, 14, 21, 28, 56, 112, 180 and 360 days.

DISCUSSION of RESULTS

Properties of scoria and blended cements. As seen from Table 1, scoria is considered as suitable material for use as pozzolan. It satisfied the standards requirements for such a material by having a combined SiO_2, Al_2O_3 and Fe_2O_3 of more than 70%, a SO_3 content of less than 4% and a loss on ignition of less than 10% (ASTM C618:2001). $SiO_{2reactive}$ content is more than 25%, as well (EN 197-1:2004). In addition, it has a strength activity index with Portland cement higher than the values specified in ASTM C618:2004. The chemical and physical properties of scoria-based blended cements are also in conformity with the standards requirements (ASTM 595:2001). Their contents of MgO and SO_3 are less than 6% and 4%, respectively. The loss on ignition is also less than 5% as specified in ASTM C595. Setting time and soundness values meet the limits specified in ASTM C595, for all binder types. The compressive strengths of blended cement mortars are lower than that of the plain Portland cement at 28 days curing. This reduction is mainly due to the slowness of pozzolanic reaction between pozzolan and CH released during cement hydration (Mindess et al. 2003), and could be due the coarser blended cement particles, as shown in Table 2.

Compressive and flexural strength of mortars. Results of compressive strength test are summarized in Table 3. As expected, the compressive strength of the concrete increases with curing time with a high rate of strength gains at early ages which gradually decrease at longer ages. Plain cement mortar specimens have higher

compressive strengths at any age when compared with blended cement mortars. The compressive strength at 7 days decreases from 30.57 to 19.99 MPa when CEM I and CEM II/B-P with 35% of scoria were used, respectively.

Table 1. Chemical composition of the used materials

Chemical composition (by mass, %)	Materials		
	Scoria*	Clinker	Gypsum
SiO_2	46.52	21.30	0.90
Al_2O_3	13.00	4.84	0.07
Fe_2O_3	11.40	3.99	0.10
CaO	10.10	65.05	32.23
CaO_f	-	2.1	-
MgO	9.11	1.81	0.20
SO_3	0.27	0.25	45.29
Loss on ignition	2.58	-	21.15
Na_2O	2.14	0.60	-
K_2O	0.77	0.28	-
Cl^-	<0.1	0.05	-
Pozzolan activity index (ASTM C 618)	79 (at 7 days) 85 (at 28 days)		

*$SiO_{2(reactive)}$=42.22% (determined in accordance with EN 196-2)

Table 2. Chemical, physical and mechanical properties of plain and blended cements

Chemical composition (%)		Chemical properties of plain and blended cements							
		C1/CEMI	C2/10%	C3/15%	C4/20%	C5/25%	C6/30%	C7/35%	C8/SRPC
SiO_2		20.69	21.59	22.35	23.25	24.00	24.33	24.61	20.72
Al_2O_3		5.09	5.20	5.68	5.73	6.55	6.80	7.39	4.33
Fe_2O_3		4.23	4.75	4.79	5.15	5.43	5.47	6.31	5.79
CaO		60.62	58.21	55.18	53.05	50.30	48.00	44.84	61.69
MgO		2.46	2.66	3.23	3.39	3.87	4.11	4.63	1.21
SO_3		2.26	2.31	2.20	2.20	2.30	2.26	2.55	2.13
Loss on ignition		1.41	1.40	1.43	1.37	1.47	1.48	1.60	2.90
Na_2O		0.60	0.71	0.83	0.94	1.07	1.16	1.31	0.21
K_2O		0.35	0.39	0.43	0.46	0.50	0.53	0.57	0.19
Cl^-		0.023	0.021	0.022	0.019	0,018	0.019	0.019	0.022
Insoluble Residue		1.03	1.58	2.09	2.51	3.48	4.08	5.33	0.36
Main compounds of clinker used in cement specimens «Based on Bogue composition »	C3S	53.36	50.55	47.74	44.94	42.13	39.32	36.51	50.16
	C2S	17.76	16.82	15.89	14.95	14.02	13.08	12.15	21.58
	C3A	5.78	5.47	5.17	4.86	4.56	4.26	3.95	1.69
	C4AF	11.53	10.93	10.32	9.71	9.11	8.50	7.89	17.60
	C3S/C2S	3.0	3.0	3.0	3.0	3.0	3.0	3.0	2.32
		Physical properties of plain and blended cements							
Specific gravity		3.13	3.09	3.05	3.02	2.99	2.98	2.96	
Initial setting (min)		151	153	153	153	152	153	158	
Final setting (min)		178	179	180	180	179	181	188	
Water demand (%)		25.1	25.2	25.2	25.4	25.4	25.4	25.5	
Soundness (mm)		0.6	0.7	0.8	0.8	0.9	1.1	0.9	
Residue on 45 µm sieve (%)		13.6	14.3	14.8	15.2	16.1	17.0	17.9	
Residue on 90 µm sieve (%)		6.4	6.2	6.4	6.5	6.7	6.9	6.8	

The relative compressive strength after 2 days curing with 35% of scoria is only 66% of that of CEM I specimens. This could be explained by the slowness of the pozzolanic reaction between the glassy phase in scoria and the CH released during cement hydration. However, due to the continuation of this reaction and the formation of a secondary C-S-H, a greater degree of hydration is achieved resulting in strengths after 90 days curing which are comparable to those of CEM I specimens. In addition, the results obtained from the flexural test showed a similar trend to that of the compressive strength, as displayed in Figure 3. The correlation between the compressive strength and the flexural strength for the entire population of test results is shown in Figure 4. The relation obtained is $f_t = 0.92\ (f_c)^{0.56}$ with a correlation factor of 0.95. This relation seems to fit well the relation proposed by (ACI 1992).

Table 3. Compressive strength of mortars.

Sample	Compressive strength (MPa)-Normalized			
	2 days	7 days	28 days	90 days
C1/CEM I (Control)	15.4-100%	30.57-100%	45.6-100%	54.48-100%
C2/10%	14.62-95%	29.33-96%	44.19-97%	53.61-98%
C3/15%	13.9-90%	27.06-89%	42.31-93%	52.66-97%
C4/20%	13.59-88%	25.43-83%	40.62-89%	52.05-96%
C5/25%	12.54-81%	23.46-77%	37.03-81%	51.3-94%
C6/30%	11.07-72%	21.26-70%	33.74-74%	49.35-91%
C7/35%	10.09-66%	19.99-65%	30.56-67%	47.57-87%

Sulfate attack. The results of the expansion test of bars immersed in 5% Na_2SO_4 solution for up to 52 weeks are shown in Figure 5. It was clearly seen form Figure 5, the use of scoria reduced expansion of the mortar bars. This reduction in expansion increased with increase in the scoria replacement level. These results were similar to those of other studies in which pozzolanic materials were used as cement replacements to improve sulfate resistance (Irassar et al. 2000; Tangchirapat et al. 2009). It should be also noted that the amount of expansion for SRPC mortar bars was very similar to that of CEM II/B mortar bars. At 26 & 52 weeks, the amount of expansion of the CEM II/B mortar bars ranged from 0.10% to 0.11% and from 0.18% to 0.19%, respectively, whereas the expansion of SRPC was 0.09% and 0.16%, respectively. This was despite the lack of C_3A in SRPC. The slightly elevated expansion noted in SRPC used in the study, which made it unsuitable for severe exposure, is possibly because the SRPC mortar contains lime and C_4AF in large proportions when compared to the CEM II/B mortars. These results confirmed earlier findings that the presence of C_3A is not the only cause of expansion due to sulfate attack (Cao et al. 1997; Tangchirapat et al. 2009).

According to ACI Committee 201, ettringite formation derived from ferroaluminate phase has also been assumed as a potential sulfate deterioration problem. The improvement of sulfate resistance by adding scoria as cement replacement can be mainly explained by the pore size refinement, the removal of lime by the pozzolanic reaction of scoria with the lime liberated during cement hydration and the C_3A dilution (Al-Amoudi 2002; Al-Dulaijan et al. 2003; Hooton & Emery 1990; Irassar et al. 2000). The pore size refinement reduced the permeability of the paste, thus limiting the ingress of sulfate ions (Irassar et al. 2000). In terms of cement

composition, C_3A is the main compound involving sulfate resistance, whereas C_4AF, an alumina bearing phase, and CH released from silicates hydration can also affect the sulfate resistance of low C_3A Portland cements (Gonzalez & Irassar 1997). On the other hand, the C_3S content was considered an important parameter on sulfate resistance of PC, too (Irassar et al. 2000). It can be noted that for CEM I of about 6% C_3A content, blending with 25% scoria content or more usually resulted in a performance similar to that of SRPC. This result is similar to that reported by (Lawrence 1990).

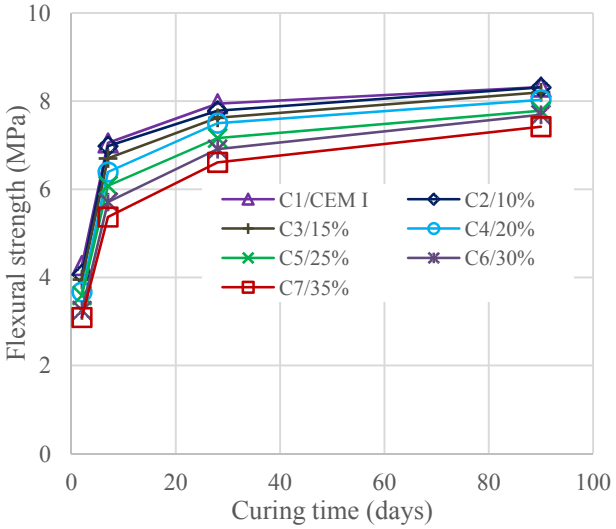

Figure 3. Development of Flexural strength with curing time

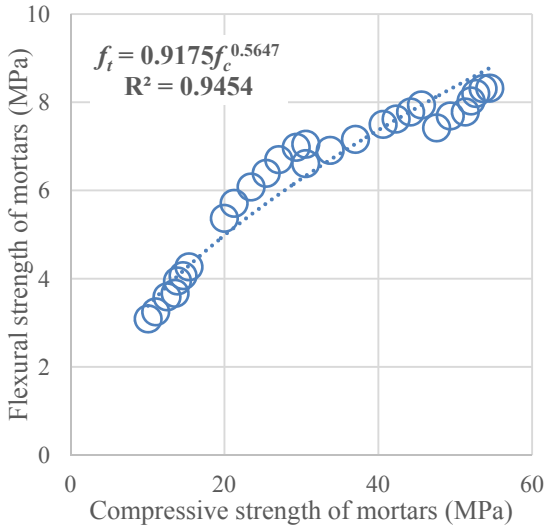

Figure 4. Correlation between compressive and flexural strength of mortars

Drying shrinkage. Figure 6 shows the results of drying shrinkage of scoria-based cement mortars. The results obtained agreed with the results published in the literature (Massazza & Costa 1979; Mehta 1981; Shannag & Yeginobali 1995). The drying shrinkage developed rapidly at an early stage, with approximately 70% of the maximum shrinkage occurring during the first 28 days. The drying shrinkage curve patterns agreed with the observations reported by (Barr et al. 2003). At 360 days, the drying shrinkage values were found similar for all binder types. These drying shrinkage values agreed with those reported in the literature (Haque & Kayali 1998; Massazza 2006; Mehta 1987). It is clearly seen from Figure 6 all scoria-based mortars exhibited shrinkage values higher than the control mortar at the early ages. However, the difference becomes marginal from 28 days of drying onward. The increase of drying shrinkage with an increase of the cement replacement level which was clearly noted, especially at early ages, might be due to (i) the pozzolanic reaction which generates an additional CSH resulting in a decrease in spacing of CSH particles; (ii) the transportation of large pores into fine pores what is called "pore size refinement". Its formation increases the capillary tension (Meddah & Tagnit-Hamou 2009; Rao 2000; South 2009; Touttanji & Bayasi 1999); (iii) the higher water demand of scoria-based cements (South 2009) as noted in Table 2; (iv) the much more porous microstructure of scoria (Massazza 1993), as seen in Figure 2. However, this increase was much lower than the maximum 0.03% allowed by ASTM C618.

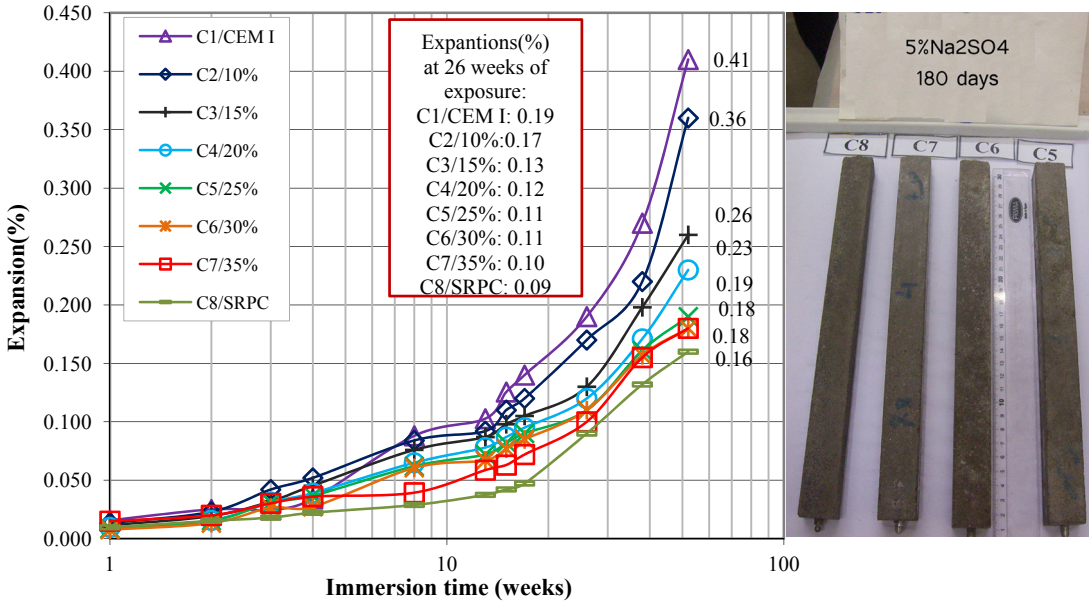

Figure 5. Length changes over time of prismatic mortars immersed in 5% Na_2SO_4

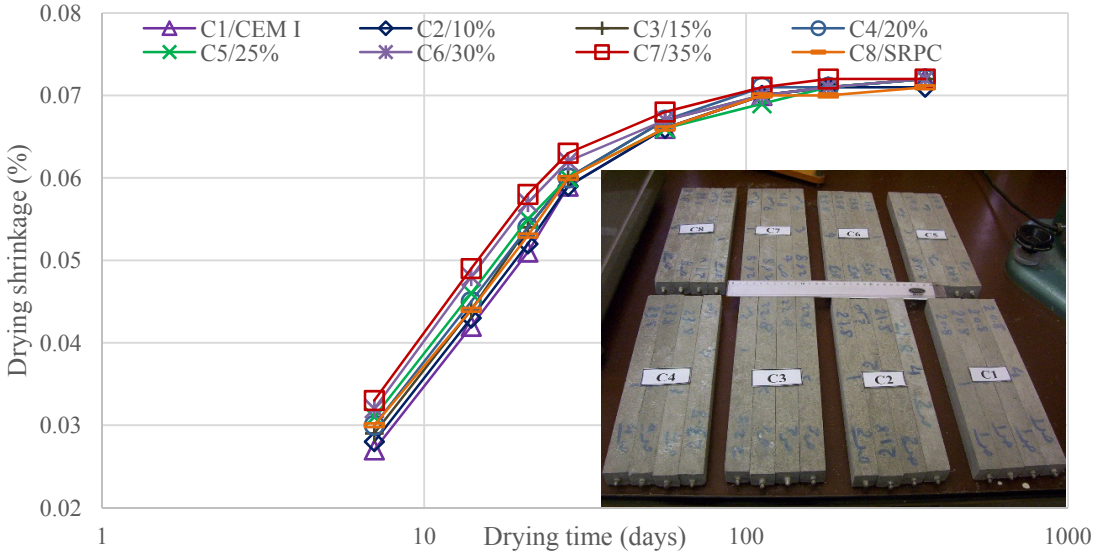

Figure 6 Drying shrinkage values of prismatic mortar specimens

Conclusion

From the experimental results, the following conclusions could be drawn:

-The studied scoria is a suitable material for use as a natural pozzolan. It satisfied the ASTM & EN requirements for such a material. The physical properties of binders containing scoria are also in conformity with the standards requirements.

-The compressive strength of mortars containing scoria-based binders was lower than that of plain cement concrete at all ages of concrete in this study. At early ages, the mortars containing CEM II/B-P binder types had compressive strengths much lower than that of plain cement concrete. However, at 90 days curing, the compressive strengths of blended cement mortars are comparable to those of plain cement concrete.

-Based on the results, blending CEM I of 6 % C_3A content, with 25% scoria content or more resulted in a performance similar to that of SRPC.
-Adding scoria as cement replacement reduced the expansion of the mortar bars exposed to sodium sulfate solution. More reduction occurs with increasing the replacement level.
-The drying shrinkage of mortar bars increases with an increase in the scoria content, especially at the early ages of drying. However, the long-term drying shrinkage of mortar bars at 360 days of drying is not affected significantly with the addition of scoria as cement replacement, particularly with up to 25% scoria content.
-Based on the results obtained, it is recommended that scoria can be used up to 25% as a partial substitute for Portland cement in production of blended cements. This addition ratio can reduce the quantity of CO_2 released by Syrian cement plants, and the consumed energy. So, production of a green concrete could be promoted.

Acknowledgement

The authors gratefully acknowledge the technical and financial support of this research from the management of General Organization for cement & Building Materials/Adra Cement Plant. Thanks are also expressed to Chemist Nazeer Adarnaly, Eng. Amjad Bernieh (Lafarge Co.) and Prof. Tamer al-Hajeh, vice-president of AIU for their appreciated help.

REFERENCES

ACI Committee 201 (1991). "Guide to durable Concrete." ACI Materials Journal, 88, 551.
ACI 363R (1992). "State of the art report on high strength concrete." American Concrete Institute, Detroit.
Al-Amoudi, OSB. (2002). Attack on plain and blended cements exposed to aggressive sulfate environments. Cement and Concrete Composites, 24, 304-316.
Al-Dulaijan, SU., Maslehuddin, M., al-Zahrani, MM., Sharif, AM., Shameem, M., Ibrahim, M. (2003). "Sulfate resistance of plain and blended cements exposed to varying concentrations of sodium sulfate." Cement and Concrete Composites, 25, 429-437.
Barr, B., Hoseinian, SB., Beygi, MA. (2003). "Shrinkage of concrete stored in natural environments." Cement and Concrete Research, 25(1)19-29.
Cao, HT., Bucea, I., Ray, A., Yozghatlian, S. (1997). The effect of cement composition and pH of environment on sulfate resistance of Portland cements and blended cements. Cement and Concrete Composites, 19(2), 161-171.
Cavdar, A, Yetgin, S. (2007). "Availability of tuffs from northeast of Turkey as natural pozzolans on cement, some chemical and mechanical relationships." Construction and Building Materials, 21, 2066-2071.
General Establishemnt of Geology and Mineral Resources in Syria (2007), Official document nr. (3207/T/9). (in Arabic).
General Establishment of Geology and Mineral Resources in Syria (2011). "A Guide for mineral resources in Syria. (in Arabic).
Ghrici, M. Kenai, S., Meziane, E. (2006). "Mechanical and durability properties of cement mortar with Algerian natural Pozzolana." Journal of Material Science, 41, 6965-6972.

Gonzalez, MA., Irassar, EF. (1997). "Ettringite formation in low C3A Portland cement exposed to sodium sulfate solution." Cement and Concrete Research, 27(7), 1061-1072.
Irassar, EF., Gonzalez, MA., Rahhal, V. (2000). "Sulfate resistance of type V cements with limestone filler and natural pozzolan." Cement and Concrete Composites, 22(5), 361-368.
Itim, A., Ezziane, K., Kadri, EH. (2011). "Compressive strength of mortar containing various amounts of mineral additions." Construction and Building Materials, 25, 3603-3609.
Lawrence, CD. (1990). "Sulfate attack on concrete." Magazine of concrete Research, 42(153), 249-264.
Massazza, F., Costa, U. (1979). "Aspects of the pozzolanic activity and properties of pozzolanic cements." II Cemento, 76, 3-18.
Massazza, F. (1993)."Pozzolanic cements." Cement & Concrete Composites, 15, 185-214
Massazza, F.(2006). "Pozzolana and pozzolanic cements." In Lea's Chemistry of cement and concrete, edited by P.C. Hewlett, Fourth edition, Elsevier.
Meddah, MS., & Tagnit-Hamou, A. (2009). Effect of mineral admixtures on hrinkage measured on massive concrete elements." Creep, Shrinkage and Durability Mechanics of Concrete and Concrete Structures–Tanabe et al. (eds), Taylor & Francis Group, London, \ ISBN 978-0-415-48508-1.
Mehta, PK. (1981). "Studies on blended Portland cements containing Santorin earth." Cement and Concrete research, 11(1981)507-518.
Mehta, PK. (1987). Pouzzolanes naturelles. In Matériaux complémentaires en cémentation pour le béton, edited by VM. Malhotra, CANMET.
Mehta PK, Monteiro PJM (2006). "Concrete: Microstructure, properties, and Materials." 3rd edition. McGraw-Hill, ISBN 0-07-146289-9.
Mindess, S., Young, JF., Darwin, D. (2003). "Concrete." 2nd Edition, Prentice Hall.
Ramezanianpour, AA., Mirvalad, SS. Aramun, E., Peidayesh, M. (2010). "Effect of four Iranian natural pozzolans on concrete durability against chloride penetration and sulfate attack." In proceedings of the 2ed international conference on sustainable construction materials and technology, 28-30 June, Ancona, Italy, edited by P. Claisse et al.
Rao, G.A. (2001). "Long-term drying shrinkage of mortar—influence of silica fume and size of fine aggregate." Cement and Concrete Research, 31(2)171–175.
Rodriguez-Camacho, RE. Uribe-Afif, R. (2002). "Importance of using natural pozzolans on concrete durability." Cement and Concrete Research, 32, 1851-1858.
Senhadji, Y, Escadeillas, G, Khelafi, H., Mouli, M. Benosman, AS. (2012). "Evaluation of natural pozzolan for use as supplementary cementitious material." European Journal of Environmental and Civil Engineering, 16(1), 77-96.
Shannag, MJ., Yeginobali, A. (1995). "Properties of paste, mortars and concretes containing natural pozzolan," Cement and Concrete Research, 25(3)647-657.
South, W. (2009). A study of the compressive strength and drying shrinkage of cementitious binders prepared using natural pozzolans. PhD Thesis, University of Wollongong, Australia.
Tangchirapat, W., Jaturapitakkul, C., Chindaprasirt, P. (2009). "Use of palm oil fuel ash as a supplementary cementitious material for producing high-strength concrete." Construction and Building Materials, 23(7), 2641-2646.
Touttanji, HA., Bayasi, Z. (1999). "Effect of curing procedures on the properties of silica fume concrete." Cement and Concrete Research, 29, 497-501.
Turanli, L., Uzal, B., Bektas, F. (2005). "Effect of large amounts of natural pozzolan addition on properties of blended cements." Cement Concrete Research, 35(6), 1106-1111.
Yang, W. (2015). "The Issues and Discussion of Modern Concrete Science." Tsinghua University Press, Beijing and Springer-Verlag Berlin Heidelberg.

Database on the Long-Term Behaviour of FRC: A Useful Tool to Achieve Overall Conclusions

P. Serna[1]; A. Llano-Torre[1]; E. García-Taengua[2]; and J. R. Martí-Vargas[1]

[1]ICITECH - Institute of Concrete Science and Technology, Universitat Politècnica de València, Camí de Vera s/n, Valencia 46022, Spain. E-mail: pserna@cst.upv.es; aillator@posgrado.upv.es; jrmarti@cst.upv.es
[2]Queen's University of Belfast, David Keir Bldg., Stranmillis Rd., BT9 5AG Belfast, U.K. E-mail: e.garcia-taengua@qub.ac.uk

Abstract

The long term behaviour of Fibre Reinforced Concrete on cracked state is an important research topic, since it is essential to understand this property when using FRC as structural material. The RILEM CCF Technical Committee was created in order to focus the efforts of all researchers on the better understanding of creep behaviour. One of the objectives of the TC was to compile a global database of results of creep test in order to analyse this phenomenon in an overall review. In order to achieve a complete enough database, several minimal variables and parameters data have been proposed on this first attempt. This first database of creep results is based on flexural creep test with different environmental conditions. In future, it can be extended to other testing methodologies. Thanks to this database, first conclusions start reveal those variables which have a higher significance level in creep deferred behaviour.

INTRODUCTION

In Fibre Reinforced Concrete (FRC) specimens at cracked state under sustained loading, creep gives a deferred crack opening in the cracked section. The control and evolution of these crack openings through time is important considering the serviceability limit state and durability of FRC elements.

Several research groups over the world focus their studies on FRC in order to achieve a better understanding the long-term behaviour of FRC in the cracked state. Tensile creep in cracked state has been studied on both cylindrical specimens (Zhao et al. 2012) and prismatic specimens (Babafemi & Boshoff 2015). Flexural creep researches are more extended. Some of these studies are focused on the material characterization (Bast et al. 2007, Zerbino & Barragán 2012); meanwhile other studies are focused in the behaviour of FRC in structural elements or beams (Buratti and Mazzotti 2012, Vasanelli et al. 2013) in addition to traditional reinforcement. Nowadays there is not yet a clear explanation on how the obtained conclusions of tensile creep test can be related with the flexural creep behaviour.

There is no standardized methodology to test FRC flexural creep behaviour in cracked state either tensile creep response. Only in Austria exist an informative

guideline in flexural creep characterization (ÖVBB-Richtlinie 2008) Different setups for the flexural creep test have been used by different authors, and therefore it is not possible to draw accurate conclusions from the comparison of results from different sources. FRCs usually shows a great variability in their mechanical properties as residual strength that contributes to the dispersion of experimental outputs.

Specific creep terminology and analysis parameters have been recently proposed by Arango et al. 2012, as an attempt to establish a basis for the purpose of standardising, for the different stages of the creep tests processes which includes pre-cracking, loading, unloading, recovery and a final bending test until failure.

The RILEM CCF TC was created in 2014 with the objectives of coordinate research efforts and compile the results of studies about creep behaviour of FRC, evaluate the structural repercussions of creep, propose unified test methods to determine the parameters characterizing creep behaviour clarifying the criteria to analyse the test results, analyse the significant variables that influence creep behaviour of cracked sections and develop practical recommendations and design criteria for structural elements. In brief, the aim is to collect all available information and knowledge about creep and coordinate on-going research efforts to produce a state-of-the-art report and RILEM recommendations

Most of the studies about creep in FRC are not covering a general review of FRC creep since they are limited to one type of fibre, concrete mix design, or a certain fibre content or level load. Moreover, research data sets described in the literature are often incomplete and contain unexpected inconsistencies. This work about the proposed database compiled from flexural creep test follows this CCF TC objective. It is large enough to provide conclusion covering all ranges of variables.

This is a first attempt to stablish the principles and basement of a database. The authors have collect their own experimental data from flexural creep tests over 5 years of researches including over 80 specimens tested with different types of fibres, concretes and environmental conditions. All the results collected were obtained following the same methodology and creep test setup. These results are consistent so that the experimental results could be easily compared.

Finally, statistical analysis has been used to obtain general conclusions and trend of all FRCs that could not be advised without an overall review. This creep database and the following extensions would be very helpful in future investigations.

OBJECTIVES AND SCOPE

This works propose the structure of a global creep test results database compiled arranged by variables and kinds of data. At this moment, this database collects results of our own flexural creep test. The establishment of certain creep specific terminology and creep parameters definition is needed in order to obtain comparable results. This database may be extended in future to other creep test methodologies y suitable to compare different criteria.

The analysis of all these independent variables and creep parameters aid to obtain a global perspective of the relations of the variables of flexural creep behaviour of FRC in cracked state. This analysis can help to predict creep response of FRC elements.

CREEP TEST METHODOLOGY

Creep test procedure. The flexural creep tests procedure was carried out on notched FRC prismatic specimens, following the standard EN 14651, which were individually pre-cracked until a certain CMOD in a 4-point bending test. Once all specimens were pre-cracked, they were transferred to the creep frames as seen in Figure 1 and tested under sustained flexural load for at least 90 days. A more detailed description of this creep test setup-up methodology is given in Arango et al. 2012 and García-Taengua et al. 2014.

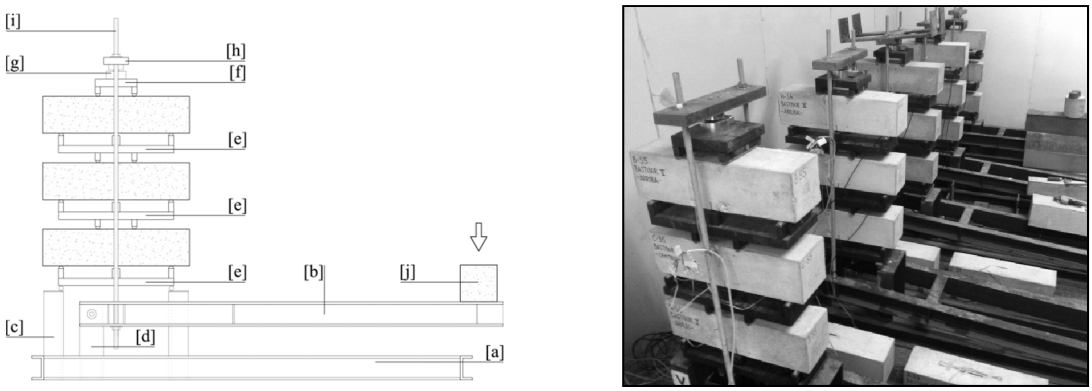

Figure 1. Flexural creep test set-up.

Variables. Main variables of these creep test are those referred to concrete like compressive strength f_c and those referred to fibres as dimensions, slenderness, material and dosage. Several types of fibres have been considered in reinforcement: steel, synthetic and glass fibres. All these variables are important to define the FRC residual behaviour but not all of them may be significant into the FRC creep behaviour.

Other variables are referred to the creep test set-up like the pre-cracking level w_p or the nominal load ratio IF_n, defined as the ratio between the load applied in creep frames to the specimens and the residual load at the pre-cracking test, usually corresponding to CMOD of 0.5 mm. That means that this load variable represents a percentage of the residual performance of each specimen.

During the creep test, variables as temperature and humidity were also continuously registered to ensure stable environmental conditions.

Creep test output data and coefficients. The idealized curve of the complete creep testing procedure is shown in Figure 2. This curve represents the three main stages of the creep test: pre-cracking stage (OC), creep stage (CF) and final bending test until failure (FH). These three curves plotted together represent the whole process of the creep test.

During the test, several parameters are measured and registered at different periods of the test. Some of main parameters of the test are also represented in Figure 2, such as the pre-cracking test crack opening w_p, pre-cracking test residual crack opening w_{pr}, instant crack opening w_{ci} and deferred crack opening w^t_{cd}. Other parameters are provided by Arango et al. 2012.

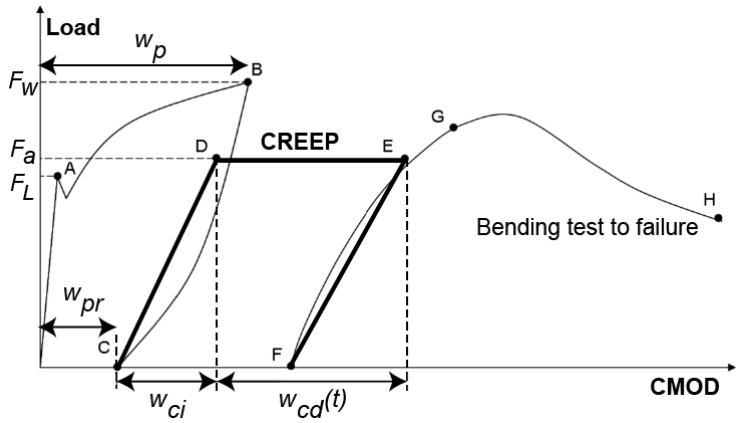

Figure 2. Idealized curve obtained in a complete testing process.

The main creep coefficients considered to evaluate creep behaviour are obtained by the experimental outputs following these expressions:

- Creep coefficient $\varphi^{o}_{w,j}$ referred to origin of the stress:

$$\varphi^{o}_{w,j} = w^{j}_{cd} / w^{o}_{ci}$$

where:

$$w^{o}_{ci} = w_{pr} + w_{ci}$$

- Creep coefficient $\varphi^{c}_{w,j}$ referred to the creep stage:

$$\varphi^{c}_{w,j} = w^{j}_{cd} / w_{ci}$$

- Crack Opening Rates COR(t_1-t_2):

$$COR^{t1-t2} = (w^{t2}_{cd} - w^{t1}_{cd}) / (t_2 - t_1)$$

All of these creep coefficients can be considered for different time periods in order to analyse the evolution of deferred strains during the test. For instance 0, 14, 30, 90, 180 and 360 days are proposed as time lapses.

CREEP DATABASE

Data groups. In order to be rigorous, it is recommended to gather all data in groups according to the information given of the data. This aggrupation aids to arrange all the data since otherwise, database will be a chaos. The first group proposal groups is: A *Identity data*, B *Environmental conditions*, C *Concrete matrix*, D *Fibres*, E *Flexural behaviour*, F *Test parameters*, G *Creep test output data* and H *Creep behaviour characterization*.

These data groups are arranged in order of appearance in the testing process, from data related to the research, specimens casting, concrete properties, testing results and final coefficients finally obtained.

It is important to clarify, that even if any data seems to be useless, all of them are designed to identify each specimen of the database and its origin in a fast and useful way. The more data provided the first time to the database, the better, since one will assure not be asked for more information in next future.

Data description. Each data group contains different items or data. All the data needed in each group is proposed in Table 1 in order to configure a database the most complete as possible.

Table 1. Listing of data, description and units of database.

N°	*Group*	*Data*	*Description*	*Units*
0.		IDRN	International Database Reference Number	
1.	A	Year	Year of realisation of creep test	yyyy
2.		Exp. campaign	Experimental campaign	--
3.		Citation Ref.	Citation Ref. / D.O.I. / Journal link	--
4.		Series	Concrete series or batch	--
5.		Name	Name/Reference of the specimen	--
6.	B	T^o	Temperature	°C
7.		RH	Relative Humidity	%
8.	C	D_{max}	Aggregate maximum diameter	mm
9.		f_{ck} / f_{ck}	Concrete Class / Targeted strength	MPa
10.		CC	Special Curing conditions: *aggressive environments*…	
11.		f_c	Compressive strength (cylindrical specimen)	MPa
12.		f_c	Compressive strength (cubic specimen)	MPa
13.	D	Material	Material of the fibres: steel synthetic, glass fibre…)	--
14.		Brand	Brand / Commercial reference	--
15.		l	Length of the fibre	mm
16.		$\emptyset$	Diameter of the fibre or diameter equivalent	mm
17.		λ	Slenderness of the fibre	--
18.		$D_{f,kg}$	Dosage in weight of fibres in concrete	kg/m^3
19.		$D_{f,\%}$	Dosage in volume of fibres in concrete	% Vol.
20.	E	F_L	Residual strength at *LOP*	MPa
21.		f_{R1}	Residual strength at *CMOD1*	MPa
22.		f_{R2}	Residual strength at *CMOD2*	MPa
23.		f_{R3}	Residual strength at *CMOD3*	MPa
24.		f_{R4}	Residual strength at *CMOD4*	MPa
25.		f_{R3} /f_{R1}	Residual strength ratio for post-crack behaviour	--
26.		*fib* Classif.	Post crack behaviour fib classification (*fib* MC 2010)	0x
27.	F	IF_n	Nominal Load Level	%
28.		F_a	Load applied	kN
29.		IF_a	Applied Load Level	%
30.		t_{max}	Total time of load applied into the specimens	days
31.	G	w_{pn}	Nominal pre-cracking expected	µm
32.		w_p	Pre-cracking test crack opening	µm
33.		w_{pr}	Pre-cracking test residual crack opening	µm
34.		w_{ci}	Loading stage instant crack opening	µm
35. to 39.		w^{j}_{cd}	Deferred crack opening at *j* days*	µm
40.		w^{tf}_{cd}	Deferred crack opening at t_f	µm
41.		w_{cui}	Instant crack opening recovery	µm
42.		w_{cud}	Deferred crack opening recovery	µm
43.		w^{tt}_{cr}	Final residual crack opening	µm
44. to 48.	H	$\varphi^{o}_{w,j}$	Creep coefficient referred to origin at *j* days*	--
49. to 53.		$\varphi^{c}_{w,j}$	Creep coefficient referred to creep stage at *j* days*	--
54. to 58.		COR^{i-j}	Crack Opening Rate from *i-j* days*	µm/day

* *Where* i *and* j *represents times lapses of 0, 14, 30, 90, 180 and 360 days.*

Although each specimen has its own name or references, a reference number inside the database is needed. Therefore, the *International Database Reference Number* or IDRN is proposed and given to each specimen provided to the database in order to identify all the specimens inside the database. *Identity data* of the experimental campaign and concrete specimens are really essential in order to identify the source and research of each specimen. These items will help after year to locate each specimen and any publication where the results appeared.

Some additional information data may be added in future updates of this database since this proposal is opened to discussion. The main goal is to achieve a useful creep test analytic tool.

Due to the large number of variables inside the database, Table 2 shows a sample extract from the database with certain of the variables values for some ID specimen.

Table 2. Sample extract of specimen data from the database.

ID	f_c	$D_{f,kg}$	IF_a	f_{R1}	f_{R3}	f_{R3}/f_{R1}	$\varphi^o_{w,90}$	$\varphi^c_{w,90}$	$COR^{0\text{-}14}$	$COR^{14\text{-}30}$	$COR^{30\text{-}90}$
43	73.7	4.5	36.0	0.7	1.0	1.301	0.200	1.410	0.80	1.21	0.72
44	73.7	4.5	42.0	0.9	1.6	1.822	0.240	1.850	1.05	1.19	0.90
45	73.7	4.5	56.0	0.9	1.5	1.690	0.300	1.910	2.23	1.22	0.87
46	70.0	9	37.0	2.3	3.5	1.506	0.350	1.070	3.33	1.51	0.95
47	70.0	9	39.0	1.9	3.9	2.016	0.240	1.050	2.19	0.94	0.75
48	70.0	9	55.0	1.2	3.9	3.353	0.180	0.880	1.67	0.54	0.45
49	70.1	3.5	39.0	1.3	0.2	0.164	0.250	1.500	2.82	1.24	--
50	70.1	3.5	40.0	1.0	--	--	--	--	3.04	2.73	5.05
51	70.1	3.5	45.0	0.7	--	--	--	--	--	--	--
52	70.4	9	40.0	3.4	5.2	1.551	0.180	0.710	2.91	1.52	0.51
53	70.4	9	39.0	3.2	4.4	1.393	0.300	0.940	2.91	1.93	0.79
54	70.4	9	39.0	3.0	4.0	1.357	0.350	1.150	2.89	2.31	1.09

This sample extract from the database helps to imagine how many data have been collected for this first attempt, but if more test results are added, it could became an essential tool for creep researchers.

ANALYSIS AND RESULTS

Once the database is compiled starts the overall analysis of creep test results. The main objective of this analysis is to evaluate the relations between the variables and the parameters of this database, identifying the variables that have a statistical significance on most of creep parameters. When these significant variables are identified, creep tests and creep parameters can be regarded in a global view and all global conclusions obtained will be very helpful in future for the design of experiments stage of new creep test.

Multiple Linear Regression. In this first analysis, a *Multiple Linear Regression* (MLR) has been applied in order to relate each creep parameter to the simple effect of the independent variables considered. These MLR models have been obtained by

means of a stepwise regression (Hair et al. 2009) considering a threshold for p-values identifying significant effects as 0.05 in all cases. That procedure assures a confidence level of 95% in all analysis.

After some preliminary analyses, as expected, a high degree of multicolinearity was detected if all similar variables were considered at the same time. It is not possible to consider all the variables in the same model, since their not being independent would compromise the reliability of any conclusion. Instead of that, different MLR modelling approaches must be considered.

In this first study, as independent variables have been taken the type of fibre, concrete compressive strength f_c, fibre content $D_{f,kg}$, and load ratio IF_a, following this general expression:

$$cp_i = K_i + a_i\, IF_a + b_i\, f_c + c_i\, D_{f,kg}$$

where cp_i refers to each creep parameter analysed; K_i is a coefficient dependent on the fibre type; a_i, b_i, and c_i are coefficients to be fitted; IF_a is the real applied load ratio in %; f_c is the compressive strength of concrete in MPa, $D_{f,kg}$ is the fibre content in kg/m^3.

The different creep parameters compared in this first approach were $\varphi^{o}_{w,90}$, $\varphi^{c}_{w,90}$, $COR^{0\text{-}14}$, $COR^{14\text{-}30}$ and $COR^{30\text{-}90}$, since they are some of the most representative parameters and all specimens have these values.

For the analysis of these creep parameters cp_i, all coefficients of variables have been estimated by least squares when the model is fitted to experimental data. The results of these significance tests on creep coefficients are summarized in Table 3. Each row of the table represents one MLR analysis by mean of one cross in case of significant effect of the variable and the R-squared value of the analysis. Blank cells in the table mean no statistically significant effects. A quick way of analyse the significance of each variable is counting the number of parameters on which each particular variable has a statistically significant effect by counting the crosses. Last row of the Tables 3 gives this count of significant effects for each variable.

Table 3. Results from MLR analyses on creep parameters: Significant variables.

	fc	$D_{f,kg}$	*IFa*	R^2
$\varphi^{o}_{w,90}$	x	x	x	0.8383
$\varphi^{c}_{w,90}$	x	x		0.7707
$COR^{0\text{-}14}$		x		0.4769
$COR^{14\text{-}30}$	x	x	x	0.4059
$COR^{30\text{-}90}$	x	x	x	0.3493
(Count)	*4*	*5*	*3*	

Results discussion. After the different analysis realized to the database, some clear tendencies can be observed plotting the equations vs. each variable. For instance, in Figure 3 are shown the evolution of the creep coefficient at 90 days referred to origin $\varphi^{o}_{w,90}$ along the range of both independent variables load ratio IF_a and compressive strength f_c. In these plots, the creep coefficient is transformed into a logarithmic parameter typified by the load ratio IF_a. In both cases, the evolution of the variable trends in a straight and continuous way what represent an exponential trend in the regular plot of the coefficient.

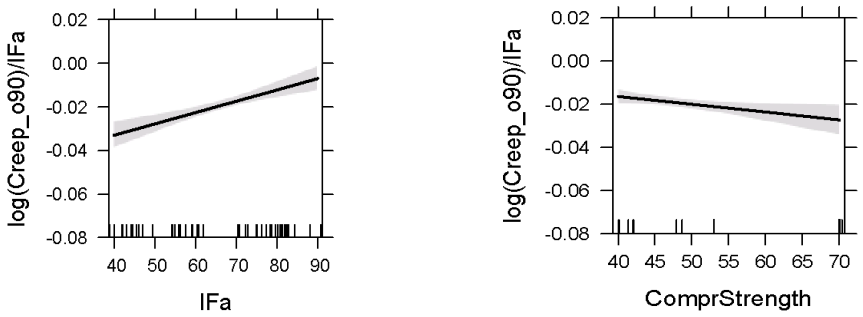

Figure 3. Tendencies of $\varphi^{o}_{w,90}$ versus the variables *IFa* and *fc*.

In case of load ratio IF_a plot, the creep parameter follows an ascendant evolution (positive), and that means that increasing the variable increases also the parameter. Therefore, that variable can be explained as statistically significant with positive sign. On the other hand, for the compressive strength f_c plot, the creep coefficient follows a descendant evolution (negative), what means that increasing the variable, the creep parameter decreases. In this case, the behaviour of this parameter shows a statistically significances of the variable in a negative way.

In a similar way, the analysis of creep coefficient referred to creep stage at 90 days $\varphi^{c}_{w,90}$, shows in Figure 4 the evolution along the variables presented with, in both cases, a clear straight and continuous tendency.

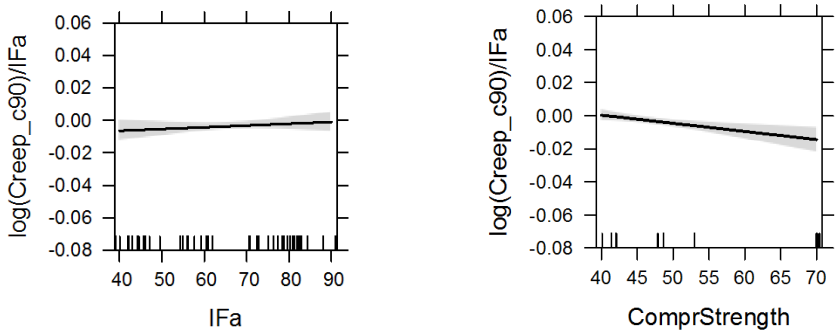

Figure 4. Tendencies of $\varphi^{c}_{w,90}$ versus the variables IF_a and f_c.

In this case, for load ratio IF_a variable plot, the creep parameter follows a straight evolution that seems to be horizontal. That justifies that the analysed variable has no statistical significance and the creep parameter remains stable in load ratio range. In the plot of compressive strength f_c variable, the creep coefficient follows a descendant evolution (negative), meaning a negative statistically significances: the higher compressive strength of the concrete, the lower creep coefficient.

The tendencies obtained in previous figures with the creep coefficient as logarithmic parameter typified by the load ratio, are confirmed in Figure 5, since a straight line turns into an exponential line if natural creep coefficients are represented. Both plots show exponential behaviours versus de load ratio variable IF_a. In case of the creep coefficient $\varphi^{o}_{w,90}$ referred to origin at 90 days, the parameter grows exponentially with the load ratio IF_a. Meanwhile, the $\varphi^{c}_{w,90}$, where the significance

was no relevant, the creep parameter values rest nearly constant even with highest levels of load ratio.

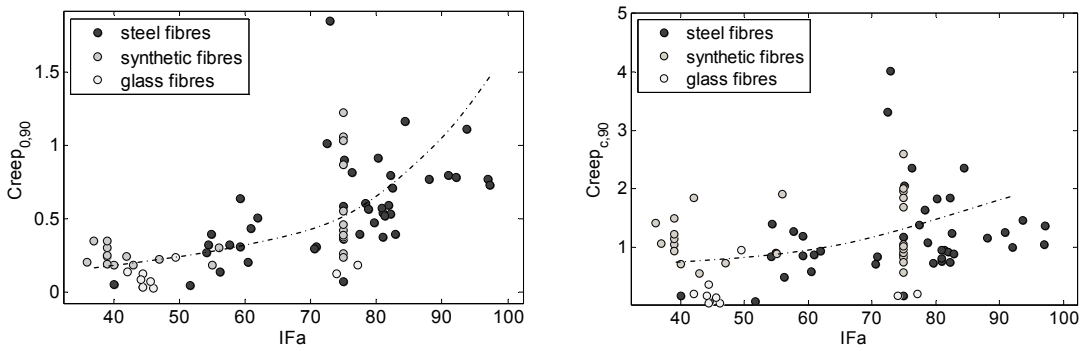

Figure 5. Evolution of $\varphi^{o}_{w,90}$ and $\varphi^{c}_{w,90}$ depending the IF_a applied.

These overall conclusions could not be obtained without this compiled database, since a high number of creep test results are needed in this kind of analysis. Moreover, each creep test gives few quantities of results in spite of their long duration, so it would be beneficial for all to compile the most creep test results as possible. The more results added to the database, the better and the closer conclusions will be obtained.

CONCLUSIONS

A first attempt of a database compilation of creep test results has been made and its subsequent analysis has made it possible to reach the following conclusions:

- Several creep testing methodologies exist making difficult the comparison between the different results. It is important to unify methodologies into a single one for each kind of creep test.
- A first proposal of a database and its structure has been made. This database is organised in data groups defined to collect comparable data.
- It is proposed a first attempt of unification of specific creep terminology and glossary for every researches and standards. This unification helps the researches avoid errors in tests comparison
- The proposed creep database is a useful tool in order to analyse global behaviour of different FRC specimens.
- An analysis of the database has been realised and first general conclusions of creep behaviour of FRC have been obtained, such as the high significance of the variables load ratio IF_a and in the creep parameters.

Everybody can participate in this database by providing their own test results and all participants will have free access to the whole database. The more results added to the database, the better and the closer conclusions will be obtained.

ACKNOWLEDGEMENTS

The authors of this work wish to thank the Spanish Ministry of Economy and Competitiveness and the European Regional Development Fund, for the following funded projects "BIA2012-35776 (FISNE)".

REFERENCES

Arango, S., Serna, P., Martí-Vargas, J. R. and García-Taengua, E. (2012). "A Test Method to Characterize Flexural Creep Behaviour of Pre-cracked FRC Specimens." *Experimental Mechanics*, 52, pp. 1067-1078.

Babafemi, A. J. and Boshoff, W. P. (2015). "Tensile creep of macro-synthetic fibre reinforced concrete (MSFRC) under uni-axial tensile loading." *Cement and Concrete Composites*, 55, pp. 62-69

Bast, T., Eder, A., and Kusterle, W. (2007). "Kriechversuche an Kunststoffmakro-faserbetonen Untersuchungen zum Langzeitverhalten von Faserbetonen unter Biegezugbeanspruchung - ein Zwischenbericht." *Faserbeton Beiträge* zum 11. Vilser Baustofftag, pp. 32-35.

Buratti N. and Mazzotti C. (2012). "Temperature effect on the long term behaviour of macro-synthetic and steel fibre reinforced concrete." In: *8th RILEM international symposium on fibre reinforced concrete: challenges and opportunities*, 19-21 September, Guimaraes, Portugal, 2012. p. 715-25.

EN 14651:2007. Test Method for Metallic Fibered Concrete - Measuring the Flexural tensile Strength (Limit of Proportionality (LOP), Residual), CEN - *European Committee for Standardization*, Brussels (2005), pp. 1-17.

fib Model Code for Concrete Structures 2010 (2013), Wiley-VCH Verlag GmbH & Co. KGaA, pp. 74-150.

García-Taengua, E., Arango, S., Martí-Vargas, J. R. and Serna, P. (2014). "Flexural creep of steel fiber reinforced concrete in the cracked state." *Construction and Building Materials*, 65, pp. 321-329.

Hair, F., Black, W., Babin, B. and Anderson, R. (2009). *Multivariate Data Analysis*, 7th edition, Prentice Hall, 2009, 816 pp.

ÖVBB-Richtlinie (2008). "*Faserbeton*", Österreichische Vereinigung für Beton- und Bautechnik, 2008, 109 pp.

Vasanelli, E., Micelli, F., Aiello, M. A. and Plizzari, G. (2013). "Long term behavior of FRC flexural beams under sustained load." *Engineering Structures*, 56, pp. 1858-1867.

Zerbino R. and Barragán B. (2012), Long-term behavior of cracked steel fiber reinforced concrete beams under sustained loading. ACI Materials Journal, 109 (2), pp. 215-224.

Zhao G, Di Prisco M. and Vandewalle L. (2012). "Experimental research on uni-axial tensile creep behaviour of pre-cracked steel fibre reinforced concrete". In: *8th RILEM international symposium on fibre reinforced concrete: challenges and opportunities*, 19–21 September, Guimaraes, Portugal, 2012. p. 760-771.

Preliminary Studies on the Effect of C&DW on the Long-Term Properties of Sustainable Self-Compacting Concrete

S. Manzi[1]; C. Mazzotti[1]; and M. C. Bignozzi[1]

[1]Department of Civil, Chemical, Environmental and Materials Engineering, University of Bologna, Viale Risorgimento 2, 40136 Bologna, Italy. E-mail: stefania.manzi4@unibo.it; claudio.mazzotti@unibo.it; maria.bignozzi@unibo.it

Abstract

The mix-design of self-compacting concrete (SCC) with both fine and coarse concrete waste from construction and demolition (C&DW) is investigated. The effects of concrete recycled aggregates on fresh state behavior and short- and long-term mechanical and physical properties of new structural SCC are investigated to ascertain the feasibility of SCC with medium-high mechanical strength. A reference SCC mix, prepared with natural aggregates and the same water/powder ratio as those prepared with recycled aggregates, is reported for comparison. An integrated approach involving porosimetric analysis and mechanical characterizations has been carried out. Porosity measurements and mechanical investigations combined with time-dependent properties, such as shrinkage and creep are reported as fundamental features to assess structural SCC behavior.

INTRODUCTION

In the last years the reuse of concrete waste from construction and demolition (C&DW) has become object of great interest in order to reduce the environmental impact related to waste disposal and natural aggregates use (Manzi et al. 2013, Mazzotti et al. 2013, Behera et al. 2014). Self-compacting concrete (SCC) represents one of the major technical innovations in the field of materials for civil engineering (Domone 2006, Nikbin et al. 2014). Its positive features mainly result from the elimination of mechanical compaction. Compared to ordinary vibrated concrete, SCC offers several advantages in terms of both technology and worker health and safety conditions. One interesting benefit is the enhancement of the working conditions in building sites, especially the suppression of health and safety issues associated with the vibration task. The possibility of employing C&DW in SCC has not been properly investigated yet. In particular, only a few studies have been made on SCC with C&DW and mainly on coarse C&DW (Kou et al. 2009, Grdic et al. 2010). Moreover, there are no data on long-term properties of SCC with concrete recycled aggregates.

In this paper, the mix-design of SCCs with both fine and coarse C&DW is investigated. Concrete waste coming from the demolition of a never finished concrete building was crushed and properly assorted to create grain size distributions suitable to produce high quality SCC for structural applications. This waste represented a very

good choice for recycling high-grade concrete in new concrete structures because at the time of demolition there were no internal partitions (i.e., gypsum, brickwork) inside the building.

The effects of both fine and coarse concrete recycled aggregates (ranging from 25 to 40 % of total amount of aggregates) on fresh state behavior and short- and long-term mechanical and physical properties of structural SCC are investigated to ascertain the feasibility of SCC with medium-high mechanical strength.

An integrated approach involving porosimetric analysis and mechanical characterizations has been carried out. Porosity measurements and mechanical investigations combined with time-dependent properties (i.e., shrinkage and creep) are reported as fundamental features to assess structural SCC behavior.

EXPERIMENTAL CAMPAIGN

Materials. Conventionally available SCC components were used to prepare the mixes. Cement type CEM II-A/LL 42.5 R and calcium carbonate were used as binder and filler, respectively, in all the SCC mixes. An acrylic based superplasticizer and a biopolymer based viscosity modifying agent (VMA) were used as admixtures in all the SCC mixes. As natural aggregates, sand (0-6 mm) and fine gravel (6-16 mm) were used with a cumulative grain size distribution (sand: 60 vol% and fine gravel 40 vol%) complying with Fuller distribution. As recycled aggregates, concrete waste coming from the demolition of a never finished Italian concrete building was used (Bari, 2006). Compressive tests made on concrete cores taken from the original building showed medium compressive strength ($f_{cm} \approx 36$ MPa). After on-site crashing treatment and steel separation, further crushing treatments were made in the laboratory to obtain three different fractions (0-4 mm, 4-8 mm and 8-16 mm), with a cumulative grain size distribution curve similar to that one of natural aggregate and to Fuller distribution (0-4 mm: 47 vol%, 4-8 mm: 21 vol% and 8-16 mm: 32 vol%). Recycled aggregates present dry bulk density values lower than natural aggregates and, correspondingly, higher values of water absorption.

Specimen preparation and testing. Starting from a reference mix-design (named S0) with 100% of natural aggregates (sand: 60 vol% and fine gravel: 40 vol%), according to obtained cumulative grain size distribution curve, two new SCC mixes were studied. A first concrete mix, named S1, was prepared replacing 25 vol% of natural aggregates (both fine and coarse) with recycled aggregates (both fine and coarse). The original proportions inside natural and recycled aggregates determined with the cumulative grain size distributions curves were maintained. A second concrete mix, named S2 was prepared replacing 40 vol% of natural aggregates (both fine and coarse) with recycled aggregates (both fine and coarse).

The studied mixes are reported in Table 1. Cement content (350 kg/m^3), filler content (220 kg/m^3), *Dmax* (16 mm) and viscosity modifying agent were maintained constant for all the SCC formulations. The same water/powder ratio (0.3) and admixtures amount were used for all the SCC formulations. Natural and recycled aggregates were used in saturated surface-dried (ssd) conditions and the mixes were prepared in a laboratory concrete mixer (190 L volume).

Table 1. Concrete mix design.

	S0	*S1*	*S2*
Cement (kg/m^3)	350	350	350
Water (kg/m^3)	179	172	172
Filler (kg/m^3)	220	220	220
Water/powder ratio	0.3	0.3	0.3
Natural aggregates[(a)] (kg/m^3)	1598	1198	959
Recycled aggregates[(a)] (kg/m^3)	0	360	577
Superplasticizer[(b)] (%)	1	1	1
VMA[(b)] (%)	0.4	0.4	0.4

[(a)]saturated surface-dried (ssd) conditions; [(b)]mass% on cement amount

The slump-flow (*SF*), flow rate (t_{500}) and J-ring test (*SFJ*) were determined according to EN 11350-8 and EN 12350-12, respectively.

For each formulation, 14 cylindrical concrete samples (diameter: 12 cm, height: 24 cm), 2 prisms (10 x 10 x 40 cm^3) and 2 cubic samples (15 x 15 x 15 cm^3) were prepared and cured for 28 days at 20 ± 1°C and R.H. > 95%, for physical and mechanical tests. Bulk density (*D*) measurement (determined by mass/volume ratio) and water absorption (*wa*) test at atmospheric pressure were performed on 2 cubic concrete samples, according to UNI 7699. Concrete strength tests were performed using a universal testing machine (4000 kN). Compressive strength (f_{cm}) was determined according to EN 12390-3 on 4 concrete cylindrical samples per mix. Secant elastic modulus (*E*) and tensile splitting strength (f_{ct}) were measured on 2 cylindrical samples, according to UNI 6556 and EN 12390-6, respectively. Three-point flexural strength (f_{cf}) was determined on 2 concrete prisms, according to EN 12390-5.

Pore size distribution was investigated by mercury intrusion porosimeter (MIP, Carlo Erba 2000), equipped with a macropore unit (Fisons 120) on samples (about 1 cm^3) representative of the cement mortar around coarse aggregates obtained by concrete cylinders after 28 days of curing.

The long-term behavior of the recycled aggregates concretes was investigated by creep and shrinkage tests. Two cylinders for each mix were subject to creep test at 28 days from casting, according to ASTM C512/C512M-10 standard, and two cylinders were subject to shrinkage test, starting after two days from casting. All the tests were performed in a climate chamber at 20 ± 1 °C and 60 % R.H. for about two years with specimens in drying conditions. The longitudinal strain variation with time of each cylinder was measured by using electrical strain gauges connected to a digital acquisition system (Mazzotti et al. 2012). For creep tests, a compression stress of about 30 % of the actual strength at the time of loading (i.e., within stress limit of linear viscoelasticity) was applied at 28 days.

RESULTS AND DISCUSSION

Fresh state behavior. Properties of the SCC mixes in the fresh state are reported in Figure 1*a*. All the mixes showed slump-flow (*SF*) > 600 mm, which is the lower limit of flowability for self-compacting concrete (UNI 11040). Both S1 and S2 mixes with fine and coarse recycled aggregates showed values of *SF* higher than the reference mix S0. This increase can be ascribed to the high water absorption capacity of the fine recycled aggregates compared to natural sand that needs a higher amount of water in the mix in order to be in the saturated surface-dried condition. This amount of water could not be held by the aggregates, thus increasing the initial flowability of the mix (Kou et al. 2009). All the investigated mixes showed values of flow rate (t_{500}) within 12", in accordance with SCC specifications (UNI 11040). The visual observation of the slump-flow diameters at the end of the flowing showed a uniform distribution of the particles in the mixes, with no evidence of segregation. As for the J-ring test, only S2 mix slightly exceeded the recommended value of *SFJ-SF* (i.e., 55 mm instead of 50 mm), while the other mixes fulfilled the Standard request (UNI 11040). The visual observation of the slump-flow diameters at the end of the flowing through obstacles showed a uniform distribution of the particles in the mixes, with no evidence of segregation. This result shows how the use of recycled aggregates for SCC could be a feasible way, even substituting a high amount of natural aggregates with C&DW.

Hardened state behavior. The physical and mechanical properties of the investigated concrete mixes after 28 days of curing are reported in Figures 1*b* and 2, respectively. All the mixes show similar values of bulk density (*D*), while a slightly increase in the water absorption (*wa*) can be observed with the increase of the recycled aggregates amount (Figure 1*b*).

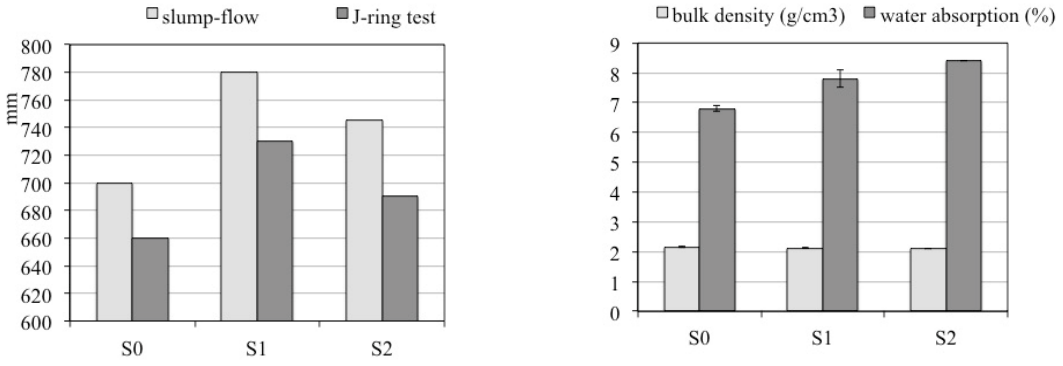

(*a*) (*b*)

Figure 1. Physical properties of the investigated mixes at the fresh (*a*) and hardened state (*b*).

The higher the recycled aggregate amount in the mix-design is, the higher the SCC compressive strength (f_{cm}) is (Figure 2*a*). This increase in terms of f_{cm} is correlated to a good adhesion between the new SCC paste and the adhered mortar of the recycled aggregates. In accordance with compressive strength, S2 samples show the highest values of elastic modulus (*E*) (≈ 28 GPa), whereas S1 samples show *E* values similar to the reference SCC, even if slightly lower (Figure 2*a*). The presence

of the adhered mortar in the recycled aggregates does not affect the elastic modulus. On the contrary, it contributes to increase f_{cm}, creating a good adhesion between the old and the new paste. In the SCC mixes, both the tensile splitting strength (f_{ct}) and the three-point flexural strength (f_{cf}) values (Figure 2*b*) slightly decrease with the increase of C&DW amount. This result is in accordance with the slightly increase of *wa* values previously obtained (Figure 1*b*).

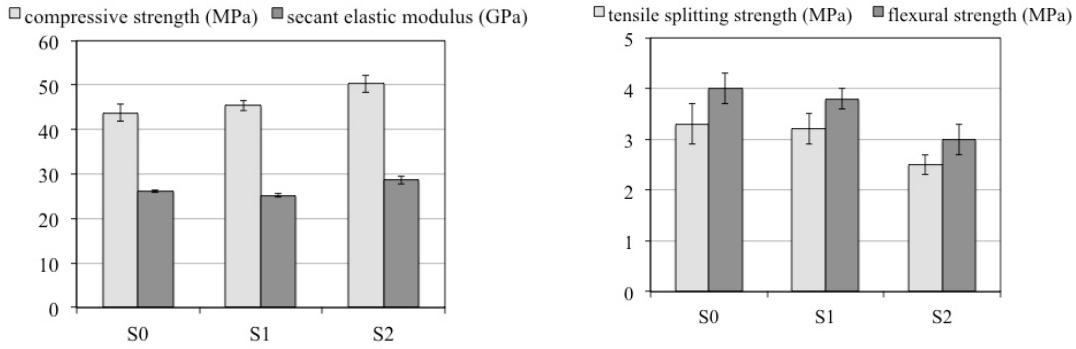

(*a*) (*b*)

Figure 2. Mechanical properties of the investigated mixes: compressive strength and secant elastic modulus (*a*), tensile splitting strength and three-point flexural strength (*b*).

Porosity. Figure 3 reports the cumulative pore size distributions, determined by MIP, for the investigated samples representative of the cement matrix porosity. All samples exhibit a negligible porosity for pores greater than 0.2 μm, whereas some small differences in pore size distribution curves are evident for pores dimension < 0.2μm. Increasing the content of recycled aggregates, total open porosity slightly increases. S0 shows the lowest total open porosity among the investigated samples. This result is in accordance with the *wa* increases (Figure 1*b*) and both f_{ct} and f_{cf} decreases (Figure 2*b*) with the C&DW increases in the SCC mixes.

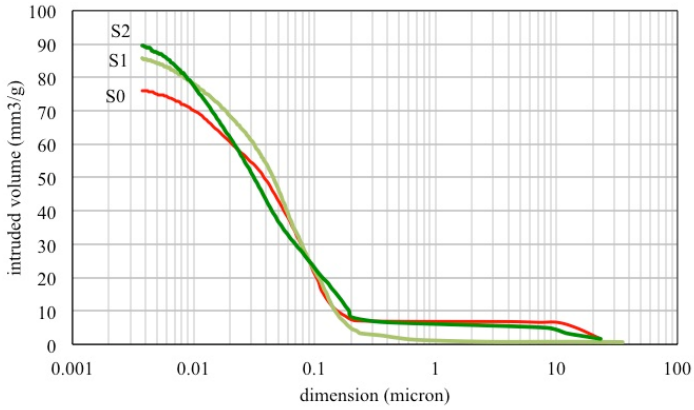

Figure 3. Pore size distribution of the investigated samples.

Long-term behavior. Figure 4 shows the long-term behavior of all the SCC mixes tested for nearly 2 years. Regarding the shrinkage behavior (autogenous and drying

contributions) all curves are similar (Figure 4*a*), showing a rapid shrinkage strain increase in the first three months. The slope of the curves decreases with time, becoming almost flat after ten months. S0 and S1 are very similar in values, while S2 exhibits the smallest strains among the investigated SCC samples, in accordance with the highest f_{cm} values (Figure 2*a*). Specific creep curves (creep strain per unit of applied stress, basic and drying contributions together) are reported in Figure 4*b*: all the curves have a similar behavior. In accordance with shrinkage curves, the presence of C&DW does not influence the specific creep behavior. The slope of the curves decreases with time. After about 4 months the creep phenomenon is less active. S2 exhibits the smallest specific creep among the investigated SCC samples, in accordance with the lowest shrinkage (Figure 4*a*) and the highest f_{cm} values (Figure 2*a*).

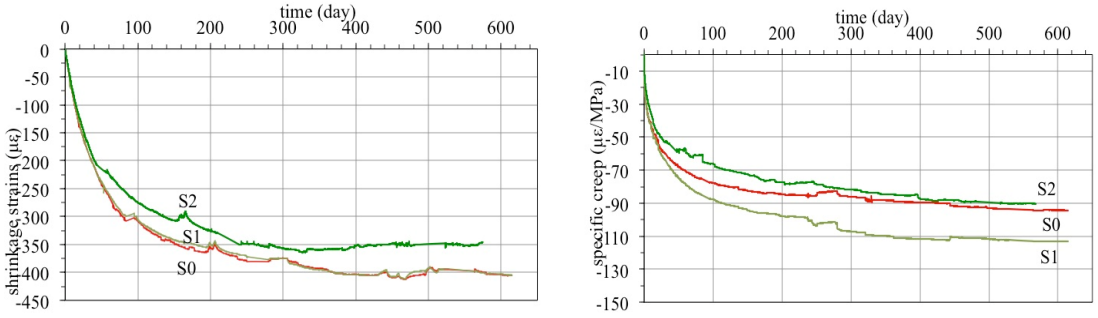

(a) (b)

Figure 4. Long-term behavior of the investigated samples: shrinkage strains (a) and specific creep (b).

CONCLUSIONS

The possibility of replacing both fine and coarse fraction of natural aggregates with C&DW in SCC mixes has been successfully investigated. The effects of both fine and coarse concrete recycled aggregates on fresh state behavior and short- and long-term mechanical and physical properties of structural SCC have been investigated to ascertain the feasibility of SCC with medium-high mechanical strength (i.e., 50 MPa). An integrated approach involving porosimetric analysis and mechanical characterizations combined with time-dependent properties (shrinkage and creep), has been successfully carried out. This work strengthens the concept of sustainability in civil constructions combining the use of coarse and fine concrete recycled aggregates to produce structural SCC with a low environmental impact.

REFERENCES

Behera, M., Bhattacharyya, S.K., Minocha, A.K., Deoliya, R. and Maiti S. (2014). "Recycled aggregate from C&D waste & its use in concrete – A breakthrough towards sustainability in construction sector: A review." *Construction and Building Material*s, 68, 501-516.

Domone, P.L. (2006). “Self-compacting concrete: An analysis of 11 years of case studies.” *Cement & Concrete Composites*, 28, 197-208.

Grdic, Z.J., Toplicic-Curcic, G.A., Despotovic I.M. and Ristic, N.S. (2010). “Properties of self-compacting concrete prepared with coarse recycled concrete aggregate.” *Construction and Building Materials*, 24, 1129-1133.

Kou, S.C. and Poon, C.S. (2009). “Properties of self-compacting concrete prepared with coarse and fine recycled concrete aggregates.” *Cement & Concrete Composites*, 31, 622-627.

Manzi, S., Bignozzi, M.C. and Mazzotti C. (2013). “Short and long-term behavior of structural concrete with recycled concrete aggregate.” *Cement and Concrete Composites*, 37, 312-318.

Mazzotti, C. and Savoia M. (2012). “An experimental campaign on the long-term properties of self compacting concretes.” *Adv Struct Eng*,15(7), 1155-1166.

Mazzotti, C., Manzi, S. and Bignozzi, M.C. (2013). “Role of recycled concrete aggregates on the long-term behavior of structural concrete.” *Mechanics and Physics of Creep, Shrinkage, and Durability of Concrete: A Tribute to Zdenek P. Bazant - Proceedings of the 9th Int. Conf. on Creep, Shrinkage, and Durability Mechanics, CONCREEP-9, Boston*, 388-395.

Nikbin, I.M., Beygi, M.H.A., Kazemi, M.T., Vaseghi Amiri, J., Rabbanifar, S., Rahmani, E.and Rahimi S. (2014). “A comprehensive investigation into the effect of water to cement ratio and powder content on mechanical properties of self-compacting concrete.” *Construction and Building Materials*, 57, 69-80.

Experimental Study on the Effects of a Loading Rate on the Shear Performance of an RC Beam

V. Piseth[1]; K. Nakarai[2]; N. Chijiwa[3]; and K. Maekawa[4]

[1]Master Student, Department of Civil and Environmental Engineering, Hiroshima University, 1-4-1, Kagamiyama, Higashi-Hiroshima 739-8527, Japan. E-mail: piseth_van@hotmail.com
[2]Associate Professor, Department of Civil and Environmental Engineering, Hiroshima University, 1-4-1, Kagamiyama, Higashi-Hiroshima 739-8527, Japan. E-mail: nakarai@hiroshima-u.ac.jp
[3]Assistant Professor, Department of Civil Engineering, Tokyo Institute of Technology, 2-12-1, Ookayama, Meguro, Tokyo 152-8550, Japan. E-mail: chijiwa@cv.titech.ac.jp
[4]Professor, Department of Civil Engineering, The University of Tokyo, 7-3-1, Hongo, Bunkyo, Tokyo 113-8654, Japan. E-mail: maekawa@concrete.t.u-tokyo.ac.jp

Abstract

Three 200x320x2300mm RC beams were tested under three different loading conditions to investigate the effects of loading rate on the shear performance of RC beam. Tested at loading rate 10mm/1hr, RC Beam 1 represents specimen under normal loading while RC Beam 2 represents specimen under slow loading at loading rate 10mm/100hr from 60kN. Tested at loading rate 10mm/100hr from 100kN, RC Beam 3 represents specimen under both normal and slow loading. The results showed that RC Beam 1, 2 and 3 had diagonal cracking load of 134.1kN, 133.6kN and 133.9kN and had ultimate failure load of 137.5kN, 146.2kN and 161.6kN respectively. Although these results indicated similar diagonal cracking strength, slow loading had influences on the ultimate failure load and crack pattern. The locations of diagonal bending crack for RC Beam 1, 2 and 3 were approximately 350mm, 530mm and 390mm from the center of the beam on the failure side. The location of bending cracks was affected by slow loading rate. As a consequence, slow loading had significant effects on the location of diagonal cracks so that it increased the ultimate failure load.

INTRODUCTION

The sustained load problem could occur in old structure constructed decades ago especially underground structure such as tunnel. In the aged structure design based on old specification, shear stress might be higher than that of the recent structure. Under this circumstance, creep shear failure might occur in the concrete structure. Rüsch (1960) studied the effects of sustained loading and loading rate on compressive strength of concrete and found that sustained loading and slower loading

rate resulted in lower ratio of concrete maximum stress to cylinder strength. Experimental work done by Sarkhosh et al. (2013) investigated shear capacity of reinforced concrete (RC) beams under sustained loading and revealed that sustained loading has no significant effect on the shear capacity. However, the loading and displacement measurement system by Sarkhosh et al. could be further improved to better understand shear performance. There are few other studies of sustained load on shear performance of RC beams and the results are inconclusive. With the improved system, different loading rates are one of the approaches to verify the sustained loading effects. Based on this consideration, the effect of loading rate on shear performance of RC beam was investigated by experimental work.

EXPERIMENTAL PROGRAM

Materials and mixture proportions. Table 1 lists the properties of the materials used in this study while Table 2 tabulates the mixture proportion for cylindrical specimens and RC beams. The water to cement ratios (W/C) adopted in this study is 0.50.

Table 1. Material properties

Materials	Type	Properties
Cement	Ordinary Portland Cement	Specific gravity: 3.04
		Specific surface area: 3650 cm2/g
Fine aggregate	Crushed quartz	Surface-dry specific gravity: 2.58
Coarse aggregate	Crushed gravel (20-05)	Surface-dry specific gravity: 2.62

Table 2. Mixture proportion

Name	W/C (%)	Design Value		s/a (%)	Unit Weight (kg/m^3)						
		Slump (cm)	Air (%)		W	C	S		G		AD
							S1	S3	G1	G3	
50NC-SL	50	8±2	4.5±1.5	44.6	170	340	503	271	537	440	SV10L

Abbreviation: water (W), sand (s), aggregate (a), gravel (G) and admixture (AD)

Cylindrical specimens and RC beams. Cylindrical specimens of diameter 100mm by height 200mm for compressive strength and Young's modulus test as well as specimens of diameter 150mm by height 200mm for splitting tensile test were prepared. The testing ages were 1, 3, 7, 28, 91, and at the loading age of the RC beams for all cylindrical specimens except day 1 for splitting tensile specimen. The size and dimension of the RC beams are shown in Figure 1 with tension reinforcement ratio of 0.8%. High strength deformed steel reinforcement (f_y=1062N/mm^2) was used in this study in order to induce shear failure.

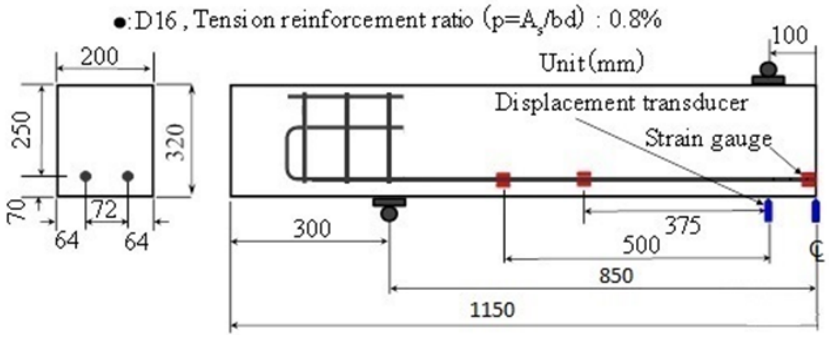

Figure 1. Outline of RC beams

Measurement system. Two concentrated load were applied on top of RC beams during testing at 100mm from center line on each side. The shear span to effective depth ratio was fixed to 3.0. Three displacement transducers were placed at the center of RC beams along bottom line to measure the average displacement. These transducers have capacity of measuring from 10mm to 50mm with minimum graduations of 0.001mm to 0.02mm. At the same time, these displacement transducers have a capacity of 25mm to 50mm with minimum graduations of 0.002mm to 0.005mm in diagonal tension direction. Additionally, they have capacity of 10 mm to 25 mm with minimum graduations of 0.001mm to 0.002mm in diagonal compression directions. Same type of transducers was used to measure vertical and horizontal displacements with capacity of 10mm to 50mm and minimum graduations of 0.001mm to 0.005mm. Displacement transducers for measurement of shear, vertical and horizontal displacements were installed on stainless steel beams with L-shape section. The details of installation of the displacement transducers are illustrated in Photo 1. Due to possibility of multiple cracks, crack widths were measured by π-shaped displacement transducers at every 100mm interval with capacity of 2 mm and minimum graduation of 0.001 mm as shown in Photo 1. Separate reinforcement strain gauges were installed at predetermined locations along reinforcement bar.

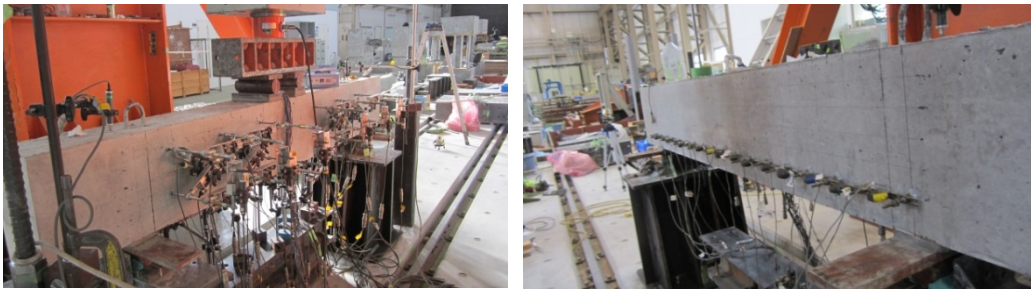

Photo 1. Overall view of RC beam set up

Loading condition of RC beam. Three RC beams were subjected to three different loading conditions until failure: normal loading rate at 10mm/1hr as RC beam 1, normal loading rate at 10mm/1hr until 60kN followed by slow loading rate 10mm/100hr as RC beam 2, and normal loading rate at 10mm/1hr until 100kN followed by slow loading rate 10mm/100hr as RC beam 3 as shown in Table 3. Before testing, all RC beams were carefully inspected and none were found to have

any cracks. During testing, the development of cracks was checked at every 10kN interval until failure after 30kN mark in order to give a clearer understanding of loading rate effect. To avoid creep effect during every crack check, the load was manually decreased to approximately 5kN from the in-progress-load. Categorized as structurally crucial crack, diagonal crack was observed to begin its development between two key intervals: 60kN and 100kN.

Table 3. Loading conditions of RC beams

Representation	Normal Loading	Slow Loading	Normal & Slow Loading
	RC beam 1	RC beam 2	RC beam 3
Normal Rate: 10mm/1hr	0kN to ultimate failure	0kN to 60kN	0kN to 100kN
Slow Rate: 10mm/100hr	-	60kN to ultimate failure	100kN to ultimate failure

RESULTS AND DISCUSSION

Mechanical properties of concrete. The results of compressive strength, Young's modulus and splitting tensile strength are shown in Table 4. Both cylindrical specimens and RC beams were prepared and sealed using aluminum tape and cured under normal room temperature. Then, the seal were removed after 28 days so that drying effect on RC beams was minimized especially during testing at loading age.

Table 4. Mechanical properties of concrete

Age	Compressive Strength	Young's Modulus	Splitting Tensile Strength
(days)	(N/mm^2)	(kN/mm^2)	(N/mm^2)
1	13.0	21.0	-
3	23.6	27.2	2.59
7	29.3	29.7	2.98
28	35.1	31.9	2.94
91	40.4	31.1	3.44
130 (loading age)	39.8	29.7	3.28

Effects of loading rate. Starting from center line, one half portion of RC beam that diagonal crack occurred was referred as failure side and the other half portion was referred as non-failure side as indicated in Photo 4. Method to determine the precise diagonal cracking load value is generally considered as critical so the combination of on-site visual observation, load-deflection curve, and shear force-shear deflection relationship were applied in all of the three RC beams. RC beam 1 had diagonal cracking load and ultimate failure load of 134.1kN and 137.5kN while RC beam 2

had diagonal cracking load and ultimate failure load of 133.6kN and 146.2kN respectively. And RC beam 3 had diagonal cracking load and ultimate failure load of 133.9kN and 161.6kN as shown in Figures 2 and 3. From load and deflection curve, diagonal cracking load was observed by the noticeable decrease of load with respect to deflection. Although this trend was valid for all RC beams, RC beam 3 showed large increase in load and deflection afterward. After diagonal cracking load of 133.6kN, RC beam 2 failed at first failure load of 135.9kN with deflection of 6.14mm. Then, RC beam 2 showed increase in load and deflection again after 9.29mm deflection until ultimate failure load. This phenomenon is due to change of failure mechanism from failure side to non-failure side in the case of RC beam 2. As a consequence, failure side on the left span of RC beam 2 could be considered as first failure and non-failure side on the right span could be considered as second-failure as shown in Photo 4. Slow loading allowed more time for beam internal structure to response to loading. However, this change was not observed in case of RC beam 3 which represented normal and slow loading. At diagonal cracking load, RC beam 1, 2 and 3 had average deflection of 5.23mm, 5.68mm and 5.63mm at the beam center respectively. At ultimate failure load, displacement transducer at beam center showed that RC beam 1, 2 and 3 had average values of 6.14mm, 13.0mm and 8.25mm respectively. The values of diagonal cracking load are again confirmed by shear force-shear displacement relationship in Figures 4 and 5 for failure and non-failure side of RC beam. From shear force and shear displacement relationship, diagonal cracking load was observed by the noticeable decrease of shear force with respect to displacement. Although this trend was valid for all RC beams, RC beam 3 showed large increase in shear force and displacement afterward. This trend is similar to load and deflection curve of RC beam 3.

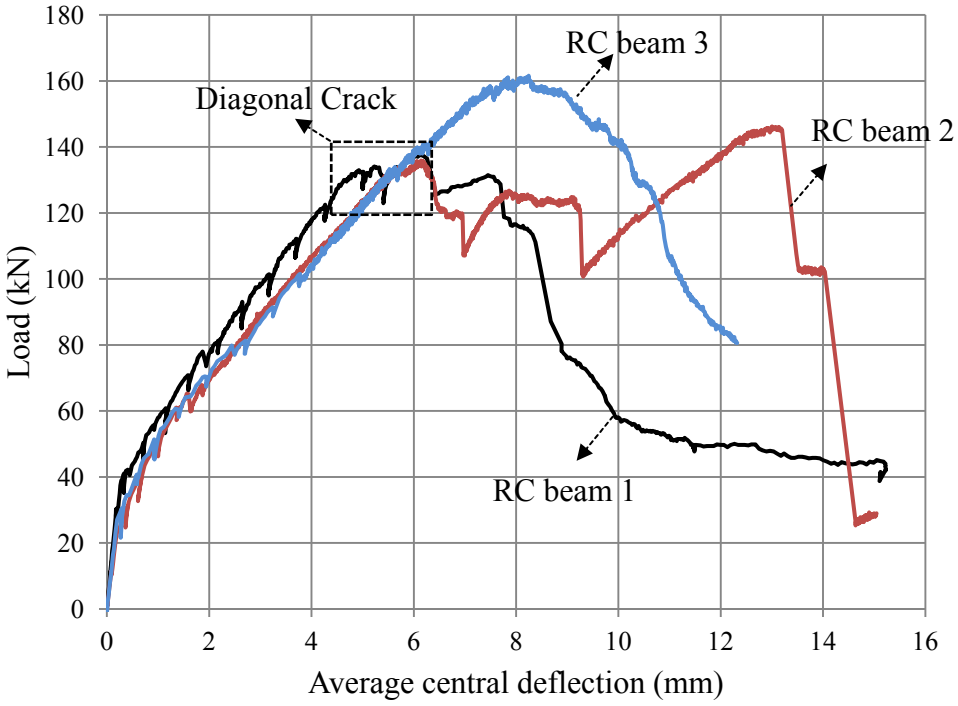

Figure 2. Load and average central deflection graph of RC beams

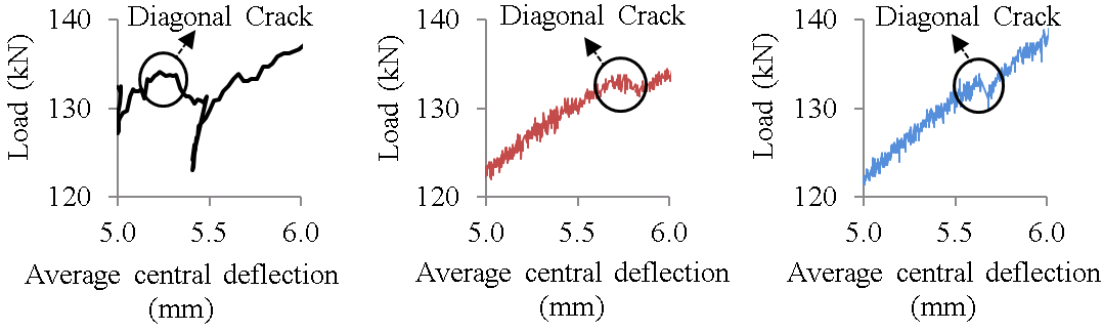

Figure 3. Close up view of diagonal cracking load of RC beams

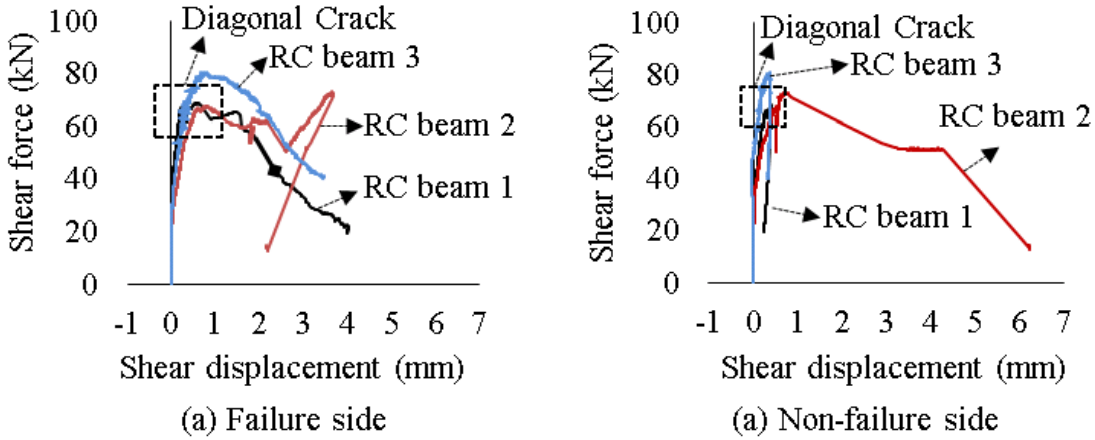

Figure 4. Shear force and shear displacement of RC beams

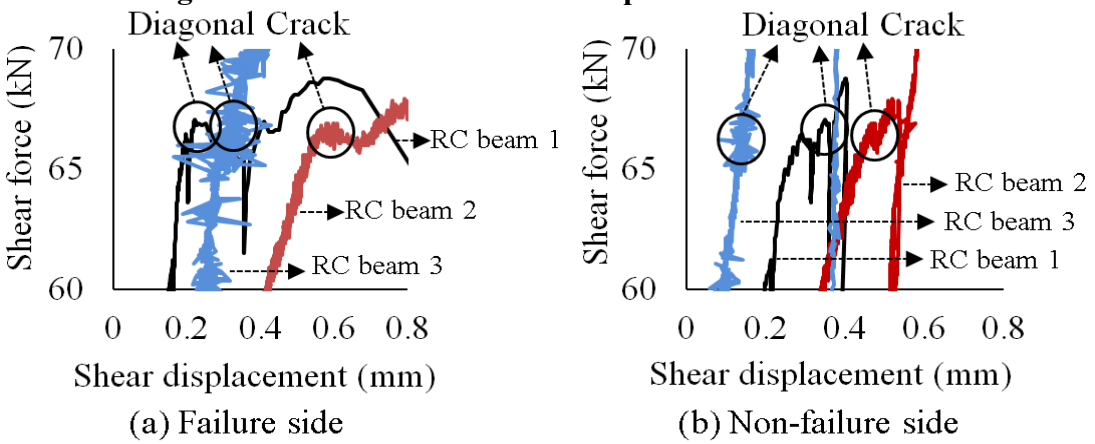

Figure 5. Close up view of shear force and shear displacement at diagonal crack

The estimated and measured values of RC beam capacity with ratio of flexural cracking moment and diagonal cracking strength are shown in Tables 5 and 6. For flexural cracking load of RC beam 1, the measured value was higher than estimated value and it was difficult to explain the cause. For RC beam 2 and 3, the measured values were smaller than estimated value and this reduction might be the effect of shrinkage after seal removal. While the estimated value of diagonal cracking load is

calculated using Niwa's equation, the ratios of estimated and measured value of diagonal cracking load are 1.23, 1.22 and 1.23 for RC beam 1, 2 and 3.

Table 5. Estimated values of RC beam capacity

Specimen Name	Estimated values			
	Flexural cracking load	Flexural cracking moment	Diagonal cracking load	Diagonal cracking strength
	$P_{cr,calc}$	$M_{cr,calc}$	$V_{c,calc}$	$\tau_{c,calc}$
	kN	kNm	kN	N/mm^2
RC Beam 1	31.4	11.7	109.1	1.1
RC Beam 2				
RC Beam 3				

Table 6. Measured values of RC beam capacity

Specimen Name	Measured values					$M_{cr,exp}/M_{cr,calc}$	$\tau_{c,exp}/\tau_{c,calc}$
	Flexural cracking load	Flexural cracking moment	Diagonal cracking load	Diagonal cracking strength	Ultimate failure load		
	$P_{cr,exp}$	$M_{cr,exp}$	$V_{c,exp}$	$\tau_{c,exp}$	$P_{ult,exp}$		
	kN	kNm	kN	N/mm^2	kN	-	-
RC Beam 1	42.2	15.8	134.1	1.341	137.5	1.35	1.23
RC Beam 2	24.5	9.2	133.6	1.336	146.2	0.78	1.22
RC Beam 3	28.2	10.6	133.9	1.339	161.6	0.90	1.23

There are large differences of ultimate failure load between the three RC beams. Both RC beam 2 and 3 had higher ultimate failure load than RC beam 1. And, both RC beam 2 and 3 that were partially subjected to slow loading rate tends to have more branched crack pattern than normal loading RC beam 1 as shown in Photos 2 and 3. This branched crack can be explained by the fact that slow loading allows more time for beam internal structure to response to loading.

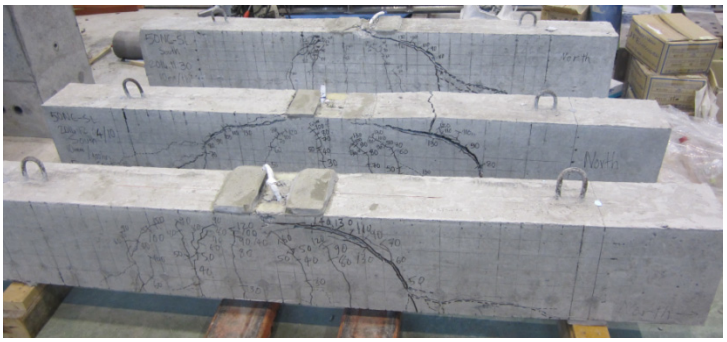

Photo 2. Overall view of cracked RC beams

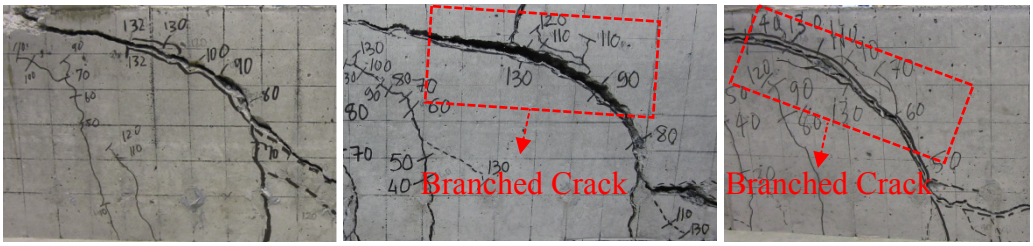

(a) RC beam 1 (b) RC beam 2 (c) RC beam 3

Photo 3. Close up view of crack pattern of RC beams

Beside diagonal cracking load and central deflection, RC specimen 1, 2 and 3 had diagonal cracking distance of approximately 350mm, 530mm and 390mm from beam center as shown in Photo 4. Represented slow loading, RC beam 2 had bending crack much further from center of the beam than those of RC specimen 1 and 3.

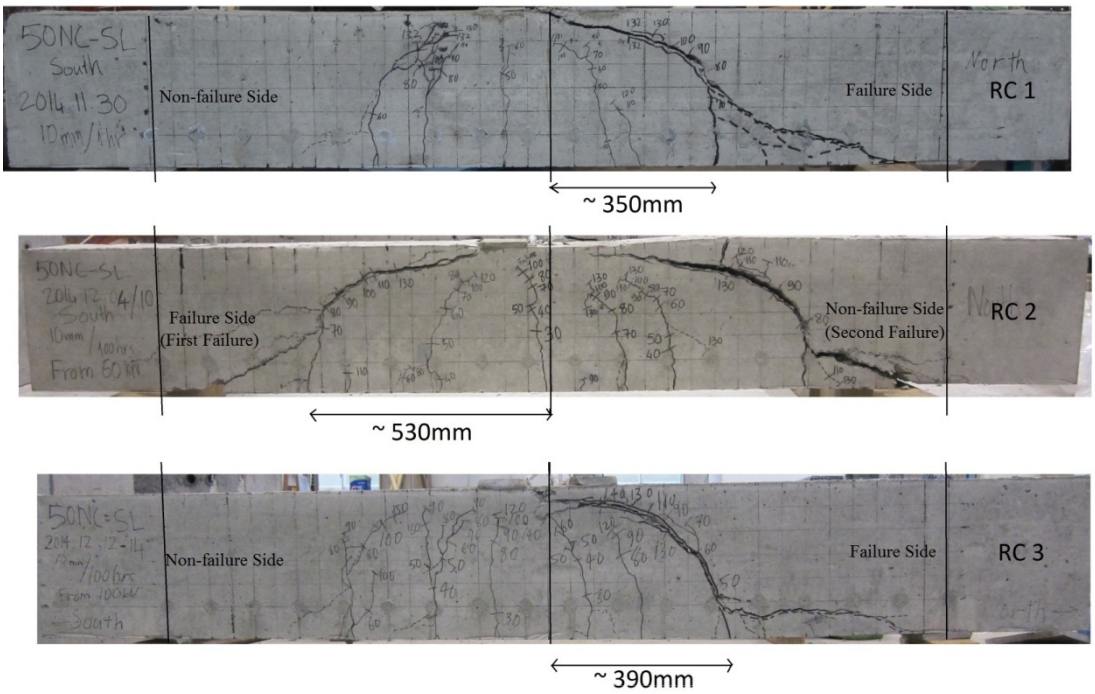

Photo 4. Location of diagonal crack and crack pattern of RC beams

CONCLUSION

Different loading rates were applied on three 200x320x2300mm RC beams to determine time-dependent effects on the shear performance. RC beam 1 represented specimen under normal loading while RC beam 2 represented specimen under slow loading. To better understand different loading rate, RC beam 3 was selected to represent specimen under slow and normal loading. Although these results indicated similar diagonal cracking load, slow loading had influences on the ultimate failure load. Slow loading allowed more time for internal beam structure to response to loading. In addition, slow loading rate affected the location of bending crack. At the same time, bending cracks directly affected diagonal cracks. As a consequence, slow

loading had significant effects on the location of diagonal cracks. Within the boundary of this study, three unanswered facts are revealed about different loading rate on shear capacity of RC beam: no significant effect on diagonal cracking load, effect on ultimate failure load, and effect on location of diagonal crack. Due to limited number of testing, additional specimens are required to get more accurate results. Since all three RC beams were tested by displacement control setting, future study will use load control setting and the effects of load control setting on shear performance of RC beam will be studied.

ACKNOWLEDGEMENT

This study is financially supported by MEXT/JSPS KAKENHI 23226011.

REFERENCES

Niwa, J., Yamada, K., Yokozawa, K., and Okamura, H. (1986), “Revaluation of the equation for shear strength of reinforced concrete beams without web reinforcement”, *Journal of Materials, Concrete Structures and Pavements*, Japan Society of Civil Engineers, No.372/V-5, pp.167-176. (in Japanese)

Rüsch, H. (1960). "Researches toward a general flexural theory for structural concrete." *ACI Journal Proceedings*. Vol. 57. No. 7. ACI.

Sarkhosh, R., Walraven, J., Den, U. J., and Braam, R. (2013). "Shear capacity of concrete beams under sustained loading." *IABSE Symposium Report*. Vol. 99. No. 31. International Association for Bridge and Structural Engineering.

Experimental Study on the Creep Behavior of Alkali-Silica Reaction (ASR) Damaged Concrete with Slow/Late Aggregates

H. Özkan[2]; H.-W. Reinhardt[1]; O. Mielich[2]

[1]Department of Construction Materials, University of Stuttgart, Germany.
[2]Materials Testing Institute University of Stuttgart, Otto-Graf-Institute, Germany.

Abstract

Concrete that has been damaged by alkali-silica reaction (ASR) is used in many cases still for a longer period of time. To calculate the residual strength and the deformation of ASR-damaged structures knowledge of the strength, of the elastic modulus and creep are required. The focus of most studies [ICAAR] is put on the damage mechanisms of expansion occurring, the crack formation and decreasing short-term strength. In addition, the concretes investigated were not made with slow/late aggregates in most cases. The research project has the goal to investigate the creep of concrete with slow/late aggregates. These react only after long-term (10 to 20 years). The slow/late aggregates stem from quartz porphyries (rhyolites), greywacke, quartzite, granite, andesite and high-grade crushed gravel from the Upper Rhine. The results presented in this study include concrete with different aggregates, namely tree alkali-sensitive ones (greywacke from the Lower Harz, quartz porphyry from the Halle Porphyry Complex and crushed gravel from the Upper Rhine valley) and one alkali-insensitive aggregate (quartz porphyry from the Black Forest).

1. INTRODUCTION

For creep of ASR damaged concrete, very few publications have been found. Herrador et al. describes tests on concrete with aggregate from granodiorite. The rock has been classified in accordance with ASTM C289 as non-reactive, since the soluble SiO_2 content was only 2.67 mmol/l. A dam created with it showed, however, after 12 years, first ASR damage. In another study of Blight, it was found that the creep of AAR damaged concrete can be two and a half to four times that of undamaged concrete.

In the present study, the results of ASR-damaged concretes made with slow/late aggregates, are discussed with respect to mechanical properties and creep.

2. MATERIALS AND METHODS

2.1 Aggregates used

Four crushed aggregates are used which are greywacke from the lower Harz (GW), quartz porphyry from the Halle Porphyry Complex (QP), quartz porphyry from the Black Forest (QP(SW)) and crushed gravel (boulders) from the Upper Rhine valley (OR). The alkali sensitivity of the rocks was assessed with the accelerated mortar test according to [Franke et al. (2004)] which is derived from [Oberholster et al. (1986)] and [RILEM (2000)]. Additionally the alkali sensitivity of the rocks was assessed within a period of 560 days with the fog chamber test at 40 °C used in Germany, similar to the internationally usual concrete prism test (RILEM AAR-3). With the mentioned tests, greywacke (GW), quartz porphyry (QP) and crushed gravel from the Upper Rhine valley (OR) were found to be ASR sensitive while quartz porphyry (QP(SW)) turned out to be insensitive.

2.2 Concrete composition

The cement used is a Portland cement CEM I 32.5 R [EN 197-1 (2000)] with 1.30% by mass Na_2O equivalent. Table 1 shows the composition of the four concrete mixes. The cement content is always 400 kg/m^3, the water-cement ratio amounts to 0.45, and the grading curve follows almost the Fuller curve with 16 mm maximum grain size. It is designated as AB 16 according to the German DIN 1045-2. 30% by vol. of the aggregates consist of non-reactive sand up to 2 mm and 40% stem from reactive and non-reactive rock with grain size 2/8 and 30% 8/16 mm resp.

Table 1: Composition of concrete mixes

Concrete indicator	Aggregate	Storage	Cement		Aggregate proportion[1)]
		40°C fog chamber	Designation	Total alkali content	
			-	M.-% $Na_2O_{equ.}$	Vol.-%
GW	crushed greywacke	x	CEM I 32.5 R	1.30	30 + 70
QP	crushed quartz porphyry	x			
OR	crushed gravel from Upper Rhine	x			
QP(SW)	crushed quartz porphyry	x			

[1)] 30 Vol.-% non-reactive sand, 70 Vol.-% reactive and non-reactive aggregates resp.

2.3 Specimens and storage conditions

Cylinders with 300 mm height and 150 mm diameter are used for the determination of the expansion. Cubes with 150 mm edge length serve for the determination of the compressive strength. Cylinders with 300 mm height and 150 mm diameter are tested in compression for the modulus of elasticity.

After mixing of each concrete mix, the specimens were stored at 20°C and 95 % RH. After 28 days of storage, the concrete cylinders were placed in a fog chamber at (40 ± 2.0) °C during 560 days. Measurements of the expansion are taken continuously up to 560 days. In addition, the specimens are visually inspected. Compressive strength and the static modulus of elasticity are determined at 28, 140, 280, and 560 days.

2.4 Creep tests

The specimens for compressive creep are cylinders with 300 mm height and 150 mm diameter. For each parameter combination, two specimens are provided. The creep tests were performed on samples that were stored 28 days at 20/95, 140 days, 280 days and 560 days in a fog chamber. Creep tests were carried out with a load corresponding to one third of the characteristic 28 days cylinder strength in a climatic chamber at a constant temperature of 23°C and 80% RH. With the creep, shrinkage/swelling of concrete cylinders of the same production under the same environmental conditions was further measured. The exposure time was 365 days for all concretes. The deformation during creep was measured at regular intervals using a dial gauge.

The test rigs for long-time creep were developed and produced at the institute. The application of the load is carried out with a hydraulic jack which can be operated with a hydraulic hand pump. After application of the load, the force is maintained by Belleville springs. The control of the applied load is measured by means of load cells. A picture of the creep rig and a detailed drawing can be seen in Figure 1.

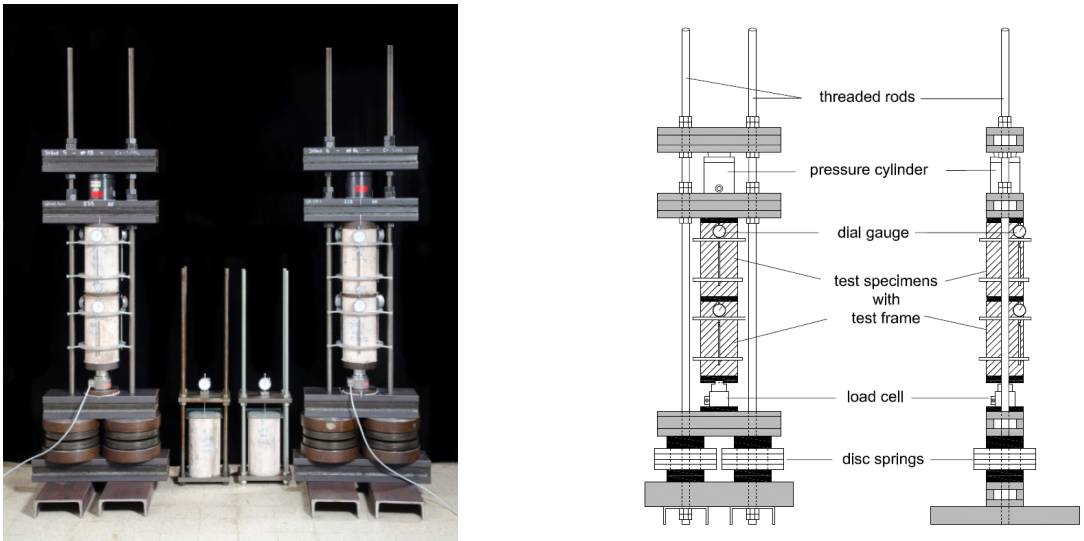

Figure 1. Test rig for compressive creep

3. RESULTS AND DISCUSSION

The results of this experimental study showed that alkali-silica reaction (ASR) affects not only the expansion behavior, but also the static modulus of elasticity and creep. All concretes investigated show an increase in the compressive strength (Table 2). The measured compressive strength values after 28 days of moist storage serve as reference values. The warm, humid environment in the fog chamber favors this increase regardless of the ASR.

Table 2: Development of compressive strength (MPa))

Aggregate type	Moist Storage	Storage time in the fog chamber in days		
	28 d	140	280	560
OR	52,1 (100)	57,9 (111)	61,5 (118)	65,4 (125)
GW	50,6 (100)	69,2 (137)	71,4 (141)	72,7 (143)
QP	53,4 (100)	69,6 (130)	74,5 (140)	81,5 (153)
QP(SW)	54,5 (100)	72,5 (133)	74,2 (136)	83,8 (154)

Also, the static modulus of elasticity of concrete with alkali-insensitive aggregate (QP(SW)) show an increase with storage period. In concrete with alkali-sensitive aggregates, the static modulus of elasticity decrease with the alkali-silica reaction (Table 3). Only if the ASR cannot proceed as a result of leaching, a renewed increase in the static modulus occurs. In Table 2, the static Young's modulus values are referred to the 28-day value (in brackets).

Table 3: Development of the static modulus of elasticity (MPa)

Aggregate type	Moist storage	Storage time in the fog chamber in days		
	28 d	140	280	560
OR	37702 (100)	15805 (42)	20750 (55)	28934 (77)
GW	40302 (100)	43391 (108)	16440 (41)	25931 (64)
QP	36031 (100)	41078 (114)	41551 (115)	22342 (62)
QP(SW)	31729 (100)	38682 (122)	39543 (125)	40191 (127)

The cylinder strains of concrete with alkali-sensitive aggregates showed major expansions or larger crack widths as opposed to concrete with alkali-insensitive aggregates. The cylinder expansion of the concrete are plotted at 40°C fog chamber storage as function of the storage period (Figure 2).

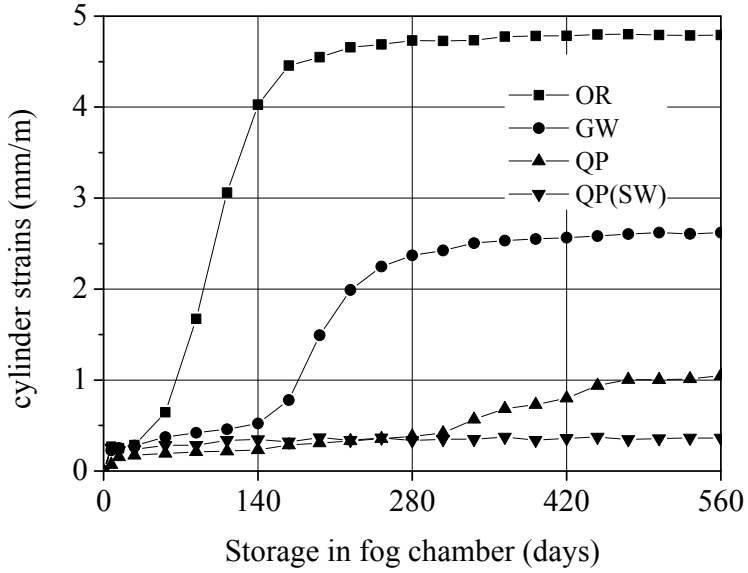

Figure 2. Strain measured on cylinder

The strains of all concretes were measured at regular intervals during the pre-damage in the fog chamber. The concrete with crushed gravel from the Upper Rhine valley as aggregate (OR) had a severe damage during storage in the 40°C fog chamber, indicating a high damage potential of the aggregate used. These concretes start after approx. 50 days to react. They reached a maximum elongation of approx. 4.8 mm/m from approx. 6-month storage period. The reaction flattens after 140 days again. The static modulus of elasticity increases from this point again (Table 3).

In case of concrete with QP however, the initial ASR induced expansion (after 12 months of storage in the fog chamber) starts to flatten approximately after 17 months of storage. The total expansion of concrete with QP reaches a value of 1 mm/m (Figure 2).

The concretes with alkali-sensitive aggregate show higher creep strain than the alkali-resistant. Depending on the progress of the AKR creep has a different course. The most damaged concrete specimens (OR and GW) have a higher creep damage than the less damaged. It is worth noting, however, that the creep strain curves after flattening (the end of the alkali-silica reaction) due to leaching becomes smaller again. There is a healing process, because without the additional alkali supply in the fog chamber ASR cannot proceed. This process causes the static modulus of elasticity to increase again and the creep to increase less.

The general trend of the concrete creep curves (Figure 3-6) corresponds well to those given in the literature on creep [Rüsch et al. (1962)].

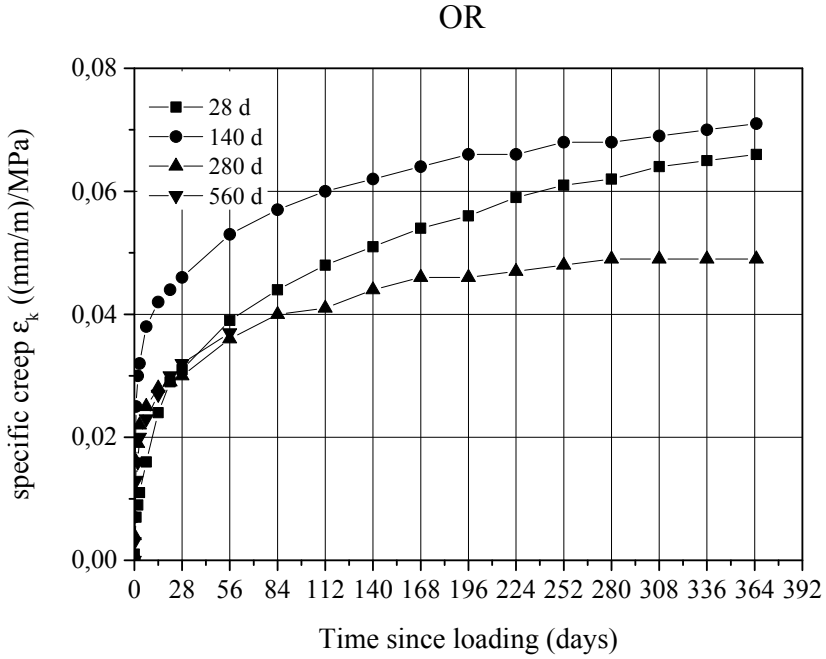

Figure 3. Specific creep of concrete with crushed gravel from the Upper Rhine valley as aggregate (OR) after different pre-storage time in fog chamber

The concretes with crushed gravel from the Upper Rhine valley as aggregate (OR) showed the largest expansions in the fog chamber. Also, these concretes show a larger creep than the other concretes. The strains due ASR achieve in this concrete its maximum after 140 days (Figure 2). Therefore, the specific creep of 140 days pre-damaged concrete samples is higher than the other concretes made with the same grain size (Figure 3). The specific creep of the sample stored 140 days in the fog chamber reached a final value of 0.071 (mm/m)/MPa after 365 days. By leaching of concrete samples no ASR takes place from that date instead, the increase of strain is idle and the static modulus of elasticity is increasing (Figure 2). Thus, the creep of concrete samples with crushed gravel from the Upper Rhine valley as aggregate (OR) are lower than the samples of 140 d fog chamber storage.

A similar trend is also evident in the concrete specimens with greywacke (GW) and quartz porphyry (QP). Up to a halt the reaction due to leaching of concrete samples creep strains are getting bigger. The concrete with greywacke (GW) as aggregate stored 280 days in fog chamber reached a maximum specific creep of 0.06 (mm/m)/MPa, whereas the concrete with quartz porphyry (QP) as aggregate reached a specific creep of 0.047 (mm/m)/MPa after 560 days of fog chamber storage.

Once the ASR cannot proceed, the change in length is to stand and static modulus increases. This makes the creep smaller.

The specific creep of the concrete samples with greywacke (GW) as aggregate (Figure 4) and quartz porphyry (QP) as aggregate (Figure 5) are shown in the following diagrams.

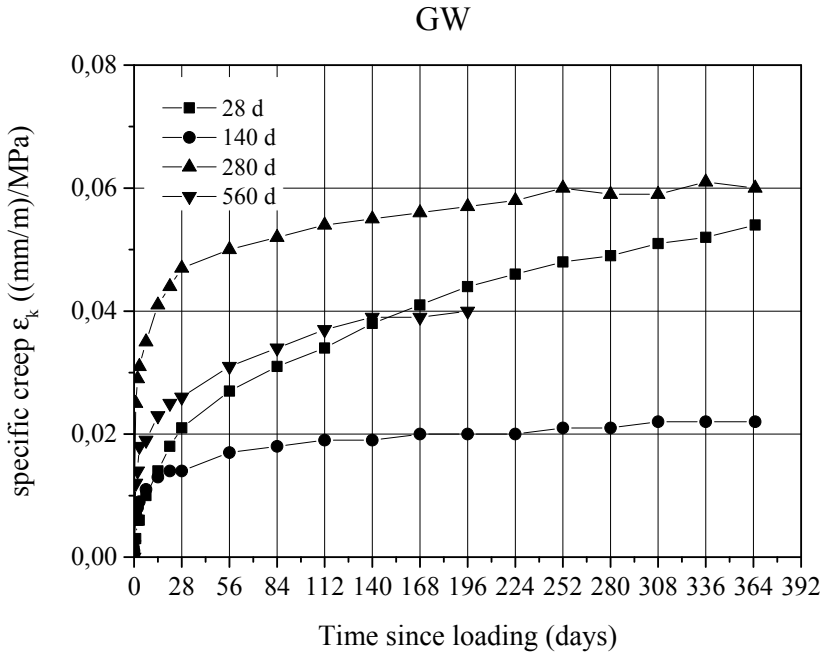

Figure 4. Specific creep of concrete with greywacke (GW) as aggregate after different pre-storage time in fog chamber

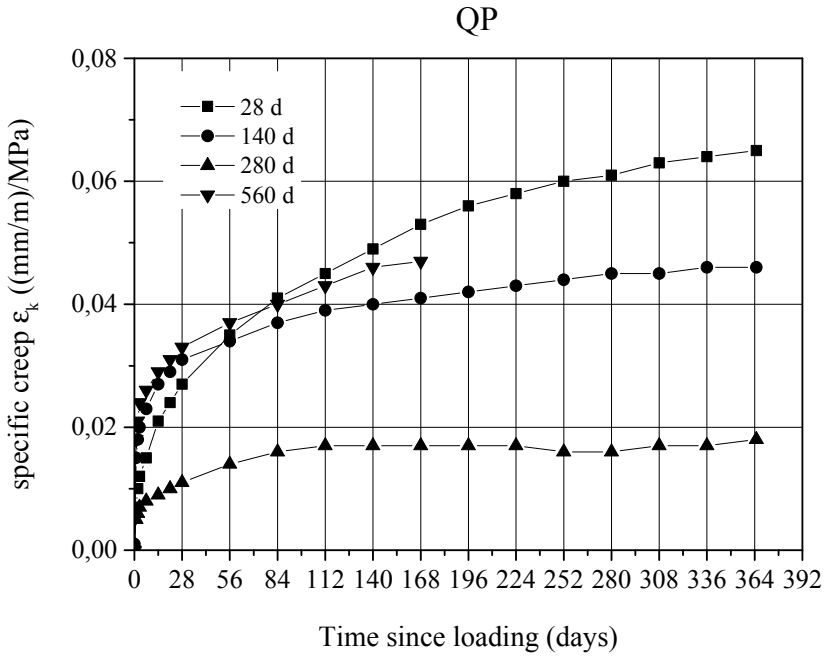

Figure 5. Specific creep of concrete with quartz porphyry (QP) as aggregate after different pre-storage time in fog chamber

In the concretes made with the quartz porphyry from the Black Forest (QP (SW)), however, the creep is getting smaller (Figure 6). These concretes were classified alkali-resistant and showed even after 560 days of storage in the chamber no damage.

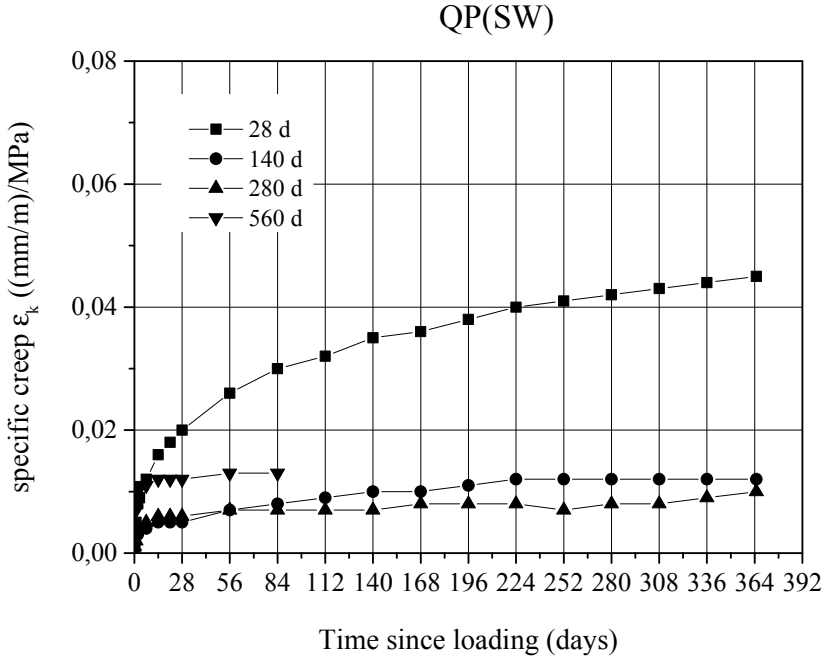

Figure 6. Specific creep of concrete with quartz porphyry from the Black Forest (QP (SW)) as aggregate after different pre-storage time in fog chamber

4. CONCLUSION

It has been shown that the static modulus of elasticity significantly depends on the storage time in the fog chamber. All the examined concretes with slow/late aggregates show an increase in the compressive strength, so it can be that compressive strength results of ASR damages concrete are misinterpreted [Mielich and Reinhardt. (2011)].

The concretes made with crushed gravel from the Upper Rhine valley (OR) and greywacke (GW) showed a strong degradation caused by ASR in warm, humid environment. The damaged concrete samples of these aggregates have a higher creep than the less or not damaged concrete.

The course of creep of concrete is dependent on the static modulus of elasticity and expansion. The creep depends mainly on the static modulus of elasticity. The smaller the static modulus of elasticity, the higher is the creep. On the other hand, with a significant increase in expansion the creep increases accordingly. It is worth noting, however, that after termination of the ASR due to the leaching, the creep of the concrete samples becomes smaller, and at the same time increases the static modulus of elasticity again.

REFERENCES

Blight, G.E. (1996). *Engineering properties of reinforced concrete damaged by AAR*. 10th Intern. Conf. on alkali aggregate reaction in concrete. Melbourne, Australia, pp. 987-994

DIN 1045 Part 2 (2008). Concrete, reinforced and prestressed concrete structures – Part 2: Concrete – Specification, properties, production and conformity – Application rules for DIN EN 206-1 (in German)

EN 197-1 Cement – Part 1 (2000). Composition, specifications and conformity criteria for common cements. German version EN 197-1:2000 + A1:2004

Franke. L, Witt, S. (2004). *Accelerated test for alkali reaction: application of an internationally recognized quick test to German conditions*. Concrete Plant + Precast Technology 70, No. 5, 14-21

Herrador, M.F., Martínez-Abella, F., Fernández-Gago, R. (2009). *Mechanical behavior model for ASR-affected dam concrete under service load: formulation and verification*. Materials & Structures 42 pp. 201-212

ICAAR (International Conference on Alkali-Aggregate Reaction in concrete). Conference Proceedings of the ICAAR since 1974

Mielich, O., Reinhardt, H.W. (2011). *Strength properties as an evaluation criterion for failure analysis of ASR-damaged concrete structures*. Bauinstandsetzen und Baudenkmalpflege 17 no. 3 / 4, pp 1-14

Oberholster, R.E., Davies, G. (1986). *An accelerated method for testing the potential alkali reactivity of siliceous aggregates*. Cement and Concrete Research 16, No. 2, 181-189

RILEM Recommended Test Method AAR-2 Detection of Potential Alkali-Reactivity of Aggregates (2000). The Ultra accelerated Mortar-bar Test. Materials and Structures 33, No. 229, 283-289

Rüsch, H, Kordina, K., Hilfsdorf, H. (1962). *Der Einfluss des mineralogischen Charakters der Zuschläge auf das Kriechen von Beton*. German Committee for Reinforced Concrete (DAfStb), Heft 146

Delayed Shear Crack Formation of Shallow RC Box Culverts in Service

N. Chijiwa[1]; X. Zhu[2]; H. Ohno[3]; S. Tanabe[4]; K. Nakarai[5]; and K. Maekawa[6]

[1]Department of Civil Engineering, Tokyo Institute of Technology, Ookayama 2-12-1-M1-21, Meguro, Tokyo 152-8552, Japan. E-mail: chijiwa@cv.titech.ac.jp
[2]Department of Civil Engineering, The University of Tokyo, Hongo 7-3-1, Bunkyo, Tokyo 113-8656, Japan. E-mail: zhu@concrete.t.u-tokyo.ac.jp
[3]Tokyo Electric Power Company, Uchisaiwai-cho 1-1-3, Chiyoda, Tokyo 100-8560, Japan. E-mail: oono.hiroki@tepco.co.jp
[4]Tokyo Electric Power Company, Uchisaiwai-cho 1-1-3, Chiyoda, Tokyo 100-8560, Japan. E-mail: tanabe.shigeru@tepco.co.jp
[5]Department of Civil Engineering, Hiroshima University, Kagamiyama 1-4-1, Higashi-Hiroshima, Hiroshima 739-8527, Japan. E-mail: nakarai@hiroshima-u.ac.jp
[6]Department of Civil Engineering, The University of Tokyo, Hongo 7-3-1, Bunkyo, Tokyo 113-8656, Japan. E-mail: maekawa@concrete.t.u-tokyo.ac.jp

Abstract

Long-term excessive deformation of underground RC box culverts in service was monitored over 20 years and its mechanism is analytically discussed in this study. The long-term excessive deformation possibly attributes to synergy effects accompanying delayed shear failure of RC slabs subjected to vertical soil pressures and the time-dependent creep-shrinkage of structural concrete. Special attention is directed to the delayed shear cracking which was actually found in real underground box culverts over the service life. The delayed shear crack is experimentally reproduced in the laboratory as well as the multi-scale computational simulation.

INTRODUCTION

Kunieda et.al (2014) reported that top slabs of shallow underground RC box culverts were seriously deformed with numerous cracking. After a few decades of service, the deflection of the top slab exceeded approximately 3 to 10 times the design prediction by the conventional codes for practice as shown in Figure 1(a). Large numbers of cracks at the inner surfaces of tunnel have also been observed as shown in Figure 1(b). The largest crack width near the haunch is 0.9mm, which is more than three times the allowable value specified (Standard Specifications for Concrete Structures – 2007 (2007)). Through the analytical approach in consideration of migration of moisture and associated shrinkage, the authors reported that long-term excessive

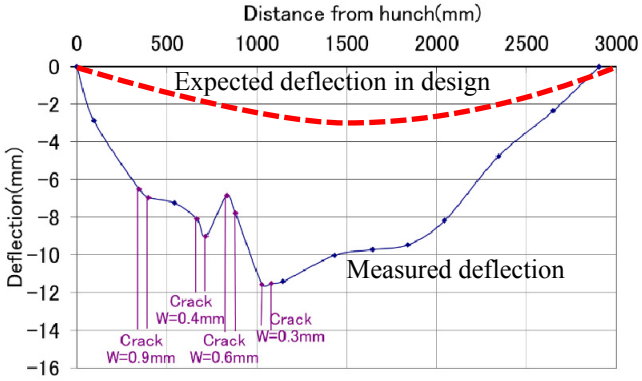

(a) Deflection of the top slab

(b) Cracks on the top slab

Figure 1 Excessive deflection and cracks of the culvert

deformation may attribute to synergy effects accompanying delayed shear failure owing to the vertical soil pressure, which can be accelerated by shrinkage and creep of structural concrete.

This conclusion is partially supported by the past studies, i.e., concrete's shrinkage and creep of the top slab possibly increases in the vertical earth pressure (Abhijit 1991, Richard 2005) acting on underground culverts caused by both uneven settlement of the foundation and RC structural deformation as a coupled action. Furthermore, the shear capacity of the RC simple beam which takes the influence of drying shrinkage is known to be reduced up to about 85% compared to the one under the sealed conditions (Mitani et al. 2011). Then, this paper aims to verify the existence of the predicted delayed shear crack, and get basic information to assess the future risk and serviceability of the underground RC culverts in line with the durability mechanics.

TARGET CULVERT

The dimensioning and detailing of the tunnel section suffering from excessive deflection are shown in Figure 2. This culvert was constructed in 1982. The thickness of the top slab is 35cm and the height of the fill above the culvert is relatively low, ranging from 5.04m to 6.98m. The dry sand is used as for backfilling material. This culvert has been used for urban utility and cabling, and it is in service as well. In order to keep the stable local ambient conditions, air ventilation is conducted with blower fan machines, and the temperature is kept about 25±2 degree Celsius. Then, the internal surfaces of the culvert have been exposed to continuous drying (RH=30±10%). The outer surface exposed to soil foundation was kept almost wet during its whole life and the ground water level is about at half of the side walls. It is

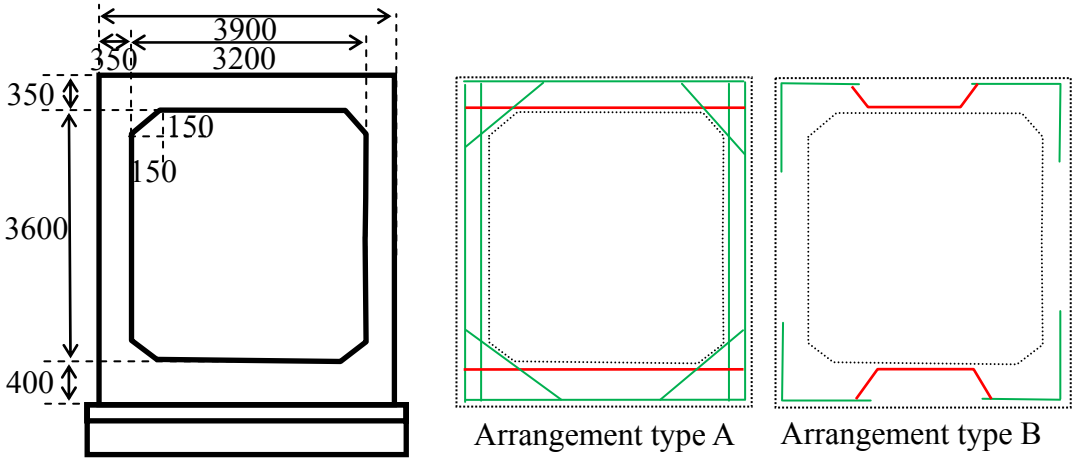

a) Shape of the culvert

b) Arrangement of steel bar
*Red:D22, Green:D19
*Type A and Type B appears each other in the pitch of 150mm

Figure 2 Design detail of the culvert

observed by the periodical monitoring that the number of cracks in the culvert has been increasing and the crack width has also become wider with time. Some cracks have reached reinforcing bars, but the steel corrosion is not observed at this moment because of less supply of moisture due to dry states. As a matter of fact, water leakage was found at several locations inside the culvert, but they are not from the top slab but the side walls and construction joints.

Characteristic values of concrete used are examined by the back-check tests of the mix proportion, and it is compared with the specified design values as shown in Table 1. Actual water to cement ratio of concrete mixture was larger than the design value, and both the compressive strength and Young's modulus are lower than the design specification. The characteristics of reinforcing bars are also examined, and its results are summarized in Table 2. The young's modulus of reinforcing bars is lower than the design value although the yield strength is larger. Working strains of the reinforcing bars on the top slab were measured by the stress release technique of destructive testing, and they are about 1000 micro in tension and it is in the elastic range.

Filled sand is cohesive, and N-value (standard penetration test) of the surrounding ground is 1 to 5 on the top slab and 0 to 2 at both sides of the culvert. From the test result of the grain size distribution, it is found that the surrounding ground consists of 4% coarse aggregate, 59-69% fine aggregate and 27-37% silt powder. The power ratio is a little bit larger than that of the normal ground. It is also confirmed that the culvert is surrounded by fully saturated ground.

Table 1 Estimated mix proportion of the concrete

		Test result	Reference
Compression Strength(N/mm^2)		24.2	Design: 24.0
Young's modulus (kN/mm^2)		16.6	JSCE standard specification:25.0
Mix Proportion	Maximum size of gravel(mm)	20-25	Design: 25
	Cement(kg/m^3)	393	Design: 285
	Water(kg/m^3)	248	Design: 154
	Fine aggregate(kg/m^3)	643	Design: 809
	Coarse aggregate(kg/m^3)	976	Design: 1076
	Water to cement ratio(%)	63.0	Design: 54.0
Fine pore	Total pore volume(ml/g)	0.129	-
	Air contents(%)	23.9	-
Carbonation depth(mm)		38.9	Cover depth: 58.6mm

Table 2 Stress condition of the reinforcement bar in the top slab

Section	Section 1	Section 2	Reference
Bar diameter	24.2		-
Estimated strength category	16.6		-
Young's modulus (kN/mm^2)	180	178	JSCE standard specification:200
Yield strength(N/mm^2)	391	391	JSCE standard specification:295
Measured stress(N/mm^2)	151	170	-
Corrosion	No	No	-

VERIFICATION FROM MATERIAL ASPECTS

As the first step, the loading condition to the RC culvert, which may possibly cause the observed crack, is discussed. The vertical soil pressure on the top slab was inversely calculated so that the computed crack width and its spacing may match the observed reality by using the in-plane flexural theory. Here, the magnitude of drying shrinkage was simply derived from the total summation of the individual crack's width. In this inverse analysis, out of plane action was neglected.

The inverse analysis indicates the soil pressure as about 3 times large as the design value. If it is true, the reinforcing bars should be close to yield or more. Even if the horizontal conferment is assumed to be 0 to 0.4 times as large as the design value, the vertical load is limited at most 2.5 to 2.5 times large. It implies that the in-plane flexural theory never comes up to the real excessive deflection even though creep and shrinkage of concrete are taken into account. It seems quite probable that other unconcerned and uninvestigated factors like non-uniform soil pressure and/or delayed shear crack propagation may unavoidable impacts as Kunieda et al. (2014) pointed

(a) Light from the span center (b) Light from the hunch side
→Same crack is shoot, but shade appears only in (a) because of the gap.

Figure 3 Transverse gap on the crack in the top slab

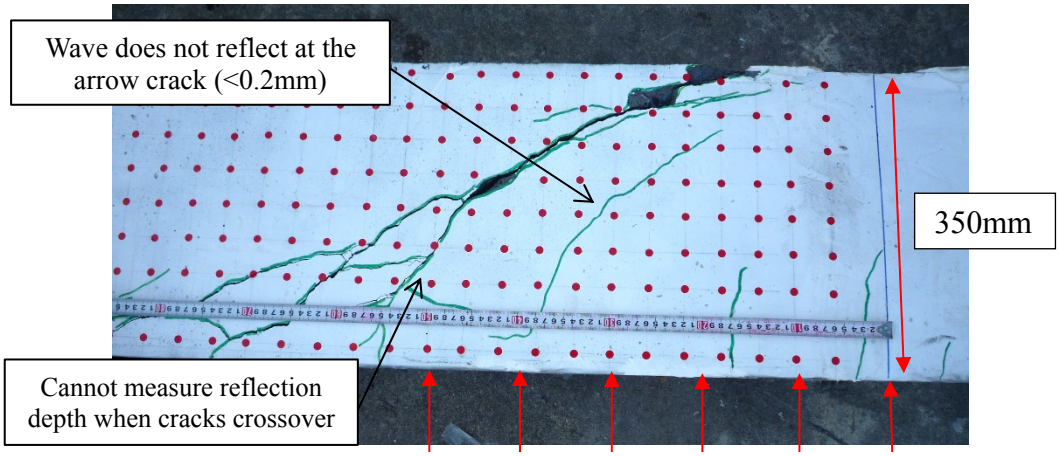

Reflection depth(mm)	OUT	256	286	303	333	357
True value(mm)	-	260	290	310	350	350

Figure 4 Verification of the elastic wave reflection test

out in the previous short discussion before the following destructive testing.

DETECTION OF DIAGONAL SHEAR CRACKING

In case of columns and beams on the ground, it is easy to detect the shear failure by visual inspection. But, for tunnels and culverts, it is impossible to directly see the diagonal shear crack. Then, for verification of the out-of-plane deformation which may be associated with diagonal shear crack propagation, the inner surface of the upper slab was carefully examined by finger-touching from inside of the culvert. The transverse gap was clearly felt by fingers as scratched or interlock, which means the

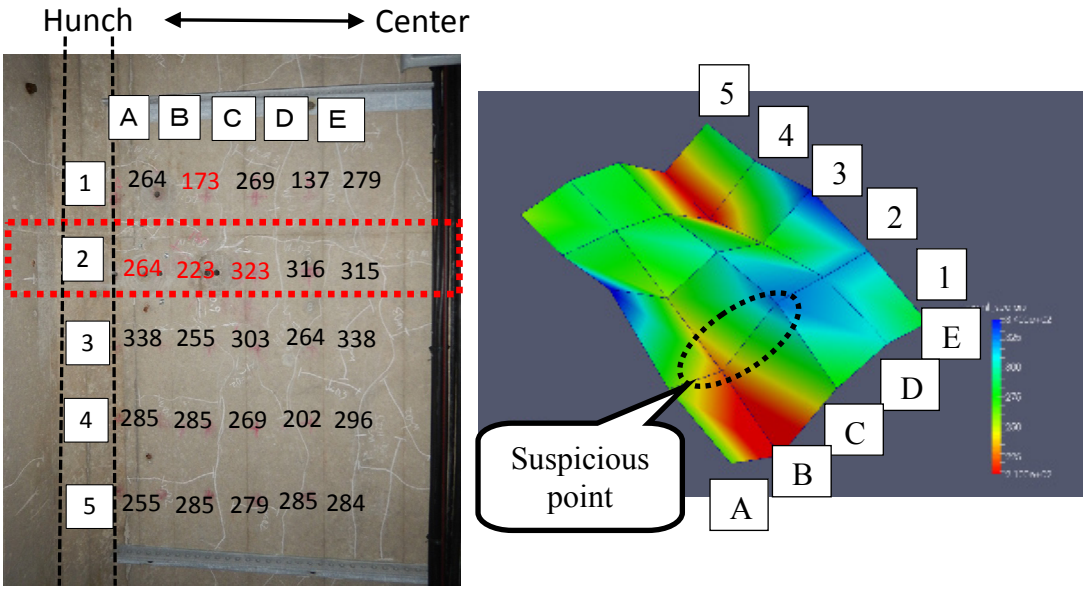

Figure 5 Contour map of the wave reflation depth in the culvert

out-of-plane deformation of cracked concrete as shown in Figure 3. This gap was observed larger near the hunch side where the greater shear force is thought to be applied than the center span. Then, this crack is highly estimated to be an extreme end of diagonal crack planes.
This transverse gap can be easily detected as well by shadows of the skew illumination as shown in Figure 3. In the case of flexural cracks without the transverse gap, no shadow is made no matter how much directions the illumination is applied. This is some sort of visual inspection to detect the out-of-plane alone.

The elastic wave reflection test (e.g. Schabowicz et al. (2012)) was also conducted at several points on the line normal to the culvert axis. If the crack is vertical bending one, the acoustic wave should reflect at about 350mm depth (opposite side of the slab thickness). But, if the crack would be inclined to the centroid axis of the slab, the reflecting depth will be smaller. Validity of the method was examined in advance by using the beam which failed in the mode of shear. Figure 4 shows the depth of wave reflection point which agrees well with the crack depth from the bottom side of the beam.

Figure 5 is the detected height map of the wave reflation depth in the culvert, and it is found that there exist some points where the wave reflection changes significantly around the point. At these points, diagonal shear crack is suspected to be present. Around the most suspicious point between 2-B to 2-C as shown in Figure 5, several micro-bore holes were drilled in about 300mm depth, and the inner surfaces were scanned by the stick scanner (Zacoeb et al. (2007)). The scanned images are shown in Figure 6, and a crack across the hole is found from this image. The enclosed shape of the crack plane is expected from the depth where the crack intersects the hole. This seems to be a typical diagonal shear crack, and it does not reach the flexural compression zone.

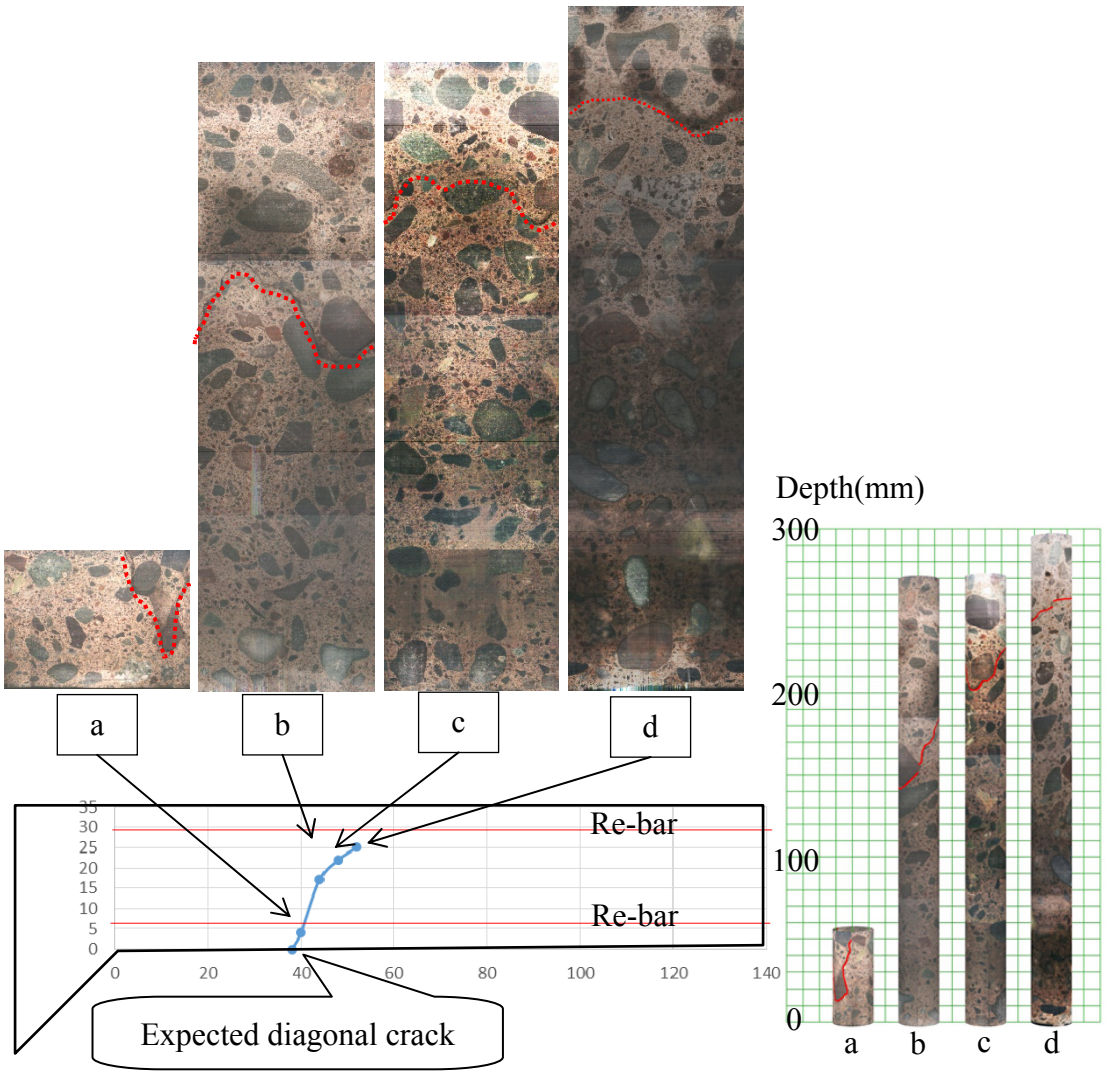

Figure 6 Image of the inner surface of the hole and expected diagonal shear crack in the top slab

With these observations, it can be concluded that the excessive deflection is caused not only by the flexural deformation associated with shrinkage and creep of concrete, but also by the propagation of diagonal shear cracks which lead to out-of-plane displacement. It is assumed that the diagonal shear crack gradually extends for about 30 years, accompanying the top slab deflection.

From the finger-touching examination of the crack and elastic wave reflection test, the diagonal shear crack seems to be formed at many places in the culvert. At this moment, they are formed locally, and not fully linked along the culvert axis. Because the vertical load on the diagonal crack position can be redistributed along the culvert axis by the three-dimensional effect, the safety of the culvert can be maintained even though the diagonal crack is locally formed. Detailed coupled analysis of the whole structures and soil foundation under static and dynamic conditions will be needed for upgrading the maintenance strategy of existing infrastructures.

CONCLUSION

The existence of the delayed shear crack is confirmed by several tests in the shallow RC box culvert. The excessive deflection of the top slab in the culvert is caused by not only by the shrinkage and creep of the concrete but also by the slip on this delayed shear crack. In order to assess the safety of the structure under static and dynamic condition, further experiments and analyses are necessary based on the facts found in this research.

ACKNOWLEDMENTS

The authors appreciate the assistance for site inspection and monitoring by Mr. Yoshimoto and Mr. Nakajima of Tokyo Electric Power Company, Mr. Takanashi of Tokyo Densetsu Service Corporation, and for the analysis by Dr. T. Mishima of Maeda Corporation. This study was financially supported by JSPS KAKENHI Grant No. 23226011.

REFERENCES

Abhijit D. and Bratish S. (1991). "Large-scale model test on square box culvert backfilled with sand", ASCE, *Journal of Geotechnical Engineering*, 117(1).

Bennett R., Wood S., Drumm E., and Rainwater N. (2005). "Vertical loads on concrete box culverts under high embankments", *J. Bridge Eng.*, 10(6), 643–649.

JSCE (Japanese Society of Civil Engineers). (2007). *Standard Specifications for Concrete Structures – 2007*, JSCE Guidelines for Concrete, No.15, JSCE, Tokyo, Japan.

Kuneda, M., Zhu, X., Nakajima, Y., Tanabe, S., and Maekawa, K. (2014). "Long-Term Serviceability and Risk Assessment of Shallow Underground RC Culverts and Tunnels", *Proceedings of the 1st Ageing of Materials & Structures 2014 Conference*, 376-383.

Mitani T., Hyodo H., Ota K., and Sato R. (2011). "Discover and the evaluation of shear strength decrease of reinforced normal-strength concrete beams", *Proceedings of JCI*, 33(2), 721-726.

Schabowicz, K. and Hola, J. (2012). "Nondestructive Elastic-Wave Tests of Foundation Slab in Office Building", *Materials Transactions, Special Issue on APCNDT 2009*, 53(2), 296-302.

Zacoeb, A. , Ishibashi, K., Ito, Y., Miyamoto, N., Sogabe, M., (2007). Development of advanced inspection device for inside concrete structures", *The 1st International Conference of European Asian Civil Engineering Forum*, D32-D38

Creep Behaviour of Concrete Structures under Lower High Temperatures (80~240 °C)

Wei Jiang[1]; Yong Yuan[2]; and Zhenghong Yang[3]

[1]School of Materials Sciences and Engineering, Tongji University, No. 4800 Cao'an Rd., Shanghai 201804. E-mail: jwsky@126.com
[1]College of Civil Engineering, Tongji University, No. 1239 Siping Rd., Shanghai 200092. E-mail: yuany@tongji.edu.cn
[3]School of Materials Sciences and Engineering, Tongji University, No. 4800 Cao'an Rd., Shanghai 201804. E-mail: yzh@tongji.edu.cn

Abstract

Some concrete structures are serviced in lower high temperature (80~240 degree C), such as nuclear containment vessels or underground structure on geothermal area. However, the creep behaviour of concrete for these special structures remains as an issue that is neglected or not implemented consideration during the design process, which may lead to inappropriate estimation for the service behavior and durability to concrete structure. Although there are already many creep models for concrete, lots of them are based on the normal temperature (20 or 23 degree C). Even though the influence of high temperature is considered in some studies, most of them are focused on the short-term creep strain under extremely high temperature. On the other hand, the widely application of lightweight aggregate concrete (LAC) brings considerable beneficial results of economy and society due to its lighter dead-weight and better thermal performance. What's more, the heat resistance of LAC is much better than the normal concrete. However, the high creep behavior of LAC is also a deterrent. Is LAC a suitable material for some special concrete structure under long term lower higher temperature? In this paper, the creep behaviour of LAC is studied at various temperatures ranging from 80 degree C to adopted maximal 240 degree C, together with the parallel test at the 20 degree C. The specimen is cylindrical, which is 100mm in diameter and 300mm in height. The compressive strength of the specimen at 28 day is 30 MPa, with the water binder ratio is 0.5. Four kinds of strain, such as the instantaneous stress-related strain, free thermal strain, transient strain and creep strain are obtained by unstressed tests, transient strain test and steady state creep test. The revised creep model will be developed to describe the sensitivity to the temperature rise under stress fields as a result of enhancement in the existing creep predication model. Finally, the microscopic observation for the specimen will be done by scanning electron microscope to obtain the microstructure evolution induced by thermal-chemo-

mechanical effects. The creep behaviour of LAC in some high temperature range is obtained in this paper. Although the research is relatively conventional, it provides an additional accuracy of creep in terms of lower high temperature (80~240 degree C) in the long term for special concrete structures, which will be demonstrated in the cracking control and durability of some special infrastructure. What's more, it also provides the possibility of thermal-chemo-mechanical analysis on the creep behaviour, and helps in analyzing the multi-scales model of the creep, which can be improved via an Arrhenius law.

INTRODUCTION

Lightweight aggregate concrete (LAC) is built up by the lightweight aggregate, such as the ceramsite. The widely application of LAC brings considerable beneficial results of economy and society due to its lighter dead-weight and better thermal performance, for example, it can save the material consumption, increase the construction efficiency, deduce the load of foundation and improve the Building insulation performance. What's more, the heat resistance of LAC is much better than the normal concrete, for the reason that the lightweight aggregate has already been high-temperature sintered (Sun et.al, 2012, Chi et al.,2014). It seems that the LAC has the lowest loss of strength above 150 degree C. (Sullivan et al,1983,1992) However, compared to the normal concrete, the high creep behavior of LAC is also a deterrent, which limits its application.

On the other hand, some concrete structures are serviced in lower high temperature (80~240 degree C), such as nuclear containment vessels or underground structure on geothermal area. However, the creep behaviour of concrete for these special structures remains as an issue that is neglected or not implemented consideration during the design process, which may lead to inappropriate estimation for the service behavior and durability to concrete structure. Although there are already many creep models for concrete, lots of them are based on the normal temperature (20 or 23 degree C). Even though the influence of high temperature is considered in some studies, most of them are focused on the short-term creep strain under extremely high temperature.

In a summary, most of the experimental results are focused on normal strength concrete and almost no research has performed on LAC, which has considerable potential for the application of some special construction that in the lower high temperature. It is thus necessary to investigate the properties of creep, including the transient strain and short-term creep strain at the lower high temperature.

MIX PROPORTION

Ordinary Portland cement CEM II 42.5 was used and fly ash was added as filler in LAC. Spherical shale ceramisite was used as the aggregate, with the bulk density is 850kg/m^3, and the apparent density is 1700kg/m^3. The aggregate did not

pre-wet before casted. Details of the constituent materials applied in this investigation are given below. The mix proportion of LAC as tests is given in Table 4 ,and its compressive strength at 28 day is 30MPa.

Table 1 Qualitative index and test result of CEM II 42.5

Basis	Specific surface	Setting time (Initial)	Setting time (Final)	Soundness	Consistency	Compressive Strength (3d)	Compressive Strength (2d)
	m^2/kg	min	min		%	MPa	MPa
GB175-2007	≥300	≥45	≤600	Qualified	——	≥17.0	≥42.5
Result	390	133	211	Qualified	27.2	31.0	46.5

Table 2 Qualitative index and test result of fly ash

Basis	Fineness（Knocking 0.045mm） %	Water demand ratio %	Moisture content %	Soundness mm
DG/TJ08-230	≤25.0	≤105	≤1.0	≤5.0
Result	22.1	98	0.1	1.0

Table 3 Gradation of lightweight aggregate (ceramsite)

Residue （by mass）/ %				
4.65 mm	16 mm	19 mm	26.5 mm	31.5 mm
100	84.8	49.3	11.2	0

Table 4 Mix proportion for lightweight aggregate concrete（kg/m3）

	Water	*Cement*	*Fly ash*	*Sand*	*Coarse aggregate*	*Admixture*
LAC	160	365	100	700	594	4.32

TEST METHOD

The concrete strain at elevated temperature consists of four terms: instantaneous stress-related strain ε_σ, free thermal strain ε_{th}, creep strain ε_{cr} and transient strain ε_{tr} ,which is expressed as:

$$\varepsilon = \varepsilon_{th}(\theta) + \varepsilon_\sigma(\sigma,\theta) + \varepsilon_{cr}(\sigma,\theta,t) + \varepsilon_{tr}(\sigma,\theta)$$

The four kinds of strain were obtained by the followed three kinds of test method: unstressed test, transient strain test, and steady state creep test. All the heating rate in the tests are 5 degree C/min

(1) Unstressed Test

The instantaneous stress-related strain of LAC at the low higher temperature is obtained in this test. The specimen is heated, without any external load, to a target temperature. The temperature is maintained until the steady-state temperature condition is achieved.

(2) Transient Strain Test

The free thermal strain and transient strain of LAC is obtained by this method. The specimen is subjected to a preload equal to the stress level is 0, 20% and 40%,

respectively. The preload is maintained while the specimen is heated to the target temperature. In order to avoid the influence of the basic creep strain on the result of transient strain, the load and temperature was kept constant for half an hour after reaching the target temperature, and then it was cooled to the ambient temperature.

(3)Steady State Creep Test

The steady state creep test was carried out to obtain the short-term creep strain of LAC. The creep strain was measured during three hours after the steady state condition was reached.

TEST SET-UP

Usually, the creep test under high temperature is carried out by the stress testing machine. Compression tests at elevated temperature can be done by a controlled heating rate, load rate and strain rate. The disadvantages of the equipment are included as follows. First, the displacement obtained is the total of the concrete specimen and the two loading platens, which must be removed during the data handling. However, the loading platens suffer complex effect of high temperature, and the result is obviously influenced by the stability of the loading platens. Second, the metal loading platens has higher thermal conductivity, which causes the heat over flow from the electric furnace by the steel plated even if the thermal insulation layer installed on the side of loading platen. For one hand, it gives rise to the uneven temperature field. On the other hand, it consumes too much power during the long term creep tests. Third, the “stress testing machine with temperature control system” is quite expensive which make against to many groups of long terms creep tests during the same time.

Equipment for the long term creep test under the lower high temperature is developed in this paper. The design idea is that only a furnace is added on the traditional creep experimental device to cover the specimen. The loading and maintain system (such as spring) is remained outside the furnace.

The interior of the furnace is cylindrical with dimensions of 212mm in diameter and 325mm in height. The furnace has two diameter 100mm openings, at the top and the bottom, to fit the loading platens. The cylinder specimen is placed at the center of the computer controlled electric furnace with the dimension of 100mm in diameter and 300mm in height. Two ring fixtures are setup up to install the LVDT with the gauge length is 200mm. Two pieces of LVDT which stand high temperature (less than 300 degree C) are selected.

One of the biggest challenges is how to select the appropriate loading platens, which must be meet the following requirement. It must have enough strength to transfer the load to the specimen; what’s more, its strength will not fall sharply in the high temperature environment. Then, lower thermal conductivity is needed in order to reduce the heat loss during the long term test.

In this research, Granite is used as the loading platens with the dimension as 100 × 100 × 10mm. Its compressive strength is 169.8MPa in normal atmospheric temperature, which is strong enough to transfer the load to the compressive creep test with the stress level under 40%. In addition, it seems that the threshold temperature is 400 degree C, which means that its strength does not diminish, even increase a bit (Xu, 2014), for the target temperature range. In addition, the thermal conductivity of Granite is 3.49W/mK, less than the Austenitic Alloy (one kind of stainless steel, commonly used in the Stress testing machine),which is 16.2 W/mK.

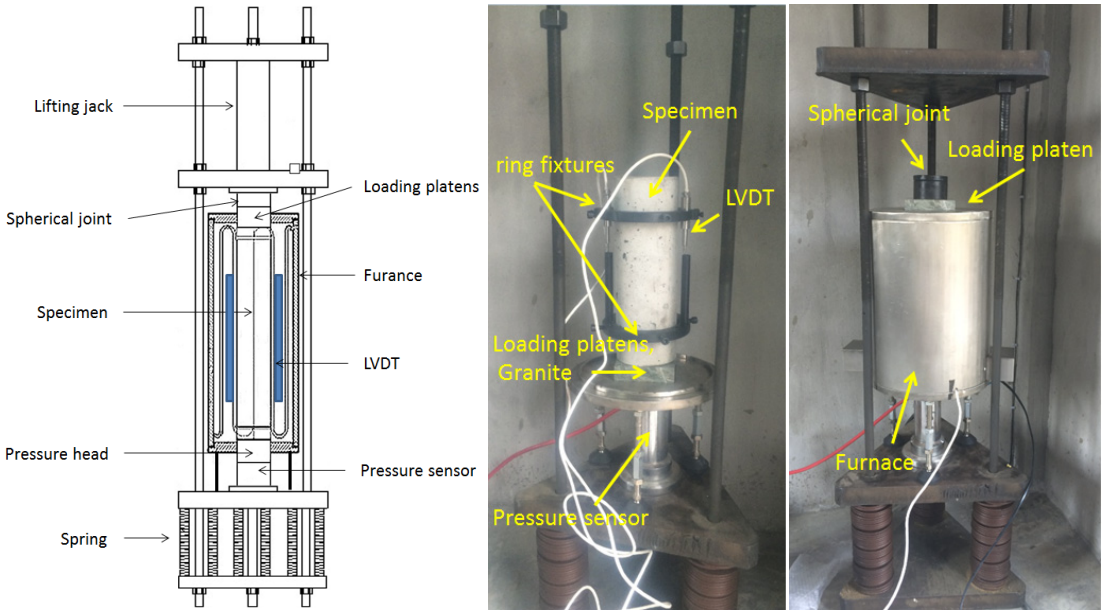

Figure 1. Equipment for the creep test under the lower high temperature

The equipment developed in this paper has the following advantages. First, the displacement measurement for the concrete is directly obtained from the center part of the specimen, which avoids the uneven temperature fields on the end, and the uncertain deformation of the loading platens. Second, this equipment is improved by the traditional force balance creep installation, which is relatively cheaper. It is possible for many groups of long term creep test at the same time.

SUMMARY

With the aim of analyzing the creep behaviour of LAC at lower high temperature, a series of tests had been carried out. To this end, the testing method and the corresponding test equipment had been developed in this paper. In future papers the results and the discussed of the creep behaviour of creep at lower high temperature will be presented. In this way using

ACKNOWLEDGEMENTS

The research was financially supported by the National Natural Science Foundation of China with grand numbers of 51308405.

REFERENCE

Chi, J.H., et al.(2014). “Research on seismic resistance and mechanic behavior of reinforced lightweight aggregate concrete walls after high temperature. ” *Fire and materials*. 38(8): 789-805

Sullivan, P. J. E, Khoury G A, Grainger B N.(1983) “Appratus for measuring the transient thermal strain behavior of unsealed concrete under constant load for temperature up to 700℃”.*Magazine of concrete research.*, 37(125):229-236

Sullivan, P. J. E. Shanshar, R.(1992) “Performance of concrete at elevated temperatures (as measuredby the reduction in compressive strength).” *Five Technology.,* 28 (3)：240-250

Sun Q, Cao W, Xue H, Zhou M, Su Q (2011). “Resistance to high temperature performance and finite element analysis on fiber reinforced lightweight aggregate concrete”. *Concrete*.,7, 23-26.

XU, X. L., Gao, F., and Zhang, Z. Z. (2014). “Research on triaxial compression test of granite after high temperatures.” *J. Rock and Soil Mechanics.,* 35(11), 3177-3183.

Sun Q, Cao W, Xue H, Zhou M, Su Q (2011). “Resistance to high temperature performance and finite element analysis on fiber reinforced lightweight aggregate concrete”. *Concrete*.,7, 23-26.

Long-Term Performance of Dry Storage Structures

Masoud Dehghani Champiri; Arezou Attar; Mohammad Hanifehzadeh;
Kaspar Willam; and Bora Gencturk

Department of Civil and Environmental Engineering, Cullen College of Engineering, University of Houston, TX. E-mail: kwillam@uh.edu

Abstract

In this paper long-term creep and shrinkage behavior of vertical dry cask structures are investigated and discussed. Environmental aging is considered in the form of deleterious mismatch effects of steel and concrete creep at the interface of two materials. Additionally, the performance in the case of a tip-over impact is studied. The aging simulations include creep and shrinkage predictions of the representative cask models for 40 years of service using the B4 creep formulation of concrete [RILEM, 2014] and the Bailey-Norton creep formulation for steel [Betten, J., 2008]. The results illustrate cask behavior for hygro-thermal-mechanical aging before it is subjected to tip-over impact. The time history results of creep and shrinkage illustrate the mismatch of deformations and residual stresses in the steel liner and contiguous concrete. Both, full bond and no bond cases are studied in order to assess progressive damage at the interface of the two materials. It is observed that the concomitant shear transfer induces significant damage in the interfacial region of the two cask components. Results of tip-over simulations show that the strains and stresses in the concrete are up to 20% different for young and aged concrete.

1. INTRUDUCTION

All U.S. nuclear power plants initially store used nuclear fuel in “spent fuel pools”. These pools are robust containment structures made of reinforced concrete several feet thick, protected by steel liners. As the pools near capacity, utilities move the older spent fuel bundles into “dry cask” storage. Fuel is typically cooled at least 5 years in the fuel pool before being transferred to dry cask storage structures. U.S. Nuclear Regulatory Commission (NRC) has authorized transfer as early as 3 years; the industry norm is about 10 years. Various types of dry cask structures exist including horizontal and vertical configurations. The most common configuration of dry cask outerpack structure is a vertical concrete hollow cylinder with a steel liner inside. Currently, the design life and licensure of dry casks is 20 years with extension to 40 years. However, in the absence of a permanent storage repository their life may be extended further after appropriate condition evaluation. The NRC guidance stated that tip-over events cannot happen on the dry cask structure (NUREG-1536, 1997 and NUREG-1567, 2000).

Normally dry storage casks are composite structures made of an inner steel liner and a concrete outerpack housing the basket of the spent nuclear fuel bundle.

The main purpose of the cask structure is to provide safe storage of spent nuclear fuel elements of low levels of radiation and temperature. Consequently, the upright storage cask structures are mainly subject to self-weight and environmental aging in addition to rare events of tip-over potentially induced by severe seismic events or man-made hazards.

The concrete outerpack may age due to different reasons including creep, shrinkage, and alkali silica reaction (ASR). ASR is not considered in this paper but detailed information about its effects can be found in Saouma and Hariri-Ardebili (2014). The effects of creep and shrinkage have been studied using B4 model (RILEM, 2014) for concrete and Norton-Bailey law (Betten, 2008) for metal creep. These laws have been implemented in COMSOL (COMSOL Multiphysics, 2015) which is capable to perform hygro-thermal-mechanical analysis. The result of this study is incorporated in the commercial code LS-DYNA version 970 (Hallquist, 2006) to assess the tip-over induced impact of the cask.

The outline of this paper is as follow: the geometry of the cask structure is explained first, secondly the material properties are presented, and then creep and shrinkage analyses of the cask are performed in COMSOL, followed by tip-over simulation in LS-DYNA. The paper concludes with a discussion of the results.

2. CASK GEOMETRY

The vertical dry cask structure considered includes the following parts: concrete outerpack, steel liner, base plate, lid assembly (lid-top, lid-bottom, concrete lid) and canister. The geometric properties are summarized in Table 1. It is noted that concrete pad, canister and subgrade soil are not modeled in COMSOL for aging simulation. The selected model cask is 2.8 times smaller than the original prototype cask but does not contain any spent fuel.

Table 1: Dimensions for simulating the contact problem for 1:2.8 scale cask

Part	Height (mm)	Length (mm)	Width (mm)	Internal radius (mm)	External radius (mm)	Thickness (mm)
Rectangular concrete pad	381.0	3810.0	3810.0	-	-	-
Subgrade soil	2540.0	7620.0	7620.0	-	-	-
Steel liner	1963.0	-	-	356.0	372.0	16.0
Concrete	1963.0	-	-	372.0	610.0	239.0
Lid-top	-	-	-	-	432.0	7.0
Lid-bottom	-	-	-	-	353.0	4.0
Lid-rib	51.0	-	-	350.0	353.0	4.0
Concrete-lid	51.0	-	-	-	350.0	350.0
Base plate	-	-	-	-	610.0	64.0
Canister	1905.0	-	-	350.0	353.0	4.0

The following assumptions are made here:

- Air outlets and inlets which are used for natural air circulation, are not model. The effect of these openings to environmental aging and impact is expected to be minor.
- Base plate is modeled as a circular solid plate. Equivalent thickness of this cylinder is calculated based on the weight of the actual base plate.
- Extra weight for dynamic similitude has been added to the concrete cask part. An equivalent mass density of concrete has been considered to include this extra mass.
- Canister is modeled as a rigid cylinder in contact with the steel liner.

3. MATERIAL PROPERTIES

Plasticity material models are applicable if the cracks in concrete are small enough and can be homogenized to satisfy the basic assumption of continuum mechanics (Fung, 1993; Chen, 1982). The cask structure is made of steel and concrete. Elastic-perfectly plastic behavior is considered for the steel parts. With regard to concrete, the three- invariant Willam-Warnke (1974) formulation is used for the failure study of the concrete cask structure in COMSOL, while concrete cap surface material model (CSCM-159) (Murray, 2007) is used for mechanical behavior of cask and pad in LSDYNA. Material properties of steel and concrete parts are shown in Table 2. Isotropic elastic material behavior is considered for soil. Modulus of elasticity, Poisson's ratio and mass density of the soil are taken as 34474 MPa, 0.3, and 1.5 gr/cm^3, respectively.

Table 2: Material properties

Structural Steel properties		Concrete properties	
Property	**Value**	**Property**	**Value**
Heat capacity at constant pressure	475 [J/(kg*K)]	Heat capacity at constant pressure	880 [J/(kg*K)]
Thermal conductivity	44.5 [W/(m*K)]	Thermal conductivity	1.8 [W/(m*K)]
Coefficient of thermal expansion	12.3E-6 [1/K]	Coefficient of thermal expansion	10E-6 [1/K]
Density	7850 [kg/m^3]	Density	2450 [kg/m^3]
Poisson's ratio	0.26	Poisson's ratio	0.15
Young's modulus	206E+9 [Pa]	Young's modulus	25E+9 [Pa]
Initial yield stress	250 [MPa]	Young's modulus-aged	28E+9 [Pa]
Lamé parameter λ	1.5E+11[Pa]	Uniaxial tensile strength	4.14 [MPa]
		Uniaxial compressive strength-cask	41.4 [MPa]
		Biaxial compressive strength	45 [MPa]
		Compressive pad strength	55 [MPa]

CEB-FIP model (2010) is used for predicting the age-dependent modulus of elasticity for concrete. The aging equation follows Eq. (1):

$$E_{ci}(t) = \left[\exp\left[s \times \left[1 - \left[\frac{28}{t/t_1}\right]^{0.5}\right]\right]\right]^{0.5} \times E_{ci} \quad (1)$$

where, s is a coefficient depending on the type of cement ($s=0.20$ for rapid hardening high strength cements; $s=0.25$ for normal and rapid hardening cements, and $s=0.38$ for low hardening cements), t is the age of concrete (days), t_1 is equal to 1 day, and E_{ci} is the modulus of elasticity of concrete at 28 days.

4. CREEP AND SHRINKAGE

4.1 Creep analysis

B4 creep model (RILEM, 2014) is applied for the creep behavior of concrete. Fig. 1 shows the creep compliance for 40 years (14 400 days). The following inputs are used in the model: Type I cement, loading at 28 days, drying begins at 28 days, 80% relative humidity, uniaxial concrete cylinder strength is 27.6 MPa, volume to surface ratio of cask equal to 192.18 mm, cement content is 219.3 kg/m^3: water-cement ratio is 0.6, and aggregate-cement ratio is 0.7.

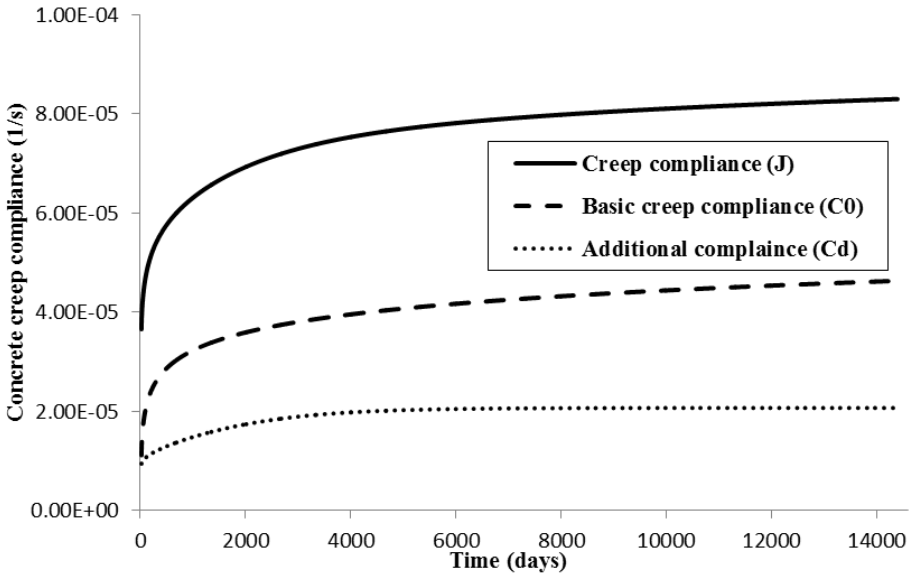

Fig. 1: Concrete creep compliance of dry cask structures for 40 years

Based on the parameters, the creep compliance can be calculated:

$$J(\hat{t},\hat{t}') = q_1 + R_T C_0(\hat{t},\hat{t}') + C_d(\hat{t},\hat{t}',\overline{t_0}) \quad (2)$$

In which q_1 is the instantaneous compliance (compliance extrapolated from compliance curves between 0.1 sec and 1 hour to zero load duration, which is independent of the age t' at loading of the compliance curve); C_0 is compliance function for basic creep (i.e., creep at constant moisture content and no moisture migration through the concrete); and C_d is the additional compliance due to simultaneous drying. The volumetric and deviatoric creep functions are according to (Bazant, 1975) assuming Poisson's ratio to remain constant.

This concrete creep behavior has been implemented in COMSOL. In addition, creep behavior of steel parts is modeled using the Norton-Bailey formulation (Betten, 2008):

$$\frac{\partial \boldsymbol{\varepsilon_c}}{\partial t} = A(\frac{\sigma_{eff}}{\sigma_{ref}})^n m \left(\frac{t + t_{shift}}{t_{ref}}\right)^{m-1} \boldsymbol{N^D}, \boldsymbol{N^D} = \frac{3}{2}\frac{dev(\boldsymbol{\sigma})}{\sigma_{eff}} \quad (3)$$

where A is the creep rate coefficient equal to 3.125E-14 1/hr, n is stress exponent equal to 5.0, m is the hardening exponent equal to 0.5 and t_{ref} is equal to 1 day. Other variables are defined based on the state of the stress during the creep process. Time hardening approach is chosen for computation of the creep and temperature dependency of the steel in this analysis.

4.2. Shrinkage analysis

B4 shrinkage model (RILEM, 2014) has been used to model the shrinkage behavior of the cask. Based on that model, the time dependence of shrinkage strain is shown in Fig. 2 for the long-term analysis of the dry cask structure in COMSOL assuming uniform drying.

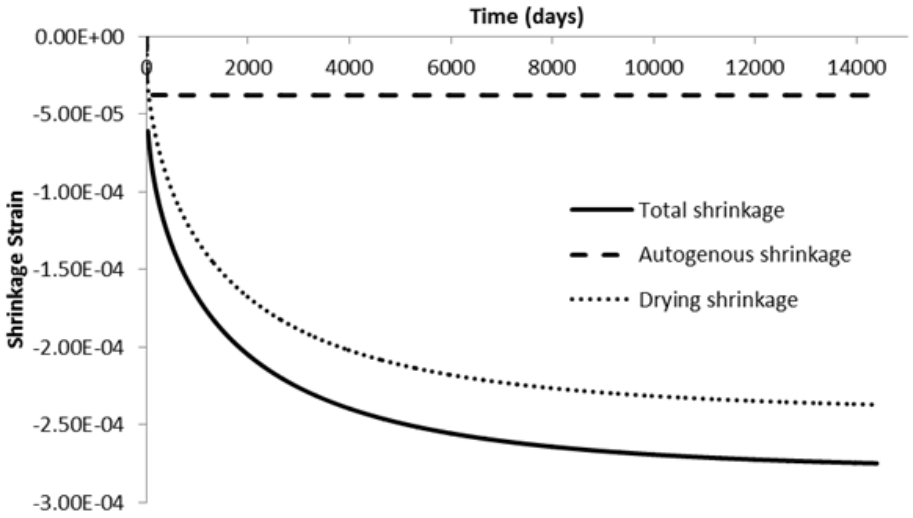

Fig. 2: Concrete shrinkage strain of dry cask structures for 40 years

4.3. Thermal analysis

The temperature gradient from the inside liner to the outside cask surface introduces thermal stresses and accelerates the creep and shrinkage processes in the cask. To this end steady state temperature conditions are assumed with 20ºC (293.15K) on the outside and 80ºC (353.15K) on the inside.

4.4. COMSOL model and results

As mentioned before, COMSOL Multiphysics software has been used to simulate the environmental aging of the dry cask structures. The dry cask structure is modeled as a 2-D axisymmetric composite solid. The concrete cask, base plate, lid assembly and steel liner are included in the model.

The thermal loading of the dry cask structures is due to high temperature exposure of the inside steel liner, near the nuclear fuel basket, while the concrete outerpack is being held at a steady outside temperature. Self-weight, temperature gradient, creep and shrinkage of the dry storage structure are being considered in this

paper before the final tip-over crash event. The bottom surface of the base plate is constrained in the vertical direction to remove rigid body translation. To incorporate the results of COMSOL into LS-DYNA, an identical finite element (FE) mesh is used in both simulations. One-point integration with hour glass control is selected for each element. The problem is solved as coupled thermo-mechanical analysis. The COMSOL model includes 8800 DOFs. Different stress level between the steel liner and the concrete along the top and bottom of the cask is shown in Fig. 3, and von-Mises stress contours are shown in Fig. 4 in two cases: (a) full bond and (b) no bond.

The Figures depict the level of von Mises stress in the steel liner which is much higher in the steel liner than in the concrete due to bond.

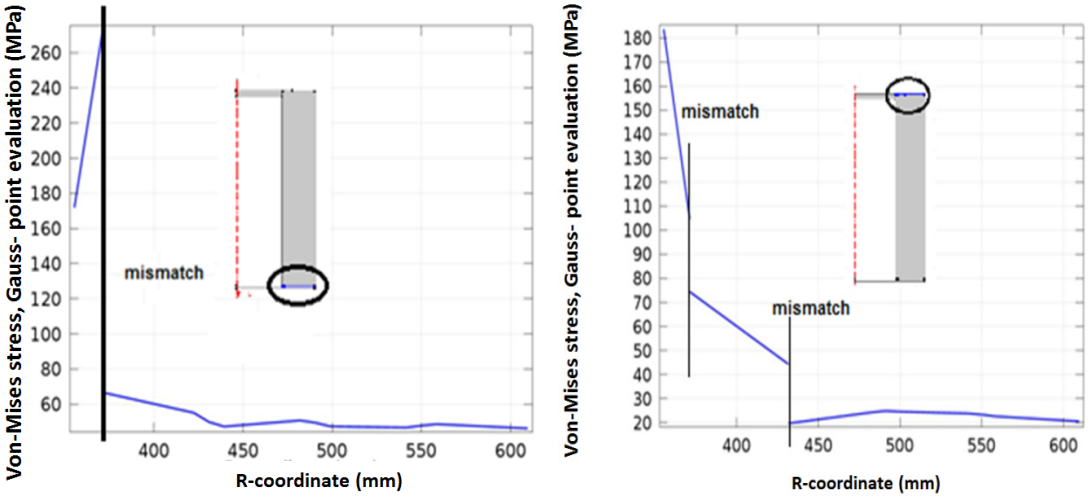

(a) von-Mises stress along the bottom surface (b) von-Mises stress along the upper surface

Fig. 3: von-Mises stress along the radial direction of the concrete cask and steel liner

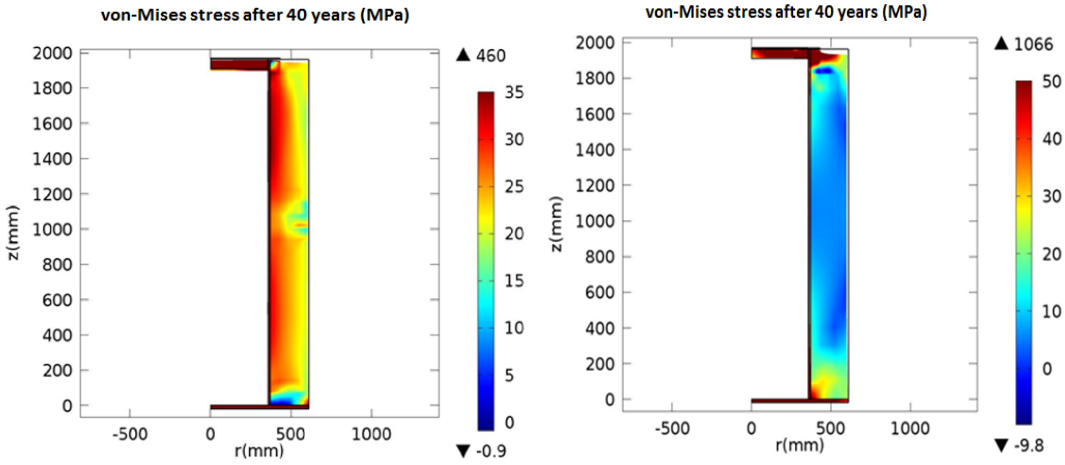

(a) Full bond (b) No bond

Fig. 4. von-Mises stress contours after 40 years.

Since the Norton-Bailey law for metal creep and the B4 model for concrete creep lead to considerable differences of creep deformations, the full bond constraint introduces shear transfer and significant damage in the interfacial region of the two cask components. The ensuing tip-over impact of the composite cask structure is

analyzed to quantify the effect of interface damage on the failure mode. Initial strains of all elements are calculated and they are input in the cask elements for LSDYNA simulation of the contact-impact problem.

5. TIP-OVER SIMULATION OF THE CASKS

The level of damage is the main focus of the tip-over simulation to evaluate the crash failure and energy dissipation while the concrete cask absorbs this energy. In the FE simulation, only half of the 3-D model cask is considered due to symmetry.

5.1 Modeling, boundary and initial conditions

The out-of-plane displacement components in the circumferential direction are restrained in the plane of symmetry. During the tip-over event, only the responses within the near field of the soil foundation are of interest. Thus, absorbing boundary conditions are imposed on the bottom of the soil foundation to avoid reflection of stress waves.

The initial strains due to creep, shrinkage, and temperature in each element, were obtained COMSOL model and were implemented in LS-DYNA as an initial strain term to simulate the long-term behavior of the cask. The cask is tilted 35 degrees as an initial condition. Surface to surface contact (Hallquist, 2006; Zhong, 1993) is used for concrete cask-pad interaction, pad-soil interaction, base plate-pad interaction, canister-base plate, and canister-liner interaction. Static and dynamic friction coefficients in the contact surface are taken equal to 0.25 (Funk, 1989). For contact between cask, steel liner and lid, tied contact surface to surface offset is used to activate penalty method instead of constraint method. The penalty method shows better behavior in most cases than the constraint method, while both of them have the same computational cost. Hourglass control is implemented using one-point integration (assumed strain co-rotational stiffness form for 2D and 3D solid elements) according to Belytschko and Bindeman (1993). This form is available for explicit solutions in LS-DYNA. In this simulation, the number of elements is $N_{ele}=17,736$, the number of nodes is $N_{node}=37,798,$ and the number of time steps is 2E+07.

5.2 Results of tip-over simulation

Three separate simulations are performed:

Case (1), impact response of the cask at 28 days assuming full bond between the cask and the liner without pre-strains due to creep and shrinkage;

Case (2), impact response considering the creep and shrinkage effects after 40 years. Initial strains include creep, shrinkage, and temperature as obtained from COMSOL which are imported into LS-DYNA assuming full bond between the cask and the liner; and

Case (3) is the same as Case (2), except for the loss of bond between the concrete outerpack and and the steel liner.

Identical contact time and effective plastic strain contours are obtained for cases (1) and (2), but different ones for case (3) as shown in Fig. 5. The internal time step of this analysis is 4.45E-08 sec. This small step size is determined by LS-DYNA for explicit time integration of two–body contact and for using the penalty method for surface-to-surface contact. This simulation takes 6 hours to complete utilizing 8

processors in parallel on a single personal computer. Contact happened at the time of 1.0165 sec (corresponding to the maximum acceleration at the tip of the cask) after starting tip-over simulation from the inclined initial condition. The effective plastic strain is a monotonically increasing scalar value which is calculated incrementally as a function of the second invariant of the plastic rate of deformation tensor. In index notation, the effective plastic strain is the integral of:

$$\varepsilon_{pl} = \int_{t_0}^{t_1} \sqrt{\frac{2}{3}(DP)_{ij}(DP)_{ij}}\,dt \tag{4}$$

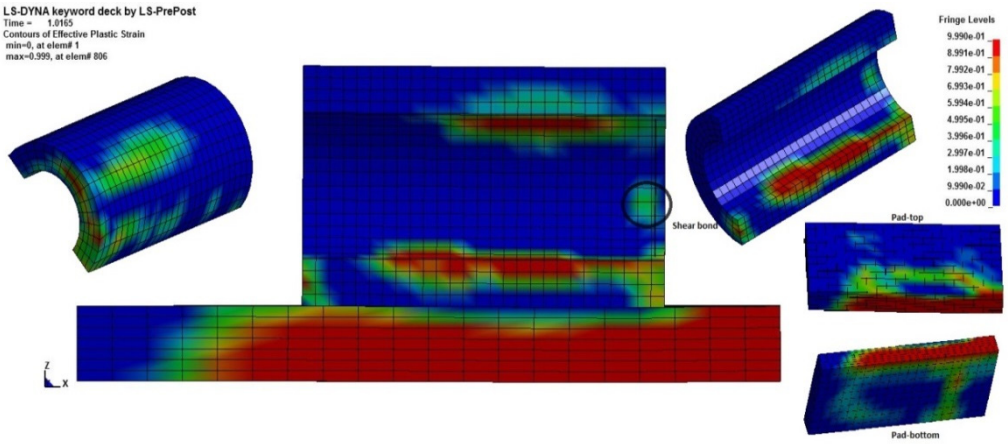

(a) Effective plastic strain contours for cases (1) and (2)

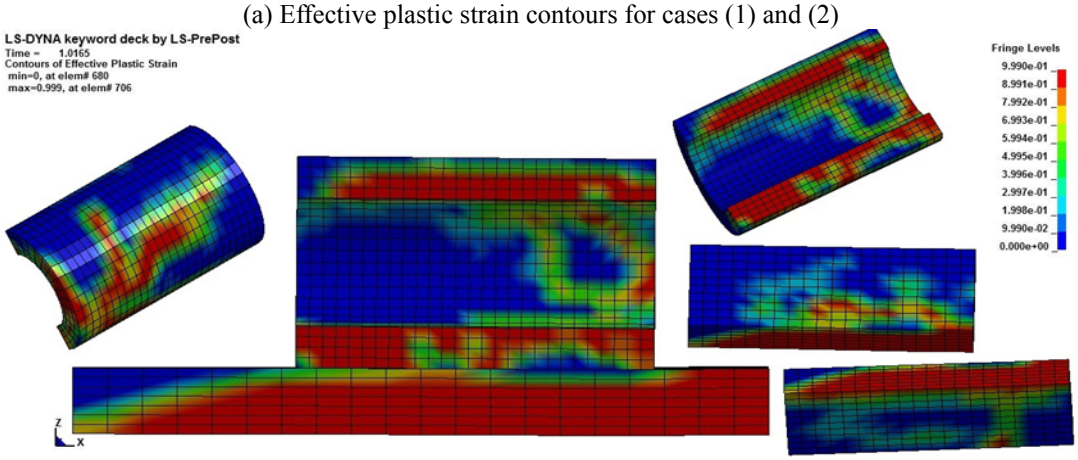

(b) Effective plastic strain contours for case (3)

Fig. 5 Contours of effective plastic strain at t=1.0165 sec.

Fig. 5 shows effective plastic strain contour after impact. It shows that internal edges of the concrete cask are subjected to large plastic deformations during this impact scenario. Shear bond failure is the major failure mode.

Tip of the cask on the contact edge is selected to illustrate the stress and strain time histories in this element. Time histories of von-Mises stress and effective plastic strain are presented in Fig. 6. Whereas the concrete tensile strength is only one-tenth of compressive strength, this element didn't exhaust the tensile capacity. However the von Mises stress exceeds the compressive strength of concrete for a short duration.

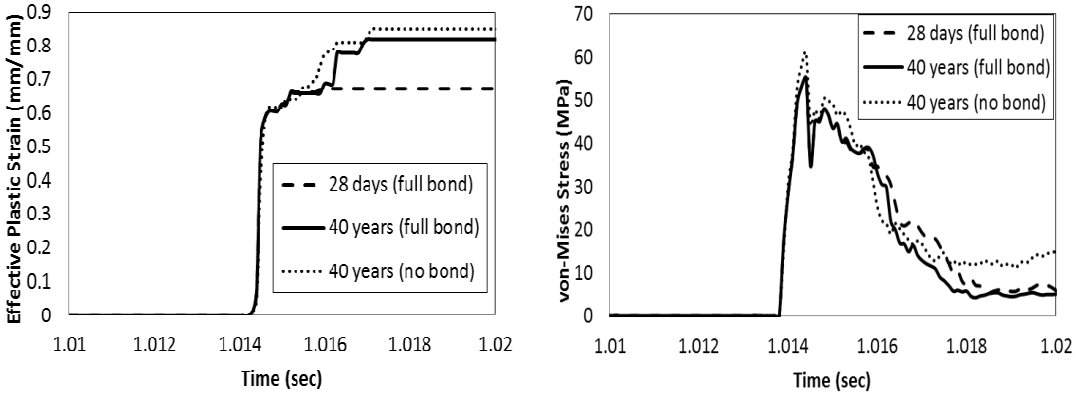

Fig. 6. Results of the tip-over simulations

As seen in Fig. 6, the 28 days and aged concrete with full bond show 10% difference in strains and stresses after contact while this difference increases to 20% for the case of no bond. The effective plastic strain reached a value of 68% at 28 days concrete, 83% of aged concrete with full bond and 86% of aged concrete without bond during contact indicating large inelastic deformations far beyond the strain level for tensile cracking and compressive crushing of concrete.

6. CONCLUSIONS

A simplified 1:2.8 scale model of the dry cask structure was studied to evaluate the long-term creep and shrinkage response. Long-term creep and shrinkage behavior of the dry cask structure were analyzed using B4 model (RILEM, 2014) for concrete and Norton-Bailey formulation for steel (Betten, 2008) with COMSOL. The results of creep and shrinkage illustrated the effect of mismatch of deformations and residual stresses in the steel liner and contiguous concrete. The Norton-Bailey law for metal (Betten, 2008) and the B4 model (RILEM, 2014) for concrete creep lead to considerable differences in deformations, the concomitant shear transfer induced significant damage in the interfacial region of the two cask components.

Initial strains due to shrinkage, creep, and temperature were calculated and input to all elements of the model in LS-DYNA which was used for explicit time integration for the impact scenario of tip-over. Strains and stresses were investigated in the critical region at the top of cask. There was negligible interpenetration during contact-impact, although the cask was subjected to considerable distress during impact. Results of the long-term predictions of dry cask comparing full bond vs. no bond show differences up to 10% in stresses, and about 20% in strains, while the failure mode remained unchanged.

ACKNOWLEDGEMENTS

This research was supported by the Nuclear Energy University Program (NEUP), contract number: 00128931. Their support is greatly acknowledged. The opinions expressed in this paper are those of the authors and do not necessarily reflect the views of the sponsor.

REFERENCES

Belytschko, T. and Bindeman, L. P. (1993). "Assumed strain stabilization of the eight node hexahedral element," *Computer Methods in Applied Mechanics and Engineering*, 105, 225-260.

Bazant, Z. P. (1975). Theory of creep and shrinkage in concrete structures, Reprinted from Mechanics Today, Vol. 2, Pergamon Press, Chapt. I, pp. 1-93, Northwestern University, Evanston, Illinois.

Betten, J. (2008). Creep Mechanics, ISBN-10: 3540850503, ISBN-13: 978-3540850502 , Auflage: 3rd ed.

Chen, W.F. (1982). Plasticity in Reinforcement Concrete. McGraw-Hill, New York.

CEB-FIP (2010). Model code for concrete structures, first draft, Bulletin d' information No. 195, Comite-Euro-International Du Beton-Federation Internationale De La Precontrainte, Paris.

COMSOL Multiphysics® (2015). The Platform for Physics-Based Modeling and Simulation, <http://www.comsol.com/comsol-multiphysics>.

Fung, Y.C. (1993). A First Course in Continuum Mechanics. Prentice-Hall, Englewood Cliffs, NJ.

Funk, R. (1989). "Shear friction transfer mechanisms for supports attached to concrete," *American Concrete International Journal,* 11 (7), 53–58.

Hallquist, J.O. (2006). LS-DYNA Theory Manual. Livermore Software and Technology Corporation (version 970).

Murray, Y.D. (2007). User manual for LS-DYNA concrete material model 159, Report No. FHWA-HRT-05-062, US department of transportation, Federal Highway Administration.

NUREG-1536 (1997). Standard Review Plan for Dry Cask Storage Systems. US Nuclear Regulatory Commission.

NUREG-1567 (2000). Standard Review Plan for Spent Fuel Dry Storage Facilities. US Nuclear Regulatory Commission.

RILEM Report (2014). Report of RILEM committee TC-MDC, Multi-decade creep mpdel B4 for concrete creep and shrinkage including multi-decade prediction: description and application, RILEM committee (Bazant, Z. P., Wender, R., Hubler, M. H.).

Saouma, V.E., Hariri-Ardebili, M. A. (2014). "A proposed aging management program for alkali silica reactions in a nuclear power plant," *Nuclear Engineering and Design,* 277 (2014) 248–264.

Willam, K.J. and Warnke, E.P. (1974). "Constitutive Model for the Triaxial Behaviour of Concrete," *Proc. Intl. Assoc. Bridge Structl. Engrs,* Report 19, Section III, Zurich, p. 30.

Zhong, Z.H. (1993). Finite Element Procedures for Contact-Impact Problems. Oxford University Press, Oxford.

Fully-coupled creep-damage models for concrete

C. F. Dunant[1] and A. Hilaire[1]

[1]Laboratory of construction materials EPFL-STI-IMX 10015 Lausanne, Switzerland
email: cyrille.dunant@epfl.ch, adrien.hilaire@epfl.ch

ABSTRACT

The long term analysis of structures and structural elements depends on accounting both for the creep stress relaxation and the development of structural cracks. The development of such cracks may take place over long periods and therefore be difficult to distinguish from the viscous effects. Modelling structures under such slow-loading conditions requires the development of appropriate numerical models for material behaviour, and novel strategies for computing the link between creep and damage. In this paper, we present a new empirical model combining both aspects. The creep component is represented here using a Maxwell chain, and the material laws are based on the modified compression field theory (MCFT) and the Mazars model. The effects of speed-of-loading are investigated, and the effect of creep on the post-peak behaviour is assessed. A particular attention is given to the implementation which integrates models developed with widely differing aims.

1 Introduction

The long-term behaviour of concrete structures is strongly dependent on creep. In the case of pre-stressed or post-tensioned structures, this aspect is critical. It is well understood that the creep causes loss of confinement, reducing the strength of the structure, and significant efforts have been devoted to establish creep models valid over long periods. Creep is also significant in the early age, and models have been developed to describe its role in preventing early-age cracking. Such models take a particular care to take into account the ageing of the material. In the medium-term, however, for loading times of less than a week on mature concrete, creep is generally not taken into account. Thus, in the laboratory, the testing of beams to failure is usually analysed using models which assume that creep is insignificant. However, for a large specimens, the test may last a number of days, with loads maintained at a number of steps for the purpose of data recording. There is a need to analyse the role of creep in such experiments.

On of the reasons creep is not considered is that the modelling of the failure behaviour of concrete is itself a very complex endeavour and further, dominates member

failure. In the case of disturbed regions however, the behaviour of the members results from a number of local failure modes: the opening of cracks, shear along these cracks, localised crushing. In such cases the precise order of the opening of the cracks as well as their positions, which is likely to be influenced by the viscous nature of the material, is critical. Here, we have implemented non-local versions of the Modified Compression Field Theory [1] and Mazars models [2], which have been extensively used to model a great number of beams and plates. The MCFT model in its original form is implemented as a non-linear elastic behaviour and is thus unsuitable for modelling load cycles combined with creep. A further modification enforces irreversibility of the damage. To compare both models better, the damage is in both cases represented by a single scalar.

Choosing a creep model is strongly dependent on the time scales considered. Here, we consider a loading time of approximately two days. Crack propagation, however may occur within seconds or less. The time range considered therefore constrains the choice of numerical model: a Maxwell chain will have to have elements with characteristic times spanning the ranges of all important phenomena: crack propagation under loading, crack propagation under constant load, creep relaxation over 2 days. All these behaviours have been implemented in AMIE[3], an open-source code developed at the laboratory of material construction, originally for the simulation of ASR at the meso-scale.

2 Materials and methods

The setup used to validate the model is a simple rectangular sample with dimensions comparable to that of a test cylinder. A simple loading case is studied, in tension with a cycle post peak. The loading scheme and dimensions of the sample are reported on Figure 1. The goal was to compare the behaviour of numerical concrete models where damage and creep are fully coupled.

Three rates of loading are studied, they are low enough to enable the development of a non-negligible creep strain. The loading parameters are detailed in the table 1.

Table 1: Parameters of the three rates of loadings

Loading rate	t_0 (d)	t_1 (d)	t_2 (d)
1	0.3	0.6	1.2
2	3	6	12
3	30	60	120

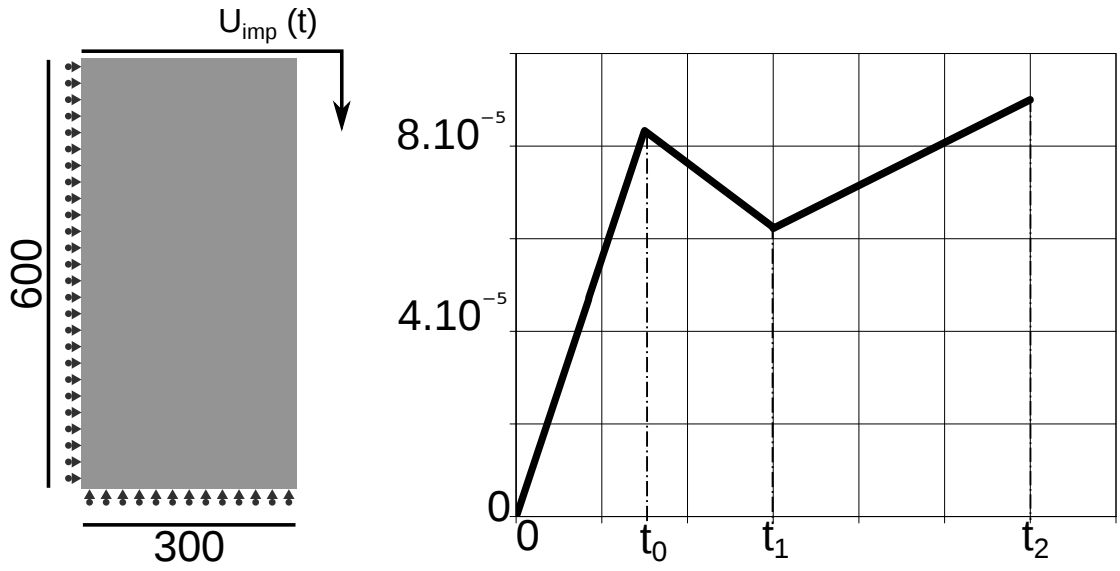

Figure 1: Setup and loading schemes.

3 Fracture behaviour

The first fracture behaviour is inspired from the MCFT [1]. This empirical behaviour is normally solved in a non-linear elastic code, using a secant stiffness approach. Although in the original version the damage is represented as a rotating crack, in this work for the sake of simplification the damage is represented using a scalar variable. This is not a disadvantage in this case as the loading does not allow crack closing and failure only happens in tension.

The principal stresses and strains (σ_1, σ_2,ϵ_1 and ϵ_2) used in the relationships described below are the smoothed non-local equivalents. The equations below are expressed such that the unit for stress is Pa.

The stress-strain relationship is described by the appropriate failure criterion.

The failure criterion used in tension depends on the proximity of reinforcement bars in tension. Two criteria are therefore defined. For unreinforced concrete, ϵ_{ch} and ϵ_{te} describe strains over which the concrete transitions to complete rupture, and ϵ_1^{crit} the critical tensile strain at cracking (f'_c in MPa). This relation is purely empirical but is commonly used in civil engineering applications.

$$\epsilon_1^{\text{crit}} = \frac{0.65|f'_c|^{0.33}}{E_0} \tag{1}$$

With E_0 the initial modulus We first define:

$$\phi_t^{\text{norebar}} = \begin{cases} 1 & \text{if } \epsilon_1 < \epsilon_1^{\text{crit}} \\ \frac{1}{1+\sqrt{k(\epsilon_1-\epsilon_1^{\text{crit}})}} & \text{if } \epsilon_1^{\text{crit}} \leq \epsilon_1 < \epsilon_{ch} \\ \frac{1}{1+\sqrt{k(\epsilon_1-\epsilon_1^{\text{crit}})}} \frac{\epsilon_{te}-\epsilon_1}{\epsilon_{te}-\epsilon_{ch}} & \text{if } \epsilon_{ch} \leq \epsilon_1 < \epsilon_{te} \\ 0 & \text{otherwise} \end{cases} \tag{2}$$

In this expression, the coefficient k is chosen so that the integral under the stress-strain curve be equal to the dissipated fracture energy at failure, assumed to be $G_f = 75$ N/m. We then get the effective limit strain, with d_t the current damage for the tensile branch:

$$\epsilon_1^{\text{crit,eff}} = \phi_t^{\text{norebar}} \frac{\sigma_1}{E_0(1-d_t)} \tag{3}$$

And the unreinforced concrete tensile criterion $\mathcal{C}_t^{\text{norebar}}$ is

$$\mathcal{C}_t^{\text{norebar}} = \begin{cases} 1 - \frac{\epsilon_1^{\text{crit,eff}}}{\epsilon_1} & \text{if } \epsilon_2 > \epsilon_1^{\text{crit,eff}} \\ -1 + \frac{\epsilon_1}{\epsilon_1^{\text{crit,eff}}} & \text{otherwise} \end{cases} \tag{4}$$

Table 2: Parameters for the MCFT simulation.

E	ν	f'_c	ϵ_2^{crit}	$\epsilon_{ch}^{\text{bare}}$	$\epsilon_{te}^{\text{bare}}$
37 GPa	0.2	37 MPa	0.0025	0.00694	0.00694×5

The second fracture behaviour is the Mazar model, which was implemented in AMIE without modifications using non-local fields for its expression instead of local ones. The evolution of the damage variable is calculated according to the following relationships where the Mazars' strain $\tilde{\epsilon}$ is introduced and ϵ_{crit} is the tensile strain threshold:

$$\tilde{\epsilon} = \sqrt{\langle\epsilon\rangle_+ : \langle\epsilon\rangle_+} \tag{5}$$

$$\begin{aligned} &\text{if } \tilde{\epsilon} > \epsilon_{crit} \text{ then } : \\ &\quad d = 1 - \frac{\epsilon_{crit}}{\tilde{\epsilon}} exp(-B_t(\tilde{\epsilon} - \epsilon_{crit})) \\ &\text{if } \tilde{\epsilon} \leq \epsilon_{crit} \text{ then } : \\ &\quad \dot{d} = 0 \end{aligned} \tag{6}$$

The damage parameters are given in the Tab. 3.

ϵ_{crit}	G_{ft}(J.m^{-2})
0.0001	10

Table 3: Damage parameters

4 Creep model

The concrete visco-elastic behaviour is represented using a generalised Kelvin-Voigt model with five branches. The numerical scheme used to model these chains is space-time finite elements. In the space-time approximation, the displacement in time of an element is linear, or put in an other way, the speed is a constant over a time slice. In this approximation, after Giorla *et al.* [4], the discretisation follows naturally from the weak form, for the elastic part, the elementary matrices corresponding to degrees of freedom i and j are:

$$\int \dot{\nabla} h_i \mathbb{C} \nabla^T h_j + \nabla h_i \mathbb{C} \dot{\nabla}^T h_j + \sum_{\text{b}} \int \dot{\nabla} h_i \mathbb{C}_b \nabla^T h_j + \nabla h_i \mathbb{C}_b \dot{\nabla}^T h_j \tag{7}$$

where the h_i are the shape function for the prismatic space-time element, and the $\mathbb{C}$ the stiffness matrices of the branches. The viscous part is:

$$\sum_{\text{b}} \int \dot{\nabla} h_i \mathbb{E}_b \dot{\nabla}^T h_j + \ddot{\nabla} h_i \mathbb{E}_b \nabla^T h_j \tag{8}$$

Where $\mathbb{E}_b$ is the dissipation matrix of the branch. In the case where the elements are linear in time, this reduces to a form which is symmetric. The parameters for the creep model used are given in the table 4. They are calibrated according to basic creep tests performed on a ordinary concrete (water/cement ratio = 0.45). The evolution of the creep strain is plotted on the figure 2.

k_0 (GPa)	τ_0 (d)	k_1 (GPa)	τ_1 (d)	k_2 (GPa)	τ_2 (d)	k_3 (GPa)	τ_3 (d)
540	0.05	390	0.5	202	5	51	50

Table 4: Table for the generalised Kelvin-Voigt chain used.

5 Solving strategy and Results

To solve for the coupled problem, it is key that the visco-elastic behaviour is taken into account in all intervals, and at the same time, that the damage can occur as soon as an element goes over its failure surface. The solution to these constraints is inspired from

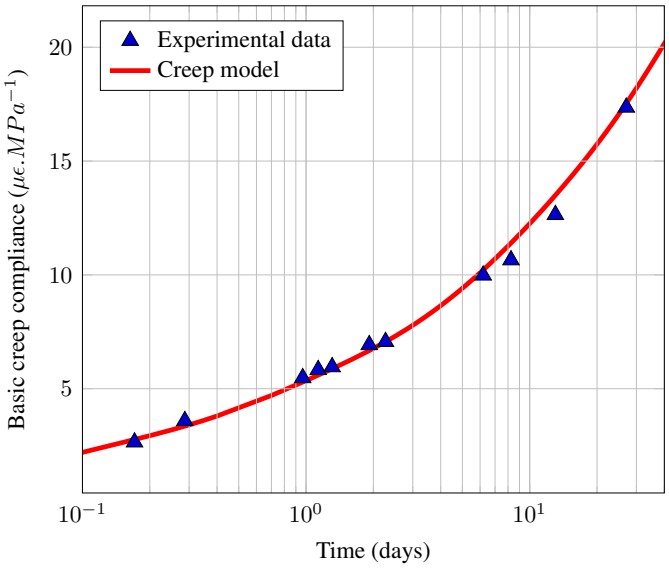

Figure 2: Creep compliance vs. time

the solving strategies introduced by Dunant *et al.* [5] as well as that of Rots [6] In the linear approximation considered for the displacements over time, it is easy, knowing the distances to the fracture surface at the beginning and end of a time slice to determine when the intercept will occur. Using this, each damage event is successively found and a small damage increment is applied in the elements at the moment where they reach their failure limit. Using this approach, the creep model is computed over each time period and thus the simulation take into account the full coupling between both the damage and the creep relaxation processes.

The behaviour as they have been implemented set limits on the possible stress and strain states of the samples, dynamic effects are neglected. Nonetheless, the stresses reached when the loading is slow are considerably lower than upon faster loading. As the stifness reduces, this becomes more sensitive post-peak. An important observation is that the measure of the peak load should take into account the time which was required for the loading. This effect has already been reported by Denarié [7]. The exact calculation of the interaction requires a precise coupling between the creep and damage processes: indeed the damage proceeds slowly, at rates comparable to the loading. Therefore, the strategy proposed in this paper is highly appropriate.

The relevance of this strategy is illustrated through the set up described previously. The stress-strain curves are plotted on the figures 3 for the two different failure criterions. Without the consideration of creep, the parameters of the two criterions imply that the two models have the same behaviour before the peak load. However, the MCFT model is more brittle then the Mazars one. The evolution of the stress versus time is

plotted on the figures 4.
The peak load depends on the loading rate of the sample regardless of the failure criterion. Nonetheless, the post-peak behavior seems to be less sensitive to the strain rate for the most brittle criterion.

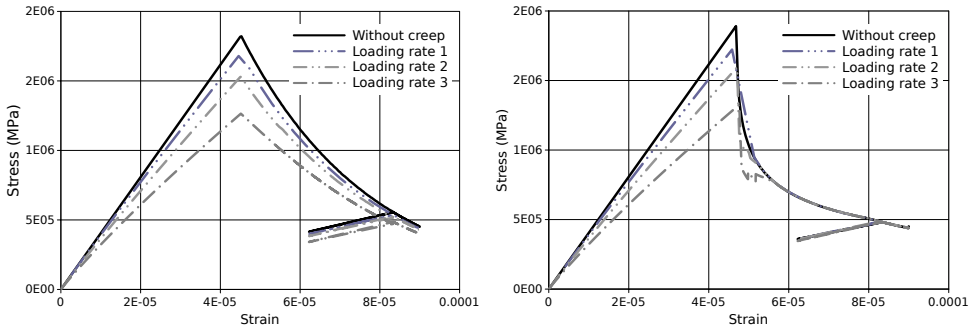

(a) Mazars failure criterion (b) MCFT failure criterion

Figure 3: Stress-strain curves for different rates of loading

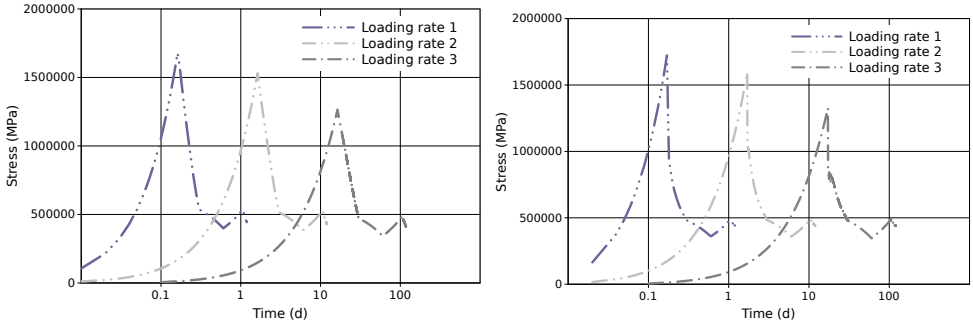

(a) Mazars failure criterion (b) MCFT failure criterion

Figure 4: Evolution of stress vs. time for different rates of loading

6 Conclusion

In this paper, it was shown that it is possible to implement a coupling between creep and damage that does not impact too much on the computational cost of the simulations. The importance of taking into account creep even for relatively short loading durations was highlighted using an extension of two widely used models for concrete.

We wish to acknoledge the Swiss Federal Office for Energy for their financial contribution to this work.

References

[1] F. J. Vecchio, "Reinforced concrete membrane element formulations," *Journal of Structural Engineering*, vol. 116, no. 3, pp. 730–750, 1990.

[2] J. Mazars, "A description of micro-and macroscale damage of concrete structures," *Engineering Fracture Mechanics*, vol. 25, no. 5, pp. 729–737, 1986.

[3] C. F. Dunant and K. L. Scrivener, "Micro-mechanical modelling of alkali–silica-reaction-induced degradation using the amie framework," *Cement and Concrete research*, vol. 40, no. 4, pp. 517–525, 2010.

[4] A. Giorla, K. Scrivener, and C. Dunant, "Finite elements in space and time for the analysis of generalised visco-elastic materials," *International Journal for Numerical Methods in Engineering*, vol. 97, no. 6, pp. 454–472, 2014.

[5] C. F. Dunant, S. P. Bordas, P. Kerfriden, K. L. Scrivener, and T. Rabczuk, "An algorithm to compute damage from load in composites," *Frontiers of Architecture and Civil Engineering in China*, vol. 5, no. 2, pp. 180–193, 2011.

[6] J. Rots, "Sequentially linear continuum model for concrete fracture," *Fracture Mechanics of*, vol. 13, 2001.

[7] E. Denarié, C. Cécot, and C. Huet, "Characterization of creep and crack growth interactions in the fracture behavior of concrete," *Cement and concrete research*, vol. 36, no. 3, pp. 571–575, 2006.